Springer Series in Optical Sciences 239

Razvan Stoian
Jörn Bonse *Editors*

Ultrafast Laser Nanostructuring

The Pursuit of Extreme Scales

Springer

Springer Series in Optical Sciences

Founding Editor

H. K. V. Lotsch, Nußloch, Baden-Württemberg, Germany

Volume 239

Editor-in-Chief

William T. Rhodes, Florida Atlantic University, Boca Raton, FL, USA

Series Editors

Ali Adibi, School of Electrical and Computer Engineering, Georgia Institute of Technology, Atlanta, GA, USA

Toshimitsu Asakura, Toyohira-ku, Hokkai-Gakuen University, Sapporo, Hokkaido, Japan

Theodor W. Hänsch, Max Planck Institute of Quantum Optics, Garching b. München, Bayern, Germany

Ferenc Krausz, Max Planck Institute of Quantum Optics, Garching b. München, Bayern, Germany

Barry R. Masters, Cambridge, MA, USA

Katsumi Midorikawa, Laser Tech Lab, RIKEN Advanced Science Institute, Saitama, Japan

Herbert Venghaus, Fraunhofer Institute for Telecommunications, Berlin, Germany

Horst Weber, Berlin, Germany

Harald Weinfurter, München, Germany

Kazuya Kobayashi, Dept. EECE, Chuo University, Bunkyo-ku, Tokyo, Japan

Vadim Markel, Department of Radiology, University of Pennsylvania, Philadelphia, PA, USA

Springer Series in Optical Sciences is led by Editor-in-Chief William T. Rhodes, Florida Atlantic University, USA, and provides an expanding selection of research monographs in all major areas of optics:

- lasers and quantum optics
- ultrafast phenomena
- optical spectroscopy techniques
- optoelectronics
- information optics
- applied laser technology
- industrial applications and
- other topics of contemporary interest.

With this broad coverage of topics the series is useful to research scientists and engineers who need up-to-date reference books.

Razvan Stoian • Jörn Bonse
Editors

Ultrafast Laser Nanostructuring

The Pursuit of Extreme Scales

Volumes I, II, and III

Springer

Editors
Razvan Stoian
Laboratoire Hubert Curien
Université Jean Monnet
Saint Etienne, France

Jörn Bonse
Bundesanstalt für Materialforschung und -prüfung (BAM)
Berlin, Germany

ISSN 0342-4111 ISSN 1556-1534 (electronic)
Springer Series in Optical Sciences
ISBN 978-3-031-14751-7 ISBN 978-3-031-14752-4 (eBook)
https://doi.org/10.1007/978-3-031-14752-4

© The Editor(s) (if applicable) and The Author(s), under exclusive license to Springer Nature Switzerland AG 2023
Chapter 31 is licensed under the terms of the Creative Commons Attribution 4.0 International License (http://creativecommons.org/licenses/by/4.0/). For further details see licence information in the chapter.
This work is subject to copyright. All rights are solely and exclusively licensed by the Publisher, whether the whole or part of the material is concerned, specifically the rights of translation, reprinting, reuse of illustrations, recitation, broadcasting, reproduction on microfilms or in any other physical way, and transmission or information storage and retrieval, electronic adaptation, computer software, or by similar or dissimilar methodology now known or hereafter developed.
The use of general descriptive names, registered names, trademarks, service marks, etc. in this publication does not imply, even in the absence of a specific statement, that such names are exempt from the relevant protective laws and regulations and therefore free for general use.
The publisher, the authors, and the editors are safe to assume that the advice and information in this book are believed to be true and accurate at the date of publication. Neither the publisher nor the authors or the editors give a warranty, expressed or implied, with respect to the material contained herein or for any errors or omissions that may have been made. The publisher remains neutral with regard to jurisdictional claims in published maps and institutional affiliations.

This Springer imprint is published by the registered company Springer Nature Switzerland AG
The registered company address is: Gewerbestrasse 11, 6330 Cham, Switzerland

Preface

Long seen as “a solution seeking a problem,” laser pulses are nowadays – more than 60 years after their first practical demonstration – paramount in shaping and structuring matter. Harnessing their capabilities to direct intense beams of light, the number of scientific and technological developments and daily-life applications is continuously increasing. Today, the presence of lasers is ubiquitous in all sites of scientific and technological interest, from the most advanced research laboratories to industrial factories and medical hospitals.

The directionality of the laser beam determines equally a local character on light-matter interaction and as such a local modification to a material target. Furthermore, the coherence of laser radiation enables near-field or far-field scattering and interference effects that widen significantly the capabilities of controlling and tracking laser-matter interactions in space and time. Already with the advent of lasers, powerful beams of light have been directed at solid materials for a variety of purposes, making this application as old as the laser itself. The roots of the major applications for laser structuring were developed already in the 1960s, setting the base of both theoretical and experimental studies on laser ablation, with the number of publications expanding explosively during the next decades.

Within this dynamic context, laser processing of materials experienced an impressive development over the years. Laser processing means specifically the capability to structure and tailor a material on its surface or even within its volume, rendering new functions and properties that are impacting the mechanical, electrical, or optical characteristics of the material. These properties are scale-dependent, generating thus over the years an equally impressive quest for spatial or temporal resolution. Therefore, the developments in laser engineering with major breakthroughs, notably in pulse duration and power, always closely accompanied the efforts in material structuring with two milestones in sight: (1) yield and (2) resolution. Every step in shrinking the laser pulse duration led to a subsequent strong-impact development in process precision – particularly when the *ultrashort* pulse durations surpassed the fundamental electron-phonon relaxation times. Thus, minimizing heat diffusion, the advent of pulses with duration smaller than molecular or lattice vibration times has managed to confine the spatial resolution to the optical diffraction limit and sometimes even beyond. The *nanoscale* was already in sight at the turn of the millennium. An important question may be raised now; is there any fundamental limit in the processing resolution, a barrier defined by the intrinsic properties of light and matter? The answer has an inherently multidisciplinary nature, following the conversion of free-propagating electromagnetic radiation into material-confined energy potentially usable to drive or transform matter, and will be the focus of the present book.

Relying on the experience and expertise of the leading researchers in the field, the present book intends to explore the current efforts in achieving laser processing resolution beyond the diffraction limit, laying down a perspective towards extreme laser nanostructuring. Following the most recent advances and developments, it puts forward a concept of *extreme processing scales* enabled by optical pulses that are able to bypass diffraction limits and achieve structuring characteristic scales beyond 100 nm. This objective can be achieved by a comprehensive understanding on how light can change matter and how, in turn, matter can change light, allowing jointly for actively controlling light and material processes. In order to give an extended perspective on the current state-of-the-art in the field of precision laser structuring, the book is divided into three main parts.

The first part of the book (Part I: Fundamental Processes) offers a perspective into the fundamentals of laser-matter interaction on extreme spatial scales, with a description of the most advanced modeling efforts in understanding energy deposition in matter, a plethora of material-relaxation pathways, as well as advanced concepts for probing and observing matter in motion. Roadmaps for energy localization will be developed, and the atomistic perspective of laser ablation visualized. Theoretical modelling enables in-depth insights on ultrafast quantum processes at the nanoscale. Laser-driven self-organization at surfaces will be dissected regarding the question of how light drives material periodic patterns down to the nanoscale, explored and transmitted to its ultimate limits of an atomic printer, and immediately complemented by the unprecedented capabilities of ultrafast in-situ observation approaches for tracking the laser-induced material response with extreme spatial and temporal resolution.

In the second part of the book (Part II: Concepts of Extreme Nanostructuring), distinct concepts will be developed and explored that allow confinement of light and harnessing of a material response restricted to nano- or mesoscopic scales at surfaces or in the volume of irradiated materials. A special focus will be on optical near-field related approaches for localizing light on scales even below the optical diffraction limit and plasmonic printing. Spatial and temporal beam-shaping and tailored interference techniques are discussed in the context of ultrashort laser pulses, and insights into some extreme states of matter realized by the tight confinement of laser energy are presented. The ultimate limits of writing waveguides in the bulk of dielectrics and for manifesting 3D-nanolithography are elucidated. Plasma-based surface treatments can significantly enhance the vertical precision of surface processing through etching processes.

Finally, the third part of the book (Part III: Applications) leads us to a number of resuming applications, unveiling the tremendous capabilities of surface functionalization through laser micro- and nanostructuring, assessing the 3D-writing of waveguides in the bulk of dielectrics or semiconductors for enabling new branches of integrated photonics, and summarizing related applications ranging from nanophotonics to nanofluidics and from optical sensing to biomedical applications, including the latest capabilities of refractive eye surgery. This part will analyze the applications' compatibility in yield and reproducibility with current industrial requirements, costs, and intellectual property aspects. It expands the involved spatial scales by more than eight orders of magnitude, when extending extremely small structures featuring sizes of few tens of nanometers to larger dimensions in the meter range.

Thus, from surfaces to the bulk, from subtractive to additive manufacturing approaches, from advanced theoretical frames to practical technological processes – we invite the readers here to an exciting journey into the varicolored landscape of extreme laser nanostructuring.

The idea of this book project was seeded in early 2020. We were delighted about the numerous and extremely positive responses from the laser-processing community, quickly receiving commitments for more than 30 individual book chapters. About 2500 communications later, the book is published. We would like to thank all authors of this book project for their insightful and detailed chapters, reviewing and reporting on this fascinating topic of the *pursuit of extreme scales in ultrafast laser nanostructuring*. Moreover, we would like to acknowledge the professional help and guidance of the staff of Springer Nature. Finally, we hope you will enjoy reading this book as much as we have enjoyed putting it together.

Saint Etienne, France Razvan Stoian
Berlin, Germany Jörn Bonse
December 2022

Contents

Volume I

Part I Fundamental Processes

1 **Insights into Laser-Matter Interaction from Inside: Wealth of Processes, Multiplicity of Mechanisms and Possible Roadmaps for Energy Localization** 3
Thibault J.-Y. Derrien, Yoann Levy, and Nadezhda M. Bulgakova

2 **The Atomistic Perspective of Nanoscale Laser Ablation** 65
Dmitry S. Ivanov, Pavel N. Terekhin, Sergey I. Kudryashov, Sergey M. Klimentov, Andrei V. Kabashin, Martin E. Garcia, Baerbel Rethfeld, and Irina N. Zavestovskaya

3 **Ultrafast Quantum Processes at the Nanoscale: Insights from Modelling** 139
Bernd Bauerhenne, Tobias Zier, and Martin E. Garcia

4 **The Universality of Self-Organisation: A Path to an Atom Printer?** 173
Serim Ilday and F. Ömer Ilday

5 **How Light Drives Material Periodic Patterns Down to the Nanoscale** 209
Anton Rudenko and Jean-Philippe Colombier

6 **In-Situ Observation of the Formation of Laser-Induced Periodic Surface Structures with Extreme Spatial and Temporal Resolution** 257
Klaus Sokolowski-Tinten, Jörn Bonse, Anton Barty, Henry N. Chapman, Saša Bajt, Mike J. Bogan, Sebastien Boutet, Andrea Cavalleri, Stefan Düsterer, Matthias Frank, Janos Hajdu, Stefan Hau-Riege, Stefano Marchesini, Nikola Stojanovic, and Rolf Treusch

7 **Probing Matter by Light** 277
Mario Garcia-Lechuga, Javier Solis, and Jan Siegel

8 **Probing Light by Matter: Implications of Complex Illumination on Ultrafast Nanostructuring** 321
Camilo Florian, Xiaohan Du, and Craig B. Arnold

9 **Imaging Dynamics of Femtosecond Laser-Induced Surface Nanostructuring** 355
Cong Cong, Ranran Fang, Anatoliy Y. Vorobyev, Mohamed ElKabbash, Subhash C. Singh, and Chunlei Guo

Volume II

Part II Concepts of Extreme Nanostructuring

10 **Macroscale Microfabrication Enabled by Nanoscale Morphological Control of Laser Internal Modification** 379
Ya Cheng, Haisu Zhang, Peng Wang, Jia Qi, Jian Xu, Xin Li, Wenbo Li, Xiaolong Li, Zijie Lin, Jinming Chen, Ming Hu, and Min Wang

11 **Optical Nanostructuring by Near-Field Laser Ablation** 411
Johannes Boneberg, Elke Scheer, and Paul Leiderer

12 **Nanoscale Plasmonic Printing** 447
Soon Hock Ng and Saulius Juodkazis

13 **Search for High-Pressure Silicon Phases: Reaching the Extreme Conditions with High-Intensity Laser Irradiation** 471
Ludovic Rapp, Takeshi Matsuoka, Konstantin L. Firestein, Daisuke Sagae, Hideaki Habara, Keiichiro Mukai, Kazuo A. Tanaka, Eugene Gamaly, Ryosuke Kodama, Yusuke Seto, Takahisa Shobu, Aki Tominaga, Lachlan Smillie, Bianca Haberl, Tatiana Pikuz, Toshinori Yabuuchi, Tadashi Togashi, Yuichi Inubushi, Makina Yabashi, Saulius Juodkazis, Dmitri V. Golberg, Andrei V. Rode, and Norimasa Ozaki

14 **Periodic Surface Structures by Laser Interference Ablation** 495
Jürgen Ihlemann, Andreas Blumenstein, Jan-Hendrik Klein-Wiele, and Peter Simon

15 **Spatial Beam Shaping with a Liquid-Crystal Spatial Light Modulator for Surface Micro- and Nanoprocessing** 533
Yoshio Hayasaki and Satoshi Hasegawa

16 **Nonstandard Light for Ultrafast Laser Microstructuring and Nanostructuring** 581
Francois Courvoisier

17 Controlled Nanostructuring of Transparent Matter with Temporal Airy Pulses 623
Thomas Winkler, Bastian Zielinski, Cristian Sarpe, Elena R. Ciobotea, Arne Senftleben, and Thomas Baumert

18 Ultraprecise Surface Processing by Etching with Laser-Induced Plasmas 653
Martin Ehrhardt, Pierre Lorenz, and Klaus Zimmer

19 Nanostructuring by Photochemistry: Laser-Induced Type A Modification 691
Lionel Canioni, Yannick Petit, and Thierry Cardinal

20 Subtractive 3D Laser Nanolithography of Crystals by Giant Wet-Chemical Etching Selectivity 725
Airán Ródenas Seguí

21 Ultrafast Meets Ultrasmall: Where Are the Limits of Ultrafast Waveguide Writing? 759
Omair Ghafur, Peter Jürgens, Laura Rammelt, and Alexandre Mermillod-Blondin

22 Multi-Photon 3D Lithography and Calcination for sub-100-nm Additive Manufacturing of Inorganics 787
Greta Merkininkaitė, Edvinas Aleksandravičius, Simonas Varapnickas, Darius Gailevičius, Simas Šakirzanovas, and Mangirdas Malinauskas

Volume III

Part III Applications

23 Creation of Material Functions by Nanostructuring 827
Marek Mezera, Camilo Florian, Gert-willem Römer, Jörg Krüger, and Jörn Bonse

24 Role of Surface Chemistry on Wettability of Laser Micro-/Nanostructured Metallic Surfaces 887
Nithin Joy and Anne-Marie Kietzig

25 Ultrafast Laser Biomimetic Micro-/Nanostructuring 921
George D. Tsibidis and Emmanuel Stratakis

26 Ultrarapid Industrial Large-Area Processing Using Laser Interference Patterning Methods 951
Andrés Fabián Lasagni, Lucinda Mulko, and Marcos Soldera

27 Internal Structuring of Semiconductors with Ultrafast Lasers: Opening a Route to Three-Dimensional Silicon Photonics 979
David Grojo, Maxime Chambonneau, Shuting Lei, Alexandros Mouskeftaras, Olivier Utéza, and Andong Wang

28 Nanoscale Sampling of Optical Signals: Application to High-Resolution Spectroscopy 1019
Guillermo Martin, Alain Morand, Myriam Bonduelle, Ciro D'Amico, Razvan Stoian, Javier Rodriguez Vazquez de Aldana, and Carolina Romero Vazquez

29 Ultrafast Laser Volume Nanostructuring of Transparent Materials: From Nanophotonics to Nanomechanics 1053
Razvan Stoian, Ciro D'Amico, Yves Bellouard, and Guanghua Cheng

30 Nanofluidics Fabricated by 3D Femtosecond Laser Processing 1085
Koji Sugioka

31 Laser Structuring for Biomedical Applications 1105
Gerda Buchberger, Martina Muck, Cristina Plamadeala, and Johannes Heitz

32 Laser Nanostructuring for SERS Applications 1167
Xiao Luo and Minlin Zhong

33 Laser Micro- and Nanostructuring for Refractive Eye Surgery 1217
Norbert Linz, Sebastian Freidank, Xiao-Xuan Liang, and Alfred Vogel

Contributors

Edvinas Aleksandravičius Laser Research Center, Physics Faculty, Vilnius University, Vilnius, Lithuania

Craig B. Arnold Princeton Institute for the Research and Technology of Materials (PRISM), Princeton University, Princeton, NJ, USA
Mechanical and Aerospace Engineering (MAE), Princeton University, Princeton, NJ, USA

Saša Bajt Center for Free-Electron Laser Science CFEL, Deutsches Elektronen-Synchrotron DESY, Hamburg, Germany
The Hamburg Centre for Ultrafast Imaging, Hamburg, Germany

Anton Barty Deutsches Elektronen-Synchrotron DESY, Hamburg, Germany

Bernd Bauerhenne Theoretical Physics and Center for Interdisciplinary Nanostructure Science and Technology (CINSaT), University of Kassel, Kassel, Germany

Thomas Baumert Institute for Physics and CINSaT, University of Kassel, Kassel, Germany

Yves Bellouard Galatea Lab, STI/IEM, Ecole Polytechnique Fédérale de Lausanne (EPFL), Neuchâtel, Switzerland

Andreas Blumenstein Institut für Nanophotonik Göttingen e.V., Göttingen, Germany

Mike J. Bogan Lawrence Livermore National Laboratory, Livermore, CA, USA

Myriam Bonduelle Université Grenoble Alpes, CNRS, IPAG, Grenoble, France

Johannes Boneberg Physics Department, University of Konstanz, Konstanz, Germany

Jörn Bonse Bundesanstalt für Materialforschung und -prüfung (BAM), Berlin, Germany

Sebastien Boutet SLAC National Accelerator Laboratory, Menlo Park, CA, USA

Gerda Buchberger Institute of Applied Physics, Johannes Kepler University (JKU) Linz, Linz, Austria

Nadezhda M. Bulgakova HiLASE Centre, FZU – Institute of Physics of the Czech Academy of Sciences, Dolní Břežany, Czech Republic

Lionel Canioni Université de Bordeaux, Talence, France

Thierry Cardinal Institut de Chimie de la Matière Condensée de Bordeaux, Université de Bordeaux, Pessac, France

Andrea Cavalleri Max Planck Institute for the Structure and Dynamics of Matter, Hamburg, Germany

Maxime Chambonneau Institute of Applied Physics, Abbe Center of Photonics Friedrich Schiller University, Jena, Germany

Henry N. Chapman Center for Free-Electron Laser Science CFEL, Deutsches Elektronen-Synchrotron DESY, Hamburg, Germany
Department of Physics, Universität Hamburg, Hamburg, Germany
The Hamburg Centre for Ultrafast Imaging, Hamburg, Germany

Jinming Chen School of Physics and Electronic Science, East China Normal University, Shanghai, China

Guanghua Cheng School of Electronics and Information, Northwestern Polytechnical University, Xi'an, Shaanxi, China

Ya Cheng School of Physics and Electronic Science, East China Normal University, Shanghai, China
Shanghai Institute of Optics and Fine Mechanics, Chinese Academy of Sciences, Shanghai, China

Elena R. Ciobotea Institute for Physics and CINSaT, University of Kassel, Kassel, Germany

Jean-Philippe Colombier Université de Lyon, UJM-Saint-Etienne, CNRS, IOGS, St-Etienne, France

Cong Cong The Institute of Optics, University of Rochester, Rochester, NY, USA

Francois Courvoisier FEMTO-ST Institute, Université de Bourgogne Franche-Comté, Besançon Cedex, France

Ciro D'Amico Laboratoire Hubert Curien, UMR 5516 CNRS, Université de Lyon, Université Jean Monnet, Saint Etienne, France

Javier Rodriguez Vazquez de Aldana Grupo de Investigacion en Aplicaciones del Laser y Fotonica, Facultad de Ciencias, Universidad de Salamanca, Salamanca, Spain

Thibault J. -Y. Derrien HiLASE Centre, FZU – Institute of Physics of the Czech Academy of Sciences, Dolní Břežany, Czech Republic

Xiaohan Du Princeton Institute for the Research and Technology of Materials (PRISM), Princeton University, Princeton, NJ, USA
Mechanical and Aerospace Engineering (MAE), Princeton University, Princeton, NJ, USA

Stefan Düsterer Deutsches Elektronen-Synchrotron DESY, Hamburg, Germany

Martin Ehrhardt Leibniz Institute of Surface Engineering (IOM), Leipzig, Germany

Mohamed ElKabbash The Institute of Optics, University of Rochester, Rochester, NY, USA

Ranran Fang The Institute of Optics, University of Rochester, Rochester, NY, USA

Konstantin L. Firestein Centre for Materials Science and School of Chemistry and Physics, Queensland University of Technology, Brisbane, QLD, Australia

Camilo Florian Princeton Institute for the Research and Technology of Materials (PRISM), Princeton University, Princeton, NJ, USA

Matthias Frank Lawrence Livermore National Laboratory, Livermore, CA, USA

Sebastian Freidank Institut für Biomedizinische Optik, Universität zu Lübeck, Lübeck, Germany

Darius Gailevičius Laser Research Center, Physics Faculty, Vilnius University, Vilnius, Lithuania

Eugene Gamaly Department of Quantum Science and Technology, Research School of Physics, The Australian National University, Canberra, ACT, Australia

Martin E. Garcia Theoretical Physics and Center for Interdisciplinary Nanostructure Science and Technology (CINSaT), University of Kassel, Kassel, Germany

Mario Garcia-Lechuga Laser Processing Group, Instituto de Óptica, IO-CSIC, Madrid, Spain

Omair Ghafur Max-Born-Institute, Berlin, Germany

Dmitri V. Golberg Centre for Materials Science and School of Chemistry and Physics, Queensland University of Technology, Brisbane, QLD, Australia

David Grojo Aix-Marseille Université, CNRS, LP3 UMR7341, Marseille, France

Chunlei Guo The Institute of Optics, University of Rochester, Rochester, NY, USA

Hideaki Habara Graduate School of Engineering, Osaka University, Suita, Osaka, Japan

Bianca Haberl Neutron Scattering Division, Neutron Sciences Directorate, Oak Ridge National Laboratory, Oak Ridge, TN, USA

Janos Hajdu Department of Cell and Molecular Biology, Uppsala Universitet, Uppsala, Sweden
The European Extreme Light Infrastructure, Institute of Physics, Academy of Sciences of the Czech Republic, Dolní Břežany, Czech Republic

Satoshi Hasegawa Center for Optical Research and Education (CORE), Utsunomiya University, Utsunomiya, Japan

Stefan Hau-Riege Lawrence Livermore National Laboratory, Livermore, CA, USA

Yoshio Hayasaki Center for Optical Research and Education (CORE), Utsunomiya University, Utsunomiya, Japan

Johannes Heitz Institute of Applied Physics, Johannes Kepler University (JKU) Linz, Linz, Austria

Ming Hu School of Physics and Electronic Science, East China Normal University, Shanghai, China

Jürgen Ihlemann Institut für Nanophotonik Göttingen e.V., Göttingen, Germany

F. Ömer Ilday Physics Department, and Electrical and Electronics Engineering Department, Bilkent University, Ankara, Turkey

Serim Ilday Faculty of Electrical Engineering and Information Technology (ETIT), Ruhr-Universität Bochum (RUB), Bochum, Germany

Yuichi Inubushi Japan Synchrotron Radiation Research Institute, Sayo, Hyogo, Japan
RIKEN SPring-8 Center, Sayo, Hyogo, Japan

Dmitry S. Ivanov P.N. Lebedev Physical Institute, Moscow, Russia

Nithin Joy McGill University, Montreal, Québec, Canada

Saulius Juodkazis Optical Sciences Centre and ARC Training Centre in Surface Engineering for Advanced Materials (SEAM), School of Science, Swinburne University of Technology, Hawthorn, VIC, Australia
Tokyo Tech World Research Hub Initiative (WRHI), School of Materials and Chemical Technology, Tokyo Institute of Technology, Meguro City, Tokyo, Japan

Peter Jürgens Max-Born-Institute, Berlin, Germany

Andrei V. Kabashin Institute of Engineering Physics for Biomedicine (PhysBio), Moscow, Russia
LP3, Aix-Marseille Université, CNRS, LP3, Campus de Luminy, Marseille, France

Anne-Marie Kietzig McGill University, Montreal, Québec, Canada

Jan-Hendrik Klein-Wiele Institut für Nanophotonik Göttingen e.V, Göttingen, Germany

Sergey M. Klimentov Institute of Engineering Physics for Biomedicine (PhysBio), Moscow, Russia

Ryosuke Kodama Graduate School of Engineering, Osaka University, Suita, Osaka, JapanInstitute of Laser Engineering, Osaka University, Suita, Osaka, Japan

Jörg Krüger Bundesanstalt für Materialforschung und -prüfung (BAM), Berlin, Germany

Sergey I. Kudryashov P.N. Lebedev Physical Institute, Moscow, Russia

Andrés Fabián Lasagni Technische Universität Dresden, Faculty of Mechanical Engineering, Institute of Manufacturing Technology, Dresden, Germany
Fraunhofer Institute for Material and Beam Technology IWS, Dresden, Germany

Shuting Lei Department of Industrial and Manufacturing Systems Engineering, Kansas State University, Manhattan, KS, USA

Paul Leiderer Physics Department, University of Konstanz, Konstanz, Germany

Yoann Levy HiLASE Centre, FZU – Institute of Physics of the Czech Academy of Sciences, Dolní Břežany, Czech Republic

Wenbo Li Shanghai Institute of Optics and Fine Mechanics, Chinese Academy of Sciences, Shanghai, China

Xiaolong Li School of Physics and Electronic Science, East China Normal University, Shanghai, China

Xin Li School of Physics and Electronic Science, East China Normal University, Shanghai, China

Xiao-Xuan Liang Institut für Biomedizinische Optik, Universität zu Lübeck, Lübeck, Germany

Zijie Lin School of Physics and Electronic Science, East China Normal University, Shanghai, China

Norbert Linz Institut für Biomedizinische Optik, Universität zu Lübeck, Lübeck, Germany

Pierre Lorenz Leibniz Institute of Surface Engineering (IOM), Leipzig, Germany

Xiao Luo Laser Materials Processing Research Center, Key Laboratory for Advanced Materials Processing Technology (Ministry of Education), School of Materials Science and Engineering, Tsinghua University, Beijing, P. R. China

Mangirdas Malinauskas Laser Research Center, Physics Faculty, Vilnius University, Vilnius, Lithuania

Stefano Marchesini SLAC National Accelerator Laboratory, Menlo Park, CA, USA

Guillermo Martin Université Grenoble Alpes, CNRS, IPAG, Grenoble, France

Takeshi Matsuoka Institute for Open and Transdisciplinary Research Initiatives, Osaka University, Suita, Osaka, Japan

Greta Merkininkaitė Faculty of Chemistry and Geoscience, Vilnius University, Vilnius, Lithuania
Femtika, Vilnius, Lithuania

Alexandre Mermillod-Blondin Max-Born-Institute, Berlin, Germany

Marek Mezera Bundesanstalt für Materialforschung und -prüfung (BAM), Berlin, Germany

Alain Morand Université Grenoble Alpes, CNRS, Grenoble INP, IMEP-LAHC, Grenoble, France

Alexandros Mouskeftaras Aix-Marseille Université, CNRS, LP3 UMR7341, Marseille, France

Martina Muck Institute of Applied Physics, Johannes Kepler University (JKU) Linz, Linz, Austria

Keiichiro Mukai Graduate School of Engineering, Osaka University, Suita, Osaka, Japan

Lucinda Mulko Technische Universität Dresden, Faculty of Mechanical Engineering, Institute of Manufacturing Technology, Dresden, Germany

Soon Hock Ng Optical Sciences Centre, School of Science, Swinburne University of Technology, Hawthorn, VIC, Australia

Norimasa Ozaki Graduate School of Engineering, Osaka University, Suita, Osaka, JapanInstitute of Laser Engineering, Osaka University, Suita, Osaka, Japan

Yannick Petit Institut de Chimie de la Matière Condensée de Bordeaux, Université de Bordeaux, Pessac, France

Tatiana Pikuz Institute for Open and Transdisciplinary Research Initiatives, Osaka University, Suita, Osaka, Japan

Cristina Plamadeala Institute of Applied Physics, Johannes Kepler University (JKU) Linz, Linz, Austria

Jia Qi School of Physics and Electronic Science, East China Normal University, Shanghai, China

Laura Rammelt Max-Born-Institute, Berlin, Germany

Ludovic Rapp Department of Quantum Science and Technology, Research School of Physics, The Australian National University, Canberra, ACT, Australia

Baerbel Rethfeld Department of Physics and Research Center OPTIMAS, Technical University of Kaiserslautern, Kaiserslautern, Germany

Andrei V. Rode Department of Quantum Science and Technology, Research School of Physics, The Australian National University, Canberra, ACT, Australia

Gert-willem Römer Chair of Laser Processing, Department of Mechanics of Solids, Surfaces & Systems (MS3), University of Twente, Enschede, The Netherlands

Anton Rudenko Arizona Center for Mathematical Sciences and College of Optical Sciences, University of Arizona, Tucson, AZ, USA

Daisuke Sagae Graduate School of Engineering, Osaka University, Suita, Osaka, Japan

Simas Šakirzanovas Faculty of Chemistry and Geoscience, Vilnius University, Vilnius, Lithuania
Department of Chemical Engineering and Technology, Center for Physical Sciences and Technology, Vilnius, Lithuania

Cristian Sarpe Institute for Physics and CINSaT, University of Kassel, Kassel, Germany

Elke Scheer Physics Department, University of Konstanz, Konstanz, Germany

Airán Ródenas Seguí Departamento de Física, Universidad de La Laguna (ULL), Tenerife, Spain
Instituto Universitario de Estudios Avanzados (IUdEA), Universidad de La Laguna, Tenerife, Spain

Arne Senftleben Institute for Physics and CINSaT, University of Kassel, Kassel, Germany

Yusuke Seto Graduate School of Science, Kobe University, Kobe, Hyogo, Japan

Takahisa Shobu Japan Atomic Energy Agency, Chiyoda City, Tokyo, Japan

Jan Siegel Laser Processing Group, Instituto de Óptica, IO-CSIC, Madrid, Spain

Peter Simon Institut für Nanophotonik Göttingen e.V., Göttingen, Germany

Subhash C. Singh The Institute of Optics, University of Rochester, Rochester, NY, USA

Lachlan Smillie Department of Quantum Science and Technology, Research School of Physics, The Australian National University, Canberra, ACT, Australia

Klaus Sokolowski-Tinten Faculty of Physics and Centre for Nanointegration Duisburg-Essen, University of Duisburg-Essen, Duisburg, Germany

Marcos Soldera Technische Universität Dresden, Faculty of Mechanical Engineering, Institute of Manufacturing Technology, Dresden, Germany

Javier Solis Laser Processing Group, Instituto de Óptica, IO-CSIC, Madrid, Spain

Razvan Stoian Laboratoire Hubert Curien, UMR 5516 CNRS, Université de Lyon, Université Jean Monnet, Saint Etienne, France

Nikola Stojanovic Deutsches Zentrum für Luft- und Raumfahrt (DLR) Berlin-Adlersdorf, Berlin, Germany

Emmanuel Stratakis Institute of Electronic Structure and Laser (IESL), Foundation for Research and Technology (FORTH), Heraklion, Crete, Greece
Department of Physics, University of Crete, Heraklion, Greece

Koji Sugioka RIKEN Center for Advanced Photonics, Wako, Saitama, Japan

Kazuo A. Tanaka Graduate School of Engineering, Osaka University, Suita, Osaka, Japan

Pavel N. Terekhin Department of Physics and Research Center OPTIMAS, Technical University of Kaiserslautern, Kaiserslautern, Germany

Tadashi Togashi Japan Synchrotron Radiation Research Institute, Sayo, Hyogo, Japan
RIKEN SPring-8 Center, Sayo, Hyogo, Japan

Aki Tominaga Japan Atomic Energy Agency, Chiyoda City, Tokyo, Japan

Rolf Treusch Deutsches Elektronen-Synchrotron DESY, Hamburg, Germany

George D. Tsibidis Institute of Electronic Structure and Laser (IESL), Foundation for Research and Technology (FORTH), Heraklion, Crete, Greece
Department of Physics, University of Crete, Heraklion, Greece

Olivier Utéza Aix-Marseille Université, CNRS, LP3 UMR7341, Marseille, France

Simonas Varapnickas Laser Research Center, Physics Faculty, Vilnius University, Vilnius, Lithuania

Carolina Romero Vazquez Grupo de Investigacion en Aplicaciones del Laser y Fotonica, Facultad de Ciencias, Universidad de Salamanca, Salamanca, Spain

Alfred Vogel Institut für Biomedizinische Optik, Universität zu Lübeck, Lübeck, Germany

Anatoliy Y. Vorobyev The Institute of Optics, University of Rochester, Rochester, NY, USA

Andong Wang Aix-Marseille Université, CNRS, LP3 UMR7341, Marseille, France

Min Wang School of Physics and Electronic Science, East China Normal University, Shanghai, China

Peng Wang Shanghai Institute of Optics and Fine Mechanics, Chinese Academy of Sciences, Shanghai, China

Thomas Winkler Department of Physics and Astronomy, Aarhus University, Aarhus C, Denmark

Jian Xu School of Physics and Electronic Science, East China Normal University, Shanghai, China

Makina Yabashi Japan Synchrotron Radiation Research Institute, Sayo, Hyogo, Japan
RIKEN SPring-8 Center, Sayo, Hyogo, Japan

Toshinori Yabuuchi Japan Synchrotron Radiation Research Institute, Sayo, Hyogo, Japan
RIKEN SPring-8 Center, Sayo, Hyogo, Japan

Irina N. Zavestovskaya P.N. Lebedev Physical Institute, Moscow, Russia
Institute of Engineering Physics for Biomedicine (PhysBio), Moscow, Russia

Haisu Zhang School of Physics and Electronic Science, East China Normal University, Shanghai, China

Minlin Zhong Laser Materials Processing Research Center, Key Laboratory for Advanced Materials Processing Technology (Ministry of Education), School of Materials Science and Engineering, Tsinghua University, Beijing, P. R. China

Bastian Zielinski Institute for Physics and CINSaT, University of Kassel, Kassel, Germany

Tobias Zier Department of Physics, University of California Merced, Merced, California, USA

Klaus Zimmer Leibniz Institute of Surface Engineering (IOM), Leipzig, Germany

Part I
Fundamental Processes

Chapter 1
Insights into Laser-Matter Interaction from Inside: Wealth of Processes, Multiplicity of Mechanisms and Possible Roadmaps for Energy Localization

Thibault J.-Y. Derrien, Yoann Levy, and Nadezhda M. Bulgakova

Abstract Short and ultrashort laser pulses are nowadays an integral part of up-to-date technological solutions in many areas from material micro-/nanoprocessing and synthesis of new materials to quantum computing and biomedicine. The number of laser applications in science and industries is growing precipitously with tendencies of enhancing laser processing precision and reproducibility toward creation of extremely tiny objects. Coupling more laser energy into a smaller material volume in a controllable way is one of the grand challenges, which can only be achieved through a deep understanding of a wealth of the laser-triggered transient processes at different spatiotemporal scales.

The objective of this chapter is to provide a review of the main fundamental linear and nonlinear processes excited by ultrafast lasers in different kinds of materials with the aim to reveal and highlight possible mechanisms, which would enable extreme localization of energy absorption. After summarizing existing knowledge on laser-induced phenomena that includes mechanisms of laser light absorption, heat transfer peculiarities, energy thermalization at ultrafast time scales, and related hydrodynamic phenomena, an overview is given on novel insights into highly nonequilibrium processes gained in recent years via quantum and molecular dynamics simulations. The fundamental part is followed by an analysis of possible techniques and processes, which could enable extreme localization of laser energy absorption both on the surface of material samples and in the bulk. Finally, as an example of laser energy localization alternating at nanoscale, laser-induced periodic surface structures (LIPSS) are discussed. The multiplicity of the mechanisms is demonstrated via a rigorous theoretical analysis and simulations.

Keywords Ultrafast laser irradiation of materials · Laser energy absorption · Linear and nonlinear processes · Surface electromagnetic waves · Material

---

T. J.-Y. Derrien · Y. Levy · N. M. Bulgakova (✉)
HiLASE Centre, FZU – Institute of Physics of the Czech Academy of Sciences, Dolní Břežany, Czech Republic
e-mail: derrien@fzu.cz; levy@fzu.cz; bulgakova@fzu.cz

© The Author(s), under exclusive license to Springer Nature Switzerland AG 2023

R. Stoian, J. Bonse (eds.), *Ultrafast Laser Nanostructuring*, Springer Series in Optical Sciences 239, https://doi.org/10.1007/978-3-031-14752-4_1

relocation · Time-dependent density-functional theory (TDDFT) · Laser-induced periodic surface structures (LIPSS)

1 Introduction

One of the main trends of modern micro-/nanotechnologies is fabricating functional objects toward smaller size, controllably and cheaper. To address such needs, the method of ultrashort laser action on materials offers exceptional opportunities among other perspective techniques due to its high flexibility in terms of irradiation parameters, cleanliness, and applicability to any material irrespective of its thermophysical and optical properties and chemical reactivity. Laser light is a versatile tool, which enables a great variety of scientific and technological applications such as gentle laser cleaning of surfaces [1], selective phase removal [2], direct writing of surface and bulk micro- and nanostructures [3, 4], synthesis of materials with new properties [5], or producing extreme stresses yielding in generation of new material phases [6]. However, still all functional capabilities of laser light are not fully explored, and even more impressive progress of laser applications in various fields of human activity can be expected in the near future [7], in particular with employing new spatiotemporally shaped laser beams [8].

Ultrafast laser irradiating a material triggers so many physical and chemical processes that it is often difficult to identify contribution of a separate process to a particular observable phenomenon as well as to the final footprint of laser action. The laser-induced processes and the corresponding fields of knowledge are shown schematically in Fig. 1.1a. In Fig. 1.1b, we specify laser-induced processes in the condensed state for different kinds of materials. Many of these processes are of high importance for achieving and controlling strong localization of laser energy coupling into a smallest possible volume. Thus, to utilize all the possibilities that are offered by a wide variety of existing and still developed lasers, a vital need is to deeply understand underlying physics and chemistry of laser-matter interaction and the material response to laser action.

In this chapter, we overview the fundamental processes in laser-irradiated solids, when laser beams are focused on the surface or inside the bulk. Many of these processes will be deeper analyzed in the following chapters of this book when considering specific phenomena. Our review does not pretend to completeness and aims to outline main concepts, approaches, and some recent findings as well as to provide core references in the field of laser modification of materials of different kinds. Also some techniques, which help or can help to better localize light absorption, will be discussed. Finally, we touch the mechanisms of laser-induced periodic surface structure (LIPSS) formation on metallic surfaces as an example of alternating localization of laser energy absorption at nanoscale. Two regimes will be considered, with strong laser ablation, when only few pulses couple with the same spot on the surface, and with low or no ablation, when LIPSS are erecting well above the initial surface level due to the oxidation process.

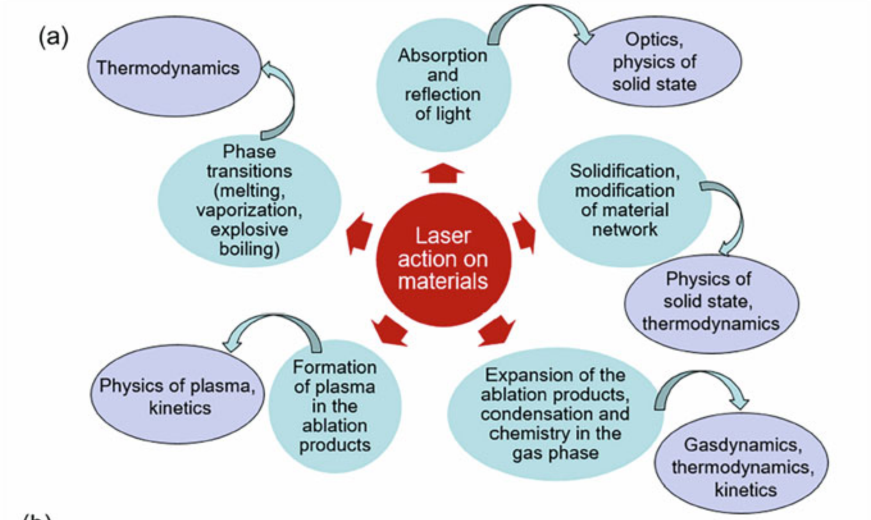
(a)
Thermodynamics
Absorption and reflection of light
Optics, physics of solid state
Phase transitions (melting, vaporization, explosive boiling)
Laser action on materials
Solidification, modification of material network
Physics of solid state, thermodynamics
Physics of plasma, kinetics
Formation of plasma in the ablation products
Expansion of the ablation products, condensation and chemistry in the gas phase
Gasdynamics, thermodynamics, kinetics

(b)

Time scale	Metals	Semiconductors	Dielectrics
During laser pulse	Laser energy absorption by conduction electrons Excitation of d-band electrons in transition metals	Photo-ionization; collisional ionization (avalanche), light absorption by excited electrons	
	Dynamic change of reflectivity		
After laser pulse	Electron-lattice thermalization		
	Phase transitions (solid-solid transitions, melting, ablation, recrystallization); generation of defect states; hydrodynamics phenomena (stress waves, acoustic waves, surface relocation of melt)		
		Ultrafast melting, photo-recombination, Auger recombination, amorphization	Free-electron trapping, photo-recombination

Fig. 1.1 (**a**) Major processes induced by laser action on materials (outlined in blue ovals) and corresponding fields of knowledge involved (text in violet ovals). (**b**) Specific laser-induced processes in the condensed state for different kinds of materials

2 Fundamental Mechanisms of Ultrashort Laser Pulses with Solids

In this section, we will start from considering the mechanisms of laser energy absorption by different materials, which predetermine spatial scales affected by laser light. For ultrashort laser pulses, due to extremely rapid energy delivery, much shorter than characteristic times of heat conductivity for spreading heat, laser-affected zones in the irradiated targets are strongly localized with a minimal residual damage. This is a prerequisite for generation of well-defined microstructures with high quality and reproducibility. Thus, finding ways toward more localized absorption that strongly depends on material properties is one of the prime tasks of laser-assisted nanotechnologies.

Laser light absorption in condensed matter is governed by electromagnetic processes of interaction between the laser electromagnetic wave and electrons on the background of an interatomic/ionic field. (Note that we do not touch here the cases of interaction of mid-infrared laser beams with covalent solids when radiation may couple with vibrational group frequencies of bonds). The electrons, which absorb laser light, are described by wave functions that give the probability density of finding them in a certain position where they are subjected to forces from fields of surrounding atoms/ions and electrons. However, the classical approach treats the electrons in solids as point objects that are a necessary requirement/simplification enabling to providing large-scale multi-physics simulations. Thus, in the first part of this chapter, we consider classical approaches for treating laser energy absorption. In ultrafast irradiation regimes, immediately after the laser energy absorption by electrons, an irradiated material occurs in a highly nonequilibrium state that is followed by thermalization of hot electrons' absorbed laser energy with surrounding material matrix (ions and atoms usually named lattice). These aspects will be shortly discussed in Sect. 2.2 with referencing to literature. Section 2.3 will dwell in more details on the electromagnetic phenomena inside and on the surface of irradiated materials. The peculiarities of postirradiation material evolution will be considered in Sect. 2.4, while in Sect. 3, we shall discuss new features of laser-matter interaction comprehended via ab-initio simulation approaches.

2.1 Mechanisms of Laser Energy Absorption: Role of Dynamic Reflectivity

In this subsection, we first shortly overview major mechanisms of laser energy absorption in various materials whose detailed descriptions can be found in extensive literature. Then an attention is given to dynamic behavior of reflectivity, which defines the fraction of the incident laser energy absorbed by the irradiated material and its initial distribution in the target that in its turn determines the following modification of material properties at temporal and spatial scales.

The main mechanisms of laser energy absorption can be considered to be well established by now. In metals, laser radiation is absorbed by conduction electrons via the inverse bremsstrahlung mechanism. The essence of this process is that an electron (or another charged particle) may absorb a photon when it collides with another charged particle or, in the other words, when it is changing its momentum upon deflection in the electric field of other particles. Thus, the absorbing particle gains energy of the absorbed photon, satisfying the energy conservation law. We note that, in transition metals, a significant number of d electrons can be excited to the conduction band, thus contributing to the optical and thermophysical properties

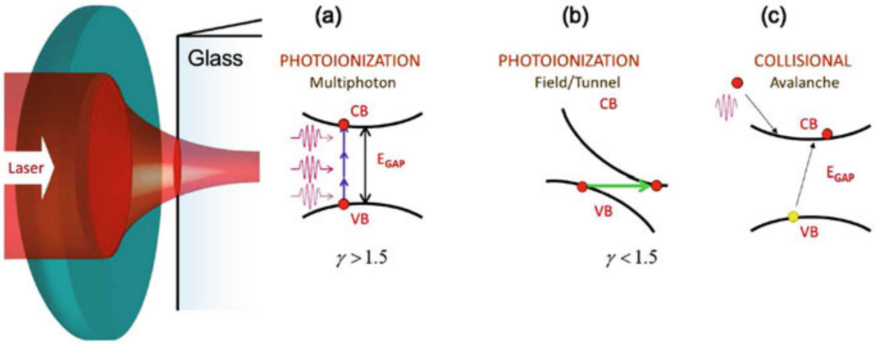

Fig. 1.2 Schematics of ultrafast laser ionization processes in transparent materials [9]. (**a**) Multiphoton ionization across the bandgap. (**b**) Tunnel ionization in strong fields. (**c**) Collisional ionization and carrier multiplication. (The figure was reprinted with permission from Stoian [9])

of the material [10]. For bandgap materials, the situation substantially differs as the electron density in the conduction band of a non-disturbed material is near-zero (in wide bandgap dielectrics) or very small (in semiconductors) to noticeably absorb radiation in the inverse bremsstrahlung process. Under intense laser irradiation, free electrons are photoexcited from the valence to the conduction band via single- or multiphoton absorption that is determined by the ratio of the bandgap to the photon energy and/or via tunneling ionization [11–13]. When a definite level of the electron density is reached (typically starting from approximately 10^{18}–10^{19} cm^{-3}), the generated conduction electrons start to efficiently absorb laser radiation via inverse bremsstrahlung (due to increased collision frequency between charged particles) and can gain enough energy to ionize neutral atoms in collisions, the process called avalanche ionization [14]. The scheme of the processes of free electron generation in dielectric materials is given in Fig. 1.2 [9].

After the laser pulse action, the generated free carriers are gradually or swiftly recombining to the ground or defect state depending on material type. In semiconductors, the main recombination process is of Auger (three-particle) type [12] although radiative recombination is also present, especially at low free electron densities [15]. In inorganic dielectrics, electron recombination proceeds usually in the form of trapping into localized states, accompanied by creation of color centers, excitons, and other defects [16, 17]. The detailed descriptions of laser energy absorption in different kinds of materials and generation of free carriers in bandgap materials can be found in [9, 18, 19].

Generation of free electrons in bandgap materials, excitation of d electron in transition metals, and heating of the electrons in the conduction band cause a dynamic change of the optical material response to laser irradiation. Swift change of reflectivity and local absorptivity during the laser action determines the final energy coupled into material and, hence, its overall subsequent evolution into a laser-modified state. Thus, accurate knowledge of the absorbed energy and its spatial distribution is a prerequisite for achieving desired modification structures, especially in micro-/nanostructuring regimes, as well as for adequate interpretation of experimental observation.

For ultrashort laser pulses, measuring of the absorbed/reflected energy evolution resolved in time and over the irradiation spot does not appear feasible at the present status of diagnostics. For metals, integral measurements of both specular and diffuse reflection [20] (Fig. 1.3) or of only specular component of reflected light [21] demonstrate a strong reduction of reflectivity at relatively high laser fluences already at single pulse irradiation. By now, many subtle details of the transient optical response of different materials undergoing strong electronic excitation are still not fully understood. Many approaches have been proposed to describe the dynamic optical properties based mostly on the Drude model including its modifications [22–27], or on its combination with the plasma theory [21, 28], and/or based on the Kubo-Greenwood formalism [25, 29, 30]. For more details, we refer the readers to these papers and to the review [31] where the majority of the existing approaches for description of material optical response to laser irradiation are overviewed for both metals and bandgap materials. We also draw attention to the verification of the Drude model using time-dependent density-functional theory simulations, which has demonstrated its validity in a wide range of laser wavelengths and intensities [32].

2.2 Nonequilibrium States: Thermalization of the Excited Systems

When a metal is subjected to a strong photon flux from the laser beam, the dense cloud of conduction electrons massively absorbs incoming photons. For ultrashort laser pulses with duration smaller than the characteristic time of the energy transfer from electrons to the ionic lattice (electron-lattice thermalization time), the electronic subsystem is strongly heated by the end of the laser pulse, while the lattice remains cold. As a result, the irradiated solid occurs in a strongly nonequilibrium condition, and it strives to attain equilibrium in the electron-lattice thermalization process. This process is in the core of the so-called two-temperature model (TTM) developed by Anisimov et al. [33] and widely used for simulations and estimations of the laser energy coupling to metallic samples [18, 19, 24, 27, 31]. The main equations of the TTM represent the heat flux equations for the electron and lattice subsystem couples via the energy coupling term, which are written in the one-dimensional form as

$$C_e \frac{\partial T_e}{\partial t} = \frac{\partial}{\partial z} K_e \frac{\partial T_e}{\partial z} - g(T_e - T_l) + S(z, t), \tag{1.1}$$

$$C_l \frac{\partial T_l}{\partial t} = \frac{\partial}{\partial z} K_l \frac{\partial T_l}{\partial z} + g(T_e - T_l). \tag{1.2}$$

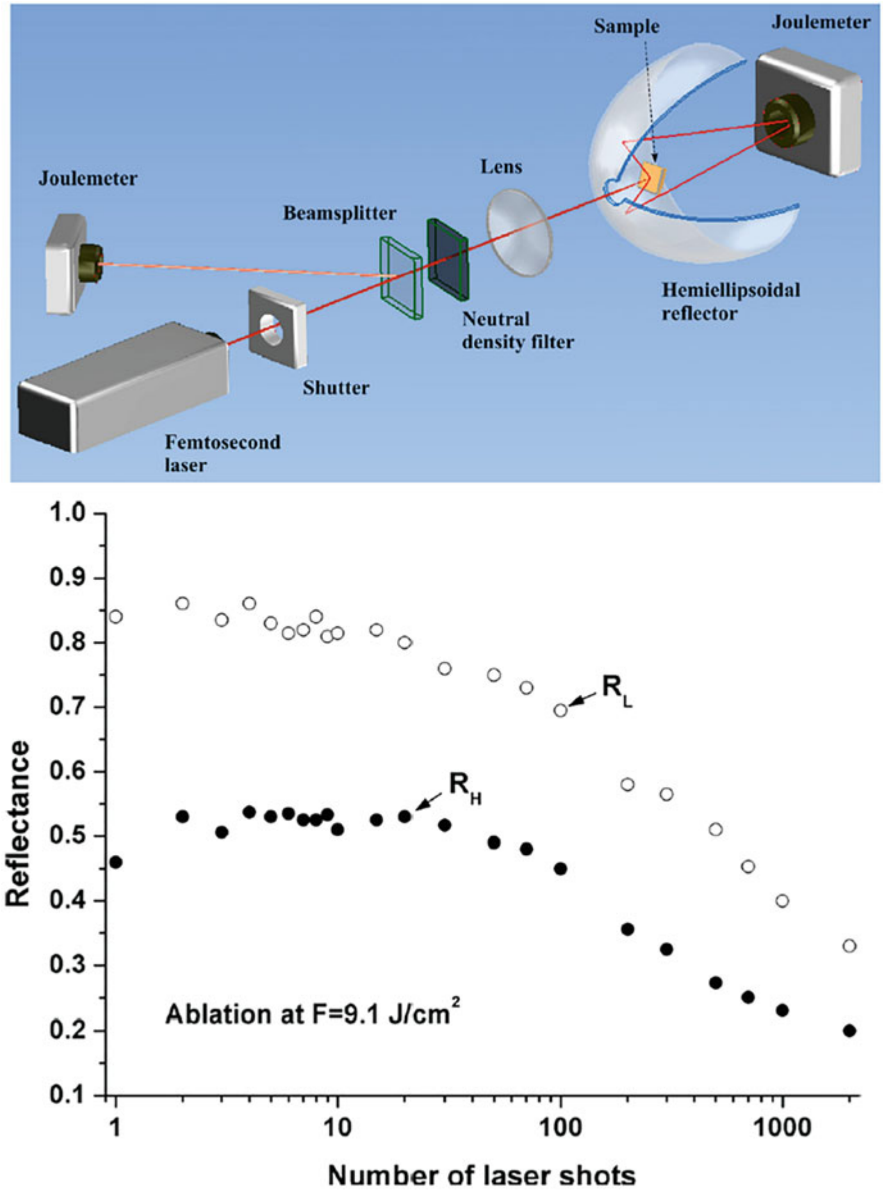

Fig. 1.3 Top: Experimental setup with hemiellipsoidal reflector for measuring integral reflectivity from laser-irradiated sample used in [20]. Bottom: High-intensity reflectance R_H(N) of copper in multipulse ablation at laser fluence $F = 9.1$ J/cm^2. Low-intensity reflectance R_L(N) is also shown, which corresponds to a single laser pulse at an attenuated laser fluence of $F_L = 0.043$ J/cm^2, being below the damage threshold. F_L was applied to probe the change in the reflectivity after each high-intensity laser shot. The figure was reprinted with permission from Vorobyev and Guo [20]

Here C_e, C_l, K_e, and K_l are the heat capacities and thermal conductivities of the electron and lattice subsystems; g is the electron-lattice coupling factor; $S(z, t)$ is the source term describing the temporal shape of the laser energy flux; and z is the coordinate directed from the target surface to the bulk. Generally, for ultrashort laser pulses, the term of heat transfer in Eq. (1.2) can be disregarded in view of a negligible contribution of lattice heat conduction on femto- and picosecond time scales. Also note that the factor g is often called the electron-phonon coupling factor as the exchange between electrons and lattice proceeds via excitation of phonons that are vibrational motion of lattice of atoms/ions or molecules constituting a solid material.

The main problem of application of the TTM to metals irradiated by ultrashort laser pulses is the necessity of the knowledge about the evolution of the material parameters under extremely nonequilibrium conditions of ultrafast laser heating. The accurate data on the heat capacities and thermal conductivities of electrons in metals as well as the factor g responsible for energy exchange between the electron and lattice subsystems are the key for successful application of the TTM for gaining a deep insight into the temperature evolution in laser-irradiated metals, of almost the same importance as the knowledge on the dynamic change of optical properties analyzed in Sect. 2.1. In many situation, the TTM simulations are performed with the simplified C_e and K_e values linearly dependent on the electron temperature and the g value to be constant, which give a good qualitative picture of the laser heating process [34]. However, for more accurate description of real experimental conditions, especially at achieving highly nonequilibrium states, more insights into the physical parameters of highly excited nonequilibrium materials are vital. An important step toward solving this problem was made by Lin et al. [10]. The authors performed simulations based on the density of states (DOS) theory to derive the heat capacities, the chemical potentials, and the electron-lattice coupling factors as a function of electron temperature for eight materials widely used in experimental studies and important for various applications. The obtained dependencies, being fitted by analytical function, can be directly used in the TTM simulations [31].

The simulations by Lin et al. [10] assume that the electrons are instantly heated to a certain temperature and are in equilibrium inside their subsystem, while the lattice remains to be cold. The question arises about the level of equilibrium within the conduction electrons at very short excitation times. As an example, for several metals (mainly noble metals), so-called ballistic transport is introduced to the TTM to account for a high-energy tail of nonequilibrium electrons at the surface layer, which swiftly transfer the absorbed energy to a certain depth of an irradiated metal (ballistic range). Usually, the contribution of ballistic electrons is described by increasing the laser energy absorption length [34]. A more sophisticated modification of the TTM to account ballistic electrons introduces an intermediate step, a heat flow equation for nonthermal electrons [35]. With such approach, the authors achieved a quantitative description of the results of photoelectron spectroscopy, additionally assuming a reduced electron-phonon coupling.

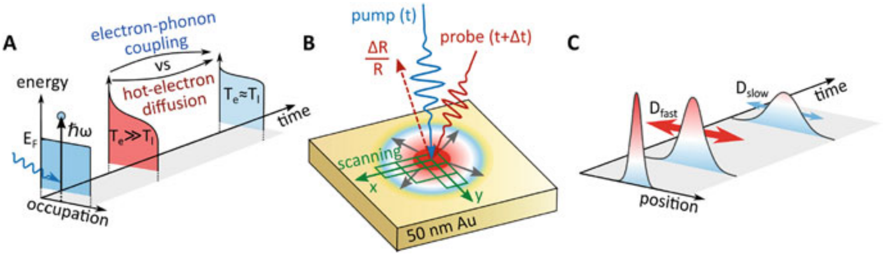

Fig. 1.4 Schematic description of scanning ultrafast thermomodulation microscopy. (**a**) The energy distribution of conduction electrons perturbed by optical excitation quickly evolves to a quasi-thermalized Fermi-Dirac distribution with high electron temperature (T_e), while the lattice temperature (T_l) stays to the ambient one. Subsequent electron-phonon coupling and hot-carrier diffusion lead to thermal equilibrium between the electron and lattice subsystems. (**b**) An optical pump pulse illuminates a thin gold film, inducing a local hot-electron distribution. The probe pulse measures the temperature-dependent transient reflectivity ($\Delta R/R$). (**c**) The spatiotemporal evolution of the photoexcited spot size is monitored to visualize hot-electron diffusion. Courtesy of A. Block [37]

Recently, Mo et al. [36] reported on the experiments exploring the ultrafast melting process in thin gold films based on time-resolved electron diffraction measurements. The experiments were supported by the TTM simulations, which have demonstrated that the electron-lattice coupling factor is overestimated by the equilibrium DOS theory whose data were reported in [10]. Block et al. [37] imaged the spatiotemporal hot-electron diffusion in thin gold films using scanning ultrafast thermomodulation microscopy. The scheme and assumptions of the method are presented in Fig. 1.4. Two distinct diffusion regimes were revealed, an initial rapid diffusion during the first few picoseconds (hot-electron regime), followed by about 100-fold slower diffusion at longer times (phonon-limited thermal diffusion regime). Applying comprehensive three-dimensional simulations based on the TTM, the authors [37] have obtained a good agreement between theory and experiment only under the assumption of a delayed electron-phonon coupling, thus further supporting an important role of nonequilibrium in ultrafast processes. We note that significant efforts have been made to better address phase transitions within the TTM framework, which was originally developed to describe solely the dynamics of sample heating upon ultrashort laser irradiation. In particular, hydrodynamic-type models, which are based on the TTM approach, were developed and successfully applied for the ultrashort irradiation conditions when the solid-liquid-vapor phase transitions occur; see, e.g., [26, 38, 39]. Such sophisticated models require a reliable equation-of-state suitable for strongly nonequilibrium regimes [40, 41].

Thus, despite a rather long history of applications of the TTM with its modifications, for example, by expanding the two-temperature model by inclusion of additional subsystems (see review [42] and references therein), this model remains important and calls for further improvements as well as for applications for other materials. As an example, in semiconductors and semimetals, the electrons and holes can be considered as separate subsystems with different temperatures so the three-temperature model has been proposed [42, 43]. The two-temperature model is also used for various bandgap materials expressed in terms of the total energies of subsystems of carriers and phonons/lattice [12, 44] in the temperature terms considering the temperature as a measure of an average energy of subsystem's elements [45].

Finally, it is necessary to mention the in-depth studies of laser-induced nonequilibrium processes in solids based on the Boltzmann equation [13], Monte Carlo method [46], and molecular dynamics approach [47, 48]. Although such approaches demand big computational resources and, hence, require access to large computational facilities, they enable in-depth considerations of underlying physics of nonequilibrium processes under the action of ultrashort laser pulses.

2.3 Electromagnetic Processes

Propagation of intense light in an external medium toward a material sample and into the sample is a trigger for a number of complex phenomena. Laser beam on its way can be disturbed by the ionization of present atomic/molecular species (e.g., ambient air, artificial gaseous atmosphere, or liquids). It was demonstrated that ionization of nitrogen in air becomes very important when laser intensity exceeds a certain threshold power, an effect that limits the energy reaching the target [49–51]. This effect becomes even more pronounced for multi-pulse irradiation regimes in view of accumulation of various metastable states of nitrogen molecules that also depends on pulse repetition rate compared to the rates of metastable states' decay [51].

Upon arrival at the sample surface, laser light couples to a surface layer, which is usually far not perfect (surface roughness, nanoparticles, various surface states/defects) that leads to light scattering and excitation of surface electromagnetic waves, also known as surface polaritons [52]. Laser light in near-infrared to ultraviolet spectral range interacts mostly with electrons in irradiated samples, and its propagation inside a particular sample depends strongly on a transient behavior of material dielectric function. While in a metal the laser intensity is usually decaying exponentially due to the free carriers' absorption, the picture is different for bandgap materials. Nevertheless, even for those transparent to the laser wavelength, i.e., when the photon energies are smaller than the bandgap, the propagation of laser beams through a dielectric or semiconducting media can induce modifications of the dielectric permittivity through several mechanisms [17, 23].

Propagation of light through transparent crystals and glasses involves a competition of several processes. While the Kerr effect results in increasing the refractive index with light intensity, free electrons generated by laser action act oppositely. They scatter the remaining part of the laser beam that is observed as a reduction of the refractive index. This counteraction of two processes, Kerr nonlinearity and plasma scattering, can lead to laser beam filamentation in transparent ionizable media [53]. Other phenomena such as Franz-Keldysh effect also lead to a modification of the refractive index that can be investigated using a perturbative approach [54].

In general, strong field effects can manifest themselves as a shift of electron energy levels due to the motion of electrons (and nuclei) in the applied field, a shift known as Stark effect. This modification of the allowed energy levels induces a transient change of the band structure, which can result in a transient reduction or increase of the bandgap [32].

In this subsection, we review first the mechanisms of light focusing and defocusing in materials due to the combined action of the Kerr and plasma scattering effects, along with the spectral dispersion and the diffraction limit of light. Then the dynamics of electron excitation in bandgap materials, which can undergo a transient metallization, is considered with insights into a microscopic role of laser polarization. The subsection ends with recalling the fundamentals of excitation of surface electromagnetic waves by intense laser light.

2.3.1 Classical Diffraction Limit and Spectral Dispersion

A first limit to the localization of light is given by the diffraction limit where the highest resolution is related to laser wavelength and refractive index of the medium n, along with numerical aperture of the objective [55]. In the Gaussian optics, it manifests itself as a purely propagative effect and can be described in the paraxial approximation via solving a nonlinear Schrödinger equation [56, 57]. The minimum spatial radius w_0 of a focused Gaussian laser beam is called the beam waist:

$$w_0 \simeq \frac{\lambda_0}{\pi \mathrm{NA}} = \frac{\lambda_0}{\pi n_0 \sin\theta}$$

where λ_0 is wavelength in vacuum, n_0 is the refractive index of a medium where the beam propagates, θ is the divergence half-angle of the beam (the far-field angle between the beam axis and a conventional beam boundary, at which the intensity drops by e^2 times compared to on-axis intensity at the same beam cross-section), and NA is numerical aperture of an optical system.

As laser light is primarily a flux of photons described by an electromagnetic waves (oriented in real space and called "polarization"), its finite pulse duration τ induces a dispersion of the photon wavelength distributed around a central value λ. This dispersion can be obtained from the Heisenberg inequality written in the form

$$\tau \cdot \delta E \geq h/4\pi,$$

where $\delta E = \delta\lambda_0 \times hc/\lambda_0^2$ is the photon energy dispersion, h is the Planck constant, c is speed of light in vacuum, and $\delta\lambda_0$ is the dispersion around the central wavelength λ_0. Using these values, the spectral width can be evaluated as $\delta\lambda = \lambda_0^2/(4\pi c\tau)$. Table 1.1 presents examples of dispersions of laser wavelengths

Table 1.1 Uncertainty of wavelength λ_0 and photon momentum $\boldsymbol{k}$ ($\delta k = 2\pi \times \delta\lambda_0/\lambda_0^2$, where $\delta\lambda_0$ is the dispersion around central wavelength λ_0) induced by the spectral width in several ultrashort pulse laser systems. The photon energy is denoted by e_{ph}

Examples of laser amplified sources	e_{ph}, eV	τ	λ_0, nm	$\lvert\delta k\rvert$, 10^4 m^{-1}	$\frac{\delta k}{k}$
Astrella, Coherent	1.55	30 fs	800 ± 5.7	5.6	0.71%
PHAROS, Light Conversion	1.20	240 fs	1030 ± 1.2	0.70	0.11%
— ” —	1.20	7 ps	1030 ± 0.04	0.02	<0.01%
PERLA C, HiLASE	1.20	2 ps	1030 ± 0.14	0.08	0.01%

and photon momenta for the laser systems, which are available at the HiLASE Centre (High-average power LASErs Centre in Dolní Břežany, Czech Republic).

2.3.2 Optical Kerr Effect

The optical Kerr effect finds its microscopic origin in the two processes, a nearly instantaneous response of bound electrons in an irradiated material to a polarized laser light [58] and a slower process of field-induced molecular reorientation/nuclear motion especially important for gases and liquids [59, 60]. These processes lead to an anisotropic optical response of materials to irradiation described using a third-order susceptibility $\chi^{(3)}$ [61]. At the macroscopic level, the Kerr effect is described as the intensity-dependent refractive index of laser-irradiated media [62]. The change of optical refractive index is expressed as

$$n = n_0 + n_2 I$$

where n_2 is nonlinear index of refraction, which can be measured experimentally (e.g., in Si [63], SiO_2, water [64]). For conventional dielectrics, n_2 is usually positive that means that an intense laser beam propagating through such a dielectric material can experience self-focusing culminating in its collapsing. The critical power of the laser beam, above which self-focusing overcomes beam diffraction and leads to collapse, can be estimated as [65]

$$P_{\mathrm{cr}} \simeq 3.72 \frac{\lambda_0^2}{8\pi n_0 n_2}.$$

Upon collapsing, due to a swift increase of the laser intensity, the media experiences ionization with the formation of a localized region of a dense free-electron plasma, which in its turn scatters (defocuses) the light. If the beam power exceeds significantly the critical power of self-focusing, the beam can again undergo self-focusing and, moreover, can experience multiple focusing-defocusing cycles (see Fig. 1.5 [53]). Filamentation is a universal phenomenon, which can be met in gases [53, 66], solids [53, 67], and liquids [68]. Controlling the laser-induced filamentation effect can offer an additional degree of freedom for tailoring photonic

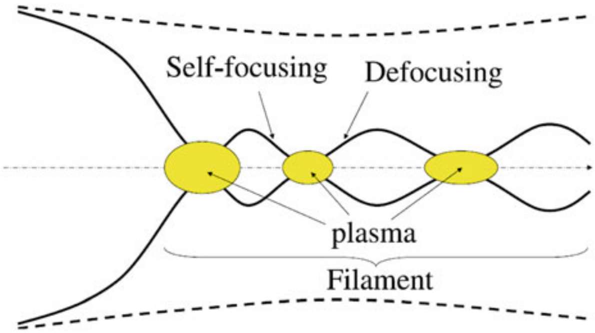

Fig. 1.5 Schematic representation of the focusing-defocusing cycles undergone by a powerful laser beam [53]. The solid curves indicate the diameter of the intense core of the beam. The dashed lines indicate the root mean square radius of the full beam. (The figure was reprinted with permission from Couairon and Mysyrowicz [53])

structures inside bulk dielectrics [67] and reducing the modification area on solid surfaces immersed in liquids [69].

2.3.3 Light Defocusing in Dielectrics

The role of local refractive index. The Drude model of light absorption by the electrons excited to the conduction zone of bandgap materials describes a decrease of the local optical refractive index [17]. At high-intensity laser irradiation, this effect leads to the formation of gradients of refractive index that can result in defocusing the laser light during the laser beam propagation [70]. The Drude contribution to the dielectric permittivity emerges from the laser-generated electric current in the irradiated medium that originates from the oscillating motion of conduction electrons inside their allowed energy bands (so-called intraband motion). We recall here the statement in the book by Boyd [62] that "the photorefractive effect is the change in refractive index of an optical material that results from the optically induced redistribution of electrons and holes. The photorefractive effect is quite different from most of the other nonlinear-optical effects described in this book in that it cannot be described by a nonlinear susceptibility $\chi^{(n)}$ for any value of n."

Thus, the so-called Drude effect of the absorption of light by free electrons on the optical refractive index can be derived from introducing an equation of motion of the conduction band electrons, which can be written as

$$m^* \frac{d}{dt}\left[N_e \boldsymbol{V}_e\right] = -\left|e\right| N_e \boldsymbol{E} - m^* N_e \nu \boldsymbol{V}_e. \tag{1.3}$$

Here m^* is an effective mass of electrons in the conduction bands with the total density N_e, $\boldsymbol{V}_e$ is their velocity, e is the electron charge, $\boldsymbol{E}$ is the electric field, and ν is the collision frequency of electrons. For an incompressible electron gas subjected to oscillations in an alternating electric field, this equation reduces to the expression of the Drude approximation with a conduction current $\boldsymbol{J}_{\text{cond}} = -\left|e\right| N_e \boldsymbol{V}_e$ that can be rewritten as

$$\boldsymbol{J}_{\text{cond}} = -\left|e\right| N_e \boldsymbol{V}_e = -\frac{\varepsilon_0}{\omega} \cdot \frac{N_e e^2}{m^* \varepsilon_0} \cdot \frac{1}{i - \frac{\nu}{\omega}} \times \boldsymbol{E} = i \varepsilon_0 \boldsymbol{E} \cdot \frac{\omega_p^2}{\omega} \cdot \frac{1}{1 + i\frac{\nu}{\omega}}, \tag{1.4}$$

where ω_p is the plasma frequency.

From the above equation of motion of the electrons with assumptions of a linearly polarized wave irradiating a crystal and an isotropic response of the electrons to the incident field, a simplified description of a scalar dielectric permittivity $\varepsilon(\omega)$ as function of laser frequency ω can be derived, which reads as [23]

$$\varepsilon(\omega) = 1 + \underbrace{\left[\varepsilon_\infty(\omega) - 1\right]}_{\text{valence band contribution}} \cdot \underbrace{\frac{N_0 - N_e}{N_0}}_{\text{band-filling effect}} - \underbrace{\frac{N_e e^2}{m^* \varepsilon_0 \omega^2} \cdot \frac{1}{1 + i\frac{\nu}{\omega}}}_{\text{Drude term}},$$

where $\varepsilon_\infty(\omega)$ is the frequency-dependent dielectric permittivity of the non-excited material. N_0 is the maximum quantity of electrons in terms of density that can populate the conduction bands of the solid. Assuming that the core levels of atoms would not contribute to the excitation of electrons (Born-Oppenheimer approximation), the density N_0 can be limited to the quantity of electrons that are initially present in the valence bands. The effective mass m^* should be taken consistently with the local electric field, presumably dependent on laser intensity [71]. The collision frequency ν is usually described assuming a Matthiessen rule, according to which collision frequencies of j processes are combined as $\nu^{-1} = \sum_j \nu_j^{-1}$. Thus, for solids, the contributions of electron-electron and electron-ion/atom collisions are included. In metals, the two limiting cases, the cold solid and the hot plasma in relatively low- and high-intensity regimes, respectively, can be used with joining them smoothly in the transition range [72], while kinetic models can be employed for dielectrics [73].

Defocusing of the Laser Beam and Ionization Instabilities At the macroscopic scale, the laser light defocusing induced by the local motion of charges in the conduction bands makes it difficult to localize the laser energy. Upon focusing the laser light, the excited electrons scatter the subsequent flux of photons, thus spreading the light away from the region of focus [70]. For writing photonic structures in bandgap materials, a stronger localization of light is usually required that can be achieved by using high NA lenses [6, 74, 75]. From the viewpoint of modeling, high NA focusing requires an extra care about choosing the simulation approach, boundary conditions, as well as stability and convergence of the applied numerical schemes [70, 75–79]. An example is given in Fig. 1.6 demonstrating comparison of application of the nonlinear Schrödinger equation and a more accurate approach based on Maxwell's equations. These particular simulations were performed for a very low energy of the laser beam focused by lens with NA = 0.8 toward fused silica depth (geometrical focus was 80 µm below the surface). At the

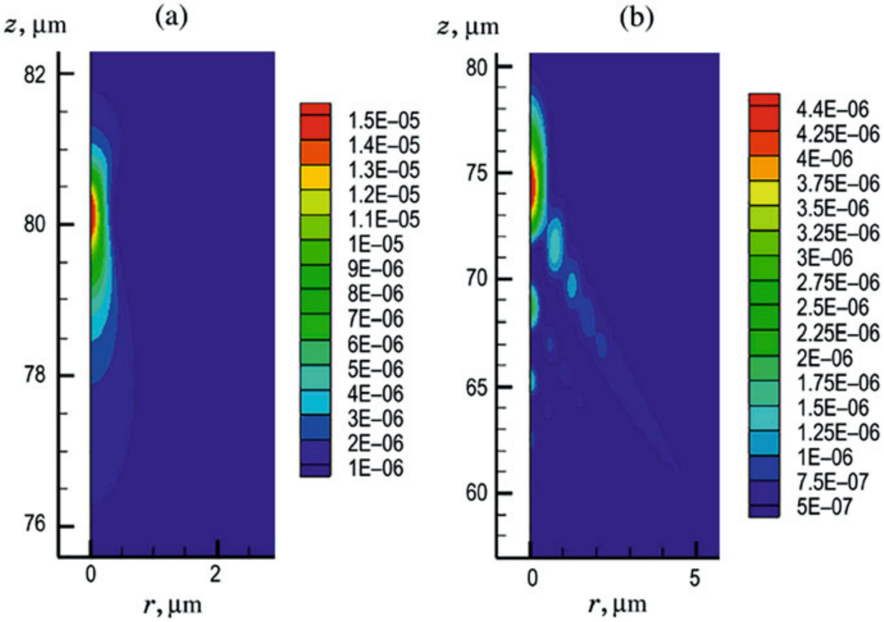

Fig. 1.6 Snapshots of laser intensity in fused silica obtained for NA = 0.8 by solving numerically (**a**) nonlinear Schrödinger equation and (**b**) Maxwell's equations. Low-energy case is presented without inducing ionization. Snapshots are given for the same time moment when the beam approached the focus zone. Pulse duration is 80 fs, and laser wavelength is 800 nm. Color scale represents the ratio of local laser intensity to the intensity, at which the Keldysh adiabaticity parameter is equal to unity [11]

applied beam energy, ionization of silica and the Kerr effect were absent; thus, the case demonstrates a pure effect of the used equations. Maxwell's equations capture well the beam diffraction, while the unidirectional Schrödinger approach yields in a smooth distribution of laser intensity nearby the focus.

2.3.4 Excitation of Electrons in Bandgap Materials

Excitation of electrons in solids (ionization from the valence band to the conduction band) by linearly polarized light is widely treated based on the theory presented in the seminal article of L. V. Keldysh [11]. The case of circular light polarization was also developed [80] using a model based on double Bessel functions inherited from atomic physics [81]. The Keldysh theory for linear polarization has been routinely implemented in many works using either a parabolic band structure [82, 83] or the Kane band structure [32, 84–86]. Note that the type of band structure affects the dependence of the transient gap energy on laser intensity. While a parabolic band structure leads to bandgap opening, a cosine band structure results in a less trivial variation [71]. As for circular polarization, it is also employed for laser material processing although not so often [87–90]. One of the reasons is that circularly polarized light excites bandgap materials less efficiently as compared to linear polarized light [91].

Figure 1.7 presents a qualitative difference in the excitation rates as a function of intensity upon irradiation of a bandgap material by (a) linearly [92] and (b) circularly [80] polarized laser beams. While the circular polarized light induces a smooth increase of the number of electrons transferred from valence to conduction bands per a time unit, the linear polarized light exhibits drops of excitation that are associated with disabling the tunneling ionization channel between two states on the occasion of the so-called Wannier-Stark localization (see Supplemental Material in [32]). Note that, using the TDDFT simulations, which takes into account several electronic bands, contrary to the two-band Keldysh model for solids, no particular drops of probability could be observed when varying the laser intensity at a given wavelength. As a result, sudden drops in ionization probability with irradiation intensity obtained using the Keldysh formalism are not observable experimentally [93], and their amplitudes look to be overestimated theoretically if an insufficient number of electronic bands is considered.

2.3.5 The Role of Laser Polarization in Excitation of Solids

As mentioned above, laser excitation of electrons inside a crystal strongly depends on laser light polarization. From the point of view of the band structure of the crystal, linear polarization leads a unidirectional transfer of momentum to the electrons [94] from $\boldsymbol{k}_e$ to $\boldsymbol{k}_e + \frac{e}{c}\boldsymbol{A}(t)$ ($\boldsymbol{A}$ is the vector potential acting on the electrons from the laser wave), while a circular polarization induces a time-dependent momentum transfer from the light to the electron in all directions. As a result, the energy levels populated by excited electrons in the band structure are very different for the cases of the linear and circular polarization. Figure 1.8 illustrates dynamics of excited electrons revealed in the TDDFT simulations of silicon irradiated by 25-fs laser pulse at 3000-nm wavelength with left-hand elliptical polarization [95]. Snapshots are given for a laser wave sub-cycle. The electron wave packet is swiftly accelerated by the vector potential of the laser field (shown by black arrow). A complex behavior of the electrons in the band structure of silicon is demonstrated, which results in many conduction bands involved in the dynamics.

On the material side, the primitive cell of a perfect bulk crystal contains a number of symmetries at equilibrium. Upon irradiation by polarized light, certain symmetries are broken [96]. This induces a transient manifestation of processes such as quantum phase transitions [97], a transient change of optical properties [98], or the transient opening of the bandgap [99]. In the real space, the light-induced symmetry breaking enables a reorganization of allowed electronic levels during the laser action. This can also cause a transient anisotropy in the light absorption [100], thus conferring an important role to the choice of crystal orientation (with respect

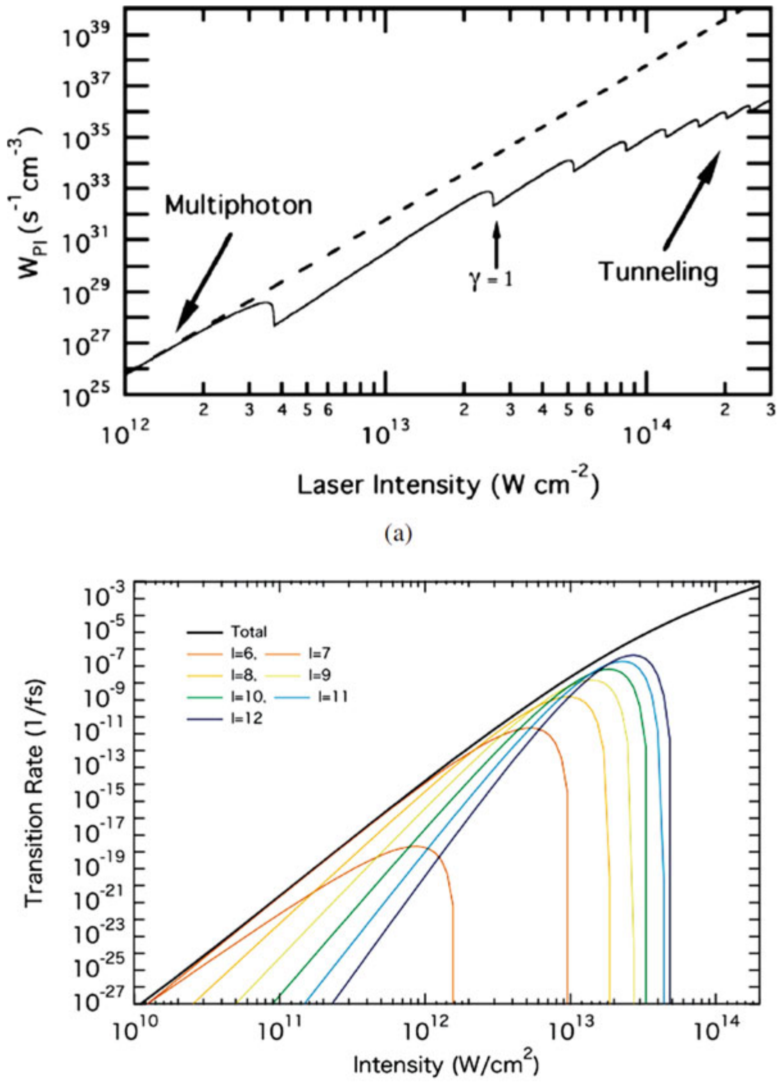

(a)

(b)

Fig. 1.7 Two-band excitation probability for transition of electrons from the valence band to conduction band for (**a**) linear polarized laser beam (800 nm wavelength, fused silica with the bandgap of 9 eV) [92] and (**b**) circular polarized light (800 nm, α-quartz) [80]. Copyright information. (**a**) was reprinted with permission from Gulley (2010) and (**b**) was reproduced with permission of Otobe et al. ©The Physical Society of Japan (2019)

to the laser polarization) for improving control over damage threshold [101] and nanostructure formation [102–104].

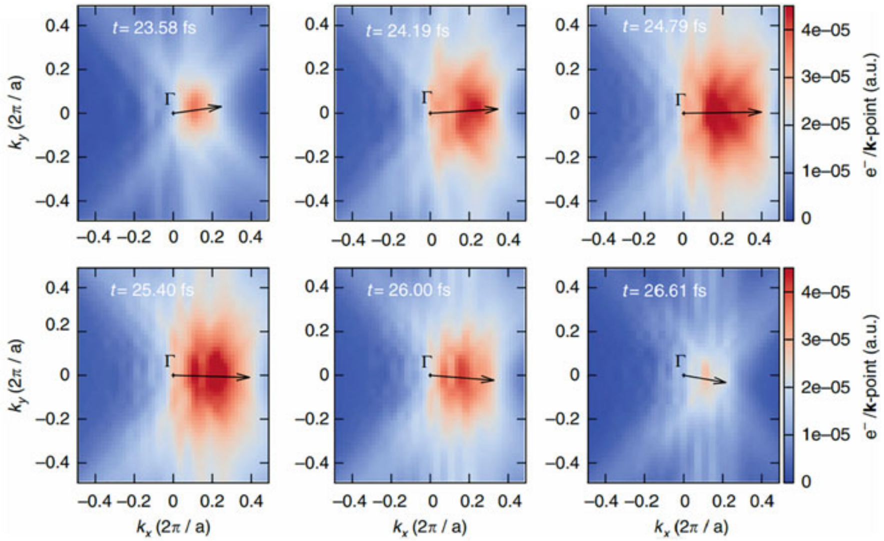

Fig. 1.8 Sub-cycle dynamics of quantum states explored by the electrons in silicon upon irradiation by laser light with left-handed elliptical polarization [95] (licensed under CC BY 4.0). Color scale represents the occupation of the electrons in the conduction bands. The arrow indicates the direction and strength of the applied vector potential. Pulse duration is 25 fs (FWHM), and laser wavelength is 3000 nm

2.3.6 Transient Reduction of Optical Penetration Depth and Light-Induced Metallization

For bandgap materials, first-principle simulations demonstrated recently that attenuation of light inside material can be well described using the Beer-Lambert law [105], provided that absorption remains metallic during the interaction. In some cases, the optical penetration depth may increase when using particular geometries [106] or if a material gains particular properties at high irradiation intensities. For example, while silicon reduces its absorption depth with increasing laser intensity, graphite can turn from a metallic to a dielectric state upon irradiation, leading to an inhomogeneous absorption profile at high intensities [107].

Out of some specific regimes and as a first approximation, the absorption of light by the free electrons can be described in the frames of the Drude model (Sect. 2.3.3). Generally, the optical penetration depth is dependent on the intensity of light and can strongly decrease upon excitation of electrons (their transition from the valence band to the conduction band). Transient metallization of bandgap materials can be described by different approaches. On the one hand, the excitation of electrons from the valence band to the conduction band in conventional materials induces manifestation of a metallic optical response when the density of excited electrons exceeds the critical plasma density at the irradiation wavelength. The dynamics of the electron excitation is usually described in the terms of the rate equations

[18, 23, 108, 109] which are often coupled with the two-temperature model modified to account for the dynamic change of the charge carrier density. Such approach in a simplified manner enables to evaluate the absorbed laser energy and its distribution in the irradiated sample that determines post-irradiation evolution of the material.

On the other hand, the electronic levels of bandgap materials can be considered from a quantum perspective that also allows to gain insight into metallization of a bandgap material by describing the ”laser dressing” effect illustrated in Fig. 1.9 [110] (see also Refs. [32, 111, 112]). An ultrafast transition from dielectric to metallic response of a material to light manifests itself as a crossing of the quasi-electronic levels when laser intensity exceeds transiently a metallization threshold. Under certain conditions, e.g., if a very short but very intense laser pulse is applied, the metallization effect in a dielectric material can be reversible at the timescale of the laser cycle [110, 113]. Arguably, such excitation effect was related to light-induced tunneling and was observed in several laser-irradiated dielectric materials [114], conferring a kind of universality to the Landau-Zener tunneling (or transient metallization) [115]. It should also be mentioned that the ultrafast metallization has been described in a number of works as an excitation of bulk polaritons [116–118].

2.3.7 Excitation of Surface Polaritons

From a classical point of view, *surface polaritons* are a kind of surface electromagnetic waves [119, 120], which play an important role in localization of laser energy absorption. At the microscopic level, when a photon excites an electron bound to an atom, they form together a quasiparticle known as plasmon polariton. This excitation is longitudinal, i.e., the polariton wavevector $\boldsymbol{k}$ and the electric field $\boldsymbol{E}$ enabling the electron-photon coupling are parallel to each other.

Polaritons can be excited both in the volume (bulk polariton) and at the surface of materials. When being close to an interface, a bulk polariton is perturbed by its presence that leads to the modification of the polariton near-field topology [121]. This in its turn results in a modification (shift) of the allowed energy quanta of the polariton. Bulk and surface polariton quanta usually have an energy of the order of electron-volt (1–10 eV) and therefore may be excited by the laser wave when irradiating solids in the range from UV to IR [122].

While some attempts to merge thermal and polaritonic models were proposed [123, 124], fully coupled microscopic descriptions are under development [125]. Classical approaches for describing the physics of plasmon polaritons include dispersion relations (deduced from simplified Maxwell’s equations) and numerical simulations of locally resolved near-fields using the method of finite-difference time-domain (FDTD). We note that the latter approach is widely employed in classical photonics and plasmonics in equilibrium situations, provided that the response of the material remains localized in space [126]. It should also be mentioned that recent progress in time-resolved photoemission electron microscopy using ultrashort laser excitation sources enables a mapping of plasmon polaritons that deepens our understanding and interpretation of the plasmonic behavior [127].

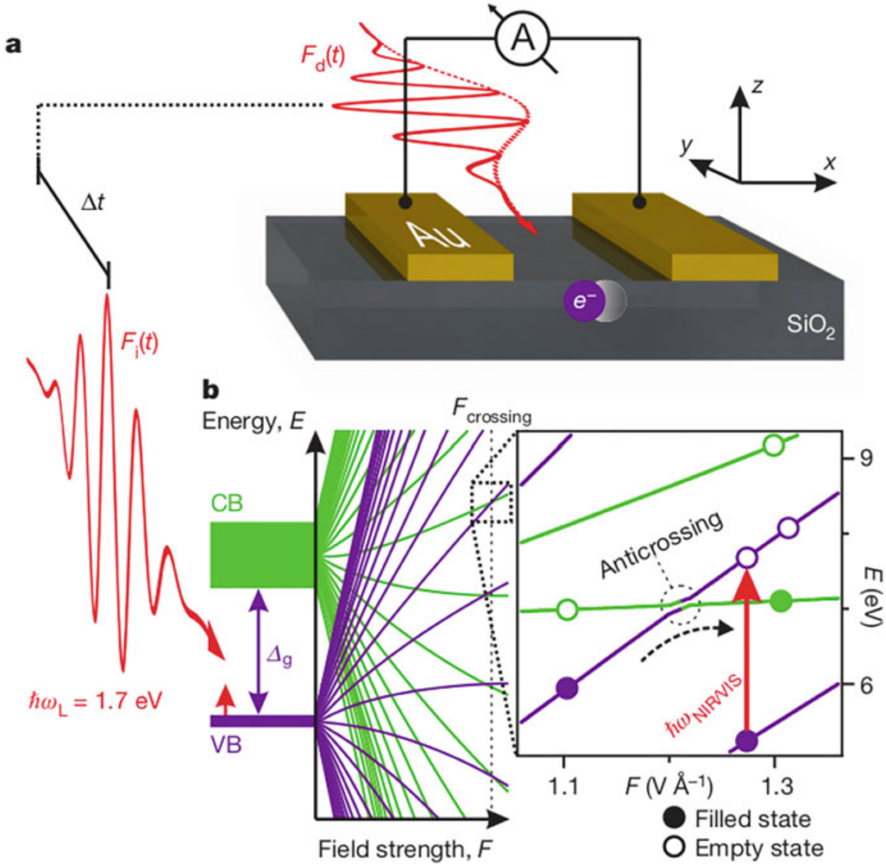
a
$F_d(t)$
A
z
y
x
Δt
Au
e^-
SiO$_2$
$F_i(t)$
$\hbar\omega_L$ = 1.7 eV
b
Energy, E
$F_{crossing}$
CB
Δ_g
VB
Field strength, F
Anticrossing
$\hbar\omega_{NIR/VIS}$
9
6
E (eV)
1.1
F (V Å^{-1})
1.3
● Filled state
○ Empty state

Fig. 1.9 (**a**) Schematic of the metal-dielectric nanojunction employed in [110] for measuring the optical-field-induced current in fused silica. (**b**) Illustration of the adiabatic energy levels of the electronic states in the valence band (VB, purple) and conduction band (CB, green) of the dielectric under the influence of a static or slowly varying strong electric field. At low fields, the valence band states are occupied, and the conduction band states are empty. As the field strength increases, the valence band and conduction band levels cross. Figure was reprinted with permission from Schiffrin et al. [110]

The Problem of Phase-Matching in Laser Processing Conditions In the classical vision, plasmon polaritons are described under an approximation of a local response of a solid to laser light that is a simplified description based on isotropic dielectric permittivities. Historically, encouraged by experimental observations of plasmonic effects (e.g., plasmonic microscopy using leaky modes [129, 130]), studies of materials with low losses were prevailing due to simplifications of the classical formalism such as neglecting the imaginary parts in the dispersion relations [130–132]. In such idealized situations, i.e., when irradiating an ideal material, the dispersion relation analysis has revealed that a far-field monochromatic light can

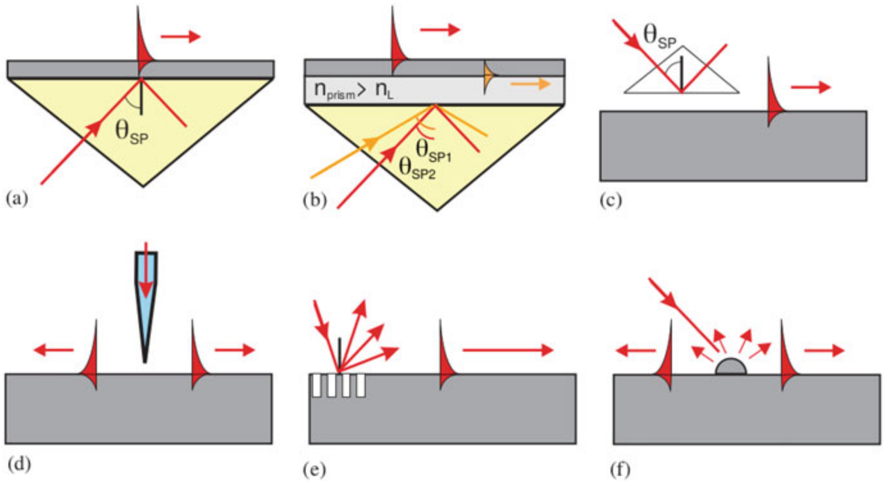

Fig. 1.10 A variety of methods to trigger phase-matching of surface plasmon polaritons with far-field laser light [128]. (**a**, **b**) Resonant coupling in Kretschmann geometry. (**c**) Resonant coupling in Otto geometry. (**d**) Nonresonant coupling using a laser-irradiated metallic tip. (**e**) Nonresonant scattering on gratings. (**f**) Nonresonant scattering on surface defects and nanoparticles. Figure was reprinted with permission from Zayats et al. [128]

couple with a near-field polariton only if a phase-matching could be achieved by using a dielectric prism, a grating, or some high-index oil [128] (see Fig. 1.10).

In the case of rough surfaces, each micro-/nanoprotrusion forming the surface roughness has a random curvature radius, thus extending the possibilities of wavenumber matching between incident light and the surface polariton waves [52]. To get some intuition on this effect, the Heisenberg uncertainty principle can be employed. The uncertainty on spatial roughness at nanometric level (e.g., various curvature radii, random spatial positions, uncertainty on shape) induces a large uncertainty δk on the scattered light wavevector k. Although being poorly controllable, surface roughness is expected to enable a facilitated coupling of the incident wave with polaritonic modes. A mild efficiency of such a coupling can be compensated by using intense laser light. Fundamentally, any asperity on a metallic surface can lead to the excitation of surface electromagnetic modes [128, 133] (see Figs. 1.10f and 1.17b). Recently, the application of asymmetric circular resonant structures, on which an ultrashort laser pulse was scattered and resolved at the femtosecond and nanometer scales, has revealed possibilities of the control offered by improved knowledge of ultrafast surface polaritonics [134].

Overall, the excitation of polaritons at materials' surfaces is rather a commonly met process (along with its physical and chemical consequences) in laser micro-/nano-engineering of surface structures. The presence of a roughness of different size and distribution over the surface (called also selvedge [52]) leads to excitation of polaritons by laser light that usually results in a periodic deposition of the laser energy, due to interference between the excited surface electromagnetic wave and the incident laser light [52]. Such interference should not be seen as a classical free-space interference of light but rather as a coupling between waves of different natures [135]. In general, the phase-matching can be obtained by the presence of a scattering center or can also be well controlled by smartly interfering beams [136, 137].

A Wide Number of Surface Electromagnetic Phenomena A survey of the large number of polaritonic quasiparticles have been recently proposed, calling for a unification of the terminology and of the theories describing the polaritonic coupling [119, 138]. While on metallic (or transiently metallized) materials, the excitation of surface plasmon polaritons is a natural phenomenon, other types of polaritons such as surface phonon polaritons or exciton polaritons can also be excited in dielectric materials [139]. Dispersion relations deduced from Maxwell's equations [140] correspond to the band structure of electrons in solids in the presence of laser light [117, 118, 141] called often "laser dressing." The transient phenomena emerging from these couplings can offer numerous possibilities for tweaking the laser energy coupling with matter in the near future.

The Role of Ohmic Losses in Laser Nanostructuring of Surfaces The lossy character of a solid leads to reduction of lifetime of excited plasmonic waves on its surface [142, 143]. Lifetimes of plasmon polaritons were found to be close to a picosecond at surfaces of so-called plasmonic materials (i.e., materials where plasmons can propagate to long distances) such as Au, Ag, Pt, Cu, and Al [132, 144], whereas short femtosecond lifetimes are usually obtained for materials exhibiting high Ohmic losses such as Mo, Ti, steel, V, W, etc. [132]. This classification correlates well with the observation of highly regular laser-induced periodic surface structures (LIPSS) (Fig. 1.11) [145]. High regularity was also confirmed for other lossy materials such as CoCrMo and CrNiMo alloys [146, 147]. An improvement of regularity proposed in [145] by reducing the applied laser wavelength and, hence, reducing the distance of propagation of plasmon polaritons for Au was recently confirmed by Liu et al. [148]. The authors write: "the findings validate that the uniformity of LSFL generated by 515 nm laser is better than that generated by 1030 nm laser." These results support the hypothesis that the formation of highly regular structures is related to the damping of excited plasmon polaritons at the surface of lossy materials [145].

Overall, the plasmon polaritons excited on surfaces of lossy materials propagate on a short distance and their energy is quickly converted into heat. This secures a low level of interaction between surface electromagnetic waves emitted randomly by numerous roughness features and, hence, a better coupling with incoming laser light. Thus, the choice of lossy materials may enable to tweak the localization of light at extreme spatial and temporal resolution.

Further Routes Toward Reduction of the Period of Polaritons Reducing the periodicity of the excited surface electromagnetic waves to extremely small scales is foreseen to be achievable by irradiation of prestructured surfaces such as near-

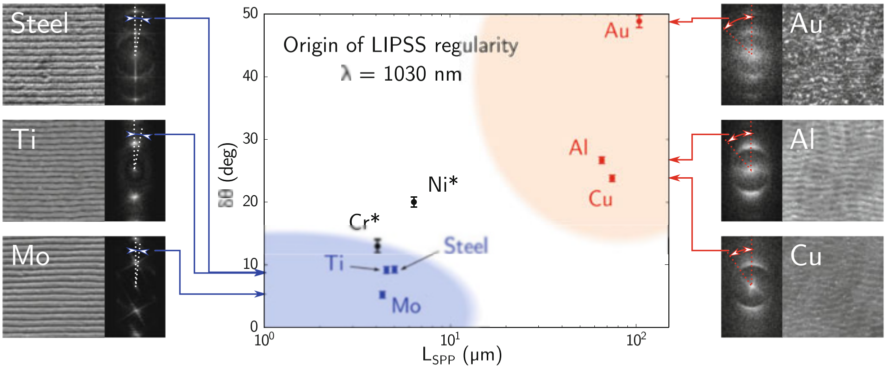

Fig. 1.11 Correlation between a characteristic distance of propagation L_{SPP} of surface plasmon polaritons (SPP) with the regularity of LIPSS produced on surfaces of several materials [145] (licensed under CC BY)

wavelength gratings. For several bandgap materials, Huang et al. have demonstrated the reduction of the polariton wavelength due to the influence of the surface geometry on the coupled surface frequency [149, 150] that leads to very small narrow periods, much below the diffraction limit.

Another way for higher localization of light in solids is employing thin films with alternating metal-dielectric properties [129, 151]. In such situations, by controlling thin-film thickness or materials' composition, several modes of surface electromagnetic waves can be excited [152, 153], some of which can become dominating. This aspect of multiplicity of the excited modes and their roles in surface periodic structuring call for further studies (see Sect. 5).

2.4 *Post-irradiation Material Evolution*

Nanostructuring of material surfaces by ultrashort laser pulses requires swift freezing, at a nanoscale, of the laser-induced nanorelief into a permanent surface modification. In most cases, formation of nanorelief is associated with a rearrangement of matter. Due to highly nonequilibrium conditions generated in a solid target upon ultrashort laser irradiation and timescales of at least several tens of picoseconds needed for any material movement larger than ~100 nm at subsonic speeds, the relocation of the material is mostly a post-irradiation dynamics. Melting and vaporization are the phase transformations of matter that are most related to material evolution/relocation upon laser irradiation. These processes usually take place during laser processing of solids, but insufficient attention is given to mechanical stresses, which however play an important role, both by deforming the laser affected zones in irradiated samples and by affecting the onset of phase transition.

2.4.1 Isochoric Heating and Stress Buildup

As already stated in Sect. 2.1, the energy of an ultrashort laser pulse is first coupling to the electrons of an irradiated solid. In this situation, the time necessary to achieve thermalization between the electrons and lattice gives a characteristic time of the material response when the energy starts to act on the core of the material.

For metallic materials, the rate of transfer of the energy from the electrons to the lattice (the coupling factor g; see Eqs. (1.1)–(1.2)) is usually of the order of 10^{16} W/m^3/K [10]. The corresponding electron-lattice coupling times $\sim C_e/g$ are of the order of a few to tens of picoseconds. Considering a typical thickness l_{heat} of several tens of nanometers for the heated layer during the coupling time[1] and the speed of sound c_s in metals in the range of (3–6) × 10^3 m/s, one can evaluate that the electron-lattice coupling time is usually of the order or shorter than the time $t \sim l_{\text{heat}}/c_s$ (about several tens of ps) required for any significant expansion/relocation of the material. In such cases, the laser heating can be considered as isochoric with the consequence of building up strong mechanical stresses within the absorption layer as it gets heated up. In some semiconductors and dielectrics, the coupling time can even be longer. For example, in Al_2O_3 and MgO, the typical recombination time of the laser-excited electrons is 100 and 50 ps, respectively [154]. However, some materials like fused silica exhibit a swift trapping process of excited electrons into excitonic states, with a characteristic time of the order of 150 fs [17]. Additionally, large bandgap materials do not strongly absorb laser light at wavelengths, whose photon energy is smaller than their bandgap (usually in the visible or near-infrared domain). At relatively small laser fluences, the light penetration depth or an effective energy deposition layer in such materials can significantly be larger than for metals. The absorbed laser energy can thus be spread over several tens of micrometers in depth, depending on the focusing conditions, thus limiting the stress confinement. Nevertheless, at high laser fluences, a thin skin (absorbing) layer is swiftly developing during irradiation [45, 109] that can be in favor of stress confinement.

When isochoric heating is realized, the conditions for mechanical stress confinement are developed. A compressive stress builds up in the swiftly heated surface region of the material that results in (i) generation of a stress wave traveling toward the depth of the material and (ii) expansion of material in the direction of the free surface that induces the propagation of a rarefaction wave following the stress (or shock) wave.

The pressure waves (shock, rarefaction) are traveling in the samples and can reflect from various boundaries and discontinuities. In particular, a compression wave traveling in the depth of the material, which undergoes melting, can reflect from the solid-melt interface. Upon reflection, the shock wave is transmitted through the interface, while a rarefaction wave is reflected. Thus, multiple reflections and interference of the waves can occur, making the dynamics complex. We refer the reader to the references [155, 156] and references therein for further details on the stress wave dynamics in laser-irradiated samples and in particular the insights from molecular dynamics simulations.

---

[1] We consider here laser pulse durations that are shorter than the electron-phonon coupling time $\tau_{\text{e-ph}}$. In general, the heating time (and the corresponding depth of the heated layer) is given by the maximum between the coupling time and the pulse duration, max $\left(\tau_{\text{e-ph}}, \tau\right)$.

The effects of the stress wave development can be clearly observed experimentally in several situations. The case of short and ultrashort pulsed laser irradiation of thin metallic films with thickness smaller than a micrometer (see Fig. 1.12a, b) is a typical example where expansion of the material, tensile stress, and a shock wave play a dominant role [157–161]. Bulging of the laser-heated area and cracking or punching of the metallic films are usual laser-induced damages in such situations.

Besides the stress waves considered above, which are mechanically affecting the irradiated zone and “shaking” the material, there is another type of stresses, which are induced by “quasi-static” temperature gradients, slowly evolving with material cooling. In particular, this concerns the stress components across the irradiation spot. Such stresses are especially important for processing of brittle refractory materials with ultrashort laser pulses. The majority of solids expand almost linearly upon heating at temperatures below their melting points. If a temperature gradient builds up at the surface or inside a material while its expansion is constrained, the thermal stress arises [163]. In practice, the situation is met virtually for any laser irradiation where the material within the laser spot of finite dimension is confined by surrounding cold material regions on the sample surface. The consequences vary however with ductility of the material, its linear thermal expansion coefficient, and the value of temperature gradient. The stress effects therefore manifest themselves

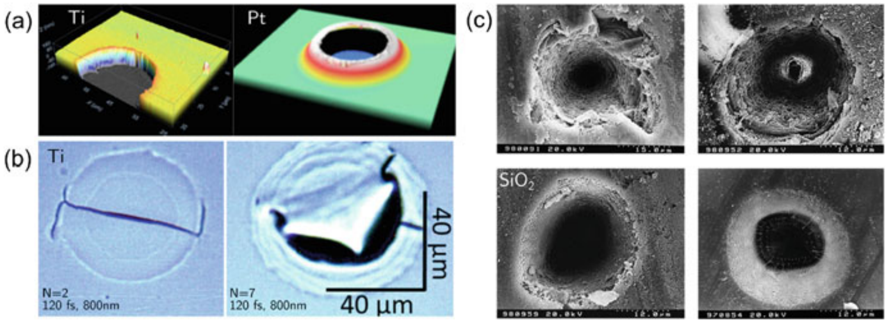

Fig. 1.12 Effects of stresses on material surfaces induced by ultrashort laser pulses. (**a**, **b**) Effects on metallic films. (**a**) 330-nm-thick Ti film (left) and 335-nm-thick Pt film (right) ablated by 1064 nm single pulses at pulse duration of 10 ps [159]. Note the difference between Ti and Pt films; the latter shows significant plastic deformations at the edges. (**b**) 300-nm-thin Ti film irradiated by several 120 fs pulses at 800 nm wavelength [161]. (**c**) Visible cracks formed on fused silica surface upon irradiation by 80 laser pulses at 790 nm wavelength with different pulse durations. From top to bottom and from left to right: 3 ps, 220 fs, 20 fs, and 5 fs [162]. (**a**) and (**c**) were reprinted with permission from Heise et al. [159] and Lenzner et al. [162], respectively. (**b**) is licensed under CC BY

mostly for refractory and brittle materials such as glass in the forms of cracks around the irradiation crater; see Fig. 1.12c [162] and also Refs. [50, 164, 165]. Techniques based on the so-called controlled fracture take even advantages of the temperature inhomogeneity to create and propagate a crack induced by the thermal gradient [166, 167].

The Case of Volumetric Modifications In the case of volumetric modification, the laser pulse is focused in the bulk of a transparent material. The matter undergoing the laser-induced changes is surrounded by a colder material that provides stress confinement and makes it possible to reach pressure levels beyond GPa around the focus [168]. Without delving into details of the electromagnetic effects occurring on the laser beam way toward the focus zone (see Sect. 2.3), we briefly present a few characteristics associated with stress.

Focusing of infrared or visible laser pulses of sub-ps duration inside wide bandgap dielectrics allows modification of the refractive index within the focal volume as was first discovered by Davis et al. [169]. This method is exploited for fabrication of waveguides and other photonics and optoelectronics structures that rely on a strong contrast of refractive index. Depending on the level of excitation reached, the irradiated material follows different relaxation routes that can yield different spatial distributions of the index of refraction with zones of lower and higher index as compared to the initial optical properties. Higher indices are generated by structural rearrangements of glass bonds, while lower index zones are created by thermal expansion or cavitations induced in the volume [57, 170]. It is clear that, in the material bulk, any local densification is automatically accompanied by a rarefaction zones in other locations to satisfy the conservation of mass since no material escapes from the modification area in the bulk. We note that, using temporally shaped laser pulses that control stress development and dynamics, it is possible to invert the natural response of optical glasses with strong thermal expansion [171]. Upon irradiation by usual Gaussian pulses (pulse sequences), such materials tend to create an extended rarefaction region with a thin compaction envelope around it. Smartly tailored laser pulses lead to a significant refractive index increase in extended focal regions, which are suitable for waveguide writing.

The stresses generated in the bulk can induce micro-explosions, yielding nano- or micro-voids where the matter locally vaporizes upon expansion (see next subsection), thus inducing plastic deformation. It is interesting to note that the pressure levels generated by a micro-explosion in the volume are found to be bouncing for a few nanoseconds before the permanent defects are imprinted in the bulk. This bouncing is associated with a densification and rarefaction of the optical index of refraction [172, 173]. Another important point concerns stress generation upon laser-induced volumetric modification in crystalline materials. A high level of localized stresses can induce birefringence and cracks produced in some crystals only along favorable directions [174].

The consequences of laser-induced stresses in the material evolution go beyond the appearance of cracks and deformation. Locally in an irradiated material, not only the temperature but also the level of stress (pressure) determines its phase and thus its ability to locally melt/ablate as is discussed in the next section.

2.4.2 Melting, Ablation, and Relocation

Here we start shortly from some general basics of thermodynamics, which can be found in textbooks on thermodynamics, in particular in [175, 176]. Melting and vaporization are often prerequisites when aiming at modifying a sample by laser, even at sub-micrometric scales. At equilibrium, for a closed system at a given pressure, when the local energy density in a material is sufficient to reach its melting temperature T_m, the phase transition occurs, consuming the latent heat of fusion L_m. At the melting temperature, the liquid and solid phase can coexist, and, once the equivalent of the latent heat is provided, the material is locally completely molten and its temperature can increase beyond T_m. The same applies for the process of vaporization by boiling with the consumption of the latent heat of vaporization at the boiling temperature. It is important to recall that the melting and boiling temperatures depend on the pressure in a thermodynamic system considered. In a thermodynamic p-T diagram, the binodal curves represent the sets of pressure and temperature where two phases (solid-liquid or liquid-vapor) coexist at equilibrium in a closed system. The Clausius-Clapeyron relation provides the dependencies by giving the local slope of the binodal curves.

Upon heating by a laser, if the changes of temperature and pressure are not too fast, the system evolution can be considered as transition through a succession of equilibrium states and the Clausius-Clapeyron relation can be applied. However, if the system (a material) is heated too fast that it cannot follow the equilibrium states, it can be superheated (also “overheated”). A solid material in this case can remain solid for a time at a temperature beyond the melting one for a given pressure culminating in a catastrophic melting [47].

Homogeneous Melting Superheated (or overheated) solids are in a metastable state, in which their properties (density, temperature) fluctuate and small regions of melt can appear randomly [155]. Each nucleus can collapse back to solid unless it reaches a critical radius. The nucleation rate is growing exponentially with the temperature, while the critical nucleus radius decreases [177]. Thus, upon irradiation of solids by ultrashort laser pulses, for energy densities above the melting threshold, significant overheating takes place, and melting occurs mainly via homogeneous nucleation [47, 177]. This scenario was supported experimentally for some metals, e.g., in [36, 178, 179] stressing the importance of the laser energy density deposited in the sample. The higher the energy density deposited in the material, the more homogeneously the nucleation proceeds. Homogeneous nucleation of molten phase in solids is widely supported by numerical investigations, see, e.g., [47, 180], showing in particular the onset of catastrophic homogeneous nucleation as soon as the superheating $(T - T_\mathrm{m})/T_\mathrm{m}$ reaches between 14% and 30%, depending on the material.

Homogeneous melting is a volumetric process, opposite to heterogeneous melting when a melting front propagates from a sample surface or a grain surface, a free surface impurities, etc. It is important to note that the melting front velocity is limited. It was shown by molecular dynamics simulations [47] that, for metals at least, heterogeneous nucleation of melt is limited in rate and the melting front velocity is typically a few percents of the speed of sound. Moreover, upon irradiation by ultrashort laser pulses, homogeneous melting does not proceed classically through a propagation of the melting fronts from the nuclei of melt [181]. Such process would require much time, similarly to the case of heterogeneous melting from surfaces or impurities. It was shown that it is rather the coalescence of the molten nuclei due to their high density, which is exponentially increasing with overheating.

Stress Relaxation and Ablation by Spallation and Phase Explosion Similar situation of overheating occurs for the vaporization process in the molten material with vapor bubbles nucleating in the overheated melt. At this stage, the pressure waves develop (see Sect. 2.4.1), which have a significant impact in the case of laser irradiation of matter by ultrashort laser pulses. In particular, a drop of pressure locally enhances the nucleation rate of vapor bubbles. This can lead to spallation when the rarefaction wave builds up in the overheated molten material. The rarefaction wave provides, in an undersurface region, a high rate of formation of vapor nuclei, which coalesce and eventually tear the melt apart, thus separating the surface liquid layer from the rest of the material [182]. For higher rates of energy deposition, the vapor nucleation rate in the molten target becomes higher so that the bubbles are formed within the whole laser-heated high-temperature layer. Under such conditions, materials disintegrate via the mechanism of phase explosion known in thermodynamics as explosive boiling [182, 183].

Relocation within Molten Material Regions Molten or softened materials can experience relocation within the laser-affected zone on the surface. Hydrodynamic instabilities and pressure-induced movements are the most common mechanisms of such relocations. We give here several examples revealing the importance of reorganization of molten material in the laser-assisted fabrication of nanostructures.

When vaporization takes place from the molten surface layer of a laser-irradiated target, the recoil pressure of the ablation products expels the deeper melt, which can solidify at the periphery of the forming crater. The relocation of the melt is very common in laser processing and, in particular, for the cases of CW, long and short (nanosecond) pulses, when the heat-affected zone and thus the molten area extend radially due to heat conduction [184, 185].

When a thin film deposited on another material experiences melting, being heated in a furnace or due to irradiation by laser or by a particle beam, the surface tension of the molten material can lead to rupturing the film, thus resulting in droplet formation [186–189]. This phenomenon is called dewetting and it is used, e.g., for preparation of catalytic nanoparticles for chemical vapor deposition (CVD) growth of carbon nanotubes [186]. An interesting effect of dewetting was observed in [190] where thin Pt films (thinner than 5 nm) deposited on silicon were irradiated by polarized laser light. The conditions to generate LIPSS are met and a periodic modulation of the temperature in the molten films is thus expected. With a surface tension strongly dependent on the temperature, platinum thin film eventually experiences dewetting into a periodic array of nanowires orienting perpendicular to the laser polarization.

Laser printing is another example of melt relocation using thin films. In some particular cases [191], a donor thin film representing a silicon-on-insulator wafer is irradiated by a laser pulse through a transparent receiver substrate to induce its melting. Densification of silicon upon melting and surface tension induce a contraction into a nanosphere that acquires extra momentum and is expelled and collected on a receiver substrate. This smart technique enables highly controllable regular arrangement of silicon nanoparticles. Similarly, nano-bump and nano-whisker structures can be achieved on thin metallic films [192, 193].

Finally, hydrodynamic instabilities can play a significant role in the surface reorganization of samples irradiated by ultrashort laser pulses [194–196]. For example, the ablative Rayleigh-Taylor instability was identified to contribute to the surface texturing of laser-irradiated metals, leading even to generation of nanoparticles [197]. Other convective instabilities related to surface tension were recently identified as responsible for the growth of micro- and submicrometer periodic structures on the surfaces of irradiated samples. In the case of thin molten layers of nickel, the Marangoni convection was found to be efficiently developing [198]. It is induced by the transverse gradients of surface temperature due to the inhomogeneous absorption of the laser energy that originates from the sample roughness. The convection can be enhanced by the rarefaction wave (unloading of the compressive stress), thus leading to the growth of surface structures. For the case of dielectrics, Gräf et al. [199] have proven the development of thermo-convective instability in a thin molten layer as a route for tuning reorganization of matter by selecting the spatial periods of LIPSS forming on the surface.

3 New Insights from TDDFT Simulations

Fundamental Aspects of Time-Dependent Density-Functional Theory The time-dependent density-functional theory (TDDFT) is a powerful tool, which enables the simulations of the dynamic evolution of electronic states under the action of ultrashort pulses of laser light [122, 200, 201]. The density-functional theory (DFT) is based on the idea that the local electron density $n(\boldsymbol{r})$ (comprising *all* the electrons whose probability distributions are present at a position $\boldsymbol{r}$) can be used as an observable value (usually resolved using x-ray diffraction [202]) to map other quantities, including energy and forces acting in atoms, molecules, and crystals. The time-dependent version of the DFT is based on a time-dependent density $n(\boldsymbol{r}, t)$ which matches the evolution of the electron density at a given position in the real space with the evolution of other observables. However, it is important to keep in mind that the memory effects cannot be captured by the evolution of the density $n(\boldsymbol{r}, t)$ using the existing approximations [203] that prevents to grasp all phenomena that can be important for the field of laser material processing. While one-to-one correspondence between the ground-state density $n(\boldsymbol{r})$ and the state of the system is secured by the Hohenberg-Kohn theorem [204], the time-dependent uniqueness and existence of such correspondence is secured by the Runge-Gross theorem [205, 206]. As a result, the DFT and the TDDFT are usually considered as being "formally exact," whereas their limitations originate from the approximations, which are necessary for solving numerically tractable problems based on nowadays computer facilities [207].

Using first-principle pseudo-potential constructed from the Dirac equation, the TDDFT enables meaningful predictions of the total density of electrons in the presence of an electric field from a strictly first-principle formalism [208, 209], still with applying a number of approximations (e.g., without phonons). The laser light that can be described either classically (using a classical electric field, or using a classical vector potential), or quantumly by using operators written in second quantization (that is beyond the scope of this chapter) [210].

A distinction should be made between the *excited* electron density, i.e., the quantity of electrons located in the conduction bands of a solid [23, 45], and the *total electron density* that comprises the conduction band electrons, the valence band electrons, and *in fine* the total electron charge density present at a given position. Note that in quantum electrodynamics, the concept of conduction bands can be defined only when considering an intuitive vision of a frozen band structure where electronic states are frozen but where operators evolve in time. The latter corresponds to a very intuitive Heisenberg vision. Conversely, in the Schrödinger vision, the conduction and valence bands are no longer defined since the electronic states evolve with time [211]. In practice, a combination of both visions can be employed.

Accessing the Dynamics of Excited Electrons upon Ultrashort Laser Irradiation The quantity of excited electrons can be accessed in different ways. The quantity of electrons present in the conduction bands at a given time moment is a gauge-dependent value. Several definitions are available for calculating the quantity of electrons present in valence bands during the irradiation of a solid, which provide the same results at the end of the laser action [200, 212]. It is then possible to calculate the number of excited electrons at the end of the laser action for various irradiation conditions that was recently realized for deducing the electron photo-ionization rates in silicon [32] along with their comparison with the Keldysh theory for solids [11, 85]. The excitation rates provided by the TDDFT are about two orders of magnitude higher than predictions of the Keldysh theory for solids. The main reason for this discrepancy was presumed to be in the limited number of bands accounted for in the Keldysh model for solids and the idealized dispersion laws (Kane and parabolic) [11, 213]. The TDDFT was also recently employed for estimating the excited electron density in the context of surface nanostructuring [214].

From the experimental point of view, a sensible progress was recently achieved in the transient measurements of the excited electron density. While past works required the adjustment of optical probes to the Drude model to access the excited electron density from pump-probe experiments [215–217], recent methods give a possibility of direct measurements of the transient excited electron density with a sub-cycle resolution [218], in line with the excited electron density obtained from the TDDFT simulations [200].

Ponderomotive Potential vs Bandgap Energy Upon irradiation of a solid by a linearly polarized laser pulse, the electrons located in a crystal are reorganizing in the real space as a function of time, intensity, and wavelength of irradiating laser wave. This also manifests itself as a reorganization of the electronic quasi-energy levels (see Sect. 2.3). Although being intuitive regarding atomic ionization, the ponderomotive potential U_{eff} (denoted as $\tilde{\Delta}$ in [11]) was sometimes associated with the transient bandgap energy of the irradiated solid. This consideration however leads to some contradictions. Firstly, following the expressions for the ponderomotive potential U_{eff} provided in the Keldysh theory (for parabolic or Kane two-band structure in crystals [11]), the U_{eff} value is increasing with laser intensity. However, the photo-ionization rate w_{PI} depends on U_{eff} only in the multiphoton ionization approximation, while in the tunneling regime, it does not depend anymore on the value of U_{eff}.

Secondly, while a two-band model describes a transient increase of the bandgap [71, 219], models with several bands or band replicates reveal a bandgap decrease and even a possibility of transient metallization [110, 111, 113] originating from the Landau-Zener tunneling effect [114]. In experiments, the transient opening of the bandgap energy was observed in some limited cases, e.g., when irradiating specific materials by circularly polarized light [99, 220], while for most materials, a closure of the bandgap is usually observed [112, 114, 221, 222]. Therefore, promising perspectives arise from beyond-two-band approximation approaches for describing ultrafast phenomena such as electron excitation [223, 224] and ultrafast phase transitions in solids.

Thus, it can be hypothesized that another understanding for the ponderomotive potential U_{eff} should be considered. In particular, the Kapitza potential can provide an insight into the effective ponderomotive energy [225].

Finite-Temperature Density-Functional Theory: Opportunities and Limits of Applicability In the last decade, the finite-temperature DFT is increasingly used, thanks to increased accessibility of computational centers and the open-access policy of codes' developers. This has made possible the calculation of the linear optical response of solids [10, 30, 226, 227] along with thermodynamical properties [10, 228].

Although the finite-temperature DFT predicts nonequilibrium crystal configurations, it is not justified that the electron distribution in a highly excited solid completely relaxes to an equilibrium state prior to inducing a phase modification. Additionally, the symmetry of the system can change during laser action, a feature that is not considered in the usual DFT.

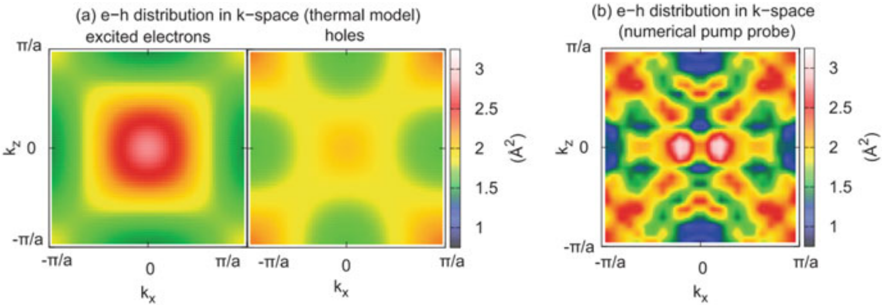

Fig. 1.13 Distribution of occupation of electron-hole states in the first Brillouin zone [230]. (**a**) Simulations performed using the finite-temperature DFT with the Fermi-Dirac distribution of electrons. (**b**) Simulations performed using the TDDFT. Figure was reprinted with permission from Sato et al. [230]

Upon construction of a ground state of a solid using the DFT, the occupation of the electronic levels has to be defined by introducing an equilibrated Fermi-Dirac distribution of electrons. The resulting finite-temperature DFT (sometimes called "thermal DFT") could be meaningful only if electrons excited by laser light are fully relaxed into a thermalized distribution. Then this approach is to be privileged for studying the situations when laser pulses have a duration longer than the electron relaxation time in the irradiated materials [227]. Such approach was successfully applied to investigate the absorption of gold with careful accounting for the spin-orbit coupling [229].

By neglecting the motion of nuclei (i.e., phonon excitation), the finite-temperature DFT assumes an equilibrium situation within the electron subsystem, while there is no equilibrium between the electrons and the lattice. On the contrary, the TDDFT does not require the assumption of a thermalized electron gas during the laser action. Figure 1.13 illustrates how the distribution of electrons and holes in the Brillouin zone of silicon calculated using the TDDFT can be considerably different after few laser cycles from that simulated in the frames of the finite-temperature DFT approach assuming the Fermi-Dirac distribution [95, 230]. Similar conclusions can be extended to metallic materials [231].

The Electron-Phonon-Photon Coupling: Still Unresolved Quantum Phenomenon Here we would like to stress a lack of knowledge about the electron-phonon coupling to account for a contribution of the lattice to the transient response of material to ultrafast laser excitation at subpicosecond timescale. While some impressive results were obtained in the last decade in simulations of phonons [232, 233], the problem of knowing how electronic wave function in the presence of phonons couples with potential energy surfaces remains open. This question is related to the exact factorization problem, which can be seen as a quantum equivalent of the two-temperature approach [234–236]. More information on quantum approaches in revealing the processes at nanoscale under ultrafast laser irradiation can be found in Chap. 3 of this book [237].

Finally, first-principle approaches, which take into account a role of photons in the description of electron-phonon coupling in a simplified manner, have been proposed [238, 239]. It should also be noted that coupling the TDDFT with the classical (Ehrenfest) molecular dynamics only accounts for forces originating from the electron motion, which remains to be resolved in the frames of quantum description of internuclei phenomena [122, 240].

Toward Large-Scale First-Principle Descriptions A high computational efficiency of molecular dynamics (MD) combined with the TTM enables to describe many nonequilibrium aspects of modifications/ablation of ultrashort laser-irradiated materials [47, 155, 241, 242]. However, for addressing nonthermal processes, introducing a first-principle description of electrons into MD would be beneficial. Notably, the development of interatomic potentials that would be dependent on the electron charge cloud around atoms appears promising. Recently, using machine learning techniques, it was proposed to construct interatomic potentials, which involve the results obtained from the first-principle simulations [243]. This promising direction would enable the possibility to address the breaking of crystal symmetry induced in solids by laser light [98].

4 Roadmaps for Laser Energy Localization

As discussed in Sect. 2, a controlled laser fabrication of nanostructures requires in many cases to drastically reduce the laser energy deposition volume. In this section, we start from basic considerations of focusing Gaussian beams. We then present advantages, which can be taken by the use of spatial and temporal beam shaping, that receive increasing interest in the community. Finally, some additional concepts are presented, which can facilitate localization of the absorbed laser energy, spatiotemporal coupling in ultrashort laser pulses, multiwavelength irradiations, and localized field enhancement by nanomaterials.

4.1 Laser Focusing and Beam Shaping

Gaussian Beam Focusing One of the most obvious ways to localize the absorbed laser energy to a small sample zone is to focus it. In the Gaussian beam optics, considering a beam of wavelength λ_0 in vacuum, a diameter D (the diameter illuminated on the lens determined by $1/e^2$ of peak intensity) and a focal length of the lens f larger than the beam diameter (small angle approximation must be valid), the beam waist w_0 (beam radius at focus) can be evaluated as $2w_0 \approx (4/\pi)\lambda_0 f/D$. Therefore, expanding the beam on the focusing lens and/or choosing a shorter f

helps to reduce the spot size. However, for wavelengths in the visible and near-IR spectral ranges, even using microscope objectives with high numerical apertures of 0.5 or larger, the typical $1/e^2$ spot diameter is larger than half a micron.

Modification of materials by ultrashort laser pulses, when material ablation or structural transformation occurs much faster than the absorbed heat would diffuse from the laser-affected zone, is governed by the laser energy density deposited locally. Using a Gaussian laser beam profile with a peak fluence only slightly above the damage threshold of an irradiated material, it is thus possible to obtain modification on scales much smaller than the beam waist $2w_0$, even down to dozens of nanometers as was first proposed by Pronko et al. [244]. Illustration of this technique is shown in Fig. 1.14 [245]. This simple smart method is applicable for different materials [245–248] and offers great opportunities for bio-applications [247] (see also review [249]). Another ingenious technique of achieving subdiffraction modification of material surfaces is using the so-called photonic nanojets generated from a dielectric microsphere illuminated by laser light [250]. This method can be referred to laser beam shaping, which in its turn offers a great variety of degrees of freedom for tailoring material properties by laser light at nanoscale.

Laser Beam Shaping Laser beam shaping (spatial, temporal, and spatiotemporal) is a powerful technique not only for enhancing the efficiency of laser processing of materials of different kind, but also it offers ways for extreme localization of light absorption with achieving high control over laser nanostructuring. One of the earliest techniques in this direction is the application of double pulses with pico- or subpicosecond separation in time. By a proper selection of the irradiation parameters, double-pulse irradiation enables generation of novel 2D surface nanomorphologies on large surface area as was shown recently by Fraggelakis et al. [251]. Another efficient method to cover large surface areas by highly reproducible nanostructures is interfering femtosecond laser beams [192, 252]. This interference method can also be used for simultaneous laser-induced forward transfer of nanoparticles into a highly ordered positioning in the receiver substrate [253].

Enhanced control over localized coupling of single laser pulses with materials can be accomplished by modification spatial and temporal beam profiles. This includes applications of Bessel [254], doughnut-shaped [255] and vortex beams [256], and temporally asymmetric femtosecond pulses [257]. More detailed information about beam shaping techniques and their applications for material structuring down to nanoscale can be found in Chaps. 15 [258] and 16 [259] of this book.

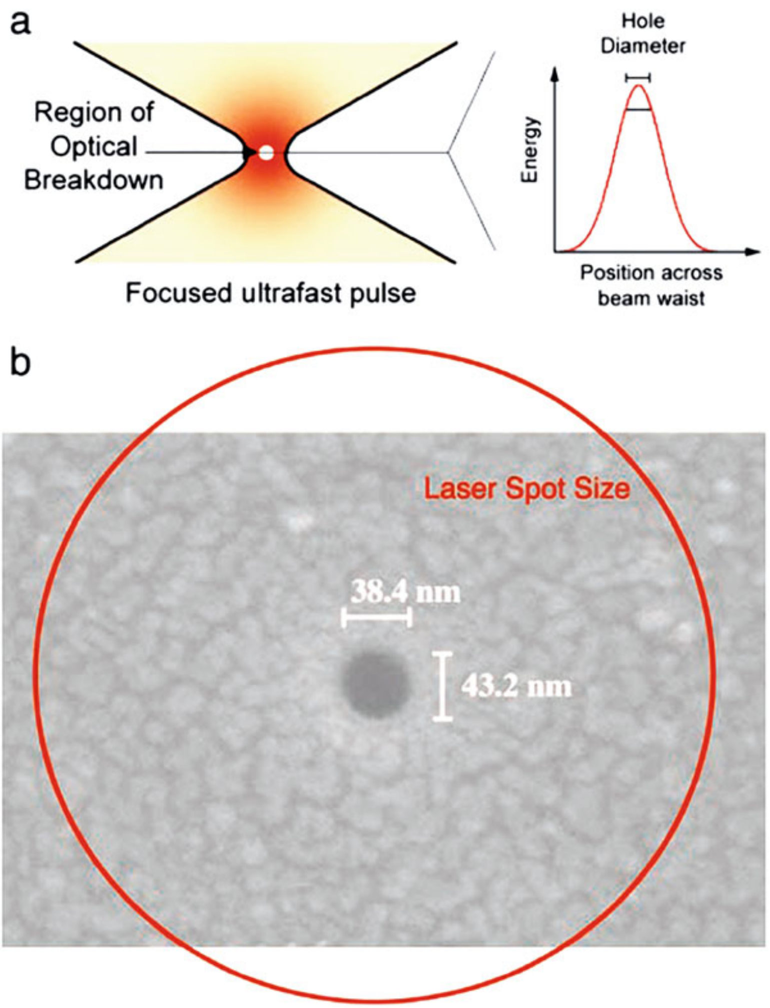
a
Region of Optical Breakdown
Focused ultrafast pulse
Hole Diameter
Energy
Position across beam waist
b
Laser Spot Size
38.4 nm
43.2 nm

Fig. 1.14 (**a**) Illustration of how an ultrashort laser pulse can create an ablation localized to a region smaller than the light resolution limit [245]. As the pulse energy is decreased, a smaller portion of focus spot exceeds the energy threshold for optical breakdown, thus allowing formation of subdiffraction features. (**b**) Example of a nanometer-scale hole in a transparent material. The red circle indicates the $1/e^2$ focus-spot size. Laser wavelength was 1053 nm and pulse duration was 800 fs. A high numerical aperture was used. Copyright (2004) National Academy of Sciences, USA

4.2 Spatiotemporal Features of Ultrashort Laser Pulses

Many experimental studies in recent years point out to an intriguing effect, symmetry breakings during nonlinear interaction of ultrashort laser pulses with materials. Dependence of the formed structures on the direction of laser scanning and polarization, an effect known as nonreciprocal writing, is one of the most commonly observed asymmetries [260–262]. This effect is attributed to the presence of the pulse-front tilt (PFT) [263] in the modifying laser beam. Usually, ultrashort laser pulses are described, assuming that the spatial dependence of the electric field is separable from the time dependence. However, spatial and temporal coordinates of ultrashort beams are coupled, resulting in the beam spatiotemporal distortions in the form of a nonzero angle between the pulse front and the direction perpendicular to the beam [264], which is evolving with beam propagation ("lighthouse effect" [265]).

Spatiotemporal couplings are sometimes referred to as "distortions," as they often yield unwanted effect. On the other hand, numerous recent studies have shown that it is possible to control and exploit these effects, for nonlinear frequency conversion, generation of terahertz or x-ray pulses, ultrafast electron diffraction, and electron acceleration [266, 267]. Also the lighthouse effect is a very promising technique for enhancing precision of material processing by "simultaneous spatial and temporal focusing (SSTF)" [268].

Recently, the consequences of the spatiotemporal couplings in ultrashort laser beams on laser-induced volumetric modification of transparent materials have been investigated numerically [269]. The model based on Maxwell's equations supplemented by the hydrodynamic-type equations for the generated free electron plasma has been applied to the case of fused silica. In view of the complexity of numerical simulations for the 3D geometry, the model was simplified to the 2D case, which has enabled to qualitatively study the influence of the pulse-front tilt components on laser energy deposition. The simulations have shown that observed asymmetries in material modifications are primarily due to the PFT, rather than the lighthouse effect. It has also been demonstrated that the presence of the PFT and its rotation during laser beam propagation inside material can lead to a higher local energy coupling as compared to the beams without spatiotemporal coupling features (see an example in Fig. 1.15).

For multipulse scenario, the model was extended for taking into account accumulation of defects [269]. In the presence of the PFT, the distribution of defects exhibits dependence on the direction of sample translation, closely mimicking the existing experimental observations. Extension of simulations to the 3D case [270] has supported the main conclusions of [269] although underlining that the wave front rotation can be important in affecting the spatiotemporal evolution of ultrafast laser pulses upon propagation in an ionizable media. Thus, the spatiotemporal coupling can serve as an additional degree of freedom for enhancing localization of laser light absorption in the regimes of direct laser writing of photonic structures inside transparent materials.

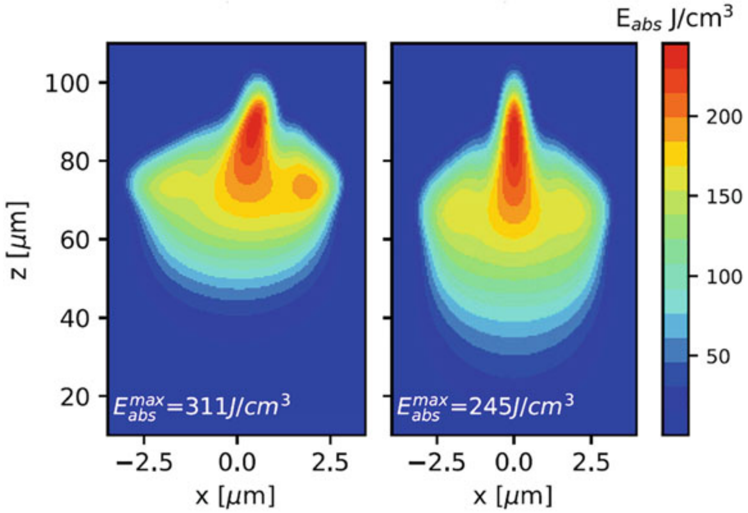

Fig. 1.15 The maps of the absorbed laser energy after propagation of focused laser beams with PFT (left) and without PFT (right) obtained in simulations. In the presented case, pulse-front rotation is absent. Maximum absorbed energies are given at the bottom of the images

4.3 Perspectives of Dual-Wavelength Laser Beams for Material Processing

Traditionally, monochromatic laser beams are used for material processing; for modifications of structural, optical, mechanical, conductive, and thermal properties of different materials; and for designing new nanostructured material systems. So far, there are a limited number of studies of bichromatic laser irradiation of materials, which however indicate dramatic effects on the surface modification. This includes improving the quality of surface nanostructuring [271], enhanced efficiency of nanoparticle production [272], improvement of the LIBS signal [273], and microfabrication of optical structures in hard materials [274]. It has also been shown that, using bi-wavelength irradiation, it is possible to localize structural modifications inside a glass in the regimes where it is difficult to do with monochromatic laser pulses [275]. Furthermore, dual-wavelength irradiation enables to control localized light absorption, in particular to achieve an overcritical free electron density inside transparent material [276]. Numerically, it was shown that, at relatively low laser fluences, dual wavelength is less efficient as compared to single-color irradiation of one of the harmonics, provided that the total laser fluence is the same. However, it was revealed that the situation can be overturned with increasing laser fluence and at a proper chosen ratio between the pulse energies [277].

Figure 1.16 presents an example of simulation results, based on the model [278], demonstrating a possibility to efficiently couple bicolor laser pulses into

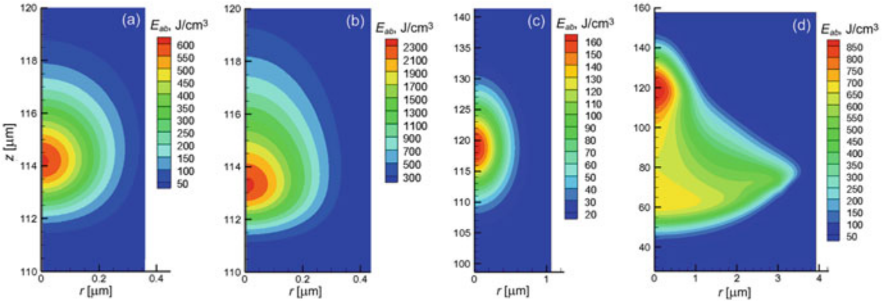

Fig. 1.16 Absorbed energy density maps inside fused silica after propagation of ultrashort laser pulses [279]. (**a**) Laser pulse at wavelength of 400 nm with energy of 6 nJ and duration of 140 fs. (**b**) The laser pulse as in (**a**) followed by the laser pulse at wavelength of 800 nm with energy 120 nJ and duration of 180 fs. Time delay between pulses is 0.8 ps. (**c**) The single laser pulse with wavelength of 800 nm at energy 120 nJ and duration of 180 fs. (**d**) The laser pulse as in (**c**) but with the energy of 1.5 μJ. Laser pulses propagate from the bottom to top. Geometrical focus of both pulses is at 120 μm from the sample surface. Laser beam waists are 0.51 μm and 2 μm for 400 nm and 800 nm, respectively. Figure was reprinted with permission from Bulgakova et al. [279]

a nanovolume upon volumetric modification of bandgap materials. The absorbed energy density maps show a dramatic effect of the second-harmonics prepulse on laser energy absorption of the fundamental-harmonics pulse at 800 nm [279]. A 6-nJ pulse at 400-nm wavelength, which only slightly excites material in front of the focus (Fig. 1.16a), provides a strong absorption of the energy from the 800-nm pulse followed with a delay of 0.8 ps (Fig. 1.16b). Remarkable is that the near-IR pulse alone is absorbed rather negligibly (Fig. 1.16c). Furthermore, increasing its energy by more than ten times results in delocalization of the absorbed energy over an extended region (Fig. 1.16d), while the local maximum of the absorbed energy density is almost three times smaller as compared to the dual-wavelength case shown in (Fig. 1.16b). Note that, in the dual-wavelength case, the region of laser energy absorption is strongly localized. These simulations point out that the dual-wavelength laser action on bandgap materials may have a high potential for controllable, highly efficient laser energy coupling.

4.4 Scattering of Light by Nanomaterials

Scattering of light by nanomaterials enables the coupling of far-field light with materials toward nanometric scales. By scattering light on a dielectric nanoparticle, light localization can scale down to 100 nm by forming an "photonic jet" that leads to the formation of nano-holes [280]. Beyond the diffraction limit, the scattering of light on nanostructured objects such as conical tips employed in atomic force tomography leads to an extreme concentration of infrared light down to few nm (see Fig. 1.17a) using plasmon polariton in metallic materials [281] or Mie resonances in

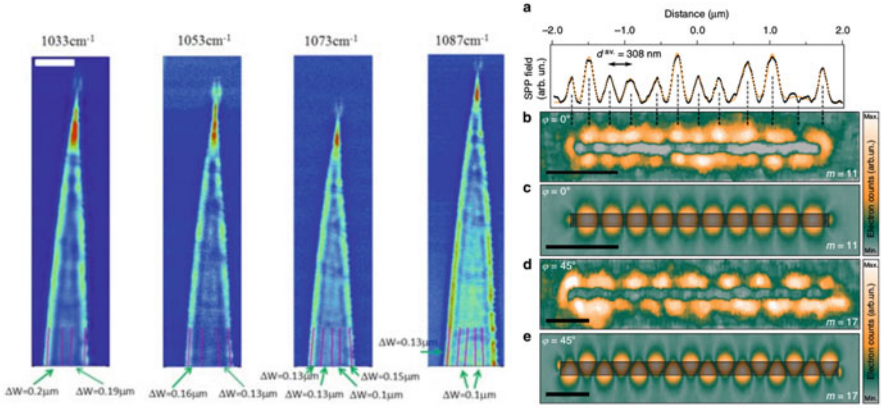

(a) (b)

Fig. 1.17 Observation of plasmon polariton in nanomaterials. (**a**) 3rd harmonic near-field signal (arb. units) from graphene on SiC for different incident light frequencies. The lower pink lines show a fitting of the near-field fringe maxima used to derive the plasmon wavelength. The figure demonstrate the sensitivity of field localization as a function of illumination wavelength (Supplementary Information in [281]). (**b**) Field localization on an Au nanowire irradiated by an fs laser pulse. A new ultrafast-imaging methodology was used, which utilizes an electron imaging filter to form a two-dimensional projection of one spatial coordinate versus electron energy [133]. (**a**) was reprinted with permission from Chen et al. [281]. (**b**) is licensed under CC BY

dielectric materials [282]. Light scattering by Au nanorods enables the experimental observation of even and odd plasmon polariton modes (see Fig. 1.17b) [133]. Finally, it is possible to maximize localization by illuminating a hollow metallic cone filled with a gas. This method enables to simultaneously couple surface plasmon polaritons generated on the metallic cone converting infrared photons to higher energies via harmonic generation in the irradiated gas [283, 284], thus outpassing the diffraction limit.

5 Laser-Induced Periodic Surface Structures (LIPSS) as Alternating Localization of Absorbed Laser Energy at Nanoscale

Since the discovery of laser-induced periodic surface structures in 1965 [285], this phenomenon is attracting considerable attention from both fundamental studies and various applications. The LIPSS research is still offering new discoveries and findings in new laser irradiation regimes. The comprehensive, deeply detailed analysis of different kinds of the LIPSS, formation mechanisms, and wide variety of applications can be found in [286, 287] and also in Chap. 5 of this book [288]. Here we will dwell on two recent findings in the two regimes of laser irradiation, which enable covering large surface areas by highly regular periodic structures upon laser scanning.

In the high-energy regime, only few laser irradiation shots are overlapping, which however result in highly ordered ripples without any bifurcation points. Such LIPSS can conventionally be called ablative as their ridges are located below the initial material surface [145]. In the low-energy regime applied to thin metallic films [153], thousands of laser pulses are overlapping on the sample surface, and the LIPSS are erecting above the initial surface. While in the high-energy irradiation regime, the surface is almost free of oxidation signs, in the low-energy regime, thin metallic films are periodically oxidized through the whole thickness. Thus, such LIPSS are called thermochemical. Both these extreme structures are explained via theories related to coupling the scattered surface electromagnetic waves with the incident laser light. The LIPSS phenomenon is a bright demonstration of laser energy localization at nanoscale in a periodic manner.

5.1 Highly Regular LIPSS in the Ablative Regime

The fabrication of highly regular periodic surface structures on surfaces of metals at high throughput [145] (see Fig. 1.11) is well correlated with materials that exhibit strong losses as stated in Sect. 2.3.7. In this subsection, we present the theory, which enables to study and predict the LIPSS regularity on surfaces of different metals.

As laser light scattering on material surfaces takes places on randomized roughness features of different size and shape, it is reasonable to assume that the scattered waves interfere in an irregular manner, thus giving rise for a randomized amplification of the local electric field on the surface. The incident polarized laser light is better coupling with the regions of amplified field, and, being chaotically distributed, such regions do not allow to build well-aligned lines of enhanced laser light absorption. From this viewpoint, a smaller propagation distance of surface scattered electromagnetic waves (we consider here surface plasmon polaritons) and, hence, smaller interference between SPPs are preferable for achieving a better LIPSS regularity. Let us discuss this aspect in more detail.

The propagation distance of SPPs at the interface between media 1 and 2 with dielectric permittivities ε_1 and ε_2, respectively, can be calculated as [130]

$$L_{\mathrm{SPP}} = \frac{1}{2 \times \mathrm{Im}\left(\beta_{\mathrm{SPP}}\right)}$$

where $\beta_{\mathrm{SPP}} = \pm\frac{\omega}{c}\sqrt{\frac{\varepsilon_1\varepsilon_2}{\varepsilon_1+\varepsilon_2}}$ is a complex-valued quantity. As the L_{SPP} value depends on the laser light frequency ω and the dielectric functions of media, it is reasonable to suggest that the LIPSS regularity can be naturally better at some wavelengths as compared to other ones. Furthermore, it can be hypothesized that the irradiation conditions exist, under which it is possible to fabricate regular LIPSS on Au, Al,

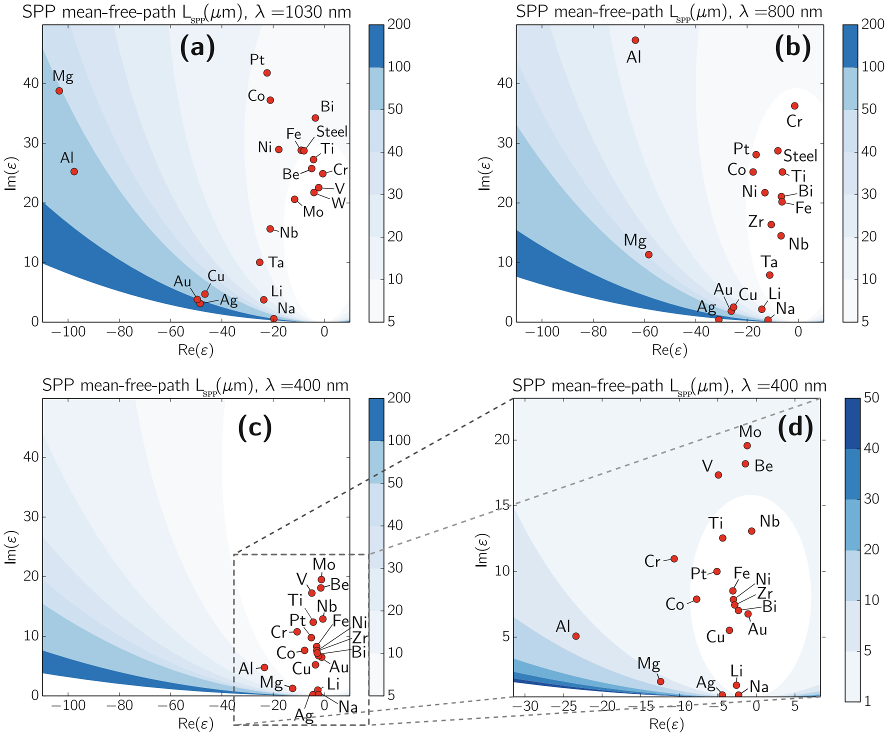

Fig. 1.18 Decay length of surface plasmon polaritons upon irradiation by laser pulses at wavelengths (**a**) 1030 nm, (**b**) 800 nm, and (**c**) 400 nm. (**d**) shows the enhanced view of (**c**). The color scale is given in μm. [145] (licensed under CC BY)

and Cu that occurs to be impossible at 1030 nm (Fig. 1.11). Figure 1.18 compares the SPP decay (propagation) distances for a number of materials at three laser wavelengths. It demonstrates that, with decreasing the laser wavelength, L_{SPP} is also decreasing for all metals that is favorable for enhancing the LIPSS regularity according to above considerations.

Under the assumption of weakly changing optical properties of metals upon femtosecond laser irradiation (a rather reasonable assumption for fluences below 1 J/cm^2 according to Refs. [20, 21, 31]), it is possible to outline a hierarchy of materials regarding formation of highly regular LIPSS on their surfaces. A simplest criterion for a classification of materials into groups, which enable and do not enable inscription of highly regular LIPSS on their surfaces, can be based on empirical observations with determining a threshold L_{SPP} value, above which structures lose their regularity. Based on the results published in Refs. [145, 289, 290] (W, Cr, Mo, Ti, steel), an empirical threshold criterion $L_{\mathrm{SPP}}^{\mathrm{th}} \approx 10\,\mu\mathrm{m}$ can be proposed. Under the condition $L_{\mathrm{SPP}} > L_{\mathrm{SPP}}^{\mathrm{th}}$ for a material irradiated at a chosen wavelength, the high

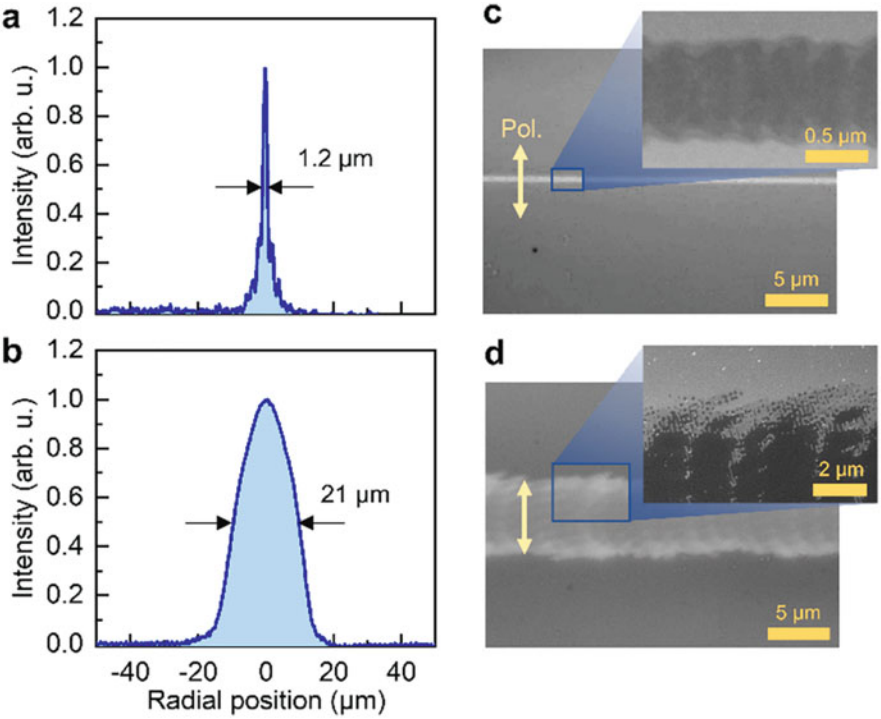

Fig. 1.19 Evidence that LIPSS formation depends on the spot size of laser beam [292]. (**a**, **b**) Beam profiles used in the laser scanning of the silicon surface. (**c**, **d**) Corresponding optical microscope images of the laser-scanned silicon surface. Insets present scanning electron microscope images. Figure was reprinted with permission from Kim et al. [292]

regular LIPSS should be difficult to obtain. In particular, it refers to good plasmonic metal such as Ag, Au, Al, and Cu (see Figs. 1.11 and 1.18).

The results presented in this subsection have initiated extensive research of the conditions for highly regular LIPSS fabrication on surfaces of different materials. Recent studies [291] offered a valuable insight into the role laser wave front quality in regular LIPSS manufacturing, stressing on the importance of spot size. The effects of the angle of incidence on the regularity of the structures have been investigated by Liu et al. [148]. Finally, Kim et al. [292] reported a way for avoiding LIPSS formation by reducing the spot size below the SPP propagation distance and below the diffraction limit (see Fig. 1.19).

5.2 Thermochemical LIPSS: Multiplicity of Polaritonic Modes in Thin Films

Laser-induced periodic surface structures, which are smaller than half of the laser wavelength, are usually named “high spatial frequency LIPSS” or HSFL [286]. Understanding of their formation mechanisms has been challenging for several decades [293–297]. In this subsection, we introduce a new insight into the mechanisms of HSFL formation on thin metallic films deposited on a glass substrate. The theoretical analysis based on the dispersion relation reveals a multiplicity of laser-excited electromagnetic modes, which can be imprinted on the metal-oxide films and some of which are well matching the periodicity of the experimentally observed HSFL [153]. The dominance of one or another mode is presumed to be determined by their lifetime and amplitude.

The Role of Number of Laser Pulses Acting on the Same Surface Area in the LIPSS Periodicity Upon increasing a number of laser pulses sequentially acting on the same surface area, a decrease in the LIPSS period is usually observed, thus evidencing a possibility to increase precision of energy deposition down to half the laser wavelength in metals [149, 298] and down to 10 nm in semiconductors and dielectrics [299, 300]. In dielectrics, the reduction of the LIPSS period is usually attributed to the change of topography of the surface from pulse to pulse and, hence, shifting the resonant spatial frequencies for plasmonic coupling. Such idea paved the way to explore the formation of various types of structures that may imply a more sophisticated classification of LIPSS than only their perpendicular or parallel orientation relative to laser polarization [301]. In the case of a low number of shots per surface area, formation of structures with periods smaller than half of laser wavelength was observed on easily oxidized metals [298, 302], in particular upon irradiation in air or in a confining medium such as water [152, 303], as well as in vacuum [296, 302, 304, 305]. The observation of HFSL self-organization upon irradiation in vacuum shows that the surface chemistry is not a necessary condition to their formation. Recently, this aspect triggered investigations, which attribute the formation mechanisms of HSFL to hydrodynamic instabilities developing at a nanometer scale [287, 306].

In this section, we focus on another case, LIPSS formation on thin metallic films deposited on glass substrates at ultrashort pulsed laser irradiation with low pulse energies, below the melting threshold, in the presence of the ambient air. Under such conditions, thousands of pulses are coupling effectively with the same surface area upon scanning the surface at low scanning velocities [153, 307]. At certain irradiation conditions, ordinary LIPSS with periods of the order of laser wavelength (low spatial frequency LIPSS or LSFL) are transforming to HSFL. The mechanisms of transformation are discussed.

The Role of Ambient Air in the Formation of Ultrasmall Periodic Structures As an example, we consider here chromium films 28-nm thick deposited on BK7 substrate

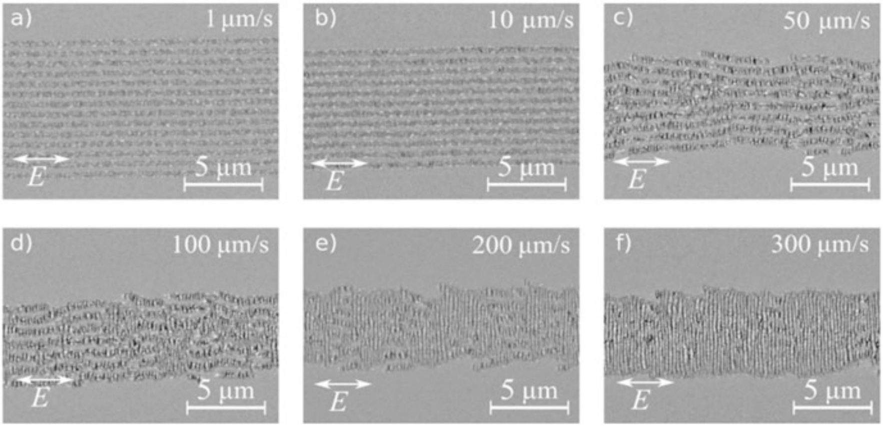

Fig. 1.20 Transformation of LSFL to HSFL formed on a Cr film of 28-nm thick deposited on BK7 with increasing the laser scanning speed [153]. Irradiation conditions are the following: laser wavelength is 1026 nm, pulse energy is 110 nJ, pulse duration is 232 fs, repetition rate is 200 kHz. Effective pulse number per surface area can be evaluated as (**a**) 3×10^6, (**b**) 3×10^5, (**c**) 6×10^4, (**d**) 3×10^4, (**e**) 1.5×10^4, and (**f**) 10^4. In all regimes, the irradiated areas are strongly oxidized up to reaching film transparency. Figure was reprinted with permission from Dostovalov et al. [153]

[153]. For such situation, a thin-film polaritonic scenario may be applied for the analysis of the observed LIPSS periodicity. We start from considering the scenarios, which could explain a gradual transformation of LSFL (Fig. 1.20a, b) to HSFL (Fig. 1.20e–f) upon increasing the scanning velocity of the laser beam:

- At low scanning velocity (1 μm/s), LIPSS with a near-wavelength period parallel to the laser polarization were observed on the surface of oxidized Cr. These LIPSS are successfully explained by using the Sipe model (see [153]);
- At high scanning velocity (100–300 μm/s), LIPSS with much smaller periods than the laser wavelength are formed perpendicularly to the laser polarization. This case is explained by the excitation of surface polaritons in the fully oxidized Cr film using a thin-film surface polariton model, which is described below.

On the Multiplicity of Modes in Thin-Film Polaritonics Utilizing a thin-film plasmonic model [130, 151] for exploring the LIPSS formation in confined systems was first proposed in Ref. [308]. This model was applied to investigate the formation of 100-nm periodic structures on laser-excited water-immersed silicon [152]. It was demonstrated that the coupling of surface plasmon polaritons generated at two interfaces leads to a strong reduction of the plasmon polariton periodicity for silicon transiently metallized by laser irradiation. In [152], only one from four possible solutions of such a complex problem [130, 151] was analyzed. However, the complete analysis of the dispersion relation in metallic films points out that other possible solutions (branches) can be also observable under some excitation conditions [129].

Upon oxidation, the multiple possible modes appear due to the multivalued character of the dispersion relation for polaritons in thin films. Assuming a homogeneous polaritonic wave number $\beta \in \mathbb{C}$ describing the state of polaritons in the system, a dispersion relation can be written to characterize the distribution of the field in the system. For a heterogeneous situation (air-thin film-glass substrate, numbered 2, 1 and 3, respectively), the dispersion relation reads as [130, 151]

$$e^{-2k_1 h} = \frac{\left(\frac{k_1}{\varepsilon_1} + \frac{k_2}{\varepsilon_2}\right) \times \left(\frac{k_1}{\varepsilon_1} + \frac{k_3}{\varepsilon_3}\right)}{\left(\frac{k_1}{\varepsilon_1} - \frac{k_2}{\varepsilon_2}\right) \times \left(\frac{k_1}{\varepsilon_1} - \frac{k_3}{\varepsilon_3}\right)} \tag{1.5}$$

where $k_j^2 = \beta^2 - \varepsilon_j \left(\frac{\omega}{c}\right)^2$ and h is the film thickness. The momentum conservation law generates several sets of solutions called the complex branches and, thus, should be rewritten as $k_j = s_j \sqrt{\beta^2 - \varepsilon_j \left(\frac{\omega}{c}\right)^2}$ where $s_j = \pm 1$ is the sign of the square root. Since three media are involved in this system, $2^3 = 8$ branches of the solution have to be considered. Since the change of sign s_1 keeps invariant the Eq. (1.5), the number of branches are reduced to 4, consistently with [129]. Hence, the possible branches are $(s_2, s_3) = (+, +)$ for bound modes, $(+, -)$ and $(-, +)$ for leaky modes, and $(-, -)$ mode for a higher-order mode that has a leaky character [309].

Numerically, each branch provides a different value of the periodicity. The remaining question is on how to identify, which branch is the one, which leads to the highest field enhancement, selecting in fine which mode is dominating in the interaction. Consistently with [129], the distribution of the field intensity at the interfaces of a thin film can be symmetric or antisymmetric, by a phase shift in the periodic energy deposited at the front- and back-side of the laser-irradiated film.

When the film is oxidized, branches of the solution of Eq. (1.5) are evolving according to changing dielectric functions upon oxidation. Figure 1.21 presents the periods of the possible surface polaritons in the Air/(Cr+Cr_2O_3+CrO_2)/BK7 system. The multiplicity of possible modes suggests a consistent explanation of the observed HSFL in the case of high number of pulses (when scanning velocity was 300 µm/s, see Fig. 1.20f) [153]. Recently, the same model was successfully applied to explain the influence of the choice of a substrate for deposition of Cr films [310].

A note should be added on the origin of the number of possible modes. It can be understood from the dispersion relation describing a symmetric configuration (e.g., air/film/air) as expressed by two equations [130, 151] written as

$$\tanh(2k_1 t) = -\left(\frac{k_2 \varepsilon_1}{k_1 \varepsilon_2}\right)^{\pm 1}. \tag{1.6}$$

Although Eq. (1.6) is a particular case of Eq. (1.5), it well reflects the nontrivial number of solutions for the dispersion relation of polaritons possible on thin films in relation to the Riemann surfaces of the tanh function.

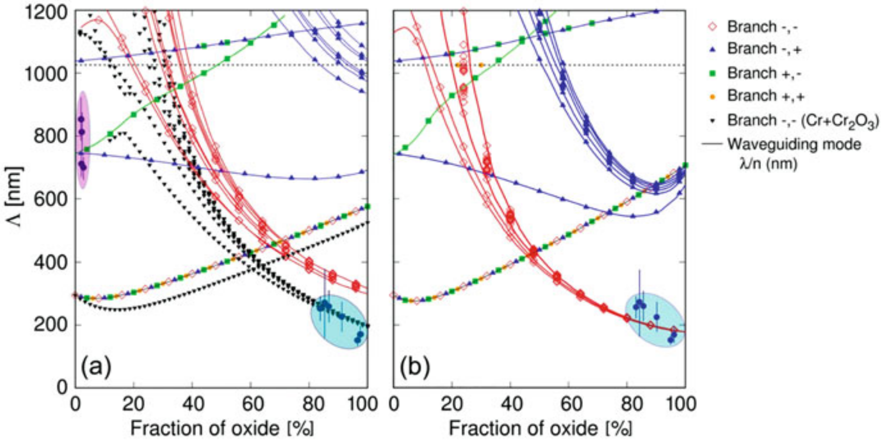

Fig. 1.21 Possible periods of surface polaritons in 28-nm thick film of Cr deposited on a BK7 substrate predicted for irradiation by a series of 1026-nm ultrashort laser pulses (see parameters in Fig. 1.20 caption) [153]. The comparison between experimental (dots with error bars) and simulation results demonstrates that the film oxidation leads to excitation of a number of surface polariton modes. The polariton mode with the smallest periodicity (200 nm) consistently explains the HSFL observed perpendicular to the laser polarization (Fig. 1.20f). In (**a**), the mixture of Cr, Cr_2O_3, and CrO_2 revealed by Raman measurements was taken account using the theory of effective optical medium. In (**b**), a porosity of the sample was additionally taken into account based on the theory of effective optical medium. Figure was reprinted with permission from Dostovalov et al. [153]

These results anticipate a high complexity of the HSFL formation in the regimes of oxidation in thin metallic films. Development of an integrated tool aiming at predicting the multiple types of LIPSS for such regimes looks to be important and would facilitate a transfer of extreme laser nanostructuring technology to industry.

6 Concluding Remarks

In this chapter, we have provided an overview of the processes, which are triggered in materials of different kinds with most of them being determining in localization of the absorbed laser energy toward the nanoscale. Some of these processes are material-specific, while others can manifest themselves transiently in any materials. At the first place, we put the processes of laser energy absorption, which predetermine the overall post-irradiation evolution of a laser-excited material. In the surface as well as in volumetric absorption of laser light, electromagnetic processes, including plasmonic phenomena, are especially important for material nanostructuring that is considered in this chapter in more detail. We have also discussed new fundamental insights into electron excitation obtained via the time-dependent density functional theory.

The sequence of the laser-induced thermal processes following light absorption is outlined that includes thermalization between the electron and lattice subsystems, generation of stresses, melting, and hydrodynamic phenomena, which are responsible for material relocation, culminating in either smoothing the laser-disturbed material surface or freezing the modification structure that depends on the irradiation conditions as well as on material properties. Then we discuss some possible ways for achieving a better localization of the energy, where tailoring the spatiotemporal profiles of laser beams (pulse shaping) appears to be the most important, attracting an intense interest of researchers. As a final point, we present the theoretical explanations of the formation of highly regular LIPSS on metallic surfaces in the two extreme regimes of irradiation when laser fluence in single pulse exceeds the material ablation threshold and is well below the melting threshold.

A deep and clear understanding of the mechanisms, and driving forces, which lead to formation on surface nanorelief or volumetric nanostructuring is critical for developing groundbreaking applications, some of which are already emerging and will be discussed in the following chapters, while many of them are waiting us in the future. Finally, we note that, from the practical point of view, a wide variety of lasers operating in different spectral ranges with ultrashort pulses offer a great flexibility for designing nanomaterials with highly functional properties, which are opening new fields of application, ranging from optics, photonics and optoelectronics to biomedical sensing, photocatalysis, and solar energy harvesting.

Acknowledgments The research of T. J.-Y. D., Y. L. and N. M. B. is financed by the European Regional Development Fund and the state budget of the Czech Republic (project BIATRI, No. CZ.02.1.01/0.0/0.0/15_003/0000445; project HiLASE CoE, No. CZ.02.1.01/0.0/0.0/15_006/0000674).

References

1. D. M. Kane (Ed.), *Laser Cleaning II* (World Scientific, Singapore, 2007)
2. J. Han, O. Malek, J. Vleugels, A. Braem, S. Castagne, Ultrafast laser selective phase removal for surface modification of nanocomposite materials. Opt. Express **29**, 24834–24845 (2021)
3. R. Buividas, M. Mikutis, S. Juodkazis, Surface and bulk structuring of materials by ripples with long and short laser pulses: recent advances. Prog. Quantum Electron. **38**, 119–156 (2014)
4. K. Phillips, H.H. Gandhi, E. Mazur, S.K. Sundaram, Ultrafast laser processing of materials: a review. Adv. Opt. Photon. **7**, 684–712 (2015)
5. D. Zhang, B. Gökce, S. Barcikowski, Laser synthesis and processing of colloids: fundamentals and applications. Chem. Rev. **117**, 3990–4103 (2017)
6. R. Buividas, G. Gervinskas, A. Tadich, B.C.C. Cowie, V. Mizeikis, A. Vailionis, D. de Ligny, E.G. Gamaly, A.V. Rode, S. Juodkazis, Phase transformation in laser-induced micro-explosion in olivine (Fe,Mg)$_2$SiO$_4$, Adv. Eng. Mater. **16**, 767–773 (2014)
7. K. Sugioka, Progress in ultrafast laser processing and future prospects. Nanophotonics **6**, 393–413 (2017)
8. F. Courvoisier, R. Stoian, A. Couairon, Ultrafast laser micro- and nano-processing with nondiffracting and curved beams. Opt. Laser Technol. **80**, 125–137 (2016)

9. R. Stoian, Volume photoinscription of glasses: three-dimensional micro and nanostructuring with ultrashort laser pulses. Appl. Phys. A **126**, 438 (2020)
10. Z. Lin, L.V. Zhigilei, V. Celli, Electron-phonon coupling and electron heat capacity of metals under conditions of strong electron-phonon nonequilibrium. Phys. Rev. B **77**, 075133 (2008)
11. L.V. Keldysh, Ionization in the field of a strong electromagnetic wave. Sov. Phys. JETP **20**, 1307–1314 (1965)
12. H.M. van Driel, Kinetics of high-density plasmas generated in Si by 1.06- and 0.53-μm picosecond laser pulses. Phys. Rev. B **35**, 8166–8176 (1987)
13. A. Kaiser, B. Rethfeld, M. Vicanek, G. Simon, Microscopic processes in dielectrics under irradiation by subpicosecond laser pulses. Phys. Rev. B **61**, 11437–11450 (2000)
14. D. Arnold, E. Cartier, Theory of laser-induced free electron heating and impact ionization in wide-band-gap solids. Phys. Rev. B **46**, 15102–15115 (1992)
15. W.P. Dumke, Spontaneous radiative recombination in semiconductors. Phys. Rev. **105**, 139–144 (1957)
16. J.P. Vigouroux, J.P. Duraud, A. Le Moel, C. Le Gressus, D.L. Griscom, Electron trapping in amorphous SiO_2 studied by charge buildup under electron bombardment. J. Appl. Phys. **57**, 5139–5144 (1985)
17. P. Martin, S. Guizard, P. Daguzan, G. Petite, P. d'Oliveira, P. Maynadier, M. Pedrix, Subpicosecond study of carrier trapping dynamics in wide-band-gap crystals. Phys. Rev. B **55**, 5799–5810 (1997)
18. N.M. Bulgakova, Fundamentals of ultrafast laser processing, in *Ultrafast Laser Processing: From Micro- to Nanoscale*, ed. by K. Sugioka, Y. Cheng Pan (Stanford Publishing, 2013), pp. 99–182
19. B. Rethfeld, D.S. Ivanov, M.E. Garcia, S.I. Anisimov, Modelling ultrafast laser ablation. J. Phys. D: Appl. Phys. **50**, 193001 (2017)
20. A.Y. Vorobyev, C. Guo, Reflection of femtosecond laser light in multipulse ablation of metals. J. Appl. Phys. **110**, 043102 (2011)
21. S.E. Kirkwood, Y.Y. Tsui, R. Fedosejevs, A.V. Brantov, V.Y. Bychenkov, Experimental and theoretical study of absorption of femtosecond laser pulses in interaction with solid copper targets. Phys. Rev. B **46**, 144120 (2009)
22. A.D. Rakić, A.B. Djurišić, J.M. Elazar, M.L. Majewski, Optical properties of metallic films for vertical-cavity optoelectronic devices. Appl. Opt. **37**, 5271–5283 (1998)
23. K. Sokolowski-Tinten, D. von der Linde, Generation of dense electron-hole plasmas in silicon. Phys. Rev. B **61**, 2643–2650 (2000)
24. Y. Ren, J.K. Chen, Y. Zhang, J. Huang, Ultrashort laser pulse energy deposition in metal films with phase changes. Appl. Phys. Lett **98**, 191105 (2011)
25. D.V. Knyazev, P.R. Levashov, Transport and optical properties of warm dense aluminum in the two-temperature regime: ab initio calculation and semiempirical approximation. Phys. Plasmas **21**, 073302 (2014)
26. S.I. Ashitkov, P.S. Komarov, V.V. Zhakhovsky, Y.V. Petrov, V.A. Khokhlov, A.A. Yurkevich, D.K. Ilnitsky, N.A. Inogamov, M.B. Agranat, Ablation of gold irradiated by femtosecond laser pulse: experiment and modeling. J. Phys. Conf. Ser. **774**, 012097 (2016)
27. J. Winter, S. Rapp, M. Schmidt, H.P. Huber, Ultrafast laser processing of copper: a comparative study of experimental and simulated transient optical properties. Appl. Surf. Sci. **417**, 2–15 (2017)
28. P.A. Loboda, N.A. Smirnov, A.A. Shadrin, N.G. Karlykhanov, Simulation of absorption of femtosecond laser pulses in solid-density copper. High Energy Density Phys. **7**, 361–370 (2011)
29. S. Mazevet, J. Clérouin, V. Recoules, P.M. Anglade, G. Zerah, Ab-initio simulations of the optical properties of warm dense gold. Phys. Rev. Lett. **95**, 085002 (2005)
30. E. Bévillon, R. Stoian, J.P. Colombier, Nonequilibrium optical properties of transition metals upon ultrafast electron heating. J. Phys.: Condens. Matter **30**, 385401 (2018)

31. M.V. Shugaev, M. He, S.A. Lizunov, Y. Levy, T.J.-Y. Derrien, V.P. Zhukov, N.M. Bulgakova, L.V. Zhigilei, Insights into laser-materials interaction through modeling on atomic and macroscopic scales, in *Advances in the Application of Lasers in Materials Science*, ed. by P. Ossi. Springer Series in Material Science, vol. 274 (Springer Nature Switzerland AG, 2018), pp. 107–148
32. T.J.-Y. Derrien, N. Tancogne-Dejean, V.P. Zhukov, H. Appel, A. Rubio, N.M. Bulgakova, Photoionization and transient Wannier-Stark ladder in silicon: first principle simulations versus Keldysh theory. Phys. Rev. B **104**, L241201 (2021)
33. S.I. Anisimov, B.L. Kapeliovich, T.L. Perel'man, Electron emission from surface of metals induced by ultrashort laser pulses. Sov. Phys. JETP **39**, 375–377 (1974)
34. S.-S. Wellershoff, J. Hohlfeld, J. Güdde, E. Matthias, The role of electron-phonon coupling in femtosecond laser damage of metals. Appl. Phys. A **69**, S99–S107 (1999)
35. M. Lisowski, P.A. Loukakos, U. Bovensiepen, J. Stähler, C. Gahl, M. Wolf, Ultrafast dynamics of electron thermalization and transport effects in Ru (001). Appl. Phys. A **78**, 165–176 (2004)
36. M.Z. Mo, Z. Chen, R.K. Li, M. Dunning, B.B.L. Witte, J.K. Baldwin, L.B. Fletcher, J.B. Kim, A. Ng, R. Redmer, A.H. Reid, P. Shekhar, X.Z. Shen, M. Shen, K. Sokolowski-Tinten, Y.Y. Tsui, Y.Q. Wang, Q. Zheng, X.J. Wang, S.H. Glenzer, Heterogeneous to homogeneous melting transition visualized with ultrafast electron diffraction. Science **360**, 1451–1455 (2018)
37. A. Block, M. Liebel, R. Yu, M. Spector, Y. Sivan, F.J. García de Abajo, N.F. van Hulst, Tracking ultrafast hot-electron diffusion in space and time by ultrafast thermomodulation microscopy. Sci. Adv. **5**, eaav8965 (2019)
38. J.-P. Colombier, P. Combis, F. Bonneau, R. Le Harzic, E. Audouard, Hydrodynamic simulations of metal ablation by femtosecond laser irradiation. Phys. Rev. B **71**, 165406 (2005)
39. M.E. Povarnitsyn, T.E. Itina, K.V. Khishchenko, P.R. Levashov, Multi-material two-temperature model for simulation of ultrashort laser ablation. Appl. Surf. Sci. **253**, 6343–6346 (2007)
40. P.R. Levashov, K.V. Khishchenko, Tabular multiphase equations of state for metals and their applications. AIP Conf. Proc. **955**, 59–65 (2007)
41. Y.V. Petrov, K.P. Migdal, N.A. Inogamov, V.V. Zhakhovsky, Two-temperature equation of state for aluminum and gold with electrons excited by an ultrashort laser pulse. Appl. Phys. B: Lasers Opt. **119**, 401–411 (2015)
42. S.L. Johnson, M. Savoini, P. Beaud, G. Ingold, U. Staub, F. Carbone, L. Castiglioni, M. Hengsberger, J. Osterwalder, Watching ultrafast responses of structure and magnetism in condensed matter with momentum-resolved probes. Struct. Dyn. **4**, 061506 (2017)
43. B. Mansart, M.J.G. Cottet, G.F. Mancini, T. Jarlborg, S.B. Dugdale, S.L. Johnson, S.O. Mariager, C.J. Milne, P. Beaud, S. Grubel, J.A. Johnson, T. Kubacka, G. Ingold, K. Prsa, H.M. Rønnow, K. Conder, E. Pomjakushina, M. Chergui, F. Carbone, Temperature-dependent electron-phonon coupling in $La_{2-x}Sr_xCuO_4$ probed by femtosecond X-ray diffraction. Phys. Rev. B **88**, 054507 (2013)
44. A. Rämer, O. Osmani, B. Rethfeld, Laser damage in silicon: energy absorption, relaxation, and transport. J. Appl. Phys. **116**, 053508 (2014)
45. N.M. Bulgakova, R. Stoian, A. Rosenfeld, I.V. Hertel, W. Marine, E.E.B. Campbell, A general continuum approach to describe fast electronic transport in pulsed laser irradiated materials: the problem of Coulomb explosion. Appl. Phys. A **81**, 345–356 (2005)
46. N. Medvedev, H.O. Jeschke, B. Ziaja, Nonthermal phase transitions in semiconductors induced by a femtosecond extreme ultraviolet laser pulse. New J. Phys. **15**, 015016 (2013)
47. D.S. Ivanov, L.V. Zhigilei, Kinetic limit of heterogeneous melting in metals. Phys. Rev. Lett. **98**, 195701 (2007)
48. D.S. Ivanov, P.N. Terekhin, S.I. Kudryashov, S.M. Klementov, A.V. Kabashin, M.E. Garcia, B. Rethfeld, I.N. Zavestovskaya, The atomistic perspective of nanoscale laser ablation, in *Ultrafast Laser Nanostructuring—The Pursuit of Extreme Scales, Chapter 2*, ed. by R. Stoian, J. Bonse (Springer, Berlin, 2022)

49. A. Becker, N. Aközbek, K. Vijayalakshmi, E. Oral, C.M. Bowden, S.L. Chin, Intensity clamping and re-focusing of intense femtosecond laser pulses in nitrogen molecular gas. Appl. Phys. B **73**, 287–290 (2001)
50. I. Mirza, N.M. Bulgakova, J. Tomášťík, V. Michálek, O. Haderka, L. Fekete, T. Mocek, Ultrashort pulse laser ablation of dielectrics: thresholds, mechanisms, role of breakdown, Sci. Rep. **6**, 39133 (2016)
51. A.V. Bulgakov, I. Mirza, N.M. Bulgakova, V.P. Zhukov, R. Machulka, O. Haderka, E.E.B. Campbell, T. Mocek, Initiation of air ionization by ultrashort laser pulses: evidence for a role of metastable state air molecules. J. Phys. D: Appl. Phys. **51**, 25LT02 (2018)
52. J.E. Sipe, J.F. Young, J.S. Preston, H.M. van Driel, Laser-induced periodic surface structure. I. Theory. Phys. Rev. B **27**, 1141–1154 (1983)
53. A. Couairon, A. Mysyrowicz, Femtosecond filamentation in transparent media. Phys. Rep. **441**, 47–189 (2007)
54. T. Otobe, Y. Shinohara, S.A. Sato, K. Yabana, Femtosecond time-resolved dynamical Franz-Keldysh effect. Phys. Rev. B **93**, 045124 (2016)
55. M. Born, E. Wolf, *Principles of Optics. Electromagnetic Theory of Propagation, Interference and Diffraction of Light*, 7th edn. (Cambridge University Press, Cambridge, 1980)
56. S.W. Winkler, I.M. Burakov, R. Stoian, N.M. Bulgakova, A. Husakou, A. Mermillod-Blondin, A. Rosenfeld, D. Ashkenasi, I.V. Hertel, Transient response of dielectric materials exposed to ultrafast laser radiation. Appl. Phys. A **84**, 413–422 (2006)
57. I.M. Burakov, N.M. Bulgakova, R. Stoian, A. Mermillod-Blondin, E. Audouard, A. Rosenfeld, A. Husakou, I.V. Hertel, Spatial distribution of refractive index variations induced in bulk fused silica by single ultrashort and short laser pulses. J. Appl. Phys. **101**, 043506 (2007)
58. M. Sheik-Bahae, D.C. Hutchings, D.J. Hagan, E.W. Van Stryland, Dispersion of bound electronic nonlinear refraction in solids. IEEE J. Quantum. Electron. **27**, 1296–1309 (1991)
59. J.W. Beams, E.O. Lawrence, On the lag of the Kerr effect. Proc. Natl. Acad. Sci. U.S.A. **13**, 505 (1927)
60. Q. Zhong, J.T. Fourkas, Optical Kerr effect spectroscopy of simple liquids. J. Phys. Chem. B **112**, 15529–15539 (2008)
61. T. Steffen, N.A.C.M. Meinders, K. Duppen, Microscopic origin of the optical Kerr effect response of CS_2-pentane binary mixtures. J. Phys. Chem. A **102**, 4213–4221 (1998)
62. R.W. Boyd, *Nonlinear Optics* (Academic Press, New York, 2008)
63. A.D. Bristow, N. Rotenberg, H.M. van Driel, Two-photon absorption and Kerr coefficients of silicon for 850–2200 nm. Appl. Phys. Lett. **90**, 191104 (2007)
64. M.J. Weber, *Handbook of Optical Materials* (CRC Press, Boca Raton, 2003)
65. J.H. Marburger, Self-focusing: theory. Prog. Quantum Electron. **4**, 35–110 (1975)
66. S.L. Chin, T.J. Wang, C. Marceau, J. Wu, J.S. Liu, O. Kosareva, N. Panov, Y.P. Chen, J.F. Daigle, S. Yuana, A. Azarm, W.W. Liue, T. Seideman, H.P. Zeng, M. Richardson, R. Li, Z.Z. Xu, Advances in intense femtosecond laser filamentation in air. Laser Phys. **22**, 1–53 (2012)
67. F. Ahmed, M. Shamim Ahsan, M. Seop Lee, M.B.G. Jun, Near-field modification of femtosecond laser beam to enhance single-shot pulse filamentation in glass medium. Appl. Phys. A **114**, 1161–1165 (2014)
68. A. Vogel, K. Nahen, D. Theisen, J. Noack, Plasma formation in water by picosecond and nanosecond Nd:YAG laser pulses—Part I: optical breakdown at threshold and superthreshold irradiance. IEEE J. Sel. Top. Quantum Electron. **2**, 847–860 (1996)
69. G. Daminelli, J. Krüger, W. Kautek, Femtosecond laser interaction with silicon under water confinement. Thin Solid Films **467**, 334–341 (2004)
70. N.M. Bulgakova, V.P. Zhukov, Y.P. Meshcheryakov, Theoretical treatments of ultrashort pulse laser processing of transparent materials: toward understanding the volume nanograting formation and "quill" writing effect. Appl. Phys. B **113**, 437 (2013)
71. V.E. Gruzdev, Photoionization rate in wide band-gap crystals. Phys. Rev. B **75**, 205106 (2007)
72. K. Eidmann, J. Meyer-ter Vehn, T. Schlegel, S. Hüller, Hydrodynamic simulation of subpicosecond laser interaction with solid-density matter. Phys. Rev. E **62**, 1202 (2000)

73. T.E. Itina, N.S. Shcheblanov, Collision frequencies and absorption calculations for ultra-short laser interactions with dielectric materials. Proc. SPIE **9065**, 906506 (2013)
74. S.S. Juodkazis, H. Misawa, E. Gamaly, B. Luther-Davies, L. Hallo, P. Nicolai, V.T. Tikhonchuk, Laser-induced microexplosion confined in the bulk of a sapphire crystal: evidence of multimegabar pressures. Phys. Rev. Lett. **96**, 166101 (2006)
75. E. Efimenko, A. Kim, M. Quiroga-Teixeiro, Ionization-induced small-scaled plasma structures in tightly focused ultrashort laser pulses. Phys. Rev. Lett. **102**, 015002 (2009)
76. E.V. Zavedeev, V.V. Kononenko, V.M. Gololobov, V.I. Konov, Modeling the effect of fs light delocalization in Si bulk. Laser Phys. Lett. **11**, 036002 (2014)
77. R. Buschlinger, S. Nolte, U. Peschel, Self-organized pattern formation in laser-induced multiphoton ionization. Phys. Rev. B **89**, 184306 (2014)
78. E.V. Zavedeev, V.V. Kononenko, V.I. Konov, Delocalization of femtosecond laser radiation in crystalline Si in the mid-IR range. Laser Phys. **26**, 016101 (2016)
79. V.P. Zhukov, N.M. Bulgakova, M.P. Fedoruk, Nonlinear Maxwell´s and Schrödinger equations for describing the volumetric interaction of femtosecond laser pulses with transparent solid dielectrics: effect of the boundary conditions. J. Opt. Technol. **84**, 439 (2017)
80. T. Otobe, Y. Shinohara, S.A. Sato, K. Yabana, Theory for electron excitation in dielectrics under an intense linear and circularly polarized laser fields. J. Phys. Soc. Jpn. **88**, 024706 (2019)
81. H.R. Reiss, V.P. Krainov, Generalized Bessel functions in tunnelling ionization. J. Phys. A: Math. Gen. **36**, 5575–5585 (2003)
82. V.E. Gruzdev, Laser-induced ionization of solids: back to Keldysh. Proc. SPIE **5647**, 480–492 (2005)
83. N.S. Shcheblanov, M.E. Povarnitsyn, P.N. Terekhin, S. Guizard, A. Couairon, Nonlinear photoionization of transparent solids: a nonperturbative theory obeying selection rules. Phys. Rev. A **96**, 063410 (2017)
84. B. Chimier, O. Utéza, N. Sanner, M. Sentis, T. Itina, P. Lassonde, F. Légaré, F. Vidal, J.C. Kieffer, Damage and ablation thresholds of fused-silica in femtosecond regime. Phys. Rev. B **84**, 094104 (2011)
85. V. Gruzdev, Fundamental mechanisms of laser damage of dielectric crystals by ultrashort pulse: ionization dynamics for the Keldysh model. Opt. Eng. **53**, 122515 (2014)
86. P. Jürgens, M. Jupé, M. Gyamfi, D. Ristau, Ultrafast polychromatic ionization of dielectric solids. Proc. SPIE **10014**, 100141C (2016)
87. O. Varlamova, Self-organized pattern formation upon femtosecond laser ablation by circularly polarized light. Appl. Surf. Sci. **252**, 4702–4706 (2006)
88. J. Reif, Femtosecond laser induced nanostructure formation: self-organization control parameters. Appl. Phys. A **92**, 1019–1024 (2008)
89. Y. Tang, J. Yang, B. Zhao, M. Wang, X. Zhu, Control of periodic ripples growth on metals by femtosecond laser ellipticity. Opt. Express **20**, 25826–25833 (2012)
90. G. Lazzini, L. Romoli, F. Tantussi, F. Fuso, Nanostructure patterns on stainless-steel upon ultrafast laser ablation with circular polarization. Opt. Laser Technol. **107**, 435–442 (2018)
91. V.V. Temnov, K. Sokolowski-Tinten, P. Zhou, A. El-Khamhawy, D. von der Linde, Multiphoton ionization in dielectrics: comparison of circular and linear polarization. Phys. Rev. Lett. **97**, 237403 (2006)
92. J.R. Gulley, W.M. Dennis, Ultrashort-pulse propagation through free-carrier plasmas. Phys. Rev. A **81**, 033818 (2010)
93. D. Grojo, S. Leyder, P. Delaporte, W. Marine, M. Sentis, O. Utéza, Long-wavelength multiphoton ionization inside band-gap solids. Phys. Rev. B **88**, 195135 (2013)
94. W.V. Houston, Acceleration of electrons in a crystal lattice. Phys. Rev. **57**, 184–186 (1940)
95. N. Tancogne-Dejean, O.D. Mücke, F.X. Kärtner, A. Rubio, Ellipticity dependence of high-harmonic generation in solids originating from coupled intraband and interband dynamics. Nat. Commun. **8**, 745 (2017)
96. D.N. Basov, R.D. Averitt, D. Hsieh, Towards properties on demand in quantum materials. Nat. Mater. **16**, 1077–1088 (2017)

97. G.E. Topp, N. Tancogne-Dejean, A.F. Kemper, A. Rubio, M.A. Sentef, All-optical nonequilibrium pathway to stabilising magnetic Weyl semimetals in pyrochlore iridates. Nat. Commun. **9**, 4452 (2018)
98. S. Yamada, K. Yabana, Symmetry properties of attosecond transient absorption spectroscopy in crystalline dielectrics. Phys. Rev. B **101**, 165128 (2020)
99. Y.H. Wang, H. Steinberg, P. Jarillo-Herrero, N. Gedik, Observation of Floquet-Bloch states on the surface of a topological insulator. Science **342**, 453 (2013)
100. M. Kozák, T. Otobe, M. Zukerstein, F. Trojánek, P. Malý, Anisotropy and polarization dependence of multiphoton charge carrier generation rate in diamond. Phys. Rev. B **99**, 104305 (2019)
101. X. Li, W. Rong, L. Jiang, K. Zhang, C. Li, Q. Cao, G. Zhang, Y. Lu, Generation and elimination of polarization-dependent ablation of cubic crystals by femtosecond laser radiation. Opt. Express **22**, 30170 (2014)
102. L. Jiang, W. Han, X. Li, Q. Wang, F. Meng, Y. Lu, Crystal orientation dependence of femtosecond laser-induced periodic surface structure on (100) silicon. Opt. Lett. **39**, 3114–3117 (2014)
103. L. Museur, G.D. Tsibidis, A. Manousaki, D. Anglos, A. Kanaev, Surface structuring of rutile TiO_2 (100) and (001) single crystals with femtosecond pulsed laser irradiation. J. Opt. Soc. Am. B **35**, 2600 (2018)
104. C. Florian, D. Fischer, K. Freiberg, M. Duwe, M. Sahre, S. Schneider, A. Hertwig, J. Krüger, M. Rettenmayr, U. Beck, A. Undisz, J. Bonse, Single femtosecond laser-pulse-induced superficial amorphization and re-crystallization of silicon. Materials **14**, 1651 (2021)
105. S.A. Sato, K. Yabana, Y. Shinohara, T. Otobe, K.-M. Lee, G. F. Bertsch, Time-dependent density functional theory of high-intensity short-pulse laser irradiation on insulators. Phys. Rev. B **92**, 205413 (2015)
106. K.-M. Lee, C. Min Kim, S.A. Sato, T. Otobe, Y. Shinohara, K. Yabana, T. Moon Jeong, First-principles simulation of the optical response of bulk and thin-film α-quartz irradiated with an ultrashort intense laser pulse. J. Appl. Phys. **115**, 053519 (2014)
107. M. Uemoto, S. Kurata, N. Kawaguchi, K. Yabana, First-principles study of ultrafast and nonlinear optical properties of graphite thin films. Phys. Rev. B **103**, 085433 (2021)
108. B.C. Stuart, M.D. Feit, S. Herman., A.M. Rubenchik, B.W. Shore, M.D. Perry, Nanosecond-to-femtosecond laser-induced breakdown in dielectrics. Phys. Rev. B **53**, 1749–1761 (1995)
109. N. Varkentina, N. Sanner, M. Lebugle, M. Sentis, O. Uteza, Absorption of a single 500 fs laser pulse at the surface of fused silica: energy balance and ablation efficiency. J. Appl. Phys. **114**, 173105 (2013)
110. A. Schiffrin, T. Paasch-Colberg, N. Karpowicz, V. Apalkov, D. Gerster, S. Mühlbrandt, M. Korbman, J. Reichert, M. Schultze, S. Holzner, J.V. Barth, R. Kienberger, R. Ernstorfer, V.S. Yakovlev, M.I. Stockman, F. Krausz, Optical-field-induced current in dielectrics. Nature **493**, 70–74 (2012)
111. M. Durach, A. Rusina, M.F. Kling, M.I. Stockman, Predicted ultrafast dynamic metallization of dielectric nanofilms by strong single-cycle optical fields. Phys. Rev. Lett. **107**, 086602 (2011)
112. C. Schmidt, J. Bühler, A.-C. Heinrich, J. Allerbeck, R. Podzimski, D. Berghoff, T. Meier, W.G. Schmidt, C. Reichl, W. Wegscheider, D. Brida, A. Leitenstorfer, Signatures of transient Wannier-Stark localization in bulk gallium arsenide. Nat. Commun. **9**, 2890 (2018)
113. M. Schultze, E.M. Bothschafter, A. Sommer, S. Holzner, W. Schweinberger, M. Fiess, M. Hofstetter, R. Kienberger, V. Apalkov, V.S. Yakovlev, M.I. Stockman, F. Krausz, Controlling dielectrics with the electric field of light. Nature **493**, 75–78 (2012)
114. O. Kwon, T. Paasch-Colberg, V. Apalkov, B.-K. Kim, J.-J. Kim, M.I. Stockman, D. Kim, Semimetallization of dielectrics in strong optical fields. Sci. Rep. **6**, 21272 (2016)
115. F. Sekiguchi, T. Mochizuki, C. Kim, H. Akiyama, L.N. Pfeiffer, K.W. West, R. Shimano, Anomalous metal phase emergent on the verge of an exciton Mott transition. Phys. Rev. Lett. **118**, 067401 (2017)

116. M. Combescot, Polariton versus optical Stark effect: an old concept revisited. Solid State Commun. **74**, 291–294 (1990)
117. M. Durach, A. Rusina, M.F. Kling, M.I. Stockman, Metallization of nanofilms in strong adiabatic electric fields. Phys. Rev. Lett. **105**, 086803 (2010)
118. V. Rokaj, M. Ruggenthaler, F.G. Eich, A. Rubio, Free electron gas in cavity quantum electrodynamics. Phys. Rev. Res. **4**, 013012 (2022)
119. V.M. Agranovich, A.A. Maradudin, D. Mills, Surface Polaritons, in *Electromagnetic Waves at Surfaces and Interfaces*. Modern Problems in Condensed Matter Physics (1982)
120. A.M. Bonch-Bruevich, M.N. Libenson, V.S. Makin, V.A. Trubaev, Surface electromagnetic waves in optics. Opt. Eng. **31**, 718–730 (1992)
121. J.E. Sipe, Surface electrodynamics: radiation fields, surface polaritons, and radiation remnants. Can. J. Phys. **63**, 104–113 (1985)
122. M.A.L. Marques, N.T. Maitra, F.M.S. Nogueira, E.K.U. Gross, A. Rubio (eds.), *Fundamentals of Time-dependent Density Functional Theory*. Lecture Notes in Physics (Springer, New York, 2011)
123. P.N. Terekhin, O. Benhayoun, S.T. Weber, D.S. Ivanov, M.E. Garcia, B. Rethfeld, Influence of surface plasmon polaritons on laser energy absorption and structuring of surfaces. Appl. Surf. Sci. **512**, 144420 (2020)
124. O. Benhayoun, P.N. Terekhin, D.S. Ivanov, B. Rethfeld, M. Garcia, Theory for heating of metals assisted by surface plasmon polaritons. Appl. Surf. Sci. **569**, 150427 (2021)
125. F. Buchholz, I. Theophilou, K.J.H. Giesbertz, M. Ruggenthaler, A. Rubio, Light-matter hybrid-orbital-based first-principles methods: the influence of the polariton statistics. J. Chem. Theory Comput. **16**, 5601–5620 (2020)
126. S. Raza, G. Toscano, A.-P. Jauho, M. Wubs, N.A. Mortensen, Unusual resonances in nanoplasmonic structures due to nonlocal response. Phys. Rev. B **84**, 121412(R) (2011)
127. P. Kahl, D. Podbiel, C. Schneider, A. Makris, S. Sindermann, C. Witt, D. Kilbane, M.H.-V. Hoegen, M. Aeschlimann, F.M. Zu Heringdorf, Direct observation of surface plasmon polariton propagation and interference by time-resolved imaging in normal-incidence two photon photoemission microscopy. Plasmonics **13**, 239–246 (2018)
128. A.V. Zayats, I.I. Smolyaninoy, A.A. Maradudin, Nano-optics of surface plasmon polaritons. Phys. Rep. **408**, 131–314 (2005)
129. J.J. Burke, G.I. Stegeman, T. Tamir, Surface-polariton-like waves guided by thin, lossy metal films. Phys. Rev. B **33**, 5186 (1986)
130. S.A. Maier, *Plasmonics, Fundamentals and Applications* (Springer, Berlin, 2007)
131. H. Raether, *Surface Plasmons on Smooth and Rough Surfaces and on Gratings* (Springer, Berlin, 1986)
132. T.J.-Y. Derrien, J. Krüger, J. Bonse, Properties of surface plasmon polaritons on lossy materials: lifetimes, periods and excitation conditions. J. Opt. **18**, 115007 (2016)
133. L. Piazza, T.T.A. Lummen, E. Quiñonez, Y. Murooka, B.W. Reed, B. Barwick, F. Carbone, Simultaneous observation of the quantization and the interference pattern of a plasmonic near-field. Nat. Commun. **6**, 6407 (2015)
134. Y. Dai, Z. Zhou, A. Ghosh, R.S.K. Mong, A. Kubo, C.-B. Huang, H. Petek, Plasmonic topological quasiparticle on the nanometre and femtosecond scales. Nature **588**, 616–619 (2020)
135. H. Liu, P. Lalanne, Microscopic theory of the extraordinary optical transmission. Nature **452**, 728–731 (2008)
136. S. Palomba, L. Novotny, Nonlinear excitation of surface plasmon polaritons by four-wave mixing. Phys. Rev. Lett. **101**, 056802 (2008)
137. J. Renger, R. Quidant, N. van Hulst, S. Palomba, L. Novotny, Free-space excitation of propagating surface plasmon polaritons by nonlinear four-wave mixing. Phys. Rev. Lett. **103**, 266802 (2009)
138. D.N. Basov, A. Asenjo-Garcia, P.J. Schuck, X. Zhu, A. Rubio, Polariton panorama. Nanophotonics **10**, 549–577 (2020)

139. D.N. Basov, M.M. Fogler, F.J. Garcia de Abajo, Polaritons in van der Waals materials. Science **354**, aag1992 (2016)
140. W.L. Barnes, A. Dereux, T.W. Ebbesen, Surface plasmon subwavelength optics. Nature **424**, 824–830 (2003)
141. S. Latini, E. Ronca, U. De Giovannini, H. Hübener, A. Rubio, Cavity control of excitons in two-dimensional materials. Nano Lett. **19**, 3473–3479 (2019)
142. R.J. Bell, R.W. Alexander, W.F. Parks, G. Kovener, Surface excitations in absorbing media. Opt. Commun. **8**, 147 (1973)
143. R.W. Alexander, G.S. Kovener, R.J. Bell, Dispersion curves for surface electromagnetic waves with damping. Phys. Rev. Lett. **32**, 154 (1974)
144. I. Razdolski, A.L. Chekhov, A.I. Stognij, A. Stupakiewicz, Ultrafast transport and relaxation of hot plasmonic electrons in metal-dielectric heterostructures. Phys. Rev. B **100**, 045412 (2019)
145. I. Gnilitskyi, T.J.-Y. Derrien, Y. Levy, N.M. Bulgakova, T. Mocek, L. Orazi, High-speed manufacturing of highly regular femtosecond laser-induced periodic surface structures: physical origin of regularity. Sci. Rep. **7**, 8485 (2017)
146. A. Möhl, S. Kaldun, C. Kunz, F. A. Müller, U. Fuchs, S. Gräf, Tailored focal beam shaping and its application in laser material processing. J. Laser Appl. **31**, 042019 (2019)
147. A. Batal, A. Michalek, A. Garcia-Giron, V. Nasrollahi, P. Penchev, R. Sammons, S. Dimov, Effects of laser processing conditions on wettability and proliferation of Saos-2 cells on CoCrMo alloy surfaces, Adv. Opt. Technol. **91**, 67–78 (2019)
148. Y.-H. Liu, K.-K. Kuo, C.-W. Cheng, Femtosecond laser-induced periodic surface structures on different tilted metal surfaces. Nanomaterials **10**, 2540 (2020)
149. M. Huang, Y. Cheng, F. Zhao, Z. Xu, The significant role of plasmonic effects in femtosecond laser-induced grating fabrication on the nanoscale. Ann. Phys.-Berlin **S25**, 74–86 (2013)
150. M. Huang, Z. Xu, Spontaneous scaling down of femtosecond laser-induced apertures towards the 10-nanometer level: the excitation of quasistatic surface plasmons. Laser Photon. Rev. **8**, 633–652 (2014)
151. B. Prade, J.Y. Vinet, A. Mysyrowicz, Guided optical waves in planar heterostructures with negative dielectric constant. Phys. Rev. B **44**, 13556 (1991)
152. T.J.-Y. Derrien, R. Koter, J. Krüger, S. Höhm, A. Rosenfeld, J. Bonse, Plasmonic formation mechanism of periodic 100-nm-structures upon femtosecond laser irradiation of silicon in water. J. Appl. Phys. **116**, 074902 (2014)
153. A.V. Dostovalov, T.J.-Y. Derrien, S.A. Lizunov, F. Přeučil, K.A. Okotrub, T. Mocek, V.P. Korolkov, S.A. Babin, N.M. Bulgakova, LIPSS on thin metallic films: new insights from multiplicity of laser-excited electromagnetic modes and efficiency of metal oxidation. Appl. Surf. Sci. **491**, 650–658 (2019)
154. P. Daguzan, S. Guizard, P. Martin, G. Petite, Time-resolved studies of free carriers in insulators, in *Ultrafast Processes in Spectroscopy*, ed. by O. Svelto, S. De Silvestri, G. Denardo. (Springer, Boston, 1996), pp. 547–551
155. D.S. Ivanov, L.V. Zhigilei, Combined atomistic-continuum modeling of short-pulse laser melting and disintegration of metal films. Phys. Rev. B **68**, 064114 (2003)
156. M.V. Shugaev, M. He, Y. Levy, A. Mazzi, A. Miotello, N.M. Bulgakova, L.V. Zhigilei, Laser-induced thermal processes: heat transfer, generation of stresses, melting and solidification, vaporization, and phase explosion, in *Handbook of Laser Micro- and Nano-Engineering*, ed. by K. Sugioka (Springer Nature Switzerland AG, 2021), pp. 83–163
157. V. Schultze, M. Wagner, Laser-induced forward transfer of aluminium. Appl. Surf. Sci. **52**, 303–309 (1991)
158. M.V. Shugaev, N.M. Bulgakova, Thermodynamic and stress analysis of laser-induced forward transfer of metals. Appl. Phys. A **101**, 103–109 (2010)
159. G. Heise, M. Domke, J. Konrad, S. Sarrach, J. Sotrop, H.P. Huber, Laser lift-off initiated by direct induced ablation of different metal thin films with ultra-short laser pulses. J. Phys. D: Appl. Phys. **45**, 315303 (2012)

160. M. Domke, L. Nobile, S. Rapp, S. Eiselen, J. Sotrop, H.P. Huber, M. Schmidt, Understanding thin film laser ablation: the role of the effective penetration depth and the film thickness. Phys. Proc. **56**, 1007–1014 (2014)
161. N.T. Goodfriend, S.V. Starinskiy, O. Nerushev, N.M. Bulgakova, A.V. Bulgakov, E.E.B. Campbell, Laser pulse duration dependence of blister formation on back-radiated Ti thin films for BB-LIFT. Appl. Phys. A **122**, 154 (2016)
162. M. Lenzner, F. Krausz, J. Krüger, W. Kautek, Photoablation with sub-10 fs laser pulses. Appl. Surf. Sci. **154–155**, 11–16 (2000)
163. W.D. Kingery, Factors affecting thermal stress resistance of ceramic materials. J. Am. Ceram. Soc. **38**, 3–15 (1955)
164. B.C. Stuart, M.D. Feit, A.M. Rubenchik, B.W. Shore, M.D. Perry, Laser-induced damage in dielectrics with nanosecond to subpicosecond pulses. Phys. Rev. Lett. **74**, 2248–2251 (1995)
165. E. Vanagas, J. Kawai, D. Tuzhilin, I. Kudryashov, A. Mizuyama, K. G. Nakamura, K.-i. Kondo, S.-Y. Koshihara, M. Takesada, K. Matsuda, S. Juodkazis, V. Jarutis, S. Matsuo, H. Misawa, Glass cutting by femtosecond pulsed irradiation. J. Micro. Nanolithogr. MEMS MOEMS **3**, 358–363 (2004)
166. T. Ueda, K. Yamada, K. Oiso, A. Hosokawa, Thermal stress cleaving of brittle materials by laser beam. CIRP Ann. **51**, 149–152 (2002)
167. K. Yamamoto, N. Hasaka, H. Morita, E. Ohmura, Three-dimensional thermal stress analysis on laser scribing of glass. Precis. Eng. **32**, 301–308 (2008)
168. E.G. Gamaly, S. Juodkazis, K. Nishimura, H. Misawa, B. Luther-Davies, L. Hallo, P. Nicolai, V.T. Tikhonchuk, Laser-matter interaction in the bulk of a transparent solid: confined microexplosion and void formation. Phys. Rev. B **73**, 214101 (2006)
169. K.M. Davis, K. Miura, N. Sugimoto, K. Hirao, Writing waveguides in glass with a femtosecond laser. Opt. Lett. **21**, 1729–1731 (1996)
170. R. Stoian, C. D'Amico, M.K. Bhuyan, G. Cheng, Ultrafast laser photoinscription of large-mode-area waveguiding structures in bulk dielectrics. Opt. Laser Technol. **80**, 98–103 (2016)
171. A. Mermillod-Blondin, I.M. Burakov, Y.P. Meshcheryakov, N.M. Bulgakova, E. Audouard, A. Rosenfeld, A. Husakou, I.V. Hertel, R. Stoian, Flipping the sign of refractive index changes in ultrafast and temporally shaped laser-irradiated borosilicate crown optical glass at high repetition rate. Phys. Rev. B **77**, 104205 (2008)
172. M. Sakakura, M. Terazima, Initial temporal and spatial changes of the refractive index induced by focused femtosecond pulsed laser irradiation inside a glass. Phys. Rev. B **71**, 024113 (2005)
173. A. Mermillod-Blondin, J. Bonse, A. Rosenfeld, I.V. Hertel, Y.P. Meshcheryakov, N.M. Bulgakova, E. Audouard, R. Stoian, Dynamics of femtosecond laser induced voidlike structures in fused silica. Appl. Phys. Lett. **94**, 041911 (2009)
174. M. Sakakura, Y. Shimotsuma, N. Fukuda, K. Miura, Transient strain distributions during femtosecond laser-induced deformation inside LiF and MgO single crystals. J. Appl. Phys. **118**, 023106 (2015)
175. V.P. Scripov, *Metastable Liquids* (Wiley, New York, 1974)
176. Y.B. Rumer, M.S. Ryvkin, *Thermodynamics, Statistical Physics and Kinetics* (Mir Publishers, Moscow, 1980)
177. B. Rethfeld, K. Sokolowski-Tinten, D. von der Linde, Ultrafast thermal melting of laser-excited solids by homogeneous nucleation. Phys. Rev. B **65**, 092103 (2002)
178. B.J. Siwick, J.R. Dwyer, R.E. Jordan, R.J.D. Miller, An atomic-level view of melting using femtosecond electron diffraction. Science **302**, 1382–1385 (2003)
179. R. Ernstorfer, M. Harb, C.T. Hebeisen, G. Sciaini, T. Dartigalongue, R.J.D. Miller, The formation of warm dense matter: experimental evidence for electronic bond hardening in gold. Science **323**, 1033–1037 (2009)
180. S.-N. Luo, T.J. Ahrens, T. Çağın, A. Strachan, W.A. Goddard, D.C. Swift, Maximum superheating and undercooling: systematics, molecular dynamics simulations, and dynamic experiments. Phys. Rev. B **68**, 134206 (2003)

181. Z. Lin, E. Leveugle, E.M. Bringa, L.V. Zhigilei, Molecular dynamics simulation of laser melting of nanocrystalline Au. J. Phys. Chem. C **114**, 5686–5699 (2010)
182. C. Wu, L.V. Zhigilei, Microscopic mechanisms of laser spallation and ablation of metal targets from large-scale molecular dynamics simulations. Appl. Phys. A **114**, 11–32 (2014)
183. N.M. Bulgakova, A.V. Bulgakov, Pulsed laser ablation of solids: transition from normal vaporization to phase explosion. Appl. Phys. A **73**, 199–208 (2001)
184. B.N. Chichkov, C. Momma, S. Nolte, F. von Alvensleben, A. Tünnermann, Femtosecond, picosecond and nanosecond laser ablation of solids. Appl. Phys. A **63**, 109–115 (1996)
185. C. Körner, R. Mayerhofer, M. Hartmann, H.W. Bergmann, Physical and material aspects in using visible laser pulses of nanosecond duration for ablation. Appl. Phys. A **63**, 123–131 (1996)
186. Y. Yao, L. K. Falk, R. E. Morjan, O. Nerushev, E.E.B. Campbell, Synthesis of carbon nanotube films by thermal CVD in the presence of supported catalyst particles. Part I: the nanotube film. J. Mater. Sci.: Mater. Electron. **15**, 583–594 (2004)
187. S.J. Henley, J.D. Carrey, S.R.P. Silva, Pulsed-laser-induced nanoscale island formation in thin metal-on-oxide films. Phys. Rev. B **72**, 195408 (2005)
188. Y. Kojima, T. Kato, Nanoparticle formation in au thin films by electron-beam-induced dewetting. Nanotechnology **19**, 255605 (2005)
189. Y. Oh, M. Lee, Single-pulse transformation of Ag thin film into nanoparticles via laser-induced dewetting. Appl. Surf. Sci. **399**, 554–564 (2017)
190. M. Dasbach, H.M. Reinhardt, N.A. Hampp, Formation of highly ordered platinum nanowire arrays on silicon via laser-induced self-organization. Nanomaterials **9**, 1031 (2019)
191. U. Zywietz, A.B. Evlyukhin, C. Reinhardt, B.N. Chichkov, Laser printing of silicon nanoparticles with resonant optical electric and magnetic responses. Nat. Commun. **5**, 3402 (2014)
192. Y. Nakata, T. Okada, M. Maeda, Nano-sized hollow bump array generated by single femtosecond laser pulse. Jpn. J. Appl. Phys. **42**, L1452–L1454 (2003)
193. F. Korte, J. Koch, B.N. Chichkov, Formation of microbumps and nanojets on gold targets by femtosecond laser pulses. Appl. Phys. A **79**, 879–881 (2004)
194. E.L. Gurevich, S.V. Gurevich, Laser induced periodic surface structures induced by surface plasmons coupled via roughness. Appl. Surf. Sci. **302**, 118–123 (2014)
195. E.L. Gurevich, Mechanisms of femtosecond LIPSS formation induced by periodic surface temperature modulation. Appl. Surf. Sci. **374**, 56–60 (2016)
196. D.V. Pavlov, S.O. Gurbatov, S.I. Kudryashov, E.L. Gurevich, A.A. Kuchmizhak, Laser-induced surface relief nanocrowns as a manifestation of nanoscale Rayleigh-Plateau hydrodynamic instability. Appl. Surf. Sci. **511**, 145463 (2014)
197. C.-Y. Shih, R. Streubel, J. Heberle, A. Letzel, M. V. Shugaev, C. Wu, M. Schmidt, B. Gökce, S. Barcikowski, L.V. Zhigilei, Two mechanisms of nanoparticle generation in picosecond laser ablation in liquids: the origin of the bimodal size distribution. Nanoscale **10**, 6900–6910 (2018)
198. A. Rudenko, A. Abou-Saleh, F. Pigeon, C. Mauclair, F. Garrelie, R. Stoian, J.-P. Colombier, High-frequency periodic patterns driven by non-radiative fields coupled with Marangoni convection instabilities on laser-excited metal surfaces. Acta Mater. **194**, 93–105 (2020)
199. S. Gräf, C. Kunz, S. Engel, T. Derrien, F. Müller, Femtosecond laser-induced periodic surface structures on fused silica: the impact of the initial substrate temperature. Materials **11**, 1340 (2018)
200. T. Otobe, M. Yamagiwa, J.-I. Iwata, K. Yabana, T. Nakatsukasa, G.F. Bertsch, First-principles electron dynamics simulation for optical breakdown of dielectrics under an intense laser field. Phys. Rev. B **77**, 165104 (2008)
201. F. Schlaepfer, M. Lucchini, S.A. Sato, M. Volkov, L. Kasmi, N. Hartmann, A. Rubio, L. Gallmann, U. Keller, Attosecond optical-field-enhanced carrier injection into the GaAs conduction band. Nat. Phys. **14**, 560–564 (2018)
202. J.M. Zuo, P. Blaha, K. Schwarz, The theoretical charge density of silicon: experimental testing of exchange and correlation potentials. J. Phys.: Condens. Matter **9**, 7541–7561 (1997)

203. N.T. Maitra, K. Burke, C. Woodward, Memory in time-dependent density functional theory. Phys. Rev. Lett. **89**, 023002 (2002)
204. P. Hohenberg, W. Kohn, Inhomogeneous electron gas. Phys. Rev. **136**, B864 (1964)
205. E. Runge, E.K.U. Gross, Density-functional theory for time-dependent systems. Phys. Rev. Lett. **52**, 997–1000 (1984)
206. C.A. Ullrich, *Time-Dependent Density-Functional Theory: Concepts and Applications* (Oxford University Press, Oxford, 2012)
207. C.A. Ullrich, Z.-H. Yang, A brief compendium of time-dependent density functional theory. Braz. J. Phys. **44**, 154–188 (2014)
208. M.J.T. Oliveira, F. Nogueira, Generating relativistic pseudo-potentials with explicit incorporation of semi-core states using APE, the atomic pseudo-potentials engine. Comput. Phys. Commun. **178**, 524–534 (2008)
209. M.A.L. Marques, M.J.T. Oliveira, T. Burnus, Libxc: a library of exchange and correlation functionals for density functional theory. Comput. Phys. Commun. **183**, 2272–2281 (2012)
210. G. Stefanucci, R.V. Leeuwen, *Nonequilibrium Many-body Theory of Quantum Systems: A Modern Introduction* (Cambridge University Press, Cambridge, 2013)
211. C. Cohen-Tannoudji, J. Dupont-Roc, G. Grynberg, *Photons and Atoms: Introduction to Quantum Electrodynamics* (Wiley, New York, 1997)
212. G. Ernotte, T.J. Hammond, M. Taucer, A gauge-invariant formulation of interband and intraband currents in solids. Phys. Rev. B **98**, 235202 (2018)
213. H. Deng, W. Guo, H. Gao, L. Li, X. Yuan, W. Zheng, X. Zu, A numerical approach for femtosecond laser-induced photoionization in solids and its application. J. Opt. **21**, 075501 (2019)
214. J.-P. Colombier, A. Rudenko, E. Silaeva, H. Zhang, X. Sedao, E. Bévillon, S. Reynaud, C. Maurice, F. Pigeon, F. Garrelie, R. Stoian, Mixing periodic topographies and structural patterns on silicon surfaces mediated by ultrafast photoexcited charge carriers. Phys. Rev. Res. **2**, 043080 (2020)
215. C. Sarpe, J. Köhler, T. Winkler, M. Wollenhaupt, T. Baumert, Real time observation of transient electron density in water irradiated with tailored femtosecond laser pulses. New J. Phys. **14**, 075021 (2012)
216. M. Lebugle, O. Utéza, M. Sentis, N. Sanner, High temporal resolution and calibration in pump-probe experiments characterizing femtosecond laser-dielectrics interaction. Appl. Phys. A **120**, 455–461 (2015)
217. K.J. Wædegaard, D.B. Sandkamm, A. Mouskeftaras, S. Guizard, P. Balling, Probing ultrashort-pulse laser excitation of sapphire: from the initial carrier creation to material ablation. Europhys. Lett. **105**, 47001 (2014)
218. P. Jürgens, B. Liewehr, B. Kruse, C. Peltz, T. Witting, A. Husakou, A. Rouzee, M. Ivanov, T. Fennel, M.J.J. Vrakking, A. Mermillod-Blondin, Characterization of laser-induced ionization dynamics in solid dielectrics. ACS Photon. **9**, 233–240 (2022)
219. U. De Giovannini, H. Hübener, A. Rubio, Monitoring electron-photon dressing in WSe_2. Nano Lett. **16**, 7993–7998 (2016)
220. E.J. Sie, J.W. McIver, Y.-H. Lee, L. Fu, J. Kong, N. Gedik, Valley-selective optical Stark effect in monolayer WS_2. Nat. Mater. **14**, 290–294 (2014)
221. F. Mahmood, C.-K. Chan, Z. Alpichshev, D. Gardner, Y. Lee, P.A. Lee, N. Gedik, Selective scattering between Floquet-Bloch and Volkov states in a topological insulator. Nat. Phys. **12**, 306–310 (2016)
222. T. Winkler, L. Haahr-Lillevang, C. Sarpe, B. Zielinski, N. Götte, A. Senftleben, P. Balling, T. Baumert, Laser amplification in excited dielectrics. Nat. Phys. **14**, 74–79 (2017)
223. E. Smetanina, P. González de Alaiza Martínez, I. Thiele, B. Chimier, A. Bourgeade, G. Duchateau, Optical Bloch modeling of femtosecond-laser-induced electron dynamics in dielectrics. Phys. Rev. E **101**, 063206 (2020)
224. T. Apostolova, B. Obreshkov, Sub-cycle dynamics of electron-hole pairs and high-harmonic generation in bulk diamond subjected to intense femtosecond laser pulse. Opt. Quantum. Electron. **50**, 1–18 (2018)

225. A. Zheltikov, Laser-induced tunneling, the Kapitza effective potential, and the limits of perturbative nonlinear optics. Opt. Express **27**, 8246 (2019)
226. H. Zhang, C. Li, E. Bevillon, G. Cheng, J.-P. Colombier, R. Stoian, Ultrafast destructuring of laser-irradiated tungsten: thermal or nonthermal process. Phys. Rev. B **94**, 224103 (2016)
227. A. Blumenstein, E.S. Zijlstra, D.S. Ivanov, S.T. Weber, T. Zier, F. Kleinwort, B. Rethfeld, J. Ihlemann, P. Simon, M.E. Garcia, Transient optics of gold during laser irradiation: from first principles to experiment. Phys. Rev. B **101**, 165140 (2020)
228. E. Bévillon, J. Colombier, V. Recoules, R. Stoian, First-principles calculations of heat capacities of ultrafast laser-excited electrons in metals. Appl. Surf. Sci. **336**, 79–84 (2015)
229. K. Glantschnig, C. Ambrosch-Draxl, Relativistic effects on the linear optical properties of Au, Pt, Pb and W. New J. Phys. **12**, 103048 (2010)
230. S.A. Sato, Y. Shinohara, T. Otobe, K. Yabana, Dielectric response of laser-excited silicon at finite electron temperature. Phys. Rev. B **90**, 174303 (2014)
231. M. Volkov, S.A. Sato, F. Schlaepfer, L. Kasmi, N. Hartmann, M. Lucchini, L. Gallmann, A. Rubio, U. Keller, Attosecond screening dynamics mediated by electron localization in transition metals. Nat. Phys. **15**, 1145–1149 (2019)
232. T. Zier, E.S. Zijlstra, M.E. Garcia, Quasimomentum-space image for ultrafast melting of silicon. Phys. Rev. Lett. **116**, 153901 (2016)
233. A. Yamada, K. Yabana, Modulation of probe signal in coherent phonon detection revisited: analytical and first-principles computational analyses. Phys. Rev. B **101**, 214313 (2020)
234. F.G. Eich, F. Agostini, The adiabatic limit of the exact factorization of the electron-nuclear wave function. J. Chem. Phys. **145**, 054110 (2016)
235. N.M. Hoffmann, H. Appel, A. Rubio, N.T. Maitra, Light-matter interactions via the exact factorization approach. Eur. Phys. J. B **91**, 180 (2018)
236. R. Requist, C.R. Proetto, E.K.U. Gross, Exact factorization-based density functional theory of electron-phonon systems. Phys. Rev. B **99**, 165136 (2019)
237. B. Bauerhenne, T. Zier, M.E. Garcia, *Ultrafast Quantum Processes at the Nanoscale: Insights from Modelling* (Springer, Berlin, 2022)
238. C.M. Bustamante, T.N. Todorov, C.G. Sánchez, A. Horsfield, D.A. Scherlis, A simple approximation to the electron-phonon interaction in population dynamics. J. Chem. Phys. **153**, 234108 (2020)
239. H.-Y. Chen, D. Sangalli, M. Bernardi, Exciton-phonon interaction and relaxation times from first principles. Phys. Rev. Lett. **125**, 107401 (2020)
240. P. Martinez, B. Rosenzweig, N.M. Hoffmann, L. Lacombe, N.T. Maitra, Case studies of the time-dependent potential energy surface for dynamics in cavities. J. Chem. Phys. **154**, 014102 (2020)
241. M.V. Shugaev, I. Gnilitskyi, N.M. Bulgakova, L.V. Zhigilei, Mechanism of single-pulse ablative generation of laser-induced periodic surface structures. Phys. Rev. B **96**, 205429 (2017)
242. C.-Y. Shih, I. Gnilitskyi, M.V. Shugaev, E. Skoulas, E. Stratakis, L.V. Zhigilei, Effect of a liquid environment on single-pulse generation of laser induced periodic surface structures and nanoparticles. Nanoscale **12**, 7674–7687 (2020)
243. B. Bauerhenne, V.P. Lipp, T. Zier, E.S. Zijlstra, M.E. Garcia, Self-learning method for construction of analytical interatomic potentials to describe laser-excited materials. Phys. Rev. Lett. **124**, 085501 (2020)
244. P.P. Pronko, S.K. Dutta, J. Squier, J.V. Rudd, D. Du, G. Mourou, Machining of sub-micron holes using a femtosecond laser at 800 nm. Opt. Commun. **114**, 106–110 (1995)
245. A.P. Joglekar, H.-H. Liu, E. Meyhöfer, G. Mourou, A.J. Hunt, Optics at critical intensity: applications to nanomorphing. Proc. Natl. Acad. Sci. U. S.A. **101**, 5856–5861 (2004)
246. B.K.A. Ngoi, K. Venkatakrishnan, B. Tan, N.R. Sivakumar, The effect of Rowland Ghost on sub-micronmachining using femtosecond pulsed laser. Opt. Express **8**, 492–496 (2001)
247. A.P. Joglekar, H.-H. Liu, G.J. Spooner, E. Meyhöfer, G. Mourou, A.J. Hunt, A study of the deterministic character of optical damage by femtosecond laser pulses and applications to nanomachining. Appl. Phys. B **77**, 25–30 (2003)

248. F. Caballero-Lucas, C. Florian, J.M. Fernández-Pradas, J.L. Morenza, P. Serra, Beam waist position study for surface modification of polymethyl-methacrylate with femtosecond laser pulses. Appl. Surf. Sci. **374**, 353–358 (2016)
249. R. Stoian, J.-P. Colombier, Advances in ultrafast laser structuring of materials at the nanoscale. Nanophotonics **9**, 4665–4688 (2020)
250. T. Uenohara, Y. Takaya, Y. Mizutani, Laser micro machining beyond the diffraction limit using a photonic nanojet. CIRP Ann. **66**, 491–494 (2017)
251. F. Fraggelakis, G. Mincuzzi, J. Lopez, I. Manek-Hónninger, R. Kling, Controlling 2D laser nano structuring over large area with double femtosecond pulses. Appl. Surf. Sci. **470**, 677–686 (2019)
252. Y. Nakata, Y. Matsuba, N. Miyanaga, Sub-micron period metal lattices fabricated by interfering ultraviolet femtosecond laser processing. Appl. Phys. A **122**, 532 (2016)
253. Y. Nakata, E. Hayashi, K. Tsubakimoto, N. Miyanaga, A. Narazaki, T. Shoji, Y. Tsuboi, Nanodot array deposition via single shot laser interference pattern using laser-induced forward transfer. Int. J. Extreme Manuf. **2**, 025101 (2020)
254. R. Stoian, M. Bhuyan, G. Cheng, G. Zhang, R. Meyer, F. Courvoisier, Ultrafast Bessel beams: advanced tools for laser materials processing. Adv. Opt. Technol. **7**, 165–174 (2018)
255. J.-H. Yoo, J.B. In, C. Zheng, I. Sakellari, R.N. Raman, M.J. Matthews, S. Elhadj, C.P. Grigoropoulos, Directed dewetting of amorphous silicon film by a donut-shaped laser pulse. Nanotechnology **26**, 165303 (2015)
256. K. Toyoda, F. Takahashi, S. Takizawa, Y. Tokizane, K. Miyamoto, R. Morita, T. Omatsu, Transfer of light helicity to nanostructures. Phys. Rev. Lett. **110**, 143603 (2013)
257. L. Englert, B. Rethfeld, L. Haag, M. Wollenhaupt, C. Sarpe-Tudoran, T. Baumert, Control of ionization processes in high band gap materials via tailored femtosecond pulses. Opt. Express **15**, 17855–17862 (2007)
258. Y. Hayasaki, S. Hasegawa, H. Zhang, Spatial beam shaping with a liquid-crystal spatial light modulator, in *Ultrafast Laser Nanostructuring—The Pursuit of Extreme Scales*, ed. by R. Stoian, J. Bonse, Chapter 15 (Springer, Berlin, 2022)
259. F. Courvoisier, Non-standard light for ultrafast laser micro- and nano-structuring, in *Ultrafast Laser Nanostructuring—The Pursuit of Extreme Scales*, ed. by R. Stoian, J. Bonse. Chapter 16 (Springer, Berlin, 2022)
260. P.G. Kazansky, W. Yang, E. Bricchi, J. Bovatsek, A. Arai, Y. Shimotsuma, K. Miura, K. Hirao, "Quill" writing with ultrashort light pulses in transparent materials. Appl. Phys. Lett. **90**, 151120 (2007)
261. D.N. Vitek, E. Block, Y. Bellouard, D. E. Adams, S. Backus, D. Kleinfeld, C.G. Durfee, J.A. Squier, Spatio-temporally focused femtosecond laser pulses for nonreciprocal writing in optically transparent materials. Opt. Express **18**, 24673–24678 (2010)
262. H. Song, Y. Dai, J. Song, H. Ma, X. Yan, G. Ma, Femtosecond laser-induced structural difference in fused silica with a non-reciprocal writing process. Appl. Phys. A **123**, 255 (2017)
263. S. Akturk, X. Gu, P. Gabolde, R. Trebino, The general theory of first-order spatio-temporal distortions of gaussian pulses and beams, Opt. Express **13**, 8642–8661 (2005)
264. S. Akturk, X. Gu, P. Bowlan, R. Trebino, Spatio-temporal couplings in ultrashort laser pulses. J. Opt. **12**, 093001 (2010)
265. J.A. Wheeler, A. Borot, S.H. Monchocé, Vincenti, A. Ricci, A. Malvache, R. Lopez-Martens, F. Quéré, Attosecond lighthouses from plasma mirrors. Nat. Photon. **6**, 829–833 (2012)
266. J.A. Fülöp, J. Hebling, Applications of tilted-pulse-front excitation, in *Recent Optical and Photonic Technologies*, ed. by K.Y. Kim (IntechOpen, 2010), pp. 207–230
267. A. Popp, J. Vieira, J. Osterhoff, Z. Major, R. Hörlein, M. Fuchs, R. Weingartner, T.P. Rowlands-Rees, M. Marti, R.A. Fonseca, S.F. Martins, L.O. Silva, S.M. Hooker, F. Krausz, F. Grüner, S. Karsch, All-optical steering of laser-wakefield-accelerated electron beams. Phys. Rev. Lett. **105**, 215001 (2010)
268. R. Kammel, R. Ackermann, J. Thomas, J. Götte, S. Skupin, A. Tünnermann, S. Nolte, Enhancing precision in fs-laser material processing by simultaneous spatial and temporal focusing. Light: Sci. Appl. **3**, e169 (2014)

269. V.P. Zhukov, S. Akturk, N.M. Bulgakova, Asymmetric interactions induced by spatio-temporal couplings of femtosecond laser pulses in transparent media. J. Opt. Soc. Am. B **36**, 1556–1564 (2019)
270. Y. Li, J. Song, Q. Zhai, W. Yin, X. Tang, Y. Dai, Effect of wavefront rotation on the photoionization process by ultrafast laser spatiotemporal focusing. J. Opt. Soc. Am. B **38**, 1040–1047 (2021)
271. T.Q. Jia, H.X. Chen, M. Huang, F.L. Zhao, J.R. Qiu, R.X. Li, Z.Z. Xu, X.K. Xe, J. Zhang, H. Kuroda, Formation of nanogratings on the surface of a ZnSe crystal irradiated by femtosecond laser pulses. Phys. Rev. B **72**, 125429 (2005)
272. M. Sakamoto, T. Tachikawa, M. Fujitsuka, T. Majama, Two-color two-laser fabrication of gold nanoparticles in a PVA film. Chem. Phys. Lett. **420**, 90–94 (2006)
273. P.K. Diwakar, S.S. Harilal, J.R. Freeman, A. Hassanein, Role of laser pre-pulse wavelength and inter-pulse delay on signal enhancement in collinear double-pulse laser-induced breakdown spectroscopy, Spectrochim. Acta B: At. Spectrosc. **87**, 65–73 (2013)
274. K. Sugioka, T. Akane, K. Obata, K. Toyoda, K. Midorikawa, Multiwavelength excitation processing using F_2 and KrF excimer lasers for precision microfabrication of hard materials. Appl. Surf. Sci. **197–198**, 814–821 (2002)
275. T. Asada, T. Tamaki, E. Nakazumi, M. Ohmura, K. Itoh, Laser-induced structural modifications inside glass using a femtosecond laser and a CO_2 laser. J. Laser Micro Nanoeng. **9**, 174–179 (2014)
276. F.V. Potemkin, B.G. Bravy, Y.I. Bezsudnova, E.I. Mareev, V.M. Starostin, V.T. Platonenko, V.M. Gordienko, Overcritical plasma ignition and diagnostics from oncoming interaction of two color low energy tightly focused femtosecond laser pulses inside fused silica. Laser Phys. Lett. **13**, 045402 (2016)
277. N.M. Bulgakova, V.P. Zhukov, A.R. Collins, D. Rostohar, T.J.-Y. Derrien, T. Mocek, How to optimize ultrashort pulse laser interaction with glass surfaces in cutting regimes? Appl. Surf. Sci. **336**, 364–374 (2015)
278. N.M. Bulgakova, V.P. Zhukov, S.V. Sonina, Y.P. Meshcheryakov, Modification of transparent materials with ultrashort laser pulses: what is energetically and mechanically meaningful? J. Appl. Phys. **118**, 233108 (2015)
279. N.M. Bulgakova, V.P. Zhukov, J. Sladek, I. Mirza, A.V. Bulgakov, Dual wavelength laser excitation of bandgap materials: challenges for efficient energy coupling, in *Conference on Lasers and Electro-Optics, OSA Technical Digest* (Optical Society of America, 2020), p. STh1H.4
280. X. Sedao, T.J.-Y. Derrien, G.R.B.E. Romer, B. Pathiraj, A.J. Huis in 't Veld, Parallel laser surface texturing by a simple transportable micro-sphere arrays. J. Appl. Phys. **112**, 103111 (2012)
281. J. Chen, M. Badioli, P. Alonso-González, S. Thongrattanasiri, F. Huth, J. Osmond, M. Spasenović, A. Centeno, A. Pesquera, P. Godignon, A. Zurutuza Elorza, N. Camara, F.J.G. de Abajo, R. Hillenbrand, F.H.L. Koppens, Optical nano-imaging of gate-tunable graphene plasmons. Nature **487** 77–81 (2012)
282. J. Bogdanowicz, M. Gilbert, N. Innocenti, S. Koelling, B. Vanderheyden, W. Vandervorst, Light absorption in conical silicon particles. Opt. Express **21**, 3891–3896 (2013)
283. S. Kim, J. Jin, Y.-J. Kim, I.-Y. Park, Y. Kim, S.-W. Kim, High-harmonic generation by resonant plasmon field enhancement. Nature **453**, 757–760 (2008)
284. I.-Y. Park, S. Kim, J. Choi, D.-H. Lee, Y.-J. Kim, M. F. Kling, M. I. Stockman, S.-W. Kim, Plasmonic generation of ultrashort extreme-ultraviolet light pulses. Nat. Photon. **5**, 677–681 (2011)
285. M. Birnbaum, Semiconductor surface damage produced by ruby lasers. J. Appl. Phys. **36**, 3688 (1965)
286. J. Bonse, S. Höhm, S.V. Kirner, A. Rosenfeld, J. Krüger, Laser-induced periodic surface structures - a scientific evergreen. IEEE J. Sel. Topics Quantum Electron. **23**, 9000615 (2017)
287. J. Bonse, S. Gräf, Maxwell meets Marangoni-a review of theories on laser-induced periodic surface structures. Laser Photon. Rev. **14**, 2000215 (2020)

288. A. Rudenko, J.-P. Colombier, How light drives material periodic patterns down to the nanoscale, in *Ultrafast Laser Nanostructuring—The Pursuit of Extreme Scales*, ed. by R. Stoian, J. Bonse. Chapter 5 (Springer, Berlin, 2022)
289. B. Öktem, I. Pavlov, S. Ilday, H. Kalaycioglu, A. Rybak, S. Yavas, M. Erdogan, F.O. Ilday, Nonlinear laser lithography for indefinitely large-area nanostructuring with femtosecond pulses. Nat. Photon. **7**, 897–901 (2013)
290. A. Ruiz de la Cruz, R. Lahoz, J. Siegel, G.F. de la Fuente, J. Solis, High speed inscription of uniform, large-area laser-induced periodic surface structures in Cr films using a high repetition rate fs laser. Opt. Lett. **39**, 2491 (2014)
291. A. San-Blas, M. Martinez-Calderon, E. Granados, M. Gómez-Aranzadi, A. Rodríguez, S.M. Olaizola, LIPSS manufacturing with regularity control through laser wavefront curvature. Surf. Interfaces **25**, 101205 (2021)
292. B. Kim, H.K. Nam, J. Ryu, Y.-J. Kim, S.-W. Kim, Non-periodic nanoscale structuring of crystalline silicon surface by using ultrashort laser pulses. Appl. Surf. Sci. **565**, 150595 (2021)
293. A.M. Ozkan, Femtosecond laser-induced periodic structure writing on diamond crystals and microclusters. Appl. Phys. Lett. **75**, 3716–3718 (1999)
294. J. Bonse, H. Sturm, D. Schmidt, W. Kautek, Chemical, morphological and accumulation phenomena in ultrashort-pulse laser ablation of TiN in air. Appl. Phys. A **71**, 657–665 (2000)
295. J. Reif, F. Costache, M. Henyk, S.V. Pandelov, Ripples revisited—non-classical morphology at the bottom of femtosecond laser ablation craters in transparent dielectrics. Appl. Surf. Sci. **197–198**, 891–895 (2002)
296. A. Borowiec, H.K. Haugen, Subwavelength ripple formation on the surfaces of compound semiconductors irradiated with femtosecond laser pulses. Appl. Phys. Lett. **82**, 4462–4464 (2003)
297. Q. Wu, Y. Ma, R. Fang, Y. Liao, Q. Yu, X. Chen, K. Wang, Femtosecond laser-induced periodic surface structure on diamond film. Appl. Phys. Lett. **82**, 1703 (2003)
298. J. Bonse, S. Höhm, A. Rosenfeld, J. Krüger, Sub-100-nm laser-induced periodic surface structures upon irradiation of titanium by Ti-sapphire femtosecond laser pulses in air. Appl. Phys. A **110**, 547–551 (2013)
299. M. Huang, F. Zhao, Y. Cheng, N. Xu, Z. Xu, Origin of laser-induced near-subwavelength ripples: interference between surface plasmons and incident laser. ACS Nano **3**, 4062–4070 (2009)
300. M. Huang, F. Zhao, Y. Cheng, N. Xu, Z. Xu, Mechanisms of ultrafast laser-induced deep-subwavelength gratings on graphite and diamond. Phys. Rev. B **79**, 125436 (2009)
301. J.Z.P. Skolski, G.R.B.E. Römer, J.V. Obona, A.J. Huis in 't Veld, Modeling laser-induced periodic surface structures: finite-difference time-domain feedback simulations. J. Appl. Phys. **115**, 103102 (2014)
302. M. Huang, F. Zhao, Y. Cheng, Z. Xu, Effects of the amorphous layer on laser-induced subwavelength structures on carbon allotropes. Opt. Lett. **37**, 677 (2012)
303. C. Wang, H. Huo, M. Johnson, M. Shen, E. Mazur, The thresholds of surface nano-/micro-morphology modifications with femtosecond laser pulse irradiations. Nanotechnology **21**, 075304 (2010)
304. G. Obara, H. Shimizu, T. Enami, E. Mazur, M. Terakawa, M. Obara, Growth of high spatial frequency periodic ripple structures on SiC crystal surfaces irradiated with successive femtosecond laser pulses. Opt. Express **21**, 26323 (2013)
305. A. Sarracino, A.R. Ansari, B. Torralva, S. Yalisove, Sub-100 nm high spatial frequency periodic structures driven by femtosecond laser induced desorption in GaAs. Appl. Phys. Lett. **118**, 242106 (2021)
306. A. Rudenko, C. Mauclair, F. Garrelie, R. Stoian, J.-P. Colombier, Amplification and regulation of periodic nanostructures in multipulse ultrashort laser-induced surface evolution by electromagnetic-hydrodynamic simulations. Phys. Rev. B **99**, 235412 (2019)
307. A.V. Dostovalov, V.P. Korolkov, K.A. Okotrub, K.A. Bronnikov, S.A. Babin, Oxide composition and period variation of thermochemical LIPSS on chromium films with different thickness. Opt. Express **26**, 7712 (2018)

308. G.A. Martsinovskii, G.D. Shandybina, D.S. Smirnov, S.V. Zabotnov, L.A. Golovan, V.Y. Timoshenko, P.K. Kashkarov, Ultrashort excitations of surface polaritons and waveguide modes in semiconductors. Opt. Spectrosc. **105**, 67–72 (2008)
309. A. Norrman, T. Setälä, A.T. Friberg, Surface-plasmon polariton solutions at a lossy slab in a symmetric surrounding. Opt. Express **22**, 4628 (2014)
310. H. Xie, B. Zhao, J. Cheng, S.K. Chamoli, T. Zou, W. Xin, J. Yang, Super-regular femtosecond laser nanolithography based on dual-interface plasmons coupling. Nanophotonics **10**, 3831–3842 (2021)

Chapter 2
The Atomistic Perspective of Nanoscale Laser Ablation

Dmitry S. Ivanov, Pavel N. Terekhin, Sergey I. Kudryashov, Sergey M. Klimentov, Andrei V. Kabashin, Martin E. Garcia, Baerbel Rethfeld, and Irina N. Zavestovskaya

Abstract Materials irradiated by ultrashort laser pulses can undergo a variety of surface relief and structural modifications due to melting, spallation, and ablation processes. The possibility of instant and localized energy deposition into materials makes the short laser pulses a perspective tool in precise material modifications under controlled conditions. Thus, with certain laser irradiation parameters, the absorbed energy can trigger one or several laser-induced phase transition processes in the solid leading to material ejection, generation of subsurface voids, or nanostructures growth on the surface. The resulting material modifications can change its topographical, morphological, magnetic, and optical properties. While the ablation and spallation processes were utilized in laser welding and drilling technology, the functionalized surfaces have found a number of applications in micro-optics,

---

D. S. Ivanov (✉) · S. I. Kudryashov
P.N. Lebedev Physical Institute, Moscow, Russia
e-mail: ivanov@uni-kassel.de; kudryashovsi@lebedev.ru

P. N. Terekhin · B. Rethfeld
Department of Physics and Research Center OPTIMAS, Technical University of Kaiserslautern, Kaiserslautern, Germany
e-mail: terekhin@physik.uni-kl.de; rethfeld@physik.uni-kl.de

S. M. Klimentov
Institute of Engineering Physics for Biomedicine (PhysBio), Moscow, Russia

A. V. Kabashin
Institute of Engineering Physics for Biomedicine (PhysBio), Moscow, Russia

LP3, Aix-Marseille Université, CNRS, LP3, Campus de Luminy, Marseille, France

M. E. Garcia
Institute of Physics and Center for Interdisciplinary Nanostructure Science and Technology (CINSaT), University of Kassel, Kassel, Germany
e-mail: m.garcia@uni-kassel.de

I. N. Zavestovskaya
P.N. Lebedev Physical Institute, Moscow, Russia

Institute of Engineering Physics for Biomedicine (PhysBio), Moscow, Russia
e-mail: zavestovskayain@lebedev.ru

© The Author(s), under exclusive license to Springer Nature Switzerland AG 2023

R. Stoian, J. Bonse (eds.), *Ultrafast Laser Nanostructuring*, Springer Series
in Optical Sciences 239, https://doi.org/10.1007/978-3-031-14752-4_2

waveguides, Raman spectroscopy, and biosensors. Generation of material modifications in a designed way, however, requires a detailed understanding of the dynamics of fast, nonequilibrium, and interrelated laser-induced processes at nanoscale. In this work, a combined particle-based mesoscopic numerical approach suitable for the investigation of ablation and nanostructuring mechanism of solids on the experimental scale is proposed. The combined model is applied to investigate the laser-induced processes and their dependences on the surrounding media and laser irradiation parameters: wavelength, pulse duration, and fluence. Good agreement between the modeling and the experimental results justifies the proposed approach as a powerful numerical tool revealing the fundamental physics of the underlying the ablation and nanostructuring processes. This will pave the way toward predesigned topography for functionalized surfaces on the nanoscales.

Keywords Laser-matter interactions · Modeling and simulations · Ultrashort laser pulses · Nanostructuring of materials · Electron-phonon interaction · Laser melting and ablation

1 Introduction

Short pulse laser nanostructuring of materials is increasingly used in biomedical and industrial applications. The possibility to activate nonequilibrium phase transformation processes with laser pulse durations shorter than the characteristic time of the electron-phonon relaxation on the nanoscale often leads to the generation of structures with unique properties and on subwavelength dimensions [1]. In particular, the generation of such laser-induced periodic surface structures (LIPSS) on different materials have found prominent applications for material surface functionalization in waveguiding [2], tribology [3, 4] magnetics [5], wetting [6, 7], and Raman spectroscopy [8]. Despite the fact that the experimental progress in nanopatterning of the variety of materials (metals, semiconductors, and dielectrics) has succeeded a significant progress during the last decade [9], the theoretical interpretation and fundamental understanding of the processes behind the nanostructure formation meet a lot of scientific discussions and sometimes controversial explanations [9, 10]. Thus, the most recent experimental works on the generation of helix structures on silicon and other materials [11–14] have met a lot of scientific interest due to new perspectives in material modification technologies, but the mechanism of their formation remains unclear due to limited knowledge of the laser-induced processes at the nanoscale responsible for the generation of such unusual structures.

In this view, the combination of theoretical modelings at different scales and utilization of variety computational methods – ab initio study [15, 16], classical molecular dynamics and Monte Carlo methods [17, 18], electrodynamics [19], and hydrodynamic approaches [20] – can shed a light on the laser-induced processes and covering wide spatial and temporal ranges. Moreover, the successful attempt in combination of the above methods within the scale of a single computational approach [21, 22], additionally reinforced with time-resolved pump-probe experiments, represents an efficient tool for studying the laser-induced processes during and after the laser-matter interaction at the nanoscale [9, 23–25].

Short laser pulse interaction with materials involves a number of concurrent processes that can be activated in a wide range of time and spatial scales [26–31]. The establishment of strong temperature and pressure gradients in material under conditions of a high degree of overheating, realized during short laser pulse heating, can induce strongly transient phase transition processes as fast as hundreds of femtoseconds with a size of nuclei as small as several interatomic distances. Since this situation is quite common in short pulse laser processing of materials, the need of robust theoretical models that could be applicable under such extreme conditions is obvious. Apparently, for its successful description, the kinetics of phase transition must be considered and compared with the experimental data. To most crucial issues related to the kinetics of phase transition, one can bring the time of homogeneous melting of a certain volume, frequency of nuclei birth in the volume, speed of interphase front propagation in heterogeneous phase grow, and formation of a Knudsen layer for the description of laser-induced melting (plume expansion). Several attempts have been recently undertaken in order to theoretically describe short pulse laser-induced nucleation mechanisms in continuum. In the theoretical work by Mei [32], classical nucleation theory of melting was able to describe melting processes in continuum and had a good comparison with experimental data on melting time of 500 ps–1 ns [33, 34] followed by the laser pulses of 100 ps–10 ns range. Thus, the continuum models based on Navier-Stokes equations on laser cutting, drilling, and welding with pulses of 1 ns and longer were successfully used in the experimental data interpretation [35–38]. For shorter laser pulses of 1 ps–100 ps, however, the melting time registered experimentally, 3 ps–15 ps, was too short for explanations based on the work presented by Mei, which is applicable for the equilibrium phase transformation processes. A more sophisticated theory of ultrashort laser-induced melting was presented in [39], where melting time due to homogeneous nucleation as a function of superheating revealed a strongly exponential dependence and explained experimental results on such short melting times measured in [40–42]. However, being very sensitive to a small variation of the input parameters, the applicability of this theory is still questionable when working with pulses of 100 fs–1 ps where the time of melting shorter than 1 ps was registered [43, 44]. Additionally, the comparison of the calculated melting time based on the theory presented in [39] with its direct measurements in molecular dynamics calculations in [45] differed by several orders of magnitude for femtosecond laser pulses. Apparently, such a big difference could not be explained by inaccuracy of the input parameters only, and a nonthermal character of laser-induced melting in ultrashort pulse experiments can be assumed [46–48]. Finally, a significant progress in understanding of nonequilibrium phase transition processes at continuum level (including melting and evaporation) was achieved in the theoretical work by Volkov and Zhigilei [30].

It is difficult, nevertheless, to treat the experimental data on short pulse laser drilling, cutting, and welding with the existing continuum models when moving toward pulses of 1 ps and shorter. Not only the mechanism of nonequilibrium, melting process is not clear in the description of continuum but the mechanism of ultrafast laser ablation, spallation, and evaporation that are massively involved into short pulse laser processing of materials aggravate the difficulties of the continuum approaches. Some of the limitations can be overcome by adding “more physics” within the framework provided by the utilized model. In particular, combining the two-temperature model (TTM) [49] for description of the electron-phonon temperature dynamics in metals followed by an ultrashort laser irradiation with the hot electron blast model [50] and thermo-elasticity equations [51] has been proven as an advanced model to investigate the conditions for nonthermal damage to thin metal films [52]. However, the impossibility to account on crystal structure, polycrystalline character of solids, and lattice defects in these continuum models is a bottleneck when considering thresholds of melting, ablation, and spallation processes.

A computational method that is suitable for the simulation of fast nonequilibrium processes and therefore can provide insights into the mechanisms of laser-metal interactions is the molecular dynamics (MD) method. The advantage of the MD method is that only details of the interatomic interaction need to be specified, and no assumptions are made about the character of the processes under study. In particular, MD has been demonstrated to be an efficient tool for a microscopic analysis of the melting mechanisms under conditions of overheating in both the bulk of a crystal [53] and in systems with free surfaces [54]. Simulations of boiling, spinodal decomposition and fragmentation of a metastable liquid [55], generation and propagation of laser-induced pressure waves [56], and laser ablation [57, 58] have also been reported. It was shown that lowering of the interatomic bonding energy in the proximity of grain boundaries and a variety of defects of polycrystalline solids act as a preferable nucleation sites during fast transformation processes and possible to investigate at atomic scale with MD approaches [59, 60].

In spite of the apparent benefit of the MD model, specifically for microscopic investigation of the nonequilibrium phase transition processes, the classical MD approach, however, is not directly applicable for the case of short pulse laser melting/spallation/ablation processes. The absence of free carriers limits the material heat conduction upon photo-excitation and results in unphysically confined thermal energy deposition within the proximity of the free surface. Several modifications have to be made in order to apply the classical MD method for simulation of laser interactions with metals. Straightforward application of the Fourier’s law or the equation of heat conduction in metals [61] implies that a complete local thermal equilibrium is reached between the electrons and phonons. This assumption is correct as soon as the duration of the laser pulse is much longer than the characteristic time of electron-phonon relaxation. For ps and fs pulses, however, the electron-phonon equilibrium cannot be assumed a priori, and the time evolution of the lattice and electron temperatures, T_l and T_e, is typically described within TTM [49].

In this chapter, therefore, we present the overview of numerical methods, combining different computational models into a single mesoscopic approach, devoted to simulate the interaction of laser pulse irradiation with a solid of different materials (metals, semiconductors, and dielectrics), in different media (vacuum or liquid), and for different purposes: melting, ablation, nanostructuring, LIPSS formation, or laser-induced nanoparticle (NP) generation due to pulsed laser ablation in liquids (PLAL) or in vacuum. The proposed approaches have been successfully utilized in a number of projects aiming on laser machining of solids, nanostructuring, and materials surface functionalization. Being applied on the experimental scale and having the results of simulations directly verified with the experimental measurements, the presented approaches can serve as a powerful numerical tool for designing the methodology for generation of structures with demanded properties (topographical, morphological, magnetic, and optical).

2 Models

2.1 Combined MD-TTM Model for Metals

In order to overcome limitations of both atomistic approach with MD and continuum model by TTM, we are developing a hybrid computational model for modeling of short laser pulse interaction with metals that combines classical MD method for simulation of nonequilibrium processes of lattice superheating and fast phase transitions with a continuum description of the laser excitation and subsequent relaxation of the conduction band electrons, based on TTM, which in 3D can be written as follows:

$$\begin{cases} C_e\left(T_e\right)\frac{\partial T_e}{\partial t} = \nabla\left(K_e\left(T_e\right)\nabla T_e\right) - G\left(T_e - T_l\right) + Q\left(\overrightarrow{\mathrm{r}}, t\right) \\ C_l\left(T_l\right)\frac{\partial T_l}{\partial t} = \nabla\left(K_l \nabla T_l\right) + G\left(T_e - T_l\right) \end{cases} \tag{2.1}$$

In this system of two diffusion differential equations, given by Eq. (2.1), for the electrons and lattice, the indexes “**e**” and “**l**” are standing for correspondingly electrons and lattice temperatures. Two subsystems are coupled via the electron-phonon interaction, described by means of the electron-phonon coupling G, and C is the heat capacity. Both G and C_e are in general functions of temperatures T_e and T_l and the free electron density n_e [62]. The conductivity of lattice is negligible as compared to the electronic one and frequently omitted. The latter, however, have a number of possible descriptions and, depending on the level of excitation and the required accuracy, can be given by a simple linear expression [63], or by plasma-like dependence [64], or by recently suggested more accurate dependence [65] on temperatures T_e, T_l, and n. Although, included into Eq. (2.1), the source term $Q(\mathbf{r},t)$ is primarily devoted for description of the laser irradiation absorption, it can also be modified and used for the energy deposition with an ion beam, as it is given by Lindhard model, for instance [66]. Alternatively, for the case of a laser spot much wider than the lateral size of the computational cell, 1D model for the heat conduction and for the source term can be used:

$$Q\left(z,t\right)=\varphi\left(1-R\left(T_e\right)\right)\alpha_{\mathrm{abs}}\exp\left(-\alpha_{\mathrm{abs}}z\right)\frac{1}{\tau}\sqrt{\frac{\sigma}{\pi}}\exp\left(-\sigma\frac{\left(t-t_0\right)^2}{\tau^2}\right)\tag{2.2}$$

whereas the modeling of structure growth with size comparable with the spot size 3D model must be utilized:

$$Q\left(\overrightarrow{r},t\right)=\frac{E}{\pi b^2}\left(1-R\left(T_e\right)\right)\alpha_{\mathrm{abs}}\exp\left(-\alpha_{\mathrm{abs}}z\right)\exp\left(-\frac{r^2}{b^2}\right)\frac{1}{\tau}\sqrt{\frac{\sigma}{\pi}}\exp\left(-\sigma\frac{\left(t-t_0\right)^2}{\tau^2}\right)\tag{2.3}$$

where ϕ is the average incident fluence, E is the energy per pulse, τ is pulse duration, and R is the reflectivity function that can depend on the level of excitation via the electronic temperature. α_{abs} is the linear absorption coefficient; $b = W_0/2$ is the half of beam waist, $\sigma = 4\ln 2$; and the pulse is centered at $t_0 = 2.5\tau$. When dealing with long pulses, however, when the density of solid can change during the pulse, the solution of differential equation with respect to intensity attenuation can be required:

$$\frac{dI\left(z,t\right)}{dz}=-\alpha_{\mathrm{abs}}I\left(z,t\right)\tag{2.4}$$

and the ballistic energy transport, if any, can be added to the effective absorption depth $\alpha_{\mathrm{abs}} = 1/(\lambda_0 + \lambda_{\mathrm{ball}})$.

On the other hand, the MD method can be formulated as simple as

$$m_i\overrightarrow{a}_i=\overrightarrow{F}_i=-\nabla U\left(\overrightarrow{r}_1,\overrightarrow{r}_{2,}\ldots\overrightarrow{r}_N\right)\tag{2.5}$$

for a system of N particles, the interatomic forces between which are determined from the gradient of the interatomic potential function $U(\mathbf{r}_1,\mathbf{r}_2,\mathbf{r}_3,\ \ldots,\mathbf{r}_N)$. This function can include a variety of terms, describing different type of interactions, and devoted to reproduce the crystal structure and the properties of the material at the equilibrium. Thus it can be given by Lennard-Jones potential for simple molecular solids (Ar, Kr) [67] or Stillinger-Weber potential for description of the opened diamond crystal structures (Si, Ge) [68], embedded atom method (EAM) to address metallic type of bonding (Au, Ni, Al) [69], or a mixture of different terms for Van der Waals, Born Mayer, and Coulomb interactions for a complex systems like ionic type of crystal or metallic glasses [70–72].

In the combined TTM-MD method [73], schematically illustrated in Fig. 2.1, MD substitutes the TTM equation for the lattice temperature. The diffusion equation for the electron temperature, T_e, is solved by a finite difference method simultaneously with MD integration of the equations of motion for atoms. The electron temperature enters a coupling term that is added to the MD equations of motion to account for the energy exchange between the electrons and the lattice via the additional friction term:

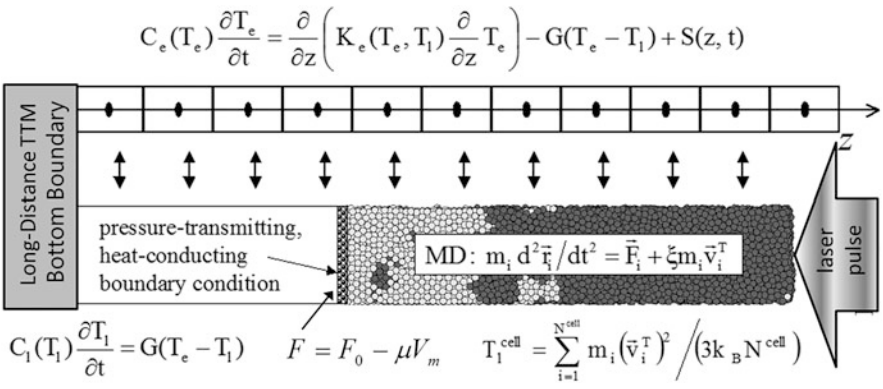
$C_e(T_e)\frac{\partial T_e}{\partial t} = \frac{\partial}{\partial z}\left(K_e(T_e, T_l)\frac{\partial}{\partial z}T_e\right) - G(T_e - T_l) + S(z, t)$
Long-Distance TTM Bottom Boundary
Z
pressure-transmitting, heat-conducting boundary condition
MD: $m_i\, d^2\vec{r}_i/dt^2 = \vec{F}_i + \xi m_i \vec{v}_i^T$
laser pulse
$C_l(T_l)\frac{\partial T_l}{\partial t} = G(T_e - T_l)$
$F = F_0 - \mu V_m$
$T_l^{cell} = \sum_{i=1}^{N^{cell}} m_i\left(\vec{v}_i^T\right)^2 / \left(3k_B N^{cell}\right)$

Fig. 2.1 Schematic representation of the combined continuum-atomistic model for simulation of laser interaction with a metal target. The evolution of electron temperature is described by a nonlinear differential equation, whereas the atomic motions are described by the MD method with an additional term, $\xi m_i \vec{v}_i^{\,T}$, added to the ordinary MD equations of motion to account for the electron-phonon coupling. The pressure-transmitting boundary additional force $F = F_0 - \mu V_m$ is added for each of the boundary monolayer m, where μ is impedance coefficient [74]. Spatial discretization in the continuum model (typically ~1 nm) and size of the atomistic region are not drawn to scale. The cells in the finite difference discretization are related to the corresponding volumes of the MD system, and the local lattice temperature, T_l^{cell}, is defined for each cell from the average kinetic energy of thermal motion of atoms. Thermal velocity of an atom is defined as $\vec{v}_i^{\,T} = \vec{v}_i - \vec{v}^{\,c}$, where $\vec{v}_i$ is the actual velocity of an atom i and $\vec{v}^{\,c}$ is the velocity of the center of mass of a cell to which atom i belongs. A Gaussian temporal profile, $S(z,t)$, is used to describe the laser excitation of the conduction band electrons. The expansion, density variations, and, at higher fluences, disintegration of the irradiated target predicted in the MD part of the model are accounted for in the continuum part of the model. A complete description of the combined TTM-MD model is given in [73]

$$m_i \frac{d^2\vec{r}_i}{dt^2} = -\operatorname{grad} U(\mathbf{r}_1, \mathbf{r}_2, \mathbf{r}_3 \ldots, \mathbf{r}_N) + \xi m_i \frac{d\vec{r}_i^{\,T}}{dt} \tag{2.6}$$

and the coefficient ξ given by the energy conservation law:

$$\xi = \mathrm{G}V_\mathrm{N}\,(T_e - T_l) / \sum_i m_i \left(\vec{v}_i^{\,T}\right)^2 \tag{2.7}$$

In this formulation we distinguish between the thermal velocities of the atoms, $\mathbf{V_i}^\mathbf{T}$, and the velocities of their collective motion. Cells in the finite difference discretization are related to the corresponding volumes in the MD system. The lattice temperature and coefficient ξ are defined for each cell of a volume V_N, and the summation in Eq. (2.7) is performed over all the atoms in a given cell. The expansion and, at higher fluences, disintegration of the irradiated target predicted in the MD part of simulation are accounted for in the continuum part of the model. The time steps in the two parts of the combined model are chosen so that one MD time step would correspond to an integer number of time steps of finite difference integration of the TTM equation for the electronic temperature, $\Delta t_{\mathrm{MD}} = n\Delta t_{\mathrm{FD}}$. In each finite difference discretization cell, the energy transferred between the electrons and the lattice due to the electron-phonon coupling is accumulated for n steps of integration and then transferred to the corresponding part of the MD system by means of the coupling term.

The MD method is used only in the very surface region of the target, where active processes of laser melting and ablation are taking place, whereas the diffusion equation for the electron temperature is solved in a much wider region affected by the thermal conduction. A special pressure-transmitting boundary condition [74] is used to imitate the propagation of the laser-induced pressure wave from the MD region of the computational cell to the continuum part of the model. The energy carried away by the wave is monitored, allowing for control of the energy conservation in the combined model. Periodic boundary conditions are imposed in the directions parallel to the surface. These conditions simulate the situation in which the laser spot diameter is large compared to the depth of the laser energy deposition, so that the effects of the edges of the laser beam can be neglected. In the part of the computational cell beyond the MD region (left part in Fig. 2.1), the energy exchange between the electrons and the lattice is described by a conventional TTM, in which the phonon contribution to the heat conduction is neglected. The temperature dependence of the lattice heat capacity, $C_l(T_l)$, obtained for the model material is approximated by a polynomial function and used in the TTM equation for the lattice temperature.

The hybrid atomistic-continuum model, briefly described above, combines the advantages of TTM and MD methods. TTM provides an adequate description of the laser energy deposition into the electronic system, energy exchange between the electrons and phonons, and fast electron heat conduction in metals, whereas the MD method is addressing the kinetics of fast nonequilibrium phase transitions with atomic resolution. Thus the model, described above, was successfully applied to study short pulse laser melting [73, 75], processes of spallation and ablation of metal targets [76, 77], and short laser pulse nanostructuring of materials on the experimental scale [78] described in the next section.

2.2 Combined MD-nTTM Model for Semiconductors

With an appropriate modification of MD-TTM, Fig. 2.1, a similar model can be composed for the investigation of short laser pulse interaction with semiconductors and insulators. In particular for semiconductors, as it was proposed in [79, 80], the continuum part of the combined model for the description of laser-generated free carriers dynamics (the electron-hole pairs with density N_e) via their common temperature value T_e can be formulated as follows:

$$\left\{\begin{array}{l} \frac{dI(z,t)}{dz} = -\left(\alpha + \alpha_{FCA}\left(\varepsilon\left(N_e\right)\right)\right) I\left(z,t\right) - \beta I^2\left(z,t\right) \\ \frac{\partial N_e}{\partial t} = \frac{\alpha I(z,t)}{h\nu} + \frac{\beta I^2(z,t)}{2h\nu} + \delta N_e - \gamma N_e^3 - \nabla \cdot \overrightarrow{J}\left(N_e, T_e, E_g\right) \\ \frac{\partial U_e\left(N_e T_e, E_g\right)}{\partial t} = \left(\alpha + \alpha_{\mathrm{FCA}}\left(\varepsilon\left(N_e\right)\right)\right) I\left(z,t\right) + \beta I^2\left(z,t\right) \\ - \nabla \cdot \overrightarrow{W}\left(N_e, T_e, E_g\right) - \frac{C_{e-h}\left(N_e, T_e, E_g\right)}{\tau_e}\left(T_e - T_l\right) \\ C_l \frac{\partial T_l}{\partial t} = \overrightarrow{\nabla} \cdot \left(\kappa \overrightarrow{\nabla} T_l\right) + \frac{C_{e-h}\left(N_e, T_e, E_g\right)}{\tau_e}\left(T_e - T_l\right) \rightarrow\rightarrow m_i \frac{d\overrightarrow{r}_i}{dt^2} \\ = - \sum\limits_{j=1,N} \overrightarrow{\nabla} U\left(\overrightarrow{r}_{ij}, T_e\right) + \xi m_i \overrightarrow{V}_i^T \end{array}\right. \tag{2.8}$$

where α, β, δ, and γ are coefficients corresponding to 1- and 2-photon absorption, impact ionization, and Auger recombination due to the irradiation of the intensity I and α_{FCA} is free carrier absorption coefficient. The systems of free carriers (electron-hole pairs) and phonons interact via the carrier-phonon coupling defined here as a ratio of free carrier's heat capacity $C_{e\text{-}h}$ and the carrier-phonon energy relaxation time τ_e. Noteworthy, the energy flux W in Eq. (2.8) includes both the carrier's flux J with the diffusion coefficient D as follows and heat diffusion defined via the conductivities of both electrons and holes as k_e and k_h:

$$\left\{\begin{array}{l} \overrightarrow{W} = \left\{E_g + 2k_B T_e\left[H_0^1\left(\eta_e\right) + H_0^1\left(\eta_h\right)\right]\right\} \overrightarrow{J} - \left(k_e + k_h\right)\nabla T_e \\ \overrightarrow{J} = -D\left\{\nabla n + \frac{N_e}{k_B T_e}\left[H_{-\frac{1}{2}}^{\frac{1}{2}}\left(\eta_e\right) + H_{-\frac{1}{2}}^{\frac{1}{2}}\left(\eta_h\right)\right]^{-1}\nabla E_g + \frac{N_e}{T_e}\left[2\frac{H_0^1(\eta_e)+H_0^1(\eta_h)}{H_{-\frac{1}{2}}^{\frac{1}{2}}(\eta_e)+H_{-\frac{1}{2}}^{\frac{1}{2}}(\eta_h)} - \frac{3}{2}\right]\nabla T_e\right\} \\ D = \frac{k_b T_e}{q_e}\frac{\mu_e \mu_h H_{\frac{1}{2}}^0\left(\eta_e\right) H_{\frac{1}{2}}^0\left(\eta_h\right)}{\mu_e H_{\frac{1}{2}}^0\left(\eta_e\right)+\mu_h H_{\frac{1}{2}}^0\left(\eta_h\right)}\left[H_{-\frac{1}{2}}^{\frac{1}{2}}\left(\eta_e\right) + H_{-\frac{1}{2}}^{\frac{1}{2}}\left(\eta_h\right)\right] \end{array}\right. \tag{2.9}$$

where μ_e and μ_h are mobilities of electrons and holes correspondingly, $H_j^i(\eta_c) = F^i(\eta_c)/F^j(\eta_c)$, and $F^j(\eta_c)$ is Fermi-Dirac integrals of order "I" of the carriers with the reduced chemical potential $\eta_e = (E_F - E_c)/kT_e$ and $\eta_h = (E_V - E_F)/kT_e$ of the corresponding electrons and holes with respect to their quasi Fermi level to the levels of conduction or valence bands. Finally, the total energy of free carriers U_e consists of both the kinetic and potential energies, which comprises the energy gap E_g (that can vary in general) as well [79]:

$$U_e = N_e E_g\left(N_e, T_e\right) + \frac{3}{2} N_e k_b T_e\left[H_{1/2}^{3/2}\left(\eta_e\right) + H_{1/2}^{3/2}\left(\eta_h\right)\right] \tag{2.10}$$

while the description of a number of parameters, entering the continuum part of the combined model, can vary and justifies either by experimental measurements [79] or theoretical calculations [81, 82]; the strategy of developing the combined model for semiconductor in the example with Si remains the same; we replace the last equation for lattice temperature with MD integrations as prescribed by Eq. (2.6), and the interatomic potential U can be used in classical Stillinger-Weber parametrization [68] or electronic temperature (and possible the electronic density)-

dependent potentials, described below. Because of the additional equation for the carrier's density, we refer to this combined method as MD-nTTM [83], and its successful application for investigation of ultrashort laser pulse melting of free standing Si films is given in the next section. Finally, it is worth mentioning that unlike a similar model for Si published in Ref. [84], where nondegenerate model based on the Boltzmann distribution of the electron-hole pairs was assumed (indicating negligible excitation), the complete description of the laser-generated free carriers dynamics via Fermi-Dirac functions was applied in [83], resulted in the applicability of the MD-nTTM model discussed here for investigation of laser melting of Si.

2.3 Combined MD-nTTM Model for Dielectric Materials

In the case of dielectric materials, although more complicated, the atomistic-continuum method on the example with SiO_2 (both crystabalite and fused silica materials) was developed and can be represented by Eq. (2.11):

$$\begin{cases} \frac{\partial I(z,t)}{\partial z} = -\sigma_6 I^6(z,t)\left(1 - \frac{N_e}{N_v - N_{tr}}\right)6h\nu - \alpha_{\text{FCA}}(\varepsilon(N_e))\, I(z,t) \\ \frac{\partial N_e}{\partial t} = \left(\sigma_6 I^6(z,t) + Q_{av}\right)\left(1 - \frac{N_e}{N_v - N_{tr}}\right) - \frac{N_e}{\tau_{tr}} - \upsilon_{\text{Auger}}(N_e) - \overrightarrow{\nabla}\cdot\overrightarrow{J} \\ \frac{\partial N_{tr}}{\partial t} = \frac{N_e}{\tau_{tr}} \\ \frac{\partial U_e}{\partial t} = \sigma_6 I^6(z,t)\left(1 - \frac{N_e}{N_v - N_{tr}}\right)6h\nu + \alpha_{\text{FCA}}(\varepsilon(N_e))\, I(z,t) \\ -\overrightarrow{\nabla}\cdot\overrightarrow{W} - \frac{C_{e-h}}{\tau_{\text{rel}}}(T_e - T_l) - Q_{tr} \\ C_l(T_l)\frac{\partial T_l}{\partial t} = \overrightarrow{\nabla} K_l \cdot \overrightarrow{\nabla} T_l + \frac{C_{e-h}}{\tau_{rel}}(T_e - T_l) + Q_{tr}^{*} \rightarrow\rightarrow m_i \frac{d\overrightarrow{r}_i}{dt^2} \\ = -\sum\limits_{j=1,N} \overrightarrow{\nabla} U\left(\overrightarrow{r}_{ij}, T_e\right) + \xi m_i \overrightarrow{V}_i^{T} \end{cases} \tag{2.11}$$

where the first equation in Eq. (2.11) is written for the intensity I attenuation of the laser pulse in the wide gap solid (~9 eV for SiO_2) that under the utilization of 775 nm laser wavelength laser irradiation assumes six-photon absorption and accounts for the dynamically changing values of valence band electrons N_v and trapped carriers N_{tr}. The second term describes free carrier absorption process, characterized by the changing free carrier absorption coefficient α_{FCA} depending on the current value of dielectric function ε. The free carriers' density N_e in the second equation is changing due to six-photon absorption, avalanche ionization process Q_{av}, trapping process, which has a characteristic time τ_{tr}, Auger recombination process described via function υ_{Auger}*(n_e)* (third term), and carrier's flux J due to free carriers' diffusion (last term). The density of trapped carriers n_{tr} is characterized by the trapping time τ_{tr} and is given by the third equation. The total energy conservation of the system is balanced here between the contribution due to electron-hole free carriers with temperature T_e and phonons with temperature T_l (fourth and fifth equations correspondingly). The free carrier flux J and energy density flux W can be calculated as it is given by Eq. (2.9). Note the energy associated with the trapping process Q_{tr}, which leaves the electronic subsystem, is accounted for in the phonon subsystem via its thermal part $Q_{tr}{}^{*}$ only, whereas the rest of it enters the atomistic description of the solid via the MD part as the excess of the potential energy due to added stresses.

While a number of parameters entering the system of Eq. (2.11) (such as Q_{tr} the heat dissipated through the trapping process) were studied by different experimental and theoretical groups**,** they can vary in analytical description depending on the investigated physics [85]. At the relatively high fluences, used in NP production due to PLAL, however, the issue regarding impact ionization process becomes more crucial. Being responsible for the development of laser-induced strong electrostatic forces and subsequent material ejection via the Coulomb explosion mechanism [46, 86], the accurate description of the ionization process yet remains uncertain. Nevertheless, while investigations including the relevant nonequilibrium electron kinetics have been done [87–91], the focused works [81, 92, 93] give promising description of the transient optical properties, nonequilibrium electron-hole carriers dynamics, and nonthermal electron-phonon coupling.

As a strategy, in the combined MD-nTTM method, the last equation of the above system (2.11) is substituted with MD integrations, where the interatomic potential can be given by the Beest, Kramer, and Santen (BKS) potential for SiO_2 [70, 94]. As an alternative to BKS potential, the modified BKS [71] or under certain conditions Tsuneyuki, Tsukada, Aoki, and Matsui (TTAM) potential [95], focusing on the reproduction of specific material properties can be applied. For fused silica material, the properties of amorphous structures can play a significant role [96]. For instance, under extreme conditions of Coulomb explosion, realized in the solid upon short pulse laser energy deposition, the initial structure of solid can affect the onset of blast expansion process. Therefore, the parametrization suggested by Carre, Horbach, Ispas, and Kob (CHIK potential) [72] could be preferable while its analytical form remains as it is of modified BKS potential, given by Eq. (2.12):

$$U\left(r_{ij}\right)=\frac{1}{4\pi\varepsilon_0}\frac{q_iq_j}{r_{ij}}+a_{ij}\exp\left(-b_{ij}r_{ij}\right)-\frac{c_{ij}}{r_{ij}^6}+f_0 4\varepsilon_{ij}\left[\left(\frac{\sigma_{ij}}{r_{ij}}\right)^{30}-\left(\frac{\sigma_{ij}}{r_{ij}}\right)^{6}\right] \tag{2.12}$$

where ε_0 is the vacuum permittivity constant and $\boldsymbol{r_{ij}}=\boldsymbol{r_j}$ - $\boldsymbol{r_i}$ is the interatomic distance between ions j and i with corresponding charges q_j and q_i and positions in space, characterized by vectors $\boldsymbol{r_j}$ and $\boldsymbol{r_i}$. The first term in Eq. (2.12) handles the long-ranged Coulomb interactions taking place in ionic crystals. The second term corresponds to the Born-Mayer repulsion on close distances. The third term describes the Van der Waals attraction between the ions, and the fourth term modifies the interatomic potential to exclude the unphysical attraction between the atoms when the distance r_{ij} becomes too small. The parameters of the potential a_{ij},

b_{ij}, c_{ij}, f_0, ε_{ij}, and ε_{ij} for O-O, Si-Si, and Si-O interactions we take as they are given for modified BKS potential and listed in Ref. [71].

2.4 Optimization of the MD-nTTM Model Performance

As an inherent limitation of the MD-nTTM methods' applicability, given by Eqs. (2.8) and (2.11), we can point out an extremely shallow, 10^{-21} s, time step (for spatial discretization of ~2–4 nm) of the continuum part of the model as compared to that in the case of metals. Namely, the negligible number of free carriers in the conduction band at the beginning of the pulse (which can be few ps in duration) limits a reliable determination of the diffusion coefficient, given by the ratio of conductivity function over the heat capacity of free carriers. Since in the beginning of the pulse both of quantities are close to zero, the uncertainty of their numerically defined ration hardly impacts the stability of the explicit numerical schemes. This problem was resolved my means of implementation semi-implicit Crank-Nicolson numerical approach, which allowed us to raise the time step up to 10^{-15} s during the solution of nTTM system, given by Eqs. (2.8) and (2.11) [97].

Also, the important point in utilization of any of the reasonable interatomic potentials for fused silica concerns the summation of long-range forces originating from Coulomb interactions [98]. As a result, a frequently used BKS potential for the MD description of SiO_2 and fused silica (which are primary targets of the proposed research) in the ground state contains a slowly decaying *1/r* term, where *r* is the interatomic distance. The applications of ordinary algorithms in this case lead to a number of operations scaling as $\sim N_{at}^2$ during the numerical processing, where N_{at} is the number of particles (atoms) in the analyzed system. This used to limit the size of systems under study and merely excluded the applicability of MD-based approaches for NP generation problems due to PLAL, where processing of large systems is necessary. This milestone, however, was successfully overcome by means of combination of few modifications. First, the Ewald method of summation of long-range interactions was utilized [99], which allowed to increase the efficiency of calculations up to that scaling as $N_{at}\mathrm{Log}(N_{at})$. Namely, the method can be significantly improved with a correct choice of σ parameter in the expression of the Coulomb total energy term:

$$
\begin{aligned}
U^{\Sigma} &= \sum_{i\neq j} \frac{q_i q_j}{r_{ij}}, \text{ where} \frac{1}{r} = \frac{f(r)}{r} + \frac{1-f(r)}{r}, \text{ and} f(r) = erfc(\sigma r) \\
&= 1 - erf(\sigma r) = 1 - \frac{2}{\pi} \iint_0^{\sigma k} \ell^{-s^2} ds \qquad (2.13)
\end{aligned}
$$

and the total energy is given by

$$
U^{\Sigma} = U^{\mathrm{real}} + U^{\mathrm{recip}} + U^{\mathrm{self}} + U^{bc} \qquad (2.14)
$$

So the total energy U^{Σ} consists of the U^{real} input due to *f(r)/r* term in Eq. 2.13, converging in real space; the U^{recip} input due to *(1-f(r))/r* term in Eq. 2.13; the self-interacting term U^{self} (for the reciprocal vector $k = 0$); and the free boundary input U^{bc} (if they are) accounting for the dipole interaction (from here, the thicker the film, the smaller the corresponding input U^{bc}). Importantly, while the value of U^{Σ} is independent on the choice of σ in Eq. (2.13), it was found that at $\sigma = 0.2$ both the real and reciprocal sums in Eq. (2.14) converge fast, and the latter has a negligible value as compared to its real contribution. This enables us to completely discard the reciprocal sum and to introduce a cutoff radius of ~11 A in the neighbor search procedure, reducing therefore the number of operations to scaling as ~N_{at} for processing the whole system.

2.5 MD-nTTM-CG Model for Materials

Furthermore, to make it even faster, this algorithm was successfully and combined with the quasi-coarse-grain dynamics (QCGD) method [100]. In particular, it allows to combine the atoms in relatively slow evolving parts of the irradiated material into larger clusters by means of grouping the initial lattice units in each directions with lattice-fold times $L_{CG} = 1, 2, 4, 8, \ldots$ Thus, the coarse graining level 2 (2 × 2 × 2 unit cells replaced by 1 coarse cell) represent 8 atoms with a single particle, level 4 (4 × 4 × 4 unit cells replaced by 1 coarse cell) represent 64 atoms with a single particle, and level 8 (8 × 8 × 8 unit cells replaced by 1 coarse cell) represent 512 atoms with a single particle. This increases the efficiency of calculations of the atomistic part of the combined MD-nTTM model on the one hand and increases the time step of the continuum part of the model (in order to keep the same particle density per 3D mesh cell) on the other hand. Finally, it was shown in Ref. [100] that the coarse graining up to level 4 is efficient and still accurate enough for considering the macroscopic evolution of the irradiated solid. However, the corresponding drop in resolution must be justified by the scale of the ongoing laser-induced processes. The procedure for deriving the corresponding scaling factors for transferring normal MD units and functions (energy, forces due to pair and EAM interactions and the electron density ρ) to their coarse grain (CG) representation for the case of embedded atom method (EAM) [69] can be described as follows [22]:

$$E_i = U_{\text{EAM}}\left(\sum_{i\neq j}\rho\left(r_{ij}\right)\right) + \frac{1}{2}\sum_{i\neq j}V_{\text{pair}}\left(r_{ij}\right) \tag{2.15}$$

The energy E_i of each atom $\underline{i}$ is given by Eq. (2.15) since EAM potential has inputs due to many-body term (first) and pair interaction (second term). Then, for representation of the coarse graining of level L_{CG}, the following procedure can be useful:

(a) The unit lattice cell a_{lat} and all the atomic positions $\overrightarrow{r}$ are scaled by L_{CG} in order to get $a_{\mathrm{lat}}^{\sim}$ and $\overrightarrow{r}^{\sim}$ in CG:
$a_{\mathrm{lat}}^{\sim} = L_{CG} a_{\mathrm{lat}}$ and $\overrightarrow{r}^{\sim} = L_{CG} \overrightarrow{r}$ and the corresponding atomic masses $m^{\sim} = L_{CG}^{3} m$

(b) $a_{\mathrm{uct-off}}^{\sim} = L_{CG} a_{\mathrm{cut-off}}$ and $r_{\mathrm{tab}}^{\sim} = L_{CG} r_{\mathrm{tab}}$ are the points in the potential table, if it is used by the code.

(c) $\rho_{\mathrm{uct-off}}^{\sim} = L_{CG}^{3} \rho_{\mathrm{cut-odd}}$ and $\rho_{\mathrm{tab}}^{\sim} = L_{CG}^{3} \rho_{\mathrm{tab}}$ are the points in the density table, if used by the code.

(d) $V_{\mathrm{pair}}^{\sim}\left(r^{\sim}\right) = L_{CG}^{3} V_{\mathrm{pair}}(r)$

(e) $F_{\mathrm{pair}}^{\sim}\left(r^{\sim}\right) = \frac{d\left(V_{\mathrm{pair}}^{\sim}(r^{\sim})\right)}{dr^{\sim}} = \frac{d\left(L_{CG}{}^{3} V_{\mathrm{pair}}(r)\right)}{d(L_{CG} r)} = L_{CG}^{2} \frac{d\left(V_{\mathrm{pair}}(r)\right)}{d(r)} = L_{CG}^{2} F_{\mathrm{pair}}(r)$

(f) $\rho^{\sim}\left(r^{\sim}\right) = L_{CG}^{3} \rho(r)$

(g) $D\rho^{\sim}\left(r^{\sim}\right) = \frac{d(\rho^{\sim}(r^{\sim}))}{d(r^{\sim})} = \frac{d\left(L_{CG}^{3} \rho(r)\right)}{d(L_{CG} r)} = L_{CG}^{2} \frac{d(\rho(r))}{d(r)} = L_{CG}^{2} D\rho(r)$ for derivative of the function $\rho(r)$

(h) $U_{\mathrm{EAM}}^{\sim}\left(\rho^{\sim}\left(r^{\sim}\right)\right) = L_{CG}^{3} U_{\mathrm{EAM}}\left(\rho(r)\right)$

(i) $F_{\mathrm{EAM}}^{\sim}\left(\rho^{\sim}\left(r^{\sim}\right)\right) = \frac{d\left(U_{\mathrm{EAM}}^{\sim}(\rho^{\sim}(r^{\sim}))\right)}{d(\rho^{\sim}(r^{\sim}))} = \frac{d\left(L_{CG}^{3} U_{\mathrm{EAM}}(\rho(r))\right)}{d\left(L_{CG}^{3} \rho(r)\right)} = \frac{d(U_{\mathrm{EAM}}(\rho(r)))}{d(\rho(r))} = F_{\mathrm{EAM}}\left(\rho(r)\right)$

Then, we solve normally the equation of motion with respect to **r~** and ρ~(r~). The connection between volumes of different L_{CG} levels and their implementation in an adaptive mode (adaptive CG volumes reorganization) is another way of improving the efficiency of processing of large systems but goes beyond the scope of this chapter. But the application of modified Ewald method, QCGD approach, and Crank-Nicolson schemes in the presented form already increases the efficiency of calculations with the number of operation scaling as ~N_{at} (number of atoms in the system) that enables the modeling of laser-induced modification of materials surfaces on the experimental dimensions.

2.6 MD-nTTM-U(T_e) Model for Materials

Finally, the description of nonthermal effects occurring upon the laser excitation of materials in a high fluence regime, as well as amorphization processes, can have a strong impact on the melting, ablation, and crystallization dynamics, especially in the case of semiconductors and dielectrics. Thus, the utilization of interatomic potentials U that accounts for ultrafast interatomic-bonding changes becomes necessary. Commonly used interatomic potentials like Stillinger-Weber [68] or Tersoff [101] for Si or modified BKS for SiO_2 [71] or CHIK potential [72] for fused silica cannot reproduce those effects since the applied potentials are only functions of the interatomic distances and have no information about the presence of hot carriers. Consequently, the applications of classical MD method, even reinforced with a number of additional physical implementations like nTTM add-ons, still yield the results considerably deviating from the experimental measurements. In particular, neglecting the nonthermal effects may result in overestimation of the melting and ablation thresholds, which makes the abovementioned potentials suitable for the case of moderate laser excitations (below the melting threshold) [102].

However, there have been recent attempts to account for the interatomic potential changes depending on the photoexcited carrier properties, taking into account the bond weakening under ultrashort laser pulse irradiation of Si [103]. Although possessing low accuracy, the potential derived in Ref. [103] is an example of the inclusion of band structure information into the classical MD approach. Some discussions about the necessary conditions to be fulfilled by such a potential in order to achieve a better accuracy have been recently reported in Ref. [104]. Aiming on elaboration of the potentials capable of describing bond weakening (hardening) processes in materials due to ultrashort laser pulse excitation, potentials fit to ab-initio MD simulations based on density functional theory (DFT) have been recently developed [105, 106]. In particular, the potentials $U(T_e)$ for Si [107] is ready for utilization and can be successfully applied in MD-nTTM calculation, where the interatomic forces, along with pair and angular dependences, are functions of the free carrier's temperature. Moreover, the recent works also resulted in the development of machine learning potentials, mostly based on feed-forward artificial neural networks [108]. The latter are extensions of the so-called high-dimensional neural network interatomic potentials [109]. The ab-initio simulations in turn can also be used for the analysis of new optical properties of the functionalized surfaces [110].

2.7 Large-Scale Applications of MD-Based Models

For a number of nanostructuring and material surface functionalization experiments, the size of laser spot becomes comparable or even smaller than the characteristic size of the modelled feature. In this case, an ordinary computational cell, limited in lateral sizes and elongated in depth (for laser energy deposition) with 1D heat conduction and carrier's diffusion model (given by Eqs. 2.1, 2.8, and 2.11), is no longer valid. Instead, to accommodate the concurrent laser-induced processes across the materials' surface and in the bulk, the computational box of lateral size large enough and the full 3D model for the heat conduction and carrier's diffusion must be applied. As a result, the number of atoms for processing in such simulations can be a few hundreds of millions and more, which makes it difficult or even impossible to process with utilization of a single processor core. Hence, the abovementioned models must be implemented in multiprocessing mode with the utilization of message passing interface (MPI) library, for instance [111].

Also, the correct choice of the computational cell geometry has a significant impact on both the accuracy of the investigated physics representation and the efficiency of calculations. Frequently, the experimental symmetries can be utilized so that the scale of the experimental measurements can be represented during the

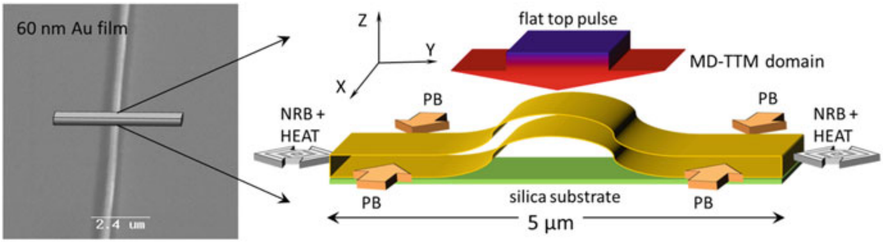

Fig. 2.2 Nanobarrier generated on the surface of a 60 nm Au film with a 30 fs flattop pulse in the experiment (left) [112] and schematic representation of the computational cell used in large-scale modeling of this process on the experimental dimensions (right). (Reprinted with permission from [113], © Springer-Verlag Berlin Heidelberg)

simulations in one or more directions. The latter allows for the direct comparison of the modeling results with the experimental measurements. Thus, in the experiments on nanobarrier-like structure generation on 60 nm gold film with 30 fs laser pulse [112], the computational cell for simulations on experimental scale can be seen in Fig. 2.2 [113]. In order to simulate the process of nanostructuring, Fig. 2.2 (left), the rectangular shape of computational cell was chosen perpendicular to the barrier-like structure. Because no temperature or pressure gradients are expected in the direction parallel to the structure, it allows to impose the periodic boundary conditions (PBC) in X, providing that the cell size in X (40 nm) is still large enough to accommodate possible formation of voids inside the bulk of materials (<20 nm), Fig. 2.2 (right). The lateral cell size in Y direction (perpendicular to the barrier structure) must be large enough to fit the laser sport (800 nm width), providing that the laser-induced elastoplastic deformations of the irradiated target in this direction will fit the computational cell as well. At the distances, where neither phase transitions nor film deformations are expected (~2.5 µm), we can set the dynamically behaving nonreflecting boundary conditions (NRB) [74] that absorb the laser-induced pressure waves, propagating outward the generated structure. Meanwhile the NRB are transparent for the heat flux, providing the cooling mechanism for the growing structure on the distance up to 50 µm. Finally, the 60 nm film is situated on imaginary silica substrate with which it weakly interacts via Lennard-Jones potential [67], in accordance with the experimental measurements on film-silica adhesion. Thus, the total computational cell in Fig. 2.2 suits the requirements on the identical comparison of the simulation results with the experiment data and can be applied in the simulation of nanostructuring phenomena in a multiprocessing regime, schematically represented in Fig. 2.3.

The whole system is divided to the equal volumes treated by N_x and N_y processor cores in X and Y direction correspondingly. The choice of a single processor core in Z direction is dictated by a more efficient use of the CPU-HOURS. Namely, the intense motion of the ablating products in upward direction will still keep processor cores equally loaded in most of the cases. In each processor core, 3D mesh is applied with the linked cell algorithm [111] for an efficient processing in

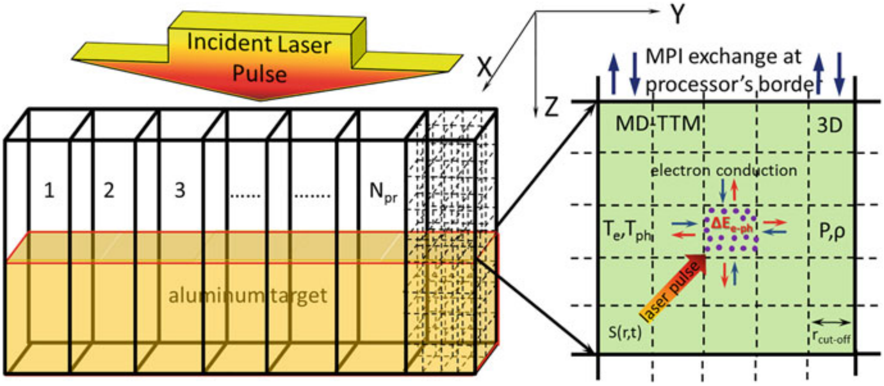

Fig. 2.3 The computational box for simulations of laser-induced materials restructuring (on the example with Al) during the laser ablation process. The box is divided to the number of subcells N_x and N_y in X and Y directions correspondingly to be processed by N_x*N_y processor cores (left). Each separate core is divided to 3D mesh and shown in 2D view (right). The corresponding MD or combined models (MD-TTM, MD-nTTM, MD-nTTM-CG) are solved for each of the mesh cell inside of each processor core, communicating between each other via MPI

parallel calculations. The 3D mesh in each processor core is generated based in the minimal cutoff distance (~0.5 nm), $r_{cut-off}$, of the potentials involved into the calculations. However, for the case of the combined methods (like MD-TTM [73, 78]), the size of mesh can be a bit large (~ 1 nm). The choice of the mesh size is justified on the one hand by its minimization for the efficient neighbor list search and calculations of forces in the MD part. On the other hand, the cell must be big enough to accommodate a group of atoms large enough (~100 atoms) to introduce their statistical description (under assumption of quasi-equilibrium) for a reliable determination of their macroscopic quantities. Furthermore, due to still limited number of particles per cell, the resulting MD noise of macroscopic properties definition can significantly impair the stability of the continuum algorithms in the combined methods. Thus, the thermophysical properties of the atomic subsystem (such as temperature and pressure) are averaged over the closest 26 neighboring cells (that totally accounts for ~2500 atoms) to suppress their value fluctuations, Fig. 2.3.

Finally, in order to run large-scale simulations and be able to model the nanostructuring processes on the experimental scale, the multiprocessing approach must be computationally efficient. The efficiency of performing the calculations in multiprocessing regime, however, essentially depends on the parallelization algorithm implementing MPI. Traditionally, the MD-based models do not belong to the group of task readily undergone to the parallelization. In particular, due to containing sequential part of ordinary and straightforward algorithms, the amount of time spent by a single processor to perform an MD step can become comparable with the time it needs for communications caused by the necessity of the sequential part exchange between the processor cores. This situation leads to saturation of the speedup process with the amount of utilized cores and reflected in the so-called Amdahl's law [114], which strictly speaking relies on the fact of the sequential part presence only without consideration of the communication procedure. In former times this law resulted in an impossibility to achieve a speedup of more than 100 times even with an infinite number of used processors. Therefore, it is important to limit the necessity of the sequential part exchange between the processor cores for the MD-based algorithm. For instance, in the numerical schemes of the MD-TTM models for simulations of nanostructuring processes, Fig. 2.2, each processor core is aware of its closest 26 neighbors only (in 3D) that basically remove the speedup limitation until the spatial scale processed by each processor becomes comparable with the size of a single 3D mesh cell, limited by the cutoff distance $r_{\text{cut-off}}$ for the selected interatomic potential, Fig. 2.3. Thus, the effective reorganization of the most time-consuming subroutines like neighbor list search and communication procedure [111], the number of operations in our codes used for simulations of the nanostructuring processes in [113], and in the those discussed in the following sections of this chapter, scales currently as ~*N/2* (where *N* is a number of particles in the system). In order words, each processor core is only away of the atoms inside of its borders plus a single layer skin of link-cells around (without knowledge of what is happening further away). This makes the size of the modelled system only limited by the available computational resources. The example of speedup of MD-TTM benchmark calculations (in FORTRAN 95), performed on Lichtenberg supercomputer TU-Darmstadt, is shown in Fig. 2.4. For the system of 100,000,000 atoms, and for the case of both blocking and nonblocking interconnect, a slight deviation from the linear dependence is noticeable above 128 processor cores. The speedup for fewer processors can be considered as strictly linear. Thus, the utilization of 1024 cores in such calculations results in a roughly 600 times speedup.

3 Laser-Induced Damage of Solids

3.1 Melting: Heterogeneous and Homogenous

Although melting is a common and well-studied phenomenon, the nature of the structural instability of a superheated crystal and the microscopic mechanisms of melting are still subjects of active scientific discussions [39, 115–117]. Recent experimental investigations combining short pulse laser irradiation with optical, X-ray, and electron diffraction time-resolved probe techniques [33, 34, 41–43, 118] have a promise of providing new insights into the melting mechanisms and kinetics. The extremely high heating rates of 10^{14} K/s and even more can be achieved by short (pico- and femtosecond) pulse laser irradiation, opening unique opportunities for investigation of the kinetic limits of achievable superheating. While the time-resolved pump-probe experiments are providing valuable information on the time scales of the laser-induced melting, a reliable interpretation of the experimental

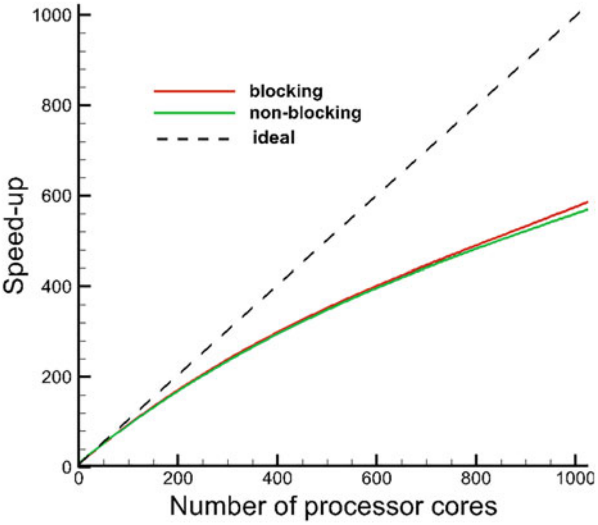

Fig. 2.4 The speedup of large-scale MD-TTM simulations, presented in this chapter, given by blocking and nonblocking interconnect on Lichtenberg supercomputer (TU-Darmstadt). The negligible difference between two regimes of the parallel runs indicates the efficiency of algorithm of communications due to MPI

observations requires a better understanding of the microscopic mechanisms of melting occurring under highly nonequilibrium conditions created in the target material by short pulse laser irradiation. Thus, in this section, we briefly report the results of MD investigation of both homogenous and heterogeneous mechanism of meting in particular under the conditions realized during short laser pulse interaction with metallic targets.

In the works reported in Ref. [119, 120], the combined MD-TTM method [73] was designed to study fast nonequilibrium phase transition processes. The objective was to investigate the applicability of the homogeneous nucleation theory [39, 121] at the strong degrees of overheating that can be achieved with short laser pulses with the MD-TTM model developed for metals [73]. The timescale of the homogeneous melting process t_M [39], the density of the liquid phase nuclei, and the evolution of the shapes of the liquid regions were investigated. Microscopic mechanism of the homogeneous melting was considered based on the results of several large-scale MD simulations performed for EAM Ni material at a high degree of superheating ($T \approx 1.2T_m$) [120]. The results of simulations revealed that the melting time predicted by the nucleation theory [39] and the one obtained from our MD simulation differ by at least four orders of the magnitude. Even though not all of the parameters in Ref. [39] can be reliably determined experimentally and even the value of melting time t_M is sensitive to the choice of the materials parameters, determined for the used EAM potential in Ref. [120], the difference in four orders of magnitude can be hardly eliminated by a simple variation of the parameters within physically reasonable limits. Therefore, the applicability of nucleation theory [39, 121] in the description of the homogeneous melting at high degrees of overheating attainable in short laser pulse nanostructuring experiments is questionable.

The mechanisms and kinetics of heterogeneous melting have been extensively studied both experimentally and theoretically, resulting in a well-established framework for semi-empirical description of the kinetics of the melting process [122–124]. Most of the investigations, however, have been focused on the regime of relatively low overheating of the liquid-crystal interface above the equilibrium melting temperature, when either the nonequilibrium kinetic description reduces to a linear relationship between the velocity of the melting front and overheating [123, 124] or the melting process is considered to be heat flow limited and the overheating is neglected altogether. The analysis of the kinetics of the melting process at strong overheating is challenging, and understanding of the kinetic limits of heterogeneous melting remains poor. In particular, in the absence of more reliable estimates, the speed of sound is often used as the limiting velocity of the melting front in interpretation of the results of short pulse laser melting experiments [118, 122], where the conditions for significant overheating can be readily achieved.

Therefore, in the series of large-scale MD-TTM simulations on EAM Ni material [119], the velocity of the melting front is measured for the conditions of a constant temperature enforced throughout the computational cell. In a real melting process, however, the energy supply to the melting region is not instantaneous but is defined by the electron thermal conductivity and electron-phonon coupling. In order to provide a realistic description of the energy supply to the melting front from the bulk of the overheated crystal (in the performed MD-TTM simulations) instead of enforcing a constant lattice temperature throughout the computational cell, a constant electron temperature at the back surface of the computational cell was maintained, while allowing both electron and lattice temperatures to evolve freely during the melting process. The results of the simulations revealed that the velocities of the heterogeneous melting front are significantly lower as compared to the ones measured in the constant lattice temperature series. The maximum velocity, measured at $1.2T_m$, is 140 m/s, less than 3% of the room temperature speed of sound in the EAM Ni crystal. Further the increase of the temperature results in a homogeneous nucleation of liquid regions inside the overheated crystal, ahead of the melting front.

The more complete analysis of the melting mechanism of free standing metallic films due to a short laser pulse irradiation is reported in [73] and compared here with that of free standing Si film under similar irradiation conditions [83], Fig. 2.5.

The application of the combined MD-TTM method revealed that in metal targets with fcc crystal, the rapidly increasing temperature results in the corresponding increase of pressure, which reinforces the crystal stability against homogeneous melting mechanism. In opposite, if the laser-induced stresses results in the generation of negative (tension) stresses inside the film, the crystal stability decrease facilitates the propagation of the solid-liquid interface during the heterogeneous melting process [75]. Alternatively, the atomistic-continuum approach MD-nTTM for silicon target was used in studying an ultrashort laser pulse melting process and

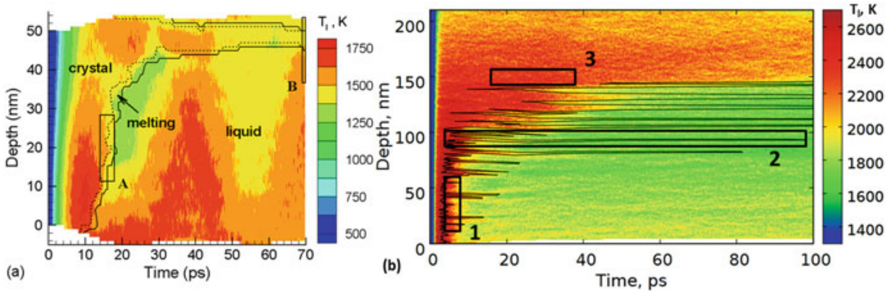

Fig. 2.5 (**a**) Contour plot of lattice temperature for simulation of laser melting of a 50 nm Ni film irradiated with a 200 fs laser pulse at an absorbed fluence of 430 J/m^2. Solid and dashed lines show the beginning and the end of the melting process. Rectangles A and B in (**a**) show the areas of homogeneous and heterogeneous melting mechanism, respectively. (**b**) Contour plots of lattice temperature, obtained from the simulation of 130 fs laser pulse focused on 2 μm Si film at the absorbed fluence 2000 J/m^2. The rectangles on plot (**b**) identify the location homogeneous (1), heterogeneous (2), and the area with rapid generation-collapse process of liquid nuclei (3). The black solid line shows the position of melting front, assuming 50% of the material is molten. For a closer look, we show the sample depth only up to 210 nm, where the phase transition processes take place. In both (**a**) and (**b**), the laser pulse is directed along the Y axes, from the bottom of the contour plots

revealed the kinetic of phase transition directly opposite to that found for metals [83]. In particular, the opened diamond crystal structure of Si tends to collapse under compression (originating from fast laser heating) and reinforces its stability under expansion (acoustic relaxation), Fig. 2.5b. This results in a deeper extension of the homogeneous melting (rectangle 1 in Fig. 2.5b) as compared to that in metals under similar irradiation conditions. Together with a long-lasting heterogeneous melting mechanism (rectangle 2 in Fig. 2.5b), the area of rapid generation-collapse process of the liquid nuclei is indicated (rectangle 3 in Fig. 2.5b). The laser-induced temperature-pressure interplay in Si results in the onset of melting process upon the increase of pressure, which at sufficiently high temperature destabilizes the crystal structure and a number of liquid nuclei is generated. The acoustic relaxation process, however, decreases the internal stresses and stabilizes the crystal structure resulting in a fast collapse of generated liquid nuclei. Given by performed MD-nTTM simulations, the detailed investigation of the kinetics of laser-induced melting in semiconductors on the example with Si is presented elsewhere [83].

In general, as it was clearly emphasized in the work by Zhigilei [77], at low laser fluences, the processes induced by the short pulse laser irradiation are limited to the melting of a surface region of the target followed by an epitaxial regrowth of the crystalline bulk of the target and complete resolidification on a timescale from hundreds of picoseconds to several nanoseconds. The kinetics of the melting process is defined by the relative contributions of the homogeneous and heterogeneous melting mechanisms. At laser fluences close to the threshold for surface melting, the fast homogeneous melting (nucleation and growth of multiple liquid regions within the overheated crystal) takes place during the first several tens of picoseconds and is immediately followed by the resolidification. At higher laser fluences, the melting proceeds in two stages, with the fast homogeneous melting followed by a slower heterogeneous melting (propagation of a well-defined liquid-crystal interface deeper into the target) that typically takes several hundreds of picoseconds. The transition to the two-stage melting process takes place when the melting front formed by the end of the homogeneous melting process is located deeper than the depth of a layer containing most of the energy deposited by the laser pulse. The heat conduction from the hot surface to the cold bulk of the target in this case results in an additional heating of the liquid-crystal interface, fueling its propagation deeper into the target.

3.2 Ablation and Spallation

Short pulse laser ablation is the phenomenon that is actively used in a broad range of applications, from surface micromachining [125] and pulsed laser deposition of thin films and coatings [126] to the design of laser plasma thrusters for small satellites [127]. The mechanisms responsible for the material removal in laser ablation include an intensive evaporation from the irradiated surface at low laser fluences and/or long pulse durations [128] an explosive decomposition of a surface region of the target into individual atoms/molecules and liquid droplets at higher fluences [129, 130], hydrodynamic sputtering [131] or expulsion of molten material due to the action of the evaporation/ablation recoil pressure [132], ejection of large droplets or fractured solid fragments caused by photomechanical effects [133–135], as well as nonthermal processes related to photochemical reactions [136] or laser-induced charging and Coulomb explosion of a surface layer of the target [137].

The explosive boiling or “phase explosion”, in particular, is commonly discussed as a primary mechanism of short pulse laser ablation of metal targets [129, 130, 138–140]. This mechanism of material ejection involves an explosive decomposition of a surface region of the target superheated beyond the limit of thermodynamic stability of the target material (above the critical point) into a two-phase mixture of liquid and vapor. Experimental observations of the onset of the ejection of liquid droplets, as well as a steep increase of the ablation rate, are often interpreted as evidence of the transition from normal vaporization to the phase explosion [130, 138, 140]. The results of molecular dynamic (MD) simulations of short pulse laser ablation [58, 77, 139, 141–143] confirm phase explosion as the dominant mechanism responsible for the material ejection at sufficiently high laser fluences (leading to the temperature of the irradiated surface above the critical point) and provide detailed information of the dynamics of the decomposition of the overheated surface region and characteristics of the ablation plume.

The fast rate of the energy deposition in short pulse laser irradiation, however, not only leads to a sharp temperature rise in the absorbing region of the target but can also result in the generation of compressive stresses [75]. The interaction of the laser-induced compressive stresses with free surface of the irradiated target can transform them to the tensile stresses of sufficient strength to cause mechanical fracture of a solid material or disruption and sputtering of a melted layer. The ejection of large liquid droplets or solid particulates caused by the relaxation of the laser-induced stresses is often called photomechanical ablation or spallation [133, 134, 144, 145].

The detailed investigation of the above processes involved into the laser-metal interaction and the resulting ablation yield was addressed in the work by Zhigilei [77] within the wide ranges of both pulse duration (1–50 ps) and the absorbed fluences (from melting to ablation thresholds), targeting different regimes of the solid damage. This research has confirmed that the maximum values of the laser-induced stresses and the contribution of photomechanical effects to the material ejection or damage are defined by the relationship between the characteristic time of the laser heating τ_{heating} and the time required for the mechanical relaxation (expansion) of the heated volume τ_{mech}. Then, for sufficiently short τ_{heating}, the heating and melting take place under nearly constant volume condition, causing a buildup of compressive stresses. In short pulse laser interactions with metals, the time of the laser heating is defined by the laser pulse duration, τ_{pulse}, or the characteristic time of the energy transfer from the excited electrons to the lattice, $\tau_{\text{e-ph}}$, whichever is longer. The condition for the generation of compressive stresses, usually referred to as the condition of the internal stress confinement [133, 134, 144], can in this case be formulated as

$$\max\left\{\tau_{\text{pulse}}, \tau_{\text{e-ph}}\right\} = \tau_{\text{heating}} \leq \tau_{\text{mech}} = {}^{L_{\text{e-diff}}}\big/_{C_s} \tag{2.16}$$

where $L_{\text{e-diff}}$ the diffusive/ballistic penetration depth of the excited electrons during the time of the electron-phonon equilibration and C_s is the speed of sound in the target material.

As a result of the research presented in Ref. [77], it was also formulated that there are mainly three regimes of the material response to the laser irradiation: melting and resolidification of a surface region of the target, photomechanical spallation of a single or multiple layers/droplets (spallation), and an explosive disintegration of a melted surface layer overheated above the limit of its thermodynamic stability (phase explosion). The last two regimes are frequently referred to as mechanical and thermal damage of the irradiated solids correspondingly and can be clearly separated by a great difference in the number of vapor atoms, massively appearing in the material ejection mechanism via explosive boiling (ablation in the regime of thermal damage).

3.3 Quality and Efficiency: Mechanical Versus Thermal Damage Regimes

From the above section and the inequality, given by Eq. (2.16), it can be preliminary deduced that for sufficiently short laser pulses that satisfy the condition for stress confinement, the fast laser energy deposition results in the build-up of strong compressive stresses in the surface region of the target. The relaxation of the laser-induced compressive stresses generates an unloading (tensile) wave propagating from the surface to the bulk of the target. When laser fluence reaches a well-defined spallation threshold value, the tensile stresses become sufficiently strong to induce nucleation, growth, and coalescence of multiple voids in the surface region of the target, leading to the separation (spallation) and ejection of a liquid layer. As the laser fluence increases above the spallation threshold, photomechanical disruption of the melted region of the target can result in the ejection of multiple layers and large liquid droplets [77]. This regime of the material processing is targeting the quality and frequently used for nanostructuring of materials with a minimum of thermal damage around the laser-induced features [23, 112, 146].

A transition to the regime of phase explosion is identified by an abrupt change in the composition of the ejected plume, from liquid layers and large droplets to a mixture of individual atoms and small clusters/droplets. The sharp (threshold-like) increase in the amount of the vapor-phase atoms at the transition from the photomechanical spallation to the phase explosion regime reflects the difference in the physical mechanisms responsible for the material ejection in these two regimes. An explosive release of vapor, rather than the relaxation of photomechanical stresses, provides the main driving force for the decomposition and collective ejection of the overheated layer of the target in the regime of phase explosion [77]. This regime of the material processing is targeting the efficiency of the ablation and frequently used for nanoparticles production with a significant thermal damage around the obtained crater [147, 148].

The processes of laser melting, spallation, and phase explosion are taking place simultaneously and are closely intertwined with each other. In particular, the onset of spallation interrupts the heat conduction from the hot surface layer separated from the bulk the target, leading to a sharp drop in the duration of the heterogeneous stage of melting and the time required for complete resolidification of the target, as well as to a decrease in the maximum melting depth observed in the simulations. The transition to the phase explosion has an opposite effect: the duration of the melting and resolidification cycle, as well as the size of the melting zone increase due to the continued interaction of the ablation plume with the surface of the target [77].

From the above discussions, it would be profitable to separate the regimes of thermal and mechanical damage and use the last one for the purpose of material surface functionalization, where the high quality of the resulting surface is essential in a number of IT- and bio-applications [4, 10, 149, 150]. In particular, the latest results on material surface nanostructuring open up new perspectives for the fabrication of surface structures with high spatial resolution. A wide range of applications through optimized light coupling in photovoltaic [151], LED [152], and detector devices [153] can benefit from the gained knowledge and allow a detailed control of the fabrication process of next-generation devices. Providing the appropriate conditions for the onset of spallation mechanism (responsible for the regime of mechanical damage), however, given by Eq. (2.16), due to uncertain

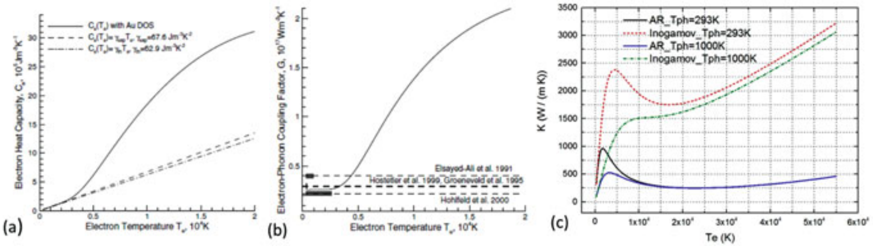

Fig. 2.6 The electron temperature dependence of on the example with gold. The electron heat capacity (**a**) and the electron-phonon coupling (**b**), published in Ref. [62] along with variety of approximations. The electron heat conductivity function plotted for two values of the lattice temperatures (300 K and 1000 K) according to the approximation by Anisimov [64] and Inogamov [73] (**c**). The latter includes the dependence on density

value of $L_{\text{e-diff}}$, is barely applicable in the material processing prediction, if speaking about the efficiency and quality.

The recently performed extensive theoretical study, however, targeted the problem of the laser-deposited energy dissipation and its effect on the induced target damage [154, 155]. Utilizing the relation $G_{\text{e-ph}} \sim C_e/\tau_{\text{e-ph}}$ [49] over the electron-phonon equilibration period $\tau_{e\text{-}ph}$, Eq. (2.16) was extended in the following form:

$$\max\left\{\tau_{\text{pulse}}, \tau_{\text{e-ph}}\right\} \approx \tau_{\text{heating}} \leq \tau_{\text{mech}} \approx \frac{L_{\text{e-diff}}}{C_s} \approx \frac{\sqrt{D_e\tau_{\text{e-ph}}}}{C_s} = \\ = \frac{\sqrt{\tau_{\text{e-ph}}k_e(F_{\text{las}})/C_e(F_{\text{las}})}}{C_s} \approx \frac{\sqrt{k_{\text{e}}(F_{\text{las}})/G_{\text{e-ph}}(F_{\text{las}})}}{C_s} \tag{2.17}$$

where k_e, $G_{\text{e-ph}}$, and C_{e} are the electron heat conductivity, the electron-phonon coupling, and the electron heat capacity functions correspondingly. From here, it is clear that, if minimizing the left side of Eq. (2.17) working with the pulses shorter than the characteristic electron-phonon equilibration time, there are two main channels for the laser-deposited energy dissipation. The first is the energy dissipation channel via the fast electron heat conduction, determining the effective energy penetration depth by the time of the electron-phonon coupling $\tau_{\text{e-ph.}}$ and correspondingly the range $L_{\text{e-diff}}$ of the established temperature and pressure gradients. And the second is the channel governed by the electron-phonon energy exchange, determining the rate of heating [156]. But what is even more important is that the material properties such as the electron heat conduction, electron heat capacity, and the strength of the electron-phonon energy coupling are strong functions of the electron temperature (Fig. 2.6) [24, 62].

Interestingly, the value of the electron heat capacity and the electron-phonon coupling, presented in Fig. 2.6 for gold, is monotonically changing (increasing or decreasing simultaneously for both) for the range of materials [62], while the electron heat conductivity function exposes different regimes depending on the electronic temperature. Moreover, the electron temperature dynamics, and its characteristic range of variation in turn, are strongly affected by the pulse

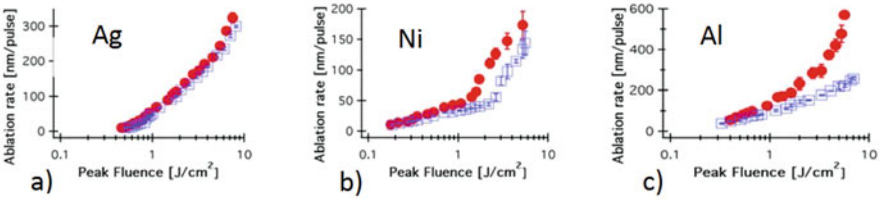

Fig. 2.7 The experimentally measured ablation rates of the selected materials Ag (**a**), Ni (**b**), and Al (**c**) versus absorbed fluence for pulse durations of 0.2 ps (circles) and 10 ps (squares) [157]

duration and the applied fluence, which gives us the possibility of manipulation with the efficiency of both channels to some extent. More precisely, applying the corresponding irradiation regime, we can either suppress or increase the amount heat dissipated through conductivity channel. Thus, for the given pulse duration, shorter than the electron-phonon relaxation time, there exists such a fluence range, where due to strong scaling of the thermal conductivity function with the induced electron temperature, one can achieve a laser energy deposition depth sufficient for the onset of the inertial stress confinement regime. The latter leads to the regime of mechanical damage, preferable for the purpose of nanostructuring of materials with minimized thermal damage.

The suggested theory fits very well to the data, obtained in the experimental works [157], and replotted here in Fig. 2.7. In this research the applied pulse durations were short, moderate, or long depending on the properties of material under ablation process. Both pulses, 0.2 ps and 10 ps, are short for Ag material, and the ablation rate exposes the more or less linear behavior with fluence indicating the photomechanical character of the damage mechanism due to realization of the inertial stress confinement conditions. For Al material, 10 ps pulse is a long one. Therefore, the conditions of inertial stress confinement will not be realized even at high fluences. Its damage mechanism, therefore, can be attributed to the photothermal character, whereas the short 200 fs pulse will trigger the photomechanical one. Finally, the Ni material with the characteristic electron-phonon relaxation time of about 10 ps is a bordering case so that both characters of the damage mechanisms are involved. In most of the experiments, however, both photomechanical and photothermal mechanisms of the material processing are involved to some extent.

3.4 All-Optical Control in Ultrashort Double-Pulse Laser Ablation Experiments

In this section we will briefly describe the research, which successfully united both theoretical investigation with MD-TTM model and the experimental results on the example of all-optical control for the ablation process in double-pulse experiments [158]. All-optical control is well known and broadly utilized in coherent interference and diffraction (multilayer [159] and multi-beam [160] interference, diffractive beam shaping and profiling [161, 162], etc.), as well as in incoherent (all-optical switching [163], dynamic laser tuning [164]) optical phenomena over the many decades. In solids, double-pulse (DP) optical control of atomic motion was demonstrated via ultrafast (typically, femtosecond/fs) laser excitation of sub-picosecond vibrations of ionic lattices at the corresponding center-zone optical-phonon frequencies due to almost instant electron-hole plasma photo-injection and its displacive modification of crystalline lattice potentials in semimetals and semiconductors [165, 166] through the optical deformation-potential electron-phonon interaction [167]. In this case, the first pump pulse started promptly the sub-picosecond lattice oscillations toward the plasma-induced new quasi-equilibrium position (atomic clocking), while the second pump pulse could enhance or cancel these oscillations, coming and modulating the atomic potential surface via in-phase or antiphase instantaneous photo-injection of electron-hole plasma [167], respectively. Recently, an extension to all-optical control of vibration in two dimensions via pulse shaping was demonstrated [110]. Similarly, high-Q (high-fidelity) coherent atomic motion at much lower acoustic-phonon frequencies and related multi-picosecond timescales was numerously revealed as long-term reverberations in thin metallic films [168] and dynamically growing melt layer on a Si surface [169], excited by fs-laser pulses; however, optical control of such acoustic oscillations was not experimentally realized so far, to our knowledge. Moreover, coherent acoustic control of DP fs-laser ablation was theoretically predicted almost decade ago [170], considering the hypothetic destructive interference interaction between the trailing tensile pressure wave from the first fs-laser pump pulse and the leading compressive pressure wave from the second fs-laser pump pulse. It was also theoretically predicted based on DFT study that one can even manipulate, using two delayed pulses, the nonthermal melting of Si [171]. The first pulse excites thermally squeezed phonons in the solid, while the second pulse can or cannot induce melting depending on the delay. By means of shifting the irradiated material out of the equilibrium and bringing it into the extreme conditions, one can utilize its unique, not met in nature, optical, electrical, and thermophysical properties [172].

Until recently, the control of ablation processes in condense matter has been demonstrated for shaped pulses or double pulses separated by sub-picosecond delay [173–175]. The control mechanism in those works was the manipulation of the nonequilibrium distribution of excited electrons. However, no control of laser ablation has been proposed relying on the mechanical relaxation pathways of the material, despite prompt optical modulation of absorbance/ablation by ultrashort shaped pulses (~1 ps) [176] and routine screening by ablative plume/plasma (~1 ns) in DP fs-laser standoff LIDAR monitoring using laser-induced breakdown spectroscopy [177]. Meanwhile, very recently some intriguing facts of strongly modulated alternating (enhanced/diminished) ablation efficiencies for ultrashort laser pulse bursts with odd and even small pulse numbers were reported [178], indicating some unidentified internal self-organization in the sequences of ultrashort laser pulses as a prerequisite for possible *all-optical ablation control*.

In this work, DP femtosecond laser ablation of thin aluminum films of variable thicknesses (up to bulk aluminum) indicated the cancellation of ablative removal at multi-picosecond inter-pulse delay times via drastically raising the corresponding DP ablation thresholds. This counterintuitive phenomenon was explored experimentally by probing multiscale transient matter states during single-pulse fs-laser ablation by time-resolved optical reflection microscopy and verifying double-pump-matter interactions via time-resolved double-pump transmission studies. In addition, to support the experimental measurements, the single-pump-prepared transient states and their interaction with the second pump pulse were theoretically characterized via a hybrid atomistic-continuum numerical approach MD-TTM, described above and applied here for theoretical interpretation of the experimental data.

Single-shot front-side ablation of fresh spots of 30–120-nm-thick Al thin films prepared by high-vacuum magnetron sputtering onto silica glass slides without any adhesive sublayers was produced by linearly polarized femtosecond laser pulses. During the experiments on double-pulse ablation, laser pulses passed a two-beam optical Michelson interferometer (Fig. 2.8a) with a 50%-transmission dielectric multilayer beam splitter and a pair of stationary and movable highly reflective (99.95%) normal-incidence dielectric multilayer mirrors, allowing to vary inter-pulse delay time τ in the range of -100 to $+8000$ ps. Prior focusing, the total double-pulse energy was reduced in the range $E = 0.1$–0.9 mJ, resulting in a sub-filamentation regime in peak pulse fluence $F_0 = E/(\pi R_{1/e}{}^2)$ up to 1.5 J/cm^2. This peak fluence value is well sufficient for spectrally resonant (at 800 nm) ablation of the Al films (Fig. 2.1b) above the corresponding thickness-dependent thresholds F_{abl} (Fig. 2.1c). The experimentally measured saturation of a single-shot threshold fluence depending on the Al film thickness [179] matched our previous theoretical predictions performed for noble (Au, Cu) and transitional (Al, Ni) metals [180]. Fluence calibration for each pump channel was based on measurements of single-shot fresh-spot ablation radii R_{abl}.

At the fixed above-threshold incident fluence $F \approx 0.8$ J/cm^2 per the pump pulse, there is a drastic radial decrease (Fig. 2.8c, 90 nm film) – up to disappearance (Fig. 2.8e, 120 nm film] – of the DP ablation spots with their measured radii R_{abl} for the all used Al films and its bulk sample versus the inter-pulse delay time τ in the range 10–100 ps. Accounting for the Gaussian fs-laser beam profile and the measured SP ablation thresholds $F_{\mathrm{abl}}(0)$ (Fig. 2.8c), the observed variations of DP ablation radii were related to the corresponding opposite trend for the DP ablation thresholds $F_{\mathrm{abl}}(\tau)$ (Fig. 2.8d, e). The possible variation reasons were supposed to be different over the different timescales [181] and even for the different film thicknesses. Note that the experimental measurements of threshold fluence for material modification, shown in Fig. 2.8c, reach a saturation value starting from some thickness, H, which corresponds to the diffusive penetration depth of the laser-deposited thermal energy by the time of the electron-phonon equilibrium. Up to that thickness, the films can be considered thin and the threshold fluence scales linearly. For thicker targets, the laser-deposited heat remains within H_{diff} distance from the surface, and the threshold fluence does not increase further. Following the method suggested in

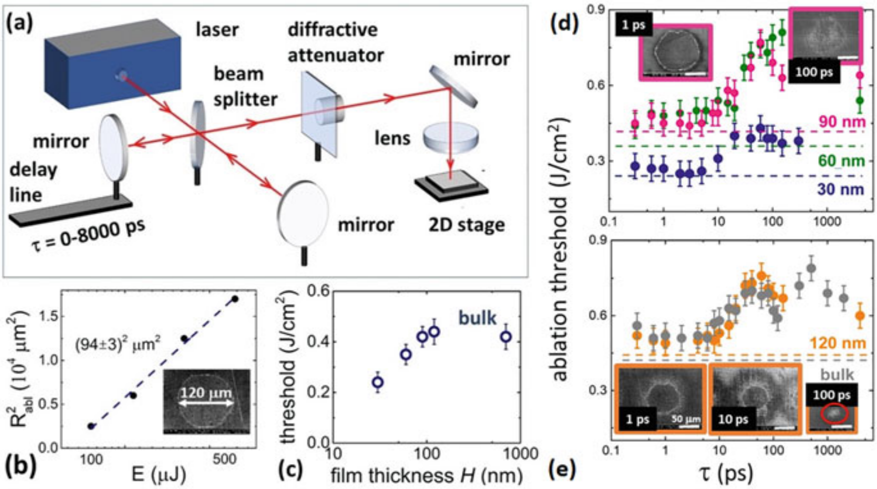

Fig. 2.8 (**a**) Schematic picture of the DP fs-laser ablation experimental setup; (**b**) fluence calibration curve $R_{\text{abl}}{}^2$ vs E with the squared 1/e-radius $R_{1/e}{}^2$ as its linear slope in $R_{\text{abl}}{}^2$-lnE coordinates (inset: top-view SEM image of the typical spallative crater) for the 30 nm Al film; (**c**) single-pump (SP) ablation threshold $F_{\text{abl}}(0)$ vs H. DP ablation thresholds F_{abl} vs delay τ: (**d**) 30-, 60-, and 90-nm-thick Al films; (**e**) 120-nm-thick film and bulk Al sample, where each threshold value was obtained over six measurements. The horizontal dashed lines exhibit the corresponding single-pump thresholds. Top-view SEM images of DP-ablation spots (fluence ≈0.8 J/cm^2 per pump pulse) are presented for different delays and film thicknesses in the corresponding colored frames. The all-scale bars are equal to 50 μm. (Reprinted with permission from [158], © Elsevier)

[180, 182], it can be estimated from the materials properties and yield the value of ~100 nm, which support our experimental data and proves the used films (30, 60, 90, and 120 nm) as thin targets [158].

To support the experimental measurements and find out their theoretical interpretation, we use MD-TTM model in a multiprocessing regime, schematically illustrated in Fig. 2.3. While the basics of this model are given in the second section of this chapter, the boundary conditions for modeling of laser interaction with Al material as well as the interatomic potential function description, its material representation properties, and of the electronic system parameters can be found in Ref. [147]. Prior the modeling the films where equilibrated at the normal conditions and placed on a silica substrate, with which they interact via Lennard-Jones potential.

Our MD-TTM modeling of fs-laser ablation of 30 nm and 90 nm Al films (with lateral dimensions of 50 nm × 50 nm) provides a deep insight into the underlying microscopic mechanism of physical processes in terms of the DP delay time τ right prior the incidence of the second pump pulse and 200 ps after it, Fig. 2.9. Here, the total DP incident fluences F_{inc} for the 30 nm and 90 nm films were chosen to exceed the minimal one at lower τ and remain less the maximal one at the inter-pulse delay τ – specifically, $0.25 < F_{\text{inc}} = 0.33 < 0.39$ J/cm^2 ($H = 30$ nm) and

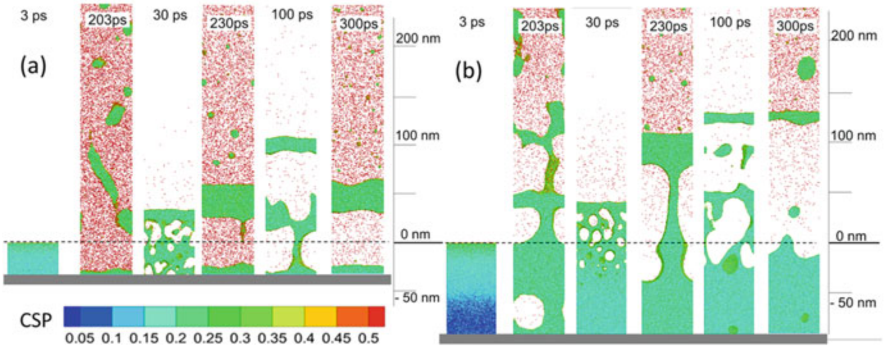

Fig. 2.9 MD-TTM atomic configuration snapshots of 30-nm- (**a**) and 90-nm- (**b**) thick Al films ablated by double 800-nm 100-fs laser pulses with the total fluence of 0.33 (**a**) and 0.6 (**b**) J/cm^2 and inter-pulse delay times of 3, 30, and 100 ps. Each pair of images in (**a**, **b**) shows the atomic configurations right prior and 200 ps after the second pump pulse. The atoms are colored by the central symmetry parameter (CSP) [183] for identification of the crystal structures as follows: solid <0.08 < defects <0.12 < liquid <0.25 < surface <0.50 < vapor. The gray line at the bottom indicates the substrate position. (Reprinted with permission from [158], © Elsevier)

$0.45 < F_{\mathrm{inc}} = 0.6 < 0.7$ J/cm^2 ($H = 90$ nm). Both these films demonstrate, after the single-pump exposure, how the second pump pulse interacts with the material at different evolution stages of its phase/aggregate state after surface heating, melting, thermal expansion, and surface vaporization (ablation). Specifically, at the moments of the second pulse arrival, the surface heating and melting ($\tau \approx 3$ ps), thermal expansion and sub-surface growth of voids ($\tau \approx 30$ ps), and the complete spallation of their topmost layers ($\tau \approx 100$ ps) can be observed (Fig. 2.9, left images in each pair). The incidence of the second pump pulse at the different instants, however, brings the very different final ablation dynamics (Fig. 2.9, right images in each pair). The absorption of the second pump pulse at $\tau \approx 3$ ps just increases the deposited volume energy density, similarly to the laser energy deposition by a single laser pulse, but at the double incident fluence, driving afterward considerable ablative removal via expulsion of vapor-droplet mixture (phase explosion) accompanied with the spallation mechanism. The second pump pulse incidence at $\tau \approx 30$ ps delay for both film thicknesses is absorbed by the volume under intensive expansion, driven by the relaxation of the laser-induced stresses (resulting from the first pulse), while the complete material removal by the spallation mechanism has not occurred at this moment yet. The second pulse laser energy deposition into the expanding volume results in its secondary heating and the subsequent relaxation of the laser-induced stresses occur in both directions (up and down) this time, causing the reversal motion of the material under ablation process, decreasing therefore the ablation efficiency and increasing the ablation threshold correspondingly. Finally, the 100-ps delay between the pump pulses results in the consequent phase explosion of the already spalled volume of the 30 and 90 nm, but its ablation cannot revert much material toward the substrate anymore.

The related analysis of the accompanying transient pressure waves reveals the effect of the heat and stress confinement in the surface layer after the second pump pulse at $\tau \approx 3$ ps and the almost total screening effect of the ablative plume for the second pump pulse at $\tau \approx 30$ ps. This can be seen in Fig. 2.10, where for the case of 90-nm-film thickness, we illustrate the very different laser-induced stresses relaxation dynamics (and the resulting dynamics of the liftoff velocity of the ablating material) inside the films for the case of pulse delay of $\tau = 3$ ps and $\tau = 30$ ps. Analyzing the pressure field evolution shown for the moment of the second pulse arrival, 10 ps and 20 ps after (when the result of fast heating is reflected via accumulation and relaxation of the internal stresses), we can extract the effect of the pulse delay during DP ablation process. Since the characteristic heating depth of the aluminum by the time of the electron-phonon equilibrium can be estimated as ~100 nm [180], the spallation mechanism is more pronounced for the thicker film thickness (90 nm).

As it was mentioned above, the DP ablation process with the pulse delay of 3 ps merely increases the laser-generated stresses inside the presurface layer of the material that later relaxes in a normal way, similarly to that due to a single-pulse regime at doubled energy. Namely, the relaxation of the laser-generated internal stresses, Fig. 2.10a, results in the propagation of the unloading pressure waves toward free surface and the substrate. The subsequent reflection of the pressure wave from the substrate induces a partial spallation of the subsurface layer, which is also accompanied by intensive evaporation due to relatively high absorbed fluence and high liftoff velocity, Fig. 2.10b.

If the second pulse delay is longer, however, the laser-induced stresses due to the first pulse have enough time for relaxation, and the second pulse therefore will be absorbed by acoustically relaxed material, which is already in the process of hydrodynamic motion (due to relaxation of the laser-induced stresses across the molten material) and the onset of the spallation mechanism of the material removal visualized via the internal voids growth (Fig. 2.10c) [77, 154, 184]. The absorbed laser energy is then transformed into additional lattice heating that in turn results in the recurrent generation of the compressive stresses, the relaxation of which is accompanied by the propagation of the pressure waves in both directions (upward and downward). This can be seen in Fig. 2.10c as a temporal increase of the internal pressure (red color) with the establishment of material motion downward observed in liftoff velocity field, Fig. 2.10d (dark blue color). The relaxation of the recurrent induced stresses is affecting the internal voids growth and altering the hydrodynamic motion of the molten matter to the opposite direction by the time of 40 ps. This is emphasized in Fig. 2.10c–d by black circles that indicates the generated voids that collapse by the time of 50 ps due to altered direction of the material motion. Subsequently, this material will be redeposited on the substrate and will undergo slow crystallization process. The resulting removed volume of the material is less than it is for the case of 3 ps second pulse delay, and the ablation threshold for the pulse delay of $\tau = 30$ ps is therefore increased. This efficient increase of the ablation threshold is governed by the same process of pressure relaxation dynamics for longer pulse delays (100 ps), however, with the effect of laser-induced stresses

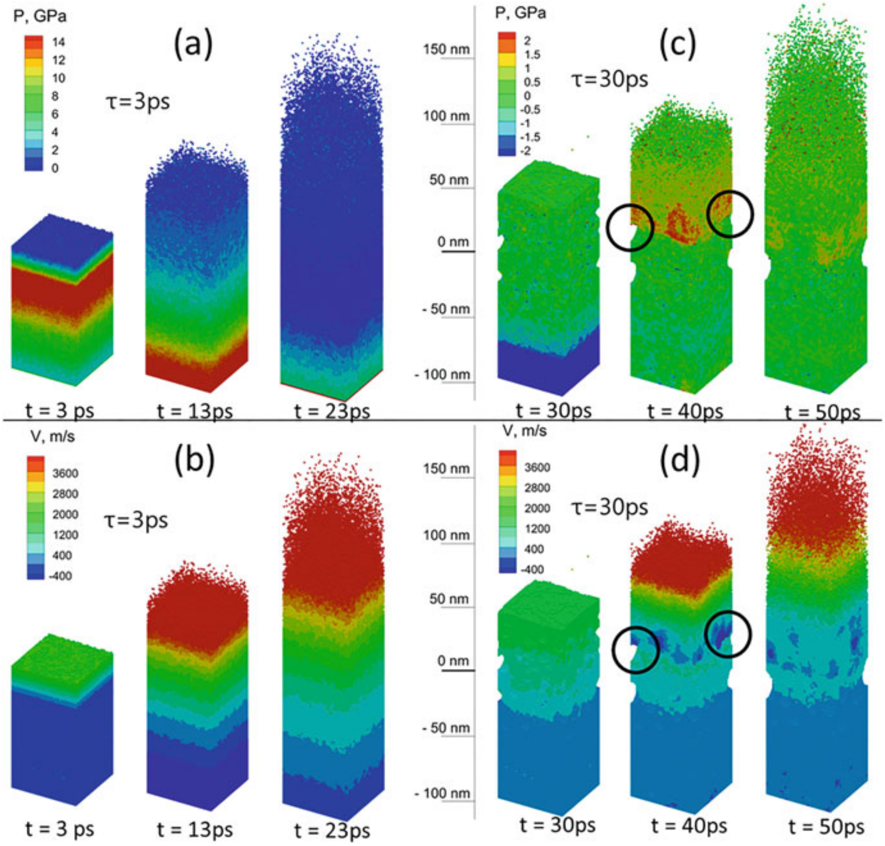
P, GPa
14
12
10
8
6
4
2
0
(a)
τ=3ps
t = 3 ps
t = 13ps
t = 23ps
150 nm
100 nm
50 nm
0 nm
- 50 nm
- 100 nm
P, GPa
2
1.5
1
0.5
0
-0.5
-1
-1.5
-2
(c)
τ=30ps
t = 30ps
t = 40ps
t = 50ps
V, m/s
3600
2800
2000
1200
400
-400
(b)
τ=3ps
t = 3 ps
t = 13ps
t = 23ps
150 nm
100 nm
50 nm
0 nm
- 50 nm
- 100 nm
V, m/s
3600
2800
2000
1200
400
-400
(d)
τ=30ps
t = 30ps
t = 40ps
t = 50ps

Fig. 2.10 Pressure and material velocity liftoff fields, illustrating the effect of the second pulse delay on the laser-induced stresses relaxation dynamics. Pressure and velocity of liftoff fields for the case of pulse delay $\tau = 3$ ps (**a**) are shown in (**a**) and (**b**), whereas the case of the second pulse delay of $\tau = 30$ ps is illustrated correspondingly in (**c**) and (**d**). For each of the case, the pressure and liftoff velocity fields are shown for the moment of second pulse arrival, 10 ps and 20 ps after. The black circles in (**c**) and (**d**) indicate the onset of spallation mechanism via internal void generation that collapses soon. (Reprinted with permission from [158], © Elsevier)

relaxation process less pronounced for visualization. The effect of ablation threshold increase in a DP experiments for thinner films (30 nm) is also less pronounced due to fast mechanical (acoustic) relaxation of the material in response to the laser heating, Eq. (2.17).

At last, the geometry of the irradiated target, and the target's thickness in particular, determines the mechanical relaxation rate and the period of laser-generated pressure wave reflections from free surfaces or the substrate (mechanical oscillation of the irradiated target). The time delay between the first and second pulses, determining the character of the efficient ablation threshold fluence change, will be different for thinner or thicker targets. This explains the periodic variation in the ablation threshold fluence depending on the film thickness and the second pulse delay measured experimentally. Nevertheless, the relaxation of the laser-induced stresses due to the first pump pulse determines the ablation threshold dynamics due to the second pulse for a range of fluences and inter-pulse delays whenever the conditions for the internal stresses confinement, given by Eq. (2.17), and their subsequent relaxation are observed.

Finally, the presented above experimental and theoretical findings were found to be consistent with the DP ablation threshold variations versus τ in Fig. 2.8. Double-pulse femtosecond laser ablation of thin aluminum films of variable thickness counterintuitively demonstrated strongly reduced and corresponding increased (60–70%) ablation thresholds over the thickness-independent inter-pulse delay in the range of 20–200 ps, enabling efficient dynamic all-optical control of ultrafast laser ablation. The successful interconnection with the experimental measurements and the applied theoretical modeling with MD-TTM model revealed a complex interplay of the laser-generated stresses relaxation dynamics and screening of the focused irradiation by the ablation products, crucially sensitive to the second pump-pulse absorption and laser-deposited energy dissipation. The results of these experimental and theoretical studies enable the manipulation of the material properties during its transient states, induced by a double-pump pulse ablation process. Thus, the dynamic all-optical control in double-pump pulse ablation experiments can find some potential technological applications.

4 Nanostructuring of Material Surfaces

4.1 Single-Pulse Nanostructuring of Metals

Research efforts toward the development of direct-write laser technologies have yielded a significant progress in fabrication of surface nano- and microstructures with spatial resolution exceeding the optical diffraction limit. The spatial resolution achievable in laser surface processing is defined by the ability to concentrate the laser energy deposition in a smallest possible domain. Several approaches have been demonstrated to be instrumental in achieving highly localized laser energy deposition, including the use of tightly focused laser beams with the peak laser fluence close to the threshold for material modification [185, 186] or utilization of the optical near field effects, for example, a local field enhancement in the vicinity of a probe tip [187–190] or a deposited nano-/microparticle [191, 192]. Following the first approach, the direct writing of ordered arrays of hollow bumps and jet-like structures on metal films of different thickness has been recently demonstrated in a number of works [112, 146, 193–195].

While the ability to generate arrays of nanoscale surface features opens up a range of opportunities for practical applications, the processes responsible for the surface nanostructuring until recently were not fully understood. Possible

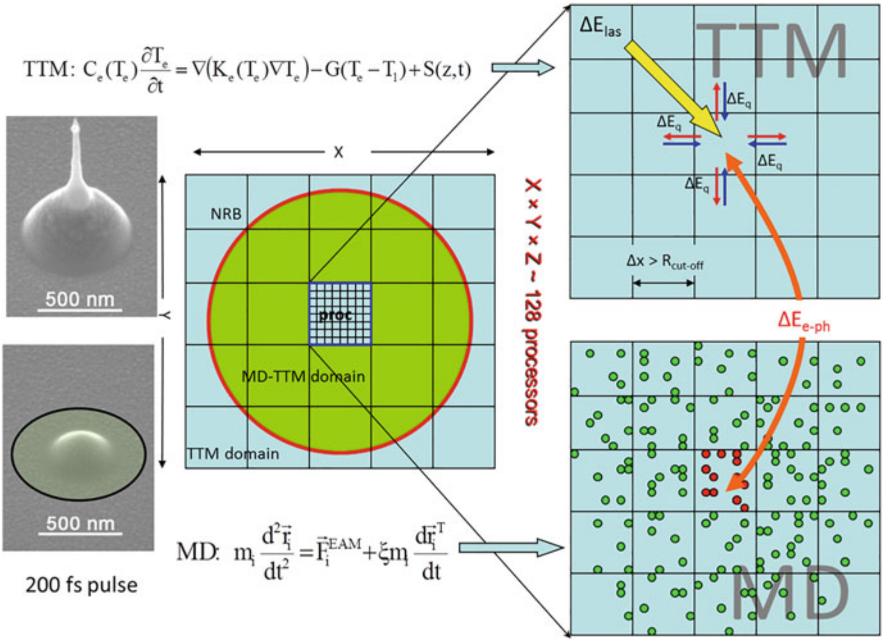
TTM: $C_e(T_e)\frac{\partial T_e}{\partial t} = \nabla(K_e(T_e)\nabla T_e) - G(T_e - T_l) + S(z,t)$
500 nm
500 nm
200 fs pulse
X
NRB
proc
MD-TTM domain
TTM domain
X × Y × Z ~ 128 processors
ΔE_{las}
TTM
ΔE_q
ΔE_q
ΔE_q
ΔE_q
$\Delta x > R_{cut\text{-}off}$
$\Delta E_{e\text{-}ph}$
MD
MD: $m_i \frac{d^2\vec{r}_i}{dt^2} = \vec{F}_i^{EAM} + \xi m_i \frac{d\vec{r}_i^{\,T}}{dt}$

Fig. 2.11 The nanobump- and nanojet-like structure, produced at Laser Zentrum Hannover by 200 fs laser pulse focused on a 60 nm Au film (left). The computational cell with circumferential nonreflecting boundary conditions (NRB) for absorption of the laser-induced pressure wave. The total cell is divided into 128 processors, and the MD-TTM model is solved in 3D mesh in each of them

mechanisms discussed in literature include Marangoni convection [193], peeling and expansion of the film due to the pressure of evaporating material [146, 195], and thermo-elastic and plastic deformation of the film suggested based on recent continuum simulations [20]. Computer modeling of the material response to short pulse laser irradiation indeed has a potential for providing information on the physical processes responsible for the formation of submicron frozen surface structures in laser nanotexturing. In this section therefore, we apply the MD-TTM method to investigate the physics underlying the formation of nanobump and nanojet structures, in particular produced at Laser Zentrum Hannover [112], Fig. 2.11 (left). Corresponding to that model, the computational cell, reinforced by MPI parallel algorithm, is schematically shown in Fig. 2.11 (right) [196].

The simulations are performed for a 20 nm Ni film deposited on a transparent substrate. The choice of Ni, rather that Au used in experiments [112], is defined by the computational necessity on the one hand, but it also allows to capture the essential driving mechanisms, responsible for the structures growth in the absence of a number of concurrent processes induced in the sample covering the experimental scale. The initial MD part of the model is a circular slab of 250 nm in diameter, where atoms are arranged in the FCC crystal structure with (001) surface oriented parallel to the substrate. The thermal and elastic properties of the Ni film are defined by the interatomic interaction potential, described in this work by the embedded-atom method (EAM) [197]. Some of the parameters of the model EAM Ni material are reported in [73] along with the parameters used in the TTM equation for the electron. The top surface of the film, exposed to the laser irradiation, is free to move, whereas the interaction of the bottom side of the film with the substrate is described by Lennard-Jones potential. The parameters of the Lennard-Jones potential are chosen to represent an adhesion of a Ni film to the substrate that is ten times weaker than the effective strength of Ni-Ni interaction (based on the experimental measurements by Laser Zentrum Hannover). The substrate is kept rigid during the simulation, and the energy exchange between the metal film and the substrate is not allowed. This assumption of the model is justified by the short characteristic time of the processes responsible for the nanobump formation and relatively slow heat exchange between a metal film and a glass substrate.

While the size of the MD part of the combined model is limited to 250 nm in diameter, the TTM equations for the electron and lattice temperatures are solved in a much wider region affected by the thermal conduction, up to 5 μm from the center in the radial direction, Fig. 2.11. A special nonreflective boundary (NRB) condition [56, 74] is applied circumferentially around the MD computational cell. This boundary condition imitates the propagation of the laser-induced radial/circular pressure wave from the MD region to the continuum part of the model and eliminates the artificial effect of the multiple reflections of the wave from the system's radial boundary.

Strong electron-phonon coupling of Ni (one order of magnitude stronger than that of Au) and negligible contribution of the ballistic energy transport (the range of ballistic electrons in Au is ~100 nm [63]) result in a fast lattice heating and a high degree of laser energy localization near the laser spot. To quantitatively characterize the extent of spatial energy redistribution during the time of the electron-phonon equilibration, one can consider the effective penetration depth of hot electrons, $L_{\text{e-diff}}$ in Eq. (2.17), introduced in Ref. [182]. Following the procedure described in [63, 180, 182], the values of $L_{\text{e-diff}}$ can be estimated to be ~50 nm for Ni and ~700 nm for Au. Thus, a 20-nm-thick Ni circular slab of 250 nm in diameter provides an adequate description of the laser-induced phase transformations and plastic deformation following a localized laser energy deposition and still contains 85,000,000 atoms, a tremendous number that could be treated in a large-scale parallel MD simulation at the time of 2005.

Since the sample size is reduced by one order of magnitude, to observe the nanostructuring process similar to [112, 193–195], the diameter of the laser beam in the MD simulation is also reduced by the same order. The simulation is performed with 200 fs laser pulse having Gaussian spatial and temporal profiles and a laser beam diameter (full width at half maximum) equal to 10 nm. Thus, the computational model can be considered to be a scaled down version of the experimental setup used in nanostructuring of Au films. While the difference in the length scale and material properties does not allow us to establish direct quantitative connections between the computational results and experimental data, the scaled down model can be expected to capture the basic mechanisms responsible for formation of the surface nanostructures.

The simulation, in the reported here work, was performed with an MPI parallel MD-TTM code optimized for the IBM eServer cluster 1350 at the National Facility at the Irish Centre for High-End Computing. Using an optimized linked list neighbor search and improved memory consumption, the code has reached a competitive (in 2005) time of ~8 μs spent by a single processor per atom per time step for the Nordsieck fifth-order predictor-corrector algorithm. The simulation was run across 128 processors and required ~1000 hours of calculations.

The results of the simulation can be seen in Fig. 2.12a–d as a sequence of the atomic snapshots. The atoms are colored by the potential energy, which allowed for distinguishing solid, liquid, surface, generated dislocations, and final internal structure of the formed nanobump. It is clearly seen that after a short melting time during the first 15 ps, the established motion of the liquid material results on the growing structure, which is completely solidified by the end of the simulation at 250 ps. For a better understanding of the mechanism of nanostructuring, however, we perform a more quantitative analysis below.

The fast localized heating of the film takes place under conditions of the partial inertial stress confinement [56, 77], discussed above in this chapter, when the heating time is shorter than the time needed for the film to expand in response to the thermoelastic stresses, given by Eq. (2.17). The confinement of the thermoelastic stresses, combined with an additional pressure coming from the suppressed volume expansion associated with the melting process (due to a positive volume of melting for fcc metals), results in the buildup of high, up to 8 GPa, compressive stresses during the first several picoseconds of the simulation, Fig. 2.12e. The relaxation of the compressive stresses proceeds by expansion in both radial direction and normal to the substrate. In the presence of the rigid substrate, the normal expansion of the film results in the upward acceleration of the film up to a velocity exceeding 300 m/s, Fig. 2.12e. The expansion of the film may be described in terms of an unloading wave propagating from the free surface toward the substrate. The reflection of the unloading (tensile) wave from the rigid substrate results in the concentration of the tensile stresses at the film-substrate interface and leads to the separation of the film from the substrate.

An apparent correlation between the time of the film acceleration and the first peak of the compressive pressure, Fig. 2.12e, provides clear evidence that the relaxation of the laser-induced compressive stresses generated under conditions of the inertial stress confinement is responsible for the initial acceleration of the central part of the film. Following the initial acceleration, the vertical velocity slowly decreases during the remaining part of the simulation, Fig. 2.12e. The decrease of the velocity is related to the resistance of the colder parts of the film to the separation from the substrate. The upward displacement of the central part of the film leads to the elastic deformation of the surrounding areas which relaxes by pooling the film back toward the substrate, Fig. 2.12a–d. In the melted part of the film, however, the initial momentum induces a hydrodynamic flow of the molten material, leading to the formation of a distinct nanobump.

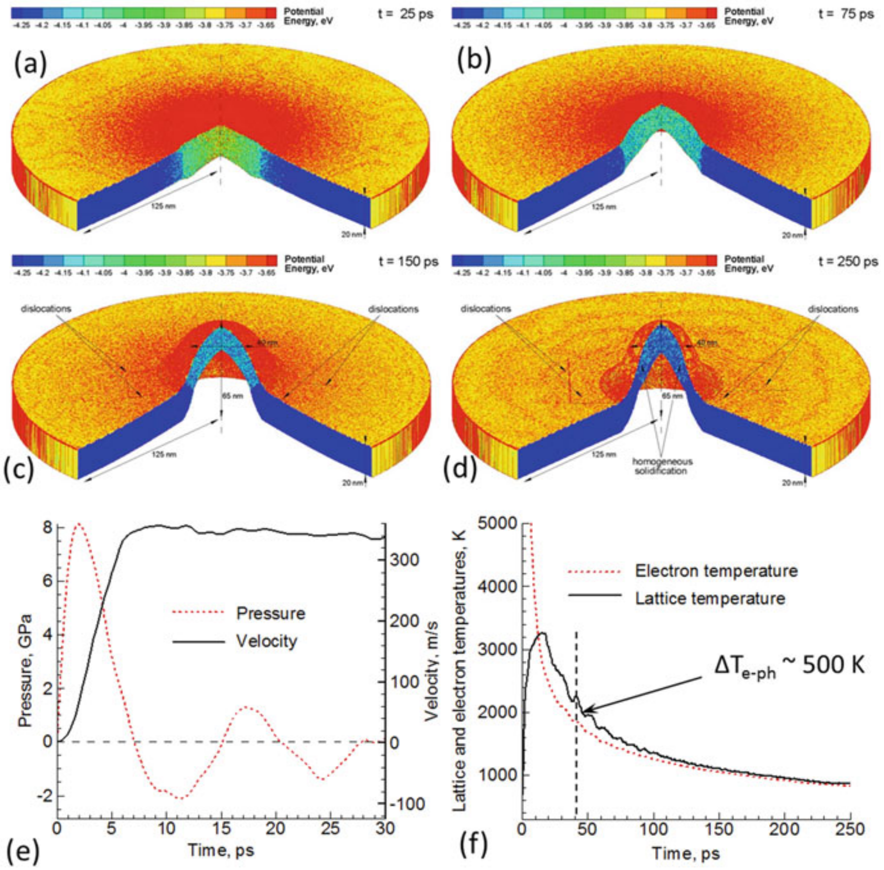

Fig. 2.12 The atomic snapshots from the simulation of nanostructuring of 20 nm Ni film of 250 nm diameter, situated on a silica substrate. The laser pulse of 200 fs is focused in a 10 nm Gaussian spot at the absorbed fluence of 3.1 J/cm^2. The atomic configurations are shown for 25 ps (**a**), 75 ps (**b**), 150 ps (**c**), and 250 ps (**d**), when the structure is completely solidified. The initial changes of pressure and velocity, averaged over a part of the film within 2 nm from the center of the laser, during the first 25 ps of the simulation are shown in (**e**). The time dependences of the electron and lattice temperatures (**f**). The maximum negative difference of ~500 K between the temperatures of electrons and lattice is indicated by dashed line at $t = 40$ ps

On the other hand, strong electron temperature gradients established in the radial direction following the initial localized laser energy deposition result in a fast cooling of the electrons and the lattice at later times. Thus, after the quick electron-phonon equilibration by 12 ps, already by the time of 40 ps, the temperature of electrons, due to fast heat condition mechanism in 2D (and in 3D in general), drops even below the lattice temperature, and the largest difference of 500 K is reached. In other words, the electrons start acting as a freezer for the molten material that results in the onset of its fast resolidification. At ~50 ps the lattice temperature at the periphery of the melted region drops below the equilibrium melting temperature, starting a slow process of epitaxial crystallization. At the same time, the fast 2D electron heat conduction continues to cool the melted region, with the lattice temperature in the center of the laser spot dropping down to T_m by 90 ps and down to $0.6T_m$ by the end of the simulation at 250 ps. At such strong undercooling, the slow epitaxial recrystallization gives way to a massive homogeneous nucleation of multiple crystallites within the undercooled liquid region, resulting in a rapid solidification of the nanobump. A detailed analysis of the solidification process producing a nanocrystalline nanobump is presented elsewhere [198].

The relaxation of the compressive stresses generated under conditions of the inertial stress confinement is identified as the main driving force responsible for the acceleration of a transiently melted region of the film which results in the bloating of a hollow nanostructure. Two-dimensional electron heat conduction provides the conditions for the fast cooling of the melted region and rapid solidification of a surface feature generated in the process of hydrodynamic motion of the liquid metal. While in the simulation discussed in this work, the growth of the nanobump stops at ~200 ps; one can expect that, at higher excitation levels, the hydrodynamic motion induced by the relaxation of the laser-induced compressive stresses may result in a stronger acceleration and a more active hydrodynamic flow leading to the emergence of jet-like structures that have been observed on top of hollow microbumps in experiments performed at sufficiently high-laser fluences [112].

4.2 Periodic Nanostructuring: Theory Versus Experiment

The ability of ultrashort laser pulses to deposit energy into a material in a highly localized way allows for a precise nanoscale surface restructuring, which makes femtosecond laser processing useful for various applications in information- and bio-technologies [199]. In particular, the capability of generating periodic structures on the submicron scale was demonstrated by obtaining material surfaces with specific morphological properties on metals [200], semiconductors [201], and dielectrics [202]. Moreover, the development of such structures was observed on both thin and thick targets [200–203]. Careful spatiotemporal design of the laser pulse was methodologically shown as an efficient tool for the creation of surfaces with demanded features [204], which is an important step toward the material surface functionalization, demanded in IT- and bio-technologies.

In order to gain the detailed knowledge on the laser-induced processes involved into the surface functionalization mechanism, in this section we perform both experimental and theoretical investigations of the formation of periodic nanostructures by UV (248 nm) single-laser pulses with a periodic sinusoidally shaped spatial intensity profile on the surface of a thick Au target, Fig. 2.13. The presented work is a unique combination of an extensive experimental investigation (performed by Institut für Nanophotonik Göttingen e.V. (Chap. 14 of this book [205]) and super-large-scale

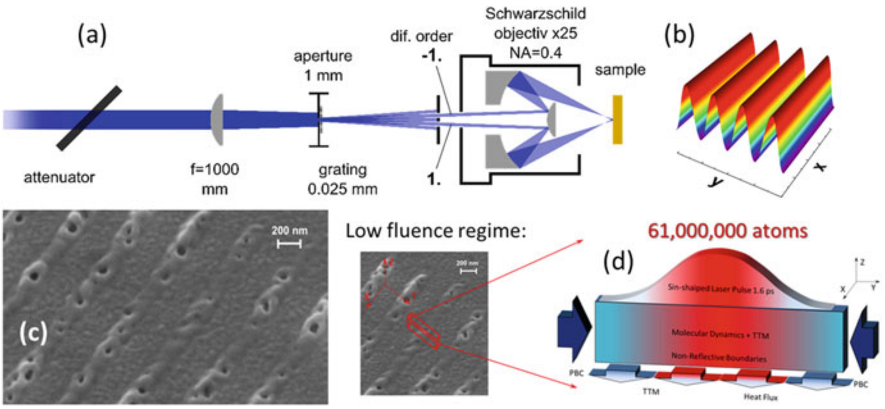

Fig. 2.13 (**a**) Mask projection setup for a periodic surface structuring of an area of 40 μm. A sinusoidal interference pattern with a period of 500 nm is obtained by using only the ±1st diffraction orders. (**b**) Schematic shape of the intensity distribution, created by an ideal single-laser pulse self-interference of two beams under a certain angle. (**c**) SEM pictures showing surface modifications from a single-laser pulse at the incident fluence of 125 mJ/cm^2 with periodic line spacing of 500 nm corresponding to the periodic irradiation pattern created by two beam interference. Small segments of a larger structured area on a thick gold sample at four different average incident fluences are shown. (**d**) Schematic representation of the computational cell used in the super-large-scale modeling of periodic nanostructuring experiments. PBs are the periodic boundaries. The nonreflective boundaries are transparent for the heat fluxes [78]

simulation of the investigated process on the experimental scale, performed on Lichtenberg Super Computer TU-Darmstadt [78].

All surface structuring experiments are accomplished by single-pulse exposure using a combination of interference and mask projection to form a large area sinusoidal intensity distribution on the sample surface, Fig. 2.13. The applied two-beam interference (resulting in the sinusoidal pattern) allows to reach the highest possible spatial intensity gradient, which is crucial for keeping the simulated volume as small as possible. The smallest available modulation period d is then only limited by the numerical aperture NA of the applied optics and the laser wavelength λ and can be expressed as $d = \lambda/2NA$. Thus, using a short wavelength of 248 nm and a large numerical aperture of $NA = 0.4$, a lower limit for the periodicity of ~310 nm is obtained. As a result, the periodically structured surface, sensitive to the applied fluence, was generated within the spot size of 40 μm [78].

The idea of modeling on the experimental scale is based on symmetry utilization of the experiment described above, see Fig. 2.13b, c. The laser beam, sinusoidally shaped in one dimension (Y), leaves a uniform laser intensity distribution in X direction. Dealing with the size of the laser spot of ~40 μm in diameter (flat top in X and sinusoidal shaped in Y), its central part will therefore not be affected by a diffusion process in X direction up to ~1 μs of the experimental time. This estimated time is confirmed in preliminary calculations using the TTM approach [49]. Considering this time as long enough for the formation and solidification of the nanostructures [113], this provides a possibility for periodic boundary (PB) conditions in X during our simulation time (up to several ns). As a result, since we do not expect any temperature and pressure gradients in the lateral direction parallel to the grating lines (X), for a simulation allowing for identical comparison with experiment, we constructed the computational cell as schematically shown in Fig. 2.13d. The Au MD supercell consisting of 61,000,000 atoms taken with dimensions of (20 × 350 x 150) nm was taken in X, Y, and Z directions, respectively. In order to avoid unnecessary and expensive MD integrations in deep bulk of the material, at a certain depth from the surface (in Z direction), we impose nonreflective boundary (NRB) conditions [56, 113]. Demanded by the investigated physics, the MD-TTM model was applied only above that limit.

Thus, the computational cell was constructed as it is shown in Fig. 2.3 and adapted for processing by 768 processor cores. The MD-TTM domain was divided into a 3D mesh with 1 nm^3 unit cell, and the thermo-physical properties of the atomic subsystem (such as temperature and pressure) were averaged over the closest 26 neighboring cells (that totally accounts for ~2500 atoms) to suppress their value fluctuations due to MD noise [73]. The complete details of the materials and the economic system parameters, as well as the modeling procedure can be found elsewhere [113, 196].

The model calculations were performed at the incident fluences of 122.5 mJ/cm^2 and 145.9 mJ/cm^2. The results of these simulations and the corresponding experimentally obtained structures are compared in Fig. 2.14. Here the SEM pictures in (a) and (b) show a view on the surface of the experimentally obtained structures, while the transmission electron microscope (TEM) *Titan E-TEM* pictures (c) and (d), as well as the atomic configuration snapshots from the simulation in (e–h) show a cross section of the material. The TEM cross section was cut by a focused ion beam (FIB) and shows the gold structure (dark region) covered by platinum (lighter speckled pattern). The platinum was deposited prior to the lamella preparation and filled all empty spaces. In both cross sections in Fig. 2.14c, d, the formation of voids (light area within the gold) as well as an uplift of material above the void can be observed at the locations of maximum fluence of the irradiating sinusoidal distribution.

In the atomic snapshots in Fig. 2.14e–h of the simulation, the atoms are colored according to the local order parameter (LOP), which is used here for quantitative analysis of the material phase due to fast nonequilibrium melting process and was described in details in Ref. [73]. The LOP parameter helps us to identify the atoms with liquid surrounding due to fast and nonequilibrium melting process (red atoms with LOP > 0.95) and also to highlight the material with somehow disturbed structures like the formation of defects, dislocation planes, and grain boundaries [198]. The atomic configurations are shown at a time of 100 ps and at 300 ps and 500 ps after the beginning of the pulse, respectively, for the lower and higher fluences. By these times the laser-induced melting process is finalized and reverts into the more slow recrystallization process by either homogeneous or heterogeneous mechanism [196]. Simultaneously, the material motion comes to rest, reflected by the liftoff velocity approaching zero. This velocity was calculated as a macroscopic quantity for each mesh cell and was monitored during the

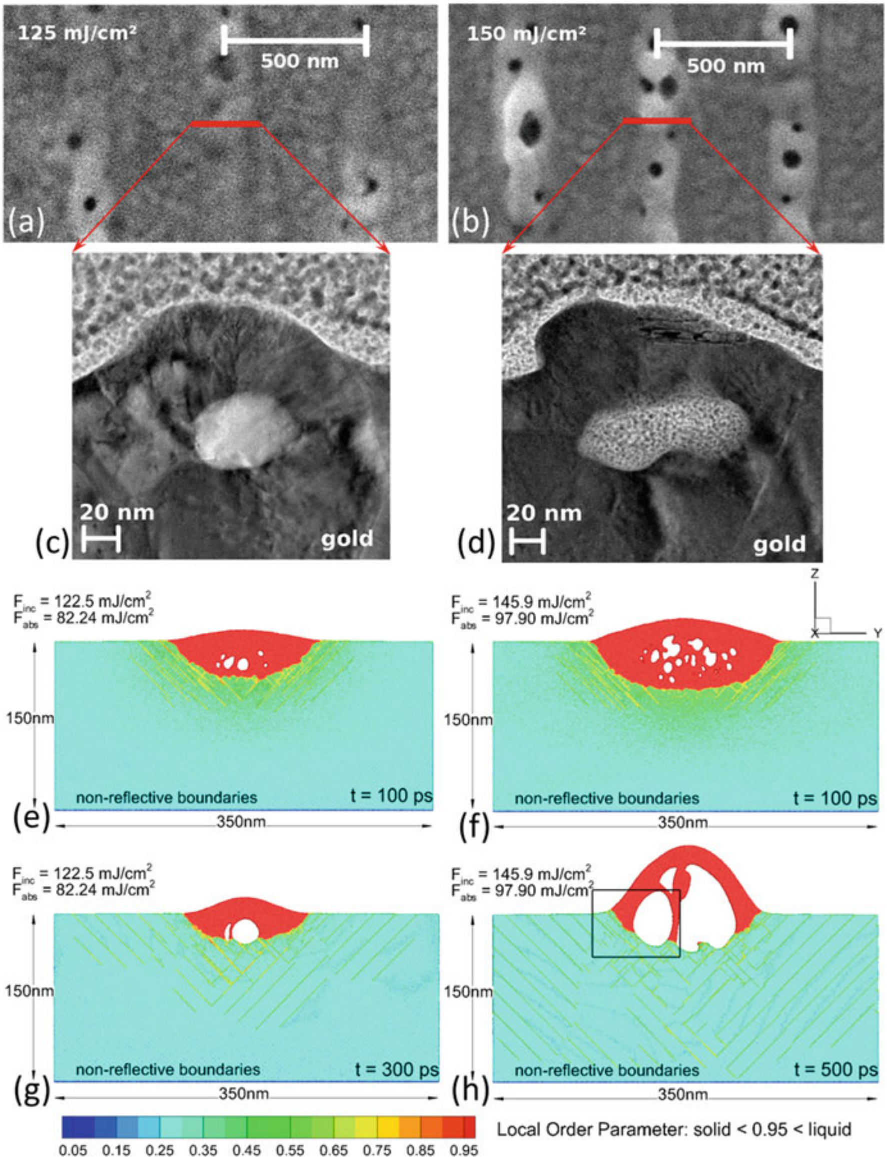

Fig. 2.14 SEM images of the 500 nm periodic structures with average incident fluences of 125 mJ/cm^2 (**a**) and 150 mJ/cm^2 (**b**). For these fluences TEM cross sections (**c**) and (**d**), respectively, were prepared with 500 nm structures by FIB. The darker areas show the gold, whereas the lighter areas show a protective platinum layer that has filled the empty spaces during the preparation process. The central 1-nm-thick slices of the atomic configuration snapshots at different times are shown in (**e**–**h**) for the incident fluences of 122.5 mJ/cm^2 (left) and 145.9 mJ/cm^2 (right). The atoms are colored according the LOP with the threshold value of 0.95 indicating atoms with liquid ambient (red) and those with a crystalline surrounding (other than red) [78]. (Reprinted with permission from [78], © American Physical Society (APS))

whole simulations. The newly formed structures with the ongoing process of recrystallization will solidify during the next tens of ns with no expected further changes in their geometry.

In general, the mechanism responsible for the nanostructuring process is similar to that described in Ref. [196] with a simplified model and later confirmed in a super-large-scale modeling of nanostructuring of thin metal films in Ref. [113]. Namely, the relaxation of the laser-induced compressive stresses generated under conditions of the inertial stress confinement [134, 155], given by Eq. (2.17), serves as the main driving force responsible for the acceleration of a transiently melted region of the target which results in the bloating of a nanostructure. Fast electron heat conduction, on the other hand, proceeding by two- or three-dimensional manner (depending on the experimental geometry), results in the electron temperature falling below the temperature of atoms in the molten volume. In this case, the electrons, due to electron-phonon energy exchange, provide the conditions for the fast cooling of melted material and rapid solidification of a surface feature generated in the process of hydrodynamic motion of the liquid material.

Nevertheless, there is an essential difference between the nanostructuring processes of thick metal targets, investigated in this work, and thin metal films investigated in Ref. [113]. In those simulations, the formation of a nanostructure was assisted with by the separation of film from a substrate. Alternatively, in the simulations shown in Fig. 2.14e–h, we observe the formation of voids at some distance beneath the surface. The reason is that in our modeling we are dealing with a thick target. Keeping in mind the aspect of the conservation of mass, this implies the formation of voids inside the material or a significant redistribution of matter along the surface in order to allow the formation of bulged nanostructures. This indeed can be confirmed by simple observation of our computed atomic configuration snapshots and our experimental results, Fig. 2.14a–h. The relaxation of the laser-induced stresses formed in the material under conditions of inertial stress confinement induces strong tensile stresses (~ −4 GPa) that in the liquid part of the material exceed the material strength (the atmospheric pressure, ~0.1 MPa is a negligible contribution here) and promote the formation of voids, the precursor of a spallation process [77, 206, 207]. The mechanism of void formation was investigated in details for metallic and molecular solids in Ref. [134]. It was found that if the conditions for inertial stress confinement are fulfilled under the applied irradiation parameters (Eq. (2.17) in Sect. 3.3 of this chapter), the critical size of voids and the rate of their nucleation are governed by the combination of both quantities of the induced tensile forces (negative pressure) and the atomic temperature. The range at which the characteristic temperature and pressure gradients are established by the time of the electron-phonon equilibrium is related to the effective laser energy deposition depth. It was shown that for short laser pulses (shorter than the characteristic electron-phonon equilibration time), this depth can be approximated as a function of the material properties at the applied fluence [155]. For the fluences used in this work, the effective laser energy deposition depth is ranging from 70 nm to 100 nm. At the material's surface, the tensile forces are diminishing, and therefore, the formation of voids is suppressed, even though the temperature is highest there. On the other hand, at deeper parts of the material, where tensile stresses can reach their maximum value, the atomic temperature may not be high enough for exceeding the material strength. The formation of the voids, therefore, takes place at some distance from the surface, but within the effective laser energy deposition depth.

Finally, the applied computational technique allowed a direct comparison of the experiment with the results of MD simulation on an atomic scale showing a very good agreement. The process of nanostructuring on thick metal targets due to an ultrashort single UV laser pulse near the damage threshold can be described as a result of three competing mechanisms. The relaxation of laser-induced compressive stresses under conditions of inertial stress confinement promotes the formation of voids inside the molten part of the material at the areas with the highest incident energy. The formation of voids relaxes the induced tensile stresses and assists in the establishment of hydrodynamic motion of the upper liquid resulting in the structure growth. Meanwhile, fast electron heat conduction in bulk of the target provides rapid cooling of the elevating structure and results in its fast resolidification. Understanding these processes on an atomic scale and being able to precisely simulate them provides a powerful tool for predicting material behavior and hence designing new nanotechnology applications.

The performed theoretical and experimental investigation of the mechanism of periodic nanostructuring also allows to take a close look at the resulting morphology of the obtained structures [23]. Figure 2.15 shows the direct comparison of the modeling results with the experimental observations for the case of 500 nm period structures formation at an incident fluence of 250 mJ/cm^2. One can see that the final structures are opened to the surface (a) and the simulation is reproducing this process (c). Amazingly, not only the formation of the wall-like structures is observed in both simulations and experiments (green lines relate the experimental observation with corresponding cross sections in the simulated structure), but even the tiny surface and subsurface nanograins, nanovoids, nanowalls, nanocolumns, and polycrystalline structures at the base of the modelled structures reveal a perfect match between the simulation and experiments at the nanoscale. Namely, the process of spallation creates an excessively rough surface with nanostructures and nanovoids, captured inside the solidified material (b). To make it clear, the corresponding nanocolumn (orange rectangle) and nanovoid structures (red rectangle) are identified and boxed in both the TEM (a) and FIB (b) pictures and related to the atomic snapshot (c). The formation of such structures perfectly agrees with recent theoretical finding presented in [208, 209].

Apart from the generation of a great number of dislocation planes, highlighted by a light blue color in Fig. 2.15c, the results of the simulation also predict the polycrystalline character of the solidified structures as it was emphasized in [198]. As it was found in [196], the fast cooling process of the developing structure is provided by the strong electronic heat conduction mechanism. Since the classical solidification is governed by the diffusion process, which takes time, the liquid can undergo a significant cooling below the equilibrium melting point by more than 20% [120]. Thus, at such strong undercooling conditions, the classical solidification process governed by the heterogeneous mechanism (propagation of the well-defined

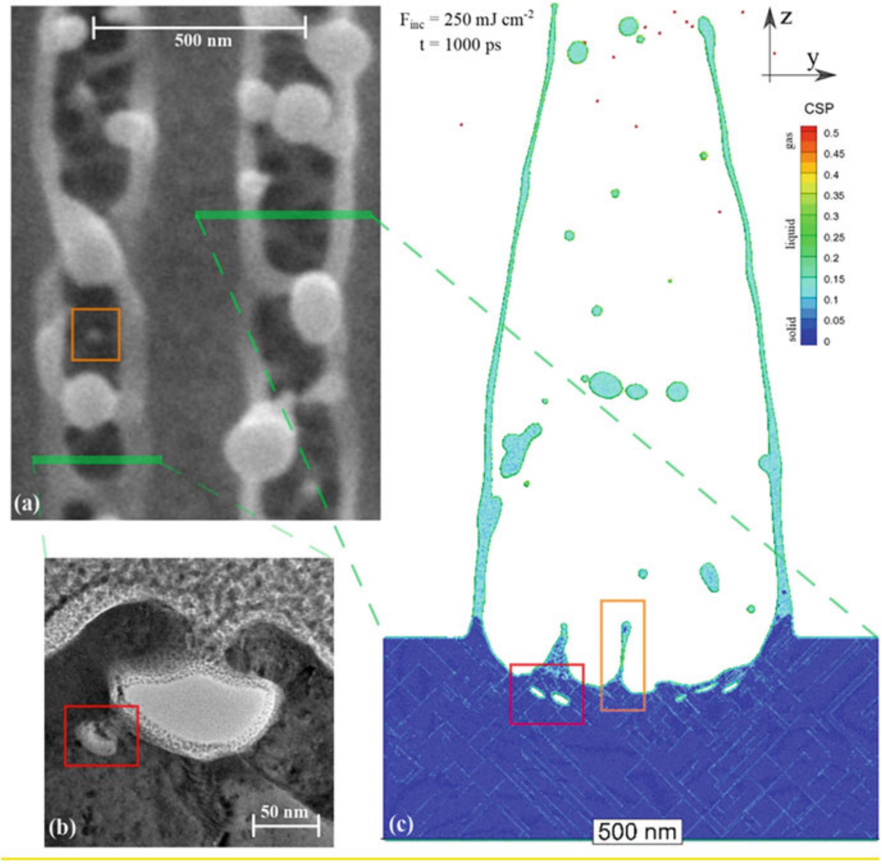

Fig. 2.15 Direct comparison of SEM top view in (**a**) and TEM cross section in (**b**) with the simulation results of the atomic configuration 40 × 500 × 200 nm^3 of 500 nm period at 1000 nm in (**c**). The atoms are colored by CSP for distinguishing a local crystal structure as follows: crystal <0.08 < defects (dislocations) < 0.11 < liquid <0.25 < surfaces <0.50 < vapor (free atoms). The process of spallation results in an opening of the generated structure and formation of a number of droplets and pillar-like structures on the remaining surface (orange rectangle). The spallation process is accompanied with the generation of subsurface voids (red rectangle) registered in both experiment and simulation and zoomed in the squared window in Fig. 2.16d below. (Reprinted from [23], Copyright 2020 under Creative Commons BY 4.0 license. Retrieved from https://doi.org/10.3390/nano10101998)

solid-liquid interface) cannot keep up due to a too high cooling rate, and the solidification process turns into a massive nucleation of the solid phase inside the liquid due to the homogeneous nucleation mechanism. This results in the formation of nanograins of the solid phase that have random orientation forming nanograin boundaries constituting the polycrystalline character of the final nanostructures. Moreover, the higher the cooling rate, the smaller the resulting nanograin size. Since the cooling rate depends on the established temperature gradient, it therefore

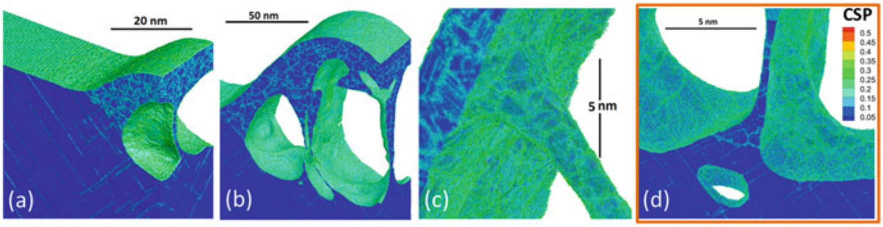

Fig. 2.16 The nanostructures generated in the simulations on periodic nanostructuring are zoomed for (**a**) the period of 270 nm at the incident fluence of 120 mJ/cm^2 and (**b**) 145 mJ/cm^2. (**c**) Structures obtained for the case of 500 nm period at the incident fluence of 160 mJ/cm^2 and (**d**) 250 mJ/cm^2. The atoms are colored by CSP parameter. (Reprinted from [23], Copyright 2020 under Creative Commons BY 4.0 license. Retrieved from https://doi.org/10.3390/nano10101998)

depends on both the physical size of the excited volume and the applied incident fluence, see Fig. 2.16.

The analysis of the generated crystal structures, presented in Fig. 2.16a–d, indicates their polycrystalline character. Apparently, the size of resulting nanocrystals depends on the cooling rate upon the onset of homogeneous nucleation. At this moment the temperature of liquid is already significantly below the equilibrium melting point, and the lower its value, the large the amount of the solid nuclei is generated, limiting therefore their final size. The temperature to which the liquid is cooled down (right before the onset of homogeneous nucleation) is determined by the initial geometry of the established electronic temperature gradients, their steepness, and the available space for the heat sink. From here we can conclude that small nanocrystals mainly constitute the nanostructures generated at a smaller period and at smaller incident fluence. The last figure in Fig. 2.16d allows for a direct comparison of the simulated bottom and subsurface structure generation, shown in an orange rectangle region in Fig. 2.15a–c. Noticeably larger size of the nanocrystals is explained by a relatively weaker cooling rate limited to the nearly 1D case due to the elongated geometry of the pillar-, column-, or wall-like structures. The detailed analysis of the experimental picture, Fig. 2.15b, indicates the polycrystalline character of the subsurface region via darker lines and spots due to different optical properties of the nanograin boundaries and the relative defects. While the experimentally observed and numerically simulated nanograin structures are in agreement with recent theoretical works [210–212], it is worth mentioning that the crystal structures obtained during the nanostructuring process due to extremely fast laser-induced cooling mechanism can be of unique character and never met in nature. Thus, generation of such structures can be of great interest for potential technological applications.

4.3 *Periodic Nanostructuring: The Effect of Liquid Environment*

This work is a successor of our previous study [23, 78] (and in the above two sections), where the mechanism of periodic nanostructuring process due to UV (248 nm) single-laser pulses (with a periodic sinusoidal-shaped spatial intensity profile on the surface of a thick Au target) was studied both experimentally and theoretically. In the present study, we focus on the new phenomena involved into the process of periodic nanostructuring under water layer. For this purpose, we perform several simulations at the incident fluences ranged from 160 to 250 mJ/cm^2, and the nanostructuring process itself will be studied with and without spatial confinement due to a layer of water situated atop the target. The experiments on nanostructuring performed in the presence of water layer on the surface revealed, in general, finer structures, less damage of the surrounding parts, and cleaner surface as that compared to the experiments performed in air or in vacuum [213–215]. The physical mechanism underlying the advantage of nanostructuring process under a layer of water, however, was not clear until recently [148, 216, 217], and essential phenomena resulting in a better quality of the structured surface obtained under conditions of spatial confinement become the main subject of this subsection [218].

From the point of theoretical study, the modeling of water is a challenging task due to specific properties of the water molecule. The existing water models [219–221], although nicely representing the water properties for particular experiments, suffer from one or another limitations depending on the assigned task details. The explicit model [219] requires very small computational time-step during the integration, which results in its high computational cost. The model reported in [220] is representing a water molecule as three particles, which is necessary for some simulations, but requires simulating quite a number of atoms, which limits the size of the total computational box. The model suggested in [221] represents the water via big (several molecules) interacting particles that results in an accurate reproduction of the water properties, but the interaction between big water particles and small metal atoms does not seem to be obvious.

In this work, therefore, we suggest a water model, representing its mechanical properties only via EAM method proposed by Zhakhovsky [222], which helps us to overcome the time-step and system size limitations on the one hand, but still allows for a straightforward analysis of the interaction between water and metal particles as the interaction between single molecules. Thus, the suggested computational approach is aiming on the identification of general effects involved in the nanostructuring process, solely caused by the mechanical action of a water layer. Such a general approach, however, is an important intermediate step, and we can directly compare the results of simulations with and without spatial confinement. A similar isolating approach was already successfully implemented in the investigation of the main mechanisms responsible for nanostructuring process in the above in Sect. 4.1. Finally, the interaction between water particles and metal atoms was assumed in a similar way proposed in [217]. A direct comparison of the final results with the experiment, therefore, has a semiquantitative character since we do not consider the optical effects due to a water layer explicitly.

To simulate the process of nanostructuring of metals under water layer, the model, therefore, is used in combination with already-developed MD-TTM computational approach, Fig. 2.3, with an additional thick water layer atop, modelled via classical MD method as it is schematically shown in Fig. 2.17 for the case of multiprocessing regime. The experimental setup is the same as in the previous two sections and schematically shown in Fig. 2.13a, b. In the present experiments, all surface patterns are accomplished by single-pulse exposure using two beams interference in order to form a large area sinusoidal intensity distribution on the sample surface, Fig. 2.17a. Both experiments and simulations were executed with a spatially modulated intensity profile with a period of 270 nm and 350 nm, respectively. The spatial irradiation geometry of the experiment combined with a properly selected model volume gives the opportunity to obtain a direct comparison of experiment and simulation of nanostructuring a thick Au target on the experimental scale, which eventually opens the way to predict properties (topological, morphological, and structural) of surface modifications for industrial applications. Thus, the surface nanostructuring simulations in this work are performed in air/vacuum and under a water layer for three different incident fluences [218].

In order to investigate the effect of water confinement on the process of periodic nanostructuring with UV 400 fs laser pulse, we performed six simulations for a set of fluences of 160, 200, and 250 mJ/cm^2 for the case Au in vacuum (the same as in air) and with a water layer atop the target. Therefore, we have a possibility for a direct comparison of the nanostructuring process for the same conditions depending on media above the target. The sample of gold was initially prepared and equilibrated at 293 K at $P = 0$ GPa. Then, the layer of water, equilibrated at the same conditions, was placed atop the gold target at the distance satisfying the minimum of the solid-liquid interface energy and relaxed for few ps. Finally, all six computational supercells were run for 1000 ps of the experimental time.

The results of modeling of the periodic nanostructuring due to a single 400 fs UV laser pulse can be seen in Fig. 2.18 as a sequence of the atomic snapshots taken at 175 ps and at the final time 1000 ps in comparison between the process in vacuum and under water layer. The mechanism of nanostructuring was already presented in previous sections and also in Ref. [196] for a general mechanisms and for the case of periodic UV nanostructuring in particular [23, 78]. Here, we mostly concentrate on the effect of water confinement.

In Fig. 2.18 we observe two atomic configurations for the structures produced in air (left) and under water confinement (right), taken correspondingly at 175 ps and 100 ps after the pulse. By means of a direct comparison of the presented snapshots, we can visualize, analyze, and understand the effect of water confinement on the process of nanostructuring. First, the water confinement due to its mechanical resistance leads to a significant suppression of the growing nanofeature that makes the final structured surface smoother as compared to that obtained in air or in vacuum. It is also visible that by the final time of 1000 ps, the effect of the water layer results in a significantly faster solidification of the growing tip of nanofeature.

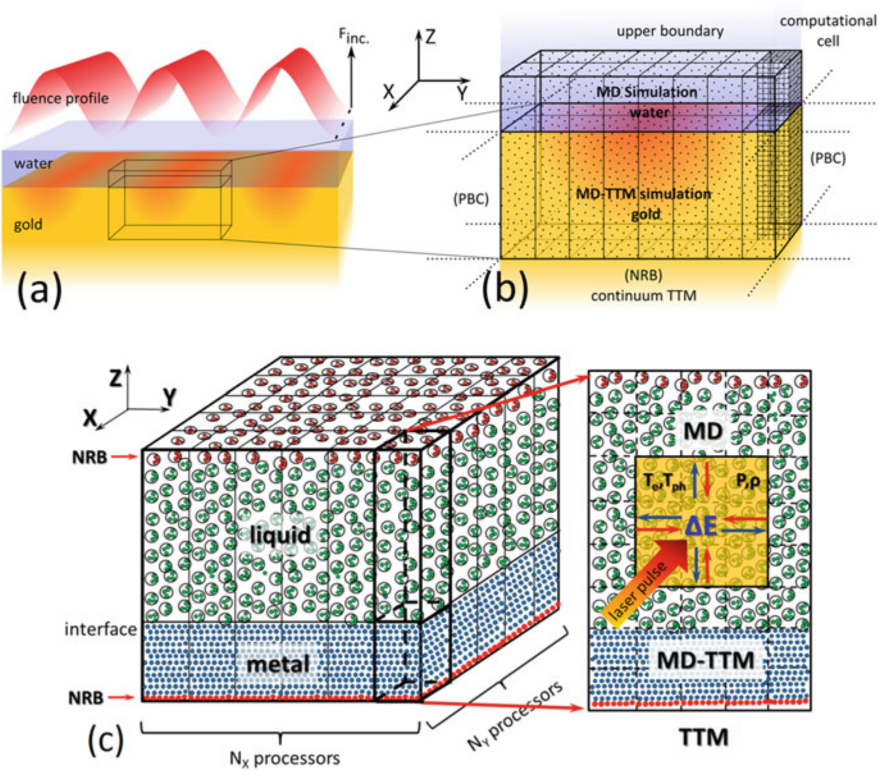
fluence profile
F_inc.
water
gold
(a)
Z
X
Y
upper boundary
computational cell
MD Simulation
water
(PBC)
(PBC)
MD-TTM simulation
gold
(NRB)
continuum TTM
(b)
Z
Y
X
NRB
liquid
interface
metal
NRB
(c)
N_X processors
N_Y processors
MD
T_e,T_ph
P,ρ
ΔE
laser pulse
MD-TTM
TTM

Fig. 2.17 Computational box for the experiment, shown in Fig. 2.13a, b for the case of water confinement, relays on the sinusoidal laser energy distribution on the target surface (**a**). The total computational cell therefore is schematically represented for multiprocessing mode in (**b**) and expanded in details in (**c**). In each particular processor core, an atomistic-continuum MD-TTM model for metal part and ordinary MD model for water part are solved in 3D space (internal mesh is shown for one processor core). Beneath the nonreflective boundaries (NRB), an ordinary TTM model is solved in continuum to account for the heat flux outward the metal surface region describing the cooling process [218]

The high rate of cooling due to electron heat conduction (inside the nanofeature) and heat losses due to vaporization losses, visible in Fig. 2.18 as red dots, facilitates the solidification process. Second, at a higher fluence (250 mJ/cm^2), the formation of debris upon the structures opening to the air may take a massive character, as seen in Fig. 2.15c. As a result of gravitation and the ablative plume expansion, the ejected metal clusters and droplets will eventually (on the millisecond time scale and longer) redeposit back on the resulting surface affecting its quality. In the case of water confinement, however, the formation of liquid metal droplets at the applied fluences is suppressed. Even at much higher applied fluences (1 J/cm^2 and above), the generated droplets constitutes the colloidal solution of NPs as it is in PLAL experiments, leaving the resulting nanostructured surface cleaner (free of

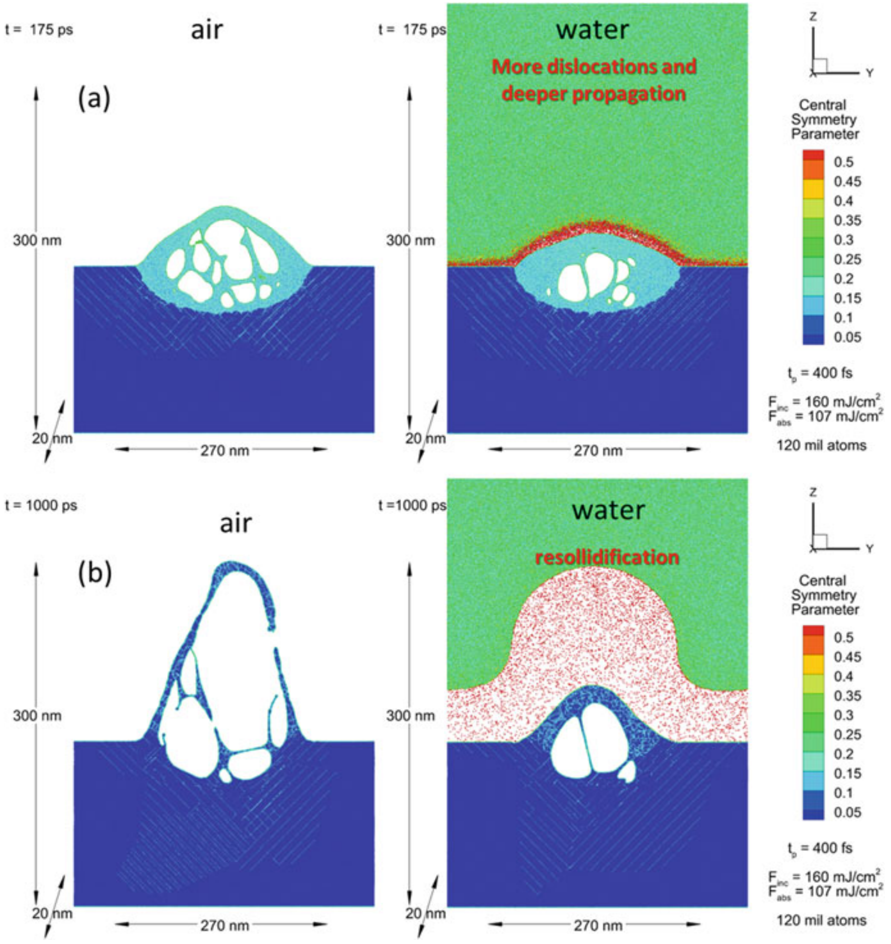
t= 175 ps
air
(a)
300 nm
20 nm
270 nm
t= 175 ps
water
More dislocations and deeper propagation
300 nm
20 nm
270 nm
Z
Y
Central Symmetry Parameter
0.5
0.45
0.4
0.35
0.3
0.25
0.2
0.15
0.1
0.05
t_p = 400 fs
F_inc = 160 mJ/cm²
F_abs = 107 mJ/cm²
120 mil atoms
t = 1000 ps
air
(b)
300 nm
20 nm
270 nm
t =1000 ps
water
resollidification
300 nm
20 nm
270 nm
Z
Y
Central Symmetry Parameter
0.5
0.45
0.4
0.35
0.3
0.25
0.2
0.15
0.1
0.05
t_p = 400 fs
F_inc = 160 mJ/cm²
F_abs = 107 mJ/cm²
120 mil atoms

Fig. 2.18 The atomic snapshots of the structured gold surface due to 400 fs laser pulse with 270 nm period intensity distribution along Y axis (Fig. 2.17a) taken at $t = 175$ ps (**a**) and at the final time 1000 ps (**b**). The same incident fluence of 160 mJ/cm^2 gives qualitatively different result for the case of structuring in air/vacuum (left) and under water layer (right). The atoms are colored by CSP for distinguishing a local crystal structure as follows: crystal <0.08 < defects (dislocations) < 0.11 < liquid <0.25 < surfaces <0.50 < vapor (free atoms)

redeposited metal debris). This can be confirmed by examination and comparison of the experimental measurements. And third, it was detected during the simulations that for the case of nanostructuring under water confinement, the propagation of dislocation planes inside the metal film, visible in Fig. 2.18 as light blue lines, is deeper and it proceeds in a greater number due to additional resistance of the water layer to the relaxation of the laser-induced stresses inside the metal film. As a result, the structures, obtained under regime of spatial confinement due to a water layer, are expected to be stronger from the point of endurance. Such process was already observed in our previous work [23, 196] and detected in short-pulse laser-peening experiments [223].

Eventually, by the time of 1000 ps, when the temperature of material constituting the forming shell is around 750 K in air, it has the value of only 600 K in water, which is much below the melting point and the elevation of the nanofeature is over (the elevation speed was monitored by the velocity filed). Under this significant undercooling (the equilibrium melting temperature of the modelled gold material is 1343 K), the solidification process takes a massive character by means of homogeneous nucleation of the solid phase. The final structures therefore exhibit polycrystalline character, as it was also registered in the above simulations.

In conclusion, it is worth mentioning that as a result of our simulations of periodic nanostructuring process with a UV laser pulse, we got a possibility for a comparison of the modeling results with the experimental data on the same scale. Because of the number of assumptions in the modeling and experimental procedure, however, the possibility of a direct comparison of the modeling and experimental results at the moment has a semiquantitative character. Nevertheless, the obtained results so far confirmed the experimental observations and explained the main reasons why the quality of generated structures under conditions of spatial confinement with a water layer in general benefits over those obtained in air or in vacuum.

5 Inclusion of Plasmonics Into MD-TTM Model

5.1 Generation of LIPSS on Metal Surfaces

Precise manufacturing of surface nanostructures is of crucial interest for both fundamental science and practical perspectives. The variety of surface functionalization possibilities open up a way for advanced nanoscale devices. Irradiation of solids by ultra-short laser pulses can lead to the spontaneous formation of laser-induced periodic surface structures (LIPSS), which are broadly applied for the surface nanostructuring. LIPSS attract considerable fundamental interest due to their many potential applications ranging from optics, mechanics, and chemistry to biology, medicine, and industry [4, 10, 149]. LIPSS are usually formed in a multi-pulse regime [10, 224, 225] or in the laser scanning regime [226, 227] when the morphology of the surface treated by the laser pulse is continuously changing from pulse to pulse. This fact has a crucial importance and can influence on the deposition and relaxation of the laser energy of the subsequent irradiation shot. Therefore, before tackling an intricate question about LIPSS formation in multi-pulse or laser scanning regimes, we aim to investigate the mechanisms for the LIPSS formation due to only a single-laser pulse [228–231]. In contrast to multi-pulse or laser scanning regimes (which are discussed in details in Chaps. 1 [232], 5 [233], and 23 [234] of this book), there are only a few studies about LIPSS formation after a single-laser pulse [235–240]. Among various theories, which were proposed to explain LIPSS formation [10, 148, 208, 225, 237, 241–246], excitation of surface plasmon polaritons (SPP) and their interference with the incoming light wave is regarded to be the most promising hypothesis for the physical origin of the LIPSS morphology [241, 242]. SPP are actively used in plasmonics at weak and moderate laser excitation conditions [247–251], but so far little attention has been given to verify the influence of SPP excitation on LIPSS formation at higher laser fluences.

SPP waves can be induced at the interface between a dielectric (air) and a conductor and propagate along it. For the excitation of the SPP, two conditions have to be met. First, the geometrical structure of the irradiated sample should provide the missing wave vector between the photon (laser pulse) and the SPP to fulfill the conservation of linear momentum. Therefore, it is possible to launch SPP waves on a sample with a step edge (Fig. 2.19a) [252, 253] because a Fourier transform of the step edge gives a continuum spectrum of momenta [230]. It means that the step edge structure is able to provide additional momentum to the light wave to excite SPP. The SPP coupling can also be realized with the help of a prism or grating [254]. Second, the dielectric function of the conducting medium, at the interface of which the SPP can be excited, must satisfy the condition on plasmonic activity that is $\mathrm{Re}(\varepsilon) < 0$, where ε is the dielectric function [254]. Simultaneous fulfillment of both conditions for the SPP excitation can be guaranteed by a step edge structure on gold used in our study. The schematic irradiation geometry is shown in Fig. 2.19a.

One can univocally determine the location of the SPP excitation at the step edge [252] for a sample geometry as in Fig. 2.19a. Generally, the SPP will be excited at both sides of the step edge, but here we are only interested in the positive x-coordinate values. An analytical function for the source term (the total input power per volume) $Q_{\mathrm{total}}(\mathbf{r},\mathrm{t})$ with $\mathbf{r}$ given by (x,y,z) in the frame of the TTM approach has been derived by explicit calculation of the electromagnetic fields of the laser and the SPP and their interference [228]. The dielectric function was assumed to be constant and taken from an experimental work [255], treating evaporated gold samples as well. At the laser wavelength 343 nm used in our experiments, we have extracted the real and imaginary parts of the dielectric function of gold as $\varepsilon'_m = -0.49$ and $\varepsilon''_m = 6.18$, respectively, which satisfy the condition on plasmonic activity $\varepsilon'_m < 0$ [254]. In contrast to the previous studies [148, 208, 237, 243], the description of the laser energy absorption, which enters the TTM part of the MD-TTM model, is given by the new source term $Q_{\mathrm{total}}(\boldsymbol{r},t)$ that includes the effect of SPP excitation on the absorbed laser energy redistribution across the surface. This plasmonic source term can also be applied for studying features of the excited SPP, for example, for investigation of the SPP properties and to discover plasmon-induced hot carriers' generation [256].

5.2 Modeling of LIPSS

LIPSS formation on material surfaces was investigated in different works [237, 243] in the framework of the TTM model [31, 49], where it was assumed that

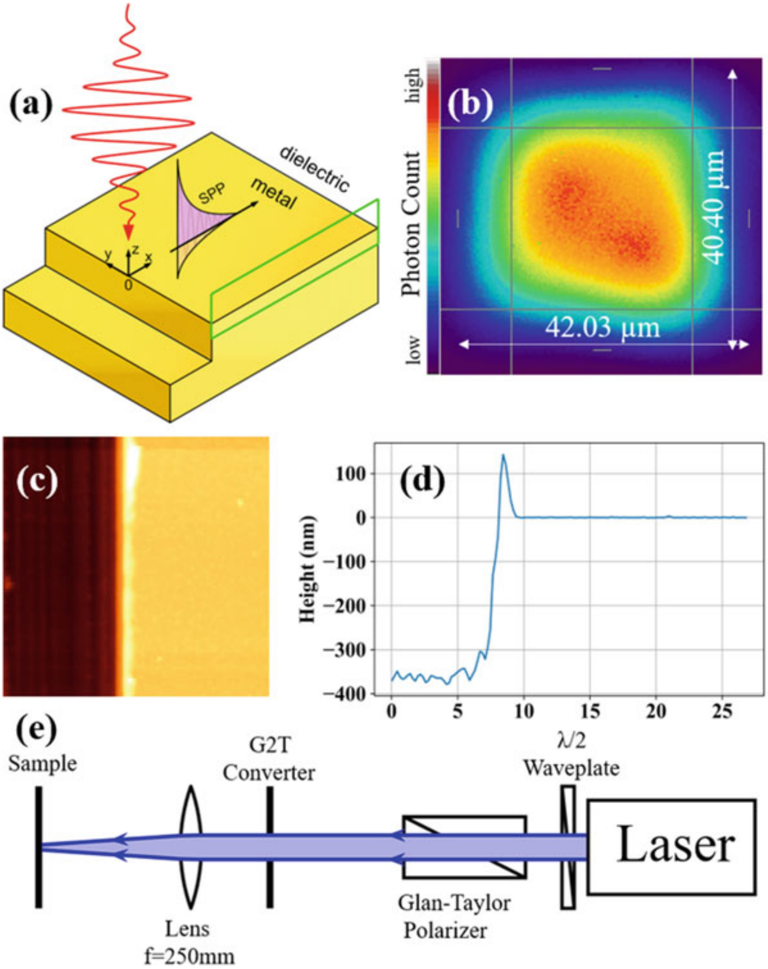
(a)
dielectric
SPP
metal
y
z
x
0
(b)
high
Photon Count
low
42.03 μm
40.40 μm
(c)
(d)
Height (nm)
100
0
−100
−200
−300
−400
0
5
10
15
20
25
(e)
Sample
G2T
Converter
λ/2
Waveplate
Laser
Lens
f=250mm
Glan-Taylor
Polarizer

Fig. 2.19 Schematic representation of the irradiated system and the experimental setup. (**a**) The schematic step edge irradiation geometry with SPP excitation. The green frame shows the simulation region for the MD-TTM. (**b**) The beam profile in the surface plane. (**c**) AFM recording of a trench (step edge) on the gold sample. (**d**) The average height profile measured by AFM. (**e**) The experimental setup

electrons absorb the laser energy in accordance with the predefined source term profile. In addition, a combined electromagnetic and thermohydrodynamic approach [245, 246] was developed. However, under extreme conditions, realized during ultrashort pulse laser heating, the classical description of laser-induced phase transition mechanism, given by Gibbs' theory or other continuum models under the assumption of local equilibrium, is no longer valid, and we apply here the MD-

TTM approach with the computational cell schematically illustrated in Fig. 2.3, for instance.

In existing approaches so far, arbitrary periodic functions in the lateral x-direction have been assumed for the source term to imitate the laser energy absorption in the frames of the TTM or MD-TTM models [148, 208, 237, 243]. As a result, such models allow to reveal relaxation dynamics of laser-induced periodic energy deposition, but they cannot inherently predict the SPP periodicity and decay length, which will influence the final morphology of LIPSS. With our approach we present a clear demonstration of the SPP nature of LIPSS formation following single-laser pulse irradiation of a step edge structure on a gold sample. In addition, our MD-TTM simulations, including the modeling of SPP excitation and subsequent interference of the SPP field with the laser field [228], provide a complete description of the growing mechanism of the experimentally obtained structures. It should be mentioned that complex prefabricated structures on the surface can result in complex electromagnetic fields [250, 257, 258], which could trigger intricate surface patterns. Here we have chosen a simple step edge structure to have the opportunity for the direct comparison of simulations with measurements on the same spatiotemporal scales.

In the applied MD-TTM, an advanced, as compared to previously developed [64], model for the electron conductivity [65] was implemented in large-scale simulations of the laser-deposited energy dissipation in the irradiated target. We applied a single 250 fs laser pulse at an incident fluence when the structures appear. The sample size for the MD-TTM simulations was 4000 nm × 10 nm × 200 nm in x, y, and z directions, respectively, consisting of 375 million atoms. The position of the step edge is located in our simulations at the center, where $x = 0$ nm and periodic boundary conditions are set in the x-direction at ±2000 nm, a distance large enough from the center to neglect the modulations in laser energy deposition due to the SPP. The NRB conditions were applied at a depth of 150 nm [74], and an ordinary TTM model was solved beneath the NRB for both electrons and phonons.

In the proposed approach, the excitation of SPP and its interference with the incident electromagnetic wave, resulting in the laser-deposited energy redistribution across the surface, is directly accounted in the source term $Q(\mathbf{r},t)$ entering the TTM part of the combined model, Eq. (2.1). The analytical form of the source was derived as divergence of the Poynting vector $\mathbf{S} = \mathbf{E} \times \mathbf{B}$ and included the complete information about the electromagnetic wave. The details on SPP source term derivation can be found elsewhere [228], and its function consists of three inputs:

$$Q_{\text{total}}\left(\overrightarrow{r}, t\right) = Q_{\text{las}-\text{las}}\left(\overrightarrow{r}, t\right) + Q_{\text{las}-\text{SPP}}\left(\overrightarrow{r}, t\right) + Q_{\text{SPP}-\text{SPP}}\left(\overrightarrow{r}, t\right) \qquad (2.18)$$

correspondingly, due to laser-laser, laser-SPP, and SPP-SPP field interference.

In the simulation, we assume the SPP coupling parameter $\beta = 0.30$ and the phase $\delta = 238.68°$ in the implemented laser source. These parameters were chosen based on preliminary calculations on the laser energy deposition coupled with the energy conservation law. The electronic temperature reaches its maximum value of

14500 K and performs roughly five modulations before it decays. Followed by the laser energy absorption, the electron-phonon equilibration takes place within the next 10 ps. A maximum lattice temperature of 3500 K is achieved in the proximity of the surface near the step edge [230].

The simulation results are shown in Fig. 2.20 as a sequence of the atomic snapshots of the target evolution. The material reorganization (surface uplift) of LIPSS formation occurs at 120 ps, when the nucleation of internal voids, due to the relaxation of the laser-induced stresses, indicates the onset of spallation. While structures are forming, the resolidification process takes place. This can be seen in Fig. 2.20 at 300 ps, 500 ps, and 1000 ps as a propagation of the solid-liquid interface toward the free surface due to the heterogeneous mechanism of solidification. Later, at 1000 ps, the resolidification process is complemented with nucleation of solid phase inside the liquid due to homogeneous solidification mechanism, when the strong cooling rate results in the local temperature drop significantly below the melting point (20–25%). The structure closest to the step edge grows up to 70 nm by the time of 1000 ps, while the third peak from the step edge has a height of 25 nm (see Fig. 2.20). The final structures profile is in good agreement with the experimental height profile shown in Fig. 2.22b. The atomic force microscope (AFM) measurement in Fig. 2.22 does not show the first two periods, and the observed height profile starts with a modulation depth of about 25 nm. The first two periods are not presented, as the structures are too irregular for precise measurement. The spatial decay of the height profile of LIPSS is governed by the laser-SPP interference part of the source term with a characteristic length $1/K_x'' = 676$ nm calculated at the experimentally applied laser wavelength 343 nm. In contrast, the classically defined SPP attenuation length [228, 254] $1/(2k'')_x = 338$ nm has a two times lower value. The calculated new surface level is elevated above its initial position before the irradiation by 2–3 nm due to material thermal expansion. However, it is challenging to measure the level of the virgin surface experimentally because of possible contamination of the surface. Therefore, we can state that this effect is too small to be measured precisely with an applied experimental setup. The formation of a number of dislocation planes is visible as light blue lines in Fig. 2.20 beginning from 300 ps due to the laser-peening process [259].

From the analysis of the simulation results, we can state that the mechanism of the formation of periodic structures (LIPSS) following laser irradiation is generally similar to that discussed in [78, 260, 261]. Namely, the SPP-assisted laser-deposited energy redistribution results in rapid periodic lattice heating, which proceeds under the conditions of internal stress confinement, Eq. (2.17). The subsequent relaxation of the laser-induced internal stresses is accompanied with a generation of a strong pressure wave through the molten material and nucleation of voids in the bulk of the material with their periodic concentration corresponding to the positions of the corresponding SPP-assisted heating peaks. Such mechanical (acoustic) relaxation of the irradiated target results in the establishment of a hydrodynamic motion in the melt and is responsible for the elevation of the forming structure. The solidification process of the growing LIPSS, on the other hand, is provided by the fast electron heat conduction in 3D [196], Sect. 4.1.

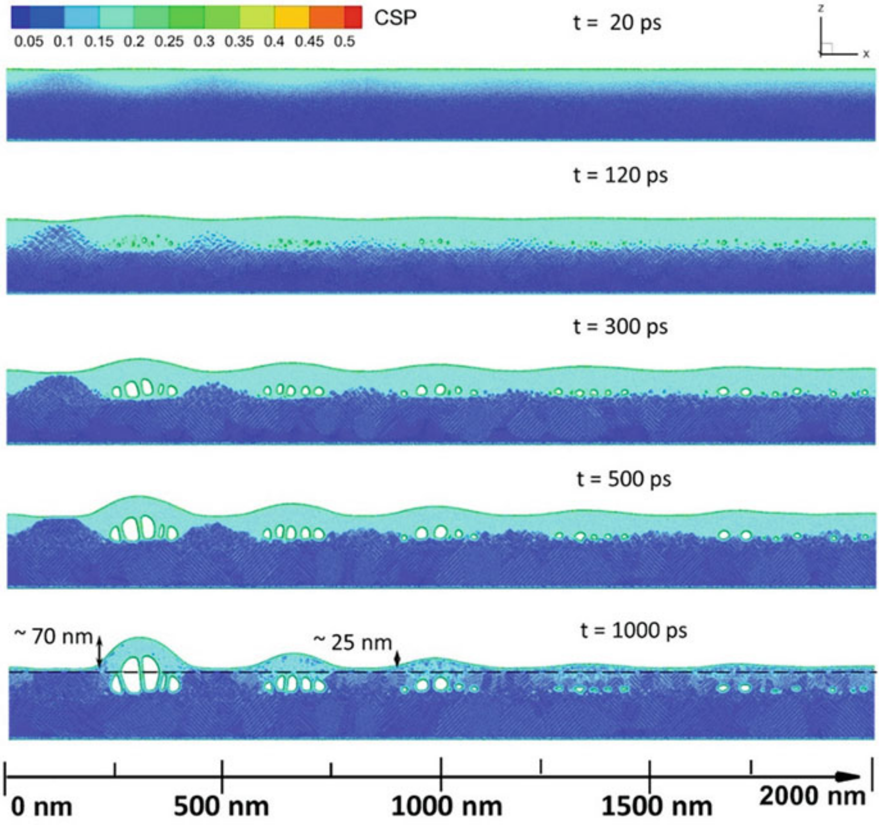

Fig. 2.20 MD-TTM simulations of LIPSS. Atomic snapshots of the Au target for the case of an incident fluence of 130 mJ/cm^2 are depicted for the times of 20 ps, 120 ps, 300 ps, 500 ps, and 1000 ps after the pulse. The atoms are colored by the central symmetry parameter (CSP) for distinguishing the local crystal structure as follows: crystal <0.08 < defects (dislocations) < 0.11 < liquid <0.25 < surfaces <0.50 < vapor (free atoms). The CSP parameter is shown in the figure as a color scale bar. The dashed line at the last snapshot indicates the sample surface before the irradiation. (Reprinted with permission from [230], © De Gruyter)

5.3 Experimental Verification

The samples used in the experiments consist of a 350-nm-thick gold layer on a glass substrate (Fig. 2.19d). Between the gold layer and the substrate, a thin chromium layer is applied to increase adhesion. The samples were manufactured via thermal evaporation. The root mean square (rms) surface roughness on the top of the gold sample was measured to be $R_{\text{rms}} = 1$ nm, with measurements taken at random positions on the sample using AFM. Such a small roughness ensures that SPP are excited only at the position of the step edge. The polarization of the laser beam is typically set to be perpendicular to the step edge (p-polarization). In addition, we have performed experiments with the laser polarization being parallel to the step edge (s-polarization), where LIPSS are not observed. Therefore, this suggests that the excitation of any other surface waves, for instance, quasi-cylindrical waves, has a negligible contribution to single-pulse LIPSS formation for a given sample geometry. Moreover, it was shown that quasi-cylindrical waves are mainly important for sub-wavelength slits or grooves [262, 263]. However, note that the contribution of quasi-cylindrical waves is increasing with increasing the laser wavelength and can be particularly important at infrared laser frequencies [263–266].

As the experimental representation of the step edge, a trench was mechanically created by scratching the surface before irradiation with the help of a sharp razor blade by loading it onto the surface using a spring to maintain a constant force. The edges of this trench are the equivalent of the step edge. The sample was moved with a constant velocity via a motorized linear stage to provide a steady trench. The prepared step edge profile can be seen in Fig. 2.19c, d. The uplifting walls at the sides of the trench have a height of about 100 nm relative to the top level of the gold surface, Fig. 2.19d.

All experimental results were produced using the third harmonic radiation of a Light Conversion Pharos PH-1-20W at 343 nm wavelength with a spectral width of about 1 nm. At the fundamental wavelength of 1030 nm, the pulse duration is 250 fs. A sketch of the experimental setup is presented in Fig. 2.19e. The experimental setup contains the laser source, a λ/2 wave plate, a Glan-Taylor polarizer to control the polarization of the beam, and a Gaussian to top-hat beam shaper (G2T) with a focusing lens ($f = 250$ mm) to produce a homogeneous, square-shaped laser spot (~40 μm at $1/e^2$ level, see Fig. 2.19b) on the sample. The laser beam was centered at the edge of the irradiated trench. We have applied only one single pulse per irradiation at normal incidence in all performed experiments. A series of single pulses were given on different positions along the trench, while the fluence was varied from shot to shot. The sample was examined by a scanning electron microscope (SEM) and an AFM.

Figure 2.21a presents the experimental results of LIPSS formation close to the rough step edge. It can be clearly seen that LIPSS structures follow the shape of the step edge rims due to SPP excited in the perpendicular directions. Figure 2.21b shows LIPSS structures at the step edge with an additional scratch nearby. Although the laser polarization is perpendicular to the step edge, we observe periodic structures parallel to the scratch on the right of it. We can decompose the laser polarization to the perpendicular and parallel components relative to the additional scratch. The perpendicular component or effective p-polarization relative to the additional scratch will cause SPP excitation, which will lead to LIPSS formation with orientation perpendicular to this effective p-polarization and parallel to the additional scratch. Therefore, the scratch direction will define the orientation of LIPSS. To make a clear comparison of the theory and the experiments and to avoid possible SPP-SPP scattering with the creation of complex absorption patterns like in the area between the step edge and the scratch in Fig. 2.21b, we tried to improve the uniformity of the step edge. On the other hand, the appropriate design

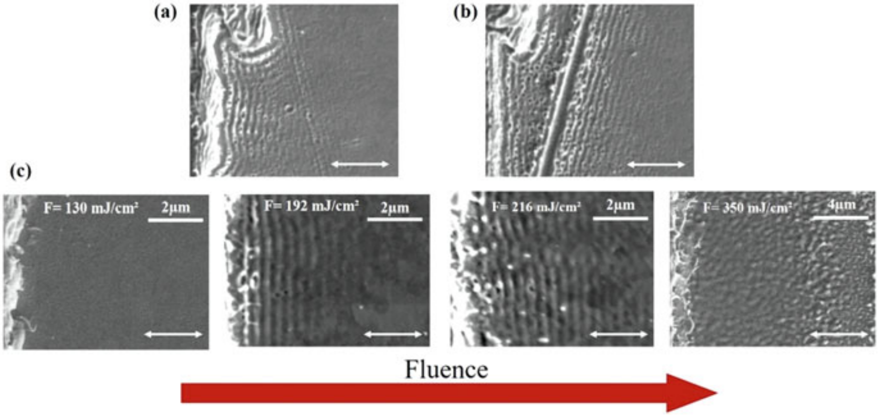

Fig. 2.21 SEM images of LIPSS with a step edge located at the very left side of each image. (**a**) SEM picture of LIPSS at the rough step edge irradiated with a fluence of $\phi = (214 \pm 22)$ mJ/cm^2. (**b**) SEM picture of LIPSS at the step edge with an additional scratch irradiated with a fluence of $\phi = (223 \pm 23)$ mJ/cm^2. (**c**) SEM pictures of LIPSS at the step edge with increasing incident fluence. The white horizontal double arrows show the direction of the laser polarization. (Reprinted with permission from [230], © De Gruyter)

of the step edges or scratches can in the future potentially result in the formation of the surface relief with demanded properties for technological applications.

The threshold of visible periodic patterns with a period of ~343 nm appears on a gold surface after laser irradiation of the step edge with a fluence of 160 mJ/cm^2. Increasing the fluence enhances the visibility of the structures (see Fig. 2.21c). Prominent LIPSS at fluences of 172 mJ/cm^2 and 192 mJ/cm^2 are shown in Fig. 2.22. In the investigated fluence range (130–350 mJ/cm^2), we observe LIPSS at fluences of 160–270 mJ/cm^2, where the LIPSS periodicity stays constant. Above 270 mJ/cm^2, we do not detect periodic structures in the final morphology (Fig. 2.21c, last). A possible explanation is that they disappear upon ablation of the surface layer [23]. We have found indications of ablation above a fluence of about 250 mJ/cm^2. AFM height profiles of LIPSS are presented in Fig. 2.22.

LIPSS are mainly divided into two groups: low-spatial-frequency LIPSS (LSFL) with a period comparable to the light wavelength and high-spatial-frequency LIPSS (HSFL) with a period comparable or smaller than half of the light wavelength [10, 148]. In the single-pulse experiments, we observe LSFL, which are oriented orthogonal to the beam polarization and have a periodicity close to the laser wavelength. We found that ablation is not required for a single-pulse LSFL formation shown in Fig. 2.22. Instead, we observe structures, which are formed by material surface reorganization (local swelling). It should be mentioned that other mechanisms of LIPSS formation, for example, mechanisms based on self-organization and instabilities in a liquid surface layer [233], can appear in the laser scanning and multi-pulse irradiation regimes. Note that we measured ablation for incident fluences higher than 250 mJ/cm^2, whereas LIPSS presented in Fig. 2.22

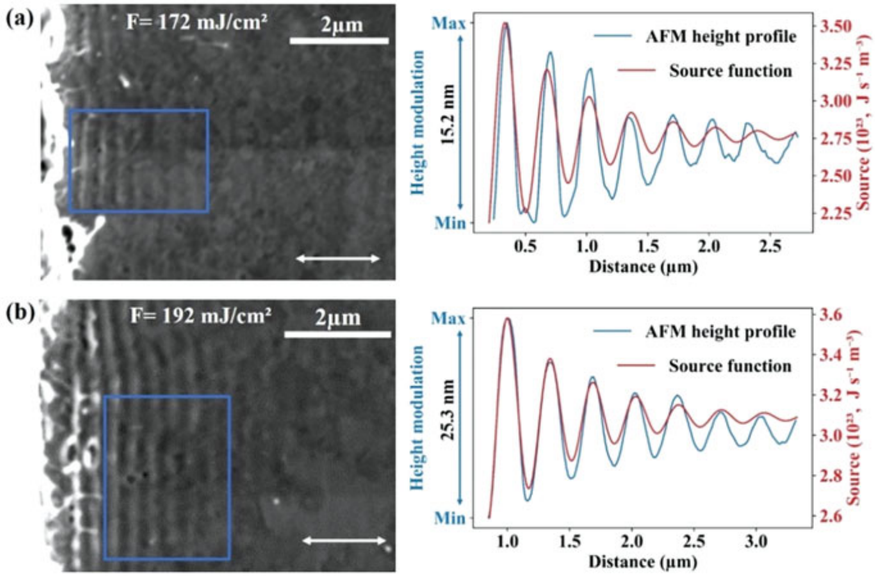

Fig. 2.22 SEM and AFM images of LIPSS with a step edge located at the very left side of each image. SEM picture of LIPSS at the edge of the trench irradiated with the fluences (**a**) $\phi = (172 \pm 9)$ mJ/cm^2 and (**b**) $\phi = (192 \pm 10)$ mJ/cm^2. The height profile of LIPSS is measured by AFM averaged over the sections indicated in the SEM pictures. The theoretical curves of the source function are also included in the figure. The white horizontal double-arrows show the direction of the laser polarization. (Reprinted with permission from [230], © De Gruyter)

have been induced with incident laser fluences 172 mJ/cm^2 and 192 mJ/cm^2. To the best of our knowledge, we have manufactured LSFL with the smallest periodicity reported so far for the single-pulse irradiation of metals in air. The only exception we are aware of is LSFL structures on Cu within the same range of periodicity (300 ± 40) nm [236].

We find excellent agreement between experiments and simulations for LIPSS periodicity: $\Lambda^{\text{exp}} = (338+/-10$ nm) and $\Lambda^{\text{theor}} = 344$ nm. This indicates that the assumption of a constant dielectric function is a good approximation for a given laser wavelength 343 nm when we compare SPP and LIPSS periods. However, special attention should be considered for larger laser wavelengths because the transient change of the optical properties of the irradiated sample could considerably modify SPP properties [267]. The spatial decay of the periodic structures away from the step edge is also in accordance with the decay of the modulated absorbed laser energy in the sample (see Fig. 2.22). However, the experimental structures experience a weaker spatial decay of the height profiles. The reason could be the nonconstant dielectric function [16, 267], resulting in an increased SPP propagation length and, therefore, its decay length. In addition, the limited size of the computational cell and utilization of nonreflective boundaries (NRB) designed for the absorption of planar pressure waves could also account for an underestimated threshold of the growing LIPSS structures. More accurate Langevin-NRB, aimed at absorbing of nonplanar laser-induced pressure waves due to periodically heated material surface, have been recently suggested in Ref. [208] and will be used in our following research. Moreover, additional investigations are necessary for a precise determination of the SPP coupling parameter β [228, 230] and hence a fully quantitative description of the LIPSS formation. Nevertheless, the direct comparison of our modeling results with our experimental findings provides a full understanding of the mechanism of the structure formation in a semiquantitative manner. Although the data calculated for 130 mJ/cm^2 match the experimental results of a slightly higher fluence of 170 mJ/cm^2, we have found a coincidence of the experimentally observed decay range of LIPSS and SPP-assisted MD-TTM simulations. Moreover, quasi-cylindrical waves can be excluded since they have a negligible contribution at low laser wavelengths [263, 265]. Therefore, we are confident to have identified SPP-laser interference as the origin of the formed LIPSS.

Based on our findings, we can elucidate the key steps leading to LIPSS formation after single-shot femtosecond irradiation of a predesigned step edge feature on gold. Initially, SPP waves are responsible for the periodic laser energy deposition and seed an opportunity that LIPSS will be formed. Although SPP can be excited at all fluences, LIPSS can be observed only in a specific laser fluence range below and around the ablation threshold. Note that the so-called ablative LIPSS [208] appear at much stronger fluences. They are caused by massive openings and expending of material, while molten walls merge in between the structures. In this work, we have shown nonablative LIPSS. These LIPSS are forming when the laser energy is high enough to create visible structures but still below the fluence of overall openings of voids inside LIPSS. It could be the reason of better regularity of LIPSS in our case in comparison with results for Au obtained in Ref. [239]. The final LIPSS relief is governed by the material elevation (local swelling or cavitation) due to the relaxation of the laser-induced stresses, triggering the spallation mechanism (mechanical rupture of the material with the formation of internal voids). In contrast, the solidification process is assisted with fast cooling due to the electron thermal conduction process. Thus, the evolution of the periodically heated material will define the LIPSS morphology. It should be mentioned that LIPSS can be created with periodicity varying in a wide range, depending on the physical properties of the sample, laser parameters, and, for instance, on the application of the external magnetic field during laser exposure [268]. In addition, it was shown in Ref. [231] that via manipulation of the laser beam profile by adjusting a fluence slope with increasing distance from the step edge, the decay of the height of the structures may be reduced or even completely eliminated, thus facilitating the formation of LIPSS with uniform heights.

6 Conclusion

In this overview, the most advanced continuous and atomistic description models were combined together to enlighten the laser-induced optical, plasmonic, melting, boiling, and ejection processes, occurring at wide spatial and temporal scales. Combining several numerical techniques into the single computational approach is envisioned as the key steps in studying the ultrashort-pulse laser modification of diverse materials in different ambient media. Furthermore, the efficient reorganization of the most time-consuming procedures in MPI implementation of the proposed models for multiprocessing allows to perform simulations on the scale directly attainable in the experiment and have the results of modeling directly compared with the experimental measurements. The applied numerical approaches have been identified as powerful numerical tools for the investigation of the nonequilibrium transient laser-induced states of materials. The proposed combined approach exhibits remarkable consistency with the experimental findings in various nanoscale laser-induced phenomena with further potential toward efficient and controllable light-driven nanostructuring and plasmonics. On the one hand, at high laser fluences (nanostructuring), future research with manipulating the laser beam profile can pave the way for LIPSS design with desired height profiles and periodicity, or, in other words, it will find a lot of applications in laser micro-engineering for manufacturing of surface structures with demanded properties. On the other hand, at low laser fluences (plasmonics), combined theoretical and experimental work, which will be focused on the details of the SPP decay mechanics on electron-hole pairs, can lead to future applications exploiting generation of hot carriers. The generation of hot carriers and the evolution of the laser-excited electronic energy distribution toward a hot Fermi distribution has also strong impact on the energy dissipation processes. Such nonequilibrium effects have not yet been included in the presented approaches.

Possible improvements of the approach presented in this chapter could include the implementation of interatomic potentials depending on the electronic temperature and/or the electronic density. In this way, the changes of the potential energy surface for the ions due to the laser excitation of electron and holes can be taken into account. Recent research on this topic is in progress. The general strategy described in this chapter assumes further combination of variety of computational techniques into mesoscopic models to fulfill the requirements of the nowadays investigations in computational materials science.

Acknowledgments We acknowledge the financial support of the Deutsche Forschungsgemeinschaft projects RE1141/14-2, IH 17/18-2, GA465/15-2, and IV122/4-1 and RFBR Project Number 20-02-00861. The MD-TTM calculations were performed at Lichtenberg Super Computer Facility TU-Darmstadt (Germany). Some simulations were executed on the high-performance cluster "Elwetritsch" through the projects TopNano and Mulan at the TU Kaiserslautern, which is a part of the "Alliance of High Performance Computing Rheinland-Pfalz." P.N.T. and B.R. kindly acknowledge the support of Regionales Hochschulrechenzentrum Kaiserslautern.

References

1. J. Bonse, J. Krüger, S. Höhm, A. Rosenfeld, Femtosecond laser-induced periodic surface structures. J. Laser Appl. **24**, 42006 (2012)
2. G.A. Martsinovskiĭ, G.D. Shandybina, D.S. Smirnov, S.V. Zabotnov, L.A. Golovan, V.Y. Timoshenko, P.K. Kashkarov, Ultrashort excitations of surface polaritons and waveguide modes in semiconductors. Opt. Spectrosc. **105**, 67–72 (2008)
3. C. Kunz, J. Bonse, D. Spaltmann, C. Neumann, A. Turchanin, J.F. Bartolomé, F.A. Müller, S. Gräf, Tribological performance of metal-reinforced ceramic composites selectively structured with femtosecond laser-induced periodic surface structures. Appl. Surf. Sci. **499**, 143917 (2020)
4. C. Florian, S.V. Kirner, J. Krüger, J. Bonse, Surface functionalization by laser-induced periodic surface structures. J. Laser Appl. **32**, 022063 (2020)
5. K. Czajkowski, M. Ratzke, O. Varlamova, J. Reif, Femtosecond-laser-induced periodic surface structures on magnetic layer targets: The roles of femtosecond-laser interaction and of magnetization. Appl. Surf. Sci. **417**, 84–87 (2017)
6. F.A. Müller, C. Kunz, S. Gräf, Bio-inspired functional surfaces based on laser-induced periodic surface structures. Materials **9**, 476 (2016)
7. S. Parvate, P. Dixit, S. Chattopadhyay, Superhydrophobic surfaces: Insights from theory and experiment. J. Phys. Chem. B **124**, 1323–1360 (2020)
8. H. Messaoudi, S. Kumar Das, J. Lange, F. Heinrich, S. Schrader, M. Frohme, R. Grunwald, Femtosecond-laser induced periodic surface structures for surface enhanced Raman spectroscopy of biomolecules, in *Progress in Nonlinear Nano-Optics*, (Springer International Publishing, Cham, 2015), pp. 207–219
9. A. Nakhoul, C. Maurice, M. Agoyan, A. Rudenko, F. Garrelie, F. Pigeon, J.-P. Colombier, Self-organization regimes induced by ultrafast laser on surfaces in the tens of nanometer scales. Nano **11**, 1020 (2021)
10. J. Bonse, S. Gräf, Maxwell meets Marangoni - a review of theories on laser-induced periodic surface structures. Laser Photon. Rev. **14**, 2000215 (2020)
11. A. Ablez, K. Toyoda, K. Miyamoto, T. Omatsu, Microneedle structuring of Si(111) by irradiation with picosecond optical vortex pulses. New J. Phys. **13**, 62006 (2020)
12. T. Omatsu, K. Miyamoto, K. Toyoda, R. Morita, Y. Arita, K. Dholakia, A new twist for materials science: The formation of Chiral structures using the angular momentum of light. Adv. Optical Mater. **7**, 1801672 (2019)
13. S. Syubaev, A. Zhizhchenko, O. Vitrik, S. Kudryashov, A. Porfiev, S. Fomchenkov, S. Khonina, A. Kuchmizhak, Zero-OAM laser printing of chiral nanoneedles. Opt. Lett. **42**, 5022–5025 (2017)
14. Y. Nakata, M. Yoshida, N. Miyanaga, Parallel fabrication of spiral surface structures by interference pattern of circularly polarized beams. Sci. Rep. **8**, 13448 (2018)
15. S.A. Centoni, B. Sadigh, G.H. Gilmer, T.J. Lenosky, T.D. de la Rubia, C.B. Musgrave, First-principles calculation of intrinsic defect formation volumes in silicon. Phys. Rev. B **72**, 195206 (2005)
16. A. Blumenstein, E.S. Zijlstra, D.S. Ivanov, S.T. Weber, T. Zier, F. Kleinwort, B. Rethfeld, J. Ihlemann, P. Simon, M.E. Garcia, Transient optics of gold during laser irradiation: From first principles to experiment. Phys. Rev. B **101**, 165140 (2020)
17. A. Zepeda-Ruiz, A. Stukowski, T. Oppelstrup, V.V. Bulatov, Probing the limits of metal plasticity with molecular dynamics simulations. Nature **550**, 492–495 (2017)
18. T. Oppelstrup, V.V. Bulatov, G.H. Gilmer, M.H. Kalos, B. Sadigh, First-passage Monte Carlo algorithm: Diffusion without all the hops. Phys. Rev. Lett. **97**, 230602 (2006)
19. A. Rudenko, C. Mauclair, F. Garrelie, R. Stoian, J.P. Colombier, Light absorption by surface nanoholes and nanobumps. Appl. Surf. Sci. **470**, 228–233 (2019)
20. Y.P. Meshcheryakov, N.M. Bulgakova, Thermoelastic modeling of microbump and nanojet formation on nanosize gold films under femtosecond laser irradiation. Appl. Phys. A Mater. Sci. Process. **82**, 363 (2005)

21. I. Milov, V. Zhakhovsky, D. Ilnitsky, K. Migdal, V. Khokhlov, Y. Petrov, N. Inogamov, V. Lipp, N. Medvedev, B. Ziaja, V. Medvedev, A. Makhotkin, E. Louis, F. Bijkerk, Two-level ablation and damage morphology of Ru films under femtosecond extreme UV irradiation. Appl. Surf. Sci. **528**, 146952 (2020)
22. S. Galitskiy, D.S. Ivanov, A.M. Dongare, Dynamic evolution of microstructure during laser shock loading and spall failure of single crystal al at the atomic scales. J. Appl. Phys. **124**, 205901 (2018)
23. A. Blumenstein, M.E. Garcia, B. Rethfeld, P. Simon, J. Ihlemann, D.S. Ivanov, Formation of periodic nano ridge patterns by ultrashort UV laser irradiation of gold. Nano **10**, 1998 (2020)
24. M.E. Povarnitsyn, N.E. Andreev, E.M. Apfelbaum, T.E. Itina, K.V. Khishchenko, O.F. Kostenko, P.R. Levashov, M.E. Veysman, A wide-range model for simulation of pump-probe experiments with metals. Appl. Surf. Sci. **258**, 9480–9483 (2012)
25. C.-Y. Shih, C. Chen, C. Rehbock, A. Tymoczko, U. Wiedwald, M. Kamp, U. Schuermann, L. Kienle, S. Barcikowski, L.V. Zhigilei, Limited elemental mixing in nanoparticles generated by ultrashort pulse laser ablation of AgCu bilayer thin films in a liquid environment: Atomistic modeling and experiments. J. Phys. Chem. C **125**, 2132–2155 (2021)
26. N. Medvedev, Z. Li, B. Ziaja, Thermal and nonthermal melting of silicon under femtosecond x-ray irradiation. Phys. Rev. B **91**, 054113 (2015)
27. T. Kramer, S. Remund, B. Jäggi, M. Schmid, B. Neuenschwander, Ablation dynamics – From absorption to heat accumulation/ultra-fast laser matter interaction. Adv. Opt. Technol **7**, 129–144 (2018)
28. T.E. Itina, J. Hermann, P. Delaporte, M. Sentis, Laser-generated plasma plume expansion: Combined continuous-microscopic modeling. Phys. Rev. E **66**, 066406 (2002)
29. N.A. Inogamov, V.A. Khokhlov, Y.V. Petrov, V.V. Zhakhovsky, Hydrodynamic and molecular-dynamics modeling of laserablation in liquid: From surf ace melting till bubble formation. Opt. Quant. Electron. **52**, 63 (2020)
30. A.N. Volkov, L.V. Zhigilei, Hydrodynamic multi-phase model for simulation of laser-induced non-equilibrium phase transformations. J. Phys. Conf. Ser. **59**, 640 (2007)
31. B. Rethfeld, D.S. Ivanov, M.E. Garcia, S.I. Anisimov, Modelling ultrafast laser ablation. J. Phys. D. Appl. Phys. **50**, 193001 (2017)
32. Q.S. Mei, K. Lu, "Melting and superheating of crystalline solids" from bulk to nanocrystals. Prog. Mater. Sci. **52**, 1175 (2007)
33. S. Williamson, G. Mourou, J.C.M. Li, Time-resolved laser-induced phase transformation in aluminum. Phys. Rev. Lett. **52**, 2364 (1984)
34. B. Lin, H.E. Elsayed-Ali, Temperature dependent reflection electron diffraction study of In(1 1 1) and observation of laser-induced transient surface superheating. Surf. Sci. **498**, 275 (2002)
35. E.W.J. Brcka, Complete description of the material transfer and the deposition by PLD of thin films of ceramic materials. Int. J. High Temp. Chem. Proc. **2**, S417 (1993)
36. M. Aden, E. Beyer, H. Kunze, G. Herziger, Laser-induced vaporization of a metal surface. Int. J. Phys. D **25**, S57 (1992)
37. W. Schulz, V. Kostrykin, H. Zefferer, D. Petring, R. Poprawe, A free boundary problem related to laser beam fusion cutting: ODE approximation. Int. J. Heat Mass Transf. **40**, 2913 (1997)
38. W. Schulz, V. Kostrykin, M. Nießen, J. Michel, D. Petring, E.W. Kreutz, R. Poprawe, Dynamics of ripple formation and melt flow in laser beam cutting. J. Phys. D. Appl. Phys. **32**, 1219 (1999)
39. B. Rethfeld, K. Sokolowski-Tinten, D. von der Linde, S.I. Anisimov, Ultrafast thermal melting of laser-excited solids by homogeneous nucleation. Phys. Rev. B **65**, 092103 (2002)
40. V. Schmidt, W. Husinsky, G. Betz, Dynamics of laser desorption and ablation of metals at the threshold on the Femtosecond time scale. Phys. Rev. Lett. **85**, 3516 (2000)
41. K. Sokolowski-Tinten, C. Blome, J. Blums, A. Cavalleri, C. Dietrich, A. Tarasevich, I. Uschmann, E. Förster, M. Kammler, M. Horn-von-Hoegen, D. von der Linde, Femtosecond X-ray measurement of Coherent lattice vibrations near the Lindemann stability limit. Nature **422**, 287 (2003)

42. B.J. Siwick, J.R. Dwyer, R.E. Jordan, R.J.D. Miller, An atomic-level view of melting using Femtosecond electron diffraction. Science **302**, 1382 (2003)
43. M.B. Agranat, S.I. Ashitkov, V.E. Fortov, A.V. Kirillin, A.V. Kostanovskii, S.I. Anisimov, P.S. Kondratenko, Use of optical anisotropy for study of ultrafast phase transformations at solid surfaces. Appl. Phys. A Mater. Sci. Process. **69**, 637 (1999)
44. K. Sokolowski-Tinten, J. Bialkowski, M. Boing, Thermal and nonthermal melting of Gallium Arsenide after Femtosecond laser excitation. Phys. Rev. B **58**, R11805 (1998)
45. Z. Lin, L.V. Zhigilei, Time-resolved diffraction profiles and structural dynamics of Ni film under short laser pulse irradiation. J. Phys. Conf. Ser. **59**, 11 (2007)
46. N.M. Bulgakova, R. Stoian, A. Rosenfeld, I.V. Hertel, E.E.B. Campbell, Electronic transport and consequences for material removal in ultrafast pulsed laser ablation of materials. Phys. Rev. B **69**, 054102 (2004)
47. P. Stampfli, K.H. Bennemann, Theory for the instability of the diamond structure of Si, Ge, and C induced by a dense electron-hole plasma. Phys. Rev. B **42**, 7163 (1990)
48. V. Recoules, J. Clérouin, G. Zérah, P.M. Anglade, S. Mazevet, Effect of intense laser irradiation on the lattice stability of semiconductors and metals. Phys. Rev. Lett. **96**, 055503 (2006)
49. S.I. Anisimov, B.L. Kapeliovich, T.L. Perel'man, Electron emission from metal surfaces exposed to ultrashort laser pulses. Zh. Eksp. Teor. Fiz **66**, 776 (1974) [Sov. Phys. JETP **39**, 375 (1974)]
50. Y. Shen, Y. Gan, W. Qi, Y. Shen, Z. Chen, Effect of the hot electron blast force on ultrafast laser ablation of nickel thin film. Appl. Opt. **54**, 1737–1742 (2015)
51. M.L. Wilkins, *Methods in Computational Physics*, vol 3 (Academic press, New York, 1964), pp. 211–261
52. J. Hohlfeld, J.G. Müller, S.-S. Wellershoff, E. Matthias, Time-resolved thermoreflectivity of thin gold films and its dependence on film thickness. Appl. Phys. A Mater. Sci. Process. **64**, 387 (1997)
53. Z.H. Jin, K. Lu, Melting of surface-free bulk single crystals. Philos. Mag. Lett. **78**, 29 (1998)
54. F.F. Abraham, J.Q. Broughton, Pulsed melting of silicon (111) and (100) surfaces simulated by molecular dynamics. Phys. Rev. Lett. **56**, 734 (1986)
55. T.A. Wm, B.L. Holian, Droplet formation by rapid expansion of a liquid. Phys. Rev. E **59**, 6742 (1999)
56. L.V. Zhigilei, B.J. Garrison, Pressure waves in microscopic simulations of laser ablation. Mater. Res. Soc. Symp. Proc. **538**, 491 (1999)
57. R.F.W. Herrmann, J. Gerlach, E.E.B. Campbell, Ultrashort pulse laser ablation of silicon: An MD simulation study. Appl. Phys. A Mater. Sci. Process. **66**, 35 (1998)
58. L.V. Zhigilei, Dynamics of the plume formation and parameters of the ejected clusters in short-pulse laser ablation. Appl. Phys. A Mater. Sci. Process. **76**, 339 (2003)
59. Z. Lin, E.M. Bringa, E. Leveugle, L.V. Zhigilei, Molecular dynamics simulation of laser melting of nanocrystalline Au. J. Phys. Chem. C **114**, 5686 (2010)
60. D.S. Ivanov, V.P. Lipp, B. Rethfeld, M.E. Garcia, Molecular-dynamics study of the mechanism of short-pulse laser ablation of single-crystal and polycrystalline metallic targets. J. Opt. Technol. **81**, 250 (2014)
61. E. Ohmura, I. Fukumoto, Modified molecular dynamics simulation on laser ablation of metal. Int. J. Japan Soc. Prec. Eng. **31**, 206 (1997)
62. Z. Lin, L.V. Zhigilei, V. Celli, Electron-phonon coupling and electron heat capacity of metals under conditions of strong electron-phonon nonequilibrium. Phys. Rev. B **77**, 075133 (2008)
63. J. Hohlfeld, S.-S. Wellershoff, J. Gudde, U. Conrad, V. Jahnke, E. Matthias, Electron and lattice dynamics following optical excitation of metals. Chem. Phys. **251**, 237–258 (2000)
64. S.I. Anisimov, B. Rethfeld, On the theory of ultrashort laser pulse interaction with a metal. Proc. SPIE Int. Soc. Opt. Eng. **3093**, 192 (1997)
65. Y.V. Petrov, N.A. Inogamov, S.I. Anisimov, K.P. Migdal, V.A. Khokhlov, K.V. Khishchenko, Thermal conductivity of condensed gold in states with the strongly excited electron subsystem. J. Phys. Conf. Ser. **653**, 012087 (2015)

66. J. Lindhard, M. Schar, Energy dissipation by ions in the keV region. Phys. Rev. **124**, 128 (1961) (1961)
67. J.E. Lennard-Jones, A.F. Devonshire, On the determination of molecular fields. II. From the equation of state of a gas. Proc. Roy. Soc. A **106**, 463 (1924)
68. F. Stillinger, T.A. Weber, Computer simulation of local order in condensed phases of silicon. Phys. Rev. B **31**, 5262 (1985)
69. V.V. Zhakhovskii, N.A. Inogamov, Y.V. Petrov, S.I. Ashitkov, K. Nishihara, Molecular dynamics simulation of femtosecond ablation and spallation with different interatomic potentials. Appl. Surf. Sci. **255**, 9592 (2009)
70. B.W.H. Van Beest, G.J. Kramer, R.A. van Santen, Force fields for silicas and aluminophosphates based on ab initio calculations. Phys. Rev. Lett. **64**, 1955 (1990)
71. C. Rajappa, S.B. Sringeri, Y. Subramanian, J. Gopalakrishnan, Universal scaling in the aging of the strong glass former SiO2. J. Chem. Phys. **140**, 244512 (2014)
72. A. Carre, J. Horbach, S. Ispas, W. Kob, New fitting scheme to obtain effective potential from Car-Parrinello molecular-dynamics simulations: Application to silica. EPL **82**, 17001 (2008)
73. D.S. Ivanov, L.V. Zhigilei, Combined atomistic-continuum modelling of short-pulse laser melting and disintegration of metal films. Phys. Rev. B **68**, 064114 (2003)
74. C. Schafer, H.M. Urbassek, L.V. Zhigilei, B.J. Garrison, Pressure-transmitting boundary conditions for molecular dynamics simulations. Comput. Mater. Sci. **24**, 421 (2002)
75. D.S. Ivanov, L.V. Zhigilei, Effect of pressure relaxation on the mechanisms of short-pulse laser melting. Phys. Rev. Lett. **91**, 105701 (2003)
76. L.V. Zhigilei, D.S. Ivanov, E. Leveugle, B. Sadigh, E.M. Bringa, Computer modeling of laser melting and spallation of metal targets, high power laser ablation V. Proc. SPIE **5448**, 505–519 (2004)
77. L.V. Zhigilei, Z. Lin, D.S. Ivanov, Atomistic modeling of short pulse laser ablation of metals: Connections between melting, spallation, and phase explosion. J. Chem. Phys. **113**, 11892 (2009)
78. D.S. Ivanov, V.P. Lipp, A. Blumenstein, V.P. Veiko, E.B. Yakovlev, V.V. Roddatis, M.E. Garcia, B. Rethfeld, J. Ihlemann, P, 78, Experimental and theoretical investigation of periodic nanostructuring of Au with UV laser near the ablation threshold. Phys. Rev. Appl. **4**, 064006 (2015)
79. H.M. van Driel, Kinetics of high-density plasmas generated in Si by 1.06- and 0.53-μm picosecond laser pulses. Phys. Rev. B **35**, 8166 (1987)
80. J.K. Chen, D.Y. Tzou, J.E. Beraun, Numerical investigation of ultrashort laser damage in semiconductors. Int. J. Heat Mass Transf. **48**, 501 (2005)
81. A. Rämer, O. Osmani, B. Rethfeld, Laser damage in silicon: Energy absorption, relaxation, and transport. J. Appl. Phys. **116**, 053508 (2014)
82. T.E. Itina, N.S. Shcheblanov, Effect of laser field on collision frequencies and absorption during ultra-short laser interactions with dielectric materials. Fundamentals of Laser-Assisted Micro- and Nanotechnologies 2013, Proc. SPIE **9065**, 906506 (2013)
83. V.P. Lipp, B. Rethfeld, M.E. Garcia, D.S. Ivanov, Atomistic-continuum modeling of short laser pulse melting of Si targets. Phys. Rev. B **90**, 245306 (2014)
84. Y. Gan, J.K. Chen, A hybrid method for integrated atomistic-continuum simulation of ultrashort-pulse laser interaction with semiconductors. Comput. Phys. Commun. **183**, 278 (2012)
85. P. Balling, J. Schou, Femtosecond-laser ablation dynamics of dielectrics: Basics and applications for thin films. Rep. Prog. Phys. **76**, 036502 (2013)
86. S. Juodkazis, K. Nishimura, S. Tanaka, H. Misawa, E.G. Gamaly, B. Luther-Davies, L. Hallo, P. Nicolai, V.T. Tikhonchuk, Laser-induced microexplosion confined in the bulk of a sapphire crystal: Evidence of multimegabar pressures. Phys. Rev. Lett. **96**, 166101 (2006)
87. B. Rethfeld, Unified model for the free-electron avalanche in laser-irradiated dielectrics. Phys. Rev. Lett. **92**, 187401 (2004)
88. A. Kaiser, B. Rethfeld, M. Vicanek, G. Simon, Microscopic processes in dielectrics under irradiation by subpicosecond laser pulses. Phys. Rev. B **61**, 11437 (2000)

89. M. Mero, A.J. Sabbah, J. Zeller, W. Rudolph, Femtosecond dynamics of dielectric films in the pre-ablation regime. Appl. Phys. A Mater. Sci. Process. **81**, 317 (2005)
90. J. Jasapara, M. Mero, W. Rudolph, Retrieval of the dielectric function of thin films from femtosecond pump-probe experiments. Appl. Phys. Lett. **80**, 2637 (2002)
91. M. Mero, J. Liu, A.J. Sabbah, J. Zeller, P.M. Alsing, J.K. McIver, W. Rudolph, J. Jasapara, Scaling laws of femtosecond laser induced breakdown in dielectric films, in *Conference on Lasers and Electro-Optics/International Quantum Electronics Conference and Photonic Applications Systems Technologies, Technical Digest (CD)*, (Optica Publishing Group, 2004) paper CThD4
92. N. Brouwer, B. Rethfeld, Transient electron excitation and nonthermal electron-phonon coupling in dielectrics irradiated by ultrashort laser pulses. Phys. Rev. B **95**, 245139 (2017)
93. A. Rämer, L. Haahr-Lillevang, B. Rethfeld, P. Balling, Modeling the transient optical parameters in laser-excited band gap materials. Opt. Eng. **56**, 011015 (2016)
94. G.J. Kramer, B.W.H. Van Beest, R.A. van Santen, Relation between crystal symmetry and ionicity in silica polymorphs. Nature **351**, 636 (1991)
95. S. Tsuneyuki, M. Tsukada, H. Aoki, Y. Matsui, First-principles interatomic potential of silica applied to molecular dynamics. Phys. Rev. Lett. **61**, 869 (1988)
96. T.F. Soules, G.H. Gilmer, M.J. Matthews, J.S. Stoken, M.D. Feit, Silica molecular dynamic force fields—A practical assessment. J. Non-Crystall. Sol. **357**, 1564 (2011)
97. V.P. Lipp, B. Rethfeld, M.E. Garcia, D.S. Ivanov, Solving a system of differential equations containing a diffusion equation with nonlinear terms on the example of laser heating in silicon. Appl. Sci. **10**, 1853 (2020)
98. A. Piróth, J. Sólyom, *Fundamentals of the Physics of Solids: Volume 1: Structure and Dynamics* (Springer Science, Budapest, 2002)
99. P. Ewald, Evaluation of optical and electrostatic lattice potentials. Ann. Phys. Leipzig. **64**, 253 (1921)
100. A.M. Dongare, Quasi-coarse-grained dynamics: Modelling of metallic materials at mesoscales. Philos. Mag. **94**, 3877–3897 (2014)
101. J. Tersoff, New empirical approach for the structure and energy of covalent systems. Phys. Rev. B **37**, 6991 (1988)
102. Y. Wang, X. Xu, L. Zheng, Molecular dynamics simulation of ultrafast laser ablation of fused silica film. Appl. Phys. A Mater. Sci. Process. **92**, 849 (2008)
103. L. Shokeen, P.K. Schelling, Thermodynamics and kinetics of silicon under conditions of strong electronic excitation. J. Appl. Phys. **109**, 073503 (2011)
104. V.P. Lipp, D.S. Ivanov, B. Rethfeld, M.E. Garcia, On the interatomic interaction potential that describes bond weakening in classical molecular-dynamic modelling. J. Opt. Technol. **81**, 254 (2014)
105. E.S. Zijlstra, T. Zier, B. Bauerhenne, S. Krylow, P.M. Geiger, M.E. Garcia, Femtosecond-laser-induced bond breaking and structural modifications in silicon, TiO2, and defective graphene: An ab initio molecular dynamics study. Appl. Phys. A Mater. Sci. Process. **114**, 1 (2014)
106. M. Kempkes, T. Zier, K. Singer, M.E. Garcia, Ultrafast nonthermal NV center formation in diamond. Carbon **174**, 524–530 (2021)
107. B. Bauerhenne, V.P. Lipp, T. Zier, E.S. Zijlstra, M.E. Garcia, Self-learning method for construction of analytical interatomic potentials to describe laser-excited materials. Phys. Rev. Lett. **124**, 085501 (2020)
108. P. Plettenberg, Neural Network Interatomic Potential for Laser-Excited Silicon, Master-Thesis, University of Kassel, 2021
109. J. Behler, M. Parrinello, Generalized neural-network representation of high-dimensional potential-energy surfaces. Phys. Rev. Lett. **98**, 146401 (2007)
110. H. Katsuki, J.C. Delagnes, K. Hosaka, K. Ishioka, H. Chiba, E.S. Zijlstra, M.E. Garcia, H. Takahashi, K. Watanabe, M. Kitajima, Y. Matsumoto, K.G. Nakamura, K. Ohmori, All-optical control and visualization of ultrafast two-dimensional atomic motions in a single crystal of bismuth. Nat. Commun. **4**, 2801 (2013)

111. M.P. Allen, D.J. Tildesley, *Computer Simulation of Liquids* (Clarendon press, Oxford, 1987)
112. A.I. Kuznetsov, J. Koch, B.N. Chichkov, Nanostructuring of thin gold films by femtosecond lasers. Appl. Phys. A Mater. Sci. Process. **94**, 221 (2009)
113. D.S. Ivanov, A.I. Kuznetsov, V.P. Lipp, B. Rethfeld, B.N. Chichkov, M.E. Garcia, W. Schulz, Short laser pulse surface nanostructuring on thin metal films: Direct comparison of molecular dynamics modeling and experiment. Appl. Phys. A Mater. Sci. Process. **111**, 675 (2013)
114. J.L. Gustafson, Reevaluating Amdahl's law. Comm. ACM **31**, 532 (1988)
115. K. Lu, Y. Li, Homogeneous nucleation catastrophe as a kinetic stability limit for superheated crystal. Phys. Rev. Lett. **80**, 4474 (1998)
116. Z.H. Jin, P. Gambsch, K. Lu, E. Ma, Melting mechanisms at the limit of superheating. Phys. Rev. Lett. **87**, 055703 (2001)
117. R.W. Cahn, Melting from within. Nature **413**, 582–583 (2002)
118. J.R. Dwyer, C.T. Hebeisen, R. Ernstorfer, M. Harb, V.B. Deyirmenjian, R.E. Jordan, R.J. Dwayne Miller, Femtosecond electron diffraction: 'Making the molecular movie'. Phil. Trans. R. Soc. A **364**, 741–778 (2006)
119. D.S. Ivanov, L.V. Zhigilei, Kinetic limit of heterogeneous melting in metals. Phys. Rev. Lett. **98**, 195701 (2007)
120. D.S. Ivanov, O. Osmani, B. Rethfeld, Computer modeling of nanostructuring on materials with tightly focused energy deposition, chapter I, in *Laser Beams: Theory, Properties, and Applications*, (Nova Science Publishers, New York, 2011)
121. J.W. Gibbs, *Collected Works*, vol 1 (Longmans, New York, 1931), pp. 55–372
122. J.Y. Tsao, M.J. Aziz, M.O. Thompson, P.S. Peercy, Asymmetric melting and freezing kinetics in silicon. Phys. Rev. Lett. **56**, 2712 (1986)
123. D.Y. Sun, M. Asta, J.J. Hoyt, Kinetic coefficient of Ni solid-liquid interfaces from molecular-dynamics simulations. Phys. Rev. B **69**, 024108 (2004)
124. F. Celestini, J.-M. Debierre, Measuring kinetic coefficients by molecular dynamics simulation of zone melting. Phys. Rev. E **65**, 041605 (2002)
125. D. Bäuerle, *Laser Processing and Chemistry* (Springer-Verlag, Berlin, Heidelberg, 2000)
126. D.B. Chrisey, G.K. Hubler, *Pulsed Laser Deposition of Thin Films* (Wiley, New York, 1994)
127. C.R. Phipps, J.R. Luke, G.G. McDuff, T. Lippert, Laser-driven micro-rocket. Appl. Phys. A Mater. Sci. Process. **77**, 193–201 (2003)
128. S.I. Anisimov, Vaporization of metal absorbing laser radiation. Sov. Phys. JETP **27**, 182–183 (1968)
129. A. Miotello, R. Kelly, Laser-induced phase explosion: New physical problems when a condensed phase approaches the thermodynamic critical temperature. Appl. Phys. A Mater. Sci. Process. **69**, S67–S73 (1999)
130. N.M. Bulgakova, A.V. Bulgakov, Pulsed laser ablation of solids: Transition from normal vaporization to phase explosion. Appl. Phys. A Mater. Sci. Process. **73**, 199–208 (2001)
131. T.D. Bennett, C.P. Grigoropoulos, D.J. Krajnovich, Near-threshold laser sputtering of gold. J. Appl. Phys. **77**, 849–864 (1995)
132. V.V. Semak, J.G. Thomas, B.R. Campbell, Drilling of steel and HgCdTe with the femtosecond pulses produced by a commercial laser system. J. Phys. D. Appl. Phys. **37**, 2925–2931 (2004)
133. G. Paltauf, P.E. Dyer, Photomechanical processes and effects in ablation. Chem. Rev. **103**, 487–518 (2003)
134. E. Leveugle, D.S. Ivanov, L.V. Zhigilei, Photomechanical spallation of molecular and metal targets: Molecular dynamics study. Appl. Phys. A Mater. Sci. Process. **79**, 1643–1655 (2004)
135. J. Yang, Y. Zhao, N. Zhang, Y. Liang, M. Wang, Ablation of metallic targets by high-intensity ultrashort laser pulses. Phys. Rev. B **76**, 165430 (2007)
136. H. Masuhara, T. Asahi, Y. Hosokawa, Laser nanochemistry. Pure Appl. Chem. **78**, 2205–2226 (2006)
137. N.M. Bulgakova, R. Stoian, A. Rosenfeld, I.V. Hertel, W. Marine, E.E.B. Campbell, A general continuum approach to describe fast electronic transport in pulsed laser irradiated materials: The problem of Coulomb explosion. Appl. Phys. A Mater. Sci. Process. **81**, 345–356 (2005)

138. K.H. Song, X. Xu, Explosive phase transformation in excimer laser ablation. Appl. Surf. Sci. **127-129**, 111–116 (1998)
139. C. Cheng, X. Xu, Mechanisms of decomposition of metal during femtosecond laser ablation. Phys. Rev. B **72**, 165415 (2005)
140. C. Porneala, D.A. Willis, Observation of nanosecond laser-induced phase explosion in aluminium. Appl. Phys. Lett. **89**, 211121 (2006)
141. L.V. Zhigilei, P.B.S. Kodali, B.J. Garrison, On the threshold behavior in the laser ablation of organic solids. Chem. Phys. Lett. **276**, 269–273 (1997)
142. L.V. Zhigilei, E. Leveugle, B.J. Garrison, Y.G. Yingling, M.I. Zeifman, Computer simulations of laser ablation of molecular substrates. Chem. Rev. **103**, 321–348 (2003)
143. E. Leveugle, L.V. Zhigilei, Molecular dynamics simulation study of the ejection and transport of polymer molecules in matrix-assisted pulsed laser evaporation. J. Appl. Phys. **102**, 074914 (2007)
144. A. Vogel, V. Venugopalan, Mechanisms of pulsed laser ablation of biological tissues. Chem. Rev. **103**, 577–644 (2003)
145. M. Kashii, Y. Hosokawa, H. Kitano, H. Adachi, Y. Mori, K. Takano, H. Matsumura, T. Inoue, S. Murakami, K. Sugamoto, H. Yoshikawa, T. Sasaki, H. Masuhara, Femtosecond laser-induced cleaving of protein crystal in water solution. Appl. Surf. Sci. **253**, 6447–6450 (2007)
146. Y. Nakata, N. Miyanaga, T. Okada, Effect of pulse width and fluence of femtosecond laser on the size of nanobump array. Appl. Surf. Sci. **253**, 6555–6557 (2007)
147. M. Iqbal, S.A. Khan, D.S. Ivanov, R.A. Ganeev, V.V. Kim, G.S. Boltaev, N.A. Abbasi, S. Shaju, M.E. Garcia, B. Rethfeld, A.S. Alnaser, The mechanism of laser assisted generation of aluminum nanoparticles, their wettability and nonlinearity properties. Appl. Surf. Sci. **527**, 146702 (2020)
148. C.-Y. Shih, I. Gnilitskyi, M.V. Shugaev, E. Skoulas, E. Stratakis, L.V. Zhigilei, Effect of a liquid environment on single-pulse generation of laser induced periodic surface structures and nanoparticles. Nanoscale **12**, 7674–7687 (2020)
149. R. Stoian, J.P. Colombier, Advances in ultrafast laser structuring of materials at the nanoscale. Nano **9**(16), 4665–4688 (2020)
150. A. Rudenko, C. Mauclair, F. Garrelie, R. Stoian, J.-P. Colombier, Self-organization of surfaces on the nanoscale by topography-mediated selection of quasicylindrical and plasmonic waves. Nano **8**, 459–465 (2019)
151. C. Eisele, C.E. Nebel, M. Stutzmann, Periodic light coupler gratings in amorphous thin film solar cells. J. Appl. Phys. **89**, 7722–7726 (2001)
152. J.-T. Chen, W.-C. Lai, Y.-J. Kao, Y.-Y. Yang, J.-K. Sheu, Laser-induced periodic structures for light extraction efficiency enhancement of GaN-based light emitting diodes. Opt. Exp. **20**, 5689–5695 (2012)
153. C. Wang, Y.-C. Chang, J. Yao, C. Luo, S. Yin, P. Ruffin, C. Brantley, E. Edwards, Surface enhanced Raman spectroscopy by interfered femtosecond laser created nanostructures. Appl. Phys. Lett. **100**, 023107 (2012)
154. D.S. Ivanov, B.C. Rethfeld, The effect of pulse duration on the character of laser heating: Photo-mechanical vs. photo-thermal damage of metal targets. Appl. Surf. Sci. **255**, 9724 (2009)
155. D.S. Ivanov, V.P. Lipp, V.P. Veiko, E. Jakovlev, B. Rethfeld, M.E. Garcia, Molecular dynamics study of the short laser pulse ablation: Quality and efficiency in production. Appl. Phys. A Mater. Sci. Process. **117**, 2133 (2014)
156. L.V. Zhigilei, D.S. Ivanov, Channels of energy redistribution in short-pulse laser interactions with metal targets. Appl. Surf. Sci. **248**, 433 (2005)
157. P.T. Mannion, S.F. Favre, D.S. Ivanov, G.M. O'Connor, T.J. Glynn, J.G. Lunney, B. Doggett, Langmuir probe investigation of plasma expansion in Femto- and Picosecond laser ablation of selected metals. J. Phys. Conf. Ser. **59**, 753 (2007)
158. S.I. Kudryashov, A.A. Samokhvalov, Y.D. Golubev, D.S. Ivanov, M.E. Garcia, V.P. Veiko, Dynamic all-optical control in ultrashort double-pulse laser ablation. Appl. Surf. Sci. **30**, 147940 (2021)

159. M. Born, E. Wolf, *Principles of Optics: Electromagnetic Theory of Propagation, Interference and Diffraction of Light* (Elsevier, Amsterdam, 2013)
160. G.M. Burrow, T.K. Gaylord, Multi-beam interference advances and applications: Nano-electronics, photonic crystals, metamaterials, subwavelength structures, optical trapping, and biomedical structures. Micromachines **2**(2), 221 (2011)
161. F. Diebel, D. Leykam, S. Kroesen, C. Denz, A.S. Desyatnikov, Conical diffraction and composite Lieb bosons in photonic lattices. Phys. Rev. Lett. **116**, 183902 (2016)
162. N.M. Litchinitser, Structured light meets structured matter. Science **337**(6098), 1054–1055 (2012)
163. K. Nozaki, T. Tanabe, A. Shinya, S. Matsuo, T. Sato, H. Taniyama, M. Notomi, Sub-femtojoule all-optical switching using a photonic-crystal nanocavity. Nat. Phot. **4**(7), 477 (2010)
164. J.D. Fowlkes, L. Kondic, J. Diez, Y. Wu, P.D. Rack, Self-assembly versus directed assembly of nanoparticles via pulsed laser induced dewetting of patterned metal films. Nano Lett. **11**(6), 2478 (2011)
165. M. Hase, K. Mizoguchi, H. Harima, S. Nakashima, M. Tani, K. Sakai, M. Hangyo, Optical control of coherent optical phonons in bismuth films. Appl. Phys. Lett. **69**(17), 2474 (1996)
166. C.A.D. Roeser, M. Kandyla, A. Mendioroz, E. Mazur, Optical control of coherent lattice vibrations in tellurium. Phys. Rev. B **70**(21), 212302 (2004)
167. S.I. Kudryashov, M. Kandyla, C. Roeser, E. Mazur, Intraband and interband optical deformation potentials in femtosecond-laser excited α-Te. Phys. Rev. B **75**, 085207 (2007)
168. A. Devos, A. Le Louarn, Strong effect of interband transitions in the picosecond ultrasonics response of metallic thin films. Phys. Rev. B **68**(4), 045405 (2003)
169. A.A. Ionin, S.I. Kudryashov, S.V. Seleznev, D.V. Sinitsyn, V.N. Lednev, S.M. Pershin, Pre-ablation electron and lattice dynamics on the silicon surface excited by a femtosecond laser pulse. JETP **121**(5), 737 (2015)
170. M.E. Povarnitsyn, T.E. Itina, K.V. Khishchenko, P.R. Levashov, Suppression of ablation in femtosecond double-pulse experiments. Phys. Rev. Lett. **103**(19), 195002 (2009)
171. T. Zier, Ab-initio analysis of the structural response of solids after femtosecond-laser-pulse excitation: From understanding towards control, PhD Dissertation, Department of Theoretical Physics University of Kassel, Germany, April (2019)
172. P. Papon, J. Leblond, P.H.E. Meijer, *The Physics of Phase Transitions: Concepts and Applications* (Springer Verlag Berlin, Heidelberg, New-York, 2002)
173. J.P. Colombier, P. Combis, A. Rosenfeld, I.V. Hertel, E. Audouard, R. Stoian, Optimized energy coupling at ultrafast laser-irradiated metal surfaces by tailoring I ntensity envelopes: Consequences for material removal from Al samples. Phys. Rev. B **74**, 224106 (2006)
174. C. Mauclair, M. Zamfirescu, J.P. Colombier, G. Cheng, K. Mishchik, E. Audouard, R. Stoian, Control of ultrafast laser-induced bulk nanogratings in fused silica via pulse time envelopes. Opt. Exp **20**, 12997–13005 (2012)
175. L. Englert, B. Rethfeld, L. Haag, M. Wollenhaupt, C. Sarpe-Tudoran, T. Baumert, Control of ionization processes in high band gap materials via tailored femtosecond pulses. Opt. Exp **15**, 17855 (2007)
176. J.P. Colombier, P. Combis, A. Rosenfeld, I.V. Hertel, E. Audouard, R. Stoian, Optimized energy coupling at ultrafast laser-irradiated metal surfaces by tailoring intensity envelopes: Consequences for material removal from Al samples. Phys. Rev. B **74**, 224106 (2006)
177. J. Penczak, R. Kupfer, I. Bar, R.J. Gordon, The role of plasma shielding in collinear double-pulse femtosecond laser-induced breakdown spectroscopy. Spectrochim. Acta B **97**, 34 (2014)
178. B. Jaeggi, S. Remund, Y. Zhang, T. Kramer, B. Neuenschwander, Optimizing the specific removal rate with the burst mode under varying conditions. J. Laser Micro/Nanoeng. **12**(3) (2017)
179. S.G. Bezhanov, P.A. Danilov, A.A. Ionin, I.V. Kiseleva, S.I. Kudryashov, S.A. Uryupin, D.A. Zayarny, Femtosecond laser induced nanostructuring of aluminum films of variable thickness. Las. Phys. Lett. **15**(1), 015901 (2018)

180. D.S. Ivanov, L.V. Zhigilei, Combined atomistic-continuum model for simulation of laser interaction with metals: Application in the calculation of melting thresholds in Ni targets of varying thickness. Appl. Phys. A Mater. Sci. Process. **79**, 977–981 (2004)
181. S.I. Kudryashov, A.A. Ionin, Multi-scale dynamics of front-side femtosecond laser heating, melting and ablation of thin supported aluminum film. Int. J. Heat Mass Transf. **99**, 383 (2016)
182. P.B. Corkum, F. Brunel, N.K. Sherman, T. Srinivasan-Rao, Thermal response of metals to ultrashort-pulse laser excitation. Phys. Rev. Lett. **61**, 2886 (1988)
183. C.L. Kelchner, S.J. Plimpton, J.C. Hamilton, Dislocation nucleation and defect structure during surface indentation. Phys. Rev. B **58**, 11085 (1998)
184. C. Wu, L.V. Zhigilei, Microscopic mechanisms of laser spallation and ablation of metal targets from large-scale molecular dynamics simulations. Appl. Phys. A Mater. Sci. Process. **114**(1), 11 (2014)
185. P.P. Pronko, S.K. Dutta, J. Squier, J.V. Rudd, D. Du, G. Mourou, Machining of sub-micron holes using a femtosecond laser at 800 nm. Opt. Commun. **114**, 106–110 (1995)
186. F. Korte, J. Serbin, J. Koch, A. Egbert, C. Fallnich, A. Ostendorf, B.N. Chichkov, Towards nanostructuring with femtosecond laser pulses. Appl. Phys. A Mater. Sci. Process. **77**, 229–235 (2003)
187. J. Jersch, F. Demming, J. Hildenhagen, K. Dickmann, Nano-material processing with laser radiation in the near field of a scanning probe tip. Opt. Laser Technol. **29**, 433–437 (1997)
188. A. Chimmalgi, T.Y. Choi, C.P. Grigoropoulos, K. Komvopoulos, Femtosecond laser aperturless near-field nanomachining of metals assisted by scanning probe microscopy. Appl. Phys. Lett. **82**, 1146–1148 (2003)
189. J. Boneberg, H.-J. Münzer, M. Tresp, M. Ochmann, P. Leiderer, The mechanism of nanostructuring upon nanosecond laser irradiation of a STM tip. Appl. Phys. A Mater. Sci. Process. **67**, 381–384 (1998)
190. S.M. Huang, M.H. Hong, Y.F. Lu, B.S. Lukyanchuk, W.D. Song, T.C. Chong, Pulsed-laser assisted nanopatterning of metallic layers combined with atomic force microscopy. J. Appl. Phys. **91**, 3268–3274 (2002)
191. S.M. Huang, M.H. Hong, B. Lukiyanchuk, T.C. Chong, Nanostructures fabricated on metal surfaces assisted by laser with optical near-field effects. Appl. Phys. A Mater. Sci. Process. **77**, 293–296 (2003)
192. Y. Lu, S.C. Chen, Nanopatterning of a silicon surface by near-field enhanced laser irradiation. Nanotechnology **14**, 505–508 (2003)
193. F. Korte, J. Koch, B.N. Chichkov, Formation of microbumps and nanojets on gold targets by femtosecond laser pulses. Appl. Phys. A Mater. Sci. Process. **79**, 879–881 (2004)
194. J. Koch, F. Korte, T. Bauer, C. Fallnich, A. Ostendorf, B.N. Chichkov, Nanotexturing of gold films by femtosecond laser-induced melt dynamics. Appl. Phys. A Mater. Sci. Process. **81**, 325–328 (2005)
195. Y. Nakata, T. Okada, M. Maeda, Nano-sized hollow bump array generated by single femtosecond laser pulse. Jpn. J. Appl. Phys. **42**, L1452–L1454 (2003)
196. D.S. Ivanov, B.C. Rethfeld, G.M. O'Connor, T.J. Glynn, A.N. Volkov, L.V. Zhigilei, The mechanism of Nanobump formation in Femtosecond pulse laser nanostructuring of thin metal films. Appl. Phys. A Mater. Sci. Process. **92**, 791 (2008)
197. X.W. Zhou, H.N.G. Wadley, R.A. Johnson, D.J. Larson, N. Tabat, A. Cerezo, A.K. Petford-Long, G.D.W. Smith, P.H. Clifton, R.L. Martens, T.F. Kelly, Atomic scale structure of sputtered metal multilayers. Acta Mater. **49**, 4005–4015 (2001)
198. D.S. Ivanov, B.C. Rethfeld, G.M. O'Connor, T.J. Glynn, Z. Lin, L.V. Zhigilei, Nanocrystalline structure of nanobump generated by localized photoexcitation of metal film. J. Appl. Phys. **107**, 013519 (2010)
199. D.W. Bäuerle, *Laser Processing and Chemistry*, 4th edn. (Springer, 2011)
200. P. Simon, J. Ihlemann, Machining of submicron structures on metals and semiconductors by ultrashort UV-laser pulses. Appl. Phys. A Mater. Sci. Process. **63**, 50 (1996)

201. J.-H. Klein-Wiele, P. Simon, Sub-100nm pattern generation by laser direct writing using a confinement layer. Opt. Exp **21**, 9017 (2013)
202. J. Ihlemann, Patterning of oxide thin films by UV laser ablation. J. Optoelectron. Adv. Mater. **7**, 1191 (2005)
203. L. Gallais, E. Bergeret, B. Wang, M. Guerin, E. Bènevent, Ultrafast laser ablation of metal films on flexible substrates. Appl. Phys. A Mater. Sci. Process. **115**, 177 (2014)
204. R. Stoian, J.P. Colombier, C. Mauclair, G. Cheng, M.K. Bhuyan, P.K. Velpula, P. Srisungsitthisunti, Spatial and temporal laser pulse design for material processing on ultrafast scales. Appl. Phys. A Mater. Sci. Process. **114**, 119 (2014)
205. A. Blumenstein, J. Ihlemann, J.-H. Klein-Wiele, P. Simon, Periodic surface structures by laser interference ablation, in *Ultrafast Laser Nanostructuring - The Pursuit of Extreme Scales*, ed. by R. Stoian, J. Bonse, (Springer, 2022)
206. N.A. Inogamov, V.V. Zhakhovskii, S.I. Ashitkov, Y.V. Petrov, M.B. Agranat, S.I. Anisimov, K. Nishihara, V.E. Fortov, Nanospallation induced by an ultrashort laser pulse. J. Exp. Theor. Phys. **107**, 1 (2008)
207. A.K. Upadhyay, N.A. Inogamov, B. Rethfeld, H.M. Urbassek, Ablation by ultrashort laser pulses: Atomistic and thermodynamic analysis of the processes at the ablation threshold. Phys. Rev. B **78**, 045437 (2008)
208. M.V. Shugaev, I. Gnilitskyi, N.M. Bulgakova, L.V. Zhigilei, Mechanism of single-pulse ablative generation of laser-induced periodic surface structures. Phys. Rev. B **96**, 205429 (2017)
209. A. Abou-Saleh, E.T. Karim, C. Maurice, S. Reynaud, F. Pigeon, F. Garrelie, L.V. Zhigilei, J.P. Colombier, Spallation-induced roughness promoting high spatial frequency nanostructure formation on Cr. Appl. Phys. A Mater. Sci. Process. **124**, 308 (2018)
210. C. Wu, M.S. Christensen, J.-M. Savolainen, P. Balling, L.V. Zhigilei, Generation of subsurface voids and a nanocrystalline surface layer in femtosecond laser irradiation of a single crystal Ag target. Phys. Rev. B **91**, 035413 (2015)
211. C. Wu, L.V. Zhigilei, Nanocrystalline and polyicosahedral structure of a nanospike generated on metal surface irradiated by a single femtosecond laser pulse. J. Phys. Chem. C **120**, 4438–4447 (2016)
212. M.V. Shugaev, C. Wu, O. Armbruster, A. Naghilou, N. Brouwer, D.S. Ivanov, T.J.-Y. Derrien, N.M. Bulgakova, W. Kautek, B. Rethfeld, L.V. Zhigilei, Fundamentals of ultrafast laser–material interaction. MRS Bullet. **41**, 960 (2016)
213. K. Miyazaki, G. Miyaji, Periodic nanostructure formation on silicon irradiated with multiple low-fluence femtosecond laser pulses in water. Phys. Proc **39**, 674 (2012)
214. B. Borchers, J. Békési, P. Simon, J. Ihlemann, Submicron surface patterning by laser ablation with short UV pulses using a proximity phase mask setup. J. Appl. Phys. **107**, 063106 (2010)
215. J.H. Klein-Wiele, P. Simon, Sub-100nm pattern generation by laser direct writing using a confinement layer. Opt. Express **21**(7), 9017–9023 (2013)
216. Y.V. Petrov, V.A. Khokhlov, V.V. Zhakhovsky, N.A. Inogamov, Hydrodynamic phenomena induced by laser ablation of metal into liquid. Appl. Surf. Sci. **492**, 285–297 (2019)
217. E.T. Karim, M. Shugaev, C. Wu, Z. Lin, R.F. Hainsey, L.V. Zhigilei, Atomistic simulation study of short pulse laser interactions with a metal target under conditions of spatial confinement by a transparent overlayer. J. Appl. Phys. **115**, 183501 (2014)
218. D.S. Ivanov, A. Blumenstein, J. Ihlemann, P. Simon, M.E. Garcia, B. Rethfeld, Molecular dynamics modeling of periodic nanostructuring of metals with a short UV laser pulse under spatial confinement by a water layer. Appl. Phys. A Mater. Sci. Process. **123**, 744 (2017)
219. H. Nada, An intermolecular potential model for the simulation of ice and water near the melting point: A six-site model of H2O. J. Chem. Phys. **118**, 7401 (2003)
220. Y. Dou, L.V. Zhigilei, Z. Postawa, N. Winograd, B.J. Garrison, Thickness effects of water overlayer on its explosive evaporation at heated metal surfaces. Nucl. Instr. Meth. B **180**, 105–111 (2001)
221. C.-Y. Shih, C. Wu, M.V. Shugaev, L.V. Zhigilei, Atomistic modeling of nanoparticle generation in short pulse laser ablation of thin metal films in water. J. Colloid Interface Sci. **489**, 3–17 (2017)

222. Development of Interatomic EAM Potentials. Available online: https://www.researchgate.net/project/Development-of-interatomic-EAM-potentials. Accessed on 30 Nov 2017
223. H. Nakano, S. Miyauti, N. Butani, T. Shibayanagi, M. Tsukamoto, N. Abe, Femtosecond laser peening of stainless steel. J. Laser Micro/Nanoeng **4**, 35 (2009)
224. C.A. Zuhlke, G.D. Tsibidis, T. Anderson, E. Stratakis, G. Gogos, D.R. Alexander, Investigation of femtosecond laser induced ripple formation on copper for varying incident angle. AIP Adv. **8**, 015212 (2018)
225. H. Zhang, J.P. Colombier, S. Witte, Laser-induced periodic surface structures: Arbitrary angles of incidence and polarization states. Phys. Rev. B **101**, 245430 (2020)
226. I. Gnilitskyi, T.J.-Y. Derrien, Y. Levy, N.M. Bulgakova, T. Mocek, L. Orazi, High-speed manufacturing of highly regular femtosecond laser-induced periodic surface structures: Physical origin of regularity. Sci. Rep. **7**, 1 (2017)
227. F. Nyenhuis, P.N. Terekhin, T. Menold, B. Rethfeld, A. Michalowski, J.A. L'huillier, Fundamentals of scanning surface structuring by ultrashort laser pulses: From electron diffusion to final morphology (2022). Preprint at https://arxiv.org/abs/2201.0824
228. P.N. Terekhin, O. Benhayoun, S.T. Weber, D.S. Ivanov, M.E. Garcia, B. Rethfeld, Influence of surface plasmon polaritons on laser energy absorption and structuring of surfaces. Appl. Surf. Sci. **512**, 144420 (2020)
229. O. Benhayoun, P.N. Terekhin, D.S. Ivanov, B. Rethfeld, M.E. Garcia, Theory for heating of metals assisted by surface plasmon polaritons. Appl. Surf. Sci. **569**, 150427 (2021)
230. P.N. Terekhin, J. Oltmanns, A. Blumenstein, D.S. Ivanov, F. Kleinwort, M.E. Garcia, B. Rethfeld, J. Ihlemann, P. Simon, Key role of surface plasmon polaritons in generation of periodic surface structures following single-pulse laser irradiation of a gold step edge. Nano **11**(2), 359–367 (2022)
231. J. Oltmanns, P.N. Terekhin, F. Kleinwort, A. Blumenstein, D.S. Ivanov, M.E. Garcia, B. Rethfeld, J. Ihlemann, P. Simon, Influence of the laser beam shape on laser-induced periodic surface structure formation assisted by surface plasmon polaritons. J. Laser Micro/Nanoeng. **16**(3), 199–204 (2021)
232. T.J.-Y. Derrien, Y. Levy, N.M. Bulgakova, Insights into laser-matter interaction from inside: Wealth of processes, multiplicity of mechanisms and possible roadmaps for energy localization, in *Ultrafast Laser Nanostructuring - The Pursuit of Extreme Scales*, ed. by R. Stoian, J. Bonse, (Springer, 2022)
233. A. Rudenko, J.P. Colombier, How light drives material periodic patterns down to the nanoscale, in *Ultrafast Laser Nanostructuring - The Pursuit of Extreme Scales*, ed. by R. Stoian, J. Bonse, (Springer, 2022)
234. M. Mezera, C. Florian, G.R.B.E. Römer, J. Krüger, J. Bonse, Creation of material functions by nanostructuring, in *Ultrafast Laser Nanostructuring - The Pursuit of Extreme Scales*, ed. by R. Stoian, J. Bonse, (Springer, 2022)
235. E.L. Gurevich, S.V. Gurevich, Laser induced periodic surface structures induced by surface plasmons coupled via roughness. Appl. Surf. Sci. **302**, 118–123 (2014)
236. S. Maragkaki, T.J.-Y. Derrien, Y. Levy, N.M. Bulgakova, A. Ostendorf, E.L. Gurevich, Wavelength dependence of picosecond laser-induced periodic surface structures on copper. Appl. Surf. Sci. **417**, 88–92 (2017)
237. E.L. Gurevich, Y. Levy, N.M. Bulgakova, Three-step description of single-pulse formation of laser-induced periodic surface structures on metals. J. Nanomater. **10**, 1836 (2020)
238. E.L. Gurevich, On the influence of surface plasmon-polariton waves on pattern formation upon laser ablation. Appl. Surf. Sci. **278**, 52–56 (2013)
239. E.L. Gurevich, Y. Levy, S.V. Gurevich, N.M. Bulgakova, Role of the temperature dynamics in formation of nanopatterns upon single femtosecond laser pulses on gold. Phys. Rev. B **95**, 054305 (2017)
240. N. Ackerl, K. Wegener, Observation of single ultrashort laser pulse generated periodic surface structures on linelike defects. J. Laser Appl. **32**, 022049 (2020)
241. J.E. Sipe, J.F. Young, J.S. Preston, H.M. van Driel, Laser-induced periodic surface structure. I. Theory. Phys. Rev. B **27**, 1141–1154 (1983)

242. J. Bonse, A. Rosenfeld, J. Krüger, On the role of surface plasmon polaritons in the formation of laser-induced periodic surface structures upon irradiation of silicon by femtosecond-laser pulses. J. Appl. Phys. **106**, 104910 (2009)
243. Y. Levy, N.M. Bulgakova, T. Mocek, Laser-induced periodic surface structures formation: Investigation of the effect of nonlinear absorption of laser energy in different materials. Proc. SPIE **10228**, 102280T (2017)
244. O. Varlamova, J. Reif, S. Varlamov, M. Bestehorn, The laser polarization as control parameter in the formation of laser-induced periodic surface structures: Comparison of numerical and experimental results. Appl. Surf. Sci. **257**, 5465–5469 (2011)
245. A. Rudenko, C. Mauclair, F. Garrelie, R. Stoian, J.P. Colombier, Self-organization of surfaces on the nanoscale by topography-mediated selection of quasi-cylindrical and plasmonic waves. Nano **8**(3), 459–465 (2019)
246. A. Rudenko, A. Abou-Saleh, F. Pigeon, C. Mauclair, F. Garrelie, R. Stoian, J.P. Colombier, High-frequency periodic patterns driven by non-radiative fields coupled with Marangoni convection instabilities on laser-excited metal surfaces. Acta Mater. **194**, 93–105 (2020)
247. Y. Fang, M. Sun, Nanoplasmonic waveguides: Towards applications in integrated nanophotonic circuits. Light Sci. Appl. **4**, e294 (2015)
248. G. Palermo, K.V. Sreekanth, N. Maccaferri, G.E. Lio, G. Nicoletta, F. De Angelis, M. Hinczewski, G. Strangi, Hyperbolic dispersion metasurfaces for molecular biosensing. Nano **10**(1), 295–314 (2021)
249. S. Kou, G. Yuan, Q. Wang, L. Du, E. Balaur, D. Zhang, D. Tang, B. Abbey, X.-C. Yuan, J. Lin, On-chip photonic Fourier transform with surface plasmon polaritons. Light Sci. Appl. **5**, e16034 (2016)
250. F. López-Tejeira, S. Rodrigo, L. Martín-Moreno, F.J. García-Vidal, E. Devaux, T.W. Ebbesen, J.R. Krenn, I.P. Radko, S.I. Bozhevolnyi, M.U. González, J.C. Weeber, A. Dereux, Efficient unidirectional nanoslit couplers for surface plasmons. Nat. Phys. **3**, 324–328 (2007)
251. T. Zang, H. Zang, Z. Xi, J. Du, H. Wang, Y. Lu, P. Wang, Asymmetric excitation of surface plasmon polaritons via paired slot antennas for angstrom displacement sensing. Phys. Rev. Lett. **124**, 243901 (2020)
252. C. Lemke, T. Leißner, A. Klick, J. Fiutowski, J.W. Radke, M. Thomaschewski, J. Kjelstrup-Hansen, H.-G. Rubahn, M. Bauer, The complex dispersion relation of surface plasmon polaritons at gold/para-hexaphenylene interfaces. Appl. Phys. B Lasers Opt. **116**, 585–591 (2014)
253. A. Klick, S. de la Cruz, C. Lemke, M. Großmann, H. Beyer, J. Fiutowski, H.-G. Rubahn, E.R. Méndez, M. Bauer, Amplitude and phase of surface plasmon polaritons excited at a step edge. Appl. Phys. B Lasers Opt. **122**, 79 (2016)
254. S.A. Maier, *Plasmonics: Fundamentals and Applications* (Springer, Berlin, 2007)
255. R.L. Olmon, B. Slovick, T.W. Johnson, D. Shelton, S.-H. Oh, G.D. Boreman, M.B. Raschke, Optical dielectric function of gold. Phys. Rev. B **86**, 235147 (2012)
256. M. Hartelt, P.N. Terekhin, T. Eul, A.-K. Mahro, B. Frisch, E. Prinz, B. Rethfeld, B. Stadtmüller, M. Aeschlimann, Energy and momentum distribution of surface Plasmon-induced hot carriers isolated via spatiotemporal separation. ACS Nano **15**, 19559–19569 (2021)
257. J. Lin, J.P.B. Mueller, Q. Wang, G. Yuan, N. Antoniou, X.-C. Yuan, F. Capasso, Polarization-controlled tunable directional coupling of Surface Plasmon Polaritons. Science **340**, 331–334 (2013)
258. S.-Y. Lee, K. Kim, G.-Y. Lee, B. Lee, Polarization-multiplexed plasmonic phase generation with distributed nanoslits. Opt. Express **23**, 15598–15607 (2015)
259. H. Wang, J. Jürgensen, P. Decker, Z. Hu, K. Yan, E.L. Gurevich, A. Ostendorf, Corrosion behavior of NiTi alloy subjected to femtosecond laser shock peening without protective coating in air environment. Appl. Surf. Sci. **501**, 144338 (2020)
260. R.D. Murphy, B. Torralva, D.P. Adams, S.M. Yalisove, Laser-induced periodic surface structure formation resulting from single-pulse ultrafast irradiation of Au microstructures on a Si substrate. Appl. Phys. Lett. **102**, 211101 (2013)

261. R.D. Murphy, B. Torralva, D.P. Adams, S.M. Yalisove, Polarization dependent formation of femtosecond laser-induced periodic surface structures near stepped features. Appl. Phys. Lett. **104**, 231117 (2014)
262. P. Lalanne, J.P. Hugonin, Interaction between optical nano-objects at metallo-dielectric interfaces. Nat. Phys. **2**, 551–556 (2006)
263. P. Lalanne, J.P. Hugonin, H.T. Liu, B. Wang, A microscopic view of the electromagnetic properties of sub-λ metallic surfaces. Surf. Sci. Rep. **64**, 453–469 (2009)
264. A.Y. Nikitin, F.J. García-Vidal, L. Martín-Moreno, Surface electromagnetic field radiated by a subwavelength hole in a metal film. Phys. Rev. Lett. **105**, 073902 (2010)
265. C.H. Gan, J.R. Pugh, M.J. Cryan, J.G. Rarity, G.R. Nash, Role of quasicylindrical waves and surface plasmon polaritons on beam shaping with resonant nanogratings in the infrared. Phys. Rev. B **89**, 201415(R) (2014)
266. E.A. Danilov, S.A. Uryupin, Competition of quasi-cylindrical and surface waves excited at the femtosecond pulse effect on the metal. Opt. Lett. **46**, 2521–2524 (2021)
267. F. Garrelie, J.P. Colombier, F. Pigeon, S. Tonchev, N. Faure, M. Bounhalli, S. Reynaud, O. Parriaux, Evidence of surface plasmon resonance in ultrafast laser-induced ripples. Opt. Express **19**, 9035–9043 (2011)
268. M. Schäfer, P.N. Terekhin, Y. Kang, G. Torosyan, X. del Arco Fargas, S. Hirtle, B. Rethfeld, J.A. L'huillier, Magnetic-field assisted laser ablation of silicon. J. Opt. Soc. Am. B **38**, E1–E6 (2021)

Chapter 3
Ultrafast Quantum Processes at the Nanoscale: Insights from Modeling

Bernd Bauerhenne, Tobias Zier, and Martin E. Garcia

Abstract Ultrashort laser pulses excite in solids and nanostructures a large amount of electrons and holes. This leads to an extreme state, which has nonequilibrium character in multiple aspects and evolves through different steps with characteristic timescales toward maximization of entropy. First, decoherence yields to random phases of the excited carriers and to a diagonal reduced density matrix, resulting in a nonequilibrium electron distribution. On a later stage, carrier-carrier collisions due to Coulomb interactions contribute to an electron and hole thermalization process, after which carrier acquire an extremely high temperature. The ions, however, remain at the initial temperature around their initial positions. The hot electrons and holes produce dramatic changes in the interactions between ions, leading to the presence of strong forces acting on the ions. As a consequence, ions move rapidly without acquiring a well-defined temperature. Depending on its lifetime, mainly determined by incoherent electron-phonon scattering, this non-thermal situation can lead to a large variety of non-thermal structural changes and to states of matter which are inaccessible at thermodynamical equilibrium.

In this chapter, we summarize a theoretical framework for describing the above sketched "non-thermal state," discuss the influence of quantum effects, explain how this state decays, enumerate a series of still open questions, and present different examples of laser-induced non-thermal effects in solids and show how they can be experimentally detected.

Keywords Femtosecond laser excitation · Electron-phonon coupling · Non-thermal phenomena · Potential energy surface · Electronic temperature · Density functional theory

---

B. Bauerhenne (✉) · M. E. Garcia
Theoretical Physics and Center for Interdisciplinary Nanostructure Science and Technology (CINSaT), University of Kassel, Kassel, Germany
e-mail: bauerhenne@uni-kassel.de; garcia@physik.uni-kassel.de

T. Zier
Department of Physics, University of California Merced, Merced, California, USA
e-mail: tzier2@ucmerced.edu

© The Author(s), under exclusive license to Springer Nature Switzerland AG 2023

R. Stoian, J. Bonse (eds.), *Ultrafast Laser Nanostructuring*, Springer Series in Optical Sciences 239, https://doi.org/10.1007/978-3-031-14752-4_3

1 Laser-Solid Interaction: Timescales, Quantum, and Quasiclassical/Classical Processes

The usage of femtosecond laser pulses allows advanced structure manipulations of solids beyond thermodynamical limits. Reason for this is the ultrashort interaction time between the laser field and the matter. During the short action of the intense laser field, the electrons undergo strong interaction, whereas there is a negligible influence on the nuclei, since the electrons are much lighter than the nuclei. In detail, the laser field excites electrons from occupied to unoccupied electronic levels (in the case of semiconductors, from the valence band to the conduction band). Besides this creation of electron-hole pairs, the laser also induces a polarization. Due to electron-electron collisions, the polarization vanishes within a time τ_{defasing} of a few femtosecond after the laser pulse. On a slightly longer timescale τ_{e-e} of typically tens to hundreds of femtoseconds, the electron-electron collisions induce a thermalization of the electrons and holes to a Fermi distribution with a high electronic temperature T_e. In contrast to this, the timescale for phonon-phonon collisions τ_{ph-ph} and for the electron-phonon collisions τ_{e-ph} is much longer and takes place on picoseconds. Thus, the equilibration of the excited electronic system and the cold ionic system needs a picosecond timescale. The electron-phonon coupling (EPC) given by electron-phonon collisions induces a decrease of T_e and heats up the ions, whereas the phonon-phonon collisions induce a thermalization of the ions to an ionic temperature T_i. In summary, the electrons reach very fast an electronic temperature T_e after an excitation with a femtosecond laser pulse, whereas a lattice or ionic temperature T_i is established much later.

In this chapter, we call “non-thermal” those transient states after laser excitation in which electrons have already thermalized but ions have not. This means that we focus on processes for which T_e is well defined (and extremely high), but for which no phonon (lattice) temperature can be determined. During those times $\tau_{e-e} < t < \tau_{ph-ph}$ after laser excitation, very exciting non-thermal phenomena take place, which are the subject of this chapter. It is important to point out here that the electron-phonon coupling time τ_{e-ph} is usually, but not always, larger than the phonon thermalization time τ_{ph-ph}. Furthermore, one does not know, so far, if non-thermal processes, taking place on timescales considerably shorter than τ_{e-ph}, have real influence on the laser processing performance and products.

2 The Generalized Born-Oppenheimer Approximation: Non-Thermal Ions Guided by Excited Electrons

In this section, we provide a mathematical description of the laser-induced nonequilibrium transient state that leads to non-thermal processes in solids and nanostructures. We introduce the concept of laser-induced potential energy surface, which arises naturally from a generalized Born-Oppenheimer approximation. But before describing the interaction of the material with the laser, we go step by step and start by the original adiabatic approximation as it was introduced for systems in the electronic ground state ($T_\mathrm{e} = 0$). We follow below the logic and notation used by Czycholl [1].

2.1 The Hamiltonian of the Solid

We consider a solid (or nanostructure) consisting of N_e electrons (with charge $-e$) and N_I ions having masses M_i and charges $Z_i\,e$ ($i = 1, \ldots N_I$). Due to charge neutrality, it must hold that $N_e = \sum_{i=1}^{N_I} Z_i$. In its nonrelativistic version, the Hamiltonian of the system can be written as

$$\hat{H} = \hat{T}_I + \hat{T}_\mathrm{e} + V_{ee} + V_{eI} + V_{II}. \tag{3.1}$$

Here, the first term corresponds to the kinetic energy of the ions, given by

$$\hat{T}_I = -\sum_{i=1}^{N_I} \frac{\hbar^2}{2M_i} \nabla^2_{\boldsymbol{R}_i}, \tag{3.2}$$

where $\nabla_{\boldsymbol{R}_i}$ refers to the gradient with respect to the coordinate $\boldsymbol{R}_i$ of the i-th ion. The second term of the Hamiltonian (3.1) stands for the kinetic energy of the electrons:

$$\hat{T}_\mathrm{e} = -\sum_{j=1}^{N_e} \frac{\hbar^2}{2\,m_\mathrm{e}} \nabla^2_{\boldsymbol{r}_j}, \tag{3.3}$$

where $\nabla_{\boldsymbol{r}_j}$ refers to the gradient with respect to the coordinate $\boldsymbol{r}_j$ of the j-th electron with mass m_e. The third term of the Hamiltonian (3.1) refers to the Coulomb interactions (repulsion) between electrons and is given by

$$V_{ee} = \sum_{j<l}^{N_e} \frac{e^2}{|\boldsymbol{r}_j - \boldsymbol{r}_l|}. \tag{3.4}$$

The last two terms of the Hamiltonian $\hat{H}$ describe the attractive interaction between electrons and ions and to the ion-ion repulsion, respectively. Both interaction terms consist of pair potentials and can be written as

$$V_{eI} = \sum_{j=1}^{N_e} \sum_{i=1}^{N_I} v_{eI}\big(|\boldsymbol{r}_j - \boldsymbol{R}_i|\big),$$

and

$$V_{II} = \sum_{i<k}^{N_I} v_{II}\big(|\boldsymbol{R}_i - \boldsymbol{R}_k|\big).$$

Note, however, that the form of the pair potentials $v_{eI}\big(|\boldsymbol{r}_j - \boldsymbol{R}_i|\big)$ and $v_{II}\big(|\boldsymbol{R}_i - \boldsymbol{R}_k|\big)$ depends on how many electrons are taken as degrees of freedom of the problem. If, for example, only the valence electrons are considered, then the ions do not only include the atomic nuclei but also the core electrons. This means that both pair potentials must include not only the Coulomb interactions but also the Pauli principle, and they acquire a more complex form, but remaining a sum of pair potentials. On the other hand, if all electrons are considered as degrees of freedom, then both potentials $v_{eI}(|\boldsymbol{r}_j - \boldsymbol{R}_i|)$ and $v_{II}(|\boldsymbol{R}_i - \boldsymbol{R}_k|)$ can be written as pure Coulomb interactions, and the corresponding terms of the Hamiltonian have the form

$$V_{eI} = \sum_{j=1}^{N_e} \sum_{i=1}^{N_I} \frac{-Z_i\, e^2}{|\boldsymbol{r}_j - \boldsymbol{R}_i|}, \tag{3.5}$$

$$V_{II} = \sum_{i<k}^{N_I} \frac{Z_i Z_k\, e^2}{|\boldsymbol{R}_i - \boldsymbol{R}_k|}. \tag{3.6}$$

Since ions are considerably heavier and consequently much slower than electrons ($m/M_i \sim 10^{-4}$), the ionic kinetic energies are orders of magnitude smaller than those of the electrons. Therefore, the term $\hat{T}_I$ is orders of magnitude smaller than the other terms of the Hamiltonian $\hat{H}$ [1, 2]. This is the basis for the adiabatic (or Born-Oppenheimer) approximation.

2.2 Born-Oppenheimer (or Adiabatic) Potential Energy Surface (PES)

In view of the above arguments, we can treat $\hat{T}_I$ as a perturbation and write

$$\hat{H} = \hat{H}_0 + \hat{T}_I.$$

$\hat{H}_0$ is thus the zeroth-order approximation of $\hat{H}$ in $\hat{T}_I$. Notice that $\hat{H}_0$ is a purely electronic Hamiltonian, with the operators $\nabla_{\boldsymbol{r}_j}$, V_{ee} acting only on the electron wave functions and the terms V_{eI} and V_{II} depending on the ionic coordinates $\{\boldsymbol{R}_i\}$ as "external parameters." Thus, for fixed ionic coordinates $\{\boldsymbol{R}_i\}$, $\hat{H}_0$ describes N_e electrons in a static potential with external parameters. The corresponding stationary Schrödinger equation reads

$$\hat{H}_0\, \phi_\alpha\big(\{\boldsymbol{r}_j\}, \{\boldsymbol{R}_i\}\big) = \Big[\hat{T}_{\mathrm{e}} + V_{ee} + V_{eI} + V_{II}\Big]\ \phi_\alpha\big(\{\boldsymbol{r}_j\}, \{\boldsymbol{R}_i\}\big)$$

$$= [\epsilon_\alpha(\{\boldsymbol{R}_i\}) + V_{II}(\{\boldsymbol{R}_i\})]\,\phi_\alpha\big(\{\boldsymbol{r}_j\},\{\boldsymbol{R}_i\}\big), \tag{3.7}$$

where the wave function ϕ_α is an eigenstate of $\hat{H}_0$, which describes all N_e electrons considered as degrees of freedom and can therefore be expressed, in a periodic solid, as a linear combination of $N_e \times N_e$ Slater determinants of Bloch functions. The eigenvalues are denoted by ϵ_α, where α labels the N_e-body quantum state described by the wave function $\phi_\alpha(\{\boldsymbol{r}_j\},\{\boldsymbol{R}_i\})$. Since V_{II} does not depend on the electronic coordinates and it is just a constant from the point of view of electrons, we write it explicitly as an additive constant in Eq. (3.7). Note that both ϵ_α and V_{II} are functions of the ionic coordinates, which formally appear as $3N_I$ external parameters. $\{\alpha\}$ is a complete set of quantum numbers and $\{\phi_\alpha\}$ a complete set of N_e-electron wave functions.

On the basis of the diagonalization of $\hat{H}_0$, we can now write down the Schrödinger equation for the complete Hamiltonian $\hat{H}$, which reads

$$\hat{H}\ \psi\big(\{\boldsymbol{r}_j\},\{\boldsymbol{R}_i\}\big) = E\ \psi\big(\{\boldsymbol{r}_j\},\{\boldsymbol{R}_i\}\big). \tag{3.8}$$

Here, $\psi\big(\{\boldsymbol{r}_j\},\{\boldsymbol{R}_i\}\big)$ refers to the complete wave function of the solid describing the N_e electrons and N_I ions. For fixed ionic coordinates, we can expand $\psi\big(\{\boldsymbol{r}_j\},\{\boldsymbol{R}_i\}\big)$ as a linear combination of the functions ϕ_α making use of the completeness of the set $\{\phi_\alpha\}$ of eigenfunctions of $\hat{H}_0$. Thus,

$$\psi\big(\{\boldsymbol{r}_j\},\{\boldsymbol{R}_i\}\big) = \sum_\alpha \chi_\alpha\big(\{\boldsymbol{R}_i\}\big)\ \phi_\alpha\big(\{\boldsymbol{r}_j\},\{\boldsymbol{R}_i\}\big). \tag{3.9}$$

Inserting Eq. (3.9) into Eq. (3.8), one obtains

$$\sum_\alpha \Big[\hat{H}_0 + \hat{T}_I - E\Big]\ \chi_\alpha\big(\{\boldsymbol{R}_i\}\big)\ \phi_\alpha\big(\{\boldsymbol{r}_j\},\{\boldsymbol{R}_i\}\big) = 0. \tag{3.10}$$

Here, the coefficients $\{\chi_\alpha\}$ of the linear expansion are functions of the ionic coordinates. This means that, for different sets of ionic coordinates $\{\boldsymbol{R}_i\}$, one obtains different values of the χ_α's.

Taking into account that the operator $\hat{T}_I$ affects both the ϕ_α's and the χ_α's, multiplying Eq. (3.10) by $\phi^*_\beta(\{\boldsymbol{r}_j\},\{\boldsymbol{R}_i\})$, and integrating over all $3\,N_e$ electronic coordinates, one obtains, after some intermediate steps and after interchanging the labels α and β,

$$\begin{aligned}\Big[\hat{T}_I + \epsilon_\alpha\big(\{\boldsymbol{R}_i\}\big) + V_{II}\big(\{\boldsymbol{R}_i\}\big)\Big]\,\chi_\alpha\big(\{\boldsymbol{R}_i\}\big)&\\ + \sum_\beta B_{\beta\alpha}\big(\{\boldsymbol{R}_i\}\big)\ \chi_\beta\big(\{\boldsymbol{R}_i\}\big)\ =\ E\,\chi_\alpha\big(\{\boldsymbol{R}_i\}\big),&\end{aligned} \tag{3.11}$$

where $B_{\beta\alpha}$ are operators acting on the ionic coordinates and therefore on the coefficients $\chi_\alpha\big(\{\boldsymbol{R}_i\}\big)$ (see [1] for the detailed expressions).

2.2.1 Adiabatic Approximation

One can easily estimate the magnitude of the terms contained in the operators $B_{\beta\alpha}$ [1]. It turns out that some of the terms scale roughly as $(m/M_i)^{3/4}$ and the others as (m/M_i) and can therefore be neglected if the velocity of the ions is small. The adiabatic approximation consists in assuming that

$$B_{\beta\alpha} \to 0. \tag{3.12}$$

Following this assumption and replacing $B_{\beta\alpha}$ by 0 in Eq. (3.11), one obtains an effective Schrödinger equation fulfilled by the coefficients $\chi_\alpha\big(\{\boldsymbol{R}_i\}\big)$ of the form

$$\Big[\hat{T}_I + U\big(\{\boldsymbol{R}_i\}\big)\Big]\,\chi_\alpha\big(\{\boldsymbol{R}_i\}\big) \;=\; E\,\chi_\alpha\big(\{\boldsymbol{R}_i\}\big), \tag{3.13}$$

with

$$U\big(\{\boldsymbol{R}_i\}\big) = \epsilon_\alpha\big(\{\boldsymbol{R}_i\}\big) + V_{II}\big(\{\boldsymbol{R}_i\}\big). \tag{3.14}$$

Note that in Eq. (3.13), the coefficients $\chi_\alpha(\{\boldsymbol{R}_i\})$ can be interpreted as the wave functions of the ions, which move under the influence of an effective potential $U(\{\boldsymbol{R}_i\})$, which is called *potential energy surface* (PES). The concept of PES is widely used and constitutes the basis for the study of ionic motion in molecular and condensed matter physics. The adiabatic approximation basically consists in assuming that, from the point of view of ions, the fast electrons adapt to any new ionic configuration immediately, modifying themselves the interaction potential between ions. The multidimensional potential energy surface (PES) $U\big(\{\boldsymbol{R}_i\}\big)$ is obtained by solving the electronic Schrödinger equation (3.7), i.e., by solving the electronic problem. In Eq. (3.14), $\epsilon_\alpha\big(\{\boldsymbol{R}_i\}\big)$ is the contribution of the fast moving electrons. This contribution can be negative (attractive, due to bonding) or positive (repulsive, due to antibonding) depending on the state α of the N_e-electron system. The different states of the N_e-electronic system are labeled with α, and for each N_e-electron state, there is a particular potential energy surface. $\alpha = 0$ corresponds to the ground state potential energy $U_0\big(\{\boldsymbol{R}_i\}\big)$, which is obtained from the ground state of $\hat{H}_0$. There is a huge amount of PESs, since already each single-electron excitation leads to a different PES. The PESs are multidimensional surfaces in a space of $3\,N_I$ dimensions. In the adiabatic approximation, there is no connection between the different PESs. They can cross with each other but there is no term connecting them. However, as soon as the factors $B_{\beta\alpha}$ (Eq. (3.11)) become different from zero, jumps between the potential surfaces induced by the motion of the ions are possible.

2.3 Effects of a fs-Laser Interaction on Matter

If a fs-laser pulse excites matter, intense electric and magnetic fields act on matter for the applied ultrashort pulse duration. Due to this, mainly the electrons are excited, since they are much lighter than the ions. Thus, the laser interaction term reads

$$\hat{H}_{\mathrm{L}} = \sum_{j=1}^{N_{\mathrm{e}}} \frac{i\,\hbar\,e}{m_{\mathrm{e}}}\,\mathbf{A}(\mathbf{r}_j,t)\cdot\nabla_{\mathbf{r}_j} + \sum_{j=1}^{N_{\mathrm{e}}} \frac{e^2}{2\,m_{\mathrm{e}}}\,\mathbf{A}^2(\mathbf{r}_j,t). \tag{3.15}$$

Here, $\mathbf{A}(\mathbf{r},t)$ denotes the vector potential of the laser field. Furthermore, the Coulomb gauge has been used, i.e., $\nabla\cdot A = 0$. Commonly, one neglects the quadratic term except in the case of extremely high intensities. Using the Born-Oppenheimer approximation, the motion of the electrons and ions is decoupled. Therefore, the Hamiltonian of the electrons in the femtosecond laser field can be written as

$$\hat{H} = \sum_{j=1}^{N_{\mathrm{e}}} \hat{H}_j^{(1)} + \sum_{j=1}^{N_{\mathrm{e}}} \hat{H}_j^{(\mathrm{L})} + \sum_{j<k}^{N_{\mathrm{e}}} \hat{V}_{jk}^{(\mathrm{int})}, \tag{3.16}$$

where

$$\hat{H}_j^{(1)} = \frac{\hbar^2}{2\,m_{\mathrm{e}}^2}\nabla_{\mathbf{r}_j}^2 + V_{\mathrm{ext}}(\mathbf{r}_j) + \frac{V_{\mathbf{nn}}}{N_{\mathrm{e}}}, \tag{3.17}$$

$$\hat{H}_j^{(\mathrm{L})} = \frac{i\,\hbar\,e}{m_{\mathrm{e}}}\,\mathbf{A}(\mathbf{r}_j,t)\cdot\nabla_{\mathbf{r}_j} + \frac{e^2}{2\,m_{\mathrm{e}}}\,\mathbf{A}^2(\mathbf{r}_j,t), \tag{3.18}$$

are one particle operators with $V_{\mathrm{ext}}(\mathbf{r}_j)$ being the external potential given by the ions and

$$\hat{V}_{jk}^{(\mathrm{int})} = \frac{e^2}{\left|\mathbf{r}_j - \mathbf{r}_k\right|}, \tag{3.19}$$

is a two particle operator describing the electron-electron interaction obeying $\hat{V}_{jk}^{(\mathrm{int})} = \hat{V}_{kj}^{(\mathrm{int})}$. Since the solid forms a periodic crystal structure, one can diagonalize the electronic Hamiltonian

$$\hat{H}_0 = \sum_{j=1}^{N_{\mathrm{e}}} \hat{H}_j^{(1)} \tag{3.20}$$

without two-electron Coulomb interaction $\hat{V}_{jk}^{(\mathrm{int})}$ and laser interaction $\hat{H}_j^{(\mathrm{L})}$. The eigenstates of $\hat{H}_0$ with eigenenergies $\varepsilon_{\ell\mathbf{k}}$ are just one-electron Bloch states $|\ell\mathbf{k}\rangle$.

Using these complete set of one-electron eigenstates, we transform the full electronic Hamilton operator (3.16) with femtosecond laser-field interaction to second quantization:

$$\begin{aligned}\hat{H} =& \sum_{\ell\mathbf{k}} \varepsilon_{\ell\mathbf{k}}\, \hat{c}^{\dagger}_{\ell\mathbf{k}}\, \hat{c}_{\ell\mathbf{k}} + \sum_{\ell\mathbf{k},\ell'\mathbf{k}'} H^{(\mathrm{L})}_{\ell\mathbf{k},\ell'\mathbf{k}'}\, \hat{c}^{\dagger}_{\ell\mathbf{k}}\, \hat{c}_{\ell'\mathbf{k}'} \\ &+ \frac{1}{2} \sum_{\ell\mathbf{k},\ell'\mathbf{k}',\ell''\mathbf{k}'',\ell'''\mathbf{k}'''} V^{(\mathrm{int})}_{\ell\mathbf{k},\ell'\mathbf{k}',\ell''\mathbf{k}'',\ell'''\mathbf{k}'''}\, \hat{c}^{\dagger}_{\ell\mathbf{k}}\, \hat{c}^{\dagger}_{\ell'\mathbf{k}'}\, \hat{c}_{\ell'''\mathbf{k}'''}\, \hat{c}_{\ell''\mathbf{k}''},\end{aligned} \tag{3.21}$$

with

$$H^{(\mathrm{L})}_{\ell\mathbf{k},\ell'\mathbf{k}'} = \sum_{\sigma} \int\limits_{\mathbb{R}^3} d^3r\; \varphi^{*}_{\ell\mathbf{k}}(\sigma,\mathbf{r}) \left(\frac{i\,\hbar\, e}{m_{\mathrm{e}}}\, \mathbf{A}(\mathbf{r},t)\cdot\nabla_{\mathbf{r}} + \frac{e^2}{2\,m_{\mathrm{e}}}\, \mathbf{A}^2(\mathbf{r},t) \right) \varphi_{\ell'\mathbf{k}'}(\sigma,\mathbf{r}) \tag{3.22}$$

and

$$\begin{aligned}V^{(\mathrm{int})}_{\ell\mathbf{k},\ell'\mathbf{k}',\ell''\mathbf{k}'',\ell'''\mathbf{k}'''} =& \sum_{\sigma,\sigma'} \int\limits_{\mathbb{R}^3} d^3r \int\limits_{\mathbb{R}^3} d^3r'\; \varphi^{*}_{\ell\mathbf{k}}(\sigma,\mathbf{r})\, \varphi^{*}_{\ell'\mathbf{k}'}(\sigma',\mathbf{r}') \times \\ &\times \frac{e^2}{|\mathbf{r}-\mathbf{r}'|}\, \varphi_{\ell''\mathbf{k}''}(\mathbf{r})\, \varphi_{\ell'''\mathbf{k}'''}(\sigma',\mathbf{r}').\end{aligned} \tag{3.23}$$

$\varphi_{\ell\mathbf{k}}(\sigma,\mathbf{r})$ denotes the Bloch electron with wave vector $\boldsymbol{k}$ in band ℓ and σ denotes the spin. Before the femtosecond laser pulse acts, the electrons form a canonical ensemble at $T_{\mathrm{e}} = 300$ K. However, a thermodynamic ensemble cannot be described by an electronic wave function, but with an electronic density matrix:

$$\hat{\rho}_e = \sum_{\alpha} p_{\alpha}\, |\Psi_{\alpha}\rangle\langle\Psi_{\alpha}|, \tag{3.24}$$

where $\{|\Psi_{\alpha}\rangle\}$ form a complete set and $0 \le p_{\alpha} \le 1$ and $\sum_{\alpha} p_{\alpha} = 1$. Thus, the electron density matrix describes the time propagation of the electronic system. At first, we neglect the complicated electron-electron interaction, so that the electronic Hamiltonian with femtosecond laser excitation is just a sum over one-particle operators. Due to this, we only need to work with the one-electron density matrix $\hat{\rho}^{(1)}_e$, which time propagation is just given by

$$\frac{\partial \hat{\rho}^{(1)}_{\mathrm{e}}}{\partial t} = -\frac{i}{\hbar}\Big[\hat{H}^{(1)}_1 + \hat{H}^{(\mathrm{L})}_1\,,\; \hat{\rho}^{(1)}_{\mathrm{e}} \Big]. \tag{3.25}$$

The femtosecond laser field described by $\hat{H}_1^{(L)}$ creates electrons above the Fermi level and holes below it. This means that it is responsible for the rapid creation of electron-hole pairs, as long as the laser pulse is acting. The probability for the creation of electron-hole pairs is proportional to the square of the absolute value of the matrix elements of $\hat{H}_1^{(L)}$, i.e., proportional to the intensity of the laser pulse. Furthermore, the laser induces a coherence—off-diagonal elements of the density matrix become nonzero. Now we consider also the up to now ignored influence of the electron-electron interaction, so that the time propagation of the one-electron density matrix $\hat{\rho}_e^{(1)}$ has to be modified to

$$\frac{\partial \hat{\rho}_e^{(1)}}{\partial t} = -\frac{i}{\hbar}\left[\hat{H}_1^{(1)} + \hat{H}_1^{(L)}\, , \, \hat{\rho}_e^{(1)}\right] \underbrace{- \frac{i}{2\hbar}\left[\hat{V}_{12}^{(int)}\, , \, \hat{\rho}_e^{(2)}\right]}_{=: \left.\frac{\partial \hat{\rho}_e^{(1)}}{\partial t}\right|_{\text{collisions}}}. \tag{3.26}$$

$\hat{\rho}_e^{(2)}$ denotes the two-electron density matrix. Now one needs the two-electron density matrix for the time propagation of the one-electron density matrix. Moreover, one needs the three-electron density matrix for the time propagation of the two-electron density matrix, and, in general, the time derivative of the n-electron reduced density matrix is related to the $(n+1)$-electron reduced density matrix. The latter is called **BBGKY hierarchy** [3]. To overcome this problem, one can use, for example, the mean field approximation, to which density functional theory belongs. Here, the two-body Coulomb interaction term is described by an effective one-particle operator, so that the electronic Hamiltonian is just a sum over one-particle operators and the term in Eq. (3.26) with the two-electron reduced density matrix is not present. We will discuss density functional theory later in more detail.

The collisions due to the electron-electron Coulomb interaction induce rapid dephasing processes, so that the laser-induced polarization goes to zero within a time $\tau_{dephasing}$, which is extremely short for high laser fluences. Therefore, one can assume that at a given time t_0 immediately after the laser pulse is over the one-electron density matrix looks like

$$\hat{\rho}_e^{(1)}(t_0) = \begin{pmatrix} \ddots & & & \\ & \rho_{kk} & 0 & \\ & & \ddots & \\ & 0 & \rho_{k'k'} & \\ & & & \ddots \end{pmatrix}, \tag{3.27}$$

where the general index k refers to the set $\{\boldsymbol{k}\nu\sigma\}$. The diagonal elements $\rho_{kk} = \hat{n}_{\boldsymbol{k}\nu\sigma}$ correspond to a nonequilibrium distribution of electrons (and holes) created by the laser pulse.

The second fastest process induced by the electron-electron Coulomb interaction is the electron thermalization, which occurs on a thermalization timescale τ_{therm}. For very low fluences, τ_{therm} is known to be of the order of 100 fs [4]. For high fluences, a carrier thermalization time faster than 25 fs in GaAs has been reported [5]. Therefore, one can assume that the diagonal elements of the density matrix, which represent a nonequilibrium electron distribution created by the laser, will rapidly converge to a Fermi-Dirac distribution, i.e.,

$$\rho_{\boldsymbol{k}\nu\sigma,\boldsymbol{k}\nu\sigma} = n_{\boldsymbol{k}\nu\sigma} = \frac{1}{\exp\Big(\beta\left(\varepsilon_{\nu\sigma}(\boldsymbol{k}) - \mu\right)\Big) + 1}, \quad \text{with } \beta = \frac{1}{k_{\mathrm{B}}\, T_{\mathrm{e}}}. \tag{3.28}$$

Here, T_{e} is the electron temperature and μ is the chemical potential. Note that T_{e} is very high (usually of the order of many thousand Kelvin) due to the large amount of energy pumped into the electronic system by the laser.

3 Finite-Temperature Density Functional Theory

After the excitation with a femtosecond laser pulse, the electrons thermalize very fast in the time τ_{therm} to a Fermi distribution with a high electronic temperature T_{e}, which remains high on a longer timescale, since the energy transfer between the electrons and the ions takes place on a picosecond timescale. The increased T_{e} causes significant changes in the electronic bonding. Using the Born-Oppenheimer approximation, the potential energy surface, on which the ions move and which is created by the electrons, changes dramatically. A system of electrons in the external potential $V_{\mathrm{ext}}(\mathbf{r})$ of the fixed nuclei at a given temperature T_{e} is thermodynamically described by the electronic density matrix $\hat{\rho}_{\mathrm{e}}$ from Eq. (3.24). Thus, we obtain the total energy of the electrons from the electronic Hamiltonian $\hat{H}_{\mathrm{e}}$ and the electronic density matrix $\hat{\rho}_{\mathrm{e}}$ by

$$\left\langle \hat{H}_{\mathrm{e}} \right\rangle_{\hat{\rho}_{\mathrm{e}}} = \left\langle \hat{T}_{\mathrm{e}} + \hat{V}_{\mathrm{int}} \right\rangle_{\hat{\rho}_{\mathrm{e}}} + \left\langle \hat{V}_{\mathrm{ext}} \right\rangle_{\hat{\rho}_{\mathrm{e}}} + \left\langle E_{\mathrm{nn}} \right\rangle_{\hat{\rho}_{\mathrm{e}}}. \tag{3.29}$$

$\hat{V}_{\mathrm{int}}$ describes the Coulomb interaction between the electrons and the constant E_{nn} accounts for the ion-ion interaction. It would be much easier to work with the electronic density:

$$\begin{aligned} n_{\mathrm{e}}(\mathbf{r}) &= \left\langle \hat{n}_{\mathrm{e}}(\mathbf{r}) \right\rangle_{\hat{\rho}_{\mathrm{e}}} \\ &= \sum_{\alpha} p_{\alpha} \left\langle \Psi_{\alpha} \middle| \hat{n}_{\mathrm{e}}(\mathbf{r}) \middle| \Psi_{\alpha} \right\rangle \\ &= \sum_{\alpha} p_{\alpha}\, n_{\mathrm{e}}^{(\alpha)}(\mathbf{r}). \end{aligned} \tag{3.30}$$

Using the latter, one obtains

$$\begin{aligned}\left\langle \hat{V}_{\text{ext}} \right\rangle_{\hat{\rho}_{\text{e}}} &= \sum_{\alpha} p_{\alpha} \left\langle \Psi_{\alpha} \middle| \hat{V}_{\text{ext}} \middle| \Psi_{\alpha} \right\rangle \\ &= \sum_{\alpha} p_{\alpha} \int_{\mathbb{R}^3} d^3 r \, V_{\text{ext}}(\mathbf{r}) \, n_{\text{e}}^{(\alpha)}(\mathbf{r}) \\ &= \int_{\mathbb{R}^3} d^3 r \, V_{\text{ext}}(\mathbf{r}) \, n_{\text{e}}(\mathbf{r}), \end{aligned} \tag{3.31}$$

and therefore, one has for the total energy

$$\left\langle \hat{H}_{\text{e}} \right\rangle_{\hat{\rho}_{\text{e}}} = \sum_{\alpha} p_{\alpha} \left\langle \Psi_{\alpha} \middle| \hat{T}_{\text{e}} + \hat{V}_{\text{int}} \middle| \Psi_{\alpha} \right\rangle + \int_{\mathbb{R}^3} d^3 r \, V_{\text{ext}}(\mathbf{r}) \, n_{\text{e}}(\mathbf{r}) + E_{\text{nn}}. \tag{3.32}$$

We observe that the operators for the kinetic energy $\hat{T}_{\text{e}}$ and for the interaction between the electrons $\hat{V}_{\text{int}}$ are universal for any system of N_{e} interacting electrons. Only the terms $V_{\text{ext}}(\mathbf{r})$ and E_{nn} differ for particular electronic systems. Fortunately, E_{nn} is just a constant, and the energy contribution of $V_{\text{ext}}(\mathbf{r})$ can be calculated from the electronic density $n_{\text{e}}(\mathbf{r})$ in a simple way. Thus, one may think that the electron density $n_{\text{e}}(\mathbf{r})$ could be used as the main variable instead of the complicated density operator $\hat{\rho}_{\text{e}}$. Indeed, in 1965, Mermin [6] introduced a theory, which describes the electronic system at temperature T_{e} with the help of the electronic density, which was the born of the finite-temperature-dependent density functional theory (DFT). In detail, Mermin proofs that the equilibrium electron density $n_{\text{e}_0}(\mathbf{r})$ determines uniquely, except for a constant, the external potential $V_{\text{ext}}(\mathbf{r})$ in the Hamiltonian $\hat{H}_{\text{e}}$ for any system of interacting electrons at a given electronic temperature T_{e}. Thus, the many-body wave functions are determined for all states (ground and excited), and the equilibrium density matrix is known, so that all properties of the system can be derived.

One calls an electron density $n_{\text{e}}(\mathbf{r})$ ρ-representable, if it can be constructed from a density operator $\hat{\rho}_{\text{e}}$. On the space of ρ-representable electron densities, Mermin introduces a universal functional for the Helmholtz free energy:

$$F_{\text{M}}\Big(n_{\text{e}}(\mathbf{r}), V_{\text{ext}}(\mathbf{r}), E_{\text{nn}}, T_{\text{e}}\Big) = \inf_{\hat{\rho}_{\text{e}} \to n_{\text{e}}(\mathbf{r})} \text{Tr}\Big(\hat{\rho}_{\text{e}} \left(\hat{T}_{\text{e}} + \hat{V}_{\text{int}} + \hat{V}_{\text{ext}}\right) + k_{\text{B}} \, T_{\text{e}} \, \hat{\rho}_{\text{e}} \, \ln\left(\hat{\rho}_{\text{e}}\right)\Big) + E_{\text{nn}} \tag{3.33}$$

using the external potential $V_{\text{ext}}(\mathbf{r})$, the nuclei interaction energy E_{nn}, and the electronic temperature T_{e}. Here, $\text{Tr}(\hat{A})$ denotes the trace of the operator $\hat{A}$ and $\inf\limits_{\hat{\rho}_{\text{e}} \to n_{\text{e}}(\mathbf{r})}$ means that the infimum is taken over all density operators $\hat{\rho}_{\text{e}}$ that generate the electron density $n_{\text{e}}(\mathbf{r})$. The above definition is meaningful, since the operators $\hat{T}_{\text{e}}$ and $\hat{V}_{\text{int}}$ are universal. For any particular $V_{\text{ext}}(\mathbf{r})$, E_{nn}, and T_{e}, which characterize the individual system, the exact equilibrium electron density $n_{\mathrm{e}_0}(\mathbf{r})$ corresponds to the ρ-representable electron density $n_{\mathrm{e}}(\mathbf{r})$ that minimizes this functional. The exact equilibrium state Helmholtz free energy of the system corresponds to the global minimum value of this functional.

Mermin's theorems state that the equilibrium electron density can be used as the main variable and that the Helmholtz free energy can be considered as a functional of the electron density. The knowledge of this functional allows to derive the equilibrium electron density and the equilibrium Helmholtz free energy. However, one has to perform a minimization over a set of electron density operators, which must be constructed from the complicated many-body wave functions of the electronic system, so that Mermin's Helmholtz free energy functional is useless for practical calculations.

Fortunately, one can apply the Kohn-Sham Ansatz from ground state DFT also to finite T_{e}'s:

1. One defines an electron density $n_{\mathrm{e}_0}(\mathbf{r})$ to be noninteracting-ρ-representable if the equilibrium electron density $n_{\mathrm{e}_0}(\mathbf{r})$ of a system of interacting electrons at a given temperature T_{e} in an external potential $V_{\mathrm{ext}}(\mathbf{r})$ is identical to the equilibrium electron density of an auxiliary system of noninteracting electrons at the temperature T_{e} in an adapted effective potential $V_{\mathrm{eff}}(\mathbf{r})$.
2. One constructs the Helmholtz free energy functional $F_{\mathrm{KS}}\big(n_{\mathrm{e}}(\mathbf{r}), V_{\mathrm{ext}}(\mathbf{r}), E_{\mathrm{nn}}, T_{\mathrm{e}}\big)$ of the system of interacting electrons at a temperature T_{e} in an external potential $V_{\mathrm{ext}}(\mathbf{r})$ with nuclei interaction energy E_{nn} as followed:

$$\begin{aligned} F_{\mathrm{KS}}\Big(n_{\mathrm{e}}(\mathbf{r}), V_{\mathrm{ext}}(\mathbf{r}), E_{\mathrm{nn}}, T_{\mathrm{e}}\Big) =& T_{\mathrm{aux}}\Big(n_{\mathrm{e}}(\mathbf{r})\Big) + E_{\mathrm{Ha}}\Big(n_{\mathrm{e}}(\mathbf{r})\Big) \\ &+ \int_{\mathbb{R}^3} d^3r\; V_{\mathrm{ext}}(\mathbf{r})\, n_{\mathrm{e}}(\mathbf{r}) + E_{\mathrm{nn}} - T_{\mathrm{e}}\, S_{\mathrm{aux}}\Big(n_{\mathrm{e}}(\mathbf{r})\Big) \\ &+ E_{\mathrm{xc}}\Big(n_{\mathrm{e}}(\mathbf{r}), T_{\mathrm{e}}\Big). \end{aligned} \tag{3.34}$$

$T_{\mathrm{aux}}\big(n_{\mathrm{e}}(\mathbf{r})\big)$ denotes the exact kinetic energy functional, and $S_{\mathrm{aux}}\big(n_{\mathrm{e}}(\mathbf{r})\big)$ denotes the exact entropy functional of the auxiliary system of noninteracting electrons. $E_{\mathrm{Ha}}\Big(n_{\mathrm{e}}(\mathbf{r})\Big)$ is the Hartree energy defined as

$$E_{\mathrm{Ha}}\Big(n_{\mathrm{e}}(\mathbf{r})\Big) = \frac{1}{2}\int_{\mathbb{R}^3} d^3r \int_{\mathbb{R}^3} d^3r'\, e^2\, \frac{n_{\mathrm{e}}(\mathbf{r})\, n_{\mathrm{e}}(\mathbf{r}')}{|\mathbf{r}-\mathbf{r}'|}. \tag{3.35}$$

$E_{\mathrm{xc}}\big(n_{\mathrm{e}}(\mathbf{r}), T_{\mathrm{e}}\big)$ is the so-called exchange-correlation functional that takes all errors into account that are introduced by using $T_{\mathrm{aux}}\big(n_{\mathrm{e}}(\mathbf{r})\big)$, $S_{\mathrm{aux}}\big(n_{\mathrm{e}}(\mathbf{r})\big)$, and $E_{\mathrm{Ha}}\big(n_{\mathrm{e}}(\mathbf{r})\big)$.

Using the system of noninteracting electrons for the calculations, using the Hartree energy to include the electron-electron interaction, and putting all errors in the exchange-correlation functional allow for practical calculations. Applying the Kohn-Sham Ansatz, one finally has to solve a Schödinger equation of a single electron in an effective potential V_{eff} (The detailed derivation can be found in Ref. [7]):

$$\left(-\frac{\hbar^2}{2m_\text{e}} \nabla_\mathbf{r}^2 + \underbrace{V_{\text{ext}}(\mathbf{r}) + \int\limits_{\mathbb{R}^3} d^3r\, e^2\, \frac{n_{\text{e}_0}(\mathbf{r})}{|\mathbf{r}-\mathbf{r}|} + V_{\text{xc}}(\mathbf{r}, T_\text{e})}_{=V_{\text{eff}}(\mathbf{r},T_\text{e})} \right) \varphi_\alpha(\mathbf{r}) = \varepsilon_\alpha\, \varphi_\alpha(\mathbf{r}). \tag{3.36}$$

$V_{\text{xc}}(\mathbf{r}, T_\text{e})$ denotes the exchange-correlation potential defined as

$$V_{\text{xc}}(\mathbf{r}, T_\text{e}) := \frac{\delta E_{\text{xc}}\Big(n_\text{e}(\mathbf{r}), T_\text{e}\Big)}{\delta n_\text{e}(\mathbf{r})} \tag{3.37}$$

and $n_{\text{e}_0}(\mathbf{r})$ denotes the equilibrium electron density. Since the latter is unknown, one starts with an initial guess. After solving Eq. (3.36), one obtains single-electron wave functions $\varphi_\alpha(\mathbf{r})$ and eigenenergies ε_α. Using these functions and energies, one can derive the related equilibrium electron density from

$$n_\text{e}(\mathbf{r}) = \sum_{\alpha=1}^{\infty} f_\alpha \left|\varphi_\alpha(\mathbf{r})\right|^2, \tag{3.38}$$

where the occupation numbers are given by the Fermi distribution:

$$f_\alpha = \frac{1}{\frac{\varepsilon_\alpha - \mu_\text{e}}{k_\text{B} T_\text{e}} + 1}. \tag{3.39}$$

The chemical potential μ_e, which is contained in the above equation, can be derived from the condition, that the total number of electrons is N_e:

$$N_\text{e} = 2 \sum_\alpha f_\alpha. \tag{3.40}$$

The factor of 2 takes into account that only two electrons can fill one orbital, one with spin up and one with spin down. Normally, the electron density $n_\text{e}(\mathbf{r})$ obtained from Eq. (3.38) is not identical to the guess put in Eq. (3.36). Thus, one put the new electron density obtained from Eq. (3.38) (or better a modified one to obtain a numerically stable iteration [8, 9]) into Eq. (3.36) and solves again for the wave functions φ_α and eigenenergies ε_α, from which one gets a new electron density.

This loop is iterated until one finds the so-called Kohn-Sham wave functions φ_α and Kohn-Sham energies ε_α, which generate an electron density from Eq. (3.38) that is identical to the electron density put in Eq. (3.36). This electron density is then the searched equilibrium electron density $n_{\mathrm{e}_0}(\mathbf{r})$. Now one can calculate the Helmholtz free energy of the interacting electrons from

$$\begin{aligned} F_{\mathrm{KS}} = & \sum_\alpha f_\alpha\, \varepsilon_\alpha + E_{\mathrm{nn}} - T_{\mathrm{e}}\, S_{\mathrm{aux}} \\ & - E_{\mathrm{Ha}}\Big(n_{\mathrm{e}_0}(\mathbf{r})\Big) - \int\limits_{\mathbb{R}^3} d^3r\; V_{\mathrm{xc}}(\mathbf{r}, T_{\mathrm{e}})\, n_{\mathrm{e}_0}(\mathbf{r}) + E_{\mathrm{xc}}\Big(n_{\mathrm{e}_0}(\mathbf{r}), T_{\mathrm{e}}\Big), \end{aligned} \tag{3.41}$$

where

$$S_{\mathrm{aux}} = -k_{\mathrm{B}} \sum_\alpha \Big(f_\alpha \ln(f_\alpha) - (1 - f_\alpha)\ln(1 - f_\alpha)\Big) \tag{3.42}$$

is the exact electronic entropy for the system of noninteracting electrons.

T_{e}-dependent DFT and ground state DFT are very popular, since very successful approaches exist for the approximation of the exchange and correlation functional $E_{\mathrm{xc}}\big(n_{\mathrm{e}}(\mathbf{r}), T_{\mathrm{e}}\big)$ as a function of the electron density $n_{\mathrm{e}}(\mathbf{r})$. Commonly, one neglects the dependence of the exchange and correlation functional on T_{e}, i.e., $E_{\mathrm{xc}} \equiv E_{\mathrm{xc}}\big(n_{\mathrm{e}}(\mathbf{r})\big)$, and uses the entropy S_{aux} of the system of non-interaction electrons for the entropy of the interacting electrons. The local density approximation (LDA) is the simplest and one of the most popular approaches for E_{xc}. LDA is based on the model system of the homogeneous electron gas in a uniform positively charged background that describes the nuclei:

$$E_{\mathrm{xc}}^{(\mathrm{LDA})}\Big(n_{\mathrm{e}}(\mathbf{r})\Big) = \int\limits_{\mathbb{R}^3} d^3r'\, n_{\mathrm{e}}(\mathbf{r}')\, \varepsilon_{\mathrm{xc}}^{(\mathrm{hom})}\big(n_{\mathrm{e}}(\mathbf{r}')\big). \tag{3.43}$$

Here, $\varepsilon_{\mathrm{xc}}^{(\mathrm{hom})}\big(n_{\mathrm{e}}(\mathbf{r}')\big)$ describes the exchange-correlation energy density of the homogeneous electron gas with electron density $n_{\mathrm{e}}(\mathbf{r}')$. Now it becomes clear why LDA is called local, because $\varepsilon_{\mathrm{xc}}^{(\mathrm{hom})}\big(n_{\mathrm{e}}(\mathbf{r}')\big)$ only depends on the electron density $n_{\mathrm{e}}(\mathbf{r}')$ at the current integration point $\mathbf{r}'$. In 1980, it was possible to calculate numerically the exact ground state energy of this model system for various electronic densities using quantum Monte Carlo methods [10]. The functional dependence was parametrized several times [11–14]. We want to note that Perdew and Wang performed the most accurate one in 1992 [14], which nowadays is always used in LDA calculations.

Besides LDA, many other functionals were developed. The natural extension of LDA is to incorporate the gradient of the electron density in the integral over the exchange-correlation energy density, which leads to the very well-known generalized gradient approximation (GGA):

$$E_{\mathrm{xc}}^{(\mathrm{GGA})}\Big(n_{\mathrm{e}}(\mathbf{r})\Big) = \int\limits_{\mathbb{R}^3} d^3r'\, n_{\mathrm{e}}(\mathbf{r}')\, \varepsilon_{\mathrm{xc}}^{(\mathrm{hom})}\big(n_{\mathrm{e}}(\mathbf{r}')\big)\, f_{\mathrm{xc}}\big(n_{\mathrm{e}}(\mathbf{r}'), \nabla n_{\mathrm{e}}(\mathbf{r}')\big). \tag{3.44}$$

Now one has to determine an approach for the additional function $f_{\mathrm{xc}}\big(n_{\mathrm{e}}(\mathbf{r}'), \nabla n_{\mathrm{e}}(\mathbf{r}')\big)$ with respect to LDA. Here, the most common approaches are BLYP [15, 16], PW91 [17], and PBE [18].

Now we want to summarize: The laser-excited PES $U\big(\{\mathbf{R}_i\}, T_{\mathrm{e}}\big) = F_{\mathrm{KS}}$ is obtained after solving the electron problem described above. The ionic coordinates $\{\mathbf{R}_i\}$ determine E_{nn} and $V_{\mathrm{ext}}(\mathbf{r})$. In the laser-excited solid and for times larger than τ_{therm}, the electrons will have a well-defined temperature T_{e}. Thus, solving the electron problem in this case means determining the function which uniquely describes electrons at a given temperature, which is the Helmholtz free energy F_{KS} of the electrons. The assumption of fast electron thermalization is justified for laser pulse intensities that excite a significant percentage of the valence electrons to the conduction band. Equation (3.41) represents a generalization of the Born-Oppenheimer approximation. Note that the usual Born-Oppenheimer approximation is recovered for $T_{\mathrm{e}} = 0$ [19]. Knowing U, one can derive the force $\mathbf{f}_i$ on atom i just by

$$\mathbf{f}_i = -\nabla_{\mathbf{R}_i} U. \tag{3.45}$$

This allows to perform molecular dynamics simulations by solving the Newton equation of motions.

It is important to point out that the functional dependence of $U\big(\{\mathbf{R}_i\}, T_{\mathrm{e}}\big)$ on the atomic positions $\{\mathbf{R}_i\}$ is strongly dominated by the electronic occupations f_α present in the first term of Eq. (3.41) and in the electronic entropy S_{aux} from Eq. (3.42). If the electronic occupations undergo strong changes, then the PES $U\big(\{\mathbf{R}_i\}, T_{\mathrm{e}}\big)$ will change significantly [19–22]. This induces dramatic changes in atomic movements and is the origin of many ultrafast phenomena, which are discussed in Sect. 7.

4 Electronic Temperature-Dependent Interatomic Potentials

T_{e}-dependent DFT allows for molecular dynamics simulations with around 1000 atoms for several picoseconds. However, the simulation of femtosecond laser material processing needs much longer timescales (nanoseconds) and the inclusion of much more atoms ($\sim 10^8$) [23]. Molecular dynamics simulations in such dimensions are only possible with classical interatomic potentials, like the Stillinger-Weber [24], Tersoff [25], or Gupta [26] potential. These interatomic potentials describe the PES of the ions with electrons at the ground state. Thus, these potentials depend only on the atomic coordinates and the electrons are not treated as degree of freedom. The treatment of electrons at the ground state is a reasonable approximation for many thermodynamical processes, where the electrons are very weakly excited. But a completely other situation arises, when a femtosecond laser pulses excite matter and the electrons are excited to very high temperatures in the order of several 10,000 K. Now the approximation of electrons being in the ground state is inappropriate. In order to solve this problem, Khakshouri et al. [27] introduced in 2008 T_e-dependent interatomic potentials, which depend besides the atomic coordinates also on the electronic temperature. They presented the first T_e-dependent interatomic potential, which was derived for the metal tungsten. They fitted the parameters of a Finnis-Sinclair potential [28] to the Helmholtz free energies of the ideal bulk bcc structure obtained from T_e-dependent DFT calculations for different lattice parameters at various T_e's. In addition, they developed a second parameterization. Here, they fitted, at various T_e's, the pressure from T_e-dependent DFT calculations of the ideal bulk bcc structure, which has the equilibrium lattice parameter at $T_e = 300$ K.

In 2015, an alternative T_e-dependent interatomic potential was developed for tungsten by Murphy et al. [29]. Again, the parameters of an extended Finnis-Sinclair potential [28] were fitted to T_e-dependent DFT Helmholtz free energies of the ideal bulk bcc structure for different lattice parameters at various T_e's. Using their potential for tungsten, Murphy et al. performed molecular dynamics simulations of a femtosecond laser excited tungsten slab. They found that the crystal structure melts, and during melting a solid-to-solid transformation from the bcc to the fcc structure occurs in parts of the slab.

Also for further metals, T_e-dependent interatomic potentials were constructed. In 2012, Norman et al. developed a T_e-dependent interatomic potential for gold [30]. The parameters of an embedded atom potential [31] were fitted to the T_e-dependent DFT Helmholtz free energies and forces of several reference structures of crystal and molten material at various T_e's. Using the new potential, Norman et al. performed molecular dynamics simulations of the femtosecond laser-driven ablation of a gold film. In 2012, Moriarty et al. developed a T_e-dependent interatomic potential for the transition metal molybdenum [32]. In contrast to the potentials mentioned above, Moriarty et al. used generalized pseudopotential theory for the construction.

The abovementioned T_e-dependent interatomic potentials were developed for metals, in which metallic bonding is dominating that can be easily described by embedded atom potentials. Due to the metallic bonding, metals prefer closed packed structures in equilibrium. Semiconductors crystallize in more complex structures like the diamond structure, as for silicon or germanium. The reason for this is a significant amount of covalent bonding. Covalent bonds are directed and, due to this, are more complicated to describe by interatomic potentials. Since silicon is one of the most important semiconductors in technology, a huge amount of different interatomic potentials were developed in the last 60 years for silicon with electron in the ground state. In 2010, Shokeen and Schelling developed the first T_e-dependent interatomic potential for silicon [33]. They used the modified Tersoff potential from Kumagai et al. [34] as a starting point. They increased the original cutoff radius from $r_{2b}^{(c)} = 0.33$ nm to $r_{2b}^{(c)} = 0.34$ nm and the parameter $r^{(1)}$ from $r^{(1)} = 0.27$ nm to $r^{(1)} = 0.31$ nm, kept six potential parameters, and set the remaining eight potential parameters T_e-dependent. The latter parameters were fitted at various T_e's to the Helmholtz free cohesive energies of the diamond-like, fcc, bcc, and sc structures at seven different lattice parameters near equilibrium. In a first step, they published the potential coefficients at four selected T_e's [33]. Then, they performed a polynomial approximation of the T_e-dependent parameters as a function of T_e in order to get a smooth T_e-dependence [35]. Using this T_e-dependent interatomic potential, they performed MD simulations of a silicon film and studied the heterogeneous and homogeneous melting and the ablation induced by femtosecond laser pulses in silicon. A drawback of these MD simulations is the violation of the energy conservation [36]. In 2018, Darkins et al. developed a second T_e-dependent interatomic potential for silicon [36]. They modified the modified Tersoff potential of Kumagai et al. [34] by introducing an additional parameter λ and an additional function Λ. They used $r_{2\mathrm{b}}^{(\mathrm{c})} = 0.34$ nm and $r^{(1)} = 0.31$ nm similar to Shokeen and Schelling, kept 12 parameters of the original modified Tersoff potential, and make λ together with the remaining two parameters A, B T_e-dependent. They fitted the parameters A, B to the T_e-dependent DFT cohesive energies of the diamond structure at various lattice parameters and T_e's. The parameter λ was fitted to the Bragg peak decay measured by Harb et al. [37, 38]. Using the new potential, Darkins et al. performed MD simulations of a silicon film excited by an intense femtosecond laser pulse; derived, among other things, the Bragg peak decay; and compared with the experimental results from Harb et al. [37, 38]. They guaranteed energy conservation in their MD simulations by introducing an additional potential energy correction term that maintains a physically realistic heat capacity of the interatomic potential during the whole simulation time.

In 2020, we published an additional T_e-dependent interatomic potential for silicon [39]. We employed a self-learning procedure that automatically adapts the functional form of the interatomic potential in order to obtain high computational efficiency and high accuracy. We fitted the atomic forces and cohesive energies of MD simulations of a thin silicon film obtained from T_e-dependent DFT calculations at various T_e's. The final potential is a polynomial with 23 T_e-dependent parameters and three constant cutoff radii. We analyzed the performance of the state-of-the-art T_e-dependent interatomic potentials for silicon versus DFT molecular dynamics simulations on Si at high T_e [40]. We found out that our interatomic potential has the best performance. In addition, we fitted the parameters of several interatomic potentials that were developed for silicon at the ground state to the atomic forces and cohesive energies obtained from T_e-dependent DFT MD simulations that were used to develop the polynomial potential. Our results showed that the reparameterized interatomic potentials do not reach the accuracy of the polynomial potential.

5 The Electron-Phonon Coupling: Toward a Thermal State

The hot electrons transfer their energy to the lattice commonly on a picosecond timescale. In order to describe this relaxation process called electron-phonon coupling, one has to go beyond the Born-Oppenheimer approximation, in which the motion of the electrons and the nuclei is decoupled. Now the defects of the periodic crystal structure related to the presence of phonons cause scattering processes of the hot Bloch electrons. We derive now the electron-phonon coupling (EPC) representation in second quantization based on Ref. [7], but with less details. In a periodic solid, a basis cell containing N_b ions is repeated in all room directions on a Bravais grid to fill the space. In order to perform calculations, one considers a finite number of atoms located in a simulation cell that contains $N_I = N_1\,N_2\,N_3\,N_b$ atoms with periodic boundary conditions. The basis cell is repeated N_1 times in x-, N_2 times in y- and N_3 times in z-direction to form the simulation cell. One can denote the nuclei coordinates as

$$\mathbf{R}_{\mathbf{n}\upsilon}(t) = \mathbf{T}_{\mathbf{n}} + \mathbf{d}_{\upsilon} + \mathbf{U}_{\mathbf{n}\upsilon}(t).$$

Here, the vectors $\mathbf{T}_{\mathbf{n}}$ form the Bravais grid, $\mathbf{d}_{\upsilon}$ describes the relative position in the basis cell, and $\mathbf{U}_{\mathbf{n}\upsilon}(t)$ is the displacement from the equilibrium position. Now we take a closer look at the external potential $\hat{V}_{\text{ext}}$ generated by the nuclei:

$$V_{\text{ext}}(\mathbf{r}_i) = \sum_{\mathbf{n}\upsilon} V^{(\upsilon)}(\mathbf{r}_i - \mathbf{R}_{\mathbf{n}\upsilon}), \tag{3.46}$$

$$V^{(\upsilon)}(\mathbf{r}_i - \mathbf{R}_{\mathbf{n}\upsilon}) = \frac{e^2\,Z_{\upsilon}}{|\mathbf{r}_i - \mathbf{R}_{\mathbf{n}\upsilon}|}. \tag{3.47}$$

A Taylor series expansion of the single nucleus potential $V^{(\upsilon)}(\mathbf{r}_i - \mathbf{R}_{\mathbf{n}\upsilon})$ with respect to the equilibrium position $\mathbf{T}_{\mathbf{n}} + \mathbf{d}_{\upsilon}$ of the considered nucleus yields

$$V^{(\upsilon)}(\mathbf{r}_i - \mathbf{R}_{\mathbf{n}\upsilon}) = V^{(\upsilon)}(\mathbf{r}_i - \mathbf{T}_{\mathbf{n}} - \mathbf{d}_{\upsilon}) - \nabla V^{(\upsilon)}(\mathbf{r}_i - \mathbf{T}_{\mathbf{n}} - \mathbf{d}_{\upsilon})^{\text{t}} \cdot \mathbf{U}_{\mathbf{n}\upsilon} + \ldots \tag{3.48}$$

Only the first term, which is independent of the displacement $\mathbf{U}_{\mathbf{n}\upsilon}$, is taken into account in the Born-Oppenheimer approximation. The second term and all following terms induce the electron-phonon coupling. If one only takes the second term into account, the electron-phonon interacting term reads

$$\hat{V}^{(\text{ep})} = \sum_{i=1}^{N_{\text{e}}} \hat{V}_i^{(\text{ep})}, \tag{3.49}$$

$$\hat{V}_i^{(\text{ep})} = -\sum_{\mathbf{n}\upsilon} \nabla V^{(\upsilon)}(\mathbf{r}_i - \mathbf{T}_{\mathbf{n}} - \mathbf{d}_{\upsilon})^{\text{t}} \cdot \mathbf{U}_{\mathbf{n}\upsilon}. \tag{3.50}$$

In second quantization, this term is denoted as

$$\hat{V}^{(\text{ep})} = \sum_{\ell\mathbf{k}} \sum_{\ell'\mathbf{k}'} V^{(\text{ep})}_{\ell\mathbf{k},\ell'\mathbf{k}'}\,\hat{c}^{\dagger}_{\ell\mathbf{k}}\,\hat{c}_{\ell'\mathbf{k}'}, \tag{3.51}$$

$$V^{(\mathrm{ep})}_{\ell\mathbf{k},\ell'\mathbf{k}'} = -\sum_{\sigma} \int\limits_{\mathbb{R}^3} d^3r\, \varphi^*_{\ell\mathbf{k}}(\sigma,\mathbf{r}) \sum_{\mathbf{n}\upsilon} \nabla V^{(\upsilon)}(\mathbf{r}-\mathbf{T}_\mathbf{n}-\mathbf{d}_\upsilon)^{\mathrm{t}} \cdot \mathbf{U}_{\mathbf{n}\upsilon}\, \varphi_{\ell'\mathbf{k}'}(\sigma,\mathbf{r}). \tag{3.52}$$

$V^{(\mathrm{ep})}_{\ell\mathbf{k},\ell'\mathbf{k}'}$ is spin diagonal, since the potential $\nabla V^{(\upsilon)}$ does not depend on the spin. Thus, the electron-phonon coupling does not change the spin. We therefore skip the spin to simplify any further analysis and perform a Fourier expansion of the single nuclei potential $V^{(\upsilon)}(\mathbf{r})$:

$$V^{(\upsilon)}(\mathbf{r}) = \sum_{\mathbf{k}''} V^{(\upsilon)}_{\mathbf{k}''}\, e^{i\,\mathbf{k}''^{\mathrm{t}}\cdot\mathbf{r}} \tag{3.53}$$

with Fourier coefficients

$$V^{(\upsilon)}_{\mathbf{k}''} = \frac{1}{\mathcal{V}_\mathrm{s}} \int\limits_{\mathcal{V}_\mathrm{s}} d^3r\, V^{(\upsilon)}(\mathbf{r})\, e^{-i\,\mathbf{k}''^{\mathrm{t}}\cdot\mathbf{r}} \tag{3.54}$$

and $\mathcal{V}_\mathrm{s}$ denotes the volume of the simulation cell. The nuclei are displaced from their equilibrium positions in the simulation cell that is periodically repeated to fill the space. Thus, the single nuclei potential $V^{(\upsilon)}(\mathbf{r})$ is not periodic with respect to the simulation cell in contrast to the total nuclei potential that is obtained from the sum over all nuclei contained in the simulation cell. Due to this, the sum over $\mathbf{k}''$ is not restricted to reciprocal lattice vectors. Using Eq. (3.53), we obtain further

$$\nabla_\mathbf{r} V^{(\upsilon)}(\mathbf{r}) = \sum_{\mathbf{k}''} V^{(\upsilon)}_{\mathbf{k}''}\, e^{i\,\mathbf{k}''^{\mathrm{t}}\cdot\mathbf{r}}\, i\,\mathbf{k}''. \tag{3.55}$$

If we insert this in Eq. (3.52), we get

$$V^{(\mathrm{ep})}_{\ell\mathbf{k},\ell'\mathbf{k}'} = \sum_{\mathbf{k}''} \int\limits_{\mathbb{R}^3} d^3r\, \varphi^*_{\ell\mathbf{k}}(\mathbf{r}) \sum_{\mathbf{n}\upsilon} V^{(\upsilon)}_{\mathbf{k}''}\, e^{i\,\mathbf{k}''^{\mathrm{t}}\cdot(\mathbf{r}-\mathbf{T}_\mathbf{n}-\mathbf{d}_\upsilon)}\, i\,\mathbf{k}''^{\mathrm{t}} \cdot \mathbf{u}_{\mathbf{n}\upsilon}\, \varphi_{\ell'\mathbf{k}'}(\mathbf{r}). \tag{3.56}$$

We transform the nuclei displacement vector $U_{\mathbf{n}\upsilon\alpha}$ to the reciprocal space and denote it in second quantization:

$$\mathbf{U}_{\mathbf{n}\upsilon} = \frac{1}{\sqrt{N_1\,N_2\,N_3}} \sum_{\mathbf{q}_{\mathbf{n}'}} \sum_{j=1}^{3\,N_\mathrm{b}} \sqrt{\frac{\hbar}{2\,m_\upsilon\,\omega_j(\mathbf{q}_{\mathbf{n}'})}} \left(\hat{b}_{j\mathbf{q}_{\mathbf{n}'}} + \hat{b}^\dagger_{j-\mathbf{q}_{\mathbf{n}'}}\right) \mathbf{e}^{(j)}_\upsilon(\mathbf{q}_{\mathbf{n}'})\, e^{i\,\mathbf{q}^{\mathrm{t}}_{\mathbf{n}'}\cdot\mathbf{T}_\mathbf{n}} \tag{3.57}$$

m_ν is the mass of the ν-th atom in the basis cell and $\omega_j(\mathbf{q}_{\mathbf{n}'})$ corresponds to the eigenfrequency of the phonon mode with wave vector $\mathbf{q}_{\mathbf{n}'}$ in band j. $\hat{b}^\dagger_{j\mathbf{q}_{\mathbf{n}'}}$ and $\hat{b}_{j\mathbf{q}_{\mathbf{n}'}}$ denote the phonon creation and annihilation operator. $\mathbf{e}^{(j)}_\upsilon(\mathbf{q}_{\mathbf{n}'})$ is the polarization vector of the phonon mode with wave vector $\mathbf{q}_{\mathbf{n}'}$ in band j. This vector is obtained by diagonalizing the dynamical matrix and describes the movement of the atoms in the basis cell for the considered phonon mode. We insert Eq. (3.57) into Eq. (3.56) and obtain

$$
\begin{aligned}
V^{(\mathrm{ep})}_{\ell\mathbf{k},\ell'\mathbf{k}'} = &- \frac{1}{\sqrt{N_1\, N_2\, N_3}} \sum_{\mathbf{q}_{\mathbf{n}'}} \sum_{\mathbf{k}''} \sum_{j=1}^{3\,N_\mathrm{b}} i \,\times \\
&\times\, \mathbf{k}''^{\mathrm{t}} \cdot \sum_{\upsilon} \mathbf{e}^{(j)}_{\upsilon}(\mathbf{q}_{\mathbf{n}'})\, V^{(\upsilon)}_{\mathbf{k}''}\, e^{-i\,\mathbf{k}''^{\mathrm{t}}\cdot \mathbf{d}_\upsilon} \underbrace{\sum_{\mathbf{T}_\mathbf{n}} e^{i\,(\mathbf{q}_{\mathbf{n}'}-\mathbf{k}'')^{\mathrm{t}}\cdot \mathbf{T}_\mathbf{n}}}_{=N_1\,N_2\,N_3\,\delta_{\mathbf{k}''\mathbf{q}_{\mathbf{n}'}+\mathbf{G}}} \times \\
&\times \int_{\mathbb{R}^3} d^3r\, \varphi^*_{\ell\mathbf{k}}(\mathbf{r})\, e^{i\,\mathbf{k}''^{\mathrm{t}}\cdot\mathbf{r}}\, \varphi_{\ell'\mathbf{k}'}(\mathbf{r}) \sqrt{\frac{\hbar}{2\,m_\upsilon\,\omega_j(\mathbf{q}_{\mathbf{n}'})}} \left(\hat{b}_{j\mathbf{q}_{\mathbf{n}'}} + \hat{b}^\dagger_{j-\mathbf{q}_{\mathbf{n}'}}\right) \\
= &- \sqrt{N_1\,N_2\,N_3} \sum_{\mathbf{q}_{\mathbf{n}'}} \sum_{\mathbf{G}} \sum_{j=1}^{3\,N_\mathrm{b}} i\,(\mathbf{q}_{\mathbf{n}'}+\mathbf{G})^{\mathrm{t}} \cdot \sum_{\upsilon} \mathbf{e}^{(j)}_{\upsilon}(\mathbf{q}_{\mathbf{n}'})\, V^{(\upsilon)}_{\mathbf{q}_{\mathbf{n}'}+\mathbf{G}}\, e^{-i\,(\mathbf{q}_{\mathbf{n}'}+\mathbf{G})^{\mathrm{t}}\cdot\mathbf{d}_\upsilon} \times \\
&\times \int_{\mathcal{V}_\mathrm{s}} d^3r\, \varphi^*_{\ell\mathbf{k}}(\mathbf{r})\, e^{i\,(\mathbf{q}_{\mathbf{n}'}+\mathbf{G})^{\mathrm{t}}\cdot\mathbf{r}}\, \varphi_{\ell'\mathbf{k}'}(\mathbf{r}) \sqrt{\frac{\hbar}{2\,m_\upsilon\,\omega_j(\mathbf{q}_{\mathbf{n}'})}} \left(\hat{b}_{j\mathbf{q}_{\mathbf{n}'}} + \hat{b}^\dagger_{j-\mathbf{q}_{\mathbf{n}'}}\right).
\end{aligned}
\tag{3.58}
$$

The $\varphi_{\ell\mathbf{k}}(\mathbf{r})$ are Bloch functions obeying

$$
\varphi_{\ell\mathbf{k}}(\mathbf{r}) = \mathrm{u}_{\ell\mathbf{k}}(\mathbf{r})\, e^{i\,\mathbf{k}^{\mathrm{t}}\cdot\mathbf{r}} \tag{3.59}
$$

with $\mathrm{u}_{\ell\mathbf{k}}(\mathbf{r}+\mathbf{T}_\mathbf{n}) = \mathrm{u}_{\ell\mathbf{k}}(\mathbf{r})$ for any vector $\mathbf{T}_\mathbf{n}$ of the Bravais grid. Now we take into account that the integral is running over the volume of the simulation cell $\mathcal{V}_\mathrm{s}$. This integral can also be done over the volume of the basis cell $\mathcal{V}_\mathrm{b}$, if one additionally sums over a given set of $N_1\,N_2\,N_3$ Bravais vectors $\mathbf{T}_\mathbf{n}$, since the basis cell is $N_1\,N_2\,N_3$ times included in the simulation cell. In this way, we obtain for the integral occurring in Eq. (3.58):

$$
\begin{aligned}
&\int_{\mathcal{V}_\mathrm{s}} d^3r\, \varphi^*_{\ell\mathbf{k}}(\mathbf{r})\, e^{i\,(\mathbf{q}_{\mathbf{n}'}+\mathbf{G})^{\mathrm{t}}\cdot\mathbf{r}}\, \varphi_{\ell'\mathbf{k}'}(\mathbf{r}) \\
&\quad = \sum_{\mathbf{T}_\mathbf{n}} \int_{\mathcal{V}_\mathrm{b}} d^3r\, \varphi^*_{\ell\mathbf{k}}(\mathbf{r}+\mathbf{T}_\mathbf{n})\, e^{i\,(\mathbf{q}_{\mathbf{n}'}+\mathbf{G})^{\mathrm{t}}\cdot(\mathbf{r}+\mathbf{T}_\mathbf{n})}\, \varphi_{\ell'\mathbf{k}'}(\mathbf{r}+\mathbf{T}_\mathbf{n}) \\
&\quad = \sum_{\mathbf{T}_\mathbf{n}} \int_{\mathcal{V}_\mathrm{b}} d^3r\, \mathrm{u}^*_{\ell\mathbf{k}}(\mathbf{r}+\mathbf{T}_\mathbf{n})\, e^{-i\,\mathbf{k}^{\mathrm{t}}\cdot(\mathbf{r}+\mathbf{T}_\mathbf{n})}\, e^{i\,(\mathbf{q}_{\mathbf{n}'}+\mathbf{G})^{\mathrm{t}}\cdot(\mathbf{r}+\mathbf{T}_\mathbf{n})}\, \mathrm{u}_{\ell'\mathbf{k}'}(\mathbf{r}+\mathbf{T}_\mathbf{n})\, e^{i\,\mathbf{k}'^{\mathrm{t}}\cdot(\mathbf{r}+\mathbf{T}_\mathbf{n})}
\end{aligned}
$$

$$= \int\limits_{\mathcal{V}_\mathrm{b}} d^3r\, e^{i\,(\mathbf{k}'-\mathbf{k}+\mathbf{q}_{\mathbf{n}'}+\mathbf{G})^\mathrm{t}\cdot\mathbf{r}}\, \mathrm{u}^*_{\ell\mathbf{k}}(\mathbf{r})\, \mathrm{u}_{\ell'\mathbf{k}'}(\mathbf{r}) \underbrace{\sum_{\mathbf{T}_\mathbf{n}} e^{i\,(\mathbf{k}'-\mathbf{k}+\mathbf{q}_{\mathbf{n}'}+\mathbf{G})^\mathrm{t}\cdot\mathbf{T}_\mathbf{n}}}_{=N_1\,N_2\,N_3\,\delta_{\mathbf{k}\mathbf{k}'+\mathbf{q}_{\mathbf{n}'}+\mathbf{G}}}$$

$$= N_1\,N_2\,N_3\,\delta_{\mathbf{k}\mathbf{k}'+\mathbf{q}_{\mathbf{n}'}+\mathbf{G}} \int\limits_{\mathcal{V}_\mathrm{b}} d^3r\, \mathrm{u}^*_{\ell\mathbf{k}'+\mathbf{q}_{\mathbf{n}'}+\mathbf{G}}(\mathbf{r})\, \mathrm{u}_{\ell'\mathbf{k}'}(\mathbf{r}). \tag{3.60}$$

We insert this into Eq. (3.58) and obtain

$$V^{(\mathrm{ep})}_{\ell\mathbf{k},\ell'\mathbf{k}'} = -\,\delta_{\mathbf{k}\mathbf{k}'+\mathbf{q}_{\mathbf{n}'}+\mathbf{G}} \sqrt{\frac{\hbar\,N_1\,N_2\,N_3}{2\,m_\upsilon\,\omega_j(\mathbf{q}_{\mathbf{n}'})}}\,N_1\,N_2\,N_3\,\times$$

$$\times \sum_{\mathbf{q}_{\mathbf{n}'}}\sum_{\mathbf{G}}\sum_{j=1}^{3\,N_\mathrm{b}} i\,(\mathbf{q}_{\mathbf{n}'}+\mathbf{G})^\mathrm{t}\cdot\sum_{\upsilon}\mathbf{e}^{(j)}_{\upsilon}(\mathbf{q}_{\mathbf{n}'})\,V^{(\upsilon)}_{\mathbf{q}_{\mathbf{n}'}+\mathbf{G}}\,e^{-i\,(\mathbf{q}_{\mathbf{n}'}+\mathbf{G})^\mathrm{t}\cdot\mathbf{d}_\upsilon}\,\times$$

$$\times \int\limits_{\mathcal{V}_\mathrm{b}} d^3r\,\mathrm{u}^*_{\ell\mathbf{k}'+\mathbf{q}_{\mathbf{n}'}+\mathbf{G}}(\mathbf{r})\,\mathrm{u}_{\ell'\mathbf{k}'}(\mathbf{r})\left(\hat{b}_{j\mathbf{q}_{\mathbf{n}'}}+\hat{b}^\dagger_{j-\mathbf{q}_{\mathbf{n}'}}\right). \tag{3.61}$$

In summary, we get finally for the electron-phonon interacting term in second quantization (here we write $\mathbf{q}$ instead of $\mathbf{q}_{\mathbf{n}'}$ in order to simplify the notation)

$$\hat{V}^{(\mathrm{ep})} = \sum_{\ell\ell'}\sum_{\mathbf{k}}\sum_{\mathbf{q}}\sum_{\mathbf{G}}\sum_{j=1}^{3\,N_\mathbf{b}} M^{(j\mathbf{q})}_{\ell\mathbf{k}+\mathbf{q}+\mathbf{G},\ell'\mathbf{k}}\left(\hat{b}_{j\mathbf{q}}+\hat{b}^\dagger_{j-\mathbf{q}}\right)\hat{c}^\dagger_{\ell\mathbf{k}+\mathbf{q}+\mathbf{G}}\,\hat{c}_{\ell'\mathbf{k}} \tag{3.62}$$

with the electron-phonon coupling matrix element

$$M^{(j\mathbf{q})}_{\ell\mathbf{k}+\mathbf{q}+\mathbf{G},\ell'\mathbf{k}} = -\sqrt{\frac{\hbar\,N_1\,N_2\,N_3}{2\,m_\upsilon\,\omega_j(\mathbf{q})}}\,N_1\,N_2\,N_3\,i\,(\mathbf{q}+\mathbf{G})^\mathrm{t}\cdot\sum_{\upsilon}\mathbf{e}^{(j)}_{\upsilon}(\mathbf{q})\,V^{(\upsilon)}_{\mathbf{q}+\mathbf{G}}\,e^{-i\,(\mathbf{q}+\mathbf{G})^\mathrm{t}\cdot\mathbf{d}_\upsilon}\,\times$$

$$\times\sum_{\sigma}\int\limits_{\mathcal{V}_\mathrm{b}} d^3r\,\mathrm{u}^*_{\ell\mathbf{k}+\mathbf{q}+\mathbf{G}}(\sigma,\mathbf{r})\,\mathrm{u}_{\ell'\mathbf{k}}(\sigma,\mathbf{r}). \tag{3.63}$$

For completeness, we again include the spin here. We conclude: the electron-phonon coupling is responsible for the following two basis processes:

(1) $\hat{b}^\dagger_{j-\mathbf{q}}\,\hat{c}^\dagger_{\ell\mathbf{k}+\mathbf{q}+\mathbf{G}}\,\hat{c}_{\ell'\mathbf{k}}$: A Bloch electron with wave vector $\mathbf{k}$ scatters and gets the wave vector $\mathbf{k}+\mathbf{q}$ by emitting of a phonon with wave vector $-\mathbf{q}$.

(2) $\hat{b}_{j\mathbf{q}}\,\hat{c}^\dagger_{\ell\mathbf{k}+\mathbf{q}+\mathbf{G}}\,\hat{c}_{\ell'\mathbf{k}}$: A Bloch electron with wave vector $\mathbf{k}$ scatters and gets the wave vector $\mathbf{k}+\mathbf{q}$ by absorbing of a phonon with wave vector $\mathbf{q}$.

During the scattering processes, the Bloch electron can change its state from ℓ to ℓ', but the spin is not changed, because $\hat{V}^{(\mathrm{ep})}$ does not act on the spin.

5.1 Electron-Phonon Coupling Strength

The electron-phonon coupling transfers energy from the hot electrons to the cold ions:

$$\frac{\partial E_\mathrm{e}}{\partial t} = \dot{E}_\mathrm{ep}, \tag{3.64}$$

$$\frac{\partial E_\mathrm{I}}{\partial t} = -\dot{E}_\mathrm{ep}. \tag{3.65}$$

Here, E_e denotes the energy of the electrons, E_I denotes the energy of the ions, and $\dot{E}_\mathrm{ep}$ is the energy transfer rate. Allen et. al. [41] firstly derive in 1987 $\dot{E}_\mathrm{ep}$ by ab initio methods for metals. Wang et al. [42] improved this approach in 1994. A detailed explanation of the improved approach was first given by Lin et al. [43] in 2008. Waldecker et al. extended this method to calculate different electron-phonon coupling constants for individual phonon branches in aluminum [44] and in antimony [45]. In 2017, Sadasivam et al. [46] extended Allens original work to derive the electron-phonon coupling constants for 12 semiconductors. Now we derive the electron-phonon coupling rate $\dot{E}_\mathrm{ep}$ from ab initio by summarizing the above studies following Ref. [7]. For this, we describe the nuclei in the harmonic approximation and the electrons in the mean field approximation by one-particle operators. Thus, the Hamiltonian reads in second quantization:

$$\hat{H}_0 = \underbrace{2\sum_{\ell\mathbf{k}} \varepsilon_{\ell\mathbf{k}}\, \hat{c}^\dagger_{\ell\mathbf{k}}\, \hat{c}_{\ell\mathbf{k}}}_{=E_\mathrm{e}} + \underbrace{\sum_{j\mathbf{q}} \hbar\,\omega_j(\mathbf{q}) \left(\hat{b}^\dagger_{j\mathbf{q}}\,\hat{b}_{j\mathbf{q}} + \frac{1}{2}\right)}_{=E_\mathrm{I}}. \tag{3.66}$$

The factor of 2 in the first term accounts that the sum over ℓ only runs over spin up states. The operator $\hat{c}^\dagger_{\ell\mathbf{k}}$ creates one electron in the Bloch state $|\ell\mathbf{k}\rangle$, and the operator $\hat{b}^\dagger_{j\mathbf{q}}$ creates one phonon in the phonon mode $j\mathbf{q}$. We define

$$E_0 = \sum_{j\mathbf{q}} \frac{\hbar\,\omega_j(\mathbf{q})}{2}$$

as the contribution of the zero point motion. We consider the electron-phonon coupling $\hat{V}^{(\mathrm{ep})}$ as a perturbation, which does not change the spin state of the Bloch electrons. Using Fermis golden rule, which proof can be found in Ref. [47], we can derive the rate equation for the electron occupation $n_{\ell\mathbf{k}}$ of the state $\ell\mathbf{k}$:

$$\frac{\partial n_{\ell\mathbf{k}}}{\partial t}$$

$$= \frac{2\pi}{\hbar} \sum_{j\mathbf{q}} \sum_{\ell'\mathbf{k}'} \left| M^{(j\mathbf{q})}_{\ell\mathbf{k},\ell'\mathbf{k}'} \right|^2 \times$$

$$\times\Big(-n_{\ell\mathbf{k}}\,(1-n_{\ell'\mathbf{k}'})\Big((n_{j\mathbf{q}}+1)\,\delta\Big(\varepsilon_{\ell\mathbf{k}}-\varepsilon_{\ell'\mathbf{k}'}-\hbar\,\omega_j(\mathbf{q})\Big)+n_{j\mathbf{q}}\,\delta\Big(\varepsilon_{\ell\mathbf{k}}-\varepsilon_{\ell'\mathbf{k}'}+\hbar\,\omega_j(\mathbf{q})\Big)\Big)$$
$$+n_{\ell'\mathbf{k}'}\,(1-n_{\ell\mathbf{k}})\Big((n_{j\mathbf{q}}+1)\,\delta\Big(\varepsilon_{\ell\mathbf{k}}-\varepsilon_{\ell'\mathbf{k}'}+\hbar\,\omega_j(\mathbf{q})\Big)+n_{j\mathbf{q}}\,\delta\Big(\varepsilon_{\ell\mathbf{k}}-\varepsilon_{\ell'\mathbf{k}'}-\hbar\,\omega_j(\mathbf{q})\Big)\Big)\Big). \tag{3.67}$$

and the rate equation for the phonon occupation $n_{j\mathbf{q}}$ of the state $j\mathbf{q}$:

$$\frac{\partial n_{j\mathbf{q}}}{\partial t}=\frac{4\pi}{\hbar}\sum_{j\mathbf{q}}\sum_{\ell'\mathbf{k}'}\left|M^{(j\mathbf{q})}_{\ell\mathbf{k},\ell'\mathbf{k}'}\right|^2 n_{\ell\mathbf{k}}\,(1-n_{\ell'\mathbf{k}'})\times$$
$$\times\Big((n_{j\mathbf{q}}+1)\,\delta\Big(\varepsilon_{\ell\mathbf{k}}-\varepsilon_{\ell'\mathbf{k}'}-\hbar\,\omega_j(\mathbf{q})\Big)-n_{j\mathbf{q}}\,\delta\Big(\varepsilon_{\ell\mathbf{k}}-\varepsilon_{\ell'\mathbf{k}'}+\hbar\,\omega_j(\mathbf{q})\Big)\Big). \tag{3.68}$$

Equations (3.67) and (3.68) form the **Bloch-Boltzmann-Peierls equations** [41]. The electron-phonon coupling-driven changes in the electron and phonon occupations are given by these rate equations, which also fulfill the energy conservation:

$$2\sum_{\ell\mathbf{k}}\varepsilon_{\ell\mathbf{k}}\,\frac{\partial n_{\ell\mathbf{k}}}{\partial t}+\sum_{j\mathbf{q}}\hbar\,\omega_j(\mathbf{q})\,\frac{\partial n_{j\mathbf{q}}}{\partial t}=0. \tag{3.69}$$

In order to determine the electron-phonon energy exchange rate

$$\dot{E}_{\mathrm{ep}}=-\frac{\partial E_{\mathrm{I}}}{\partial t}=-\sum_{j\mathbf{q}}\hbar\,\omega_j(\mathbf{q})\,\frac{\partial n_{j\mathbf{q}}}{\partial t},$$

we take a closer look at $\frac{\partial n_{j\mathbf{q}}}{\partial t}$ from Eq. (3.68):

$$\begin{aligned}-\frac{\partial n_{j\mathbf{q}}}{\partial t}=&\frac{4\pi}{\hbar}\sum_{\ell\mathbf{k}}\sum_{\ell'\mathbf{k}'}\left|M^{(j\mathbf{q})}_{\ell\mathbf{k},\ell'\mathbf{k}'}\right|^2\Big(-(n_{j\mathbf{q}}+1)\,n_{\ell\mathbf{k}}\,(1-n_{\ell'\mathbf{k}'})\,\delta\Big(\varepsilon_{\ell\mathbf{k}}-\varepsilon_{\ell'\mathbf{k}'}-\hbar\,\omega_j(\mathbf{q})\Big)\\&+n_{j\mathbf{q}}\,n_{\ell\mathbf{k}}\,(1-n_{\ell'\mathbf{k}'})\,\delta\Big(\varepsilon_{\ell\mathbf{k}}-\varepsilon_{\ell'\mathbf{k}'}+\hbar\,\omega_j(\mathbf{q})\Big)\Big)\\=&\frac{4\pi}{\hbar}\sum_{\ell\mathbf{k}}\sum_{\ell'\mathbf{k}'}\left|M^{(j\mathbf{q})}_{\ell\mathbf{k},\ell'\mathbf{k}'}\right|^2\Big(-(n_{j\mathbf{q}}+1)\,n_{\ell'\mathbf{k}'}\,(1-n_{\ell\mathbf{k}})\,\underbrace{\delta\Big(\varepsilon_{\ell'\mathbf{k}'}-\varepsilon_{\ell\mathbf{k}}-\hbar\,\omega_j(\mathbf{q})\Big)}_{=\delta\left(\varepsilon_{\ell\mathbf{k}}-\varepsilon_{\ell'\mathbf{k}'}+\hbar\,\omega_j(\mathbf{q})\right)}\\&+n_{j\mathbf{q}}\,n_{\ell\mathbf{k}}\,(1-n_{\ell'\mathbf{k}'})\,\delta\Big(\varepsilon_{\ell\mathbf{k}}-\varepsilon_{\ell'\mathbf{k}'}+\hbar\,\omega_j(\mathbf{q})\Big)\Big)\\=&\frac{4\pi}{\hbar}\sum_{\ell\mathbf{k}}\sum_{\ell'\mathbf{k}'}\left|M^{(j\mathbf{q})}_{\ell\mathbf{k},\ell'\mathbf{k}'}\right|^2\Big(-(n_{j\mathbf{q}}+1)\,n_{\ell'\mathbf{k}'}\,(1-n_{\ell\mathbf{k}})+n_{j\mathbf{q}}\,n_{\ell\mathbf{k}}\,(1-n_{\ell'\mathbf{k}'})\Big)\times\\&\times\,\delta\Big(\varepsilon_{\ell\mathbf{k}}-\varepsilon_{\ell'\mathbf{k}'}+\hbar\,\omega_j(\mathbf{q})\Big).\end{aligned}$$

Due to

$$-(n_{j\mathbf{q}}+1)\,n_{\ell'\mathbf{k}'}\,(1-n_{\ell\mathbf{k}})+n_{j\mathbf{q}}\,n_{\ell\mathbf{k}}\,(1-n_{\ell'\mathbf{k}'})=(n_{\ell\mathbf{k}}-n_{\ell'\mathbf{k}'})\,n_{j\mathbf{q}}-n_{\ell'\mathbf{k}'}\,(1-n_{\ell\mathbf{k}})$$

we get

$$\begin{aligned}-\frac{\partial n_{j\mathbf{q}}}{\partial t}=&\frac{4\pi}{\hbar}\sum_{\ell\mathbf{k}}\sum_{\ell'\mathbf{k}'}\left|M^{(j\mathbf{q})}_{\ell\mathbf{k},\ell'\mathbf{k}'}\right|^2\Big((n_{\ell\mathbf{k}}-n_{\ell'\mathbf{k}'})\,n_{j\mathbf{q}}-n_{\ell'\mathbf{k}'}\,(1-n_{\ell\mathbf{k}})\Big)\times\\ &\times\,\delta\Big(\varepsilon_{\ell\mathbf{k}}-\varepsilon_{\ell'\mathbf{k}'}+\hbar\,\omega_j(\mathbf{q})\Big).\end{aligned}$$

Using this, we obtain for the electron-phonon coupling energy transfer rate

$$\begin{aligned}\dot{E}_{\mathrm{ep}}=&-\sum_{j\mathbf{q}}\hbar\,\omega_j(\mathbf{q})\,\frac{\partial n_{j\mathbf{q}}}{\partial t}\\ =&\frac{4\pi}{\hbar}\sum_{j\mathbf{q}}\sum_{\ell\mathbf{k}}\sum_{\ell'\mathbf{k}'}\hbar\,\omega_j(\mathbf{q})\left|M^{(j\mathbf{q})}_{\ell\mathbf{k},\ell'\mathbf{k}'}\right|^2\Big((n_{\ell\mathbf{k}}-n_{\ell'\mathbf{k}'})\,n_{j\mathbf{q}}-n_{\ell'\mathbf{k}'}\,(1-n_{\ell\mathbf{k}})\Big)\times\\ &\times\,\delta\Big(\varepsilon_{\ell\mathbf{k}}-\varepsilon_{\ell'\mathbf{k}'}+\hbar\,\omega_j(\mathbf{q})\Big).\end{aligned}\tag{3.70}$$

Now we assume thermal equilibrium of the electrons and phonons. Thus, the electronic occupations $n_{\ell\mathbf{k}}$, $n_{\ell'\mathbf{k}'}$ follow a Fermi distribution $f_{\mathrm{F}}(\varepsilon_{\ell\mathbf{k}},T_{\mathrm{e}})$, $f_{\mathrm{F}}(\varepsilon_{\ell'\mathbf{k}'},T_{\mathrm{e}})$ with the electronic temperature T_{e}, and the phonon occupation $n_{j\mathbf{q}}$ follows a Bose-Einstein distribution $f_{\mathrm{B}}\big(\hbar\,\omega_j(\mathbf{q}),T_{\mathrm{i}}\big)$ with nuclei temperature T_{i}. Then we get

$$\begin{aligned}\dot{E}_{\mathrm{ep}}=&\frac{2\pi}{\hbar}\sum_{j\mathbf{q}}\sum_{\ell\mathbf{k}}\sum_{\ell'\mathbf{k}'}\hbar\,\omega_j(\mathbf{q})\left|M^{(j\mathbf{q})}_{\ell\mathbf{k},\ell'\mathbf{k}'}\right|^2\delta\Big(\varepsilon_{\ell\mathbf{k}}-\varepsilon_{\ell'\mathbf{k}'}+\hbar\,\omega_j(\mathbf{q})\Big)\times\\ &\times\Big(\Big(f_{\mathrm{F}}(\varepsilon_{\ell\mathbf{k}},T_{\mathrm{e}})-f_{\mathrm{F}}(\varepsilon_{\ell'\mathbf{k}'},T_{\mathrm{e}})\Big)f_{\mathrm{B}}\big(\hbar\,\omega_j(\mathbf{q}),T_{\mathrm{i}}\big)-f_{\mathrm{F}}(\varepsilon_{\ell'\mathbf{k}'},T_{\mathrm{e}})\Big(1-f_{\mathrm{F}}(\varepsilon_{\ell\mathbf{k}},T_{\mathrm{e}})\Big)\Big).\end{aligned}\tag{3.71}$$

The above equation is used by Sadasivam et al. [46] to derive the electron-phonon coupling constant for semiconductors. The drawback of this equation is related to the fact that a huge amount of different phonon modes and electronic states must be taken into account in the sums. For metals, it was possible to reduce the calculation effort by introducing further approximations [41–43]: Due to

$$f_{\mathrm{F}}(\varepsilon',T)\Big(1-f_{\mathrm{F}}(\varepsilon,T)\Big)=\Big(f_{\mathrm{F}}(\varepsilon,T)-f_{\mathrm{F}}(\varepsilon',T)\Big)f_{\mathrm{B}}(\varepsilon'-\varepsilon,T)$$

we get

$$\begin{aligned}\dot{E}_{\text{ep}} =& \frac{2\pi}{\hbar}\sum_{j\mathbf{q}}\sum_{\ell\mathbf{k}}\sum_{\ell'\mathbf{k}'}\hbar\,\omega_j(\mathbf{q})\left|M^{(j\mathbf{q})}_{\ell\mathbf{k},\ell'\mathbf{k}'}\right|^2\delta\Big(\varepsilon_{\ell\mathbf{k}}-\varepsilon_{\ell'\mathbf{k}'}+\hbar\,\omega_j(\mathbf{q})\Big)\times\\ &\times\Big(f_{\text{F}}(\varepsilon_{\ell\mathbf{k}},T_{\text{e}})-f_{\text{F}}(\varepsilon_{\ell'\mathbf{k}'},T_{\text{e}})\Big)\Big(f_{\text{B}}\big(\hbar\,\omega_j(\mathbf{q}),T_{\text{i}}\big)-f_{\text{B}}\big(\varepsilon_{\ell'\mathbf{k}'}-\varepsilon_{\ell\mathbf{k}},T_{\text{e}}\big)\Big).\end{aligned} \tag{3.72}$$

Since the density of states $\mathfrak{D}(E_{\text{F}})$ at the Fermi energy E_{F} is bigger than zero in a metal, Allen defines the **electron-phonon spectral function** [41]:

$$f_{\text{epsf}}(\varepsilon,\varepsilon',\omega)=\frac{2}{\hbar\,\mathfrak{D}(E_{\text{F}})}\sum_{\ell\mathbf{k}}\sum_{\ell'\mathbf{k}'}\left|M^{(j\mathbf{q})}_{\ell\mathbf{k},\ell'\mathbf{k}'}\right|^2\delta\big(\varepsilon_{\ell\mathbf{k}}-\varepsilon\big)\,\delta\big(\varepsilon_{\ell'\mathbf{k}'}-\varepsilon'\big)\,\delta\Big(\omega_j(\mathbf{q})-\omega\Big) \tag{3.73}$$

and uses this new definition for the electron-phonon coupling rate:

$$\begin{aligned}\dot{E}_{\text{ep}} =& \pi\,\mathfrak{D}(E_{\text{F}})\int_0^\infty d\omega\int_{-\infty}^\infty d\varepsilon\int_{-\infty}^\infty d\varepsilon'\,f_{\text{epsf}}(\varepsilon,\varepsilon',\omega)\,\hbar\,\omega\,\delta(\varepsilon-\varepsilon'+\hbar\,\omega)\times\\ &\times\Big(f_{\text{F}}(\varepsilon,T_{\text{e}})-f_{\text{F}}(\varepsilon',T_{\text{e}})\Big)\Big(f_{\text{B}}\big(\hbar\,\omega,T_{\text{i}}\big)-f_{\text{B}}\big(\varepsilon'-\varepsilon,T_{\text{e}}\big)\Big)\\ =& \pi\,\mathfrak{D}(E_{\text{F}})\int_0^\infty d\omega\int_{-\infty}^\infty d\varepsilon\,f_{\text{epsf}}(\varepsilon,\varepsilon+\hbar\,\omega,\omega)\,\hbar\,\omega\times\\ &\times\Big(f_{\text{F}}(\varepsilon,T_{\text{e}})-f_{\text{F}}(\varepsilon+\hbar\,\omega,T_{\text{e}})\Big)\Big(f_{\text{B}}\big(\hbar\,\omega,T_{\text{i}}\big)-f_{\text{B}}\big(\hbar\,\omega,T_{\text{e}}\big)\Big).\end{aligned} \tag{3.74}$$

Furthermore, one defines the **Eliashberg function**:

$$f_{\text{El}}(\omega)=f_{\text{epsf}}(E_{\text{F}},E_{\text{F}},\omega). \tag{3.75}$$

The electron energies commonly vary in the eV range and the phonon energies vary commonly in the meV range. Thus, one can perform the following approximations [42, 43]:

$$f_{\text{epsf}}(\varepsilon,\varepsilon+\hbar\,\omega,\omega)\approx\frac{\mathfrak{D}(\varepsilon)\,\mathfrak{D}(\varepsilon+\hbar\,\omega)}{\mathfrak{D}(E_{\text{F}})^2}\,f_{\text{El}}(\omega) \tag{3.76}$$

$$\begin{aligned}f_{\text{F}}(\varepsilon,T_{\text{e}})-f_{\text{F}}(\varepsilon+\hbar\,\omega,T_{\text{e}})\approx& f_{\text{F}}(\varepsilon,T_{\text{e}})-\left(f_{\text{F}}(\varepsilon,T_{\text{e}})+\frac{\partial f_{\text{F}}(\varepsilon,T_{\text{e}})}{\partial\varepsilon}\,\hbar\,\omega\right)\\ =&-\hbar\,\omega\,\frac{\partial f_{\text{F}}(\varepsilon,T_{\text{e}})}{\partial\varepsilon}\end{aligned} \tag{3.77}$$

and

$$\mathfrak{D}(\varepsilon + \hbar\,\omega) \approx \mathfrak{D}(\varepsilon). \tag{3.78}$$

Using these approximations, the electron-phonon coupling rate transforms to

$$\dot{E}_{\mathrm{ep}} = -\frac{\pi}{\mathfrak{D}(E_{\mathrm{F}})} \int\limits_{0}^{\infty} d\omega\, f_{\mathrm{El}}(\omega)\, (\hbar\,\omega)^2 \Big(f_{\mathrm{B}}\big(\hbar\,\omega, T_{\mathrm{i}}\big) - f_{\mathrm{B}}\big(\hbar\,\omega, T_{\mathrm{e}}\big)\Big) \times$$

$$\times \int\limits_{-\infty}^{\infty} d\varepsilon\, \mathfrak{D}(\varepsilon)^2\, \frac{\partial f_{\mathrm{F}}(\varepsilon, T_{\mathrm{e}})}{\partial \varepsilon}. \tag{3.79}$$

By dividing the phonon modes in different groups of phonon branches, Waldecker et al. [44, 45] define an individual ionic temperature $T_{\mathrm{i}}^{(b)}$ for each phonon branch.

Using this temperature, Waldecker introduces an individual electron-phonon coupling rate $E_{\mathrm{ep}}^{(b)}$ for each phonon branch by integrating in the above equation only over the related phonon modes. Commonly, one defines the **electron-phonon coupling constant** G_{ep} from

$$\dot{E}_{\mathrm{ep}} = -G_{\mathrm{ep}}\, N_{\mathrm{at}}\, (T_{\mathrm{e}} - T_{\mathrm{i}}). \tag{3.80}$$

6 Physical Picture of Femtosecond Laser Excitation

In view of the above discussion, one can understand the mechanisms for laser-induced structural changes by using a simple physical picture (see Fig. 3.1): Before laser excitation, the solid is in thermodynamical equilibrium at a low initial (lattice and electronic) temperature ($T_{\mathrm{i}} \leq 300K$). This means that electrons fill mainly the states below the Fermi level. The resulting ground state potential landscape $U_0(\{\boldsymbol{R}_i\}, T_{\mathrm{e}} = 300\,\mathrm{K})$ shows minima at the crystal lattice sites. Atoms are sitting on these sites and therefore no forces act on them. However, the situation changes dramatically when the solid becomes excited by a laser pulse, which creates a considerable amount of electron-hole pairs. This means that the electronic occupations $n_{\nu\boldsymbol{k}}(t)$ change. Consequently, the functional form of $U(\{\boldsymbol{R}_i\}, T_{\mathrm{e}})$ undergoes quantitative and qualitative changes, which results in the shifting of the minima, or their disappearance for very high fluences [48]. Since these modifications occur on a timescale which is much shorter than the reaction time of the lattice, the atoms remain during the laser puse in their positions, most of them no longer minima of the new potential landscape. Therefore, forces now act on the atoms, which start to move [49]. As a consequence of the laser excitation, the system is in an extreme nonequilibrium state in which electrons are very hot while the lattice remains cold.

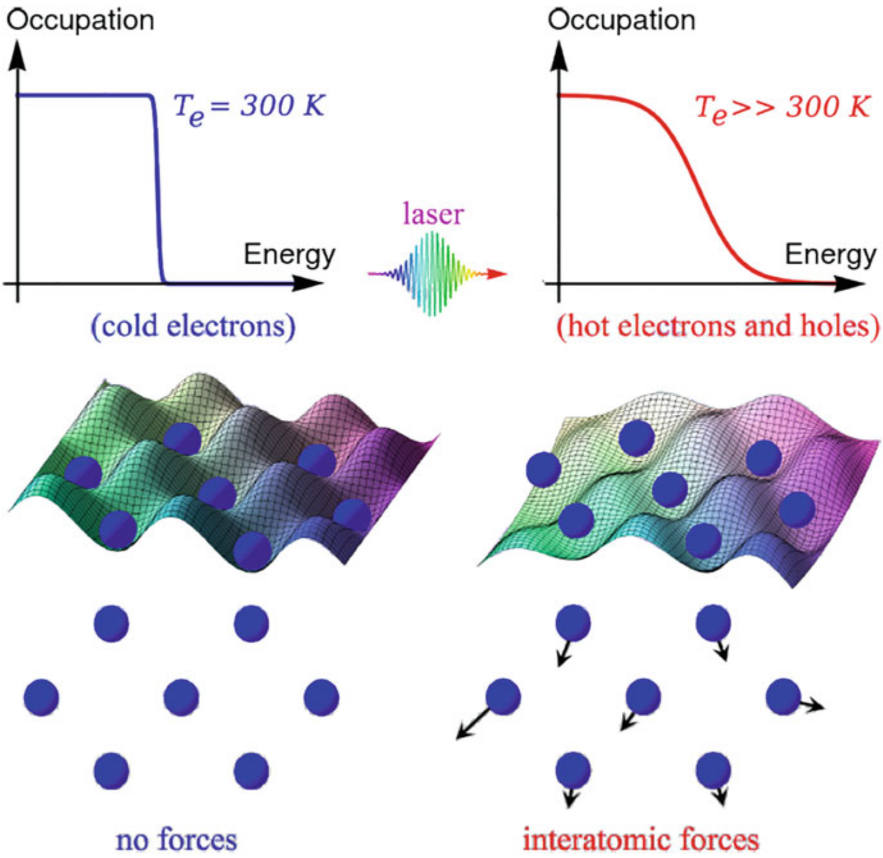

Fig. 3.1 Before the femtosecond laser pulse, the solid is in thermal equilibrium. Thus, the electrons form a Fermi distribution and the ions are located at the minimum of the PES. An intense femtosecond laser pulse strongly couples to the electrons in the solid and produces excited electron and hole pairs. These thermalize within a short time to a Fermi distribution with a high electronic temperature. The PES changes significantly due to the hot electrons, so that the ions start to move non-thermally

This may lead to a variety of laser-induced structural events. Due to the electron-phonon coupling, the state with hot electrons and cold ions decays on a picosecond timescale.

It is important to point out that the approach described above for obtaining the laser-excited PES is not the only possible one. The assumption that electrons acquire a well-defined temperature during the first stages of the laser-induced lattice dynamics was used for some molecular dynamics simulations [50, 51] and by us for the construction of excited PESs [52, 53]. Fahy and coworkers use for semiconductors and semimetals a constraint model in which it is assumed that electrons and holes thermalize separately and acquire two different chemical potentials [54]. We discussed in Ref. [55] and Ref. [56] the drawbacks of this assumption for semimetals in general and also for semiconductors excited by very intense laser pulses. We have also compared the behavior of phonon softening assuming one and two chemical potentials in Ref. [57].

Another possible starting point for the calculation of the laser-excited PES is to assume that the electronic entropy remains constant. This idea was implemented by Stampfli and Bennemann [19, 20, 58] and by us [55, 56, 59]. In that case, the thermodynamical function which is relevant for the construction of the laser-excited PES is the total energy.

Finally, molecular dynamics simulations were performed in which the absorbed energy is the quantity which does not change during the first stages of the laser-induced lattice dynamics. Those simulations take the laser pulse explicitly into account. Examples are the works by Jeschke et al. [21, 22, 48, 60, 61].

7 Ultrafast Structural Phenomena Driven by Quantum or Non-Thermal Effects

Ultrafast phenomena occurring on times $t < \tau_{e-ph}$ have been investigated with the help of pump-probe measurements since the 1980s [62]. An impressive example of those studies is the time-resolved measurement of the laser-induced ultrafast melting of Bi, performed by R. D. Miller and coworkers [63]. With the help of ultrafast electron crystallography, they could show that the timescale for non-thermal melting can be as fast as half of the period of the $\mathrm{A}_1 g$ optical phonon. It is clear that in this case, melting is non-thermal, since phonons have no possibility to thermalize on such a short time. When melting or other laser-induced structural phase transitions take place on times $\tau_{e-e} < t < \tau_{ph-ph}$, the ionic motion is mostly driven by changes in the potential energy surface (PES).

Silvestrelli et al. performed MD simulations of femtosecond laser-excited silicon using T_e-dependent DFT [50, 64]. They realized that silicon melts within hundred femtoseconds after the laser excitation, which is called non-thermal melting. We further analyzed the atomic motions and found that in silicon the non-thermal melting occurs in three stages [65]: At first, the atoms move super diffusive, until the scattering rate of the atoms increases significantly. Due to this, the time-dependent mean square displacements of the atoms start to increase more slowly, which corresponds to a fractional diffusive motion. Finally, the mean square displacements increase linearly indicating a normal diffusive motion of the atoms. The dramatic changes in the PES of Si were directly observed in the calculations of Recoules et al. [66]. They derived the phonon bandstructure of silicon before and after a femotsecond laser excitation with T_e-dependent DFT and found a laser-induced decrease of the phonon frequencies; especially the acoustic phonon frequencies become negative indicating a lattice instability. Thus, the femtosecond laser excitation induces a bond softening. In other materials, like gold, a femtosecond laser excitation can induce a bond hardening, i.e., the phonon frequencies increase [66].

Using ultrafast x-ray diffraction, Harb et al. [38] measured an ultrafast decay of the Bragg peak intensities of a silicon film after an intense femtosecond laser pulse excitation, which proves the theoretical predictions of non-thermal melting in silicon. Such a laser-induced ultrafast melting could also be time-resolved measured in bismuth by Sciaini et al. [63].

Besides the above described solid-to-liquid transition, a femtosecond laser can also induce an ultrafast solid-to-solid transition. Antimony and bismuth crystallize in the A7 structure under ambient conditions. Here, the atoms form hexagonal planes, which are stacked on top of each other with alternating distances. This difference between the plane distances is called a Peierls distortion and is described by the so-called Peierls parameter. In 2009, Fausti et al. studied femtosecond laser pulse excited antimony using picosecond Raman scattering and found a laser-induced reversible transition from the A7 to a structure with lower symmetry [67]. In 2018, Teitelbaum et al. [68] measured a laser-induced solid-to-solid phase transition in bismuth from the A7 structure to a structure with higher symmetry by applying dual echelon femtosecond single-shot spectroscopy [69]. The excitation by a femotsecond laser pulse induces in VO_2 a phase transition between the monoclinic M1-phase to a rutile R-phase [70]. These measurements show that a femtosecond laser pulse may change the PES in such a way that a different crystal structure becomes the minimum.

A further effect of a femtosecond laser pulse is the excitation of coherent phonons in selected materials [71, 72].

The first molecular dynamics (MD) simulations with T_e-dependent DFT were performed by Alavi et al. in 1994 for a dense, hot hydrogen gas [73]. Later, Silvestrelli et al. performed MD simulations of the ultrafast melting of silicon (Si) [50, 64] and graphite [74] at increased T_e. Many more calculations using T_e-dependent DFT followed [65, 66].

8 Open Questions

In this chapter, we have described the theoretical framework to treat laser-induced ultrafast thermal and non-thermal structural phenomena. We have shown that an approach based on Mermin's functional [6] for the Helmholtz free energy of electrons and holes is the most realistic one, since it accounts for the fact that the excited carriers lose quantum coherence and thermalize quickly after being excited by the photons. Of course, many further efforts are still necessary to obtain a full ab initio description of the structural changes starting from the excitation process. The coupling of the laser pulse and electrons was quasi-empirically taken into account in the first simulations using the tight-binding method for describing electrons (see, for instance, Ref. [75]). The vector potential of the laser field was taken into account by modifying the hopping elements through a Peierls substitution. Nowadays, the coupling of light with electrons can be very accurately taken into account in the framework of the time-dependent density functional theory (TDDFT), developed by

Runge and Gross [76]. Details of the theory can be read in many books and reviews (see, for instance, [77]). TDDFT yields a good quantum description of the excitation process including many-photon absorption. It has, however, a problem. The excited state cannot thermalize in the framework of TTDFT. This happens because the method relies on the time evolution of a Slater determinat, i.e., of a pure state. But the thermalized state is a mixed state. And since the quantum evolution operator is unitary, a pure state cannot evolve into a mixed state, and the thermalization cannot be achieved without further modifications of the method. For the moment, TDDFT yields excellent results for describing laser-induced currents and magnetization dynamics in solids [78, 79] as well as laser-induced dynamics in molecules, where the thermalization problem is less crucial [80]. The loss of coherence comes through carrier-carrier and carrier-phonon collisions. The latter were described in detail in this chapter. In order to describe the carrier-carrier collisions at a good theoretical level, Boltzmann approaches, or at least approaches considering rate equations for the electron occupations [81], must be considered. Notice that those approaches can be then combined with DFT and the forces acting on the ions during electron thermalization can then be obtained. Such approaches are in progress in our group in collaboration with B. Rethfeld's group in Kaiserslautern. Further combination with TDDFT will allow in the near future to describe the laser-induced structural changes of solids from the photon absorption up to the mechanical relaxation on ab initio level.

References

1. G. Czycholl, *Theoretische Festkörper Physik Band 1*, 4th edn. (Springer, Berlin, 2016)
2. E.S. Zijlstra, M.E. Garcia, *Laser-induced Softening of Lattice Vibration Dynamics at Sold State Surfaces and Interfaces*, vol. 1, ed. by U. Bovensiepen, H. Petek, M. Wolf (Wiley, Weinheim, 2010)
3. M. Bonitz, *Quantum Kinetic Theory*, 2nd edn. (Springer, New York, 2016)
4. T. Elsaesser, J. Shah, L. Rota, P. Lugli, Initial thermalization of photoexcited carriers in gaas studied by fem-tosecond luminescence spectroscopy. Phys. Rev. Lett. **66**, 1757 (1991)
5. W.H. Knox, D.S. Chemla, G. Livescu, J.E. Cunningham, J.E. Henry, Femtosecond carrier thermalization in dense fermi seas. Phys. Rev. Lett. **61**, 1290–1293 (1988)
6. N. David Mermin, Thermal properties of the inhomogeneous electron gas. Phys. Rev. **137**, A1441 (1965)
7. B. Bauerhenne, *Materials Interaction with Femtosecond Lasers*, 1st edn. (Springer, Berlin, 2021)
8. P. Pulay, Convergence acceleration of iterative sequences: The case of SCF iteration. Chem. Phys. Lett. **73**, 393 (1980)
9. G.P. Kerker, Efficient iteration scheme for self-consistent pseudopotential calculations. Phys. Rev. B **23**, 3082 (1981)
10. D.M. Ceperley, B.J. Alder, Ground state of the electron gas by a stochastic method. Phys. Rev. Lett. **45**, 566–569 (1980)
11. S.H. Vosko, L. Wilk, M. Nusair, Accurate spin-dependent electron liquid correlation energies for local spin density calculations: a critical analysis. Can. J. Phys. **58**(8), 1200–1211 (1980)
12. J.P. Perdew, A. Zunger, Self-interaction correction to density-functional approximations for many-electron systems. Phys. Rev. B **23**, 5048–5079 (1981)
13. L.A. Cole, J.P. Perdew, Calculated electron affinities of the elements. Phys. Rev. A **25**, 1265–1271 (1982)

14. J.P. Perdew, Y. Wang, Accurate and simple analytic representation of the electron-gas correlation energy. Phys. Rev. B **45**, 13244–13249 (1992)
15. A.D. Becke, Density-functional exchange-energy approximation with correct asymptotic behavior. Phys. Rev. A **38**, 3098–3100 (1988)
16. C. Lee, W. Yang, R.G. Parr, Development of the colle-salvetti correlation-energy formula into a functional of the electron density. Phys. Rev. B **37**, 785–789 (1988)
17. J.P. Perdew, J.A. Chevary, S.H. Vosko, K.A. Jackson, M.R. Pederson, D.J. Singh, C. Fiolhais, Atoms, molecules, solids, and surfaces: Applications of the generalized gradient approximation for exchange and correlation. Phys. Rev. B **46**, 6671–6687 (1992)
18. J.P. Perdew, K. Burke, M. Ernzerhof, Generalized gradient approximation made simple. Phys. Rev. Lett. **77**, 3865–3868 (1996)
19. P. Stampfli, K.H. Bennemann, Theory for the instability of the diamond structure of Si, Ge, and C induced by a dense electron-hole plasma. Phys. Rev. B **42**, 7163 (1990)
20. P. Stampfli, K.H. Bennemann, Dynamical theory of the laser-induced lattice instability of silicon. Phys. Rev. B **46**, 10686 (1992)
21. H.O. Jeschke, M.E. Garcia, K.H. Bennemann, Time-dependent energy absorption changes during ultrafast lattice deformation. J. Appl. Phys. **91**, 18–23 (2002)
22. H.O. Jeschke, M.E. Garcia, M. Lenzner, J. Bonse, J. Krüger, W. Kautek, Theoretical description of the ultrafast ablation of diamond and graphite: dependence of thresholds on pulse duration. Appl. Surf. Sci. **197–198**, 839–844 (2002)
23. D.S. Ivanov, V.P. Lipp, A. Blumenstein, F. Kleinwort, V.P. Veiko, E. Yakovlev, V. Roddatis, M.E. Garcia, B. Rethfeld, J. Ihlemann, P. Simon, Experimental and theoretical investigation of periodic nanostructuring of au with ultrashort uv laser pulses near the damage threshold. Phys. Rev. Applied **4**, 064006 (2015)
24. F.H. Stillinger, T.A. Weber, Computer simulation of local order in condensed phases of silicon. Phys. Rev. B **31**, 5262–5271 (1985)
25. J. Tersoff, Empirical interatomic potential for silicon with improved elastic properties. Phys. Rev. B **38**, 9902–9905 (1988)
26. R.P. Gupta, Lattice relaxation at a metal surface. Phys. Rev. B **23**, 6265–6270 (1981)
27. S. Khakshouri, D. Alfè, D.M. Duffy, Development of an electron-temperature-dependent interatomic potential for molecular dynamics simulation of tungsten under electronic excitation. Phys. Rev. B **78**, 224304 (2008)
28. M.W. Finnis, J.E. Sinclair, A simple empirical n-body potential for transition metals. Philos. Mag. A **50**(1), 45–55 (1984)
29. S.T. Murphy, S.L. Daraszewicz, Y. Giret, M. Watkins, A.L. Shluger, K. Tanimura, D.M. Duffy, Dynamical simulations of an electronically induced solid-solid phase transformation in tungsten. Phys. Rev. B **92**, 134110 (2015)
30. G.E. Norman, S.V. Starikov, V.V. Stegailov, Atomistic simulation of laser ablation of gold: Effect of pressure relaxation. J. Exp. Theor. Phys. **114**(5), 792–800 (2012)
31. M.S. Daw, M.I. Baskes, Semiempirical, quantum mechanical calculation of hydrogen embrittlement in metals. Phys. Rev. Lett. **50**, 1285–1288 (1983)
32. J.A. Moriarty, R.Q. Hood, L.H. Yang, Quantum-mechanical interatomic potentials with electron temperature for strong-coupling transition metals. Phys. Rev. Lett. **108**, 036401 (2012)
33. L. Shokeen, P.K. Schelling, An empirical potential for silicon under conditions of strong electronic excitation. Appl. Phys. Lett. **97**(15), 151907 (2010)
34. T. Kumagai, S. Izumi, S. Hara, S. Sakai, Development of bond-order potentials that can reproduce the elastic constants and melting point of silicon for classical molecular dynamics simulation. Comput. Mater. Sci. **39**(2), 457–464 (2007)
35. L. Shokeen, P.K. Schelling, Thermodynamics and kinetics of silicon under conditions of strong electronic excitation. J. Appl. Phys. **109**(7), 073503 (2011)
36. R. Darkins, P.-W. Ma, S.T. Murphy, D.M. Duffy, Simulating electronically driven structural changes in silicon with two-temperature molecular dynamics. Phys. Rev. B **98**, 024304 (2018)
37. M. Harb, R. Ernstorfer, T. Dartigalongue, C.T. Hebeisen, R.E. Jordan, R.J.D. Miller, Carrier relaxation and lattice heating dynamics in silicon revealed by femtosecond electron diffraction. J. Phys. Chem. B **110**(50), 25308–25313 (2006)

38. M. Harb, R. Ernstorfer, C.T. Hebeisen, G. Sciaini, W. Peng, T. Dartigalongue, M.A. Eriksson, M.G. Lagally, S.G. Kruglik, R.J.D. Miller, Electronically driven structure changes of si captured by femtosecond electron diffraction. Phys. Rev. Lett. **100**, 155504 (2008)
39. B. Bauerhenne, V.P. Lipp, T. Zier, E.S. Zijlstra, M.E. Garcia, Self-learning method for construction of analytical interatomic potentials to describe laser-excited materials. Phys. Rev. Lett. **124**, 085501 (2020)
40. B. Bauerhenne, M.E. Garcia, Performance of state-of-the-art force fields for atomistic simulations of silicon at high electronic temperatures. The European Physical Journal Special Topics **227**(14), 1615–1629 (2019)
41. P.B. Allen, Theory of thermal relaxation of electrons in metals. Phys. Rev. Lett. **59**, 1460–1463 (1987)
42. X.Y. Wang, D.M. Riffe, Y.-S. Lee, M.C. Downer, Time-resolved electron-temperature measurement in a highly excited gold target using femtosecond thermionic emission. Phys. Rev. B **50**, 8016–8019 (1994)
43. Z. Lin, L.V. Zhigilei, V. Celli, Electron-phonon coupling and electron heat capacity of metals under conditions of strong electron-phonon nonequilibrium. Phys. Rev. B **77**, 075133 (2008)
44. L. Waldecker, R. Bertoni, R. Ernstorfer, J. Vorberger, Electron-phonon coupling and energy flow in a simple metal beyond the two-temperature approximation. Phys. Rev. X **6**, 021003 (2016)
45. L. Waldecker, T. Vasileiadis, R. Bertoni, R. Ernstorfer, T. Zier, F.H. Valencia, M.E. Garcia, E.S. Zijlstra, Coherent and incoherent structural dynamics in laser-excited antimony. Phys. Rev. B **95**, 054302 (2017)
46. S. Sadasivam, M.K.Y. Chan, P. Darancet, Theory of thermal relaxation of electrons in semiconductors. Phys. Rev. Lett. **119**, 136602 (2017)
47. W. Greiner, *Quantum Mechanics An Introduction*, 4th edn. (Springer, New York, 2000)
48. H.O. Jeschke, M.E. Garcia, K.H. Bennemann, Microscopic analysis of the femtosecond graphitization of diamond. Phys. Rev. B **60**, R3701–R3704 (1999)
49. H.O. Jeschke, M.E. Garcia, *Ultrafast structural changes induced by femtosecond laser pulses*, in *Nonlinear Optics, Quantum Optics and Ultrafast Phenomena with X-rays*, ed. by B.W. Adams (Kluwer Academic Publishers, Boston/Dordrecht/London, 2003)
50. P.L. Silvestrelli, A. Alavi, M. Parrinello, D. Frenkel, Ab initio molecular dynamics simulation of laser melting of silicon. Phys. Rev. Lett. **77**, 3149–3152 (1996)
51. K. Zickfeld, M.E. Garcia, K.H. Bennemann, Theoretical study of the laser-induced femtosecond dynamics of small si$_n$ clusters. Phys. Rev. B **59**, 13422–13430 (1999)
52. N. Huntemann E.S. Zijlstra, M.E. Garcia, Laser-induced solid-solid phase transition in as under pressure: a theoretical prediction. New J. Phys. **10**, 033010 (2008)
53. J. Walkenhorst E.S. Zijlstra, M.E. Garcia, Anharmonic noninertial lattice dynamics during ultrafast nonthermal melting of INSB. Phys. Rev. Lett. **101**, 135701 (2008)
54. P. Tangney, S. Fahy, Calculations of the a_1 phonon frequency in photoexcited tellurium. Phys. Rev. Lett. **82**, 4340–4343 (1999)
55. L.L. Tatarinova E.S. Zijlstra, M.E. Garcia, Laser-induced phonon-phonon interactions in bismuth. Phys. Rev. B **74**, 220301 (2006)
56. S.L. Johnson, P. Beaud, C.J. Milne, F.S. Krasniqi, E.S. Zijlstra, M.E. Garcia, M. Kaiser, D. Grolimund, R. Abela, G. Ingold, Nanoscale depth-resolved coherent femtosecond motion in laser-excited bismuth. Phys. Rev. Lett. **100**, 155501 (2008)
57. B Bauerhenne, M.E. Garcia, Universal behavior of the band gap as a function of the atomic mean-square displacement in laser-excited silicon. Advanced Optical Technologies **9**(3), 145–153 (2020)
58. K.H. Bennemann, P. Stampfli, Time dependence of the laser-induced femtosecond lattice instability of Si and GaAs: Role of longitudinal optical distortions. Phys. Rev. B **49**, 7299 (1994)
59. L.L. Tatarinova E.S. Zijlstra, M.E. Garcia, Ab-initio study of coherent phonons excited by femtosecond laser pulses in bismuth. Proc. SPIE **6261**, 62610R (2006)

60. M.E. Garcia, H.O. Jeschke, K.H. Bennemann, Theory for the ultrafast dynamics of excited clusters: interplay between elementary excitations and atomic structure. Appl. Phys. B **71**, 361–371 (2000)
61. H.O. Jeschke, M.E. Garcia, K.H. Bennemann, Theory for the ultrafast ablation of graphite films. Phys. Rev. Lett **87**, 015003 (2001)
62. G.A. Morou C.B. Harris, E.P. Ippen, A.H. Zewail, *Ultrafast Phenomena VII.* Series in Chemical Physics (Springer, Berlin, 1990)
63. G. Sciaini, M. Harb, S.G. Kruglik, T. Payer, C.T. Hebeisen, F.-J. Meyer zu Heringsdorf, M. Yamaguchi, M. Horn-von Hoegen, R. Ernstdorfer, R.J.D. Miller, Electronic acceleration of atomic motions and disordering in bismuth. Nature(London) **56**, 458 (2009)
64. P.L. Silvestrelli, A. Alavi, M. Parrinello, D. Frenkel, Structural, dynamical, electronic, and bonding properties of laser-heated silicon: An ab initio molecular-dynamics study. Phys. Rev. B **56**, 3806–3812 (1997)
65. E.S. Zijlstra, A. Kalitsov, T. Zier, M.E. Garcia, Fractional diffusion in silicon. Adv. Mater. **25**(39), 5605–5608 (2013)
66. V. Recoules, J. Clérouin, G. Zérah, P.M. Anglade, S. Mazevet, Effect of intense laser irradiation on the lattice stability of semiconductors and metals. Phys. Rev. Lett. **96**, 055503 (2006)
67. D. Fausti, O.V. Misochko, P.H.M. van Loosdrecht, Ultrafast photoinduced structure phase transition in antimony single crystals. Phys. Rev. B **80**, 161207 (2009)
68. S.W. Teitelbaum, T. Shin, J.W. Wolfson, Y.-H. Cheng, I.J. Porter, M. Kandyla, K.A. Nelson, Real-time observation of a coherent lattice transformation into a high-symmetry phase. Phys. Rev. X **8**, 031081 (2018)
69. T. Shin, J.W. Wolfson, S.W. Teitelbaum, M. Kandyla, K.A. Nelson, Dual echelon femtosecond single-shot spectroscopy. Rev. Sci. Instrum. **85**(8), 083115 (2014)
70. S. Wall, D. Wegkamp, L. Foglia, K. Appavoo, J. Nag, R.F. Haglund Jr, J. Stähler, M. Wolf, Ultrafast changes in lattice symmetry probed by coherent phonons. Nat. Commun. **3**, 721 (2012)
71. K. Sokolowski-Tinten, C. Blome, J. Blums, A. Cavalleri, C. Dietrich, A. Tarasevitch, I. Uschmann, E. Forster, M. Kammler, M. Horn-von Hoegen, D. von der Linde. Femtosecond x-ray measurement of coherent lattice vibrations near the lindemann stability limit. Nature **422**, 287–289 (2003)
72. K. Ishioka, M. Kitajima, O.V. Misochko, Coherent A1g and Eg phonons of antimony. J. Appl. Phys. **103**(12), 123505 (2008)
73. A. Alavi, J. Kohanoff, M. Parrinello, D. Frenkel, Ab initio molecular dynamics with excited electrons. Phys. Rev. Lett. **73**, 2599–2602 (1994)
74. P.L. Silvestrelli, M. Parrinello, Ab initio molecular dynamics simulation of laser melting of graphite. J. Appl. Phys. **83**(5), 2478–2483 (1998)
75. T. Dumitrică, R.E. Allen, Femtosecond-scale response of gaas to ultrafast laser pulses. Phys. Rev. B **66**, 081202 (2002)
76. E. Runge, E.K.U. Gross, Density-functional theory for time-dependent systems. Phys. Rev. Lett. **52**, 997–1000 (1984)
77. M.E. Casida, M. Huix-Rotllant, Progress in time-dependent density-functional theory. Annu. Rev. Phys. Chem. **63**(1), 287–323 (2012)
78. G. Wachter, C. Lemell, J. Burgdörfer, S.A. Sato, X.-M. Tong, K. Yabana, Ab initio simulation of electrical currents induced by ultrafast laser excitation of dielectric materials. Phys. Rev. Lett. **113**, 087401 (2014)
79. F. Siegrist, J.A. Gessner, M. Ossiander, C. Denker, Y.-P. Chang, M.C. Schröder, A. Guggenmos, Y. Cui, J. Walowski, U. Martens, J.K. Dewhurst, U. Kleineberg, M. Münzenberg, S. Sharma, M. Schultze, Light-wave dynamic control of magnetism. Nature **571**(7764), 240–244 (2019)
80. J. Krumland, A.M. Valencia, S. Pittalis, C.A. Rozzi, C. Cocchi, Understanding real-time time-dependent density-functional theory simulations of ultrafast laser-induced dynamics in organic molecules. J. Chem. Phys. **153**(5), 054106 (2020)
81. B. Rethfeld, Unified model for the free-electron avalanche in laser-irradiated dielectrics. Phys. Rev. Lett. **92**, 187401 (2004)

Chapter 4
The Universality of Self-Organisation: A Path to an Atom Printer?

Serim Ilday and F. Ömer Ilday

Abstract More than 30 years ago, Donald Eigler and Erhard Schweizer spelt the letters IBM by positioning 35 individual xenon atoms at 4 K temperature using a scanning tunnelling microscope. The arrangement took approximately 22 h. This was an outstanding demonstration of control over individual atoms. Since then, 3D printers developed into a near-ubiquitous technology. Nevertheless, with typical resolutions in the micrometres, they are far from the atomic scale of control that the IBM demonstration seemed to herald. Even the highest resolution achieved with ultrafast lasers driving two-photon polymerisation barely reaches 100 nm, three orders of magnitude distant from the atomic scale. Here, we adopt a long-term view when we ask about the possibility of a 3D atom printer, which can build an arbitrarily shaped object of macroscopic dimensions with control over its atomic structure at room temperature and within a reasonable amount of time. After discussing the state-of-the-art technology based on direct laser writing, we identify three fundamental challenges to overcome. The first is the *fat fingers problem*, which refers to laser wavelengths being much larger than the size of the atoms. The second one is *complexity explosion*, namely, the number of processing step scales with the inverse cube of the resolution, leading to prohibitively long processing times. The third challenge is the increasing strength of random fluctuations as the size of the smallest volume element to be printed approaches the atomic scale. This requires control over the fluctuations, which we call *mischief of fluctuations*. Although direct-writing techniques offer sufficient resolution, speed, and excellent flexibility for the mesoscopic scale, each of the three fundamental problems above appears enough to render the atomic scale unreachable. Each of these arise out of

---

S. Ilday (✉)
Faculty of Electrical Engineering and Information Technology (ETIT), Ruhr-Universität Bochum (RUB), Bochum, Germany
e-mail: serim.ilday@rub.de

F. Ö. Ilday
Physics Department, and Electrical and Electronics Engineering Department, Bilkent University, Ankara, Turkey
e-mail: ilday@bilkent.edu.tr

© The Author(s), under exclusive license to Springer Nature Switzerland AG 2023

R. Stoian, J. Bonse (eds.), *Ultrafast Laser Nanostructuring*, Springer Series in Optical Sciences 239, https://doi.org/10.1007/978-3-031-14752-4_4

a need to control each atom individually and with precision. In contrast, the three challenges of direct writing are not fundamental limitations to self-organisation, this chapter proposes a potential path to a 3D atom printer, where laser-driven self-organisation can complement direct-writing techniques by bridging the atomic and mesoscopic scales.

Keywords Self-organisation · Self-assembly · 3D printing · Additive manufacturing · Ultrafast lasers · Laser-material processing · Pattern formation

1 Introduction

In a 1990 paper published in *Nature*, D. Eigler and E. Schweizer demonstrated the astounding capability of controlling individual atoms [1]. Their demonstration of spelling the letters IBM with 35 Xe atoms was revolutionary, inspiring, and raised high hopes that we might, after all, assemble custom-designed structures and functionalities atom-by-atom (Fig. 4.1a). Around the same time, this vision was popularised through a futuristic device called the Replicator in the science-fiction TV series *Star Trek: The Next Generation* (Fig. 4.1b). A *Replicator* is a fictional machine that can synthesise any inanimate object with molecular precision. In principle, the spelling of IBM with 35 Xe atoms constituted a solid scientific basis for anticipating a *Replicator* being built in the future. Three decades after the IBM demonstration, so-called 3D printers that can create arbitrarily shaped objects form a mature technology, some of which are, incidentally, branded as *Replicators*.

However, present-day 3D printers can print using typically single or a few different materials, mainly metal alloys or plastics. Their resolutions are in the 20 μm to 1 mm range. The better resolutions are obtained using laser-based melting of the material, limiting them mainly to metals and metal alloys despite ongoing efforts to broaden the material compatibility [2–7]. Only the most sophisticated printers based on ultrafast lasers driving multiphoton-induced polymerisation can reach the mesoscopic scale with resolutions ranging from ∼150 nm [8–10] to a micron [11, 12]. Unfortunately, the multiphoton polymerisation technique is even more limited in the materials it can print. Examples of the state-of-the-art 3D printing methodologies are provided in Fig. 4.2 [13–16], which were also discussed in a recent feature article [17].

The current state of the art is far from the possibilities heralded by the IBM demonstration or the fictional *Replicator* technology. They fail most strikingly in two aspects, spatial resolution and limited material choices. Despite the significant interest and rapid progress in 3D printing, it is an open question whether reaching the atomic scale and universality in materials is merely a matter of more time and better engineering.

Can we anticipate progress that eventually leads to the capability to print a complex structure, perhaps, a biological tissue, by assembling it atom-by-atom? Any biological tissue comprises enormous complexity, organised into different structures from the tissue level to the individual cells, which, in turn, contain

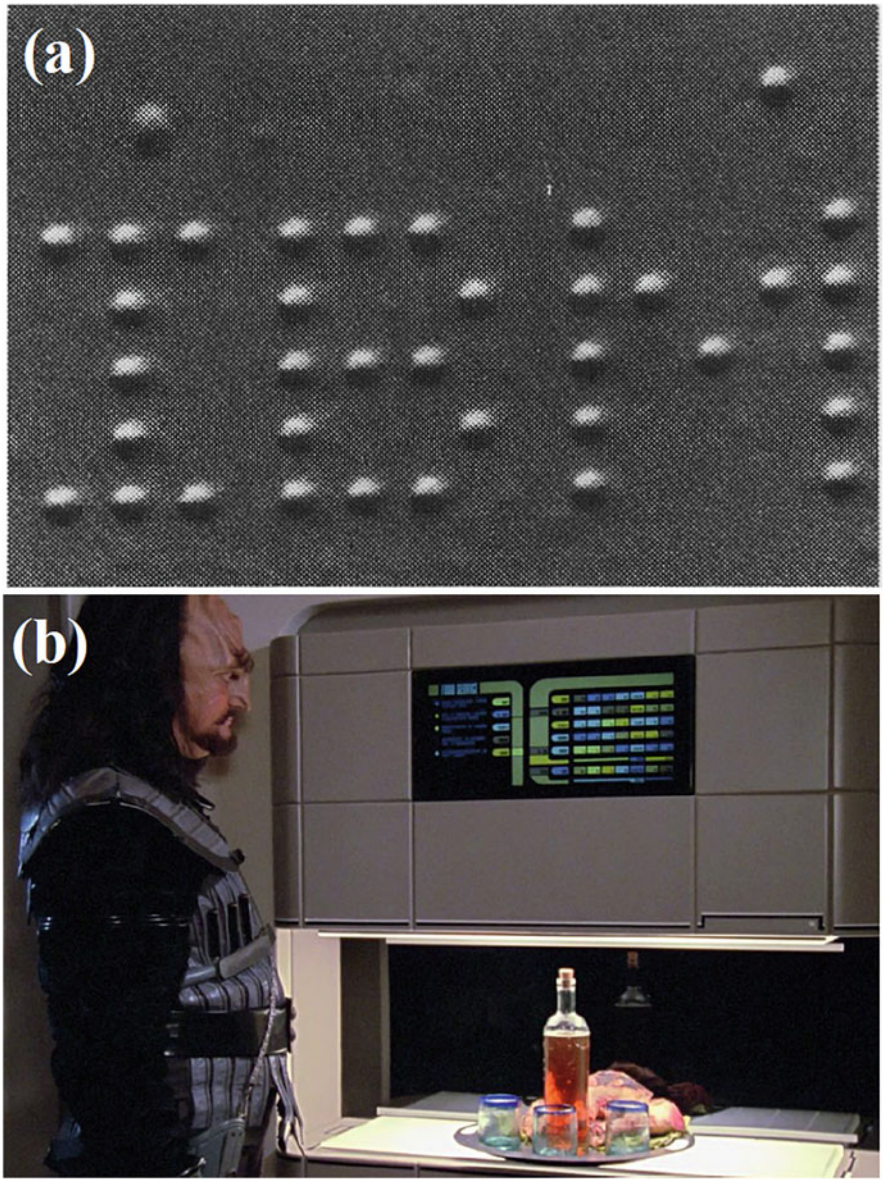

Fig. 4.1 The letters IBM were spelt with 35 Xe atoms in 1990 [1] (Image Credit: IBM). (**b**) The image of a plate of food synthesised by a Replicator as imagined in the science-fictional production, Star Trek (Image Credit: Paramount Television)

subcellular structures that are themselves complex combinations of hundreds of biomolecules. These wildly varying structures exist in a state of homeostasis, locally resisting the deleterious effects of the second law of thermodynamics

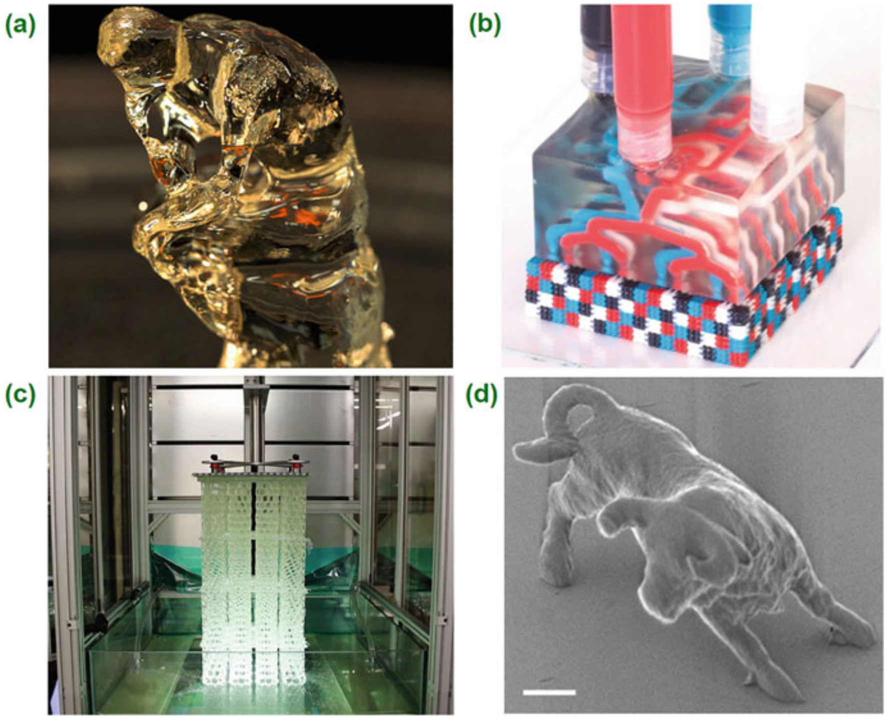

Fig. 4.2 (**a**) 3D printed 40-millimetres-tall version of Auguste Rodin's The Thinker using computed axial lithography [13] (Image Credit: University of California at Berkeley). (**b**) Multilateral multi-nozzle 3D printing of several millimetres-large voxelated structures using four different materials [14] (Image Credit: Harvard University). (**c**) Large-volume 3D printing of a meters-long polyurethane acrylate lattice from a liquid interface [15] (Image Credit: Northwestern University). (**d**) Micro-nano-fabrication of a bull structure at sub-diffraction-limit resolution using two-photon polymerisation technique (Scale bar 2 μm) [16]. Credit: Osaka University

through continuous processing of matter and an energy flux [18]. They are dynamic and adaptive, capable of autocatalysis, autoinhibition, self-healing, self-replication, regeneration, and reproduction. Unlike the atoms spelling out IBM, which could only be maintained in that configuration by cooling the sample to 4 K, biological tissue thrives at temperatures in the range of 300 K, where the thermal fluctuations are extreme at the atomic level [19].

Nevertheless, the molecular machinery that maintains a 1-mm^3 slab of tissue is well adapted to, and in fact, evolved to exploit these fluctuations [20]. It is imperative to recognise that nothing about its structure or molecular machinery is controlled precisely down to the individual atom. Some 10^{21} atoms participate in this dynamic steady state, and their assembly and continuous rearrangements are far from error-free. Still, a diverse network of feedback loops called the metabolism keeps both the structure and the machinery running successfully [21]. Even if we ignore these amazing dynamic features, its vast structural complexity exceeds, by a considerable margin, anything that we have been able to manufacture to date.

Our purpose in this chapter is to provide a perspective for a possible pathway that could eventually enable a technology to print arbitrarily shaped objects of macroscopic dimensions with control over its atomic structure at room temperature, a 3D atom printer, if you will. We will argue that recent developments in laser physics and technology and self-organisation methods can be exploited to merge top-down and bottom-up approaches into a single device that could bridge the gap between the atomic and mesoscopic scales. Section 2 will give a brief introduction to the state-of-the-art direct laser writing technology and bring forwards the possibility of merging additive and subtractive manufacturing methods using, what we refer to as the *Omni-modality* approach. Section 3 will stress that regardless of advanced engineering, the top-down manufacturing methods will always be limited in reaching the atomic scale by the three fundamental challenges and bring forwards laser-driven self-organisation techniques to help overcome these challenges and complement them. Finally, Sect. 4 will give a perspective on an atom printer's practicality, design, and potential and outline its working principles that combine top-down and bottom-up approaches.

2 The State-of-the-Art Direct Laser Writing Technology

The fabrication of the majority of small-scale engineered structures is based on transferring or impressing a structure from a previously prepared mould or mask to the target material or using direct, point-by-point processing of the material(s) involved to define the structure. The former defers the problem to creating a mould or a mask. This approach works best (and exceptionally well for microelectronics) when many identical copies of a single structure are made. The latter can be further divided into additive or subtractive techniques. While many alternative technologies compete in both categories, arguably the best-known methods are conventional mechanical techniques (limited to $>100\,\mu\text{m}$ scale) and laser removal for the subtractive approach [22–24]. Most additive manufacturing solutions rely on low-cost, low-resolution 3D printers that melt and resolidify plastic derivatives for the consumer market and laser-based 3D printers that generally build out of metal alloys for the professional market [25, 26]. Both subtractive and additive manufacturing techniques work best in the micron scale and above, and the mesoscopic scale of 0.1–$1\,\mu\text{m}$ continues to be the domain of high-end niche applications. In addition to the additive and subtractive techniques, a third possibility is what we refer to as the *Omni-modality* approach, where both methods are seamlessly interchanged within the same manufacturing platform. This approach is best suited to laser technology, where recent inventions [27] make it practical to use a single laser for both processes. Despite the convenience of this approach, it alone does not remove the limitations on the resolution that additive and subtractive techniques suffer from, which will be discussed in Sect. 3.

2.1 Additive Manufacturing

Additive manufacturing is regarded as an essential component of the so-called 4th Industrial Revolution, speeding time to market, enhancing productivity and flexibility, and reducing the use of resources. While it is a fast-growing area, the share of additive manufacturing in the global market remains low. This is due to various challenges, such as the high cost of the investment; lack of fast, scalable, serial production workflows; issues with repeatability, quality, and standardisation; and limited possibilities for materials to be printed. While many of these immediate limitations will likely be solved with further engineering effort, the restriction to printing resolution stands out as a fundamental problem. By printing resolution, we refer to the size of the smallest independently printable volume element or the voxel size. In additive manufacturing, which is based on direct writing, a lower limit to the voxel size is set by the size of the energy source activating the process, which is the spot size of the optical beam in the case of laser-based 3D printers. This, in turn, is limited by diffraction to a few 100 nm using optical wavelengths. In the vast majority of the cases, the practical resolution limits are much larger, at $10\,\mu\text{m}$ or even larger. A continuous-wave (CW) laser is commonly used as a precise heat source to melt or sinter the target material, which may be in wire or powder form. Technical factors, such as the size of the powder particles or the diameter of the wire, set the printing resolution. With these techniques, currently achieved resolutions are >20–$30\,\mu\text{m}$ for the powder method and $>200\,\mu\text{m}$ for the wire method, which are much higher than the fundamental limits set by optical diffraction.

The highest resolutions in 3D printing are achieved with the so-called multiphoton polymerisation technique [28]. This technique uses a polymer that is initially in liquid form. It can be solidified through a polymerisation process using light of sufficient photon energy, often near the ultraviolet (UV). For the activation of the polymerisation process, a laser with twice or even triple of the activation wavelength is used. This way, the activation is achieved only by nonlinear optical processes known as two- or three-photon absorption. Such a process requires the nearly simultaneous participation of two or three photons, respectively, the rate of which, in turn, is proportional to the square or the cube of the beam's intensity. As a result of this nonlinear dependency, the activation only occurs near the focal point and is avoided along the beam before or after the focus. This increased localisation compared to linear absorption is the key to the excellent resolutions obtained with this method and has the same physical basis as in multiphoton microscopy [29–31].

Furthermore, the lateral resolution, namely, the smallest lateral size of the material that can be polymerised, is effectively set by the diffraction limit of the multiphoton wavelength rather than that of the exciting laser. This corresponds to half or a third of the excitation wavelength for two- and three-photon processes, respectively. Since the nonlinear absorption process requires extremely high peak powers, ultrafast lasers producing femtosecond pulses are used. It is only this method where printing resolutions are indeed low enough to be limited by optical diffraction. The current state of the art corresponds to a repeatably achievable lateral resolution of ~150 nm, although even 50-nm features have been reported [8].

2.2 Subtractive Manufacturing

Subtractive manufacturing, where the desired object is obtained by removing unneeded parts from a larger object, remains the dominant manufacturing method when the required number of units of the shape is too low for moulding, casting, and similar mechanisms to be practical. In addition to various mechanical techniques, laser processing of materials is ubiquitous. An incredibly diverse set of industrial manufacturing processes, notably cutting, drilling, marking, metals, glass, plastics, ceramics, and semiconductors, are switching from more mechanical techniques to lasers due to their greater precision, freedom from wear, and ease of automation.

Lasers can be grouped according to their temporal characteristics, namely, continuous-wave (CW), nanosecond-pulsed, and ultrafast (sub-picosecond pulses). The laser-material interaction process is purely thermal for CW lasers. With nanosecond pulses, the laser power during a pulse is orders of magnitude higher than the average power. Material removal is through a form of vaporisation, known as ablation. Laser energy is better localised, but the heat-affected zone, where temperatures reach melting levels, is still 0.1–1 mm. The interaction of ultrashort pulses is markedly different. Energy delivery is so fast that the electrons, to which the laser energy is first coupled, cannot reach thermal equilibrium even with their atoms during the pulse. Often, there is no discernible heat zone; ultrafast ablation offers tangible benefits in quality and precision.

Due to their low costs, CW lasers are the most commonly used lasers in subtractive manufacturing. This approach's typical precision and resolutions are in the 0.1–1-mm range. Nanosecond lasers offer better resolutions due to better containment of thermal effects but rarely get better than the 10–100-μm range. Ultrafast lasers provide the greatest precision in micromachining, where structures are as fine as ~1 μm can be controllably and repeatably removed, although 10 μm is more typical. The smallest structures obtained without using near-field effects are in the range of several 100 nm.

A significant advantage of subtractive techniques is that virtually any material can be processed with a matching technique. It is not that there are no limitations. For example, CW lasers are effective only on sufficiently absorbing materials at their wavelengths, and mechanical drilling of brittle materials is tricky, but there is using a suitable technique available. In particular, ultrafast micromachining is nearly universal, from metals to semiconductors and glass to plastics and even biological tissue. This is so because the process of ultrafast ablation is mainly independent of the linear optical properties of the material, allowing even transparent materials to be removed. Also, the nearly complete avoidance of heating means that even thermally sensitive materials can be processed, albeit at low speeds. However, subtractive techniques lack the flexibility of additive manufacturing in creating arbitrarily shaped structures. A line of sight is needed for access, and complex shapes with voids may not be permissible. Furthermore, subtractive processing involves, by definition, the removal of material, which is often discarded. As such, it is highly wasteful.

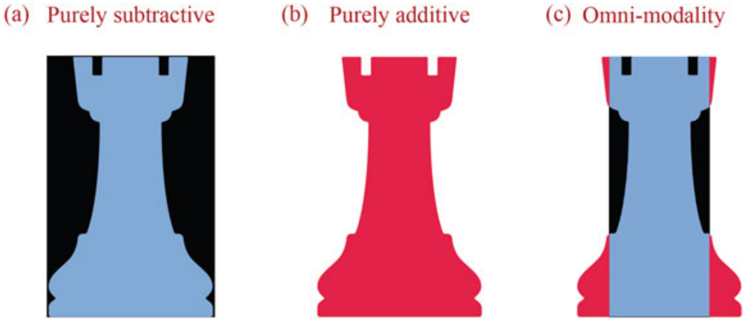

Fig. 4.3 (**a**) In subtractive manufacturing, a 3D object is created by removing it from an encompassing block. (**b**) Purely additive manufacturing starts from scratch, layer-by-layer printing the desired object by combining microscopic-sized parts. A depiction of the *Omni-modality* approach to laser-based manufacturing that seamlessly integrates additive and subtractive manufacturing around a single laser: (**c**) We start from an intermediate-sized block. Then, certain parts are removed, and certain features are added by 3D printing. The size of the original block is freely chosen to minimise the consumption of resources, including energy and time

2.3 The Omni-modality *Approach: Merging of the Additive and Subtractive Manufacturing*

Given the relative advantages and disadvantages of additive and subtractive techniques, we propose to combine them through the use of a single, versatile laser, which exploits the collective ultrafast pulse-matter interactions, and is capable of efficiently performing both techniques. We refer to this approach as the *Omni-modality* approach. One major reason is to reduce manufacturing time and material usage. The benefit of the combined use is a result of geometry in this case. As illustrated in Fig. 4.3, a given object that needs to be created is often of irregular geometry, such that starting from a larger volume into which the intended shape fits requires the removal of substantial volumes (Fig. 4.3a). In contrast, a purely additive approach requires printing the entire object, which is likely to be time-consuming (Fig. 4.3b). Therefore, a logical alternative is to start from an optimally sized block, from which relatively little material has to be removed, and a similarly small amount of additional structure needs to be printed (Fig. 4.3c). Moreover, the combined application of both techniques has various synergistic benefits that transcend increased speed and reduced waste. For instance, the final surface quality achieved with the additive techniques requires post-treatment, which could be improved in situ using the flexibility to use ablation, melting and resolidification, or surface structuring, in any order, according to the need. The latter can include texturing for functionalisation. For example, self-organised patterns[32] may be created on a surface to control its wettability, tribological [33, 34], and biological [35] properties.

2.4 An **Omni-modality** *Laser to Exploit the Collective Ultrafast Pulse-Matter Interactions*

The *Omni-modality* approach is already achievable, but it would require the integration of multiple lasers, significantly increasing the complexity. This is so because lasers used for additive and subtractive processes, particularly ultrafast micromachining, are entirely different from those used for additive manufacturing. Based on our recent invention of the ablation-cooled laser-material removal technique [27], it is now possible to use the same laser for a wide variety of laser-matter interactions. Stated simply, the interactions for additive processes are based on thermal effects, except for the polymerisation method. At the same time, ultrafast micromachining works best in the so-called nonthermal mode, which means heating the nearby areas is avoided. From a physics point of view, the key feature of the ablation-cooled regime is that many, typically thousands of pulses, interact and ablate the material collectively. By judiciously exploiting the *collective* nature of the process, it is possible to alter the interaction physics. Before clarifying this, we will briefly discuss ultrafast ablation and the ablation-cooled regime.

Ultrafast ablation is the most precise mechanism of material removal using a laser beam. The electrons absorb a laser beam's energy first, which transfers to their atoms within a few picoseconds. Femtosecond pulse-material interactions are known as nonthermal because the electrons and the atoms reach equilibrium after the pulse ends. In reality, the terminology of nonthermal is not accurate, as a thermal process does occur at the point of light absorption. A better expression would be nonthermal equilibrium as the aspect that truly distinguishes ultrafast ablation from longer-pulsed or CW lasers is that the electron and atom temperatures are far from thermal equilibrium with each other during the pulse. Regardless of this sidenote on terminology, ultrafast ablation allows for the best localisation of the laser's effect. Surrounding regions of the material that are as close as a few micrometres can be prevented from heating substantially as the part of the material at focus is ablated.

Despite the advantages, ultrafast lasers remain a niche technology compared to the nanosecond and CW lasers despite their supreme precision because ultrafast micromachining is slow and inefficient. The fundamental reason for the low efficiency and speed is the Beer-Lambert law, which stipulates the exponential absorption of light (Fig. 4.4a). Ablation occurs only where the absorbed energy exceeds a threshold. As a result, ablation depth increases logarithmically with pulse energy [36], limiting efficiency.

The exponential tail below the threshold becomes excess heat (Fig. 4.4a, green-shaded region). In the commonly used method of ultrafast ablation, the material is allowed to cool by diffusion of this excess heat to surrounding regions before the next pulse arrives. Typically, the repetition rate is in the kHz range and rarely exceeds 1 MHz. Therefore, the time between the pulses ranges from a microsecond up to a millisecond. If the repetition rate is too high, heat accumulation occurs, and even though femtosecond pulses are used, damage to surrounding regions is observed. In practice, the peak power of the pulses is chosen to be well above the

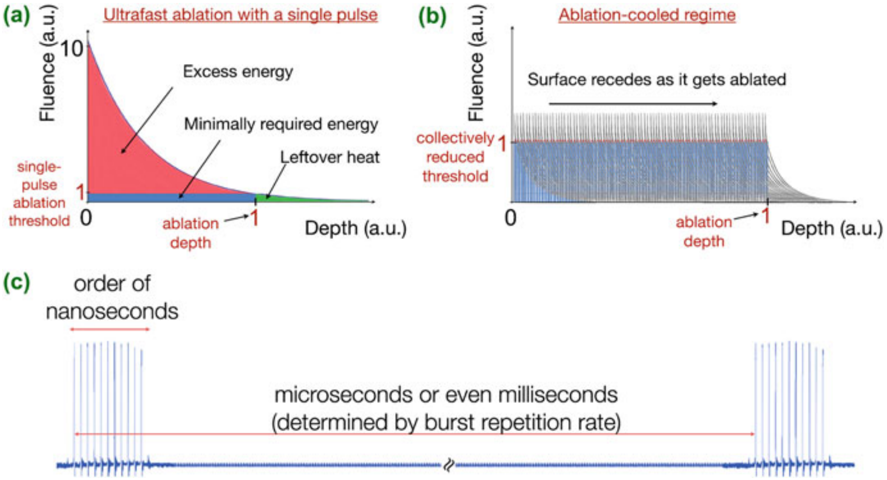
(a)
Ultrafast ablation with a single pulse
Fluence (a.u.)
10
Excess energy
Minimally required energy
Leftover heat
single-pulse ablation threshold
1
0
ablation depth
1
Depth (a.u.)
(b)
Ablation-cooled regime
Fluence (a.u.)
Surface recedes as it gets ablated
collectively reduced threshold
1
0
ablation depth
1
Depth (a.u.)
(c)
order of nanoseconds
microseconds or even milliseconds
(determined by burst repetition rate)

Fig. 4.4 (**a**) Depiction of energy absorption during ultrafast ablation with a single pulse, which avoids collateral heat damage but suffers from low efficiency. (**b**) In contrast, in the ablation-cooled regime, numerous pulses achieve higher efficiency through collective ablation, and the total energy under the many pulses is closer to the minimum energy within the blue-shaded area. (**c**) The temporal profile of a burst train is shown. The burst width is commonly 10–100 ns, and the time between successive bursts is given by the inverse of the burst repetition rate. This figure depicts a burst containing only ten pulses for clarity. Typically, we use bursts containing thousands of individual pulses and the repetition rate within each burst is up to 100 GHz

ablation threshold to minimise the fraction of energy that is left behind in the form of excess heat. However, the fixed exponential form of the absorption necessarily means that much of the absorbed energy becomes extra kinetic energy for the particles to be ejected (Fig. 4.4a, red-shaded region). The resulting logarithmic scaling of the ablated amount with respect to the pulse energy drastically reduces the efficiency of the ablation. Therefore, the exponential form of the Beer-Lambert law limits the repetition rate, and the rate at which material can be removed without causing cumulative heating.

The ablation-cooled laser-material removal method [27, 37] is qualitatively different because thousands of ultrafast pulses, which have extremely short time gaps between them, *collectively* ablate the material (Fig. 4.4b). We use repetition rates up in the multi-GHz range, up to 50 GHz. The delay between pulses is so short that the heat left behind each pulse cannot diffuse before the next pulse arrives, and the temperature at beam focus becomes a *nonlinear iterative* function of all the previous pulses. Excess heat is extracted during ablation to replace diffusion as the dominant heat transfer mechanism, which is the origin of the term *ablation cooling*. We have reported >10-fold higher efficiency with up to 1000 times lower pulse energies. Each pulse is far below the threshold for ablating the material individually.

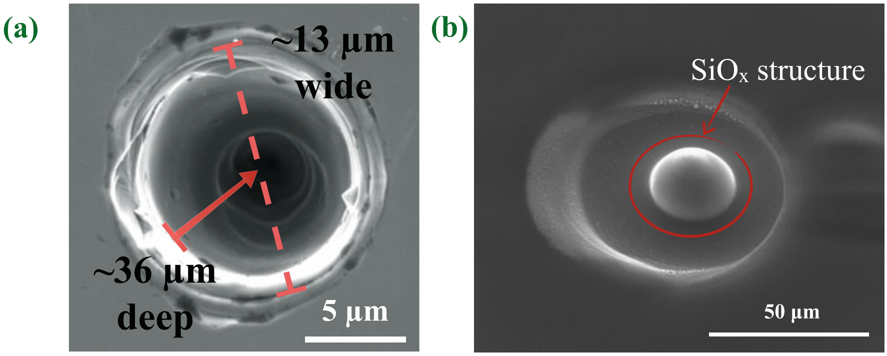

Fig. 4.5 Same sample, same laser, different parameters: (**a**) Top view of the crater created by a single burst as a record-efficient ultrafast ablation of crystalline Si. (**b**) The purely thermal activation of SiO$_x$ growth is induced by keeping the GHz-train of pulses below the ablation threshold. The average power, spot size at focus, wavelength, and pulse duration were approximately the same in both cases. The main difference was the duty cycle of the bursts, which, in turn, changes the pulse energies. The laser is switched from one mode of operation to the other by purely electronic means

An important consequence of the collective ablation is that by changing certain pulse parameters, such as the repetition rate, the interaction can easily be taken below the ablation threshold without changing the average power applied. Once below the threshold, the collective interaction can be switched from a heat-accumulation-free ultrafast interaction to a purely heating mode, even though the pulses are still ultrafast. We can regard this mode as a quasi-CW mode. We have developed a versatile laser system that can electronically switch between different operational modes, namely, a purely thermal excitation mode and an ultrafast ablation mode are well suited to additive and subtractive manufacturing, respectively. The details of the laser setup are beyond the scope of this chapter and will be discussed elsewhere. This laser is based on a so-called burst-mode fibre laser, which was pioneered by one of us [38, 39]. Bursts refer to groups of high-repetition-rate pulses, followed by a long gap of no emission before another burst is produced (Fig. 4.4c). We have shown, experimentally, that the same laser can enact efficient ultrafast ablation and non-ablating thermal excitation by purely electronic reconfiguration of the temporal sequence of the pulses (Fig. 4.5).

In addition to additive and subtractive manufacturing, a third type of laser processing is surface treatment or functionalisation. This can take multiple forms. The most straightforward applications include smoothening a rough surface either by selective melting and resolidification or ultrafast ablation. However, there are exciting additional possibilities that introduce functionalisation, namely, creating a surface texture or structure that achieves a predesigned function. Examples include self-organised patterns (Fig. 4.6a) [32] that may be created on a surface to control its wettability (Fig. 4.6b), tribological [33, 34], and biological [35] properties.

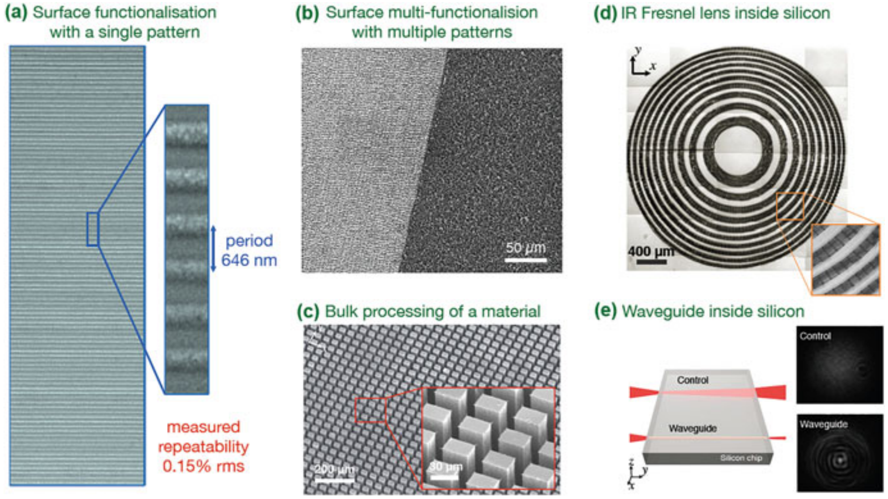
(a) Surface functionalisation with a single pattern
period 646 nm
measured repeatability 0.15% rms
(b) Surface multi-functionalision with multiple patterns
50 μm
(d) IR Fresnel lens inside silicon
y
x
400 μm
(c) Bulk processing of a material
200 μm
30 μm
(e) Waveguide inside silicon
Control
Waveguide
Silicon chip
Control
Waveguide
y
x

Fig. 4.6 Examples of surface and bulk functionalisation using 2D and 3D nonlinear laser lithography technique. Scanning electron microscope images of highly uniform self-organised (**a**) TiO_x nanostructures on titanium [32], (**b**) SiO_x nanostructures on silicon, and (**c**) rectangular blocks carved inside silicon [40]. Optical images of (**d**) an IR Fresnel lens and (**e**) a waveguide written deep inside silicon without processing its surfaces [40]

Furthermore, bulk materials can also be processed to functionalise materials [40] for certain optical, electrical, and optoelectronic applications as can be seen from Fig. 4.6c–e.

3 Three Fundamental Challenges and Laser-Driven Self-Organisation as a Remedy

Despite the rapid progress in 3D printing technologies, three fundamental challenges strongly limit the current paths towards approaching atomic resolution due to technological improvements. Instead, a radically different approach is necessary that circumvents these challenges. Before we propose the use of self-organisation as a possible path, we will discuss these three challenges.

3.1 The Fat Fingers *Problem* ($\lambda \gg a_0$)

As discussed in the preceding section, current approaches to creating arbitrarily shaped objects in a 3D printer are based on what is known as direct writing. Most of the laser-based techniques have micron-scale features sizes. The best resolution or the smallest voxel sizes are obtained using ultrafast lasers driving multiphoton-based polymerisation. In either case, the smallest feature sizes that can be written are ultimately limited by the wavelength of the light, and in the range of several microns for general-use techniques and can approach 100 nm in the case of two-photon polymerisation or laser ablation with very tight focusing. Specific workarounds have been proposed, using plasmonics [41], metamaterials [42], or implementation of super-resolution microscopy techniques [43, 44]. Still, they each introduce new and stringent limitations [45], and the improvements are short of what is needed to approach the atomic scale. The wavelength of light imposes a fundamental barrier that is about several orders of magnitude distant from the inter-atomic distances. We succinctly summarise the fundamental origins of this limitation by the inequality, $\lambda \gg a_0$, where λ is the wavelength of the laser and a_0 is the Bohr radius that sets the order of magnitude scale for the inter-atomic distances.

3.2 The Explosion of Complexity *Problem*

It is conceivable that the *fat fingers problem* will be overcome in the future, for example, with the development of practical x-ray lasers or through the use of electron beams instead of lasers. That possibility prompts us to consider the formidable limitation of the *explosion of complexity*: As the feature size is scaled down, the number of points that must be processed increases cubically for 3D structures. Consider an object of 1 mm^3 in volume, a rather modest size. At present, carving out or additively building such a structure at 1-μm resolution is possible but requires an order of 10^9 steps. Approaching the atomic scale, order of 1 Å, increases the number of steps to 10^{21}, which is in the realm of science fiction. At a rate of a million steps per second, the point-by-point processing of a 1-mm^3 structure at atomic resolution would take millions of years. Even if massive parallelisation and tremendous increases in the speed of processing each point can be anticipated, reaching the capability to process such astronomical numbers of points unlikely to become feasible within the foreseeable future. Equally importantly, the necessity of point-by-point processing of each atom is extremely questionable. One evident reason is that even the spatially most complex materials, such as biological tissue, harbour large amounts of repetition and redundancy. Moreover, the third challenge leads us to question the utility of atom-by-atom processing, even if it becomes feasible and practical.

3.3 The Mischief of Fluctuations

The IBM demonstration was achieved at the cryogenic temperature of 4 K because the random motion of atoms becomes increasingly strong, as temperatures close to room temperature are approached. Therefore, a scaling down of the direct writing approach would have to confront increasingly strong fluctuations. This problem is exacerbated by the fact that the most straightforward solution to the limitations of diffraction is to use lasers with shorter wavelengths, even x-rays to reach the atomic scale. However, this means increasing photon energies, which would transfer even more energy to the atoms, increasing their kinetic motion, not to mention that the atoms would be ionised. Therefore, any method that aims to achieve a particular organisation at the atomic scale has to be compatible with the inevitable thermal motion as the atoms are directed towards a particular atomic structure.

Given these three strong limitations that arise from the physics at play, it is difficult to believe that the currently dominant approach to 3D printing and micromachining, namely, direct writing, can reach the atomic scale, and remain practical, in the foreseeable future, if ever. These difficulties motivate the central thesis of this chapter that self-organisation may be a viable route towards achieving control over the atomic structure.

3.4 Laser-Driven Self-Organisation as a Remedy

Nature demonstrates self-organised pattern formation [46–48] from the atomic to astronomic scales (Fig. 4.7), where the basic units of each physically different system assemble and form structure. Although they are often used interchangeably, and there are efforts to construct formal definitions [49], self-assembly and self-organisation fundamentally refer to the same phenomena of emergent complexity through spontaneous aggregation. Therefore, we will use self-organisation as an encompassing term that includes self-assembly.

The oldest publication documenting observation of self-organised pattern formation in a laboratory setting, as opposed to a natural occurrence, is, to our knowledge, that of convection cells in liquids, and dates to 1901 [53]. The first report of specifically laser-induced self-organised pattern formation is from 1965 [54]. Today, self-organisation has been documented and studied in numerous laboratory systems. Since the earliest studies, self-organisation has been primarily investigated for chemical systems [55–57], which has been later extended to other physical systems [58–63], and fields of engineering [64, 65] and social sciences [66]. There is vast literature on self-organisation with beautiful examples. Unfortunately, it remains mainly a phenomenon observed when encountered, often with fascination. Its deliberate use to achieve technological functions is relatively rare, which we attribute to the lack of a general theoretical framework that allows the prediction of the conditions, such as a set of externally controllable parameters, that will result in a self-organised system to reach a pre-selected pattern. Often one is required to laboriously search for the right conditions or settings in a large parameter and phase space. Despite the enormous progress in self-organisation, the most severe unresolved difficulty from the perspective of a 3D atom printer is the specificity of self-organisation processes. For such a printer to be practical, it should offer near-

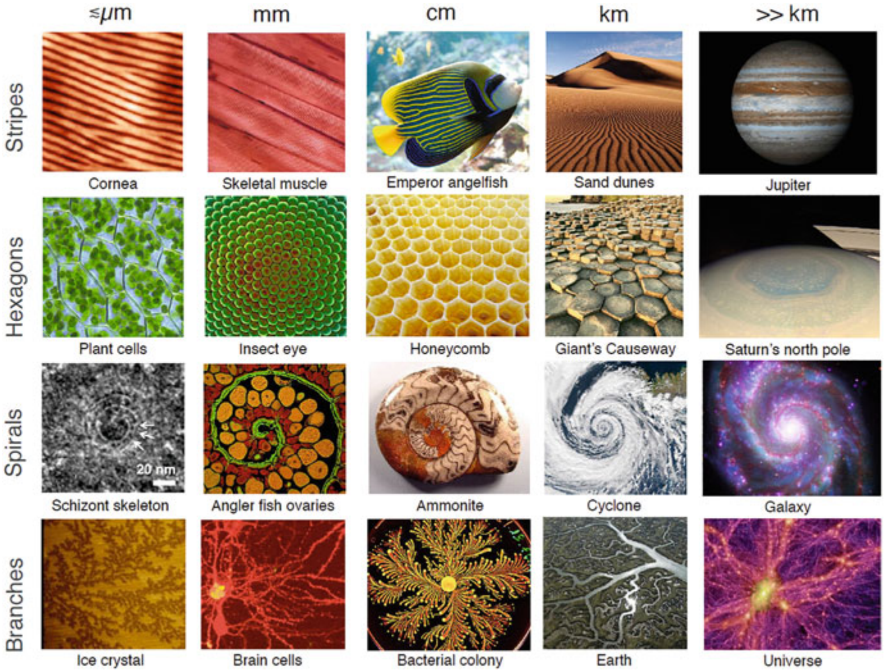
≤μm
mm
cm
km
>> km
Stripes
Hexagons
Spirals
Branches
Cornea
Skeletal muscle
Emperor angelfish
Sand dunes
Jupiter
Plant cells
Insect eye
Honeycomb
Giant's Causeway
Saturn's north pole
Schizont skeleton
20 nm
Angler fish ovaries
Ammonite
Cyclone
Galaxy
Ice crystal
Brain cells
Bacterial colony
Earth
Universe

Fig. 4.7 Similar self-organised geometric patterns are observed across a wide range of spatial scales: cornea [50], skeletal muscle (Image Credit: Michael Abbey), emperor angelfish (Image Credit: Kasper Hareskov Tygesen), sand dunes (Great Sand Dunes National Park; Image credit: Jack Brauer), Jupiter (Image Credit: NASA), plant cells (Image Credit: Kristian Peters), insect eye (Diamondback moth; Image credit: David Scharf), honeycomb (Image Credit: Cordelia Molloy), Giant's Causeway (Image Credit: The Independent), Saturn's north pole (Image credit: NASA), schizont skeleton [51], angler fish ovaries (Image Credit: Michael Gakuran), ammonite fossil (Image Credit: Unknown), cyclone (Image Credit: NASA), galaxy (The Whirlpool Galaxy; Image Credit: NASA), ice crystals [52], brain cells (Image credit: Mark Miller, Brandeis University), bacterial colony (Image Credit: Eshel Ben-Jacob), Earth (Salt marshes, Coto Doñana National Park; Image Credit: Unknown), universe (Computer simulation by The Virgo Consortium; Image credit: The New York Times). This collage is inspired by Philip Ball's book titled *Patterns in Nature*

universality or at least an extensive library of material compositions and atomic structures that can be assembled. Unfortunately, self-organisation literature is by and large material-, size-, shape-, and interaction-specific.

Each demonstration of self-organisation, so far, resulted from carefully engineered inter-particle interactions, interactions between the particle system and its environment, and the external energy source, which prevents constructing a general theoretical framework for self-organised systems. For instance, it is common to engineer the interactions between colloidal particles by decorating them with (bio)chemicals (e.g., Janus particles [67], DNA origami [68] techniques, and alike) or by promoting specific chemical bondings between certain molecules [57]. It is

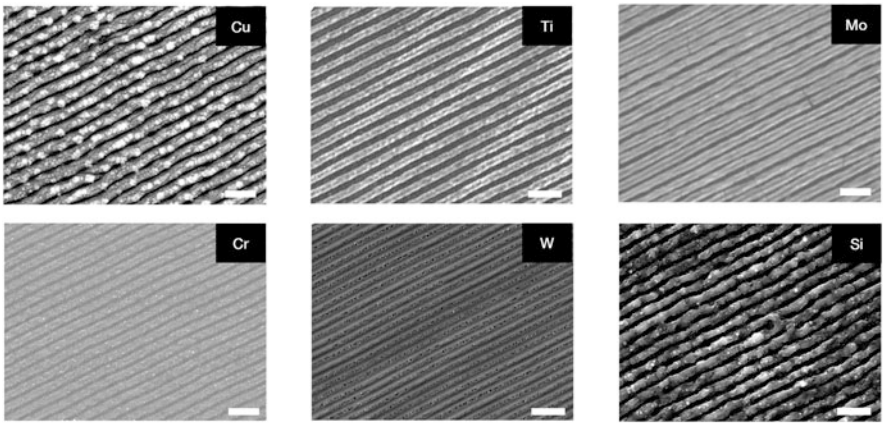

Fig. 4.8 The universality of nonlinear laser lithograph (NLL) [32] is demonstrated on various materials

also popular to engineer the chemical composition of the liquid solutions to direct the movements of such functionalised particles [69]. Other engineered interactions involve particles that can only respond to a specific external energy source, such as a nanoparticle swarm that moves only in the presence of a magnetic field [70], or micron-sized robots that could only be controlled by the electrical signals emitted by an electronic device [71]. All these engineered interactions render the principles leading to self-organisation specific to the materials or chemical used, kind of the external energy source, or to experimental conditions.

As illustrated through the geometric patterns of Fig. 4.7, self-organisation occurs over vastly different physical scales but yields similar features in these unrelated systems. A most pertinent question is whether we can harness this capacity to achieve a high degree of independence of directed self-organised systems from their specifics. This is a matter of great practical importance as it would address one of the most limiting aspects of the self-organised approach, namely, that virtually every experiment has to be redesigned when the materials or the interactions involved are changed.

There is accumulating evidence that the answer may be affirmative, as demonstrated through both NLL [32] and universal dissipative self-assembly [62] methods we introduced to the scientific literature. We have already confirmed that NLL is able to produce the same structures using Ti, Mo, W, Cr, Cu, Al, Si, GaAs, and glass, some of which can be found in Fig. 4.8.

Even more dramatically, we have achieved self-assembly of ∼3-nm-large CdTe quantum dots suspended in water (or various chemicals), 500-nm-large polystyrene spheres in water, 0.7-μm-large soft spheres of *Micrococcus luteus* and ∼1-μm by ∼2-μm in size, rod-like *Escherichia coli* bacterial cells, ∼5-μm elliptical *Saccharomyces cerevisiae* yeast cells, and ∼15-μm-large MCF10A normal human breast cells, which obey the same physical rules (Fig. 4.9) [62]. In all of these

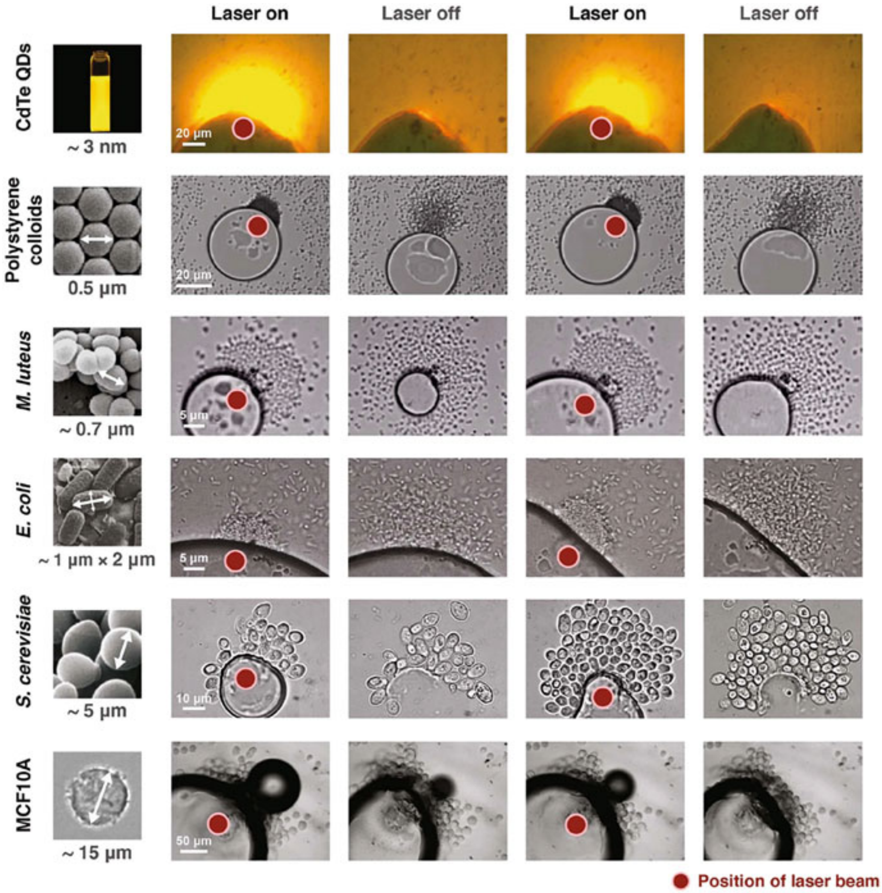
Laser on
Laser off
Laser on
Laser off
CdTe QDs
~ 3 nm
20 μm
Polystyrene colloids
0.5 μm
20 μm
M. luteus
~ 0.7 μm
5 μm
E. coli
~ 1 μm × 2 μm
5 μm
S. cerevisiae
~ 5 μm
10 μm
MCF10A
~ 15 μm
50 μm
● Position of laser beam

Fig. 4.9 Dissipative self-assembly universality demonstrated with various particles and organisms [62]

examples, a few experimental parameters, such as laser power, naturally need to be adapted to achieve optimal results. Still, the same qualitative self-organised behaviour is observed, which suggests a high degree of universality and material independence. Setting aside the promising experimental demonstrations, these two methods and other model systems with dissimilar dynamics have to be further studied to formalise a general theoretical framework to create design recipes for an atom printer.

The following subsection provides arguments on how ultrafast lasers are outstanding candidates as model systems to study self-organisation and also tools to drive it. We will further discuss how they help address the three fundamental challenges we identified at the beginning of this section.

3.5 The Promise of Ultrafast Lasers

The (passive) modelocking of lasers is arguably the most successful application of human-made self-organisation. First demonstrated in 1964 [72], passive modelocking developed to underlie the science and technology of ultrafast optics with diverse applications, including precision material processing, optical imaging, frequency combs, and high-field physics, among many others. At its core, modelocking is the self-organised formation of ultrafast pulses in a laser cavity, which is achieved because the frequency modes of the laser cavity experience higher net laser gain when they mutually lock up in phase [73]. Perhaps because of its success, the fact that self-organisation underlies the generation of ultrafast pulses through modelocking may be overlooked [74]. This is a pity since the modelocking of lasers is an excellent model system for 1D self-organisation that can be described with a master equation introduced by Hermann A. Haus in 1991 [75]. The recent advent of spatiotemporal modelocking extends it to 2D and 3D self-organisation. We envision that such efforts may even build upon Haus' master equation as an important step towards a general theory of self-organisation.

Self-organisation is dissipative. From the perspective of nonlinear systems, Liouville's theorem shows that conservative systems cannot support attractors to which an extended portion of the phase space decisively converges. Similarly, the sustained temporal evolution of a statistical system requires detailed balance to be broken; a self-organised process needs to be driven away from thermal equilibrium by an external energy flux accompanied by dissipation. Numerous mechanisms can introduce gradients in temperature, pressure, concentration, probabilities, or any other parameter that is relevant to that particular system. In *Nature*, this source can be, for instance, the Sun, or tidal and geological heating, or chemical reactions, as in ATP synthesis by electrochemical gradients [76]. In the laboratory, it can be electrical, optical, a plasma source (e.g., magnetrons in a vacuum system), and chemical reactions, or a laser. Fundamentally, which energy source is used does not matter; the important thing is to create gradients in transition/interaction probabilities. Nevertheless, among these, lasers, particularly ultrafast lasers, stand out with a unique combination of advantages.

Ultrafast lasers can induce spatiotemporal thermal gradients on the materials they interact with. Single or multiphoton absorption at a material converts the energy of the pulses into nearly instantaneous local heating, which can be used to create highly configurable adjustable spatiotemporal thermal gradients. The material could be a metal, semiconductor, glass, ceramic, a polymer [32], colloidal solution of nanoparticles [58, 62] or living organisms [62], a transparent material [40], and a thin film grown under vacuum [77], among other possibilities. Peak thermal gradients of $>10^7$ K/mm can momentarily be achieved using ultrashort pulses despite delivering only minuscule amounts of energy (nanojoules per pulse).

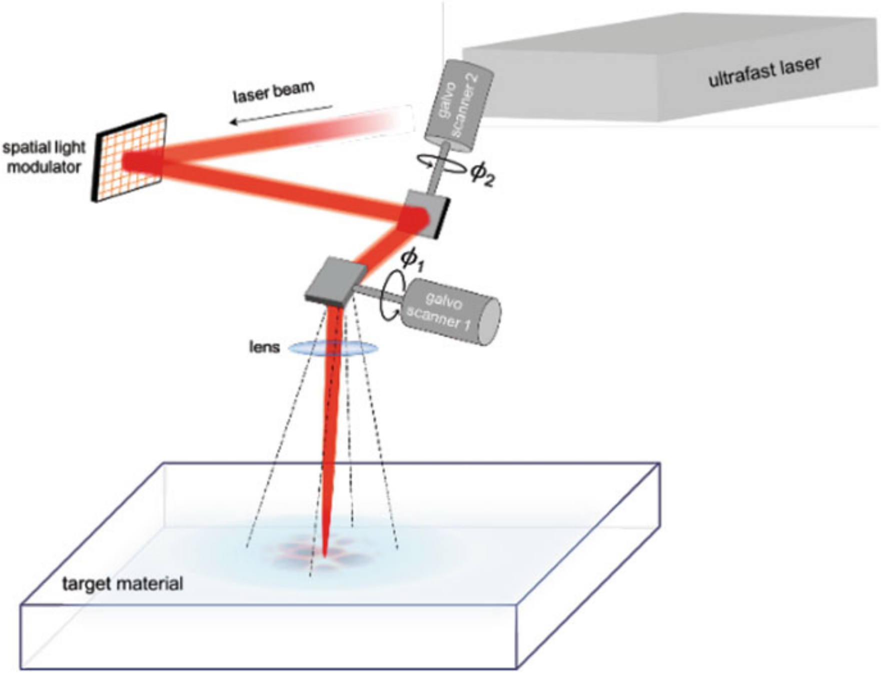

Fig. 4.10 The most common method of using an ultrafast laser coupled to a rapid beam scanner followed by a lens or objective that focusses the beam on the target material. Shown here are a two-axis galvanometric scanner that allows beam displacement within ∼1ms and a spatial light modulator that allows wavefront and beam shaping, as well as displacement

Laser power, thus the rate of energy delivery, can be electronically adjusted in nanoseconds. The beam from a modelocked ultrafast laser can be shaped to produce any desired shape at focus, limited only by diffraction, using the millions of pixels of a spatial light modulator as actuators [62]. The focussed beam can then be moved to any point on the surface or at any depth in the case of a transparent target within microseconds to milliseconds [40]. Using these capabilities, one can create nearly arbitrarily sculptured, highly precise, and extraordinarily steep thermal gradients (Fig. 4.10).

Nevertheless, the advantages of ultrafast lasers in the creation of steep thermal gradients appear to have been underappreciated, and the overwhelming majority of their usage focussed on ultrafast measurements of transient phenomena and excitation of multiphoton processes, e.g., for microscopy, or, even more commonly, to ablate materials [78, 79]. The last one is merely an extreme consequence of creating a large thermal gradient.

3.6 Overcoming the Fat Fingers *Problem*

In self-organisation, the entire structure, from its finest features to the overall pattern, is determined by the nonlinear interactions. As such, there is no need for the energy source, say, the laser beam, to be localised at the same scale as the finest features to be created. Often, the pattern formation is driven by a thermal, chemical, and another gradient, which is not even in the plane of the patterns. Consider the Rayleigh-Bènard convection cells, which are fluid patterns that form due to a uniform temperature difference along the direction *perpendicular* to the plane of the patterns [46].

Using well-controlled spatiotemporal thermal gradients to direct self-organisation provides a most interesting but hitherto unrecognised route towards beating the diffraction limit. The beam size is not relevant to the smallest features of the pattern. Still, it does limit the size of the pattern or the smallest distance over which one self-organised pattern can turn into a different one. In simpler terms, the diffraction limits the smallest spatial region within which the structure can be controlled independently, which limits the smallest voxel size. Even within the confines of this limitation, the smallest region, where a given self-organised structure is controllably created, can be substantially smaller.

Consider a dynamic process that leads to a particular self-organised material that adopts a given atomic structure only over a finite temperature range, $\varDelta T = T_{\max} - T_{\min}$. Diffraction limits the smallest spot that a laser beam can be focussed to, known as the Abbe limit [80]. The thermal gradient generated by the absorption of a short laser pulse is given by the ratio of the temperature difference created by the absorption of a laser pulse to the beam spot size. Diffusion reduces this gradient over time, but in the time scales relevant to ultrashort pulses and processes, the thermal gradients that can be reached with a diffraction limited beam can be nearly as much as $(T_c - T_o)/d \approx T_c/d$, where T_c is the critical temperature beyond which ablation occurs (in the range of 10^4 K), T_o is the ambient temperature (say, $\sim$300 K), and $d = \lambda/(2NA)$ is the Abbe limit (for green light, $\sim$250 nm), where NA is the numerical aperture. For a sufficiently fast process for which we can ignore the effects of diffusion, our hypothetical self-organised structure can be confined within a spatial region of size $d\varDelta T/T_c$. Since it is possible that $\varDelta T/T_c << 1$, the fundamental limits to spatial localisation of self-organised material forms are not strongly limited by diffraction, and feature sizes considerably smaller than the diffraction limit are, in theory, achievable. It should be emphasised that creating a structure confined to a slice along the slope of a diffraction-limited beam is not independently controllable and will apply to specialised usage scenarios. It is safe to consider the diffraction limit as the smallest voxel size for all intents and purposes. However, as discussed below, the self-organised structure within each voxel is not limited by diffraction. Substantial control over the atomic structure appears to be entirely possible. In Fig. 4.11, we present examples from our recent work, conducted in this direction.

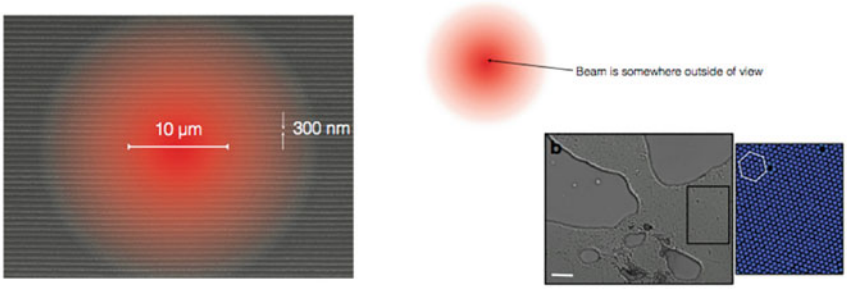

(a) Structures much smaller than the beam:

(b) When the beam is not even near:

10 µm
300 nm
Beam is somewhere outside of view
b

(c) Structures far beyond the diffraction limit:

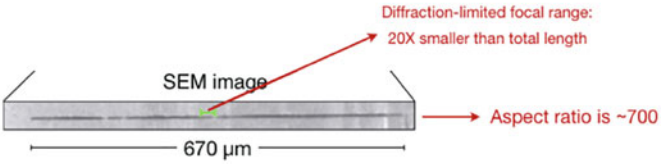

Diffraction-limited focal range:
20X smaller than total length
SEM image
Aspect ratio is ~700
670 µm

(d) Control over structure in the few nanometer range with a laser

(e) With magnetrons:

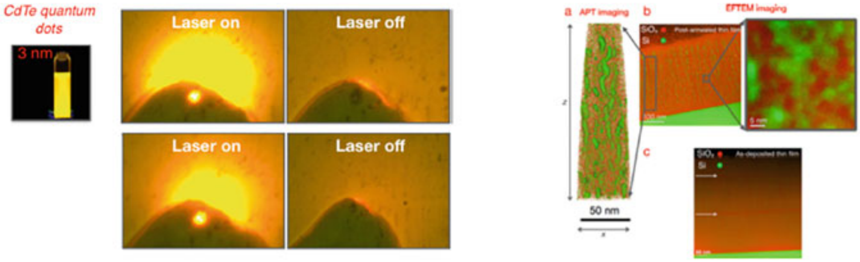

CdTe quantum dots
3 nm
Laser on
Laser off
Laser on
Laser off
a APT imaging
b
EFTEM imaging
SiO2
Si
Post-annealed thin film
c
As-deposited thin film
50 nm

Fig. 4.11 A representative selection of recent experimental demonstrations showing fine control in the microscopic even few-nanometre range can be achieved without requiring energy flux with comparable foci. (**a**) Laser-induced periodic surface structures (LIPSS) with unprecedented uniformity and repeatability formed by scanning a Gaussian beam over the surface, known as nonlinear laser lithography (NLL) [32], is shown in comparison to the much larger beam used to create them. (**b**) A colloidal aggregate is formed by the dissipative self-assembly method shown [58], where the laser beam driving the process does not even necessarily overlap with the aggregate. (**c**) In-chip self-organised line formation *via* NLL forming structures far beyond the diffraction limit [40]. (**d**) Even ∼3 nm-large quantum dots can be collected with the dissipative self-assembly method61 shown in (**b**), where in both cases, the features of the self-organised pattern are determined by the interaction dynamics and not the size of the laser beam. (**e**) Even crude spatiotemporal thermal gradients can lead to controlled atom-by-atom formation of a complex structure, an anisotropic random network of Si quantum dots. The network is anisotropic at the mesoscopic scale but isotropic in the nanoscale of ∼10 nm, confirmed by atom probe tomography (APT) of structure and independently by energy-filtered transmission electron microscopy (EFTEM). A control experiment -c- proves that the origin of the multiscale structure is the spatial thermal gradient [81]

In nonlinear laser lithography (NLL) [32, 40] and numerous related works, the laser beam is homogenous and much larger (by 10–100 times) than the periodic structures that are self-organised, which are, in fact, smaller than even the laser's wavelength (Fig. 4.11a and 4.11c). This decoupling of the smallest features and the spatial localisation of the laser beam is even more dramatic in the case of dissipative colloidal self-assembly [58, 62] (Fig. 4.11b and d). In this case, the self-organised aggregate is not even directly underneath the laser beam but typically displaced considerably, confined within a cavity bubble. The laser-induced Marangoni flows give rise to the aggregation process through drag forces [58, 62]. Furthermore, since the drag force is equally present for small and large particles, we have shown that the same self-assembly process works with CdTe quantum dots, as small as 3 nm, which are nearly four orders of magnitude smaller than the size of the laser beam. The laser-based control in the examples given above involves thermal gradients with a relatively high spatiotemporal resolution, whereby it was possible to achieve control over the self-organised patterns. However, it is possible to influence the atomic-scale arrangement even by using thermal gradients with low spatial resolution along one direction (Fig. 4.11e) [81].

It is often the case that a steady state of a self-organised system is born out of fluctuations that grow through a positive feedback mechanism (also known as amplified fluctuations [82]), which is counterbalanced by a negative feedback mechanism that is initially non-existent or negligibly weak, but becomes important once the amplitude characterising this state grows beyond a certain size. Thus, a steady state is a dynamic balance that continues to exist in the presence of fluctuations. Luck or serendipity has nothing to do with achieving these results as the self-organisation in these different systems is guided by controlling the intrinsic feedback mechanisms *via* a few external parameters. The key is to identify the positive and negative feedback loops and to which control parameter(s) and in what way they are responding. Here, a positive feedback loop refers to the situation where a certain change in the initial status of a system induces further changes, often leading to an exponential growth of the tiniest variation that typically arises from fluctuations, noise. An especially well-known example is the onset of coherent laser oscillation starting from spontaneous emission in an optical cavity that provides feedback. Eventually, a saturation mechanism (a negative feedback loop) is induced, slowing down the growth rate. A negative feedback loop acts to oppose a change, and it is known as an inhibitory process in chemistry and biology. Negative feedback is the predominant form of external feedback applied in engineering applications, often to reduce noise. Positive feedback is regarded as a source of instability and is desperately avoided. Our interest here is when both positive and negative feedback are internal and intrinsic to the system's dynamics. Figure 4.12 shows the depictions of the processes that resulted in the self-organisation of structures shown in Fig. 4.12. Below, we will describe the intrinsic feedback mechanisms guiding self-organisation.

The main reason for picking these model systems as case studies is that they are entirely as different from each other in physical details. At the same time, self-organisation is born out of amplified fluctuations and guided by their intrinsic feedback mechanisms. Another reason for choosing them is that each is more conveniently described by one of the two major classes of theoretical models commonly used to describe pattern formation. These are, namely, models based on an interaction kernel (involving integro-differential or integro-difference equations) or a generalised reaction-diffusion model (a Turing-like instability, involving partial differential equations) [83]. We should stress that these formalisms are interchangeable and do not represent any fundamental differences.

Nonlinear laser lithography (NLL) judiciously exploited intrinsic feedback mechanisms to achieve self-organised structures of extremely periodic structures with uniformity (as characterised by Allan deviation) of 0.1 nm for structures with a period of 700 nm measured over long distances (extending over 100s of μm) [32]. The top row of Fig. 4.12a shows the interaction of femtosecond pulses with the material surface. Each pulse scatters from the pre-existing roughness on the surface or by the nanostructures if already formed. The scattered light, propagating as surface waves, interferes with each other. At the points of constructive interference, the intensity is higher, which modifies the surface. The modified surface scatters the lights of the next pulse differently, which reinforces further modification, constituting a positive feedback mechanism. The bottom row depicts the negative feedback that regulates the growth of the structures. Atmospheric oxygen cannot penetrate through the growing oxide structure, limiting the reaction and preventing further growth of the structure. In the 3D-NLL case (Fig. 4.12b), a self-focusing laser beam modifies the interior of the silicon chip without leaving any damage to its surfaces (positive feedback loop). The refractive index of the modified regions changes, which shifts the focal point of the iterative pulses and limits further growth of the self-organised structures (negative feedback).

Similar to the NLL case, dissipative self-assembly of colloids (Fig. 4.12c) benefits from the feedback mechanisms, where ultrafast pulses create nonlinear thermal gradients, which, together with the surface effects, give rise to Marangoni flows [58, 62]. A positive feedback mechanism occurs between the fluid flows that drag the colloidal particles and promote aggregation of the particles. The growth of the aggregates is counterbalanced by strong Brownian motion, which functions as a limiting force to the growing aggregates. In the vacuum deposition case shown in Fig. 4.12d, deposition of Si and SiO_2 from two targets that were activated by magnetrons, "rained down" on a substrate at the bottom of a vacuum chamber. A spatial gradient formed in the vertical (growth) direction of the substrate because of the steep temperature difference between the "hot" atoms and molecules that were energised by the magnetrons, and the cold substrate, which was kept at room temperature. By controlling the power of the magnetrons for each of the targets, the energies of the Si atoms and the SiO_2 molecules were controlled. Here, we promoted nanocrystal growth in the vertical direction to decrease the onset of percolation for achieving a network structure where individual quantum dots are connected by Si bridges (positive feedback). We also limited full phase separation of metastable oxides into Si and SiO_2 to avoid further growth of QD diameters (negative feedback).

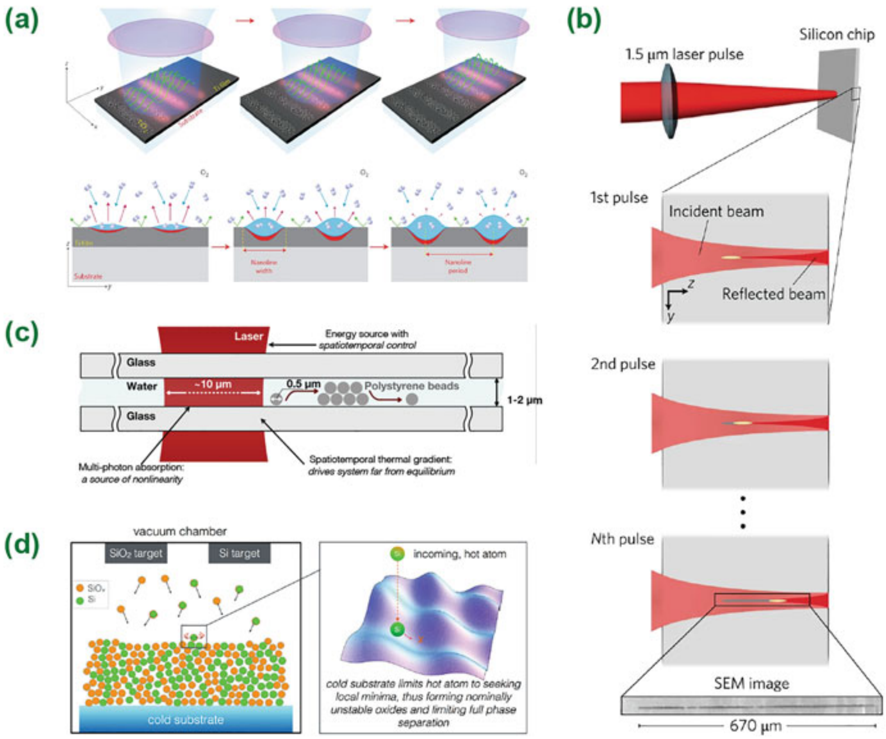
(a)
(b)
Silicon chip
1.5 μm laser pulse
1st pulse
Incident beam
Reflected beam
z
y
2nd pulse
Nth pulse
SEM image
670 μm
(c)
Laser
Energy source with spatiotemporal control
Glass
Water
~10 μm
0.5 μm
Polystyrene beads
1-2 μm
Glass
Multi-photon absorption: a source of nonlinearity
Spatiotemporal thermal gradient: drives system far from equilibrium
(d)
vacuum chamber
SiO₂ target
Si target
SiOₓ
Si
cold substrate
incoming, hot atom
cold substrate limits hot atom to seeking local minima, thus forming nominally unstable oxides and limiting full phase separation

Fig. 4.12 Schematic representations of methods that lead to self-organised structures shown in Fig. 4.10. (**a**) 2D-NLL [32], (**b**) 3D-NLL [40], (**c**) dissipative self-assembly of colloids [58, 62], (**d**) self-assembly of Si atoms in a vacuum chamber [81]

In all these examples, the fundamental reason why self-organisation works so well is that the feedback mechanisms driving the processes are nonlocal. Nonlocality refers to the situation where the feedback mechanisms acting at a particular point in space depend not only on the characteristics of that point but also over an extended region surrounding that point. This dependence can be described most conveniently in an integral form using a kernel that characterises the nonlocal nature of the interaction, not only for the examples we have shown in Fig. 4.11 but also for diverse systems, ranging from self-organised vegetation patterns [63] to spin glass systems.

3.7 Overcoming the Explosion of Complexity

Unlike the case of direct writing methods discussed in Sect. 2, when thousands of particles [58, 62], or even an astronomical number of atoms [32, 40, 81] self-organise into a predetermined pattern, there is no need to control individual particles. The concept of self-organisation relies on the possibility that the system of interest, which typically has numerous degrees of freedom, can somehow be directed using just a handful of control parameters. This becomes possible if nearly all of the internal degrees of freedom become locked to each other by the nonlinear interactions following the "slaving principle" developed by H. Haken in the 1960s and 1970s [84, 85]. The particular pattern itself is selected by choosing suitable values for one or at most a few parameters. Because the slaving principle eliminates the need to control a vast number of degrees of freedom, the number of required processing steps is reduced to adjusting a few control parameters. This, in turn, reduces the time needed to print a structure in case of a printer exploiting self-organisation. In a sense, self-organisation automatically achieves a vast degree of parallelisation, as the internal degrees of freedom organise themselves through their nonlinear interactions [62, 86].

The locking of the internal degrees of freedom is best illustrated by the well-studied example of locking of the frequency modes in a laser during the onset of modelocking [74]. A laser's cavity imposes discrete longitudinal modes, equally spaced in frequency. In an ordinary multimode laser, a number of these modes are excited and oscillate independently of each other with random relative phases. In the case of modelocking, thousands to millions of modes spontaneously lock up, i.e., they develop fixed phase relationships. This corresponds to forming a coherent structure in time, namely, an ultrashort pulse. Various interrelated formulations have been developed, whereby differential equations are typically used by taking the continuum limit of the vast number of modes. To better illustrate the slaving principle, here, we retain the discrete modes [87]. The electric field within the cavity can be written as

$$E(z,t) = \sum_m a_m(t) e^{-i(\omega_0+\omega_R m)t} e^{(k_0+\Delta k m)z} + c.c., \tag{4.1}$$

where $\Delta k = 2\pi/L$, $\omega_R = \nu_g \Delta k$ and k_0 and ω_0 are the central wavenumber and frequency, respectively. Then, the equations of evolution for these modes can be written as

$$\dot{a}_m = (i\gamma_d - \gamma_g)m^2 a_m + (i\gamma_k - \gamma_s) \sum_{j-k+l=m}^{N} a_j a_k^* a_l + g a_m, \tag{4.2}$$

where the parameters γ_d, γ_g, γ_k, γ_s, and g correspond to various effects, such as gain, nonlinearities, and N, which is the maximum number of frequency modes the laser cavity supports. Modelocking is obtained for certain values of these parameters. A special case with an analytic solution is the formation of a soliton-like pulse [88]. All the $2N$ degrees of freedom corresponding to the amplitude and phase of a_m become fixed, save for noise due to quantum fluctuations or of technical origin. In the time domain, a pulse emerges with the form, $A_p \mathrm{sech}(t/\tau_p)$, where A_p

and τ_p are its amplitude and temporal width, respectively, as determined collectively by a_m. In this case, the so-called soliton area theorem provides a straightforward relation that we can conveniently use to illustrate the principle of slaving. The amplitude and temporal width of the soliton are interrelated by $A_p^2 \tau = \gamma_d / \gamma_k$, and the energy of the soliton is $E_p = A_p^2 \tau_p$, where, in both cases, we neglected proportionality constants of the order of 1. Let's take a moment to contemplate this result. A modelocked laser contains very many modes or degrees of freedom. After the onset of modelocking, a coherent structure arises. Its emergent characteristics, such as width and amplitude, are determined collectively by these many degrees of freedom. A handful of parameters influence these characteristics; for instance, by controlling the pump power of the laser, which sets E_p and by changing the dispersion of the cavity, γ_d, we can independently set the amplitude and width of the pulse. This is how up to millions of degrees of freedom, a_m, become fixed up to an overall phase. Furthermore, the overall macroscopic characteristics of the pulse can be controlled through the two parameters of pump power and dispersion alone.

3.8 Taming the **Mischief of Fluctuations**

The importance of fluctuations seems to have been appreciated mainly when it was desired to suppress them. The notion that fluctuations can be an excellent control tool appears to go unnoticed. This is hardly surprising given that the principal aim of the large engineering field of control theory is to suppress noise. While this is undoubtedly desirable for linear and near-equilibrium systems, as we will argue below, this is not always the case for self-organisation, where noise, fluctuations, defects, and all other incoherent modulations (or even coherent ones) can increase robustness, improve evolutionary fitness, and enhance functionality or are outright necessary for emergence.

When a spatiotemporal energy flux is introduced to a system at thermal equilibrium, first, dissipation breaks detailed balance, leading to a net flow (of mater, chemical reactions, trajectories of particles, probabilities, etc.) both in space and in time. This leads to significant amplification of the fluctuations, often called critical fluctuations or giant number fluctuations. Unlike in closed systems (already at or approaching thermal equilibrium), the fluctuations become correlated in open systems (sustained far from equilibrium), ergo do not satisfy the central limit theorem. As a result, not only is time-reversibility broken, but new forms of nonlinearities arise from the newly formed correlations. Under such conditions, the system is not stationary; it is driven from one state to another. The number of states that a complex system can be driven to is directly related to its nonlinear interactions with the net flux. High nonlinearity translates into an expanding phase space with an abundant number of states. However, opening up the phase space to exploration by the system does not guarantee that the system will be able to visit a wide variety of states. For that, it needs fluctuations. Fluctuations have to

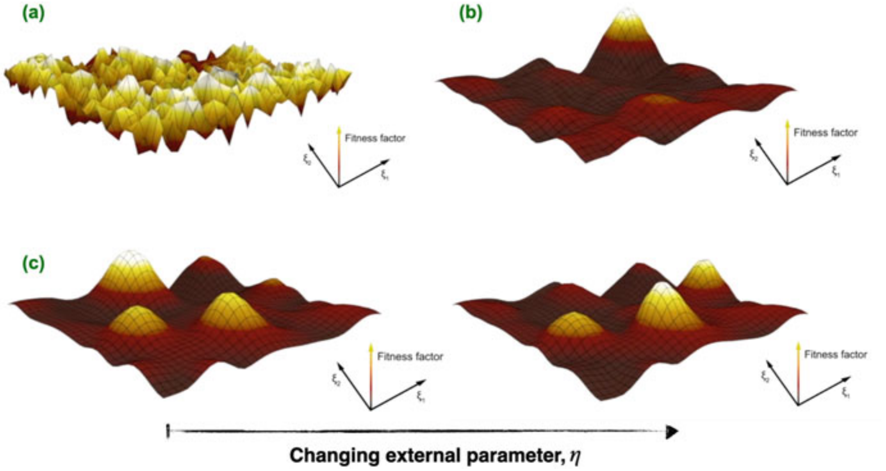

Fig. 4.13 (**a**) A Badlands landscape has many peaks of comparable size, whereas (**b**) a Fujiyama fitness landscape has a dominating peak. In the context of a 3D atom printer, an intermediate landscape with several peaks corresponding to a different atomic structure is of greater interest. The most prominent peak must have a sufficient margin. The fluctuations must be present and strong enough to ensure that the system reliably converges to the most prominent peak each time it is started from different initial coordinates. (**c**) By changing the control parameters, such as the power of the laser beam that drives the self-organised process, the landscape is deformed to make the peak corresponding to the desired atomic structure as the most prominent peak

be strong enough to "shake" the phase space to turn the static steady states into dynamic ones so that there is no single thermodynamic minimum energy state but a multitude of them, constantly evolving. Undisputedly, there is no static energy landscape anymore; instead, borrowing the concept from evolutionary biology, there is a "fitness landscape."

Fitness landscapes are useful conceptual tools for understanding the evolution of a self-organising system [89, 90], first introduced by John Maynard Smith in 1970. A fitness landscape can be thought of as a generalisation of the potential surfaces for conservative mechanical systems. In evolutionary biology, fitness represents the net reproductive rate, determining the success of a particular genomic sequence in a population. The coordinates of this landscape correspond to the different configurations of the genomic sequence. Unlike the mechanical analogy, the landscape is not static but changes dynamically as the system evolves. A population, an ensemble of many individual organisms with different genomic sequences, tend to evolve towards higher fitness values. In the analogy to an evolving self-organising system, the landscape coordinates correspond to different values in the system's phase space. In place of fitness, we have the growth rate of a given pattern. In both cases, the system tries to climb the peaks in their high-dimensional landscapes.

These fitness landscapes may have many peaks of comparable size, known as a Badlands landscape (Fig. 4.13a), or it can have a single peak, known as a Fujiyama landscape (Fig. 4.13b). Without fluctuations, a self-organised system will get stuck to whichever peak it happens to start close to, where each peak corresponds to a different self-organised pattern. The initial condition for a self-organised system corresponds to different starting coordinates in this landscape. Unless there is a single peak, as in the Fujiyama landscape, different initial conditions will lead to different peaks or patterns. Given our interest in controlling self-organisation to achieve a pattern, i.e., an atomic structure, of our choosing, it is imperative that the parameters must be chosen such that there are multiple peaks in the landscape. Control of self-organisation can be understood in this analogy as changing the control parameters, such as the laser power, thus deforming the landscape to make a different peak, the tallest peak (Fig. 4.13c). However, it is not guaranteed the system will find its way to the tallest peak, where there are multiple peaks. A rougher landscape is much more complex for the self-organising system to climb as the smaller local peaks form traps that the system cannot escape. In practice, this means that a different self-organised pattern, i.e., atomic structure, from what was intended may be erroneously obtained due to slight variations in the initial conditions. This is highly undesirable for the 3D atom printer.

Fluctuations come to our aid here. Any perturbation due to the fluctuations can be thought of as a little kick in the phase space, which can dislodge the system from being trapped at a small peak, allowing the self-organising system to explore its landscape more fully and evolve to the tallest peak. In this case, quite contrary to the case of direct writing, the presence of fluctuations is not detrimental but essential for the self-organisation to develop near independence from the initial conditions and to exhibit universality. Furthermore, since the fluctuations are part of the intrinsic feedback loops in complex natural systems and our experimental designs (Figs. 4.11 and 4.12), there is no need to suppress or control them extensively.

4 From Self-Organisation to a 3D Atom Printer

In this final section, we discuss how a 3D atom printer may be constructed with the aid of self-organisation. As mentioned in Sect. 2, 3D printer technology based on direct writing is highly developed and versatile at the microscopic scale but can barely reach the mesoscopic scale. Three hard limitations arising from fundamental physical effects prevent further scaling down the resolution. At the same time, as discussed in Sect. 3, laser-driven self-organisation is not directly limited by the same three challenges. As a result, self-organisation could allow the creation of materials with control over the structure down to the atomic scale.

In *Nature*, highly complex structures spontaneously arise through self-organisation (Fig. 4.7). This is observed ubiquitously at all scales. The most elaborate structures ever observed are, arguably, those of biological organisms and, among them, probably, the brain. Biological structures grow through what may be thought of as a myriad network of multiple self-organised processes, often arranged hierarchically and developed by evolution over aeons. The relatively simpler inorganic but highly complex structures and living organisms prove that

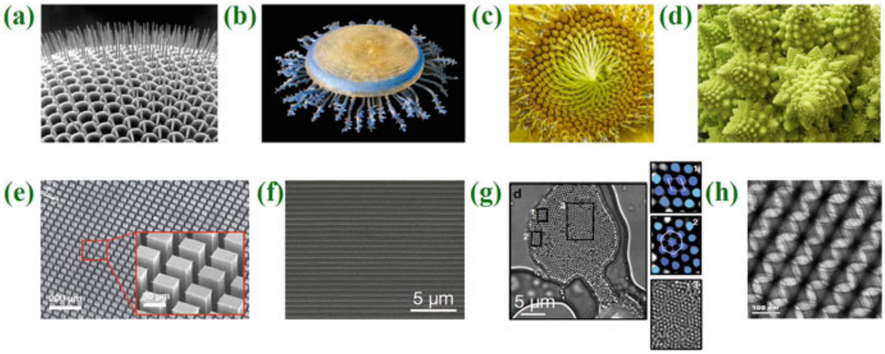

Fig. 4.14 Examples to self-organised structures exhibited by living organisms: (**a**) fly eye (Image Credit: Unknown), (**b**) jellyfish *Porpita mediterranea* (Image Credit: Max Mackenzie), (**c**) sunflower (Image Credit: Unknown), (**d**) cauliflower (Image Credit: WindyPower, Deviant Art). Examples of self-organised structures we have created in the laboratory: (**e**) 3D structures created in silicon [40], (**f**) 2D patterns created on titanium [32], (**g**) self-assembled colloids [58], (**h**) a self-assembled hierarchical zeolite structure

complex structures can be created purely by self-organisation. We believe that a 3D printer operating similarly is possible, where the printing processes do not involve point-by-point processing at any step or scale, quite unlike existing 3D printers. Instead, the intended object is printed entirely by self-organised processes, which are still externally driven. The conditions and the parameters that drive vary over time, but with the complete elimination of the point-by-point process, the final resolution of the structure is not explicitly determined at all. However, our present understanding of self-organised processes is in its infancy. We have barely begun to understand how to steer a single self-organised process to achieve a specific pattern. Complex self-organisation at multiple scales requires hierarchical self-organisation, which is even less understood. The perspective for a 3D atom printer that we discuss here is that of a simpler, less ambitious but better-understood arrangement. In this case, self-organisation has the more modest role of bridging the mesoscopic scale, where a direct writing approach is permissible, and the nanometric and atomic scales (Fig. 4.14).

In order to make our discussion more concrete, we next discuss the broad outlines of a specific implementation of a 3D atom printer that could be built using existing technology. We consider a setup (Fig. 4.15) that is broadly based on our earlier demonstration of vacuum deposition with a static spatial thermal gradient [81] but introduces the dynamic spatiotemporal thermal gradients of the dissipative dynamic self-assembly [58, 62]. The elements making up the material to be deposited are generated by ablation from targets inside the chamber. There may be multiple targets, but we depict two here for simplicity. These targets may be, for instance, Si and SiO_2 [81]. Ablation of atoms from these targets may be by magnetrons or pulsed lasers for greater flexibility. In the latter case, as many targets can be addressed as needed by an additional arm of the same laser that drives the self-organisation

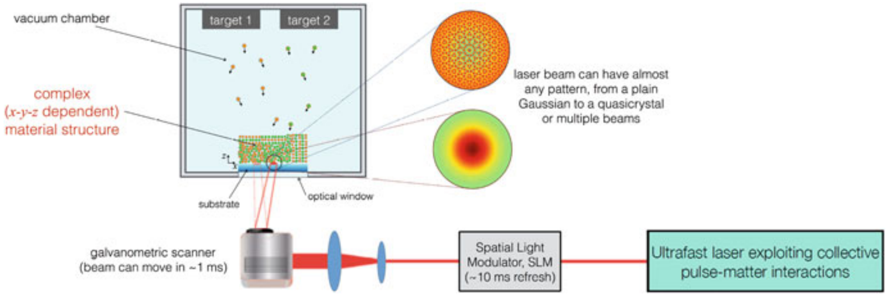
vacuum chamber
target 1
target 2
complex
(x-y-z dependent)
material structure
laser beam can have almost
any pattern, from a plain
Gaussian to a quasicrystal
or multiple beams
substrate
optical window
galvanometric scanner
(beam can move in ~1 ms)
Spatial Light
Modulator, SLM
(~10 ms refresh)
Ultrafast laser exploiting collective
pulse-matter interactions

Fig. 4.15 A possible implementation of a 3D atom printer using vacuum deposition. Multiple material targets are used as sources of the different atoms and molecules for the intended composition. These targets could be activated by magnetrons or by a pulsed laser. The 3D object is printed on a substrate layer by layer. The atomic structure and composition are controlled by spatiotemporal thermal gradients formed on the substrate using dynamically controlled structured light from an ultrafast laser

process. This way, the ablation starting and stopping times of each target can be precisely controlled synchronously with the beam pattern applied to the object's surface being printed.

The spatial thermal gradients on the surface of the object will be determined by the laser beam, which can be structured to create virtually any pattern. The diffraction limit only limits the most miniature scale of these patterns, but as we have discussed in the previous section, this does not preclude control over the atomic structure. The main imprint of diffraction will be to limit the minimum distance between two regions of different intended atomic structures. This is nearly the same limit as the voxel size, i.e., the smallest independently addressable region.

During any layer-by-layer deposition process, the growth direction is mapped to time, as in the common forms of 3D printing and vacuum deposition. This mapping readily creates an additional opportunity for bypassing the optical diffraction limit. The speed at which the driving laser beam is reconfigured compared to the deposition rate sets a lower limit to the spatial resolution along the vertical direction. Currently, spatial light modulators (SLMs) offer the highest number of independent actuators, but they are relatively slow with refresh rates of $\sim$10 ms. Deformable mirror and MEMS technologies provide response times of $\sim 10\,\mu$s. They have relatively fewer (several thousands instead of several millions), but still a large number of actuators. Even at the present speed limits, hardly an atomic layer is deposited within the timescale for being able to reconfigure the laser beam. Furthermore, it is reasonable to expect significant advances in these parameters. Therefore, the printing resolution is not limited by diffraction or laser physics, rather by the dynamics of the deposition and following self-organisation processes. In theory, control down to the single atomic layer is plausible under the right conditions.

Next, we discuss how the *explosion of complexity* is circumvented in this implementation, which paves the way to reasonable printing times for macroscopic objects. We aim to provide an order of magnitude calculation to illustrate that reasonable printing times are feasible. Consider, again, the same vacuum deposition setup of Fig. 4.15. Even disregarding likely progress in the deformable mirror or SLM technologies, the former allows to reconfigure the spatial thermal gradients on the surface within $\sim 10\,\mu\text{s}$. If the deposition rate is adjusted to one atom layer on average during this time, printing rates of ~ 0.1 mm/s are already conceivable while updating the structured laser field once per printing of each atomic layer. Thus, a 1-mm-thick structure could be printed over a few minutes. The lateral size of the object does not impact the processing time as long as it is not wider than the field of view covered by the structured laser beam. Therefore, 3D structures approaching a 1 mm^3 in size could conceivably be printed in the timescale of minutes. As discussed in Sect. 3, the expected time for an equivalent-sized object is many orders of magnitude longer if attempting to process point by point in atomic-scale resolution, even if it were possible.

Finally, the impact of fluctuations is entirely different in the case of self-organisation. When no attempt is made to control the exact position and state of the individual particles, the fluctuations play an integral and welcome role in many self-organised or other feedback-driven and iterative processes. There is no a priori reason to avoid or suppress them, and there are many cases where the presence and characteristics of the fluctuations can alter the dynamically preferred atomic arrangement. Access to atomic structures that are not reachable through near-equilibrium states can enable new functionalities, for example, through noise-induced transitions [91].

Overall, we believe there is a possible path towards a 3D atom printer by fully exploiting self-organisation. The entirely self-organised creation of a complex 3D object, much as the organic growth of a biological organisation, except that the details are externally steered rather than set by its evolutionary history, is a distant possibility. We believe that our present understanding of the fundamentals of self-organisation is too primitive even to conjecture on this possibility beyond expressing our belief that it should be possible. However, as discussed above, exploiting self-organisation to bridge the gap between the mesoscopic scale, where direct writing is possible, and the atomic scale, appears to us a perfectly viable path. We further believe that the first demonstration of such a device could be achieved within a decade. To this end, we need a more advanced understanding of the physics of laser-driven self-organisation. We will also need better experimental tools. These tools include interaction chambers, which may not be limited to traditional vacuum deposition techniques but may include, for example, microplasmas for highly reactive species. However, the most important role will likely be played by ultrafast lasers designed specifically for driving self-organised processes in the matter they interact with, possibly by exploiting collective pulse-matter interactions tailored to achieve a degree of separate control over the electron and atom (lattice) temperatures.

In concluding, we look forwards to an exciting decade of a creative combination of curiosity-driven fundamental advances in self-organisation physics with advanced laser technologies and innovative developments in 3D printing and material deposition techniques that could lead to disruptive and immediate industrial applications.

Acknowledgments The authors acknowledge funding the European Research Council (ERC) through the Ph.D. (grant no. 853387) NLL (grant no. 617521), the UniLase (grant no. 101055055), and the SUPERSONIC (grant no. 966846) projects and the TÜBİTAK—The Scientific and Technological Research Council of Turkey through projects no. 20AG024 and 20AG001.

References

1. D.M. Eigler, E.K. Schweizer, Positioning single atoms with a scanning tunnelling microscope. Nature **344**, 524–526 (1990)
2. D.G. Moore, L. Barbera, K. Masania, A.R. Studart, Three-dimensional printing of multicomponent glasses using phase-separating resins. Nat. Mater. **19**, 1–7 (2020)
3. D. Zhang, X. Liu, J. Qiu, 3D printing of glass by additive manufacturing techniques: a review. Front. Optoelectron. **14**, 263–277 (2021)
4. H. Wang et al., 3D Printing of transparent spinel ceramics with transmittance approaching the theoretical limit. Adv. Mater. **33**, 2007072 (2021)
5. B. Zhang et al., Three-dimensional printing of large-scale, high-resolution bioceramics with micronano inner porosity and customized surface characterization design for bone regeneration. ACS Appl. Mater. Interfaces **14**(7), 8804–8815 (2022)
6. S. Murphy, A. Atala, 3D bioprinting of tissues and organs. Nat. Biotechnol. **32**, 773–785 (2014)
7. A.S. Gladman, E.A. Matsumoto, R.G. Nuzzo, L. Mahadevan, J.A. Lewis, Biomimetic 4D printing. Nature Mater. **15**, 413–418 (2016)
8. M. Emons et al., Two-photon polymerization technique with sub-50 nm resolution by sub-10 fs laser pulses. Opt. Mater. Exp. **2**(7), 942–947 (2012)
9. K. Obata, A. El-Tamer, L. Koch, U. Hinze, B.N. Chichkov, High-aspect 3D two-photon polymerization structuring with widened objective working range (WOW-2PP). Light Sci. Appl. **2**, e116 (2013)
10. X. Wen, B. Zhang, W. Wang et al., 3D-printed silica with nanoscale resolution. Nature Mater. **20**, 1506–1511 (2021)
11. H.B. Sun et al., Arbitrary-lattice photonic crystals created by multiphoton microfabrication. Opt. Lett. **26**, 325–327 (2001)
12. S.K. Saha et al., Scalable submicrometer additive manufacturing. Science **366**, 105–109 (2019)
13. B.E. Kelly et al., Volumetric additive manufacturing via tomographic reconstruction. Science **363**, 1075–1079 (2019)
14. M.A. Skylar-Scott et al., Voxelated soft matter via multimaterial multinozzle 3D printing. Nature **575**, 330–335 (2019)
15. D.A. Walker et al., Rapid, large-volume, thermally controlled 3D printing using a mobile liquid interface. Science **366**, 360–364 (2019)
16. S. Kawata et al., Finer features for functional microdevices. Nature **412**, 697–698 (2001)
17. Zastrow, M., 3D printing gets bigger, faster and stronger. Nature **578**, 20–23 (2020)
18. E. Schrödinger, *What is Life?* (Cambridge University Press, Cambridge, 1944)
19. P.C. Bressloff, *Stochastic Processes in Cell Biology* (Springer, Berlin, 2014)
20. P.M. Hoffmann, *Life's Ratchet: How Molecular Machines Extract Order from Chaos* (Basic Books, 2012)

21. U. Alon, *An Introduction to Systems Biology* (Chapman and Hall/CRC, 2006)
22. J. Cheng et al., A review of ultrafast laser materials micromachining. Opt. Laser Technol. **46**, 88–102 (2013)
23. K. Sugioka, Y. Cheng, Ultrafast lasers—reliable tools for advanced materials processing. Light Sci. Appl. **3**, 1–12 (2014)
24. W.M. Steen, Laser material processing—an overview. J. Opt. A: Pure Appl. Opt. **5**, S3 (2003)
25. E.O. Olakanmi, R.F. Cochrane, K.W. Dalgarno, A review on selective laser sintering/melting (SLS/SLM) of aluminium alloy powders: Processing, microstructure, and properties. Prog. Mater. Sci. **74**, 401–477 (2015)
26. S. Kaierle et al., Review on laser deposition welding: from micro to macro. Phys. Proc. **39**, 336–345 (2012)
27. C. Kerse et al., Ablation-cooled material removal with ultrafast bursts of pulses. Nature **537**, 84–88 (2016)
28. B.H. Cumpston et al., Two-photon polymerization initiators for three-dimensional optical data storage and microfabrication. Nature **398**, 51–54 (1999)
29. C. Xu, F.W. Wise, Recent advances in fibre lasers for nonlinear microscopy. Nature Photon. **7**, 875–882 (2013)
30. W. Denk, J.H. Strickler, W.W. Webb, Two-photon laser scanning fluorescence microscopy. Science **248**, 73–76 (1990)
31. W. Zong et al., Fast high-resolution miniature two-photon microscopy for brain imaging in freely behaving mice. Nat. Methods **14**, 713–719 (2017)
32. B. Öktem et al., Nonlinear laser lithography for indefinitely large-area nanostructuring with femtosecond pulses. Nat. Photon. **7**, 897–901 (2013)
33. L. Orazi et al., Nonlinear laser lithography to control surface properties of stainless steel. CIRP Ann. Manuf. Technol. **64**, 193–196 (2015)
34. I. Gnilitskyi et al., Nano patterning of AISI 316L stainless steel with nonlinear laser lithography: sliding under dry and oil-lubricated conditions. Tribol. Int. **99**, 67–76 (2016)
35. M. Erdoğan et al., Texturing of titanium (Ti6Al4V) medical implant surfaces with MHz-repetition-rate femtosecond and picosecond Yb-doped fiber lasers. Opt. Exp. **19**, 10986–96 (2011)
36. S. Nolte et al., Ablation of metals by ultrashort laser pulses. JOSA B **14**, 2716–2722 (1997)
37. P. Elahi et al., High-power Yb-based all-fiber laser delivering 300 fs pulses for high-speed ablation-cooled material removal. Opt. Lett. **43**, 534–535 (2018)
38. H. Kalaycioğlu, P. Elahi, O. Akcaalan, F.Ö Ilday, High-repetition-rate ultrafast fiber lasers for material processing. IEEE J. Sel. Top. Quantum Electron. **24**, 1–12 (2018)
39. H. Kalaycioğlu, K. Eken, F.Ö Ilday, Fiber amplification of pulse bursts up to 20 μJ pulse energy at 1 kHz repetition rate. Opt. Lett. **36**, 3383–5 (2011)
40. O. Tokel et al., In-chip microstructures and photonic devices fabricated by nonlinear laser lithography deep inside silicon. Nature Photon. **11**, 639–635 (2017)
41. L. Pan et al., Maskless plasmonic lithography at 22 nm resolution. Sci. Rep. **1**, 175 (2011)
42. Z. Liu, H. Lee, Y. Xiong, C. Sun, X. Zhang, Far-field optical hyperlens magnifying sub-diffraction-limited objects. Science **315**, 1686–364 (2007)
43. S.W. Hell, Far-field optical nanoscopy. Science **316**, 1153–1158 (2007)
44. E.F. Matlin, L.J. Zipp, Imaging arbitrary incoherent source distributions with near quantum-limited resolution. Sci. Rep. **12**, 2810 (2022)
45. J. Fischer, M. Wegener, Three-dimensional optical laser lithography beyond the diffraction limit. Laser Photon. Rev. **7**, 22–44 (2012)
46. M.C. Cross, P.C. Hohenberg, Pattern-formation outside of equilibrium. Rev. Mod. Phys. **65**, 851–1112 (1993)
47. M. Cross, H. Greenside, *Pattern Formation and Dynamics in Nonequilibrium Systems* (Cambridge University Press, Cambridge, 2009)
48. P. Ball, *Patterns in Nature* (University of Chicago Press, Chicago, 2016)
49. J.D. Halley, D.A. Winkler, Consistent concepts of self-organization and self-assembly. Complexity **14**, 10–17 (2008)

50. A. Blagodatski, A. Sergeev, M. Kryuchkov, Y. Lopatina, V.L. Katanaev, Diverse set of Turing nanopatterns coat corneae across insect lineages. PNAS **112**, 34 (2015)
51. J.M. Watermeyer et al. A spiral scaffold underlies cytoadherent knobs in Plasmodium falciparum-infected erythrocytes. Blood **127**, 343–351 (2015)
52. P. Bampoulis, D. Lohse, H.J.W. Zandvliet, B. Poelsema, Coarsening dynamics of ice crystals intercalated between graphene and supporting mica. Appl. Phys. Lett. **108**, 011601 (2016)
53. H. Bénard, Les tourbillons cellulaires dans une nappe liquide. - Méthodes optiques d'observation et d'enregistrement. J. Phys. Théor. Appl. **10**, 254–266 (1901)
54. Birnbaum, M. Semiconductor surface damage produced by ruby lasers. J. Appl. Phys. **36**, 3688–3689 (1965).
55. B.P. Belousov, Periodicheski deistvuyushchaya reaktsia i ee mekhanism (Periodically acting reaction and its mechanism). Sbornik referatov po radiotsionnoi meditsine, 1958 (Collection of abstracts on radiation medicine, 1958) (1959), pp. 147–145
56. A.M. Zhabotinsky, Periodical process of oxidation of malonic acid solution. Biofizika **9**, 306–311 (1964)
57. J. Lv et al., Self-assembled inorganic chiral superstructures. Nat. Rev. Chem. **6**, 125–145 (2022)
58. S. Ilday et al., Rich complex behaviour of self-assembled nanoparticles far from equilibrium. Nat. Commun. **8**, 14942 (2017)
59. T. Otsuka, Y. Tsunoda, T. Abe, N. Shimizu, P. Van Duppen, Underlying structure of collective bands and self-organization in quantum systems. Phys. Rev. Lett. **123**, 222502 (2019)
60. M. Mameia, R. Menezes, R. Tolksdorf, F. Zambonelli, Case studies for self-organization in computer science. J. Sys. Archit. **52**, 443–460 (2006)
61. E. Karsenti, Self-organization in cell biology: a brief history. Nat. Rev. Mol. Cell. Biol. **9**, 255–262 (2008)
62. G. Makey et al., Universality of dissipative self-assembly from quantum dots to human cells. Nat. Phys. **16**, 795–801 (2020)
63. S.A. Levin, Self-organization and the emergence of complexity in ecological systems. BioScience, **55**, 1075–1079 (2005)
64. J. Lee et al., Production of tunable nanomaterials using hierarchically assembled bacteriophages. Nat. Protoc. **12**, 1999–2013 (2017)
65. A. Rizzo et al., Polarized light emitting diode by long-range nanorod self-assembling on a water surface. ACS Nano **3**, 1506–1512 (2009)
66. H. Ulrich, G.J.B. Probst, *Self-Organization and Management of Social Systems* (Springer, Berlin, 1984)
67. A. Walther, A.H.E. Müller, Janus particles: synthesis, self-assembly, physical properties, and applications. Chem. Rev. **113**, 5194–5261 (2013)
68. S. Dey et al., DNA origami. Nat. Rev. Methods Primers **1**, 13 (2021)
69. J. Palacci, S. Sacanna, A.P. Steinberg, D.J. Pine, P.M. Chaikin, Living crystals of light-activated colloidal surfers. Science **339**, 936–940 (2013)
70. J. Yu et al., Ultra-extensible ribbon-like magnetic microswarm. Nat. Commun. **9**, 3260 (2018)
71. R. Rubenstein, A. Cornejo, R. Nagpal, Programmable self-assembly in a thousand-robot swarm. Science **345**, 795–799 (2014)
72. L.E. Hargrove, R.L. Fork, M.A. Pollack, Locking of HeNe laser modes induced by synchronous intracavity modulation. Appl. Phys. Lett. **5**, 4–5 (1964)
73. H.A. Haus, Mode-locking of lasers. IEEE J. Sel. Top. Quantum Electron. **6**, 1173–1185 (2000)
74. F.Ö Ilday, Mode-locking dissected. Nat. Phys. **16**, 504–505 (2020)
75. H.A. Haus, Structures for additive pulse mode locking. J. Opt. Soc. Am. B **8**(10), 2068 (1991)
76. C. von Ballmoos, A. Wiedenmann, P. Dimroth, Essentials for ATP synthesis by F1F0 ATP synthases. Annu. Rev. Biochem. **78**, 649–672 (2009)
77. D.B. Chrisey, G.K. Hubler, *Pulsed Laser Deposition of Thin Films* (Wiley, New York, 1994)
78. K.C. Phillips, H.H. Gandhi, E. Mazur, S.K. Sundaram, Ultrafast laser processing of materials: a review. Adv. Opt. Photon. **7**, 629–684 (2015)

79. E.G. Gamaly, A.V. Rode, B. Luther-Davies, Ultrafast ablation with high-pulse-rate lasers. Part I: theoretical considerations. J. Appl. Phys. **85**, 4213–4221 (1999)
80. M. Born, E. Wolf, *Principles of Optics: Electromagnetic Theory of Propagation, Interference and Diffraction of Light* (Cambridge University Press, Cambridge, 1999)
81. S. Ilday et al. Multiscale self-assembly of silicon quantum dots into an anisotropic three-dimensional random network. Nano Lett. **16**, 1942–1948 (2016)
82. G. Nicolis, I. Prigogine, *Self-Organization in Nonequilibrium Systems* (Wiley, New York, 1977)
83. F. Borgogno, P. D'Odorico, F. Laio, L. Ridolfi, Mathematical models of vegetation pattern formation in ecohydrology. Rev. Geophys. **47**, 1–36 (2009)
84. H. Haken, Cooperative phenomena in systems far from thermal equilibrium and in nonphysical systems. Rev. Mod. Phys. **47**, 67–121 (1975)
85. H. Haken, Slaving principle revisited. Phys. D: Nonlinear Phenom. **97**, 95–103 (1996)
86. S. Ilday, Mapping uncharted territory. Inference: Int. Rev. Sci. **6**, 4 (2022). https://doi.org/10.37282/991819.22.10
87. A. Gordon, B. Fischer, Phase transition theory of many-mode ordering and pulse formation in lasers. Phys. Rev. Lett. **89**, 103901 (2002)
88. H.A. Haus, Theory of modelocking with a fast saturable absorber. J. Appl. Phys. **46**, 3049–3058 (1975)
89. P.A. Romero, F.H. Arnold, Exploring protein fitness landscapes by directed evolution. Nat. Rev. Mol. Cell Biol. **10**, 866–876 (2009)
90. M.A. Nowak, R.M. May, Evolutionary games and spatial chaos. Nature **359**, 826–829 (1992)
91. C. van den Broeck, J.M.R. Parrondo, R. Toral, Noise-induced nonequilibrium phase-transition. Phys. Rev. Lett. **73**, 3395–3398 (1994)

Chapter 5
How Light Drives Material Periodic Patterns Down to the Nanoscale

Anton Rudenko and Jean-Philippe Colombier

Abstract Ultrashort laser pulses enable efficient energy confinement down to the nanoscale, inducing extreme thermodynamic conditions in condensed matter. In contrast to longer pulse excitation, high-energy gradients are established, able to trigger nonlinear phenomena and instabilities that result from multiphysics coupling from the atomic to the macroscale. Self-organization of matter into periodic nanoscale patterns under multipulse laser excitation is one of the most intriguing manifestations of these phenomena with a wide range of potential applications in optics and mechanics, and of a fundamental scientific interest. This chapter provides an overview of the relevant processes with a particular emphasis on material modifications occurring in dielectrics, semiconductors, or metals and a critical assessment and discussion of plausible scenarios of matter reorganization toward periodic nanoscale patterns. Relying on representative experimental observations, proposed explanations are supported by numerical simulations. The dynamic interplay between light and matter evolution is explored to pave the way for structuring self-arranged surfaces on dimensions well below the diffraction limit and reaching the sub-100-nm feature size. Open questions and unexplored directions of possible further research work are outlined along the lines of the chapter.

Keywords Self-organization · Dissipative structures · Laser-induced periodic surface structures · Laser-induced ripples · Ultrafast phenomena

---

A. Rudenko
Arizona Center for Mathematical Sciences and College of Optical Sciences, University of Arizona, Tucson, AZ, USA

J.-P. Colombier (✉)
Université de, UJM-Saint-Etienne, CNRS, IOGS, St-Etienne, France
e-mail: jean.philippe.colombier@univ-st-etienne.fr

© The Author(s), under exclusive license to Springer Nature Switzerland AG 2023

R. Stoian, J. Bonse (eds.), *Ultrafast Laser Nanostructuring*, Springer Series in Optical Sciences 239, https://doi.org/10.1007/978-3-031-14752-4_5

1 Introduction

The light-induced formation of arranged, assembled, and self-organized structures on solid surfaces has a steady stream of deepened and extended research activity due to the ever-growing technological importance of on-demand tailored nanomaterials and surface functionalization [1–4]. As well, when dealing with a large concentration of interacting nanoobjects that compose the nanopatterns, properties differing from the bulk counterparts result from their collective response. Requiring advanced fundamental and technological knowledge, the control of light interaction at the nanoscale is crucial as it drives nanopatterns' formation and growth [5, 6]. These patterns correspond to regular spatial distributions of domains, serving as templates replicated to define the surface texture. Nowadays, highly efficient surface manufacturing is then envisioned hierarchically across scales, from the collection of atoms to the macroscale. Gradients in the dissipated energy strongly determine also the geometrical and physicochemical features and potential abilities of patterns. Furthermore, the technological process able to reduce topography size down to its ultimate scaling limit is a primary driver of progress in nanoscience. The nanometer scale represents a cornerstone to achieve matter manipulation with an unprecedented accuracy that can be offered and standardized by ultrafast laser process [7]. A key point is the interaction of light with matter, which is governed by feedback, i.e., light will shape matter and in return that will reshape light. New behaviors emerging from nanoobject are steadily unraveled, generally attributed to collective response on mesoscopic scales. Different material properties can thus be defined by structuring at this scale, designing new thermal, mechanical, bactericidal, or optical characteristics [8–10].

Prigogine coined the term *dissipative structures* to periodic patterns that occur in open systems far from equilibrium structures [11]. They are distinguished from those appearing under equilibrium as dissipative structures continuously export entropy in order to maintain their organization. Under an external energy flux, they consist of an evolution process where development of complex structures takes place primarily in and through the system itself in order to dissipate this energy. Laser-induced self-organization of matter is an unambiguous nanometric manifestation of dissipative structures that form periodically as the system is brought far from equilibrium by the pulse-burst laser when a steady state becomes unstable. The incoming coherent laser light drives the surface out-of-equilibrium and forces spontaneous ordering to occur. Driven by internal variation processes mainly caused by surface fluctuations' roughness, the selective retained ordered configuration is finally defined by counterintuitive stochastic thermodynamics. The photoexcited material continuously decreases its thermodynamical entropy, exporting entropy excess to the surrounding environment. Confusingly, stochastic thermodynamics seems to contradict the least-action principle for conservative systems and the maximum entropy production principle [12, 13]. This way, in response to the photon flux, the surface progressively creates dissipative structures capable of minimizing the free energy of the system and dissipating the absorbed energy more

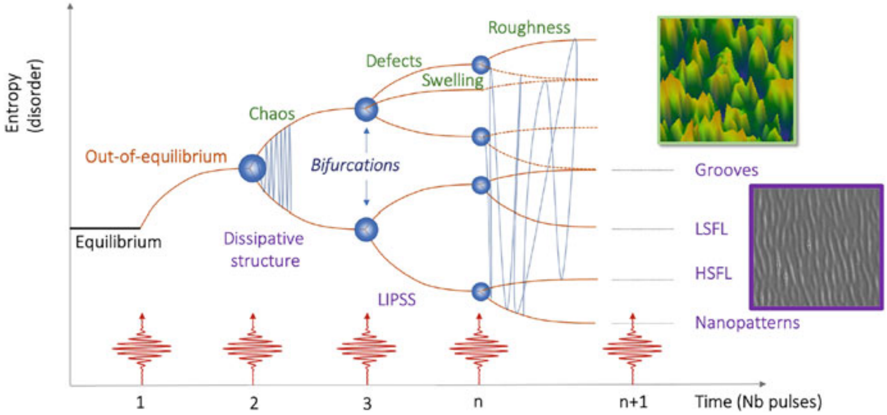

Fig. 5.1 Bifurcation diagram in laser-induced surface structures. Consecutive photon energy absorption and dissipation processes are associated with disorder at different scales generating defects or roughness. After going through bifurcations and chaotic zones, structures that are much more dynamic and stable emerge, and the laser beam becomes a source of order when the system moves away sufficiently from equilibrium, forming LIPSS

and more efficiently. This creation of surface corresponds to self-organization in order to maximize entropy exporting rate. After relaxation and resolidification, the system is considered to be self-organized as a global pattern has emerged solely from interactions among the lower-level units of the surface using only local thermomechanical information [14].

Upon CW to ultrafast laser irradiation in sub- and near-ablation regime, dissipative structures emerge far from equilibrium when a steady state becomes unstable at critical bifurcation points as shown in Fig. 5.1. The bifurcation diagram illustrates the evolving material undergoing entropy production and flow induced by light. Upon repetitive excitation, thermal-induced stresses yield crystal defects or void formation in the lattice inducing an irreversible damage of the surface [15, 16]. This mechanical effect refers to lattice distortion and swelling as a first step of disordered material response [17, 18]. Rapidly, surface processes are activated, and roughness is formed from intricate and unpredictable patterns. The characteristics of nanoscale surface morphology are defined by the competition between the evolution of transient liquid structures and the rapid resolidification of the surface region. Growth of topography driven by nucleation, cavitation, and thermocapillary forces, inducing drops and bubbles actuation, is compensated by surface tension effects that smooth out the molten surface features against viscosity. The solidification front propagation freezes finally the dynamic system with an inhomogeneous velocity depending on the local crystallographic orientation of the crystal-liquid interface [19, 20].

The patterns consist mostly in fingerprints of coherent light [21, 22] that result from well-ordered structures with laser polarization-related orientations and wavelength-related periods. Features are tunable by dose adjustment and multipulse interaction that offers broad possibilities for laser-induced nanostructuring. Laser-induced periodic structures (LIPSS) shape reproducible patterns due to their correspondence to steady states frozen by the liquid-solid phase transition. In particular, upon dynamic coupling of light with light-shaped topography [23, 24], ultrashort laser processing has a strong ability to generate high-temperature gradients sculpting locally the material but also triggering instabilities that can be frozen via fast lattice cooling and resolidification. This imprints chaotic time-dependent state before evolving into a self-organized structures as a steady state.

The scale of structuring, the minimal feature size, and the resulting morphologies and topographies define the function that can be attached to the structured material. This function pertains to optical, mechanical, or contact properties of the processed materials, upgrading the relevant performance, e.g., optical efficiency, mechanical strength, or contact attributes. The patterns with dimensions far beyond the diffraction limit, relying on nonradiative waves inducing short gradient scale length, are promising for numerous applications in photonics, mechanics, and biomedical applications [4]. To achieve the regular nanopatterns with dimensions much smaller than the laser wavelength, this chapter will develop the nature and the origin of the physical mechanism behind the surface nanofeatures. The question *how to access the nanoscale manufacturing by ultrafast light?* will be addressed. To respond to this, the discussion will offer a realistic outlook of the global material response, combining electromagnetic and hydrodynamic surface response on nanoscopic lengths. Finally, the potential of achieving designed vectorial patterns at the ultimate scale is discussed.

2 Self-Organization in Laser-Induced Dissipative Structures

Progress in manufacturing, energy conversion, or transportation is closely tied to the ability to manipulate bulk and surface material properties at the nanoscale. Creating regularly nanostructured materials can strongly impact multifold aspects of our technological environment, with artificial materials engineered to have surface properties non-existing in nature. Material functionalization relies on the creation of local modifications, which enable an enhancement of intrinsic material characteristics or performing a specific function in the mechanical, electrical, chemical, or optical domains. The challenge is to design local properties so that efficient functions can be added to processed materials.

The interaction of intense femtosecond laser pulses with rough surfaces and inhomogeneous volumes offers the possibility to induce straightforwardly spatial optical resonances in the near-field and coherent light-wave scattering [25]. This enables localizing light beyond the diffraction limit, presenting a real potential of direct nanostructuring with spatial order and tunable physical characteristics by optical means. Ultrafast dynamics of irradiated materials can spontaneously drive predictable physical transformations, triggering a remarkable onset of alternating properties with well-defined periodicity and contrast as illustrated in Fig. 5.2.

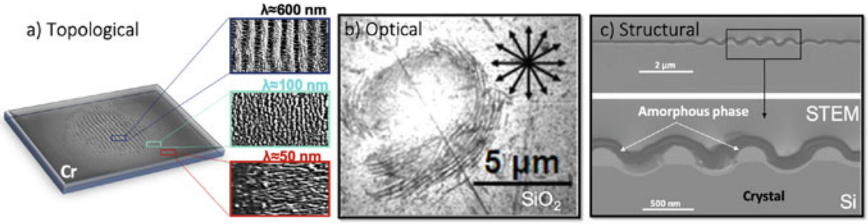

Fig. 5.2 Laser-induced periodic patterns formed by alternating topography on Cr from Ref. [20] (copyright 2018 Springer Science), optical index changes on SiO_2 from Ref. [28] (copyright 2013 Optical Society of America), and structural phases on Si from Ref. [27]. Surface and bulk nanostructures consist of manifestation of self-organization effects with controllable features as orientation that can be tuned by the polarization of the electric field. Transiently surface and volume inhomogeneities serve as fluctuations and noise that triggered ordered configuration with coherent light coupling

Unconventional combination of topographies, optical indices, and structural phases controlled at nanometer scales upgrade surface and bulk functionalities. New features of the treated material result in both the type of properties and the scale of the induced changes for applications in emerging technologies as photonics, sensors, wettability, or nano-fluidics requiring structuring with high aspect ratio, gradients, and anisotropy. The property may be exotic for the selected material, with nonstandard crystalline states, strongly accrediting functionalization potential [26, 27].

Under ultrafast laser irradiation, the final states are related mainly to the degree of nonequilibrium and to the intrinsic material relaxation paths. These define electronic and structural transitions determining permanent material alterations. Consequently, many states in the thermodynamic phase space may be reached by developing synergies between light and matter. Near the fluence threshold modification of most materials, a periodic alignment of surface ripples can be generated, referred to laser-induced periodic surface structures (LIPSS). These (quasi-)periodic lines are a universal phenomenon gaining an increasing attraction since the synergy between light and matter develops spontaneously and coherently with a free evolution process. Also, formed in a broad range of pulse durations, starting from continuous to femtosecond irradiation, the advent of ultrafast laser sources has renewed interest in LIPSS as grating-like structures can be generated in a simple single-step process, with a large range of periods. Moreover, with light sources enabling nonlinear interaction, LIPSS can be formed on almost any materials [29], metals, semiconductors, and dielectrics as shown in Fig. 5.2, even those having a bandgap greater than the laser wavelength [30]. Alongside this, the complex irregular topography of the surface and inhomogeneity of the volume has shown to allow the generation of complex intensity patterns far beyond the diffraction limit in irradiated areas. Due to a substantial energy confinement in time and space, ultrafast irradiation constitutes a powerful driving force for reduced-scale structuring.

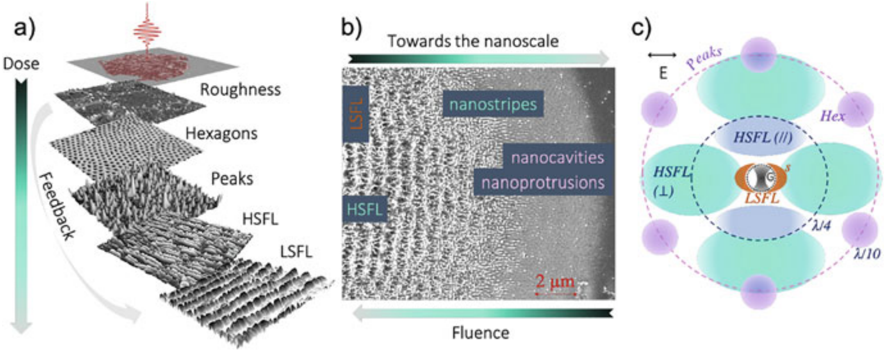

Fig. 5.3 Laser-induced periodic surface structures as a function of feedback (**a**). For low laser fluence below ablation regime, patterns as hexagons and high-density peaks can be formed at the nanoscale. In case of the polarization orients the pattern by near-field coupling, HSFLs are formed. For higher fluence, LSFL and grooves are generated in ablation regime. Nanoregimes of self-organization can coexist on a single impact, following the Gaussian fluence distribution (**b**). Fourier transform representation of the main patterns generated on the surface (**c**). HSFL can exhibit parallel or perpendicular orientations to the polarization, depending on the roughness features. Labels *Hex* and *Peak* refer to hexagonal nanocavities and nanopeaks, respectively, with both sub-100nm periodicities

In a multipulse irradiation regime, Fig. 5.3 illustrates how the consecutive laser pulses impact a surface. Nanostructuring patterns are reproducible due to their correspondence to steady states frozen by a phase transition for a given dose value, depending both on local fluence and number of pulses. The local photoexcited area is constantly modified by the previous pulses and is roughened constantly, from an initially quasi-flat surface to transiently growing disturbances [31, 32]. Incident light is then scattered by surface inhomogeneities and interferes coherently with these scattered waves, and LIPSS can be generated with different periodic scales on the irradiated surface, involving polarization effects on the freshly formed roughness centers [24, 33]. Radiative and nonradiative modes of light coupling drive the periods and the orientation of the patterns via energy absorption distribution and subsequent gradients. While multiple patterns have been observed experimentally in laser-irradiated surfaces, their occurrence has primarily been explained by different theoretical models that will be developed in the next sections.

Slightly sub-wavelength-sized ripples, termed low-spatial frequency LIPSS (LSFL), were first observed by Birnbaum [34], and until the mid-1980s, a model was developed attributing the phenomenon to a modulated energy input, which was ascribed to an interference of the incident wave with surface scattered electromagnetic waves [21, 35]. For irradiation with an angle of incidence normal to the surface, LSFL typically shows periods close to or slightly smaller than the laser wavelength ($\lambda/2 \leq \Lambda_{LSFL} \leq \lambda$), while HSFL exhibits periods considerably smaller than the irradiation wavelength ($\Lambda_{HSFL} < \lambda/2$). HSFLs are mainly formed for the shortest pulse durations ranging from fs to ps. Far beyond the diffraction limit, spontaneous periodic nanostructures as nanopeaks and hexagonal nanocavities were also recently reported with a period below 100 nm and a unit size around 20 nm. As most of the sub-wavelength structures are oriented by the laser polarization, a crossed-polarization strategy is employed to form 2D LIPSS. Finally, LIPSS with periodicities larger than the laser wavelength, generally called "grooves," can be generated when increasing the incident pulse energy. Grooves can be oriented parallel or perpendicular to the electric field polarization. Across the laser spot produced by a beam of Gaussian spatial intensity distribution, the LIPSS features can change abruptly between very fine structures in the edge region of lower intensity to a coarser structure in the central part of the impact as shown in Fig. 5.3b. To resume most of the structures' orientation and periodicity, the different kinds of LIPSS are indicated in Fig. 5.3c in the Fourier space.

Various self-organization regimes can be triggered depending both on the laser parameters (wavelength, fluence, number of pulses, pulse duration, polarization states) and the initial surface conditions as topography, crystal defects, and inhomogeneous response of local crystallographic grains [19, 32, 36]. Periodic patterns correspond to distinct dissipative structures ordered through fluctuations inherent to surface, bulk, and even laser energy distribution. Each of them is caused by intensive light energy exchange with the remaining material that consists of the dissipative environment. Forming far from equilibrium, complex patterns of structures emerge for given dose conditions. Their growth, amplification, and regulation are then carried out by successive pulses that fuel natural selection. As long as the thermomechanical distributions induced by light absorption follow the inhomogeneous topography, next pulse fosters the formed pattern by a positive feedback. In the opposite case, e.g., as material removal or slow liquid flow occurs, negative feedback stabilizes configurations. Either of feedbacks provides the configuration with a selective advantage over competing self-organization regimes. One can notice that all the intricacies such as sensitivity to initial roughness and crystal orientations can be attributed to the initial material fluctuations that can undergo local nonlinearity influencing the interplay of positive and negative feedback cycles. Finally, the observed patterns with reproducible features are associated with classifiable processes of light energy deposition and material relaxation in the heat-affected regions that trigger and regulate a well-defined self-organization, as developed in the next sections.

3 Nanoscale Phenomena in Ultrafast LIPSS Formation

This section focuses on the nanoscale phenomena induced by single and multiple ultrashort laser irradiation of solid materials and underlines the potential role of these phenomena in self-organization of LIPSS. Some of these phenomena are novel in the context of laser material processing and specific due to the unique possibilities of ultrashort lasers to confine intense light and heat at nanoscale or due to the repetitive multipulse nature of light-matter interaction, whereas others have been widely discussed in various fields of research including nonlinear optics, nanophotonics, plasmonics, heat transport, fluid dynamics, etc. The main goal here is not only to overview the recent theoretical and experimental achievements in understanding of the formation processes of the variety of ultrashort LIPSS but also to make a potential link between different fields of light-matter interaction at the nanoscale and the field of ultrashort laser material processing sharing similar concepts and phenomena.

The important feature of ultrashort laser-matter interaction is the possibility to consider separately the processes of the energy deposition (light-matter interaction) and the hydrodynamic processes in the heat-affected regions. This fact is valid as long as the pulse duration does not exceed few picoseconds, corresponding to the timescale of electron-phonon relaxation and lattice heating. However, the self-organization of LIPSS typically occurs within multiple pulse irradiation. The laser-affected surface or bulk are modified (subjected to irreversible damage) pulse-by-pulse, and the topography evolves from pristine material toward the regular structures. From this perspective, at the beginning of each pulse, the light interacts with newly established nanostructures, and the modifications taken place as a result of the previous laser pulse interaction influence the energy deposition of the next laser pulse. Therefore, although the first subsection is fully devoted to light-matter interaction with the nanostructures during laser pulse excitation, the considered surface topography would also include the features commonly produced by hydrodynamics upon material excitation by previous laser pulses. Similarly, the second part focuses on the variety of hydrodynamic processes and the role of irreversible damage in the genesis and evolution of the nanostructures, but considers the inhomogeneous energy absorption by preexisting nanoscale features. Finally, the scenarios currently proposed to explain the particular types of the nanostructures on dielectric, semiconductor, or metal surfaces based on the discussed physical phenomena are detailed in a separate part of this chapter.

The variety of theoretical and numerical approaches developed in order to simulate the involved phenomena has been recently discussed in the review paper [37] and introduced in Chapter 1 by Derrien et al. For the sake of clarity, we briefly summarize here the existing models describing light-matter interaction during the laser pulse excitation and the following hydrodynamics. The involved parts (optical, thermalization, hydrodynamics) are indicated in Fig. 5.4.

The optical part of the laser-matter interaction problem requires coupling of 3D light propagation with a comprehensive material response. Linear propagation in an inhomogeneous medium is described by full-vector Maxwell equations that can be solved by finite-difference time-domain (FDTD) method [38], compatible with the nano-/microscales of interest. Generally, there is no exact analytic solution to the problem (except Mie theory of scattering by a single homogeneous sphere [39]); however, there is a wide range of models considering specific partial solutions, for instance, Sipe's theory for inhomogeneous scattering from nanoscale surface roughness [21], surface plasmon theories [40, 41], solutions for a single Hertzian dipole near the metal surface [42], the grating theory [43], discrete dipole and effective medium theory [44], etc. Each of these approaches is capable of describing

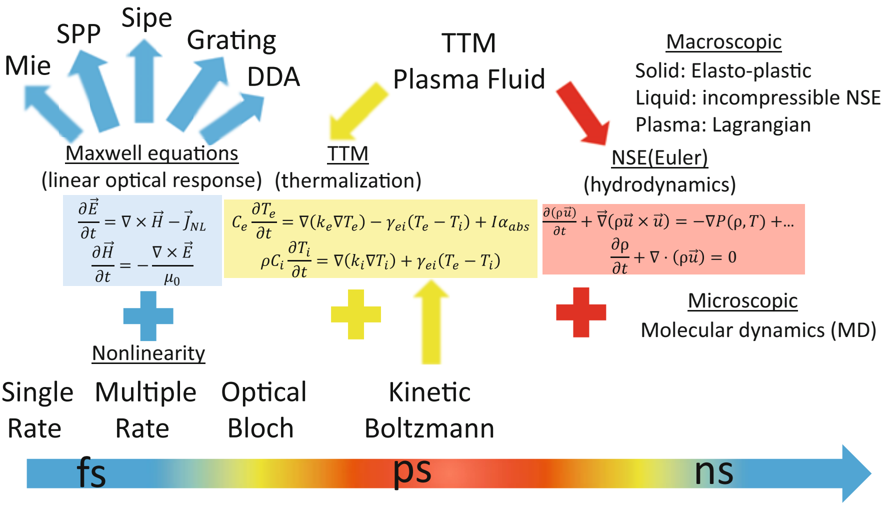
Mie
SPP
Sipe
Grating
DDA
TTM
Plasma Fluid
Macroscopic
Solid: Elasto-plastic
Liquid: incompressible NSE
Plasma: Lagrangian
Maxwell equations
(linear optical response)
TTM
(thermalization)
NSE(Euler)
(hydrodynamics)
$\frac{\partial \vec{E}}{\partial t} = \nabla \times \vec{H} - \vec{J}_{NL}$
$\frac{\partial \vec{H}}{\partial t} = -\frac{\nabla \times \vec{E}}{\mu_0}$
$C_e \frac{\partial T_e}{\partial t} = \nabla(k_e \nabla T_e) - \gamma_{ei}(T_e - T_i) + I\alpha_{abs}$
$\rho C_i \frac{\partial T_i}{\partial t} = \nabla(k_i \nabla T_i) + \gamma_{ei}(T_e - T_i)$
$\frac{\partial(\rho\vec{u})}{\partial t} + \vec{\nabla}(\rho\vec{u} \times \vec{u}) = -\nabla P(\rho, T) + \ldots$
$\frac{\partial \rho}{\partial t} + \nabla \cdot (\rho \vec{u}) = 0$
Microscopic
Molecular dynamics (MD)
Nonlinearity
Single Rate
Multiple Rate
Optical Bloch
Kinetic Boltzmann
fs
ps
ns

Fig. 5.4 Schematics of numerical/analytical models for ultrashort laser-matter interaction. The linear optical part includes Maxwell equations, Mie theory, SPP (surface plasmon polariton) theory, Sipe's model, grating theory, and DDA (discrete dipole approximation). Nonlinearity can be modeled by single or multiple rate or optical Bloch equations. The thermalization part is described by TTM (two-temperature model for electrons and ions), TTM plasma fluid models, or kinetic Boltzmann equation. Finally, the hydrodynamic part includes macroscopic NSE (Navier-Stokes equations) or microscopic MD (molecular dynamics method). The bottom arrow and the corresponding colors indicate the timescales (femto-, pico-, nano-) of the relevant processes modeled by these approaches

physics within its domain of validity but may potentially overlook the details of more complex light propagation problems. The nonlinear optical response can be incorporated to FDTD via the nonlinear currents $\mathbf{J}_{\mathbf{NL}}$ and might include (in the order of increasing complexity) effective permittivity constants upon laser excitation [22, 45], the Drude model and a single rate equation for the macroscopic electron density evolution [46, 47], energy-resolved multiple rate equations [48, 49], two-temperature plasma fluid models [50–52], nonequilibrium kinetic Boltzmann [53–55] and Maxwell-Bloch approaches [56–58], or (time-dependent) density functional theory simulations [27, 59]. The latter three approaches are expected to provide more precise insight into the optical response under nonequilibrium ultrashort laser excitation.

The hydrodynamics involved in intense femtosecond laser excitation can be modeled by microscopic or macroscopic approaches and requires coupling with one of the previously mentioned optical models to describe the appropriate initial conditions. Molecular dynamics (MD) is a complementary atomistic tool to understand the order to disorder state transition in laser ablation. Although limited to hundreds of nanometer spatial scales (in 3D) and strongly dependent on the choice of the specific interatomic potential (which are better explored for metals, but rather complex for dielectrics/semiconductors), the numerical results provide detailed atomic resolved information about the laser-induced modifications [15, 20, 60]. The atomistic perspective of nanoscale ablation is reviewed in Chapter 2 by Ivanov et al., where MD approach is applied in combination with energy deposition and two-temperature excitation models to explore surface modification mechanisms at nanoscale. The macroscopic hydrodynamic simulations based on Navier-Stokes equations are capable of elucidating the role of each involved phenomena separately, can be applied on microscales, and, therefore, are solved within the same mesh grid as FDTD but require sufficient numerical accuracy and stability and sophisticated boundary conditions to resolve the phase transitions. Thus, different approaches/numerical schemes might be required to treat accurately different phases: elastoplastic models for a solid state [61–63], incompressible Navier-Stokes for melt flow dynamics [64, 65], compressible Navier-Stokes with the appropriate equation-of-state for phase transitions [66, 67], and the hydrodynamic equations in Lagrangian form for strong ablation and plasma plume expansion [68, 69]. The alternative methods based on the statistical nature of the phenomena include particle-in-cell (PIC) [70] and Monte Carlo methods [71], as well mesh-free smoothed particle hydrodynamics methods [72] but are less explored in the context of ultrashort laser-induced modifications.

3.1 How Light Sees the Nanostructures

In order to understand the possible origin of inhomogeneity in the energy deposition on the surface or in the bulk of a solid material, it is helpful to discuss firstly the light interaction with single imperfections, i.e., nanoholes, nanobumps, nanoparticles, or nanovoids. These features are the counterparts of surface or bulk roughness [73] and might be as well induced by laser irradiation, as explained in the hydrodynamic subsection. The qualitative picture of light interaction with these nanofeatures remains unchanged as long as they are much smaller than the laser wavelength (therefore, a few tens of nanometers dimensions in case of irradiation by ultraviolet-infrared laser pulses). The interest in single inhomogeneities in the frame of laser material processing is related to several notable properties of light interaction in this specific regime resulting in light and heat confinement, reduction of the ablation threshold, periodic and polarization-dependent modulation of the energy deposition, and a pronounced role of inter-pulse and intra-pulse feedbacks, summarized in Fig. 5.5, affecting the evolution of the surface topography. Generally, the electromagnetic feedbacks are provided by changes in size, shape, or concentration of the imperfections and in the optical properties of laser-excited solids.

Light Confinement Firstly, the light is confined to the surface of these imperfections and the local fields can be significantly enhanced at the nanoscale. This is particularly relevant in case of metal nanoparticles which exhibit a strong localized surface plasmon resonance, i.e., collective oscillation of electrons at the interface of the nanoparticle. Similar features are pronounced for surface imperfections, i.e.,

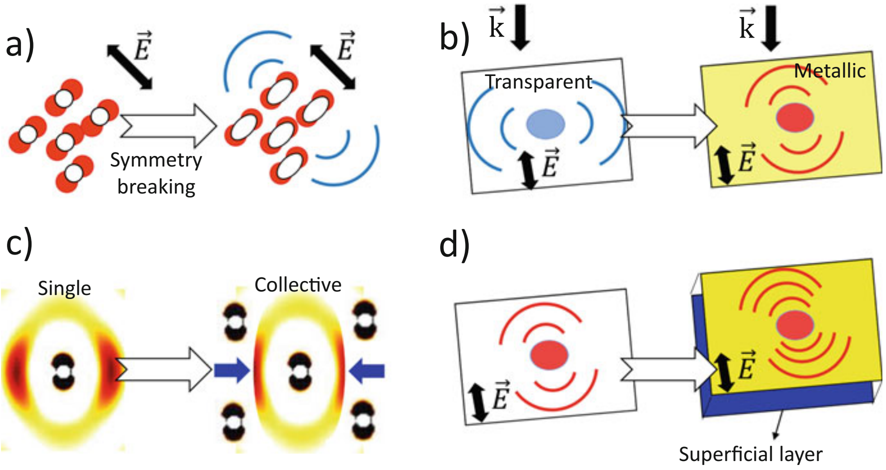

Fig. 5.5 Schematics of potential feedbacks playing the role in the onset of the interference periodic patterns originated from inhomogeneities. (**a**) Symmetry breaking by local field enhancement and changes in the scattering behavior of the nanostructures provided by intra-pulse (via local optical breakdown) or inter-pulse (via local material removal) feedbacks. (**b**) Transient changes in material properties resulting in quasi-metallic optical response. (**c**) Collective effects contributing to a blueshift of the resonant wavelength. (**d**) Formation of a superficial layer (oxidation; dense electron plasma formation), changing the optical response on the laser-irradiated interface

nanoholes and nanobumps, where the local field is strongly enhanced in the material [33, 74]. For convenience, the intensity distributions underlying the nanoscale light confinement properties are qualitatively shown in the upper row of Fig. 5.6 for a single nanohole and nanobump beneath transparent glass and metallic steel surfaces. In case of metals, the direct consequence is the strong absorption of light and localized heating at the interface of such inhomogeneities, as well as the enhanced nonlinearity. In case of transparent materials, the field enhancement may result in the localized optical breakdown, i.e., if the intensity is high enough, the electrons are transferred to the conduction band and the created electron plasma acquires quasi-metallic properties and absorbs light. This way, the light interaction with imperfections of different origins results in pronounced hot spots on the surface or in the bulk of solids. Importantly, we discuss here the three-dimensional effects related to the presence of inhomogeneities which exhibit several unique properties and 3D spatial complexity. In addition, the light can be also *homogeneously* confined, for example, along the metal interface due to light penetration depth limited by $\approx$ 10 nm scale or due to the formation of an absorbing electron plasma in photoexcited transparent solids.

Polarization Memory Secondly, the nanofeatures exhibit polarization-dependent response to the incoming light. For instance, the local field is enhanced along the polarization direction in case of metal nanoparticles in a transparent medium.

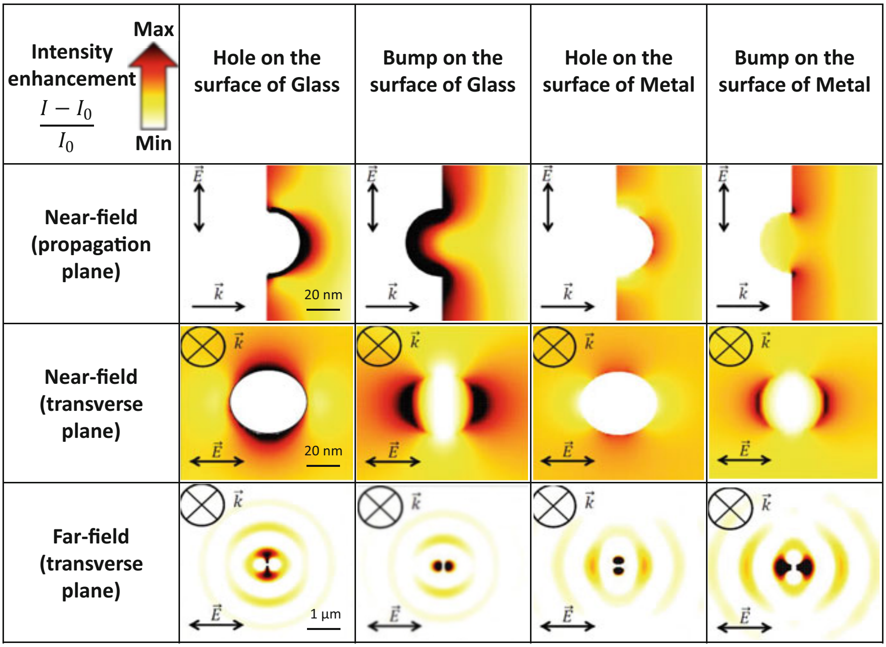

Fig. 5.6 Table summarizes and compares the qualitative behavior of the interference patterns in propagation (upper row) and transverse planes (middle and bottom rows) below the laser-irradiated surfaces of glass (fused silica) and metal (stainless steel) for a single hemispherical nanohole and nanobump. The directions of the electric field **E** and light propagation **k**, as well as the dimension scales, are indicated in the figures. Quantitative results are provided in Ref. [33]. Copyright 2019 Elsevier

In contrast, the field is enhanced perpendicular to the laser polarization if the refractive index of the particle is lower than the one of the surrounding medium, for example, a nanovoid structure inside glass. On the interface, this index-related dependency results in qualitatively different local field distributions below surface nanoholes and nanobumps, as shown in the middle row of Fig. 5.6, perpendicular (for a nanohole) or parallel (for a nanobump) to the laser polarization. The concept of polarization memory is important due to the fact that independent of spatial positions, exact shape or size, the imperfections are subjected to the identical field and matter response. The equally oriented localized modifications can contribute to the symmetry breaking of the initially homogeneous or random system. As a result, the polarization-dependent near-field response provides conditions for intra-pulse feedback (excitation of free carriers and growth of oriented nanoplasmas) or for inter-pulse feedback (selected local material removal) in multipulse laser-matter interaction. The concept is illustrated in Fig. 5.5a and further developed in the context of light interaction with asymmetric nanostructures.

Asymmetric Inhomogeneities Local modifications driven by a polarization-dependent near-field optical response can reshape the inhomogeneities. The origin of possible modifications is discussed in the next subsection, where the most pronounced scenarios include local melting (commonly observed in reshaping of nanoparticles by laser pulses) and near-field ablation. The ellipsoid asymmetric shape may qualitatively change the optical response of the nanostructure, reinforcing the scattering parallel to the direction of elongation. As a result, the periodic energy deposition is prioritized within one direction, in contrast to the symmetric spherical wave (in the bulk of solid). Consequently, irradiation by multiple pulses with one laser polarization provides then a positive feedback for the evolution of the nanostructures.

The concept of such feedback was firstly proposed in order to explain the evolution of self-organized nanogratings in fused silica bulk [75–77]. The local field enhancement near single inhomogeneities causes local optical breakdown and formation of nanoplasmas that further expand in nanoplanes perpendicular to the laser polarization following the optical field pulse-by-pulse via intra-pulse feedback. The concept was supported by numerical simulations and further applied to surface nanogratings, sharing a similar formation mechanism [47, 78]. Recent experimental observations of perpendicularly oriented nanovoid structures exhibiting birefringence in the bulk of glasses irradiated by multiple ultrashort laser pulses [79] provide evidence for the involvement of near-field effects in the symmetry breaking of the material optical response.

Polarization-dependent elongated nanovoids were also observed on the metal surface subjected to multiple pulse ultrashort laser irradiation, indicating the possible contribution of local field enhancement to the material damage at the nanoscale [16]. Moreover, recent simulations have indicated that the contributions from both intra-pulse (electron plasma kinetics) and inter-pulse (void structure cavitation) feedbacks are involved in the successive topography evolution and establishment of regular and highly periodic nanostructures in the bulk of fused silica [80].

Periodic Patterns Finally, the inhomogeneities scatter light and the interference of the scattered and the incident waves results in a standing wave pattern determined by the properties of the incoming light (laser wavelength) and of the medium (refractive index). In the bulk of transparent solids, these radiative features are described within the concept of Mie scattering from an homogeneous sphere [39]. They represent periodic spherical waves with λ/n periodicity in the plane perpendicular to the light propagation, where λ is the laser wavelength and n is the refractive index of the medium. In the limit of a sphere of radius $R \ll \lambda$, the scattering has properties of Rayleigh scattering, with the intensity decaying as $\propto 1/R^2$. The optical response, however, is more complex in case of scattering from a surface imperfection, i.e., nanohole or nanobump, and can be no more described by analytical Mie theory but requires numerical computation of Sommerfeld integrals or using numerical electromagnetic solvers. Nevertheless, analytical approximations exist for a dipole close to the interface [42], indicating the involvement of both evanescent and radiative diffraction modes in the interference patterns. Furthermore, the analytical method allows for classification of surface electromagnetic wave contributions in the general case of a plasmonic nanostructure at metallic surfaces, including quasi-cylindrical waves, surface plasmon polaritons (SPPs), and Norton waves [81, 82]. The dominant contribution of each counterpart depends on the optical properties of the medium and on the distance from the imperfection. The general trend is that the periodic interference patterns have asymmetric amplitudes of field enhancement parallel or perpendicular to the laser polarization. These ones change from the dominantly parallel to the field vector and λ/n periodicity for air-transparent solid interfaces to dominantly perpendicular and $\approx \lambda$ periodicity for air-metallic interfaces. For example, the intensity patterns near a single nanohole and nanobump beneath transparent glass and metal steel surfaces are shown in the lower row of Fig. 5.6. The polarization-dependent behavior of the radiative patterns is independent of the nature of inhomogeneity, but only defined by the properties of the medium [33].

Surface Plasmon Excitation Surface plasmon polaritons (SPPs) are propagating waves along a metal-dielectric interface with a spatial period of $\lambda_{SPP} = \lambda/Re(\sqrt{\epsilon_1\epsilon_2/(\epsilon_1+\epsilon_2)})$, where λ is the light wavelength and ϵ_1 and ϵ_2 are the indexes of metal and dielectric materials (see [40] and discussion in Ref. [41] for specific materials). In order to couple with the incident light, the SPPs should be excited by surface inhomogeneities at normal incidence. Several approaches were developed in order to take into account surface roughness and angle dependency [83, 84], which influence quantitatively the periodicity and lead to deviations from the expressions for a pure metal-dielectric interface. Additionally, it is worth noting that the interference patterns include SPPs as a part of the solution and the evanescent waves can play a non-negligible additional role, correcting the spatial periodicity as a function of distance from the excited inhomogeneities [24]. In the particular case of interface between air and plasmonic metals (gold, silver, etc.) at infrared-optical wavelengths, $\lambda_{SPP} \approx \lambda$ for both solutions, resulting in the interference patterns dominantly oriented perpendicular to the laser polarization with almost constant period at a certain distance from the inhomogeneity. However, the deviations in amplitude and field extrema positions near the inhomogeneity are apparent even for metals like stainless steel, with separate and total contributions from SPPs and quasi-cylindrical waves in the propagation plane shown in Fig. 5.7a–c and in the transverse planes in Fig. 5.7e. The combination of the contributions of evanescent and plasmonic waves still results in the field maxima separated by $\approx \lambda$ but with a shift $\approx 3\lambda/4$ from the position of the inhomogeneity as indicated in Fig. 5.7d, as well as different damping properties of the waves at a distance from the excited surface nanohole [24].

Surface or bulk roughness (consisting mainly of nanofeatures) is the main factor to explain the transition from homogeneous to quasiperiodic-, wavelength-, and polarization-dependent energy deposition on the evolving topography upon multipulse laser irradiation [85]. The theory of inhomogeneous scattering of light by surface nanoroughness in the context of LIPSS was pioneered by Sipe et al. [21], proposing the spatial k-vector dependencies as a function of the filling factor, laser

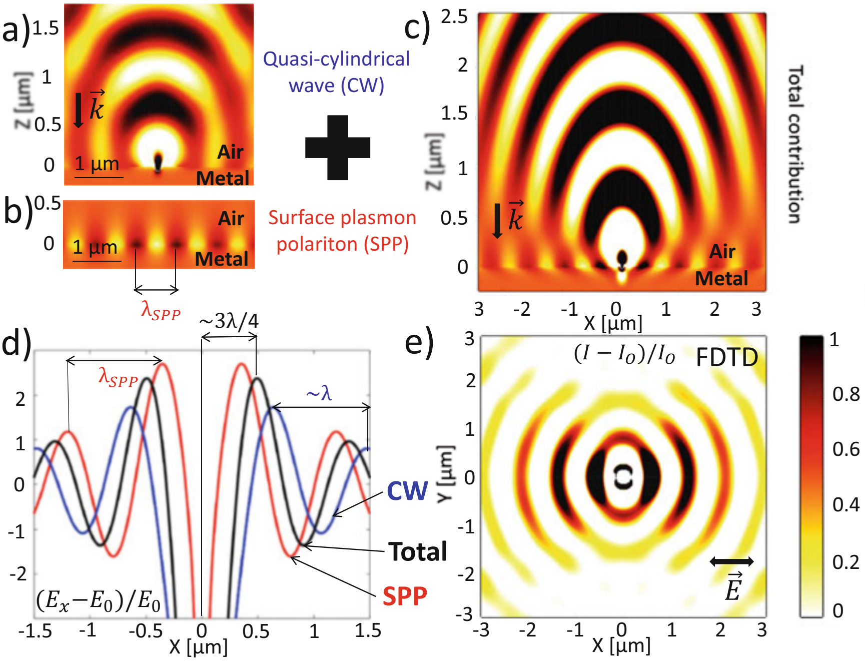

Fig. 5.7 Contributions of quasi-cylindrical wave (a, CW blue) and surface plasmon polaritons (b, SPP red) excited by a single nanohole on stainless steel surface to total scattered field (c, total black) are shown separately in the propagation plane (**a**)–(**c**) and quantified in (**d**). (**e**) The interference pattern generated underneath the nanohole in the transverse plane. The directions of the electric field **E** and light propagation **k**, as well as the dimension scales, are indicated in the figures. $Z = 0$ corresponds to the air-metal interface and (0, 0, 0) to the nanohole center. More detailed description can be found in Ref. [24]. Copyright De Gruyter 2019

wavelength, and the material properties. Two general solutions dominant in case of dielectrics (parallel to the polarization, periodicity $\approx \lambda/n$) and metals (perpendicular to the polarization, periodicity $\approx \lambda_{SPP}$) were specified, finding good agreement with commonly observed LSFL (low-spatial-frequency LIPSS). It is worth noting that intense ultrashort laser interaction with single prefabricated asymmetric ridges, trenches, grooves, and stepped microstructures resulting in pronounced periodic interference patterns concentrated around the inhomogeneity and single pulse-induced material modifications were investigated by several groups [86–88]. These experiments support the involvement of different types of surface electromagnetic waves (parallel or perpendicular oriented patterns) in the energy deposition process and provide the opportunity to analyze the formation mechanisms within a single pulse excitation, i.e., without inter-pulse feedback.

Transient Optical Properties In the regime of a laser pulse energy sufficient to modify the pristine material, the propagation of the laser pulse and the light-matter interaction are no longer linear. During the energy deposition, the electron-phonon system is in strong nonequilibrium. Excitation processes in dielectrics and semiconductors represented by photo- and avalanche ionization result in an abrupt transition from a transparent material to a strongly absorbing electron plasma with quasi-metallic properties. The excited metals also exhibit a strong thermal nonlinearity, which potentially can even modify the optical response from a non-plasmonic to a plasmonic state [89]. These nonlinearities influence the energy deposition dynamics and the optical response of inhomogeneities.

In the context of LIPSS, the effective transient refractive index changes induced by photoexcitation of free carriers in dielectrics and semiconductors were proposed to change the nanostructure periodicity as well as the orientation of patterns due to the transition to a quasi-metallic state (concept of the intra-pulse feedback illustrated in Fig. 5.5b). First theoretical approaches were based on Sipe's theory for inhomogeneous absorption with transient optical properties changing according to the level of excitation (electron density) [90, 91]. The transient inhomogeneous energy deposition was also modeled by full-vector Maxwell equations, initially assuming the photoexcitation being not coupled to the laser pulse propagation [45, 92]. The intra-pulse feedback was further considered, where the field and the transient optical properties were coupled through nonlinear propagation in the bulk and at the surface of materials [27, 47, 49, 78].

Collective Effects in Optical Response Upon multipulse irradiation, the surface topography evolves, and the changes in its individual features and their collective interactions might affect the global optical response of the system and the periodicity of LIPSS (concept illustrated in Fig. 5.5c). There are three different aspects that have been considered here: the random distribution and concentration of individual scattering centers [24, 31, 49], bulk or surface roughness [21, 83, 84], and a grating structure itself [93, 94], considering that the self-organization has already taken place. From a macroscopic point of view, surface roughness is regarded as the potential driver of the surface plasmon resonance blueshift toward smaller periods [83]. From a microscopic point of view, the shift in the resonant wavelength is related to dipole-dipole coupling in metal nanostructures, resulting in a blueshift with decreasing center-to-center distance between dipoles [24, 95]. In a recent work applying photoemission electron microscopy, the correlation between individual nanohole inter-distance and the LIPSS period has been evidenced [31]. Finally, for a regular grating structure, the surface plasmon resonance can blueshift with increasing depth of the grating. Huang et al. [93] proposed that the period of LIPSS would evolve according to this blueshift. Another interesting phenomenon arising with increasing depth of the metal gratings is the possibility of grating splitting by the intensity enhancement strictly at the tip of the nanostructure [96–99]. In this case, multiple irradiation results in grating periods reduced by a factor of $2 \approx \lambda/2$.

Positive and Negative Feedbacks Once the nanostructures are preformed, the light interaction might provide positive (constructive) or negative (destructive) feedback for the following evolution during successive laser pulse irradiation. Generally, the simplified feedback mechanisms are the material removal in the maxima of the intensity ("ablation") or the material addition in these maxima (commonly referred as "expansion") [92, 100]. The hydrodynamic effects are detailed in the next subsection and might be much more complex, but the examples of "ablation" are phase explosion/evaporation of the overcritical temperature surface layers or material removal caused by recoil pressure or Marangoni forces [67, 101], whereas "expansion" occurs during material swelling [17, 67]. From the electromagnetic point of view, the "ablation" provides positive feedback for the growth of periodic nanostructures oriented perpendicularly to the laser polarization and negative for the parallel ones [24, 45, 92]. In contrast, the "expansion" feedback is beneficial for the growth of parallel oriented LIPSS [100]. More precisely, LSFL on metals and semiconductors (or HSFL on dielectric/metal surfaces), having orientation perpendicular to the laser polarization, are reinforced by positive "ablation" feedback [24, 45, 92], but LSFL on wide bandgap dielectrics (and parallel HSFL on metal surfaces) can grow only under positive "expansion" feedback [100]. More details concerning the specific types of LIPSS are provided in a separate section. Additionally, it is worth noting that the action of these feedback mechanisms is inverted by applying cross-polarized laser beams, which can result in the erasure of the created nanostructures on the surface or in the bulk of materials [102–105].

Superficial Nanolayer Laser-matter interaction might result in the establishment of new interfaces between excited or modified material and the medium, which is unaffected by laser irradiation. These interfaces exhibiting abrupt contrast of refractive indices may influence the light propagation and, as a result, the orientation and the periodicity of the interference patterns (concept illustrated in Fig. 5.5d). Note that surface roughness itself (pristine or created by laser irradiation, including periodic surface structures) was considered in several papers as a nanolayer with effective medium properties or air volume fraction [106–109], which is a rough approximation, valid only for low filling factors in volume and slight perturbations of the optical properties.

Excitation of SPPs at the interface of a thin nanolayer of a dense electron plasma and non-excited material was proposed as the origin of sub-wavelength patterns in Ref. [106]. This scenario relies on quasi-metallic properties of the homogeneous plasma layer that allow for $\lambda_{SPP} \ll \lambda$.

Considering multipulse irradiation, the chemical reactions initiated by previous pulses may result in the formation of a thin nanoscale oxide layer at the top of the metal surfaces with different optical properties than of the pristine material [108, 110, 111]. Such configuration with the intermediate properties modeled by an effective porous medium was proposed to modify the periodicity of surface electromagnetic waves down to the nanoscale and, consequently, the periodic energy deposition perpendicular to the laser polarization by the following pulses. In contrast, recent experiments have provided no evidence for a clear relation between an oxide layer and the formation of patterns with sub-wavelength periodicity [111]. Additionally, a different type of patterns below the oxide layer with the parallel orientation and a periodicity $\approx \lambda/n$ (n is the refractive index of the oxide layer) was observed experimentally and interpreted by the interference patterns calculated by full-vector Maxwell simulations with structured surface and a 100-nm-thick, transparent oxidation layer on the top of it [110].

3.2 How the Hydrodynamics Creates/Amplifies the Inhomogeneity

After a brief introduction in light-matter interaction during laser excitation, we discuss the possible pathways to permanent modifications at the nanoscale on the surface and in the bulk after ultrashort laser pulse exposure. We note here that some types of the modifications might be relevant only for specific materials. For example, low refractive index changes are commonly induced by multipulse irradiation of glasses [112]; transitions from solid to an amorphous material with different material properties upon laser irradiation are evidenced for silicon [113]; oxidation chemical processes might occur on a thin nanoscale surface layer of metals [108, 110], etc. Nevertheless, we focus here on the processes that are common for the majority of materials, which are summarized in Fig. 5.8. Generally, the permanent modifications are then the consequence of phase transitions induced by pure thermal (direct heating) or thermomechanical (pressure wave propagation driven by temperature gradients) effects. These processes are pronounced in case of ultrashort pulse irradiation due to ultrafast energy deposition (timescales smaller than for thermal diffusion and pressure wave dissipation processes), and, as a result, heat and stress confinement that lead to abrupt irreversible nanoscale modifications. Importantly, the underlined modifications occur on the timescales from tens of picoseconds to hundreds of nanoseconds, followed by fast resolidification, imprinting the organized structures on the surface or in the bulk of materials. The hydrodynamic phenomena on these scales have been recently evidenced by double-pulse experiments with the appropriate delays, showing the pronounced sensitivity of the final surface topography to the respective delays [31, 32, 114–116], and by time-resolved diffraction signals [78].

Melting Non-ablative modifications that do not necessarily require the laser pulse energies exceeding the material ablation threshold can be initiated by laser-induced local melting. The nanoscale melt layer on the surfaces of dielectrics, semiconductors, or metals can be affected by nanoscale forces of different origins that further result in destabilization of the layer, fluid flow above the initial surface, and material rearrangement followed by fast resolidification. The timescale of resolidification typically limits the action of forces at the nanoscale. For instance, the gravitation forces exerted on a melt layer provide negligible acceleration to affect the melt flow, whereas the van der Waals forces would necessitate a material, staying in a liquid phase for milliseconds [117]. One could mention the Marangoni forces caused by surface tension gradients, the forces driven by phase transitions and density gradients, i.e., subsurface cavitation, evaporation (recoil pressure forces),

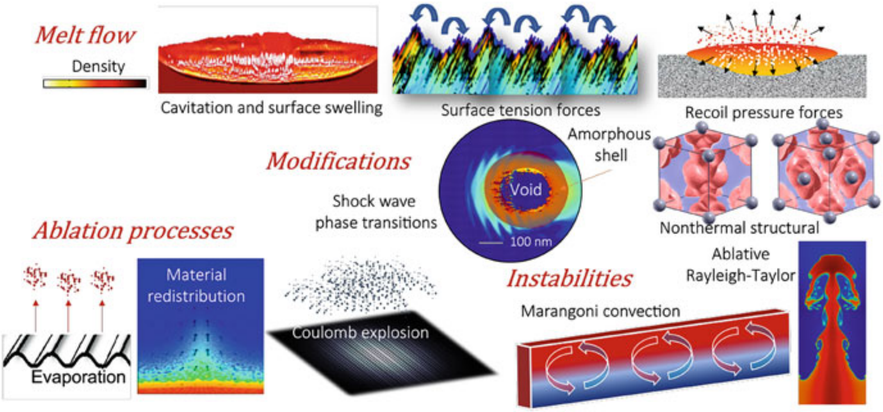
Melt flow
Density
Cavitation and surface swelling
Surface tension forces
Recoil pressure forces
Modifications
Amorphous shell
Void
100 nm
Shock wave phase transitions
Nonthermal structural
Ablation processes
Evaporation
Material redistribution
Coulomb explosion
Instabilities
Ablative Rayleigh-Taylor
Marangoni convection

Fig. 5.8 Physical phenomena resulting in material modifications under ultrashort laser excitation: melt flow driven by internal forces (rarefaction/surface tension/recoil pressure), pressure wave propagation and nonthermal processes, surface ablation, and hydrodynamic instabilities (convection Marangoni and Rayleigh-Taylor instability from Ref. [141]). Copyright Elsevier 2019

and resolidification as the potential drivers of the melt flow upon femtosecond laser excitation [118, 119]. The involvement of Marangoni forces, surface swelling due to formation of subsurface cavities and recoil pressure in the melt flow dynamics, and laser ablation processes is evidenced by the observation of material redistribution above the initial surface level [17, 120]. Additionally, more exotic phenomena comprising hydrodynamic instabilities in a thin liquid layer are possible in the regimes of femtosecond laser pulse excitation.

Hydrodynamic Instability Nanoscale instabilities on the laser-excited surfaces are the main drivers of material arrangement in periodic patterns, different from the ones imposed by the laser beam interference. Several specific conditions are required to initiate a hydrodynamic instability: initial perturbations, destabilizing force acting against the imposed temperature or density gradients, and satisfactory conditions for the instability growth. The concept of self-organization to explain the periodic surface morphology was firstly formulated in the frame of a defect deformation instability of the surface relief described by Kuramoto-Sivashinsky equations [121–123]. This scenario is based on nucleation, diffusion, and erosion of mobile point defects (adatom vacancies, electron-hole pairs, etc.) induced by the laser in a thin surface layer that can cooperatively arrange in the periodically ordered distributions, including LIPSS or hexagonal structures [121]. The empirical equation used in numerical simulations is widely applied for a dimensionless mathematical analysis of Turing patterns in the systems out-of-equilibrium [124]. However, the parameters are a priori unknown and not directly related to measurable material properties. Nevertheless, the concept of defect-deformation might be interesting along with the recent observations of low-fluence periodic structuring on the atomic level [125], discussed in the subsection “Alternative Mechanisms.”

On the other side, similar self-organized patterns can be formed by hydrodynamic instabilities having well-established physical origins, namely, Bénard-Marangoni and Rayleigh-Taylor instabilities.

The Marangoni instability was firstly realized in a convection experiment while heating a liquid with a free upper surface from below, where the liquid flow driven by surface tension gradient (Marangoni) forces arranges into hexagons (the fluid rises in the center and descends along its six sidewalls) [126]. The opposite behavior is observed in gases with the fluid descending in the center of the hexagons. The symmetry can be inverted by multiple effects, including temperature-dependent viscosity, thermal conductivity, and density—the main physical properties of the liquid layer [127]. Upon bifurcation, the hexagons transform into quasiperiodic stripes, which is another stable solution of the convection problem [128]. The classical Bénard-Marangoni problem cannot be directly applied to the laser ablation problem because the vertical temperature gradient is directed toward the free surface and the Marangoni critical number is too low to produce the instability [118, 119]. Nevertheless, the instability can be caused by horizontal temperature (and surface tension) gradients created by inhomogeneous energy deposition. The strong perturbation perpendicular to the interface results from melt flow driven by phase transitions below the surface (subsurface cavitation). This effect is responsible for compressible fluid dynamics with deformable surfaces—a more complex dynamic problem, where the condition of the critical Marangoni number is no more relevant [129]. The modification takes place in the form of hydrothermal waves caused by polarization-dependent disturbances (intensity, temperature, surface tension) on the laser-excited surface. The instability wavelength is proportional to the thickness of melt layer, and the time required for the development lies within $\approx$ 100 ps, faster than the expected cooling time of the laser-excited materials [119]. The Marangoni convection instability has been proposed to be involved in the formation of grooves and spikes driven by temperature gradients induced by preexisting near-wavelength LIPSS [130–132], in the formation of sub-wavelength HSFL initiated by gradients caused by polarization-dependent absorption of random nanoholes and nanobumps [119], and be responsible for the crown-like reliefs in nanosecond laser-produced rims [133].

Ablative and rarefaction forces may accelerate a lighter fluid (vapor, cavity) into a heavier one (liquid), which potentially results in the development of Rayleigh-Taylor instabilities (accompanied by the Richtmyer-Meshkov instability if the acceleration is impulsive or by the Kelvin-Helmholtz instability if there is a velocity difference across the interface between two fluids) [134, 135]. This instability takes place naturally at different scales from atomic to astrophysical and is commonly observed in laser inertial confinement fusion and explosive combustion. The consequence of such instability is the growth of "mushroomlike" spikes and bubbles at the interface between two fluids and their turbulent mixing. Pressure gradients during laser ablation reach several gigapascals. An acceleration produced by the recoil pressure would be strong enough to cause instability on pico-/nanosecond timescales and nano-/micrometer spatial scales [118, 119, 136]. However, several factors including surface tension have a stabilizing effect, and further observations and numerical simulations in the ablative regimes are required to elucidate the potential role of Rayleigh-Taylor instabilities in ultrashort laser-matter interactions.

Plastic Deformation Shock wave propagation in the bulk of solid materials results in plastic deformation. In glasses and crystals, this effect may lie at the origin of refractive index changes [137]. In metals, the compressive residual stresses induced by a shock wave result in material hardening and modify the material properties, improving the resistance to fatigue, known as laser shock peening [138]. Depending on shock strength, the modifications may vary from low refractive index changes to exotic nanoscale dense phases observed in the experiments of microexplosion in the bulk of transparent solids [139, 140]. The modifications can be involved in the establishment of periodic volume structures. For instance, laser-induced nanogratings consist of nanolayers with contrasted refractive index changes, corresponding to densified and rarefied material [77].

Cavitation and Nucleation Independent of the nature of the irradiated material (dielectrics, semiconductors, metals), the material failure can occur via thermomechanical pathways resulting in an abrupt phase transition through cavitation (subjected to the critical negative pressure) or through nucleation (subjected to the critical high temperature). Cavitation is often the consequence of the rarefaction induced by pressure waves in ultrashort laser processing of surfaces and bulk materials. In this case, the confined modifications are established on nano-/micrometer spatial scales in tens of picosecond timescales [16, 60, 67, 142]. Along with the thermomechanical processes, the modifications can be driven by nucleation processes [66, 143]. Nanoscopic void-like structures observed below the laser-irradiated surfaces [16, 144] or in the bulk of transparent materials [79, 145] play an important role in multipulse feedback and successive energy deposition [67, 143], as well as for the destabilization of a thin melt layer [119]. In a recent work, subsurface cavitation and material swelling processes have been proposed to play the key role in the formation of LSFL induced by femtosecond laser excitation of surface plasmon polaritons from a gold step edge [146]. The continuous growth of nanocavities in melt flow was observed in molecular dynamics simulations beneath the metal surface [60, 142] and also simulated by Rayleigh-Plesset equations in the bulk of fused silica [143].

Phase/Coulomb Explosion Phase explosion is considered to be one of the major surface ablation and material removal mechanisms [147]. Additionally, the phenomenon of Coulomb explosion relying on breaking bonds of solids by repulsive Coulomb forces is potentially involved upon intense femtosecond laser excitation of dielectrics and semiconductors, although it is inhibited in metals by the high mobility of the conduction band electrons [148]. Both of these mechanisms were proposed to participate in LIPSS formation at the nanoscale [70, 101, 149–152]. Shugaev et al. performed molecular dynamics simulations with periodic pulse energy modulation, where $\approx$ 600 nm liquid wall structure and $\approx$ 100 nm frozen protrusion above the initial surface upon resolidification are formed at the predefined intensity minima [151]. This scenario underlying the pronounced role of the material redistribution in the lower part of the ablation plume upon single pulse excitation differs from the one considered in classical ablation models with dominantly material removal of the overcritical surface layers corresponding to the intensity maxima [33, 118, 152] or the melt flow driven to colder regions by the ablative recoil pressure forces [101]. Concerning the Coulomb explosion scenario, the periodic modulation was proposed to originate from the energy deposition by surface plasma wave inducing inhomogeneous free carrier density profiles and resulting in periodic explosion of localized ion clouds [70, 149, 150]. The multitude of proposed mechanisms emphasizes the need to consider the actual energy pulse deposition, the microscopic (molecular dynamics or particle-in-cell methods) or the macroscopic (compressible Navier-Stokes equations) hydrodynamics, and the multipulse feedbacks within one single coupled approach.

Multipulse Laser Ablation Attempt to address multipulse laser ablation processes in its full dynamic complexity has been made in recent works considering Maxwell equations for the energy deposition on the laser-modified surface coupled with macroscopic compressible Navier-Stokes equations [67, 80, 119].

In the first work, both the mechanical (cavitation and spallation by negative pressure) and the thermal (phase explosion lose to the critical temperature) processes were considered to be relevant on metal surfaces. General trends of femtosecond irradiation are summarized in Fig. 5.9, classified by required laser fluence and number of applied pulses. The first pulse results in subsurface cavitation on the nanoscale, formation of a microvoid below the surface, or thermal ablation depending on laser fluence. The corresponding lattice density snapshots are illustrated at the bottom of Fig. 5.9. The typical optical responses of the deformed surfaces are sketched in the upper row corresponding to the second pulse irradiation. Among them, local field enhancement by created subsurface voids is underlined. The next upper row details the typical surface profile developing after irradiation with several pulses, consisting of surface nanoroughness and ripples. Then, the mechanisms of periodic structure regulation are detailed in the upper part of Fig. 5.9. For near-threshold fluences, the hydrodynamic scenario is expected, where the cavitation takes place in the melted tips of the nanostructures, which are further removed by the following pulses due to strong local field enhancement on subsurface nanovoids. For higher fluences, the electromagnetic feedback dominates over the hydrodynamic processes, resulting in shape modification of ripples and a homogeneous distribution of the absorbed energy over the whole surface.

The Marangoni effects, defined by surface tension gradients, were added in Ref. [119] via specific Marangoni boundary conditions on the surface. The simulations showed the possibility of femtosecond laser nanostructuring by melt flow above the initial surface and the development of a hydrodynamic instability in a thin melt layer. Importantly, these nanoscale effects are accompanied by laser ablation through subsurface cavitation and material removal in the intensity maxima discussed in Fig. 5.9, which explains the mixed morphologies of LIPSS (including LSFL and HSFL) evolving with the number of applied pulses.

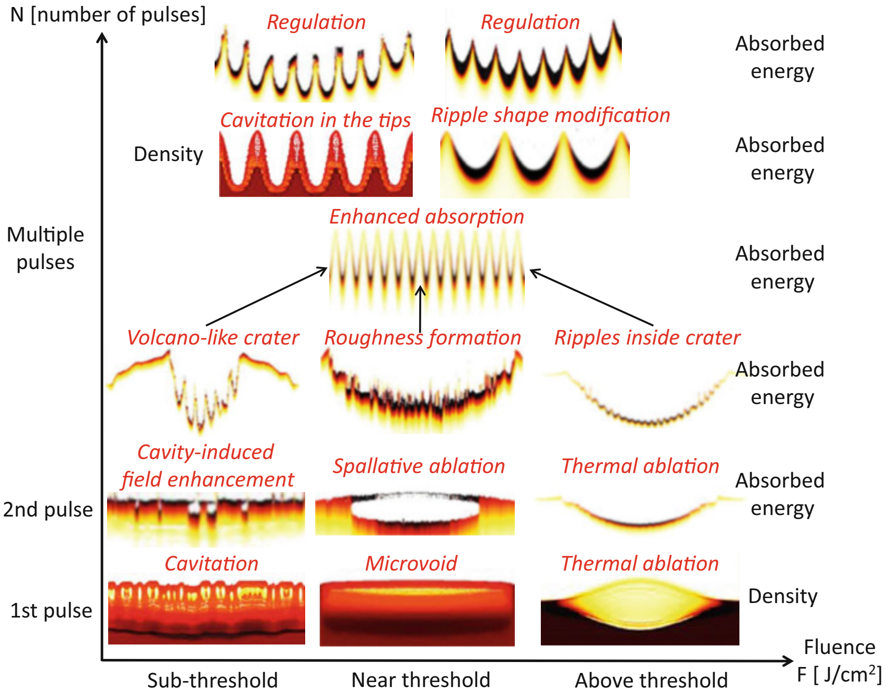
N [number of pulses]
Regulation
Regulation
Absorbed energy
Cavitation in the tips
Ripple shape modification
Density
Absorbed energy
Enhanced absorption
Multiple pulses
Absorbed energy
Volcano-like crater
Roughness formation
Ripples inside crater
Absorbed energy
Cavity-induced field enhancement
Spallative ablation
Thermal ablation
Absorbed energy
2nd pulse
Cavitation
Microvoid
Thermal ablation
Density
1st pulse
Fluence F [J/cm^2]
Sub-threshold
Near threshold
Above threshold

Fig. 5.9 Schematics of coupled electromagnetic and hydrodynamic processes upon multipulse femtosecond laser irradiation as a function of laser fluence and number of applied pulses. Absorbed energy is calculated by Maxwell equations, whereas density snapshots are obtained by solution of compressible Navier-Stokes equations detailed in Ref. [67]. Reprinted figure with permission from A. Rudenko et al., Phys. Rev. B 99, 235412, 2019. Copyright 2019 by the American Physical Society

Finally, the recent work [80] devoted to femtosecond laser-induced modifications in the bulk of fused silica (without free surfaces) points out the relevance of pressure wave-driven cavitation processes in the onset of periodic volume nanogratings. In this case, the constructive feedback is provided by combined local field enhancement, electron plasma growth, and cavitation induced by negative pressures.

Nonthermal Phase Transitions Additionally, nonthermal phase transitions (melting, ablation) can be induced in semiconductors and metals after strong electronic excitation of the material with intense femtosecond laser pulses [153–156]. Remarkably, such processes may also result in drastic changes from hexagonal to cubic solid phases and in mechanical expansion of finite-size metal nanoclusters or nanoparticles [156]. The possibility to trigger ultrafast allotropic transitions in transition metals under femtosecond laser irradiation has been intensively investigated by means of ab initio calculations [157–159]. Before thermal solid-to-liquid transformations, electronic heating can drastically modify screening, charge distribution, and atomic binding features, potentially triggering structural modifications in the solid phase. The relevance of nonthermal processes in multipulse ultrashort pulse irradiation of surfaces with nanoscale roughness still remains to be elucidated. The examples of laser-induced nonthermal effects in solids and a theoretical framework to investigate these processes are detailed in Chapter 3 by Bauerhenne et al.

Alternative Mechanisms A recent report [125] suggests that both reversible and irreversible nanoscale periodic surface patterns can be induced by electrostatic stress-induced cold viscous flow from charged defects excited by laser pulse energies few orders below the ablation threshold. Under the applied laser irradiation conditions ($F \approx$ mJ/cm^2), nonlinear absorption is estimated to be negligible to induce any heat-driven modifications. The authors question whether an alternative scenario of material modification is possible via a nonthermal mechanism originating from low carrier excitation in dielectrics [125]. On metal surfaces, the nanoscopic surface modifications in the form of adatom and vacancy clusters have been evidenced, applying fluences of the same order of magnitude or lower, much below the melting threshold [160]. Understanding the mechanisms responsible for the onset of irreversible modifications at the nanoscale is particularly relevant to the regime of multiple pulse irradiation, where significant changes in the surface topography may accumulate pulse-by-pulse following the inter-pulse feedback and roughness amplification.

4 Universality of LIPSS: From Dielectrics to Metals

After having introduced the major physical effects involved in LIPSS formation, we focus on the particular types of periodic nanostructures on dielectric, semiconductor, and metal surfaces and in the bulk of transparent solids. We summarize the recent numerical achievements and point out where sufficient agreement is achieved and where open questions still remain. A detailed literature survey on the experimental observations of LIPSS created on specific materials can be found in a recent review [161].

4.1 Dielectrics

Commonly observed periodic nanostructures on the surface of transparent glasses and crystals (dielectrics) include LSFL($\|$, λ/n), with an orientation parallel to the laser polarization and near-wavelength periodicity, and HSFL($\perp$, $\ll \lambda/n$) with an orientation perpendicular to the laser polarization and sub-wavelength periods [78, 91]. The latter orthogonal nanostructures are also formed deep in the bulk of glasses and crystals by self-organization, representing volume nanogratings, which exhibit strong refractive index contrast and birefringence [75–77].

LSFL First observation and explanation of near-wavelength ripples with λ/n periods along the polarization direction dates back to the early 1980s, considering scattering from an individual shallow scratch on the dielectric interface [163]. Sipe's theory for inhomogeneous scattering from a rough surface [21] includes this solution for transparent materials and was later used to analyze experimental results. As the refractive index n primarily decreases upon the excitation of free carriers, the periodicity increase, observed experimentally, was attributed to the transient behavior of the excited dielectrics [91]. The interference patterns originating from light interaction with rough surfaces and having an orientation parallel to the laser polarization and near-wavelength periodicity were obtained by full-vector electromagnetic simulations, confirming the increasing periodicity with the increasing excitation rate (free carrier density) [92]. The electron plasma kinetics was further coupled to propagation codes to explore the variety of patterns forming after single pulse excitation due to intra-pulse feedback. Generally, electron plasma patterns with a better regularity are reproduced well below ($\approx$ 200 nm) the initial surface level [47, 78]. The material modification toward regular LSFL in this case should involve significant ablation and removal of the upper surface layers [78]. The multipulse evolution of LSFL, however, still remains to be elucidated because a simple ablation feedback cannot explain the growth of the nanostructures oriented parallel to the electric field.

HSFL In the latest works with nonlinear propagation coupled to electron plasma kinetics [47, 78], LSFL patterns were obtained simultaneously with other type of ripples (HSFL) with the orientation perpendicular to the laser polarization and sub-wavelength periodicity, in agreement with several experiments [78, 91, 164]. Figure 5.10a shows the experimental SEM image with both types of LIPSS indicated and the electron plasma distributions simulated by a full-vector Maxwell propagation code coupled with a rate equation for the electron density kinetics. Essentially, the orientation and the periodicity of patterns are in good agreement with the experiments, and the complex morphology with coexisting patterns can be explained by partial removal of the upper surface layers during laser ablation. The evolution of HSFL nanostructures involves electron plasma growth deep below the laser-irradiated surface or inside the bulk of transparent materials. The origin of the regularity and periodicity has different interpretations in the literature. One of the proposed scenarios relies on the excitation of SPPs with a wavelength significantly smaller than the laser wavelength corresponding to a plasmonic wave at the interface between a highly excited overdense plasma and weakly excited material [106, 109, 165] or the surrounding medium (air, water) [166, 167]. According to the Drude model and the expression for the SPP wavelength, the period then continuously decreases with increasing excitation rate (electron density) [106, 166, 167]. The described concept corresponds to the intra-pulse feedback in Fig. 5.5d with a laser-induced superficial plasma layer on the top of the surface. On one side, the exact optical properties of an electron plasma nanolayer of the laser-excited surface are difficult to verify experimentally. On the other side, the simulations indicate that quasiperiodic nanoplasmas form already at carrier densities much lower than

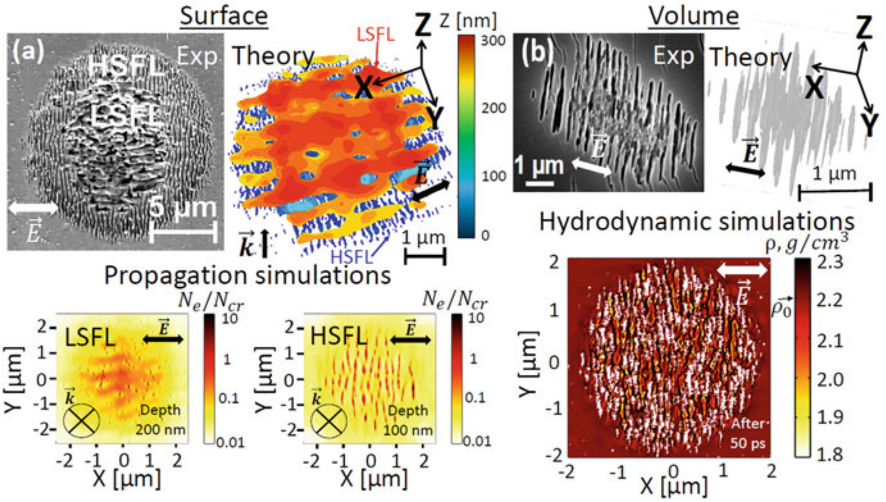

Fig. 5.10 LIPSS on the surface (**a**) and in the bulk (**b**) of fused silica. The experimental "Exp" SEM images of the topography after multiple ultrashort laser pulse excitation are provided from Ref. [78] (**a**) and from Ref. [162] (**b**). Copyright 2012 Optical Society of America. (**a**) The simulation results of electron plasma patterns beneath fused silica surface, corresponding to LSFL and HSFL ripples, are shown. The electron density N_e is normalized to the critical value N_{cr} in vacuum, and the values $N_e > 10^{20}$ cm^{-3} are plotted on 3D image. Simulation details can be found in Ref. [78]. Copyright 2017 Springer Nature. (**b**) The 3D image of the electron plasma pattern (values $N_e > 0.5N_{cr}$) in the bulk of fused silica is plotted, and the 2D hydrodynamic snapshot of the glass density is provided, indicating modifications (cavitation, melting, and densification) upon $N = 7$ pulse irradiation 50 ps after pulse excitation. The pristine density of fused silica ρ_0 is indicated on the scale. Simulation details are provided in Ref. [80]. Copyright Wiley-VCH 2021

required for the excitation of SPPs (and the periods are independent of the exact value of electron density—inhomogeneous distributions are considered) [47, 78]. Additionally, propagating waves with extreme sub-wavelength periods cannot fully couple with the incident light due to the contribution of other surface waves with approximately wavelength periodicity and strong damping on rough surfaces [27]. As a result, even at extreme excitation conditions at the interface of transparent materials (when SPPs are excited), the only interference patterns that are supported in the bulk have a periodicity close to the wavelength in the medium [46, 49, 109]. Different scenario invokes a symmetry breaking by polarization-dependent near fields at single inhomogeneities in the bulk or at the surface [46, 76, 78], initiation of structure growth (within a single pulse, growth of individual nanoplasmas; within multiple pulses, growth of individual nanovoid structures), and then a selective process of multiple interference supporting the amplification of nanograting periods corresponding to a fraction of the laser wavelength in the medium λ/n [46, 49], $\lambda/2n$ [47, 49, 78, 168], $\lambda/3n$ etc. [49, 169]. This concept should generally include both intra- and inter-pulse feedbacks, illustrated in Fig. 5.5a, successively improving the structure regularity with the number of applied pulses, and does not necessarily involve the excitation of SPPs in contrast to the firstly proposed concept [78]. The spacing between electron plasma nanogratings was shown to correlate with the concentration of the inhomogeneities (nanovoids), indicating that the period reduction might originate from an increasing number of laser-induced nanoscopic modifications with increasing number of applied pulses [49]. Recent multipulse simulations, which couple the electron plasma kinetics with hydrodynamics on longer timescales [80], provide a realistic description of the evolution of volume nanogratings in the bulk of fused silica. The extended approach not only explains the intermediate regimes when polarization-dependent ellipsoidal nanovoids are created [79], but also how the high regularity is achieved and which transient and permanent modifications take place during multiple pulse laser processing. The calculated three-dimensional void structures are similar to the ones observed experimentally [162], both shown in Fig. 5.10. The hydrodynamic snapshot at the bottom of the figure reveals a complex interplay between the involved void cavitation processes (white color, low density), melting and fluid flow (intermediate liquid density), and densification (black color, high density). Nanoscale subsurface cavitation can be potentially involved as well in the formation of HSFL on the surface of dielectrics, although it is not regarded as necessary condition [47].

Grooves In addition, grooves($\|$, $\gg \lambda$) parallel to the laser polarization and having periods exceeding the laser wavelength were reported if high number of pulses are applied. These surface structures were attributed to a convection instability driven by parallel hydrothermal waves in high-viscosity fused silica [132]. Tsibidis et al. proposed that the convection instability was caused by preexisting LSFL($\|$, λ/n) on the fused silica surface. The increasing periods of both LSFLs and grooves with increasing fluence or number of applied pulses observed in the experiment were related to incubation effects [132]. The hydrodynamic scenario for groove formation is plausible here; nevertheless, the multipulse evolution of the surface topography and the successive energy deposition (Tsibidis et al. considered Sipe's efficacy theory to describe the light interaction with microscopic roughness) as well as the role of the considered processes (Marangoni, recoil pressure, or gravitational forces) involved in the critical number (and the period) definition remain to be clarified.

4.2 Semiconductors and Metals

Generally, there is no sharp boundary between dielectrics and semiconductors. Therefore, lower bandgap semiconductors may react in a similar way to wide bandgap dielectrics at high excitation levels. In case of low bandgap materials (silicon, germanium, zinc oxide etc.), commonly observed periodic structures are LSFL($\perp$, $\approx \lambda$) perpendicular to the laser polarization with near-wavelength periodicity, HSFL($\|$, $\perp$, $\ll \lambda/n$) parallel or perpendicular to the laser polarization and deep sub-wavelength periodicity, and grooves($\|$, $\gg \lambda$) parallel to the laser polarization and periods exceeding the laser wavelength [27, 64, 90, 93, 131, 170].

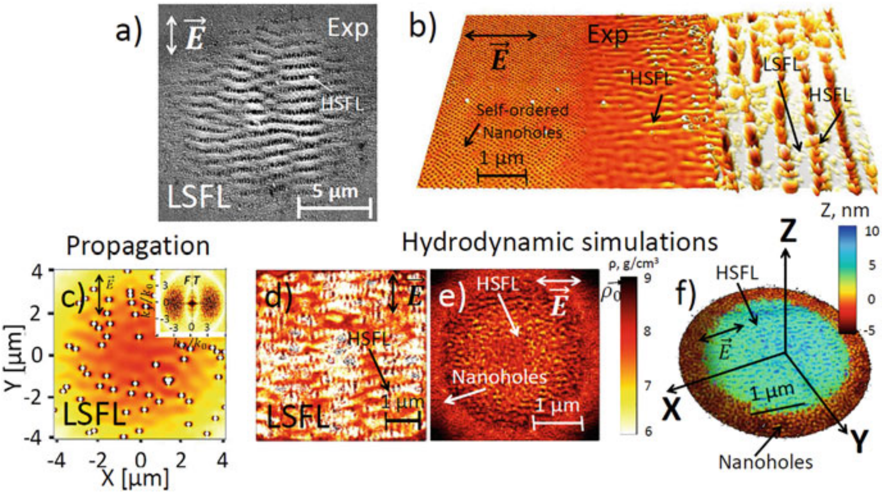

Fig. 5.11 LIPSS on the surface of metal (nickel). The experimental "Exp" SEM images of the topography after multiple ultrashort laser pulse excitation are provided from Ref. [16] (**a**) and from Ref. [119] (**b**). (**c**) The interference patterns calculated by Maxwell equations beneath metal surface, showing pronounced LSFL patterns. Simulation details are provided in Ref. [16]. Adapted with permission from ACS Photonics 2018, 5, 4, 1418–1426. Copyright 2018 American Chemical Society. (**d**), (**e**) Density snapshots 100 ps after pulse excitation of nickel surface, indicating simultaneous formation of HSFL, LSFL, and self-organized nanoholes. The details of hydrodynamic simulations are from Ref. [119]. The pristine density of nickel ρ_0 is indicated on the scale. (**f**) 3D snapshot of nickel density, showing the surface topography after laser pulse irradiation from Ref. [119].Copyright 2020 Elsevier

The indicated types of LIPSS observed on semiconductor surfaces are commonly also created by multiple irradiation of metal surfaces [20, 29, 152]. Therefore, some of the proposed formation mechanisms are relevant to both, semiconductors and metals.

LSFL The orientation and the periodicity of the near-wavelength LIPSS are commonly explained by Sipe's theory with transient quasi-metallic homogeneous properties of the electron plasma for semiconductors [22, 90, 170] and electronically modified optical properties for metals [45] or SPP theories on a flat plasma-air (or metal-air) interface [64, 93, 171]. The near-wavelength quasiperiodic interference patterns perpendicular to the laser polarization can be obtained by solving full-vector Maxwell propagation equations beneath rough surface with nanometric holes or bumps, resembling the experimentally observed LSFL as shown in Fig. 5.11a, c. The debate is still open regarding the necessary involvement of surface plasmons [27, 172], as long as both features (orientation and periodicity) can be interpreted by the interference of the incident light with non-plasmonic evanescent waves in an electron plasma approaching metallic densities, which are, however, not sufficient to excite surface plasmons at the plasma-air interface [22, 27, 45]. We note that the discrepancy is due to multiple factors, including limited applicability of the SPP excitation criterion for a flat interface; transient optical changes in the spatially inhomogeneous electron plasma kinetics, which are not necessarily characterized by an instantaneous Drude response with a certain electron density; contributions from evanescent surface waves; and the evolving changes of the surface topography upon irradiation with multiple pulses. In case of plasmonic metals, SPPs are likely to contribute strongly to the spatially periodic energy deposition [24, 94, 146]. The application of advanced models for the nonlinear optical response of laser-excited surfaces including semiconductor Maxwell-Bloch equations [56, 57] or nonequilibrium approaches including the interband and intraband transitions in metals [50, 51, 55] can potentially provide deeper insight and resolve some of the remaining issues.

The decreasing period of LSFLs with increasing number of applied pulses (tendency commonly observed for both laser-excited semiconductors [64, 93, 173] and metals [31, 93, 94, 152]) was interpreted by considering inter-pulse feedback mechanisms on the evolving surface topography. For instance, according to the grating-assisted SPP theory [93], the periodicity would adapt to the changes of the surface plasmon resonance with the increasing depth of the ripple gratings. Such an interpretation does not explain how a grating with one fixed period would transform into grating with a different one and was not supported numerically by electromagnetic calculations with multipulse material removal feedback [24, 92]. Alternative explanations were based on the angle dependence [92], the transient changes of the optical properties of metals [94], and the displacement of molten material by surface tension forces from the protruded hills toward the wells of ripples [64]. Recently, numerical simulations were performed on the surface topography evolution from its pristine roughness toward well-ordered grating structures [24]. The established periodicity after tens of pulses was found well below the SPP wavelength, independent of the ripple depth, transient changes of the optical properties, without strong angle dependence in the center of the crater and potential melt flow dynamics. The blueshift toward smaller periods was explained by the involvement of evanescent quasi-cylindrical waves, which have a significant contribution to absorption near the individual nanoholes (or Hertzian dipoles on the surface) and reduce the resonant wavelength from near-wavelength $\approx \lambda$ to sub-wavelength $\approx 3\lambda/4$ via collective dipole-dipole coupling [24, 31].

Another commonly observed dependence is the increasing period with the increasing laser fluence and a saturation near $\approx \lambda$ [64, 88, 152, 171, 174]. In case of semiconductors, this behavior was explained by the increase of surface plasmon wavelength with the electron density of the excited transient plasma [64, 171]. This scenario might be not applicable in the case of metals due to a different evolution of the transient optical properties upon the electronic excitation. Nevertheless, the laser excitation was proposed to modify the plasma frequency of metals [174], or to affect the permittivity of laser-excited metals through two-photon absorption [88], causing the potential increase in the predicted grating spacing. Both approaches rely on empirical hypothesized dependencies, supported neither by the experimental evidence nor by Maxwell-based propagation simulations (to model the interference between incident and transiently scattered waves). Quantum-based models taking into account both intraband and interband transitions in laser-excited metals [175] or ab initio simulations [176] coupled with appropriate propagation solvers [55] should be applied here to get an accurate description and deeper understanding of the transient optical properties and the pulse energy deposition at laser-excited metal surfaces. An alternative interpretation relies on the fact that at high laser fluence, the ablation (and melting) takes place all along the surface (at the tips and at the bottom of the surface nanoholes) and favors, therefore, the role of long-distance interference maxima rather than local field effects. These maxima would have a regular periodicity close to $\approx \lambda$, and the nanohole coupling effects, contributing to a resonance blueshift, would be negligible [24]. This way, the period increase with increasing laser fluence may have a fully electromagnetic explanation (applicable to metals and semiconductors), without the involvement of specific transient changes of the optical properties.

A different aspect of LSFLs formation concerns the involved hydrodynamics: whether the structures are formed by material ablation, by material swelling, or by melt flow dynamics without involvement of strong ablation. For instance, structures above the initial surface level were observed on silicon surfaces [27, 64], which supports the involvement of melt dynamics. Nevertheless, the mechanisms leading to surface modification may vary and likely depend on the laser fluence (being either in the sub-ablative or ablative regime). In this context, the emergence of LIPSS on metal surfaces has been attributed to different material removal processes, including cavitation and spallative ablation [20, 67, 146], phase explosion and material redistribution [151], or even the Coulomb explosion mechanism [70]. Hydrodynamic scenarios encompassing different inter-pulse feedbacks (positive or negative) may affect the properties of ripples, resulting in the amplification and growth of the structures [67], but also changes in ripple periods [24, 64], or their partial erasure [143].

HSFL The formation mechanisms of ripples with much smaller periodicity (HSFLs), perpendicular or parallel to the laser polarization, have been debated in the literature and have different interpretations. In some works, a similar mechanism as for the formation of LSFLs, which relies on the excitation of sub-wavelength SPPs, was proposed (sometimes involving second harmonic generation of incident laser radiation or LSFL splitting) [98, 166, 177]. Clearly, the nanostructures with orientation parallel to the laser polarization cannot be explained by such scenario, as well as the possibility of creating structures with mixed types of orientation [20]. Sipe's theory, commonly applied to interpret LSFLs, fails here. However, full-vector electromagnetic calculations indicate that the high-frequency polarization response underneath rough surface may originate from near-field local effects near individual nanoholes or nanobumps [33, 45, 92]. For clarity, a spatial Fourier transform from the typical interference patterns is shown in Fig. 5.11c. This response contains a variety of high frequencies but is a priori random, although coherent [45]. It is worth noting that both orientations with respect to the laser polarization are possible depending on the nature of the inhomogeneities [33]. Recently, coupled electromagnetic-hydrodynamic simulations have shown that the regularity originates not from the interference patterns but is rather a consequence of the hydrodynamic convection instability in a thin melt layer destabilized by the excited pressure wave [119]. Such scenario considers a hierarchy of coupled effects. First, the near-field enhancement near individual inhomogeneities contributes to a polarization-dependent energy deposition and oriented temperature gradients. Second, the laser-excited pressure wave destabilizes the melt layer pushing it upward from the interface. At the interface, the surface tension forces driven by polarization-dependent temperature gradients redistribute the molten material above the interface following the hydrothermal waves. Periodic structures appear as a consequence of the convection instability with a characteristic period proportional to the melt layer thickness [119]. When both electromagnetic and hydrodynamic approaches are coupled together, inter-pulse feedback mechanisms can be included to describe multipulse irradiation. As a result, even complex ripple morphologies consisting of mixed LSFL and HSFL structures on nickel surface or hexagonal nanoholes as shown in Fig. 5.11a, b have been reproduced by 3D numerical simulations. For instance, Fig. 5.11d shows a metal density snapshot with near-wavelength LSFL patterns having purely electromagnetic origin is covered by cross-oriented HSFL structures of a smaller period having hydrodynamic origins. Figure 5.11e, f details the density and the 3D surface topography after single pulse excitation with sub-ablation fluence, where the HSFL structures are evidenced in the center and surrounded by self-ordered quasi-hexagonal nanoholes. Similar configurations were observed experimentally [117], as shown in Fig. 5.11b.

Hexagonal Structures The abovementioned hexagonal nanostructures deserve particular attention. Until recently, hexagonal arrangements (holes, pores, particles, spikes) were observed only in a few works with nanosecond lasers and had micrometer sizes [130, 136, 178, 179]. These self-organized structures were attributed to Marangoni convection [130, 179] and Rayleigh-Taylor [136] hydrodynamic instabilities. Recently, similar structures have been observed also at the nanoscale by applying double pulses with picosecond to nanosecond time delays [32, 115–117, 180]. In case of long time delays, the electron dynamics induced by the second laser pulse occurs to be uncoupled from the electronic excitation by the first pulse (considering that the thermal equilibrium is reached within a ten picosecond timescale). This fact indicates that the final morphology is the result of melt flow driven by temperature gradients (and is, therefore, of hydrodynamic origin rather than of electromagnetic one). Nevertheless, the coupling through laser-excited carriers is possible for shorter delays close to one picosecond [116], and the dynamic approaches considering both pulse propagation and electron plasma fluid dynamics might be helpful to elucidate the relevant effects upon double pulse excitation.

Grooves The emergence of grooves($\|$, $\gg \lambda$) on metal and semiconductor surfaces, commonly lying above the LSFL structures created by previous laser pulses [131, 152, 170], was interpreted by two different mechanisms. In the first scenario, the appearance of structures with periods larger than laser wavelength was attributed to the interference patterns of light [45, 92, 170]. The grooves themselves consist of the aggregates of nanoparticles which are fused together [170]. Electromagnetic simulations with multipulse ablation feedback indicate that with increasing size of the nanoparticles and a positive feedback, quasiperiodic patterns with supra-wavelength periods and an orientation parallel to the laser polarization appear on the surface [45]. The origin of the orientation and the periodicity were not clearly explained in these works, however can be understood intuitively. Because the energy deposition below the particles has a dominant enhancement parallel to the laser polarization (similar to the surface nanobumps [33]), positive feedback reinforces scattering parallel to the structures and results in the development of elongated ridges of large dimensions, producing maxima of interference patterns at supra-wavelength distance from them [33]. The second scenario proposed by Tsibidis et al. relies on the Marangoni convection instability in the form of hydrothermal waves that drive the melt flow perpendicular to the previously formed LSFLs($\perp$, $\approx \lambda$) or parallel to the laser polarization [131]. As a result, the LSFLs are suppressed, whereas large-scale grooves and spikes above the surface are created by melt flow with dimensions defined by the critical Marangoni number [131]. Groove period dependencies both on the number of applied pulses and laser fluence obtained experimentally on metal surface agreed with the predictions of the hydrodynamic model [152].

5 From the Diffraction Limit to the Nanoscale Control of the Periodic Patterns

To achieve regular nanopatterns with dimensions much smaller than the laser wavelength, the electromagnetic fields should act in synergy with the thermomechanical material response discussed previously. In this section, we analyze the factors that make it possible to form such patterns at the nanoscale. For metals and excited bandgap materials with metallic-like optical properties, evanescent waves are spatially confined to surface or bulk nanofeatures, and the initial roughness and homogeneity of the irradiated sample are a crucial point [32]. To reach the nanoscale on a structured surface, thin film deposition, electropolishing, or a rigorous mechanical polishing is required to prepare the surface with an average roughness below 10 nm. Since Sipe's work and selvedge-light coupling theory, it is clearly established that the roughness layer lays a central role in the formation of LIPSS [21, 25]. An induced transient roughness is necessary both for the excitation and the scattering of surface waves but will also condition the nonradiative fields and, therefore, the transverse temperature gradients.

5.1 From Light Energy Confinement to Thermal Gradients

The specificities of ultrashort laser interaction rely on the possibility to dissipate the energy at the record nanoscales limiting the energy carried away by shock propagation, radiation effects, and thermal diffusion. The absorbed light is confined in a thickness corresponding to the skin depth, typically a few tens of nm for metallic surfaces. For the light scattered by nanoreliefs, the decay depends directly on the size of the nanorelief as expressed by the inverse-square dependence of the Rayleigh law discussed in Sect. 3. Feature scale smaller than the laser wavelength samples coherently scatters the optical field, creating a polarization-dependent distribution of the nonradiative pattern, as shown in Fig. 5.6. This defines the 3D near-field confinement and the corresponding gradients around pristine and preformed surface cavities, bumps, or nanostructures. The electromagnetic energy coupled to electrons is quasi-instantaneously transformed into (electronic) heat by electron-electron Coulomb interactions with elastic and inelastic relaxation times in the femtosecond range [181]. Depending on the electron-phonon (*e-ph*) coupling strength, electronic energy is then transferred to lattice heat within a few picoseconds, establishing high-temperature gradients $\nabla T = \nabla T_L + \nabla T_T$ where ∇T_L, perpendicular to the irradiated surface, stands for longitudinal gradients and ∇T_T the transversal ones. This electron-phonon nonequilibrium stage is decisive since heat is efficiently and rapidly transported away from excited region by hot electron collisions, which smooths the energy gradients. The duration of this stage is limited by the *e-ph* relaxation time impacting severely the size of the heated region. This effect is strongly dependent not only on the initial electron structure of the material but also on its evolution. Photoexcited bandgap materials are expected to be less thermally insulating as electrons from the valence band are excited to the conduction band and transition metals are strongly affected by d-band electron scattering dynamics [182–184]. The mean free path determines the electron diffusion depth and thus the confinement length and the temperature gradients [185].

Role of Longitudinal Temperature Gradients ∇T_L are typically determined by the optical skin depth in the tens of nm scale for metals or 100 nm for strongly photoexcited bandgap surfaces. This length represents the minimal confinement size and, depending on the fluence, is generally enhanced by electronic transport before relaxation with phonons is complete [185]. As the difference between the melting temperature and the temperature sustainable by the material before turning into plasma is around 10^3 K, the longitudinal gradients reach $\nabla T_L^{max} \simeq 10^{11}$ K m^{-1}.

High longitudinal temperature gradients lead to the formation of a melted nanolayer and to significant changes of the fluid density induced by the propagating shock wave. Subsurface cavitation occurs on the timescale of a few tens of picoseconds below the surface at distances comparable to the light absorption depth. Successive pulses couple to nanocavities inducing the redistribution of optical fields around the nanovoids. This results in confinement of the absorption energy in the vicinity of the nanocavity and acts as inter-pulse feedback. Local cavitation occurs in tiny volumes in a self-organized and periodic arrangement, and the thermomechanical effects conserve light spatial arrangements. Adding to this localized cavitation process, frozen nanojets at the edges of exploding nanovoids are generated if light coupling is stronger. They consist of nanopeak structures that emerge from the resolidified melt [16]. If the lifetime of this molten layer is sufficient, local nanovoids trapped beneath the surface coalesce and the mechanical stress can induce the disruption of the thin layer, causing surface detaching by spallation [20].

Transverse Temperature Gradients Transverse temperature gradients are directly defined by the size of the near-field absorption around the roughness as nonradiative fields decrease as $\sim 1/r^2$ from the nanorelief [39]. The optical properties of the material around the scattered nanoobject strongly impact the distribution and the size of the generated heat affected zone surrounding the protrusion or the hole. A similar order of magnitude can be reached for ∇T_T^{max} compared to ∇T_L^{max}, depending on the degree of heating above the melting temperature and superheating of the material can occur in short timescale. Both longitudinal and transverse gradients relax simultaneously and can trigger oriented nanoscale effects. When they act collectively with a similar contribution, convective flows develop and ordered polygonal nanopatterns can be formed, induced by the natural relaxation of the irregular wavy structures excited at the surfaces [117].

Variations of temperature, induced by the inhomogeneous light coupling in the liquid regions, provide the driving force for buildup surface tension gradients. The flow in the incompressible liquid, induced by transverse temperature gradients $\nabla_T T$ along the free surface, is usually directed from hot to cold areas of the surface, which corresponds to thermocapillary convection [186, 187]. Capillary phenomena are not only driven by surface tension heterogeneities or gradients but also when interphase boundaries possess considerable curvature. Light-induced sharp roughness fosters this during multipulse irradiation regime. The surface profile is then sculpted by melt flow until the material resolidification sets in, after which the nanoreliefs are imprinted on the surface. Pressure gradients, induced by $\nabla_L T$-generated differences of the density inside the liquid, underlying shock and rarefaction waves, can amplify the convective flows by Rayleigh-Bénard like or even Rayleigh-Taylor instabilities as shown in Fig. 5.12 [119].

5.2 *How to Drive the Thermal Gradient Direction*

Oriented self-organization indicates that the complex electromagnetic interactions, mainly based on the spatial coherence of the laser field and the local field enhancement, govern the gradients. Laser pulse duration and sequence can also drive the dynamics of energy deposition, affecting the underlying mechanisms that determine the surface modification. This is achievable through a precise

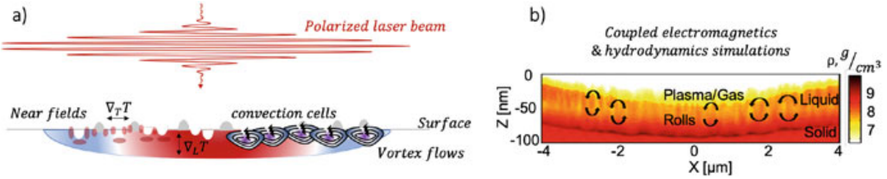

Fig. 5.12 (**a**) Scheme of the polarization dependence of the near-field absorption around nanoroughness. The oriented electromagnetic response induces instabilities and nanometric convection cells by local transverse and longitudinal temperature gradients. (**b**) Simulations of surface density after 25 ps upon ultrashort laser irradiation calculated by 3D-FDTD coupled to hydrodynamics revealing convective flows induced by vortex flows in irradiated Ni from Ref. [119]. Copyright 2020 Elsevier

control of the electronic or the relaxation dynamics of the irradiated materials. The potential of ultrafast laser irradiation lies in the capability to induce a strong electronic photoexcitation that alters the band structure [27, 183]. This offers unique possibilities to manipulate material properties on ultrafast timescales as a high perturbation of the electronic structure is able to deform a crystal lattice up to a nonclassical phase transition or disordered states as experimentally evidenced by ultrafast structural probes [188, 189]. On picosecond timescale, the laser pulse directly interacts with the nascent melt or plasma.

Control of the Temporal Sequence of Excitation The control of light-induced processes can be achieved, and particular states of matter can be accessed adjusting the energy delivery rate in real time. This leads to significant perspectives for laser-induced structures, e.g., structures with well-defined spatial distribution, structural phase transitions in polymorphic materials, plasmonic or magnetic switching properties, and reversible surface crystallographic rearrangements with custom properties. Temporal control enables also precise design of properties of relevant surfaces in the sub-μm range. Theoretically designed thermodynamic states showing a significant increase in the excitation of a solid surface or in a nascent plasma state have been obtained by adaptive feedback loops [190, 191]. Genetic algorithms and evolutionary strategies were performed on spatial beam engineering and hydrodynamic numerical approach to determine shapes of optimal pulses on the tens of picosecond scale able to upgrade quality and throughput in material structuring by optimizing thermodynamic pathways. Further control by optimizing the irradiation sequence retains also the mechanisms of control exploiting the coherence of the laser field. Double-pulse experiments with varying time delay between two fs-laser pulses offer an experimental method to control LIPSS features and their dynamics affecting the formation mechanisms by modifying the feedback. Numerous experiments with double-pulse sequences of femtosecond pulses were performed on metals [192], semiconductors [193], and dielectrics [78]. A delayed action of cross-polarized laser pulse has also been shown to overcome the anisotropic polarization response of the surface as shown in Fig. 5.11 where 2D patterns were formed at the nanoscale for a specific delay [32, 117]. This has also been observed on the microscale [115], showing that the polarization effects are suppressed with a temporal manipulation strategy of the laser pulse to influence the self-organized liquid flows.

Control of the Polarization States Direct femtosecond laser surface structuring based on optical vortex beams with different spatial distributions of the state of polarization offered new opportunities to generate complex and unconventional surface structures. The most straightforward method to structure light is to add a complex helical phase or a spatially variant phase shift by using a spiral phase plate or a spatial light modulator. By means of a q-plate characterized by a topological charge, different states of an optical vortex beam carrying an orbital angular momentum can generate various regular surface patterns on surfaces and in the bulk [194, 195]. LSFL and HSFL with radial and azimuthal polarized beams can be easily obtained experimentally and reproduced by electromagnetic FDTD simulations. The orientation of both kinds of patterns follows the local polarization direction of the beams as shown in Fig. 5.13 a–d. Polarization-dependent azimuthal-varying nanostructuring was also reported within bulk fused silica bulk [28, 196]. The results of electromagnetic simulations with a radially polarized beam inducing

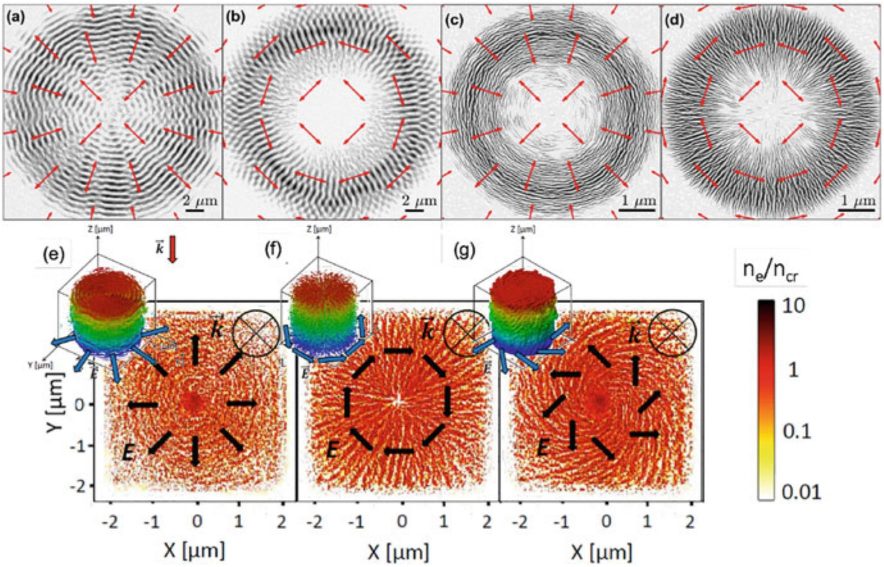

Fig. 5.13 Simulations of surface topographies and bulk nanogratings resulting in local complex polarization states of vectorial beams. LSFLs on Cr (**a**), (**b**) and HSFLs on excited Si (**c**), (**d**) are observed for radially polarized (**a**), (**c**) and azimuthally polarized (**b**), (**d**) beams at normal incidence. LSFLs and HSFLs exhibit orientations perpendicular to the local electric field vector from Ref. . [99]. Electronic distribution induced by radial (**e**), azimuthal (**f**), and spiral (**g**) polarization irradiation inside SiO_2 bulk photoexcited by a 120 fs laser pulse and calculated by 3D-FDTD. Reproduced from Ref. [169] with permission from Japan Laser Processing Society

ringlike self-organization are shown in Fig. 5.13 e–g. The azimuthal polarization beam creates radially oriented nanoplasmas that elongate perpendicular to the local laser polarization [169]. The coupling between nonradiative light modes in the presence of nanometric surface roughness is then able to trigger unconventional structures at the ultimate scale.

6 Conclusion

As light confinement gets extreme, ultrafast irradiation induces a locally nonlinear regime of excitation by inhomogeneous multiphoton absorption in bandgap materials and local field enhancement in metals. Both drive the matter far from equilibrium, in conditions of surface complexity emergence at the nanoscale. This is sustained by light-induced nonequilibrium thermodynamics able to create a plethora of processes within the excited region. They mostly rely on the propagation and interaction of shock and rarefaction waves but also on the generation of low viscosity phases in condensed matter that induce fracture, cavitation, and nanovoid formation. These effects strongly limit the energy transport and the absorbed energy stays confined well below the hundreds of nanometer length scale during the interaction process. To achieve surface design at the nanometric scale, a key process is then the interrelation between matter and light or feedback, namely, how light will shape matter and how in return structured matter will reshape light.

For irradiated corrugated and pre-structured surfaces, surface waves including evanescent cylindrical waves, surface plasmon polaritons, or local field enhancements limit the dimension of the light coupling. This coupling generates radiative response in the photoexcited nanoreliefs as cavities, bumps, trapped voids, nanoparticles, etc., and more efficiently a nonradiative contribution that allows near-field nanostructuring. Squeezing light into tiny, sub-wavelength-scale spaces results in unusual behaviors generating self-assembly of structures at surface and in the bulk with an unprecedented uniformity on extreme scales. To bypass the diffraction limit bottleneck for large-scale manufacturing, self-organization process can then be exploited by tuning subtly the excitation and relaxation pathways. As confined optical responses are critically dependent on the physical processes induced by light that can be guided in time and space, near-field and optical nonlinearities have to be generated as a function of the expected hydrodynamic response. To optimize structuring in terms of uniformity, yield, and scale, an optimal control approach has still to be developed by spatiotemporal beam engineering. Control of the spatiotemporal energy distribution relies on the vectorial design of nonstandard and non-diffractive beams through tailored modulation of amplitude, phase, and polarization of the light fields. Temporally, a synchronization of the laser energy delivery rate with the material dynamic response, essentially enhancing the energy coupling and regulating the hydrodynamic instabilities, could be achieved. This will optimize laser interactions and therefore, lead to an essential upgrade in laser processing beyond the current state of the art moving to a new technological field combining nanophotonics, plasmonics, extreme physics, and metastructures.

Acknowledgments This work was supported by an Air Force Office of Scientific Research award Grant No. FA9550-19-1-0032, by the IMOTEP project within the program "Investissements d'Avenir" operated by ADEME and by the LABEX MANUTECH-SISE (ANR-10-LABX-0075) of the Université de Lyon, within the program "Investissements d'Avenir" (ANR-11-IDEX-0007) operated by the French National Research Agency (ANR). Numerical calculations have been performed using HPC resources from GENCI-TGCC and CINES, project gen7041.

References

1. K. Ariga, J.P Hill, M.V. Lee, A. Vinu, R. Charvet, S. Acharya, Challenges and breakthroughs in recent research on self-assembly. Sci. Technol. Adv. Mater. **9**, 014109 (2008)
2. A. Ranella, M. Barberoglou, S. Bakogianni, C. Fotakis, E. Stratakis, Tuning cell adhesion by controlling the roughness and wettability of 3D micro/nano silicon structures. Acta Biomater. **6**(7), 2711–2720 (2010)
3. M. Malinauskas, A. Žukauskas, S. Hasegawa, Y. Hayasaki, V. Mizeikis, R. Buividas, S. Juodkazis, Ultrafast laser processing of materials: from science to industry. Light: Science and Applications **5**(8), e16133–e16133 (2016)
4. J. Bonse, S. Höhm, S.V. Kirner, A. Rosenfeld, J. Krüger, Laser-induced periodic surface structures—A scientific evergreen. IEEE J. Sel. Top. Quantum Electron. **23**(3), 9000615 (2017)
5. K. Sugioka, Y. Cheng, Femtosecond laser three-dimensional micro-and nanofabrication. Appl. Phys. Rev. **1**(4), 041303 (2014)
6. K. Sugioka, Y. Cheng, Ultrafast lasers—reliable tools for advanced materials processing. Light: Science and Applications **3**(4), e149–e149 (2014)
7. R. Stoian, J.-P. Colombier, Advances in ultrafast laser structuring of materials at the nanoscale. Nanophotonics **9**(16), 4665–4688 (2020)
8. B. Dusser, Z. Sagan, H. Soder, N. Faure, J.-P. Colombier, M. Jourlin, E. Audouard, Controlled nanostructures formation by ultra fast laser pulses for color marking. Opt. Express **18**(3), 2913–2924 (2010)
9. J.-M. Guay, A.C. Lesina, G. Côté, M. Charron, D. Poitras, L. Ramunno, P. Berini, A. Weck, Laser-induced plasmonic colours on metals. Nat. Commun. **8**(1), 16095 (2017)
10. E.P. Ivanova, J. Hasan, H.K. Webb, G. Gervinskas, S. Juodkazis, V.K. Truong, A.H.F. Wu, R.N. Lamb, V.A. Baulin, G.S. Watson, et al. Bactericidal activity of black silicon. Nat. Commun. **4**(1), 2838 (2013)
11. I. Prigogine, P. Van Rysselberghe, Introduction to thermodynamics of irreversible processes. J. Electrochem. Soc. **110**(4), 97C (1963)
12. E.T. Jaynes, The minimum entropy production principle. Annu. Rev. Phys. Chem. **31**(1), 579–601 (1980)
13. R.G. Endres, Entropy production selects nonequilibrium states in multistable systems. Sci. Rep. **7**(1), 14437 (2017)
14. V.V. Isaeva, Self-organization in biological systems. Biol. Bull. **39**(2), 110–118 (2012)
15. X. Sedao, M.V. Shugaev, C. Wu, T. Douillard, C. Esnouf, C. Maurice, S. Reynaud, F. Pigeon, F. Garrelie, L.V. Zhigilei, J.-P. Colombier, Growth twinning and generation of high-frequency surface nanostructures in ultrafast laser-induced transient melting and resolidification. ACS Nano **10**(7), 6995–7007 (2016)
16. X. Sedao, A. Abou Saleh, A. Rudenko, T. Douillard, C. Esnouf, S. Reynaud, C. Maurice, F. Pigeon, F. Garrelie, J.-P. Colombier, Self-arranged periodic nanovoids by ultrafast laser-induced near-field enhancement. ACS Photonics **5**(4), 1418–1426 (2018)
17. J.-M. Savolainen, M.S. Christensen, P. Balling, Material swelling as the first step in the ablation of metals by ultrashort laser pulses. Phys. Rev. B **84**(19), 193410 (2011)

18. M.V. Shugaev, M. He, Y. Levy, A. Mazzi, A. Miotello, N.M. Bulgakova, L.V. Zhigilei, *Laser-Induced Thermal Processes: Heat Transfer, Generation of Stresses, Melting and Solidification, Vaporization, and Phase Explosion* (Springer, Cham, 2021), pp. 83–163
19. X. Sedao, C. Maurice, F. Garrelie, J.-P. Colombier, S. Reynaud, R. Quey, F. Pigeon, Influence of crystal orientation on the formation of femtosecond laser-induced periodic surface structures and lattice defects accumulation. Appl. Phys. Lett. **104**(17), 171605 (2014)
20. A. Abou-Saleh, E.T. Karim, C. Maurice, S. Reynaud, F. Pigeon, F. Garrelie, L.V. Zhigilei, J.P. Colombier, Spallation-induced roughness promoting high spatial frequency nanostructure formation on Cr. Appl. Phys. A **124**(4), 208 (2018)
21. J.E. Sipe, J.F. Young, J.S. Preston, H.M. van Driel, Laser-induced periodic surface structure. I. theory. Phys. Rev. B **27**(2), 1141 (1983)
22. J.Z.P. Skolski, G.R.B.E. Römer, J. Vincenc Obona, V. Ocelik, J.Th.M. De Hosson, et al. Laser-induced periodic surface structures: Fingerprints of light localization. Phys. Rev. B **85**(7), 075320 (2012)
23. B. Öktem, I. Pavlov, S. Ilday, H. Kalaycıoğlu, A. Rybak, S. Yavaş, M. Erdoğan, F. Ömer Ilday, Nonlinear laser lithography for indefinitely large-area nanostructuring with femtosecond pulses. Nat. Photonics **7**(11), 897 (2013)
24. A. Rudenko, C. Mauclair, F. Garrelie, R. Stoian, J.-P. Colombier, Self-organization of surfaces on the nanoscale by topography-mediated selection of quasi-cylindrical and plasmonic waves. Nanophotonics **8**(3), 459–465 (2019)
25. H.M. Van Driel, J.E. Sipe, J.F. Young, Laser-induced periodic surface structure on solids: a universal phenomenon. Phys. Rev. Lett. **49**(26), 1955 (1982)
26. C. Li, G. Cheng, X. Sedao, W. Zhang, H. Zhang, N. Faure, D. Jamon, J.-P. Colombier, R. Stoian, Scattering effects and high-spatial-frequency nanostructures on ultrafast laser irradiated surfaces of zirconium metallic alloys with nano-scaled topographies. Opt. Express **24**(11), 11558–11568 (2016)
27. J.-P. Colombier, A. Rudenko, E. Silaeva, H. Zhang, X. Sedao, E. Bévillon, S. Reynaud, C. Maurice, F. Pigeon, F. Garrelie, et al. Mixing periodic topographies and structural patterns on silicon surfaces mediated by ultrafast photoexcited charge carriers. Phys. Rev. Res. **2**(4), 043080 (2020)
28. R. Stoian, K. Mishchik, G. Cheng, C. Mauclair, C. D'Amico, J.-P. Colombier, M. Zamfirescu, Investigation and control of ultrafast laser-induced isotropic and anisotropic nanoscale-modulated index patterns in bulk fused silica. Opt. Mater. Express **3**(10), 1755–1768 (2013)
29. J. Bonse, J. Krüger, S. Höhm, A. Rosenfeld, Femtosecond laser-induced periodic surface structures. J. Laser Appl. **24**(4), 042006 (2012)
30. A. Borowiec, H.K. Haugen, Subwavelength ripple formation on the surfaces of compound semiconductors irradiated with femtosecond laser pulses. Appl. Phys. Lett. **82**(25), 4462–4464 (2003)
31. A. Abou Saleh, A. Rudenko, L. Douillard, F. Pigeon, F. Garrelie, J.-P. Colombier, Nanoscale imaging of ultrafast light coupling to self-organized nanostructures. ACS Photonics **6**(9), 2287–2294 (2019)
32. A. Nakhoul, C. Maurice, M. Agoyan, A. Rudenko, F. Garrelie, F. Pigeon, J.-P. Colombier, Self-organization regimes induced by ultrafast laser on surfaces in the tens of nanometer scales. Nanomaterials **11**(4), 1020 (2021)
33. A. Rudenko, C. Mauclair, F. Garrelie, R. Stoian, J.P. Colombier, Light absorption by surface nanoholes and nanobumps. Appl. Surf. Sci. **470**, 228–233 (2019)
34. M. Birnbaum, Semiconductor surface damage produced by ruby lasers. J. Appl. Phys. **36**(11), 3688–3689 (1965)
35. Z. Guosheng, P.M. Fauchet, A.E. Siegman, Growth of spontaneous periodic surface structures on solids during laser illumination. Phys. Rev. B **26**(10), 5366 (1982)
36. X. Sedao, C. Maurice, F. Garrelie, J.-P. Colombier, S. Reynaud, R. Quey, G. Blanc, F. Pigeon, Electron backscatter diffraction characterization of laser-induced periodic surface structures on nickel surface. Appl. Surf. Sci. **302**, 114–117 (2014)

37. J. Bonse, S. Gräf, Maxwell meets Marangoni—A review of theories on laser-induced periodic surface structures. Laser Photonics Rev. **14**(10), 2000215 (2020)
38. U.S. Inan, R.A. Marshall, *Numerical Electromagnetics: The FDTD Method* (Cambridge University, Cambridge, 2011)
39. G. Mie, Beiträge zur Optik trüber Medien, speziell kolloidaler Metallösungen. Annalen der Physik **330**(3), 377–445 (1908). https://doi.org/10.1002/andp.19083300302
40. A.V. Zayats, I.I. Smolyaninov, A.A. Maradudin, Nano-optics of surface plasmon polaritons. Phys. Rep. **408**(3–4), 131–314 (2005)
41. T.J.Y. Derrien, J. Krüger, J. Bonse, Properties of surface plasmon polaritons on lossy materials: lifetimes, periods and excitation conditions. J. Opt. **18**(11), 115007 (2016)
42. A.Y. Nikitin, F.J. García-Vidal, L. Martín-Moreno, Surface electromagnetic field radiated by a subwavelength hole in a metal film. Phys. Rev. Lett. **105**(7), 073902 (2010)
43. J. Chandezon, M.T. Dupuis, G. Cornet, D. Maystre, Multicoated gratings: a differential formalism applicable in the entire optical region. J. Opt. Soc. Am. **72**(7), 839–846 (1982)
44. V.A. Markel, Introduction to the Maxwell Garnett approximation: tutorial. J. Opt. Soc. Am. A **33**(7), 1244–1256 (2016)
45. H. Zhang, J.-P. Colombier, C. Li, N. Faure, G. Cheng, R. Stoian, Coherence in ultrafast laser-induced periodic surface structures. Phys. Rev. B **92**(17), 174109 (2015)
46. R. Buschlinger, S. Nolte, U. Peschel, Self-organized pattern formation in laser-induced multiphoton ionization. Phys. Rev. B **89**(18), 184306 (2014)
47. J.-L. Déziel, L.J. Dubé, S.H. Messaddeq, Y. Messaddeq, C. Varin, Femtosecond self-reconfiguration of laser-induced plasma patterns in dielectrics. Phys. Rev. B **97**(20), 205116 (2018)
48. B. Rethfeld, Unified model for the free-electron avalanche in laser-irradiated dielectrics. Phys. Rev. Lett. **92**, 187401 (2004)
49. A. Rudenko, J.-P. Colombier, T.E. Itina, From random inhomogeneities to periodic nanostructures induced in bulk silica by ultrashort laser. Phys. Rev. B **93**(7), 075427 (2016)
50. A. Marini, M. Conforti, G.D. Valle, H.W. Lee, T.X. Tran, W. Chang, M.A. Schmidt, S. Longhi, P.St.J. Russell, F. Biancalana, Ultrafast nonlinear dynamics of surface plasmon polaritons in gold nanowires due to the intrinsic nonlinearity of metals. New J. Phys. **15**(1), 013033 (2013)
51. P. Bresson, J.-F. Bryche, M. Besbes, J. Moreau, P.-L. Karsenti, P. G. Charette, D. Morris, M. Canva, Improved two-temperature modeling of ultrafast thermal and optical phenomena in continuous and nanostructured metal films. Phys. Rev. B **102**, 155127 (2020)
52. B. Morel, R. Giust, K. Ardaneh, F. Courvoisier, A solver based on pseudo-spectral analytical time-domain method for the two-fluid plasma model. Sci. Rep. **11**(1), 3151 (2021)
53. B. Rethfeld, A. Kaiser, M. Vicanek, G. Simon, Ultrafast dynamics of nonequilibrium electrons in metals under femtosecond laser irradiation. Phys. Rev. B **65**(21), 214303 (2002)
54. N. Brouwer, B. Rethfeld, Transient electron excitation and nonthermal electron-phonon coupling in dielectrics irradiated by ultrashort laser pulses. Phys. Rev. B **95**(24), 245139 (2017)
55. A. Rudenko, J.V. Moloney, Coupled kinetic Boltzmann electromagnetic approach for intense ultrashort laser excitation of plasmonic nanostructures. Phys. Rev. B **104**, 035418 (2021)
56. R. Buschlinger, M. Lorke, U. Peschel, Light-matter interaction and lasing in semiconductor nanowires: A combined finite-difference time-domain and semiconductor Bloch equation approach. Phys. Rev. B **91**, 045203 (2015)
57. J.R. Gulley, D. Huang, Self-consistent quantum-kinetic theory for interplay between pulsed-laser excitation and nonlinear carrier transport in a quantum-wire array. Opt. Express **27**(12), 17154–17185 (2019)
58. E. Smetanina, P.G. de Alaiza Martínez, I. Thiele, B. Chimier, A. Bourgeade, G. Duchateau, Optical Bloch modeling of femtosecond-laser-induced electron dynamics in dielectrics. Phys. Rev. E **101**(6), 063206 (2020)
59. K. Yabana, T. Sugiyama, Y. Shinohara, T. Otobe, G.F. Bertsch, Time-dependent density functional theory for strong electromagnetic fields in crystalline solids. Phys. Rev. B **85**(4), 045134 (2012)

60. M.V. Shugaev, L.V. Zhigilei, Thermodynamic analysis and atomistic modeling of subsurface cavitation in photomechanical spallation. Comput. Mater. Sci **166**, 311–317 (2019)
61. Y.P. Meshcheryakov, M.V. Shugaev, T. Mattle, T. Lippert, N.M. Bulgakova, Role of thermal stresses on pulsed laser irradiation of thin films under conditions of microbump formation and nonvaporization forward transfer. Appl. Phys. A **113**(2), 521–529 (2013)
62. S. Najafi, A.S. Arabanian, R. Massudi, Comprehensive modeling of structural modification induced by a femtosecond laser pulse inside fused silica glass. J. Phys. D: Appl. Phys. **49**(25), 255101 (2016)
63. R. Beuton, B. Chimier, J. Breil, D. Hébert, K. Mishchik, J. Lopez, P.H. Maire, G. Duchateau, Thermo-elasto-plastic simulations of femtosecond laser-induced multiple-cavity in fused silica. Appl. Phys. A **124**(4), 124 (2018)
64. G.D. Tsibidis, M. Barberoglou, P.A. Loukakos, E. Stratakis, C. Fotakis, Dynamics of ripple formation on silicon surfaces by ultrashort laser pulses in subablation conditions. Phys. Rev. B **86**(11), 115316 (2012)
65. A.N. Volkov, L.V. Zhigilei, Melt dynamics and melt-through time in continuous wave laser heating of metal films: Contributions of the recoil vapor pressure and marangoni effects. Int. J. Heat Mass Transfer **112**, 300–317 (2017)
66. M.E. Povarnitsyn, T.E. Itina, M. Sentis, K.V. Khishchenko, P.R. Levashov, Material decomposition mechanisms in femtosecond laser interactions with metals. Phys. Rev. B **75**(23), 235414 (2007)
67. A. Rudenko, C. Mauclair, F. Garrelie, R. Stoian, J.-P. Colombier, Amplification and regulation of periodic nanostructures in multipulse ultrashort laser-induced surface evolution by electromagnetic-hydrodynamic simulations. Phys. Rev. B **99**(23), 235412 (2019)
68. J.-P. Colombier, P. Combis, F. Bonneau, R. Le Harzic, E. Audouard, Hydrodynamic simulations of metal ablation by femtosecond laser irradiation. Phys. Rev. B **71**(16), 165406 (2005)
69. M.E. Povarnitsyn, N.E. Andreev, E.M. Apfelbaum, T.E. Itina, K.V. Khishchenko, O.F. Kostenko, P.R. Levashov, M.E. Veysman, A wide-range model for simulation of pump-probe experiments with metals. Appl. Surf. Sci. **258**(23), 9480–9483 (2012)
70. M. Djouder, O. Lamrous, M.D. Mitiche, T.E. Itina, M. Zemirli, Electromagnetic particle-in-cell (PIC) method for modeling the formation of metal surface structures induced by femtosecond laser radiation. Appl. Surf. Sci. **280**, 711–714 (2013)
71. T.E. Itina, J. Hermann, P. Delaporte, M. Sentis, Laser-generated plasma plume expansion: Combined continuous-microscopic modeling. Phys. Rev. E **66**(6), 066406 (2002)
72. P. Koukouvinis, N. Kyriazis, M. Gavaises, Smoothed particle hydrodynamics simulation of a laser pulse impact onto a liquid metal droplet. PloS One **13**(9), e0204125 (2018)
73. N. Bloembergen, Role of cracks, pores, and absorbing inclusions on laser induced damage threshold at surfaces of transparent dielectrics. Appl. Opt. **12**(4), 661–664 (1973)
74. J. Le Perchec, P. Quemerais, A. Barbara, T. Lopez-Rios, Why metallic surfaces with grooves a few nanometers deep and wide may strongly absorb visible light. Phys. Rev. Lett. **100**(6), 066408 (2008)
75. Y. Shimotsuma, P.G. Kazansky, J. Qiu, K. Hirao, Self-organized nanogratings in glass irradiated by ultrashort light pulses. Phys. Rev. Lett. **91**(24), 247405 (2003)
76. V.R. Bhardwaj, E Simova, P.P. Rajeev, C. Hnatovsky, R.S. Taylor, D.M. Rayner, P.B. Corkum, Optically produced arrays of planar nanostructures inside fused silica. Phys. Rev. Lett. **96**(5), 057404 (2006)
77. R. Taylor, C. Hnatovsky, E. Simova, Applications of femtosecond laser induced self-organized planar nanocracks inside fused silica glass. Laser Photonics Rev. **2**(1–2), 26–46 (2008)
78. A. Rudenko, J.-P. Colombier, S. Höhm, A. Rosenfeld, J. Krüger, J. Bonse, T.E. Itina, Spontaneous periodic ordering on the surface and in the bulk of dielectrics irradiated by ultrafast laser: a shared electromagnetic origin. Sci. Rep. **7**(1), 12306 (2017)
79. M. Sakakura, Y. Lei, L. Wang, Y.-H. Yu, P.G. Kazansky, Ultralow-loss geometric phase and polarization shaping by ultrafast laser writing in silica glass. Light: Science and Applications **9**(1), 15 (2020)

80. A. Rudenko, J.-P. Colombier, T.E. Itina, R. Stoian, Genesis of nanogratings in silica bulk via multipulse interplay of ultrafast photo-excitation and hydrodynamics. Adv. Opt. Mater. **9**(20), 2100973 (2021)
81. P. Lalanne, J.P. Hugonin, H.T. Liu, B. Wang, A microscopic view of the electromagnetic properties of sub-l metallic surfaces. Surf. Sci. Rep. **64**(10), 453–469 (2009)
82. A.Y. Nikitin, S.G. Rodrigo, F.J. García-Vidal, L. Martín-Moreno, In the diffraction shadow: Norton waves versus surface plasmon polaritons in the optical region. New J. Phys. **11**(12), 123020 (2009)
83. A. Alekseevich Ionin, S.I. Kudryashov, S.V. Makarov, A.A. Rudenko, S.V. Seleznev, D.V. Sinitsyn, T.P. Kaminskaya, V.V. Popov, Nonlinear evolution of aluminum surface relief under multiple femtosecond laser irradiation. JETP Lett. **101**(5), 350–357 (2015)
84. Y. Fuentes-Edfuf, J.A. Sánchez-Gil, C. Florian, V. Giannini, J. Solis, J. Siegel, Surface plasmon polaritons on rough metal surfaces: Role in the formation of laser-induced periodic surface structures. ACS Omega **4**(4), 6939–6946 (2019)
85. A. Barborica, I.N. Mihailescu, V.S. Teodorescu, Dynamical evolution of the surface microrelief under multiple-pulse-laser irradiation: An analysis based on surface-scattered waves. Phys. Rev. B **49**, 8385–8395 (1994)
86. G. Obara, N. Maeda, T. Miyanishi, M. Terakawa, N.N. Nedyalkov, M. Obara, Plasmonic and Mie scattering control of far-field interference for regular ripple formation on various material substrates. Opt. Express **19**(20), 19093–19103 (2011)
87. R.D. Murphy, B. Torralva, D.P. Adams, S.M. Yalisove, Laser-induced periodic surface structure formation resulting from single-pulse ultrafast irradiation of Au microstructures on a Si substrate. Appl. Phys. Lett. **102**(21), 211101 (2013)
88. K. Cheng, J. Liu, K. Cao, L. Chen, Y. Zhang, Q. Jiang, D. Feng, S. Zhang, Z. Sun, T. Jia, Ultrafast dynamics of single-pulse femtosecond laser-induced periodic ripples on the surface of a gold film. Phys. Rev. B **98**(18), 184106 (2018)
89. E. Bévillon, J.P. Colombier, V. Recoules, H. Zhang, C. Li, R. Stoian, Ultrafast switching of surface plasmonic conditions in nonplasmonic metals. Phys. Rev. B **93**, 165416 (2016)
90. J. Bonse, A. Rosenfeld, J. Krüger, On the role of surface plasmon polaritons in the formation of laser-induced periodic surface structures upon irradiation of silicon by femtosecond-laser pulses. J. Appl. Phys. **106**(10), 104910 (2009)
91. S. Höhm, A. Rosenfeld, J. Krüger, J. Bonse, Femtosecond laser-induced periodic surface structures on silica. J. Appl. Phys. **112**(1), 014901 (2012)
92. J.Z.P. Skolski, G.R.B.E. Römer, J. Vincenc Obona, A.J. Huis in't Veld, Modeling laser-induced periodic surface structures: Finite-difference time-domain feedback simulations. J. Appl. Phys. **115**(10), 103102 (2014)
93. M. Huang, F. Zhao, Y. Cheng, N. Xu, Z. Xu, Origin of laser-induced near-subwavelength ripples: interference between surface plasmons and incident laser. ACS Nano **3**(12), 4062–4070 (2009)
94. F. Garrelie, J.-P. Colombier, F. Pigeon, S. Tonchev, N. Faure, M. Bounhalli, S. Reynaud, O. Parriaux, Evidence of surface plasmon resonance in ultrafast laser-induced ripples. Opt. Express **19**(10), 9035–9043 (2011)
95. J.A. Jenkins, Y. Zhou, S. Thota, X. Tian, X. Zhao, S. Zou, J. Zhao, Blue-shifted narrow localized surface plasmon resonance from dipole coupling in gold nanoparticle random arrays. The Journal of Physical Chemistry C **118**(45), 26276–26283 (2014)
96. S. Hou, Y. Huo, P. Xiong, Y. Zhang, S. Zhang, T. Jia, Z. Sun, J. Qiu, Z. Xu, Formation of long- and short-periodic nanoripples on stainless steel irradiated by femtosecond laser pulses. J. Phys. D: Appl. Phys. **44**(50), 505401 (2011)
97. J.-W. Yao, C.-Y. Zhang, H.-Y. Liu, Q.-F. Dai, L.-J. Wu, S. Lan, A.V. Gopal, V.A. Trofimov, T.M. Lysak, High spatial frequency periodic structures induced on metal surface by femtosecond laser pulses. Opt. Express **20**(2), 905–911 (2012)
98. M. Huang, Y. Cheng, F. Zhao, Z. Xu, The significant role of plasmonic effects in femtosecond laser-induced grating fabrication on the nanoscale. Annalen der Physik **525**(1–2), 74–86 (2013)

99. H. Zhang, J.-P. Colombier, S. Witte, Laser-induced periodic surface structures: Arbitrary angles of incidence and polarization states. Phys. Rev. B **101**(24), 245430 (2020)
100. J.-L. Déziel, J. Dumont, D. Gagnon, L.J. Dubé, S.H. Messaddeq, Y. Messaddeq, Constructive feedback for the growth of laser-induced periodic surface structures. Phys. Status Solidi C **13**(2–3), 121–124 (2016)
101. I. Gnilitskyi, V. Gruzdev, N.M. Bulgakova, T. Mocek, L. Orazi, Mechanisms of high-regularity periodic structuring of silicon surface by sub-mhz repetition rate ultrashort laser pulses. Appl. Phys. Lett. **109**(14), 143101 (2016)
102. R.S. Taylor, C. Hnatovsky, E. Simova, P.P. Rajeev, D.M. Rayner, P.B. Corkum, Femtosecond laser erasing and rewriting of self-organized planar nanocracks in fused silica glass. Opt. Lett. **32**(19), 2888–2890 (2007)
103. F. Zimmermann, A. Plech, S. Richter, A. Tünnermann, S. Nolte, On the rewriting of ultrashort pulse-induced nanogratings. Opt. Lett. **40**(9), 2049–2052 (2015)
104. Y. Lei, N. Zhang, J. Yang, C. Guo, Femtosecond laser eraser for controllable removing periodic microstructures on Fe-based metallic glass surfaces. Opt. Express **26**(5), 5102–5110 (2018)
105. W. Zhang, Q. Zhai, J. Song, K. Lou, Y. Li, Z. Ou, Q. Zhao, Y. Dai, Manipulation of self-organized nanograting for erasing and rewriting by ultrashort double-pulse sequences irradiation in fused silica. J. Phys. D: Appl. Phys. **53**(16), 165106 (2020)
106. L. Wang, Q.-D. Chen, X.-W. Cao, R. Buividas, X. Wang, S. Juodkazis, H.-B. Sun, Plasmonic nano-printing: large-area nanoscale energy deposition for efficient surface texturing. Light: Science and Applications **6**(12), e17112 (2017)
107. H.U. Lim, J. Kang, C. Guo, T.Y. Hwang, Manipulation of multiple periodic surface structures on metals induced by femtosecond lasers. Appl. Surf. Sci. **454**, 327–333 (2018)
108. A.V. Dostovalov, T.J.-Y. Derrien, S.A. Lizunov, F. Přeučil, K.A. Okotrub, T. Mocek, V.P. Korolkov, S.A. Babin, N.M. Bulgakova, LIPSS on thin metallic films: New insights from multiplicity of laser-excited electromagnetic modes and efficiency of metal oxidation. Appl. Surf. Sci. **491**, 650–658 (2019)
109. V.B. Gildenburg, I.A. Pavlichenko, Internal surface plasmon excitation as the root cause of laser-induced periodic plasma structure and self-organized nanograting formation in the volume of transparent dielectric. Nanomaterials **10**(8), 1461 (2020)
110. C. Florian, J.-L. Déziel, S.V. Kirner, J. Siegel, J. Bonse, The role of the laser-induced oxide layer in the formation of laser-induced periodic surface structures. Nanomaterials **10**(1), 147 (2020)
111. P. Dominic, F. Bourquard, S. Reynaud, A. Weck, J.-P. Colombier, F. Garrelie, On the insignificant role of the oxidation process on ultrafast high-spatial-frequency LIPSS formation on tungsten. Nanomaterials **11**(5), 1069 (2021)
112. K.M. Davis, K. Miura, N. Sugimoto, K. Hirao, Writing waveguides in glass with a femtosecond laser. Opt. Lett. **21**(21), 1729–1731 (1996)
113. J. Jia, M. Li, C.V. Thompson, Amorphization of silicon by femtosecond laser pulses. Appl. Phys. Lett. **84**(16), 3205–3207 (2004)
114. M. Gedvilas, J. Mikšys, G. Račiukaitis, Flexible periodical micro-and nano-structuring of a stainless steel surface using dual-wavelength double-pulse picosecond laser irradiation. RSC Adv. **5**(92), 75075–75080 (2015)
115. F. Fraggelakis, G. Mincuzzi, J. Lopez, I. Manek-Hönninger, R. Kling, Controlling 2D laser nano structuring over large area with double femtosecond pulses. Appl. Surf. Sci. **470**, 677–686 (2019)
116. M. Mastellone, A. Bellucci, M. Girolami, V. Serpente, R. Polini, S. Orlando, A. Santagata, E. Sani, F. Hitzel, D.M. Trucchi, Deep-subwavelength 2D periodic surface nanostructures on diamond by double-pulse femtosecond laser irradiation. Nano Lett. **21**(10), 4477–4483 (2021)
117. A. Abou Saleh, A. Rudenko, S. Reynaud, F. Pigeon, F. Garrelie, J.-P. Colombier, Sub-100 nm 2D nanopatterning on a large scale by ultrafast laser energy regulation. Nanoscale **12**(12), 6609–6616 (2020)

118. E.L. Gurevich, Mechanisms of femtosecond LIPSS formation induced by periodic surface temperature modulation. Appl. Surf. Sci. **374**, 56–60 (2016)
119. A. Rudenko, A. Abou-Saleh, F. Pigeon, C. Mauclair, F. Garrelie, R. Stoian, J.-P. Colombier, High-frequency periodic patterns driven by non-radiative fields coupled with Marangoni convection instabilities on laser-excited metal surfaces. Acta Mater. **194**, 93–105 (2020)
120. A. Ben-Yakar, A. Harkin, J. Ashmore, R.L. Byer, H.A. Stone, Thermal and fluid processes of a thin melt zone during femtosecond laser ablation of glass: the formation of rims by single laser pulses. J. Phys. D: Appl. Phys. **40**(5), 1447 (2007)
121. V.I. Emel'yanov, D.M. Seval'nev, Defect-deformational Kuramoto-Sivashinsky equation and formation of surface nano-and microstructures under the laser and ion-beam irradiation. Laser Phys. **21**(3), 566–575 (2011)
122. O. Varlamova, J. Reif, S. Varlamov, M. Bestehorn, The laser polarization as control parameter in the formation of laser-induced periodic surface structures: Comparison of numerical and experimental results. Appl. Surf. Sci. **257**(12), 5465–5469 (2011)
123. O. Varlamova, C. Martens, M. Ratzke, J. Reif, Genesis of femtosecond-induced nanostructures on solid surfaces. Appl. Opt. **53**(31), I10–I15 (2014)
124. M.C. Cross, P.C. Hohenberg, Pattern formation outside of equilibrium. Rev. Mod. Phys. **65**, 851–1112 (1993)
125. H. Li, J. Qin, Z. Cao, Z. Su, Laser-induced reversible and irreversible surface nanostructuring. Adv. Mater. Interfaces **8**(7), 2001945 (2021)
126. J.R.A. Pearson, On convection cells induced by surface tension. J. Fluid Mech. **4**(5), 489–500 (1958)
127. F.H. Busse, The stability of finite amplitude cellular convection and its relation to an extremum principle. J. Fluid Mech. **30**(4), 625–649 (1967)
128. Q. Ouyang, H.L. Swinney, Transition from a uniform state to hexagonal and striped Turing patterns. Nature **352**(6336), 610–612 (1991)
129. L.E. Scriven, C.V. Sternling, On cellular convection driven by surface-tension gradients: effects of mean surface tension and surface viscosity. J. Fluid Mech. **19**(3), 321–340 (1964)
130. I. Ursu, I.A. Dorobantu, I.N. Mihailescu, M. Vlad, F. Spineanu, A.M. Prokhorov, V.I. Konov, V.N. Tokarev, Possible mechanism for laser-induced two-dimensional periodic structures by analogy with the Bénard effect. Opt. Lett. **14**(16), 853–855 (1989)
131. G.D. Tsibidis, C. Fotakis, E. Stratakis, From ripples to spikes: A hydrodynamical mechanism to interpret femtosecond laser-induced self-assembled structures. Phys. Rev. B **92**(4), 041405 (2015)
132. G.D. Tsibidis, E. Skoulas, A. Papadopoulos, E. Stratakis, Convection roll-driven generation of supra-wavelength periodic surface structures on dielectrics upon irradiation with femtosecond pulsed lasers. Phys. Rev. B **94**, 081305(R) (2016)
133. Y.N. Kulchin, O.B. Vitrik, A.A. Kuchmizhak, V.I. Emel'Yanov, A.A. Ionin, S.I. Kudryashov, S.V. Makarov, Formation of crownlike and related nanostructures on thin supported gold films irradiated by single diffraction-limited nanosecond laser pulses. Phys. Rev. E **90**(2), 023017 (2014)
134. H.-J. Kull, Theory of the Rayleigh-Taylor instability. Phys. Rep. **206**(5), 197–325 (1991)
135. O. Schilling, Progress on understanding Rayleigh–Taylor flow and mixing using synergy between simulation, modeling, and experiment. J. Fluids Eng. **142**(12), 120802 (2020)
136. X.Y. Chen, J. Lin, J.M. Liu, Z.G. Liu, Formation and evolution of self-organized hexagonal patterns on silicon surface by laser irradiation in water. Appl. Phys. A **94**(3), 649–656 (2009)
137. S.S. Fedotov, L.N. Butvina, A.G. Okhrimchuk, Plastic deformation as nature of femtosecond laser writing in YAG crystal. Sci. Rep. **10**(1), 19385 (2020)
138. A. Nakhoul, A. Rudenko, X. Sedao, N. Peillon, J.P. Colombier, C. Maurice, G. Blanc, A. Borbély, N. Faure, G. Kermouche, Energy feedthrough and microstructure evolution during direct laser peening of aluminum in femtosecond and picosecond regimes. J. Appl. Phys. **130**(1), 015104 (2021)
139. A. Vailionis, E.G. Gamaly, V. Mizeikis, W. Yang, A.V. Rode, S. Juodkazis, Evidence of superdense aluminium synthesized by ultrafast microexplosion. Nat. Commun. **2**(1), 445 (2011)

140. L.A. Smillie, M. Niihori, L. Rapp, B. Haberl, J.S. Williams, J.E. Bradby, C.J. Pickard, A.V. Rode, Exotic silicon phases synthesized through ultrashort laser-induced microexplosion: Characterization with raman microspectroscopy. Phys. Rev. Mater. **4**(9), 093803 (2020)
141. N. Fleischmann, S. Adami, N.A. Adams, Numerical symmetry-preserving techniques for low-dissipation shock-capturing schemes. Comput. Fluids **189**, 94–107 (2019)
142. S.V. Starikov, V.V. Pisarev, Atomistic simulation of laser-pulse surface modification: predictions of models with various length and time scales. J. Appl. Phys. **117**(13), 135901 (2015)
143. A. Rudenko, J.-P. Colombier, T.E. Itina, Nanopore-mediated ultrashort laser-induced formation and erasure of volume nanogratings in glass. Phys. Chem. Chem. Phys. **20**(8), 5887–5899 (2018)
144. A.A. Ionin, S.I. Kudryashov, A.E. Ligachev, S.V. Makarov, L.V. Seleznev, D.V. Sinitsyn, Nanoscale cavitation instability of the surface melt along the grooves of one-dimensional nanorelief gratings on an aluminum surface. JETP Lett. **94**(4), 266–269 (2011)
145. M. Lancry, B. Poumellec, J. Canning, K. Cook, J.-C. Poulin, F. Brisset, Ultrafast nanoporous silica formation driven by femtosecond laser irradiation. Laser Photonics Rev. **7**(6), 953–962 (2013)
146. P.N. Terekhin, J. Oltmanns, A. Blumenstein, D.S. Ivanov, F. Kleinwort, M.E. Garcia, B. Rethfeld, J. Ihlemann, P. Simon, Key role of surface plasmon polaritons in generation of periodic surface structures following single-pulse laser irradiation of a gold step edge. Nanophotonics **11**(2), 359–367 (2022)
147. L.V. Zhigilei, Z. Lin, D.S. Ivanov, Atomistic modeling of short pulse laser ablation of metals: connections between melting, spallation, and phase explosion. J. Phys. Chem. C **113**(27), 11892–11906 (2009)
148. R. Stoian, A. Rosenfeld, D. Ashkenasi, I.V. Hertel, N.M. Bulgakova, E.E.B. Campbell, Surface charging and impulsive ion ejection during ultrashort pulsed laser ablation. Phys. Rev. Lett. **88**, 097603 (2002)
149. S. Sakabe, M. Hashida, S. Tokita, S. Namba, K. Okamuro, Mechanism for self-formation of periodic grating structures on a metal surface by a femtosecond laser pulse. Phys. Rev. B **79**(3), 033409 (2009)
150. M. Huang, F. Zhao, Y. Cheng, N. Xu, Z. Xu, Mechanisms of ultrafast laser-induced deep-subwavelength gratings on graphite and diamond. Phys. Rev. B **79**(12), 125436 (2009)
151. M.V. Shugaev, I. Gnilitskyi, N.M. Bulgakova, L.V. Zhigilei, Mechanism of single-pulse ablative generation of laser-induced periodic surface structures. Phys. Rev. B **96**, 205429 (2017)
152. G.D. Tsibidis, A. Mimidis, E. Skoulas, S.V. Kirner, J. Krüger, J. Bonse, E. Stratakis, Modelling periodic structure formation on 100Cr6 steel after irradiation with femtosecond-pulsed laser beams. Appl. Phys. A **124**(1), 27 (2018)
153. A. Rousse, C. Rischel, S. Fourmaux, I. Uschmann, S. Sebban, G. Grillon, P. Balcou, E. Förster, J.-P. Geindre, P. Audebert, et al., Non-thermal melting in semiconductors measured at femtosecond resolution. Nature **410**(6824), 65–68 (2001)
154. S.K. Sundaram, E. Mazur, Inducing and probing non-thermal transitions in semiconductors using femtosecond laser pulses. Nat. Mater. **1**(4), 217–224 (2002)
155. Y. Tanaka, S. Tsuneyuki, Possible electronic entropy-driven mechanism for non-thermal ablation of metals. Appl. Phys. Express **11**(4), 046701 (2018)
156. N. Medvedev, I. Milov, Nonthermal phase transitions in metals. Sci. Rep. **10**(1), 12775 (2020)
157. Y. Giret, S.L. Daraszewicz, D.M. Duffy, A.L. Shluger, K. Tanimura, Nonthermal solid-to-solid phase transitions in tungsten. Phys. Rev. B **90**(9), 094103 (2014)
158. E. Bévillon, J.-P. Colombier, R. Stoian, First-principles assessment of potential ultrafast laser-induced structural transition in Ni. Appl. Surf. Sci. **374**, 365–369 (2016)
159. S.T. Murphy, Y. Giret, S.L. Daraszewicz, A.C. Lim, A.L. Shluger, K.Tanimura, D.M. Duffy, Contribution of electronic excitation to the structural evolution of ultrafast laser-irradiated tungsten nanofilms. Phys. Rev. B **93**(10), 104105 (2016)
160. C. Zaum, N. Osterloh, R. Darkins, D.M. Duffy, K. Morgenstern, Real-space observation of surface structuring induced by ultra-fast-laser illumination far below the melting threshold. Sci. Rep. **11**, 13269 (2021)

161. J. Bonse, S.V. Kirner, J. Krüger, *Laser-Induced Periodic Surface Structures (LIPSS)* (Springer International Publishing, Cham, 2021), pp. 879–936
162. C. Mauclair, M. Zamfirescu, J.-P. Colombier, G. Cheng, K. Mishchik, E. Audouard, R. Stoian, Control of ultrafast laser-induced bulk nanogratings in fused silica via pulse time envelopes. Opt. Express **20**(12), 12997–13005 (2012)
163. P. Temple, M. Soileau, Polarization charge model for laser-induced ripple patterns in dielectric materials. IEEE J. Quantum Electron. **17**(10), 2067–2072 (1981)
164. X. Shi, L. Jiang, X. Li, S. Wang, Y. Yuan, Y. Lu, Femtosecond laser-induced periodic structure adjustments based on electron dynamics control: from subwavelength ripples to double-grating structures. Opt. Lett. **38**(19), 3743–3746 (2013)
165. Z. Li, Q. Wu, X. Jiang, X. Zhou, Y. Liu, X. Hu, J. Zhang, J. Yao, J. Xu, Formation mechanism of high spatial frequency laser-induced periodic surface structures and experimental support. Appl. Surf. Sci. **580**, 152107 (2022)
166. G. Miyaji, K. Miyazaki, K. Zhang, T. Yoshifuji, J. Fujita, Mechanism of femtosecond-laser-induced periodic nanostructure formation on crystalline silicon surface immersed in water. Opt. Express **20**(14), 14848–14856 (2012)
167. S.K. Das, H. Messaoudi, A. Debroy, E. McGlynn, R. Grunwald, Multiphoton excitation of surface plasmon-polaritons and scaling of nanoripple formation in large bandgap materials. Opt. Mater. Express **3**(10), 1705–1715 (2013)
168. R. Buividas, M. Mikutis, S. Juodkazis, Surface and bulk structuring of materials by ripples with long and short laser pulses: Recent advances. Prog. Quantum Electron. **38**(3), 119–156 (2014)
169. A. Rudenko, J.-P. Colombier, T.E. Itina, Influence of polarization state on ultrafast laser-induced bulk nanostructuring. J. Laser Micro/Nanoeng. **11**(3), 304–311 (2016)
170. S. He, J.J.J. Nivas, K.K. Anoop, A. Vecchione, M. Hu, R. Bruzzese, S. Amoruso, Surface structures induced by ultrashort laser pulses: Formation mechanisms of ripples and grooves. Appl. Surf. Sci. **353**, 1214–1222 (2015)
171. T.J.-Y. Derrien, T.E. Itina, R. Torres, T. Sarnet, M. Sentis, Possible surface plasmon polariton excitation under femtosecond laser irradiation of silicon. J. Appl. Phys. **114**(8), 083104 (2013)
172. M. Garcia-Lechuga, D. Puerto, Y. Fuentes-Edfuf, J. Solis, J. Siegel, Ultrafast moving-spot microscopy: Birth and growth of laser-induced periodic surface structures. ACS Photonics **3**(10), 1961–1967 (2016)
173. J. Bonse, J. Krüger, Pulse number dependence of laser-induced periodic surface structures for femtosecond laser irradiation of silicon. J. Appl. Phys. **108**(3), 034903 (2010)
174. K. Okamuro, M. Hashida, Y. Miyasaka, Y. Ikuta, S. Tokita, S. Sakabe, Laser fluence dependence of periodic grating structures formed on metal surfaces under femtosecond laser pulse irradiation. Phys. Rev. B **82**(16), 165417 (2010)
175. A.A. Yurkevich, S.I. Ashitkov, M.B. Agranat, Permittivity of gold with a strongly excited electronic subsystem. Phys. Plasmas **24**(11), 113106 (2017)
176. E. Bévillon, R. Stoian, J.-P. Colombier, Nonequilibrium optical properties of transition metals upon ultrafast electron heating. J. Phys. Condens. Matter **30**(38), 385401 (2018)
177. R. Le Harzic, D. Dörr, D. Sauer, F. Stracke, H. Zimmermann, Generation of high spatial frequency ripples on silicon under ultrashort laser pulses irradiation. Appl. Phys. Lett. **98**(21), 211905 (2011)
178. Y. Kawakami, E. Ozawa, Self-assembled coherent array of ultra-fine particles on single-crystal tungsten substrate using SHG Nd: YAG laser. Appl. Phys. A **71**(4), 453–456 (2000)
179. J.-G. Son, J.W. Choi, O. Seo, D.-K. Ko, et al., Morphology evolution of self-organized porous structures in silicon surface. Results in Physics **12**, 46–51 (2019)
180. J.-M. Romano, A. Garcia-Giron, P. Penchev, S. Dimov, Triangular laser-induced submicron textures for functionalising stainless steel surfaces. Appl. Surf. Sci. **440**, 162–169 (2018)
181. H.-T. Chang, A. Guggenmos, S.K. Cushing, Y. Cui, N.U. Din, S.R. Acharya, I.J. Porter, U. Kleineberg, V. Turkowski, T.S. Rahman, et al. Electron thermalization and relaxation in laser-heated nickel by few-femtosecond core-level transient absorption spectroscopy. Phys. Rev. B **103**(6), 064305 (2021)

182. E. Bévillon, J.-P. Colombier, V. Recoules, R. Stoian, Free-electron properties of metals under ultrafast laser-induced electron-phonon nonequilibrium: A first-principles study. Phys. Rev. B **89**(11), 115–117 (2014)
183. E.P. Silaeva, E. Bévillon, R. Stoian, J.-P. Colombier, Ultrafast electron dynamics and orbital-dependent thermalization in photoexcited metals. Phys. Rev. B **98**(9), 094306 (2018)
184. N. Medvedev, I. Milov, Electron-phonon coupling in metals at high electronic temperatures. Phys. Rev. B **102**(6), 064302 (2020)
185. J.-P. Colombier, F. Garrelie, N. Faure, S. Reynaud, M. Bounhalli, E. Audouard, R. Stoian, F. Pigeon, Effects of electron-phonon coupling and electron diffusion on ripples growth on ultrafast-laser-irradiated metals. J. Appl. Phys. **111**(2), 024902 (2012)
186. H.C. Kuhlmann, Thermocapillary flows in finite size systems. Math. Comput. Modell. **20**(10-11), 145–173 (1994)
187. V.G. Levich, V.S. Krylov, Surface-tension-driven phenomena. Annu. Rev. Fluid Mech. **1**(1), 293–316 (1969)
188. A.M. Lindenberg, J. Larsson, K. Sokolowski-Tinten, K.J. Gaffney, C. Blome, O. Synnergren, J. Sheppard, C. Caleman, A.G. MacPhee, D. Weinstein, et al., Atomic-scale visualization of inertial dynamics. Science **308**(5720), 392–395 (2005)
189. V.R. Morrison, R.P. Chatelain, K.L. Tiwari, A. Hendaoui, A. Bruhács, M. Chaker, B.J. Siwick, A photoinduced metal-like phase of monoclinic VO_2 revealed by ultrafast electron diffraction. Science **346**(6208), 445–448 (2014)
190. J.P. Colombier, E. Audouard, R. Stoian, Laser pulses designed in time by adaptive hydrodynamic modeling for optimizing ultra-fast laser–metal interactions. Appl. Phys. A **110**(3), 723–729 (2013)
191. J.-P. Colombier, P. Combis, E. Audouard, R. Stoian, Guiding heat in laser ablation of metals on ultrafast timescales: an adaptive modeling approach on aluminum. New J. Phys. **14**(1), 013039 (2012)
192. J. Kim, S. Na, S. Cho, W. Chang, K. Whang, Surface ripple changes during Cr film ablation with a double ultrashort laser pulse. Opt. Lasers Eng. **46**(4), 306–310 (2008)
193. S. Höhm, A. Rosenfeld, J. Krüger, J. Bonse, Area dependence of femtosecond laser-induced periodic surface structures for varying band gap materials after double pulse excitation. Appl. Surf. Sci. **278**, 7–12 (2013)
194. A. Rubano, F. Cardano, B. Piccirillo, L. Marrucci, Q-plate technology: a progress review. J. Opt. Soc. Am. B **36**(5), D70–D87 (2019)
195. J.J.J. Nivas, S. He, A. Rubano, A. Vecchione, D. Paparo, L. Marrucci, R. Bruzzese, S. Amoruso, Direct femtosecond laser surface structuring with optical vortex beams generated by a q-plate. Sci. Rep. **5**(1), 17929 (2015)
196. C. Hnatovsky, V.G. Shvedov, W. Krolikowski, The role of light-induced nanostructures in femtosecond laser micromachining with vector and scalar pulses. Opt. Express **21**(10), 12651–12656 (2013)

Chapter 6
In-Situ Observation of the Formation of Laser-Induced Periodic Surface Structures with Extreme Spatial and Temporal Resolution

Klaus Sokolowski-Tinten, Jörn Bonse, Anton Barty, Henry N. Chapman, Saša Bajt, Mike J. Bogan, Sebastien Boutet, Andrea Cavalleri, Stefan Düsterer, Matthias Frank, Janos Hajdu, Stefan Hau-Riege, Stefano Marchesini, Nikola Stojanovic, and Rolf Treusch

Abstract Irradiation of solid surfaces with intense ultrashort laser pulses represents a unique way of depositing energy into materials. It allows to realize states of extreme electronic excitation and/or very high temperature and pressure and to drive materials close to and beyond fundamental stability limits. As a consequence, structural changes and phase transitions often occur along unusual pathways and under strongly nonequilibrium conditions. Due to the inherent multiscale nature—both temporally and spatially—of these *irreversible* processes, their direct experimental observation requires techniques that combine high temporal resolution with the appropriate spatial resolution and the capability to obtain good quality data on a single pulse/event basis. In this respect, fourth-generation light sources, namely, short wavelength and short pulse free electron lasers (FELs), are offering new and fascinating possibilities. As an example, this chapter will discuss the results of scattering experiments carried out at the FLASH free electron laser at DESY (Hamburg, Germany), which allowed us to resolve laser-induced structure formation at surfaces on the nanometer to submicron length scale and in temporal regimes ranging from picoseconds to several nanoseconds with sub-picosecond resolution.

Keywords Laser-induced periodic surface structures (LIPSS) · Capillary waves · Time-resolved scattering · Pump-probe experiments · Free electron laser

---

K. Sokolowski-Tinten (✉)
Faculty of Physics and Centre for Nanointegration Duisburg-Essen, University of Duisburg-Essen, Duisburg, Germany
e-mail: klaus.sokolowski-tinten@uni-due.de

J. Bonse
Bundesanstalt für Materialforschung und –prüfung (BAM), Berlin, Germany
e-mail: joern.bonse@bam.de

© The Author(s), under exclusive license to Springer Nature Switzerland AG 2023
R. Stoian, J. Bonse (eds.), *Ultrafast Laser Nanostructuring*, Springer Series in Optical Sciences 239, https://doi.org/10.1007/978-3-031-14752-4_6

1 Introduction

Irradiation of solid surfaces with intense ultrashort laser pulses represents a unique way of depositing energy into materials. It allows to realize states of extreme electronic excitation and/or very high temperature and pressure and to drive materials close to and beyond fundamental stability limits. As a consequence, structural changes and phase transitions often occur along unusual pathways and under strongly nonequilibrium conditions [1].

Moreover, such laser-solid interactions at high intensities and fluences are not only interesting from a fundamental physics point of view but represent also the basis for numerous applications of lasers for materials processing and synthesis (e.g., see Part 3 of this book and references therein). In this general context, the formation of so-called **l**aser-**i**nduced **p**eriodic **s**urface **s**tructures (LIPSS) or ripples

---

A. Barty · S. Düsterer · R. Treusch
Deutsches Elektronen-Synchrotron DESY, Hamburg, Germany
e-mail: anton.barty@desy.de; stefan.duesterer@desy.de; rolf.treusch@desy.de

H. N. Chapman
Center for Free-Electron Laser Science CFEL, Deutsches Elektronen-Synchrotron DESY, Hamburg, Germany

Department of Physics, Universität Hamburg, Hamburg, Germany

The Hamburg Centre for Ultrafast Imaging, Hamburg, Germany
e-mail: henry.chapman@cfel.de

S. Bajt
Center for Free-Electron Laser Science CFEL, Deutsches Elektronen-Synchrotron DESY, Hamburg, Germany

The Hamburg Centre for Ultrafast Imaging, Hamburg, Germany
e-mail: sasa.bajt@desy.de

M. J. Bogan · M. Frank · S. Hau-Riege
Lawrence Livermore National Laboratory, Livermore, CA, USA
e-mail: mbogan@tractionondemand.com; frank1@llnl.gov; hauriege1@llnl.gov

S. Boutet · S. Marchesini
SLAC National Accelerator Laboratory, Menlo Park, CA, USA
e-mail: sboutet@slac.stanford.edu; smarches@slac.stanford.edu

A. Cavalleri
Max Planck Institute for the Structure and Dynamics of Matter, Hamburg, Germany
e-mail: andrea.cavalleri@mpsd.mpg.de

J. Hajdu
Department of Cell and Molecular Biology, Uppsala Universitet, Uppsala, Sweden

The European Extreme Light Infrastructure, Institute of Physics, Academy of Sciences of the Czech Republic, Dolní Břežany, Czech Republic
e-mail: janos.hajdu@icm.uu.se

N. Stojanovic
Deutsches Zentrum für Luft- und Raumfahrt (DLR) Berlin-Adlersdorf, Berlin, Germany
e-mail: nikola.stojanovic@dlr.de

represent an interesting and very common case under typical processing conditions, namely, irradiation of *real* (i.e., rough) surfaces with multiple/many pulses.

LIPSS have been first reported in 1965 by Birnbaum [2] on semiconductors irradiated with pulses from a free-running ruby laser (≈200 μs duration). Since then the topic has attracted continuous interest, not only to understand the basic mechanisms that lead to these sub-micrometer to nanoscale surface modifications, but also because LIPSS are considered as a versatile tool to achieve nanoscale structuring/patterning and functionalization of surfaces for a variety of applications (see [3] and references therein, as well as Chap. 23 of this book by Mezera et al.).

LIPSS have been observed on almost all kinds of materials and with any kind of laser. Depending on the LIPSS periodicity, different mechanisms are discussed in the very extensive literature. Meanwhile accepted is the view that LIPSS with a periodicity of the order of the laser wavelength (so-called low spatial frequency LIPSS: LSFL) can be attributed to the interference between the incident laser wave and waves scattered/excited at the surface leading to an intensity modulation and thus to a (periodically) modulated energy deposition [4]. In 1983, Sipe et al. [5] have developed this picture into a rigorous electromagnetic model which is frequently used and has been further developed since then [6–8].

More recently and so far only after irradiation with multiple ultrashort laser pulses, LIPSS with a periodicity much smaller than the laser wavelength have been observed. The mechanisms which lead to these high spatial frequency LIPSS (HSFL) are not fully clear yet. HSFL have been, for example, attributed to near-field scattering and interference effects [9] in conjunction with surface second harmonic generation (e.g., [6, 10, 11]), but also self-organization processes have been proposed [12, 13]. Very recently, a coupled electromagnetic-hydrodynamic mechanism was proposed, where thermocapillary melt flows (Marangoni convection instability) that are initiated by spatial gradients caused by polarization-dependent absorption at random nanobumps and nanoholes cause the formation of HSFL [14].

However, it is not the purpose of this contribution to discuss in detail all models and controversies about LIPSS (for reviews of the current understanding, the reader is referred to [15–17] and references therein), but to reveal and emphasize the *dynamical* aspects of LIPSS formation. In the vast majority of published work, LIPSS have been studied *post mortem* through an analysis of the permanent modifications of the irradiated surface. A comparatively small number of time-resolved experiments addressing both, the nanosecond [18–22] and the femtosecond and picosecond time range [23–29], have been performed. Using optical probing, direct imaging [24–29] and diffraction/scattering techniques [18–23] have been applied. However, the spatial resolution was limited by the optical probe wavelength which made it difficult/impossible to follow the transient structural evolution of the laser-irradiated surface on sub-micrometer to nanometer length scales. For a more general discussion on time-resolved optical probing, the reader is referred to Chap. 7 (M. Garcia-Lechuga et al.) of this book.

Here we present results of time-resolved scattering experiments performed at the extreme ultraviolet (XUV) free electron laser (FEL) FLASH at DESY in Hamburg (Germany) [30]. The unique combination of short wavelength, ultrashort pulse duration, and high photon flux has opened up new and exciting possibilities since it allows the investigation of *irreversible* processes with high temporal resolution and the appropriate nanoscale spatial resolution. We make use of these possibilities to study in the time domain the formation of LIPSS at the surface of laser-excited thin silicon films.[1]

2 Time-Resolved XUV Scattering at FLASH

The FLASH free electron laser at DESY (Hamburg/Germany) was the first FEL operating at wavelengths below 50 nm [30]. It has been available to users since 2005 serving a broad scientific community interested in atomic, molecular, and cluster physics, high-energy-density research, dynamics at surfaces and diffraction imaging with high spatial resolution (see [32, 33] and references therein).

To address the particular topic of this contribution, namely, the dynamics of nanoscale structure formation at laser-irradiated surfaces, we carried out a series of time-resolved laser pump XUV scattering probe experiments to follow the laser-induced changes with femtosecond temporal and nanometer spatial resolution. A schematic of the experimental setup is shown in Fig. 6.1.

Experiments were performed at beamline BL2 [34], and FLASH was operated in the single-bunch ultrashort-pulse mode, providing pulses at a wavelength of 13.5 nm, a pulse duration of 10–20 fs and a mean pulse energy of about 20 μJ (corresponding to $>10^{12}$ XUV photons per pulse). These pulses were focused onto

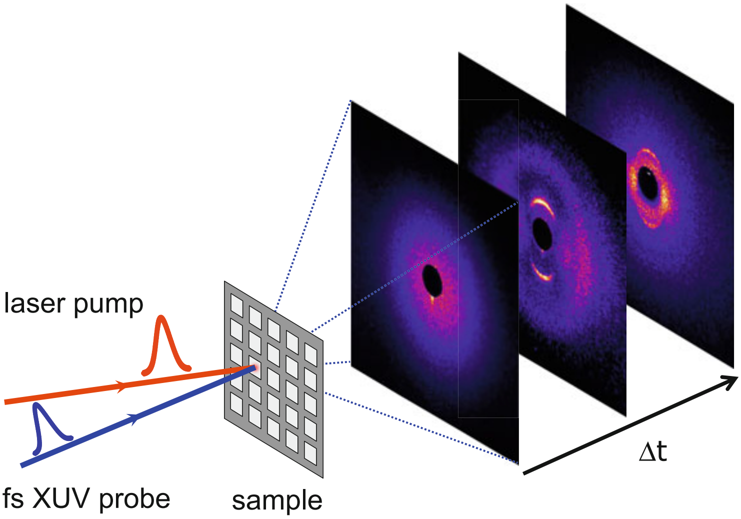

Fig. 6.1 Schematic of the time-resolved single-pulse scattering experiment performed at the XUV free electron laser FLASH

the sample under study (see below) to a spot size of approximately 20 μm full width at half maximum (FWHM).

---

[1] Some of these results have been presented earlier in [31].

Scattering experiments were carried out in a normal-incidence transmission geometry. A 45° graded multilayer mirror with a central hole was used to selectively collect the radiation scattered by the sample and direct it onto a XUV-sensitive CCD detector while blocking at the same time any background scattering, plasma emission from the target, etc., as well as the direct beam (which passed through the central hole). At $\lambda_{\mathrm{XUV}} = 13.5\,\mathrm{nm}$, this diffraction setup allowed to measure scattering patterns over a spatial frequency range (spatial frequency $q = (2\pi/\lambda_{\mathrm{XUV}}) \cdot sin(\theta)$; θ diffraction angle) from $\pm 10\ \mu\mathrm{m}^{-1}$ (determined by the size of the central hole) to $\pm 110\,\mu\mathrm{m}^{-1}$ (detector size), providing an effective spatial resolution of better than 50 nm [35]. For further details, the reader is referred to [36, 37].

Samples comprised polycrystalline silicon films with 100 nm thickness deposited onto arrays of free-standing, 20-nm-thick Si_3N_4 membranes supported by a silicon wafer frame. Such target arrays allowed replacement of the sample between consecutive exposures, because single-pulse irradiation with both, the optical laser and the FEL, leads to irreversible sample modifications (e.g., its destruction).

These samples have been irradiated with 12 ps, 523 nm laser pulses [38] at an angle of incidence of 47° (normally p-polarized) and an incident fluence of about 1.7 J/cm^2 (pump beam size on the sample $30 \times 40\,\mu\mathrm{m}^2$ FWHM), well above the ablation threshold of $\lesssim 0.5\,\mathrm{J/cm}^2$. The delay time Δt between the optical pump and the XUV probe was varied over a range from -50 ps to 4.5 ns with a help of a mechanical delay line.

For each delay time, three to five diffraction images have been recorded (each on a fresh sample window), and the data were averaged to increase the signal-to-noise ratio. Frequently, detector images without pump and probe, pump only, and probe only have been recorded to allow for background correction as well as to characterize the scattering of the non-excited samples.

3 Experimental Results

As first results, we present here data obtained on a 100-nm-thick polycrystalline silicon film, deposited on $100 \times 100\,\mu\mathrm{m}^2$ sized Si_3N_4 membrane windows. Figure 6.2 shows a sequence of transient scattering patterns for different pump-probe delay times. The intensity scale of the false-color representation is in arbitrary units, but the same for all frames/delays. The black disk in the center of each image represents the “beam stop” realized by the hole in the XUV multilayer mirror. The projection of the pump laser beam polarization (p-pol.) onto the sample surface is indicated by the vertical solid white bar in the first frame of Fig. 6.2.

Before discussing the temporal evolution of these scattering patterns, we want to emphasize their “grainy” structure, which represent speckles due to the spatially coherent XUV illumination. From the average speckle size $\delta q_S \approx 0.4\,\mu\mathrm{m}^{-1}$,

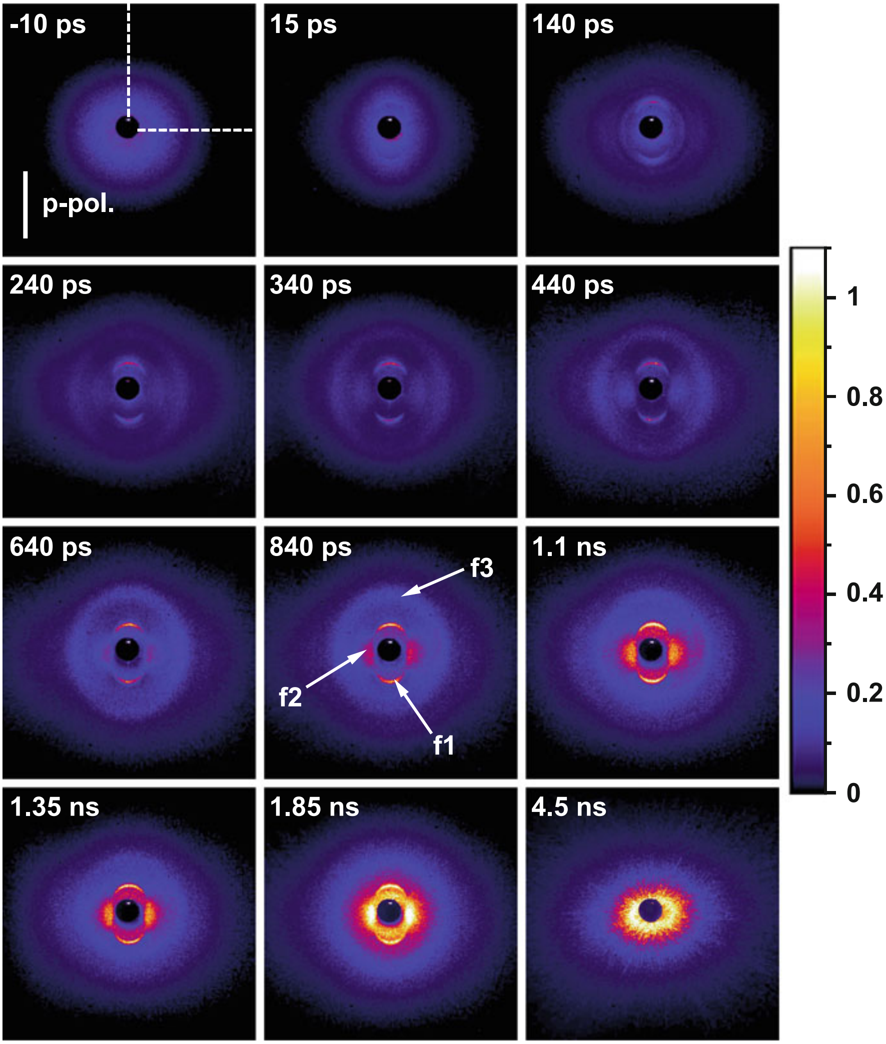

Fig. 6.2 Transient scattering patterns (in false-color representation) of a 100 nm polycrystalline Si-film on a 20 nm Si_3N_4 membrane (size: $100 \times 100\,\mu m^2$) as a function of delay time Δt between the 12 ps, 523 nm optical pump pulse (fluence $\approx 1.7\,J/cm^2$), and the 10–20 fs, 13.5 nm XUV probe pulse. Displayed spatial frequency range (horizontal and vertical): $-92\,\mu m^{-1}$ to $+92\,\mu m^{-1}$; intensity scale in arbitrary units, but the same for all frames; solid white bar in the first frame: direction of laser polarization (projection onto the surface)

the diameter d of the coherently illuminated sample area can be estimated as $d = 2\pi/\delta q_S \approx 16\,\mu m$, which agrees well with the nominal XUV spot size of $20\,\mu m$ on the sample, highlighting the high spatial coherence of the FEL radiation [39].

The diffraction pattern prior to excitation (-10 ps delay) does reveal that the polycrystalline silicon film has a transverse structure (e.g., grain size) on a hundred nm length scale (as inferred from the width of the measured distribution). Already shortly after excitation, changes of the scattering patterns can be recognized, and three distinct features, in the following denoted as f1, f2, and f3 (marked in the frame for $\Delta t = 840$ ps), develop on different timescales. The most prominent transient feature—f1—is the strong arc-shaped diffraction peaks at $q_v \approx \pm 21\,\mu\mathrm{m}^{-1}$ in the vertical direction. They indicate the formation of a well-oriented structure (perpendicular to the laser polarization) with ≈ 300 nm periodicity. Feature f2 corresponds to the (broader) diffraction peaks at $q_h \approx \pm 15$–$25\,\mu\mathrm{m}^{-1}$ along the horizontal direction (at later times close to the beam stop). Additionally, a broad, ringlike diffraction feature (f3) can be recognized. It has an elliptical shape with (at $\Delta t = 840$ ps) vertical and horizontal half axes of $\approx 43\,\mu\mathrm{m}^{-1}$ and $\approx 36\,\mu\mathrm{m}^{-1}$, corresponding to real space periodicities of ≈ 146 nm and ≈ 175 nm, respectively.

More detailed/quantitative information about the temporal evolution of the different diffraction features is presented in Fig. 6.3. The top row depicts vertical (a) and horizontal (b) cross sections along the white-dashed lines, as shown in the first frame of Fig. 6.2, for selected pump-probe time delays. The bottom row displays time dependencies of (c) the integrated diffraction signal of f1 (red), f2 (blue), and f3 (green), of (d) the (vertical) real space periodicities Λ_{f1} (red) and Λ_{f3} (green) of features f1 and f3, respectively, and of (e) the peak width (FWHM) of f3 (open circles) along the vertical direction and, derived from this width, the effective size of the corresponding *structurally coherent* sample area (filled squares; explanation see below).

Feature f1 starts to form already during the pump laser pulse (2nd frame in Fig. 6.2; green trace $I\ (q_v)$ in Fig. 6.3a). Its intensity increases with time (red curve in Fig. 6.3c) and it persists until the whole sample starts to disintegrate (last frame in Fig. 6.2, $\Delta t = 4.5$ ns). Moreover, there is a continuous shift in the peak position indicating an increase of its characteristic periodicity Λ_{f1} (red trace in Fig. 6.3d) with time. Feature f2 becomes visible after about 300 ps and its intensity increases subsequently (green trace in Fig. 6.3c). Simultaneously, f2 moves toward smaller q, but an accurate determination of the peak position as a function of delay time is difficult since at early delays, it overlaps with feature f3, while at later delays, it is partially blocked by the beam stop. The elliptical ring feature f3 starts to develop after approximately 100 ps, is most visible after a few hundred ps, and does not persist as long as features f1 and f2. Moreover, its peak position changes with time, being constant for about 400 ps before starting to shift to smaller q_v, which corresponds to an increasing real space periodicity Λ_{f3} (green trace in Fig. 6.3d). Also the width of the ringlike feature f3 changes with time, being constant again for approximately 400 ps followed by a linear decrease, which could be followed until f3 has almost vanished after about 1.4 ns.

All quantities shown in Fig. 6.3c–e for the different features reveal essentially a two-stage evolution of the whole process. During the first stage, up to about 0.4 ns the intensity of f1 and f3 increases, while the intensity of f2 is low. During the same time, Λ_{f1} increases, but Λ_{f3} stays constant. For delay times $\Delta t > 0.4$ ns (stage

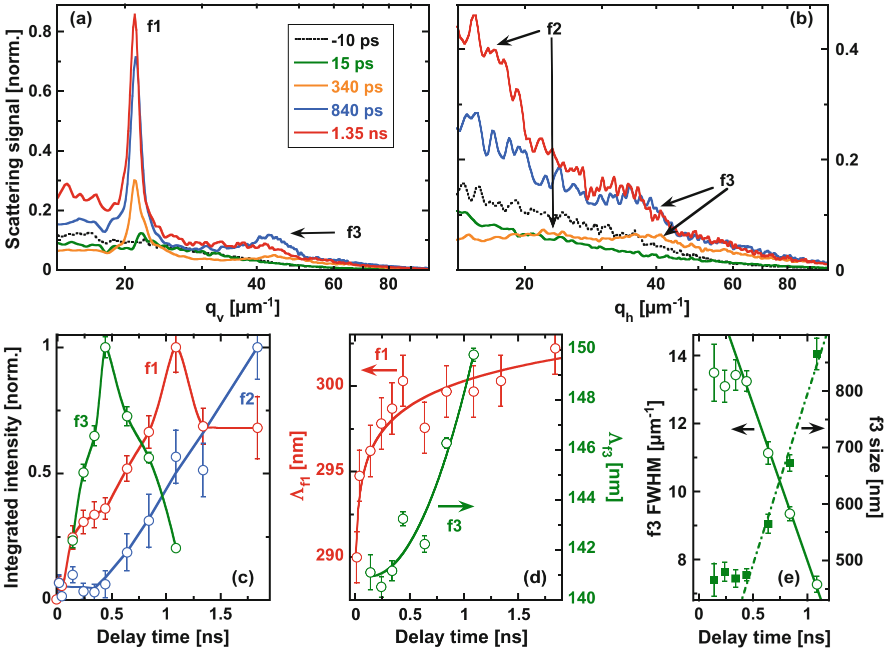

Fig. 6.3 Top row: (**a**) Vertical ($I\ (q_v)$) and (**b**) horizontal ($I\ (q_h)$) cross sections along the white-dashed lines, as shown in the first frame of Fig. 6.2, for selected pump-probe delay times. Bottom row: (**c**) Integrated intensity of the characteristic features f1 (red), f2 (blue), and f3 (green), (**d**) real space periodicities Λ_{f1} of feature f1 (red, left axis) and Λ_{f3} of feature f3 (in vertical direction, green, right axis), (**e**) FWHM of feature f3 (open circles, left axis) and the derived size of the corresponding *structurally coherent* sample area (full squares, right axis), all as a function of pump-probe delay time. The solid curves in (**c**) and (**d**) are a guide to the eye; the curves in (**e**) represent linear fits to the data points at late delay times

2), f1 exhibits a further increase in intensity, which levels off around 1 ns, while the intensity of f2 starts to continuously increase, and f3 decreases in intensity. Similarly, while Λ_{f1} remains essentially constant, Λ_{f3} increases and the f3 peak width decreases.

4 Discussion and Interpretation of the Transient Scattering Patterns

Before discussing and interpreting the experimental results, we would like to point out that *any* spatially dependent modulation of the optical properties (in the XUV!) of the laser-excited material will result in scattering of the probe beam. Such modulation can be caused by a variety of processes, such as electronic excitation, ionization, heating, but also changes in density and surface topography due to material expansion and ablation. Therefore, it is a priori difficult if not impossible to disentangle these processes from the scattering data without further knowledge, for example, through their characteristic timescales. Most likely, the scattering observed at early delay times has to be attributed to electronic excitation and melting of the material, whereas at later times, density modulations and changes of the surface topography due to expansion and ablation dominate.

To interpret the experimental data and the different diffraction features, we apply first the intuitive model of interference between the incident laser field and surface scattered/excited waves since it allows simple predictions on the periodicity and angular orientation of the resulting LIPSS. This is illustrated in Fig. 6.4 where $\mathbf{k}_p$ denotes the in-surface component of the wave-vector $\mathbf{k}_i$ of the incident pump laser beam ($k_p = k_i \cdot \sin(\alpha)$; α: angle of incidence) and $\mathbf{k}_s$ the wave-vector of a scattered/excited wave propagating along the surface.

While $\mathbf{k}_s$ can have, in principle, any in-plane direction, its length is determined by the particular nature of the scattering/excitation process. Often it has been found that $k_s \approx k_i$ and the LIPSS wave-vector $\mathbf{q}_l$ is then given by $\mathbf{q}_l = \pm(\mathbf{k}_p + \mathbf{k}_s)$. Therefore, all possible $\mathbf{q}_l$ lie on two intersecting circles with radius $k_p \approx k_i$ centered at $\pm\mathbf{k}_p$. Moreover, in many experiments (e.g., [40]), three dominating LIPSS modes were found for p-polarized light. The first two modes $q_l^{\pm}$ correspond to $\mathbf{k}_s$ parallel or antiparallel to $\mathbf{k}_p$, and the third mode q_l^0 to the intersection points of the two circles. For these cases, $q_l^{\pm} = (k_i \pm k_p) = k_i \cdot (1 \pm \sin(\alpha))$ and $q_l^0 = k_i \cdot \cos(\alpha)$, which results in $q_l^+ = 20.8\,\mu\text{m}^{-1}$, $q_l^- = 3.2\,\mu\text{m}^{-1}$, and $q_l^0 = 8.1\,\mu\text{m}^{-1}$ here. The corresponding LIPSS periodicities $\Lambda_l = 2\pi/q_l$ are $\Lambda_l^+ = 302\,\text{nm}$, $\Lambda_l^- = 1.95\,\mu\text{m}$, and $\Lambda_l^0 = 780\,\text{nm}$. While q_l^- and q_l^0 are blocked by the beam stop, it seems natural to identify the arc-shaped diffraction feature f1 as segments of the intersecting

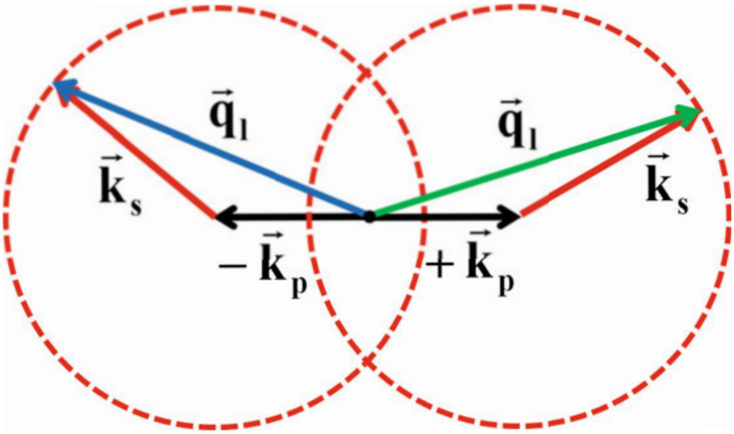

Fig. 6.4 Interference model for LIPSS generation: $\mathbf{k}_p$, in-surface component of the wave-vector $\mathbf{k}_i$ of the incident pump laser beam with $k_p = k_i \cdot \sin(\alpha)$; $\mathbf{k}_s$, wave-vector of a scattered/excited wave propagating along the surface; $\mathbf{q}_l$, LIPSS wave-vector

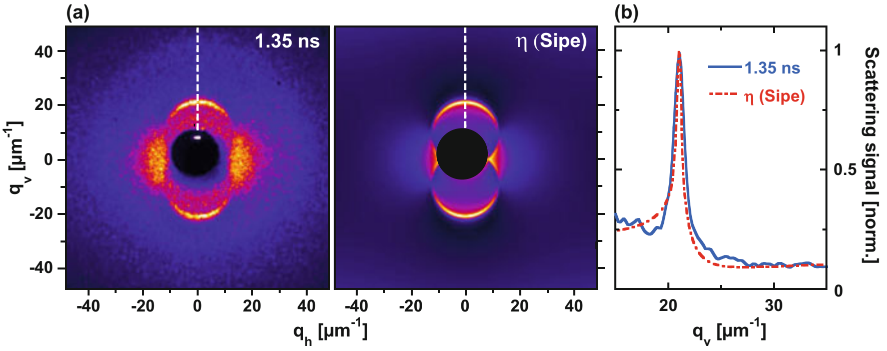

Fig. 6.5 (**a**) Comparison of the transient scattering pattern measured at $\Delta t = 1.35\,\text{ns}$ and calculations of the so-called efficacy factor η based on the model by Sipe et al. [5]. (**b**) Vertical cross sections (normalized) in the vicinity of the q_l^+-peak (red, $\eta\,(q_v)$; blue, $I\,(q_v, 1.35\,\text{ns})$

circles and the f1-peak in the circles and the f1-peak in the $I\,(q_v)$-profiles (Fig. 6.3a) as the q_l^+ LIPSS mode.

Going beyond the simplified interference model, the theory of Sipe et al. is applied [5, 41]. It allows to calculate the so-called efficacy factor $\eta(\mathbf{q})$, which is proportional to the spatially varying deposition of the laser pulse energy (represented in Fourier space). Among other factors, it depends on the optical constants of the irradiated material (for further details, the reader is referred to [41, 42]). Figure 6.5a compares the transient scattering pattern measured at $\Delta t = 1.35\,\text{ns}$ to a calculated distribution of η for the parameters of our experiment (i.e., laser wavelength, polarization, and angle of incidence) using the optical constants of liquid Si as input.

The agreement between the calculated efficacy factor and the measured scattering pattern is striking and almost quantitative (at least in certain q-ranges) as indicated by the vertical cross sections around the q_l^+-peak shown in Fig. 6.5b. This unambiguously confirms the assignment of f1 made above. In the classification of the recent LIPSS literature [17], f1 is associated with type-s LSFL. It should be noted that the good agreement between the calculated η and the measured experimental diffraction pattern is achieved only when using the optical constants of liquid Si (which is metallic) as input. Given the high pump fluence well above the melting and ablation threshold, this appears not surprising because melting will occur already during the 12 ps duration laser pulse.

However, the efficacy factor $\eta\,(\mathbf{q})$ does not provide information on how and on which timescales such a modulated energy deposition transforms into modifications of the sample properties and morphology responsible for the transient scattering measured in the experiment. Moreover, the Sipe model, as applied here, does not take into account changes of the sample (morphology, optical properties) during irradiation, which are very likely to occur for the conditions of our experiment (12 ps pulse duration, high fluence) when the material transforms already during the pulse from a cold solid, over a hot, electronically excited semiconductor into a metallic liquid. Such changes will definitely influence the process of LIPSS formation (e.g., Bonse et al. [42] have argued for the case of fs laser-excited Si that changes of the optical properties caused by the formation of a dense electron-hole plasma can change the LIPSS periodicity).

However, we believe that the increase of the real space periodicity Λ_{f1} of the f1 feature (Fig. 6.3d) observed here is only an apparent one since this would imply a corresponding expansion of the LIPSS pattern over the whole pump laser spot size of 40 µm in horizontal direction, requiring lateral expansion velocities initially in excess of 5 km/s, which appears unrealistic.

Pfau et al. [43] have observed changes of positions of diffraction peaks of similar magnitude (i.e., a few percent) in time-resolved magnetic scattering experiments (performed also at FLASH) during the ultrafast, laser-induced demagnetization of a thin-film Co/Pt multilayer. These samples exhibit a pronounced “wormlike” structure of domains with opposite magnetization, which gives rise to a characteristic diffraction ring. The peak position of this diffraction ring shifts to lower q within a few hundred femtoseconds after laser excitation, which is attributed to changes of the scattering form factor due to a smoothing of the magnetization profile at the domain boundary caused by spin-dependent carrier transport.

We think a similar form factor effect is responsible for the observed shift of the f1 peak—although on a very different timescale. The spatially periodic energy deposition (as described by the efficacy factor) transfers—very likely in a nonlinear fashion—into a corresponding modulation of the material properties (e.g., temperature, melt depth), thus imposing lateral gradients of these properties. These will smooth out with time due to lateral transport (e.g., heat conduction), which may affect the form factor in a similar way as discussed in [43].

Considering only Fig. 6.5, it is tempting to interpret f2 also with the help of the Sipe model and the efficacy factor as the “tail” of scattering signal originating from the vicinity of $\mathrm{q}_l^0/\mathrm{q}_l^-$. We exclude this explanation because the f2 feature appears significantly later than f1 and is initially well separated from the beam stop (see the orange $I\ (q_h)$-trace in Fig. 6.3) and thus q_l^0. However, the limited signal-to-noise ratio of the data in the q-range of the f2 feature does not allow for further quantitative analysis, so we refrain from speculating on its physical origin at this point.

Similarly, the calculated η does not account for the elliptical f3 feature, which is strongest for $\Delta t < 1\,\mathrm{ns}$ and which has almost vanished at $\Delta t = 1.35\,\mathrm{ns}$. As a possible origin of the f3 feature, we suggest the formation of capillary waves at the surface of the laser-molten silicon film [19, 21], presumably excited through the recoil of ablating material. This scenario is supported by the timescales of the appearance of this feature at delay times $\Delta t \approx 100\,\mathrm{ps}$ [44]. For a quantitative analysis, we neglect gravitational forces (i.e., large capillary constant $a = \sqrt{\frac{2\sigma}{g\rho}}$ [45]; g gravitational acceleration, σ surface tension, ρ density) and apply the dispersion relation of capillary waves in the short wavelength limit (eq. 62.3 in [45]). This results in an oscillation period $T = \sqrt{\frac{\Lambda^3\rho}{2\pi\sigma}}$ (Λ wavelength of the capillary waves).

Identifying Λ with $\Lambda_{f3} \approx 140\,\text{nm}$ at early delay times (stage 1) and using published values for the density $\rho = 2.52\,\text{g/cm}^3$ and the surface tension $\sigma = 0.874\,\text{kg/s}^2$ of liquid silicon at the melting point [46], we obtain a half oscillation period of $T/2 \lesssim 0.6\,\text{ns}$, in reasonable agreement with the temporal evolution (rise and subsequent decay) of the intensity of the f3 feature [19]. Within this picture, f3 does not reappear since these short wavelength capillary waves are damped by viscous forces with a damping time $\tau_D = \frac{\rho\Lambda^2}{8\pi^2\eta} \approx 2.8\,\text{ns}$ ($\eta \approx 0.8\,\text{mPa·s}$: dynamic viscosity of liquid silicon [47]) and additionally laser-induced ablation decomposes the molten silicon film on the ns timescale. With respect to the observed time-dependent increase of Λ_{f3}, similar form factor changes might be responsible as discussed above for the LIPSS periodicity Λ_{f1}.

Finally, we interpret the peak width w (FWHM) of the f3 feature, as depicted by the open circles in Fig. 6.3e, in a Scherrer-like approach [48] as a measure of the size $s \approx 2\pi/w$ of the area, where capillary waves are *coherently* excited. This size (filled squares in Fig. 6.3e) has an approximately constant value of 470 nm during stage 1, but increases linearly with a slope of $v = 600\,\text{m/s}$ (dashed-dotted curve in Fig. 6.3e) during stage 2. Within the capillary wave picture, v corresponds to twice the group velocity v_G of the excited waves assuming that the initial excitation area expands radially by capillary wave propagation. However, one must take into account that the value of a (and thus v) derived from the f3 peak width w with the equation above tends to overestimate the actual size for two reasons [49]: (i) The Scherrer equation includes a pre-factor K, which depends on the shape of the scattering object and is usually somewhat smaller than 1; (ii) the determined value of a represents in our case (2D scattering objects) an area-weighted mean value, which depends on the size distribution (unknown), but emphasizes larger *particles*. Therefore, $v/2 = 300\,\text{m/s}$ represents actually an upper boundary for the group velocity v_G of capillary waves, which can be theoretically calculated from the dispersion relation as $v_G = d\omega/dk = \frac{3}{2} \cdot \sqrt{\frac{2\pi\sigma}{\rho\Lambda}}$. Using again the published values for density ρ and surface tension σ of liquid silicon [46], we obtain $v_G \approx 180\,\text{m/s}$, in reasonable agreement with the upper boundary $v/2 = 300\,\text{m/s}$ determined from the observed decrease of the f3 peak width.

In summary, although we ignore any temperature-dependent changes of the thermophysical material properties, the simple capillary wave picture provides a surprisingly good quantitative description of the temporal evolution of the f3 feature. However, two questions remain unanswered: (i) What mechanism selects the observed wavelength Λ_{f3} and (ii) why is the f3 diffraction ring elliptical? As we will argue in the next section, both effects may be related to the f1 feature and the formation of type-s LSFL.

5 Polarization Dependence

The Sipe model allows predictions how the LIPSS formation depends on laser polarization [5, 40]. In particular, it is expected (and has been experimentally confirmed) that upon rotation of the pump laser polarization, the arc segments, where $\eta(\mathbf{q})$ is maximum, rotate as well. To validate this, the XUV scattering on a similar 100-nm-thick Si film for similar[2] excitation conditions as above has been measured for three different polarization directions (p-, s-, and 45°-polarization). Data for a pump-probe delay of $\Delta t = 340\,\text{ps}$ are shown in Fig. 6.6.

It has to be noted that these measurements have been performed with silicon films deposited on smaller, $20 \times 20\,\mu\text{m}^2$-sized Si_3N_4 membranes. Diffraction from the edges of the membranes is responsible for the very intense vertical and horizontal streaks (white), which partially overlap with the different scattering features discussed above. However, in complete agreement with the Sipe model, the f1 feature moves along the two intersecting circles depicted in Fig. 6.4 and is weakest for s-polarized pump light. Although the f2 feature is not visible for s-polarized excitation, presumably because the scattering intensity is low (as for f1) and superimposed by the strong scattering from the membrane edges, Fig. 6.6 clearly demonstrates that the diffraction features f2 and f3 change their orientation as well. However, while the motion of f1 is centered around $\pm\mathbf{k}_p$, f2 and f3 rotate around the origin $\mathbf{q} = 0$. As such, the elliptical f3 feature keeps its large axis always

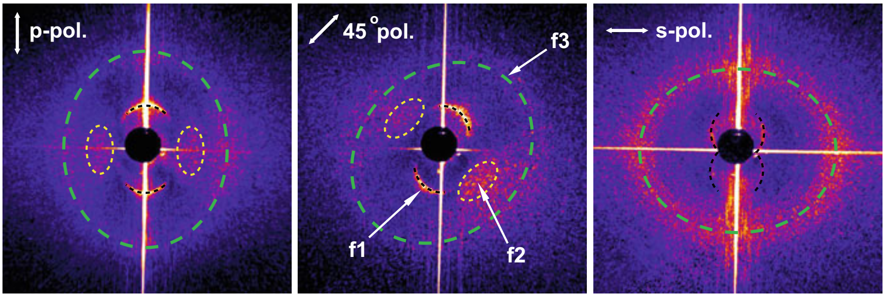

Fig. 6.6 Transient scattering patterns of a 100 nm polycrystalline Si film (on a $20 \times 20\,\mu\text{m}^2$, 20-nm-thick Si_3N_4 membrane) measured 340 ps after excitation with a 12 ps, 523 nm laser pulse (fluence $\approx 2\,\text{J/cm}^2$) for different polarization directions (left, p-pol.; middle, 45°-pol.; right, s-pol.). The black, yellow, and green dashed curves mark the characteristic diffraction features f1, f2, and f3, respectively. Please note that the intensity scale has been adjusted for each image separately in order to make the different diffraction features clearly visible. The overall scattering intensity is decreasing by changing the pump polarization from p to s

parallel to the linear laser beam polarization (the aspect ratio does not change), while the f2 feature is always oriented perpendicular to it.

---

[2] For the measurements with 45°- and s-polarized pumping, we increased the laser fluence to the maximum available level of about $2.2\,\text{J/cm}^2$ to account at least partly for the increased reflection losses compared to pumping with p-polarized light.

To explain this behavior, one has to consider that the modulated energy deposition at the spatial frequency q_l^+ of the f1 feature, which leads to LIPSS formation, also imposes an overall asymmetry of the transient material properties and consequently in the material dynamics between directions along and perpendicular to the pump laser polarization. Since the f1 feature appears first (already during the pulses), it may be not surprising that the processes leading to the f2 and f3 diffraction features depend on the pump pulse polarization in the observed manner (rotation with the polarization, ellipticity of f3), although f2 and f3 are not accounted for by the efficacy factor $\eta\,(\mathbf{q})$. In fact, in Chap. 5 of this book, Rudenko and Colombier discuss various mechanisms (e.g., near-field effects) that lead to a polarization-dependent symmetry breaking and thus preferred orientation of the evolving structures. In addition, it is noteworthy that $\Lambda_{f3} \approx \Lambda_{f1}/2$, which points toward a further connection between the f1 and f3 features, suggesting that the so far not understood selection of wavelength within the capillary wave picture is also related to the periodically modulated energy deposition.

6 Higher-Order LIPSS

In this section, we discuss results from a scattering experiment in a similar experimental geometry, but using single 50 fs, 800 nm, and p-polarized laser pulses at an angle of incidence of 45° (p-pol.) for the excitation of approximately $5 \times 5\,\mu\text{m}^2$ sized Si patches of 100 nm thickness deposited on free-standing 20-nm-thick Si_3N_4 membranes (see inset in the upper-left frame in Fig. 6.7) at a fluence again well above the ablation threshold. For several reasons not be discussed here, we were not able to perform systematic measurements, but only to record a limited number of scattering patterns. A short sequence of those are shown in Fig. 6.7 for different pump-probe time delays. As in Fig. 6.2, the projection of the pump laser beam polarization (p-pol.) onto the sample surface is indicated by the vertical solid white bar in the first frame of Fig. 6.7.

Please note that in order to make diffraction features at larger scattering angles visible (e.g., scattering pattern at $\Delta t = 0.4$ ns), high FEL intensities were required leading to saturation of the detector closer to the beam stop. The saturated region was smeared out further in vertical direction due to the read-out process of the CCD detector.

The upper-left pattern measured at negative time delay shows the scattering of the unperturbed Si patch. Two features of the scattering patterns measured at positive delay times are particularly noteworthy:

(1) The f1 feature, which is characteristic for type-s LSFL as predicted by the Sipe model, is observed even after excitation with a single fs pulse. Since the pump spot size on the sample is larger than the actual sample size, we

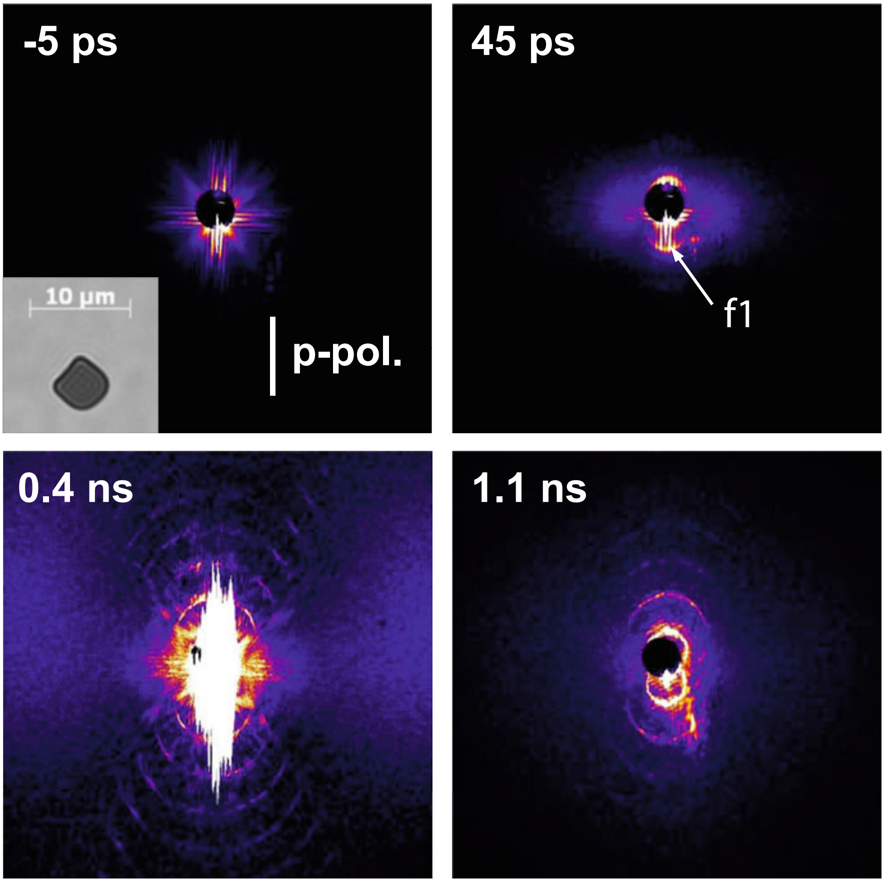

Fig. 6.7 Transient scattering pattern of 5 × 5 µm^2 sized Si patches of 100 nm thickness deposited on free-standing 20-nm-thick Si_3N_4 membranes after excitation with a 50 fs, 800 nm laser pulse for different pump-probe delay times; solid white bar in the first frame: direction of laser polarization (projection onto the surface). The inset in the upper-left frame shows an optical micrograph of a typical sample

attribute this to efficient scattering of the pump radiation at the edges of the Si patch, similar to the observations on surfaces, which have been intentionally pre-structured/scratched [26, 29].

(2) As is best visible in the two scattering patterns at larger delays, not only the fundamental of the f1 feature is observed but also higher diffraction orders (we were able to detect scattering up to the 9th order) indicating that the spatial modulation of the material properties that give rise to the scattering of the XUV probe pulse is non-sinusoidal. These higher orders are observed at longer delay times and can be, therefore, very likely associated with changes of the sample morphology due to a spatially modulated ablation of the material. Since ablation

exhibits generally a nonlinear dependence on fluence (e.g., threshold behavior), a non-sinusoidal surface morphology will develop even for a sinusoidally modulated energy deposition leading to higher-order diffraction.

We would like to emphasize that these results, although not yet systematic, specifically highlight the advantage of probing the LIPSS dynamics with short wavelength radiation. Higher-order transient diffraction from LIPSS has so far been reported only in the work by Keilmann [19], who observed second-order LIPSS diffraction after excitation with a CO_2 laser (wavelength 10.6 μm). In all other studies, the accessible momentum transfer range was not sufficient to capture these details.

7 Summary and Outlook

The formation of LIPSS (and structure formation in general) at laser-irradiated surfaces represents a complex multiscale problem in terms of the relevant length and timescales, as well as the underlying physical processes, posing extreme challenges for their experimental and theoretical investigation.

On the experimental side, techniques are required that combine high temporal resolution down to the femtosecond range with the appropriate spatial resolution on the nanometer to micrometer scale. Furthermore, these techniques need to be applied under highly irreversible conditions where single pulse laser excitation leads to significant permanent changes of the irradiated surface area.

In this contribution, we have presented a set of time-resolved scattering experiments using femtosecond XUV pulses from a FEL that allowed us to follow directly structure formation at the surface of thin silicon films after irradiation with picosecond optical laser pulses on sub-micrometer to nanometer length scales.

Although the measured data reveal a complex evolution both, in time and momentum space, the main aspects are accounted for by the LIPSS model of Sipe et al. [5], which is confirmed almost quantitatively. However, the additional diffraction features observed here and their complex temporal evolution reveal the relevance of other processes (e.g., excitation of capillary waves).

Due to time constraints—the presented data represent results from approx. 48 h of FEL beamtime—more detailed and systematic studies had not been possible. Nevertheless, our experiments represent the first step towards more thorough investigations of nanoscale structure formation (incl. LIPSS) at laser-irradiated surface on extreme time and length scales that have not been accessible before.

While the extension of these experiments toward shorter probing wavelengths will enable measurements with even higher spatial resolution, the application of a grazing-incidence scattering geometry [50] will allow to study the surfaces of bulk materials, a situation more typical/relevant in *real-life* laser processing. Similarly, the technique can be also applied in the multi-pulse excitation regime by pre-structuring the surface through irradiation with N laser pulses and probing the transient changes induced by the $(N + 1)$ excitation pulse, as has been done in all-optical pump-probe experiments (e.g., [23, 25]). On the other hand, 3D tomography using multiple probe pulses at different angles of incidence may provide volumetric information.

Moreover, experimental schemes that make use of the very high spatial coherence of the FEL radiation, like coherent diffraction imaging [37] and photon correlation spectroscopy (e.g., [51, 52]), can provide additional opportunities. In fact, during the same beamtime, where the data presented here have been measured, we have additionally used both techniques to follow in real space with nanometer resolution and on picosecond timescales the laser-induced destruction of a fabricated nanostructure [35].

With respect to the theoretical description of these processes, such experiments, in particular if scattering intensities can be properly calibrated/normalized, should provide important benchmark data for the sophisticated hybrid electromagnetic and hydrodynamic continuum models (see, e.g., [14] and Chap. 5 of this book) that have been developed recently.

Acknowledgments We are deeply indebted to Bruce Woods for his inventive engineering solutions that were critical for the success of these experiments, and his skill and efficiency in managing the construction of the instrumentation. We dedicate this to his memory. We also thank H. Ehrke, M. M. Seibert, and R. Tobey for their help during the experiment. This work was financially supported by the following agencies: the *Deutsche Forschungsgemeinschaft* (DFG, German Research Foundation) through the Collaborative Research Centre (CRC) 1242 (project number 278162697, project C01 *Structural Dynamics in Impulsively Excited Nanostructures*); the German Federal Ministry of Education and Research (FSP 301, grant 05KS7PG1); the US Department of Energy (DOE), Lawrence Livermore National Laboratory; the National Science Foundation Center for Biophotonics, University of California, Davis; the Advanced Light Source and National Centre for Electron Microscopy, Lawrence Berkeley National Laboratory, under contract DE-AC03-76SF00098; the Natural Sciences and Engineering Research Council of Canada (NSERC Postdoctoral Fellowship to M.J.B.); the Sven and Lilly Lawskis Foundation (doctoral fellowship to M.M.S.); the US Department of Energy Office of Science to the Stanford Linear Accelerator Center; the European Development Fund (structural dynamics of biomolecular systems—ELIBIO, CZ.02.1.01/0.0/0.0/15_003/0000447); the European Union (TUIXS); the Swedish Research Council; the Swedish Foundation for International Cooperation in Research and Higher Education; and the Swedish Foundation for Strategic Research. This work was performed under the auspices of the US DOE by Lawrence Livermore National Laboratory in part under contract W-7405-Eng-48 and in part under contract DE-AC52-07NA27344.

References

1. B. Rethfeld, K. Sokolowski-Tinten, D. von der Linde, S.I. Anisimov, Appl. Phys. A: Mater. Sci. Process. **79**, 767 (2004). https://doi.org/10.1007/s00339-004-2805-9
2. M. Birnbaum, J. Appl. Phys. **36**(11), 3688 (1965). https://doi.org/10.1063/1.1703071
3. C. Florian, S.V. Kirner, J. Krüger, J. Bonse, J. Laser. Appl. **32**(2), 022063 (2020). https://doi.org/10.2351/7.0000103
4. D.C. Emmony, R.P. Howson, L. J. Willis, Appl. Phys. Lett. **23**(11), 598 (1973). https://doi.org/10.1063/1.1654761

5. J.E. Sipe, J.F. Young, J.S. Preston, H.M. van Driel, Phys. Rev. B **27**, 1141 (1983). https://doi.org/10.1103/PhysRevB.27.1141
6. D. Dufft, A. Rosenfeld, S.K. Das, R. Grunwald, J. Bonse, J. Appl. Phys. **105**(3), 034908 (2009). https://doi.org/10.1063/1.3074106
7. J.Z.P. Skolski, G.R.B.E. Römer, J.V. Obona, V. Ocelik, A.J. Huis in 't Veld, J.T.M. De Hosson, Phys. Rev. B **85**, 075320 (2012). https://doi.org/10.1103/PhysRevB.85.075320
8. S. Höhm, A. Rosenfeld, J. Krüger, J. Bonse, J. Appl. Phys. **112**, 014901 (2012). https://doi.org/10.1063/1.4730902
9. A. Rudenko, J.P. Colombier, S. Höhm, A. Rosenfeld, J. Krüger, J. Bonse, T.E. Itina, Sci. Rep. **7**, 12306 (2017). https://doi.org/10.1038/s41598-017-12502-4
10. T.Q. Jia, H.X. Chen, M. Huang, F.L. Zhao, J.R. Qiu, R.X. Li, Z.Z. Xu, X.K. He, J. Zhang, H. Kuroda, Phys. Rev. B **72**, 125429 (2005). https://doi.org/10.1103/PhysRevB.72.125429
11. X. Guo, R. Li, Y. Hang, Z. Xu, B. Yu, H. Ma, B. Lu, X. Sun, Mater. Lett. **62**, 1769 (2008). https://doi.org/10.1016/j.matlet.2007.09.082
12. F. Costache, S. Kouteva-Arguirova, J. Reif, Appl. Phys. A: Mater. Sci. Process. **79**, 1429 (2004). https://doi.org/10.1007/s00339-004-2803-y
13. J. Reif, O. Varlamova, F. Costache, Appl. Phys. A: Mater. Sci. Process. **92**, 1019 (2008). https://doi.org/10.1007/s00339-008-4671-3
14. A. Rudenko, A. Abou-Saleh, F. Pigeon, C. Mauclair, F. Garrelie, R. Stoian, J.P. Colombier, Acta Mater. **194**, 93 (2020). https://doi.org/10.1016/j.actamat.2020.04.058
15. J. Bonse, S. Höhm, S.V. Kirner, A. Rosenfeld, J. Krüger, IEEE J. Sel. Top. Quantum Electron. **23**, 9000615 (2017). https://doi.org/10.1109/JSTQE.2016.2614183
16. J. Bonse, Nanomaterials **10**, 1950 (2020). https://doi.org/10.3390/nano10101950
17. J. Bonse, S. Gräf, Laser Photon. Rev. **14**, 2000215 (2020). https://doi.org/10.1002/lpor.202000215
18. D.J. Ehrlich, S.R.J. Brueck, J.Y. Tsao, Appl. Phys. Lett. **41**, 630 (1982). https://doi.org/10.1063/1.93631
19. F. Keilmann, Phys. Rev. Lett. **51**, 2097 (1983). https://doi.org/10.1103/PhysRevLett.51.2097
20. J.F. Young, J.S. Preston, J.E. Sipe, H.M. van Driel, Phys. Rev. B **27**, 1424 (1983). https://doi.org/10.1103/PhysRevB.27.1424
21. J.F. Young, J.E. Sipe, H.M. van Driel, Phys. Rev. B **30**, 2001 (1984). https://doi.org/10.1103/PhysRevB.30.2001
22. T.D. Lee, H.W. Lee, C.H. Nam, J.K. Kim, C.O. Park, J. Appl. Phys. **71**, 4208 (1992). https://doi.org/10.1063/1.350799
23. S. Höhm, A. Rosenfeld, J. Krüger, J. Bonse, Appl. Phys. Lett. **102**, 054102 (2013). https://doi.org/10.1063/1.4790284
24. R.D. Murphy, B. Torralva, D.P. Adams, S.M. Yalisove, Appl. Phys. Lett. **103**, 141104 (2013). https://doi.org/10.1063/1.4823588
25. X. Jia, T.Q. Jia, N.N. Peng, D.H. Feng, S.A. Zhang, Z.R. Sun, J. Appl. Phys. **115**, 143102 (2014). https://doi.org/10.1063/1.4870445
26. K.R.P. Kafka, D.R. Austin, H. Li, A.Y. Yi, J. Cheng, E.A. Chowdhury, Opt. Express **23**, 19432 (2015). https://doi.org/10.1364/OE.23.019432
27. M. Garcia-Lechuga, D. Puerto, Y. Fuentes-Edfuf, J. Solis, J. Siegel, ACS Photon. **3**, 1961 (2016). https://doi.org/10.1021/acsphotonics.6b00514
28. K. Zhou, X. Jia, T. Jia, K. Cheng, K. Cao, S. Zhang, D. Feng, Z. Sun, J. Appl. Phys. **121**, 104301 (2017). https://doi.org/10.1063/1.4978375
29. J. Liu, X. Jia, W. Wu, K. Cheng, D. Feng, S. Zhang, Z. Sun, T. Jia, Opt. Express **26**, 6302 (2018). https://doi.org/10.1364/OE.26.006302
30. V. Ayvazyan, N. Baboi, J. Bähr, V. Balandin, B. Beutner, A. Brandt, I. Bohnet, A. Bolzmann, R. Brinkmann, O. Brovko, J. Carneiro, S. Casalbuoni, M. Castellano, P. Castro, L. Catani, E. Chiadroni, S. Choroba, A. Cianchi, H. Delsim-Hashemi, G.D. Pirro, M. Dohlus, S. Düsterer, H. Edwards, B. Faatz, A. Fateev, J. Feldhaus, K. Flöttmann, J. Frisch, L. Fröhlich, T. Garvey, U. Gensch, N. Golubeva, H.J. Grabosch, B. Grigoryan, O. Grimm, U. Hahn, J. Han, M. v. Hartrott, K. Honkavaara, M. Hüning, R. Ischebeck, E. Jaeschke, M. Jablonka, R. Kam-

mering, V. Katalev, B.K.S. Khodyachykh, Y. Kim, V. Kocharyan, M. Körfer, M. Kollewe, D. Kostin, D. Krämer, M. Krassilnikov, G. Kube, L. Lilje, T. Limberg, D. Lipka, F. Löhl, M. Luong, C. Magne, J. Menzel, P. Michelato, V. Miltchev, M. Minty, W. Möller, L. Monaco, W. Müller, M. Nagl, O. Napoly, P. Nicolosi, D. Nölle, T.N. nez, A. Oppelt, C. Pagani, R. Paparella, B. Petersen, B. Petrosyan, J. Pflüger, P. Piot, E. Plönjes, L. Poletto, D. Proch, D. Pugachov, K. Rehlich, D. Richter, S. Riemann, M. Ross, J. Rossbach, M. Sachwitz, E.L.Saldin, W. Sandner, H. Schlarb, B. Schmidt, M. Schmitz, P. Schmüser, J. Schneider, E. Schneidmiller, H.J. Schreiber, S. Schreiber, A. Shabunov, D. Sertore, S. Setzer, S. Simrock, E. Sombrowski, L. Staykov, B. Steffen, F. Stephan, F. Stulle, K. Sytchev, H. Thom, K. Tiedtke, M. Tischer, R. Treusch, D. Trines, I. Tsakov, A. Vardanyan, R. Wanzenberg, T. Weiland, H. Weise, M. Wendt, I. Will, A. Winter, K. Wittenburg, M. Yurkov, I. Zagorodnov, P. Zambolin, K. Zapfe, Eur. Phys. J. D **37**, 297 (2006). https://doi.org/10.1140/epjd/e2005-00308-1

31. K. Sokolowski-Tinten, A. Barty, S. Boutet, U. Shymanovich, H. Chapman, M. Bogan, S. Marchesini, S. Hau-Riege, N. Stojanovic, J. Bonse, Y. Rosandi, H.M. Urbassek, R. Tobey, H. Ehrke, A. Cavalleri, S. Düsterer, H. Redlin, M. Frank, S. Bajt, J. Schulz, M. Seibert, J. Hajdu, R. Treusch, C. Bostedt, M. Hoener, T. Möller, AIP Conf. Proc. **1278**, 373 (2010). https://doi.org/10.1063/1.3507123
32. C. Bostedt, H.N. Chapman, J.T. Costello, J.R. Crespo López-Urrutia, S. Düsterer, S.W. Epp, J. Feldhaus, A. Föhlisch, M. Meyer, T. Möller, R. Moshammer, M. Richter, K. Sokolowski-Tinten, A. Sorokin, K. Tiedtke, J. Ullrich, W. Wurth, Nucl. Instrum. Methods Phys. Res. A **601**, 108 (2009). http://doi.org/10.1016/j.nima.2008.12.202. Special issue in honour of Prof. Kai Siegbahn
33. J. Rossbach, J.R. Schneider, W. Wurth, Phys. Rep. **808**, 1 (2019). https://doi.org/10.1016/j.physrep.2019.02.002
34. K. Tiedtke, A. Azima, N. von Bargen, L. Bittner, S. Bonfigt, S. Düsterer, B. Faatz, U. Frühling, M. Gensch, C. Gerth, N. Guerassimova, U. Hahn, T. Hans, M. Hesse, K. Honkavaar, U. Jastrow, P. Juranic, S. Kapitzki, B. Keitel, T. Kracht, M. Kuhlmann, W.B. Li, M. Martins, T. Núñez, E. Plönjes, H. Redlin, E.L. Saldin, E.A. Schneidmiller, J.R. Schneider, S. Schreiber, N. Stojanovic, F. Tavella, S. Toleikis, R. Treusch, H. Weigelt, M. Wellhöfer, H. Wabnitz, M.V. Yurkov, J. Feldhaus, New J. Phys. **11**, 023029 (2009). https://doi.org/10.1088/1367-2630/11/2/023029
35. A. Barty, S. Boutet, M.J. Bogan, S. Marchesini, K. Sokolowski-Tinten, N. Stojanovic, R. Tobey, H. Ehrke, A. Cavalleri, S. Düsterer, M. Frank, S. Bajt, B.W. Woods, M.M. Seibert, J. Hajdu, R. Treusch, H.N. Chapman, Nat. Photon. **2**, 415 (2008). https://doi.org/10.1038/nphoton.2008.128
36. S. Bajt, H.N. Chapman, E.A. Spiller, J.B. Alameda, B.W. Woods, M. Frank, M.J. Bogan, A. Barty, S. Boutet, S. Marchesini, S.P. Hau-Riege, J. Hajdu, D. Shapiro, Appl. Opt. **47**, 1673 (2008). https://doi.org/10.1364/AO.47.001673
37. H.N. Chapman, A. Barty, M.J. Bogan, S. Boutet, M. Frank, S.P. Hau-Riege, S. Marchesini, B.W. Woods, S. Bajt, W.H. Benner, R.A. London, E. Plönjes, M. Kuhlmann, R. Treusch, S. Düsterer, T. Tschentscher, J.R. Schneider, E. Spiller, T. Möller, C. Bostedt, M. Hoener, D.A. Shapiro, K.O. Hodgson, D. van der Spoel, F. Burmeister, M. Bergh, C. Caleman, G. Huldt, M.M. Seibert, F.R. Maia, R.W. Lee, A. Szoke, N. Timneanu, J. Hajdu, Nat. Phys. **2**, 839 (2006). https://doi.org/10.1038/nphys461
38. H. Redlin, A. Al-Shemmary, A. Azima, N. Stojanovic, F. Tavella, I. Will, S. Düsterer, Nucl. Instr. Meth. Phys. Res. A **635**, S88 (2011). https://doi.org/10.1016/j.nima.2010.09.159
39. A. Singer, I.A. Vartanyants, M. Kuhlmann, S. Duesterer, R. Treusch, J. Feldhaus, Phys. Rev. Lett. **101**, 254801 (2008). https://doi.org/10.1103/PhysRevLett.101.254801
40. J.F. Young, J.S. Preston, H.M. van Driel, J.E. Sipe, Phys. Rev. B **27**, 1155 (1983). https://doi.org/10.1103/PhysRevB.27.1155
41. J. Bonse, M. Munz, H. Sturm, J. Appl. Phys. **97**, 013538 (2005). https://doi.org/10.1063/1.1827919
42. J. Bonse, A. Rosenfeld, J. Krüger, J. Appl. Phys. **106**, 104910 (2009). https://doi.org/10.1063/1.3261734

43. B. Pfau, S. Schaffert, L. Müller, C. Gutt, A. Al-Shemmary, F. Büttner, R. Delaunay, S. Düsterer, S. Flewett, R. Frömter, J. Geilhufe, E. Guehrs, C.M. Günther, R. Hawaldar, M. Hille, N. Jaouen, A. Kobs, K. Li, J. Mohanty, H. Redlin, W.F. Schlotter, D. Stickler, R. Treusch, B. Vodungbo, M. Kläui, H.P. Oepen, J. Lüning, G. Grübel, S. Eisebitt, Nat. Commun. **3**, 1100 (2012). https://doi.org/10.1038/ncomms2108
44. K. Sokolowski-Tinten, J. Bialkowski, A. Cavalleri, D. von der Linde, Appl. Surf. Sci. **127-129**, 755 (1998). https://doi.org/10.1016/S0169-4332(97)00736-8
45. L.D. Landau, E.M. Lifshitz, *Fluid Mechanics*. Course of Theoretical Physics, vol. 6, 2nd edn. (Pergamon, 1987)
46. S. Nakamura, T. Hibiya, Int. J. Thermophys. **13**, 1061 (1992). https://doi.org/10.1007/BF01141216
47. K.W. Kolasinski, Curr. Opin. Solid State Mater. Sci. **11**, 76 (2007). https://doi.org/10.1016/j.cossms.2008.06.004
48. P. Scherrer, Nachrichten Gesellschaft der Wissenschaften zu Göttingen (Mathematisch-Physikalische Klasse, 1918), pp. 98–100
49. J.I. Langford, A.J.C. Wilson, J. Appl. Crystallogr. **11**, 102 (1978). https://doi.org/10.1107/S0021889878012844
50. L. Randolph, M. Banjafar, T.R. Preston, T. Yabuuchi, M. Makita, N.P. Dover, C. Rödel, S. Göde, Y. Inubushi, G. Jakob, J. Kaa, A. Kon, J.K. Koga, D. Ksenzov, T. Matsuoka, M. Nishiuchi, M. Paulus, F. Schon, K. Sueda, Y. Sentoku, T. Togashi, M. Vafaee-Khanjani, M. Bussmann, T.E. Cowan, M. Kläui, C. Fortmann-Grote, A.P. Mancuso, T. Kluge, C. Gutt, M. Nakatsutsumi Phys. Rev. Research **4**, 033038 (2022). https://doi.org/10.1103/PhysRevResearch.4.033038
51. W. Roseker, S.O. Hruszkewycz, F. Lehmkühler, M. Walther, H. Schulte-Schrepping, S. Lee, T. Osaka, L. Strüder, R. Hartmann, M. Sikorski, S. Song, A. Robert, P.H. Fuoss, M. Sutton, G.B. Stephenson, G. Grübel, Nat. Commun. **9**, 1704 (2018). https://doi.org/10.1038/s41467-018-04178-9
52. Y. Sun, G. Carini, M. Chollet, F.J. Decker, M. Dunne, P. Fuoss, S.O. Hruszkewycz, T.J. Lane, K. Nakahara, S. Nelson, A. Robert, T. Sato, S. Song, G.B. Stephenson, M. Sutton, T.B. Van Driel, C. Weninger, D. Zhu, Phys. Rev. Lett. **127**, 058001 (2021). https://doi.org/10.1103/PhysRevLett.127.058001

Chapter 7
Probing Matter by Light

Mario Garcia-Lechuga, Javier Solis, and Jan Siegel

Abstract The success of ultrafast laser processing strategies to fabricate reproducible nanostructures below the diffraction limit was possible in part by understanding the complex material transformation pathways triggered by laser pulses. A continuously growing scientific community has focused on the development of experimental techniques, mostly based on probing matter by light, to unravel the underlying interaction mechanisms. Often supported by theoretical modelling, these techniques have greatly contributed to today's understanding of laser-matter interaction and enabled the identification of processing conditions that would have hardly been identified with empirical parameter scans. In this chapter, we review these light-based probing techniques, which interrogate in-situ the transient state of matter throughout its transformation from the initial state to the final state. Each technique is introduced and discussed in terms of its suitability for measuring certain transient changes induced, its spatial and temporal resolution, and is accompanied by results that illustrate its potential. Finally, a few examples of the applicability of some of these techniques in an industrial environment are given.

Keywords Time-resolved microscopy · Femtosecond laser · Pump-probe · Laser-matter interaction · Laser processing · LIBS

1 Introduction

Since the invention of lasers, they have become an essential tool both in scientific research and industrial development due to the unique properties of laser radiation. The way energy deposition with lasers can be controlled enables reaching interaction levels from the excitation of a single atom to the extreme relativistic regime. As a direct consequence, high-precision materials structuring is possible,

---

M. Garcia-Lechuga · J. Solis · J. Siegel (✉)
Laser Processing Group, Instituto de Óptica, IO-CSIC, Madrid, Spain
e-mail: mario.garcia.lechuga@csic.es; j.solis@csic.es; j.siegel@csic.es

© The Author(s), under exclusive license to Springer Nature Switzerland AG 2023

R. Stoian, J. Bonse (eds.), *Ultrafast Laser Nanostructuring*, Springer Series
in Optical Sciences 239, https://doi.org/10.1007/978-3-031-14752-4_7

even at the nanoscale [1]. The spectrum of achievable laser-induced modifications is manifold, ranging from ablation (ejection of material) to subtler structural changes (melting, solidification, density changes, modifications in the crystal structure, phase segregation, etc.). Applications ranging from surface functionalization by nano- and microscale texturing to the generation of nanoparticles or the direct writing of photonic structures are thus feasible.

The physical mechanisms underlying these applications are as broad as the type of materials that can be processed by lasers. In each case, different processes will occur over a certain time scale leading to transient changes in the material properties, from the carrier excitation stage to the final chemical/morphological/structural changes induced. These transient changes very often manifest in changes of the optical properties, which enable them to be detected using light-based techniques.

In this first section, we will briefly describe the origin of the optical properties of materials, the mechanisms that cause optical changes upon laser irradiation, and the measurable optical parameters that enable the characterization of the transient and permanent modifications induced.

1.1 Brief Review of Light Interaction with Matter

Light propagation in materials can be described by Maxwell equations, no matter the complexity of solving them under many circumstances (anisotropic materials, nanomaterials, ultrashort-pulsed beams, nonlinearities, etc.). In this section, considering the context of laser processing, some simplifications are introduced. First, magnetic media are not considered; therefore, the wave equation for the electric field, $\overrightarrow{E}(x, y, z, t)$, is expressed as [2]

$$\nabla \times \left(\nabla \times \overrightarrow{E}\right) + \frac{1}{c^2}\frac{\partial^2 \overrightarrow{E}}{\partial t^2} = -\frac{1}{c^2\epsilon_0}\frac{\partial^2 \overrightarrow{P}}{\partial t^2} - \frac{1}{c^2\epsilon_0}\frac{\partial \overrightarrow{J}}{\partial t} \tag{7.1}$$

being c the speed of light in free space and ϵ_0 the permittivity of free space. The two terms on the right-hand side are called source terms and are related to the optical properties of the material. $\overrightarrow{P}$ is the polarization of the material, and the first term thus accounts for the light interaction with bound electrons (i.e., electrons in the valence band of a solid). $\overrightarrow{J}$ corresponds to the electric current density, and the second term is thus associated to the behavior of free electrons in the presence of an external electric field. Therefore, the first term is mostly relevant for nonconductive materials and the second one for conductive ones.

For the case of an isotropic medium, the propagation of a monochromatic electromagnetic wave can be expressed through a simplified wave equation

$$\nabla^2 \overrightarrow{E} = -\frac{\omega^2}{c^2} \cdot \epsilon(\omega) \cdot \overrightarrow{E} \tag{7.2}$$

with ω being the angular frequency of the E-field wave and ϵ the dielectric function of the material. This function is directly linked to the complex refractive index, $\widetilde{n}$, by the expression

$$\epsilon\left(\omega\right)=\tilde{n}^2=\left(n+i\kappa\right)^2 \tag{7.3}$$

with n being the real part of the refractive index and κ the extinction coefficient of the material. In the frame of laser processing of materials, the extinction coefficient κ is a key factor, since it determines whether there is or not (linear) laser energy deposition in the material upon laser irradiation.

In a metal, light is absorbed by the free electrons via inverse bremsstrahlung. In a perfect dielectric material, there are no electrons in the conduction band to be accelerated by the field, and absorption is produced only when the photon energy is above the material bandgap (E_{gap}). This results in the generation of quasi-free electrons due to transitions from the valence to the conduction band. In narrow bandgap semiconductors (e.g., silicon, $E_{\text{gap}} = 1.1$ eV), absorption starts in the infrared region, while in wide band-gap semiconductors and dielectrics (optically transparent materials as sapphire,$E_{\text{gap}} = 8.8$ eV), absorption requires photon energies in the deep UV region. Additionally, absorption may occur via nonlinear ionization when irradiating with high-intensity laser pulses [3], something particularly relevant for laser processing of transparent materials. The required intensities should be above 10^{14} W/cm^2 [4], which are nowadays routinely achieved with commercial amplified ultrafast lasers (sub-picosecond pulse duration). From a theoretical point of view, the generation of free electrons by the strong-field ionization mechanisms (multiphoton absorption and tunneling ionization) is well described in the frame of the Keldysh formalism [5], described in more detail also in Chap. 1 of this book.

The indicated changes in the electron population in the energetic bands of the material due to light absorption has a direct impact on its optical properties, making the dielectric function to become time dependent, $\epsilon(\omega, t)$. As already mentioned, one of the most relevant transient effects of laser-matter interaction is the generation of free-carriers, which modifies the refractive index. This modification can be expressed by using the Drude-Lorentz model

$$\tilde{n}^2=\tilde{n}_0^2-\Delta\tilde{n}_{\text{Drude}}^2 \tag{7.4}$$

$\tilde{n}_0$ being the complex refractive index of the material before excitation and $\Delta\tilde{n}_{\text{Drude}}$ the contribution of the free electrons generated, which can be expressed as

$$\Delta\tilde{n}_{\text{Drude}}^2=\frac{N_e}{N_c}\frac{1}{1+i/\left(\omega\cdot\tau\right)} \tag{7.5}$$

with N_e being the free electron density, τ the scattering time of free electrons, and N_c the so-called critical electron density. This parameter is given by the expression $N_c = m^*\epsilon_0\omega^2/e^2$, with m^* being the reduced mass of the electron and e the charge of the electron. This transient change in the optical properties caused by free-carrier generation is especially relevant in dielectrics. The excited material becomes absorbing due to the presence of free-carriers. The photo-generated free- or quasi-free-carriers may further absorb energy by inverse bremsstrahlung, thus increasing their kinetic energy. Once this energy becomes larger than the bandgap, the free electrons can inelastically collide with an electron in the valence band and promote it to the conduction band. This additional ionization mechanism is normally referred to as impact or avalanche ionization. The free electron dynamics, including both strong-field and impact ionization, can be modelled by using either single- or multi-rate equations [6, 7].

Along with the photo-generation of free electrons, there are other mechanisms that may induce transient changes in the optical properties upon excitation. Among them, the nonlinear Kerr effect triggers an instantaneous increase of the refractive index that is proportional to the intensity of the incoming laser pulse [8]. Additionally, the formation of self-trapped excitons (STEs) may take place, especially in materials with a small elastic constant, like fused silica and alkali halides. In STEs, excitons are strongly bound and localized near a single atom [9], although there is a certain controversy about their efficiency as an energy relaxation mechanism [10, 11]. Moreover, the elevated temperatures and pressures the material may experience upon laser exposure may also affect its optical properties [12]. Material heating, melting, flow, evaporation, re-solidification, and permanent structural or topographic changes will obviously affect optical properties. Finally, along with changes in the dielectric function, carrier relaxation may induce light emission from out-of-equilibrium states. Even at low excitation levels, the spectral and intensity analysis of the emitted light can be of relevance for accessing the composition and thermodynamic state of the material upon irradiation [13]. At higher intensities, plasma (light) and particle emission analysis provides a wealth of information regarding the interactions, as discussed in more detail in Sect. 2.1.

1.2 Concept of Probing Matter by Light

The characterization of permanent optical changes in the processed material allows accessing in a simple way modifications that can be of scientific or industrial interest. They may include subtle changes in the surface topography or much stronger ones such as ablated craters which provide information directly related to the processing quality. In this section we focus on the concept of optical probing techniques for which the detected light wavelength is the same as the incident probe wavelength. Other powerful probing techniques do not belong to this category, such as Raman spectroscopy techniques, which are discussed, for instance, in [14].

Optical microscopy is arguably the simplest technique for a quick and visual analysis of the produced changes. Among the different optical microscopy modalities, bright-field microscopy is the most commonly used one. Depending on the illumination configuration, it allows assessing the material reflectivity and transmissivity. These two macroscopic magnitudes, reflectivity and transmissivity, are essential to retrieve the optical changes produced after excitation. Reflectivity, when illuminating the surface at normal incidence, is given by

$$R = \left| \frac{\tilde{n}_2 - \tilde{n}_1}{\tilde{n}_2 + \tilde{n}_1} \right|^2 \tag{7.6}$$

with $\tilde{n}_1$being the complex refractive index of the medium of incidence (normally air: $\tilde{n}_1 \approx 1$) and $\tilde{n}_2$ the complex refractive index of the material under study. Reflectivity depends both on the real part and imaginary part (extinction coefficient) of the refractive index. The separation of both contributions to the complex refractive index from a reflectivity measurement at a single angle of incidence is not possible. However, by combining reflectivity and transmission measurements, this difficulty can be solved since transmissivity is given by the attenuation of light propagating through the material (only κ dependent). This behavior is mathematically described by the Beer-Lambert law:

$$I(z) = I_0 \cdot e^{-\alpha z} \tag{7.7}$$

where I is the intensity of the light propagating inside the material along the z-axis, I_0 is the intensity at the surface, and α is the absorption coefficient, defined as $\alpha = 2\omega\kappa/c$. The inverse of the absorption coefficient is the so-called skin penetration depth ($\delta = \alpha^{-1}$).

This methodology to retrieve n and κ is limited to materials with low attenuation or thin layer thickness. An alternative to fully retrieve the dielectric function is the use of ellipsometry, which measures the change of polarization upon reflection at different angles of incidence for a single or multiple wavelengths. From the measured changes (and in most cases supported by additional modelling), it is possible to invert the Fresnel equations [2] and to obtain the values of n and κ at the single or multiple wavelengths (spectroscopic ellipsometry) used.

In the above description, the analysis of light properties after interacting with a material has been focused only on the analysis of changes in the amplitude of the illumination beam, either in reflection or in transmission. The analysis of phase shifts in the light-material interaction provides an additional route to access to the optical properties of the material. The characterization of the phase is achieved by using interferometric layouts that are described next.

Figure 7.1 shows several images of modified regions produced upon exposure to a single femtosecond laser pulse above the modification threshold. The images were recorded in reflection illuminating with a blue LED ($\lambda = 460 \pm 25$ nm). The images show, along with an ablation crater and surrounding material debris, a set of contrasted annular rings within the irradiated region. This optical effect is due, as sketched on the right-hand side of the figure, to an interferential phenomenon (Newton's rings) arising from the presence of a thin heat-affected layer underneath the crater. The illumination beam is reflected both at the top and bottom interface of

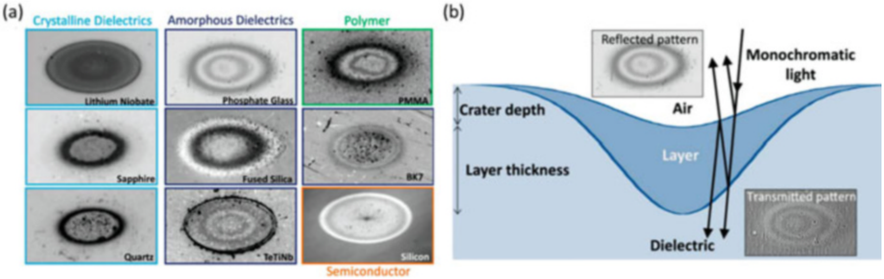
(a)
Crystalline Dielectrics
Amorphous Dielectrics
Polymer
Lithium Niobate
Phosphate Glass
PMMA
Sapphire
Fused Silica
BK7
Quartz
TeTiNb
Silicon
Semiconductor
(b)
Reflected pattern
Monochromatic light
Crater depth
Air
Layer thickness
Layer
Transmitted pattern
Dielectric

Fig. 7.1 (**a**) Optical microscopy images at 460 nm illumination wavelength of irradiated regions (ultrashort laser pulse at 800 nm) for different materials. (**b**) Scheme of the multilayer interference system in the irradiated region, where examples of the images in reflection and transmission are shown. (Adapted with permission from [16] © The Optical Society)

this layer, introducing an optical path difference (OPD) between the two reflected beams. The OPD is proportional to the real part of refractive index (n_l) and the thickness of the layer (d_l):

$$\mathrm{OPD} = 2 \cdot n_l \cdot d_l \tag{7.8}$$

The factor of 2 accounts for the full round trip of the beam reflected at the bottom interface of the layer. Constructive interference occurs when the two beams are in phase (a phase difference equal to 2π or a multiple), which occurs when the OPD is equal to the illumination wavelength or a multiple of it. Therefore, by counting the number of Newton's rings and their corresponding position, it becomes possible to characterize the optical thickness ($n_l \cdot d_l$) of the layer at each position. The deconvolution of index and depth requires an additional analysis of the optical contrast of the rings and a comparison with simulations based on the optical behavior of thin films [15].

The characterization of the OPD in different regions of the irradiated zone allows thus extracting important properties of the modified material. This characterization is especially relevant when the induced modifications show low optical contrast (small changes in reflectivity and transmission). The group of techniques specially designed for characterizing the spatial distribution of the OPD are usually referred to as quantitative-phase microscopy. The usual configuration is based on a Mach-Zehnder interferometer, as sketched in Fig. 7.2a, in which the interference pattern generated by the phase difference of a reference beam and a beam traversing the sample is imaged onto a charge-coupled device (CCD) camera. This technique (in transmission configuration) requires the sample to be transparent at the illumination wavelength. In the example shown in Fig. 7.2, infrared light was used to record the changes induced after irradiation of a silicon sample [17]. Figure 7.2b shows the differences between a conventional intensity image (at the top) and a phase image

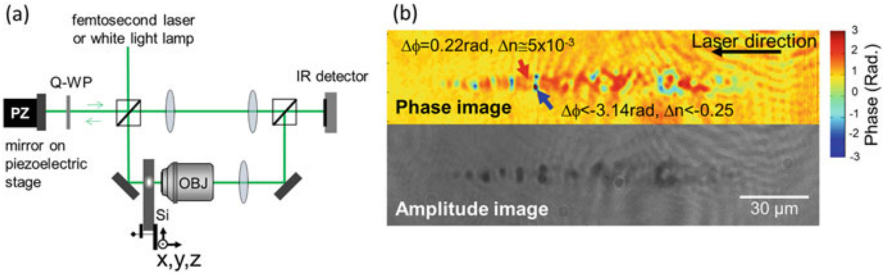

Fig. 7.2 (**a**) Schematic view of an experimental arrangement for quantitative-phase microscopy with infrared illumination. (**b**) Comparison between an amplitude image (top) and a phase image (bottom) of laser-generated microstructures inside a silicon sample. The regions marked with colored numbers correspond to positive (1 and 3) and negative (2) phase shift values. Provided by authors of [17]

(at the bottom). The phase image allows observing negative or positive phase-shift regions that can be respectively associated to densified or porous regions.

An additional and extremely useful interferometric technique is the so-called white light interference microscopy, or simply optical profilometry. This technique uses an interferometric microscope objective (Mirau objective), in which an interference pattern is formed because of the OPD between a reference beam and the beam reflected at sample surface. By unwrapping the phase-shift image, information about the surface topography with nanometric depth resolution can be extracted.

In summary, in this section we have presented different optical methods that allow accessing the changes produced in the material. The exemplified changes here are of permanent nature, but, as already indicated, they have their origin in transient phenomena (free electron generation, material melting, etc.). Thus, the use of techniques like the ones described here and adding temporal resolution capabilities enables the characterization of transient phenomena that eventually lead to the final material modification.

2 In-Situ Probing Technique

As indicated in Sect. 1.2, the concept underlying the use of optical probes to analyze light-matter interaction is using a secondary, weak light source (probe beam) to interrogate the optical properties of the material irradiated by a high-intensity (pump) laser pulse. This can be done using experimental layouts with spatial and/or temporal resolution. In the spatial case, this provides information about the optical properties of the material modified by the laser or the role of the local fluence of the pump laser in the process. In the temporal one, we acquire, for instance, information regarding the electron density evolution and the eventual structural changes induced upon carrier relaxation. In what follows, we will make a somewhat artificial distinction between what we will call “real-time optical measurements” with ns (and sub-nanosecond) resolution and “time-resolved ultrafast optical measurements” with ps and fs resolution.

In the former, (“real-time techniques”) we have access to the evolution of an optical property of the irradiated surface by using a continuous or relatively long pulsed optical probe beam and a sufficiently fast recording device (i.e., fast photodiode plus oscilloscope). Therefore, single pulse events can be recorded at once over a pre-established temporal window, no matter if the material undergoes a permanent transformation. This approach can be performed by using either point like probes (i.e., the probe light beam is focused inside a larger pump laser excited region) or image-based techniques (see Sect. 2.6 on ultrafast continuous imaging (*UCI*) techniques). In the second type (“time-resolved”), the surface is excited multiple times and interrogated with a pulsed optical probe to reconstruct the evolution of the optical property by scanning the temporal delay between the pump and the probe pulses. The temporal resolution of the measurement will be given by the width of the probe pulse (in most cases). If the material does not return to its initial state upon irradiation, the temporal reconstruction of the property of interest (i.e., reflectivity) makes it necessary to move the sample to a fresh region before each new pump laser pulse exposure.

The use of optical probes to analyze the temporal evolution of the laser-excited material is nearly as old as lasers are. Most likely, the first “real-time reflectivity measurements” performed upon laser excitation of a solid were reported in 1964 by researchers from the Hughes Aircraft Company [18]. They measured the temporal evolution of the reflectivity of several semiconductors (Ge, Si, InP, etc.) excited by single ns ruby laser pulses. Figure 7.3 (left) shows the experimental setup they used. Apart from the type of photodetectors used (photomultiplers), the layout has not changed much since then for this type of measurements. Interestingly, the authors of this work were not that much interested in the structural changes induced in the material but in the use of crystalline semiconductors as passive Q-switch elements in a pulsed laser cavity. The measured reflectivity evolution for the case of Ge is shown at the right of the figure, showing a reflectivity plateau for fluences above ~0.3 J/cm^2 that nowadays we would identify as laser-induced surface melting.

Since the publication of this early work, many research papers have reported on the temporal evolution of the optical properties of laser-excited materials in a variety of experimental configurations, using different interrogation parameters (reflectivity, transmission, luminescence, intensity, phase, refractive index, linear and nonlinear susceptibilities, etc.). In this section, we will review a number of them, including both point-probing (Sects. 2.2 and 2.3) and image-based (Sects. 2.4, 2.5, and 2.6) techniques. An initial sub-section devoted to laser-induced breakdown spectroscopy (Sect. 2.1) has been included, as it can be considered as a special class, a “self-probing” technique.

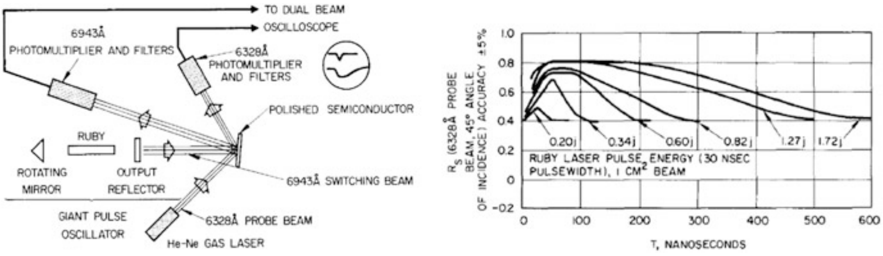
TO DUAL BEAM
OSCILLOSCOPE
6943Å
PHOTOMULTIPLIER AND FILTERS
6328Å
PHOTOMULTIPLIER
AND FILTERS
POLISHED SEMICONDUCTOR
RUBY
ROTATING
MIRROR
OUTPUT
REFLECTOR
6943Å SWITCHING BEAM
GIANT PULSE
OSCILLATOR
6328Å PROBE BEAM
He-Ne GAS LASER
R_S (6328Å PROBE BEAM, 45° ANGLE OF INCIDENCE) ACCURACY ±5%
1.0
0.8
0.6
0.4
0.2
0
-0.2
0.20j
0.34j
0.60j
0.82j
1.27j
1.72j
RUBY LASER PULSE ENERGY (30 NSEC PULSEWIDTH), 1 CM² BEAM
0
100
200
300
400
500
600
T, NANOSECONDS

Fig. 7.3 (Left) Experimental apparatus for measuring the temporal evolution of the reflectivity of a switched semiconductor. (Right) Time dependence of the reflectivity R_s of mechanically polished Ge excited by a giant (30 ns) ruby laser pulse. (Reprinted from [18] with the permission of AIP Publishing)

2.1 Self-Probing: Laser-Induced Breakdown Spectroscopy

Laser-induced Breakdown Spectroscopy (LIBS) is a powerful optical technique for noncontact, remote analysis of the chemical composition of materials. The concept is based on irradiating the specimen of interest with a high-energy laser pulse and measuring the emission spectrum of the laser-induced ablation plasma formed near the material surface, which contains the fingerprint of the elemental composition. The history of LIBS, reviewed in detail in the excellent book by Cremers and Radziemski [19], began almost immediately after the invention of the laser. In 1963, in Debras-Guedon and Liodec published the first analytical use of lasers for spectrochemical analysis of surfaces [20]. Soon after, Runge et al. published a work employing a pulsed laser for direct excitation of steel, reporting a linear relationship of the nickel and chromium content with the intensities of the corresponding characteristic emission line, which demonstrated the potential of the technique of quantitative analysis via calibration [21]. Time-resolved studies of the emission spectra appeared soon after, which aided in the discrimination against bremsstrahlung, featuring a continuous spectrum. While in the early days such measurements were quite complex, the enormous progress in detector development, offering gated, intensified charge-coupled devices (ICCDs) or electron-multiplying CCDs (EMCCDs), greatly contributed to the progress in LIBS. Since the early 1990s, the scientific activity in the field has been (and still is) rising exponentially. One of the main reasons is the strong interest for a variety of industrial sectors, as detailed in [22].

It needs to be stressed here that it is not only the composition of the material of interest that can be extracted by this technique. LIBS, with its different modalities, constitutes a powerful tool for visualizing a wealth of different laser-matter interaction processes and has the ability to quantify numerous properties of the laser-generated plasma. Thanks to this ability, it can be considered a self-probing technique, that is, the same laser pulse that interacts with the material is used to probe the generated plasma by exciting it for spectral measurements. In the following sections, a brief summary of the most important LIBS-based methods to quantify the properties of the ablation plasma is given.

2.1.1 Determining Electron Densities of a Laser-Induced Ablation Plasma

The dominant contributions to line broadening in a LIBS plasma are the Doppler effect and the Stark effect. The Doppler width $\Delta\lambda_D$ of an emission line λ_0 depends only on the absolute temperature T and the atomic weight M of the emitting species, according to the following equation [19]:

$$\Delta\lambda_D = \left(8k_BT * \ln 2/Mc^2\right)^{1/2}\lambda_0 \tag{7.9}$$

with k_B being the Boltzmann constant. In most cases of laser-produced plasmas, Doppler broadening is much smaller than broadening by the Stark effect, which is caused by collisions of the emitting species with electrons, and to a lesser extent by collisions with ions. Measuring stark-broadened line widths $\Delta\lambda_S$ can be used under certain conditions to calculate the electron density N_e in plasmas according to the following relation [23]:

$$\Delta\lambda_S = 2W \times \left(N_e/10^{16}\right)[\text{Å}] \tag{7.10}$$

where W is an electron impact parameter, which is a weak function of the temperature and only changes by a factor less than 2 over the temperature range 10.000–80.000 K. It should be noted that the FWHM line width $\Delta\lambda_S$ in Eq. (7.10) is given in Å and N_e in cm^{-3}. However, in the case of strong emission lines, an additional line-width broadening mechanism is often present, which is self-absorption of the light emitted from one atomic species and re-absorbed by another species. This effect causes an overestimation of the electron density but can be detected by a careful analysis of the line shape, which features a change in the spectral line shape and often take the form of a top-hat-shaped profile or even central dip. Since self-absorption severely affects the results obtained from plasma analysis, for precision studies, it is recommendable to perform them only on optically thin plasmas, where the emitted radiation traverses and escapes from the plasma without significant absorption or scattering.

2.1.2 Thermodynamic Equilibrium and Determining Electron Temperature

An important condition for being able to determine other plasma properties, such as electron speeds or populations of energy levels, is the presence of thermodynamic equilibrium. Only then, these properties can be described through the concept of temperature, which is accessible to LIBS. However, this condition is rarely fulfilled for the entire lifetime of the plasma or for its complete spatial extension. Therefore, the concept of local thermodynamic equilibrium (LTE) has been introduced, which reduces this requirement to a small region. LTE can typically be assumed after a certain time, when a sufficient number of collisions have occurred to thermalize the plasma [19]. Once it can be assumed that LTE exists, the distribution of several quantities depends only on the electron temperature T_e of the ablation plasma, which can be determined by measuring the ratio of two line intensities from successive ionization stages of the same element [23]. From LIBS measurements it is also possible to determine temperatures of atom, ions, and the ionization equilibrium, as well as vibrational and rotational temperatures [19].

2.1.3 Temporally and Spectrally Resolved Imaging of Laser-Induced Plasmas

In view of the space constraints of this section, we would like to give just a single example for an experimental LIBS configuration and results obtained, reported by our group [24]. It is by no means representative or provides the most groundbreaking results but shows a combination of a conventional point-probing LIBS configuration with a time-resolved imaging configuration to provide temporal, spectral, and spatial information. The basic principle of the setup (sketched in Fig. 7.4a) consists of an ArF excimer laser (193 nm, 20 ns) incident at an angle on the target of interest, which is placed in a vacuum chamber with controlled gas pressure such that the ablated material (electron plasma, neutrals, ions) can expand from the surface. A 4f imaging system is installed in order to project the ablation plume onto the entrance slit of an imaging spectrograph, whose exit plane is recorded by a gated ICCD camera with adjustable exposure time (down to 30 ns).

The purpose of the periscope is to rotate the plume image in such a way that the expansion axis lies along the slit axis, thus preserving this spatial information as the vertical direction of the recorded image. The horizontal axis corresponds to the wavelength of the emitted light, dispersed by the diffraction grating inside the spectrograph. This technique has been applied to the study of the ablation and expansion dynamics of several materials at different ambient gas pressures with some results being shown in Fig. 7.4b–e) [24–26].

2.2 Real-Time Point-Probing with ns and Sub-ns Temporal Resolution

Before describing ultrafast resolution point-probing techniques in Sect. 2.3, it is worth taking a look at their lower-resolution antecessors, "real-time" optical measurements" with ns (and sub-nanosecond) resolution. In this respect, it should be noted that well before the successful development of the first solid state, chirped

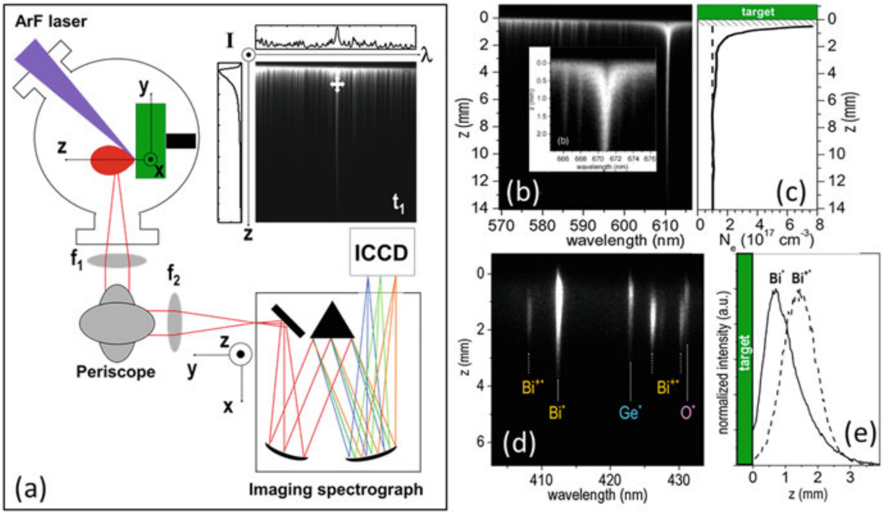
ArF laser
y
z
x
f1
f2
Periscope
z
y
x
I
λ
z
t1
ICCD
Imaging spectrograph
(a)
0
2
4
6
8
10
12
14
z (mm)
(b)
570
580
590
600
610
wavelength (nm)
target
(c)
0
2
4
6
8
N_e (10^{17} cm^{-3})
z (mm)
0
2
4
6
z (mm)
Bi+*
Bi*
Ge*
Bi+*
O*
(d)
410
420
430
wavelength (nm)
normalized intensity (a.u.)
target
Bi*
Bi+*
(e)
0
1
2
3
z (mm)

Fig. 7.4 (**a**) Experimental setup for spatial-spectral imaging of laser-induced plasmas with temporal resolution. (**b**) Time-integrated spatial-spectral image of the expanding $LiNbO_3$ plasma in vacuum, obtained by irradiating the target with a single-laser pulse. (**c**) Electron density N_e extracted from the 610.3 nm line in (**b**) as a function of distance z to the target. The shaded area in (**b**) very close to the surface (0.5–0 mm) indicates the region of self-absorption. (**d**) Time-gated ($\Delta t = 100$ ns, $t = 200$ ns) spatial-spectral image of the expanding plasma obtained by irradiating a $Bi_{12}Ge_1O_{20}$ target. (**e**) Transient spatial distributions of Bi neutrals (Bi* line at 412.2 nm) and Bi ions (Bi^{+*} line at 425.9 nm) extracted taken from (**d**). (Reprinted with permission from [24] © Elsevier)

pulse fs-laser amplifiers based on Ti:Sapphire crystals [27] for materials processing applications, ns laser lasers were routinely used for semiconductors processing [28, 29].

The first works on laser annealing of crystal damage in ion-implanted semiconductors date from the late seventies [30, 31]. The physical mechanisms underlying this process were the subject of an intense debate in the subsequent years. This debate boosted an enormous amount of experiments aimed at clarifying the role of carrier excitation and relaxation in the structural transformations induced in semiconductors upon short pulse (typically ns) laser irradiation. Their common denominator was the determination in "real time" of the temporal evolution of a given material property upon irradiation. Among them, experiments involving optical probes were particularly successful and included reflectivity [32, 33], reflectivity at multiple wavelengths [34], transmission [35], Raman [36], interferential [37], photoluminescence (self-probing) [38], and ellipsometry measurements [39]. Although not strictly "optical," ns-resolution "real-time" measurements using a point-probing scheme were carried out by using electron [40] or X-ray beams for diffraction [41] or absorption measurements [42]. Around the mid-1980s, it was more or less generally recognized that ns laser-induced annealing of semiconductors was mediated by the formation of a thermal molten layer at the material surface that propagated inward, leading to the redistribution of ion-implanted dopants. This brief overview on early “real-time optical” point-probing measurements would not be complete without mentioning that electrical probe measurements [43, 44] were, along with ultrafast time-resolved measurements (Sect. 2.3), crucial in elucidating the controversy between the thermal [45, 46] and plasma models [47, 48] for laser annealing with ns-laser pulses. Obviously, the references above quoted are far from being an exhaustive selection since more than 1400 research papers on laser annealing of semiconductors were published just from 1978 to 1988.

In the subsequent years, real-time ns-resolution optical measurements were also crucial in the analysis of the variety of solidification scenarios that appear when ns and ps laser pulses interact with semiconductors, especially in thin film configuration (either amorphous or crystalline) on substrates with different thermal conductivities. Interfacial amorphization [49], inhomogeneous melting [50], bulk amorphization [51], surface-initiated solidification [52, 53], bulk solidification and explosive crystallization [54], propagation of molten buried layers [55], and recalescence phenomena [56] upon ns and ps laser processing were a subject of intense research. A very interesting approach developed for thin films on transparent substrates was the simultaneous use of front- and back-surface reflectivity measurements upon laser exposure, as shown in [57].

The use of point-probing measurements in the analysis of the dynamics of phase transitions associated to phase change optical recording materials [58, 59] has also been extremely successful. The use of real-time optical measurements provided an ideal alternative to differential scanning calorimetry, analyzing thermally induced phase transitions occurring in transformation windows from 1 to 10^4 μs over micron-size-irradiated regions, as first shown in [60]. The demonstration of ultrashort pulse-induced reversible phase transitions in phase change materials [61] evidenced the need of increasing the time resolution of “real-time” point-probe measurements to the sub-nanosecond regime not only in the case of phase change materials but also in rapid solidification phenomena induced with ps laser pulses [62]. This can be achieved by using single-shot streak cameras to detect sample reflectivity or transmission changes for bursts of ps-probe pulses closely spaced in time [63] or using a relatively long (~1 μs), single-mode, temporally square probe laser pulse to achieve a temporal resolution close to 10 ps [64]. This approach was also used to analyze ultrafast phase transitions in InP [65] but resulted especially useful to demonstrate for the first-time reversible (amorphization and crystallization) phase transitions in GeSb films irradiated with ps pulses occurring over a time window of less than 400 ps [66]. The same approach of optimizing latent heat release and heat flow in the thin film structure was later on used in GeSbTe films to demonstrate ps-laser pulse-driven, reversible phase-change optical recording and resolve the respective phase transformation times [67].

Although the above examples can be considered as “historical,” phase change materials, specially chalcogenides, are still very attractive for a wealth of applications, and real-time reflectivity measurements are still an essential tool for the investigation, for instance, of multilevel recording applications [68] or tunable

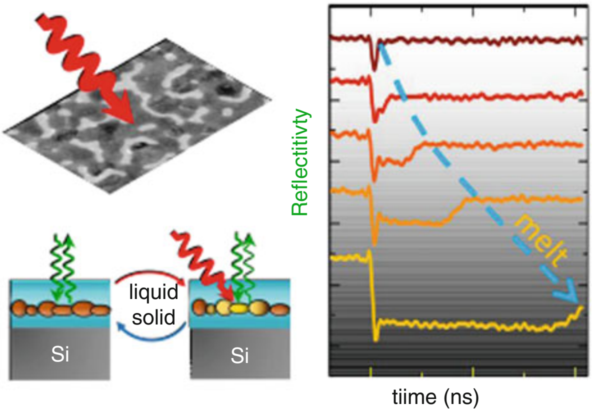

Fig. 7.5 Laser-induced transient phase change of an embedded single layer of near-coalescence Bi nanostructures (random metasurface) from solid to liquid and back to solid upon cooling. The ns pump pulse is indicated in red the cw probe beam in green. The graph displays real-time reflectivity measurements of the phase transitions at different pulse energies. The lower reflectivity is a signature of the molten phase. (Reprinted with permission from [71] © Wiley)

nanophotonics [69]. The same applies to other applications related to laser-induced phase transitions like the assessment of novel mechanisms in during the formation of the so-called laser-induced periodic surface structures (LIPSS, see also Chap. 23) in semiconductors [70] or the investigation of reversible laser-induced switching in random metasurfaces based on disordered bismuth nanostructures [71]. The latter study (c.f. Fig. 7.5) demonstrates how this technique is capable of quantifying the melt duration even for an ultrathin Bi nanoparticle layer (5 nm thick), demonstrating tunability over a range of 10–700 ns by changing the pump fluence. The pump laser-induced transient state of low reflectivity can be exploited for the fabrication of nanophotonic switching devices.

2.3 Ultrafast Point-Probing: From the Visible to the X-Ray Regime

Given the immense advances in ultrafast science over the last decades and the scope of the book, we will limit this section to review some time-resolved (pump-probe) optical techniques and experiments with fs-resolution in point-probing configuration, involving the interaction with condensed systems. We will therefore not comment on pump-probe experiments in the fields of femtochemistry [72], ultrahigh intensity interactions [73], attoscience [74, 75], and related fields. On the other hand, the availability of ultrafast image-based techniques [76, 77] (see Sect. 2.4) generated an essential step in our comprehension of ultrafast interactions in condensed systems, beyond the information derived from point-probing experiments.

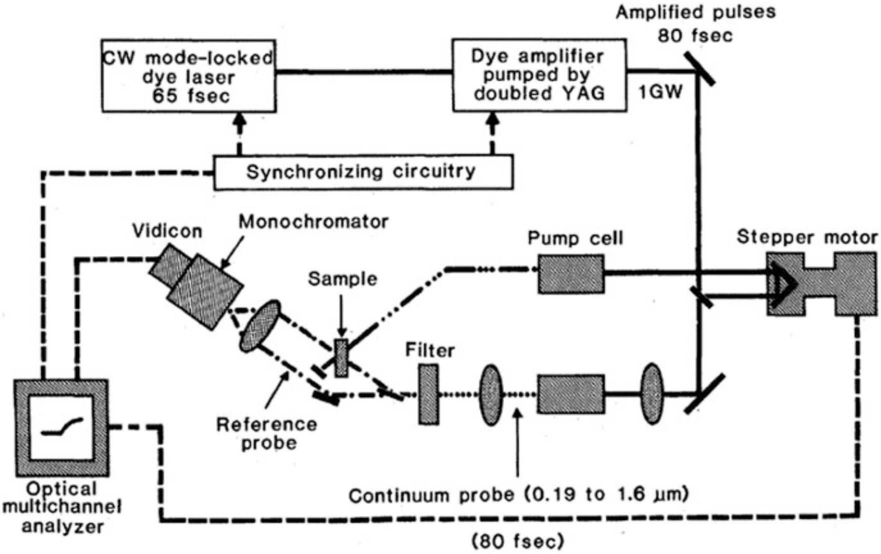
Amplified pulses
80 fsec
CW mode-locked dye laser 65 fsec
Dye amplifier pumped by doubled YAG
1GW
Synchronizing circuitry
Vidicon
Monochromator
Pump cell
Stepper motor
Sample
Filter
Reference probe
Optical multichannel analyzer
Continuum probe (0.19 to 1.6 μm)
(80 fsec)

Fig. 7.6 Schematic of apparatus for femtosecond time-resolved spectroscopy according to the description in reference [79]. Notice the use of probe pulses extracted from a supercontinuum source

For what concerns the early use of optical point-probing measurements with ps- and fs-resolution, it is remarkable that already in the late seventies, a number of techniques based on this scheme were already well established and applied to the study of a variety dynamic processes [78]. In 1983, Charles Victor Shank from Bell Labs published a small review in Science entitled “Measurement of ultrafast phenomena in the femtosecond time domain” [79], where the expected developments of fs-resolution spectroscopy were envisaged. Optical reflectivity, transmission, and absorption point-probing measurements, using not only monochromatic sources but also white light continuum sources (see for instance [80]), were already available in 1983. Figure 7.6 shows a typical layout of a point-probing, pump-probe fs-resolution experiment. The amplified laser pulse is split in a lower- and higher-energy component that reaches the sample after passing through a variable delay line. The lower energy pulse interrogates the excited region (in this case its transmission relative to a reference probe) at a selected delay with respect to the pump pulse, enabling the reconstruction of the measured property evolution as a function of time.

When the process is reversible, it is possible to use a static sample, something not possible when analyzing phenomena involving structural transformations for which, during the experiment, a fresh region of the sample needs to be exposed for every measurement. The same year (1983), Shank and coworkers published two crucial papers for the comprehension of ultrafast laser-induced phase transitions in semiconductors. In one case they used multiple wavelengths from a white light continuum source [81] to measure the reflectivity evolution of the fs-laser-irradiated surface; in the second case, they employed second-harmonic generation [82] as a point-like probes. Both papers proved by means of different methods the formation of a highly excited, disordered structural state of Si within a fraction of a picosecond upon excitation, followed by a transition to ordinary molten silicon in a few picoseconds. Figure 7.7 shows a polar plot of the second-harmonic intensity generated at the surface showing a strong decrease of the intensity (at $\varphi = 120°$) consistent with a strong perturbation of the ternary symmetry of the <111> Si surface within about 240 fs. The formation of an isotropic surface of molten Si is found to require a longer time, about 3 ps.

These two works were the first demonstration of the existence of a nonthermal ultrafast melting process in Si upon irradiation with sub-picosecond laser pulses. This phenomenon was later on observed in other semiconductors, like GaAs [83, 84], but also in other materials, like chalcogenide-based films for optical recording [85]. Related to this topic of ultrafast phase transitions, electronic excitation-enhanced crystallization in amorphous GeSb films excited with fs-laser pulses was demonstrated in 1996 [86].

Along with these two techniques (multi-wavelength reflectivity and second-harmonic point-probing), the development of other ultrafast point-probing techniques like time-resolved ellipsometry and dielectric function measurements enabled the access to a more detailed view of the evolution of the optical properties of the irradiated material. The first single wavelength ellipsometry measurements with ps resolution date from 1974 [87]. The extension to the fs-regime had to wait for nearly 20 years [Choo 1993]. This technique has recently been revisited to enable spectroscopic ellipsometry measurements with a resolution close to 100 fs over a spectral interval of 1.3–3.6 eV [88]. A direct measurement of the evolution of the dielectric function of materials with fs resolution upon irradiation was first reported in 1997 [89]. Figure 7.8 shows the setup as described in [90]. Reflectance is measured at two different angles over the white light continuum spectrum generated in a CaF_2 crystal. The measured values are used to determine the dielectric function by numerically inverting the Fresnel equations for reflectivity. This technique enabled to further confirm [77] the existence of electronic excitation-induced lattice disorder in GaAs [91] and was also used to analyze the presence of ultrafast phase transitions in GeSb films [92] upon fs laser excitation.

Although X-ray point probes are not strictly speaking "optical" probes, they have also been extremely successful in the analysis of structural transformation dynamics upon fs-laser excitation. In this respect, it is worth noting that there is only an indirect relationship between the optical and structural properties of crystals. This makes fs-resolved X-ray diffraction [93, 94] the only technique that may provide direct information about the structural dynamics, even at the nanoscale [95]. This topic is reviewed in detail along with other X-ray experiments in Chap. 6.

To conclude this subsection, it must be emphasized that optical point-probing, pump-probe experiments are also a useful tool for the time-resolved analysis of carrier and structural transformation dynamics in reversible structural changes. They have been thoroughly used, for instance, in highly correlated materials [96] and also

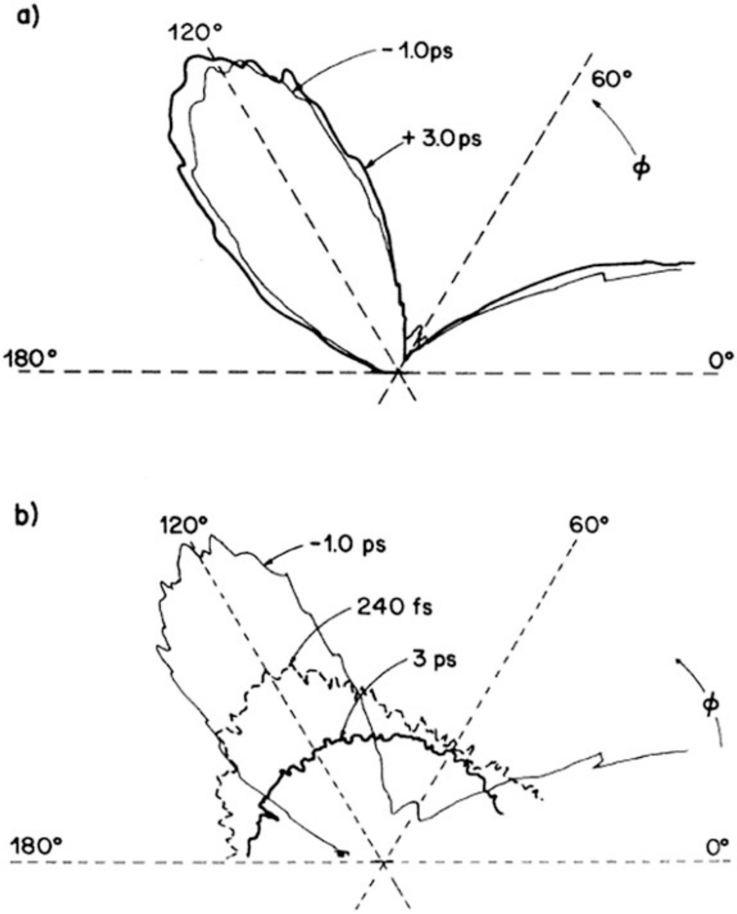

Fig. 7.7 (**a**) Polar plot of the second-harmonic intensity in Si as a function of time and angle (φ) for low pump energy, 0.5 E_{th}. (**b**) Polar plot of the second-harmonic intensity as a function of time and angle (φ) for pump energy 2.0 E_{th}. E_{th} is the surface amorphization threshold of Si at 620 nm (90 fs pulse duration). (Reprinted with permission from [82] © (1983) by the American Physical Society)

(beyond the optical regime) in THz spectroscopy [97] for the analysis of carrier dynamics in photovoltaics [98]. A particularly relevant application in the study of ultrafast dynamics has been their use for the study of coherent optical phonons (COPs). Optical phonons are called coherent when the oscillation phase is kept constant in a time range longer than the vibration period. An ultrashort laser pulse can excite coherent optical phonons through the sudden modification in free-carrier density and electron temperature, which perturbs the interatomic potential. This results in a displacement of the atoms, acting like an external force on the vibrational degrees of freedom [99]. Since COPs occur on an atomic-scale, X-rays are the

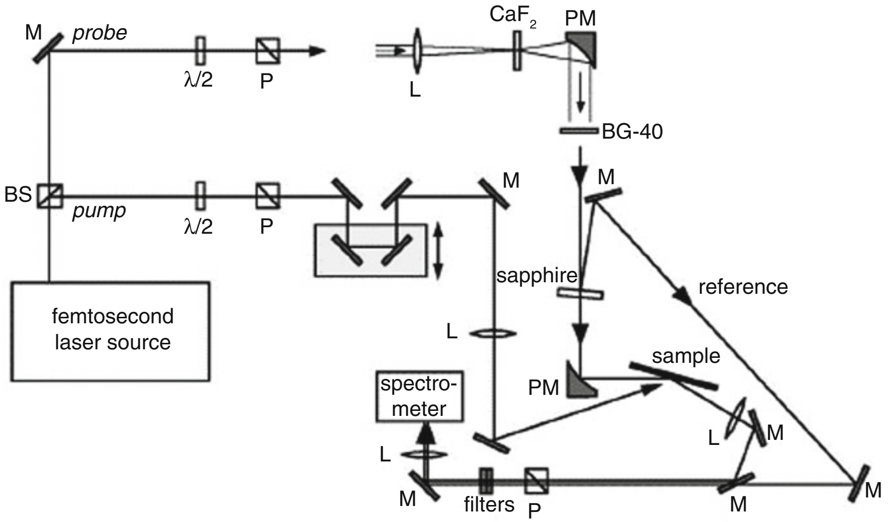

Fig. 7.8 Scheme of the setup for time-resolved dielectric function measurements by dual-angle reflectometry. BS polarizing beam splitter; M flat mirror; PM parabolic mirror; L lens; P polarizer; and λ/2 half-wave plate. (Reprinted from [90] with the permission of AIP Publishing)

ideal tool to follow the related lattice dynamics [100]. However, optical probes may be used to detect and analyze coherent optical phonons due to the changes in reflectivity associated to Raman active vibrations. This feature has been used to analyze coherent phonon dynamics in a variety of systems including, among others, phase change materials [101] in amorphous and crystalline phase [102].

2.4 *Ultrafast Surface Microscopy*

In 1985, M.C. Downer, R.L. Fork, and C.V. Shank introduced a novel technique, combining a pump-probe approach with optical microscopy [76, 103]. This new experimental system was presented as the natural evolution of the previous work of C.V. Shank et al. [81], in which point-probing reflectance was monitored with a photodiode. The interest of this technique lies in two main aspects. First, it provides direct images of the surface, which makes the qualitative analysis of the transformation dynamics simpler than in other techniques. Second, it gives simultaneously access to the reflectivity evolution of the material both in time, t, and space, r. That way, the material response at different local fluences is obtained since the beam profile normally shows a spatial Gaussian distribution. Figure 7.9a shows a set of recorded images upon excitation of crystalline silicon with an 80 fs pulse at 620 nm.

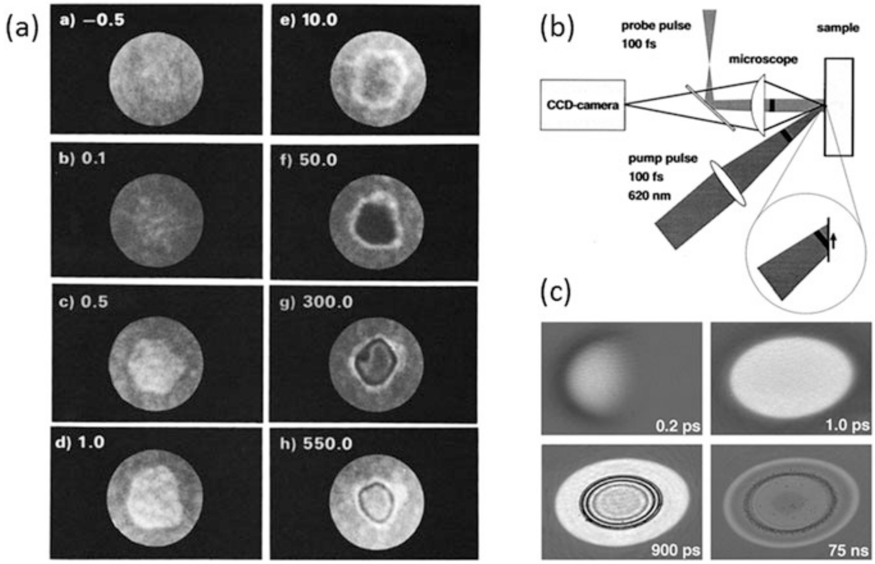

Fig. 7.9 (**a**) Images of the evolution of the surface reflectivity of a silicon sample after irradiation. The numbers in each image correspond to the temporal delay (in picoseconds) after excitation. (Reprinted with permission from [103] © Springer). (**b**) Sketch of time-resolved microscopy. In this particular case, the pump pulse reaches the sample at an oblique angle and the probe pulse normal to the surface. (Reprinted with permission from [104] © Elsevier). (**c**) Time-resolved images (time delay labelled on each image) of the surface of a silicon wafer after irradiation. Frame size 220 μm × 300 μm. (Reprinted with permission from [105] © (1998) by the American Physical Society)

A step forward in the development of this technique was made in 1997 by D. von der Linde, K. Sokolowski-Tinten, and coworkers [105, 106], by capturing the evolution of the reflectivity with a CCD camera instead of photographic paper, while reversing the angle of incidence of the pump and probe beam. The experimental setup is sketched in Fig. 7.9b. This technique resulted in high-quality digital images, as shown in the Fig. 7.9c for a silicon sample, which allowed better quantitative analysis by digital processing. As a first example of the high-spatial and temporal resolution, the image recorded at a delay 0.2 ps resolves the *landing* of the pump pulse (incident from the left). Since the incidence angle of the pump beam was 45°, the left part of the image first experiences a change of reflectivity triggered by the generation of free electrons. From the Fresnel equation and Lorentz-Drude modelling, it is possible to estimate the temporal evolution of free electron density. A second example, demonstrating the huge potential of this technique to unravel ultrafast laser-matter interaction mechanisms, is the observation of transient Newton rings at delays on a scale of hundreds of picoseconds (900 ps in the image of Fig. 7.9c). The rings are formed by constructive and destructive interference of the probe light partially reflected at the top and bottom interface of an expanding layer of ablated material. The analysis of the number of rings at different time delays allowed to measure the expansion velocity of the ablating layer (~1000 km/h) and enabled to assess the thermodynamical mechanisms responsible for the ablation process (isochoric heating, adiabatic expansion, rarefaction wave propagation, phase explosion) [104].

Beyond the study of electronic excitation-induced disorder (nonthermal melting) [77, 107, 108], time-resolved microscopy has mainly focused on the study of the ablation dynamics of materials, which, as indicated above, is a process where matter is subjected to extreme thermodynamic conditions. In the case of dielectrics, fs-resolved microscopy has the additional advantage of facilitating the analysis of nonlinear absorption mechanisms. Several research groups have investigated the ablation dynamics of dielectrics, including the fs-resolved microscopy studies in sapphire, fused silica, quartz, or lithium niobate among others by authors of this chapter [109–111]. Figure 7.10a shows three snapshots of a fused silica surface recorded at different time delays after irradiation, together with the temporal evolution of the reflectivity at different positions (local fluences). At ultrashort time delays, a strong transient increase in surface reflectivity (up to five times) is observed, reaching its maximum at several some 100 s of femtoseconds after the arrival of the pump pulse. This delay in the occurrence of the reflectivity maximum implies a delay in reaching the maximum free electron density after pulse absorption, stressing the important role of impact ionization in the carrier excitation process. Further studies in dielectrics allowed to observe the formation of transient Newton rings also in other dielectrics [112], as shown in Fig. 7.10b. This observation indicates that some of the main physical mechanisms underlying ultrafast ablation are material independent.

This technique has also been used to characterize the temporal dynamics of other types of material transformations, for instance, for the case of crystalline silicon with a micrometric dielectric sphere placed on the surface (c.f. Fig. 7.10c). This experiment allowed to characterize the effect of strong local field enhancement (near field) on laser material processing [113], an effect that is discussed in more detail in Chaps. 8 and 11. Another example is illustrated in Fig. 7.10d, showing time-resolved images that reveal the formation dynamics of a thin heat-affected layer at the surface of phosphate glass. This sub-ablative effect, as demonstrated by the laser-induced surface elevation in AFM image (instead of depression), is quantified via image analysis (contrast and number of Newton's rings) and optical modelling. It should be noted that the time window to observe this effect lies in the 100 s of nanosecond's range after irradiation, which required the implementation of a long optical delay line, implemented by means of optical fibers for the probe beam [114]. Finally, Fig. 7.10e shows transient reflectivity images of the material transformation pathway, leading to the formation of laser-induced periodic surface structures (LIPSS) on silicon. It has to be emphasized that these structures are formed by the effect of multiple pulse irradiation. The experiment, using a special layout ("moving spot") enabled to demonstrate that the LIPSS formation process in this case is initiated by free electron generation leading to nonthermal melting, liquid phase overheating, and rapid solidification into the amorphous phase [115].

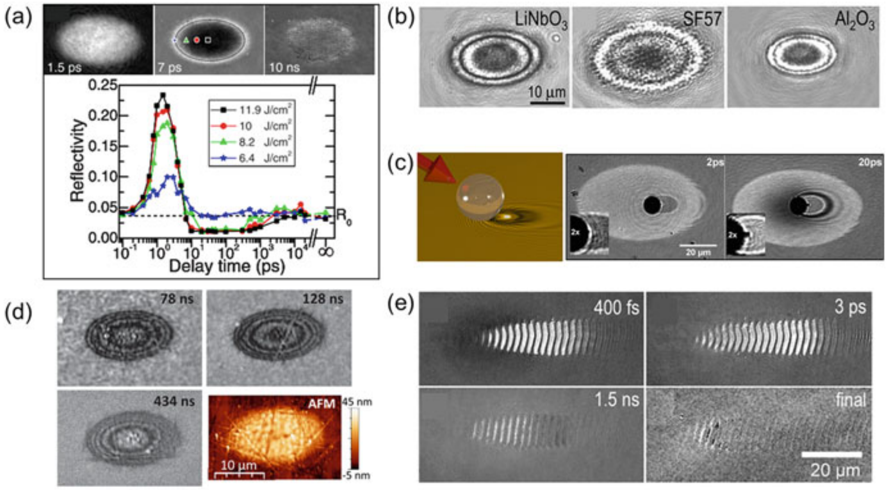

Fig. 7.10 (**a**) Time-resolved reflectivity images and their temporal evolution upon single pulse fs laser excitation of fused silica. The analysis is performed at different radial positions, corresponding to local fluences that range from close to the ablation threshold (blue stars) to well above (black squares). (Reprinted with permission from [109] © The Optical Society). (**b**) Time-resolved reflectivity images of laser-irradiated dielectrics recorded with sub-nanosecond time delays ($LiNbO_3$ at 315 ps, SF57 glass at 415 ps, and Al_2O_3 (sapphire) at 215 ps), featuring transient Newton's rings. (Reprinted from [112] with the permission of AIP Publishing). (**c**) Left. Schematic view of the spatial intensity distribution in the vicinity of a micrometric spherical particle irradiated by the laser at oblique angle. Right. Surface reflectivity images at the particle location for two different delays (indicated). Image from [113]. (**d**) Time-resolved reflectivity images at different time delays after irradiation of a phosphate glass with fluences below the ablation threshold. The bottom right frame shows an atomic force microscope (AFM) image of the permanent surface modification induced. (Adapted from [114] with permission from the authors). (**e**) In-situ microscopy images of the silicon surface recorded at different delay times during laser writing of self-organized amorphous fringes (LIPSS). (Reprinted with permission from [115] © 2016 American Chemical Society)

Before describing more complex ultrafast time-resolved imaging techniques, we will briefly revise some other recent results derived from time-resolved microscopy experiments. Winkler and co-workers [116] observed and characterized laser amplification in excited dielectrics. In a pump-probe experimental configuration in which the sample surface was imaged from the backside, it was observed that the probe beam was coherently amplified while propagating inside an excited dielectric. This amplification starts to increase around 100 to 200 fs after excitation and is sustained for several tens of picoseconds in a thin sapphire sample. Pan and coworkers [117], using a setup similar to the one sketched in Fig. 7.10c, have recently studied the transformation dynamics of molybdenum disulfide, a semiconductor material attracting considerable interest because of its potential applications in optoelectronics. More recently, Xie and coworkers [118] have used time-resolved microscopy to characterize a pump-induced transient micro-grating generated by the Kerr effect. This strategy is proposed as a solution for the determination of an absolute pump-probe delay and pulse-front tilt detection.

Although time-resolved microscopy has been demonstrated to be a very powerful technique, the obtained information corresponds to changes in the amplitude of the illumination beam (reflection or transmission) alone. In order to access other optical parameters (polarization or phase with spectral resolution), it is necessary to use alternative approaches. Different experimental strategies, combining the use of time-resolved microscopy with the determination of additional parameters, have been developed. The most relevant ones can be grouped into time-resolved ellipsometry and time-resolved interferometry experiments, as described in more detail in the following sections, together with time-resolved imaging of non-specular scattered light with is described in detail in Chap. 9.

Ellipsometry encompasses techniques that analyze the intensity and state of polarization of a light beam after it has been reflected off a surface, allowing access to the dielectric function of the material under study. Wang and Downer [119] carried out the first work on single-wavelength ellipsometry with temporal resolution upon material excitation with fs laser pulses. More recently, different groups have proposed the combination of ellipsometry and time-resolved microscopy, the so-called ultrafast pump-probe imaging ellipsometry [120–122]. In this particular case, the approach is based on the use of a single wavelength and different incidence angles. The procedure consists in recording a set of images for each time delay, polarizer and analyzer settings for different angles. By analyzing the reflectivity of the images at different angles, local ellipsometry measurements as a function of time are obtained. From these data, and the application of Fresnel equations, the components of the time-dependent complex refractive index can be retrieved. This technique is especially useful for characterizing events occurring in the timescale up to 10s of picoseconds after irradiation, where the images recorded with the conventional time-resolved microscopy are usually dark, either due to interferential effects (destructive interference) or absorptive process. The determination of the transient complex refractive index allows to extract the optical penetration depth and assess the roles of absorption and interference in the observed behavior.

Another alternative to determine the dielectric function (spectroscopic approach) has recently been proposed in [123]. In this case, the s and p components of the polarization of the probe beam at different delays and as a function of the probe wavelength are measured. The experimental setup is shown in Fig. 7.11a along with an inset showing two example images. The temporal evolution of the reflectivity intensity for each of the polarization components is plotted in Fig. 7.11b for each probe wavelength. The results extracted from this analysis allowed to discover a possible additional absorption channel for p-polarized light.

In the above description, the shown techniques are based on directly recording the reflected or transmitted light from an illuminated surface (area), allowing to access the amplitude or polarization of the electric field. Another relevant property of the field is the phase, which can be retrieved by interferometric techniques. In the following paragraphs, three different approaches for time-resolved interferometry will be revisited. In the first one, an evolution of conventional fs-resolved

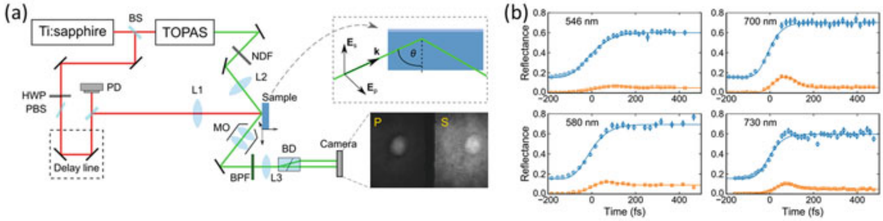

Fig. 7.11 (**a**) Pump-probe setup for measuring simultaneously s- and p-polarized reflectance. The probe wavelength is tunable by making use of an opto-parametric amplifier. Before the CCD, a beam displacer (BD) separates the reflected s and p components, being recorded simultaneously. (**b**) Time-dependent s- and p-reflectance data (blue circles and orange squares, respectively) at different probe wavelengths. (Adapted with permission from [123] © (2020) by the American Physical Society)

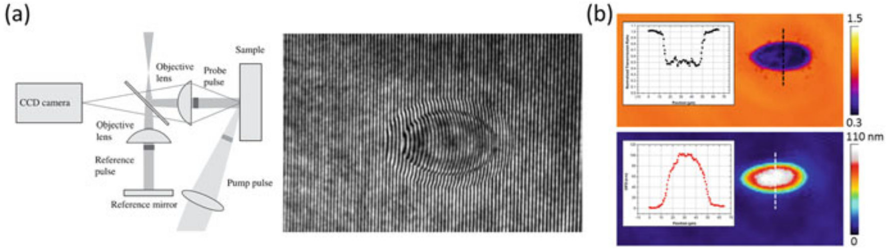

Fig. 7.12 (**a**) Left. Setup for ultrafast interferometry with imaging configuration. Right. Transient interferometric image of an ablating GaAs <100> surface excited with $F = 1.4\ \mathrm{F_{abl}}$, recorded at a temporal delay of 1.4 ns. Reprinted with permission from [124] © Springer. (**b**) Example of the spatial information on transmission and optical path difference (OPD) extracted after recording with a wavefront sensor the probe beam transmitted through an excited Nb_2O_5 film (delay of 18 picoseconds). (Adapted from conference presentation by authors of ref. [126], available at https://www.fresnel.fr/perso/gallais/)

microscopy incorporating a Michelson interferometer [124, 125] was developed. The corresponding setup is shown in Fig. 7.12a. On the right side of the same figure, an image of the recorded interference pattern for a delay of 1.4 ns after irradiation of GaAs with a single femtosecond pulse is shown. From these images and their analysis, it is possible to distinguish phase contributions induced by changes in the optical constants and surface deformation.

A different strategy was followed in [127], where the intensity and phase of the probe beam after interacting with the excited material is recorded with a 2D-wavefront sensor instead of a regular CCD. After mathematical processing, these two quantities can be separated into two different images, one accounting for the absorption (top image in Fig. 7.12b) and one representing the optical path difference (OPD) (bottom image in Fig. 7.12b).

The two techniques described above correspond to interferometry measurements in the space domain. A different approach is frequency-domain interferometry,

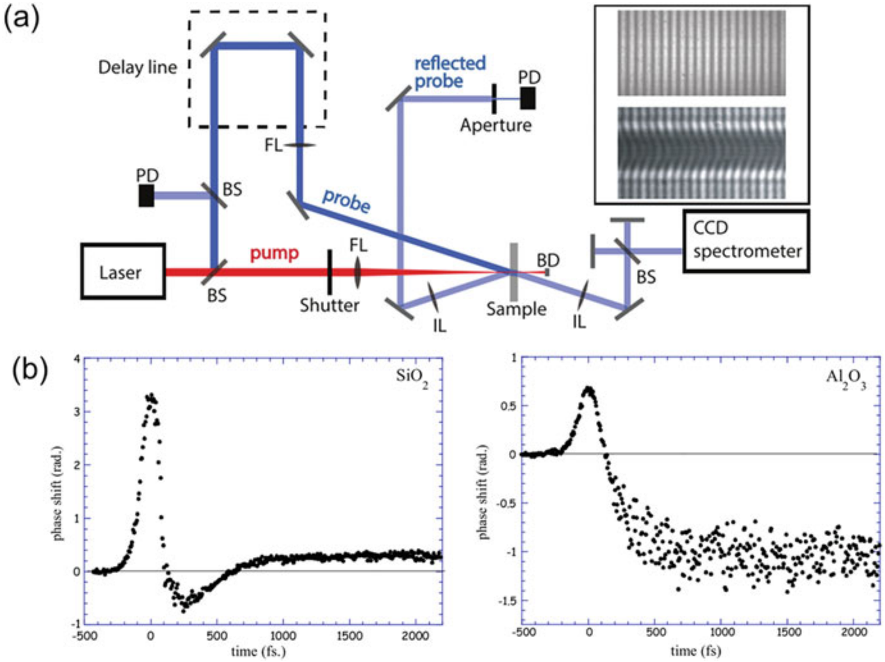
(a)
Delay line
FL
PD
BS
Laser
BS
pump
Shutter
FL
probe
reflected probe
PD
Aperture
IL
Sample
BD
IL
BS
CCD spectrometer
(b)
SiO2
phase shift (rad.)
time (fs.)
-500
0
500
1000
1500
2000
-1
0
1
2
3
4
Al2O3
phase shift (rad.)
time (fs)
-1.5
-1
-0.5
0
0.5
1

Fig. 7.13 (**a**) Schematic of a time-resolved interferometry setup. BS beam splitter. FL focusing lens. IL imaging lens. PD photodiode. BD beam dump. The inset shows two examples of CCD images recorded with (bottom) and without (top) laser excitation. (Reprinted with permission from [130] © IOP Publishing) (**b**) Temporal evolution of the measured phase shift in fused silica (SiO_2) and sapphire (Al_2O_3). The pump irradiation intensities are well below the ablation threshold fluence. (Reprinted with permission from [131] © Springer-Nature)

as first reported in this field by Audebert and coworkers [128, 129] and further exploited and improved by the group of Guizard [130, 131]. As shown in Fig. 7.13a, the experimental setup includes an interferometer and a spectrograph with a CCD. The Michelson interferometer is located behind the sample and splits the probe beam in two parts. The interferometer is slightly misaligned, projecting onto the spectrograph slit the two beams laterally displaced. This causes that one beam to act as a probe beam, carrying information of the excited region, and the other as a reference beam, carrying information of the non-excited region. Both beams enter the spectrograph, and the spectral interference pattern is imaged onto a CCD. Figure 7.13a also includes two examples of interference images recorded with the CCD, situated at the spectrograph output. The upper image shows a featureless interference pattern, corresponding to a situation of negative time delay (probe beam arrives earlier). In contrast, the lower image corresponds to a situation after excitation, leading to a strong distortion (phase shift) and change of intensity (absorption) in the fringes.

Figure 7.13b shows a plot of the phase shift evolution as a function of time for two different materials: fused silica (SiO_2) and sapphire (Al_2O_3). The phase shift is directly related to the change of the real part of the refractive index [131]. At ultrashort time delays, a positive phase shift is attributed to the nonlinear optical behavior of bound electrons (nonlinear Kerr effect), caused by the presence of the intense excitation beam. This effect is observed in both materials (see Fig. 7.13b). The observation of the Kerr effect allows to precisely determine the arrival time of the pump pulse to the sample surface. Immediately afterward, a negative contribution to the refractive index that leads to a negative phase shift is caused by the photo-generated electrons (N_e), as already described in the Drude-Lorentz model. This decrease of the phase shift due to the generation of free electrons is observed after the Kerr effect in both materials. Finally, a recovery of the phase shift to positive values is observed for fused silica, as opposed to the case of sapphire. The recovery in silica is due to the formation of self-trapped excitons (STE), which contributes to an increase of the refractive index.

When used in transmission, frequency domain interferometry also provides information about the absorption experienced by probe beam, thus giving access to the imaginary part of the refractive index. However, this approach has two main disadvantages. First, only transparent materials or very thin films on transparent substrates can be studied. Second, the sampling beam does not only probe the surface (where the energy deposition is highest) but also probes laser-induced changes occurring in deeper regions, effectively providing and average measurement over the interaction depth. This problem, and the related ambiguities, can be sorted out combining in the same setup femtosecond-resolved microscopy and frequency-domain interferometry, as reported in [11].

2.5 *Ultrafast Shadowgraphy*

The most basic configuration of ultrafast shadowgraphy is actually very similar to the transmission probing configuration of laser-induced surface changes presented in Sect. 2.4. A typical ultrafast surface microscopy configuration that can be rapidly switched between reflectivity and transmission modes has been reported in [132], based on a probing incidence either from the front side or the back side of the sample. Yet, most ultrafast shadowgraphy studies employ a configuration in which the pump beam and the probe beam enclose an angle of 90°, which corresponds to a side view of a laser-matter interaction region. With this configuration, a variety of different mechanisms can be investigated, of which the most frequent ones are summarized in the following subsections:

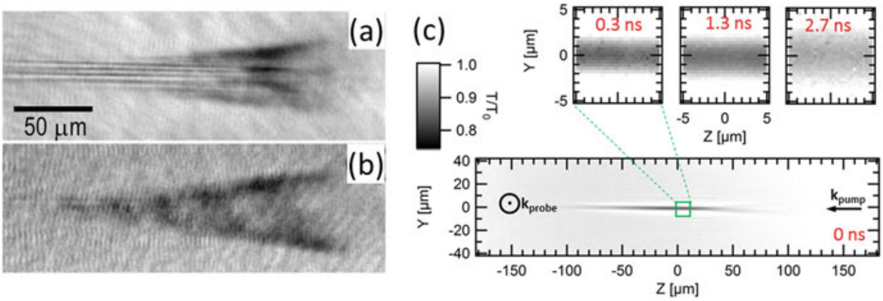

Fig. 7.14 (**a**, **b**) Shadowgraphs recorded inside phosphate glass upon irradiation with single pump laser pulses ($\lambda = 800$ nm). (**a**) corresponds to a pulse duration of $\tau = 100$ fs, whereas (**b**) to $\tau = 270$ fs. The pump pulse propagates from left to right the 400 nm; $\tau = 100$ fs probe pulse is incident from behind. Reprinted from [133] with the permission of AIP Publishing. (**c**) Shadowgraphs recorded in bulk silicon after the irradiation with a single pulse ($\lambda = 1300$ nm, $\tau = 90$ fs). For increasing time delays (bottom part), diffusion of free electrons is observed. The laser pulse propagates from right to left. (Provided by the authors of [136])

2.5.1 Electron Plasma Formation Dynamics Inside Materials

Employing ultrafast shadowgraphy, numerous groups have investigated the plasma formation and relaxation dynamics of laser-excited regions inside a material. One example can be found in [133], in which the technique was applied to investigate nonlinear propagation, excitation, and modification inside phosphate glass. In this study, a train of fs laser pulses was focused 1.56 mm below the surface while transversally displacing the sample, which led to the inscription of optical waveguides. Figure 7.14a, b display shadowgraphs of individual pulse recorded at different time delays, visualizing regions where free electrons are generated (dark regions) during pump pulse propagation. The corresponding electron density can be estimated by means of quantifying the local absorption and applying a simple Drude model. Moreover, in (a) the presence of pronounced beam filamentation can be appreciated, as well as the distorsion of the focal volume (expected to be of elliptical rather than arrow head shape). Filamentation can be avoided by a slightly increasing the pulse duration, as demonstrated in (b). Focal volume distortion, caused by pre-focal depletion, is more difficult to prevent but can be minimized by a reduction of pulse energy and multiple overwriting at lower energies. Both strategies were shown to greatly improve waveguide performance [133]. Other groups have investigated by means of shadowgraphy filamentation behavior and electron dynamics in more complex situations, such as double pulses and multiple pulses [134].

An interesting modality of the basic shadowgraphy setup has been introduced by Sun et al. [135]. By means of dividing the probe beam after the sample in two, and spatially overlapping the probed region with a non-probed region on the CCD camera (similar to the technique introduced in Sect. 2.5 [11]), additional information can be extracted. In particular, the transient change of the real part of the refractive index as well as the electron-electron collision time for a given pump energy can be extracted. Alternatively, phase contrast microscopy also provides access to the time-resolved changes of the refractive index [136].

Even more challenging is the investigation of these processes in semiconductors that are nontransparent to visible light. Pioneering work in this field has been performed by the group of Grojo, applying femtosecond-resolved shadowgraphy to the study of fs excitation inside bulk silicon [137]. This study required the use of pump and probe wavelengths in the spectral range where silicon becomes transparent ($\lambda > 1100$ nm), as well as the use of cameras with infrared sensitivity. Figure 7.14c displays typical time-resolved shadowgraphs, revealing that the laser-excited electron plasma is very elongated, in part due to the strong refraction of silicon, increasing significantly its width at longer delays, which is indicative of radial electron diffusion.

2.5.2 Surface Ablation and Shockwave Expansion

Besides exploiting shadowgraphy for resolving ultrafast plasma formation and relaxation dynamics, the technique has been widely applied to the study of a number of other processes. In particular, surface ablation and the accompanying shockwaves expanding in the surrounding air, as well as stress waves inside the material, have been the focus of interest since long. While the shock waves can also be studied to some extend with ultrafast surface microscopy (see Sect. 2.4), the information obtained is rather limited. Ultrafast shadowgraphy has the advantage of providing a side view of the expanding wave and thus directly yielding quantitative information about the axial expansion velocities. An example can be seen in Fig. 7.15a–d, showing different stages of the expansion of a shockwave in air, accompanied by a stress front propagating into the material along the direction of the long-lived filament, formed at an early stage [138].

Although so far rarely used for the study of ultrafast laser-induced processes, the work of the Vogel group should be included in this section. They developed advanced microscopy techniques for shadowgraphy. Figure 7.15e–g displays shadowgraphs recorded with different modalities, clearly demonstrating the enormous contrast enhancement and revealing features that are not seen with standard shadowgraphy [139].

2.6 Ultrafast Continuous Imaging (UCI) Techniques

The previously discussed time-resolved techniques can be grouped in those offering the complete temporal evolution for a single-laser excitation event (Sect. 2.2) and those that record only one time-gated signal at a given delay value per laser pulse (Sects. 2.1, 2.3, 2.4, and 2.5). The latter requires therefore exposure to many laser pulses at different pump-probe delays in order to reconstruct the complete temporal

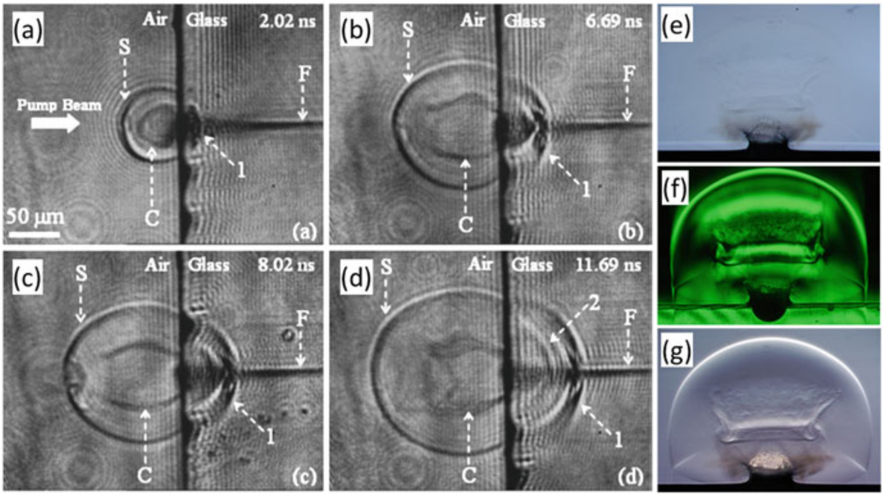

Fig. 7.15 (**a**–**d**) Shadowgraphs recorded at an air/silica interface upon irradiation with a single pump laser pulse ($\lambda = 800$ nm, $\tau = 100$ fs) at $F = 40$ J/cm^2. S shockwave front; C contact front; 1: first stress wave front; 2: second stress wave front; F filament. Reprinted from [138] with the permission of AIP Publishing [138]. (**e**–**g**) Shadowgraphs recorded at the air/water interface upon irradiation with a single pump laser pulse ($\lambda = 2940$ nm, $\tau = 80$ ns, $F = 5.4$ J/cm^2) from the top, recorded at a delay of 2300 ns. The different appearance is caused by the different imaging modalities used. (**e**) Bright-field shadowgraphy. (**f**) Dark-field shadowgraphy. (**g**) Combined Hoffmann modulation shadowgraphy combined with a knife-edge technique. (Provided by author of ref. [139])

evolution. Time-gated techniques offer a far superior temporal resolution than real-time techniques, but the inherent need for multiple laser exposure can be a serious limitation. While single-pulse-induced dynamics can in principle be investigated with time-gated techniques by exciting a previously unexposed region for each delay time, this method requires the absence of significant pump pulse fluctuations and a spatially homogeneous sample, which is sufficiently large for exposure to numerous (typically $N = 20$–100) spatially separated laser excitation spots (typical diameter $d = 20$–100 µm, separation $s = 2{*}d$). Yet this requirement to the sample cannot always be met. In particular, this is an issue for samples that are not sufficiently homogeneous (e.g., often the case for thin films grown by certain techniques in research labs), costly to be fabricated in such a size (e.g., samples produced by electron/ion beam lithography), inherently inhomogeneous samples (e.g., biological samples), or evolving samples (e.g., living tissue, chemical reactions).

Motivated by this need for high temporal resolution techniques with true single pulse measurement capability, a range of advanced techniques has recently been developed, often termed as continuous optical imaging techniques. The basic concept that most of them share is the use of a single excitation pulse to induce the transformation, combined with multiple probe pulses arriving at different time delays, which can be distinguished and separated by their individual spatial positions, angles, wavelengths, states of polarization, or spatial frequencies. An exception is a technique that does not require probe pulses but relies on the detection of luminescence or scattered pump light [140], explained in more detail at the end of this section.

In the following, we summarize them and briefly explain the basic measurement principles. A more detailed overview can be found in the excellent reviews of Guo et al. [141, 142], Liang et al. [143], and Mikami et al. [144]. There are undoubtedly other powerful techniques in this very active field of research that do not fall in this categorization and which we left out here in order to not exceed the length of this section.

2.6.1 Spatial Division UCI

In the pioneering work of the Nelson group [145], a true single pulse point-probing technique was introduced. By means of introducing two specially designed optical components in the probe beam path, sketched in Fig. 7.16a, the so-called echelons, the large-diameter probe beam, could be subdivided into 20 × 20 sub-beams, each with a different optical delay with respect to the pump pulse. After probing the sample, the beam was sent to a CCD camera for recording. The technique also includes an elegant method for normalizing the spatial intensity inhomogeneities of the probe beam, by generating a reference image of a fraction of the sub-divided beam that had not probed the sample, and which is simultaneously recorded by the CCD camera. The echelons were designed to yield a delay step size of 25 fs, and the useful delay window achieved was 10 ps. The results obtained in their study of chemical reactions allowed a single pulse real-time transmission measurement with high temporal resolution and extremely low noise (as low as 0.1% of the transmitted probe light intensity) [145].

A straight-forward further development of this technique, coined multiframe femtosecond time-resolved optical polarography (M-FTOP), was reported by Wang et al. [147]. The authors traded the high-single-pulse sampling capability for gaining 2D spatial resolution by using a single echelon only, which allowed the 2D imaging of an fs laser beam propagating in a transparent material (c.f. Fig. 7.16c). Since the echelon generated a spatially dependent probe pulse arrival at the propagation/imaging plane, snapshots at different delay times, spaced by 0.96 ps, could be recorded with a single camera upon single-pulse irradiation, as shown in Fig. 7.16d. It should be noted that it is the Kerr effect that causes the propagating pulse to be visible to the recording CCD, inducing a transient birefringence in the material, which is detected by introducing crossed polarizers in the setup.

2.6.2 Temporal Wavelength Division UCI

One of the drawbacks of the space division–based methods described in the previous section is the use of a physical echelon, which leads to a fixed delay between probe

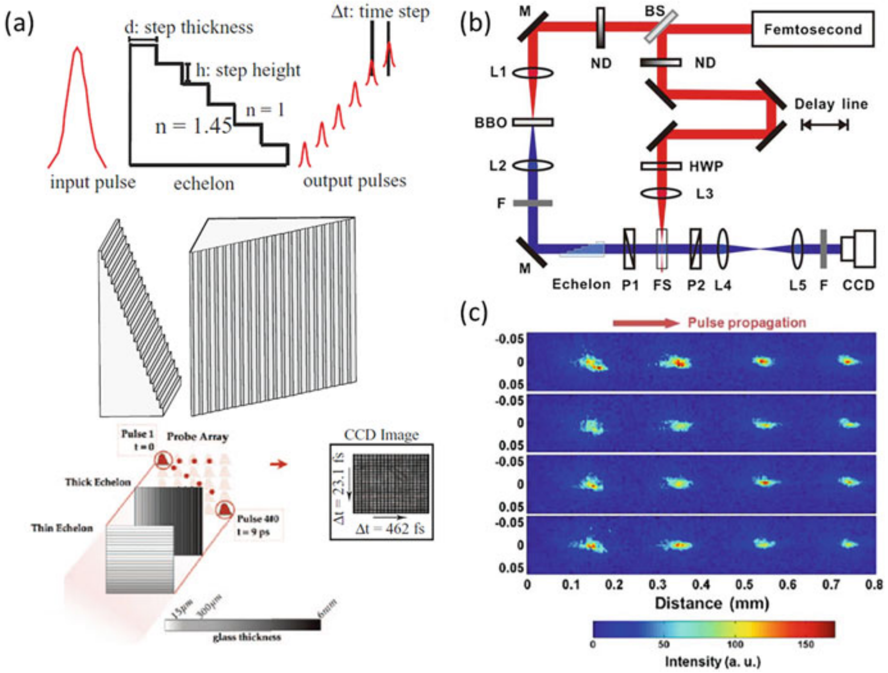
(a)
d: step thickness
h: step height
n = 1.45
n = 1
Δt: time step
input pulse
echelon
output pulses
Pulse 1
t = 0
Probe Array
Thick Echelon
Thin Echelon
Pulse 440
t = 9 ps
CCD Image
Δt = 23.1 fs
Δt = 462 fs
15μm
300μm
6mm
glass thickness
(b)
M
ND
BS
Femtosecond
L1
ND
Delay line
BBO
L2
HWP
L3
F
M
Echelon
P1
FS
P2
L4
L5
F
CCD
(c)
Pulse propagation
-0.05
0
0.05
0
0.1
0.2
0.3
0.4
0.5
0.6
0.7
0.8
Distance (mm)
0
50
100
150
Intensity (a. u.)

Fig. 7.16 UCI techniques based on spatial division and representative results. (**a**) Concept of the technique reported in [145, 146]. Reprinted with permission from [146] © AIP Publishing. (**b**) Sketch of the technique reported in [147] and (**c**) results obtained. Each row corresponds to the data obtained in a single pulse experiment. The different rows show data taken under the same conditions and the differences seen are caused by pulse fluctuations, underling the importance of UCI techniques. (Reprinted with permission from [147] © The Optical Society)

pulses that depends on the design of the echelon. A powerful technique reported in 2014 that allows a dynamical tuning of the interpulse delay is the so-called sequentially timed all-optical mapping photography (STAMP) [148]. Considerably more complex, the technique can be divided in three main steps required to prepare a suitable probe pulse train, as sketched in Fig. 7.17. In the first step, a single ultrashort probe pulse is stretched by means of introducing spectral chirp to a length that covers the desired temporal window of the process studied. To this end, the use of a glass rod allows stretching within the fs domain, whereas the use of a prism pair gives access to a ps temporal window, and the propagation of the pulse in a long fiber offers access to an ns temporal window. The second step consists in splitting this continuous chirped pulse into individual daughter pulses with a user-defined temporal spacing, employing a temporal pulse shaper based on a grating pair, a spatial light modulator and a 4-f imaging system. As a consequence of the initial spectral chirped pulse, the different pulse segments have different wavelengths (within the spectral bandwidth of the original ultrashort pulse). The third step, employed after probing the dynamics of the material, exploits

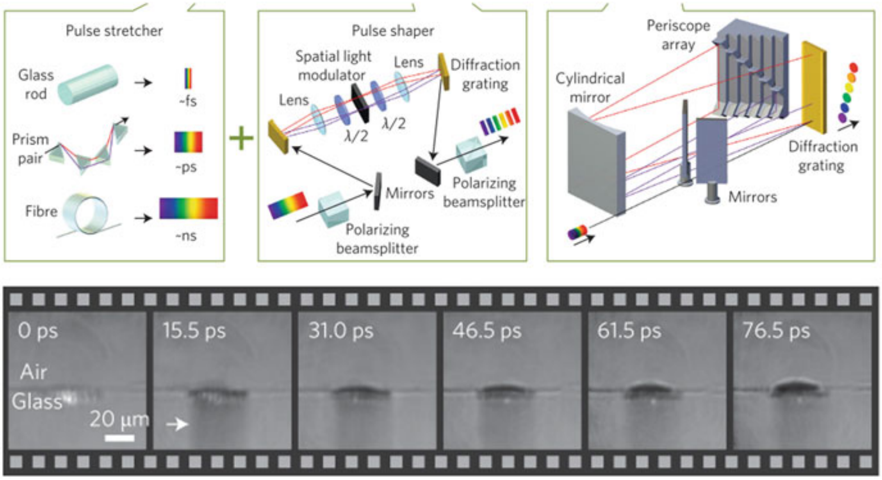
Pulse stretcher
Glass rod
~fs
Prism pair
~ps
Fibre
~ns
Pulse shaper
Spatial light modulator
Lens
Lens
Diffraction grating
λ/2
λ/2
Mirrors
Polarizing beamsplitter
Polarizing beamsplitter
Periscope array
Cylindrical mirror
Diffraction grating
Mirrors
0 ps
15.5 ps
31.0 ps
46.5 ps
61.5 ps
76.5 ps
Air
Glass
20 µm

Fig. 7.17 UCI technique STAMP based on temporal division and representative results. Top row: Different steps of modifications applied to the probe pulse (left) pulse stretcher (middle) pulse shaper to generate daughter pulses (right) spatial mapping device, placed after probing the sample. Bottom row: Results of an ablation study in glass, showing the generation of a plasma filament and the generation and expansion of a plume caused by laser irradiation. (Reprinted from [148] by permission from Springer-Nature)

this wavelength difference of the pulse segments by introducing a diffraction grating to diffract them at different angles in the horizontal plane. Afterward, the pulses multi-pass through an optical system based on a cylindrical mirror and periscope array, whose function is to separate the image-encoded daughter pulses with high spectral resolution without image distortion and optical loss, displacing them in the vertical direction and eventually reaching the CCD sensor to record a single multiframe image.

This technique has been applied to the study of several laser-matter interaction mechanisms, including the surface ablation on a glass substrate as shown in Fig. 7.17, as well as the high temporal resolution visualization of lattice vibrational waves in $LiNbO_3$ [148]. Since then, several modalities of this technique, such as spatially filtered STAMP [149], have been developed and applied to capture, for instance, the dynamics of the crystalline-to-amorphous phase transition of $Ge_2Sb_2Te_5$. A recent directly related technique, also based on temporally stretching the probe pulse and using different spectral bands that are temporally separated, is “Framing imaging based on non-collinear optical parametric amplification (FINCOPA)” [150]. The technique also employs step 1 of the STAMP technique but avoids step 2 (generating separated daughter pulses with a pulse shaper) through optical parametric amplification of different spectral bands of the probe pulse (after passing the sample) with a pump pulse to generate a time-gated image. The drawback of this technique is the experimental complexity and the need for multiple CCD cameras.

2.6.3 Angle Division UCI

UCI methods based on angle division rely on the acquisition of interferometric images captured simultaneously at different angles with a single CCD camera. One example is the so-called all-optical coaxial frame imaging (OCFI), in which a train of probe pulses coaxially illuminates the target and generates multiple holograms via interference with multiple reference pulses, individually delayed to span the time window of interest [151]. The authors demonstrate the potential of this technique by recording multiple time-gated images of different single pulse laser-matter interaction processes, such as surface ablation in aluminum foil and ionization in air. The advantage of this holography based technique, related to the non-UCI spectral imaging interferometry technique described in Sect. 2.4 [11], is the direct access to the phase, which allows a measurement of the real part of the refractive index.

Another angle division UCI technique is "single-shot frequency-domain tomography (SFDT)" [152]. Here, five probe pulses with different projection angles are overlapped both spatially and temporally at the target for continuous imaging of a transient, which was measured using spectral imaging interferometry. Applied to the study of laser pulse propagation in fused silica, the technique is able to record movies of the diffraction, self-focusing and filamentation via reconstruction by inverse-Fourier-transform of the hologram area associated with each probe pulse, and applying a tomographic image reconstruction algorithm.

2.6.4 Spatial Frequency Division UCI

The principle underlying spatial frequency division is the encoding of unique periodic modulations (spatial frequencies) in the beam profiles of each probe pulse in order to be able them. One such technique, "femtosecond videography for atomic and molecular dynamics (FRAME)" [153], employs this concept in a very similar way as done in structured illumination microscopy, where it is used for eliminating out-of-focus light [154, 155]. In FRAME, multiple probe pulses with the user-desired temporal separation are generated with a beam splitter configuration. Introducing ronchi (bar) gratings with different rotation positions in each arm, each probe pulse is encoded with its own fringe pattern with a unique orientation. This strategy allows detection of all probe pulses with a single camera since the individual images can be extracted via Fourier transformation and filtering.

Another UCI technique based on spatial frequency division is "time-resolved holographic polarization microscopy (THPM)," which can image the amplitude and phase distributions of two orthogonal polarization states of an ultrafast event [156].

2.6.5 Receive-Only (Passive) UCI

In contrast to the previously listed concepts of UCI, based on different encoding and reading strategies of a probe pulse train, other methods have been reported that rely on the detection of luminescence or scattered pump light using a detector with high temporal resolution, not requiring the use of probe pulses (receive-only, passive). An excellent review on these techniques can be found in [143]. Among them, one of the pioneering techniques in this field has been developed by Gao and co-workers [140], termed compressed ultrafast photography (CUP), which employs a digital micro-mirror device for spatial encoding and a streak camera for adding temporal resolution. The input image of an ultrafast moving object is encoded with a pseudo-random binary pattern and then temporally dispersed along a spatial axis using a streak camera with an open slit, equivalent to a temporal shearing operation. By applying a CUP reconstruction algorithm, the encoded spatio-temporal images recorded by the streak camera can be transformed into a time sequence of snapshots of the moving object. The system is able to capture a single, nonrepetitive event at up to 100 billion frames per second with up to 350 frames per acquisition. The authors have beautifully demonstrated its performance by imaging the propagation of a laser pulse in different materials, its reflection at a mirror, and its refraction at a glass interface, including others.

3 In-Situ Process Monitoring in Technological Laser Processing Applications

Industrial applications of advanced laser processing have been boosted by the widespread availability of Yb-based fiber lasers, reaching 100 s of μJ pulse energies, at 10s of MHz repetition rates and average powers well exceeding 100 W [157]. Chapter 26 provides a detailed view regarding ultra-rapid industrial large area processing by different approaches. While the wealth and potential of the different in-situ probing techniques discussed in the previous sections is without doubt enormous, their application to real-world industrial laser processing is still in its infancy. The major handicaps preventing their widespread use are experimental complexity, slow feedback, and lack of automation. However, some of the techniques have been successfully implemented for industrial processing, and a few examples are given in the next sections.

3.1 Specificity in Laser Cleaning and Art Restauration

Laser cleaning aims at the removal of contaminant particles or layers, which represents a major challenge in several industrial fields [158]. Removal of graffiti from walls is probably the most well-known application in which dedicated companies offer their service since long. The relative simplicity of this particular application is given by the self-regulation principle: in most cases the contaminating layer absorbs the laser light stronger than the uncontaminated material, which causes the removal process to stop automatically without supervision or control. However, most other laser cleaning applications require a real-time control of the removal process in order to avoid damage of the underlying material.

A particularly relevant sector is art restauration, in which unwanted damage needs to be avoided. Here, laser-induced breakdown spectroscopy (LIBS, see Sect. 2.1) has found its way due to the simple experimental configuration. Employing moderate power lasers, compact fiber optic spectrometers, and raster scanning optics, automatic data acquisition and real-time spectral analysis is possible. The beauty of the technique is that it inflicts minimal damage and not only provides the spectral fingerprint of the contaminated material but also of the underlying material to be preserved, enabling authentication, dating, and conservation in cultural heritage and archaeology [159]. Yet, it is vital to identify the optimum laser cleaning methodology/parameters for a given material, in order to prevent unwanted side effects to occur, such as darkening [160].

3.2 Monitoring the Depth and Side Wall Smoothness in Laser Drilling

Laser drilling of different materials has been implemented in the industry for decades. While drilling with ultrafast lasers is still not widespread due to the much higher photon cost, the unique properties of ultrashort laser pulses enable the fabrication of structures with much higher precision and nanometer size and in transparent materials that cannot be processed with longer pulse lasers [161, 162]. Real-time control of the hole features during the drilling process is therefore of strong interest for industry in order to ensure maximum efficiency and precision. In 2005, Kamiya et al. introduced simple real-time monitoring method to quantify the hole depth during femtosecond laser drilling by analyzing the interference between the processing pulse reflected from sample material and a reference pulse in a Mach-Zehnder interferometer [163]. The depth resolution depends on the laser bandwidth and was 5.5 micrometers in their case.

Another method to quantify the ablation rate is based on a side view configuration (see Sect. 2.5), as reported, for instance, in [164] for a transparent material. The advantage of this approach is the simultaneous monitoring of the side walls (at least in one plane), that is, how conical the shape of the hole becomes. Döring and coauthors [165] demonstrated that this approach can also be used for some semiconductors, using an illumination source at 1060 nm to image the evolution of the hole shape and depth during percussion drilling in silicon. A further advantage of the shadowgraphy approach is the access to transient plasma dynamics, which provides a means for processing parameter optimization. However, this approach is only valid for materials that offer a transparency regime that allows real-time imaging.

In the context of image-based monitoring of femtosecond laser machining, strong effort is being made by many groups to develop feedback algorithms in order to compensate for laser energy fluctuations or surface layers of unknown thickness (rust). Ideally, an approach without the need to model complex laser-matter interaction process is needed, operating purely with pattern recognition. Mills et al. have introduced a machine learning algorithm based on a neural network that was trained to determine the particular laser parameters that led to optimized ablation of nickel and fused silica samples [166].

Other strategies for real-time monitoring of hole drilling are based on LIBS. Asimellis et al. [167] reported a near-real-time method to determine the layer thickness on electroplated coin blanks during the drilling process via monitoring relative emission-line intensities from key probe elements via successive laser ablation pulses. A similar strategy has been applied to a very different field, laser surgery. Huang and co-workers achieved real-time identification of different tissue types by employing LIBS and spectral recognition algorithms [168]. Their system provides a powerful surgical tool for precise microsurgery applications with real-time feedback.

3.3 Welding Quality Control

Undoubtedly, one of the most important industrial applications of laser materials processing has been metal welding. A large number of publications have described different online monitoring techniques. The more conventional systems use acoustic waves, photo-detectors sensitive in different spectral regions [169], in-situ imaging with CCD or CMOS cameras, pyrometers, or plasma charge sensors [170]. Advanced layouts may include a combination of optical wavelength selective point-probing sensors and spectrometers, UV-visible imaging, high-speed imaging [171], and even X-ray imaging systems [172] as shown in Fig. 7.18. In the case of X-rays, synchrotron-based ultrahigh-speed imaging has also been used to quantify the phenomenon of "keyhole" formation during laser melting of metals [173]. Also recently, optical coherence tomography has been used to monitor in-situ the surface topography of the processing zone, as well as the surrounding area during laser welding [174].

Unlike metals, in the case of glasses, the need for ultrafast lasers for welding is a must due to their optical properties. The first work on glass welding dates back to the early 2000s [175], although the realization of industrially compatible approaches required the further development of high repetition rate Yb-based lasers [176]. Indeed, these sources have enabled a wealth of in-situ imaging pump-probe techniques for industrial processing, as shown in [177]. Among them, pump-probe imaging has been successfully used in laser glass welding [178] and also in glass

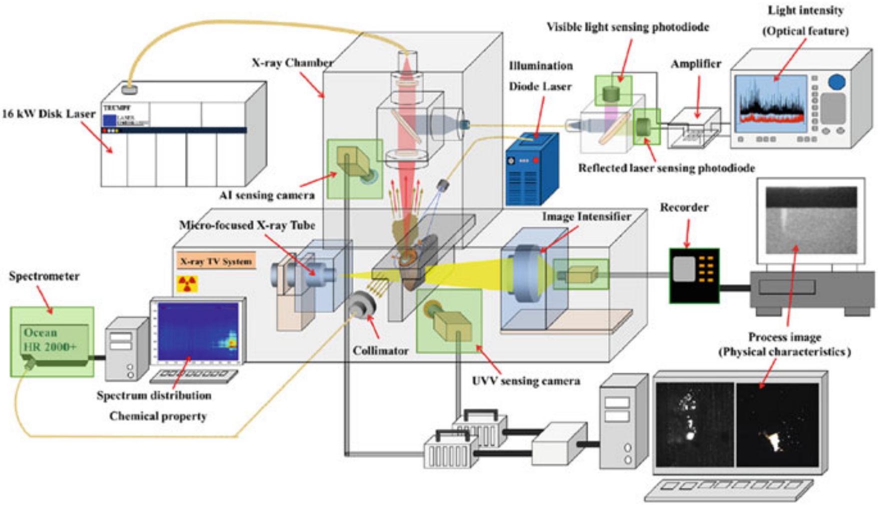
16 kW Disk Laser
X-ray Chamber
Visible light sensing photodiode
Light intensity
(Optical feature)
Illumination
Diode Laser
Amplifier
Reflected laser sensing photodiode
AI sensing camera
Micro-focused X-ray Tube
X-ray TV System
Image Intensifier
Recorder
Spectrometer
Ocean
HR 2000+
Collimator
Process image
(Physical characteristics)
UVV sensing camera
Spectrum distribution
Chemical property

Fig. 7.18 Experimental setup of the measurement system based on multiple sensors during laser welding. (Reprinted with permissions from [172] © Elsevier)

processing approaches involving spatial and temporal shaping of the processing lasers [179].

4 Outlook

The field of probing matter with light during the interaction of a laser pulse with a material system is vast, and this chapter can only give a glimpse of the exciting work performed by a steadily growing scientific community. For obvious space limitation reasons, it is not possible to cite in this review chapter every possible work related to this broad subject, and for sure there are many non-deliberate omissions in it. Still, the subtitle of this book, *The Pursuit of Extreme Scales*, deserves a few additional comments on the exploration of the limits in the spatial and temporal domains.

The impressive advances reached in the field of near field microscopy (and their related local spectroscopies) has enabled the achievement of imaging at spatial resolutions in the few nm to tens of nm range, depending on the approach used (aperture or apertureless scanning near-field optical microscopy, SNOM) [180]. The combination of ad hoc tip fabrication methodologies [181] and the use of adaptive approaches [182] has enabled reaching extreme spatial resolutions also in the so-called tip-enhanced nano-spectroscopies [183]. At the same time, this has enabled reaching extreme enhancement values in tip-enhanced photoluminescence (TEPL) and tip-enhanced Raman spectroscopy (TERS).

The combination of ultrashort laser pulses and light localization phenomena appears therefore as a natural way to move toward higher spatial and temporal resolution limits during the study of light-matter interactions using light probes. Indeed, such a combination has found an ever-increasing number of fundamentally relevant applications that go well beyond the development of fs-resolution, time-resolved SNOM [184, 185]. As described by Lienau and coworkers in ref. [186], "When illuminating metallic nanostructures with ultrashort, femtosecond light pulses, local field intensities are easily reached that are sufficient to generate high harmonic radiation or to propel electrons out of these particles, generating new nanoscale sources of femtosecond electron bunches of potential interest for future applications in ultrahigh time resolution electron microscopy or diffraction [. . .]. Hybrid nanostructures, comprising metals, semiconductors and/or molecular aggregates may find entirely new applications in ultrafast switching or for designing new classes of photonic transistors with unprecedented sensitivity [. . .]." This kind of interactions have led to the relatively recent development of the so-called strong field nano-optics [187] with extremely relevant applications, including the development of new types of ultrafast electron microscopes with unprecedented spatial, temporal, and energy resolution.

With regard to the latter application, along with the combination of light localization phenomena with ultrashort laser pulses, one can naturally think of combining pulsed electron bunches with ultrafast lasers to image the morphological/structural evolution of a laser-excited material at extreme spatial and temporal scales. While this idea is not new at all, and although it does not involve probing matter by light but with electrons, the relation of it with fast and ultrafast laser sources is strong. The first works aimed at developing a "time-resolved" transmission electron microscope using pulsed electron and laser sources date from the early 2000s with the pioneering works by Bostanjoglo [188]. Only 10 years later, the so-called 4D electron microscopy [189] was a reality, and several works have already shown electron imaging and diffraction with temporal resolution in the 100 s of fs range [190–192]. The advances, challenges, and perspectives of 4D electron microscopy have been recently reviewed in ref. [193], with the prospect of achieving Å–fs–meV resolution in the future.

All these recent advances in the development of time-resolved probing with light and electron sources will strongly contribute to unravel the underlying mechanisms of complex interaction pathways. Thanks to this steady growth, combined with decreasing equipment costs and increasing interest of the different technology sectors, the future of in-situ process monitoring for fundamental research and real-world applications is bright. We can certainly expect that nanostructuring with ultrafast lasers will strongly benefit from the increasing capabilities of in-situ monitoring techniques.

References

1. W.M. Steen, J. Mazumder, *Laser Material Processing* (Springer, London, 2010)
2. G.R. Fowles, *Introduction to Modern Optics* (Dover Publications, 1975)
3. R.W. Boyd, *Nonlinear Optics* (Academic Press, 2008)
4. F. Krausz, T. Brabec, Rev. Mod. Phys. **72**, 545 (2000)
5. L.V. Keldysh, Sov. Phys. JETP **20**, 1307 (1965)
6. B. Stuart, M. Feit, S. Herman, A. Rubenchik, B. Shore, M. Perry, Phys. Rev. B Condens. Matter **53**, 1749 (1996)
7. B. Rethfeld, Phys. Rev. B **73**, 035101 (2006)
8. R.W. Boyd, G.L. Fischer, Encycl. Mater. Sci. Technol. Second Ed, 6237 (2001)
9. S.S. Mao, F. Quéré, S. Guizard, X. Mao, R.E. Russo, G. Petite, P. Martin, 1695 (2004). Appl. Phys. A Mater. Sci. Process. **797**, 79 (2004)
10. F. Quéré, S. Guizard, P. Martin, G. Petite, O. Gobert, P. Meynadier, M. Perdrix, Appl. Phys. B Lasers Opt. **68**, 459 (1999) 1999 683
11. M. Garcia-Lechuga, L. Haahr-Lillevang, J. Siegel, P. Balling, S. Guizard, J. Solis, Phys. Rev. B **95**, 214114 (2017)
12. E.G. Gamaly, A.V. Rode, Prog. Quantum Electron. **37**, 215 (2013)
13. M. Gaft, R. Reisfeld, G. Panczer, *Modern Luminescence Spectroscopy of Minerals and Materials* (Springer-Verlag, Berlin/Heidelberg, 2005)
14. R.R. Jones, D.C. Hooper, L. Zhang, D. Wolverson, V.K. Valev, Nanoscale Res. Lett. **14**, 231 (2019)
15. F. Abelès, M.L. Thèye, Surf. Sci. **5**, 325 (1966)
16. J. Hernandez-Rueda, J. Siegel, M. Garcia-Lechuga, J. Solis, J. Opt. Soc. Am. B **31**, 1676 (2014)
17. Q. Li, M. Chambonneau, M. Chanal, D. Grojo, Appl. Opt. **55**, 9577 (2016)
18. W.R. Sooy, M. Geller, D.P. Bortfeld, Appl. Phys. Lett. **5**, 54 (1964)
19. D.A. Cremers, L.J. Radziemski, *Handbook of Laser-Induced Breakdown Spectroscopy*, 2nd edn. (Wiley, 2013)
20. J. Debras-Guédon, N. Liodec, Comptes Rendus l'Académie Des Sci. **257**, 3336 (1963)
21. E.F. Runge, R.W. Minck, F.R. Bryan, Spectrochim. Acta **20**, 733 (1964)
22. S. Legnaioli, B. Campanella, F. Poggialini, S. Pagnotta, M.A. Harith, Z.A. Abdel-Salam, V. Palleschi, Anal. Methods **12**, 1014 (2020)
23. F.J. Gordillo-Vázquez, A. Perea, J.A. Chaos, J. Gonzalo, C.N. Afonso, Appl. Phys. Lett. **78**, 7 (2001)
24. J. Siegel, G. Epurescu, A. Perea, F.J. Gordillo-Vázquez, J. Gonzalo, C.N. Afonso, Spectrochim. Acta - Part B At. Spectrosc. **60**, 915 (2005)
25. J. Siegel, G. Epurescu, A. Perea, F.J. Gordillo-Vázquez, J. Gonzalo, C.N. Afonso, Opt. Lett. **29**, 2228 (2004)
26. G. Epurescu, J. Siegel, J. Gonzalo, F.J. Gordillo-Vázquez, C.N. Afonso, Appl. Phys. Lett. **87**, 1 (2005)
27. J. Squier, D. Harter, F. Salin, G. Mourou, Opt. Lett. **16**, 324 (1991)
28. C. W. White (ed.), *Laser and Electron Beam Processing of Superconductors*, 1st edn. (Academic Press, Orlando, 1980)
29. Y. R. T. Wood, R. F, C. W. White (eds.), *Laser Part. Beams*, vol 4 (1986), p. 321
30. P. Baeri, S.U. Campisano, G. Foti, E. Rimini, Appl. Phys. Lett. **33**, 137 (1978)
31. I.B. Khaibullin, E.I. Shtyrkov, M.M. Zaripov, M.F. Galyautdinov, G.G. Zakirov, Sov. Phys. Semicond. **11**, 190 (1977)
32. D.H. Auston, C.M. Surko, T.N.C. Venkatesan, R.E. Slusher, J.A. Golovchenko, Appl. Phys. Lett. **33**, 437 (1978)
33. D.H. Lowndes, R.F. Wood, Appl. Phys. Lett. **38**, 971 (1981)
34. M.I. Nathan, R.T. Hodgson, E.J. Yoffa, Appl. Phys. Lett. **36**, 512 (1980)
35. D.H. Lowndes, Phys. Rev. Lett. **48**, 267 (1982)

36. H.W. Lo, A. Compaan, Phys. Rev. Lett. **44**, 1604 (1980)
37. K. Murakami, H. Itoh, K. Takita, K. Masuda, Phys. B+C **117–118**, 1024 (1983)
38. D.H. Lowndes, G.E. Jellison, R.F. Wood, Phys. Rev. B **26**, 6747 (1982)
39. G.E. Jellison, D.H. Lowndes, Appl. Phys. Lett. **51**, 352 (1987)
40. R.S. Becker, G.S. Higashi, J.A. Golovchenko, Phys. Rev. Lett. **52**, 307 (1984)
41. D.M.B.C. Larson, C.W. White, T. S. Noggle **48**, 337 (1982)
42. K. Murakami, H.C. Gerritsen, H. van Brug, F. Bijkerk, F.W. Saris, M.J. van der Wiel, Phys. Rev. Lett. **56**, 655 (1986)
43. G.J. Galvin, M.O. Thompson, J.W. Mayer, R.B. Hammond, N. Paulter, P.S. Peercy, Phys. Rev. Lett. **48**, 33 (1982)
44. G.J. Galvin, M.O. Thompson, J.W. Mayer, P.S. Peercy, R.B. Hammond, N. Paulter, Phys. Rev. B **27**, 1079 (1983)
45. R.F. Wood, G.E. Giles, Phys. Rev. B **23**, 2923 (1981)
46. R.F. Wood, J.R. Kirkpatrick, G.E. Giles, Phys. Rev. B **23**, 5555 (1981)
47. J.A. Van Vechten, R. Tsu, F.W. Saris, D. Hoonhout, Phys. Lett. A **74**, 417 (1979)
48. J.A. Van Vechten, R. Tsu, F.W. Saris, Phys. Lett. A **74**, 422 (1979)
49. M.O. Thompson, J.W. Mayer, A.G. Cullis, H.C. Webber, N.G. Chew, J.M. Poate, D.C. Jacobson, Phys. Rev. Lett. **50**, 896 (1983)
50. J. Solis, C.N. Afonso, J. Appl. Phys. **69**, 2105 (1991)
51. T. Sameshima, S. Usui, J. Appl. Phys. **74**, 6592 (1993)
52. J.J.P. Bruines, R.P.M. Van Hal, H.M.J. Boots, W. Sinke, F.W. Saris, Appl. Phys. Lett. **48**, 1252 (1986)
53. J. Siegel, J. Solis, C.N. Afonso, F. Vega, J. Bankmann, O. Martínez Sacristán, K. Sokolowski-Tinten, J. Appl. Phys. **89**, 3642 (2001)
54. M.O. Thompson, G.J. Galvin, J.W. Mayer, P.S. Peercy, J.M. Poate, D.C. Jacobson, A.G. Cullis, N.G. Chew, Phys. Rev. Lett. **52**, 2360 (1984)
55. F. Vega, N. Chaoui, J. Solis, J. Armengol, C.N. Afonso, J. Appl. Phys. **97**, 103519 (2005)
56. S.R. Stiffler, M.O. Thompson, P.S. Peercy, Phys. Rev. B **43**, 9851 (1991)
57. J. Boneberg, P. Leiderer, Phys. Status Solidi Appl. Res. **166**, 643 (1998)
58. M. Wuttig, N. Yamada, Nat. Mater. **6**, 824 (2007)
59. M. Le Gallo, A. Sebastian, J. Phys. D. Appl. Phys. **53**, 213002 (2020)
60. C.J. van der Poel, J. Mater. Res. **3**, 126 (1988)
61. C.N. Afonso, J. Solis, F. Catalina, C. Kalpouzos, Appl. Phys. Lett. **60**, 3123 (1992)
62. J. Siegel, J. Solis, C.N. Afonso, Appl. Surf. Sci. **154**, 130 (2000)
63. Y. Kanemitsu, H. Kuroda, S. Shionoya, Jpn. J. Appl. Phys. **23**, 618 (1984)
64. J. Solis, J. Siegel, C.N. Afonso, Rev. Sci. Instrum. **71**, 1595 (2000)
65. J. Bonse, S.M. Wiggins, J. Solis, J. Appl. Phys. **96**, 2352 (2004)
66. J. Siegel, C.N. Afonso, J. Solis, Appl. Phys. Lett. **75**, 3102 (1999)
67. J. Siegel, A. Schropp, J. Solis, C.N. Afonso, M. Wuttig, Appl. Phys. Lett. **84**, 2250 (2004)
68. S. Wen, Y. Meng, M. Jiang, Y. Wang, Sci. Rep. **8**, 4979 (2018)
69. S. Abdollahramezani, O. Hemmatyar, H. Taghinejad, A. Krasnok, Y. Kiarashinejad, M. Zandehshahvar, A. Alù, A. Adibi, Nanophotonics **9**, 1189 (2020)
70. N. Casquero, Y. Fuentes-Edfuf, R. Zazo, J. Solis, J. Siegel, J. Phys. D. Appl. Phys. **53**, 9 (2020)
71. M. Alvarez-Alegria, J. Siegel, M. Garcia-Pardo, F. Cabello, J. Toudert, E. Haro-Poniatowski, R. Serna, Adv. Opt. Mater. **10**, 2101405 (2022)
72. A.H. Zewail, J. Phys. Chem. A **104**, 5660 (2000)
73. G.A. Mourou, T. Tajima, S.V. Bulanov, Rev. Mod. Phys. **78**, 309 (2006)
74. P.H. Bucksbaum, Science (80-.) **317**, 766 (2007)
75. A. Nayak, M. Dumergue, S. Kühn, S. Mondal, T. Csizmadia, N.G. Harshitha, M. Füle, M. Upadhyay Kahaly, B. Farkas, B. Major, V. Szaszkó-Bogár, P. Földi, S. Majorosi, N. Tsatrafyllis, E. Skantzakis, L. Neoričić, M. Shirozhan, G. Vampa, K. Varjú, P. Tzallas, G. Sansone, D. Charalambidis, S. Kahaly, Phys. Rep. **833**, 1 (2019)
76. M.C. Downer, R.L. Fork, C.V. Shank, J. Opt. Soc. Am. B **2**, 595 (1985)

77. K. Sokolowski-Tinten, J. Bialkowski, M. Boing, A. Cavalleri, D. von der Linde, Phys. Rev. B **58**, R11805 (1998)
78. S. L. Shapiro (ed.), *Ultrashort Light Pulses* (Springer, Berlin Heidelberg, 1977)
79. C.V. Shank, Science **219**, 1027 (1983)
80. A. Brodeur, S.L. Chin, Phys. Rev. Lett. **80**, 4406 (1998)
81. C.V. Shank, R. Yen, C. Hirlimann, Phys. Rev. Lett. **50**, 454 (1983)
82. C.V. Shank, R. Yen, C. Hirlimann, Phys. Rev. Lett. **51**, 900 (1983)
83. P. Saeta, J.-K. Wang, Y. Siegal, N. Bloembergen, E. Mazur, Phys. Rev. Lett. **67**, 1023 (1991)
84. K. Sokolowski-Tinten, J. Bialkowski, D. von der Linde, Phys. Rev. B **51**, 14186 (1995)
85. K. Sokolowski-Tinten, J. Solis, J. Bialkowski, J. Siegel, C.N. Afonso, D. von der Linde, *Tech. Dig. 1998 EQEC. Eur. Quantum Electron. Conf. (Cat. No.98TH8326)* (IEEE, 1998), p. 234
86. J. Solis, C. Afonso, S. Hyde, N. Barry, P. French, Phys. Rev. Lett. **76**, 2519 (1996)
87. D.H. Auston, C.V. Shank, Phys. Rev. Lett. **32**, 1120 (1974)
88. S. Richter, M. Rebarz, O. Herrfurth, S. Espinoza, R. Schmidt-Grund, J. Andreasson, Rev. Sci. Instrum. **92**, 033104 (2021)
89. J.P. Callan, A.M.-T. Kim, L. Huangt, E.N. Glezer, E. Mazur, MRS Online Proc. Libr. **481**, 395 (1997)
90. C.A.D. Roeser, A.M.-T. Kim, J.P. Callan, L. Huang, E.N. Glezer, Y. Siegal, E. Mazur, Rev. Sci. Instrum. **74**, 3413 (2003)
91. L. Huang, J.P. Callan, E.N. Glezer, E. Mazur, Phys. Rev. Lett. **80**, 185 (1998)
92. J.P. Callan, A.M.-T. Kim, C.A.D. Roeser, E. Mazur, J. Solis, J. Siegel, C.N. Afonso, J.C.G. de Sande, Phys. Rev. Lett. **86**, 3650 (2001)
93. A.H. Chin, R.W. Schoenlein, T.E. Glover, P. Balling, W.P. Leemans, C.V. Shank, Phys. Rev. Lett. **83**, 336 (1999)
94. C.W. Siders, A. Cavalleri, K. Sokolowski-Tinten, C. Tóth, T. Guo, M. Kammler, M. Horn Von Hoegen, K.R. Wilson, D. Von Der Linde, C.P.J. Barty, Science (80-.) **286**, 1340 (1999)
95. T. Frigge, B. Hafke, T. Witte, B. Krenzer, C. Streubühr, A. Samad Syed, V. Mikšić Trontl, I. Avigo, P. Zhou, M. Ligges, D. Von Der Linde, U. Bovensiepen, M. Horn-Von Hoegen, S. Wippermann, A. Lücke, S. Sanna, U. Gerstmann, W.G. Schmidt, Nature **544**, 207 (2017)
96. C. Giannetti, M. Capone, D. Fausti, M. Fabrizio, F. Parmigiani, D. Mihailovic, Adv. Phys. **65**, 58 (2016)
97. H.A. Hafez, X. Chai, A. Ibrahim, S. Mondal, D. Férachou, X. Ropagnol, T. Ozaki, J. Opt. **18**, 093004 (2016)
98. M.B. Johnston, L.M. Herz, Acc. Chem. Res. **49**, 146 (2016)
99. J. Hernandez-Rueda, A. Savoia, W. Gawelda, J. Solis, B. Mansart, D. Boschetto, J. Siegel, Appl. Phys. Lett. **98**, 251906 (2011)
100. P. Beaud, S.L. Johnson, A. Streun, R. Abela, D. Abramsohn, D. Grolimund, F. Krasniqi, T. Schmidt, V. Schlott, G. Ingold, Phys. Rev. Lett. **99**, 174801 (2007)
101. M. Forst, T. Dekorsy, C. Trappe, M. Laurenzis, H. Kurz, B. Béchevet, Appl. Phys. Lett. **77**, 1964 (2000)
102. N. Stojanovic, D. von der Linde, K. Sokolowski-Tinten, U. Zastrau, F. Perner, E. Förster, R. Sobierajski, R. Nietubyc, M. Jurek, D. Klinger, J. Pelka, J. Krzywinski, L. Juha, J. Cihelka, A. Velyhan, S. Koptyaev, V. Hajkova, J. Chalupsky, J. Kuba, T. Tschentscher, S. Toleikis, S. Düsterer, H. Redlin, E. Förster, R. Sobierajski, R. Nietubyc, M. Jurek, D. Klinger, J. Pelka, J. Krzywinski, L. Juha, J. Cihelka, A. Velyhan, S. Koptyaev, V. Hajkova, J. Chalupsky, J. Kuba, T. Tschentscher, S. Toleikis, S. Düsterer, H. Redlin, Appl. Phys. Lett. **89**, 89 (2006)
103. M.C. Downer, R.L. Fork, C.V. Shank, *Ultrafast Phenom. IV* (Springer, Berlin, Heidelberg, 1984), pp. 106–110
104. D. von der Linde, K. Sokolowski-Tinten, Appl. Surf. Sci. **154–155**, 1 (2000)
105. K. Sokolowski-Tinten, J. Bialkowski, A. Cavalleri, D. von der Linde, A. Oparin, J. Meyer-ter-Vehn, S. Anisimov, Phys. Rev. Lett. **81**, 224 (1998)
106. D. von der Linde, K. Sokolowski-Tinten, J. Bialkowski, Appl. Surf. Sci. **109–110**, 1 (1997)
107. K. Sokolowski-Tinten, J. Solis, J. Bialkowski, J. Siegel, C.N. Afonso, D. von der Linde, Phys. Rev. Lett. **81**, 3679 (1998)

108. J. Siegel, W. Gawelda, D. Puerto, C. Dorronsoro, J. Solis, C.N. Afonso, J.C.G. De Sande, R. Bez, A. Pirovano, C. Wiemer, J. Appl. Phys. **103**, 023516 (2008)
109. D. Puerto, J. Siegel, W. Gawelda, M. Galvan-Sosa, L. Ehrentraut, J. Bonse, J. Solis, J. Opt. Soc. Am. B **27**, 1065 (2010)
110. J. Hernandez-Rueda, D. Puerto, J. Siegel, M. Galvan-Sosa, J. Solis, Appl. Surf. Sci. **258**, 9389 (2012)
111. M. Garcia-Lechuga, J. Solis, J. Siegel, Appl. Phys. A Mater. Sci. Process. **124**, 221 (2018)
112. M. Garcia-Lechuga, J. Siegel, J. Hernandez-Rueda, J. Solis, Appl. Phys. Lett. **105**, 112902 (2014)
113. P. Kühler, D. Puerto, M. Mosbacher, P. Leiderer, F.J.G. de Abajo, J. Siegel, J. Solis, Beilstein J. Nanotechnol. **4**, 501 (2013)
114. M. Garcia-Lechuga, J. Solis, J. Siegel, Appl. Phys. Lett. **108**, 171901 (2016)
115. M. Garcia-Lechuga, D. Puerto, Y. Fuentes-Edfuf, J. Solis, J. Siegel, ACS Photonics **3**, 1961 (2016)
116. T. Winkler, L. Haahr-Lillevang, C. Sarpe, B. Zielinski, N. Götte, A. Senftleben, P. Balling, T. Baumert, Nat. Phys. **14**, 74 (2018)
117. C. Pan, L. Jiang, J. Sun, Q. Wang, F. Wang, K. Wang, Y. Lu, Y. Wang, L. Qu, T. Cui, Light Sci. Appl. **9**, 80 (2020)
118. C. Xie, R. Meyer, L. Froehly, R. Giust, F. Courvoisier, Light Sci. Appl. **10**, 126 (2021)
119. X.Y. Wang, M.C. Downer, Opt. Lett. **17**, 1450 (1992)
120. S. Rapp, M. Kaiser, M. Schmidt, H.P. Huber, Opt. Express **24**, 17572 (2016)
121. J. Winter, S. Rapp, M. Spellauge, C. Eulenkamp, M. Schmidt, H.P. Huber, Appl. Surf. Sci. **511**, 145514 (2020)
122. J. Winter, S. Rapp, M. Schmidt, H.P. Huber, Appl. Surf. Sci. **417**, 2 (2017)
123. S.H. Møller, S.T. Andersen, P. Balling, Phys. Rev. Res. **2**, 043010 (2020)
124. V.V. Temnov, K. Sokolowski-Tinten, P. Zhou, D. von der Linde, Appl. Phys. A Mater. Sci. Process. **78**, 483 (2004)
125. V.V. Temnov, K. Sokolowski-Tinten, P. Zhou, D. von der Linde, J. Opt. Soc. Am. B **23**, 1954 (2006)
126. L. Gallais, S. Monneret, Opt. Lett. **41**, 3245 (2016)
127. P. Bon, G. Maucort, B. Wattellier, S. Monneret, Opt. Express **17**, 13080 (2009)
128. P. Audebert, P. Daguzan, A. Dos Santos, J.C. Gauthier, J.P. Geindre, S. Guizard, G. Hamoniaux, K. Krastev, P. Martin, G. Petite, A. Antonetti, Phys. Rev. Lett. **73**, 1990 (1994)
129. J.P. Geindre, A. Mysyrowicz, A. Dos Santos, P. Audebert, A. Rousse, G. Hamoniaux, A. Antonetti, F. Falliès, J.C. Gauthier, Opt. Lett. **19**, 1997 (1994)
130. K.J. Wædegaard, D.B. Sandkamm, A. Mouskeftaras, S. Guizard, P. Balling, Europhys. Lett. **105**, 47001 (2014)
131. A. Mouskeftaras, S. Guizard, N. Fedorov, S. Klimentov, Appl. Phys. A Mater. Sci. Process. **110**, 709 (2013)
132. D. Puerto, W. Gawelda, J. Siegel, J. Bonse, G. Bachelier, J. Solis, Appl. Phys. A Mater. Sci. Process. **92**, 803 (2008)
133. W. Gawelda, D. Puerto, J. Siegel, A. Ferrer, A.R. De La Cruz, H. Fernández, J. Solis, Appl. Phys. Lett. **93**, 93 (2008)
134. F. Wang, C. Pan, J. Sun, Q. Wang, Y. Lu, L. Jiang, Opt. Express **27**, 10050 (2019)
135. Q. Sun, H. Jiang, Y. Liu, Z. Wu, H. Yang, Q. Gong, Opt. Lett. **30**, 320 (2005)
136. A. Mermillod-Blondin, J. Bonse, A. Rosenfeld, I.V. Hertel, Y.P. Meshcheryakov, N.M. Bulgakova, E. Audouard, R. Stoian, Appl. Phys. Lett. **94**, 041911 (2009)
137. A. Mouskeftaras, M. Chanal, M. Chambonneau, R. Clady, O. Utéza, D. Grojo, Appl. Phys. Lett. **108**, 41107 (2016)
138. H. Hu, X. Wang, H. Zhai, N. Zhang, P. Wang, Appl. Phys. Lett. **97**, 061117 (2010)
139. A. Vogel, I. Apitz, S. Freidank, R. Dijkink, Opt. Lett. **31**, 1812 (2006)
140. L. Gao, J. Liang, C. Li, L.V. Wang, Nature **516**, 74 (2014) 5167529
141. B. Guo, J. Sun, Y.F. Lu, L. Jiang, Int. J. Extrem. Manuf. **1**, 032004 (2019)

142. B. Guo, *Handb. Laser Micro-Nano-Engineering* (Springer International Publishing, Cham, 2020), pp. 1–51
143. J. Liang, L.V. Wang, Opt **5**(9), 1113–1127 (2018)
144. H. Mikami, L. Gao, K. Goda, Nanophotonics **5**, 441 (2016)
145. P.R. Poulin, K.A. Nelson, Science (80-.) **313**, 1756 (2006)
146. T. Shin, J.W. Wolfson, S.W. Teitelbaum, M. Kandyla, K.A. Nelson, Rev. Sci. Instrum. **85**, 083115 (2014)
147. X. Wang, L. Yan, J. Si, S. Matsuo, H. Xu, X. Hou, Appl. Opt. **53**, 8395 (2014)
148. K. Nakagawa, A. Iwasaki, Y. Oishi, R. Horisaki, A. Tsukamoto, A. Nakamura, K. Hirosawa, H. Liao, T. Ushida, K. Goda, F. Kannari, I. Sakuma, Nat. Photonics **8**, 6 (2014)
149. T. Suzuki, R. Hida, Y. Yamaguchi, K. Nakagawa, T. Saiki, F. Kannari, Appl. Phys. Express **10**, 092502 (2017)
150. X. Zeng, S. Zheng, Y. Cai, Q. Lin, J. Liang, X. Lu, J. Li, W. Xie, S. Xu, Adv. Photonics **2**, 1 (2020)
151. C. Li, G. Cheng, X. Sedao, W. Zhang, H. Zhang, N. Faure, D. Jamon, J.-P. Colombier, R. Stoian, Opt. Express **24**, 11558 (2016)
152. Z. Li, R. Zgadzaj, X. Wang, Y.-Y. Chang, M.C. Downer, Nat. Commun. **5**, 3085 (2014)
153. A. Ehn, J. Bood, Z. Li, E. Berrocal, M. Aldén, E. Kristensson, Light Sci. Appl. **6**, e17045 (2017)
154. M.A.A. Neil, R. Juškaitis, T. Wilson, Opt. Lett. **22**, 1905 (1997)
155. M.J. Cole, J. Siegel, S.E. Webb, R. Jones, K. Dowling, P.M. French, M.J. Lever, L.O. Sucharov, M.A. Neil, R. Juskaitis, T. Wilson, Opt. Lett. **25**, 1361 (2000)
156. Q.-Y. Yue, Z.-J. Cheng, L. Han, Y. Yang, C.-S. Guo, Opt. Express **25**, 14182 (2017)
157. G. Chang, Z. Wei, IScience **23**, 101101 (2020)
158. D.M. Kane, *Laser Cleaning II* (World Scientific Publishing Co, 2007)
159. A. Botto, B. Campanella, S. Legnaioli, M. Lezzerini, G. Lorenzetti, S. Pagnotta, F. Poggialini, V. Palleschi, J. Anal. At. Spectrom. **34**, 81 (2019)
160. P. Pouli, M. Oujja, M. Castillejo, Appl. Phys. A Mater. Sci. Process. **106**, 1062 (2011) 447 (2011)
161. R. Stoian, J.-P. Colombier, Nanophotonics **9**, 4665 (2020)
162. R. Osellame, G. Cerullo, R. Ramponi, *Femtosecond Laser Micromachining* (Springer, Berlin Heidelberg, 2012)
163. M. Kamiya, S. Aoshima, Rev. Laser Eng. **33**, 685 (2005)
164. D. Grossmann, M. Reininghaus, C. Kalupka, M. Jenne, M. Kumkar, Opt. Express **25**, 28478 (2017)
165. S. Döring, S. Richter, S. Nolte, A. Tünnermann, Opt. Express **18**, 20395 (2010)
166. B. Mills, D.J. Heath, J.A. Grant-Jacob, Y. Xie, R.W. Eason, J. Phys. Photonics **1**, 015008 (2018)
167. G. Asimellis, A. Giannoudakos, M. Kompitsas, Appl. Opt. **46**, 935 (2007)
168. H. Huang, L.-M. Yang, S. Bai, J. Liu, J. Biomed. Opt. **20**, 028001 (2015)
169. P. De Bono, C. Allen, G. D'Angelo, A. Cisi, J. Laser Appl. **29**, 022417 (2017)
170. J. Shao, Y. Yan, J. Phys. Conf. Ser. **15**, 101 (2005)
171. S.M. Robertson, A.F.H. Kaplan, J. Frostevarg, J. Manuf. Process. **67**, 91 (2021)
172. D. You, X. Gao, S. Katayama, J. Mater. Process. Technol. **219**, 209 (2015)
173. R. Cunningham, C. Zhao, N. Parab, C. Kantzos, J. Pauza, K. Fezzaa, T. Sun, A.D. Rollett, Science (80-.) **363**, 849 (2019)
174. C. Stadter, M. Schmoeller, M. Zeitler, V. Tueretkan, U. Munzert, M.F. Zaeh, J. Laser Appl. **31**, 022408 (2019)
175. T. Tamaki, W. Watanabe, J. Nishii, K. Itoh, Jpn. J. Appl. Phys. **44**, L687 (2005)
176. S. Richter, S. Döring, A. Tünnermann, S. Nolte, Appl. Phys. A Mater. Sci. Process. **103**, 257 (2011)
177. M. Jenne, F. Zimmermann, D. Flamm, D. Großmann, J. Kleiner, M. Kumkar, S. Nolte, J. Laser Micro Nanoeng. **13**, 273 (2018)

178. A. Gruber, F. Zimmermann, M. Jenne, D.G. Grossmann, M. Kumkar, in *Laser Appl. Microelectron. Optoelectron. Manuf. XXIII*, ed. by B. Neuenschwander, G. Račiukaitis, T. Makimura, C. P. Grigoropoulos, (SPIE, 2018), p. 051906-1–6
179. M. Jenne, D. Flamm, M. Faber, D. Grossmann, J. Kleiner, F. Zimmermann, M. Kumkar, S. Nolte, in *Laser-Based Micro- Nanoprocessing XIII*, ed. by U. Klotzbach, R. Kling, A. Watanabe, (SPIE, 2019), p. 109061G-1–7
180. P. Bazylewski, S. Ezugwu, G. Fanchini, Appl. Sci. **7**, 973 (2017)
181. W.-S. Chang, S. Bauerdick, M.S. Jeong, Ultramicroscopy **108**, 1070 (2008)
182. D.Y. Lee, C. Park, J. Choi, Y. Koo, M. Kang, M.S. Jeong, M.B. Raschke, K.D. Park, Nat. Commun. **12**, 1 (2021)
183. K.D. Park, M.A. May, H. Leng, J. Wang, J.A. Kropp, T. Gougousi, M. Pelton, M.B. Raschke, Sci. Adv. **5**, 1 (2019)
184. R.V. Ovali, R. Sahin, A. Bek, M.E. Tasgin, Appl. Phys. Lett. **118** (2021)
185. M. Wagner, Z. Fei, A.S. McLeod, A.S. Rodin, W. Bao, E.G. Iwinski, Z. Zhao, M. Goldflam, M. Liu, G. Dominguez, M. Thiemens, M.M. Fogler, A.H. Castro Neto, C.N. Lau, S. Amarie, F. Keilmann, D.N. Basov, Nanophotonics Lett. **14**, 894 (2014)
186. C. Lienau, M.A. Noginov, M. Lončar, J. Opt. (United Kingdom) **16**, 13 (2014)
187. P. Dombi, Z. Pápa, J. Vogelsang, S.V. Yalunin, M. Sivis, G. Herink, S. Schäfer, P. Groß, C. Ropers, C. Lienau, Rev. Mod. Phys. **92**, 1 (2020)
188. O. Bostanjoglo, R. Elschner, Z. Mao, T. Nink, M. Weingärtner, Ultramicroscopy **81**, 141 (2000)
189. A.H. Zewail, Science **328**, 187 (2010)
190. D.J. Flannigan, A.H. Zewail, Acc. Chem. Res. **45**, 1828 (2012)
191. L. Piazza, D.J. Masiel, T. LaGrange, B.W. Reed, B. Barwick, F. Carbone, Chem. Phys. **423**, 79 (2013)
192. T. LaGrange, B.W. Reed, M.K. Santala, J.T. McKeown, A. Kulovits, J.M.K. Wiezorek, L. Nikolova, F. Rosei, B.J. Siwick, G.H. Campbell, Micron **43**, 1108 (2012)
193. W.A. Curtis, D.J. Flannigan, Phys. Chem. Chem. Phys. **23**, 23544 (2021)

Chapter 8
Probing Light by Matter: Implications of Complex Illumination on Ultrafast Nanostructuring

Camilo Florian, Xiaohan Du, and Craig B. Arnold

Abstract Pushing the limits of precision and reproducibility in ultrafast laser-based nanostructuring requires detailed control over the properties of the illumination. Most traditional methods of laser-based manufacturing rely on the simplicity of Gaussian beams for their well-understood propagation behavior and ease of generation. However, a variety of benefits can be obtained by moving beyond Gaussian beams to single or multiple tailored beams working toward optimal spatial and temporal control over the beam profiles. In this chapter, we center our attention on methods to generate and manipulate complex light beams and the resulting material interactions that occur in response to irradiations with these non-traditional sources. We begin with a discussion on the main differences between Gaussian and more complex light profiles, describing the mechanisms of phase and spatial control before narrowing the discussion to approaches for spatial structuring associated with materials processing with ultrashort laser pulses. Such structuring can occur in both far-field propagating architectures, considering rapidly varying spatial profiles generated mechanically or optically, as well as near-field, non-propagating beams associated with plasmonic and dielectric systems. This chapter emphasizes some of the unique abilities of complex light to shape materials at the nanoscale from a fundamental perspective while referencing potential applications of such methods.

Keywords Gaussian beam · Top-hat · Annular beams · Vortex beams · Bessel beams · Airy beams · Plasmonic focusing · Dielectric microlenses · Time-dependent structured profiles · Dual-laser beam processing · Dual-laser

---

C. Florian (✉)
Princeton Institute for the Research and Technology of Materials (PRISM), Princeton University, Princeton, NJ, USA
e-mail: camilofb1@gmail.com

X. Du · C. B. Arnold
Princeton Institute for the Research and Technology of Materials (PRISM), Princeton University, Princeton, NJ, USA

Mechanical and Aerospace Engineering (MAE), Princeton University, Princeton, NJ, USA
e-mail: xiaohand@princeton.edu; cbarnold@princeton.edu

© The Author(s), under exclusive license to Springer Nature Switzerland AG 2023

R. Stoian, J. Bonse (eds.), *Ultrafast Laser Nanostructuring*, Springer Series in Optical Sciences 239, https://doi.org/10.1007/978-3-031-14752-4_8

additive manufacturing · Direct laser-interference patterning · Laser-induced forward transfer · Resonant focal scanning · TAG lens

1 Introduction: Traditional Illumination Versus Spatially Structured Light

The Gaussian Beam

The most commonly used laser beam shape for many micromachining applications is the Gaussian distribution. It is not a surprise since the vast majority of laser cavities are designed to operate at or near the fundamental transverse electromagnetic mode (TEM00) which corresponds to a Gaussian. One clear advantage from the mathematical standpoint is that its Fourier transform is also Gaussian, meaning that it is possible to keep a Gaussian distribution even after the beam passes through focusing elements such as lenses and objectives. Therefore, its implementation in laser processing systems can be done in most cases without the need for beam shaping techniques [15]. With regard to materials processing applications, there are three general parameters that are considered important due to their influence on the final features imprinted by the laser radiation. The first one, known as the *confocal parameter*, is the distance range along the propagation axis where the energy can be confined. The second, the *beam divergence*, depends on how the beam changes along the propagation axis. Finally, it is important to know the *minimum spot size* where the energy can be localized. For obvious reasons, when micro- or nano-machining is desired, these beam dimensions play an important role in the final modification that is ultimately achievable in the irradiated material. These parameters can be deduced from the mathematical expression that describes an electric field propagating along the Z axis ($E(r,z)$) of a linearly polarized Gaussian beam distribution in the Z direction as shown in Eq. (8.1) [66]:

$$E\left(r,z\right)=E_0\frac{w_0}{w(z)}\exp\left(\frac{-r^2}{w(z)^2}\right)\exp\left[-i\left(kz+k\frac{r^2}{2R(z)}-\varphi(z)\right)\right], \tag{8.1}$$

where z is the position on the propagation Z axis, w_0 is the waist radius, i is the unit imaginary number, r is the radial distance from the center (Eq. 8.2), and k is the wave number (Eq. 8.3).

$$r=\sqrt{x^2+y^2}, \tag{8.2}$$

$$k=\frac{2\pi}{\lambda}. \tag{8.3}$$

The beam radius along the axis propagation, $w(z)$ can be expressed as a function of a parameter known as Rayleigh length:

$$w(z) = w_0 \sqrt{1 + \left(\frac{z}{z_r}\right)^2}. \tag{8.4}$$

The Rayleigh length is the distance from the position of the minimum beam waist, w_0, along the propagation axis until which the cross-section of the beam doubles, or the beam radius increases by a factor $\sqrt{2}$:

$$z_R = \frac{\pi {w_0}^2}{\lambda}. \tag{8.5}$$

The *confocal parameter* is defined as two times the Rayleigh length, $2z_R$, and is usually used to indicate the spatial range along the propagation axis where the energy can be confined.

The radius of curvature of the wave front for distances larger than the Rayleigh length (in the far-field region) is defined as

$$R(z) = z\left[1 + \left(\frac{z_R}{z}\right)^2\right]. \tag{8.6}$$

Finally, an additional phase shift that occurs when a Gaussian beam is being focused is known as the Gouy phase, and it can be described as

$$\varphi(z) = \tan^{-1}\left(\frac{z}{z_R}\right). \tag{8.7}$$

When the beam propagates from the focal plane further than the Rayleigh length (Eq. 8.5), i.e., in the far-field, a non-ideal Gaussian beam expands laterally far from the beam waist. The resulting angle difference measured from the position of the minimum beam waist, w_0, is known as the *beam divergence angle* θ. In the case of Gaussian beams, the beam quality factor M^2 allows us to describe how far from an ideal Gaussian distribution a real laser beam is when it propagates to infinity. For ideal diffraction-limited Gaussian beams, $M^2 = 1$, while for real beams, $M^2 > 1$.

$$M^2 = \frac{\pi w_0 \theta}{\lambda}, \tag{8.8}$$

$$\theta = \frac{M^2 \lambda}{\pi w_0}. \tag{8.9}$$

Gaussian beams are characterized by having low divergence, which allows focusing the energy from these beams in very small volumes. A good approximation for the *minimum spot size*, d_{f}, that it is possible to achieve with a Gaussian beam that is being focused through a focusing lens with numerical aperture NA, can be expressed as

$$d_{\mathrm{f}} \approx 2\frac{\lambda M^2}{\pi NA}. \tag{8.10}$$

Traditionally, the corresponding intensity distribution $I(r, z)$ for Gaussian beams is given by Eq. (8.11) of the modulus squared of the electromagnetic field (Eq. 8.1) with the impedance of the medium in which the field is propagating η (for propagation in vacuum $\eta = \eta_0 \approx 377\ \Omega$). A plot of the intensity profile corresponding to a Gaussian beam is included in Table 8.1 at the end of Sect. 2.

$$I\,(r, z) = \frac{|E\,(r, z)|^2}{2\eta}. \tag{8.11}$$

Implications for Materials Processing

The modification of materials with high spatial resolution typically requires high effective numerical aperture systems to confine a Gaussian beam into the smallest possible voxel. For example, light from an infrared laser of wavelength 1027 nm with Gaussian distribution and beam quality factor $M^2 = 1.1$, focused through a lens system with NA = 0.55 (commonly found in 50× microscope objectives), is axially confined to around 6 µm (Eq. 8.5) and laterally to 1.43 µm (Eq. 8.10). When the irradiation is done at the surface level of a static sample, the resulting material modification will follow a crater-like morphology. For modifications in bulk, such as in the particular case of transparent materials, it is actually possible to produce a modification whose geometry will closely follow the voxel dimensions.[1] Figure 8.1 shows the different ablated morphologies created by a single shot of femtosecond laser for surface and bulk modification over a sample of polymethyl methacrylate (PMMA). When the voxel of the focused beam is located close to the surface, only a superficial crater-like modification is produced. However, when the voxel is located slightly beneath the surface, the irradiation produces a modification in the bulk of the material following the dimensions and shape of the focused beam voxel.

From an application point of view, it will be possible to modify a material with a focused Gaussian beam as far as the material surface is located within the focused voxel location, and the intensity there is adequate to modify it. Nevertheless, this is not always the case, especially for non-flat surfaces with high roughness, which are abundant in many materials processing industrial applications. The challenge

---

[1] The resulting modification size and shape will be strongly influenced by the light-matter interaction.

Table 8.1 Intensity distributions and propagation along the Z-axis of the different beam distributions of Sect. 2

Description	Intensity distributions	Propagation
Gaussian: Intensity peak located at the center from where the intensity decreases radially	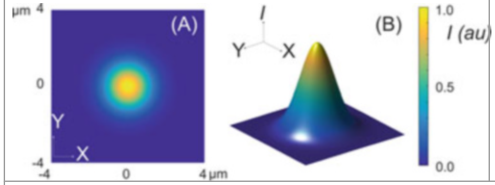	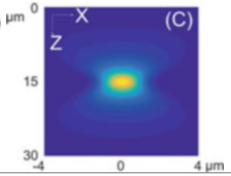
	The minimum modified feature is achieved laterally and axially only when the beam's high-intensity location matches the position of interest. Oftentimes, positioning is challenging, especially with high NA optics	
Annular-vortex: High-intensity region that follows a doughnut shape with an intensity minimum at the geometric center. It could be produced by intensity distribution changes of light phase modifications	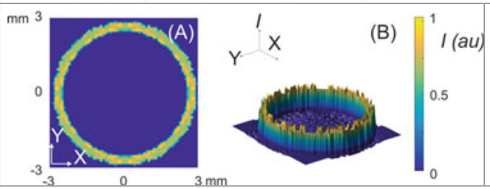	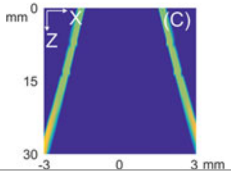
	The modification in the material follows a ring shape. Contrary to Gaussian beams, the material will not exhibit modifications at the central region of the irradiated area. The beam propagation in this case depends on the way it was generated. In this particular case, the beam generation followed the optical system showed in Fig. 8.3	

(continued)

Table 8.1 (continued)

Description	Intensity distributions	Propagation
Bessel: High-intensity central lobe surrounded by concentric rings with less intensity. Propagation could be several micrometers while keeping a rather constant intensity distribution	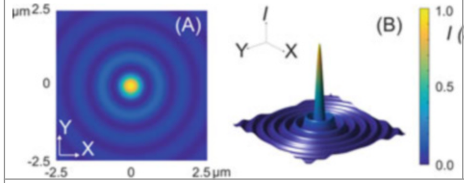	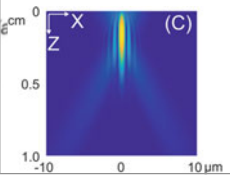
	The modification occurs over longer axial ranges compared to conventional processing with Gaussian beams. Depending on the energy used and the material bandgap, it would be possible to produce modifications only with the central lobe	
Airy: Intensity peak follows a curved trajectory along the propagation axis. Similarly, as with Bessel beams, propagation could range several millimeters	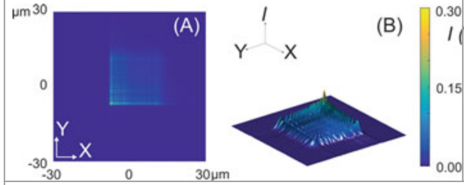	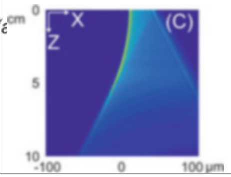
	Contrary to Bessel beams, materials modified with this distribution will show curved modifications along the propagation direction. It provides longer axial ranges for processing compared to regular Gaussian beams	

The plots for each beam intensity distribution are simulations of (A) the top view of the XY plane, (B) 3D representation, and (C) XZ projection showing the propagation along the Z axis. Images credits, Camilo Florian

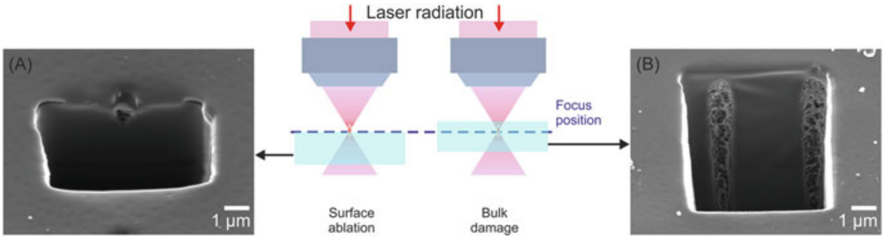

Fig. 8.1 SEM images of laser irradiations from a single femtosecond laser pulse (1027 nm, 450 fs) focused through a NA = 0.55 microscope objective (**a**) at the surface and (**b**) slightly beneath the surface of a sample of poly-methyl methacrylate (PMMA). A focused ion beam was used to selectively ablate material to show the axial extend of the beam modification. The images were acquired with an incident angle of 45° to visualize the walls of the FIB-ablated area. (Florian et al. [22], Copyright (2015), with permission from Elsevier)

here is maintaining an accurate alignment between the material of interest and the location of the focused voxel. Although this could be solved by using high-accuracy positioning stages, they could considerably increase the overall production costs and extend the processing times. For this reason, modifications on the laser beam intensity and propagation constitute robust alternatives to extend the advantages of traditional Gaussian sources.

Structured Light: Beyond Gaussian Beams
Among the different variations that could be performed over a beam of light to increase the efficiency toward the micro- and nanofabrication of materials, we could classify the most widespread methods into two groups: (i) techniques that rely on spatial intensity distribution changes only (in far and near-field configurations) and (ii) time-dependent structured profiles that could modify the beam intensity distribution, its propagation, and/or its interaction with matter.

In the first group, the objective is to *spatially modify the shape of the intensity profile* to meet the conditions for the final processing requirements. A good example widely used in materials processing applications is the *top-hat beam* [62]. Its formation comes from a simple modification to a Gaussian beam where the final spatial distribution forms a homogeneous intensity plateau at the center. This plateau can modify materials, producing well-defined modification sizes, shapes, and depths, while at the same time being practically independent of the laser energy used. It is particularly convenient when different material thicknesses need to be processed while maintaining the same modification dimensions. We will discuss different spatial beam shapes in the far-field in Sect. 2 and near-field configurations in Sect. 3 that offer advantages over Gaussian beams in terms of higher spatial resolution features or longer fabrication axial ranges.

In the second group, the *time-dependent structured profiles* consist of a rapid modification to the beam intensity profile, its propagation, or its interaction dynamics with matter. As an example of these profiles, the use of a tunable acoustic gradient of index (TAG) lens in a regular direct-laser writing system can induce rapidly varying intensity profiles over extended axial ranges, providing axially longer working distances compared with traditionally focused Gaussian beams at operational oscillation frequencies over ~140 KHz [14]. The rapidly changing properties of the beam in time enables the use of these types of complex beams in advanced materials processing applications, as we will develop further in Sect. 4. Finally, this chapter will close by providing an overview of the presented beam-shaping techniques and their standpoints for the machining of materials toward the pursuit of extremely small scales.

2 Far-Field Approaches

2.1 Top-Hat Beams

One method for the generation of a top-hat intensity distribution is the use of a diffractive mask placed in the propagation path of a Gaussian beam to form an Airy pattern that will be subsequently focused through a lens [62]. The distribution at the focal plane corresponds to a circular beam with a homogeneous intensity area forming a plateau. Contrary to a Gaussian beam distribution, the edges of this intensity distribution are sharp, forming the characteristic hat shape as it is illustrated in Fig. 8.2. In comparison with Gaussian beams, the quality factor M^2 is usually over 10, which does not enable tight focusing or axial confinement (Eqs. 8.5 and 8.10). Despite that, the advantages that can be retrieved from the homogeneous intensity plateau in materials processing applications could be exploited for laser cutting [62], laser annealing [51], and pulsed laser deposition [10], to name a few. Also, this beam distribution is useful for several imaging applications, since the homogeneous intensity area can illuminate a specific area of interest homogeneously [61]. Regarding the final modification of materials with this type of beam, Fig. 8.2 includes a comparison that shows the typical formation of a crater-like modification from a Gaussian beam and the squared well-like modification from a top-hat distribution.

2.2 Annular and Vortex Beams

Gaussian beams could also be modified to form *annular beam distributions* that correspond to doughnut-shaped intensity profiles in which the intensity peak is arranged in a shape of a ring with a minimum at the center. Similarly, as for the production of a top-hat beam, when an Airy pattern is focused through a focusing lens, at positions before the focal plane, an annular intensity distribution can be formed, as illustrated in Fig. 8.2 [54]. Commonly, applications for annular beams can be found in illumination systems, since it is possible to induce changes over

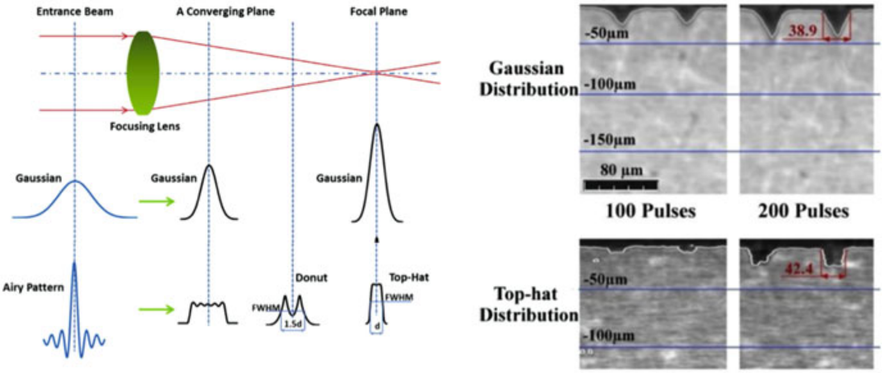
Entrance Beam
A Converging Plane
Focal Plane
Focusing Lens
Gaussian
Gaussian
Gaussian
Airy Pattern
Donut
FWHM
1.5d
Top-Hat
FWHM
d
Gaussian Distribution
-50µm
38.9
-100µm
-150µm
80 µm
100 Pulses
200 Pulses
Top-hat Distribution
-50µm
42.4
-100µm

Fig. 8.2 Gaussian and Airy patterns focused through a regular lens, producing Gaussian and top-hat intensity distributions, respectively, at the focal plane. On the right, a side view optical image shows the corresponding material ablation on a sample of silicon nitride, after the irradiation with 100 and 200 pulses. It can be seen how in the case of the top-hat profile, the ablation follows the squared beam shape in comparison with the Gaussian counterpart. (Reprinted from Nasrollahi et al. [54], Copyright (2020), with permission from Elsevier)

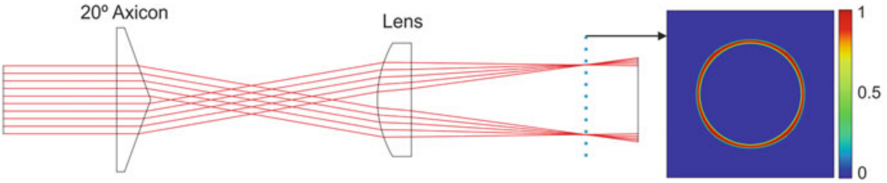
20° Axicon
Lens
1
0.5
0

Fig. 8.3 Optical ray tracing for a system with an axicon combined with a focusing lens. An annular beam is formed at the lens focal plane. The normalized intensity distribution at this position is plotted in false colors at the right. (Images credits, Camilo Florian)

a ring-shaped region while keeping the center unaffected. This effect is exploited in the super-resolution microscopy technique STED [35]. For material processing, the machining application should require the fabrication of ring-like modifications like the one shown in Fig. 8.3. An example can be found in the propelling of materials induced by blister-assisted laser-induced forward transfer (BA-LIFT) [71, 74]. In that particular case, the generation of a ring-like modification at the interface between a polymer layer and a transparent substrate generates a protrusion that propels the liquid forward over longer-than-usual distances without compromising the spatial resolution of the transferred material.

On a similar trend, a *vortex beam* can also produce the same doughnut-shaped intensity. However, its origin extends more than regular intensity distribution changes. In this case, it is the light phase that is customized to change along the beam propagation direction, following a twisted phase trajectory that results in the cancellation of certain light waves, producing a region with zero intensity at the center, as it can be seen in Fig. 8.4 [68]. Experimentally, it can be produced

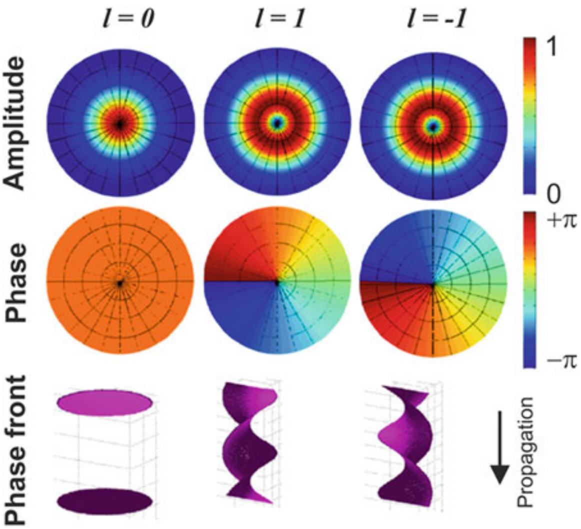

Fig. 8.4 Examples of Laguerre-Gauss modes and superpositions of opposite-sign modes *l*. First row: amplitude distributions of the electric field. Second row: phase distributions. Third row: shape of the phase front as it propagates. (Reprinted from Spinello et al. [68], Copyright (2016), with permission from Elsevier)

with a Gaussian beam passing through an optical device that modifies its phase, changing its effective intensity distribution [80]. Different methods can be used for the creation of such beams, requiring in some cases additional optical elements such as phase plates [32], q-plates [2, 55], spatial light modulators [1], deformable mirrors [29], birefringent liquid crystals [27] and s-plates [73], or by using different oscillation modes generated inside a laser cavity.

From the point of view of the spatial intensity distributions, annular beams and these particular vortex beams with a doughnut shape can be equivalent. The radical difference could be found when the polarization of the vortex beam is modified, in which case the beam is known as a vector-vortex beam. When a material interaction is triggered by certain polarization from the vortex beam, the interaction from an annular beam compared with a polarized vortex beam results to be substantially different, as it is illustrated with two irradiation examples in Fig. 8.5. In this figure, the modification with a regular annular beam produced a ring-shaped modification that is not modified in the center, where the intensity minimum is located. In contrast, the modification with a vector-vortex beam could induce the formation of superficial structures in the irradiated area, whose orientation depends on the local polarization of the beam. In this particular case, the vector-vortex beam has azimuthal polarization, producing concentric micrometric ring-like structures perpendicular to the polarization. Vortex beams have been extensively used in a wide variety of applications [65], including the generation of optical traps [26, 30] and the laser processing of materials for biomimetic applications [67].

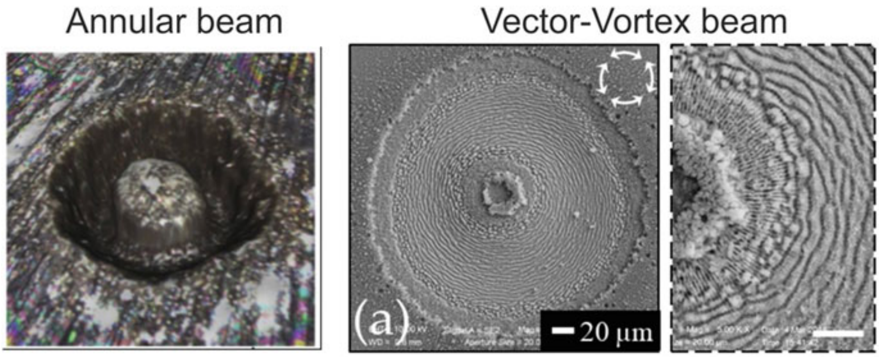

Fig. 8.5 On the left, an optical image from the irradiation of a silicon nitride sample with an annular beam distribution, produced at a position before the focal plane of an optical system that focalizes an Airy pattern, as illustrated in Fig. 8.2. (Reprinted from Nasrollahi et al. [54], Copyright (2020), with permission from Elsevier). On the right, an SEM micrograph shows the modification on a silicon sample using a vector-vortex beam with azimuthal polarization as indicated by the white arrows. The fabricated microstructures are defined by the polarization direction. (Image adapted with permission from Nivas and Amoruso [56] under Copyright license CC BY 4.0)

2.3 Non-diffractive Bessel and Airy Beams

Certain complex beams are known to be non-diffractive or quasi non-diffractive, resulting in an ability to reconstruct around obstacles and maintain a focused intensity distribution over long axial distances. However, in reality, non-diffractive beams experience some degree of diffraction due to the finite optics size and beam energy, but their experimental equivalent still offers their characteristic advantages in terms of extended confocal parameters.

Among the non-diffractive beams, the *Bessel beam distribution* exhibits a high-intensity central peak surrounded by less intense concentric rings. Depending on the way these beams are generated, the axial region where the intensity distribution remains approximately constant could range from microns up to several millimeters depending on the optical configuration. Modifications achieved by this type of beam are found primarily in laser-cutting and laser-marking applications, where it is possible to process millimeter-thick substrates with only one single laser pulse [16].

For this particular beam distribution, the electric field follows the zeroth-order Bessel function of the first kind J_0. This description corresponds to a high-intensity central peak that is the product of a superposition of plane waves with wave vectors forming a cone around the propagation axis that can be exploited for materials processing over large axial distances [11]. Experimentally, the equation that describes such beams where $r^2 = x^2 + y^2$ represents the radial distance from the center and $k^2 = {k_\mathrm{z}}^2 + {k_\mathrm{r}}^2$ is the wave vector is given by

$$E\left(r, t\right) = A_0 \exp\left(ik_\mathrm{z}z\right) J_0\left(k_\mathrm{r}r\right). \tag{8.12}$$

An approximation of a Bessel beam distribution can be produced experimentally using a Gaussian beam in combination with an aperture [18], an axicon [57, 70], a digitally controlled refractive device [5], and tunable acoustic gradient (TAG) lenses [48], or other methods [15]. Perhaps, the most cost-efficient way to generate a Bessel beam distribution is by using an axicon. However, it requires delicate alignment in order to avoid distortions. Table 8.1 displays the plots of a Bessel distribution using a wedge axicon angle $\alpha = 2°$ that corresponds at the same time to the angle between the z and r components of the wave vector k [24].

Similarly, useful parameters for material processing applications in the case of Bessel beam distributions are the Rayleigh length z_R and the diameter of the central lobe d_f [47]:

$$z_\mathrm{R} \approx \frac{D}{2\,(n-1)\tan(\alpha)}, \tag{8.13}$$

$$d_\mathrm{f} \approx \frac{2.405\alpha}{k\,(n-1)\tan(\alpha)}. \tag{8.14}$$

n is the refractive index of the axicon material, and D is the diameter of the beam entering the axicon. It is important to note here that in the case of Bessel beams generated with an axicon, both the Rayleigh length and the minimum size of the central lobe depend strongly on the axicon wedge angle. Also, when compared with the values that are possible to reach with a Gaussian beam, the Rayleigh length, in this case, is several orders of magnitude longer, while keeping a rather constant and small central lobe diameter. This characteristic is exploited in materials processing applications that require elongated energy volumes in the axial direction for the control of particles in optical trapping systems [30, 50] or the ablation of thick substrates with a single laser pulse [11, 34]. Figure 8.6 contains an SEM image from a transversal cut on an irradiated silicon sample where a conventional Bessel beam was used. In this case, it is possible to see the modification from the main Bessel beam lobe, as well as the three first surrounding annular rings that propagate vertically downward. For comparison with a regular Gaussian beam, the intensity profile and propagation of a Bessel beam are included in Table 8.1.

Another example of a non-diffractive beam is the *Airy beam distributions*. Here, the beam appears to be following a curved path along the propagation axis. In this case, the intensity maxima transversely "accelerate" during their propagation, resulting in a curved trajectory. The intensity distribution of an Airy beam consists of a main lobe that holds the intensity peak preceded by a series of adjacent and gradually less intense peaks that propagate without diffraction. Normally, if there are no changes in the refractive index of the propagating medium, the intensity centroid of an optical beam should move in a straight line [19]. This particular property of Airy beams allows the beam to propagate around physical obstacles and reconstruct the intensity distribution at later axial positions. For this reason, Airy beams are

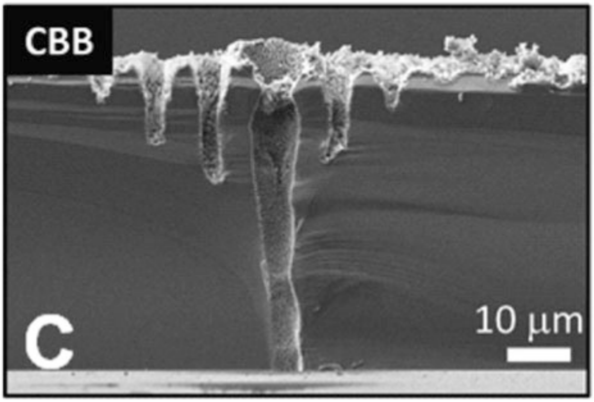

Fig. 8.6 Material modification with a conventional Bessel beam "CBB" on a silicon substrate. (Image adapted with permission from He et al. [34] under Copyright license CC BY)

often called self-healing beams. This property can be exploited for light propagation in turbulent media without compromising the final beam intensity distribution.

An example of an Airy beam generated by using a Gaussian beam ($w_0 = 3$ mm) passing through a cubic phase mask is displayed in Table 8.1, which includes the intensity distributions at the XY plane and its propagation along the Z axis. It is important to note that the intensity maxima exhibit a curved trajectory and its length is significatively larger than its Gaussian or Bessel counterparts. In this case, the beam propagation is plotted over a distance of 10 cm. In the particular case of materials processing, it is important to note that significant energy losses are present, especially when compared with the incoming Gaussian laser beam, which makes the use of this type of beam for limited materials processing applications, including the modification of glass [28] and diamond [46] to name a few. A transverse view of a sample irradiated with an Airy beam after one, two, and five passes over a silicon sample is shown in Fig. 8.7. The resulting material modification follows the distribution of the beam intensity maxima, which curves along the propagation axis, consequently modifying the material following a curve.

Other applications for this type of beam can be found in telecommunications [83], optical trapping systems [82], and imaging techniques [33], to name a few. A complete set of applications on materials micromachining of materials with Bessel and Airy beams could be found in Chap. 16.

2.4 Holography Approaches

All the previously mentioned intensity distributions can be achieved by holographic approaches. Here, an initial beam, usually with a Gaussian distribution, interacts with a mask or, more commonly, a digital optical device such as a spatial light

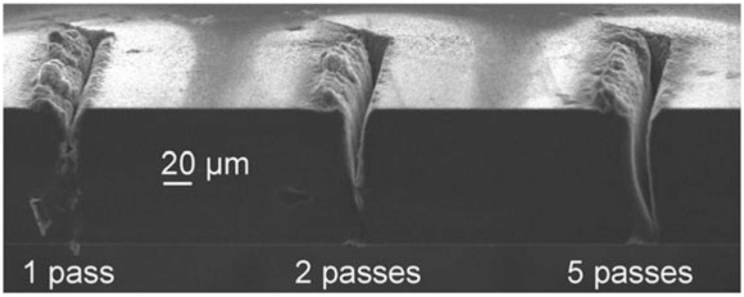

Fig. 8.7 Evolution with the number of passes of the produced machining of curved trenches in silicon using accelerating Airy beams. (Reprinted from Mathis et al. [46], with the permission of AIP Publishing)

modulator or a digital micromirror array [25] for a user-defined change of its amplitude and/or phase. The general idea is the generation of additional wavefronts that will ultimately interfere at a certain plane along the propagation axis, generating an interference pattern that will contain the desired beam distribution. The implementation of computer-controlled digital devices allows for flexibility in the creation of intensity distributions, enabling the creation of complex forms, as can be seen in Fig. 8.8, where spatially structured beams suitable for marking the surface of a material were generated using a spatial light modulator [43, 84]. In short, this flexibility allows holographic approaches to create virtually any beam distribution. However, there are some limitations in terms of the maximum energy available after the beam shaping process as well as considerations for the damage threshold for the holographic-generating device. Despite this, the use of holographic approaches for materials processing is sometimes desired, because with these methods, it is possible to create multiple laser beams that can be used for parallelized processing, increasing the overall processing speed [12, 45].

3 Near-Field Approaches

Near-field optics describes and exploits light-matter interactions at a nanometer scale, where the optical field is evanescent rather than propagating. Thus, it is not subject to the classical diffraction limit, allowing outstanding spatial resolution and enhanced intensity that can be used in applications for plasmonics, microscopy, nano-photonics, and nano-fabrication. In general, any monochromatic light can be represented by an electric field $E(r)$ with spatially dependent amplitude $A(r)$ and phase $\phi(r)$ of the vector components of the field, following Eq. (8.15):

$$E(r) = A(r)\mathrm{e}^{i\phi(r)} = \int_{-\infty}^{\infty} E_{\mathrm{k}}\mathrm{e}^{ik.r}dk, \tag{8.15}$$

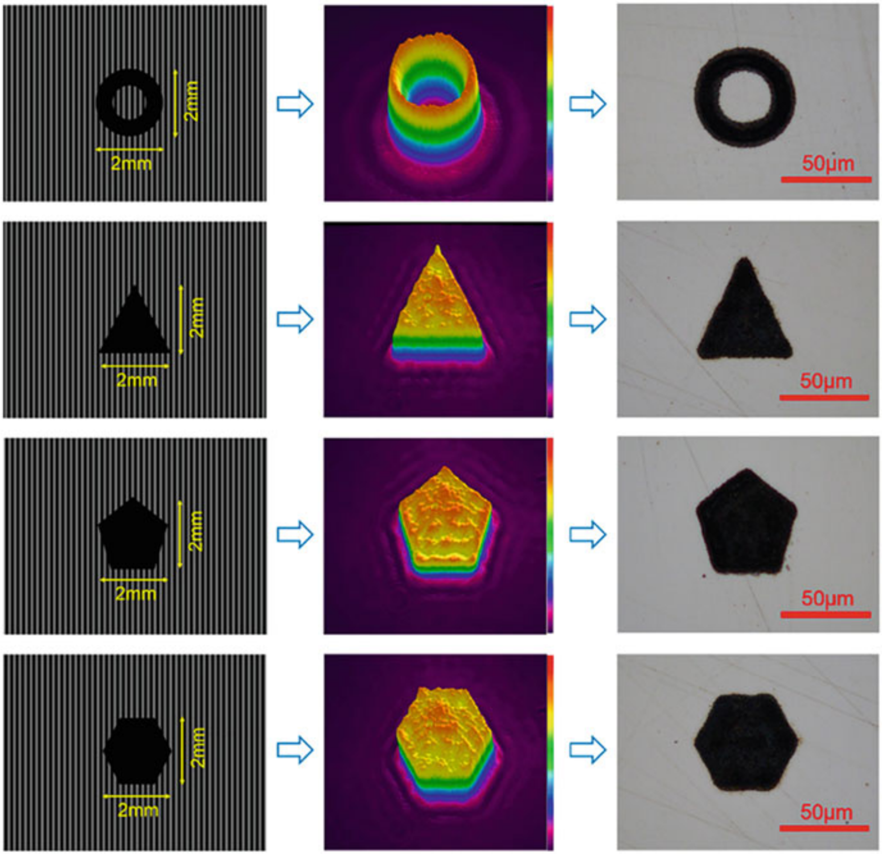

Fig. 8.8 Spatially structured beams formed from different mask spatial distributions by the incidence of a Gaussian beam on a spatial light modulator (left) with the corresponding image of the beam on a CCD camera (center) and the corresponding modification on the surface of a stainless-steel polished sample. (Reprinted from Liu et al. [43], Copyright (2018), with permission from Elsevier)

where r represents the spatial position and E_k is the complex amplitude of the wavevector k:

$$k = \frac{2\pi n}{\lambda} = \sqrt{k_x^2 + k_y^2 + k_z^2}. \tag{8.16}$$

The real part of the refractive index is represented by n and the light wavelength by λ. The Z component of the wavevector has a non-zero imaginary component when $k_x^2 + k_y^2 > k_0$, and therefore, any imaginary components in Eq. (8.15) will have an exponentially decaying amplitude with an increase in distance. The near-field that is localized within less than a wavelength distance from the surface of interest evolves toward propagating far-field radiation that contains information from the material at the surface, with resolutions below the diffraction-limited maximum resolution of the far-field [4].

In this subsection, we briefly review two well-established techniques to manipulate the near-field in the nanoscale, including plasmonic approaches such as scanning near-field optical microscopy (SNOM) probes and dielectric-based approaches such as the use of optically trapped dielectric microspheres. Additional details will be presented in Chap. 11.

3.1 Plasmonic-Based Approach: SNOM Probes

In scanning near-field optical microscopy (SNOM), the generation of near-field light can take place by using two different sets of methods. The first general set is aperture-based approaches that consist in the use of a probe with an aperture whose size is smaller than the laser wavelength used to illuminate the sample. Here the near-field radiation is scattered back to be detected as far-field radiation following a configuration as the one shown in Fig. 8.9a. A second general set of methods consists in aperture-less approaches, where the near-field light is emitted from the surface due to external illumination that is scattered off of a sharp tip to be detected likewise in the far-field [4]. The use of the same principle as the one for imaging structures with nanometer resolution, but for the modification of materials, has been demonstrated with different photosensitive materials, polymers, metals, and semiconductors, to name a few [60]. Here, when the near-field enhancement overcomes the required ablation fluence for a given material, it is possible to produce permanent modifications with nanometer resolution and high reproducibility. Figure 8.9a shows a system that incorporates an *SNOM aperture-based probe* to generate the near-field radiation over a photosensitive polymer material. The modifications produced are included in Fig. 8.9b, where a set of craters were characterized via AFM. From the topography data, profiles that reveal the depth of the modifications are extracted along the line of craters, showing modifications of ~500 nm in diameter and ~75 nm in depth.

Additional methods to shape light in the near-field can profit from plasmonic interaction based on the use of different geometries of antennas, in which the near-field enhancement is larger compared to values reached with circular geometry probes. Among these configurations, there are several approaches based on *plasmonic lensing structures* initially designed for imaging applications that consist in concentric ring gratings with defined refractive indexes for the detection of the near-field at the vicinity of the structures of interest offering nanometer resolutions [6, 20]. For material processing, due to the extremely small cavity sizes of plasmonic lenses, the intensity enhancement could be up to 100 times higher than the laser radiation impinging on the structures. When the appropriate system is used, the energy could be focused in the near-field to spots smaller than 100 nm [69].

Alternatively, *bow-tie antennas* are widely employed in plasmonic structures for material processing. When combined with femtosecond laser pulses, they generate

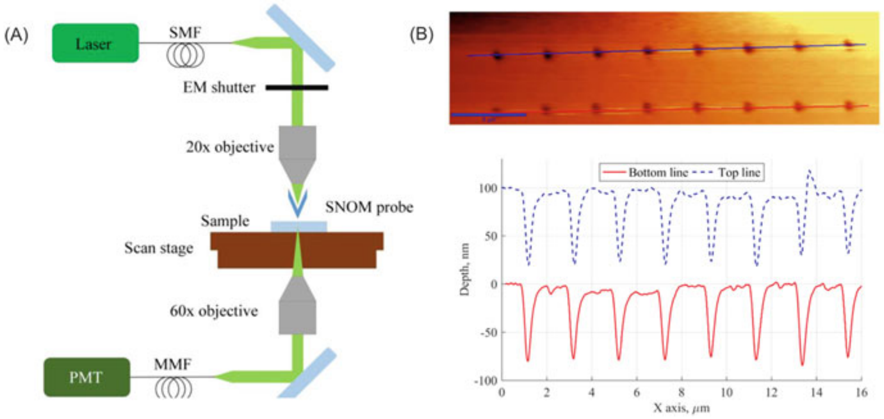
(A)
Laser
SMF
EM shutter
20x objective
SNOM probe
Sample
Scan stage
60x objective
PMT
MMF
(B)
Bottom line
Top line
Depth, nm
100
50
0
-50
-100
0
2
4
6
8
10
12
14
16
X axis, μm

Fig. 8.9 (**a**) Schematic representation of the SNOM experimental setup. (**b**) AFM topography data of the irradiation experiments performed on a photoresist deposited on quartz, including a cross-sectional profile along the marked blue and red lines. (Image adapted with permission from Roszkiewicz et al. [60] under Copyright license CC by 4.0)

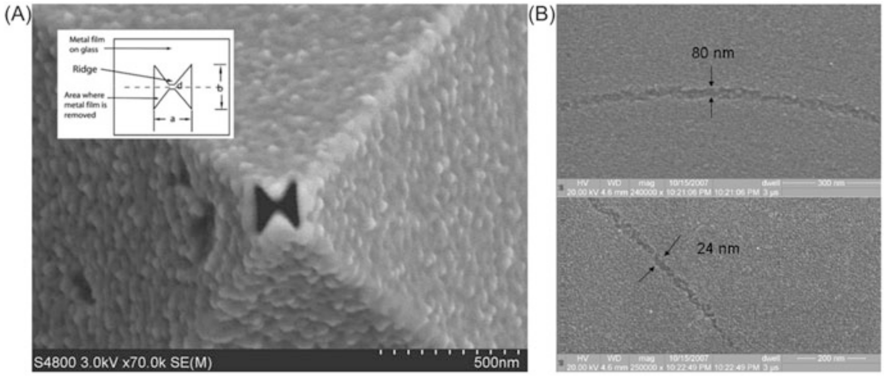
(A)
Metal film on glass
Ridge
Area where metal film is removed
a
b
d
S4800 3.0kV x70.0k SE(M)
500nm
(B)
80 nm
24 nm

Fig. 8.10 (**a**) SEM image of a bow-tie aperture on an AFM probe with an inset of idealized geometry. (**b**) SEM of circle pattern showing top and side sections of a circle. (Reproduced from the Open Access paper Murphy-dubay et al. [52], ©2008 Optical Society of America)

highly confined intensity peak distributions suitable for nanopatterning applications. The advantage is attributed to a field concentration in the gap between the ridges of the antenna. Figure 8.10 includes SEM micrographs that display the bow-tie antenna fabricated on the tip of an AFM cantilever. This particular system was used in the femtosecond-based nanopatterning of a positive photoresist Shipley (S1805) with features as small as 24 nm in width, following at the same time a curve trajectory (Fig. 8.10b). The enhancement is finally produced by the propagation of the fundamental electric-magnetic field TEM10 mode. Ultimately, the intensity variation is different depending on the geometry of the SNOM probe [31, 38, 39, 52].

3.2 Dielectric-Based Approach: Optical-Trap-Assisted Nanopatterning

One of the first experimental demonstrations on the use of near-field enhancements produced by certain particles was reported during the development of techniques for cleaning semiconductor surfaces with laser light. The idea was to use loosely focused laser beams to generate a catapulting effect to detach particles from the surface of expensive substrates [36]. Unfortunately, for its original application, this catapulting effect led to unwanted substrate permanent nanometric modifications. Later, this idea of exploiting the field enhancements was developed into particle- and tip-assisted nanofabrication techniques in which different and numerous research groups have contributed to the understanding of the interaction of matter with light at these extremely small scales [40, 42, 44, 72, 79].

As a particular example of these techniques, the use of *dielectric microspheres* positioned conveniently near a substrate could exhibit the near-field radiation enhancements for processing materials in the nanoscale [50]. Here, radiation coming from a laser source passing through the microsphere can be focused onto very small focal volumes, enhancing the near-field between the microsphere and the substrate of interest. If the intensity reached is high enough, the material can be permanently modified, exhibiting subwavelength spatial resolution. In this particular case, the dielectric microlens behaves as an aperture that allows the subsequent focusing of light, as it is shown in Fig. 8.11. In this figure, an optically trapped dielectric microsphere in water is used to enhance the near-field radiation in the vicinity of a polyimide film and a silicon substrate. The lateral positioning of the microsphere relative to the irradiated sample is performed by piezo-actuated stages. The axial distance of the microsphere is kept constant as a product of the double-layer repulsive potential between the microsphere and the substrate, as well as an optical force pushing the microsphere toward the substrate [7, 21, 50]. The constant balance between attraction and repulsion preserves the same microsphere-substrate distance at all times without feedback control mechanisms. This is possible due to the nature of the Bessel beam optical trap that allows for a large axial trapping region where the optical force on the microlens is practically constant. Depending on the irradiation conditions, it is possible to produce craters in the material by ablating the material in selected positions (Fig. 8.11d) or to induce material swelling for the formation of nano-cones (Fig. 8.11e).

A summary of the intensity distributions used in the above near-field approaches is arranged in Table 8.2. From here, different approaches based on the use of dielectric objects have emerged for applications in materials processing and imaging [9]. A complete description of available techniques and historic development of applications that use near-field radiation for the modification of materials is included in Chap. 11.

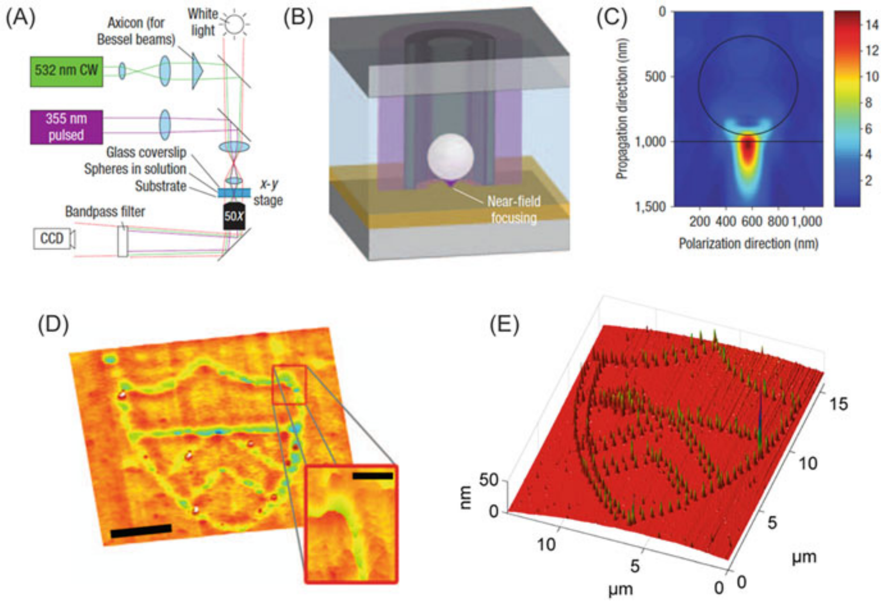
(A)
Axicon (for Bessel beams)
White light
532 nm CW
355 nm pulsed
Glass coverslip
Spheres in solution
Substrate
x-y stage
50X
Bandpass filter
CCD
(B)
Near-field focusing
(C)
Propagation direction (nm)
0
500
1,000
1,500
200 400 600 800 1,000
Polarization direction (nm)
14
12
10
8
6
4
2
(D)
(E)
nm
50
0
10
5
0
μm
15
10
5
0
μm

Fig. 8.11 (**a**) Schematic of the experimental setup including a trapping laser (green) and a processing laser (purple). The white light is used for real-time video acquisition with the 50× objective and the CCD camera. (**b**) Sketch of the irradiation process with an optically trapped sphere near the polyimide surface (orange) in the trapping laser (green). The processing beam (purple) covers an area larger than the microsphere, but it only reaches fluences above the threshold for modification in positions directly beneath the microsphere. (**c**) FDTD simulation of the intensity passing through a 0.76 μm microsphere in water above the polyimide substrate. The plane shown is parallel to the propagation and electric field polarization directions. (**d**) AFM image of a Princeton University logo nanopatterned on the polyimide layer. In this case, a fluence of 3 mJ/cm^2 was used to produce trenches by overlapping consecutive laser pulses. Main scale bar, 2 mm; inset scale bar, 1 mm (**a**–**d**). (Reprinted with permission from McLeod and Arnold [50], Copyright 2008, Springer Nature). (**e**) AFM image of a Princeton University logo made of nano-cones on a silicon sample produced at a fluence of 7.3 mJ/cm^2 with a polystyrene microsphere. (Reprinted with permission from Chen et al. [7], Copyright 2017, Laser Institute of America)

4 Time-Dependent Structured Profiles

In addition to the static structured light approaches discussed in the previous section, there exist ultrafast beam structuring methods that exploit system or material properties that evolve over time. Depending on the specific application, it is possible to induce (i) transient absorption regimes caused by the action of two adequately separated beams in time or space, (ii) interference between two or more laser beams, or (iii) rapid variation of focus produced by an ultrafast varifocal lens, all of which are aimed toward the production of high-spatial-resolution features. In the following subsections, we will discuss how these time-dependent structured profiles can be used in different laser-based processing techniques.

Table 8.2 Intensity distributions and propagation along the Z-axis of the three different beam distributions from Sect. 3

Description	Intensity distributions
SNOM probes: Here, the field enhancement is produced between the material and the probe for distances smaller than the laser wavelength used. The intensity forms a narrow filament in the near-field that disperses in the far-field	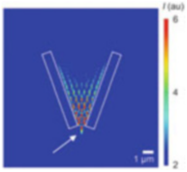 The field enhancement exploited for materials processing is produced by approaching the SNOM probe close to the surface of the material of interest. In that way, the resolution enhancement is combined with an intensity increase that allows the machining of materials with high spatial resolution. The dimensions are considerably smaller than the Gaussian counterparts
Bow-tie antennas: The field enhancement is produced in the tight separation between the triangular structures as a product of plasmon resonances at the structure's surface	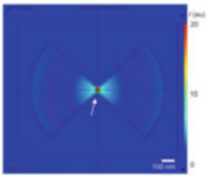 The field enhancement in bow-tie antennas configurations can be used for nanopatterning applications over extended areas when the antenna is mounted in a scanning-compatible device, as shown in Fig. 8.10
Dielectric microsphere: The intensity distribution used for materials processing is formed after the dielectric microsphere. The voxel is known as a photonic nano-jet, due to its small dimensions	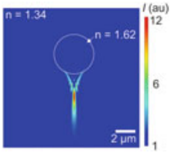 The final intensity distribution dimensions used for materials processing depend on the wavelength used, the refractive index ratio between light propagation media/microsphere and the distance between the microlens surface and the sample of interest

Images credits, Camilo Florian

4.1 Dual-Laser Beam Processing (DLBP) and Dual-Laser Additive Manufacturing (DLAM)

Multiple beams enable us to create material modifications that are not possible to produce with regular single-beam processing. The resulting interaction between more than one beam extends the benefits for different materials processing applications toward higher spatial resolutions either from a subtractive or additive process.

Dual-laser beam processing (*DLBP*) of materials follows a subtractive approach based on the same principle as the super-resolution fluorescence microscopy technique STED [35]. In DLBP, two different laser beams irradiate the sample at the same position, one with Gaussian spatial and temporal distribution and pulse energy above the material's bandgap to promote electrons from the valence band to the conduction band, and a second one with doughnut-shaped spatial profile and Gaussian temporal profile and pulse energy lower than the material's bandgap to promote the depletion of the previously excited electrons back to the valence band, as it is illustrated in Fig. 8.12. Due to the doughnut-shaped spatial distribution, after the depletion process took place, in the central part, unirradiated by this second beam, excited electrons are located in a significatively smaller region. If a third Gaussian pulse reaches the sample when this transient regime is present, the excited electrons in the conduction band can be easily ablated with a wavelength that would otherwise be transmitted by the sample, reducing the final feature size. This induced transient state occurs within the duration of the laser pulses and can be controlled by shifting the pulse delays in a controlled way [77]. It was determined that the best inter-pulse delay for the realization of the smallest features corresponds to $+5$ ns (Fig. 8.12c), since a combination of heat and excited carriers increases absorption for the implemented laser wavelengths.

Additive manufacturing techniques can also take advantage of multiple laser beams to modify and control the material processing. For instance, in laser powder bed fusion, the fabrication of metallic 3D objects is achieved by selectively melting irradiated areas in a bottom-up configuration following a layer-by-layer approach. In order to increase the fabrication speeds in this type of additive manufacturing technique, parallelization using *dual-laser additive manufacturing* (*DLAM*) approaches is often preferred [78]. However, different variables should be considered for a correct application of the approach, including the geometrical distribution of the laser beams with respect to the final fabricated feature and the thermal processes associated with the interaction of different laser beams as heat sources. By controlling these parameters, it is possible to exploit regions of already melted material to modify how the melted pool will cool down and solidify. Following this approach, it is possible to modify and control the thermal evolution of the fusion process and fabricate morphologies and structures that otherwise would be difficult to produce with conventional single-beam powder bed melting approaches [81]. Figure 8.13a shows a schematic layout of the geometry used to create two parallel metallic lines. When the hatch distance between them is reduced,

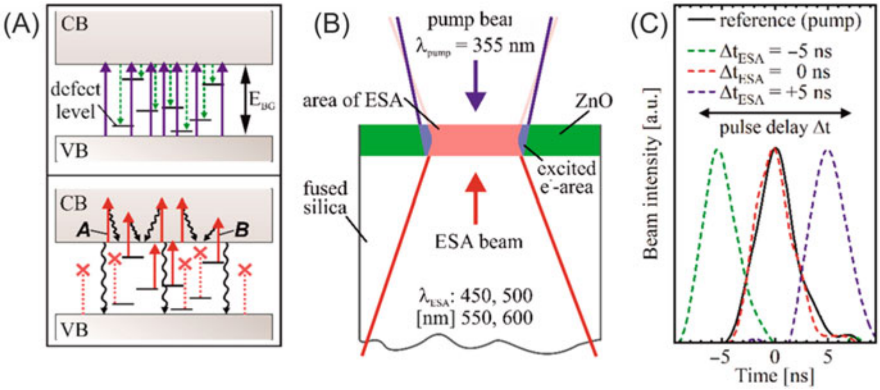
(A)
CB
defect level
E_{BG}
VB
CB
A
B
VB
(B)
pump beam
λ_{pump} = 355 nm
area of ESA
ZnO
fused silica
excited e⁻-area
ESA beam
λ_{ESA}: 450, 500 [nm] 550, 600
(C)
reference (pump)
Δt_{ESA} = −5 ns
Δt_{ESA} = 0 ns
Δt_{ESA} = +5 ns
pulse delay Δt
Beam intensity [a.u.]
−5
0
5
Time [ns]

Fig. 8.12 (**a**) Illustration of the excited state absorption (ESA)-based ablation process. The upper part shows the excitation from the valence band (VB) to the conduction band (CB) and the bottom part shows the ESA in solid arrows. (**b**) Sketch of a 1-mm-thick sample cross-section (white) covered by a thin layer of ZnO (green). The pump beam impinges the sample from the top and the ESA beam from the bottom, as indicated by the arrows. (**c**) Pulse delays (dashed lines) and their temporal overlap with respect to the pump pulse (solid black line). (Image adapted with permission from Wenisch et al. [77] under Copyright license CC by 4.0)

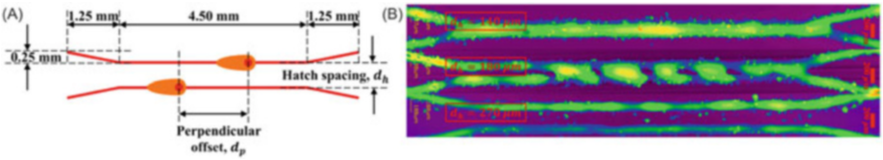
(A)
1.25 mm
4.50 mm
1.25 mm
0.25 mm
Hatch spacing, d_h
Perpendicular offset, d_p
(B)
d_h = 140 μm
d_h = 180 μm
d_h = 270 μm

Fig. 8.13 (**a**) Schematic diagram defining hatch spacing and perpendicular offset in the experiment. The red lines will correspond to lines that protrude~~s~~ from the surface as a product of melting a metallic powder bed. (**b**) Lines with different hatch distances are produced and characterized via laser scanning confocal microscopy. (Reprinted from Zhang et al. [81], Copyright (2020), with permission from Elsevier)

the two lines coalesce into an intermediate reproducible state of periodic structures of melted material, as it can be observed in Fig. 8.13b.

Interestingly, depending on the perpendicular offset, for two identical beams, it is possible to observe two types of material coalescence; for no perpendicular offset, the coalescence follows a heat-to-head fashion, where each individual molten pool interacts with each other forming material bulges with a certain periodicity but no preferential orientation. In the second situation, when the perpendicular offset is increased, the interaction follows a head-to-tail fashion, resulting in a clear orientation of the periodic structures of the molten pools [81].

4.2 Direct Laser-Interference Patterning (DLIP) and Laser-Induced Forward Transfer (LIFT)

When the interaction between more than one beam occurs within a determined spatial region during a short timeframe, it is possible to induce interference between the implicated beams. Similarly, as with dual-laser beam processing approaches, this interference can be exploited for the processing of materials following subtractive and additive modes.

Direct laser-interference patterning (*DLIP*) foundation principles are based in a technique called laser interference lithography (LIL) [63], originally used as a maskless large area photolithography technique for the formation of periodic nanometric-scale patterns. DLIP uses higher-intensity lasers compared to LIL, and it is also a maskless processing technique that exploits the light coherence to induce spatially controlled intensity patterns for the fabrication of micro- and nanometer-scale periodic structures. The process consists in the interference of two or more coherent laser beams on the surface of the material of interest. In such cases, the intensity pattern periodicity depends on the wavelength used and the incident angles of the incoming laser beams. The shape of the resulting pattern can be defined by changing the relative phase between the incident beams, and its intensity can be modulated by the polarization of each participant beam.

The intensity pattern $I(x,y)$ at the surface for two equal beams with top hat intensity is given by Eq. (8.17) [13, 58]:

$$I\left(x,y\right)=2I_0\left[1+\cos\left(\frac{4\pi\sin\theta}{\lambda}x\right)\right], \tag{8.17}$$

where I_0 is the peak intensity of each of the two incident laser beams, λ is the laser wavelength, and θ is the beam's angle of incidence with respect to the surface. For the case of a Gaussian spatial distribution, the intensity pattern is the following:

$$I\left(x,y\right)=4I_0\exp\left[\left[-2\left(\frac{4x^2}{d_x^2}+\frac{4y^2}{d_y^2}\right)\right]\cdot\left[1+\cos\left(\frac{4\pi\sin\theta}{\lambda}x\right)\right]\right]. \tag{8.18}$$

For the interference system, it is also possible to calculate the expected period Λ with Eq. (8.19):

$$\Lambda=\frac{\lambda}{2\sin\left(\frac{\theta}{2}\right)}. \tag{8.19}$$

An example of the calculated and measured intensity patterns is included in Fig. 8.14, where it is also possible to see the ablation on stainless steel using two different pulse energies.

Increasing the number of beams participating in the interference produces more complex intensity patterns; for instance, in planar configurations, three beams can

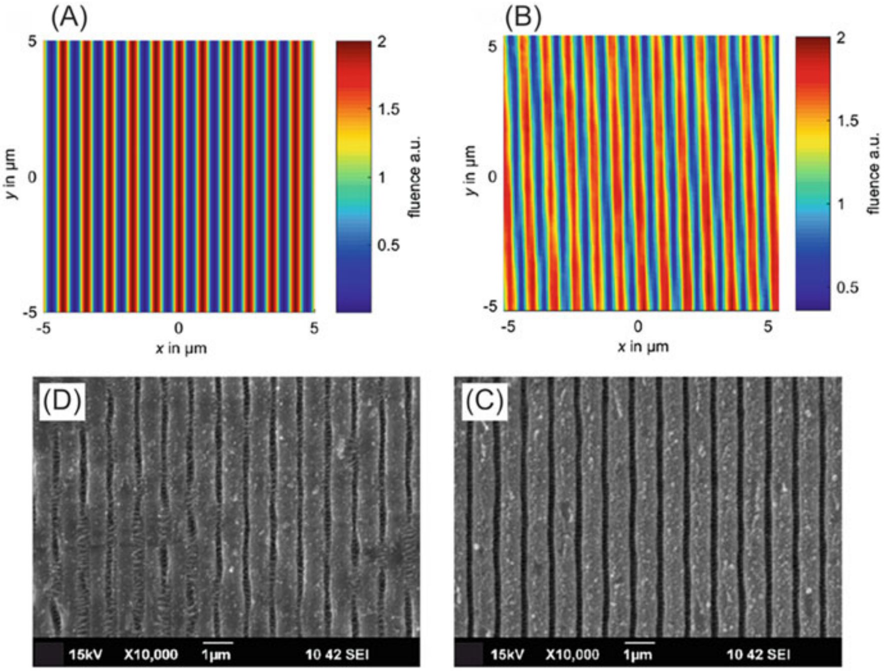

Fig. 8.14 Calculated (**a**) and measured (**b**) intensity patterns at the sample surface. The corresponding irradiations in stainless steel are presented as SEM micrographs in (**c**) for pulse energy $E_\text{p} = 7.2$ µJ and (**d**) for $E_\text{p} = 9$ µJ. (Image adapted with permission from Peter et al. [58] under Copyright license CC by 4.0)

produce a two-dimensional dot pattern, while four beams can be used to produce a line pattern with thinner and higher peaks and thicker areas of low intensity than a two-beam pattern [41, 59]. An example for non-planar beams is included in Fig. 8.15a, producing an intensity pattern that corresponds to multiple spots separated longitudinally by a period Λ. The product of the irradiation on titanium with this intensity profile can be seen in the SEM micrograph of Fig. 8.15b, where multiple spots were irradiated to cover a whole area. When the irradiation takes place with ultrashort-pulsed lasers, the formation of low- and high-spatial-frequency LIPSS (LSFL and HSFL) can also be induced, as shown in Fig. 8.15c. Detail applications for the use of these hierarchical structures will be extensively discussed in Chap. 26.

Printing of materials under a regular *laser-induced forward transfer* (*LIFT*) process occurs when a focused laser beam is irradiated over a material of interest that is often disposed as thin layers (solid, liquid, or intermediate viscosity pastes) [3, 64]. The irradiation leads to a microexplosion that impulses tiny amounts of the material toward a receptor substrate placed conveniently close by. The resulting feature forms one printed pixel per laser pulse with micrometer resolutions [23, 75, 76]. Recently, direct laser-interference patterning (DLIP) was implemented to

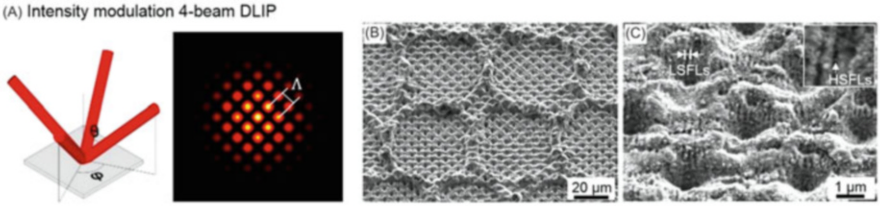

Fig. 8.15 (**a**) Illustration of beams impinging on the sample simultaneously from different angles and the resulting calculated intensity pattern from black (no intensity) to yellow (high intensity). (**b**) Hierarchical surface structure on titanium produced with the intensity pattern shown in (**a**). (**c**) High-magnification image showing also the LIPSS features (LSFLs in the image and HFSLs in the inset). (Image adapted with permission from Zwahr et al. [85] under Copyright license CC by 4.0)

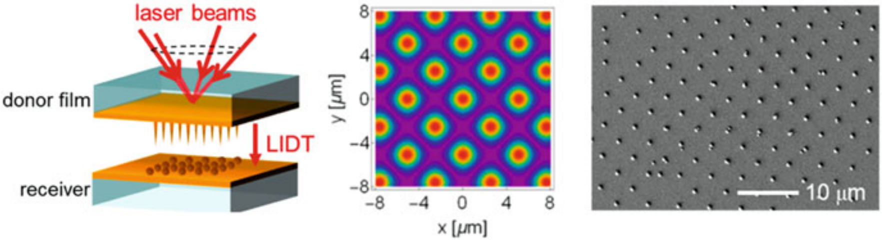

Fig. 8.16 Illustration of the four-beam interference at the interface of the donor substrate and the thin film of the material of interest. The intensity profile corresponds to the simulated intensity at the same position. On the left, a SEM micrograph displays gold pixels symmetrically spaced printed over a receptor substrate. (Image adapted with permission from Nakata et al. [53] under Copyright license CC by 4.0)

generate an intensity pattern distribution corresponding to a matrix of pulses like the one shown in Fig. 8.16. Each individual intensity dot can propel material toward an acceptor substrate while keeping the same spatial distribution even considering the drag resistance under ambient air conditions, as reported in [53]. In this particular case, the propelled material was disposed in thin films of noble metals, including platinum and gold. The resulting printed pixels in the case of the gold donor substrate correspond to pixels in the shape of sub-micron-sized dots that follow the same spatial distribution of the used intensity distribution profile, as shown in Fig. 8.16.

4.3 Resonant Focal Scanning

Another important method of beam control for optimal laser processing is the use of ultrahigh-speed scanning of the focus in order to create a quasi-line focus or other complex beam shape. There are few technologies able to scan at sufficiently high speed [37]. One type of ultrafast variable focus optic is a resonant scanning device

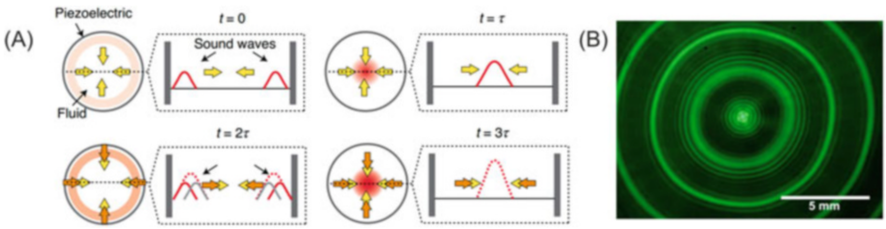

Fig. 8.17 (**a**) Schematic of the model based on considering the TAG as a resonator. Cylindrical waves travel back and forth in the TAG lens, interfering with each other and producing periodic changes in the lens optical power every 2 τ. (Image reproduced with permission from Duocastella and Arnold [16]; permission conveyed through Copyright Clearance Center, Inc). (**b**) Beam distribution measured after 80 cm from the TAG lens using a Gaussian-collimated beam as input beam. The piezoelectric frequency is 299.7 kHz. (Image reproduced with the permission of AIP Publishing from McLeod and Arnold [49])

known as a tunable acoustic gradient of refractive index (TAG) lens. These lenses are optical devices that use acoustic waves inside a liquid to modulate the local density, producing spatially and temporally varying refraction index changes that can be exploited for lensing effects (Fig. 8.17a) [37, 48]. The oscillation frequency is driven by an external voltage source whose amplitude influences the focusing-defocusing power of the lens. Due to the local refractive index changes, the liquid changes the light propagation path as shown in Fig. 8.17b. The frequency of operation of the TAG lens ranges several hundreds of kHz, and the specific working frequencies depend on the geometry of the piezoelectric itself.

The use of this type of lens presents advantages for the processing of materials, since it is possible to dynamically displace the intensity distribution along the beam axis over longer distances compared with regular direct writing systems. Therefore, it is possible to modify samples without the need of sample repositioning [14, 17]. Figure 8.18 shows the intensity distribution for a nanosecond laser-marking system that implements a regular marking system and one that incorporates a TAG lens. The range of positions along the beam axis where the intensity is high enough to produce damage in the sample is larger in the case of the system with a working TAG lens. This allows the marking of the surface of a stepped sample without the need for sample repositioning, as shown in Fig. 8.18c, thanks to the axial scanning performed by the TAG lens.

Another advantage of using a resonant scanning system is an increase of ablation efficiency provided by the rapidly scanning focal position. Conventional direct-laser writing systems used for the ablation of materials usually rely on the use of higher numerical apertures to produce modification with high spatial resolution. The use of higher numerical apertures means that the axial region where the energy is focused is smaller. When the machining of samples in depth > Rayleigh length is needed, the sample position should be carefully maintained to benefit from the small focal volume; as material is removed, it is important to continue to adjust the location of the laser focus to follow the change in topography of the workpiece [8].

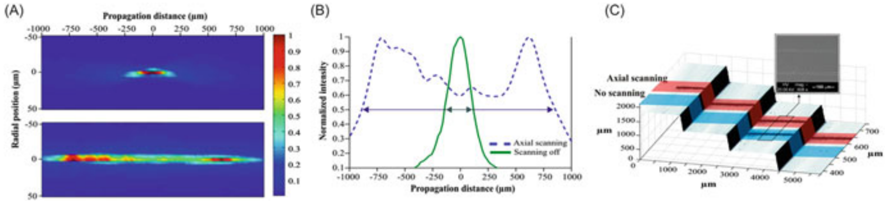

Fig. 8.18 (**a**) Intensity distribution of the laser beam propagation without and with axial scanning (TAG lens amplitude 10Vpp) after a microscope objective (5×, NA = 0.13). (**b**) Intensity profiles at the center (radial position = 0 μm) along the axial direction. (**c**) Machining with and without a TAG lens on a silicon-stepped surface. When there is no axial scanning, the system marks the surface only in one step, whereas with the axial scanning provided by a working TAG lens is possible to mark all the surfaces without requiring sample repositioning over an extended axial distance of 2 mm. The inset corresponds to an SEM micrograph with the widths of both modifications at the indicated step. (Reprinted from Duocastella and Arnold [17], with the permission of AIP Publishing)

However rapid resonant focal scanning obviates the need for such detailed feedback and control of the sample surface location. Figure 8.19a shows the comparison of the ablation with a nanosecond laser of a square of 200 × 200 μm^2 on a silicon sample with and without the TAG lens after three consecutive scans. In particular, the vertical profiles show a lack of ablated material in the case of the regular marking system without the TAG lens, whereas in the case with a working TAG lens, it is possible to ablate homogeneously over the whole area. This effect is produced because the scanning lens irradiates the material with different effective numerical apertures (or different focal lengths) per cycle defined by the amplitude of the oscillation. Therefore, the irradiation takes place with different spot sizes that increase material ablation when the fluence is high enough [8].

Optimization of a resonant scanning machining system can be performed by properly selecting the rate between the frequency of the marking laser and the frequency of operation of the scanning element. If the factor between these two parameters is an integer, the focal positions of the irradiated pulses will be the same, and no axial scanning will be induced. For all the other cases, the frequency mismatch will ensure that a pulse reaches the sample at different locations for each pulse interacting with the surface. Figure 8.19b shows an irradiation experiment in a cube of borosilicate glass using the same laser repetition rate (1000 Hz) and different TAG lens operating frequencies [14]. Here, the sample is scanned at the same speed laterally, and the images are acquired from a lateral perspective. Depending on the machining application, the right number of pulses per cycle could be customized by the proper selection of the TAG lens operational frequency, increasing the number of pulses that effectively reach the sample per TAG lens cycle.

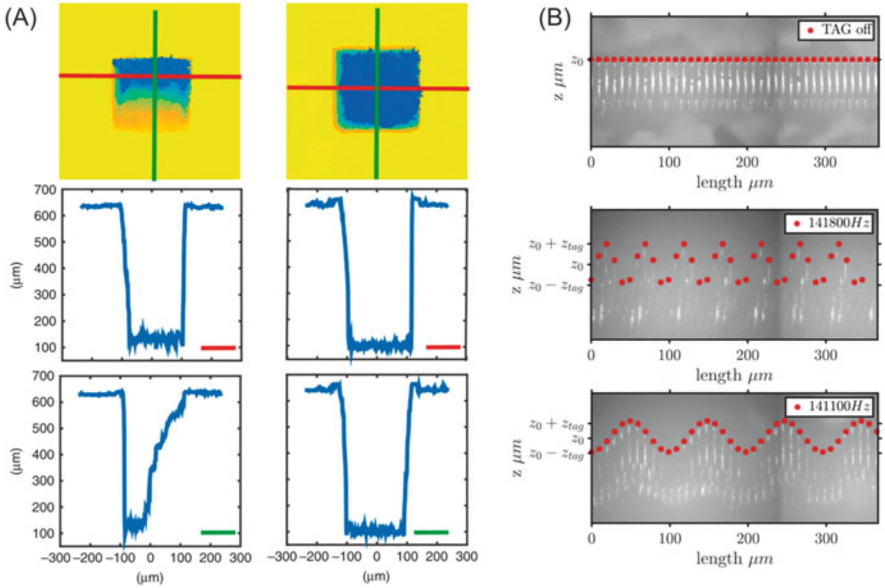

Fig. 8.19 (**a**) Ablation of 200 × 200 μm^2 squares on a 500-μm-thick silicon sample after three consecutive scans without (left) and with a TAG lens (right). The second row shows horizontal cross-section profiles indicated by the red lines. The third row similarly shows vertical profiles indicated by the green lines. (Image adapted with permission from Chen et al. [8] under Copyright license CC by 4.0). (**b**) Optical microscopy images from a lateral perspective of femtosecond laser modifications in a borosilicate glass cube without (top) and with an axial scanning frequency of 141,800 Hz and five pulses per cycle (middle) and 141,100 Hz and ten pulses per cycle (bottom). (Image reprinted from Du et al. [14], Copyright (2021), with permission from Elsevier)

5 Conclusions and Perspectives

This chapter reviews techniques for creating and using spatially structured beams from a fundamental perspective, as well as the resulting material interactions that occur. Generally speaking, the three key parameters which influence the final features of laser material processing are the confocal parameter, the beam divergence, and the minimum spot size. These parameters describe how traditional Gaussian beams focus energy into a small voxel and make surface or bulk modifications to materials, following closely the voxel dimensions; however, we discuss how it is possible to control and modify these parameters in order to create more complex beam architectures with beneficial performance in laser processing applications. Such spatially and temporally structured beam profiles are classified as varying the spatial intensity distributions in the far-field, the near-field, and temporally varying profiles. We show several examples of how to exploit these time-dependent profiles in subtractive and additive processing techniques. The development and advances of current and future laser-based micro- and nanofabrication techniques rely on our ability to accurately control and modify the optical properties of an incident beam of light and through techniques such as those described in this chapter, great advances in materials processing continue to be made.

Acknowledgments C.F. acknowledges the support from the European Commission through the Marie Curie Individual Fellowship – Global grant No. 844977. Also, to G. Mao for the support and useful conversations.

References

1. O.J. Allegre, W. Perrie, S.P. Edwardson, G. Dearden, K.G. Watkins, Laser microprocessing of steel with radially and azimuthally polarized femtosecond vortex pulses. J. Opt. **14**(8), 085601 (2012). https://doi.org/10.1088/2040-8978/14/8/085601
2. K.K. Anoop, A. Rubano, R. Fittipaldi, X. Wang, D. Paparo, A. Vecchione, L. Marrucci, R. Bruzzese, S. Amoruso, Femtosecond laser surface structuring of silicon using optical vortex beams generated by a q-plate. Appl. Phys. Lett. **104**(24), 241604 (2014). https://doi.org/10.1063/1.4884116
3. C.B. Arnold, P. Serra, A. Piqué, Laser direct-write techniques for printing of complex materials. MRS Bull. **32**(1), 23–31 (2007). https://doi.org/10.1557/mrs2007.11
4. P. Bazylewski, S. Ezugwu, G. Fanchini, A review of three-dimensional scanning near-field optical microscopy (3D-SNOM) and its applications in nanoscale light management. Appl. Sci. **7**(10), 973 (2017). https://doi.org/10.3390/app7100973
5. N. Chattrapiban, E.A. Rogers, D. Cofield, W.T. Hill III, R. Roy, Generation of nondiffracting Bessel beams by use of a spatial light modulator. Opt. Lett. **28**(22), 2183–2185 (2003). https://doi.org/10.1364/OL.28.002183
6. P. Chaturvedi, W. Wu, V.J. Logeeswaran, Z. Yu, M.S. Islam, S.Y. Wang, R.S. Williams, N.X. Fang, P. Chaturvedi, W. Wu, V.J. Logeeswaran, Z. Yu, M.S. Islam, A smooth optical superlens. Appl. Phys. Lett. **96**(4), 043102, 35–38 (2010). https://doi.org/10.1063/1.3293448
7. T.-H. Chen, Y.-C. Tsai, R. Fardel, C.B. Arnold, Generation of nanoscale anticounterfeiting patterns on silicon by optical trap assisted nanopatterning. J. Laser Appl. **29**(1), 012006 (2017). https://doi.org/10.2351/1.4966590
8. T.-H. Chen, R. Fardel, C.B. Arnold, Ultrafast z-scanning for high-efficiency laser micro-machining. Light Sci. Appl. **7**(4), 17181 (2018). https://doi.org/10.1038/lsa.2017.181
9. L. Chen, Y. Zhou, R. Zhou, M. Hong, Microsphere—toward future of optical microscopes. IScience **23**(6), 101211 (2020). https://doi.org/10.1016/j.isci.2020.101211
10. D.B. Chrisey, G.K. Hubler, *Pulsed Laser Deposition of Thin Films* (Wiley, 1994)
11. F. Courvoisier, J. Zhang, M.K. Bhuyan, M. Jacquot, J.M. Dudley, Applications of femtosecond Bessel beams to laser ablation. Appl. Phys. A Mater. Sci. Process. **112**(1), 29–34 (2013). https://doi.org/10.1007/s00339-012-7201-2
12. J. Cugat, A.R. de la Cruz, R. Sole, A. Ferrer, J.J. Carvajal, X. Mateos, J. Massons, J. Solis, G. Lifante, F. Diaz, M. Aguilgo, Femtosecond-laser microstructuring of ribs on active (Yb,Nb):RTP/RTP planar waveguides. J. Lightwave Technol. **31**(3), 385–390 (2013). https://doi.org/10.1109/JLT.2012.2230615
13. C. Daniel, F. Mücklich, Z. Liu, Periodical micro-nano-structuring of metallic surfaces by interfering laser beams. Appl. Surf. Sci. **208–209**(1), 317–321 (2003). https://doi.org/10.1016/S0169-4332(02)01381-8
14. X. Du, S.Y. Kang, C.B. Arnold, Optimization of ultrafast axial scanning parameters for efficient pulsed laser micro-machining. J. Mater. Process. Technol. **288**, 116850 (2021). https://doi.org/10.1016/j.jmatprotec.2020.116850

15. M. Duocastella, C.B. Arnold, Bessel and annular beams for materials processing. Laser Photonics Rev. **6**(5), 607–621 (2012). https://doi.org/10.1002/lpor.201100031
16. M. Duocastella, C.B. Arnold, Transient response in ultra-high speed liquid lenses. J. Phys. D. Appl. Phys. **46**(7), 075102 (2013). https://doi.org/10.1088/0022-3727/46/7/075102
17. M. Duocastella, C.B. Arnold, Enhanced depth of field laser processing using an ultra-high-speed axial scanner. Appl. Phys. Lett. **102**(6), 061113 (2013). https://doi.org/10.1063/1.4791593
18. J. Durnin, Exact solutions for nondiffracting beams I the scalar theory. J. Opt. Soc. Am. A **4**(4), 651–654 (1987). https://doi.org/10.1364/josaa.4.000651
19. N.K. Efremidis, Z. Chen, M. Segev, D.N. Christodoulides, Airy beams and accelerating waves: An overview of recent advances. Optica **6**(5), 686–701 (2019). https://doi.org/10.1364/OPTICA.6.000686
20. N. Fang, X. Zhang, Imaging properties of a metamaterial superlens. Appl. Phys. Lett. **82**(2), 161–163 (2003). https://doi.org/10.1063/1.1536712
21. R. Fardel, Y.C. Tsai, Y.T. Craig, Microbead dynamics in optical trap assisted nanopatterning. Appl. Phys. A Mater. Sci. Process. **112**, 23–28 (2013). https://doi.org/10.1007/s00339-012-7200-3
22. C. Florian, F. Caballero-Lucas, J.M. Fernández-Pradas, S. Bosch, J.L. Morenza, P. Serra, Femtosecond laser surface ablation of polymethyl-methacrylate with position control through z-scan. J. Phys. D. Appl. Phys. **48**(33), 335302 (2015). https://doi.org/10.1088/0022-3727/48/33/335302
23. C. Florian, S. Piazza, A. Diaspro, P. Serra, M. Duocastella, Direct laser printing of tailored polymeric microlenses. ACS Appl. Mater. Interfaces **8**(27), 17028–17032 (2016). https://doi.org/10.1021/acsami.6b05385
24. Q. Fontaine, H. Hu, S. Pigeon, T. Bienaimé, E. Wu, E. Giacobino, A. Bramati, Q. Glorieux, Attenuation-free non-diffracting Bessel beams. Opt. Express **27**(21), 30067–30080 (2019). https://doi.org/10.1364/oe.27.030067
25. A. Forbes, Structured light from lasers. Laser Photonics Rev. **13**(11), 1900140 (2019). https://doi.org/10.1002/lpor.201900140
26. D. Gao, W. Ding, M. Nieto-Vesperinas, X. Ding, M. Rahman, T. Zhang, C. Lim, C.-W. Qiu, Optical manipulation from the microscale to the nanoscale: Fundamentals, advances and prospects. Light Sci. Appl. **6**(9), e17039 (2017). https://doi.org/10.1038/lsa.2017.39
27. S. Ge, P. Chen, Z. Shen, W. Sun, X. Wang, W. Hu, Y. Zhang, Y. Lu, Terahertz vortex beam generator based on a photopatterned large birefringence liquid crystal. Opt. Express **25**(11), 12349–12356 (2017). https://doi.org/10.1364/OE.25.012349
28. M. Gecevičius, M. Beresna, R. Drevinskas, P.G. Kazansky, Airy beams generated by ultrafast laser-imprinted space-variant nanostructures in glass. Opt. Lett. **39**(24), 6791–6794 (2014). https://doi.org/10.1364/OL.39.006791
29. L. Gong, Y. Ren, W. Liu, M. Wang, M. Zhong, Z. Wang, Y. Li, Generation of cylindrically polarized vector vortex beams with digital micromirror device. J. Appl. Phys. **116**(18), 183105 (2014). https://doi.org/10.1063/1.4901574
30. Z. Gong, Y. Le Pan, G. Videen, C. Wang, Optical trapping and manipulation of single particles in air: Principles, technical details, and applications. J. Quant. Spectrosc. Radiat. Transf. **214**, 94–119 (2018). https://doi.org/10.1016/j.jqsrt.2018.04.027
31. R. Guo, E.C. Kinzel, Y. Li, S.M. Uppuluri, A. Raman, X. Xu, Three-dimensional mapping of optical near field of a nanoscale bowtie antenna. Opt. Express **18**(5), 4961–4971 (2010). https://doi.org/10.1364/OE.18.004961
32. Z. Guo, H. Liu, L. Xiang, L. Chen, J. Yang, J. Wen, Y. Shang, T. Wang, F. Pang, Generation of perfect vortex beams with polymer-based phase plate. IEEE Photon. Technol. Lett. **32**(10), 565–568 (2020). https://doi.org/10.1109/LPT.2020.2985745
33. Y. Guo, Y. Huang, J. Li, L. Wang, Z. Yang, J. Liu, X. Peng, W. Yan, J. Qu, Deep penetration microscopic imaging with non-diffracting airy beams. Membranes **11**(6), 391 (2021). https://doi.org/10.3390/membranes11060391

34. F. He, J. Yu, Y. Tan, W. Chu, C. Zhou, Y. Cheng, K. Sugioka, Tailoring femtosecond 1.5-µm Bessel beams for manufacturing high-aspect-ratio through-silicon vias. Sci. Rep. **7**(1), 40785 (2017). https://doi.org/10.1038/srep40785
35. S.W. Hell, J. Wichmann, Breaking the diffraction resolution limit by stimulated emission: Stimulated-emission-depletion fluorescence microscopy. Opt. Lett. **19**(11), 780–782 (1994). https://doi.org/10.1364/OL.19.000780
36. K. Imen, S.J. Lee, S.D. Allen, Laser-assisted micron scale particle removal Laser-assisted micron scale particle removal. Appl. Phys. Lett. 58, 203–205 (1991). https://doi.org/10.1063/1.104923
37. S.Y. Kang, M. Duocastella, C.B. Arnold, Variable optical elements for fast focus control. Nat. Photonics **14**(9), 533–542 (2020). https://doi.org/10.1038/s41566-020-0684-z
38. E.C. Kinzel, X. Xu, Extraordinary infrared transmission through a periodic bowtie aperture array. Opt. Lett. **35**(7), 992–994 (2010). https://doi.org/10.1364/OL.35.000992
39. A. Kumar, K.H. Hsu, K.E. Jacobs, P.M. Ferreira, N.X. Fang, Direct metal nano-imprinting using an embossed solid electrolyte stamp. Nanotechnology **22**(15), 155302 (2011). https://doi.org/10.1088/0957-4484/22/15/155302
40. P. Kühler, F.J. García de Abajo, J. Solis, M. Mosbacher, P. Leiderer, C.N. Alfonso, J. Siegel, Imprinting the optical near field of microstructures with nanometer resolution. Small **5**(16), 1825–1829 (2009). https://doi.org/10.1002/smll.200900393
41. A. Lasagni, C. Holzapfel, F. Mücklich, Periodic pattern formation of intermetallic phases with long range order by laser interference metallurgy. Adv. Eng. Mater. **7**(6), 487–492 (2005). https://doi.org/10.1002/adem.200400206
42. P. Leiderer, J. Boneberg, V. Dobler, M. Mosbacher, H.-J. Muenzer, N. Chaoui, J. Siegel, J. Solis, C.N. Alfonso, T. Fourrier, G. Schrems, D. Baeuerle, Laser-induced particle removal from silicon wafers. Proc. SPIE **4065**, 249–259 (2000). https://doi.org/10.1117/12.407353
43. D. Liu, Y. Wang, Z. Zhai, Z. Fang, Q. Tao, W. Perrie, S.P. Edwarson, G. Dearden, Dynamic laser beam shaping for material processing using hybrid holograms. Opt. Laser Technol. **102**, 68–73 (2018). https://doi.org/10.1016/j.optlastec.2017.12.022
44. B.S. Luk'Yanchuk, N. Arnold, Z. Wang, M.H. Hong, Three-dimensional effects in dry laser cleaning. Appl. Phys. A Mater. Sci. Process. **77**, 209–215 (2003). https://doi.org/10.1007/s00339-003-2139-z
45. J. Martínez de Mendívil, J. Hoyo, J. Solís, M.C. Pujol, M. Aguiló, F. Díaz, G. Lifante, Channel waveguide fabrication in KY(WO4)2 combining liquid-phase-epitaxy and beam-multiplexed femtosecond laser writing. Opt. Mater. **47**, 304–309 (2015). https://doi.org/10.1016/j.optmat.2015.05.046
46. A. Mathis, F. Courvoisier, L. Froehly, L. Furfaro, M. Jacquot, P.A. Lacourt, J.M. Dudley, Micromachining along a curve: Femtosecond laser micromachining of curved profiles in diamond and silicon using accelerating beams. Appl. Phys. Lett. **101**(7), 071110 (2012). https://doi.org/10.1063/1.4745925
47. D. McGloin, K. Dholakia, Bessel beams: Diffraction in a new light. Contemp. Phys. **46**(1), 15–28 (2005). https://doi.org/10.1080/0010751042000275259
48. E. McLeod, A.B. Hopkins, C.B. Arnold, Multiscale Bessel beams generated by a tunable acoustic gradient index of refraction lens. Opt. Lett. **31**(21), 3155–3157 (2006). https://doi.org/10.1364/ol.31.003155
49. E. McLeod, C.B. Arnold, Mechanics and refractive power optimization of tunable acoustic gradient lenses. J. Appl. Phys. **102**(3), 033104 (2007). https://doi.org/10.1063/1.2763947
50. E. McLeod, C.B. Arnold, Subwavelength direct-write nanopatterning using optically trapped microspheres. Nat. Nanotechnol. **3**(7), 413–417 (2008). https://doi.org/10.1038/nnano.2008.150
51. M. Miyasaka, J. Stoemenos, Excimer laser annealing of amorphous and solid-phase-crystallized silicon films. J. Appl. Phys. **86**(10), 5556 (1999). https://doi.org/10.1063/1.371560
52. N. Murphy-dubay, L. Wang, E.C. Kinzel, S.M.V. Uppuluri, X. Xu, Nanopatterning using NSOM probes integrated with high transmission nanoscale bowtie aperture. Opt. Express **16**(4), 2584–2589 (2008). https://doi.org/10.1364/OE.16.002584

53. Y. Nakata, K. Tsubakimoto, N. Miyanaga, A. Narazaki, T. Shoji, Y. Tsuboi, Laser-induced transfer of noble metal nanodots with femtosecond laser-interference processing. Nanomaterials **11**(2), 1–10 (2021). https://doi.org/10.3390/nano11020305
54. V. Nasrollahi, P. Penchev, A. Batal, H. Le, S. Dimov, K. Kim, Laser drilling with a top-hat beam of micro-scale high aspect ratio holes in silicon nitride. J. Mater. Process. Technol. **281**, 116636 (2020). https://doi.org/10.1016/j.jmatprotec.2020.116636
55. J.J.J. Nivas, S. He, Z. Song, A. Rubano, A. Vecchione, D. Paparo, L. Marrucci, R. Bruzzese, S. Amoruso, Femtosecond laser surface structuring of silicon with Gaussian and optical vortex beams. Appl. Surf. Sci. **418**, 565–571 (2017). https://doi.org/10.1016/j.apsusc.2016.10.162
56. J.J.J. Nivas, S. Amoruso, Generation of supra-wavelength grooves in femtosecond laser surface structuring of silicon. Nanomaterials **11**, 174 (2021). https://doi.org/10.3390/nano11010174
57. H.D. Nguyen, X. Sedao, C. Mauclair, G. Bidron, N. Faure, E. Moreno, J.-P. Colombier, R. Stoian, Non-diffractive Bessel beams for ultrafast laser scanning platform and proof-of-concept Side-Wall polishing of additively manufactured parts. Micromachines **11**(11), 974 (2020). https://doi.org/10.3390/mi11110974
58. A. Peter, A.H.A. Lutey, S. Faas, L. Romoli, V. Onuseit, T. Graf, Direct laser interference patterning of stainless steel by ultrashort pulses for antibacterial surfaces. Opt. Laser Technol. **123**, 105954 (2020). https://doi.org/10.1016/j.optlastec.2019.105954
59. E. Rebollar, M. Castillejo, Laser interactions with organic/polymer materials, in *Handbook of Laser Micro- and Nano-Engineering*, (Springer, Cham, 2020). https://doi.org/10.1007/978-3-319-69537-2_13-1
60. A. Roszkiewicz, A. Jain, M. Teodorczyk, W. Nasalski, Formation and characterization of hole nanopattern on photoresist layer by scanning near-field optical microscope. Nanomaterials **9**(10), 1452 (2019). https://doi.org/10.3390/nano9101452
61. C.J. Rowlands, F. Ströhl, P.P.V. Ramirez, K.M. Scherer, C.F. Kaminski, Flat-field super-resolution localization microscopy with a low-cost refractive beam-shaping element. Sci. Rep. **8**(1), 5630 (2018). https://doi.org/10.1038/s41598-018-24052-4
62. S. Rung, M. Rexhepi, C. Bischoff, R. Hellmann, Laserscribing of thin films using top-hat laser beam profiles. J. Laser Micro/Nanoeng. **8**(3), 309–314 (2013). https://doi.org/10.2961/jlmn.2013.03.0021
63. J.H. Seo, J.H. Park, S.I. Kim, B.J. Park, Z. Ma, J. Choi, B.K. Ju, Nanopatterning by laser interference lithography: Applications to optical devices. J. Nanosci. Nanotechnol. **14**(2), 1521–1532 (2014). https://doi.org/10.1166/jnn.2014.9199
64. P. Serra, A. Piqué, Laser-induced forward transfer: Fundamentals and applications. Adv. Mater. Technol. **4**(1), 1800099 (2019). https://doi.org/10.1002/admt.201800099
65. Y. Shen, X. Wang, Z. Xie, C. Min, X. Fu, Q. Liu, M. Gong, X. Yuan, Optical vortices 30 years on: OAM manipulation from topological charge to multiple singularities. Light Sci. Appl. **8**(1), 90 (2019). https://doi.org/10.1038/s41377-019-0194-2
66. W.T. Silfvast, *Laser Fundamentals* (Cambridge University Press, 2004). https://doi.org/10.1017/CBO9780511616426
67. E. Skoulas, A. Manousaki, C. Fotakis, E. Stratakis, Biomimetic surface structuring using cylindrical vector femtosecond laser beams. Sci. Rep. **7**, 45114 (2017). https://doi.org/10.1038/srep45114
68. F. Spinello, C.G. Someda, R.A. Ravanelli, E. Mari, G. Parisi, F. Tamburini, F. Romanato, P. Coassini, M. Oldoni, Radio channel multiplexing with superpositions of opposite-sign OAM modes. AEU-Int. J. Electron. C. **70**(8), 990–997 (2016). https://doi.org/10.1016/j.aeue.2016.03.017
69. W. Srituravanich, L. Pan, Y. Wang, C. Sun, D.B. Bogy, X. Zhang, Flying plasmonic lens in the near field for high-speed nanolithography. Nat. Nanotechnol. **3**(12), 733–737 (2008). https://doi.org/10.1038/nnano.2008.303
70. N. Stsepuro, P. Nosov, M. Galkin, G. Krasin, M. Kovalev, S. Kudryashov, Generating bessel-gaussian beams with controlled axial intensity distribution. Appl. Sci. **10**(21), 7911 (2020). https://doi.org/10.3390/app10217911

71. H. Suhara, J. Aoto, M. Iwata, Printing method for long flight distance by laser-induced forward transfer. J. Laser Micro Nanoeng. **15**(2), 143–149 (2020). https://doi.org/10.2961/jlmn.2020.02.2012
72. S. Surdo, M. Duocastella, A. Diaspro, Nanopatterning with photonic nanojets: Review and perspectives in biomedical research. Micromachines **12**(3), 256 (2021). https://doi.org/10.3390/mi12030256
73. Y. Tang, W. Perrie, D. Rico Sierra, Q. Li, D. Liu, S.P. Edwardson, G. Dearden, Laser–material interactions of high-quality ultrashort pulsed vector vortex beams. Micromachines **12**(4), 376 (2021). https://doi.org/10.3390/mi12040376
74. E. Turkoz, S. Kang, L. Deike, C.B. Arnold, Subthreshold laser jetting via flow-focusing in laser-induced forward transfer. Phys. Rev. Fluids **3**, 082201 (2018). https://doi.org/10.1103/PhysRevFluids.3.082201
75. E. Turkoz, A. Perazzo, H. Kim, H.A. Stone, C.B. Arnold, Impulsively induced jets from viscoelastic films for high-resolution printing. Phys. Rev. Lett. **120**(7), 074501 (2018). https://doi.org/10.1103/PhysRevLett.120.074501
76. E. Turkoz, S. Kang, X. Du, L. Deike, C.B. Arnold, Reduction of transfer threshold energy for laser-induced jetting of liquids using faraday waves. Phys. Rev. Appl. **11**(5), 054022 (2019). https://doi.org/10.1103/PhysRevApplied.11.054022
77. C. Wenisch, S. Engel, S. Gräf, F.A. Müller, Dual laser beam processing of semiconducting thin films by excited state absorption. Materials **14**(5), 1256 (2021). https://doi.org/10.3390/ma14051256
78. C.Y. Yap, C.K. Chua, Z.L. Dong, Z.H. Liu, D.Q. Zhang, L.E. Loh, S.L. Sing, Review of selective laser melting: Materials and applications. Appl. Phys. Rev. **2**(4), 041101 (2015). https://doi.org/10.1063/1.4935926
79. Z.B. Wang, N. Joseph, L. Li, B.S. Luk'Yanchuk, A review of optical near-fields in particle/tip-assisted laser nanofabrication. J. Mech. Eng. Sci. **224**, 1113–1127 (2010). https://doi.org/10.1243/09544062JMES1766
80. X. Wang, Z. Nie, Y. Liang, J. Wang, T. Li, B. Jia, Recent advances on optical vortex generation. Nanophotonics **7**(9), 1533–1556 (2018). https://doi.org/10.1515/nanoph-2018-0072
81. W. Zhang, W. Hou, L. Deike, C.B. Arnold, Using a dual-laser system to create periodic coalescence in laser powder bed fusion. Acta Mater. **201**, 14–22 (2020). https://doi.org/10.1016/j.actamat.2020.09.071
82. Z. Zheng, B.F. Zhang, H. Chen, J. Ding, H.T. Wang, Optical trapping with focused airy beams. Appl. Opt. **50**(1), 43–49 (2011). https://doi.org/10.1364/AO.50.000043
83. G. Zhu, Y. Wen, X. Wu, Y. Chen, J. Liu, S. Yu, Obstacle evasion in free-space optical communications utilizing airy beams. Opt. Lett. **43**(6), 1203–1206 (2018). https://doi.org/10.1364/ol.43.001203
84. P. Zupancic, P.M. Preiss, R. Ma, A. Lukin, M. Eric Tai, M. Rispoli, R. Islam, M. Greiner, Ultra-precise holographic beam shaping for microscopic quantum control. Opt. Express **24**(13), 13881–13893 (2016). https://doi.org/10.1364/OE.24.013881
85. C. Zwahr, R. Helbig, C. Werner, A.F. Lasagni, Fabrication of multifunctional titanium surfaces by producing hierarchical surface patterns using laser based ablation methods. Sci. Rep. **9**(1), 6721 (2019). https://doi.org/10.1038/s41598-019-43055-3

Chapter 9
Imaging Dynamics of Femtosecond Laser-Induced Surface Nanostructuring

Cong Cong, Ranran Fang, Anatoliy Y. Vorobyev, Mohamed ElKabbash, Subhash C. Singh, and Chunlei Guo

Abstract Over the past years, direct femtosecond laser surface processing has distinguished itself from other conventional laser ablation methods and becomes an important method to create surface structures at nano- and microscales due to its flexibility, simplicity, and controllability in creating various types of nano-/microstructures that are suitable for a wide range of applications. Significant advancements were made recently in applying this technique to altering optical properties of metals and semiconductors, such as highly absorptive or novel materials with wetting properties ranging from superhydrophilic to superhydrophobic.

To explore the dynamics of surface nanostructuring, here we describe some recent progresses on a scattered-light-based optical imaging technique which allows the capture of the complete temporal and spatial evolution of the femtosecond laser-induced morphological surface structural dynamics of metals from start to finish, that is, from the initial transient surface fluctuations, through melting and ablation, to the end of resolidification.

The formation dynamics of the surface structures at different length scales and the sequence of their appearance changes with laser fluence are discussed. The mechanisms driving each of these dynamic steps are discussed.

Keywords Ultrafast dynamics · Imaging · Nanostructuring · Transient surface structure

1 Introduction of Nanostructuring

Surface morphology plays a key role in determining the optical, mechanical, wetting, chemical, biological, and other properties of a solid surface. Recently, femtosecond laser surface nanostructuring has emerged as a novel and versatile

---

C. Cong · R. Fang · A. Y. Vorobyev · M. ElKabbash · S. C. Singh · C. Guo (✉)
The Institute of Optics, University of Rochester, Rochester, NY, USA
e-mail: ccong@ur.rochester.edu; anatoliy.vorobyev@rochester.edu; mke23@case.edu; ssingh49@UR.Rochester.edu; chunlei.guo@rochester.edu

© The Author(s), under exclusive license to Springer Nature Switzerland AG 2023
R. Stoian, J. Bonse (eds.), *Ultrafast Laser Nanostructuring*, Springer Series in Optical Sciences 239, https://doi.org/10.1007/978-3-031-14752-4_9

way for producing a large variety of surface nanostructures enabling a wide range of applications in photonics, plasmonics, optoelectronics, biochemical sensing, micro/nano-fluidics, optofluidic, biomedicine, and other areas [1]. The advantages of femtosecond laser surface patterning include ability of processing nearly all types of materials (metals, semiconductors, glasses, and polymers), capability of processing nonplanar surfaces, ability of producing nanostructures on surface areas from nanoscale to macroscale, and maskless single-step processing at a high speed under normal ambient conditions, without needing a clean room environment [2, 3].

With the advent of femtosecond lasers, the potential for femtosecond lasers in ablation-based micro- and nano-processing has been demonstrated [1, 4–7]. Initially, a number of techniques using femtosecond lasers assisted by other techniques were developed for surface nanostructuring and nanopatterning of solids, such as near-field nanomachining [8], laser-assisted chemical etching [9], and deposition from femtosecond laser-ablated plumes [10]. It was also found that laser-induced periodic surface structures that had previously been generated using long-pulsed lasers can also be produced by femtosecond laser pulses on nearly all types of materials, including semiconductors [11–14], dielectrics [2, 3, 15], and metals [16–18]. More recently, direct femtosecond laser processing stood out as a new field for surface nanostructuring and nanopatterning due to its flexibility, simplicity, and capability of producing a large variety of surface structures suitable for a wide range of application [1, 6]. Figure 9.1 shows some typical nano- and microscale images following femtosecond laser irradiation [6].

With the development of femtosecond laser nanostructuring, novel materials have been created such as black silicon [9], black and colored metals [16, 19, 20], colored silicon [21], and materials with strong hydrophobicity [7, 22–24], hydrophilicity [25] and even with the extreme of liquid-transporting superwicking effect [26, 27]. Figure 9.2 shows some typical laser-processed material: colored metals [1], superhydrophilic surface [6], and superhydrophobic surface [7]. Furthermore, it has been demonstrated that the femtosecond laser-induced surface structures can be successfully used for significant enhancement of X-ray generation [28], photoelectron emission [29], and thermal radiation from incandescent light sources [30]. Biological applications have also been explored with surface nanopatterning [31–33].

2 Selected Ultrafast Imaging Methods

To explore the dynamics process of nanostructuring, time-resolved imaging techniques are required. Ultrafast morphological and crystalline structural dynamics have been studied using various techniques, including optical imaging [34–40], X-ray diffraction [41, 42], electron diffraction [43], and diffractive XUV imaging [44].

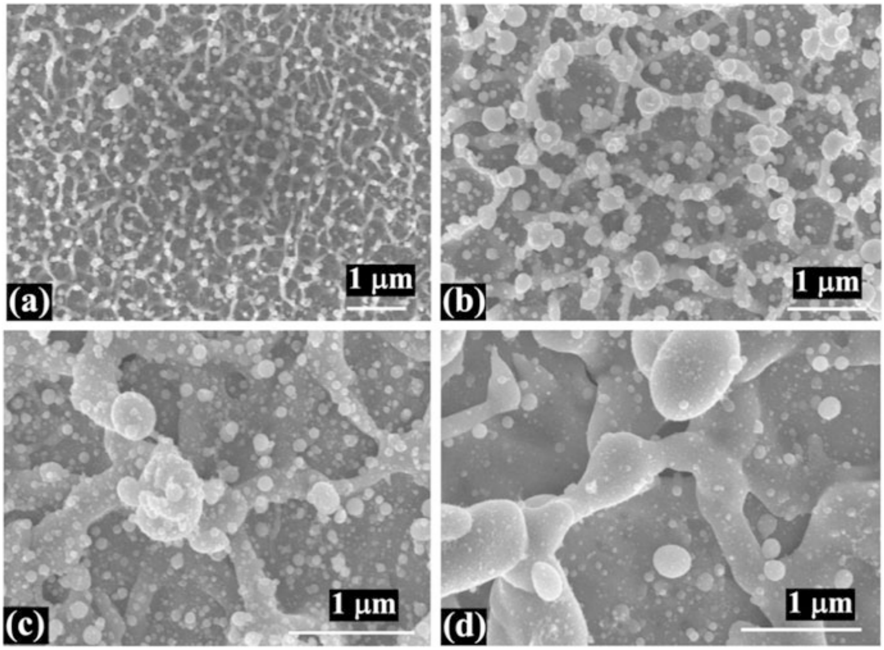

Fig. 9.1 Typical nano- and microscale images following direct femtosecond laser processing. SEM images of irradiated copper following ablation (**a**) after 1 shot featuring only random nanostructures in the form of nanoprotrusions and nanocavities, (**b**) surface after 2 shots featuring only random nanostructures in the form of spherical nanoprotrusions and nanocavities, (**c**) surface after 10 shots featuring both nano- and microstructures, and (**d**) surface after 1000 shots showing microstructures being dominating. (Reprinted with permission from Ref. [6])

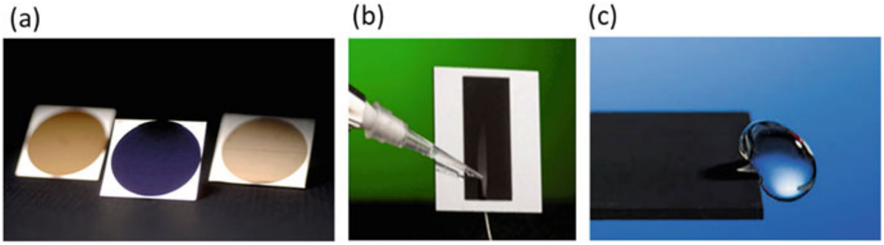

Fig. 9.2 Femtosecond laser produced (**a**) colored metals [1], (**b**) superhydrophilic surface [6], and (**c**) superhydrophobic surface [7]

2.1 Ultrafast Optical Imaging

Optical imaging can be achieved by collecting specular reflections [34–40], which is more suitable for resolving relatively large changes in reflection, such as formation of Newton rings [35–39]. K. Sokolowski-Tinten et al. used a pump pulse to excite

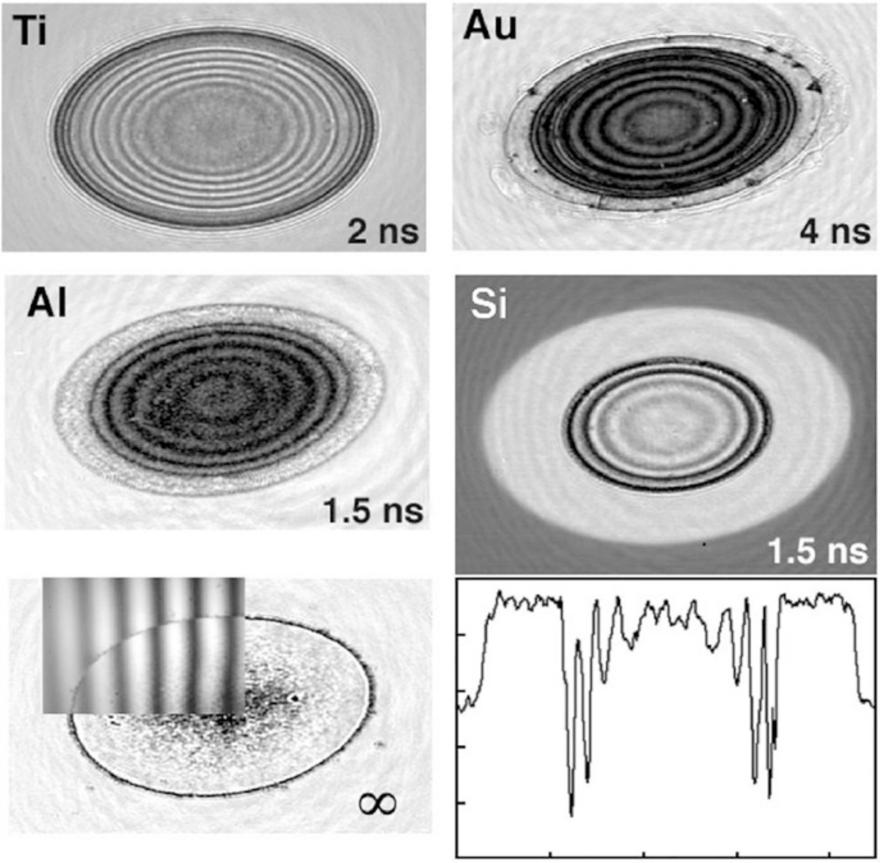

Fig. 9.3 Depth measurements through interference patterns in ultrafast imaging: top and center row: ring patterns on Ti, Au, Al, and Si with the certain delay time after the ablation. Bottom left: final surface structure of the Al film. Inset: interferogram. Bottom right: reflectivity profile for Si. (Reprinted with permission from Ref. [37])

a surface layer and initiate the ablation and then used a weak, time-delayed probe pulse to illuminate the sample surface and observed with a high-resolution optical microscope. Figure 9.3 shows the depth measurements through interference patterns in ultrafast imaging [37]. The surface profile corresponding to the transient status with different delay time can be determined by the interference ring distribution, enabling to identify the characteristic stages of the conversion of solid material into hot fluid matter undergoing ablation.

However, the strong background of specular reflections could make it difficult to discern small changes in reflection, which are often associated with nano-/microstructure formation, making it less suitable to implement in the nanostructuring field.

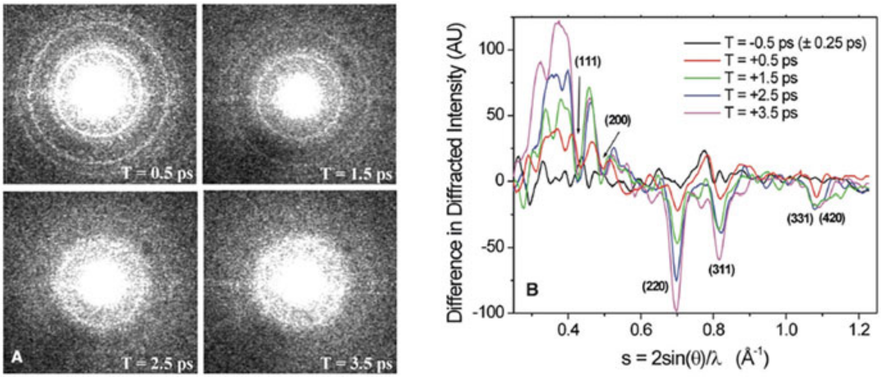

Fig. 9.4 Femtosecond electron diffraction study of an ultrafast solid-liquid phase transition in polycrystalline Al. (**a**) Sequence of diffraction patterns taken at pump-probe delay intervals (T) through the phase transition. (**b**) Radial average of the difference in diffracted intensity at different time delay. (Reprinted with permission from Ref. [43])

2.2 Ultrafast X-Ray and Electron Diffraction Imaging

Ultrafast X-ray and electron diffraction studies are more suitable for investigating long-range disorder phenomena in crystalline materials, such as melting. B. J. Siwick et al. [43] used 600-femtosecond electron pulses to study the structural evolution of aluminum (Al) during an ultrafast laser-induced solid-liquid phase transition. They observed the loss of long-range order of Al and the appearance of liquid structure by using femtosecond electron diffraction. As shown in Fig. 9.4a, the first four rings in the diffraction pattern are associated with the fcc lattice structure, which are clearly depicted at the delay time of 0.5 ps after ablation, indicating that the melting has not happened yet. At the delay time of 3.5 ps after ablation, only a single broad ring was visible, corresponding to the characteristic of liquid phase.

P. Baum et al. [45] used four-dimensional (4D) femtosecond electron diffraction method to visualize transitional structures from the initial monoclinic to the final tetragonal phase in crystalline vanadium dioxide, induced by near-infrared excitation. Three-dimensional Bragg diffraction patterns were also revealed to resolve the displacement of atoms. Figure 9.5 shows the crystal structures of vanadium dioxide phases and the Bragg diffraction patterns observed by the researchers. Figure 9.5a represents the crystal structure of monoclinic, low-temperature, and the rutile, high-temperature phase, while Fig. 9.5b shows the typical diffraction patterns observed by ultrafast electron crystallography of various crystal surfaces and zone axes.

In a more recent work, using coherent diffraction imaging with femtosecond X-ray free-electron laser (FEL), A. Barty et al. [46] captured time series snapshots of a solid evolution in ultrafast time scale with a temporal resolution of 10 ps. FEL beam is transmitted through the sample with a certain delay after the ablation caused by the visible pump laser, carrying information about the transient sample structure to

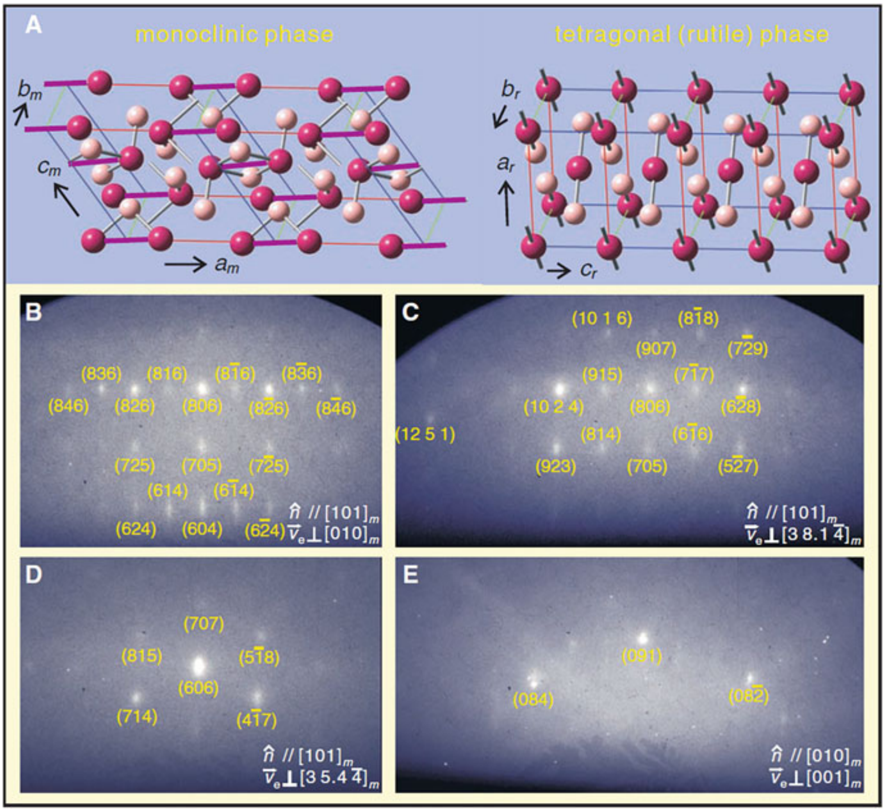
A
monoclinic phase
tetragonal (rutile) phase
b_m
c_m
a_m
b_r
a_r
c_r
B
(836) (816) (8$\bar{1}$6) (8$\bar{3}$6)
(846) (826) (806) (8$\bar{2}$6) (8$\bar{4}$6)
(725) (705) (7$\bar{2}$5)
(614) (6$\bar{1}$4)
(624) (604) (6$\bar{2}$4)
$\hat{n}$ // [101]$_m$
$\vec{v}_e \perp$ [010]$_m$
C
(10 1 6) (8$\bar{1}$8)
(907) (7$\bar{2}$9)
(915) (7$\bar{1}$7)
(10 2 4) (806) (6$\bar{2}$8)
(12 5 1)
(814) (6$\bar{1}$6)
(923) (705) (5$\bar{2}$7)
$\hat{n}$ // [101]$_m$
$\vec{v}_e \perp$ [3 8.1 $\bar{4}$]$_m$
D
(707)
(815) (5$\bar{1}$8)
(606)
(714) (4$\bar{1}$7)
$\hat{n}$ // [101]$_m$
$\vec{v}_e \perp$ [3 5.4 $\bar{4}$]$_m$
E
(091)
(084) (08$\bar{2}$)
$\hat{n}$ // [010]$_m$
$\vec{v}_e \perp$ [001]$_m$

Fig. 9.5 Crystal structures of vanadium dioxide phases (**a**) and observed Bragg diffraction (**b**–**e**). (Reprinted with permission from Ref. [45])

the CCD detector. The real images were able to be reconstructed from the diffraction patterns at a relatively high spatial resolution due to the short wavelength of the FEL beam.

On the other hand, in some required experiments, the retrieval through diffraction images may become increasingly more difficult and less reliable at longer time delays. Diffractive imaging using time-resolved coherent XUV scattering in a transmission geometry can also be applied for indirect imaging, in which a real image was reconstructed from a diffraction pattern [44].

3 Ultrafast Pump-Probe Scatter Light Imaging

Although X-ray diffraction imaging provides a high spatial resolution of the target, it also requires extensive image reconstruction algorithms that is challenging for delay times longer than 1 ns [46–48]. In addition, the intensity of the X-ray probe is often higher than the ablation threshold of imaged materials, making it impossible to determine the resolidification dynamics [47, 48]. For ultrafast electron diffraction imaging, although the melting process and phase transition can be inferred from the diffraction patterns [45], this technique is not a direct imaging method, and the actual form of sample cannot be visualized through this method. More recently, an ultrafast optical imaging technique was developed to investigate the structural dynamics of metals by utilizing scattered light instead of specular reflections [48–50]. Here, we will describe a scattered-light imaging technique that provides a near-zero background and high contrast, allowing to obtain high-quality real-space images of the structural dynamics of metals and resolve the complete temporal and spatial evolution of fs laser-induced morphological surface structure formation in laser-metal interactions [48–50].

3.1 Experimental Setup

The ultrafast pump-probe imaging setup is depicted in Fig. 9.6a [48–50]. An amplified Ti:sapphire laser system was used. A pump beam induced the formation of surface structures on zinc (Zn) and produced nano-/microstructures by a single laser pulse at a fluence in the range of 0.1–1.0 J cm^{-2}, under which extensive nano-/microstructure formation was observed [6].

For controlling the delay time between the pump and probe pulses, an optical delay line was used to provide various time delays, ranging from 0 to 408 ns, between the pump and probe pulses, shown in Fig. 9.6a represented by several mirrors [48–50]. A delay of 408 ns was achieved by allowing the beam to propagate over 120 m through multiple reflections. A zero delay was achieved by using the autocorrelation technique through using a BBO crystal.

After passing the delay line, the probe pulse was directed onto the BBO crystal to generate second harmonics at 400 nm. A blue band-pass filter was used to block the fundamental light after the BBO crystal and only let the 400-nm wavelength laser passing through. The 400-nm probe pulse was incident on the sample at an angle of 18°. A 50-mm (numerical aperture = 0.25) long-working-distance objective was used to image the sample surface onto the sensor of a CCD camera. The imaging optics used could resolve both nanoclusters and microstructures. More details about the measurements can be found in Ref. [49]. The formation dynamics of the transient surface structures at different delays can be tracked, and the effect of the laser fluence on their evolution can be identified, including transient surface structural fluctuations and solidification.

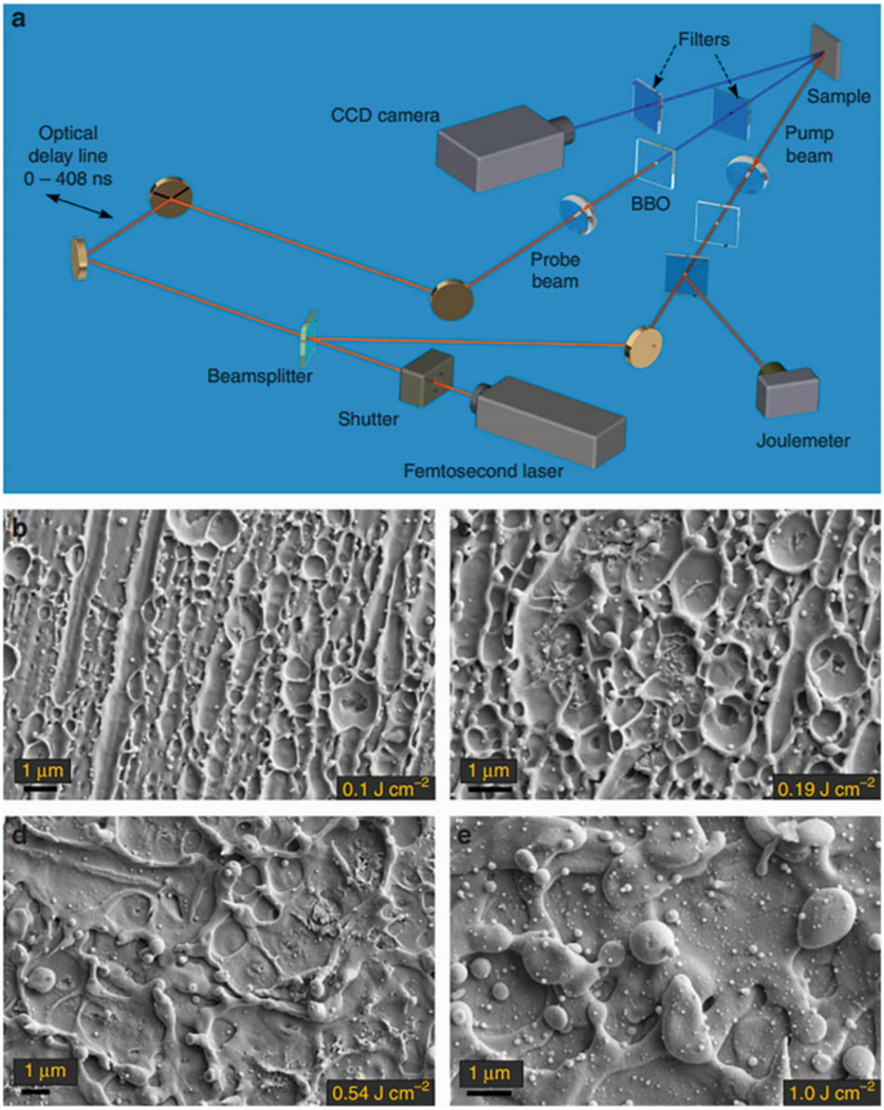
a
Filters
Sample
CCD camera
Pump beam
Optical delay line 0 – 408 ns
BBO
Probe beam
Beamsplitter
Shutter
Joulemeter
Femtosecond laser
b
1 µm
0.1 J cm^{-2}
c
1 µm
0.19 J cm^{-2}
d
1 µm
0.54 J cm^{-2}
e
1 µm
1.0 J cm^{-2}

Fig. 9.6 (**a**) Ultrafast pump-probe imaging setup. (**b**–**e**) SEM images of surface nano-/microstructures of Zn in the center of the irradiated spot at various laser fluences, as indicated in the figure. (Reprinted with permission from Ref. [49])

3.2 Reflectance Measurements

To characterize the optical reflection variation from a surface, as the surface was irradiated with a high-intensity laser beam, and the surface reflectance at a given fluence was crucial for the discussion, the surface reflectance was also collected at different fluences by using a hemi-ellipsoidal reflector to record both the specular and diffuse light reflection [49, 51]. Samples were placed at the internal focal point of the reflector. The reflected light was collected at the external focal point of the reflector, and its energy E_R could be measured by using a joulemeter. The reflectance $R = E_R/E_I$ was obtained from the measured E_R and E_I.

3.3 Characterization of Surface Structures

The researchers then used a scanning electron microscope (SEM) and a three-dimensional laser scanning microscope to examine the laser-induced surface nano-/microstructures after the resolidification of the surface, shown in Fig. 9.6b–e [49].

4 Nanostructuring Imaging Results and Discussions

The researchers measured the single-pulse damage threshold of the Zn sample to be 22 mJ cm^{-2}, which was determined based on the first appearance of surface modification observed under an optical microscope [49]. They also found out that nanostructures always dominate at lower fluences, while microstructures dominate at higher fluences [49], proved by Fig. 9.6b–e, which described the typical surface nano-/microstructures produced in the center of the ablated spot at various laser fluences.

To further explore the dynamics, Fig. 9.7 shows the transient structures of Zn at different delays for laser fluences of 0.1 J cm^{-2}, which are approximately four times larger than the damage threshold [49, 50]. The authors determined that the surface structures began to appear at a time delay of 400 ps, shown in Fig. 9.7c, but a comparison with the structures observed a long time after the laser pulse ($t = \infty$, from Fig. 9.7d) revealed that the two images show nearly no resemblance. The comparison indicated that the material in the irradiated spot was not yet solidified, resulting in the surface structures observed at this delay being transient. Another comparison of Fig. 9.7e, f revealed some similarity at the periphery of the irradiated spot, showing that the transient structures began to solidify at 527 ps and with increasing of delay time; the solidified area increased as well. About 90% of the surface structures were frozen at $t = 50$ ns, shown in Fig. 9.7g, h. The structures became identical to their final configuration at 124 ns, indicating that the surface structures were completely solidified at the time, shown in Fig. 9.7i, j [49].

For a fluence of 0.1 J cm^{-2}, they also found that the surface structures were dominated by extensive nanostructures with dimensions between 30 and 500 nm, and some microstructures, shown in Fig. 9.6b [49]. To fully characterized the surface structural evolution dynamics, three characteristic times were defined to evaluate the process [49, 50]:

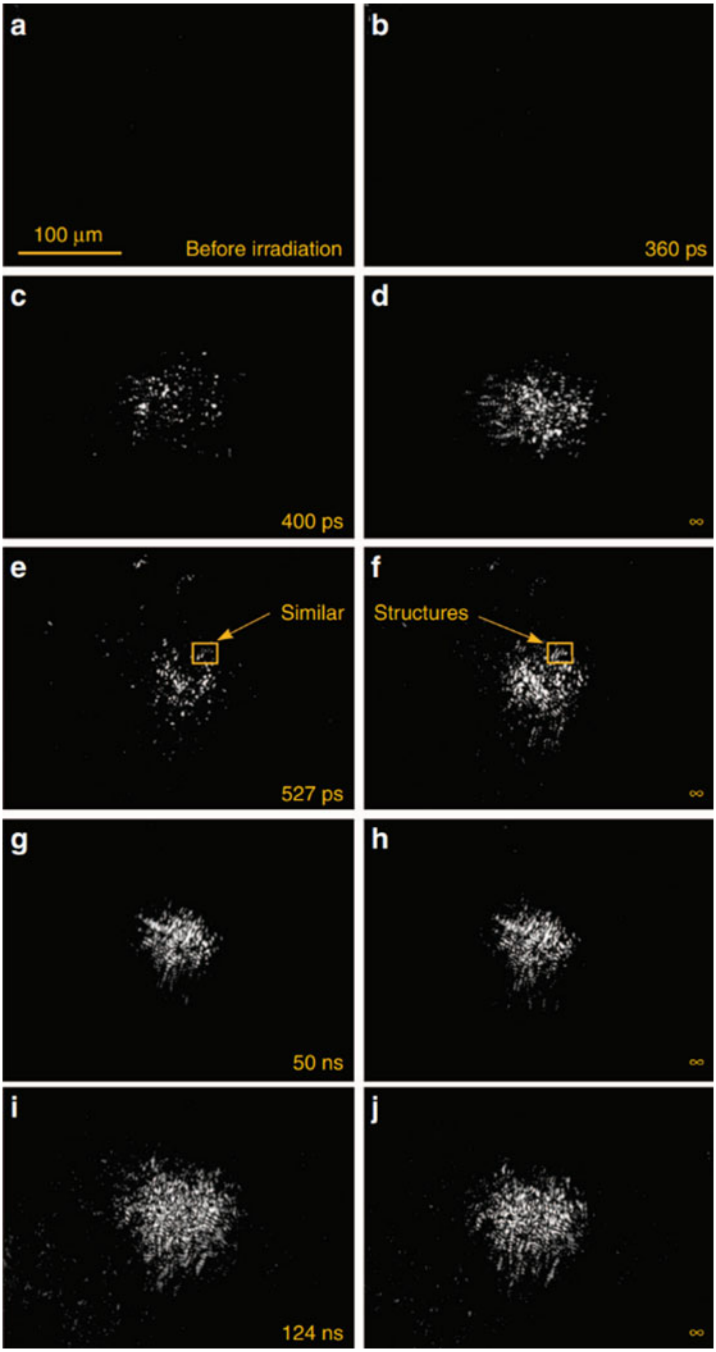
a
100 µm
Before irradiation
b
360 ps
c
400 ps
d
∞
e
Similar
527 ps
f
Structures
∞
g
50 ns
h
∞
i
124 ns
j
∞

Fig. 9.7 (**a–j**) A comparison of transient surface structures observed at various delay times and final solidified structures following a pump pulse at a fluence of 0.10 J cm^{-2}. (Reprinted with permission from Ref. [49])

Table 9.1 Measurements and estimates regarding surface structural dynamics [49]

F (J cm^{-2})	t_1 (ps)	t_2 (ns)	t_3 (ns)	R	T_m (K)	t_{cool} (ns)	Ablation mechanism
0.022	–	–	–	0.57	890	–	Damage threshold
0.10	400	0.527	123.8	0.57	2970	32	Spallation
0.14	300	0.86	322	0.57	4080	41	Phase explosion
0.19	200	1.3	–	0.57	5430	50	
0.26	100	2.8	–	0.56	7320	62	
0.34	50	5	–	0.57	9480	74	
0.54	–	9.3	–	0.57	14,880	101	
0.78	–	50	–	0.55	22,330	130	
1.0	–	124	–	0.56	28,580	156	
1.1	–	–	–	0.5	–	–	Solid-density plasma regime
1.8	–	–	–	0.33	–	–	

- t_1: the time at which transient surface structures first appear
- t_2: the time at which solidification begins
- t_3: the time at which the surface structures become completely solidified

Three characteristic times were summarized for different pump fluences in Table 9.1 [49]. Fs laser-excited surface structure formation had been studied for semiconductors [36, 37], where the time required for complete solidification in silicon was found to have an upper value about 75 ns, much shorter than the analyzed data of Zn.

The mechanism of the transient surface structure formation and its associated start time, t_1, is the first to be discussed. A more previous research had shown that the characteristic time for surface melting following the ultrafast laser irradiation of Zn was about 3 ps at laser fluences of 0.1–0.15 J cm^{-2} [52]. However, the data showed that the onset of transient surface structure formation occurred at about 400 and about 300 ps at laser fluences of 0.1 and 0.14 J cm^{-2}, respectively [49].

They believed that the time difference suggested that the irradiated surface did not undergo a morphological change immediately after melting; instead, there was a time delay between the melting process and the hydrodynamic motion of the melted material that results in the transient morphological fluctuations observed on the surface. Generally, transient structural fluctuations could be induced by the flow of the melted material due to a temperature gradient (the Marangoni effect) and the flow due to laser-induced stresses in the melted surface layer. To identify whether the Marangoni effect plays the key role, they estimated the characteristic timescale t_M of the Marangoni effect through the formula [53]:

$$t_{\mathrm{M}} = \frac{\eta L^2}{|\gamma_T|\, T_{\mathrm{m}} h} \tag{9.1}$$

where η is the dynamic viscosity of the melt, L is the typical radial dimension, h is the average melt depth, T_{m} is the melting point of the metal, and $|\gamma_T| = |d\gamma/dT|$ represents the absolute value of the temperature coefficient of the surface tension γ. By using the values of $\eta = 2.5 \times 10^{-3}$ Pa s [54], $|\gamma_T| = 0.25 \times 10^{-3}$ N m^{-1} K^{-1} [55], $T_{\mathrm{m}} = 693$ K, and $L = 200$ nm and assumed $h = 30$ nm, they got $t_{\mathrm{M}} \approx 20$ ns to be the obtained result, which is two orders of magnitude larger than the observed values of t_1 [49]. Therefore, they proved that the Marangoni effect did not appear to be the primary cause of the onset of the transient surface structures. However, this did not exclude the Marangoni effect as a factor affecting the formation of surface structures at longer timescales.

Following high-intensity ultrashort laser pulse heating and as a result of isochoric heating, a highly pressurized melted surface layer can be formed, which also had been theoretically predicted in more previous work [56, 57]. Pressure relaxation in this melted layer will induce hydrodynamic motion, resulting in morphological fluctuations on the surface. The timescale of those morphological fluctuations is governed by the speed of sound in the melted material [57] and can be estimated as $t_{\mathrm{P}} \approx L/v_{\mathrm{sl}}$, where v_{sl} represents the speed of sound in liquid Zn, as the value is 3.8×10^3 m s^{-1} [58] in solid Zn, and the speed of in liquid metals is 1.5 times smaller than that in solids. Therefore, assuming $v_{\mathrm{sl}} = 2.3 \times 10^3$ m s^{-1} and again using the typical radial dimension $L = 200$ nm found from Fig. 9.6b, $t_{\mathrm{P}} \approx 90$ ps was obtained, which is on the same timescale as the measured t_1 values [49].

In general, melting occurs at laser fluences near the damage threshold, and ablation occurs at higher fluences. The laser fluence was more than four times greater than the damage threshold [49]. The start time of transient surface structure formation, t_1, was associated with ablation driven by pressure relaxation in the surface layer, as determined by the Fig. 9.8, whereas Fig. 9.8 presents t_1 and t_2 as functions of the laser fluence. Also from the figure, t_1 decreases with laser fluence, which indicates an earlier onset of ablation due to higher pressure in the surface layer [49].

Figure 9.9 shows a series of time-resolved surface images acquired at various delays following pump pulse irradiation at a higher fluence of 0.78 and 1.0 J cm^{-2} separately [49, 50]. Counterintuitively, it can be seen that transient surface structures first appeared at the edge of the irradiated spot and formed a ring, in contrast to what occurred under ablation at lower laser fluences, for which the transient structures first appear in the center (from Fig. 9.7c) [49, 50]. Over time, the transient surface structures moved toward the center. At 5–9.3 ns, the center of the irradiated spot was covered with structures. The solidification of the transient surface structures began at about 124 ns, as indicated by the resemblance to the final image. At the longest delay investigated in the experiments (408 ns), they found out that the solidification was not fully completed, as a difference was still existing between Fig. 9.9k, l. Then

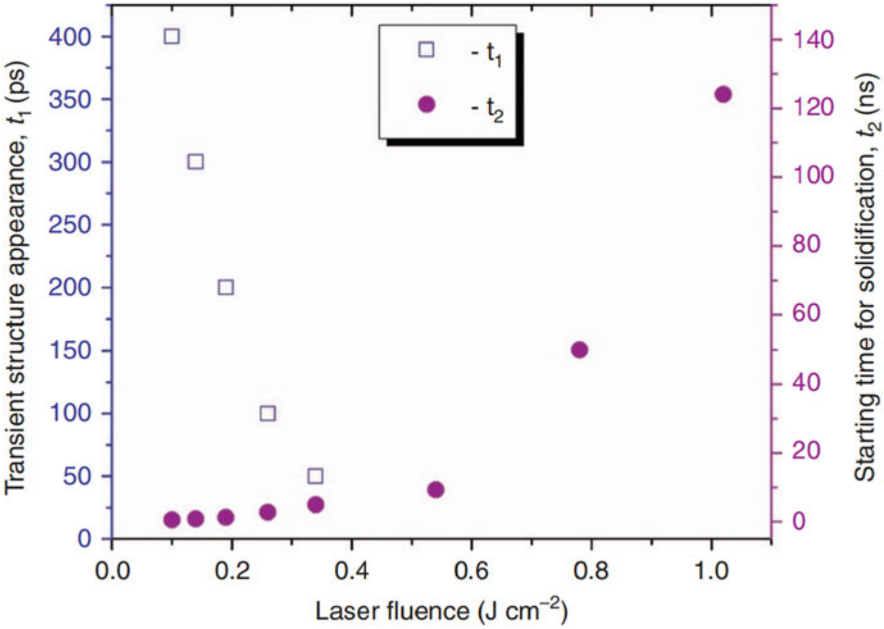

Fig. 9.8 Time at which transient surface structures appear, t_1, and start time of solidification, t_2, as functions of laser fluence. (Reprinted with permission from Ref. [49])

they made a comparison of Figs. 9.7 and 9.9 and showed that the spatial sequencing of the transient structures before solidification varied with the laser fluence. To further understand this dependence, the authors considered the surface images to be acquired at a fixed delay time of 527 ps, but at different laser fluences, as shown in Fig. 9.10, a transition can be seen from first emergence of the transient structures in the center to first emergence at the edge that occurs at 0.54 J cm^{-2}. the SEM images presented in Fig. 9.6 to show that at this laser fluence, the surface structures in the center changed from being mostly nanostructures to being mostly microstructures, corresponding to the CCD images [49].

At these higher laser fluences, nanostructures could be produced at the edge of the ablated spot because of the Gaussian profile of the laser beam. Therefore, the spatial evolution of the ring surface pattern observed between 300 ps and 2.8 ns in Fig. 9.9 is attributed to the fact that nanostructures first form at the surrounding area, and the center region is later populated with microstructures; with regard to the timescale of morphological fluctuations ($t_P \approx L/v_{sl}$), the time required to form nanostructures (corresponding to smaller L) was shorter than that required to form microstructures (corresponding to larger L) [49]. Another possible explanation for the central dark spot is that the formation of highly light-absorptive matter in the central part of the interaction area was possibly due to the formation of an ablation plasma that masks the surface structures. Over time, such an ablation plasma would become more transparent, and the surface structures in the central part of the ablated

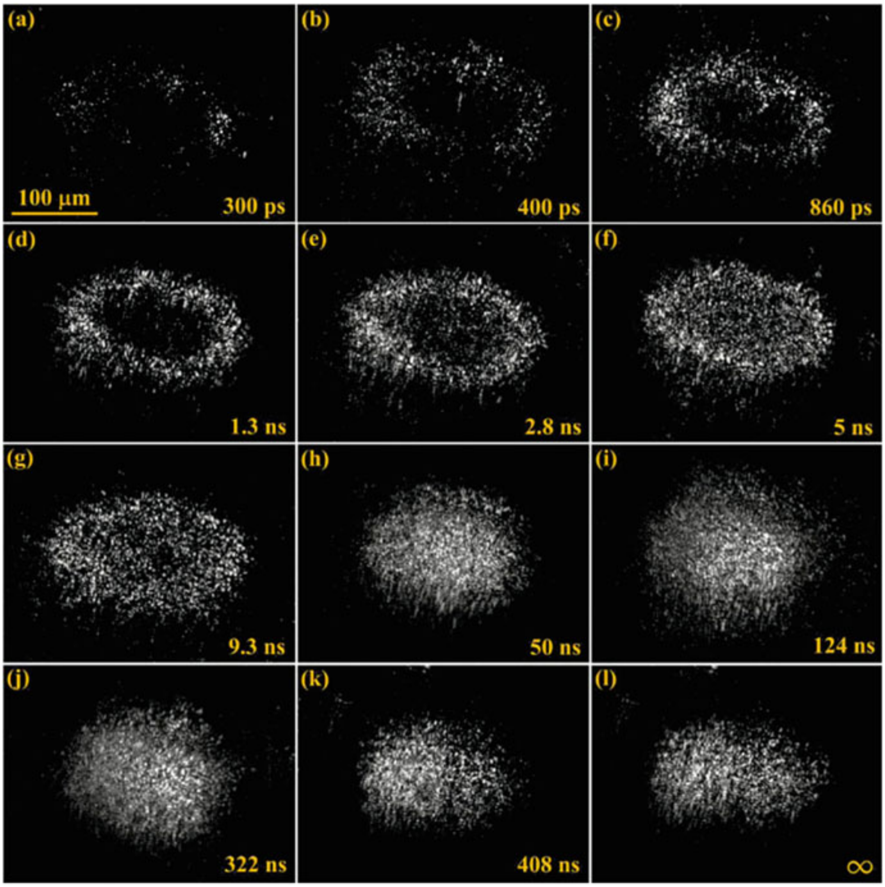

Fig. 9.9 (**a**–**l**) CCD images of a Zn surface at various delay times following a pump pulse at a fluence of 0.78 J cm^{-2}. (Reprinted with permission from Ref. [49])

area would become more visible [49, 50]. The absorption of laser light by an ablation plasma has been previously observed in more previous research of double-pulse ablation studies [59, 60].

Several possible ablation mechanisms exist [56, 57, 61–63] to describe the mechanisms of the evolution of the transient surface structures from their first appearance (t_1) up through the onset of solidification (t_2), including evaporation [62], thermomechanical fragmentation/spallation [56, 57], and phase explosion [56, 63]. The maximum lattice temperature T_m should also be estimated to identify the ablation mechanisms that were responsible to the former observations [52, 64]:

$$T_\mathrm{m} = T_0 + \frac{F_\mathrm{A}}{c_i} \frac{\beta\alpha}{\beta + \alpha}, \beta = \sqrt{\frac{g}{\kappa}} \tag{9.2}$$

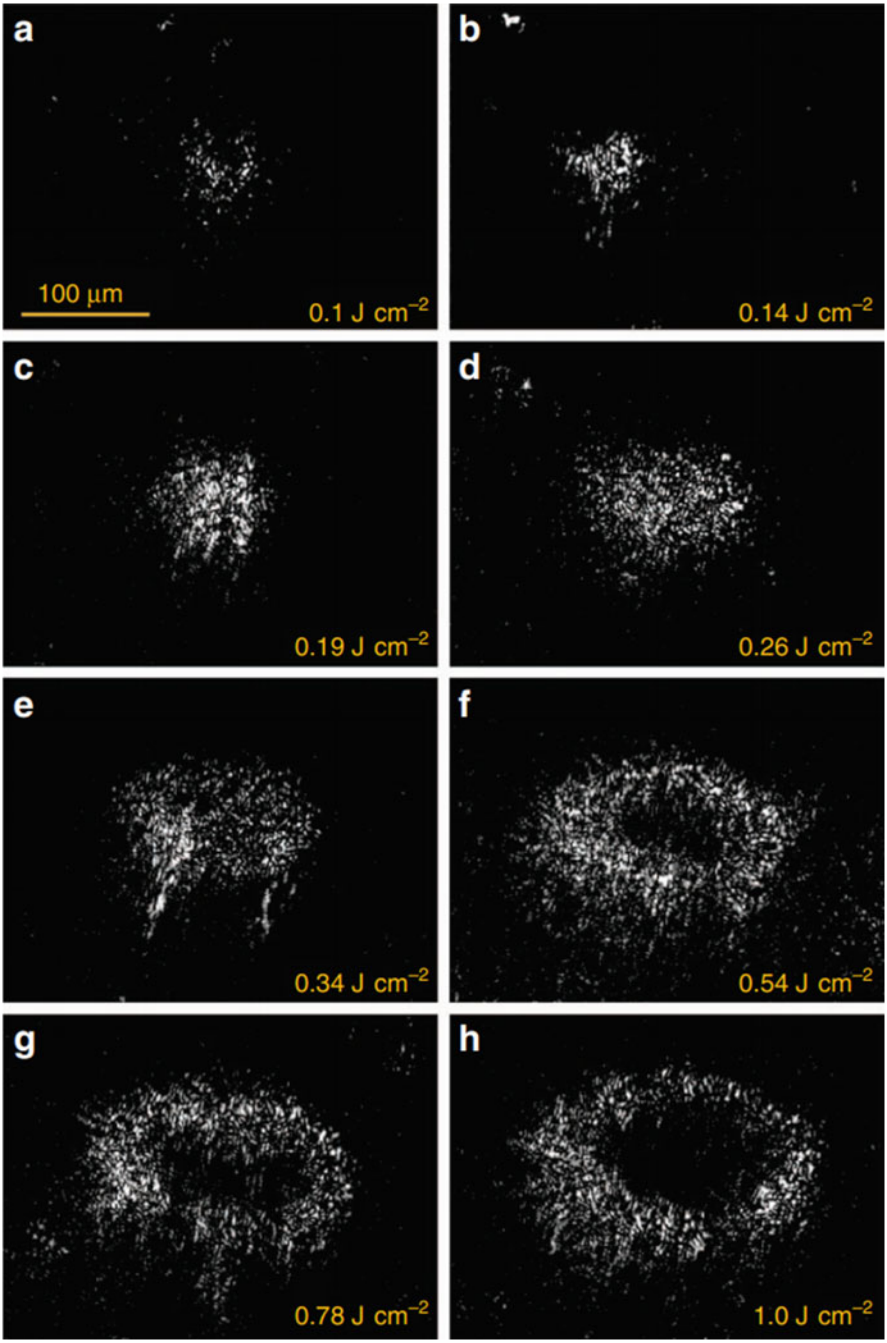
a
100 µm
0.1 J cm−2
b
0.14 J cm−2
c
0.19 J cm−2
d
0.26 J cm−2
e
0.34 J cm−2
f
0.54 J cm−2
g
0.78 J cm−2
h
1.0 J cm−2

Fig. 9.10 (**a**–**h**) CCD images of Zn surfaces at a fixed delay time of 527 ps following pump pulses at various laser fluence values. (Reprinted with permission from Ref. [49])

where T_0 is the room temperature, c_i is the specific heat of the lattice, α is the light attenuation coefficient, g is the electron-phonon coupling factor, κ is the thermal conductivity, and $\phi_A = (1 - R)\phi$ is the absorbed laser fluence [51], where R is the reflectance of Zn at the wavelength of the laser used. The reflectance of a metal surface depends on its condition after polishing, the angle of the incident light, and the laser fluence. The key to obtaining a reliable estimate of the surface temperature was to accurately determine the value of the sample reflectance under the experimental conditions. To do so, they performed a rigorous surface reflectance measurement by using a hemi-ellipsoidal collector to collect both the specular and diffuse reflected light [49, 51]. The measured reflectance in a fluence range of 0.01–1.0 J cm^{-2} was $R = 0.55$–0.57, shown in Table 9.1 [49]. Table 9.1 also shows the surface temperatures estimated by using $T_0 = 300$ K, $c_i = 2.78 \times 106$ J m^{-3} K^{-1}, $\alpha = 7.5 \times 10^7$ m^{-1}, $g = 6 \times 10^{16}$ W m^{-3} K^{-1} [65], and $\kappa = 116$ W m^{-1} K^{-1} [49]. At the damage threshold laser fluence of 0.022 J cm^{-2}, T_m was estimated to be 890 K, only slightly higher than the melting point of Zn (693 K), indicating that (Eq. 9.2) provided a reasonable estimation of the surface temperature.

At $\phi = 0.1$ J cm^{-2}, the surface temperature was estimated to be 2970 K, exceeding the boiling point of Zn (1180 K), and this laser fluence was in the ablation regime [49]. At laser fluences of 0.14 J cm^{-2} or above, the estimated surface temperatures are above the thermodynamic critical point T_c (3190 K), indicating that the laser-excited material becomes a supercritical fluid (with no distinction between the liquid and vapor phases). The authors discussed that the surface temperature for ablation at $F = 0.1$ J cm^{-2} could lead to either vaporization [62] or thermomechanical fragmentation/spallation [49, 56, 57]. However, it is believed that the predominant contribution to ablation was from thermomechanical fragmentation/spallation, whereas the role of vaporization was not essential [66]. Therefore, it is believed that the results at a fluence of 0.1 J cm^{-2} were mostly related to ablation through the spallation mechanism. In the spallation regime, an ultrashort laser pulse induces fast isochoric heating of the surface layer [56, 57, 67–69], which causes a buildup of high stress, cavitation, nanofoam formation, and thermomechanical spallation (ablation) of a liquid layer on the surface due to the relaxation of tensile stresses developed in the surface layer.

In a more recent follow-up work, the same research lab used a similar ultrafast imaging technique to record the spatiotemporal evolution of the nanostructures induced by femtosecond laser ablation [48]. The evolution underwent melting, spallation, and resolidification process. Finite-difference time-domain (FDTD) simulation was also performed and showed consistency with molecular dynamics simulations, showing that the photomechanical spallation was leading the melting of nanostructure for a few picoseconds. Figure 9.11 shows the difference of FDTD calculation of scattering through liquid and solid Zn sphere and schematics of photomechanical spallation process in surface nanostructures which was done in the work [48].

For an incident laser fluence of higher than 0.14 J cm^{-2}, the surface temperature is estimated to be significantly higher than 0.9 T_c [49], which is the characteristic threshold temperature for phase explosion [63]. Phase explosion occurs at laser

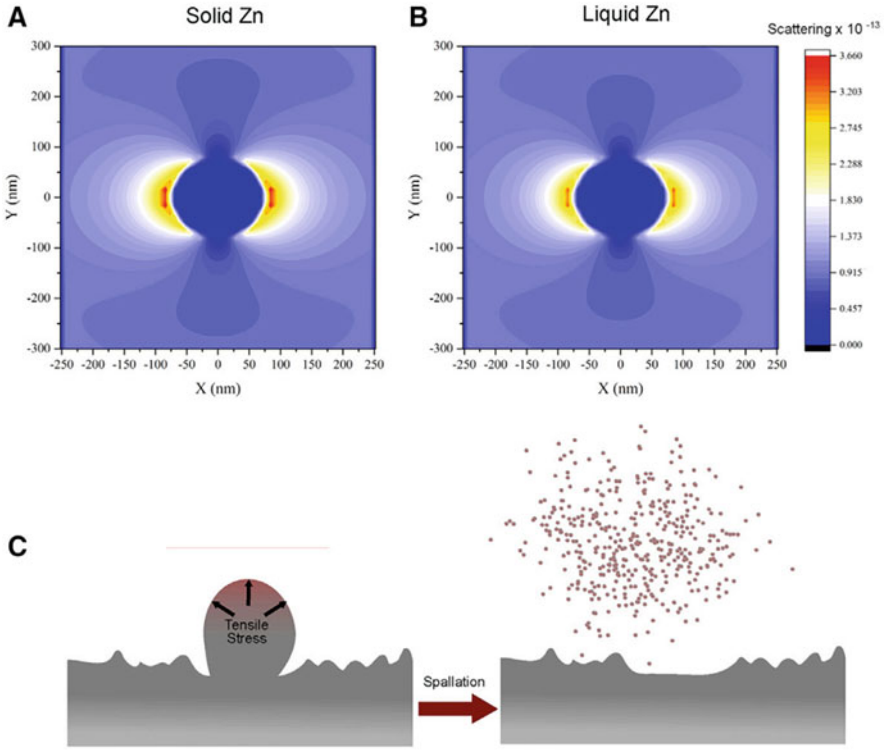
A
Solid Zn
B
Liquid Zn
Scattering x 10^-13
3.660
3.203
2.745
2.288
1.830
1.373
0.915
0.457
0.000
Y (nm)
X (nm)
300
200
100
0
-100
-200
-300
-250 -200 -150 -100 -50 0 50 100 150 200 250
C
Tensile Stress
Spallation

Fig. 9.11 (**a**, **b**) FDTD calculation of scattering from a 150 nm (**a**) solid Zn sphere and (**b**) liquid Zn sphere. (**c**) Schematics of photomechanical spallation process in surface nanostructures. (Reprinted with permission from Ref. [48])

fluences below those for substantial ionization and plasma formation [69]. It is known that plasma formation causes a significant decrease in reflectance [49, 51, 70]. The reflectance measurements recorded in Table 9.1 shows that a significant decrease in the reflectance of the Zn surface occurs at laser fluences above 1.1 J cm^{-2}. The result indicates that in the laser fluence range of 0.14–1.1 J cm^{-2}, ablation is primarily caused by phase explosion. Therefore, the authors inferred that the transient structural dynamics between t_1 and t_2 originate from either the spallation mechanism or the phase explosion mechanism, depending on the laser fluence [49]. As shown in Fig. 9.8, both t_1 and t_2 depend on the laser fluence. The start time of solidification, t_2, increases with laser fluence, indicating that a longer time is required for solidification to occur at a higher laser fluence [49].

The discussion of mechanism of complete solidification and its associated time, t_3, was also put forward [49]. After ablation, rapid cooling due to high electronic heat conduction causes solidification of the melted surface layer, giving rise to permanent surface structures. The cooling and resolidification of the melted surface layer in the spallation regime had been previously modeled by using the atomistic molecular dynamics method combined with a continuum-level two-temperature model by other researchers [67, 68]. In those more previous works, the complete resolidification time was predicted to be 2.5 ns for Al [67] and 1.4–1.7 ns for Ag [68]. Those timescales were approximately two orders of magnitude smaller than the observed complete solidification time, t_3, for Zn. It is generally believed that the cooling of an ultrafast laser-heated metal surface is dominated by thermal conduction [52, 64]. Under these conditions, the cooling time t_{cool} is estimated to be [52]

$$t_{\mathrm{cool}} = \frac{\delta^2}{4\chi}, \delta = \left(\frac{18 I_{\mathrm{A}} k}{g^2 T_0}\right)^{\frac{1}{3}} \tag{9.3}$$

where χ is the thermal diffusivity and I_{A} is the absorbed laser intensity. The estimated values of t_{cool} for Zn are also shown in Table 9.1, where it can be seen that t_{cool} is significantly shorter than t_3 from observation. Following this way, both the model predictions [67, 68] and the estimation based on the equation predicted significantly faster cooling than the observation in the experiments, indicating that the current understanding of the rapid cooling process was incomplete [49]. To explain this discrepancy, it was suggested that the slower cooling process was due to an enhanced thermal coupling [49], which had previously been observed and modeled [71, 72], where it was found that a significant amount of thermal energy remains in a metal following fs laser ablation, as the transfer time of thermal energy from the ablation plume back to the sample is much longer than the laser pulse duration in the time domain. The speculation was supported by other researchers of residual thermal coupling in the ablation of Zn [71], which indicated that the starting point of the enhanced thermal coupling occurs at $\phi = 0.45$ J cm^{-2} and is correlated with an abrupt increase in the start time of solidification, t_2, where $\phi >$ 0.54 J cm^{-2}, shown in Fig. 9.8 [49]. Moreover, the heating of a sample through the transfer of energy from the ablation plasma was found to cause ultradeep drilling of the material in more previous research [73]. In addition to the enhanced thermal coupling, surface cooling can also be slowed by the latent heat of resolidification and by exothermic chemical reactions induced during laser ablation [74]. In one example of the large contribution of chemical sources of energy, this contribution has been shown to reach up to 30% of the incident laser energy during the nanosecond laser ablation of Zn in air [74].

5 Summary and Outlook

In conclusion, by using the ultrafast pump-probe imaging technique, the researchers have captured and visualized the complete temporal and spatial evolution of the fs laser-induced surface structural dynamics of metals. The transient surface structures were found by the researchers to first appear at a delay time on the order of 100 ps, and this is attributed to ablation driven by pressure relaxation in the surface layer. At lower laser fluences that favor nanostructure formation, the transient surface structures first appear in the central portion of the ablated spot. At higher laser fluences that favor microstructure formation, nanostructures first emerge at the periphery, and the center region is later populated with microstructures [49].

The visualization and control of surface structural dynamics not only are of fundamental importance for understanding the fs laser-induced responses of materials but also pave the way for the design of new material functionalities through surface structuring.

References

1. A.Y. Vorobyev, C. Guo, Direct femtosecond laser surface nano/microstructuring and its applications. Laser Photonics Rev. **7**, 385–407 (2013)
2. Y. He, J. Zhang, S. Singh, E. Garcell, A.Y. Vorobyev, B. Lam, Z. Zhan, J. Yang, C. Guo, Maskless laser nano-lithography of glass through sequential activation of multi-threshold ablation. Appl. Phys. Lett. **114**, 133107 (2019)
3. J. Zhang, C. Cong, C. Guo, Single-step maskless nano-lithography on glass by femtosecond laser processing. J. Appl. Phys. **127**, 163102 (2020)
4. P. Pronko, S. Dutta, J. Squier, J. Rudd, D. Du, G. Mourou, Machining of sub-micron holes using a femtosecond laser at 800 nm. Opt. Commun. **114**, 106–110 (1995)
5. F. Korte, J. Serbin, J. Koch, A. Egbert, C. Fallnich, A. Ostendorf, B. Chichkov, Towards nanostructuring with femtosecond laser pulses. Appl. Phys. A **77**, 229–235 (2003)
6. A.Y. Vorobyev, C. Guo, Femtosecond laser nanostructuring of metals. Opt. Express **14**, 2164–2169 (2006)
7. A. Vorobyev, C. Guo, Multifunctional surfaces produced by femtosecond laser pulses. J. Appl. Phys. **117**, 033103 (2015)
8. S. Nolte, B. Chichkov, H. Welling, Y. Shani, K. Lieberman, H. Terkel, Nanostructuring with spatially localized femtosecond laser pulses. Opt. Lett. **24**, 914–916 (1999)
9. C. Wu, C. Crouch, L. Zhao, J. Carey, R. Younkin, J. Levinson, E. Mazur, R. Farrell, P. Gothoskar, A. Karger, Near-unity below-band-gap absorption by microstructured silicon. Appl. Phys. Lett. **78**, 1850–1852 (2001)
10. A. Pereira, A. Cros, P. Delaporte, S. Georgiou, A. Manousaki, W. Marine, M. Sentis, Surface nanostructuring of metals by laser irradiation: Effects of pulse duration, wavelength and gas atmosphere. Appl. Phys. A **79**, 1433–1437 (2004)
11. A. Borowiec, H.K. Haugen, Subwavelength ripple formation on the surfaces of compound semiconductors irradiated with femtosecond laser pulses. Appl. Phys. Lett. **82**, 4462–4464 (2003)
12. J. Bonse, M. Munz, H. Sturm, Structure formation on the surface of indium phosphide irradiated by femtosecond laser pulses. J. Appl. Phys. **97**, 013538 (2005)
13. F. Costache, S. Kouteva-Arguirova, J. Reif, Sub–damage–threshold femtosecond laser ablation from crystalline Si: Surface nanostructures and phase transformation. Appl. Phys. A **79**, 1429–1432 (2004)
14. A. Vorobyev, C. Guo, Direct creation of black silicon using femtosecond laser pulses. Appl. Surf. Sci. **257**, 7291–7294 (2011)
15. A. Kabashin, M. Charbonneau-Lefort, M. Meunier, R. Leonelli, Effects of deposition and post-fabrication conditions on photoluminescent properties of nanostructured Si/SiOx films prepared by laser ablation. Appl. Surf. Sci. **168**, 328–331 (2000)

16. A. Vorobyev, C. Guo, Enhanced absorptance of gold following multipulse femtosecond laser ablation. Phys. Rev. B **72**, 195422 (2005)
17. Y.P. Meshcheryakov, N. Bulgakova, Thermoelastic modeling of microbump and nanojet formation on nanosize gold films under femtosecond laser irradiation. Appl. Phys. A **82**, 363–368 (2006)
18. D.S. Ivanov, B. Rethfeld, G.M. O'Connor, T.J. Glynn, A.N. Volkov, L.V. Zhigilei, The mechanism of nanobump formation in femtosecond pulse laser nanostructuring of thin metal films. Appl. Phys. A **92**, 791–796 (2008)
19. A.Y. Vorobyev, C. Guo, Colorizing metals with femtosecond laser pulses. Appl. Phys. Lett. **92**, 041914 (2008)
20. A.Y. Vorobyev, C. Guo, Femtosecond laser blackening of platinum. J. Appl. Phys. **104**, 053516 (2008)
21. A.Y. Vorobyev, C. Guo, Antireflection effect of femtosecond laser-induced periodic surface structures on silicon. Opt. Express **19**, A1031–A1036 (2011)
22. T. Baldacchini, J.E. Carey, M. Zhou, E. Mazur, Superhydrophobic surfaces prepared by microstructuring of silicon using a femtosecond laser. Langmuir **22**, 4917–4919 (2006)
23. M. Barberoglou, V. Zorba, E. Stratakis, E. Spanakis, P. Tzanetakis, S.H. Anastasiadis, C. Fotakis, Bio-inspired water repellent surfaces produced by ultrafast laser structuring of silicon. Appl. Surf. Sci. **255**, 5425–5429 (2009)
24. E. Fadeeva, S. Schlie, J. Koch, B.N. Chichkov, A.Y. Vorobyev, C. Guo, *Contact Angle, Wettability and Adhesion*, vol 6 (VSP/Brill, 2009)
25. A. Vorobyev, C. Guo, Water sprints uphill on glass. J. Appl. Phys. **108**, 123512 (2010)
26. S.C. Singh, M. ElKabbash, Z. Li, X. Li, B. Regmi, M. Madsen, S.A. Jalil, Z. Zhan, J. Zhang, C. Guo, Solar-trackable super-wicking black metal panel for photothermal water sanitation. Nat. Sustain. **3**, 938–946 (2020)
27. A.Y. Vorobyev, C. Guo, Laser turns silicon superwicking. Opt. Express **18**, 6455–6460 (2010)
28. R.V. Volkov, D.M. Golishnikov, V.M. Gordienko, A.B. Savel'ev, Overheated plasma at the surface of a target with a periodic structure induced by femtosecond laser radiation. J. Exp. Theor. Phys. Lett. **77**, 473–476 (2003)
29. T.Y. Hwang, A.Y. Vorobyev, C. Guo, Surface-plasmon-enhanced photoelectron emission from nanostructure-covered periodic grooves on metals. Phys. Rev. B **79**, 085425 (2009)
30. A.Y. Vorobyev, V.S. Makin, C. Guo, Brighter light sources from black metal: Significant increase in emission efficiency of incandescent light sources. Phys. Rev. Lett. **102**, 234301 (2009)
31. S.A. Jalil, M. Akram, J.A. Bhat, J.J. Hayes, S.C. Singh, M. ElKabbash, C. Guo, Creating superhydrophobic and antibacterial surfaces on gold by femtosecond laser pulses. Appl. Surf. Sci. **506**, 144952 (2020)
32. E. Fadeeva, V.K. Truong, M. Stiesch, B.N. Chichkov, R.J. Crawford, J. Wang, E.P. Ivanova, Bacterial retention on superhydrophobic titanium surfaces fabricated by femtosecond laser ablation. Langmuir **27**, 3012–3019 (2011)
33. A. Cunha, A.-M. Elie, L. Plawinski, A.P. Serro, A.M.B. do Rego, A. Almeida, M.C. Urdaci, M.-C. Durrieu, R. Vilar, Femtosecond laser surface texturing of titanium as a method to reduce the adhesion of Staphylococcus aureus and biofilm formation. Appl. Surf. Sci. **360**, 485–493 (2016)
34. M. Downer, R.L. Fork, C.V. Shank, Femtosecond imaging of melting and evaporation at a photoexcited silicon surface. J. Opt. Soc. Am. B **2**, 595–599 (1985)
35. J. Bonse, G. Bachelier, J. Siegel, J. Solis, H. Sturm, Time-and space-resolved dynamics of ablation and optical breakdown induced by femtosecond laser pulses in indium phosphide. J. Appl. Phys. **103**, 054910 (2008)
36. D. Von der Linde, K. Sokolowski-Tinten, The physical mechanisms of short-pulse laser ablation. Appl. Surf. Sci. **154**, 1–10 (2000)
37. K. Sokolowski-Tinten, J. Bialkowski, A. Cavalleri, D. von der Linde, A. Oparin, J. Meyer-ter-Vehn, S. Anisimov, Transient states of matter during short pulse laser ablation. Phys. Rev. Lett. **81**, 224 (1998)

38. J. Bonse, G. Bachelier, J. Siegel, J. Solis, Time-and space-resolved dynamics of melting, ablation, and solidification phenomena induced by femtosecond laser pulses in germanium. Phys. Rev. B **74**, 134106 (2006)
39. M. Domke, S. Rapp, M. Schmidt, H.P. Huber, Ultrafast pump-probe microscopy with high temporal dynamic range. Opt. Express **20**, 10330–10338 (2012)
40. J. Hernandez-Rueda, D. Puerto, J. Siegel, M. Galvan-Sosa, J. Solis, Plasma dynamics and structural modifications induced by femtosecond laser pulses in quartz. Appl. Surf. Sci. **258**, 9389–9393 (2012)
41. C.W. Siders, A. Cavalleri, K. Sokolowski-Tinten, C. Tóth, T. Guo, M. Kammler, M.H. Von Hoegen, K.R. Wilson, D. von der Linde, C.P. Barty, Detection of nonthermal melting by ultrafast X-ray diffraction. Science **286**, 1340–1342 (1999)
42. A. Rousse, C. Rischel, S. Fourmaux, I. Uschmann, S. Sebban, G. Grillon, P. Balcou, E. Förster, J.-P. Geindre, P. Audebert, Non-thermal melting in semiconductors measured at femtosecond resolution. Nature **410**, 65–68 (2001)
43. B.J. Siwick, J.R. Dwyer, R.E. Jordan, R.J.D. Miller, An atomic-level view of melting using femtosecond electron diffraction. Science **302**, 1382–1385 (2003)
44. K. Sokolowski-Tinten, A. Barty, S. Boutet, U. Shymanovich, H. Chapman, M. Bogan, S. Marchesini, S. Hau-Riege, N. Stojanovic, J. Bonse, Y. Rosandi, H.M. Urbassek, R.A. Tobey, H. Ehrke, A. Cavalleri, S. Düsterer, H. Redlin, M. Frank, S. Bajt, J. Schulz, M. Seibert, J. Hajdu, R. Treusch, C. Bostedt, M. Hoener, T. Möller, Short-pulse laser induced transient structure formation and ablation studied with time-resolved coherent XUV-scattering. MRS Online Proc. Libr. **1230**, 1–6 (2009)
45. P. Baum, D.-S. Yang, A.H. Zewail, 4D visualization of transitional structures in phase transformations by electron diffraction. Science **318**, 788–792 (2007)
46. A. Barty, S. Boutet, M.J. Bogan, S. Hau-Riege, S. Marchesini, K. Sokolowski-Tinten, N. Stojanovic, H. Ehrke, A. Cavalleri, S. Düsterer, Ultrafast single-shot diffraction imaging of nanoscale dynamics. Nat. Photonics **2**, 415–419 (2008)
47. J. Spence, Ultrafast diffract-and-destroy movies. Nat. Photonics **2**, 390–391 (2008)
48. M. ElKabbash, R. Fang, A. Vorobyev, S.A. Jalil, S. Chamoli, B. Lam, S. Singh, C. Guo, Imaging nanostructure phase transition through ultrafast far-field optical ultra-microscopy. Cell Rep. Phys. Sci. **2**, 100651 (2021)
49. R. Fang, A. Vorobyev, C. Guo, Direct visualization of the complete evolution of femtosecond laser-induced surface structural dynamics of metals. Light Sci. Appl. **6**, e16256–e16256 (2017)
50. R. Fang, A.Y. Vorobyev, S.C. Singh, C. Guo, Ultrafast microscopy in resolving femtosecond laser-induced surface structuring. Jpn. J. Appl. Phys. **57**, 08PF04 (2018)
51. A. Vorobyev, C. Guo, Reflection of femtosecond laser light in multipulse ablation of metals. J. Appl. Phys. **110**, 043102 (2011)
52. M. Agranat, S. Ashitkov, V. Fortov, A. Kirillin, A. Kostanovskii, S. Anisimov, P. Kondratenko, Use of optical anisotropy for study of ultrafast phase transformations at solid surfaces. Appl. Phys. A **69**, 637–640 (1999)
53. J. Bonse, S. Wiggins, J. Solis, Phase transitions induced by femtosecond laser pulse irradiation of indium phosphide. Appl. Surf. Sci. **248**, 151–156 (2005)
54. M.J. Assael, I.J. Armyra, J. Brillo, S.V. Stankus, J. Wu, W.A. Wakeham, Reference data for the density and viscosity of liquid cadmium, cobalt, gallium, indium, mercury, silicon, thallium, and zinc. J. Phys. Chem. Ref. Data **41**, 033101 (2012)
55. K. Nogi, K. Ogino, A. McLean, W. Miller, The temperature coefficient of the surface tension of pure liquid metals. Metall. Trans. B **17**, 163–170 (1986)
56. E. Leveugle, D.S. Ivanov, L.V. Zhigilei, Photomechanical spallation of molecular and metal targets: Molecular dynamics study. Appl. Phys. A **79**, 1643–1655 (2004)
57. N. Inogamov, A.Y. Faenov, V. Zhakhovskii, I.Y. Skobelev, V. Khokhlov, Y. Kato, M. Tanaka, T. Pikuz, M. Kishimoto, M. Ishino, Interaction of short laser pulses in wavelength range from infrared to X-ray with metals, semiconductors, and dielectrics. Contrib. Plasma Physics **51**, 361–366 (2011)
58. D.R. Lide, *CRC Handbook of Chemistry and Physics*, vol 85 (CRC Press, 2004)

59. A. Semerok, C. Dutouquet, Ultrashort double pulse laser ablation of metals. Thin Solid Films **453**, 501–505 (2004)
60. M. Povarnitsyn, T. Itina, K. Khishchenko, P. Levashov, Suppression of ablation in femtosecond double-pulse experiments. Phys. Rev. Lett. **103**, 195002 (2009)
61. N.M. Bulgakova, R. Stoian, A. Rosenfeld, I.V. Hertel, *Laser-Surface Interactions for New Materials Production* (Springer, 2010), pp. 81–97
62. S.I. Anisimov, B. Luk'Yanchuk, Selected problems of laser ablation theory. Physics-Uspekhi **45**, 293 (2002)
63. A. Miotello, R. Kelly, Critical assessment of thermal models for laser sputtering at high fluences. Appl. Phys. Lett. **67**, 3535–3537 (1995)
64. S.I. Anisimov, B. Rethfeld, *Nonresonant Laser-Matter Interaction (NLMI-9)* (International Society for Optics and Photonics, 1997), pp. 192–203
65. M.V. Shugaev, N.M. Bulgakova, Thermodynamic and stress analysis of laser-induced forward transfer of metals. Appl. Phys. A **101**, 103–109 (2010)
66. N. Inogamov, V. Zhakhovskii, V. Khokhlov, Jet formation in spallation of metal film from substrate under action of femtosecond laser pulse. J. Exp. Theor. Phys. **120**, 15–48 (2015)
67. N.A. Inogamov, V.V. Zhakhovsky, V.A. Khokhlov, S.I. Ashitkov, Y.N. Emirov, K.V. Khichshenko, A.Y. Faenov, T.A. Pikuz, M. Ishino, M. Kando, *Journal of Physics: Conference Series* (IOP Publishing, 2014), p. 012041
68. C. Wu, M.S. Christensen, J.-M. Savolainen, P. Balling, L.V. Zhigilei, Generation of subsurface voids and a nanocrystalline surface layer in femtosecond laser irradiation of a single-crystal Ag target. Phys. Rev. B **91**, 035413 (2015)
69. L.V. Zhigilei, Z. Lin, D.S. Ivanov, Atomistic modeling of short pulse laser ablation of metals: Connections between melting, spallation, and phase explosion. J. Phys. Chem. C **113**, 11892–11906 (2009)
70. S. Kirkwood, Y. Tsui, R. Fedosejevs, A. Brantov, V.Y. Bychenkov, Experimental and theoretical study of absorption of femtosecond laser pulses in interaction with solid copper targets. Phys. Rev. B **79**, 144120 (2009)
71. A. Vorobyev, C. Guo, Enhanced energy coupling in femtosecond laser-metal interactions at high intensities. Opt. Express **14**, 13113–13119 (2006)
72. N. Bulgakova, V. Zhukov, A. Vorobyev, C. Guo, Modeling of residual thermal effect in femtosecond laser ablation of metals: Role of a gas environment. Appl. Phys. A **92**, 883–889 (2008)
73. N.M. Bulgakova, A.B. Evtushenko, Y.G. Shukhov, S.I. Kudryashov, A.V. Bulgakov, Role of laser-induced plasma in ultradeep drilling of materials by nanosecond laser pulses. Appl. Surf. Sci. **257**, 10876–10882 (2011)
74. A.Y. Vorobyev, I. Dorofeev, M. Libenson, Concerning the chemical source of energy in a laser flare. Sov. Tech. Phys. Lett. **18**, 172–173 (1992)

Part II
Concepts of Extreme Nanostructuring

Chapter 10

Macroscale Microfabrication Enabled by Nanoscale Morphological Control of Laser Internal Modification

Ya Cheng, Haisu Zhang, Peng Wang, Jia Qi, Jian Xu, Xin Li, Wenbo Li, Xiaolong Li, Zijie Lin, Jinming Chen, Ming Hu, and Min Wang

Abstract Over the past decades, ultrafast laser internal modification has become a widely adopted approach to enable three-dimensional (3D) micromachining of transparent materials into sophisticated structures and devices with the extreme geometrical flexibility. Owing to the linear diffraction and nonlinear self-focusing effects, it is extremely challenging to maintain the high longitudinal resolution when focusing deeply into the transparent substrates for achieving macroscale microfabrication, i.e., fabrication of objects of centimeter-level heights without sacrificing the micrometer-scale resolution. We overcome this tremendous difficulty using loosely focused picosecond laser pulses, which, surprisingly, offer focal-volume-invariant modification deeply inside fused silica glass and give rise to the formation of extended nanocracks preferentially oriented along the laser scan direction. We show that the combination of these two advantages uniquely allows efficient macroscale microfabrication as demanded by various applications such as 3D glass printing and flow chemistry.

Keywords Ultrafast laser internal modification · Selective chemical etching · Macroscale microfabrication · 3D glass printing · Flow chemistry application

---

Y. Cheng (✉)
School of Physics and Electronic Science, East China Normal University, Shanghai, China

Shanghai Institute of Optics and Fine Mechanics, Chinese Academy of Sciences, Shanghai, China
e-mail: ya.cheng@siom.ac.cn

H. Zhang · J. Qi · J. Xu · X. Li · X. Li · Z. Lin · J. Chen · M. Hu · M. Wang
School of Physics and Electronic Science, East China Normal University, Shanghai, China
e-mail: hszhang@phy.ecnu.edu.cn; jqi@phy.ecnu.edu.cn; jxu@phy.ecnu.edu.cn; xli@phy.ecnu.edu.cn; 823166915@qq.com; urnor@icloud.com; jmchen@phy.ecnu.edu.cn; mhu@phy.ecnu.edu.cn; mwang@phy.ecnu.edu.cn

P. Wang · W. Li
Shanghai Institute of Optics and Fine Mechanics, Chinese Academy of Sciences, Shanghai, China
e-mail: wangpeng2015@siom.ac.cn; lwb199267@sina.com

© The Author(s), under exclusive license to Springer Nature Switzerland AG 2023

R. Stoian, J. Bonse (eds.), *Ultrafast Laser Nanostructuring*, Springer Series in Optical Sciences 239, https://doi.org/10.1007/978-3-031-14752-4_10

1 Introduction

Focusing high-power ultrafast laser into transparent materials launches an abundant of chemical, physical, and thermomechanical processes around the laser focus. Such photo-initiated reactions facilitate determinative and highly localized modification within the transparent materials, enabling three-dimensional (3D) micromachining of the materials into sophisticated structures and devices with the extreme geometrical flexibility and superior functionality. Ultrafast laser internal modification underpins the field of high-resolution 3D material machining [1, 2], benefiting a broad spectrum of applications ranging from micro-optoelectromechanics and biomimetic device to massive data storage and quantum information technology [3–6]. The ultrashort pulse duration minimizes collateral thermal damages accompanying laser-material interactions in the conventional nanosecond regime, and meanwhile, the corresponding ultrahigh peak intensity facilitates efficient energy deposition by free carrier absorption irrespective of the bandgap of the material under processing [7]. Since the initial free carriers are generated by the nonlinear photoionization of homogeneous valence band electrons instead of randomly distributed extrinsic defects and impurities, ultrafast laser-induced photo-absorption possesses a deterministic threshold which is inherently confined within the focal volume [8]. The localized energy deposition and internal modification by tightly focused ultrafast laser thus feature a micro-to-nanoscale processing resolution roughly determined by the geometrical size of the laser focus [9].

High-precision ultrafast laser inscription necessitates the judicious design of the illumination technique of the ultrafast laser into the transparent substrate, in order to mitigate a multitude of deleterious effects such as linear diffraction/dispersion, geometrical aberration, nonlinear self-focusing, plasma defocusing/shielding, thermal accumulation, and mechanical stress. Tremendous efforts have been put to control the delivery of ultrafast laser into bulk materials, in order to optimize the laser-material interactions and corresponding internal modifications under specific targets. Both active control schemes, including slit shaping [10], double-pulse excitation [11], Bessel beam [12], simultaneous spatiotemporal focusing [13], and passive optimization loops by adaptive wavefront corrections or temporal shaping with spatial light modulators [14–17], are demonstrated to obtain the desired laser processing resolutions within few millimeters' depth inside bulk materials. However, in the scenario of fabricating centimeter-scale height macro-objects utilizing a low numerical aperture (NA) lens of a long working distance, all the methods mentioned above degrade rapidly. Since the transversal and longitudinal sizes of the focus are respectively proportional to NA^{-1} and NA^{-2} of the focal lens in the linear regime [18], the use of low-NA lens largely increases the attainable focal size especially for the longitudinal dimension. The spherical aberration induced by the index mismatch at the interface and the nonlinear distortions at high-input powers necessitated by the low-NA focusing [19–21] can further spoil the laser-material interaction which can only be compensated by pulse shaping to a limited extent (An in-depth discussion on the encountered limitations and their work-arounds can be found in Chap. 21 of this book).

On the other hand, since the very first demonstration of selective etching of ultrafast laser modified regions inside fused silica glass [22], ultrafast laser induced chemical etching (ULICE) has been intensively investigated to become a versatile method of subtractive manufacturing and rapid prototyping of embedded microfluidic channels and free-form functional components based on transparent substrates [23]. The laser-modified region features diverse chemical, physical, and mechanical transformations including electronic defects, nanopores, lattice disruption, and thermomechanical stress [24], lending itself more susceptible to the chemical etchant compared to the pristine region and thus being selectively etched to form internal hollow structures. Strong anisotropy exists in the chemical etching of ultrafast laser-induced modifications inside a majority of transparent materials, which manifests itself as the polarization-sensitive etching efficiency of the laser-modified region along different scanning directions [25]. Systematic studies pinpoint the formation of nanogratings aligned perpendicular to the polarization direction of the laser, which can suppress or enhance the reaction and refreshment of the etchant within the modified region, as the main origin of the etching anisotropy [26, 27]. Continuous efforts have been put to enhance the etching efficiency and meanwhile alleviate the etching anisotropy of the ULICE process, aiming for sophisticated 3D fabrication capability with complex geometries [28–31] (interested readers are welcome to read Chap. 30 of this book for further information about the ULICE process).

Owing to the unfavorable distortion of the focal profile when focusing deeply into the transparent substrates, as well as the limited chemical etching efficiency and etching anisotropy of ultrafast laser internal modification, 3D manufacturing objects of large heights by ULICE is conceived as a formidable task with rare attempts. In this chapter, we will introduce our recent endeavors for 3D macroscale microfabrication of various functional components, enabled by the nanoscale morphological control of laser internal modification through the delicate spatiotemporal manipulation of laser-material interactions [32–34]. A new laser-material interaction regime is identified with the highly confined modification arising from the self-regulated multiple-pulse interactions mediated by accumulated material changes [35]. Our results reveal a focal-volume-invariant modification deeply inside the fused silica glass, which not only enhances the overall chemical etching rate but also eliminates the etching anisotropy of the laser internal modification within the full range of the glass. As a result, our findings facilitate high-precision, large-scale, and high-throughput manufacturing of geometrically complex glass components at uniform micron resolutions in all three dimensions. The demonstrated multiscale processing capability, from the nanometer to the centimeter range, holds great promise in laser 3D printing, flow chemistry control, and biomimetic engineering.

The organization of this chapter is as follows. Fundamental processes underlying ultrafast laser internal modification in transparent materials will be briefly introduced in Sect. 1, with emphasis on the morphology transformation of laser-induced modification when the pulse durations are stretched from femtosecond (fs) to picosecond (ps) regimes. The nanoscale morphology change of the ultrafast laser internal modification is carefully examined at variable pulse durations in Sect. 2, providing clear evidences of enhanced etching efficiency and suppressed anisotropy for the selective chemical etching of the laser-modified regions by ps pulses of well-controlled durations. The unprecedented control of both the transverse and longitudinal processing resolutions in large-scale glass samples by loosely focused ps pulses is demonstrated in Sect. 3, and elaborated ultrafast pump-probe microscopy is utilized to investigate the underlying mechanism for the observed depth-insensitive laser internal modification. Applications profited by the established macroscale ultrafast laser microfabrication are discussed in Sect. 4, and concluding remarks and perspectives are given in Sect. 5.

1.1 Concept of Ultrafast Laser Internal Modification

Nonlinear photo-absorption emerges when focusing high-power ultrafast laser into the substrates which are transparent to the laser wavelength, i.e., the bandgap E_g of the substrate material is higher than the incident photon energy hv (v is the laser frequency and h is the Planck constant), forming localized internal modification around the laser focus and leaving remaining substrate intact. Nonresonant photoionization of valence band electrons at high laser intensities, which was first predicted by Keldysh in 1960s [36], provides the initial "seed" electrons for photo-absorption. Avalanche ionization by collisions between laser-heated conduction band electrons and bound valence band electrons enables a quick multiplicity of electrons in the conduction band [37]. The synergetic actions of photoionization and avalanche ionization rapidly increase the conduction band electron density, and plasma absorption will dominate the energy deposition process when approaching to the critical electron density ($\sim 10^{21}$ cm^{-3} for 1 μm laser wavelength) [38]. In the meantime, due to the ultrashort duration of the laser pulse, only the electrons within the focal volume are heated to very high temperatures while the material lattice remains cold, which essentially decouples the electron-lattice energy exchange and thermomechanical response with the nonlinear photo-absorption, ensuring the nonthermal nature of ultrafast laser-material interaction [39]. Moreover, due to the sharp thresholds for photoionization in wide-bandgap dielectrics (Eg >> hv), highly confined free-carrier generation and internal modification with feature sizes far below the diffraction limit of the incident laser are expected [8, 9]. More information about the fundamental processes for laser-material interaction can be found in Chap. 1 of this book.

Distinct physical evolution and relaxation pathways after the interaction of the ultrafast laser pulse can be triggered around the laser focus depending on the spatiotemporal distribution of laser energy deposition, rendering diverse types of permanent internal modification which are discussed in next paragraphs.

1.2 Categorization of Typical Morphologies Including Refractive Modification, Nanograting Formation, and Nano-void Formation Induced by Ultrafast Laser Pulses

The ultrafast laser internal modification can be generally categorized into three regimes with corresponding typical morphologies described as below [40].

1. Low-Energy Regime: Smooth Refractive Index Change

   In this regime, the deposited energy is too low to drive substantial thermo-mechanical transformations of the lattice, and alternatively an electronic defect initiated localized melting, and rapid resolidification dominates the post-pulse relaxation [39], which can induce gentle perturbations to the lattice with slight structural compaction, or rarefaction depends on the specific physiochemical property of the substrate material. Given the smooth refractive index change induced in this regime, various in-volume photonic components can be fabricated including optical waveguides [41, 42], fiber gratings [43], and Fresnel waveplates [44]. The optical microscope image of a femtosecond laser-written waveguide inside bulk glass is shown in Fig. 10.1a.
2. Medium-Energy Regime: Nanograting Formation

   The formation of periodic arrays of planar nanostructures, or the well-known nanograting, has been ubiquitously observed at the ultrafast laser-modified regions with moderately high-energy deposition [45]. Furthermore, nanogratings are well self-organized under the illumination of multiple laser pulses and long-range sample scanning. Atomic force microscope (AFM) images of the laser-induced nanogratings in fused silica are shown in Fig. 10.1b. The orientation of these nanogratings perpendicular to the polarization direction of the laser strongly pinpoints the presence of plasmonic enhancement of local electric fields responsible for the produced subwavelength features, though the detailed physical mechanisms still elude researchers with hot controversy [46–48].

   Prosperous applications of the laser-induced nanograting have been demonstrated in the recent decade. Profited by the strong form birefringence of these nanogratings, hyperdimensional data storage and polarization vortex waveplates are realized [5, 49, 50]. Besides, long-range self-organized nanograting can enhance the contrast of selective chemical etching which facilitates fabrication of high-aspect-ratio microfluidic channels [51–53]. Furthermore, sub-50 nm width microchannels are reliably inscribed thanks to the combination of threshold effect and nanograting formation [9, 54]. The field of ultrafast laser-induced nanograting is still in hot development.
3. High-Energy Regime: Micro-explosion and Nano-void Formation

   In this regime, a large fraction of laser pulse energy is deposited in the focus, inducing local pressure higher than the Young's modulus and the formation of shock wave which expels the central material outward and leaves a rarefied core and even a nano-void in the focus [55, 56]. Scanning electron microscope

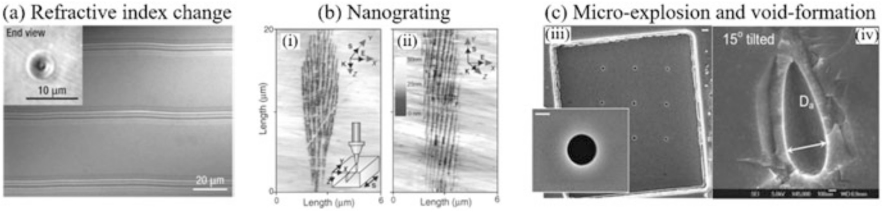

Fig. 10.1 Morphological images corresponding to the three types of ultrafast laser internal modification. (**a**) Optical microscope image of a femtosecond-laser-micromachined waveguide inside bulk glass, with the inset shows the end face of the waveguide. (Reprinted with permission from Schaffer et al. [42] © The Optical Society). (**b**) Atomic force microscope images of chemically etched laser-modified regions, with (i) the cross-sectional view and (ii) the top-view images of the laser-modified region. (Reprinted figure with permission from Bhardwaj et al. [46] Copyright (2021) by the American Physical Society). (**c**) SEM images of femtosecond laser produced voids in sapphire, with (iii) the top-view SEM image of an array of voids and (iv) the side-view SEM image of a laser-affected region after a brief etching in hydrofluoric acid. (Reprinted figure with permission from Juodkazis et al. [56] Copyright (2021) by the American Physical Society)

(SEM) images of laser-induced voids in sapphire are shown in Fig. 10.1c. This modification type is useful for data storage and photonic bandgap materials [57–59].

1.3 Transformation from Self-Organized Nanograting to Preferentially Oriented Nanocracks with Picosecond Laser Pulses of Well-Controlled Pulse Durations

The spatiotemporal profile of the ultrafast laser is of equivalent significance for the attainable internal modification besides the total pulse energy. Various processes are involved during the laser-material interaction which have complicated spatiotemporal responses, such as photoionization, collisional heating, avalanche ionization, self-focusing, and plasma defocusing. Conjugated effects between the excited processes provide ample options to control the ultrafast laser internal modification by spatiotemporal shaping.

Recently, we found that by continuously tuning the duration of the ultrafast laser, the laser internal modification features a gradual transformation from the periodic nanograting oriented vertical to the laser polarization to the extended nanocracks preferentially along the laser scanning direction [32]. Apparently, these nanocracks imply the contribution of efficient energy deposition which induces large though highly confined thermomechanical stress to locally crack the irradiated material following the scanning of the laser focus. Consequently, by solely controlling the duration of ultrafast laser (which is quite convenient to implement by adjusting the grating pair separation of the output compressor employed in high-power ultrafast laser amplifier systems), different internal modification types can be obtained in order to satisfy variable requirements for post-processing selective chemical etching. This efficient temporal control of the ultrafast laser internal modification will be introduced in detail in the following sections.

2 Dependence of Nanoscale Morphology on the Pulse Duration of the Ultrafast Laser

The nanoscale morphology of the ultrafast laser internal modification is systematically examined in this section. The pulse duration dependence of nanoscale morphological transformation of the laser-modified region from periodic nanogratings to preferentially oriented nanocracks is established by ex situ imaging and measurements [32]. Morphology-dominated selective chemical etching is investigated to demonstrate a unique and superior etching regime of enhanced efficiency and suppressed anisotropy.

2.1 Experimental Setup

The experimental schematic is depicted in Fig. 10.2a. The ultrashort laser pulses provided by a high-power ultrafast laser system (Light Conversion, Pharos-20 W), with a central wavelength of 1028 ± 5 nm, repetition rates from 1 kHz to 1 MHz, and variable pulse durations ranging from 270 fs to 10 ps, were employed for laser direct writing in the fused silica glass samples (Corning 7980) with a size of $10 \times 10 \times 2$ mm^3. The laser beam was focused 300 μm beneath the glass surface by a microscope objective lens with $\mathrm{NA} = 0.45$, and the incident pulse energies were adjusted by a variable neutral density filter. To characterize the morphologies of internal modifications induced by various combinations of pulse duration, polarization state, and pulse energy, groups of straight lines with a length of 10 mm and a line spacing of 50 μm were scanned under different processing conditions. Five lines were written under the same condition for each group, in order to reduce the fluctuations of the measurements by averaging the data obtained from the individual lines in the same group.

After the laser irradiation, the glass samples were grinded and polished to remove the ends of the laser-written tracks as the focal spot of the laser beam was distorted by the sample edges due to refractive index mismatch at glass/air interfaces. To monitor the morphology of laser internal modification, the irradiated samples were polished to expose the modified regions, and a brief chemical wet etching in a potassium hydroxide (KOH) solution was employed to disclose the nanoscale morphologies in the modified structures. Besides, selective chemical etching of

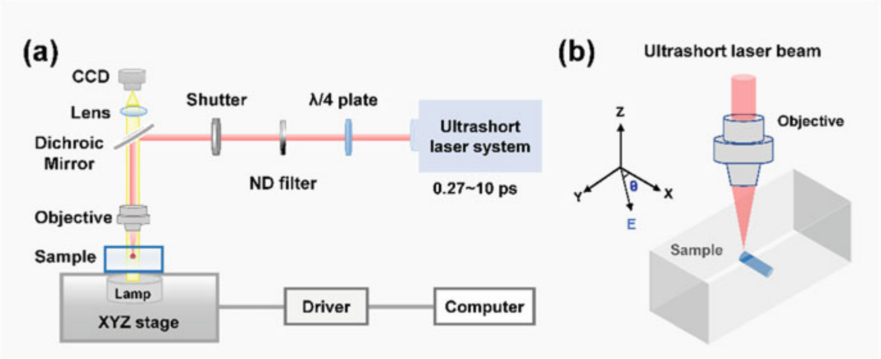

Fig. 10.2 (**a**) The experimental schematic for the ultrafast laser internal modification at variable pulse durations. (**b**) The definition of laser scanning direction and the polarization direction. (Reprinted with permission from Li et al. [32] © 2019 Elsevier B.V)

the laser-modified regions at different processing conditions was also investigated by immersion of the irradiated samples in a 10 mol/L KOH solution hosted in an ultrasonic bath at 85 °C for 1 h.

2.2 Results

The SEM images of the laser written tracks at the fixed single-pulse energy (8 μJ) but different pulse durations are shown in Fig. 10.3. The repetition rate and the scanning velocity were maintained at 50 kHz and 500 μm/s, respectively. Three polarization states of the laser beam were selected to examine the polarization dependence of the laser internal modification. The left and middle columns correspond to linear polarizations, and the last column corresponds to circular polarization. The angle θ between the polarization direction and the laser scanning direction is labelled for the linear polarization cases.

It can be clearly seen that when irradiated with linearly polarized fs laser pulses, periodic nanogratings aligned vertical to the polarization direction are formed in fused silica (see the left and middle panels of Fig. 10.3a). Besides, random nanostructures are observed by switching the linear polarization to the circular polarization, as shown in the right panel of the Fig. 10.3a. These results are consistent with the previous reports on the fs laser-induced nanograting in fused silica [25–30]. Moreover, when the fs laser pulses are stretched to 1 ps and 2 ps as shown in Fig. 10.3b, c, randomly distributed nanocracks mixed with self-organized nanogratings emerge in the laser-modified region. These random nanocracks prevail against the nanogratings as the pulse duration is further stretched to 4 ps (see Fig. 10.3d). The laser-modified regions feature interconnected nanocracks preferentially oriented along the scanning direction irrespective of the polarization states of the

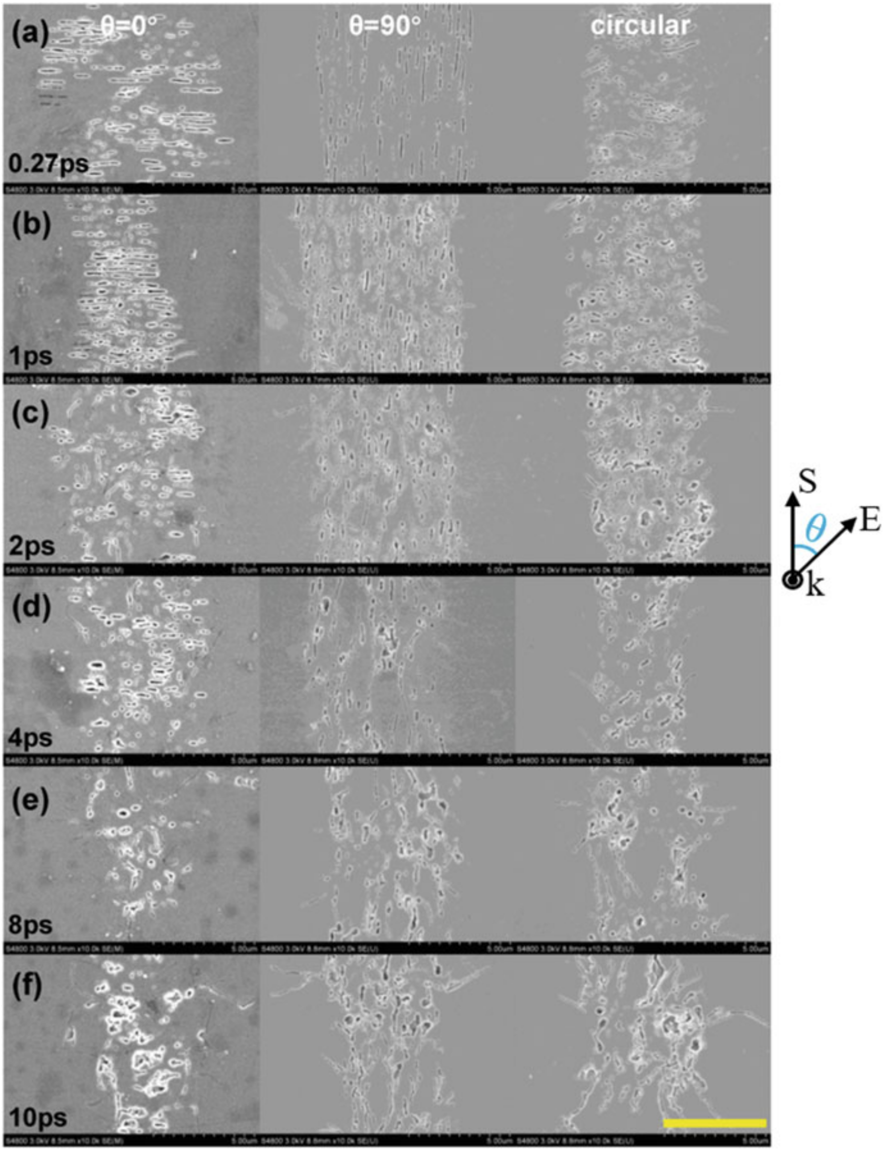
(a)
θ=0°
θ=90°
circular
0.27ps
(b)
1ps
(c)
2ps
(d)
4ps
(e)
8ps
(f)
10ps
S
θ
E
k

Fig. 10.3 SEM images of the irradiated area at different pulse durations and different polarization conditions at 8 μJ. (**a**) 0.27 ps; (**b**) 1 ps; (**c**) 2 ps; (**d**) 4 ps; (**e**) 8 ps; (**f**) 10 ps. The relation between the laser incident direction (k), polarization direction (E), and scanning direction (S) is depicted in the right. Polarization angle is denoted in each panel. Scale bar is 5 μm. (Reprinted with permission from Li et al. [32] © 2019 Elsevier B.V)

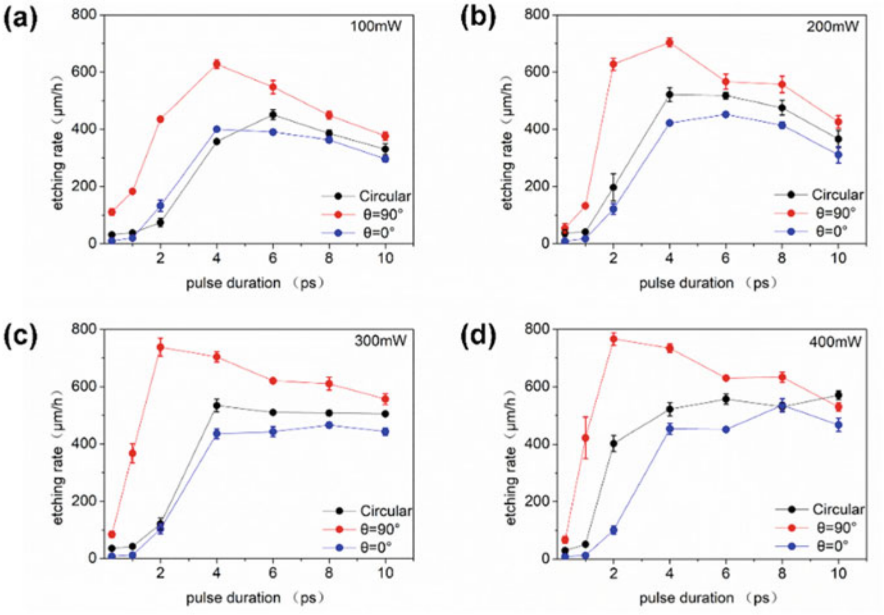

Fig. 10.4 Etching rates of laser-modified lines in fused silica versus pulse durations at different polarization states and pulse energies: (**a**) 2 μJ; (**b**) 4 μJ; (**c**) 6 μJ; (**d**) 8 μJ. (Reprinted with permission from Li et al. [32] © 2019 Elsevier B.V)

incident laser, as long as the pulse duration is longer than 4 ps as shown in Fig. 10.3e, f.

The chemical etching rates of the laser internal modification under different processing conditions are shown in Fig. 10.4. It can be easily noticed that at the same pulse energy, the etching rate of the ps laser-induced modification increases by one order of magnitude compared to that of the fs laser-induced modification. This can be well anticipated since ps laser induces large-scale nanocracks which can promote the penetration, reaction, and refreshment of the etchant solution. Meanwhile, the etching anisotropy for different polarization states is largely reduced for the ps laser-induced modification, which is easily understood since the nanocracks are always aligned to the laser scanning direction by the ps laser. In the contrary, the nanogratings induced by the fs laser will promote or block the continuous flow of the etchant depending on the relative orientation of the polarization direction and the scanning direction [25–27].

2.3 Discussion

The physical mechanism behind the transition of the laser-induced morphology of laser internal modification from polarization-orientated nanogratings to extended nanocracks along the scanning direction needs further clarification. It might be associated with the different energy absorption levels as well as the thermal stress relaxations in the interaction of ps laser with the transparent dielectrics as compared with the fs laser interaction counterpart [60–63]. We speculate that the possible reason for the absence of the self-organized nanogratings may result from the increased interaction time of single pulses. To a certain extent, the extension of the pulse duration in 4–10 ps regime could further enhance the energy deposition of single pulses inside bulk fused silica to a critical level for generating volumetric expansion and localized melting as well as prolonging the cooling time for thermal diffusion around the focus, both of which could cause the possible corruption or reconfiguration of laser-induced modification (e.g., nanogratings).

Meanwhile, as compared with the typical fs regime, with the increase of pulse duration in 4–10 ps regime, the accumulation of thermal stress in the interfaces between laser-modified regions and unmodified regions may promote the generation of seeded defects and subsequent developments of chaotic nanocracks around the focal volume. Although it was reported that the nanograting structures could still be formed even with 8 ps pulses at a higher repetition rate (200 kHz) when a high-NA (NA = 0.65) objective lens was used [61], the results presented here are different since the laser-affected zones are relatively large due to the use of a lower objective lens (NA = 0.45) and rapid thermal diffusion is much difficult since the thermal conductivity of bulk fused silica is very low (1.38 W/m·K). The high stress is also indicated by the fact that the nanocracks in the laser-modified regions are preferentially oriented along the laser scan direction when irradiated with the circularly polarized pulses (Fig. 10.3d–f). Nevertheless, from an application of point of view, this interaction regime enabled with the picosecond laser pulses for polarization-insensitive space-selective etching is of great use for fabrication of 3D microstructures in fused silica, as the necessity of dynamic adjustment of direction of the laser polarization is eliminated for fabricating geometrically complex structures.

3 Improvement of Longitudinal Resolution with Loosely Focused Picosecond Laser Pulses

As already emphasized in the introduction of this chapter, ultrafast laser internal modification based on low-NA focusing facilitates a long working distance suitable for large-scale sample fabrication, though at the unfavorable cost of expanded focus size and compromised processing resolution especially for the longitudinal direction. In this section, we demonstrate that this tough problem can be overcome by adopting ps laser pulses for internal modification deep inside the substrate (fused silica): a homogeneous microscale processing resolution is maintained in all three dimensions among the full range of the macroscale glass sample irrespective of the adverse linear and nonlinear distortions which spoil the focusing of the laser beam. Underlying mechanisms are investigated with the help of ultrafast pump-probe transverse microscopy, which implies a novel laser-material interaction regime demanding further systematic researches.

3.1 Localized Internal Modification Along the Propagation Direction with Loosely Focused Picosecond Pulses

To examine the fabrication resolutions offered by loosely focusing the picosecond laser pulses into fused silica as a function of focal depth, we inscribed multiple lines as schematically illustrated in Fig. 10.5. A 5× objective lens (M Plan Apo NIR, Mitutoyo Corporation) with NA = 0.14 was used to focus the laser beam into the glass sample. The objective lens features a long working distance of 37.5 mm, enabling the fabrication of structures with heights up to 5 cm in fused silica. The lines, which were inscribed at different scan speeds and depths within fused silica, were organized into two grid arrays oriented in *X* and *Y* directions, as shown in Fig. 10.5a, b, respectively. The scan speed and the depth of the focal position can be identified for each inscribed line, as indicated in Fig. 10.5. The average laser power was fixed at 1.65 W in the writing of the lines in both of the two arrays, and the laser pulses were always polarized along the Y direction. The results in Fig. 10.5 were obtained using laser pulses negatively chirped to 10 ps. However, the same results can also be obtained if one chooses to use positively chirped pulses as long as the pulse duration is in the proper range. We noticed that the cross section of all the inscribed lines showed a similar geometry of a nearly circular shape, which are insensitive to scan speed, depth of focal position, as well as the direction of laser writing. The difference is that with an increasing scan speed, the color in the cross section captured under the microscope in a reflective mode becomes lighter, indicating that a weaker modification of fused silica will be generated with the decrease of the irradiation dose at the increasing scan speed. Since, in the 3D glass printing by the ULICE process, a chemical wet etching must be carried out for selective removal of the modified fused silica by the laser pulses, it is important to examine the cross section of hollow channels produced after the chemical wet etching in KOH solution, as shown in the outmost column on the right-handed side of Fig. 10.5a, b, respectively. The lateral and axial resolutions revealed by all the cross-sectional micrographs are ~20 μm, despite the fact that the lines are inscribed at various depths across a range of 5 cm. This means that the fabrication can maintain an unchanged resolution from the bottom to the top of the glass without the additional need of compensation of the aberration originated from the refractive

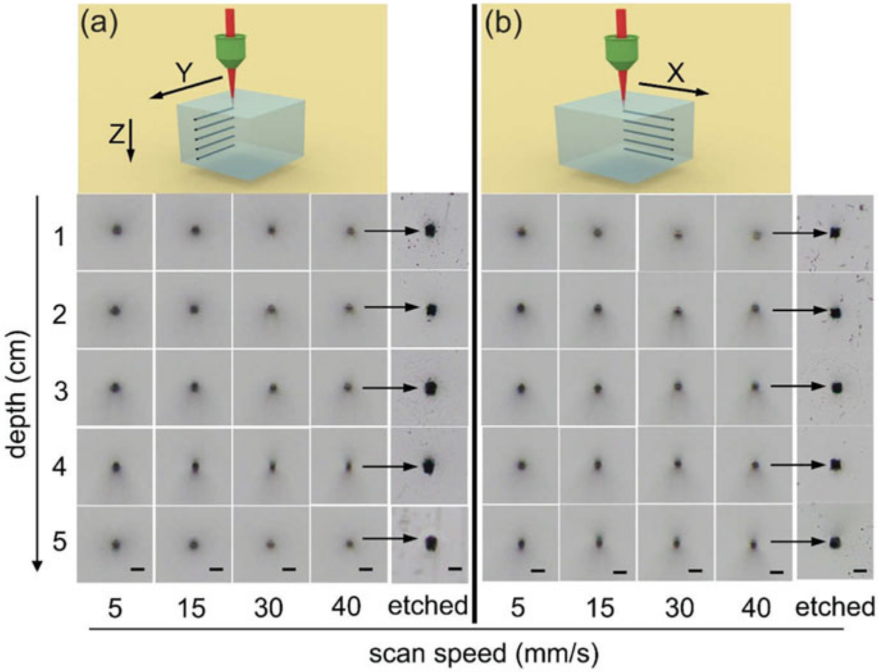

Fig. 10.5 The fabrication resolution offered by loosely focusing ps laser pulses into fused silica. Schematic illustration and cross-sectional optical micrographs of the lines written along the (**a**) *Y* and (**b**) *X* directions. The laser polarization is along the *X* direction. Cross-sectional micrographs of the hollow channels produced by chemically etching the inscribed lines are shown in the last column of (**a**, **b**), respectively. Scale bar, 25 μm. (Reprinted with permission from Wang et al. [82])

index mismatch between air and glass. This amazing characteristic is of great value for 3D microprinting in glass with the ULICE [33].

3.2 Mechanism Investigation

Suppression of the longitudinal extension of internal modification induced by a single laser pulse through adaptive temporal shaping has been demonstrated before [14]. The optimized pulse shape found by the feedback loop is identical to a stretched picosecond pulse. Pertinent theoretical works have pointed out that in comparison to femtosecond pulses, picosecond pulses at the same energy can deliver higher fluences into much narrower region around the laser focus, due to the reduced self-focusing effects and prefocal energy depletions, as well as the shortened plasma defocusing events which increase the effective irradiation of material around the focus [62]. Meanwhile, few-ps pulses compete well with fs pulses in the context of minimum collateral damages during the laser-material interaction, considering the

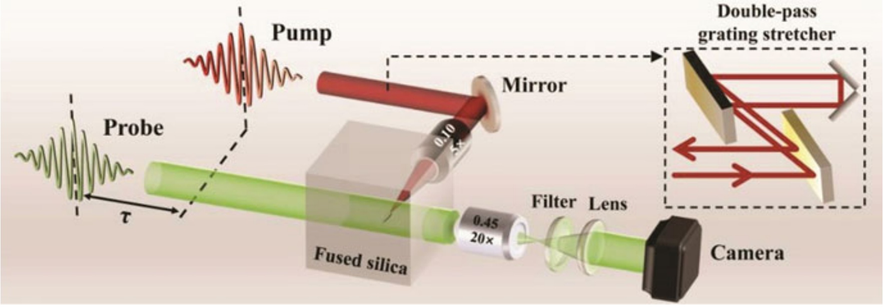

Fig. 10.6 Schematic of the transverse pump-probe microscopy

sluggish thermomechanical responses of irradiated materials in few hundreds of ps to a few ns [64].

To investigate the underlying mechanism of the observed exceptional laser inscription in the picosecond regime, transverse pump-probe microscopy is employed to visualize the spatiotemporal plasma dynamics and structural transformation in the laser-excited glass with both femtosecond and picosecond pulses [35]. The experimental schematic is shown in Fig. 10.6. Briefly, 370 fs laser pulses at 1030 nm wavelength were split into the pump and the probe. The pump pulse was loosely focused (NA = 0.10) at ~10 mm depth inside the fused silica glass after passing the double-pass grating stretcher for pulse-duration manipulation, while the probe pulse was mechanically delayed and frequency doubled to 515 nm and then used as the strobing light to illuminate the pump interaction volume from the transverse direction (see Fig. 10.6).

Ultrafast pump-probe microscopy has been widely employed for investigating the transient dynamics following laser excitation and revealing the physical pathways responsible for the final material modification in various kinds of glasses [65–67]. Consistent understanding is established in the context of single-pulse interaction with initially intact samples. Transient transmission images captured by single-shot probe pulses at different delays with respect to the pump pulse are shown for the pump pulse duration of 370 fs in Fig. 10.7a and 10 ps in Fig. 10.7b, respectively. Pump pulses incident from the left are set at the same energy (20 μJ) for both durations. At first glance, different plasma generation sequences can be clearly noticed by comparing the transient images taken at short delays shown in Fig. 10.7a, b, where free electrons generated by the pump pulse induce remarkable absorption of the traversing probe pulse. Plasma absorption commences around the geometrical focus at the leading edge of the 10-ps pump pulse and extends toward the pump incident direction following the peak and trailing edge of the pulse, whereas the prefocal plasma generation with subsequent forward growth along the pump incident direction is established by the 370-fs pump pulse. This is in well consistence with the moving breakdown model predicting opposite optical breakdown sequences for femtosecond and picosecond laser pulses [68, 69].

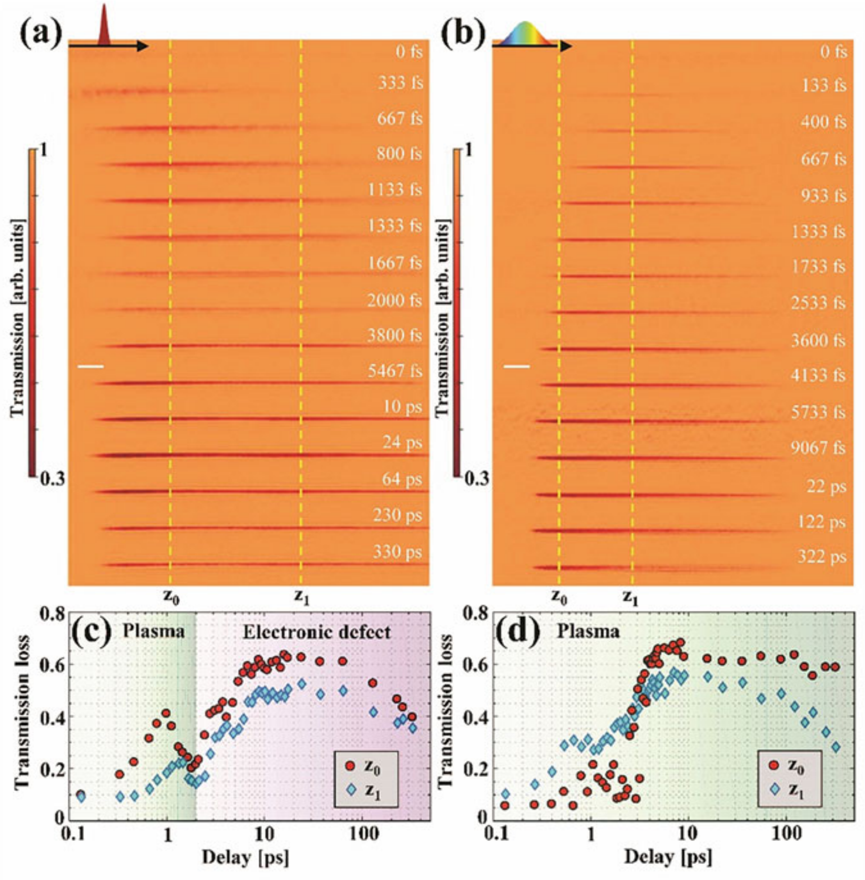

Fig. 10.7 Transverse pump-probe microscopy in the single-pulse interaction regime. The transient transmission images are captured for the 370-fs pump pulse (**a**) and the 10-ps pump pulse (**b**). Two straight cuts of the transient images are plotted in (**c**) and (**d**). The pump pulse energy is kept at 20 μJ for both durations. The delay of the probe pulse with respect to the pump pulse is labelled in the right parts of (**a**) and (**b**). The scale bars in (**a**) and (**b**) are 20 μm

Two vertical cuts along the transient images are plotted in Fig. 10.7c, d, where z_0 denotes the axial position corresponding to the maximum transmission loss, and z_1 represents the expected location of the geometrical focus. It can be clearly seen that the plasma absorption is quickly quenched in 1 ps for the 370-fs pump case. Free electrons injected into the conduction band of fused silica are previously found to be quickly trapped in ~150 fs by the deformed lattice potential due to the weakening of Si-O bonds [70], forming immobile electron-hole pairs localized at specific lattice sites – the self-trapped excitons (STE). Considering the limited temporal resolution determined by the durations of both the pump pulse and the probe pulse to be around

300 fs, the observed plasma decay could be ascribed to the fast STE formation after the passage of the 370-fs pump pulse.

The STEs further relax into a variety of point defects such as the well-known nonbridging oxygen hole centers (NBOHC) and the oxygen deficiency centers (ODC) in fused silica [71, 72]. The strong revival of transmission loss starting from ~3.0 ps in Fig. 10.7a can be ascribed to the scattering as well as absorption induced by electronic defects. Notably, the transient images are changed from the absorption dominated to the diffraction dominated if one compares the images taken before 1133 fs and after 3.8 ps. Negative refractive index changes originating from transient electronic defects have been previously identified in UV laser-illuminated fused silica [65]. The measured behavior in this work is consistent with these results. Nevertheless, the electronic defects here play a stronger effect on the traversing probe pulse compared to free electron plasma generated at short delays, which has to be identified by further sophisticated methods besides the transient transmission imaging. Moreover, defect accumulation induces large displacement and localized heating of the lattice, leading to the buildup of thermoelastic stress and acoustic wave formation [62]. Thermal annihilation of electronic defects and slow release of thermal stress ensues in a few hundreds of ps to a few nanoseconds, which is manifested as the partial recovery of transmission after 100 ps in Fig. 10.7c.

On the contrary, the lack of rapid electron trapping during and after the 10-ps pump pulse as revealed by the lack of obvious transmission recovery shown in Fig. 10.7b, d indicates that the coupling between the laser and the glass lattice is such strong that the lattice is severely distorted being unable to trap electrons. It is well accepted that picosecond pulses with adequate intensities can provide sufficient acceleration of free electrons generated by direct photoionization through the inverse bremsstrahlung. The avalanche ionization emerges for the high-energy portion of heated electrons with excess energy than the bandgap. The combined action of both ionization processes induces continuous increase of free electron density as well as the collisional heating of both electrons and lattice during the pump pulse. Consequently, a long-lived plasma absorption tail lasting hundreds of ps is observed in Fig. 10.7d.

Remarkedly, the observed plasma absorption and structural transformation regions induced by single pump pulses shown in Fig. 10.7 follow the highly elliptical laser focal profile at the low-NA focusing, with subtle differences arising from the prefocal energy depletions and nonlinear propagation effects due to the competition of self-focusing and plasma defocusing setting in at high laser powers [21, 73, 74]. This confirms the incapability of single-pulse interaction in concentrating laser energy for sufficient internal modification, signifying the accumulation effect of multiple-pulse interactions in the laser internal modification process.

Further pump-probe microscopy is focused on the accumulation effect of laser-material interaction [75–77]. To this end, each glass site is pre-irradiated by certain number of pump pulses, after which the transient plasma and structural dynamics induced by the succeeding pulse is captured at various delays of probe pulses. The pump pulse energy is kept at 20 μJ for both durations. The transmission images

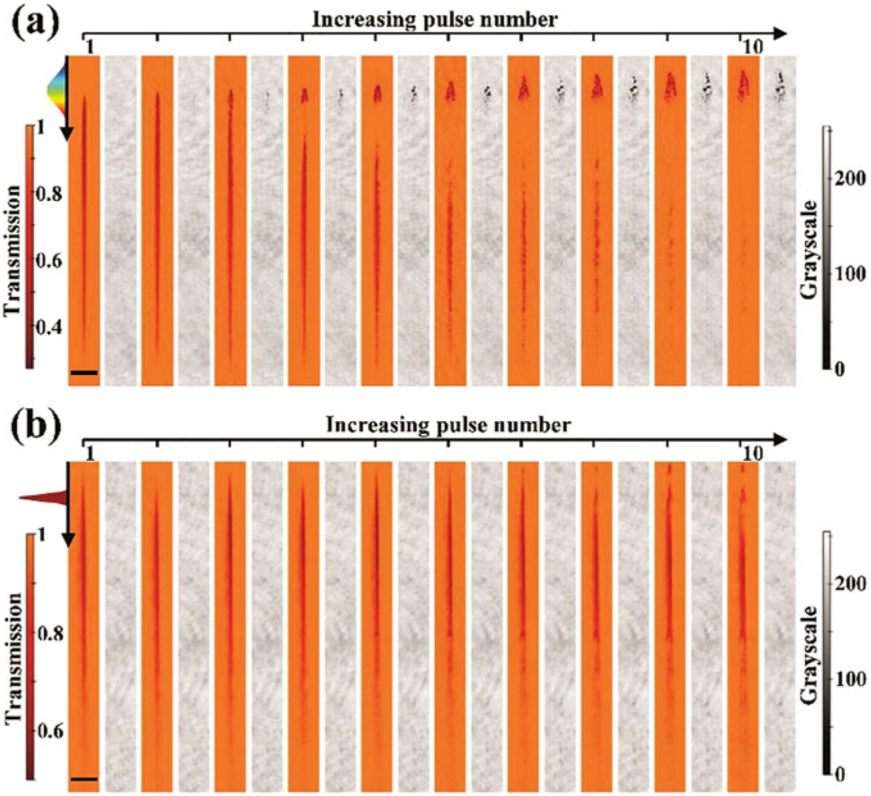

Fig. 10.8 (**a**, **b**) Transverse pump-probe microscopy in the multi-pulse interaction regime. The transient transmission images and corresponding static micrographs for material modifications are shown for the 10-ps pump pulse (**a**) and the 370-fs pump pulse (**b**). The scale bars in (**a**) and (**b**) are 20 μm

taken at the delays corresponding to the maximum plasma generation are rendered in pseudo-colors and shown in Fig. 10.8a, b for the 10-ps and 370-fs pump pulses, respectively. Each transient image is normalized with the image taken before the incoming pump pulse. Permanent material modifications after each pump pulse are also measured and shown as grayscale graphs in Fig. 10.8a, b. Distinct features are unfolded as the spatial shift and confinement of plasma absorption regions toward the incident direction following the interactions of 10-ps pump pulses, while similar spatial extensions of plasma generated by each single pulse irrespective of previous exposures are observed for the 370-fs pump pulses. It implies that the propagation of subsequent pulses through the region modified by previous pulses is arrested for the 10-ps pump pulse. Meanwhile, severe material disruptions induced by 10-ps pump pulses are present at regions corresponding to the localized plasma absorption in the transient images. On the contrary, the apparent incapability of energy concentration by irradiation with multiple femtosecond pulses causes the final material modification weakly detectable as shown in Fig. 10.8b.

It is clearly unveiled that the incubation effect plays a significant role in laser-glass interactions with picosecond pulses. The electron binding energy in the irradiated part of glass is reduced compared to the pristine position [78, 79], due to the presence of defect centers, structural rearrangement, as well as mechanical damage after laser exposure. Photoionization in the modified region is then activated at a lower-intensity threshold, facilitating quick generation of free electrons in the leading edge of excitation pulse. As a result, collisional heating of free electrons by inverse bremsstrahlung is enhanced by the remaining pulse. Avalanche ionization by those electrons with kinetic energies in excess of the bandgap of the irradiated region (~9 eV for pristine fused silica) renders rapid multiplications of free electrons in the conduction band [80]. Since picosecond pulses can provide sufficient acceleration of free electrons generated by direct photoionizations due to the long-lasting electric field, their interaction with the irradiated region is quite susceptible to the intrinsic defects left by previous pulses. Moreover, the electron-ion/lattice energy exchange also occurs during the picosecond pulse [39, 56], which can increase the energy coupling efficiency through local lattice vibration and temperature elevation. The efficient energy deposition is further supported by the observation of bright plasma continuum emissions emanated from the localized material modification region driven by multiple picosecond pulses instead of femtosecond pulses. Consequently, highly selective spatial energy concentrations are realized by accumulated positive feedbacks from material changes during the multiple pulse interactions in the picosecond regime.

To further test the paradigm of cumulative light concentration, the material modifications generated by continuous exposures of picosecond pulses are investigated, and the corresponding transient plasma images are also captured for comparison. The single-pulse energy is set to 10 μJ to approximate the inscription conditions in Fig. 10.5. It is clearly seen in Fig. 10.9a that disruptive material damages appear after irradiation by five 10-ps laser pulses, and the corresponding plasma absorption regions are gradually shifted and localized toward the incident laser pulses. The location of laser focus is estimated from the transient plasma images induced by the first few pulses and shown as the white dashed line in Fig. 10.9a. Unexpectedly, the optical breakdown region is continuously extended above the laser focus with increasing exposures of laser pulses and the laser-modified region is stabilized in space after deposition of 2×10^5 pulses (see the second row in Fig. 10.9a). Additional exposures induce no effects in the irradiated region, indicating that the local laser intensity falls below the optical breakdown threshold due to the far distance from the focus. The stable material modification is characterized by a longitudinal length of 160 μm and a transversal width around 15 μm.

The presented results in Fig. 10.9a seem contradictory with the demonstrated highly confined material modification shown in Fig. 10.5. The essential difference is that the glass sample is kept static under the illumination of laser pulses in Fig. 10.9a, while a rapid scanning of the glass sample across the laser focus is utilized for inscribing straight lines in Fig. 10.5. The direct comparison between these two different inscription conditions is shown in Fig. 10.9b. Remarked differences are

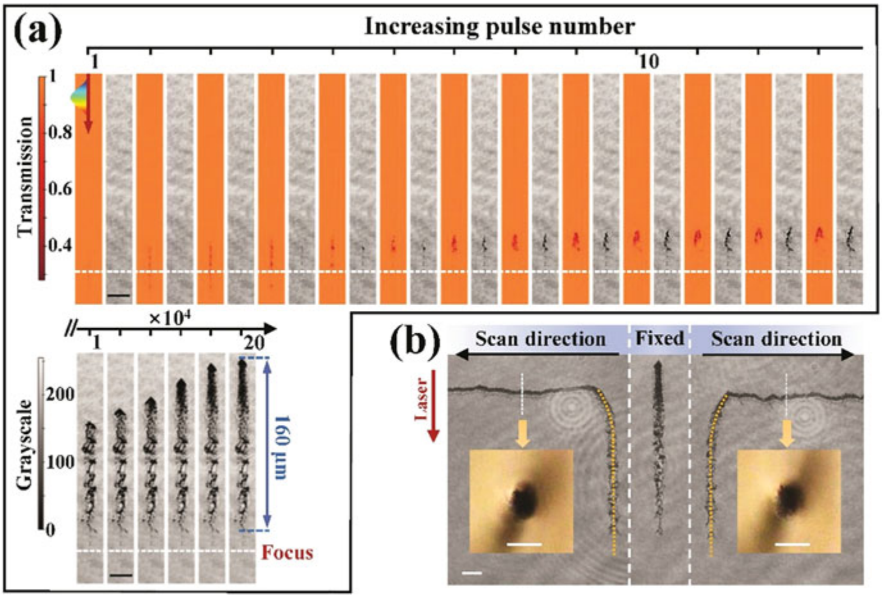

Fig. 10.9 (**a**) The transient transmission images and corresponding static micrographs for material modifications induced by 10-ps pump pulses. (**b**) Static micrographs for the material modifications generated in scanned sample compared to fixed sample. The laser repetition rate and scanning velocity are 200 kHz and 10 mm/s, respectively. The scale bars in both figures are 20 μm

clearly identified: the elongated material modification is obtained when the sample is fixed, while the upper part of stable material modification is turned by 90° toward the scanning direction of the laser focus. Laser-modified regions during sample movements are well confined within a spherical cross section of ~20 μm diameter as shown in the insets of Fig. 10.9b. It should be noted that the vertical fluctuation of the laser-inscribed tracks shown in Fig. 10.9b is due to the instability of the utilized motor stage for sample scanning, which can be minimized by using a high-stability motion stage as illustrated later.

The observed motion-determined picosecond laser inscription is quite surprising compared to the conventional knowledges concerning the laser-material interaction and machining. For example, the morphologies of laser-modified regions are found to be sensitive to the scanning direction in the context of nanograting formation and quill writing [45, 46, 81], due to the polarization-dependent surface plasmonic enhancement and the pulse front tilt, respectively. However, the motion control in these embodiments only determines the connections between adjacent modified regions, not strikingly changes the spatial distribution of material modification compared to the static case.

On the other hand, illuminating clues can be conceived based on the pump-probe microscopy results on static samples. It is well revealed in Figs. 10.8 and 10.9 that strong incubation effects exist for the laser-material interaction in the picosecond regime: picosecond pulses are concentrated on material changes induced by previous exposures far before reaching the focus. When the moving sample is exposed to the picosecond pulses, the irradiated regions for each pulse are dispersed along the scanning direction, with the mutual overlap between adjacent pulses depending on the scanning velocity and the repetition rate of the laser pulse train. Therefore, each pulse will be concentrated around the modified region by previous pulses as a sequential deposition along the scanning direction, producing well-confined material modifications and inhibiting the otherwise longitudinal growth of material modifications in the static case. It should be noted that further systematic studies and theoretical modeling, besides the empirical and qualitative discussions described in this section, are highly demanded for a thorough understanding of the underlying physics of the picosecond laser inscription.

4 Applications

Benefitting from the robust processing resolution and the superior post-processing chemical etching both provided by the picosecond laser internal modification as elaborated in the last two sections, macroscale microfabrication of geometrically complex samples and functional components is expected to promote a broad spectrum of applications, including large-scale 3D printing, optofluidic integration, flow chemistry control, and micro-optoelectromechanics. Two representative application cases are given in this section.

4.1 3D Printing Application

There are basically four steps for the 3D printing of glass objects by the discovered ps laser internal modification and ensuing selective chemical etching [82], as shown in Fig. 10.10. First of all, a digital model of the desired 3D structure is generated as stereolithography (STL) files. The STL files are firstly covered by a cuboid frame and then undergo a subtraction operation. Afterwards, the 3D models are sliced into horizontal planes with a fixed slice thickness, and the planes are further decomposed into lines. The second step is the ultrafast laser irradiation of the glass sample. The sample is scanned across the laser focus along the lines generated in the previous step from bottom to top in a layer-by-layer manner. Thirdly, the samples irradiated by the focused laser pulses are polished to remove the outer areas. Typically a few millimeters thick areas are polished. The outer areas near the vertical sidewalls of the cubic sample could not be sufficiently modified by the laser irradiation because of the distortion of the focal spot caused by the air-glass interface at the sidewalls. Finally, the polished samples are immersed in a wet etching bath of potassium hydroxide (KOH) with a concentration of 10 mol/L at a temperature of 90 °C for tens of hours to selectively remove the irradiated regions.

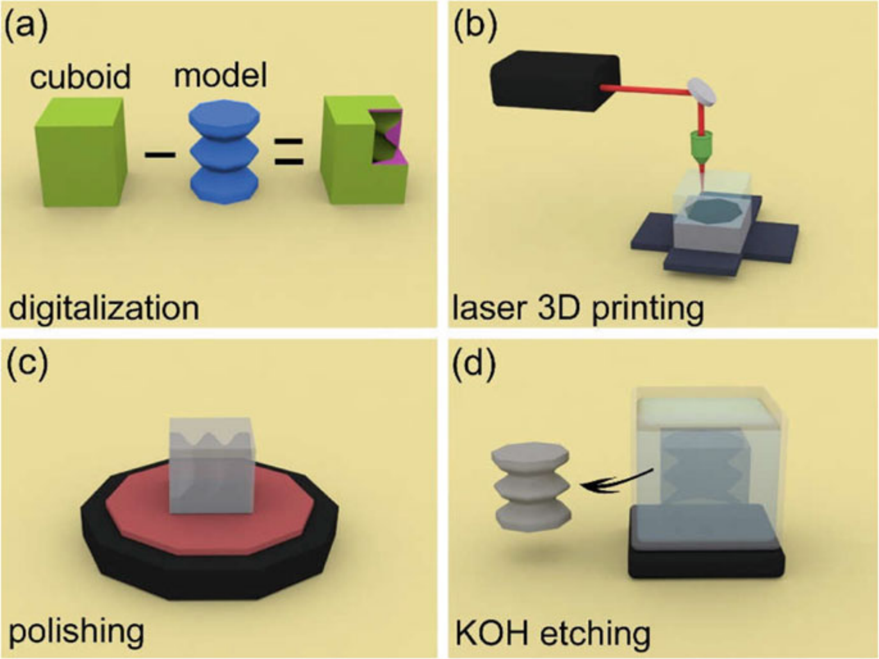

Fig. 10.10 The four steps in the 3D glass microprinting: (**a**) digitalization of the 3D model, (**b**) scanning of the laser beam along the pre-designed paths, (**c**) mechanical polishing, (**d**) removal of the irradiated materials with chemical etching. (Reprinted with permission from Wang et al. [82])

We have successfully employed the above procedures for a series of 3D printed macroscale objects and functional components [33]. Figure 10.11 shows a 3.8 cm high sculpture, which is a statue of *Confucius*. The model of the sculpture is shown in Fig. 10.11a, and the front and back sides of the printed sculpture are presented in Fig. 10.11b, c. Figure 10.11d shows an enlarged part of the model in Fig. 10.11a. For comparison, the 3D profile of the printed sculpture captured by laser confocal microscopy is illustrated in Fig. 10.11e. The details of the decorative pattern on the cloth and the left hand hanging behind his body are shown in Fig. 10.11f, g, respectively. It proves that the entire sculpture is printed with a decent fabrication resolution from the top to bottom.

Recently, a macroscale sculpture reproducing the Chinese treasure, *four-sheep statue*, is also fabricated in a 4 cm-height fused silica glass [35]. The pictures of the fabricated sculpture are shown in Fig. 10.12, with the digital model depicted in (a) the fabricated sculpture from the inclined view and the front view shown in (b–c), and the zoom-in details demonstrated in the insets, (d) the attached decorative pattern, (e) the lateral protrusion, and (f–g) the horns of the front dragon and the corner sheep. The high-fidelity duplicate of the exquisite Chinese treasure proves the excellent capability of the established 3D large-scale glass printing technique. It should be noted that although the surface of the whole sculpture appears smooth,

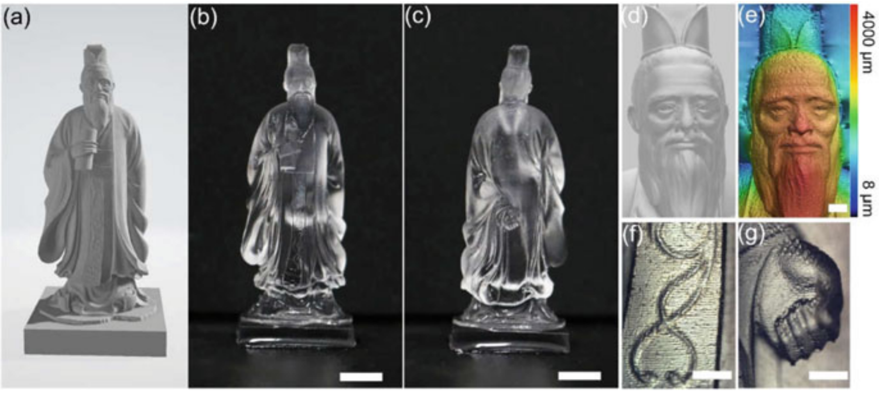

Fig. 10.11 A laser printed sculpture of *Confucius* in fused silica. (**a**) The model and the (**b**) front, (**c**) back sides of the sculpture. (**d**) An enlarged part of the model in (**a**). (**e**) 3D profile of the printed sculpture captured by laser confocal microscopy. (**f**) The details of the decorative pattern on the cloth. (**g**) The left hand hanging behind his body. Scale bar in (**b**, **c**): 5 mm, (**e**–**g**): 1 mm. (Reprinted and adapted with permission from Wang et al. [33])

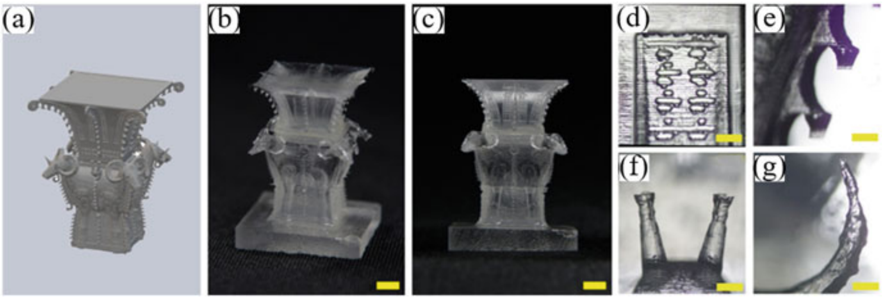

Fig. 10.12 Digital camera images of the fabricated *four-sheep statue* object. (**a**) the digital model of *four-sheep statue*, (**b**–**c**) the inclined view and the front view of the fabricated sculpture, (**d**–**g**) the zoom-in details. The scale bars are 5 mm for (**b**–**c**) and 500 μm for (**d**–**g**)

it does not reach the level of the mirrorlike surface quality typically produced with mechanical polishing. Improvement on the surface quality is possible with elaborated post-annealing or CO_2 laser polishing, which requires much effort to optimize and will be investigated in the future.

Besides, we have also demonstrated an air turbine with movable parts directly fabricated within glass without any assembling process [33]. The model of the air turbine is illustrated in Fig. 10.13a, b. As shown by Fig. 10.13b, the micromachine is composed of an air fan, one driving gear and two driven gears, as well as two cams. The driving gear is fabricated with the turbine fan as an integral component to ensure a robust physical connection between the gear and the turbine fan. The two driven gears can be wound by the driving gear when an airflow drives the fan to rotate. Each of the driven gears is connected with a cam. The laser-printed air turbine is

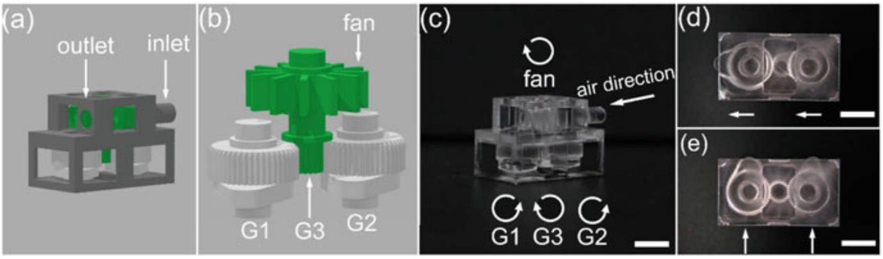

Fig. 10.13 A laser-printed air turbine. (**a**) The air turbine model. Inlet and outlet for air injection are indicated. (**b**) The interior of the turbine including a turbine fan, a driving gear (G3), and two driven gears (G1 and G2). Each of G1 and G2 is connected with a cam. (**c**) Digital camera image of the fabricated turbine. The air direction and rotation direction of the fan, as well as the rotation directions of G1, G2, and G3 from a top view, are all indicated by the curved arrows in (**c**). (**d**) The initial position of the two cams is pointing to the left as indicated by the two arrows. (**e**) Both the cams are rotated in a clockwise direction by 90° as a result of the injected airflow. Scale bar: 5 mm. (Reprinted with permission from Wang et al. [33])

presented in Fig. 10.13c. The micromachine is functional as we can rotate the cams by injecting the airflow from the inlet. The synchronized motion of the two cams is evidenced by the images in Fig. 10.13d, e, in which the orientations of the cams are changed as indicated by the white arrows. Thanks to the capability of fabricating the large glass objects at the high resolution, the demonstrated technique offers potential for manufacturing precision instruments, tools, and machines in various research and application fields.

At last, we show the fabrication of 3D printed glass macroscale objects with embedded free-form 3D microfluidic networks [34]. A bioinspired blood vessel structure encapsulated in a 3D printed glass hand has been designed, as shown in Fig. 10.14a, b. To fabricate 3D uniform glass microchannels with centimeter-scale length, introduction of a string of extra-access ports along the microfluidic channels has been adopted for ensuring homogeneous fabrication of the channels during the chemical etching. An embedded micropattern including a microchannel and several tens of extra-access ports was first created inside glass using the ultrashort pulse laser direct writing, and then the surrounding area of the hand model was modified by the same laser beam in a 3D programmable manner. After that, the laser-modified glass sample was chemically etched until all the laser-irradiated regions were fully removed.

Figure 10.14c presents a fabricated hand model with a size of about ~3 cm × 2.7 cm × 1.1 cm, in which fingernails and some skin texture patterns on the hand back can be clearly distinguished due to the high resolution down to several tens of micrometers. Moreover, the embedded microchannel patterns including open extra-access ports and three openings below the hand can be observed. Finally, all extra-access ports were sealed by CO_2 laser defocusing irradiation to form a 3D close microchannel encapsulated in the hand model with only three openings as shown in Fig. 10.14d. Further microfluidic experiments confirmed that the

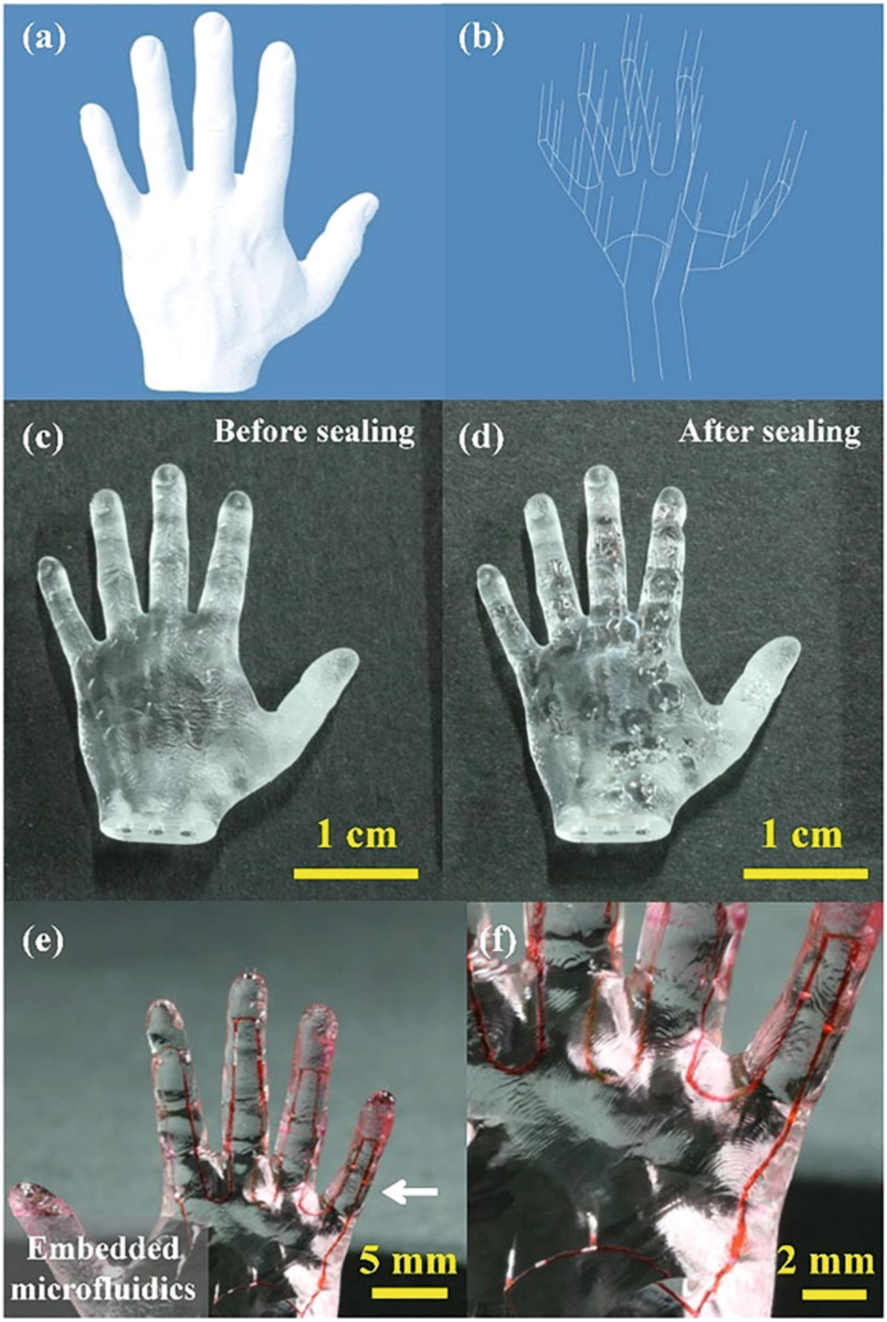
(a)
(b)
(c)
Before sealing
1 cm
(d)
After sealing
1 cm
(e)
Embedded microfluidics
5 mm
(f)
2 mm

Fig. 10.14 Schematics of (**a**) a 3D hand model and (**b**) an embedded microchannel pattern for ultrafast laser-induced chemical etching. Pictures of 3D printed bioinspired glass hand with encapsulated channels and extra-access ports (**c**) before and (**d**) after CO_2 laser sealing. (**e**) 3D microfluidic demonstration of the hand based on combination of 3D glass subtractive printing and hybrid laser microfabrication. (**f**) Close-up image of a part of the hand as indicated by a white arrow in (**e**). (Reprinted with permission from Lin et al. [34] © 2020 WILEY-VCH Verlag GmbH & Co. KGaA, Weinheim)

encapsulated microchannel with sealed extra-access ports are fully through hollow structure without any leakage (see Fig. 10.14e). Especially, the microfluidic circuit can be clearly visualized inside the close-up image of fingers (see Fig. 10.14f). We expect that this approach based on combination of the ULICE and CO_2 laser-induced melting will be beneficial for the development of novel lab-on-a-chip and biochip devices for promoting the understandings of causes of human diseases such as cancers and cardiovascular diseases.

4.2 Flow Chemistry Industrial Application

Besides enabling 3D printing of macroscale glass structures with micrometer resolutions in a subtractive manner, the ps laser internal modification followed by selective chemical etching also allows customized fabrication of large-scale and high-precision microfluidic structures with 3D configurations for flow chemistry applications. In the context of flow chemistry, the chemical reactions are performed in a continuously flowing stream rather than in the traditional batch reactor system, which exhibits great advantages for the promotion of chemical reactions such as enhanced heat and mass transfer, and high selectivity in a clean and safe way [83]. Continuous-flow microreactors which consist of a series of mixing units allow efficient manipulation of the fluids inside microchannels in a precise and flexible fashion, which are now playing an important role in flow chemistry. Extension of widely used 2D to 3D configurations and incorporation of multiple functionalities into microreactors will bring new opportunities for innovative development of continuous-flow manufacturing of biopharmaceuticals and fine chemicals [84]. Figure 10.15 shows a typical example of ultrafast laser-fabricated glass microreactor based on the proposed technique. The total size of the fabricated reactor is 15 cm by 12 cm (Fig. 10.15a). As illustrated in Fig. 10.15b, the reactor structure mainly consists of three-layer microfluidic structures: the top, the middle, and the bottom layers. Both the top and bottom layers are planar channels that provide homogeneous control of the temperature of the whole reactor. And the middle layer is a 3D complex channel including a series of micro-mixing units with 3D configurations based on Baker’s transformation principle for providing high-performance continuous-flow reaction. Moreover, the microreactor can be further scaled up to construct a continuous-flow manufacturing system with high throughput for industrial application as demonstrated in Fig. 10.16.

Benefitting from the features of microfluidic structures with 3D configurations, the reaction rate in glass microreactors fabricated by ultrafast laser can be highly promoted, which is advantageous for the application in flow chemistry. One example is the solid-liquid synthesis of gadopentetate dimeglumine, which is the most widely used magnetic resonance imaging (MRI) contrast agent [85]. With an ultrafast laser-fabricated microreactor, highly efficient mixing and movement of the solid-liquid mixtures can be significantly enhanced due to 3D shear flow and vigorous turbulence. The interface of the solid-liquid phase can be enlarged, leading to the

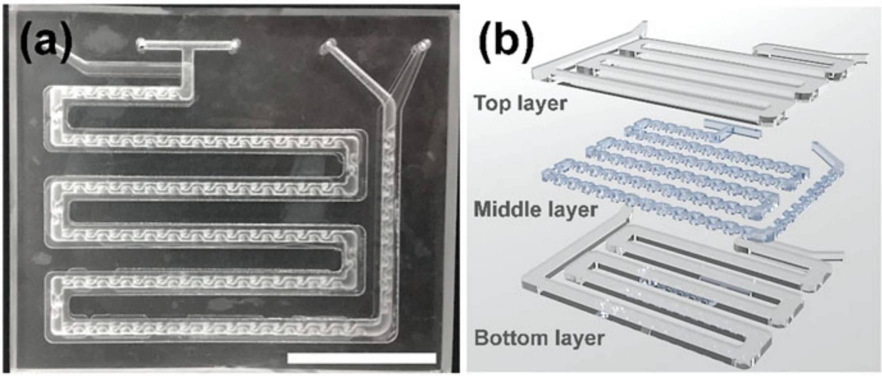

Fig. 10.15 Ultrafast laser-fabricated 3D glass microreactor. (**a**) Photograph of a glass microreactor with a 3D configuration (the total size of the reactor is 15 cm by 12 cm). Scale bar: 5 cm. (**b**) Schematic of the reactor structure, which consists of three layers: one planar microchannel in the top layer for temperature control, a complex microchannel including a series of 3D mixing units in the middle layer for continuous-flow reactions based on fast mixing, and another planar microchannel in the bottom layer for temperature control

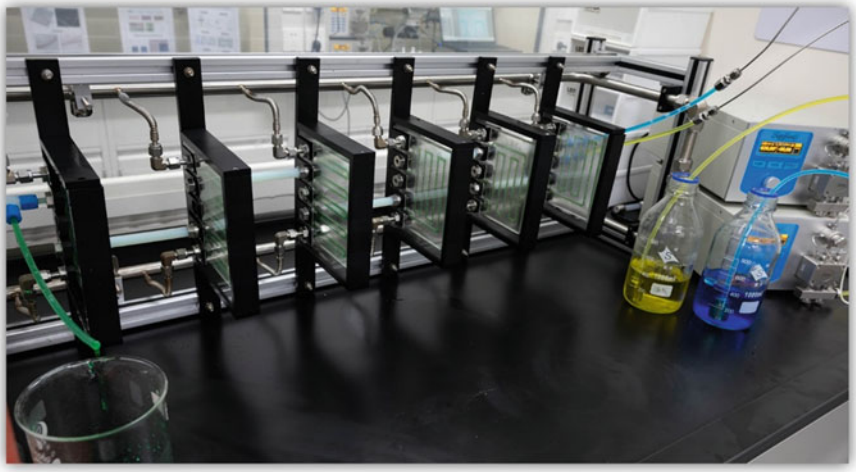

Fig. 10.16 Photograph of a continuous-flow manufacturing system constructed by a series of ultrafast laser-fabricated glass microreactors

enhanced mixing effect and mass transfer inside the reactor. The in-line analytical results of the ultraviolet-visible (UV-vis) spectrometer showed a significantly higher reaction rate compared with the round-bottom flask system. Moreover, controllable synthesis of PEG (polyethylene glycol)-mediated mineralization of zeolitic imidazolate framework-8 (ZIF-8) biocomposites, which have recently been proved to be useful in drug and vaccine delivery, has been achieved using a 3D glass microreactor

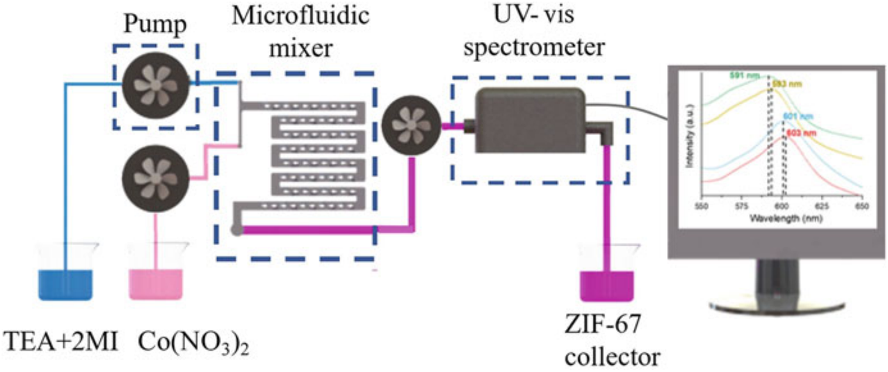

Fig. 10.17 Schematic of continuous-flow synthesis system. The reactants are pumped into a microreactor including the microfluidic mixer. Then, the produced crystals flow through the channel and are pumped into the UV-vis spectrometer for an in-line absorption test. The peak position of the absorption spectrum varies according to the size of the crystals; thus the sizes of the crystals can be read out automatically. (Reprinted with permission from Li et al. [87] © 2020 Chinese Chemical Society and Institute of Materia Medica, Chinese Academy of Medical Sciences. Published by Elsevier B.V)

[86]. The obtained result can be extended to the community of vaccine particles by automated and remote synthesis and leading toward the future personalized synthesis of therapeutics. In addition, continuous-flow synthesis of ZIF-67 crystals using an ultrafast laser-fabricated microreactor and in-line monitoring of size-controlled synthesis through UV-vis absorption spectra have been demonstrated as shown in Fig. 10.17 [87]. The size of the crystals correlates to the dosage amount of the triethylamine in the flow synthetic environment. The absorption peak position of the UV-vis absorption spectra is linearly related to the size of ZIF-67 crystals. The products of continuous-flow synthesis are of the typical shape of ZIF-67 as shown in SEM images of Fig. 10.18. Statistic sizes of the ZIF-67 crystals were collected by measuring rhombic dodecahedron particles in each SEM image. The measured sizes from SEM images are consistent with the estimated sizes based on the in situ UV-vis spectra, thus in situ UV-vis spectra can be used to estimate the sizes of the final products. The ZIF-67 crystals were converted into nanoporous carbon particles and showed size-dependent performance in Na-ion battery and in Mg/H2O seawater battery.

5 Conclusion and Outlook

The researches on the ultrafast laser internal modification have boomed in the recent decade, stimulated by the strong application-driven impetus from a plethora of technological demands for high-throughput, high-precision, and

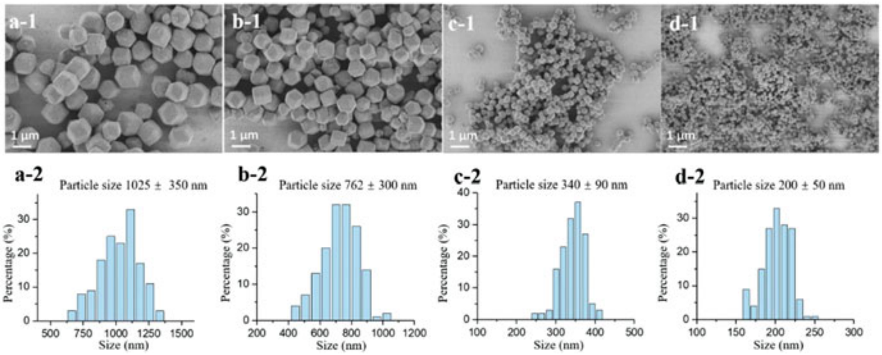

Fig. 10.18 SEM images and particle sizes of the ZIF-67 particles synthesized by continuous-flow synthesis. Particles with statistic sizes of (**a**) ~1025 nm; (**b**) ~762 nm; (**c**) ~340 nm; and (**d**) ~200 nm. Fifty particles were measured in each case. (Reprinted with permission from Li et al. [87] © 2020 Chinese Chemical Society and Institute of Materia Medica, Chinese Academy of Medical Sciences. Published by Elsevier B.V)

high-scalability macroscale manufacturing at micro-to-nanoscale resolution. The macroscale microfabrication technique by picosecond laser-induced selective chemical etching demonstrated in this chapter makes a substantial step toward the industry-compatible laser micromanufacturing. Picosecond laser internal modification provides two key advantages compared to the femtosecond laser internal modification: focal-volume-invariant modification deeply inside transparent substrates and superior selective chemical etching with enhanced efficiency and suppressed anisotropy. These unique properties enabled the unprecedented application of ultrafast laser-induced chemical etching for macroscale fabrication of objects with centimeter-level heights without sacrificing the micrometer-scale resolution.

From the fundamental physics point of view, the laser-material interaction revealed in this chapter features the exceptional multi-pulse effect for picosecond laser inscription in fused silica glass, strongly differing from the conventional incubation and thermal accumulation effect for laser-material interaction in the multi-pulse deposition regime. Transverse pump-probe microscopy is employed to reveal the plasma and structural dynamics deep inside the glass excited by loosely focused laser pulses of different durations, supporting the self-regulated energy concentration of multiple few-picosecond pulses irrespective of the focal depths. The discovered ultrafast laser-material interaction provides renewed and vigorous impetus to the long-standing study of materials exposed to high-power pulsed radiations. At the same time, this observation brings an unprecedented method for laser printing of macroscale glass objects at robust microscale resolutions with arbitrary geometrical complexities, holding fascinating perspectives in massive manufacturing of diverse devices of significant scientific and technical importance, including microfluidic chips, biomimetic components, and large-scale micro-optoelectromechanics.

References

1. R.R. Gattass, E. Mazur, Nat. Photonics **2**, 219–225 (2008). https://doi.org/10.1038/nphoton.2008.226
2. K. Sugioka, Y. Cheng, Appl. Phys. Rev. **1**, 041303 (2014). https://doi.org/10.1063/1.4904320
3. M. Malinauskas, A. Žukauskas, S. Hasegawa, Y. Hayasaki, V. Mizeikis, R. Buividas, S. Juodkazis, Light Sci. Appl. **5**, e16133 (2016). https://doi.org/10.1038/lsa.2016.133
4. J. Bauer, S. Hengsbach, I. Tesari, R. Schwaiger, O. Kraft, Proc. Natl. Acad. Sci. U. S. A. **111**, 2453–2458 (2014). https://doi.org/10.1063/1.5114955
5. J. Zhang, M. Gecevičius, M. Beresna, P.G. Kazansky, Phys. Rev. Lett. **112**, 033901 (2014). https://doi.org/10.1103/PhysRevLett.112.033901
6. A. Crespi, R. Osellame, R. Ramponi, V. Giovannetti, R. Fazio, L. Sansoni, F. De Nicola, F. Sciarrino, P. Mataloni, Nat. Photonics **7**, 322–328 (2013). https://doi.org/10.1038/nphoton.2013.26
7. B.C. Stuart, M.D. Feit, A.M. Rubenchik, B.W. Shore, M.D. Perry, Phys. Rev. Lett. **74**, 2248–2251 (1995). https://doi.org/10.1103/PhysRevLett.74.2248
8. A.P. Joglekar, H.H. Liu, E. Meyhofer, G. Mourou, A.J. Hunt, Proc. Natl. Acad. Sci. U. S. A. **101**, 5856–5861 (2004). https://doi.org/10.1073/pnas.0307470101
9. Y. Liao, Y. Shen, L. Qiao, D. Chen, Y. Cheng, K. Sugioka, K. Midorikawa, Opt. Lett. **38**, 187–189 (2013). https://doi.org/10.1364/OL.38.000187
10. Y. Cheng, K. Sugioka, K. Midorikawa, M. Masuda, K. Toyoda, M. Kawachi, K. Shihoyama, Opt. Lett. **28**, 55–57 (2003). https://doi.org/10.1364/OL.28.000055
11. L. Englert, M. Wollenhaupt, L. Haag, C. Sarpe-Tudoran, B. Rethfeld, T. Baumert, Appl. Phys. A Mater. Sci. Process. **92**, 749–753 (2008). https://doi.org/10.1007/s00339-008-4584-1
12. M.K. Bhuyan, F. Courvoisier, P.A. Lacourt, M. Jacquot, R. Salut, L. Furfaro, J.M. Dudley, Appl. Phys. Lett. **97**, 081102 (2010). https://doi.org/10.1109/URSIGASS.2011.6050591
13. F. He, H. Xu, Y. Cheng, J. Ni, H. Xiong, Z. Xu, K. Sugioka, K. Midorikawa, Opt. Lett. **35**, 1106–1108 (2010). https://doi.org/10.1364/OL.35.001106
14. A. Mermillod-Blondin, C. Mauclair, A. Rosenfeld, J. Bonse, I.V. Hertel, E. Audouard, R. Stoian, Appl. Phys. Lett. **93**, 021921 (2008). https://doi.org/10.1063/1.2958345
15. A. Mermillod-Blondin, I.M. Burakov, Y.P. Meshcheryakov, N.M. Bulgakova, E. Audouard, A. Rosenfeld, A. Husakou, I.V. Hertel, R. Stoian, Phys. Rev. B **77**, 104205 (2008). https://doi.org/10.1103/PhysRevB.77.104205
16. P.S. Salter, A. Jesacher, J.B. Spring, B.J. Metcalf, N. Thomas-Peter, R.D. Simmonds, N.K. Langford, I.A. Walmsley, M.J. Booth, Opt. Lett. **37**, 470–472 (2012). https://doi.org/10.1364/OL.37.000470
17. Y.C. Chen, P.S. Salter, S. Knauer, L. Weng, A.C. Frangeskou, C.J. Stephen, S.N. Ishmael, P.R. Dolan, S. Johnson, B.L. Green, G.W. Morley, M.E. Newton, J.G. Rarity, M.J. Booth, J.M. Smith, Nat. Photonics **11**, 77–80 (2017). https://doi.org/10.1038/nphoton.2016.234
18. R. Osellame, G. Cerullo, R. Ramponi, *Femtosecond Laser Micromachining: Photonic and Microfluidic Devices in Transparent Materials Ch. 1* (Springer Science & Business Media, New York, 2012). https://doi.org/10.1007/978-3-642-23366-1
19. P. Török, P. Varga, Z. Laczik, G.R. Booker, J. Opt. Soc. Am. A **12**, 325 (1995). https://doi.org/10.1364/JOSAA.12.000325
20. C. Hnatovsky, R.S. Taylor, E. Simova, V.R. Bhardwaj, D.M. Rayner, P.B. Corkum, J. Appl. Phys. **98**, 013517 (2005). https://doi.org/10.1007/s00339-006-3590-4
21. A. Couairon, A. Mysyrowicz, Phys. Rep. **441**, 47–189 (2007). https://doi.org/10.1016/j.physrep.2006.12.005
22. A. Marcinkevičius, S. Juodkazis, M. Watanabe, M. Miwa, S. Matsuo, H. Misawa, J. Nishii, Opt. Lett. **26**, 277–279 (2001). https://doi.org/10.1364/OL.26.000277
23. S. Juodkazis, K. Yamasaki, V. Mizeikis, S. Matsuo, H. Misawa, Appl. Phys. A Mater. Sci. Process. **79**, 1549–1553 (2004). https://doi.org/10.1007/s00339-004-2845-1

24. Y. Bellouard, A. Said, M. Dugan, P. Bado, Opt. Express **12**, 2120–2129 (2004). https://doi.org/10.1364/OPEX.12.002120
25. C. Hnatovsky, R.S. Taylor, E. Simova, V.R. Bhardwaj, D.M. Rayner, P.B. Corkum, Opt. Lett. **30**, 1867–1869 (2005). https://doi.org/10.1364/OL.30.001867
26. C. Hnatovsky, R.S. Taylor, P.P. Rajeev, E. Simova, V.R. Bhardwaj, D.M. Rayner, P.B. Corkum, Appl. Phys. Lett. **87**, 014104 (2005). https://doi.org/10.1063/1.1991991
27. C. Hnatovsky, R.S. Taylor, E. Simova, P.P. Rajeev, D.M. Rayner, V.R. Bhardwaj, P.B. Corkum, Appl. Phys. A Mater. Sci. Process. **84**, 47–61 (2006). https://doi.org/10.1007/s00339-006-3590-4
28. R. Taylor, C. Hnatovsky, E. Simova, Laser Photonics Rev. **2**, 26–46 (2008). https://doi.org/10.1002/lpor.200710031
29. K.C. Vishnubhatla, N. Bellini, R. Ramponi, G. Cerullo, R. Osellame, Opt. Express **17**, 8685–8695 (2009). https://doi.org/10.1364/OE.17.008685
30. S. Kiyama, S. Matsuo, S. Hashimoto, Y. Morihira, J. Phys. Chem. C **113**, 11560–11566 (2009). https://doi.org/10.1021/jp900915r
31. V. Stankevič, J. Karosas, G. Račiukaitis, P. Gečys, Micromachines **11**, 483 (2020). https://doi.org/10.3390/mi11050483
32. X. Li, J. Xu, Z. Lin, J. Qi, P. Wang, W. Chu, Z. Fang, Z. Wang, Z. Chai, Y. Cheng, Appl. Surf. Sci. **485**, 188–193 (2019). https://doi.org/10.1016/j.apsusc.2019.04.211
33. P. Wang, W. Chu, W. Li, Y. Tan, F. Liu, M. Wang, J. Qi, J. Lin, F. Zhang, Z. Wang, Y. Cheng, Micromachines **10**, 565 (2019). https://doi.org/10.3390/mi10090565
34. Z. Lin, J. Xu, Y. Song, X. Li, P. Wang, W. Chu, Z. Wang, Y. Cheng, Adv. Mater. Technol. **5**, 1900989 (2020). https://doi.org/10.1002/admt.201900989
35. H. Zhang, P. Wang, W. Chu, J. Yu, W. Li, J. Qi, Z. Wang, Y. Cheng, et al. arXiv:2004.03894 (2020). https://arxiv.org/abs/2004.03894
36. L.V. Keldysh, Ionization in the field of a strong electromagnetic wave. Sov. Phys. JETP **20**, 1307–1314 (1965)
37. D. Du, X. Liu, G. Korn, J. Squier, G. Mourou, Appl. Phys. Lett. **64**, 3071–3073 (1994). https://doi.org/10.1063/1.111350
38. A.C. Tien, S. Backus, H. Kapteyn, M. Murnane, G. Mourou, Phys. Rev. Lett. **82**, 3883–3886 (1999). https://doi.org/10.1103/PhysRevLett.82.3883
39. S.S. Mao, F. Quéré, S. Guizard, X. Mao, R.E. Russo, G. Petite, P. Martin, Appl. Phys. A Mater. Sci. Process. **79**, 1695–1709 (2004). https://doi.org/10.1007/s00339-004-2684-0
40. K. Itoh, W. Watanabe, S. Nolte, C.B. Schaffer, MRS Bull. **31**, 620–625 (2006). https://doi.org/10.1557/mrs2006.159
41. K. Davis, K. Miura, N. Sugimoto, K. Hirao, Opt. Lett. **21**, 1729 (1996). https://doi.org/10.1364/ol.21.001729
42. C.B. Schaffer, A. Brodeur, J.F. García, E. Mazur, Opt. Lett. **26**, 93–95 (2001). https://doi.org/10.1364/OL.26.000093
43. Y. Kondo, K. Nouchi, T. Mitsuyu, M. Watanabe, P.G. Kazansky, K. Hirao, Opt. Lett. **24**, 646–648 (1999). https://doi.org/10.1364/OL.24.000646
44. E. Bricchi, J.D. Mills, P.G. Kazansky, B.G. Klappauf, J.J. Baumberg, Opt. Lett. **27**, 2200–2202 (2002). https://doi.org/10.1364/OL.27.002200
45. Y. Shimotsuma, P.G. Kazansky, J. Qiu, K. Hirao, Phys. Rev. Lett. **91**, 247405 (2003). https://doi.org/10.1103/PhysRevLett.91.247405
46. V.R. Bhardwaj, E. Simova, P.P. Rajeev, C. Hnatovsky, R.S. Taylor, D.M. Rayner, P.B. Corkum, Phys. Rev. Lett. **96**, 057404 (2006). https://doi.org/10.1103/PhysRevLett.96.057404
47. M. Beresna, M. Gecevičius, P.G. Kazansky, T. Taylor, A.V. Kavokin, Appl. Phys. Lett. **101**, 053120 (2012). https://doi.org/10.1063/1.4742899
48. A. Rudenko, J.P. Colombier, T.E. Itina, Phys. Rev. B **93**, 075427 (2016). https://doi.org/10.1103/PhysRevB.93.075427
49. M. Beresna, M. Gecevičius, P.G. Kazansky, Opt. Mater. Express **1**, 783–795 (2011). https://doi.org/10.1364/OME.1.000783

50. M. Beresna, M. Gecevičius, P.G. Kazansky, Adv. Opt. Photon. **6**, 293–339 (2014). https://doi.org/10.1364/AOP.6.000293
51. V. Maselli, J.R. Grenier, S. Ho, P.R. Herman, Opt. Express **17**, 11719–11729 (2009). https://doi.org/10.1364/OE.17.011719
52. Y. Liao, J. Song, E. Li, Y. Luo, Y. Shen, D. Chen, Y. Cheng, Z. Xu, K. Sugioka, K. Midorikawa, Lab Chip **12**, 746–749 (2012). https://doi.org/10.1039/C2LC21015K
53. K. Sugioka, J. Xu, D. Wu, Y. Hanada, Z. Wang, Y. Cheng, K. Midorikawa, Lab Chip **14**, 3447–3459 (2014). https://doi.org/10.1039/C4LC00548A
54. Y. Liao, J. Ni, L. Qiao, M. Huang, Y. Bellouard, K. Sugioka, Y. Cheng, Optica **2**, 329–334 (2015). https://doi.org/10.1364/OPTICA.2.000329
55. E.N. Glezer, E. Mazur, Appl. Phys. Lett. **71**, 882–884 (1997). https://doi.org/10.1063/1.119677
56. S. Juodkazis, K. Nishimura, S. Tanaka, H. Misawa, E.G. Gamaly, B. Luther-Davies, L. Hallo, P. Nicolai, V.T. Tikhonchuk, Phys. Rev. Lett. **96**, 166101 (2006). https://doi.org/10.1103/PhysRevLett.96.166101
57. E.N. Glezer, M. Milosavljevic, L. Huang, R.J. Finlay, T.-H. Her, J.P. Callan, E. Mazur, Opt. Lett. **21**, 2023–2025 (1996). https://doi.org/10.1364/OL.21.002023
58. M. Deubel, G.V. Freymann, M. Wegener, S. Pereira, K. Busch, C.M. Soukoulis, Nat. Mater. **3**, 444–447 (2004). https://doi.org/10.1038/nmat1155
59. S. Juodkazis, V. Mizeikis, H. Misawa, J. Appl. Phys. **106**, 051101 (2009). https://doi.org/10.1063/1.3216462
60. I.M. Burakov, N.M. Bulgakova, R. Stoian, A. Mermillod-Blondin, E. Audouard, A. Rosenfeld, A. Husakou, I.V. Hertel, J. Appl. Phys. **101**, 043506 (2007). https://doi.org/10.1063/1.2436925
61. C. Corbari, A. Champion, M. Gecevičius, M. Beresna, Y. Bellouard, P.G. Kazansky, Opt. Express **21**, 3946–3958 (2013). https://doi.org/10.1364/OE.21.003946
62. P.K. Velpula, M.K. Bhuyan, F. Courvoisier, H. Zhang, J.P. Colombier, R. Stoian, Laser Photonics Rev. **10**, 230–244 (2016). https://doi.org/10.1002/lpor.201500112
63. K. Bergner, B. Seyfarth, K.A. Lammers, T. Ullsperger, S. Döring, M. Heinrich, M. Kumkar, D. Flamm, A. Tünnermann, S. Nolte, Appl. Opt. **57**, 4618–4632 (2018). https://doi.org/10.1364/AO.57.004618
64. M. Sakakura, M. Terazima, Phys. Rev. B **71**, 024113 (2005). https://doi.org/10.1103/PhysRevB.71.024113
65. D.G. Papazoglou, S. Tzortzakis, Opt. Mater. Express **1**, 625 (2011). https://doi.org/10.1364/OME.1.000625
66. D. Grossmann, M. Reininghaus, C. Kalupka, M. Kumkar, R. Poprawe, Opt. Express **24**, 023221 (2016). https://doi.org/10.1364/OE.24.023221
67. M.K. Bhuyan, M. Somayaji, A. Mermillod-Blondin, F. Bourquard, J.P. Colombier, R. Stoian, Optica **4**, 951–958 (2017). https://doi.org/10.1364/OPTICA.4.000951
68. F. Docchio, P. Regondi, M.R.C. Capon, J. Mellerio, Appl. Opt. **27**, 3661–3668 (1988). https://doi.org/10.1364/AO.27.003661
69. D.X. Hammer, E.D. Jansen, M. Frenz, G.D. Noojin, R.J. Thomas, J. Noack, A. Vogel, B.A. Rockwell, A.J. Welch, Appl. Opt. **36**, 5630–5640 (1997). https://doi.org/10.1364/AO.36.005630
70. P. Audebert, P. Daguzan, A. Dos Santos, J.C. Gauthier, J.P. Geindre, S. Guizard, G. Hamoniaux, K. Krastev, P. Martin, G. Petite, A. Antonetti, Phys. Rev. Lett. **73**, 1990 (1994). https://doi.org/10.1103/PhysRevLett.73.1990
71. L. Skuja, J. Non-Cryst. Solids **239**, 16 (1998). https://doi.org/10.1016/S0022-3093(98)00720-0
72. J.W. Chan, T.R. Huser, S.H. Risbud, D.M. Krol, Appl. Phys. A Mater. Sci. Process. **76**, 367–372 (2003). https://doi.org/10.1007/s00339-002-1822-9
73. D.M. Rayner, A. Naumov, P.B. Corkum, Opt. Express **13**, 3208–3217 (2005). https://doi.org/10.1364/OPEX.13.003208
74. A. Couairon, L. Sudrie, M. Franco, B. Prade, A. Mysyrowicz, Phys. Rev. B **71**, 125435 (2005). https://doi.org/10.1103/PhysRevB.71.125435

75. A. Rosenfeld, M. Lorenz, R. Stoian, D. Ashkenasi, Appl. Phys. A Mater. Sci. Process. **69**, S373–S376 (1999). https://doi.org/10.1007/s003390051419
76. G. Raciukaitis, M. Brikas, P. Gecys, M. Gedvilas, *Proc. SPIE 7005, High-Power Laser Ablation VII* (2008), p. 70052L. https://doi.org/10.1117/12.782937
77. F. Bauer, A. Michalowski, T. Kiedrowski, S. Nolte, Opt. Express **23**, 1035 (2015). https://doi.org/10.1364/OE.23.001035
78. P.P. Rajeev, M. Gertsvolf, E. Simova, C. Hnatovsky, R.S. Taylor, V.R. Bhardwaj, D.M. Rayner, P.B. Corkum, Phys. Rev. Lett. **97**, 253001 (2006). https://doi.org/10.1103/PhysRevLett.97.253001
79. D. Grojo, M. Gertsvolf, S. Lei, T. Barillot, D.M. Rayner, P.B. Corkum, Phys. Rev. B **81**, 212301 (2010). https://doi.org/10.1103/PhysRevB.81.212301
80. B. Rethfeld, Phys. Rev. Lett. **92**, 187401 (2004). https://doi.org/10.1103/PhysRevLett.92.209901
81. P.G. Kazansky, M. Beresna, Top. Appl. Phys. **123**, 127 (2012). https://doi.org/10.1007/978-3-642-23366-1_6
82. P. Wang, W. Chu, X. Li, Z. Lin, J. Xu, H. Zhang, Y. Cheng, *Proc. SPIE 11268, Laser-Based Micro- and Nanoprocessing XIV* (2020), p. 1126808. https://doi.org/10.1117/12.2542020
83. F. Gomollón-Bel, Chem. Int. **41**, 12–17 (2019). https://doi.org/10.1515/ci-2019-0203
84. Y. Cheng, W. Zhu, X. Qian, *Beyond Limits Manufacturing: Mass Customization of Factory-on-a-Chip for Flow Chemistry in 70 Years of Excellence: ECNU's Ongoing Commitment to Cutting-Edge, Cross-Disciplinary Research* (Science/AAAS, Washington DC, 2021), pp. 17–19
85. D. Yin, Y. Li, L. Xia, W. Li, W. Chu, J. Yu, M. Wu, Y. Cheng, M. Hu, Chin. Chem. Lett. **33**, 1077–1080 (2022). https://doi.org/10.1016/j.cclet.2021.05.073
86. M. Wu, L. Xia, Y. Li, D. Yin, J. Yu, W. Li, N. Wang, X. Li, J. Cui, W. Chu, Y. Cheng, M. Hu, Chin. Chem. Lett. **33**, 497–500 (2022). https://doi.org/10.1016/j.cclet.2021.07.004
87. W. Li, Y. Li, W. Zhang, D. Yin, Y. Cheng, W. Chu, M. Hu, Chin. Chem. Lett. **32**, 1131–1134 (2021). https://doi.org/10.1016/j.cclet.2020.09.039

Chapter 11
Optical Nanostructuring by Near-Field Laser Ablation

Johannes Boneberg, Elke Scheer, and Paul Leiderer

Abstract The interaction of short, intense laser pulses with nanoparticles on a surface leads to laterally tightly confined, strongly enhanced electromagnetic fields below and around the nano-objects, which can easily give rise to nanoablation. This effect can be exploited for structuring substrate surfaces on a length scale well below the diffraction limit, one to two orders smaller than the incident laser wavelength. We report on structure formation by laser ablation in the optical near field of both dielectric and metallic nano-objects, the latter allowing even stronger and more localized enhancement of the electromagnetic field due to the excitation of plasmon modes. In the course of time, various improvements have been added to this technique, so that also more complex and even arbitrary structures can be produced by means of nanoablation. The near-field patterns generated on the surface can be read out with high-resolution techniques like scanning electron microscopy and atomic force microscopy and provide thus a valuable tool – in conjunction with numerical calculations like finite-difference time-domain (FDTD) simulations – for a deeper understanding of the optical and plasmonic properties of nanostructures and their applications.

Keywords Optical nanostructuring · Nanoablation · Optical near-field enhancement · Nanosphere lithography · Dielectric microlenses · Photonic nanojets · FDTD simulations · Plasmon resonance imaging

1 Introduction

In classical optics, light cannot be focused to a scale significantly smaller than its wavelength. This is commonly known as the “diffraction limit” and represents a major obstacle in using standard optical methods for the preparation of nano-

---

J. Boneberg · E. Scheer · P. Leiderer (✉)
Physics Department, University of Konstanz, Konstanz, Germany
e-mail: Johannes.Boneberg@uni-Konstanz.de; Elke.Scheer@uni-konstanz.de;
Paul.Leiderer@uni-konstanz.de

© The Author(s), under exclusive license to Springer Nature Switzerland AG 2023

R. Stoian, J. Bonse (eds.), *Ultrafast Laser Nanostructuring*, Springer Series
in Optical Sciences 239, https://doi.org/10.1007/978-3-031-14752-4_11

structures or the integration of optical components into nano-devices. Although it is true that today's semiconductor industry can produce features in the low nanometer range by sophisticated photolithography techniques, this requires extreme efforts and is not a suitable application, for example, for simple, quick nanostructuring of surfaces. Therefore, alternative optical methods which provide access to the sub-wavelength regime are of great interest.

The first concept for a device that allows optical experiments below the diffraction limit was described by E.H. Synge in 1928 [1] and realized by D.W. Pohl, W. Denk, and M. Lanz in 1984 [2]. The principle of this so-called scanning near-field optical microscope (SNOM) is to scan a sub-wavelength aperture across the sample (for details, see also Chap. 8 of this book). A further development is the aperture-less SNOM (aSNOM), where the strong concentration of the electric field in the vicinity of scattering objects, the "optical near-field," is used [3]. In particular, *metallic* nano-structures are very efficient scatterers for wavelengths close to the plasmonic resonances of their conduction electrons and have been used as antennas for surface-enhanced Raman scattering (SERS) [4, 5], for optical pumping of nanoscale objects like quantum dots [6], and for extreme light confinement for nonlinear effects [7–9]. One of the first attempts to exploit this antenna or "lightning-rod" effect for the nanostructuring of surfaces was reported in 1996 by Jersch and Dickmann [10]. These authors illuminated the metal tip of a scanning tunneling microscope with the pulses of a Nd:YAG laser (pulse duration 10 ns) and generated in this way hole- or hillock-like structures in the nanometer range. Soon afterward it was shown, however, that these features were not produced by the high electric field at the tip apex but by the thermal expansion of the illuminated tip, which led to a momentary mechanical contact between tip and sample [11–13]. Only several years later, structuring through field enhancement at the tips of scanning probe microscopes was unequivocally demonstrated [14–18]. In order to disentangle structuring effects due to optical near fields from those originating from a pulsed mechanical contact between tip and sample, one can use proper nanoparticles deposited on the surface instead of a scanning probe tip (which, despite its nanometer-size tip radius, is a macroscopic object). Effects of thermal expansion are then considerably smaller. This will be shown in Sect. 3.2 of this chapter.

Similar to metallic structures, also small *dielectric* objects can be used for nanostructuring by means of their optical near fields. Mostly micro- and nanospheres have been utilized for this purpose so far. The application for generating sub-wavelength structures has in this case been found more or less accidentally in the context of laser-induced removal of contaminant particles from surfaces which are required to be extremely clean, like silicon wafers in the semiconductor industry. This so-called dry laser cleaning (DLC) was conceived at the beginning of the 1990s by the groups of A. Tam and S. Allen [19, 20] as a contactless cleaning technique. The basic idea of DLC was to illuminate the contaminated wafer with a short laser pulse and use the very fast thermal expansion and subsequent deceleration of the surface to detach the particles by inertial forces. Although this laser cleaning method proved to be quite efficient for particle removal, systematic investigations revealed that the dominating mechanism was not the laser-induced thermal expansion but

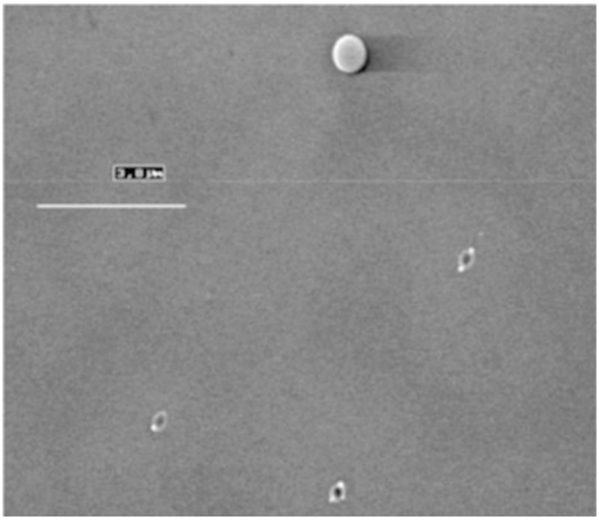

Fig. 11.1 Scanning electron micrograph (SEM) of a cleaned area (DLC, laser pulse duration $\tau = 30$ ps, wavelength $\lambda = 583$ nm) of a silicon sample intentionally contaminated with 800-nm polystyrene spheres. Elliptical holes can be found over the illuminated region, and also a remaining particle can be seen. The scale bar has a length of 3.8 µm. (Figure reproduced with permission from Ref. [21])

the local ablation of the substrate underneath the particles under the influence of the strong near-field enhancement, as shown in Fig. 11.1 [21]. The damage in the wafer resulting from the ablation was, of course, inacceptable as a cleaning concept for the semiconductor industry, and therefore this method is not used nowadays, at least not to our knowledge. However, the observation of nanoholes produced by dry laser cleaning was the starting point of nanostructuring by optical near fields of dielectric micro- and nanospheres. This topic is discussed in Sect. 2, whereas Sect. 3 is devoted to plasmonic particles.

2 Optical Near Fields of Dielectric Nanostructures

2.1 Dielectric Particles: Theory and Simulations

The scattering of light by a homogeneous spherical scatterer has been analytically solved already one century ago by the physicist Gustav Mie [22], as described in detail by Barber and Hill [23]. Mie did his original calculations for colloidal suspensions of metal particles, which have a complex refractive index. For simplicity, we will restrict ourselves in this Sect. 2 to dielectric particles with a real refractive index n, like silica or polystyrene (PS), which are the most used ones in the experiments described below. Following Mie, one considers a sphere with diameter *d,* which is irradiated by a plane electromagnetic wave. The incident wave is partly scattered by the sphere, and it partly penetrates into its interior. The total electric field $\boldsymbol{E}_{\text{tot}}$ is therefore a superposition of the incident electric field $\boldsymbol{E}_{\text{i}}$, a scattered wave $\boldsymbol{E}_{\text{s}}$, and the field in the interior of the sphere $\boldsymbol{E}_{\text{int}}$. Due to the spherical symmetry of the problem, these contributions can be expanded in terms of vector spherical harmonics. The coefficients of this expansion contain the diameter of the particles in form of the dimensionless Mie (or size) parameter [24]:

$$\beta := \frac{kd}{2} = \frac{\pi N d}{\lambda}, \tag{11.1}$$

where λ is the light wavelength in vacuum and k and N are the light wave vector and the refractive index of the surrounding medium.

For large spheres ($x \gg 1$), the particle focuses the incident wave on its shadow side, acting like a spherical lens. The distance of the focus from the surface of the sphere can be calculated by means of spherical optics [25]:

$$f = d\,\frac{2-n}{4\,(n-1)}. \tag{11.2}$$

For silica ($n = 1.45$) and PS ($n = 1.58$), this yields for f the values 0.30 d and 0.18 d, respectively. An example of a Mie calculation for a PS sphere with a diameter of 50 μm is shown in Fig. 11.2, which confirms the result from Eq. 11.2. The field intensity in the focus is in this case enhanced by a factor of 2000 compared to the incident intensity. The bigger a particle is compared to the wavelength, the better is the focusing and hence the maximum intensity in the focus, because diffraction will play less and less a role. Superimposed on this behavior are maxima in the intensity due to optical resonance modes of the sphere [26].

Such strong enhancement by microlenses has given rise to a number of applications, both for the optical near-field structuring described below and for a number of other topics, particularly nonlinear phenomena on a micron scale. The first near-field structuring experiments were reported in the year 2000 [21, 27], and in 2004 the name "photonic nanojet" was coined for the light distribution in the focus depicted in Fig. 11.2 [28]. Since then, a number of reviews about applications of photonic nanojets have appeared, two recent ones in Refs. [29–31].

For spheres with a small size parameter ($d < \lambda$), the electric near field has a completely different spatial distribution, given by the field of an electric dipole [32]:

$$\boldsymbol{E} = \boldsymbol{E}i + \frac{1}{4\pi\varepsilon_0}\left[\frac{3\,(\boldsymbol{r}\boldsymbol{p})\,\boldsymbol{r}}{r^5} - \frac{\boldsymbol{p}}{r^3}\right] \tag{11.3}$$

with the dipole moment

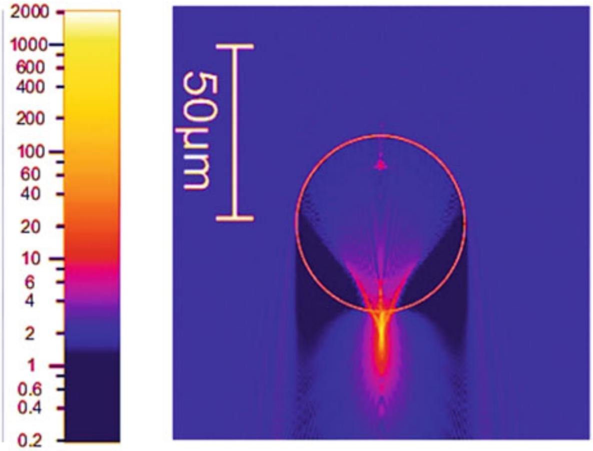

Fig. 11.2 Mie calculation of the optical near-field intensity of a spherical transparent particle with a refractive index $n = 1.58$ and a diameter $d \gg \lambda$, placed in vacuum. The scale on the color code gives the enhancement factor

$$\boldsymbol{p} = \frac{1}{2}\pi \varepsilon_0 d^3 \boldsymbol{E}_i \frac{\varepsilon - 1}{\varepsilon + 2}, \tag{11.4}$$

where $\varepsilon = n^2$ is the relative dielectric constant of the particle. At a small distance, the evanescent, exponentially decaying part of the electric field has a dominant influence on the field distribution, as seen in Fig. 11.3: The intensity is no longer peaked in the forward direction but has two side lobes, oriented along the polarization of the electric field. For the maximal field intensity enhancement ξ^2 at the surface of the sphere, one obtains from Eq. (11.3):

$$\xi^2 = (E/E_i)^2 = \left(\frac{3\varepsilon}{\varepsilon + 2}\right)^2 \tag{11.5}$$

The resulting values for ξ^2 are 2.36 and 2.77, respectively, for the dielectric constants ε of silica and PS, and are thus much smaller than for big spheres. Besides, the enhancement factor in this size parameter regime does *not* any longer depend on the sphere diameter.

The dipole radiation emitted from an oscillating dipole given by Eq. 11.3 exhibits an interesting difference between the near- and the far field: in the near field, where the evanescent part of the field dominates, the spatial energy density is nearly exclusively determined by the square of the electric field, E^2, whereas in the far field the energy density consists to equal parts of the electric and magnetic field contributions [32].

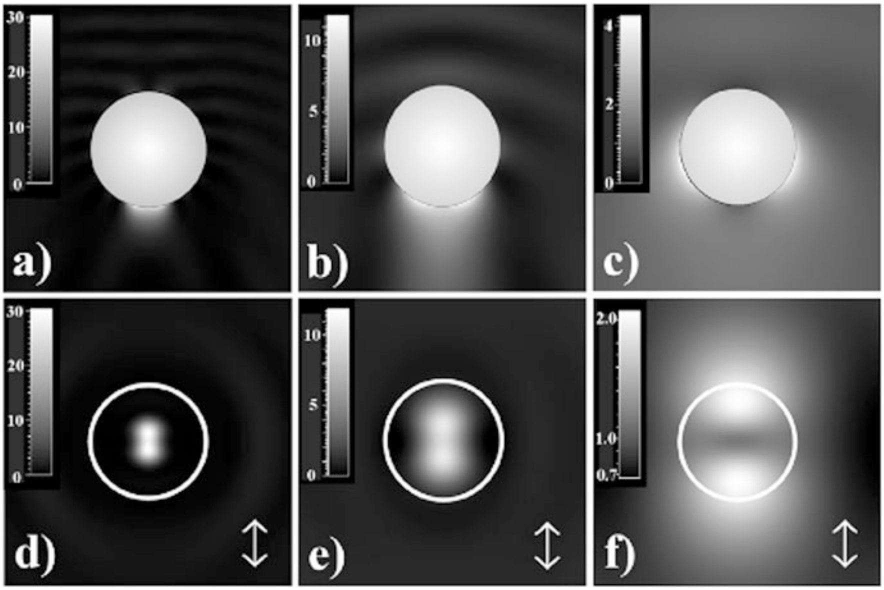

Fig. 11.3 Normalized field intensities calculated according to Mie theory for different-sized spheres that are irradiated with light at a wavelength $\lambda = 800$ nm. The diameters of the spheres with a refractive index $n = 1.58$ (PS) are 1700 nm (**a**, **d**), 800 nm (**b**, **e**), and 320 nm (**e**, **f**). Plotted is the intensity in a cross-section as seen from the side (**a**–**c**) and in the plane of the substrate surface as seen from above (**d**–**f**). The light field enters from the top, and the polarization vector of the electric field is indicated by an arrow. The displayed areas are 5100×5100 nm^2, 2400×2400 nm^2, and 960×960 nm^2, respectively. (Figure reproduced with permission from Ref. [21])

The Mie treatment described so far applies to a sphere in a homogeneous medium, whereas in the optical structuring experiments presented below the particles, whose near fields are exploited, are located on or close to a sample surface. Taking this into account requires semi-analytical field calculations, for example, the multiple-multipole (MMP) technique [33] which has been applied by R. Pack and R. Wannemacher to the case of PS particles on a Si substrate (Fig. 11.4) [34]. Typically, in the presence of a substrate with a refractive index $n > 1$ the enhancement in the center is higher than for the Mie solution, the width is smaller, and the dipole pattern can disappear nearly completely for certain size parameters (like in Fig. 11.4c for the 800 nm sphere). More information about the treatment beyond the Mie theory of a particle on a surface is given in Ref. [26]. More recently, purely numerical methods have also been used to calculate the near-field distribution of spheres, like the finite-difference time-domain (FDTD) technique, which will be addressed in more detail in Sect. 3.

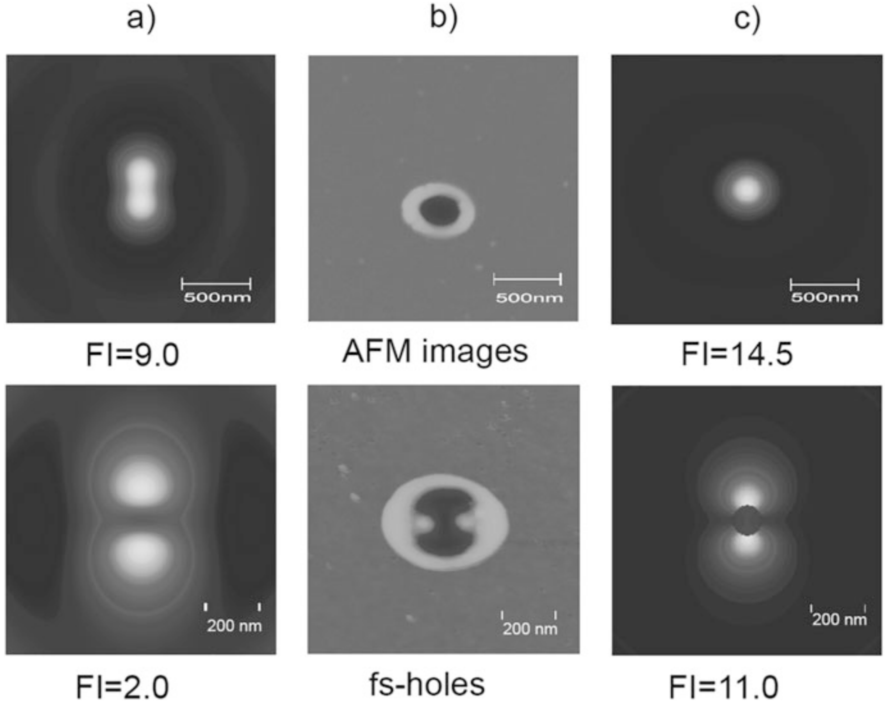

Fig. 11.4 Field intensity enhancement and ablation pattern underneath colloidal particles with diameters of 800 nm (top) and 320 nm (bottom) on a silicon substrate. The direction of the electrical field is orientated in the vertical direction. (**a**) Calculated field enhancement according to Mie theory, that is, neglecting the influence of the substrate; (**b**) AFM images of the ablation patterns resulting from illumination by a fs laser pulse (experiment); (**c**) Calculation including the influence of the substrate [34]. The gray scales in the calculations are the same as in Fig. 11.3. (Figure reproduced with permission from Ref. [34])

2.2 *Dielectric Particles: Experiments*

As already mentioned in the introduction, the first indications for nanostructuring of surfaces in the near field of dielectric particles came from experiments in the context of dry laser cleaning (Fig. 11.1). As shown above, the intensity underneath the particles can be enhanced by orders of magnitude and can thus be above the ablation threshold of the Si substrate, even if the incident laser fluence is well below this threshold. This gives rise to the observed nanoholes seen in Fig. 11.1, which are nanoscopic ablation craters generated by the optical near field.

Such craters are illustrated in more detail in Fig. 11.5, again for a Si surface. In this example, 1700 nm spheres and laser pulses with 150 fs at a wavelength of 800 nm were used [21]. The triangular pattern of holes was generated by a cluster of six particles, which had formed as a result of attractive capillary forces during sample preparation. This tendency of monodisperse colloidal spheres to aggregate

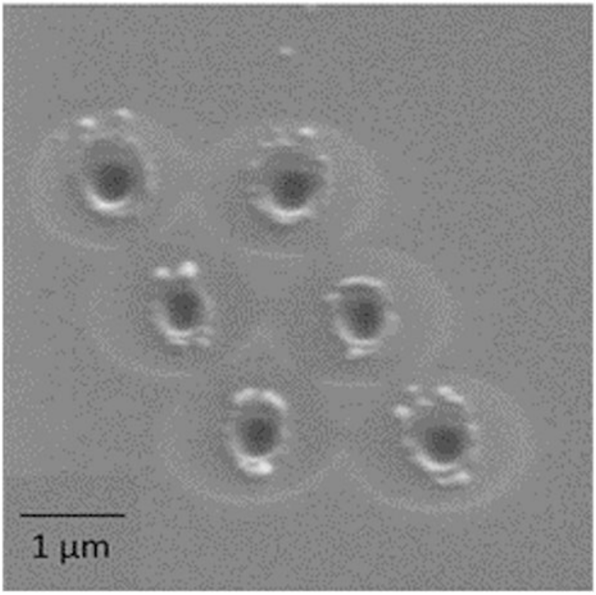

Fig. 11.5 SEM image of holes generated during dry laser cleaning of a silicon surface with a fs laser pulse (150 fs, $\lambda = 800$ nm) by an aggregate of six 1700 nm PS spheres. (Figure reproduced with permission from Ref. [21])

in regular arrays was used later, as shown below, to build masks which allow one to pattern large areas in a one-step process with a single laser pulse. The diameter of the near field created holes in Fig. 11.5 is 300 nm and is thus somewhat smaller than $\lambda/2$, the traditional diffraction limit in the far field.

In addition to the craters, the SEM picture in Fig. 11.5 reveals faint, disklike features with a diameter of 1700 nm around each of these holes. This contrast results from a thin (10 nm) SiO_2 layer that had been evaporated onto the sample after the deposition of the particles, but before the laser pulse, to mark the original particle positions as a "footprint." A scan across the sample surface showed that for every such footprint the laser-induced particle removal was accompanied by crater formation [35]. The dominating mechanism of "dry laser cleaning" in these experiments was, therefore, not the thermal expansion of the substrate, as initially assumed [20], but the ejection of the material below the spheres [21].

The ejection process can also explain the "splashes" found around each crater in Fig. 11.5. Whereas the ablation of the material occurs on a very short timescale, the particle itself hardly moves during that process. The ablated Si material is therefore squeezed out sideways and partly reacts with the surrounding air. The "caldera" around the craters thus consists mainly of SiO_x, as confirmed by chemical etching [36]. Caldera formation can be avoided, if the colloid particles are placed at some distance from the substrate utilizing a spacer [37] or by inclined irradiation of the particles [38], as shown in Fig. 11.6. In Fig. 11.6a sphere was irradiated from the

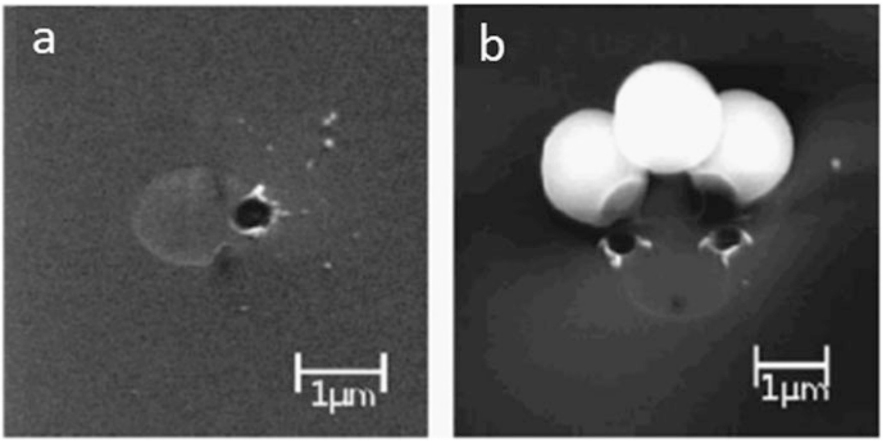

Fig. 11.6 SEM images of holes generated during dry laser cleaning of a silicon surface with a fs laser pulse ($\tau = 150$ fs, $\lambda = 800$ nm). (**a**) Laser beam incident at an angle of 45° from the left side; (**b**) 45° incidence from the back. (Figure reproduced with permission from Ref. [38])

left at an angle of incidence of 45°. The ablation hole is therefore not in the center but at the right edge of the particle's footprint. Figure 11.6b gives another example of nanoablation at inclined irradiation; here, an aggregate of three particles detached only partly, and traces of the substrate material on the two spheres which generated ablation holes are clearly visible. The third sphere is somewhat smaller and left only a barely visible round mark with 0.2 µm diameter in the substrate. A more detailed description of ablation effects upon inclined irradiation of nanospheres has been presented by Wang et al. [39].

Influence of particle size The holes in Figs. 11.5 and 11.6 were generated by the near field of particles larger than the light wavelength; the size parameter therefore had values well above 1. The holes are in this case nearly circular in shape. For smaller spheres, the Mie calculations shown in Figs. 11.3 and 11.4 predict pronounced anisotropies if linearly polarized light is used for the irradiation. This is experimentally confirmed, as shown by the AFM image in Fig. 11.4b, which displays a dumbbell-like pattern for 320 nm particles illuminated with 800 nm light. The similarity between the simulated and the experimental patterns in Fig. 11.4 suggested that local ablation of a smooth silicon substrate can be used to image the optical near-field distribution of nanoscopic objects. This aspect will be further discussed in Sect. 3.

The calculations in Figs. 11.3 and 11.4 indicate not only the development of an anisotropy in the near-field distribution but also a strong reduction of the maximum near-field enhancement as the size parameter is reduced. Also this aspect has been corroborated by experiment: since particle removal in a DLC process is dominated by the material ablation underneath the particle, the threshold for removal is a measure of the onset of near-field ablation. Experimentally, the incident

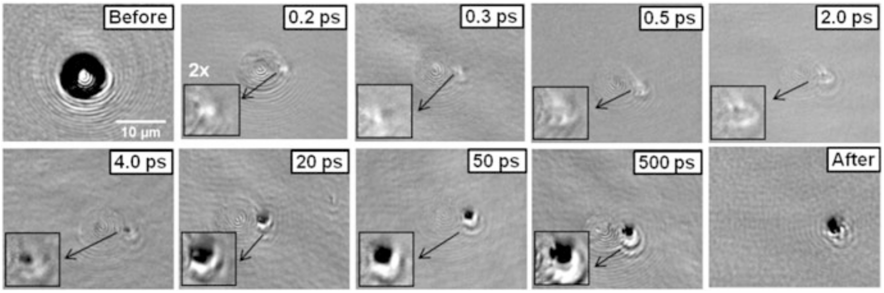

Fig. 11.7 Femtosecond-resolved ablation dynamics of Si in the near field of a small dielectric sphere, appearing as a black disk in the top-left frame. Shown are surface reflectivity images at the particle location for different time delays (indicated in the upper right corners) upon exposure to a 120 fs-laser pulse incident from the left at an angle of 54°. Except for the images corresponding to the surface before and after the arrival of the laser pulse, the images have been normalized to an image obtained blocking the pump pulse to minimize the scattering effects caused by the 7.9 µm-diameter particle. Zooms (2×) have been applied to the relevant part of the images and pasted as insets. (Figure reproduced from [40] (©2013 P. Kühler et al., distributed under the terms of the Creative Commons Attribution 2.0 Generic License, https://creativecommons.org/licenses/by/2.0))

fluence values for the DLC threshold were found to be 11, 25, and 80 mJ/cm^2 for particles with 1700, 800, and 320 nm diameter, respectively [35]. Since one would expect that the value of the cleaning threshold is inversely proportional to the field enhancement, this tendency agrees qualitatively quite well with the enhancements calculated in Fig. 11.3a–c.

Temporal development of near-field induced structure formation In order to gain information about the timescale of the near-field structuring process, microscopy in the femtosecond to picosecond range is required. This has been achieved by employing a pump-probe technique, as illustrated in Fig. 11.7 for the formation of a hole in a Si substrate in the focus of a microsphere, irradiated by a 120 fs laser pulse at a wavelength of 800 nm [40]. The sphere diameter was 7.9 µm, the size parameter thus $\beta = 30$. An oblique angle of incidence of 54° was used, so that the location of the focus on the substrate was not covered by the sphere, but was optically accessible from above. As mentioned before, on such short timescales, the sphere does not move noticeably; it could therefore be eliminated from the frames between 0.2 and 500 ps by subtracting the image where the ablation pulse was blocked. Already at a delay of 0.2 ps, a bright spot appears at the location of the focus, which is interpreted as evidence for the formation of a dense electron-hole plasma. At a delay of 4 ps, this formerly bright region has become dark, a signature of ablation. After about 10 ps, the image hardly changes anymore, showing that the ablation has been completed. An overview of the mechanisms and dynamics of near-field-induced ablation has been presented by Plech et al. [36].

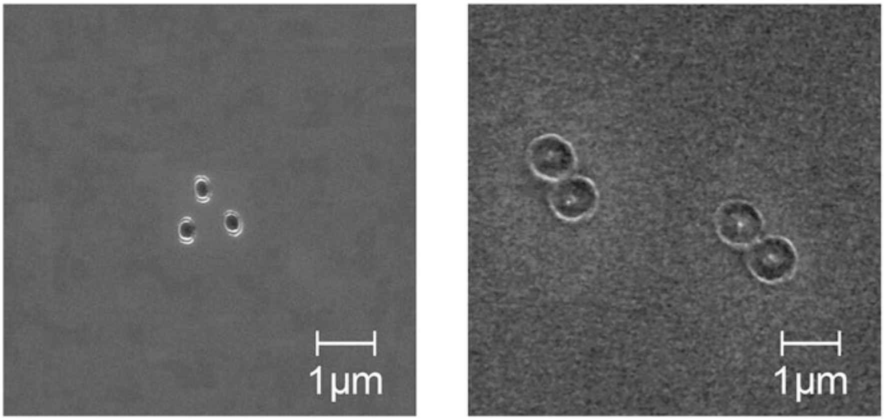

Fig. 11.8 SEM image of near-field induced holes created by irradiating clusters of 800 nm PS spheres on silicon (left). Trimer irradiated with a 100 fs pulse; (right) two dimers irradiated with an 8 ns pulse. The wavelength was in both cases $\lambda = 800$ nm. (Image adapted with permission from Ref. [34])

Whereas for laser pulses in the regime of femtoseconds up to a few picoseconds, the holes generated at the surface of bulk Si are caused by a nanoablation process and typically have steep walls and a diameter of about the enhanced field distribution, irradiation of the same sample with nanosecond pulses leads to structures with a quite different shape: They are shallow, and their diameter can be several times larger (see Fig. 11.8b). A rim surrounds the depression in the surface, and in the center a hillock-like feature appears, sometimes also referred to as nanobump or nanocone [41–45]. This change in shape compared to fs pulses as in Fig. 11.8a can partly be explained by the lateral heat flow in the substrate, which on a nanosecond timescale cannot be neglected anymore. The decisive parameter is the thermal diffusion length $l = 2(D\tau)^{½}$ (where D is the thermal diffusion coefficient and τ is the laser pulse duration). For Si, one obtains a value $l \approx 1$ µm for $\tau = 8$ ns. In addition to the spreading of heat, also melting and lateral flow of the molten material under the influence of capillary forces, the Marangoni effect and the density difference between solid and liquid Si play a role in the structure formation [32]. For *thin films* on solid substrates, a further mechanism coming into play is dewetting [46], which depends on the Hamaker constants of film and substrate. Even nanosecond pulses can then give rise to well-defined holes with sharp edges in the film, as shown in Fig. 11.9 [47].

Nanostructuring of regular hole arrays The examples so far show the formation of individual holes or small hole clusters in the optical near field of colloid spheres. If one is rather interested in a regular array of holes, one can make use of the tendency of monodisperse colloid suspensions to form densely packed layers by self-assembly, as already mentioned above. Under appropriate conditions, these layers can extend over areas in the cm^2 range [48–51]. Using their near fields,

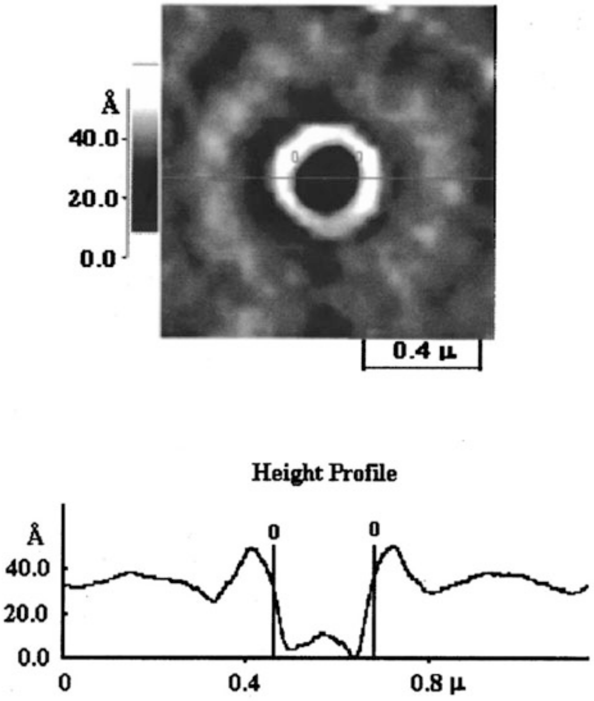

Fig. 11.9 AFM image and depth profile of a pit in a 35-nm thick Al film on silicon, formed after the illumination of a 0.95 µm SiO_2 particle by a single nanosecond pulse with a fluence of 300 mJ/cm^2 (KrF excimer laser, $\lambda = 248$ nm, $\tau = 23$ ns). (Reprinted from Ref. [47], with the permission of AIP Publishing)

millions of nanoholes can be generated with just one laser pulse. An example is depicted in Fig. 11.10, again for a Si substrate. By selecting the proper colloid sphere size and laser intensity, one can choose the holes' diameter, depth, and distance over a wide range.

Numerous groups have used this technique for surface patterning [34, 37, 41, 44, 47, 52–60]. By choosing proper conditions, regular arrays of holes with diameters well below 100 nm can be generated, as shown in Fig. 11.11 [52], and even smaller holes down to a diameter of 30 nm have been reported [47]. The method is quite versatile and applicable to many substrates. Besides Si, other semiconductors like Ge, GaAs, InAs, and InP have been structured [32], but also glass [58, 60] and polymers [37, 56, 59], as well as thin metal films [47, 58] and silicon membranes [61] (Fig. 11.12).

More complex or even arbitrary-shaped periodic patterns can be generated by irradiating substrates immersed in liquids (together with the attached particle mask) or by using variable angles of the incident laser beam. In the first case, applied by Ulmeanu et al. [62, 63], the structures resulting from laser irradiation depend –

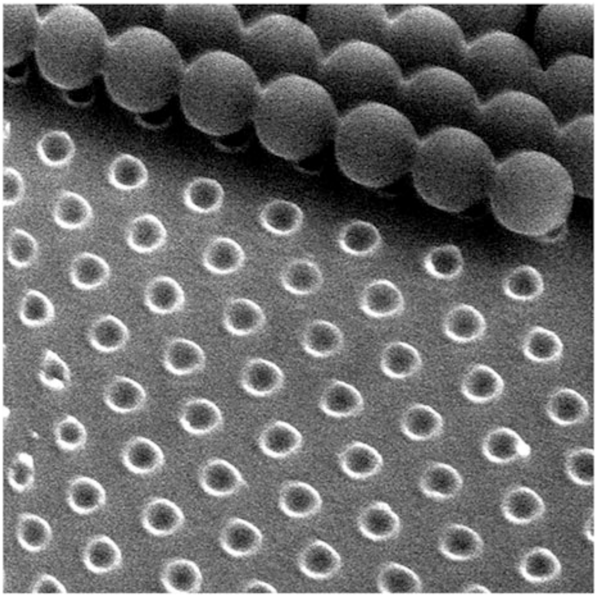

Fig. 11.10 Nanohole pattern generated by illuminating an ordered array of PS microspheres with a single laser pulse ($\tau = 150$ fs, $\lambda = 800$ nm). Some remaining spheres are also seen. (Sphere diameter 800 nm; similar images are shown in [34])

apart from the parameters already mentioned – also on the difference between the refractive index of the particles and the surrounding liquid medium. The principle of variable oblique irradiation, as used by Guo et al. [64], is shown in Fig. 11.13, together with an experimental example of a 20-nm thick eutectic $Sb_{20}Tb_{30}$ film supported by a polycarbonate substrate and structured by a ns laser pulse.

Even more flexibility for patterning by the optical near field of microspheres has been demonstrated by the group of Arnold et al. by means of an optical trap [65, 66]. In this approach an individual sphere was held by optical tweezers, and structuring was achieved by a ns KrF laser, moving the sample at the focal distance under the sphere in the desired manner by means of a translation stage. In this way, arbitrary patterns with a minimum width given by the focus size of the microsphere can be generated. This principle was extended to parallel structuring by an array of traps, each filled with a microbead [67]. More details about this technique can be found in Chap. 8 “Probing Light by Matter: Implications of Complex Illumination on Ultrafast Nanostructuring.”

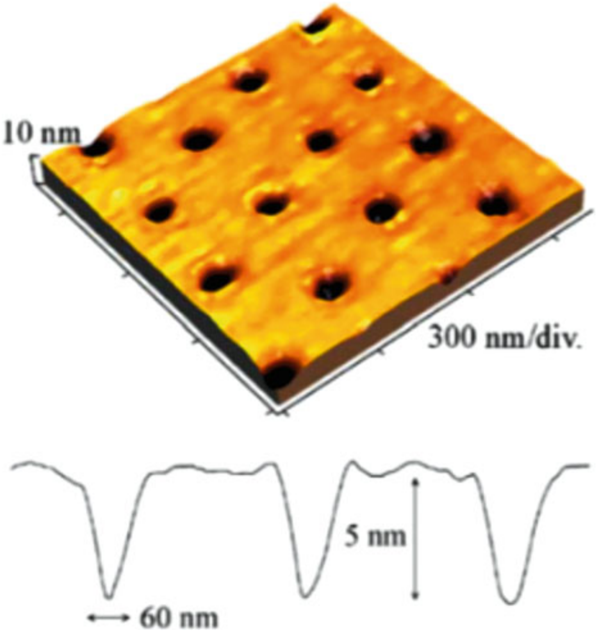

Fig. 11.11 Silicon nanoholes fabricated on a (100) Si surface by using a single-shot 265.7-nm Ti:sapphire laser radiation ($\tau = 300$ fs, fluence 15 ± 3.5 mJ/cm^2) together with a regular lattice of SiO_2 microspheres ($r = 150$ nm). The width of the holes at FWHM (full width half maximum) is 57 ± 6.5 nm and their depth with respect to the original silicon surface 6 ± 1 nm. (Reprinted by permission from [52])

3 Optical Near Fields of Plasmonic Nanostructures

The optical near fields of metallic nanostructures are typically dominated by plasmonic excitations of the conduction electrons. As will be shown below, the resonances can give rise to strong near-field enhancements localized on an even distinctly smaller length scale than for the dielectric particles. We first provide a short account of the simulations and then present an overview of the experimental results. Localization of light at the nanoscale due to plasmonic effects is also discussed in Chap. 12 on plasmonic nanoprinting.

3.1 Plasmonic Particles: Simulations

A theoretical description of the near-field enhancement of metallic spheres was already included in Mie's original theory [22] introduced in Sect. 2, which also holds for suspensions of spherical *metallic* colloids. However, many plasmonic nano-objects which are interesting for applications deviate substantially from the

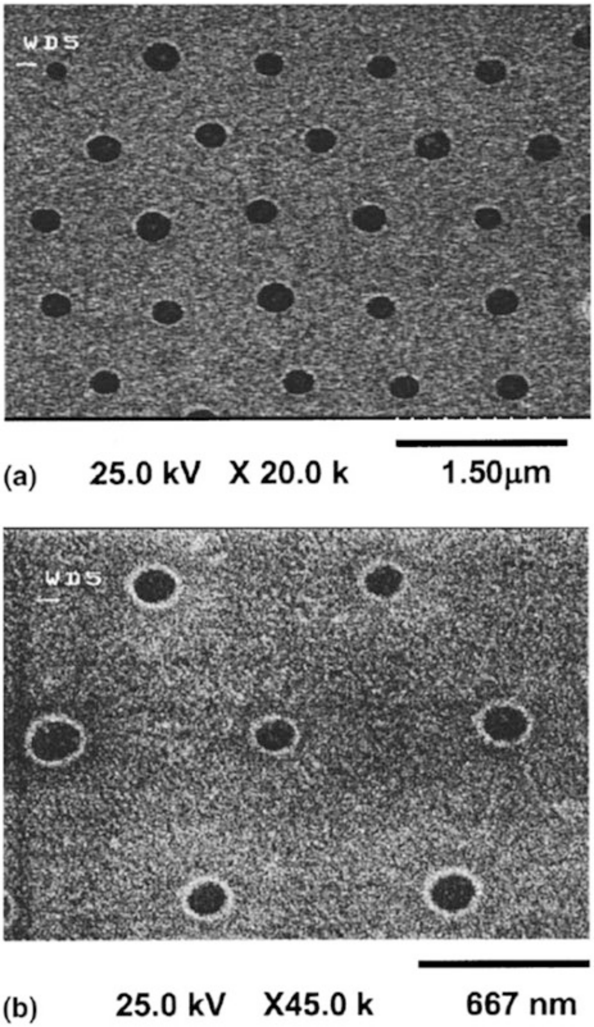

Fig. 11.12 (**a**) and (**b**) SEM images of a periodic pit array in a 35-nm thick Al film on silicon, formed after the illumination of an array of 0.95 µm SiO_2 particles by a single pulse with a fluence of 300 mJ/cm^2 (KrF excimer laser, $\lambda = 248$ nm, $\tau = 23$ ns). (Reprinted from Ref. [47], with the permission of AIP Publishing)

simple spherical symmetry, such as triangular, bow tie, and rodlike structures. For those, numerical methods have been developed, like the discrete dipole approximation (DDA) and the finite-difference time-domain (FDTD) simulations. Since FDTD has been used most frequently in the literature, we give here a brief description of this approach as an example of the numerical strategies. Information on DDA can be found in [68].

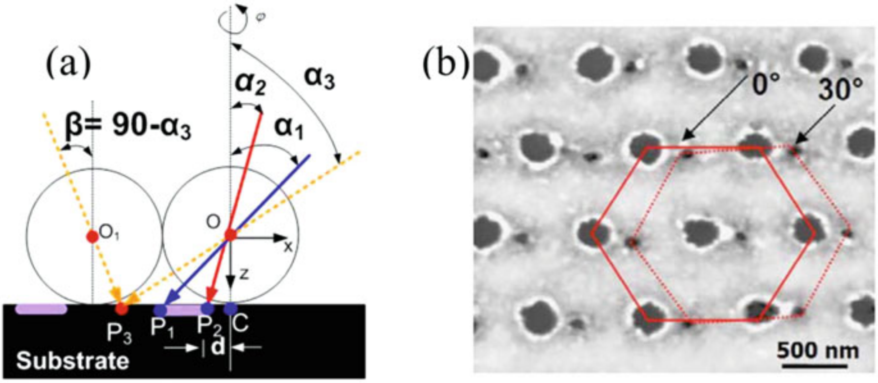

Fig. 11.13 (**a**) Schematic diagram of the experimental configuration for direct laser writing of nanoline arrays on a $Sb_{70}Tb_{30}$ substrate surface; (**b**) SEM image of two hexagonal nanodot arrays ablated by a single KrF laser pulse ($\lambda = 248$ nm, pulse width 15 ns) at an incident angle of 0° (with a fluence of 6.5 mJ/cm^2) and 30° (with a fluence of 1.0 mJ/cm^2), respectively. (Reprinted from Ref. [64], with the permission of AIP Publishing)

FDTD was introduced in 1966 by K. S. Yee [69] as a method for solving the time-dependent Maxwell equations in complex systems, which are analytically not accessible. The nanostructure and its surroundings are discretized into a grid of cells. In this way, the temporal and spatial derivatives can be approximated as difference quotients, for which the differential equations for each time step and every cell are solved. This approach allows one to simulate not only idealized but also realistic nanostructures. In Fig. 11.14a we show as an example an AFM image of a gold triangle, prepared by colloid lithography (to be described in Sect. 3.2). Figure 11.14b is the corresponding model structure, used as an input for calculating the distribution of plasmonic excitations in this object. Details of the experimental triangle, like the curvature of the corners, the profile of the edges, and the surface roughness can be included in the simulation, which, as it turns out, has a considerable influence on the coupling between the triangle and the incident light wave. Compared to an idealized structure, these modifications partly shift and partly broaden the plasmonic resonance and thus can be responsible for a decrease of the field enhancement in the hotspots. Also, details of the substrate could in this case be chosen realistically, e.g., a 1.5-nm thick SiO_2 layer on top of bulk Si, as determined by ellipsometry [70].

The field intensity calculated for such a triangle using the FDTD program of Lumerical Inc. is shown in Fig. 11.15a. The side length of the triangle is 550 nm and its height 40 nm, and the laser irradiation is vertical with 800-nm light. The field intensity is averaged over the whole triangle height and normalized by the incident intensity. As a comparison with a somewhat smaller dielectric sphere with 320 nm diameter in Fig. 11.3 shows, the field enhancement for these metallic triangles is much more localized and can also be much more pronounced. The FDTD simulations in addition allow one to gain information about the dissipated energy in

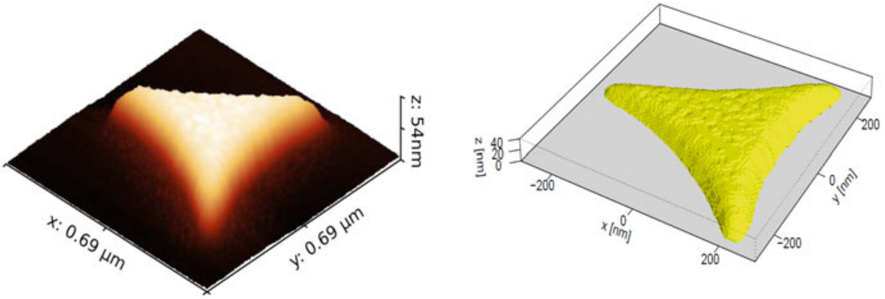

Fig. 11.14 (left) 3D image of a gold triangle prepared by colloid lithography; (right) model of such a triangle, on which the simulations displayed in Fig. 11.15 were carried out

the plasmonic structure and also about the electric field vectors. Both quantities are shown for the same triangle in Fig. 11.15b, c. The spatially resolved dissipation will be relevant for the local melting experiments discussed further below.

3.2 Plasmonic Particles: Experiments

Standard techniques for the fabrication of plasmonic nanostructures are electron-beam and focused-ion-beam lithography, which have been used for disklike, triangular, bow tie, and rodlike nanoantennas and even more complex shapes [71]. An alternative method for many investigations, which is fast and much less costly, is colloid lithography, based on the colloid monolayers introduced in Sect. 2. These layers can serve as an evaporation mask for preparing triangular nanostructures in quite a versatile way. The size and thickness of the triangles can be chosen from nanometers up to microns by selecting the size of the spheres and the evaporation conditions, and the area to be covered by the structures in a parallel process can be as large as the whole colloid mask. An important feature is that the triangles generated in this fashion can have tip radii as small as 5 nm [72], a value that is not easily reached by conventional lithographic techniques. Figure 11.16 shows an array of nanotriangles produced in this way. In the following, we will first focus on the near-field ablation patterns generated by these triangular structures and will then discuss some of the other shapes of plasmonic structures.

Triangular structures A first example for nanoablation by the near field of plasmonic triangles like the ones in Fig. 11.16 is shown in Fig. 11.17. The material of the triangles was gold, as in most experiments in this section, owing to its superior plasmonic properties and resistance against corrosion. The substrate was again a Si wafer, and single pulses of a fs laser at a wavelength of 800 nm served as light source. The intensity of the pulse was below the damage threshold of bare silicon. Consequently, the silicon substrate remained undamaged in most of the irradiated

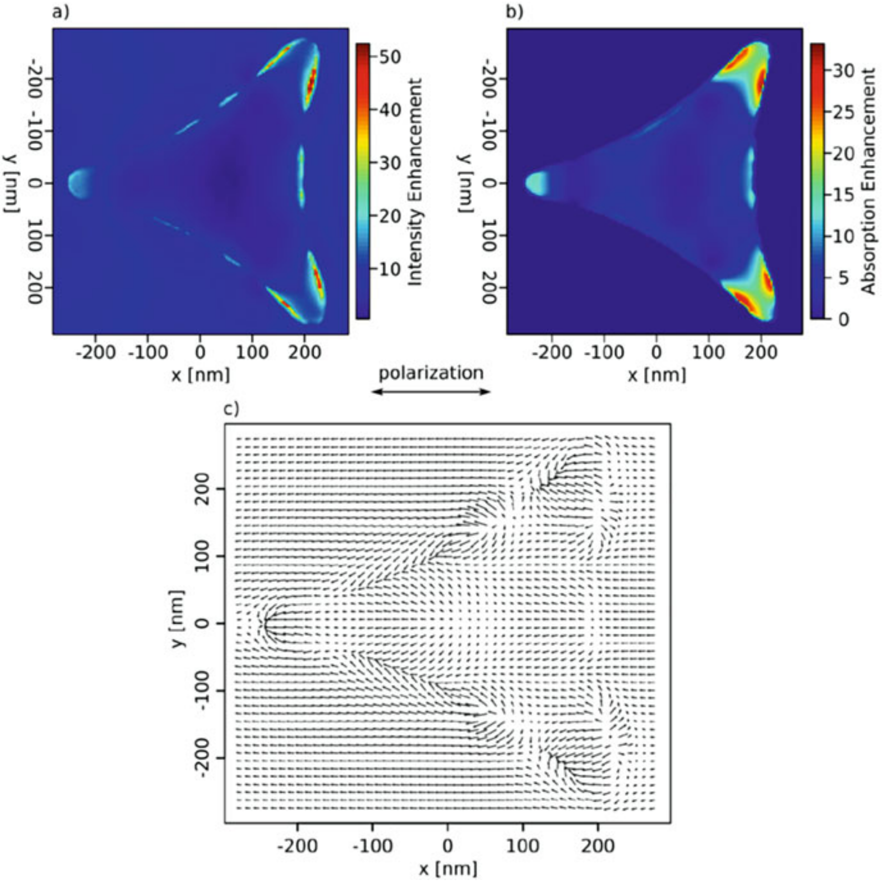

Fig. 11.15 (**a**) Calculated field intensity enhancement, (**b**) dissipation, and (**c**) electric field vector distribution for a nanotriangle like in Fig. 11.14b. The polarization of the incident laser radiation was here horizontal. The simulation volume was 1 × 1 × 1.2 μm^3 with “perfectly matched layer” boundary conditions. The meshing was set to automatic mode far from the triangle, and a manually refined mesh with a cell size of 1.3 × 1.3 × 0.5 nm^3 was added around the particle [70]

area, although the Au triangles were removed by applying the light pulse [73]. Small ablation craters are only seen at some of the positions of the former triangle corners. Like the nanoablation craters of dielectric spheres, these holes are surrounded by rims of ablated material. The crater-caldera structure becomes even more obvious when the remaining gold clusters in Fig. 11.17b are removed by chemical etching (Fig. 11.17c). The radius of curvature at the tips of the holes in Fig. 11.17 has been determined as 5 nm, similar to the tip radius of the original gold triangles. This is distinctly smaller than the minimum hole radii reported for the near-field ablation of *dielectric* spheres, which illustrates the potential of plasmonic particles for generating structures in the low nm range. A similar ablation experiment with

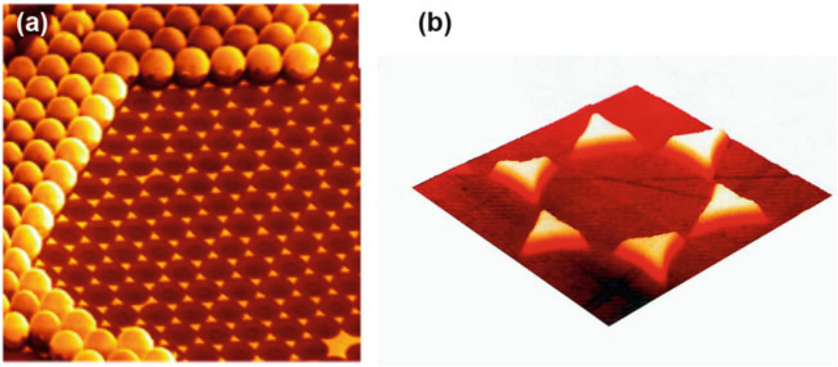

Fig. 11.16 (**a**) SEM image of a regular array of triangular nanostructures prepared by colloid lithography. The colloid monolayer used as an evaporation mask has only been partly removed in this case, the size of the spheres is 1500 nm; (**b**) detail of the hexagonal triangle array from (**a**) AFM image. The scale in vertical direction is enlarged compared to the scale in plane

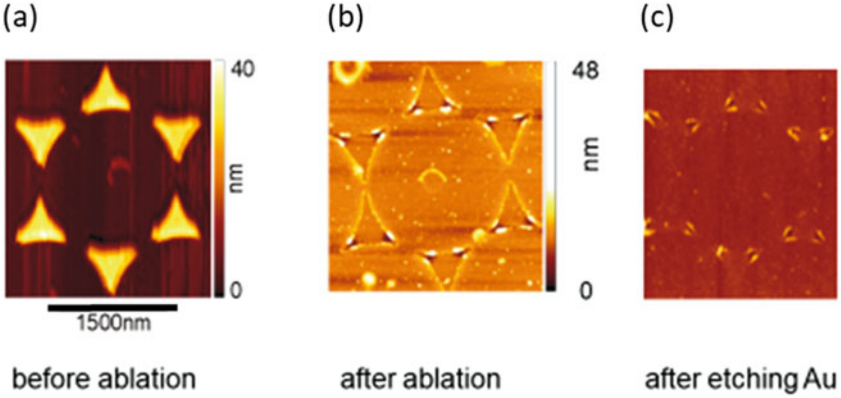

Fig. 11.17 AFM image of gold triangles on silicon, side length 450 nm, 25 nm thick. (**a**) as prepared; (**b**) after irradiation with one laser pulse (laser source: Ti:sapphire laser, $\tau = 150$ fs, $\lambda = 800$ nm) (**c**) after chemical removal of the gold. Light polarization vertical (indicated by the arrow on the right side). In (**b**) the former positions of the gold triangles are outlined as contours, formed by gold clusters which developed in the evaporation process through the colloid mask. (Image adapted from [72], with the permission of AIP Publishing)

gold triangles, but on glass instead of silicon, was carried out by Jamali et al. [74], as shown in Fig. 11.18.

The ablation patterns in Figs. 11.17 and 11.18 are a clear demonstration of the field enhancement at sharp tips of metallic structures. Since ablation only occurs under and near the plasmonic particle where the field enhancement is high enough, these patterns represent nonlinear "contact photographs" of the near-field distribution. They can reveal rather fine details, in Fig. 11.17 with a resolution of better than 1/50 of the incident light wavelength [72]. This makes the method useful

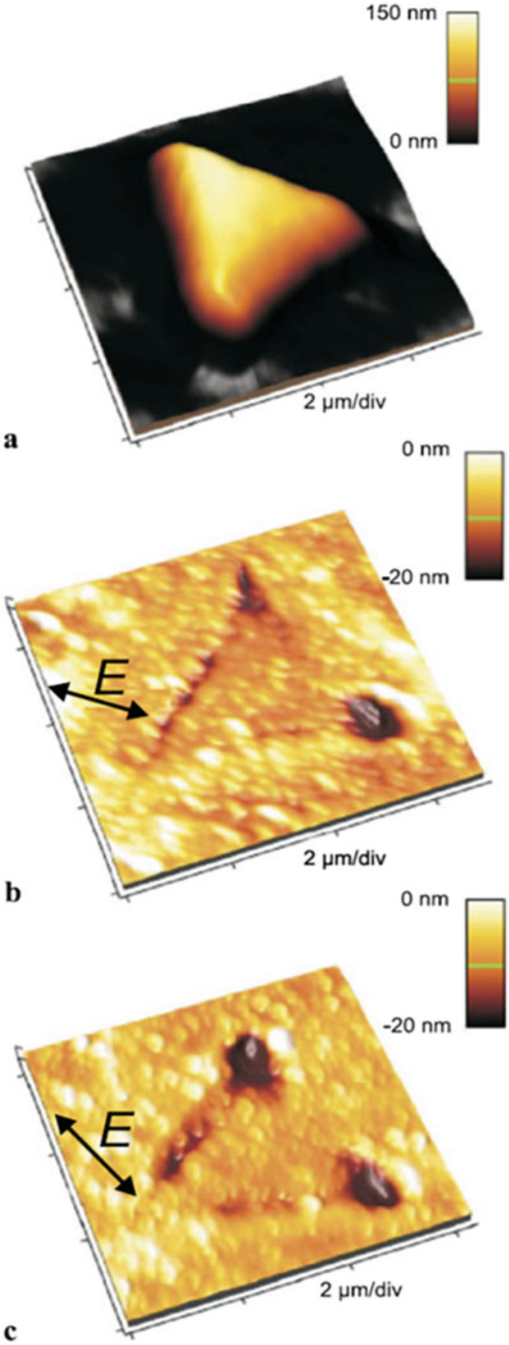

Fig. 11.18 (**a**) AFM image of a single triangular gold nanoparticle on glass before laser treatment. (**b**, **c**) AFM images of the sample after illumination with a single linearly polarized laser pulse with $\tau = 35$ fs. The black arrows indicate the polarization direction of the laser light (note: according to the authors, the scale in plane has to be corrected from 2 μm/div to 0.2 μm/div (T. Baumert, private communication, 2021)). (Reprinted by permission from [74])

for comparisons and cross-checks with simulations of optical near-field distributions like DDA and FDTD. In contrast to the aSNOM, which is also used as a tool for optical near-field imaging, a probe tip is not required, and thus possible distortions of the intensity distribution close to the probe are avoided. This kind of photography adds to other powerful methods for imaging optical near fields which do not rely on a probe tip, for example, two-photon polymerization [75–77], photochemical imaging [78], phase change in certain chalcogenide films [79, 80], parabolic-mirror-based confocal microscopy [81], spatially resolved third harmonic emission [8], and photoelectron microscopy (PEEM) [82–84]. Nanoablation imaging as introduced here is among the techniques with the highest resolution, it has the advantage of relative simplicity, and it is applicable under ambient conditions and to any smooth substrate. Besides silicon and glass, also polymer coatings have since been used to map the field enhancement around nanostructures [85].

It has already been pointed out in Sect. 3.1 that details of the geometry of simulated plasmonic structures can have a significant influence on the near-field distribution. This holds particularly for the hotspots and hence also for possible applications, for example, as nanoantennas. One of these details can be illustrated already by the ablation pattern shown in Fig. 11.17: In this image, the ablation holes do not appear at all triangle corners but only at those pointing sideways (for vertically polarized light). In simulations [86] the positions of the hotspots were just opposite, namely, at the triangle corners pointing up and down. These simulations were, for simplicity, carried out with equilateral triangles with *straight* edges instead of the slightly curved contours of the experimental structures prepared by colloid lithography. Only later it was noticed that the plasmonic resonances are strongly affected by this – at first glance – minor difference. This is shown in Fig. 11.19 by simulations of both kinds of triangular structures and for two orientations with respect to the polarization of the incident light. The differences between the two triangle types are apparent.

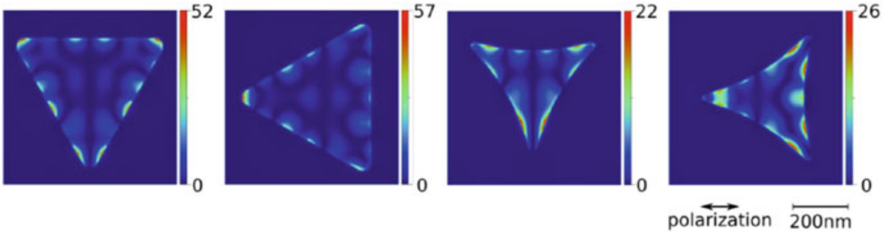

Fig. 11.19 FDTD calculations of two different types of nanotriangles with straight and curved edges. The field intensity enhancement was extracted in a plane between the SiO_2 layer (thickness 2.4 nm) and the Si substrate below the triangle. The simulation volume was $3 \times 3 \times 6\ \mu m^3$ with "perfectly matched layer" boundary conditions. The meshing was set to automatic mode far from the triangle, and a manually refined mesh with a cell size of $2 \times 2 \times 0.5\ nm^3$ was added around the particle [70]

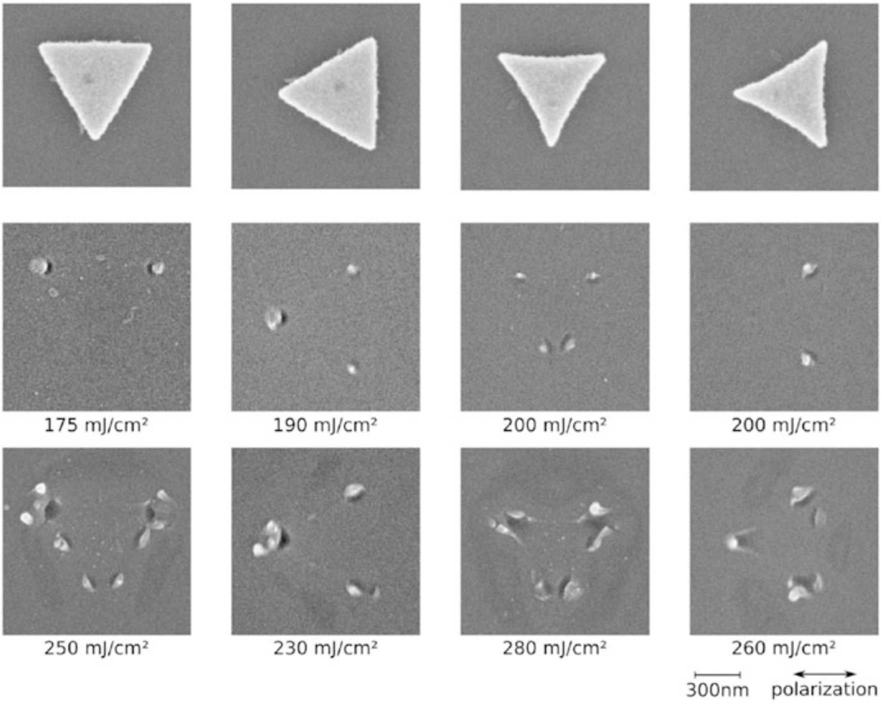

Fig. 11.20 SEM micrographs of structures as shown in Fig. 11.19, prepared by electron beam lithography, and their corresponding ablation patterns on a silicon substrate for two orientations with respect to the polarization of the incident light. The laser wavelength was 800 nm, the pulse duration is 150 fs, and the local incident fluence is indicated below each frame [70]

An experimental confirmation of this result is presented in Fig. 11.20. E-beam lithography has been applied in this case to fabricate both the straight-edged and the curved-edged triangular structures with thickness and tip distances corresponding to those in the simulations of Fig. 11.19. Again, for each triangle type, two orientations with respect to the incident light have been studied (top row). The middle row shows ablation patterns just slightly above the local ablation threshold and the bottom row at a slightly higher intensity in order to image also weaker hotspot features. One notices excellent agreement in the hotspot positions between simulation and experiment, which underlines the complementary nature of these two approaches to gain information about optical near-field patterns.

The somewhat complex near-field patterns in Figs. 11.19 and 11.20 arise from higher multipole modes, which are excited if the size of the nanostructure is larger than the fundamental plasmon mode. This is demonstrated in Fig. 11.21 by the comparison of the calculated near-field patterns of 540 and 85 nm nanotriangles. For the latter, the exciting laser wavelength is close to the resonance of the primary (dipolar) mode, as seen from the optical absorption spectra above the simulated enhancement distributions. The dipole resonance of the larger particles, however,

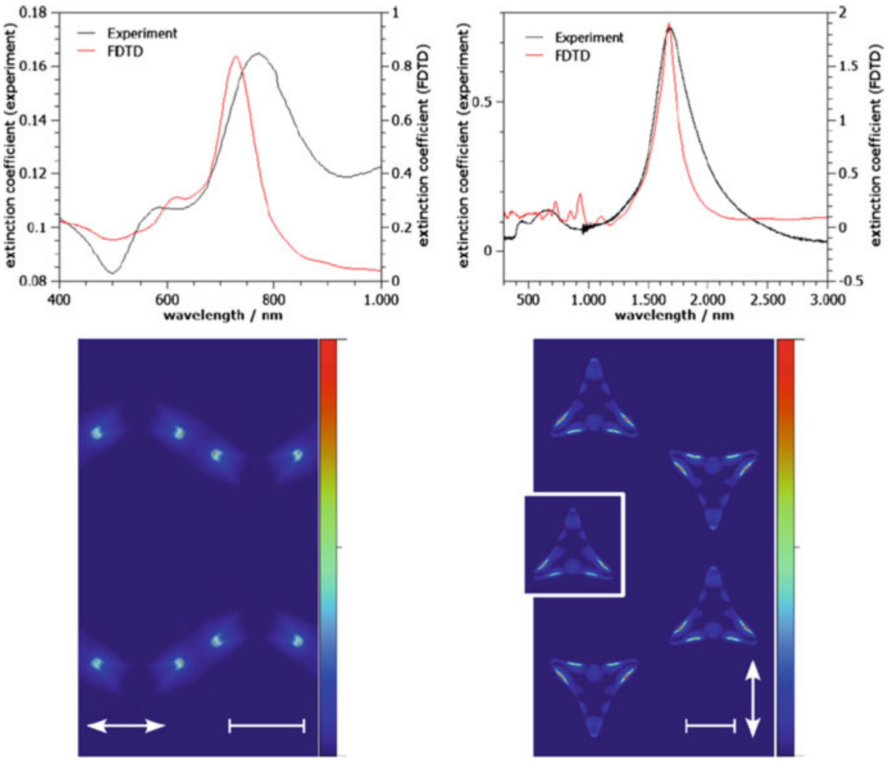

Fig. 11.21 Measured and FDTD-simulated absorption spectra for 85 nm (left) and 540 nm (right) nanotriangles on glass with the corresponding calculated scattered field intensities (normalized to the incoming field) for 800-nm irradiation on silicon. Small inset: calculated field distribution for a single 540-nm triangle. The double-headed arrows give the direction of the polarization of the incident laser light. Scale bars: 100 nm (left) and 300 nm (right). False-color rulers: 0 to 255 (left) and 0 to 30 (right). (Reprinted by permission from [87])

would only be excited by a wavelength in the infrared around 1700 nm. Also for these simulations, a comparison with laser-induced ablation patterns has been made (Fig. 11.22). Again, the patterns from experiment and simulation are in convincing agreement.

In order to check whether the neighboring particles in the hexagonal triangle array produced by colloid lithography influence the near-field distribution, both individual triangles and arrays were studied. The inset in Fig. 11.21 (right) shows no significant difference between the two, which means that the coupling to surrounding particles plays a minor role in these arrays, in line with experimental findings [86].

For many applications of plasmonic nanostructures, like nonlinear phenomena where high field intensities are required, a quantity as crucial as the distribution of the near fields is the maximum enhancement factor that is reached in the hotspots.

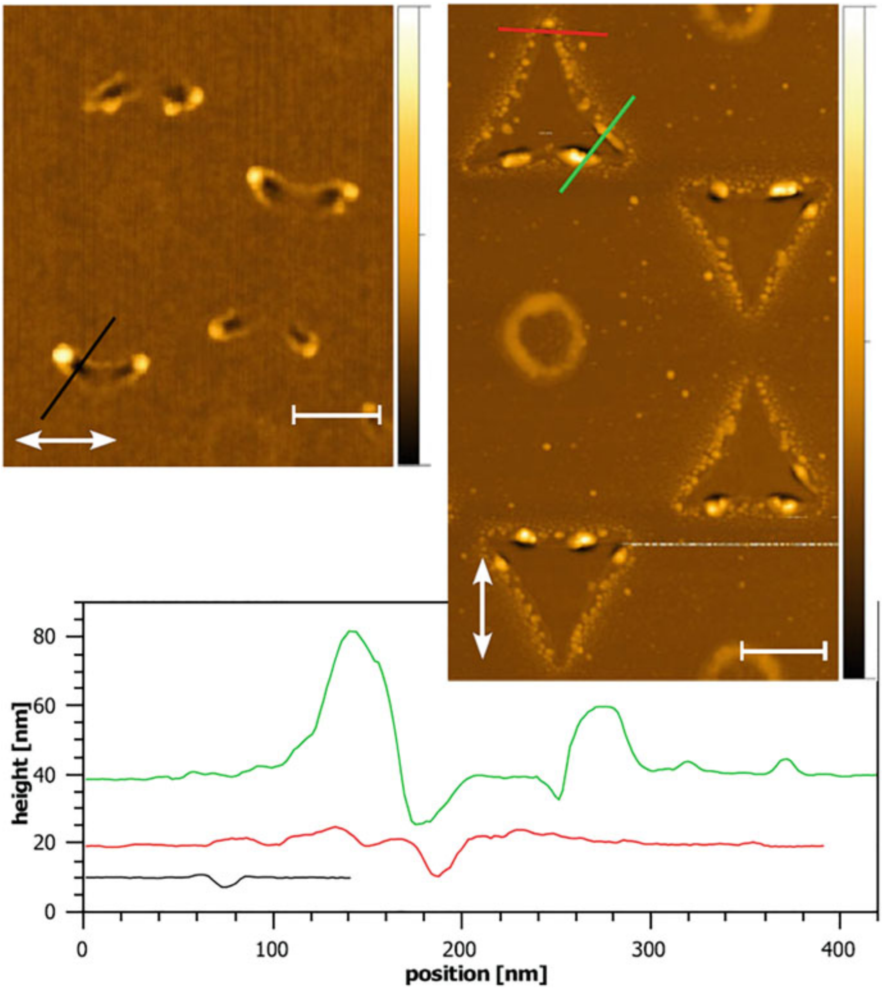

Fig. 11.22 AFM images of the ablation pattern for nanotriangles with a side length of 85 nm (left) and 540 nm (right) on a silicon substrate ($\tau = 150$ fs, $\lambda =$ nm,). The left sample had to be cleaned using the snow jet technique before the AFM scan; therefore the gold clusters around the contour of the original triangle positions are missing. The position of the height profile is depicted in the AFM image with a bar in the corresponding color. In the graph, the profiles are shown with an arbitrary offset. The double-headed arrows give the direction of the polarization of the incident laser light. Scale bars: 100 nm (left) and 300 nm (right). False-color rulers: 0 nm to 10 nm (left) and 0 nm to 70 nm (right). Reprinted by permission from [87]

Estimates on these values can be obtained by comparing ablation thresholds with and without particles [88, 89]. The agreement between these experimental enhancement results and the simulations is up to now mostly in the order-of-magnitude range only. Obviously, details like tip radius, edge shape, and roughness

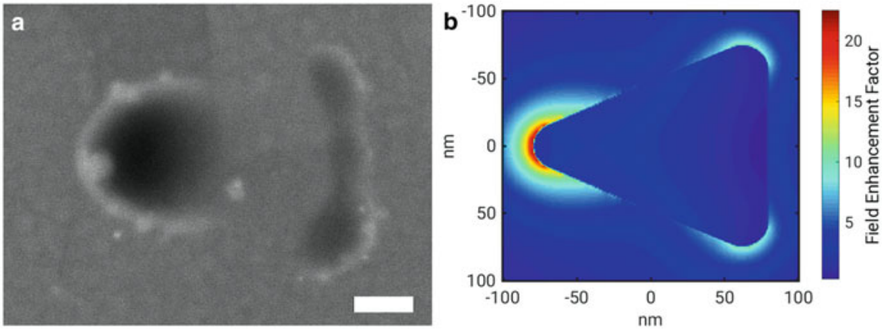

Fig. 11.23 (**a**) SEM image of the contour of a gold triangle after the exposure with 40 fs laser pulses at a central wavelength of 803 nm and a fluence of 114.3 mJ/cm^2 (scale bar 50 nm); (**b**) FDTD simulated electric field enhancement for the triangular nanoparticle [90]

play an even bigger role here than for the contours of the near-field patterns. In the few investigations that exist, the experimental enhancement factors are typically well below the calculated ones. For some triangular structures, the values derived by the ablation method were found to be a factor of 2 to 5 below the simulation results [70].

Another important aspect for the application of nonlinear plasmonics is the unwanted modification of the metallic particles near the hotspots when they are irradiated by high laser intensities. The evolution of this breakdown induced by femtosecond pulses has been studied recently by Nagy et al. for gold triangles which were about a factor of 2 smaller than those in Figs. 11.19 and 11.20 [90]. Also in these experiments, precise nanolithographic mapping of the near-field distribution via ablation was observed (Fig. 11.23), and again the comparison with the simulation reveals the high level of agreement. An example of the modification of triangle tips by the field enhancement in the plasmonic hotspots is shown in Fig. 11.24 [87]. In this case, the laser pulse duration was distinctly longer (300 ps); therefore instead of ablation, the dominating mechanism was local melting of the metal structure in the hotspots.

The ablation experiments with plasmonic nanotriangles described above aimed mainly at imaging the near-field hotspots and at developing a good understanding in comparison with simulations. However, this method also lends itself for intentional nanostructuring of surfaces, particularly since a large variety of patterns can be generated. Figures 11.25 and 11.26 show examples where Au nanotriangles prepared by colloid lithography have been exploited to pattern glass surfaces [91, 92]. Essential parameters for the pattern fabrication are the fluence, polarization, angle of incidence and duration of the laser pulse, the size and shape of the plasmonic structures, and the substrate's refractive index. Based on simulations reliable predictions are now feasible about the ablation pattern that will be generated by particular plasmonic structures, which will help optimize these structures for the

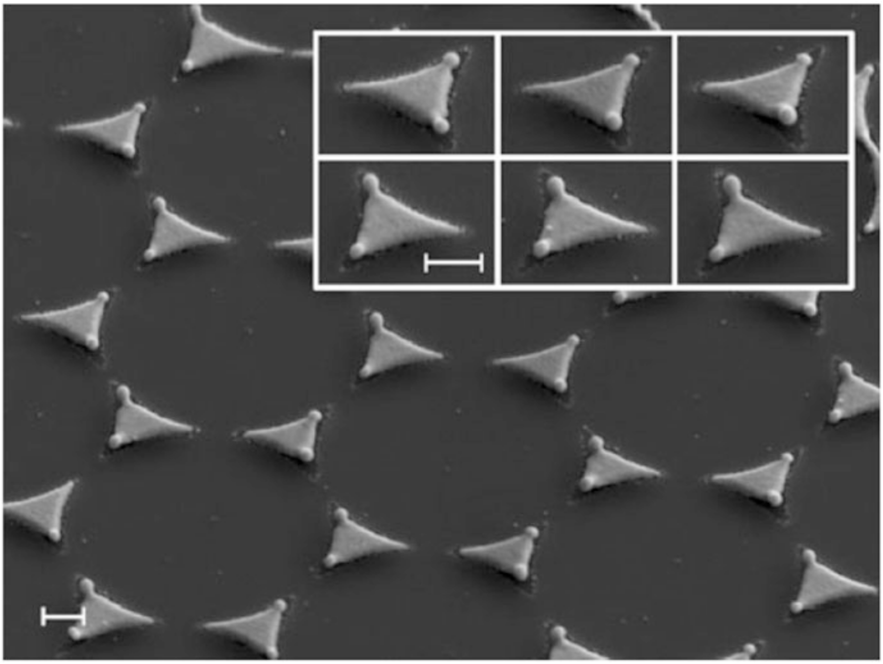

Fig. 11.24 SEM image of modified gold nanotriangles (produced with 1740 nm colloids) after irradiation with a single ps laser pulse ($\tau = 300$ ps, $\lambda = 800$ nm). Laser polarization in horizontal direction, scale bars: 300 nm. The two rows in the inset show triangles with two different orientations, demonstrating that even details of the molten structures at the hotspots are similar for triangles with the same orientation. (Reprinted by permission from [87])

desired results. More details on plasmonic nanoprinting are presented in Chap. 12 of this book.

Non-triangular particle shapes In addition to triangular particles, there are also a number of investigations of patterns generated with other plasmonic structures like metallic spheres, rods, and bow tie antennas [70, 88, 89, 93–101]; see also Chap. 8 of this book. Nanohole fabrication by spherical gold particles was reported by Nedyalkov et al. [89, 99]. These authors found that the holes had an elongated shape in the direction of the incident laser polarization, analogous to the pattern of small dielectric spheres, but with a much higher enhancement factor. For 200-nm spheres, the values were 26 in the simulation and 7.5 in the experiment. In a similar investigation by Eversole et al., the influence of *inclined* incidence was studied for both s- and p-polarized laser light. These authors found good agreement between simulated and experimental enhancement factors, and in some cases the measured values were even higher than the theoretical ones. An AFM image of an ablation crater and the corresponding profile are shown in Fig. 11.27 [88]. Hashimoto et al. report the formation of holes less than 10 nm in diameter in borosilicate glass

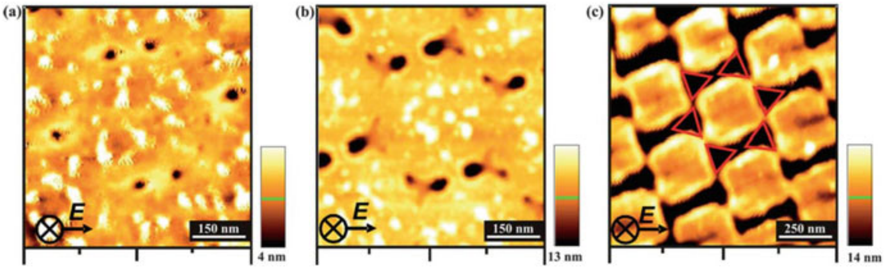

Fig. 11.25 AFM images of nanopatterns generated on a fused silica substrate with a single pulse of a Ti:sapphire laser ($\tau = 35$ fs, $\lambda = 790$ nm) in a region of low (**a**), medium (**b**), and high (**c**) laser fluence. The applied pulse energy was $E = 0.16$ mJ. The red triangles (right image) indicate the original position of the triangular nanoparticles on the substrate prior to irradiation. For clarity reasons, the red triangles have been drawn larger than the original nanoparticles, which, in fact, have a tip-to-tip distance of approximately 100 nm. The black arrows indicate the polarization direction of the incoming laser light. (Used with permission of Royal Society of Chemistry (Great Britain) from [91]; permission conveyed through Copyright Clearance Center, Inc.)

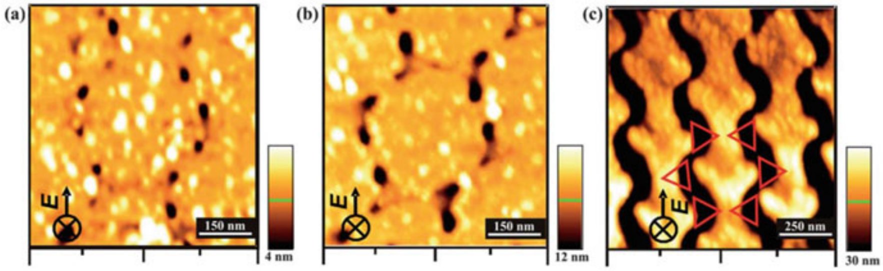

Fig. 11.26 AFM images of nanopatterns generated like in Fig. 11.25, but with a different laser polarization, in a region of low (**a**), medium (**b**), and high (**c**) laser fluence. The applied pulse energy was $E = 3.8$ mJ. The red triangles (right image) indicate the original position of the triangular nanoparticles on the substrate prior to irradiation. The black arrow indicates the polarization direction of the laser light. (Used with permission of Royal Society of Chemistry (Great Britain) from [91]; permission conveyed through Copyright Clearance Center, Inc.)

when they irradiated 40-nm Au spheres with a ns laser beam [96, 97]. Laser-induced ablation by plasmonic gold nanorods has been studied by Harrison and Ben-Yakar [94, 95] and by Boulais, Robitaille et al. [93, 101]. Typical aspect ratios of the rods were around 2, and the long axes were around 60 to 90 nm. The holes generated with these rods were on the order of the size of the plasmonic structures, as seen in Fig. 11.28.

Since most of these nanoablation experiments had been done on Si substrates, Ref. [101] addresses the question which mechanism eventually limits the minimum structure size that can be reached on this substrate. As the authors point out, the key difference between conventional laser ablation [102, 103] and nanoablation is the tight localization of the energy absorption in the latter, which can be significantly

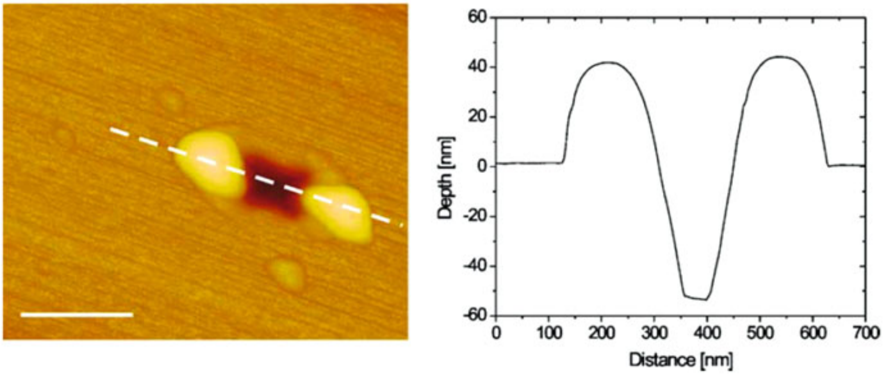

Fig. 11.27 AFM images of nanocraters ablated by 150-nm gold nanoparticles on silicon (100) and corresponding cross section as found along the white dotted line. The laser pulse duration was 220 fs, the wavelength 780 nm, and the fluence 128 mJ/cm^2; the light was s-polarized at 45° incident angle. The scale bar is 200 nm. (Reprinted by permission from Ref. [88])

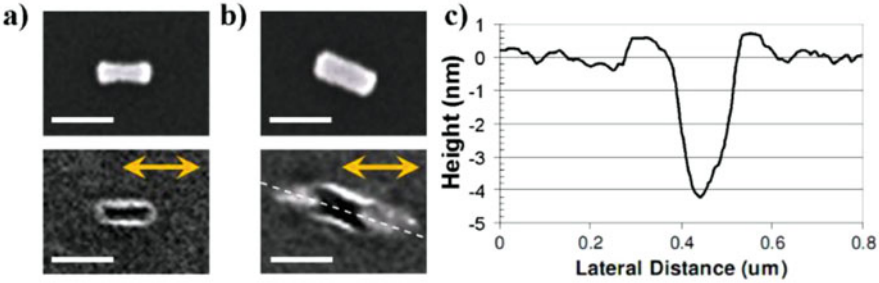

Fig. 11.28 Nanoscale ablation site and depth profile: SEM images of the nanorods before and after laser irradiation at a local effective fluence of (**a**) 54 mJ/cm^2, right at the ablation threshold, and (**b**) 218 mJ/cm^2. The scale bars correspond to 75 nm, and the yellow arrows indicate the incident polarization. (**c**) The depth profile of the ablation site shown in (**b**), along the long axis shown with the dotted line as obtained using AFM. Note the different scales for the horizontal and vertical axes in (**c**) [94]

smaller than the diffusion length of the charge carriers in the Si substrate. Carrier diffusion will therefore limit the achievable ablation feature size. In an investigation of near-field ablated holes in the gap of an optical bow tie antenna, Kolloch and Dickreuter et al. [70, 104] reached a similar conclusion. Other materials, where this broadening mechanism is absent, might allow the fabrication of even smaller structures by means of laser ablation.

4 Conclusion

The generation of nanostructures on solid surfaces utilizing local ablation in optical near fields of nano-objects is an efficient and straightforward process. It allows one to fabricate holes in many substrates, including dielectrics, semiconductors, and metals. The diameters of these structures can be distinctly smaller than given by the diffraction limit in the far field.

Although the first experiments on nanoablation in the tightly focused beam waist of dielectric micro- and nanospheres – today known as photonic nanojets – date back about two decades, they are still of interest today. An attractive property of the monodisperse colloidal spheres that have been used in many investigations is the tendency of these particles to form well-ordered monolayers over large areas in the cm^2 range. Therefore, an enormous number of periodically arranged submicron holes can be generated with such monolayers in a one-step process by illumination with a single short laser pulse, mostly in the femtosecond or picosecond range. Also, structures more complex than just round holes can be fabricated with this technique by using refined irradiation conditions like inclined incidence at variable angles.

Compared to dielectric spheres, the optical near fields of *metallic* nanostructures can be confined even more, in particular close to sharp corners, due to the resonant excitation of localized plasmons. Ablation structures with sizes smaller than 10 nm have been reported for this method. The field enhancement that can be reached at these hotspots is vital for numerous applications like sensors, surface-enhanced Raman scattering, and nonlinear optics and is an essential topic in modern plasmonics. The nanoablation technique has been successfully applied for imaging the optical near-field distribution of plasmonic particles, and in conjunction with simulations such as FDTD, a state has been reached that allows a reliable prediction of the near-field landscape.

Acknowledgments We appreciate numerous discussions with the groups of Carmen Afonso, Jan Siegel and Javier Solis (Madrid), Dieter Bäuerle (Linz) and Roland Oltra (Dijon), and also with Andrew C. Tam (San Jose), Minghui Hong, and Boris Luk'yanchuk (Singapore), Anton Plech (Karlsruhe), Andreas Pack and Reinhold Wannemacher (Chemnitz), and Hiroaki Misawa, Kosei Ueno, and Saulius Juodkazis (Sapporo) and their teams. In our group in Konstanz, we are in particular indebted to our master and PhD students Christof Bartels, Micha Bertsch, Simon Dickreuter, Julia Gleixner, Johannes Graf, Juliane König-Birk, Andreas Kolloch, Paul Kühler, Mario Mosbacher, Hajo Münzer, and Michael Ochmann.

References

1. E. Synge, A suggested method for extending microscopic resolution into the ultra-microscopic region. Philos. Magazine Ser **7**(6), 35, 356 (1928). https://doi.org/10.1080/14786440808564615
2. D. Pohl, Optical stethoscopy: Image recording with resolution λ/20. Appl. Phys. Lett. **44**, 651 (1984). https://doi.org/10.1063/1.94865

3. R. Hillenbrand, F. Keilmann, P. Hanarp, D.S. Sutherland, J. Aizpurua, Coherent imaging of nanoscale plasmon patterns with a carbon nanotube optical probe. Appl. Phys. Lett. **83**, 368 (2003). https://doi.org/10.1063/1.1592629
4. A.D. McFarland, M.A. Young, J.A. Dieringer, R.P. Van Duyne, Wavelength-scanned surface-enhanced Raman excitation spectroscopy. J. Phys. Chem. B **109**, 11279 (2005). https://doi.org/10.1021/jp050508u
5. S. Nie, S.R. Emory, Probing single molecules and single nanoparticles by surface-enhanced Raman scattering. Science **275**, 1102 (1997). https://doi.org/10.1126/science.275.5303.1102
6. J.N. Farahani, D.W. Pohl, H.-J. Eisler, B. Hecht, Single quantum dot coupled to a scanning optical antenna: A tunable superemitter. Phys. Rev. Lett. **95**, 017402 (2005). https://doi.org/10.1103/PhysRevLett.95.017402
7. T. Hanke, G. Krauss, D. Traeutlein, B. Wild, R. Bratschitsch, A. Leitenstorfer, Efficient non-linear light emission of single gold optical antennas driven by few-cycle near-infrared pulses. Phys. Rev. Lett. **103**, 257404 (2009). https://doi.org/10.1103/PhysRevLett.103.257404
8. T. Hanke, J. Cesar, V. Knittel, A. Trügler, U. Hohenester, A. Leitenstorfer, R. Bratschitsch, Tailoring spatiotemporal light confinement in single plasmonic nanoantennas. Nano Lett. **12**, 992 (2012). https://doi.org/10.1021/nl2041047
9. J.A. Schuller, E.S. Barnard, W. Cai, Y.C. Jun, J.S. White, M.L. Brongersma, Plasmonics for extreme light concentration and manipulation. Nat. Mater. **9**, 193 (2010). https://doi.org/10.1038/nmat2630
10. J. Jersch, K. Dickmann, Nanostructure fabrication using laser field enhancement in the near field of a scanning tunneling microscope tip. Appl. Phys. Lett. **68**, 868 (1996). https://doi.org/10.1063/1.116527
11. J. Boneberg, M. Tresp, M. Ochmann, H.-J. Münzer, P. Leiderer, Time resolved measurements of the response of a STM tip upon illumination with a nanosecond laser pulse. Appl. Phys. A Mater. Sci. Process. **66**, 615–619 (1998a). https://doi.org/10.1007/s003390050722
12. J. Boneberg, H.-J. Münzer, M. Tresp, M. Ochmann, P. Leiderer, The mechanism of nanostructuring upon nanosecond laser irradiation of a STM tip. Appl. Phys. A Mater. Sci. Process. **67**, 381 (1998b). https://doi.org/10.1007/s003390050789
13. R. Huber, M. Koch, J. Feldmann, Laser-induced thermal expansion of a scanning tunneling microscope tip measured with an atomic force microscope cantilever. Appl. Phys. Lett. **73**, 2521 (1998). https://doi.org/10.1063/1.122502
14. A. Chimmalgi, T.Y. Choi, C.P. Grigoropoulos, K. Komvopoulos, Femtosecond laser aperturless near-field nanomachining of metals assisted by scanning probe microscopy. Appl. Phys. Lett. **82**, 1146 (2003). https://doi.org/10.1063/1.1555693
15. A. Chimmalgi, C. Grigoropoulos, K. Komvopoulos, Surface nanostructuring by nano−/femtosecond laser-assisted scanning force microscopy. J. Appl. Phys. **97**, 104319 (2005). https://doi.org/10.1063/1.1899245
16. S.M. Huang, M.H. Hong, Y.F. Lu, B.S. Luk'yanchuk, W.D. Song, T.C. Chong, Pulsed-laser assisted nanopatterning of metallic layers combined with atomic force microscopy. J. Appl. Phys. **91**, 3268 (2002b). https://doi.org/10.1063/1.1448882
17. Y.F. Lu, Z.H. Mai, Y.W. Zheng, W.D. Song, W.K. Chim, Nanostructure fabrication using pulsed lasers in combination with a scanning tunneling microscope: Mechanism investigation. Appl. Phys. Lett. **76**, 1200 (2000b). https://doi.org/10.1063/1.125982
18. Z.H. Mai, Y.F. Lu, S.M. Huang, W.K. Chim, Mechanism of laser-induced nano modification on hydrogen-passivated Si(100) surfaces underneath the tip of an scanning tunneling microscope. J. Vac. Sci. Technol. **B18**, 1853 (2000). https://doi.org/10.1116/1.1303815
19. K. Imen, S.J. Lee, S.D. Allen, Laser-assisted micron scale particle removal. Appl. Phys. Lett. **58**, 203 (1991). https://doi.org/10.1063/1.104923
20. A.C. Tam, W.P. Leung, W. Zapka, W. Ziemlich, Laser-cleaning techniques for removal of surface particulates. J. Appl. Phys. **71**, 3515 (1992). https://doi.org/10.1063/1.350906
21. P. Leiderer, J. Boneberg, V. Dobler, M. Mosbacher, H.-J. Münzer, N. Chaoui, J. Siegel, J. Solis, C.N. Afonso, T. Fourrier, G. Schrems, D. Bäuerle, Laser-induced particle removal from Silicon wafers, in *High Power Laser Ablation III, April 24–28, 2000, C.R. Phipps ed., Proc. SPIE4065, 249*, (2000). https://doi.org/10.1117/12.407353

22. G. Mie, Articles on the optical characteristics of turbid tubes, especially colloidal metal solutions. Ann. Phys. **25**, 377 (1908). https://doi.org/10.1002/andp.19083300302
23. P.W. Barber, S.C. Hill, *Light Scattering by Particles: Computational Methods* (World Scientific, 1990). https://doi.org/10.1142/0784
24. H.M. Nussenzveig, W.J. Wiscombe, Efficiency factors in Mie scattering. Phys. Rev. Lett. **45**, 1490 (1980). https://doi.org/10.1103/PhysRevLett.45.1490
25. L. Bergmann and C. Schäfer, Lehrbuch der Experimentalphysik: Bd. III Optik (Walter de Gruyter, 1987)
26. B.S. Luk'yanchuk, M. Mosbacher, Y.W. Zheng, H.-J. Münzer, S.M. Huang, M. Bertsch, W.D. Song, Z.B. Wang, Y.F. Lu, O. Dubbers, J. Boneberg, P. Leiderer, M.H. Hong, T.C. Chong, Optical resonance and near-field effects in dry laser cleaning, in *Laser Cleaning*, ed. by B. Lukyanchuk, (World Scientific, 2002), p. 106
27. Y.F. Lu, L. Zhang, W.D. Song, Y.W. Zheng, B.S. Luk'yanchuk, Laser writing of a subwavelength structure on silicon (100) surfaces with particle-enhanced optical irradiation. JETP Lett. **72**, 457 (2000a). https://doi.org/10.1134/1.1339899
28. Z. Chen, A. Taflove, V. Backman, Photonic nanojet enhancement of backscattering of light by nanoparticles: A potential novel visible-light ultramicroscopy technique. Opt. Express **12**, 1214 (2004). https://doi.org/10.1364/OPEX.12.001214
29. B.S. Luk'yanchuk, R. Paniagua-Domínguez, I. Minin, O. Minin, Z. Wang, Refractive index less than two: Photonic nanojets yesterday, today and tomorrow. Opt. Mater. Express **7**, 1820 (2017). https://doi.org/10.1364/OME.7.001820
30. S. Surdo, M. Duocastella, A. Diaspro, Nanopatterning with photonic Nanojets: Review and perspectives in biomedical research. Micromachines **12**, 256 (2021). https://doi.org/10.3390/mi12030256
31. M. Terakawa, N.N. Nedyalkov, Near-field optics for nanoprocessing. Adv. Opt. Technol. **5**, 17 (2016). https://doi.org/10.1515/aot-2015-0054
32. H.-J. Münzer, Laserinduzierte Nanostrukturierung von Oberflächen, PhD dissertation, (Konstanz 2001)
33. C. Hafner, *The Generalized Multipole Technique for Computational Electromagnetics* (Artech House, Inc., 1990)
34. H.-J. Münzer, M. Mosbacher, M. Bertsch, O. Dubbers, F. Burmeister, A. Pack, R. Wannemacher, B. U. Runge, D. Bäuerle, J. Boneberg and P. Leiderer, Optical near-field effects in surface nanostructuring and laser cleaning, Proc. SPIE 4426, 180 (2002)
35. M. Mosbacher, H.-J. Münzer, J. Zimmermann, J. Solis, J. Boneberg, P. Leiderer, Optical field enhancement effects in laser-assisted particle removal. Appl. Phys. A Mater. Sci. Process. **72**, 41 (2001). https://doi.org/10.1007/s003390000715
36. A. Plech, P. Leiderer, J. Boneberg, Femtosecond laser near field ablation. Laser Photon. Rev. **3**, 435–451 (2009). https://doi.org/10.1002/lpor.200810044
37. R. Denk, K. Piglmayer, D. Bäuerle, Laser-induced nanopatterning of PET using a-SiO_2 microspheres. Appl. Phys. A Mater. Sci. Process. **74**, 825 (2002). https://doi.org/10.1007/s003390201295
38. H.-J. Münzer, M. Mosbacher, M. Bertsch, J. Zimmermann, P. Leiderer, J. Boneberg, Local field enhancement effects for nanostructuring of surfaces. J. Microsc. **202**, 129 (2001). https://doi.org/10.1046/j.1365-2818.2001.00876.x
39. Z.B. Wang, M.H. Hong, B.S. Luk'yanchuk, Y. Lin, Q.F. Wang, T.C. Chong, Angle effect in laser nanopatterning with particle-mask. J. Appl. Phys. **96**, 6845 (2004). https://doi.org/10.1063/1.1786652
40. P. Kühler, D. Puerto, M. Mosbacher, P. Leiderer, F.J. Garcia de Abajo, J. Siegel, J. Solis, Femtosecond-resolved ablation dynamics of Si in the near field of a small dielectric particle. Beilstein J. Nanotechnol. **4**, 501 (2013). https://doi.org/10.3762/bjnano.4.59
41. S.M. Huang, Z. Sun, B.S. Luk'yanchuk, M.H. Hong, L.P. Shi, Nanobump arrays fabricated by laser irradiation of polystyrene particle layers on silicon. Appl. Phys. Lett. **86**, 161911 (2005). https://doi.org/10.1063/1.1886896

42. F. Lang, M. Mosbacher, P. Leiderer, Near field induced defects and influence of the liquid layer thickness in Steam Laser Cleaning of silicon wafers. Appl. Phys. A Mater. Sci. Process. **77**, 177 (2003). https://doi.org/10.1007/s00339-003-2101-0
43. M. Mosbacher, V. Dobler, M. Bertsch, H.-J. Münzer, J. Boneberg, P. Leiderer, Laser cleaning of silicon wafers: Prospects and problems, in *Surface Contamination and Cleaning*, ed. by K. L. Mittal, vol. 1, (2003), p. 311
44. X.C. Wang, H.Y. Zheng, C.W. Tan, F. Wang, H.Y. Yu, K.L. Pey, Fabrication of silicon nanobump arrays by near-field enhanced laser irradiation. Appl. Phys. Lett. **96**, 084101 (2010). https://doi.org/10.1063/1.3327513
45. G. Wysocki, R. Denk, K. Piglmayer, N. Arnold, D. Bäuerle, Single-step fabrication of silicon-cone arrays. Appl. Phys. Lett. **82**, 692 (2003). https://doi.org/10.1063/1.1538347
46. J. Bischof, D. Scherer, S. Herminghaus, P. Leiderer, Dewetting modes of thin metallic films: Nucleation of holes and spinodal dewetting. Phys. Rev. Lett. **77**, 1536 (1996). https://doi.org/10.1103/PhysRevLett.77.1536
47. S.M. Huang, M.H. Hong, B.S. Luk'yanchuk, Y.W. Zheng, W.D. Song, Y.F. Lu, T.C. Chong, Pulsed laser-assisted surface structuring with optical near-field enhanced effects. J. Appl. Phys. **92**, 2495 (2002a). https://doi.org/10.1063/1.1501768
48. F. Burmeister, C. Schäfle, B. Keilhofer, C. Bechinger, J. Boneberg, P. Leiderer, From mesoscopic to nanoscopic surface structures: lithography with colloid monolayers. Adv. Mater. **10**, 495 (1998). https://doi.org/10.1002/(SICI)1521-4095(199804)10:6<495::AID-ADMA495>3.0.CO;2-A
49. H.W. Deckman, J.H. Dunsmuir, Natural lithography. Appl. Phys. Lett. **41**, 377 (1982). https://doi.org/10.1063/1.93501
50. U.C. Fischer, H.P. Zingsheim, Submicroscopic pattern replication with visible light. J. Vac. Sci. Technol. **19**, 881 (1981). https://doi.org/10.1116/1.571227
51. A. Kosiorek, W. Kandulski, P. Chudzinski, K. Kempa, M. Giersig, Shadow nanosphere lithography: Simulation and experiment. Nano Lett. **4**, 1359 (2004). https://doi.org/10.1021/nl049361t
52. D. Brodoceanu, L. Landström, D. Bäuerle, Laser-induced nanopatterning of silicon with colloidal monolayers. Appl. Phys. A Mater. Sci. Process. **86**, 313 (2007). https://doi.org/10.1007/s00339-006-3781-z
53. K.L.N. Deepak, D. Grojo, L. Charmasson, P. Delaporte, O. Utéza, M. Dussauze, E. Fargin, Fabrication of microcraters on silicon substrate by UV nanosecond phononic nanojets from microspheres. UVX **2012**, 02003 (2013). https://doi.org/10.1051/uvx/201302003
54. S.M. Huang, Z. Sun, Y.F. Lu, Nanofabrication by laser irradiation of polystyrene particle layers on silicon. Nanotechnology **18**, 025302 (2007). https://doi.org/10.1088/0957-4484/18/2/025302
55. Y. Lu, S.C. Chen, Nanopatterning of a silicon surface by near-field enhanced laser irradiation. Nanotechnology **14**, 505 (2003). https://doi.org/10.1088/0957-4484/14/5/305
56. K. Piglmayer, R. Denk, D. Bäuerle, Laser-induced surface patterning by means of microspheres. Appl. Phys. Lett. **80**, 4693 (2002). https://doi.org/10.1063/1.1489085
57. H. Takada, M. Obara, Fabrication of hexagonally arrayed nanoholes using femtosecond laser pulse ablation with template of subwavelength polystyrene particle array. Jap. J. Appl. Phys. **44**, 7993 (2005). https://doi.org/10.1063/1.350906
58. M. Ulmeanu, M. Zamfirescu, L. Rusen, C. Luculescu, A. Moldovan, A. Stratan, R. Dabu, Structuring by field enhancement of glass, Ag, Au, and Co thin films using short pulse laser ablation. J. Appl. Phys. **106**, 114908 (2009). https://doi.org/10.1063/1.3264833
59. O. Watanabe, T. Ikawa, M. Hasegawa, M. Tsuchimori, Y. Kawata, Nanofabrication induced by near-field exposure from a nanosecond laser pulse. Appl. Phys. Lett. **79**, 1366 (2001). https://doi.org/10.1063/1.1398326
60. Y. Zhou, M.H. Hong, J.Y.H. Fuh, L. Lu, B.S. Luk'yanchuk, Z.B. Wang, L.P. Shi, T.C. Chong, Direct femtosecond laser nanopatterning of glass substrate by particle-assisted near-field enhancement. Appl. Phys. Lett. **88**, 023110 (2006). https://doi.org/10.1063/1.2163988

61. S. Juodkazis, Y. Nishi, H. Misawa, V. Mizeikis, O. Schecker, R. Waitz, P. Leiderer, E. Scheer, Optical transmission and laser structuring of silicon membranes. Opt. Express **17**, 15308 (2009). https://doi.org/10.1364/OE.17.015308
62. M. Ulmeanu, P. Petkov, D. Ursescu, V.A. Maraloiu, F. Jipa, E. Brousseau, M.N.R. Ashfold, Pattern formation on silicon by laser-initiated liquid-assisted colloidal lithography. Nanotechnology **26**, 455303 (2015). https://doi.org/10.1088/0957-4484/26/45/455303
63. M. Ulmeanu, P. Petkov, D. Ursescu, F. Jipa, R. Harniman, E. Brousseau, M.N.R. Ashfold, Substrate surface patterning by optical near field modulation around colloidal particles immersed in a liquid. Opt. Express **24**, 27340 (2016). https://doi.org/10.1364/OE.24.027340
64. W. Guo, Z.B. Wang, L. Li, D.J. Whitehead, B.S. Luk'yanchuk, Z. Liu, Near-field laser parallel nanofabrication of arbitrary-shaped patterns. Appl. Phys. Lett. **90**, 243101 (2007). https://doi.org/10.1063/1.2748035
65. R. Fardel, E. McLeod, Y. Tsai, C.B. Arnold, Nanoscale ablation through optically trapped microspheres. Appl. Phys. A Mater. Sci. Process. **101**, 41 (2010). https://doi.org/10.1007/s00339-010-5792-z
66. E. McLeod, C.B. Arnold, Subwavelength direct-write nanopatterning using optically trapped microspheres. Nat. Nanotechnol. **3**, 413 (2008). https://doi.org/10.1038/nnano.2008.150
67. E. McLeod, C.B. Arnold, Array-based optical nanolithography using optically trapped microlenses. Opt. Express **17**, 3640 (2009). https://doi.org/10.1364/OE.17.003640
68. E.M. Perassi, J.C. Hernandez-Garrido, M.S. Moreno, E.R. Encina, E.A. Coronado, P.A. Midgley, Using highly accurate 3D nanometrology to model the optical properties of highly irregular nanoparticles: A powerful tool for rational design of plasmonic devices. Nano Lett. **10**, 2097–2104 (2010). https://doi.org/10.1021/nl1005492
69. K. Yee, Numerical solution of initial boundary value problems involving Maxwell's equations in isotropic media. IEEE Trans. Antennas Propag. **14**, 302 (1966). https://doi.org/10.1109/TAP.1966.1138693
70. S. Dickreuter, J. Gleixner, A. Kolloch, J. Boneberg, E. Scheer, P. Leiderer, Mapping of plasmonic resonances in nanotriangles. Beilstein J. Nanotechnol. **4**, 588 (2013). https://doi.org/10.3762/bjnano.4.66
71. A. Merlen, F. Lagugne-Labarthet, Imaging the optical near field in Plasmonic nanostructures. Appl. Spectr. **68**, 1307 (2014). https://doi.org/10.1366/14-07699
72. P. Leiderer, C. Bartels, J. König-Birk, M. Mosbacher, J. Boneberg, Imaging optical near-fields of nanostructures. Appl. Phys. Lett. **85**, 5370 (2004). https://doi.org/10.1063/1.1819990
73. W. Huang, W. Qian, M.A. El-Sayed, Gold nanoparticles propulsion from surface fueled by absorption of femtosecond laser pulse at their surface Plasmon resonance. J. Am. Chem. Soc. **128**, 13330 (2006). https://doi.org/10.1021/ja064328p
74. A.A. Jamali, B. Witzigmann, R. Morarescu, T. Baumert, F. Träger, F. Hubenthal, Local near field assisted ablation of fused silica: An experimental and theoretical study. Appl. Phys. A Mater. Sci. Process. **110**, 743 (2013). https://doi.org/10.1007/s00339-012-7135-8
75. T. Geldhauser, S. Ikegaya, A. Kolloch, N. Murazawa, K. Ueno, J. Boneberg, P. Leiderer, E. Scheer, H. Misawa, Visualization of near-field enhancements of gold triangles by nonlinear photopolymerization. Plasmonics **6**, 207 (2011). https://doi.org/10.1007/s11468-010-9189-9
76. N. Murazawa, K. Ueno, V. Mizeikis, S. Juodkazis, H. Misawa, Spatially selective nonlinear Photopolymerization induced by the near-field of surface Plasmons localized on rectangular gold Nanorods. J. Phys. Chem. C **113**, 1147 (2009). https://doi.org/10.1021/jp809623y
77. K. Ueno, S. Juodkazis, T. Shibuya, Y. Yokota, V. Mizeikis, K. Sasaki, H. Misawa, Nanoparticle plasmon-assisted two-photon polymerization induced by incoherent excitation source. J. Am. Chem. Soc. **130**, 6928 (2008). https://doi.org/10.1021/ja801262r
78. C. Hubert, A. Rumyantseva, G. Lerondel, J. Grand, S. Kostcheev, L. Billot, A. Vial, R. Bachelot, P. Royer, S. Chang, S.K. Gray, G.P. Wiederrecht, G.C. Schatz, Near-field photochemical imaging of noble metal nanostructures. Nano Lett. **5**, 615 (2005). https://doi.org/10.1021/nl047956i

79. P. Kühler, F.J. Garcia de Abajo, J. Solis, M. Mosbacher, P. Leiderer, C. Afonso, J. Siegel, Imprinting the optical near field of microstructures with nanometer resolution. Small **5**, 1825 (2009). https://doi.org/10.1002/smll.200900393
80. P. Kühler, F.J. Garcia de Abajo, P. Leiprecht, A. Kolloch, J. Solis, P. Leiderer, J. Siegel, Quantitative imaging of optical near fields. Opt. Express **20**, 22063 (2012). https://doi.org/10.1364/OE.20.022063
81. L.E. Hennemann, A. Kolloch, A. Kern, J. Mihaljevic, J. Boneberg, P. Leiderer, A. Meixner, D. Zhang, Assessing the plasmonics of gold nano-triangles with higher order laser modes. Beilstein J. Nanotechnol. **3**, 674 (2012). https://doi.org/10.3762/bjnano.3.77
82. M. Aeschlimann, M. Bauer, D. Bayer, T. Brixner, F.J. de Abajo, W. Pfeiffer, M. Rohmer, C. Spindler, F. Steeb, Adaptive subwavelength control of nano-optical fields. Nature **446**, 301 (2007). https://doi.org/10.1038/nature05595
83. C.M. Scheffler, R.C. Word, R. Könenkamp, Controlling electric field and photoemission at the tips of triangular gold antennas. Plasmonics **16**, 371 (2021). https://doi.org/10.1007/s11468-020-01292-7
84. Q. Sun, K. Ueno, H. Yu, A. Kubo, Y. Matsuo, H. Misawa, Direct imaging of the near field and dynamics of surface plasmon resonance on gold nanostructures using photoemission electron microscopy. Light: Sci. Appl **2**, e118 (2013). https://doi.org/10.1038/lsa.2013.74
85. J. Fiutowski, C. Maibohm, J. Kjelstrup-Hansen, H.-G. Rubahn, Laser ablation of polymer coatings allows for electromagnetic field enhancement mapping around nanostructures. Appl. Phys. Lett. **98**, 193117 (2011). https://doi.org/10.1063/1.3591972
86. J. Boneberg, J. König-Birk, H.-J. Münzer, P. Leiderer, K. Shuford, G.C. Schatz, Optical near-fields of triangular nanostructures. Appl. Phys. A Mater. Sci. Process. **89**, 299–303 (2007). https://doi.org/10.1007/s00339-007-4138-y
87. A. Kolloch, T. Geldhauser, K. Ueno, H. Misawa, J. Boneberg, A. Plech, P. Leiderer, Femtosecond and picosecond near-field ablation of gold nanotriangles: Nanostructuring and nanomelting. Appl. Phys. A Mater. Sci. Process. **104**, 793–799 (2011). https://doi.org/10.1007/s00339-011-6443-8
88. D. Eversole, B. Luk'yanchuk, A. Ben-Yakar, Plasmonic laser nanoablation of silicon by the scattering of femtosecond pulses near gold nanospheres. Appl. Phys. A Mater. Sci. Process. **89**, 283–291 (2007). https://doi.org/10.1007/s00339-007-4166-7
89. N.N. Nedyalkov, H. Takada, M. Obara, Nanostructuring of silicon surface by femtosecond laser pulse mediated with enhanced near-field of gold nanoparticles. Appl. Phys. A Mater. Sci. Process. **85**, 163 (2006a). https://doi.org/10.1007/s00339-006-3679-9
90. B.J. Nagy, Z. Pápa, L. Péter, C. Prietl, J.R. Krenn, P. Dombi, Near-field-induced femtosecond breakdown of Plasmonic nanoparticles. Plasmonics **15**, 335 (2020). https://doi.org/10.1007/s11468-019-01043-3
91. R. Moraretscu, L. Englert, B. Kolaric, P. Damman, R.A.L. Vallée, T. Baumert, F. Hubenthal, F. Träger, Tuning nanopatterns on fused silica substrates: A theoretical and experimental approach. J. Mater. Chem. **21**, 4076 (2011). https://doi.org/10.1039/c0jm03829f
92. F. Hubenthal, R. Moraretscu, L. Englert, L. Haag, T. Baumert, F. Träger, Parallel generation of nanochannels in fused silica with a single femtosecond laser pulse: Exploiting the optical near fields of triangular nanoparticles. Appl. Phys. Lett. **95**, 063101 (2009). https://doi.org/10.1063/1.3186787
93. E. Boulais, A. Robitaille, P. Desjeans-Gauthier, M. Meunier, Role of near-field enhancement in plasmonic laser nanoablation using gold nanorods on a silicon substrate: Comment. Opt. Express **19**, 6177–6178 (2011). https://doi.org/10.1364/OE.19.006177
94. R.K. Harrison, A. Ben-Yakar, Role of near-field enhancement in plasmonic laser nanoablation using gold nanorods on a silicon substrate. Opt. Express **18**, 22556 (2010). https://doi.org/10.1364/OE.18.022556
95. R.K. Harrison, A. Ben-Yakar, Role of near-field enhancement in plasmonic laser nanoablation using gold nanorods on a silicon substrate: Reply. Opt. Express **19**, 6179 (2011). https://doi.org/10.1364/OE.19.006179

96. S. Hashimoto, T. Uwada, M. Hagiri, H. Takai, T. Ueki, Gold nanoparticle-assisted laser surface modification of borosilicate glass substrates. J. Phys. Chem. C **113**, 20640 (2009). https://doi.org/10.1021/jp905291h
97. S. Hashimoto, T. Uwada, M. Hagiri, R. Shiraishi, Mechanistic aspect of surface modification on glass substrates assisted by single shot pulsed laser-induced fragmentation of gold nanoparticles. J. Phys. Chem. C **115**, 12, 4986 (2011). https://doi.org/10.1021/jp106830x
98. S. Imamova, N. Nedyalkov, A. Dikovska, P. Atanasov, M. Sawczak, R. Jendrzejeski, G. Sliwinski, M. Obara, Near field properties of nanoparticle arrays fabricated by laser annealing of thin Au and Ag films. Appl. Surf. Sci. **257**, 1075 (2010). https://doi.org/10.1016/j.apsusc.2010.08.016
99. N. Nedyalkov, T. Sakai, T. Miyanishi, M. Obara, Near field properties in the vicinity of gold nanoparticles placed on various substrates for precise nanostructuring. J. Phys. D. Appl. Phys. **39**, 5037 (2006b). https://doi.org/10.1088/0022-3727/39/23/021
100. N. Nedyalkov, T. Sakai, T. Miyanishi, M. Obara, Near field distribution in two dimensionally arrayed gold nanoparticles on platinum substrate. Appl. Phys. Lett. **90**, 123106 (2007). https://doi.org/10.1063/1.2715103
101. A. Robitaille, É. Boulais, M. Meunier, Mechanisms of plasmon-enhanced femtosecond laser nanoablation of silicon. Opt. Express **21**, 9703 (2013). https://doi.org/10.1364/OE.21.009703
102. J. Bonse, S. Baudach, J. Krüger, W. Kautek, M. Lenzner, Femtosecond laser ablation of silicon—Modification thresholds and morphology. Appl. Phys. A Mater. Sci. Process. **74**, 19–25 (2002). https://doi.org/10.1007/s003390100893
103. D. von der Linde, K. Sokolowski-Tinten, J. Bialkowski, Laser-solid interaction in the femtosecond time regime. Appl. Surf. Sci. **109/110**, 1 (1997). https://doi.org/10.1016/S0169-4332(96)00611-3
104. A. Kolloch, Plasmon resonances for Sub-100 nm silicon ablation: Quantitative measurement and nanometer-scale ablation mechanism, PhD Dissertation (Konstanz 2012) http://nbn-resolving.de/urn:nbn:de:bsz:352-231938

Chapter 12
Nanoscale Plasmonic Printing

Soon Hock Ng and Saulius Juodkazis

Abstract Nanoscale structuring/printing is of interest for a range of applications in 3D subtractive and additive manufacturing ($3D^{\pm}$). Basic principles of light field enhancement and control at the nanoscale are overviewed in this chapter for bulk, surface, and localised plasmons (1D, 2D, and 3D localisation, respectively). All these plasmons are resonant phenomena that have common Lorentzian spectral line shape that relates refractive and absorption properties as well as defining the phase of transmitted and scattered light. Localisation of light at the nanoscale creates the possibility of modification with matching resolution. Harnessing this light enhancement can be demonstrated as a "nano-pen" for direct write nanolithography.

Keywords Plasmonics · Nanoscale · Ablation · Direct laser write

1 Why Plasmonic?

Light–matter interaction is determined by the relative permittivity (dielectric function) of a material $\varepsilon(\omega)|_{t_0}$ at the wavelength of light λ and at a particular moment in time t_0 from the material side; $\omega = 2\pi c/\lambda$ with c being speed of light. The light intensity $I(t) \equiv \mathbf{E}(t)^2$ is defined by its electric field $\mathbf{E}$ at that selected moment in time t_0 and defines how much light's energy is absorbed, reflected, scattered, and transmitted. All the portions of the absorbed, transmitted, and reflected light obey energy conservation $A + R + T = 100\%$. The real and imaginary parts of the permittivity $\varepsilon \equiv \varepsilon_1 + i\varepsilon_2$ define the dispersion- and absorption-related response of a material; permittivity is related to complex refractive index $\sqrt{\varepsilon} \equiv \tilde{n} = (n + i\kappa)$. In such a description, a strongly nonlinear response of a material in the field of a high intensity laser pulse is given by the instantaneous value of ε (or $\tilde{n}$). For a material exposed to a short pulse of high intensity, electrons are generated by linear

---

S. H. Ng · S. Juodkazis (✉)
Optical Sciences Centre, School of Science, Swinburne University of Technology, Hawthorn, VIC, Australia
e-mail: soonhockng@swin.edu.au

© The Author(s), under exclusive license to Springer Nature Switzerland AG 2023

R. Stoian, J. Bonse (eds.), *Ultrafast Laser Nanostructuring*, Springer Series in Optical Sciences 239, https://doi.org/10.1007/978-3-031-14752-4_12

and nonlinear mechanisms of absorption. Light propagation and absorption in such a photo-excited state are described by nonlinear optical methods until this solid-state plasma state transitions into a true ionised plasma state defined by dielectric breakdown at $\varepsilon = 0$.

The most interesting and highly dynamic changes to material relevant to the discussion here occur during transition to plasma and pre-breakdown conditions. In the case of ultra-short sub-1-ps pulses of high intensity, the transition from solid to plasma state can be very fast, occurring over several optical cycles (~3 fs) at the laser wavelength $\lambda \approx 1$ µm. It is no surprise that a complete understanding of complex spatio-temporal phenomena evolving in time and along the light propagation direction inside excited micro-volumes attracts interest and is analysed via increasingly sophisticated experimental techniques.

In the process of defining the scope of this discussion, how it pertains to light–matter interactions within a photo-excited focal volume and transition from a dielectric to a metallic state $1 < \varepsilon < 0$, we in fact discuss plasma-related phenomena occurring on the inner surface dielectric (transparent) host volume. Hence, the word plasmonic is well aligned to such field of research and applications.

As an example, plasmonic printing is contactless method for modification of materials, which harnesses the localisation of light to a sharp tip or nanoparticle this is in close proximity to the sample. Such printing can be nanoscale, with sub-wavelength feature sizes below the classical optical resolution limit $\sim 0.6\lambda/NA$, defined by the numerical aperture NA of the lens used. True nanoscale localisation by this plasmonic printing can be achieved when the modified volume is constrained to dimensions smaller than 100 nm along all axes, thus nanoscale.

In experiments with light–matter interactions, when ultra-short sub-1-ps laser pulses create sub-wavelength and nanoscale patterns (nanoprints) on surfaces and interfaces, the surface waves at those interfaces are discussed. The interfaces can be a natural boundary at sample's surface with its environment (air, gas, liquid, other solid) or can be created inside a transparent host medium at the focal region where photo-excitation creates a highly conductive (plasma) volume via absorption and ionisation. In both cases, the interface between materials with different permittivities has to be analysed, accounting for fast changing permittivities. Such analysis is presented next, considering explicitly the interface between two mediums with complex permittivities.

2 Surface Plasmon Polariton (SPP)

As a surface wave, light bound to the collective oscillation of surface charge, the surface plasmon polariton (SPP) can exist at the interface of metal and dielectric (media 1 and 2 in Fig. 12.1). Dispersion relation ω vs. wave number $k = 2\pi/\lambda$ is found from the solution of the wave Helmholtz equation. The electrical E-field of the SPP wave has a form $E_x e^{i\beta x} e^{-k_z z}$, describing propagation along x-direction with a propagation constant β (the wavevector):

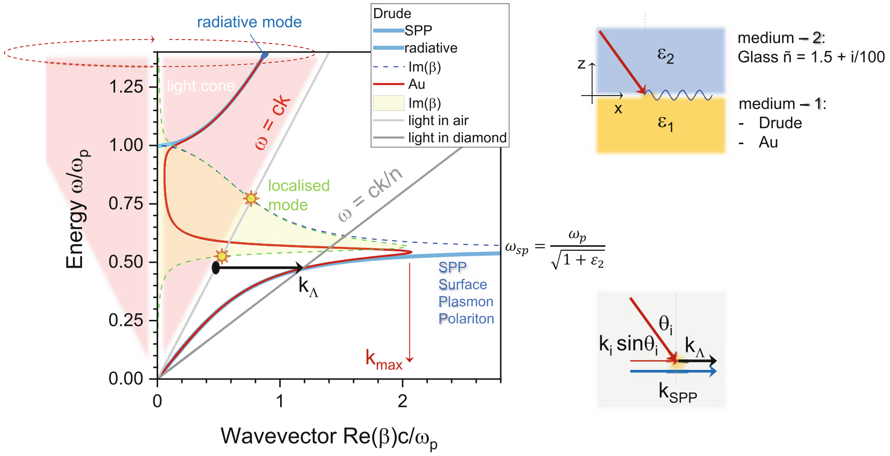

Fig. 12.1 Dispersion $\omega(k)$ relations for Drude models: lossless and Au at the metal–glass interface; ω_p is the plasma frequency and glass has a refractive index of $n = 1.5 + i/100$. Phase-matching diagram $k_{SPP} = k_i \sin\theta_i + k_\Lambda$ to launch surface plasmon polariton (SPP) with a grating (or prism) introducing k_Λ; k_i, θ_i are the wavevector of incident light and angle of incidence, respectively (right-bottom inset). A refractive index of a $n = 2.5$ dielectric (e.g., a diamond prism) for the light line $\omega = (c/n)k$ is shown. Dashed lines are ω vs. $Im(\beta)$ (non-propagating localised mode), where β is the propagation constant or SPP wavevector (Eq. (12.1)) at the metal–glass interface. An asymptotic frequency of surface plasmon is ω_{sp} for the lossless Drude plasma (no electron damping $Im(\varepsilon_D) = 0$; medium - 1); ε_2 is the permittivity of glass (medium - 2). Insets show diagrams of interaction zone (right-top) with scattering of a dipole nature providing redirection and wave matching

$$\beta = k_0\sqrt{\frac{\varepsilon_1\varepsilon_2}{\varepsilon_1+\varepsilon_2}}, \tag{12.1}$$

where $k_0 = 2\pi/\lambda$ is the wavevector of incident light (k_i in Fig. 12.1). The SPP, an evanescent field, exponentially decays into the surrounding media 1 and 2 with its own $k_z^{(1,2)}$. As the SPP approaches the surface plasmon frequency, $\omega_{sp} = \omega_p/\sqrt{1+\varepsilon_2}$, where the plasma frequency $\omega_p = \sqrt{N_e e^2/(\varepsilon_0 m)}$ (also referenced as bulk plasmon) is defined by electron density N_e, electron charge, and mass e, m, respectively, and permittivity of free space ε_0—the permittivity of metal (negative) has the same absolute value as the dielectric host $\varepsilon_1(\omega) + \varepsilon_2 = 0$ and the group velocity of the SPP $v_g \to 0$ (a standing wave).

Figure 12.1 shows dispersion relations (Eq. (12.1)) for the metal–glass (2-1) interface where metal (1) is modelled by the Drude model and its adaptation to the Au [1]. Dielectric medium (2) is glass-like with permittivity $\varepsilon_2 \equiv \tilde{n}^2 = (1.5 + i/100)^2$. The Drude model is useful to understand the underlying physics of SPP dispersion. The plasma of a free electron gas in the fixed ion background that provides a restoring action for the oscillation is described by the permittivity separated into real and imaginary parts (ε_1 medium in Fig. 12.1):

$$\varepsilon(\omega) = 1 - \frac{\omega_p^2}{\omega^2 + i\gamma\omega} = \left(1 - \frac{\omega_p^2\tau^2}{1+\omega^2\tau^2}\right) + i \times \frac{\omega_p^2\tau}{\omega(1+\omega^2\tau^2)}, \tag{12.2}$$

where $\tau = 1/\gamma$ is the lifetime of the electron plasma oscillation defined by its collision frequency γ. At low frequencies $\omega < \omega_p$, metallic plasma behaves like a metal (are reflective). Closer to ω_p, the product $\omega\tau \gg 1$, and the damping of oscillations is negligible and $\varepsilon(\omega)$ (Eq. (12.2)) is dominated by the real part defined by the undamped free electron plasma $\varepsilon(\omega) = 1 - \omega_p^2/\omega^2$. This ideal condition of the Drude model $\varepsilon_D(\omega)$ is plotted in Fig. 12.1. It has both the SPP mode for the lower frequency branch discussed above and the high-frequency $\omega/\omega_p > 1$, where plasma is optically transparent and has dispersion of $\omega^2 = \omega_p^2 + k^2c^2$ for transverse traveling waves with group velocity $v_g = d\omega/dk < c$. This branch of dispersion is less relevant to the discussion here where radiative E-fields escape the light–matter interaction volume. The radiative modes are confined inside the light cone around the $Energy$-axis with boundary if the light line $\omega = ck$ (shaded region in Fig. 12.1). This light cone with x as a radial coordinate also defines all the possible projections of the wavevector k for transverse waves at a specific wavelength (or ω). Such presentation is useful for the discussion of the phase-matching conditions necessary to launch the surface bound transverse TM-mode SPP wave. Phase matching is provided by scattered light along the direction of SPP wave. Scattering provided by roughness, which can be actual surface roughness, caused by an unevenness of permittivity, or can be dipole scattering of a nanoscale localised absorber, e.g., a nanoparticle. For a controlled launch of a SPP, such phase matching is provided by a wavevector of a grating or under total internal reflection at a specific angle of incidence θ_i. Regardless of the phase- matching mechanism, it is marked as k_Λ. A diamond prism can provide the required wavevector deficit from the light cone in air, to the SPP mode at the intersection point with the light line, in a medium of refractive index $n = 2.5$ (diamond); see Fig. 12.1.

Plasmonic (Olympic) metals Au, Ag, Cu can be modelled with the Drude model at lower frequencies when interband electronic transitions do not place (up to 1 eV energy). This is called the Drude–Sommerfeld-free electron model. For gold, the best fit of experimentally measured permittivity to Eq. (12.2) is achieved with $E = \hbar\omega_p = 8.5$ eV and $\tau = 14$ fs [1]. These values are close to other reported data and were used for the Au dispersion plot shown in Fig. 12.1. The time constant τ is a fit parameter that reflects cumulative charge scattering interactions. With this Drude–Sommerfeld model of Au permittivity, the dispersion dependence of a SPP mode on an Au–glass interface has a strong overlap with the lossless Drude model; however, there is a distinct maximum value of the wavevector $k_{max} = 2\pi/Re(\beta)$. k_{max} is proportional to τ. The k_{max} for Au with $\hbar\omega_p = 8.5$ eV [1] (Fig. 12.1) corresponds to smallest wavelength of SPP of $\lambda_{sp} = 70.6$ nm. The value of $2\pi/Re(\beta)$ is usually used to define the period of laser imprinted ripples also called light-induced periodic surface structures (LIPSS), even though they can be formed inside materials or sub-surface as discussed next.

3 Photo-Generated Plasma

3.1 Permittivity Defined by the Electron Density N_e and Collision Rate ν

Conditions required to launch a SPP at a metal (or a plasma)—dielectric interface are described above (Sect. 2). They are dictated by the electron density N_e that defines the plasma frequency ω_p and relaxation time presented by an effective τ. Under irradiation of a high intensity 1–100 TW/cm^2 ultra-short laser pulse, a dielectric or semiconductor can be converted into a metallic state with $0 < \varepsilon < 1$, and dielectric breakdown can be induced at the focal spot defined by $\varepsilon = 0$. This fast material transformation during sub-1-ps pulse can be considered as a material of changing state (dielectric–metal—Die–Met [2]). Once an $\varepsilon < 1$ region focal volume is created, a SPP at the interface with a dielectric host can be launched. For the surface of a dielectric or semiconductor in the focal region of a high intensity pulse, two interfaces have to be considered, one at the internal interface between the host and surface bound Die–Met, as well as Die–Met with ambient air (Fig. 12.2).

In a similar way as the Drude model is modified to define permittivity of Au with two parameters ω_p and τ, it can be used for semiconductors and dielectrics that have a large real part of permittivity (refractive index), which decreases under photo-generation of electrons [2]:

$$\varepsilon = \left[(\varepsilon_i - 1)\frac{N_e}{N_a}\right] + \left[1 - \frac{N_e}{N_{cr}(1 + i\nu/\omega)}\right], \tag{12.3}$$

where $N_a = \rho N_A/M$ is the atomic density expressed via mass density ρ, Avogadro number N_A, and the molar mass M, $N_{cr} = \varepsilon_0\omega^2 m/e^2$ is the critical number density, and ν is the effective collision frequency (its dependence on N_e and temperature of electrons T_e are discussed below). The N_e is a source of electrons upon optical exci-

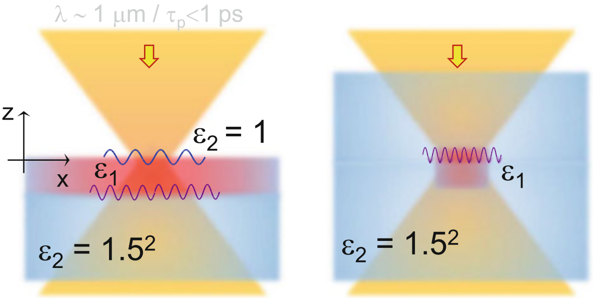

Fig. 12.2 Geometry of interfaces between photo-excited material transitioning via a dielectric–metal (Die–Met–red region) state of permittivity with focal spot placed on the surface or inside a transparent medium (permittivity $\varepsilon_2 = 1.5^2$ of a glass-like host–blue region)

tation. Equation (12.3) is derived by making use of identity $\omega_p^2/\omega^2 = N_e/N_{cr}$. [3] The first term in brackets [...] describes the reduction of unperturbed permittivity due to induced polarisation of the material, while the second [...] term is Drude like due to electronic part of the permittivity. The N_{cr} defines electron density at which the material becomes reflective, i.e., the plasma frequency equals the frequency of light. For example, for the $\lambda = 1030$ nm, wavelength $N_{cr} = 1.05 \times 10^{21}$ cm^{-3}. The collision rates in laser-induced electrically neutral (electron and ion number density are the same) plasmas [4] at the equilibrated electron and ion temperature have comparable rates for electron–electron (*ee*) and electron–ion (*ei*) momentum exchange $\nu_{ee} \sim \nu_{ei}/\sqrt{2}$ [4]. For the energy vs. momentum exchange rate $\nu^{(K)}$ vs. $\nu^{(p)}$ (*ei* case): $\nu^{(K)} = \frac{2m_i}{m_e+m_i}\nu^p$, where masses of ions and electrons are m_i and m_e, respectively, while for the *ee* case $\nu^{(K)} = \nu^{(p)}$. During thermalisation, hot electrons transfer energy to ions at rate $\nu^{(K)} = \frac{2m_e}{m_i}\nu^{(p)}$ [4]. The thermalisation time is reciprocal to the exchange rate discussed above.

Collision Rates [3] The elastic momentum exchange rate or collision rate ν_{col} of electrons is effectively a constant due to collisions with the lattice (phonons), neutrals, electrons, and ions [3]. The following estimates are obtained for numerical modelling and follow Ref. [3]. The collision rate is dependent on concentration and temperature increasing in intensity as both do. The quasi-neutrality between electrons and ions $N_e = N_i$ is maintained [3]. When $N_e \ll N_a$, electron–phonon interactions dominate, and at room temperature, $\nu_{e-ph} \approx k_B T/\hbar = 3.79 \times 10^{13}$ s^{-1}, [3], where k_B is the Boltzmann's constant. The electron–ion Coulomb collisions increase with density towards the upper physical limit $\nu_{e-i}^{max} \approx v_e/d \approx 10^{16}$ s^{-1}, where v_e is the electron velocity and d is the interatomic distance $d = 1/\sqrt[3]{\frac{3N_a}{4\pi}}$. The Coulomb collisions increase with laser pulse intensity and dominate at the ablation threshold when first ionisation occurs, i.e., $N_e \approx N_a$. The maximum rate of collisions $\nu_{e-i}^{max} = v_e^{max}/d$, where the velocity $v_e^{max} = \sqrt{2(J_i + \epsilon_B)/m_e}$, J_i is the ionisation potential, and ϵ_B is the binding energy (the enthalpy of formation, the heat of sublimation, or latent heat [5]—for example, for Si $\epsilon_B = 4.62$ eV/atom). The electron energy at the ablation threshold is equal to the sum $J_i + \epsilon_B$. This amount of electron energy is sufficient to break bonds inside the solid.

With increasing laser intensity and temperature, the collision rate decreases as in an ideal plasma $\nu_{e-i} \propto N_e/T_e^{3/2}$. The collision rate $\nu_{eff} = N_e \sigma_\Sigma v_e$ is defined by the sum of cross sections σ_Σ of the contributing processes in momentum transfer from electrons to ions. The description above justifies definition of collision rate as

$$\nu_{\mathrm{col}}(N_e) = \nu_{e-ph}^{min} + \nu_{e-i}^{max}\frac{N_e}{N_a}. \tag{12.4}$$

SiO$_2$ Case Next, estimates are made for SiO$_2$: $d \approx 0.575$ nm (with mass density $\rho = 2.2$ g/cm^3, molar mass $M = 28 + 2 \times 16 = 60$ g/mol), $\epsilon_B = 3.7$ eV/atom [6] with the larger ionisation potential of oxygen $J_i = 13.6$ eV (for Si $J_i = 8.15$ eV) used for the estimate of $\nu_{e-i}^{max} = 4.29 \times 10^{15}$ s^{-1} with velocity $v_e^{max} = 2.47 \times$

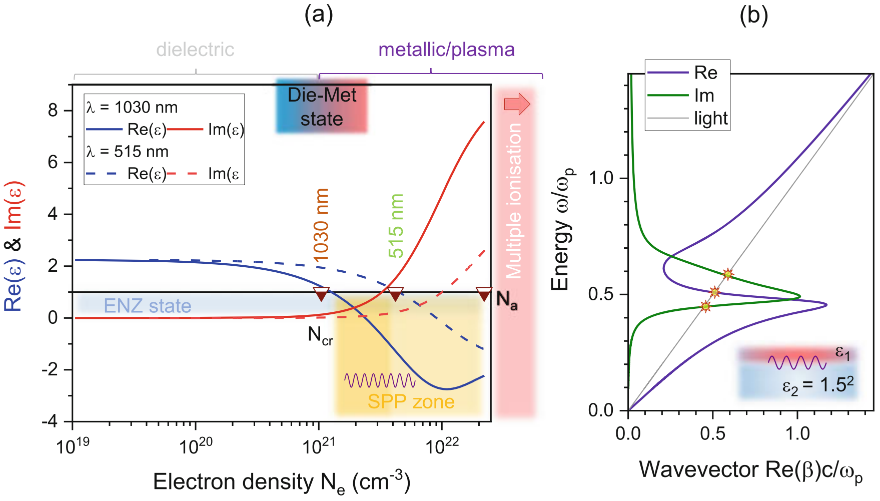

Fig. 12.3 Dielectric–metal transition (Die–Met). (**a**) Silica SiO_2 under increasing generation of electrons N_e [cm^{-3}]; starting refractive index $\sqrt{\varepsilon} = 1.5$; the critical densities of electrons N_{cr} for two wavelengths $\lambda = 1030$ nm (1.05×10^{21} cm^{-3}) and 515 nm (4.20×10^{21} cm^{-3}) are shown by markers on the $Re(\varepsilon) = 1$ line separating dielectric–metallic state (Die–Met transition). The atomic density of SiO_2 $N_a = 2.21 \times 10^{22}$ cm^{-3} is the limit of the curves. Calculations were made with Eqs. (12.2) and (12.4) with parameters evaluated in Sect. 3. (**b**) Equation (12.1) plotted for the epsilon-near-zero (ENZ) material at N_{cr} with ω_p for $\lambda = 1030$ nm (Eq. (12.3)) interfaced with silica $\sqrt{\varepsilon_1} = 1.5 + i/100$; light line is for air. Markers show intersection locations of the propagating surface wave SPP and localised $Im(\beta)$ vs. ω (see also Chapter 29_Stoian)

10^6 m/s. Evolution of permittivity of SiO_2 under increasing ionisation during a high intensity pulse is calculated with Eq. (12.2) using electron density dependence of collision rate $\nu_{col}(N_e)$ (Eq. (12.4)) and is plotted in Fig. 12.3.

3.2 Dielectric-to-Metal Transition: Permittivity Analysis

Figure 12.3a illustrates the change in permittivity ε from a dielectric to a metallic plasma state using collision rate estimates provided above. This qualitative picture of light–matter interaction shows the region where the interface can be formed supporting the SPP mode between plasma $Re(\varepsilon) < 1$ and surrounding glass (or air), see Fig. 12.2. For a shorter wavelength, the photo-excited region is partly transparent up to larger electron density due to larger N_{cr}. Calculations shown in Fig. 12.3a were carried out to the point of first ionisation of atoms, i.e., the N_a of SiO_2. At high light intensity, multiple ionised plasma is attainable [7, 8], and its density and temperature will define the actual collision rate that was only estimated qualitatively for herein. However, the physical picture of collision-rate-controlled permittivity changes is shown here with conditions of SPP creation at the interface between plasma and surroundings. It is instructive prediction of SPP on plasma of critical density N_{cr} on glass $\varepsilon_2 = (1.5 + i/100)^2$ shown in Fig. 12.3b. The dispersion plot of normalised energy ω vs. $Re(\beta)$ and $Im(\beta)$ resembles a Lorentzian spectral line shape of dispersion $D(\omega)$ and absorbance $A(\omega)$, respectively [9]. The dispersion dependence of the surface bound propagating SPP wave (real β) and non-propagating surface bound (imaginary β) is close together in both energy and wavevector space at the intersection with free space light. Such intersection indicates the possibility to couple the free propagating light into those modes and relax the required phase- matching conditions described for SPP launched on the lossless Drude plasma (Fig. 12.1). Such dispersion/absorption spectral line shape resembles a dipole response. During exposure of the dielectric medium to a high intensity ultra-short laser pulse, the plasma density evolves quickly, creating a constantly changing plasma density. Its temperature and collision rates are all important to the discussion of SPP launch at the interface. The spatial extent of such an interface and energy absorption is also directly linked to the ε as is analysed next.

Permittivity given by Eq. (12.2) defines a state of photo-excited material at which a SPP wave can be launched. Metal-like permittivity $1 > Re(\varepsilon) > 0$ created by a laser pulse defines region of interest at this epsilon-near-zero (ENZ) condition that is efficient in light energy absorption. The rate of absorption and its spatial location are important for interface formation required for the SPP. Also, the phase of light upon reflection from the boundary between different refractive index materials changes in a step-like manner. The phase of the reflected field E_R (incidence from air $n = 1$) onto material of index n is defined by $E_R = -\frac{n-1}{n+1}E_{in}$, where E_{in} is the incident E-field and the "−" sign defines the opposite phase or the π-shift. For $n > 1$, there is a π-shift between the incident and reflected E-fields. Since the real part of refractive index of ENZ $n < 1$, there is no phase change between E_R and E_{in}. Figure 12.4 illustrates light incidence on the micro-cylinders of higher and lower refractive index embedded inside glass. These volumes are similar to those that occur when laser pulses are tightly focused using objective lenses of numerical aperture $NA \approx 1$ in the wavelength range from visible to near IR. Formation of interference fringes at different distances from the front surface of these cylinders is a demonstration of the phase change. This illustration shows that phase changes around the interfaces that support SPP modes can alter light intensity distribution, intensity causing a different absorption and plasma density.

3.3 Energy Deposition at the ENZ Conditions ($\varepsilon \to 0$)

This section describes how a material is changed via permittivity evolution with larger electron density N_e and simultaneously changing collision rate ν. The conditions discussed are at high electron densities around the critical plasma density at the laser wavelength $0.1 < \frac{N_e}{N_{cr}} < 10$. At around N_{cr}, SPP conditions can be created for the interface of excited plasma in contact with a dielectric host (Fig. 12.3b).

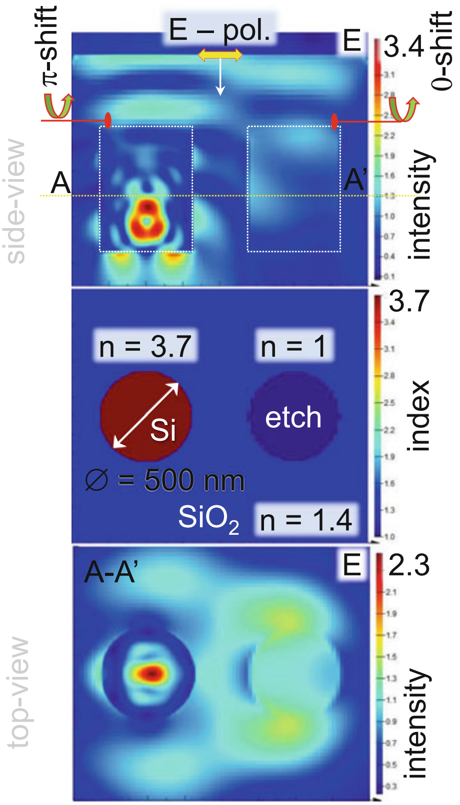

Fig. 12.4 Numerical modelling of plane wave propagation through micro-cylinders of Si and empty space (etch with refractive index $n = 1$) inside a glass host ($n = 1.4$); wavelength $\lambda = 767$ nm. Calculations were made by finite-difference time-domain (FDTD) simulations (Lumerical). Panels show light field enhancement; incident field is a linearly polarised plane wave with $|\mathbf{E}| = 1$. Phase π-shift occurs upon reflection from a higher refractive index material

Surfaces discussed in plasmonic nanoprinting look like the ablated Si shown in Fig. 12.5 with different periods of semi-regular patterns of ripples—light-induced periodic surface structures (LIPSS). Ripples can be formed on the surface or inside the volume of dielectrics or semiconductors. Small sub-wavelength ripples on the surface and especially inside the bulk are particular for exposure by high intensity ultra-short laser pulses. Surface patterns are formed by ablation—Latin word for removal—which means that material has enough deposited/absorbed energy to loose solid-state material cohesion (overcome the binding energy $\epsilon_B \sim 5$ eV/atom) and to be ionised with ionisation energies $J_i > 10$ eV/atom. Exciting solid-state matter and exceeding energy deposition required for each phase transition—from melting, evaporation ($\sim \epsilon_B$), to ionisation (J_i), and plasma—within a sub-1-ps pulse are a very fast process since typical lattice vibrations are on the order of few picoseconds and do not mediate energy deposition by sub-1-ps pulsed during the laser pulse itself. The energy deposition by absorbance A is linked to the reflectance R in the overall energy balance $A + R + T = 100\%$, where T is the transmittance. How much light is absorbed and reflected is all defined by the permittivity ε of the

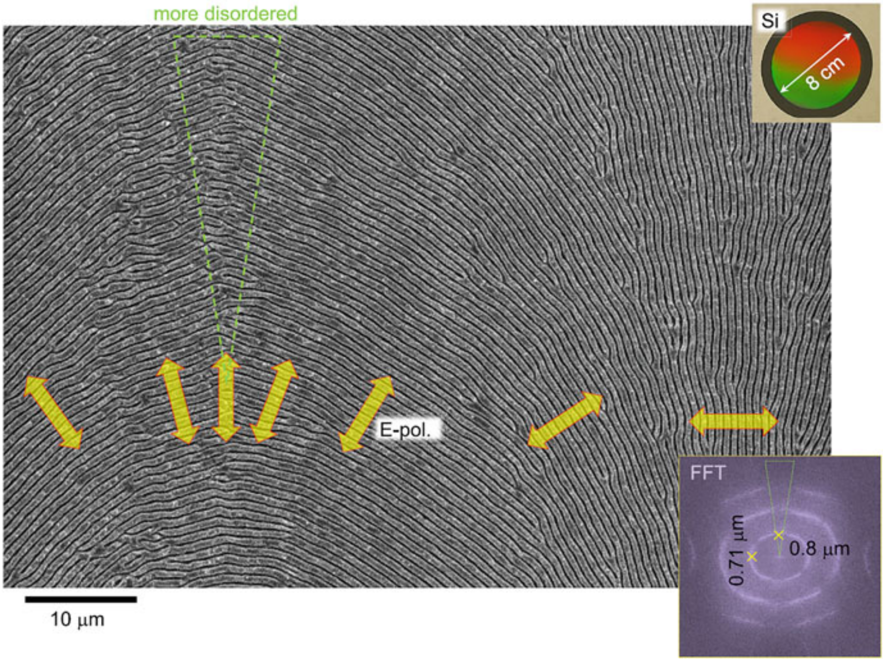

Fig. 12.5 SEM image of large area nanoprinting of ripples on Si by ultra-short laser pulses: wavelength $\lambda = 1030$ nm, repetition rate $\nu = 100$ kHz, an overlap of 10 pulses per 1 µm, a scan speed of $v_s = 0.1$ mm/s, focusing with numerical aperture $NA = 0.26$, pulse energy $E_p = 10$ µJ, polarisation rotation 2° per micrometre of travel. Laser beam was focused with an added cylindrical lens of $f = 80$ mm defining the ablation area of $\sim 400 \times 5$ μm^2 on the sample (elongated along polarisation). Photo inset is for linear scan without polarisation rotation [10]

material. As discussed above, ε changes during a laser pulse since electrons are fast in following the E-field of the incident light.

For light incident from air ($n = 1$) onto a material with refractive index ($n + i\kappa$), the Fresnel coefficients define R at angle of incidence θ_i, and for the normal incidence $\theta_i = 0$, it is $R = \frac{(n-1)^2+\kappa^2}{(n+1)^2+\kappa^2}$. For insignificant transmission $T \rightarrow 0$ in an absorbing medium (optically thick), $A = 1 - R$ and is $A = \frac{4\kappa^2}{(n+1)^2+\kappa^2}$. From Eq. (12.3), we can calculate which portion of light is absorbed at different electron densities leading to the ENZ conditions. If the starting material has $n = 1.5$ (e.g., silica glass), at N_{cr} for $\lambda = 1030$ nm, one finds $\sqrt{\varepsilon} = n + i\kappa = 0.34 + i \times 0.19$. Thus $A = 73.8\%$, which is a substantial energy deposited to the target with the depth of absorption (skin depth for the intensity $I = |E|^2$) defined as $l_{ab} = \frac{c}{2\omega\kappa} = \frac{\lambda}{4\pi\kappa} = 427$ nm. At $N_e = N_{cr}/2$, the most efficient energy deposition takes place, with $A = 97.5\%$. At larger plasma density, $N_e = 2N_{cr}$, $\tilde{n} = 0.25 + i \times 0.91$, $A = 41.8\%$, and deposition depth $\text{ł}_{ab} = 90$ nm (10% of λ). Shallow energy deposition is favourable for formation of an interface supporting the SPP mode.

When the plasma frequency approaches that of the collision rate $\omega_p \approx \nu_{\mathrm{col}}$, optical constants of plasma become [6]

$$Re(\varepsilon) \approx \frac{\omega^2}{\omega_p^2} \sim \frac{N_{cr}}{N_e}; \quad Im(\varepsilon) \approx \frac{\omega_p}{\omega}\left(1 + \frac{\omega^2}{\omega_p^2}\right)^{-1}; \quad n \approx \kappa = \sqrt{Im(\varepsilon)/2} = \sqrt{\frac{\omega_p}{2\omega}}, \tag{12.5}$$

i.e., $n \approx \kappa$ as in the example above or glass at electronic density of $2 \times N_{cr}$ with metallic state of $n < 1$.

Ablation threshold fluence for dielectrics Φ_{th} [J/cm^2] is predicted from considering that the pulse energy is absorbed by electrons in the skin depth l_{ab} and is in excess of the bonding energy and ionisation potential $(\epsilon_B + J_i)$ [6]:

$$\Phi_{th}^{Die} = I_{th} t_p = \frac{3}{4}(\epsilon_B + J_i)\frac{l_{ab} N_e}{A}, \tag{12.6}$$

where t_p is the pulse duration and I_{th} [W/cm^2] is the pulse intensity (irradiance). Considering the upper bound estimate with $J_i = 13.6$ eV/atom for oxygen and full ionisation of the material $(N_e = N_a)$, one finds that for A and l_{ab} at N_{cr}, $\Phi_{th}^{Die} = 2.65$ J/cm^2 for silica. It is very close to the experimentally determined value of 2 J/cm^2. This is a reasonable estimate since A and l_{ab} are strongly inversely dependent on N_e, and the experimentally determined threshold fluence is only obtained at $1.1 N_{cr}$.

3.4 Electron Photo-Generation

The peak intensity of an ultra-short laser pulse (assumed to be Gaussian) is double the average intensity I_p. The absorbed energy is defined by the absorbance A, and the absorbed energy density [J/cm^3] at the end of the laser pulse is $W_a = A\Phi_p / l_{ab}$, where the fluence $\Phi_p = \int_0^{t_p} I_p(t)dt$. The electron density N_e at the end of the pulse is defined by $\int_0^{t_p} I_p(t)dt$. The average intensity of the laser pulse is $I_a = c\varepsilon_0 E_0^2/2 \equiv cB_0^2/(2\mu_0) \equiv E_0 B_0/(2\mu_0)$, where E_0 is the amplitude of the electric field strength [V/m], $B_0 = E_0/c$ is the maximum magnetic field strength [T], and ε_0, μ_0 are the permittivity and permeability of the free space, respectively. The generation of electrons by laser pulses changes in time with the instantaneous intensity $I \propto EB$.

The energy change during one collision is $\Delta\epsilon_e = \frac{2\epsilon_{osc}\omega^2}{\nu_{\mathrm{col}}^2 + \omega^2}$, defined via the effective electron collision frequency and electron quiver energy $\epsilon_{osc} = \frac{e^2 E^2}{4 m_e \omega^2}$, where electron mass and charge are m_e and e, respectively. When both the electron energy $\epsilon_e = \frac{A}{l_{abs} N_e}\int_0^{t_p} I_p dt$ and $\Delta\epsilon_e \approx \epsilon_{osc}$ (the energy gained per electron in a single collision is comparable to that of the oscillation) are larger than the photon energy, then $\gamma \equiv \epsilon_e \Delta\epsilon_e/(\hbar\omega)^2 > 1$ and classical multi-photon absorption determines the ionisation rate—the so-called large frequency and moderate (low) field condition. When $\gamma \ll 1$, the tunnelling ionisation becomes dominant (quantum case), i.e., low-frequency, high-field conditions. At the intensity of 13 TW/cm^2, which is typical for the breakdown threshold in silica and sapphire, $\gamma = 2$. Avalanche ionisation, which is present at typical ∼TW/cm^2 irradiance at ambient conditions (especially at the longer near-IR wavelengths), is the dominant factor due to the avalanche rate scaling as λ^2.

To estimate the electron density at the end of a high intensity ultra-short laser pulse—$1 - 10$ TW/cm^2 and up to tens-of-TW/cm^2 reaching dielectric breakdown of a dielectric host (at $Re(\varepsilon) = 0$)—the multi-photon ionisation and impact (or avalanche) rates of electron generation w_{mpi} and w_{imp}, respectively, can be calculated by Gamaly et al. [6]

$$w_{mpi} \approx \omega n_{ph}^{3/2} \left(\frac{\epsilon_{osc}}{2J_i}\right)^{n_{ph}}, \tag{12.7}$$

$$w_{imp} \approx \frac{\epsilon_{osc}}{J_i} \left(\frac{2\omega^2 \nu_{\text{col}}}{\omega^2 + \nu_{\text{col}}^2}\right), \tag{12.8}$$

where $n_{ph} = J_i/\hbar\omega$ is the number of photons necessary for atom ionisation.

These rate estimates are valid for N_e excitation in the ENZ range (ENZ is $Re(\varepsilon) = 0$) and generation of electrons progress as [6]

$$\frac{dN_e}{dt} = N_e w_{imp} + N_a w_{mpi}, \tag{12.9}$$

which has a solution with an initial electron density N_0:

$$N_e = \left(N_0 + \frac{N_a w_{mpi}}{w_{imp}}[1 - e^{-w_{imp}t}]\right) e^{w_{imp}t}. \tag{12.10}$$

Here we reflect on the above formulae that provides the possibility of estimating electron density N_e at any time across the lifetime of the laser pulse. The N_e depends on the pulse intensity I_p and is linked to the electron collision rates in plasma ν_{col}, which tends to saturate as it approaches that of laser the frequency $\nu_{\text{col}} \approx \omega$. Due to shallow energy deposition into skin depth $l_{ab} \leq 100$ nm $\ll \lambda$, an interface between the host dielectric and metallic plasma state of Die–Met is created during the laser pulse. Such an interface can support the SPP mode that has wavelength determined from the maximum of $Re(\beta) = 2\pi/\lambda_{sp}$, which is a standing wave ($v_g \to 0$). Figure 12.3b shows that at N_{cr}, when Die–Met transition into the metallic state $\varepsilon < 1$ takes place, the dispersion dependencies ω vs. $Re(\beta)$ and ω vs. $Im(\beta)$ for surface bound propagating SPP and non-propagating modes, respectively, resemble dispersion $D(\omega)$ and absorption $A(\omega)$ line shapes of the Lorentzian oscillator. The most efficient electron generation (large A) is at $N_{cr}/2$, and the most shallow energy

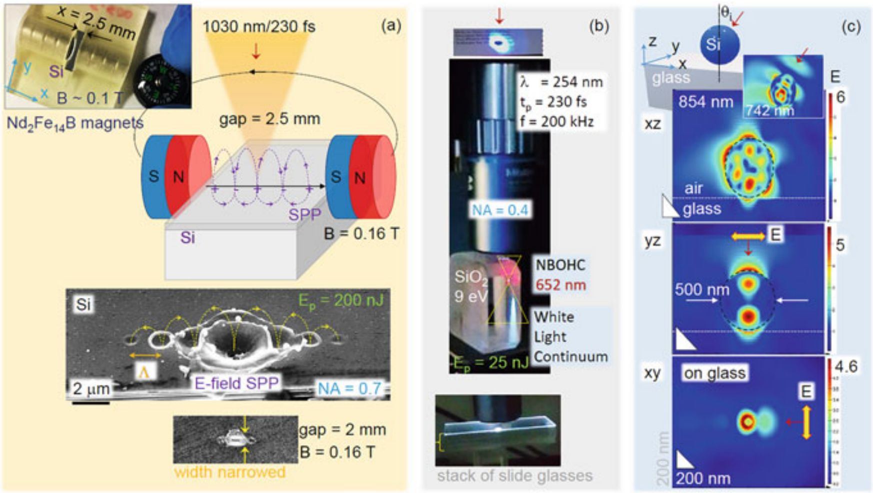
(a)
x = 2.5 mm
y
Si
x
B ~ 0.1 T
Nd2Fe14B magnets
1030 nm/230 fs
gap = 2.5 mm
S N
S N
SPP
Si
B = 0.16 T
Si
Ep = 200 nJ
Λ
2 μm
E-field SPP
NA = 0.7
gap = 2 mm
B = 0.16 T
width narrowed
(b)
λ = 254 nm
tp = 230 fs
f = 200 kHz
NA = 0.4
SiO2
9 eV
NBOHC
652 nm
White
Light
Continuum
Ep = 25 nJ
stack of slide glasses
(c)
θi
z y x
Si
glass
854 nm
742 nm
E
6
xz
air
glass
yz
E
5
500 nm
xy
on glass
E
4.6
200 nm
200 nm

Fig. 12.6 On-surface and in-volume nanoscale modifications/printing. (**a**) Single pulse ablation pit at the focal spot of $1.22\lambda/NA = 1.8$ μm diameter with SPP-type imprint $\Lambda \sim 1$ μm along magnetic B-field lines; E-field lines of the SPP mode are shown by dashed lines. Light intensity was ~43 TW/cm^2/pulse. (**b**) Bond breaking in fused silica SiO$_2$ detectable by luminescence of non-bridging oxygen hole centre (NBHC) Si-O· (bond breaking Si-O··Si); intensity $I_p \approx$ 23.1 TW/cm^2/pulse. Threshold of observable luminescence was 0.2 nJ/pulse or 0.18 TW/cm^2. (**c**) FDTD calculated E-field enhancement at different cross sections of a Si-sphere of 0.5 μm diameter of glass under a slanted $\theta_i = 30°$ incidence. See text for details

deposition $l_{an} < 100$ nm is at $2N_{cr}$. This takes place at a small portion of the entire sub-1-ps pulse with an optical cycle ~ 3 fs.

The discussion in this section was focused on dielectrics and further developed for metals, with the main difference being that the ablation threshold occurs when the absorbed energy is in excess of the binding energy and electron work function $(\epsilon_B + \phi_{esc})$ [6]. The analysis presented was applied to the discussion of experimentally observed small-period ripple (LIPSS) formation in GaN as a SPP mode imprint on the plasma–GaN interface under irradiation from the air side [11]. The ripple period is taken as $\Lambda = \lambda_{sp}/2$ and is presented as a standing wave imprint or a formation of two counter-propagating SPPs forming a stationary interference field with period $\Lambda = \lambda_{sp}/(2\sin\frac{\theta}{2}) = \lambda_{sp}/2$ for the mutual angle between two SPP waves $\theta = \pi$. The orientation and direction of SPPs are defined by the polarisation of the incident E-field (only TM mode can launch the SPP [12]) and energy-axis mirror symmetry presented by the light cone in Fig. 12.1.

Figure 12.6a shows a laser ablated pit made with a single 1030 nm/230 fs pulse, focused into a 1.8 μm-diameter area with the sample placed inside magnetic B-field [13]. The signature of the SPP-affected Si–air surface is evident and up to 10 times larger than the original energy deposition area. SEM images revealed the period of the pattern as $\Lambda \approx \lambda_{sp}/2 \sim 1$ μm aligned along B-field. In a stronger B-field (smaller gap x in (a)), ablation structures become elongated and narrowed as would be expected from a smaller cyclotron radius—electrons move along magnetic field lines in a spinning trajectory of radius $r_c = \frac{mv}{qB}$.

Another example where plasmonic formation character is discussed is the 3D patterning of sub-wavelength ($\lambda/20 - \lambda/4$) structures of period $\Lambda = 20 - 200$ nm inside the volume of glass or crystal under multi-pulse exposure (see Chapters 5_Rudenko and 10_Cheng). Formation of the plasma region (required for the Die–Met change in permittivity) in the tightly focused laser pulse starts from direct bond breakage upon electronic excitation. In wide bandgap materials such as fused silica $E_g \approx 9$ eV, cleaving of Si-O-Si bonds and creation of non-bridging oxygen hole centres (NBOHC) Si-O· [14] are visualised by the emission of 1.9 eV red light. This occurs in the focal volume of the fs-laser pulse at the wavelength corresponding to $E_g/2$, when two-photon absorption of the silica host is induced (Fig. 12.6b). Nanogratings perpendicular to the linear polarisation of the incident light are formed in the focal region and can be patterned via beam/sample scanning over the required region with 3D direct write flexibility (similar as ripples on Si surface shown in Fig. 12.5).

For both surface and bulk irradiation at ENZ conditions (Fig. 12.6a,b), coupling of the laser pulse at normal incidence into SPP mode requires phase matching (Fig. 12.1), which is relaxed when redirection/scattering light source becomes small, sub-wavelength. For example, a nanoparticle can act as a dipole and redirect light into the surface wave SPP (plasmonic response of a nanoparticle is discussed in Sect. 4). Figure 12.6c shows light field redistribution and enhancement of a 1-µm-diameter Si- sphere on glass ($n = 1.5$) under a linearly polarised wave at an angle of incidence $\theta_i = 30°$. Central cross sections and intensity maps at the glass interface reveal light localisation to tens-of-nm and its redirection, including reflection. This illustration shows that nanoscale localisation of light is expected for objects with size comparable to the wavelength and focal volumes of tightly focused laser pulses with lateral cross section $\sim \lambda/NA$ (a diffraction- limited focal spot). Considering the resonant nature of such scattering, it is strongly dependent on angle of incidence and the wavelength linked to the permittivities in the interaction region. Again, it is an illustration that permittivity guides the light–matter interaction, which is constant theme of this chapter. The permittivity considered here (Eq. (12.3)) can also include Kerr nonlinearity by setting $\varepsilon_{nl} = \varepsilon_K I$ with $\varepsilon_K = 2\sqrt{\varepsilon_i} n_2$ [cm^2/W] [3].

4 Nanoparticles in High Intensity Laser Field

Next, light interaction with true nanoscale sized particles $\leq$100 nm is discussed. The fast evolving light energy deposition, from defect generation (Fig. 12.6b) to dielectric breakdown $Re(\varepsilon) = 0$, occurs during only a fraction of the ultra-short laser pulse $t_p \approx 300$ fs. It is instructive to analyse light interaction with plasmonic (metallic or plasma) nano-volume; the collective effects of light scattering by nanoparticles at the ripple LIPSS formation conditions are actively discussed in Chapter 5_Rudenko.

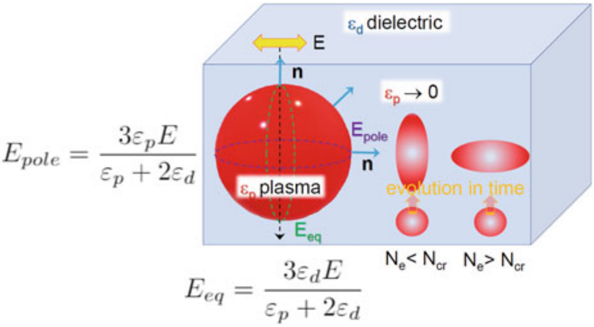
ε_d dielectric
E
n
$\varepsilon_p \rightarrow 0$
E_{pole}
n
ε_p plasma
evolution in time
E_{eq}
$N_e < N_{cr}$
$N_e > N_{cr}$
$E_{pole} = \frac{3\varepsilon_p E}{\varepsilon_p + 2\varepsilon_d}$
$E_{eq} = \frac{3\varepsilon_d E}{\varepsilon_p + 2\varepsilon_d}$

Fig. 12.7 Schematics of the local fields E_{eq} and E_{pole} near plasma nano-sphere dependent on ε_r, according to Eq. (12.14). Depending on the plasma density, the local field will be larger at equator or poles driving ionisation of host material at the interface

Analytical formulas describing the local field distribution around plasma nanospheres are derived following tutorial Ref. [15] with the notations given in Fig. 12.7. It was previously discussed [16] that a plasma nano-sphere can be created in a subsurface volume under irradiation by high intensity laser pulses and be related to ripples = formation [17].

As a model, let us consider plasma-like nano-spheres $\sim$20 nm that are surrounded by a dielectric environment with their size being much smaller compared to the laser wavelength ($\lambda \sim 1\ \mu$m), so electrostatic theory can be used to determine local field distribution around the plasma nano-sphere (Fig. 12.7). This field distribution drives evolution of ionisation and plasma formation upon absorption of the incident laser pulse at the plasma–host interface.

Electrical potential φ_{out} outside the dielectric sphere with radius R in the presence of uniform external electric field **E** can be expressed as [15]

$$\varphi_{out} = -\mathbf{E}r\cos\Theta + \frac{\varepsilon_r - 1}{\varepsilon_r + 2}\frac{|\mathbf{E}|R^3}{r^2}\cos\Theta, \tag{12.11}$$

where Θ is the angle between external electric field **E** and normal of the sphere surface **n**, and $\varepsilon_r = \frac{\varepsilon_p}{\varepsilon_d}$ is the relative permittivity expressed as the ratio between plasma's ε_p and dielectric ε_d surrounding. The φ_{out} potential describes a superposition of the applied E-field (by light) and that of a dipole located at the particle's centre. The formula for the corresponding local electric field outside the sphere E_{loc} in polar coordinates (unit vectors $\mathbf{e_r}$, $\mathbf{e_\theta}$) is calculated using $E_{loc} = -\nabla\varphi_{out}$ equation, which results in

$$E_{loc} = \frac{3\mathbf{E}}{\varepsilon_r + 2}(\varepsilon_r\cos\Theta e_r - \sin\Theta e_\theta). \tag{12.12}$$

The local field outside the plasma sphere near the equator, E_{eq} (at $\Theta = \pi/2$), and poles, E_{pol} ($\Theta = 0,\ \pi$), is respectively

$$E_{eq} = \frac{3\mathbf{E}}{\varepsilon_r + 2}, \quad E_{pole} = \frac{3\varepsilon_r \mathbf{E}}{\varepsilon_r + 2}, \tag{12.13}$$

or using ε_d and ε_p takes form:

$$E_{eq} = \frac{3\varepsilon_d \mathbf{E}}{\varepsilon_p + 2\varepsilon_d}, \quad E_{pole} = \frac{3\varepsilon_p \mathbf{E}}{\varepsilon_p + 2\varepsilon_d}. \tag{12.14}$$

The absolute value of Eq. (12.12) is given by

$$E_{loc} = \frac{3\mathbf{E}}{\varepsilon_r + 2}\sqrt{1 + (\varepsilon_r^2 - 1)\cos^2\Theta} \quad , \tag{12.15}$$

or using ε_d and ε_p:

$$E_{loc} = 3\mathbf{E}\frac{\sqrt{\varepsilon_d^2 - (\varepsilon_d^2 - \varepsilon_p^2)\cos^2\Theta}}{\varepsilon_p + 2\varepsilon_d}. \tag{12.16}$$

The local field enhancement factor, D, defined as the ratio between fields near equator and poles, is equal to the ratio between dielectric material and plasma permittivity:

$$D = \frac{E_{eq}}{E_{pol}} = \frac{\varepsilon_d}{\varepsilon_p} = \frac{1}{\varepsilon_r}, \tag{12.17}$$

where ε_r is a relative permittivity. For a metallic/plasma nano-volume in a dielectric host under critical plasma conditions, $0 < \varepsilon_r < 1$ (or $0 < \varepsilon_p < \varepsilon_d$). Under these conditions, the local E-field is stronger near the equator compared to the poles; hence, $D > 1$ (Fig. 12.7). Plasma permittivity depends on electron density $\varepsilon_p = 1 - N_e/N_{cr}$ and is decreasing upon photo-excitation. As N_e increases and plasma permittivity ε_p decreases, it reaches 0 at breakdown. At this condition, Eq. (12.17) predicts that field enhancement, D, is at a maximum. If critical electron density is further increased, D decreases, and at $\varepsilon_r < -1$, field becomes stronger near poles and plasma growth direction changes from normal to parallel to the surface (Fig. 12.7). The local field can also be presented via the enhancement factor $L = \frac{3}{\varepsilon_r + 2}$, which is explicitly presented via permittivities in Eq. (12.14). The local field enhancement is directly related to the surface-enhanced Raman scattering (SERS).

It is noteworthy that the local field E_{eq} or E_{pole} is growing at the $-|\varepsilon_p| = 2\varepsilon_d$, the so-called Frölich condition when the denominator in Eq. (12.14) approaches zero. The local E-field bound to the interfaces of micro-volumes can reach large enhancements of 10 – 50 times and localisation down to tens-of-nm as shown by FDTD, which is exact the solution of Maxwell's equations (Figs. 12.4 and 12.6c).

Light scattering from single 100-nm-diameter nano-spheres of different materials is shown in Fig. 12.7 calculated by FDTD (Lumerical). The pattern of dipole scattering emerges around the laser-driven plasmon, localised on the nano-sphere, i.e., light is not emitted along the dipole axis (E-polarisation) and has a toroidal distribution perpendicular to the dipole. A perfect electrical conductor represents material with **E** = 0 within it and has 100% reflection and 0% absorption. The empty space (etch) sample simulates an empty nano-sphere inside glass host. At $\lambda = 925$-nm wavelength, all 100-nm spheres show the same geometry of light redistribution around it. However, the empty (etch) sample shows light intensity is enhanced inside it as compared to the glass side of the interface (similar case is discussed in Sect. 5 for nano-hole on a surface). The calculated cross sections have extensions smaller than the wavelength of light and show how such oscillating dipoles act for light redirection and can deliver the required phase matching (Fig. 12.1). Nanoparticles smaller than the wavelength of light have scattering C_{sc} and absorption C_a cross sections dependent on the polarisability α [12] (Fig. 12.8):

$$C_{sc} = \frac{1}{6\pi}\left(\frac{2\pi}{\lambda}\right)^4 |\alpha|^2; \quad C_a = \frac{2\pi}{\lambda} Im(\alpha); \quad \alpha = 3V\frac{\varepsilon_m - \varepsilon_d}{\varepsilon_m + 2\varepsilon_d}, \tag{12.18}$$

where V is the volume of nanoparticle with permittivity ε_m in the dielectric host ε_d. The plasmon resonance localised on a nanoparticle is dependent on the particle size and shape. For spherical metallic nanoparticles, the Maxwell–Garnett (MG)

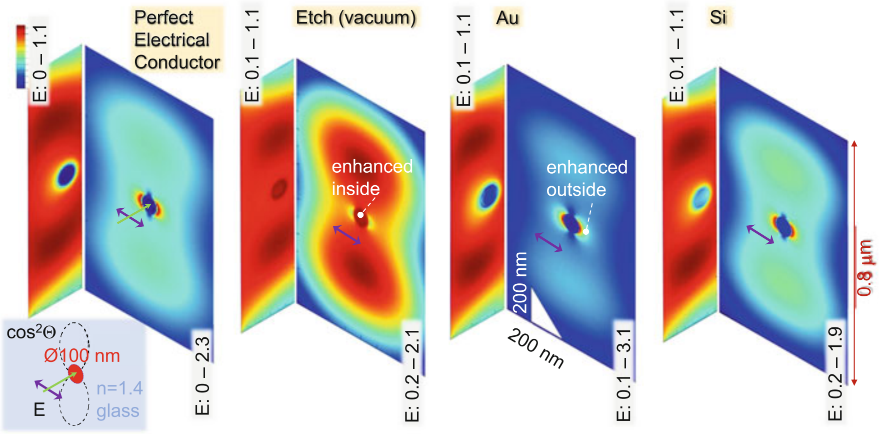

Fig. 12.8 FDTD simulation of light field distribution around 100-nm-diameter nanoparticles of different materials inside silica glass ($n = 1.4$). Incident plane wave of linearly polarised light of wavelength 925 nm; E-field of the incident light $|E_0| = 1$, Si and Au properties are from the Lumerical database. Dipole scattering nature is recognisable as a $\cos^2\theta$ intensity profile; the vertical extension of the image is $\sim \lambda$

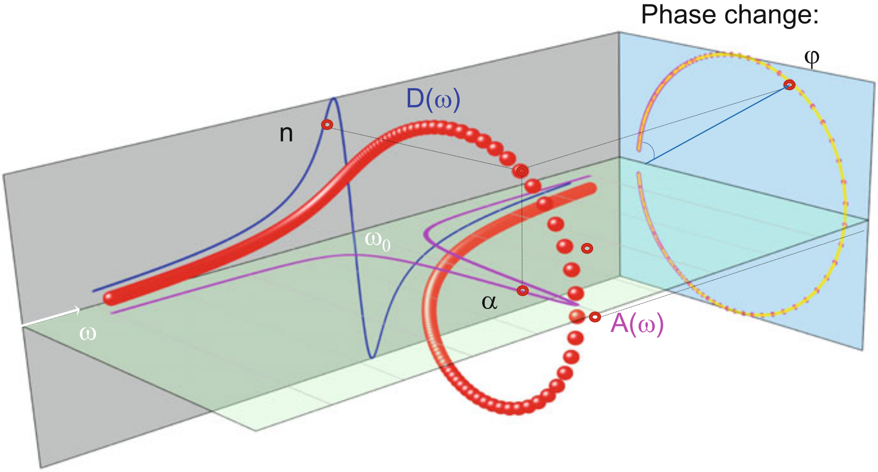

Fig. 12.9 Absorption $A(\omega) = \tau/(1+(\omega-\omega_0)^2\tau^2)$ and dispersion $D(\omega) = (\omega-\omega_0)\tau^2/(1+(\omega-\omega_0)^2\tau^2)$ line shapes for the Lorentzian oscillator near resonance ω_0 [9]; τ is the relaxation time. Real part of the refractive index n and imaginary part κ are inter-related; absorption coefficient $\alpha = 4\pi\kappa/\lambda$ [cm^{-1}]

medium theory defines the effective permittivity dependent on the volume fraction F of nanoparticles as $\varepsilon_{MG} = \varepsilon_d \frac{3+2F\alpha'}{3-F\alpha'}$, where α' is the constant proportional to the polarisability of nanoparticles [18]. The resonant plasmon absorption wavelength of the localised plasmon is then given as [18]

$$\lambda_{3D} = \lambda_p \sqrt{1 + \left(\frac{F+2}{1-F}\right) n_s^2}, \qquad (12.19)$$

where n_s is the refractive index surrounding MG medium. This wavelength and the corresponding frequency can be considered as a localised 3D plasmon, while the SPP mode is the 2D plasmon and bulk plasmon with λ_p (ω_p frequency, e.g., $\lambda_p = 131$ nm for Au). In all those cases of 1D, 2D, and 3D plasmonic resonances, the absorbance spectral line shape can be considered as the Lorentzian where the real and imaginary parts of the refractive index (and permittivity) are inter-related as shown in the complex plane presentation (Fig. 12.9) to reveal phase evolution in the vicinity of resonance [9].

5 Nanolithography by Direct Write with Optical Near Field

The localisation and enhancement of light intensity within a hollow 100-nm-diameter nano-void (vacuum case in Fig. 12.8) make it possible to ionise the inner

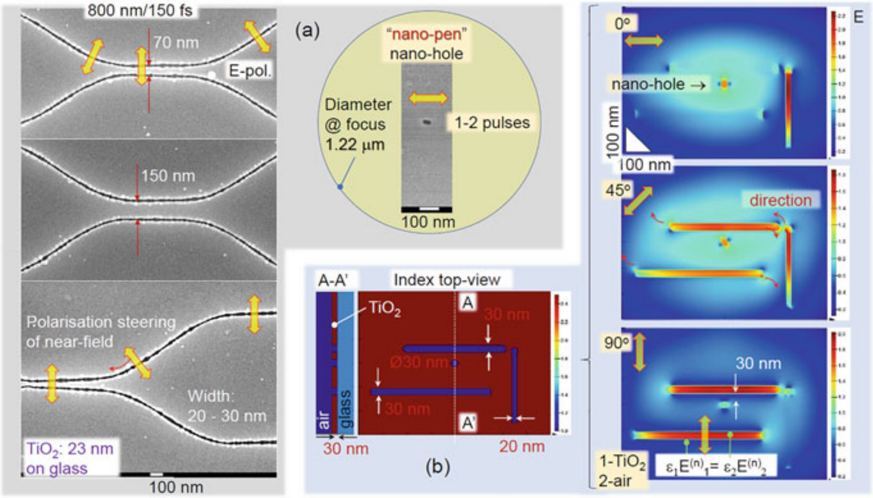
800 nm/150 fs
70 nm
E-pol.
150 nm
Polarisation steering of near-field
Width: 20 - 30 nm
TiO$_2$: 23 nm on glass
100 nm
(a)
"nano-pen" nano-hole
Diameter @ focus 1.22 μm
1-2 pulses
100 nm
A-A'
Index top-view
TiO$_2$
A
30 nm
Ø30 nm
30 nm
A'
air
glass
30 nm
20 nm
(b)
0°
nano-hole →
100 nm
100 nm
45°
direction
90°
30 nm
1-TiO$_2$
2-air
$\varepsilon_1 E^{(n)}_1 = \varepsilon_2 E^{(n)}_2$
E

Fig. 12.10 Nano-hole—"nano-pen" [19]: polarisation steering of optical near field (experiment (**a**) and numerical model (**b**)). (**a**) SEM images of nano-grooves ablated by near field enhanced inside a nano-hole, which was initiated by irradiation of 1-2 threshold intensity pulses. (**b**) FDTD light field enhancement simulations for nano-grooves and a nano-hole showing E-field enhancement dependent on polarisation (**a** cool–hot colour scale); wavelength of light $\lambda = 794$ nm and a refractive index of TiO$_2$, and glass substrates were set to $n = 2.5$ and 1.4 values, respectively (see text for details)

glass–vacuum interface. This is similar to the ionisation of the surrounding host by a metallic/plasma nanoparticle (Fig. 12.7; the interface from the outside of nanoparticle). It is exactly this principle of light localisation and enhancement inside a nano-hole 20–30 nm in diameter that was used as a "nano-pen", which inscribed nano-grooves of the similar $\sim 20 - 30$-nm width throughout the entire thickness of a TiO$_2$ film of 23 nm deposited on a glass substrate [19]. This direct write nanolithography (Fig. 12.10a) is realised as a "nano-pen", which is steered by linear polarisation of a fs-laser beam focused onto a 1.2 μm focal spot ($NA = 0.8$, $\lambda = 0.8$ μm) with a nano-film of titania acting as a "resist". Interestingly, nano-grooves can be written as close as width of the groove. The reason for such performance is revealed by the FDTD simulations in Fig. 12.10b. A nano-hole (at the centre of the calculation field) of 30-nm diameter, along with grooves with orientations (vertical or horizontal), widths (20 or 30 nm), and end shapes (rounded or rectangular) was illuminated at $\lambda = 794$ nm by a plane wave (no focusing). Light field enhancement inside the nano-hole and nano-grooves depends on mutual orientation of linear polarisation (E-field) and the nano-void. For the nano-hole, the light intensity is the largest inside it and has a sudden drop just across the interface into titania along the E-field orientation. For nano-grooves, enhancement is expressed more when the groove is perpendicular to the polarisation. For grooves aligned to the E-field, there is almost no enhancement (barely recognisable in Fig. 12.10b).

In both nano-hole and nano-groove cases, the reason for light enhancement and its polarisation dependence is the boundary condition to the normal components for the displacement $D^{(n)}$. $D_2^{(n)} - D_1^{(n)} = \sigma$ for the interface between two materials titania (1) and air (2), where σ is the surface charge density (unbound charges or free); another condition is continuity of the tangential components $E_1^{(t)} = E_2^{(t)}$. For the dielectrics discussed here, $\sigma = 0$ and $\varepsilon_1 E_1^{(n)} = \varepsilon_2 E_2^{(n)}$. This boundary condition is based on the E-field strength that is the product of $\mathbf{E} \cdot \mathbf{n_{12}} = E \cos\theta$. With $\mathbf{n_{12}}$ being the normal to the interface, it defines the steering capability of the optical near field upon illumination (see arrow markers in $\theta = \pi/4$ calculated light field in Fig. 12.10b). The intensity $I \equiv \mathbf{E}^2$ and the dipole pattern of intensity $\cos^2\theta$ open the possibility to redirect the maximum intensity at the interface by changing the linear polarisation orientation of the illumination. For the titania–air boundary ($n_1 = 2.5$ vs. $n_2 = 1$), the light intensity inside the air gap (2) is enhanced with respect to the field inside titania (1) by $I_2 = |E_2|^2 = \left(\frac{n_1^2}{n_2^2}\right)^2 E_1^2 \approx 39 I_1$. This is immense enhancement in the near field and is harnessed to ablate nano-grooves by direct laser writing (Fig. 12.10a). Figure 12.10b also reveals that close proximity ablation of nano-grooves does not cause light field enhancement between the nano-hole and nano-groove (see $\theta = \pi/2$ panel). Conversely, a lower light field intensity occurs between them. The FDTD calculations are made for plane wave incidence, while the actual nano-ablation (a) was made with a focused fs-laser beam into a $\sim 1.2\ \mu$m focal spot (see circle in (a) overlaid with SEM image of nano-hole). When the laser pulse energy was changed by only ~10%, no ablation of pristine titania film took place. The enhancement in a nano-hole by more than 20% above or below the ablation threshold can be well controlled during writing. This experimental observation is well supported by the FDTD intensity distribution maps at the tips of grooves (sharp or rounded tips do not cause fundamental differences in steering and enhancement of the near fields).

Direct fs-laser writing at the nanoscale using optical near-field enhancement, which is directed and steered by the polarisation orientation of the incoming beam, has the distinct advantage of avoiding proximity effects encountered in particle beam lithographies (electron and ion e/i)—where resist exposure by secondary electrons reduce resolution. Noteworthy, even though the single feature size in e/i-beam lithographies can be a few nm, the resolution when two lines/dots have to be defined close together in the resist suffers from the proximity effects. In the as-described nano-pen lithography (branded as optical-focused ion beam (O-FIB) [19]), the proximity issue is resolved naturally, and laser focal spot does not determine the resolution of nano-patterning. This approach is vacuum-less and can be carried out with indefinite write fields (no stitching required). There is a good practical tolerance of nano-pen writing for the axial displacement of laser focus due to the focal spot having typical $axial/lateral \sim 3\ \mu\text{m}/1\ \mu\text{m}$ dimensions. Hence, the technique is applicable to curved surfaces and works with dry optics ($NA < 1$) required for fast beam/sample scanning. The demonstrated principle used a 23-nm-thick titania film on glass [19]. This helped produce a large field enhancement $n^4 \approx 40$ due to large refractive index $n = 2.5$ of titania. However, the demonstrated principle of the enhancement is present even for a nano-hole on the surface of any material. It is best illustrated in the 3D void case in Fig. 12.8 where the nano-void is surrounded by the same host medium. A single nano-line was recorded using ablation on sapphire [20] by starting with ablation of ripples and reducing the laser pulse energy to form a single nano-groove. It is noteworthy that there is no E-field enhancement expanding into substrate (Fig. 12.10b) or air (not shown here for brevity), which is a welcome feature. This is especially relevant for electronic materials that can be damaged with high-energy ∼100 keV electron beams used in high-resolution e-beam lithography or material implantation as is the case for i-beam lithography [21].

In order to guide nano-ablation to within the hole/groove, the working recipe for this optical direct write near-field nano-pen is: 1. make a seed nano-hole/void, 2. use at slightly lower laser pulse energy during scanning/writing, 3. steer the ablation trace by polarisation of incoming laser beam. Polarisation steering was the same as for surface patterning (Fig. 12.5) control by rotating a $\lambda/2$-waveplate along the scan trajectory. With increasing complexity and versatility of combined electron, ion, photon micro-fabrication tools [22], there are different methods for how to create a seed nano-hole to be used in nano-pen writing. Such a nano-hole is a structure that grows into ripples under multiple irradiations as shown in lithium niobate [23] (see Chapters 11_Boneberg and 8_Florian for material modification by near-fields enhanced by nanoparticles).

Writing speed can be high and almost debris-free due to minute material removal. The velocity of air molecules at normal conditions is $v_{rms} = \sqrt{3k_BT/m}$, i.e., 480 m/s for O_2 and 510 m/s for N_2. During a laser pulse of $t_p = 1$ ps, N_2 molecules only move 0.5 nm. The free path of molecules is $l_f = 1/(\sqrt{2}\pi n_0\sigma) = k_BT/(\sqrt{2}\pi p\sigma)$, where the n_0 is the number density of molecules, $\sigma = a^2$ is the cross section of molecules defined by their size a, p is the pressure, k_B is the Boltzmann constant, and T is the absolute temperature. The value of $l_f \approx 60$ nm in air with $n_0 = 2.69 \times 10^{19}$ cm^{-3}. During a sub-1-ps laser pulse used to write 20-nm width lines, the movement of molecules in air is less than 0.5 nm under ambient conditions. The cross sections for the light–matter interaction volume are smaller than l_f^3, and so there is an equivalence to close-to-vacuum conditions during laser fabrication during this nano-pen writing. Low molecular number density in the light–matter interaction volume is always advantageous for high-precision nanofabrication and nanolithography.

6 Localisation of Energy Deposition

The common feature of the plasmonic nature of nanoprinting is the 3D localisation of energy deposition into the skin depth $l_{ab} = \lambda/(4\pi\kappa)$. How much light energy is absorbed is also dependent on the portion of reflected light $R = f(n,\kappa)$. In the case of nanolithography with a nano-pen, light localisation was delivered by an empty/void nanostructure. In all the 3D, 2D, and 1D cases discussed, optical near field is the way for light concentration and localisation. We have shown that the volumetric energy density $Energy/Volume$ ~J/mm^3 is the right measure for the additive mode of 3D$^{(+)}$ printing by ultra-short laser pulses [24], e.g., in the case of polymerisation.

In the case of ablation (3D$^-$ fabrication), fine tuning of the optimum ablation rate is achieved by changing the pulse number per irradiation spot, using beam scanning [25], and control over the number of pulses per burst [26]. For comparison of different fabrication conditions, the volume [mm^3] ablated per 1 W average power per min: V_a ~mm^3/W/min ~ mm^3/(W.s) ~ mm^3/J is used. This is the ablated volume per energy delivered by the laser for subtractive machining (3D$^{(-)}$ printing). It is not surprising that accounting for the energy deposition in the light–matter interaction volume is the essential measure for both the additive and subtractive 3D$^{(+)}$ and 3D$^{(-)}$ modes of 3D fabrication.

New modes of laser operation bring the capability of combining ultra-short pulses into MHz-GHz bursts with a controlled number of pulses per burst [26]. It was shown that this burst mode of operation delivers ablation rates for metal and dental tissue on the order of 3 mm^3/min. This is the rate that reaches that of current electrical discharge machining/grinding (EDM/G) computer numerical control (CNC) tools. This parity between material removal rate by discharge spark and laser beam was achieved in 2016. The burst mode advantage is the ability to fine tune material removal to the most efficient fluence [J/cm^2] [27], which was empirically determined to be $e^2 = 7.4$ times larger than the ablation threshold for the given material [28]. This scaling is consistent with optical energy delivery into the skin depth, rather than ablation via heating of the irradiated and surrounding volume, which is the case for longer pulses.

Among other examples of plasmonic modification of materials are photo-reduction of Ag in a polymer and SPP imprint [29], localised plasmon-induced polymerisation in nano-gaps [30, 31], and polymerisation enhancement at the tips of black-Si [32].

7 Conclusions and Outlook

Since the year 2000, the average laser power of ultra-short (sub-1 ps)-pulsed lasers has increased as $Power = 2^{N/2}$ with N—the number of the years from beginning of the trend, which parallels Moore's law for the number of transistors in an integrated circuit (based on amplitude report of ultra-short laser product line [33]). Parallels can be drawn between photons and transistors, with laser units reducing in size while increasing the number of photons in time (intensity in the number of photons per time $N \times \hbar\omega/t_p$ [W]). Miniaturisation has been the driving force of Moore's law for last 50 years in microelectronics. One can expect the same impact for ultra-short-pulsed lasers, increasing and expanding laser processing for high-speed and large surface areas (or volume modification). Ultra-short laser pulses can control energy deposition in both time and space down to the nanoscale, driving local modification via melting, evaporation, and ablation. With this flexibility, applications are expected to grow.

Acknowledgments This work was supported by the ARC Discovery DP190103284 and Linkage LP190100505 projects. SJ is grateful to Workshop of Photonics for the technology transfer project and fs-laser industrial 3D printing setup based on PHAROS laser.

References

1. R.L. Olmon, B. Slovick, T.W. Johnson, D. Shelton, S.-H. Oh, G.D. Boreman, M.B. Raschke, Optical dielectric function of gold. Phys. Rev. B **86**, 235147 (2012)
2. E.G. Gamaly, A.V. Rode, Ultrafast re-structuring of the electronic landscape of transparent dielectrics: new material states (Die-Met). Appl. Phys. A **124**, 278 (2018)
3. E.G. Gamaly, A.V. Rode, Transient optical properties of dielectrics and semiconductors excited by an ultrashort laser pulse. J. Opt. Soc. Am. B **31**, C36 (2014)
4. R. Parker, *Introduction to Plasma Physics I* (MIT OpenCourseWare, MIT, Lecture notes, 2006)
5. B. Farid, R.W. Godby, Cohesive energies of crystals. Phys. Rev. B **43**, 14248–14250 (1991)
6. E.G. Gamaly, A.V. Rode, B. Luther-Davies, V.T. Tikhonchuk, Ablation of solids by femtosecond lasers: Ablation mechanism and ablation thresholds for metals and dielectrics. Phys. Plasmas **9**, 949 (1991).
7. S. Juodkazis, K. Nishimura, S. Tanaka, H. Misawa, E.E. Gamaly, B. Luther-Davies, L. Hallo, P. Nicolai, V. Tikhonchuk, "Laser-induced microexplosion confined in the bulk of a sapphire crystal: Evidence of multimegabar pressures. Phys. Rev. Lett. **96**, 166101 (2006)
8. E.E. Gamaly, S. Juodkazis, K. Nishimura, H. Misawa, B. Luther-Davies, L. Hallo, P. Nicolai, V. Tikhonchuk, Laser-matter interaction in a bulk of a transparent solid: confined microexplosion and void formation. Phys. Rev. B **73**, 214101 (2006)
9. A.G. Marshall, Dispersion vs. absorption (DISPA): A magic circle for spectroscopic line shape analysis. Chemom. Intell. Lab. Syst. **3**, 261–275 (1988).
10. L. Wang, Q.-D. Chen, X.-W. Cao, R. Buividas, X. Wang, S. Juodkazis, H.-B. Sun, Plasmonic nano-printing: large-area nanoscale energy deposition for efficient surface texturing. Light: Sci. Appl. **6**, e17112 (2017)
11. K. Miyazaki, G. Miyaji, Nanograting formation through surface plasmon fields induced by femtosecond laser pulses. J. Appl. Phys. **114**, 153108 (2013).
12. S.A. Maier, *Plasmonics: Fundamentals and Applications*. (Springer, Berlin, 2007)
13. J. Maksimovic, S. Ng, T. Katkus, B. Cowie, S. Juodkazis, External field-controlled ablation: Magnetic field. Nanomaterials **9**, 1662 (2019)
14. S.S. Mao, F. Qu(́e)r(́e), S. Guizard, X. Mao, R.E. Russo, G. Petite, P. Martin, Dynamics of femtosecond laser interactions with dielectrics. Appl. Phys. A **79**, 1695–1709 (2004)
15. L. Grechko, V. Sugakov, O. Tomasevich, A. Fedorchenko, *Sbornik zadach po teoreticheskoj fizike* (Vysshajashkola, Moskva (in Russian), 1972)
16. R. Buividas, L. Rosa, R. Šliupas, T. Kudrius, G. Šlekys, V. Datsyuk, S. Juodkazis, "Mechanism of fine ripple formation on surfaces of (semi)transparent materials via a half-wavelength cavity feedback. Nanotechnology **22**, 055304 (2011)
17. R. Buividas, M. Mikutis, S. Juodkazis, External field-controlled ablation: Magnetic field. Prog. Quantum Electron. **38**, 119–156 (2014)
18. V.N. Rai, A.K. Srivastava, C. Mukherjee, S.K. Deb, Surface enhanced absorption and transmission from dye coated gold nanoparticles in thin films. Appl. Optics **51**, 2606–2015 (2012)

19. Z.-Z. Li, L. Wang, H. Fan, Y.-H. Yu, Q.-D. Chen, S. Juodkazis, H.-B. Sun, O-FIB: far-field-induced near-field breakdown for direct nanowriting in an atmospheric environment. Light Sci. Appl. **9**, 41 (2020)
20. R. Buividas, S. Rekštytė, M. Malinauskas, S. Juodkazis, Nano-groove and 3D fabrication by controlled avalanche using femtosecond laser pulses. Opt. Mat. Express **3**, 1674–1686 (2013)
21. G. Seniutinas, A. Balčytis, I. Rėklaitis, F. Chen, J. Davis, C. David, S. Juodkazis, Tipping solutions: emerging 3D nano-fabrication/-imaging technologies. Nanophotonics **6**, 923–941 (2017)
22. M.P. Echlin, M. Straw, S. Randolph, J. Filevich, T.M. Pollock, The TriBeam system: Femtosecond laser ablation in situ SEM. Mater. Charact. **100**, 1–12 (2015)
23. H. Shimizu, G. Obara, M. Terakawa, E. Mazur, M. Obara, Evolution of femtosecond laser-induced surface ripples on lithium niobate crystal surfaces. Appl. Phys. Express **6**, 112701 (2013)
24. E. Skliutas, M. Lebedevaite, E. Kabouraki, T. Baldacchini, J. Ostrauskaite, M. Vamvakaki, M. Farsari, S. Juodkazis, M. Malinauskas, Polymerization mechanisms initiated by spatio-temporally confined light. Nanophotonics **10**, 1211–1242 (2021)
25. E. Vanagas, J. Kawai, D. Tuzilin, I. Kudryashov, A. Mizuyama, K.G. Nakamura, K.-I. Kondo, S.-Y. Koshihara, M. Takesada, K. Matsuda, S. Juodkazis, V. Jarutis, S. Matsuo, H. Misawa, Glass cutting by femtosecond pulsed irradiation. J. Microlith. Microfab. Microsyst. **3**, 358–363 (2004)
26. C. Kerse, H. Kalaycıoğlu, P. Elahi, B. Çetin, D. Kesim, O. Akçaalan, S. Yavaş, M. Aşık, B. Öktem, H. Hoogland, R. Holzwarth, F. Ilday, Ablation-cooled material removal with ultrafast bursts of pulses. Nature **537**, 84–88 (2016)
27. D. Förster, B. Jäggi, A. Michalowski, B. Neuenschwander, Review on experimental and theoretical investigations of ultra-short pulsed laser ablation of metals with burst pulses. Materials **14**, 3331 (2021)
28. N. Hodgson, A. Steinkopff, S. Heming, H. Allegre, H. Haloui, T. Lee, M. Laha, J. VanNunen, Ultrafast laser machining: process optimization and applications, in *SPIE Laser Applications in Microelectronic and Optoelectronic Manufacturing (LAMOM) XXVI*, vol. 11673 (SPIE, Bellingham, Washington, USA, 2021) pp. 11673–08
29. Y.-K. Sun, L. Wang, M. Kamano, S. Juodkazis, Plasmonic nano-imprinting by photo-doping. Opt. Lett. **43**, 3786–3789 (2018)
30. K. Ueno, S. Juodkazis, T. Shibuya, Y. Yokota, V. Mizeikis, K. Sasaki, H. Misawa, Nanoparticle plasmon-assisted two-photon photopolymerization induced by incoherent excitation source. J. Am. Chem. Soc. **130**, 6928–6929 (2008)
31. K. Ueno, S. Juodkazis, T. Shibuya, V. Mizeikis, Y. Yokota, H. Misawa, Nano-particle-enhanced photo-polymerization. J. Phys. Chem. C **113**, 11720–11724 (2009)
32. A. Žukauskas, M. Malinauskas, A. Kadys, G. Gervinskas, G. Seniutinas, S. Kandasamy, S. Juodkazis, "Black silicon: substrate for laser 3D micro/nano-polymerization. Optics Express **21**, 6901–6909 (2013)
33. E. Mottay, Femtosecond lasers for high throughput surface engineering, in *SPIE Photonics West Industry*, vol. 11768 (SPIE, Bellingham, 2021), pp. 11768–11707

Chapter 13

Search for High-Pressure Silicon Phases: Reaching the Extreme Conditions with High-Intensity Laser Irradiation

Ludovic Rapp, Takeshi Matsuoka, Konstantin L. Firestein, Daisuke Sagae, Hideaki Habara, Keiichiro Mukai, Kazuo A. Tanaka, Eugene Gamaly, Ryosuke Kodama, Yusuke Seto, Takahisa Shobu, Aki Tominaga, Lachlan Smillie, Bianca Haberl, Tatiana Pikuz, Toshinori Yabuuchi, Tadashi Togashi, Yuichi Inubushi, Makina Yabashi, Saulius Juodkazis, Dmitri V. Golberg, Andrei V. Rode, and Norimasa Ozaki

Abstract Controlling electronic and optical properties of semiconducting materials could substantially expand their functionality and enable new pathways for the formation of 'smart' materials for emerging innovative applications. An emerging new path for the synthesis of exotic silicon (Si) polymorphs is irradiation of bulk diamond-cubic Si by ultrashort laser pulses at relativistic intensity above 10^{19} W/cm^2. Exotic polymorphs are formed due to interaction with MeV-energy electrons generated in laser-produced high-temperature plasma state. The unusual Si structures are found in the form of 5–10 nm nanoparticles confined deep in the bulk of 500-μm-thick Si samples. Raman spectroscopy, electron microscopy and X-ray diffraction studies provide an unequivocal evidence of exotic Si phase formation. A key advantage of such relativistic irradiation lies thereby in the fact that large quantities of such exotic Si is synthesised embedded within the bulk diamond-cubic Si and that further the formed Si polymorphs are stable at ambient temperature and pressure. They are thus available for further studies for electronic applications in selective band gap engineering.

L. Rapp (✉) · E. Gamaly · L. Smillie · A. V. Rode
Department of Quantum Science and Technology, Research School of Physics, The Australian National University, Canberra, ACT, Australia
e-mail: ludovic.rapp@anu.edu.au

T. Matsuoka · T. Pikuz
Institute for Open and Transdisciplinary Research Initiatives, Osaka University, Suita, Osaka, Japan

K. L. Firestein · D. V. Golberg
Centre for Materials Science and School of Chemistry and Physics, Queensland University of Technology, Brisbane, QLD, Australia

© The Author(s), under exclusive license to Springer Nature Switzerland AG 2023

R. Stoian, J. Bonse (eds.), *Ultrafast Laser Nanostructuring*, Springer Series in Optical Sciences 239, https://doi.org/10.1007/978-3-031-14752-4_13

Keywords Laser-matter interaction at relativistic laser intensity · High-temperature laser-produced plasma · Relativistic electrons · Silicon crystal phases · Phase transformation

1 Introduction

Atoms in common crystals begin to rearrange into new positions under elevated pressure, which results in materials exhibiting unusual properties, and the science of matter formed in these extraordinary new atomic arrangements is now questioning some of our fundamental understanding of physics and chemistry [1–6]. Syntheses of these unconventional polymorphs can only be met through the application of extreme conditions, such as high pressure and temperature, which enable access to new exotic states of matter formed away from equilibrium of the elemental free energy landscape. Local potential energy minima then allow to preserve such new metastable substances for further characterisation and exploitation.

Silicon (Si) is the second-most abundant element on our planet (after oxygen), and fundamental studies of Si allow understanding the evolution of terrestrial planets [7, 8]. It is also an important technological material as it is the most widely used semiconductor. The silicon phases are interesting owing to their electronic

---

D. Sagae · H. Habara · K. Mukai · K. A. Tanaka
Graduate School of Engineering, Osaka University, Suita, Osaka, Japan
e-mail: norimasa.ozaki@eie.eng.osaka-u.ac.jp

R. Kodama · N. Ozaki (✉)
Graduate School of Engineering, Osaka University, Suita, Osaka, Japan

Institute of Laser Engineering, Osaka University, Suita, Osaka, Japan
e-mail: norimasa.ozaki@eie.eng.osaka-u.ac.jp

Y. Seto
Graduate School of Science, Kobe University, Kobe, Hyogo, Japan

T. Shobu · A. Tominaga
Japan Atomic Energy Agency, Chiyoda City, Tokyo, Japan

B. Haberl
Neutron Scattering Division, Neutron Sciences Directorate, Oak Ridge National Laboratory, Oak Ridge, TN, USA

T. Yabuuchi · T. Togashi · Y. Inubushi · M. Yabashi
Japan Synchrotron Radiation Research Institute, Sayo, Hyogo, Japan

RIKEN SPring-8 Center, Sayo, Hyogo, Japan

S. Juodkazis
Optical Sciences Centre and ARC Training Centre in Surface Engineering for Advanced Materials (SEAM), School of Science, Swinburne University of Technology, Hawthorn, VIC, Australia

Tokyo Tech World Research Hub Initiative (WRHI), School of Materials and Chemical Technology, Tokyo Institute of Technology, Meguro City, Tokyo, Japan

properties, which are determined by details of their atomic structures [4, 5]. The energy landscape of Si is rich of local minima, which is a reason for a very strong polymorphism. At least 14 polymorphs of Si have experimentally been made [4–6, 9], suggesting that additional structures may also be kinetically stable at ambient conditions. In the search for such structures, metastable and recoverable to ambient conditions, many highly useful allotropes of Si have been predicted, especially allotropes useful for photovoltaics [10].

In general, the methods used for studying material transformation under high pressure and temperature could be performed in static conditions in diamond anvil cell (DAC) [2], or by nanoindentation [11, 12], and in dynamic conditions of strong shock waves generated by explosives and Mega-Joule-class ns pulse lasers [13]. Applying static pressure gives a possibility for in situ study of the phase transitions at elevated pressure and temperature. However, the synthesis of exotic metastable phases by standard high-pressure devices is limited; it is usually insufficient to overcome the very strong kinetic barriers. The highest pressure of 640 GPa in DAC was demonstrated recently using superhard micro-ball nanodiamonds [14], and a combination of 377 GPa and 5700 K, close to those in Earth's inner core, was recreated in laboratory conditions in a laser-heated diamond-anvil cell [15]. The upper level for high pressure is set by the strength of diamond at about 1 TPa.

Phase transitions into new states at pressure above 1 TPa but in transient conditions have been studied in direct laser drive shock wave compression. These studies uncover the high-pressure equation of state and isentropic sound speed up to 2.1 TPa [13]. The phase transitions into high-pressure polymorphs are evident from the velocity interferometry. The flexibility of adjusting laser pulses energy, temporal shape, duration and intensity allows to precisely control shock wave loading for probing different thermodynamic spaces. The strain rates induced in laser-generated shock waves vary from about 10^6 to 10^9 s^{-1}, and the shock durations, ranging from less than 100 ps to more than 100 ns, permit the evaluation of a wide range of materials on a microscale to a mesoscale (sub-grain size, single crystal to pseudo-bulk) [16].

The existing experimental data on Si below 250 GPa and equation-of-state studies helped to develop the *first-principles* construction of a high-pressure-temperature (*P-T*) phase diagram of Si up to 4 TPa, which shows good agreement between the experiments and predictions for melting temperature and phase transition points [17]. The high *P-T* diagram revealed the existence of stable Si phases at multi-TPa conditions. A double hexagonal close-packed (dhcp) structure has been found to be thermodynamically and dynamically stable at relatively low-pressure range around 52 GPa and 500 K, supporting earlier computational predictions [18]. In addition, the results showed the existence of an anomalous sequence of face-centred cubic (fcc) to body-centred cubic (bcc) to simple cubic (sc) transitions beyond 2.8 TPa – see Fig. 13.1. The observed melting temperatures are consistently ~50–150 K lower than the theoretical predictions due to anisotropic defect-laden imperfections in the crystals used in the experiments [17].

The shock waves induced by laser direct drive or laser-launched flyer plate are broadening the range of states and spatial/temporal scales for studying mechanical

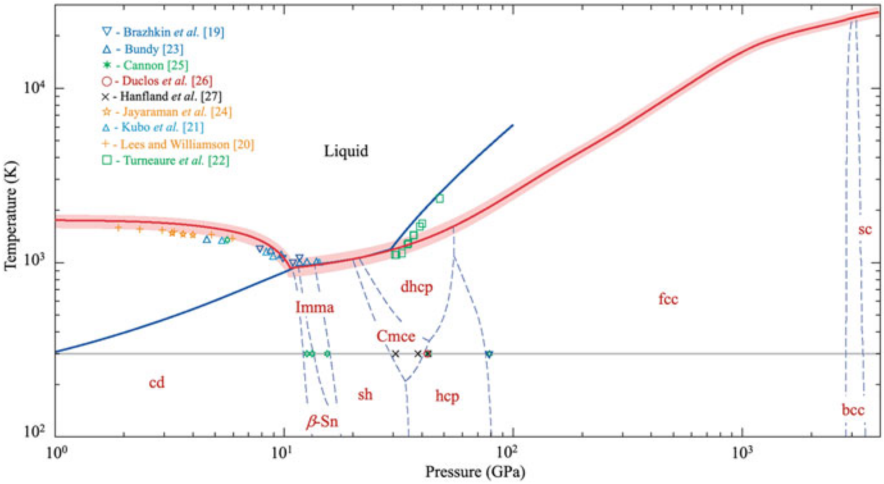

Fig. 13.1 Pressure-temperature (*P*-*T*) phase diagram of silicon predicted using first-principles methodology. Here, the grey horizontal line represents the $T = 300$ K isotherm, whereas the solid blue line represents the principal shock Hugoniot. The discrete data points, which are also labeled in the legend, correspond to experimentally observed phase-transition points [19–21]. (Adopted from Ref. [17] with permission)

properties such as plasticity and spallation, high-pressure physics and chemistry. However, the lifetime of new high-pressure polymorphs is way too short for practical utilisation of their unusual electronic and structural properties.

There were several successful attempts to utilise ultrashort laser pulses for forming new structure by irradiating crystal surfaces. Polymorphs with altered band structure have been realised by ultra-fast laser microstructuring and hyperdoping silicon surfaces in the presence of SF_6 [22, 23], by inducing surface defects and formation of a metastable body-centred cubic (bc8-Si) and a rhombohedral (r8-Si) polymorph [24, 25]. All these transformations however occur in a thin, up to 500-nm thick, surface layer. This bottleneck has indeed been a major inhibitor toward commercial use of these intriguing exotic Si polymorphs.

Recently, a new path to form new high-pressure/temperature conditions has been developed to combine the best of both worlds, an ultrashort pulse laser-induced microexplosion in confined geometry [26–29]. The tight focusing of the laser pulse deep inside a transparent crystal allows achieving the absorbed energy density in excess of several MJ/cm^3, higher than the strength of any material, in a sub-micron volume surrounded by the pristine solid. The ability to achieve this high level of energy density comes from the extremely short timescale of ultrashort laser pulses. Just 1 μJ of laser energy delivered into a focal volume of <1 μm^3 within a time shorter than 1 ps (1 ps = 10^{-12} s) immediately leads to an energy density above 1 MJ/cm^3 [26–29]. The crucial element here is that the energy from electromagnetic field of laser radiation into the electron subsystem is deposited faster than it can

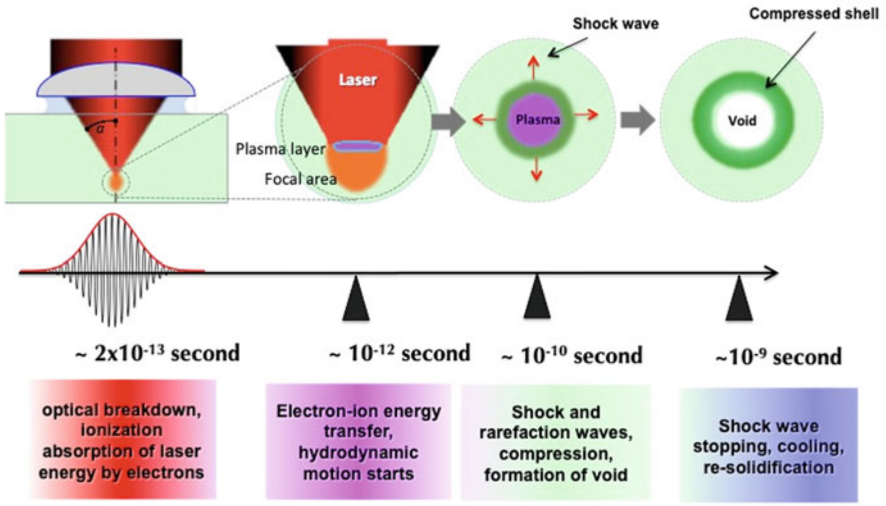
Shock wave
Compressed shell
Laser
Plasma layer
Focal area
Plasma
Void
α
~ 2x10-13 second
~ 10-12 second
~ 10-10 second
~10-9 second
optical breakdown, ionization absorption of laser energy by electrons
Electron-ion energy transfer, hydrodynamic motion starts
Shock and rarefaction waves, compression, formation of void
Shock wave stopping, cooling, re-solidification

Fig. 13.2 The sequence of physical processes with related time scales as a result of ultrashort laser-induced microexplosion confined inside the solid. (Adopted from Ref. [28] with permission)

transfer to the lattice through the electron-ion collisions and faster than it can dissipate through electronic heat conduction [30].

The complex processes are schematically presented in Fig. 13.2. A few picoseconds after the intense ultrashort sub-picosecond pulse, the absorbed laser energy transfers from the heated electrons to the ions, and a strong shock wave accompanied by a rarefaction wave starts expanding away from the focal volume. The extremely high heating rates up to 10^{17-18} K/s (>10 eV in <100 fs) create the solid density plasma at the temperature of a few tens of electronvolts ($\sim 5 \times 10^5$ K). The pressure/temperature conditions created in the microexplosion are similar to those in hot cores of planets, termed as warm dense matter (WDM) [31]. The material converted to high pressure/temperature solid density plasma is then transformed into the novel solid phase during the ultra-fast cooling and re-structuring, and the record-fast quenching rates $\sim 10^{15}$–10^{16} K/s lead to unusual solid-plasma-solid transformation paths, overcoming kinetic barriers to the formation of previously unknown high-pressure material phases. The shock wave moves the material away from the energy-absorbed volume and, after decelerating and stopping, forms an empty void surrounded by a shell of compressed material. The pressure-modified material converted to the novel phases is formed. All transformed material remains confined inside the bulk of undamaged surrounding material, ready for further studies.

The confined geometry conditions for producing high-pressure silicon structures have been realised by focusing ultrashort laser pulses on Si-surface buried under a 10–μm-thick oxidised layer [32, 33]. Several new phases were identified from the electron diffraction spectra and using the complementary ab initio random structure searches in the laser-modified volume in Si in these experiments [32, 34]. The searches found two new energetically competitive tetragonal structures, st12-Si with 12 atoms and indirect band gap between 1.1 eV [35] and 1.67 eV [36] and bt8-Si with 16 atoms per unit cell and predicted to be a low-band gap semiconductor. Traces of two other tetragonal phases with 32 atoms in their unit cells have been detected in the same laser-modified zones. One of those has been predicted to be suitable for solar applications due to a quasidirect band gap of close to 1.3 eV [4]. In addition, the electron diffraction data also reveal the presence of other as yet unidentified Si phases. We note that some of the unidentified reflections disappeared from the diffraction patterns taken from the same sites 2 weeks after sample preparation. However, the bt8- and st12-related diffraction spots were retained more than a year after the initial observation.

Intriguingly, the diffraction analysis demonstrated that the formation of bt8 and st12 polymorphs is dependent on laser fluence. While the lower fluence of 48 J/cm^2 resulted in predominantly st12-Si phase with formation energy of 0.139 eV/atom relative to dc-Si, a higher fluence of 96 J/cm^2 yielded predominantly bt8-Si with 0.146 eV/atom, demonstrating a possibility to control the formation of desirable metastable phase by varying the irradiating laser fluence.

A major difficulty in studying and utilisation of these new polymorphs with their unusual properties is the very low quantity of new material produced. Estimates from high-resolution transmission electron microscopy (TEM) images [32, 37] suggest that the amount of new phase produced in a single laser shot is of the order of ~10^{-15} g – 10^{-14} g, which makes it extremely difficult to detect and characterise their unusual structural and electronic properties.

While formation of large number of microexplosion sites using high-repetition rate, up to 10^6 pulses per second and higher, laser system is potentially a way to increase the total quantity of high-pressure phases, the relative volume of these new allotropes in the bulk is only in a sub-micron shell surrounding the microexplosion site. Simple increase of laser pulse energy in microexplosion experiments also has its own constraints, as the imperfections in the material due to colour centres, dislocations in crystal lattice and unpaired dangling bonds reduce the capacity of material to withstand high pressure. These defects reduce the strength of material and lead to subsequent formation of cracks, which channel away the energy of the expanding shock wave, decrease the pressure at the front of the shock wave and impede the material compression [26, 33, 37].

Increasing the amount of new material converted into unconventionally structured crystal lattices requires the development of ways to alter a much larger volume of Si structure in the ultrashort time. Here, we explore a new way to deposit significant amount of energy into a bulk of silicon crystal in an ultrashort period of time via the generation of high-energy electrons at a relativistic intensity of laser radiation [38, 39]. Electrons at mega-electron volt (MeV) energy levels with a speed close to the speed of light penetrate deep into the bulk of materials. For example, the stopping range of penetration for 1 MeV electrons in Si is about 2.3 mm [40]. This clearly allows for laser synthesis of exotic Si materials at greater thickness than the previously achieved within a 500 nm thin layers close to the surface. We analyse the physical processes involved in the transition to the relativistic regime of laser interaction with matter and the resulting possibility for the conversion of silicon into new crystal structures at considerable larger quantity, all preserved in the original crystal matrix.

To understand the formation of unusual Si phases, we analyse the volume of material affected by MeV-energy electrons exposed to the high-laser-intensity experimental conditions. Analysis of TEM images and X-ray diffraction (XRD) provides compelling evidence for the formation of metastable Si phases. Reaching the unexplored domain of laser interaction with material at relativistic laser intensities opens new pathways for material phase transformations and localised band-gap engineering at the nanoscale.

2 Experiment

2.1 Laser Irradiation Conditions

A 40 TW Ti:Sapphire laser system with a double-chirped pulse amplification configuration (Pulsar, Amplitude Technology Co.) was used in the experiments [41]. The front-end laser system adapted a double CPA layout with crossed polarised rotation to suppress amplified spontaneous emission (ASE) intensity [42]. The laser pulse duration was 25 fs, the wavelength 800 nm, and the pulse energy was up to ~1 J. The shot-to-shot laser energy fluctuation was 2%. A pair of gratings was used to compress the laser pulse to 25 fs in FWHM. The pulse duration was measured by self-referenced spectral interferometry (Wizzler by Fastlight). The intensity contrast ratio was determined by a third-order cross-correlation (Sequoia by Amplitude Tech.). The averaged energy contrast, i.e. the energy ratio of the ASE in the temporal range between -70 ps and -20 ps before the pulse peak to the main peak power, was measured to be 7.7×10^{-10}.

The 25-fs pulse was focused onto Si wafers using an off-axis parabolic mirror with a reflected focal length of 165 mm, off-axis angle 32.5° and f-number 3.7 (NA = 0.135) – see Fig. 13.3. The Si wafer was a boron-doped high-purity diamond-cubic-silicon <100> crystal with electrical resistivity 1–20 Ohm × cm and thickness of 525 μm. The angle of incidence of the linearly p-polarised pulses on the sample was 53.4°, resulting in an elliptical focal spot size of 14 μm × 3 μm at FWHM, which corresponds to surface area $S_{\text{foc}} = 3.3 \times 10^{-7}$ cm^2. A laser intensity of up to 7.5×10^{19} W/cm^2 was reached at maximal pulse energy of 616 mJ, which corresponds to a laser fluence of up to 1.87 MJ/cm^2 on the sample surface (Fig. 13.3). The energy level of ASE generated a laser fluence of about 1.44 mJ/cm^2 at an intensity below ~7×10^7 W/cm^2 before the arrival of the 25 fs pulse, well below the ablation threshold of 0.3 J/cm^2 for Si at 10-ps pulse length (see, for example, [43]). Thus, the high energy contrast provided assurance of the absence of any surface modification before the arrival of the 25-fs pulse.

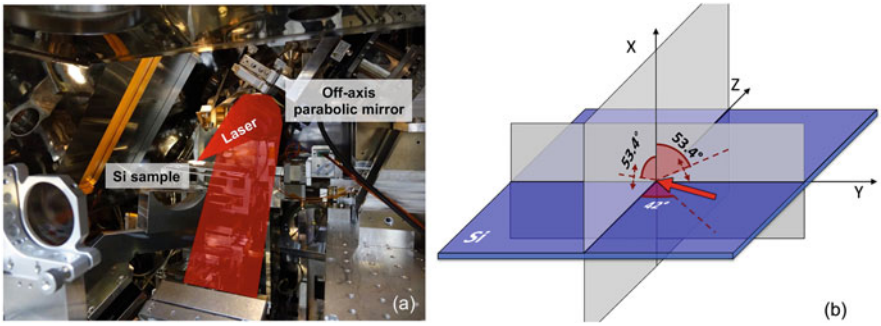

Fig. 13.3 Irradiation of an Si target with 25-fs linearly polarised pulses with *p*-component at 53.4° to the target surface: (**a**) focusing arrangement showing the focusing off-axis parabolic mirror and the Si target, (**b**) geometry of laser pulse orientation relative to the axes of Si crystal; Si [100] orientation is along the *X*-axis; Si [110] is in *Y*-*Z* plane

2.2 Irradiated Sample Characterisation

2.2.1 Optical Microscopy

Visual inspection of samples after the experiment shows that a rather large amount of material has been ablated from the front surface of the samples. The samples irradiated by 0.616 J pulses demonstrate spallation from the rear surface, while samples irradiated by lower energy pulses of 62 mJ have no indication of spallation. The effect of spallation is illustrated in Fig. 13.4, where optical images of the front and the rear surfaces of one of the samples are shown. The depth of the spallation crater is ~106 μm. There are clearly visible cracks in the crystal spreading away from the craters. That gave us an opportunity to analyse the material not only on the crater floor and the floors of spallation but also within the bulk of material.

The ablated craters on the Si surface were characterised by a 3D laser scanning confocal microscope (Keyence VK-9710) based on 408 nm laser source. The ablated volume of the crater formed by the highest pulse energy of 616 mJ and intensity $I_{\text{las}} = 7.5 \times 10^{19}$ W/cm^2 was measured to be ~8.72×10^{-5} cm^3. The dependencies of the ablated depth and crater size on pulse energy are presented in Fig. 13.4.

2.2.2 Raman Micro-Spectroscopy

The surfaces of such processed Si crystals, namely, the floor of the crater and the spalled region, were surveyed and examined by Raman spectroscopy. In addition, the Si sample broken along the crack through the ablated area provided an opportunity to characterise the volume between the crater and the spalled area produced by the laser-generated shock wave.

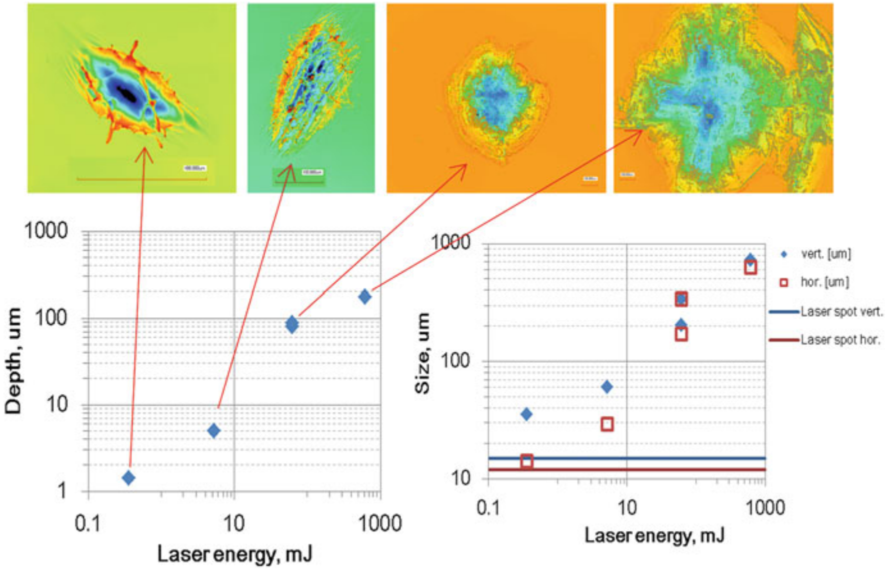

Fig. 13.4 Depth and size of the ablated crater measured by confocal optical profilometer, with corresponding profilometer images. The red and blue lines in the right panel indicate the laser focal spot size in X-direction (blue line) and in Y-Z plane (red line) indicated in Fig. 13.3b

Raman characterisation of the bulk of the sample between the ablated and spalled craters was performed with a Renishaw InVia Reflex Raman spectrometer. Spectra were obtained with 532 nm and 633 nm lasers using ×20, 0.25-NA (Olympus SLMPLN 20X) where a large depth of field provided more leniency in the focus of the Raman laser across the rough surfaces. We note here that the new Si allotropes may only be visible when and if they are present in a sufficiently large, larger that 100-nm, fraction of the sampled material [32, 44, 45]. Further, only Si allotropes with a band gap can readily be detected with Raman spectroscopy in small samples. If structures without band gap (or under such stress that band gaps are reduced to naught) are present, they may thus not be detected by this probe. Raman spectra were collected on a Peltier-cooled CCD detector with 1200 and 2400 lines/mm gratings. The relative precision of locating peaks is within 0.1–0.5 cm^{-1}, where the variation is dependent the peak strength relative to any overlapping peaks. Analysis was performed using the Wires 4 software package. After a linear baseline subtraction, the peaks were fitted with mixed Gaussian-Lorentzian curves.

Two types of modification were observed in the Raman spectra, the shift of Raman peaks from their known unstressed positions and the presence of new peaks attributed to Si allotropes and some additional disordered silicon – see Fig. 13.5. Note that it is not clear from Raman spectroscopy if this is truly amorphous Si (a-Si) or nanocrystalline Si consisting of crystal small enough to allow for the breakdown on quantum confinement. These are observed on the ablated crater floor and in the

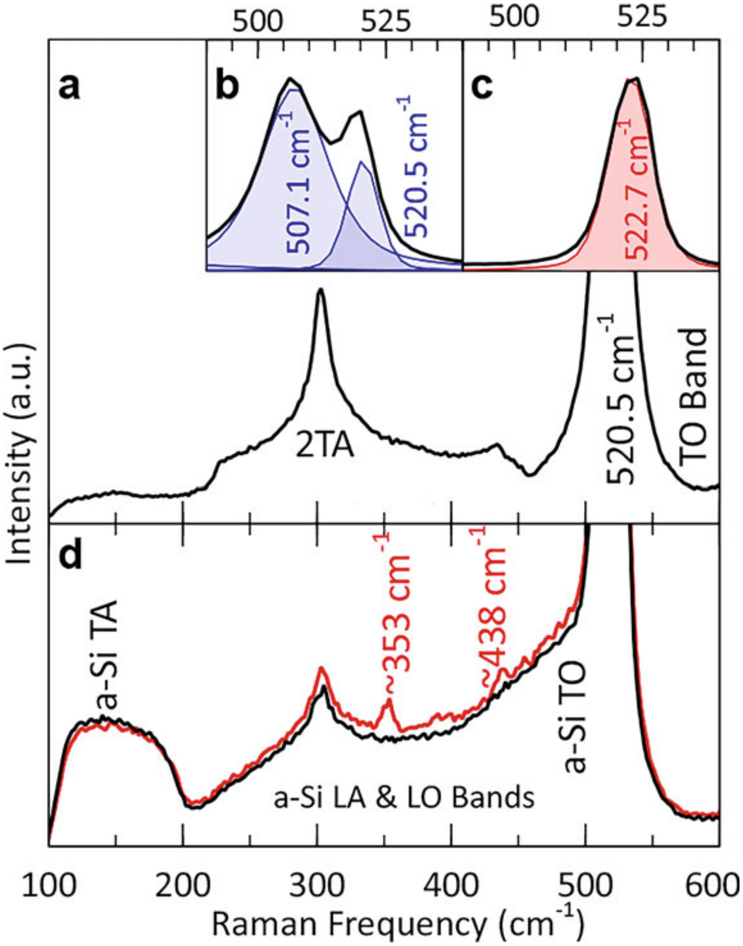

Fig. 13.5 Raman spectra collected from laser-irradiated Si sample. (**a**) example of dc-Si as recorded from the ablated crater surface of the sample irradiated at 7.5 × 10^{19} W/cm^2; (**b**) a component of the TO band shifted from 520.5 cm^{-1} to 507.1 cm^{-1} due to tensile strain and/or nanocrystallinity (curve fitting in blue); (**c**) the TO band shifted from 520.5 cm^{-1} to higher wavenumbers due to compressive strain (curve fitting is in red) by about 2.2 cm^{-1}. This corresponds to ~0.7–1.0 GPa; (**d**) spectra from disordered Si in black, and with additional peaks at 353 cm^{-1} and 438 cm^{-1} from a crystalline bt8/bc8/r8-Si allotrope, shown in red

surface of the crack in between the ablated and spalled craters. The spalled surface, however, indicates only the presence of the original unstressed dc-Si structure.

Distinct instances of Si allotropes were clearly found in a sample irradiated at 7.5 × 10^{19} W/cm^2. While the most common occurrence was disordered Si, several peaks in addition to the presence of disordered and fully crystalline dc-Si are evident in Fig. 13.5a. First, the peak at 522.7 cm^{-1} can be explained by a compressive stress, which causes the transverse optical (TO) band of dc-Si to shift to higher wavenumbers [46, 47]. Modified material that can manifest itself in the dc-Si TO band has shifted to higher wavenumbers above 520.5 cm^{-1} (a shift to 522.7 cm^{-1} is shown in Fig. 13.5c). The observed Raman shift of the one-phonon band of Si is indicative of a local residual compressive strain with a pressure range from 0.7 to 1.0 GPa [46, 47]. It is noteworthy that a distinct level of compressive stress is seen rather than a continuum of increasing stresses. The reason for this is still unclear. Shifts to lower wavenumbers (507.1 cm^{-1}, Fig. 13.5b) were also observed. These could be attributed toto tensile stress and/or nanocrystallinity [47, 48] or also to the presence of a hexagonal phase of Si such as 2H or 4H Si. Such hexagonal structures typically form upon thermal annealing of an exotic Si phase recovered from high pressure.

Figure 13.5d shows a spectrum, containing both disordered Si and dc-Si (in black). Two additional peaks at approximately 353 cm^{-1} and 438 cm^{-1} are commonly associated with the closely related bc8-Si/bt8-Si and r8-Si metastable phases (shown in red, Fig. 13.5d) [33]. The bc8-Si structure typically transforms from r8-Si as Si fully decompresses from high pressure [49]. However, with only two relatively weak intensity peaks, it was not possible to confidently associate these peaks specifically to the bc8-Si, bt8-Si and r8-Si phases. Recently, a number of other potential pressure-induced allotropes with similar Raman signals have been discussed [10, 32, 33]. These include bt8-Si, which we have previously demonstrated experimentally [32], and a range of other tetragonal structures that might be possibly formed [10, 33]. The physics of this phenomenon is rather nontrivial: the bc8-like superstructures appear as regularly ordered patterns of switchable atomic strings, preserving everywhere the energetically favourable tetrahedral coordination of silicon atoms. The variety of superstructures arises because each string can be switched between two states independently of the others. In addition to the known bc8, bt8 and r8 crystals, 128 tetrahedral structures with 16 (6 phases), 24 (22 phases) and 32 (100 phases) atoms per primitive cell are generated and studied; most of them are new ones [10].

Nonetheless, Raman examination has revealed evidence of laser-induced transformations, and these are now further investigated using X-ray diffraction analysis and electron microscopy.

2.2.3 X-Ray Diffraction Analysis with Cu-K_α Radiation

The 2D patterns of X-ray diffraction of the sample were measured using a Rigaku SmartLab diffractometer under Cu-K_α radiation at 1.54 Å (40 kV, 40 mA). A CBO-f poly-capillary was used to converge parallel line focus beam to a point focus, tailored by a 0.5 mm height limiting slit and a 0.5 mm incident slit. A Hypix3000 detector was used in 2D scanning mode 121.7 mm away from the sample. The sample area was aligned on a Chi-Phi cradle stage, both drives of which were continuously oscillating during data collection to randomise crystal orientations experimentally. The 2D XRD pattern from 10° to 90° 2θ was integrated into 1D data at a step size 0.01° 2θ/step using Rigaku 2DP v2.1.6 software, followed by the phase identification against ICDD PDF-4+ database in Diffrac.EVA v5 software.

The 2D patterns from X-Ray micro-diffraction of the sample area of interest and 1D pattern integrated from the 2D data are demonstrated in Fig. 13.6. XRD analysis reveals that apart from the peaks originated from cubic Si, additional XRD peaks are seen at 2θ of 32.27°, 33.51°. 35.35° (interplanar distances $d = 2.77$ Å, 2.67 Å and 2.54 Å, respectively). Such angles correspond reasonably well to the d-spacings in several metastable phases, for instance for the bc8 phase d [211] = 2.71 Å, for the st12 phase d [201] = 2.62 Å and d [210] = 2.54 Å, while for the bt8 phase d [112] = 2.68 Å [10, 32, 49]. The results of these preliminary tests are indication of the presence of exotic pressure-induced polymorphs of Si although additional data is required for full structure determination. To confirm this observation, further studies of the samples exposed to 61.6 mJ pulse energy have been performed at the Spring-8 synchrotron 30 keV X-ray source. The details are in the next section.

2.2.4 X-Ray Diffraction with 30 KeV Synchrotron Radiation

X-ray diffraction was performed in the end station of the BL22XU beamline in SPring8 synchrotron. The experimental arrangement and schematics are shown in Fig. 13.7. The X-ray beam of 30.047 ± 0.048 keV was shaped to a 50 µm square shape by two square slits located upstream of the sample. The first slit limited the beam aperture, and the second slit cut the scattered X-ray from the first slit to prevent stray X-ray on sample. The X-ray was irradiated to the spalled side of the sample to minimise the X-ray path inside the bulk of Si sample. The crater centre was placed on the X-ray beam centre. The transmitted X-ray was detected by an 0D detector and the sample was positioned at the maximum X-ray transmittance; the accuracy of the location in the crater is 50 µm.

A 2D X-ray detector (PILATUS3 R 300 K by DECTRIS) was used to detect the diffracted X-rays from the sample. The camera was fixed at the location such that the camera length (distance between the sample and the camera detection plane) of 254.14 ± 0.2 mm and the angle of $2\theta_0$ of 16°. The pixel size of the detector was 0.172 μm^2. The X-ray incidence angle to the sample was varied by two rotation stages (ϕ, ω angles). Two experimental runs were performed. In the first run, the angle ϕ was varied from $-10°$ to 10° with a step of 5°, and angle ω was varied from $-5°$ to 5° with a step of 0.1°. In the second run the angle ϕ was fixed at 15° and the angle ω was varied from 1.5° to 2.5° with a step of 0.1°. The sample was exposed for 100 s at each set of angles (ϕ, ω).

The XRD images indicate the presence of signatures of metastable silicon structures all deep inside the Si crystal (Fig. 13.8). These structures are potentially the tetragonal bt8-Si (with an $I4_1/a$ space group that is structurally an intermediate state between β-Sn-Si ($I4_1/amd$ space group) and bc8-Si ($Ia\text{-}3$ space group) or also the similarities bc8-Si itself. Further, the presence of r8-Si ($R\text{-}3$ space group) and st12-Si ($P4_32_12$ space group) cannot be excluded [10, 32, 33, 49]. Further study of such a sample to assemble of full diffraction data set is required in order to perform

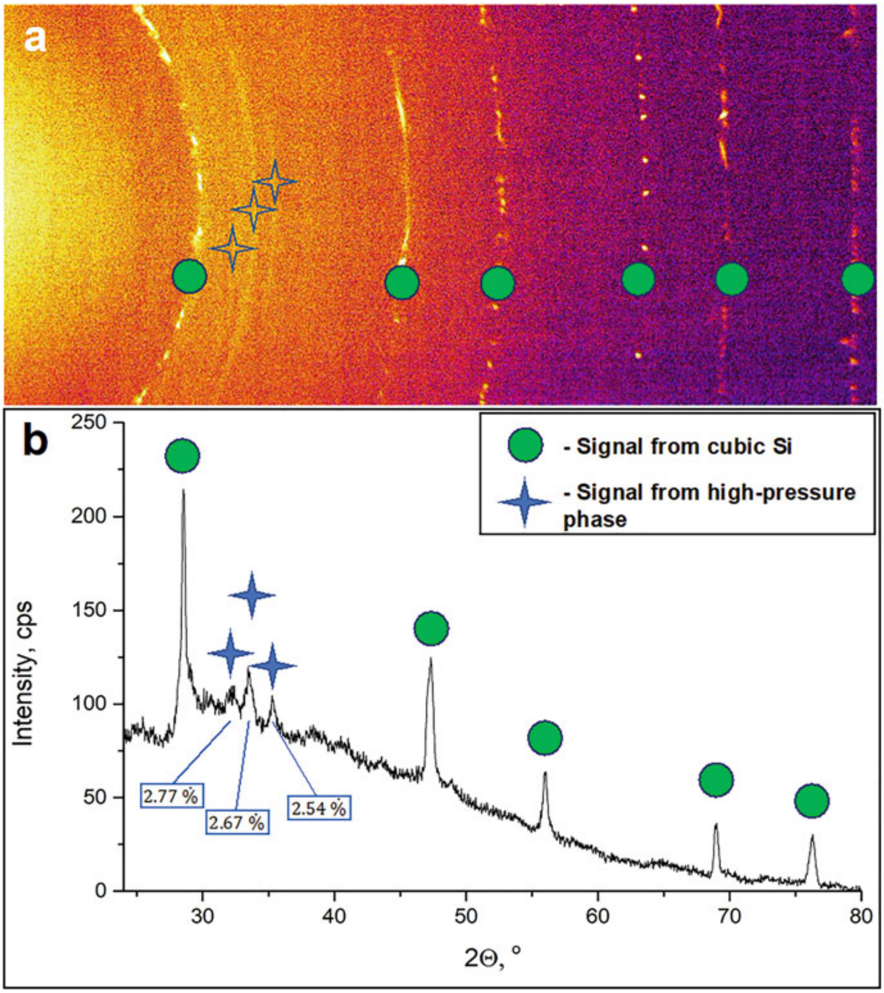

Fig. 13.6 X-ray diffraction analysis of the Si sample. (**a**) 2D patterns of X-ray micro-diffraction of the interested tip area on the sample; (**b**) 1D spectral pattern integrated from the 2D data

more quantitative structure data analysis. Nonetheless, the data clearly show that exotic Si phases as recovered from pressure are also synthesised through relativistic irradiation.

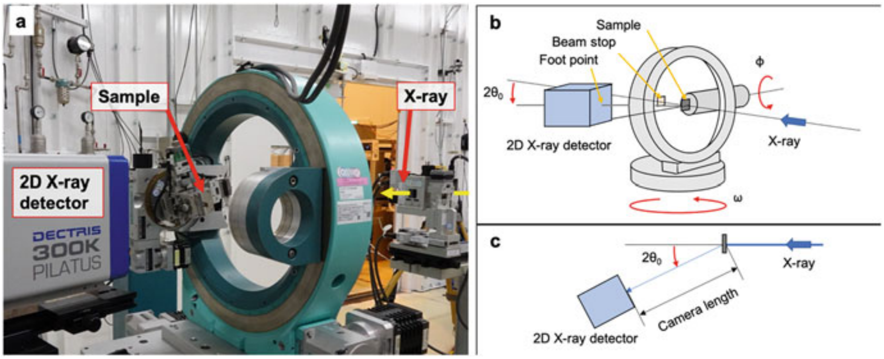
a
Sample
X-ray
2D X-ray detector
DECTRIS
300K
PILATUS
b
Sample
Beam stop
Foot point
2θ0
ϕ
2D X-ray detector
X-ray
ω
c
2θ0
X-ray
Camera length
2D X-ray detector

Fig. 13.7 Experimental chamber and schematics of X-ray diffraction analysis of the BL22XU beamline in SPring-8 synchrotron. (**a**) arrangement in the experimental chamber. (**b**) schematic of the experimental configuration with a top-view shown in (**c**)

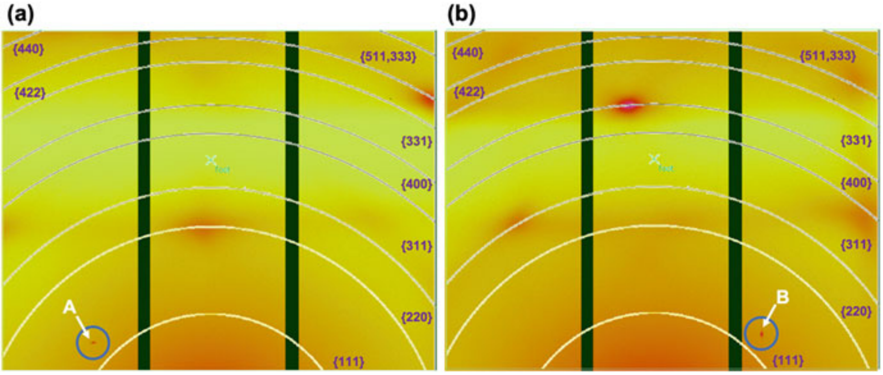

Fig. 13.8 XRD images in logarithmic intensity scale of Si sample irradiated at pulse energy of 61.6 mJ with overlaid dc-Si lines; the 2θ direction is in radially outward. (**a**) spot 'A' in the XRD image corresponding to a *d*-spacing of 2.71 Å, e.g. from the bt8/bc8-Si [211] structure. (**b**) spot 'B' in the XRD image corresponding to *d*-spacing of 2.68 Å, e.g. from the bt8-Si [112]. The cross point in all images is the foot point as described in Fig. 13.7; the black stripes are the 'dead' areas of the detector

3 Discussion

The results of Raman spectroscopy and X-ray diffraction provide convincing evidence of the formation of pressure-induced metastable silicon polymorphs deep in the bulk of a silicon sample irradiated by a laser pulse at relativistic intensity. This is a considerable step forward in the synthesis of large volumes of such materials. Further, our investigations give now insight into the sequence of the intertwined physical processes induced by the intense 25 fs pulse at and above relativistic intensity. This is detailed now:

3.1 Absorption of Laser Radiation and Ionisation at Relativistic Intensity

The maximum laser intensity at the pulse energy of 0.616 J is $I_{\text{las}} = 7.5 \times 10^{19}$ W/cm^2, well above the relativistic intensity threshold for $\lambda = 800$ nm laser (2.15×10^{18} W/cm^2) [50, 51]. The characteristics of the strength of relativistic laser field are expressed as the dimensionless amplitude of the laser electric field, $a_0 = e\overline{A}/m_{\text{e}}c^2$, and the ponderomotive potential $p_{\text{pm}} = m_{\text{e}}c^2\left[\left(1 + a_0^2\right)^{1/2} - 1\right]$, where e is the electron charge, $\overline{A}$ is the vector-potential connected to the electric field amplitude $\overline{E}$ by the relation $\overline{E} = -\frac{1}{c}\frac{\partial \overline{A}}{\partial t}$ [52]. In the case of low intensity, $a_0 << 1$, the above formula for the ponderomotive potential reduces to what conventionally called the electron's oscillation energy in the high frequency field. Expression of the dimensionless field amplitude through the intensity is

$$a_0 = \frac{e}{m_{\text{e}}\, c\, \omega}\left(\frac{8\pi\ I_{\text{las}}}{c}\right)^{1/2}; \tag{13.1}$$

where ω is the laser frequency. For the intensity $I_{\text{las}} = 7.5 \times 10^{19}$ W/cm^2, $a_0 = 5.915$ and the ponderomotive potential $p_{\text{pm}} = 2.558$ MeV. As $a_0 > 1$, the interaction proceeds in the ultra-relativistic regime.

The obliquely incident linearly polarised ultra-relativistic beam with p-component at 53.4° to the target surface (see Fig. 13.3b) interacts with the Si surface ionizing the sample by the over-the-barrier ionisation mechanism, allegedly stripping all of 14 electrons from Si-atom. The total ionisation losses are 4.66 keV per atom during the pulse.

3.2 Acceleration of Electrons

The laser pulse penetrates the solid to the depth of c/ω_{pe}, where ω_{pe} is the electron plasma frequency for the relativistic case. Note that the ponderomotive force oscillates with the double of laser frequency, 2ω. That means the magnetic force of the relativistic beam pushes the group of electrons inside the sample, accelerating them twice every laser cycle. The pressure of light, which is momentum transfer from the photons to electrons during the pulse, may induce the ion motion only in the condition when the pulse duration is longer than the time for establishing the electron-ion electrostatic coupling. Calculations by Wilks et al. [38] demonstrated that the relativistic beam produces so-called hole boring, i.e. the ion charge density depression inside the target, during the time $t = 189 \times (\omega)^{-1}$. In our experiments the comparable time $t = 58.9 \times (\omega)^{-1}$ is almost three times shorter, suggesting much lower suppression. Hence, even at the relativistic intensity of 7.5×10^{19} W/cm^2 and pulse duration 25 fs the laser-plasma interaction time is too short to drag the ions by the electrostatic force, imposed by the light pressure-driven relativistic electrons $(\omega)^{-1}$. However, the high-energy tail of hot electrons, with the energy up to MeV and higher, penetrates the solid during the laser pulse and distributes the absorbed laser energy into a volume much larger than that limited by the spot size on the surface and the skin layer depth into the target [53].

The intensity scaling suggests the energy in the high-energy tail of electron energy distribution is proportional to the ponderomotive potential in the following form [38, 54]:

$$kT_{\mathrm{h}} \cong p_{\mathrm{pm}} = m_{\mathrm{e}}c^2\,(\gamma - 1) = 511\left[\left(1 + 0.73\ I_{18}\lambda^2\right)^{1/2} - 1\right]\mathrm{keV}; \tag{13.2}$$

where I_{18} is the intensity in the units of [10^{18} W/cm^2] and λ is in [μm]. In our experiments $I_{18} = 75$, thus the energy in the hot electrons is $kT_{\mathrm{h}} = 2.56$ MeV that is close to the estimated above ponderomotive potential.

The trajectory of electron in strong linearly polarised field at relativistic intensity has a shape of figure-eight, moving at the average electron velocity. The longitudinal displacement is proportional to the magnetic force, $[e \times (v \times B)]/c \propto a_0^2$; $(v \propto a_0)$, which is proportional to a_0^2, whereas the transverse displacement along the electric field scales up with a_0. Therefore, at $a_0 > 1$ the longitudinal momentum becomes much larger than the transverse one. The electromagnetic wave hitting the solid surface transfers the photon's momentum to *electrons* in a medium by the action of the magnetic force, i.e. by the light pressure. The light pressure P_{las} of a photon's beam equals to the momentum $\eta_{\mathrm{abs}}E_{\mathrm{las}}/c$ transferred per unit of surface S_{foc} and per unit of time t_{p} is $P_{\mathrm{las}} = (2 - \eta_{\mathrm{abs}})I_{\mathrm{las}}/c$, where η_{abs} is the absorption coefficient. Taking $\eta_{\mathrm{abs}} = 0.74$ [55] at the maximum intensity in our experimental conditions, the light pressure imposed on electrons is 3.15×10^{15} Pa.

The force $(v \times B)$ created by the over-the-barrier ionisation acts on the electrons swiftly, accelerating them in the direction of the laser beam. Due to the oblique incidence, this force has two components, along the surface of the sample and perpendicular to the surface, making the electrons trajectories rather complicated. The electron motion is the source of the relativistic nonlinear effects [56], and the nonlinearity of the electron orbits enhances the laser-matter interactions. The electron orbits exhibit remarkable chaos within a single optical cycle. This strong orbital nonlinearity is responsible for the efficient absorption of the laser energy within a few optical cycles. In the case considered here, the 25 fs pulse duration equals to nearly ten optical cycles ($2\pi/\omega = 2.66$ fs). Thus, the main absorption mechanism is apparently plasma heating by the oscillating component of the pondermotive force of intense laser light, the $j \times B$ heating [54, 56]. The conversion efficiency of laser energy to electrons increases with laser intensity from about 20% to 30% at the relativistic intensity up to 80% at ten times higher level.

It was found by Santala et al. [57] that for shallow plasma density gradients the fast electron angular distribution becomes random. The authors suggested that $j \times B$ heating in the long-scale plasma supports this observation. According to particle-in-cell calculations of Santala et al. at the intensity 10^{20} W/cm^2, the additional electrons beam is generated in the direction of the obliquely incident laser beam propagation. The conditions in our experiments are reasonably alike Santala et al., experiments and calculations. Therefore, the shallow plasma gradients along with the orbital nonlinearities contribute into almost isotropic electrons angular distribution produced ablation in a volume several orders of magnitude larger than the interaction zone.

In these conditions the ponderomotive scaling significantly exaggerates the hot electrons temperature. The scaling and discussion in Mordovanakis et al. [58] suggest that at the ultra-relativistic intensity the hot electrons temperature scales as $T_\mathrm{h} \propto \left[I_{18}\lambda_\mu^2\right]^\alpha$, where $\alpha = 0.33 – 0.64$. Results of our experiments suggest the following scaling for hot electrons in the considered case:

- at $a_0 \geq 1.0$, $T_\mathrm{h} \approx 118\ (\mp 5) \times \left[I_{18}\lambda_\mu^2\right]^{0.64\mp 0.05}$keV; for $I_{18} = 75$ and $\lambda = 0.8$ μm, $T_\mathrm{h} = 1.405$ MeV;
- at $a_0 >> 1$, $T_\mathrm{h} \approx 290 \times \left[I_{18}\lambda_\mu^2\right]^{1/3}$keV; for $I_{18} = 75$ and $\lambda = 0.8$ μm, $T_\mathrm{h} = 1.054$ MeV.

Summing up the above analysis, one can conclude that the energy distribution of the electrons entering from the absorption zone into the solid sample can be characterised by two temperatures. The major part of the electrons has temperature 0.1–0.3 keV, while the relatively small part of the electrons in the high-energy tail has energy around 1 MeV. The angular distribution of electrons is apparently isotropic. By the end of 25 fs-long pulse, a large part of electrons energy is confined in a few cubic microns volume of the interaction zone, creating the strong electron pressure gradient at the boundary. The isochoric heating of the solid by the fast electrons is accompanied by much slower shock wave created by the electronic pressure gradient.

3.3 Energy Deposition as Point Explosion

The energy of a 25 fs-short ultra-relativistic pulse is absorbed by electrons within a volume of less than a cubic micron, while the ions remain cold during the pulse. However, the laser-affected and -ablated volume embraces a few cubic millimetres. A steep electronic pressure gradient establishes by the end of the pulse at the boundary of the interaction volume. The pressure gradient drives the ions' motion through the cold solid as a shock wave. Boschetto et al. [59] found that the low energy fs-short pulse excites phonons by the electronic pressure gradient. Recently, it was demonstrated that the ultra-relativistic fs-short pulse generates the blast wave [60]. The energy deposition region is much smaller than the laser-affected volume, and the pulse duration is much shorter than the time span of material modification process by the absorbed laser energy.

For the above reasons, it is appropriate to describe the major features of the process in time and space by the analytic solution to the strong spherical point explosion problem [61–63]. In this solution, the initial cold pressure in a material before the shock is neglected. The solution to the problem provides scaling laws for the distance of the shock front from the source R, velocity v_{sw} and pressure P_{sw} at the shock wave front as follows:

$$R = \left(\frac{5}{2}a\right)^{2/5} \times t^{2/5};\ v_{\mathrm{sw}} = a \times R^{-3/2};\ P_{\mathrm{sw}} = \frac{2\rho_0 a^2}{(\gamma + 1)\, R^3}; \tag{13.3}$$

where a is the explicit function of the initial parameters, absorbed energy E_{abs}, initial density r_0 and adiabatic constant of the material γ:

$$a = \left(\frac{E_{\mathrm{abs}}}{\rho_0}\right)^{1/2} \times \left\{\frac{3}{4\pi} \frac{(\gamma - 1)\,(\gamma + 1)^2}{(3\gamma - 1)}\right\}^{1/2}. \tag{13.4}$$

Conventionally, in cold solid-state material $\gamma \cong 3$, so the scalings are transformed as follows:

$$R_{\mathrm{sw}} = 1.39 \times \left(\frac{E_{\mathrm{abs}}}{\rho_0}\right)^{1/5} \times t^{2/5},\ v_{\mathrm{sw}} = 0.91 \times \left(\frac{E_{\mathrm{abs}}}{\rho_0}\right)^{1/2} \times R^{-3/2};\ \text{and}\ P_{\mathrm{sw}} \approx \frac{0.45 E_{\mathrm{abs}}}{R^3}; \tag{13.5}$$

were time is in [s], distance in [cm] and energy in [erg] units.

Let’s estimate the pressure that would be brought by the point explosion to the distance comparable to the depth of the craters for the experiments at 61.6 mJ (relativistic case) and 616 mJ per pulse (ultra-relativistic cases) at the bottom of the ablated crater. The depth of the crater is the length of the shock wave propagation from the focal point to the stopping point where it converts into acoustic wave. Following Eq. (13.5) and taking the shock wave distance as the crater depth $R_{616} = 175$ µm at 616 mJ, one gets a pressure $P_{616} = 50$ GPa and the time $t_{616} = 11$ ns to reach the shock wave stopping point. For the case of 61 mJ and $R_{61.6} = 82.9$ µm, the pressure at the stopping point and shock wave propagation time, correspondingly, are $P_{61.6} = 48.7$ GPa and $t_{616} = 11$ ns. This pressure is lower than the bulk Young’s modulus of ~165 GPa given for ideal silicon structure and could be attributed to a deviation of the shock wave from spherical expansion. Note that in both ultra-relativistic and relativistic cases (616 mJ and 61.6 mJ), the same pressure is predicted at the bottom of the crater, though in ultra-relativistic case it is reached at the depth of more than two times deeper into the sample. Hence, the point explosion scenario gives physically and semi-quantitatively correct picture of the formation and propagation of the laser-generated shock wave at relativistic and ultra-relativistic laser intensity.

One can see that the shock wave arriving at the bottom of the crater in the ultra-relativistic case has a pressure of the order of the cold pressure in a solid crystal. Note, that at the same time the ablation occurs by the rarefaction wave followed by the front of the shock wave, so that the real pressure at the front is higher. Hence, propagating a relatively weak shock wave with a front pressure below the Young modulus of Si of $E = 165$ GPa through the intact part of the sample and producing spallation at the back of the sample is feasible.

It is instructive to apply the simple analytics of point explosion scalings to predict the results of experiments Santos et al., [60]. According to Eq. (13.5), the resulted pressure of 40 TPa in experiments of irradiating 19-μm-thick Al foil is achieved in 49 ps, which is in semi-quantitative agreement with the authors hydrodynamic simulations indicating that 14 TPa pressure was achieved in a few ps.

3.4 Spallation from Compressive Stress

Spallation was observed only at the highest energy of the pulse of 0.616 J; there was no spallation at the rear surface of 525-μm-thick Si sample at 61.6 mJ pulse energy. The depth of the spallation crater is ~106 μm and the effect is illustrated in Fig. 13.4.

The part of the sample under the crater remains solid indicating that the shock wave pressure was below the Young's modulus of Si crystal, and therefore was non-destructive. The absorbed energy density, i.e. the absorbed energy *per* atom, was relatively low in the ~300-μm solid path of the 525-μm-thick Si sample as the electrons' stopping range is of the order of 6–8 mm for the 2–3 MeV electrons [64]. Hence, the absorbed ultra-relativistic electrons generated quite a moderate energy density due to extremely long stopping range. The collision of ultra-relativistic electron with Si atom proceeds as elastic scattering on each of the atomic electrons [65]. The breaking of the inter-atomic bonds allegedly occurs during this event. The ablation process starts from the upper surface of the sample propagating inside the sample. The ablation boundary moves inside the sample with velocity slightly exceeding the sound velocity in Si. The recoil pressure of expanding plasma vapours at the ablation boundary drives the weak shock wave inside a solid. The process resembles that occurring in the spherical laser fusion pellet when the ablated part of the outer shell implodes the rest of the shell mass to the centre of symmetry [66–68]. The difference is that in laser fusion the sum of the thermal pressure and recoil pressure drives the shock into the cold material, while in the case of ultra-relativistic ablation the recoil pressure drives a shock wave into the fast-electron preheated mass of the solid material.

At the pulse energy 62 mJ and intensity 7.5×10^{18} W/cm^2, slightly above the relativistic threshold, there was no spallation at the rear side of 525-μm-thick sample. The electrons generated at above relativistic intensity limit transfer their energy over the thickness of the unbroken part of the sample, rising the ions' energy to a few eV level and pressure around few tens of GPa to initiate the observed phase transformations. The material integrity is violated close to the free surface and a part of the sample expands producing the spallation crater. However, the electrons with the energy $\leq$0.5 MeV at the intensity below the relativistic limit cannot preheat the 300-μm thick intact part of the sample.

4 Conclusions

In summary, we demonstrate the processes of exotic phase formation in Si irradiated by ultrashort laser pulses at relativistic intensity. The exceptional conditions in such ultrashort laser experiments are the presence of relativistic electrons generated in laser-produced plasma, which penetrates inside the bulk. As a result, the ultrashort laser energy is deposited in much larger volume of the material, providing favourable conditions for large volume formation of such unconventional polymorphs. The compressive pressure at the front of the shock wave propagating through the crystal is strong enough to induce high-pressure silicon phase transitions into the metallic regime above ~11 GPa. The part of the material below the bottom of the ablation crater remained intact after the experiment at the intensity below ~7.5×10^{18} W/cm^2 (below 1.87×10^5 J/cm^2). We note here that the exotic Si allotropes were found on the ablation crated bed and in the bulk of Si affected by the relativistic electrons (those with the energy above 0.5 MeV). There were no exotic phases found on the bed of the spallation crater. Raman analysis proved the presence of residual stress inside the sample. The XRD analysis revealed that these inclusions were formed by known Si phases such as bc8, bt8 or st12 although full structure determination will require further data. The ability to maintain a remnant compressive stress in the dc-Si is, however, significant. It is also conceivable that some of the exotic crystal phases created in the far from equilibrium conditions of this work also require large remnant stresses to be preserved in the sample after laser modification. Large residual stress will clearly impact the optical and electrical properties by shifting the band gap of novel silicon phases. Further insights could be gained on the temporal dimension of the Si phase transitions during laser irradiation with coaxial pump (fs-optical)-probe (fs-X-ray) experiments using ultrashort 10 fs X-ray-free electron laser beam as described in [69]. Our results demonstrate the ability of ultra-fast lasers to locally modify the electronic properties of Si with submicrometric precision and will advance potential strategies for nanoelectronics through the incorporation of such nanostructures into semiconductor devices.

Acknowledgements This research was supported by the Australian Government through the Australian Research Discovery Project funding scheme (Project DP170100131). K.L.F and D.G are grateful to the Australian Research Council (ARC) for granting the Laureate fund No. FL160100089, to Central Analytical Research Facility of Queensland University of Technology for technical support, and acknowledge the facilities and technical assistance of the Australian Microscopy & Microanalysis Research Facility at the Centre for Microscopy and Microanalysis, The University of Queensland. B. H. was supported by resources at the Spallation Neutron Source and the High Flux Isotope Reactor, DOE Office of Science User Facilities operated by the Oak Ridge National Laboratory (ORNL). The XRD experiments were performed at BL22Xu in SPring-8 with the approval of JAEA (Proposal No. 2018A-E15) and the approval of the Japan Synchrotron Radiation Research Institute (JASRI) (Proposal Nos. 2018A3738).

Competing Interests The authors declare no competing interests.

References

1. P.F. McMillan, New materials from high pressure experiments: Challenges and opportunities. High Press. Res. **23**, 7–22 (2003)
2. P.F. McMillan, Pressing on: The legacy of Percy W. Bridgman. Nat. Mater. **4**, 715–718 (2005)
3. L. Zhang, Y. Wang, J. Lv, Y. Ma, Materials discovery at high pressure. Nat. Rev. Mater. **2**, 17005 (2017)
4. Q. Zhu, A.R. Oganov, A.O. Lyakhov, X. Yu, Generalized evolutionary metadynamics for sampling the energy landscapes and its applications. Phys. Rev. B **92**, 024106 (2015)
5. M. Amsler, S. Botti, M.A.L. Marques, T.J. Lenosky, S. Goedecker, Low-density silicon allotropes for photovoltaic applications. Phys. Rev. B **92**, 014101 (2015)
6. A. Mujica, C.J. Pickard, R.J. Needs, Low-energy tetrahedral polymorphs of carbon, silicon, and germanium. Phys. Rev. B **91**, 214104 (2015)
7. E.J. Davies, P.J. Carter, S. Root, R.G. Kraus, D.K. Spaulding, S.T. Stewart, S.B. Jacobsen, Silicate melting and vaporization during rocky planet formation. J. Geophys. Res. Planets **125**, e2019JE006227 (2020)
8. J.E. Chambers, Making more terrestrial planets. Icarus **152**, 205 (2001)
9. B. Haberl, T.A. Strobel, J.E. Bradby, Pathways to exotic metastable silicon allotropes. Appl. Phys. Rev. **3**, 040808 (2016)
10. V.E. Dmitrienko, V.A. Chizhikov, An infinite family of bc8-like metastable phases in silicon. Phys. Rev. B **101**, 245203 (2020)
11. S. Wong, B. Haberl, B. Johnson, A. Mujica Fernaud, M. Guthrie, J. McCallum, J. Williams, J. Bradby, Formation of an r8-dominant Si material. Phys. Rev. Letters **122**, 105701 (2019)
12. S. Wong, B. Haberl, B. Johnson, A. Mujica Fernaud, M. Guthrie, J. McCallum, J. Williams, J. Bradby, Thermal evolution of the indentation-induced phases of silicon. J. Appl. Phys. **126**, 105901 (2019)
13. B.J. Henderson, M.C. Marshall, T.R. Boehly, R. Paul, C.A. McCoy, S.X. Hu, D.N. Polsin, L.E. Crandall, M.F. Huff, D.A. Chin, J.J. Ruby, X. Gong, D.E. Fratanduono, J.H. Eggert, J.R. Rygg, G.W. Collins, Shock-compressed silicon: Hugoniot and sound speed up to 2100 GPa. Phys. Rev. B **103**, 094115 (2021)
14. L. Dubrovinsky, N. Dubrovinskaia, V.B. Prakapenka, A.M. Abakumov, Implementation of micro-ball nanodiamond anvils for high-pressure studies above 6 Mbar. Nat. Commun. **3**, 1163 (2012)
15. S. Tateno, K. Hirose, Y. Ohishi, Y. Tatsumi, The structure of iron in Earth's inner core. Science **330**, 359–362 (2010)
16. S.N. Luo, D.C. Swift, T.E. Tierney IV, D.L. Paisley, G.A. Kyrala, R.P. Johnson, A.A. Hauer, O. Tschauner, P.D. Asimow, Laser-induced shock waves in condence matter: Some techniques and applications. High Pressure Res. **24**, 409–422 (2004)
17. R. Paul, S.X. Hu, V.V. Karasiev, Crystalline phase transitions and vibrational spectra of silicon up to multiterapascal pressures. Phys. Rev. B **100**, 144101 (2019)
18. C. Li, C. Wang, J. Han, L. Yan, B. Deng, X. Liu, A comprehensive study of the high-pressure–Temperature phase diagram of silicon. J. Mater. Sci. **53**, 7475 (2018)
19. V.V. Brazhkin, A.G. Lyapin, S.V. Popova, R.N. Voloshin, Nonequilibrium phase transitions and amorphization in Si, Si/GaAs, Ge, and Ge/GaSb at the decompression of high-pressure phases. Phys. Rev. B **51**, 7549 (1995)
20. J. Lees, B.H.J. Williamson, Combined very high pressure/high temperature calibration of the tetrahedral anvil apparatus, fusion curves of Zinc, Aluminium, Germanium and Silicon to 60 kilobars. Nature **208**, 278 (1965)
21. A. Kubo, Y. Wang, C.E. Runge, T. Uchida, B. Kiefer, N. Nishiyama, T.S. Duffy, Melting curve of silicon to 15 GPa determined by two-dimensional angle-dispersive diffraction using a kawai-type apparatus with x-ray transparent sintered diamond anvils. J. Phys. Chem. Solids **69**, 2255 (2008)

22. C.H. Crouch, J.E. Carey, M. Shen, E. Mazur, F.Y. Génin, Infrared absorption by sulfur-doped silicon formed by femtosecond laser irradiation. Appl. Phys. A **79**, 1635–1641 (2004)
23. B. Franta, E. Mazur, S.K. Sundaram, Ultrafast laser processing of silicon for photovoltaics. Int. Mater. Rev. **63**, 227–240 (2018)
24. M.J. Smith, M.-J. Sher, B. Franta, Y.-T. Lin, E. Mazur, S. Gradečak, The origins of pressure-induced phase transformations during the surface texturing of silicon using femtosecond laser irradiation. J. Appl. Phys. **112**, 083518 (2012)
25. M.J. Smith, M.-J. Sher, B. Franta, Y.-T. Lin, E. Mazur, S. Gradečak, Improving dopant incorporation during femtosecond-laser doping of Si with a Se thin-film dopant precursor. Appl. Phys. A Mater. Sci. Process. **114**, 1009–1016 (2014)
26. S. Juodkazis, K. Nishimura, S. Tanaka, H. Misawa, E.G. Gamaly, B. Luther-Davies, L. Hallo, P. Nicolai, V.T. Tikhonchuk, Laser-induced microexplosion confined in the bulk of a sapphire crystal: Evidence of multimegabar pressures. Phys. Rev. Lett. **96**, 166101 (2006)
27. E.G. Gamaly, S. Juodkazis, K. Nishimura, H. Misawa, B. Luther-Davies, L. Hallo, P. Nicolai, V.T. Tikhonchuk, Laser-matter interaction in a bulk of a transparent solid: Confined microexplosion and void formation. Phys. Rev. B **73**, 214101 (2006)
28. E.G. Gamaly, L. Rapp, V. Roppo, S. Juodkazis, A.V. Rode, Generation of high energy density by fs-laser induced confined microexplosion. New J. Phys. **15**, 025018 (2013)
29. E.G. Gamaly, S. Juodkazis, A.V. Rode, Extreme energy density confined inside a transparent crystal: Status and perspectives of solid-plasma-solid transformations. Nano **8**, 555 (2018)
30. E.G. Gamaly, A.V. Rode, Physics of ultra-short laser interaction with matter: From phonon excitation to ultimate transformations. Prog. Quant. Electron. **37**, 215–323 (2013)
31. R.P. Drake, High-energy-density physics. Phys. Today **63**(6), 28–33 (2010)
32. L. Rapp, B. Haberl, C.J. Pickard, J.E. Bradby, E.G. Gamaly, J.S. Williams, A.V. Rode, Experimental evidence of new tetragonal polymorphs of silicon formed through ultrafast-laser-induced confined microexplosion. Nat. Commun. **6**, 7555 (2015)
33. L.A. Smillie, M. Niihori, L. Rapp, B. Haberl, J.S. Williams, J.E. Bradby, C.J. Pickard, A.V. Rode, Exotic silicon phases synthesised through ultrashort laser-induced microexpolsion: Characterisation with Raman microspectroscopy. Phys. Rev. Mater. **4**, 093803 (2020)
34. C.J. Pickard, R.J. Needs, Ab initio random structure searching. J. Phys. Condens. Matter **23**, 053201 (2011)
35. J.D. Joannopoulos, M.L. Cohen, Electronic properties of complex crystalline and amorphous phases of Ge and Si. I. Density of states and band structures. Phys. Rev. B **7**, 2644 (1973)
36. B.D. Malone, J.D. Sau, M.L. Cohen, *Ab initio* survey of the electronic structure of tetrahedrally bonded phases of silicon. Phys. Rev. B **78**, 35210 (2008)
37. A. Vailionis, E.G. Gamaly, V. Mizeikis, W. Yang, A.V. Rode, S. Juodkazis, Evidence of superdense aluminium synthesized by ultrafast microexplosion. Nat. Commun. **2**, 445 (2011)
38. S.C. Wilks, W.L. Kruer, M. Tabak, A.B. Langdon, Absorption of ultra-intense laser pulses. Phys. Rev. Lett. **69**, 1383 (1992)
39. G.A. Mourou, T. Tajima, S.V. Bulanov, Optics in the relativistic regime. Rev. Mod. Phys. **78**, 309 (2006)
40. https://physics.nist.gov/PhysRefData/Star/Text/ESTAR.html
41. D. Strickland, G. Mourou, Compression of amplified chirped optical pulses. Opt. Commun. **55**, 447 (1985)
42. N. Khodakovskiy, M.P. Kalashnikov, E. Gontier, F. Falcoz, P.-M. Paul, Degradation of picosecond temporal contrast of Ti:sapphire lasers with coherent pedestals. Opt. Lett. **41**, 4441–4444 (2016)
43. B. Luther-Davies, A.V. Rode, N. Madsen, E.G. Gamaly, Picosecond high repetition rate pulsed laser ablation of dielectrics: The effect of energy accumulation between pulses. Opt. Eng. **44**, 051102 (2005)
44. L. Bressel, D. de Ligny, E.G. Gamaly, A.V. Rode, S. Juodkazis, Observation of O_2 inside voids formed in GeO_2 glass by tightly-focused fs-laser pulses. Opt. Mater. Express **1**, 1150–1157 (2011)

45. N. Varkentina, M. Dussauze, A. Royon, M. Ramme, Y. Petit, L. Canioni, High repetition rate femtosecond laser irradiation of fused silica studied by Raman spectroscopy. Opt. Mater. Express **6**, 79–90 (2016)
46. T.P. Mernagh, L.-G. Liu, Pressure dependence of Raman phonons of some group IVA (C, Si, and Ge) elements. J. Phys. Chem. Solids **52**, 507 (1991)
47. V. Paillard, P. Puech, M.A. Laguna, P. Temple-Boyer, B. Caussat, J.P. Couderc, B. de Mauduit, Resonant Raman scattering in polycrystalline silicon thin films. Appl. Phys. Lett. **73**, 1718 (1998)
48. V. Paillard, P. Puech, M.A. Laguna, R. Carles, B. Kohn, F. Huisken, Improved one-phonon confinement model for an accurate size determination of silicon nanocrystals. J. Appl. Phys. **86**, 1921 (1999)
49. J.-T. Wang, C. Chen, H. Mizuseki, Y. Kawazoe, Kinetic origin of divergent decompression pathways in silicon and germanium. Phys. Rev. Lett. **110**, 165503 (2013)
50. T. Tajima, J.M. Dawson, Laser electron accelerator. Phys. Rev. Lett. **43**, 267 (1979)
51. S.V. Bulanov, N.M. Naumova, F. Pegoraro, Interaction of an ultrashort, relativistically strong laser pulse with an overdense plasma. Phys. Plasmas **1**, 745 (1994)
52. L.D. Landau, E.M. Lifshitz, *The Classic Theory of Fields* (Pergamon Press, Oxford, 1980)
53. D. Umstadter, Relativistic laser-plasma interaction. J. Phys. D Appl. Phys. **36**, R151–R165 (2003)
54. P. Gibbon, *Short Pulse Laser Interaction with Matter. An Introduction* (Imperial College Press, London, 2005)
55. P.K. Singh, Y.Q. Cui, A. Adak, A.D. Lad, G. Chatterjee, P. Brijesh, Z.M. Sheng, G.R. Kumar, Contrasting levels of absorption of intense femtosecond laser pulses by solids. Sci. Rep. **5**, 17870 (2015)
56. Y. Kishimoto, T. Tajima, T., in *High Field Science*, ed. by T. Tajima, K. Mima, H. Baldis, (Plenum Press, New York, 1999), p. 85
57. M.I.K. Santala, M. Zepf, I. Watts, F.N. Beg, E. Clark, M. Tatarakis, K. Krushelnick, A.E. Dangor, T. McCanny, I. Spencer, R.P. Singhal, K.W.D. Ledingham, S.C. Wilks, A.C. Machacek, J.S. Wark, R. Allott, R.J. Clarke, P.A. Norreys, Effect of the plasma density scale length on the direction of fast electrons in relativistic laser-solid interactions. Phys. Rev. Lett. **84**, 1459–1462 (2000)
58. A.G. Mordovanakis, P.-E. Masson-Laborde, J. Easter, K. Popov, B. Hou, G. Mourou, W. Rozmus, M.G. Haines, J. Nees, K. Krushelnick, Temperature scaling of hot electrons produced by a tightly focused relativistic-intensity laser at 0.5 kHz repetition rate. Appl. Phys. Lett. **96**, 071109 (2010)
59. D. Boschetto, E.G. Gamaly, A.V. Rode, B. Luther-Davies, D. Glijer, T. Garl, O. Albert, A. Rousse, J. Etchepare, Small atomic displacements recorded in bismuth by the optical reflectivity of femtosecond laser-pulse excitations. Phys. Rev. Lett. **100**, 027404 (2008)
60. J.J. Santos, B. Vauzour, M. Touati, L. Gremillet, J.-L. Feugeas, T. Ceccotti, R. Bouillaud, F. Deneuville, V. Floquet, C. Fourment, M. Hadj-Bachir, S. Hulin, A. Morace, P. Nicolaï, P. d'Oliveira, F. Reau, A. Samaké, O. Tcherbakoff, V.T. Tikhonchuk, M. Veltcheva, D. Batani, Isochoric heating and strong blast wave formation driven by fast electrons in solid-density targets. New J. Phys. **19**, 103005 (2017)
61. Y.B. Zel'dovich, Y.P. Raizer, *Physics of shock waves and high-temperature hydrodynamic phenomena* (Dover, New York, 2002)
62. L.I. Sedov, *Similarity and Dimensional Methods in Mechanics* (Academic Press, New York, 1959)
63. G.G. Chernyi, Hypersonic flow around a slender blunt cone. Dokl. Akad. Nauk USSR **115**, 681–683 (1957)
64. W.L. Kruer, K. Estabrook, J×B heating by very intense laser light. Phys. Fluids **28**, 430 (1985)
65. https://physics.nist.gov/PhysRefData/Star/Text/intro.html
66. V.B. Berestetzki, E.M. Lifshits, L.P. Pitaevskii, *Quantum Electrodynamics*, 2nd edn. (Elsevier, Oxford, 1982)

67. R.P. Drake, *High-Energy-Density Physics: Foundation of Inertial Fusion and Experimental Astrophysics*, 2nd edn. (Springer, Switzerland, 2018)
68. Y.V. Afanas'ev, E.G. Gamaly, O.N. Krokhin, V.B. Rozanov, Stationary model of the "corona" of spherical targets. Journ. Exper. Theor. Physics **44**, 311–316 (1976).; Y.V. Afanas'ev, E.G. Gamaly, O.N. Krokhin, V.B. Rozanov, Acceleration, implosion and stability of a laser-irradiated plane layer. Prikl. Mat. Mekh. **39**, 451 (1975); (in Russian)
69. V. Anand, J. Maksimovic, T. Katkus, S.H. Ng, O. Ulcinas, M. Mikutis, J. Baltrukonis, A. Urbas, G. Slekys, H. Ogura, D. Sagae, T. Pikuz, T. Somekawa, N. Ozaki, A. Vailionis, K. Glazebrook, J.P. Brodi, L. Rapp, A.V. Rode, E.G. Gamaly, S. Juodkazis, All femtosecond optical pump and X-ray probe: Holey-axicon for free electron lasers. J. Phys. Photonics **3**, 024002 (2021)

Chapter 14
Periodic Surface Structures by Laser Interference Ablation

Jürgen Ihlemann, Andreas Blumenstein, Jan-Hendrik Klein-Wiele, and Peter Simon

Abstract Interference of two or more overlapping coherent laser beams leads to a spatially periodic intensity modulation. Placing a material surface at this position and applying a sufficiently high intensity level will lead to a permanent surface modification, e.g., a periodic relief structure. The coherent beams are usually generated by splitting of one beam into several partial beams and recombining them on the material surface. In order to obtain specific intensity distributions, the partial beams can be manipulated concerning their amplitude, phase, and polarization. Various arrangements for beam splitting and recombination are presented. Amplitude or phase gratings, diffractive or refractive elements, or spatial light modulators are used. The obtainable minimal feature size depends on the wavelength and the interference angle of the beams. Structure details of the periodic patterns depend on the beam parameters, the material, and the environment. Grooves, ridges, bumps, spikes, droplets, and subsurface voids are observed. Such periodic patterns give rise to numerous applications in various fields like photonics, fraud protection, electronics, fluidics, tribology, and medicine. Examples are diffractive marking or changing the cell growth properties on medical implants.

Keywords Periodic surface structures · Laser interference ablation · Direct laser interference patterning · Mask imaging · Two-grating interferometer

1 Introduction

In the overwhelming variety of laser-generated nanostructures, there is a special class of structures devoting particular attention, namely, periodic surface structures. In this case, a topographic feature, we can call it a "unit cell," is repeated in a one- or two-dimensional array along the surface of a work piece. Such a regular

---

J. Ihlemann (✉) · A. Blumenstein · J.-H. Klein-Wiele · P. Simon
Institut für Nanophotonik Göttingen e.V., Göttingen, Germany
e-mail: juergen.ihlemann@ifnano.de; andreas.blumenstein@ifnano.de; jhkw@ifnano.de; peter.simon@ifano.de

© The Author(s), under exclusive license to Springer Nature Switzerland AG 2023

R. Stoian, J. Bonse (eds.), *Ultrafast Laser Nanostructuring*, Springer Series
in Optical Sciences 239, https://doi.org/10.1007/978-3-031-14752-4_14

arrangement of strictly repeated features gives rise to specific advantages. First, the properties of the surface are uniform across the entire processed area thus providing an unrivaled reproducibility of the addressed functionality. Second, particular functionalities can be obtained (e.g., diffractive/interference effects), which would be otherwise unavailable.

A direct intuition of this insight relates to the usual fabrication strategy of periodic surface structures: they are typically created using the interference of light. With this strategy, it is straightforward to generate a regularly repeated arrangement of alternating constructive and destructive interference. Applying such a pattern as irradiation field having a peak intensity exceeding the ablation threshold of a material, a permanent periodic surface pattern will result.

Laser interference ablation with ultrashort pulses has been first introduced in 1996 by using fs-excimer laser systems [1]. Later, starting around the year 2000 [2], with the emergence of Ti:sapphire lasers, these sources have been extensively applied giving rise to a rapidly increasing number of publications in this field, covering numerous aspects of the technology. Several points will be detailed in the next sections, including basic considerations of multi-beam interference (Sect. 2), various optical arrangements for the creation of simple or complex interference patterns (Sect. 3), investigation of the structure formation mechanisms (Sect. 4), and applications of the created periodic structures (Sect. 5).

In addition to the work described under these categories, there are quite a number of publications discussing further interesting facets of the field. These include addressing the effect of heat accumulation during interference patterning [3], discuss the benefits of using double pulses to increase the level of control over the structure formation [4], investigate the possibilities of improving the structuring efficiency [5] and homogeneity [6], and report on time resolved reflectivity mapping during structure formation [7]. The next sections will give an overview of the most important aspects of periodic nanostructures created by laser interference ablation. At the end (Sect. 6), future perspectives of this exciting field will be shortly discussed.

2 Basic Considerations Concerning Pulse Propagation and Laser Interference Patterns

It is well known, that interference of two or more overlapping coherent laser beams leads to a spatially periodic intensity modulation. In the simplest situation, combining two beams (Fig. 14.1), the resulting interference pattern yields an intensity distribution with a sinusoidal shape (described in detail later in this chapter).

Placing a material surface at this position and applying a sufficiently high intensity level, this will lead to a permanent surface modification, e.g., a periodic relief structure. The coherent beams are usually generated by splitting one beam

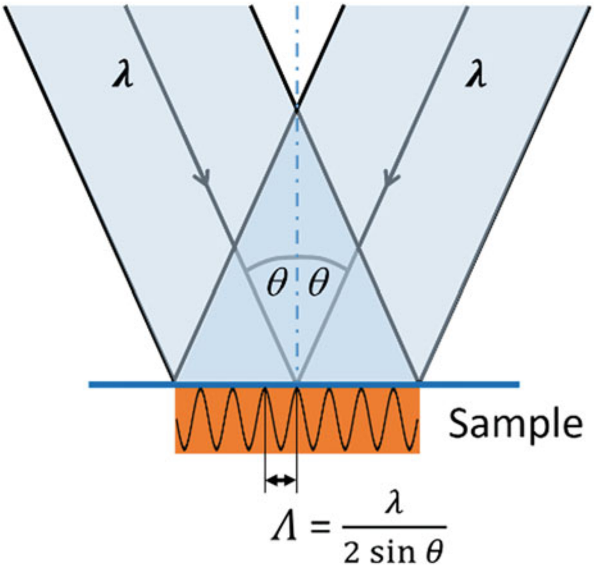

Fig. 14.1 Schematic representation of pattern formation by two-beam interference

into several partial beams. This is accomplished by reflective or diffractive beam splitters (Fig. 14.2). The partial beams are recombined on the material surface by an arrangement of mirrors or by an optical system imaging the plane of the beam splitter on the surface.

The applied beam splitting and beam combination strategy has an essential impact on the quality of the obtained interference pattern, as addressed in Fig. 14.2. Figure 14.2a displays the situation in which reflective beam splitting/beam combination is used. Although the setup is very simple and requires no special components, it suffers from severe limitations. First, for an arbitrary ray in the beam (dashed line in Fig. 14.2a), no spatial overlap is ensured in the target plane, thus imposing a stringent requirement for the spatial coherence of the beam. This problem could be solved by adding one more mirror to one of the arms, thus implementing a differing number of reflections in the arms. However, this would make the setup more complex and difficult to align. In addition, there is another problem, which is inherent to this arrangement. The pulse fronts (dotted line) of the partial beams enclose an angle in the target plane, leading to a limited extension of the interaction zone for ultrashort pulses, as was already discussed in [8] and [9]. On the contrary, the scheme displayed in Fig. 14.2b comprising a diffractive beam splitter (e.g., a transmission grating) and an *achromatic* imaging of the beam splitting plane onto the target plane is free of both previously mentioned limitations. The achromatic imaging ensures that the pulse front stays parallel to the phase front [10]. For all rays in the beam perfect overlap is obtained in the target plane. Consequently, even with ultrashort pulses full temporal overlap of the colliding

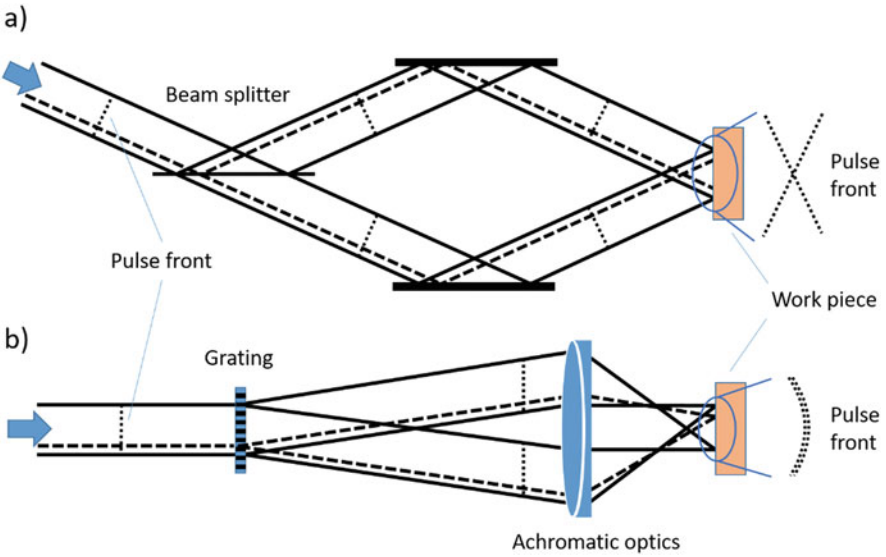

Fig. 14.2 Beam splitting strategies based on (**a**) reflective versus (**b**) diffractive beam splitting

pulses is provided in the target plane over the entire area of interference. The pulse fronts of the partial beams remain parallel to the beam splitting plane upon propagation up to the imaging optics and will be curved behind the optics. In this case, no delay occurs between the partial beams at any position and therefore perfect interference is obtained all across the beam. However, because of the curved phase front and therefore curved pulse front, various rays in the beam reach the target at slightly different times. In some experiments, it is important to ensure the shortest possible interaction time of the ultrashort pulse with the target, which requires a plane pulse front being parallel to the sample surface.

The arrangement displayed in Fig. 14.3 fulfills all these requirements. In this arrangement, a field lens is used to illuminate the beam splitting element (grating) with a converging beam. If the focal plane of the field lens coincides with the back focal plane of the imaging optics, the rays behind the imaging optics will be collimated. Consequently, the phase front, and because of the achromatic feature of the imaging optics also the pulse front will be plane, without curvature.

The use of achromatic imaging optics not only insures a control of the pulse front being parallel to the phase front. It also avoids unwanted chromatic spread of the image points and hence a deterioration of the image quality, when using ultrashort pulses with a broad spectral bandwidth. It is worth mentioning that reflecting optics are generally free from chromatic aberration and are therefore particularly suitable for such applications. Amako et al. also addressed this problem and proposed a simple optical scheme for chromatic-distortion compensation when splitting and re-combining femtosecond beams by using a pair of diffractive optical elements [11].

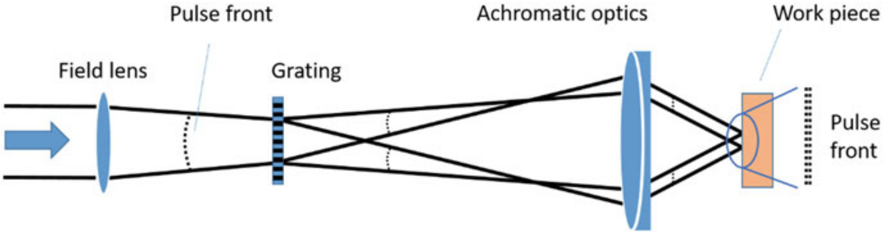

Fig. 14.3 Beam splitting and beam combination strategy maintaining plane pulse front on target

Using multiple beam interference, in order to obtain specific patterns, the partial beams can be manipulated concerning their propagation direction, amplitude, phase, and polarization. If more than two partial beams are generated, the selection or blocking of particular beams enhances the variety of complex interference patterns.

In a general case, the stationary (time integrated) intensity distribution $I(\mathbf{r})$ for multi-beam interference of n beams is calculated as

$$I\left(\mathbf{r}\right) = \left\langle \left|\mathbf{E}_1\left(\mathbf{r}\right) + \mathbf{E}_2\left(\mathbf{r}\right) + \mathbf{E}_3\left(\mathbf{r}\right) \cdots + \mathbf{E}_n\left(\mathbf{r}\right)\right|^2 \right\rangle, \tag{14.1}$$

where

$$\mathbf{E}_i = \mathbf{E}_{i,0} e^{i\left(\mathbf{k}_i \mathbf{r} - \omega t + \phi_i\right)} \qquad \text{with} \qquad i = 1 \rightarrow n \tag{14.2}$$

are the electric field amplitude vectors, $\mathbf{k}_i$ the wave vectors, and ϕ_i the initial optical phases of the interfering beams.

In the simplest case, just having two interfering beams with identical amplitudes propagating in the z-y plane (Fig. 14.4), the description is strongly simplified:

$$\mathbf{k}_{1,z} = \mathbf{k}_{2,z}, \tag{14.3}$$

$$\left|\mathbf{k}_{1,z}\right| = \left|\ \mathbf{k}_{2,z}\right| = k_z, \tag{14.4}$$

$$\mathbf{k}_{2,y} = -\mathbf{k}_{1,y}, \tag{14.5}$$

$$\left|\mathbf{k}_{2,y}\right| = \left|-\mathbf{k}_{1,y}\right| = k_y = k \sin\theta = \frac{2\pi}{\lambda} \sin\theta. \tag{14.6}$$

The resulting electric field (the sum of the two interfering fields) is then

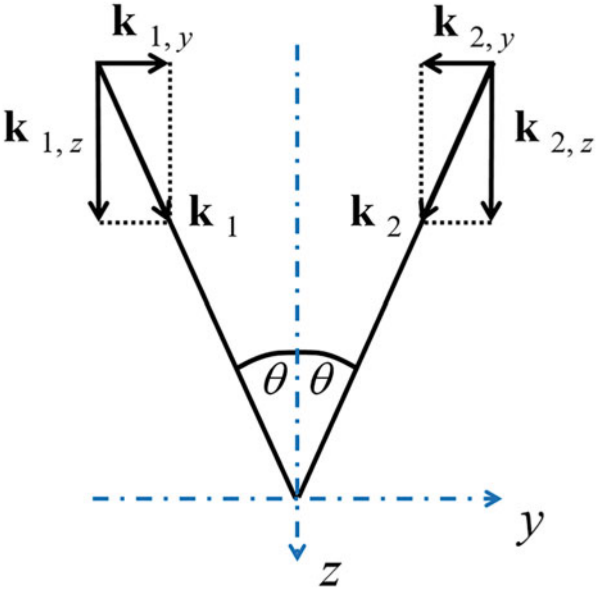

Fig. 14.4 Wave vector configuration in two-beam interference

$$\mathbf{E} = \mathbf{E}_0 \left(e^{ik_y y} + e^{-ik_y y}\right) e^{i(k_z z - \omega t + \phi)} = \mathbf{E}_0 \cdot 2\cos\left(k_y y\right) \cdot e^{i(k_z z - \omega t + \phi)}, \tag{14.7}$$

yielding an intensity distribution along the y-axis as

$$I \propto E_0^2 \left(\cos k_y y\right)^2 = E_0^2 \left(1 + \cos 2k_y y\right). \tag{14.8}$$

Substituting (14.5) into (14.7) yields

$$I \propto E_0^2 \left(1 + \cos 2\left(\frac{2\pi}{\lambda}\sin\theta\right) y\right) = E_0^2 \left(1 + \cos\frac{2\pi}{\Lambda} y\right). \tag{14.9}$$

Thus the intensity oscillates along the y-axis with a period of

$$\Lambda = \frac{\lambda}{2\sin\theta}. \tag{14.10}$$

In the above consideration, it is assumed that the beams are fully coherent and their amplitudes are equal. The situation changes, if these conditions are not fulfilled. In case of unequal amplitudes of the interfering beams, Eq. 14.8 converts to

$$I \propto E_{1,0}^2 + E_{2,0}^2 + 2E_{1,0}E_{2,0}\left(\cos 2k_y y\right), \tag{14.11}$$

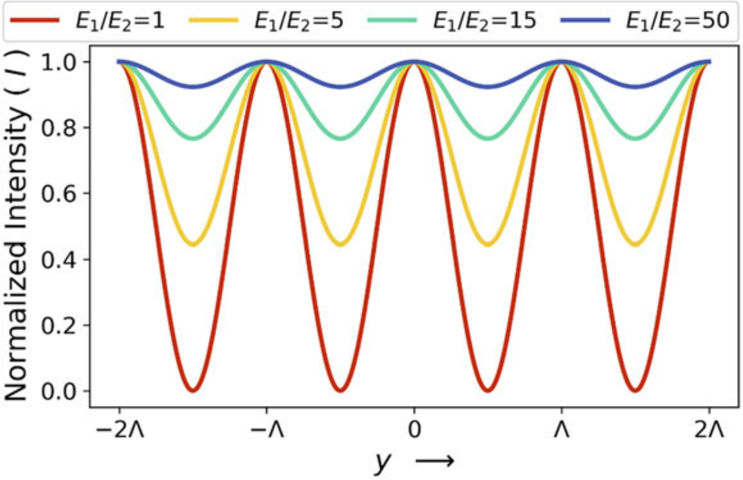

Fig. 14.5 Intensity distribution (along the ***y***-axis) across the resulting interference pattern in case of two interfering beams (according to Fig. 14.4) for various ratios of the field strengths (E_1/E_2) of the partial beams

where E_1 and E_2 are the field strengths of the two interfering beams. Figure 14.5 displays the resulting intensity distribution along the y-axis for various E_1/E_2 ratios.

Evidently, besides using standard diffraction gratings, the diffractive splitting of an incoming beam can also be accomplished by applying special diffractive optical elements (DOE) [12–14]. A more advanced approach uses spatial light modulators as variable (addressable) DOEs to create a computer-generated hologram (CGH) [15–17] for creating the desired interference patterns.

As already mentioned, applying an irradiation with a periodic modulation of the lateral intensity distribution with sufficiently high fluence to overcome the modification threshold of a material, a permanent periodic pattern will be created on the surface. The ultrashort pulse duration ensures a rapid energy deposition and keeps the so-called heat-affected zone (HAZ) small, so that a very high spatial resolution can be achieved for virtually all materials. However, depending on the physical details of the interaction between the light field and the medium, the shape of the created pattern may more or less follow the form of the fluence distribution (Fig. 14.6), or it can substantially differ from that (Fig. 14.7). The relevant parameters are the photon energy and the pulse duration of the irradiation, the number of applied pulses, plus the free carrier concentration and the band structure of the material, responsible for vaporization, melting, or hydrodynamic motion on an atomic scale. In metals, for instance, the free carriers absorb the incoming photons, and transfer their energy to the lattice after the electron-phonon relaxation time, which is typically in the range of a couple of picoseconds. Therefore, once the pulse duration is below the electron-phonon relaxation time, further reduction of the pulse length does not make any difference.

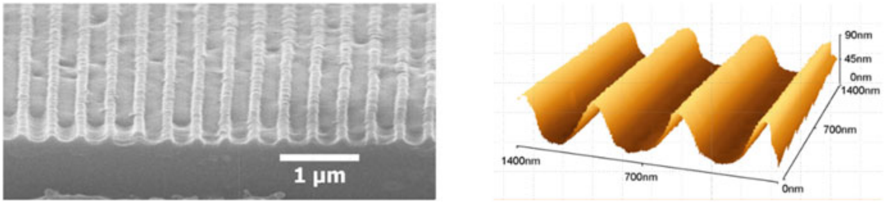

Fig. 14.6 Periodic pattern with period $\Lambda = 360$ nm on $LiNbO_3$, laser parameters: 248 nm, 500 fs, 170 mJ/cm^2, 5 pulses. (Reprinted by permission from Springer [18])

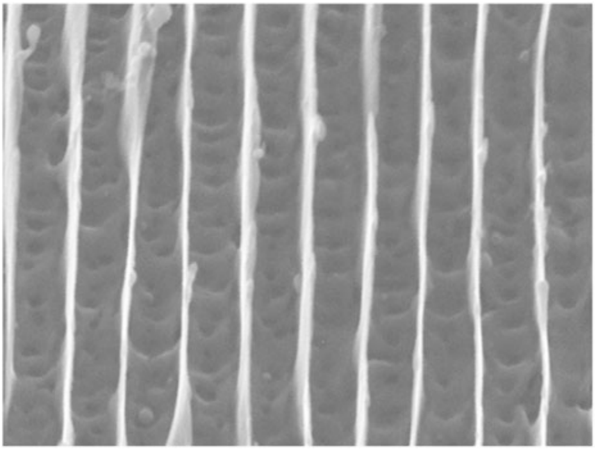

Fig. 14.7 Periodic pattern with $\Lambda = 360$ nm on Cu, laser parameters: 248 nm, 500 fs, 0.6 J/cm^2, 1 pulse. (Reprinted from [19], with permission from Elsevier)

The situation is completely different for materials without free carriers, especially for transparent dielectrics. In this case, reduction of the pulse duration, even down to the few-cycle regime, is advantageous because it increases the peak intensity of the pulses, which is a key parameter for multiphoton absorption [20]. A strong localized absorption is essential for high precision fabrication. Further considerations related to the physical mechanism of laser ablation can be found in Chap. 1.

3 Beam Delivery Methods for Two- and Multi-Beam Interference Ablation

There are essentially two methods for generating interferometric structures by direct short-pulse laser ablation.

(a) *Imaging*

The laser beam is split into multiple beams by means of a diffractive optical element (DOE), e.g., a transmission grating which is placed in the object plane of an imaging optics. The selected partial beams are then recombined in the image plane located on the sample surface.

(b) *Non-imaging*

The beam is split into multiple beams by a diffractive, refractive, or reflective beam splitter. The partial beams are recombined on the sample surface via a set of mirrors or gratings.

Additionally, the use of computer-generated holograms or the utilization of the interference field in the proximity of a diffractive mask is possible.

3.1 Imaging Methods

As mentioned in the Sect. 2, the requirements regarding spatial coherence are significantly reduced, when the plane of the emergence of the interfering beams is imaged to a plane where these emerging beams are recombined and interfere with each other. The simplest setup is given by a linear diffraction grating "mask," which is imaged with a single optical element onto the work piece. If diffraction orders ≥ 2 do not enter the aperture of the optical element, and if the zero-order beam is blocked (or suppressed by the design of the mask), the basic version of two-beam interference is accomplished. This has been realized for the first time for ultrashort pulse ablation by using a transmission grating as a mask in combination with a Schwarzschild-type reflective objective for mask projection on the work piece (Fig. 14.8). The use of a reflective instead of a refractive objective provides the following advantages:

- High transmission and high damage threshold (no glass in beam path, which could exhibit high (two-photon) absorption, especially in the UV)
- Aberration free (achromatic due to pure reflection)
- Large working distance compared to refractive objectives of comparable numerical aperture

Such a setup has been used for the nano patterning of copper and silicon surfaces with a period of about 360 nm [1].

Replacing the linear grating by another, e.g., crossed grating pattern, two-dimensional patterns like hole arrays are obtained [21]. Repeating the irradiation after a sub-period displacement of the mask, intricate features like double hole arrays are possible [22]. Using a phase mask instead of an amplitude mask, the processing efficiency can be increased significantly [23]. Even more sophisticated patterns can be generated, if the diffractive mask is split into two elements. Two linear masks, whose mutual distance D and rotational orientation can be varied,

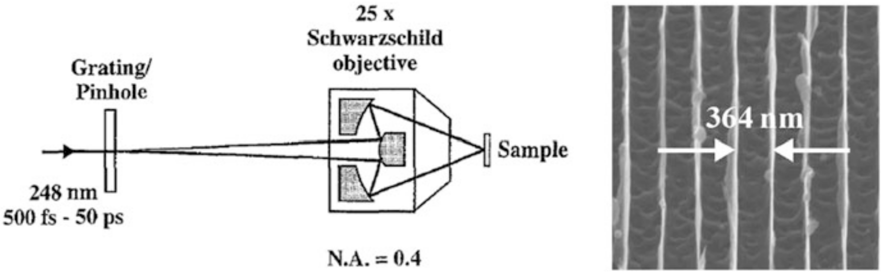
25 x
Schwarzschild
objective
Grating/
Pinhole
Sample
248 nm
500 fs - 50 ps
N.A. = 0.4
364 nm

Fig. 14.8 Setup for grating projection with a Schwarzschild objective (left) and a periodic pattern obtained by single pulse irradiation of copper (248 nm, 5 ps, 0.6 J/cm^2) (right). (Reprinted by permission from Springer [1])

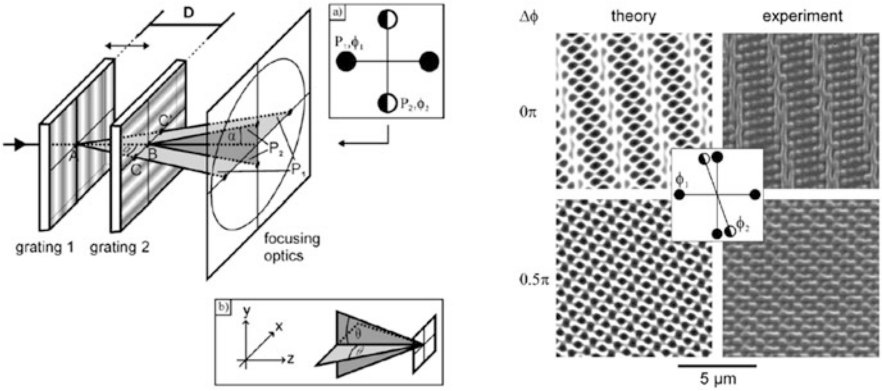
D
a)
P1,φ1
P2,φ2
A
B
C
C'
α
P2
P1
grating 1
grating 2
focusing
optics
b)
y
x
z
θ
Δφ
theory
experiment
0π
0.5π
φ1
φ2
5 μm

Fig. 14.9 Setup for phase-controlled multiple beam interference with an adjustable diffractive delay generator (left). Comparison of calculated and experimentally obtained patterns on polycarbonate (248 nm, 500 fs) (right). (Reprinted from [24], with the permission of AIP Publishing)

are able to create a huge variety of complex interference patterns [24]. The path difference between the zero-order and the +/− first-order beams generated at the first grating and propagating under an angle θ amounts to $\Delta L = D(1/\cos\theta - 1)$ at the position of the second grating. This corresponds to a phase difference of $\Delta\varphi = 2\pi\ \Delta L/\lambda$ (with wavelength λ), which remains constant throughout the further beam propagation and can be precisely tuned by varying the distance D. Thus, by varying distance and rotation angle, the resulting interference pattern can be changed to a large extent. Figure 14.9 displays the basic grating configuration and a comparison of calculated and ablated patterns obtained by six-beam interference. The experimental patterns have been obtained on a polycarbonate sample using 248 nm/500 fs laser pulses.

An even more complex pattern generator comprising two or more adjustable diffractive elements and a beam selector enabling the blocking of specific partial beams has been applied for the complex patterning of steel surfaces [25]. In this

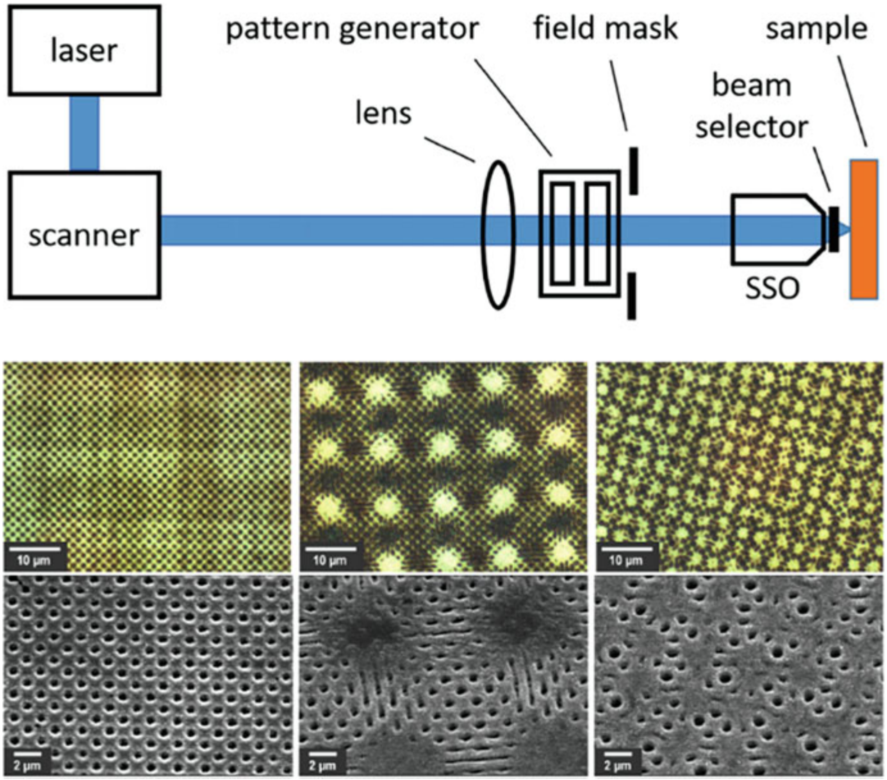

Fig. 14.10 Top: Optical system for the fabrication of diffractive patterns. One element of the pattern generator as well as the beam selector can be rotated around the optical axis. SSO Schwarzschild objective. The length of the setup from the pattern generator to the sample amounts to 350 mm. Bottom: Light microscopy (top row) and scanning electron microscopy (bottom row) images of three holographic marks that were fabricated with different configurations of the pattern generator. Left: 4 beams, single phase mask; middle: 12 beams, rotation angle 10° between the two phase masks; right: 12 beams, rotation angle 30°. (Reprinted from [25])

case, a 355 nm/9 ps laser has been used in combination with a beam scanner, which scans the beam over the whole processing field of the Schwarzschild objective (Fig. 14.10).

Instead of using a single optical element for the projection of the diffractive element, also the imaging with two lenses in a 4f-configuration can been applied [26]. The two lenses of focal length f_1 and f_2 are placed in a distance of $f_1 + f_2$, resulting in a magnification factor of f_2/f_1. This way, a diffractive element creating four diffracted beams has been projected on a stainless steel surface to produce hole arrays with periods in the range 1.5 to 2.2 µm (Fig. 14.11).

A similar arrangement has been applied for the fabrication of hexagonal lattice structures utilizing six interfering beams [27]. Such a setup can be extended in order to gain more pattern flexibility. By inserting small glass plates into the

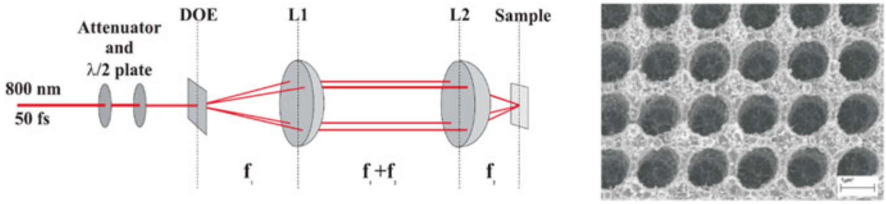
Attenuator
and
λ/2 plate
DOE
L1
L2
Sample
800 nm
50 fs
f1
f1+f2
f2

Fig. 14.11 Setup of a 4f imaging system (left) and a periodic hole pattern obtained in stainless steel by four-beam interference (800 nm, 50 fs, 0.2 J/cm^2, 200 pulses) (right). (Reprinted from [26])

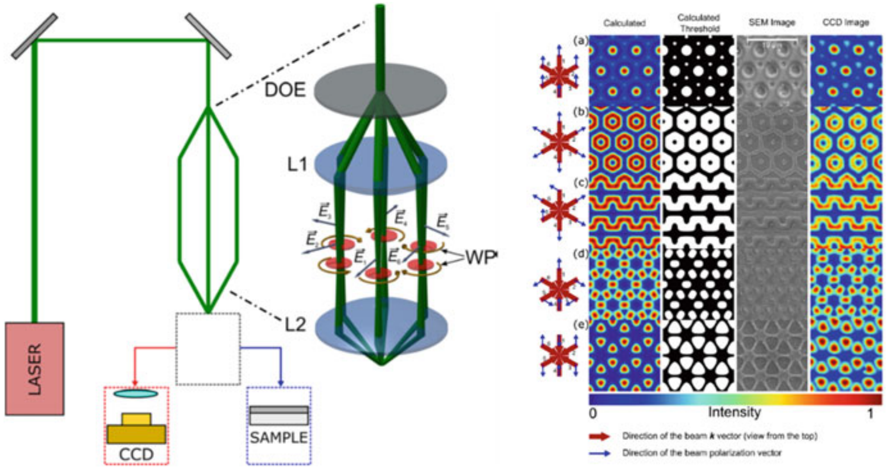
LASER
CCD
SAMPLE
DOE
L1
L2
WP
E1
E2
E3
E4
E5
E6
Calculated
Calculated Threshold
SEM Image
CCD Image
(a)
(b)
(c)
(d)
(e)
0
Intensity
1
Direction of the beam k vector (view from the top)
Direction of the beam polarization vector

Fig. 14.12 Left: Setup for pattern generation using polarization control. Right: Calculated and experimentally fabricated complex patterns in a Cr-film obtained by 532 nm/ 300 ps laser ablation under variation of the polarization. (Reprinted with permission from [29]. Copyright 2017, Laser Institute of America)

separated partial beams between the two lenses, each diffracted partial beam can be individually manipulated in intensity and phase [28]. The phase shift is adjusted by tilting the 1-mm-thick glass plates. A tilting accuracy of 0.1° is required to obtain a phase shifting accuracy of 30 nm. By inserting rotatable half-wave plates instead of simple glass plates, the polarization of each individual beam can be manipulated [29]. Various patterns as shown in Fig. 14.12 are obtained this way using six-beam interference.

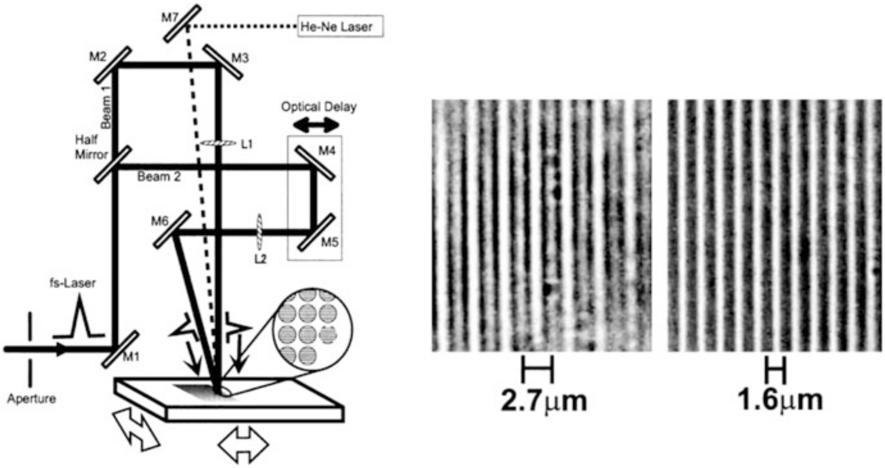

Fig. 14.13 Left: Mirror arrangement for non-imaging two-beam interference. Right: Surface relief gratings fabricated on sapphire using this arrangement. (Reprinted by permission from Springer [2])

3.2 *Non-Imaging Methods*

If the generation and recombination of two or more beams are performed in a non-imaging setup, several measures have to be taken in order to ensure high contrast interference patterns. This has been demonstrated for the case of two-beam interference using a 800 nm/100 fs laser for the fabrication of surface relief gratings on transparent dielectrics like glasses and crystalline metal oxides [2] and SiO_2 thin films [30]. An arrangement of mirrors has to be provided so that rays originating from the same beam area overlap on the target surface (Fig. 14.13). Furthermore, one of the two beams is guided through a variable optical delay line, so that the temporal overlap of both beams can be precisely adjusted. Structure periods around 2 μm are obtained on spots of 50–100 μm diameter. Crossed grating structures are obtained by double exposure in two directions orthogonal to each other [31]. Arrangements with movable mirrors enable the variation of the structure period [32].

Such a two-beam interference setup can be used for some kind of holographic data storage. A “data mask” containing specific information is inserted in one beam path, whereas the other beam serves as reference beam [33]. The resulting interference pattern (hologram) contains the data information, which can be reconstructed by irradiation with the reference beam (Fig. 14.14).

The generation and superposition of two coherent beams can also be accomplished in a common path configuration, where two (partial) mirrors are positioned in close proximity, so that both reflected beams take nearly the same beam path [34]. However, for a 200 fs pulse, the induced path difference must not exceed 60 μm to ensure temporal overlap on the work piece. A Michelson interferometer with

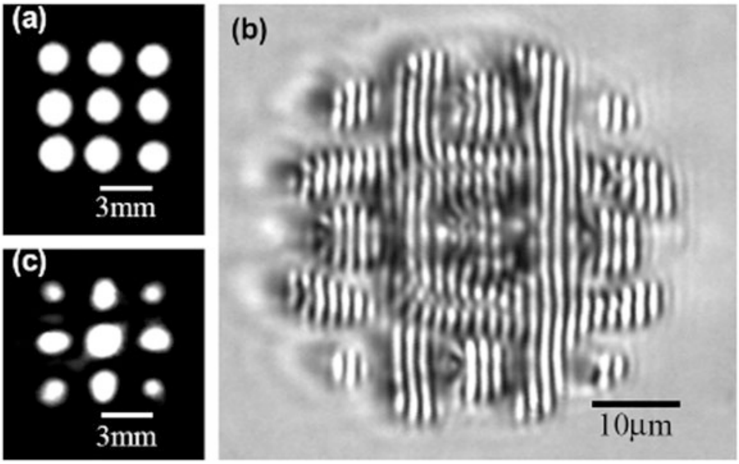

Fig. 14.14 Holographic data storage on the surface of PMMA. (**a**) The data mask. (**b**) The corresponding hologram recorded with the pulse energy of each beam of ~80 µJ (800 nm, 130 fs). (**c**) The reconstruction image of the data mask. (Reprinted from [33])

slightly tilted mirrors has also been used to create linear and (by double exposure) two-dimensional gratings [35].

By interference patterning with two beams, whose polarization can be individually adjusted by a combination of Wollaston prisms and wave plates, the polarization dependence of the grating depth has been investigated [36]. It could be shown that p-polarization of both beams leads to the deepest gratings in silicon, when ablating with 800 nm/200 fs laser pulses.

Also in the non-imaging case, the generation of two or more interfering beams can be accomplished with diffractive instead of reflective beam splitters [5]. Instead of using refractive or reflective optics to recombine the multiple beams, this recombination can also be accomplished by diffractive means. In a simple configuration, the two first-order beams generated at a linear transmission grating G1 with period p are again diffracted at a second grating G2 with period $p/2$. If the lines of both gratings are oriented parallel to each other, and the distance between G1 and G2 is d, an interference pattern with period $p/2$ is obtained at the same distance d behind G2 [37] (Fig. 14.15). Using an appropriate focusing optics to obtain sufficiently high fluence, a line pattern can be ablated. Due to the use of two successively passed gratings, such an arrangement is achromatic; the characteristics of the diffraction pattern do not depend on the wavelength (bandwidth) or the coherence properties of the laser pulses. With this method, sub-500 nm grating periods on stainless steel have been obtained using 248 nm/500 fs laser pulses [38]. Two-dimensional gratings have been fabricated this way by double exposure [39].

An extension of this method to fabricate large area hole arrays has been applied in [41]. In this case, four beams generated at a crossed grating are recombined by

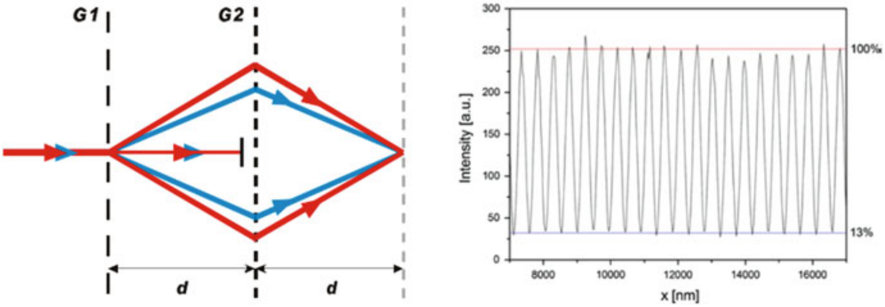

Fig. 14.15 Left: Two-grating interferometer scheme. (Taken from [40]). Right: Intensity distribution in the work piece plane recorded with a monitoring system. (Reprinted by permission from Springer [39])

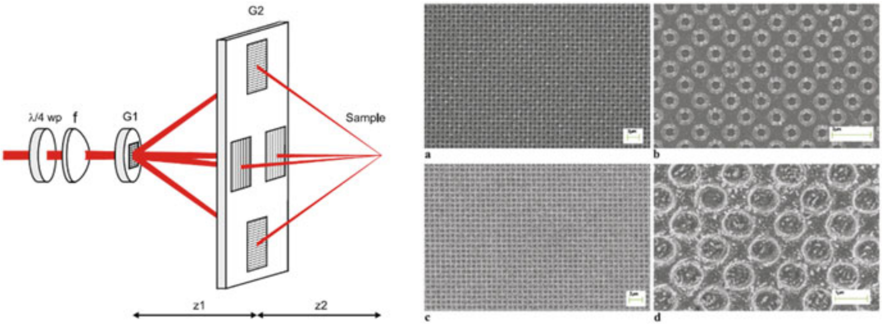

Fig. 14.16 Left: Two-grating interferometer setup for the fabrication of hole arrays using femtosecond laser pulses. Right: Hole arrays made by femtosecond laser (800 nm) ablation using the two-grating interferometer. (**a**, **b**) Silicon, (**c**, **d**) steel. (**a**) 50 pulses with 0.2 J/cm^2, (**b**) single pulse with 1 J/cm^2, (**c**) and (**d**) 500 pulses with 0.2 J/cm^2. (Reprinted by permission from Springer [41])

four suitably orientated linear gratings (one for each beam) fabricated on a single substrate to facilitate easy adjustment (Fig. 14.16).

Laser interference ablation is possible even without any imaging or recombining optical system behind the diffractive beam splitter (mask). If the work piece is positioned close behind this mask, the diffracted beams are not yet separated, and their interference pattern is present in this so-called proximity position. Several requirements have to be fulfilled in order to generate a periodic ablation pattern on the work piece by this method:

1. The distance between mask and work piece has to be limited to a value, where coherent overlap of the diverging diffractive beams is ensured. This value depends on the beam size and the diffraction angle.
2. The ablation threshold of the material to be ablated has to be lower compared to that of the mask material, as there is no geometrically caused reduction of the fluence like in the case of imaging or focusing.

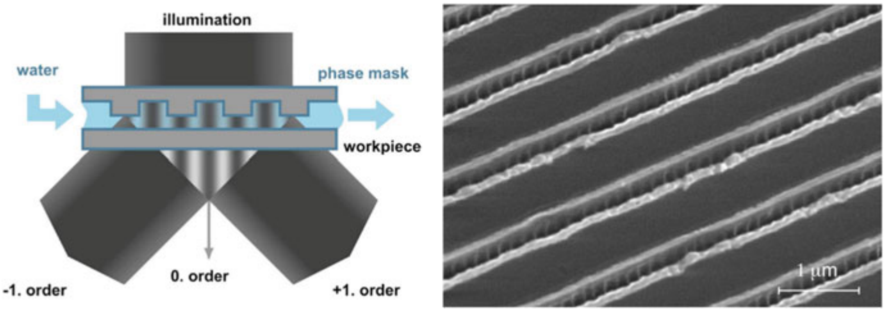

Fig. 14.17 Left: Proximity configuration of laser interference ablation. Right: Ablation pattern on silicon obtained in this configuration. Laser parameters: 248 nm, 1.3 ps, 120 mJ/cm^2, 20 pulses. (Reprinted from [42], with the permission of AIP Publishing)

3. Any disturbing effect of the zero-order beam has to be minimized, as a residual zero-order beam cannot be blocked between mask and work piece.
4. Care has to be taken that ablated material does not contaminate or even damage the nearby mask.

All these requirements are fulfilled in the example presented in [42] (Fig. 14.17):

1. The distance between mask and work piece is adjusted to 130 µm.
2. The mask is a fused silica phase mask; fused silica has a significantly higher ablation threshold than most other materials.
3. The disturbing effect due to the modulation of the interference pattern in z-direction originating from the residual zero-order beam is eliminated by moving the work piece during laser processing slightly in z-direction (in the µm range) averaging out any otherwise arising inhomogeneity.
4. The space between phase mask and work piece is flushed with water during processing. This way ablated material is carried away and cannot contaminate the mask.

Besides using strictly periodic phase masks to create one- or two-dimensional patterns, also pixel-based diffractive optical elements (DOE) or computer-generated holograms (CGH) are used for the fabrication of periodic patterns. Such a CGH has been applied in combination with a UV-fs-laser (248 nm, 500 fs). It was designed to generate a 25 × 25 spot array in the object plane, which was then imaged onto the work piece creating a 25 × 25 hole array in polyimide [43] and steel [44]. In addition to static CGH, variable CGH based on spatial light modulators are applied for periodic patterning [45, 46]. For further details see Chap. 15.

4 Structure Details on the Sub-Period Scale

The variety of applications of periodic surface structures results from the utilization and control of surface features, like nm thick side walls, spikes, well-defined ridges, or tiny drilled holes. A specific surface functionalization, like hydrophobicity or a diffractive effect, can require complex surface features. To actively control them is a big challenge, where many factors are relevant, the material itself, the beam parameters, and the environment. After understanding the structuring process in detail, it is even possible to produce numerous details smaller than half the wavelength in a controlled manner. Even a simple sinusoidal interference pattern can create complex surface details. When varying the fluence along two dimensions, the feature complexity is further increased [24, 47].

On the submicron scale, the formation of grooves, ridges, bumps, spikes, droplets, and subsurface voids is observed, indicating that contributions like lateral material movement may play an important role [48]. Irradiation with a line pattern results in the evolution of grooves with protruding side walls [49]. Thin films may disintegrate and form nanowires and nanodots [50, 51] or nanospikes [52]. As one of the main driving mechanisms responsible for the nanostructures growth, the relaxation of the laser-induced stresses has been identified, that are generated in the vicinity of the target's surface as a result of the laser heating [53–55].

The shape of the final nanostructures depends on the material as well as on the laser parameters, the dynamic change of the reflectivity of the material [56, 57], the geometrical parameters of the irradiation pattern, and the number of applied pulses. For single pulse irradiation, a detailed description of the evolution process of the resulting features can be obtained by molecular dynamics (MD)-based simulations [58, 59].

An interference pattern on a glass, a semiconductor, or a metal surface induces completely different material response resulting from the differing material parameters. A particularly important factor influencing the ablation result is the applied laser fluence. Even small variations in the amount of energy deposited at a surface may change the resulting features dramatically. As a typical example for the behavior of a metal, the ultrashort laser pulse-induced nanostructure formation on gold is discussed here in more detail. Using two-beam interference (laser parameters: 248 nm, 1.6 ps), a sine-shaped line profile with a period of 350 nm is projected onto the surface. The structure formation process is categorized in four main fluence regimes, which apply in principle to a wide range of metals and are shown in Fig. 14.18: (a) the damage threshold, leading to a surface swelling; (b) melting, corresponding to void formation beneath the surface; (c) the onset of spallation, manifesting in droplet and wall formation at the sides of the opening groove; and (d) the process of phase explosion, where broad surface melting and ejection of disintegrated single atoms is taking place, producing an irregular surface. These distinctions are following a description by Zhigilei et al. [60] and are based on detailed molecular dynamics–two temperature model (MD-TTM) [59] (see also

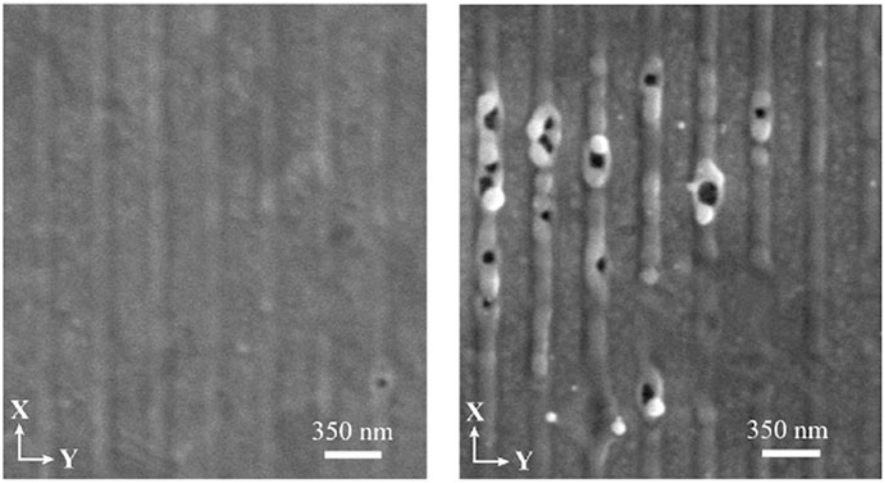

(a) damge threshold - swelling (b) melting - void formation

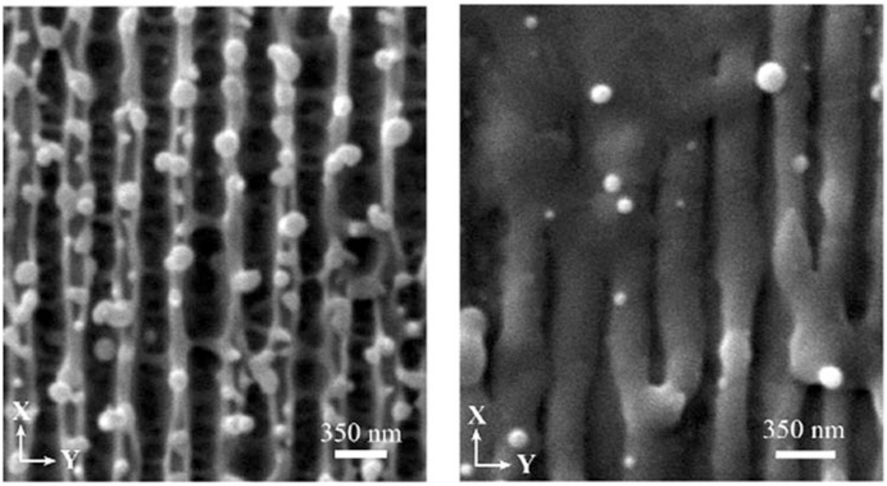

(c) spallation - droplets (d) phase explosion - broad melting

Fig. 14.18 Surface topography obtained on gold after single pulse irradiation with a 350-nm period line pattern. (**a**) Surface swelling at 100 mJ/cm^2, (**b**) void formation at 150 mJ/cm^2, (**c**) wall formation at 200 mJ/cm^2, (**d**) broad melting at 350 mJ/cm^2. (Reprinted from [61])

Chap. 2). The specific processes occurring in these fluence regimes are explained in the following.

Damage threshold, surface swelling Above an average incident fluence of 100 mJ/cm^2 as shown in Fig. 14.18a, an uplift of material can be observed. It occurs in periodic lines at a corridor where the fluence exceeds the damage threshold

(210 mJ/cm^2 for gold at 248 nm). The suggested mechanism is a laser-induced fast and localized melting which leads to a sudden volume increase, since liquid gold is less dense than gold in the crystalline phase, as discussed similarly for Ni by D. S. Ivanov et al. [53, 62, 63]. This upward movement is the strongest in the center where the deepest melting into the bulk occurs. Some small voids might form temporarily in the overheated melt, increase the upward directed movement, and release stress/pressure of the material. When recrystallization starts from the bottom and the sides, the original level of the surface at the sides of uplifted material is decreased, and mass conservation is preserved, observable in Fig. 14.18a and further described in [61].

Melting, void formation At an incident fluence of ~150 mJ/cm^2, a localized melting is induced sufficient to create voids, partly beneath the surface and partly opened up, Fig. 14.18b, while in the first case an uplift is observed; in the latter a hole is created. The void opening is accompanied by a material transfer in x- and y-direction and can induce an agglomeration to a droplet at the surface, near to the formed cavity. At these conditions, however, no material is spalled from the surface, concluded from the absence of debris around the structured area.

Spallation, droplet and wall formation In Fig. 14.18c grooves along the peak fluence with subfeatures at the sides are visible, formed at an incident fluence of 200 mJ/cm^2. The features can be described as walls, bulges, droplets, and melt splashes. MD-TTM suggest the following mechanisms for their formation: the melt is overheated and explosive boiling is observed [60, 64], manifesting in a significant number of gaseous bubbles opening near the surface in the center of the simulation volume. This is accompanied by a temporal volume increase leading to an uplift of the complete simulation volume. Recrystallization is starting from the bottom of the sample leaving only a molten semicircle. This shape can be explained by the combination of the sinusoidal shape of energy deposition and a smearing of the absorbed energy due to heat diffusion. In the upper part of the molten semicircle, the volume increases, and explosive boiling leads to material ejection in a plume. In the center of this plume of uplifting material, surrounded by two walls of molten gold, droplets of detached melt are visible, which will ultimately leave the surface. On the ground of the well (Fig. 14.18c) where material is partly ejected, thin filaments of gold have been solidified, with a few tens of nm thickness caused by a fast cooling process in the metal, due to high electron mobility [61].

Phase explosion, broad melting At an incident average fluence of ~350 mJ/cm^2, the complete sample surface is at least temporarily molten, and the material located at the peak intensity positions undergoes phase explosion. A distinct structure formation is partly hindered, and the simulation suggests that the ballistic range of the electrons is mainly determining the melting radius around the peak of the fluence profile [65]. At a certain periodicity, most of the surface is molten and the grooves are not becoming deeper.

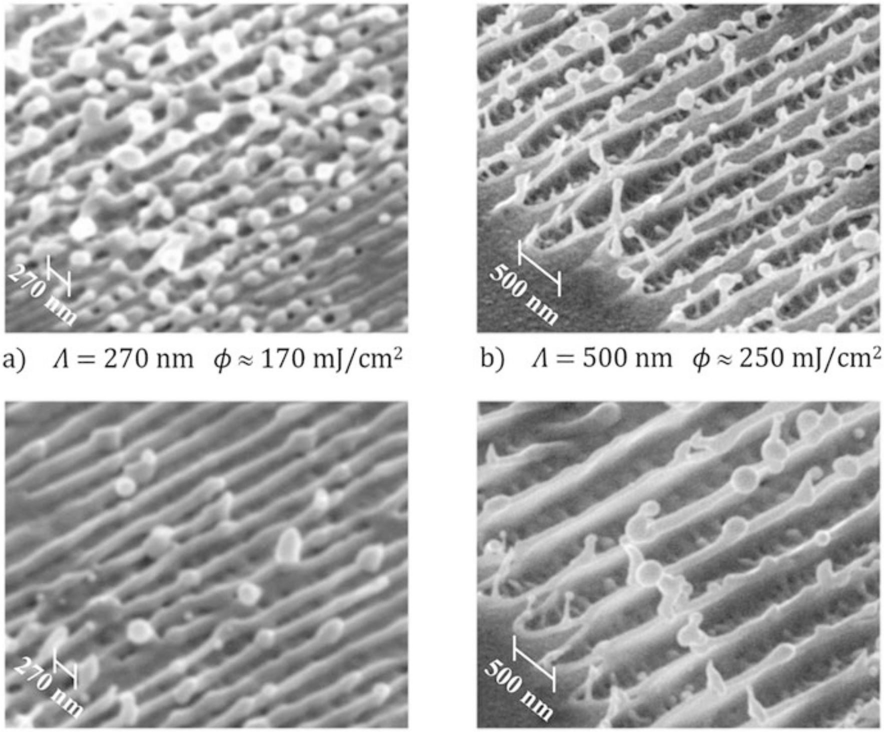

a) $\Lambda = 270$ nm $\phi \approx 170$ mJ/cm^2 b) $\Lambda = 500$ nm $\phi \approx 250$ mJ/cm^2

c) $\Lambda = 270$ nm $\phi \approx 300$ mJ/cm^2 d) $\Lambda = 500$ nm $\phi \approx 400$ mJ/cm^2

Fig. 14.19 Periodic patterns obtained with periods of 270 nm in (**a**) and (**c**) and 500 nm in (**b**) and (**d**) at various fluences. SEM images taken at a tilt angle 45°, the period is indicated by the scale bars. For larger periods, a higher fluence is required to obtain nanoridges composed of two collided walls. (Reprinted from [61])

When aiming for nm-sized periodic structures in metals and semiconductors, the heat diffusion limits the minimal obtainable structure size. The energy deposition needs to be on a time scale below the heat diffusion time. At spallation conditions (around 200 mJ/cm^2), the influence of the structure period Λ is investigated for $\Lambda = 270$ nm and $\Lambda = 500$ nm. These two periods are compared for two different fluence regimes, and the differences, especially in the groove spacing and nano-feature formation, are pointed out. In Fig. 14.19a the smaller of the two structure periods is shown at 170 mJ/cm^2. At these parameters groove formation with distinct walls and a high density of droplets is observed. The walls are colliding in a line along the lowest fluence of the profile. In the right corner in Fig. 14.19a, the fluence was lower; therefore, grooves are partly not even opened up. When comparing this structure to the larger period of $\Lambda = 500$ nm in Fig. 14.19b, some differences can be observed. Even though also groove formation is observed, space of undamaged surface is visible between the grooves; the wall-like features at the side of the groove are not colliding with each other like in (a), even though the fluence in (b) is significantly higher than in (a). When the fluence of the 500 nm structure is raised to 400 mJ/cm^2 also at this large structure period, the walls are colliding, forming a single feature between them. The walls contain material that has been laterally moved perpendicular to the grating lines and are standing higher than the original surface, as observed in Fig. 14.19d in the front left. The density of features at the surface seems reduced at this high fluence which might be due to a spallation of a significant amount of melt from the grooves. Also at the smaller structure in (c) the amount of droplets is significantly reduced compared to (a), however the walls are not as high as in (d), and they show a more bulge shape than a sharp thin wall-like shape. A possible explanation for these significant differences between structuring periods of 270 nm and 500 nm is that the gradient of the fluence profile is roughly twice as high in the smaller applied fluence profile.

Numerous other works also addressed the formation of structural details on various materials. With single pulses of a 560 fs/1030 nm-laser in a two-beam interference configuration, a line pattern with 720 nm period has been obtained on silicon [66]. At low fluence, the material exhibits some swelling on the lines of maximum intensity. Increasing the fluence, ablation grooves develop which are bordered by ridges protruding 3–4 nm over the original surface (Fig. 14.20). It is supposed that the protrusions originate from material expansion during resolidification of the melt or by oxidation of the heated, but not ablated silicon.

Detailed studies of multi-beam interference on gold films have been performed by Nakata et al. with laser pulses of about 200 fs at 800 nm. At low fluence, at the positions of maximum intensity (square array in the case of four-beam interference), bumps in the 57-nm thin gold films are observed [67]. Increasing the fluence slightly, drops develop and after further increase, whiskers or spikes are formed (Fig. 14.21). At the highest applied fluence, hole arrays are formed with the holes at the positions of maximum intensity. Using six-beam interference, a similar behavior on a hexagonal array has been demonstrated [27]. The spike formation is explained by the so-called solid-liquid-solid (SLS) mechanism [68]: the locally melted gold film detaches from the substrate forming a bump and by surface tension a melt droplet. By pinching off this droplet and quick freezing, a spiky structure with more than 1 μm height and roughly 100 nm width remains. However, height of the spike and curvature radius of the tip depend critically on the applied fluence ranging from about 120 to 150 mJ/cm^2. Using back side irradiation of the metal film through the substrate (the configuration typical for laser-induced forward transfer (LIFT)), the droplets pinched off can be transferred to a receiver substrate leading to regular arrays of gold nanodots [69].

In the case of surface patterning of soda lime glass with a picosecond laser at 532 nm, ripples (LIPSS) are found as a substructure of the rather coarse periodic line or dot pattern created by interference patterning [70]. The chosen fluences were close to 2 J/cm^2, where multiphoton absorption is expected. Aspect ratios of only <0.3 have been obtained, and chipping occurs with increasing irradiation dose. Also in the case of stainless steel, an interference pattern can be combined

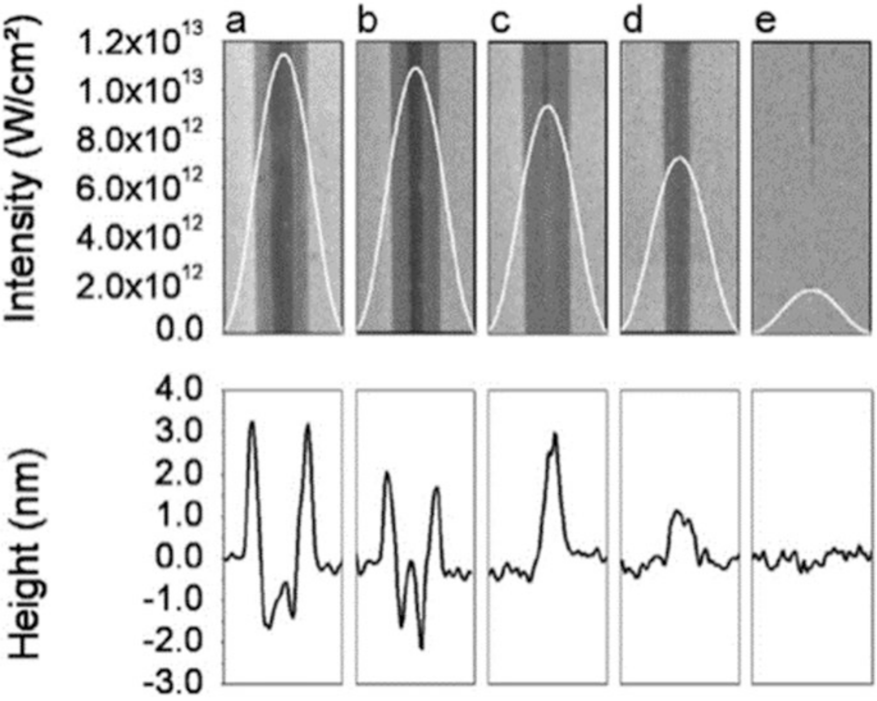

Fig. 14.20 Intensity profiles, SEM images, and AFM profiles at various positions of the interference spot on silicon with 720 nm period. (Reprinted from [66], with permission from Elsevier)

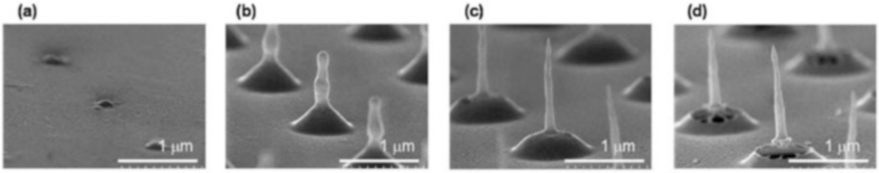

Fig. 14.21 Four-beam interference pattern on a thin gold film. Variation of the fluence: (**a**) 90,6 mJ/cm^2, (**b**) 125 mJ/cm^2, (**c**) 136 mJ/cm^2, (**d**) 148 mJ/cm^2. (Reprinted from [68], with permission from Elsevier)

with a ripple pattern. When the polarization is set in that way that the ripples develop perpendicular to the interference lines, a two-dimensional array of droplet-like pillars is obtained [71]. It was found that high fluences favor the interference structure formation, whereas low fluences lead predominantly to ripples, so that a fine tuning is necessary to obtain the desired pattern. Using a ps laser at 355 nm, hierarchical patterns consisting of a 650 nm period interference pattern and a 75 nm LIPSS pattern have been obtained in indium tin oxide thin films [72]. Depending on the beam polarization, the LIPSS substructure is parallel or perpendicular to the interference pattern. Also for these material and laser parameters, interference ablation is the dominant mechanism under high fluence conditions, while LIPSS formation is dominant at lower fluences. Similar hierarchical patterns composed of interference and ripple structure have been observed by 800 nm/100 fs-irradiation of stainless steel [73].

The importance of lateral material flow has been demonstrated for the case of 70 ps-laser structuring of steel at 532 nm [74]. At moderate fluences (around 1 J/cm^2), four-beam interference leads to a two-dimensional array of holes; as expected, the holes appear at the positions of maximum intensity. Increasing the fluence, the rims around the holes grow and the rims of neighboring holes merge to form a grid-like pattern. At the highest applied fluence of >25 J/cm^2, pillars of up to 400 nm height grow at the crossing points of the grid. The process is explained by the flow of molten material from the spots of highest local intensity to those of minimum intensity. This becomes possible by the comparatively long pulse duration of 70 ps.

Dimple arrays with 600 nm period have been generated on silicon by four-beam interference ablation at 532 nm and 515 nm with pulse durations of 300 fs, 300 ps, and 35 ns [75]. Whereas at 300 fs a well-defined hole array is formed, at 35 ns only very shallow dimples are obtained. The behavior is simulated in terms of nanoscale thermal diffusion. A thermal modulation depth is defined and classified into three regions: *ultrafine ablation*, *ablation and melting*, and *melting*. In the case of *ultrafine ablation* (300 fs), the material in the minima of the irradiation pattern remains at room temperature, whereas the material in the maxima is mainly vaporized. On the other hand, in the case of *melting* (35 ns), the material melts over the whole surface and no solid material is left. In this case, only shallow topographies are possible. At 300 ps, elevated bumps in the dimples are observed. The formation mechanism of these bumps is still unclear, but their appearance is a further indication of the dominant role of complex material flow leading to specific substructures.

By controlling the polarization of the individual interfering beams, complex substructures of the interference pattern can be created [29]. This has been demonstrated for six-beam interference of a 532 nm laser with 300 ps pulse duration on chromium films on glass. Excellent match between calculated and experimental results has been achieved. A further approach utilizes the fine tuning of the phase of the individual interfering beams by tilting inserted glass plates [28]. This way interference patterns with a complex unit cell and correspondingly complex surface patterns can be created.

Creating an interference pattern on copper with a 100 fs/800 nm-laser, accumulation of copper oxide (CuO, Cu_2O) mainly on the hills of the structure is observed [76]. This is explained by preferential redeposition of ablated and then oxidized material on the top of the pattern.

A further method to influence the structure details of laser interference ablation is the irradiation under confinement, i.e., a covering (transparent) material above the irradiated surface. The influence of a 400-nm-thick polymethylmethacrylate film deposited on Ni- and Si-surfaces has been investigated [77]. Without this

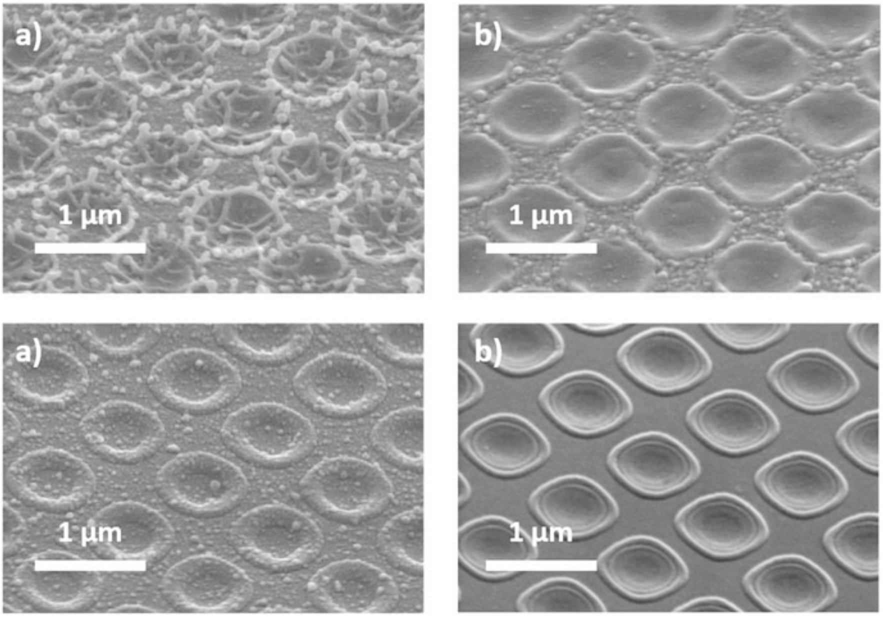

Fig. 14.22 Single pulse patterns obtained (**a**) without and (**b**) with confinement film. Top: Ni, 1.1 J/cm^2; bottom: Si, 0.3 J/cm^2. (Reprinted from [77])

confinement film, after single pulse irradiation, the interference pattern generated with a 500 fs/248 nm-laser is deteriorated by a lot of droplets and splashes, which are completely absent when the confinement film is applied (Fig. 14.22). Then, without this disturbing spatter, very fine sub-structures like 80 nm wide lines and 30 nm wide spaces can reproducibly be generated. Also in the case of gold, the strong droplet formation in vacuum or air environment can be suppressed by a water film confinement leading to a smoother surface [78].

Many of the structure details originate from the specific conditions of the moving melt. Surface tension leads to droplet formation; lateral movement leads to ridge formation; separating or colliding material fractions cause specific topographies, which cannot be directly derived from the laser intensity profile without regarding material properties and motion dynamics. Though lateral material movement is also observed in the case of sub-ps pulses, extended material flow over several µm becomes possible only for pulse duration of at least some ten picoseconds. This is indicated by the results of a comparative study using 0.5, 5, and 50 ps [19]. Sharp, narrow ridges are formed at 0.5 and 5 ps, whereas significant broadening is observed at 50 ps.

5 Applications of Periodic Surface Patterns in Optics, Fluidics, Life Science, and Tribology

Applications of ultrashort pulse-generated periodic nanostructures can be categorized in optically/electromagnetically effective and in mechanically/chemically effective cases.

5.1 Optically/Electromagnetically Effective Applications

In optical applications, the light diffraction at periodic nanostructures is utilized for guiding light into desired directions, i.e., to enhance or suppress propagation of light of specific wavelengths in specific directions. A grating like periodic pattern can be utilized for coupling light into planar waveguides. Planar waveguides consist of highly refractive optical films on dielectric substrates. Due to a high index contrast between film and substrate or film and environment (air), sub-micron film thicknesses are applied for efficient monomode guiding of visible or NIR light.

The coupling of light into such waveguides is carried out by means of diffraction gratings generated in the substrate or in the film. Ta_2O_5 is a waveguide material which is often used because of its high refractive index of $n = 2.2$ in the visible range. Gratings with 500 nm period have been generated by irradiation with 500-fs laser at 248 nm wavelength in Ta_2O_5 [79]. A single pulse at 100 mJ/cm^2 leads to a modulation depth of 10 nm, by repeated irradiation a modulation depth of 200 nm can be obtained. Similar results have been obtained using the same laser system for the patterning of $LiNbO_3$, a material used for waveguides as well with a refractive index of $n = 2.3$. A grating with 360 nm period and 80 nm modulation depth has been obtained by single pulse exposure [18]. Coupling and decoupling of HeNe laser light via gratings in $LiNbO_3$ created by a 800-nm-fs-laser has been demonstrated [31].

A periodic hole array with holes of 1 μm diameter and 2 μm depth in stainless steel causes a strong reduction of the surface reflectance leading to a virtually black surface. The fabrication of such a surface has been demonstrated by using four-beam interference with 800 nm, 50 fs pulses [26]. In addition to increased absorption, also increased light emission of a material can be obtained by generating a suitable surface structure, which reduces the losses by total internal reflection. The luminous InGaN-layer of a LED chip has been patterned with a two-dimensional pattern of μm-sized holes by four-beam interference using a 500 fs laser emitting at 248 nm [80]. This way the light extraction efficiency could be increased by a factor of two. By covering the structured surface with a special resin, a total enhancement of more than three has been obtained.

A special configuration of a two-grating interferometer has been applied for the fabrication of diffractive surface marks on silicon and steel [41]. The femtosecond laser beam (800 nm wavelength) is split into four beams by a diffractive optical

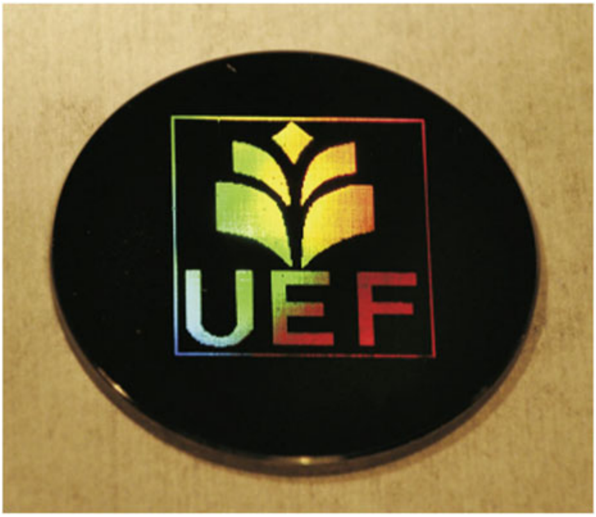

Fig. 14.23 Logo of the University of Eastern Finland made by using two-dimensional two-grating interference method on stainless steel. Sample diameter: 2 inch. (Reprinted by permission from Springer [41])

element (first grating) (Fig. 14.16). The second (recombining) grating is divided into four areas with linear gratings. Two of them recombine the horizontally diffracted beams and the other two the vertically diffracted ones. By adjusting periods and distances (see Sect. 3), the four-beam interference leads to the formation of a 2D hole pattern with a period of 780 nm on the sample surface. By stitching of 170 μm spots, each irradiated with 25 pulses of 0.8 J/cm^2 fluence, a colorful iridescent logo could be fabricated on a stainless steel surface (Fig. 14.23). In contrast to one-dimensional line patterns, which are hardly visible, if the viewing direction is not optimal, this 2D dot pattern can be viewed practically from all directions.

By using two diffraction gratings with variable distance and rotation angle, a huge variety of interference patterns can be generated [25]. This variety can be further enhanced by selecting or blocking particular beams (Fig. 14.10). In combination of such a pattern generator with a picosecond UV-laser (355 nm), a large number of surface topographies with sub-micron feature size can be fabricated directly on metallic surfaces, e.g., on stainless steel. Irradiation of such surface patterns with coherent light leads to characteristic diffraction patterns that can be analyzed by a camera-based reader (Fig. 14.24). This concept can be applied for security labelling and product traceability.

Surface texturing is an important process in Si thin film photovoltaics, e.g., for minimizing reflection losses. ZnO:Al, which is often used as transparent conductive oxide for the front contact of thin film cells, cannot be textured with good control by chemical etch processes. Therefore, laser patterning can provide the texture necessary for enhanced light trapping. By using a 10 ps–355 nm laser and single

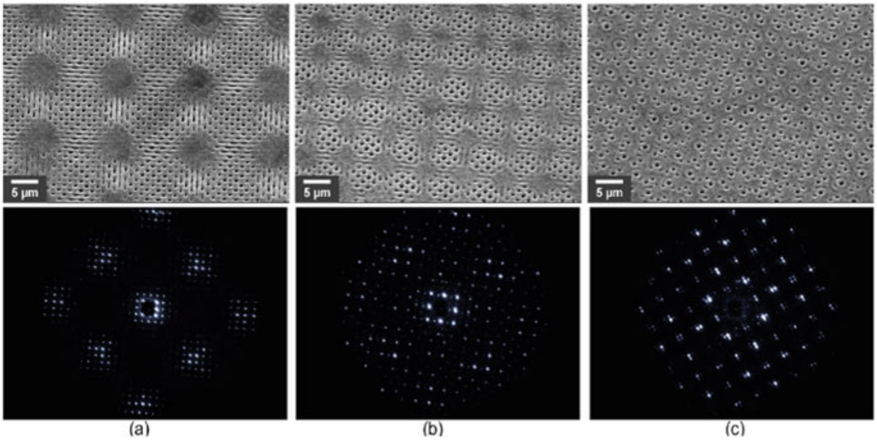

Fig. 14.24 Scanning electron microscopy (top) and diffraction pattern (bottom) images of holographic marks that were fabricated by interference of 12 beams from a pattern generator comprising two phase gratings and a beam selector. Rotation angle between the two phase gratings: (**a**) 8°; (**b**) 16°; (**c**) 35°. (Reprinted from [25])

pulse two-beam interference, a grating of 120 nm depth could be created in ZnO:Al [81]. Large area texturing is obtained by scanning the laser running at high repetition rate over the sample using a movable stage. The structured films show a moderate increase in sheet resistance and no loss in transmittance. The laser interference patterning is therefore a suitable method for films that cannot be textured by etching processes.

Two-beam interference of a 35 fs–800 nm laser pulse has been used to write a binary grating of zones with alternatively oriented magnetization in the ferromagnetic amorphous alloy GdFeCo [82]. A periodicity of 2.5 μm could be obtained by using mask projection with a suitable phase mask. Each laser pulse leads to the local reversion of the magnetic domains in the irradiated area enabling the overwriting of an existing configuration. The authors claim that by manipulating the wavefront of one or both partial beams using a 2D-SLM, 10^6 individually addressable domains could be switched all optically at a rate of 0.6 Gb/s.

5.2 Mechanically/Chemically Effective Applications

Grating patterns on soda lime glass have been fabricated by two- and four-beam interference of a ps laser at 532 nm [70]. As glasses are very transparent in the visible spectral range, the ablation process is based on nonlinear absorption. Structure periods between 2.3 and 9 μm have been obtained, however with substantial surface roughness. These deterministic patterns are partially superimposed by a LIPSS pattern with a period around 300 nm. This surface texture exhibits an increased hydrophilic behavior. In some cases, even super-hydrophilicity with contact angles below 5° has been obtained. Such super-hydrophilic glass surfaces can be used, e.g., in antifogging and self-cleaning applications.

Stainless steel, invar, and tungsten have been patterned by two-beam interference with a picosecond laser (1.7 ps) at 1030 nm wavelength [83]. High pulse energies up to 3 mJ enable sufficient fluence on a large elliptical spot of 1 mm × 0.2 mm size, so that a high process speed up to 200 cm^2/min can be reached. The surface pattern with 2.6 μm period is superimposed by high spatial frequency and low spatial frequency LIPSS. Further hierarchical structures consisting of deterministic microscale gratings with nanoscale protrusions are supposed to cause the observed super-hydrophobicity with contact angles $\geq$150 for all investigated materials.

Large-scale production of patterned surfaces is possible by the structuring of molds and reproduction of the surface pattern via processes like hot embossing or injection molding. A periodic hole array fabricated in a steel mold has been fabricated by an ultrashort pulse UV laser (248 nm, 1 ps) [44]. In this case, a multispot beam pattern for parallel hole drilling has been generated by a pixelated diffractive optical element. 25 × 25 holes of 5 μm diameter with an aspect ratio >1 could be generated simultaneously. By variothermal injection molding, a spike array on a polypropylene surface is produced, which exhibits excellent superhydrophobicity with a contact angle >160° (Fig. 14.25). Also gratings with 1.5 μm period and an aspect ratio >1 have been generated in metallic injection molds [84]. This way diffractive security labels enabling fraud resistance and product traceability can be easily molded in plastic parts. A tool life of more than two million molding cycles has been obtained. Further investigations show that even sub-micron-period structures can be transferred into polypropylene by injection molding [85].

The possibility of roll-to-roll hot-embossing of polymer foils with laser-patterned Ni-sleeves has been demonstrated [86]. A picosecond laser at 1064 nm wavelength is used to generate a two-beam interference pattern with a pitch between 1.5 and 6 μm, which is superimposed by LIPSS structures with 800 nm and 160 nm. The embossed replica in a PET foil contains the interference patters (albeit with a reduced height compared to the Ni-sleeve in the case of small periods), but the 800 nm period is only partially and the 160 nm period is not transferred into the polymer.

Antibacterial surfaces on stainless steel have been generated by creating 1D and 2D-gratings (holes or cones) by two-beam interference with a ps-laser at 1030 nm wavelength [87]. In order to obtain the 2D patterns, two exposures with orthogonal orientation of the sample and suitable polarization were applied. The pattern parameters (period and depth) were optimized in such a way that the contact points of the bacteria cells to the surface are minimized. Reduction of bacteria retention of 70–80% in the case of S. aureus and even more than 99% in the case of E. coli compared to unstructured reference samples could be obtained. It turned out that interference processing provides greater flexibility than LIPSS for tailoring the specific characteristics appropriate for antibacterial surfaces.

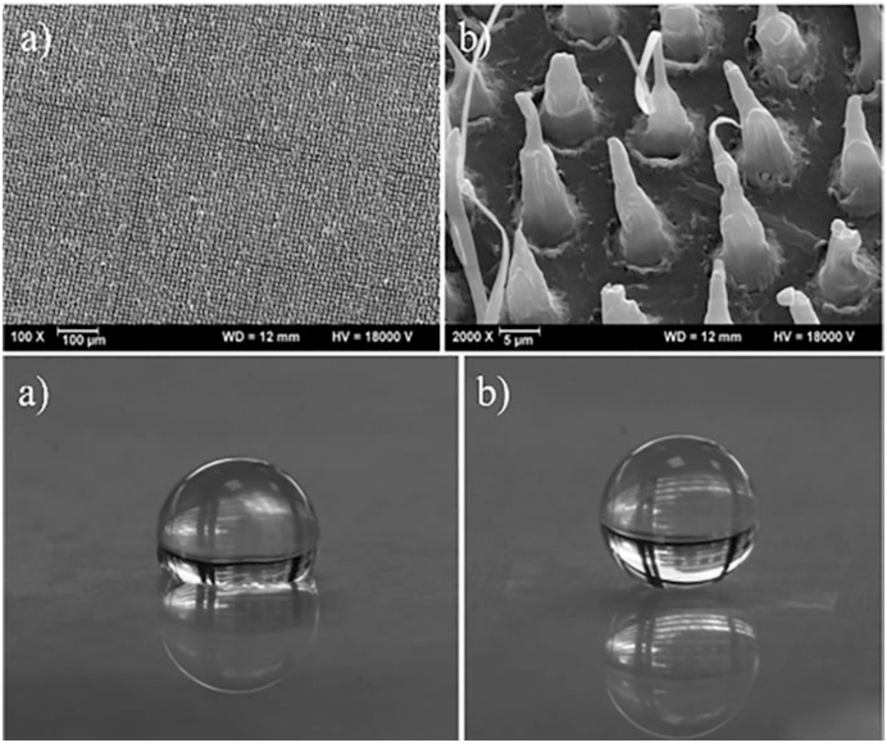
a)
100 X 100 µm WD = 12 mm HV = 18000 V
b)
2000 X 5 µm WD = 12 mm HV = 18000 V
a)
b)

Fig. 14.25 *Top:* SEM pictures of a polypropylene (PP) replica of a laser-patterned steel mold obtained by variothermal injection molding. Period ~13 μm, base diameter of the pins ~5 μm. (**a**) overview, (**b**) close up view of (**a**). *Bottom:* Contact angle measurement on a replicated PP sample, (**a**) without and (**b**) with surface texture. (Reprinted by permission from Springer [44])

The antibacterial property of a copper surface against Escherichia coli is enhanced by a periodic groove pattern with 2 μm wide and 1 μm deep grooves made by interference processing using a 100 fs laser operating at 800 nm [88]. The width of the grooves is in the scale range of single bacteria cells. A reduction of bacterial cell viability of up to 15 times in comparison with a smooth copper surface has been achieved.

Reduced cell adhesion is also essential in the case of so-called trauma implants. These implants, made of stainless steel or titanium, are used as immobilization aids after bone fracture and have to be removed surgically after healing of the fracture. This is sometimes difficult due to the strong integration with the bone tissue. Therefore, periodic surface micro- and nanostructures are ablated on the implant surface in order to influence cell adhesion and facilitate removal. In a systematic parameter study, various patterns have been created on stainless steel and titanium by interference ablation with a picosecond laser emitting at 355 nm wavelength

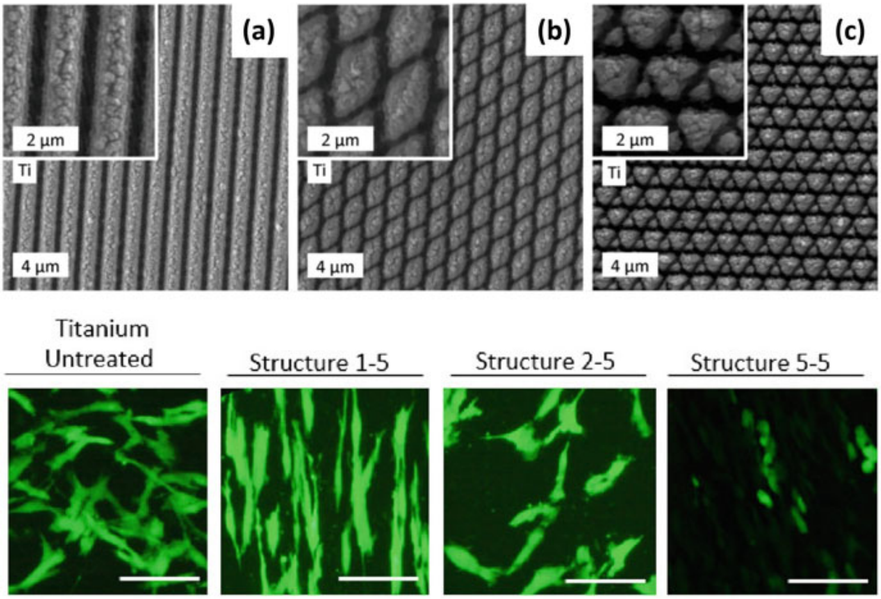

Fig. 14.26 Scanning electron microscopy (SEM) examination of nanostructures on titanium (**a**–**c**) plates. The following structures are shown: (**a**): 1-5; (**b**): 2-5; (**c**): 5-5. The influence of nanostructures on cell morphology. Whole plates of titanium were structured, and SCP1 cell morphology was analyzed 48 h after cell seeding. The structure 1-5 lead to elongated and linearized cell morphology on titanium plates. The structure 2-5 had only minor effects on cell morphology, while the structure 5-5 resulted in smaller and rounded cell phenotypes. (Reprinted from [89])

[89]. The patterns are composed of linear gratings with 1.5 μm period generated by two-beam interference and superposition of 1, 2, or 3 linear gratings under variation of their respective orientation (Fig. 14.26). Reduced cell adhesion was found for four out of 30 investigated structure types, while cell morphology was influenced by two structures. Strong effects on cell adhesion were observed especially for deep structures, while only minor effects were detected for shallow structures.

A 100 fs/800 nm laser has been used to fabricate groove patterns in yttria-stabilized tetragonal zirconia polycrystal (Y-TZP, dental zirconia) by two-beam interference [90]. This material is used for several components applied in restorative dentistry, e.g., for dental implants. The aim is to improve the capacity of the material to osteointegrate, i.e., to establish a good implant-to-bone contact. Surface patterns with 3 μm period and 1 μm depth as well as with 10 μm period and 3 μm depth have been prepared. This topographical pattern was combined with a biochemical modification in form of a peptide-based platform. Whereas the grooves mainly influence the contact guidance (cell alignment, elongation, and migration), the peptide platform improved cell adhesion and generated the osteogenic potential (Fig. 14.27). Alumina toughened zirconia (ATZ) is another material used in dental

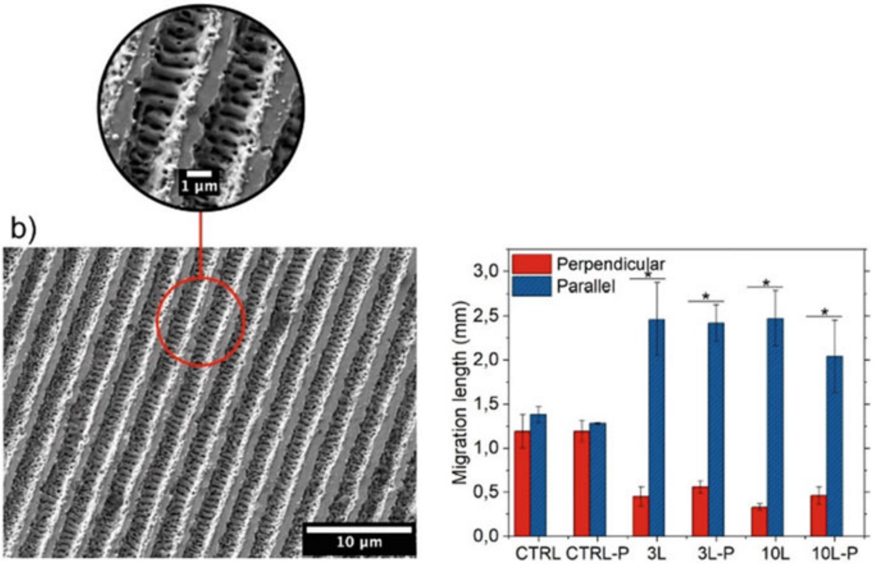

Fig. 14.27 *Left:* FESEM micrograph of a Y-PZT surface with a 3 µm period groove pattern. *Right:* Migration length (mm) for the studied specimens in two directions: parallel and perpendicular to the grooves (3 L = 3 mm period, 10 L = 10 µm period). In CTRL specimens (without grooves) two orthogonal directions were chosen arbitrarily. * indicates statistical differences between the migration length in the parallel and the perpendicular direction for a particular specimen. (Reprinted from [90], with permission from Elsevier)

and maxillofacial applications. Due to evenly dispersed alumina particles in the zirconia matrix, its strength exceeds that of pure ZrO_2. By generating a groove pattern with 10 µm period using 560 fs pulses at 1030 nm wavelength, cell attachment and alignment could be modified, and a faster and greater osteogenic differentiation of human mesenchymal stem cells (hMSC) has been obtained [91].

Periodic surface patterns can also influence the friction behavior of surfaces. For the friction behavior of 100Cr6 steel, a comparative study of the influence of surface patterns made by laser beam interference ablation (LBIA) and those by creating laser-induced low spatial frequency LIPSS (LSFL) has been performed [92]. Both experiments were performed with a similar laser of 220–250 fs pulse duration, but at different wavelengths (343 nm for LBIA and 1030 nm for LIPSS). Though the structure periods are rather similar, the tribological behavior is different, presumably due to the higher aspect ratio of the LBIA-pattern (Fig. 14.28). In the case of a lubricated surface, the coefficient of friction (COF) increases for LBIA compared to a smooth reference surface, whereas it mostly decreases in case of LIPSS. In the case of a dry surface, the behavior is just the other way round (Table 14.1).

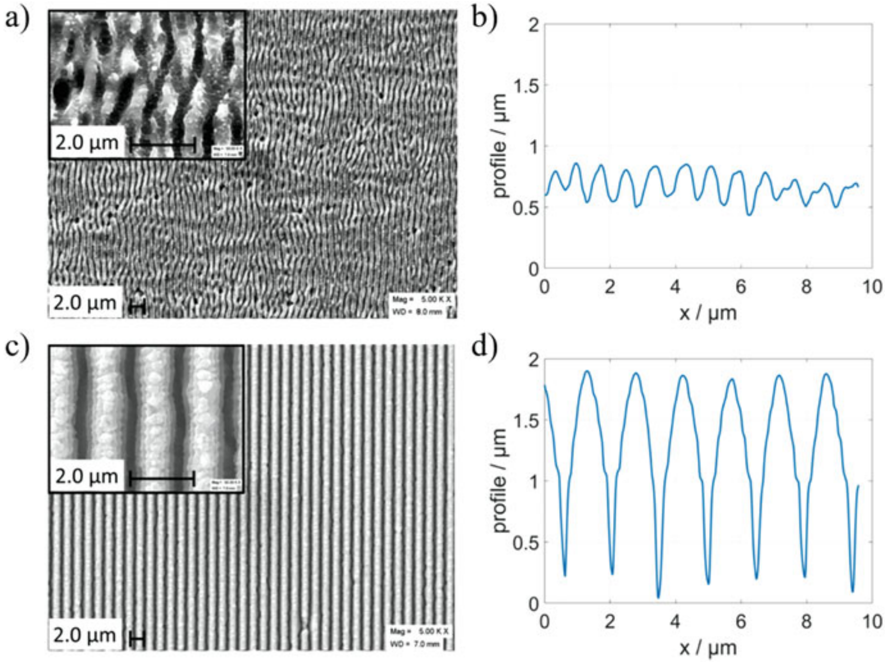

Fig. 14.28 Laser-based surface modification using the LSFL and LBIA method. SEM image of LSFL (**a**) reveals a mostly vertical orientation of the structures, and the corresponding AFM profile (**b**) shows the height profile. Structures fabricated by LBIA show a high homogeneity in the SEM image (**c**) and the AFM profile (**d**). (Reprinted from [92])

Table 14.1 Summarized modification possibilities with respect to a polished reference surface indicating no influence (0), increase (+), strong increase (++), decrease (−), and strong decrease (− −) of the coefficient of friction

	Dry				Lubricated			
Ball	LBIA		LSFL		LBIA		LSFL	
	90	0	90	0	90	0	90	0
Steel	0	− −	+	+	++	+	0	−
WC	−	− −	++	+	+	++	− −	− −

Reprinted from [92]

6 Perspectives of Laser Interference Ablation

The rapid advancement of high power ultrashort pulse lasers massively challenges the entire field of surface fabrication technology. Nowadays, femtosecond laser sources emerge whose average power exceed the kilowatt level and their single pulse energy is often in the multi-millijoule range [93–95]. Conventional irradiation schemes comprising beam focusing or mask projection completely fail to handle the enormous power of such laser systems.

This problem was already recognized, and corresponding novel irradiation strategies have been proposed and tested. All these strategies share a common philosophy: parallelization of the surface irradiation. This means that the high power laser beam is subdivided in many individual beams, each of them carrying only a fraction of the total power and acting in a parallel fashion. For the realization of a parallel processing scheme, there are several approaches.

Typically, diffractive optical elements are used to split the high power beam, and these can further be manipulated by spatial light modulators (SLM) combined with a scanner system or even with a multitude of scanners [96].

Contemporary and future setups have to address numerous issues related to potential damage of optics and layers, heat management at components with residual absorption, and ensuring a high level of flexibility by creating arbitrary patterns or periodic structures.

Up to now, laser fabrication of periodic nanostructures has not reached a level of industrial application because of lacking an appropriate throughput. We anticipate that combining the interference techniques discussed in this chapter with future massive parallelization of the irradiation will lead to a wide-spread application of the technology in tribology, functionalization of surgical implants, and surface marking. For an overview of large area applications, please see Chap. 26.

Moreover, we foresee that there will be a great demand to combine all the abovementioned capabilities with additional pulse compression techniques to allow in future the high throughput processing of any material with very high precision applying high average power ultrashort pulses with durations down to the few-cycle regime [97, 98].

Acknowledgments Financial support by the Deutsche Forschungsgemeinschaft, project IH 17/18-2 is gratefully acknowledged.

References

1. P. Simon, J. Ihlemann, Machining of submicron structures on metals and semiconductors by ultrashort UV-laser pulses. Appl. Phys. A Mater. Sci. Process. **63**(5), 505–508 (1996)
2. K. Kawamura, T. Ogawa, N. Sarukura, M. Hirano, H. Hosono, Fabrication of surface relief gratings on transparent dielectric materials by two-beam holographic method using infrared femtosecond laser pulses. Appl. Phys. B Lasers Opt. **71**(1), 119–121 (2000)
3. N. Schröder, G. Vergara, B. Voisat, A.F. Lasagni, Monitoring the heat accumulation during fabrication of surface micro-patterns on metallic surfaces using direct laser interference patterning. J. Laser Micro Nanoeng. **15**(2), 150–157 (2020)
4. F. Fraggelakis, G.D. Tsibidis, E. Stratakis, Tailoring submicrometer periodic surface structures via ultrashort pulsed direct laser interference patterning. Phys. Rev. B **103**(5), 54105 (2021)
5. C. He, K. Vannahme, A. Gillner, High-efficiency sub-micrometer multi-beam interference structuring for large-scale surface using ultrashort laser pulses. J. Laser Micro Nanoeng. **14**(1), 95–99 (2019)
6. B. Lechthaler, C. Pauly, F. Mücklich, Objective homogeneity quantification of a periodic surface using the Gini coefficient. Sci. Rep. **10**, 14516 (2020)

7. M. Wang, Q. Guo, S. Wang, W. Zhu, F. Tian, Y. Wei, P. Ji, X. Li, J. Yang, Interference femtosecond laser stamping of micro-grating structures and time-resolved observation of its dynamics. Opt. Express **28**(12), 18376 (2020)
8. A.A. Maznev, T.F. Crimmins, K.A. Nelson, How to make femtosecond pulses overlap. Opt. Lett. **23**(17), 1378 (1998)
9. Y. Nakata, T. Okada, M. Maeda, Lines of periodic hole structures produced by laser ablation using interfering femtosecond lasers split by a transmission grating. Appl. Phys. A Mater. Sci. Process. **77**(3–4), 399–401 (2003)
10. Z. Bor, Distortion of femtosecond laser pulses in lenses and lens systems. J. Mod. Opt. **35**(12), 1907–1918 (1988)
11. J. Amako, K. Nagasaka, N. Kazuhiro, Chromatic-distortion compensation in splitting and focusing of femtosecond pulses by use of a pair of diffractive optical elements. Opt. Lett. **27**(11), 969 (2002)
12. T. Kondo, S. Matsuo, S. Juodkazis, H. Misawa, Femtosecond laser interference technique with diffractive beam splitter for fabrication of three-dimensional photonic crystals. Appl. Phys. Lett. **79**(6), 725–727 (2001)
13. G. Lee, S.H. Song, C.-H. Oh, P.-S. Kim, Arbitrary structuring of two-dimensional photonic crystals by use of phase-only Fourier gratings. Opt. Lett. **29**(21), 2539 (2004)
14. Y. Kuroiwa, N. Takeshima, Y. Narita, S. Tanaka, K. Hirao, Arbitrary micropatterning method in femtosecond laser microprocessing using diffractive optical elements. Opt. Express **12**(9), 1908 (2004)
15. Y. Hayasaki, T. Sugimoto, A. Takita, N. Nishida, Variable holographic femtosecond laser processing by use of a spatial light modulator. Appl. Phys. Lett. **87**, 031101 (2005)
16. N. Sanner, N. Huot, E. Audouard, C. Larat, J.-P. Huignard, B. Loiseaux, Programmable focal spot shaping of amplified femtosecond laser pulses. Opt. Lett. **30**(12), 1479 (2005)
17. S. Hasegawa, Y. Hayasaki, Adaptive optimization of a hologram in holographic femtosecond laser processing system. Opt. Lett. **34**(1), 22 (2009)
18. K. Chen, J. Ihlemann, P. Simon, I. Baumann, W. Sohler, Generation of submicron surface gratings on LiNbO3 by ultrashort UV laser pulses. Appl. Phys. A Mater. Sci. Process. **65**(4–5), 517–518 (1997)
19. P. Simon, J. Ihlemann, Ablation of submicron structures on metals and semiconductors by femtosecond UV-laser pulses. Appl. Surf. Sci. **109–110**, 25–29 (1997)
20. M. Lenzner, J. Krüger, S. Sartania, Z. Cheng, C. Spielmann, G. Mourou, F. Kautek, Femtosecond optical breakdown in dielectrics. Phys. Rev. Lett. **80**(18), 4076–4079 (1998)
21. J. Bekesi, J.-H. Klein-Wiele, D. Schaefer, J. Ihlemann, P. Simon, Surface texturing of metals with submicron precision using a short-pulse UV laser, in *Third International Symposium on Laser Precision Microfabrication, Proc. SPIE*, vol. 4830, (2003), p. 497
22. J.-H. Klein-Wiele, P. Simon, Sub-wavelength pattern generation by laser direct writing via repeated irradiation. Opt. Express **21**(1), 626 (2013)
23. J. Ihlemann, J.H. Klein-Wiele, J. Bekesi, P. Simon, UV ultrafast laser processing using phase masks. J. Phys. Conf. Ser. **59**(1), 449–452 (2007)
24. J.H. Klein-Wiele, P. Simon, Fabrication of periodic nanostructures by phase-controlled multiple-beam interference. Appl. Phys. Lett. **83**(23), 4707–4709 (2003)
25. J.-H. Klein-Wiele, T. Fricke-Begemann, P. Simon, J. Ihlemann, Complex diffractive surface patterns on metals by UV-ps laser ablation. Opt. Express **27**(20), 28902 (2019)
26. K. Paivasaari, J.J.J. Kaakkunen, M. Kuittinen, T. Jaaskelainen, Enhanced optical absorptance of metals using interferometric femtosecond ablation. Opt. Express **15**(21), 13838 (2007)
27. Y. Nakata, M. Yoshida, K. Osawa, N. Miyanaga, Fabricating a regular hexagonal lattice structure by interference pattern of six femtosecond laser beams. Appl. Surf. Sci. **417**, 69–72 (2017)
28. B. Voisiat, M. Gedvilas, S. Indrišiunas, G. Raciukaitis, Flexible microstructuring of thin films using multi-beam interference: Ablation with ultrashort lasers. J. Laser Micro Nanoeng. **6**(3), 185–190 (2011)

29. S. Indrišiūnas, B. Voisiat, M. Gedvilas, G. Račiukaitis, New opportunities for custom-shape patterning using polarization control in confocal laser beam interference setup. J. Laser Appl. **29**(1), 011501 (2017)
30. K.I. Kawamura, N. Sarukura, M. Hirano, H. Hosono, Holographic encoding of fine-pitched micrograting structures in amorphous SiO_2 thin films on silicon by a single femtosecond laser pulse. Appl. Phys. Lett. **78**(8), 1038–1040 (2001)
31. M. Hirano, K.I. Kawamura, H. Hosono, Encoding of holographic grating and periodic nanostructure by femtosecond laser pulse. Appl. Surf. Sci. **197–198**, 688–698 (2002)
32. K. Venkatakrishnan, N.R. Sivakumar, C.W. Hee, H. Tan, W.L. Liang, G.K. Gan, Direct fabrication of surface-relief grating by interferometric technique using femtosecond laser. Appl. Phys. A Mater. Sci. Process. **77**(7), 959–963 (2003)
33. Y. Li, K. Yamada, T. Ishizuka, W. Watanabe, K. Itoh, Z. Zhou, Single femtosecond pulse holography using polymethyl methacrylate. Opt. Express **10**(21), 1173 (2002)
34. K. Venkatakrishnan, N.R. Sivakumar, B. Tan, Fabrication of planar gratings by direct ablation using an ultrashort pulse laser in a common optical path configuration. Appl. Phys. A Mater. Sci. Process. **76**(2), 143–146 (2003)
35. V. Oliveira, N.I. Polushkin, O. Conde, R. Vilar, Laser surface patterning using a Michelson interferometer and femtosecond laser radiation. Opt. Laser Technol. **44**(7), 2072–2075 (2012)
36. C.W. Hee, B.K.A. Ngoi, L.E.N. Lim, K. Venkatakrishnan, W.L. Liang, Effect of polarization on femtosecond pulsed laser ablation of surface relief gratings using a novel interferometer. Opt. Laser Technol. **37**(2), 93–98 (2005)
37. J. Bekesi, J. Meinertz, J. Ihlemann, P. Simon, Fabrication of large-area grating structures through laser ablation. Appl. Phys. A Mater. Sci. Process. **93**(1), 27–31 (2008)
38. J. Bekesi, J. Meinertz, J. Ihlemann, P. Simon, Grating interferometers for efficient generation of large area grating structures via laser ablation. J. Laser Micro Nanoeng. **2**(3), 221–224 (2007)
39. J. Bekesi, P. Simon, J. Ihlemann, Deterministic sub-micron 2D grating structures on steel by UV-fs-laser interference patterning. Appl. Phys. A Mater. Sci. Process. **114**(1), 69–73 (2014)
40. J. Bekesi, J. Meinertz, P. Simon, J. Ihlemann, Sub-500-nm patterning of glass by nanosecond KrF excimer laser ablation. Appl. Phys. A Mater. Sci. Process. **110**(1), 17–21 (2013)
41. J.J.J. Kaakkunen, K. Paivasaari, P. Vahimaa, Fabrication of large-area hole arrays using high-efficiency two-grating interference system and femtosecond laser ablation. Appl. Phys. A Mater. Sci. Process. **103**(2), 267–270 (2011)
42. B. Borchers, J. Bekesi, P. Simon, J. Ihlemann, Submicron surface patterning by laser ablation with short UV pulses using a proximity phase mask setup. J. Appl. Phys. **107**(6), 063106 (2010)
43. J.J.J. Kaakkunen, J. Bekesi, J. Ihlemann, P. Simon, Ablation of microstructures applying diffractive elements and UV femtosecond laser pulses. Appl. Phys. A Mater. Sci. Process. **101**(2), 225–229 (2010)
44. J. Bekesi, J.J.J. Kaakkunen, W. Michaeli, F. Klaiber, M. Schoengart, J. Ihlemann, P. Simon, Fast fabrication of super-hydrophobic surfaces on polypropylene by replication of short-pulse laser structured molds. Appl. Phys. A Mater. Sci. Process. **99**(4), 691–695 (2010)
45. Y. Hayasaki, M. Nishitani, H. Takahashi, H. Yamamoto, A. Takita, D. Suzuki, S. Hasegawa, Experimental investigation of the closest parallel pulses in holographic femtosecond laser processing. Appl. Phys. A Mater. Sci. Process. **107**(2), 357–362 (2012)
46. Q. Zhou, W. Yang, F. He, R. Stoian, R. Hui, G. Cheng, Femtosecond multi-beam interference lithography based on dynamic wavefront engineering. Opt. Express **21**(8), 9851 (2013)
47. J.H. Klein-Wiele, J. Bekesi, P. Simon, Sub-micron patterning of solid materials with ultraviolet femtosecond pulses. Appl. Phys. A Mater. Sci. Process. **79**(4–6), 775–778 (2004)
48. N.A. Inogamov, V.V. Zhakhovsky, V.A. Khokhlov, Y.V. Petrov, K.P. Migdal, Solitary nanostructures produced by ultrashort laser pulse. Nanoscale Res. Lett. **11**(1), 1–13 (2016)
49. O. Apel, F. Beinhorn, J. Ihlemann, J.H. Klein-Wiele, G. Marowsky, P. Simon, Periodic nanostructures. Z. Phys. Chem. **214**(9), 1233–1250 (2000)
50. E. Molotokaite, M. Gedvilas, G. Račiukaitis, V. Girdauskas, Picosecond laser beam interference ablation of thin metal films on glass substrate. J. Laser Micro Nanoeng. **5**(1), 74–79 (2010)

51. T. Höche, R. Böhme, J.W. Gerlach, F. Frost, K. Zimmer, B. Rauschenbach, Semiconductor nanowires prepared by diffraction-mask-projection excimer-laser patterning. Nanomaterials Lett. **4**(5), 895–897 (2004)
52. Y. Nakata, Y. Matsuba, N. Miyanaga, Sub-micron period metal lattices fabricated by interfering ultraviolet femtosecond laser processing. Appl. Phys. A Mater. Sci. Process. **122**(5), 1–6 (2016)
53. D.S. Ivanov, B. Rethfeld, G.M. O'Connor, T.J. Glynn, A.N. Volkov, L.V. Zhigilei, The mechanism of nanobump formation in femtosecond pulse laser nanostructuring of thin metal films. Appl. Phys. A Mater. Sci. Process. **92**(4), 791–796 (2008)
54. S.I. Ashitkov, P.S. Komarov, A.V. Ovchinnikov, E.V. Struleva, V.V. Zhakhovskii, N.A. Inogamov, M.B. Agranat, Ablation and nanostructuring of metals by femtosecond laser pulses. Quantum Electron. **44**(6), 535–539 (2014)
55. S.I. Anisimov, V.V. Zhakhovsky, N.A. Inogamov, S.A. Murzov, V.A. Khokhlov, Formation and crystallisation of a liquid jet in a film exposed to a tightly focused laser beam. Quantum Electron. **47**(6), 509–521 (2017)
56. C. Fourment, F. Deneuville, D. Descamps, F. Dorchies, S. Petit, O. Peyrusse, B. Holst, V. Recoules, Experimental determination of temperature-dependent electron-electron collision frequency in isochorically heated warm dense gold. Phys. Rev. B **89**, 161110(R) (2014)
57. A. Blumenstein, E.S. Zijlstra, D.S. Ivanov, S.T. Weber, T. Zier, F. Kleinwort, B. Rethfeld, J. Ihlemann, P. Simon, M.E. Garcia, Transient optics of gold during laser irradiation: From first principles to experiment. Phys. Rev. B **101**(16), 165140 (2020)
58. D.S. Ivanov, L.V. Zhigilei, Combined atomistic-continuum modeling of short-pulse laser melting and disintegration of metal films. Phys. Rev. B **68**(6), 64114 (2003)
59. D.S. Ivanov, V.P. Lipp, A. Blumenstein, F. Kleinwort, V.P. Veiko, E. Yakovlev, V. Roddatis, M.E. Garcia, B. Rethfeld, J. Ihlemann, P. Simon, Experimental and theoretical investigation of periodic nanostructuring of Au with ultrashort UV laser pulses near the damage threshold. Phys. Rev. Appl. **4**, 064006 (2015)
60. L.V. Zhigilei, Z. Lin, D.S. Ivanov, Atomistic modeling of short pulse laser ablation of metals: Connections between melting, spallation, and phase explosion. J. Phys. Chem. C **113**(27), 11892–11906 (2009)
61. A. Blumenstein, M.E. Garcia, B. Rethfeld, P. Simon, J. Ihlemann, D.S. Ivanov, Formation of periodic nanoridge patterns by ultrashort single pulse UV laser irradiation of gold. Nanomaterials **10**(10), 1–14 (2020)
62. D.S. Ivanov, L.V. Zhigilei, Effect of pressure relaxation on the mechanisms of short-pulse laser melting. Phys. Rev. Lett. **91**(10), 105701 (2003)
63. D.S. Ivanov, A.I. Kuznetsov, V.P. Lipp, B. Rethfeld, B.N. Chichkov, M.E. Garcia, W. Schulz, Short laser pulse nanostructuring of metals: Direct comparison of molecular dynamics modeling and experiment. Appl. Phys. A Mater. Sci. Process. **111**(3), 675–687 (2013)
64. B. Rethfeld, D.S. Ivanov, M.E. Garcia, S.I. Anisimov, Modelling ultrafast laser ablation. J. Phys. D. Appl. Phys. **50**(19), 193001 (2017)
65. J. Hohlfeld, S.S. Wellershoff, J. Güdde, U. Conrad, V. Jähnke, E. Matthias, Electron and lattice dynamics following optical excitation of metals. Chem. Phys. **251**(1–3), 237–258 (2000)
66. V. Oliveira, R. Vilar, R. Serra, J.C. Oliveira, N.I. Polushkin, O. Conde, Sub-micron structuring of silicon using femtosecond laser interferometry. Opt. Laser Technol. **54**(1), 428–431 (2013)
67. Y. Nakata, N. Shimada, Y. Matsuba, N. Miayanaga, Fabrication and applications of periodic nanostructures formed by interfering femtosecond laser proccessing, in *Proceedings of ICALEO 2014*, (2014), pp. 965–970
68. Y. Nakata, N. Miyanaga, K. Momoo, T. Hiromoto, Solid-liquid-solid process for forming free-standing gold nanowhisker superlattice by interfering femtosecond laser irradiation. Appl. Surf. Sci. **274**, 27–32 (2013)
69. Y. Nakata, E. Hayashi, K. Tsubakimoto, N. Miyanaga, A. Narazaki, T. Shoji, Y. Tsuboi, Nanodot array deposition via single shot laser interference pattern using laser-induced forward transfer. Int. J. Extrem. Manuf. **2**(2), 1–6 (2020)

70. M. Soldera, S. Alamri, P.A. Sürmann, T. Kunze, A.F. Lasagni, Microfabrication and surface functionalization of soda lime glass through direct laser interference patterning. Nanomaterials **11**, 129 (2021)
71. S. Alamri, F. Fraggelakis, T. Kunze, B. Krupop, G. Mincuzzi, R. Kling, A.F. Lasagni, On the interplay of DLIP and LIPSS upon ultra-short laser pulse irradiation. Materials (Basel). **12**(7), 1018 (2019)
72. N. Charipar, R.C.Y. Auyeung, H. Kim, K. Charipar, A. Piqué, Hierarchical laser patterning of indium tin oxide thin films. Opt. Mater. Express **9**(7), 3035–3045 (2019)
73. D.W. Müller, T. Fox, P.G. Grützmacher, S. Suarez, F. Mücklich, Applying ultrashort pulsed direct laser interference patterning for functional surfaces. Sci. Rep. **10**(1), 3647 (2020)
74. B. Voisiat, S. Milles, A.F. Lasagni, Impact of molten pool dynamics on resultant surface structures during direct laser interference patterning. J. Laser Micro Nanoeng. **16**(1), 30–35 (2021)
75. M. Gedvilas, S. Indrišiunas, B. Voisiat, E. Stankevičius, A. Selskis, G. Račiukaitis, Nanoscale thermal diffusion during the laser interference ablation using femto-, pico-, and nanosecond pulses in silicon. Phys. Chem. Chem. Phys. **20**(17), 12166–12174 (2018)
76. D.W. Müller, A. Holtsch, S. Lößlein, C. Pauly, C. Spengler, S. Grandthyll, K. Jacobs, F. Mücklich, F. Müller, In-depth investigation of copper surface chemistry modification by ultrashort pulsed direct laser interference patterning. Langmuir **36**(45), 13415–13425 (2020)
77. J.-H. Klein-Wiele, P. Simon, Sub-100nm pattern generation by laser direct writing using a confinement layer. Opt. Express **21**(7), 9017 (2013)
78. D.S. Ivanov, A. Blumenstein, J. Ihlemann, P. Simon, M.E. Garcia, B. Rethfeld, Molecular dynamics modeling of periodic nanostructuring of metals with a short UV laser pulse under spatial confinement by a water layer. Appl. Phys. A Mater. Sci. Process. **123**(12), 744 (2017)
79. F. Beinhorn, J. Ihlemann, P. Simon, G. Marowsky, B. Maisenhölder, J. Edlinger, D. Neuschäfer, D. Anselmetti, Sub-micron grating formation in Ta_2O_5 -waveguides by femtosecond UV-laser ablation. Appl. Surf. Sci. **138–139**(1–4), 107–110 (1999)
80. K. Tanaka, K. Yamae, J. Oota, M. Kubo, J.H. Klein-Wiele, P. Simon, Study on improving the light extraction efficiency from a LED chip by relief structures on the surface of the InGaN thin film induced by Femto-second excimer laser ablation. J. Japan Soc. Precis. Eng. **77**(4), 400–404 (2011)
81. S. Ring, B. Stannowski, F. Fink, R. Schlatmann, Micro gratings written in ZnO:Al thin films using picosecond UV-laser interference patterning. Phys. Status Solidi - Rapid Res. Lett. **7**(9), 635–638 (2013)
82. C.S. Davies, J. Janušonis, A.V. Kimel, A. Kirilyuk, A. Tsukamoto, T. Rasing, R.I. Tobey, Towards massively parallelized all-optical magnetic recording. J. Appl. Phys. **123**, 213904 (2018)
83. P. Hauschwitz, D. Jochcová, R. Jagdheesh, M. Cimrman, J. Brajer, D. Rostohar, T. Mocek, J. Kopeček, A. Lucianetti, M. Smrž, Large-beam picosecond interference patterning of metallic substrates. Materials (Basel). **13**, 4676 (2020)
84. J.-H. Klein-Wiele, F. Kleinwort, P. Simon, Schlechte Karten für Produktpiraterie. Mikroproduktion, 04/60-62 (2018)
85. A.H.A. Lutey, G. Lazzini, L. Gemini, A. Peter, V. Onuseit, J. Graus, F. Fuso, R. Kling, L. Romoli, Insight into replication effectiveness of laser-textured micro and nanoscale morphology by injection molding. J. Manuf. Process. **65**, 445–454 (2021)
86. V. Lang, A. Rank, A.F. Lasagni, Large area one-step fabrication of three-level multiple-scaled micro and nanostructured nickel sleeves for roll-to-roll hot embossing. Adv. Eng. Mater. **19**(8), 1700126 (2017)
87. A. Peter, A.H.A. Lutey, S. Faas, L. Romoli, V. Onuseit, T. Graf, Direct laser interference patterning of stainless steel by ultrashort pulses for antibacterial surfaces. Opt. Laser Technol. **123**, 105954 (2020)
88. D.W. Müller, S. Lößlein, E. Terriac, K. Brix, K. Siems, R. Moeller, R. Kautenburger, F. Mücklich, Increasing antibacterial efficiency of Cu surfaces by targeted surface functionalization via ultrashort pulsed direct laser interference patterning. Adv. Mater. Interfaces **8**, 2001656 (2021)

89. K.O. Böker, F. Kleinwort, J.H. Klein-Wiele, P. Simon, K. Jäckle, S. Taheri, W. Lehmann, A.F. Schilling, Laser ablated periodic nanostructures on titanium and steel implants influence adhesion and osteogenic differentiation of mesenchymal stem cells. Materials (Basel). **13**, 3526 (2020)
90. J. Minguela, D.W. Müller, F. Mücklich, L. Llanes, M.P. Ginebra, J.J. Roa, C. Mas-Moruno, Peptidic biofunctionalization of laser patterned dental zirconia: A biochemical-topographical approach. Mater. Sci. Eng. C **125**, 112096 (2021)
91. A. Carvalho, L. Cangueiro, V. Oliveira, R. Vilar, M.H. Fernandes, F.J. Monteiro, Femtosecond laser microstructured Alumina toughened Zirconia: A new strategy to improve osteogenic differentiation of hMSCs. Appl. Surf. Sci. **435**, 1237–1245 (2018)
92. S. Rung, K. Bokan, F. Kleinwort, S. Schwarz, P. Simon, J.H. Klein-Wiele, C. Esen, R. Hellmann, Possibilities of dry and lubricated friction modification enabled by different ultrashort laser-based surface structuring methods. Lubricants **7**, 43 (2019)
93. P. Russbueldt, T. Mans, J. Weitenberg, H.D. Hoffmann, R. Poprawe, Compact diode-pumped 1.1 kW Yb:YAG Innoslab femtosecond amplifier. Opt. Lett. **35**(24), 4169 (2010)
94. M. Müller, M. Kienel, A. Klenke, T. Gottschall, E. Shestaev, M. Plötner, J. Limpert, A. Tünnermann, 1 kW 1 mJ eight-channel ultrafast fiber laser. Opt. Lett. **41**(15), 3439 (2016)
95. T. Dietz, M. Jenne, D. Bauer, M. Scharun, D. Sutter, A. Killi, Ultrafast thin-disk multi-pass amplifier system providing 1.9 kW of average output power and pulse energies in the 10 mJ range at 1 ps of pulse duration for glass-cleaving applications. Opt. Express **28**(8), 11415 (2020)
96. J. Finger, M. Hesker, High power ultrashort pulse laser processing using a flexible multibeam approach. J. Phys. Photonics **3**, 021004 (2021)
97. T. Nagy, S. Hädrich, P. Simon, A. Blumenstein, N. Walther, R. Klas, J. Buldt, H. Stark, S. Breitkopf, P. Jójárt, I. Seres, Z. Várallyay, T. Eidam, J. Limpert, Generation of three-cycle multi-millijoule laser pulses at 318 W average power. Optica **6**(11), 1423 (2019)
98. M. Müller, J. Buldt, H. Stark, C. Grebing, J. Limpert, Multipass cell for high-power few-cycle compression. Opt. Lett. **46**(11), 2678 (2021)

Chapter 15
Spatial Beam Shaping with a Liquid-Crystal Spatial Light Modulator for Surface Micro- and Nanoprocessing

Yoshio Hayasaki and Satoshi Hasegawa

Abstract Spatial beam shaping is very important to perform material laser processing with high quality and high throughput. The spatial beam shaping can be performed by passive and active optical components. The passive optical components including refractive optical elements such as an ordinary lens, microlens array, cylindrical lens, axicon lens, aperture, and diffractive optical elements such as a diffractive lens, grating, and hologram are normally used without paying a special attention for specially designed shapes. The active optical components, including an active lens, beam scanners, beam deflector, and a spatial light modulator (SLM). The SLM is very useful to modulate an incident laser beam, especially an arbitrary and variable spatial beam shaping generated with a computer-generated hologram (CGH) displayed on a liquid-crystal SLM (LCSLM), which is the main topics in this chapter, will offer attractive for a next-generation laser processing and have been widely expanded to many applications. In this chapter, the principle, features, and useful techniques of the spatial beam shaping based on a CGH on LCSLM will be described, and some experimental results using femtosecond laser pulses will be demonstrated.

Keywords Computer-generated holography · Spatial light modulator · Parallel laser beams · Aberration compensation · Adaptive optics · Three-dimensional focus beam · Feedback control of laser beams

1 Introduction

Femtosecond laser processing is a promising tool for fabricating novel and useful structures on the surfaces of and inside materials. An enormous number of pulse

---

Y. Hayasaki (✉) · S. Hasegawa
Center for Optical Research and Education (CORE), Utsunomiya University, Utsunomiya, Japan
e-mail: hayasaki@cc.utsunomiya-u.ac.jp; hasegawa_s@cc.utsunomiya-u.ac.jp

© The Author(s), under exclusive license to Springer Nature Switzerland AG 2023

R. Stoian, J. Bonse (eds.), *Ultrafast Laser Nanostructuring*, Springer Series in Optical Sciences 239, https://doi.org/10.1007/978-3-031-14752-4_15

irradiation points will be required for fabricating actual two-dimensional (2D) and three-dimensional (3D) structures with millimeter to centimeter scale, because the femtosecond laser processing can make structures with high resolution of $\lambda/10 \sim \lambda/2$. For instance, if a 1 cm^2 area of material surface is processed at intervals of 1 μm, the number of processing points is 10^8. If a laser with a repetition rate of 1 MHz is used, laser processing would take 100 seconds. Therefore, the throughput of femtosecond laser processing must be improved for practical applications, because the throughput is directly connected to the cost that is important in the technological fight for survival.

One promising method to improve the throughput is laser processing with spatially shaped pulses, especially a method based on a computer-generated hologram (CGH) displayed on a spatial light modulator (SLM), called holographic laser processing [1]. The method has also been applied to shaped beam fabrication [2] and single-shot three-dimensional (3D) fabrication [3].

In this section, the main topics will be the holographic laser processing using a commercially available liquid-crystal SLM (LCSLM). The principle, features, optical systems, and CGH design methods will be described, and some experimental demonstrations will be also described.

2 Optical Components for Spatial Beam Shaping

2.1 Classification of Optical Components

Optical components for spatial beam shaping are classified into passive and active types. The typical passive optical components are an aperture (optical mask), beam splitters, a lens array, and diffractive optical elements (DOEs). And the typical active optical components are a LCSLM, deformable mirror (DM), and digital micromirror device (DMD). These optical components are used in combinations effectively.

2.2 Passive Optical Components for Spatial Beam Shaping

An aperture (an optical mask) is used to control the amplitude of light. The optical mask including a circular aperture, a slit, or a specific pattern causes loss of light but is an easy and effective implementation. The optical mask is placed at the conjugate image plane, the spatial frequency plane, or the pupil plane. When the optical mask is placed at the Fourier plane, the beam diameter and the Rayleigh length of the focused pulse are controlled [4, 5]. In ordinary focusing, such as focusing of a Gaussian pulse by an objective lens, the focusing volume has different lengths in the lateral and axial directions, and laser processing produces a fabricated structure that depends on the focusing volume. Therefore, in the fabrication of an optical waveguide, the beam is reduced in size in one direction by an aperture, and the difference between the lateral and axial lengths is minimized. The same effect can be achieved with a cylindrical lens [6]. A dark-ring mask and an annular mask at the pupil plane of an objective lens can be used to obtain smaller fabricated structures in glass based on the principle of superresolution [7].

Beam splitters can easily form parallel pulses without introducing large changes in the spatial and temporal properties of the pulses. The method allows highly flexible pulse manipulation because of the ease of inserting other optical components. There is no fundamental limit to the number of divided pulses, but a high degree of parallelism increases the costs of the optical components and decreases the system stability. One important optical arrangement for parallel processing is interference exposure for making periodic structures [8–10]. A combination of this arrangement with a special prism has been employed to minimize the pitch [11].

Lens arrays can easily form many focal spots at regular intervals [12, 13] and are useful components for fabricating identical structures in parallel. The intensity of the focal spots is proportional to the incident laser power entering the pupils of the individual lenses; therefore, the uniformity of the illumination light on the lens array is extremely important for fabricating uniform parallel structures. The lens array was used with the LCSLM for functional parallel processing [14].

Diffractive optical elements (DOEs) are effective for producing arbitrary spatial patterns. In laser processing systems, DOEs are used for beam combining and beam branching [15]. Beams from three diffraction gratings with different directions, used instead of a prism combiner, have been made to interfere on a sample for fabricating a periodic structure via photopolymerization [16]. DOEs inherently have spatial dispersion, and since ultrashort pulses have broadband, so this optical system is suitable for pulse lengths down to sub-picosecond level [17]. An optical system composed of a diffractive beam splitter and telescope optics interferes among ultrashort pulses without spectral dispersion in a wide area. Another approach for compensating for spectral dispersion is to use a combination of two DOEs to perform parallel multifocal processing with femtosecond pulses [18–21]. The spatial spectral dispersion along the radial direction can be minimized by the dispersion compensation method. A diffractive equivalent axicon lens has been used to fabricate a micro-channel with a high aspect ratio [22–25]. The large-volume ablation of glass using femtosecond Bessel pulses was explained by rapid expansion due to heating, with subsequent cavitation.

2.3 Active Optical Components for Spatial Beam Shaping

An LCSLM that is originally developed as a key device to actively and dynamically control light in displays and optical information processing has recently been used in imaging systems, optical tweezers, and laser processing systems. There were many types historically, but at present, a liquid crystal on silicon SLM (LCOS-SLM), which has nematic LC molecules sandwiched by a silicon-based circuits for addressing and transparent electrode on a glass substrate, is widely commercialized. The main feature is to perform phase modulation with low loss of light and is frequently used as a device for modulating spectral phase in a pulse shaper and as a device for displaying CGHs. The LCSLM is a key device in material laser processing; therefore, it will be described in detail in a later section.

A DM was originally developed for adaptive optics in astronomy, and small-scale devices were developed for use in observation of the human retina. Recently, commercial products have become available at a relatively low price. The number of pixels is not so large compared with an LCSLM, so it is difficult to generate a complex optical pattern, but they can be used for spatial deformation of pulses [26] and aberration compensation in laser processing systems. These devices are effective for real-time, adaptive wavefront control because the response speed is faster than that of nematic LCSLMs. The DM was used with the LCSLM for a control of the pulse duration at the focus point [27].

A DMD was originally developed for a projector display. It is also widely commercialized. The ordinary DMD has a huge number of micromirrors fabricated by the microelectromechanical systems (MEMS) technology. The micromirrors are individually tilted by an electronical control; therefore, they perform a spatial intensity modulation of a collimated illumination laser beam. One of the good features is high frame rate. Recently at an R/D level, a DMD with a piston movement was developed for a spatial phase modulation.

In the use of the above active optical components, **c**oordinated control of scanning devices, such as galvanometer scanners and motor- and piezo-driven stages, under the cooperation with the holographic processing is very important for industrial laser processing [28–30].

3 Optical Setups for Spatial Beam Shaping with CGH

Figure 15.1 shows optical setups for spatial beam shaping in holographic laser processing, which are classified into three types according to the positional relationship between the target and the CGH. The target is located on the image plane, the Fresnel plane, and the Fourier plane of the CGH.

Figure 15.1a shows the image-plane type. When the target is placed at the image plane of the CGH [31], the irradiation beam is divided into multiple beams by a diffractive beam splitter, which is a kind of hologram. The diffracted beams form an interference pattern on the target through a 4*f* imaging system. Selecting the necessary diffracted beams with a spatial frequency filter placed at the Fourier plane allows variable interference patterning [32–36]. An advantage of this method is its suitability for processing a periodic structure over a large area. The spatial frequency filter is space-invariant; that is to say, the effect it has on the incident light does not differ from location to location. If a space-variant structure is required, the desired period and direction are applied at the desired position in the diffractive

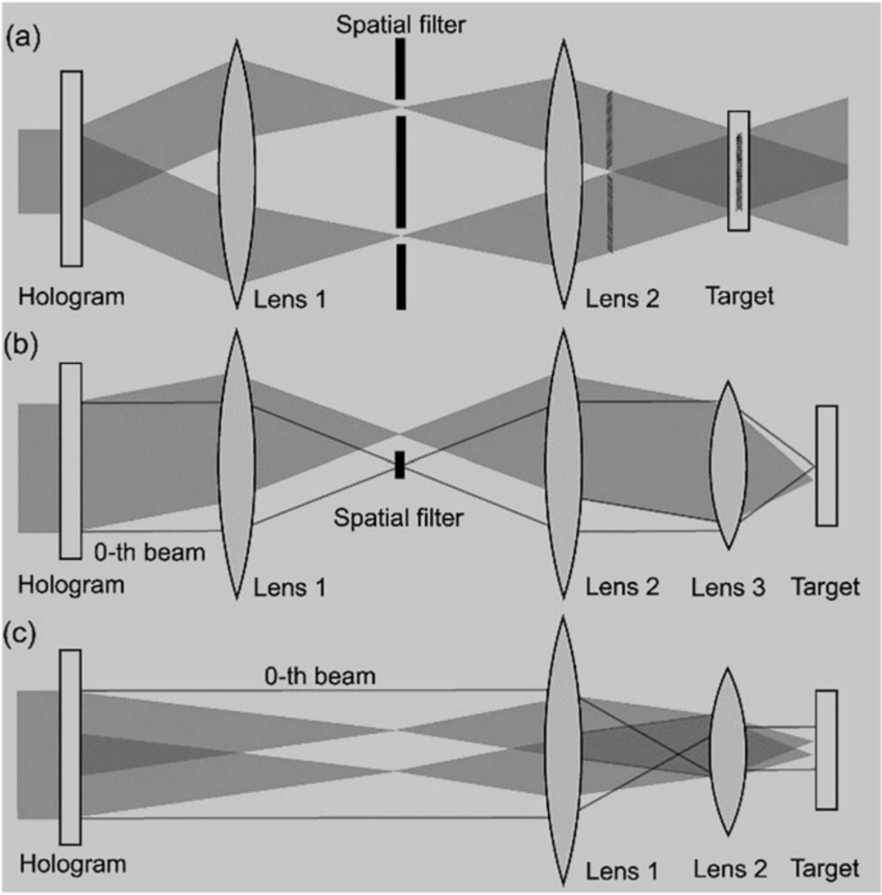
(a)
Spatial filter
Hologram
Lens 1
Lens 2
Target
(b)
Spatial filter
0-th beam
Hologram
Lens 1
Lens 2
Lens 3
Target
(c)
0-th beam
Hologram
Lens 1
Lens 2
Target

Fig. 15.1 Three types of the optical setups for holographic laser processing, with a target placed at (**a**) the image plane, (**b**) the Fourier plane, and (**c**) the Fresnel plane of the CGH

beam splitter. This type is very useful to a controllable and complex beam shaping, although it has loss of light [37–39].

Figure 15.1b shows the Fourier-plane type. When the target is placed at the Fourier plane of the CGH displayed on the LCSLM, a Fourier transform type of CGH, which is called as the Fourier CGH, is used. The Fourier CGH with high quality in the beam shape and light-use efficiency can be designed with low computational cost by using optimization techniques. The zero-order beam that causes undesired processing is zero theoretically, however it is difficult to achieve the zero according to the performance of an LCSLM. A straightforward method for removing it is to obstruct with a spatial filter on the Fourier plane. Shift-variant parallel femtosecond laser processing with a fixed hologram [15] and variable holograms [1–3] has been demonstrated with this optical system.

Now we discuss the details of the optical setup using Fig. 15.1b. In the optical system using the Fourier CGH, the relation between the beam diffraction position r, defined as a distance from the optical axis, and a spatial frequency component of the CGH, σ, is as follows. In this explanation, the CGH is a simple grating. A general CGH is described by a superposition of gratings with different spacing and direction; therefore, the discussion using the simple grating does not lose generality. When light with center wavelength λ_c is diffracted by fringes with spatial frequency σ on the LCSLM, the diffraction angle θ is given by $\theta = \sin^{-1}(\sigma\lambda_c)$ [40, 41]. Then, the diffraction position r on the focal plane (the Fourier plane) of the lens with a focal length f is

$$r = f \tan\left[\sin^{-1}(\sigma\lambda_c)\right] = f\left[\sigma\lambda_c + (\sigma\lambda_c)^3/2 + \cdots\right]. \tag{15.1}$$

If $\sigma\lambda_c$ is sufficiently smaller than 1 (~2×10^{-2} in a real system), then r is approximated as

$$\begin{aligned} r &= f\sigma\lambda_c/M \\ &= f\sigma_{\mathrm{OL}}\lambda_c \end{aligned}, \tag{15.2}$$

where M is a newly introduced magnification given by the reduction optics to match the size of the imaged CGH to the pupil of the objective lens (OL) (indicated as lens 3 in Fig. 15.1b), and σ_{OL} is the spatial frequency on the pupil plane. In general, the CGH size which depends of the size of LCSLM is bigger than the pupil, and $M =$ ~0.5 in our system. This equation indicates the diffraction point is proportional to f and σ_{OL}, if the light source with λ_c is given. Then, the focal spot diameter, d_{Airy}, at the sample plane is calculated for the full width at half maximum (FWHM) of the Airy disk pattern by the ordinary diffraction theory as

$$d_{\mathrm{Airy}} =\sim \lambda_c/\mathrm{NA}_{\mathrm{eff}}, \tag{15.3}$$

where $\mathrm{NA}_{\mathrm{eff}} = R_{\mathrm{OL}}/f$ is the effective numerical aperture at the OL's pupil. The beam radius on the pupil, R_{OL}, is also rewritten with the effective size of CGH on the pupil plane as

$$R_{\mathrm{OL}} = N_p/(2\sigma_{\mathrm{OL}}), \tag{15.4}$$

where N_p is the side number of the pixels of LCSLM. From Eqs. (15.2), (15.3), and (15.4),

$$r = (N_p/2)\ d_{\mathrm{Airy}} \tag{15.5}$$

is obtained, and the change of the diffraction position for the parameters of the optical system is accompanied by the change of the beam diameter. Consequently, the diffraction position is decided by only σ_{OL}, as indicated by Eq. (15.2).

This paragraph indicates almost same discussion with above paragraph, but notes the description in another form for further understanding, although it is a bit redundant. A CGH with $N_\mathrm{p} \times N_\mathrm{p}$ pixels is displayed on an area of the LCSLM with a dimension of $W \times W$. The maximum frequency of the CGH is $\sigma_\mathrm{max} = N_\mathrm{p}/(2\,W)$ (σ_max is the maximum of σ_OL). The CGH is imaged on the OL's pupil plane with magnification $M = f_2/f_1$, where f_2 and f_1 are the focal lengths of lens 1 and lens 2, respectively. The side length of the OL's pupil plane is $W_\mathrm{OL} = WM$. Therefore, the minimum step size in the spatial frequency domain is $1/W_\mathrm{OL} = 1/(WM)$. Consequently, the equivalent pixel size p_s on the sample plane is geometrically calculated as

$$p_\mathrm{s} = \frac{\lambda_\mathrm{c} f_\mathrm{OL}}{W_\mathrm{OL}} = \frac{\lambda_\mathrm{c} f_\mathrm{OL} f_1}{W f_2}, \tag{15.6}$$

where f_OL is the focal length of OL. From Eqs. (15.2), (15.4), (15.5), and $R_\mathrm{OL} = W_\mathrm{OL}/2$, d_airy is almost equal to $2p_\mathrm{s}$. It is important to select M so as to adjust the size of the imaged CGH to the diameter of the OL's pupil, $W_\mathrm{OL} = 2\mathrm{NA}_\mathrm{OL} f_\mathrm{OL}$. Then NA_eff is nearly equal to NA_OL, and therefore, the focal spot diameter is minimized.

Figure 15.1c shows the Fresnel-plane type. When the target is placed at the Fresnel plane of the hologram, the Fresnel transform hologram can be used, as is done for focal spot shaping [2]. The zero-order beam is background light of the diffraction peaks. In the case of a transparent material, the femtosecond laser processing is based on a multiphoton process, so that the background light does not contribute to the processing. To change the axial position (depth) without any mechanical movements and to realize 3D parallel processing with a single shot, a Fresnel transform hologram is required [3]. The focus diameter of the hologram lens is the same as that given by Eq. (15.12). The maximum numerical aperture of the hologram lens is determined by the pixel size p, namely, $\mathrm{NA}^{(\mathrm{max})} = \lambda_\mathrm{c}/(2p)$. The minimum focus diameter is almost the same as the pixel size p. In Fig. 15.1c, the focal spot is reduced to the diffraction limit with a set of reduction optics.

Next, a spatial spectral dispersion will be discussed as indicated with the gray lines in Fig. 15.2. The Fourier CGH intrinsically has spatial spectral dispersion because the CGH is the same as a diffraction grating as indicated before, so that the focal spot has spatial broadening Δr given by

$$\Delta r = f_\mathrm{OL} \sigma_\mathrm{OL} \Delta\lambda = (\Delta\lambda/\lambda_\mathrm{c})\, r, \tag{15.7}$$

where $\Delta\lambda$ is the spectral width of laser source, typically a femtosecond laser. This equation indicates that Δr depends on only r if the light source is given with fixed λ_c and $\Delta\lambda$. To give an example, a femtosecond laser with $\lambda_\mathrm{c} = 1000$ nm and $\Delta\lambda = 10$ nm is used, $\Delta r = 1\ \mu\mathrm{m}$ for $r = 100\ \mu\mathrm{m}$.

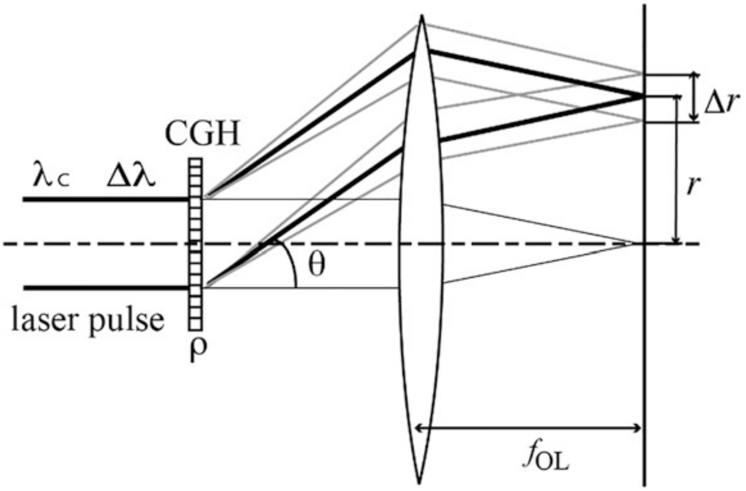

Fig. 15.2 Relation between the spatial frequency of the Fourier CGH and the diffraction point and the spatial-spectral dispersion of the diffracted pulse for a femtosecond laser pulse with a broadband spectrum

4 Liquid-Crystal Spatial Light Modulator (LCSLM)

4.1 Important Performance of LCSLM

An LCSLM should have the maximum phase modulation of more than 2π to generate a desired pattern with high-light use efficiency using a CGH. A typical commercially available LCSLM has a temporal response of several 10 fps (frames per second) and several 10 lp/mm (line pairs per millimeter). Recently, LCSLMs with several 100 fps and with 4 K × 2 K pixels are released, so the alternatives became wide, although the prices are still high. We will need to consider the following performances according to applications.

#1 Reflectance
A reflectance of commercially available LCSLMs is 80–98% which depends on a type of the mirror and its aperture ratio. The metal mirror has broadband and relatively low reflectance, and inversely the dielectric mirror has narrowband and high reflectance. The maximum reflectance is decided by the aperture ratio, because the reflectance of the dielectric mirror is more than 99%. An LCSLM with a dielectric mirror should be used in laser processing applications, because an irradiation power to the LCSLM is very high.

#2 Surface Structure
An LCSLM has no flat surface in the order of wavelength, so the surface structure should be compensated at the same time as the input image is given. The focus beam

is deformed, if a user pays no attention of the surface structure, namely, applies no compensation.

#3 Input Signal-to-Phase Modulation Property

An LCSLM has an individual input signal-to-phase modulation property, which is not linear. So, a user needs to measure the property in advance and make a calibration curve to obtain a desired phase modulation for an input digital video signal. In some cases, it may be optimized by a maker of the LCSLM at the time of shipment. Furthermore strictly speaking, the property is not spatially uniform; therefore the compensation should apply for the respective pixels.

#4 Spatial Frequency Response

An LCSLM has a spatial frequency response that is high in the low spatial frequency region and low in the high spatial frequency region as a low-pass filter like. It should be also considered. A method for solving the difficult to use according to the spatial frequency response will be described in Sect. 6.1.

The above surface structure, input signal-to-phase modulation property including the surface structure, and the spatial frequency response of the LCSLM should be compensated to generate the desired profile of the diffraction light intensity. Therefore, a user needs to measure them in advance. For a commercial product, the compensation procedure may be prepared by a maker of LCSLM. They will be automatically corrected by an in-system optimization of CGH, which will be described in detail later.

4.2 *Mathematical Model of LCSLM and Its Characteristics*

The spatiotemporal dynamics of an actual phase $u(\mathbf{r},t)$ at a position $\mathbf{r}$ and a time t in the LCSLM is frequently expressed by an exponential relaxation with a transverse diffusion for an ideal phase $u_{\mathrm{ideal}}(\mathbf{r},t)$ as

$$\tau_{\mathrm{LCSLM}} \nabla \partial u\left(\mathbf{r},t\right)/\partial t = -u\left(\mathbf{r},t\right) + l_{{\mathrm{LCSLM}}^2} \nabla^2 \perp u\left(\mathbf{r},t\right) + u_{\mathrm{ideal}}\left(\mathbf{r},t\right), \tag{15.8}$$

where τ_{LCSLM} is a time constant of LCSLM, $\nabla^2{}_\perp$ is the transverse Laplacian in the x and y directions, and l_{LCSLM} is a parameter corresponding to a diffusion length in the diffusion equation, which is related to the spatial frequency response of the actual LCSLM [42, 43]. u_{ideal} is given with an intensity-to-phase modulation f_{LCSLM} for an electric input signal $e(\mathbf{r},t)$ as

$$u_{\mathrm{ideal}}\left(\mathbf{r},t\right) = f_{\mathrm{LCSLM}}\left[e\left(\mathbf{r},t\right)\right] + u_0\left(\mathbf{r}\right) \tag{15.9}$$

where $u_0(\mathbf{r})$ is an initial phase which is spatially nonuniform and is different for an individual device. If an ideal LCSLM without the spatial frequency response

($l_{\mathrm{LCSLM}} = 0$), the temporal dynamics of the phase $u(t)$ can be expressed by

$$\tau_{\mathrm{LCSLM}} \nabla \partial u_{\mathrm{c}}(t)/\partial t = u_{\mathrm{c}}(t) + f_{\mathrm{LCSLM}}\left[e_{\mathrm{c}}(t)\right], \tag{15.10}$$

where the subscript c means a spatially uniform state. When a step function ($e_{\mathrm{c}}(t) = 0$, if ($t < 0$), $e_{\mathrm{c}}(t) = e_{\mathrm{cs}}$, else) is given to this system, the behavior is obtained as

$$u_{\mathrm{c}}(t) = f_{\mathrm{LCSLM}}\left(e_{\mathrm{cs}}\right)\left[1 - \exp\left(-t/\tau_{\mathrm{LCSLM}}\right)\right], \tag{15.11}$$

τ is known from the temporal change of $u_{\mathrm{c}}(t)$ and f_{LCSLM} is known by measuring $u_{\mathrm{c}}(t)_{t \to \infty}$.

The Fourier transform analysis is applied to solve Eq. (15.8), and for simplicity, one-dimensional signals are considered. Here the Fourier transform is denoted as F, and the Fourier transforms of $U(k, t) = F\{u(x, t)\}$ and $U_{\mathrm{ideal}}(k, t) = F\{u_{\mathrm{ideal}}(x, t)\}$ are given; the Fourier transform of Eq. (15.1) is calculated as

$$\tau_{\mathrm{LCSLM}} dU\left(k, t\right)/dt = -H^{-1}(k)\ U\left(k, t\right) + U_{\mathrm{ideal}}\left(k, t\right), \tag{15.12}$$

where

$$H(k) = 1/\left(1 + l_{\mathrm{LCSLM}} k\right) \tag{15.13}$$

that is the transform function of LCSLM. It is sufficient. After sufficient times passed under a temporally constant input $u_{\mathrm{s}}(x)$ is given, that is, the steady state $U_{\mathrm{s}}(k)$ when $dU(k,t)/dt = 0$ is described as

$$U_{\mathrm{s}}(k) = H(k) U_{\mathrm{ideal}}(k). \tag{15.14}$$

This equation indicates that high-resolution components of an input image to the LCSLM decays even if the input image is ideal. It also indicates that the spatial frequency property is characterized by only l_{LCSLM}. Consequently, a regulation of $U_{\mathrm{ideal}}(k)$ gives the desired phase distribution $U_{\mathrm{s}}(k)$, if l_{LCSLM} can be known. In an actual research site, it will be required to know τ_{LCSLM}, l_{LCSLM}, f_{LCSLM}, and $u_0(\mathbf{r})$ of the LCSLM that you use.

5 Experimental Optical Setups for Holographic Laser Processing

Figure 15.3 shows the experimental optical setups for holographic femtosecond laser processing. These optical setups mainly consist of an amplified femtosecond laser system, an LCSLM, and a relay optics. In our research group, two kinds of

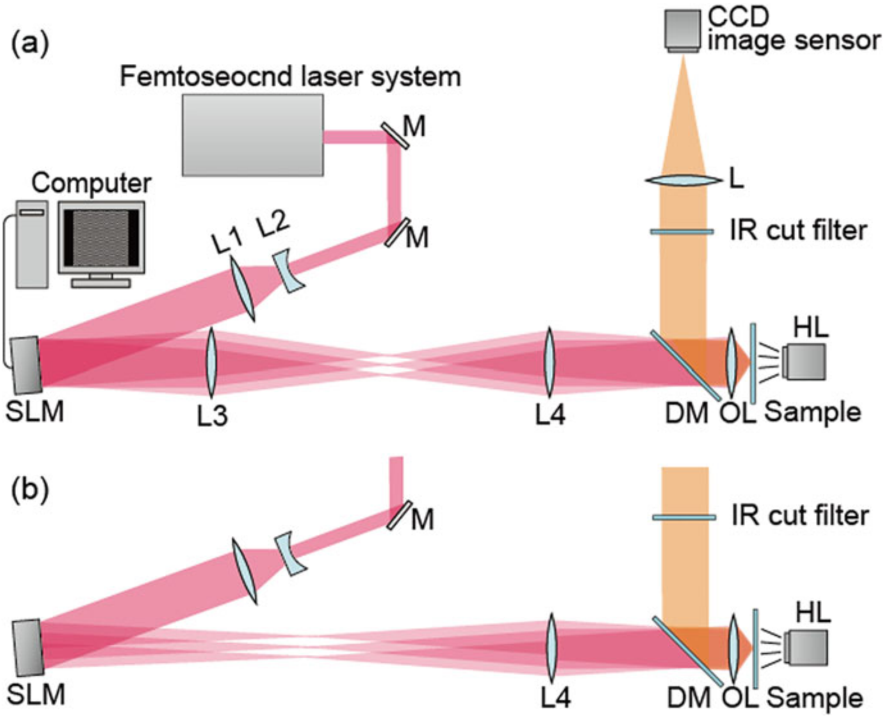

Fig. 15.3 Holographic femtosecond laser processing systems with (**a**) the Fourier CGH and (**b**) the Fresnel CGH

the femtosecond laser systems are mainly used. The first one is an 1 kHz–1 mJ-Ti:sapphire amplified femtosecond laser system with a center wavelength of 800 nm and a pulse duration of 45 fs, because the 1 kHz was indicated at the front and the second one is 10 kH–1 mJ-Yb:KGW laser with 1030 nm and 155 fs. The LCSLM was mainly a PPM (programmable phase modulator) (Hamamatsu Photonics) until 2010 and, at the later time, an LCOS-SLM (Hamamatsu Photonics, X10468).

The laser pulses emitted from the laser source are firstly collimated with a set of negative and positive lenses to fit the beam size to the aperture of the LCSLM, which is typically a ~10 mm square. The collimated laser pulse is diffracted by the CGH displayed on the LCSLM. There are two types of the optical systems after the beam diffraction. They are the Fourier type shown in Fig. 15.3a and the Fresnel type shown in Fig. 15.3b.

In the Fourier-type optical system, the diffracted beam forms a designed processing pattern at the Fourier plane of lens 3 (L3). The 0-th order light was obstructed at the Fourier plane by a thin metal wire, because the diffraction efficiency is high (70 to more than 90%, according to the reconstruction patterns) but a non-zero 0-th light exists. The processing pattern was reduced with lens4 (L4) and a microscope objective lens (OL). A set of L3 and L4 was decided to image the aperture of

LCSLM on the pupil of the OL, and typically it had $M = 1/2$ magnification in our systems. A user should need to be careful for the magnification according to the OL that the user selects. The OL with NA of 0.2–1.2 was selected according to applications.

The irradiation energy at the sample was given by the product of the energy measured before introducing the laser pulse into the OL and the transmittance of the OL. The transmittance of an ordinary commercialized, not specialized OL was not so high in near infrared region, especially in the wavelength region of ~1 μm, typically from 0.5 to 0.8. The sample is set on a three-dimensional motorized stage. The axial and lateral processing position of the sample is controlled by the computer-controlled motorized and piezoelectric stages. To observe laser processing of the sample, the sample was illuminated with a halogen lamp (HL) or a LED lamp, and a CCD or CMOS image sensor captured images of the sample via a dichroic mirror (DM) and an infrared (IR) cut filter.

In the Fresnel-type system, the diffracted beam forms a designed processing pattern at the Fresnel plane to arrange the focusing points in 3D. When the target is placed at the Fresnel plane of the hologram, the Fresnel transform hologram can be used, as is done for focal spot shaping. The 0-th order beam is the background light of the diffraction peaks. In the case of a transparent material, the femtosecond laser processing is based on a multiphoton process, so that the background light does not contribute to the processing. To change the axial position (depth) without any mechanical movements and to realize 3D parallel processing with a single shot, a Fresnel transform hologram is required. The maximum numerical aperture of the hologram lens is determined by the pixel size p, namely, $\mathrm{NA}^{(\max)} = \lambda_c/(2p)$. The minimum focus diameter is almost the same as the pixel size p. The focal spot is reduced to the diffraction limit with a set of reduction optics.

Figure 15.4 shows the experimental setup with two LCSLMs for generating a vector beam. The pulse was collimated and given to the first LCSLM (SLM1), which displayed CGH1 for applying a spatial phase modulation (wavefront modulation) to the linearly polarized light. The HWP was arranged with an angle of $\pi/8$ to rotate

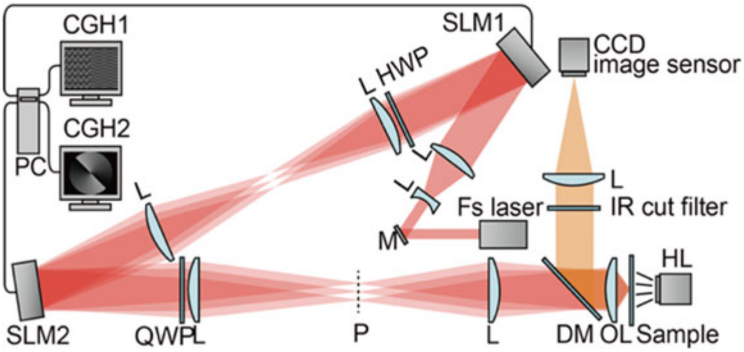

Fig. 15.4 Holographic vector-wave femtosecond laser processing system

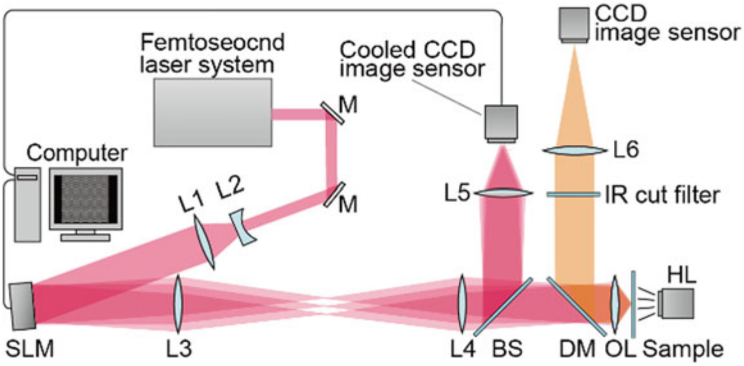

Fig. 15.5 Holographic femtosecond laser processing system with a beam observation module for the in-system optimization of CGH

the linear polarization angle by $\pi/4$. And the pulse was given to the second LCSLM (SLM2) located at the image plane of SLM1. It displayed CGH2 for applying a phase delay between two orthogonal components, that is, polarization modulation. The circular or elliptical polarization reflected from SLM2 was converted to linear polarized light using a QWP set to an angle of $\pi/4$. The reconstructed spot array with a desired polarization distribution was irradiated to a sample through an imaging optics. The observation optical system was same as indicated before.

Figure 15.5 shows the holographic laser processing system with the in-system optimization of a CGH. The optical system had a beam observation module (BOM) for observing the CGH reconstruction. The BOM was composed of a beam sampler (BS) for dividing the CGH reconstruction, a Fourier lens, and a CCD or CMOS image sensor.

6 Experimental Demonstrations of Holographic Laser Processing

6.1 Parallel Beams Generated with Compensation of LCSLM's Property [44]

Figure 15.6a, b show a CGH designed to generate ten diffraction peaks and its computer reconstruction. The intensity profile of the reconstruction is also indicated. The minimum and maximum spatial frequencies of the diffraction peaks were 1.59 and 4.96 lp/mm, respectively. In the computer reconstruction, the uniformity of peak intensities U_{PI} was 99.97%, and the diffraction efficiency η was 95.8%, demonstrating that the CGH calculated with the optimal-rotation-angle (ORA) method [45] had high-uniformity diffraction peaks. Here, the uniformity is defined

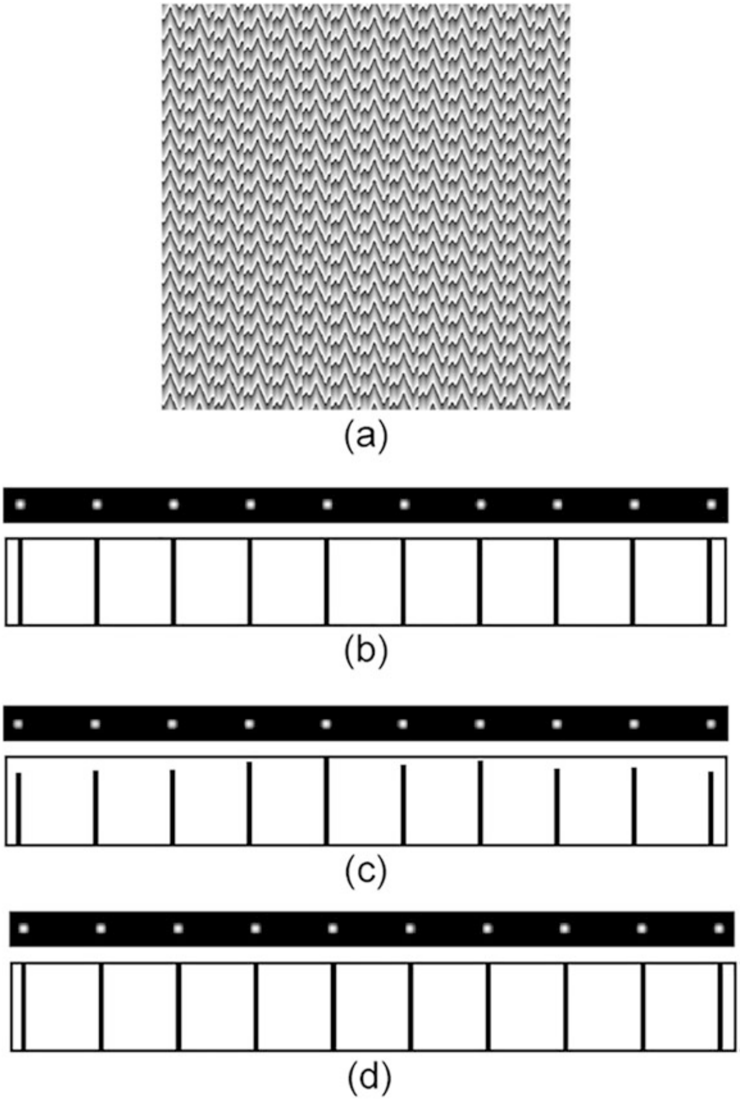

Fig. 15.6 (**a**) CGH for generating ten beams, (**b**) computed reconstruction of the CGH and the intensity profile, and (**c**) computed reconstruction of the CGH taking into account the spatial frequency response of the LCSLM and the intensity profile. (**d**) A computed reconstruction of a CGH with compensation of spatial frequency response of the LCSLM and the intensity profile. (Adapted with permission from Ref. [46] (c) The Optical Society)

by the ratio of the minimum peak intensity $I_{\min}$ to the maximum peak intensity $I_{\max}$ in the reconstruction as

$$U_{\mathrm{PI}} = I_{\min}/I_{\max}, \tag{15.15}$$

and η is defined by the first-order diffracted light intensity I_1 and the 0-th order light intensity I_0 when the LCSLM does not display a CGH as

$$\eta = I_1/I_0. \tag{15.16}$$

As you can see, the peaks are delta function in this calculation, because the CGH has no aperture. In an actual optical system, the aperture with a finite size exists; the peaks have a finite width, typically the diffraction limit width. In the experiments, the intensity is measured with the summation of the light intensities at around each focus spot.

Figure 15.6c shows the computer reconstruction of the CGH with the spatial frequency response of the LCSLM and its intensity profile, respectively. In this calculation, the CGH displayed on the LCSLM was simulated under the setting of $l_{\mathrm{LCSLM}} = 16$ µm. It is not shown in this figure, because it looked almost the same as the CGH shown in Fig. 15.6a, although they were different strictly. $U_{\mathrm{PI}} = 82\%$ and $\eta = 70\%$. The diffraction peaks with high spatial frequency decreased with dependent on the spatial frequency response characterized with $l = 16$ µm.

Figure 15.6d shows a computer reconstruction of a CGH optimized in consideration with the spatial frequency response of the LCSLM. $U_{\mathrm{PI}} = 99.9\%$ and $\eta = 69.2\%$. The optimization method improved U_{PI} drastically without any decrease of η.

Figure 15.7 shows the experimental results of the holographic laser processing. The sample was an ordinary glass microscope cover slip (Matsunami), subjected to ultrasonic cleaning in ethanol and pure water. Observation of the processed area was performed by an optical microscope with transmission and reflection illumination (Olympus, BX60). An atomic force microscope (AFM; Digital Instruments, Dimension3100) and a scanning electron microscope (SEM; Hitachi, S4700) were also used to observe the processed area.

Figure 15.7a shows the optical reconstruction of the CGH without compensation and the intensity profile. The intensity profile was obtained from the maximum value in each column. Here, $U_{\mathrm{PI}} = 74\%$ and $\eta = 60\%$. U_{PI} was smaller than that of the computer reconstruction; in particular, there was a large decrease of the diffraction peaks at high spatial frequency. Therefore, the actual l_{LCSLM} was larger than that used in the computer simulation ($l_{\mathrm{LCSLM}} = 16$ µm). Figure 15.7b shows a transmission microscope image of the processed area. Figure 15.7c shows an AFM image of the processed area. The irradiation energy was 1.9 µJ. From the AFM observation, the processed structure was cavities surrounded by a ring-shaped protrusion, debris, and small droplets on the glass surface. The minimum diameter $d_{\min}$ and maximum diameter $d_{\max}$ were 0.94 µm and 1.24 µm, respectively. The uniformity of the diameter, $U_{\mathrm{D}} = d_{\min}/d_{\max}$, was 76%.

Figure 15.7d shows the optical reconstruction of the CGH with compensation and the intensity profile. Here, $U_{\mathrm{D}} = 91\%$ and $\eta = 61\%$. U_{D} was improved. Figure 15.7e shows a transmission microscope image of the processed area. From the AFM observation shown in Fig. 15.7f, $d_{\min} = 0.87$ µm and $d_{\max} = 1.03$ µm,

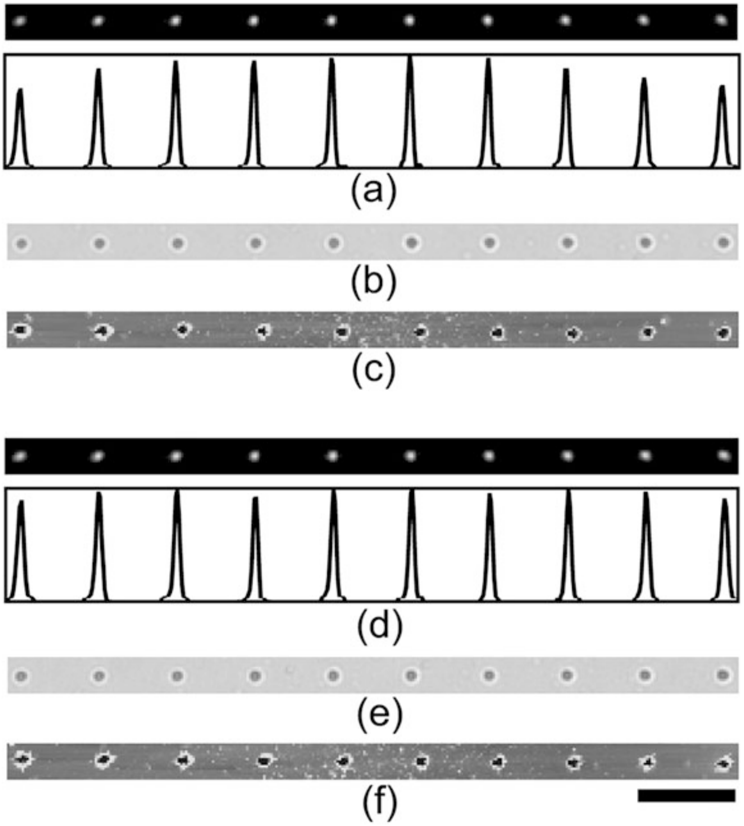

Fig. 15.7 (**a**) Optical reconstruction of CGH without compensation and the intensity profile, (**b**) its transmission microscope image, and (**c**) its AFM image. (**d**) Optical reconstruction of CGH with compensation and the intensity profile, (**e**) its transmission microscope image, and (**f**) its AFM image. The scale bar is 10 μm. (Adapted with permission from Ref. [46] (c) The Optical Society)

respectively. Here, U_D was improved to 84% by the compensation of the spatial frequency response.

6.2 Three Dimensionally Arranged Focusing Spots [46]

6.2.1 Three-Dimensional Microfabrication with Multi-Pulse Irradiations

Figure 15.8 shows the experimental results of 3D microfabrication inside a glass. The microfabrication was performed with three shots of the laser pulses using three CGHs without axial translation of the sample. Figure 15.8a shows the

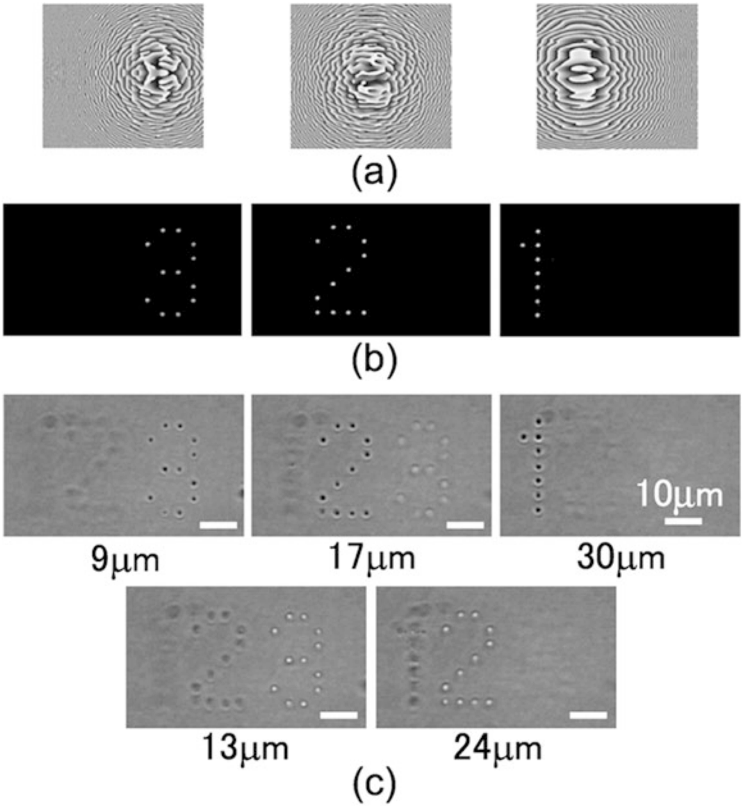

Fig. 15.8 (**a**) CGHs generating focal points at focal lengths of 1800, 2000, and 2400 mm, (**b**) optical reconstructions of the CGHs, and (**c**) transmission microscope images of 3D fabrications using 3 CGHs. (Reprinted with permission from Ref. [46] (c) The Optical Society)

CGHs designed to generate 12, 12, and 8 diffraction peaks, and having focal lengths of 1800, 2000, and 2400 mm, respectively. Figure 15.8b shows the optical reconstructions of the CGHs. The respective U_{PI} were 92%, 93%, and 83%, and the respective η were 73%, 71%, and 68%. In the transmitted optical microscope observation of the fabricated area, when the axial movements of the microscope stage were 9, 17, and 30 μm inside the glass from the position the sample surface was focused, the structures were observed as the dark spots, as shown in Fig. 15.8c. It also shows the optical microscope observation at the stage movements of 13 and 24 μm for the easy observation of the 3D structures. The irradiation energies were 7.3, 7.0, and 6.9 μJ, respectively.

6.2.2 Three-Dimensional Microfabrication with Single-Pulse Irradiation

Figure 15.9 shows an experimental result of 3D microfabrication with a single pulse. Figure 15.9a shows CGH designed to generate 32 diffraction peaks, and having focal lengths of 1800, 2000, and 2400 mm, respectively. Figure 15.9b shows the optical reconstructions of the CGH. The respective U_{PI} were 89%, 88%, and 83%. The total η was 68%. The uniformity depended on the number of the diffraction peaks. Therefore, as the diffraction peaks increase, U_{PI} was reduced. The upper three images in Fig. 15.9c show the transmitted optical microscope observation of the fabrication area, when the axial movements of the microscope stage were 7, 18, and 29 μm inside the glass from the position the sample surface was focused, the

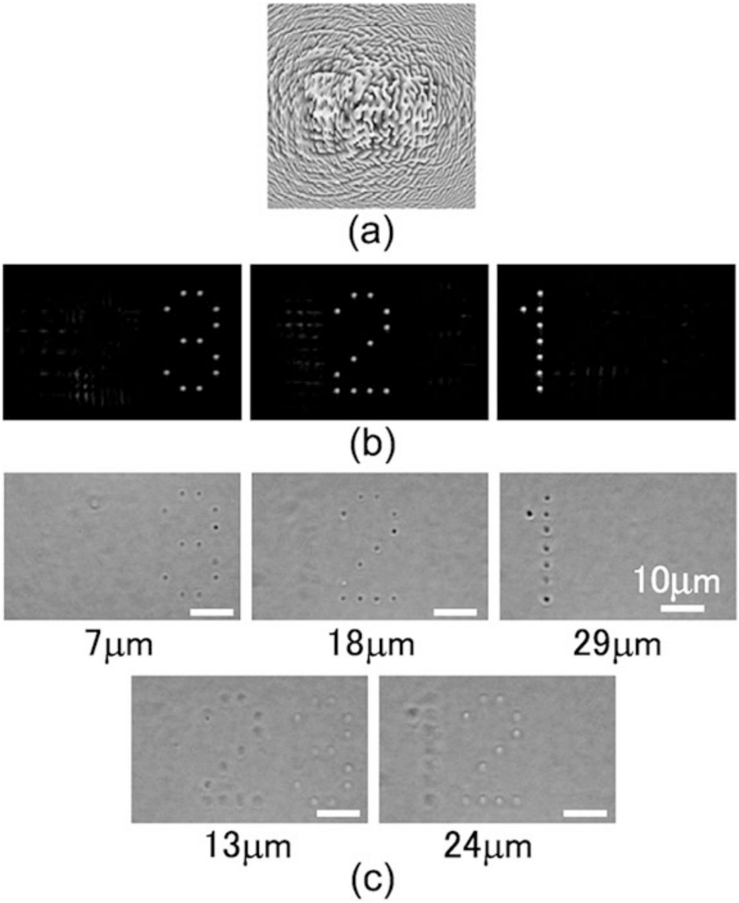

Fig. 15.9 (**a**) CGH having focal lengths of 1800, 2000, and 2400 mm in different areas, (**b**) optical reconstructions of the CGH, and (**c**) transmission microscope images of 3D parallel fabrication using a CGH. (Reprinted with permission from Ref. [46] (c) The Optical Society)

structures were observed as the dark spots. The lower two images in Fig. 15.9c show the transmitted optical microscope observation between the upper three images in Fig. 15.9c. The irradiation energy was 18 μJ.

6.3 *Line-Shaped Beam [47]*

6.3.1 Design of a Line-Shaped Beam with a Window Function

The linear fabrication used by a diffractive cylindrical lens (DCL) is most simple demonstration of the Fresnel CGH. The phase distribution of a DCL for generating a line-shaped beam is described by

$$u\,(x,y) = w(x)\left(\frac{ky^2}{2f}\right) \bmod\ (2\pi) \tag{15.17}$$

where $w(x)$ is a window function with a value from 0 to 1, $k = 2\pi/\lambda$ is the wave number, and f is the focal length. Figure 15.10 shows three types of DCLs, having different $w(x)$, and their computational reconstructions. When $w(x)$ was a rectangular function given by

$$w_{\text{rect}}(x) = \begin{cases} 1 \text{ if } 0 \le x < 1 \\ 0 \qquad \text{else} \end{cases}, \tag{15.18}$$

the diffraction image was a long line-shaped beam, but oscillations due to diffraction caused by the edges of the aperture were present, as shown in Fig. 15.10a. A

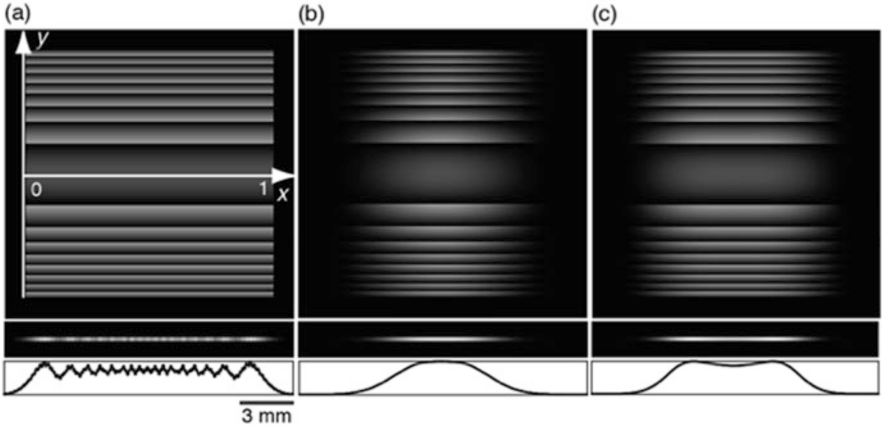

Fig. 15.10 Phase distributions of DCLs with (**a**) w_{rect}, (**b**) w_{hann}, and (**c**) w_{mak}, and their computational reconstructions. (Adapted with permission from Ref. [47] (c) The Optical Society)

smoothly decaying window function suppresses diffraction from the edges. A Hann window, which is a well-known window function, is described by

$$w_{\text{hann}}(x) = \begin{cases} \frac{1}{2}(1 - \cos 2\pi x) & \text{if } 0 \leq x < 1 \\ 0 & \text{else} \end{cases}. \tag{15.19}$$

A modified form of the Akaike window is described by

$$w_{\text{mak}}(x) = \begin{cases} w_{\text{akaike}}(4x) & \text{if } 0 < x < 0.125 \\ 1 & \text{if } 0.125 < x < 0.875 \\ w_{\text{akaike}}\{4(x - 0.750)\} & \text{if } 0.875 < x < 1 \\ 0 & \text{else} \end{cases}, \tag{15.20}$$

where $w_{\text{akaike}}(x) = 0.625–0.5\cos(2\pi x)–0.125\cos(4\pi x)$ is the Akaike window. As a result, the diffraction pattern also decayed smoothly toward the outside without any oscillations, as shown in Fig. 15.10b, c, respectively. w_{hann} was adopted for comparison, because it is one of the window functions that is frequently used. It gave a shorter line-shaped beam and a gentle decay of the intensity. In a number of experimental trials for making a better function, the window function w_{mak} produced a line-shaped beam which was long and showed smooth changes.

6.3.2 Nonparabolic Term

In general, a femtosecond laser pulse has an intensity distribution, typically, the Gaussian distribution. In order to make a line beam with both shape edges, the method for adding nonparabolic term to a parabolic cylindrical lens. Figure 15.11a, b show a phase distribution of a parabolic cylindrical lens with different focal lengths along two-orthogonal directions and its reconstruction. The phase distribution is described as

$$u(x, y) = \left(k\frac{x^2}{2f_x} + k\frac{y^2}{2f_y}\right) \bmod (2\pi) \tag{15.21}$$

The illumination beam had the Gaussian intensity distribution; therefore, the reconstruction of the cylindrical lens had also the Gaussian profile. Figure 15.11c, d show a phase distribution of a parabolic cylindrical lens added the nonparabolic phase distribution described as

$$u(r) = \left[u(\mathrm{x}, y) + A_2r^2 + A_3r^3 + A_4r^4 + \cdots\right] \bmod (2\pi), \tag{15.22}$$

where $r = (x^2 + y^2)^{1/2}$ is the distance from the optical axis, and A_n ($n = 2, 3, 4$ ....) are constants. The reconstruction became a flat distribution, as shown in Fig.

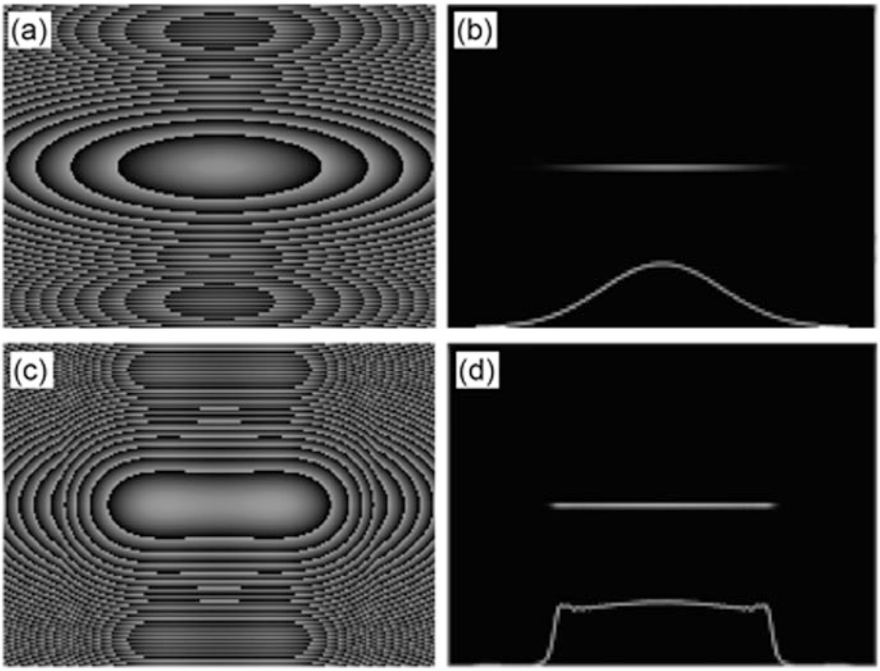

Fig. 15.11 (**a**) Parabolic DCL with different focal lengths along two-orthogonal directions and (**b**) its reconstruction. (**c**) Parabolic cylindrical lens added the nonparabolic phase distribution and (**d**) its reconstruction

15.11d. This method gives higher light-use efficiency than the method using the window functions.

6.3.3 Microfabrications Using a Line Beam

Figure 15.12 shows SEM images of the area processed with a line-shaped femtosecond laser pulse. The target material was super white crown glass (B270, Schott). Laser processing was performed using holographic cylindrical lenses with window functions w_{rect}, w_{hann}, and w_{mak}, while changing the irradiation energy. In the case of w_{rect}, as shown in Fig. 15.12a, the fabricated line structure had large variations. In the case of w_{hann}, the length became longer and the uniformity was improved. The use of w_{mak} formed a line structure with a length of 42 μm and a width of 0.58 μm when $E = 4.9$ μJ, as shown in Fig. 15.12c.

Figure 15.13 shows wide laser peeling using a line-shaped beam generated by a holographic cylindrical lens. The sample was an ITO film coated on a glass substrate. Figure 15.13a shows the holographic cylindrical lens with w_{mak}. Figure 15.13b shows the optical reconstruction and its profile captured at the focal plane. The laser peeling shown in Fig. 15.13c was performed with $E = 2.7$ μJ, a pulse

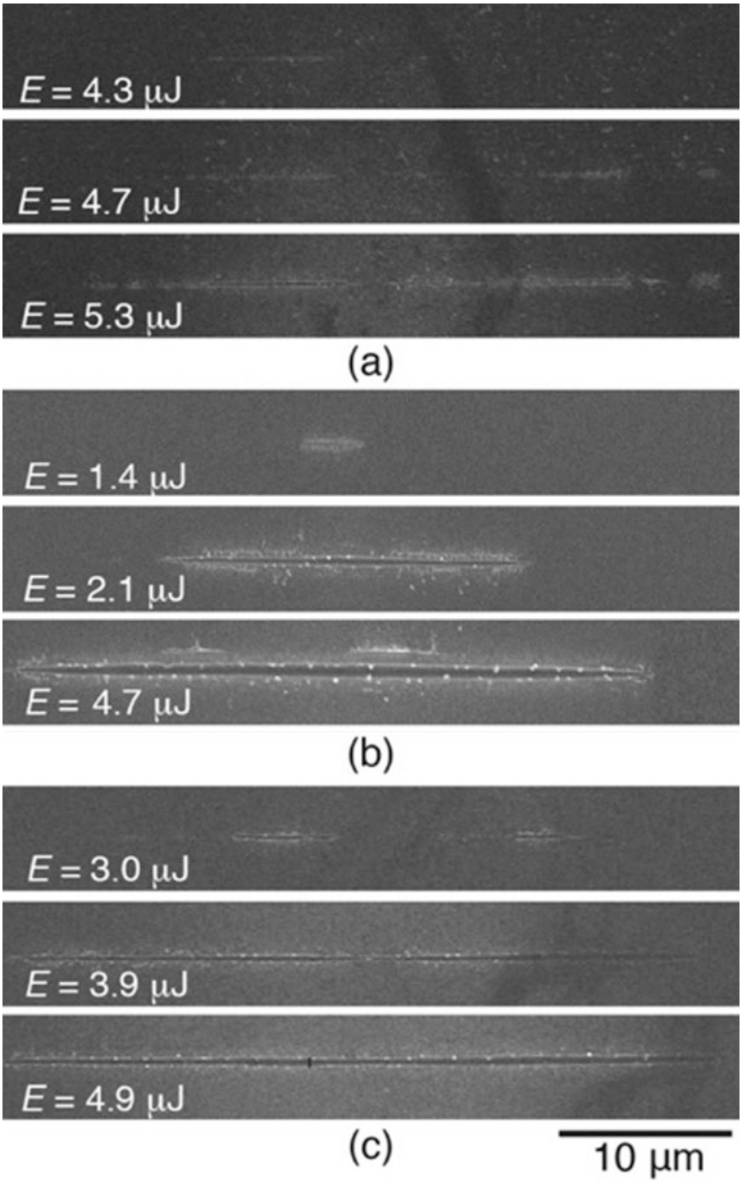
E = 4.3 μJ
E = 4.7 μJ
E = 5.3 μJ
(a)
E = 1.4 μJ
E = 2.1 μJ
E = 4.7 μJ
(b)
E = 3.0 μJ
E = 3.9 μJ
E = 4.9 μJ
(c)
10 μm

Fig. 15.12 SEM images of structure processed using holographic cylindrical lenses with window functions (**a**) w_{rect}, (**b**) w_{hann}, and (**c**) w_{mak}, respectively. E means the irradiation energy on the sample plane. (Reprinted with permission from Ref. [47] (c) The Optical Society)

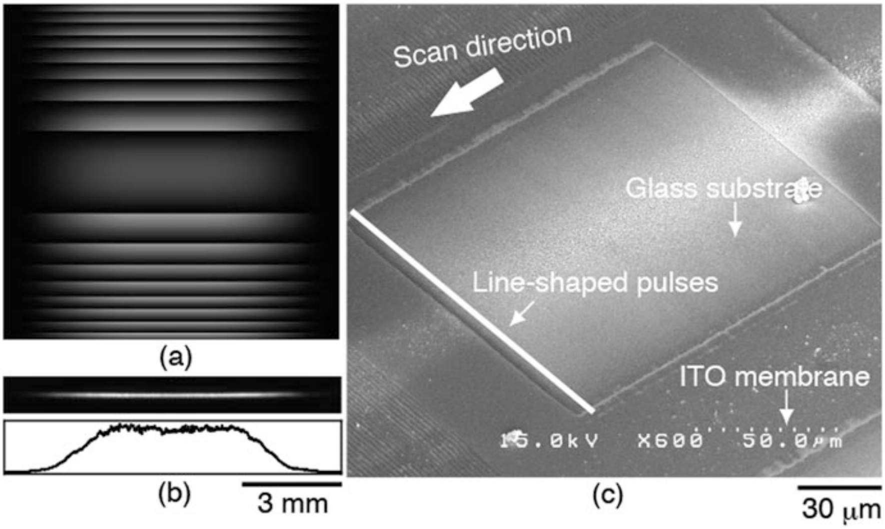

Fig. 15.13 (**a**) Phase distribution of holographic cylindrical lens and (**b**) its optical reconstruction. (**c**) Line-shaped laser peeling of ITO membrane on glass substrate. (Reprinted with permission from Ref. [47] (c) The Optical Society)

repetition frequency of 50 Hz, and a sample scanning speed of $v_{\mathrm{scan}} = 2\ \mu\mathrm{m/s}$. The threshold power for laser peeling of the ITO membrane, $E_{\mathrm{th}}{}^{(\mathrm{ITO})}$, was 0.5 µJ, which was one-sixth of the ablation threshold of the super white crown glass ($E_{\mathrm{th}}{}^{(\mathrm{glass})} = 3.0\ \mu\mathrm{J}$). When $E = 1.4\ \mu\mathrm{J}$, at a scanning speed of $v_{\mathrm{scan}} = 25\ \mu\mathrm{m/s}$ or higher (an irradiation interval of 500 µm), the ITO membrane was partially removed in the form of a periodical grating, that is, the peeling operation failed. When $E = 2.7\ \mu\mathrm{J}$ (10% smaller than the ablation threshold of the glass), at $v_{\mathrm{scan}} = 25\ \mu\mathrm{m/s}$ the ITO membrane was completely removed. When $E > E_{\mathrm{th}}{}^{(\mathrm{glass})}$, the glass substrate was damaged, as expected. In summary, suitable conditions for laser peeling were an energy E slightly smaller than the ablation threshold of the substrate and an irradiation interval smaller than the width along the short axis (0.58 µm in this experiment). It was found that little debris around the fabricated area was observed. The debris was removed by the beam itself.

6.4 Vector Beam [41, 48]

6.4.1 Design of Vector Beam

A full control of degrees of freedom in the light, including amplitude, phase, and polarization is important for opening up a wide variety of new applications of femtosecond laser processing. It means exploiting the nature of light as a vector wave and is called vector-wave control.

The optical setup for the vector-wave control mainly consists of a pair of SLMs, a half-wave plate (HWP), and a quarter-wave plate (QWP). When the Jones matrixes of these optical elements are defined as S, H, and Q, respectively, the Jones vector of the output beam, E_{out}, for the linear polarized input beam $E_{\text{in}} = (1, 0)^{\text{T}}$ is expressed as

$$E_{\text{out}} = Q_{\pi/4} S_a H_{\pi/8} S_b E_{\text{in}} = \frac{1}{2} \begin{bmatrix} \exp\left[-i\left(a+b-\pi/2\right)\right] + \exp\left[-ia\right] \\ -\exp\left[-i\left(a+b\right)\right] - \exp\left[-i\left(a-\pi/2\right)\right] \end{bmatrix} \tag{15.23}$$

where the subscripts on H and Q are the azimuthal angles at the respective wave plates, and the subscripts a and b are the phases applied to the pair of SLMs, respectively. a is the sum of the components of the CGH, a_{CGH}, and for polarization modulation, α_{pol}. Here, the phases on the SLMs to $a = a_{\text{CGH}} + a_{\text{POL}} = a_{\text{CGH}} - \theta$ and $b = 2\theta + \pi/2$ were set. Equation (15.23) is rewritten as

$$E_{\text{out}} = \exp\left(-ia_{\text{CGH}}\right) \begin{bmatrix} \cos\theta \\ \sin\theta \end{bmatrix} \tag{15.24}$$

This equation indicates that a_{CGH} and a_{POL} decide the beam formation and its polarization, so this system generates a vector beam.

6.4.2 Microfabrications Using a Vector Beam

Figure 15.14 shows the generations of a radial, an azimuth, and windmill polarization beams. Figure 15.14a shows CGHs for generating the radial polarization beam. The gray scale represents the phase from 0 to 2π. Figure 15.14b shows the optical reconstruction on the Fourier plane P. The white arrows indicate the polarization direction. The reconstruction had a doughnut shape because the beam center had a phase and polarization singularity. Figure 15.14c shows the SEM images with top and bird’s eye view of the structure fabricated by the radial polarization beam. E = 270 nJ and the pulse shot number of 10,000. The pitch of nanostructures was ~180 nm. The orientation of the spatial wave vector of the nanostructures coincides with the polarization direction at each position. Figure 15.14d–f show the case of the azimuth polarization beam. Figure 15.14g–i show the case of the windmill polarization beam. Interestingly, it was found three different types of spatially complex nanostructure on the sidewall of the hole.

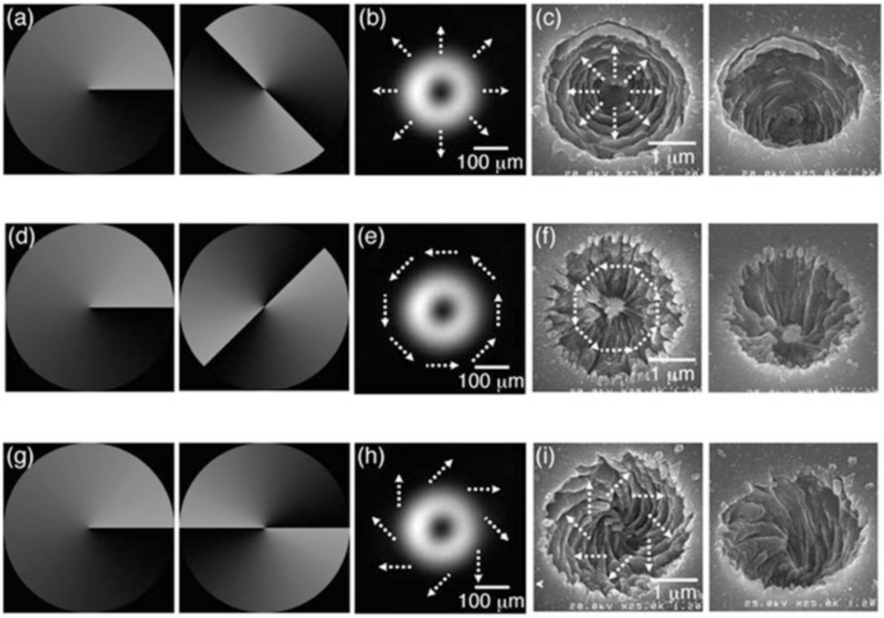

Fig. 15.14 Generations of cylindrical vector beams. (**a**–**c**) Radial polarization beam, (**d**–**f**) azimuth polarization beam, and (**g**–**i**) windmill polarization beam. From the left, two phase modulation distributions (CGHs) for the wavefront and polarization modulations, and the optical reconstruction, the SEM images from a top and bird's eye view of fabricated structure are indicated

6.5 Ring-Shaped Beam [49]

6.5.1 Design of Diffraction-Limited Ring-Shaped Beam

A laser beam with the ring-shaped intensity distribution will be useful to make a through or non-through hole on a wide variety of materials. The ring-shaped beam is formed with a combination of an axicon lens (conical-shape lens) and an ordinary lens in general. The ring-shaped beam has twice the beam width of the diffraction limit and anisotropic intensity distributions in axial and lateral. To make the beam width with the diffraction limit will improve the fabrication speed. And to make isotropic intensity distributions will be effective for an application, for example, to fabricate a straight hole with a vertical wall.

Figure 15.15 shows optical setups for obtaining a ring-shaped beam. Figure 15.15a shows an ordinary refractive axicon lens for generating the ring-shaped beam. The phase distribution u_0 and the complex amplitude U_0 behind the axicon is expressed by

$$U_0(r) = A(r)\exp\left[i\left(c_0\frac{r}{R_{\text{axicon}}} + \theta_0\right)\right] \tag{15.25}$$

where $r = (x^2 + y^2)^{1/2}$ is the position in a cylindrical coordinate system, c_0 is a constant (negative value), θ_0 is an initial phase, R_{axicon} is the radius of the axicon, and A is an amplitude distribution of an irradiation beam. An intensity distribution of a ring-shaped beam I is expressed by

$$I_0(\rho) = |F[U_0(r)]|^2, \tag{15.26}$$

where σ is the position in Fourier plane and F denotes the Fourier transform.

A diffractive axicon shown in Fig. 15.15b has the complex amplitude U_1 behind the diffractive axicon are expressed by

$$U_1(r) = A(r) \exp\left[i \left(c_0 \frac{r}{R_{\text{axicon}}} + \theta_1 \right) \bmod (2\pi) \right] \tag{15.27}$$

respectively, mod is the remainder (modulo) operator. In this case, a Bessel beam that has a longitudinal axial beam is also obtained at position between the diffractive axicon and a lens. The Bessel beam is undesirable for some applications because the lens may be damaged by irradiation with the Bessel beam in the case of a high-power laser. One way to avoid such damage is to design a negative diffractive axicon, as shown in Fig. 15.15c. The complex amplitude U_2 behind the diffractive axicon are expressed by

$$U_2(r) = A(r) \exp\left[i \left(c_0 \frac{r}{R_{\text{axicon}}} + \theta_2 \right) \bmod (2\pi) \right] \tag{15.28}$$

respectively. In this case, there is no damage to the lens; however, the beam width of the ring-shaped beam is theoretically two times larger than the diffraction limit, because the actual NA of the diffraction light is half compared with that of normal focusing using a lens. The resulting decrease in resolution may be a disadvantage for some applications. The setups in Fig. 15.13a, b have also the same issue.

To overcome this issue, a radial grating as shown in Fig. 15.13d was used. The phase distribution ϕ_3 and the complex amplitude U_3 behind the axicon is expressed by

$$U_3(r) = A(r) \exp\{\arg[U_1(r) + U_2(r)]\} \tag{15.29}$$

By the coherent superposition of U_1 and U_2, a diffraction-limited ring beam is theoretically obtained because the actual NA of the diffraction light is the same as that of a beam formed by focusing using a normal lens. In the profile of ϕ_3, the radial grating has binary phase levels of 0 and π. Therefore, the diffraction efficiency of the ring beam is theoretically 81%. An intensity distribution of a diffraction-limited ring beam I_3 is obtained by Fourier transform of U_3. Consequently, a calculation of Eq. (15.29) is equivalent to the binary coding processing of the diffractive axicon with the phase delay in Eqs. (15.27) or (15.28). However, a regulation of the phase

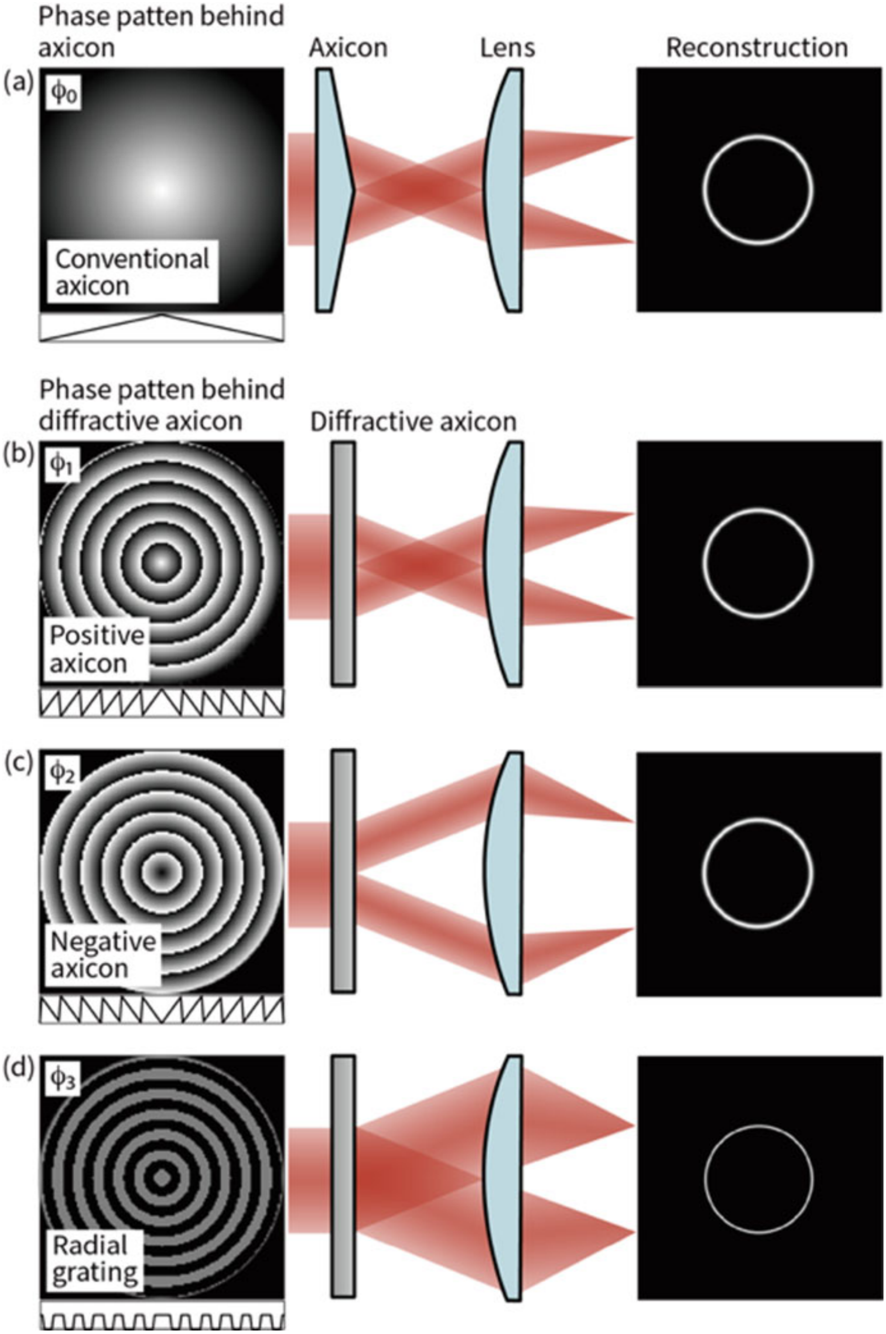
Phase patten behind axicon
Axicon
Lens
Reconstruction
(a)
ϕ_0
Conventional axicon
Phase patten behind diffractive axicon
Diffractive axicon
(b)
ϕ_1
Positive axicon
(c)
ϕ_2
Negative axicon
(d)
ϕ_3
Radial grating

Fig. 15.15 Phase patterns behind each axicon and their reconstructed patterns. (**a**) Ordinary refractive axicon lens. (**b**) Positive diffractive axicon lens. (**c**) Negative diffractive axicon lens. (**d**) Radial grating. (Reprinted with permission from Ref. [49] (c) The Optical Society)

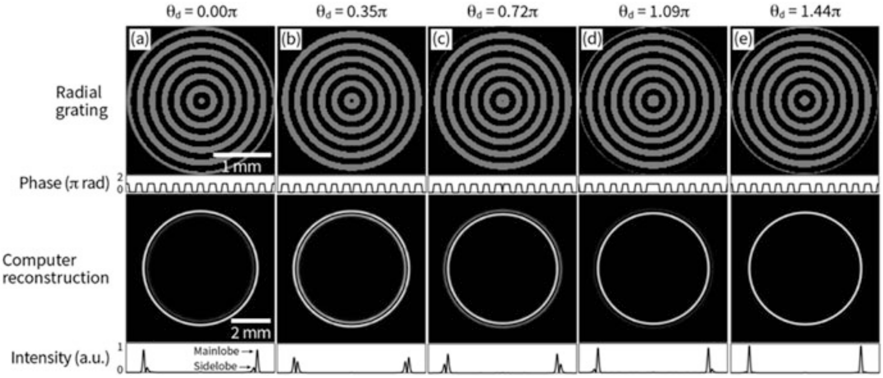

Fig. 15.16 Radial gratings and their reconstructions versus the phase difference θ_d. θ_d was set to (**a**) 0.00π, (**b**) 0.35π, (**c**) 0.72π, (**d**) 1.09π, and (**e**) 1.44π. (Reprinted with permission from Ref. [49] (c) The Optical Society)

delay becomes important to obtain the high-quality ring beam compared with the conventional binary diffractive axicon.

A sidelobe occurs near the main lobe in the ring-shaped beam as a side effect of diffraction-limited resolution. The sidelobe may decrease the accuracy and the resolution in some applications. The origin of the sidelobe is interference between two diffraction beams from the radial grating composed of a coherent superposition of positive and negative diffractive axicons (Fig. 15.15b, c). The position and intensity of the sidelobe changed with the phase difference $\theta_\text{d} = \theta_1 - \theta_2$ in reference to Eqs. (15.27) and (15.28). Therefore, the sidelobe can be efficiently suppressed by regulating θ_d. Figure 15.16 shows radial gratings and their computer reconstructions versus the phase difference θ_d. In this experiment, the spatial frequency ν and the constant c_0 of the radial grating were set to 5 lp/mm and 60π, respectively. The intensity profile was normalized by 1.05 times the maximum intensity. With increasing θ_d, the phase of the binary profile was laterally shifted, and the intensity of the sidelobe was slightly changed, as shown in the figure.

Figure 15.17 shows a computer simulation of the light propagation of the ring-shaped beam along the optical axis. Figure 15.17a, b are the light propagation from the positive and the negative diffractive axicons, respectively. The focused beams were slightly inclined with respect to the optical axis. Figure 15.17c indicates the light propagation from the radial grating with $\theta_\text{d} = 1.44\pi$. The z-axis profile was well-confined compared with the axicons. The reason for this is the interference between the two diffraction beams with slight tilts. Figure 15.17d shows the peak intensity in these z-axis profiles. The peak position in the radial grating was consistent with the intersection of the peak positions for the diffractive axicons. The depth of focus (DOF), that is, the FWHM in the z-axis profile, for the radial grating was four times smaller compared with the diffractive axicons.

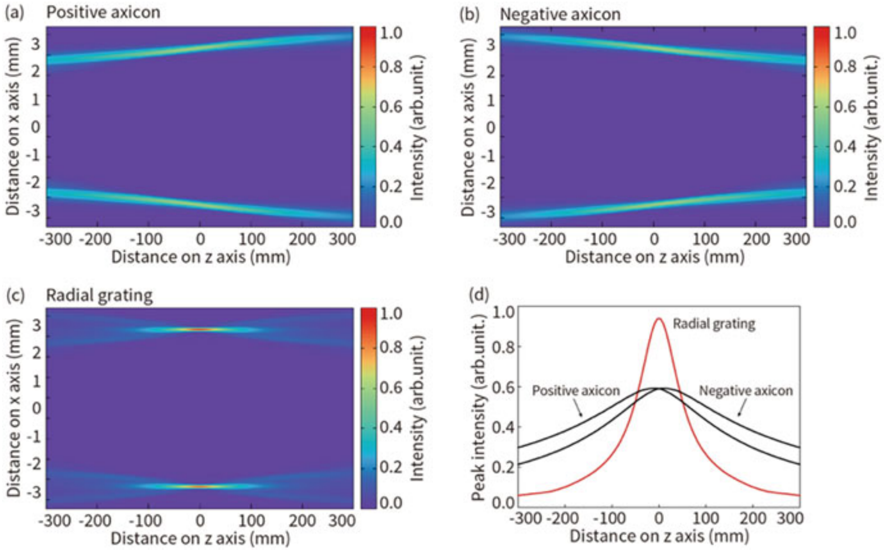

Fig. 15.17 Intensity profile of the ring beam versus the distance on the z-axis in the case of (**a**) the positive axicon, (**b**) the negative axicon, and (**c**) the radial grating. (**d**) Peak intensities in the profiles versus the distance on the z-axis. (Reprinted with permission from Ref. [49] (c) The Optical Society)

6.5.2 Microfabrication Using a Ring Beam

Figure 15.18 shows the result of through-hole processing using the diffraction-limited ring-shaped beam. A 60× objective lens (OL; Edmund) with a numerical aperture (NA) of 0.85 was used. The ring-shaped beam was focused at 2 μm inside the sample surface. In order to demonstrate laser processing in water, a water immersion OL (60×, NA = 1.0; Olympus, LUMPLFLN 60XW) was also used. The sample was a polyethylene naphthalate (PEN) film with a thickness of 4 μm. The figure indicates the optical reconstructions of the ring-shaped beam and the optical microscope images of the structures fabricated by the ring-shaped beam irradiation as a function of pulse energy E, respectively. The optical reconstruction was captured by a charge-coupled device (CCD) image sensor (BITRAN, BU-40 L) at the focal plane of the lens just after the reflection from the LCOS-SLM. Laser processing was performed with five pulse shots and gradually increasing E. In the image of the fabricated structure, the annular dark area is due to light scattering from the structure. The circular dark hole indicates that through-hole processing was successfully achieved. In each θ_d, a minimum E required to perform through-hole processing (image surrounded by a red border) were 22.1, 24.5, and 20.5 μJ, respectively. This means that the pulse energy was efficiently focused to the main lobe while suppressing the sidelobe by optimizing the ring-shaped beam.

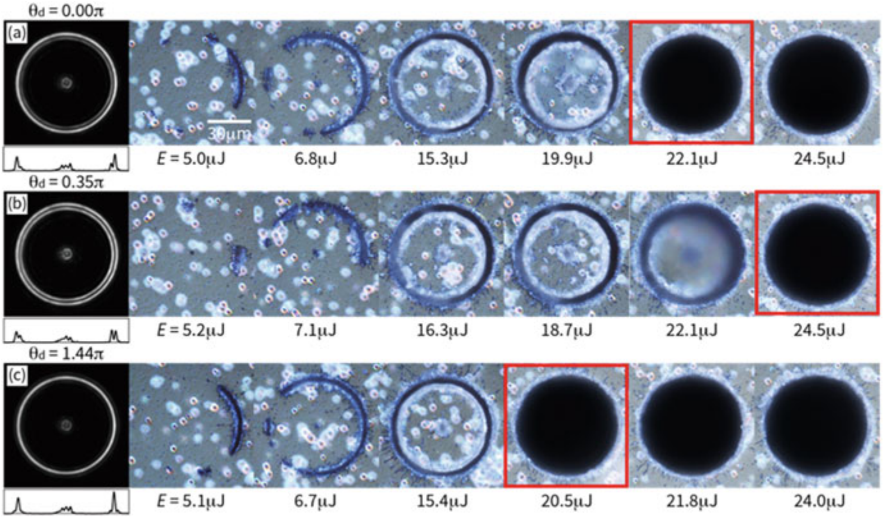

Fig. 15.18 Optical reconstructions of the ring-shaped beams and optical microscope images of the structures fabricated by their reconstruction versus the phase difference θ_{d}. θ_{d} was set to (**a**) 0.00, (**b**) 0.35, and (**c**) 1.44π. (Reprinted with permission from Ref. [49] (c) The Optical Society)

6.5.3 Comparison of Structure Fabricated by Ring-Shaped Beam and Circularly Scanned Beam

In order to analyze the morphological structure fabricated by the ring-shaped beam irradiation, laser processing with a circularly scanned spot beam was performed by way of comparison. Figure 15.19a, b show the intensities and height images obtained with the confocal microscope and top view and perspective view images obtained with the SEM in the structures fabricated by the circularly scanned beam and the ring-shaped beam, respectively. In the case of the scanned spot beam, the number of pulse shots required to fabricate the annular structure was 571 in total. The frequency of the pulse shots and E were set to 60 Hz and 105 nJ, respectively. The lateral shift distance of the focus spot was set to the FWHM of the focus spot. In the results, two types of debris were observed. One was sub-micro debris distributed across a wide area, which was clearly observed in the intensity image of the confocal microscope and SEM images. The sub-micro debris was produced by the subsequent pulse irradiating the melt-solidification structure generated by the previous pulse. The other was micro debris densely deposited on either side of the structure, which was observed in the height image of the confocal microscope and SEM images. The micro debris was derived from aggregation due to melting of the sub-micro debris produced by the subsequent pulse irradiation. The bottom of the figure shows the SEM image of the structure fabricated with $E = 131$ nJ. The pulse energy was near the threshold energy to perform through-hole processing. From the image, a lot of sub-micro debris were observed around the structure.

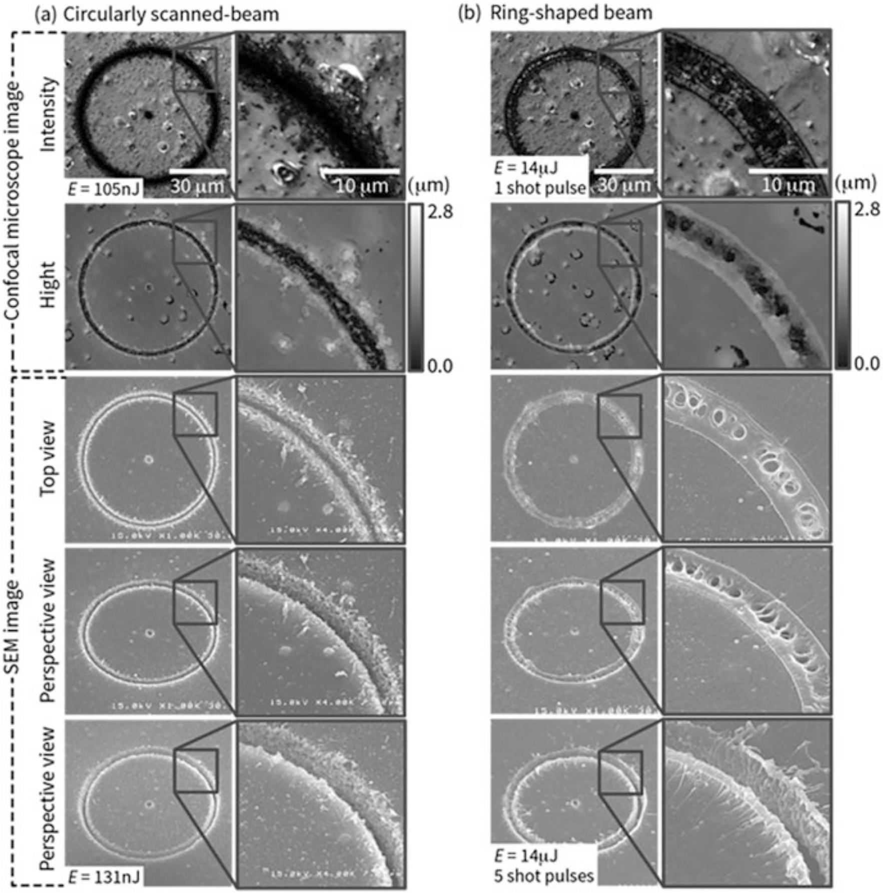
(a) Circularly scanned-beam
(b) Ring-shaped beam
Confocal microscope image
Intensity
Hight
SEM image
Top view
Perspective view
Perspective view
E = 105nJ
30 μm
10 μm
(μm)
2.8
0.0
E = 14μJ
1 shot pulse
E = 131nJ
E = 14μJ
5 shot pulses

Fig. 15.19 Intensity and height images obtained with the confocal microscope and top view and perspective view images of the SEM for the structures fabricated by (**a**) the circularly scanned spot beam and (**b**) the ring-shaped beam. (Reprinted with permission from Ref. [49] (c) The Optical Society)

In the case of the ring-shaped beam, single-shot pulse irradiation was performed. The energy E was set to 14 μJ and was controlled to obtain a structure with a size comparable to that produced by the scanned spot beam. From the result, the sub-micro debris around the annular structure was significantly reduced because the subsequent pulse did not destroy the melt-solidification structure on the underside of the groove observed in the height image of the confocal microscope and perspective view of SEM image. The debris scattered in inward and outward directions perpendicular to the annular structure was also observed in the intensity image of the confocal microscope and was estimated as having a low height from the height image. This structure was specific to single-shot laser processing. The bottom of the figure shows the SEM image of the structure fabricated with $E = 14$ μJ and pulse shot number of 5. The pulse energy and the pulse shot number were also near the threshold values to perform through-hole processing with the ring-shaped beam. From the image, a few sub-micro debris were observed around the structure. Therefore, the roughness near the laser irradiation area was reduced compared with the case of the scanned spot beam.

6.6 Focused Beam with Sub-Diffraction Limit [50]

6.6.1 Design of Sub-Diffraction Limit Focusing

A focused spot size is essentially limited by the diffraction of light, which depends on the wavelength of the light and the numerical aperture (NA) of the focusing lens. In the case of laser material processing, an effective NA that depends on the diameter of the beam irradiating the lens may be more practical than the NA of the focusing lens, because the beam diameter is actually set to less than the pupil size of the lens in order to avoid energy loss. On the other hand, there is a trade-off between the spot size and the field of view (FOV). The FOV is also important for performing processing of large areas using a high-speed optical scanner. Consequently, to generate a sub-diffraction-limit spot whose diameter is smaller than the diffraction limit while maintaining a wide FOV is effective in industrial applications.

A novel algorithm for designing a CGH for generating a sub-diffraction-limit spot with regulation of the light intensity of the surrounding spots was proposed. The CGH design algorithm based on the amplitude optimization around diffraction spots has been demonstrated [51] to avoid a distortion of diffraction spots. Our algorithm was based on proximity complex amplitude optimization between diffraction spots. To demonstrate the effectiveness of the algorithm, a sub-diffraction-limit spot was applied to femtosecond laser processing. To the best of our knowledge, this is the first demonstration of femtosecond laser processing using this kind of sub-diffraction-limit spot. In the experiment, we found that the beam diameter of the sub-diffraction-limit spot was 0.60 times smaller than the diffraction-limit spot. Furthermore, the diameter of the structure processed by the sub-diffraction-limit spot was also reduced to 0.39 times thanks to the nonlinearity of femtosecond laser processing. Fortunately, a certain level of light intensity of the surrounding spots had no effect on the results of laser processing because the intensities of the surrounding spots were lower than the damage threshold of the target sample. Finally, as a supplementary experiment, light patterns formed with combinations of connected and unconnected surrounding spots were demonstrated by using the proposed algorithm. The pattern formed by connected surrounding spots had a spot size comparable to the diffraction limit.

Figure 15.20 shows CGHs together with intensity and phase distributions of their reconstructions. The upper and lower rows indicate computer and experimental reconstructions, respectively. The experimental reconstruction was captured by a charge-coupled device (CCD) image sensor (BITRAN, BU-40 L) on the focal plane

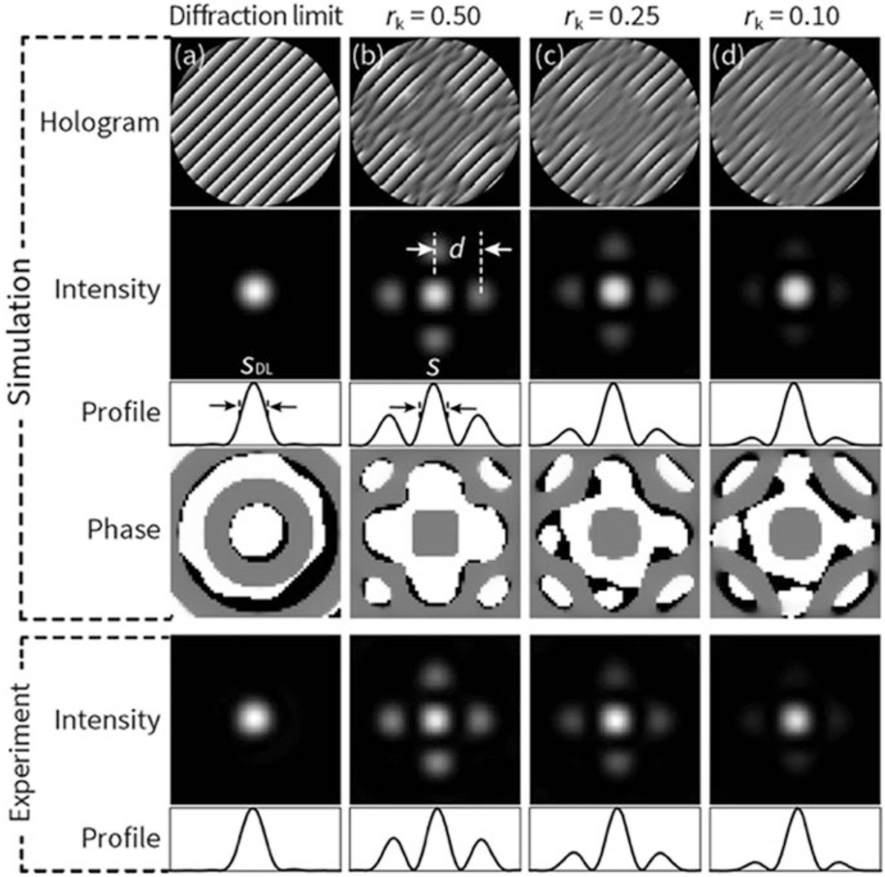

Fig. 15.20 CGHs together with intensity and phase images of computer and experimental reconstructions in the case of (**a**) a diffraction-limit spot and (**b**–**d**) sub-diffraction-limit spots with r_n of 0.50, 0.25, and 0.10, respectively. (Reprinted with permission from Ref. [50] (c) The Optical Society)

of the lens after reflection at the SLM. Figure 15.20a shows the result in the case of a conventional diffraction-limit spot, which was used by way of comparison. The full width at half maximum (FWHM) of the diffraction-limit spot in the intensity profile was defined as w_{DL}. Figure 15.20b–d show the results in the case of sub-diffraction-limit spots with r_n of 0.50, 0.25, and 0.10, respectively. The distance between the center and surrounding spots was defined as d. The FWHM of the sub-diffraction-limit spot was defined as w_{SDL}. d and w_{SDL} were normalized by w_{DL} as $d_{\mathrm{norm}} = d/w_{\mathrm{DL}}$ and $w_{\mathrm{norm}} = w_{\mathrm{SDL}}/w_{\mathrm{DL}}$, respectively, where d_{norm} was fixed to 1.75. From the results, a ratio of the energy contained in the center spot in Fig. 15.20b compared to that in Fig. 15.20a was 0.17 in the simulation. Furthermore, the simulation agreed well with the experiment. From the phase image in the case of the

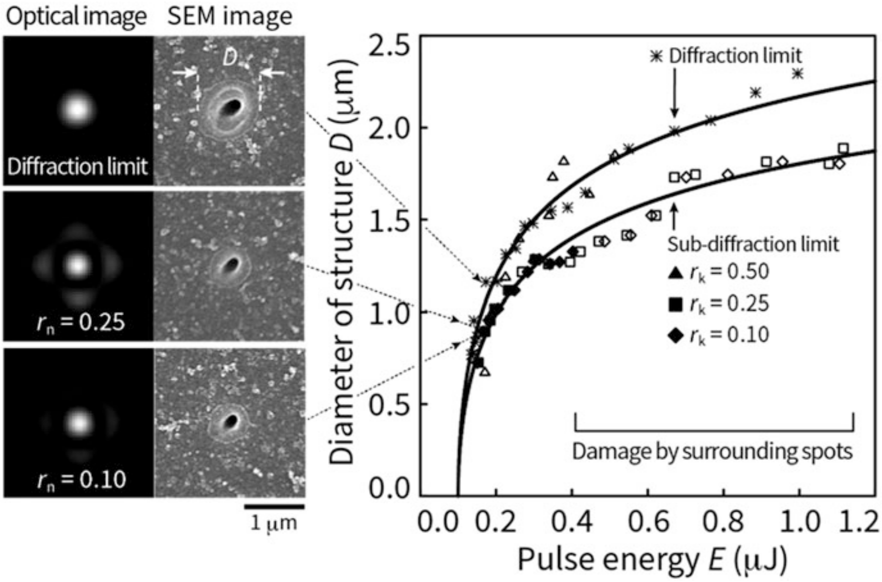

Fig. 15.21 (**a**) Diameter of fabricated structure versus E of the spot with the diffraction limit spot and sub-diffraction-limit spots with r_n of 0.50, 0.25, and 0.10, respectively, when dnorm was fixed to 1.25. (Adopted with permission from Ref. [50] (c) The Optical Society)

sub-diffraction-limit spot, the phase difference between the center and surrounding spots was successfully fixed to π.

6.6.2 Microfabrications Using a Sub-Diffraction Limit-Focused Beam

Femtosecond laser processing with the sub-diffraction-limit spot was demonstrated. Figure 15.21a shows the diameter of the fabricated structure, D, versus the pulse energy, E, when d_{norm} was fixed to 1.25. The inset indicates an optical reconstruction of the CGH and an SEM image of the fabricated structure in each plot. D was measured from an SEM image of the structure. Laser processing was performed by single-shot pulse irradiation on the glass surface. The solid line in the figure represents analytical values calculated using

$$D = \omega\left[2\ln\left(\frac{E}{E_{\text{th}}}\right)\right]^{1/2}, \tag{15.30}$$

which is based on the assumption that the intensity distribution of the focused spot is Gaussian. Here, $\omega = 0.41\lambda/\text{NA}$ is the Gaussian radius of the focused spot in the diffraction limit. $E_{\text{th}} = 0.1$ μJ is the threshold pulse energy required to fabricate the structure. The asterisks, triangles, squares, and diamonds indicate the results using the conventional diffraction-limit spot and the sub-diffraction-limit spots with r_n of 0.50, 0.25, and 0.10, respectively. In the case of the diffraction-limit spot, the plot corresponded to the solid line with NA = 0.32 because the experiment was performed using an OL with effective NA = 0.32. When $E < 4E_\mathrm{th}$, laser processing by the surrounding spots was successfully suppressed. Fortunately, a certain level of light intensity on the surrounding spots had no effect on the processing result because the peak intensity of the surrounding spots was lower than the damage threshold of the glass sample. When $4E_\mathrm{th} < E$, an open plot means that the structure was undesirably fabricated by the surrounding spots. When r_n was set to 0.50 (triangles), laser processing by the surrounding spots was always performed for a wide range of E. Consequently, the plot in the case of the sub-diffraction-limit spot demonstrated higher resolution than that of the diffraction-limit spot with variation of E. Furthermore, the plot practically corresponded to the solid line with NA = 0.39.

6.6.3 Beam Shaping with the Diffraction Limit Size

Figure 15.22 shows focused beams generated by the proposed method. The upper left image indicates the conventional diffraction-limit spot. The other patterns indicate the results obtained by combining connected and unconnected surrounding spots. In the cases of spot connection and disconnection, the phase difference between surrounding spots was set to zero and π, respectively. By regulating the constraint in the algorithm, unique patterns with spot sizes comparable to the diffraction limit were arbitrarily generated. The square-shaped pattern (center of Fig. 15.22) was composed of nine (3 × 3) spots, including 1 center and 8 surrounding spots, where d_norm, r_n, and the phase difference between center and surrounding spots were set to 0.88, 1.0, and 0π, respectively. Therefore, the proposed method will be useful for generating not only sub-diffraction-limit spots but also these kinds of unique patterns.

7 In-System Optimization of CGH

7.1 *Importance of In-System Optimization of CGH*

Even if a CGH is optimized to have a diffraction efficiency of more than 99% and a uniformity of more than 99% in a computer, the reconstruction of the CGH in an actual optical system degrades due to static and dynamic imperfections of the optical system. The static imperfections are a non-flat intensity profile of laser beam (typically Gaussian profile and the differ from the ideal Gaussian), optical system aberrations such as spherical aberration originating from a refractive index mismatch between the immersion medium of an objective lens and a target material

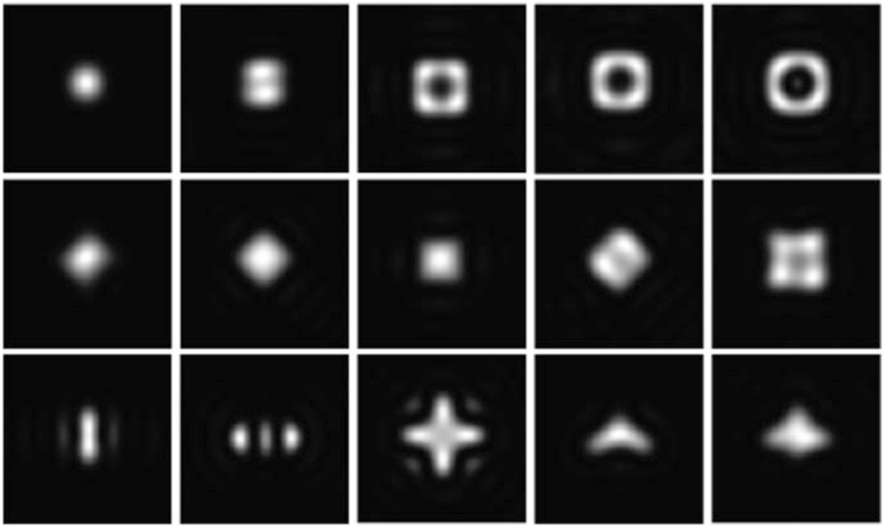

Fig. 15.22 Focused beams generated connected and unconnected surrounding spots. (Reprinted with permission from Ref. [50] (c) The Optical Society)

[52, 53], the spatial frequency response of the LCSLM, and the nonlinearity and its spatial variation of an input-to-phase modulation property of LCSLM [36, 38]. In addition, it is difficult to identify slight misalignments, dusts on optics, and wavefront distortion in the target material in advance. The dynamic imperfections are pointing and shape fluctuation of laser beam**,** temporal fluctuations of LCSLM, small movements of optics caused by micro tremors, air disturbance and dusts in air, and some other changes according to external disturbance and temperature change.

7.2 Pre- and In-Process Optimization of CGH

In order to compensate for the above static and dynamic imperfections, a method that performs optimization of the CGH in a laser processing system, called in-system optimization, was developed [54–57]. The in-system optimization enabled parallel laser processing with more than 1000 focus spots [58]. To compensate static imperfections, the in-system optimization of a CGH was firstly performed, and afterwards the laser processing was performed. The scheme is called as a pre-process optimization. Furthermore, to compensate for unpredictable dynamic imperfections was performed a continuous optimization of a CGH during laser processing, which was called as in-process optimization [59]. These in-system optimization automatically cancels out imperfections.

7.3 In-System and Pre-Processing Optimization of CGH

7.3.1 Optimization of a CGH with More Than 1000 Parallel Beams [58]

Figure 15.23a shows an optical reconstruction of a CGH optimized only in a computer, which is the conventional method, and its intensity profile on the line indicated by the gray arrow. The number of parallel beams N_{parallel} was 1005. The CGH optimization with 100 iterations is required about 124 minutes in the case of a CGH with 800 × 600 pixels. The central spot in the reconstruction was the non-diffracted 0-th order light. The uniformity U, defined as the ratio of the maximum and the minimum peak intensities in the reconstruction, was 0.32. The average (AVG) and the standard deviation (SD) of the peak intensities were 116 and 27, respectively. The intensity I was measured as an 8-bit signal for the captured image obtained by the cooled CCD image sensor. The actual quality of the reconstruction was low, although the reconstruction in the computer had $U > 0.99$. In particular, the peak intensities in the high-spatial-frequency region were obviously low, as a result of the poor spatial frequency response of the SLM.

Figure 15.23b shows the optical reconstruction optimized only in the computer and its intensity profile, in the case where the spatial frequency response of the SLM in the computational reconstruction was taken into account. The optical reconstruction was also degraded to $U = 0.46$, AVG = 176, and SD = 23, due to unknown properties of the optical system, although the beams arranged in a high-spatial-frequency area were improved. The reconstruction in the computer was also degraded to $U = 0.81$ (see the solid curve in Fig. 15.23d) because of mutual interference between the sidelobes and high-order diffraction peaks.

Figure 15.23c shows the optical reconstruction of the CGH optimized using the in-system optimization. U was improved to 0.84 (see the filled circles in Fig. 15.23d). This value was comparable to the computational reconstruction in which the spatial frequency response of the SLM was taken into account, with AVG = 131 and SD = 4. In particular, the intensities in the high-frequency region were significantly enhanced.

Figure 15.23d shows the change of U with increasing number of iterations in the CGH optimization process. The solid line indicates the optimization process in the computer with the spatial frequency response of the SLM taken into account, shown in Fig. 15.23b. The filled circles indicate the process with the in-system optimization, shown in Fig. 15.23c. They showed almost the same performance. This means that the in-system optimization reached the limit of the optical system performance. This is the first demonstration of CGH optimization for multiple beams with a high degree of parallelism with high uniformity.

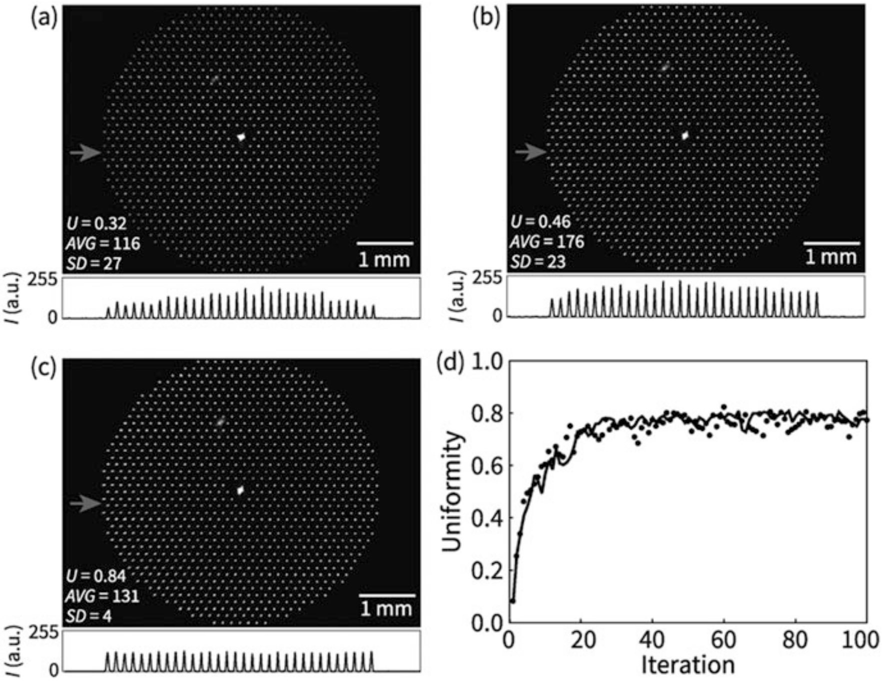

Fig. 15.23 Optical reconstructions of CGH optimized (**a**) only in the computer and (**b**) by the computational reconstruction with the spatial response characteristic of SLM and (**c**) the in-system optimization. (**d**) Change of the uniformity in the reconstruction for iteration in the optimization of (**b**) (solid lines) and (**c**) (filled circles), respectively. (Reprinted with permission from Ref. [58] (c) The Optical Society)

7.3.2 Massively Parallel Laser Processing Using In-System Optimization of a CGH

Figure 15.24 shows massively parallel femtosecond laser processing of a glass surface. The parallel beams shown in Fig. 15.3 were used. Figure 15.24a shows optical microscope images of the structure processed by the reconstruction shown in Fig. 15.23a. The processing was performed with five pulse shots with gradually increasing average pulse energy E_{sample}. In the images, the gray and white circles indicate positions with and without a pit fabricated by the pulse irradiation. In the inset of the figure, N_{pit} indicates the number of fabricated pits. Mainly the center part of the reconstruction was processed, despite the increase of E_{sample}.

Figure 15.24b shows optical microscope images of the structure processed by the reconstruction shown in Fig. 15.23b. The processing was discretely performed in the reconstruction with the increase of the E_{sample} because the intensity distribution became more uniform.

Fig. 15.24 (**a**–**c**) Optical microscope images of the structure processed using the reconstruction of Fig. 15.23a–c, respectively. (**d**) Number of fabricated pits N_{pit} versus the average pulse energy E_{sample} in the case using the reconstruction without (Fig. 15.23a, b) and with (Fig. 15.23c) the in-system optimization, respectively. (Reprinted with permission from Ref. [58] (c) The Optical Society)

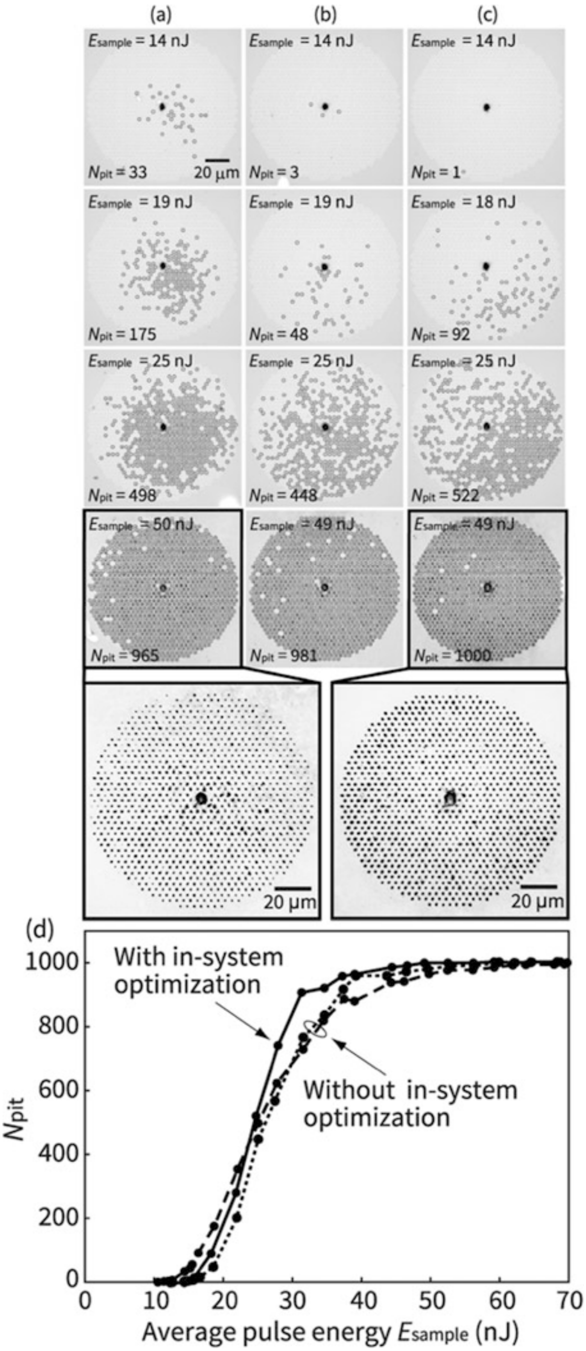

Figure 15.22c shows optical microscope images of the structure processed by the reconstruction shown in Fig. 15.23c. The two images arranged below the figure are magnified optical microscope images showing the results without and with the in-system optimization when E_{sample} was set to 50 and 49 nJ, respectively. Improved quality in the fabricated structure was experimentally demonstrated.

Figure 15.24d shows N_{pit} versus E_{sample} without (dashed and dot lines) and with (solid line) the in-system optimization, corresponding to Fig. 15.23a–c, respectively. In the results without the optimization, $R_{\mathrm{E}} = 0.16$ and 0.24, corresponding to the dashed and dotted lines, respectively, where R_{E} represents the ratio between the minimum energy required to process a single pit and the minimum energy required to make $N_{\mathrm{pit}} = N_{\mathrm{parallel}}$. In the result obtained with the optimization, R_{E} was improved to 0.29. As a result of the optimization, the energy required to fabricate over 1000 pits was decreased from 69 nJ and 60 nJ to 49 nJ, respectively.

The maximum value of the diffraction area was predictable from the spatial frequency response of the LCSLM. However, the minimum value of p_{d} was 2.5 times larger than the value of our previous work. The reason for the discrepancy was assumed to be as follows. In the previous work, the minimum $p_{\mathrm{d}} = 2.8$ was evaluated from the optical reconstruction captured by an image sensor. When p_{d} was set to 3.0, the quality of the fabricated structure was unexpectedly undesirable due to mutual interference between the sidelobes of the diffraction beam. This is because the energy required to fabricate the glass sample is quite high compared with that required to capture the reconstruction. Therefore, the minimum p_{d} in the actual laser processing is usually larger than that evaluated from the optical reconstruction.

Massively parallel femtosecond laser processing with more than 1000 beams was demonstrated. The number of parallel beams, N_{parallel}, which is related to the processing throughput, is mathematically given by the number of pixels in the SLM, imaged on the pupil plane of the objective lens and the distance parameter, p_{d}, which is obtained by dividing the distance between adjacent beams by the diffraction-limited beam diameter. N_{parallel} and p_{d} were limited by the spatial frequency response of the LCSLM and the diffraction limitation of the focused beam, respectively. In our system, the maximum values of N_{parallel} and p_{d} were experimentally estimated to be 250 and 7.00, respectively. Based on these parameters, the maximum N_{parallel} was calculated to be 1189 by using an analytical equation.

In massively parallel laser processing of glass samples, it was experimentally demonstrated that in-system optimization of the CGH is a key method in realizing 1 k-laser processing. In the case of laser processing with $N_{\mathrm{parallel}} = 1005$, 1005 pits were successfully fabricated with irradiation pulse energies of $E_{\mathrm{sample}} = 59$ nJ at the sample plane and $E_{\mathrm{SLM}} = 0.337$ mJ at the LCSLM plane. The energy at the LCSLM plane was sufficiently less than the damage threshold of the LCSLM.

7.4 Parallel Focused Beams with Three-Dimensional Arrangement

7.4.1 Optimization Procedure of CGH

The CGH calculation was performed by using a modified version of the weighted iterative Fourier transform (WIFT) method [60]. The processes of optical reconstruction of the CGH in the laser processing system, detection of the reconstruction, and recalculation of the CGH were iteratively performed based on the rewritable capability of the LCOS-SLM while the laser processing was being performed. The target patterns were parallel beams with uniform intensity. The estimation of the reconstruction was performed based on the uniformity $U_\mathrm{I} = I_\mathrm{min}/I_\mathrm{max}$, where I_min and I_max are the minimum and the maximum intensities in all the diffraction peaks, respectively.

In this section, we will introduce the principle of 3D reconstructions and optimization methods and give the simulation results to verify the feasibility of the method. We take use the angular spectrum (AS) method [61, 62] to realize the 3D distribution; in theory, the spectrum in the image plane A can be calculated by multiplying the spectrum in the object plane A_0 with the angular spectrum propagator H, that is expressed as $A = A_0 * H$, where

$$H\left(\sigma_x, \sigma_y; z\right) = \exp\left[jkz\sqrt{1 - (\lambda\sigma_x)^2 - \left(\lambda\sigma_y\right)^2}\right], \tag{15.31}$$

where σ_x and σ_y are the spatial frequencies for each direction and z is an axial distance of the beam propagation. The conversion from the spatial domain to the spatial frequency domain is easily obtained by the fast Fourier transform (FFT) calculation. Furthermore, multiple CGHs with different z can be calculated, and then the phase information in these CGHs needs to be superimposed to synthesize a u_sum that can generate 3D reconstructions. This synthesis process is performed by the summation process of the phase distribution expressed as

$$u_\mathrm{sum} = u_1 + u_2 + \cdots + u_m, \tag{15.32}$$

where u_m is the phase distribution for m-th focal planes and the spatial coordinates omitted for simplifications. This formula $\mathrm{mod}(u_\mathrm{sum}, 2\pi)$ is then used to filter out the overflow phase values in order to avoid the distortion of the reconstructions when displaying the CGH on the LCSLM.

After realizing the design of CGH containing 3D reconstructions, due to the imperfections of the optical system, there are differences in the intensity of diffraction spots, so the next step needs to be considered is the uniformity optimization between them. Here, we take use a modified version of the WIFT algorithm to optimize the intensity distribution for each iteration. This optimization algorithm is based on iterative calculation method; in each iteration, different weight values

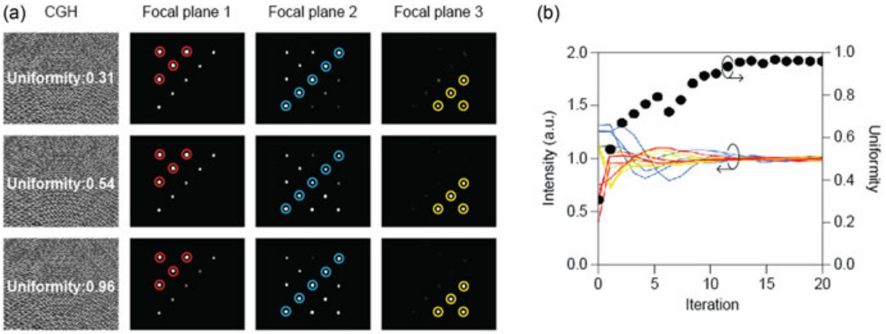

Fig. 15.25 (**a**) Schematic of the optimization results of CGHs and corresponding 3D optical reconstructions. The red, blue, and yellow circles are used to distinguish the optical reconstructions at different focal planes. (**b**) Intensity of all diffractions for the optimization iterations (indicated with corresponding color lines) and the uniformity of them the (indicated with black-dots)

will be assigned to each light spot. The reduced light intensity will be allocated to the spot with weak intensity, which is realized in the form of allocating larger weight value, so as to adjust the intensity difference between the light spots, that is, adjusting the uniformity between them. The optimization method for 3D reconstructions is to collect the spot intensity information in each focal plane in each iteration and finally carry out unified weight value distribution processing; then the uniformity between the light spots will be significantly improved after a limited times of iterations.

Both the computer optimization and the optimization in the optical system are calculated in the computer based on this method. The difference is the acquisition of light intensity. In the simulation, the light intensity is calculated by FFT. However, in the actual optical system, after the diffracted beams are focused by the lens, the focal spots are collected by image sensor and then transmitted to the computer for processing. In addition, the implementation method in the optical system is to use the image sensor that is fixed on the linear stage to move to different focal planes along the optical axis then to collect three-dimensional light intensity data.

7.4.2 Microfabrication Using a CGH that Performs a 3D Focusing

Figure 15.25a shows the schematic of the optimization results of CGHs and corresponding 3D optical reconstructions. Figure 15.25b shows the intensity of the respective peak intensity and their uniformity The color lines represent the intensity changes of the optical reconstructions, and the black-dotted lines indicate the variations of the uniformity. The spacing between the focal planes is 4 mm, and all the 3D patterns were optimized 20 times using our in-system optimization method.

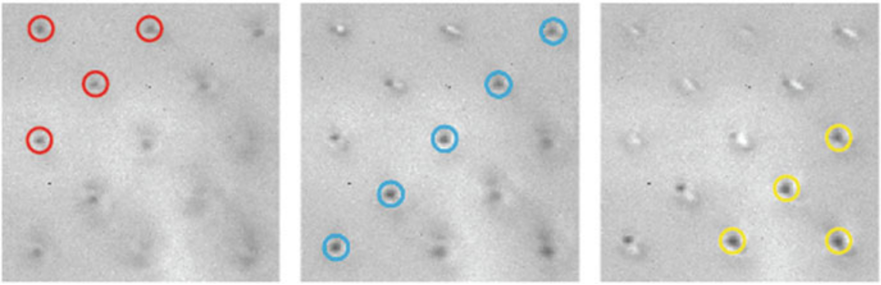

Fig. 15.26 Experimental results of 3D holographic processing. The red, blue, and yellow circles mark the micro-holes processed on different layers inside the glass. The total pulse energy of the 13 focal spots of each pattern was 6.5 μJ, and so the average energy of each spot was 0.50 μJ, which was a little higher than the fabrication threshold of 0.30 μJ inside the glass sample. And the interval between the processing layers is 6.4 μm

Initially, the intensities of the optical reconstructed spots at focal plane 2 and focal plane 3 are weaker than that at focal plane 1, especially the bottom right corner one at focal plane 2 and the one at focal plane 3. The initial uniformity was 0.31. After 20 times of the optimization, the uniformity reached to 0.97; it can be seen that both the spot size and intensity have been significantly improved.

Figure 15.26 shows the results of holographic processing using the optimal CGHs. The red, blue, and yellow circle areas mark the micro-holes processed on different layers inside the glass. The total pulse energy of the 13 focal spots of each pattern was 6.5 μJ, and so the average energy of each spot was 0.50 μJ, which was a little higher than the fabrication threshold of 0.30 μJ inside the glass sample. And the interval between the processing layers was 6.4 μm. As a direct proof, it can be seen from the figure, the 3D optical reconstructed spots can be processed at different layers after being introduced inside the glass material by a single irradiation. That is, the original 2D pattern can be transformed into 3D distribution of various patterns, and the arbitrariness and flexibility of holographic laser processing can be greatly improved. And we believe that this is very helpful to expand the application range of laser processing.

8 Summary

Spatial beam shaping based on the computer-generated hologram was displayed on a spatial light modulator. The principle, features, and useful techniques of the holographic femtosecond laser processing were described. The experimental results of the femtosecond laser processing with parallel beams, line-shaped beam, circular-shaped beam, and vector beam were demonstrated. These beam shaping will be promising for performing a valuable and high-speed fabrication of the complex optical structures in large area, especially, industrial applications. In addition, it needs to investigate the interactions between a variety of materials and the spatially and temporally shaped beams much more. The knowledge will be further enhanced ultrashort pulse laser processing. Now a beam design for each application is important, and it is not so easy because of the number of beam parameters is increased. An on-going research project is an automatic design of spatial beam shaping in two and three dimensions.

References

1. Y. Hayasaki, T. Sugimoto, A. Takita, N. Nishida, Variable holographic femtosecond laser processing by use of a spatial light modulator. Appl. Phys. Lett. **87**, 031101 (2005)
2. N. Sanner, N. Huot, E. Audouard, C. Larat, J.P. Huignard, B. Loiseaux, Programmable focal spot shaping of amplified femtosecond laser pulses. Opt. Lett. **30**, 1479–1481 (2005)
3. S. Hasegawa, Y. Hayasaki, N. Nishida, Holographic femtosecond laser processing with multiplexed phase Fresnel lenses. Opt. Lett. **31**, 1705–1707 (2006)
4. Y. Cheng, K. Sugioka, K. Midorikawa, M. Masuda, K. Toyoda, M. Kawachi, K. Shihoyama, Control of the cross-sectional shape of a hollow microchannel embedded in photostructurable glass by use of a femtosecond laser. Opt. Lett. **28**, 55–57 (2003)
5. M. Ams, G.D. Marshall, D.J. Spence, M.J. Withford, Slit beam shaping method for femtosecond laser direct-write fabrication of symmetric waveguides in bulk glasses. Opt. Express **13**, 5676–5681 (2005)
6. G. Cerullo, R. Osellame, S. Taccheo, M. Marangoni, D. Polli, R. Ramponi, P. Laporta, S.D. Silvestri, Femtosecond micromachining of symmetric waveguides at 1.5 mm by astigmatic beam focusing. Opt. Lett. **27**, 1938–1940 (2002)
7. M. Merano, G. Boyer, A. Trisorio, G. Chériaux, G. Mourou, Superresolved femtosecond laser ablation. Opt. Lett. **32**, 2239–2242 (2007)
8. K. Kawamura, T. Ogawa, N. Sarukura, M. Hirano, H. Hosono, Fabrication of surface relief gratings on transparent dielectric materials by two-beam holographic method using infrared femtosecond laser pulses. Appl. Phys. B Lasers Opt. **71**, 119–121 (2000)
9. L. Wu, Y. Zhong, C.T. Chan, K.S. Wong, G.P. Wang, Fabrication of large area two- and three-dimensional polymer photonic crystals using single refracting prism holographic lithography. Appl. Phys. Lett. **86**, 241102 (2005)
10. M. Lei, B. Yao, R.A. Rupp, Structuring by multi-beam interference using symmetric pyramids. Opt. Express **14**, 5803–5811 (2006)
11. T.M. Bloomstein, M.F. Marchant, S. Deneault, D.E. Hardy, M. Rothschild, 22-nm immersion interference lithography. Opt. Express **14**, 6434–6443 (2006)
12. S. Matsuo, S. Juodkazis, H. Misawa, Femtosecond laser microfabrication of periodic structures using a microlens array. Appl. Phys. A Mater. Sci. Process. **80**, 683–685 (2005)
13. J. Kato, N. Takeyasu, Y. Adachi, H.B. Sun, S. Kawata, Multiple-spot parallel processing for laser micronanofabrication. Appl. Phys. Lett. **86**, 044–102 (2005)
14. P.S. Salter, M.J. Booth, Addressable microlens array for parallel laser microfabrication. Opt. Lett. **36**, 2302–2304 (2011)
15. Y. Kuroiwa, N. Takeshima, Y. Narita, S. Tanaka, K. Hirao, Arbitrary micropatterning method in femtosecond laser microprocessing using diffractive optical elements. Opt. Express **12**, 1908–1915 (2004)
16. A. Shishido, I.B. Diviliansky, I.C. Khoo, T.S. Mayer, S. Nishimura, G.L. Egan, T.E. Mallouk, Direct fabrication of two-dimensional titania arrays using interference photolithography. Appl. Phys. Lett. **79**, 3332–3334 (2001)
17. J.H. Klein-Wiele, P. Simon, Fabrication of periodic nanostructures by phase-controlled multiple-beam interference. Appl. Phys. Lett. **83**, 4707–4709 (2003)

18. J. Amako, K. Nagasaka, N. Kazuhiro, Chromatic-distortion compensation in splitting and focusing of femtosecond pulses by use of a pair of diffractive optical elements. Opt. Lett. **27**, 969–971 (2002)
19. G. Mínguez-Vega, J. Lancis, J. Caraquitena, V. Torres-Company, P. Andrés, High spatiotemporal resolution in multifocal processing with femtosecond laser pulses. Opt. Lett. **31**, 2631–2633 (2006)
20. G. Mínguez-Vega, E. Tajahuerce, M. Fernández-Alonso, V. Climent, J. Lancis, J. Caraquitena, P. Andrés, Dispersion-compensated beam-splitting of femtosecond light pulses: Wave optics analysis. Opt. Express **15**, 278–288 (2007)
21. L. Martínez-León, P. Clemente, E. Tajahuerce, G. Mínguez-Vega, O. Mendoza-Yero, M. Fernández-Alonso, J. Lancis, V. Climent, P. Andrés, Spatial-chirp compensation in dynamical holograms reconstructed with ultrafast lasers. Appl. Phys. Lett. **94**, 011104 (2009)
22. J. Amako, D. Sawaki, E. Fujii, Microstructuring transparent materials by use of nondiffracting ultrashort pulse beams generated by diffractive optics. J. Opt. Soc. Am. B **20**, 2562–2568 (2003)
23. F. Courvoisier, P.A. Lacourt, M. Jacquot, M.K. Bhuyan, L. Furfaro, J.M. Dudley, Surface nanoprocessing with nondiffracting femtosecond Bessel beams. Opt. Lett. **34**, 3163–3165 (2009)
24. M.K. Bhuyan, F. Courvoisier, P.A. Lacourt, M. Jacquot, L. Furfaro, M.J. Withford, J.M. Dudley, High aspect ratio taper-free microchannel fabrication using femtosecond Bessel beams. Opt. Express **18**, 566–574 (2010)
25. M.K. Bhuyan, F. Courvoisier, P.A. Lacourt, M. Jacquot, R. Salut, L. Furfaro, J.M. Dudley, High aspect ratio nanochannel machining using single shot femtosecond Bessel beams. Appl. Phys. Lett. **97**, 81–102 (2010)
26. R.R. Thomson, A.S. Bockelt, E. Ramsay, S. Beecher, A.H. Greenaway, A.K. Kar, D.T. Reid, Shaping ultrafast laser inscribed optical waveguides using a deformable mirror. Opt. Express **16**, 12786–12793 (2008)
27. B. Sun, P.S. Salter, M.J. Booth, Pulse front adaptive optics: A new method for control of ultrashort laser pulses. Opt. Express **23**, 19348 (2015)
28. Z. Kuang, W. Perrie, J. Leach, M. Sharp, S. Edwardson, M. Padgett, G. Dearden, K. Watkins, High throughput diffractive multi-beam femtosecond laser processing using a spatial light modulator. Appl. Surf. Sci. **255**, 2284–2289 (2008)
29. Z. Kuang, D. Liu, W. Perrie, S. Edwardson, M. Sharp, E. Fearon, G. Dearden, K. Watkins, Fast parallel diffractive multi-beam femtosecond laser surface micro-structuring. Appl. Surf. Sci. **255**, 6582–6588 (2009)
30. K.L. Wlodarczyk, J.J.J. Kaakkunen, P. Vahimaa, D.P. Hand, Efficient speckle-free laser marking using a spatial light modulator. Appl. Phys. A Mater. Sci. Process. **116**, 111–118 (2014)
31. A.A. Maznev, T.E. Crimmins, K.A. Nelson, How to make femtosecond pulses overlap. Opt. Lett. **23**, 1378–1380 (1998)
32. H.B. Sun, Y. Xu, S. Juodkazis, K. Sun, M. Watanabe, S. Matsuo, H. Misawa, J. Nishii, Arbitrary-lattice photonic crystals created by multiphoton microfabrication. Opt. Lett. **26**, 325–327 (2001)
33. T. Kondo, S. Matsuo, S. Juodkazis, H. Misawa, Femtosecond laser interference technique with diffractive beam splitter for fabrication of three-dimensional photonic crystals. Appl. Phys. Lett. **79**, 725–727 (2001)
34. Y. Nakata, T. Okada, M. Maeda, Fabrication of dot matrix, comb, and nanowire structures using laser ablation by interfered femtosecond laser beams. Appl. Phys. Lett. **81**, 4239–4242 (2002)
35. Y. Li, W. Watanabe, K. Yamada, T. Shinagawa, K. Itoh, J. Nishii, Y. Jiang, Holographic fabrication of multiple layers of grating inside soda-lime glass with femtosecond laser pulses. Appl. Phys. Lett. **80**, 1508–1510 (2002)
36. K. Venkatakrishnan, N.R. Sivakumar, C.W. Hee, B. Tan, W.L. Liang, G.K. Gan, Direct fabrication of surface-relief grating by interferometric technique using femtosecond laser. Appl. Phys. A Mater. Sci. Process. **77**, 959–963 (2003)

37. Z. Kuang, J. Li, S. Edwardson, W. Perrie, D. Liu, G. Dearden, Ultrafast laser beam shaping for material processing at imaging plane by geometric masks using a spatial light modulator. Opt. Lasers Eng. **70**, 1–5 (2015)
38. D. Liu, Y. Wang, Z. Zhai, Z. Fang, Q. Tao, W. Perrie, S.P. Edwarson, G. Dearden, Dynamic laser beam shaping for material processing using hybrid holograms. Opt. Laser Technol. **102**, 68–73 (2018)
39. Y. Nakata, K. Osawa, N. Miyanaga, Utilization of the high spatial-frequency component in adaptive beam shaping by using a virtual diagonal phase grating. Sci. Rep. **9**, 4640 (2019)
40. Y. Hayasaki, M. Nishitani, H. Takahashi, H. Yamamoto, A. Takita, D. Suzuki, S. Hasegawa, Experimental investigation of the closest parallel pulses in holographic femtosecond laser processing. Appl. Phys. A **107**, 357–362 (2012)
41. S. Hasegawa, Y. Hayasaki, Holographic vector wave femtosecond laser processing. Int. J. Optomechatronics **18**, 73–88 (2014)
42. Y. Hayasaki, H. Yamamoto, N. Nishida, Optical dependence of spatial frequency of formed patterns on focusing deviation in nonlinear optical ring resonator. Opt. Commun. **151**, 263–267 (1998)
43. Y. Hayasaki, H. Yamamoto, N. Nishida, Self-scanning of isolated spots in a nonlinear optical system with two-dimensional feedback. J. Opt. Soc. Am. B **17**, 1211–1215 (2000)
44. K. Chaen, H. Takahashi, S. Hasegawa, Y. Hayasaki, Display method with compensation of the spatial frequency response of a liquid crystal spatial light modulator for holographic femtosecond laser processing. Opt. Commun. **280**, 165–172 (2007)
45. J. Bengtsson, Kinoform design with an optimal-rotation-angle method. Appl. Opt. **33**, 6879–6884 (1994)
46. H. Takahashi, S. Hasegawa, Y. Hayasaki, Holographic femtosecond laser processing using optimal-rotation-angle method with compensation of spatial frequency response of liquid crystal spatial light modulator. Appl. Opt. **46**, 5917–5923 (2007)
47. S. Hasegawa, K. Shiono, Y. Hayasaki, Femtosecond laser processing with a holographic line-shaped beam. Opt. Express **3**, 23185–23194 (2015)
48. S. Hasegawa, Y. Hayasaki, Polarization distribution control of parallel femtosecond pulses with spatial light modulators. Opt. Express **21**, 12987–12995 (2013)
49. S. Hasegawa, H. Ito, H. Toyoda, Y. Hayasaki, Diffraction-limited ring beam generated by radial grating. OSA Continuum **1**, 283–294 (2018)
50. S. Hasegawa, H. Takahashi, M. Ota, D. Barada, Y. Ogura, J. Tanida, Y. Hayasaki, Spatial phase shaping of ultrashort pulses to overcome the diffraction limit. OSA Continuum **2**, 3240–3250 (2019)
51. Y. Ogura, M. Aino, J. Tanida, Design and demonstration of fan-out elements generating an array of subdiffraction spots. Opt. Express **22**, 25196–25207 (2014)
52. H. Itoh, N. Matsumoto, T. Inoue, Spherical aberration correction suitable for a wavefront controller. Opt. Express **17**, 14367–14373 (2009)
53. B.P. Cumming, A. Jesacher, M.J. Booth, T. Wilson, M. Gu, Adaptive aberration compensation for three-dimensional micro-fabrication of photonic crystals in lithium niobate. Opt. Express **19**, 9419–9425 (2011)
54. S. Hasegawa, Y. Hayasaki, Adaptive optimization of a hologram in holographic femtosecond laser processing system. Opt. Lett. **34**, 22–24 (2009)
55. S. Hasegawa, Y. Hayasaki, Second harmonic optimization of computer-generated hologram. Opt. Lett. **36**, 2943–2945 (2011)
56. N. Matsumoto, T. Inoue, T. Ando, Y. Takiguchi, Y. Ohtake, H. Toyoda, High-quality generation of a multispot pattern using a spatial light modulator with adaptive feedback. Opt. Lett. **37**, 3135–3137 (2012)
57. M. Silvennoinen, J. Kaakkunen, K. Paivasaari, P. Vahimaa, Parallel femtosecond laser ablation with individually controlled intensity. Opt. Express **22**, 2603–2608 (2014)
58. S. Hasegawa, H. Ito, H. Toyoda, Y. Hayasaki, Massively parallel femtosecond laser processing. Opt. Express **24**, 18513–18524 (2016)

59. H. Zhang, S. Hasegawa, H. Takahashi, H. Toyoda, Y. Hayasaki, In-system optimization of a hologram for high-stability parallel laser processing. Opt. Lett. **45**, 3344–3347 (2020)
60. R. Di Leonardo, F. Ianni, G. Ruocco, Computer generation of optimal holograms for optical trap arrays. Opt. Express **15**, 1913–1922 (2007)
61. J.W. Goodman, *Introduction to Fourier Optics*, 2nd edn. (McGraw-Hill, New York, 1996)
62. L. Yu, M.K. Kim, Wavelength-scanning digital interference holography for tomographic three-dimensional imaging by use of the angular spectrum method. Opt. Lett. **30**, 2092–2094 (2005)

Chapter 16
Nonstandard Light for Ultrafast Laser Microstructuring and Nanostructuring

Francois Courvoisier

Abstract Ultrashort laser pulses have revolutionized laser-matter interaction because they can deposit energy at extremely small scales. High-speed and controlled nanostructuring has become possible both at the surface of materials and inside transparent materials. Here, a specific class of beams is reviewed: the "Bessel beams" that are quasi-invariant along the propagation. They provide new avenues for controlling laser-matter interaction at extreme nanometric scales at the surface of materials but also within the bulk of transparent dielectrics. Of particular interest is the possibility to generate nanostructures with extremely high aspect ratio—length divided by diameter—, up to several 10,000:1 using single ultrafast laser pulses. The generation of nanoplasma using quasi-non-diffracting beams provides access to extreme material states and opens a drastically new regime for material nanostructuring. This chapter reviews the state of the art of the fundamental concepts of Bessel beams and their applications, particularly for high aspect ratio nanostructuring, drilling, and stealth dicing. More complex beam shapes, based on the same concept of conical flow of light, offer new perspectives for materials processing.

Keywords Bessel beams · Diffraction-free beams · Ultrafast laser beam shaping · High aspect ratio · Stealth dicing · Curved beams

1 Introduction

Chirped pulse amplification has enabled an evolution in laser structuring. High-energy, ultrafast laser pulses, i.e., with pulse duration typically between 50 fs to some tens of picoseconds, can generate a highly excited free electron gas in the cold lattice. This is possible not only in metals but also in dielectrics, thanks to

---

F. Courvoisier (✉)
FEMTO-ST Institute, Université de Bourgogne Franche-Comté, Besançon Cedex, France
e-mail: francois.courvoisier@femto-st.fr

© The Author(s), under exclusive license to Springer Nature Switzerland AG 2023

R. Stoian, J. Bonse (eds.), *Ultrafast Laser Nanostructuring*, Springer Series in Optical Sciences 239, https://doi.org/10.1007/978-3-031-14752-4_16

the nonlinear ionization. At the surface of materials, the ultrafast character of the energy deposition produces a high contrast between the excited zone and the non-excited material. This opens the possibility to structure materials at the micrometer or nanometer scale. This chapter will particularly emphasize the structuring of transparent materials bulk at this extreme scale. One of the key aspects of the possibility to excite transparent materials via nonlinear ionization is that energy can be stored inside the bulk of the material with no modification on other surfaces. Femtosecond and picosecond lasers have therefore found a large number of applications during the last decade.

While early works were dedicated to inscribing in materials the tiniest modifications using highly focused Gaussian beams, it has been then recognized that beam shaping could bring new opportunities. Chapters 15 and 26 discuss the applications of beam shaping for laser micro structuring and nanostructuring. This chapter focuses on a specific class of beam shapes which is the “non-diffracting” or “diffraction-free” beams. The terminology has been brought by Durnin when introducing the zeroth-order Bessel beam which is a propagation-invariant solution to the wave equation [1]. The specificity of this beam is that it can maintain an extremely narrow focus, even below the wavelength, on extremely long distances, well beyond the limitation of the Rayleigh range. In solid dielectrics, the zeroth-order Bessel beam has close links with the filamentation of ultrafast pulses.

A first class of applications therefore lies in the use of this propagation invariance to circumvent the technical issue of maintaining the workpiece surface within the laser focus. A second very important property of Bessel beams is that their nonlinear propagation inside transparent materials can be also invariant, in contrast with the nonlinear propagation of Gaussian beams which is conventionally much more difficult to control. It will be seen that the second property allows for depositing energy highly homogeneously along extremely long distances. The generation of extremely high aspect ratio nanostructures can be performed even using a single-laser pulse. This has opened a large number of new applications. Among them, high-speed (meter per second) glass separation with a non-ablative process has attracted an enormous attention for obvious applications to mass fabrication of touchscreens, consumer electronics and, more recently, high-speed cutting of windshields and window glass. This field of research has rapidly evolved from the first reviews [2–6].

In this chapter, Sect. 2 describes non-diffracting Bessel beams, how they can be shaped, and the applications of their extended focal zone to laser surface microstructuring and nanostructuring. Section 3 discusses the propagation of intense ultrashort pulses inside the bulk of transparent dielectrics. The nonlinear propagation of Bessel beams corresponds to the asymptotic behavior of the filamentation process of a Gaussian pulse. It is shown that Bessel-shaped pulses can generate plasma rods with nanometric diameter over a length of several tens of micrometers to centimeters. The relaxation of a nanoplasma rod inside the transparent material can generate an index modification, nano-gratings, or a void. The physics of the interaction and of the void formation will be discussed. Section 4 reviews the applications to high aspect ratio microstructuring and nanostructuring of transparent dielectrics, with a particular emphasis on stealth dicing. Section 5 is dedicated to the new perspectives in the field: additional beam engineering maintains the diffraction-free character without the cylindrical symmetry of the initial Bessel beam. Tailoring the beam structure can improve the stress field, with important applications to stealth dicing. Another important perspective is to engineer the ultrafast laser beam such that it can produce curved profiles inside the transparent material: this can be used to avoid mechanical chamfering that is conventionally used to avoid chipping of glass.

2 Propagation of Non-diffracting Beams in Vacuum: Application to Surface Laser Nanopatterning

This section first describes what are non-diffracting Bessel beams and the means to generate them. Then, the applications of their extended focus to surface nanostructuring are reviewed.

2.1 Non-diffracting Beams and Spatial Beam Shaping of Ultrashort Pulses

2.1.1 Basics of Bessel Beams

A Bessel beam can be seen as a cylindrically symmetric interference field: it is the coherent superposition of an infinite set of plane waves whose wavevectors are distributed on the generatrix of a cone. Durnin has formalized the Bessel beam as a solution to the Helmholtz equation: this solution is featured by an intensity distribution that is invariant along the propagation direction [1].

The monochromatic field scalar amplitude of the zeroth-order Bessel beam reads in cylindrical coordinates as:

$$A(r, z, t) = A_0 J_0\left(\frac{2\pi}{\lambda} \sin\gamma r\right) e^{i\frac{2\pi}{\lambda}\cos\gamma z} \tag{16.1}$$

where λ is the wavelength, A_0 is constant, and γ is defined as the cone angle. This is the angle made by the wavevector with respect to the optical axis: the wavevector has a radial component $k_r^0 = \frac{2\pi}{\lambda}\sin\gamma$ and a longitudinal component $k_z^0 = \frac{2\pi}{\lambda}\cos\gamma$. It is apparent from the above equation that the intensity $|A|^2$ of the field is invariant with z.

Obviously, this solution carries infinite energy. In practice, the transverse profile is apodized, and the length of the Bessel beam is therefore limited. To simplify the terminology, no difference will be made between the ideal Bessel beams and

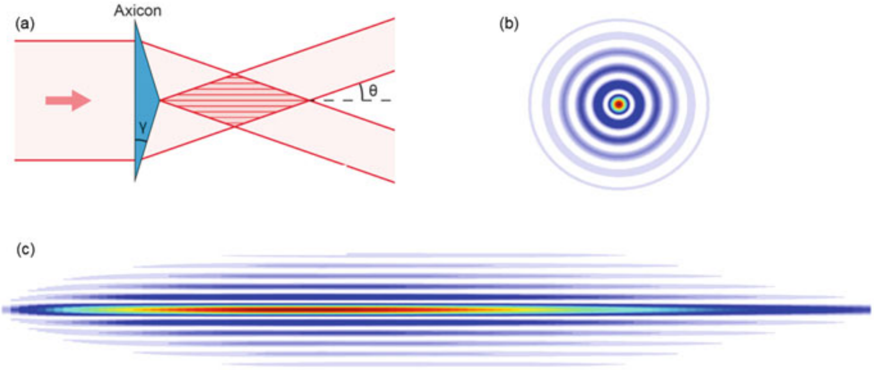

Fig. 16.1 (**a**) A Bessel beam is a cylindrically symmetric field of interference and can be, for instance, generated using an axicon lens. (**b**) Example of a transverse cross section of the intensity distribution. (**c**) Longitudinal cross section of the intensity distribution. The intensity scales from blue (low) to red (high)

the experimentally realized ones. In addition, unless explicitly specified, the zeroth-order Bessel beam will be called "Bessel beam."

Figure 16.1 shows how the interference field defines the length over which the Bessel beam exists. It is also apparent that the number of lobes around the central core is, during the propagation, progressively increasing and then decreasing. The Bessel zone length is typically defined by $Z_{\max} \sim w/\tan\gamma$, where w is typically the waist of the input Gaussian beam.

Within the Bessel range, since the angle made by the interfering waves does not change along propagation, the central lobe diameter is invariant. The full width at half maximum of the central lobe intensity profile is $0.36\lambda/\sin\gamma$, and the first zero of the intensity is given by $r_0 = 0.38\lambda/\sin\gamma$. In the Fourier space, i.e., the far field, the Bessel beam intensity distribution is a ring, peaked at $k_r = k_r^0$, with a thickness inversely proportional to the length of the Bessel zone.

A Bessel-Gauss beam is one of the experimentally realizable Bessel beams. It can be generated by shaping a Gaussian beam using an axicon. The on-axis intensity distribution of a Bessel-Gauss beam propagating in a medium of index n with a cone angle γ in the medium can be expressed using the input power P_0 and waist w_0 of the Gaussian beam using the following expression, within the paraxial approximation [7, 8]:

$$I_{\text{on-axis}}(z) = 8\pi P_0 n z \frac{\sin^2\gamma}{\lambda w_0^2} e^{-2(z\sin\gamma/w_0)^2} \tag{16.2}$$

In the close vicinity of the central lobe, one can therefore approximate the Bessel-Gauss beam intensity profile to $I(r,z) = I_{\text{on-axis}}(z)|J_0(k_r^0 r)|^2$.

While for a Gaussian beam the Rayleigh range shortens when the beam is more focused, i.e., when the waist is smaller, the situation is very different for a Bessel beam since the cone angle γ and the waist w are two independent parameters. Therefore, the central core width can be down to nearly $\lambda/2$, while the Bessel zone length can be arbitrarily chosen—obviously within the limits of the numerical aperture of the optics.

The Bessel beam can also be seen as an elongated focus, as it was initially shown by McLeod [9]. The energy flow is conical, and, within a geometric optics point of view, the energy is focused onto a segment instead of a point for the Gaussian beam. Increasing the length of the Bessel beam by a factor 10 only requires to increase the waist in a similar factor, and if one wants to maintain the peak intensity, the input power must be adequately increased.

2.1.2 Spatiotemporal Structure

The spatiotemporal structure of the Bessel beam created using an ultrafast pulse is a coherent superposition of monochromatic Bessel beam amplitudes. The relationship between the different components is determined by the way the pulse is shaped. For instance, axicons or spatial light modulators do not create the same spatiotemporal structure [10]. However, to the best of our knowledge, the exact spatiotemporal structure of the Bessel beam has no impact on laser nanostructuring. This is why, in the following, the pulses will be treated using monochromatic approximation.

2.1.3 Presence of Interfaces

Importantly, when the beam crosses a flat interface at normal incidence such as air dielectric or dielectric air, the transverse profile does not change. This is because the radial wavevector is preserved [11]. The Bessel zone length is increased by a factor n, the refractive index of the medium. It is also important to highlight the fact that the far field of the Bessel beam is composed only of a thin radial spectrum implies that the Bessel beam is much less sensitive to spherical aberration when the beam is focused inside a dielectric medium. This is an important benefit in comparison with Gaussian beams which are distorted in this situation.

2.1.4 Bessel Beam Generation

Bessel beams can be generated using several means. All are intended to apply a conical phase onto the Gaussian laser beam: spatial light modulators (SLM) [12, 13], diffractive optical elements [14, 15], transmissive [16–19], or reflective axicons [20]. However, it is conventionally difficult to obtain high cone angle after such shaping means. Spatial light modulators and diffractive optical elements are limited to cone angles below some mrad. The fabrication of axicons is also technically very difficult, particularly when the cone angle is above some degrees. The mechanical turning often induces defects in the symmetry around the optical axis [21]. In addition,

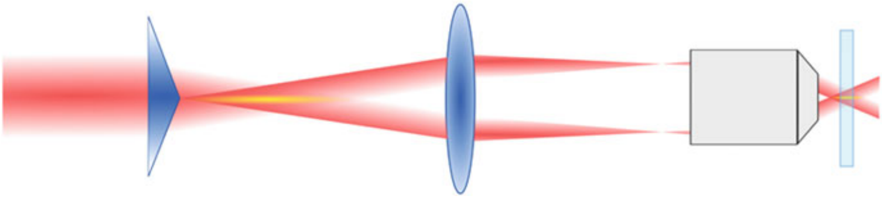

Fig. 16.2 Setup used to increase the cone angle of a primary Bessel beam. The lens and microscope objective are placed in a 2f-2f configuration to image the primary Bessel beam. Copyright Remi Meyer

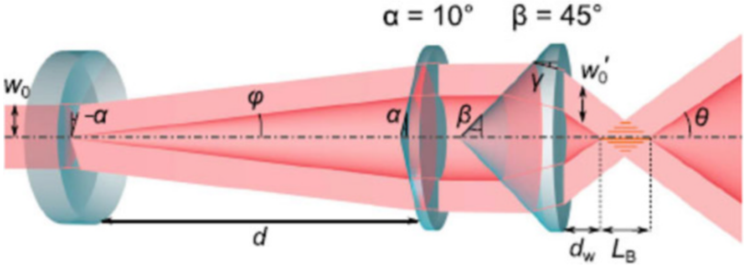

Fig. 16.3 Setup to generate extended Bessel beams with high cone angles and a long working distance (indicated as d_w). Reprinted figure with permission from [27]

the tip of the axicon is very often rounded, which generates a spherical wave co-propagating and interfering with the Bessel beam [22, 23]. Recently developed laser-based techniques avoid the defect of cylindrical asymmetry due to the mechanical interaction between the tool and the workpiece [24, 25].

As it will be seen in Sect. 3.4, the applications to nanostructuring often require strong focusing typically above 10 to 20°. Most of the high-angle Bessel beam generators are similar to the one shown in Fig. 16.2. They are based on imaging a first Bessel beam using a 2f-2f telescopic arrangement which magnifies the cone angle at the cost of reducing the beam length by the square of the magnification. With this kind of architecture, the Bessel zone length is typically below a few hundreds of micrometers for a cone angle exceeding 10°.

Recently, a new kind of architecture has been developed to reach Bessel zone lengths of several millimeters. A first version has been developed by Chebbi et al. [26]. This has been recently improved in [27] to avoid any intermediate focusing. As shown in Fig. 16.3, the first two axicons are complementary and create a wide annulus of light that is further focused using a very high-angle axicon.

The intensity over the optical axis of Bessel-Gauss beams varies smoothly. By controlling the diffraction efficiency of the phase mask applied by spatial light modulators or diffractive optical elements, it is possible to generate Bessel beams where the on-axis intensity is nearly constant over a segment, which is important for applications to laser nanostructuring [28, 29]. A new approach using geometrical phase optics has been developed for the same purpose in reference [30].

2.2 Extended Focal Length and Applications to Surface Structuring

Ultrafast laser ablation is characterized by a very marked threshold. Nanostructuring is made possible by adjusting the sample area over which the fluence exceeds the ablation threshold. Nanostructures can be processed with diameters even well below the wavelength [31]. For this application, the laser distribution must have strong gradients. This is conventionally performed using tightly focused Gaussian beams, as shown in Fig. 16.4a. However, in this case, the longitudinal positioning range over which the surface of the solid can be nanostructured is on the same order of magnitude as the diameter of the structures. This renders the sample positioning critical which is generally an obstacle to large area processing for real-life applications.

In this context, the quasi-arbitrary length of the Bessel zone allows fully lifting this constraint. A number of works have demonstrated surface nanostructuring using Bessel-Gauss beams, including processing of non-flat samples or opto-perforation of cells, in which position is inherently difficult to control [18]. The submicron ablation of indium tin oxide (ITO) has been demonstrated by Sahin [32], and Doan et al. demonstrated the ablation of transparent conductive oxide through the substrate, so as to improve the final surface quality [33]. The extended Bessel zone allows for compensating flatness and thickness variation of the sample. The same property holds for higher order Bessel beams, used by Wetzel to process graphene [34], and holds more generally for all extended interference fields [35, 36]. Recently, the process has been extended to homogeneously write nano-ripples at the surface on a highly curved sample [37], as shown in Fig. 16.4b.

The longitudinal invariance of a Bessel beam is also useful to produce high aspect ratio microstructures inside metallic or dielectric materials by percussion drilling. Indeed, even when it is partially obstructed, the Bessel beam maintains its structure, obviously over a shorter length. Alexeev et al. demonstrated that a Bessel beam maintains a higher intensity over a longer length than Gaussian beams when propagating inside a deep channel made inside a metallic sample [38]. It is also noticeable that tapering occurs very frequently on most high aspect ratio structures in opaque materials [39]. In diamond, graphitization occurs very rapidly after few laser pulses, such that tapering also occurs when drilling trenches [40, 41].

Another important property of Bessel beams is that they are self-healing: after an obstacle, the intensity maximum reconstructs because of the conical flow of light. Nguyen et al. have used this property, in addition to the extended Bessel zone, to create high aspect ratio microstructures in additive manufacturing. The presence of the powder only moderately effects the beam structure [42].

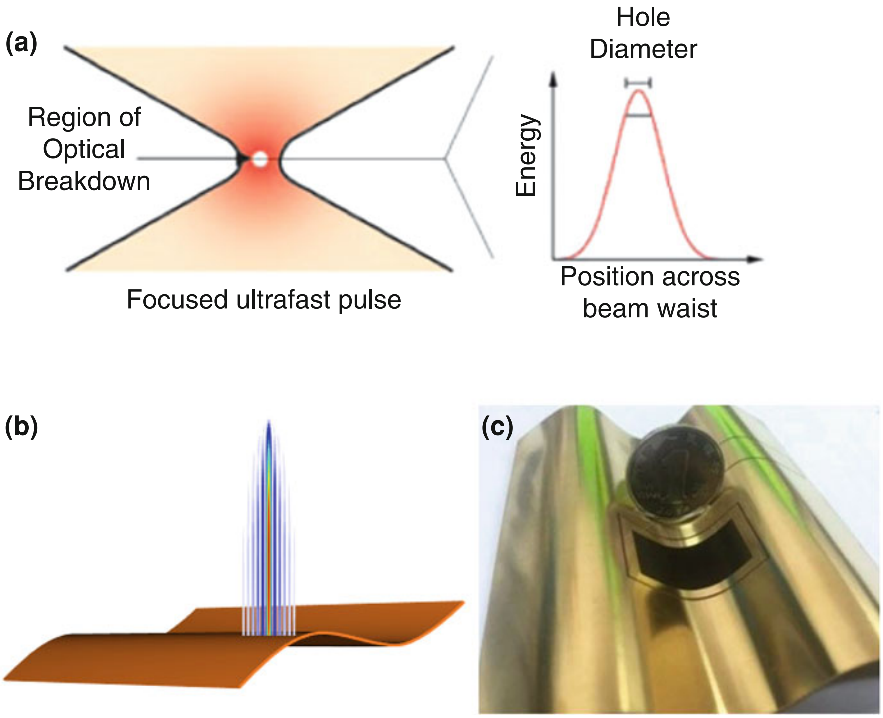

Fig. 16.4 (**a**) Optical breakdown can be induced on lateral dimension much smaller than the spot size, but it also implies that the longitudinal extent over which the sample surface is placed is restricted to the same order of magnitude [31]. (**b**,**c**) The central lobe of diffraction-free Bessel beam provides a large longitudinal range where identical illumination conditions can be obtained. Li et al. demonstrated homogeneous laser nanoprocessing on non-flat sample [37]. (**a**) Reprinted figure with permission from [31]. Copyright (2004) National Academy of Sciences, USA. (**c**) Reprinted figure with permission from [37]. Copyright The Optical Society

3 Non-diffracting Beams for High Aspect Ratio Nano-structuring the Bulk of Transparent Materials

The most striking benefits with Bessel beams in terms of laser materials processing lie in the processing of transparent materials, particularly in a near-single burst illumination regime. This section discusses the propagation of relatively high-intensity pulses, from regimes where they are used for two-photon photopolymerization to regimes where the laser-deposited energy density is high enough to open a void inside the transparent solid. The related applications will be discussed in the next section.

3.1 Propagation in the Bulk of Transparent Dielectrics and Nanoplasma Formation

When propagating inside a transparent dielectric, ultrashort pulses undergo the nonlinear self-focusing Kerr effect, and if the intensity is sufficiently high, an electron-hole plasma is generated. This plasma both partially absorbs and defocuses the pulse. These multiple effects are obviously highly nonlinear: the filamentation regime where all these effects are combined is very difficult to predict and to scale. Gaussian beams in the filamentation regime undergo a strong spatial and spectral reshaping [43]. The physics of the nonlinear propagation of Bessel beams differs significantly from the one of Gaussian beams. It has been described in detail by Polesana et al. [44].

In a pure Kerr medium, in the absence of losses, an ultrafast Bessel beam undergoes reshaping by four-wave mixing. Several new spatio-spectral components are generated: a wave parallel to the optical axis and a wave with the radial wavevector $\sqrt{2}k_r^0$ [45]. Engineering the spatial spectrum of the Bessel pulse can stabilize the beam [46, 47], but, with the perspective of laser structuring, most of the stabilization can come from nonlinear losses occurring within the central core. Porras et al. demonstrated the existence of stationary solutions, i.e., propagation-invariant, based on a conical flow of light associated with nonlinear losses, even in the presence of Kerr effect. These solutions can be seeded using Bessel beams. Noticeably, the stationary regime exists when both cone angle and nonlinear losses are sufficiently high. The non-stationary regime of the filamentation of Bessel beams can be associated with the periodic formation of plasma with applications to the imprinting of periodic marks inside fused silica [45].

When the cone angle is sufficiently high, the impact of Kerr effect becomes negligible. The length over which an optical ray crosses a high-intensity region is limited to about 1 μm, which implies that the accumulated Kerr phase is close to zero. In addition, when the cone angle is high enough, stabilization occurs from the high nonlinear losses due to nonlinear ionization and plasma absorption [44]. In this case, a plasma rod can be generated within the central core of the Bessel beam. The plasma density is highly homogeneous, and the applications reviewed below take benefit of this homogeneity.

Garzillo and co-workers experimentally compared the propagation of femtosecond and picosecond pulses in BK7 glass [48]: the picosecond regime seemed to be more stable than the femtosecond one. In practice, picosecond pulses undergo less spectral reshaping and less plasma defocusing. Another argument was raised by the group of R. Stoian (Univ. Lyon-Saint Etienne, France): using numerical simulations shown in Fig. 16.5, the group pointed out that the higher peak power of femtosecond pulses tend to enable ionization over a wider transverse distance than the picosecond ones. The picosecond regime therefore seems more favorable to a higher localization of energy deposition within the Bessel beam central lobe. It should be however noted that the vertical scales of the graphs are not identical: the higher dynamical range for the case of 1.8 ps pulses makes it in fact difficult to quantitatively compare. More investigations are therefore needed.

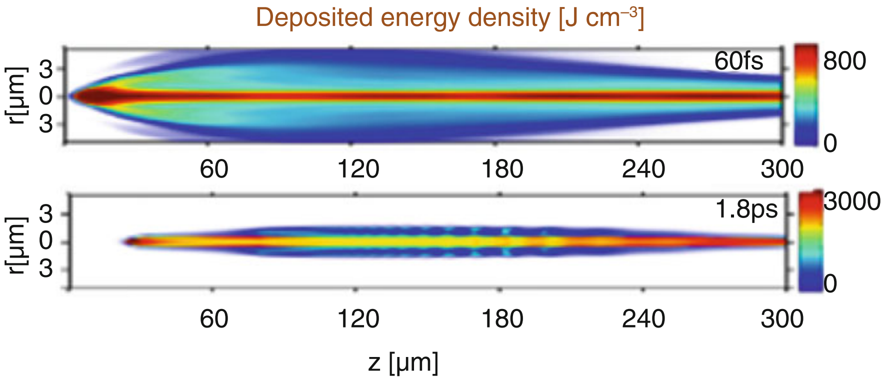

Fig. 16.5 Comparison of energy deposition by a Bessel beam within fused silica using nonlinear Schrödinger equation for a single pulse of duration 60 fs pulse (top) and 1.8 ps (bottom). Reprinted figure with permission from [49]. Note that the color bars are different. The energy density in the picosecond case seems less homogeneous

It is worth noticing that these results are formulated on simulations based on paraxial nonlinear Schrödinger equation. It is an approximation to Maxwell's equations obtained after neglecting longitudinal components of the field, and the plasma is treated as a static medium of permittivity fixed by Drude model [50]. This approach eliminates the possibility of modeling plasma waves. Although these approximations are extremely useful to model the filamentation dynamics inside solids [43, 51], they are in fact no longer valid under strong focusing conditions to model the interaction with nanoscaled plasmas. This is even more true when the plasma density reaches the critical density, at which the permittivity turns to zero. Beuton et al. predicted with a full Maxwell code the possibility of reaching overcritical plasma densities [52]. The additional effect of resonance absorption has been very recently demonstrated to occur in these conditions for a femtosecond Bessel beam: most of the absorption is collisionless [53]. This is an effect which was not captured by the models described above, and that will be discussed at the end of this section.

3.2 Link to the Filamentation of Gaussian Beams

The propagation of Bessel beams inside solid dielectrics has been popularized because it is a close cousin of the filamentation of Gaussian beams. More precisely, during the nonlinear filamentation process, Gaussian beams self-reshape into Bessel-like beams [54]. Filaments and Bessel beams in the presence of nonlinear losses are both characterized by an intense central core, surrounded by an energy reservoir. Nonlinear stationary Bessel beams can be seen as the asymptotic structure

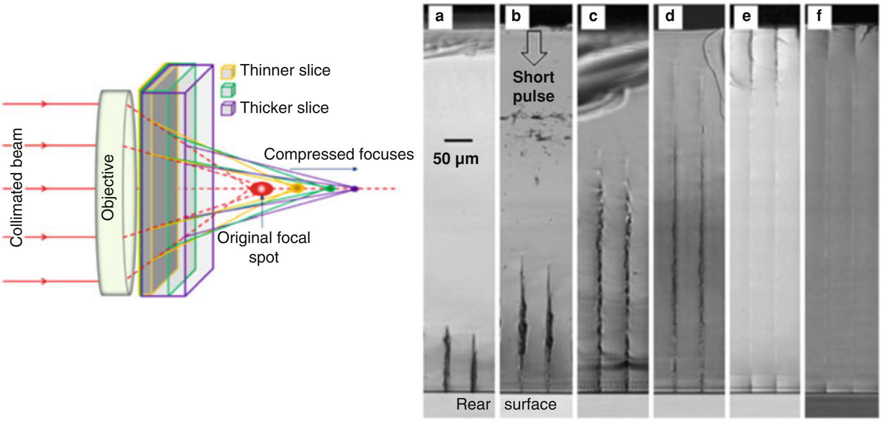

Fig. 16.6 (Left) Concept of the spherical aberration induced by a thick glass slide inserted after the focusing objective (right) views of cleaved surfaces of the longest single-shot voids fabricated with different inserted glass plate thickness: (**a**) no glass, (**b**) 1 mm, (**c**) 2 mm, (**d**) 3 mm, (**e**) 5 mm, (**f**) 6 mm. Reprinted figure with permission from [58]

of filamentation after a long propagation distance where the dynamics becomes stationary, i.e., propagation-invariant.

To efficiently trigger filamentation, most authors use high-power pulses or bursts of pulses with either moderate focusing to induce a dynamic reshaping by Kerr effect or, more often for laser structuring applications, a relatively high focusing associated with spherical aberration [55–57]. Spherical aberration focuses the field components with the strongest radial wavevectors first, while the weakest radial wavevector components are focused at longer propagation distances. This way, a Gaussian beam with spherical aberration closely resembles to a Bessel beam (see Fig. 16.6(left)). Ahmed et al. exploited this property by inserting a thick plate of fused silica between the focusing lens and the transparent workpiece where the filamentation had to be created [58] (Fig. 16.6(right)). This enables a high degree of control of the filamentation, very close to what be achieved using geometrical optics to control the position of the Bessel beam. Recently, Alimohammadian et al. used conical phases in the Fourier space to strengthen the filamentation and to longitudinally shift the position of the filament inside transparent materials by several hundreds of micrometers [59, 60].

3.3 *High Aspect Ratio Index Modification*

Using a Bessel beam with moderately high fluence (typ. 10^{13} W.cm^{-2}), a subcritical plasma is generated inside transparent dielectrics. This has been characterized, for instance, by Velpula et al. using a two-color time-resolved microscopy [61]. The

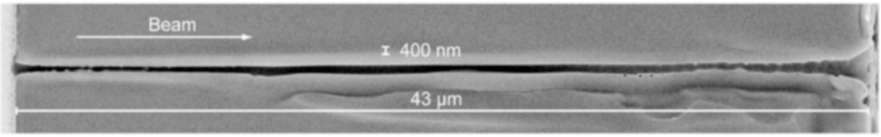

Fig. 16.7 High aspect ratio nanochannel generated by a single pulse of a Bessel beam with cone angle 11° in glass. Reprinted figure with permission from [8]

plasma of excited free electrons relax as heat or via self-trapping which induce structural rearrangements as described in [62] to yield positive or negative index modifications depending on the material and the relaxation pathway. This regime was used in early works to generate a homogeneous index modification inside glass [63, 64] by using low cone angles.

3.4 High Aspect Ratio Nanovoid Formation

3.4.1 Single-Shot Drilling

Interestingly, if the input pulse energy and the focusing of the Bessel beam are strong enough, a single-laser pulse is enough to generate a high aspect ratio nanovoid inside glass, which was first demonstrated in our group [8]; it is shown in Fig. 16.7. With Gaussian beams, void opening was also observed previously, but much stronger focusing is required, typically with numerical apertures close or above one [65, 66].

The filamentation regime where a Gaussian beam nonlinearly self-transforms to generate a relatively homogeneous nanoplasma can also deposit sufficient energy density to open elongated nanovoids, for instance, in PMMA [56] or glass [59, 60, 67].

One can remark here that this regime is significantly different from what can be generated using temporal Airy pulses, where it is the plasma dynamics that induces a spatial reshaping. This generates an elongated filament, typically on the order of 30 μm , and a high aspect ratio channel close to the surface of glass [68, 69]. This regime is reviewed in detail in Chap. 17.

The observation of these high aspect ratio voids with nanoscale diameter, under scanning electron microscopy (SEM), is particularly challenging. Several techniques have been developed throughout the years: initially, Bhuyan et al. were mechanically cleaving the channels. To increase the reliability of the imaging, focused ion beam (FIB) milling was used later [70]: using the ion beam, a large cuvette is first drilled in the vicinity of the void, providing access to the SEM beam to image the vertical plane containing the longitudinal cross section of the void. Then, a very fine approach, removing progressively the material by vertical layers of typically 40 nm and intermediate imaging, allows imaging the nanoscale void with high resolution. Importantly, this process is overall very long (≈ 1h per void),

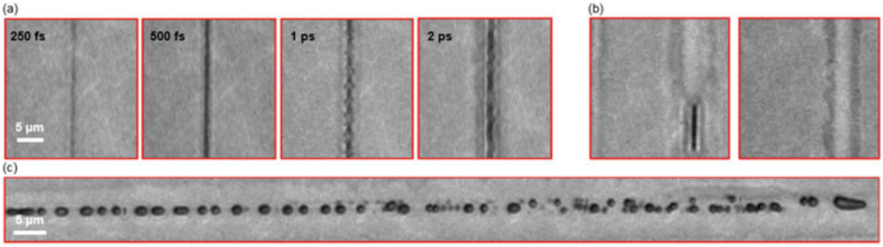

Fig. 16.8 (**a**) Different morphologies of material modification after single-shot Bessel beam illumination with the same pulse energy with different pulse durations. (**b**) Modification inside Gorilla glass, for a 3 ps pulse, at two different positions inside the sample. (**c**) Same as in (**b**) with three times higher pulse energy. Reprinted figure with permission from [73]

limited to depths of approximately 30 µm, and the void channel must be perfectly perpendicular to the sample surface such that the FIB beam milling is parallel to the high aspect ratio void. Very recently, Chen et al. developed an efficient technique to overcome those difficulties: the drilling of void channel is repeated at different longitudinal positions inside the sample, and then fine polishing of the sample surface provides access to the transverse cross section of the voids at different heights using SEM. A 3D reconstruction is then possible [71].

High aspect ratio void formation has been observed in a very large number of transparent materials, such as fused silica, different glasses, chalcogenide glasses, and PMMA, ZnS [72] , and even in materials as hard as sapphire [70]. The void opening requires a strong gradient of energy deposition, associated with relatively fast cooling. Importantly, the modification produced inside the transparent material is not always a void particularly at the highest energies. In this case, it is very often that irregular bubbles form in the position of the Bessel beam central core. This typically occurs when a relatively large diameter of material has been melt around the void. Depending on the material, the highest energies can be associated with the formation of an index modification on a large diameter. Figure 16.8 shows several types of modifications created in different materials with various parameters.

3.4.2 Influence of Pulse Duration

Figure 16.9 compares the modification created in sapphire for two different pulse durations under relatively strong focusing ($\gamma = 26°$ in air). In the femtosecond case (top left), the void channel is free from apparent defects under SEM imaging, while the picosecond case (top right) shows a much wider heat-affected zone and redeposited nanoparticles. In the latter case, it is apparent that the void opening was associated with a transient hot vapor phase where nanoparticles could nucleate. It is still unclear which of the picosecond or the femtosecond case is associated with the highest energy density. Void formation in the femtosecond case is still under debate as it will be seen below.

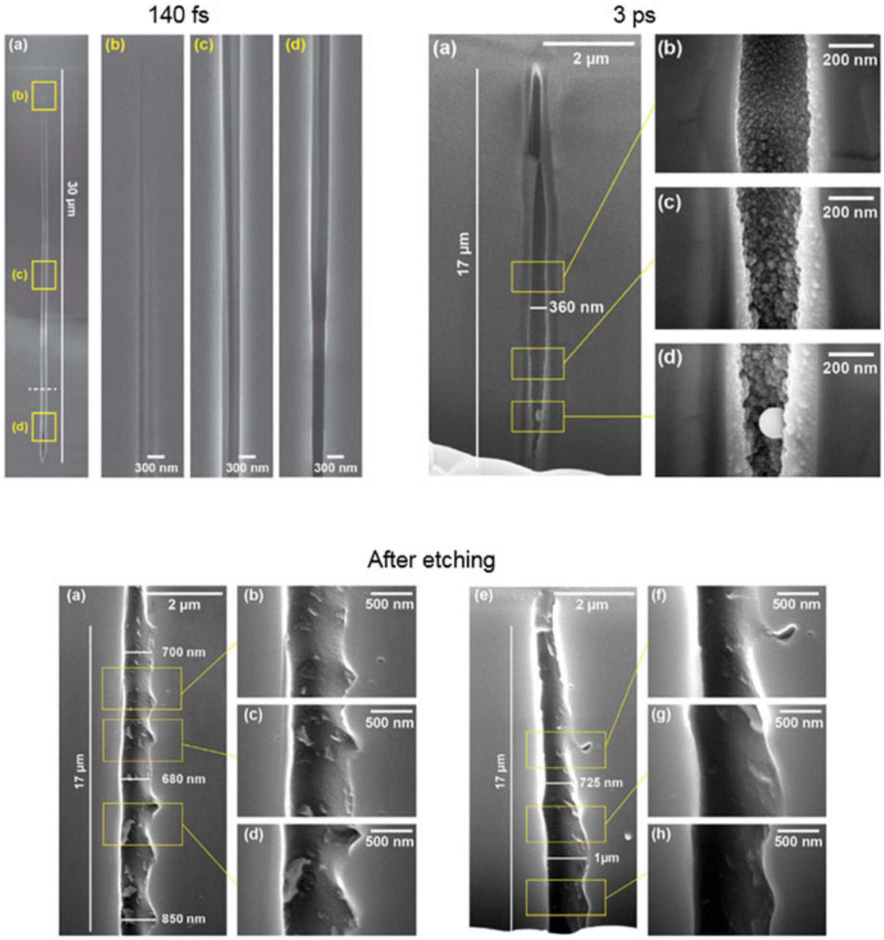
140 fs
(a)
(b)
(c)
(d)
30 µm
300 nm
300 nm
300 nm
3 ps
(a)
2 µm
17 µm
360 nm
(b)
200 nm
(c)
200 nm
(d)
200 nm
After etching
(a)
2 µm
700 nm
680 nm
850 nm
17 µm
(b)
500 nm
(c)
500 nm
(d)
500 nm
(e)
2 µm
725 nm
1µm
17 µm
(f)
500 nm
(g)
500 nm
(h)
500 nm

Fig. 16.9 High aspect ratio nanovoids generated in the bulk of sapphire in the single-pulse regime using a Bessel beam with cone angle 14°. (Left column) pulse duration of 140 fs; (right column) pulse duration of 3 ps; (top row) SEM imaging after FIB milling; (bottom row) after HF etching of the FIB-milled structures. The picosecond case shows a larger heat-affected zone and cracks. Adapted figure with permission from [70]

It is important to remark that high aspect ratio nanovoids can be created using both femtosecond and picosecond pulse durations, but, in the femtosecond regime, stronger focusing is needed (cone angle typically above 10° inside the solid). In this high focusing condition, voids could be opened using pulse durations down to 50 fs, where, conventionally, avalanche ionization cannot be triggered. This shows that the physics of the interaction, at least in the femtosecond regime, is not yet fully understood. In glass and fused silica, picosecond pulses generally yield modifications that are more visible under conventional microscopy: they are probably wider and show a wider heat-affected zone. Some modifications extend several micrometers away from the channel center (see, for instance, Fig. 16.2 of reference [74]).

3.4.3 Bursts

It can be interesting to investigate the reduction of peak power by splitting the pulse into several sub-pulses so as to reduce nonlinear ionization in the outer lobes of the Bessel beam.

In the void formation regime in glass, our group has investigated the effect of splitting the femtosecond pulse in two equal sub-pulses, separated by durations between 0 and 500 ps [75]. Below a pulse separation of approximately 10 ps, the morphology and length of the void were varying shot to shot. But interestingly, above a pulse separation of 10 ps, the voids that were formed could have increased diameter in comparison with a single-shot case, and smaller energies could give rise to smaller diameter voids. In this case, a diameter close to 100 nm could be reached.

Using absorption measurements, it was shown that the overall absorption was not increasing in comparison with the single-pulse case. Therefore, the increase of drilling efficiency is due to an increased energy density deposited by the sequence of two pulses. The material after the first shot undergoes a progressive transformation on a scale of typically 10 ps: in this hot dense state, the material is highly absorbing. This result matches the pump-probe measurements of Garcia-Lechuga at the surface of fused silica [76] as well as simulation results predicting the transformation of fused silica into warm dense matter when the laser-deposited energy density reaches several MJ/kg [77, 78] as it is the case after the first pulse the Bessel beam configuration [75]. This state is long-living, probably more than several nanoseconds [79], which is why the enhancement of drilling efficiency is observed for bursts of pulses separated by up to several tens of ns as characterized by Kumkar et al. [80, 81] and frequently used in the application of stealth dicing, which is described in the next section.

Depending on the exact geometrical configuration, some transient wave-guiding effect has been observed, to increase the length of the modification. This is possible for relatively low cone angles, where the beam can be trapped into the waveguide created by the first pulse [82]. More generally, burst pulse configuration can benefit of the heat accumulation to create wider and stronger modifications. Although the burst configuration has been successfully used for stealth dicing, systematic comparisons of the diameter evolution with the burst parameters have still to be performed.

3.4.4 Pulse Polarization

In fused silica and glass, no effect of the pulse polarization has been yet observed. Although it can slightly modify the ablation threshold because of the difference in nonlinear ionization cross sections, the cross sections of the channels are circular whatever the polarization. In contrast, in sapphire, voids generated using a linear polarization, in the femtosecond regime, have an elliptical transverse cross section, oriented perpendicularly to the polarization direction [53]. The ellipticity can be used to control the formation of cracks [70]. In the picosecond regime, for pulse durations above 600 fs, high-power Bessel beams create cracks in several directions, which indicates that the void cross section is circular [83].

3.4.5 Heat-Affected Zone

The formation of high aspect ratio voids fully enclosed in sapphire or glass demonstrates that part of the material is compressed around the void. In the case of sapphire, Rapp et al. evaluated the compression ratio to ∼15% [70].

Recently, using FIB milling and chemical etching, Zhang et al. characterized that around the 290 nm-diameter void channel drilled in fused silica with 4 ps pulses, the material is annealed over a diameter of ∼ 2 µm, corresponding to the Bessel beam core, and cracks develop only at a further distance, typically 2 µm (see Fig. 16.10) [84]. These micro-cracks are key for the application to stealth dicing mentioned in Sect. 4.

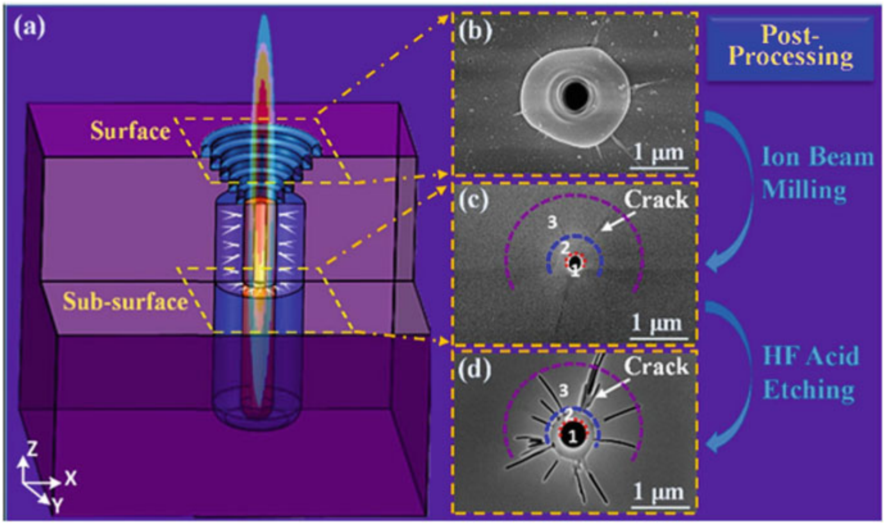

Fig. 16.10 SEM imaging of a void transverse cross section inside fused silica. In (**c**), the void is inside the red dotted line (1), the annealed region (2) is enclosed in the blue circle, and the third region with cracks is within the purple circle. (**d**) Shows the same area after HF etching to reveal the cracks. Reprinted figure with permission from [84]

3.5 Physics of Energy Deposition and Void Opening: Current Challenges

The physics of the energy deposition process is particularly difficult to characterize because of the nanometric value of the characteristic scales involved. A very interesting discussion on experimental flaws is provided in Section II.B of reference [85]. This field has been very active in the recent years, with several techniques that were developed to characterize the nonlinear pulse propagation and energy deposition inside transparent dielectrics. Bergner et al. developed a pump-probe microscopy technique to image the filamentation of 6 ps pulses [86]. Their technique was capable to retrieve the local index of refraction. This technique was particularly efficient to show the impact of Kerr effect ahead of the focal region, the buildup of the plasma which particularly extends in time toward the laser source. One can notice also that their results demonstrate that the region where the maximal temperature is reached, around the Gaussian beam focus, is maintained hot during several nanoseconds at least, in agreement with the results mentioned in Sect. 3.4. This is the region where the strongest material modification is observed. The spatial resolution of this technique is unfortunately not enough to characterize the formation of nanovoids.

As it was mentioned earlier in Sect. 3.1, the energy deposition during the pulse propagation has not yet been completely modeled. The computationally efficient models using nonlinear Schrödinger equation cannot describe the detail of the physics occurring when submicron plasma is generated. Using first-principle particle-in-cell numerical simulations that are based on solving Maxwell's equations together with particles trajectories [87, 88], our group has recently demonstrated that a very important absorption mechanism was collisionless, which is conventionally very difficult to capture using simulations [53]. This collisionless absorption is a combination of two effects. The first is resonance absorption: when a p-polarized pulse impinges on a plasma ramp, the pulse is deviated at the so-called turning point where the density reaches $\rho = \rho_c \cos i$, where ρ_c is the critical density and i the incidence angle on the plasma. (Note that for Bessel beams, the turning point shifts away from the optical axis when the cone angle $\gamma = \pi/2 - i$ is decreased). The evanescent field created from the turning point tunnels to the critical density point where it can resonantly excite electrostatic plasma waves—also named Langmuir or longitudinal waves in the literature [88]. If the turning point and critical point are close enough, the conversion efficiency can be very important, typically up to 60% [89]. The second effect is the damping of the plasma wave by several plasma wave-particle interaction processes such as Landau damping and transit acceleration. These interactions are collisionless processes [88]. Overall, in conditions close to the regime of nanovoid formation with femtosecond pulses (e.g., [8] and [70]), our simulations demonstrated that over 90% of the absorption is collisionless. This shows that most of the literature models still have to be adapted to fully interpret the dynamics of plasma buildup and laser-plasma interaction during the pulse propagation.

After the energy has been deposited in the form of an electron-hole plasma inside the dielectric, a number of relaxation processes take place. They highly depend on the energy density that was deposited by the laser pulse. For relatively low ionization degree, the free electron relaxation involves phonon excitation, generation of self-trapped excitons, themselves relaxing in the form of structural deformations. However, for the case of void opening, it is more likely that high energy densities are involved. When the ionization percentage typically reaches 20% (see the case of silicon in reference [90]), lattice disordering can occur at ultrafast scales [91], yielding bandgap shrinking, as observed recently in fused silica by Winkler et al. [92].

A number of experiments corroborate the fact that a fast transition to a hot state arise approximately in the picosecond scale after the laser pulse. Somayaji et al. reported the absence of trapping at the sub-picosecond scale in fused silica [79], while the trapping of free carriers occurs within 150 fs in the case of weak ionization [93]. The same authors also reported photoluminescence and spectrally resolved photoluminescence at the ns scale, demonstrating a phase on the order of 5000 K, well above the boiling point of silica and close to its critical point [94]. This is consistent with the observation of a transformation at ps-scale toward a regime of warm dense matter by Hoyo et al. [75] as well with the refractive index measurements on the filamentation of picosecond Gaussian beams of reference [86]. Heat diffusion occurs during several hundreds of nanoseconds, in association with potential phase changes.

Two scenarii were discussed for the actual opening of the void structure. References [95] and [65], considering the voids formed by tightly focused Gaussian beams, first hypothesized a mechanism where the pressure reached by the plasma creates a microexplosion that compresses the solid material around. Numerical simulations based on elastoplastic modeling including the equation of state of fused silica showed the feasibility of this mechanism for an ultrafast Bessel pulse. In this mechanism, the void would open on timescales of several hundreds of picoseconds [52, 96].

Bhuyan et al. used phase contrast microscopy to characterize the dynamics of plasma and void formation using femtosecond and picosecond pulses, shaped as Bessel beams [97, 98]. The measurements shown in Fig. 16.11 seem to show that the void opening takes place between 1 to several milliseconds after the laser pulse. A second mechanism has therefore been suggested: cavitation could occur within an overheated liquid [98]. Similar dynamics is observed using picosecond pulses [79]. However, the experimental setup cannot distinguish the radial distribution of the index of refraction. It is possible that the high temperature reached around the microexplosion site, with a high positive refractive index contribution, could mask part of the process at early times. For now, the differences observed between the femtosecond and picosecond regime in terms of void morphology (Fig. 16.9) are not yet fully explained. More experimental and simulation works are required to fully answer this question. Finally, one can remark that, in the case that warm dense matter is actually generated in the relaxation of the plasma, this state of matter is still challenging to model and is not described by the Drude model [99].

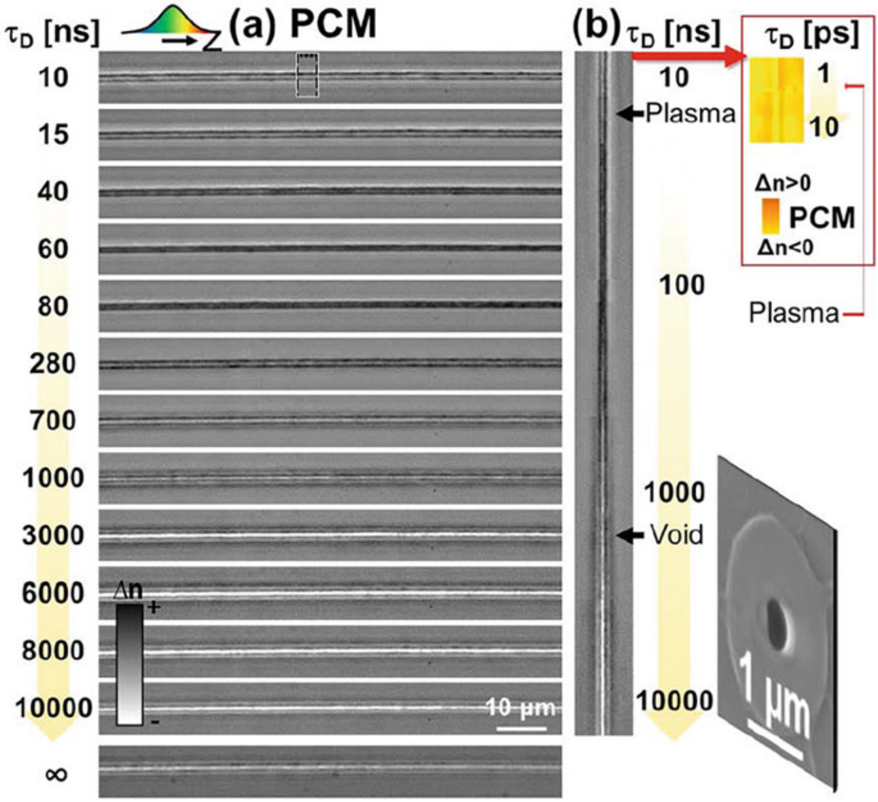
τD [ns]
z
(a) PCM
10
15
40
60
80
280
700
1000
3000
6000
8000
10000
∞
Δn
+
-
10 μm
(b) τD [ns]
10
Plasma
100
1000
Void
10000
τD [ps]
1
10
Δn>0
PCM
Δn<0
Plasma
1 μm

Fig. 16.11 (**a**) Time-resolved sequence of phase contrast imaging corresponding to the appearance of a high aspect ratio void inside fused silica after illumination by a chirped pulse of 5 ps duration (propagation from left to right). (**b**) Concatenation of crosscuts of the images of (**a**) to show the evolution of the dynamics in time (log scale). The inset shows the dynamics at early times in identical conditions, from [98]. Reprinted figure with permission from [79]

4 Applications to High Aspect Ratio Nanostructuring

Ultrafast non-diffracting Bessel beams have been successfully used in a number of applications where high aspect ratio microstructure or nanostructures are required.

4.1 Two-Photon Photopolymerization

Two-photon photopolymerization is a powerful fabrication technique to produce almost arbitrary-shaped components and tools, scaling from millimeters to sub-micrometer, useful to a wide range of applications [100–102]. However, point-by-point irradiation is a very slow process. Zeroth and higher-order Bessel beams have been used to parallelize the process and produce two- or three-dimensional structures by avoiding the translation of the beam in one or more directions (see [2] and references therein, [103, 104]).

4.2 Index Modifications and Gratings

At low fluence, the long, subcritical plasma channels created by ultrafast pulses shaped as Bessel beams in the single-shot or multishot regime induce a local modification of the index of refraction. These modifications are highly homogeneous and can be positive or negative depending on the material [105]. Glass photosensitivity can also be used to control the laser-induced modifications [106]. High aspect ratio smooth modifications were successfully used to generate volumetric Bragg gratings in PMMA, PDMS, or fused silica by a number of different groups [107–110]. Because of the width of the heat-affected zone, the modifications cannot be processed arbitrary close to each other, and the laser inscription often imposes operating on higher order of the Bragg grating. Still, the reflectivity of these gratings could reach up to 90% [110]. Reference [111] demonstrates extremely efficient passband and stop bands nearly with transmission of, respectively, nearly 100% and 0%.

The stress field induced within the material by the laser-induced modifications can interestingly be shaped to generate engineered optical anisotropies. In this context, Bessel beam provides a means to create optically thick modifications [112].

High aspect ratio modifications in fused silica and glass can be etched using hydrofluoric acid (HF) or potassium hydroxide (KOH), so as to serve for microfabrication purposes. Several works have been performed to increase the etching efficiency, particularly using double-pulse illumination to benefit from the localized absorption of self-trapped excitons [113, 114].

Finally, one can remark that in a near ablation regime, using a high number of pulses, self-organized nanovoids appear. They are shaped as lamellas oriented perpendicular to the polarization. Bessel beams allow for generating such gratings over extended volumes, as shown and modeled by Rudenko et al. [115, 116]. They find applications in laser fabrication of photonic components with space-varying anisotropy.

4.3 Laser Welding

Joining materials is required in almost all fabrication fields and scales. Because it is highly flexible and contact-free, laser welding is obviously highly attractive. Ultrashort laser pulses allow for welding glass and more generally transparent materials between themselves as well as glass with another material. The ultrashort character of the pulses provides, via nonlinear ionization, the ability to control in three dimensions the position of the heat source. However, welding requires generally a relatively large volume of molten material to fill the small gap between the parts to be joined. Filamentation and Bessel beams are ideally positioned to locally fuse the transparent material over an elongated volume and relax, in addition, the constraint on surface positioning. The idea has been very early developed by Tamaki et al. and further developed by several groups [117–119]. The use of actual Bessel beams is more recent [120]. Importantly, the joined parts can become as strong as the bulk material itself. The illumination strategy, including heat accumulation using long burst, is an important factor to release the constraints and improve the stiffness of the weld parts [119]. Hecker et al. highlighted the role of the conical structure of the Bessel beam to maintain a homogeneous illumination during melting [121].

4.4 Nanovoids for Photonics

To build in-line spectrometers, it is necessary to have the means to extract a fraction of the light traveling inside optical waveguides. High aspect ratio nanovoids can be used as very efficient scattering centers for this purpose. The high index contrast provided by the void highly increases the efficiency for the light extraction in comparison with a more conventional index modification on the order of 10^{-2}. This has been nicely demonstrated to build spectrometers for astro-photonics, operating in the mid-infrared window, with waveguides and light extraction written inside a chalcogenide glass [122, 123] as illustrated in Fig. 16.12. Using a similar approach, reference [124] demonstrates very strong Bragg resonances for Bragg filters in the telecommunications window. The group of P. Herman, Toronto, corrected the aberration due to the curvature of optical fibers to laser-inscribe a chirped array of high aspect ratio nanovoids on a relatively short extent of the waveguide, not only to extract light out of the waveguide but also to focus the output-coupled light directly onto a camera without a lens. In this case, the nanovoids were also enlarged using chemical etching [125].

A second application of nanovoids is the fabrication of photonic crystals. However, as already mentioned, it is difficult to process voids very close to each other because of the diameter of the heat-affected zone and because the previously drilled channels impact on the Bessel beam propagation. However, for this application, it is not necessary that the aspect ratio is extremely high. Liu et al. have engineered the Bessel beam length to reduce the aspect ratio and produce relatively compact photonic crystals [126, 127]. In addition, at the air-solid interface, the voids often show a trumpet-like profile. A nonhomogeneous diameter is obviously detrimental for photonic crystals. The same authors have polished the surface of the sample after laser processing to obtain highly homogeneous nanostructures [127].

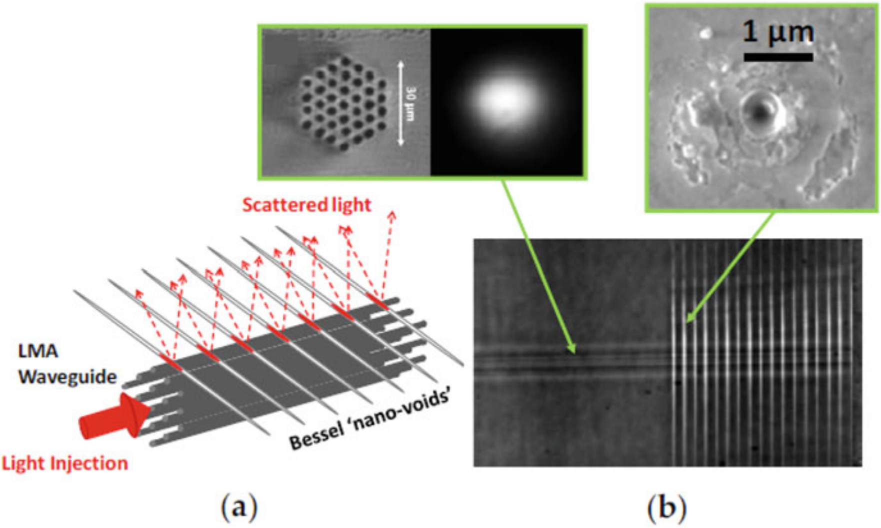

Fig. 16.12 Concept (left) and images of a photonic crystal waveguide structure inside chalcogenide glass (top images). The Bessel-induced nanovoids are used as scattering centers to couple light out of the waveguide. Reprinted figure with permission from [123]

4.5 Drilling and Cutting of Glass and Sapphire

High-speed cutting and drilling of glass are essential for a large number of mass fabrication applications, particularly in the field of microelectronics and consumer electronics. The need is to drill and/or separate glass sheets with a thickness comprised between some tens to several hundred micrometers. The resistance of glass should be preserved; it should be free of chipping with limited number of defects in the vicinity of the cut surface.

4.5.1 Drilling

It has been recently demonstrated that Bessel beams allow for cutting the whole thickness of glass slide, by translating the Bessel beam onto a trajectory while the beam is positioned such as to cross both front and exit surfaces. With this strategy, it was possible to obtain non-tapered, vertical walls for cutting of contours and opening, in transparent materials, circular holes of several tens of micrometers in diameter. An example of diamond drilling is presented in Fig. 16.13. Noticeably, the burst regime, although improving the ablation rate, is not always the best option to obtain the highest quality structures [128–130]. An improvement of the ablation efficiency can be obtained using double pulses with a typical delay of 50 ps, which corresponds to the lifetime of self-trapped excitons [114] (in this case, the

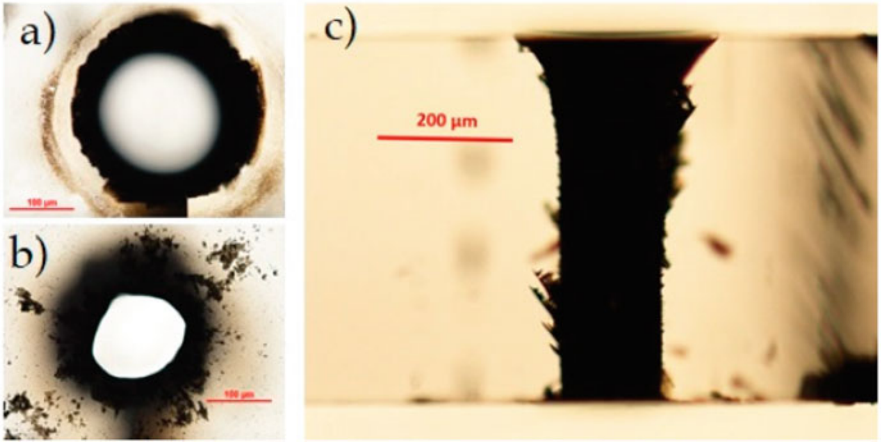

Fig. 16.13 Characterization by optical microscopy of a through-hole drilled inside 500 µm-thick diamond, using 100 writing circles. (**a**) Top, (**b**) bottom, and (**c**) lateral views. Reprinted figure with permission from [130]

pulse energy is usually lower than the one needed to open a void in single shot). An alternative approach to linear beam shaping is to produce, by nonlinear pulse propagation into a water film flowing on a workpiece, a filament, which is then used to process the workpiece. Water also contributes to material removal [131].

To increase the ablation removal rate while drilling high aspect ratio craters in glass, Ito et al. have used the superposition of a femtosecond laser filament to a continuous-wave beam at 1064 nm wavelength [132, 133]. The free electrons generated inside the filament absorb the continuous laser light efficiently. The high amount of energy absorbed over a cylinder inside glass opens an ablation crater with a diameter of 10 µm and a length of ∼130 µm in 40 ms .

4.5.2 Transparent Material Separation Without Ablation: Stealth Dicing

Stealth dicing of glass is probably one of the most important commercial applications of ultrafast lasers in the last decade. Although the material to separate is at millimeter thickness scale, it is the control of laser-induced nanometric modifications that enable a drastically new regime of separation. Stealth dicing was initially developed to cut silicon wafers at high speed [134]. It consists of generating a plane of defects within the depth of a brittle material to cut and, in a second step, of applying a stress such that a fracture propagates through the defects and cleaves the workpiece. In the initial technology, the laser was a nanosecond infrared source, and the modifications in silicon were extending over some tens of micrometers.

A similar technique was developed by Ahmed et al. for glass separation with micrometric resolution [58, 136]. In this case, the modifications were based

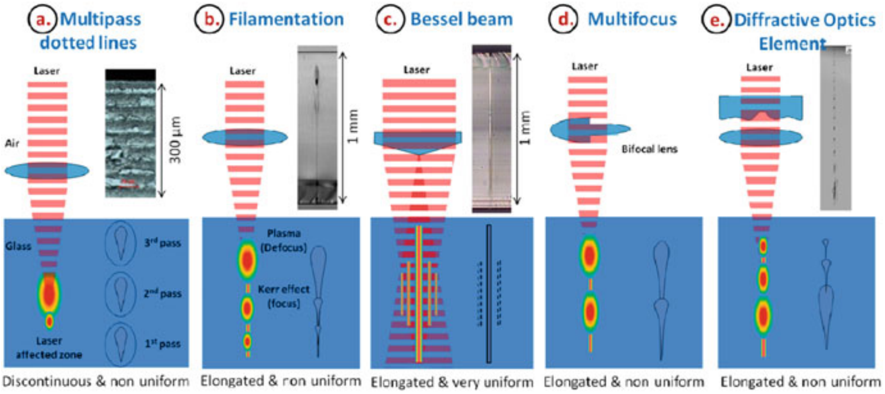
a. Multipass dotted lines
b. Filamentation
c. Bessel beam
d. Multifocus
e. Diffractive Optics Element
Laser
Air
300 µm
Glass
3rd pass
2nd pass
1st pass
Laser affected zone
Laser
1 mm
Plasma (Defocus)
Kerr effect (focus)
Laser
1 mm
Laser
Bifocal lens
Laser
Discontinuous & non uniform
Elongated & non uniform
Elongated & very uniform
Elongated & non uniform
Elongated & non uniform

Fig. 16.14 Different strategies for ultrafast laser inscription of modifications inside glass for stealth dicing. Reprinted figure with permission from [135]

on the filamentation of ultrashort pulses. Figure 16.14 compares different types of modifications tested to reach high-speed and high-quality cutting. A typical separation between the high aspect ratio voids is ∼5–25µm, such that a laser source with repetition rate of several 100s kHz allows for processing glass at a speed on the order of 1 m/s. Apart from speed, the benefit is the quasi-absence of dust particles since it is not really an ablative process. The kerf is zero and, in optimal conditions, the method is free from chipping.

First implementations of Bessel beams in this field were performed by Tsai [137] and Bhuyan [138]. The main benefit is to produce a highly homogeneous stress distribution along the material thickness, which is crucial to maintain a high cut quality for tempered glass [138]. In this reference, the authors demonstrated from mechanical cleaving that the optimal beam position was fully inside the sample and used single pulses with a pulse duration of 11 ps. Cutting was achieved at a speed of 270 mm/s.

Overall, the cutting can be along straight or curved paths [80], and the surface quality is conventionally relatively rough (typ. between 0.5 µm and several µm). It is highly linked to the extension of internal cracks [67] and therefore to the illumination parameters as described in [135]. Particularly, the use of bursts and thermal load can benefit to the cleaving operation [80] but requires fine adjustment, for instance, using a dash line strategy [135].

As for the second step, the cleaving operation, several approaches were used: most research groups used mechanical flexure, whereas CO_2 laser provides highly repeatable conditions [67, 139]; it can be also noted that tempered glass is internally stressed by the chemical treatment such that it self-cleaves.

Although the stealth dicing technology has promptly emerged and attracted the interest of a large number of research groups and companies, only few publications quantitatively compared the different techniques. Li et al. compared filamentation-based cleaving of glass to laser surface scribing and to combinations of filamentation and V-groove scribing, against a number of criteria: cleaving guidance, reproducibility, breaking force, morphology of the cut surface, and flexural strength of the cut parts. Using a single-pulse filamentation, the assistance of a V-groove was found to improve the cutting quality. Overall, the best results were found for a burst-mode filamentation, when the filament is formed fully inside the 1 mm-thick glass sample. The authors reported submicron roughness of the cleaved facets, with the nicest edges and a flexural strength nearly equal to the pristine reference material [140]. Dudutis et al. quantitatively compared Bessel beam-based stealth dicing using sub-picosecond pulses with more conventional glass cutting techniques such as laser-based rear-side machining, mechanical scribe and cleave, water jet cutting, or diamond saw cutting [141]. Their analysis also involved a number of criteria, including residual stress. The Bessel beam approach provided the results with the less residual surface cracks and chipping. Yet as the flexural strength of the cut samples is less than for conventional rear-side machining, the regime of pulse duration and energy used here with the Bessel beam creates a large heat-affected zone and cracks extending over several tens of micrometers, which are very likely fragilizing the cut material. Shorter pulse durations tend to minimize the damaged region. One can remark that the procedure used to apply the stress that separates the samples appears to be an important parameter although the field is yet lacking of published studies.

4.5.3 Thick Glass Cutting

Most of the previously mentioned work dealt with the cutting of relatively thin flat glass sheets, with thickness ranging from 30 μm to approximately 2 mm, because the typical Bessel zone or filament length is on the order of 200–700 μm. Cutting of multi-mm-thick glass requires other strategies. A first approach is to generate multiple modification surfaces, on top of each other to cover most of the glass thickness in multiple passes. This approach obviously decreases the overall process throughput and requires a fine alignment of the planes written on top of each other, which needs high repeatability translation stages.

A second approach is to extend the Bessel zone length to multi-millimeter scale so as to enable cutting using a single-laser pass. Extending the beam length using the same cone angle imposes to increase the pulse energy in the same ratio as the length increase. For multi-mm-long ranges, the burst energy should be on the order of 1 mJ. It is difficult to use such energy in the conventional telescopic setup used to magnify the cone angle (see Sect. 2.1) mostly because of the risk of optical damage to the second lens. Indeed, as the Bessel zone extends, its Fourier transform is thinner, with a much higher energy than for the processing of thin samples. To avoid the use of the 2f-2f setup, high apex angle axicons were used to shape the ultrafast laser beam.

To increase the working distance to several millimeters, the three-axicon shaping technique of reference [26] was implemented to produce 8 mm-long modifications in glass [142]. (One can remark that in [143], a single axicon is used, with obvious limitation on the working distance, but mJ pulses used enabled cutting 8 mm glass in single pass.) The setup was slightly improved using a pair of negative and positive axicons to avoid any intermediate hotspots or focusing [27] (see Sect. 2). With this approach, extremely thick glass, up to 1 cm thickness, could be cleaved using the stealth dicing technique [27]. Noticeably, the aspect ratio of the nanovoids, using the same geometry, has been scaled from 100:1 in [8] to 30,000:1 in [27]. Very thick glass cutting opens new opportunities to reduce costs for window glass processing in a context where better insulating windows are required to limit our carbon footprint.

5 Perspectives

Thick and thin glass processing using diffraction-free Bessel beams has been very active in the recent years. Even more recently, a number of new orientations have attracted attention. It was realized that shaping the central lobe of the Bessel beam could enhance the performances of stealth dicing. The stealth dicing technique has also been widened to curved glass cutting. New strategies are being developed to cut glass with curved surface in a single pass, and finally, the family of Bessel beams has been generalized to create almost arbitrary transverse cross sections that propagate preserving the conical flow and longitudinal invariance.

5.1 Crack Formation

Micro-crack formation seems to be the mechanism allowing material separation where the stress-induced fracture propagates through the laser-induced crack network. The transient stress and crack propagation imaging has been reported in [144, 145]. Cracks with a transverse extension of several tens of micrometers can be produced using high-energy pulses, particularly when using relatively long pulse duration. Increasing the crack extent allows for increasing the channel to channel distance and, while this increases the surface roughness, straightforwardly improves the process speed.

In sapphire, cracks can be generated following the crystal axes. Rapp et al. demonstrated that using approximately ten times the energy needed to produce a nanochannel in single shot, cracks extending over $\sim$ 20 µm were generated in a star-shape following the three axes of the hexagonal lattice [83]. Interestingly, below a pulse duration of $\sim$ 600 fs, only a single crack is generated, perpendicular to the polarization axis. This can be understood from the elliptical transverse shape of the nanovoid formed in the femtosecond regime (see Sect. 3.5). Polarization could then be used to control the crack direction, although a nontrivial coupling exists with the stress induced by formerly drilled nanochannels. These results were also confirmed in reference [146], in which cutting of sapphire along a curved path is demonstrated at 500 mm/s (see Fig. 16.15).

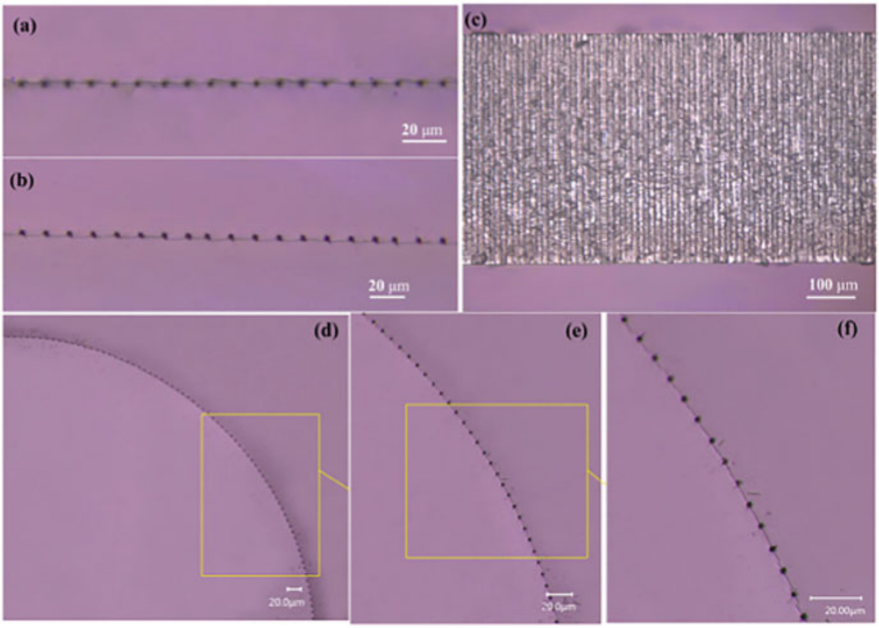

Fig. 16.15 Control of the formation of cracks after Bessel beam illumination. The cutting speed is 0.5 m/s. The images show optical microscopy characterization of the sample. (**a**, **b**) Top and bottom views before cleavage of a line-type modification. (**c**) View of the cleaved surface of the line-type modification. (**d**–**f**) Top views of a curvilinear cleave with different magnifications. The radius of curvature is 500 μm. Reprinted figure with permission from [146]

In glass, the transverse cross section of the channels does not show any ellipticity. This can be controlled using a specific beam shape, for instance, by producing an elliptical Bessel beam, formed by filtering part of the intensity ring distribution in the Fourier space [147] or by using more complex beam shaping approaches [148, 149] or simply using imperfect axicons or an axicon with a tilt [21, 150, 151]. The elliptical cross section of the channels increases the stress along the major axis of the ellipse. This improves the cleavability of the material and the flexural strength of the cut material [152]. Another similar approach using multiple cavities has been suggested and modeled in reference [153].

Another way of controlling the crack formation and improving the process throughput is the use of a dash line strategy where groups of channels are processed and a crack joins the groups during material separation. This strategy improves guiding the overall fracture, particularly for the separation of materials cut along curved paths [135].

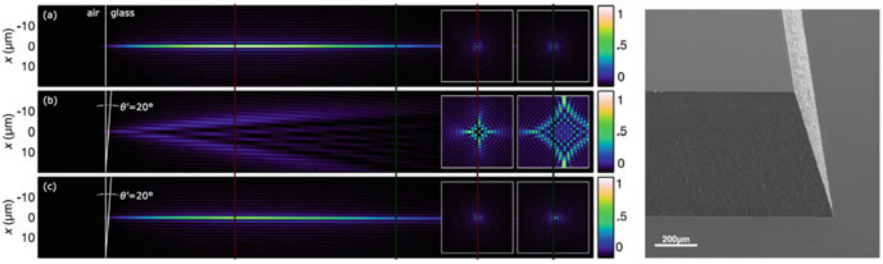

Fig. 16.16 (left) Simulation of Bessel beam intensity distribution inside glass: (**a**) if the glass surface is normal to the beam axis, (**b**) if the surface is tilted by 20°, (**c**) same as (**b**) but the Bessel beam is pre-corrected. (Right) Example of glass cutting with a tilt of 30° with respect to the normal. Reprinted figure with permission from [154]. Copyright The Optical Society

5.2 Aberration Correction for Non-flat Glass Cutting

The applications of glass cutting are by far limited to neither flat glass nor vertical cutting. Glass vertically cut at 90° from its surface can undergo chipping or breaking when handled because of stress accumulation at the corners. However, the beam inclination that is necessary to create beveled edges induces a strong beam distortion, as can be observed from Fig. 16.16 (middle left). The subsequent intensity drop within the beam prevents nanochannel drilling. Jenne et al. compensated the aberration due to the inclined glass surface using a phase mask computed with a decomposition of the aberration on Zernike polynomials [154]. Successful cutting with 30° tilt angle is shown in Fig.16.16 (right). A more precise aberration correction was developed in reference [139], where the aberration is computed by inverse propagation. In this reference, the phase mask is additionally engineered to produce an elliptical Bessel beam.

A similar problem arises to cut curved surfaces such as glass tubes for ampoules or syringes. Flamm et al. applied a quadratic phase compensation to preserve the shape of the Bessel beam inside a curved glass article. Figure 16.17 compares the beam intensity distribution produced within glass without and with the aberration correction. Obviously, the correction is dependent on the curvature of the article [155].

The cut parts of the tube shown in Fig. 16.17 have been removed using laser illumination with the corrected Bessel beam and chemical etching. This overall demonstrates the usefulness and flexibility of laser structuring using non-diffracting Bessel beams.

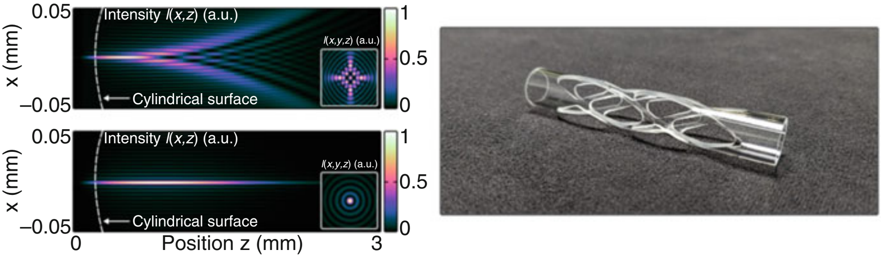

Fig. 16.17 (left) Simulation of Bessel beam intensity distribution inside curved glass, before (top) and after correction (bottom). (Right) Complex contour cutting from a glass tube. Etching is used after laser illumination to enable material removal. Reprinted figure with permission from [155]

5.3 Laser Processing of Curved Structures

This section discusses the application to edge chamfering that is necessary for glass handling and reducing the stress accumulation within the corners, as mentioned in Sect. 5.2. Instead of the three passes at three different angles that are necessary to cut and chamfer glass in a bull-nose shape, it would be desirable to have a process performing this operation in a single step. A fully curved profile would even more reduce the stress confinement due to sharp angles. In this context, other classes of extended beams, i.e., accelerating beams and, in more general, beams with a curvature, can offer new opportunities.

Self-accelerating beams are beams which produce an interference pattern that laterally shifts along a curve during propagation. A first version, the “Airy beam,” was produced using a third-order phase and an optical Fourier transformation [156]. It was early used to produce curved plasma channels in air [157, 158]. By recognizing that accelerating beams are caustics, it is in fact possible to largely extend the self-acceleration property to arbitrary curved trajectories, which can even extend to the non-paraxial regime [159–164].

First applications to curved laser micromachining were developed by Mathis et al. where accelerating beams were used for edge polishing and curved trench opening [163, 165] and to inscribe a curved damage inside glass [161]. A challenging issue in the field is the generation of curvatures with large radius. This requires very large extents of the third-order phase applied in the Fourier plane as well as optics with large pupils: the beams developed by Mathis et al. could be curved only over a distance of typically 50 to 70 µm while reaching a tilt of $\pm \sim 45°$ (see Fig. 16.18 (left) [163]). Recently, using a similar approach, Sohr et al. demonstrated curved modifications of 700 µm glass that could be etched, with a maximal tilt of $\sim 18°$, as shown in Fig. 16.18 (right) [166].

To circumvent the abovementioned difficulty of phase extent to create an accelerating beam with large maximal tilt to process glass with thickness of several hundreds of micrometers to millimeters, a new strategy was developed in [167].

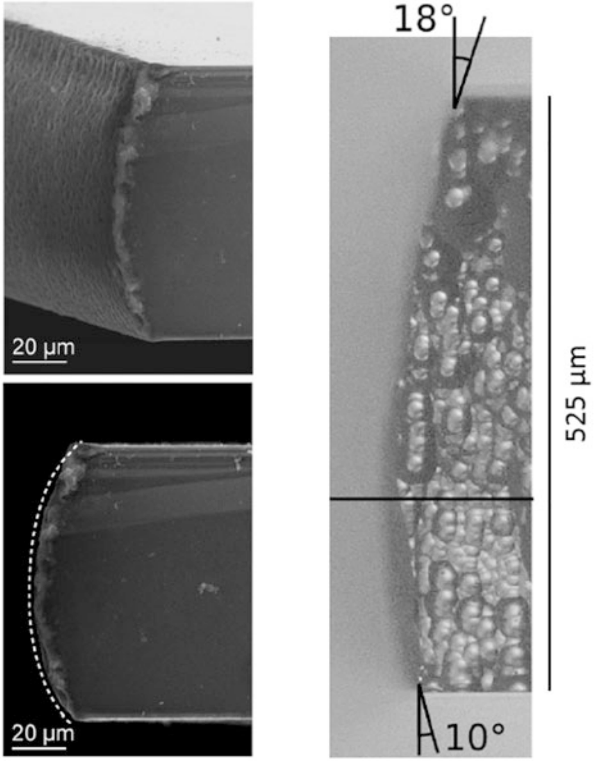

Fig. 16.18 (left) Curved edge processing of 50 μm-thick silicon using an accelerating beam. Reprinted figure with permission from [163]; (right) two-step curved edge processing in glass: laser illumination using an accelerating beam is used before chemical etching to enable material separation. Reprinted and adapted figure with permission from [166]. Copyright The Optical Society

The concept, as shown in Fig. 16.19, is to generate a series of focii positioned on a curved trajectory. Very large tilt angles can be reached as can be seen in Fig. 16.19 (right).

5.4 *Bessel-Like Beams and Applications*

Most of the works discussed up to here were based on zeroth-order Bessel beams. However, it is easy to understand that higher-order Bessel beams or other beam shapes could offer interesting perspectives in the field of laser micromachining and nanomachining.

Jukna et al. demonstrated that higher-order Bessel beams can sustain—if the cone angle is sufficiently high—the same propagation-invariant regime as the one

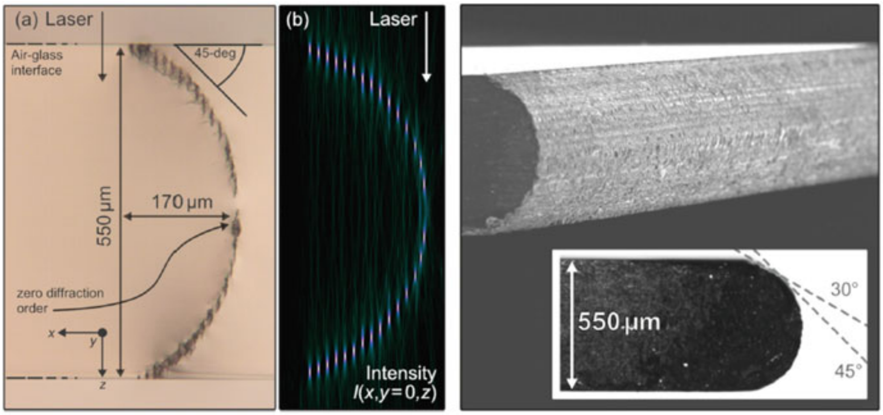

Fig. 16.19 Curved edge processing using a series of focii distributed over a half-circle. Material separation is obtained after chemical etching. Reprinted figure with permission from [167]

generated by zeroth-order Bessel beams [168]. Higher-order Bessel beams have been tested by several groups for laser processing. However, a key aspect is that at the high power necessary to induce material modification, the cone angle generally used can be insufficient to prevent nonlinear modulation instability. It tends to split the main intensity ring [169]. As shown in [170], the main ring of the higher-order Bessel can split into multiple hotspots during the propagation. Jedrkiewicz et al. reported single-shot induced tubular modifications in glass using higher-order Bessel beams in the picosecond regime [171]. In the femtosecond regime, modifications are visible only at the surface. In reference [172], azimuthal and radial polarizations of a first-order Bessel beam have been compared in the context of picosecond laser crack formation inside glass. It was shown the most prominent effect is in fact the intensity asymmetries of the beam.

A new class of Bessel-like beams has been introduced by Jenne et al. with a generalization of the azimuthal phase applied [148, 149]. The phase of an nth-order Bessel beam is, in radial coordinates(r, φ):

$$\Psi(r, \varphi) = \frac{2\pi}{\lambda} \sin \gamma r + n\varphi \tag{16.3}$$

This generates a beam with a transverse intensity profile close to $|J_n(r)|^2$ function. The first term is responsible for the conical structure of the beam, while the second determines the transverse position of the intensity maxima, since they are the points of constructive interference. The concept introduced by Jenne and Flamm is to modify the second term, following [148, 149]:

$$\Psi(r, \varphi) = \frac{2\pi}{\lambda} \sin \gamma r + \Theta(\varphi) \tag{16.4}$$

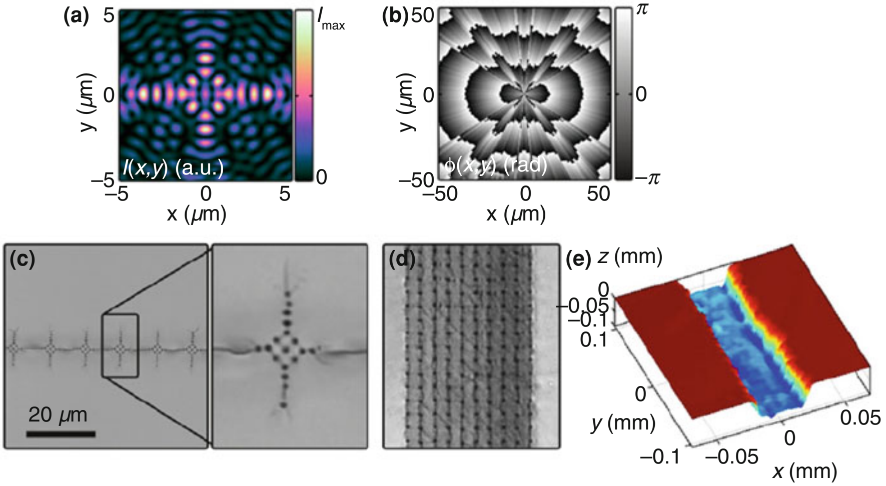

Fig. 16.20 (**a**) Cross section of a Bessel-like beam generated using the phase mask shown in (**b**). (**c**) SEM view of a series of ultrafast laser-induced material modifications and cracks using the beam shape (**a**). (**d**) After scanning the beam over a series of lines, a square array of cracks and channels is created. (**e**) shows the profile of a trench after chemical etching of the sample shown in (**d**). Reprinted figure with permission from [155]

where Θ is an arbitrary function. With this approach, the group developed beam shapes that can efficiently control the formation of well-oriented extended cracks. The use of asymmetrically shaped central lobe of Bessel beam [149] confirms the results of Meyer et al. [152].

Figure 16.20 demonstrates that Bessel-like shaping opens a very large number of possibilities to engineer the stress distribution inside glass, obviously not limited to glass cleaving applications.

Other approaches have also been used to engineer Bessel beams while preserving their non-diffracting properties, such as superpositions of laterally shifted Bessel vortices [173], superpositions of vortices [174], or the synthesis of non-diffracting Mathieu and Weber beams [175]. Using superimposed vortex orders, Yu et al. reduced the intensity of the side lobes which was successfully applied to surface nanostructuring with reduced limitation on the fluence in the central peak, as shown in Fig. 16.21 [176].

6 Conclusion

As a conclusion, ultrafast laser beam shaping as quasi-diffraction-free Bessel beams that propagate in a conical flow has enabled the development of drastically new laser nanostructuring applications, down to the extreme regime of 100 nm laser

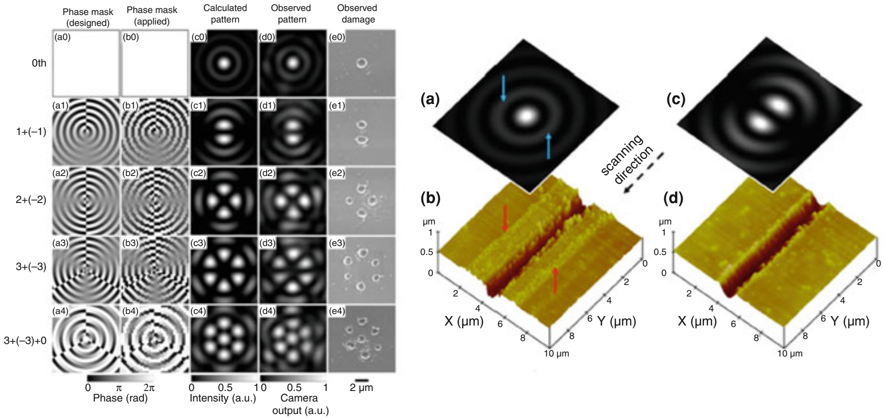

Fig. 16.21 (left) Superpositions of different Bessel beams leads to multiple spots and can be used to process material surface; (right) trench nanomachining using an engineered Bessel-like beam can reduce the damage produced by side lobes. Reprinted figure with permission from [176]

structuring and extremely high aspect ratio up to 30,000 to 1. The strength of the approach is that these extreme scales are also very well adapted for real-life technological applications. The very long focal region of Bessel beams releases the constraint on ultraprecise sample positioning when nanostructuring, non-flat surfaces can be processed. Inside solids, the laser beam shaping enables the generation of extended index modification, photopolymerization, or void formation with applications in photonics or to high-speed thin or thick glass cutting. This chapter has also reviewed recent new directions of the field where new beam shapes are being developed, maintaining the conical flow property, but where the transverse intensity distribution is engineered to control targeted effects with enhanced transverse directionality. The recent generalization of Bessel beams and the development of non-diffracting caustics [177] open a new toolbox to control matter at extreme scales and extreme regimes with ultrafast laser pulses.

It is no doubt that next generation of very high-power, kilowatt-class lasers will offer new opportunities for further developments since the extended focus of Bessel and Bessel-like beams requires more energy and higher average power [178]. On a fundamental side, the nanometric scale of the laser-induced plasmas inside dielectrics still represents a challenge for the laser-matter interaction in this regime, but recent results make us oversee that extreme states can be reached using these beam shapes with both fundamental and technological impacts. Warm dense matter can be generated over extremely long distances using only a tabletop laser, in contrast with much more complex high-energy sources currently used. On the technological aspects, the extreme pressures and temperatures reached within the materials over lengths at centimeter-scale can offer also very interesting perspectives in terms of new material synthesis [179].

Acknowledgments FC acknowledges the financial supports of the European Research Council (ERC) 682032-PULSAR, Region Bourgogne-Franche-Comte and Agence Nationale de la Recherche (EQUIPEX+ SMARTLIGHT platform ANR-21-ESRE-0040), I-SITE BFC project (contract ANR-15-IDEX-0003), and the EIPHI Graduate School ANR-17-EURE-0002.

References

1. J. Durnin, J.J. Miceli, J.H. Eberly, Diffraction-free beams. Phys. Rev. Lett. **58**, 1499–1501 (1987)
2. M. Duocastella, C. Arnold, Bessel and annular beams for materials processing. Laser Photon. Rev. **6**, 607–621 (2012)
3. F. Courvoisier, R. Stoian, A. Couairon, Ultrafast laser micro- and nano-processing with nondiffracting and curved beams. Opt. Laser Technol. **80**, 125–137 (2016)
4. R. Stoian, M.K. Bhuyan, G. Zhang, G. Cheng, R. Meyer, F. Courvoisier, Ultrafast Bessel beams: advanced tools for laser materials processing. Adv. Opt. Technol. **7**, 165–174 (2018)
5. R. Stoian, Volume photoinscription of glasses: three-dimensional micro- and nanostructuring with ultrashort laser pulses. Appl. Phys. A Mater. Sci. Process. **126**, 438 (2020)
6. F. Courvoisier, Ultrafast laser micro-nano structuring of transparent materials with high aspect ratio, in *Handbook of Laser Micro- and Nano-Engineering* (Springer International Publishing, 2020), pp. 1–37
7. V. Jarutis, R. Paškauskas, A. Stabinis, Focusing of Laguerre–Gaussian beams by axicon. Optics Communications **184**, 105–112 (2000)
8. M.K. Bhuyan, F. Courvoisier, P.A. Lacourt, M. Jacquot, R. Salut, L. Furfaro, J.M. Dudley, High aspect ratio nanochannel machining using single shot femtosecond Bessel beams. Appl. Phys. Lett. **97**, 081102 (2010)
9. J.H. McLeod, The axicon: A new type of optical element. J. Opt. Soc. Am. **44**, 592 (1954)
10. L. Froehly, M. Jacquot, P.A. Lacourt, J.M. Dudley, F. Courvoisier, Spatiotemporal structure of femtosecond Bessel beams from spatial light modulators. J. Opt. Soc. Am. A **31**, 790 (2014)
11. P. Brandão, D. Pires, Transmission and reflection of vector Bessel beams through an interface between dielectrics. Phys. Lett. A **381**, 813–816 (2017)
12. N. Chattrapiban, E.A. Rogers, D. Cofield, I. Wendell T. Hill, R. Roy, Generation of nondiffracting Bessel beams by use of a spatial light modulator. Optics Letters **28**, 2183 (2003)
13. A. Vasara, J. Turunen, A.T. Friberg, Realization of general nondiffracting beams with computer-generated holograms. J. Opt. Soc. Am. A **6**, 1748 (1989)
14. J. Amako, D. Sawaki, E. Fujii, Microstructuring transparent materials by use of nondiffracting ultrashort pulse beams generated by diffractive optics. J. Opt. Soc. Am. B **20**, 2562 (2003)
15. S.N. Khonina, V.V. Kotlyar, R.V. Skidanov, V.A. Soifer, K. Jefimovs, J. Simonen, J. Turunen, Rotation of microparticles with Bessel beams generated by diffractive elements. J. Modern Opt. **51**, 2167–2184 (2004)
16. R. Grunwald, U. Neumann, V. Kebbel, H.J. Kühn, K. Mann, U. Leinhos, H. Mischke, D. Wulff-Molder, Vacuum-ultraviolet beam array generation by flat micro-optical structures. Optics Letters **29**, 977 (2004)
17. T. Grosjean, S.S. Saleh, M.A. Suarez, I.A. Ibrahim, V. Piquerey, D. Charraut, P. Sandoz, Fiber microaxicons fabricated by a polishing technique for the generation of Bessel-like beams. Applied Optics **46**, 8061 (2007)
18. X. Tsampoula, V. Garceés-Chavez, M. Comrie, D.J. Stevenson, B. Agate, C.T.A. Brown, F. Gunn-Moore, K. Dholakia, Femtosecond cellular transfection using a nondiffracting light beam. Appl. Phys. Lett. **91**, 053902 (2007)
19. S. Akturk, B. Zhou, M. Franco, A. Couairon, A. Mysyrowicz, Generation of long plasma channels in air by focusing ultrashort laser pulses with an axicon. Optics Communications **282**, 129–134 (2009)

20. P. Boucher, J.D. Hoyo, C. Billet, O. Pinel, G. Labroille, F. Courvoisier, Generation of high conical angle Bessel–Gauss beams with reflective axicons. Applied Optics **57**, 6725 (2018)
21. J. Dudutis, P. Gečys, G. Račiukaitis, Non-ideal axicon-generated Bessel beam application for intra-volume glass modification. Optics Express **24**, 28433 (2016)
22. O. Brzobohatý, T. Cižmár, P. Zemánek, High quality quasi-Bessel beam generated by round-tip axicon. Optics Express **16**, 12688 (2008)
23. T. Čižmár, K. Dholakia, Tunable Bessel light modes: engineering the axial propagation. Optics Express **17**, 15558 (2009)
24. S. Schwarz, G.L. Roth, S. Rung, C. Esen, R. Hellmann, Fabrication and evaluation of negative axicons for ultrashort pulsed laser applications. Optics Express **28**, 26207 (2020)
25. S. Schwarz, S. Rung, C. Esen, R. Hellmann, Rapid fabrication of precise glass axicon arrays by an all laser-based manufacturing technology. J. Laser Appl. **32**, 012001 (2020)
26. B. Chebbi, S. Minko, N. Al-Akwaa, I. Golub, Remote control of extended depth of field focusing. Optics Communications **283**, 1678–1683 (2010)
27. R. Meyer, L. Froehly, R. Giust, J.D. Hoyo, L. Furfaro, C. Billet, F. Courvoisier, Extremely high-aspect-ratio ultrafast Bessel beam generation and stealth dicing of multi-millimeter thick glass. Appl. Phys. Lett. **114**, 201105 (2019)
28. I. Ouadghiri-Idrissi, R. Giust, L. Froehly, M. Jacquot, L. Furfaro, J.M. Dudley, F. Courvoisier, Arbitrary shaping of on-axis amplitude of femtosecond Bessel beams with a single phase-only spatial light modulator. Optics Express **24**, 11495–11504 (2016)
29. R. Dharmavarapu, S. Bhattacharya, S. Juodkazis, Diffractive optics for axial intensity shaping of Bessel beams. J. Opt. (UK) **20**, 085606 (2018)
30. P. Gotovski, P. Šlevas, E. Nacius, V. Jukna, S. Orlov, J. Baltrukonis, O. Ulčinas, T. Gertus, Formation of optical needles by Pancharatnam-Berry phase element for laser-induced modifications in transparent materials, in *Laser-based Micro- and Nanoprocessing XIV*, vol. 11268, ed. by U. Klotzbach, A. Watanabe, R. Kling (International Society for Optics and Photonics (SPIE), 2020), pp. 357–365
31. A.P. Joglekar, H. h. Liu, E. Meyhofer, G. Mourou, A.J. Hunt, Optics at critical intensity: Applications to nanomorphing. Proc. Natl. Acad. Sci. **101**, 5856–5861 (2004)
32. R. Sahin, I. Kabacelik, Nanostructuring of ito thin films through femtosecond laser ablation. Appl. Phys. A Mater. Sci. Process. **122**, 314 (2016)
33. D.H. Doan, R. Iida, B. Kim, I. Satoh, K. Fushinobu, Bessel beam laser-scribing of thin film silicon solar cells by ns pulsed laser. J. Thermal Sci. Technol. **11**, 11 (2016)
34. B. Wetzel, C. Xie, P.A. Lacourt, J.M. Dudley, F. Courvoisier, Femtosecond laser fabrication of micro and nano-disks in single layer graphene using vortex Bessel beams. Appl. Phys. Lett. **103**, 241111 (2013)
35. B. Voisiat, M. Gedvilas, S. Indrišiūnas, G. Račiukaitis, Picosecond-laser 4-beam-interference ablation as a flexible tool for thin film microstructuring. Physics Procedia **12**, 116–124 (2011)
36. S. Alamri, A.F. Lasagni, Development of a general model for direct laser interference patterning of polymers. Optics Express **25**, 9603 (2017)
37. X. Li et al., Creating a three-dimensional surface with antireflective properties by using femtosecond-laser Bessel-beam-assisted thermal oxidation. Optics Letters **45**, 2989 (2020)
38. I. Alexeev, K.H. Leitz, A. Otto, M. Schmidt, Application of Bessel beams for ultrafast laser volume structuring of nontransparent media. Physics Procedia **5**, 533–540 (2010)
39. Y. Matsuoka, Y. Kizuka, T. Inoue, The characteristics of laser micro drilling using a Bessel beam. Appl. Phys. A Solids Surf. **84**, 423–430 (2006)
40. O. Jedrkiewicz et al., Pulsed Bessel beam-induced microchannels on a diamond surface for versatile microfluidic and sensing applications. Opt. Mater. Exp. **7**, 1962 (2017)
41. S. Kumar et al., Laser surface structuring of diamond with ultrashort Bessel beams. Scientific Reports **8**, 14021 (2018)
42. H.D. Nguyen et al., Non-diffractive Bessel beams for ultrafast laser scanning platform and proof-of-concept side-wall polishing of additively manufactured parts. Micromachines **11**, 974 (2020)

43. A. Couairon, A. Mysyrowicz, Femtosecond filamentation in transparent media. Physics Reports **441**, 47–189 (2007)
44. P. Polesana, M. Franco, A. Couairon, D. Faccio, P.D. Trapani, Filamentation in Kerr media from pulsed Bessel beams. Phys. Rev. A **77**, 043814 (2008)
45. E. Gaizauskas et al., Discrete damage traces from filamentation of Gauss-Bessel pulses. Optics Letters **31**, 80 (2006)
46. I. Ouadghiri-Idrissi, J.M. Dudley, F. Courvoisier, Controlling nonlinear instabilities in Bessel beams through longitudinal intensity shaping. Optics Letters **42**, 3785 (2017)
47. I. Ouadghiri-Idrissi, J.M. Dudley, F. Courvoisier, Control of spatial four-wave-mixing efficiency in Bessel beams using longitudinal intensity shaping. Phys. Rev. A **100**, 043804 (2019-10)
48. V. Garzillo et al., Optimization of laser energy deposition for single-shot high aspect-ratio microstructuring of thick BK7 glass. J. Appl. Phys. **120**, 013102 (2016)
49. P.K. Velpula, M.K. Bhuyan, C. Mauclair, J.P. Colombier, R. Stoian, Role of free carriers excited by ultrafast Bessel beams for submicron structuring applications. Optical Engineering **53**, 076108 (2014)
50. L. Sudrie et al., Femtosecond laser-induced damage and filamentary propagation in fused silica. Phys. Rev. Lett. **89**, 4135 (2002)
51. S. Tzortzakis et al., Self-guided propagation of ultrashort IR laser pulses in fused silica. Phys. Rev. Lett. **87**, 213902 (2001)
52. R. Beuton et al., Numerical studies of dielectric material modifications by a femtosecond Bessel–Gauss laser beam. Appl. Phys. A Mater. Sci. Process. **127**, 334 (2021)
53. K. Ardaneh et al., A new route to high energy density inside the bulk of transparent materials (2021). arXiv:2109.00803
54. D. Faccio et al., Kerr-induced spontaneous Bessel beam formation in the regime of strong two-photon absorption. Optics Express **16**, 8213 (2008)
55. L. Luo et al., Formation of diversiform microstructures in wide-bandgap materials by tight-focusing femtosecond laser pulses. J. Opt. A Pure Appl. Optics **4**, 105–110 (2001)
56. S. Sowa, W. Watanabe, J. Nishii, K. Itoh, Filamentary cavity formation in poly(methyl methacrylate) by single femtosecond pulse. Appl. Phys. A **81**, 1587–1590 (2005)
57. J. Song et al., Formation mechanism of self-organized voids in dielectrics induced by tightly focused femtosecond laser pulses. Appl. Phys. Lett. **92**, 092904 (2008)
58. F. Ahmed, M.S. Ahsan, M.S. Lee, M.B.G. Jun, Near-field modification of femtosecond laser beam to enhance single-shot pulse filamentation in glass medium. Appl. Phys. A **114**, 1161–1165 (2013)
59. E. Alimohammadian, E. Ertorer, E.M. Uzeda, J. Li, P.R. Herman, Inhibition and enhancement of linear and nonlinear optical effects by conical phase front shaping for femtosecond laser material processing. Scientific Reports **10**, 21528 (2020)
60. E. Alimohammadian, E. Ertorer, P.R. Herman, Conical phase front and aberration beam shaping for manipulating femtosecond laser chemical etching. Opt. Mater. Exp. **11**, 2432 (2021)
61. P.K. Velpula et al., Spatio-temporal dynamics in nondiffractive Bessel ultrafast laser nanoscale volume structuring. Laser Photon. Rev. **10**, 230–244 (2016)
62. R. Stoian, M.K. Bhuyan, A. Rudenko, J.P. Colombier, G. Cheng, High-resolution material structuring using ultrafast laser non-diffractive beams. Adv. Phys. X **4**, 1659180 (2019)
63. A. Marcinkevicius, S. Juodkazis, S. Matsuo, V. Mizeikis, H. Misawa, Application of Bessel beams for microfabrication of dielectrics by femtosecond laser. Jpn. J. Appl. Phys. **40**, L1197–L1199 (2001)
64. V. Zambon, N. McCarthy, M. Piché, Fabrication of photonic devices directly written in glass using ultrafast Bessel beams, in R. Vallée, et al. (eds.) *Photonics North 2008*, vol. 7099 (International Society for Optics and Photonics (SPIE), 2008), pp. 720–724
65. S. Juodkazis et al., Laser-induced microexplosion confined in the bulk of a sapphire crystal: Evidence of multimegabar pressures. Phys. Rev. Lett. **96**, 166101 (2006)

66. S. Juodkazis, H. Misawa, T. Hashimoto, E.G. Gamaly, B. Luther-Davies, Laser-induced microexplosion confined in a bulk of silica: Formation of nanovoids. Appl. Phys. Lett. **88**, 201909 (2006)
67. F. Werr et al., Surface probing of ultra-short-pulse laser filament cut window glass and the impact on the separation behavior. Adv. Eng. Mater. **22**, 2000471 (2020)
68. N. Götte et al., Temporal Airy pulses for controlled high aspect ratio nanomachining of dielectrics. Optica **3**, 389 (2016-04)
69. S. Winkler et al., Transient response of dielectric materials exposed to ultrafast laser radiation. Appl. Phys. A Solids Surf. **84**, 413–422 (2006)
70. L. Rapp et al., High aspect ratio micro-explosions in the bulk of sapphire generated by femtosecond Bessel beams. Scientific Reports **6**, 34286 (2016)
71. T. Chen et al., Reconstructing of embedded high-aspect-ratio nano-voids generated by ultrafast laser Bessel beams. Micromachines **11**, 671 (2020)
72. G.Y. Chang, Y.H. Wang, G.H. Cheng, Writing nanopores on a ZnS crystal with ultrafast Bessel beams. Chinese Optics **14**, 213–225 (2021)
73. C. Vetter et al., High aspect ratio structuring of glass with ultrafast Bessel beams. Materials **14**, 6749 (2021)
74. M. Lamperti et al., Invited article: Filamentary deposition of laser energy in glasses with Bessel beams. APL Photonics **3**, 120805 (2018)
75. J. del Hoyo, R. Meyer, L. Furfaro, F. Courvoisier, Nanoscale confinement of energy deposition in glass by double ultrafast Bessel pulses. Nanophotonics **10**, 1089–1097 (2020)
76. M. Garcia-Lechuga et al., Simultaneous time-space resolved reflectivity and interferometric measurements of dielectrics excited with femtosecond laser pulses. Phys. Rev. B **95**, 214114 (2017)
77. A. Denoeud et al., Metallization of warm dense SiO2 studied by XANES spectroscopy. Phys. Rev. Lett. **113**, 116404 (2014)
78. K. Engelhorn et al., Electronic structure of warm dense silicon dioxide. Phys. Rev. B **91**, 214305 (2015)
79. M. Somayaji et al., Multiscale electronic and thermomechanical dynamics in ultrafast nanoscale laser structuring of bulk fused silica. Scientific Reports **10**, 15152 (2020)
80. M. Kumkar et al., Comparison of different processes for separation of glass and crystals using ultrashort pulsed lasers, in *Frontiers in Ultrafast Optics: Biomedical, Scientific, and Industrial Applications XIV*, vol. 8972, ed. by A. Heisterkamp, P.R. Herman (International Society for Optics and Photonics (SPIE), 2014), pp. 161–176
81. K. Mishchik et al., Improved laser glass cutting by spatio-temporal control of energy deposition using bursts of femtosecond pulses. Optics Express **25**, 33271 (2017)
82. S. Karimelahi, L. Abolghasemi, P.R. Herman, Rapid micromachining of high aspect ratio holes in fused silica glass by high repetition rate picosecond laser. Appl. Phys. A **114**, 91–111 (2013)
83. L. Rapp et al., High speed cleaving of crystals with ultrafast Bessel beams. Optics Express **25**, 9312 (2017)
84. G. Zhang et al., Thermal and mechanical limitations to processing resolution in volume non-diffractive ultrafast laser structuring. Appl. Surf. Sci. **570**, 151170 (2021)
85. N.M. Bulgakova, V.P. Zhukov, S.V. Sonina, Y.P. Meshcheryakov, Modification of transparent materials with ultrashort laser pulses: What is energetically and mechanically meaningful? J. Appl. Phys. **118**, 233108 (2015)
86. K. Bergner et al., Spatio-temporal analysis of glass volume processing using ultrashort laser pulses. Applied Optics **57**, 4618 (2018)
87. T.D. Arber et al., Contemporary particle-in-cell approach to laser-plasma modelling. Plasma Phys. Controll. Fusion **57**, 113001 (2015)
88. W. Kruer, *Physics of Laser Plasma Interactions* (CRC Press, 2019)
89. N. Denisov, On a singularity of the field on an electromagnetic wave propagated in an inhomogeneous plasma. J. Exp. Theor. Phys. **4**, 544 (1957)

90. P. Stampfli, K.H. Bennemann, Dynamical theory of the laser-induced lattice instability of silicon. Phys. Rev. B **46**, 10686–10692 (1992)
91. B. Rethfeld, D.S. Ivanov, M.E. Garcia, S.I. Anisimov, Modelling ultrafast laser ablation. J. Phys. D Appl. Phys. **50**, 193001 (2017)
92. T. Winkler et al., Laser amplification in excited dielectrics. Nature Physics **14**, 74–79 (2017-09)
93. S. Mao et al., Dynamics of femtosecond laser interactions with dielectrics. Appl. Phys. A Solids Surf. **79**, 1695–1709 (2004)
94. R.G. Kraus et al., Shock vaporization of silica and the thermodynamics of planetary impact events. J. Geophys. Res. Planets **117**, E09009 (2012)
95. E.N. Glezer, E. Mazur, Ultrafast-laser driven micro-explosions in transparent materials. Appl. Phys. Lett. **71**, 882 (1997)
96. R. Beuton et al., Thermo-elasto-plastic simulations of femtosecond laser-induced structural modifications: Application to cavity formation in fused silica. J. Appl. Phys. **122**, 203104 (2017)
97. M.K. Bhuyan, P.K. Velpula, M. Somayaji, J.P. Colombier, R. Stoian, 3D nano-fabrication using controlled Bessel-glass interaction in ultra-fast modes. J. Laser Micro Nanoeng. **12**, 274–280 (2017)
98. M.K. Bhuyan et al., Ultrafast laser nanostructuring in bulk silica, a "slow" microexplosion. Optica **4**, 951 (2017)
99. M. Bonitz et al., Ab initio simulation of warm dense matter. Phys. Plasmas **27**, 042710 (2020)
100. K. Sugioka, Y. Cheng, Ultrafast lasers—reliable tools for advanced materials processing. Light Sci. Appl. **3**, e149 (2014)
101. M. Malinauskas et al., Ultrafast laser processing of materials: From science to industry. Light Sci. Appl. **5**, e16133 (2016)
102. F. Sima, K. Sugioka, Ultrafast laser manufacturing of nanofluidic systems. Nanophotonics **10**, 2389–2406 (2021)
103. M. Manousidaki, D.G. Papazoglou, M. Farsari, S. Tzortzakis, Long-scale multiphoton polymerization voxel growth investigation using engineered Bessel beams. Opt. Mater. Exp. **9**, 2838 (2019)
104. H. Cheng et al., Generation of Bessel-beam arrays for parallel fabrication in two-photon polymerization. J. Laser Appl. **33**, 012040 (2021)
105. C. Mauclair et al., Excitation and relaxation dynamics in ultrafast laser irradiated optical glasses. High Power Laser Sci. Eng. **4**, e46 (2016)
106. X. Wang et al., Photochemical response triggered by ultrashort laser Gaussian-Bessel beams in photo-thermo-refractive glass. Optics Express **28**, 31093 (2020)
107. M. Mikutis, T. Kudrius, G. Šlekys, D. Paipulas, S. Juodkazis, High 90% efficiency Bragg gratings formed in fused silica by femtosecond Gauss-Bessel laser beams. Opt. Mater. Exp. **3**, 1862 (2013)
108. Y. Matushiro, W. Watanabe, Femtosecond laser processing of polymethyl methacrylate with an axicon. J. Laser Micro Nanoeng. **11**, 59–65 (2016)
109. W. Watanabe, Y. Matushiro, K. Hatanaka, S. Juodkazis, Regeneration of a grating in PMMA inscribed by femtosecond laser Bessel beam. J. Laser Micro Nanoeng. **12**, 102–106 (2017)
110. K. Homma, W. Watanabe, Fabrication of PDMS-based volume Bragg gratings by stitching of femtosecond laser filament. Jpn. J. Appl. Phys. **60**, 032003 (2021)
111. D. Gailevičius, V. Purlys, K. Staliunas, Photonic crystal spatial filters fabricated by femtosecond pulsed Bessel beam. Optics Letters **44**, 4969 (2019)
112. Q. Sun, T. Lee, M. Beresna, G. Brambilla, Control of laser induced cumulative stress for efficient processing of fused silica. Scientific Reports **10**, 3819 (2020)
113. Z. Wang et al., High-throughput microchannel fabrication in fused silica by temporally shaped femtosecond laser Bessel-beam-assisted chemical etching. Optics Letters **43**, 98 (2017)
114. D. Chu, P. Yao, X. Sun, K. Yin, C. Huang, Ablation enhancement of fused silica glass by femtosecond laser double-pulse Bessel beam. J. Opt. Soc. Am. B **37**, 3535 (2020)

115. A. Rudenko, J.P. Colombier, T.E. Itina, Influence of polarization state on ultrafast laser-induced bulk nanostructuring. J. Laser Micro Nanoeng. **11**, 304–311 (2016)
116. G. Cheng et al., Embedded nanogratings in bulk fused silica under non-diffractive Bessel ultrafast laser irradiation. Appl. Phys. Lett. **110**, 261901 (2017)
117. T. Tamaki, W. Watanabe, J. Nishii, K. Itoh, Welding of transparent materials using femtosecond laser pulses. Jpn. J. Appl. Phys. **44**, L687–L689 (2005)
118. W. Watanabe, S. Onda, T. Tamaki, K. Itoh, J. Nishii, Space-selective laser joining of dissimilar transparent materials using femtosecond laser pulses. Appl. Phys. Lett. **89**, 021106 (2006)
119. S. Richter, F. Zimmermann, R. Eberhardt, A. Tünnermann, S. Nolte, Toward laser welding of glasses without optical contacting. Appl. Phys. A **121**, 1–9 (2015)
120. G. Zhang, R. Stoian, W. Zhao, G. Cheng, Femtosecond laser Bessel beam welding of transparent to non-transparent materials with large focal-position tolerant zone. Optics Express **26**, 917 (2018)
121. S. Hecker, M. Blothe, T. Graf, Reproducible process regimes during glass welding by bursts of subpicosecond laser pulses. Applied Optics **59**, 11382 (2020)
122. G. Martin et al., Near infrared spectro-interferometer using femtosecond laser written gls embedded waveguides and nano-scatterers. Optics Express **25**, 8386 (2017)
123. C. D'Amico, G. Martin, J. Troles, G. Cheng, R. Stoian, Multiscale laser written photonic structures in bulk chalcogenide glasses for infrared light transport and extraction. Photonics **8**, 211 (2021)
124. G. Zhang, G. Cheng, M. Bhuyan, C. D'Amico, R. Stoian, Efficient point-by-point Bragg gratings fabricated in embedded laser-written silica waveguides using ultrafast Bessel beams. Optics Letters **43**, 2161 (2018)
125. K.M. Aghdami, A. Rahnama, E. Ertorer, P.R. Herman, Laser nano-filament explosion for enabling open-grating sensing in optical fibre. Nature Communications **12**, 6344 (2021)
126. X. Liu et al., Front-surface fabrication of moderate aspect ratio micro-channels in fused silica by single picosecond Gaussian–Bessel laser pulse. Appl. Phys. A Mater. Sci. Process. **124**, 206 (2018)
127. X. Liu et al., Truncated Gaussian-Bessel beams for short-pulse processing of small-aspect-ratio micro-channels in dielectrics. Optics Express **27**, 6996 (2019)
128. O. Jedrkiewicz, D. Valetti, P.D. Trapani, Etching and drilling of through-holes in thin glass by means of picosecond Bessel beams. SN Appl. Sci. **1**, 1267 (2019)
129. V.V. Belloni, V. Sabonis, P.D. Trapani, O. Jedrkiewicz, Burst mode versus single-pulse machining for Bessel beam micro-drilling of thin glass: study and comparison. SN Appl. Sci. **2**, 1589 (2020)
130. V.V. Belloni, M. Bollani, S.M. Eaton, P.D. Trapani, O. Jedrkiewicz, Micro-hole generation by high-energy pulsed Bessel beams in different transparent materials. Micromachines **12**, 455 (2021)
131. S. Butkus, D. Paipulas, R. Sirutkaitis, E. Gaižauskas, V. Sirutkaitis, Rapid cutting and drilling of transparent materials via femtosecond laser filamentation. J. Laser Micro Nanoeng. **9**, 213–220 (2014)
132. Y. Ito, R. Yoshizaki, N. Miyamoto, N. Sugita, Ultrafast and precision drilling of glass by selective absorption of fiber-laser pulse into femtosecond-laser-induced filament. Appl. Phys. Lett. **113**, 061101 (2018)
133. Y. Ito, R. Shinomoto, A. Otsu, K. Nagato, N. Sugita, Dynamics of pressure waves during femtosecond laser processing of glass. Optics Express **27**, 29158 (2019)
134. M. Kumagai et al., Advanced dicing technology for semiconductor wafer—stealth dicing. IEEE Trans. Semiconduct. Manuf. **20**, 259–265 (2007)
135. K. Mishchik et al., Dash line glass- and sapphire-cutting with high power USP laser, in *Frontiers in Ultrafast Optics: Biomedical, Scientific, and Industrial Applications XVI*, vol. 9740, ed. by A. Heisterkamp, P.R. Herman, M. Meunier, S. Nolte (International Society for Optics and Photonics (SPIE), 2016), pp. 91–106
136. F. Ahmed, M.S. Lee, H. Sekita, T. Sumiyoshi, M. Kamata, Display glass cutting by femtosecond laser induced single shot periodic void array. Appl. Phys. A **93**, 189–192 (2008)

137. W.J. Tsai, C.J. Gu, C.W. Cheng, J.B. Horng, Internal modification for cutting transparent glass using femtosecond Bessel beams. Optical Engineering **53**, 051503 (2013)
138. M.K. Bhuyan et al., High-speed laser-assisted cutting of strong transparent materials using picosecond Bessel beams. Appl. Phys. A Mater. Sci. Process. **120**, 443–446 (2015)
139. C. Ungaro et al., Using phase-corrected Bessel beams to cut glass substrates with a chamfered edge. Applied Optics **60**, 714 (2021)
140. J. Li, E. Ertorer, P.R. Herman, Ultrafast laser burst-train filamentation for non-contact scribing of optical glasses. Optics Express **27**, 25078 (2019)
141. J. Dudutis et al., In-depth comparison of conventional glass cutting technologies with laser-based methods by volumetric scribing using Bessel beam and rear-side machining. Optics Express **28**, 32133 (2020)
142. K. Bergner et al., Scaling ultrashort laser pulse induced glass modifications for cleaving applications. Applied Optics **57**, 5941 (2018)
143. A. Feuer, J.U. Thomas, C. Freitag, R. Weber, T. Graf, Single-pass laser separation of 8 mm thick glass with a millijoule picosecond pulsed Gaussian–Bessel beam. Appl. Phys. A Mater. Sci. Process. **125**, 332 (2019)
144. M. Jenne et al., Multi pulse pump-probe diagnostics for development of advanced transparent materials processing. J. Laser Micro Nanoeng. **13**, 273–279 (2018)
145. M. Jenne et al., Pump-probe microscopy of tailored ultrashort laser pulses for glass separation processes, in *Laser-based Micro- and Nanoprocessing XIII*, vol. 10906, ed. by U. Klotzbach, A. Watanabe, R. Kling (International Society for Optics and Photonics (SPIE), 2019), pp. 219–225
146. T. Liu, H. Wei, J. Wu, J. Lu, Y. Zhang, Modulation of crack formation inside single-crystal sapphire using ultrafast laser Bessel beams. Opt. Laser Technol. **136**, 106778 (2021)
147. R. Meyer et al., Single-shot ultrafast laser processing of high-aspect-ratio nanochannels using elliptical Bessel beams. Optics Letters **42**, 4307 (2017)
148. D. Flamm et al., Generalized non-diffracting beams for ultrafast materials processing. in *Frontiers in Ultrafast Optics: Biomedical, Scientific, and Industrial Applications XX*, vol. 11270, ed. by P.R. Herman, M. Meunier, R. Osellame (International Society for Optics and Photonics (SPIE), 2020), pp. 68–75
149. M. Jenne et al., Facilitated glass separation by asymmetric Bessel-like beams. Optics Express **28**, 6552 (2020)
150. J. Dudutis, R. Stonys, G. Račiukaitis, P. Gečys, Aberration-controlled Bessel beam processing of glass. Optics Express **26**, 3627 (2018)
151. J. Dudutis, R. Stonys, G. Račiukaitis, P. Gečys, Glass dicing with elliptical Bessel beam. Opt. Laser Technol. **111**, 331–337 (2019)
152. R. Meyer, R. Giust, M. Jacquot, J.M. Dudley, F. Courvoisier, Submicron-quality cleaving of glass with elliptical ultrafast Bessel beams. Appl. Phys. Lett. **111**, 231108 (2017)
153. R. Beuton et al., Thermo-elasto-plastic simulations of femtosecond laser-induced multiple-cavity in fused silica. Appl. Phys. A Mater. Sci. Process. **124**, 324 (2018)
154. M. Jenne et al., High-quality tailored-edge cleaving using aberration-corrected Bessel-like beams. Optics Letters **43**, 3164 (2018)
155. D. Flamm et al., Structured light for ultrafast laser micro- and nanoprocessing. Optical Engineering **60**, 025105 (2021)
156. G.A. Siviloglou, D.N. Christodoulides, Accelerating finite energy Airy beams. Optics Letters **32**, 979 (2007)
157. P. Polynkin, M. Kolesik, J.V. Moloney, G.A. Siviloglou, D.N. Christodoulides, Curved plasma channel generation using ultraintense Airy beams. Science **324**, 229–232 (2009-04)
158. M. Clerici et al., Laser-assisted guiding of electric discharges around objects. Science Advances **1**, e1400111 (2015)
159. S. Vo, K. Fuerschbach, K.P. Thompson, M.A. Alonso, J.P. Rolland, Airy beams: a geometric optics perspective. J. Opt. Soc. Am. A **27**, 2574 (2010)
160. E. Greenfield, M. Segev, W. Walasik, O. Raz, Accelerating light beams along arbitrary convex trajectories. Phys. Rev. Lett. **106**, 213902 (2011)

161. L. Froehly et al., Arbitrary accelerating micron-scale caustic beams in two and three dimensions. Optics Express **19**, 16455 (2011)
162. F. Courvoisier et al., Sending femtosecond pulses in circles: highly nonparaxial accelerating beams. Optics Letters **37**, 1736 (2012)
163. A. Mathis et al., Arbitrary nonparaxial accelerating periodic beams and spherical shaping of light. Optics Letters **38**, 2218 (2013)
164. M.A. Alonso, M.A. Bandres, Generation of nonparaxial accelerating fields through mirrors. i: Two dimensions. Optics Express **22**, 7124–7132 (2014)
165. A. Mathis et al., Direct machining of curved trenches in silicon with femtosecond accelerating beams. JEOS:RP **8**, 13019 (2013)
166. D. Sohr, J.U. Thomas, S. Skupin, Shaping convex edges in borosilicate glass by single pass perforation with an Airy beam. Optics Letters **46**, 2529 (2021)
167. D. Flamm et al., Protecting the edge: Ultrafast laser modified c-shaped glass edges. J. Laser Appl. **34**, 012014 (2022)
168. V. Jukna et al., Filamentation with nonlinear Bessel vortices. Optics Express **22**, 25410 (2014)
169. C. Xie et al., Tubular filamentation for laser material processing. Scientific Reports **5**, 8914 (2015)
170. W. Cheng, P. Polynkin, Micromachining of borosilicate glass surfaces using femtosecond higher-order Bessel beams. J. Opt. Soc. Am. B **31**, C48 (2014)
171. O. Jedrkiewicz, S. Bonanomi, M. Selva, P.D. Trapani, Experimental investigation of high aspect ratio tubular microstructuring of glass by means of picosecond Bessel vortices. Appl. Phys. A Mater. Sci. Process. **120**, 385–391 (2015)
172. J., Baltrukonis, O. Ulčinas, S. Orlov, V. Jukna, Void and micro-crack generation in transparent materials with high-energy first-order vector Bessel beam. J. Opt. Soc. Am. B **37**, 2121 (2020)
173. E. Nacius et al., Spatially displaced and superposed Bessel beams for transparent material laser micro-processing. J. Opt. Soc. Am. B (2021)
174. P. Šlevas, S. Orlov, E. Nacius, O. Ulčinas, Azimuthally modulated axicon vortical beams for laser microprocessing. Optics Communications **505**, 127509 (2022)
175. S. Orlov, A. Juršenas, E. Nacius, Optical Bessel-like beams with engineered axial phase and intensity distribution. J. Laser Micro Nanoeng. **13**, 244–248 (2018)
176. X. Yu, C.A. Trallero-Herrero, S. Lei, Materials processing with superposed Bessel beams. Appl. Surf. Sci. **360**, 833–839 (2016)
177. A. Zannotti, C. Denz, M.A. Alonso, M.R. Dennis, Shaping caustics into propagation-invariant light. Nature Communications **11**, Article number: 3597 (2020)
178. T. Dietz et al., Ultrafast thin-disk multi-pass amplifier system providing 19 kW of average output power and pulse energies in the 10 mJ range at 1 ps of pulse duration for glass-cleaving applications. Optics Express **28**, 11415 (2020)
179. A. Vailionis et al., Evidence of superdense aluminium synthesized by ultrafast microexplosion. Nature Communications **2**, Article number: 445 (2011)

Chapter 17
Controlled Nanostructuring of Transparent Matter with Temporal Airy Pulses

**Thomas Winkler, Bastian Zielinski, Cristian Sarpe, Elena R. Ciobotea,
Arne Senftleben, and Thomas Baumert**

Abstract Ultrashort near-infrared femtosecond laser pulses have become the tool of choice for high-precision processing of transparent ultrawide bandgap materials, ranging from material ablation, amorphization, waveguide writing to optical data storage. The processing precision with ultrashort laser pulses is fundamentally limited in the lateral direction by diffraction, while self-absorption and self-reflection are limiting the achievable depth. In this chapter, we present one of the possible pathways to overcome these limits by utilizing temporal pulse-shaping technology. In the following, we review and discuss the main light-matter interaction mechanisms, multiphoton and avalanche excitation, and how ultrashort and temporally shaped femtosecond laser pulses address them differently, allowing the control over the spatial carrier distribution and the subsequent material processing. We demonstrate the potential of temporal pulse shaping as a tool for controlled nanostructuring below the typical limits by discussing our in situ and postmortem experimental and numerical studies on the spatial distribution of laser excitation in water, high-aspect-ratio structuring of fused silica, and the optoporation of cells.

Keywords Laser material processing · Femtosecond spectroscopy · Dielectrics · Fused silica · Sapphire · Nanostructuring · Temporal pulse shaping · Cell poration · Biophysics

---

T. Winkler (✉)
Department of Physics and Astronomy, Aarhus University, Aarhus C, Denmark
e-mail: winkler@phys.au.dk

B. Zielinski · C. Sarpe · E. R. Ciobotea · A. Senftleben · T. Baumert
Institute of Physics and CINSaT, University of Kassel, Kassel, Germany

© The Author(s), under exclusive license to Springer Nature Switzerland AG 2023
R. Stoian, J. Bonse (eds.), *Ultrafast Laser Nanostructuring*, Springer Series
in Optical Sciences 239, https://doi.org/10.1007/978-3-031-14752-4_17

1 Introduction to Nanostructuring of Transparent Matter with Temporally Adapted Pulses

Material processing based on ultrashort laser pulses in the near infrared has become a well-established field that has emerged over the last decades [1–3] and enables key technologies for a variety of applications ranging from micro- and nano processing of dielectric materials for photonics to medical and biological research. Based on the precision of laser ablation due to a strongly reduced heat-affected zone that is unattainable by other technologies, femtosecond laser processing remains the tool of choice. In recent years, the limits of the processing precision have experienced significant shifts by temporal, spatial, and combined pulse-shaping techniques, as demonstrated in Chaps. 8, 16, 28, and 33.

In contrast to spatial pulse-shaping techniques, which – as the name suggests – influence the ablation characteristics by varying the incident fluence/intensity distribution (e.g., by using non-diffracting Bessel beams [4]), temporal pulse shaping addresses the interplay of different excitation mechanisms in transparent matter to manipulate and control the ablation characteristics such as the removal rate or enabling sub-diffraction-limited ablation, while maintaining the classical Gaussian spatial beam profile and propagation properties. Over the years, temporal pulse shaping has developed from straightforward Michelson interferometer-based double pulses with variable inter-pulse delay (e.g., [5–7]) or simple stretching/chirping of pulses using gratings or prisms (e.g., [8, 9]) to the application of complex temporal and polarization forms created by liquid-crystal display (LCD)-based pulse shapers (see [10–13] and references therein). These techniques address the manipulation of the light-matter interaction on relatively short timescales and thus influence the initial step of electron plasma formation. Similarly, the creation of bursts of closely spaced pulses (nanoseconds) at high repetition rates, commonly referred to as "burst mode," has enabled another pathway of processing through addressing the interplay between excitation and heating with a high throughput at relatively low costs [14–17].

In this chapter, we will demonstrate an approach to control the precision of laser processing of transparent materials, temporally asymmetric-shaped laser pulses, that is, *temporal Airy pulses* (TAP).

In the subsequent sections, we will discuss the current understanding about why asymmetric-shaped laser pulses are a perfect tool for precision processing of transparent matter. Measuring and modeling how these laser pulses interact and address the different interaction mechanisms at play in water, sapphire, and fused silica lays the foundation of our understanding which in turn enables sophisticated applications, exemplified by our studies on single-cell optoporation.

2 Fundamentals of Energy Deposition by Temporally Shaped Femtosecond Laser Pulses into Dielectrics

In this section, we discuss the fundamental light-matter interaction mechanisms that allow for the excitation of carriers in ultrawide bandgap dielectrics by near-infrared femtosecond laser pulses, being the first step in every ablation process, strong field and avalanche excitation [18]. Subsequent, we discuss spatially resolved real-time measurements of the excitation of water by ultrashort femtosecond and temporal Airy pulses and compare the experimental results with numerical simulations, demonstrating the unique spatial carrier distribution that can be achieved by temporal pulse shaping.

2.1 Seed and Heat Mechanism by Strong Field and Avalanche Excitation

To enable the processing of transparent materials with femtosecond laser pulses, a sufficient amount of energy needs to be deposited by a laser pulse, causing permanent changes to the material, such as refractive index modification [19–21], amorphization of crystalline material [22, 23], or the permanent removal of such (i.e., ablation) [24, 25]. Typically, near-infrared femtosecond laser pulses of wavelengths around 800 nm are used for processing purposes. Consequentially, the photon energy of only 1.5 eV is insufficient to simply excite valence band electrons into the conduction band across the bandgap of usually around 6–12 eV, depending on the dielectric material. However, sufficiently high intensities of the laser pulse allow for the simultaneous absorption of multiple photons by valence band electrons to be promoted into the conduction band, naming it multiphoton excitation [26]. While initially the number of photons required for the multiphoton process is simply given by the ratio of the bandgap energy to the photon energy, for increasing intensity of the pump pulse, the quiver energy of the electrons increases the apparent bandgap energy of the material (i.e., the ponderomotive energy shift) [18, 26]. Thus, the multiphoton process can change the order of nonlinearity during the temporal profile of an intense laser pulse. At an even higher intensity, the chances of tunnel excitation/ionization increase substantially [26]. Here, valence band electrons tunnel across the gap due to the tilted potential following the strong electric field of the laser pulse.

The electrons promoted to the conduction band via strong-field excitation act as a seed for a secondary excitation channel, avalanche excitation [18]. The quasi-free electrons in the conduction band can absorb single photons from the near-infrared laser pulse via inverse bremsstrahlung absorption, gaining kinetic energy. Once the kinetic energy of the conduction band electron exceeds the bandgap energy of the material, another valence band electron can be promoted to the conduction band via impact excitation, leaving two electrons close to the bottom of the conduction band, ready to repeat the process. Thus, impact excitation can lead to a self-reenforcing multiplication of the conduction band electron density, giving the process its well-known name.

For a more detailed review of the excitation pathways in dielectric materials, we refer to Balling and Schou [18] and the references therein.

The change in the electron density as a function of time $N_e(t)$ is typically described by a rate equation in the form of [18]:

$$\frac{\partial N_e(t)}{\partial t} = \eta_{\mathrm{SFE}}(t) + \eta_{\mathrm{AE}}(t) \tag{17.1}$$

where the first part describes the rate of carrier excitation by strong-field excitation (SFE) whereas the second term describes the contribution by avalanche excitation.

While there exists a manifold of theoretical descriptions of both contributions, the Keldysh formalism [26, 27] and the multiple rate equation model [28, 29] are currently the most commonly used models for strong-field and avalanche excitation, respectively. However, recently, a novel and powerful approach to model the avalanche excitation process – a dynamical rate equation model – was introduced by Déziel et al. [30].

In order to draw a simple picture, we limit ourselves to a phenomenological description of the processes via the following rate equation:

$$\frac{\partial N_e(t)}{\partial t} \propto \frac{N_{e\mathrm{Max}} - N_e}{N_{e\mathrm{Max}}} \left(\sigma_n I^n(t) + \alpha I(t) N_e(t)\right) \tag{17.2}$$

with σ_n, the n-th order multiphoton excitation coefficient and α, the avalanche excitation coefficient. $I(t)$ is the time-dependent intensity of the exciting laser pulse. As the excitation of free carriers will diminish the amount of available valence band electrons, a stagnation factor $N_e/N_{e\mathrm{Max}}$ – given as the ratio of current to maximum available electrons for excitation ($N_{e\mathrm{Max}}$) – is introduced.

The limits of Eq. (17.2) become immediately apparent, exemplified in the inability to capture changing orders of the multiphoton process due to the bandgap increase by ponderomotive energy shifts or by increasing probability of tunneling excitation. Another limitation of Eq. (17.2) is the description of avalanche excitation, as here the intensity interacts with the current electron density. However, after each free-carrier-absorption event, the electron must scatter for momentum conservation [18]. Thus, the actual impact excitation process is delayed with respect to the exiting laser pulse. While the proper description in keeping track of the how many conduction electrons have how much kinetic energy is well established by using a multiple or dynamical rate equation model as mentioned above, we make use of an approach first introduced by Vogel and coworkers [31]. By introducing a retardation time:

$$t_{\mathrm{ret}} = t - n' \cdot \tau \tag{17.3}$$

with n' the number of photons required to obtain sufficient energy for impact excitation, being approx. 1.5× the bandgap energy [32] and the time between scattering events τ (i.e., the electron scattering time), we rewrite Eq. (17.2) to be:

$$\frac{\partial N_e(t)}{\partial t} \propto \frac{N_{e\mathrm{Max}} - N_e}{N_{e\mathrm{Max}}} \left(\sigma_n I^n(t) + \alpha\ I(t)\ N_e\left(t_{\mathrm{ret}}\right)\right) \tag{17.4}$$

Thus, the light field at time t only creates avalanche excitation with conduction band electrons present at the time t_{ret}.

Although Eq. (17.4) is a strong simplification of the complex excitation processes, we will demonstrate in the subsequent sections that this description of the excitation in the moderate excitation regime can capture the physics involved in the interaction of temporally asymmetric-shaped femtosecond laser pulses. From Eq. (17.4) it already becomes clear that depending on the duration or the temporal shape of an incident exciting laser pulse multiphoton and avalanche excitation are addressed very differently.

This aspect can be best illustrated by comparing the time-dependent conduction band carrier density created by two temporal Airy pulse of opposite temporal shape, as they have the same energy and peak intensity – thus allowing for a fair comparison.

While there exist many ways to temporally shape laser pulses, spectral phase modulation remains the only way to precisely shape the temporal profile of ultrashort laser pulses [33]. Here, different spectral components of femtosecond laser pulse are delayed with respect to each other, that is, by applying a spectral phase modulation. Typically described in a Taylor expansion around the central angular frequency of the laser pulse, the second order phase term will lead to a group delay dispersion (GDD), that is, a classical chirp of the pulse, while the third order term ("third order dispersion") causes the creation of asymmetric temporal Airy pulses, whose envelope is described by an Airy function with an exponential decay [34]. A complete mathematical description of spectral pulse shaping with an in-depth discussion can be found in [35].

Figure 17.1 shows the intensity profile of two temporal Airy pulses created with a third-order dispersion term of $+6 \times 10^5$ fs^3 (red line) and -6×10^5 fs^3 (blue line). The asymmetric pulses consist of a main pulse with a subsequent train of pulses with ever decreasing intensity and sub-pulse separation. The sign of the phase simply flips the temporal profile, making the temporal Airy pulse with a negative phase start with the least intense sub-pulse.

Figure 17.1 also demonstrates how these two temporal Airy pulses with equal pulse energy and peak intensities will create a significantly different carrier density in a dielectric material. We calculated the time-dependent conduction band electron density using Eq. (17.4) with details given in [36].

Using the positive TAP pulse, we observe a sharp increase in carrier density at the beginning of the pulse which is mainly produced by SFE (red dashed labeled $N_e{}^+$(SFE) in Fig. 17.1) and that each of the pulses of the train further increases

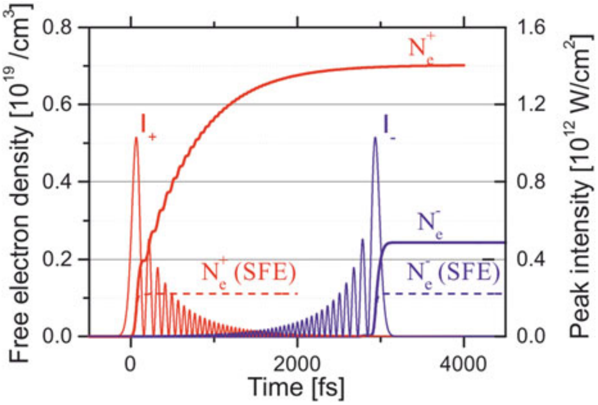

Fig. 17.1 Calculated time-dependent conduction band electron density N_e taking multiphoton and avalanche ionization into account (solid lines) for positive (red curves, index +) and negative (blue curves, index −) TAP pulses with a third-order dispersion coefficient of ±600000 fs^3 (applied to an initial pulse with 30 fs FWHM). The contribution by pure multiphoton ionization is indicated as well (dashed lines $N_e^{\pm}$ (SFE)). The corresponding transient intensities of the modulated pulses are also presented (I_+, I_-). The curves for negative shaped pulses are offset by 3 ps in time for better visualization. (Reproduced from Sarpe et al. [36]. © IOP Publishing and Deutsche Physikalische Gesellschaft. Reproduced by permission of IOP Publishing. All rights reserved)

the carrier density by AI reaching the maximum carrier density at the end of the pulse. The negative TAP pulse, on the other hand, creates a significantly smaller final carrier density, despite the equal energy and peak intensity. It does, however, create the same number of free carriers via SFE (blue dashed line $N_e{}^{-}$(SFE)), but only at the very end of the main pulse, meaning only a small fraction of avalanche excitation can take place. In this example, the train of smaller pulses of the negative TAP is not absorbed at all, and the final sub-pulse acts similar to an ultrashort laser pulse.

The slow rise in carrier density over the course of the temporal profile of the positive TAP pulse delivers significant advantages over Gaussian-shape ultrashort laser pulses where the carrier density rises very fast at the much higher peak intensities. We will explore and discuss the superiority of positive TAP pulses in the excitation and ablation of transparent laser pulses based in the subsequent chapters.

2.2 Real-Time Spatially Resolved Measurements of Energy Deposition in Water

With the excitation of any dielectric material, that is, the promotion of valence band electrons to the conduction band, a change in the optical properties is induced. While usually being transparent to visible light due to a large bandgap energy, the creation of a high charge carrier density will provide the dielectric material with metallic properties. It is also the first step in the processing of materials, as the charge carriers are the mediators in the energy transfer from the laser pulse to the material that can cause permanent changes, for example, the formation of defects, ablation, or bubble formation (cavitation) in the case of water. Consequentially, the density of the charge carriers and their spatial distribution in the interaction area of the laser pulse are decisive for the result of any modification process.

2.2.1 Optical Properties of Excited Dielectrics

To create the fundamental understanding of laser energy deposition with TAP pulses and to directly observe the impact of temporal pulse shaping on the spatial properties of the laser excitation, we performed time and spatially resolved pump-probe measurement on liquid water. The choice of liquid water as the sample system is based on three aspects: First, water can be treated as an amorphous semiconductor and shares the main excitation pathways and optical properties with its solid cousins, for example, sapphire; second, using liquid water makes it easy to have an unlimited sample supply and to provide a fresh sample volume for each laser pulse; lastly, studying the excitation of water is of high interest for any biological or medical related applications, as we will discuss in Sect. 3.

The optical properties of an excited dielectric material are typically well captured by the Drude model, providing the complex dielectric function for a material with a magnetic permeability of 1 [37]:

$$\varepsilon\left(\omega\right) = \varepsilon_b - \frac{\omega_{\mathrm{pl}}^2}{\omega^2 + i\omega\tau^{-1}}, \tag{17.5}$$

where ε_b is the dielectric constant of the unexcited material, where the second part describes the contribution by the quasi-free electrons with τ the electron scattering time, ω the angular frequency of the incident light field, and ω_{pl} the plasma frequency, given by [37]:

$$\omega_{\mathrm{pl}} = \frac{N_e e^2}{m_e \varepsilon_0}, \tag{17.6}$$

where e is the elementary charge, m_e the conduction band electron mass, and ε_0 the vacuum permittivity.

It is important to note that the scattering time of the conduction electrons is also dependent on the carrier density, as a higher carrier density will decrease the time between scattering events. In general, the scattering time τ (inverse of the scattering rate γ) is expressed in terms of a constant electron-phonon (*e*–*p*) term and a carrier density or electron temperature-dependent carrier-carrier scattering term (*c*–*c*) [18]:

$$\tau(N) = \frac{1}{\gamma(N)} = \frac{1}{\gamma_{e-p}} + \frac{1}{\gamma_{c-c}(N)} \tag{17.7}$$

In case a large fraction of valence band electrons is excited, their contribution to the dielectric background of the unexcited material vanishes, and as such, an alternative description for the dielectric "constant" (ε_b) must be incorporated into the dielectric function (Eq. 17.5). Guizard et al. suggested a description derived from the Clausius-Mossotti equation [38].

While the complex dielectric function can be accessed, for example, by time-resolved ellipsometry measurements, as demonstrated, for example, by Møller et al. [39], our experiments, discussed below are only able to access the real and imaginary part of the complex refractive index.

The complex dielectric function and the complex refractive index, $\tilde{n}$, are related via [37]:

$$\sqrt{\varepsilon} = \tilde{n} = n + \mathrm{i}k \tag{17.8}$$

With n the real, and k, the imaginary part of the complex refractive index.

From Eqs. (17.5) and (17.8), it becomes clear that the creation of a high carrier density will lead to a decrease in the real part of the refractive index, while the imaginary part, linked to the absorption coefficient $\alpha = 2k\omega/c$, increases.

2.2.2 Measuring Optical Properties of Laser-Excited Dielectrics: Imaging Spectral Interferometry

To measure changes of the dielectric function and the refractive index modifications of an excited dielectric material, optical pump-probe spectroscopy has proven to be an excellent tool. While straightforward time-resolved transmission/absorption and reflection measurements can be used to track the overall charge carrier dynamics, information about the real part of the refractive index cannot be obtained. In addition, these techniques often lack high sensitivities for excitation densities far below the ablation threshold.

Interferometric measurement techniques, on the other hand, can provide complete information about changing optical properties, allowing the measurement of both the real part of the complex absorption index and the imaginary part at the same time.

In spatial interferometry [40], samples are placed in one arm of a Mach-Zehnder interferometer and are excited by a strong ultrashort laser pulse. The interferometric images are then produced by the interference of the probe pulse passing through the dielectric sample with a reference pulse propagating in the other arm of the interferometer. The phase and amplitude obtained by direct evaluation or via Fourier analysis of the interference picture provide the complex refractive index of the excited dielectric sample. While spatial interferometry has the ability to monitor the excitation dynamics on long timescales due to the possibility of a very long arm length in the interferometer, the experimental setup is complicated and sensitive to the ambient conditions of the experiment, like air turbulences, temperature fluctuations, or mechanical vibrations.

Spectral interferometry [41–43] is, on the other hand, a technique which combines the advantages of spatial interferometry but with a much reduced experimental effort. Here, probe and reference pulses co-propagate through a dielectric sample, only separated by a fixed time delay. The excitation by the pump pulse is placed after the reference but before the probe pulse. Typically, probe and reference pulses are created by using a Michelson interferometer-based arrangement [44, 45], but we will present a simpler and more stable common-path setup below. After interaction with the excited sample, the pulses are sent to an imaging spectrometer, where a frequency-domain interference is produced. Even though the pulses are well separated in time, spatially splitting the spectrum into separate spectral components detected by the spectrometer (-pixel) leads to interference because the temporal length of an ultrashort laser pulse is defined by its bandwidth. Each pixel detects just a small partial bandwidth, and therefore the individual pulses are stretched enough to interfere. The shift of the interference fringe mini/maxima and the change of their contrast, compared to interference without excitation, give direct access to the changed real and imaginary part of the refractive index the probe pulse experiences after excitation, as we will discuss further below. One limitation of spectral interferometry is usually the temporal window available for a direct measurement of the changed optical properties. Unfortunately, a large temporal separation between reference and probe pulse requires a high-resolution spectrometer to allow the interference of both pulses within the spectrometer. While the often used semi-common-path arrangements of a Michelson-type interferometer for spectral interferometry brings advantages compared to the Mach-Zehnder type, mechanical stability remains one of the downsides of both approaches.

As we want to study the effects of temporally asymmetric-shaped laser pulses, which extend to a few picoseconds as seen in Fig. 17.1, we utilized a measurement scheme [36, 46–48] that allows a wide measurement window of 6.5 ps and excellent spectral resolution. At the same time, our approach has no need for a physical interferometry setup.

Figure 17.2 shows the principal setup of our ultra-stable common-path imaging spectral interference setup, as presented, and discussed in more detail in [36, 47, 48]. We utilize 800 nm, 30 fs femtosecond laser pulses provided by a Femtolasers Femtopower Pro Amplifier System which are split into a pump and probe (and reference) arm. In the probe arm, which can be delayed with respect to the pump arm using a high-precision motorized delay stage, we frequency double the fundamental beam in a β-BBO crystal and pre-compress it in a prism compressor, allowing for close to bandwidth-limited pulses in the interaction area.

Afterwards, we split the 400 nm beam into a pair of pulses in a 12.5 mm thick birefringent α-BBO crystal (in Fig. 17.2 α-BBO 1). The pulses have orthogonal

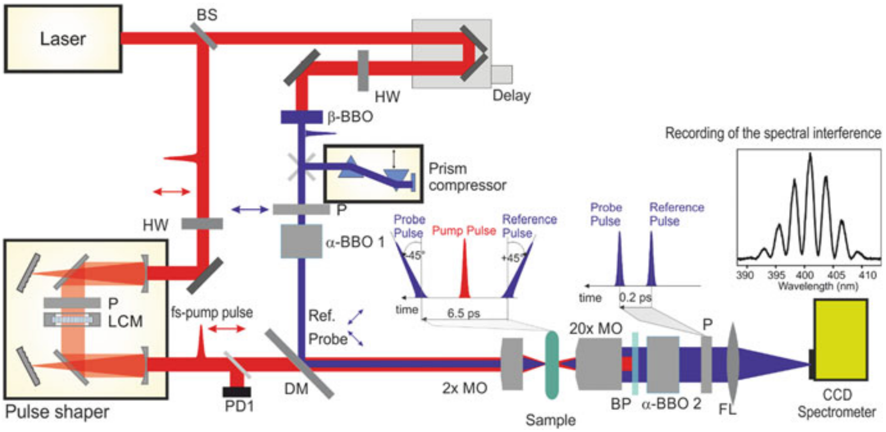
Laser
BS
HW
Delay
β-BBO
Prism
compressor
Recording of the spectral interference
HW
P
α-BBO 1
Probe Pulse
Pump Pulse
Reference Pulse
-45°
+45°
time
6.5 ps
Probe Pulse
Reference Pulse
time
0.2 ps
390 395 400 405 410
Wavelength (nm)
P
LCM
fs-pump pulse
Ref.
Probe
20x MO
P
Pulse shaper
PD1
DM
2x MO
Sample
BP
α-BBO 2
FL
CCD
Spectrometer

Fig. 17.2 Experimental setup – description in the text: BS, beam splitter. HW, half waveplate; P, polarizer; LCM, liquid-crystal modulator. DM, dichroic mirror; MO, microscope objective; BP, Bandpass filter; FL, focusing lens. A time-delayed pulse is frequency doubled to 400 nm and passes through a birefringent crystal α-BBO 1. This one creates a pair of orthogonally polarized pulses with a separation of 6.5 ps. The reference and probe pulses propagate through the interaction area together with the pump and probe, the changes in the optical properties. A second birefringent crystal α-BBO 2 decreases the temporal separation between the blue pulses to 0.2 ps. After passing through a polarizer the frequency-domain interference pattern is recorded – sketched above the CCD spectrometer. (Adapted from Winkler et al. [47] with permission from Elsevier)

polarization to each other and ±45° relative to the pump pulse. The resulting reference and probe pulse are separated by a temporal distance of 6.5 ps with a FWHM pulse duration of approx. 40 fs, respectively. Both pulses are focused together with the temporally shaped fundamental 800 nm pump pulse of 30 fs FWHM onto the surface of a free-flowing water jet, using a long working distance apochromatic microscope objective (Mitutoyo M Plan APO 2×). The jet is produced by pumping double-deionized water through a polished stainless steel nozzle and has an average thickness of 121.3 µm with a variation of ±0.5 µm, obtained by several measurements at the same position using the spectral interference signal from the internally reflected pulse. A sufficient flow rate of the water allows for a fresh volume of water each time the laser is fired (1 kHz repetition rate).

The pump arm of the setup contains a liquid-crystal modulator-based home-build pulse shaper [33], which we use to apply the strong third-order dispersion to create the temporal Airy pulses, as described in Sect. 2.1. At the same time, we make use of a thin-film polarizer in the pulse shaper and a motor-controlled half-wave plate to adjust the pump pulse energy. Afterwards, pump and probe beam are recombined by a dichroic beam splitter and focused onto the water jet.

After the pump pulse excited the water jet, it is removed from the beamline by a bandpass filter (40 nm FWHM, centered at 400 nm), inhibiting it from entering into an infinity-corrected long-working-distance apochromatic microscope objective (Mitutoyo M Plan APO 20×). Focused on the front surface of the water jet, this objective collects reference and probe pulse.

As the temporal separation of 6.5 ps is too large to allow the observation of spectral interference in our spectrometer, we utilize a second alpha-BBO crystal to reduce the temporal separation of the 400 nm pulses. By orienting the 12.2 mm thick crystal such that reference and probe are now propagating through the opposite axis compared to the first crystal, we reduce the temporal separation to only 200 fs. Using a polarizer, set to a vertical polarization, we allow for the detection of the interference pattern (see Fig. 17.2). Afterwards, both pulses are imaged onto the entrance slit of an imaging spectrometer (Princeton Instruments 320) using a 400 mm focusing lens, providing an overall magnification of the imaging system of 40×. Thanks to the cooled 2D CCD array of the spectrometer, the spectral information can be detected simultaneously along a line through the beam profile. Here, 128 pixels are available for the spatial and 1024 pixels for the spectral detection. This technique allows to record the spectral interference signal as a function of the radial position across the excitation region. A fraction of the reference probe beam is imaged onto a CCD camera, which allows for a high precision in overlapping pump and probe beam on the surface of the water jet. It is important to notice that the beam sizes of pump and probe pulse were chosen such that the Rayleigh range of both pulses exceeded the water jet's thickness by more than one order of magnitude, ensuring a homogeneous illumination of the jet.

In the previous section, we described the impact of the excitation of electrons into the conduction band on the complex dielectric function and consequentially the real and imaginary part of the refractive index. Using our time-resolved spectral interferometry setup, we probe the difference of the refractive indices between excited and unexcited state [36, 47]:

$$\Delta\tilde{n}(N) = \tilde{n}(N) - \tilde{n}\,(N = 0) = -\frac{1}{2n_0}\left(\frac{\omega_{pl}}{\omega}\right)^2 \frac{1}{1-(i\omega\tau)^{-1}} \tag{17.9}$$

with $n_0 = \sqrt{\varepsilon_B}$.

It is important to note that the probe pulse measures the accumulated refractive index change throughout the water jet, thus being unable to provide a spatial resolution in depth. Consequentially could different distributions of refractive index change lead to the same overall refractive index change, as discussed in detail below.

The two main observations from the interference pattern mentioned above, fringe shift and fringe contrast, relate to the real and complex part as follows:

The Phase Shift

The lowered real part of the complex refractive index (due to the excitation of carriers) leads to a higher phase velocity of the probe pulse in the water jet which results in a decreased temporal separation between the probe and reference pulse. This reduced temporal separation is measured as a phase shift $\Delta\Phi$ in the spectral interference pattern (i.e., a shift of the position of the interference minima/maxima) and is highly dependent on the carrier density and the thickness of the sample L [36, 47]:

$$\Delta\Phi(N) = \frac{2\pi}{\lambda}\int_{z=0}^{L} \mathrm{Re}\left(\Delta\widetilde{n}(N)\right) dz \tag{17.10}$$

The Optical Density

The increased absorption by free carriers leads to the absorption of the probe pulse (a reduction in interference contrast) and is typically given as the optical density via the relation [36, 47]:

$$\mathrm{OD} = -\ln T = \frac{4\pi}{\lambda}\int_{z=0}^{L} \mathrm{Im}\left(\Delta\widetilde{n}(N)\right) dz \tag{17.11}$$

where T is the transmission.

While the reflectivity at the surface of the water jet is also impacted by the change in the refractive index, at excitation densities well below the ablation threshold, its impact onto the measured optical density/absorption can be neglected, and absorption inside the sample dominates the change in transmission.

Although both values, phase shift and optical density, can be extracted right away from the interference pattern, as mentioned above, the Fourier-transform analysis provides a significant improvement allowing for a much more sensitive and reliable evaluation of the abovementioned properties. A detailed description of the data evaluation can be found in [36, 47, 48].

2.2.3 Spatially Resolved Measurement of Laser Excitation in Water with Ultrashort and Temporal Airy Pulses

To demonstrate the peculiarities of laser excitation with temporal Airy pulses, we compare the excitation created by a 30 fs 800 nm bandwidth-limited laser pulse and a positive temporal Airy pulse. From the temporal profile of both pulse shapes (a symmetrical Gaussian beam with a FWHM of 30 fs and the positive TAP pulse shown in Fig. 17.1), it becomes apparent that the temporal evolution of the electron density created by each of the pulses is very different. Unfortunately, is it not possible to fully resolve the initial temporal change of the refractive index (increase absorption and decrease of the phase shift) of both pulse shapes precisely, as the measured signal is overlapped by the optical Kerr effect [36, 48]: This pump-pulse intensity-dependent increase in the real part of the refractive index will hide the actual phase shift and optical density evolutions until the pump pulse has passed. Thus, we will discuss the results obtained shortly after the pump pulse

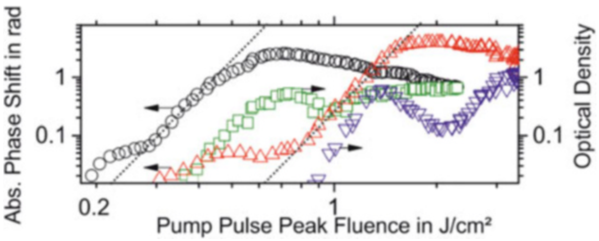

Fig. 17.3 Measured pump-pulse fluence-dependent excitation of liquid water: Black circles, absolute phase shift for BWL pulses; red up pointed triangles, absolute phase shift for TAP pulses; green squares, optical density for BWL pulses; purple down pointing triangles, optical density for TAP pulses. The time delays at which the measurements were taken are 1.5 ps for the BWL and 3 ps for the TAP pulses, respectively The black dotted lines indicate a power- law scaling of 6. Please note that the measured phase shift is negative. (Reproduced from Winkler et al. [47] with permission from Elsevier)

has passed. This allows to measure the optical properties before significant carrier recombination and diffusion, which is typically set on a 10s to 100s of picosecond timescale, as measured in our earlier work [36]. The results discussed below were obtained in a close collaboration with the research group of Peter Balling at Aarhus University.

As a first step in understanding the excitation of water, we will concentrate on the pump-pulse fluence dependence thus the dependence on the number of conduction band electrons within the sample. Figure 17.3 shows the locally measured phase shift and the optical density as a function of the pump pulse peak fluence for both pulse shapes. The first observation made is that the detection of a change in the phase shift (black circles, red triangles) happens at a significantly lower excitation fluence compared to the measured optical density (green squares, blue down pointing triangles). This is due to the much higher sensitivity of the measurement to the real part of the dielectric function compared to the imaginary part (absorption).

In addition, we make two major observations:

1. *The threshold for excitation and the subsequent change of phase shift and optical density is significantly higher for the TAP pulse compared to the BWL.*

The black dotted lines in Fig. 17.3 indicate a power-law scaling with the order of 6, perfectly fitting a multiphoton process involving six 800 nm photons, with a photon energy of 1.55 eV, to promote electrons across the estimated bandgap energy of around 8.3–9.5 eV [49, 50]. The reason for the difference in the excitation thresholds can be found in the significantly different peak intensity of the two pulse shapes. The peak of the main pulse of the TAP pulse train has roughly only 1/6th of the intensity compared to the BWL pulse. Consequentially, the required fluence to initiate multiphoton excitation (as the seed for avalanche processes) is higher for the TAP pulse. This has been discussed in more detail in our previous work [36].

In addition, we observe a small increase in phase shift starting at very low excitation fluences and stagnating until the main excitation takes place (indicated by the black dotted line, which follows a power-law scaling of 6). This low stagnating signal is indicative for a lower-order excitation process from a low-density reservoir, such as solvated electrons [49, 51], which have caught large attention throughout recent years, and which added to the intense discussions about the bandgap energy of water [49–51]. However, it also becomes apparent that the density of carriers injected via this pathway are too low to initiate a subsequent excitation process via the avalanche process, hence the stagnation of the signal for increasing carrier density. We estimate the carrier density of the low-density reservoir to be 1.4×10^{18} cm^{-3} under the assumption of a constant electron density throughout the water jet (Eq. 17.10).

2. *The maximum change in phase shift and optical density is significantly higher for TAP compared to BWL pulses.*

To understand how the TAP pulse can – irrespectively of the peak fluence/excitation strength – create a much higher phase shift and optical density throughout the water jet, we will make use of our simplified rate equation model described in Sect. 2.1. To model the experimental observations, we calculate the excitation throughout the material for a Gaussian laser pulse in space and time, taking into account the absorption of the exciting pulse by multiphoton and free carrier excitation [47], as described in Sect. 2.1. Due to the large waist of the beam (approx. 24 μm), its Raileigh range is an order of magnitude larger than the thickness of the water jet, allowing to calculate the excitation for each radial component separately, strongly reducing the computational effort. Afterwards we calculate the accumulated phase shift and optical density by the probe pulse according to Eqs. (17.10) and (17.11).

Figure 17.4 shows the calculated carrier density distribution in the water jet for both the BWL and the TAP pulse as a function of the radial position at the surface (**a**) and as a function of depth at the center of the beam (**b**). While the depth-dependent distribution (**b**) caused by the BWL pulse (black curve) shows that with increasing depth the carrier density drastically decreases, the TAP pulse (grey dashed curve) shows a quite different distribution. Although the general behavior remains the same, for an equal carrier density at the surface, the electron density is much higher throughout the material causing a larger accumulated local phase shift.

The reason for this behavior can be found in the unique temporal profile of the TAP pulse, already discussed in Sect. 2. As the carrier density only slowly increases with time and is delayed due to peculiarities of the avalanche excitation process, the highest carrier density will overlap with the least intense parts of the pulse, allowing it to propagate deep into the material. The BWL on the other hand causes a rapid excitation of the large fraction of carriers directly at the surface of the water jet leading to a strong absorption of the pump pulse preventing it to propagate deep into the material. While a simply chirped pulse would certainly lead to similar results, it is important to notice that the pulse energy required would be significantly higher, as the first, low-intensity half of the pulse duration usually does not lead to an excitation (similar to the negative TAP, see Fig. 17.1) and only the peak part and subsequent rest of the pulse are absorbed. This aspect is further discussed in Sect. 3.

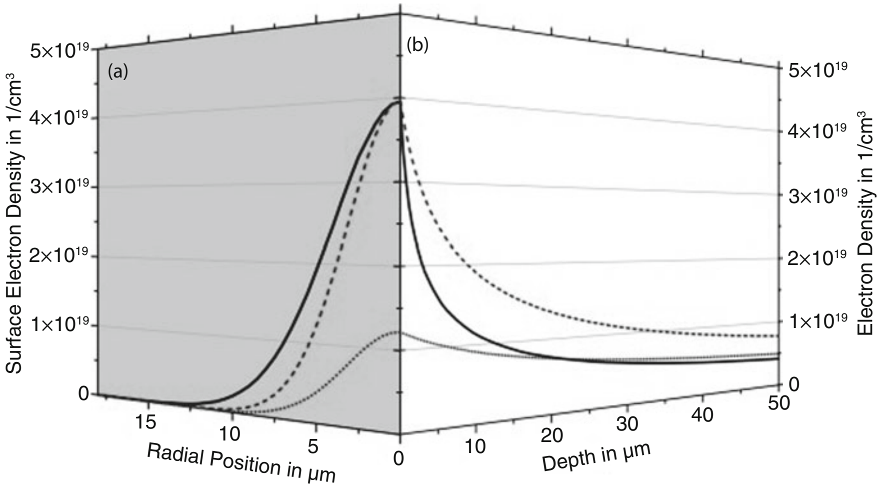

Fig. 17.4 Simulated radially and depth-dependent phase shift for BWL (black) and TAP (red) laser pulses: (**a**) radially dependent phase shift for, equal phase shift (compared to the BWL) at $r = 0$ µm (grey dotted line). Equal electron density at $r = 0$ µm (grey dashed line). (**b**) Depth-dependent conduction band electron density at the center of the laser pulse ($r = 0$ µm) for the same cases as in (**a**). Detailed information about the simulations are given in [47]. (Reproduced from Winkler et al. [47] with permission from Elsevier)

The dependence of the excitation on the local pump pulse fluence, discussed above, also heavily influence the radial distribution of the carrier density, as typically Gaussian beam profiles are used for laser excitation and material processing. Figure 17.4a shows the calculated radial dependence on the carrier density at the surface of the water jet using BWL (black line) and TAP (grey dashed line) pulses. While with increasing radial position (and thus lower local fluence), the surface carrier density strongly decreases for both pulse shapes (starting at the same value in the center), it decreases more quickly for the TAP pulse compared to the BWL pulse, strongly reducing the excited area by approx. a factor of 2.

To confirm that our simulations capture the influence of the temporal pulse shape on the spatial carrier distribution throughout the water jet, we compare it to the phase shift measured along the radius of the pump pulse using our imaging setup described above.

Figure 17.5b shows the radial distribution of the measured phase shift using the BWL (black circles) and TAP pulse (red triangles) and the corresponding simulations (black solid and red dashed lines) for the case of an equally strong carrier density at the surface in the center of the laser pulse. We observe an excellent agreement between simulation and experiment which proves the significantly larger phase shift in the center by the larger integrated carrier density of the TAP pulse. In addition, a narrower phase shift distribution for the latter is observed.

Furthermore, it is interesting to discuss the results where an equal phase shift by both pulses is obtained, as this can wrongly be identified as the case in which the

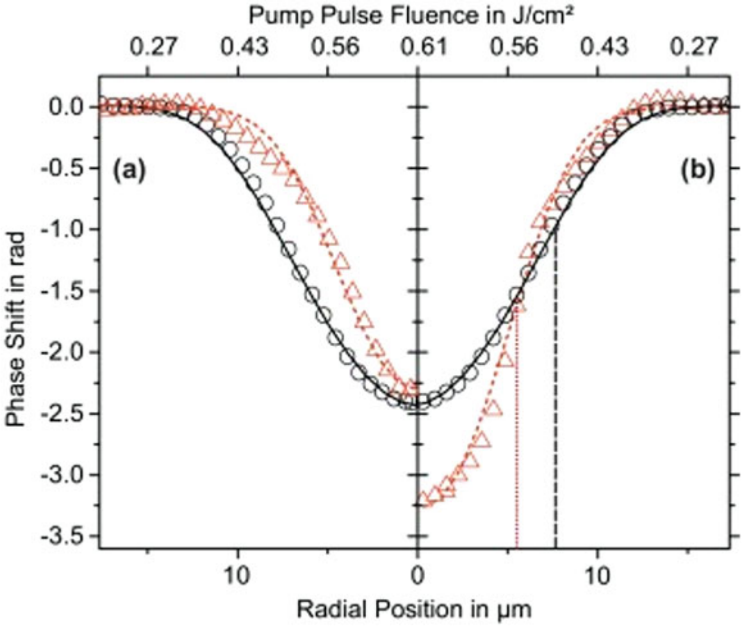

Fig. 17.5 Measured (symbols) and simulated (lines) radially dependent phase shift for BWL (black) and TAP (red) laser pulses: (**a**) equal measured phase shift at $r = 0$ μm for both pulse shapes. For the TAP the fluence is increased by a factor of 2.2. (**b**) Equal simulated electron density at the surface at $r = 0$ μm for both pulse shapes. The fluence for TAP is increased by a factor of 2.5. Black dashed and red dotted vertical lines indicate the radius at which the phase shift decreased to half of the minimum value. The simulation details can be found here [47]. (Reproduced with permission from Winkler et al. [47] with permission from Elsevier)

material is brought into the same excitation conditions. Here we had to choose an excitation fluence of the TAP pulse 2.2× higher compared to the BWL. The results are shown in Fig. 17.5a, and again, very good agreement between measurement and simulation for both pulse shapes are obtained, confirming that the simple model captures the interplay between multiphoton and avalanche excitation. From Fig. 17.4b (grey dotted line), we observe that the carrier densities at the surface leading to an equal measured phase shift in the center are four times lower than the density created by the BWL pulse. However, it can also be seen that the phase shift deep inside the water jet are actually higher for the TAP pulse compared to the BWL.

Overall, our spatially resolved measurements on water demonstrate that temporal Airy pulses advantageously make use of the heat and seed model, allowing the pulse to create a high carrier density deep into the material over a smaller area, causing a "needlelike" excitation profile in strong contrast to the excitation by the BWL that has a larger lateral but much smaller longitudinal extension thereby allowing material processing only close to the surface and with less spatial resolution than the TAP.

3 Proof of Principle: Nanostructuring of Solid Dielectrics at the Nanoscale with Temporal Airy Pulses

We have discussed the initial step in the processing of dielectric materials, the carrier excitation and the impact of temporal pulse shaping on its spatial properties. Here, we will demonstrate the long-lasting impact of the initial carrier distribution by discussing material processing experiments in which positive TAP pulses are able to create deeper and thinner ablation structures in sapphire and fused silica.

The results presented in the upcoming Sects. 3.1 and 3.2 were obtained in a close collaboration with the research groups of Javier Solis and Jan Siegel at the Spanish National Research Council, as well as with the group of Hartmuth Hillmer at the University of Kassel, respectively.

3.1 Postmortem Measurements of Laser Ablation in Sapphire

To link the carrier excitation distribution discussed in the last section to permanent material modifications, we performed single-shot laser processing experiments on crystalline sapphire [52]. Sapphire, a crystalline solid dielectric with a high bandgap (approx. 10 eV), shares the main excitation pathways with water and thus provides the perfect platform to demonstrate the possibilities of the TAP pulses and to link the initial carrier distribution to the final ablation profile. Using the same pulse-shaping approach as in our water experiments, BWL and TAP pulses are tightly focused onto the surface of a sapphire sample and the resulting hole structures are investigated postmortem via atomic force microscopy.

Figure 17.6 shows AFM images and profiles of hole structures obtained by a single BWL (at 89 nJ) and TAP (at 97 nJ). It can be seen that for the TAP pulse a smaller hole diameter with a larger depth compared to the BWL pulse is obtained, thus representing a similar profile to what has been obtained in the spectral interference measurements. Even if the pulse energy would be tuned for the BWL to create a smaller diameter to match the TAP hole surface diameter, the depth would reduce significantly as well, giving the TAP a unique ablation profile. These measurements demonstrate and confirm that the electronic excitation mechanisms observed in the real-time measurements in water are at play in the permanent material modification of solid dielectrics. Note that both processes occur on timescales separated by many orders of magnitude.

Overall are these observations very similar to experiments performed on another high-bandgap dielectric material, fused silica. While AFM measurements demonstrate that surface ablation can also be achieved one order below the diffraction limit [53], a look into the depth of the material reveals unique feature of utilizing temporal Airy pulses.

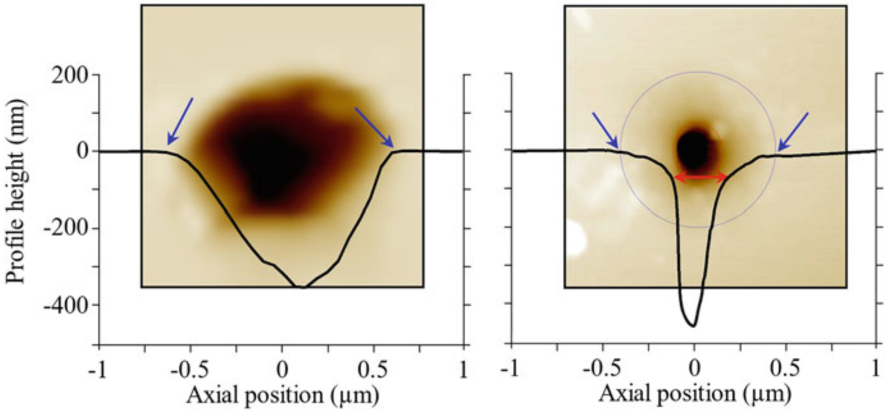

Fig. 17.6 AFM micrographs overlaid with depth cross sections (black line) of two craters produced using a BWL pulse at 89 nJ (left) and a positive TAP pulse at 97 nJ (right), both with a beam diameter of 1.4 μm. The arrows and dotted lines indicate the border of the different ablation regimes, evidenced as a slope change in the depth cross sections. (Adapted from Hernandez-Ruenda et al. [52], Copyright 2015 American Chemical Society)

3.2 High-Aspect Ratio Ablation Structures in Fused Silica

Another material well-suited for processing with temporal Airy pulses is fused silica. In contrast to water or sapphire, conduction band electrons are – shortly after excitation – quickly captured into self-trapped exciton states on a typical timescale of 100–200 fs [45, 48]. The self-trapped excitons, which are energetically localized in the middle of the bandgap, typically only contribute with a positive refractive index modification to the optical properties and do not absorb single photons in the visible or near-UV spectral range [54]. While the trapping of electrons has no or only little impact on the excitation profile and energy deposition into the material by ultrashort BWL laser pulses, the dynamics are heavily changed for the temporal Airy pulses as electrons are being trapped continuously during the interaction with the pulses. This is especially important, as trapped electrons can be excited back into the conduction band via multiphoton and avalanche excitation [34, 54].

As the required energy and thus the number of photons for promoting electrons from the trapping states to the conduction band is smaller (only 5.4 eV) compared to the main excitation channel from the valence to the conduction band (9 eV), the TAP pulse can efficiently deposit energy deep into the material [34]. This is because the cross section for a multiphoton process heavily decreases with the order of photons required to drive the process. At the same time, excitonic trapping will keep the overall conduction band carrier density low, leading to only a small amount of free carrier absorption [34]. The complex interaction between excitation, trapping, and re-excitation strongly enhances the spatial features brought by the TAP pulse (and thus its energy deposition into the material) which is demonstrated in Fig. 17.7.

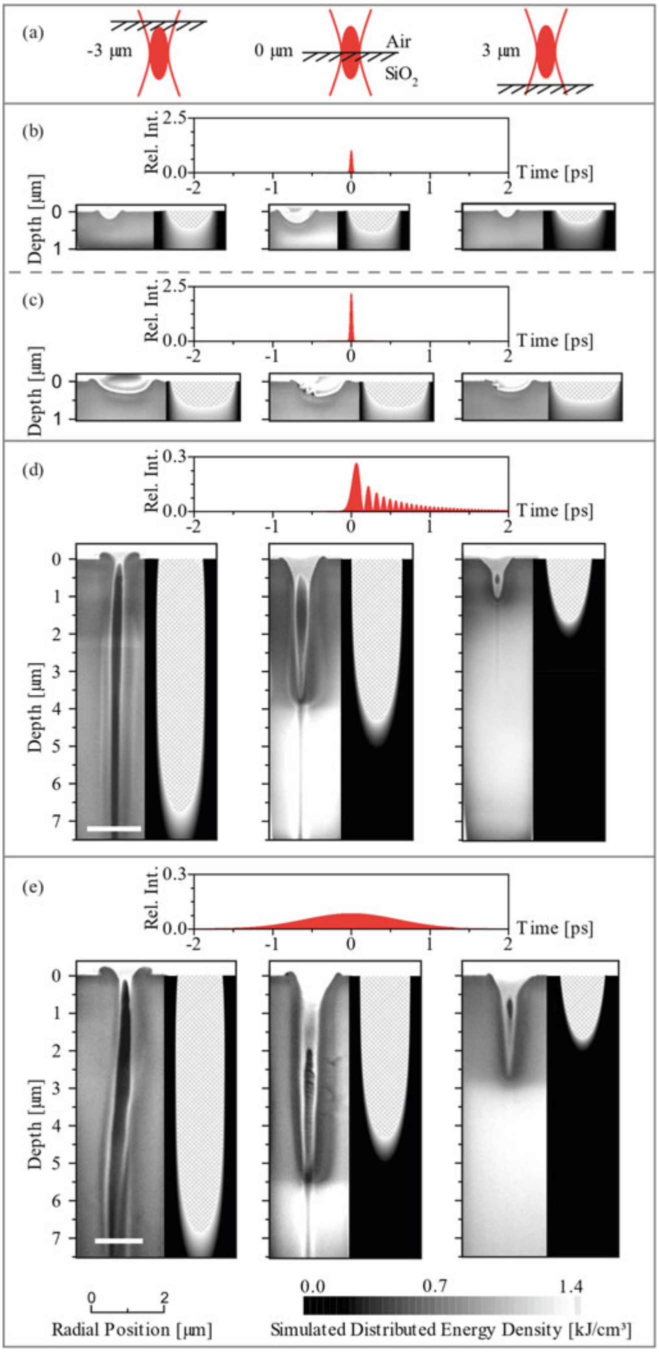
(a)
-3 μm
0 μm
Air
SiO$_2$
3 μm
(b)
(c)
(d)
(e)
Rel. Int.
2.5
0.3
0.0
Time [ps]
-2
-1
0
1
2
Depth [μm]
0
1
2
3
4
5
6
7
0
2
Radial Position [μm]
0.0
0.7
1.4
Simulated Distributed Energy Density [kJ/cm³]

The difference in the ablation characteristics of BWL and TAP pulses under different focus positions (below, at or above the surface) are shown in Fig. 17.7b–d. These side views of the ablation structures were obtained by focused ion beam milling and scanning electron microscopy.

Figure 17.7b exemplifies that BWL pulses only create a shallow ablation structure, reaching only a couple of hundreds of nm into the fused silica (independent on the focus position). Even if the pulse energy is increased by a factor of 2.5 (Fig. 17.7c), thus 5× higher than the ablation threshold, the depth of the ablation structure does not increase, while the lateral ablation radius grows. This behavior is not only linked to a strong absorption and self-reflection of the BWL pulse due to the excitation of the fused silica close to the surface but also by a strong absorption in the air above the sample. Our simulations of the ablation region (shaded area) – shown to the right of the SEM images – take the latter effect into account and are able to capture the stagnation of the hole depth by the BWL laser pulse [34].

In Fig. 17.7d, hole structures obtained with a single TAP pulse, with a pulse energy 2.5× above the ablation threshold, for the three focus positions are shown. It becomes immediately clear that the TAP pulse is able to create a needle-shaped high-aspect-ratio ablation structure reaching ratios up to 30:1 (depth to channel width). While the simulations are not able to fully predict the ablation diameter – possibly due to not all of the material being ejected, as well as refraction and propagation effects not being considered – the depth predictions fit exceptionally well (see [34] and the corresponding supplementary material for additional data and in-depth discussions). This demonstrates that due to the continuous trapping of carriers, the TAP pulse is able to penetrate deep into the material depositing a huge amount of energy by having a low peak intensity, making it the perfect tool for high-aspect-ratio material processing, avoiding large absorption above and inside the material. An important observation made from our experiments and simulations is that the ablation depth achieved by the TAP pulse is directly linked to its Rayleigh

Fig. 17.7 Machining results for (**b**), (**c**) bandwidth-limited pulses, (**d**) TAPs with a third-order dispersion coefficient of 6×10^5 fs^3, and (**e**) temporally symmetric chirped pulses with a second-order dispersion coefficient of 1.5×10^4 fs^2 at three different focus positions with respect to the surface of the fused silica sample as indicated in (**a**). For each focus position, scanning electron microscope images of cross sections obtained by focused ion beam (FIB) milling (left) are compared to simulations (right). The shaded areas in the simulation areas indicate where an – for the ablation required – energy of at least 1.4 kJ/cm^3 was deposited by the laser pulse. Experiments in (**b**), (**d**), and (**e**) were performed at approximately 2.5× above the ablation threshold energy for the corresponding pulse shape. Results for bandwidth-limited pulses approximately six times above their threshold and corresponding to the same pulse energy as used for shaped pulses in (**d**) are displayed in (**c**) showing shallow structures. The peak intensities of the applied pulses in the pulse pictograms are normalized to the simulated BWL shown in (**b**). The dark-shaded areas around the holes in the scanning electron microscope images are attributed to densified material after material processing. Vertical white lines in the middle column in (**d**) and (**e**) are FIB milling artifacts, and horizontal white bars in (**d**) and (**e**) indicate the measured hole depth. (Reproduced from Götte et al. [34] with permission from the Optical Society America)

range, thus purely defined by the spot size and wavelength and not related to any filamentation phenomena [55, 56].

In Sect. 2 we discussed that laser pulses with long-pulse durations should – in principle – be able to produce the same excitation volume compared to TAP+, just at the price of a higher pulse energy, as nearly half of the pulse is waisted before the intensity is high enough to reach the threshold for strong-field excitation. In the case of the processing of fused silica, however, the simply longer pulses have more than just the energetic disadvantage. Figure 17.7e shows the ablation structures obtained with a symmetrically stretched – by applying a linear chirp – pulse with the same statistical pulse duration (i.e., the time in which light is present) as the TAP+ pulse. While we observe that the stretched pulse is also able to create deep ablation channels, it is obvious that the channel width is larger (reducing the aspect ratio) and the hole structure is not as "clean" as the ones created by the TAP pulses. The reason for this reduced processing quality and precision can be related to two main aspects: 1. The continuous presence of the light field will lead to conduction band electrons gaining much higher kinetic energies, leading to a larger diffusion volume of the carriers and consequentially an energy that is deposited over a larger radius, while the TAP+ pulse causes a much more localized energy input, as electrons are trapped close to their excitation location. 2. Femtosecond laser amplifier systems often suffer from a slight spatial chirp (i.e., the distribution of frequencies across the spatial beam profile). Thus, when temporally stretched (chirped) pulses are used, there is a slight temporal delay between different spatial parts of the beam, exciting and ablating the material inhomogeneously as, for example, higher photon energies lead to a slightly lower ablation threshold compared to parts of the beam where first low-energy photons arrive, adding to the asymmetric shape of the ablation structure [57].

4 Optoporation of Biological Cells with Temporal Airy Pulses

After having demonstrated the control of direct nanostructuring of solid dielectrics, we will now take a look at nanostructuring of biological cells in an aqueous environment, where the damage to the cell's membrane is mediated by the excitation of water and consequent generation of cavitation bubbles. Here, the control over the shape of the excited region by temporal pulse shaping, discussed in Sect. 2, offers significant advantages regarding targeting the cell membrane. The results discussed below were obtained in close collaboration with the group of Jean Pierre Wolf at University of Geneva, Switzerland [58, 59].

Introducing foreign molecules into living cells is an important part of the toolbox of biologists. While the cell membrane is permeable for some molecules, non-permeable molecules must be delivered by artificial means (transfection) like transient chemical bond breaking or physical disruption of the membrane. Next to established large-scale technologies like electrophoresis or viral vectors, ultrashort laser pulses can be used to create a transient pore in the cell membrane through which molecules can enter the cell. In a microscope setup, it is possible to target single cells.

For an extensive review of different poration techniques and their application in different areas of research, including femtosecond laser-based techniques, see, for example [60–63]. The pathway from laser excitation of water to the generation of cavitation bubbles and how they can disturb the cell membrane is laid out in [31] and in Chap. 33.

Depending on the pulse parameters (energy, number of pulses, wavelength, pulse length), two regimes of laser-cell membrane interaction for optoporation can be differentiated, chemically induced damage with a large number of low intensity pulses, where the energy absorbed by the water can, for example, create free radicals that destruct the cell membrane, or damage by cavitation bubbles, where the high local excitation of the water by a high-intensity pulse is so strong that short-lived bubbles form and cause physical stress to the membrane [31]. In the following we will discuss poration with a single femtosecond laser pulse with energies above the reported intensity threshold for bubble formation in water with ultrashort 800 nm femtosecond laser pulses (10^{14} W/cm^2).

When focusing the laser with a high numerical aperture microscope objective onto the cell, the affected region is micrometer sized while the irregularly shaped cells can be several tens of micrometer in size. As a test system, we use the well-known HeLa cervical cancer cells (HeLa meaning Henrietta Lacks, the person from whom the line of cells was started in 1951) [64–66]. These cells exhibit a fried egg shape where the majority of the cell is relatively flat with a height of 5–7 μm and the nucleus forming a high point bulging upwards as sketched in Fig. 17.8. To target a cell's membrane with a laser beam on these scales, precise positioning in all three spatial dimensions is necessary. This can be challenging and time-consuming. As discussed above, the width and length of the excited region can be controlled by tuning the temporal shape of the laser pulse, especially featuring the needle-shaped interaction region achieved with TAP pulses. This high spatial aspect ratio reduces the need for exact targeting in vertical direction while keeping the affected volume small.

We have investigated the effect of temporal pulse shaping on the laser-cell membrane interaction of HeLa cells in water. In a first study, fixed cells were processed, and the resulting damage was analyzed with SEM [59]. In a second step, the same nanostructuring was applied to living cells, and the poration efficiency and survivability were evaluated with fluorescent dyes [58].

In both studies, a monolayer of HeLa cells was grown on a substrate and processed with single laser pulses by raster scanning at a fixed vertical position. The 30 fs, 800 nm pulses were focused with a 40×, 0.75 NA water immersion objective to a focal spot with an assumed beam waist of 0.7 μm. The vertical position of the focus was set at 6 μm above the substrate surface and corresponds to the mean thickness of the layer of cells. The matrix pattern of laser shot position had a shot-to-shot distance of 7.5 μm. For the SEM analysis of the fixed cells, reference marks

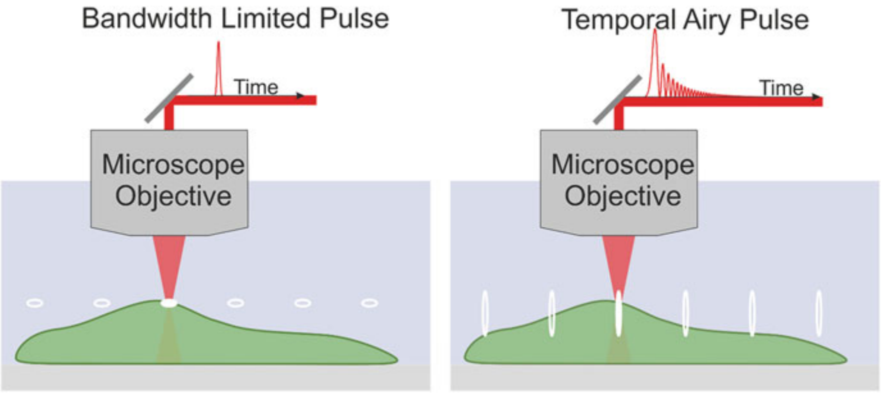

Fig. 17.8 Sketch of irregularly shaped HeLa cell (green) and focused 800 nm laser beams (red) using bandwidth-limited pulses (left) and positive TAP (right). The use of TAPs assures high-aspect-ratio needlelike excitation regions in the surrounding water for every laser shot as sketched in white and therefore provides a higher chance to porate the membrane of the cell in comparison to the highly localized excitation by the BWL pulse (left)

and labeling were placed into the glass cover slip in a 100 μm distance around the matrix to locate the matrix positions in the later analysis. It is interesting to note that much higher pulse energies are needed for processing of the glass substrate than for processing the cell membrane (1 μJ compared to around 100 nJ for cells). When using BWL pulses, the localized excitation in the water medium is so high that big cavitation bubbles and shock waves lead to the detachment of several cells in a significant radius. This was prevented by using TAP+ pulses with a third-order dispersion coefficient of only 100 kfs^3 and focusing directly onto the surface of the glass substrate.

For the processing of fixed and living cells, BWL (bandwidth limited pulses), TAP+ (temporal Airy pulse with a third-order dispersion of +600,000 fs$^{3)}$, TAP- (temporal Airy pulses with a third-order dispersion of −600,000 fs^3), and GDD (linearly positively chirped pulses with a group delay dispersion of +15,000 fs^2) were used.

4.1 *Optoporation of Fixed Cells: Efficiency and Morphology*

In Fig. 17.9a, we present the results of the first study on fixed HeLa cells analyzed with SEM [59]. Each Harvey ball represents the ratio of successful poration for up to 32 laser spots with identical parameters (shot locations that hit a gap in the monolayer of HeLa cells were excluded from the analysis).

For the onset of poration, TAP- needs the highest pulse energy (90 nJ). For GDD around 80 nJ are needed and 40 nJ for BWL. With just 30 nJ, TAP+ requires the least energy. For all pulse shapes, increasing the pulse energy to twice the respective

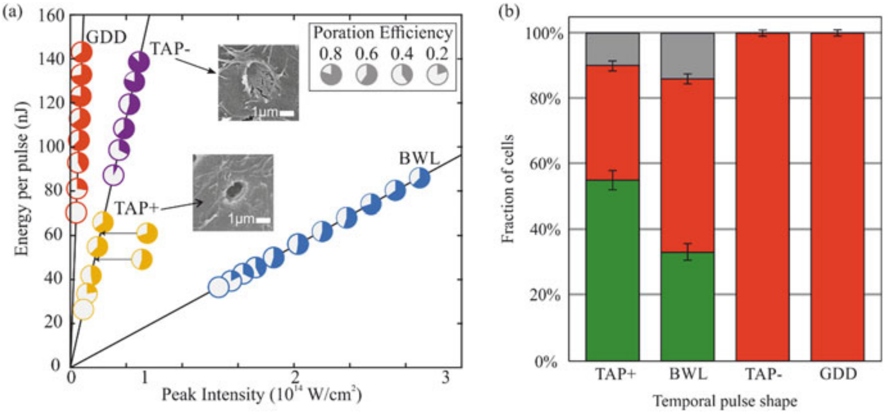

Fig. 17.9 (**a**) Poration efficiency of fixed HeLa cells irradiated with BWL (bandwidth limited), TAP+ (temporal Airy pulse with a third-order dispersion of +600,000 fs^3), TAP- (temporal Airy pulses with a third-order dispersion of −600,000 fs^3), and GDD (linearly positively chirped pulses with a group delay dispersion of +15,000 fs^2). For each pulse shape and single pulse energy, a Harvey ball represents the experimentally found poration efficiency. The black lines show the energy-dependent peak intensity of a pulse depending on its shape. (**b**) Fraction of successfully porated cells during laser treatment (green bar) and cells alive after 4 hours (green plus red bar). Grey represents detached cells. All four temporal pulse shapes BWL (bandwidth limited), TAP+ (temporal Airy pulse with a third-order dispersion of +600,000 fs^3), TAP- (temporal Airy pulses with a third-order dispersion of −600,000 fs^3), and GDD (linearly positively chirped pulses with a group delay dispersion of +15,000 fs^2) were applied with the same energy of 75 nJ per pulse. (Adapted with permission from (**a**) Richter et al. [54] and (**b**) Couairon et al. [55]. Copyright 2015 and 2018 American Chemical Society)

threshold enhances the poration efficiency to roughly 75%. Taking into account the temporal shape of the pulses, all shaped pulses show significantly lower peak intensities compared to the BWL pulse. For poration efficiency around 60%, the peak intensity of TAP+ is one-order magnitude below that one of BWL.

The analysis by SEM enables us to categorize the type of damage caused by the single laser pulses. The differentiation is done between ablation type damage (round holes), recess damage (disturbed membrane structure), and larger cracks. One-shot location can exhibit more than one type of damage at the same time, for example, a visible hole with cracks forming at the edges. For the cracks it must be noted that they might have formed or been enhanced during the preparation of the samples for the SEM. The most notable observation is that TAP+ pulses mainly produce ablation type damage and TAP- irregular recess type damage (see inset images in Fig. 17.9a). This points to two different situations during excitation and consequent cavitation bubble-mediated disruption of the cell membrane. The TAP+ causes precise, strong but spatially confined damage which is big enough for large molecules or even nanoparticles to enter the cell.

4.2 Optoporation of Living Cells: Survivability

From the SEM imaging, we can get information about the surface of the cell. But the needlelike excited region of shaped pulses makes it more likely that the excited region and consequent cavitation bubble-induced damage reach into the cell. To study the possible toxicity of the poration with shaped laser pulses, we performed the same nanostructuring on living HeLa cells [58]. The combination of three different fluorescent markers enabled us to identify the poration efficiency and survivability 4 hours after the laser treatment, by applying them before, during, and after the laser, respectively. All three dyes have different wavelengths, are imaged simultaneously in a nonlinear fluorescence microscope and hundreds of cells analyzed by automated segmentation.

As Fig. 17.9b shows, at a mid-range pulse energy of 75 nJ, the BWL and TAP+ display poration efficiencies of 33% and 55%, respectively. Nearly all cells survived the laser treatment in the investigated time window of 4 hours, independent of the poration success. For TAP- and GDD, the chosen pulse energy was too low to achieve poration.

Choosing TAP+ for single-cell single-pulse optoporation can provide high poration efficiency and viability of the cells by controlling the shape of the region in which nanostructuring of the cell membrane takes place. In cases where a layer of cells is scanned or single cells (or parts of cells) are targeted, the needle-shaped affected zone lifts constraints on vertical targeting and could significantly speed up these procedures.

5 Summary and Further Application Opportunities

In this chapter, we have demonstrated that the utilization of temporal Airy pulses (TAP) is a unique technique for the controlled processing of transparent matter with its unique high-aspect ratio needlelike excitation shape, ranging from applications in permanent laser ablation to the optoporation of biological tissue. We, however, imagine that the spatial control of carrier excitation by temporal pulse shaping to be of beneficial use in further applications as exemplified below.

A direct application of the elongated excitation region could be the enhancement of optical gain from multiphoton-stimulated emission processes in excited dielectric materials, such as sapphire [48] and fused silica [67]: Here, the conduction band carrier density or density of self-trapped excitons act as an energetically and spatially localized gain medium for an intense near-UV probe pulse. We have already demonstrated that control of spatial excitation distribution by temporal Airy pulses can be used to increase the gain length and consequentially increase the obtainable amplification by a factor of 3 compared to the excitation with bandwidth-limited femtosecond laser pulses.

The utilization of the needlelike excitation shape offered by TAP pulses in sapphire and fused silica could also offer an additional degree of freedom either in the writing of optical waveguides or the creation of microfludic structures, where typically ultrashort laser pulses are used in combination with the translation of the sample. Besides, TAP pulses could also find application in low-bandgap materials, such as classical semiconductors, where femtosecond laser pulses are utilized for 3D silicon photonics, discussed in detail in Chap. 27. In addition, we do see further applications in terms of biomedical and genetic research, where the tunable excitation depth/aspect ratio as well as the reduced peak intensities could be beneficial for an improved processing efficiency while reducing collateral damage.

Acknowledgments The authors are grateful for the close collaborations with the research groups of Hartmuth Hillmer and Thomas Kussreow (University of Kassel), Peter Balling (Aarhus University), Jean Pierre Wolf (University of Geneva), as well as Javier Solis and Jan Siegel (Spanish National Research Council), leading to the results discussed in this chapter. We also thank Bärbel Rethfeld (University of Kaiserslautern) for many fruitful discussions.

The authors acknowledge financial support from the Deutsche Forschungsgemeinschaft (DFG). Thomas Winkler received funding from the European Union's Horizon 2020 research and innovation program under Marie Skłodowska-Curie Grant Agreement No. 838772.

References

1. S. Lei, X. Zhao, X. Yu, et al., Ultrafast laser applications in manufacturing processes: A state-of-the-art review. ASME. J. Manuf. Sci. Eng. **142**(3), 031005 (2020)
2. M. Malinauskas, A. Žukauskas, S. Hasegawa, et al., Ultrafast laser processing of materials: From science to industry. Light Sci. Appl. **5**, e16133 (2016)
3. K. Sugioka, Y. Cheng, Ultrafast lasers—Reliable tools for advanced materials processing. Light Sci. Appl. **3**, e149 (2014)
4. M.K. Bhuyan, F. Courvoisier, P.A. Lacourt, et al., High aspect ratio nanochannel machining using single shot femtosecond Bessel beams. Appl. Phys. Lett. **97**, 081102 (2010)
5. I.H. Chowdhury, X. Xu, A.M. Weiner, Commercial and biomedical applications of ultrafast lasers III. High-power lasers and applications, in *SPIE2003*, (San Jose, CA, 2003), p. 138
6. I.H. Chowdhury, X. Xu, Ultrafast double-pulse ablation of fused silica. Appl. Phys. Lett. **86**, 151110 (2005)
7. Y. Qi, Q. Hongxia, W. Qinxin, et al., The influence of double pulse delay and ambient pressure on femtosecond laser ablation of silicon. Opt. Laser Technol. **66**(2015), 68–77 (2015)
8. D. Giguère, G. Olivié, F. Vidal, et al., Laser ablation threshold dependence on pulse duration for fused silica and corneal tissues: Experiments and modeling. J. Opt. Soc. Am. A **24**, 1562–1568 (2007)
9. E. Terasawa, T. Shibuya, D. Satoh, et al., Pulse duration dependence of ablation threshold for fused silica in the visible femtosecond regime. Appl. Phys. A Mater. Sci. Process. **126**, 446 (2020)
10. N. Götte, T. Kusserow, T. Winkler, et al., Temporally shaped femtosecond laser pulses for creation of functional sub-100 nm structures in dielectrics, in *Optically Induced Nanostructures: Biomedical and Technical Applications*, ed. by K. König, A. Ostendorf, (De Gruyter, Berlin, 2015)
11. R. Stoian, J.-P. Colombier, Advances in ultrafast laser structuring of materials at the nanoscale. Nanophotonics **9**(16), 4665–4688 (2020)

12. K. Sugioka, Progress in ultrafast laser processing and future prospects. Nanophotonics **6**(2), 393–413 (2017)
13. K. Sugioka, M. Meunier, A. Piqué (eds.), *Laser Precision Microfabrication* (Springer Berlin Heidelberg, Berlin, Heidelberg, 2010)
14. G. Bonamis, K. Mishchick, E. Audouard, et al., High efficiency femtosecond laser ablation with gigahertz level bursts. J. Laser Appl. **31**, 022205 (2019)
15. M. Domke, V. Matylitsky, S. Stroj, Surface ablation efficiency and quality of fs lasers in single-pulse mode, fs lasers in burst mode, and ns lasers. Appl. Surf. Sci. **505**, 144594 (2020)
16. C. Javaux Léger, K. Mishchik, O. Dematteo-Caulier, et al. Laser-based micro- and nanoprocessing IX, in *SPIE2015*, (SPIE LASE, San Francisco, 2015), p. 93510M
17. F. Zimmermann, S. Richter, S. Döring, et al., Ultrastable bonding of glass with femtosecond laser bursts. Appl. Opt. **52**, 1149–1154 (2013)
18. P. Balling, J. Schou, Femtosecond-laser ablation dynamics of dielectrics: Basics and applications for thin films. Rep. Prog. Phys. **76**(3), 036502 (2013)
19. L. Capuano, R. Pohl, R.M. Tiggelaar, et al., Morphology of single picosecond pulse subsurface laser-induced modifications of sapphire and subsequent selective etching. Opt. Express **26**, 29283–29295 (2018)
20. M. Macias-Montero, F. Muñoz, B. Sotillo et al., Element migration and local refractive index control in silicate glass by femtosecond laser induced element redistribution, in *2021 Conference on Lasers and Electro-Optics Europe and European Quantum Electronics Conference, OSA Technical Digest*, (Optica Publishing Group, 2021)
21. A. Reupert, M. Heck, S. Nolte, et al., Angular scattering pattern of femtosecond laser-induced refractive index modifications in optical fibers. Adv. Opt. Mater. **8**, 2000633 (2020)
22. C. Florian, D. Fischer, K. Freiberg, et al., Single femtosecond laser-pulse-induced superficial amorphization and re-crystallization of silicon. Materials **14**(7), 1651 (2021)
23. M. Garcia-Lechuga, N. Casquero, A. Wang, et al., Deep silicon amorphization induced by femtosecond laser pulses up to the mid-infrared. Adv. Opt. Mater. **9**, 2100400 (2021)
24. M. Garcia-Lechuga, O. Utéza, N. Sanner, D. Grojo, Evidencing the nonlinearity independence of resolution in femtosecond laser ablation. Opt. Lett. **45**, 952–955 (2020)
25. B. Guo, J. Sun, Y. Lu, L. Jiang, Ultrafast dynamics observation during femtosecond laser-material interaction. Int. J. Extreme Manuf. **1**, 032004 (2019)
26. L.V. Keldysh, Ionization in the field of a strong electromagnetic wave. Sov. Phys. JETP **20**, 5 (1965)
27. P. Balling, Laser coupling and relaxation of the absorbed energy: Metals, semiconductors, and dielectrics, in *Handbook of Laser Micro- and Nano-Engineering*, ed. by K. Sugioka, (Springer, Cham, 2020)
28. B.H. Christensen, P. Balling, Modeling ultrashort-pulse laser ablation of dielectric materials. Phys. Rev. B **79**, 155424 (2009)
29. B. Rethfeld, Unified model for the free-electron avalanche in laser-irradiated dielectrics. Phys. Rev. Lett. **92**, 187401 (2004)
30. J.-L. Déziel, L.J. Dubé, C. Varin, Dynamical rate equation model for femtosecond laser-induced breakdown in dielectrics. Phys. Rev. B **104**, 045201 (2021)
31. A. Vogel, J. Noack, G. Hüttman, G. Paltauf, Mechanisms of femtosecond laser nanosurgery of cells and tissues. Appl. Phys. B **81**, 1015–1047 (2005)
32. B.K. Ridley, *Quantum Processes in Semiconductors* (Oxford University Press, Oxford, 2013)
33. J. Köhler, M. Wollenhaupt, T. Bayer, et al., Zeptosecond precision pulse shaping. Opt. Express **19**(12), 11638–11653 (2011)
34. N. Götte, T. Winkler, T. Meinl, et al., Temporal Airy pulses for controlled high aspect ratio nanomachining of dielectrics. Optica **3**(4), 389–395 (2016)
35. M. Wollenhaupt, A. Assion, T. Baumert, in *Springer Handbook of Lasers and Optics*, ed. by F. Träger, (Springer, New York, 2007), p. 937
36. C. Sarpe, J. Köhler, T. Winkler, et al., Real-time observation of transient electron density in water irradiated with tailored femtosecond laser pulses. New J. Phys. **14**, 075021 (2012)

37. M. Born, E. Wolf, A.B. Bhatia, et al., *Principles of Optics* (Cambridge University Press, Cambridge, 2013)
38. S. Guizard, A. Semerok, J. Gaudin, et al., Femtosecond laser ablation of transparent dielectrics: Measurement and modelisation of crater profiles. Appl. Surf. Sci. **186**, 1–4 (2002)
39. S.H. Møller, S.T. Andersen, P. Balling, Transient optical properties of highly excited dielectric materials: Apparent birefringence and delayed reflectivity increase. Phys. Rev. Res. **2**, 043010 (2020)
40. V.V. Temnov, K. Sokolowski-Tinten, P. Zhou, D. von der Linde, Ultrafast imaging interferometry at femtosecond-laser-excited surfaces. J. Opt. Soc. Am. B **23**(9), 1953–1964 (2006)
41. C. Froehly, A. Lacourt, J.C. Viénot, Time impulse response and time frequency response of optical pupils.:Experimental confirmations and applications. Nouv. Rev. Opt. **4**, 183 (1973)
42. C. Iaconis, I.A. Walmsley, Spectral phase interferometry for direct electric-field reconstruction of ultrashort optical pulses. Opt. Lett. **23**(10), 792–794 (1998)
43. L. Lepetit, G. Chériaux, M. Joffre, Linear techniques of phase measurement by femtosecond spectral interferometry for applications in spectroscopy. J. Opt. Soc. Am. B **12**(12), 2467–2474 (1995)
44. D. Dempsey, G.C. Nagar, C.K. Renskers, et al., Single-shot ultrafast visualization and measurement of laser-matter interactions in flexible glass using frequency domain holography. Opt. Lett. **45**(5), 1252–1255 (2020)
45. S.S. Mao, F. Quéré, S. Guizard, et al., Dynamics of femtosecond laser interactions with dielectrics. Appl. Phys. A Mater. Sci. Process. **79**, 1695–1709 (2004)
46. M.A. van Dijk, M. Lippitz, D. Stolwijk, M. Orrit, A common-path interferometer for time-resolved and shot-noise-limited detection of single nanoparticles. Opt. Express **15**(5), 2273–2287 (2007)
47. T. Winkler, L. Haahr-Lillevang, C. Sarpe, et al., Probing spatial properties of electronic excitation in water after interaction with temporally shaped femtosecond laser pulses: Experiments and simulations. Appl. Surf. Sci. **374**, 235–242 (2016)
48. T. Winkler, L. Haahr-Lillevang, C. Sarpe, et al., Laser amplification in excited dielectrics. Nat. Phys. **14**, 74–79 (2018)
49. N. Linz, S. Freidank, X.-X. Liang, A. Vogel, Wavelength dependence of femtosecond laser-induced breakdown in water and implications for laser surgery. Phys. Rev. B **94**, 024113 (2016)
50. O. Marsalek, C.G. Elles, P.A. Pieniazek, et al., Chasing charge localization and chemical reactivity following photoionization in liquid water. J. Chem. Phys. **135**, 224510 (2011)
51. K. Siefermann, Y. Liu, E. Lugovoy, et al., Binding energies, lifetimes and implications of bulk and interface solvated electrons in water. Nat. Chem. **2**, 274–279 (2010)
52. J. Hernandez-Ruenda, N. Götte, J. Siegel, et al., Nanofabrication of tailored surface structures in dielectrics using temporally shaped femtosecond-laser pulses. ACS Appl. Mater. Interfaces **7**(12), 6613–6619 (2015)
53. L. Englert, M. Wollenhaupt, L. Haag, et al., Material processing of dielectrics with temporally asymmetric shaped femtosecond laser pulses on the nanometer scale. Appl. Phys. A Mater. Sci. Process. **92**, 749 (2008)
54. S. Richter, F. Jia, M. Heinrich, et al., The role of self-trapped excitons and defects in the formation of nanogratings in fused silica. Opt. Lett. **37**, 482–484 (2012)
55. A. Couairon, L. Sudrie, M. Franco, et al., Filamentation and damage in fused silica induced by tightly focused femtosecond laser pulses. Phys. Rev. B **71**, 125435 (2005)
56. K. Liao, W. Wang, X. Mei, B. Liu, Fabrication of millimeter-scale deep microchannels in fused silica by femtosecond laser filamentation effect. Opt. Laser Technol. **142**, 107201 (2021)
57. V.P. Zhukov, S. Akturk, N.M. Bulgakova, Asymmetric interactions induced by spatio-temporal couplings of femtosecond laser pulses in transparent media. Opt. Soc. Am. B **36**, 1556–1564 (2019)
58. G. Campargue, B. Zielinski, S. Courvoisier, et al., Live cells assessment of opto-poration by a single femtosecond temporal Airy laser pulse. AIP Adv. **8**, 125105 (2018)
59. S. Courvoisier, N. Götte, B. Zielinski, et al., Temporal Airy pulses control cell poration. APL Photonics **1**, 046102 (2016)

60. H.G. Breunig, A. Uchugonova, A. Batista, K. König, High-throughput continuous flow femtosecond laser-assisted cell optoporation and transfection. Microsc. Res. Tech. **77**(12), 974–979 (2014)
61. H.G. Breunig, A. Uchugonova, A. Batista, K. König, Cell optoporation with a sub-15 fs and a 250-fs laser. J. Biomed. Opt. **21**(6), 060501 (2016)
62. B. Duckert, S. Vinkx, D. Braeken, M. Fauvart, Single-cell transfection technologies for cell therapies and gene editing. J. Control. Release **330**, 963–975 (2021)
63. M.P. Stewart, R. Langer, K.F. Jensen, Intracellular delivery by membrane disruption: Mechanisms, strategies, and concepts. Chem. Rev. **118**(16), 7409–7531 (2018)
64. G. Gey, Basic principles of cancer cell culture. Cancer Res. **12**, 264 (1952)
65. B.P. Lucey, W.A. Nelson-Rees, G.M. Hutchins, Henrietta Lacks, HeLa cells, and cell culture contamination. Arch. Pathol. Lab. Med. **133**(9), 1463–1467 (2009)
66. R. Skloot, *The Immortal Life of Henrietta Lacks* (Crown Publ, New York, 2010)
67. T. Winkler, P. Balling, B. Zielinski, et al., Unveiling nonlinear regimes of light amplification in fused silica with femtosecond imaging spectroscopy. Phys. Rev. Res. **2**, 023341 (2020)

Chapter 18
Ultraprecise Surface Processing by Etching with Laser-Induced Plasmas

Martin Ehrhardt, Pierre Lorenz, and Klaus Zimmer

Keywords Laser · Plasma · Dry etching · Reactive gas · Optical breakdown · Low damage · Ultraprecise surface machining

1 Introduction to Ultraprecise Surface Machining with Pulsed Lasers

The term ultraprecise surface machining (UPSM) is related to the ever-increasing request of higher precision of surfaces that is driven by the increasing demands on the performance of surfaces in all areas of applications, ranging from microelectronics to optics and precision mechanics. The term UPSM was introduced by T. Taniguchi in 1983 [1] due to the increasing importance of shrinking the critical sizes below the micrometer level in the microelectronic industry. Already this time, beam technologies were identified to meet the requirements of UPSM. In particular, UPSM calls for deterministic processing of surfaces to a very high vertical (and sometimes also lateral) accuracy that needs to be much less than 1 nm for specific applications like Extreme UltraViolet Lithography (EUVL) across the full spatial frequency range, while depth precision below 10-nm rms is sufficient for many applications. This first chapter focuses on basic principles and examples for ultraprecise machining with lasers.

M. Ehrhardt (✉) · P. Lorenz · K. Zimmer
Leibniz Institute of Surface Engineering (IOM), Leipzig, Germany
e-mail: Martin.ehrhardt@iom-leipzig.de; Pierre.lorenz@iom-leipzig.de;
Klaus.zimmer@iom-leipzig.de

© The Author(s), under exclusive license to Springer Nature Switzerland AG 2023
R. Stoian, J. Bonse (eds.), *Ultrafast Laser Nanostructuring*, Springer Series
in Optical Sciences 239, https://doi.org/10.1007/978-3-031-14752-4_18

1.1 Requirements of Ultraprecise Surface Machining for Optical Applications

The traditional processes considered to be UPSM are, for instance, grinding, polishing, honing, and single-point diamond turning. The surface roughness and the surface/subsurface damage are important characteristics defining the surface integrity in UPSM [2]. The surface integrity has a great impact on a part's functionality and includes, in general, all physical, mechanical, metallurgical, compositional, chemical, and biological properties; it is also currently determined by surface (crystallographic) texture, chemical composition, microstructure, hardness, and stress distribution. Hence, to fulfill the application-specific surface integrity requirements, UPSM calls for processing at an atomic-level accuracy. For various applications like optics, the traditional measure of figure and roughness are still significant representations of the surface integrity.

There is a strong correlation between the sharpness of the tool edge (chipping tool or grinding particle) and the surface roughness/subsurface damage. For instance, the remaining subsurface damage for mechanical, chipping-based diamond ductile machining of brittle material is in the range of 50 nm and requires post polishing [3]. Traditional chip cutting technologies cannot meet the requested atomic-level processing of UPSM as the tool-edge geometry should attribute to the same level of accuracy, and the cutting edge needs to overcome the bonding forces between atoms in a crystal. A minimum cutting-chip thickness of 1 nm was achieved for metals [4].

Although polishing is capable of achieving low surface roughness, subsurface damage due to cracks, redeposited material, or incorporated abrasive particles cannot be avoided [5–9]. Therefore, the challenge for mechanical chipping-based methods of UPSM is the reduction of the subsurface damage. Hence, the measurement, control, and minimization of subsurface defects and modifications are among the key issues in UPSM [4]. The increasing demands of UPSM call for improvements of all aspects of fabrication, such as processing, machinery, and surface characterization. In particular, any mechanical forces during the processing cause certain deviations from the desired shape of the surface in relation to the stiffness of the machine components. Improvements can be achieved by completion of such machines by in-process measurements and closed-loop control systems. There are several approaches to support abrasive processes in parts by chemical processes or by energy beams, e.g., lasers [10], to enhance the surface integrity after machining.

Beam technologies like ion-, plasma- or laser-beam processing are advantageous because they enable a forceless impact of the beam tool to the surfaces and thus reduce the requirements on the UPSM equipment. Very early ion beam figuring (IBF) was identified and applied to the UPSM of optical surfaces [1]. The generation of low-energy (<5 keV) ion beams require high vacuum so that ion beam processing technologies are performed in vacuum vessels that house complex equipment for handling optics during processing. The energy of the accelerated particles of the ion beam induces physical processes at the surface that cause a directionality of the machining but may induce surface defects and modifications. In conjunction with reactive gases, the synergistic effects of the chemistry provided by reactive species and the directionality of the beam enable reactive ion beam etching processes that have higher etching rate and less surface damage than conventional (nonreactive) processes and can also be used for high-quality pattern transfer for optical applications [11–13].

The etching rate of plasma-based etching methods increases by increasing the gas pressure due to the higher species density, but an increasingly isotropic etching results due to the reduced mean free path length. Specific approaches like atmospheric pressure plasma jet etching (APPJ) enable UPSM without vacuum conditions but work reliably only for selected materials as a consequence of the governing chemical material removal mechanisms. The plasma jet allows for good conditions for local etching to achieve figuring of, e.g., free-form surfaces [11], due to the small and well-defined footprint of the plasma jet. In addition to ion and plasma beams, high-photon-energy laser pulses are identified as a tool for precise surface machining as demonstrated for the processing of organic materials [3].

In general, current ultraprecision machining technologies can achieve high surface quality and surface integrity. The processing efficiency is commonly rather low as the material removal rate is, and probably must be, low to enable the required depth precision and surface quality. Hence, the goals for further UPSM developments are the exploration and development of processing methods that offer simultaneous ultrahigh precision, low surface damage, high process reliability, and good cost-efficiency. In particular, multidisciplinary approaches involving physics, chemistry, and material science, including mechanical and nanotechnological fields, can offer new opportunities for the development of new manufacturing processes [4].

Three pillars can be identified that determine the success of UPSM:

(i) The interaction of the tool with the material must fulfill the requirements of atomic-level material removal, including the reduction of material alterations/modifications to the atomic level;
(ii) Optimized machining strategy for a well-defined process, reducing all stochasticity and systematic process deviations;
(iii) In-process measurements of process parameters and surface properties to enable closed-loop adjustment of the process parameters to the in situ measured deviations from the target parameter.

The subaperture imperfections of optical surfaces may be categorized into deviations of the *figure* (low spatial frequency roughness (LSFR)), the *waviness* figure (mid-spatial frequency roughness (MSFR)), and the *roughness* of the surface (high spatial frequency roughness (HSFR)). Usually, the waviness and roughness are mainly determined by the inherent material removal mechanisms of the machining process used, while the tool and the machining strategy determine the achievable precision of the surface figure. In addition, all types of surface and subsurface defects need to be considered as they have an important impact on the machining process as well as on applications; this holds true for mechanical as well as beam-based machining methods.

1.2 Laser-Based Techniques for Ultraprecise Surface Machining

Laser beams are used in many industrial applications, including micro-structuring, cutting, dicing, and scribing, and can be applied for the processing of a diversity of materials, for example, metals, ceramics, glass, plastics, and composites. Laser machining is characterized by several advantages, such as the absence of tool wear, tool breakage, chatter, machine deflection, and mechanically induced material damage, phenomena that are usually associated with traditional machining processes.

Hence, laser beam technology provides excellent conditions for UPSM as the tool is not in mechanical contact with the surface, and the surface can be inspected during machining, which enables additional means for in-process measurement and process control. Further, the machining strategy can be arbitrarily designed as the beam tool can be controlled spatially and temporally with high precision. The removal processes at the atomic level are an important requirement for UPSM. They depend on the interaction mechanisms with which the material removal is realized.

In Fig. 18.1, typical laser material removal approaches for precise surface machining are sketched, which are laser ablation, laser backside etching, laser chemical etching, and laser-induced plasma etching, which will be reviewed later. The dominating laser-induced mechanisms addressing the material removal are substantially different according to the irradiation geometry, the photon interaction conditions, as well as all subsequent secondary processes. In terms of the contribution to the material removal mechanism, physical and chemical processes can be distinguished. The sketched laser processes feature vastly different contributions of chemical and physical processes to the material removal mechanism as seen in Fig. 18.1, where from (a) to (d), the contribution of physical impact reduces and chemical

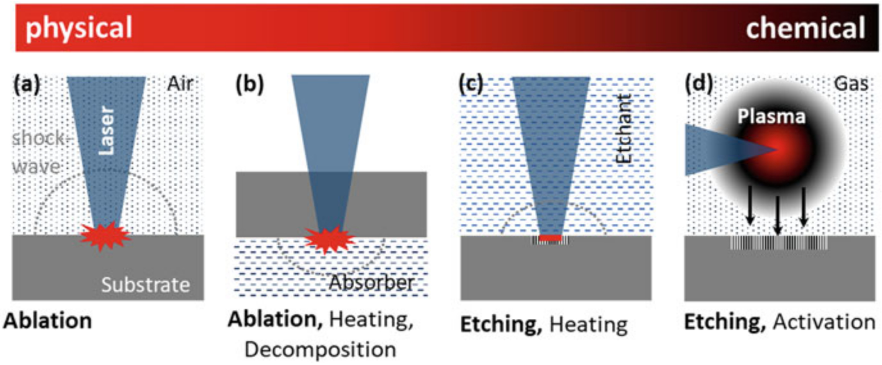

Fig. 18.1 Specific approaches to laser-based surface machining: (**a**) laser ablation, (**b**) laser-induced backside wet etching, (**c**) laser chemical etching, (**d**) laser-induced plasma etching (LIPE). According to the applicable laser-induced mechanism, it can be classified as physically or chemically dominant

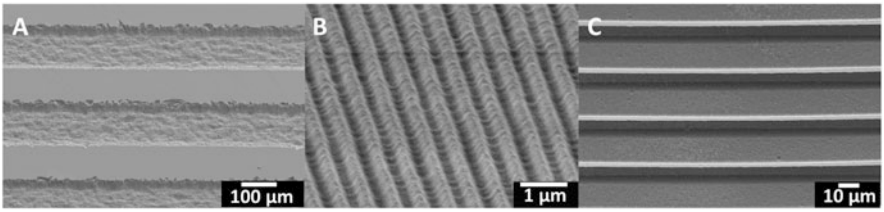

Fig. 18.2 Selected approaches for laser -based UPSM of SiO_2. (**a**) Laser ablation with UV picosecond laser pulses, (**b**) laser-induced backside etching using UV nanosecond laser pulses, (**c**) laser-induced plasma etching using femtosecond laser pulses for igniting the plasma in a CF_4 atmosphere in combination with a hard mask. (Image (**b**) is reproduced from Zimmer et al. [22] under license CC BY 3.0)

processes increases. As an example, SiO_2 surfaces after machining by laser ablation, laser backside etching, and laser-induced plasma etching are shown in Fig. 18.2. In the following section, we will review the most suitable methods enabling UPSM.

Laser ablation is the standard approach for micro-processing with a pulsed laser, including drilling, cutting, scribing, and surface texturing. It is characterized by fast material ejection from the surface by explosive processes driven by the high energy densities absorbed near the material surface. The most important parameters determining the achievable surface quality of laser ablation of a specific material are given by the material properties, the wavelength and pulse duration of the laser radiation, which in turn determines the volume and strength of the laser photons' interaction with the material. The penetration depth and the energy absorbed in the material govern the secondary processes following the primary material ejection due to ablation. More details can be found in Chaps. 2 and 9.

Ultrashort laser pulses provide, in comparison to longer pulse durations, preferred conditions for UPSM due to the required low fluences to achieve ablation, the very limited thermal diffusion length, and the reduced thermal impact on the remaining material after ablation. The laser ablation-related surface modifications include the following:

(i) Subsurface damage: Typical experimentally determined values for subsurface damage in crystalline materials (Si, SiC) are in the range of 30–50 nm and comprise amorphization, dislocations, and stacking faults [14, 15].

(ii) Surface corrugations: For laser material interaction, at least two of the manifold mechanisms for roughness and waviness generation are the formation of laser-induced periodic surface structures (LIPSS) [16] due to ultrashort laser irradiation and rim formation at ns-laser ablation due to melting processes. The rim height can vary strongly with the material. For silicon, heights between 100 and 500 nm were found [17]. The LIPSS amplitude depends on the laser irradiation parameters (λ, t_p, and N) and material properties. The LIPSS roughness ranges were measured from 60 nm (248 nm, 20 ns) to 70 nm [18, 19] for polymers and to approx. 200 nm (800 nm, 150 fs) for metals [20].

(iii) Surface deviations due to the inhomogeneities of the laser tool's footprint or overlapping footprints during scanning of the surface by discontinuous laser-driven material removal [14, 15, 21].

The ablation rate, which is usually in the range of 100 nm, provides a measure for the achievable surface figure and the surface waviness as the result of the machining strategies, including pulse and scan overlap. While the latter can be optimized by technical means, the fundamental limits of realizable precision are given by the ablation characteristics, particularly the subsurface damage, material ablation rate, and surface corrugations. Therefore, the availability of appropriate processes that inherently enable a high-quality surface machining is indispensable.

The term "laser-induced chemical etching" (LICE) refers to techniques of chemical etching by liquids or gases that are stimulated by laser photons. The etching is induced or enhanced by laser photons within the laser spot that activate the etchant, the sample surface, or both. These processes can be of photothermal or photochemical nature and are based on electronic and thermal excitation processes by UV, VIS, or IR laser radiation [23].

Experimental results show that the basic mechanism of material removal by LICE is a chemical reaction of activated species with the substrate material forming volatile or solvable reaction products that desorb from the surface [24, 25]. Some limitations are related to (i) the need for hazardous gases or liquids and (ii) the availability of suitable material-etchant combinations that enable volatile/solvable products that are formed by the chemical reactions at the surface. Localized as well as areal etching can be achieved for perpendicular and parallel laser beam irradiation configurations, respectively [26], though most often, direct surface irradiation is utilized for UPSM. Often the chemical surface reactions govern the material removal process, but the complete LICE mechanism comprises further processes like provision of new etchants, adsorption of etchants, desorption of products, etc. They must be considered in the process evaluation as they also determine the surface integrity.

Laser-induced etching can be divided into wet and dry, depending on the phase of the etchant. For laser-induced wet chemical etching (LIWCE), the etching process is performed in a liquid etchant, e.g., HCl or KOH [27, 28]. During this process, the laser usually heats the substrate surface locally, which results in enhanced etching due to the higher laser-induced surface temperatures. In addition to localized laser heating, the preferred chemical etching of laser-induced defects and modifications has been shown. The strong increase in the etching rate (up to 1000) by locally formed femtosecond laser-induced defects radiation can lead to highly localized etchings. With this method, microstructures with a very high aspect ratio can be generated in optical materials, e.g., SiO_2 or sapphire, after appropriate laser modification [29, 30]. In Chaps. 19 and 20 of the book, a detailed overview of chemically assisted laser processing can be found.

Dry-LICE is less examined and only a limited number of studies has been published so far [25, 26, 31]. Typical gaseous etchants often contain halides or halogenated compounds that form halogen radicals by photoexcitation with UV laser wavelengths. The etching rate for ns-pulse laser sources is usually in the range of 1 nm/pulse, which accounts for several atomic layers. Laser wavelengths in the visible or UV-wavelength are needed to excite the etching gas molecules. An example for dry-LICE is the etching of crystalline Si with Cl_2 [32–34] and SF_3 [32].

With the reduction of the reactant supply or the occurrence of self-limiting processes, atomic-level chemical processing can be realized. Atomic layer etching processes were studied with and without photon (laser) assistance. A spontaneous adsorption process is used, resulting in the formation of chemically bonded etchants that can be stimulated for desorption by thermal energy, light, or laser pulses. For laser-enhanced atomic layer etching of GaAs with chlorine using 248-nm laser pulses at 13 mJ/cm^2, an etching rate of 0.2 nm/cycle, which is similar to the lattice constant, was found [11]. Therefore, laser-induced chemical etching can be applied for UPSM of certain materials, but the hazardous etchants and the usual high selectivity of photochemical need to be considered.

Another approach to UPSM is laser-induced backside etching. A number of backside etching techniques have been studied for machining of transparent dielectrics by pulsed laser radiation. The process design requires the transparency of the substrate to be machined, the penetration of the substrate by the laser beam, and the strong absorption of the laser photons near the rear side surface of the sample that is in contact with an absorbing solid, liquid, or gaseous material. Results of these backside etching techniques called *laser-induced backside wet etching* (LIBWE), *laser-induced backside dry etching* (LIBDE), and *laser etching at a surface-absorbed layer* (LESAL) are summarized in Ref. [35].

The mechanism of these backside etching techniques comprises laser-induced physical and chemical processes. The chemical decomposition processes of the absorbing material, the case of LIBWE often a hydrocarbon solvent and facilitated by laser-induced photochemical or photothermal processes, lead to the formation of carbon products. They can attach to or are incorporated into the samples' rear-side surface.

Alteration of material properties, e.g., absorption coefficient, near the surface can enhance laser photon absorption, resulting in enhanced ablation of this modified, strongly absorbing surface layer. The localization of the laser photon interaction at the modified near-surface material together with the rear-side irradiation changes the ablation processes from inherent material ablation to a film-type ablation. Such effects are known from selective ablation or delamination of thin absorbing films from transparent substrates [36, 37]. This can lead to a high-surface-precision process featuring smooth surfaces and low damage. Therefore, the material removal rate of the LIBWE processes is mainly determined by the modification depth of the surface. The typical experimental material removal rates for backside etching techniques are around 100, 20, and 1 nm/pulse for LIBDE [38–40], LIBWE [22, 41–43], and LESAL [44, 45], respectively [35]. The surface roughness of backside etching techniques is rather low and can reach 1-nm rms in the case of LESAL. Reasons for the low roughness are the strong modification-confined absorption, the low etching rates [22, 38–45], and LIBWE-inherent smoothing processes [46]. An accumulation of process- or material-initiated roughness/waviness contributions can be expected with increasing pulse numbers.

The surface damage/modification depth for LIBWE was determined via Rutherford backscattering spectrometry (RBS) and UV/VIS absorption measurements. In both cases a damage depth in the range of 15 nm was found, which is similar to the depth of etching [47].

Laser-induced plasma-assisted ablation (LIPPA) is a laser-induced backside etching method in which the absorbing material is not directly attached to the substrate [48, 49]. The absorbing material and the substrate have a gap of few tens of micrometers. Due to the ablation of the absorbing material with nanosecond or femtosecond laser pulses, a plasma is generated, which reaches the substrate surface. Due to the interaction of the highly energetic species of the plasma and the surface, etching can be achieved. The typical etching rate is 50 nm/pulse [50]. The plasma interaction additionally causes a film deposition made of material from the ablated material. This laser-plasma-deposited film can be used for the metallization of surfaces [51, 52].

In addition, there are several other approaches that combine traditional microelectronic etching processes with laser methods. Laser-assisted plasma etching, one of these examples, combines HF plasma etching processes with pulsed or CW laser irradiation of the sample surface [53–55]. The laser radiation is used to locally increase the etching rate by thermal activation of the appropriate chemical reactions of plasma-generated, reactive species with the sample material. Similar to the directionality of reactive ion beam etching (RIBE), laser processing can cause anisotropy in plasma etching by continuously removing the deposited polymer passivation layer from a substate, enabling the reaction of reactive species without penetration of the passivation layer [54].

Comparing UV and VIS laser irradiation with energy densities well below the laser modification threshold of the studied Si clearly shows the thermal mechanism of the etching enhancement due to the laser heating of the Si. For transparent SiO_2, in contrast, no etching enhancement was observed. It was proposed that due to the laser irradiation, directionality and material selectivity can be achieved. In this context, less (sub-)surface damage can be expected in comparison to ion-based anisotropic etching, since laser photons have almost no momentum [55].

Another approach to laser assistance of plasma processes is the combination of atmospheric pressure plasma jet etching with pulsed laser irradiation. The goal of increasing the absorption of a glass surface by the plasma jet to enhance the laser ablation was substantially achieved but with a low degree of convergence [56, 57]. Commonly, atmospheric plasma jet etching with gases containing fluorine causes a chemical reaction that transforms the surface atoms into volatile products. For simple materials, this works well [58, 59]. However, many important materials, like technical glasses, include additives that form nonvolatile products during the plasma jet etching. These nonvolatile products can form a residual layer that prevents high-quality etching. This porous residue layer reduces the etching rate, results in higher roughness, and can be considered as a layer of near-surface defects. However, it has been shown that a cyclic process of atmospheric plasma jet etching and UV-nanosecond pulse laser irradiation is effective to remove these plasma jet-generated residues by laser ablation [60, 61]. In Table 18.1 an overview of reported surface properties for UPSM achieved by the different laser-based methods is given.

1.3 Laser Polishing

Although UPSM machining is possible with the laser-based processes given in Table 18.1, often a smooth surface finish is needed after patterning or figuring. Typical abrasive-based polishing processes such as diamond grinding [69, 70], micro grinding [69, 70], and magnetorheological finishing [71] can be applied for finishing. However, long lead time, the discussed subsurface damage, and the compatibility to beam technologies make these techniques less suited. Contact-less beam-based polishing processes can be performed with ion beams [72–75], plasma jets [76], and laser beams [77–81]. The mechanism of these polishing processes depends on the interaction process of the beam tool with the surface material and can be of atomic, physical, or chemical nature. For laser-based UPSM patterning or figuring techniques, post processing with lasers is most suited [79].

The most common laser polishing process is based on surface softening/melting using a focused beam of a high-power CW laser or short-pulsed laser, which is scanned across the surface in a specific pattern. The initial roughness of the surface is reduced due to mass flow within the melt that is driven by surface tension, thereby causing the smoothing effect. With laser polishing, a variety of materials such as glass [79, 80], plastics [82], and metals [77] could be processed, and a significant reduction of surface roughness has been achieved. However, due to the high thermal load of the surface and the phase transitions during laser polishing, the thermal gradient and the generated stress can induce micro-cracks at and near the surface [83]. Furthermore, the generation of rims, waviness, and ripple-like structures at the surface due to the hydrodynamic effects of the molten material that are frozen during resolidification can often not be avoided [84, 85].

Laser polishing with nanosecond laser pulses is mostly demonstrated for metal surfaces [86, 87]. The short pulse lengths are used to limit the thermal impact in relation to the overall heating of the workpiece, minimizing the heat-affected zone, the reduction of the applied laser power, and the limitation of the melting depth. Although ultrashort laser pulses are known for nonthermal material processing by multiphoton absorption or nonthermal melting, thermal effects can be induced due to heat accumulation at multipulse irradiation. In general, the nonlinear absorption processes at ultrashort laser pulses limit the heat penetration and enable processing of both opaque and transparent materials. Therefore, for polishing of surface with ultrashort laser pulse, high pulse repetition rates were studied. The polishing of tool steel in [88] is an example of laser polishing using ultrashort laser pulses. In this study, a reduction of the surface roughness from the original $S_a = 0.6\ \mu\text{m}$ to $S_a = 0.3\ \mu\text{m}$ could be reported. Laser polishing was also applied to laser-written glass microstructures to smooth the laser ablation-related roughness to optical

Table 18.1 Overview on reported surface properties important for UPSM

Process	Quantification	Material removal rate	Material	Medium	Roughness RMS (nm)	Laser	Reference
USPL-Ablation	Pulse	135–324 (nm/Pulse)	Si	Air	20–100	Ti:Sapphire	[17, 24]
LIBWE	Pulse	5–30 (nm/Pulse)	SiO_2	Toulene	10–30	KrF	[62]
LESAL	Pulse	1–10 (nm/Pulse)	SiO_2	Toulene (Vapor)	1–2	KrF	[45]
LIBDE	Pulse	10–100 (nm/Pulse)	SiO_2	Metal	2–10	KrF	[63]
LIPAA	Pulse	10–100 (nm/Pulse)	SiO_2	Metal	18–100	Nd:YAG	[64]
Laser wet etching	Time	~15 (µm/s)	Si	KOH	20–40	Ytterbium-Fiber	[24, 65]
Laser dry etching	Time	10–20 (nm/Pulse)	Si	Cl_2	50–100	KrF+/ArF+	[33, 66]
ALE	Pulse	~0.2 (nm/Pulse)	InP/GaAs	Cl_2		KrF+/ArF+	[67]
LIPE	Time	~1.5 (µm/min)	SiO_2	CF_4	1–2	Ti:Sapphire	[68]

quality. For millimeter-size axicons, a surface roughness of approx. 35 nm has been achieved [89].

An example of laser polishing in the extreme scale is reported in [90]. Here an ablation-based laser polishing process on Ge is reported using femtosecond laser radiation: it was shown that by removing 6 nm of the surface material the original optical quality surface roughness of <1 nm could be maintained during the material removal process.

2 Laser-Induced Reactive Plasma Etching

Laser-induced chemical etching and laser hybrid etching processes enable machining with good surface quality that cannot be reached by standard laser ablation. However, all these methods require the direct activation of the involved material, i.e., the reactive gas, the sample material, or both.

It has been proven that plasma processes can lead to high-quality surfaces while using less-dangerous gases without the requirement of expensive equipment. In particular, atmospheric-pressure plasma jets (APPJ) have proven their applicability to UPSM [58, 91, 92]. The plasma in industrial processes were ignited by electrical energy, e.g., by microwave or RF excitation. However, the walls of the equipment can cause plasma contaminations or plasma-borne particles. Further, for surface machining, the plasma generator needs to be moved along a path for surface figuring, which limits the speed of machining and implies limitations of the machining strategy.

However, focused laser radiation can also be used for the ignition of plasmas by optical breakdown. Plasma can be ignited by laser radiation in materials if the laser pulse power density exceeds a certain value to generate sufficient free carriers in a material. Once the carrier density exceeds the critical density, plasma is formed by optical breakdown. Optical breakdown can be observed in solid [93, 94], liquid [95–98], and gaseous media [99–103].

A useful definition of the optical breakdown in gases is that the electron density must exceed a threshold of ~10^{14} cm^{-3} [99]. The ionization of a gas in the strong electric field of a laser spot can occur due to two main processes: multiphoton ionization due to the absorption of several photons simultaneously or impact ionization by accelerated energetic electrons. The combination of both processes can result in an avalanche ionization where seed electrons generated by multiphoton ionization processes are accelerated by the strong electric field provided by the laser in the focal region. If the accumulated energy is high enough, collision can cause impact ionization of other atoms or molecules with the result of new free electrons. All ionization mechanisms can contribute according to the material and laser irradiance to the free electron density in the gas that finally results in the formation of plasma.

In Fig. 18.4 the laser-induced plasma is visible as a luminescent region in the gas. The processes involved in the optical breakdown are very complex, and detailed investigations have been performed since the invention of short-pulse lasers. Optical breakdown and plasma ignition are related to extreme conditions like high temperatures, extreme pressures, and high electric fields; all processes have an extremely high dynamic range during the laser pulse. More details on laser-induced optical breakdown in gases can be found in references [99, 104–107]. Up to now, these laser plasmas in gases were used mostly for analytic purposes, e.g., laser-induced breakdown spectroscopy (LIBS) [108] or as sparks in combustion engines [109].

Ignition of laser-induced plasma in gases is strongly dependent on the laser parameters, i.e., wavelength, pulse duration, and pulse power, as well as on the characteristic parameters of the surrounding gas, e.g., ionization energy and gas pressure. For nanosecond laser pulses, typical pulse energies of tens to 100 mJ are required for the plasma ignition in air [110–112]. After sufficient seed electrons are available, the subsequent parts of the nanosecond laser pulse can interact with the electrons in the plasma by inverse bremsstrahlung and enable further energy absorption by the plasma, resulting in higher temperatures and degrees of ionization. For nanosecond laser pulses, the high pulse energy required for igniting the plasma in combination with the inverse bremsstrahlung effect results in a large, excited volume, a highly energetic plasma, and strong secondary effects like shock waves that might damage the sample material.

Experiments on laser-induced plasma etching of SiO_2 in N_2 and air atmosphere using nanosecond laser pulses have been reported by Elhadj et al. [113]. Well-defined, high-quality machining could not be achieved due to thermal effects and shock waves that result in surface damage by melting and crack formation [113]. To avoid these unwanted side effects, plasma ignition with ultrashort laser pulses and optical breakdown at low laser pulse energies with stable, well-defined plasma formation is preferred. Ultrashort laser pulses provide preferred conditions for laser-induced plasma generation for precise machining of materials. Typical pulse energies are in the range of 10^{15} W/cm^2 for igniting a plasma by ultrashort laser pulses [99]. Hence, results on laser-induced plasma etching at atmospheric pressure using reactive gas mixtures were reported only recently [68, 114, 115].

3 Experimental Results on Laser-Induced Plasma Etching

Laser-induced plasma etching (LIPE) is a rather new approach for etching/machining of surfaces involving complex physical-chemical mechanisms by combining rapidly expanding laser-induced non-equilibrium plasma at atmospheric pressure and chemical reactions of the plasma-activated species with the substrate surface. Hence, the underlying mechanisms are complex, and only selected processes involved in the mechanism will be discussed. As the quality of the surface etched by the laser-induced plasma is high, this machining approach will be discussed here from the perspective of UPSM applications.

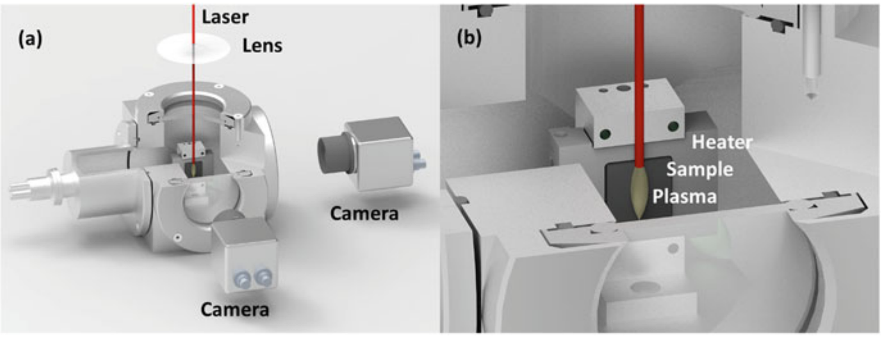

Fig. 18.3 (**a**) Sketch of the chamber for the basic studies of the LIPE process. The two cameras are used for determining the distance of the plasma to the sample. The chamber with the sample is mounted on stages so it can be moved relative to the fixed laser focal point that defines the plasma. (**b**) The magnified image of (**a**) shows sketched plasma in front of the sample on top of the heated sample holder. An optical image of laser-induced plasma in front of a substrate is shown in Fig. 18.4

The main components of LIPE experiments are as follows: (I) an ultrashort pulse laser source including optics for igniting the plasma, (II) a system for moving the laser-induced plasma relative to the sample surface, and (III) a system for maintaining/controlling other experimental parameters, for instance, the etching gas composition by a gas handling system, the pressure, the gas flow, and the sample temperature. Typically, the experiments were performed at or near atmospheric pressure. However, selected experiments were performed in a pressure range of ~400 to ~2000 mbar. Typical gases/gas mixtures used for LIP etching are CF_4 or CF_4/O_2, SF_6 or CHF_3 for dielectric materials, and air or O_2 for polymers. A femtosecond or picosecond laser source has been used for igniting the plasma in order to reduce mechanical and thermal stress load of the substrate due to shock waves and direct radiation. In order to avoid a direct contact of the laser beam with the substrate, the laser beam is aligned parallel to the substrate surface and focused through a window by a lens. The distance between the plasma and the substrate as well as the position and size of the plasma is monitored by cameras (Fig. 18.3). In Fig. 18.3, a typical setup used for LIPE is shown, with which the essential dependencies of the LIPE process are studied. Typically, the experiments were performed at an absolute pressure of 850 ± 50 mbar. Either pure CF_4 or a mixture of CF_4/O_2 has been used as etching gas. The chamber includes a sample holder with an integrated silicon nitride resistance heater that can operate in a temperature range of RT to ~500 °C. The chamber can be evacuated to low vacuum and could also withstand slight overpressure, if desired. A femtosecond laser having a pulse length of 150 fs, a wavelength of $\lambda = 775$ nm, and a pulse repetition rate of $\nu = 1$ kHz provides a maximum pulse energy of $E = 1$ mJ. The laser beam was focused inside the chamber by a lens (outside the chamber) having a focal length of 60 mm.

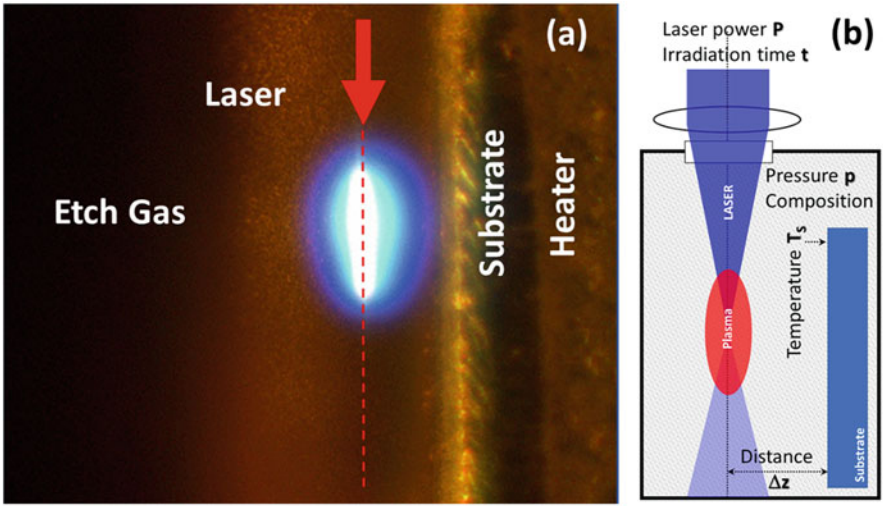

Fig. 18.4 (**a**) Optical image of a laser-induced plasma in front of a substrate surface during the LIPE process using CF_4 etching gas. The laser beam propagation and the center of the LIP are indicated. (**b**) Sketch of the experimental situation including the main parameters that influence the LIPE

The spot size and Rayleigh length of the laser focus are $r_g = 6.5$ μm and $l_{Ry} = 137$ μm, respectively, which results in a maximum power density of ~5×10^{15} W/cm^2 in the focal position. This value significantly exceeds the threshold for laser ignition of plasma in gases. The laser pulse energy and the focal length determine the size of the initially excited plasma volume. The visually observed size of the plasma increases with increasing pulse energy. Due to the caustic near the laser focus, the critical power density for plasma ignition can be exceeded already before the focal point [66, 73]. As the laser photon absorption and plasma scattering processes cause the reduction of laser power, the laser plasma can move in front of the laser focal point with increasing laser pulse energy. The temporal development of the plasma after ignition is very complex and depends on a variety of other parameters, such as the gas composition and gas pressure [116]. In Fig. 18.4 an image of typical plasma in front of a sample is shown.

4 Parameter Dependencies of Si and SiO_2 Etching

The characteristic dependence of LIPE on selected parameters has been studied for key materials such as Si and SiO_2 because they have manifold applications requiring high-quality surfaces. Because of the high sensitivity of chemical etching processes to any surface defects, such as surface contaminations, roughness, or structural defects, the sample has been cleaned carefully before the LIPE process.

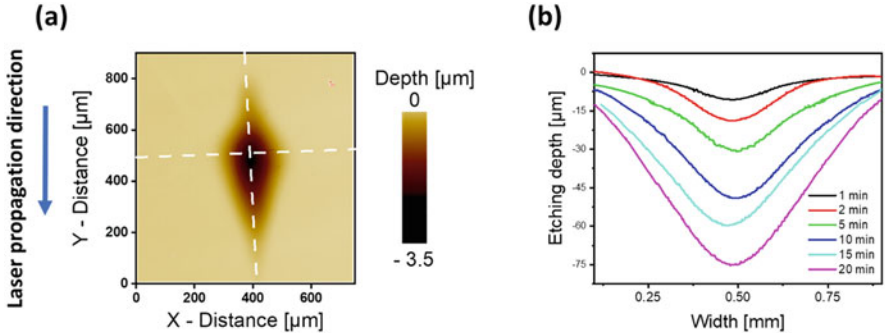

Fig. 18.5 (**a**) Contour plot of an LIPE-etched SiO_2 surface. Reproduced from Ehrhardt et al. [68] under license CC-BY-ND 4.0. The etching grove was measured by white light interferometry (WLM). The white dashed lines indicate the main and minor axes of the elliptically shaped etching groove. (**b**) Cross section along the main axes of an etching groove etched by LIPE in Si. The different cross sections represent different etching times. (Reproduced from Heinke et al. [114] under license CC BY-ND 4.0)

The following two-step clean process has been used for the SiO_2 and Si surfaces: (1) washing in a solution of 1-ml NH_4OH, 2-ml H_2O_2, and 40-ml H_2O and (2) ultrasonic cleaning at 50 °C in a solution of 1-ml HCl, 2-ml H_2O_2, and 8-ml H_2O for 20 min. Subsequently, the samples were rinsed with de-ionized (DI) water and dried thereafter by spin-off and heating for 3 min at 115 °C on a hot plate. The samples can be stored for a few days in a dry atmosphere before they are applied for LIPE studies [117].

One of the most important characteristics of UPSM processes is the etching rate that determines the etching speed for a series of laser pulses and the minimal achievable etching depth. The latter limits the achievable depth accuracy of laser-based surface machining processes. The average etching rate is calculated by dividing the maximum etching depth by the etching time or applied laser pulse number, respectively. Further, the stability of the material removal process – this can be related to the so-called incubation process known from laser ablation – needs to be considered for areal machining tasks. If needed, the machining strategy needs to be adopted to potential alterations of the material removal or etching rate. Hence, the etching rate knowledge is key for UPSM process applications.

In Fig. 18.5, a typical LIPE etching groove, having an elliptical shape with a short and a long axis, called the footprint of the machining processes, is shown exemplarily. Typically, the center of the footprint is the deepest point of the etching. The major and minor axes have typical length of around 700 and 300 µm, respectively. However, the length ratio of the major/minor axes can vary strongly with the specific parameter set used for LIPE. Cross sections along the major axes of grooves etched in silicon, shown in Fig. 18.5, indicate that the shape changes for different etching times. In general, the footprint of LIPE is only weakly correlated with the laser spot size, in contrast to laser ablation processes, but is similar to the

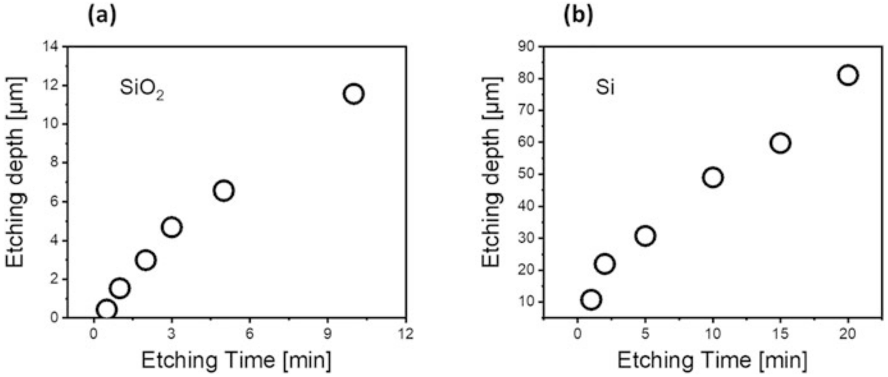

Fig. 18.6 Etching depth after LIPE in the dependence of the etching time used. The image (**a**) shows a typical curve for SiO_2 [68] and the image (**b**) for Si [114]. (Reproduced from Ehrhardt et al. [68] and Heinke et al. [114] under license CC BY-ND 4.0)

size and shape of the visible plasma plume. The footprint is related to the reaction speed of the reactive species near the surface that are generated near the focal point and redistributed due to the dynamics of the expanding plasma and diffusion processes.

Therefore, the footprint of the etching is wider and differently shaped compared to the focal region. The chemical etching reaction at the surface can be described by an Arrhenius equation (compare Eq. (18.1)) with the reactive species density and the surface temperature as the key parameters of the reaction rate. Reactive species and their temperatures may be affected by the plasma as discussed later. However, as the surface temperature can be considered to be almost constant – the laser does not hit the sample surface – the footprint of the etchings is a manifestation of the temporally integrated density of reactive species impacting the surface. Thus, all parameters affecting the etching rate also change the footprint. LIPE represents a unique mechanism that comprises a sequence of processes that finally result in surface material removal by chemical reactions.

In Fig. 18.6, the etched depth in dependence of the etching time is shown for silicon and silicon dioxide. The etching depth increases almost linearly with etching time. The slope of the etching rate alters slightly at the beginning of the etching process: for short etching times, a higher slope, which is equivalent to the etching rate, is found.

For silicon the average etching rate first increases up to ~3 min and then decreases slightly and thereafter forms a plateau as depicted in Fig. 18.7. The etching rate can be converted into an etching depth per laser pulse as the plasma decay time of $\ll 100\ \mu s$ is much less than the temporal pulse interval of 1 ms. According to Fig. 18.7, typical achieved etching depths for SiO_2 using a single laser pulse are in the range of 0.01–0.03 nm, which is much less than the lattice constant of silicon of approx. 0.5 nm. Hence, on average several laser pulses and in consequence plasma flashes are needed to remove an atomic layer from the sample surface.

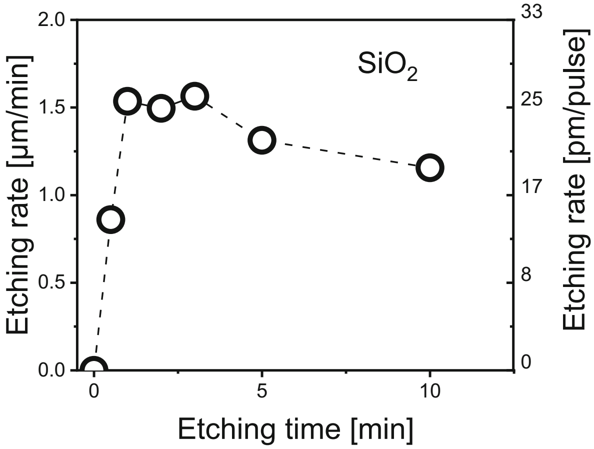

Fig. 18.7 Typical dependency of the etching rate on the etching time for SiO_2. The left scale shows the average etching rate per min, the right scale shows the average etching rate per applied laser pulse. (Reproduced from Ehrhardt et al. [68] under license CC BY-ND 4.0)

Such an almost linear increase in the etching depth as well as the low single-pulse etching depth can be observed for all simple materials if an appropriate etchant is applied. Good depth control due to the subatomic etching depth per pulse as well as a sufficiently high average etching rate for high laser repetition rates can be achieved. A particular depth distribution for applications can be achieved by controlling the laser pulse generation along the machining path. These characteristics qualify LIPE as an ideal tool for UPSM because the needed precision, a high etching rate, and good control of the etching depth can be achieved by adjusting the pulse repetition rate.

Etching is caused by complex interactions of several influencing factors and various processes of the etching process. In general, with the first laser pulse, the whole system is disturbed and changes at prolonged etching to a new quasi-equilibrium state in relation to gas-phase composition, sample substrate composition/structure, and the chemical processes involved in etching. In particular, the actual gas composition changes due to the LIPE and the stimulated chemical processes in the gas phase (homogeneous reactions, decomposition, etc.) and at the sample surface (heterogeneous reactions, etching product formation). The feed of fresh gas and the exhaust of used gas will determine the species concentration near the sample surface, in addition to LIPE gas phase and surface reactions. At the sample surface, the coverage with adherent molecules (e.g., SiO_2 in the case of silicon, airborne contaminations, or etching products) and the sample surface structure have an impact on the surface reactions. To make matters more complicated, the surface structure is affected by the sample's initial finishing processes and thus may include various defects and subsurface damage. Each of these processes needs a specific activation energy that can be provided by thermal processes or photons such that the speed of the surface reactions and, therefore, the LIPE etching rate depends also on the temperature.

After starting the etching process, the substrate's surface temperature can increase continuously due to additional heating from the laser-induced plasma until equilibrium is reached. Higher temperatures will accelerate chemical processes, in particular those featuring strong temperature dependence. Besides heating by plasma particles, the surface processes are affected by a significant amount of UV and soft X-radiation, which is generated in the plasma. These additional high-energy photons can initiate photochemical processes and reactions. It was shown that photogenerated carriers can enhance the etching of silicon for a low-pressure CF_4/O_2 plasma [53]. Such processes provide additional reaction paths that can contribute to the whole etching mechanism. For instance, the high-energy radiation alters and weakens the bonds of the substrate material that, e.g., promotes a preferential chemical attack of the reactive species from the plasma. Furthermore, plasma heating as well as high-energy radiation causes the removal of surface contaminants, such as fluoropolymers or oxides, which hinder the etching process.

Prolonged etching results in the decrease in the etching rate for several reasons. The main factor is the increase in the distance between the plasma and the surface due to the material removal as etching progresses. A larger distance of the plasma to the sample surface results in less-effective heating and irradiation of the surface by the plasma. In addition, less and differently activated species can be expected as the species need more time to diffuse to the surface. For example, deexcitation induces collisions with neutral gas molecules. However, because the change in the etching rate is related to the change in the distance of the laser-ignited plasma to the substrate surface, the etching rate reduction can be compensated by technical means. SiO_2 etching by LIPE with a CF_4 plasma, having a rate of 0.015–0.028 nm per pulse, is similar to photochemical laser dry etching with CF_2Cl_2 and CF_2Br_2, having a rate of 0.02–0.05 nm per pulse [24]. This can be an indication for similarities of the rate-limiting process.

The relationship between the etching rate and the plasma distance is remarkably linear for the etching of Si with LIPE in the CF_4/O_2 atmosphere, as Fig. 18.8 shows. For these conditions, etching has been experimentally observed up to a distance of ~225 μm between the plasma and the substrate surface. The transport of reactive species to the substrate surface is based on fluid flow and diffusion processes. These transport processes affect the distribution and the time delay between generation of the species and their interaction with the sample surface. This also means that due to the collisions with other molecules during diffusion, very different species arrive at the surface, and those may not be capable to etch but may cause deposition. Further, the plasma-generated reactive species have a low kinetic energy near the sample surface because the free mean path at atmospheric pressure is less than 1 μm. As a result, anisotropic (directional) etching or sputter effects can be ruled out as dominating etching mechanisms. A decrease in the silicon etching rate with the increase in the distance between a laser-activated volume and the surface was found for CO_2 laser dry – LICE with NF_3 [32]. In this case, a rather linear relationship

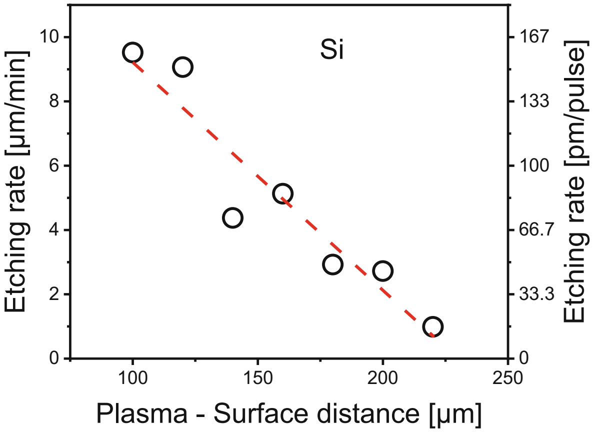

Fig. 18.8 Etching rate in dependence of the plasma-surface distance for silicon. The plasma-surface distance was measured from the center of the plasma to the substrate surface. (Reproduced from Heinke et al. [114] under license CC BY-ND 4.0)

to the pulse energy and reciprocal function to the laser beam-substrate distance was experimentally found.

The differences between LIPE and dry-LICE with NF_3 must be discussed mainly in relation to the chemical reaction paths and the excitation volume. The much-smaller excited volume at LIPE favors deactivation processes, and the used etching gases CF_4 cause not only etching reactions with silicon but also polymerization reactions, forming protective layers on the sample surface. Both reaction paths are in concurrence at the sample surface, and once the etching reaction is not dominant, polymerization reactions can suddenly terminate etching.

For chemical-reaction-dominated etching methods, temperature is one of the main factors that influence the material removal rate. According to the transition state theory, the rate of a chemical reaction increases with the increase in temperature and becomes noticeable after a specific activation energy is exceeded. For the simplest case of heterogeneous chemical reactions at the substrate, the reaction rate K is usually governed by the Arrhenius equation:

$$K = A \exp\left(-\frac{E_a}{R\,T}\right) \tag{18.1}$$

where the pre-exponential factor A is related to the number of potential reaction sites at the surface, meaning, for instance, specific reactive species hitting/adsorbing the surface, E_a is the activation energy for this reaction, R is the universal gas constant, and T is the surface temperature. The two main experimentally accessible parameters influencing the reaction rate of the reaction under consideration are the number of species arriving at the surface and surface temperature. However, it is necessary to keep in mind that

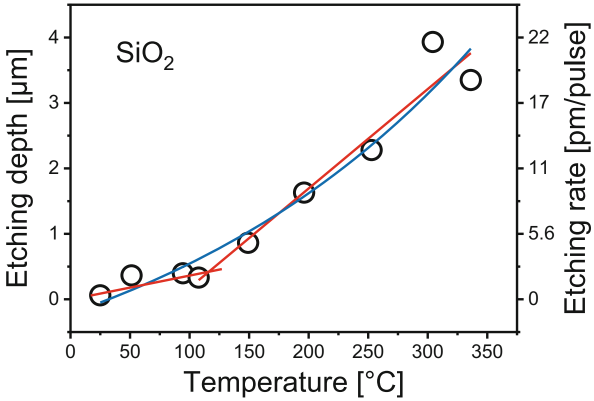

Fig. 18.9 Etching depth and etching rate in dependence of the substrate temperature for SiO$_2$ after an etching time of 3 min. The two red lines are linear fits of the experimental date for a low temperature range and high temperature range, respectively. The blue line is a fit of Eq. (18.1) to the data

- different species arriving at the surface,
- all other processes in the reaction mechanism can also be limiting the reaction rate at the surface,
- different processes can be influenced by one experimental parameter, and,
- the dynamics of the laser-induced processes imply that we deal with a nonstationary process.

In Fig. 18.9, the experimental data for the temperature dependence of the etching depth and fitted linear and exponential dependencies are shown. The two linear fits intersect also for other materials near 100 °C which can be interpreted as a transition temperature.

The characteristic etching depth dependence of LIPE on the temperature has been fitted by Arrhenius Eq. (18.1). The accuracy of the fit is rather good, and the results indicate an activation energy for the LIP SiO$_2$-etching process of 18 kJ/mol. This is a fairly low activation energy but is typical for plasma etching processes as comparisons with other etching processes show. An activation energy of 18 kJ/mol was measured for low-pressure SiO$_2$ etching with a CF$_4$/O$_2$ gas mixture regardless of the difference in the etching rate [118]. It was suggested that the rate-limiting reaction is the reaction of SiO$_2$ with F*. Despite there being good agreements, other rate-limiting processes with a low activation energy can also be considered as an explanation, such as the adsorption of species or the desorption of reaction products. In addition to thermally activated processes, synergistic effects with radiation-related activation can occur as already mentioned.

The main chemical reaction paths for CF$_4$ plasma etching of Si are summarized in refs. [119, 120]. These reaction mechanisms have been proposed for low-pressure plasma etching. The similarity of activation energies, however, suggests that similar chemical reactions dominate the etching process for LIPE at atmospheric pressure.

As mentioned, the optical breakthrough due to the high electric field of the laser causes the ionization of etching gas components. During collisions of charged particles, many processes occur. The main mechanism for CF_4 decomposition based on electron impact is

$$e + CF_4 \rightarrow CF_4^* \rightarrow CF_3^* + F + e \tag{18.2}$$

Further important reactions for fluorine generation are

$$e + CF_4 \rightarrow CF_3 + F + e \tag{18.3}$$

$$e + CF_4 \rightarrow CF_3 + F^* \tag{18.4}$$

and the detachment reaction

$$CF_3^* + F \rightarrow CF_2 + 2F \tag{18.5}$$

In the presence of oxygen, the following reaction is likely besides the reaction of atomic oxygen with CF_4 [121]:

$$CF_3 + O_2 \rightarrow COF_2 + OF \tag{18.6}$$

The following two paths can also be a source of fluorine because the OF radical is highly reactive [121]:

$$CF_3 + OF \rightarrow COF_2 + 2F \tag{18.7}$$

$$OF + OF \rightarrow O_2 + F_2^* \rightarrow O_2 + 2F \tag{18.8}$$

Volatile products that can leave the surface need to be formed by the reaction of surface atoms with excited species generated in the plasma. The main reaction contributing to the etching of silicon that forms volatile SiF_4 can be summarized as follows [121]:

$$4F + Si \rightarrow SiF_{4\ (gas)} \tag{18.9}$$

Hence, the dominant etchant for Si in a CF_4 plasma is atomic fluorine.

In addition to chemical reactions to form etchants, other reaction paths can result in polymerization reactions. Such polymerization processes can cause the formation of a fluoropolymer layer on the substrate surface [119, 122, 123] that sticks well to the surface and can result in masking. One example is as follows:

$$n\ CF_3 \rightarrow [-CF_2-]_n\ (P) + n\ F \tag{18.10}$$

A thin layer of this fluoropolymer can already influence or prevent etching of the substrate surface as the direct attack of the activated etchants is inhibited, in particular for low kinetic energy of the reactive etchants.

To reduce or suppress such polymer film formation on the sample surface, oxygen in different forms is added to the etching gas, leading to the formation of volatile carbon-containing products such as CO, CO_2, and COF_2. This means fluoropolymer deposits from CF_4 LIP contain carbon. The addition of oxygen to CF_4 gas mixtures can reduce the polymerization on the surface with results in a better, more stable, and high-quality etching.

The intensive UV and soft X-ray irradiation from the laser-induced plasma close to the surface may also influence the decomposition of fluoropolymer layers [124]. Besides the plasma characteristic and gas composition, the substrate properties, e.g., the crystal orientation, also determine the LIPE process. The measurement of the etching rate for crystalline silicon with different crystal orientations shows an orientation-dependent etching rate with the highest and lowest etching rate being observed for <111> and <110> wafers [114], respectively. Such differences in the etching rate are known from wet and low-pressure dry etching processes and can be related to different activation energies needed for etching these crystal surfaces.

The etching depth of SiO_2 increases with higher pulse energies after exceeding a threshold energy as shown in Fig. 18.10. A linear increase in the etching rate with the laser pulse energy has been observed for LIPE of different materials. The threshold is clearly determined by the laser plasma ignition and the etching rate enhancement by the stronger plasma excitation. Experimentally, the increase in the luminous plasma volume with the laser pulse energy was observed, as expected. The higher energy should cause a brighter plasma with a higher density of reactive species. Such an increase in the reactive species density with the input power is regularly observed in low-pressure CF_4/O_2 plasmas [125]. Similar effects are also expected in the case of laser-induced plasma with increasing laser pulse energy [99]. In contrast to continuous RF-pumped plasmas, laser-induced plasmas should feature a nonlinear transfer of the laser pulse energy to plasma excitation because the laser photon absorption is already nonlinear, and the power density varies in the focal region. Therefore, only a fraction of the pulse energy, for instance, only 10%, is absorbed by the gas and contributes to plasma formation at $E = 600\ \mu J$ [99]. Hence, the reasons for the linear slope are not clear but might be related to other rate-limiting processes of the whole LIPE mechanism.

In addition to energetic considerations of plasma formation, the high spatial and temporal dynamics of these laser-induced plasmas need to be considered for the discussion of all experimental data as the plasma influences various factors of the mechanism simultaneously.

With the goal of investigating the dynamics of the laser-induced plasma, short-exposure snapshots of the LIP without a substrate were taken across a wide LIP parameter range using different delay and exposure times. The optical emission of the laser-induced plasma, seen in Fig. 18.11 for three characteristic delay times, shows an ellipsoidal plasma. Detailed studies show complicated morphological changes in the plasma plume from the beginning of the optical breakdown in the

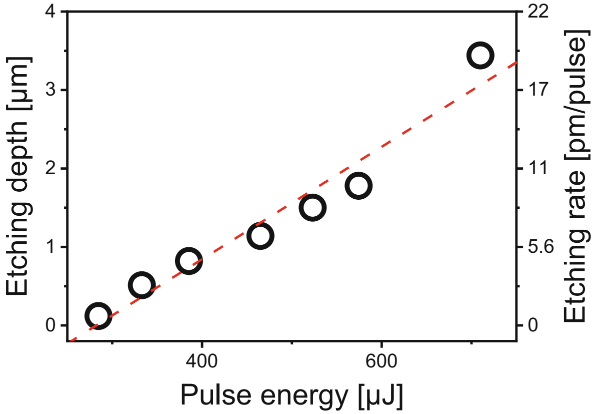

Fig. 18.10 Etching depth and etching rate of SiO_2 in dependence of the laser pulse energy after 3-min LIPE processing. (Reproduced from Ehrhardt et al. [68] under license CC BY 4.0)

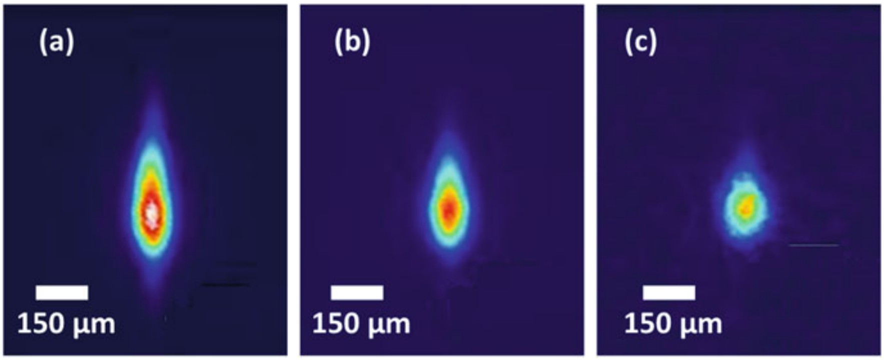

Fig. 18.11 High-speed images of a laser-induced plasma in CF_4. The images were taken at (**a**) the start of the plasma, (**b**) 1000 ns, and (**c**) 25,000 ns after applying the laser pulse. After ~6 µs, no plasma could be detected. (Note, the intensity is coded in false colors)

focal region to the quenching of the plasma that depend strongly on the laser parameter used as well as on the etch gas composition [116]. The plasma is at this stage of thermal nature.

The footprint of LIP etchings, as seen in Fig. 18.5a, can be related to the plasma dynamics. The ellipsoidal part can be related to highly excited reactive species or secondary radiations from the laser-induced plasma. The central feature of the footprint along the laser path may be discussed with the early generated plasma portions that decay quickly outside the central plasma plume.

Hence, the focusing conditions, the laser parameters, but also the plasma dynamics determine the footprint. Furthermore, when designing a footprint, the spatial-temporal plasma dynamics need to be considered. For instance, plasma ignited with a high numerical aperture lens needs lower laser pulse energy and has a smaller size and altered dynamics. All these substantial changes result in alteration of the etching rate and the footprint shape. The design of determined footprints that are useful for UPSM may be realized by designing a real or virtual laser spot shape.

Typical materials that have been studied with LIPE are SiO_2 [68], Si [114] SiC, TiO_2, and Ge [115]. However, also organic materials, polymers, composite material, e.g., SiC-SiC [126], or technical glasses can be processed by LIPE under UPSM requirements.

The general requirement for materials applicable to LIPE processes is the possibility of forming volatile products with plasma-activated etchants. For LIPE processes, suitable gases react inherently with the sample surface, forming gaseous, volatile products. In the case of LIPE, the etchants are formed only within the plasma region so that the etching gas(mixture) can be inert.

Typical etching gases containing halogen compounds were used for plasma etching of oxides. With CF_4-containing gas mixtures, in addition to silicon-containing materials, a wide variety of materials can be etched as compiled in Table 18.2.

These materials, listed in Table 18.2, show similar correlations between laser etching parameters and etching results compared to the demonstrated results in the case of using appropriate etching gases.

For polymers like polyimide (PI), oxygen is needed for the formation of reactive species that oxidize the carbon of the polymer resulting in the formation of carbon oxide and water. Hence, PI can be machined very well with LIPE using air without heating of the substrate, though the etching rate can be significantly increased when using a pure oxygen atmosphere and moderate heating (150 °C). Aluminum cannot be LIP-etched by CF_4/O_2 mixtures as the formed aluminum fluoride is not volatile at the etching temperatures used and thus forms a protective film screening the surface from the attack of reactive species.

5 Characterization of Etched Surfaces

In addition to the processing speed given by the etching rate, there are several other factors that determine the applicability of the LIPE process for UPSM. They are the ablation depth per laser pulse, which determines the achievable depth precision of the LIPE process; the structural and morphological surface characteristics; the remaining chemical modification; and the achieved surface roughness. In order to have a reliable LIPE process and also high surface quality, it is required that the surface of the substrate is free of contamination because the LIPE process is highly selective. Hence, a pre-processing cleaning step, as described in Sect. 4, is recommended.

Table 18.2 Summary of materials and processes that were etched by laser-induced plasma (Note, the etching rate is given in pm/pulse)

Material	Etching rate (µm/min)	Etching rate (pm/pulse)	Etching gas	Etching temperature (°C)	Pulse energy (µJ)	Plasma-substrate distance (µm)
Ge	5.6	93	30% vol. O_2/70% vol. CF_4	200	750	100
TiO_2	4.2	70	30% vol. O_2/70% vol. CF_4	200	710	100
SiC	1.5	25	30% vol. O_2/70% vol. CF_4	200	735	100
SiO_2	1.4	23	100% vol. CF_4	200	710	100
Polyimide	10.3	172	100% vol. O_2	160	630	100
Si	7.0	117	17% vol. O_2/83% vol. CF_4	330	880	140
Al_2O_3	X	X	30% vol. O_2/70% vol. CF_4	200	700	100
GaAs	X	X	30% vol. O_2/70% vol. CF_4	200	710	100
N-BK7	3.3	55	30% vol. O_2/70% vol. CF_4	310	750	100

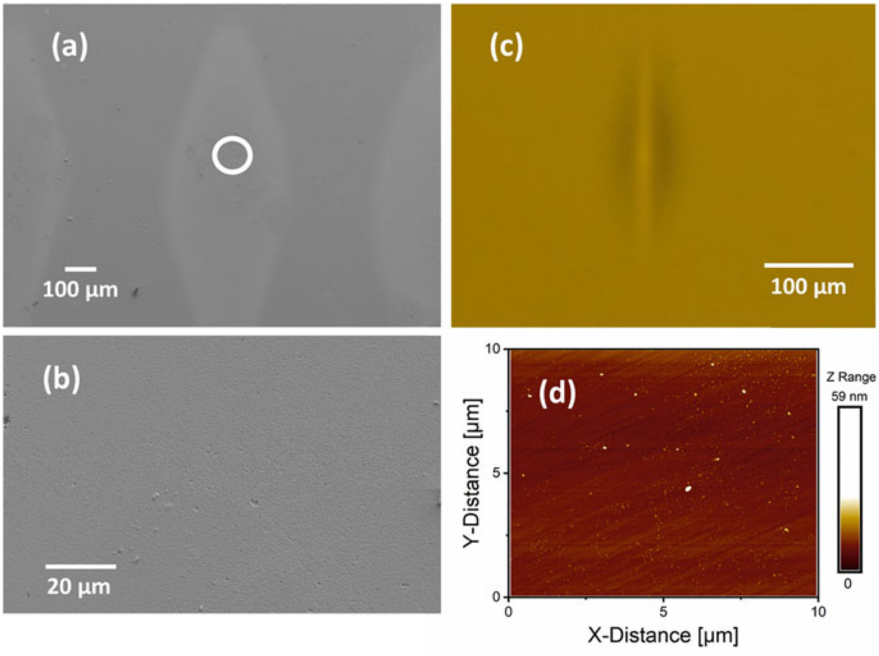

Fig. 18.12 Images of an LIPE-processed SiO_2 surface. In images (**a**) and (**c**), the whole etching groove is imaged by SEM and optical microscope, respectively. Images (**b**) and (**d**) show magnified sections of the marked area of image (**b**) measured by SEM and AFM, respectively. (Reproduced from works of Ehrhardt et al. [68] under license CC BY 4.0)

5.1 Morphology

A typical appearance of LIP-etched silica surfaces without further pre- or post-processing, e.g., cleaning or coating, imaged by different imaging methods is shown in Fig. 18.12. The SEM images (a, b) show an etched spot with two magnifications that features an increased secondary emission yield probably due to the microroughness of the surface seen in (b).

Holes and peaks, which both represent the roughness, can be attributed to the different etching rates of the surface. A faster etching forming the holes may be related to near-surface defects that provide a reduced activation energy for chemical etching processes. In contrast, the hills may be related to some surface contaminations originating from previous processes such as abrasive particles from the polishing process, or dust particles. Either way, they cause masking during etching. Despite the microroughness, the optical microscope image (c) shows a smooth surface. The AFM image (d) also shows these roughness features. A typical surface roughness of an etching groove with a depth of ~2 µm is in the range of 1–1.5 nm rms (AFM, 10 × 10 µm). As LIPE is an isotropic etching process, in a homogeneous, isotropic material, such as fused silica, holes and peaks change in size and develop to a rather wavy surface with the tendency of smoothing.

The formation of specific surface morphologies and increased surface roughness due to changed etching conditions have been observed because any compositional, structural, or directorial inhomogeneities can cause etching rate alterations. For instance, the development of pyramidal structures has been observed for LIPE of single crystalline silicon at specific conditions (CF_4/O_2 gas). The different, orientation-dependent etching rates are the main reason for their formation [114]. As a consequence, such etching rate differences can result in topographical roughness and waviness development for prolonged etching of polycrystalline or highly defective materials.

Different materials feature specific etching rates, as given in Table 18.2. The etching rate of composite materials should be related to the composition-weighted etching rates of the components. However, LIPE experiments with BK7, a glass composed of SiO_2 and different metal oxides, show a different scenario. According to the composition of the glass, a porous residue layer of metal fluorides, which are not volatile etching products, is formed. The porous film cannot be etched by the CF_4 plasma species and grows with etching time. Therefore, any material with compositional inhomogeneities, even at the atomic level, can form specific surface features including films or roughness when etching with certain etching gases. For microscopic composites like fiber-reinforced materials, the components are etched according to their etching rate. Jagged surface morphologies with a very distinct textured surface according to the microstructure of the composite were observed [126]. These topographies can also comprise undercuts in consequence of the isotropic LIP etching process.

As a consequence, the formation of any solid composite material – also for the surface region – comprising of etchable and stable components should be avoided during LIPE. Such a process has been observed for germanium at nonoptimized etching parameters, where an access of oxygen can result in GeO coalescence and the formation of surface adherend nano-sized particles. These results show also that LIPE is an atomic-level process driven by laser-excited reactive species and not a collective reaction of the absorbed laser photons.

5.2 Surface Analytics

The integrity of the processed surface is an important issue for UPSM. Compositional and structural modifications, including any subsurface defects and films, have to be avoided or reduced as much as possible. The contaminations from secondary reactions of the plasma with the chamber wall or other equipment parts can be neglected, as the plasma is small, and far away from these equipment's parts, it shows a reduction of its activity/reactivity after short distances. The risk of contamination by etching products or fluoropolymer films at nonoptimized etching conditions has already been mentioned.

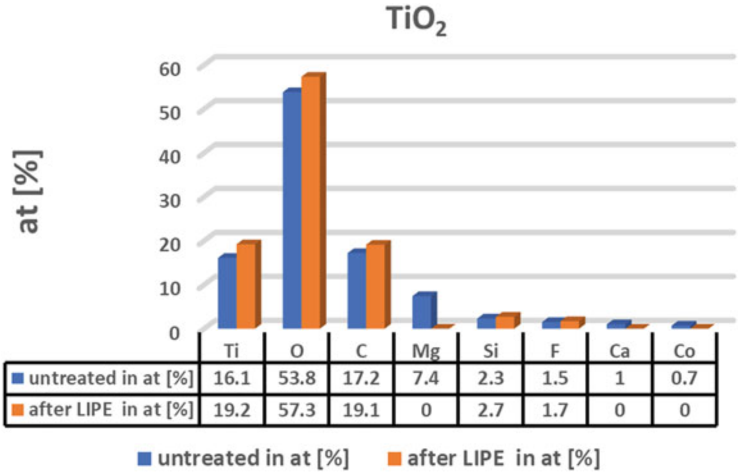

	Ti	O	C	Mg	Si	F	Ca	Co
■ untreated in at [%]	16.1	53.8	17.2	7.4	2.3	1.5	1	0.7
■ after LIPE in at [%]	19.2	57.3	19.1	0	2.7	1.7	0	0

Fig. 18.13 Composition of a TiO_2 surface before and after LIPE processing determined with XPS. Due to the LIPE processing, many of the impurities in the surface were removed. The LIPE etching was performed in CF_4/O_2 at atmospheric pressure and standard condition

X-ray photoelectron spectroscopy (XPS) analyses of LIP-etched surfaces, e.g., Si, SiO_2, and TiO_2, show a similar carbon concentration before and after etching. In many cases, it was found that an LIPE-processed surface has less contamination and impurities than the pristine surface despite the applied pre-etching cleaning. The composition of a TiO_2 surface before and after LIPE processing is shown in Fig. 18.13 exemplarily. It can be noticed that the amount of typical surface impurities is reduced due to the etching process. However, fluorine appears at the etched surface as a result of the applied CF_4 gas and non-desorbed etching products.

In comparison to other atmospheric plasma etching methods [127, 128], a unique characteristic of the LIPE is the absence of a fluoropolymer film formation at the sample surface [115] despite some fluorine also being found by XPS analysis. The reason for this effect is still under discussion, but the main argument for the small amount of fluorine occurrence on the etched surface is the significant higher plasma temperature. It leads to a high degree of the decomposition of the etching gas and reduces polymerization reactions. UV and X-ray radiation from the plasma may contribute to the decomposition of deposited organic materials on the surface. Laser-induced plasma temperatures of up to 6000 K and 12,000 K have been measured shortly after the laser ignition in air and argon gas [116]. Such high plasma peak temperatures may, in addition to the exposure by high-energy photons, remove any adsorbed/deposited fluorocarbon molecules.

Depth profiles of the material composition of etched germanium surfaces, taken by secondary ion-mass spectroscopy (SIMS), show some enrichment of fluorine and carbon at and around the etching groove. It can be concluded that a fluorocarbon film of some-nm thickness forms around the etching grove, whereas in the etched area,

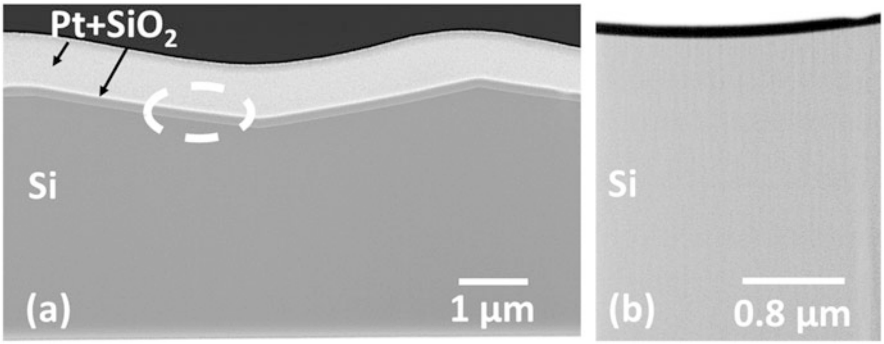

Fig. 18.14 TEM images of a cross section of an LIPE-processed Si surface. The Si was covered for cross-section preparation by a SiO_2 and Pt protection layer. Image (**b**) displays the magnified section of the image (**a**) marked area. The black layer is the deposited protection layer on top of the Si surface after LIP etching

the fluorine penetrates the Ge and forms sub-stochiometric Ge-fluoride that cannot yet desorb.

For UPSM processing, the reduction of subsurface damage is one of the key parameters. Structural examination of crystalline silicon, which was LIP-etched under typical conditions, was performed using cross-sectional TEM analyses. The images showed that typical defects related to laser ablation, such as resolidified material, cracks, stress, and dislocations, cannot be detected for LIP-etched silicon. Silicon crystallinity is maintained up to the surface except for an extremely thin layer containing oxide and fluoride. In Fig. 18.14, exemplary TEM images of a cross-sectioned, LIP-etched Si surface are shown. No subsurface defects have been generated due to the LIPE process. This is in strong contrast to the defect formation at direct laser ablation.

A comparison of physically dominated laser ablation processes and the chemically dominated LIP etching process shows clearly that the latter reduces subsurface damage dramatically. Hence, the principal characteristics of the LIPE process fulfill the requirements of UPSM of surfaces.

6 Future Requirements on Ultraprecise Surface Machining

The main future requirement of UPSM is the further improvement of important surface characteristics, such as atomic-level smoothness, angstrom-level depth control, and neglectable/no defects near the surface. In addition, there are technical requests in high-quality machining of smaller areas due to small devices or requests for diffractive, hybrid, or integrated optical surfaces. Atomically smooth and precise surfaces are related to the requirements of shorter wavelengths in EUV and X-ray optics for beam lines as well as in microelectronics where surface processing

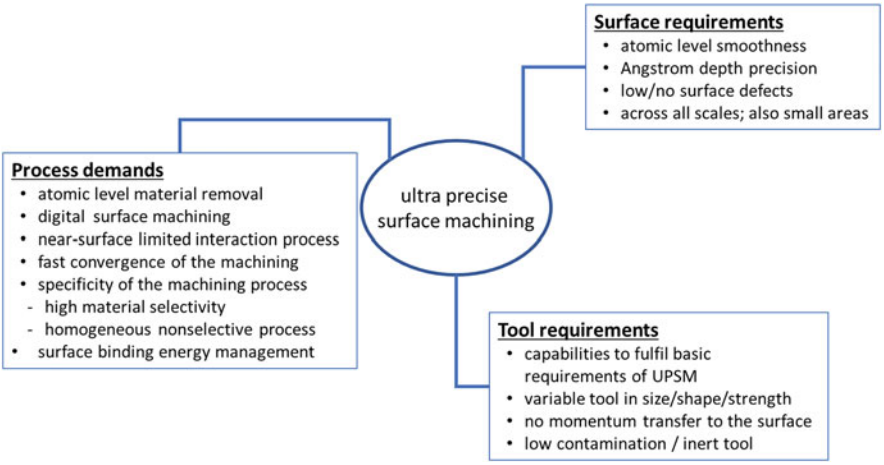
Surface requirements
• atomic level smoothness
• Angstrom depth precision
• low/no surface defects
• across all scales; also small areas
Process demands
• atomic level material removal
• digital surface machining
• near-surface limited interaction process
• fast convergence of the machining
• specificity of the machining process
- high material selectivity
- homogeneous nonselective process
• surface binding energy management
ultra precise surface machining
Tool requirements
• capabilities to fulfil basic requirements of UPSM
• variable tool in size/shape/strength
• no momentum transfer to the surface
• low contamination / inert tool

Fig. 18.15 Schematic representation of the further requirements on ultraprecise surface machining technologies

requires extreme control due to the reduction of the critical device dimensions and active film thickness. Defect scenarios are also important for mechanical applications as the surface properties determine important properties like friction, wear, and crack propagation.

The tool should be qualified to fulfill the requirements of UPSM as outlined in previous sections. This means, for instance, that the footprint should be adjustable during machining and that the material removal rate should be controllable as the process progresses. This will also allow to design efficient machining strategies adaptable to the aim of the machining and to the surface design and enable a single-step machining with high effort and convergence. Figure 18.15 presents a schematic summary of the various aspects that are necessary for future UPSM technologies.

A possible approach to fulfill the multiple requirements of UPSM are the management of the composition and surface binding energy of the last monolayer at the surface that can be reaction products. This management gives atomic-level precision in general but needs suitable interaction processes. One general approach is provided by atomic layer deposition or etching processes that are thermally activated chemical processes on specific materials on large areas. Energy-selective activation of such processes would allow us to distinguish between tool interactions with the surface and with the subsurface material.

7 Summary and Conclusions

Ultrahigh-precision surface machining is increasingly needed in various application fields due to the future demands on the surface quality related to any nanotechnological development. Traditional technologies can be complemented by beam technologies, as has been shown, but laser beam-based methods enabling atomic-level processing accuracy are rarely found. With this goal, different laser-processing approaches to achieve high depth control and defect-less surface machining are first reviewed.

Ultrahigh surface qualities are often not achievable with physical-based laser machining approaches due to the high energy densities involved in the processing mechanism that triggers several critical secondary processes, in particular subsurface defect formation. On the other hand, laser-induced chemical machining often needs aggressive chemicals. A carefully designed machining process and a selection of suitable materials are needed and given those difficulties, limitation in applications exists. The combination of different interaction mechanisms for ultraprecise surface machining is favorable if processes are combined that are complimentary, i.e., they support each other in a specific manner. The advantages of both physical and chemical processes can be combined, tuned, and utilized in specific sequences to fulfill application-specific requirements of UPSM in a more precise way, e.g., for the processing of optics.

Therefore, recent results on laser-induced plasma etching were summarized, and the capabilities of this technology for UPSM were shown. Technologies that combine physical and chemical mechanisms can benefit from the advantages of both, bringing UPSM to a new level.

Acknowledgments The help of Robert Heinke, Andriy Lotnyk, Jens Bauer, and Mohammad Afaque Hossain with the experiments is highly acknowledged. The work was funded in parts by the Deutsche Forschungsgemeinschaft (DFG, German Research Foundation) – No. 392226212.

References

1. N. Taniguchi, Current status in, and future trends of, ultraprecision machining and ultrafine materials processing. CIRP Ann. **32**, 573–582 (1983)
2. D.A. Lucca, E. Brinksmeier, G. Goch, Progress in assessing surface and subsurface integrity. CIRP Ann. **47**, 669–693 (1998)
3. J. Corbett, P.A. McKeown, G.N. Peggs, R. Whatmore, Nanotechnology: International developments and emerging products. CIRP Ann. **49**, 523–545 (2000)
4. Z. Zhang, J. Yan, T. Kuriyagawa, Manufacturing technologies toward extreme precision. Int. J. Extreme Manuf. **1**, 022001 (2019)
5. M. Pfiffer, J.L. Longuet, C. Labrugère, E. Fargin, B. Bousquet, M. Dussauze, S. Lambert, P. Cormont, J. Néauport, Characterization of the polishing-induced contamination of fused silica optics. J. Am. Ceram. Soc. **100**, 96–107 (2017)
6. Y. Lee, Evaluating subsurface damage in optical glasses. J. Eur. Opt. Soc.-Rapid Publ. **6**, 11001 (2011)
7. G. Ghosh, A. Sidpara, P. Bandyopadhyay, Review of several precision finishing processes for optics manufacturing. J. Micromanuf. **1**, 170–188 (2018)
8. M. Shaw, Precision finishing. CIRP Ann. **44**, 343–348 (1995)

9. K.-M. Han, S.-Y. Han, S. Sahir, N.P. Yerriboina, T.-G. Kim, N. Mahadev, J.-G. Park, Contamination mechanism of ceria particles on the oxide surface after the CMP process. ECS J. Solid State Sci. Technol. **9**, 124004 (2020)
10. J.C. Rozzi, F.E. Pfefferkorn, Y.C. Shin, F.P. Incropera, Experimental evaluation of the laser assisted machining of silicon nitride ceramics. J. Manuf. Sci. Eng. Trans. ASME **122**, 666–670 (2000)
11. T. Arnold, G. Böhm, R. Fechner, J. Meister, A. Nickel, F. Frost, T. Hänsel, A. Schindler, Ultra-precision surface finishing by ion beam and plasma jet techniques-status and outlook. Nucl. Instrum. Methods Phys. Res., Sect. A **616**, 147–156 (2010)
12. A. Schindler, T. Hänsel, D. Flamm, W. Frank, G. Böhm, F. Frost, R. Fechner, F. Bigl, B. Rauschenbach, Ion beam and plasma jet etching for optical component fabrication, in *Lithographic and Micromachining Techniques for Optical Component Fabrication*, (SPIE Optics + Photonics, 2001)
13. F. Dieter, H. Thomas, S. Axel, N. Andreas, H.J. Thomas, Reactive ion beam etching: A fabrication process for the figuring of precision aspheric optical surfaces in fused silica. Proc. SPIE **3739**, 167–175 (1999)
14. M.P. Echlin, M.S. Titus, M. Straw, P. Gumbsch, T.M. Pollock, Materials response to glancing incidence femtosecond laser ablation. Acta Mater. **124**, 37–46 (2017)
15. K. Werner, V. Gruzdev, N. Talisa, K. Kafka, D. Austin, C.M. Liebig, E. Chowdhury, Single-shot multi-stage damage and ablation of silicon by femtosecond mid-infrared laser pulses. Sci. Rep. **9**, 19993 (2019)
16. J. Bonse, S. Höhm, S.V. Kirner, A. Rosenfeld, J. Krüger, Laser-induced periodic surface structures&; a scientific evergreen. IEEE J. Sel. Top. Quantum Electron. **23**, 9000615 (2017)
17. S. Lee, D. Yang, S. Nikumb, Femtosecond laser micromilling of Si wafers. Appl. Surf. Sci. **254**, 2996–3005 (2008)
18. X. Lu, Q. Lu, Z. Zhu, Alignment mechanism of a nematic liquid crystal on a pre-rubbed polyimide film with laser-induced periodic surface structure. Liq. Cryst. **30**, 985–990 (2003)
19. Y. Kalachyova, O. Lyutakov, P. Slepicka, R. Elashnikov, V. Svorcik, Preparation of periodic surface structures on doped poly(methyl metacrylate) films by irradiation with KrF excimer laser. Nanoscale Res. Lett. **9**, 591 (2014)
20. J.P. Colombier, F. Garrelie, N. Faure, S. Reynaud, M. Bounhalli, E. Audouard, R. Stoian, F. Pigeon, Effects of electron-phonon coupling and electron diffusion on ripples growth on ultrafast-laser-irradiated metals. J. Appl. Phys. **111**, 024902 (2012)
21. M. Schade, O. Varlamova, J. Reif, H. Blumtritt, W. Erfurth, H.S. Leipner, High-resolution investigations of ripple structures formed by femtosecond laser irradiation of silicon. Anal. Bioanal. Chem. **396**, 1905–1911 (2010)
22. K. Zimmer, R. Böhme, Laser-induced backside wet etching of transparent materials with organic and metallic absorbers. Laser Chem. **2008**, 170632 (2008)
23. T. Chuang, Laser-induced chemical etching of solids: Promises and challenges. MRS Online Proc. Libr. **29**, 185–194 (1983)
24. D. Bäuerle, *Laser Processing and Chemistry* (Springer Science & Business Media, 2013)
25. A.K. Nath, Laser etching and dry processing. Bull. Mater. Sci. **11**, 159–166 (1988)
26. L.J. Richter, R.R. Cavanagh, Mechanistic studies of photoinduced reactions at semiconductor surfaces. Prog. Surf. Sci. **39**, 155–226 (1992)
27. M. Hermans, J. Gottmann, F. Riedel, Selective, laser-induced etching of fused silica at high scan-speeds using KOH. J. Laser Micro/Nanoeng. **9**, 126–131 (2014)
28. P. Lim, J. Brock, I. Trachtenberg, Laser-induced etching of silicon in hydrofluoric acid. Appl. Phys. Lett. **60**, 486–488 (1992)
29. L. Capuano, R. Tiggelaar, J. Berenschot, J. Gardeniers, G. Römer, Fabrication of millimeter-long structures in sapphire using femtosecond infrared laser pulses and selective etching. Opt. Lasers Eng. **133**, 106114 (2020)
30. X.-W. Cao, Y.-M. Lu, H. Fan, H. Xia, L. Zhang, Y.-L. Zhang, Wet-etching-assisted femtosecond laser holographic processing of a sapphire concave microlens array. Appl. Opt. **57**, 9604–9608 (2018)

31. F. Houle, Basic mechanisms in laser etching and deposition. Appl. Phys. A **41**, 315–330 (1986)
32. J. Brannon, Chemical etching of silicon by CO_2-laser-induced dissociation of NF_3. Appl. Phys. A **46**, 39–50 (1988)
33. R. Kullmer, D. Bäuerle, Laser-induced chemical etching of silicon in chlorine atmosphere. Appl. Phys. A **43**, 227–232 (1987)
34. S. Affrossman, R. Bailey, C. Cramer, F. Cruickshank, J. Macallister, J. Alderman, Laser photochemical etching of silicon. Appl. Phys. A **49**, 533–542 (1989)
35. K. Zimmer, M. Ehrhardt, R. Böhme, Laser-induced backside wet etching: Processes, results, and applications, in *Laser Ablation in Liquids*, ed. by G. Yang, (Pan Stanford Publishing Singapore, 2012), pp. 1013–1132
36. R. Delmdahl, R. Pätzel, J. Brune, Large-area laser-lift-off processing in microelectronics. Phys. Procedia **41**, 241–248 (2013)
37. R. Delmdahl, R. Pätzel, J. Brune, R. Senczuk, C. Goßler, R. Moser, M. Kunzer, U.T. Schwarz, Line beam processing for laser lift-off of GaN from sapphire. Phys. Status Solidi A **209**, 2653–2658 (2012)
38. B. Hopp, T. Smausz, C. Vass, G. Szabó, R. Böhme, D. Hirsch, K. Zimmer, Laser-induced backside dry and wet etching of transparent materials using solid and molten tin as absorbers. Appl. Phys. A **94**, 899–904 (2009)
39. Y. Pan, M. Ehrhardt, P. Lorenz, B. Han, B. Hopp, C. Vass, X. Ni, K. Zimmer, Influence of the confinement on laser-induced dry etching at the rear side of fused silica. Appl. Phys. A **122**, 365 (2016)
40. B. Hopp, C. Vass, T. Smausz, Z. Bor, Production of submicrometre fused silica gratings using laser-induced backside dry etching technique. J. Phys. D. Appl. Phys. **39**, 4843 (2006)
41. Y. Kawaguchi, H. Niino, T. Sato, A. Narazaki, R. Kurosaki, A deep micro-trench on silica glass fabricated by laserinduced backside wet etching (LIBWE). J. Phys. Conf. Ser. **59**, 080 (2007)
42. M. Ehrhardt, G. Raciukaitis, P. Gecys, K. Zimmer, Microstructuring of fused silica by laser-induced backside wet etching using picosecond laser pulses. Appl. Surf. Sci. **256**, 7222–7227 (2010)
43. J. Wang, H. Niino, A. Yabe, One-step microfabrication of fused silica by laser ablation of an organic solution. Appl. Phys. A Mater. Sci. Process. **68**, 111–113 (1999)
44. R. Böhme, K. Zimmer, D. Ruthe, B. Rauschenbach, Backside etching at the interface to diluted medium with nanometer etch rates. J. Laser Micro/Nanoeng. **1**, 190–194 (2006)
45. R. Böhme, K. Zimmer, Low roughness laser etching of fused silica using an adsorbed layer. Appl. Surf. Sci. **239**, 109–116 (2004)
46. R. Böhme, J. Zajadacz, K. Zimmer, B. Rauschenbach, Topography and roughness evolution of microstructured surfaces at laser-induced backside wet etching. Appl. Phys. A **80**, 433–438 (2005)
47. K. Zimmer, R. Böhme, D. Ruthe, B. Rauschenbach, The influence of laser-induced surface modifications on the backside etching process. Appl. Surf. Sci. **253**, 6588–6594 (2007)
48. J. Zhang, K. Sugioka, K. Midorikawa, Laser-induced plasma-assisted ablation of fused quartz using the fourth harmonic of a Nd+: YAG laser. Appl. Phys. A **67**, 545–549 (1998)
49. S. Xu, B. Liu, C. Pan, L. Ren, B. Tang, Q. Hu, L. Jiang, Ultrafast fabrication of micro-channels and graphite patterns on glass by nanosecond laser-induced plasma-assisted ablation (LIPAA) for electrofluidic devices. J. Mater. Process. Technol. **247**, 204–213 (2017)
50. B. Hopp, T. Smausz, T. Csizmadia, C. Vass, T. Csako, G. Szabo, Comparative study of different indirect laser-based methods developed for microprocessing of transparent materials. J. Laser Micro/Nanoeng. **5**, 80–85 (2010)
51. X. Lu, F. Jiang, T. Lei, R. Zhou, C. Zhang, G. Zheng, Q. Wen, Z. Chen, Laser-induced-plasma-assisted ablation and metallization on C-plane single crystal sapphire (c-Al_2O_3). Micromachines (Basel) **8**, 300 (2017)

52. Y. Hanada, K. Sugioka, H. Takase, H. Takai, I. Miyamoto, K. Midorikawa, Selective metallization of polyimide by laser-induced plasma-assisted ablation (LIPAA). Appl. Phys. A **80**, 111–115 (2005)
53. W. Holber, G. Reksten, R. Osgood Jr., Laser-enhanced plasma etching of silicon. Appl. Phys. Lett. **46**, 201–203 (1985)
54. J.A. Peck, D.N. Ruzic, Sub-damage-threshold plasma etching and profile tailoring of Si through laser-stimulated thermal desorption. J. Vac. Sci. Technol. A **36**, 021301 (2018)
55. J.A. Peck, D.N. Ruzic, Mechanism behind dry etching of Si assisted by pulsed visible laser. J. Appl. Phys. **122**, 173304 (2017)
56. S. Brückner, J. Hoffmeister, J. Ihlemann, C. Gerhard, S. Wieneke, W. Viöl, Hybrid laser-plasma micro-structuring of fused silica based on surface reduction by a low-temperature atmospheric pressure plasma. J. Laser Micro/Nanoeng. **7**, 73 (2012)
57. J. Hoffmeister, C. Gerhard, S. Brückner, J. Ihlemann, S. Wieneke, W. Viöl, Laser micro-structuring of fused silica subsequent to plasma-induced silicon suboxide generation and hydrogen implantation. Phys. Procedia **39**, 613–620 (2012)
58. H. Paetzelt, G. Böhm, T. Arnold, Etching of silicon surfaces using atmospheric plasma jets. Plasma Sources Sci. Technol. **24**, 025002 (2015)
59. T. Arnold, G. Böhm, I.M. Eichentopf, M. Janietz, J. Meister, A. Schindler, Plasma Jet Machining: A novel technology for precision machining of optical elements. Vak. Forsch. Prax. **22**, 10–16 (2010)
60. F. Kazemi, T. Arnold, P. Lorenz, M. Ehrhardt, K. Zimmer, Residual layer removal of technical glass resulting from reactive atmospheric plasma jet etching by pulsed laser irradiation. Plasma Chem. Plasma Process. **40**, 1241–1251 (2020)
61. F. Kazemi, T. Arnold, P. Lorenz, M. Ehrhardt, K. Zimmer, Combined reactive plasma jet-laser etching method for technical optical glass containing metal oxides. Appl. Surf. Sci. **551**, 149339 (2021)
62. G. Yang, *Laser Ablation in Liquids: Principles and Applications in the Preparation of Nanomaterials* (CRC Press, 2012)
63. B. Hopp, C. Vass, T. Smausz, Laser induced backside dry etching of transparent materials. Appl. Surf. Sci. **253**, 7922–7925 (2007)
64. H. Liu, W. Lin, M. Hong, Hybrid laser precision engineering of transparent hard materials: Challenges, solutions and applications. Light. Sci. Appl. **10**, 162 (2021)
65. R. Gutfeld, R. Hodgson, Laser enhanced etching in KOH. Appl. Phys. Lett. **40**, 352–354 (1982)
66. W. Pfleging, D. Wesner, E. Kreutz, CCl_4-assisted CF_4 etching of silicon in a microwave-assisted LDE (laser dry etching)-process. Appl. Surf. Sci. **96**, 496–500 (1996)
67. M. Ishii, T. Meguro, K. Gamo, T. Sugano, Y. Aoyagi, Digital etching using KrF excimer laser: Approach to atomic-order-controlled etching by photo induced reaction. Jpn. J. Appl. Phys. **32**, 6178–6181 (1993)
68. M. Ehrhardt, P. Lorenz, B. Han, K. Zimmer, Laser-induced reactive microplasma for etching of fused silica. Appl. Phys. A **126**, 842 (2020)
69. W.B. Rowe, *Principles of Modern Grinding Technology* (William Andrew, 2013)
70. R.I. King, R.S. Hahn, *Handbook of Modern Grinding Technology* (Springer Science & Business Media, 2012)
71. W.I. Kordonski, S. Jacobs, Magnetorheological finishing. Int. J. Mod. Phys. B **10**, 2837–2848 (1996)
72. T. Hänsel, F. Frost, A. Nickel, T. Schindler, Ultra-precision surface finishing by ion beam techniques. Vak. Forsch. Prax. **19**, 24–30 (2007)
73. Y.-S. Ghim, S.-J. You, H.-G. Rhee, H.-S. Yang, Y.-W. Lee, Ultra-precision surface polishing using ion beam figuring, in *6th International Symposium on Advanced Optical Manufacturing and Testing Technologies: Advanced Optical Manufacturing Technologies*, (International Society for Optics and Photonics, 2012), p. 84161O

74. A. Schindler, T. Hänsel, F. Frost, R. Fechner, G. Seidenkranz, A. Nickel, H.-J. Thomas, H. Neumann, D. Hirsch, R. Schwabe, Ion beam finishing technology for high precision optics production, in *Optical Fabrication and Testing*, (Optical Society of America, 2002), p. OTuB5
75. A. Schindler, T. Hänsel, M. Zeuner, G. Seidenkranz, Ion beam figuring and ion beam polishing production tools-processing technology included-for customized solutions, in *Optical Fabrication and Testing*, (Optical Society of America, 2000), p. OWA6
76. T. Arnold, G. Böhm, H. Paetzelt, New freeform manufacturing chain based on atmospheric plasma jet machining, in *Freeform Optics*, (Optical Society of America, 2015), p. FTh1B.3
77. A. Temmler, E. Willenborg, K. Wissenbach, Laser polishing, in *Laser Applications in Microelectronic and Optoelectronic Manufacturing (LAMOM) XVII*, (International Society for Optics and Photonics, 2012), p. 82430W
78. L.L. Taylor, J. Qiao, J. Qiao, Femtosecond laser polishing of optical materials, in *Optifab 2015*, (International Society for Optics and Photonics, 2015), p. 96330M
79. C. Weingarten, A. Schmickler, E. Willenborg, K. Wissenbach, R. Poprawe, Laser polishing and laser shape correction of optical glass. J. Laser Appl. **29**, 011702 (2017)
80. F. Vega, N.B. Lupon, J.A. Cebrian, F. Laguarta, Laser application for optical glass polishing. Opt. Eng. **37**, 272–279 (1998)
81. S. Mohajerani, E.V. Bordatchev, O.R. Tutunea-Fatan, Recent developments in modeling of laser polishing of metallic materials. Lasers Manuf. Mater. Process. **5**, 395–429 (2018)
82. Y. Chai, R.W. Li, D.M. Perriman, S. Chen, Q.-H. Qin, P.N. Smith, Laser polishing of thermoplastics fabricated using fused deposition modelling. Int. J. Adv. Manuf. Technol. **96**, 4295–4302 (2018)
83. F. Laguarta, N. Lupon, J. Armengol, Optical glass polishing by controlled laser surface-heat treatment. Appl. Opt. **33**, 6508–6513 (1994)
84. C. Nüsser, J. Kumstel, T. Kiedrowski, A. Diatlov, E. Willenborg, Process-and material-induced surface structures during laser polishing. Adv. Eng. Mater. **17**, 268–277 (2015)
85. A. Temmler, E. Willenborg, K. Wissenbach, Design surfaces by laser remelting. Phys. Procedia **12**, 419–430 (2011)
86. T.L. Perry, D. Werschmoeller, N.A. Duffie, X. Li, F.E. Pfefferkorn, Examination of selective pulsed laser micropolishing on microfabricated nickel samples using spatial frequency analysis. J. Manuf. Sci. Eng. **131**, 021002 (2009)
87. T.L. Perry, D. Werschmoeller, X. Li, F.E. Pfefferkorn, N.A. Duffie, Pulsed laser polishing of micro-milled Ti6Al4V samples. J. Manuf. Process. **11**, 74–81 (2009)
88. A. Sassmannshausen, A. Brenner, J. Finger, Ultrashort pulse laser polishing by continuous surface melting. J. Mater. Process. Technol. **293**, 117058 (2021)
89. S. Schwarz, S. Rung, C. Esen, R. Hellmann, Fabrication of a high-quality axicon by femtosecond laser ablation and CO(2) laser polishing for quasi-Bessel beam generation. Opt. Express **26**, 23287–23294 (2018)
90. L.L. Taylor, J. Xu, M. Pomerantz, T.R. Smith, J.C. Lambropoulos, J. Qiao, Femtosecond laser polishing of germanium. Opt. Mater. Express **9**, 4165–4177 (2019)
91. T. Arnold, G. Böhm, Application of atmospheric plasma jet machining (PJM) for effective surface figuring of SiC. Precis. Eng. **36**, 546–553 (2012)
92. J. Jeong, S. Babayan, V. Tu, J. Park, I. Henins, R. Hicks, G. Selwyn, Etching materials with an atmospheric-pressure plasma jet. Plasma Sources Sci. Technol. **7**, 282 (1998)
93. N. Bloembergen, Laser-induced electric breakdown in solids. IEEE J. Quantum Electron. **10**, 375–386 (1974)
94. F. Docchio, C. Sacchi, J. Marshall, Experimental investigation of optical breakdown thresholds in ocular media under single pulse irradiation with different pulse durations. Lasers Ophthalmol. **1**, 83–93 (1986)
95. C.-H. Fan, J.P. Longtin, Modeling optical breakdown in dielectrics during ultrafast laser processing. Appl. Opt. **40**, 3124–3131 (2001)
96. S.I. Kudryashov, V.D. Zvorykin, Microscale nanosecond laser-induced optical breakdown in water. Phys. Rev. E **78**, 036404 (2008)

97. A. Vogel, K. Nahen, D. Theisen, J. Noack, Plasma formation in water by picosecond and nanosecond Nd: YAG laser pulses. I. Optical breakdown at threshold and superthreshold irradiance. IEEE J. Sel. Top. Quantum Electron. **2**, 847–860 (1996)
98. J. Noack, A. Vogel, Laser-induced plasma formation in water at nanosecond to femtosecond time scales: Calculation of thresholds, absorption coefficients, and energy density. IEEE J. Quantum Electron. **35**, 1156–1167 (1999)
99. W. Hu, Y.C. Shin, G. King, Effect of air breakdown with a focusing lens on ultrashort laser ablation. Appl. Phys. Lett. **99**, 234104 (2011)
100. J.K. Koga, K. Moribayashi, Y. Fukuda, S.V. Bulanov, A. Sagisaka, K. Ogura, H. Daido, M. Yamagiwa, T. Kimura, T. Fujikawa, Simulation and experiments of the laser induced breakdown of air for femtosecond to nanosecond order pulses. J. Phys. D. Appl. Phys. **43**, 025204 (2009)
101. F. Morgan, L. Evans, C.G. Morgan, Laser beam induced breakdown in helium and argon. J. Phys. D. Appl. Phys. **4**, 225 (1971)
102. X.-L. Liu, X. Lu, X. Liu, T.-T. Xi, F. Liu, J.-L. Ma, J. Zhang, Tightly focused femtosecond laser pulse in air: From filamentation to breakdown. Opt. Express **18**, 26007–26017 (2010)
103. V.V. Bukin, S.V. Garnov, A.A. Malyutin, V.V. Strelkov, Femtosecond laser optical gas breakdown microplasma: The ionisation and postionisation dynamics. Quantum Electron. **37**, 961 (2007)
104. P. Schaaf, *Laser Processing of Materials: Fundamentals, Applications and Developments* (Springer Science & Business Media, 2010)
105. I.U.P. Raĭzer, *Laser-Induced Discharge Phenomena* (Consultants Bureau, 1977)
106. M. Niemz, Threshold dependence of laser-induced optical breakdown on pulse duration. Appl. Phys. Lett. **66**, 1181–1183 (1995)
107. R. Tambay, R. Thareja, Laser-induced breakdown studies of laboratory air at 0.266, 0.355, 0.532, and 1.06 μm. J. Appl. Phys. **70**, 2890–2892 (1991)
108. A.W. Miziolek, V. Palleschi, I. Schechter, *Laser Induced Breakdown Spectroscopy* (Cambridge university press, 2006)
109. M.H. Morsy, Review and recent developments of laser ignition for internal combustion engines applications. Renew. Sust. Energ. Rev. **16**, 4849–4875 (2012)
110. R. Tambay, D.V.S. Muthu, V. Kumar, R. Thareja, Laser induced air breakdown using 0.355, 0.532, and 1.06 μm radiation. Pramana – J. Phys **37**, 163–166 (1991)
111. K.A. Hamam, L.H. Gaabour, Y.E. Gamal, Numerical modeling for investigating the optical breakdown threshold of laser-induced air plasmas at different laser characteristics. Phys. Plasmas **24**, 073515 (2017)
112. M. Thiyagarajan, J.E. Scharer, Experimental investigation of 193-nm laser breakdown in air. IEEE Trans. Plasma Sci. **36**, 2512–2521 (2008)
113. S. Elhadj, I.L. Bass, G.M. Guss, M.J. Matthews, Laser-induced gas plasma etching of fused silica under ambient conditions. Laser-Induced Damage Opt. Mater. **8530**, 853022 (2012)
114. R. Heinke, M. Ehrhardt, P. Lorenz, K. Zimmer, Dry etching of monocrystalline silicon using a laser-induced reactive micro plasma. Appl. Surf. Sci. Adv. **6**, 100169 (2021)
115. M. Ehrhardt, P. Lorenz, J. Bauer, R. Heinke, M.A. Hossain, B. Han, K. Zimmer, Dry etching of germanium with laser induced reactive micro plasma. Lasers Manuf. Mater. Process. **8**, 237–255 (2021)
116. A.M. Hossain, M. Ehrhardt, M. Rudolph, D. Kalanov, P. Lorenz, K. Zimmer, A. Anders, Dynamics and 2D temperature distribution of plasma obtained by femtosecond laser-induced breakdown. J. Phys. D. Appl. Phys. **55**, 125204 (2021)
117. K. Reinhardt, W. Kern, *Handbook of Silicon Wafer Cleaning Technology* (Elsevier Science, 2008)
118. Y. Horiike, M. Shibagaki, A new chemical dry etching. Jpn. J. Appl. Phys. **15**, 13 (1976)
119. A. Fridman, *Plasma Chemistry* (Cambridge University Press, 2008)
120. D. Edelson, D.L. Flamm, Computer simulation of a CF_4 plasma etching silicon. J. Appl. Phys. **56**, 1522–1531 (1984)

121. C. Mogab, A. Adams, D. Flamm, Plasma etching of Si and SiO_2—The effect of oxygen additions to CF_4 plasmas. J. Appl. Phys. **49**, 3796–3803 (1978)
122. W. Stoffels, E. Stoffels, K. Tachibana, Polymerization of fluorocarbons in reactive ion etching plasmas. J. Vac. Sci. Technol. A **16**, 87–95 (1998)
123. S. Arai, K. Tsujimoto, S. Tachi, Deposition in dry-Etching gas plasmas. Jpn. J. Appl. Phys. **31**, 2011 (1992)
124. W. Schwarzenbach, J. Derouard, N. Sadeghi, Treatment of organic polymer surfaces by CF_4 plasmas: Etching by fluorine atoms and influence of vacuum ultraviolet radiation. J. Appl. Phys. **90**, 5491–5496 (2001)
125. I. Chun, A. Efremov, G.Y. Yeom, K.-H. Kwon, A comparative study of $CF_4/O_2/Ar$ and $C_4F_8/O_2/Ar$ plasmas for dry etching applications. Thin Solid Films **579**, 136–143 (2015)
126. K. Zimmer, M. Ehrhardt, P. Lorenz, X. Wang, P. Wang, S. Sun, Etching of SiC–SiC-composites by a laser-induced plasma in a reactive gas. Ceram. Int. **48**, 90–95 (2022)
127. J.-P. Booth, Optical and electrical diagnostics of fluorocarbon plasma etching processes. Plasma Sources Sci. Technol. **8**, 249 (1999)
128. G. Cunge, J. Booth, CF_2 production and loss mechanisms in fluorocarbon discharges: Fluorine-poor conditions and polymerization. J. Appl. Phys. **85**, 3952–3959 (1999)

Chapter 19
Nanostructuring by Photochemistry: Laser-Induced Type A Modification

Lionel Canioni, Yannick Petit, and Thierry Cardinal

Abstract The femtosecond direct laser writing technique provides a robust and efficient way to directly inscribe embedded 3D photonic devices in bulk glasses. Following direct laser writing, a local optical properties change is induced that is generally classified under three distinguished types (type I, type II, and type III). Each type allows for the fabrication of its own variety of 3D photonic components.

Glasses containing photosensitive metal salts such as silver open a whole field of tailored optical applications. This photosensitivity allows for fine control of the defects generated during femtosecond laser interaction. In practice, direct laser writing induces the creation of a new type of optical properties change, called type Argentum (Type A). It is based on the development of silver clusters that allow the creation of many optical properties such as positive refractive index (RI) change, fluorescence, and second-order nonlinear properties at the nanoscale. In this chapter, we report that type Argentum modifications could be triggered in silver-containing glasses by finely choosing the inscription parameters. The multiphysical mechanisms of optical properties changes and the consequences on the regimes of interaction will be discussed. The numerous applications of the Type A laser modification will be addressed.

Keywords Photosensitive glasses · Type A laser modification · Second-order nonlinear optical properties (χ^2) · Molecular clusters · Luminescent properties · Nanoparticle

---

L. Canioni (✉)
Université de Bordeaux, Talence, France
e-mail: lionel.canioni@u-bordeaux.fr

Y. Petit · T. Cardinal
Institut de Chimie de la Matière Condensée de Bordeaux, Université de Bordeaux, Pessac, France

© The Author(s), under exclusive license to Springer Nature Switzerland AG 2023

R. Stoian, J. Bonse (eds.), *Ultrafast Laser Nanostructuring*, Springer Series in Optical Sciences 239, https://doi.org/10.1007/978-3-031-14752-4_19

Direct laser writing (**DLW**) has been an exponentially growing research field during the last two decades, by providing an efficient and robust way to directly address three dimensional (3D) structures in transparent materials such as glasses using femtosecond laser pulses. This competitive aspect makes the DLW technique suitable for future technological transfer to advanced industrial manufacturing. Generally, DLW in glasses induces physical changes such as permanent local refractive index (RI) modifications that have been classified under three distinct types type I, type II, and type III, corresponding, respectively, to homogeneous RI change, birefringence, and voids.

In glasses with embedded silver ions Ag^{+}, when silver is abundant enough to be a constituent element of the glass network, such photosensitized glasses experiment specific permanent modification under femtosecond laser irradiation, corresponding to so-called femto-produced-photo-luminescent glasses (referred to as FPL glasses hereafter). Indeed, DLW induces the creation of fluorescent silver clusters ${Ag_m}^{x+}$ at the vicinity of the interaction laser voxel. In this chapter, we present a new type of RI change, called Type A, for Argentum, which is based on the creation of the photoinduced silver clusters that lead to changes of the linear positive and nonlinear optical RI in FPL glasses. Such Type A I does correspond to a new type of RI modifications, as the laser inscription regime clearly differs from that of other types, especially that of type I. Taking benefit of this new DLW regime in FPL glasses, Type A laser modification has been successfully used so far for integrated optics application.

1 Key Properties of Nanostructuring by Photochemistry

1.1 Laser Structuring of Glasses

Photosensitivity is the ability of an element to react to light. Generally speaking, we can separate the modifications caused by the interaction between glass and light into two categories. On one hand, one can consider the modifications on the glass network itself: we speak then of intrinsic photo-structuring. On the other hand, one can address the modifications on the impurities or dopants present in the glass: this is called extrinsic photo-structuring.

The photosensitivity of a glass is an intrinsic characteristic of its composition. It can be an expected or unexpected consequence. With the evolution of photonics and especially lasers, the scientific community has introduced the notion of photo-structuring, which is the intended exploitation of the photosensitivity of glass to create active optical systems. Depending on the size of the induced modifications, we can speak of micro-structuring or nano-structuring. Photo-structuring is the spatially controlled and deliberate modification of the properties of a material by using its photosensitivity.

1.2 The Photosensitive Glasses

The first photosensitive glasses date back to the end of the 1940s in the United States. At that time, the improvement of photographic films was an important subject of research and several ways appeared to solve the problem of the durability of the supports. Indeed, at that time, and it is still current, the “photo paper” is made of silver halide crystals suspended in a fragile protective gelatinous matrix often responsible for the premature aging of photographic plates. In 1947, Corning engineers, and more precisely S.D. Stookey, developed a photosensitive glass to overcome the fragility of the photographic emulsion and to increase the lifetime of the photographic support. This glass is an alkaline earth silicate doped with a photosensitive agent (silver, gold, or copper), an optical sensitizer (cerium), and a thermo-reducing agent (tin or antimony).

In the case of Stookey, the glass is irradiated with ultraviolet radiation to form a latent image. The UV radiation is absorbed by the cerium ions which ionize. Electrons are then ejected from the cerium ions and reduce the surrounding Ag^+ ions to neutral metal atoms Ag^0. The information of the recorded image is then contained in the distribution of these metal ions, but this image is latent because the Ag^0 species do not produce any visible change. To make this latent image visible, it is necessary to perform a thermal treatment of the glass, so that the heat facilitates the diffusion of Ag^+ ions so as to aggregate with the Ag^0 producing a precipitation of metallic particles. These metallic particles provide strong dielectric contrast with the surrounding glass, including a different RI and additional absorption response of the visible light: this dielectric contrast at the nanoscale generates at the macroscopic scale a composite metal/glass effective medium, forming then a visible and therefore revealed image [78].

1.3 Short State of the Art in Femtosecond Laser-Induced Photochemistry

Since Hill in 1978, photo-structuring has evolved a lot, and it has even become a field rich in applications since the generalization of very short pulse lasers [37]. In fact, the use of focused femtosecond pulses with energies of a few hundred nanojoules has become the preferred tool to modify the physical properties of materials in three dimensions. The selection of such a technology in the framework of photo-structuring is due to its capacity to produce an energy deposit on a volume lower than the classical limits of diffraction, thanks to mutli-photon absorption due to nonlinear effect. Among all the physical properties that can be modified, the RI is the easiest and historically the first to have been studied, in order to fabricate waveguides [27]. If the regime of very short pulses has allowed many advances, it is important to optimize the irradiation conditions according to the application envisaged and for a given material.

Fused silica is by far the most studied material in the literature. Nevertheless, although its study is interesting from a fundamental point of view, this material is not always the most suitable for applications. In fact, to improve the applications, the irradiation conditions and the intrinsic properties of the material must be optimized in order to produce the specifically desired response to the femtosecond laser exposure. This is how a branch of materials chemistry dedicated to the production of glasses specifically designed to be photo-structured was developed. Materials doped with photosensitive ions in different matrices (glasses and polymers) are particularly relevant because they can be developed to respond optimally to femtosecond pulses and decrease the energy cost needed to induce changes. They can be specifically designed to exhibit a large RI change after laser irradiation and appropriate heat treatment [75]. They can also exhibit other optical property changes such as plasmon band absorption [63, 87], luminescence [12, 28, 69], and optical nonlinear properties [18, 21, 26, 49, 53, 54, 61].

Femtosecond laser-induced photochemistry (f-LIP) has been shown in many homogeneous materials such as glasses, polymers, and crystals. In fact, the application of f-LIP has been explored in a wide range of glass matrices from commercial or specific developments: silicates [9, 26, 38, 39, 62, 63, 66], aluminosilicates also known as Foturan glass [19, 43, 74], aluminates [65, 67], borates [74], aluminoborates [49], and phosphates [12, 18, 40, 44, 50, 51, 69, 84–86]. F-LIP has also been demonstrated in polymers and crystalline matrices, such as polymeric gelatins [34, 35] and zeolites [23–25]. The irradiated or structured materials can be doped with noble metal ions Cu^{2+} [9, 38], Ag^{+} [12, 13, 15, 18–20, 34, 38, 39, 43, 67, 75, 78], and Au^{+} [66, 78]; other transitional metal ions such as Fe^{3+}, Mn^{3+} [67], or Ti^{3+} [26]; or finally with rare earths Sm^{3+} [64, 74], Eu^{2+} [65], and Eu^{3+} [42, 67]. These materials show an intrinsic response to intense laser irradiation. However, in order to improve the laser-matter interaction, some of them are prepared to obtain better modification possibilities by the use of thermo-reductive agents: for example, tin and antimony [43, 78] or photo-sensitizers like Ce^{3+} [19, 20, 43, 78].

1.4 Phenomenology of Interaction Processes

The interaction of these photosensitive materials with the femtosecond regime is a particularly studied field at present. The understanding of the physical processes involved and the associated characteristic times are a crucial point [8, 33, 46, 72, 79]. It is accepted in the scientific community that when a single high fluence pulse from a femtosecond laser interacts with a material, some of the following phenomena take place: First, the laser energy is absorbed by the material and generates photoelectrons. These electrons then transfer their kinetic energies to the lattice, producing heat. Finally, this heat diffuses and the material heats up. The melting or the explosion of the material that follows gives, respectively, the responses of types I and III. For photochemical reactions, the control of the temperature increase due to the accumulation pulse after pulse is important because such a temperature increase is the parameter that determines then the diffusion of chemical species by the induced thermal gradient [12]. This diffusion then influences the kinetics of the reactions, possibly including both the induced local concentrations of reactants and/or the thermal activation of the involved kinetic constants.

2 FPL Glasses

2.1 Glass Composition

The first FPL glass studied in [12, 13, 15, 44, 45, 68] given access to Type A laser modification is a zinc phosphate glass containing silver and gallium. Table 19.1 summarizes the different constituents of this glass and their functions.

The photosensitive element is silver oxide Ag_2O. Silver, like copper and gold, has an electronic structure with a d^{10} valence layer which makes their luminescence properties very dependent on their environment and pairing. Gold, copper, and silver are therefore good photosensitizing candidates. However, gold is difficult to introduce into glasses in high concentration and copper, when introduced into a glass, dismutes into Cu^+ and $Cu_2{}^+$. Only Cu^+ is luminescent and $Cu_2{}^+$ has a wide absorption band covering the visible and causing self-absorption phenomena. Silver has therefore been chosen as a photosensitive agent.

Concerning the matrix and taking again the classification explained above, the phosphate ions (P_2O_5) are the formative oxides. They are oxides whose unit is the tetrahedron PO_4. They form the vitreous network. A phosphate-type glass material has been chosen, as opposed to silicate glasses, because phosphate glasses are known for their ability to harbor high concentrations of silver ions [48]. To meet the stability requirements, modifying zinc oxides, ZnO, are added to this structural network. The main disadvantage of phosphates is their ability to be corroded by water. The addition of modifiers, such as SiO_2, TiO_2, Nb_2O_5, Al_2O_3, Fe_2O_3, PbO, and ZnO, improves the chemical durability by limiting the influence of water. Nevertheless, most of these elements are also photosensitive with individual spectral ranges that overlap that of silver. The choice was therefore made to select zinc oxide, whose photosensitivity is low, in order to simplify the understanding of laser-glass interactions by limiting the interacting elements. Moreover, a zinc phosphate

Table 19.1 The components of FPL glass and their functions. The x value indicates the variations in the different compositions used in the past

Compound	Function	Molar percentage of reactant
P_2O_5	Glass matrix (*phosphate*)	40
ZnO	Glass matrix (*oxyde of zinc*)	55
Ag_2O	Stabilizer and photosensitive element	x
Ga_2O_3	Stabilizer	5-x

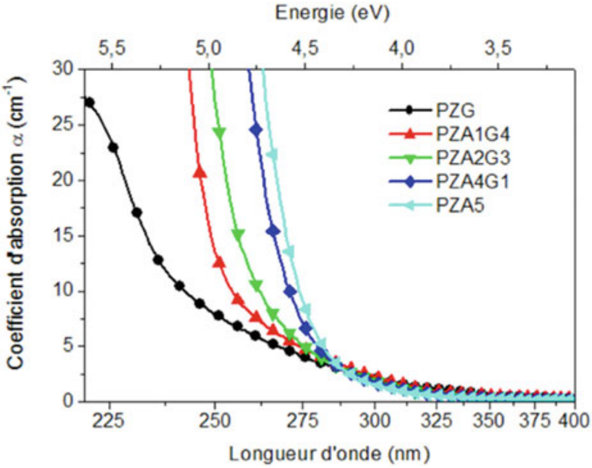

Fig. 19.1 UV absorption spectra of FPL glass as a function of the amount of silver; the cyan curve represents a molar percentage of silver reagent of 5%, the blue-navy curve 4%, the green curve 3%, and the red curve 1%; the black curve represents the glass without silver. The increase of the molar % of silver is done at the expense of that of gallium which passes from 5% to 0%. One observes a displacement of the absorption front towards the left with the increase of the molar % of silver [52]

glass has a matrix bandgap at higher energy than that involved in silver excitation spectroscopy; this allows laser-induced interactions to primarily target the single silver chemical element, as detailed hereafter [16].

2.2 *FPL Absorption Spectra*

The absorption spectra for different silver concentration is illustrated in Fig. 19.1. The compositions presented here belong to the system $40P_2O_5$-55ZnO-(**5-*x***)Ag_2O-***x***Ga_2O_3 with *x* varying from 0 to 5. (1-*x*) representing the molar percentage of silver reagents.

The PZG glass (zinc gallium phosphate, thus without silver) absorbs very little and has a UV transparency window down to 270 nm. We observe the beginning of an abrupt absorption front at about 240 nm. However, an average absorption is observed between 230 and 280 nm; this absorption has been attributed to the presence of defects and impurities in very small quantities in the glass, of the order of a few tens of ppm [16]. For compositions that contain silver, the spectrum presents a very strong absorption front with a high saturation in the UV. The more the molar percentage of silver increases, the more this front move towards the low energies (high wavelengths). We conclude that the amount of silver in the glass

Table 19.2 Non-exhaustive list of distinct FPL glasses investigated

Glass composition/name	Laser parameters	Glass family	Year	Ref
$40P_2O_5$-55ZnO-$1Ga_2O_3$-4 Ag_2O/**PZG**	9 MHz @1030 nm writing speed 10–600 μm/s fluorescence and RI change	Phosphates	2009	[12, 15]
$12Al_2O_3$-$10Na_2O$-$70P_2O_5$-$0.5Ag_2O$	250 kHz @800 nm writing speed 150 μm/s silver nanoparticles (NPs)		2013	[80]
70 Pb_2O_7-30 WO_3-AgCl	kHz and MHz @1030 nm silver nanoparticles (NPs) and waveguides		2014	[6]
$0.55Ag_2O$-$0.45P_2O_5$ and $0.5Ag_2O$-$0.1Nb_2O_5$-$0.4P_2O_5$	250 kHz @800 nm writing speed 2.5 μm/s color centers and luminescent silver NPs		2015	[83]
$19Ga_2O_3$-$78NaPO_3$-$3Ag_2O$/**GPN**	250 kHz @800 nm writing speed Nanograting formation	Gallophosphate	2014	[81]
Commercial glasses with thermally injected silver (sodo-calcite glass and SIMAX borosilicate glass)	9 MHz @1030 nm writing speed 10–100 μm/s fluorescence	Commercial	2016	[76]
$40P_2O_5$-55ZnO-$4Ag_2O$-$1Ga_2O_3$	100 kHz @1030 nm. Luminescent silver NPs and birefringent μ-regions		2016	[41]
55ZnO-$41P_2O_5$-$4Ag_2O$	@1030 nm. Creation of ring-shaped fluorescent silver clusters and silver NPs simultaneously		2017	[73]

shifts its absorption front towards high wavelengths. This is consistent with the photosensitive properties of the silver ion injected into the glass matrix.

The FPL glasses were developed first by the Institute of Chemistry of the condensed Matter of Bordeaux (ICMCB) in 2009. Even though, other research groups have developed FPL glasses, and reported works with femtosecond laser modification are listed in Table 19.2.

2.3 *Intrinsic Luminescence of FPL Glasses*

In the FPL glasses without silver, no luminescence is detected whatever the excitation conditions. The introduction of silver oxide in the phosphate glass composition lead to luminescence properties associated to the silver ion presence [16]. The first band corresponds to the isolated Ag^+ ions present in the glass matrix after the addition of Ag_2O in the glass composition, with typical excitation and emission bands centered at 240 and 290 nm, respectively. The second luminescence, at lower energies, is preponderant in FPL glasses with high silver concentration. It is typically observed for excitation at 260 nm and emission at 380 nm, and this band is assigned to the $4d^{10} \rightarrow 4d^9\ 5s$ transition. Note that the energy of the $4d^9\ 5s$ state in the case of Ag^+ is influenced by the environment of the cation. Thus, this band can be shifted by changing the mole percentage of silver or by adding different dopants such as SiO_2 or Al_2O_3 [10]. The latter is associated with the presence of Ag^+-Ag^+ pairs in glasses where silver is in high concentration and is weaker than that of Ag^+ [11]. Such pairs correspond to close Ag^+ ions showing electrostatic interaction without forming through a molecular dimer. Silver environments referring to isolated Ag^+ ions or to Ag^+-Ag^+ pairs have been clearly observed, which are distinctly referred to as site A and site B, respectively [58]. Such a distinction for pristine silver-containing glasses is of importance as it will further affect significantly the photosensitivity under femtosecond laser irradiation.

2.4 Femtosecond Laser Inscription in FPL Glass

The FPL glass is irradiated with a near-infrared femtosecond laser and focused by a microscope objective. The irradiation is then performed with different parameters: repetition rate, number of pulses, and irradiance. It is then demonstrated that the laser-matter interaction is done by a nonlinear irradiation with 4-photon interaction [12] with a femtosecond laser, at high repetition rate and at a wavelength of 1030 nm. Due to the strong nonlinearity of the absorption phenomenon, the interaction takes place only inside the focusing voxel, allowing a three-dimensional energy deposition in the glass.

The pattern used to test the interaction is an array of 35 irradiation spots placed on a grid: each column uses a different irradiance from 8 to 14 TW/cm^2, each line puts a different number of pulses in the glass, from 100 pulses to one million pulses (see Fig. 19.2a). White light and fluorescence imaging show four response ranges for the material. In one region above 12 TW/cm^2, changes in the RI and explosions are observed (see Fig. 19.2b). In a second, for lower irradiances and 10^6 pulses, we observe a localized index change without explosion or thermal modified zone. The rest of the bright field image shows very small RI change. Fluorescence imaging shows that the first two zones emit strong fluorescence. The third area shows no index change but intense fluorescence (see Fig. 19.2c). The last zone is located for irradiances below 12 TW/cm^2 and a number of pulses lower than 10^4 and for which we detect neither change of index nor fluorescence.

The imaging of the glass reveals the appearance of fluorescent structures in three dimensions inside the glass. Excitation of these structures by UV and near UV light (360–450 nm) causes an intense emission of white light. Confocal fluorescence microscopy imaging is performed showing that the luminous structures have a tube shape, narrowed at the ends, in the direction of the laser propagation (see Fig. 19.3).

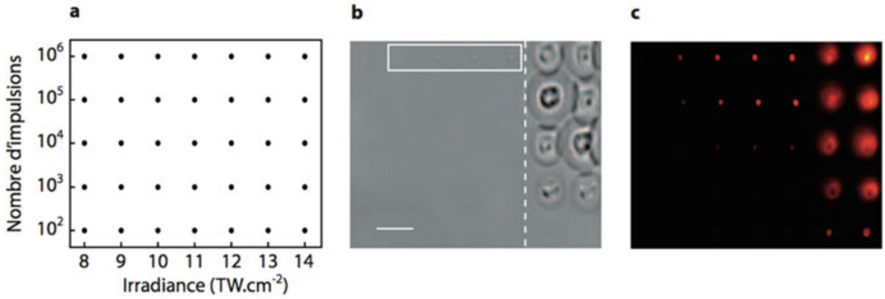

Fig. 19.2 Irradiation of a PZG glass by femtosecond IR laser – 1030 nm, 10 MHz. (**a**) Experimental design: variation of the number of pulses (from 102 to 106) and of the irradiance (from 8 to 14 TW.cm^{-2}). (**b**) Image by bright field microscopy. Dotted line: damage threshold. Boxed area: RI change. (**c**) Image by fluorescence microscopy ($\lambda_{\text{exc}} = 405$ nm). Scale: bar = 20 μm. (Reproduced from Ref. [Bellec10])

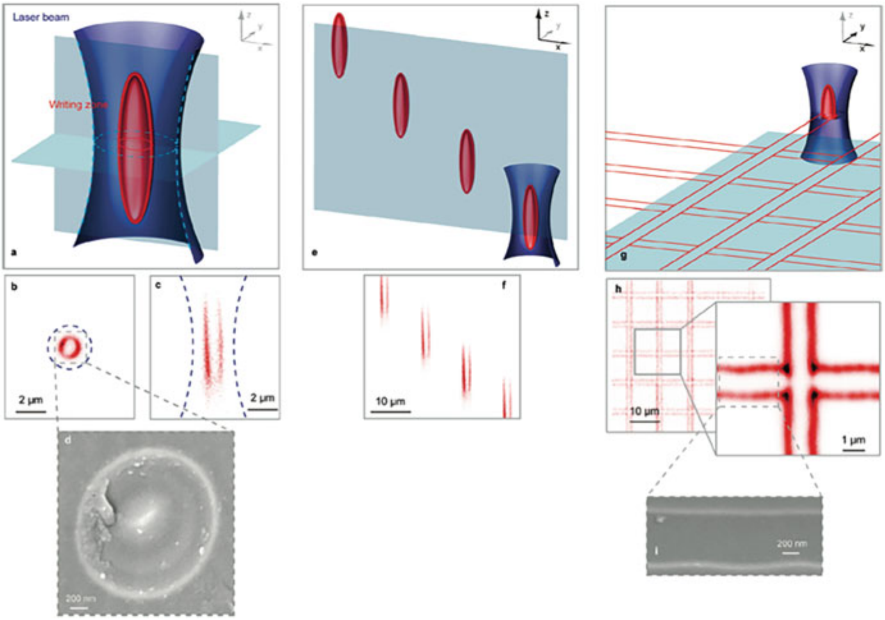

Fig. 19.3 Typology of the different structures in the FPL glass for a stationary focal point (**a**), at different depths (**e**) and in translation in the same plane (**g**). Fluorescence images (exc 405 nm) of structures in the xy (**b**,**h**) and xz (**c**,**f**) planes. Insets (**d**,**i**) are HRSEM images of images (**b**) and (**h**). (Reproduced from Ref. [13])

Each irradiation on a stationary point gives an equivalent tube. The thickness of the wall of the tube is estimated to be 250 nm. The different nonlinear processes structure well below the diffraction limit.

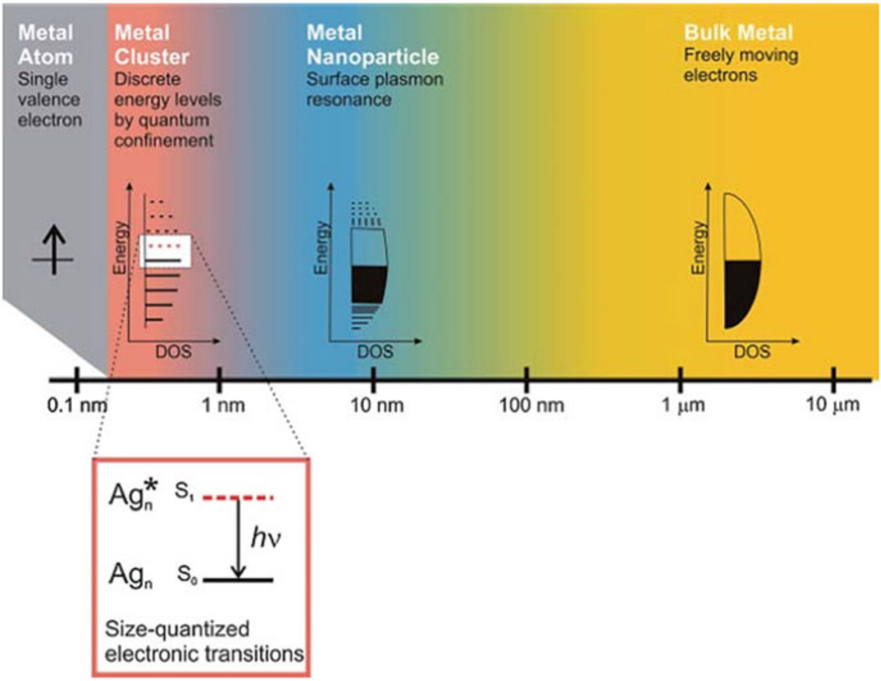
Metal Atom
Single valence electron
Metal Cluster
Discrete energy levels by quantum confinement
Metal Nanoparticle
Surface plasmon resonance
Bulk Metal
Freely moving electrons
Energy
DOS
0.1 nm
1 nm
10 nm
100 nm
1 µm
10 µm
Ag$_n^*$ S$_1$
hν
Ag$_n$ S$_0$
Size-quantized electronic transitions

Fig. 19.4 The effect of size for metals. While metals and metal nanoparticles exhibit continuous energy bands, aggregates exhibit discrete energy levels. (Reproduced from Ref. [30])

The photoinduced structures are composed of $Ag_m{}^{x+}$ silver aggregates [18]. Metal aggregates are groupings of a few atoms of a metal with specific properties. Indeed, the electronic and optical properties of metallic particles depend very much on their size, especially at the nanometer scale [30]. Metals, when they are at the macroscopic scale, are good electrical conductors and optical reflectors, due to the large number of free electrons. On the other hand, metallic nanoparticles have intense colors due to their surface plasmon resonance. When the size of the elements goes down to the nanometer level, the band structure becomes discontinuous and organized in discrete energy levels, similar to some extent to that of molecules. These particles thus behave like molecules and no longer show plasmonic properties, but they can interact with light via electronic transitions between energy levels, resulting in intense absorption and emission with few ns lifetime (see Fig. 19.4).

The fluorescence properties of photoinduced aggregates in FPL glass (intensity, spectrum, and lifetime) depend on the laser parameters in different ways during irradiation. The fluorescence intensity depends linearly on the laser irradiance and logarithmically on the number of pulses deposited in the glass. It also highlights the importance of the repetition rate in the creation of fluorescence, proving the existence of a temporal accumulation effect that can affect the temperature in the

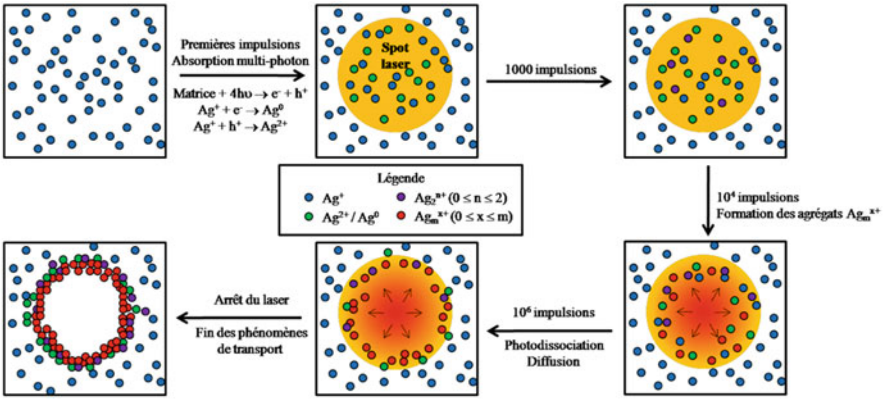
Premières impulsions
Absorption multi-photon
Matrice + 4hυ → e⁻ + h⁺
Ag⁺ + e⁻ → Ag⁰
Ag⁺ + h⁺ → Ag²⁺
Spot laser
1000 impulsions
Légende
Ag⁺
Ag₂ⁿ⁺ (0 ≤ n ≤ 2)
Ag²⁺ / Ag⁰
Agₘˣ⁺ (0 ≤ x ≤ m)
10⁴ impulsions
Formation des agrégats Agₘˣ⁺
10⁶ impulsions
Photodissociation
Diffusion
Arrêt du laser
Fin des phénomènes de transport

Fig. 19.5 Proposed mechanism leading to the formation of photoinduced structures [12, 15]

glass. These measurements lead to the proposal of a mechanism explaining the appearance of the aggregates.

To better understand the laser-glass interaction and the spatial distribution morphology of the silver clusters, a theoretical model [76, 77] was presented by our group explaining the different physical mechanisms involved in the formation of silver clusters. Such a very complete model was a new numerical approach as it was describing the controlled material aging under many-pulse glass irradiation, by simultaneously taking into account physical laser-matter interaction, material diffusion processes an chemical reactivity. Indeed, the model takes into account the different nonlinear photoionization processes, laser energy deposition followed by laser heating of the sample, diffusion ions, kinetic reactions and photo dissociation of metallic species [76]. The different physical mechanisms responsible for the formation of silver clusters (taken from Ref. [76]) are presented briefly herein. However, for more details, the reader is referred to reference [76]. First, a reservoir of free electrons is generated during the laser pulse: yellow circle that corresponds to the radial distribution of the free electrons as shown in Fig. 19.5. The formation of silver atoms Ag^0 starts to take place ($Ag^+ + e^- \rightarrow Ag^0$) where the concentration of free electrons is at its peak. During the formation of Ag^0, holes are trapped by silver ions Ag^+: $h^+ + Ag^+ \rightarrow Ag^{2+}$ and the product is assumed not to be mobile. In fact, Ag^{2+} should be considered as a hole trapped in proximity of a silver ion Ag^+ instead of a doubly ionized silver ion. Thus, the mobility of such pair is negligible compared to the mobility of silver ions Ag^+, due to its delocalization around the phosphate chains that form the glass network. The reaction $e^- + Ag^+ \rightarrow Ag^0$ ends when the concentration of free electrons vanishes. At that moment, the spatial distribution of Ag^0 corresponds to the slightly diffused distribution of preexisting free electrons. The absorption of the laser pulse induces a temperature increase in the voxel region resulting in thermal and concentration diffusions. The diffusion of Ag^0 is highly activated by the temperature (even with moderate temperature increases much below the glass transition temperature) and gradient of concentration which allows for these species to meet with Ag^+ ions and to take part in the following kinetic reaction: $Ag^0 + Ag^+ \rightarrow Ag^{2+}$. The red circle reproduces the beginning of the reaction in the area of maximal concentration of Ag^0. The reaction of the first stage of silver cluster formation $Ag^0 + Ag^+ \rightarrow Ag^{2+}$ ends when the concentration of silver atoms Ag^0 wears off. So, the spatial distribution of Ag^{2+} corresponds slightly to the spatial distribution of preexisting Ag^0. The trapping process and reactions are so fast that the concentration of free electrons, holes, and Ag^0 wears off before the next laser pulse. The following laser pulse dissociates the silver clusters in the center by photo-dissociation where the laser pulse is so intense. The next laser pulse again creates a reservoir of free electrons which triggers kinetic reactions responsible for the formation of silver clusters. The previously mentioned cycle repeats itself from one pulse to another and the non-dissociated silver clusters progressively gather on the periphery of the laser beam forming a ring-shaped structure [12, 13, 29, 70, 76] following a train of pulses. Thus, the fast diffusing of free electrons destroys the initial spatial charge neutrality of the electron-hole plasma inside the focal spot and creates an ambipolar electric field. It accelerates the diffusion. Therefore, the electron-hole trapping process provides the formation of frozen charge redistribution in space and corresponding radial static electric field $\overrightarrow{E}_{\text{dc}}$ [76], as experimentally reported [22, 53, 54].

This mechanism of writing allows to inscribe structures much below the wavelength. Indeed, the width of the structured areas (see HRSEM image in Fig. 19.3h) is about 100 nm. By multipass laser inscription and lateral displacement of few hundred of nm, it is possible to take advantage of the inscription and erasure threshold. This has been demonstrated for the formation of high periodicity photonic structures, with periods down to 200 nm.

2.5 Laser Parameter Window for Writing in FPL Glasses

The study consisted in irradiating the glass with different laser irradiances for different laser repetition rates and monitoring the fluorescence intensity emitted by the structures under 405 nm excitation while collecting emitted fluorescence in a spectral range between 450 and 750 nm [16]. The results are presented in color scale in Fig. 19.6: the lowest fluorescence intensity is represented in white, the highest in black, and the intermediate intensities in gradient red. The highest fluorescence intensity was observed at the highest irradiance possible at 11 TW.cm^{-2} below the explosion threshold and for a number of pulses of 10^7. Two conclusions could be derived. In order to create silver clusters, a large number of pulses is required as well as the right laser irradiance. The fluorescence intensity depends linearly on the irradiance while depending logarithmically on the number of pulses [69, 13]. The second conclusion implies that a high repetition rate laser is required in order to activate and create the silver clusters. When using a low repetition rate laser, the creation of silver clusters is possible but requires a longer

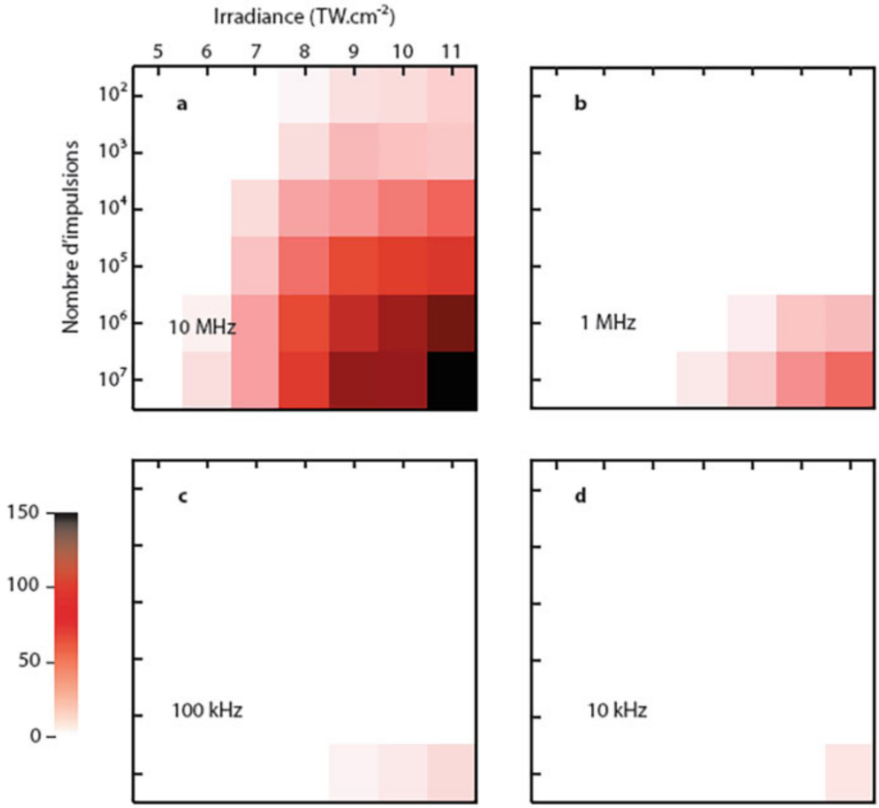

Fig. 19.6 Fluorescence intensity as a function of the laser irradiance and number of pulses for different laser repetition rates (**a**) 10 MHz (**b**) 1 MHz (**c**) 100 kHz (**d**) 10 kHz. (Taken from Ref. [14])

time of exposure which limits the writing process. A minimum number of pulses is required in order to trigger the diffusion and photochemistry of silver cluster creation.

2.6 *Temperature Reached During Femtosecond Irradiation*

There are two temperature factors during irradiation: the temperature of the glass before irradiation and the heat increase supplied by the energetic laser deposition. The second is more complex and has been discussed from a theoretical point of view [76]. To summarize, all the energy absorbed by the glass, which is not consumed by structuring or reemitted as light radiation, ends up heating the material.

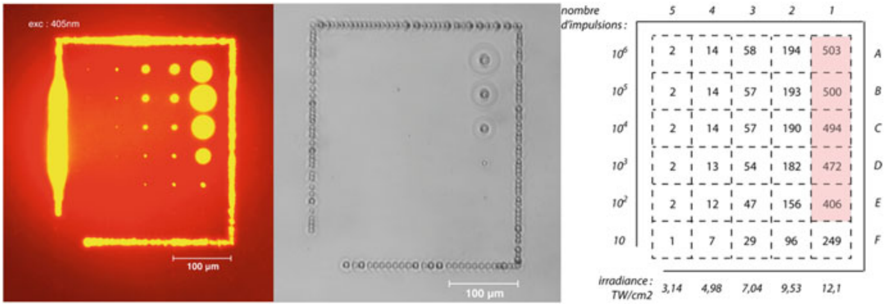

nombre d'impulsions :	5	4	3	2	1	
10^6	2	14	58	194	503	A
10^5	2	14	57	193	500	B
10^4	2	14	57	190	494	C
10^3	2	13	54	182	472	D
10^2	2	12	47	156	406	E
10	1	7	29	96	249	F
irradiance : TW/cm2	3,14	4,98	7,04	9,53	12,1	

Fig. 19.7 Left, fluorescence image of the irradiation array; excitation, 405 nm; collection, visible spectrum. Center, transmission white light image; right, increase in glass temperature at the center of the focal point as a function of writing parameters. Pink boxes indicate the area where the increase is above the glass transition temperature (375 °C). (Reproduced from Ref. [52])

Using this model, we can establish the laser-related temperature increases in each of the cells of our irradiation matrix. These temperatures are noted in Fig. 19.7. We can see that the E1 box allows under laser irradiation to exceed the glass transition temperature of this FPL glass ($T_g = 375$ °C) which is translated on the figure by a change of RI of the type I glass. Moreover, the nucleation process to form silver aggregates starts at a temperature elevation of 50 °C.

Laser structuring of FPL glasses can therefore be considered as a nonthermal process because it can be obtained for very moderate local temperature increase, with resulting temperatures much below the glass transition temperature of the glass.

2.7 Inhibition Mechanism of Laser Inscription: Thermal Constraint and UV Co-illumination Scheme

As shown in previous paragraphs, laser inscription in FPL glasses is associated with the selective laser activation of photochemistry of silver species, without significantly affecting the glass matrix itself. Such a photochemical modification is shown to occur in a nonthermal process, namely, with very moderate local temperature increase, much below the glass transition temperature (as shown in Fig. 19.7).

DLW at room temperature leads to a given efficiency of creation of molecular silver clusters in FPL glasses. One can wander what the influence of the initial glass temperature is. Does a higher initial temperature of the FPL glass favor the mobility of silver ions Ag^+ and neutral atoms Ag^0 and thus the creation of highly fluorescent silver clusters? Oppositely, does it thermally reduce the lifetime of intermediate silver species that behavior as preliminary species to initiate the clustering process of molecular silver species, and thus does it contribute to limit the efficiency of global cluster creation?

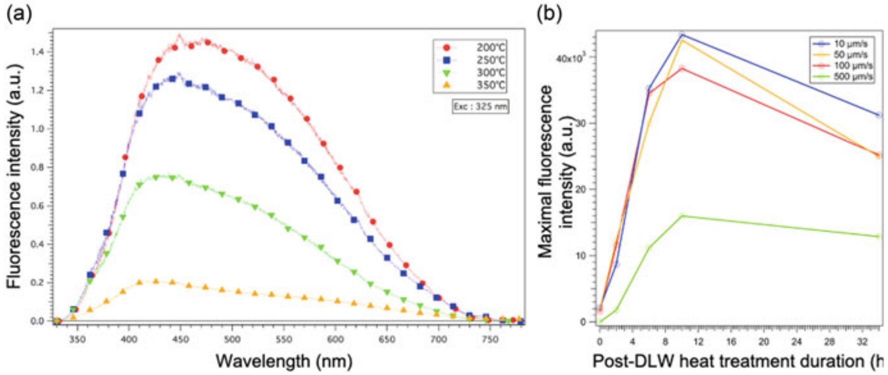

Fig. 19.8 (**a**) Fluorescence spectra of silver clusters (excitation at 325 nm) created from 4 TW/cm^2 laser irradiance and sample velocity of 220 µm/s in a silver-containing zinc phosphate FPL glass, and dependence with the external in-situ glass temperature during DLW. (**b**) Maximal fluorescence intensity after post-DLW heat treatment process [52]

Figure 19.6 had shown that the decrease of the laser repetition rate reduces the efficiency of silver cluster creation because it allows for the relaxation and partial vanishing of intermediate species between two successive pulses. Indeed, lower repetition rates lead to weaker pulse-to-pulse local concentrations of elementary bricks such as Ag^0. As a consequence, this limits the initial sequence $Ag^+ + Ag^0 \rightarrow Ag_2{}^+$ that stands for the formation of the smallest silver clusters $Ag_2{}^+$, which limits then the subsequent growth of larger and more stable silver clusters.

Applying thermal constraint at the FPL glass substrate during DLW has shown to decrease the overall efficient of fluorescent silver clusters, as shown in Fig. 19.8a with non-corrected spectra [52]. Even though all the spectral components of the fluorescence emission of laser-induced silver clusters are not equally affected, external thermal heating of the FPL glass during DLW reduces intermediate species such as trapped charges and intermediate color centers such as Ag^{2+} and Ag^0. Such thermal behavior is similar to thermal de-trapping of swallow traps, such as those produced by nanosecond UV illumination. As partial conclusion, thermal constraint with higher FPL glass temperature behaves such as inter-pulse glass accelerated aging and thus similar to the laser repetition rate reduction. On the other hand, post-DLW heat treatment allows for the subsequent growth of larger silver clusters, once large-enough molecular silver species have been created, as shown in Fig. 19.8b. At some point, one observes a fluorescence quenching due to the beginning of phase transformation of very larger fluorescent clusters into non-fluorescent metallic silver nanoparticles [52].

Preheating the FPL glass prior to DLW partially inhibits the formation of fluorescent silver clusters, while post-DLW thermal treatment allows for the thermal growth of the laser-induced clusters.

The intermediate bricks, including swallow traps such as Ag^0 mostly, are of prime importance to further grow larger and stable silver clusters. The influence

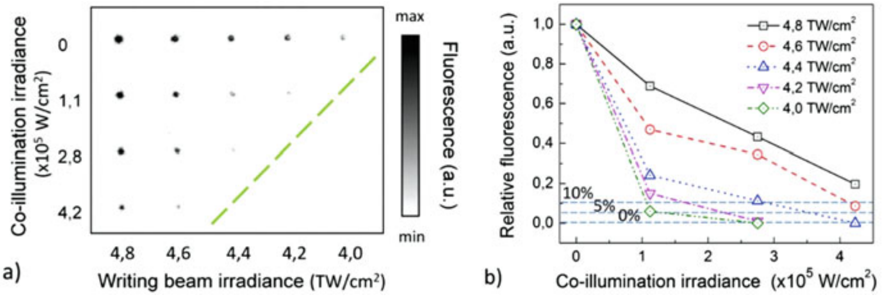

Fig. 19.9 (**a**) Interaction matrix of dual-color direct laser writing, with a fs writing beam (800 nm, 145 fs, 10^5 pulses) and a simultaneously shined UV laser diode ($\lambda_{\text{inhibition}} = 394$ nm, cw), being observed in broad-field fluorescence imaging ($\lambda_{\text{excitation}} = 405$ nm and $\Delta\lambda_{\text{collection}} = 450$–$750$ nm). (**b**) Integrated fluorescence intensity of each point, enabling an inhibition effect up to 100% [57]

of such intermediate species has been emphasized both with decreasing the laser repetition rate and with the environment temperature increase of the FPT glass. Another demonstration has been brought by means of dual-color illumination scheme. Indeed, cw UV co-illumination with tunable power during DLW has led to the tunable control of DLW efficiency of fluorescent silver clusters, as shown in Fig. 19.9a. The amplitude analysis of the inscribed fluorescence response even demonstrates an experimental access to a total inhibition of silver cluster DLW, as shown in Fig. 19.9b [57]. Indeed, UV co-illumination appears to give access to the de-trapping of electron from an individual silver element with $Ag^0 + \hbar\omega_{UV} \rightarrow Ag^+ + e^-$ or to photo-dissociate the smallest and thus weakest silver clusters, namely, Ag_2^+ with $Ag_2^+ + \hbar\omega_{UV} \rightarrow Ag^+ + Ag^0$. Inhibition of DLW efficiency is more favorably close to the laser threshold inscription, namely, when multiphoton energy deposition does not generate too many free charges and preliminary bricks to be cancelled out by UV co-illumination. Beyond the interest for the understanding of the preliminary steps of silver cluster creation and growth during DLW, such local inhibition of DLW could further be used for super-resolution optical lithography in FPL glasses, similar to what has already been achieved in organic polymers by STED-like optical lithography [32].

Dual-color scheme with UV co-illumination during DLW process allows for the tunable control and up to the total inhibition of the creation efficiency of silver clusters.

2.8 Distinct DLW Regimes in FPL Glasses Giving Rise to Type A or Type I Glass Modifications

The selective laser activation of the silver photochemistry and associated optical contrast (excitation, fluorescence, plasmonic behavior, nonlinear optical response,

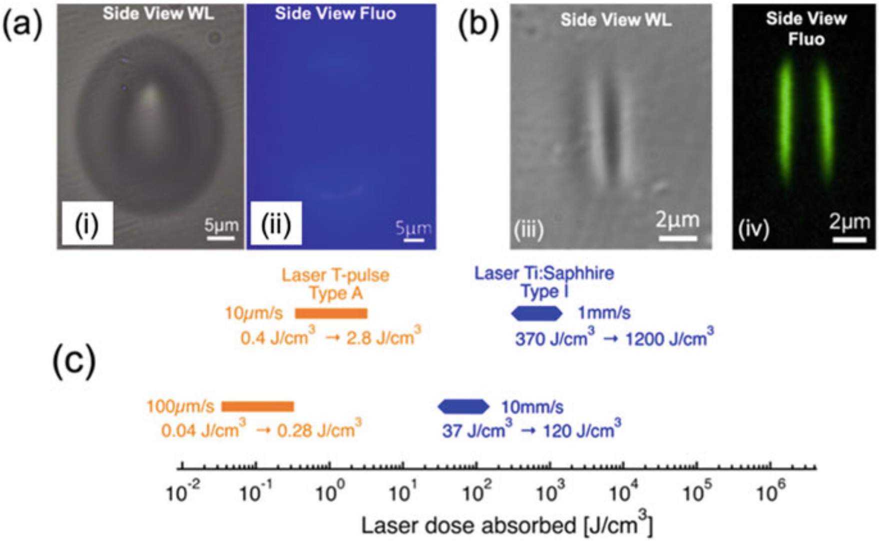

Fig. 19.10 (**a**, **b**) Side view of white-light illumination of (**a**.**i**) a type I waveguide and of (**b**.**iii**) a Type A waveguide; (**a**, **b**) side view of fluorescence image of (**a**.**ii**) a type I waveguide and of (**b**.**iv**) a Type A waveguide. Two different morphologies were observed for each type of modification. The difference of the color of fluorescence is due to different high pass filters used in each observation. (**c**) Calculated laser dose absorbed as a function of the used range of writing speed, resulting from the two distinct lasers used for the writing process of the two distinct types: (orange) T-pulse 200 laser used for the inscription of Type A modification, (blue) Ti:sapphire laser used for the type I modification [3]

RI modification) requires high repetition rates and the cumulative behavior of many-pulse irradiation. However, high irradiances typically ranging on the 5–10 TW/cm^2 correspond to moderate energy deposition and limited temperature increase (a few tens of degrees) much below the glass transition temperature. As a consequence, the DLW regime for Type A appears as a counterintuitive regime since it behaves as a nonthermal regime, especially without thermal over-/under-densification of the glass matrix after DLW, as shown in Fig. 19.10a [3].

However, FPL glasses can undergo DLW regime for type I inscription. In this case, much higher peak energies are required, leading thus to a much higher temperature increase despite lower repetition rates, as shown in Fig. 19.10b. Globally, cumulated energy deposition is much higher to access type I modification compared to what needed for Type A modification, as shown in Fig. 19.10c. In the case of type I irradiation regime in FPL glasses, the residual silver photochemistry is very marginal compared to what can be produced in the Type A irradiation regime, at least in silver-containing zinc phosphate glasses.

Type A is indeed a new type of glass modification based of the selectively laser-activated photochemistry of silver, while letting the glass matrix unaffected. Such Type A irradiation regime corresponds to much lower cumulated energy deposition than that needed to access type I, corroborating the fact that Type A regime corresponds to a counterintuitive but nonthermal regime.

3 Type A Optical Properties

3.1 Refractive Index Modification

To investigate the RI modification, labeled Δn, created inside an FPL glass following laser-glass interaction, a cartography of square linear structures of 100 × 100 µm is performed, as shown in Fig. 19.11. The irradiance and the writing speed were changed during the writing, from 6 to 10 TW/cm^2 (from 280 to 470 mW average power measured after the microscope objective), while the writing speed was varied between 10 and 50 µm/s corresponding to 1.7×10^6 and 3.3×10^5 deposited pulses, respectively, as shown in Fig. 19.11. Top view of fluorescent images under 480 nm excitation reveals the written structures as shown in Fig. 19.11a. The fluorescence intensity of the written structures exhibits a variation as a function of the laser parameters which was also previously reported by our group [13, 69]: the higher the laser irradiance and/or the number of pulses, the greater the resulting fluorescence intensity.

A pop-up image of the written structure (b) of Fig. 19.11 reveals a positive optical path difference (OPD), i.e., positive Δn correlated to the spatial distribution of the silver cluster as shown in Fig. 19.11b (to be compared with Fig. 19.11a). Based on the phase contrast images and given the depth of the structures, the quantitative value of Δn of the written structures could be ascertained. Figure 19.11c shows

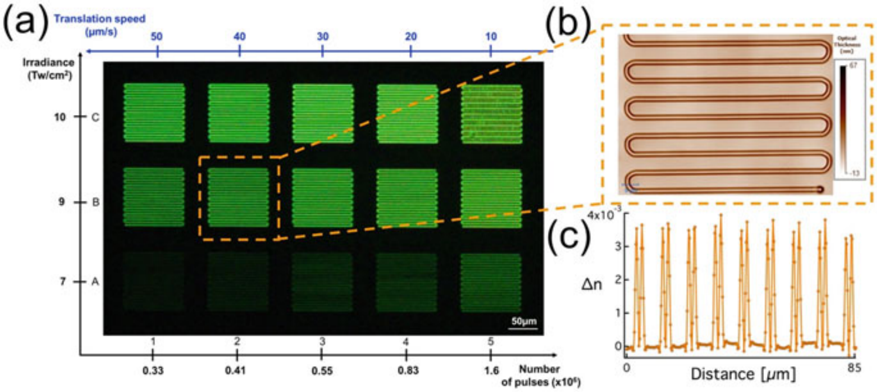

Fig. 19.11 (**a**) Fluorescence image (λ_{ex} = 480 nm, λ_{em} = 550 nm) of the written cartography. Writing irradiances are presented along the vertical axis, while the number of pulses appears along the horizontal axis. (**b**) Pop-up of the phase image under white-light illumination of the B2 structure. (**c**) Positive RI change (Δn) determined from the phase image of B2 [1]

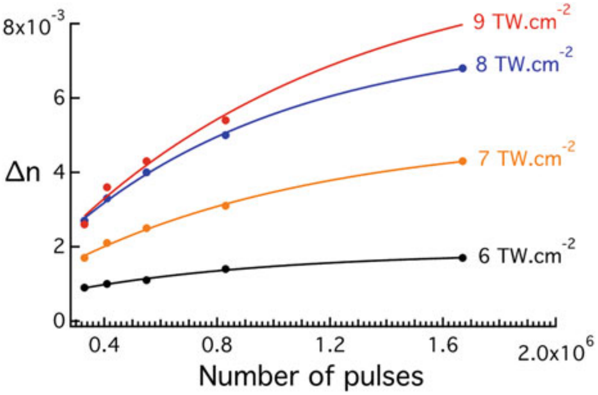

Fig. 19.12 RI change variation (Δn) as a function of the number of pulses and laser irradiance. Δn increases as a function of the laser parameters. Laser repetition rate 9.8 MHz [1]

the Δn profile determined from the phase image in Fig. 19.11b. One can observe that every laser passage results in two positive Δn peaks spatially correlated to the spatial distribution of the silver clusters. This proves that the photoinduced silver clusters are responsible for the positive Δn following DLW.

A study shows that Δn increases as a function of the number of deposited pulses as well as the laser irradiance. This result is expected, since a larger number of deposited pulses contributes to an increase in the local temperature (well below the glass transition temperature T_g). This moderate increase in temperature allows the thermal activation of the migration of silver ions as well as the chemical reactivity leading to the formation of a larger number of silver clusters [12, 76], which results in a higher Δn. The same scenario applies for increasing the laser irradiance: the higher the irradiance, the greater the formation of silver clusters, as previously reported [13]. The Δn increases from 9×10^{-4} up to 8×10^{-3} in this case (Fig. 19.12), Δn up to 2×10^{-2} in the considered silver-containing zinc phosphate glass: such Δn values are to be compared to those obtained in fused silica going from 1.3×10^{-3} up to 1.7×10^{-2} with type I modifications [7, 31]. These Δn values make thus Type A modifications competitive in terms of perspectives of photonic applications, as further detailed in this chapter.

3.2 Second-Order Nonlinear Optical Properties (X^2)

Normally, glass as a centrosymmetric material exhibits no second harmonic generation response. However, based on the electric field $\overrightarrow{E_{dc}}$ generated by the movement on the charged species, an effective second harmonic generation response has been observed [22, 53, 54]. The process of creation of silver clusters inside silver-containing glasses gives rise to a static electric-field-induced second harmonic

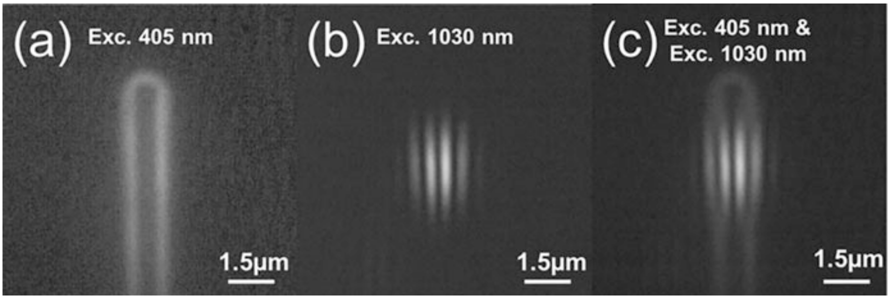

Fig. 19.13 (**a**) Fluorescence pattern of a written line under 405 nm excitation; (**b**) four-line of electric field induced second harmonic generation (EFISHG) under 1030 nm femtosecond laser excitation (**c**) superposition of the fluorescence and EFISHG correlated patterns under 405 and 1030 nm excitation. (Taken from Ref. [54])

generation (EFISHG), which corresponds to the coupling of such static electric field with the third-order nonlinear susceptibility and leads thus to an effective second-order nonlinear susceptibility. Such a coupling may be interpreted as a local centrosymmetry breaking as the structured glass gets a local polar orientation due to the imprinted static and intense buried electric field. Following DLW of linear structures and under 1030 nm excitation, EFISHG patterns were observed as shown in Fig. 19.13a that shows the typical cluster distribution under UV excitation while Fig. 19.13c shows the superposition of the fluorescence and EFISHG patterns showing correlated but distinct spatial distributions [54]. Those results exhibit an advantage for FPL glasses representing a second harmonic response following DLW which is not common in other glasses. Such a second-order nonlinear patterning appeared to be remarkably stable in silver-containing zinc phosphate glasses as long as glass is kept at temperatures below T_g. In case the reader is interested, the following readings [22, 53, 54] are recommended. Note that the locally distributed creation of silver clusters also contributed to the strong local enhancement of third-order nonlinearity while considering resonant third-harmonic generation [18].

3.3 The Principal Types of Created Molecular Clusters and Their Luminescent Properties

The photoinduced silver clusters $Ag_m{}^{x+}$ generally exhibit two main absorption bands around 290 and 345 nm [12, 47, 60] related to the creation of $Ag_\alpha(1)$ and $Ag_\alpha(2)$ clusters, respectively [47]. These clusters show a broadband fluorescence emission under UV-blue excitation, as shown in Fig. 19.14, with lifetimes ranging in the ns range. $Ag_\alpha(1)$ and $Ag_\alpha(2)$ could be the dominating clusters exhibiting the two dominating absorption bands. Also other types of clusters are generated following

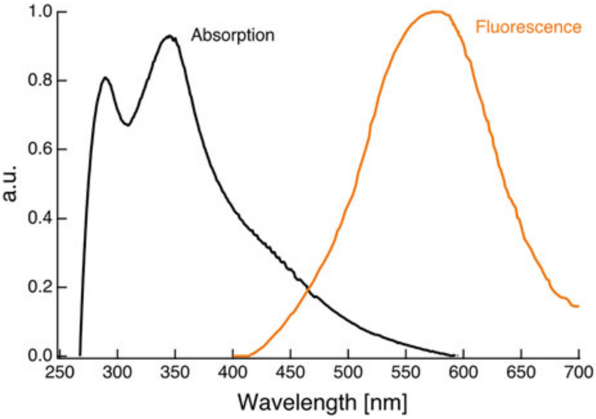

Fig. 19.14 Absorption (black) of the photoinduced silver clusters following laser irradiation exhibiting two main absorption bands around 290 and 345 nm. Fluorescence emission (orange) under blue-light excitation at 405 nm [2]

Table 19.3 Different silver (Ag) species identified following DLW in silver-containing glasses as reported in [47]

Ag specie	Amplitude	Position [nm]	Position [eV]	FWHM [nm]	FWHM [eV]
Ag_α (1)	0.103 ± 0.001	287 ± 2	4.32 ± 0.06	35 ± 4	0.5 ± 0.02
$Ag_2{}^+$	0.104 ± 0.001	302 ± 3	4.1 ± 0.08	34 ± 4	0.45 ± 0.02
Ag_α (2)	0.42 ± 0.005	340 ± 2	3.64 ± 0.04	56 ± 6	0.57 ± 0.015
Ag^0	0.084 ± 0.001	387 ± 4	3.2 ± 0.06	57 ± 5	0.47 ± 0.014
Ag_n	0.049 ± 0.003	442 ± 1	2.8 ± 0.01	73 ± 7	0.45 ± 0.012

DLW that were identified in a previous report from [47] and presented in Table 19.3.

Based on the differential silver cluster absorption with respect to the pristine glass, one can note that the silver clusters exhibit a large absorbance cross section, spanning from the UV to the visible range. To further support our hypothesis that the silver clusters are responsible for the Δn in our glasses, a Kramers-Kronig (K-K) analysis was conducted on the differential absorption spectrum of the silver clusters (Fig. 19.15a) to determine the associated Δn (Fig. 19.15b). A positive Δn was calculated and measured over the whole visible (VIS)-near infrared (NIR) ranges exhibiting a maximum value, in this case of 2.5×10^{-3} at $\lambda = 365$ nm. Such K-K analysis retrieves the experimental Δn values measured elsewhere from direct phase microscopy imaging, which makes the analysis robust and allows for concluding that the formation of new species, namely, silver clusters, supports local enhancement of polarizability and thus of the local RI change.

In Type A laser modification, Δn is not based on a standard index modification of the glass matrix itself due to the laser-induced modifications of the local density as it is the case for *type I* modification. Here, we report that the Δn produced is based

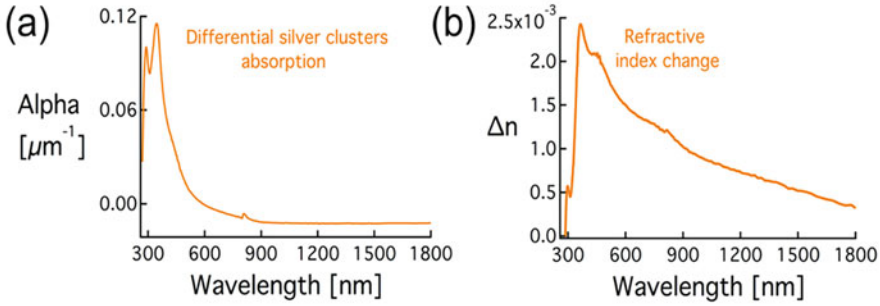

Fig. 19.15 (**a**) Silver cluster differential absorption spectrum as a function of the wavelength showing two main absorption bands near 290 and 350 nm. (**b**) RI change (Δn) determined from the spectrum shown in (**a**) based on a Kramers-Kronig analysis, considering the filling factor of the silver clusters' spatial distribution. DLW parameters: 7 TW/cm^2–40 µm/s

on the localized laser-induced creation of a new chemical silver species with the creation of new chemical bounds and with enlarged molecular electric polarizability, locally leading to an increase in the electric susceptibility and associated refraction index change.

3.4 Nanoparticle Development by Thermal Annealing Following a Type A Interaction

The concept of reduction/growth is fully accepted, this being analogous to the theory of nucleation/growth of crystals [17]. Thus, the development of nanoparticles is based on a first step of reduction of silver ions followed by a second step corresponding to the thermal growth of these nanoparticles. To initiate the reduction/growth process of nanoparticles from FPL glasses, it is possible to use the nonlinear absorption of the femtosecond laser beam. The heat accumulation being generally too low in this case, only the reduction phase is mostly accessible by laser. A subsequent phase is often necessary, which corresponds to an additional thermal annealing in order to carry out the nanoparticle growth step [47]. In FPL glasses of lanthanum borogermanate and germano-gallate, it was shown (Fig. 19.16) that the reduction and growth phase can be realized directly by femtosecond laser interaction. Nanoparticles of small sizes (3 nm) with a conversion rate of 52% from silver to nanoparticle phase were achieved.

Type Argentum (Type A) index modification can be performed in FPL glass with relatively low incident laser irradiation around 7 TW/cm^2, taking advantage of tailored materials with sensitizing agents. Type A DLW structures was demonstrated, which has been intensively investigated in terms of spatial 3D distributions of associated linear (absorption, excitation, emission, and lifetime, index modification)

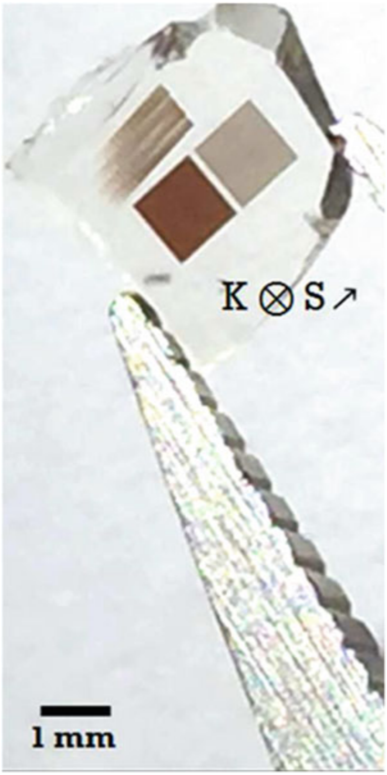

Fig. 19.16 Direct laser precipitation of metallic silver nanoparticles in a GGN glass doped with 2 mol% Ag_2O after laser structuring of 1 mm^2 square with parameters: fluences from 39 to 79 J/cm^2 [82] applications of Type A modifications and outlook

and nonlinear (SHG and THG) micro-spectroscopies. All these properties can be used for optical applications. The first one concerns volume structuring.

3.5 Volume Modification: Data Storage

High-density optical data storage (**ODS**) techniques have been actively investigated to overcome storage-capacity and lifetime limitations of conventional storage media such as CDs and DVDs for archiving purpose. Type A DLW of fluorescent hollow cylindrical structures was demonstrated, which has been intensively investigated in terms of spatial 3D distributions of associate linear and nonlinear optical properties [58, 59]. Indeed, these fluorescent structures show an increasing readout fluorescence emission while DLW intensity increases [58, 69]. An accelerated aging test, carried out in a climatic test chamber at 100 °C for 3100 h, revealed long-term storage capability of this Type A approach, with unmodified optical performance and fluorescence spectrum changes less than 1% [71]. The three-layer images, inscribed by Royon et al. 11 years ago, are still perfectly observable [69].

On the same idea, more recently, 5D ODS technique [55] on fluorescence intensity and ellipse orientation of data storage units by using Type A DLW in FPL glass was achieved. Fluorescence intensity modulation (4-bit encoding upon 16 intensity levels), obtained by controlling the incident laser irradiance, was used to provide one dimension to ODS, in addition to the three spatial coordinates. In order to increase the experimental degrees of freedom, the hollow cylindrical structure was transformed into a hollow ellipse structure by anamorphic focusing of the fs laser, leading to 4-bit encoding upon 16 orientation levels. Two different 4-bit bitmap images of 100 × 100 pixels have been embedded into one single image in such glasses by multiplexing 16 levels of the laser intensity and 16 levels of the ellipse orientation. The readout process has also been addressed, so as to independently retrieve the two incident images [55].

3.6 *Integrated Optics: Waveguide, Surface Waveguides, Directional Couplers, Beam Splitters, WBG*

Waveguides In order to illustrate the potential of Type A process for practical applications, a first approach took place by writing 7-mm-long waveguides 160 μm below the surface in FPL glass. The DLW of the waveguide was demonstrated using 1030 nm laser setup and a 20×-0.4 NA Mitutoyo microscope objective Fig. 19.17, left). The laser irradiance used was 8 TW/cm^2 with a writing speeds of 10 μm/s. Then the sample was rotated 90° for top laser injection and bottom collection of the guided light as shown in Fig. 19.17a and left.

Figure 19.17b shows one of the higher-order guided mode profiles following laser injection. One can observe that the guided mode profile is supported by the two fluorescent planes, i.e., the two planes of silver clusters, therefore providing another proof that the silver clusters are responsible for the Δn in silver-containing

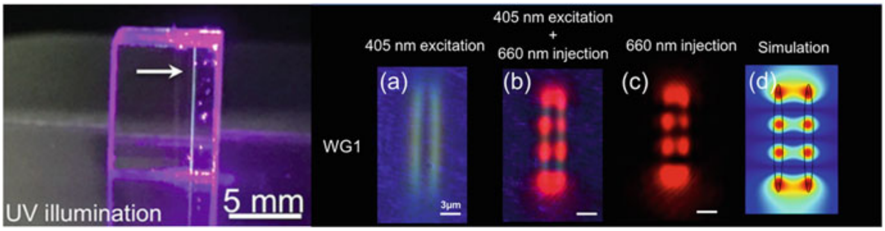

Fig. 19.17 Left, picture of the bulk sample under UV excitation ($\lambda_{ex} = 405$ nm) highlighting the fluorescence of the waveguide (indicated by the white arrow). Cross-section view of fluorescence under UV side excitation ($\lambda_{exc} = 405$ nm) of (**a**) superimposed near-field mode profile and fluorescence features for (**b**) near-field mode profile for a high-order propagating mode of (**c**) simulated mode profile using LUMERICAL for (**d**). DLW parameters for WG1: 8 TW/cm^2–10 μm/s [2]

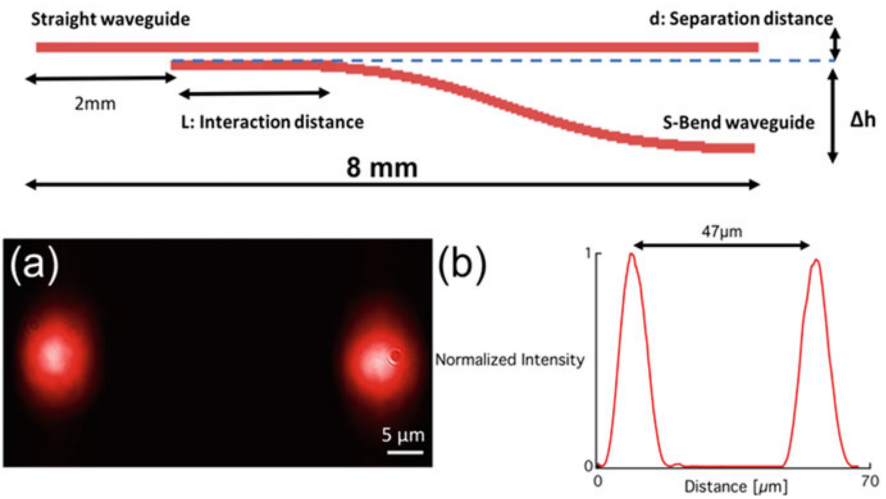

Fig. 19.18 Sketch of the coupler consisting of straight and S-bend waveguides. (**a**) Near-field mode profiles of the output of the coupler; (**b**) normalized intensity of the mode profiles indicating the creation of a 50–50 coupler. DLW parameters: 10.8 TW/cm^2–40 µm/s [1, 2]

glasses, as correlatively shown in Fig. 19.17a–c. Figure 19.17d shows the simulated modes, accordingly. This waveguide exhibited a Δn of 4.5 × 10^{-3}.

Couplers, Y junction Using the multipass laser writing, single-mode waveguides, Y junctions, and evanescent couplers have been demonstrated by Type A laser modification. Different asymmetric Y junctions were fabricated in [56]. For each case, the split ratios were adjusted to 50–50%, 43–57%, 33–67%, 27–73%, 22–78%, and 4–96% by adjusting laser writing intensity and number of laser pass.

Evanescent coupler with S-bend waveguide were also demonstrated, as shown in Fig. 19.18 [2].

Surface waveguides Taking advantage of the low pulse energy inscription regime of Type A compared to type I, laser writing on the glass surface is demonstrated with no need for additional processing. For sensing applications, near-surface waveguides were written in FPL glass. Based on this approach, an RI sensor was created in a 1 cm glass chip that shows a double resonance response shape. An increase of ~50% in the transmission followed by a decrease of ~66% was observed for a 4-mm-long oil droplet deposition on the surface (n_{oil} = 1.602 and 1.604, respectively). These surface waveguides remarkably show a non-null sensitivity for oil indices below the glass index, even for indices down to the 1.33–1.37 range compatible with biological and environmental applications [4, 5].

WBG Type A multipass laser inscription of fluorescent silver clusters opens a route for the fabrication of sub-wavelength periodic RI structures and thus for written WBG with first-order Bragg resonances down to the visible range. Figure 19.19a shows the inscription of periodic structures, demonstrating the creation of a sub-diffraction period through the multipass approach. The process of waveguide Bragg grating is a two-step process, starting first by the line-by-line successive inscription of the Bragg grating with the selective period and then followed by the inscription of the waveguide, thanks to a single laser pass perpendicular to the grating, as illustrated in Fig. 19.19b.

Examples of WBGs transmission spectra in a silver-containing gallophosphate glass, showing first-order resonance at 736.4, 796.3, and 856.1 nm, are shown in Fig. 19.20. Note that transmission dropped down to 25% with 500-µm-long WBGs, corresponding of a 75% filtering over such a short distance.

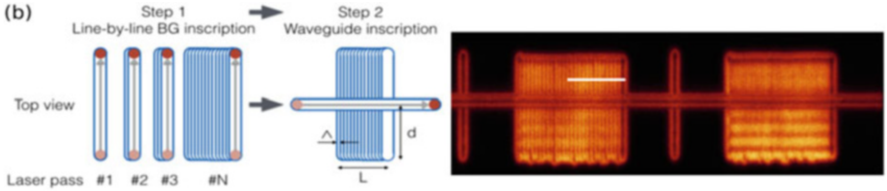

Fig. 19.19 (**b**) Schematic representation of the two-step process to write distributed feedback reflectors thanks to the Bragg grating architecture. (**a**) High-resolution confocal fluorescence image of periodic (Λ = 375 and 250 nm) WBG with crossing waveguide. White bar 5 µm

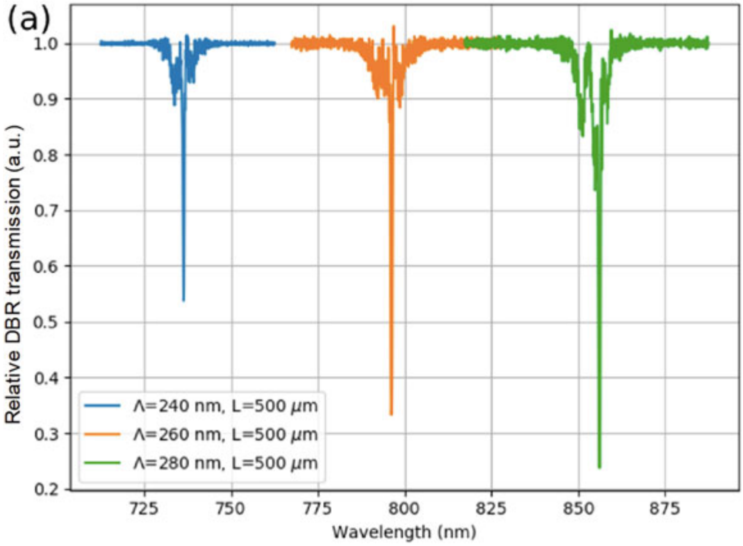

Fig. 19.20 (**a**) Transmissions of 500 µm grating length in Type A waveguide, grating periodicity (Λ = 240, 260, 28 nm) with corresponding first-order Bragg resonance λ_B peaking at 736.4, 796.3 and 856.1 nm, respectively

3.7 Controlled Nanograting

The LIPSS, laser-induced periodic surface structures, are today a very general term allowing to describe periodic structures on the surface of materials resulting from an unspecified laser radiation. With the industrial development of lasers with ultrashort pulses, structures with high-spatial frequency were highlighted. The periodicity of these structures is much smaller than the wavelength of the structuring laser. The term nanograting is then proposed by different research groups to define the

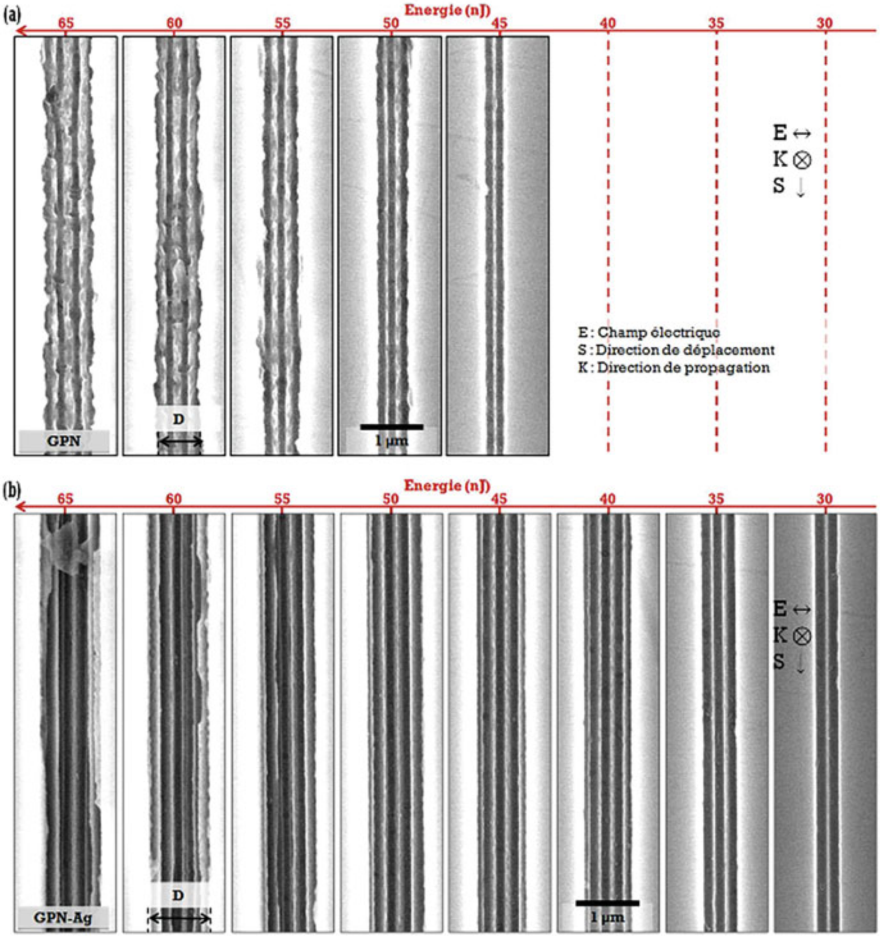
(a)
Energie (nJ)
65
60
55
50
45
40
35
30
E ↔
K ⊗
S ↓
E : Champ électrique
S : Direction de déplacement
K : Direction de propagation
GPN
D
1 µm
(b)
Energie (nJ)
65
60
55
50
45
40
35
30
E ↔
K ⊗
S ↓
GPN-Ag
D
1 µm

Fig. 19.21 SEM images (in secondary electron emission mode) of the nanostructures induced by different laser irradiations above the damage threshold on the sample surface of (**a**) GPN and (**b**) GPN-Ag glasses [81, 82]

structures induced by the strong focusing of a femtosecond laser on the surface, but also in the volume of a material.

In FPLs, the action of silver is responsible for the enhancement of multiphoton absorption during laser structuring, thus inducing very different behaviors during the laser writing processes of the nanograting. Such an influence has been the subject of remarkable results. The series of images in Fig. 19.21a, b, show the top views and the physical transverse profiles of the nanostructures, 1 year after the femtosecond laser irradiation at constant speed of a GPN matrix (without silver) and a GPN-Ag FPL glass, respectively. Such an observation reflects a good stability in time of such nanometric structures, potentially compatible with the realization of robust photonic devices based on nanograting. In order to evaluate the smoothing improvement of the nanograting in FPL glass, the standard deviation averaged over the entire profile is calculated. This evaluation leads to an estimate of the quality factor always higher than 1, even reaching $Q = 2$ (Fig. 19.21b), quantitatively demonstrating the improvement of the homogeneity of nanograting assisted by the introduction of silver. Another effect of silver photosensitivity is that the laser threshold is reduced. It takes almost twice as much energy to obtain the same nanograting in silver-free glass.

4 Outlook

Type A RI modification has been demonstrated in many glass matrices containing silver ions (FPL glasses). In these FPL glasses, the silver ion in high concentration allows by fs laser interaction to nucleate silver clusters with remarkable properties. The strong polarizability of these clusters results in an important increase of the RI, as well as strong luminescence when illuminated in the UV. The spatial localization and the sub-lambda size of the cluster distributions allow numerous applications in photonics. The main advantage of the Type A modification is the moderate laser intensity used, which allows an interaction without thermally affected zones and therefore contributes to excellent quality of the inscribed structures (optical quality equivalent to that of the pristine glass). The uniformity and availability of silver reservoir allows for a complete control of the inscription parameters and high inscription rates. The management of the silver reservoir can be further tailored by preparing specialty FPL glasses by correlating glass structure and optical behavior under femtosecond laser inscription [36]. Rewriting is possible as long as the silver reservoir is not consumed and very high recurrence lasers can be used without any degradation in the inscribed feature. The high throughput capability opens up all kinds of applications for inscription of adapted waveguides of complex topology, controlled tridimensional photonics structure down to 100 nm resolution, and surface inscription or controlled surface ablation, which is possible.

References

1. A. Abou Khalil, J.-P. Bérubé, S. Danto, J.-C. Desmoulin, T. Cardinal, Y. Petit, R. Vallée, L. Canioni, Direct laser writing of a new type of waveguides in silver containing glasses. Sci. Rep. **7**, 11124 (2017)
2. A. Abou Khalil, Direct Laser Writing of a new type of optical waveguides and components in silver containing glasses, PhD dissertation, University of Bordeaux, France and University of Laval, Québec, Canada, 2018
3. A. Abou Khalil, J.-P. Bérubé, S. Danto, T. Cardinal, Y. Petit, L. Canioni, R. Vallée, Comparative study between the novel type A and the standard Type I refractive index change created by direct laser writing in silver containing glasses. Opt. Mater. Express **9**(6), 2640–2651 (2019)
4. A. Abou Khalil, P. Lalanne, J.-P. Bérubé, Y. Petit, R. Vallée, L. Canioni, Direct laser writing of a novel refractive index sensor. Opt. Express **27**(22), 31130–31143 (2019)
5. A. Abou Khalil, W. Gebremichael, Y. Petit, L. Canioni, Refractive index change measurement by quantitative microscopy phase imaging for femtosecond laser written structures. Opt. Commun. **485**, 126731 (2021)
6. J.M.P. Almeida, P.H.D. Ferreira, D. Manzani, M. Napoli, S.J.L. Ribeiro, C.R. Mendonça, Metallic nanoparticles grown in the core of femtosecond laser micromachined waveguides. J. Appl. Phys. **115**, 193507 (2014)
7. M. Ams, G.D. Marshall, M.J. Withford, Study of the influence of femtosecondlaser polarisation on direct writing ofwaveguides. Opt. Express **14**(26), 13158–13163 (2006)
8. M. Ams, G.D. Marshall, P. Dekker, M. Dubov, V.K. Mezentsev, I. Bennion, M.J. Withford, Investigation of ultrafast laser–photonic material interactions: Challenges for directly written glass photonics. IEEE J. Sel. Top. Quantum Electron. **14**(5), 1370–1378 (2008)
9. S.D. Stookey, Ind. Eng. Chem., 1–6 (1949)
10. I. Belharouak, C. Parent, B. Tanguy, G. Le Flem, M. Couzi, Silver aggregates in photoluminescent phosphate glasses of the Ag2O–ZnO–P2O5'system. J. Non Cryst. Solids **244**, 238–249 (1999)
11. I. Belharouak, H. Aouad, M. Mesnaoui, M. Maazaz, C. Parent, B. Tanguy, P. Gravereau, G. Le Flem, Crystal structure and luminescence properties of silver in AgM(PO3)3 (M=Mg, Zn, Ba) polyphosphates. J. Solid State Chem. **145**, 97–103 (1999)
12. M. Bellec, A. Royon, B. Bousquet, K. Bourhis, M. Treguer, T. Cardinal, M. Richardson, L. Canioni, Beat the diffraction limit in 3D direct laser writing in photosensitive glass. Opt. Express **17**(12) (2009)
13. M. Bellec, A. Royon, K. Bourhis, J. Choi, B. Bousquet, M. Treguer, T. Cardinal, J.-J. Videau, M. Richardson, L. Canioni, 3D patterning at the nanoscale of fluorescent emitters in glass. J. Phys. Chem. C **114**, 15584–15588 (2010)
14. M. Bellec, Nanostructuration par laser femtoseconde dans un verre photo-luminescent, PhD dissertation, Université de Bordeaux, France, 2010
15. K. Bourhis, A. Royon, M. Bellec, J. Choi, A. Fargues, M. Treguer, J.-J. Videau, D. Talaga, M. Richardson, T. Cardinal, L. Canioni, Femtosecond laser structuring and optical properties of a silver and zinc phosphate glass. J. Non-Cryst. Solids **356**, 2658–2665 (2010)
16. K. Bourhis, Photostructuration par laser infrarouge femtoseconde de verres photosensibles de phosphates de zinc, d'argent et de gallium, Université de Bordeaux, France, 2011
17. G. Cao, *Nanostructures & Nanomaterials: Synthesis, Properties and Application* (Imperial College Press, 2004)
18. L. Canioni, M. Bellec, A. Royon, B. Bousquet, T. Cardinal, Three-dimensional optical data storage using third-harmonic generation in silver zinc phosphate glass. Opt. Lett. **33**, 360–362 (2008)
19. Y. Cheng, K. Sugioka, M. Masuda, K. Shihoyama, K. Toyoda, K. Midorikawa, Optical gratings embedded in photosensitive glass by photochemical reaction using a femtosecond laser. Opt. Express **11**, 1809–1816 (2003)

20. Y. Cheng, K. Sugioka, K. Midorikawa, M. Masuda, K. Toyoda, M. Kawachi, K. Shihoyama, Three-dimensional micro-optical components embedded in photosensitive glass by a femtosecond laser. Opt. Lett. **28**, 1144 (2003)
21. J. Choi, M. Bellec, K. Bourhis, A. Royon, L. Canioni, T. Cardinal, E. Fargin, V. Rodriguez, M. Dussauze, A. Delestre, M. Richardson, Femtosecond laser induced micro-structured silver containing glass as an engineered nonlinear optical material, in *Advances in Optical Materials*, paper AWB3, (2009)
22. J. Choi, M. Bellec, A. Royon, K. Bourhis, G. Papon, T. Cardinal, L. Canioni, M. Richardson, Three-dimensional direct femtosecond laser writing of second-order nonlinearities in glass. Opt. Lett. **37**(6), 1029–1031 (2012)
23. G. De Cremer, Y. Antoku, M. Roeffaers, M. Sliwa, J. Van Noyen, S. Smout, J. Hofkens, D.E. De Vos, B.F. Sels, T. Vosch, Photoactivation of Silver-Exchanged Zeolite A. Angew. Chem. **47**, 2813–2816 (2008)
24. G. De Cremer, E. Coutiño-Gonzalez, M.B.J. Roeffaers, B. Moens, J. Ollevier, M. Van der Auweraer, R. Schoonheydt, P.A. Jacobs, F.C. De Schryver, J. Hofkens, D.E. De Vos, B.F. Sels, T. Vosch, Characterization of fluorescence in heat-treated silver-exchanged zeolites. J. Am. Chem. Soc. **131**, 3049–3056 (2009)
25. G.D. Cremer, E. Coutiño-Gonzalez, M.B.J. Roeffaers, D.E.D. Vos, J. Hofkens, T. Vosch, B.F. Sels, In situ observation of the emission characteristics of zeolite-hosted silver species during heat treatment. ChemPhysChem **11**(8), 1627–1631 (2010)
26. Y. Dai, B. Zhu, J. Qiu, H. Ma, B. Lu, B. Yu, Space-selective precipitation of functional crystals in glass by using a high repetition rate femtosecond laser. Chem. Phys. Lett. **443**, 253–257 (2007)
27. K. Davis, K. Miura, N. Sugimoto, Writing waveguides in glass with a femtosecond laser. Opt. Lett. **21**(21), 1729–1731 (1996)
28. G. De Cremer, B. Sels, J. Hotta, M.B.J. Roeffaers, E. Bartholomeeusen, E. Coutiño-Gonzalez, V. Valtchev, D.E. De Vos, T. Vosch, J. Hofkens, 2010 optical encoding of silver zeolite microcarriers. Adv. Mater. **22**(9), 957–960 (2010)
29. J.-C. Desmoulin et al., Femtosecond laser structuring of silver-containing glass: Silver redistribution, selective etching, and surface topology engineering. J. Appl. Phys. **118**(21), 213104 (2015)
30. I. Díez, R.H.A. Ras, Fluorescent silver nanoclusters. Nanoscale **3**, 1963–1970 (2011)
31. S.M. Eaton et al., High refractive index contrast in fused silica waveguides by tightly focused, high-repetition rate femtosecond laser. J. Non-Cryst. Solids **357**(11–13), 2387–2391 (2011)
32. J. Fisher, M. Wegener, Opt. Mater. Express **1**, 614 (2011)
33. R.R. Gattass, E. Mazur, Femtosecond laser micromachining in transparent materials. Nat. Photonics **2**, 219–225 (2008)
34. T. Gleitsmann, B. Stegemann, T.M. Bernhardt, Femtosecond-laser-activated fluorescence from silver oxide nanoparticles. Appl. Phys. Lett. **84**, 4050–4052 (2004)
35. T. Gleitsmann, T.M. Bernhardt, L. Woste, Luminescence properties of femtosecond-laser-activated silver oxide nanoparticles embedded in a biopolymer matrix. Appl. Phys. A Mater. Sci. Process. **82**, 125–130 (2005)
36. T. Guérineau, L. Loi, Y. Petit, S. Danto, L. Canioni, T. Cardinal, Structural influence on the femtosecond laser ability to create fluorescent patterns in silver-containing sodium-gallium phosphate glasses. Opt. Mater. Express **8**(12), 3748–3760 (2018)
37. K.O. Hill, Y. Fujii, D.C. Johnson, B.S. Kawasaki, Photosensitivity in optical fiber waveguides: Application to reflection filter fabrication. Appl. Phys. Lett. **32**(647), 647–649 (1978)
38. B. Hua, Y. Shimotsuma, M. Nishi, K. Miura, Micro-modification of metal-doped glasses by a femtosecond laser. J. Laser Micro/Nanoeng. **2**(1), 36–39 (2007)
39. Y. Kondo, K. Miura, T. Suzuki, H. Inouye, Three-dimensional arrays of crystallites within glass by using non-resonant femtosecond pulses. J. Non-Cryst. Solids **253**(1–3), 143–156 (1999)
40. T. Kurobori, W. Zheng, C. Zhao, *Silver-Activated Radiophotoluminescent Glass: Band Assignments and a Novel Readout System Using a Modulated UV Laser Diode IOP Conference Series: Materials Science and Engineering*, vol 15 (IOP Publishing, 2010), p. 012026

41. A.S. Lipat'ev et al., Formation of luminescent and birefringent microregions in phosphate glass containing silver. Glas. Ceram. **73**(7–8), 277–282 (2016)
42. Y. Liu, M. Shimizu, B. Zhu, Y. Dai, B. Qian, J. Qiu, Y. Shimotsuma, K. Miura, K. Hirao, Micromodification of element distribution in glass using femtosecond laser irradiation. Opt. Lett. **34**, 136–138 (2009)
43. M. Masuda, K. Sugioka, Y. Cheng, N. Aoki, M. Kawachi, K. Shihoyama, K. Toyoda, H. Helvajian, K. Midorikawa, 3-D microstructuring inside photosensitive glass by femtosecond laser excitation. Appl. Phys. A Mater. Sci. Process. **76**, 857–860 (2003)
44. C. Maurel, T. Cardinal, M. Bellec, L. Canioni, B. Bousquet, M. Treguer, J.J. Videau, J. Choi, M. Richardson, Luminescence properties of silver zinc phosphate glasses following different irradiations. J. Lumin. **129**, 1514–1518 (2009)
45. C. Maurel, Verres pour la Photostructuration, PhD Dissertation, Université de Bordeaux, France, 2009
46. S.S. Mao, R.F. Qu, S. Guizard, X. Mao, R.E. Russo, G. Petite, P. Martin, Dynamics of femtosecond laser interactions with dielectrics. Appl. Phys. A Mater. Sci. Process. **79**, 1695–1709 (2004)
47. N. Marquestaut, Y. Petit, A. Royon, P. Mounaix, T. Cardinal, L. Canioni, Three-dimensional silver nanoparticle formation using femtosecond laser irradiation in phosphate glasses: Analogy with photography. Adv. Funct. Mater. **24**(37), 5824–5832 (2014)
48. M. Mesnaoui, M. Maazaz, C. Parent, B. Tanguy, G. Le Flem, Spectroscopic properties of Ag+ ions in phosphate glasses of NaPO3−AgPO3 system. Eur. J. Solid State Inorg. Chem. **29**, 1001–1013 (1992)
49. K. Miura, J. Qiu, T. Mitsuyu, K. Hirao, Space-selective growth of frequency-conversion crystals in glasses with ultrashort infrared laser pulses. Opt. Lett. **25**, 408 (2000)
50. Y. Miyamoto, T. Yamamoto, K. Kinoshita, S. Koyama, Y. Takei, H. Nanto, Y. Shimotsuma, M. Sakakura, K. Miura, K. Hirao, Emission mechanism of radiophotoluminescence in Ag-doped phosphate glass. Radiat. Meas. **45**, 546–549 (2010)
51. Y. Miyamoto, K. Kinoshita, S. Koyama, Y. Takei, H. Nanto, T. Yamamoto, M. Sakakura, Y. Shimotsuma, K. Miura, K. Hirao, Emission and excitation mechanism of radiophotoluminescence in Ag + −activated phosphate glass. Nucl. Instrum. Methods Phys. Res., Sect. A **619**, 71–74 (2010)
52. G. Papon, Nanostructuration des propriétés optiques linéaires et non linéaires d'un verre photosensible par laser femtoseconde, PhD dissertation, University of Bordeaux, France, 2012
53. G. Papon et al., Fluorescence and second-harmonic generation correlative microscopy to probe space charge separation and silver cluster stabilization during direct laser writing in a tailored silver-containing glass. Opt. Mater. Express **3**(11), 1855 (2013)
54. G. Papon, N. Marquestaut, Y. Petit, A. Royan, M. Dussauze, V. Rodriguez, T. Cardinal, L. Canioni, Femtosecond single-beam direct laser poling of stable and efficient second-order nonlinear optical properties in glass. J. Appl. Phys. **115**(11), 113103 (2014)
55. C.H. Park, Y. Petit, S.H. Park, L. Canioni, Micromachines **11**, 1026 (2020)
56. C-H. Park, Study on nonlinear multi-dimensional direct laser writing by using ultrashort high power laser, PhD dissertation, University of Bordeaux, France and Yonsei University, South Korea, 2020
57. Y. Petit, K. Mishchik, N. Varkentina, N. Marquestaut, A. Royon, I. Manek-Hönninger, T. Cardinal, L. Canioni, Dual-color control and inhibition of direct laser writing in silver-containing phosphate glasses. Opt. Lett. **40**(17), 4134–4137 (2015)
58. Y. Petit, S. Danto, T. Guérineau, A.A. Khalil, A. Le Camus, E. Fargin, G. Duchateau, J. Bérubé, R. Vallée, Y. Messaddeq, On the femtosecond laser- induced photochemistry in silver-containing oxide glasses: mechanisms, related optical and physico-chemical properties, and technological applications. Adv. Opt. Technol. **7**(5), 291–309 (2018)
59. Y. Petit, C.-H. Park, J.-M. Mok, E. Smetanina, B. Chimier, G. Duchateau, T. Cardinal, L. Canioni, S.-H. Park, Ultrashort laser induced spatial redistribution of silver species and nano-patterning of etching selectivity in silver- containing glasses. Opt. Express **27**(10), 13675 (2019)

60. L.A. Peyser et al., Photoactivated fluorescence from individual silver nanoclusters. Science **291**(5501), 103–106 (2001)
61. A. Podlipensky, J. Lange, G. Seifert, H. Graener, I. Cravetchi, Second-harmonic generation from ellipsoidal silver nanoparticles embedded in silica glass. Opt. Lett. **28**, 716–718 (2003)
62. A. Podlipensky, V. Grebenev, G. Seifert, H. Graener, Ionization and photomodification of Ag nanoparticles in soda-lime glass by 150 fs laser irradiation: A luminescence study. J. Lumin. **109**, 135–142 (2004)
63. A. Podlipensky, A. Abdolvand, G. Seifert, H. Graener, Femtosecond laser assisted production of dichroitic 3D structures in composite glass containing Ag nanoparticles. Appl. Phys. A Mater. Sci. Process. **80**, 1647–1652 (2004)
64. J. Qiu, K. Miura, T. Suzuki, T. Mitsuyu, Permanent photoreduction of Sm3+ to Sm2+ inside a sodium aluminoborate glass by an infrared femtosecond pulsed laser. Appl. Phys. Lett. **74**, 10 (1999)
65. J. Qiu, P.G. Kazanski, J. Si, K. Miura, T. Mitsuyu, K. Hirao, A.L. Gaeta, Memorized polarization-dependent light scattering in rare-earth-ion-doped glass. Appl. Phys. Lett. **77**, 1940–1942 (2000)
66. J. Qiu, X. Jiang, C. Zhu, H. Inouye, J. Si, K. Hirao, Optical properties of structurally modified glasses doped with gold ions. Opt. Lett. **29**, 370–372 (2004)
67. J. Qiu, K. Miura, K. Hirao, Femtosecond laser-induced microfeatures in glasses and their applications. J. Non-Cryst. Solids **354**, 1100–1111 (2008)
68. A. Royon, Nonlinear femtosecond near infrared laser structuring in oxide glasses, PhD dissertation, Université de Bordeaux, France, 2009
69. A. Royon, K. Bourhis, M. Bellec, G. Papon, B. Bousquet, Y. Deshayes, T. Cardinal, L. Canioni, Silver clusters embedded in glass as a perennial high capacity optical recording medium. Adv. Mater. **22**, 5282–5286 (2010)
70. A. Royon, Y. Petit, G. Papon, M. Richardson, L. Canioni, Femtosecond laser induced photochemistry in materials tailored with photosensitive agents. Opt. Mater. Express **1**(5), 866–882 (2011)
71. A. Royon, K. Bourhis, L. Béchou, T. Cardinal, L. Canioni, Y. Deshayes, Durability study of a fluorescent optical memory in glass studied by luminescence spectroscopy. Microelectron. Reliab. **53**(9–11), 1514–1518 (2013)
72. C.B. Schaffer, A. Brodeur, E. Mazur, Laser-induced breakdown and damage in bulk transparent materials induced by tightly focused femtosecond laser pulses. Meas. Sci. Technol. **12**, 1784 (2001)
73. G.Y. Shakhgildyan et al., One-step micro-modification of optical properties in silver-doped zinc phosphate glasses by femtosecond direct laser writing. J. Non-Cryst. Solids **481**, 634–642 (2018)
74. Y. Shimotsuma, M. Sakakura, K. Miura, J. Qiu, P.G. Kazansky, K. Fujita, K. Hirao, Application of femtosecond-laser induced nanostructures in optical memory. J. Nanosci. Nanotechnol. **7**, 94–104 (2007)
75. L.A. Siiman, J. Lumeau, L.B. Glebov, Nonlinear photosensitivity of photo-thermo-refractive glass by high intensity laser irradiation. J. Non-Cryst. Solids **354**, 4070–4074 (2008)
76. E. Smetanina, B. Chimier, Y. Petit, N. Varkentina, E. Fargin, L. Hirsch, T. Cardinal, L. Canioni, G. Duchateau, Modeling of cluster organization in metal-doped oxide glasses irradiated by a train of femtosecond laser pulses. Phys. Rev. A **93**(1), 013846 (2016)
77. E. Smetanina, B. Chimier, Y. Petit, A. Royon, T. Cardinal, L. Canioni, G. Duchateau, Laser writing of nonlinear optical properties in silver-doped phosphate glass. Opt. Lett. **42**(9), 1688–1691 (2017)
78. S.D. Stookey, Photosensitive glass. Ind. Eng. Chem. **41**(4), 856–861 (1949)
79. B. Stuart, M. Feit, S. Herman, A. Rubenchik, Nanosecond-to-femtosecond laser-induced breakdown in dielectrics. Phys. Rev. B, 1–13 (1996)
80. Z. Tu, Y. Teng, J. Zhou, S. Zhou, J. Qiu, Micro-modification of luminescence property in Ag+-doped phosphate glass using femtosecond laser irradiation. J. Non-Cryst. Solids **383**, 161–164 (2014)

81. M. Vangheluwe, F. Liang, Y. Petit, P. Hée, Y. Ledemi, S. Thomas, E. Fargin, T. Cardinal, Y. Messaddeq, L. Canioni, R. Vallée, Enhancement of nanogratings formation assisted by silver ions in a sodium gallophosphate glass. Opt. Lett. **39**(9), 5191–5494 (2014)
82. M. Vangheluwe, Etude de la structuration laser femtoseconde multi- échelle de verres d'oxydes dopés à l'argent, PhD dissertation, University of Bordeaux, France and University of Laval, Québec, Canada, 2015
83. A.A. Vasileva, I.A. Nazarov, P.K. Olshina, A.V. Povolotskiy, I.A. Sokolov, A.A. Manshina, Structural features of silver-doped phosphate glasses in zone of femtosecond laser-induced modification. J. Solid State Chem. **230**, 56–60 (2015)
84. Y. Watanabe, G. Namikawa, T. Onuki, K. Nishio, T. Tsuchiya, Photosensitivity in phosphate glass doped with Ag+ upon exposure to near-ultraviolet femtosecond laser pulses. Appl. Phys. Lett. **78**, 2125–2127 (2001)
85. W. Zheng, T. Kurobori, Assignments and optical properties of X-ray-induced colour centres in blue and orange radiophotoluminescent silver-activated glasses. J. Lumin. **131**, 36–40 (2011)
86. W. Zheng, T. Kurobori, Y. Miyamoto, H. Nanto, T. Yamamoto, Formation and assignment of silver defect centres in phosphate glass induced by femtosecond laser pulses. Radiat. Meas. **46**, 1402–1405 (2011)
87. P. Zijlstra, J.W.M. Chon, M. Gu, Five-dimensional optical recording mediated by surface plasmons in gold nanorods. Nature **459**, 410–413 (2009)

Chapter 20
Subtractive 3D Laser Nanolithography of Crystals by Giant Wet-Chemical Etching Selectivity

Airán Ródenas Seguí

Abstract Since the advent of ultrashort pulse lasers (τ_p ~ 100 fs), one of the long-standing goals of laser scientists has been the opening of a new field of 3D micro- and nano-engineering of materials, thanks to the inherent capability of ultrashort pulses to modify the inner volume of any material. Achieving this goal has however proved to be extremely challenging for decades and has been hampered by many fundamental and technical difficulties. This scientific endeavour has pushed our understanding of a wide variety of issues related to how ultrashort pulses non-linearly interact with matter and how matter is transformed on different time and space scales. In this chapter, we focus on a new piece of this puzzle: how nanoconfined photomodified volumes inside matter can have greatly enhanced chemical reactivities, this creating a new type of 3D nanolithographic technique with the potential to revolutionize our current nanotechnology. Along this chapter, a review of the seminal works that have led to our current knowledge is given, and some of the current key technical limitations for nanostructuring will be described. A special emphasis will also be put on what is not yet well understood, the grey areas where future important discoveries may arise towards achieving the extreme nanoscales.

Keywords Nanostructuring · Nanotechnology · Nanolithography · Three-dimensional lithography · Nanophotonics · Laser processing · Ultra-fast laser processing

---

A. Ródenas Seguí (✉)
Departamento de Física, Universidad de La Laguna (ULL), Tenerife, Spain

Instituto Universitario de Estudios Avanzados (IUdEA), Universidad de La Laguna, Tenerife, Spain
e-mail: arodenas@ull.edu.es

© The Author(s), under exclusive license to Springer Nature Switzerland AG 2023

R. Stoian, J. Bonse (eds.), *Ultrafast Laser Nanostructuring*, Springer Series in Optical Sciences 239, https://doi.org/10.1007/978-3-031-14752-4_20

1 Subtractive 3D Laser Nanostructuring of Materials: Historical Context

> In the year 2000, when they look back at this age, they will wonder why it was not until the year 1960 that anybody began seriously to move in this direction –R. P. Feynman, 1959 (*There's Plenty of Room at the Bottom*)

Since the first demonstration of laser action on May 16, 1960, by Theodore H. Maiman [1], lasers would ignite the imagination of scientists and engineers for decades. Today, a myriad of technological applications of lasers have literally transformed all fields of science and technology, from fundamental medicine and physics to manufacturing, sensing and communications, to mention a few. Back in 1960, the concept of *miniaturization* was already on the rise across technologies and manufacturing [2]; the *micro* world was already a clear future business. To push things even further, the legendary talk "*There's Plenty of Room at the Bottom*" given by Richard P. Feynman on 1959 December 29 would be the kick-start of a revolutionary new field on which subsequent generations of scientists would strive tirelessly: *nanotechnology* [3].

There is therefore little doubt that since the laser was conceived, the idea of laser sculpting matter with nanometric precision had sparked. Today, the scientific efforts of generations are beginning to bear fruit: Nanostructuring materials, even in 3D, is beginning to be within our grasp.

1.1 Femtosecond Lasers: Driving Materials Processing

The science of lasers has been the defining factor driving the fundamental developments in laser materials processing [4, 5]. For ultrashort pulse laser generation, continuous-wave mode-locking has been the main enabling technique. In this lasing regime, a laser gain medium is optically pumped continuously, and many axial cavity modes are locked together in phase, forming an ultrashort pulse with duration inversely proportional to the spectral width of all the phase-locked axial modes. If the laser was demonstrated in 1960, it took only 4 years for the demonstration of mode-locking [6], even if those first mode-locked lasers were Q-switched mode-locked lasers, with inconvenient instabilities related to the Q-switching process. From the 1970s to the 1980s, dye lasers would be the main laser instrument in all ultrashort pulse laser-enabled fundamental sciences. In 1974, the first sub-ps passively mode-locked dye laser was demonstrated [7], and in 1981, sub-100 fs colliding-pulse mode-locked (CPM) dye lasers were demonstrated [8]. Undoubtedly, the CPM dye laser would be omnipresent across the 80s. And still, a giant leap was going to happen at the end of the decade that would change laser science and technology forever: From 1985 to 1992 (in just 8 years), the field of ultrashort pulse lasers would be deeply transformed by five fundamental breakthroughs:

- The discovery of Ti:sapphire solid-state laser crystal by Moulton in 1982 and its development across the 80s [9]
- The demonstration of optical chirped pulse amplification (CPA) by D. Strickland and G. Mourou in 1985 [10]
- The development of high-power laser-pumping diodes in the late 80s
- The discovery of Kerr-lens mode-locking (KLM) of Ti:sapphire lasers by Spence et al. in 1991 [11]
- The invention of the semiconductor saturable absorber mirror (SESAM) by U. Keller et al. in 1992 [12]

These advancements, together with tremendous work on mode-locking at the time [13], have driven the field of ultrashort pulse laser processing to its present state and, together with some subsequent competing technologies (such as industrial ultrashort pulse fibre lasers, or Yb:KGW mode-locked solid-state lasers), are the scientific foundation of most of the key advancements in the field of high precision laser materials processing.

While subtractive laser nanostructuring of solid media had been pursued since the laser was invented, doing it with (1) arbitrary design and (2) high enough fidelity[1] has only been possible for the case of surface interaction processes, that is, surface laser processing and lithography (2D). Surface nanostructuring is a different problem to processing the inner 3D volume of solid media, and it has its own wide set of industrial and technological applications. To achieve both features previously mentioned on the 3D space inside a material is however a fundamentally different process than doing it on a surface interface. In 2019, arbitrary 3D subtractive laser nanostructuring of solid-state laser crystals with features down to 100 nm was first reported [14], this being a technique that fulfilled both requirements previously mentioned for a true 3D nanoprocessing. The next section succinctly summarizes the key research advancements and directions that led to this innovation, across three decades of work by researchers from around the world.

1.2 Initial Approaches to 3D Laser Nanostructuring of Solids

Mimicking nature with its exhibition of three-dimensional nanofabrication, as with the vivid colours of photonic nanostructures within insects and birds [15, 16], has proved to be both a great source of inspiration, as well as a tremendous scientific challenge. The primary goal is to fabricate intricate 3D nanostructures with bespoke functions, as, for example, 3D-ordered photonic bandgap structures (PBG) with seamlessly integrated nanostructured optical waveguides, nanogratings, microresonators and lasers, or many other sub-wavelength engineered photonic or multifunctional elements. To fabricate such structures, first it is required to have *3D design freedom* and a high fabrication *fidelity* as previously mentioned. Secondly, to bring the technology to industry for a real-world application, *scalability* (from the nanoscale to the mm and cm scale) is also key. As we will see along this chapter, lasers can be a formidable tool to achieve all these three key features.

---

[1] That is, a fidelity that permits the device to operate as devised within small functional tolerances. Typically for a nanophotonic structure functioning in the visible or near-IR range, a standard deviation tolerance of around ~15 nm can be enough.

In the following, we briefly try to review the fundamental works and advances that led to the present state of the art in the subject of this chapter, for which we revise the three seminal approaches for 3D laser nanoprocessing of materials that led to current subtractive 3D laser nanolithography of solid media, later described.

1.2.1 Multiphoton Polymerization (MPP): 3D Printing Nanostructures

A very hot topic of research across the 80s was optical data storage. The workhorse ultrashort pulse laser (τ_p ~ 100 fs) in that decade was the CPM dye laser mentioned earlier. This early type of mode-locked laser enabled the first report in 1991 by Strickler and Webb [17] of 3D nanoprocessing media in the form of two-photon polymerized (2PP) 3D voxel arrays, for 3D refractive optical data recording and reading. The potential of using ultrashort pulse lasers and nonlinear absorption processes in transparent media would be more clear 6 years later when Maruo et al. demonstrated that 2PP can be used for achieving true 3D lithography [18], by means of a mode-locked Ti:sapphire solid-state laser, a laser technology that is still used today 30 years after its invention. Soon after this key seminal work by the group of Satoshi Kawata, Straub and Gu demonstrated for the first time that 3D photonic bandgap (PBG) structures (so-called photonic crystals) with high-order stopgaps in the near-IR can be fabricated by 2PP [19]. Shortly after this, Deubel et al. would demonstrate that adding supporting walls to the plastic 3D PBG microstructures greatly increases their mechanical stability and quality [20], and in less than 3 years, the key achievement of fabricating an all-silicon inverse 3D PGB structure would also be reported, by means of a 2PP step followed by several post-processing steps to add silicon and remove the polymer [21].

Today, ultrashort pulse laser MPP has become a flourishing commercial technology and has also achieved deep sub-diffraction optical resolution with feature size of 9–52 nm two-line resolution, as recently demonstrated by the group of Min Gu [22], a resolution comparable to electron-beam lithography. In 2021, a new revolutionary photoresist developed for several years by the group of Martin Wegener in close collaboration with chemists was reported to allow for a new sequential absorption process, namely, “two-step absorption” instead to two-photon absorption has even allowed 3D laser “nanoprinting” to be done with inexpensive blue laser diodes [23]. The technique has now been assimilated as a branch of 3D printing as it is a layer-by-layer additive technique. The recognized limitations of this printing approach are that the resulting 3D microstructures are pieces isolated in space that generally need supporting walls to be fabricated [24], this impeding its implementation within existing other heterogeneous microsystem platforms. Critically, the polymeric pieces also suffer from shrinkage and still have low optical damage thresholds, all these issues, together with the problem of scalability, impeding its implementation in technology.

Despite these drawbacks, the key properties of 3D MPP laser technology (nanoscale spatial resolution, design freedom and material composition flexibility) have recently been used to make groundbreaking advances in materials science that were previously impossible and deserve mention here. By means of clever combinations of MPP with diverse advanced additive manufacturing techniques, a fundamental new class of materials has started to be investigated: micro- and nano-architected materials. Seminal works have been done by the group of Julia Greer [25–27]. These are materials whose mechanical properties are defined a priori and then fabricated through a multiscale physically informed design process. This new class of materials produce breakthrough advances across many manufacturing technologies, from ultralightweight and damage-tolerant materials to biomedical, biochemical and micromechanical devices, safe and efficient energy storage, nanophotonics and many others.

The further interested reader should refer to Chapter 22 "*Multiphoton 3D Lithographyand Calcination for Sub-100-nm Additive Manufacturing of Inorganics*" by M. Malinauskas et al.

1.2.2 The "Microexplosion" Method

In the same way that MPP 3D laser nanolithography arose around 1997 following investigations on laser 3D optical data storage (see previous section), studies on direct volume nanostructuring of transparent solid media with ultrashort pulse lasers (τ_p ~ 100 fs) also kick-started approximately the same year 1996 when the group of Eric Mazur first reported on direct data storage and retrieval with high refractive index contrast irreversible voxels inscribed inside transparent dielectric substrates (sapphire, quartz, fused silica and various glasses and plastics) [28, 29]. Glezer et al. did those experiments using the recently developed CPA mode-locked Ti:Sa laser technology mentioned before. They reported that microexplosions could produce structures with apparent diameters of only 200 nm and suggested that a likely mechanism for the creation of permanent voxels inside a wide variety of different dielectrics could be the microexplosion that occurs inside the material once the energy from the laser pulse is transferred to the lattice through a given combination of multiphoton absorption and avalanche ionization. Contrary to what occurs on surface, in this case, microexplosions take place in absence of ablation because the excited region is inside the material, this creating high temperature and pressure waves, leaving radially stratified regions of lower and higher density. This initial works would be the first of many investigations on these phenomena, with efforts mainly directed towards (1) understanding the new physics underlying these new types of experiments and (2) investigating its potential application towards novel optical applications.

With the beginning of the twenty-first century and following four decades of intense laser science (since its invention in 1960), new reviews were published updating the knowledge on the major physical processes describing ultrashort pulse laser-matter interactions [30–32]. These new reviews incorporated valuable new experimental knowledge acquired, thanks to the instrumental reliability of the new solid-state mode-locked Ti:sapphire laser technology that was originated the decade before (~1991), showing how laser technology leaps always pay back with important advances in the core fundamental sciences.

In 2003, Gorelik et al. [33] reported initial investigations on the structural modifications inside a transparent crystal (quartz), showing by means of transmission electron microscopy how modifications performed at the microexplosion regime involve the formation of amorphous volumes surrounded by extended strong strain fields; this extended stress fields producing particularly large refractive index changes (Δn ~ 0.01) on the flanks of continuously written longitudinal tracks, and observation which would create further interest for the fabrication of embedded channel optical waveguides. In 2004, Shaffer et al. [34] reported one of the first comprehensive studies on the morphology of single-pulse femtosecond laser-induced structural changes in the bulk of transparent materials, showing the key roles of pulse energy and numerical aperture (NA) of the focusing lens in controlling the types of non-linear light-matter interaction phenomena and the final volume and morphologies of modifications. Relevant for nanostructuring, they also confirmed how, when using very tight focusing lenses (1.4 NA), the pulse energy thresholds for structural change can be lower than 5 nJ, this allowing the use of unamplified lasers. In 2005, G. Zhou and M. Gu [35] reported on how microexplosions inside ferroelectric anisotropic crystals like lithium niobate are highly dependent on the pulse propagation and polarization directions, relative to the crystal axes, yielding different modification thresholds as well as different apparent diameters. In 2006, Juodkazis et al. [36] reported that extremely high pressures and temperatures (~10 TPa and 0.5 MK) can be produced inside sapphire by 800 nm single pulses with 100 nJ energy and 200 fs duration. The same year, Zhou and Gu [37] also reported that microexplosions inside lithium niobate can be arranged to conform PBG structures, with stopgaps in the 2 μm near-IR region, and Ródenas et al. [38] would report in 2009 how tuning the 3D lattice structure (face-centred cubic fct or face-centred tetragonal fct) and the lattice parameter allows to obtain stopgaps in the near-IR range from 1.0 to 2.5 μm, this matching with the various emission bands from Er^{3+}:Yb^{3+} codoped lithium niobate crystals.

The limitations of performing a high density of microexplosions within solid optical media are primarily related to the large stress fields that surround each voxel due to plastic lattice deformation and the crack propagation entailed by lattice bond breaking at the peak strain points at voxels apexes. By the end of decade, it would be clear that laser-induced stress is a serious detrimental effect of tight focusing and microexplosions. A new approach capable of minimizing all the lattice collateral damage around nanovoxels would be needed to bypass this bottleneck for the true 3D nanostructuring of solid optical media.

S. Juodkazis and co-authors [39] published a key observation that opened the avenue to 3D processing of transparent materials in 2006: They showed the first results on fabricating empty micropores (~0.63 μm diameter inside sapphire) with an ultra-high chemical wet-etching selectivity of ~8 × 10 [3] between amorphous and crystalline volumes, this allowing to fabricate hollow microchannels with 3D arbitrary architectures. The continuous etching of the micropores was observed to critically depend on the degree of pulse overlapping along a scan: Within the experimental conditions of the laser setup used (150 fs, 1 kHz, 1.35 NA), it was observed that if the pulse separation was smaller than 100 nm (approximately 1/4 of the laser spot diameter at the focal point, ~0.42 μm), the wet etching of channels became impossible, but with a pulse separation of ~200 nm, channels would etch with maximal etching rate. It was not the first report on wet-etching microchannels in solid media as it was reported 5 years after the chemical wet etching of fs-pulse laser-written tracks inside silica glass was originally reported [40], although with very poor selectivity of only ~1.4.

1.2.3 Nanograting Phenomena

The appearance of micrometric regions with nanogratings at the focal volume of ultrashort laser pulses within solid media was first reported in 2003 by Y. Shimotsuma, P. Kazansky, J. Qiu and K. Hirao [41]. These researchers observed periodic nanostructures within micrometre-sized regions inside silica glass, after irradiation with a focused beam of 150 fs pulses at 800 nm wavelength from a CPA mode-locked Ti:sapphire laser, with pulse energies of 1 μJ and above. Since then, nanograting phenomena has been studied very extensively in many optical materials (glasses and crystals) both from the fundamental point of view as well as for its technological applications, such as optical data recording. The method allows to produce nanogratings within solids with a high index of refraction contrast, and with grating cross-sections on the nanometre scale along the periodicity axis, but on the microscale on the other two axes. Since the nanoscale features are not truly 3D, we consider this technique a very particular case of volume nanostructuring. The origin of volume nanograting phenomena is yet not entirely understood in all materials, apparently depending on a balancing act between purely electromagnetic phenomena and structural properties of matter response, this being out of the scope of this chapter. We refer the interested reader in nanogratings to Chaps. 1, 4, 5, 6, 23 and 30.

2 Chemistry Meets Lasers: Laser-Enhanced Wet-Chemical Etching Selectivity

> The fact is, that it is impossible to say to what degree of perfection Lithography can be carried: its process being entirely chemical, is open to innumerable improvements –C. Hullmandel, 1824 (*The Art of Drawing on Stone*)

2.1 Differential Wet-Chemical Etching of Crystals

At the end of the nineteenth century in 1890, Becke [42] reported on the difference in chemical etching rates along different directions on a crystal. To put this finding in context, T. Edison had just patented the incandescent light bulb only some years before (1879), the discovery by J. J. Thomson of the electron had not even taken place yet [43] and X-rays were yet completely unknown, as W. C. Röntgen would report them in 1895 [44]. Before X-ray crystallography would arise later in 1912 [45], the wet-chemical etching of crystals was therefore an important technique for the advancement of crystallography. 40 years later in the decade of 1950s, a renewed interest in wet-etching crystals appeared, in relation with the interest in growing high-quality crystals and the understanding that etch pits appeared at lattice dislocations. Across the 60s up until today, wet-chemical etching has been particularly studied for the development of the semiconductor industry, lithography and microtechnology in general.

Probably the first monographic books on the science of etching post-dislocations in crystals are those of Pshenichnov [46] (1974) and Heimann [47] (1975), and the later book of Sangwal [48] (1987) is probably the first in English. As K. Sangwal described, removal of material from an interface requires energy, which can be expended by mechanical, thermal or chemical means. The wet-chemical removal of material usually involves using a liquid that can react with the crystal and yield reaction products, and it is usually called "etching" because it can reveal structural defects and microstructures within the solid crystal. "Selective etching" refers to the process where the efficiency of material removal depends on the local microstructure and defects, defining "preferential" and "non-preferential" etching processes. Preferential wet-chemical etching of crystals usually occurs at lattice defects such as dislocations, producing characteristic surface pits, and it is a classic procedure to reveal the crystalline structure of materials (topographies arise revealing definite crystallographic orientations). Figure 20.1 shows a 3D laser-written and wet-etched nanopore inside a YAG crystal, where extensive wet-etching ends up revealing the characteristic lattice planes of the YAG garnet structure.

The chemical polishing of crystals was developed during the 1960s, in efforts to produce high-quality crystal surfaces with low strain or, for example, to obtain thin crystal slices for observation under transmission electron microscope (TEM). Hot phosphoric acid was used by Tighe to chemically polish single-crystal Al_2O_3 (sapphire) [49] and by Basterfield [50] in 1969 to etch different garnets, such as YIG and YAG (both rare-earth doped and undoped). In 1975, Miller [51] also studied the effect of phosphoric acid concentration on the etching of GGG. More recently in the 2000s, the wet etching of laser crystals has also been studied for the optimization of the crystal's mechanical strength [52, 53], or more recently to thin single-crystal sapphire optical fibres down to 10 μm diameters [54].

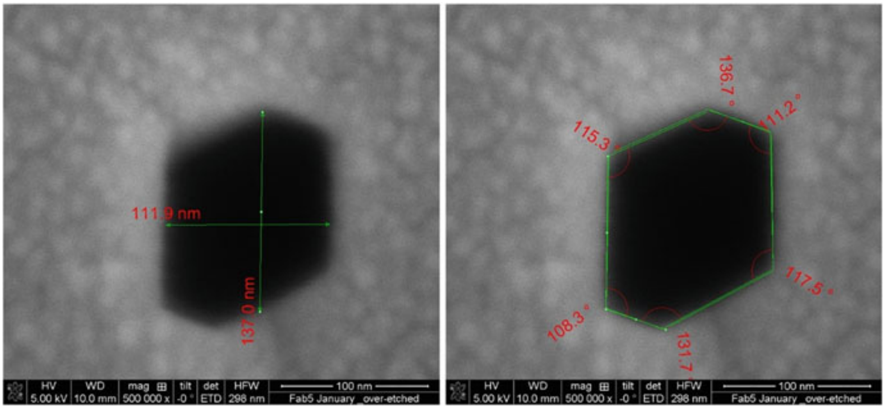

Fig. 20.1 Wet-etched nanopores fabricated by 3D laser nanolithography: crystalline planes of single-crystal YAG are revealed due to preferential etching, after the inner laser-written track is etched out first. Nanopores were etched in orthophosphoric acid solution (50% w/w) at 90 °C for 5 days. The observed surface roughness outside the pore is due to gold sputtering for SEM. Results from H2020-LASERLAB IV GA-654148. (see further results in Sect. 3.2)

2.2 Wet-Chemical Etching of Impurity Distributions in Crystals

With the advent of microtechnology in the 60s and nanotechnology later in the 80s, top-down lithographic techniques and its science received increased attention. So-called "dry-etching" techniques, such as focused ion beam (FIB), electron-beam writing (EBW), reactive-ion etching (RIE), inductively coupled plasma (ICP) etching and other technologies such as scanning probe lithographies (SPL), have been developed across decades. These techniques are usually considered anisotropic and highly directional and share a common history of development with the semiconductor industry and with photolithography. For the sake of brevity, we will not discuss these surface dry-etching techniques here; we direct the reader to specialized reviews and books on these subjects by recognized experts [55–60].

As soon as crystal defects were observed to etch selectively at increased rates, new approaches to wet-chemical etch single-crystal surfaces were developed for application in microtechnology. It is important to note that defects in crystals may be classified as chemical impurities (1), non-stoichiometry (2) and lattice defects (3). Lattice defects, as described by Sangwal, are "point defects (interstitials, vacancies, substitutions and antisites), line defects (dislocations), surface defects (crystal surfaces, grain boundaries, twin boundaries, stacking faults, domain boundaries, homo- and heterojunctions, growth striatums, growth sector boundaries, etc.), and volume defects (inclusions, precipitates and point-defect clusters)". Non-stoichiometry and intrinsic lattice defects are not straightforward to produce in a reproducible and controlled manner at the micro- and nanoscale, but extrinsic crystal defects, that is, the insertion of impurities across the surface of a material (by means such as proton exchange or ion implantation/diffusion), have been investigated extensively since the 70s, with the aim of performing micro and nanolithography in the surface of crystals. Some seminal or representative works on the enhanced wet-chemical etching selectivity of transparent dielectric crystals such as sapphire, YAG or lithium niobate by extrinsic impurity defects will be here briefly cited.

The differential wet-chemical etching of ion implanted (II) garnets was reported by Johnson et al. in 1973 [61]. II with H, He and Ne ions was selectively performed at the microscale by using photoresists as masks, and once the photoresist was removed, the crystals were etched in phosphoric acid at different temperatures. The observed increase in etching rates was proportional to the damage concentration, achieving up to three orders of magnitude increase (~2×10^3) in etching rate between damaged and undamaged material. Later, with the advent of integrated optics in the 80s–90s, the fabrication of optical channel waveguides on the surface of electro-optic crystals as lithium niobate also received attention. Mizuuchi et al. [62] reported in 1990 the HF acid wet-chemical etching of proton exchanged (PE) areas in $LiNbO_3$, finding that the etch ratio between H^+-$LiNbO_3$ and $LiNbO_3$ could be of up to ~10^3. The HF etching of Si implanted sapphire was also investigated by Ishida et al., reporting in 1996 an enhanced etch rate of ~10 nm per min of Si implanted regions [63], probably having a modified aluminosilicate composition ($Al_2O_3 \cdot SiO_2$). McHargue et al. reported [64] in 1997 an extended investigation on the HNO_3:HF wet etching of amorphized sapphire by means of ion bombardment with different impurity species (Cr, Zr, Sn) as well as with stoichiometric implant of Al + O, finding an etch rate of impurity amorphized regions of ~90 nm per minute. The same year, Nunn et al. reported [65] a method to greatly improve the surface quality of polished Nd:YAG crystals. Acknowledging that mechanical polishing leads to a 1 μm surface layer with ~10^6 more dislocations than that of high-quality crystals, the removal of this micron layer was studied by means of thermal annealing as well as Ne implantation, and phosphoric acid etching at 40 °C. The wet-etching rate of just polished YAG was of ~0.06 nm/min; polished and implanted was of ~17.5 to ~36 nm/min; polished, annealed and implanted was of ~22.5 to ~33.3 nm/min; and yielding rate enhancements of up to ~600. Crunteanu et al. reported in 2003 the He^+ implantation and H_3PO_4 etching of sapphire, observing enhanced etch rates of ~19 nm/min [66].

Lastly, in 2008, an HF acid wet-chemical etching rate enhancement of 3.2×10^4 was found by Ofan et al. [67] in 400 nm thick subsurface layers in $LiNbO_3$ crystals deeply implanted with He^+ ions and annealed to 200 °C. The origin of the etching of this subsurface layers appears to be at the generation of a dense network on nanocracks or "domains" visible under the optical microscope, which greatly enhance the transport of the etching solution across the plane, with an enhanced etch rate of 3.2 μm/min against an etch rate of 0.1 nm/min for the background. This is the highest wet-chemical etching selectivity that we know of, besides that of nanopore formation in 3D laser nanolithography as shown later.

2.3 Wet-Chemical Etching of 3D fs-Pulse Laser-Written Crystals

Femtosecond-pulse laser irradiation of transparent solids and wet-chemical etching of the irradiated volumes have been investigated since at least 2001, when the groups of S. Juodkazis, H. Misawa and J. Nishii in Japan reported on the 3D microfabrication of 10 µm width channel architectures inside fused silica, the amorphous phase of SiO_2, with 1 kHz, 120 fs, 795 nm laser pulses [40]. A maximal etching rate of 6.5 µm/h was observed, with the etching rate of undamaged silica glass remaining of 4.5 µm/h, for the given aqueous solution of 5% HF under room temperature conditions. We do not know of earlier successful experiments on 3D fs-laser structuring and wet-chemical etching of solids. After this and some other first studies on glasses, the first report on the 3D wet-chemical etching of fs-laser irradiated crystals may be that of Saulius Juodkazis and Hiroaki Misawa's group in 2005 [39]. In this seminal work, Juodkazis et al. revealed how sub-bandgap fs-pulse lasers (1 kHz, E_p ~ 20 nJ, ϕ ~ 5 J/cm^2, I_0 ~ 22 TW/cm^2, $v = 375$ µm/s) can modify the lattice structure of a sapphire crystal, converting single-crystal regions to amorphous or polycrystalline ones with submicron spatial resolution. The first microfluidic channels were there demonstrated in a crystal, and the minimal hollow channel cross-sections were of ~0.6 µm, although with a very high degree of roughness of ~120 nm. The maximal etching rate observed along the microchannels was of 83 nm/min in 10% HF aqueous, and the observed etch rate of non-irradiated crystals was of <0.01 nm/min. A high selectivity of at least 8.3×10^3 was obtained. In this seminal finding, Juodkazis et al. would be the first to study in detail and report that an enhanced wet-chemical etching with selectivity close to 10^4 can be achieved due to either laser-induced amorphization, high defect concentration or chemical modification of the crystals volume. In 2006, the same group further reported on another key finding regarding the wet etching of laser-written solids: the 3D wet etching of fs-laser written channels in quartz crystal [68], the crystalline phase of SiO_2. Authors observed that fs-laser amorphized channels inside the volume of crystalline SiO_2 would etch at ~50 µm/h, around 10 times faster than previously observed by the same authors in similar 3D channels written in a material with the same composition but different lattice structure (fused silica SiO_2 glass), in the same wet-etching conditions of 5% HF at room temperature conditions. The etching rates of unmodified quartz was observed to strongly depend on the crystal axis: 0.06 ± 0.03 µm/h along the *c*-axis, and a negligible rate perpendicular to it (≤ 0.01 µm/h), therefore yielding theoretical etch selectivities of up to ~5×10^3 if channels were written along c-axis and of ~833 otherwise, although authors reported selectivities >300 for the actual channels. These results showed the degree of complexity of the full process of wet-chemical etching fs-pulse laser photomodified materials, as it combines non-linear light-matter interactions with chemical processes at the micro- and nanoscale. The exploration and understanding of this complexity therefore offer a large opportunity for the discovery of new forms of nanotechnology.

Following these seminal discoveries by Juodkazis, Misawa and colleagues, additional work would be reported from 2007 to around 2013 on etching laser-written crystals. The first microscale objects (rotators) microfabricated inside a crystal (sapphire) by high-selectivity wet-chemical etching fs-pulse written structures were demonstrated by Matsuo et al. [69] in 2007. The KOH wet-chemical etching of fs-laser written sapphire was demonstrated by Juodkazis et al. in 2008 [70]. Wortmann et al. first reported the inscription of self-assembled nanogratings in sapphire and reported the fabrication of microchannels with aspect ratios of more than 1000 (length per width) [71]. In 2009, J. Siebenmorgen and co-authors from the groups of G. Huber, S. Nolte and A. Tünnermann reported the H_3PO_4 wet etching (85%, 50 °C) of fs-laser written single scans (1 kHz, 775 nm) in the strong damage regime typically called Type-II ($E_p = 1$ μJ, $\phi \sim 70$ J/cm^2, $I_0 = 200$ TW/cm^2, $v = 10$ μm/s) in Nd:YAG [72], with etching rates of up to 5 μm/h at the first 19 h. The use of UV ps-pulse laser writing for 3D wet-chemical etching inside sapphire crystals was also reported by R. Moser et al. in 2011 [73]. Matsuo et al. [74] also reported in 2011 the selective etching of fs-laser modified microchannels in CaF_2 crystals, with etchants of aqueous solutions of nitric acid, sulfuric acid and hydrogen chloride, while no signature of etching was observed for MgF_2.

Although performed in glass (fused silica) and not in a crystal (the type of material subject of this chapter), Sheeba Rajesh and Yves Bellouard reported in 2011 a relevant finding regarding the inner mechanisms that fundamentally drive the optimal wet etching of fs-pulse laser-written microchannels [75]: They found that the laser-deposited energy density (i.e., the total deposited energy per unit surface across a laser scan) has a characteristic effect on the etching rate of single scans, which is independent of the laser repetition rate, at least below the thermal accumulation regime. The hypothesis drawn by Bellouard and Rajesh for this effect is that once a laser pulse has an energy above the threshold for photo-modification, the higher the number of pulses, the more densification and stress build-up will occur, this enhancing the wet-chemical etching rate. As the modifications performed by Rajesh and Bellouard with low numerical aperture lenses produced very elongated voxels with sharp apexes at the top and bottom of the transverse scans, these sharp apexes entailed large peak stress values (tensile/compressive for the transverse/longitudinal components of the stress tensor relative to the elongation axis of the tracks) [76]. The localized high stress points eventually also lead to localized nanocracks as the stress induced goes above the local lattice bond's resistance (i.e., the plastic deformation limit) at the nanoscale. In the case of glass, this threshold is observed to occur at low deposited energy values and makes the large, stored stress to relax, this diminishing the etch rate that makes a plateau for increasing deposited energy. Importantly, this finding on the influence of the laser-deposited energy on wet etch rate of microchannels is yet to be studied in detail in crystals, as far as we know.

In 2013, Choudhury, Ródenas and co-authors from A. K. Kar's group reported the first wet-chemical etching of multiscanned channels (100 μm wide) inside laser-active Nd:YAG crystals for optofluidic application (where overlapping pulses allow larger processed volumes and the presence of small multiscan separations of around 1 μm significantly affect both the stress induced and the etching behaviour as compared to single scans) [77]. The wet etching was demonstrated at the low-damage photo-modification regime and at high-repetition rate for the first time, for minimizing stress accumulation and cracking (500 kHz, $E = 0.16$ μJ, $\phi \sim 1.8$ J/cm^2, $I_0 = 4$ TW/cm^2, $v = 8$ mm/s). This photo-modification regime is usually called Type I, and it is characterized by an increase in the index of refraction (both in the visible and IR ranges) demonstrated by the fact that the photomodified region acts as a step-index channel waveguide fabrication. In the case of YAG crystals, it was first reported by the same authors in 2011 [78], with similar fabrication parameters (100 kHz, $E = 0.3$ μJ, $\phi \sim 7.7$ J/cm^2, $I_0 = 11$ TW/cm^2, $v = 0.5$ mm/s). The 50% H_3PO_4 (90 °C) wet-chemical etching of large microchannels inside Nd:YAG was also demonstrated with this technique. The origin of the selectivity was moreover investigated by micro-luminescence and micro-Raman analysis prior to etching, confirming that the enhanced etching rate is originated by both modified lattice bonds (strained lattice) with characteristic higher reactivity as well as by nanocracks that favour the penetration depth of the acid solution into the crystal volume.

After 2013, research on fs-laser fabrication of microchannels inside crystals stalled, but some years later, more researchers began to investigate the wet-etching process of microchannels inside YAG crystals: In 2017, Hasse, Kränkel and Calmano reported on the first detailed investigation [79] on the dependence of etching rate, selectivity and roughness of etched surfaces on processing parameters such laser pulse energy, scan speed, acid solution and temperature, for the low-repetition rate regime at 1 kHz. Authors found wet-chemical etch rates of around 13 μm/h for the first 18 h, almost independently of pulse energy (0.2–0.5 μJ). They also reported that the etching length of microchannels appears to follow a Brownian motion square root dependency with time ($L^2 = 2Dt^{\alpha}$, $\alpha = 1$), when etching with 85% H_3PO_4 at 135 °C. In December 2018, the giant wet-etching selectivity (10^5) of 100 nm mm-long nanopores inside crystals YAG and sapphire crystals was reported by A. Ródenas et al. [14], which is separately discussed in the next section, and it is the subject of this chapter. But more research on larger micrometric channels are continued to be done.

In 2019, Hasse, Huber and Kränkel additionally reported a microchannel study in YAG with 1 kHz fs-laser [80], showing selectivities of up to 680 and studying the wet etching for both H_3PO_4 solution and H_3PO_4:H_2SO_4 water solutions. Selectivity was observed to increase the lower the temperature and did not vary significantly with etching agent, whereas diffusivity (D) was observed to increase with temperature and with lower viscosity acid solutions as (1:1) H_3PO_4:H_2SO_4. In 2020, J. Lv et al. also reported [81] on the fabrication (1 kHz amplified Ti:sapphire fs-laser) of microstructured optical waveguides in YAG, with wet-etched 2 μm wide and 16 μm high microchannels, which wet etch rates of 58 μm/h (first 3 h) and 26 μm/h (18 h), in H_3PO_4 solution. In 2021, Hasse, Kip and Kränkel further reported a more optimal 22% H_3PO_4 24% H_2SO_4 wet etch solution [82]. The diluted mixture enabled an increased wet etch rate of ~300 μm/h (1 h) and ~64 μm/h (20 h), demonstrating the selective etching of 9.6 mm long, 1 μm wide and 18 μm high microchannels in 23 days of wet etching, by etching from both channel sides. The temporal evolution of the wet etching of these microchannels was also observed to belong to a superdiffusion-driven model (α ~ 1.4) for the first time. The same year, the same authors also reported on the measurement of the internal roughness of these microchannels by means of precision saw dicing [83]. They found the minimum roughness values in their experimental conditions to be of 27 ± 3 nm for 43% H_3PO_4 48% H_2SO_4 (83 °C) solution. In 2021, the manufacturing of cm-scale Nd:YAG cylindrical rods (1 mm diameter) was also first demonstrated by Smith et al. [84], by means of fs-pulse laser writing with 500 kHz, 250 fs pulses, and by wet-chemical etching with a 50% nitric acid solution at 100 °C. In 2022, Zhou et al. also reported on the writing (Bessel-beam axicon focusing and 1 kHz amplified Ti:sapphire fs-pulse laser) and wet etching of ZnSe crystals [85], using a solution concentration ratio and etching time of NH_4OH (28%):H_2O_2 (26%) = 1:3 and 20 min (with the solution concentration referring to the mass fraction of the solution and the solution ratio to the volume ratio of the solution). Authors reported an etch rate of ~104 nm/s for photomodified regions and of ~3.5 nm/s for unmodified, this yielding a selectivity of only ~30. In 2022, A. G. Okhrimchuk et al. also reported [86] on the fabrication of low-loss near-IR (1.55 μm) and mid-IR (3.39 μm) cladding channel waveguides in Nd:YAG crystals with a 15 kHz fs-pulse laser, and by wet-chemical etching (40 days wet etching in water solutions of H_3PO_4 and H_2SO_4) forming large microchannels along the [111] crystal axis to obtain 65 μm wide, highly symmetric hexagonal hollow channels, with facets defined by the well-known inherent crystallographic differential etching rates of the crystal.

3 Giant Wet-Etching Selectivity of Nanopores Inside Crystals

The development of the reliable technique for three-dimensional femtosecond-pulse laser nanolithography of crystals was a 7-year research project, finally published in December 2018 [14]. The work demonstrated feasibility of cm-scale 3D nanostructuring of crystals, with 100 nm nanopore widths, and etching selectivities of 3.6×10^5. These three features (scalability, spatial resolution and giant selectivity) configure a technique with a great potential for a new generation of nanophotonic devices monolithically fabricated within key optical materials as sapphire and YAG. This section deals with the state-of-the-art results and what are the current limits either in understanding of the process or in the quality of the results regarding the nanoscale engineering capability (fidelity, roughness, spatial resolution, fabrication times, thermal resistance). The 3D design capabilities and the selectivity behaviour are also analysed compared to other wet-chemical etching processing techniques on the same type of crystalline materials.

3.1 Discovery and First Results

The very first experiments on 3D nanolithography of crystals were done in 2011–2012 at Heriot-Watt University (Scotland, UK), under an individual postdoctoral fellowship from the MICINN science ministry of Spain in 2009. These experiments were thought and designed at the light of previous work on 3D laser writing microexplosions inside YAG crystals for the fabrication of photonic bandgap structures [87] by A. Rodenas and M. Gu group, a work that led to the conclusions that such a technique fundamentally fails due to the response of the material: large laser-induced stress fields and accompanying bond breaking, this impeding the fabrication of large index contrast lattices at the submicron scale. The first experiments on nanoscale laser-writing and wet-chemical etching hollow nanopores in a YAG crystal were done in October 2011 (see Fig. 20.2). A series of tracks were laser written at varying depths, speeds and powers, with an IMRA μJewel D400 fibre laser system emitting linearly polarized pulses at 1047 nm wavelength, with a repetition rate of 500 kHz, a pulse duration of 350 fs and with circular polarization set with a quarter-wave plate before the focusing lens. An overfilled 100X 1.4 NA oil immersion Olympus UPlanSAPO microscope objective was used, after a 5X laser beam expansion section.

Absence of Measurable Pore Tapering and mm-Scale Nanopores The state-of-the-art before 2019 for 3D microfabrication in optical media with 3D laser writing and etching was set by the microfabrication of channels with cross-sectional widths on the micron scale, with a characteristic tapering on the entrance facets so that channels would have a conical cross-section. A. Crespi et al. [88] showed in fact that in glass (fused silica and alumino-borosilicate glasses), the aspect ratio (AR) of an etched conical channel (length over radius as defined in their work) can be estimated in first order of approximation to be proportional to the ratio of etching rates of the photomodified and the bulk glasses (the selectivity, S) in the form $S = \sqrt{\mathrm{AR}^2 + 1}$, under the assumption that the two etching rates are constant in time. Contrary to the observed wet-etching behaviour in micron-scale channels, from the initial experiment of nanopores in YAG, no tapering or conicity could be observed by optical means, as shown in Fig. 20.2. This surprising observation shows that the formation mechanism of nanopores is qualitatively different to that of microchannels, possibly due to a nanoscale confinement and the enhancement of chemical reactivity, this being an area where further research is clearly needed. Figure 20.2 shows the first microscope images of etched nanopores. Optical characterization of nanopores was done by visible-light transmission optical microscopy with the same 100X 1.4 NA objective used for fabrication. An average nanopore's length of ~0.3 mm was observed after a 12 h bath in 50% H_3PO_4 water solution (average of 25 μm/h over 12 h), and almost independently of nanopore depth from surface (15–40 μm), scan speed (1–0.1 mm/s), scan direction and pulse energy (48–20 nJ). The wet-chemical etching selectivity was not directly measured at the time, as it needs SEM images of nanopores taken at large differences in

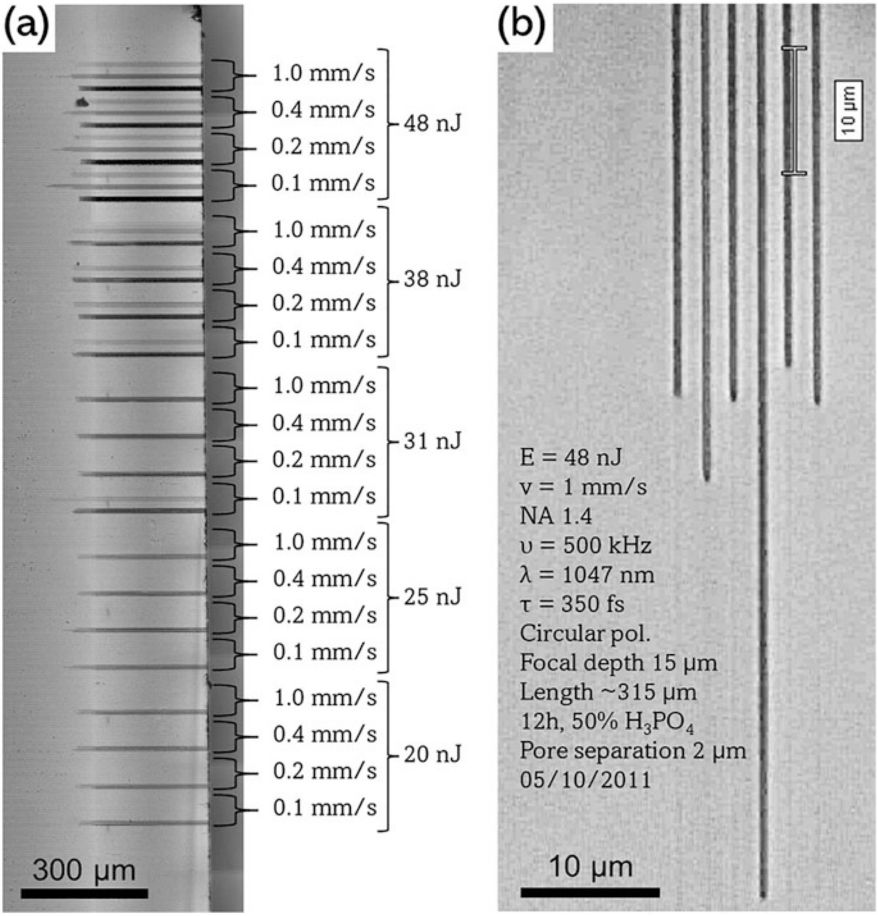
(a)
1.0 mm/s
0.4 mm/s
0.2 mm/s
0.1 mm/s
48 nJ
1.0 mm/s
0.4 mm/s
0.2 mm/s
0.1 mm/s
38 nJ
1.0 mm/s
0.4 mm/s
0.2 mm/s
0.1 mm/s
31 nJ
1.0 mm/s
0.4 mm/s
0.2 mm/s
0.1 mm/s
25 nJ
1.0 mm/s
0.4 mm/s
0.2 mm/s
0.1 mm/s
20 nJ
300 μm
(b)
10 μm
E = 48 nJ
v = 1 mm/s
NA 1.4
υ = 500 kHz
λ = 1047 nm
τ = 350 fs
Circular pol.
Focal depth 15 μm
Length ~315 μm
12h, 50% H₃PO₄
Pore separation 2 μm
05/10/2011
10 μm

Fig. 20.2 Optical transmission image of the first etched nanopores inside a YAG crystal in 2011. **(a)** After 12 h of wet etching, around 0.3 mm long pores were found, almost independently of speed (1–0.1 mm/s) and pulse energy (20–48 nJ). **(b)** For each speed, three depths (15, 25, 40 μm) were tested, with six equal power, speed and depth pores on each, 2 μm separation between each track and opposite consecutive scan directions (zigzag writing)

etching time to characterize the lateral etching rate of unmodified crystals under the wet-chemical etching conditions and solutions used.

Size and Cross-Sections of Hollow Nanopores Figure 20.3a shows an array of ~210 nm width nanopores spaced by 2 μm and filled with fluorescent rhodamine water solution, probing that nanopores are empty for the first time. Figure 20.3b show the SEM image of the group of six nanopores written with 18 nJ pulse energy, and a scan speed of 0.1 mm/s, at 15.5 μm depth. The image shows an array of pores at a portion of the crystal that was accidentally cleaved during mechanical

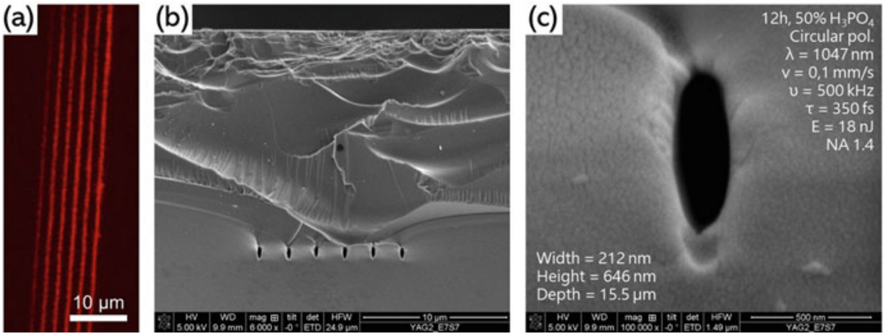

Fig. 20.3 An optical image of luminescence from an array of ~210 nm width nanopores spaced by 2 μm and filled with fluorescent rhodamine water solution probes that nanopores are empty for the first time (**a**). SEM image of the group of six nanopores written with 18 nJ pulse energy, and a scan speed of 0.1 mm/s, at 15.5 μm depth (**b**). Close-up of a single nanopore (**c**)

polishing. The cleavage reveals the strong stress fields and cracks propagating from the top apexes of pores, which are the closer to the crystal surface. A nanopore width of 212 nm and height of 646 nm was measured, corresponding to a pore aspect ratio of 3.0 (height/width), as expected for this type of focusing objective and similar to those obtained in multiphoton polymerization (see Sect. 1.2.1 and references therein).

Aberrations of the Focal Volume The main fabrication difficulty found in these first experiments was the limited focal depth available to fabrication, due to aberrations produced by the used high-NA objective (1.4 NA) in YAG crystals (with an isotropic index of refraction of 1.81 at 1 μm wavelength). Aberrations in these first experiments had a twofold detrimental effect: first, limiting the fabrication depths to around 20 μm, this increasing the probability of crystal cracking because of stress build-up in the fabricated lattices, and second, the shape of pores departs from the ideal elliptical one to a complex multi-foci shape. The fine evolution of nanopore shape with the focal depth, in these seminal experiments, is shown in Fig. 20.4. The pore cross-section is modulated by apparent multi-foci that spread the energy across the focal axis and greatly increase the pore aspect ratio. It is important to note that these pore cross-sections correspond to scanned lines at a speed of 0.1 mm/s, for which there is a high pulse overlapping and a nominal pulse-to-pulse separation of only 0.2 nm. No single pulse experiments were done, which could likely present a very different shape. Also, each pore was written with a different laser power to compensate for the diminished peak intensity as the point spread function (PSF) is further aberrated the deeper the writing was performed. Figure 20.4 also shows that nanopores can have fine spatial details at least on the ~40 nm scale, which is the observed width of the neck's gaps between multi-foci. This was a first indication that the intrinsic fs-pulse laser photomodification process of crystals can be defined on the nanoscale and in 3D if the laser pulse energy can be confined at the nanoscale.

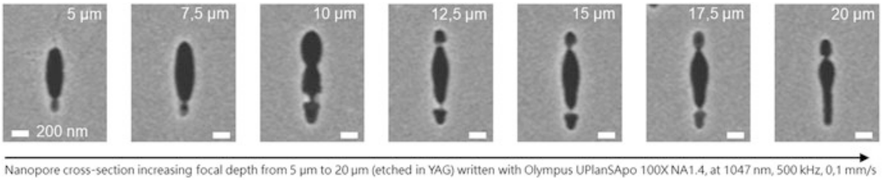
5 µm
7,5 µm
10 µm
12,5 µm
15 µm
17,5 µm
20 µm
200 nm
Nanopore cross-section increasing focal depth from 5 µm to 20 µm (etched in YAG) written with Olympus UPlanSApo 100X NA1.4, at 1047 nm, 500 kHz, 0,1 mm/s

Fig. 20.4 SEM images of nanopores written at different depths with an Olympus UPlanSApo 100X 1.4 NA objective. The top and bottom "necks" have around 40 nm widths, are due to aberrations that modulate the PSF of the focal volume and show how fine features on the nanoscale can be defined with this 3D photomodification technique if the field is engineered to have high spatial localization

3.2 State-of-the-Art

Following the initial studies in 2011–2012, two projects were initiated at the end of 2015 dedicated to further develop this nanofabrication technique, H2020-LASERLAB IV-Europe (GA 654148) followed by EXTREMELIGHT (H2020-MSCA-IF-2016, GA 747055) where an in-depth work was performed to evaluate the potential of the technique for 3D nanostructuring for advanced nanophotonics. These projects were done at the group of R. Osellame at the IFN-CNR (Milano, Italy). Here, we detail some of the key observations made at that time.

Overlapping of Single Scans The fabrication of overlapping nanopores is a key aspect for the definition of arbitrary 3D architectures, not only consisting of nanopores but also of wider structures or even planes. Overlapping of laser-written tracks in general however tends to produce bond breaking due to accumulated stress, as well as to shape irregularities between subsequent track overlaps, due to distortions of the focal volume. Initial results in 2015 showed that when using low pulse energies (E_p ~ 15 nJ), detrimental effects can be greatly reduced and sub-μm rectangular pores can be fabricated. Nanopores were written using a commercial Yb:KYW 400 fs pulse laser system (HighQ Spirit One) at 500 kHz, with circular polarization, 1 mm/s speeds and a 60X 1.42 NA PlanApoN Olympus objective. The use of this objective with aberration correction allowed to nanostructure crystals at larger depths of around 35 μm, as compared to other high NA objectives previously used, as shown in Fig. 20.4. Figure 20.5a shows single scans written in opposite directions at a depth of 32 μm, with pore aspect ratios (height/width) of 2.9 and widths on the 250 nm level. Figure 20.5b shows a multiscan pore written with the same parameters but at a larger depth of 39 μm, with a scan separation of 100 nm and 9 scans. The pore has a width of 1041 nm and a height of 644 nm. Mechanical polishing was noticed to induce some superficial cracking at the bottom side of the multiscanned pore. The ripple undulation produced by top apexes on individual laser scans performed at opposite directions (*zigzag writing*) was measured to be of ~29 nm peak to valley, primarily due to the large scan separation of 100 nm that exposes the top tips of individual single scans, clearly seen in Fig. 20.5b.

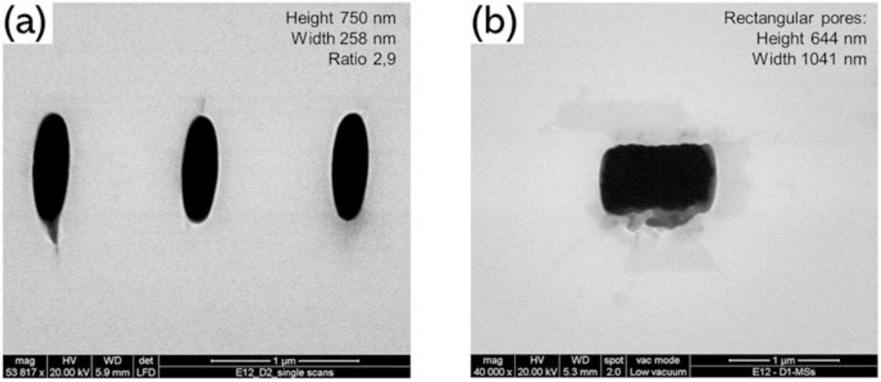

Fig. 20.5 Single (**a**) and multiscans (**b**) performed in YAG crystals at 500 kHz repetition rate and 1 mm/s scan speeds

Polarization State Effects The polarization state of photons focused on tight conditions (1.4 NA) determines to a very high degree the nonlinear absorption mechanisms of the dielectric medium and is known to strongly affect the cascade of matter excitation processes, that is, the response of the medium, as well as the varying electromagnetic pulse spatial shape and temporal dynamics within the focal volume. These dynamical processes are still neither understood nor numerically simulated to match experimental results, which typically show a very large dependence of the final modified volume with it. Femtosecond-pulse laser polarization effects were investigated both for single scans and multiscans. In the multiscan regime, where cumulative effects magnify the different photomodification processes driven by different fs-pulse photon polarization states, large differences in results were obtained for linear polarizations across or along the line scans as well as for circular polarization. Figure 20.6 shows multiscanned pores written with three different polarization states: circular and linear perpendicular and parallel to scan directions (assigned to be along an arbitrary x axis). For each polarization arrangement, three different laser powers were tested, and for each power, two multiscan pores were written (nine scans separated by 100 nm) with all scans written along equal direction (either $+x$ or $-x$). It was observed that different polarizations have different focus shifts inside the crystal, that is, different effective focal depths, and have also different characteristic pulse energy photomodification thresholds. Interestingly, pores written with a linear polarization perpendicular to scans appeared to have a larger pulse energy threshold of 24 nJ, while pores written with circular or linear polarization parallel to scans appeared to have thresholds well below 24 nJ but higher than 12 nJ.

Preferential Wet Etching of Non-photomodified YAG The wet-chemical etching of nanopores is mainly defined by the photomodified regions, which have an enhanced etching rate originated by both modified bonds (strained lattice) with

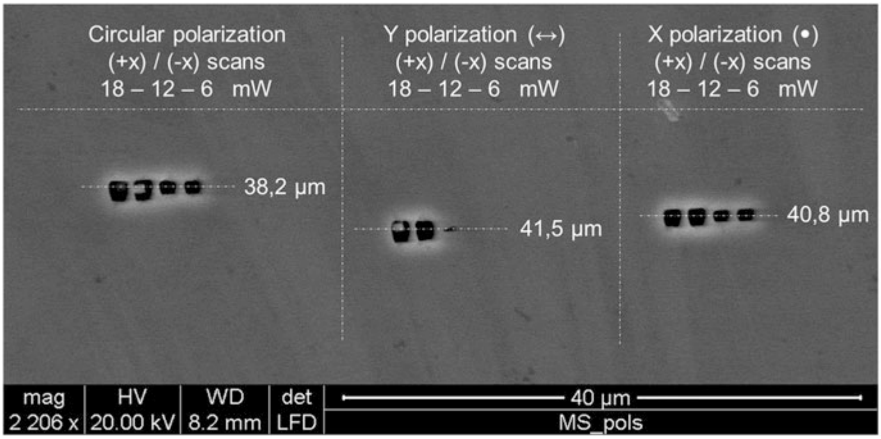

Fig. 20.6 Study of multiscanned square-shaped submicron channels inside YAG crystals for different polarizations and equivalent parameters as those in previous figures

higher reactivity as well as by possible nanocracks that would also favour the penetration depth of the acid solution into the crystal volume, as originally reported by Choudhury et al. in 2013 [77]. The etching rate of unmodified YAG is very slow on the contrary, and it was determined to be ~0.36 ± 0.23 nm/h by Ródenas et al. [14] by averaging many different experiments along different crystalline directions. This mean value only reveals the order of magnitude of the wet-chemical etch rate for a given solution and temperature and does not give information on the anisotropic nature of the process, which only reveals itself when etching beyond 100 h or more (for low concentration solutions at 70 °C temperature as in this case).

Indeed, the etching rate of non-photomodified YAG can be as low as ~0.08 nm/h as shown in Fig. 20.7, from seminal works done within the H2020-LASERLAB-IV project. In this first study on the preferential etching of YAG volume surrounding hollow nanopores, the etching rate was studied with SEM imaging to reveal the slow etch rate of the single crystal. Nanopores were first long etched (70 h) to remove all the photomodified volume that etches fast and presents lattice dislocations in its surroundings, which will also etch preferentially. Figure 20.7a shows a nanopore completely etched in this way. Further etching steps for 48 h and 94 h were performed to show the anisotropic etching of unmodified surrounding YAG volume. This long etching is preferential along lattice defects such as across different crystal planes, where the rate is constant; therefore, it reveals lattice planes, as seen in Fig. 20.7b. Although the assignment of the exact lattice planes within the YAG cubic lattice was not done, the etch rate of unmodified YAG was measured to be of ~0.08 nm/h across the horizontal plane of the nanopores perpendicular to one of the lattice planes, this being the rate at which each side of the pore etches away.

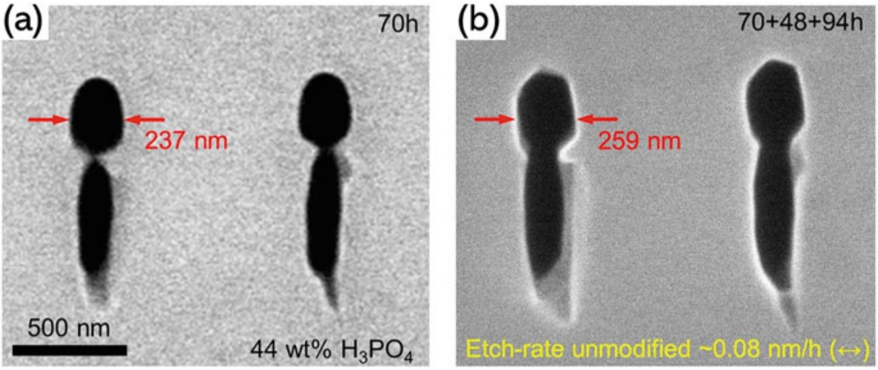

Fig. 20.7 Wet-chemical etching of nanopores: Photomodified shapes are revealed for etching times lower than around 100 h (**a**). Preferential etching can be observed for longer times (**b**), leaving well-defined pore shapes and planar walls

Further studies were performed on microstructured optical waveguides (MOWs), which are nanopore 2D lattices with a central defect that forms a channel waveguide core in the same way as in a photonic crystal fibre (PCF) or a microstructured optical fibre (MOF). Figure 20.8 shows the result from both a short 1 h and a long 10 days etching of a MOW with a pore spacing of 1 µm in the horizontal plane (perpendicular to writing direction) and a vertical spacing between layers of 1 µm. The average cross-sectional size of pores etched for only 1 h was measured to be of 329 ± 13 nm in width (↔) and of 915 ± 21 nm in height (↕), the standard error deviation being primarily given by the lack of resolution of the 22,288X magnification SEM image used (Fig. 20.8b). With subsequent etching of 10 days (240 h), an average pore width of 373 ± 11 nm (↔) and height of 924 ± 10 nm (↕) were obtained for pores from the same depth in the MOW, measured with a higher magnification (40,000X) SEM image Fig. 20.8d. From these measurements, two differential etch rates were measured of ~0.04 nm/h (↕) and ~0.18 nm/h (↔), with a standard deviation of ±0.13 nm/h. These results showed that further engineering of the nanopore shapes can be performed by utilizing this anisotropic behaviour.

Thermal Resistance of Nanotrack Photomodifications As explained, photomodified volumes consist of strained lattice at the nanoscale, although the exact type of bond distortions is yet now known. The thermal annealing of photomodified volumes was also studied prior to etching, by means of annealing samples at high temperature with optical microscope evaluation between each step. The same MOW structures as shown in Fig. 20.8 were also written on four separate crystals as these thick lattices are easily seen under optical transmission imaging, and each crystal sample was annealed for a different temperature. No modification in terms of optical contrast of the image was identified, up to temperatures of 700 °C, with annealing steps of 8 h, as shown in Fig. 20.9. This reveals that photomodified regions are very stable, this being consistent with the creation of strained bonds.

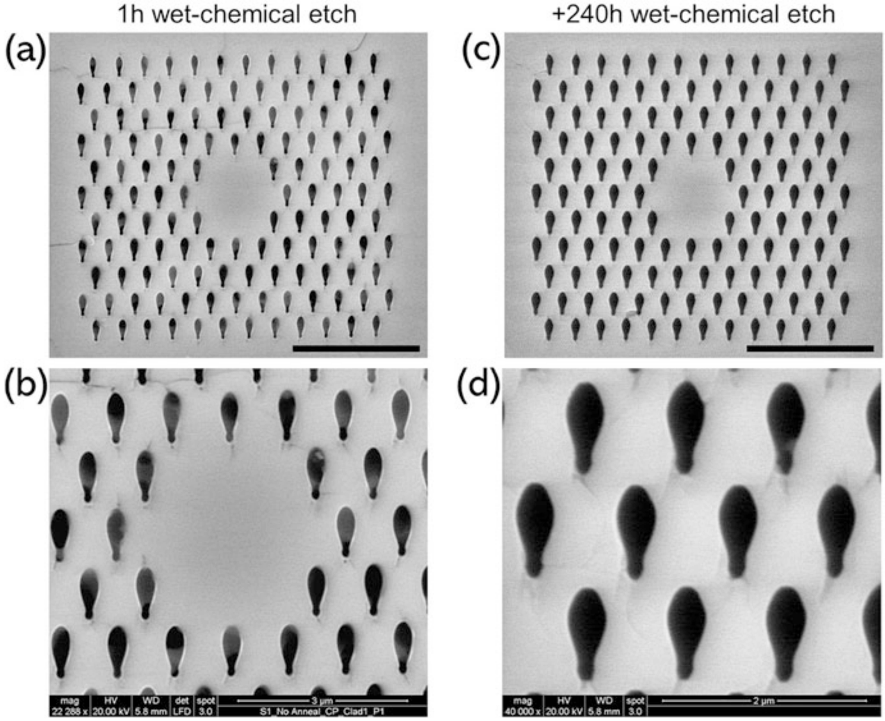
1h wet-chemical etch
+240h wet-chemical etch
(a)
(c)
(b)
(d)
mag 22 288 x HV 20.00 kV WD 5.8 mm det LFD spot 3.0
3 µm
S1_No Anneal_CP_Clad1_P1
mag 40 000 x HV 20.00 kV WD 5.8 mm spot 3.0
2 µm

Fig. 20.8 Preferential wet-chemical etching of nanopores: engineering the shape of nanopores by preferential wet etching. One hour of etching (**a**) and +240 h of etching (**b**). Respective magnified views of pores (**c**, **d**)

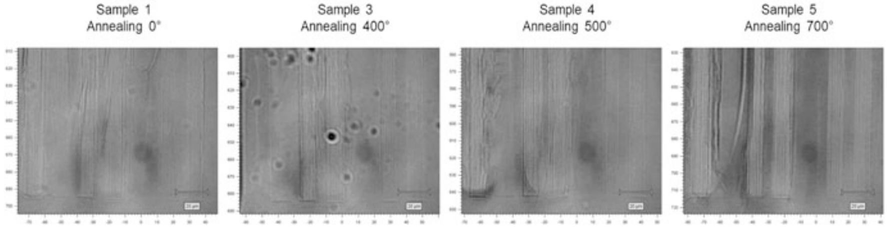
Sample 1
Annealing 0°
Sample 3
Annealing 400°
Sample 4
Annealing 500°
Sample 5
Annealing 700°

Fig. 20.9 Study on the thermal resistance of as-written volumes. 2D lattices of photomodified nanotracks (MOWs) are observed under the optical transmission microscope to equally refract light irrespective of thermal annealing treatments of up to 700 °C

Large In-Depth Nanostructuring The nanostructuring of optical crystals such as YAG and sapphire by means of high-NA focusing optics and fs-pulses has the main drawback of a limited fabrication depth at which tight focusing can be performed, as discussed previously. The focusing optics used and the type of correction for aberrations of these optical systems is critical for 3D laser nanostructuring.

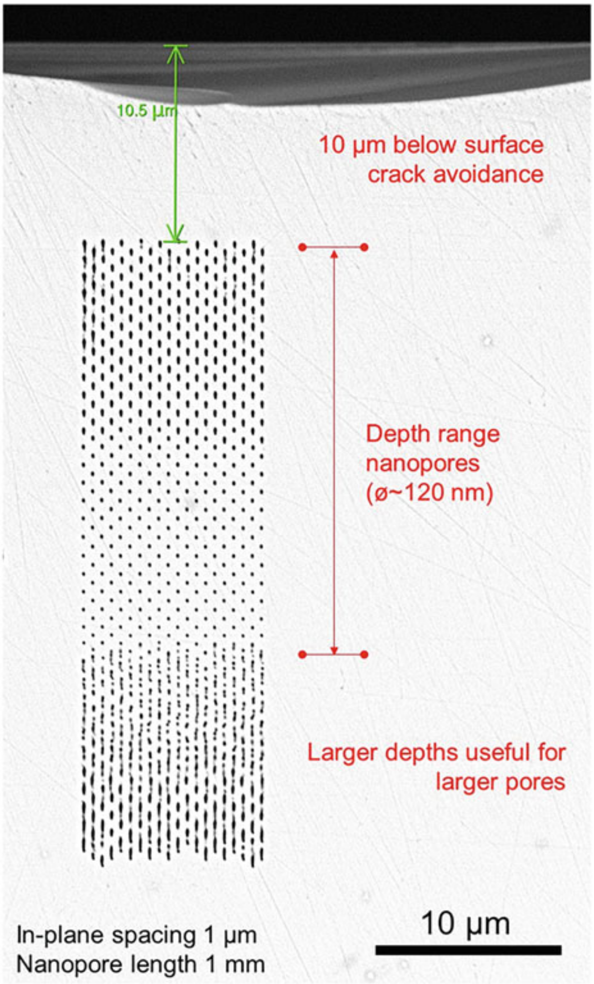
10.5 µm
10 µm below surface
crack avoidance
Depth range
nanopores
(ø~120 nm)
Larger depths useful for
larger pores
In-plane spacing 1 µm
Nanopore length 1 mm
10 µm

Fig. 20.10 Study of fabrication depths inside YAG crystals. Parameters as described in text

Within the LASERLAB IV and EXTREMELIGHT projects, a 60X 1.42 NA PlanApoN Olympus objective was used, which gave a sufficient depth range for nanofabrication of around 30 µm, from surface to beyond 20 µm in depth. Figure 20.10 shows a depth study performed with circularly polarized pulses, and a lattice with nanopore in-plane separations of 1 µm, with nanopores written at close to threshold pulse energies for each given depth.

As it is seen in Fig. 20.10, 10 µm wide lattices buried 10 µm below surface can be fabricated in absence of cracking, this being a very important feature for fabricating functional devices. Nanopores in the central region of the lattices can have average diameters of 120 nm and almost circular cross-section, a feature that

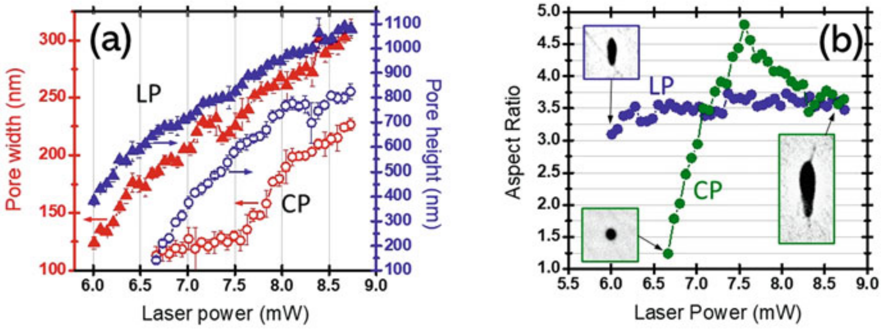

Fig. 20.11 Nanopores written at 500 kHz and 1 mm/s in YAG crystals. Nanopore cross-section size dependence of laser power for both linear polarization (LP) and circular polarization (CP) (**a**). Dependence of the nanopore aspect ratio (height divided by width across the cross-section of the pores) with laser power, for both types of laser polarization (**b**)

was only observed for circular polarization. At depths beyond 30 μm, this fine nanostructuring with ~120 nm circular pore cross-sections and 1 μm lattice spacings becomes however difficult, due to distortion of the focal point spread function by aberrations and presence of multi-foci. This limitation is only for nanostructures however, as if larger pores on the submicron size or larger are required and the available depth is greater and of up to 200 μm, physically limited by the working distance of the objective.

Pore Size and Cross-Section Dependence on Laser Power and Polarization The evolution of nanopore cross-sectional size and height/width aspect ratio was characterized in detail, for both circular and linear (parallel to scan) polarizations, at 25 μm focal depths and after 1 h of wet-chemical etching, which yielded typical nanopore lengths of around 100 μm. Figure 20.11a shows the power dependence of nanopore widths (red) and heights (blue) for linear (LP) and circular (CP) polarizations. Figure 20.11b shows the dependence of pore aspect ratio for linear and circular polarizations. The threshold for nanopore etching in YAG with linear polarization was found to be slightly lower than for circular. The threshold laser power (measured after the focusing lens) was of ~6 mW, corresponding to E_p ~ 12 nJ, ϕ ~1.8 J/cm^2 and I_0 ~ 5.1 TW/cm^2, for a 500 kHz pulse train, 350 fs pulse duration and 1 mm/s scan speed. These values of laser fluence ϕ and peak intensity I_0 are almost identical to those previously reported in 2013 by Choudhury et al. [80] for laser writing large multiscan regions with low NA focusing optics (0.4 NA) for subsequent wet-chemical etching and the fabrication of large 100 μm wide hollow channels. This suggests a common mechanism for fs-pulse laser modification and enhanced wet etching of the photomodified crystal lattice. It was also demonstrated that quasi-circular nanopore cross-sections (1.15 aspect ratio) can be achieved with circular polarization and power close to threshold. This aspect ratio can be further engineered by further wet etching by means of utilizing the previously observed anisotropic wet etching of YAG across different lattice directions.

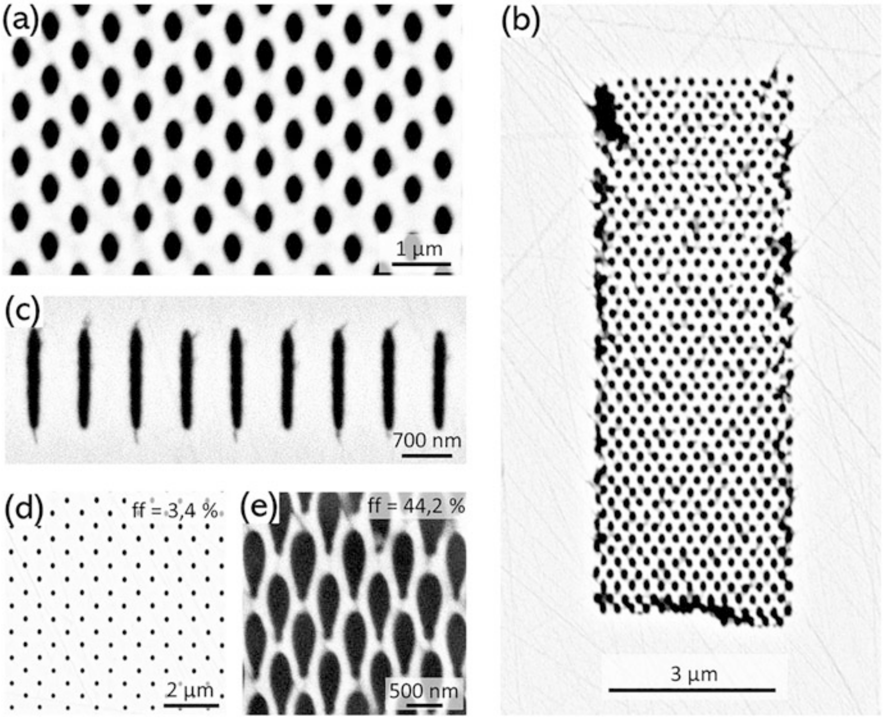

Fig. 20.12 Fabrication of ordered 2D lattices of nanopores (**a**) and (**b**), sub-wavelength gratings with bespoke pore heights and shapes (**c**) and lattices with filling factors from 3.4% up to 44.2% (**d**, **e**). More details in the text

Fabrication of Ordered Lattices with mm Lengths and Nanopores: The fabrication of a diverse range of nanopore lattices was studied, with all lattices having around 1 mm length after etching for more than 100 h. Figure 20.12a shows nanopores etched for 120 h with average widths of 257 ± 7 nm and heights of 454 ± 13 nm (aspect ratios of 1.8), which had initial aspect ratios of 2.7 after only 2 h of etching. Figure 20.12b shows a hexagonal lattice with a spacing of 250 nm, and nanopores with mean widths of 109 ± 8 nm, and heights of 125 ± 10 nm (aspect ratios of 1.15). Surface cracking after mechanical polishing of the crystals is also observed, primarily within the boundaries between lattice and bulk crystal. This suggests that nanostructured lattices can well sustain induced stress, and future strategies to avoid this cracking could be adopted at the light of these results, such as incorporating stress-relief boundaries with a gradient air filling factor decreasing towards the bulk. Figure 20.12c shows vertically overlapping nanopores after 2 h of etching, with a spacing of 700 nm, average widths of 131 ± 5 nm and heights of 1300 ± 35 nm, and this grating can diffract light at almost 100% efficiency, as discussed in the next section.

Control of Air Filling Actor Within Nanostructured Crystals Figure 20.12d shows an example of a lattice with 1 µm spacing and a low pore filling fraction of 3.4%. This lattice does not present cracking, thanks to the large spacing, and by further, wet etching the air filling factor can be finely increased towards high values, thanks to the slow etch rate of the crystal (from ~0.04 to ~0.18 nm/h in average depending on crystal axis). Figure 20.12e shows a lattice with a higher air nanopore filling fraction of 44.2%, which produces the crystal volume within the lattice to be formed by nanolayers with thickness of 150 nm, which extends for 1 mm. This lattice provides proof that large-scale (mm-scale and beyond) nanostructuring of hard and brittle materials is possible with 3D nanolithography for future advanced nanotechnologies.

Giant Selectivity and Nanopore Wet- Etching Rates in YAG and Sapphire The wet etching of nanopores inside YAG crystals was reported to produce 129 µm long nanopores in 1 h, with the standardized parameters of 1.42 NA, 0.5 MHz, 350 fs, circular polarization, 1030 nm wavelength, 1 mm/s speeds and etching at 75 °C with H_3PO_4 44 wt% with magnetic stirrer. Attending to the observed anisotropic wet etching of unmodified YAG volumes (see Fig. 20.8), an average rate of 0.11 nm/h can be used as reference value for non-modified YAG surrounding nanopores. However, a larger statistical study performed with more structures [14] yielded a higher value of 0.36 nm/h. The wet-chemical etching selectivity of these nanopores, that is, the ratio between the longitudinal etch rates of nanopores and that of its surrounding volume, analysed by SEM, was therefore estimated to be around 3.6×10^5–1.2×10^6, depending on the crystallographic cut of the YAG sample and the etch rate of non-modified crystal along directions perpendicular to the pore. The same study was also performed in z-cut sapphire (but etching with an HF solution), for which a superdiffusion-driven ($\alpha \sim 1.65$) behaviour was measured for the length evolution of nanopores with etching time, shown here in Fig. 20.13a. Cross-sections on etched nanopores inside sapphire are shown in Fig. 20.13b. These studies gave maximum pore etch rates of 79 µm/h for the first 1 h of etching and average etch rates of non-photomodified sapphire of 0.34 nm/h, this yielding an approximate selectivity of 2.3×10^5, surprisingly analogous to that of YAG considering that different crystals and acid solutions are used. The similar selectivity in both crystals points to a common physico-chemical origin, possibly related to both the nanoconfinement scale of these pores (widths ~200 nm) and their high etch rates on the 100 µm/h level (related to a high diffusivity along the nanopore longitudinal axis). A detailed study on the etching mechanisms as a function of pore size, laser parameters and etching solution and its general optimization for technological applications is therefore of prime interest, and this is another topic that deserves deep investigation, as those before mentioned.

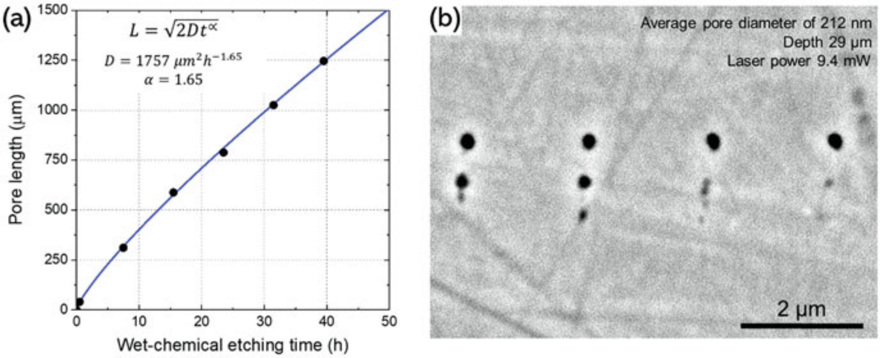

Fig. 20.13 Characterization of the temporal dynamics of wet-chemical etching of nanopores inside sapphire (**a**) and their pore cross-sections (**b**)

3.3 Technological Impact

The 3D nanostructuring of high-quality optical crystals such as garnets (YAG, YIG, etc.) and sapphire holds tremendous interest in the fields of passive optics, laser and optoelectronic applications. The most difficult test for a lithographic nanostructuring technique is the measurement of the optical capabilities of a device design to work in sub-wavelength mode, that is, where functionality is driven by a strong modulation of the index of refraction (dielectric/air/dielectric/air...) with a pitch on the nanoscale. Ródenas et al. incorporated to their seminal demonstration of 3D fs-laser nanolithography [14] the fabrication of two fundamental photonic structures whose working principle relies on the generation of sub-wavelength resonant modes: a high-efficiency sub-wavelength diffraction grating and a microstructured optical waveguide (MOW) designed to confine 1.55 μm wavelength propagation modes to a 1 μm cavity. Figure 20.14a shows a photograph of a centimetre-long 700 nm pitch grating under visible light illumination, and Fig. 20.14b shows the measured and calculated absolute diffraction efficiencies of a sub-wavelength grating (700 nm pitch) at 1070 nm wavelength. The inset shows a detail by SEM imaging of the fabricated grating, where it is seen that efficiency can reach values of 100% (theoretically), this being impossible with non-embedded gratings. Figure 20.14c shows a MOW with a hexagonal structure, a 500 nm horizontal pore-to-pore spacing, a mean pore size of 166 × 386 nm^2 and 4 mm length. Figure 20.14d aand e shows the numerically simulated intensity mode profile at 1.55 μm with FWHMs of 862 nm (vertical) and 972 nm (horizontal) and the measured diffraction-limited near-field image of the waveguide output mode measured at 1.55 μm, with an experimental FWHM of ~1.5 μm, which is limited by the resolution of the imaging lens.

The described 3D laser nanolithography technique is in its early stages of development, and therefore, the potential technologies that could be developed are diverse. Novel applications in crystalline 3D nanophotonics and nonlinear optics

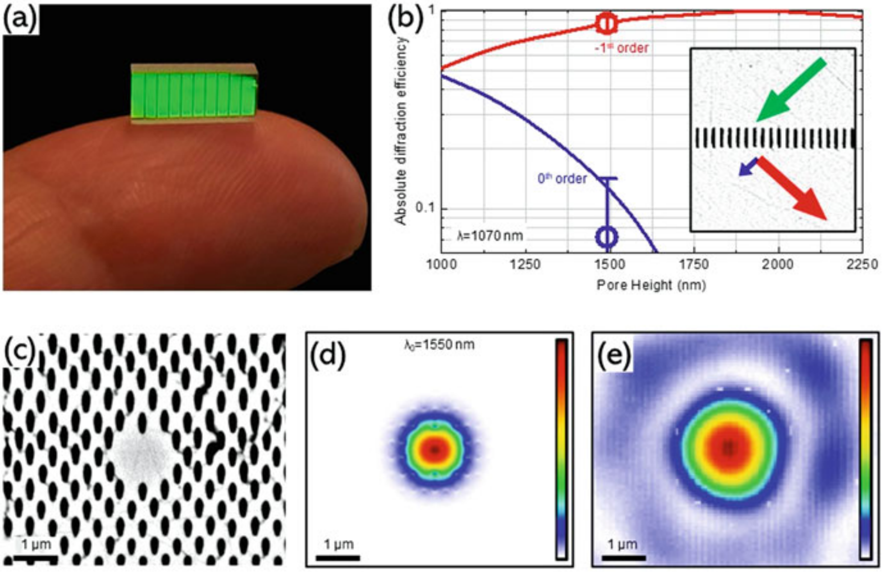

Fig. 20.14 Examples of prototype structures inside YAG crystals. (**a**) Image of a cm-scale nanograting. (**b**) Calculated efficiency of sub-wavelength volume gratings shown in the inset. (**c**) A microstructured optical waveguide (MOW) inside YAG. (**d**) Calculated and € measured mode intensity profile of the MOW (**e**) at 1.55 µm wavelength

for application in harsh and extreme environments have been the ultimate goal of the LASERLAB IV and EXTREMELIGHT projects where the technique was developed, but the 3D nanostructuring of crystals also opens up new routes to design fundamentally new monolithic solid-state lasers transforming the traditional cavity elements (such as mirrors, gratings, metalenses, dispersion elements, fibres and microfluidic cooling channels) onto embedded functionalities within the crystals, as well as to novel microresonators concepts benefiting from the 3D design flexibility inside the crystals. The prospect of producing large nanostructured laser volumes also further opens the potential for new applications in ultra-strong deformable laser nanofibres. Besides optics and photonics, the fundamental structuring capability of the technique and the good and well-known physical properties of sapphire and garnets also offer opportunities for the fabrication of highly complex crystalline components for specialized industries.

4 Towards the Extreme Scales: The Need for Discovery

One of the most exciting parts of doing research is not knowing what future discoveries may come. We can however give an educated guess on what can be expected based on the fundamental observations made so far. Having demonstrated

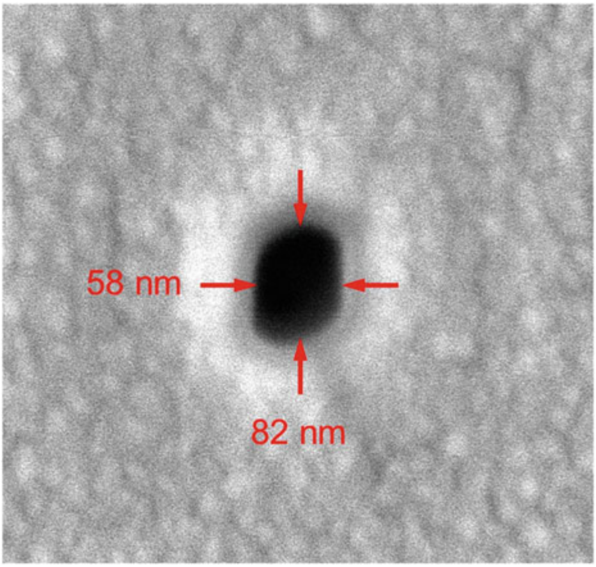

Fig. 20.15 Nanopore written inside YAG crystals with threshold pulse energy and etched long enough to reveal crystalline planes due to preferential wet etching along dislocations between planes within the non-photomodified volume that surrounds the written nanopore

that nanopores with mm-scale lengths and widths on the 100 nm level are now feasible, it can be expected that dimensions below this level will be seen in the near future. Authors have already produced nanopores with widths of 58 nm, as shown in Fig. 20.15, due to aberrated focal intensity distributions in YAG crystals producing ultra-small secondary spots along the focal axis (see also Fig. 20.4), this demonstrating that once the optical means for producing tight focal spots below this level are found, the discovered 3D nanolithography technique will probably allow to produce 3D structures with feature sizes on extreme scales. To reach these levels systematically and with high fidelity, new improved fs-pulse lasers will be needed with output power stabilities beyond what is currently possible, and improved wet-chemical etching processes will be required to finely control nanoscale etched features across macroscopic scales. Novel photomodification regimes exploiting new available lasers are also expected to produce advancements, thanks to laser-induced temperature control means, such as burst modes and on-the-fly repetition rate changes, or by means of simultaneous illumination with diverse beams for a decoupled parameters control. And furthermore, more advancements will come as well from performing dynamic control of beam parameters such as polarization, numerical aperture (beam width), scan speed and overlapping, as well as controlling the orientation of the crystals for an improved processing and testing diverse crystal compositions. The building blocks are therefore already there. We just need imagination, invention and discovery.

Acknowledgements A. R. is deeply thankful to D. Jaque, M. Gu, A. K. Kar, R. Osellame, G. Corrielli and P. Paie for their key contributions in the shaping of the work here described. Further acknowledgements are also given to S. Juodkazis for fruitful comments from 2009 on the wet etching of tracks in crystals written at 1 kHz repetition rates and to S. John for his comments on the study of photonic bandgaps in 3D nano-architected YAG crystals. A. R. also acknowledges support from "Fondo Social Europeo" (FSE), "Fondo Europeo de Desarrollo Regional" (FEDER), "Agencia Canaria de Investigación Innovación y Sociedad de la Información" (ACIISI), "Agencia Estatal de Investigación" (AEI/10.13039/501100011033, PID2019-107335RA-I00, RYC-2017-21618, 2021010102 and EIS-2021-10) and NANOtec, INTech, Cabildo de Tenerife.

References

1. T. Maiman, Stimulated optical radiation in ruby. Nature **187**, 493–494 (1960). https://doi.org/10.1038/187493a0
2. H. D. Gilbert (ed.), *Miniaturization* (Wiley-VCH, 1961)
3. N. Taniguchi, On the basic concept of nano-technology, in *Proceedings of the International Conference on Production Engineering, Part II*, (Japan Society of Precision Engineering, Tokyo, 1974)
4. U. Keller, *Ultrafast Lasers: A Comprehensive Introduction to Fundamental Principles with Practical Applications* (Springer, 2021)
5. R. Thomson, C. Leburn, D. Reid (eds.), *Ultrafast Nonlinear Optics* (Springer, New York, 2013)
6. L.E. Hargrove, R.L. Fork, M.A. Pollack, Locking of He–Ne laser modes induced by synchronous intracavity modulation. Appl. Phys. Lett. **5**, 4 (1964)
7. C.V. Shank, E.P. Ippen, Subpicosecond kilowatt pulses from a modelocked cw dye laser. Appl. Phys. Lett. **24**, 373–375 (1974)
8. R.L. Fork, B.I. Greene, C.V. Shank, Generation of optical pulses shorter than 0.1 ps by colliding pulse modelocking. Appl. Phys. Lett. **38**, 617–619 (1981)
9. P.F. Moulton, Spectroscopic and laser characteristics of Ti:Al2O3. J Opt Soc Am B **3**, 125–132 (1986)
10. D. Strickland, G. Mourou, Compression of amplified chirped optical pulses. Opt. Commun. **55**(6), 447–449 (1985)
11. D.E. Spence, P.N. Kean, W. Sibbett, 60-fsec pulse generation from a self-modelocked Ti:Sapphire laser. Opt. Lett. **16**, 42–44 (1991)
12. U. Keller, D.A.B. Miller, G.D. Boyd, T.H. Chiu, J.F. Ferguson, M.T. Asom, Solid state low-loss intracavity saturable absorber for Nd:YLF lasers: An antiresonant semiconductor Fabry-Perot saturable absorber. Opt. Lett. **17**, 505–507 (1992)
13. H.A. Haus, Mode-locking of lasers. IEEE J. Sel. Top. Quantum Electron **6**(6), 1173–1185 (2000)
14. A. Ródenas, M. Gu, G. Corrielli, P. Paiè, S. John, A.K. Kar, R. Osellame, Three-dimensional femtosecond laser nanolithography of crystals. Nat. Photonics **13**(2), 105–109 (2019)
15. Y. Kobayashi, R. Ohnuki, S. Yoshioka, Discovery of I-WP minimal-surface-based photonic crystal in the scale of a longhorn beetle. J. R. Soc. Interface **18**, 20210505 (2021)
16. V. Saranathan, S. Narayanan, A. Sandy, E.R. Dufresne, R.O. Prum, Evolution of single gyroid photonic crystals in bird feathers. Proc. Natl. Acad. Sci. **118**(23), e2101357118 (2021)
17. J.H. Strickler, W.W. Webb, Three-dimensional optical data storage in refractive media by two-photon point excitation. Opt. Lett. **16**(22), 1780–1782 (1991)
18. S. Maruo, O. Nakamura, S. Kawata, Three-dimensional microfabrication with two-photon-absorbed photopolymerization. Opt. Lett. **22**(2), 132–134 (1997)
19. M. Straub, M. Gu, Near-infrared photonic crystals with higher-order bandgaps generated by two-photon photopolymerization. Opt. Lett. **27**(20), 1824–1826 (2002)

20. M. Deubel, G. Von Freymann, M. Wegener, S. Pereira, K. Busch, C.M. Soukoulis, Direct laser writing of three-dimensional photonic-crystal templates for telecommunications. Nat. Mater. **3**(7), 444–447 (2004)
21. M. Hermatschweiler, A. Ledermann, G.A. Ozin, M. Wegener, G. von Freymann, Fabrication of silicon inverse woodpile photonic crystals. Adv. Funct. Mater. **17**(14), 2273–2277 (2007)
22. Z. Gan, Y. Cao, R.A. Evans, M. Gu, Three-dimensional deep sub-diffraction optical beam lithography with 9 nm feature size. Nat. Commun. **4**(1), 1–7 (2013)
23. V. Hahn, T. Messer, N.M. Bojanowski, et al., Two-step absorption instead of two-photon absorption in 3D nanoprinting. Nat. Photonics **15**, 932–938 (2021)
24. A.J. Gross, K. Bertoldi, Additive manufacturing of nanostructures that are delicate, complex, and smaller than ever. Small **15**(33), 1902370 (2019)
25. L.R. Meza, S. Das, J.R. Greer, Strong, lightweight, and recoverable three-dimensional ceramic nanolattices. Science **345**(6202), 1322–1326 (2014)
26. A. Vyatskikh, S. Delalande, A. Kudo, X. Zhang, C.M. Portela, J.R. Greer, Additive manufacturing of 3D nano-architected metals. Nat. Commun. **9**(1), 1–8 (2018)
27. J.R. Greer, Julia Greer answers questions about additive manufacturing. Nat. Commun. **11**, Art-No (2020)
28. E.N. Glezer, M. Milosavljevic, L. Huang, R.J. Finlay, T.H. Her, J.P. Callan, E. Mazur, Three-dimensional optical storage inside transparent materials. Opt. Lett. **21**(24), 2023–2025 (1996)
29. E.N. Glezer, E. Mazur, Ultrafast-laser driven micro-explosions in transparent materials. Appl. Phys. Lett. **71**(7), 882–884 (1997)
30. C.B. Schaffer, A. Brodeur, E. Mazur, Laser-induced breakdown and damage in bulk transparent materials induced by tightly focused femtosecond laser pulses. Meas. Sci. Technol. **12**(11), 1784 (2001)
31. S. Juodkazis, S. Matsuo, H. Misawa, V. Mizeikis, A. Marcinkevicius, H.B. Sun, Y. Tokuda, M. Takahashi, J. Nishii, Application of femtosecond laser pulses for microfabrication of transparent media. Appl. Surf. Sci. **197**, 705–709 (2002)
32. E.G. Gamaly, S. Juodkazis, K. Nishimura, H. Misawa, B. Luther-Davies, L. Hallo, P. Nicolai, V.T. Tikhonchuk, Laser-matter interaction in the bulk of a transparent solid: Confined microexplosion and void formation. Phys. Rev. B **73**(21), 214101 (2006)
33. T. Gorelik, M. Will, S. Nolte, A. Tuennermann, U. Glatzel, Transmission electron microscopy studies of femtosecond laser induced modifications in quartz. Appl. Phys. A **76**(3), 309–311 (2003)
34. C.B. Schaffer, A.O. Jamison, E. Mazur, Morphology of femtosecond laser-induced structural changes in bulk transparent materials. Appl. Phys. Lett. **84**(9), 1441–1443 (2004)
35. G. Zhou, M. Gu, Anisotropic properties of ultrafast laser-driven microexplosions in lithium niobate crystal. Appl. Phys. Lett. **87**(24), 241107 (2005)
36. S. Juodkazis, K. Nishimura, S. Tanaka, H. Misawa, E.G. Gamaly, B. Luther-Davies, L. Hallo, P. Nicolai, V.T. Tikhonchuk, Laser-induced microexplosion confined in the bulk of a sapphire crystal: Evidence of multimegabar pressures. Phys. Rev. Lett. **96**(16), 166101 (2006)
37. G. Zhou, M. Gu, Direct optical fabrication of three-dimensional photonic crystals in a high refractive index LiNbO3 crystal. Opt. Lett. **31**(18), 2783–2785 (2006)
38. A. Rodenas, G. Zhou, D. Jaque, M. Gu, Rare-earth spontaneous emission control in three-dimensional lithium Niobate photonic crystals. Adv. Mater. **21**(34), 3526–3530 (2009)
39. S. Juodkazis, K. Nishimura, H. Misawa, T. Ebisui, R. Waki, S. Matsuo, T. Okada, Control over the crystalline state of sapphire. Adv. Mater. **18**(11), 1361–1364 (2006)
40. A. Marcinkevičius, S. Juodkazis, M. Watanabe, M. Miwa, S. Matsuo, H. Misawa, J. Nishii, Femtosecond laser-assisted three-dimensional microfabrication in silica. Opt. Lett. **26**(5), 277–279 (2001)
41. Y. Shimotsuma, P.G. Kazansky, J. Qiu, K. Hirao, Self-organized nanogratings in glass irradiated by ultrashort light pulses. Phys. Rev. Lett. **91**(24), 247405 (2003)
42. F. Becke, Tschermarks. Min. Petr. Mitteil. **11**, 349 (1890)
43. J.J. Thomson, Cathode rays. The Electrician **39**, 104, also published in: In Proceedings of the Royal Institution, vol. 30, (1897), pp. 1–14

44. W.K. Röntgen, Über eine neue Art von Strahlen: vorläufige Mitteilung. Sitzungsber. Phys. Med. Gesell. (1895)
45. W. Friedrich, P. Knipping, M.V. Laue, *Interferenz-Erscheinungen bei Röntgenstrahlen Sitzungsberichte der Mathematisch-Physikalischen Classe der Königlich-Bayerischen Akademie der Wissenschaften zu München* (1912)
46. Y.P. Pshenichnov, *Vyavlenie Tonkoi Structury Kristallov (Revelation of the Fine Structure of Crystals)* (Metallurgia, Moscow, 1974)
47. R.B. Heimann, *Auflösung von Kristallen – Theorie und Technische Anwendung* (Springer, New York, 1975).; Russ. Transl., *Rastvorenie Kristallov* (Nedra, Leningrad, 1979)
48. K. Sangwal, *Etching of Crystals; Theory, Experiment, and Application*, vol. 15 aus, der Reihe: Defects in solids, ed. by S. Amelinckx, J. Nihoul (North-Holland, Amsterdam, Oxford, New York, Tokyo, 1987)
49. N.J. Tighe, Jet thinning device for preparation of Al2O3 electron microscope specimens. Rev. Sci. Instrum. **35**(4), 520–521 (1964)
50. J. Basterfield, The chemical polishing of yttrium iron garnet. J. Phys. D. Appl. Phys. **2**(8), 1159 (1969)
51. D.C. Miller, The etch rate of gadolinium gallium garnet in concentrated phosphoric acid of varying composition. J. Electrochem. Soc. **120**(12), 1771 (1973)
52. M. Gerber, T. Graf, Optimum parameters to etch Nd: YAG crystals with orthophosphoric acid H_3PO_4. Opt. Laser Technol. **33**(7), 449–453 (2001)
53. R. Feldman et al., Effect of hot acid etching on the mechanical strength of ground YAG laser elements. J. Phys. Chem. Solids **69**(4), 839–846 (2008)
54. S. Yang et al., Fiber Bragg grating fabricated in micro-single-crystal sapphire fiber. Opt. Lett. **43**(1), 62–65 (2018)
55. C.A. Mack, *Field Guide to Optical Lithography* (SPIE Press, 2006)
56. Ivo Utke, Stanislav Moshkalev, and Phillip Russell, (2012). Nanofabrication Using Focused Ion and Electron Beams Principles and Applications
57. R. Garcia, A.W. Knoll, E. Riedo, Advanced scanning probe lithography. Nat. Nanotechnol. **9**(8), 577–587 (2014)
58. U. Okoroanyanwu, *Molecular Theory of Lithography* (SPIE Press, 2015)
59. U. Okoroanyanwu, *Chemistry and Lithography: The Chemical History of Lithography*, 2nd edn. (SPIE Press, 2020)
60. D. Teresa, J. María, *Nanofabrication: Nanolithography Techniques and Their Applications* (IOP Publishing, 2020)
61. W.A. Johnson, J.C. North, R. Wolfe, Differential etching of ion-implanted garnet. J. Appl. Phys. **44**(10), 4753–4757 (1973)
62. K. Mizuuchi, K. Yamamoto, T. Taniuchi, High-efficiency coupling of laser diodes in tapered proton-exchanged waveguides. Electron. Lett. **26**, 1992–1994 (1990)
63. M. Ishida et al., A new etching method for single-crystal Al_2O_3 film on Si using Si ion implantation. Sensors Actuators A Phys. **53**(1–3), 340–344 (1996)
64. C.J. McHargue et al., Etching of amorphous Al_2O_3 produced by ion implantation. Nucl. Instrum. Methods Phys. Res., Sect. B **127**, 596–598 (1997)
65. P.J.T. Nunn, J. Olivares, L. Spadoni, P.D. Townsend, D.E. Hole, B.J. Luff, Ion beam enhanced chemical etching of Nd: YAG for optical waveguides. Nucl. Instrum. Methods Phys. Res., Sect. B **127**, 507–511 (1997)
66. A. Crunteanu, G. Jänchen, P. Hoffmann, M. Pollnau, C. Buchal, A. Petraru, D.P. Shepherd, Three-dimensional structuring of sapphire by sequential $He+$ ion-beam implantation and wet chemical etching. Appl. Phys. A **76**(7), 1109–1112 (2003)
67. A. Ofan, O. Gaathon, L. Vanamurthy, S. Bakhru, H. Bakhru, K. Evans-Lutterodt, R.M. Osgood Jr., Origin of highly spatially selective etching in deeply implanted complex oxides. Appl. Phys. Lett. **93**(18), 181906 (2008)
68. S. Matsuo, Y. Tabuchi, T. Okada, S. Juodkazis, H. Misawa, Femtosecond laser assisted etching of quartz: Microstructuring from inside. Appl. Phys. A **84**(1), 99–102 (2006)

69. S. Matsuo, Y. Shichijo, T. Tomita, S. Hashimoto, Laser fabrication of ship-in-a-bottle microstructures in sapphire. JLMN **2**, 114–116 (2007)
70. S. Juodkazis, Y. Nishi, H. Misawa, Femtosecond laser-assisted formation of channels in sapphire using KOH solution. Phys. Status Solidi RRL **2**(6), 275–277 (2008)
71. D. Wortmann, J. Gottmann, N. Brandt, H. Horn-Solle, Micro-and nanostructures inside sapphire by fs-laser irradiation and selective etching. Opt. Express **16**(3), 1517–1522 (2008)
72. J. Siebenmorgen, K. Petermann, G. Huber, K. Rademaker, S. Nolte, A. Tünnermann, Femtosecond laser written stress-induced Nd: Y3Al5O12 (Nd: YAG) channel waveguide laser. Appl. Phys. B **97**(2), 251–255 (2009)
73. R. Moser, N. Ojha, M. Kunzer, U.T. Schwarz, Sub-surface channels in sapphire made by ultraviolet picosecond laser irradiation and selective etching. Opt. Express **19**(24), 24738–24745 (2011)
74. S. Matsuo, K. Iwasa, T. Tomita, S. Hashimoto, T. Okada, Femtosecond laser-assisted etching of fluoride crystals. J. Laser Micro Nanoeng. **6**(3), 245–248 (2011)
75. S. Rajesh, Y. Bellouard, Towards fast femtosecond laser micromachining of fused silica: The effect of deposited energy. Opt. Express **18**(20), 21490–21497 (2010)
76. H.D. Nguyen, A. Ródenas, J.R.V. de Aldana, J. Martínez, F. Chen, M. Aguiló, et al., Heuristic modelling of laser written mid-infrared $LiNbO_3$ stressed-cladding waveguides. Opt. Express **24**(7), 7777–7791 (2016)
77. D. Choudhury, A. Rodenas, L. Paterson, F. Díaz, D. Jaque, A.K. Kar, Three-dimensional microstructuring of yttrium aluminum garnet crystals for laser active optofluidic applications. Appl. Phys. Lett. **103**(4), 041101 (2013)
78. A. Rodenas, A. Benayas, J.R. MacDonald, J. Zhang, D.Y. Tang, D. Jaque, A.K. Kar, Direct laser writing of near-IR step-index buried channel waveguides in rare earth doped YAG. Opt. Lett. **36**(17), 3395–3397 (2011)
79. K. Hasse, C. Kränkel, T. Calmano, Selective etching of fs-laser written structures in $Y_3Al_5O_{12}$, in *The European Conference on Lasers and Electro-Optics*, (Optical Society of America, 2017), p. CM_P_13
80. K. Hasse, G. Huber, C. Kränkel, Selective etching of fs-laser inscribed high aspect ratio microstructures in YAG. Opt. Mater. Express **9**, 3627–3637 (2019)
81. J. Lv, B. Hong, Y. Tan, F. Chen, J.R.V. de Aldana, G.P. Wang, Mid-infrared waveguiding in three-dimensional microstructured optical waveguides fabricated by femtosecond-laser writing and phosphoric acid etching. Photonics Res. **8**(3), 257–262 (2020)
82. K. Hasse, D. Kip, C. Kränkel, Influence of diluted acid mixtures on selective etching of MHz- and kHz-fs-laser inscribed structures in YAG. Opt. Mater. Express **11**(5), 1546–1554 (2021)
83. K. Hasse, D. Kip, C. Kränkel, Selective etching of 10 MHz repetition rate fs-laser inscribed tracks in YAG, in *EPJ Web of Conferences*, vol. 255, (EDP Sciences, 2021), p. 10003
84. N.A. Smith et al., Nd: YAG laser rod manufactured by femtosecond laser-induced chemical etching. Optical Materials Express **11**(12), 3946–3953 (2021)
85. S. Zhou et al., High-aspect-ratio ZnSe microstructure generated by spatially shaped femtosecond laser writing assisted with wet chemical etching. Opt. Laser Technol. **147**, 107687 (2022)
86. A.G. Okhrimchuk, A.D. Pryamikov, V.V. Likhov, D.S. Dobrovolskii, A.V. Shestakov, G.Y. Orlova, A.N. Romanov, Inscription of a waveguide in YAG: Nd crystal with a cladding composed by crystalline hollow channels. Opt. Mater. Express **12**(4), 1609–1616 (2022)
87. A. Ródenas, G. Zhou, D. Jaque, M. Gu, Direct laser writing of three-dimensional photonic structures in Nd: Yttrium aluminum garnet laser ceramics. Appl. Phys. Lett. **93**(15), 151104 (2008)
88. A. Crespi, R. Osellame, F. Bragheri, Femtosecond-laser-written optofluidics in alumino-borosilicate glass. Opt. Mater. X **4**, 100042 (2019)

Chapter 21
Ultrafast Meets Ultrasmall: Where Are the Limits of Ultrafast Waveguide Writing?

**Omair Ghafur, Peter Jürgens, Laura Rammelt,
and Alexandre Mermillod-Blondin**

Abstract Femtosecond laser direct writing (FsLDW) of optical waveguides in dielectrics has the potential to enable the direct fabrication of extremely complex three-dimensional networks of optical waveguides in the volume of any transparent dielectric material. Such a capability is unique, suggesting that ultrafast lasers could be the enabling technology required to build the photonic circuitry of the approaching quantum era. However, at the present time, FsLDW has yet to supersede established conventional techniques, such as two-dimensional lithography or ion exchange, which offer intrinsically less flexibility. The main reason for this is that the unique features of FsLDW have tended to hamper its practical implementation and adoption. In the first section of this chapter, we present the mechanisms governing energy deposition during laser writing and review some practical strategies employed to optimize the energy coupling. In the second section, the pervasiveness of thermal processes in the formation of waveguides is discussed. We show the extent to which ultrafast lasers as pure heat sources constitute a mixed blessing but one which can be systematically managed.

Keywords Laser material processing · Femtosecond laser writing · Photonic integrated circuits · Integrated optics · Waveguides

1 Introduction

Optical waveguides can be broadly defined as optical structures relying on guided propagation to direct light to one desired location. By their very nature, optical waveguides represent a fundamental constituent building block of optical circuitry. Simply integrating several waveguides in one substrate allows the construction of

---

O. Ghafur · P. Jürgens · L. Rammelt · A. Mermillod-Blondin (✉)
Max-Born-Institute, Berlin, Germany
e-mail: Omair.Ghafur@mbi-berlin.de; juergens@mbi-berlin.de; rammelt@mbi-berlin.de; mermillod@mbi-berlin.de

© The Author(s), under exclusive license to Springer Nature Switzerland AG 2023

R. Stoian, J. Bonse (eds.), *Ultrafast Laser Nanostructuring*, Springer Series
in Optical Sciences 239, https://doi.org/10.1007/978-3-031-14752-4_21

circuits able to complete a wealth of basic tasks, with applications ranging from telecommunications [1] to sensing [2].

In the context of optical processing, the most important figure of merit of a waveguide is the insertion loss, which includes losses due to both coupling and propagation, being defined as the overall loss of signal power observed when inserting the waveguide into an optical circuit. The key factor in minimizing insertion losses is mode matching; this implies that, ideally, a waveguide structure, to be used in an integrated optical circuit, should support the same propagation mode (e.g., mode size and mode shape, numerical aperture, effective refractive index) as the nearest upstream optical component. Typically, waveguide fabrication techniques aim to produce smooth optical structures supporting circular modes (mostly achieved with a circular waveguide cross section in the micron range), low losses, high-refractive-index contrast in the guiding layer, polarization independence, and broad wavelength operation. In the context of this chapter, we emphasize the limits and the extreme aspects of FsLDW on the *fabrication* of optical waveguides. The reader is invited to consult Ref. [3] for a discussion on the important topic of losses in optical waveguides.

The fabrication of optical waveguides has been demonstrated in a wide range of transparent substrates including glasses, crystals, and polymers [4–7]. Basically, the high refractive index of the guiding region might be obtained either by depositing a high refractive index material on a substrate or by direct refractive index modification [8]. Thin film deposition can be realized either by vapor deposition or by sputtering, while refractive index modification involves either ion doping (by ion exchange or ion implantation) or photo-induced refractive index changes, either by UV irradiation or with the help of ultrashort laser pulses, which is the fabrication method discussed in that chapter. Since the first demonstration of ultrafast waveguide writing (FsLDW) in 1996 [9], considerable progress has been made in understanding, optimizing, and refining this method of waveguide production. As of today, FsLDW is the most efficient method for the three-dimensional fabrication of complex photonic networks. Among its many advantages, FsLDW is a single-step process, is maskless, and does not require a clean room environment.

Typically in FsLDW, the waveguides are produced by focusing an ultrashort pulse (with a sub-ps duration) in the host substrate. The sample is usually translated in a direction transverse to the propagation axis of the focused laser beam (see Fig. 21.1a,b), although photoinscription in the longitudinal configuration (i.e., with a sample translated in the direction of propagation) is also possible [10, 11], as shown in Fig. 21.1c. In the so-called type I regime of laser-matter interaction, the high refractive index region appears in the photoexcited volume, as shown in Figs. 21.1a and c. In type II regime (see Fig. 21.1b), the laser-matter interaction scenario is different. The laser-induced structural modifications lead to material damage [12], and the guiding region appears at some distance from the laser focus, typically under the form of a (light-guiding) stress field [4]. In such a scenario, type II microstructures play the role of a stressor.

The onset of permanent structural modifications requires an external field strength sufficient to detach outermost valence electrons from their parent atoms.

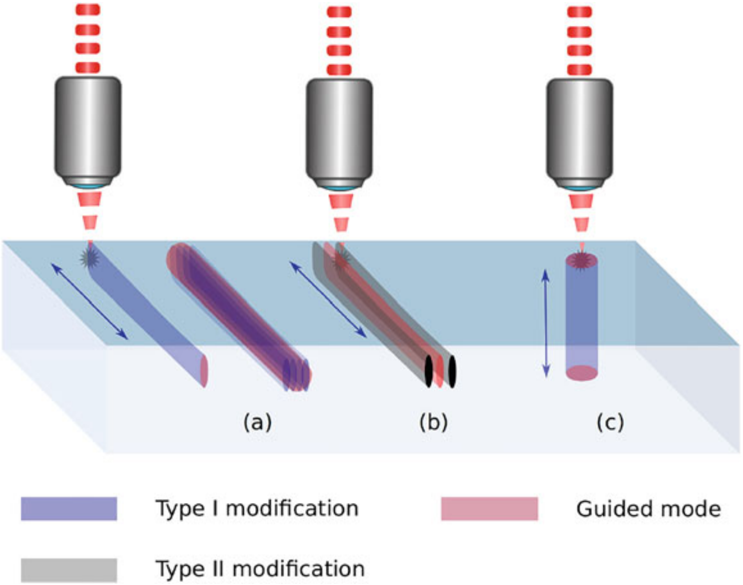

Fig. 21.1 Experimental setup used for ultrafast waveguide writing (FsLDW) in tight focusing conditions. Schematic representation of a waveguide based on (**a**) type I modifications induced in a transverse configuration, (**b**) type II modifications induced in a transverse configuration, and (**c**) type I modifications generated in a longitudinal writing scheme. Note that the number and locations of microstructures can vary depending on the optical properties (e.g., refractive index, mode size, polarization sensitivity) desired. The blue arrows indicate the direction of the sample translation

The exact modification threshold is of course highly material-dependent but usually close to the ≈1 V/Å reported for fused silica [13]. In order to obtain such an electric field magnitude, it is necessary to tightly concentrate the electromagnetic radiation from the laser with the help of fairly high numerical aperture (NA) focusing optics (usually, NA > 0.5). The energy is then coupled from the laser beam to the material via the formation of an electron-hole plasma. Permanent material lattice alterations (and hence, ultimately, refractive index changes) eventually take place as a result of the plasma relaxation through multiple channels, such as electron-phonon coupling (and subsequent thermal effects), creation of point defects, and matrix reorganization.

Despite the apparent simplicity of FsLDW, its unique 3D fabrication capability, and its versatility, FsLDW still faces a number of challenges before it can supplant the standard approaches of ion exchange or thin film deposition which are currently prevalent in industry for waveguide fabrication. In this book chapter, we attempt to clarify the limitations associated with femtosecond laser writing of waveguides. These limitations are intimately linked to the specifics of the material modification mechanisms underlying FsLDW, but we also emphasize that systematic workarounds exist.

This chapter is organized into two parts. In the first part, we examine the consequences of tight focusing and nonlinear propagation on the morphology of the focal volume, and we discuss to what extent concentrating (and propagating) the electromagnetic field to reach the material modification threshold results in intrinsic limitations. Part one is concluded by a review of experimental strategies which have been developed to overcome these limitations. The second part is dedicated to the study of thermal effects in FsLDW. The origin of the relevant thermal processes is detailed, and their role in the formation of the waveguide structure is discussed. Finally, we consider how thermal processes might fundamentally restrict the capabilities of FsLDW. For each limitation identified, we review the corresponding technical workaround.

2 Limitations Associated with Tight Focusing and Nonlinear Propagation in Ultrafast Waveguide Writing

The focal volume effects studied in this chapter play an acute role, especially in type I regime of laser-matter interaction, where the light-guiding region coincides with the laser-irradiated volume and hence the shape of the focal volume directly determines the symmetry of the final waveguide cross section.

In the following section, we first examine linear effects on the focal volume originating from tight focusing and the wavefront distortions induced by the presence of a planar interface. In the second part, we proceed to discuss the evolution of the beam profile that occurs when the laser pulse propagation becomes nonlinear.

2.1 Linear Effects

2.1.1 Gaussian Beam Focusing

The general action of a tightly focusing lens on a coherent laser beam corresponds to a linear transformation from a coherent plane wave to one with a spherical curvature. The transverse intensity distribution from the majority of laser resonators corresponds to a Gaussian function that reads [14]:

$$I(r,z) = \frac{2P_0}{\pi w(z)^2}\exp\left[-2\left(\frac{r}{w(z)}\right)^2\right], \tag{21.1}$$

where P_0 is the total power of the beam and $w(z)$ represents the radius at which the intensity equals $1/e^2$ ($\approx 13.5\%$) times the maximum on axis.

Upon focusing in a medium with a homogeneous and isotropic refractive index n, the Gaussian character of the transverse intensity distribution of the incident laser beam is preserved. The corresponding radius w_0 of the beam at the focal plane can be simply expressed as [15]:

$$w_0 = \frac{\lambda}{\pi \mathrm{NA}}. \tag{21.2}$$

Here, λ is the central wavelength of the laser, and NA is the numerical aperture defined as:

$$\mathrm{NA} = n \sin\alpha, \tag{21.3}$$

where α is the angle of the steepest ray with respect to the optical axis (see, for instance, Fig. 21.3). However, in the direction of propagation of the laser (corresponding to the z-axis), the intensity distribution has a Lorentzian profile which is characterized by the Rayleigh length z_r, defined as the distance where the area of the beam has doubled, and is given by:

$$z_r = \frac{\pi w_0^2}{\lambda}. \tag{21.4}$$

As a result, the three-dimensional intensity distribution of a focused spherical Gaussian beam in a homogeneous medium is elongated in the direction of the z-axis, corresponding to a prolate spheroid. To characterize the asymmetry of the focal volume, one can define an aspect ratio AR such as:

$$\mathrm{AR} = \frac{\mathrm{FWHM_z}}{\mathrm{FWHM_r}} = \frac{2z_r}{w_0\sqrt{2\ln 2}} = \frac{n}{\mathrm{NA}}\frac{2}{\sqrt{2\ln 2}}, \tag{21.5}$$

where $\mathrm{FWHM_z}$ and $\mathrm{FWHM_r}$ correspond to the full width at half maximum of the intensity distribution in the z and r directions, respectively.

To provide an example, we have simulated the beam propagation around the focal plane when focusing in air by using the Fresnel-Kirchhoff diffraction formula. The simulation results shown in Fig. 21.2 were obtained with the help of the Lightpipes package [16].

2.1.2 Focusing Through a Planar Air-Dielectric Interface

The simple operation of focusing a laser beam through a planar interface between two media with different refractive indices produces wavefront distortions. As the converging beam crosses the refractive index interface, it experiences spherical aberrations. Here, we use the term spherical aberration to refer to the fact that the spatial phase of the transmitted beam significantly departs from a purely spherical phase. As the pulse propagates in the second medium, these phase distortions translate into an evolution of the spatial intensity profile which ultimately results

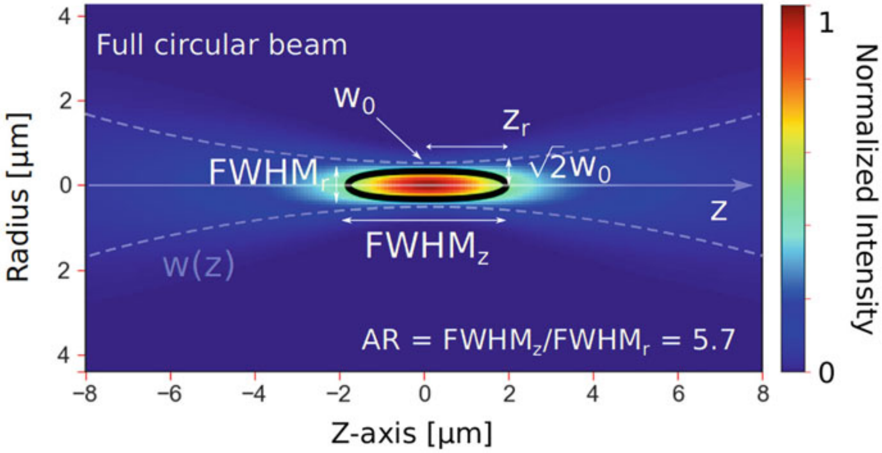

Fig. 21.2 Numerical simulation showing the intensity distribution near the focal plane (located at $z = 0$), along the propagation axis of a Gaussian beam, in vacuum (no interface), obtained using the LightPipes package [16]. The laser wavelength was 800 nm, and the beam radius was 2.2 mm at $1/e^2$ before focusing with a numerical aperture of 0.46. A black contour line is drawn at an intensity of half of the maximum on-axis intensity. The figure is labeled with typical beam parameters used to characterize lasers with Gaussian intensity distributions, as defined in the text. In a typical transverse FsLDW geometry, the waveguide would be written out of the page, and the pictured intensity distribution would determine the waveguide cross section. AR represents the aspect ratio of the focal volume

in an elongation of the focal volume along the axis of propagation and hence a decrease of the maximum on-axis intensity.

The amount of focal distortion introduced depends on (1) the magnitude of the refractive index mismatch at the interface, (2) the focusing strength (corresponding to the NA of the focusing optics), and (3) the distance to focus d_f. The distance to focus (sometimes called writing depth or working depth) simply corresponds to the distance between the interface (located at $z = z_0$) and the paraxial focus according to:

$$d_\mathrm{f} = n\overline{z_0 f_0} = \overline{z_0 f_p}, \tag{21.6}$$

where n is the refractive index of the sample and $\overline{z_0 f_0}$ corresponds to the (signed) distance between the interface and the focus in the absence of interface f_0 (see Fig. 21.3). By convention, signed distances are positive in the direction of propagation of the laser.

In the typical situation where a laser beam is focused through an air/dielectric interface (i.e., with refractive indices of 1.0 and n, respectively), the focal elongation due to spherical aberrations l_sa reads [17]:

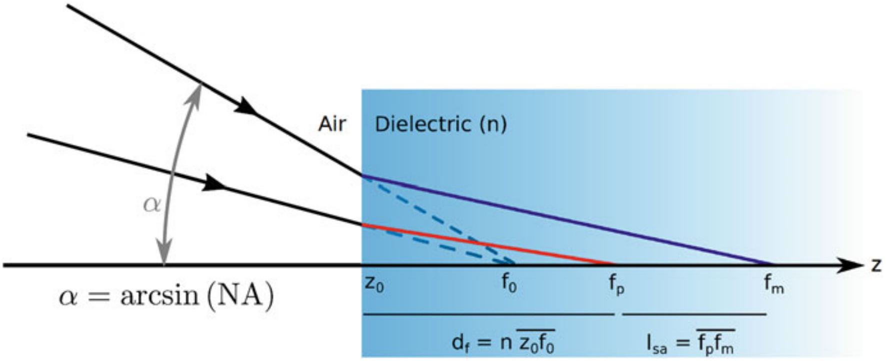

Fig. 21.3 Schematic representation of the evolution of paraxial and marginal rays when focusing through a planar air/dielectric interface located at a coordinate z_0. In the absence of interface, all rays converge at f_0. Paraxial and marginal rays intercept the axis at locations f_p and f_m, respectively. Adapted with permission from [18] ©The Optical Society

$$l_{\mathrm{sa}} = \frac{\mathrm{d_f}}{n}\left(\sqrt{\frac{n^2 - \mathrm{NA}^2}{1 - \mathrm{NA}^2}} - n\right). \tag{21.7}$$

The degradation of the AR due to such a focus elongation is particularly detrimental for writing waveguides in the transverse configuration since it directly influences the ellipticity of the modified region and therefore the ellipticity of the supported waveguide modes. In the longitudinal writing scheme, the degradation of the AR continuously varies with the writing depth. As a result, the peak intensity also depends on the depth with drastic consequences on the uniformity and nature of the laser-induced structural transformations.

In practice, d_{f} should be chosen so that the intensity on axis $I_{r=0}$ is at least 0.9 times the maximum intensity on axis in the absence of spherical aberrations. When focusing a laser pulse from air to fused silica with a NA $\sim$ 0.45, using this criterion provides a maximum distance to focus on ca. 200 μm [19]. Thus, there are limits to the depths at which FsLDW can be used.

2.2 Nonlinear Effects: Self-Focusing, Plasma Formation, and Filamentation

In addition to the linear effects presented in the previous section, the high intensities encountered when tightly focusing ultrafast pulses equally trigger a nonlinear material response to the incident laser field. This response is dominated by the response of the bound electrons and the generation of free carriers. The result is a drastic alteration of the effective material properties experienced by the laser field, i.e., the effective instantaneous dielectric constant and hence refractive index. This self-action of the laser field mediated by the material response can profoundly affect the energy deposition into the volume of the material.

2.2.1 Nonlinear Response of the Bound Electrons

As the laser pulse approaches the focal region, the local intensity increases dramatically, and the response of the material evolves from linear to nonlinear. The first observable source of nonlinearity arises from the bound electrons (also known as the Kerr response). Instead of the (small) proportional variation of the materials electronic polarization in the linear regime, in the nonlinear regime, the material polarization is driven such that it oscillates at frequencies corresponding to harmonics of the laser frequency. As a consequence, the local dielectric permittivity (and therefore the effective refractive index n_{eff}) does not only depend on the laser frequency but can also be described as a function of the laser intensity I according to:

$$n_{\text{eff}}(r,t) = n_0 + n_2 I(r,t), \tag{21.8}$$

where n_0 is the standard refractive index of the material in the linear regime and n_2 represents the intensity-dependent, nonlinear contribution of the bound electrons to the refractive index.

The consequences of a variation of the refractive index during the laser pulse manifest in both frequency and spatial domains. In the frequency domain, a time-dependent refractive index results in a time-dependent phase $\varphi(t)$ and a symmetric broadening of the spectral content of the pulse according to $w(t) = d\varphi/dt$. This nonlinear phenomenon is known as self-phase modulation (SPM). SPM typically only plays a marginal role in the context of FsLDW. The spatial counterpart of SPM, however, is called self-focusing and deserves special attention because it results in an important redistribution of the local intensity profile during propagation of the ultrafast pulse. In the spatial domain, $n_{\text{eff}}(t)$ follows the Gaussian profile of the laser beam and is therefore higher on the axis than in its surroundings. Such a refractive index profile is the optical equivalent of a converging lens and results in the laser pulse undergoing self-focusing. By analogy with linear optics, one can define an effective self-focusing focal length f_{sf} and obtain a rough estimate of the importance of self-focusing by comparing f_{sf} and f_{ext}, the focal length of the external focusing element. The self-focusing length can be derived using Fermat's principle as [20]:

$$f_{\text{sf}} = w\sqrt{\frac{n_0}{2n_2 I_0}} \tag{21.9}$$

where I_0 is the on-axis intensity and w is the beam waist before entering the material. The role played by self-focusing is more pronounced when f_{sf} is comparable to

f_{ext}, so that a direct scaling between the radius of the laser-inscribed microstructures and the strength of the external focusing optics is not straightforward at all.

An important feature to note is that self-focusing can lead to the eventual collapse of a laser beam into a self-trapped mode of propagation where self-focusing counterbalances spreading due to diffraction. The critical threshold for collapse, P_{cr}, depends on the incident beam power (not on the beam intensity) and sets an upper bound for the optical power which can be effectively propagated in a dielectric medium [21]:

$$P_{\mathrm{cr}} = C \frac{\lambda^2}{4\pi n_0 n_2}. \tag{21.10}$$

In this expression, the material's properties are taken into account through n_0 and n_2, and the laser's properties are included by considering the wavelength λ and the constant C, a coefficient depending on the beam profile. The analytical expression $C = 1.22\pi^2/8$ (initially derived for a Townes beam) provides P_{cr} within a ca. 10% accuracy for a broad family of laser beams including Gauss and super Gauss beam profiles [21].

2.2.2 Free Carrier Generation

When the local electric field strength approaches $\approx$1 V/Å, bound electrons can gain enough energy from the laser field and can be promoted from the valence to the conduction band by strong field ionization (SFI). SFI is inherently a highly nonlinear process, and as such, it also has strong consequences on the energy deposition. The fundamental reason is that SFI behaves as a threshold process: free carriers only appear *where* and *when* the local intensity exceeds the ionization threshold I_{th}. In wide bandgap dielectrics, I_{th} is typically on the order of a few TW/cm^2. In the context of non-ablative laser processing, there is strictly speaking no ionization event (since there is no electron leaving the target), but owing to the delocalization of the charge taking place when carriers are injected into the conduction band, the carriers are said to be free or quasi-free, and the term "ionization" is widely used in the laser processing community. We emphasize that the formalism used to describe SFI is similar in the ablative and non-ablative regimes and the reader is welcome to refer to the first part of this book for more information.

The electrons produced by SFI can be further accelerated by the laser field (via inverse Bremsstrahlung [22]) and produce more (quasi-)free carriers via collisional ionization (aka avalanche ionization). In solids, these two processes occur concomitantly, during the presence of the laser pulse, which greatly complicates their respective identification. As of today, the relative importance of SFI compared to electron-electron impact ionization is still not clear, but recently, an optical signature which characterizes only the SFI contribution has been demonstrated [23]. Beyond its utility for accurate plasma diagnostics, such an observable is more generally useful for material characterization: since SFI seeds the electron-electron impact ionization process, the optical signature of SFI can be exploited to anticipate the occurrence of catastrophic optical damage in optical components.

2.2.3 Filamentation

Qualitatively, the presence of free carriers results in a refractive index decrease with a magnitude that depends (nonlinearly) on the plasma density [24]. Since the plasma density depends on the local intensity, the refractive index in the presence of free carriers is smaller on the optical axis. As a consequence, the laser pulse propagates in a medium which is equivalent to a diverging lens, and the trailing edge of the incoming laser pulse experiences defocusing from the plasma produced by the leading edge of the pulse. As a result, the local intensity rapidly decreases, plasma formation stops, and self-focusing plays an increasingly important role, confining the electromagnetic energy above the ionization threshold. As this sequence repeats, the laser pulse undergoes a series of refocusing and defocusing events leading to the so-called filament propagation. In the context of direct laser writing of waveguides, filament propagation could be exploited to produce long straight optical structures. However, the high nonlinearities which underlie the plasma formation and pulse evolution make a precise control of the laser-matter interaction extremely challenging.

2.3 Practical Strategies for Optimizing the Energy Deposition in the Volume

In this subsection, we discuss the two distinct approaches usually employed to optimize the energy confinement in the volume of dielectrics. In Sect. 2.3.1, we present experimental strategies based on altering the amplitude and/or phase profile of a laser beam at the entrance pupil of the focusing objective. The approach described in Sect. 2.3.2 is dramatically different. It exploits the time-bandwidth properties of ultrafast pulses to obtain a high intensity near the focal plane only and requires one to modify the properties of the laser beam before it enters the focusing system.

2.3.1 Pupil Engineering

Modification of the Entrance Pupil

Modifying the shape of the entrance pupil of the focusing system to influence the intensity distribution in the focal plane is perhaps the most popular approach employed to reduce the aspect ratio of the elongated focal volume seen in Fig. 21.1.

For instance, one can use the widely spread “slit beam shaping method” which consists in placing a one-dimensional adjustable slit in the entrance pupil of the focusing optics to improve the aspect ratio of the focal volume.

The possibility to control the ellipticity of the longitudinal cross section of a focused laser beam by truncating the transverse profile was first introduced by Cheng et al. [25], as schematized in Fig. 21.4a. This concept was later elaborated on by Salter et al. [26] who employed a spatial light modulator (SLM) to actively tailor the longitudinal cross section of the focused beam during the waveguide writing process. In order to quantify the effect of clipping the transverse profile of a beam with an adjustable slit, we have simulated the beam propagation using the Fresnel-Kirchhoff diffraction formula [16]. We have chosen typical parameters for laser direct writing of waveguides (see, for instance, Ams et al. [27]), i.e., a laser wavelength of 800 nm, a beam radius of 2.2 mm at $1/e^2$, and focusing optics with a numerical aperture of 0.46 in a medium with $n = 1.54$, representative for technical glasses. The results are shown in Fig. 21.4b. Since a fully numerical approach was used, we were able to account for an input beam with a truncated Gaussian intensity profile. In Ref. [27], the authors simulated the elongation of the focal volume based on the analytical solutions corresponding to an input beam with an elliptical Gaussian intensity distribution.

Incidentally, we note that considering a truncated Gaussian beam appears to provide a better agreement with the experimental results compared to a simplified

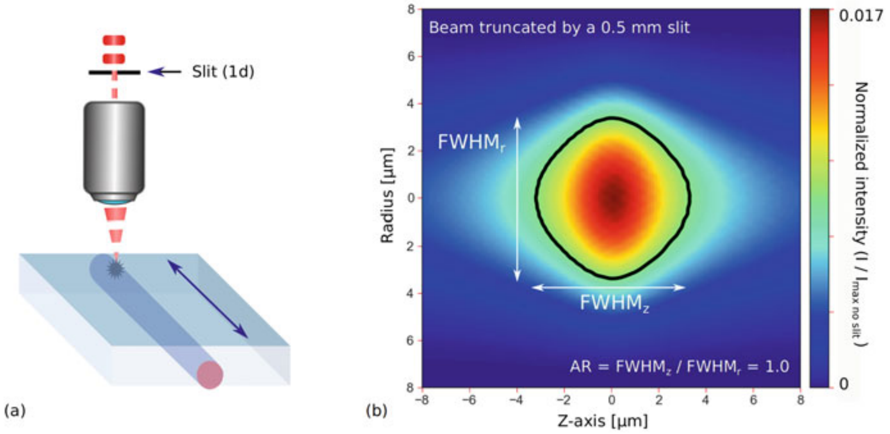

Fig. 21.4 (**a**) Experimental setup for the slit beam shaping method. (**b**) Numerical simulation showing the intensity distribution along the propagation axis of a Gaussian beam truncated by a 0.5 mm slit, obtained with the LightPipes package [16]. Except for the presence of a slit, the simulation parameters are the same as described in Fig. 21.2. A black contour line is drawn at half of the peak intensity. The figure is labeled with typical analytical quantities used to characterize Gaussian beams, as defined in the text. In a typical FsLDW geometry, the waveguide would be written in the direction out of the page, and the profile pictured would determine its cross section. Note the decrease of the peak intensity from 1.0 (obtained with the full beam) to 0.017

analytical analysis, i.e., our simulations predict that a 0.5 mm wide slit results in a quasi-circular waveguide cross section. This result tends to be confirmed by the experimental observations [27], whereas the analytical approach predicts an optimal slit width of 0.63 mm. Since truncating the beam with a slit simultaneously decreases the transmitted power and increases the beam area near the focal plane, the maximum peak intensity drastically drops. In our example, the peak intensity drops from 1.0 (in the absence of slit, see Fig. 21.2) to 0.017.

Finally, we mention that besides the popular beam shaping slit method, using an annular pupil equally stands as an appealing option, particularly in the presence of spherical aberrations [28], mainly because annular focusing results in a drastic reduction of the angular spectrum. More specifically, the paraxial (near-axis) rays are blocked in the annular pupil, thereby strongly reducing the distance between the marginal focus and the (new, quasi-)paraxial focus while preserving the (transverse) focal spot size. Experimentally, annular focusing naturally happens when using reflective focusing optics based on a Cassegrain design since in such a configuration the paraxial rays are actually back-reflected by the primary mirror.

Dynamic Wavefront Correction

Instead of modifying the transmission in the entrance pupil, one can attempt to compensate for the focus elongation created by the presence of spherical aberrations by moving a specific group of lens constituting the focusing system with the help of the so-called coverslip correction collar. Correction collars provide a good wavefront compensation but are limited to one specific writing depth. As pointed out in Ref. [29], dynamic wavefront correction can be obtained with the help of a customized motorized apparatus.

Another correction approach relies on using adaptive optical elements such as spatial light modulators (SLMs), deformable mirrors, or digital mirrors to compensate for aberrations [30]. In this scenario, the phase map produced on the adaptive element is usually imaged onto the entrance pupil plane of the focusing objective. This allows for dynamic wave front correction and therefore laser direct writing at different focusing depths [30, 31]. As an example, in Fig. 21.5, we show a comparison between microstructures generated at different depths (cf. Eq. 21.6) with and without pre-correction of the spatial phase in a Bk7 sample. The phase maps were applied with a SLM. The optimal phase maps were obtained with the help of an evolutionary algorithm. The fitness function was defined such as to minimize the axial extent of the modified region [31]. These results show that applying the proper phase correction enables to confine the energy deposition by pre-compensating the depth-dependent phase distortions experienced by the laser beam. Since SLMs are programmable elements, it is possible to change dynamically the wavefront correction as the writing depths change, for instance, to optimize the energy deposition when writing waveguides in a longitudinal configuration, as illustrated in Fig. 21.5b.

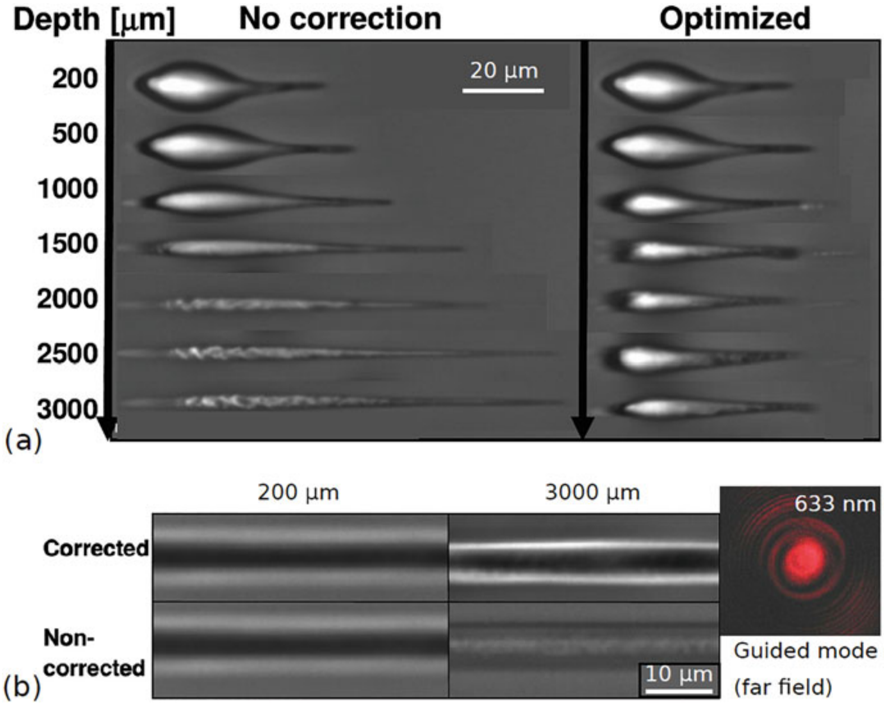

Fig. 21.5 Dynamic wavefront correction applied to longitudinal waveguide writing in Bk7. (**a**) Phase contrast microscopy pictures of laser-induced structures produced at different depths without (left) and with (right) phase pre-compensation for wavefront distortions. The phase pre-compensation was applied with the help of a spatial light modulator. The corresponding phase maps were obtained as a result of an optimization procedure based on an evolutionary algorithm. (**b**) Dynamic wavefront correction during laser writing in a longitudinal configuration. Left: microstructures obtained with and without phase correction. Right: far field intensity distribution of the guided modes supported by the waveguide fabricated with the help of dynamic wavefront corrections. Reprinted with permission from [31] ©The Optical Society

2.3.2 Simultaneous Spatial and Temporal Focusing

The method of simultaneous spatial and temporal focusing (SSTF) was initially developed in the context of multiphoton imaging [32] and transposed to microprocessing applications shortly after, to fabricate microfluidic channels with a circular cross section [33].

The principle of SSTF is to spatially separate the different spectral components of the ultrafast beam before focusing. In such a scheme, the spectral components recombine in the focal plane only, and as a result, the initial temporal profile of the pulse is recomposed in a small region near the focal plane only. Such an approach has the unique advantage of significantly reducing the maximum intensity occurring during the pulse propagation to the focus and therefore mitigates all nonlinear effects associated with ultrafast pulse propagation in materials. When applied to dielectric microprocessing, SSTF resulted in a twofold reduction of the plasma channel's length with respect to conventional focusing [34] and enabled processing through thick transparent samples [35].

Finally, Lanier and Gulley have studied numerically the combination of SSTF and annular focusing. In their experimental scheme, the incoming ultrafast pulse is first radially dispersed and then focused by an optical system with an annular entrance pupil [36]. Their results indicate that combining annular focusing and SSTF results in a localization of ionization peaks on sub-micrometer scales.

3 Laser-Induced Thermal Processes in the Direct Laser Writing of Waveguides: Virtues and Drawbacks

The physical processes leading to waveguide formation are multiple. An exhaustive enumeration of all the process involved is beyond the scope of this chapter. However, in a first attempt to categorize, one might note that two guiding scenarios emerge. In the first category, light is guided by the laser-irradiated region. Such waveguides are usually described as type I waveguides, because the laser-induced structural modifications do not create optical damage in the substrate [12]. Type I waveguides have been mostly observed in amorphous materials (such as fused silica), although some early reports suggest their presence in $LiNbO_3$ as well [37, 38]. The second category of laser-induced waveguides belongs to type II family of optical structures, formed during the process of laser-induced optical damage occurring near the guiding region. Such optical structures are mostly (but not only) encountered in crystals. The guiding mechanism at play might, for instance, rely on the presence of a stress field in the vicinity of the irradiated region. A judicious irradiation strategy (involving, for instance, multiple individual laser-induced structures) allows the resulting stress field to be tailored for guiding of light. As a main advantage, the direct laser writing of waveguides in type II scheme offers an outstanding process versatility, enabling direct laser fabrication of waveguiding microstructures in almost any crystal [4].

In this chapter, we examine the role of thermal process in the formation of both type I and type II structures. Firstly, we emphasize that laser heating is omnipresent, regardless of the final irradiation product. Secondly, we study the role of heat in both scenarios of material modification and emphasize the extent to which heat is a mixed blessing, that is, in the sense that thermal processes lie at the heart of material modification but also limit the capabilities of FsLDW.

3.1 The Origin of Thermal Effects

Once the laser energy has been coupled into the material via the creation of an electron-hole plasma, the energy stored in the quasi-free carrier bath is redistributed via three main relaxation channels. The first channel is radiative carrier recombination, resulting in the emission of photons. Generally speaking, the emission of photons upon carrier recombination is not expected to play a dominant role in inducing permanent structural modifications in the material. However, it does constitute a useful observable for precisely determining the locus of energy deposition. The second relaxation channel is the formation of point defects; these allow energy to be stored in local deformations of the atomic lattice. The third main relaxation process is the dissipation of energy via electron-phonon coupling, a process which results in a temperature elevation of the lattice. The rate of energy transfer (related to the electron-phonon coupling strength) is highly material-dependent but is generally fast, with characteristic timescales on the ps to sub-ps range [39].

The respective contribution of these relaxation channels is very difficult to disentangle since they are intimately linked. For instance, in Sect. 3.2, we show how the presence of lattice vibrations influences the creation of point defects in fused silica. However, as a main message, the current understanding of the physical processes underlying structural modification indicates that the production of heat is inevitable during FsLDW. Indeed, a scenario where the laser energy would exclusively be consumed to induce permanent structural modifications via pure electronic reorganization has never been demonstrated experimentally. Naturally, some trends can be expected. As mentioned in Sect. 2, the energy coupling from the laser to the target as well as the subsequent structural modifications are ignited by the creation of an electron-hole plasma and rely on the production of quasi-free carriers by strong field ionization, which is an intensity-dependent process, not an energy-dependent one. In this respect, the laser pulse duration seems like a legitimate control parameter to tune the amount of energy (and therefore the amount of heat) coupled into the target substrate. However, a nonzero temperature elevation of the material occurs, regardless of the briefness of the irradiating pulse duration, as shown in Fig. 21.6, where we present phase contrast microscopy pictures of laser-induced damages in the bulk of Bk7 after irradiation with a sub-10 fs duration. These results were obtained by accumulating N laser pulses at a repetition rate of 0.4 MHz. The focusing system involves reflective elements only (to preserve the pulse duration in the focal plane), and it had a numerical aperture of 0.5. Spherical aberrations and pulse distortions were kept at a minimal level by focusing at a depth of ca. 150 μm. Under such focusing conditions, the intensity distribution around the focal plane is expected to be similar to the one shown in Fig. 21.2 (neglecting the presence of nonlinear effects), with a characteristic size on the order of 1 micron in the radial direction. Strikingly, even at a modest number of laser pulses (N =10,000), the modified region extends over 20 μm in the radial direction and gradually expands as the number of pulses increases. This result indicates that the temperature distribution at the end of the excitation sequence depends on the

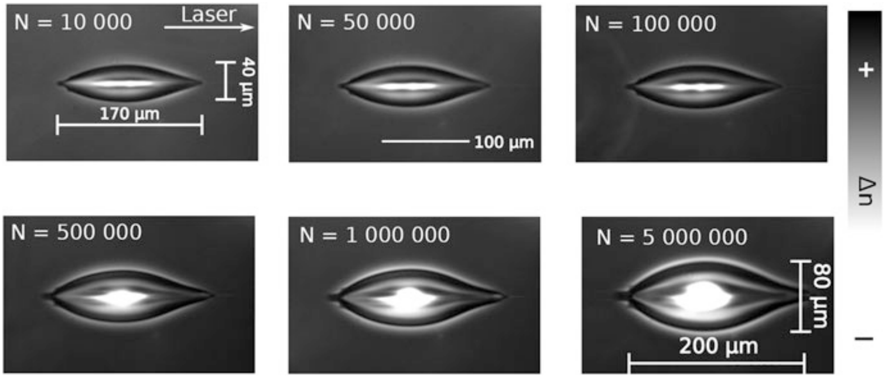

Fig. 21.6 Phase contrast microscopy pictures of laser-induced modifications obtained by accumulating N laser pulses at the same location in the volume of Bk7. The pulse duration was sub-10 fs at a repetition rate of 0.4 MHz and the pulse energy was ≈ 2.2 µJ

number of laser pulses and therefore that pulse-to-pulse heat accumulation occurs, i.e., the material does not have enough time to cool between two consecutive laser pulses.

3.2 The Ultrafast Laser Used as a Pure Heat Source

3.2.1 Single-Pulse Irradiation

A unique aspect of the laser-matter interaction, in the sub-picosecond regime, is that the energy transfer from the electron to the lattice happens before heat diffusion begins. The main consequence is an optimal on-axis temperature elevation. For instance, in fused silica, micro-Raman measurements have suggested that temperatures as high as 2700–3100 K are attained after irradiation with a single 2 µJ laser pulse [40]. In addition, the tight focusing conditions employed in FsLDW result in an energy deposition confined near the optical axis. The radial size of the laser induced by a focusing a single pulse is typically of one to a few micrometers which results in considerable temperature gradients. We recall that the cooling speed $\partial T/\partial t$ is directly proportional to the temperature gradient $\nabla^2 T(x, y, z)$:

$$\frac{\partial T}{\partial t} = D_{\mathrm{th}} \nabla^2 T(x, y, z), \tag{21.11}$$

where the proportionality coefficient D_{th} corresponds to the thermal diffusivity of the material (in units of $\mu\mathrm{m}^2\mathrm{s}^{-1}$) and is related to the material's thermal conductivity κ, to the mass density ρ, and to the heat capacity c_p according to:

$$D_{\mathrm{th}} = \frac{\kappa}{\rho c_{\mathrm{p}}}. \tag{21.12}$$

With D_{th} on the order of 0.5 $\mu\mathrm{m}^2\mathrm{s}^{-1}$ for technical glasses and initial on-axis temperatures in the range of $\approx$ 1000–3000K [40], extreme cooling rates on the order of 10^9 $\mathrm{K.s}^{-1}$ arise. To provide an example, that is comparable to the cooling rate of the universe ca. 1–100 s after the big bang.

Experimentally, heat flows in fs-laser-irradiated glasses have been studied by analyzing the morphology of the laser-induced footprint [41], by the transient lens method [42] , by pump-probe interferometry [43], or, more recently, with the help of time-resolved phase contrast microscopy [44].

The principle of time-resolved phase contrast microscopy is to exploit the temperature dependence of the refractive index $n(T)$. In most glasses, n increases with T which provides a clear contrast associated with the temperature distribution in the sample. The illumination of the microscope is ensured by a random laser synchronized with the excitation pulse in a pump-probe scheme [45]. Using a random laser as an illumination source has many advantages, such as providing a speckle-free background, high intensity, and exposure times on the order of a few nanoseconds [46].

The exquisite sensitivity of phase contrast microscopy to minute changes in the refractive index makes it an outstanding tool for visualizing the temperature evolution around the irradiated region. For instance, this method is able to resolve heat dissipation from the onset of thermal diffusion (i.e., a few ns after irradiation) until the completion of sample cooling (up to a few μs after irradiation) while also including the capability to spatially resolve the expansion dynamics of the heat front in various technical glasses. In particular, these studies have confirmed that evolution of the heat front (characterized by its radius r_{h}) can be reasonably approximated by:

$$r_h(t) = \sqrt{r_{h0}^2 + 4D_{th}t}. \tag{21.13}$$

A phase contrast snapshot of the laser-induced region is shown in Fig. 21.7a. It was acquired 1.35 μs after laser excitation of a fused silica sample by a single 70 fs laser pulse with an energy of 2.5 μJ. The red halo appearing around the optical axis shows the heat-affected zone. Panel (b) shows the aspect of the laser-induced modification after full relaxation, and the photoexcited region is represented in (c). The evolution of the heated radius observed experimentally (i.e., the radial extent of the red halo) is reported in Fig. 21.7d, together with the best least square fit of Eq. 21.13 to the experimental data. The best fit is obtained for $D_{\mathrm{th}} = 0.78\,\mu\mathrm{m}^2\mu\mathrm{s}^{-1}$, in good agreement with the value provided by the glass manufacturer ($D_{\mathrm{th}} = 0.80\,\mu\mathrm{m}^2\mu\mathrm{s}^{-1}$).

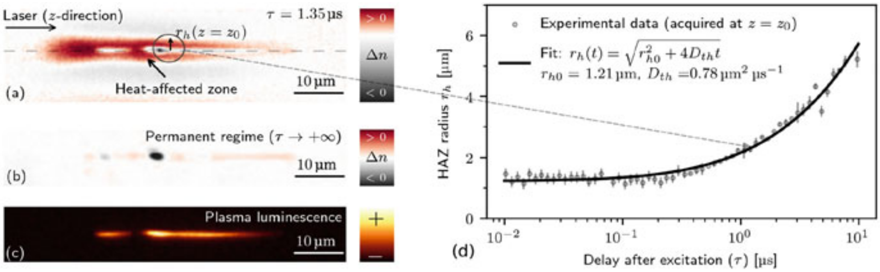

Fig. 21.7 Time-resolved imaging of thermal transients in fused silica. (**a**) Time-resolved phase contrast microscopy picture acquired 1.35 μs after excitation. (**b**) Laser-induced track in the permanent regime. (**c**) Plasma luminescence indicating the morphology of the photoexcited region. (**d**) Evolution of the radius of the heat-affected zone. The solid line represents the best least-squares fit of Eq. 21.13 to the experimental data. Reprinted by permission from Springer Nature [44]

3.2.2 Multipulse Irradiation

The control of the temperature elevation in the sample can be significantly improved by working in the multipulse irradiation scheme. When relying on multipulse irradiation, one critical parameter is the laser repetition rate. This follows from Eq. 21.13, where it can be seen that the delay between heating pulses provides some control over the width of the final irradiation product.

In general, the repetition rate of the laser should be chosen and optimized such that the temporal separation between two consecutive pulses is of the same order as the sample's cooling time (typically on the sub to the few µs timescale). This corresponds to repetition rates ranging from a few hundreds of kHz to a few MHz. In a first approximation, one can consider temperature independent thermal coefficients and write the temperature elevation in the sample after irradiation with a total number of N_{tot} laser pulses as [47]:

$$\Delta T(r, z, t) = \sum_{N=0}^{N=N_{\mathrm{tot}}} \Delta T_1\left(r, z, t - \frac{N}{\nu}\right), \tag{21.14}$$

where $\Delta T_1(r, z)$ is the temperature elevation due to a single pulse. When the final temperature exceeds the glass transition temperature T_g (ranging from ca. 600°C for multicomponent silicate glasses [48] to 1100°C for pure fused silica [49]), the local properties of the glass and, in particular, the ion mobility change drastically. Under the influence of a variety of forces (e.g., electrostatic forces, temperature gradients, concentration gradients, thermomechanical waves, etc.), the ions constituting the glass migrate into the melt. After rapid quenching due to the extreme cooling rates at play, exotic structural configurations can appear. Moreover, by alternating phases of heating and cooling, i.e., in the so-called burst processing mode, this thermal processing regime offers an outstanding degree of flexibility, with the potential to drive the sample through nonconventional thermodynamic paths.

One clear example where control of temperature gradients is of fundamental significance is the phenomenon of thermophoresis [50], an effect causing the different species present in the glass melt to move along temperature gradients, which eventually leads to species separation on the microscale. A recent study has demonstrated that a judicious choice of the sample's chemical composition enables the production of waveguides, by thermophoretic writing, with a refractive index contrast as high as 0.025 [51].

Yet another example of temperature control in multipulse irradiation is in the writing of waveguides in crystals, where a direct microdensification based on electronic excitations and smooth lattice reorganization (i.e., type I waveguides) is difficult to trigger. Instead of relying on smooth modifications induced in the photoexcited region, the waveguiding structure is obtained by inducing a tailored stress field with the help of multiple laser-induced structures called stressors. In this context, the fine control offered by the thermal accumulation mode enables the accurate manipulation of the stress state induced in the material [52], allowing the photoinscription of waveguides in almost any crystal [4]. Manipulating the stress field with the help of advanced structuring schemes is also applicable to amorphous glasses, and recently, such an approach was successfully demonstrated in fused silica [53].

In conclusion, the multipulse irradiation regime, at high repetition rates, enables a uniquely refined degree of control over the laser-induced temperature gradients and hence the structural modifications which are created by FsLDW.

3.3 *Limitations Associated with Thermal Processes and Their Possible Workarounds*

In what follows, we deliberately put the emphasis on the adverse role of thermal effects in the frame of ultrafast waveguide writing and show to what extent thermal processes can, in some scenarios, appear as a limitation.

In the first part, we select the process of laser-induced point defect formation in fused silica to illustrate that an excess of heat is sometimes counterproductive. In this scenario, thermally induced lattice vibrations can partially erase the local lattice deformations which are actually considered to be precursors to the further structural modifications leading to the local index modification in the material. In the second part, we consider the problem of heat dissipation on a wider scale and examine the limitations imposed by the presence of thermal stress. In the context of laser processing, thermal stress refers to the internal stress in the sample which results from laser-induced thermal expansion, followed by rapid cooling [47]. As such, thermal stress can expand well beyond the photo-irradiated area [47, 54]; this is in contrast to the in-plane stress created by the formation of self-ordered nanoplanes [55, 56] which result in the so-called form-induced birefringence.

3.3.1 Self-Annealing of Point Defects: The Example of Fused Silica

Formation and Relaxation of Self-Trapped Excitons (STEs) in Fused Silica

The formation of self-trapped excitons (STEs) represents an important relaxation channel in strongly coupled, wide bandgap dielectrics such as fused silica [57–60]. As a preliminary remark, we remind that even under its amorphous form, the fused silica lattice exhibits a medium-range order [61], and in what follows, the terminology *crystalline lattice* applies equally to amorphous or crystalline quartz.

Excitons can be defined as electrically neutral quasiparticles formed by a bound electron-hole pair. In general, excitons have a nonzero mobility, allowing them to diffuse from one unit cell to another. The relaxation of an exciton involves a stabilization [62] (as opposed to diffusion) of the hole under the influence of a potential trap. In fused silica, these potential traps appear when the position of one oxygen atom deviates from its position in a perfect crystal. Such a scenario is called exciton localization by disorder [63].

The presence of STEs induces important distortions of the crystal lattice [64], and the relaxation of these STEs further results in the formation of point defects such as E' centers (oxygen vacancies) and non-bridging oxygen hole centers (NBOHCs) with energy levels located deep within the bandgap, as represented in Fig. 21.8a.

Thermally Induced Detrapping of Excitons

Until recently, the self-trapping rate in SiO_2 was assumed to be independent of the excitation intensity and of the carrier density. However, recent studies have reported an intensity-dependent trapping rate (see Fig. 21.8b) that was attributed to vibration-induced back conversion of STEs into quasi-free electron-hole pairs and a reduction of the trapping probability [65]. This was caused by the high ponderomotive energy associated with the comparably long laser wavelength used in this study ($\lambda = 2100$ nm). The effect of thermal detrapping is well studied in the scientific literature (see, for example, [66, 67]) indicating that an abundance of vibrational energy prevents the efficient modification of the structural properties of the solid.

3.3.2 Thermal Stress

Polarization Dependence of fs-Laser-Induced Optical Structures in Straight Waveguides

The presence of stress may pose serious challenges in the context of waveguiding because the presence of a stress field results by definition in a nonhomogeneous and possibly anisotropic refractive index distribution. This observation applies to all classes of waveguides, regardless of the fabrication method. For this reason, the

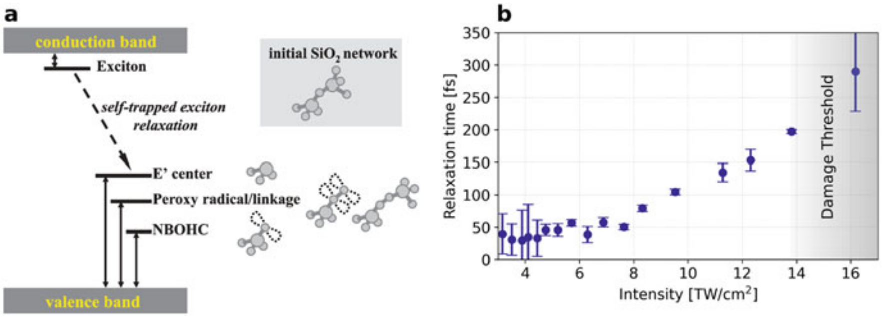

Fig. 21.8 Illustration of point defect formation through the relaxation of self-trapped excitons. (**a**) Energy diagram of light-induced defect formation in SiO_2 together with the molecular structure associated with the formation of point defects. Reprinted by permission from Springer Nature [62]. (**b**) Ultrafast relaxation time of an electron-hole plasma generated in fused silica as a function of laser intensity. Reprinted from [65], with the permission of AIP Publishing

relations between stress and waveguiding properties have been extensively studied in the broad context of optical waveguiding [68].

Isotropic stress (mostly appearing in type I modifications) is co-substantial to laser-induced microcompaction, with little to no consequence on the polarization behavior of the optical structures. Anisotropic stress, however, is typically observed in type II regime and results in highly polarization-dependent properties. In particular, anisotropic stress is observed in the so-called double-line configuration, where the waveguiding region is formed by the superposition of two stress fields created by two distinct laser-written microstructures used as stressors [4, 69], such as depicted in Fig. 21.1b. One common workaround is to use not only two but a multitude of stressors distributed in a circular configuration (as exemplified in Fig. 21.9a), at the expense of an increased fabrication time, a larger laser footprint, and a higher risk of impairing the mechanical integrity of the substrate (e.g., crack formation).

Curved Waveguides

One important limitation of FsLDW occurs when fabricating curved (or bent) waveguides. Bent waveguides are the building blocks of the so-called S-shaped structures which are commonly used in integrated optics to laterally displace the guided beam. Obtaining radii of curvature (ROC) as small as possible enables a higher integration density and ultimately a drastic reduction of the photonic chip footprint. The minimum ROC attainable while retaining low-loss waveguiding mainly depends on the waveguide lateral dimension D_{co} and on the refractive index difference Δn between the indices of the core and the cladding. In the context of FsLDW, Δn ranges from ca. 0.001 to 0.01, and D_{co} is typically on the order of a few microns. Bent waveguides with such parameters are in principle capable

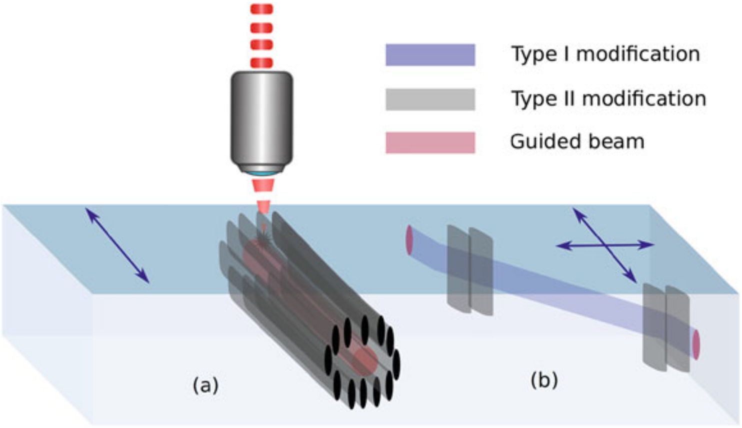

Fig. 21.9 Scheme illustrating the presence of multiple stressors used to tailor the stress distribution in the waveguiding region in the case of (**a**) a straight waveguide and (**b**) a curved waveguide. The blue arrows indicate the direction of the sample translation

of providing low-loss (≈ 0.087 dB), monomode waveguiding at a wavelength of 633 nm down to ROCs as small as 1 mm [70]. However, the ROC values usually encountered in the literature lie in the range of one to several tens of mm (see, for instance, [71–74]). The reasons for this modest performance have not yet been fully elucidated. As a tentative explanation, one might consider that according to the Fourier law, the kinetics of heat dissipation strongly depends on the temperature gradient. Consequently, the cooling rates in the inner and in the outer arcs of the structure are different which results in uneven thermal stress fields and a nonsymmetric index profile.

Following the strategies developed to overcome stress-induced birefringence in straight waveguides (see previous paragraph), bend losses can be significantly reduced (from ≈ 2.7 dB to ≈ 0.3 dB according to [75]) by judiciously placing stressors near the bent waveguide (see Fig. 21.9b for an illustration of that concept).

Another approach consists in erasing the residual stress present around the irradiated region with the help of an advanced annealing strategy [71]. Beyond the fact that a second fabrication step is de facto required, additional studies would be needed to possibly extend this method to a broad selection of substrate materials.

Observation of Long-Range Stress in Waveguide Lattices

Waveguide lattices are periodic arrays of waveguides with a separation such as to allow partial evanescent coupling. The distance between two neighboring waveguides is typically in the 10 µm range. Lately, waveguide lattices have triggered a tremendous interest in the research community at least for two reasons. Firstly, waveguide lattices enable to finely engineer the dispersion and diffraction of light and observe nonconventional light propagation schemes [76, 77]. Secondly, these systems can be used as powerful quantum simulators, thereby enabling the experimental verification of theoretical predictions otherwise hard to verify [78].

Although conventional 1D lithography [76] and photorefractive induction [79] were used as pioneering methods, FsLDW has gained considerable attention, mostly thanks to its three-dimensional and rapid prototyping capabilities [80].

Recently, studies carried out on laser-induced waveguide arrays in a gallium lanthanum sulfide glass have shown that laser-induced neighboring waveguides fabricated in the very same irradiation conditions can exhibit different propagation constants [81]. Such a discrepancy is attributed to a perturbation of the refractive index distribution due to the presence of a long-range stress arising from the nearest (laser-induced) waveguide. As a workaround, the authors have demonstrated the possibility to play on the scanning velocity during FsLDW to optimize the stress distribution and increase the overall symmetry of the waveguide array.

Processing Near Interfaces

Surface waveguides are crucial components required to expand the capabilities of photonic integrated circuits because they interface their environment with the internal optical circuitry. For instance, surface waveguides can be used as evanescent field (bio-)sensors [82, 83] or as couplers for photon-plasmon interactions [84]. Furthermore, the combination of a surface waveguide and a plasmonic transducer provides an attractive platform for surface plasmon resonance sensing, an increasingly popular method for virus detection [85, 86].

In addition to the consequences on the optical properties of the laser-induced microstructures, thermal stress can also impair the mechanical properties of the sample. In particular, thermal stress results in surface swelling [55], surface cracking [87], and ablation [88], especially when microprocessing non-doped glasses near the surface up to focusing depths of 75 μm as shown in Fig. 21.10. That behavior might be problematic when working in thin samples. One possible explanation is that the modest thermal conductivity of air (a factor of ca. 60 compared to fused silica) does not allow efficient heat dissipation and leads to an important accumulation of the thermal load near the surface.

Several strategies have been proposed to photoinscribe waveguides on the surface of glassy substrates. The first approach uses ion-doped glasses as a host, either to improve the photosensitivity (for instance, by adding silver ions [90]) or to improve the mechanical resistance of the substrate to thermal stress (tempered glass) [87] (see Fig. 21.10). One limitation of this approach is that the doping agents can exhibit optical activity (fluorescence or photoluminescence emission) which might degrade the quality of the desired optical signal. Another method consists in bonding an index-matched glass coverslip onto the surface of the sample [91]. However, this approach seems challenging to apply to nonplanar geometries. Finally, direct laser writing of surface waveguides in pure fused silica has been successfully demonstrated by focusing few-cycle pulses (i.e., with a

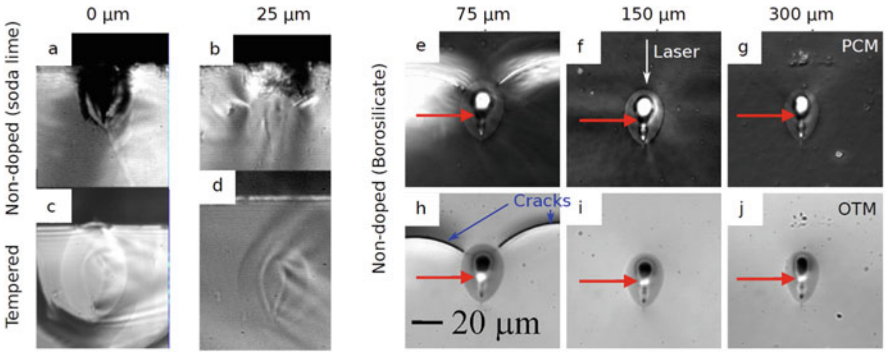

Fig. 21.10 Examples of ablation (left) and crack formation (right) when working near the surface. The laser is focused from the top. The distance between the top of the optical microstructure and the surface is indicated on top of the pictures. Red arrows indicate guiding regions (**a**–**d**): FsLDW in soda lime glass (**a**, **b**) and in a tempered glass (**c**, **d**). Reprinted with permission from [87] ©The Optical Society. (**e**–**j**): Phase contrast (PCM, panels **e**–**g**) and optical transmission microscopy (OTM, panels **h**–**j**) micrographs of laser-induced waveguides in a non-doped borosilicate glass for different writing depths. Increasing the writing depth to ca. 150 µm or more (see **f**–**g** and **i**–**j**) provides a damage-free result. Adapted with permission from [89] ©The Optical Society

duration $<$ 10 fs) at grazing incidence directly on the sample's surface [11] (see Fig. 21.11b–d). Since less energy is necessary to trigger structural modifications in the few-cycle regime (because the extremely short-pulse duration allows one to easily obtain the intensities required for SFI), the associated thermal effects are in turn greatly reduced. The interaction regime triggered in such an experimental scheme is characterized by the absence of ablation and the presence of surface microcompaction as determined by micro-Raman measurements. In contrast to the +250 nm surface swelling observed when using longer pulses [55] (see Fig. 21.11a), atomic force microscopy measurements of the sample's surface topography reveal the presence of a -10 nm variation in the center of the few-cycle irradiated region, as shown in Fig. 21.11b.

4 Conclusion

In this chapter, the limits of ultrafast waveguide writing were examined. Firstly, we have emphasized that the tight focusing of ultrashort laser pulses results in an asymmetric focal volume because (1) the NA of dry focusing systems is limited, (2) the presence of a planar air/dielectric interface in the region where the laser beam converges results in spherical aberrations, and (3) the nonlinear response of the material, combined with the macroscopic polarization and generation of quasi-free carriers, alters the profile upon propagation. Secondly, we have emphasized the omnipresence of heat production during direct laser writing and proposed

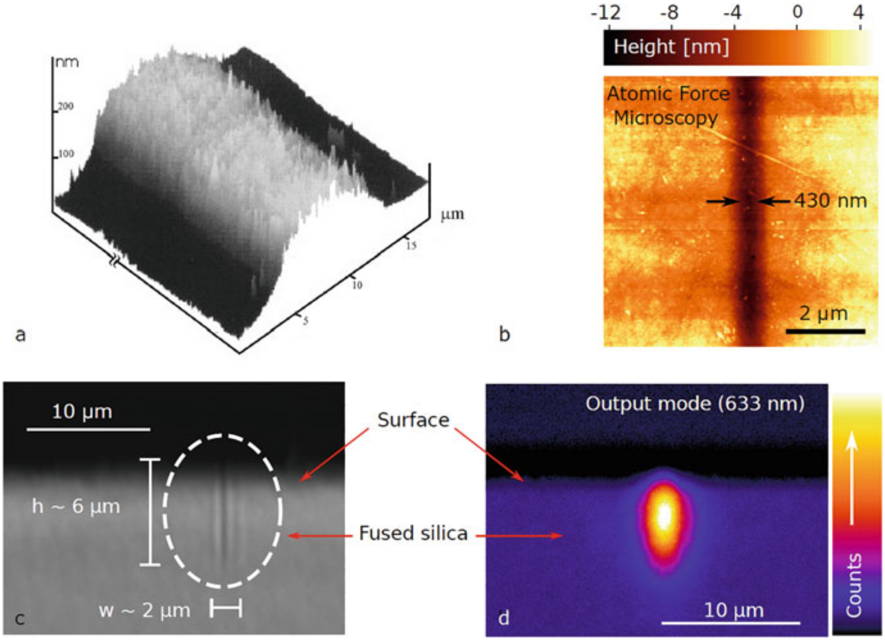

Fig. 21.11 (**a**) Surface swelling reported upon FsLDW with 50 fs pulses at normal incidence. Reprinted with permission from [55] ©The Optical Society. (**b**–**d**): results obtained with few-cycle pulses at grazing incidence. (**b**) Atomic force microscopy topography variations of the irradiated surface. (**c**) Side view of the laser-induced microstructure and (**d**) corresponding guided mode at 633 nm. Panels (**b**–**d**) reprinted with permission from [11] ©The Optical Society

experimental strategies to visualize the evolution of the heat-affected zone. We have established that the associated thermal stress can be either beneficial or detrimental.

The conjugated effects of these two aspects impose some limitations on direct laser waveguide writing: (1) it is difficult to produce mode-matched, polarization-independent waveguides with a round cross section, (2) curved waveguides with low losses and small ROC are hard to fabricate, (3) writing waveguides deep into the volume is not straightforward, and (4) the photoinscription of surface waveguides in non-doped glasses requires using few-cycle pulses or, when possible, the adjunction of an index-matched top layer.

In this chapter, we have evidenced that femtosecond laser direct writing of optical waveguides in dielectrics possesses limitations which arise from the fundamental processes at play. However, for each limitation identified, workaround strategies have been developed by researchers. As a main outlook, one should retain that a combination of the continuous improvement of the laser sources (either few-cycle and/or possibly in the UV region) and adaptive optical components (such as SLMs) together with a better understanding of the basic mechanisms underlying the laser-matter interaction will help sustain the development of smart strategies to continue improving the capabilities of ultrafast writing of waveguides.

References

1. K. Okamoto, in *Fundamentals of Optical Waveguides (Second Edition)*, ed. by K. Okamoto, 2nd edn. (Academic Press, Burlington, 2006), pp. 417–534
2. A.L. Washburn, R.C. Bailey, Analyst **136**(2), 227 (2011)
3. R.G. Hunsperger, *Losses in Optical Waveguides* (Springer New York, New York, NY, 2009), pp. 107–128
4. F. Chen, J.R.V. de Aldana, Laser Photonics Rev. **8**(2), 251 (2014)
5. A. Baum, P.J. Scully, M. Basanta, C.L.P. Thomas, P.R. Fielden, N.J. Goddard, W. Perrie, P.R. Chalker, Opt. Lett. **32**(2), 190 (2007)
6. C. Florea, K.A. Winick, J. Lightwave Technol. **21**(1), 246 (2003)
7. H. Ma, A. Jen, L. Dalton, Adv. Mater **14**(19), 1339 (2002)
8. G.C. Righini, A. Chiappini, Opt. Eng. **53**, 53 (2014)
9. K.M. Davis, K. Miura, N. Sugimoto, K. Hirao, Opt. Lett. **21**(21), 1729 (1996)
10. M. Beresna, M. Gecevičius, P.G. Kazansky, Adv. Opt. Photon. **6**(3), 293 (2014)
11. F.J. Furch, W.D. Engel, T. Witting, A. Perez-Leija, M.J.J. Vrakking, A. Mermillod-Blondin, Opt. Lett. **44**(17), 4267 (2019)
12. S. Gross, M. Dubov, M.J. Withford, Opt. Express **23**(6), 7767 (2015)
13. A. Schiffrin, T. Paasch-Colberg, N. Karpowicz, V. Apalkov, D. Gerster, S. Muhlbrandt, M. Korbman, J. Reichert, M. Schultze, S. Holzner, J.V. Barth, R. Kienberger, R. Ernstorfer, V.S. Yakovlev, M.I. Stockman, F. Krausz, Nature **493**(7430), 70 (2013)
14. S.A. Self, Appl. Opt. **22**(5), 658 (1983)
15. V. Diez-Blanco, J. Siegel, A. Ferrer, A. Ruiz de la Cruz, J. Solis, Appl. Phys. Lett. **91**(5), 051104 (2007)
16. G. Vdovin, F. van Goor, *Lightpipes: Beam Propagation Toolbox*. https://opticspy.github.io/lightpipes
17. Q. Sun, H. Jiang, Y. Liu, Y. Zhou, H. Yang, Q. Gong, J. Opt. A Pure Appl. Opt. **7**(11), 655 (2005)
18. N. Huot, R. Stoian, A. Mermillod-Blondin, C. Mauclair, E. Audouard, Opt. Express **15**(19), 12395 (2007)
19. C. Hnatovsky, R.S. Taylor, E. Simova, V.R. Bhardwaj, D.M. Rayner, P.B. Corkum, J. Appl. Phys. **98**(1), 013517 (2005)
20. R.W. Boyd, in *Nonlinear Optics (Fourth Edition)*, ed. by R.W. Boyd, 4th edn. (Academic Press, 2020), pp. 321–380
21. G. Fibich, A.L. Gaeta, Opt. Lett. **25**(5), 335 (2000)
22. R. Cauble, W. Rozmus, Phys. Fluids (United States) **28**(11), 759 (1985)
23. P. Jürgens, B. Liewehr, B. Kruse, C. Peltz, D. Engel, A. Husakou, T. Witting, M. Ivanov, M.J.J. Vrakking, T. Fennel, A. Mermillod-Blondin, Nat. Phys. **16**(10), 1035 (2020)
24. K. Sokolowski-Tinten, D. von der Linde, Phys. Rev. B **61**, 2643 (2000)
25. Y. Cheng, K. Sugioka, K. Midorikawa, M. Masuda, K. Toyoda, M. Kawachi, K. Shihoyama, Opt. Lett. **28**(1), 55 (2003)
26. P.S. Salter, A. Jesacher, J.B. Spring, B.J. Metcalf, N. Thomas-Peter, R.D. Simmonds, N.K. Langford, I.A. Walmsley, M.J. Booth, Opt. Lett. **37**(4), 470 (2012)
27. M. Ams, G.D. Marshall, D.J. Spence, M.J. Withford, Opt. Express **13**(15), 5676 (2005)
28. S.H. Wiersma, T.D. Visser, P. Török, Pure Appl. Opt. J. Eur. Opt. Soc. A **7**(5), 1237 (1998)
29. J. Gottmann, M. Hörstmann-Jungemann, M. Hermans, D. Beckmann, J. Laser Micro/Nanoeng. **4**, 192 (2009)
30. P.S. Salter, M.J. Booth, Light Sci. Appl. **8**(1), 110 (2019)
31. C. Mauclair, A. Mermillod-Blondin, N. Huot, E. Audouard, R. Stoian, Opt. Express **16**(8), 5481 (2008)
32. G. Zhu, J. van Howe, M. Durst, W. Zipfel, C. Xu, Opt. Express **13**(6), 2153 (2005)
33. F. He, H. Xu, Y. Cheng, J. Ni, H. Xiong, Z. Xu, K. Sugioka, K. Midorikawa, Opt. Lett. **35**, 1106 (2010)

34. R. Kammel, R. Ackermann, J. Thomas, J. Gotte, S. Skupin, A. Tunnermann, S. Nolte, Light Sci. Appl. **3**, e169 (2014)
35. D.N. Vitek, D.E. Adams, A. Johnson, P.S. Tsai, S. Backus, C.G. Durfee, D. Kleinfeld, J.A. Squier, Opt. Express **18**(17), 18086 (2010)
36. T.E. Lanier, J.R. Gulley, J. Opt. Soc. Am. B **33**(2), 292 (2016)
37. J. Burghoff, S. Nolte, A. Tünnermann, Appl. Phys. A **89**(1), 127 (2007)
38. H.T. Bookey, R.R. Thomson, N.D. Psaila, A.K. Kar, N. Chiodo, R. Osellame, G. Cerullo, IEEE Photon. Technol. Lett. **19**(12), 892 (2007)
39. A. Mermillod-Blondin, J. Bonse, A. Rosenfeld, I.V. Hertel, Y.P. Meshcheryakov, N.M. Bulgakova, E. Audouard, R. Stoian, Appl. Phys. Lett. **94**(4), 041911 (2009)
40. T. Yoshino, Y. Ozeki, M. Matsumoto, K. Itoh, Jpn. J. Appl. Phys. **51**(10R), 102403 (2012)
41. M. Shimizu, M. Sakakura, M. Ohnishi, M. Yamaji, Y. Shimotsuma, K. Hirao, K. Miura, Opt. Express **20**(2), 934 (2012)
42. M. Sakakura, M. Terazima, Y. Shimotsuma, K. Miura, K. Hirao, Opt. Express **15**(25), 16800 (2007)
43. V.V. Kononenko, E.V. Zavedeev, M.I. Latushko, V.I. Konov, Laser Phys. Lett. **10**(3), 036003 (2013)
44. J. Bonse, T. Seuthe, M. Grehn, M. Eberstein, A. Rosenfeld, A. Mermillod-Blondin, Appl. Phys. A **124**(1), 60 (2017)
45. A. Mermillod-Blondin, H. Mentzel, A. Rosenfeld, Opt. Lett. **38**, 4112 (2013)
46. B. Redding, M.A. Choma, H. Cao, Nature Photonics **6**, 355 (2012)
47. M. Shimizu, M. Sakakura, M. Ohnishi, Y. Shimotsuma, T. Nakaya, K. Miura, K. Hirao, J. Appl. Phys. **108**(7), (2010)
48. V.M. Fokin, E.D. Zanotto, J.W. Schmelzer, J. Non-Cryst. Solids **321**(1), 52 (2003)
49. R. Brückner, J. Non-Cryst. Solids **5**(2), 123 (1970)
50. S. Duhr, D. Braun, Proc. Natl. Acad. Sci. **103**(52), 19678 (2006)
51. M. Macias-Montero, F. Muñoz, B. Sotillo, J. del Hoyo, R. Ariza, P. Fernandez, J. Siegel, J. Solis, Sci. Rep. **11**(1), 8390 (2021)
52. Y. Bellouard, A. Champion, B. McMillen, S. Mukherjee, R.R. Thomson, C. Pépin, P. Gillet, Y. Cheng, Optica **3**(12), 1285 (2016)
53. Q. Sun, T. Lee, M. Beresna, G. Brambilla, Sci. Rep. **10**(1), 3819 (2020)
54. B. Poumellec, L. Sudrie, M. Franco, B. Prade, A. Mysyrowicz, Opt. Express **11**(9), 1070 (2003)
55. V.R. Bhardwaj, P.B. Corkum, D.M. Rayner, C. Hnatovsky, E. Simova, R.S. Taylor, Opt. Lett. **29**(12), 1312 (2004)
56. Y. Shimotsuma, M. Sakakura, P.G. Kazansky, M. Beresna, J. Qiu, K. Miura, K. Hirao, Adv. Mater. **22**(36), 4039 (2010)
57. C. Itoh, K. Tanimura, N. Itoh, J. Phys. C Solid State Phys. **21**(26), 4693 (1988)
58. P. Audebert, P. Daguzan, A. Dos Santos, J.C. Gauthier, J.P. Geindre, S. Guizard, G. Hamoniaux, K. Krastev, P. Martin, G. Petite, A. Antonetti, Phys. Rev. Lett. **73**, 1990 (1994)
59. P. Martin, S. Guizard, P. Daguzan, G. Petite, P. D'Oliveira, P. Meynadier, M. Perdrix, Phys. Rev. B **55**, 5799 (1997)
60. S. Guizard, P. Martin, P. Daguzan, G. Petite, P. Audebert, J.P. Geindre, A.D. Santos, A. Antonnetti, Europhys. Lett. (EPL) **29**(5), 401 (1995)
61. P.H. Gaskell, D.J. Wallis, Phys. Rev. Lett. **76**, 66 (1996)
62. S.S. Mao, F. Quéré, S. Guizard, X. Mao, R.E. Russo, G. Petite, P. Martin, Appl. Phys. A **79**(7), 1695 (2004)
63. A.J. Fisher, W. Hayes, A.M. Stoneham, Phys. Rev. Lett. **64**, 2667 (1990)
64. A.N. Trukhin, Nucl. Instrum. Methods Phys. Res. Sect. B **91**(1), 334 (1994)
65. P. Jürgens, M. Vrakking, A. Husakou, R. Stoian, A. Mermillod-Blondin, Appl. Phys. Lett. **115**(19), 191903 (2019)
66. J. Zhang, S. Taylor, W. Eccleston, J. Appl. Phys. **72**(4), 1429 (1992)
67. K. Said, G. Moya, A.S. Ahmed, G. Damamme, A. Kallel, Appl. Surf. Sci. **361**, 226 (2016)
68. M. Huang, Int. J. Solids Struct. **40**(7), 1615 (2003)
69. A. Courvoisier, M.J. Booth, P.S. Salter, Appl. Phys. Lett. **109**(3), 031109 (2016)

70. E.A.J. Marcatili, Bell Syst. Tech. J. **48**(7), 2103 (1969)
71. A. Arriola, S. Gross, N. Jovanovic, N. Charles, P.G. Tuthill, S.M. Olaizola, A. Fuerbach, M.J. Withford, Opt. Express **21**(3), 2978 (2013)
72. L.A. Fernandes, J.R. Grenier, P.R. Herman, J.S. Aitchison, P.V.S. Marques, Opt. Express **19**(13), 11992 (2011)
73. I.V. Dyakonov, I.A. Pogorelov, I.B. Bobrov, A.A. Kalinkin, S.S. Straupe, S.P. Kulik, P.V. Dyakonov, S.A. Evlashin, Phys. Rev. Appl. **10**, 044048 (2018)
74. G. Corrielli, S. Atzeni, S. Piacentini, I. Pitsios, A. Crespi, R. Osellame, Opt. Express **26**(12), 15101 (2018)
75. Z. Liu, Y. Liao, Z. Fang, W. Chu, Y. Cheng, Sci. China Phys. Mech. Astron. **61**(7), 70322 (2018)
76. H.S. Eisenberg, Y. Silberberg, R. Morandotti, A.R. Boyd, J.S. Aitchison, Phys. Rev. Lett. **81**, 3383 (1998)
77. D.N. Christodoulides, F. Lederer, Y. Silberberg, Nature **424**(6950), 817 (2003)
78. A. Szameit, S. Nolte, J. Phys. B At. Mol. Opt. Phys. **43**(16), 163001 (2010)
79. J.W. Fleischer, M. Segev, N.K. Efremidis, D.N. Christodoulides, Nature **422**(6928), 147 (2003)
80. T. Meany, M. Gräfe, R. Heilmann, A. Perez-Leija, S. Gross, M.J. Steel, M.J. Withford, A. Szameit, Laser Photon. Rev. **9**(4), 363 (2015)
81. R. Diener, S. Nolte, T. Pertsch, S. Minardi, Appl. Phys. Lett. **112**(11), 111908 (2018)
82. A.M. Hutchinson, Mol. Biotechnol. **3**(1), 47 (1995)
83. M. Estevez, M. Alvarez, L. Lechuga, Laser Photon. Rev. **6**(4), 463 (2012)
84. X. Guo, M. Qiu, J. Bao, B.J. Wiley, Q. Yang, X. Zhang, Y. Ma, H. Yu, L. Tong, Nano Lett. **9**(12), 4515 (2009)
85. A.M. Shrivastav, U. Cvelbar, I. Abdulhalim, Communications Biology **4**(1), 70 (2021)
86. M. Soler, M.C. Estevez, M. Cardenosa-Rubio, A. Astua, L.M. Lechuga, ACS Sensors **5**(9), 2663 (2020). PMID: 32786383
87. J. Lapointe, M. Gagné, M.J. Li, R. Kashyap, Opt. Express **22**(13), 15473 (2014)
88. G.A. Torchia, P.F. Meilán, A. Rodenas, D. Jaque, C. Mendez, L. Roso, Opt. Express **15**(20), 13266 (2007)
89. S.M. Eaton, M.L. Ng, J. Bonse, A. Mermillod-Blondin, H. Zhang, A. Rosenfeld, P.R. Herman, Appl. Opt. **47**, 2098 (2008)
90. A. Abou Khalil, J.P. Bérubé, S. Danto, J.C. Desmoulin, T. Cardinal, Y. Petit, R. Vallée, L. Canioni, Sci. Rep. **7**(1), 11124 (2017)
91. J.P. Bérubé, R. Vallée, Opt. Lett. **41**(13), 3074 (2016)

Chapter 22
Multi-Photon 3D Lithography and Calcination for sub-100-nm Additive Manufacturing of Inorganics

Greta Merkininkaitė, Edvinas Aleksandravičius, Simonas Varapnickas, Darius Gailevičius, Simas Šakirzanovas, and Mangirdas Malinauskas

Abstract Development of 3D micro-/nanostructures leads to device miniaturization, enhanced function, and advanced integration opportunities in the fields of photonics, micro-fluidics, micro-mechanics, micro-electronics, and micro-optics. Multi-photon lithography (also widely known as two-photon polymerization) as a laser direct writing technique offers the flexibility to rapidly prototype 3D structure for additive manufacturing. Recent developments of this ultrafast laser technique together with the advances in material science allowed routine 3D printing of inorganic structures via a combination of mask-less photopolymerization and thermal post-treatment (pyrolysis and/or calcination). The present achievements are very promising for technical applications where highly resilient structures (made out of inert and durable materials) are required to withstand harsh environments, for high-intensity optics applications in open space industry.

In this chapter, the physical and chemical principles for 3D nanostructuring of inorganics are covered via laser lithography of hybrid and composite materials with subsequent post-treatment. The most recent advances are overviewed, and the major achievements are highlighted including resilient sub-100-nm feature fabrication made of crystalline nanostructures, with a high refractive index and transparency.

G. Merkininkaitė
Faculty of Chemistry and Geoscience, Vilnius University, Vilnius, Lithuania

Femtika, Vilnius, Lithuania
e-mail: greta.merkininkaite@chgf.vu.lt

E. Aleksandravičius · S. Varapnickas · D. Gailevičius · M. Malinauskas (✉)
Laser Research Center, Physics Faculty, Vilnius University, Vilnius, Lithuania
e-mail: edvinas.aleksandravicius@ff.vu.lt; simonas.varapnickas@ff.vu.lt;
darius.gailevicius@ff.vu.lt; mangirdas.malinauskas@ff.vu.lt

S. Šakirzanovas
Faculty of Chemistry and Geoscience, Vilnius University, Vilnius, Lithuania

Department of Chemical Engineering and Technology, Center for Physical Sciences and Technology, Vilnius, Lithuania
e-mail: simas.sakirzanovas@chf.vu.lt

© The Author(s), under exclusive license to Springer Nature Switzerland AG 2023
R. Stoian, J. Bonse (eds.), *Ultrafast Laser Nanostructuring*, Springer Series
in Optical Sciences 239, https://doi.org/10.1007/978-3-031-14752-4_22

Advances and limitations within the context of the emerging trends and potential near-future applications are discussed in detail.

Keywords Ultrafast laser · 3D nanostructuring · Two-photon polymerization · Non-linear lithography · Post-processing · hybrid polymers; SZ2080$^{\mathrm{TM}}$ · Inorganics

Abbreviations

3D	Three dimensional
λ	Wavelength
τ	Pulse duration
f	Frequency
P_{avg}	Average measured laser beam power
v	Scan velocity
AAAPs	α-amino-alkylaceto-phenones
AESO	Acrylated epoxidized soy oil
D	Donor
DFW	Dynamic fabrication window
DH	Donor hydrogen
DIW	Extrusion-based direct ink writing
DLP	Digital light processing
fs	Femtosecond
FW	Fabrication window
HAPs	Hydroxy-aceto-phenones
IJP	Inkjet-based inkjet printing
LDW	Laser direct write
M	Monomer
MEMS	Microelectromechanical systems
MMMP	Methyl-1-(4-methylthio)phenyl-2-morpholinopropan-1-one
MPL	Multi-photon lithography
NEMS	Nanoelectromechanical systems
PI	Photoinitiator
R	Radical
SL	Stereolithography
STED	Stimulated emission depletion
TPP	Two-photon polymerization

1 Introduction

Multi-photon 3D lithography [1] (specifically, two-photon polymerization TPP [2]) is already a well-established technique among scientists and readily available in the industry [3]. Its versatility meets the requirements for a plethora of micro- and nano-scale applications where true 3D structures and high-feature definition are needed [4]. It can be extended to larger dimensions of up to mm-scales (upscaled) with a wide variety of materials to choose from [5, 6].

By definition, the outcomes of the photopolymerization processes are inherently related to the spectrum of cross-linkable materials. The materials can be purely organic or at least have some organic constituents [7]. This is indeed acceptable to a great extent for prototyping and additive manufacturing of micro-optics, nanophotonics, micro-fluidics, micro-mechanics, biomedicine, sensor, and diverse templating (master or mask-making) applications [8]. However, organic or enhanced hybrid organic–inorganic resins have limited their laser direct write (LDW) empowered advantages for manufacturing complex architectures and especially integrated devices. Such devices must feature high performance and durability under harsh conditions.

On the other hand, glasses, ceramics, and crystals offer unique properties as technical materials for high resilience, transparency, and low-inertia materials. Thus, technology for making inorganic structures has been developed to meet these needs. The first example is sol–gel (solid–gel) chemistry and its combination with high-temperature post-processing. The former relates to pyrolysis (from the Greek-derived element *pyro*—fire and *lysis*—separating) and calcination (derives its name from the Latin *calcinare*—meaning to burn lime). Pyrolysis starts from $>400\,^\circ$C with an inertial atmosphere (vacuum, nitrogen, argon) as organic molecules are chemically altered and then evaporate. In contrast, calcination typically requires a higher temperature and an air (oxidative) atmosphere to change the material to a completely inorganic substance. In addition, these are not the only observable effects. For sol–gel resists, designed for multi-photon polymerization, heat treatment with increasing temperature causes an increase in the cross-linking degree (hard bake), partial material removal, and densification together with geometrical downscaling. Furthermore, at elevated temperatures $>1000\,^\circ$C) inorganic glass–ceramic material phases can be observed followed by the emergence of crystalline phases. This, besides being a very interesting study object on its own, together with the inevitable shrinkage, can produce unique advantages (or disadvantages). It may depend on the application; however, this offers simultaneous geometry and material tuning to produce devices unachievable using different methods.

Up to now, the 3D printing of sol–gel materials and manufacturing of inorganic structures were limited to the micro-scale. However, recent advances in femtosecond laser material processing enabled research achieving features on the nano-scale. With a combination of ultrafast lasers (both, short pulses and high repetition rates), the 3D lithography is becoming a precision additive manufacturing tool with ∼100-nm spatial definition (resolution) on demand (see for instance Chap. 12

by S. Juodkazis). And combined with pyrolysis/calcination post-treatment enables reaching extreme scales of sub-100 nm and fabrication of true inorganic features. This is a milestone achievement in ultrafast laser nanostructuring, and in the following sections will be discussed in detail in respect of physical–chemical principles, technological realization, examples of novel emerging applications, and a future outlook.

1.1 Physical Principles of Nano-Localized Photopolymerization

A non-linear thresholded photoresponse of polymeric material is exploited for the laser direct write (LDW)) 3D nanopolymerization [6, 8] as shown in Fig. 22.1. The photo-excitation of the organic monomer (prepolymer) molecules can be utilized as a linear, non-linear, super-linear light–matter interaction via single-photon, two-photon, three-photon absorption mechanisms. Additionally, during exposure, avalanche ionization and thermal accumulation might occur. The interplay between these processes is not trivial. To illustrate this, one could consider the process of two-photon polymerization. In theory, if the photon energy is at least half of the energy bandgap, two-photon absorption could be responsible for the irreversible modification converting monomers to polymers through radical polymerization (or adequate cross-linking reactions). In practice, it rarely occurs exclusively and competes with single- or three-photon absorption (depending on the applied exposure wavelength) and avalanche ionization (depends mostly on pulse duration) as well as thermal accumulation (depends a lot on pulse repetition rate). This topic is still under debate, as diverse light sources, polymer materials, and photo-initiating systems, or even exposure strategies have been exploited. Although the technique is being widely used and commercially established, still intensive research effort is being invested to better understand the fundamental processes. This is illustrated in some recent prominent review papers on that topic [6, 9]. Furthermore, a decade-long dispute about the dominant mechanisms is still in progress via original research dedicated papers [10, 11].

Nevertheless, most often a local localized photo-chemical modification (Fig. 22.2) can be achieved by optimizing light exposure parameters. Usually, this includes intensity I [W/cm^2] and corresponding energy dose D [J] for the specific material to fit within the fabrication window (FW, or a dynamic DFW taking into account the ratio of damage and initiation thresholds). Fine-tuning these values can ensure fine 3D structuring (Fig. 22.4). The final feature dimensions and resulting resolution will depend on the interplay between laser exposure (I, D), material response (sensitivity, diffusion), and geometrical rigidity (architecture)—thus in turn will be defined by physical, chemical, and engineering thresholds [6]. The routinely observed spatial dimensions of single voxels are down to 100-nm lateral and 300-nm longitudinal dimensions. And the production throughput can reach tens of thousands of individual voxels per second, which makes it an extremely efficient precision additive manufacturing tool [5, 12].

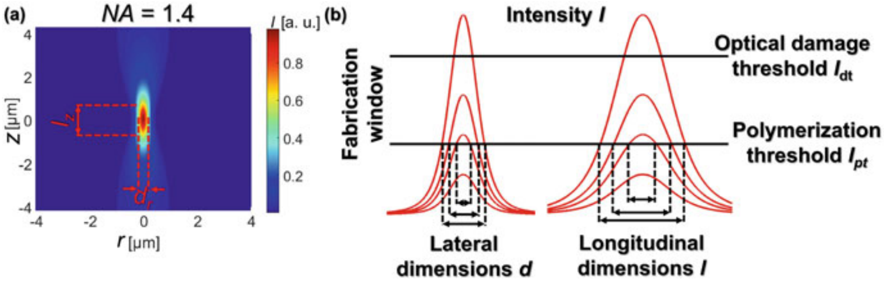

Fig. 22.1 Non-linear thresholded photoresponse of a photopolymer (prepolymer) material confined by the incident light' s intensity spatial distribution. (**a**) Light intensity distribution using NA = 1.4 immersion oil objective. The photomodified volume is defined by the lateral d_r and axial l_z isointensity region exceeding the non-linear absorption threshold (corresponding to the highest photon density). The *voxel* (volumetric pixel) is elongated along beam propagation direction following the incident energy density distribution. r and z depict realistic probable dimensions in spatial units, while I is normalized. (**b**) Scaling by intensity tuning: lateral and longitudinal dimensions, respectively. By adjusting the incident laser I fitting within the polymerization threshold (irreversible photomodification) and damage threshold (bubbling, explosions, uncontrolled burning), one can linearly vary the cross-linked volume from sub-wavelength to wavelength dimensions (lateral). The axial dimensions will be enlarged depending on the focusing optics and will follow quadratic dependence on NA. Figure adapted from [6], courtesy of Mr. E. Skliutas

1.2 Chemical Principles of Thresholded Photopolymerization

The photopolymerization process from a chemical perspective is based on the interaction between light radiations with photoinitiator and monomer. The mechanism of free radical polymerization is shown in Fig. 22.2. Free radical polymerization consists of four fundamental steps: initiation, propagation, chain transfer, and termination.

Initiation involves the formation of radicals followed by the absorbance of photons. Initiators must have an intense tendency to split into two fragments with unpaired electrons after absorption of the required energy photon. The most commonly used initiating molecules are photochemically degradable aldehydes or ketones[14]. In general, cleavage occurs at any weak bond but usually takes place at the α—position of the carbonyl group and less frequently at the β—cleavage Fig. 22.2b. The main effective chemical families of such type photoinitiators are: hydroxy-aceto-phenones, benzylketals, benzoin derivatives, α-amino-alkylaceto-phenones, phosphine oxides, α-haloaceto-phenones, trichloro-methyl-S-triazine, and others [13]. Chemical formulas of all structures (photoinitiators and monomers) are shown in Sect. 2 (Table 22.1). Basically, following radicals generation, active species then react with any monomer having an activated double bond such as α, β—unsaturated aldehydes/ketones, acrylates, vinyl esters, vinyl sulfones, imidazoles, maleimides, etc. During this process, a photoinitiator free radical adds one of the electrons to the double bond of monomer, and the remaining electron becomes the new free radical $(\mathrm{R}_{(1)} - \mathrm{M})^*$. In this way, chain initiation consists of two described steps (Fig. 22.2a), initiation part).

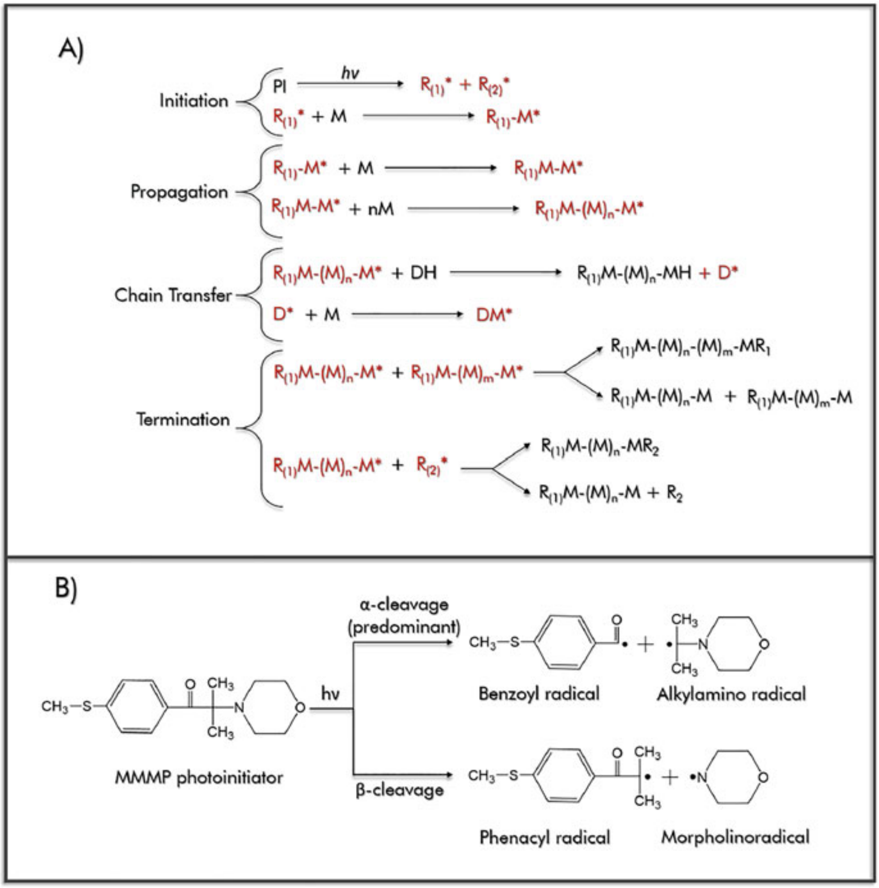
A)
Initiation
PI
hv
R(1)* + R(2)*
R(1)* + M
R(1)-M*
Propagation
R(1)-M* + M
R(1)M-M*
R(1)M-M* + nM
R(1)M-(M)n-M*
Chain Transfer
R(1)M-(M)n-M* + DH
R(1)M-(M)n-MH + D*
D* + M
DM*
Termination
R(1)M-(M)n-M* + R(1)M-(M)m-M*
R(1)M-(M)n-(M)m-MR1
R(1)M-(M)n-M + R(1)M-(M)m-M
R(1)M-(M)n-M* + R(2)*
R(1)M-(M)n-MR2
R(1)M-(M)n-M + R2
B)
MMMP photoinitiator
hv
α-cleavage (predominant)
Benzoyl radical
Alkylamino radical
β-cleavage
Phenacyl radical
Morpholinoradical
CH3—S
O
CH3
N
O

Fig. 22.2 (**a**) Steps of the free radical polymerization including initiation, propagation, chain transfer, and termination. PI, photoinitiator; M, monomer; D, donor; R, radical. Red markings show the active ingredient that is either causing the reaction or the result of it. (**b**) Photocleavage example of methyl-1-(4-methylthio)phenyl-2- morpholinopropan-1-one (MMMP) photoinitiator. Figure reproduced from [13]

During propagation, a polymer increases its chain length by the fast and progressive addition of monomers to the growing polymer chain keeping active centers. Ideally, the propagation step would continue until all monomers are consumed. However, pairs of radicals also tend to react with each other, annihilating their activities. Such behavior is called termination and is schematically depicted in Fig. 22.2a termination part.

Short polymer chains can be formed due to side reaction called chain transfer. This reaction can be caused by a small molecule, such as chain transfer agent, solvent, initiator, monomer or polymer, which in the scheme corresponds to DH (Fig. 22.2a), chain transfer). Chain transfer effect results in the destruction of one

Table 22.1 Possible photoinitiators and monomers families for UV lithography

Nr.	PI group name	PI structure	Monomer name	Monomer structure
1.	Hydroxy-aceto-phenones (HAPs)	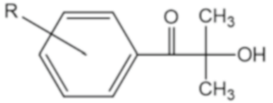 [R: H, alkyl, hydroxyalkryloxy]	α, β-unsaturated aldehydes	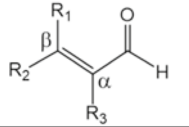
2.	Benzylketals	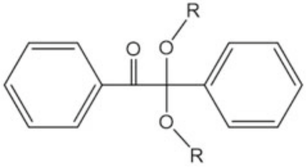 [R: alkyl]	α, β-unsaturated ketones	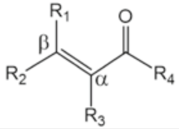
3.	Benzo-phenone	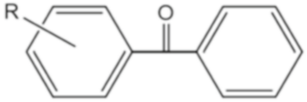 [R: H, phenyl, tolythio]	α, β-unsaturated acrylates	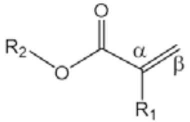

(continued)

Table 22.1 (continued)

Nr.	PI group name	PI structure	Monomer name	Monomer structure
4.	Benzoin derivatives	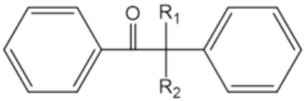 [R_1: H, OH, CH_3, alkoxy, -O-CH_2CH_2-O-, R_2: H, CH_3, O-CH_3, C_2H_5]	Vinyl esters	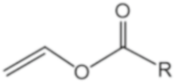
5.	α-amino-alkylaceto-phenones (AAAPs)	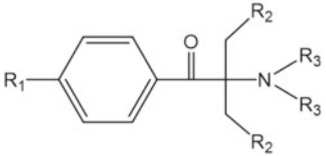 [R_1: H, -CH_3O, CH_3S, $(CH_3)_2N$, R_2: H, C_6H_5, $CH_2{=}CH$, R_3: CH_3, -$C_2H_4OC_2H_4$-]	Imidazoles	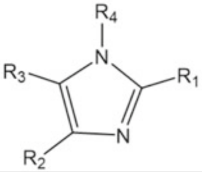
6.	Phosphine oxides	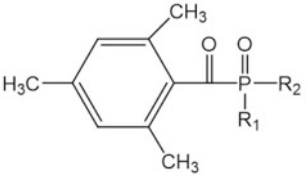 [R_1: alkyl, alkyloxy, benzyl, R_2: phenyl, ethoxy]	Vinyl sulfones	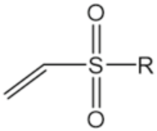

7.	α-haloaceto-phenone	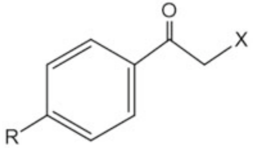 [R: alkyl, aryl, ether, (hetero)cycloalkyl, OH, X: Cl, Br]	Maleimides	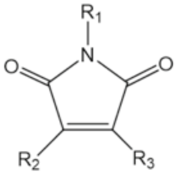
8.	Trichloro-methyl-S-triazine	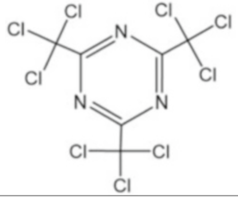 Cl Cl Cl N Cl Cl Cl N N Cl Cl Cl	Epoxides	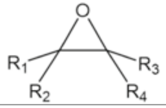

radical, but also the creation of another radical in contrast to the other modes of termination. In many cases, however, a newly created radical is unable to propagate further [15].

1.3 Laser 3D Lithography as Nano-Scale Additive Manufacturing

Combining ultrafast laser excitation with localized photopolymerization chemistry together, it can be successfully employed for LDW 3D nanolithography, in other words—optical 3D nanoprinting of cross-linkable materials. To achieve this on a basic level, a system comprising a pulsed-laser source, beam delivery/focusing, and scanning means must be used, see Fig. 22.3. Such systems are fully compatible with hybrid polymers, especially sol–gel synthesized, which can be optimized for perfect LDW 3D production due to their easy sample handling and exposure trajectory while being in a gel state, chemical wet development and superior mechanical properties to survive the whole process till revealing intricate 3D object. Finally,

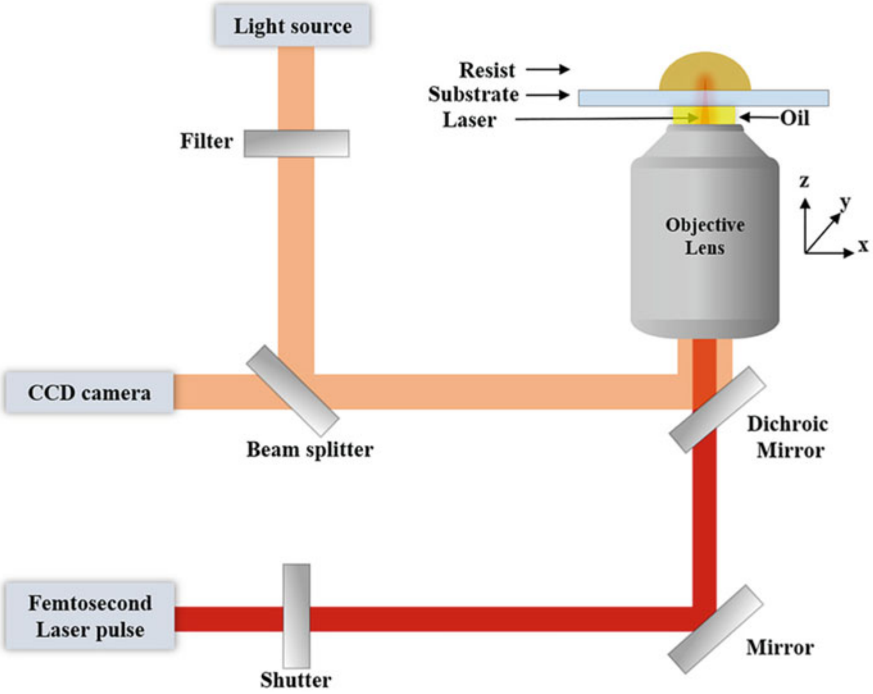
Light source
Resist
Substrate
Laser
Oil
Filter
Objective Lens
z
y
x
CCD camera
Beam splitter
Dichroic Mirror
Femtosecond Laser pulse
Shutter
Mirror

Fig. 22.3 Simplified schematic of a direct laser lithography (DLL) system operating in MPL high-resolution mode employing immersion oil objective lens. Taken from [16]

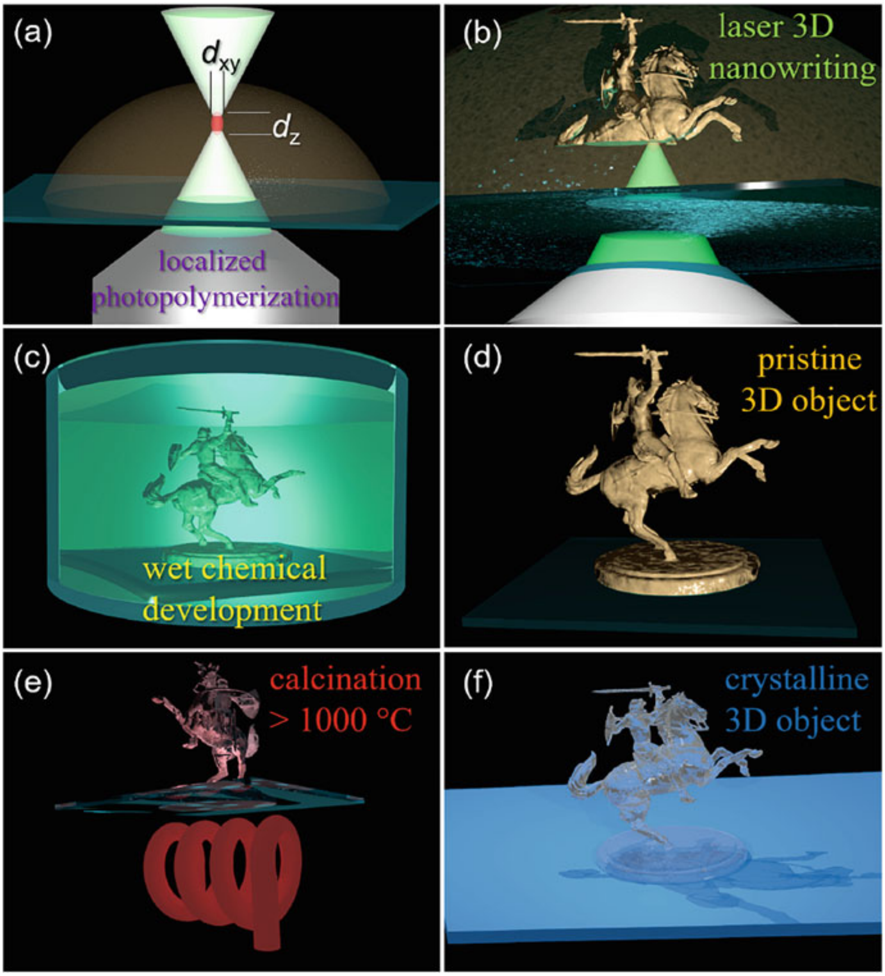
(a)
d_{xy}
d_z
localized photopolymerization
(b)
laser 3D nanowriting
(c)
wet chemical development
(d)
pristine 3D object
(e)
calcination > 1000 °C
(f)
crystalline 3D object

Fig. 22.4 Illustration of LDW process and heat treatment. (**a**) shows the basic building block of the structure—the "voxel" characterized by its transverse and longitudinal dimensions, (**b**) is the process of sequentially scanning the prepolymer and forming the desired structure, (**c**) is the development process to remove the unexposed material, (**d**) 3D polymeric structure, (**e**) calcination via thermal post-processing as a route for ceramic 3D nanostructures production, (**f**) shows crystalline 3D structure

the produced structures can serve as templates for various post-processing solutions including plasma etching, metal sputtering, atomic layer deposition, replications, infiltration as well as a sequence of them. For the context of this chapter's scope, it is important that heat treatment for enhanced cross-linking [17], down-scaling [18], chemical decomposition [19], and phase change is possible [20]. The typical sequenced protocol scheme is shown in Fig. 22.4. Altogether, it can be readily exploited for LDW as a method for additive manufacturing of inorganic substances at a nano-scale dimension. In contrast, only subtractive nanolithography was available up to now (as described in Chap. 20 by A. Rodenas).

2 Materials and Methods

Hybrid metal-organic prepolymers are outstanding materials for 3D laser printing applications. These compounds have excellent properties for fabrication, such as photosensitivity to radiation, transparency, and homogeneity. Additionally, 3D structures, manufactured from hybrids, can be converted into glass–ceramic or crystalline materials by heat treatment. Such 3D ceramic structures due to their good mechanical, thermal, and chemical properties are one of the sought-after engineering materials. Most hybrid preceramic polymers are metal-organic compounds derived from silicon with additional backbone chains consisting of carbon (C), nitrogen, oxygen (O), boron or metal atoms, such as: Hf, Zr, Al, Ti, Ge, V, Ce, Mo, Sn, Fe, Co, Ni, Pd, Pt, Cu, Ag, Au, W, etc. [21]. The backbone is connected to the side groups, which are mainly organic. The most common side groups are alkyl, vinyl, aryl, epoxy, and any other organic group, which can be involved in the photopolymerization (Fig. 22.5) [22].

In addition to homogeneous hybrid materials, composites are also used to obtain functionally structured ceramics. Generally, composites involve liquid or semi-liquid systems dispersed with fine ceramic particles as a feedstock or metal-organic resins, either in the form of inks or pastes. Polymer and ceramic particle composites are based on metal or semi-metal oxides, carbides, borides, nitrides, glass grains dispersed in organic monomers, such as oxymethylene, olefins, propylene or ethylene, urethanes, amides, ethers, esters, and acrylates (Fig. 22.5) [24].

However, composites have many disadvantages compared to hybrid organometallic monomer resins: the resolution of structures made of composites is limited by the particle size and the tendency to scatter light. Also, it is difficult to obtain a mixture of substances that is stable over a long period of time. Meanwhile, structures after heat treatment tend to shrink disproportionately in some directions, becoming porous or acquiring defects. The following light-based methods are commonly used in additive manufacturing for such materials formation: stereolithography (SL)-digital light processing (DLP) and two-photon polymerization (TPP), along with inkjet-based inkjet printing (IJP) and extrusion-based direct ink writing (DIW) [24, 25]. Indeed, the most promising method for obtaining high resolution and functionality for the production of ceramics is laser two-photon polymerization of monolithic hybrid materials with pyrolysis [20].

2.1 Synthesis of Hybrid Materials and Composites

Laser two-photon polymerization technology has the benefit of being able to use a wide range of materials [26]. The requirements for materials suitable for two-photon polymerization are very minimal: they must be transparent to the laser wavelength and must possess the characteristics for multi-photon absorption, which induces photopolymerization [27, 28]. In order to apply pyrolysis to the structures thus produced and convert them into pure inorganic ceramics or crystals, the chemical chain of materials must contain parts that do not tend to decompose to gas at high temperatures. Such materials are composites with inorganic nano/micro-particles or hybrid metal-organic prepolymers that are discussed in the previous paragraph and schematically depicted in Fig. 22.5, while their potential transformations into pottery are indicated by pink arrows. The sol–gel synthesis method is the most suitable and best studied method for the production of hybrid materials [29].

In brief, the sol–gel process entails preparing a precursor mix (a sol or a solution), which transforms into a more solid-like substance upon evaporation of the solvent, dehydration, and chemical cross-linking of its solid, liquid, or dissolved components [30]. Sols or solutions can often be transformed into ceramics through gel-like intermediates at temperatures that are significantly lower than the ones employed in traditional processing [29]. This occurs because the precursors used

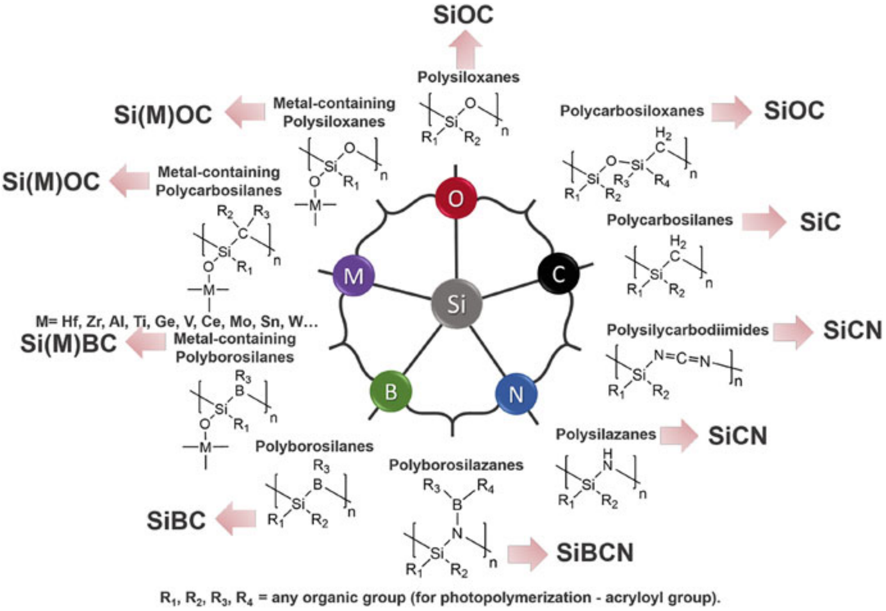
SiOC
Polysiloxanes
Si(M)OC
Metal-containing Polysiloxanes
Polycarbosiloxanes
SiOC
Si(M)OC
Metal-containing Polycarbosilanes
Polycarbosilanes
SiC
O
C
M
Si
B
N
M= Hf, Zr, Al, Ti, Ge, V, Ce, Mo, Sn, W...
Si(M)BC
Metal-containing Polyborosilanes
Polysilycarbodiimides
SiCN
Polysilazanes
SiCN
Polyborosilanes
Polyborosilazanes
SiBC
SiBCN
R₁, R₂, R₃, R₄ = any organic group (for photopolymerization - acryloyl group).

Fig. 22.5 Possible common types of silicon-based hybrid organometallic polymers in the Si-Me–O–C–N–B system used as precursors for ceramics. Reproduced from [23]

are intermixed at a molecular level and can react chemically to form a network of chemical bonds, a basis of ceramic materials.

To make it easier to understand the synthesis methodology, we present Fig. 22.6 as an example and discuss it below. The sol–gel process begins with the stabilization of an alkoxide of metal/semi-metal by organic molecules that are used as complexing ligands to provide chemical control over hydrolysis and condensation reactions, leading to form a stable suspension [31].

In the case of photocurable resins synthesis, organic acid having acryloyl group, for example, methacrylic acid, should be added to produce stable, photo-active, able to participate in photopolymerization precursors. Stabilization is carried out slowly by dropwise adding the organic acid to the alkoxide. After photopolymerization, hydrolysis is performed. During hydrolysis, water reacts nucleophilically with metal alkoxide to form hydroxide groups through the alkoxy groups contained in the metal alkoxide precursor. Acids or bases are used as catalysts for these reactions. The way the reaction occurs and its kinetic properties are principally influenced by the catalyst, the nature of the alkoxide group, and the employed solvent. Stabilized and hydrolyzed alkoxides of metals or semi-metals are added dropwise to each other. Typically, the alkoxide of the more active metal is added dropwise to the more passive one, thus forming a liquid solution–sol. The natural phenomenon that follows hydrolysis of alkoxide precursors is condensation (also called polycondensation or inorganic polymerization). In this process, hydroxyl groups react with each other to form oxo bridges (-M–O–M-) in combination with the simultaneous elimination of either a water or alcohol molecule [31–33]. In the presence of solvents and alcohol formed after hydrolysis, the condensation procedure is accelerated by heating ($\sim$90 °C), depending on the solvents and alcohol formed after hydrolysis; as a result, the gels are sufficiently rigid and clear, so they can be polymerized with appropriate radiation [32]. Additionally, a photoinitiator may be added to the sol, depending on the employed light source.

2.2 Thermal Post-Processing Techniques for 3D Nanostructures

Commonly, hybrid organometallic 3D objects have similar mechanical properties to organic structures [34, 35]. However, hybrids have one major advantage—they can transform into pure inorganic amorphous, glassy, or crystalline structures [19, 20, 36]. As a result, the amplitude of the application of such structures increases significantly. Therefore, here we will describe the post-processing of 3D hybrid structures to obtain inorganic-amorphous or crystalline structures (see Fig. 22.7). We will use the well-known and widely used SZ2080$^{\mathrm{TM}}$ [37] material to illustrate the processes.

The transformation of SZ2080$^{\mathrm{TM}}$ from polymer to amorphous glass–ceramic was studied and described by Gailevičius et al. [19]. Subsequently, Merkininkaitė

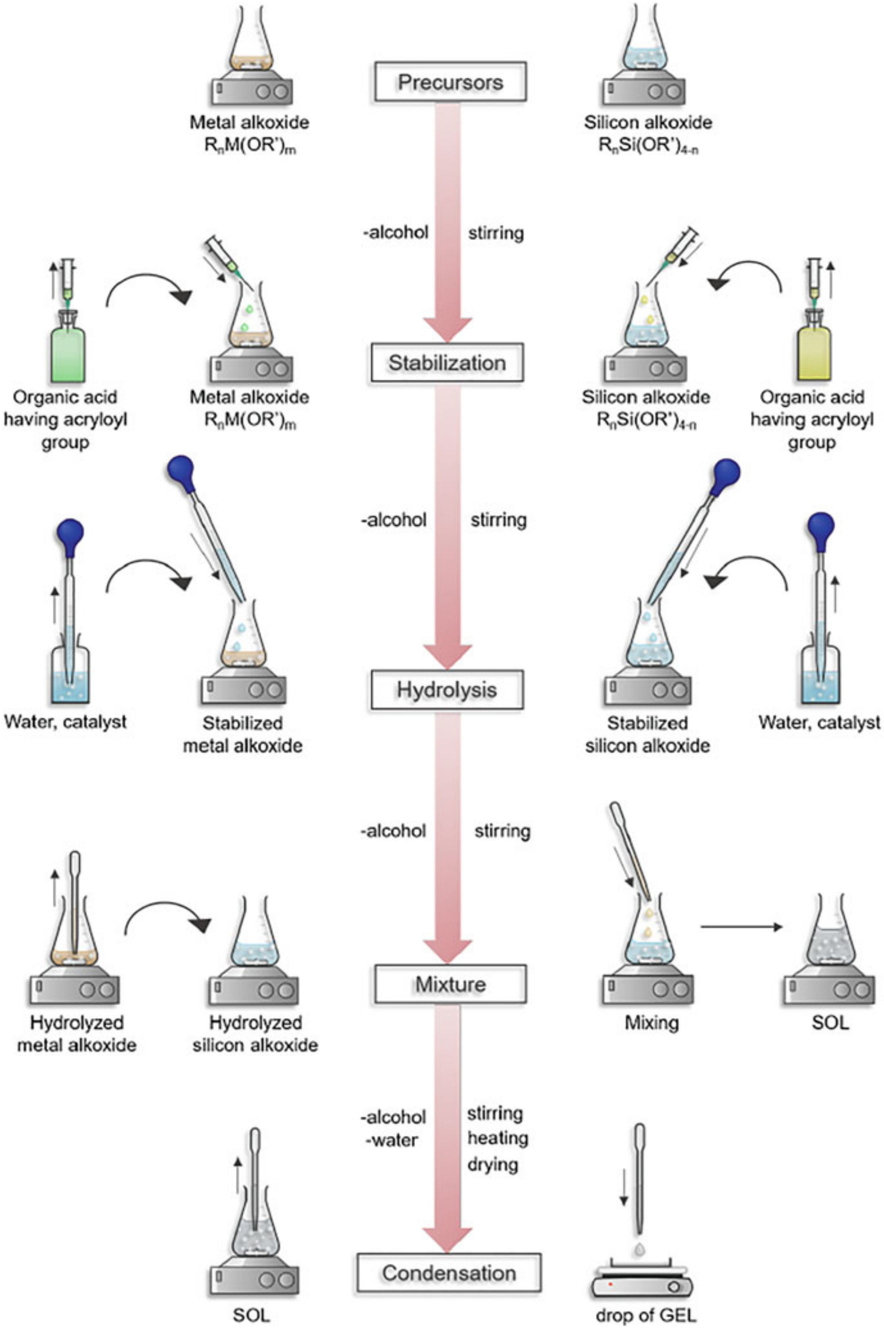
Precursors
Metal alkoxide
$R_nM(OR')_m$
Silicon alkoxide
$R_nSi(OR')_{4-n}$
-alcohol
stirring
Stabilization
Organic acid having acryloyl group
Metal alkoxide
$R_nM(OR')_m$
Silicon alkoxide
$R_nSi(OR')_{4-n}$
Organic acid having acryloyl group
-alcohol
stirring
Hydrolysis
Water, catalyst
Stabilized metal alkoxide
Stabilized silicon alkoxide
Water, catalyst
-alcohol
stirring
Mixture
Hydrolyzed metal alkoxide
Hydrolyzed silicon alkoxide
Mixing
SOL
-alcohol
-water
stirring
heating
drying
Condensation
SOL
drop of GEL

Fig. 22.6 Scheme of sol–gel synthesis of silicon-based organometallic prepolymer for laser photopolymerization. The scheme was prepared using free online chemix.org software

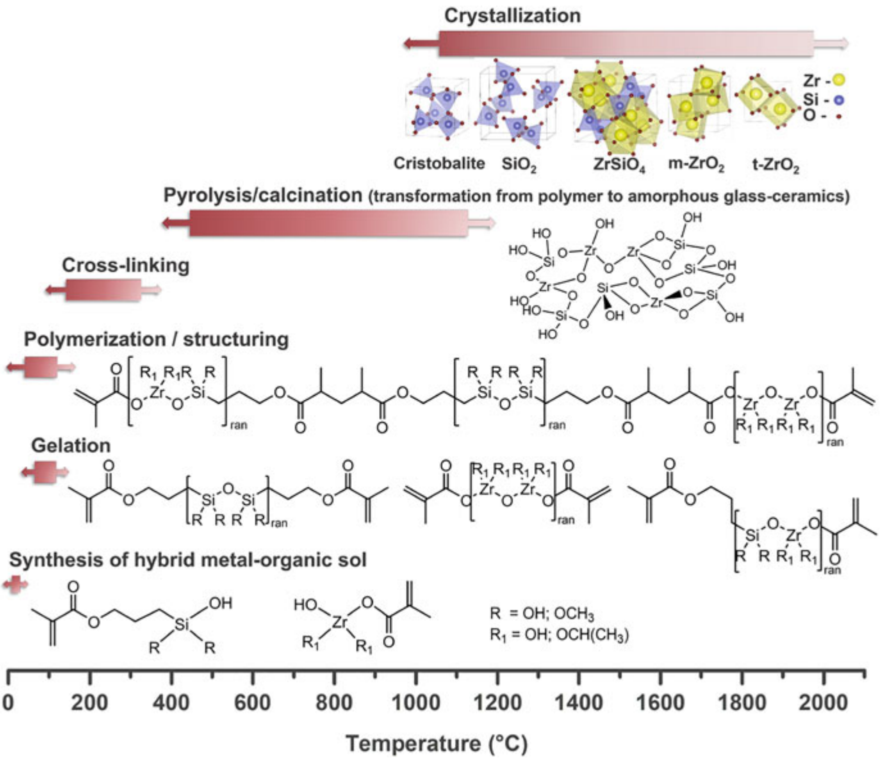
Crystallization
Zr -
Si -
O -
Cristobalite
SiO2
ZrSiO4
m-ZrO2
t-ZrO2
Pyrolysis/calcination (transformation from polymer to amorphous glass-ceramics)
Cross-linking
Polymerization / structuring
Gelation
Synthesis of hybrid metal-organic sol
R = OH; OCH3
R1 = OH; OCH(CH3)
0
200
400
600
800
1000
1200
1400
1600
1800
2000
Temperature (°C)

Fig. 22.7 Thermal transformation steps from synthesis to crystallization in Si–Zr organometallic system. Chemical structures and crystal lattices were reproduced from [19] and [20], respectively

et al. [20] investigated the dependence of crystallization on different variations in material composition and annealing temperature.

Fabrication of 3D inorganic derivatives commonly includes the following steps: First, synthesis of hybrid metal-organic prepolymer (sol- if metals alkoxides and/or siloxanes as precursors are used in the sol–gel method for the manufacture of the substance). Second, gelation, if necessary, depending on the precursors, is usually carried out at temperatures close to the boiling points of the solvents, and third photopolymerization is one of the methods that is visually explained in Fig. 22.4, or alternatively any other approach to obtain a 3D shape can be implemented. The early presented three steps are thoroughly described in the previous section.

Before the transformation of precursors into ceramic materials, a series of reactions, resulting in changes of composition and properties that are responsible for maintaining the shape after heat treatment, should be performed. Such a process is called cross-linking and can be initiated under different mechanisms [38]. Based on the chemical features of precursors, cross-linking occurs upon exposure to light or selective laser curing (the described case of photopolymerization), thermal effect (150 °C −400 °C), electron-beam curing, chemical stimuli, and reactive plasma based on NH_3, CH_4, N_2, H_2, H_2O, O_2, SiH_4, BH_3 gases for cross-linking at low temperatures (<200 °C). Thermal cross-linking after photopolymerization is the most attractive and best studied for hybrid metal-organic materials. This technique induces hydrosilylation (Si-H/vinyl groups), transamination (evolution of amines, ammonia, or oligomeric silazanes), thermal polymerization (vinyl or allyl groups), and dehydrocoupling (Si-H/Si-H or Si-H/N-H groups) reactions causing the formation of organic/inorganic networks [22, 36] and slight structure densification.

The following high-temperature methods (usually at temperatures above 400 °C) for the organic–inorganic transformation of polymers into an amorphous glass, ceramics, or crystalline structures are pyrolysis, calcination, and crystallization. The parameters of structures after heating, such as structures of chemical composition, density, ceramic yield, shape, defects population, surface morphology, crystallinity are mainly influenced by the composition of the initial material, heating temperature, and its rate of rising and holding times, heating atmosphere, overpressure, or vacuum [39]. Such transformations involve the decomposition or rearrangement of chemical bonds, the formation of new chemical bonds, and the removal of the organic part from the matter. Usually, weight loss can reach $\approx 30\%$ [40] of the initial weight, while linear shrinkage $\approx 40\%$ [19] (linear shrinkage). Most of the precursors (individually for each composition) become amorphous glass/ceramic up to 1100 °C, and crystallization begins at higher temperatures (typically from 1200 °C or the onset of crystallization can begin even at 2000 °C). The atmosphere has the most influential effect on the composition of the resulting ceramics. In an oxidizing environment, organic material is removed in the form of CO and CO_2 gas, so it is essential to adjust the rate of temperature rise to avoid porosity developing on the surface of the structure. In this case, oxides of metals or semi-metals are most likely to form, as well as using the SZ2080^{TM} (see Fig. 22.7) as a precursor. The formation of free carbon in the structure is promoted by heating in an inert atmosphere such as Ar or N. Additionally, added pressure has been proven to result in high free carbon content, since it hinders carbothermal reactions at high temperatures. Contrary, heating in a vacuum or reducing atmosphere (H_2 or NH_3) promotes carbothermal reactions, resulting in the release of free carbon [22].

In summary, the optimal conditions for polymer-to-ceramic conversion extensively depend not only on the original precursor composition, but also on the atmosphere, heating rate, temperature, and many other factors. This is opening for new directions and applications of laser-made micro-optics under harsh conditions such as high-intensity radiation, temperature, acidic environment, pressure variations, which include open space, astrophotonics, and remote sensing.

3 Trends and Technical Applications

Here we provide some most promising trends and directly benefiting fields of applications, where specifically sub-100-nm scales/definition and extreme conditions such as temperature, pressure, mechanical, optical and chemical environment are

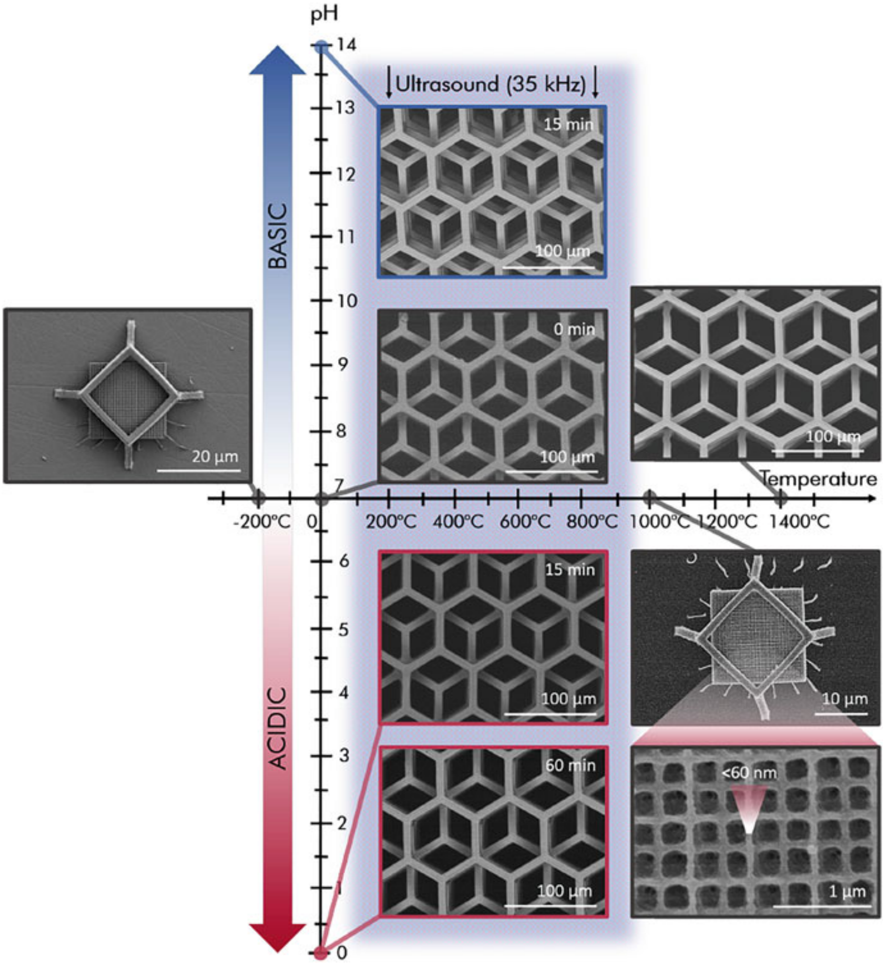
pH
14
13
12
11
10
9
8
7
6
5
4
3
2
1
0
BASIC
ACIDIC
Ultrasound (35 kHz)
15 min
0 min
15 min
60 min
100 µm
20 µm
10 µm
1 µm
<60 nm
Temperature
-200°C
0
200°C
400°C
600°C
800°C
1000°C
1200°C
1400°C

Fig. 22.8 Resistance of ceramic/crystalline 3D nano/micro-derivatives to aggressive chemicals, temperature, and ultrasound in Si/ZrO_2 system. Figure produced using results from [20]

playing critical roles. A graphically visualized map of 3D nanostructure resiliency is shown in Fig. 22.8, which confirms that ceramic micro–nano 3D structures withstand a wide range of temperatures (at least from −200 °C to 1400 °C), remain stable, and maintain sub-100-nm resolution throughout the pH range even under ultrasonic exposure. Technical applications are separated into these sub-topics: micro-optics, nanophotonics, micro-/nano-fluidics, micro-mechanics, and nano-electronics. We foresee that these fields will feature face the most benefit and list the current milestone achievements together with important details.

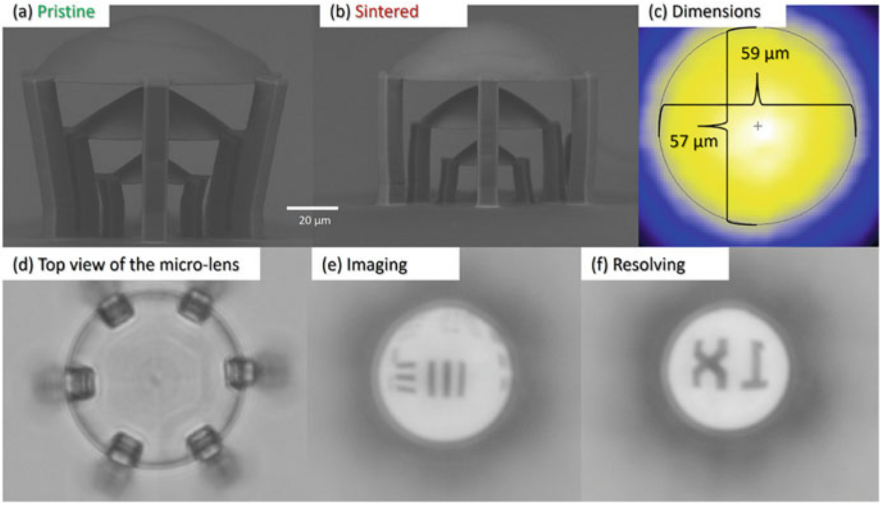

Fig. 22.9 An SEM image of compound micro-optical component stacked of 3 aspheric lenses: (**a**) pristine and (**b**) sintered. Geometrical characterization of the single lens diameter by optical profilometer (**c**), and its top view under OM (**d**). Validation of the same calcinated micro-lens imaging and resolving properties using 1951 USAF test target—imaged group 6 element 7 corresponds to the resolution of 4.39 µm (228 lp/mm). As shown, the geometrical and material properties such as projected lens shape and optical transparency are preserved for quality functional performance. Figure adapted from [41], courtesy of Ms. D. G. Hernandez

3.1 Micro-Optics

For instance, a pilot study on laser 3D printing of inorganic free-form micro-optics was experimentally validated by the author group of this chapter. Ultrafast laser nanolithography was employed for structuring hybrid organic–inorganic material SZ2080^{TM} and followed by high-temperature calcination (~1000 °C) post-processing. The combination allowed the production of true 3D architectures and the heat treatment resulted in converting the material into a highly transparent inorganic substance. The produced miniature optical elements were characterized, and their optical performance was demonstrated (Fig. 22.9).

Finally, the concept was validated for manufacturing compound optical components such as stacked lenses [41]. This is extremely attractive for the implementation of LDW lithography-made glass optics in material processing, remote sensing, and astrophotonics. Within the limitation of the employed techniques and equipment in the referenced study, the refractive index n could not be precisely estimated, yet the preliminary measuring indicated an averaged value of $\approx$1.609, which was reasonable and matched well with the $n = 1.617$ as previously reported for non-structured material in the literature [42]. The calcinated micro-lenses imaging and resolving properties were certified by 1951 USAF test target—imaged group 6 element 7 corresponding to a resolution of 4.39 µm (228 lp/mm) that is matching with the reported data obtained with polymer micro-optics [43].

3.2 Nanophotonics

Additive manufacturing at small scales enables advances in 3D nanophotonic systems as a choice of high-refractive-index materials is limited especially. A recently developed process to fabricate complex 3D architectures out of fully dense titanium dioxide (TiO_2) with a $n = 2.3$ and nanosized critical dimensions required for subwavelength structures. The transmission electron microscopy analysis proved this material to be a rutile phase of nanocrystalline TiO_2, with an average grain size of 110 nm and <1% porosity. Proof-of-concept woodpile 3D architectures with 300–600-nm beam dimensions exhibited a full photonic bandgap centered at 1.8–2.9 µm, as was revealed by Fourier-transform infrared spectroscopy and matching with plane wave expansion simulations [44]. The whole route protocol and resulting structures are shown in Fig. 22.10.

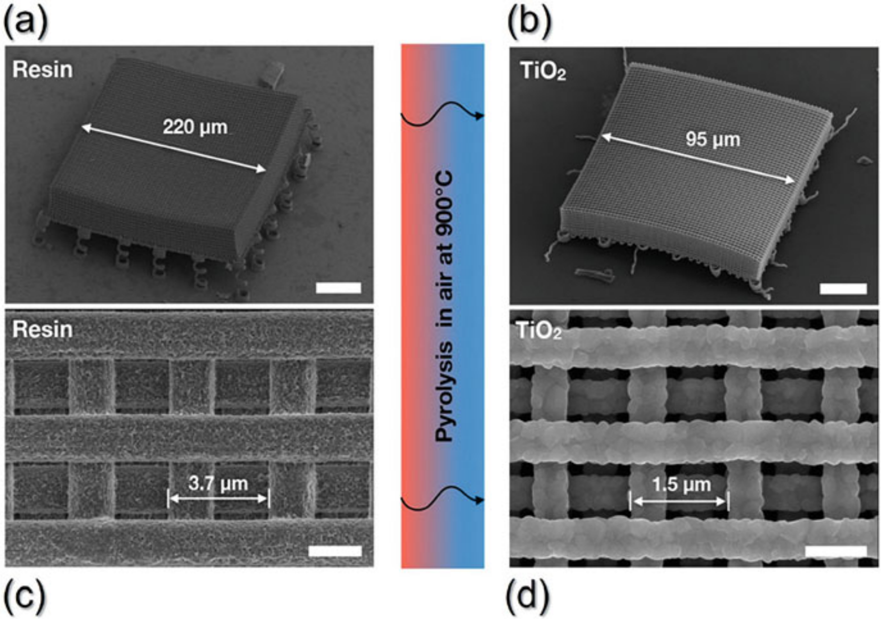

Fig. 22.10 Schematic representation of laser additive manufacturing of TiO_2 3D nanoarchitectures by SEM images. (**a**) Woodpile architectures were supported by a set of springs that decouple them from the substrate. (**b**) Titania woodpile structure was formed by calcination of the preceramic part. Representative TiO_2 magnified view before (**c**) and after (**d**) calcination at 750–900 °C. Scale bars are: (**a**) –50 µm, (**b**) –20 µm, (**c**) and (**d**) –2 µm, H – 1 µm [44]. Reproduced with permission from the American Chemical Society. Copyright ©2020 by ACS

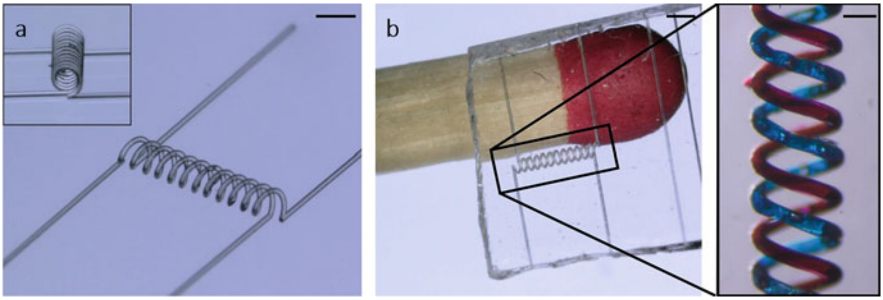

Fig. 22.11 Glass templates produced by LDW and thermal treatment: (**a**) Intertwined spirals (scale: 900 µm). (**b**) Resulting intertwined micro-fluidic spiral channels in fused-silica glass with a channel width of 74 µm. The channels were filled with dyes (see inset, scale: 140 µm). As can be seen, the 3D structures can be replicated with high fidelity and no deformations [45]. Reprinted with permission from Nature Communications. Copyright ©2019 by Nature Communications

3.3 Micro-Fluidics

Micro-fluidics is another field that is greatly benefiting from the true 3D shaping of glass structures. The topic, its challenges, and achievements are described in more detail by K. Sugioka in Chap. 30 of this book. Here we want to exemplify the fabrication of arbitrary three-dimensional suspended hollow microstructures in transparent fused-silica glass as a result of bench-marking current state of the art [45]. A micro-fluidic 3D intertwined mixer is shown in Fig. 22.11. The reported results were achieved by mixing SiO_2 nanopowder in the organic binder resin instead of sol–gel chemistry-derived hybrid photopolymer.

3.4 Micro-Mechanics

Ultrafast LDW multi-photon lithography opened a new dimension for the mechanical material engineering based on nano-architectured additive manufacturing [47]. High-porosity (low mass density) objects with optimized internal 3D geometries in combination with thermal treatment enable the production of ductile, ultrastrong polymer-derived nanoceramics [46]. As an example, mechanical performance in SiOC nanolattices is shown in Fig. 22.12. SiOC is reported as the strongest, stiffest, and most resilient two-photon polymerizable material with pillars up to 20 µm in diameter displayed plastic deformation and strength >7 GPa. The developed 200-nm feature sizes were printed, with only 30% shrinkage upon pyrolysis.

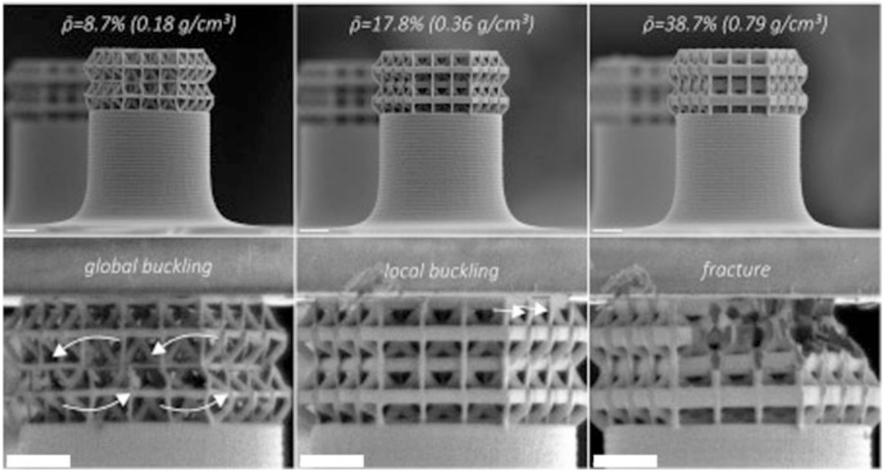

Fig. 22.12 Mechanical characterization of SiOC nanolattices: 3D structures before mechanical characterization (top) and at the moment of failure (bottom). Scale bars are all 5 μm.[46] Reprinted with permission from Elsevier. Copyright ©2019 by Elsevier

3.5 Nano-Electronics

For true 3D micro-/nano-electronic applications, conductive microstructures containing gold can be fabricated by simultaneous photopolymerization and photoreduction LDW and pyrolysis. E. Blasco et al. have reported employing a photoresist consisting of water-soluble polymers and a gold precursor. The fabricated microstructures showed good conductivity and were successfully deployed for 3D connections between gold pads [48]. Though the ultrafast laser 3D lithography in combination with calcination is a relatively young and rapidly emerging field, that is studied in its feasibility sense, yet at the same time, it already produces some functional prototypes, such as ZnO-based UV photodetection with a large current on/off ration and high cycling stability [30]. This is of crucial importance for next-generation MEMS/NEMS and energy storage devices.

3.6 Sub-100-nm Challenges: Comparison of Current Achievements

In Fig. 22.13, essential publications in the LDW 3D lithography of inorganics are marked and dated accordingly. As an important criterion, the reports are ranked in resolution (feature dimension), specifically thresholding on sub-100-nm scale. Another plot represents the growing number of citations that shows increasing interest in the field. It is noted that during recent years the amount of original

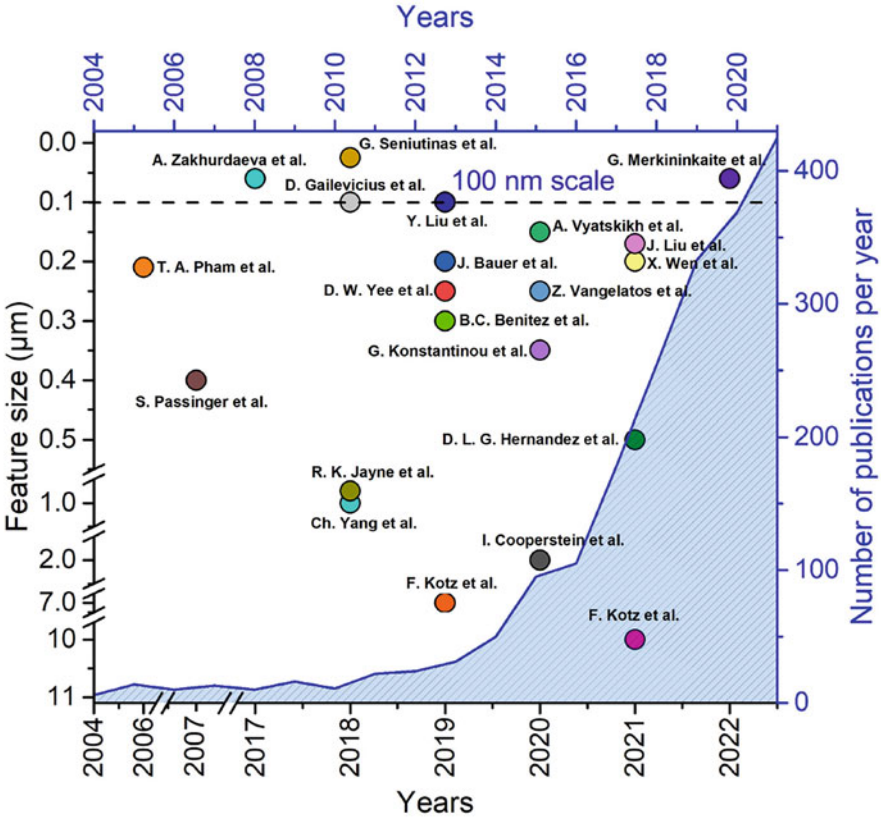

Fig. 22.13 Current achievements of 3D inorganic structure resolution in 3D lithography (corresponds to the black coordinate axis) and the number of publications per year (corresponds to the blue coordinate axis). The number of publications resulting from a search with keywords "3D, ceramic, printing" on scopus.com website, from 2004 to the December 2021 [18–20, 30, 41, 44–46, 49–61]

publications increases, and the density of the achievements concentrates toward the 100-nm benchmark, with sub-100 nm being repeatedly reached.

Sub-100-nm features can be fabricated using the stimulated emission depletion (STED) technique, which requires a more sophisticated two-wavelength laser setup and materials rather prepared suitable for that specific lithography purpose [62, 63], yet not for their functionality. Additionally, reaching dimensions below 60 nm is still not trivial task as shown in Fig. 22.14d), though it dramatically helps improving resolution to nearly 100 nm [63, 64]. While plasma etching helps fining the features (g) and pyrolysis/calcination offers downscaling (i–j), the later one is also converting the material into inorganic substances, which is way more useful for many technical applications. And as seen in (j), the achieved fine features are off-comparable dimensions to STED-made, yet without specific material optimization

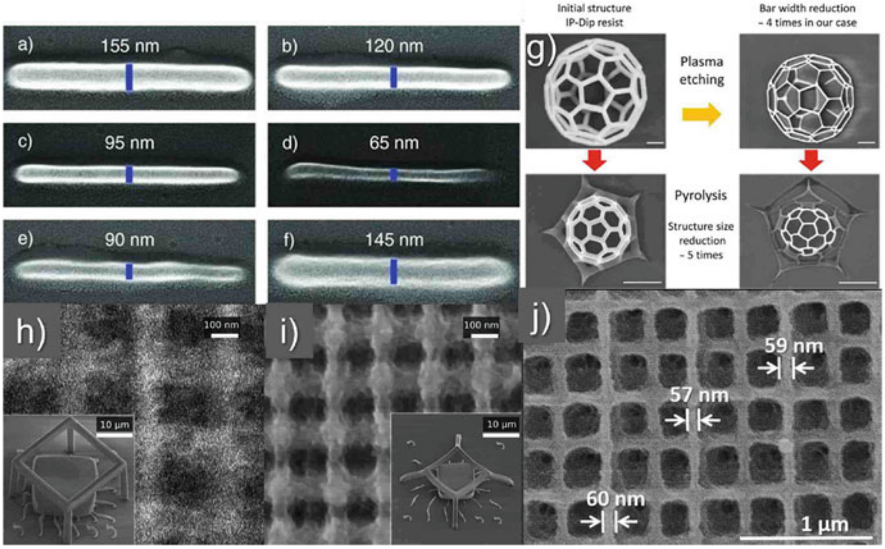
a) 155 nm
b) 120 nm
c) 95 nm
d) 65 nm
e) 90 nm
f) 145 nm
Initial structure IP-Dip resist
g)
Plasma etching
Bar width reduction ~ 4 times in our case
Pyrolysis
Structure size reduction ~ 5 times
h)
100 nm
10 µm
i)
100 nm
10 µm
j)
59 nm
57 nm
60 nm
1 µm

Fig. 22.14 Current achievements of sub-100-nm features via STED lithography (**a**–**f**), plasma- and pyrolysis-assisted post-processing solutions (**g**), and (**h**–**j**), and inorganic structures obtained via calcination approach. Note that STED technique allowed achieving of 65-nm features of organic materials as shown in (**d**), yet further variations of depletion power resulted in enlargement of the primitive structures (**e**–**f**). In (**h**), a lattice structure out of SZ2080$^{\text{TM}}$ before and (**i**) after calcination is shown, with line widths reaching below 100 nm already in inorganic glass–ceramic material, whereas with the material tuned for inorganic substance, outcome results in reproducibly reached 60-nm homogeneous lines in a well-ordered lattice geometry, shown in (**j**). Scale bars represent 1 µm in (**g**). [18–20, 62]

and upgrading of setup to a multi-color exposure are not required. Finally, the calcination route ensures complete material conversion to inorganics, thus avoiding the variation of polymer degree of conversion that depends on exposure dose [65] and removes the photoinitiator in case it was used in the photoresin [41].

Currently, pure organic plant-derived resins compared to commercially available petroleum-based resins are offering competitive performance in material photosensitivity, mechanical properties, achievable 100-nm feature sizes [66], and even can offer naturally inherent bactericidal properties [67]. ~100-nm suspended rods were made from vegetable oils thiol-ene/thiol-epoxy resins developed for the LDW 3D lithography as shown in Fig. 22.15a. We foresee that such resins can be exploded for calcination purposes too, thus potentially enabling sub-100-nm features while involving only sustainable material processing.

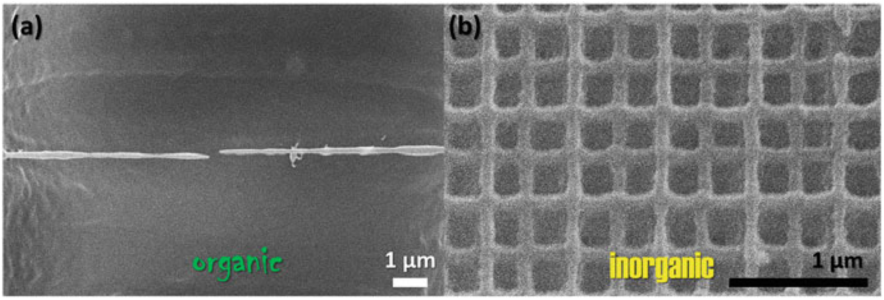

Fig. 22.15 ~100-nm suspended rods fabricated out of organic materials and ~65-nm line width reproducible inorganic template derived out of Si9:Zr1, (**a**) and (**b**), respectively [20, 66]. Both examples show that the LDW 3D multi-photon lithography (MPL) technique is readily available for sub-100-nm 3D fabrication out of diverse materials ranging from pure organic to completely inorganic via photopolymerization route

3.7 Emerging Applications

Table 22.0 summarizes the current achievements where LDW 3D lithography was used in combination with thermal post-treatment: reference, year, materials used, details of processing protocol, achieved dimensions, and targeted applications. As it is seen, various femtosecond laser setups of different wavelengths and pulse durations as well as repetition rates were applied, without a clear discrimination of 515-nm *vs.* 780–800-nm wavelengths and 100 fs *vs.* 300 fs pulse durations as well as 200 kHz or 80 MHz. Thus it can be deduced that the initial dimensions of the 3D structure, specific material, and optimized calcination protocol are determining the final dimensions of the produced feature. It should be noted that not all the groups were aiming for the highest resolution, rather for the specific application. On the other hand, supporting techniques such as helium-assisted microcasting can be used for employing hollow polymer templates for filling it with glass slurry and sequentially removing the template completely [100]. This results into fused-silica structures where the laser 3D structured polymer serves just as a sacrificial structure. Thus it is fascinating to see the approaches developed in ceramic industry are being re-implemented for micro- and nano-scales.

Figure 22.16 depicts of expected emerging laser and calcination made 3D nanostructured ceramic properties related to inherent material chemical compositions. Namely, thermal conductivity, chemical reactivity (inertness), optical, mechanical, and electromagnetic characteristics can have pronounced discrete values demanded by specific applications. The developments described in this chapter are compatible with the technology's capability of making multi-material polymer 3D structures [101], thus empowering to make multi-material inorganic–organic or inorganic–inorganic structures [49].

Finally, the eco-innovative aspect based on plant-derived optically 3D printable resins allows merging bio-renewable resources with the discussed calcination

Table 22.0 Current achievements of 3D inorganic structure resolution in 3D lithography

Nr.	Ref. year	Final material	Post-processing	Laser parameters and setup	Feat. size, nm	Applications
1.	[20] 2022	SiO_2, $ZrSiO_4$, t-ZrO_2, m-ZrO_2	Heating, air, 1 h at 1000 °C, heating rate 5 °C/min.	Direct laser writing, $\tau = 300$ fs, $\lambda = 515$ nm, $f = 200$ kHz, $P_{avg} = 64\,\mu$W, 100x 1.4 NA objective, $v = 200\,\mu$m/s, $h = 0.1\,\mu$m (in both, x and y axes)	60	3D ceramic nanostructures that are resistant to extreme low and high temperatures and aggressive chemicals
2.	[30] 2021	Metal oxide semiconductors (e.g., ZnO and Co_3O_4)	Heating, O_2, 550 °C for 30 min, heating rate 20 °C/s	Homemade TPP system. A Ti: sapphire fs laser, $\lambda = 780$ nm, $\tau = 100$ fs, $f = 80$ MHz, 40x 1.3 NA objective, $P_{avg} = 7 - 20$ mW, $v = 0.5$–5 mm/s.	170	Optoelectronic and semiconductor devices
3.	[41] 2021	SiO_2, ZrO_2	Heating, air, raising the temperature for 12 h until reaching 1100 °C and maintaining it for 3 h	$\lambda = 515$ nm of a Yb:KGW laser Pharos (Light Conversion Ltd.), $\tau = 300$ fs, $f = 200$ kHz, 63x 1.4 NA objective.	500	Micro-optics that are resistant to: high-intensity radiation, temperature, acidic environment, pressure variations
4.	[61] 2021	SiO_2 doped with Er^{3+}, Eu^{3+}, Tm^{3+}, Nd^{3+}, and Yb^{3+}	Heating, nitrogen, 1300 °C for 240 min, heating rate 1 °C/s	Commercial 2PP AM system Nanoscribe Photonic Professional GT, 63x 1.4 NA or 25x 0.8 NA objectives, $\lambda = 780$ nm, $\tau = 100$ fs, $P_{avg} = 15 - 20$ mW, $v = 4 - 5$ mm/s	200	Optical applications: active photonics, non-Hermitian photonics, and quantum devices

5.	[60] 2021	Fused silica	Heating, samples sintered in vacuum at a pressure of 5 × 10^{-2} mbar, 2 h at 1300 °C. The heating and cooling rate was 3 K/min	Commercial lithography system Photonic Professional GT2 (Nanoscribe GmbH, Germany), 10 × 0.3 NA objective (from Nanoscribe GmbH, Germany), $\lambda = 780$ nm, slicing 5 µm, h=1 µm, $v = 100$ mm/s, and laser power 80%	10,000	High-resolution glass components including optics, photonics, functional and engineered surfaces as well as lab-on-a-chip, life sciences, and biomedical engineering
6.	[56] 2020	Zr-DMAEMA	Laser extreme pyrolysis. Lighthouse Sprout-C 4 W, $\lambda = 532$ nm, $P_{\text{avg}} = 5$–10 mW	FemtoFiber pro NIR laser, $\lambda = 780$ nm, $\tau = 100$ fs, $f = 80$ MHz, 100 × 1.4 NA objective	250	Tailored scaffolds for artificial tissue and 3D patterning of local hierarchical nanofeatures for 3D complex biomimetic materials and structures
7.	[52] 2020	SiOC	Heating, argon, the temperature was increased to 200 °C with a hold time of 2 h and 1000 °C for 1 h, 5 °C/min	Nanoscribe Professional GT. The laser source is an ultrafast Er:doped fiber laser system from Toptica Photonics AG, $\lambda = 780$ nm, $\tau = 100$ fs, $f = 80$ MHz, 63 x 1.4 NA objective, $P_{\text{avg}} = 15$ mW, $v = 6$ µm/s	349	Ceramic-based micro-nozzle for micro-droplets delivery or micro-manipulation that can be realized and provide high robustness and chemical resistance
8.	[44] 2020	Rutile TiO_2	Heating, air, 750–900 °C for 1 h, 3 °C/min	A commercially available two-photon lithography system-Photonic Professional GT, Nanoscribe GmbH. $P_{\text{avg}} = 12.5$–20 mW and $t_{ex} = 0.5 \times 10$ ms	150	Fabrication of components for micro-optics or 3D MEMS

(continued)

Table 22.2 (continued)

Nr.	Ref. year	Final material	Post-processing	Laser parameters and setup	Feat. size, nm	Applications
9.	[49] 2020	YAG, Nd:YAG	Heating, air, 200 °C for 2 h, 520 °C for 2 h, 620 °C for 2 h for amorphous inorganic, further 920–1500 °C 5 h for polycrystalline, 0.6 °C/min	Photonic Professional GT printer (Nanoscribe GmbH, Germany). 25x objective	2000	Optical components in high-intensity laser systems, which require heat resistance, or light sources in optical circuits
10.	[58] 2019	IP-Dip	Heating, argon, 450 °C for 12, 17 or 2 min, 10 °C/min	Photonic Professional GT, $\lambda = 780$ nm, 63x 1.4 NA objective, $P_{\text{avg}} = 16 - 27$ mW, $v = 15$ mm/s	100	Integrated optical components, 3D photonic integrated circuitry, anti-counterfeiting security labels, dye-free structural color printing
11.	[57] Nano-engineering 2019	SU-8	Heating, nitrogen, 300 °C 1 h, 900 °C 1 h, 5 °C/min	Coherent Mira 900D, $\lambda = 800$ nm, $\tau = 150$ fs, $f = 76$ MHz, 100 x 1.4 NA objective	300	Carbon nanowires: label-free impedance-based nanobiosensors, nanoparticle-based gas sensors, and electrochemical immunosensors
12.	[45] 2019	IP-S template, fused silica	Heating, air, 600 °C, 0.5 °C/min thermal debinding, 1300 °C, 3 °C/min sintering	Photonic Professional GT, 0.8 NA objective	7000	Micro-fluidics, flow-through synthesis, photonics or waveguiding applications in optics, and photonics

13.	[46] 2019	SiOC	Heating, vacuum, 1000 °C for 1 h. Heating at 1 °C/min. Cooling at 3 °C/min	Photonic Professional GT, FemtoFiber pro NIR laser, $\lambda = 780$ nm, $\tau = 100$ fs, $f = 80$ MHz, 63 x 1.4 NA objective, $\upsilon = 10$ µm/s, $P_{avg} = 16$–36 mW for octet lattices (with 200-nm lines)	200	Engineering applications, ranging from automotive to aerospace and energy systems
14.	[51] 2019	Metal oxide (ex. ZnO)	Heating, air, 500 °C, heating at 0.5 °C/min, cooling at 2 °C/min	Photonic Professional GT, 63 x 1.4 NA objective	250	Nanoelectromechanical system (NEMS), desulfurization agent, UV photodetector
15.	[19] 2018	Glass–ceramic, cristobalite SiO_2 and tetragonal ZrO_2	Heating, air, 1000–1500 °C	$\tau = 300$ fs, $\lambda = 515$ nm, $f = 200$ kHz objectives from 0.8 to 1.4 NA	100	Chemically resilient and high-temperature optical elements for sensors
16.	[55] 2018	IP-Dip, PEG-DA, PETA	–	Nanoscribe Photonic Professional GT, $\lambda = 780$ nm, 63 x 1.4 NA objective	950	Microstructures for IR imaging or deformable microscaffolds for living cell studies

(continued)

Table 22.2 (continued)

Nr.	Ref. year	Final material	Post-processing	Laser parameters and setup	Feat. size, nm	Applications
17.	[18] 2018	IP-Dip, SZ2080	Heating, nitrogen flow 100 sccm, 250 °C 1 h, 350 °C 1 h, 690 °C 1 h, Heating rate 5 °C/min. Plasma etching	Photonic Professional GT, Femtolasers fusion, $\lambda = 800$ nm, $f = 75$ MHz, $\tau = 20$ fs, 100x 1.4 NA objective	25	Micro-optical elements and 3D templates or microscaffolds for cell studies
18.	[50] 2018	Glassy carbon	Pyrolysis by rapid thermal processing	Nanoscribe direct write laser lithography system	1000	Carbon microelectrodes
19.	[53] 2017	Glassy carbon	Heating, vacuum, 900 °C	Nanoscribe 2PP setup, $P_{\text{avg}} = 30$–33.6 mW, $v = 25$ mm/s	60	Carbon-microelectromechanical systems (Carbon-MEMS) and nanoelectromechanical systems (Carbon-NEMS)
20.	[54] 2007	Anatase, rutile TiO_2	Heating, 450 °C anatase. 650 °C rutile	Spectra Physics Tsunami, $\lambda = 780$ nm, $\tau = 120$ fs, $f = 80$ MHz, 100x 1.35 NA objective	400	3D inorganic photonic crystals
21.	[59] 2006	SiCN	Heating, nitrogen, 600 °C for 2 h, temperature rate 2 °C/min	Ti:sapphire laser, $\lambda = 780$ nm, $\tau = 100$ fs, $f = 80$ MHz, 1.4 NA objective, $P_{\text{avg}} = 100$ mW, t_{ex}=1 ms	210	3D ceramic structures such as: tribological MEMS and chemical-resistant micro-fluidics

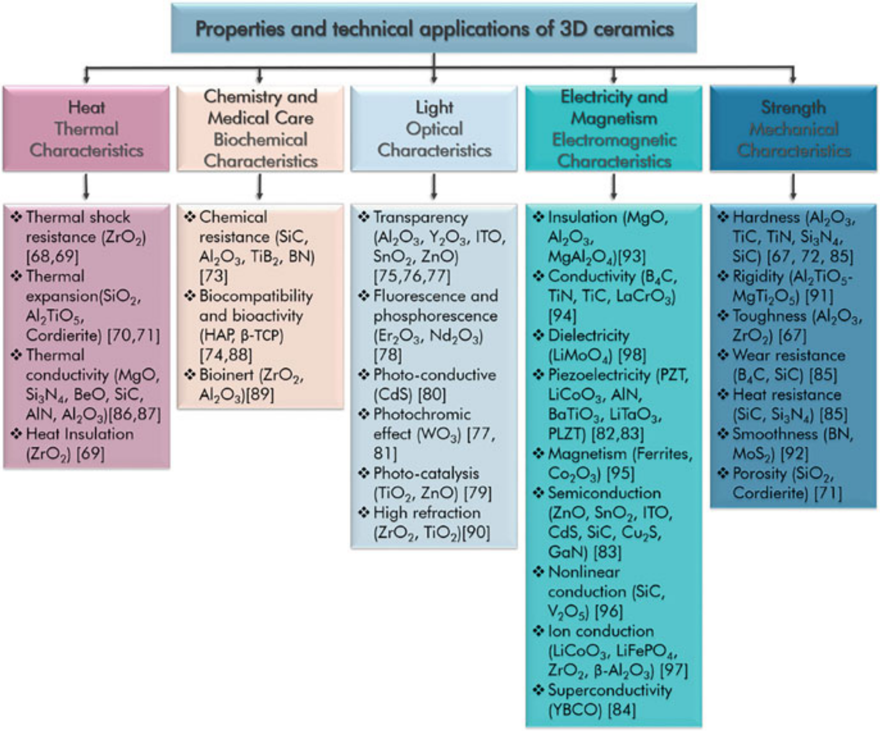
Properties and technical applications of 3D ceramics
Heat Thermal Characteristics
Chemistry and Medical Care Biochemical Characteristics
Light Optical Characteristics
Electricity and Magnetism Electromagnetic Characteristics
Strength Mechanical Characteristics
❖ Thermal shock resistance (ZrO_2) [68,69]
❖ Thermal expansion(SiO_2, Al_2TiO_5, Cordierite) [70,71]
❖ Thermal conductivity (MgO, Si_3N_4, BeO, SiC, AlN, Al_2O_3)[86,87]
❖ Heat Insulation (ZrO_2) [69]
❖ Chemical resistance (SiC, Al_2O_3, TiB_2, BN) [73]
❖ Biocompatibility and bioactivity (HAP, β-TCP) [74,88]
❖ Bioinert (ZrO_2, Al_2O_3)[89]
❖ Transparency (Al_2O_3, Y_2O_3, ITO, SnO_2, ZnO) [75,76,77]
❖ Fluorescence and phosphorescence (Er_2O_3, Nd_2O_3) [78]
❖ Photo-conductive (CdS) [80]
❖ Photochromic effect (WO_3) [77, 81]
❖ Photo-catalysis (TiO_2, ZnO) [79]
❖ High refraction (ZrO_2, TiO_2)[90]
❖ Insulation (MgO, Al_2O_3, $MgAl_2O_4$)[93]
❖ Conductivity (B_4C, TiN, TiC, $LaCrO_3$) [94]
❖ Dielectricity ($LiMoO_4$) [98]
❖ Piezoelectricity (PZT, $LiCoO_3$, AlN, $BaTiO_3$, $LiTaO_3$, PLZT) [82,83]
❖ Magnetism (Ferrites, Co_2O_3) [95]
❖ Semiconduction (ZnO, SnO_2, ITO, CdS, SiC, Cu_2S, GaN) [83]
❖ Nonlinear conduction (SiC, V_2O_5) [96]
❖ Ion conduction ($LiCoO_3$, $LiFePO_4$, ZrO_2, β-Al_2O_3) [97]
❖ Superconductivity (YBCO) [84]
❖ Hardness (Al_2O_3, TiC, TiN, Si_3N_4, SiC) [67, 72, 85]
❖ Rigidity (Al_2TiO_5-$MgTi_2O_5$) [91]
❖ Toughness (Al_2O_3, ZrO_2) [67]
❖ Wear resistance (B_4C, SiC) [85]
❖ Heat resistance (SiC, Si_3N_4) [85]
❖ Smoothness (BN, MoS_2) [92]
❖ Porosity (SiO_2, Cordierite) [71]

Fig. 22.16 Properties of 3D ceramics and their immediate possible and future potential technical applications [68–99]

method—as the organic matter is only used for templating and is evaporated eventually, thus it can allow selection of bio-based resins (such as derived from vegetable oils for instance) instead of petroleum ones [66]. As an example, an AESO (acrylated epoxidized soy oil)-based resin containing a natural diluent ethyl lactate can inherit up to 89% of the renewable carbon and offer multi-scale and multi-platform optical 3D structurability ranging from sub-micron to super-millimeter dimensions [102].

4 Summary and Conclusions

Here we have summarized recent advances and state of the art on ultrafast LDW lithography and its employment for additive manufacturing of 3D inorganic nanostructures. A specific focus was provided for material diversity, application impact, and sub-100-nm fabrication challenges. We included the combinations of precision optical 3D printing of hybrid organic–inorganic/composite materials followed by high-temperature thermal post-treatment, which empowers fabrication of complex architectures and true glass, ceramic, and even crystalline structures. The synergistic developments in laser technology and material sciences are already leading to immediate applications in micro-optics, nano-fluidics, micro-mechanics, and nano-electronic fields. Together it joins the flexibility of 3D micro-/nano-prototyping with high performance, heavy-duty cycle, and high-resilience integrated devices.

In brief, a conclusion can be made that the LDW 3D nanolithography is no longer limited to (photo-)polymer materials as in combination with calcination technique it allows additive manufacturing of a wide variety of organics materials (including renewable plant-derived resins) that can be converted into diverse and functional inorganics. The possibility of the technology to make multi-material polymer-based 3D structures is also valid for making multi-material 3D inorganics. We emphasize that besides material conversion from hybrid to inorganic, the approach established a reliable route for downscaling the structures. This is of great interest as the LDW 3D MPL alone is struggling to reach below 100-nm features in a routine manner. Yet with the 40–60% feature reduction without the loss of geometry, it makes it viable for technology to produce complex shaped geometries and highest optically true 3D printable resolution. Additionally, the material densification while sintering is offering benefits of surface self-smoothing, which is important for micro-optics, nanophotonics, and fluidic applications. And finally, this is an indirect way to avoid the photoinitiators, which may be used during the exposure stage, but are removed while calcination. It makes a significant in material-structure optimization for delicate functions, such as artificially engineered refractive index by metamaterial geometries [103], and at the same time heavy-duty technical practical applications [104] such as ultra-compact wide-angle cameras based on multi-aperture free-form optical designs [105]. From the advances in 3D additive manufacturing perspective, its active micro-optics and nanophotonics or highly integrated systems including both of them are foreseen to benefit the most in the nearest future.

Acknowledgments We kindly acknowledge Dr. Maria Farsari (IESL-FORTH) and Prof. Saulius Juodkazis (SUT) for valuable information and fruitful discussions regarding materials and sintering processes. We are heartily thankful to PhD. students Edvinas Skliutas (VU) and Diana Laura Gonzalez Hernandez (at a time VU) for their help with SEM and contribution of some items presented in this chapter.

References

1. J. Stampfl, R. Liskas, A. Ovsianikov, *Multiphoton Lithography* (Wiley, London, 2016)
2. S. Maruo, O. Nakamura, S. Kawata, Three-dimensional microfabrication with two-photon-absorbed photopolymerization. Opt. Lett. **22**, 132–134 (1997)
3. K. Sugioka, Hybrid femtosecond laser three-dimensional micro-and nanoprocessing: a review. Int. J. Extrem. Manuf. **1**, 012003 (2019)

4. M. Mangirdas, A. Žukauskas, S. Hasegawa, Y. Hayasaki, V. Mizeikis, R. Buividas, S. Juodkazis, Ultrafast laser processing of materials: from science to industry. Light Sci. Appl. **5**, 16133 (2016)
5. L. Jonušauskas, D. Gailevičius, S. Rekštytė, T. Baldacchini, S. Juodkazis, M. Malinauskas, Mesoscale laser 3D printing. Opt. Exp. **27**(11), 15205–15221 (2019)
6. E. Skliutas, M. Lebedevaite, E. Kabouraki, T. Baldacchini, J. Ostrauskaite, M. Vamvakaki, M. Farsari, S. Juodkazis, M. Malinauskas, Polymerization mechanisms initiated by spatio-temporally confined light. Nanophotonics **10**(4), 1211–1242 (2021)
7. T. Baldacchini, *Three-Dimensional Microfabrication Using Two Photon Polymerization: Fundamentals, Technology, and Applications* (Elsevier, Amsterdam, 2015)
8. L. Yang, F. Mayer, U.H.F. Bunz, E. Blasco, M. Wegener, Multi-material multi-photon 3D laser micro- and nanoprinting. Light Adv. Manuf. **2**, 2021020003 (2021)
9. P. Kiefer, V. Hahn, M. Nardi, L. Yang, E. Blasco, C. Barner-Kowollik, M. Wegener, Sensitive photoresists for rapid multiphoton 3D laser micro- and nanoprinting. Adv. Opt. Mater. **8**, 2000895 (2020)
10. M. Malinauskas, A. Žukauskas, G. Bičkauskaitė, R. Gadonas, S. Juodkazis, Mechanisms of three-dimensional structuring of photo-polymers by tightly focussed femtosecond laser pulses. Opt. Exp. **18**(10), 10209–10221 (2010)
11. V. Hahn, T. Messer, N. Maximilian Bojanowski, E.R. Curticean, I. Wacker, R.R. Schroder, E. Blasco, M. Wegener, Two-step absorption instead of two-photon absorption in 3D nanoprinting. Nat. Photon. **15**, 932–938 (2021)
12. V. Hahn, P. Kiefer, T. Frenzel, J. Qu, E. Blasco, C. Barner-Kowollik, M. Wegener, Rapid assembly of small materials building blocks (voxels) into large functional 3D metamaterials. Adv. Func. Mater. **30**, 1907795 (2020)
13. M. Lago, A. Rodriguez, R. Sendón, J. Bustos, M. Nieto, P. Paseiro, Photoinitiators: a food safety review. Food Addit. Contam. A: Chem. Anal. Control Exposure Risk Assess. **32**, 779–798 (2015)
14. T. Bérces, *Chapter 3. The Decomposition of Aldehydes and Ketones*, volume 5 of Comprehensive Chemical Kinetics (Elsevier, Amsterdam, 1972)
15. E. Andrzejewska, *Three-Dimensional Microfabrication Using Two-photon Polymerization*. Micro and Nano Technologies (William Andrew Publishing, Oxford, 2016)
16. I. Bernardeschi, M. Ilyas, L. Beccai, A review on active 3D microstructures via direct laser lithography. Adv. Intell. Syst. **3**(9), 2100051 (2021)
17. J. Bauer, A.G. Izard, Y. Zhang, T. Baldacchini, L. Valdevit, Thermal post-curing as an efficient strategy to eliminate process parameter sensitivity in the mechanical properties of two-photon polymerized materials. Opt. Exp. **28**(14), 20362–20371 (2020)
18. G. Seniutinas, A. Weber, C. Padeste, I. Sakellari, M. Farsari, C. David, Beyond 100nm resolution in 3D laser lithography—post processing solutions. Microelectron. Eng. **191**, 25–31 (2018)
19. D. Gailevičius, V. Padolskytė, L. Mikoliānaitė, S. Šakirzanovas, S. Juodkazis, M. Malinauskas, Additive-manufacturing of 3D glass-ceramics down to nanoscale resolution. Nanoscale Horizons **4**, 647–651 (2019)
20. G. Merkininkaite, E. Aleksandravicius, M. Malinauskas, D. Gailevicius, S. Sakirzanovas, Laser additive manufacturing of Si/ZrO$_2$ tunable crystalline phase 3D nanostructures. Opto-Electron. Adv. **5**, 210077 (2022)
21. E. Balčiūnas, S.J. Baldock, N. Dreižė, M. Grubliauskaitė, S. Coultas, D.L. Rochester, M. Valius, J.G. Hardy, D. Baltriukienė, 3D printing hybrid organometallic polymer-based biomaterials via laser two-photon polymerization. Polym. Int. **68**(11), 1928–1940 (2019)
22. G. Barroso, Q. Li, R.K. Bordia, G. Motz, Polymeric and ceramic silicon-based coatings—a review. J. Mater. Chem. A **7**, 1936–1963 (2019)
23. R.K. Gupta, R. Mishra, S. Kumar, A. Ranjan, L. M. Manocha, N. Eswara Prasad, *Development of Polycarbosilane PCS Polymer and PCS-Derived SiC Fibers and Their Composites* (Springer, Berlin, 2020)
24. Z. Chen, Z. Li, J. Li, C. Liu, C. Lao, Y. Fu, C. Liu, Y. Li, P. Wang, Y. He, 3D printing of ceramics: a review. J. Eur. Ceram. Soc. **39**(4), 661–687 (2019)

25. P.A. Mathews, S. Koonisetty, S. Bhardwaj, P. Biswas, R. Johnson, P. Gadhe, Patent trends in additive manufacturing of ceramic materials (2020)
26. G. Merkininkaitė, D. Gailevičius, S. Šakirzanovas, L. Jonušauskas, Polymers for regenerative medicine structures made via multiphoton 3D lithography. Int. J. Polym. Sci. **2019**, 3403548 (2019)
27. M. Farsari, M. Vamvakaki, B. Chichkov, Multiphoton polymerization of hybrid materials. J. Opt. **12**, 124001 (2010)
28. M. Malinauskas, M. Farsari, A. Piskarskas, S. Juodkazis, Ultrafast-laser micro/nano-structuring of photo-polymers: a decade of advances. Phys. Rep. **533**, 1–31 (2013)
29. G.J. Owens, R.K. Singh, F. Foroutan, M. Alqaysi, C.M. Han, C. Mahapatra, H.W. Kim, J.C. Knowles, Sol–gel based materials for biomedical applications. Progr. Mater. Sci. **77**, 1–79 (2016)
30. J. Liu, Y. Liu, C. Deng, K. Yu, X. Fan, W. Zhang, Y. Tao, H.e Hu, L. Deng, W. Xiong, 3D printing nano-architected semiconductors based on versatile and customizable metal-bound composite photoresins. Adv. Mat. Tech. **7**(6) 2101230 (2022)
31. J. Livage, Sol-gel synthesis of hybrid materials. Bull. Mater. Sci. **22**, 201–205 (1999)
32. M. Oubaha, Introduction to hybrid sol-gel materials, in *World Scientific Reference of Hybrid Materials* (2019), pp. 1–36
33. B.L. Rivas, B.F. Urbano, J. Sánchez, Water-soluble and insoluble polymers, nanoparticles, nanocomposites and hybrids with ability to remove hazardous inorganic pollutants in water. Front. Chem. **6**, 320 (2018)
34. S. Fafenrot, N. Grimmelsmann, M. Wortmann, A. Ehrmann, Three-dimensional (3D) printing of polymer-metal hybrid materials by fused deposition modeling. Materials **10**(10), 1199 (2017)
35. E. Balčiūnas, S. Baldock, N. Dreize, M. Grubliauskaitė, S. Coultas, D. Rochester, M. Valius, J. Hardy, D. Baltriukiene, 3D printing hybrid organometallic polymer-based biomaterials via laser two-photon polymerisation. Polym. Int. **68**, 08 (2019)
36. Q. Wen, Z. Yu, R. Riedel, The fate and role of in situ formed carbon in polymer-derived ceramics. Progr. Mater. Sci. **109**, 100623 (2020)
37. A. Ovsianikov, J. Viertl, B. Chichkov, M. Oubaha, B. Maccraith, I. Sakellari, A. Giakoumaki, D. Gray, M. Vamvakaki, M. Farsari, C. Fotakis, Ultra-low shrinkage hybrid photosensitive material for two-photon polymerization microfabrication. ACS Nano **2**, 2257–2262 (2008)
38. P. Colombo, G. Mera, R. Riedel, G.D. Soraru̇, Polymer-derived ceramics: 40 years of research and innovation in advanced ceramics. J. Am. Ceram. Soc. **93**, 1805–1837 (2010)
39. P. Colombo, G. Mera, R. Riedel, Gian D. Sorarú, Polymer-derived ceramics: 40 years of research and innovation in advanced ceramics. J. Am. Ceram. Soc. **93**(7), 1805–1837 (2010)
40. L. Jonušauskas, D. Gailevicius, L. Mikoliunaite, D. Sakalauskas, S. Sakirzanovas, S. Juodkazis, Optically clear and resilient free-form μ-optics 3D-printed via ultrafast laser lithography. Materials **10**, 12 (2017)
41. D.L.G. Hernandez, S. Varapnickas, G. Merkininkaite, A. Ciburys, D. Gailevičius, S. Sakirzanovas, S. Juodkazis, M. Malinauskas, Laser 3D printing of inorganic free-form micro-optics. Photonics **8**(12), 577 (2021)
42. M. Nogami, Glass preparation of the ZrO_2-SiO_2 system by the sol-gel process from metal alkoxides. J. Non-Crystall. Sol. **69**, 415–423 (1985)
43. M. Schmid, F. Sterl, S. Thiele, A. Herkommer, H. Giessen, 3D printed hybrid refractive/diffractive achromat and apochromat for the visible wavelength range. Opt. Lett. **46**(10), 2485–2488 (2021)
44. A. Vyatskikh, R.C. Ng, B. Edwards, R.M. Briggs, J.R. Greer, Additive manufacturing of high-refractive-index, nanoarchitected titanium dioxide for 3D dielectric photonic crystals. Nano Lett. **20**(5), 3513–3520 (2020)
45. K. Arnold, S. Sevim, J. Puigmartí–Luis, A. Quick, M. Thiel, A. Hrynevich, P.D. Dalton, D. Helmer, B.E. Rapp, F. Kotz, P. Risch, Fabrication of arbitrary three-dimensional suspended hollow microstructures in transparent fused silica glass. Nat. Commun. **10**(1439) (2019)

46. J. Bauer, C. Crook, A.G. Izard, Z.C. Eckel, N. Ruvalcaba, T.A. Schaedler, L. Valdevit, Additive manufacturing of ductile, ultrastrong polymer-derived nanoceramics. Matter **1**(6), 1547–1556 (2019)
47. Z. Vangelatos, H.-M. Sheikh, P.-S. Marcus, C.-P. Grigoropoulos, V.-Z. Lopez, G. Flamourakis, M. Farsari, Strength through defects: A novel Bayesian approach for the optimization of architected materials. Sci. Adv. **7**, 2218 (2021)
48. E. Blasco, J. Muller, P. Muller, V. Trouillet, M. Schon, T. Scherer, C. Barner-Kowollik, M. Wegener, Fabrication of conductive 3D gold-containing microstructures via direct laser writing. Adv. Mater. **28**, 3592–3595 (2016)
49. C. Ido, I.S.R.K. Chaitanya, B. Alisa, L. Uriel, M. Shlomo, 3D printing of micrometer-sized transparent ceramics with on-demand optical-gain properties. Adv. Mat. **32**(28), 2001675 (2020)
50. Y. Cheng, C. Qun, P. Pumidech, L. Scott, G. Mallikarjunarao, L. Nickolay, V.B. Jill, 3D-printed carbon electrodes for neurotransmitter detection. Angew. Chem. Int. Ed. **57**(43), 14255–14259 (2018)
51. D.W. Yee, M.L. Lifson, B.W. Edwards, J.R. Greer, Additive manufacturing of 3D-architected multifunctional metal oxides. Adv. Mater. **31**(33), 1901345 (2019)
52. G. Konstantinou, E. Kakkava, L. Hagelüken, P. Vallachira W. Sasikumar, J. Wang, M.G. Makowska, G. Blugan, N. Nianias, F. Marone, H. Van Swygenhoven, J. Brugger, D. Psaltis, C. Moser, Additive micro-manufacturing of crack-free PDCs by two-photon polymerization of a single, low-shrinkage preceramic resin. Addit. Manuf. **35**, 101343 (2020)
53. A. Zakhurdaeva, P.I. Dietrich, H. Hölscher, Ch. Koos, J.G. Korvink, S. Sharma, Custom-designed glassy carbon tips for atomic force microscopy. Micromachines **8**(9), 285 (2017)
54. S. Passinger, M. Saifullah, C. Reinhardt, K.R.V Subramanian, B. Chichkov, M. Welland, Direct 3D patterning of TiO_2 using femtosecond laser pulses. Ad. Mat. **19**, 1218–1221 (2007)
55. R.K. Jayne, Th. J. Stark, J.B. Reeves, D.J. Bishop, A.E. White, Dynamic actuation of soft 3D micromechanical structures using micro-electromechanical systems (MEMS). Adv. Mater. Technol. **3**(3), 1700293 (2018)
56. Z. Vangelatos, L. Wang, C.P. Grigoropoulos, Laser pyrolysis for controlled morphing and chemical modification on 3D microlattices. J. Micromech. Microeng. **30**, 055008 (2020)
57. B. Cardenas-Benitez, C. Eschebaum, D. Mager, J. Korvink, M. Madou, U. Lemmer, I. De Leon, S.O. Martinez-Chapa, Pyrolysis-induced shrinking of three-dimensional structures fabricated by two-photon polymerization: experiment and theoretical model. Microsyst. Nanoeng. **5**, 1–13 (2019)
58. Y. Liu, H. Wang, J. Ho, R. Ng, R. Ng, V. Hall-Chen, E. Koay, Z. Dong, H. Liu, C.W. Qiu, J. Greer, J. Yang, Structural color three-dimensional printing by shrinking photonic crystals. Nat. Commun. **10**, 1–8 (2019)
59. T.A. Pham, D.-P. Kim, T.-W. Lim, S.-H. Park, D.-Y. Yang, K.-S. Lee, Three-dimensional SiCN ceramic microstructures via nano-stereolithography of inorganic polymer photoresists. Adv. Funct. Mater. **16**(9), 1235–1241 (2006)
60. F. Kotz, A.S. Quick, P. Risch, T. Martin, T. Hoose, M. Thiel, D. Helmer, B.E. Rapp, Two-photon polymerization of nanocomposites for the fabrication of transparent fused silica glass microstructures. Adv. Mat. **33**(9), 2006341 (2021)
61. W. Wang, F. Ye, S. Yue, H. Guo, G. Gao, Y. Zhao, Q. Fang, C. Nguyen, X. Zhang, J. Bao, J.T. Robinson, P.M. Ajayan, J. Lou, X. Wen, B. Zhang, 3D-printed silica with nanoscale resolution. Nat. Mater. **20**, 1506–1511 (2021)
62. J. Fischer, G. von Freymann, M. Wegener, The materials challenge in diffraction-unlimited direct-laser-writing optical lithography. Adv. Mater. **22**, 3578–3582 (2010)
63. J. Fischer, M. Wegener, Three-dimensional optical laser lithography beyond the diffraction limit. Laser Photon. Rev. **7**, 22–44 (2013)
64. R. Wollhofen, J. Katzmannn, C. Hrelescu, J. Jacak, T.A. Klar, 120 nm resolution and 55 nm structure size in STED-lithography. Opt. Exp. **21**, 10831–10840 (2013)
65. A. Zukauskas, I. Matulaitiene, D. Paipulas, G. Niaura, M. Malinauskas, R. Gadonas, Tuning the refractive index in 3D direct laser writing lithography: towards GRIN microoptics. Laser. Photon. Rev. **9**(6), 706–712 (2015)

66. S. Grauzeliene, A. Navaruckiene, E. Skliutas, M. Malinauskas, A. Serra, J. Ostrauskaite, Vegetable oil-based thiol-ene/thiol-epoxy resins for laser direct writing 3D micro-/nano-lithography. Polymers **13**, 872 (2021)
67. A. Navaruckiene, E. Skliutas, S. Kasetaite, S. Rekstyte, V. Raudoniene, D. Bridziuviene, M. Malinauskas, J. Ostrauskaite, Vanillin acrylate-based resins for optical 3D printing. Polymers **12**(2), 397 (2020)
68. P. Boch, J.-C Niepce, *Ceramic Materials: Processes, Properties and Applications* (2010)
69. J. Binner, M. Porter, B. Baker, J. Zou, V. Venkatachalam, V.R. Diaz, A. D'Angio, P. Ramanujam, T. Zhang, T.S.R.C. Murthy, Selection, processing, properties and applications of ultra-high temperature ceramic matrix composites, UHTCMCs—a review. Int. Mater. Rev. **65**(7), 389–444 (2020)
70. R. Bermejo, L. Llanes, P. Supancic, T. Lube, Thermal shock behaviour of an Al_2O_3/ZrO_2 multilayered ceramic with residual stresses due to phase transformations. Key Eng. Mater. **290**, 191–198 (2005)
71. W. Liu, Y. Xie, Z. Deng, Y. Peng, J. Dong, Z. Zhu, D. Ma, Z. Yi, G. Zhang, X. Wang, Preparation of Al_2TiO_5 ceramic fibers and thermal expansion, insulation, and strength of ZrO_2-Al_2TiO_5 fiberboards (2021)
72. Z.L. Belal M.S. Elmaghraby, A.I.M. Ismail, Thermal expansion, physico-mechanical properties and microstructure of cordierite synthesized from different starting materials. Int. Ceram. Rev. **64**, 209–213 (2015)
73. E. Bajraktarova Valjakova, V. Korunoska-Stevkovska, B. Kapusevska, N. Gigovski, C. Bajraktarova Misevska, A. Grozdanov, Contemporary dental ceramic materials, a review: Chemical composition, physical and mechanical properties, indications for use. Open Access Macedonian J. Med. Sci. **6**, 1742 (2018)
74. E. Moustafa, Hybridization effect of BN and Al_2O_3 nanoparticles on the physical, wear, and electrical properties of aluminum AA1060 nanocomposites. Appl. Phys. A, **127**, 1–9 (2021)
75. Q. Chen, B. Zou, Q. Lai, Y. Wang, R. Xue, H. Xing, X. Fu, C. Huang, P. Yao, A study on biosafety of HAP ceramic prepared by SLA-3D printing technology directly. J. Mech. Behav. Biomed. Mater. **98**, 327–335 (2019)
76. H.M. Oh, Y.J. Park, H.N. Kim, J.W. Ko, H.K. Lee, Effect of milling ball size on the densification and optical properties of transparent Y_2O_3 ceramics. Ceram. Int. **47**(4), 4681–4687 (2021)
77. A. Solodar, R. Drevinskas, P. Kazansky, I. Abdulhalim, A. Cerkauskaite, Ultrafast laser induced nanostructured ITO for liquid crystal alignment and higher transparency electrodes. Appl. Phys. Lett. **113**, 081603 (2018)
78. T.D. Nguyen, L.P. Yeo, T.C. Kei, D. Mandler, S. Magdassi, A.I.Y. Tok, Efficient near infrared modulation with high visible transparency using SnO_2–WO_3 nanostructure for advanced smart windows. Adv. Opt. Mater. **7**(8), 1801389 (2019)
79. L. Wang, B. Lu, X. Liu, Y. Shi, J. Li, Y. Liu, Fabrication and upconversion luminescence of novel transparent Er_2O_3 ceramics. J. Eur. Ceram. Soc. **40**(4), 1767–1772 (2020)
80. K. Hashimoto, H. Irie, A Fujishima, TiO_2 photocatalysis: a historical overview and future prospects. Jpn. J. Appl. Phys. **44**(12), 8269–8285 (2005)
81. H. Yin, A. Akey, R. Jaramillo, Large and persistent photoconductivity due to hole-hole correlation in CdS. Phys. Rev. Mater. **2**, 084602 (2018)
82. Y. Yao, D. Sang, L. Zou, Q. Wang, C. Liu, A review on the properties and applications of WO_3 nanostructure based optical and electronic devices. Nanomaterials **11**(8), 2136 (2021)
83. S. Trolier-McKinstry, S. Zhang, A.J. Bell, X. Tan, High-performance piezoelectric crystals, ceramics, and films. Annu. Rev. Mater. Res. **48**(1), 191–217 (2018)
84. B. Szafraniak, Ł. Fuśnik, J. Xu, F. Gao, A. Brudnik, A. Rydosz, Semiconducting metal oxides: $SrTiO_3$, $BaTiO_3$ and $BaSrTiO_3$ in gas-sensing applications: a review. Coatings **11**(2) (2021)
85. D. Mendes, D. Sousa, An. C. Cerdeira, L. C.J. Pereira, A. Marques, J. Murta-Pina, A. Pronto, I. Ferreira, Low-cost and high-performance 3D printed YBCO superconductors. Ceram. Int. **47**(1), 381–387 (2021)

86. Z. Chen, Z. Li, J. Li, C. Liu, Ch. Lao, Y. Fu, C. Liu, Y. Li, P. Wang, Y. He, 3D printing of ceramics: a review. J. Eur. Ceram. Soc. **39**(4), 661–687 (2019)
87. K. Watari, High thermal conductivity non-oxide ceramics. J. Ceram. Soc. Jpn. **109**(1265), S7–S16 (2001)
88. S. Thapliyal, *Manufacturing and characterization of a 3D-printable, antibacterial, magnesium oxide nanoparticles reinforced ABS filament*. Ph.D. Thesis, 04 2017
89. B. Leukers, H. Gülkan, S. Irsen, S. Milz, C. Tille, H. Seitz, M. Schieker, Biocompatibility of ceramic scaffolds for bone replacement made by 3D printing. Materialwiss. Werkstofftech. **36**, 781–787, 12 (2005)
90. X. Du, S. Fu, Y. Zhu, 3D printing of ceramic-based scaffolds for bone tissue engineering: an overview. J. Mater. Chem. B **6**, 06 (2018)
91. K. Weber, D. Werdehausen, P. König, S. Thiele, M. Schmid, M. Decker, P.W. De Oliveira, A. Herkommer, H. Giessen, Tailored nanocomposites for 3D printed micro-optics. Opt. Mater. Exp. **10**(10), 2345–2355 (2020)
92. T. Shimazu, H. Maeda, E.H. Ishida, M. Miura, N. Isu, A. Ichikawa, K. Ota, High-damping and high-rigidity composites of Al_2TiO_5–$MgTi_2O_5$ ceramics and acrylic resin. J. Mater. Sci. **44**, 93–101 (2009)
93. J. Wang, Extrusion-based 3D printing of macro/microstructures for advanced lithium/sodium batteries (2019)
94. Z. Liu, J. Yu, P. Li, W. Xiaolong, Z. Yusong, X. Chu, X. Wang, H. Li, Z. Wu, Band alignments of -Ga_2O_3 with MgO, Al_2O_3 and $MgAl_2O_4$ measured by X-ray photoelectron spectroscopy. J. Phys. D Appl. Phys. **52**, 295104 (2019)
95. C. Han, R. Babicheva, J. Dong Qiu Chua, U. Ramamurty, S. B. Tor, C. N. Sun, K. Zhou, Microstructure and mechanical properties of (TiB+TiC)/Ti composites fabricated in situ via selective laser melting of Ti and B_4C powders. Addit. Manuf. **36**, 101466 (2020)
96. K.A. Hamzah, C.K. Yeoh, M.M. Noor, P.L. Teh, Y.Y. Aw, S.A. Sazali, W.M.A.W. Ibrahim, Mechanical properties and thermal and electrical conductivity of 3D printed ABS-copper ferrite composites via 3D printing technique. J. Thermoplast. Compos. Mater. **35**(1), 3–16 (2022)
97. R. Venkatkarthick, J. Qin, A new 3D composite of V_2O_5-based biodegradable ceramic material prepared by an environmentally friendly thermal method for supercapacitor applications. Environ. Technol. Innovation **22**, 101474 (2021)
98. Li B. Chen Z. Mi S.-Lao C. Liu C., Cheng X, Fabrication and characterization of 3D-printed highly-porous 3D $LiFePO_4$ electrodes by low temperature direct writing process. Materials **8**, 934 (2017)
99. M. Väätäjä, H. Kähäri, K. Ohenoja, M. Sobocinski, J. Juuti, H. Jantunen, 3D printed dielectric ceramic without a sintering stage. Sci. Rep. **8**, 10 (2018)
100. J. Kopfler, T. Frenzel, J. Schamlian, M. Wegener, Fused-silica 3D chiral metamaterials via helium-assisted microcasting supporting topologically protected twist edge resonances with high mechanical quality factors. Adv. Mater. **33**, 2103205 (2021)
101. S. Rekstyte, E. Kaziulionyte, E. Balciunas, D. Kaskelyte, M. Malinauskas, Direct laser fabrication of composite material 3D microstructured scaffoldings. J. Laser Micro. Nanoen. **9**, 25–30 (2014)
102. E. Skliutas, M. Lebedevaite, S. Kasetaite, S. Rekstyte, S. Lileikis, J. Ostrauskaite, M. Malinauskas, A bio-based resin for a multi-scale optical 3D printing. Sci. Rep. **10**, 9758 (2020)
103. T. Gissibl, S. Thiele, A. Herkommer, H. Giessen, Sub-micrometre accurate free-form optics by three-dimensional printing on single-mode fibres. Nat. Commun. **7**, 11763 (2016)
104. A. Butkute, L. Cekanavičius, G. Rimselis, D. Gailevicius, V. Mizeikis, A. Melninkaitis, T. Baldacchini, L. Jonusauskas, M. Malinauskas, Optical damage thresholds of microstructures made by laser three-dimensional nanolithography. Opt. Lett. **45**, 13–16 (2020)
105. A. Toulouse, J. Drozella, P. Motzfeld, N. Fahrbach, V. Aslani, S. Thiele, H. Giessen, A.M. Herkommer, Ultra-compact 3D-printed wide-angle cameras realized by multi-aperture freeform optical design. Opt. Exp. **30**, 707–720 (2022)

Part III
Applications

Chapter 23
Creation of Material Functions by Nanostructuring

Marek Mezera, Camilo Florian, Gert-willem Römer, Jörg Krüger, and Jörn Bonse

Abstract Surface nanostructures provide the possibility to create and tailor surface functionalities mainly via controlling their topography along with other chemical and physical material properties. One of the most appealing technologies for surface functionalization via micro- and nanostructuring is based on laser processing. This can be done either via direct contour-shaping of the irradiated material using a tightly focused laser beam or in a self-ordered way that allows employing larger laser beam diameters along with areal scanning to create a variety of laser-induced periodic surface structures (LIPSS). For the latter approach, particularly ultrashort pulsed lasers have recently pushed the borders across long-lasting limitations regarding the minimum achievable feature sizes and additionally boosted up the production times. This chapter reviews the plethora of recently investigated applications of LIPSS—for example, via imposing diffractive or plasmonic structural colors, the management of liquids and surface wetting properties, biomedical and bioinspired functionalities, beneficial effects in tribology for reducing friction and wear, the manipulation of optical scattering and absorption in photovoltaics, or the modification of magnetic or superconducting surface properties in other energy applications. The footprint of the LIPSS-based technology is explored in detail regarding the current state of industrialization, including an analysis of the market and associated LIPSS production costs.

M. Mezera · J. Krüger · J. Bonse (✉)
Bundesanstalt für Materialforschung und -prüfung (BAM), Berlin, Germany
e-mail: joerg.krueger@bam.de; joern.bonse@bam.de

C. Florian
Princeton Institute for the Research and Technology of Materials (PRISM), Princeton University, Princeton, NJ, USA
e-mail: camilofb1@gmail.com

G.-w. Römer
Chair of Laser Processing, Department of Mechanics of Solids, Surfaces & Systems (MS3), University of Twente, Enschede, The Netherlands
e-mail: g.r.b.e.romer@utwente.nl

© The Author(s), under exclusive license to Springer Nature Switzerland AG 2023

R. Stoian, J. Bonse (eds.), *Ultrafast Laser Nanostructuring*, Springer Series in Optical Sciences 239, https://doi.org/10.1007/978-3-031-14752-4_23

Keywords Laser-induced periodic surface structures (LIPSS) · Surface functionalization · Nanostructures · Microstructures · Laser processing · Bioinspired surfaces · Surface wetting

1 Introduction: Laser-Induced Periodic Surface Structures–LIPSS

Laser-induced periodic surface structures (LIPSS) were reported for the first time more than 50 years ago [1]. Already during their early times, it became clear that LIPSS are a universal phenomenon that occurs when intense and coherent laser radiation is interacting with the surface of solids [2]. Depending on the polarization state of the laser radiation (linear, circular, radial, vector states carrying an angular momentum, etc.), the formed LIPSS can exhibit very different surface morphologies and geometrical characteristics, for example, spatial periods, modulation depths, aspect ratios, orientations, etc. (for a detailed classification of LIPSS, see the following Sect. 1.1).

During the last decades, the topic of LIPSS has evolved into a scientific evergreen [3]. While during the 1980s the fundamental theories on LIPSS were successfully developed [4], the LIPSS phenomenon itself was rather considered as curiosity that finally did not enter the stage of practical applications. Later, starting around the turn of the millennium—with the broader availability of ultrashort pulsed laser systems in research laboratories—the topic has experienced again a vivid revival. From that time on, lots of scientific research has again focused on the fundamental formation mechanisms of LIPSS, particularly when created with femtosecond laser pulses. In that case, the stages of energy deposition to the solid driving the material into a strongly excited state and the stage of subsequent matter reorganization are temporally well separated. For detailed review articles on the origin of LIPSS, the reader is referred to [3, 5–11] and to Chap. 1 (Derrien et al.), Chap. 2 (Ivanov et al.), and Chap. 5 (Rudenko et al.) of this book. Moreover, during the last 5 to 10 years, a systematic screening of potential applications of LIPSS was performed [7, 10, 12–18], pointing toward many different scientific and practical aspects of LIPSS.

The following chapter aims to provide a comprehensive review on the variety of different surface functionalizations that can be created through LIPSS. These specific surface functions finally can be transferred into various applications in optics, fluidics, medicine, tribology, energy saving, etc.

1.1 Zoology of LIPSS

In this section, the variety of different kinds of self-organized laser-induced surface structures is presented, providing a systematic and strict classification of LIPSS along with current terminologies that can be found in the literature. We focus particularly on *low spatial frequency LIPSS* (LSFL), *high spatial frequency LIPSS* (HSFL), and *triangular nanopillars* (TNP) and explain how these subwavelength structures can be distinguished from supra-wavelength *grooves* and more irregular *spikes* structures.

Depending on the laser processing strategy ("spot processing" vs. "scanning processing" of lines or larger areas) and the specific laser irradiation parameters (fluence, number of pulses, spatial beam profile, etc.), structures of a single type of LIPSS, spatially separated regions of distinct LIPSS, or even multiple mixed types of LIPSS or hierarchical surface structures may be simultaneously observed [10].

In a strict classification, LIPSS represent a 1D- or sometimes 2D-quasiperiodic grating structure and are usually classified with respect to their spatial period Λ (compared to the irradiation wavelength λ), their relation to the laser beam polarization (linear, circular, etc.), and their depth-to-period aspect ratio A.

Low Spatial Frequency LIPSS (LSFL)

The most prominent type of LIPSS that was historically observed first in 1965 by Birnbaum [1] are LSFL. For radiation that is incident normal to the surface of a solid (angle of incidence $\theta = 0°$), LSFL typically have periods close to or somewhat smaller than the laser irradiation wavelength λ used to create them ($\lambda/2 \leq \Lambda_{\mathrm{LSFL}} \leq \lambda$) and an aspect ratio A typically <1. These structures usually form in the ablative regime at fluence levels up to several times the ablation threshold (material specific), although also melting-induced or oxidative LSFL were reported [3]. For strongly absorbing materials such as metals or semiconductors, LSFL are typically oriented perpendicular to the linear laser beam polarization (type LSFL-I), while for weakly absorbing wide band gap dielectrics, they are typically parallel to it (type LSFL-II). Note that the numbering of the different types of LIPSS with Roman letters (-I/-II) follows the historic order of observation.

The dissimilarity of both types of LSFL arises from the different coherent optical scattering mechanisms involved in their formation. LSFL-I originate from the excitation of so-called *Surface Electromagnetic Waves* (SEWs) [19, 20], such as *Surface Plasmon Polaritons* (SPPs) and the optical interference of their electromagnetic fields with the incident laser beam itself, resulting in a spatially modulated pattern of the locally deposited optical energy that finally translates into a periodically corrugated surface topography [9, 21]. For p-polarized laser radiation, the surface grating relief then exhibits spatial periods close to the wavelength ($\Lambda_{\mathrm{LSFL\text{-}I,p}} \sim \lambda/[1 \pm \sin(\theta)]$). In contrast, for dielectrics, the LSFL-II are seeded some hundreds of nanometers below the surface and originate from the interference of the incident (propagating) laser radiation with light coherently scattered at the surface roughness (via radiative fields that are propagating toward the far-field region) [22]. Via multiple laser pulse irradiation and incubation effects in the material (inter-pulse feedback), the LSFL-II signature emerges at the surface once the covering near-surface material is removed through ablation ($\Lambda_{\mathrm{LSFL\text{-}II}} \sim \lambda/\{n[1 \pm \sin(\theta)]\}$, with n being the (real valued) refractive index of the dielectric [6]).

Figure 23.1 exemplifies LSFL-I that were formed at the surface of a niobium metal sheet upon scanning fs-laser pulse irradiation in air environment [790 nm,

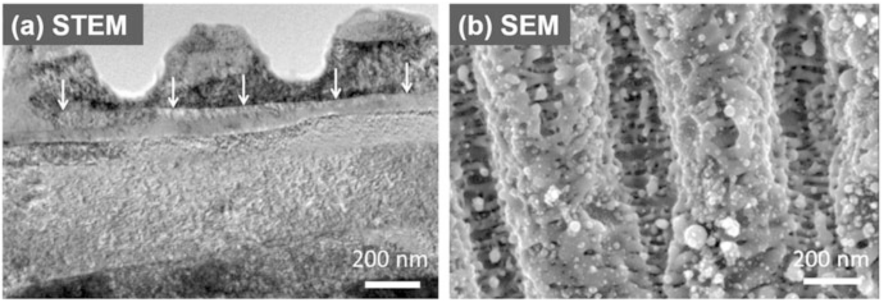

Fig. 23.1 (**a**) STEM micrograph of the cross-sectional surface profile of LSFL-I on polycrystalline niobium [790 nm, 30 fs, 1 kHz]. (**b**) Top-view SEM micrograph of the corresponding surface structures. The white arrows in (**a**) mark at the boundary between laser-affected zone and non-affected bulk material. (Reprinted (adapted) from [23], Cubero et al., Surface superconductivity changes of niobium sheets by femtosecond laser-induced periodic nanostructures, Nanomaterials (Basel, Switzerland) **10**:2025, Copyright 2020 under Creative Commons BY 4.0 license. Retrieved from https://doi.org/10.3390/nano10122525)

30 fs, 1 kHz, [23]]. Figure 23.1a shows a scanning transmission electron micrograph (STEM) of a cross-sectional cut through the surface of the processed LSFL. It can be observed that the LSFL-I are almost sinusoidal with a period of ~570 nm and a modulation depth of ~300 nm. Note the fine boundary (marked by five white arrows) that separates the laser-affected region from the non-affected polycrystalline niobium bulk material underneath. Supposedly, the niobium surface was melted up to this boundary during the fs-laser scan processing, resulting in a resolidified superficial layer of 40 to 300 nm here [23]. Figure 23.1b provides a corresponding top-view scanning electron micrograph of the LSFL-I.

High Spatial Frequency LIPSS (HSFL)

HSFL typically have periods smaller than half of the irradiation wavelength ($\Lambda_{\text{HSFL}} < \lambda/2$) and are oriented either parallel or perpendicular to the laser beam polarization (material dependent). They are formed at fluence levels very close to the damage threshold of the irradiated material and predominantly for ultrashort pulse durations in the fs- to ps-range. Two types are usually distinguished.

HSFL-I are mainly observed on transparent materials (dielectrics and semiconductors). They consist of very narrow periodic grooves having individual widths of a few tens of nanometers only, while their depth can reach up to several hundreds of nanometers. Given their large aspect ratio $A > 1$, some authors call these nanostructures *"deep subwavelength ripples/structures"*. For (semi)transparent materials and normal incident laser radiation, HSFL-I usually exhibit spatial periods of $\Lambda_{\text{HSFL-I}} \sim \lambda/(2n)$, with n being the refractive index of the material. HSFL-I originate from the near-(sub)surface interference of the incident (propagating) laser radiation with light coherently near-field scattered at nanoscale surface corrugations (via non-radiative fields confined to the near-field region of the scattering centers) [22].

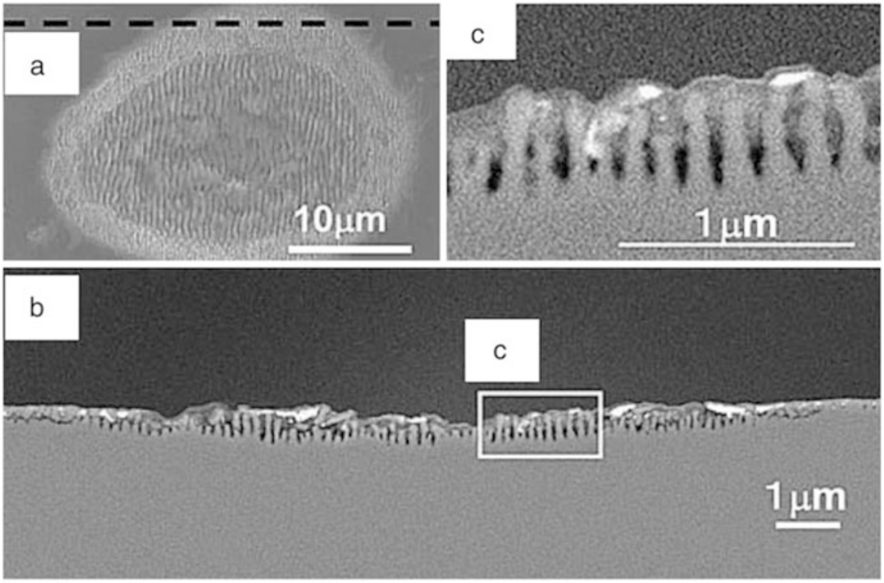

Fig. 23.2 (**a**) Top-view SEM image LSFL-I (center) and HSFL-I (periphery) on SiC. The dashed black line marks the position where the cross-sectional profiles (**b**, **c**) were acquired [800 nm, 150 fs, 50 Hz]. (**b**) Cross-sectional SEM micrograph of the whole irradiated spot. (**c**) Detailed magnification of selected area (**c**) marked in (**b**). Taken from [24]. (Reprinted by permission from Springer-Verlag: Applied Physics A **97**:271–276 (Cross-sectional morphological profiles of ripples on Si, SiC, and HOPG, Tomita, T. et al.), Copyright (2009))

Figure 23.2 demonstrates the large depth-to-period aspect ratio *A* of the HSFL-I (b,c) that were formed in the periphery of an LSFL-I covered ablation crater (a) at the surface of a silicon carbide (SiC) crystal after spot processing by fs-laser pulses in air [800 nm, 150 fs, 50 Hz [24]].

In contrast, HSFL-II have depths of only a few tens of nanometers and spatial periods of the order of ~100 nm. Hence, the resulting aspect ratio is far smaller than one ($A \ll 1$). These shallow structures are often observed on metal surfaces, and different formation mechanisms were suggested, including surface oxidation or twinning effects.

From the three observations that both types of HSFL mainly form upon irradiation with ultrashort laser pulses, are strictly related to the direction of the linear laser beam polarization, and have a lower period limit of a few tens of nanometers (caused by thermal diffusion effects washing out too small spatial modulations during the electron-phonon relaxation stage), it was concluded that ultrafast energy deposition dominates their formation [3]. However, for the HSFL-II, recent numerical 3D *Finite-Difference Time-Domain* (FDTD) calculations [25] combined with a numerical solution of the *Navier-Stokes equations* point toward a complex interplay of coherent electromagnetic scattering and subsequent thermoelastic and hydrodynamic effects, all triggered by the strong ultrafast laser excitation of the solid [26] (see also Chap. 5 (Rudenko et al.)).

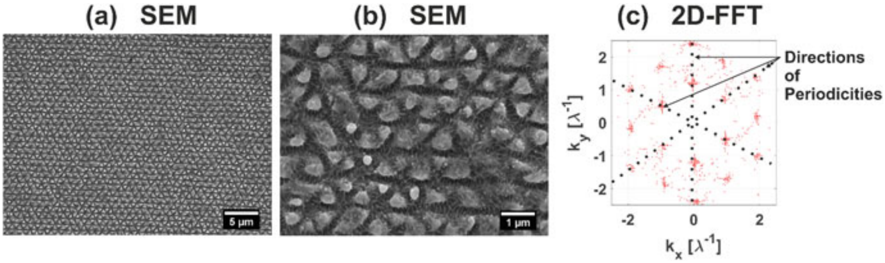

Fig. 23.3 (**a**, **b**) Top-view SEM micrographs of TNPs processed on CoCrMo-alloy upon scan processing with circularly polarized ps-laser pulses [1030 nm, 6.7 ps, 400 kHz]. (**c**) 2D-FFT of the micrograph shown in (**a**) indicating a hexagonal symmetry of the TNP arrangement along with spatial periods of Λ_{TNP} ~ 860 nm. (Adapted and reprinted from [31], van der Poel et al., Fabricating Laser-Induced Periodic Surface Structures on Medical Grade Cobalt–Chrome–Molybdenum: Tribological, Wetting and Leaching Properties, Lubricants (Basel, Switzerland) **7**:70, Copyright 2019 under Creative Commons BY 4.0 license. Retrieved from https://doi.org/10.3390/lubricants7080070)

Triangular Nanopillars (TNPs)

Starting in 2018, another characteristic surface morphology was reported by several groups for the irradiation of different metals by ultrashort laser pulses in a scan-processing geometry under specific laser processing conditions [27–31]. These surface structures consist of nanometric triangular-shaped nanopillars as building blocks for hexagonally arranged meta-units that finally form a large area 2D-grating at the laser-processed surface. Therefore, this type of LIPSS is referred to either as *"triangular nanopillars"* (TNPs) or as "*hexagonally arranged nano-triangles*" in the pertinent literature. While in Romano et al. [30] the TNPs were realized on stainless steel with multiple circularly polarized fs-laser pulses at high repetition rate (1032 nm, 310 fs, 250 kHz), Liu et al. [28] reported their formation on tungsten surfaces upon low repetition rate (800 nm, 50 fs, 1 kHz) double-fs-pulse irradiation using cross-polarized linear polarization and an inter-pulse delay of ~1 ps and with cylinder lens focusing. Fraggelakis et al. [32] used high repetition rate (1030 nm, 350 fs, 100 kHz) double-fs-pulses with circular counter rotating polarizations and inter-pulse delays up to a few nanoseconds and with spherical lens focusing for their processing. Later, van der Poel et al. [31] generated these TNPs on a cobalt-chrome-molybdenum-alloy (CoCrMo) with multiple circularly polarized ps-laser pulses (1030 nm, 6.7 ps, 400 kHz). An example from that work is provided in Fig. 23.3, where two top-view SEM micrographs (a,b) are shown that were taken at different magnifications. Figure 23.3c is a 2D-Fast Fourier Transform (2D-FFT) of the micrograph displayed in (a), representing a 2D-histogram (map) of the spatial frequencies contained in the transformed image. The characteristic arrangement of the pronounced peaks in Fig. 23.3c reflects the hexagonal symmetry of the TNP-grating structure, while their positions indicate very similar spatial periods of Λ_{TNP} ~ 860 nm found in several directions here.

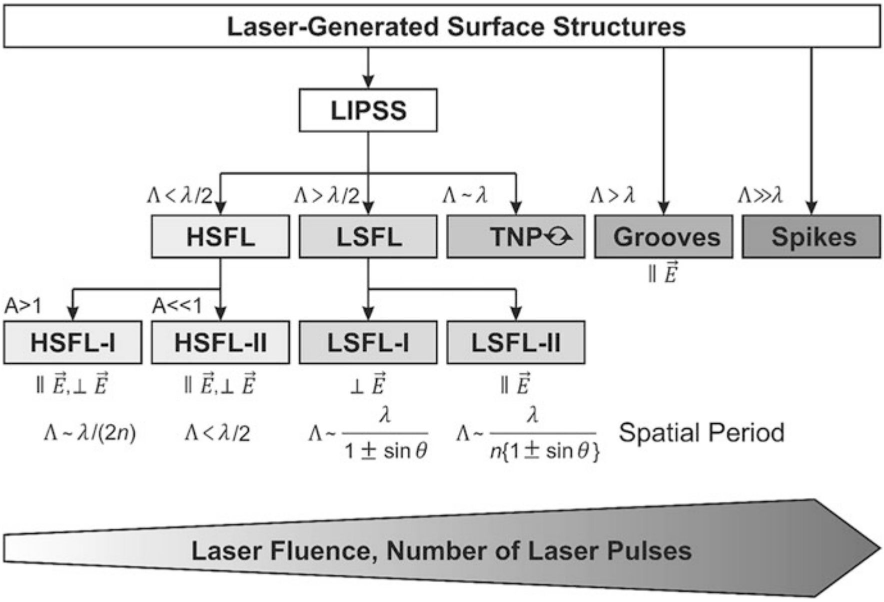
Laser-Generated Surface Structures
LIPSS
Λ<λ/2
Λ>λ/2
Λ~λ
Λ>λ
Λ≫λ
HSFL
LSFL
TNP
Grooves
Spikes
∥ E
A>1
A<<1
HSFL-I
HSFL-II
LSFL-I
LSFL-II
∥ E, ⊥ E
∥ E, ⊥ E
⊥ E
∥ E
Λ~λ/(2n)
Λ<λ/2
Λ~λ/(1±sinθ)
Λ~λ/(n{1±sinθ})
Spatial Period
Laser Fluence, Number of Laser Pulses

Fig. 23.4 Classification of laser-generated surface structures. (Adapted from [29])

The physical origin of the TNPs is currently vividly discussed in the scientific community. Since their spatial periods are very close to that of the LSFL-I when formed at the same material ($\Lambda_{\mathrm{TNP}} \approx \Lambda_{\mathrm{LSFL\text{-}I}}$), it is reasonable that an SPP-based formation mechanism should be invoked for their explanation [28, 33, 34]. Additionally, a nonlinear hydrodynamic convection flow mechanism was proposed to be relevant [32] (see also Chap. 5 (Rudenko et al.)).

Classification of Laser-Generated Surface Structures
Figure 23.4 orders the plethora of different laser-generated surface structures in a single scheme. The branch of the LIPSS was discussed already in detail in the previous subsections. Apart from the LIPSS, also supra-wavelength *grooves* ($\Lambda_{\mathrm{grooves}} > \lambda$) were observed, typically featuring an orientation parallel to the laser beam polarization and periods in the few micrometers range. Even larger structural sizes are observed for the irregular *spikes* morphology (sometimes referred to as *micro-cones*), which exhibit a very weak correlation to the polarization only and "periods" up to some tens of micrometers ($\Lambda_{\mathrm{spikes}} >> \lambda$).

The general requirements on the laser fluence and the number of laser pulses for the generation of the different surface nano- and microstructures are indicated by the arrow in the bottom part of Fig. 23.4. For a more detailed discussion of the specific formation mechanisms of grooves and spikes, the reader is referred to the specialized literature [9, 18, 29, 35].

1.2 Physical and Chemical Properties of LIPSS

In this section, physical and chemical surface properties are discussed that may be altered and controlled through LIPSS for creating specific surface functions. Figure 23.5 summarizes the different properties that are discussed in more detail in the following two subsections *Physical Properties* and *Chemical Properties*.

Physical Properties

LIPSS can create various specific physical surface properties. The most obvious one is the characteristic grating-like *surface topography* that is describing the interface between the sample material and the ambient environment. Since the formation of LIPSS includes a complex chain of different stages, starting with the optical material excitation via absorption by the electrons of the solid, followed by the transfer of the energy from the electrons to the lattice of the solid, and a cascade of subsequent relaxation processes, such as melting, ablation, solidification in

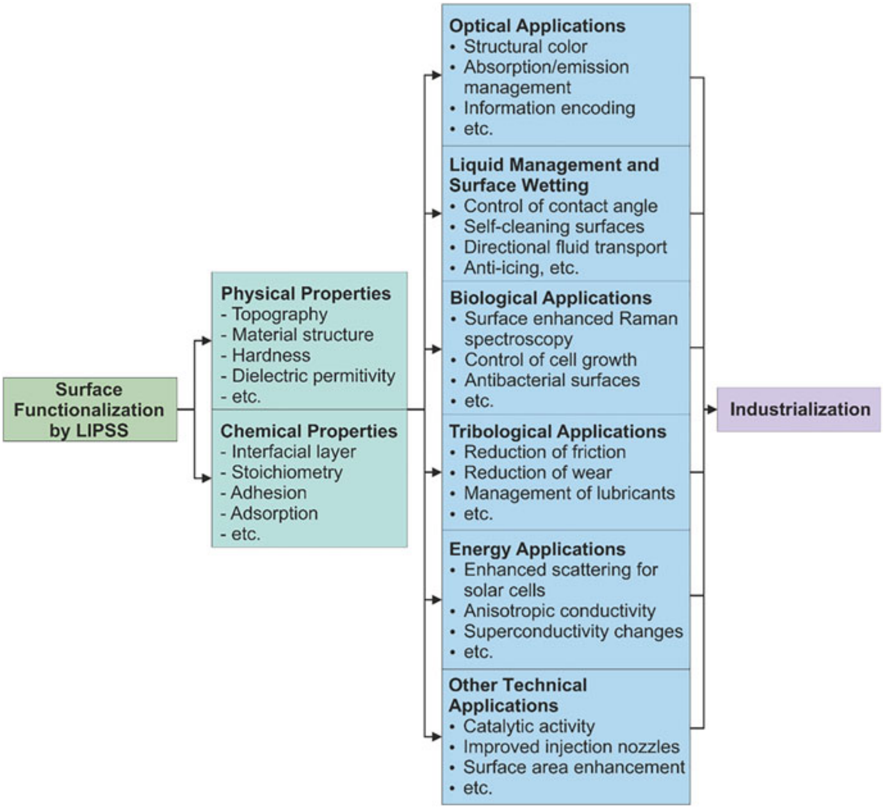
Surface Functionalization by LIPSS
Physical Properties
- Topography
- Material structure
- Hardness
- Dielectric permitivity
- etc.
Chemical Properties
- Interfacial layer
- Stoichiometry
- Adhesion
- Adsorption
- etc.
Optical Applications
• Structural color
• Absorption/emission management
• Information encoding
• etc.
Liquid Management and Surface Wetting
• Control of contact angle
• Self-cleaning surfaces
• Directional fluid transport
• Anti-icing, etc.
Biological Applications
• Surface enhanced Raman spectroscopy
• Control of cell growth
• Antibacterial surfaces
• etc.
Tribological Applications
• Reduction of friction
• Reduction of wear
• Management of lubricants
• etc.
Energy Applications
• Enhanced scattering for solar cells
• Anisotropic conductivity
• Superconductivity changes
• etc.
Other Technical Applications
• Catalytic activity
• Improved injection nozzles
• Surface area enhancement
• etc.
Industrialization

Fig. 23.5 Scheme of properties affected by LIPSS and resulting applications for surface functionalization, providing the frame for this book chapter. (Inspired by [13])

amorphous or crystalline states, etc. [9, 36], it becomes obvious that also structural material properties can be altered through the laser processing of LIPSS. As consequence, for example, the materials hardness [37], the dielectric permittivity [38], the electric conductivity [39], surface superconductivity [23], etc. can be locally modified through the presence of LIPSS, featuring specific applications in tribology, photonics, or electronics [10, 13, 16].

Chemical Properties

Apart from changes of physical properties, the formation of LIPSS is usually accompanied by chemical surface alterations, particularly if the laser processing is performed in air environment—a requirement that is strongly demanded for large area or industrial laser processing. Most prominently, typically surface oxidation occurs since high transient temperatures are reached in the reactive atmosphere air upon the processing of LIPSS [14, 15, 40, 41]. Hence, in an interfacial surface layer, the chemical composition of the irradiated material may change.

Apart from intrinsic stoichiometric material alterations, other topography- and roughness-related effects can be rendered possible through LIPSS: the enlarged surface area of the LIPSS allows molecules, such as hydrocarbons, to adsorb from the ambient environment [42–44]. Through such “aging” effects, even a transition from an initially hydrophilic surface into a superhydrophobic state can manifest—without any significant change of the surface topography. For many biomedical or healthcare applications, such topographic and surface wetting effects are particularly relevant for the controlled adhesion (repellent or adducent) of specific biological cells or even for the prevention of the formation of bacterial biofilms [45, 46]. On the other hand, the LIPSS-enhanced total surface area can help to increase the efficiency of catalytic chemical reactions [47].

From all these effects, different fields of surface functionalization can be identified that are discussed in the following Sect. 2 *Application of LIPSS*, including *Optical Applications* (Sect. 2.1), *Liquid Management and Surface Wetting* (Sect. 2.2), *Biological Applications* (Sect. 2.3), *Tribological Applications* (Sect. 2.4), *Energy Applications* (Sect. 2.5), and *Other Technical Applications* (Sect. 2.6). Finally, Sect. 3 analyzes the current state of *Industrialization* of LIPSS, providing a *Market Analysis* (Sect. 3.1), some quantitative estimates of the *Production Costs* (Sect. 3.2), and a compilation of the actual LIPSS-related *Patent Situation* (Sect. 3.3).

2 Applications of LIPSS

As outlined in the previous section, LIPSS exhibit some very specific intrinsic properties that can be used to create and tailor very different surface functionalities. Most of them finally fall back either to the topographic characteristics of LIPSS or to the specific surface chemistry involved during their formation (or even later). These surface functionalities enabled various applications that were studied already in detail in the context of LIPSS.

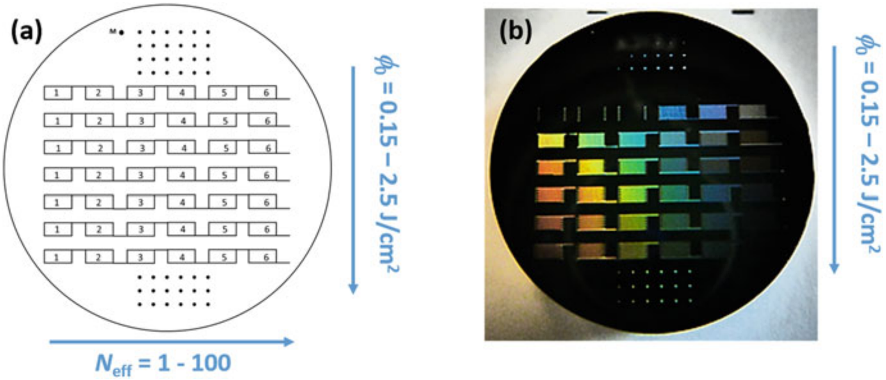

Fig. 23.6 (**a**) Scheme of laser processing. (**b**) Photograph of a polished 100Cr6 steel sample (24 mm diameter) after fs-laser processing [800 nm, 30 fs, 1 kHz] of spots, lines, and areas. The colors arise from optical diffraction of ambient light at laser-generated LSFL. (© 2016 IEEE. Reprinted, with permission, from [3], Bonse, J., et al., Laser-induced periodic surface structures—A scientific evergreen, IEEE J. Sel. Top. Quantum Electron, 2017, **23**:9000615)

2.1 Optical Applications

In this section, optical applications of laser-induced nanostructures on surfaces and subsurface layers are addressed. It is discussed that laser-induced periodic surface structures (LIPSS, ripples), nanostructure-textured microgrooves, and nanospikes can lead to diffractive structural coloring effects on metals (via ripples), modify the optical absorption of metal or semiconductor surfaces toward "black" materials (via microgrooves), or can decrease the reflectance on dielectrics leading to an antireflection effect (via nanospikes). Apart from optical emission and absorption management, safety tags can be realized via near surface 3D self-organization of nanocomposite films.

Structural Color

LIPSS with periods of the order of visible wavelengths can efficiently act as optical diffraction gratings and, thus, generate structural colors for optical applications. While some applications require the processing of individual spots or tailored lines, most of these utilizations rely on the homogeneous processing of LIPSS on large surface areas. Usually, this is implemented through laser scanners realizing a relative motion between the focused laser beam and the workpiece.

Figure 23.6 exemplifies the processing of spots, lines, and areas on a polished steel surface; see the scheme in Fig. 23.6a. For a fixed laser source (wavelength and pulse duration), the period of the LIPSS can be controlled by the laser fluence (ϕ_0) and the effective number of laser pulses per beam spot diameter (N_{eff}). On the sample, individual spots and lines connecting the areas generated through a meandering line-wise motion were processed by a Ti:Sapphire fs-laser system.

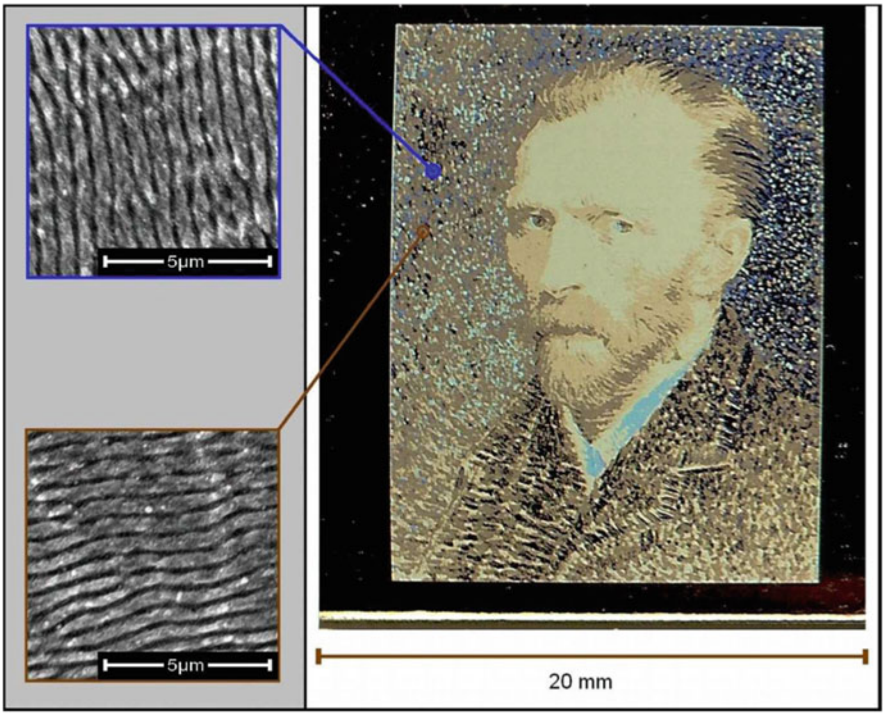

Fig. 23.7 Photograph (right) of a polished 316L stainless steel sample after fs-laser processing [800 nm, 150 fs, 5 kHz] of a miniaturized self-portrait of the painter Vincent van Gogh. The insets (left) are top-view scanning electron micrographs of LSFL with two different local orientations. (Reprinted with permission from [48], © Optical Society of America)

Depending on the LIPSS period, different structural colors appear as result of optical diffraction upon illumination of the sample with a white light source. This is demonstrated in Fig. 23.6b where color effects can be seen for the structured areas, lines, and even spots.

A pioneering work demonstrating the application of LIPSS for color marking and decoration purposes was presented by Dusser et al. [48] encoding a miniaturized, colored picture of the painter van Gogh on a steel surface; see Fig. 23.7. The color variation was implemented by a variation of the orientation of LSFL for a fixed angle of observation here.

For a more detailed discussion of structural color, the reader is referred to the recent review article of Liu et al. [17] and the references included.

Absorption and Emission Management

Hierarchical micro-nanostructures (e.g., microgrooves and spikes) largely increase the effective surface of a sample. Due to locally non-normal incident rays and multiple reflections, these surface topographies can cause an increase in the absorption of light. This effect is visualized in Fig. 23.8 for nanostructure-textured

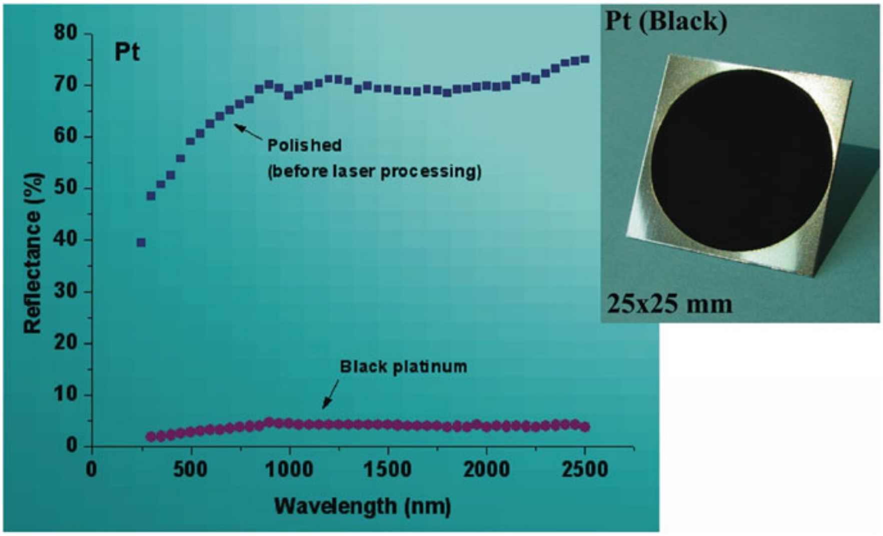

Fig. 23.8 Photograph of a fs-laser processed [800 nm, 65 fs, 1 kHz] "black platinum" sample covered with nanostructure-textured microgrooves (right). The corresponding total hemispherical reflectance spectrum is shown (left, violet full circles) along with a measurement of the polished surface as a reference (left, blue full squares). (Reprinted from [7] by permission from Wiley-VCH-Verlag GmbH: Laser Photonics Rev. **7**:285–307 (Direct femtosecond laser surface nano/microstructuring and its applications, Vorobyev, A.Y. and Guo, C.), Copyright (2012))

microgrooves on platinum forming a "black metal" [7]. The figure compares the spectral dependence of the reflectance of the polished Pt surface (full squares) with that of a fs-laser processed black Pt surface (full circles). The latter surface exhibits hemispherical reflectances of less than 5% in the ultraviolet to infrared spectral range (~250 nm to 2500 nm). The inset provides a picture of the corresponding laser-processed black Pt sample.

Regarding the emission management, Kirchhoff's law can be exploited. It states that the emittance of a surface equals its absorbance in thermal equilibrium. Hence, surfaces of increased absorption simultaneously feature an elevated emission. The effect can be used, for example, for filaments of incandescent lamps. This application has been demonstrated in a tungsten filament lamp increasing its optical emission efficiency by a factor of three in the visible range compared to an untreated filament [49].

For transparent materials, optical scattering effects can be used to create omnidirectional broadband antireflective surfaces [18]. Papadopoulos et al. [50] used circularly polarized fs-laser pulses to generate randomly arranged nanospikes for mimicking the wing of the butterfly *Greta oto*. These laser-generated structures exhibit random height and widths distributions in the few hundreds of nanometer range, resulting in surface reflectance levels down to 1% in the visible spectrum.

Information Encoding

Different technical approaches were employed to realize the encoding of information through self-organized nanostructures, for example, for security tag applications. Apart from the obvious application of using a long-lasting structural coloring to avoid falsification of (Canadian) coins [51], more complex laser processing strategies were suggested by the groups around N. Destouches and J. Siegel [52–54]. The technique applies silver salts embedded into (meso-)porous titania films to create layered and LIPSS periodically arranged Ag nanoparticle systems that can be used for multiplexed image encoding for brand identification, authentication of goods, and smart visual effects [53].

Figure 23.9a–c sketches the encoding of two distinct grating structures that can be processed in different depths in a mesoporous Ag:TiO_2 film on glass upon high-repetition rate fs-laser pulse exposure (500 kHz) at different scanning speeds, that is, "low speed" (LS) and "high speed" (HS). The gratings arise from a plasmonically driven precipitation of Ag nanoparticles within the titania matrix, along with Ostwald ripening effects, resulting in a complex 3D arrangement of differently sized Ag nanostructures (for details, see [52]). These effects can be used for encoding several pictures in a multiplexed way that can be optically read out under different rotational angles; see Fig. 23.9d–f. Such an image encoding could be used for ID cards, etc.

2.2 *Liquid Management and Surface Wetting*

In this section, wetting and liquid management applications of laser-induced micro- and nanostructures on surfaces are addressed. That is, besides surface chemistry, specific surface morphologies, including laser-induced periodic surface structures (LIPSS, ripples), can be exploited to tune and optimize the wetting properties of a surface. First, the physics governing surface wetting is addressed briefly. Next, examples are discussed showing that surface textures (including LIPSS) can be used to create surfaces that are self-cleaning or allow to direct fluids, show reduced adhesion to liquid food, reduce drag, reduce the *Leidenfrost temperature*, and, last but not least, show anti-icing properties.

Physics Governing Surface Wetting

Wettability of a solid surface is the degree to which a surface can get wet by a liquid. The wetting properties of a liquid (droplet) on a solid surface and in a gaseous environment (a so-called solid-liquid-vapor system) are typically quantified by contact angle measurements; see Fig. 23.10a. In this figure, the balance of capillary forces acting at the liquid-solid-vapor interface results in the so-called *Young's contact angle* θ_{Y} [57], which is related to the interfacial surface tension γ_{vs} of the vapor-solid, γ_{sl} of the solid-liquid, and γ_{lv} of the liquid-vapor, which are related as $\cos(\theta_{\mathrm{Y}}) = (\gamma_{\mathrm{vs}} - \gamma_{\mathrm{sl}})/\gamma_{\mathrm{lv}}$. The interfacial surface tensions are chemical material parameters [58].

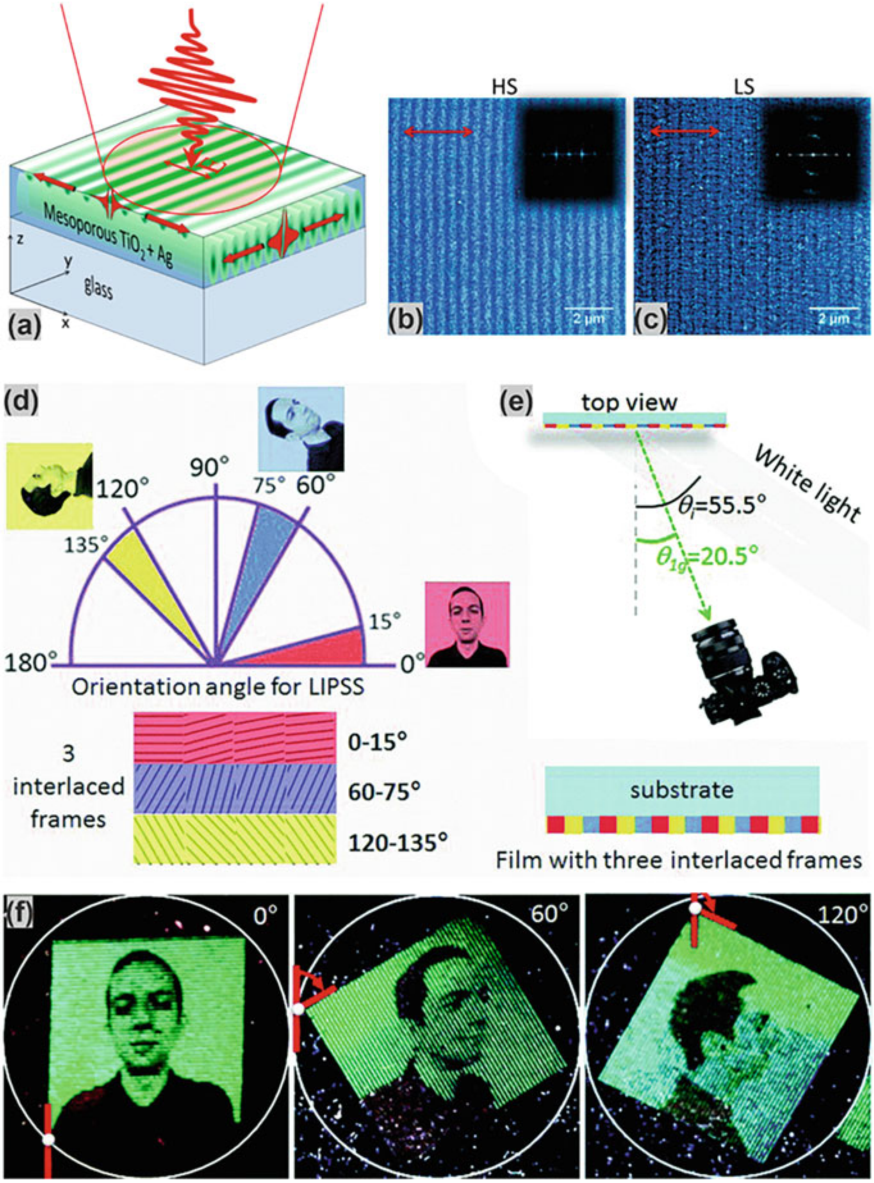
(a)
E
Mesoporous TiO2 + Ag
glass
z
y
x
HS
LS
(b)
(c)
2 µm
2 µm
(d)
90°
120°
75°
60°
135°
15°
180°
0°
Orientation angle for LIPSS
3 interlaced frames
0-15°
60-75°
120-135°
(e)
top view
White light
θi=55.5°
θ1g=20.5°
substrate
Film with three interlaced frames
(f)
0°
60°
120°

Fig. 23.9 (**a**) Scheme of laser-induced 3D self-organization in the mesoporous Ag:TiO$_2$ nanocomposite film. Linearly polarized laser pulses [515 nm, 370 fs, 500 kHz] excite simultaneously a surface wave and a guided wave, both propagating in perpendicular directions. The waves interfere with the incident pulse and cause an intensity modulation either close to the film surface parallel to the polarization or within the film perpendicular to it. Both interference patterns feature different spatial periods. (**b**, **c**) Top-view micrographs of structures "HS" (**b**; processed with high speed of 100 mm/s) and "LS" (**c**; processed with a low speed of 10 mm/s) and their respective 2D Fourier transforms (inset). The linear

If the liquid is water, a (flat) surface is referred to as hydrophilic if $\theta_Y < 90°$ and hydrophobic, that is, water repellent, if $\theta_Y > 90°$. A surface is considered superhydrophobic if $\theta_Y > 150°$. If a surface repels oily liquids, it is referred to as oleophobic [59] and omniphobic if it repels all types of liquids. A superhydrophobic surface is usually only achieved if a roughness (texture) is present on the surface. In the latter case, θ_Y cannot be calculated using the above equation, but still the contact angle can be measured and is then referred to as the *Apparent Contact Angle* (APCA) [18]. Depending on the wetting state (or wetting regime), the APCA can be calculated using one of two models. If the liquid (droplet) is in full contact with the surface of the solid, the Wenzel model applies [60]; see Fig. 23.10b. If the liquid does not fully penetrate into the "valleys" of the surface roughness but rests on the peaks of the texture, the Cassie-Baxter model applies [61]; see Fig. 23.10c. In this figure, the location of the contact line between the liquid and the solid is determined by the slope of the texture and the local Young's contact angle on the slope; see Fig. 23.10c. The steeper the slope, the higher the contact line (closer to the peak) and therefore the less the liquid-solid contact area. As a result, a droplet easily rolls off when the surface is tilted. Surface properties like self-cleaning, anti-icing, and microfluidic applications are attributed to this small liquid-solid contact area. In the case of water, effects of increased APCA, when compared to flat surfaces, occur at micrometer scale roughness levels. If on this roughness scale an additional nanometer scale roughness is superimposed, the APCA can be even further increased due to the increased local slopes of the nanometer roughness; see Fig. 23.10d. The self-cleaning properties of the lotus leaf are attributed to this dual roughness scale; see Fig. 23.10e. When designing a surface topology for improved wetting applications, LIPSS can be exploited on top of a micrometer scale texture to obtain a dual-scale roughness; see Fig. 23.10f–g. Many industrial processes and applications of LIPSS to adapt surface wetting of a surface or for liquid management are inspired by engineered replication of biological systems, such as the lotus leaf

◄

Fig. 23.9 (continued) polarization direction is indicated by the red double arrows. (Images (**a**–**c**) reprinted with permission from [52] (Liu et al., Three-dimensional self-organization in nanocomposite layered systems by ultrafast laser pulses, ACS Nano **11**:5031–5040). Copyright (2017) American Chemical Society). (**d**–**f**) Inscription of multiple "hidden" images. (**d**) Angular ranges of LIPSS used to encode the 256 grey levels of each image. The three raster images have been interlaced and printed as different fames onto a 1.18 cm^2 surface. The red, blue, and yellow colors represent false colors used for interlacing. The three frames contain gratings whose orientation varies (red: 0°–15°; blue: 60°–75°; yellow:120°–135°). (**e**) Scheme of the setup used for taking photographs of the sample, indicating the incidence angle θ_i of the white light collimated beam and the angle θ_{1g} of the first diffraction order in the plane of incidence for green light at a wavelength of 537 nm. (**f**) Photographs of the sample printed onto a polycarbonate substrate recorded for three different azimuthal angles upon rotating the sample in its plane. Three different images appear at 0°, 60°, and 120°, respectively. (Images (**d**–**f**) republished with permission of Royal Society of Chemistry, from [53], Laser-driven plasmonic gratings for multiple image hiding, Sharma, N., et al., Mater. Horiz. **6**: 978–983, 2019; permission conveyed through Copyright Clearance Center, Inc.)

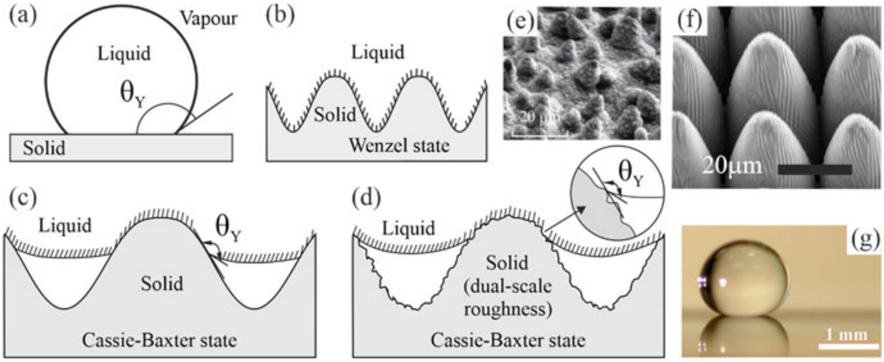

Fig. 23.10 (**a**) Definition of contact angle θ_Y [°] of a liquid (droplet) resting on a flat solid in a gaseous environment (solid-liquid-vapor system). (**b**) Wenzel state, in which the liquid fully wets the surface. (**c**) Cassie-Baxter state, in which air is trapped below the liquid. (**d**) Liquid on a hierarchical (here dual-scale) surface topology composed of micrometer and nanometer scale surface roughness, resulting in increased Apparent Contact Angle (APCA). (**e**) SEM micrograph of the surface topology of a lotus leaf composed of nanometer-sized "hairs" on top of micrometer-sized "pillars" showing hydrophobic and self-cleaning properties. (**f**) SEM micrograph of a laser-processed surface resulting in a dual-scale surface texture—that is, microscale pillars superimposed with LIPSS, replicating the surface topography of a lotus leaf. (**g**) A water drop, with a large APCA, sitting on top of a laser dual-scale surface texture. (Images (**a**–**d**) and (**f**) and (**g**) adapted and reprinted by permission of [55]. Image (**e**) adapted from [56], Barthlott et al., Plant Surfaces: Structures and Functions for Biomimetic Innovations, Nano-Micro Lett. **9**:23, Copyright 2016 under Creative Commons BY 4.0 license. https://doi.org/10.1007/s40820-016-0125-1)

[18, 62, 63]. Also, many biomedical applications of LIPSS rely (partly) on surface wetting; see Sect. 2.3.

Self-Cleaning

Contaminants and debris on the surface of a product, such as tiles, textiles, and solar panels, can negatively influence not only its main function but can also induce other effects such as tear and wear. It should be noted that, for optical applications such as solar panels or window glass, (super)hydrophobicity and transparency are competitive properties because for roughness levels exceeding about 100 nm, optical transparency is compromised due to light scattering [62]. A self-cleaning surface will reduce time and, therefore, costs associated with active cleaning procedures. If a surface exhibits (super)hydrophobic behavior, water droplets easily roll off the surface and will pick up and carry away surface contaminants. Several authors, including Jagdheesh et al. and Piccolo et al., found that LIPSS increase the (apparent) contact angle on various materials up to tens of percent when compared to "flat" or micrometer textured surface morphologies [64, 65]. Milles et al. [66] characterized the self-cleaning property of superhydrophobic hierarchical surface textures on aluminum, created by *direct laser writing* (DLW, using $\lambda = 1064$ nm and 8 ns and 14 ns pulse durations), *direct laser interference patterning* (DLIP), and LIPSS (using $\lambda = 1064$ nm and 10 ps pulse duration), which were contaminated

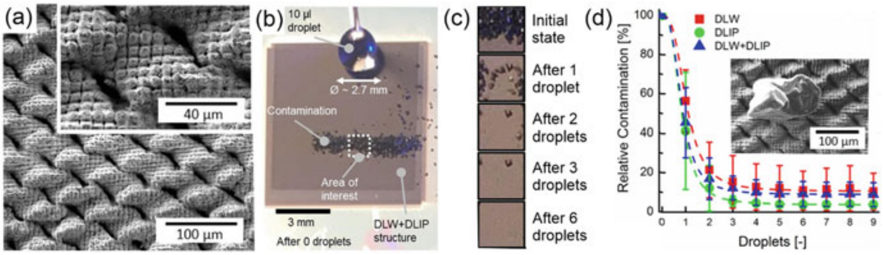

Fig. 23.11 (**a**) Top-view SEM micrograph of a hierarchical surface texture resulting from the combination of DLW, DLIP, and LIPSS showing self-cleaning properties. (**b**) Test setup used to assess self-cleaning properties of various surface textures. (**c**) The amount of particles on the region of interest was measured after each droplet rolled off. (**d**) Relative amount of particles in various textures as functions of the number of rolled-off droplets. (Reprinted and adapted from [66], Appl. Surf. Sci., Vol. **525**, Milles et al., Characterization of self-cleaning properties on superhydrophobic aluminum surfaces fabricated by direct laser writing and direct laser interference patterning, 146518, Copyright (2020), with permission from Elsevier)

with various particles including polyamide (PA) particles (~100 µm); see Fig. 23.11. Several droplets of 10 µl deionized water were dropped on contaminated laser-structured samples, which were tilted to allow droplet to roll off the sample and pick up the particles; see Fig. 23.11b. After each droplet, the number of particles on the region of interest was measured; see Fig. 23.11c. The authors found high self-cleaning efficiencies of the DLW + DLIP + LIPSS structures with a remaining contamination as low as 1% when 100 µm diameter MnO_2 and PA particles were used; see Fig. 23.11d.

Fluidic Transport

In nature, hierarchical surface textures on the mm to nm scale are known to direct liquid flow. For example, the skin texture of moisture-harvesting lizards living in arid regions consists of microstructured overlapping scales with capillary channels in between [67]. The (micro)structure (10 mm to 30 µm) on the lizard scale "holds" a water film through which the skin can become super wettable. Due to the combination of capillary channels and the microstructured scales, liquid is collected as well as transported to the snout of the animal. Such surface properties can be exploited industrially, for example for the transport of cooling lubricants [68] or lubricants in tribological applications; see Sect. 2.4. Hermens et al. [67] employed a ps pulsed laser source at 532 nm wavelength to texture 16MnCr5 steel surfaces in order to mimic the scales and capillary channels of a desert horned lizard; see Fig. 23.12a, b. The unidirectional transport of liquid, over distances in the range of centimeters, in/on such a surface texture is attributed to the network of interconnected capillaries that narrow and widen periodically. The authors characterized the liquid transport properties by depositing droplets of cooling lubricant K-40 at one side of the surface and observe the liquid transport using a video camera. It was found that the liquid propagates, from left to right in Fig. 23.12c, at 0.49 mm/s velocity.

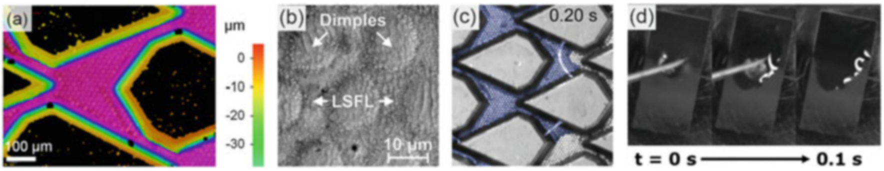

Fig. 23.12 (**a**) 3D surface topography of micrometer-sized six-sided textured polygons ("scales"), with in-between capillary "channels" consisting of micrometer-sized dimples (diameter ~10 μm) covered by sub-micrometer LSFL. (**b**) SEM micrograph (detail) of the surface texture in the capillary channels. (**c**) Image of lubricant K-40 (artificially colored blue) at 0.2 seconds after a droplet was deposited near the left side of the image. (**d**) Sequence photographs (top-view) demonstrating the unidirectional flow of a water droplet, placed in the center of a gradient of surface textures (top: spikes, bottom: LSFL) on steel. (Images (**a**–**c**) reprinted from [67], Appl. Surf. Sci., Vol. **418**, Hermens et al., Mimicking lizard-like surface structures upon ultrashort laser pulse irradiation of inorganic materials, 499–507, Copyright (2016), with permission from Elsevier. Image (**d**) taken from [69]. (Reprinted by permission from Springer-Verlag GmbH: Applied Physics A **123**:754 (Mimicking bug-like surface structures and their fluid transport produced by ultrashort laser pulse irradiation of steel, Kirner, S.V. et al.), Copyright (2017))

As another example, Kirner et al. applied a 170 fs pulsed laser source at $\lambda = 1026$ nm to texture the surface of 42CrM04 steel with a gradient of surface morphologies ranging from LSFL over grooves to spikes (see Sect. 1.1), by varying the laser fluence from 0.07 J/cm^2 (bottom of the rectangle) to 1.05 J/cm^2 (top of the rectangle), in order to mimic the transport properties of the skin of a bark bug (*Aradidae*) [69]. It was found, using video recordings, that, when applying an 8 μl droplet of deionized water in the center of the textured surface, shortly after laser processing, the liquid quickly spread at ~75 mm/s toward the area covered by spikes, and not to the area covered by grooves or LSFL; see Fig. 23.12d.

Another facet related to the transport of fluids is the laser-based creation of *superwicking* surfaces. For this functionality, the combination of capillary forces, for example, in laser-generated parallel microgrooves, along with the philicity of the nanostructure-covered inner channel surfaces can effectively transport liquids even against gravity [70]; see Fig. 23.13.

Different applications based on such superwicking surface functionality were proposed and demonstrated already. Due to the capillary action, a liquid drop quickly spreads on the wicking surface and forms a thin film over a large surface area, finally resulting in efficient evaporation. Taking benefit of such a transport of water against gravity and the simultaneously strongly enhanced absorption of laser-processed black metals for optical radiation in the visible and infrared spectral range (see Sect. 2.1), Singh et al. [71] demonstrated a solar-trackable superwicking black metal panel for photothermal water sanitation and desalination (see Fig. 23.14).

On laser-processed aluminum, such superwicking surface functionalities even persist for water at elevated temperatures up to 120 °C and may have applications in boilers with enhanced critical heat flux or in heat exchangers for enhancing energy efficiency in power generation [72].

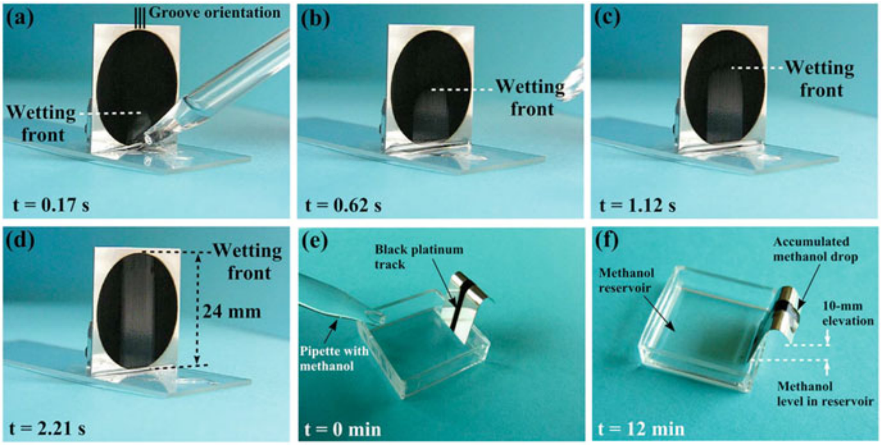
(a)
Groove orientation
Wetting front
t = 0.17 s
(b)
Wetting front
t = 0.62 s
(c)
Wetting front
t = 1.12 s
(d)
Wetting front
24 mm
t = 2.21 s
(e)
Black platinum track
Pipette with methanol
t = 0 min
(f)
Accumulated methanol drop
Methanol reservoir
10-mm elevation
Methanol level in reservoir
t = 12 min

Fig. 23.13 (**a–d**) Photographs showing the methanol transport against gravity on a vertically standing laser-processed black platinum surface. (**e–f**) Photographs showing the vertical transport of methanol and liquid accumulation across a sample edge. (Reprinted from [70], Vorobyev et al., Metal pumps liquid uphill, Appl. Phys. Lett. **94**:224102 (2009)], with the permission of AIP Publishing)

Anti-adhesive Packaging for Liquid Food

Viscous liquids, which adhere to packaging surfaces of, for example, food, cosmetics, and agrochemical products lead to wastage, an increase of recycling costs, and consumer annoyance. Inspired by the *Nepenthes* pitcher plant, Karkantonis et al. created lubricant-impregnated textured surfaces (LIS) to improve the shedding behavior of polymer surfaces of viscous liquids [73]. In this approach, the lubricant is chosen such that it wets the micro/nanotextured surface instead of repelling it, and such that the viscous liquid, which is to be repelled, is immiscible with the lubricant. A 310 fs pulsed laser source ($\lambda = 1030$ nm) was applied to texture an X6Cr17 stainless steel surface with a dual-scale texture consisting of a micrometric hatch pattern and LIPSS; see Fig. 23.15a. This surface morphology was subsequently replicated in sheets of polystyrene (PS) and polypropylene (PP) by hot embossing. Silicone oil was selected as the lubricant.

The shedding behavior of various liquids was assessed by exposing the LIS polymer samples in various liquids, including honey, milk, and ketchup. Figure 23.15b shows photographs of a submerging test of polypropylene samples in honey. The authors found that LIPSS-LIS-treated thermoplastics demonstrated anti-adhesive properties even after 50 cycles with all tested liquids, while there was a slight stickiness on the dual-scale-LIS substrates after 43 and 20 dipping cycles in milk and honey, respectively.

Drag Reduction

Drag is a force acting on a (solid) object when it moves in a fluid and acts in opposite direction to the relative motion of the object in the fluid. Drag reduction is beneficial

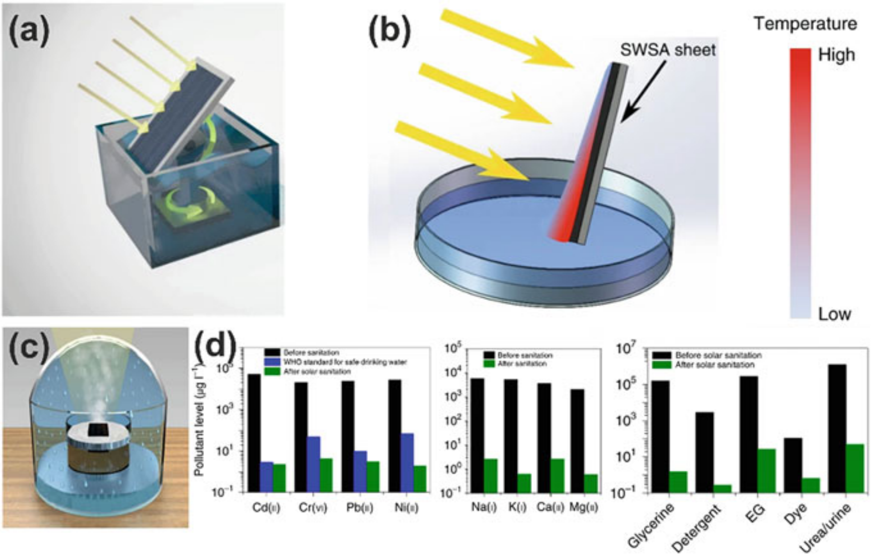

Fig. 23.14 (**a**) Schematics of a sun-tracking superwicking and super light-absorbing (SWSA) aluminum solar-based water sanitizer that (**b**) promotes interfacial heating while ensuring that water is continuously transported across the solar absorber. (**c**) Schematic of the water sanitation/desalination setup. (**d**) Water sanitation of various heavy metals, salts, and industrial/domestic/human water pollutants (EG: ethylene glycol). (Reprinted (adapted) from [71], Singh et al., Solar-trackable super-wicking black metal panel for photothermal water sanitation. Nat. Sustain. **3**:938–946, Copyright 2020 under Creative Commons BY 4.0 license. Retrieved from https://doi.org/10.1038/s41893-020-0566-x)

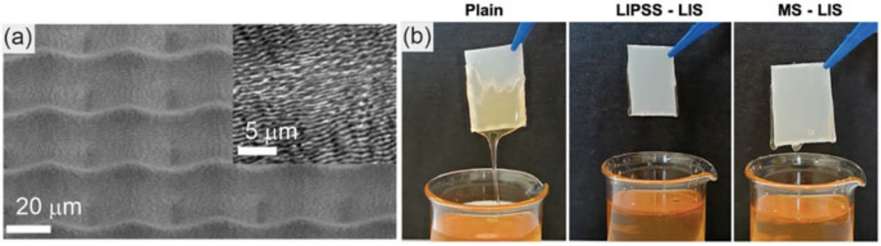

Fig. 23.15 (**a**) SEM micrograph of dual-scale laser-textured steel surface, consisting of a micrometric hatch pattern and LIPSS (insert). (**b**) Photographs of the dripping behavior of PP samples (impregnated with silicone oil) after submergence in honey; left: non-textured plain sample; center: sample covered with LIPSS; right: sample with dual-scale roughness. (Images adapted and reprinted from [73], Surf. Coat. Technol., Vol. **399**, Karkantonis et al., Femtosecond laser-induced sub-micron and multi-scale topographies for durable lubricant impregnated surfaces for food packaging applications, 126166, Copyright (2020), with permission from Elsevier)

in, for example, biomedical devices (e.g., in lab-on-a-chip applications), swimsuits, piping to transport liquids, ship hulls, and aerospace industry [62]. Compared to flat surfaces, reduction of drag can be achieved by surface textures because a shear-free

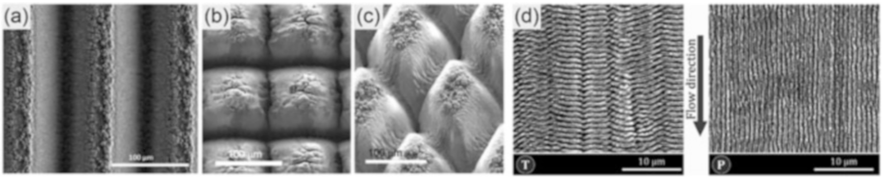

Fig. 23.16 (**a**–**c**) SEM micrographs of various multiscale surface morphologies for liquid drag reduction, consisting of micrometer scaled patterns superimposed by LIPSS on the slide walls and nanoparticles on the peaks. (**d**) SEM micrographs of LSFL on mold steel aiming a drag reduction in polymer injection molding. (Images (**a**–**c**) republished with permission of Royal Society of Chemistry, from [75], Drag reduction on laser-patterned hierarchical superhydrophobic surfaces, Ahmmed, K.M.T. and Kietzig. A.-M., Soft Matter **12**:4912–4922, 2016; permission conveyed through Copyright Clearance Center, Inc. Image (**d**) adapted and reprinted from [76], CIRP Annals, Vol. **67**, Sorgato et al., Effect of different laser-induced periodic surface structures on polymer slip in PET injection moulding, 575–578, Copyright (2018), with permission from CIRP)

boundary condition occurs at the air-liquid menisci in the Cassie-Baxter state [74]; see Fig. 23.10c, d and the no-slip condition between the liquid and the roughness peaks of texture [75]. Hence, reducing the relative fraction of the (textured) solid surface that is in contact with the liquid will result in drag reduction. Drag reduction can be quantified by measuring the so-called slip length of the (textured) solid, for example, using a rheometer or *Particle Image Velocimetry* (PIV). A large (effective) slip length reduction implies a large drag reduction. Therefore, Tanvi Ahmmed and Kietzig applied a <85 fs pulsed 800 nm laser source to texture the surface of pure copper with various micrometer scale patterns, including parallel lines (grate structures; see Fig. 23.16a) and various pillar structures (square and rhombic shaped; see Fig. 23.16b, c) all of which the sidewalls were found to be covered with LIPSS and the peaks with nanoparticles [75].

Next, the samples were coated with fluoroalkylsilane in order to chemically enhance the hydrophobicity of the surface. The authors employed water and a rheometer to quantify the slip lengths by calculating from measured torques at different shear rates. The slip length on a smooth (untextured) hydrophobic surface is small and varies from nm to a few µm [75]. The authors found significantly larger slip lengths of their laser-structured samples, varying from 70 µm to about 140 µm.

As another example, Sorgato et al. employed an 8 ps, 1064 nm laser source to cover mold steel with LSFL (see Fig. 23.16d) in order to reduce the drag of a polymer (PET) in an injection molding setup [76]. That is, because especially in injection molding of small plastic parts, for example, in electronic packaging applications, drag is high. Therefore, high pressures are required to fill the mold. The authors covered mold insert with two different orthogonal orientations of LSFL, parallel (P) and transverse (T) to the flow direction of the polymer; see Fig. 23.16d. It was found that LSFL transverse to the melt flow have a negligible effect on the injection pressure, whereas LSFL parallel to the flow direction was found to reduce the required injection pressure up to 23%.

Leidenfrost Effect

If a liquid droplet is applied on a surface that is significantly hotter than the boiling point of the liquid, an insulating vapor “cushion” forms below the droplet, such that it hovers over the solid and does evaporate slowly. This phenomenon is known as the *Leidenfrost effect*. By applying a surface texture, the Leidenfrost temperature—that is, the critical temperature of the solid over which the Leidenfrost effect occurs—reduces [55, 77, 78]. The roughness level required to reduce the Leidenfrost temperature for water is in the μm range [55, 78]. Moreover, based on the Leidenfrost effect, asymmetric surface textures, such as a sawtooth profile, can be exploited to direct the movement of droplets, even against gravity, similar to the superwicking effect (see above). These movements are induced by pressure gradients introduced by the asymmetric inclination of the surface morphology, as well as due to rotation of droplets due to Marangoni flows. These effects, and the reduction of the Leidenfrost temperature, have potential applications in, for example, *lab-on-a-chip* devices and piping to transport liquids, as it reduces drag. Dubnack et al. employed a 300 fs, 1025 nm wavelength laser source to cover the tips of a sawtooth profile in aluminum with LSFL; see Fig. 23.17a [77]. The samples were coated with fluorooctyltriethoxysilane to increase the hydrophobicity chemically. Next, the authors measured the temperature that initiated a water droplet (volumes 60 to 200 μl) to start moving. This temperature was found to equal about 170 °C for the texture without LIPSS and only about 115 °C for the textures with LIPSS; see Fig. 23.17c.

Anti-icing

Ice (frost, glaze, rime, snow) can cause problems when it adheres and accumulated on solar panels, aircraft, wind turbines, and power or communication lines, to name a few [79]. Anti-icing properties can be obtained by increasing the surface roughness of a substrate in order to increase the hydrophobicity of the surface. Designing a (super)hydrophobic surface aims at increasing the time delay in the solidification of water, promotes roll-off of water before freezing occurs (see self-cleaning), and reduces adhesion of ice after it formed on the surface [79]. A reduction of the

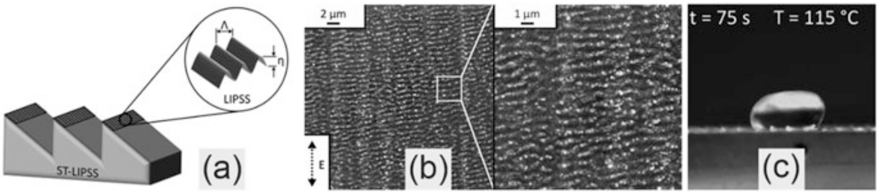

Fig. 23.17 (**a**) Millimetric sawtooth surface profile covered with LIPSS to accelerate water based on the Leidenfrost effect. (**b**) SEM micrographs of the LSFL on the tips of the sawtooth surface profile on the aluminum substrate. (**c**) Frame from a video sequence showing a moving droplet (starting from the left of the frame) at a reduced Leidenfrost temperature. (Reprinted from [77], Appl. Surf. Sci., Vol. **532**, Dubnack et al., Laser-induced Leidenfrost surfaces, 147407, Copyright (2020), with permission from Elsevier)

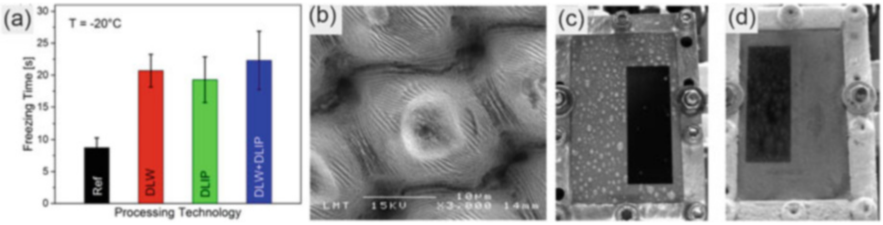

Fig. 23.18 (**a**) Average freezing time of water droplets on an untreated reference, DLW, DLIP, and DLW + DLIP + LSFL structures. (**b**) Top-view SEM micrograph of a steel surface texture consisting of 20 µm pitched pillars covered with LSFL. (**c**) Photograph of the FOTS-coated laser-textured steel sample, 10 seconds after the rain test. The laser-textured area (black) of several cm^2 in size is almost completely free of frozen droplets. (**d**) Photograph of the FOTS-coated laser-textured steel sample after the rime test. (Image (**a**) reprinted from [80], Milles et al., Fabrication of superhydrophobic and ice-repellent surfaces on pure aluminum using single and multiscaled periodic textures, Sci. Rep. **9**:13944, Copyright 2019 under Creative Commons BY 4.0 license. Retrieved from https://doi.org/10.1038/s41598-019-49615-x. (Images (**b**–**d**) adapted and reproduced from [81], Römer et al., Ultra short pulse laser generated surface textures for anti-ice applications in aviation. Proceedings International Congress on Applications of Lasers & Electro-Optics (ICALEO), 2–5 Nov., Orlando, USA, p. 30–37 (2009), https://doi.org/10.2351/1.5061570 with the permission of the Laser Institute of America)

relative solid fraction of the surface in contact with the water droplet(s) promotes anti-icing properties. A low relative solid fraction is achieved in the Cassie-Baxter state (see Fig. 23.10c, d), which lowers the heat conduction between the droplet and the surface, promotes roll-off, and reduces ice adhesion, when compared to the Wenzel state and to flat or smooth surfaces.

Milles et al. assessed the freezing time of water droplets on aluminum surfaces covered with hierarchical surface textures created using the same techniques (DLW and DLIP) and laser systems as described above (see self-cleaning) [80]. The freezing time of the DLW structures, DLIP structures, and the hierarchical structures (DLW + DLIP + LSFL; see Fig. 23.11a) was measured by imaging the solidification of 8 µl water droplets on the surface in air of −20 °C; see Fig. 23.18a. As can be observed from this graph, the freezing time of the droplet on the hierarchical structure (22.3 s) is about 2.6 times longer than on the smooth reference sample (8.7 s). Furthermore, the authors found that 13 µl droplets, when dropped from a height of 20 mm on samples cooled down to −20 °C, would only bounce on the hierarchical structures, but not on the DLW structures, nor the DLIP structures. Droplet rebounding was found to increase the freezing time.

Römer et al. studied the roll-off of water droplets on a laser-textured stainless steel sample in a representative rain test and a rime test [81]. To that end, the authors employed a 7 ps, 1030 nm wavelength laser to create a hierarchical surface texture consisting of pillars (height 20 µm, pitch 20 µm) covered with LSFL; see Fig. 23.18b. The pitch of the pillars was chosen such that several peaks will support a water droplet in the Cassie-Baxter state; see Fig. 23.10d. Next the surface was covered by a Perfluorinated OctylTrichloro-Silane (FOTS) coating to increase the hydrophobicity of the surface chemically. After the rain test (water droplets at −0 °C, climate chamber at −5 °C, 9 m/s wind speed, which are icy conditions for airplanes) of 10 seconds, a photograph was taken; see Fig. 23.18c. It was found that the laser-textured area is almost completely free of frozen droplets. Further, it was found, in a rime ice test, that the laser-textured surface only slightly slows down the formation of rime; see Fig. 23.18d. The latter can be attributed to the fact that the diameter of water droplets forming rime is (much) smaller than the pitch of the pillars in Fig. 23.18b.

2.3 Biological Applications

In this section, biological applications of laser-induced surface structures are addressed. It will be discussed that LIPSS can be used to control the adhesion and growth of bacterial films and affect the alignment of cells on medical implants. Moreover, LIPSS can be used in biochemistry for significantly enhancing Raman spectroscopic signals in *lab-on-a-chip* devices.

Biofilm Growth Control

Most common issues with prosthetics, such as, for example, dental implants [82], hip and knee prosthetics [83], as well as biomedical devices such as catheters, cardiac pacemakers, and stents [84], are joint infections and thrombosis. This causes additional hospitalization and costs and may end lethal in the worst case. A solution to this problem could be the implementation of antibacterial surfaces on such devices.

The wings of butterflies and cicadas as well as the skins of geckos show antibacterial properties mainly due to well-ordered micro- and nanostructures [85]. LIPSS on different stainless steel alloys [86–95] and various types of polymers [84, 96] have shown similar antibacterial properties.

It is to be believed that the laser process leads to an oxidation of metal surfaces, which may act bactericidal [86, 92]. Additionally, it may be concluded that the presence of a topographic surface relief with characteristic dimensions smaller than the bacterium size and with very dense features reduces the contact area between bacteria and the surface, inhibiting bacterial colonization and reducing bacteria retention [86, 87, 89, 92, 94, 96]. However, this depends on the sizes and shapes of the bacteria as shown in Fig. 23.19 by Epperlein et al. [88]. That figure shows fluorescence microscopy images of corrosion-resistant steel (V4A) samples partially covered with LIPSS (LSFL) with a period of about 700 nm, colonized for (a) 18 hours with *Escherichia coli* and (b) 20 hours with *Staphylococcus aureus*. It can be observed that the rod-shaped *E. coli* bacteria (with dimensions of ca. 0.5 µm × 2 µm) exhibit reduced adhesion on the LIPSS-covered area, whereas the spherically shaped *S. aureus* bacteria (diameter 0.5–1 µm) show increased adhesion on the LIPSS-covered area. It was stated by the authors that the increased adhesion

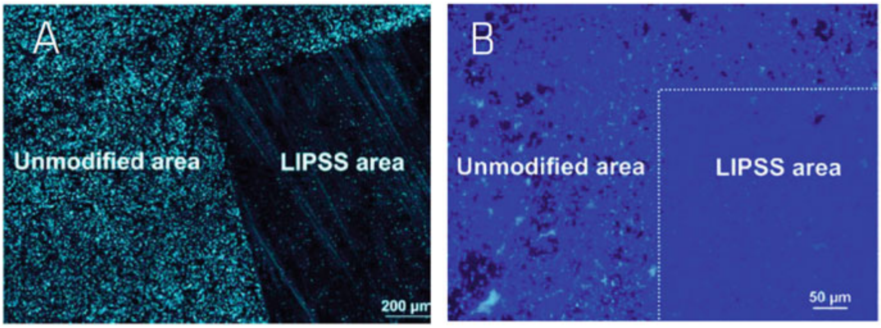

Fig. 23.19 Fluorescence microscope images of steel samples (V4A), partially processed with LSFL and subsequently colonized with dye-stained (**a**) *E. coli* bacteria after incubating of 18 h and (**b**) *S. aureus* bacteria after incubating of 20 h. (Reprinted from [88], Appl. Surf. Sci., Vol. **418**, Epperlein et al., Influence of femtosecond laser produced nanostructures on biofilm growth on steel, 420–424, Copyright (2017), with permission from Elsevier)

results from the bacteria shape aligning with the direction of the nanostructures and hence increases the contact area between bacteria and surface [88].

Hierarchical micro-/nanostructures consisting of a combination of micro-sized structures covered with nanoscaled features can also act bactericidal, as was shown, for example, by Luo et al. [90]. Figure 23.20b shows *E. coli* on different types of laser-induced surface structures on titanium. That is, “type 1” consists of LSFL with a spatial period of about 400 nm, “type 2” contains LSFL interrupted by shallow sinusoidal grooves with a distance of about 1 µm, and “type 3” is composed of LSFL with a period of about 500 nm interrupted by grooves that are about 200 nm deeper than the grooves of type 2. All three structure types show an antibacterial effect, as can be summarized in Fig. 23.20a, showing the reduction of bacteria counts in percentage of the three surface structure types compared to polished titanium as a reference. All three types also show bactericidal effects, with structure type 3 showing the highest bacteria reduction by 56%. The proportion of live and dead bacteria after incubation time varies for the surface topographies. It can be observed in Fig. 23.20b that the bacteria tend to form clusters of several bacteria (highlighted by a yellow circle) on structure type 1 (LSFL) in order to prevent rupturing. Cluster formation was observed less on type 2 and 3, but the bacteria were located more at the bottom of the grooves, especially for type 3. Rupturing of the bacteria is caused either on top of nanostructures, which leads to a platy form, or between two microstructures, leading to a lacerated form. For surface texture type 1, mostly platy ruptured dead bacteria were observed, whereas for structure type 3, the lacerated form is primarily present [90].

Conceptually, different surface roughness or nanoscale topography-mediated effects can be distinguished that may all lead to a reduced bacterial colonization, for example:

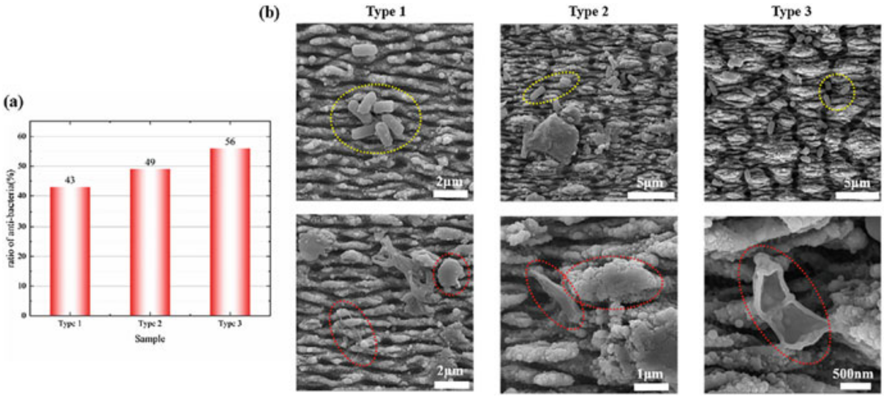

Fig. 23.20 (**a**) Antibacterial ratio (the total dead cells on LIPSS of the total cell numbers on polished titanium) for *E. coli* of three types of laser-induced surface structures. (**b**) Top-view SEM images of bacterial cells adhesion states for three types of surface morphologies after 24 h of bacterial cell culture. Yellow ellipses show survival strategies such as cluster formation over several LIPSS ridges or cells lying between the LIPSS maintaining their original shape. Red ellipses show two types of dead cells including platy form and lacerated form. The platy form means the dead cells spread wrapping the top of surface structures, and the lacerated form represents the stretched dead cells hanging between the surface structures. (Reprinted from [90], Opt. Laser Technol., Vol. **124**, Luo et al., Biocompatible nano-ripples structured surfaces induced by femtosecond laser to rebel bacterial colonization and biofilm formation, 105973, Copyright (2019), with permission from Elsevier)

- Bactericidal effects, where sharp or nanometric spiky features of the surface topography can perforate the cell membrane [97]
- Obstruction or hampering of proliferation of bacterial cells, for example, through their spatial confinement [98]
- Reduced adhesion of bacterial cells during the early stage of biofilm formation
- Etc.

In the latter context, surface topography-induced hydrophobicity can feature a low surface wettability and low surface energy to promote a low drag surface under flow conditions that is finally preventing microbial colonization at the surface through the reduced strength of adhesion of the bacteria to surface [99].

Moreover, very recently, Richter et al. [100] demonstrated that a repellence of *E. coli* bacteria of up to ~90% can be obtained by controlling the spatial period of UV ns-laser-processed sub-micrometric LSFL on polyethylene terephthalate (PET) foils. This study pointed out that the efficiency of bacteria-repellent surfaces can be significantly improved when surface nanostructures impair the adhesion for bacterial nanofiber appendages, such as pili. These pili typically feature diameters of less than 10 nm and are establishing bacterial cell-surface and cell-cell contacts as seen in the SEM micrographs shown in Fig. 23.21.

It must be noted that certain micro- and nanostructures are not well suited for metal-on-polymer-bearing surfaces in joint prosthetics due to increased friction and

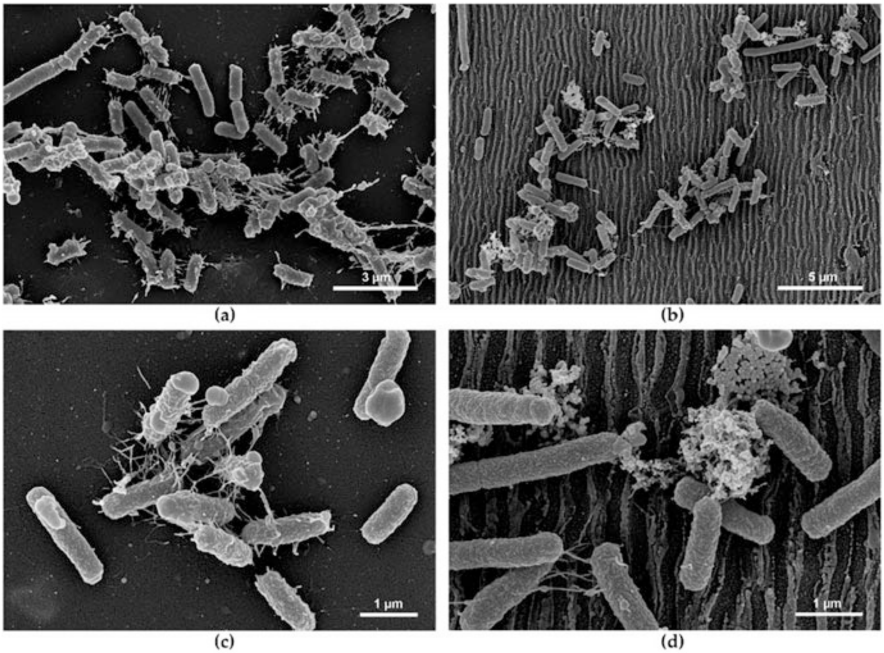

Fig. 23.21 SEM micrographs of *E. coli* bacteria on (**a**, **c**) non-irradiated (flat) PET and (**b**, **d**) laser-structured PET covered with LSFL of <300 nm spatial period. Note the different scale bars. (Reprinted from [100], Richter et al., Spatial Period of Laser-Induced Surface Nanoripples on PET Determines *Escherichia coli* Repellence. Nanomaterials **11**:3000 (2021), Copyright 2021 under Creative Commons BY 4.0 license. Retrieved from https://doi.org/10.3390/nano11113000)

abrasion, which results in a shortening of the lifetime of the joint prosthetics [31]. Nonetheless, for static implants, laser surface texturing can offer a valid technique to control biofilm growth on the implant surfaces. Moreover, in aqueous media, surface wetting effects of the laser-processed surfaces (see Sect. 2.2) may be relevant for bacterial film formation.

Cell Growth and Alignment

Another reason to add surface micro- and nanostructures on medical devices is to control the growth and alignment of biological tissue at the implant surface (see also Chap. 31 (Buchberger et al.)). While an accelerated and aligned cell growth for improved osseointegration is preferable for the interface between bone tissue and load-bearing implants, such as dental implants or hip joint prosthetics [101], a decreased cell growth of fibroblasts is desired for other implants that are intended to be removed after some time, such as catheters, cardiac pacemakers, or contraceptives [102].

One of the standard materials for dental and orthopedic implants is Ti6Al4V titanium alloy because of its excellent mechanical properties such as low weight, high

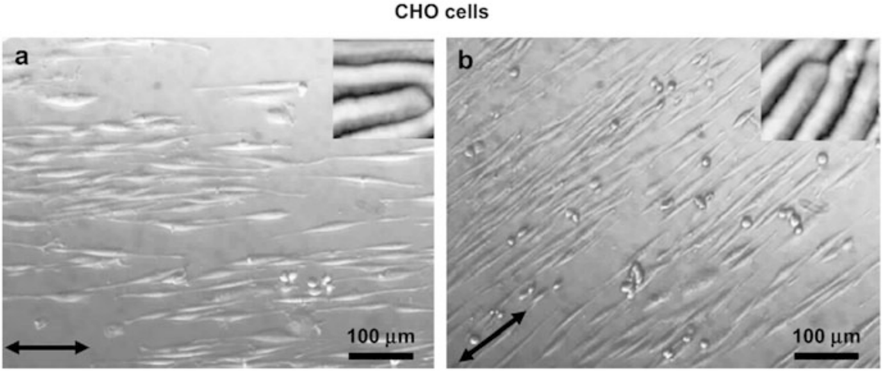

Fig. 23.22 Phase contrast optical micrographs of CHO-K1 cells (**a**) 27 h and (**b**) 52 h after seeding on PS foils laser processed at an angle of incidence of $\theta = 45°$. Arrows indicate the direction of the LIPSS. In the insets, typical magnified atomic force microscopy images (1.4 μm × 1.4 μm) of the LIPSS-textured PS foils are shown. (Reprinted from [106], Biomaterials, Vol. **29**, Rebollar et al., Proliferation of aligned mammalian cells on laser-nanostructured polystyrene, 1796–1806, Copyright (2008), with permission from Elsevier)

corrosion resistance and hardness but is also a bioinert material that osseointegration abilities could be further improved to reduce the possibility of long-term implant failure [101]. Polystyrene is a widely used biomaterial for cell culture applications for its non-toxicity and low production costs, but its hydrophobic surface hinders cell adherence and growth [103]. Therefore, the relatively fast, contactless one-step LIPSS processing is a viable choice for enhancing biocompatibility via topographical and chemical changes due to the fact that it can be applied on a wide range of materials, ranging from strong absorbing metals to transparent polymers [102, 104, 105].

It was shown that regular nanostructures (LSFL) on titanium alloys and polystyrene increase the growth rate, adhesion, and density of mammalian cells [106], osteoblastic cells [101], glioma cells [103], and fibroblastic cells [105]. Moreover, the cells align parallel to the LSFL ridges, and their shape elongates along the latter. Figure 23.22 by Rebollar et al. [106] exemplifies the elongating and parallel aligning of mammalian cells along LSFL processed by ns-UV laser radiation on polystyrene surfaces. This alignment occurred for LIPSS periods above a critical, cell-type-specific value.

In contrast, laser-generated hierarchical micrometric spikes covered by nanometric LSFL on titanium alloys and silicon wafers [107] can suppress the growth of fibroblasts, particularly if an additional anodization step is performed after the laser processing [102, 108, 109]. It was shown by Klos et al. [110] that cell growth, adhesion, and migration toward predetermined areas can be controlled by a site-selective combination of nanometer-scaled LSFL and micrometer-scaled spikes.

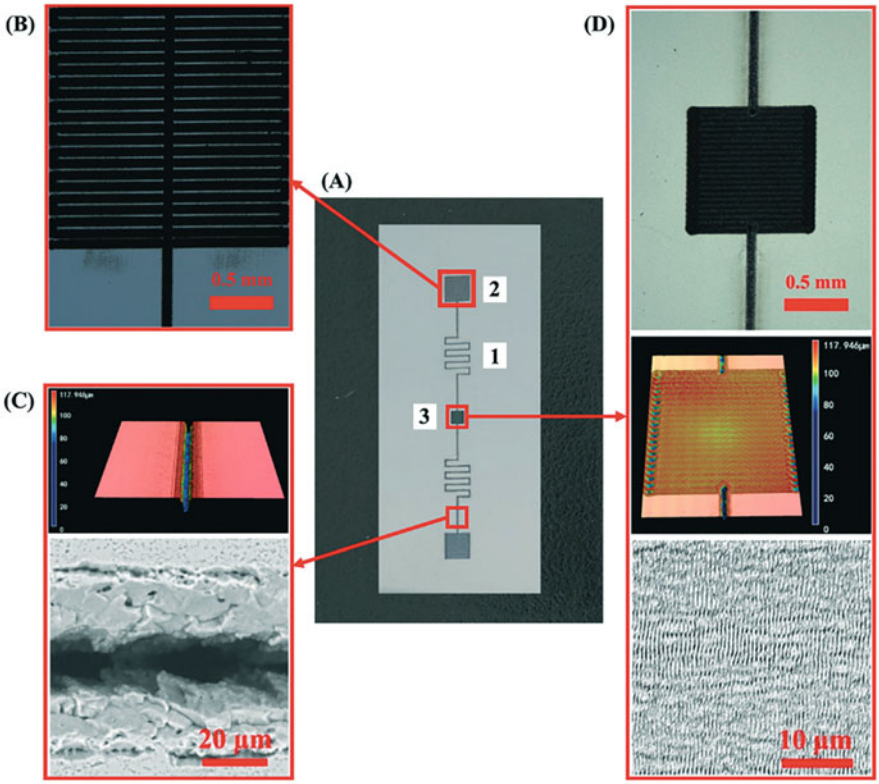

Fig. 23.23 (**a**) Photograph of the whole microfluidic platform. (**b**) Optical image of the 2 × 2 mm^2 square inlet. (**c**) 3D topography and SEM images of the microchannel. (**d**) Optical, 3D topography, and SEM images of the SERS active site. (Republished with permission of Royal Society of Chemistry, from [113], A self-driven microfluidic surface-enhanced Raman scattering device for Hg^{2+} detection fabricated by femtosecond laser, Li, X., et al., Lab on a Chip **20**:414–423, 2020; permission conveyed through Copyright Clearance Center, Inc.)

SERS Lab-on-a-Chip

It was shown by several authors [111–113] that LIPSS on suitable materials can be beneficial for surface-enhanced Raman scattering (SERS), leading to a sensitivity increasement of up to 2000 times compared with flat samples [111]. The approach may be useful for applications in food safety, biosciences, and eco-pollution. Moreover, given its flexibility, laser processing is an outstanding candidate for SERS lab-on-a-chip products due to its ability to structure complex shapes [112] and its simple, precise, and controllable process for achieving fluidic inlets, hydrophilic liquid, self-propagating microchannels, and LIPSS using a single laser processing setup [113]. An example of such a laser-processed SERS *lab-on-a-chip* is shown in Fig. 23.23 [113] where (A) shows an overview over the whole chip, (B) shows a liquid inlet, (C) shows the microchannels, and (D) shows the LIPSS-processed SERS active site.

This concept of spatially confining and transporting the chemical analyte through laser-textured surfaces can be even extended by combining it with the idea of evaporational concentration enhancement. This approach was realized by Hu et al. [114] via fs-laser processing of polytetrafluoroethylene to generate extremely superhydrophobic surfaces. For the spatial confinement of analyte droplets, small square-shaped areas of the surface remained unprocessed and served as “trapping areas” for the analyte. In combination with evaporation concentration of the analyte, for example, rhodamine 6G dye molecules with a concentration of 10^{-6} M, it was shown that the corresponding spectroscopic intensity detected via the SERS effect can be enhanced by up to two orders of magnitude on the laser-fabricated samples when compared to the non-processed surface. Pavliuk et al. demonstrated an easy-to-implement laser-printed device for ultrasensitive SERS-based identification of various analytes dissolved in water droplets at trace concentrations sensitivity levels down to 10^{-12} M [115].

2.4 Tribological Applications

This section provides a brief survey on how LIPSS-covered surface can provide beneficial tribological properties, for example, for the reduction of the coefficient of friction (CoF) or the wear between different solid bodies being in mechanical contact—or even for the manifestation of a passive directional transport of liquid lubricants toward the tribological contact area. Such a reduction of the CoF, even if nominally small, may have a tremendous potential for energy (fuel) saving and CO_2 reduction when accumulated over the entire lifetime of technical devices [116]. Simultaneously, the reduction of wear can significantly increase the servicing intervals and enhance the devices life cycles. Hence, tribological applications of LIPSS and other tailored microstructures bear an enormous societal and economic potential.

Reduction of Friction and Wear

It is a perception of paramount importance that properties such as the CoF (often referred to via the symbol μ) or wear rates are not simply material properties but must be considered as system properties [117]. A tribological system usually consists of (at least) two bodies being in touch with each other via their surfaces—either through a conformal or a nonconformal contact, featuring locally potentially very complex and even transient (multi-)contact areas. Moreover, some macroscopic forces are typically acting between the two bodies (e.g., shear forces or a normal force F_N), among other relevant environmental parameters, such as the temperature, humidity, etc. Additionally, there may be a liquid or solid lubricant added in the tribological contact region (e.g., graphite, grease, oil, water, etc.). Often, the relative motion between the two bodies can be further characterized through their relative velocities v_{rel}, some specific stroke trajectories and lengths S, or even varying

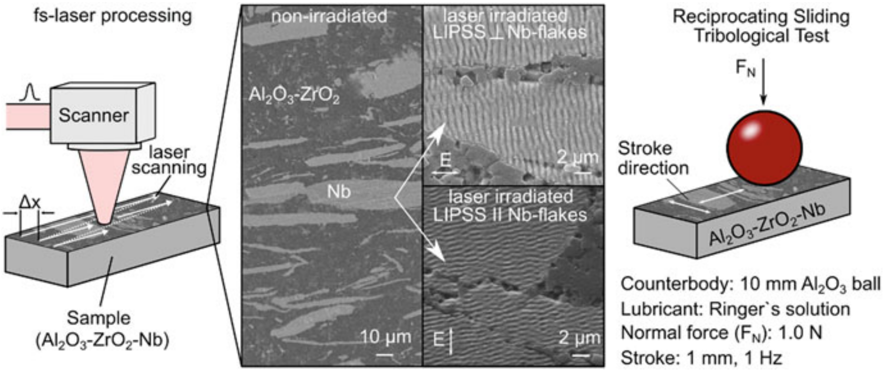
fs-laser processing
Scanner
laser scanning
Δx
Sample (Al2O3-ZrO2-Nb)
non-irradiated
Al2O3-ZrO2
Nb
10 µm
laser irradiated LIPSS ⊥ Nb-flakes
E
2 µm
laser irradiated LIPSS II Nb-flakes
E
2 µm
Reciprocating Sliding Tribological Test
FN
Stroke direction
Al2O3-ZrO2-Nb
Counterbody: 10 mm Al2O3 ball
Lubricant: Ringer`s solution
Normal force (FN): 1.0 N
Stroke: 1 mm, 1 Hz

Fig. 23.24 Scheme of fs-laser processing and reciprocating sliding tribological tests (RSTT) on selectively LIPSS-structured Al_2O_3-ZrO_2-Nb composites. (Reprinted from [127], Appl. Surf. Sci., Vol. **499**, Kunz et al., Tribological performance of metal-reinforced ceramic composites selectively structured with femtosecond laser-induced periodic surface structures, 143917, Copyright (2019), with permission from Elsevier)

operational modes of relative motion (rotating, reversing, reciprocating), a certain number of repetitive sliding cycles, etc. Many of these complex conditions can be set up, controlled, and tested with so-called tribometers [117].

Several authors already reported an improved tribological performance of LIPSS-covered surfaces on different materials, in various non-lubricated or lubricated tribological test conditions [118–124], and upon exploring some specific applications, including the improvement of mechanical seals [125] and the optimization of the performance of cutting tools [126], medical implant materials [31, 127], etc. Summarizing this research, the basic ideas of using LIPSS for tribological applications are related to (i) a change in the geometrical contact area or roughness, (ii) a confinement of the lubricant in the valleys of the LIPSS being in tribological contact—acting as reservoir, and (iii) an enhanced wetting of the lubricants at the laser-processed surfaces, or even laser-induced (iv) chemical or (v) structural surface modifications, such as oxidation or graphitization, that may (vi) additionally improve the efficiency of wear-reducing additives contained in many commercial lubricants. For more details on the tribological properties of LIPSS, the reader is referred to the pertinent literature here, such as Refs. [10, 37].

In the following, three specific examples of beneficial tribological performances of LIPSS-processed surfaces through a reduction of the CoF are presented in Figs. 23.24, 23.25, 23.26, and 23.27. These results demonstrate some prominent tribological test geometries/conditions, that is, linearly reversing *ball-on-disk* tests (referred to as reciprocating sliding tribological tests, RSTT; see Fig. 23.24, right) and rotating *pin-on-disk* (Fig. 23.26, left) or *ring-on-disk* (Fig. 23.27b) tests.

Figure 23.24 summarizes the galvanometer laser scanner-based processing of LIPSS on a Al_2O_3-ZrO_2-Nb dielectric-metal composite material (left). The fs-laser irradiation conditions were chosen to selectively form LSFL only on the elongated Nb-flakes of the composite (middle). These laser-processed samples were

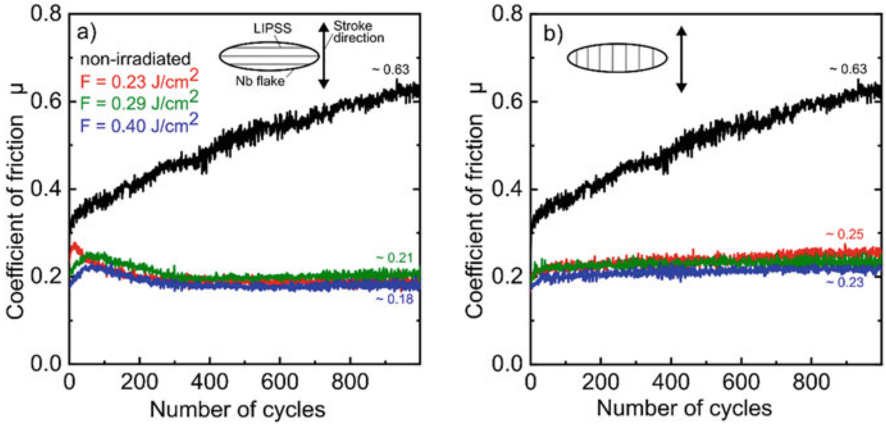

Fig. 23.25 Coefficient of friction (μ) vs. the number of RSTT sliding cycles for selectively LIPSS-structured Al_2O_3-ZrO_2-Nb composite surfaces (see Fig. 23.21) upon fs-laser processing with three different peak fluence values (0.23 J/cm^2, 0.29 J/cm^2, 0.40 J/cm^2) along with a reference of the nonirradiated material. The insets indicate the direction of the LIPSS (LSFL) with respect to the stroke direction used in the RSTT ((**a**): perpendicular, (**b**): parallel). (Reprinted from [127], Appl. Surf. Sci., Vol. **499**, Kunz et al., Tribological performance of metal-reinforced ceramic composites selectively structured with femtosecond laser-induced periodic surface structures, 143917, Copyright (2019), with permission from Elsevier)

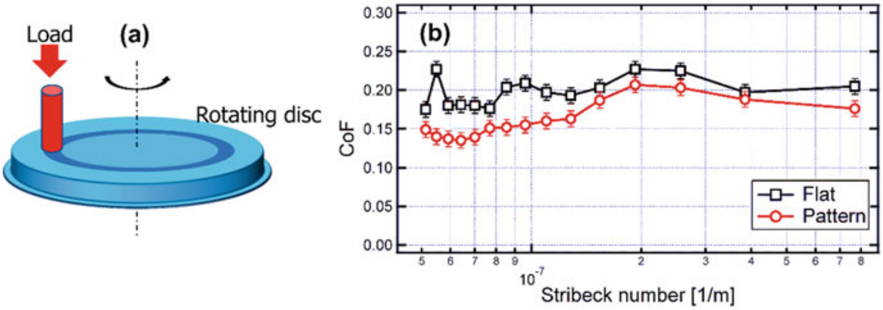

Fig. 23.26 (**a**) Scheme of pin-on-disk tribological test. (**b**) Stribeck curve of LIPSS (LSFL, referred to as "pattern") on stainless steel along with a reference curve for a polished (flat) surface. (Reprinted from [121] Gnilitskyi et al., Tribological Properties of High-Speed Uniform Femtosecond Laser Patterning on Stainless Steel, Lubricants (Basel, Switzerland) **7**:83, Copyright 2019 under Creative Commons BY 4.0 license. Retrieved from https://doi.org/10.3390/lubricants7100083)

subsequently subjected to linear reciprocating sliding tribological tests (RSTT: 1 Hz reversing frequency, $F_N = 1.0$ N normal force) against a 10-mm-diameter ball of polished Al_2O_3, employing a stroke length of $S = 1$ mm and a direction perpendicular to the elongated direction of the metal flakes in a Ringer solution as aqueous lubricant (right) [127].

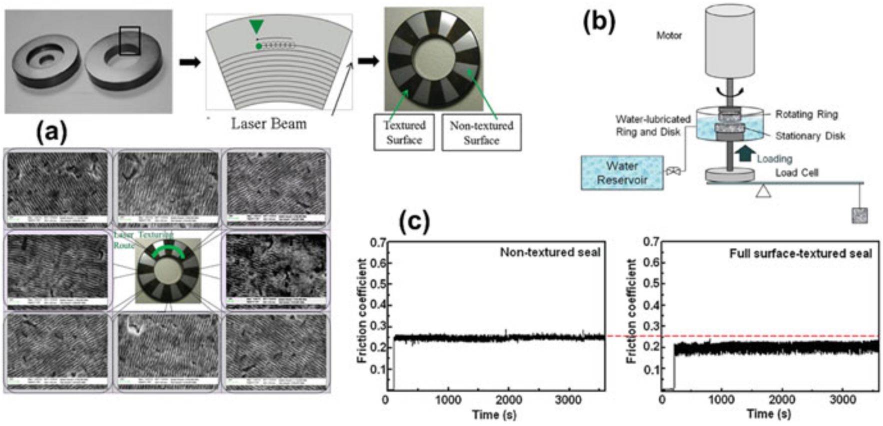

Fig. 23.27 (**a**) SiC seal consisting of two disks, of which one was fs-laser textured with LIPSS on eight individual segments. (**b**) Scheme of water-lubricated ring-on-disk tribometer. (**c**) CoF vs. operational time of the tribometer for a non-textured seal (left) and a LIPSS-textured seal (right). Image (**a**–**c**) taken from [125]. (Reprinted by permission from Springer-Verlag: Applied Physics A **107**:345–350 (Microstructure and lubricating property of ultra-fast laser pulse textured silicon carbide seals, Chen, C.Y. et al.), Copyright (2012))

The results of the RSTT for samples processed with a fs-laser [1025 nm, 300 fs, 1 kHz] at three different laser peak fluence levels along with that of a nonirradiated (polished) reference are presented in Fig. 23.25. The graphs show the CoF vs. the number of sliding cycles (here, up to 1000) for stroke directions either perpendicular to the LSFL ridges or parallel to it. In both cases, an up to a factor of three reduced CoF can be seen for the LSFL-covered Nb-flake samples when compared to the polished reference surface.

A similar beneficial tribological effect of LIPSS was reported by Gnilitskyi et al. [121] for fs-laser-processed [1030 nm, 213 fs, 600 kHz], initially polished stainless steel (X5CrNi1810) samples when tested in a pin-on-disk test against a 2-mm-diameter pin of chrome steel (100Cr6) in a commercial engine oil as a lubricant [$F_N = 0.5$ to 7.5 N, $v_{rel} = 7$ mm/s]. Figure 23.26 shows the so-called *Stribeck curve* (CoF vs. Stribeck number) of the fs-laser processed and a polished surface, acquired in the regime of boundary lubrication to mixed lubrication. The Stribeck number $SN = \eta \times v_{rel}/P$ considers the dynamic viscosity η of the oil, the relative velocity v_{rel} between the pin and the rotating disc surface, and the areal pressure P. In the entire tested range of SN, a reduction of the CoF by 10% to 25% can be seen in Fig. 23.26b when comparing the results of the LSFL-covered surface (red open circles) with that of the polished reference (black open squares). Simultaneously, a reduction of the wear by ~65% was found [121].

A beneficial effect through LIPSS was also reported by Chen et al. [125], studying the CoF of partially fs-laser-processed [800 nm, 120 fs, 1 kHz], initially polished silicon carbide (SiC) surface (Fig. 23.27a) in a ring-on-disk tribological test

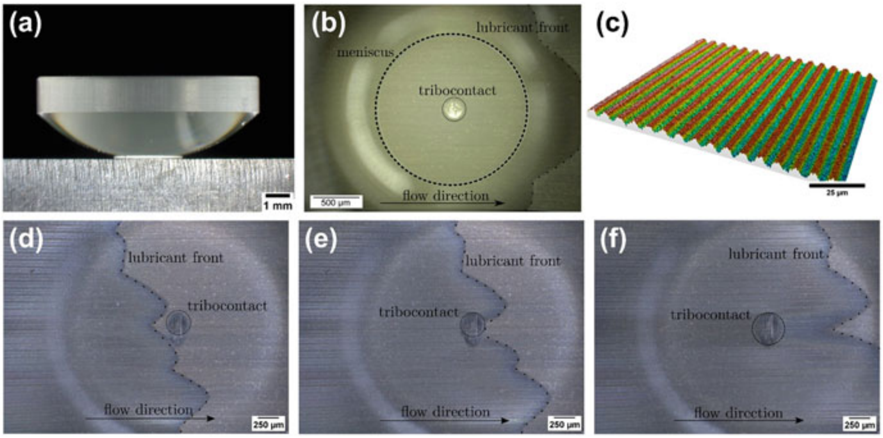
(a)
1 mm
(b)
lubricant front
meniscus
tribocontact
500 µm
flow direction
(c)
25 µm
(d)
lubricant front
tribocontact
flow direction
250 µm
(e)
lubricant front
tribocontact
flow direction
250 µm
(f)
lubricant front
tribocontact
flow direction
250 µm

Fig. 23.28 (**a**) Side view of the laser-processed sample (bottom) and a transparent glass lens (top) made for in-situ observation of the lubricant fluid flow into the tribocontact (middle). (**b**) Through-the-lens microscopic imaging of the tribocontact (central bright disk) centered in the meniscus of lubricant confined between the lens and the sample. (**c**) Surface topography of ps-DLIP-generated parallel microchannels on stainless steel for a passive directed lubricant (PAO) transport. (**d**–**f**) Temporal evolution of the PAO transport into the tribocontact area through capillary forces within the horizontally oriented microchannels. (Reprinted from [128], Stark et al., Avoiding Starvation in Tribocontact Through Active Lubricant Transport in Laser Textured Surfaces, Lubricants (Basel, Switzerland) **7**:54, Copyright 2019 under Creative Commons BY 4.0 license. Retrieved from https://doi.org/10.3390/lubricants7060054)

configuration in water environment (Fig. 23.27b). The CoF of such a fully textured SiC seal is ~20% smaller than that of a conventional polished one (Fig. 23.27c).

Management of Lubricants

Stark et al. [128] explored another tribological situation related to starvation lubrication conditions (Fig. 23.28). The authors demonstrated through in-situ optical microscopy and with a rotating ball-on-three-plates tribometer that parallel microchannels with periods of a few micrometers and depths below 1.5 μm generated by direct laser interference patterning (DLIP; 1030 nm, 6 ps, 400 kHz) on a stainless steel (X90CrMoV18) surface can induce a directed passive flow of lubricant (here polyalphaolefin oil, PAO, at room temperature) directly into the <250 μm diameter tribological contact area [128]. The effect is mainly driven by capillary forces of the lubricant within the microchannel surface structure (see also Sect. 2.2).

2.5 Energy Applications

The ever-growing world's energy needs constantly open multidisciplinary challenges for researchers and engineers when developing efficient methods and infrastructures to harvest, transport, and store energy. Laser micro- and nanoprocessing of materials via LIPSS constitutes a versatile processing method with potential to surface functionalization for certain energy applications. The fabrication of LIPSS can modify surface properties by producing topographical changes (either to enhance optical absorption/transmission/scattering, to alter electronic properties such as the electric conductivity, or to increase the effective surface area for surface-based chemical processes) or by inducing localized chemical changes as a product of the modulated laser fluence imprint. In the following, a set of applications will be discussed where LIPSS influence the final material-device functionality including solar cells, heterogeneous conductive structures on indium-doped tin oxide (ITO) substrates, superconductive surfaces, and enhanced battery storage capabilities.

Solar Cells

The fabrication of solar cells usually requires the assembling of at least three materials disposed as stacked layers: a top transparent electric contact, followed by a doped semiconductor, and finally a back electric contact. The processing of LIPSS improves the overall efficiency by modifying one of the layered materials in basically two ways: by modifying transparent surfaces to increase light transmission into the semiconductor active layer [129–131] and by inducing localized chemical changes in the semiconductor active material [132, 133].

One of the first experimental realizations of LIPSS on fully functional organic solar cells is presented in Fig. 23.29. The general thin-film solar cell architecture is illustrated in Fig. 23.29a. In this case, laser irradiation from a pulsed ns-Nd:YAG laser with an output wavelength of 532 nm (second harmonic) is directed over Poly(3-hexylthiophene) thin films (P3HT) previously deposited onto an ITO substrate. For details on the specific layer chemical compositions and thicknesses, see [132]. The morphology of the LIPSS was characterized by atomic force microscopy (AFM) data, showing parallel polymeric line structures with height variations of about ~100 nm and spatial periods corresponding to ~430 nm (Fig. 23.29b). The efficiency of regular and LIPSS-based solar cells was characterized by current vs. voltage (I-V) curves (Fig. 23.29c). From the reported data, such a LIPSS-corrugated solar cell features an overall increase of 10% efficiency with respect to the same solar cell composition/architecture without LIPSS.

Anisotropic Electric Conductivity

LIPSS fabrication on electrically conductive thin film surfaces has potential for the fabrication of individual parallel and periodic conductive surface filaments that can be used for energy transport applications in the micro- to nanoscale. This potential has been reported on LIPSS fabricated on ITO thin films deposited on glass with electrical characterizations via AFM conductivity measurements [134]. It was demonstrated that partial segregation of the conducting domains toward the

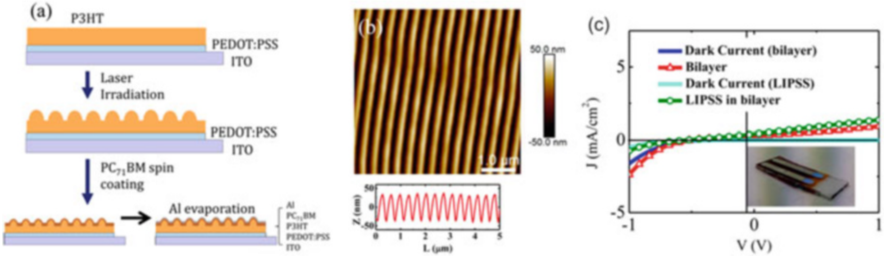

Fig. 23.29 (**a**) Scheme of the bilayer device architecture tested for photovoltaic characterization. (**b**) Surface topography of the P3HT surface just after laser irradiation. A cross-sectional height profile of the LIPSS is provided at the bottom of the image. (**c**) *I*-*V* characteristics of the LIPSS solar cell in the dark and under illumination. Note that the current (*I*) is transformed here into the current density *J*. (Reprinted with permission from [132] (Cui et al., Laser-induced periodic surface structures on P3HT and on its photovoltaic blend with $PC_{71}BM$, ACS Appl. Mater. Interfaces **8**:31894–31901). Copyright (2016) American Chemical Society)

valleys of the LIPSS could induce preferential (anisotropic) electrical conductivity along the LIPSS ridges.

The experimental realization with direct electrical characterization via macroscopic and microscopic four-point probe resistivity measurements was reported in [39]. Here, LIPSS with spatial periods of about ~900 ± 50 nm are responsible for resistivity differences longitudinally ("Micro-L") or transversally ("Micro-T") to the LIPSS orientation. The anisotropy is naturally imposed by the LIPSS orientation, and a wide range of resistivities are feasible mainly due to changes in the crystalline structure of the ITO layers as a result of the femtosecond pulses interaction. The actual micro-characterization via the four-point probe method is displayed in Fig. 23.30a, where the microprobes are placed longitudinally and transversally to the LIPSS orientation. The current vs. voltage (*I*-*V*) curves for two areas fabricated by a low (LF: 0.64 J/cm^2) and a high (HF: 0.89 J/cm^2) peak laser fluence level are presented in Fig. 23.30b, c, respectively. In both graphs, the slopes of the lines correspond to the electric resistivity in each case, showing clear differences between Micro-L and Micro-T characterization. In particular, for the low fluence sample, there is a slope difference of a factor of two, higher for the Micro-L configuration than for the Micro-T one. These findings suggest that the presence of anisotropic conductivity is induced due to a combination between the LIPSS topography and local resistivity changes due to the laser irradiation.

Surface Superconductivity

Femtosecond laser irradiation for the fabrication of LIPSS can be used to modify the magnetic responses of a material. This opens widely unexplored possibilities in terms of the final surface properties that can be accessible through surface processing techniques based on LIPSS. Recently, it has been demonstrated that magnetic responses obey topographical and chemical changes induced by the laser treatments including LIPSS [135, 136]. For applications where the material's

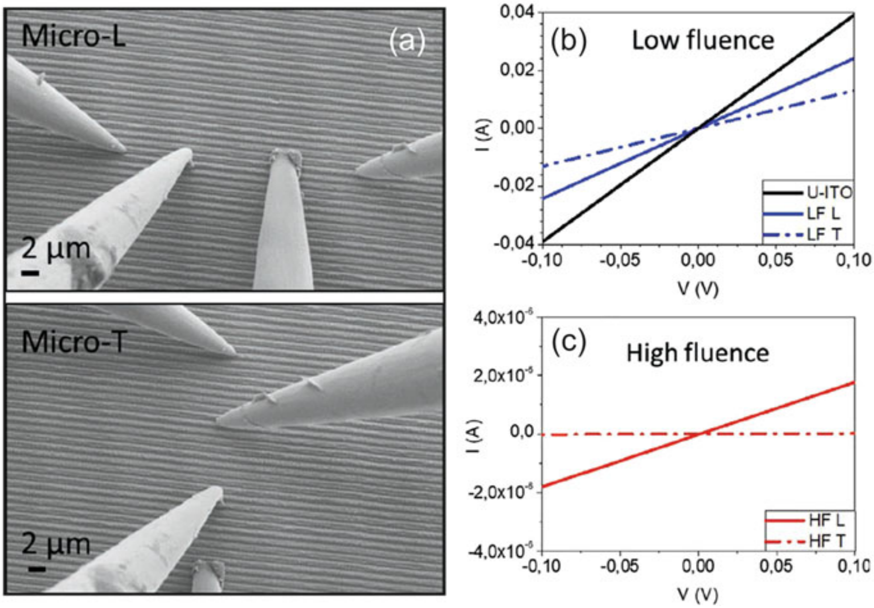

Fig. 23.30 (**a**) Micro-configuration four-point probe measurements. The actual distance between the electrodes is determined from SEM images. Fingertip-like metallic electrodes are carefully located at the ridges of the structures. (**b**), (**c**) *I*-*V* curves measured for the low fluence (LF) conditions in the macro-configuration and for high-fluence (HF) conditions in the micro-configuration, with the electrodes aligned longitudinally (Micro-L) and transversally (Micro-T) to the LIPSS direction. The *I*-*V* curve of a non-irradiated film is included as reference in (**b**). (Reprinted from [39], Lopez-Santos et al. Anisotropic resistivity surfaces produced in ITO films by laser-induced nanoscale self-organization, Adv. Opt. Mater. **9**:2001086, Copyright 2020 under Creative Commons BY 4.0 license. Retrieved from https://doi.org/10.1002/adom.202001086)

magnetic response is a defining factor, such as surface superconductivity, the realization of LIPSS constitutes an important parameter to study.

The realization of LIPSS on superconductor materials such as niobium has been reported in [23, 137], where direct current (DC) magnetization and alternating current (AC) susceptibility measurements at cryogenic temperatures with external magnetic fields of different amplitude and orientation were analyzed and reported for samples with and without LIPSS, produced in different atmospheres, as indicated in Fig. 23.31a–d. The electric characterizations demonstrated a correlation of the surface superconducting properties and the LIPSS orientation. In fact, the upper critical field, H_{c2}, was found not to be affected by the LIPSS, but the surface critical field, H_{c3}, presented higher values when the external magnetic field (H) was set parallel to the LIPSS orientation (Fig. 23.31e). Hence, it is possible to define a preferred superconductivity direction by the orientation of the imprinted structures at the surface. Interestingly, despite the induced effects of laser irradiation

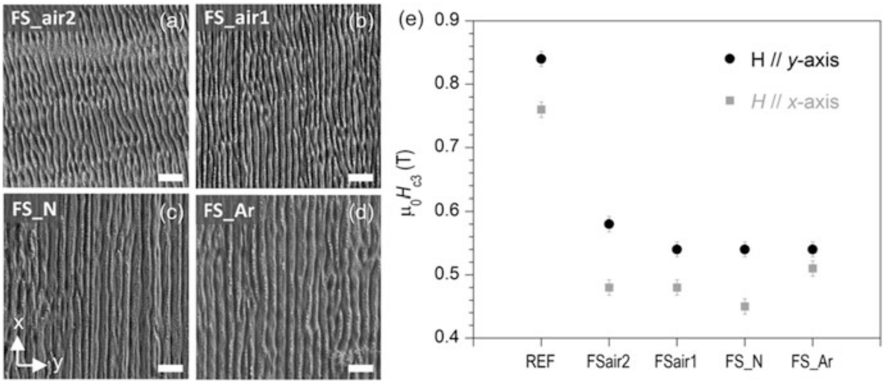

Fig. 23.31 SEM micrographs (secondary electrons) of the fs-laser-irradiated surfaces produced under different gaseous atmospheric conditions: (**a**) and (**b**) in air, (**c**) in nitrogen, and (**d**) in argon. The scale bar corresponds to 2 μm for all micrographs. The rolling direction of the pristine Nb sheet material is parallel to the *y*-axis in all samples, except for FS_air2 in (**a**), where it is parallel to *x*. (**e**) Critical surface fields, $\mu_0 H_{c3}$, of all analyzed samples. (Reprinted from [23], Cubero et al. Surface superconductivity changes of niobium sheets by femtosecond laser-induced periodic nanostructures, Nanomaterials (Basel, Switzerland) **10**:2025, Copyright 2020 under Creative Commons BY 4.0 license. Retrieved from https://doi.org/10.3390/nano10122525)

on the surface superconducting properties, the H_{c3} values are almost unaffected by differences in the LIPSS period [23].

Energy Storage

The functionalization of nickel metal electrodes acting as a cathode material optimized via LIPSS for micro-batteries applications has been reported in [138]. It was demonstrated that the fabrication of LIPSS at throughputs of 4 cm^2/s constitutes a valuable and fast one-step approach for reliable and reproducible micro-scale surface modifications on nickel-based batteries electrodes.

The morphology of the fabricated LIPSS via SEM micrographs is displayed in Fig. 23.32a–d, showing structures with periods around ~1 μm. Cyclic voltammetry characterization with LIPSS-covered and non-irradiated nickel samples showed that the anodic peak current density of the laser-processed sample at electric potentials between 0.35 V and 0.40 V (Fig. 23.32e) was over 2.5 times larger than the equivalent peak current density for the unprocessed nickel electrode (25.6 mA/cm^2 against 9.9 mA/cm^2). This is translated into net charge densities of 1.2 mC/cm^2 for the unprocessed nickel foil and 4 mC/cm^2 for the processed sample. This increase in electrochemical activity is attributed, on one hand, to an overall increase of the effective surface area relative to a non-modified nickel surface and, on the other, to chemical changes in the form of thicker oxide layers that may benefit the overall performance. Different fs- and ps-laser-processing conditions to produce the LIPSS were also studied, including laser wavelengths (532 nm, 775 nm, and 1064 nm), in order to identify the influence of the different topographies/periods on the maximum

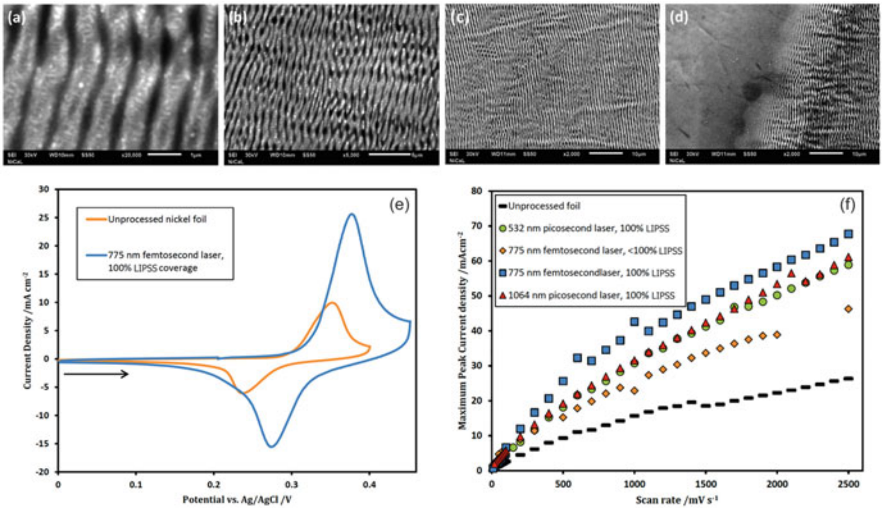

Fig. 23.32 (**a**–**c**) Top-view scanning electron micrographs of LIPSS fabricated with a laser wavelength of 1064 nm on nickel surfaces under different magnifications. (**d**) SEM micrograph centered in the boundary of laser processing, showing a relatively planar non-irradiated nickel surface (left) and the LIPSS (right). (**e**) Cyclic voltammetry at 500 mV/s of a LIPSS-covered nickel electrode (blue curve) and a non-irradiated nickel foil electrode as reference (orange curve). (**f**) Anodic peak current density values for full range of scan rates and irradiation wavelengths. "% LIPSS" corresponds to the LIPSS coverage across the nickel surface. (Reprinted from [138], Neale et al., Electrochemical performance of laser microstructured nickel oxyhydroxide cathodes, J. Power Sources **271**:42, Copyright 2014 under Creative Commons BY 3.0 license. Retrieved from https://doi.org/10.1016/j.jpowsour.2014.07.167)

peak current density achieved. It was demonstrated that the percentage of surface coverage influences the electrode performance, as it can be observed in the data plotted in Fig. 23.32f.

2.6 Other Technical Applications

This section is dedicated to LIPSS applications, which do not fall in one of the other application areas mentioned above. It will be discussed that LIPSS can improve the performance of piercing punch tools as well as the improvement of gasoline injection nozzles and the catalytic activities of electrodes.

Improved Piercing Punch Tool Performance

It was demonstrated by Aizawa et al. [139] that the LIPSS nanostructure pattern processed on the curved surface area of a diamond-coated cylindrical WC (Co) punch tool was transcribed onto the sidewall of the concurrent metal sheet piercing hole during the punching process, which finally leads to a smoother metal sheet hole

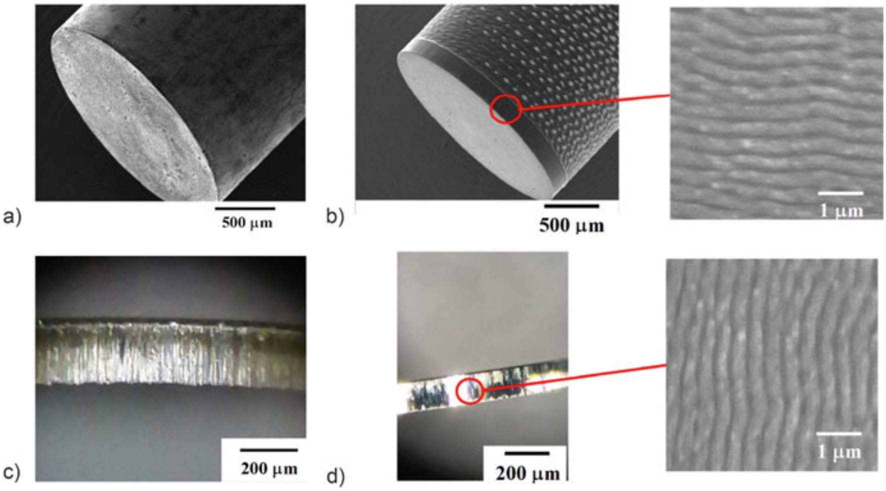

Fig. 23.33 (**a**) SEM micrograph of unstructured CVD (Chemical Vapor Deposition)-diamond-coated WC punch tool. (**b**) SEM micrograph of laser-structured CVD (Chemical Vapor Deposition)-diamond-coated WC punch tool with magnified inlet of LIPSS. (**c**) Side view of hole with rough surface punched by unstructured WC punch tool. (**d**) Side view of hole punched by laser-structured WC punch tool with smooth area with magnified inlet of SEM micrograph showing imprinted microstructures onto the punched sidewall. (Reprinted from [139], Aizawa et al., Simultaneous Nano-Texturing onto a CVD-Diamond Coated Piercing Punch with Femtosecond Laser Trimming, Appl. Sci. (Basel, Switzerland) **10**:2674, Copyright 2020 under Creative Commons BY 4.0 license. Retrieved from https://doi.org/10.3390/app10082674)

surface. Figure 23.33 illustrates SEM micrographs of the diamond-coated punch tool without (a) and with LIPSS (b), as well as images of the pierced metal hole surface after punching it without (c) and with LIPSS (d).

Improved Gasoline Injection Nozzles

LIPSS in the spray hole of gasoline direct injection nozzles enhance the atomization process of the fuel by decreasing the average droplet size of about 10% and by simultaneously increasing the spray angle by 20% with respect to regular laser trepanned holes [140]. Figure 23.34 shows SEM micrographs of a cross-section of a fs-laser drilled spray hole with the corresponding LIPSS on the inner surface of the hole [140]. Furthermore, fs-laser drilled spray holes covered with LIPSS consist of smaller surface features than compared to micro-Electrical Discharge Machining (µ-EDM) or Laser Micro-Jet (LMJ) machining, at which the process-related craters (µ-EDM) and grooves (LMJ) are in the scale of several micrometers and produce the sharpest edges with a radius of less than 1 µm, while the µ-EDM edge radius typically lies between 2 and 4 µm and LMJ produces unwanted and uncontrollable protrusions [141].

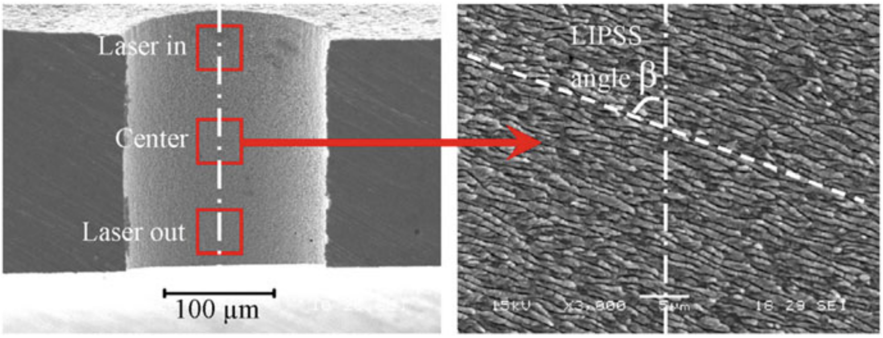

Fig. 23.34 SEM micrographs of a cross-section of a fs-laser drilled spray hole (left) and the magnified nanostructures in the center of the surface of the spray hole (right). (Reprinted from [140], CIRP Annals, Vol. **63**, Romoli, et al., Ultrashort pulsed laser drilling and surface structuring of microholes in stainless steels, 229–232, Copyright (2014), with permission from CIRP)

Increased Catalytic Activity
The fabrication of LIPSS typically leads to an increase of the nanoscale surface roughness and the total surface area. Therefore, LIPSS can enhance the catalytic activity [138, 47], depending on the specific interfacial interactions and chemical reactions. It was found by Lange et al. that the electrochemical activity in the oxygen reduction reaction on laser-processed platinum plates increased by a factor of 1500 [47].

3 Industrialization

This section sheds some light on the current state of industrialization of LIPSS by briefly analyzing the available market segment (Sect. 3.1), providing examples for estimating the production costs of LIPSS based on the currently available technology (Sect. 3.2), and giving a survey on patent applications that are relying on LIPSS (Sect. 3.3).

3.1 Market Analysis

Although LIPSS and their applications have been extensively studied, their practical manufacturing has not yet emerged from an experimental status (*Technology Readiness Levels* of TRL 3 to 5) into industrial applications (TRL > 5). A main reason for this obstacle is the relatively low areal processing rate when scanning the pulsed laser beam across the surface of the workpiece via galvanometer scanners, which typically offer scan velocities up to 10 m/s in a line. However, upcoming modern laser systems with high average laser powers in the kilowatt regime with pulse repetition frequencies in the megahertz range in combination with polygon scanners with scan velocities up to 1000 m/s [142] open the door for achieving industrial rate processing times [143, 144]. Currently, the areal LIPSS processing rates are at the m^2/min level [144]. It can, however, be expected that future improvements in ultrafast laser technology that are enabling high energy laser pulses at (burst) repetition frequencies in the Gigahertz range [145] along with advanced laser scanner technologies and in combination with smart scanning strategies for controlling the residual heat load to the laser irradiated material will enable areal LIPSS processing rates at the m^2/s level [12].

Moreover, it must be noted that the specific LIPSS processing parameters presented in most scientific publications were not optimized for enabling the lowest overall processing time for the used laser wavelength and the given material. A method to predict the laser processing parameters for optimized production rates given the used laser and material was provided by Mezera et al. [104].

Nevertheless, there are many applications that do not rely on large area processing but on the tailored marking of goods, tools, etc. One example is given by medical tools used in surgery that must be trackable during their entire lifetime, for example, by marking serial numbers, bar codes, or data matrix codes with high optical contrast. For that application, an industrial process relying on ultrashort laser-generated LIPSS named “black marking” was already established by the industry. The ultrafast laser blackened surface regions feature good corrosion resistance when a chromium containing steel is used [146].

In regard of the rapid developments on the laser market, it is worth noting that the average power of ultrashort lasers is obeying an analogon to the famous Moore’s law that was framing the developments in the field of computer technology for decades: a doubling of complexity every 2 years. More precisely, [147] underlined that since the year 2000, the increase of the average laser power of ultrashort (sub-ps) pulsed lasers can be described by a power law, that is, a growth rate ~$2^{Q/2}$ with Q being the number of the years from beginning of the trend—consistently with the data presented in [148].

It is difficult to establish accurate forecasts toward a precise market analysis. However, the prices for ultrafast laser have been dropping in recent years [149] and, just as a landmark, the worldwide annual growth rate of the revenue created by lasers in the market segment of fine metal processing is estimated to be 9.4% during the next 5 years, raising from a level of ~420 million USD in 2019 up to ~700 million USD in 2025 [149]. Considering the wide fields of applications, the emerging upscaling of the LIPSS manufacturing process to industrial demands, the dropping costs for ultrashort pulsed lasers and scanners, and that first companies offering laser-based surface functionalization as a commercial service, it is only a matter of time until LIPSS are a standard industrial manufacturing technique.

3.2 Production Costs

In order to estimate the overall fabrication costs per area required to fabricate LIPSS, it is necessary to consider the individual costs for a basic set of devices and optical elements needed for the configuration of a standard laser direct writing setup. Usually, an ultrashort pulsed laser source provides a continuous train of pulses that will be directed to the surface of the material of interest after passing through a focusing element. Ultimately, the deposited energy dose (sometimes referred to as *accumulated laser fluence*) is given by product of the laser fluence ϕ_0 and the effective number of laser pulses N_{eff} that are hitting the surface per spot area unit ($\phi_{\text{acc}} = \phi_0 \times N_{\text{eff}}$). For a single scanned line, the latter is given by a relation between the laser pulse repetition frequency and the scanning speed for a given laser spot geometry at the focus (see Eq. (23.1)). In traditional systems, the laser beam remains static and translation stages position the sample at user-defined positions and speeds. However, the increasing availability of high-repetition rate ultrashort lasers imposes a minimum laser scanning speed that is hard to reach by regular mechanical translation stages. For this reason, high-repetition rate lasers are usually combined with fast laser scanners based on a set of individually controlled galvanometric or on polygonal mirrors. The laser scanning systems are subsequently coupled with F-theta lenses to guarantee the same focusing conditions even over extended surface areas.

Table 23.1 summarizes the general requirements and estimated prices for the given elements. It is important to note that the operational costs (physical space required, energy consumption, insurances, local regulations taxes, and operator salary) are not included in this estimation, mainly because these values depend on the country where the laser processing system is located. A generalized total cost estimation over a return-on-investment period of 5 years for three-axes laser processing systems based on galvanometric or polygonal mirrors currently is ~254,000,- € and ~294,000,- €, respectively.

The relation between the number of effective pulses per beam spot diameter ($N_{\text{eff\_1D}}$), the laser beam waist radius at the material surface (w_0), the laser pulse repetition frequency (ν), and scan velocity (v_{scan}) is generally described by the Eq. (23.1):

$$N_{\text{eff1D}} = \frac{2 * w_0 * v}{v_{\text{scan}}}, \tag{23.1}$$

According to [150], it is possible to fabricate low spatial frequency LIPSS (LSFL) on steel with a high-repetition rate laser using $N_{\text{eff\_1D}} = 10$. With this value and considering a laser beam waist radius $w_0 = 50\ \mu\text{m}$, and a galvanometric scanner operating at $v_{\text{scan}} = 15$ m/s, the maximum laser repetition frequency is $\nu = 1.5$ MHz according to Eq. (23.1). Under these conditions, it is theoretically possible to reach throughputs (areal processing rates) of 0.45 m^2/h. On the other hand, regular polygonal scanners operating at 50 m/s with the same beam waist

Table 23.1 Elements needed for a general laser processing system and its estimation price on the market (information consulted on May 26, 2021)

Category	Element/device	Features	Average price estimation (2021)
Laser system (Ls)	High-repetition rate ultrashort laser	IR wavelength, rep. frequency <5 MHz, pulse energy <100 μJ, pulse duration ~500 fs	~180,000 €
Scanner (Sc)	(a) Galvanometric mirror-based scanner + F-theta lens with AR coating	<15 m/s	~10,000 €
	(b) Polygonal mirror-based scanner	48–256 m/s	~50,000 €
Safety (Sf)	Radiation safety and dosage control	Lead blinds, passive dosimeters	~5000 €
	Air filtering, exhaust system	Mobile station	~3000 €
	Eye protection	Safety goggles	~1000 €
Maintenance (Ma)	General maintenance and technical service	Filters, chiller refrigeration liquids, eventual system optimization	~5000 €/year
Miscellaneous (Ms)	Optical elements	Mirrors, mounts	~5000 €
	Translation stages	Independent *X-Y-Z* axes	~5000 €/per axis
	Optical table	Optical table with active isolation legs	~10,000 €

at the surface allow for a laser repetition frequency of $\nu = 5$ MHz while keeping $N_{\text{eff\_1D}} = 10$, resulting in throughputs of 1.5 m^2/h. Note that for polygonal scanners operating at 950 m/s, recently processing rates of ~1.5 m^2/min were demonstrated for large area surface texturing of metals [144].

For this calculation, we assumed irradiations over a squared area of 1 m × 1 m accounting a total of 20,000 parallel lines of 1 m in length and 100 μm in width, all separated at a line distance $\Delta = 50$ μm (50% lateral beam overlap). Also, for the mirrors positioning times, 100 ms for polygonal mirrors and 333 ms for galvanometric mirrors (~5 times the processing time, 1 m/v_{scan}) per line were assumed.

For an estimation of the total laser-processing time, we consider a time t_{year} corresponding to the average number of working days per year, for example, $t_{\text{year}} = 260$, and we assume that the system operational (production) time is in average $t_{\text{op}} = 18$ h per day. In order to estimate the *"photonic costs"* to produce LSFL under the above specified conditions following a similar calculation as in [151], a return-on-investment period of 5 years ($p = 5$) was considered. The formula for this calculation is included in Eq. (23.2) and considers the cost listed in Table 23.1:

$$\text{Photonic costs}\left[\text{€}/\text{m}^2\right] = \frac{\text{Total setup price}}{\text{Total throughput}} = \frac{Ls + Sc + Sf + Ma * p + Ms}{\left(\frac{1200 * w_0 * v * \Delta}{N_{\text{eff 1D}}}\ \frac{\text{s}}{\text{h}}\right) * t_{\text{op}} * t_{\text{year}} * p}, \tag{23.2}$$

In conclusion, for a typical current ultrashort laser processing system that uses a galvanometric scanner, the photonic costs for the processing of LSFL are ~24 €/m^2, and for a polygonal scanner ~9 €/m^2.

3.3 *Patent Situation*

The technological advancements for industrial interests are usually considered for publication as a patent rather than scientific papers, in order to grant intellectual property rights to the inventors and developers of such technology for protecting their business. Importantly, patent publications are distinctly different from scientific literature, especially because of the economic and legal interests that are at play. Since the granting of a patent is country specific, and there are different stages that such patent documents will pass, we focus our attention here in publicly accessible patent applications—regardless of its legal approval status. The following Table 23.2 lists a number of published patents where LIPSS are used. Wherever possible, just the international WO patent number is provided. If not available, the European or national patent numbers are given. Regarding the use of the LIPSS, the type of application is additionally specified.

4 Outlook

More than 50 years after their discovery, the topic of LIPSS moved from the field of fundamental research toward a preindustrial stage that is currently screening systematically a plethora of possible applications—all are enabled through a remarkable variety of different surface functions of LIPSS (see Fig. 23.5 to recall the content of this chapter). In view of the rapid ongoing progress of laser and scanner technology that further reduces the production costs of LIPSS and simultaneously boost up the manufacturing rates, it can be expected that during the coming 5 years, some industrial applications of LIPSS will be realized that will enter our daily life.

Table 23.2 Compilation of patents (patent number, title, type of application, publication date) that include the formation of LIPSS within its description and the claims included in the patent application. The list is ordered by the publication dates ranging from 04/2004 to 04/2021

Patent number	Title	Application	Publication date
WO2004035255	Cyclic structure formation method and surface treatment method	LIPSS fabrication	29/4/2004
WO2006027850	Method for enhancing adhesion of thin film	Surface adhesion	16/3/2006
WO2006065356	Applications of LIPSS in polymer medical devices	Antibacterial surfaces	22/6/2006
WO2007012215	Method and device for the defined structuring of a surface with a laser unit	LIPSS fabrication	1/2/2007
WO2008097374	Ultrashort duration laser methods for the nanostructuring of materials	LIPSS fabrication	14/8/2008
CN101319347	Method for crystal surface self-organizing growth of fine nanostructure with femtosecond laser	LIPSS fabrication	10/12/2008
US20080299408	Femtosecond laser pulse surface structuring methods and materials resulting therefrom	LIPSS fabrication	04/12/2008
WO2009090324	Method and device for marking a surface using controlled periodic nanostructures	Marking	23/7/2009
WO2009117451	Laser-based material processing methods and systems	LIPSS fabrication	24/09/2009

WO2012019741	Method for producing embossing tools for microstructure elements using ultrashort laser pulses	Surface adhesion	16/2/2012
EP2692855	Surface structuring for cytological and/or medical applications	Antibacterial surfaces	17/7/2013
US2014083984	Formation of laser-induced periodic surface structures (LIPSS) with picosecond pulses	LIPSS fabrication	27/3/2014
WO2014102008	Method for producing structures on a surface of a workpiece	LIPSS fabrication	3/7/2014
WO2014111697	Measurement scale	Optical	24/7/2014
WO2014111696	A method of reading data represented by a periodic, polarizing nanostructure	Data storage	24/7/2014
KR1427688*	Laser processing device and processing method	LIPSS fabrication	1/8/2014
RU2544892	Method of producing micro- and nanostructures of surface of materials	LIPSS fabrication	20/3/2015
US20150136226	Superhydrophobic surfaces and methods for producing superhydrophobic surfaces	Surface wetting	21/5/2015
WO2016039419	Method for forming surface structure of zirconia-based ceramic and zirconia-based ceramic	LIPSS fabrication	17/3/2016

(continued)

Table 23.2 (continued)

Patent number	Title	Application	Publication date
WO2016090496	Laser-induced metallic surface coloration processes, metallic nanoscale structures resulting therefrom, and metallic products produced thereby	Optical	16/06/2016
WO2017053198	Femtosecond laser-induced formation of single crystal patterned semiconductor surface	LIPSS fabrication	30/3/2017
WO2017063844	Method for producing a scattering optical unit, scattering optical unit, and lamp having a scattering optical unit	Optical	20/4/2017
WO2017153750	Method of reducing photoelectron yield and/or secondary electron yield of a ceramic surface; corresponding apparatus and product	Surface enhancement	14/09/2017
WO2018010707	Method and system of ultrafast laser writing of highly regular periodic structures	LIPSS fabrication	18/1/2018
US20180117797	Methods of making hydrophobic contoured surfaces and hydrophobic contoured surfaces and devices made therefrom	Surface adhesion	3/5/2018
WO2018100952	Method for manufacturing transfer mold roll having fine periodic structure and transfer mold roll	Surface adhesion	7/6/2018
US 10,876,193	Method and apparatus for structural coloration of metallic surfaces	Optical	1/1/2019
CN109132998	Method for inducing periodic surface structure of transparent dielectric material with single-pulse nanosecond laser	Wetting and cell adhesion	4/1/2019

US20190054571	Nanosecond laser-based high-throughput surface nanostructuring (NHSN) process	LIPSS fabrication	21/2/2019
US20190168905	Beverage container with internal antimicrobial texture	Antibacterial surfaces	6/6/2019
WO2019141626	Mold for injection molding processes and molding process using the mold	Surface adhesion	25/7/2019
WO2019166836	Using lasers to reduce reflection of transparent solids, coatings, and devices employing transparent solids	Optical	6/9/2019
WO2020003090	A component of a mold for molding preforms, a mold for molding preforms, and a process for obtaining the component	Surface adhesion	2/1/2020
WO2020012137A1	Process for nanostructuring the surface of a material by laser; assembly allowing this process to be implemented	LIPSS fabrication	16/1/2020
WO2020039217	Laser fabricated superoleophilic metallic component with oil retention properties for friction reduction	Friction reduction	27/2/2020
KR1020200053368	Metal surface color implementing method and metal plate with surface color implemented thereon	Optical	18/5/2020
CN111168233	Method for inducing periodic structure on surface of optical glass by picosecond laser	Optical	19/5/2020

(continued)

Table 23.2 (continued)

Patent number	Title	Application	Publication date
WO2020104370	Sensor device and method for producing a sensor device	Surface wetting	28/5/2020
CN111250874	Method of multi-pulse picosecond laser-induced semiconductor material periodic surface structure	LIPSS fabrication	9/6/2020
US20200198063	Method for manufacturing substrate with transparent conductive film, substrate with transparent conductive film, and solar cell	Optical	25/6/2020
KR102131165	Laser-marking method using surface reflectance control	Optical	7/7/2020
US 10,786,874 B2	Femtosecond laser pulse surface structuring methods and materials resulting therefrom	LIPSS fabrication	29/09/2020
US 10,876,193 B2	Nanostructured materials, methods, and applications	LIPSS fabrication	29/12/2020
WO2021041166	Elements for mitigating electron reflection and vacuum electronic devices incorporating elements for mitigating electron reflection	Optical	4/3/2021
WO2021048704	Method of gluing metal parts	Surface adhesion	18/3/2021
US20210121983A1	Process for nanostructuring the surface of a material by laser context and technological background	LIPSS fabrication	25/3/2021

Acknowledgments The authors acknowledge the projects Laser4Fun, CellFreeImplant, BioCombs4Nanofibers, and LaserImplant. These projects have received funding from the European Union's Horizon 2020 research and innovation program under grant agreements No. 675063 (Laser4Fun, https://www.laser4fun.eu), No. 800832 (CellFreeImplant), No. 862016 (BioCombs4Nanofibers, http://biocombs4nanofibers.eu), and No. 951730 (LaserImplant, http://laserimplant.eu). C.F. acknowledges the Individual Fellowship Marie Skłodowska-Curie project FOCUSIS under grant agreement No. 844977.

References

1. M. Birnbaum, Semiconductor surface damage produced by ruby lasers. J. Appl. Phys. **36**, 3688–3689 (1965). https://doi.org/10.1063/1.1703071
2. H.M. van Driel, J.E. Sipe, J.F. Young, Laser-induced periodic surface structures on solids: A universal phenomenon. Phys. Rev. Lett. **49**, 1955–1958 (1982). https://doi.org/10.1103/PhysRevLett.49.1955
3. J. Bonse, S. Höhm, S.V. Kirner, A. Rosenfeld, J. Krüger, Laser-induced periodic surface structures – A scientific evergreen. IEEE J. Sel. Top. Quantum Electron. **23**, 9000615 (2017). https://doi.org/10.1109/JSTQE.2016.2614183
4. J.E. Sipe, J.F. Young, J.S. Preston, H.M. van Driel, Laser-induced periodic surface structure. I. Theory. Phys. Rev. B **27**, 1141–1154 (1983). https://doi.org/10.1103/PhysRevB.27.1141
5. J. Bonse, J. Krüger, S. Höhm, A. Rosenfeld, Femtosecond laser-induced periodic surface structures. J. Laser Appl. **24**, 042006 (2012). https://doi.org/10.2351/1.4712658
6. A.E. Siegman, P.M. Fauchet, Stimulated Wood's anomalies on laser-illuminated surfaces. IEEE J. Quantum Electron. **22**, 1384–1403 (1986). https://doi.org/10.1109/JQE.1986.1073133
7. A.Y. Vorobyev, C. Guo, Direct femtosecond laser surface nano/microstructuring and its applications. Laser Photonics Rev. **7**, 385–407 (2013). https://doi.org/10.1002/lpor.201200017
8. M.J. Abere, M.L. Zhong, J. Krüger, J. Bonse, Ultrafast laser-induced morphological transformations. MRS Bull. **41**, 969–974 (2016). https://doi.org/10.1557/mrs.2016.271
9. J. Bonse, S. Gräf, Maxwell meets Marangoni – A review of theories on laser-induced periodic surface structures. Laser Photonics Rev. **14**, 2000215 (2020). https://doi.org/10.1002/lpor.202000215
10. J. Bonse, S.V. Kirner, J. Krüger, Laser-induced periodic surface structures (LIPSS), Ch. 23, pp. 879–936, in *Handbook of Laser Micro- and Nano-Engineering*, ed. by K. Sugioka, (Springer, Cham, 2021) https://doi.org/10.1007/978-3-030-63647-0_17
11. R. Buividas, M. Mikutis, S. Juodkazis, Surface and bulk structuring of materials by ripples with long and short laser pulses: Recent advances. Prog. Quantum Electron. **38**, 119–156 (2014). https://doi.org/10.1016/j.pquantelec.2014.03.002
12. J. Bonse, Quo Vadis LIPSS? — Recent and future trends on laser-induced periodic surface structures. Nanomaterials **10**, 1950 (2020). https://doi.org/10.3390/nano10101950
13. C. Florian, S.V. Kirner, J. Krüger, J. Bonse, Surface functionalization by laser-induced periodic surface structures. J. Laser Appl. **32**, 022063 (2020). https://doi.org/10.2351/7.0000103
14. C. Florian, J.L. Déziel, S.V. Kirner, J. Siegel, J. Bonse, The role of the laser-induced oxide layer in the formation of laser-induced periodic surface structures. Nanomaterials **10**, 147 (2020). https://doi.org/10.3390/nano10010147
15. C. Florian, R. Wonneberger, A. Undisz, S.V. Kirner, K. Wasmuth, D. Spaltmann, J. Krüger, J. Bonse, Chemical effects during the formation of various types of femtosecond laser-generated surface structures on titanium alloy. Appl. Phys. A Mater. Sci. Process. **126**, 266 (2020). https://doi.org/10.1007/s00339-020-3434-7
16. S. Gräf, Formation of laser-induced periodic surface structures on different materials: Fundamentals, properties and applications. Adv. Opt. Technol. **9**, 11–39 (2020). https://doi.org/10.1515/aot-2019-0062

17. H. Liu, W. Lin, M. Hong, Surface coloring by laser irradiation of solid substrates. APL Photonics **4**, 051101 (2019). https://doi.org/10.1063/1.5089778
18. E. Stratakis, J. Bonse, J. Heitz, J. Siegel, G.D. Tsibidis, E. Skoulas, A. Papadopoulos, A. Mimidis, A.-C. Joel, P. Comanns, J. Krüger, C. Florian, Y. Fuentes-Edfuf, J. Solis, W. Baumgartner, Laser engineering of biomimetic surfaces. Mater. Sci. Eng. R **141**, 100562 (2020). https://doi.org/10.1016/j.mser.2020.100562
19. S.A. Akhmanov, V.I. Emelyanov, N.I. Koroteev, V.N. Seminogov, Interaction of powerful laser radiation with the surfaces of semiconductors and metals: Nonlinear optical effects and nonlinear optical diagnostics. Sov. Phys. Usp. **28**, 1084–1124 (1985). https://doi.org/10.1070/PU1985v028n12ABEH003986
20. A.M. Bonch-Bruevich, M.N. Libenson, V.S. Makin, V.V. Trubaev, Surface electromagnetic waves in optics. Opt. Eng. **31**, 718–730 (1992). https://doi.org/10.1117/12.56133
21. J. Bonse, A. Rosenfeld, J. Krüger, On the role of surface plasmon polaritons in the formation of laser-induced periodic surface structures upon irradiation of silicon by femtosecond-laser pulses. J. Appl. Phys. **106**, 104910 (2009). https://doi.org/10.1063/1.3261734
22. A. Rudenko, J.-P. Colombier, S. Höhm, A. Rosenfeld, J. Krüger, J. Bonse, T.E. Itina, Spontaneous periodic ordering on the surface and in the bulk of dielectrics irradiated by ultrafast laser: A shared electromagnetic origin. Sci. Rep. **7**, 12306 (2017). https://doi.org/10.1038/s41598-017-12502-4
23. Á. Cubero, E. Martínez, L.A. Angurel, G.F. de la Fuente, R. Navarro, H. Legall, J. Krüger, J. Bonse, Surface superconductivity changes of niobium sheets by femtosecond laser-induced periodic nanostructures. Nanomaterials **10**, 2525 (2020). https://doi.org/10.3390/nano10122525
24. T. Tomita, R. Kumai, S. Matsuo, S. Hashimoto, M. Yamaguchi, Cross-sectional morphological profiles of ripples on Si, SiC, and HOPG. Appl. Phys. A Mater. Sci. Process. **97**, 271–276 (2009). https://doi.org/10.1007/s00339-009-5364-2
25. J.Z.P. Skolski, G.R.B.E. Römer, J.V. Obona, V. Ocelik, A.J. Huis in ‘t Veld, J.T.M. De Hosson, Laser-induced periodic surface structures: Fingerprints of light localization. Phys. Rev. B **85**, 075320 (2012). https://doi.org/10.1103/PhysRevB.85.075320
26. A. Rudenko, A. Abou-Saleh, F. Pigeon, C. Mauclair, F. Garrelie, R. Stoian, J.-P. Colombier, High-frequency periodic patterns driven by non-radiative fields coupled with Marangoni convection instabilities on laser-excited metal surfaces. Acta Mater. **194**, 93–105 (2020). https://doi.org/10.1016/j.actamat.2020.04.058
27. F. Fraggelakis, G. Mincuzzi, J. Lopez, R. Kling, I. Manek-Hönninger, Controlling micron and submicron scale laser induced surface structures on stainless steel with industrial femtosecond lasers. J. Laser Micro/Nanoeng. **13**, 206–210 (2018). https://doi.org/10.2961/jlmn.2018.03.0010
28. Q. Liu, N. Zhang, J. Yang, H. Qiao, C. Guo, Direct fabricating large-area nanotriangle structure arrays on tungsten surface by nonlinear lithography of two femtosecond laser beams. Opt. Express **26**, 11718–11727 (2018). https://doi.org/10.1364/OE.26.011718
29. M. Mezera, Picosecond Laser-Induced Periodic Surface Structures – Process Strategies for Metals, Silicon and Polymers, PhD Thesis, University of Twente, The Netherlands, 2020. https://doi.org/10.3990/1.9789036550529
30. J.-M. Romano, A. Garcia-Giron, P. Penchev, S. Dimov, Triangular laser-induced submicron textures for functionalising stainless steel surfaces. Appl. Surf. Sci. **440**, 162–169 (2018). https://doi.org/10.1016/j.apsusc.2018.01.086
31. S.H. van der Poel, M. Mezera, G.R.B.E. Römer, E.G. de Vries, D.T.A. Matthews, Fabricating laser-induced periodic surface structures on medical grade cobalt–chrome–molybdenum: Tribological, wetting and leaching properties. Lubricants **7**, 70 (2019) https://doi.org/10.3390/lubricants7080070
32. F. Fraggelakis, G. Mincuzzi, J. Lopez, I. Manek-Hönninger, R. Kling, Controlling 2D laser nano structuring over large area with double femtosecond pulses. Appl. Surf. Sci. **470**, 677–686 (2019). https://doi.org/10.1016/j.apsusc.2018.11.106

33. V.S. Makin, Y.I. Pestov, R.S. Makin, The mechanism of formation of nanostructures of hexagonal symmetry on surfaces of metals by a sequence of doubled ultrashort pulses of radiation of orthogonal polarization. Opt. Spectrosc. **128**, 264–268 (2020). https://doi.org/10.1134/S0030400X20020149
34. N. Zhang, S.-C. Chen, Formation of nanostructures and optical analogues of massless Dirac particles via femtosecond lasers. Opt. Express **28**, 36109–36121 (2020). https://doi.org/10.1364/OE.403336
35. J.J. Nivas, S. Amoruso, Generation of supra-wavelength grooves in femtosecond laser surface structuring of silicon. Nanomaterials **11**, 174 (2021). https://doi.org/10.3390/nano11010174
36. D. Bäuerle, *Laser Processing and Chemistry*, 4th edn. (Springer, Berlin, 2011). https://doi.org/10.1007/978-3-642-17613-5
37. J. Bonse, S.V. Kirner, M. Griepentrog, D. Spaltmann, J. Krüger, Femtosecond laser texturing of surfaces for tribological applications. Materials **11**, 801 (2018). https://doi.org/10.3390/ma11050801
38. T.Y. Hwang, C. Guo, Angular effects of nanostructure-covered femtosecond laser induced periodic surface structures on metals. J. Appl. Phys. **108**, 073523 (2010). https://doi.org/10.1063/1.3487934
39. C. Lopez-Santos, D. Puerto, J. Siegel, M. Macias-Montero, C. Florian, J. Gil-Rostra, V. López-Flores, A. Borras, A.R. González-Elipe, J. Solis, Anisotropic resistivity surfaces produced in ITO films by laser-induced nanoscale self-organization. Adv. Opt. Mater. **9**, 2001086 (2021). https://doi.org/10.1002/adom.202001086
40. S.V. Kirner, T. Wirth, H. Sturm, J. Krüger, J. Bonse, Nanometer-resolved chemical analyses of femtosecond laser-induced periodic surface structures on titanium. J. Appl. Phys. **122**, 10490 (2017). https://doi.org/10.1063/1.4993128
41. S.V. Kirner, N. Slachciak, A.M. Elert, M. Griepentrog, D. Fischer, A. Hertwig, M. Sahre, I. Dörfel, H. Sturm, S. Pentzien, R. Koter, D. Spaltmann, J. Krüger, J. Bonse, Tribological performance of titanium samples oxidized by fs-laser radiation, thermal heating, or electrochemical anodization. Appl. Phys. A Mater. Sci. Process. **124**, 326 (2018). https://doi.org/10.1007/s00339-018-1745-8
42. P. Gregorčič, Comment on "Bioinspired reversible switch between underwater superoleophobicity/superaerophobicity and oleophilicity/aerophilicity and improved antireflective property on the nanosecond laser-ablated superhydrophobic titanium surfaces". ACS Appl. Mater. Inter. **13**, 2117 (2021). https://doi.org/10.1021/acsami.9b23462
43. A.M. Kietzig, S.G. Hatzikiriakos, P. Englezos, Patterned superhydrophobic metallic surfaces. Langmuir **25**, 4821–4827 (2009). https://doi.org/10.1021/la8037582
44. N. Yasumaru, E. Sentoku, J. Kiuchi, Formation of organic layer on femtosecond laser-induced periodic surface structures. Appl. Surf. Sci. **405**, 267–272 (2017). https://doi.org/10.1016/j.apsusc.2017.02.084
45. M. Larrañaga-Altuna, A. Zabala, I. Llavori, O. Pearce, T.D. Nguyen, J. Caro, H. Mescheder, J.L. Endrino, G. Goel, W.N. Ayre, R.K. Seenivasagam, D.K. Tripathy, J. Armstrong, S. Goel, Bactericidal surfaces: An emerging 21st-century ultra-precision manufacturing and materials puzzle. Appl. Phys. Rev. **8**, 021303 (2021). https://doi.org/10.1063/5.0028844
46. S. Zheng, M. Bawazir, A. Dhall, H.-E. Kim, L. He, J. Heo, G. Hwang, Implication of surface properties, bacterial motility, and hydrodynamic conditions on bacterial surface sensing and their initial adhesion. Front. Bioeng. Biotechnol. **9**, 643722 (2021). https://doi.org/10.3389/fbioe.2021.643722
47. K. Lange, M. Schulz-Ruhtenberg, J. Caro, Platinum electrodes for oxygen reduction catalysis designed by ultrashort pulse laser structuring. ChemElectroChem **4**, 570–576 (2017). https://doi.org/10.1002/celc.201600630
48. B. Dusser, Z. Sagan, H. Soder, N. Faure, J.-P. Colombier, M. Jourlin, E. Audouard, Controlled nanostructures formation by ultra fast laser pulses for color marking. Opt. Express **18**, 2913–2924 (2010). https://doi.org/10.1364/OE.18.002913

49. A.Y. Vorobyev, V.S. Makin, C. Guo, Brighter light sources from black metal: Significant increase in emission efficiency of incandescent light sources. Phys. Rev. Lett. **102**, 234301 (2009). https://doi.org/10.1103/PhysRevLett.102.234301
50. A. Papadopoulos, E. Skoulas, A. Mimidis, G. Perrakis, G. Kenanakis, G.D. Tsibidis, E. Stratakis, Biomimetic omnidirectional antireflective glass via direct ultrafast laser nanostructuring. Adv. Mater. **31**, 1901123 (2019). https://doi.org/10.1002/adma.201901123
51. J.-M. Guay, A. Calà Lesina, G. Côté, M. Charron, D. Poitras, L. Ramunno, P. Berini, A. Weck, Laser-induced plasmonic colours on metals. Nat. Commun. **8**, 16095 (2017). https://doi.org/10.1038/ncomms16095
52. Z. Liu, J. Siegel, M. Garcia-Lechuga, T. Epicier, Y. Lefkir, S. Reynaud, M. Bugnet, F. Vocanson, J. Solis, G. Vitrant, N. Destouches, Three-dimensional self-organization in nanocomposite layered systems by ultrafast laser pulses. ACS Nano **11**, 5031–5040 (2017). https://doi.org/10.1021/acsnano.7b01748
53. N. Sharma, M. Vangheluwe, F. Vocanson, A. Cazier, M. Bugnet, S. Reynaud, A. Vermeulin, N. Destouches, Laser-driven plasmonic gratings for hiding multiple images. Mater. Horiz. **6**, 978–983 (2019). https://doi.org/10.1039/C9MH00017H
54. N. Sharma, N. Destouches, C. Florian, R. Serna, J. Siegel, Tailoring metal-dielectric nanocomposite materials with ultrashort laser pulses for dichroic color control. Nanoscale **11**, 18779 (2019). https://doi.org/10.1039/C9NR06763A
55. D. Arnaldo del Cerro, Picosecond pulsed laser microstructuring of metals for microfluidics. PhD-thesis. University of Twente, the Netherlands (2014). https://doi.org/10.3990/1.9789036537261
56. M. Barthlott, M. Mail, K. Koch, Plant surfaces: Structures and functions for biomimetic innovations. Nano-Micro. Lett. **9**, 23 (2017). https://doi.org/10.1007/s40820-016-0125-1
57. T. Young, An essay on the cohesion of fluids. Phil. Trans. R. Soc. Lond. **95**, 65–87 (1805). https://doi.org/10.1098/rstl.1805.0005
58. A. Samanta, Q. Wang, S.K. Shaw, H. Ding, Roles of chemistry modification for laser textured metal alloys to achieve extreme surface wetting behaviors. Mater. Des. **192**, 108744 (2020). https://doi.org/10.1016/j.matdes.2020.108744
59. T. Tuteja, W. Choi, M. Ma, G.C. Rutledge, G.H. McKinley, R.E. Cohen, Designing superoleophobic surfaces. Science **318**, 1618–1622 (2007). https://doi.org/10.1126/science.1148326
60. R.M. Wenzel, Resistance of solid surfaces to wetting by water. Ind. Eng. Chem. **28**, 988–994 (1936). https://doi.org/10.1021/ie50320a024
61. A.B.D. Cassie, S. Baxter, Wettability of porous surfaces. Trans. Faraday Soc. **40**, 546–551 (1944). https://doi.org/10.1039/TF9444000546
62. S. Nishimoto, B. Bhushan, Bioinspired self-cleaning surfaces with superhydrophobicity, superoleophobicity, and superhydrophilicity. RSC Adv. **3**, 671–690 (2013). https://doi.org/10.1039/C2RA21260A
63. J. Yong, F. Chen, Q. Yang, X. Hou, Femtosecond laser controlled wettability of solid surfaces. Soft Matter **11**, 8897–8906 (2015) https://doi.org/10.1039/c5sm02153g
64. R. Jagdheesh, B. Pathiraj, E. Karatay, G.R.B.E. Römer, A.J. Huis in 't Veld, Laser-induced nanoscale superhydrophobic structures on metal surfaces. Langmuir **27**, 8464–8469 (2011). https://doi.org/10.1021/la2011088
65. L. Piccolo, M. Sorgato, A. Batal, S. Dimov, G. Lucchetta, D. Masato, Functionalization of plastic parts by replication of variable pitch laser-induced periodic surface structures. Micromachines **11**, 429 (2020). https://doi.org/10.3390/mi11040429
66. S. Milles, M. Soldera, T. Kuntze, A.F. Lasagni, Characterization of self-cleaning properties on superhydrophobic aluminum surfaces fabricated by direct laser writing and direct laser interference patterning. Appl. Surf. Sci. **525**, 146518 (2020). https://doi.org/10.1016/j.apsusc.2020.146518
67. U. Hermens, S.V. Kirner, C. Emonts, P. Comanns, E. Skoulas, A. Mimidis, H. Mescheder, K. Winands, J. Krüger, E. Stratakis, J. Bonse, Mimicking lizard-like surface structures upon ultrashort laser pulse irradiation of inorganic materials. Appl. Surf. Sci. **418**, 499–507 (2017). https://doi.org/10.1016/j.apsusc.2016.12.112

68. P. Comanns, K. Winands, M. Pothen, R.A. Bott, H. Wagner, W. Baumgartner, The Texas horned lizard as model for robust capillary structures for passive directional transport of cooling lubricants. Proc. SPIE **9797**, 979711 (2016). https://doi.org/10.1117/12.2218873
69. S.V. Kirner, U. Hermens, A. Mimidis, E. Skoulas, C. Florian, F. Hischen, C. Plamadeala, W. Baumgartner, K. Winands, H. Mescheder, J. Krüger, J. Solis, J. Siegel, E. Stratakis, J. Bonse, Mimicking bug-like surface structures and their fluid transport produced by ultrashort laser pulse irradiation of steel. Appl. Phys. A Mater. Sci. Process. **123**, 754 (2017). https://doi.org/10.1007/s00339-017-1317-3
70. A.Y. Vorobyev, C. Guo, Metal pumps liquid uphill. Appl. Phys. Lett. **94**, 224102 (2009). https://doi.org/10.1063/1.3117237
71. S.C. Singh, M. ElKabbash, Z. Li, X. Li, B. Regmi, M. Madsen, S.A. Jalil, Z. Zhan, J. Zhang, C. Guo, Solar-trackable super-wicking black metal panel for photothermal water sanitation. Nat. Sustain. **3**, 938–946 (2020). https://doi.org/10.1038/s41893-020-0566-x
72. R. Fang, X. Zhang, J. Zheng, Z. Pan, C. Yang, L. Deng, R. Li, C. Lai, W. Yan, V.S. Maisotsenko, A.Y. Vorobyev, Superwicking functionality of femtosecond laser textured aluminum at high temperatures. Nanomaterials **11**, 2964 (2021). https://doi.org/10.3390/nano11112964
73. T. Karkantonis, A. Gaddam, T.L. See, S.S. Joshi, S. Dimov, Femtosecond laser-induced submicron and multi-scale topographies for durable lubricant impregnated surfaces for food packaging applications. Surf. Coat. Technol. **399**, 126166 (2020). https://doi.org/10.1016/j.surfcoat.2020.126166
74. R. Jagdheesh, B. Pathiraj, A. Gomez Marin, D. Arnaldo del Cerro, R.G.H. Lammertink, D. Lohse, A.J. Huis in ’t Veld, G.R.B.E. Römer, Ultra fast laser machined hydrophobic stainless steel surface for drag reduction in laminar flows. Proceedings of the 11th International Symposium on Laser Precision Microfabrication (LPM), June 7–10, Stuttgart, Germany (2010)
75. K.M.T. Ahmmed, A.-M. Kietzig, Drag reduction on laser-patterned hierarchical superhydrophobic surfaces. Soft Matter **12**, 4912–4922 (2016). https://doi.org/10.3390/mi5041219
76. M. Sorgato, D. Masato, G. Lucchetta, L. Orazi, Effect of different laser-induced periodic surface structures on polymer slip in PET injection moulding. CIRP Ann. **67**, 575–578 (2018). https://doi.org/10.1016/j.cirp.2018.04.102
77. O. Dubnack, C. Kunz, S. Gräf, F.A. Müller, Laser-induced Leidenfrost surfaces. Appl. Surf. Sci. **532**, 147407 (2020). https://doi.org/10.1016/j.apsusc.2020.147407
78. A.G. Marín, D. Arnaldo del Cerro, G.R.B.E. Römer, B. Pathiraj, A.J. Huis in ’t Veld, D. Lohse, Capillary droplets on Leidenfrost micro-ratchets. Phys. Fluids **24**, 122001 (2012). https://doi.org/10.1063/1.4768813
79. A. Volpe, C. Gaudiuso, A. Ancona, Laser fabrication of anti-icing surfaces: A review. Materials **13**, 5692 (2020). https://doi.org/10.3390/ma13245692
80. S. Milles, M. Soldera, B. Voisiat, A.F. Lasagni, Fabrication of superhydrophobic and ice-repellent surfaces on pure aluminium using single and multiscaled periodic textures. Sci. Rep. **9**, 13944 (2019). https://doi.org/10.1038/s41598-019-49615-x
81. G.R.B.E. Römer, D. Arnaldo del Cerro, R.C.J. Sipkema, M.N.W. Groenendijk, A.J. Huis in ‘t Veld, Ultra short pulse laser generated surface textures for anti-ice applications in aviation. Proceedings International Congress on Applications of Lasers & Electro-Optics (ICALEO), 2–5 Nov., Orlando, USA, p. 30–37 (2009). https://doi.org/10.2351/1.5061570
82. A. Hanif, S. Qureshi, Z. Sheikh, H. Rashid, Complications in implant dentistry. Eur. J. Dent. **11**, 135–140 (2017) https://dx.doi.org/10.4103%2Fejd.ejd_340_16
83. C.A.M. Löwik, F.C. Wagenaar, W. van der Weegen, R.W. Poolman, R. Nelissen, S.K. Bulstra, Y. Pronk, K.M. Vermeulen, M. Wouthuyzen-Bakker, I. van den Akker-Scheek, M. Stevens, P.C. Jutte, LEAK study: Design of a nationwide randomised controlled trial to find the best way to treat wound leakage after primary hip and knee arthroplasty. BMJ Open **7**, e018673 (2017). https://doi.org/10.1136/bmjopen-2017-018673
84. R.Y. Siddiquie, A. Gaddam, A. Agrawal, S.S. Dimov, S.S. Joshi, Anti-biofouling properties of femtosecond laser-induced submicron topographies on elastomeric surfaces. Langmuir **36**, 5349–5358 (2020). https://doi.org/10.1021/acs.langmuir.0c00753

85. A. Tripathy, P. Sen, B. Su, W.H. Briscoe, Natural and bioinspired nanostructured bactericidal surfaces. Adv. Colloid Interf. Sci. **248**, 85–104 (2017). https://doi.org/10.1016/j.cis.2017.07.030
86. C.-W. Chan, L. Carson, G.C. Smith, A. Morelli, S. Lee, Enhancing the antibacterial performance of orthopaedic implant materials by fibre laser surface engineering. Appl. Surf. Sci. **404**, 67–81 (2017). https://doi.org/10.1016/j.apsusc.2017.01.233
87. A. Cunha, A.-M. Elie, L. Plawinski, A.P. Serro, A.M. Botelho do Rego, A. Almeida, M.C. Urdaci, M.-C. Durrieu, R. Vilar, Femtosecond laser surface texturing of titanium as a method to reduce the adhesion of *Staphylococcus aureus* and biofilm formation. Appl. Surf. Sci. **360**, 485–493 (2016). https://doi.org/10.1016/j.apsusc.2015.10.102
88. N. Epperlein, F. Menzel, K. Schwibbert, R. Koter, J. Bonse, J. Sameith, J. Krüger, J. Toepel, Influence of femtosecond laser produced nanostructures on biofilm growth on steel. Appl. Surf. Sci. **418**, 420–424 (2017). https://doi.org/10.1016/j.apsusc.2017.02.174
89. E. Fadeeva, V.K. Truong, M. Stiesch, B.N. Chichkov, R.J. Crawford, J. Wang, E.P. Ivanova, Bacterial retention on superhydrophobic titanium surfaces fabricated by femtosecond laser ablation. Langmuir **27**, 3012–3019 (2011). https://doi.org/10.1021/la104607g
90. X. Luo, S. Yao, H. Zhang, M. Cai, W. Liu, R. Pan, C. Chen, X. Wang, L. Wang, M. Zhong, Biocompatible nano-ripples structured surfaces induced by femtosecond laser to rebel bacterial colonization and biofilm formation. Opt. Laser Technol. **124**, 105973 (2020). https://doi.org/10.1016/j.optlastec.2019.105973
91. A.H.A. Lutey, L. Gemini, L. Romoli, G. Lazzini, F. Fuso, M. Faucon, R. Kling, Towards laser-textured antibacterial surfaces. Sci. Rep. **8**, 10112 (2018). https://doi.org/10.1038/s41598-018-28454-2
92. D.W. Müller, S. Lößlein, E. Terriac, K. Brix, K. Siems, R. Moeller, R. Kautenburger, F. Mücklich, Increasing antibacterial efficiency of Cu surfaces by targeted surface functionalization via ultrashort pulsed direct laser interference patterning. Adv. Mater. Interfaces **8**, 2001656 (2020). https://doi.org/10.1002/admi.202001656
93. V. Selvamani, A. Zareei, A. Elkashif, M.K. Maruthamuthu, S. Chittiboyina, D. Delisi, Z. Li, L. Cai, V.G. Pol, M.N. Seleem, R. Rahimi, Hierarchical micro/mesoporous copper structure with enhanced antimicrobial property via laser surface texturing. Adv. Mater. Interfaces **7**, 1901890 (2020). https://doi.org/10.1002/admi.201901890
94. V.K. Truong, H.K. Webb, E. Fadeeva, B.N. Chichkov, A.H. Wu, R. Lamb, J.Y. Wang, R.J. Crawford, E.P. Ivanova, Air-directed attachment of coccoid bacteria to the surface of superhydrophobic lotus-like titanium. Biofouling **28**, 539–550 (2012). https://doi.org/10.1080/08927014.2012.694426
95. C. Zwahr, R. Helbig, C. Werner, A.F. Lasagni, Fabrication of multifunctional titanium surfaces by producing hierarchical surface patterns using laser based ablation methods. Sci. Rep. **9**, 6721 (2019). https://doi.org/10.1038/s41598-019-43055-3
96. K. Schwibbert, F. Menzel, N. Epperlein, J. Bonse, J. Krüger, Bacterial adhesion on femtosecond laser-modified polyethylene. Materials **12**, 3107 (2019) https://dx.doi.org/10.3390%2Fma12193107
97. A. Elbourne, R.J. Crawford, E.P. Ivanova, Nano-structured antimicrobial surfaces: From nature to synthetic analogues. J. Colloid Interface Sci. **508**, 603–616 (2017). https://doi.org/10.1016/j.jcis.2017.07.021
98. U. Mahanta, M. Khandelwal, A.S. Deshpande, Antimicrobial surfaces: A review of synthetic approaches, applicability and outlook. J. Mater. Sci. **56**, 17915–17941 (2021). https://doi.org/10.1007/s10853-021-06404-0
99. D.P. Linklater, V.A. Baulin, S. Juodkazis, R.J. Crawford, P. Stoodley, E.P. Ivanova, Mechano-bactericidal actions of nanostructured surfaces. Nat. Rev. Microbiol. **19**, 8–22 (2021). https://doi.org/10.1038/s41579-020-0414-z
100. A.M. Richter, G. Buchberger, D. Stifter, J. Duchoslav, A. Hertwig, J. Bonse, J. Heitz, K. Schwibbert, Spatial period of laser-induced surface Nanoripples on PET determines *Escherichia coli* repellence. Nanomaterials **11**, 3000 (2021). https://doi.org/10.3390/nano11113000

101. C. Li, Y. Yang, L. Yang, Z. Shi, P. Yang, G. Cheng, In vitro bioactivity and biocompatibility of bio-inspired Ti-6Al-4V alloy surfaces modified by combined laser micro/nano structuring. Molecules **25**, 1494 (2020). https://doi.org/10.3390/molecules25071494
102. J. Heitz, C. Plamadeala, M. Muck, O. Armbruster, W. Baumgartner, A. Weth, C. Steinwender, H. Blessberger, J. Kellermair, S.V. Kirner, J. Krüger, J. Bonse, A.S. Guntner, A.W. Hassel, Femtosecond laser-induced microstructures on Ti substrates for reduced cell adhesion. Appl. Phys. A Mater. Sci. Process. **123**, 734 (2017). https://doi.org/10.1007/s00339-017-1352-0
103. X. Wang, C.A. Ohlin, Q. Lu, J. Hu, Cell directional migration and oriented division on three-dimensional laser-induced periodic surface structures on polystyrene. Biomaterials **29**, 2049–2059 (2008). https://doi.org/10.1016/j.biomaterials.2007.12.047
104. M. Mezera, G.R.B.E. Römer, Model based optimization of process parameters to produce large homogeneous areas of laser-induced periodic surface structures. Opt. Express **27**, 6012–6029 (2019). https://doi.org/10.1364/OE.27.006012
105. S. Petrovic, D. Perusko, A. Mimidis, P. Kavatzikidou, J. Kovac, A. Ranella, M. Novakovic, M. Popovic, E. Stratakis, Response of NIH 3T3 fibroblast cells on laser-induced periodic surface structures on a 15x(Ti/Zr)/Si multilayer system. Nanomaterials **10**, 2531 (2020). https://doi.org/10.3390/nano10122531
106. E. Rebollar, I. Frischauf, M. Olbrich, T. Peterbauer, S. Hering, J. Preiner, P. Hinterdorfer, C. Romanin, J. Heitz, Proliferation of aligned mammalian cells on laser-nanostructured polystyrene. Biomaterials **29**, 1796–1806 (2008). https://doi.org/10.1016/j.biomaterials.2007.12.039
107. A. Ranella, M. Barberoglou, S. Bakogianni, C. Fotakis, E. Stratakis, Tuning cell adhesion by controlling the roughness and wettability of 3D micro/nano silicon structures. Acta Biomater. **6**, 2711–2720 (2010). https://doi.org/10.1016/j.actbio.2010.01.016
108. P. Fosodeder, W. Baumgartner, C. Steinwender, A.W. Hassel, C. Florian, J. Bonse, J. Heitz, Repellent rings at titanium cylinders against overgrowth by fibroblasts. Adv. Opt. Technol. **9**, 113–120 (2020). https://doi.org/10.1515/aot-2019-0070
109. S.A. Lone, M. Muck, P. Fosodeder, C.C. Mardare, C. Florian, A. Weth, J. Krüger, C. Steinwender, W. Baumgartner, J. Bonse, J. Heitz, A.W. Hassel, Impact of femtosecond laser treatment accompanied with anodization of titanium alloy on fibroblast cell growth. Phys. Status Solidi A **217**, 1900838 (2020) https://doi.org/10.1002/pssa.201900838
110. A. Klos, X. Sedao, T.E. Itina, C. Helfenstein-Didier, C. Donnet, S. Peyroche, L. Vico, A. Guignandon, V. Dumas, Ultrafast laser processing of nanostructured patterns for the control of cell adhesion and migration on titanium alloy. Nanomaterials **10**, 864 (2020). https://doi.org/10.3390/nano10050864
111. R. Buividas, P.R. Stoddart, S. Juodkazis, Laser fabricated ripple substrates for surface-enhanced Raman scattering. Ann. Phys. **524**, L5–L10 (2012). https://doi.org/10.1002/andp.201200140
112. H.W. Chang, Y.C. Tsai, C.W. Cheng, C.Y. Lin, Y.W. Lin, T.M. Wu, Nanostructured Ag surface fabricated by femtosecond laser for surface-enhanced Raman scattering. J. Colloid Interface Sci. **360**, 305–308 (2012). https://doi.org/10.1016/j.jcis.2011.04.005
113. X. Li, G. Yuan, W. Yu, J. Xing, Y. Zou, C. Zhao, W. Kong, Z. Yu, C. Guo, A self-driven microfluidic surface-enhanced Raman scattering device for Hg^{2+} detection fabricated by femtosecond laser. Lab Chip **20**, 414–423 (2020). https://doi.org/10.1039/c9lc00883g
114. X. Hu, R. Pan, M. Cai, W. Liu, X. Luo, C. Chen, J. Guochen, M. Zhong, Ultrafast laser micro-nano structured superhydrophobic teflon surfaces for enhanced SERS detection via evaporation concentration. Adv. Opt. Technol. **9**, 89–100 (2020). https://doi.org/10.1515/aot-2019-0072
115. G. Pavliuk, D. Pavlov, E. Mitsai, O. Vitrik, A. Mironenko, A. Zakharenko, S.A. Kulinich, S. Juodkazis, S. Bratskaya, A. Zhizhchenko, A. Kuchmizhak, Ultrasensitive SERS-based plasmonic sensor with analyte enrichment system produced by direct laser writing. Nanomaterials **10**, 49 (2020). https://doi.org/10.3390/nano10010049
116. K. Holmberg, A. Erdemir, Influence of tribology on global energy consumption, costs and emissions. Friction **5**, 263–284 (2017). https://doi.org/10.1007/s40544-017-0183-5

117. H. Czichos, K.-H. Habig, *Tribologie-Handbuch – Tribometrie, Tribomaterialien, Tribotechnik*, 4th edn. (Springer Vieweg, Wiesbaden, 2015)
118. J.J. Ayerdi, N. Slachciak, I. Llavori, A. Zabala, A. Aginagalde, J. Bonse, D. Spaltmann, On the role of a ZDDP in the tribological performance of femtosecond laser-induced periodic surface structures on titanium alloy against different counterbody materials. Lubricants **7**, 79 (2019). https://doi.org/10.3390/lubricants7090079
119. J. Bonse, R. Koter, M. Hartelt, D. Spaltmann, S. Pentzien, S. Höhm, A. Rosenfeld, J. Krüger, Femtosecond laser-induced periodic surface structures on steel and titanium alloy for tribological applications. Appl. Phys. A Mater. Sci. Process. **117**, 103–110 (2014). https://doi.org/10.1007/s00339-014-8229-2
120. J. Eichstädt, G.R.B.E. Römer, A.J. Huis in't Veld, Towards friction control using laser-induced periodic surface structures. Phys. Proced. **12**, 7–15 (2011). https://doi.org/10.1016/j.phpro.2011.03.099
121. I. Gnilitskyi, A. Rota, E. Gualtieri, S. Valeri, L. Orazi, Tribological properties of high-speed uniform femtosecond laser patterning on stainless steel. Lubricants **7**, 83 (2019). https://doi.org/10.3390/lubricants7100083
122. A. Mizuno, T. Honda, J. Kiuchi, Y. Iwai, N. Yasumaru, K. Miyazaki, Friction properties of the DLC film with periodic structures in nano-scale. Tribol. Online **1**, 44–48 (2006). https://doi.org/10.2474/trol.1.44
123. M. Pfeiffer, A. Engel, H. Gruettner, K. Guenther, F. Marquardt, G. Reisse, S. Weissmantel, Ripple formation in various metals and super-hard tetrahedral amorphous carbon films in consequence of femtosecond laser irradiation. Appl. Phys. A Mater. Sci. Process. **110**, 655–659 (2013). https://doi.org/10.1007/s00339-012-7146-5
124. J.J. Yu, Y.F. Lu, Laser-induced ripple structures on Ni-P substrates. Appl. Surf. Sci. **148**, 248–252 (1999). https://doi.org/10.1016/S0169-4332(98)00900-3
125. C.Y. Chen, C.J. Chung, B.H. Wu, W.L. Li, C.W. Chien, P.H. Wu, C.W. Cheng, Microstructure and lubricating property of ultra-fast laser pulse textured silicon carbide seals. Appl. Phys. A Mater. Sci. Process. **107**, 345–350 (2012). https://doi.org/10.1007/s00339-012-6822-9
126. N. Kawasegi, H. Sugimori, H. Morimoto, N. Morita, I. Hori, Development of cutting tools with microscale and nanoscale textures to improve frictional behavior. Precis. Eng. **33**, 248–254 (2009). https://doi.org/10.1016/j.precisioneng.2008.07.005
127. C. Kunz, J. Bonse, D. Spaltmann, C. Neumann, A. Turchanin, J.F. Bartolomé, F.A. Müller, S. Gräf, Tribological performance of metal-reinforced ceramic composites selectively structured with femtosecond laser-induced periodic surface structures. Appl. Surf. Sci. **499**, 143917 (2020). https://doi.org/10.1016/j.apsusc.2019.143917
128. T. Stark, T. Kiedrowski, H. Marschall, A.F. Lasagni, Avoiding starvation in tribocontact through active lubricant transport in laser textured surfaces. Lubricants **7**, 54 (2019). https://doi.org/10.3390/lubricants7060054
129. T. Knüttel, S. Bergfeld, S. Haas, Laser texturing of surfaces in thin-film silicon photovoltaics — A comparison of potential processes. J. Laser Micro. Nanoeng. **8**, 222–229 (2013). https://doi.org/10.2961/jlmn.2013.03.0007
130. P. Liu, W. Wang, A. Pan, Y. Xiang, D. Wang, Periodic surface structures on the surface of indium tin oxide film obtained using picosecond laser. Opt. Laser Technol. **106**, 259–264 (2018). https://doi.org/10.1016/j.optlastec.2018.04.019
131. F. Nigo, M. Hashida, M. Tsukamoto, S. Sakabe, M. Kusaba, Reflectance and crystallinity of silicon solar cells with LIPSS produced by XeCl excimer laser pulses. App. Phys. A **126**, 129 (2020). https://doi.org/10.1007/s00339-020-3305-2
132. J. Cui, A. Rodríguez-Rodríguez, M. Hernández, M.C. García-Gutiérrez, A. Nogales, M. Castillejo, D. Moseguí González, P. Müller-Buschbaum, T.A. Ezquerra, E. Rebollar, Laser-induced periodic surface structures on P3HT and on its photovoltaic blend with $PC_{71}BM$. ACS Appl. Mater. Interfaces **8**, 31894–31901 (2016). https://doi.org/10.1021/acsami.6b09053
133. A. Rodriguez-Rodriguez, E. Rebollar, T. Ezquerra, M. Castillejo, J.V. Garcia-Ramos, M.C. Garcia-Gutierrez, Patterning conjugated polymers by laser: Synergy of nanostructure forma-

tion in the all-polymer heterojunction P3HT/PCDTBT. Langmuir **34**, 115–125 (2018). https://doi.org/10.1021/acs.langmuir.7b03761

134. E. Gutierrez-Fernandez, I. Gabaldon-Saucedo, A. Rodriguez-Rodriguez, E. Solano, M.C. Garcia-Gutierrez, A. Nogales, A. Cirera, T. Ezquerra, E. Rebollar, Laser nanostructuring of thin films of PEDOT:PSS on ITO: Morphology, molecular structure and electrical properties. Appl. Surf. Sci. **509**, 145350 (2020). https://doi.org/10.1016/j.apsusc.2020.145350
135. K. Czajkowski, M. Ratzke, O. Varlamova, J. Reif, Femtosecond-laser-induced periodic surface structures on magnetic layer targets: The roles of femtosecond-laser interaction and of magnetization. Appl. Surf. Sci. **418**, 84–87 (2017). https://doi.org/10.1016/j.apsusc.2017.03.148
136. E. Sanchez, G. Rodriguez-Rodriguez, R. Aragon, M. Arranz, E. Rebollar, M. Castillejo, J. Colino, Anisotropy engineering of soft thin films in the undulated magnetic state. J. Magn. Magn. Mater. **514**, 167149 (2020). https://doi.org/10.1016/j.jmmm.2020.167149
137. A. Cubero, E. Martínez, L.A. Angurel, G.F. de la Fuente, R. Navarro, H. Legall, J. Krüger, J. Bonse, Effects of laser-induced periodic surface structures on the superconducting properties of Niobium. Appl. Surf. Sci. **508**, 145140 (2020). https://doi.org/10.1016/j.apsusc.2019.145140
138. A.R. Neale, Y. Jin, J. Ouyang, S. Hughes, D. Hesp, V. Dhanak, G. Dearden, S. Edwardson, L.J. Hardwick, Electrochemical performance of laser micro-structured nickel oxyhydroxide cathodes. J. Power Sources **271**, 42–47 (2014). https://doi.org/10.1016/j.jpowsour.2014.07.167
139. T. Aizawa, S. Tomomi, K. Yoshihiro, I. Tadahiko, Simultaneous nano-texturing onto a CVD-diamond coated piercing punch with femtosecond laser trimming. Appl. Sci. **10**, 2674 (2020). https://doi.org/10.3390/app10082674
140. L. Romoli, C.A.A. Rashed, G. Lovicu, G. Dini, F. Tantussi, F. Fuso, M. Fiaschi, Ultrashort pulsed laser drilling and surface structuring of microholes in stainless steels. CIRP Ann. **63**, 229–232 (2014). https://doi.org/10.1016/j.cirp.2014.03.053
141. L. Romoli, G. Lovicu, C.A.A. Rashed, G. Dini, M. De Sanctis, M. Fiaschi, Microstructural changes induced by ultrashort pulsed lasers in microdrilling of fuel nozzles. Proc. CIRP **33**, 508–513 (2015). https://doi.org/10.1016/j.procir.2015.06.064
142. A. Streek, U. Loeschner, R. Liebers, Ultrafast laser machining: High-rate laser microprocessing handles large-area substrates. Laser Focus World (October, 2019). https://www.laserfocusworld.com/lasers-sources/article/14039800/highrate-laser-microprocessing-handles-largearea-substrates
143. F. Fraggelakis, G. Mincuzzi, J. Lopez, I. Manek-Hönninger, R. Kling, Texturing metal surface with MHz ultra-short laser pulses. Opt. Express **25**, 18131–18139 (2017). https://doi.org/10.1364/OE.25.018131
144. J. Schille, L. Schneider, S. Mauersberger, S. Szokup, S. Höhn, J. Pötschke, F. Reiß, E. Leidich, U. Löschner, High-rate laser surface texturing for advanced tribological functionality. Lubricants **8**, 33 (2020). https://doi.org/10.3390/lubricants8030033
145. K. Mishchik, G. Bonamis, J. Qiao, J. Lopez, E. Audouard, E. Mottay, C. Hönninger, I. Manek-Hönninger, High-efficiency femtosecond ablation of silicon with GHz repetition rate laser source. Opt. Lett. **44**, 2193–2196 (2019). https://doi.org/10.1364/OL.44.002193
146. C. Neugebauer, D. Aalderink, E. Maurer, B. Faisst, A. Budnicki, Ultrafast lasers for precise and corrosion free marking on chirurgical steels. Proc. SPIE **10092**, 1009204 (2017). https://doi.org/10.1117/12.2252029
147. M. Han, D. Smith, S.H. Ng, V. Anand, T. Katkus, S. Juodkazis, Ultra-short pulse lasers – materials – applications. Eng. Proc. **11**, 44 (2021). https://doi.org/10.3390/ASEC2021-11143
148. J. Schille, U. Löschner, Ultrashort pulse lasers in high-rate laser micro processing – Quo vadis? Adv. Opt. Techn. **10**, 233–237 (2021). https://doi.org/10.1515/aot-2021-0049
149. Strategies unlimited: The worldwide market for lasers - trends and five-year forecast (2019–2025). (2020). https://store.strategies-u.com/products/the-worldwide-market-for-lasers-market-review-and-forecast-2020.html

150. C. Florian, E. Skoulas, D. Puerto, A. Mimidis, E. Stratakis, J. Solis, J. Siegel, Controlling the wettability of steel surfaces processed with femtosecond laser pulses. ACS Appl. Mater. Interfaces **10**, 36564–36571 (2018). https://doi.org/10.1021/acsami.8b13908
151. J. Bonse, R. Koter, M. Hartelt, D. Spaltmann, S. Pentzien, S. Höhm, A. Rosenfeld, J. Krüger, Tribological performance of femtosecond laser-induced periodic surface structures on titanium and a high toughness bearing steel. Appl. Surf. Sci. **336**, 21–27 (2015). https://doi.org/10.1016/j.apsusc.2014.08.111

Chapter 24
Role of Surface Chemistry on Wettability of Laser Micro-/Nanostructured Metallic Surfaces

Nithin Joy and Anne-Marie Kietzig

Abstract Over the past few decades, short and ultrashort pulsed lasers have been used extensively to manipulate the surface properties of almost all solid materials. Among them, the pulsed laser-generated superhydrophobic/superhydrophilic surfaces have attracted considerable interest from both research and industry owing to their potential in self-cleaning, anticorrosion, anti-biofouling, and deicing applications. A transition in the surface wettability from (super)hydrophilicity to (super)hydrophobicity of laser micro-/nanostructured metallic surfaces over time has been reported by many authors over the past decade. These studies suggest the critical role of surface chemistry in controlling the final wetting state of laser-textured metallic surfaces. In this chapter, we demonstrate how surface chemistry varies over time after being exposed to ambient air, liquids, gases, and heat treatments and how those changes result in wettability transitions. The suggested mechanisms leading to the transition from (super)hydrophilicity to (super)hydrophobicity are reviewed. The reliability and reproducibility of X-ray photoelectron spectroscopy and contact angle measurement data are assessed. Finally, the existing challenges in describing the phenomenon of wettability transition and future prospects for explaining the wettability transition are presented.

Keywords Pulsed laser machining · Superhydrophobic/superhydrophilic surfaces · Wettability transition · Surface topography · Surface chemistry · Organic matters · Surface oxidation

1 Introduction

The biological, electrical, mechanical, optical, tribological, and wetting properties of a solid target surface can be regulated by manipulating the surface topography

---

N. Joy · A.-M. Kietzig (✉)
McGill University, Montreal, Québec, Canada
e-mail: anne.kietzig@mcgill.ca

© The Author(s), under exclusive license to Springer Nature Switzerland AG 2023

R. Stoian, J. Bonse (eds.), *Ultrafast Laser Nanostructuring*, Springer Series in Optical Sciences 239, https://doi.org/10.1007/978-3-031-14752-4_24

and surface chemistry. Controlling surface wettability is crucial for many industrial applications that count on self-cleaning, anti-icing, anticorrosion, antimicrobial, and/or drag-reducing properties. A surface with a water contact angle greater than 150° and a contact angle hysteresis of less than 10° is said to be superhydrophobic, while a superhydrophilic surface possesses a water contact angle of less than 10°. Generally, surface chemistry along with surface topography plays a crucial role in controlling the wetting property of a solid surface [1]. Over the past decades, numerous approaches have been established to modify the topography and chemistry of solid surfaces including anodization [2], chemical etching [3], layer-by-layer deposition [4], lithography [5], plasma etching [6, 7], chemical vapor deposition [8], and electrodeposition [9]. Alike processing methods typically involve multiple complicated fabrication steps, possibly vacuum equipment and non-green chemical treatments, which thus limit their broad applicability [1]. In contrast, short and ultrashort pulsed laser micro-/nanomachining that has by now been well established as a flexible and unique technique to alter the topography and chemistry of a wide range of solid surfaces including metals, semiconductors, and polymers [10] is a simple, single-step, contactless, mask-less, controllable, high-resolution, and environment-friendly processing technique [1, 10]. Detailed mechanisms of how the ultrashort pulses interact with solid surfaces to produce various nanostructures are presented in Chaps. 1, 2 and 5. With respect to surface wettability of a wide variety of laser-processed metallic surfaces, many research groups have reported on their initial superhydrophilic response upon laser machining and the subsequent wettability transition from superhydrophilicity to hydrophobicity (or even superhydrophobicity) when exposed to various conditions (ambient air, liquid, gas, and heat). In particular, the topography and chemistry of a given solid target surface are the two key factors that influence its wetting behavior. Many reports demonstrated that the surface topography of laser-textured metallic surfaces remains unaltered over time [11–16]. Accordingly, research efforts in the last decade have focused on elucidating changes in surface chemistry of laser-irradiated metals [17–22]. A variety of elemental analysis methods, including XPS, EDX, FT-IR, AES, and XRD, have been used to identify the elemental composition of laser-machined surfaces in an effort to elucidate and understand the underlying mechanism and driving forces of this wettability transition. The purpose of this chapter is to review the most important works that have considerably contributed to the present understanding on the influence of surface chemistry on the wettability transition of metals upon laser machining, to outline controversies and highlight the persisting gaps in knowledge.

2 Wettability Transition Upon Ambient Air Exposure

In 2009, Kietzig et al. first reported the wetting transition of a laser-processed metallic surface with exposure to ambient air over time [11]. Kietzig et al. micromachined various alloy surfaces by raster scanning femtosecond laser pulses. Immediately after the laser processing, all the samples exhibited a superhydrophilic

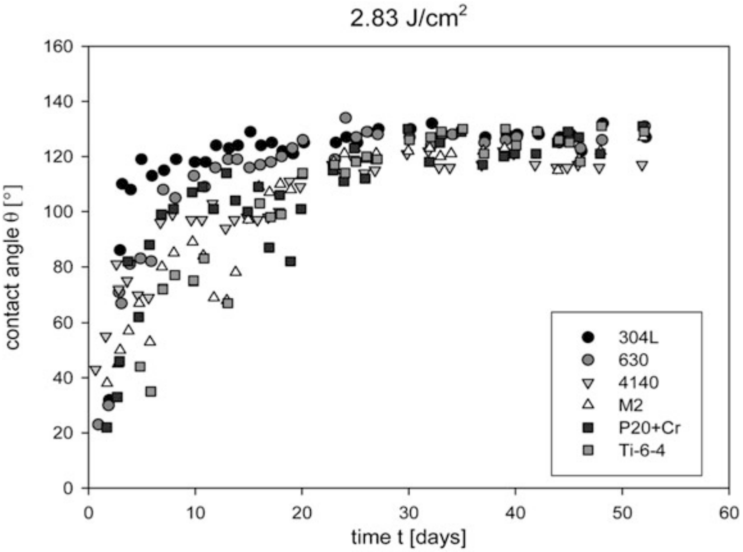

Fig. 24.1 Contact angle evolution over time of different metal alloys. (Reprinted from Kietzig et al. [11] with permission from ACS)

wetting response. An increase in measured contact angles was observed over time until the samples reached a stable hydrophobic or almost superhydrophobic state after days to weeks as depicted in Fig. 24.1. Elemental surface analysis was carried out by X-ray photoelectron spectroscopy (XPS) on the untreated surface and on all laser-processed samples. A comparison of the XPS spectra immediately after the laser treatment and after 52 days of air exposure highlights that the relative amount of carbon on the sample surface had increased. Since these findings have been published, many other studies have confirmed the general observation that when laser-machined metallic surfaces are exposed to ambient air for an extended period, they generally transition in their surface wetting response from (super)hydrophilic to (super)hydrophobic while their ablated surface texture remains unchanged [11]. Hence, solely a change in surface chemistry is responsible for the wettability transition.

Kietzig et al. performed a follow-up study in 2011 wherein they considered five different metallic substrates of high purity [12]. The surface texture and the time required to reach a steady wetting state varied from one metal to another. XPS analysis upon reaching steady state demonstrated an increased carbon-to-metal ratio for all substrates in comparison to the respective readings before laser machining. The authors therewith reiterate their original hypothesis that the origin of and driving force for the changes in surface chemistry and related wetting response lies with laser-created lattice defects, such as oxygen-deficient metal oxide layers, in the metallic crystal structure. Kietzig et al. [12] further highlighted that if the laser-machined surface is favorably textured such that it can possibly promote air-trapping, then the changes in surface chemistry can result in a switch of the dominant wetting mechanism from the homogeneously wetting Wenzel [23] to the air-trapping Cassie-Baxter [24] wetting state.

Bizi-Bandoki et al. (2013) were the first to carry out a more thorough chemical analysis attempting to identify the functional groups responsible for the observed wettability transition over time on femtosecond laser-processed metallic surfaces [25]. XPS analysis of all sample surfaces was performed before laser processing and after the measured contact angles had reached their respective steady states. The surface chemistry analysis of the studied aluminum alloy substrate confirmed the observations previously made by Kietzig et al. [11]; the carbon content on the surface increased from 55 at% before laser machining to 67 at% 6 days after laser irradiation (Fig. 24.2a). The XPS analysis further revealed the presence of hydrophobic functional groups, primarily the methyl (CH_3) group, to which the wettability transition to highly hydrophobic is attributed. On the contrary to the observations made on the aluminum alloy surface, the laser-treated stainless steel surface presented a reduction in the carbon content once the surface contact angle had stabilized compared to the surface before treatment (68 at% to 56 at%) as illustrated in Fig. 24.2b. The authors propose that water molecules present on the surface before laser treatment were removed through the laser process, which in turn renders the surface less polar and more hydrophobic. It remains unclear how this explanation for the stainless steel sample relates to the results obtained for the aluminum alloy.

In early 2015, Long et al. published a study that presents thorough elemental analyses on picosecond laser-machined metallic surfaces that were stored in different atmospheres after laser irradiation [13, 26]. Alike previous studies, the authors' XPS investigation concentrates on the relative magnitude of the carbon-to-metal ratio. Yet, this ratio is interpreted as an indicator for the amount of organic compounds adsorbed on the metallic surface. Furthermore, the authors extend the analysis by also considering the ratio of C–C to C–H bonds, which provides an indicator of the polarity of absorbed organic compounds. A low carbon-to-metal and low C–C to C–H bond ratio is thus characteristic for the highly hydrophilic surfaces observed shortly after laser machining, whereas upon the transition to (super)hydrophobicity, the laser-machined surfaces rather present a higher carbon-to-metal and also a higher C–C to C–H bond ratio. Interestingly, while a significant increase in the carbon-to-metal ratio with time was observed for the samples stored in ambient air, the C–C to C–H bond ratio found on surfaces kept in air was similar to (for Al) [13] or lower than (for Cu) [26] the reading of pristine surfaces. The C–C to C–H bond ratio, however, showed a significant increase if storage conditions favored the absorption of long-chain organic matter. In conclusion, the authors suggest that the absorption of organic compounds with long alkyl chains should be favored when highly hydrophobic surfaces are desired. Long et al. briefly address Lewis acid/base reactions as a possible explanation for the underlying driving force yet conclude that alike reactions would progress considerably faster than what is typically observed for the wettability transition on laser-machined metals.

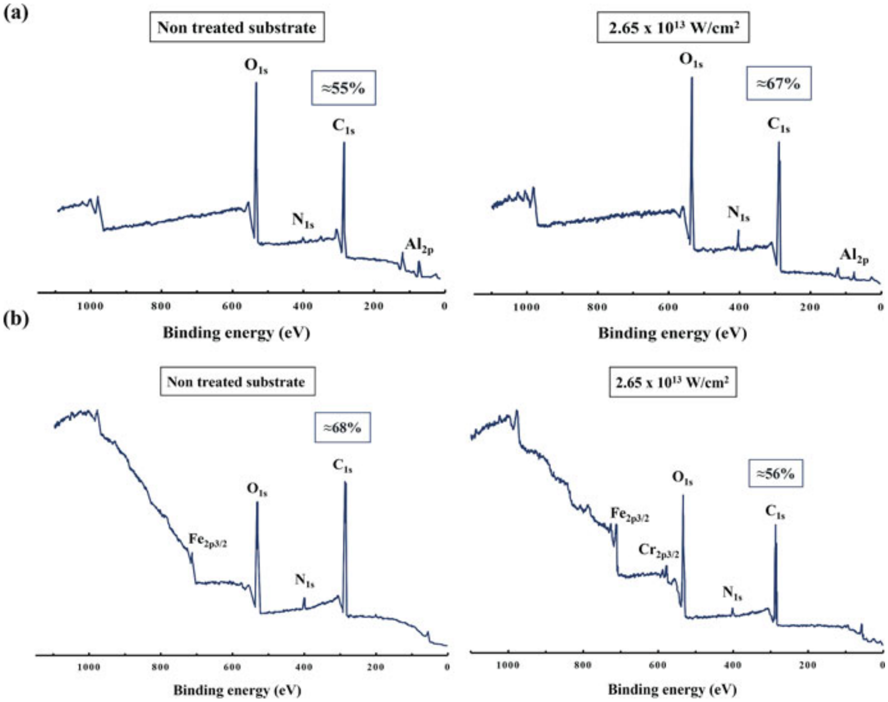

Fig. 24.2 XPS spectra before and after femtosecond laser processing of (**a**) aluminum alloy and (**b**) stainless steel. (Reproduced from Bizi-Bandoki et al. [25] with permission from Elsevier)

Toward the end of 2015, a different working hypothesis based on partial deoxidation was presented by Ta et al., who investigated the wettability transition on Cu and brass samples [14]. The authors explained the initial hydrophilic response with the formation of layers of CuO and ZnO over the textured surface by the interaction between freshly ablated (and thus exposed) copper and zinc with oxygen from the ambient air. The presence of hydrophilic CuO along with the surface roughness is understood to cause the initially observed (super)hydrophilicity. The partial deoxidation of CuO to Cu_2O upon air exposure was proposed as the significant factor contributing to the observed wettability transition, where CuO is considered as a hydrophilic and Cu_2O as a hydrophobic molecule. Yet EDX elemental analysis revealed a reduction in the surface oxygen level of less than 1% (20.2–19.5%) for the samples irradiated at higher fluence after 38 days of ambient air exposure. Although Long et al. previously proposed the significance of adsorption of organic matters on the wettability transition on Cu [26], the authors did not assess or comment on possible changes in surface carbon. However, the authors extended their study to wetting tests with a methanol/water solution in an effort to test the applicability of nanosecond laser-textured brass surfaces as chemical sensors. They observed a reduction in the contact angle of the methanol/water solution with increasing methanol concentration. Furthermore, the superhydrophobicity of the laser-textured surface was lost after the sensing test, clearly indicating that the methanol solution chemically modified the surface. Upon continued air exposure, the authors again observed an increase in the contact angle, but the transition was extremely slow. The authors have not commented on how the surface chemistry was modified by the methanol/water solution and why the wettability transition slowed down after the sensing test.

Several months later, in summer 2016, Boinovich et al. [27] reinterpreted the results and data presented by Ta et al. [14] and critically commented on the original authors' key findings. Boinovich et al. highlight that pure metals and their oxides are hydrophilic and have a water contact angle of under 90°. According to the XRD data, the freshly laser-processed Cu surface comprises both CuO and Cu_2O, with an increase in Cu_2O compared to the unprocessed surface, yet the surface stayed extremely hydrophilic. This casts doubt on Ta et al.'s suggested partial deoxidation explanation for the wettability transition ($CuO \rightarrow Cu_2O$). Boinovich et al. also reconsider Ta et al.'s methanol experiments and present an argument for their findings: exposing laser-processed surfaces to methanol, which is an excellent solvent for many organic compounds, is anticipated to result in the removal of organic matters from the aged surface, and ultimately in a more hydrophilic response from the surface. This very first solvent experiment on a laser-machined surface indirectly confirms the idea that the wettability transition may be ascribed to the adsorption of organic molecules on the laser-machined surface, even if the original authors did not recognize it. Finally, the considerably slower wettability transition of the methanol-cleaned sample reported by Ta et al. was also explained by Boinovich et al.: laser processing renders a metallic surface to be in a highly nonequilibrium state directly after the irradiation exposure as characterized by many high-energy surface defects. During the exposure to a solvent, the surface is already allowed to relax and thus reduce its overall Gibb's free energy. Thus, the authors described the trigger of the slow wettability transition as "*after washing out the airborne organics with a methanol solution droplet, their re-adsorption on the surface is driven by a lower energy gain at a partially relaxed surface*" [27].

Also in 2016 and based on Long et al.'s work [13], Jagdheesh et al. significantly contribute to the understanding of the wettability transition with their experiments on aluminum [28]. Alike Bizi-Bandoki et al.'s [25] steel sample, the authors observe a reduction in the carbon content upon laser processing their aluminum substrate. Their explanation is based on the consideration that the measured carbon content on unprocessed samples is derived from hydro-carbonaceous contamination resulting from the exposure to the atmosphere and cleaning steps involving organic solvents. Further, they highlight that the oxygen-to-metal ratio on laser-machined surfaces exceed the expected stoichiometric relationship for Al_2O_3, which they attribute to the presence of aluminum hydroxide oxide (AlO(OH)) following a hydroxylation reaction with absorbed water molecules from the ambient atmosphere. Jagdheesh et al.'s important contribution to the research field is the elaborate explanation of the surface chemical reactions responsible for the observed wettability transition. In this regard, the authors extend Long et al.'s considerations and highlight that

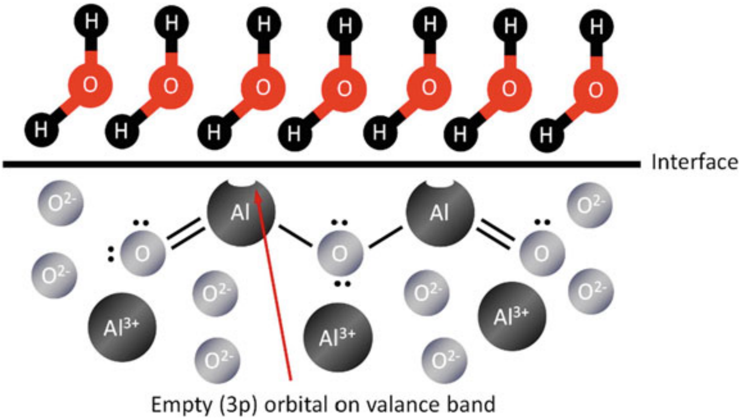

Fig. 24.3 Schematic illustration of molecules/atoms state of the fresh Al-II surface. (Reprinted from Yang et al. [29] with permission from Elsevier)

the presence of a high number of coordinatively unsaturated ions is typical for transition metal oxides. Upon laser machining, a metallic surface is thus expected to present a considerable amount of metal cations acting as Lewis acids and oxygen anions acting as Lewis bases as illustrated in Fig. 24.3. These Lewis acid/base pairs promote the dissociation of water molecules from the ambient surroundings upon adsorption into hydroxides (OH anions) and hydrogen cations, which are then available for reaction with the unsaturated ions of the metal oxide layer.

The authors indicate that such hydroxylation occurs very rapidly. Furthermore, Jagdheesh et al. [28] briefly present two possible routes for subsequent surface reactions: (1) with the presence of abundant water molecules, the already formed hydroxylated layer on the oxide surface adsorbs a second layer of water through strong hydrogen bonding; (2) the hydroxyl group present on the oxide surface significantly contributes to the chemisorption of organic matter resulting in a surface polarity reduction and finally leading to a wettability transition.

In 2017, Cardoso et al. [15] summarized the considerations of Long et al. [13] and Jagdheesh et al. [28] and elaborate systematically on the mechanism responsible for the change in surface chemistry that causes the transition in the wetting state. XPS analyses carried out on an untreated sample, a laser-machined sample that has previously reached hydrophobicity and a laser-machined hydrophilic sample that had been stored in a polystyrene container, lead the authors to the following conclusions: organic molecules present on the untreated sample are removed during the laser-machining process; the freshly laser-textured surface is then passivated by the formation of a metal oxide layer. During this oxide layer formation process, various metal and oxide ions remain unsaturated and thus act as Lewis acid and Lewis base pairs; upon further exposure to air, hydroxylation of the acid/base pairs from airborne water occurs. Yet the progressive evolution of surface wettability upon ambient air exposure is not directly caused by the rapid hydroxylation process.

Rather, the authors suggest that upon air exposure, organic molecules such as carboxylates present in air moisture (as formic acid and acetic acid) are chemisorbed to the laser-machined hydroxylated oxide surface. Equation (24.1) represents the proposed chemisorption process that occurs on laser-treated metal surfaces when the samples are exposed to ambient air:

$$\mathrm{RCOOH\,(g)} + \text{metal–OH} \rightarrow \text{RCOO–metal} + \mathrm{H_2O} \tag{24.1}$$

Thus, nonpolar carboxylates or more broadly nonpolar hydrocarbons that chemisorb or adsorb to the hydroxylated metal oxide effectively depolarize the respective surface, that is, reduce the total surface free energy. The observed wettability transition can be attributed to this surface depolarization.

In 2019, Exir and Weck [16] extended from Long et al.'s [26] studies on copper samples and Jagdheesh et al.'s [28] and Cardoso et al.'s [15] work with aluminum and aluminum alloy samples to titanium. Their careful XPS analyses compare the chemical composition of a freshly ablated surface with one after 45 days and another after 1 year of ambient air exposure, which is among the longest periods studied. Following the logic put forward by Long et al. [13], the authors consider changes in the ratio of C–C to C–H bonds "*as an indicator to probe the nature of the surface wettability.*" Since the different samples showed only marginal differences in this ratio, the authors hypothesize that the unique electronic structure of TiO_2 and Ti_2O_3 played a considerable role in the reported wettability transition on titanium. From the comparison of high-resolution XPS spectra of Ti2p, a reduction in the concentration of Ti^{3+} (thus in Ti_2O_3) and an increase of Ti^{4+} (as in TiO_2) have been observed upon ambient air exposure over time. While the origin of such changes in the oxide structure remains unexplained, the authors highlight that Ti_2O_3 exhibits many coordinatively unsaturated sites, which act as Lewis acid/base pairs as has previously been shown for copper and aluminum oxides. In contrast to the previously established theory based on the surface hydroxylation, the authors attribute the imminent hydrophilic response upon laser machining to the hydration of the electron-deficient titanium ion (Fig. 24.4a) and thus do not consider a dissociative adsorption reaction as suggested by Jagdeesh et al. Further, Exir and Weck contrast the particular electronic structure of TiO_2 to that of Ti_2O_3 and outline that the octet of electrons in the outer orbital of the $3s^2p^6$ shell protects the empty 3D orbital of the Ti atoms from interaction. Accordingly, and as illustrated in Fig. 24.4b, the authors conclude that again no hydroxylation occurs but rather a hydration structure with water hydrogen oriented toward the titanium surface is assumed to be the prime factor causing the hydrophobic response after ambient air exposure. The extreme nonwetting response that was reported with a water contact angle of 153° 1 year after laser machining is attributed to the combined effect of surface chemistry and texture leading to the Cassie-Baxter wetting state. Contact angle hysteresis measurements have not been provided to prove the Cassie-Baxter wetting state on the investigated surfaces (of typical laser-induced periodic surface structure (LIPSS) topography). Yet following the arguments already provided by Boinovich et al. [27] to the work presented by Ta et al. [14], it is well known that

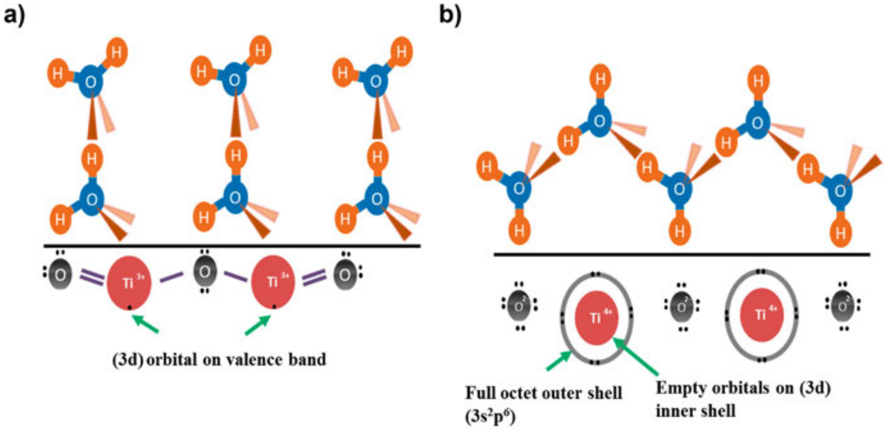
a)
b)
H
O
Ti3+
Ti4+
O2-
(3d) orbital on valence band
Full octet outer shell (3s²p⁶)
Empty orbitals on (3d) inner shell

Fig. 24.4 Schematic of the orientation of water molecules next to the (**a**) hydrophilic surface and (**b**) hydrophobic surface. (Reprinted from Exir and Weck [16] with permission from Elsevier)

clean metal oxides are hydrophilic and thus present a water contact angle of <90°. Considering the wavy topography of LIPSS, it remains unclear how the chemistry of TiO_2 alone, that is, without further adsorption/chemisorption of carbonaceous compounds, can be responsible for the claimed Cassie-Baxter wetting state.

In summary, to explain the wettability transition observed on laser-machined metallic surfaces, researchers have presented two prominent theories: the accumulation of airborne nonpolar carbonaceous molecules on laser-textured metal surfaces after days of ambient air exposure is proposed as the primary reason for the observed wettability transition; others have hypothesized that the partial deoxidation of laser-treated metal oxide surfaces causes the changes from (super)hydrophilicity to (super)hydrophobicity. Irrespective of the explanation, it is expected that the processing environment influences the initial chemical state and wettability response of the laser-processed surface. Furthermore, the previously discussed studies have already highlighted that the exposure environment after the completion of the laser-machining process also affects the final wettability response. Generally, in the previously presented studies, laser machining and subsequent sample exposure is performed under laboratory conditions with limited details provided about the specific working environment (temperature and humidity) and ambient air composition. Generally, it takes a relatively long time for laser-processed metallic surfaces to reach a steady wetting state under ambient air exposure, and the time (days) varies with type of metal. Disparities in the reported wettability transition time for alike metal surfaces might be caused by seasonal changes in one research location or climate differences when comparing results from different research groups. In the following two subchapters, we direct our discussion to studies that employed a specifically controlled processing and/or exposure environment in an effort to influence the surface's wettability response.

3 Machining Under Controlled Processing Conditions

Laser machining in different processing environments not only affects the surface chemistry but also influences the surfaces' topography because of the different optical properties of different background gases. Accordingly, the direct comparisons of contact angle values as indicators of the surface chemistry after laser processing in different environments must be made with this compounded effect in mind.

Guan et al. laser machined stainless steel and Al alloy surfaces within a well-sealed chamber in Ar, N_2, O_2, air and under vacuum [30]. Samples were stored in ambient air before and after laser processing. The study focuses especially on achieving superhydrophilicity for a prolonged period. Regardless of the processing environment, all surfaces exhibited superhydrophilicity immediately after the laser treatment. For the Al alloy samples, a distinct hierarchy in transition rate can be observed as a function of the processing environment (Table 24.1). After 10 days, surfaces treated under vacuum, O_2, and air are still hydrophilic while those processed in Ar and N_2 environment have already reached a hydrophobic wetting state. The stainless steel samples processed in the different environments exhibit a similar but slower trend with the exception of the air-processed sample, which remains superhydrophilic even after 10 days (Table 24.1). Although the authors stated that the difference in water solubility between Fe and Al oxides was responsible for the material dependency, the exact cause and effect relationship of the substrate material dependence remains unclear.

As proposed previously, upon laser machining, a metallic surface exhibits a significant amount of reactive sites, that is, Lewis acid/base pairs [13, 28]. The actual number of such coordinatively unsaturated ions available for further reaction depends on the machining environment. Thus, machining in an inert gas environment (Ar, vacuum) is expected to result in a maximum number of reactive

Table 24.1 Contact angle (°) evolution as a function of store time in different conditions for Al alloy and stainless steel, respectively

	4 h	2 days	3 days	1 week	10 days
Al alloy					
Vacuum	0	0	0	9	18
O_2	0	0	10	17	25
Air	0	5	11	19	31
N_2	0	28	45	75	101
Ar	0	36	58	80	117
Stainless steel					
Vacuum	0	0	0	0	0
O_2	0	0	0	18	21
Air	0	0	0	0	0
N_2	0	0	16	23	53
Ar	0	0	27	74	105

Reproduced from Guan et al. [30] with permission of the Elsevier sites. A higher number of reactive sites promotes the hydroxylation process, which in turn supports the chemisorption of organic matter upon exposure to air. Following this logic, the short wettability transition time observed for Ar can be readily explained. Similar results could be expected for laser machining in a vacuum as this theoretically also constitutes an inert environment. XPS analysis, however, revealed a higher concentration of polar functional C=O bonds for Al alloy and stainless steel surfaces machined under vacuum. The presence of such polar functional groups can likely be attributed to undesired contamination of the vacuum environment (the particularities of the resulting surface chemistry after vacuum exposure are discussed in greater detail in a later section). It is to note that the authors neither specify the purity of the gases nor the quality of the vacuum. The wettability transition results for metal samples processed in N_2 are not further addressed by the authors. Yet it is expected that the formation of metal nitrides plays a role in the observed results.

In 2019, Pou et al. [31] extended Guan et al.'s [30] study by using the same processing gases but also including CO_2 in their experiments with stainless steel. This study's focus lies on enhancing hydrophobicity by selectively choosing the processing environment. The minimum purity of the five processing gases used was reported as 99.5%. In contrast to Guan et al.'s study, the experiments were carried out under continuous gas flow. According to SEM images and roughness measurements, the micro-topography and roughness of the processed surfaces are similar regardless of the machining environment. However, the authors highlight the morphological differences in the submicron regime observed on surfaces processed in O_2 and Ar. Surfaces processed in O_2 have surface cracks and periodic nano-ripples, whereas surfaces processed in Ar have smooth grooves. As a result of the high-temperature processes that occurred during laser machining, the authors presume that oxide layers are formed, which results in surface cracks. Therefore, variations in the submicron topography could contribute to differences in the surface chemical composition. Similar to Guan et al. [30], the surface machined under an Ar environment showed the highest hydrophobicity compared with the surfaces machined under other processing environments: on the surface machined in Ar (125 ± 2°), the contact angle is significantly higher than that measured on the surface processed in N_2 (83 ± 9°). Yet it was unclear from the report how much time elapsed between processing and contact angle measurements. XPS analysis carried out 7 days after laser processing reveals clear differences in the atomic oxygen and nitrogen to Fe ratios as a function of the processing environment. The relative amount of oxides and nitrides with respect to Fe [(O + N)/Fe] on the laser-treated surface was proposed as the wettability control. A minimum (O + N)/Fe content appeared on the surfaces treated in Ar and N_2, and a maximum was observed for surfaces treated in O_2 and air. In addition, a maximum amount of nonpolar carbon, C–C and C–H bonds was measured on the surface machined in N_2, whereas the least amounts were measured for the surfaces processed in O_2. According to Long et al. [13], a higher carbon-to-metal ratio and a greater C–C and C–H bond ratio lead to a greater contact angle. However, the current results showed a greater contact angle for the Ar-processed samples than for the N_2-processed samples, yet the N_2-

processed sample shows a higher carbon-to-metal ratio and a greater C–C and C–H bond ratio. Hence, the ((O + N)/Fe) ratio fails as a wettability control indicator for Ar-processed samples.

In summary, the two prominent reports on surface chemistry and wettability upon laser processing in different environments highlight that machining in an inert environment, such as Ar, results in a faster wettability transition. Even though neither report went into great detail in their proposed explanation, we suspect that an inert environment, as opposed to a reactive one, results in a greater number of reactive sites where hydroxylation can occur.

4 Postprocessing Exposure to Controlled Conditions

Previously discussed studies have shown that the wettability transition that occurs while the metal is exposed to ambient air continues over a prolonged period of several days to weeks. The following section highlights research efforts targeted on increasing the measured steady-state contact angle and tailoring the transition time from (super)hydrophilicity to (super)hydrophobicity by targeted exposure to different liquids, gases, and possible heat treatments. It is to note that the studies discussed in the following are based on the laser process being carried out in ambient air unless explicitly stated otherwise.

4.1 Liquids

Carboxylic acids, such a lauric acid, readily form monolayers on the surface of aluminum and its oxides. As these monolayers are comprised of long alkyl chains, with a terminal methyl group facing outward, they are inherently hydrophobic. In their important contribution from 2015, Long et al. [13] leveraged this phenomenon to rapidly fabricate superhydrophobic surfaces. They submerged freshly laser-irradiated aluminum samples in a lauric acid-ethanol solution for 30 min at room temperature. After being rinsed with ethanol and dried in an oven at 80 °C for 15 min, the surfaces present sessile water contact angles of 154 ± 3°. The XPS data further confirms the adsorption of organic species onto the surface, where the carbon-to-aluminum ratio increases from 0.65 (pristine surface) to 3.14.

The laser processing of brass surfaces in air followed by postprocess exposure to various liquids in comparison to ambient air exposure has been reported by Yan et al. in 2018 [32]. Laser-processed samples were submerged in vinegar, sodium bicarbonate (0.07 g/ml), isopropyl alcohol (IPA), and salt water (0.07 g/ml) for 3 h before being exposed to ambient air. Figure 24.5 shows the contact angle evolution of laser-textured brass surfaces after immersion in various solutions. The laser-treated brass showed hydrophobicity (108°) immediately after immersion in the IPA solution and reached a steady wetting state of 131° after 3 days of air exposure.

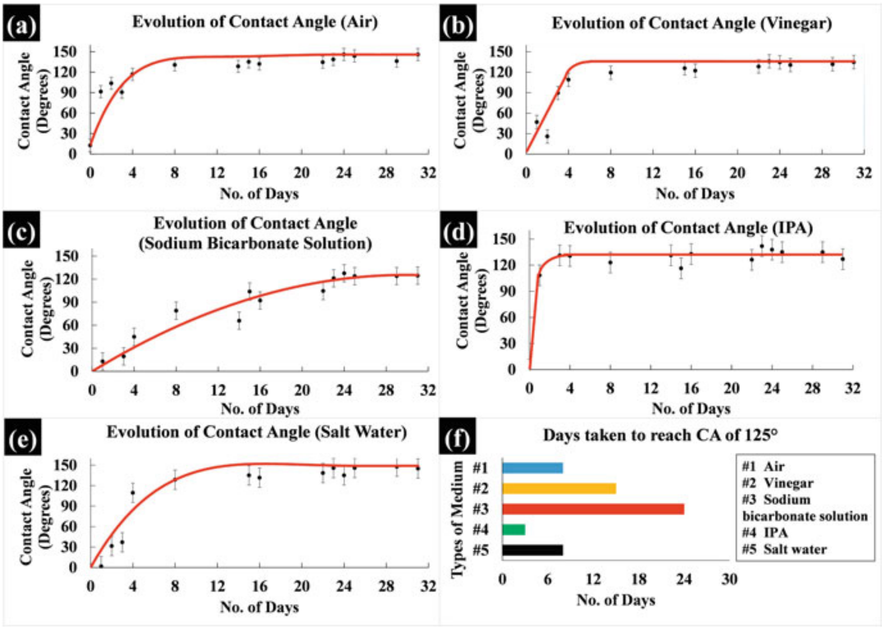

Fig. 24.5 Contact angle evolution of the laser-textured brass surfaces over time. (**a**) Exposed to air, immersed into (**b**) vinegar, (**c**) sodium bicarbonate solution, (**d**) IPA, and (**e**) salt water. (**f**) Days taken to reach CA of 125°. (Reprinted from Yan et al. [32] with permission of the Elsevier)

Directly after immersion in salt water, vinegar, and sodium bicarbonate, the respective samples presented as hydrophilic. Nevertheless, the samples attained a contact angle of 125° within 8 (salt water), 15 (vinegar), and 24 (sodium bicarbonate) days after exposure to air. Notably, the control surface that had been directly exposed to air after laser irradiation developed into a stable hydrophobic surface (with contact angle >125°) at a similar rate than the saltwater sample (8 days) and thus faster than the surface that had been immersed in the sodium bicarbonate solution (15 days). SEM analysis provided evidence that the sodium bicarbonate solution considerably altered the surface morphology of the laser-processed sample, growing spiky flowerlike structures from typical laser-induced bumpy structures. According to the authors, the other samples showed no notable differences in morphology upon immersion. As mentioned earlier, absolute values of the contact angles should not be directly compared between samples of different morphology. XPS analysis was only provided for the air-exposed sample, and differences in chemical composition were briefly commented based on EDS spectra. A detailed discussion of differences in the surface chemistry caused by the different immersion media is lacking, yet along the theories introduced here in earlier sections, the authors conclude that the adsorption of organic matter upon air exposure contributes to the contact angle evolution. No clear explanations are provided for the differences in reaction rate.

In 2020, Schnell et al. [33] explicitly investigated the influence of a variety of chemical solvents on the wetting properties of laser-textured surfaces over time. After laser processing, Ti6Al4V samples were immersed for 15 min in an ultrasonic bath with the respective high purity solvent (water, ethanol, acetone, IPA, hexane) before being stored in ambient air. The surfaces exposed to hexane showed a hydrophobic response already after 1 day of air storage, while the surfaces cleaned in alcohol (ethanol and IPA) still remained superhydrophilic (Fig. 24.6). After 14 days of air exposure, the hexane sample, which showed the fastest wettability evolution, reached the highest contact angle among the samples exposed to different solvents. Interestingly, the IPA exposed sample, which showed the slowest wettability evolution, reached third rank among the highest contact angles after 14 days of air storage. That contradicts the observation of Yan et al. [32], although there is a significant difference in immersion treatment conditions (15 min in an ultrasonic bath vs. 180 min of immersion). With reference to especially Long et al.'s work [13], the XPS analysis is focused on the carbon-to-metal ratio and on the atomic percentage of C–C and C–H bonds, as indicators for surface wettability. The authors conclude that long-chain alkanes, like hexane, permanently bond to the laser-irradiated metal and quickly and fully saturate all available reactive sites available from an initial hydroxylation reaction, which thus results in the rapid decrease in wettability and subsequent stable nonwetting even after 14 days of storage. Schnell et al. [33] also briefly comment on the volatility of hexane. Undoubtedly, the high vapor pressure of some solvents will affect the composition of the ambient air near the sample directly after removal of the metallic substrate from the respective liquid. A more detailed discussion is provided in a later section that discusses the influence of different gaseous exposure conditions. On the contrary to the samples exposed to hexane, alcohol-immersed samples are hypothesized to keep a thin film of alcohol molecules on their surface for a prolonged time, such that their highly polar hydroxyl group (OH) induces a superhydrophilic wetting response until organic molecules from the ambient air adsorb onto the surface.

While the authors reference previous work that indicated the importance of surface hydroxylation upon laser processing, the discussion of the similarities and differences in the wettability evolution of the chemically considerably different media, acetone, and water is limited to an indication of a shorter alkyl chain length of possible airborne contaminants dissolved in the respective liquids. The particularly low contact angles measured upon water immersion is not further addressed.

4.2 Gases

In their prominent studies from 2015, Long et al. also presented a comprehensive investigation to ascertain the effect of several gas exposure conditions (Air, CO_2, N_2, O_2, organic) on the wettability of laser-textured pure metal surfaces (Al and Cu) [13, 26]. Figure 24.7a illustrates the measured water contact angles of the laser-textured Al samples kept under various ambient conditions for 8 and 30 days, while Fig. 24.7b shows contact angle measurements on Cu samples after 8 days of storage. The Al samples that were kept in an organic-rich environment (0.5 mL

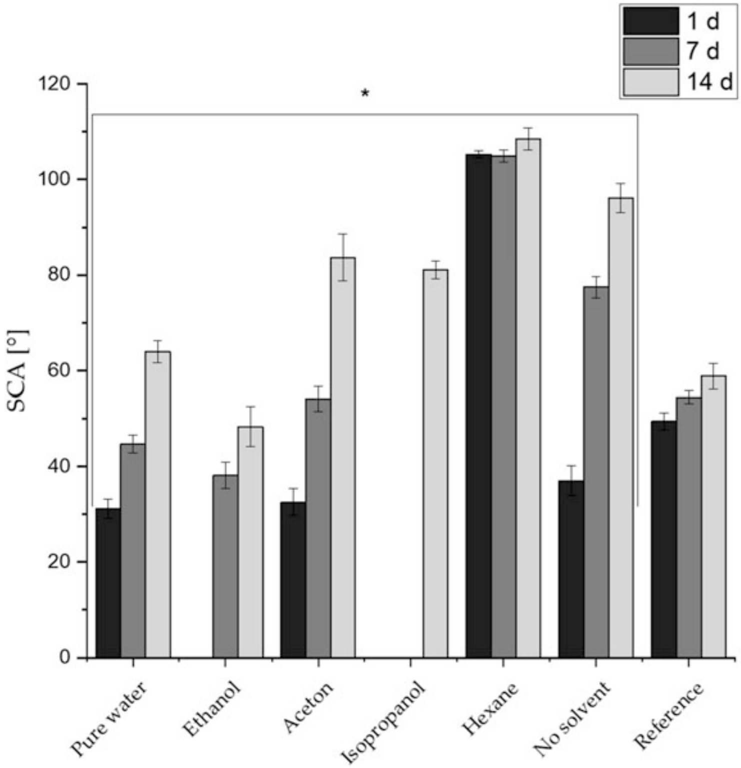

Fig. 24.6 Static contact angles (SCA) on reference (polished, unstructured, and water rinsed) and laser-processed specimens as a function of time and cleaning solvent. (Reprinted from Schnell et al. [33] with permission from MDPI)

4-methyloctanoic acid place in a 15 L container) demonstrated a swift transition to superhydrophobicity after 8 days. XPS analysis indicates that the carbon-to-aluminum ratio for the surface stored in the organic-rich atmosphere (1.77) is similar to that for the surface stored in ambient air (1.72). Despite the fact that the organic environment contains more organic matter than ambient air, the overall amount of adsorption does not rise considerably. The findings on Al surfaces hint that the adsorption of organics that are in the gas phase is restricted to particular maxima, but adsorption from liquid solutions (lauric acid-ethanol solutions; ratio of 3.14) have increased efficacy. Similar to Al samples, the Cu samples that were stored in an organic-rich environment (0.2 g vacuseal grease) demonstrated a brisk transition to hydrophobicity after 8 days. However, laser-processed Al and Cu samples kept in pure O_2 and N_2 remain hydrophilic after 30 and 8 days of exposure, respectively. Even after extended storage in CO_2, O_2, and N_2 for 30 days, the laser-treated Al surface maintained its superhydrophilic properties. Early studies proposed the decomposition of CO_2 to carbon with oxygen-deficient oxides as a factor for

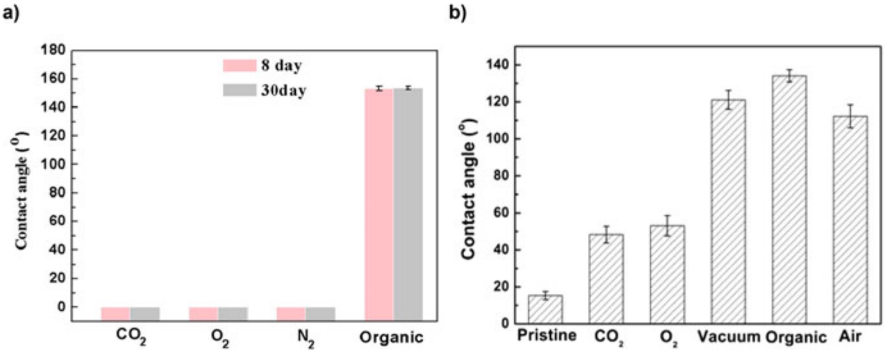

Fig. 24.7 Contact angles of the (**a**) Al samples stored in different atmosphere for 8 and 30 days (Reprinted from Long et al. [13] with permission of the Elsevier) and (**b**) Cu samples stored in different atmosphere for 8 days. (Reprinted from Long et al. [26] with permission of the AIP Publishing)

the slow transition in wettability of laser-textured metals [11]. But the proposed mechanism cannot be pertinent for this study. Contrarily, Cu surfaces stored in CO_2 and O_2 for 8 days exhibited a slight increase in the contact angle (48.3 ± 4.5°). Nevertheless, the discussion is limited only to CO_2 exposure for both the Al and Cu. XPS analysis indicates a minimum carbon-to-metal ratio and C–C and C–H bond ratio for the surface stored in CO_2, which attributed the superhydrophilicity and hydrophilicity, respectively, for Al and Cu.

Additionally, the study carried out by Cardoso et al. [15] identified an important relation between the sample storage conditions and the evolution of contact angles upon laser machining. The authors' samples were stored under three different conditions: directly exposed to air, within a polyethylene ziplock bag, and inside a polystyrene box (both filled with lab air) and subject to repeated contact angle measurements (Fig. 24.8). The authors indicate that the laser-processed sample stored in the ziplock bag was processed under different machining conditions, thus resulting in a different topography. Furthermore, the ziplock bag did not provide a perfect seal, allowing for limited airflow. Under consideration of these aspects, the authors conclude that the polyethylene bag slowed the wetting transition process, which took 7 days to attain hydrophobicity, in comparison to the sample exposed to air that already exhibited high hydrophobicity on day 4. The sample stored in a polystyrene box did not achieve hydrophobic characteristics even after 15 days. This observation is attributed to the better air seal provided by the polystyrene box in comparison to the poorer sealing ziplock bag, which allowed for some airflow.

Overall, it can be concluded that laser-processed metallic surfaces exhibit a strong hydrophobic response when kept in an environment that provides abundant nonpolar and long-chain organic compounds. Early studies proposed the decomposition of CO_2 to carbon with oxygen-deficient oxides as a factor for the slow transition in wettability of laser-textured metals [11]. However, the results stemming from experiments with CO_2 as the processing environment [31] or the deliberate

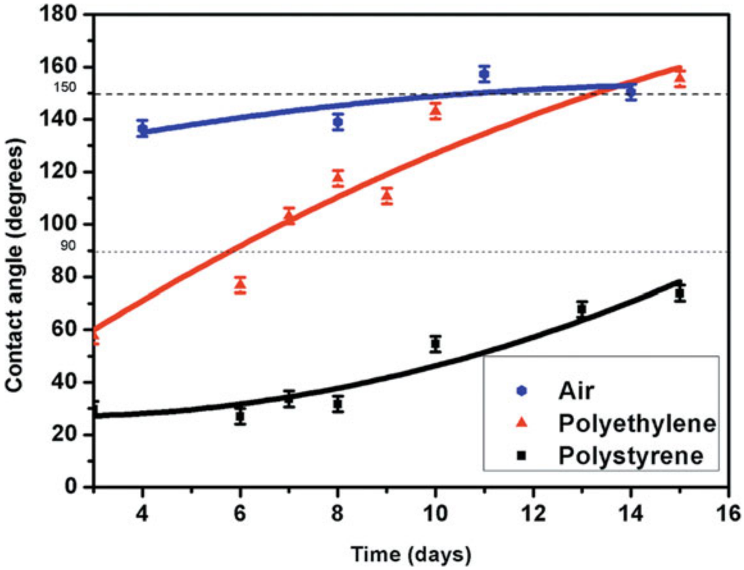

Fig. 24.8 Comparison of contact angle values of sample stored in polyethylene bag and samples kept inside a polystyrene box and air. Samples depicted for all conditionings were wet and measured every day. (Reprinted from Cardoso et al. [15] with permission from RSC)

exposure environment [13] have indicated that CO_2 exposure does not particularly favor the wettability transition. The results from Pou et al. indicate that the surface machined in CO_2 remained hydrophilic; however, the report does not indicate how much time elapsed between the processing and the contact angle measurements. Figure 24.7, which summarizes results from Long et al.'s studies, indicates that their Al surface exposed to CO_2 for 30 days remained superhydrophilic [13], whereas the Cu surface showed a moderately increased contact angle after 8 days of exposure [26]. This has further been confirmed in studies where both the processing and exposure environment have been controlled.

Lehr and Kietzig who laser machined Ti surfaces in a variety of processing environments (O_2, N_2, H_2O) and subsequently exposed them to pure O_2, CO_2, and H_2O for 18 h found no statistically significant increase in the measured contact angle upon postprocessing exposure to CO_2 in comparison to other exposure environments [34]. Yet as discussed earlier, the surface topology of the different samples was slightly affected by the processing environment, which limits a direct comparison of measured contact angles.

Likewise, Landis et al. laser machined Ti surfaces in O_2, N_2, and a mixture of O_2 and N_2 (~air composition) to study the effect of the gas composition on the surface morphology, the surface chemistry, and the stability of the machined structures [35]. As opposed to Lehr and Kietzig's study [34], the surface morphology of laser-machined Ti surfaces (LIPSS) remained comparable under various gas compositions and varying total pressure (0.01–500 Torr). XPS measurements, however, revealed that background gases and pressure influence the chemical composition of LIPSS surfaces. Surfaces that were machined in O_2 exhibited only titanium and oxygen, indicating the formation of TiO_2. The surface machined in N_2 contained titanium, oxygen, and nitrogen, denoting the growth of TiN. As a result of argon sputtering, oxygen was removed in significant amounts while nitrogen retained its original amount, indicating that nitrogen has been incorporated into the titanium lattice. Furthermore, the results suggest that the presence of O_2 in the machining condition inhibits the incorporation of N_2 [35].

Wood et al. [36], who carried out the laser process with and without a continuous CO_2 flow, confirmed that machining under a continuous flow of CO_2 does not affect the measured contact angles. However, laser-processed surfaces that were placed inside a CO_2-rich reactor and kept at an elevated temperature and pressure (60 °C and 20 PSI) for 30 days exhibited a higher contact angle in contrast with the surfaces not being postprocessed. Whether this result can be attributed to the direct exposure to CO_2 or is rather to be attributed to organic contamination in the reactor that is available for adsorption or chemisorption to the surface aided by the increased temperature and pressure remains unexplored. In the following section, more detail is provided on studies carried out in closed reactors at reduced pressure.

4.3 Vacuum

A number of studies have commented on the influence of residence in vacuum on the wettability transition of laser-processed samples [26, 37, 38]. Figure 24.7b illustrates Long et al.'s [26] findings that indicates that the laser-processed Cu surface stored in a vacuum for 8 days resulted in a greater measured contact angle (121.1 ± 5.1°) than the comparable sample stored in ambient air (112 ± 6.2°). According to XPS data, the carbon-to-copper ratio was markedly enhanced for the samples stored in the vacuum atmosphere for 8 days. The highest relative ratio of nonpolar C–C and C–H bonds was also measured on these vacuum-stored surfaces, which explains the hydrophobic response. A mechanical vacuum pump was used to create the supposedly inert vacuum atmosphere, and the authors elaborate that oil contamination from the pump actually leads to a storage environment rich in organic compounds.

Similarly, Jagdheesh et al. [37] found in 2017 that stainless steel samples that were laser machined in ambient air but stored in a high vacuum (10^{-4} Pa) for 15–90 min underwent prompt modifications to superhydrophobicity. Samples stored for 30 min and above became extremely nonwetting such that dispensing water droplets onto the surface became difficult. XPS measurements were performed on the non-laser-processed material (reference material), fresh laser-machined sample, and sample stored in a high vacuum for 30 min. Comparing the spectra obtained before and after vacuum storage, a surge in the C 1s peak intensity was observed, which is attributed to the adsorption of organic matter during vacuum storage. As Long et al. [26] concluded earlier, the authors highlight that organic matter adsorbing from ambient CO_2, airborne hydrocarbons, or oil pumps might pollute the inside walls of a vacuum chamber and is then readily available to chemisorb to the hydroxylated laser-processed surface. Thereby, the polarity of the sample surfaces is reduced resulting in a wettability transition. The authors also consider that the water vapor partial pressure impacted organic matter chemisorption. The very low water vapor partial pressure at a high vacuum environment hinders the adsorption of water molecules, thus reducing the passivation of the hydroxyl sites, which subsequently allows for efficient chemisorption of organic matter to such a degree that the surface energy of the sample is considerably lowered within only 15–30 min.

In a recent contribution, Khan et al. [38] observed a similar trend for laser-processed stainless steel and Cu meshes. After 4 h of vacuum storage, the machined surfaces became superhydrophobic and superoleophilic. Alike Jagdheesh et al.'s [37] study attributes the much faster transition in the wettability state to the reduction in ambient humidity within the vacuum chamber in contrast to aging in an ambient atmosphere. On the contrary, Guan et al.'s study [30] highlights that metal surfaces machined in a vacuum environment and subsequently exposed to air retain high hydrophilicity over 10 days. Possibly, this observation can be explained by a vacuum system that has been contaminated with polar molecules.

The term “vacuum” is defined as a space where matter does not exist or where the pressure is so low that particles cannot influence processes taking place. The “vacuum” applied in all of the above studies appears not to be inert but, on the contrary, contains substantial concentrations of various organic matter, which dramatically alters the surface chemistry of the stored samples. These observations suggest that the quality of the vacuum atmosphere, which may vary from one vacuum system to the next, has a significant impact on the wettability transition. Accordingly, diligence in the reporting of experimental parameters and care in the setup of experimental campaigns greatly influence the reproducibility of samples' wetting response. The actual influence of an “inert environment” might better be assessed in an inert gas rather than a possibly contaminated vacuum.

5 Heat Treatments

Beyond the deliberate exposure of laser-processed samples to specific chemical species, many reports have attempted to achieve a faster wetting transition based on low temperature treatment of various laser-processed metallic surfaces [39–44]. From fundamental chemical kinetics and the Arrhenius equation, it is well known that elevated temperatures lead to increased reaction rates. Thus, it is expected that the surface chemistry of the laser-machined metallic surface is affected by a heat treatment postprocess. Several studies have shown that low temperature heat treatments in air after laser machining favor the wettability transition of the initially (super)hydrophilic surface to a (super)hydrophobicity [45–48]. Contrarily, high temperature treatment [13, 26] in air or hot water exposure [47, 49] results in superhydrophilic wetting.

5.1 Air

Ngo et al. extensively studied the impact of various heat treatments on the final wetting state of laser micro-/nanomachined metallic surfaces [46–48]. The authors used a simple low-temperature annealing treatment after their laser-machining process to accelerate the observed wettability transition of various laser-irradiated samples, such as stainless steel [46], Al [47, 48], Ti [48], and Cu [48]. In all studies, a dramatic reduction in the transition time from several days (30 days) to several hours has been achieved by employing the low temperature annealing treatment after laser machining. Ngo et al.'s study on laser-processed stainless steel surfaces indicates a hydrophobic response after already 2 h and subsequently superhydrophobicity after 4 h of heat treatment at 100 °C. No significant changes of the contact or sliding angle were observed with longer heat treatment durations (6–20 h) or subsequent air exposure for 14 days. For their stainless steel surface, the authors adopt the theory of CO_2 being decomposed to carbon in the presence of active magnetite to explain the wettability transition, as initially proposed by Kietzig et al. [11] In 2018, Ngo et al. extended their studies to investigate the influence of various temperatures on wettability transition times on three different highly pure metallic surfaces and found that the optimum annealing temperature and the annealing time are material dependent [48]. For Al and Ti, the wettability transition time decreases with increasing annealing temperature (100–200 °C). Cu surfaces followed a similar trend up to 150 °C; however, at higher temperatures (200 °C), they exhibited a longer wettability transition time. Upon annealing at 200 °C, Ti and Al surfaces exhibited a contact angle of 150° after 30 and 90 min, respectively. The Cu sample took a minimum of 120 min of annealing at 150 °C to reach the same wettability. In the context of this study, the authors present FT-IR measurements, which validate the existence of hydroxyl functional groups on laser-ablated Al and Ti surfaces that are considered to initiate the adsorption of organic matter upon exposure to ambient air. The heat treatment is understood to accelerate the adsorption of hydrophobic organic matter on the laser-processed surfaces [48]. Similar to Al and Ti, Cu also presents functional hydroxyl groups prior to the heat treatment. FT-IR analysis further confirms the presence of a small peak corresponding to methyl groups (CH_3). Yet a comparison of FT-IR results on Cu before and after heat treatment reveals no significant differences pointing to the adsorption of organic matter, which lets the authors to rule out organic layer adsorption as a reason for the wettability transition. Rather, the authors highlight that EDS analysis indicated a noticeable rise in the Cu concentration on the laser-processed surface after heat treatment. Hence, the authors revert in their discussion to Ta et al.'s [14] theory of partial deoxidation of CuO to Cu_2O to account for the transition in the wetting state. While Ngo and Chun's studies present different mechanisms for different materials, they highlight however that irrespective of the metallic nature of the sample, its wettability transition upon laser processing can be accelerated by low temperature heat treatment in air. However, the authors did not elaborate on the material-specific variables that decide upon the underlying reaction mechanism and thus cause the differences in the observed transition temperatures and annealing times.

In addition and now extending the temperature range under consideration, several researchers have noticed a wettability transition from superhydrophobicity to superhydrophilicity upon sufficiently high-temperature treatments for various laser-processed metallic surfaces: Al [13, 29], Cu [26], and brass [43]. Long et al. thermally annealed (250 °C for 20 min) superhydrophobic Al [13] samples that had been kept in air for 30 days and Cu [26] samples that had been stored in the vacuum for 8 days. Both Al [13] and Cu [26] retrieved their original superhydrophilic responses that had been observed immediately after laser machining. As evidenced by XPS spectra, annealing effectively reduces the carbon-to-metal ratio and decreases in the C–C and C–H bond ratio owing to partial removal of organic matter. Thus, the observed reduction in the nonpolar components explains this reverse wettability transition.

Building upon the studies by Ngo and Chun and Long et al., Li et al. [43] observed a reversible wettability transition on laser-processed brass surfaces upon heat treatment. The laser-processed superhydrophilic sample was rendered superhydrophobic when the surface was heated at a temperature of ~150 °C for 4 h. The superhydrophobic surface regained its initial superhydrophilic wetting response when it was heated to a temperature above 250 °C for 1 h. The heating-reheating cycles were carried out ten times with good reproducibility of the measured contact angles for both wetting states, as depicted in Fig. 24.9. The authors, who observed change in the C–C and C–H bond ratio with the heat treatments, argue that increasing heating time and temperature up to 150 °C leads to an increase in the mobility of airborne organic molecules, which accordingly increases the chemical and physical adsorption of airborne organic components. Consequently, the superhydrophilic surfaces gradually become superhydrophobic. Contrarily at a high temperature (above 250 °C), the carboxylates that form on the superhydrophobic surface become unstable. As a result of the increased mobility of the adsorbed molecules, the hydrogen bond tends to break. Thus, the nonpolar carbonaceous species are decomposed and thus removed from the surface, resulting in the observed considerably lower water contact angle.

5.2 Water

Further of interest are studies that consider rendering laser-processed metallic surfaces stably superhydrophilic through a simple short-term (few hours) boiling water treatment. As previously mentioned, in their original studies, Kietzig et al. report on soaking metallic surfaces that had been laser processed in ambient air in boiling water for 2 days to render the surfaces superhydrophilic [11]. In an application study with laser-machined surfaces of different wettability published by White et al. in 2013 [50], the researchers highlight that laser machining a titanium surface under high humidity (>80%) and subsequently storing it for 24 h in warm

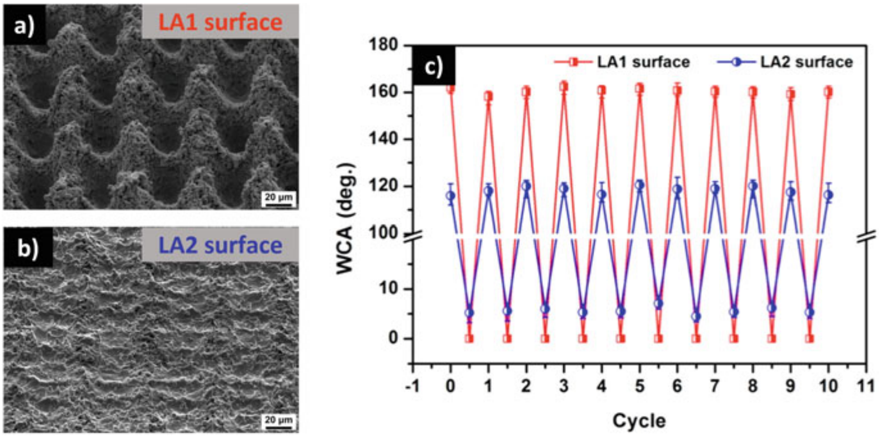

Fig. 24.9 SEM images of (**a**) LA1 surface and (**b**) LA2 surface and (**c**) reversible wettability transition between superhydrophobicity and superhydrophilicity of the LA1 surface and that between hydrophobicity and hydrophilicity of the LA2 surface during alternate heating-reheating cycles. (Reproduced from Li et al. [43] with permission of the Elsevier)

water conserves the superhydrophilicity of the surface. A thorough explanation with respect to the underlying surface chemistry was provided in Cardoso et al.'s study in 2017 [15]. The authors suggest that upon the rapid hydroxylation of the Lewis acid/base pairs, the availability of abundant water molecules results in the formation of strong hydrogen bonds between the initial hydroxyl groups and non-dissociated water molecules. This leads to the presence of a secondary adsorbed water layer, which effectively limits the adsorption of hydrocarbons and thus also limits the attainable steady-state contact angle.

In the context of their heat treatment studies, Ngo and Chun observed a similar wetting response on laser-processed aluminum samples [47]. The sample immersed in boiling water for 2 h attained superhydrophilicity and maintained it for more than 2 months. Based on their EDS, XRD, and FT-IR analyses, the authors attribute the stable superhydrophilicity after the boiling water treatment to the presence of AlOOH and Al_2O_3 and propose that the reaction between aluminum and boiling water forms a highly hydrophilic pseudo-boehmite nanostructure as shown in reaction Eq. (24.2).

$$\mathrm{Al} + 2\,\mathrm{H_2O} \rightarrow \mathrm{AlOOH} + 3/2\,\mathrm{H_2} \tag{24.2}$$

In 2019, Cheng et al. investigated the influence of water bath temperature (50 and 100 °C) on the transition in wetting state of already air-exposed (7 days) hydrophobic laser-processed Cu surfaces [49]. Surfaces treated for 1 h in a high temperature water bath (100 °C) are rendered more hydrophilic than their low temperature (50 °C) counterparts. Upon subsequent air exposure, all surfaces gradually transition to lower wettability again, with samples treated in 100 °C water exhibiting lower steady-state contact angles than those treated at 50 °C. Similar to Al, it is postulated that the hydroxylation reaction between the hot water and the copper leads to the formation of $Cu(OH)_2$. Auger Electron Spectroscopy (AES) confirms that the $Cu(OH)_2$ concentration increased considerably after the water bath treatment at 100 °C, while the sample treated at 50 °C showed a minor increase in intensity compared to before treatment.

Recent work by Wood et al. (2021) considers LIPSS structures on stainless steel surfaces stored in boiling water for 48 h, which rendered them highly hydrophilic ($21 \pm 5°$) [36]. In contrast with the earlier studies, after exposure to lab air for 30 days, the authors observed an appreciable increase in the measured contact angle ($50 \pm 3°$). The authors conclude that 48 h of storing the sample in boiling water is not sufficient to reach superhydrophilicity. The slow reaction between the LIPSS surface and the boiling water in comparison with the earlier studies [47, 49] is attributed to the low ablation depth resulting from processing with a fluence near the ablation threshold. Such processing conditions are suggested to result in a lesser number of reactive sites available for hydroxylation on the metallic surface.

Previous studies showed that the normal aging of metallic surfaces through oxidation and contamination triggers an increase in the contact angle. It is possible that normal aging is responsible for the observed increase in contact angle. Other studies have indicated that water-boiled laser-machined samples showed no change in contact angle after being exposed to ambient conditions. However, the ambient conditions where the samples are stored are not explicitly described.

The previous section illustrates that heat treatments of moderate temperatures accelerate reaction rates as expected. Depending on the nature of the exposure medium reactive sites on the surface are deactivated, and the chemisorbed or adsorbed molecules dictate the resulting wettability response.

Overall, it has become evident that reactive sites created during the laser process are subject to deactivation by reaction with different species present in the postprocessing exposure environment. The polarity of the chemisorbed or adsorbed functional groups is ultimately decisive for the wettability response of the laser-processed surface. Considering that the average laboratory environment typically consists of a mix of different gases with traces of various vapors and organic contaminants, it is evident that the different species in the exposure environment ultimately compete for reaction with the reactive surface. All studies presently known to the authors involve the exposure of the sample surfaces to ambient air of unreported composition. Consideration of this circumstance might help in comparing and interpreting seemingly contradictory results presented by different research groups.

In such an effort, we interpret results presented by Cardoso et al. [15] who also reported on the effect of the presence of water molecules during the wettability transition. Over the course of 37 days, two laser-machined samples were repeatedly tested for their contact angle alongside two aged samples that had never before come into contact with water. All test samples had been stored in polystyrene containers filled with ambient lab air of unknown composition. As illustrated in Fig. 24.10, the repeatedly wetted samples exhibited a typical transition of wettability from hydrophilicity to hydrophobicity, whereas for the previously unexposed samples,

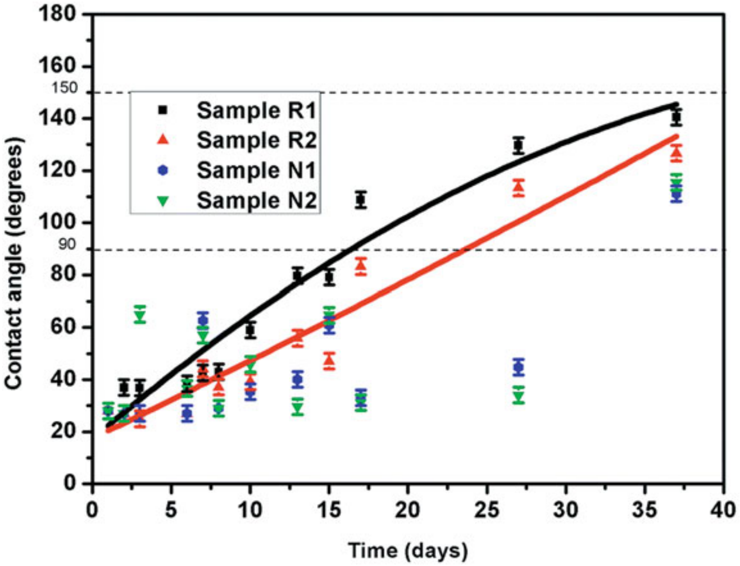

Fig. 24.10 Time evolution of SCA values of samples. Displayed in black and red (samples R1 and R2), patterns were repeatedly measured, and in blue and green (samples N1 and N2), two new patterns were measured each day. Both samples were stored in polystyrene containers. (Reprinted from Cardoso et al. [15] with permission from RSC)

no clear trend is observed over 37 days with overall random hydrophilic wettability results. While there was little discussion of the observed results by the authors, we suggest that the explanation lies in the repeated exposure to ambient laboratory conditions. The sample that was repeatedly tested on the contact angle goniometer had to be manipulated in ambient air. Furthermore, opening and closing the polystyrene storage container led to an exchange of the air composition within the container. Adsorption of organic matter onto the laser-machined surface from the ambient air was such facilitated. On the contrary, the sample that has been left inside its polystyrene container without intermitted exposure to air or exchange of the storage air only had a limited number of alike contaminants in its atmosphere available for interaction with the surface.

6 Fluence

Although there are only a limited number of studies carried out on understanding the influence of laser fluence on wettability transition, they do cover both the short (nanosecond) and ultrashort (picosecond and femtosecond) pulse regimes. Among others, Kietzig et al. [11], Bizi-Bandoki et al. [25], Ta et al. [14], Cardoso et al. [15], and Milles et al. [51] investigated the influence of applied laser fluence on wettability transition on laser-processed metallic surfaces. Irrespective of the applied laser fluence, most studies provide evidence that the samples become highly hydrophilic immediately after laser irradiation. Kietzig et al. [11] observed that surfaces subjected to low fluence from a femtosecond laser reach a steady wetting state faster than the sample irradiated at higher fluences. All the samples treated at a lower fluence achieved at least 63% of their steady-state contact angle only 1 day after the femtosecond laser irradiation. In contrast, samples irradiated with higher fluences became hydrophobic much slower. Ta et al. [14] observed a similar trend on nanosecond laser-irradiated Cu and brass surfaces, with samples irradiated with higher fluence exposing lower steady-state contact angles. Cu irradiated at a comparatively higher fluence took almost 30 days to reach the steady state, while their lower fluence counterparts took only 11 days. Irrespective of the applied fluence, the laser-treated brass surfaces achieved steady wetting after about 11 days of ambient exposure. According to the EDX results, the surface oxygen concentration increased from 3.6% for the untreated brass substrate to 9.0% and 20.2% 4 h after laser machining with fluences of 55 and 75 J/cm^2, respectively. With subsequent air exposure for 38 days, surface oxygen concentrations decreased on the brass samples and a fluence dependency was observed. For fluences of 55, 65, and 75 J/cm^2, the oxygen concentrations decreased from 9.0 to 4.5%, 19.8 to 16.2%, and 20.02 to 19.5%, respectively. The authors have not elaborated on why and how fluence affects the increase and decrease in oxygen concentration for fresh and aged laser-treated surfaces, respectively. Yet stemming from the earlier discussion, we conclude that the increased O_2 response directly after machining results from the newly exposed and oxidized surface.

In 2018, Milles et al. [51] investigated the influence of cumulated fluence on surface wettability of laser-textured substrates produced by direct laser interference patterning (DLIP) with a picosecond laser. Laser interference ablation methods that can result in periodic surface structures are described in Chap. 14. The authors have observed two different groups of samples with different behaviors as a function of cumulated fluence. The first group corresponds to a rather low cumulated fluence range (between 1 and 40 J/cm^2), and the second group resulted from machining with much higher cumulated fluences (between 150 and 270 J/cm^2). The samples in the first group showed a strong hydrophobic response after 5 days. No significant changes were observed after 11 days, but a spread in the recorded contact angle was found after 21 days (98–150°). Samples machined with low cumulated fluence (less than 33 J/cm^2) displayed a decrease in contact angle after 20 days of air exposure despite no significant decline in atomic carbon concentration (88 at% to 84 at% for 4.8 J/cm^2). In contrast, samples treated with the higher fluences remained hydrophilic after 5 days of exposure but became increasingly hydrophobic (>146°) upon 11, 21, and 28 days of exposure. The observed differences in the wetting response of the two groups were correlated to the respective surface chemistry. While the authors concentrate their discussion on differences in the carbon content response from the XPS, their tabulated results allow consideration of the carbon-to-oxygen and carbon-to-metal ratios. After 2 and 20 days of exposure, significant differences in the surface carbon content for structures produced in the two fluence ranges were observed. At low fluence (4.8 J/cm^2), the carbon-to-metal ratio decreases from 98.1 to 60.4 from the second to the twentieth day of exposure. For high fluence (271.3 J/cm^2), it increases slightly from 3.0 to 3.3. No data is provided that allows for an assessment of the C–C to C–H bond ratio. However, the carbon-to-oxygen ratio for the low fluence sample decreases from 8.2 to 6.0 throughout the exposure, while the high fluence sample presents a slight increase from 1 to 1.1 for the same ratio.

In 2020, Florian et al. investigated the influence of applied laser fluence on the formation of graded oxide layers and adsorption of carbonaceous molecules from the atmosphere on the laser-machined Ti alloy surfaces [52]. The authors laser machined three different types of structures by varying the peak fluence (ϕ_0) and number of effective pulses (N): (1) LIPSS (ϕ_0 – 0.5 J/cm^2, N – 40), (2) grooves (ϕ_0 – 2.5 J/cm^2, N – 100), and spikes (ϕ_0 – 3.0 J/cm^2, N – 400). Following the glow-discharge optical emission spectroscopy (GD-OES) results, the polished Ti alloy surface was found to have a native oxide layer thickness of ~10 nm. The native oxide layer thickness increased from ~10 nm for the polished surface to ~40, ~60, and ~165 nm for LIPSS, grooves, and spikes, respectively. Also, a minimum carbon concentration was observed on the polished surface, whereas the maximum concentration was detected on the spike surface. According to the authors, increased surface roughness and porosity cause increased adsorption of carbonaceous contaminants onto the surface [52].

To a certain extent, the differences in wetting behavior with cumulated fluence are thoroughly explained with the observed changes in surface chemistry in conjunction with the topography of the respective laser-created textures. That is, (1) higher fluence laser texturing results in coarser surfaces with relatively larger surface area available for the formation of polar metal oxides, which thus show a more hydrophilic response immediately after laser texturing in comparison to lower-fluence machined surfaces, and (2) coarser, possibly air-trapping surface textures take longer to transition to low wettability as more surface area needs to be covered by organic matter. The observed incidences of increasing wettability with time remain however unexplained in this study.

In summary, it is important to acknowledge the fluence dependency of the surface chemistry response of laser-processed metallic surfaces to get a full understanding of their wetting transition.

7 Probing Surface Chemistry

In addition to the different perspectives taken in this chapter on the chemical effects in laser surface structuring, we want to close with some critical considerations on the particularities of probing surface chemistry of laser-structured surfaces.

X-ray photoelectron spectroscopy (XPS) is the most extensively used method for surface analysis. It can be applied to a wide variety of materials and can extract quantitative information on the surface's chemical composition and prevalent functional groups within the topmost 5 nm of the given surface. Many of the reports discussed above have utilized XPS to retrieve the elemental composition along with the chemical state of laser-processed surfaces. In some cases, the reliability and reproducibility of XPS results may however have been affected by the scanning strategy employed during laser processing, which prescribes whether the laser energy is distributed uniformly over the surface or not. Spot size, pulse overlap, and scan line overlap in comparison to the size of the probing X-ray beam will have a major influence on the XPS results, especially considering that most laser pulses come with a Gaussian spatial intensity distribution. Homogeneous structures are created when the laser energy is applied uniformly over the surface [11, 12, 25, 53]. However, many previously discussed studies report on the surface chemistry of laser-inscribed structures (e.g., grid patterns [15, 37], micropillars [28], microchannels [28], microburrs [46–48]), whose SEM images clearly indicate spatial variations that might possibly influence the surface chemistry response (Fig. 24.11).

If we exemplarily consider a raster scanning protocol for a grid pattern with hatch distances larger than the ablated line width, then we note that substantial regions on the surface remain pristine and possibly only show few redeposited nanoparticle debris [15, 28, 37, 46–48]. On the other hand, scan line intersections receive twice the fluence compared with the individual scan lines, which causes visibly deeper ablation craters at the intersections. Therefore, an individual repeat unit of the grid pattern contains various zones where the laser fluence is imparted differently, that is, the non-laser-processed region, regions of scan line intersections, the scan line groove center, and the groove ridge, which both according to the Gaussian beam profile experience at least a 2D fluence distribution. Thus, if the experimental protocol enables to perform sensitive chemical analysis exclusively on a particular region of interest, all previous sections of this chapter suggest that we should expect to find different chemical responses from the different surface regions of such laser-inscribed patterns. In this context, Ngo and Chun's EDS analyses

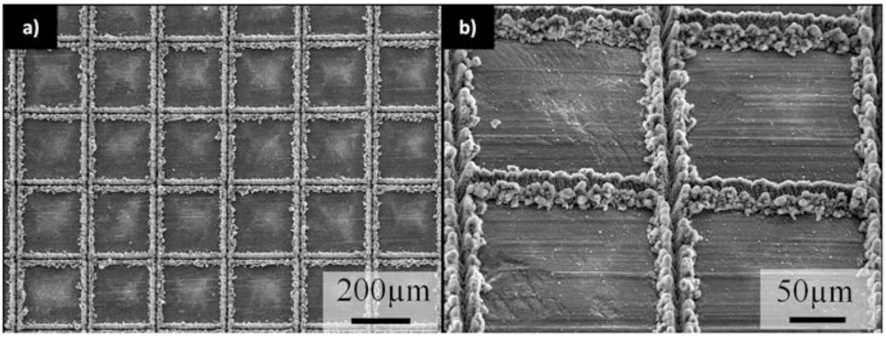

Fig. 24.11 Typical SEM images (**a**) top view and (**b**) enlarged tilted images of an aluminum surface just after laser ablation. (Reprinted from Ngo and Chun [47] with permission from Elsevier)

on laser-ablated microburr structures and adjacent nonirradiated surfaces indicate a clear difference in the carbon content on the μ-burrs after the heat treatment, whereas no changes were noted for the nonirradiated surfaces [48]. However, when performing a chemical analysis with a probing X-ray beam of fixed beam diameter possibly only 5–10 times the hatch distance, the problem arises how to determine from which region the response signal is collected and how to assure that an alike section of the surface is probed in comparative studies among different samples. None of the studies carried out on alike laser-inscribed surfaces provides sufficient experimental detail to judge how the authors have addressed this concern. It is thus possible that the reported XPS data constitutes either a single random sample of the underlying inhomogeneous surface or an average response from different regions with unreported sample size, which might not be representative for the whole sample. Nonetheless, some publications use various analytical tools to perform a more detailed analysis of the surface chemistry of laser-machined surfaces [52, 54]. For example, Kirner et al. showed that by using AES (Auger electron spectroscopy), it was possible to analyze the chemical composition of individual ridges and valleys of nano-sized features such as HSFLs and LSFLs [54]. However, these studies have not coupled the observed surface chemistry results to surface wettability.

Similarly, care should be taken in carrying out and reporting contact angle measurements. The most widely used and easiest method to quantify static, advancing, and receding contact angles is contact angle goniometry. All the studies that are described in this chapter use contact angle measurements to assess the surface wettability of laser-processed metallic surfaces. The reliability and reproducibility of the result of the measurement can, however, be controlled and influenced by a variety of factors, such as surface contamination, humidity and temperature of the measurement environment, elapsed time between laser machining and contact angle measurements, and postprocessing steps employed directly after laser machining (e.g., ultrasonication, plasma treatment).

It is evident from earlier sections of this review that the duration of the laser process and the elapsed time between laser processing and contact angle measurements play a role in the contact angle result, as these factors are decisive on how long a given surface can possibly interact with a given environment. Furthermore, ambient conditions during contact angle goniometry are well known to affect the measurement. In 2012, Kietzig et al. highlighted the influence of ambient humidity during contact angle measurements specifically for laser-processed metallic surfaces [12].

Yet even before actually carrying out contact angle goniometry or XPS analysis, researchers need to decide how to assess the wettability and surface chemistry of their laser-processed substrates, and there exists an inherent trade-off: either the surface is first cleaned from redeposited nanoparticles or nanoparticles remain on the substrate during analysis. Schnell et al. (2020) revealed that the final wettability of laser-processed metallic surface is greatly affected by the solvent used to clean the surface [33]. On the contrary, Wood et al. (2021) recently indicated that the presence of redeposited nanoparticles and nanoparticle agglomerates also affects the wettability of laser-processed surfaces [36]. Wood et al.'s results also revealed that the gas flow rate during laser processing influences nanoparticle agglomeration. Nanoparticle agglomerates change in their appearance from spiderweb-like structures to large cloud-like flakes when the flow rate increases [36]. Consequently, any surface analysis measurements carried out on laser-processed surfaces without prior removal of loose nanoparticles through, for example, sonication in a solvent will reflect the wettability or surface chemistry of the agglomerate system and not that of the machined surface. Furthermore, the nanoparticle agglomerates are redistributed or washed away by the first contact with a water droplet. Thus, replicate measurements for contact angle analysis on surfaces without prior nanoparticle removal need to be carried out in such a way that they constitute true replicates.

In light of these considerations, we note that few of the studies reviewed here conducted alike postprocessing steps, and several failed to sufficiently report the employed experimental details so that detailed comparative assessments of how different factors contributed to the contact angle measurement are not easily made.

Overall, an understanding of this uncertainty inherent to the analysis method used in many of the above discussed studies can possibly elucidate certain contradictions in the results presented by different research groups.

8 Conclusion and Future Outlook

Controlling the wettability of a surface is crucial in applications that require possibly hierarchical surface features including self-cleaning, anti-icing, anticorrosion, antimicrobial, and drag reduction. A solid surface's wetting property is influenced considerably by surface topography and surface chemistry. It is well established that short and ultrashort pulsed laser micro-/nanomachining is a versatile and unique way of altering the topography and chemistry of solid surfaces. The wettability of laser-machined surfaces undergoes a transition from superhydrophilicity to hydrophobicity (or even superhydrophobicity) upon exposure to a variety of conditions (ambient air, liquid, gas, and heat). In this chapter, we highlighted the present state of knowledge, described the gaps in knowledge, and identified the controversies concerning the influence of surface chemistry on the wettability transition of metals during laser machining. Under ambient air exposure, laser-processed metallic surfaces take a considerable amount of time to reach a steady wetting state; depending on the type of metal, the duration (days) varies. In an environment with abundant nonpolar and long-chain organic compounds, laser-processed metallic surfaces demonstrated a rapid transition to (super)hydrophobicity. Low-temperature heat treatments in air after laser machining promote the transition from an initially hydrophilic surface to a hydrophobic surface. On the other hand, high-temperature processing in air or hot water exposure results in superhydrophilic wetting. The surfaces subjected to low fluences from a short and ultrashort laser reach a steady wetting state faster than samples irradiated at higher fluences. The wettability of laser-processed surfaces is ultimately determined by the polarity of the chemisorbed or adsorbed functional groups. The wettability transition observed on laser-machined metallic surfaces has been explained by two prominent theories: (1) the accumulation of nonpolar carbonaceous molecules on laser-treated metal surfaces after several days of exposure to various conditions was proposed as the primary cause of the observed wettability transition, and (2) the partial deoxidation of laser-treated metal oxide surfaces causes the changes from (super)hydrophilicity to (super)hydrophobicity.

Despite this, there are uncertainties associated with both the reported exposure conditions and characterization. Most of the previously presented studies performed laser machining and subsequent sample exposure under laboratory conditions with little information provided about the specific working environment (temperature and humidity) and ambient air composition. Accordingly, it is not possible to directly compare the reported wettability transition times even for similar metal surfaces from different research groups. Consequently, the reproducibility of a samples' wetting responses is highly affected by the level of diligence in reporting experimental parameters and careful settings of experiments. Therefore, laser machining and exposure to well-known, controlled environments will be critical to assessing the effects of various elements and species on wettability transitions in the future. In addition, the vacuum used for assessing inert storage conditions is often not actually inert but, on the contrary, seemingly contains considerable amounts of organic matter from storage chamber walls or vacuum pump oil that drastically alters the surface chemistry of the samples. As opposed to a contaminated vacuum, an inert gas might be a better way to evaluate the actual impact of an "inert environment."

Surface chemistry analysis and wettability assessment are typically performed with XPS and contact angle goniometry, respectively. However, the reproducibility and reliability of XPS results may be affected by the scanning strategy employed during laser processing, which governs whether the laser energy is distributed uniformly over the surface or not (laser-inscribed patterns). We, therefore, need a sensitive chemical analysis protocol that can be applied to user-defined areas since the distinct surface regions of laser-inscribed patterns are foreseen to have different chemical responses. Additionally, the reliability and reproducibility of the contact angle measurements can be influenced by a combination of factors (surface contamination, temperature, humidity, postprocessing steps, etc.). Thus, obtaining an accurate replica of the contact angle measurements on surfaces requires a detailed description of the experimental conditions used where several authors failed in the past to sufficiently report the employed experimental details.

References

1. K.M. Tanvir Ahmmed et al., Fabrication of micro/nano structures on metals by femtosecond laser micromachining. Micromachines **5**, 1219–1253 (2014)
2. W. Liu et al., Fabrication of the superhydrophobic surface on aluminum alloy by anodizing and polymeric coating. Appl. Surf. Sci. **264**, 872–878 (2013)
3. J.H. Kim, A. Mirzaei, H.W. Kim, S.S. Kim, Facile fabrication of superhydrophobic surfaces from austenitic stainless steel (AISI 304) by chemical etching. Appl. Surf. Sci. **439**, 598–604 (2018)

4. J. Bravo, L. Zhai, Z. Wu, R.E. Cohen, M.F. Rubner, Transparent superhydrophobic films based on silica nanoparticles. Langmuir **23**, 7293–7298 (2007)
5. H.J. Choi, S. Choo, J.H. Shin, K.I. Kim, H. Lee, Fabrication of superhydrophobic and oleophobic surfaces with overhang structure by reverse nanoimprint lithography. J. Phys. Chem. C **117**, 24354–24359 (2013)
6. A. Satyaprasad, V. Jain, S.K. Nema, Deposition of superhydrophobic nanostructured Teflon-like coating using expanding plasma arc. Appl. Surf. Sci. **253**, 5462–5466 (2007)
7. P. Dimitrakellis, E. Gogolides, Hydrophobic and superhydrophobic surfaces fabricated using atmospheric pressure cold plasma technology: A review. Adv. Colloid Interf. Sci. **254**, 1–21 (2018)
8. W. Sun et al., Fabrication of polydimethylsiloxane-derived superhydrophobic surface on aluminium via chemical vapour deposition technique for corrosion protection. Corros. Sci. **128**, 176–185 (2017)
9. Z. Chen, L. Hao, A. Chen, Q. Song, C. Chen, A rapid one-step process for fabrication of superhydrophobic surface by electrodeposition method. Electrochim. Acta **59**, 168–171 (2012)
10. A.Y. Vorobyev, C. Guo, Direct femtosecond laser surface nano/microstructuring and its applications. Laser Photonics Rev. **7**, 385–407 (2013)
11. A.M. Kietzig, S.G. Hatzikiriakos, P. Englezos, Patterned superhydrophobic metallic surfaces. Langmuir **25**, 4821–4827 (2009)
12. A.M. Kietzig, M.N. Mirvakili, S. Kamal, P. Englezos, S.G. Hatzikiriakos, Laser-patterned super-hydrophobic pure metallic substrates: Cassie to Wenzel wetting transitions. J. Adhes. Sci. Technol. **25**, 2789–2809 (2012)
13. J. Long, M. Zhong, H. Zhang, P. Fan, Superhydrophilicity to superhydrophobicity transition of picosecond laser microstructured aluminum in ambient air. J. Colloid Interface Sci. **441**, 1–9 (2015)
14. D.V. Ta et al., Nanosecond laser textured superhydrophobic metallic surfaces and their chemical sensing applications. Appl. Surf. Sci. **357**, 248–254 (2015)
15. J.T. Cardoso et al., Influence of ambient conditions on the evolution of wettability properties of an IR-, ns-laser textured aluminium alloy. RSC Adv. **7**, 39617–39627 (2017)
16. H. Exir, A. Weck, Mechanism of superhydrophilic to superhydrophobic transition of femtosecond laser-induced periodic surface structures on titanium. Surf. Coat. Technol. **378**, 124931 (2019)
17. E. Skoulas, A. Manousaki, C. Fotakis, E. Stratakis, Biomimetic surface structuring using cylindrical vector femtosecond laser beams. Sci. Rep. **7**, 45114 (2017)
18. V.D. Ta et al., Laser textured superhydrophobic surfaces and their applications for homogeneous spot deposition. Appl. Surf. Sci. **365**, 153–159 (2016)
19. X. Yan et al., Atmosphere-mediated superhydrophobicity of rationally designed micro/nanostructured surfaces. ACS Nano **13**, 4160–4173 (2019)
20. U. Trdan, M. Hočevar, P. Gregorčič, Transition from superhydrophilic to superhydrophobic state of laser textured stainless steel surface and its effect on corrosion resistance. Corros. Sci. **123**, 21–26 (2017)
21. A.H.A. Lutey et al., Towards Laser-Textured Antibacterial Surfaces. Sci. Rep. **8**, 10112 (2018)
22. C. Sciancalepore, L. Gemini, L. Romoli, F. Bondioli, Study of the wettability behavior of stainless steel surfaces after ultrafast laser texturing. Surf. Coat. Technol. **352**, 370–377 (2018)
23. R.N. Wenzel, Resistance of solid surfaces to wetting by water. Ind. Eng. Chem. **28**, 988–994 (1936)
24. R.H. Dettre, R.E. Johnson Jr., Contact angle hysteresis II. Contact angle measurements on rough surfaces, in *Advances in Chemistry*, vol. 43, (American Chemical Society, 1964), pp. 136–144
25. P. Bizi-Bandoki, S. Valette, E. Audouard, S. Benayoun, Time dependency of the hydrophilicity and hydrophobicity of metallic alloys subjected to femtosecond laser irradiations. Appl. Surf. Sci. **273**, 399–407 (2013)
26. J. Long, M. Zhong, P. Fan, D. Gong, H. Zhang, Wettability conversion of ultrafast laser structured copper surface. J. Laser Appl. **27**, S29107 (2015)

27. L.B. Boinovich, A.M. Emelyanenko, K.A. Emelyanenko, A.G. Domantovsky, A.A. Shiryaev, Comment on nanosecond laser textured superhydrophobic metallic surfaces and their chemical sensing applications by Duong V. Ta, Andrew Dunn, Thomas J. Wasley, Robert W. Kay, Jonathan Stringer, Patrick J. Smith, Colm Connaughton, Jonathan D. Shephard. Appl. Surf. Sci. **379**, 111–113 (2016)
28. R. Jagdheesh, M. Diaz, J.L. Ocaña, Bio inspired self-cleaning ultrahydrophobic aluminium surface by laser processing. RSC Adv. **6**, 72933–72941 (2016)
29. Z. Yang, X. Liu, Y. Tian, Insights into the wettability transition of nanosecond laser ablated surface under ambient air exposure. J. Colloid Interface Sci. **533**, 268–277 (2019)
30. Y.C. Guan et al., Fabrication of metallic surfaces with long-term superhydrophilic property using one-stop laser method. Mater. Des. **78**, 19–24 (2015)
31. P. Pou et al., Laser texturing of stainless steel under different processing atmospheres: From superhydrophilic to superhydrophobic surfaces. Appl. Surf. Sci. **475**, 896–905 (2019)
32. H. Yan, M.R.B. Abdul Rashid, S.Y. Khew, F. Li, M. Hong, Wettability transition of laser textured brass surfaces inside different mediums. Appl. Surf. Sci. **427**, 369–375 (2018)
33. G. Schnell, C. Polley, S. Bartling, H. Seitz, Effect of chemical solvents on the wetting behavior over time of femtosecond laser structured Ti6Al4V surfaces. Nano **10**, 1241 (2020)
34. J. Lehr, A.M. Kietzig, Dependence of capillary forces on relative humidity and the surface properties of femtosecond laser micromachined titanium. J. Colloid Interface Sci. **448**, 356–366 (2015)
35. E.C. Landis, K.C. Phillips, E. Mazur, C.M. Friend, Formation of nanostructured TiO 2 by femtosecond laser irradiation of titanium in O 2. J. Appl. Phys. **112**, 2–7 (2012)
36. M.J. Wood, P. Servio, A.-M. Kietzig, The tuning of LIPSS wettability during laser machining and through post-processing. Nano **11**, 973 (2021)
37. R. Jagdheesh, M. Diaz, S. Marimuthu, J.L. Ocana, Robust fabrication of μ-patterns with tunable and durable wetting properties: Hydrophilic to ultrahydrophobic via a vacuum process. J. Mater. Chem. A **5**, 7125–7136 (2017)
38. S.A. Khan et al., Expedited transition in the wettability response of metal meshes structured by femtosecond laser pulses for oil-water separation. Front. Chem. **8**, 768 (2020)
39. D. Patil, S. Aravindan, M. Kaushal Wasson, V. Perumal, P.V. Rao, Fast fabrication of superhydrophobic titanium alloy as antibacterial surface using nanosecond laser texturing. J. Micro Nano-Manuf. **6**, 011002 (2018)
40. D. Rico Sierra, S.P. Edwardson, G. Dearden, Laser surface texturing of titanium with thermal post-processing for improved wettability properties. Procedia CIRP **74**, 362–366 (2018)
41. Y. Wan, C. Xi, H. Yu, Fabrication of self-cleaning superhydrophobic surface on stainless steel by nanosecond laser. Mater. Res. Express **5**, 115002 (2018)
42. D. Wei et al., Anti-corrosion behaviour of superwetting structured surfaces on Mg-9Al-1Zn magnesium alloy. Appl. Surf. Sci. **483**, 1017–1026 (2019)
43. X. Li et al., Reversible wettability transition between superhydrophilicity and superhydrophobicity through alternate heating-reheating cycle on laser-ablated brass surface. Appl. Surf. Sci. **492**, 349–361 (2019)
44. L. Ma et al., Hybrid nanosecond laser processing and heat treatment for rapid preparation of super-hydrophobic copper surface. Metals **9**, 668 (2019)
45. D.M. Chun, C.V. Ngo, K.M. Lee, Fast fabrication of superhydrophobic metallic surface using nanosecond laser texturing and low-temperature annealing. CIRP Ann. – Manuf. Technol. **65**, 519–522 (2016)
46. C.V. Ngo, D.M. Chun, Fast wettability transition from hydrophilic to superhydrophobic laser-textured stainless steel surfaces under low-temperature annealing. Appl. Surf. Sci. **409**, 232–240 (2017)
47. C.V. Ngo, D.M. Chun, Control of laser-ablated aluminum surface wettability to superhydrophobic or superhydrophilic through simple heat treatment or water boiling post-processing. Appl. Surf. Sci. **435**, 974–982 (2018)

48. C.-V. Ngo, D.-M. Chun, Effect of heat treatment temperature on the wettability transition from hydrophilic to superhydrophobic on laser-ablated metallic surfaces. Adv. Eng. Mater. **20**, 1701086 (2018)
49. H.-C. Cheng, T.-L. Chang, C.-S. Lin, P.-H. Chen, Wettability of laser-textured copper surface after a water-bath process. AIP Adv. **9**, 125140 (2019)
50. B. White, A. Sarkar, A.M. Kietzig, Fog-harvesting inspired by the Stenocara beetle – an analysis of drop collection and removal from biomimetic samples with wetting contrast. Appl. Surf. Sci. **284**, 826–836 (2013)
51. S. Milles, B. Voisiat, M. Nitschke, A.F. Lasagni, Influence of roughness achieved by periodic structures on the wettability of aluminum using direct laser writing and direct laser interference patterning technology. J. Mater. Process. Technol. **270**, 142–151 (2019)
52. C. Florian et al., Chemical effects during the formation of various types of femtosecond laser-generated surface structures on titanium alloy. Appl. Phys. A Mater. Sci. Process. **126**, 266 (2020)
53. J. Lehr et al., The influence of the gas environment on morphology and chemical composition of surfaces micro-machined with a femtosecond laser. Appl. Surf. Sci. **320**, 455–465 (2014)
54. S.V. Kirner, T. Wirth, H. Sturm, J. Krüger, J. Bonse, Nanometer-resolved chemical analyses of femtosecond laser-induced periodic surface structures on titanium. J. Appl. Phys. **122**, 104901 (2017)

Chapter 25
Ultrafast Laser Biomimetic Micro-/Nanostructuring

George D. Tsibidis and Emmanuel Stratakis

Abstract Nature provides an abundance of functional surfaces as a direct consequence of evolutionary pressure that forces them to demonstrate adaptation to environmental conditions and outstanding performance. Such response is facilitated by the presence of self-assembled and highly self-organized hierarchical nanosized structures on the species surface. As a result of the paramount significance of the impact of the topography on the species' natural adaptation, a transfer of the paradigm (biomimetism) into artificial materials is desirable. To fabricate the surfaces of artificial materials and emulate their response, laser-based techniques are employed to produce biomimetic structures of desirable complexity. The dominant methodologies to produce such surface patterns are either through a self-organization manner and the fabrication of the so-called Laser-Induced Periodic Surface Structures (LIPSS) or via appropriate modulation of the laser intensity by involving two or more coherent laser pulses that interfere generating a periodic intensity (Direct Laser Interference Patterning, DLIP). This chapter reviews the irradiation schemes and the physical mechanisms that have been proposed to investigate the formation of complex biomimetic structures with special emphasis on the LIPSS and DLIP techniques. A number of parameters and conditions are discussed that influence the shape and type of the induced structures. Apart from the conventional techniques in the determination of the laser parameters toward fabricating structures with desirable features, a novel and fast approach based on advanced artificial intelligence tools is presented and discussed. Potential applications of the produced nanopatterned topographies are additionally demonstrated.

Keywords Biomimetic surfaces · Laser processing · Modelling surface micro-/nanopatterning · Laser-Induced Periodic Surface Structures · Predictive modelling

---

G. D. Tsibidis · E. Stratakis (✉)
Institute of Electronic Structure and Laser (IESL), Foundation for Research and Technology (FORTH), Heraklion, Crete, Greece

Department of Physics, University of Crete, Heraklion, Greece
e-mail: tsibidis@iesl.forth.gr; stratak@iesl.forth.gr

© The Author(s), under exclusive license to Springer Nature Switzerland AG 2023

R. Stoian, J. Bonse (eds.), *Ultrafast Laser Nanostructuring*, Springer Series in Optical Sciences 239, https://doi.org/10.1007/978-3-031-14752-4_25

1 Introduction

The exploration and replication of biological systems with desired properties is popularly termed as *biomimetics* (from the Greek word *bios*, meaning life, and *mimesis*, meaning to imitate) [1, 2]. Biomimetics, a term attributed to Otto Schmidt [3], involves the application of lessons, concepts, and underlying principles from the natural world into the engineered world.

Biological systems have, for almost 4 billion years, evolved to function and provide unique solutions for complex problems that are smart, energy efficient, agile, adaptable, fault tolerant, eco-friendly, and multifunctional. Such solutions emerged as a direct consequence of evolutionary pressure that, typically, forces natural species to become highly optimized and efficient. On the other hand, natural processes result in sophisticated structures that utilize complex interplay between surface topography and functionalities. For example, nano- or microscale patterned surfaces or topographies that have different length scales superimposed on one another (hierarchical) are common in nature, which lead to many interesting possibilities when developing novel synthetic materials in an abundance of technological applications [1, 2].

Transferring the natural functionalities to the fabrication of technological designs, several methodologies have been developed to facilitate the formation of bioinspired surfaces exhibiting hierarchical structuring at length scales ranging from hundreds of nanometers to several micrometers. Laser processing excels over a variety of patterning methodologies such as mechanical, chemical, and electric discharge texturing as it allows local modifications with a large degree of control over the shape and size of the features, which are formed, and a broader range of sizes, which can be fabricated. Besides this, laser structuring techniques can be readily incorporated to computer-aided design and manufacture systems for complex and customized surface texture designs and subsequently reproducible and cost-effective fabrication. This can give rise to a versatile class of laser-based rapid prototyping texturing systems that could potentially be commercialized for mass production and thus attract considerable attention in the following years. To fabricate the surfaces of artificial materials and emulate their response, laser-based techniques are employed to produce biomimetic structures of desirable complexity. The dominant methodologies to produce such surface patterns are either through a self-organization manner and the fabrication of the so-called Laser-Induced Periodic Surface Structures (LIPSS) or via appropriate modulation of the laser intensity by involving two or more coherent laser pulses that interfere generating a periodic intensity (Direct Laser Interference Patterning, DLIP). This chapter reviews the current state of the art of laser processing methodologies used for the fabrication and engineering of biomimetic surfaces to realize extraordinary optical, mechanical, chemical, wetting, and biological-active properties for numerous applications. The focus is centered on the irradiation schemes and the physical mechanisms that have been proposed to investigate the formation of complex biomimetic structures with special emphasis on the LIPSS and DLIP techniques. Special focus is also drawn on an emerging field, the predictive modelling through the investigation of the performance of representative statistical and machine learning-based algorithms in forecasting the outcome of laser processing on a range of materials. Certainly, the success of the integration of biologically inspired designs into future viable commercial applications or other technological challenges is pertinent to the capacity to replicate efficiently patterns that appear in nature. Thus, an overview over the most relevant applications to date is briefly discussed while some emerging future prospects and emerging possibilities are also presented.

2 Functionalities of Patterned Surfaces on Natural Species

The special functionalities of certain organisms found in nature are usually not governed by the intrinsic property of materials but are more likely pertinent to the presence of microstructures and nanostructures on the surface of those species. With respect to the topographies found in the natural surfaces, sophisticated designs have been developed through a biologically controlled self-assembly procedure over billions of years adapting to the environmental conditions. Such adaptive and responsive self-assembly is provided by means of a hierarchical self-organization and optimization of the biological material at each level of hierarchy, so as to yield outstanding performance. There are many excellent published studies and reviews that address both the impressive properties of the nano-/microstructured patterned surfaces of biological species as well as the adoption of bioinspired designs for a number of purposes, usually, related to certain applications (see, e.g., [1, 2] and references therein). According to those reports, multifunctionality in natural materials is quite common, and properties such as thermal insulation, high adhesion strengths or even reversible adhesion, aerodynamic or hydrodynamic lift, incredible mechanical or structural strength, friction enhancement/reduction, self-assembly, antireflection and structural color (Fig. 25.1), self-cleaning, drag reduction (Fig. 25.2), self-healing, or impressive wetting properties (such as super-hydrophobicity/super-hydrophilicity) are only some examples of the properties of these materials. It is evident that the aforementioned functionalities are correlated to the features of the topographies, and these paradigms are possible of commercial interest [1, 2, 10].

3 Laser Fabrication of Biomimetic Structures

Due to a plethora of impressive properties exhibited by various species in nature, the capability to design and fabricate biomimetic structures on artificial materials is of significant importance as it would provide a virtually endless potential for the development of novel artificial materials and systems with advanced functionalities. In the past decades, femtosecond laser pulses have become an effective tool in

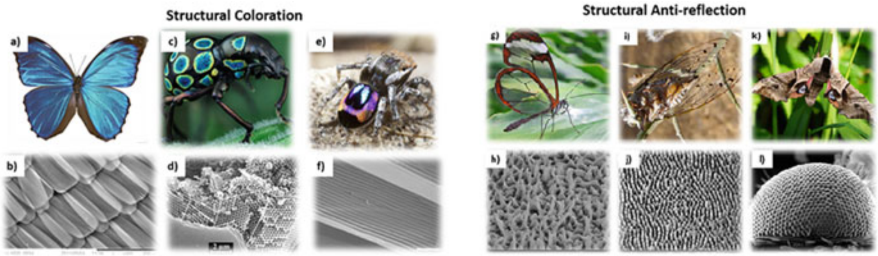

Fig. 25.1 Examples of biological systems with optical properties such as structural coloration and structural antireflection (first row shows various insects, while second row in the above figure illustrates the patterned surface of the insects (**a**) licensed by Didier Descouens/CC-BY-SA-4.0 (Wikimedia Commons). (**b**) was reprinted with permission from Rashmi Nanjundaswamy/Lawrence Hall of Science CC BY-NC-SA 3.0 US. (**c**) was reprinted with permission from Javier Rupérez, Spanish photographer specializing in extreme macrophotography (www.javier-ruperez.com). (**d**) was reprinted with permission from Welch et al. [6] from American Physical Society. (**e**, **f**) was reprinted with permission from Hsiung et al. [7] from Springer Nature (Creative Commons CC BY 4.0). (**g**) was licensed by David Tiller CC BY-SA 3.0 (Wikimedia Commons). (**h**) was reprinted with permission from Siddique et al. [8] and licensed by Radwanul H., CC BY-SA 3.0 (Wikimedia Commons). (**i**) was licensed by Gail Hampshire CC BY-SA 2.0 (Wikimedia Commons). (**j**) was reprinted with permission from Papadopoulos et al. [9] by John Wiley & Sons. (**k**) and licensed by Ben Sale CC BY-SA 2.0 (Wikimedia Commons). (**l**) was licensed by Dartmouth college)

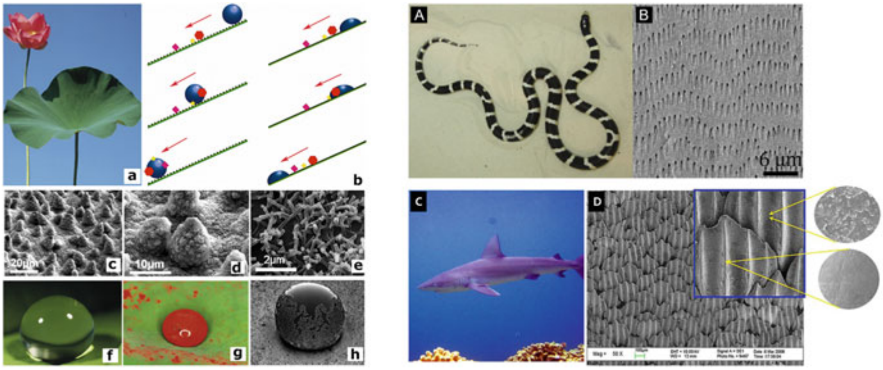

Fig. 25.2 Examples of biological systems with water repellence (**a**–**h**). (Reprinted with permission from Koch et al. [11] Copyright (2008) by Elsevier) and drag reduction ((**A**, **B**) were taken from [12] licensed under Creative Commons 2.0 from Beilstein Journal of Technology. (**C**) was reprinted with permission from Stratakis et al. [2] Copyright (2020) by Elsevier). (**D**) was reprinted with permission from Pu et al. [13] under CC BY 3.0 license. (**c**), (**d**), (**e**), (**B**), and (**D**) illustrate the patterned surface, while (**a**), (**A**), and (**C**) show the species; (**b**), (**f**), (**g**), and (**h**) demonstrate water repellence

laser processing and produce bioinspired topographies on artificial materials such as metals, semiconductors, dielectrics, ceramics, and polymers. The advantage of the laser-based techniques is due to their capacity in precise materials' micro-

/nano-fabrication with an impressive contribution to major advances in science, technology, and industry [2, 15–19].

3.1 Laser-Induced Periodic Surface Structures (LIPSS)

One particular type of patterns comprising the Laser-Induced Periodic Surface Structures (LIPSS) is the most common type of topography that can be fabricated via irradiation of solids' surfaces by Gaussian beams [2, 20]. In principle, these self-assembled textures are classified according to their size and orientation (Figs. 25.3 and 25.4 [2, 20]); more specifically, depending on the laser wavelength, λ, the period of the induced structures Λ may vary from (i) deep/shallow subwavelength ($\Lambda << \lambda/2$), termed as High Spatial Frequency LIPSS (HSFL) [20, 21] to (ii) subwavelength ($\lambda/2 < \Lambda < \sim\lambda$), coined as Low Spatial Frequency LIPSS (LSFL) [22, 23].

The characteristics of laser-induced periodic surface structures (ripples) are strongly dependent on the irradiated solid [20, 24]. For strongly absorbing materials such as metals or highly excited semiconductors, near wavelength-sized LSFL-I (Fig. 25.4a) are generated with an orientation perpendicular to the laser beam polarization [24–26]. Apart from the dielectric function of the material [24–26], other parameters that influence the periods of the induced structures are the energy

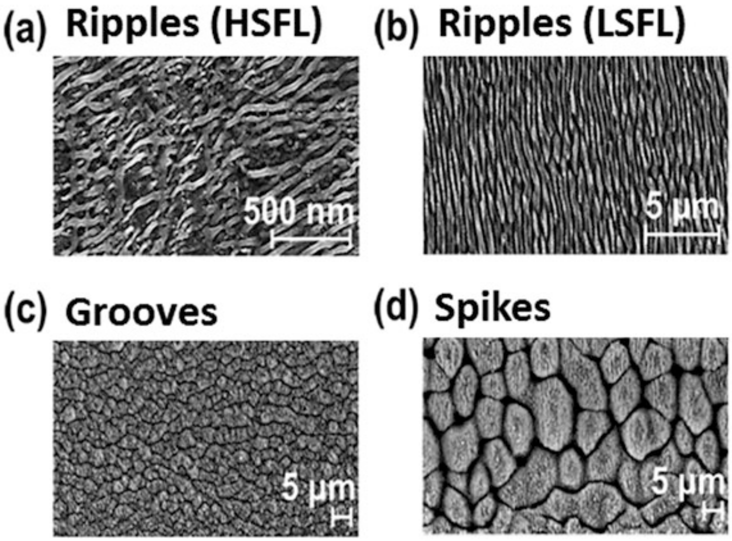

Fig. 25.3 Top-view scanning electron microscopy images of four characteristic surface morphologies observed upon femtosecond laser scan processing of a steel surface. (Reprinted with permission from Hermens et al. [14] Copyright (2016) by Elsevier)

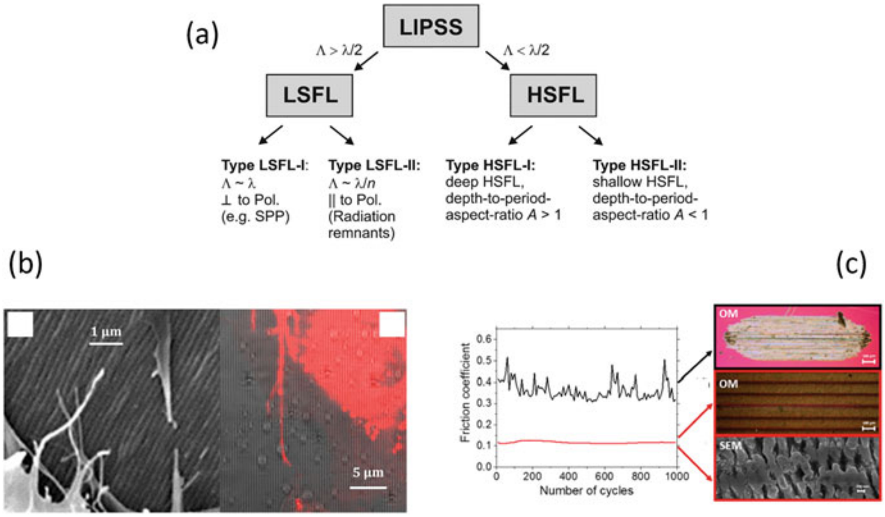
(a)
LIPSS
Λ > λ/2
Λ < λ/2
LSFL
HSFL
Type LSFL-I:
Λ ~ λ
⊥ to Pol.
(e.g. SPP)
Type LSFL-II:
Λ ~ λ/n
|| to Pol.
(Radiation remnants)
Type HSFL-I:
deep HSFL,
depth-to-period-aspect-ratio A > 1
Type HSFL-II:
shallow HSFL,
depth-to-period-aspect-ratio A < 1
(b)
1 μm
5 μm
(c)
Friction coefficient
0.0
0.1
0.2
0.3
0.4
0.5
0.6
0
200
400
600
800
1000
Number of cycles
OM
OM
SEM

Fig. 25.4 (**a**) LIPSS Classification. (Reprinted with permission from Bonse et al. [20] Copyright (2017) by IEEE), (**b**). (Reprinted with permission from Stratakis et al. [2] Copyright (2020) by Elsevier), (**c**) impact of topography on friction. (Reprinted with permission from Bonse et al. [30] Copyright (2014) by Springer Nature)

dose [22, 27], fluence [27], and surface roughness [26, 28, 29]. These structures are observed in the ablative regime for fluences up to several times above the damage threshold of the material. By contrast, at lower fluences (close to the ablation threshold), shallow HSFL-II (Fig. 25.4a) are formed [20]. A different scenario occurs for weakly absorbing materials (i.e., dielectrics). In that case, subwavelength-sized LSFL-II (Fig. 25.4a) structures are formed with an orientation parallel to the orientation of the laser beam and periodicity close to λ/n, with n being the refractive index of the material [21, 31, 32]. The corresponding HSFL-I (Fig. 25.4a) are normally oriented perpendicular to the polarization direction [21, 31]. With respect to the impact of LIPSS patterns, Fig. 25.4b, c illustrate two examples of the benefit of fabricating nano-/micro-sized topographies: (i) activation of proliferative nuclear signaling in biological cells [2] and (ii) improvement of tribological performance [30].

One very important attribute of the LSFL and HSFL structures is that their orientation is directly dependent on the polarization orientation that indicates that electromagnetic mechanisms predominantly account for the formation leading to a spatially preferential modulated energy deposition and absorption [20, 21]. With respect to the comparison of absorption in various materials and the induced structures, in highly absorbed materials of semiconductors, excitation of the solid and the interference of the incident beam with excited Surface Plasmon modes (SP) constitutes the predominant mechanism that leads to LSFL-I [24, 25, 33, 34]. By contrast, the LSFL-II represents the result of the so-called Radiation Remnants that

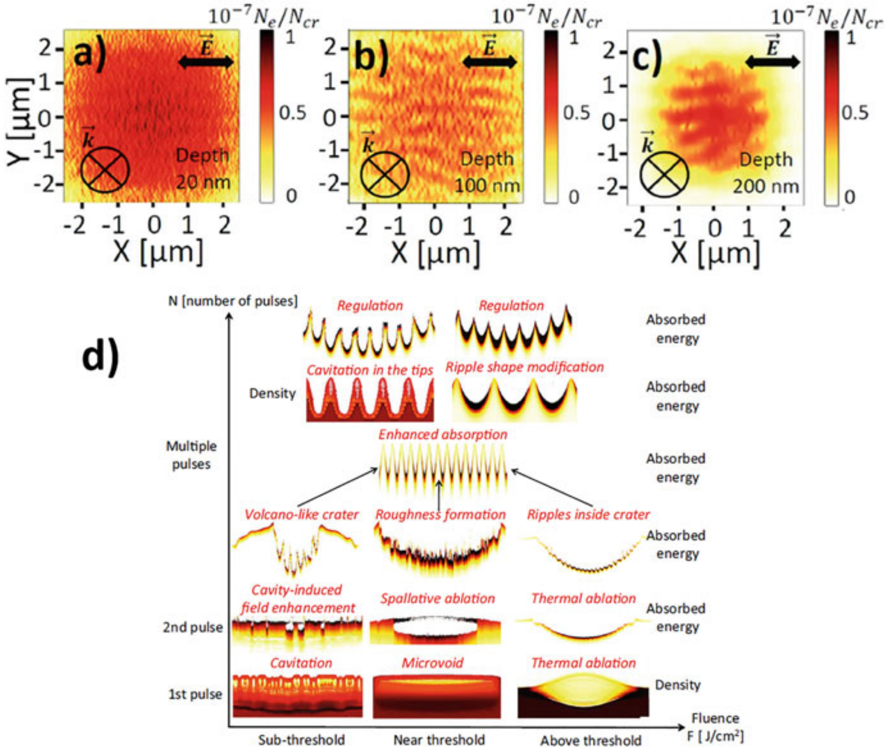

Fig. 25.5 (**a–c**) Top view of electron density distribution calculated by 3D-FDTD calculations coupled with electron density equation (for SiO2) at various depths. (Reprinted with permission from Rudenko et al. [21] under Creative Commons Attribution 4.0 International License). (**d**) Schematics of coupled electromagnetic and hydrodynamic processes upon multipulse femtosecond laser irradiation of metals as a function of laser fluence and number of applied pulses. (Reprinted with permission from Rudenko et al. [40]. Copyright (2019) by the American Physical Society)

are nonpropagating electromagnetic mode close to the rough surface that interfere with the incident beam [20, 35, 36]. Finally, the formation of HSFL is closely related to the interference of the incident beam with the radiation scattered at the rough surface [34]. Over the past years, a series of approaches attempted to unveil the role of local electromagnetic fields in the formation of both HSFL and LSFL surface structures through the employment of advanced Finite Difference Time Domain (FDTD) numerical schemes to solve Maxwell equations (Fig. 25.5a–c) [21, 34, 37–40].

On the other hand, to provide a detailed description of the interpulse effects (i.e., for repetitive irradiation), apart from electromagnetic origin of the LIPSS, a precise quantification of the induced topographies requires a multiscale analysis of the physical phenomena that take place upon irradiation of a solid with femtosecond pulses. Such phenomena comprise the precise estimation of the spatiotemporal

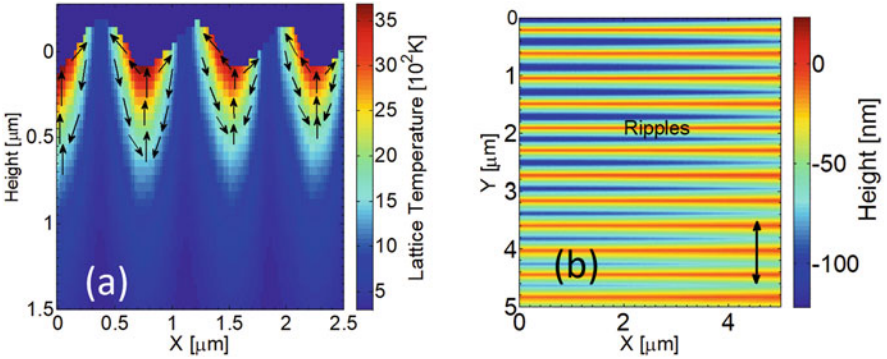

Fig. 25.6 (**a**) Simulated experiment for melt displacement (for Si). (Reprinted with permission from Tsibidis et al. [41]. Copyright (2015) by the American Physical Society). (**b**) Ripple profile. (Reprinted with permission from Tsibidis et al. [27]. Copyright (2017) by Springer Nature)

absorbed laser energy profile, the excitation of the irradiated material [42, 43], description of relaxation processes, incorporation of ablation effects [44], phase changes [45, 46], hydrodynamical movement, and resolidification in a continuous way to account for the topography response when subsequent pulses irradiate the material. Especially, various hydrodynamic models were developed to describe the evolution of the surface morphology and LIPSS formation. One approach was based on Kuramoto-Sivashinsky that assumed self-organization processes [47]; however, the underlying theoretical approach was not sufficient to correlate the laser conditions with the induced surface morphology. By contrast, more advanced models have been developed to describe the hydrothermal dynamics of incompressible Newtonian fluids through the solution of Navier-Stokes (Figs. 25.5d and 25.6) [21, 23, 27, 33, 36, 48–51]. More specifically, a sketch of the potential topographies that can be fabricated following a coupling of electrodynamic and hydrodynamic processes upon multipulse femtosecond laser irradiation of solids is illustrated in Fig. 25.5d that shows that the laser parameters (i.e., laser fluence and number of applied pulses) influence the roughness of the induced topographies. A precise investigation of the dynamics of the produced hydrothermal waves has been followed (Fig. 25.6a) [41] to describe the process toward the fabrication of LIPSS topographies (Fig. 25.6b) [27]. The arrows in Fig. 25.6a indicate the direction of movement due to processes related to surface tension and temperature gradients. The periodicity of the hydrothermal waves that is also linked with the periodicity of the produced LIPSS (Fig. 25.6b) originates from electromagnetic effects (i.e., scattered waves off corrugated surfaces or surface plasmon waves) and interference with the incident beam. Further discussion on the fundamental processes of LIPSS formation and the role of electromagnetic effects is presented in Chap. 5 (by Rudenko and Colombier).

3.2 Grooves

Other ordered surface structures (Fig. 25.3c) characterized by a supra-wavelength period ($\Lambda > \lambda$) and a preferential alignment parallel to the laser polarization typically develop at larger irradiance levels or for higher number of laser pulses [36, 41, 52, 53]. These supra-wavelength structures were not included in the previous classification of LIPSS, and they are termed as *grooves*. Grooves have been observed in semiconductors (Si, InP, etc.) [41, 52, 54] and dielectrics [36], and their formation has been predominantly attributed to hydrodynamic processes (Fig. 25.7) [36, 41, 52]. In contrast to the thermocapillary waves that are developed and lead to the formation of LSFL structures, convection rolls are produced (Fig. 25.7a) that force the molten material to move perpendicularly to the orientation of ripples (which are produced at lower fluences and smaller energy dose). A systematic analysis of the dynamics of the fluid movement indicates that stable solutions for the formation of grooves occur if these structures have periodicities larger than the laser wavelength (Fig. 25.7b) [41]. Experimental observations confirm the orientation and size of grooves (Fig. 25.7c) [41]. To evaluate the impact of topographies covered with grooves, experiments on PET have indicated that the presence of supra-wavelength structures on PET can enhance hydrophobicity (Fig. 25.7d, e) [2].

More recently, the formation of supra-wavelength structures on metals (e.g., steel) has also been reported [27]. However, the formation of these supra-wavelength

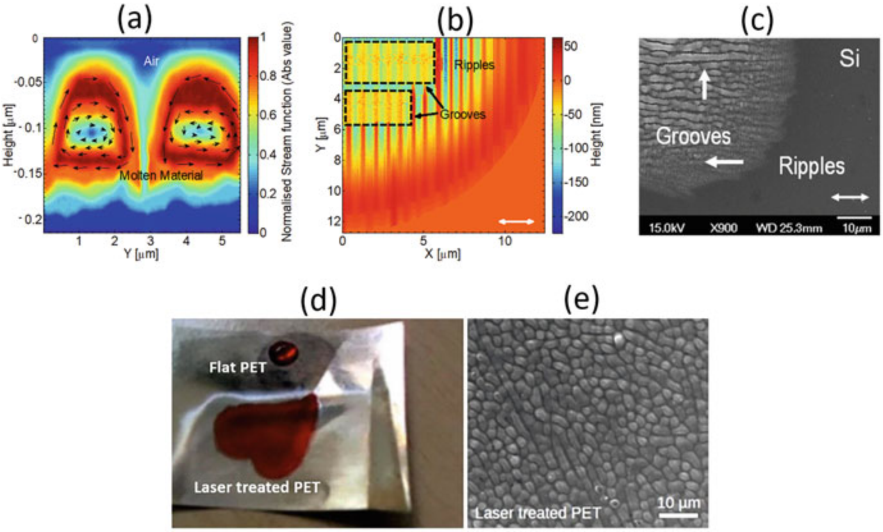

Fig. 25.7 (**a**) Convection roll and melt displacement, (**b**) simulation results for grooves and ripples, (**c**) SEM image for Si, and (**d**–**e**) wetting by laser-induced microstructures. ((**a**–**c**) was reprinted with permission from Tsibidis et al. [41]. Copyright (2015) by the American Physical Society, (**d**) and (**e**) was reprinted with permission from Stratakis et al. [2]. Copyright (2020) by Elsevier)

structures and their dependence on the various experimental parameters has yet to be investigated in all types of materials. For example, in semiconductors, the grooves period increases as a function of the number of laser pulses [41, 52], contrary to what is typically observed for ripples. This appears to indicate grooves formation might also involve further mechanisms that deserve careful investigations. A systematic analysis of the hydrothermal wave strengths that are developed as the energy dose increases is capable to account for the evolution of the periods Λ.

3.3 Spikes

Arrays of conical protrusions (spikes) have been reported (see [2] and references therein) when surfaces are repeatedly irradiated with high-fluence femtosecond laser pulses. In regard to the formation of biomimetic spikelike protrusions, various strategies have been proposed. The most straightforward relies on a line-wise movement of a focused laser beam across the surface at a certain velocity achieving an effective number of pulses per beam spot diameter [14], while a different approach assumes the employment of high repetition rate lasers [55]. On the other hand, Zuhlke et al. [56] presented two distinct spike formation scenarios through below (or above) surface growth (BSG or ASG) (Fig. 25.8a, b). While the BSG scenario is predominantly caused by electromagnetic scattering/absorption effects, the ASG scenario is generally explained by the formation of thermocapillary effects and the development of hydrodynamic melt-flow. In regard to potential use of spike-covered topographies on artificial materials, it has been deduced (Fig. 25.8c–f) that the proliferation behavior of individual cell populations is affected by the size and density of spikes on a patterned surface [57]. This suggests that such patterns could be used to optimize implant materials and especially their surfaces aiming to improve properties such as antibacterial efficacy, wound healing, or accelerated tissue formation.

Simulations have been performed to explain the spike formation on semiconductors [41]. It has been shown that at high fluences, a combination of ablative and hydrothermal effects accounts for the excitation of capillary waves that lead to the formation of such protrusions (Fig. 25.9a), which are validated from experimental data (Fig. 25.9b) [41]. According to current state-of-the-art theoretical models, the topography that has been produced at lower fluences or number of pulses is an essential ingredient to force molten material to form protrusions [41]. Nevertheless, given the significance of topography coverage with spikelike structures to the demonstration of impressive biomimetic functionalities, more fundamental research is required to elucidate in more detail the underlying physical mechanisms of the formation of these structures.

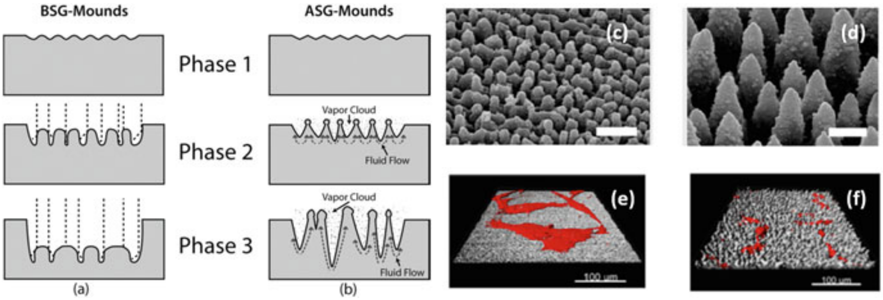

Fig. 25.8 Scheme of the formation of spikes through BSG (**a**) or ASG (**b**). (Reprinted with permission from Zhulke et al. [56]. Copyright (2013) by Optical Society of America). (**c**–**f**) Spike impact on the cell proliferation (reprinted with permission from Schaeske et al. [57]. Copyright (2020) by MDPI)

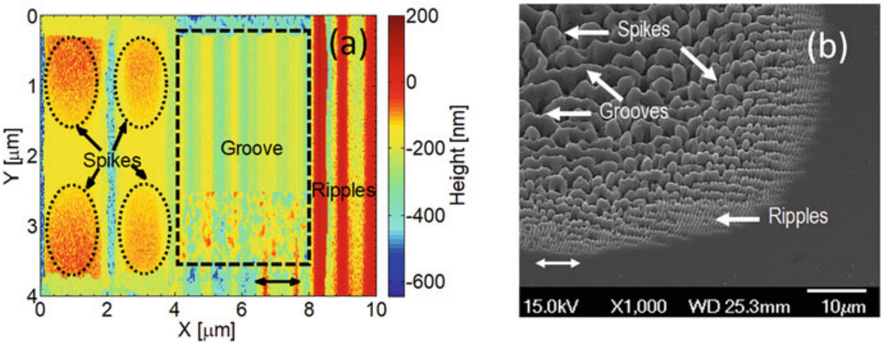

Fig. 25.9 Spikes, grooves, and rippled formed on silicon: (**a**) simulated results and (**b**) SEM image. (Reprinted with permission from Tsibidis et al. [41]. Copyright (2015) by the American Physical Society)

3.4 Complex Patterns Closer to Biomimetic Features

Ultrafast laser processing has been turned out to constitute a valuable and efficient method toward the realization of biomimetic surfaces that can mimic both the surface topographies and functional characteristics of species found in nature. The topographies that have been presented in the previous sections have, in principle, been fabricated through the employment of linearly polarized beams of Gaussian intensity spatial profiles. To enhance the complexity of the fabricated structures, various schemes have been developed: (i) use of radially or azimuthally polarized beams to produce more complex topographies (Fig. 25.10a) (i.e., leading to contact angle variation with increased roughness (Fig.25.10b)) [58], (ii) modulation of the interplay between pulse delays in double pulse experiments (Fig. 25.10c) (i.e., exhibiting enhanced iridescence (Fig. 25.10d) that is a property that can be used for holographic or counterfeit applications) [59], and (iii) the employment of circularly

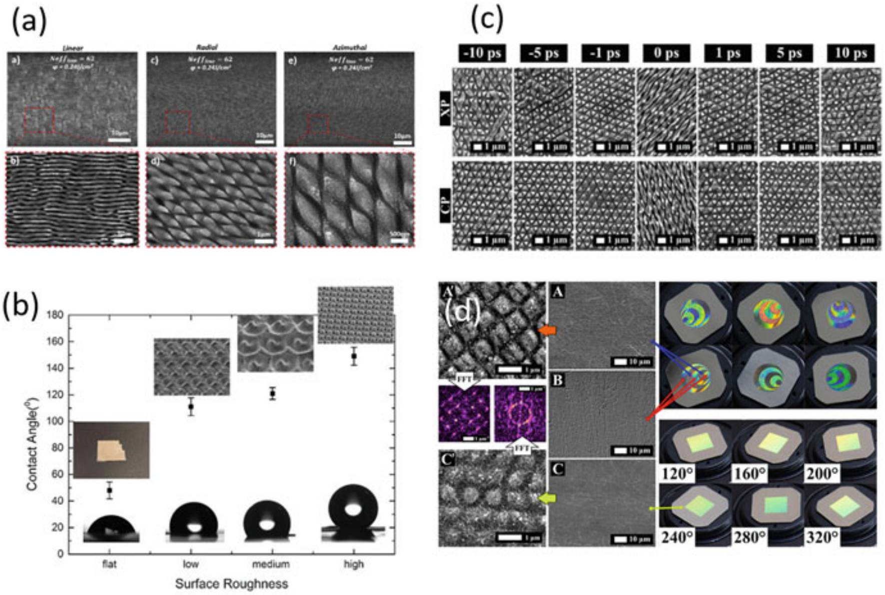

Fig. 25.10 (**a**) SEM images of nickel depicting line scans produced with linearly, radially, azimuthally polarized femtosecond beams and (**b**) contact angle variation as a function of the surface roughness and the type of the induced topography ((**a**, **b**) are reprinted with permission from Skoulas et al. [58] under Creative Commons Attribution 4.0 International License). (**c**) Top view of topographies on stainless steel attained in double pulse experiments for various pulse separation values and polarization states (XP and CP stand for double linearly and counter-rotating circularly polarized beams, respectively) and (**d**) holographic applications ((**c**, **d**) are reprinted with permission from Fraggelakis et al. [59] Copyright (2018) by Elsevier)

polarized beams that led to the fabrication of randomly distributed nanopillar-like morphologies that mimic the cicada wings and lead to impressive antireflective properties (Fig. 25.11) [9].

3.5 Direct Laser Interference Patterning

3.5.1 Fundamentals of DLIP-Based Nanostructuring

Direct Laser Interference Patterning (DLIP) constitutes an alternative and high-resolution method for producing micro-/nanoscale large area surface structures on metallic, semiconducting, and polymeric targets. In contrast to previous methodologies, this technique is based on the fabrication of a periodic interference pattern through the employment of a series of overlapping coherent beams (Fig. 25.12) [4, 60–62]. Further discussion on DLIP is presented in Chap. 14 (by Ihlemann et al.) and Chap. 26 (by Lasagni et al.). As mentioned in the previous sections, a

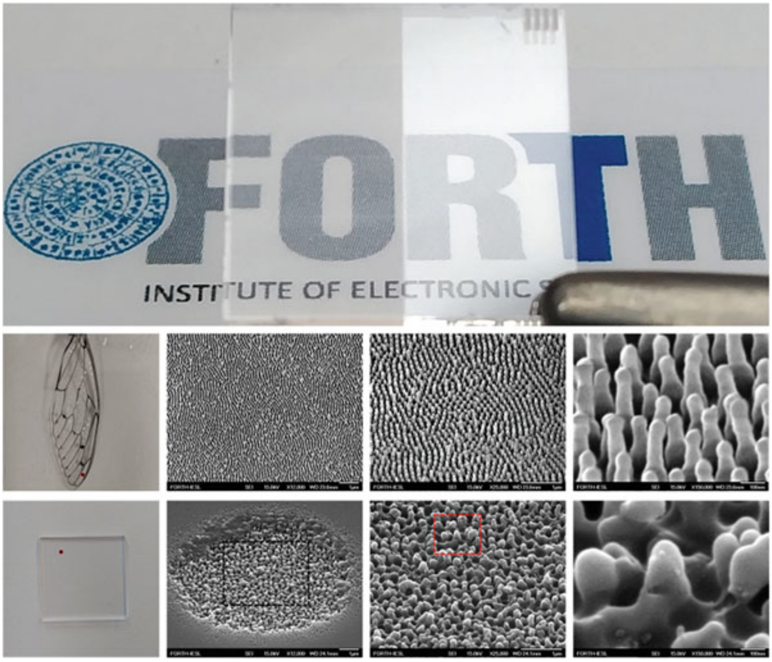

Fig. 25.11 First row: Antireflective properties of treated glass. Second row: Cicada wing and wing surface pattern. Third row: Impact of nanopillar-like morphologies on fused silica with circularly polarized beams. (Reprinted with permission from Papadopoulos et al. [9] Copyright (2019) by Wiley)

crucial parameter that plays an important role in the induced topography features is the energy deposition, and therefore, complex irradiation schemes and intensity profiles are expected to influence to a great extent the spatial profile of the absorbed energy. As a result, the use of interfering beams could provide a solution toward this direction.

DLIP is based on the superposition of the electric field vectors of coherent beams. The electric field of a light wave n is equal to $\vec{E}_n = A_n \vec{p}_n e^{i\left(\omega t - \vec{k}_n \cdot \vec{r}\right)}$ where A_n is the amplitude, $\vec{p}_n$ is the polarization vector, $\vec{k}_n$ (i.e., $\left|\vec{k}_n\right| \equiv k = \frac{2\pi}{\lambda}$) stands for the wavevector, $\vec{r}$ is the position vector, and ω is the angular frequency. It is noted that the resulting interference pattern for N beams is calculated through the expression $\vec{E}_{\text{total}} = \sum_{n=1}^{N} \vec{E}_n$. Each laser beam irradiates the material at an incident angle with the vertical axis equal to θ_n and azimuthal angle φ_n. It is assumed that all laser beams are linearly polarized, and the polarization direction is the same for all DLIP beams. The total spatial intensity distribution is, then,

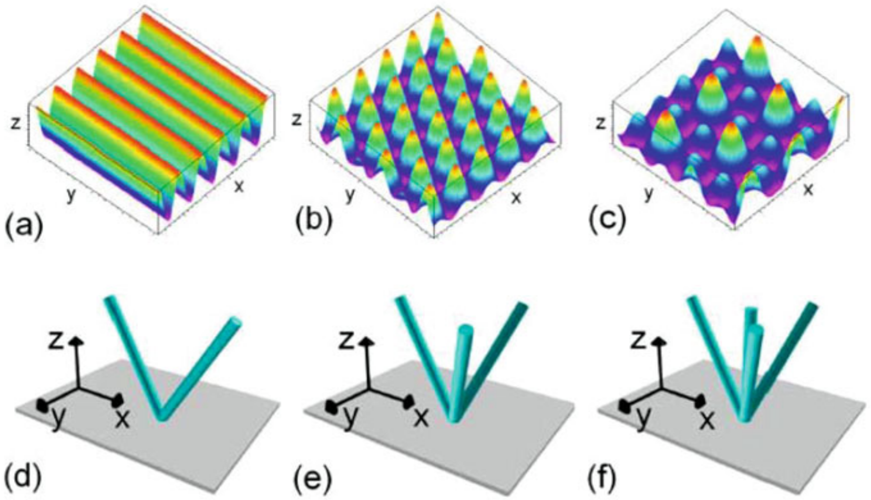

Fig. 25.12 Calculated intensity distribution for two- (**a**), three- (**b**), and four (**c**)-beam interference; (**d–f**) correspond to the respective beam configurations. (Reprinted with permission from Rosenkranz et al. [62]. Copyright (2016) by MDPI)

provided by the formula $I_0 = c\,\varepsilon_0 \left|\vec{E}_{\text{total}}\right|^2/2$, where c and ε_0 stand for the speed of light and dielectric vacuum permittivity, respectively. For interference with *two* ($\varphi_1 = \varphi_2 = 0$, and $\theta_1 = \theta_2 = \theta$) and *four* beams ($\varphi_1 = \varphi_2 = 0$, $\varphi_3 = \varphi_4 = \pi/2$, $\theta_1 = \theta_2 = \theta_3 = \theta_4 = \theta$), the following total intensities are $I_0^{(2)}$and $I_0^{(4)}$ on the surface of the material, respectively,

$$\begin{aligned} I_0^{(2)} &\sim I_1\,[1 + \cos(2kx\sin\theta)] \\ I_0^{(4)} &\sim I_1\left\{\left[1 + \frac{1}{2}\cos(2kx\sin\theta) + \frac{1}{2}\cos(2ky\sin\theta) + 2\cos(kx\sin\theta)\cos(ky\sin\theta)\right]\right\} \end{aligned} \tag{25.1}$$

where I_1 is the intensity of each of the constituent laser beams of the DLIP in which a Gaussian envelope is included ($\sim e^{-2\left(\frac{x^2+y^2}{w_0^2}\right)}$) with a 1/e^2 Gaussian spot radius equal to w_0. A Cartesian coordinate system is used (x,y,z). It is evident that the choice of θ_n can be used to define the periodicities of the interference pattern. More specifically, for two-beam DLIP, a sinusoidal of periodicity equals to $\Lambda_{\text{DLIP}} = \frac{\lambda}{(2\sin\theta)}$ along x-axis, or for a four-beam DLIP, a dot-type intensity distribution of periodicity equals to $\Lambda_{\text{DLIP}} = \frac{\lambda}{(\sin\theta)}$ along x-axis and y-axis and a secondary $\Lambda_{\text{DLIP}} = \frac{1}{\sqrt{2}}\frac{\lambda}{(\sin\theta)}$along the direction defined by $\hat{x} + \hat{y}$ ($\hat{x}$, $\hat{y}$ are unit vectors).

As a result, the production of a predefined surface topography can be tailored by the angle of incidence of the constituent beams [4]. These aspects have showed that DLIP is capable to offer great flexibility in the production of complex hierarchical functional structures for potential applications [62–65].

Nevertheless, despite the extensive research that has been conducted toward investigating the surface patterns textured with DLIP, a detailed analysis of the underlying physical mechanisms that account for the structure formation is generally unexplored [4, 60–67]. In a recent study [66], a thermal model has been introduced to calculate the thermal response of metallic materials following irradiation of a flat surface with a *single* DLIP pulse. It is known that the generation of sub-micrometer periodic structures as a result of irradiation with laser femtosecond pulses requires exposure to subsequent many pulses (see [2] and references therein); thus, an accurate model needs to take into account the influence of a varying corrugation on the energy absorption and therefore the role of interpulse morphological changes [23, 32].

On the other hand, a consistent approach of the description of the physical mechanisms that leads to surface patterning can only be derived through a consistent multiscale approach that efficiently incorporates all physical processes related to energy absorption, mass removal (i.e., ablation), phase change, fluid hydrodynamic movement, and resolidification mechanisms. Experimental evidence has also demonstrated the crucial role of the microfluidic motion on 2D-LIPSS formation [59]. As surface texturing is a multipulse process, the fundamentals of the formation of the various structures require a thorough knowledge of both intra- and interpulse physical effects [23, 36] as well as a precise evaluation of the absorbed laser energy to accurately describe the generation of laser-induced structures.

In a recent study [4], an experimental and theoretical approach has been presented to illustrate the plethora of the underlying complex physical processes. Special emphasis has been focused on the description of (i) the energy absorption of a liquid material assuming a dynamical change of the optical parameters [69, 70], (ii) electron excitation and dynamics, (iii) mass removal, and (iv) hydrodynamical phenomena that determine the surface topography following a multipulse process. This investigation attempted to shed light on the crucial contribution of hydrodynamical phenomena (Fig. 25.13) to DLIP-assisted pattern formation (Fig. 25.14) that has been proposed in previous reports [60]. In regard to potential use of topographies on artificial materials produced with DLIP technologies, it has been deduced (Fig. 25.15) that cell growth/migration is promoted in every direction on unstructured topographies (Fig. 25.15a). By contrast, patterned topographies hint at a cell migration in directions parallel to the patterned surface (Fig. 25.15b) [68]. Furthermore, it has been shown (see discussion in the next section) that a combination of DLIP and double pulses can lead to more complex topographies that resemble natural topographies.

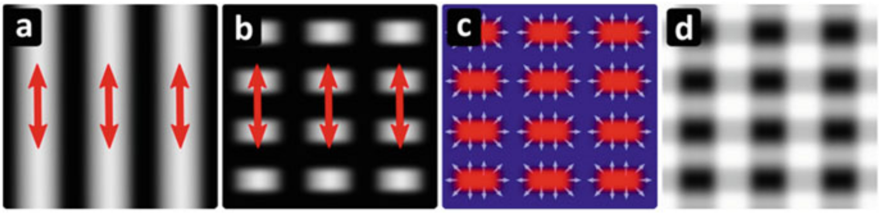

Fig. 25.13 Simultaneous formation of LIPSS and DLIP structures. (**a**) DLIP pattern on the surface. (**b**) Absorbed light intensity on the surface through SPP excitation. (**c**) Hot (red) and cold (blue) areas resulting from absorption of light intensity pattern shown in (**b**). Material flow is represented by white arrows. (**d**) Surface relief resulting from the movement in (**c**). (Reprinted with permission from Alamri et al. [60] Copyright (2019) by MDPI)

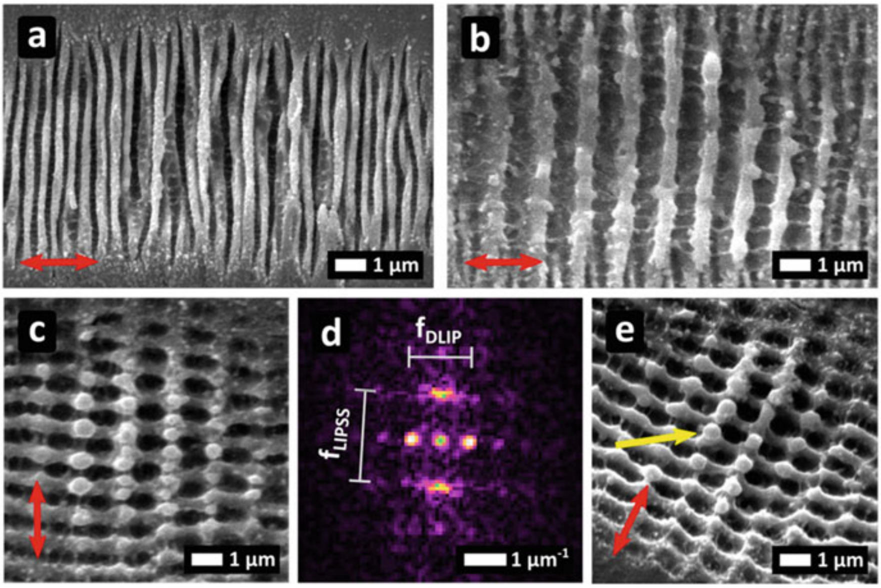

Fig. 25.14 Stainless steel substrates-irradiated fs DLIP pulses at various fluences (**a**), (**b**), (**d**), (**e**). (**c**) is FFT of (**c**). Red double-headed arrow indicates the laser polarization. Yellow arrow shows a protrusion. (Reprinted with permission from Alamri et al. [60]. Copyright (2019) by MDPI)

3.5.2 Control of Pattern Complexity via DLIP and Double Pulses

One aspect that is of paramount importance both from a fundamental and application point of view is the combined action of DLIP and Double Pulse (DP) irradiation. In a number of reports, temporally shaped femtosecond laser pulses have been employed to control thermal effects and improve micro-/nanoscale material processing. It was shown that DP methodology can be used to tailor the surface pattern features by controlling heat localization [71, 72]. Certainly, an interesting issue is whether a combined action of a DLIP and DP technique could present

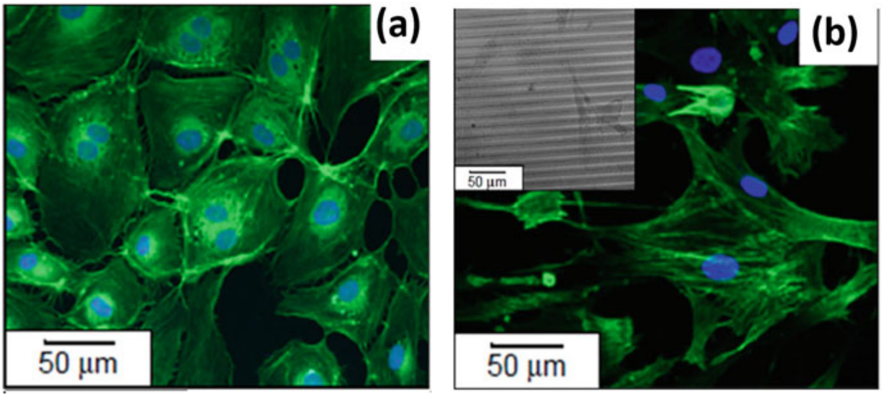

Fig. 25.15 Cell migration on unstructured (**a**) or patterned with DLIP technology (**b**) surface (inset in (**b**) shows the shape of the pattern). (Reprinted with permission from Marczak et al. [68]. Copyright (2014) by Optica Applicata under CC-BY 4.0)

a novel methodology toward controlling further the ultrafast processes that lead to surface patterning. More specifically, in a complementary way, DLIP could be employed to set the initial conditions of the structure formation process while the DP could allow a control over the evolution of the microfluidic surface reorganization. To account for the capability to intervene in the material reorganization process, a detailed description of the fundamental mechanisms that determine the surface topography has recently been investigated [4, 5]. To this end, both single (SP) and temporally delayed DLIP double pulses (DP) are used (Figs. 25.16 and 25.17) to estimate the influence of different absorption and excitation levels when the second of the DP irradiates a material in molten phase. Thus, appropriately, large temporal separation (~500 ps) has been used to ensure molten material is irradiated while excitation level is substantially low at the time the second pulse heats the material. To illustrate the role of the periodicities of the interference patterns on the surface features (i.e., frequencies of induced structures, height, ablated depth, complexity of sub-micrometer periodic structures, etc.), a DLIP technique with variable induced periodicity Λ_{LIPSS} is used while a multiscale model is presented that incorporates the influence of electrodynamical effects (i.e., excitation of Surface Plasmon Polaritons, SPP) on the formation of the surface topography. According to the results of the investigation, distinctly different morphologies are attained assuming two- or four-beam DLIP (Fig. 25.17). In another study [5], a similar investigation indicated that combining Gaussian beams with DLIP in double-pulse trains enables the generation of unique submicron surface topographies with increased complexity. Results showed that the order of the Gaussian and DLIP pulses in train sequences influences the final surface profile attained (Fig. 25.18) (in the first column, G stands for the Gaussian beam while $H(V)$ stand for DLIP beams leading to horizontally (vertically) oriented periodic intensity profile; the superscripts-double-headed arrows correspond to the polarization of each beam)

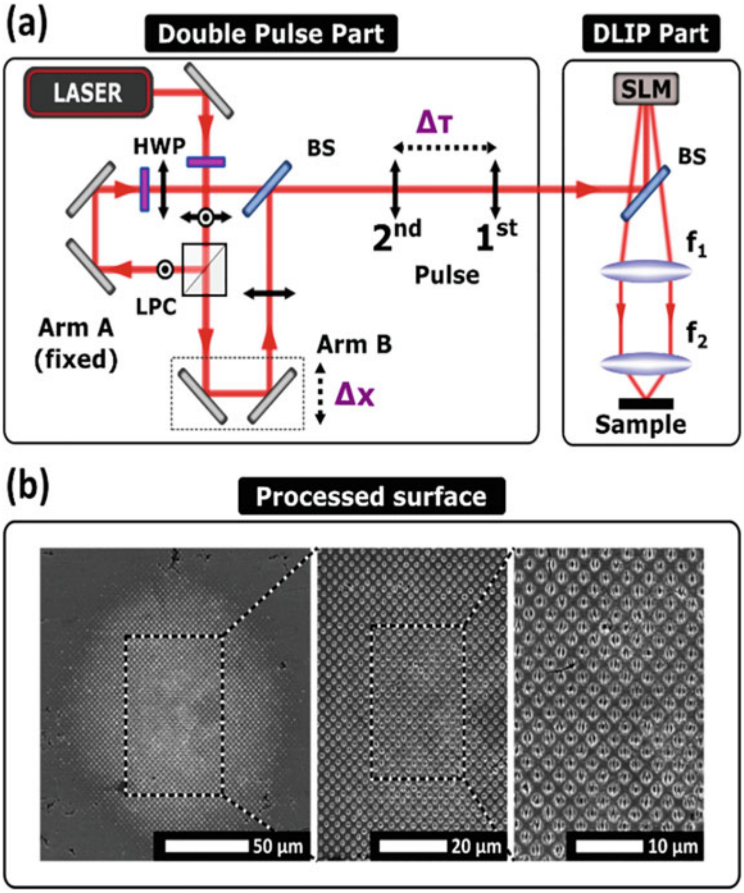
(a)
Double Pulse Part
DLIP Part
LASER
HWP
BS
ΔT
2nd
1st
Pulse
LPC
Arm A
(fixed)
Arm B
Δx
SLM
BS
f1
f2
Sample
(b)
Processed surface
50 μm
20 μm
10 μm

Fig. 25.16 (**a**) Experimental setup of combined DLIP and DP. (**b**) Surface processed with four beams with $\theta_n = 19 \pm 0.5\,^\circ$, NP = 50, and 42 μJ. (Reprinted with permission from Fraggelakis et al. [4]. Copyright (2021) by the American Physical Society)

[5]. Furthermore, experimental results and multiscale modelling revealed that both the spatial intensity of the two pulses, as well as hydrodynamical effects, have a significant impact on the pattern features (first and fifth columns in Fig. 25.18 show the experimental and simulations results). Results emphasized the capability to actively tailor the microfluidic melt motion that dominates the structure formation process, via controlling the applied temperature gradient's temporal profile (third and fourth column in Fig. 25.18). More importantly, the unique irradiation schemes discussed, here, lead to the generation of novel complex morphologies comprising features in multiple length scales (first column in Fig. 25.18). This demonstrates an unparalleled capacity toward tailoring laser-induced morphology and obtaining complex topographies for a variety of applications. Thus, DLIP technology offers a

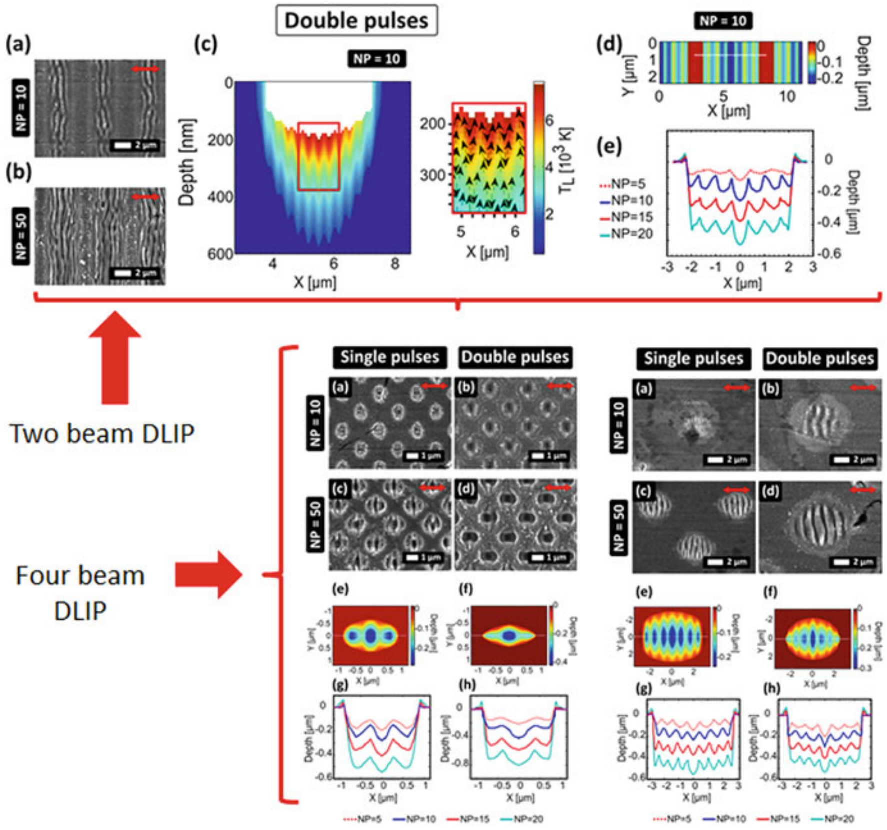

Fig. 25.17 LIPSS formation following irradiation with single and DP DLIP. (Reprinted with permission from Fraggelakis et al. [4]. Copyright (2021) by the American Physical Society)

unique capacity to fabricate patterns of a plethora of length scales and features as seen in nature (Fig. 25.18).

4 Tailoring the Nanostructuring Process Through Advanced Predictive Tools

The theoretical approaches that are usually followed in laser processing are based on materials modelling and investigation of the underlying physical mechanisms of laser-matter interaction. They have been a powerful tool that provides key information for tailoring the surface or structural topographies of materials. They are aimed to constitute a cost-effective method that allows the minimization of the use of trial-and-error schemes aiming to reduce the need for an increasing number

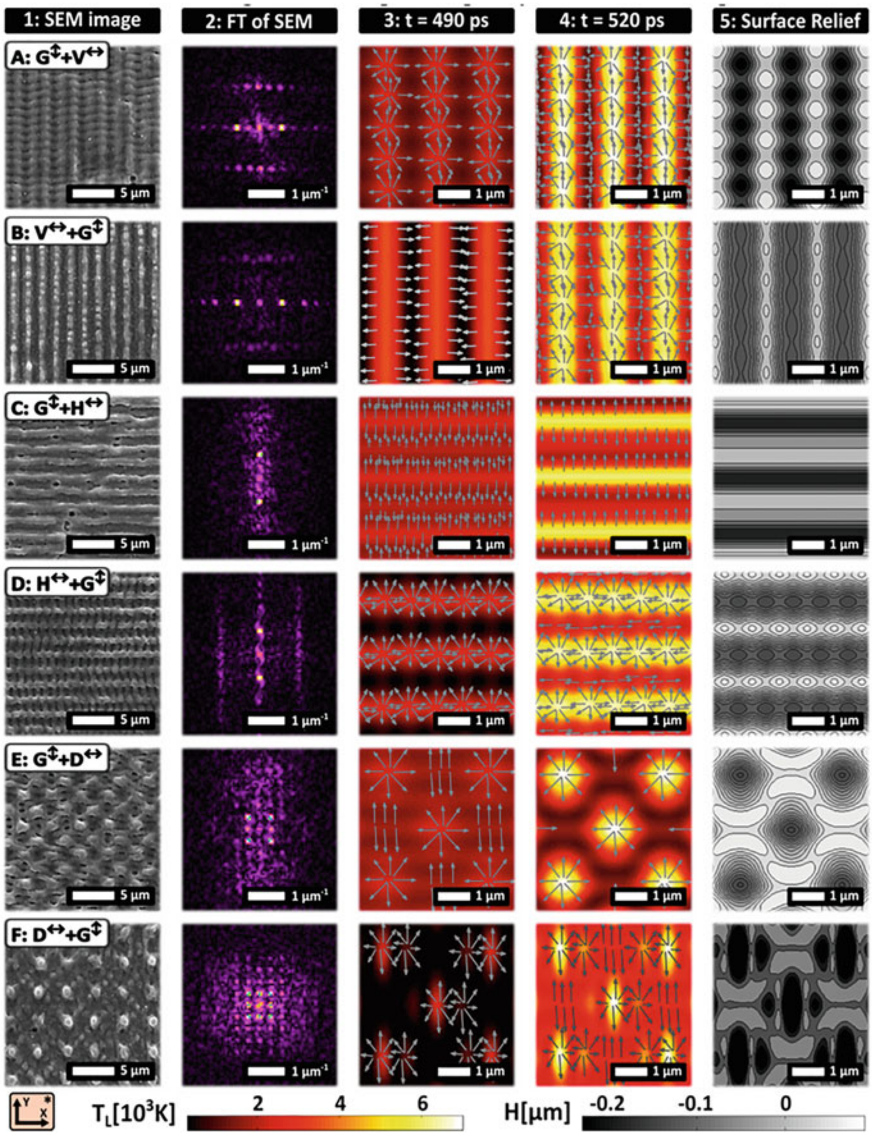

Fig. 25.18 SEM images of the double pulse irradiation schemes used (1st column) together with the respective FFT analysis (2nd column) and simulation results (columns 3–5). The pulse profile and the order are indicated in the legends of the 1st column, while the superscript arrows indicate the pulse polarization in each case. The total energy of the double-pulse pair is 80 µJ/pulse and NP = 50 pulses. Simulation results are shown in each case, just before (3rd column, $\Delta\tau = 490$ ps) and right after (4th column, $\Delta\tau = 520$ ps) the arrival of the second pulse. The final morphology predicted by the simulation experiment is shown in the 5th column (contour plots to illustrate the height). The arrows in the 3rd and 4th column provide a guide to eye representation of the fluid transport direction. The color bars at the bottom of the figure provide the temperature (3rd and 4th columns) and height (5th column) values range. (Reprinted with permission from Fraggelakis et al. [5])

of experiments. In principle, the employment of materials modelling is especially versatile, and it can offer a solution toward controlling the output procedure through a systematic exploration of the usually complex physical processes that occur during the manufacturing processes [20, 23, 41, 42, 73, 74]. Nevertheless, despite the significance originated from the use of materials modelling, the complexities due to the need of a large number of simulated experiments in which multiscale physical models are involved downgrade the benefit of the methodology as it leads to slow decision-making. Furthermore, the manifold of the set of laser parameter values that should be spanned to derive a database of feature characteristics is usually very large that eventually requires vast execution times even at very powerful computer systems. More specifically, laser conditions that can be tailored to produce site-specific topographies can include parameters such as the laser energy, wavelength, polarization, pulse duration (or pulse separation in train of pulses), energy dose, material type, angle of incidence, etc. Due to the increased complexity, data-driven strategies can be proposed as a solution to correlate feature characteristics and manufacturing process parameters in a more efficient way. To this end, more advanced predictive modelling schemes have started to be developed and used that are based on artificial intelligence algorithms. Predictive modelling represents an emerging field that combines existing and novel methodologies aimed to rapidly understand physical mechanisms and concurrently develop new materials, processes, and structures.

An abundance of predictive modelling approaches based on machine learning (ML) techniques have been used for material processing. In Raccuglia et al. [75], a ML model datasets of “failed” experiments were used to train the algorithms to predict reaction outcomes for the crystallization of templated vanadium selenites. In another study, laser-based manufacturing was facilitated with the employment of ML schemes to improve geometric accuracy of the fabricated parts [76]. On the other hand, an increase in the accuracy and the need for prediction of distortion quantification in the fabricated materials were further facilitated with the employment of a deep learning approach. Furthermore, big-data analysis strategies were developed by Tani and Kobayashi [77] to describe the impact of the surface topography on the laser ablation process. In another work, neural network-based approaches were used (Mills et al. [78, 79]) to explore the morphology features of an induced 3D surface profile of a substrate after being laser fabricated with a single laser pulse, for random laser spatially shaped intensity profiles. On the other hand, Agrawal et al. [80] predicted the fatigue strength of steels. Both physics-based and data-driven approaches were used to correlate properties of alloys and manufacturing process parameters.

Inspired by the above studies and challenges, a complementary laser manufacturing processing and discovery with data-driven analysis was recently proposed to describe LIPSS formation on solids [81]. Certainly, experimental measurements and simulation results constitute a valuable collection of information, which remains mostly unexploited when the response of a solid to intense irradiation schemes are investigated. Predictive modelling through the utilization of statistical and machine learning models offers an efficient approach to encode the accumulated experience and knowledge from previous experiments into a mathematical model and, subsequently, be able to extrapolate into unexplored conditions. Thus, ML models can be used to function as trainable parametric models that aim to perform a learning task such as classification or regression [82]. As a result, ML models can be regarded as a function or a mapping that transforms the input to an output. In order to accurately learn the mapping between the input variables (e.g., laser fabrication conditions) and the output property (e.g., the observed material structure as labeled by the experts), an optimization procedure can be defined and followed. In Ref. [81], various simple ML models were used that were trained and evaluated on three materials (silicon, titanium alloy, and stainless steel) for which both simulated end experimental results (Figs. 25.19 and 25.20) are available for various types of structures fabricated with the use of femtosecond pulses (i.e., ripples, grooves, spikes). Performance results indicate that simpler predictive models with a curated and well-educated preprocessing step enjoyed the highest accuracy (Fig. 25.20) (in Ref. [81], the ML-related terminology and a detailed procedure of the analysis are presented). Certainly, the amount of training data is a crucial factor that needs to be determined in order to allow an efficient feature classification through an automated procedure. In a second stage, the experimental data are augmented with simulation data extracted from multiscale modelling on the physical processes originated from the laser-material interaction. This approach further enabled the study of the effect of sample size on predictive performance, upon retraining the ML models. The study indicates that the use of a larger sample size, especially, at or close to the transition boundaries, significantly benefits the predictive models' accuracy (Fig. 25.21).

Finally, quantification of the uncertainty regions was proposed, where the predictive models are not certain about the outcome (Fig. 25.22) [81]. Since the studied ML models generate a probability distribution of the structures for each sample, uncertainty quantification is calculated using the so-called information entropy function [83]. The inverse of the information entropy can be used to correlate with a measure of certainty indicator. A detailed description of the steps followed to train the predictive modelling algorithm with a set of experimental and simulated data and the efficiency of the various machine learning algorithms is presented in Ref. [81]. Therefore, departing from the traditional selection of optimal input laser parameters for a given output, usually performed manually through an expensive trial-error method, ML techniques can be implemented to calibrate laser parameters in a more automatic, faster, and easier fashion than the existing practices. Results for two laser parameters (i.e., fluence and number of pulses [81]) demonstrated that the ML forecasting model exhibits very good accuracy and capability toward predicting the occurrence of all three types of self-assembled structures efficiently. The approach achieved a successful quantification of the uncertainty of each region related to particular structures and each material while automatically estimated the most uncertain points. A future extension to the model could be related to a fully automated process of structure-type identification through image processing tools and structure labeling to efficiently explore the parameter space. There is no doubt that the approach requires further validation and possibly more development. However, the aforementioned results show that the predictive design and ML-based

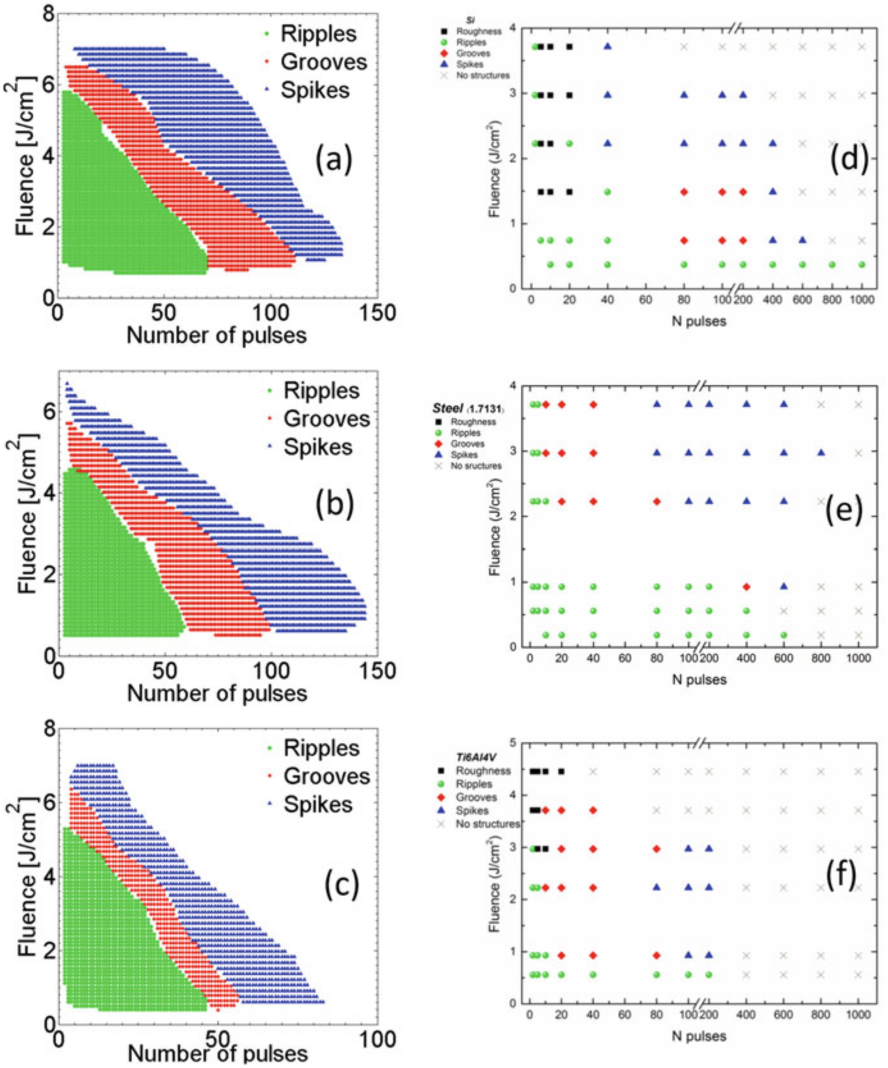

Fig. 25.19 LIPSS structures at various fluence and energy dose values for three materials (silicon: first row, (**a**) and (**d**) steel: second row, (**b**) and (**e**) titanium: third row (**c**) and (**f**)). Classification has been performed through physical modelling (left column) (**a**), (**b**) and (**c**) or analysis of experimental data (right column) (**d**), (**e**) and (**f**). (Reprinted with permission from Velli et al. [81]. Copyright (2020) by American Institute of Physics)

methodologies are expected to transform surface patterning techniques by making it more data-driven while providing routes for optimization of low-cost fabrication of products with desired properties.

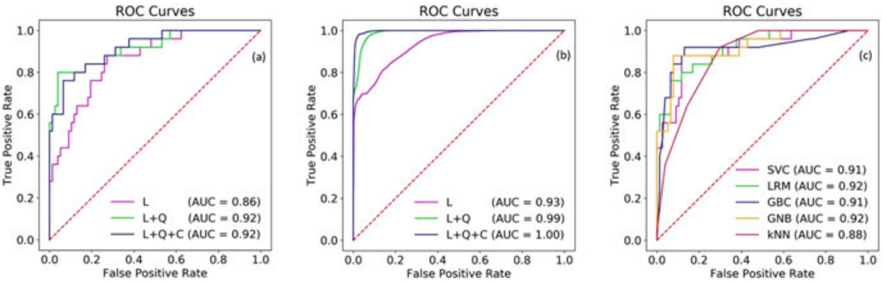

Fig. 25.20 Performance assessment models on constructed features for experimental data (**a**), simulated data (**b**), and predictive models on experimental data (**c**). (Reprinted with permission from Velli et al. [81]. Copyright (2020) by American Institute of Physics). Results are for silicon

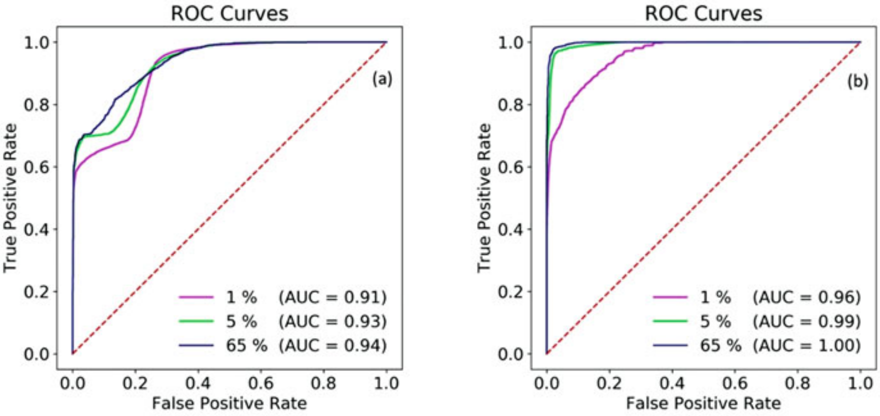

Fig. 25.21 Performance assessment models assuming the effect of sample size and linear regression model (**a**) linear features and (**b**) linear + cubic + quadratic features. (Reprinted with permission from Velli et al. [81]. Copyright (2020) by American Institute of Physics). Results are for silicon

5 Applications of Biomimetic Nanostructures

The various self-organized or biomimetic structures discussed in the previous sections can be fabricated in most types of materials such as metals, dielectrics, semiconductors, and polymers, which unveils the universality of the fabrication technique. On the other hand, depending on the laser conditions and experimental setups, the level of complexity of the fabricated topographies that can be reached makes the patterns as ideal candidates for usage in a wide range of technological applications. Figure 25.23 shows an overview of identified scientific and industrial applications of a plethora of biomimetic structures. In a recent paper [2], a vast list of published works that review the state-of-the-art and specific applicability of particular biomimetic patterns in each field is presented. Notably, the number

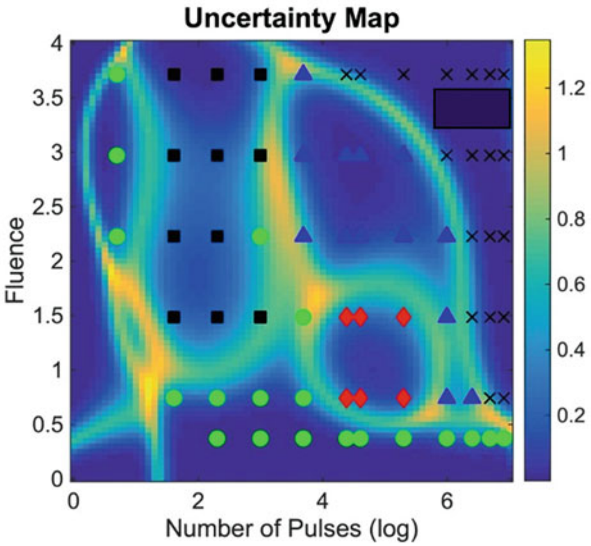

Fig. 25.22 Uncertainty quantification using multinomial logistic regression as predictive model. The annotation of the surface structures (e.g., dots, squares, crosses, etc.) in the above figure is the same as in Fig. 25.19d. Linear, quadratic, and cubic features are employed as input in the multinomial logistic regression model. (Reprinted with permission from Velli et al. [81]. Copyright (2020) by American Institute of Physics). Results are for silicon

of potential of applications continues to grow with the continuous research on the techniques to increase the complexity and functionality of the topographies. Further discussion on applications of biomimetic structures is presented in Chap. 23 (by Mezera et al.).

Certainly, the biomimetic structural features (i.e., type, periodicity, density, geometric characteristics) of the topographies fabricated with laser techniques are related to the aimed functionality of the processed material (i.e., antireflection, water repellency, corrosion resistance, iridescence, anti-icing, bactericidal, fog collection, directed fluid transport, hydrophobicity, hydrophilicity, friction reduction, antifouling, etc.). Therefore, depending on the functionality, ripples of periodicities between ~100 nm and ~1 μm, spikes, and pillar-like structures of the size of some micrometers and some hundreds of nanometers, respectively, have been fabricated on various artificial materials (see a more detailed description in Table 1 in Ref. [2]) while more complex, hierarchical, topographies have also been produced. As precision constitutes a crucial parameter in the fabrication condition, it is evident that apart from the need to develop advanced modelling schemes to describe laser matter interaction and patterning processes, data-driven strategies (see Sect. 4) represent a powerful tool to produce topographies with desired features.

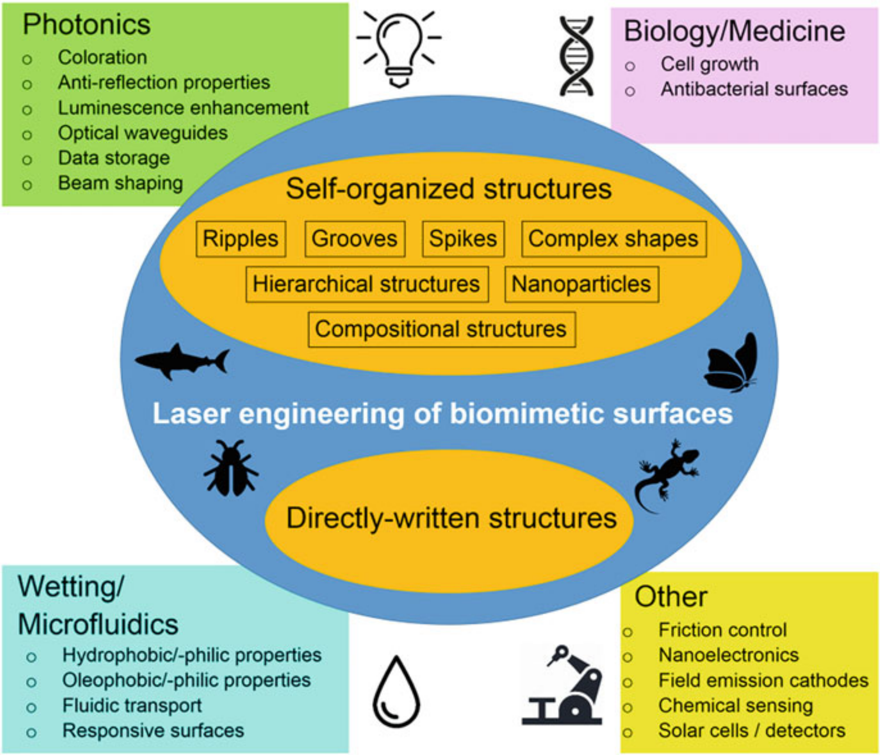
Photonics
Coloration
Anti-reflection properties
Luminescence enhancement
Optical waveguides
Data storage
Beam shaping
Biology/Medicine
Cell growth
Antibacterial surfaces
Self-organized structures
Ripples
Grooves
Spikes
Complex shapes
Hierarchical structures
Nanoparticles
Compositional structures
Laser engineering of biomimetic surfaces
Directly-written structures
Wetting/ Microfluidics
Hydrophobic/-philic properties
Oleophobic/-philic properties
Fluidic transport
Responsive surfaces
Other
Friction control
Nanoelectronics
Field emission cathodes
Chemical sensing
Solar cells / detectors

Fig. 25.23 Overview of different applications of laser-fabricated biomimetic surfaces. (Reprinted with permission from Stratakis et al. [2]. Copyright (2020) by Elsevier)

6 Conclusions-Outlook

The exciting properties of nano/micro nanopatterned surfaces on biological species found in nature, the principal approaches toward transferring this knowledge to artificial materials, and some representative current and potential applications have been reviewed. The features of the surfaces of the biological species that have been developed in an evolutionary way to adapt the functionalities to environmental changes presented a virtual endless potential of technological ideas for the improvement of material performance or design of new materials. Thus, learning from the extraordinary properties originating from the characteristics of the surface topographies provides inspiration and opens new trends for innovation for a variety of technological applications.

Laser systems present unique capabilities for precise large-scale and high-throughput precise fabrication. On the other hand, improvement in the structuring resolution to scales down to lower than 100 nm and the minimization of thermal damage effects are provided with the employment of advanced femtosecond laser sources. In particular, a standing question in regard to the formation of periodic structures of sub-100 nm is firstly whether electromagnetic phenomena such as radiation attenuation and scattering effects set limits to the minimum sizes of the spatial period [84]. Furthermore, it is important to explore whether matter reorganization-related effects such as hydrodynamic processes require a minimum spatial frequency of the hydrothermal waves to lead to periodic structures.

Further advances in the laser processing are also facilitated with a continuous improvement of such laser systems and modalities: (i) high repetition fs or high power laser systems, (ii) employment of laser sources with very energetic beams (i.e., XUV), and (iii) ability to tailor the spatiotemporal beam profile and production of complex polarization states and energy deposition locally are expected to expand the range of complexity and novelty (i.e., in terms of potential applications) of biomimetic textures.

It is evident that the wealth of arising possibilities in laser-based manufacturing and nanofabrication and the number of approaches toward producing sophisticated topographies could be assisted through a systematic way of classification of methodologies for a fast, efficient, and automated way, avoiding expensive and questionable trial-and-error techniques. Thus, with regard to future prospects, apart from the need for the production of novel laser sources, digital-based techniques and artificial intelligence methodologies are expected to enhance the innovation capacity of laser manufacturing potential; thus, this emerging field constitutes a powerful tool designed for simulating and testing new techniques and methods, developing new advanced materials and products, and exploring new directions in the field of laser materials processing and manufacturing.

References

1. E.I. Stratakis, V. Zorba, *Nanotechnologies for the Life Sciences* (Wiley-VCH Verlag GmbH & Co. KGaA, 2007)
2. E. Stratakis et al., Mater. Sci. Eng. R: Rep. **141**, 100562 (2020)
3. M. Salta, J.A. Wharton, P. Stoodley, S.P. Dennington, L.R. Goodes, S. Werwinski, U. Mart, R.J.K. Wood, K.R. Stokes, Philos. Trans. R. Soc. A **368**, 4729 (2010)
4. F. Fraggelakis, G.D. Tsibidis, E. Stratakis, Phys. Rev. B **103**, 054105 (2021)
5. F. Fraggelakis, G.D. Tsibidis, E. Stratakis, Opto-Electron. Adv **5**, 210052 (2022)
6. V. Welch, V. Lousse, O. Deparis, A. Parker, J.P. Vigneron, Phys. Rev. E **75**, 041919 (2007)
7. B.K. Hsiung et al., Nat. Commun. **8**, 2278 (2017)
8. R.H. Siddique, G. Gomard, H. Holscher, Nat. Commun. **6**, 6909 (2015)
9. A. Papadopoulos, E. Skoulas, A. Mimidis, G. Perrakis, G. Kenanakis, G.D. Tsibidis, S. E, Adv. Mater. **31**, 1901123 (2019)
10. T. Sullivan, I. O'Callaghan, Biomimetics **5**, 58 (2020)
11. K. Koch, B. Bhushan, W. Barthlott, Prog. Mater. Sci. **54**, 137 (2009)
12. M.J. Baum, L. Heepe, E. Fadeeva, S.N. Gorb, Beilstein J. Nanotech **5**, 1091 (2014)
13. X. Pu, G.J. Li, H.L. Huang, Biol. Open **5**, 389 (2016)
14. U. Hermens et al., Appl. Surf. Sci. **418**, 499 (2017)
15. A.Y. Vorobyev, C. Guo, Laser Photonics Rev. **7**, 385 (2012)

16. V. Zorba, E. Stratakis, M. Barberoglou, E. Spanakis, P. Tzanetakis, S.H. Anastasiadis, C. Fotakis, Adv. Mater. **20**, 4049 (2008)
17. V. Zorba, L. Persano, D. Pisignano, A. Athanassiou, E. Stratakis, R. Cingolani, P. Tzanetakis, C. Fotakis, Nanotechnology **17**, 3234 (2006)
18. J.-C. Diels, W. Rudolph, *Ultrashort Laser Pulse Phenomena: Fundamentals, Techniques, and Applications on a Femtosecond Time Scale*, 2nd edn. (Elsevier/Academic Press, Amsterdam/Boston, 2006)
19. E.L. Papadopoulou, A. Samara, M. Barberoglou, A. Manousaki, S.N. Pagakis, E. Anastasiadou, C. Fotakis, E. Stratakis, Tissue Eng. Part C-Me **16**, 497 (2010)
20. J. Bonse, S. Höhm, S.V. Kirner, A. Rosenfeld, J. Krüger, IEEE J. Sel. Top. Quant **23**, 9000615 (2017)
21. A. Rudenko, J.P. Colombier, S. Höhm, A. Rosenfeld, J. Krüger, J. Bonse, T.E. Itina, Sci. Rep-Uk **7**, 12306 (2017)
22. J. Bonse, J. Krüger, S. Höhm, A. Rosenfeld, J. Laser Appl. **24**, 042006 (2012)
23. G.D. Tsibidis, M. Barberoglou, P.A. Loukakos, E. Stratakis, C. Fotakis, Phys. Rev. B **86**, 115316 (2012)
24. J.E. Sipe, J.F. Young, J.S. Preston, H.M. van Driel, Phys. Rev. B **27**, 1141 (1983)
25. J. Bonse, A. Rosenfeld, J. Krüger, J. Appl. Phys. **106**, 104910 (2009)
26. Y. Fuentes-Edfuf, J.A. Sánchez-Gil, M. Garcia-Pardo, R. Serna, G.D. Tsibidis, V. Giannini, J. Solis, J. Siegel, Appl. Surf. Sci. **493**, 948 (2019)
27. G.D. Tsibidis, A. Mimidis, E. Skoulas, S.V. Kirner, J. Krüger, J. Bonse, E. Stratakis, Appl. Phys. A **124**, 27 (2017)
28. M. Huang, F.L. Zhao, Y. Cheng, N.S. Xu, Z.Z. Xu, ACS Nano **3**, 4062 (2009)
29. X. Sedao et al., ACS Photon. **5**, 1418 (2018)
30. J. Bonse, R. Koter, M. Hartelt, D. Spaltmann, S. Pentzien, S. Hohm, A. Rosenfeld, J. Kruger, Appl. Phys. A-Mater. Sci. Proc **117**, 103 (2014)
31. S. Höhm, A. Rosenfeld, J. Krüger, J. Bonse, J. Appl. Phys. **112**, 014901 (2012)
32. G.D. Tsibidis, E. Stratakis, Sci. Rep-Uk **10**, 8675 (2020)
33. G.D. Tsibidis, E. Skoulas, E. Stratakis, Opt. Lett. **40**, 5172 (2015)
34. A. Rudenko, C. Mauclair, F. Garrelie, R. Stoian, J.P. Colombier, Appl. Surf. Sci. **470**, 228 (2019)
35. J.E. Sipe, H.M. Vandriel, J.F. Young, Can. J. Phys. **63**, 104 (1985)
36. G.D. Tsibidis, E. Skoulas, A. Papadopoulos, E. Stratakis, Phys. Rev. B **94**, 081305(R) (2016)
37. J.Z.P. Skolski, G.R.B.E. Romer, A.J.H. i'nt Veld, V.S. Mitko, J.V. Obona, V. Ocelik, J.T.M. De Hosson, J. Laser Micro Nanoeng. **5**, 263 (2010)
38. J.Z.P. Skolski, G.R.B.E. Romer, J.V. Obona, V. Ocelik, A.J.H. i'nt Veld, J.T.M. De Hosson, Phys. Rev. B **85**, 075320 (2012)
39. A. Rudenko, J.-P. Colombier, T.E. Itina, Phys. Rev. B **93**, 075427 (2016)
40. A. Rudenko, C. Mauclair, F. Garrelie, R. Stoian, J.P. Colombier, Phys. Rev. B **99**, 235412 (2019)
41. G.D. Tsibidis, C. Fotakis, E. Stratakis, Phys. Rev. B **92**, 041405(R) (2015)
42. B. Rethfeld, M.E. Garcia, D.S. Ivanov, S. Anisimov, J. Phys. D. Appl. Phys. **50**, 193001 (2017)
43. S.I. Anisimov, B.L. Kapeliovich, T.L. Perel'man, Zhurnal Eksperimentalnoi Teor. Fiz **66**, 776 (1974) Sov. Phys. Tech. Phys. 11, 945 (1967)
44. B. Gaković, G.D. Tsibidis, E. Skoulas, S.M. Petrović, B. Vasić, E. Stratakis, J. Appl. Phys. **122**, 223106 (2017)
45. D.S. Ivanov, Z. Lin, B. Rethfeld, G.M. O'Connor, T.J. Glynn, L.V. Zhigilei, J. Appl. Phys. **107**, 013519 (2010)
46. D.S. Ivanov, L.V. Zhigilei, Phys. Rev. B **68**, 064114 (2003)
47. O. Varlamova, J. Reif, S. Varlamov, M. Bestehorn, in *Progress in Nonlinear Nano-Optics*, ed. by S. Sakabe, C. Lienau, R. Grunwald, (Springer International Publishing, 2015), p. 3
48. G.D. Tsibidis, E. Stratakis, J. Appl. Phys. **121**, 163106 (2017)
49. A. Margiolakis, G.D. Tsibidis, K.M. Dani, G.P. Tsironis, Phys. Rev. B **98**, 224103 (2018)
50. E. Petrakakis, G.D. Tsibidis, E. Stratakis, Phys. Rev. B **99**, 195201 (2019)

51. A. Rudenko, C. Mauclair, F. Garrelie, R. Stoian, J.-P. Colombier, Nanophotonics-Berlin **8**, 459 (2019)
52. E. Allahyari, J. Jj Nivas, E. Skoulas, R. Bruzzese, G.D. Tsibidis, E. Stratakis, S. Amoruso, Appl. Surf. Sci. **528**, 146607 (2020)
53. J.J. Nivas, S. He, A. Rubano, A. Vecchione, D. Paparo, L. Marrucci, R. Bruzzese, S. Amoruso, Sci. Rep-Uk **5**, 17929 (2015)
54. S. He, J.J.J. Nivas, K.K. Anoop, A. Vecchione, M. Hu, R. Bruzzese, S. Amoruso, Appl. Surf. Sci. **353**, 1214 (2015)
55. C. Florian, E. Skoulas, D. Puerto, A. Mimidis, E. Stratakis, J. Solis, J. Siegel, ACS Appl. Mater. Interfaces **10**, 36564 (2018)
56. C.A. Zuhlke, T.P. Anderson, D.R. Alexander, Opt. Express **21**, 8460 (2013)
57. J. Schaeske, E. Fadeeva, S. Schlie-Wolter, A. Deiwick, B.N. Chichkov, A. Ingendoh-Tsakmakidis, M. Stiesch, A. Winkel, Int. J. Mol. Sci. **21**, 8442 (2020)
58. E. Skoulas, A. Manousaki, C. Fotakis, E. Stratakis, Sci. Rep-Uk **7**, 45114 (2017)
59. F. Fraggelakis, G. Mincuzzi, J. Lopez, I. Manek-Honninger, R. Kling, Appl. Surf. Sci. **470**, 677 (2019)
60. S. Alamri, F. Fraggelakis, T. Kunze, B. Krupop, G. Mincuzzi, R. Kling, A.F. Lasagni, Materials (Basel) **12**, 1018 (2019)
61. B. Voisiat, A.I. Aguilar-Morales, T. Kunze, A.F. Lasagni, Materials (Basel) **13**, 200 (2020)
62. A. Rosenkranz, M. Hans, C. Gachot, A. Thome, S. Bonk, F. Mücklich, Lubricants **4**, 2 (2016)
63. S. Milles, M. Soldera, B. Voisiat, A.F. Lasagni, Sci. Rep-Uk **9**, 13944 (2019)
64. S. Alamri, A.I. Aguilar-Morales, A.F. Lasagni, Eur. Polym. J. **99**, 27 (2018)
65. A. Peter, A.H.A. Lutey, S. Faas, L. Romoli, V. Onuseit, T. Graf, Opt. Laser Technol. **123**, 105954 (2020)
66. M. Bieda, M. Siebold, A.F. Lasagni, Appl. Surf. Sci. **387**, 175 (2016)
67. D.W. Müller, T. Fox, P.G. Grützmacher, S. Suarez, F. Mücklich, Sci. Rep-Uk **10**, 3647 (2020)
68. J. Marczak, J. Kusinski, R. Major, A. Rycyk, A. Sarzynski, M. Strzelec, K. Czyz, Opt. Appl. **44**, 575 (2014)
69. E. Bevillon, R. Stoian, J.P. Colombier, J. Phys. Condens. Matter **30**, 385401 (2018)
70. E. Siegel, Phys. Chem. Liq. **5**, 9 (1976)
71. M. Barberoglou, G.D. Tsibidis, D. Gray, E. Magoulakis, C. Fotakis, E. Stratakis, P.A. Loukakos, Appl. Phys. Mater. Sci. Process. **113**, 273 (2013)
72. T.J.Y. Derrien, J. Kruger, T.E. Itina, S. Höhm, A. Rosenfeld, J. Bonse, Opt. Express **21**, 29643 (2013)
73. T.J.Y. Derrien, T.E. Itina, R. Torres, T. Sarnet, M. Sentis, J. Appl. Phys. **114**, 083104 (2013)
74. Z. Lin, L.V. Zhigilei, V. Celli, Phys. Rev. B **77**, 075133 (2008)
75. P. Raccuglia et al., Nature **533**, 73 (2016)
76. J. Francis, L.K. Bian, Manuf. Lett. **20**, 10 (2019)
77. S. Tani, Y. Kobayashi, Appl. Phys. A-Mater. Sci. Process **124**, 265 (2018)
78. B. Mills, D.J. Heath, J.A. Grant-Jacob, R.W. Eason, Opt. Express **26**, 17245 (2018)
79. D.J. Heath, J.A. Grant-Jacob, Y.H. Xie, B.S. Mackay, J.A.G. Baker, R.W. Eason, B. Mills, Opt. Express **26**, 21574 (2018)
80. A. Agrawal, P.D. Deshpande, A. Cecen, G.P. Basavarsu, A.N. Choudhary, S.R. Kalidindi, Integrat. Mater. Manufact. Innov. **3**, 90 (2014)
81. M.C. Velli, G.D. Tsibidis, A. Mimidis, E. Skoulas, Y. Pantazis, E. Stratakis, J. Appl. Phys. **128**, 183102 (2020)
82. C.M. Bishop, *Pattern Recognition and Machine Learning* (Springer, New York, 2006) Information science and statistics
83. C.E. Shannon, Bell Syst. Tech. J. **27**, 379 (1948)
84. J. Bonse, S. Gräf, Nanomaterials **11**, 3326 (2021)

Chapter 26
Ultrarapid Industrial Large-Area Processing Using Laser Interference Patterning Methods

Andrés Fabián Lasagni, Lucinda Mulko, and Marcos Soldera

Abstract Fabrication of two- and three-dimensional structures in the micro- and nano-range allows a new degree of freedom for the design of materials by tailoring desired material properties and, thus, obtaining enhanced functionalities. Such complex designs are only possible using novel fabrication techniques with high resolution, even in the nanoscale range. Additionally, the implementation of methods capable to produce the mentioned structures into industrial applications requires the ability to process large areas at high throughputs. An innovative solution for high-speed surface patterning of periodic structures is laser-based interferometric methods, such as laser interference lithography (LIL) and Direct Laser Interference Patterning (DLIP). Here, periodic structures can be produced in different materials by overlapping a certain number of laser beams over the material's surface. These methods are introduced in this chapter, showing different processing systems and configurations, demonstrating the possibility for the fast and precise tailoring of material surface microstructures and topographies on industrial relevant scales. Finally, several application examples are described.

Keywords Direct Laser Interference Patterning (DLIP) · Laser interference lithography (LIL) · Large-area surface processing · Applications of surface nanostructures · Roll-to-roll fabrication

---

A. F. Lasagni (✉)
Technische Universität Dresden, Faculty of Mechanical Engineering, Institute of Manufacturing Technology, Dresden, Germany

Fraunhofer Institute for Material and Beam Technology IWS, Dresden, Germany
e-mail: andres_fabian.lasagni@tu-dresden.de

L. Mulko · M. Soldera
Technische Universität Dresden, Faculty of Mechanical Engineering, Institute of Manufacturing Technology, Dresden, Germany

© The Author(s), under exclusive license to Springer Nature Switzerland AG 2023

R. Stoian, J. Bonse (eds.), *Ultrafast Laser Nanostructuring*, Springer Series in Optical Sciences 239, https://doi.org/10.1007/978-3-031-14752-4_26

1 Introduction

Laser interference technologies are able to merge the technological and economical aspects required in order to manufacture surface architectures at the nano/micro level using a top-down methodology [1]. While the concept of interference is a long-standing one, dating back to Young's famous double-slit experiment in 1801, it was not until around 1970 that a laser source was used on a photoresist material to create holograms and interference diffraction gratings. This was the beginning of what is today known as laser interference lithography [2]. Since then, laser interference lithography (LIL) has proven to be a suitable patterning tool for the development of periodic structures [3–5]. The principle of LIL is based on the interference of two or more coherent laser beams to form a horizontal standing wave for a grating pattern that can be recorded on a photosensitive layer, such as a photoresist. In the case of negative photoresist (e.g., one of the most popular is the SU-8 epoxy-based negative photoresist, developed by IBM in the late 1980s [6]), the photosensitive material is reinforced, either polymerized or cross-linked, at the positions of the laser interference maxima. Then, the application of a developer will detach only the regions that were not exposed to light, resulting in a topographical variation [7].

A plethora of lithographic methods are currently available, such as X-ray lithography, electron beam lithography (EBL), ion beam lithography (IBL), and, more recently, nanoimprint lithography [8–10]. During the last decades, the boom and bust in popularity of each technology have mainly depended on their performance, productivity, and cost of operation and implementation. In turn, LIL has significant improvements over other serial lithography methods, such as higher efficiency and easier scalability, low cost and high throughput, the absence of surface contamination (as the material is polymerized and does not ablate), the ability to produce patterns over large areas (up to thousands of mm in diameter), as well as software-controlled repeatable patterns (with different periods, feature sizes, and pattern shapes) [4].

Later in time, with the emergence of laser systems with sufficient pulse energy, another interference technique was developed [11], which made it possible to modify the topography of the material directly, without the need of an intermediate photoresist mask and subsequent development steps. Hence, the method has been called Direct Laser Interference Patterning (DLIP) [12–17]. Like laser-based manufacturing methods, laser radiation has the capability to be used for enabling a variety of metallurgical processes, such as melting, recrystallization, or crystallization of amorphous materials. This feature was extensively studied in the 90s in silicon materials for the development of thin-film electronic devices [11, 18, 19]. Additionally, the formation of intermetallic phases and grain size architectures has been reported in metals as well as thin films [20, 21].

A primary condition for achieving the periodic structure by DLIP is that the target material absorbs radiation at the working wavelength of the laser. The laser must also provide sufficient energy per unit area or fluence, called threshold fluence, to be able to ablate the material directly. This threshold fluence can vary from only some µJ to a few J, depending on the material and used pulse duration. Concerning the mechanism underlying the structuring process, depending on the kind of laser radiation-material interaction, the microstructuring process can be essentially photothermal or predominantly photochemical, as well as a combination of both (photophysical ablation) [22, 23].

In this chapter, the capabilities and possibilities of LIL and DLIP methods are depicted. Firstly, the fundamental concepts for high-throughput processing using laser interference concepts are presented. It includes a brief description of the LIL equipment, which involves, for example, the so-called Lloyd's mirror interferometer. Then, the most common DLIP configurations as well as scanner-based DLIP optics will be discussed. Later on, a section of this chapter is dedicated to the DLIP processing of embossing tools, including plate-to-plate (P2P) and roll-to-roll (R2R) configurations. Afterward, a few applications of surface micro-/nanostructures produced by ultrarapid methods are summarized. Last but not least, the challenges of moving laser interference techniques to an extreme large scale will be discussed.

2 Concepts for High-Throughput Processing

2.1 Large-Area Laser Interference Lithography

The LIL [4, 7] is a patterning method in which a photoresist is irradiated by two or more overlapping coherent light beams. In this way, the polymerization of the photoresist follows a repetitive pattern produced by the interference of the laser beams. This maskless fabrication process is also called interferometric lithography (IL) or holographic lithography [24–28].

Substrates patterned with LIL have been employed in a wide range of application fields including NIR photodetectors [29], superhydrophobic surfaces with tunable adhesion [30], and light-trapping concepts for solar cells [31]. In addition, this technology has been used to produce templates for assembling nanostructures for plasmonics [32], photonic crystals, and SERS (Surface Enhanced Raman Spectroscopy) sensors [33].

The most relevant parameters controlling a LIL process are the exposure dosage, laser power, and the overlapping angle between the interfering beams. Additionally, reflections at the photoresist/substrate as well as at the photoresist/air interfaces need to be carefully considered to minimize unwanted second-order modulations that could lead to a nonuniform topography. To attend to this issue, antireflective coatings have been deposited between the substrate and photoresist (bottom antireflection coating or BARC) and also onto the photoresist (top antireflection coating or TARC) [2]. The minimum spatial period of repetitive structures fabricated with typical LIL methods is in the sub-micrometer range (i.e., 150–300 nm) using UV laser sources [2]. Remarkably, areas up to 1.2 m × 1.2 m have been structured with

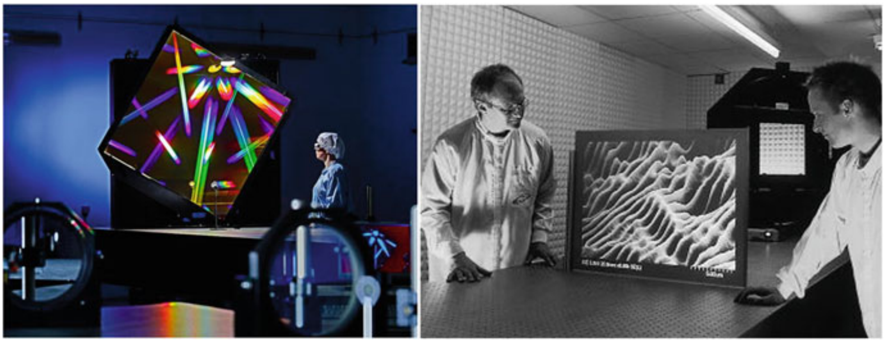

Fig. 26.1 Photograph of large-scale surface textures by LIL. Left: A hexagonal grid with a period of 1 μm has been produced on 1.2 × 1.2 m^2 [35]. (© 2019, NNT 2019. Right: 0.5 m^2 masterplate with asymmetrical microstructures used as a projector. Both images were taken at Fraunhofer ISE [36] © 2004, Society of Photo-Optical Instrumentation Engineers (SPIE))

feature sizes down to 100 nm [34–36]. Figure 26.1 shows two photographs for a better impression of the large areas that current LIL technology can achieve.

The simplest experimental setup for LIL is the single-beam Lloyd's mirror interferometer (see Chap. 14 for additional information) [37]. The laser source must be selected so that its wavelength matches the absorption and sensitivity characteristics of the photoresist, and its coherence length is long enough to overcome the optical path length difference. Pulsed lasers have coherence lengths in the order of their pulse length, whereas continuous wave (CW) lasers have a very long coherence length (of several meters). Besides, the exposure dose from CW lasers can be easily adjusted by controlling the exposure time [2, 38]. Upon irradiating the sample, the spatial intensity modulation of the interference pattern is then transferred to the photoresist.

Figure 26.2 shows diverse examples of repetitive nano-/microstructures fabricated by LIL. For instance, a line-like texture etched on silicon after overlapping two laser beams on a photoresist is shown in Fig. 26.2a [7]. Namely, after a few minutes of UV light exposure, followed by photoresist development and chemical etching, the periodic modulation of the interference pattern was transferred to the silicon substrate. Different approaches can be followed to increase the complexity of the patterned structures.

For example, rotating the substrate at a given angle and re-irradiating, it gives rise to different surface structures like pillars or dots with quadratic or hexagonal periodicity, depending on the type of photoresist (negative or positive) and the number of rotation and re-irradiation steps and exposure time [2, 7]. Figure 26.2b, c show periodic arrays of pillars and dots, respectively, which were fabricated after rotating the sample 90° degrees between two sequential exposures keeping the same periodicity. In the example displayed in Fig. 26.2b, a positive photoresist was used, implying that the exposed material at the interference maxima positions was degraded and removed in the development step. Following this trend, using the

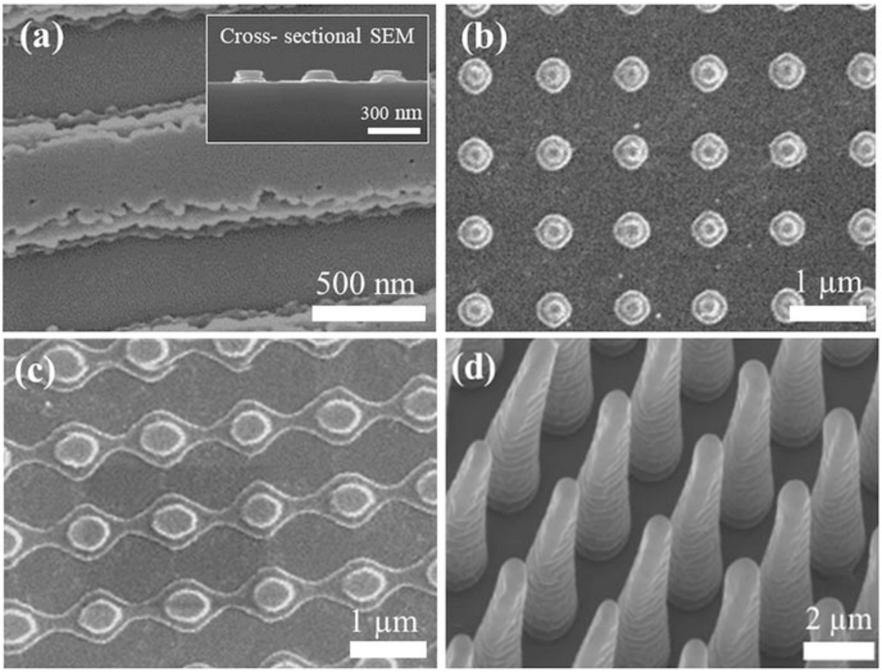

Fig. 26.2 (**a**) Line-like surface texture fabricated on Si using two-beam interference single-exposure LIL followed by photoresist development and chemical etching. Pillar structures produced by a double exposure with 90° sample rotation of a positive photoresists and exposure time of (**b**) 3 min and (**c**) 6 min [7]. (©2008 Elsevier B.V). (**d**) PEG-DA pillars fabricated with a four-beam LIL configuration using an fs-laser source [39]. (©2019, WILEY-VCH Verlag GmbH & Co. KGaA, Weinheim)

same system but increasing the exposure time, the material continued to degrade forming a dot-like structure. Thus, in the LIL process, a repetitive inverse structure is achieved (Fig. 26.2c). On the contrary, when a negative photoresist is exposed, the material is strengthened by photopolymerization or cross-linking and retained again after development. Thus, in the LIL process, a hollow-type repetitive inverse structure is achieved.

Another strategy to increase the complexity of the structures is to overlap more than two coherent beams on the sample. As explained in Chap. 14 (J. Ihlemann et al., "Periodic surface structures by laser interference ablation"), this enables the formation of a wide range of geometries, even by interfering with only three or four beams. Figure 26.2d shows an example of structures on polyethylene glycol diacrylate (PEG-DA) hydrogel mixed with a photoinitiator (camphorquinone) produced by overlapping four laser beams with pulse durations in the fs regime [39]. The spatial period measured on the sample was 2.85 μm, which is slightly shorter than the calculated period of 2.96 μm.

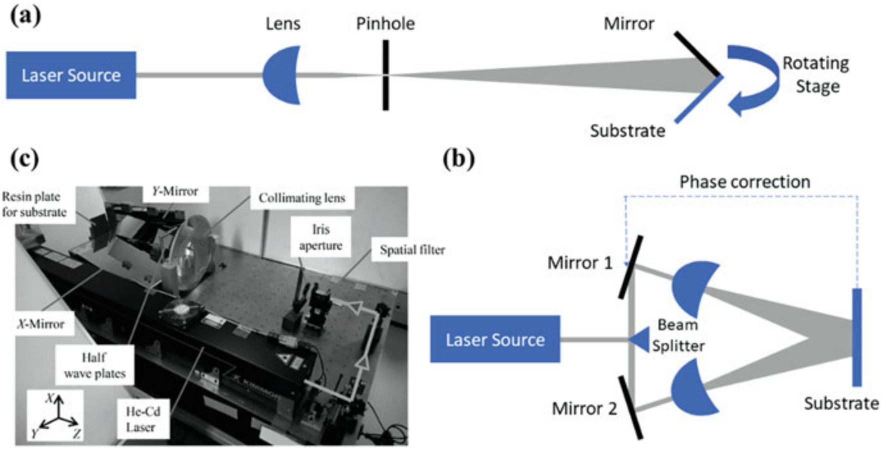
(a)
Laser Source
Lens
Pinhole
Mirror
Rotating Stage
Substrate
(c)
Resin plate for substrate
Y-Mirror
Collimating lens
Iris aperture
Spatial filter
X-Mirror
Half wave plates
X
Y
Z
He-Cd Laser
(b)
Phase correction
Mirror 1
Laser Source
Beam Splitter
Mirror 2
Substrate

Fig. 26.3 (**a**) Working principle of Lloyd's mirror interferometer with the required optical components to produce a two-beam interference pattern with long coherent Gaussian laser beam, (**b**) schematics of a dual-beam interferometer with its optical components, and (**c**) photograph of Lloyd's mirror interferometer system on a vibration-dumped table [40]. (©2017, Elsevier, Inc.)

For industrial processing (patterning areas larger than 10 cm^2), two optical configurations for LIL patterning are commonly used. One of them is the above-mentioned Lloyd's mirror interferometer setup, which employs a laser with a long coherence length and Gaussian profile. As shown in Fig. 26.3a, the laser beam is focused by a lens on a pinhole to create a diverging laser beam and then directed toward the sample and a mirror, which are placed perpendicular to each other [2]. In this way, the second beam is created from the reflection at the mirror and directed toward the sample to produce the interference pattern. This concept can thus be considered as a one-beam interferometer. Furthermore, the period of the resulting line-like pattern can be tuned by rotating the substrate-mirror assembly (the direction of rotation is indicated by the arrow in Fig. 26.3a). To achieve a high contrast in the interference pattern, the laser beam must be s-polarized so that the incident and reflected beams have their polarization vectors in the same direction. However, this method has some drawbacks that limit its use for large-scale applications. As large-area mirrors with a very smooth surface finish are extremely expensive and difficult to handle, the irradiated area is typically limited to a few cm^2. As commented above, this setup is not convenient for ultrashort pulse laser sources featuring short coherence lengths because the optical delay cannot be adjusted [41]. Figure 26.3b shows a photograph of a Lloyd's mirror interferometer system [40].

Alternatively, a dual-beam interferometer can be used to pattern large areas. In this setup, the primary beam is split into two sub-beams utilizing a beam splitter. Then, the secondary beams are expanded and directed toward the sample where they recombine, as shown in Fig. 26.3c. For obtaining a uniform interference pattern on the sample, the intensity of the individual sub-beams and their profile (e.g., Gaussian) must be equal, and the path length difference must be significantly shorter than the coherence length of the laser radiation [2]. The beam quality can be further improved by using a pinhole and aligning the beams to the substrate.

As the sub-beams have different optical paths, the quality of the resulting interference pattern is very sensitive to airflow, which can yield a significant phase difference between the beams. To overcome this problem, a phase correction system must be included in the interferometer setup. In Fig. 26.3c, a simple yet effective solution is implemented by translating Mirror 1 to the optimum position, as is illustrated by the dashed line.

It is worth pointing out that if the spatial period has to be modified, the mirrors must be repositioned so that the desired overlap angle can be set. The difficulty of this procedure lies in the fact that normally, the mirrors are moved manually and the optical setup must be realigned.

The drawbacks of LIL are the limitations regarding the layout and the profile of the structure. In principle, the pattern of the microstructure cannot vary significantly in the structured area, but several patterns can be superposed on top of each other. In addition, high stability of the optical assembly during exposure is required. Exposure times can be relatively large due to the limited laser power. For example, for the treatment of a $600 \times 800\ \text{mm}^2$ area, exposure times range from 20 to 60 minutes, depending on the depth of the structure. Thus, unstable conditions during exposure will result in microstructures with a low aspect ratio [36].

The dual-beam setup described before has been also implemented for the direct processing of materials. This is the case of the DLIP method developed in the 90s as was described in Sect. 1 [11]. The main difference is that the beams are not expanded before reaching the substrate (as in Fig. 26.3c) in order to have sufficient laser fluence to be able to ablate or modify the material's surface.

2.2 Scanner-Based Direct Laser Interference Patterning

For reaching a higher performance in terms of patterning area and throughputs as well as to allow automatic control of the spatial period, other concepts have been developed in the case of the DLIP technique [42, 43]. In this case, the setup consists of a laser source (e.g., providing ns or ps pulses) and different optical elements for beam splitting and beam guidance (such as beam expander, diffractive optical element (DOE), and prism). The schematic of the scanner-based DLIP configuration is shown in Fig. 26.4a. Firstly, to enlarge the laser spot and produce a slightly divergent beam, the emitted laser radiation is guided into a beam expander. Then, a DOE splits the laser beam into two equally energetic sub-beams followed by a prism, which parallelizes them. Adjusting the distance between the prism and the DOE allows to vary the beam separation, which in turn changes the overlap angle (interference angle) and permits, after calibrating the setup, to modify the spatial period with high precision. Next, a galvanometer scanner equipped with an f-theta

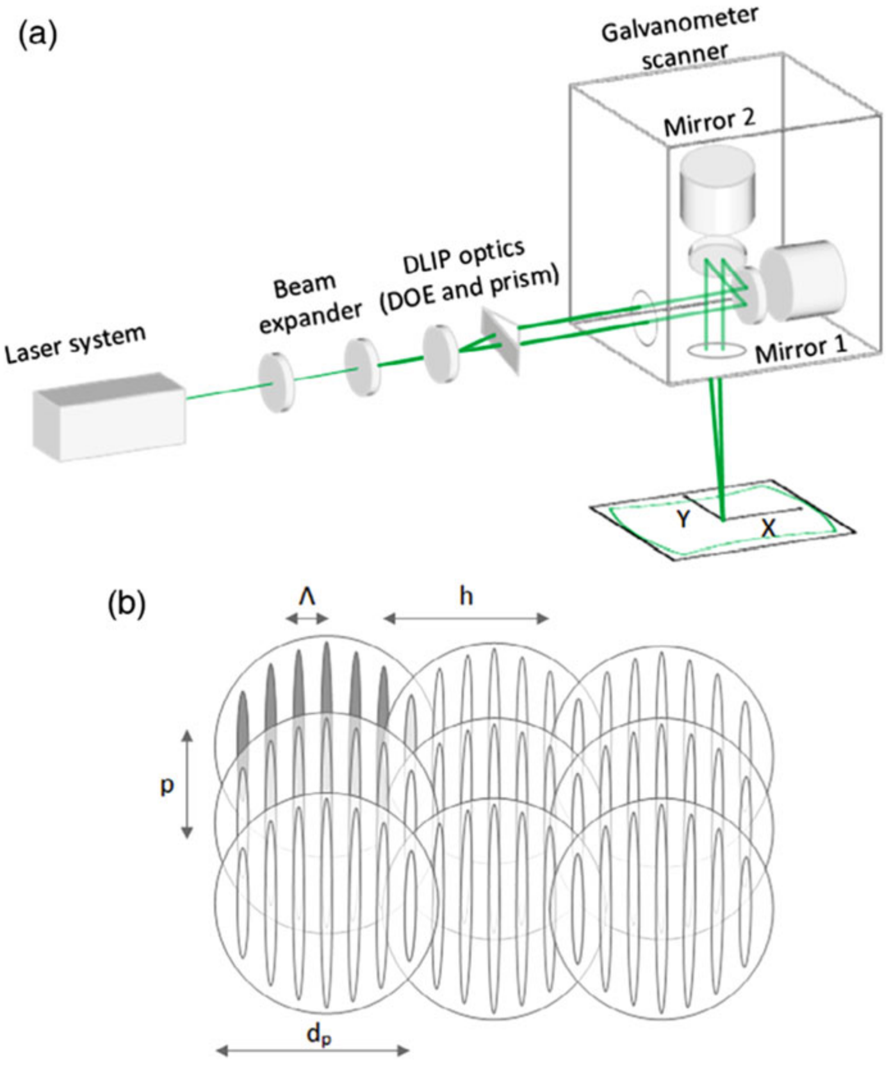
(a)
Galvanometer scanner
Mirror 2
DLIP optics (DOE and prism)
Beam expander
Laser system
Mirror 1
Y
X
(b)
Λ
h
p
d_p

Fig. 26.4 (**a**) DLIP setup with a laser system and a galvanometer scanner and (**b**) process strategy for producing homogeneous microstructures [42]. (©2021 The Authors, Advanced Engineering Materials published by Wiley-VCH GmbH)

lens is used to very fast render the sub-beams over the substrate and simultaneously overlay them producing the interference pattern [42].

For producing the different microstructures, the movement of the mirrors must be coordinated with the repetition frequency of the laser. To achieve homogeneous and deep line-like structures, the interfering spot also called holographic pixel (corresponding to the area at which both laser sub-beams are focused) can be overlapped in the vertical and horizontal directions. This is exemplarily shown in Fig. 26.4b, where "d_p" is the diameter of the DLIP area and "Λ" the spatial period. In the vertical direction, the DLIP spots can be separated by a distance "*p*" resulting in different overlaps that are parallel to the interference lines. Moreover, the DLIP areas can be overlapped horizontally at a certain distance, which is known as the hatch distance "*h*." This displacement is perpendicular to the direction of the interference lines and must be set to an integer of Λ (e.g., 2Λ, 3Λ, 4Λ ...) so that the intensity maximum positions are overlapped and thus avoiding the deterioration of the structure produced in the previous step.

The scan field provided by this setup is controlled by the different elements used, which are mainly the size of the galvanometer mirrors, the separation distance between the parallel beams, and the focal distance of the f-theta objective. For instance, the latest was evaluated using a Scanlab intelliSCAN 30 scanner, with a focal length of 100 mm and a beam aperture of 30 mm [42]. A total of six different scan fields with spatial periods ranging from 2.9 to 12.8 μm were fabricated. As an example, photographs of the scanned fields of steel surfaces together with a scanning electron microscope (SEM) image of a single DLIP spot for a spatial period of 6.9 μm are shown in Fig. 26.5. The laser used had a pulse duration of 5 ns, a frequency of 3.5 kHz, and a working wavelength of 527 nm. The processing rate was c.a. 7.7 cm^2/min.

By visually analyzing the scan fields, the following features can be seen, as long as one or more laser beams are directed onto a plane with a two-mirror system. Firstly, the size of the maximum scanning field depends on the scanning angles of the mirrors and the scanner objective. Secondly, the distance traveled by the laser beam between mirror 1 (see Fig. 26.4) and the image field produces a distortion of the image field, as has been reported by someone else for the Direct Laser Writing (DLW) method [44]. However, by using commercial image field corrections given by the scanner supplier, the distortion of the image field can be corrected. Furthermore, the scan fields showed a typical barrel-shaped image field distortion (Fig. 26.5a) caused by the f-theta objective, regardless of the spatial period interference used.

For larger spatial periods (>6.9 μm), shorter separations between the parallelized beams are needed (see Fig. 26.5a). In consequence, larger areas can be treated using the DLIP-scanner configuration. Meanwhile, for smaller periods, the spacing between the beams would increase and the modified area would decrease. For example, for a spatial period as small as 2.9 μm, the distance between the two partial beams was 1.82 cm, resulting in a scanning field area of 21.47 cm^2. In contrast, for a spatial period of 12.8 μm, which has the smallest distance between the laser beams (0.41 cm), the scan field area is 38.48 cm^2 [42].

Regarding quality and topographical parameters of the produced patterns, from previous investigations [43], it is known that the most important parameter influencing the structure depth is the number of superimposed laser pulses or cumulated fluence, which is controlled by the different percentage of pulse overlap used. This effect is shown in Fig. 26.5b, for the spatial period of 6.9 μm. The results show that a maximum structure depth of approximately 6 μm was reached when using 13

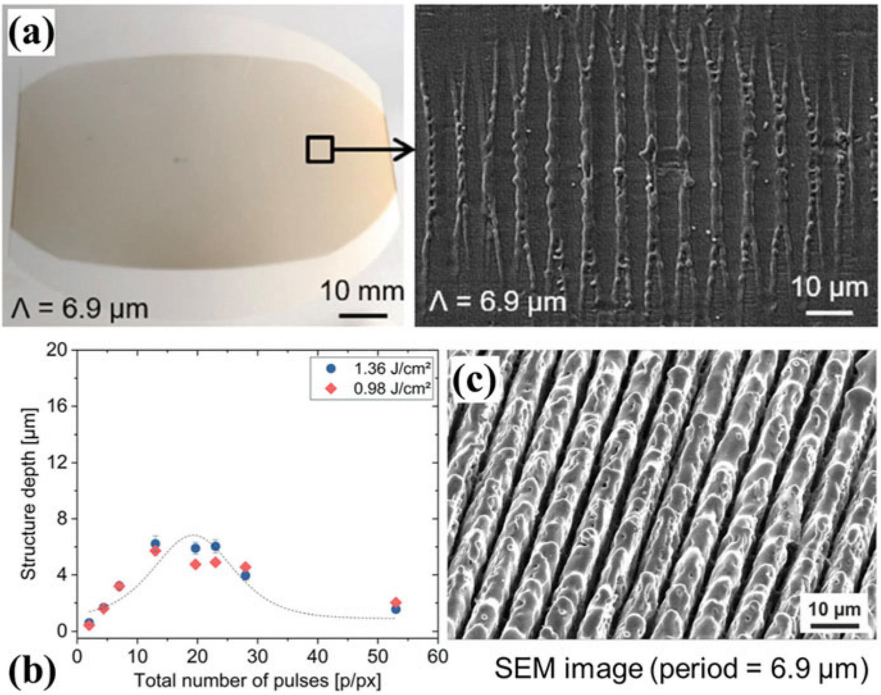

Fig. 26.5 (**a**) Optical (left) and SEM (right) images of the DLIP-treated scan fields of stainless steel for a spatial period of 6.9 µm. (**b**) Structure depth as a function of the total number of pulses applied for a spatial period of 6.9 µm and (**c**) SEM image of the line-like pattern resulting from 13 pulses [42]. (©2021 The Authors, Advanced Engineering Materials published by Wiley-VCH GmbH)

to 25 pulses independently of the laser fluence used (0.98 and 1.36 J/cm^2). Figure 26.5c shows an example of a line-like structure produced in steel using 13 pulses. The use of a larger number of overlap pulses produces a decrease in the structure depth, which is typical when ns pulses are utilized [45]. Due to the flexibility of the developed configuration, this equipment can be utilized to produce decorative elements as will be described in Sect. 3.4.

2.3 Processing of Embossing Tools

In recent years, various DLIP systems have been developed, including 3D workstations, which allow the treatment of large parts such as sleeves or cylinders for R2R processing. For instance, one such system permits the treatment of cylindrical parts up to 600 mm in length and 350 mm in diameter [46, 47]]. The system can be equipped with both ns and ps-laser sources, and different optical heads can be

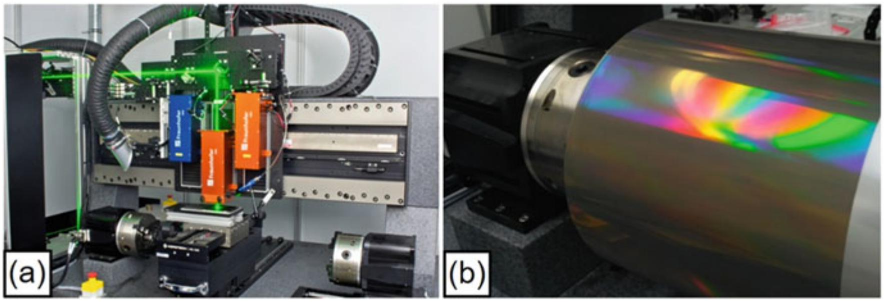

Fig. 26.6 (**a**) Large-area DLIP system for 2D and 3D parts (TU-Dresden, Fraunhofer IWS). The system consists of three different DLIP optics, for 355 nm, 532 nm, and 1064 nm wavelengths. (**b**) DLIP-treated seamless sleeve (300 mm in diameter and 300 mm in length) processed at 5700 mm^2/min (using only 10 W of IR laser power) [48]. (©2018 by the authors. Licensee MDPI, Basel, Switzerland)

utilized (see Fig. 26.6a). It can be also used to treat planar surfaces, with dimensions up to 600 mm × 300 mm. To enable a proper overlap of the interfering laser beams on the workpiece, the optical heads are mounted on independent linear stages that can move in Z-direction. For the treatment of a certain area on the metallic substrate, the optical head is translated by an additional linear stage in X-direction, while the cylindrical workpiece is moved by a rotary axis relative to the treating optical assembly. The 3D DLIP system shown in Fig. 26.6a is equipped with a picosecond-pulsed Nd:YAG slab solid-state laser emitting near-infrared radiation of a wavelength of 1064 nm, as well as their second (532 nm) and triple harmonics (355 nm) (Edgewave, Germany).

To improve the process throughput, it is necessary to increase the linear speed at the sleeve surface, which is directly correlated to the angular speed of the rotational axis. An example of a treated nickel sleeve is shown in Fig. 26.6b, which was rotated at 60.8 RPM, corresponding to a linear speed of 57.15 m/min (approximately 1 m/s) [48]. By setting the repetition rate of the laser to 30 kHz and using a beam diameter of 190 μm, an overlap of 74% between the pulses can be calculated. Simultaneously, the DLIP optical head was moved over the cylinder (along its axial direction) at a constant speed of 6 mm/min. This results in a hatch distance of 100 μm between the DLIP tracks. As it can be seen in Fig. 26.6b, characteristic rainbow colors are observed (pattern of colors ranging from violet to red in increasing wavelength order), which is typical for periodic patterns with spatial periods of a few micrometers (in this case, 1.4 μm) [49, 50]. The image also denotes the high homogeneity of the obtained structure. Furthermore, using the abovementioned parameters, the sleeve could be processed in only 50 min, resulting in an impressive throughput of 5700 mm^2/min (the total treated area was ~2827 cm^2).

The treated Ni sleeves can be used in R2R hot-embossing systems to pattern polymer foils at typical Web speeds between 1 and 50 m/min. In this way, and considering a polymer foil of, for example, 300 mm in width, throughputs up to 15

m^2/min are feasible. The processing of polymer foils using the produced sleeves is shown in Sect. 3.3, including also an application example of DLIP-processed sleeves and their implementation in R2R processing.

In addition to cylindrical tools, DLIP can be also used to treat 2D flat surfaces for P2P hot embossing, as has been reported in [51]. Stamps for hot embossing are usually made of silicon, metals, photoresists, and epoxy resins. Particularly, metal molds offer significant advantages, as they can withstand higher pressures and temperatures and retain their structures after a larger number of cycles. It is also worth mentioning that most metals can also be used in large-area sleeves for R2R hot embossing. Although nickel is one of the most widely used metals as stamps due to its durability, ease of cleaning, lack of oxidation, and compatibility with many polymers, it is toxic and may cause skin allergies upon contact. Therefore, Cr and Cu were proposed as alternative candidates for DLIP-patterned stamps in a comparison study. Here, periodic hole-like textures were directly fabricated onto Cr, Cu, and Ni sheets by overlapping four beams from a ps-laser source at a wavelength of 532 nm. Screening experiments sweeping the cumulated fluence revealed the conditions by which the structure depth can be controlled. Furthermore, a process parameter window for each material could be established for obtaining smooth craters sidewalls, which are desired for embossing soften polymers. Among the three processed materials, the Cr stamp showed the best processability, higher texture uniformity, and smooth sidewalls. Figure 26.7 shows profiles extracted from optical confocal images of the three stamps with similar structure depths, i.e., 1.34 μm for Cr (10 pulses at a fluence of 2.9 J/cm^2), 1.18 μm for Ni (120 pulses at a fluence of 1.6 J/cm^2), and 1.31 μm for Cu (80 pulses at a fluence of 1.6 J/cm^2) together with profiles of the corresponding replicas on polymethyl methacrylate (PMMA) after the hot-embossing step. As can be seen, the replica from the Cr stamp showed the best uniformity and smoother micropillar surface, whereas the other imprints had jagged sidewalls and poor homogeneity. The optimum Cr stamp was also used to imprint other polymers, namely, polyethylene terephthalate (PET) and polycarbonate (PC) with very different glass transition temperatures (81 °C for PET and 147 °C for PC), yielding also replicas with smooth sidewalls and structure depths similar to the stamp, as shown in the confocal images and corresponding profiles of Fig. 26.7b [52].

These imprinted polymers featured enhanced surface properties that can be exploited in many different application fields where large-area functional polymers are needed at low patterning costs. Examples of such applications are antibacterial surfaces, optoelectronic devices, decorative or anti-counterfeit holographic features, biomedical devices, or easy-to-clean surfaces. For instance, the PET and PMMA replicas shown in Fig. 26.7 have shown a significant increase in the static water contact angle of more than 55° for both polymers, reaching a maximum contact angle of 139° on structured PET. The dynamic water contact angles measurements revealed a relatively high hysteresis between 20° and 40°, which implies that the water droplet had a high adhesion to the surface. The combination of high static water contact angles and high adhesion is a characteristic of the rose petal, a natural

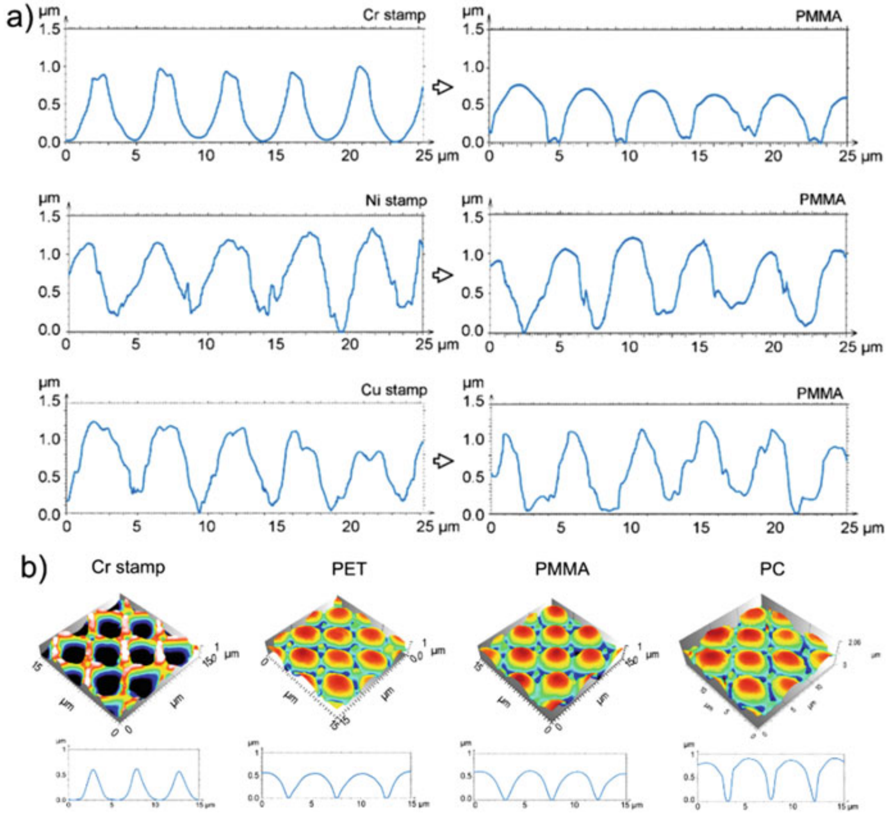

Fig. 26.7 (**a**) Profiles extracted from confocal images taken on Cr, Ni, and Cu stamps structured by DLIP together with the profiles of corresponding imprints on PMMA [51]. (**b**) Confocal images and profiles of a Cr stamp and imprints on PET, PMMA, and PC [52]. (© 2020, Society of Photo-Optical Instrumentation Engineers (SPIE))

nano-/microstructured surface that was recently found of technological relevance, for example, for friction reduction [53].

3 Applications of Surface Nanostructures

3.1 Direct Treatment of Dental Implants

Regenerative medicine and tissue engineering are multidisciplinary fields that seek to design materials that temporarily or permanently replace diseased or damaged tissues, favoring their regeneration [54]. One of the main obstacles to overcome in biomedical titanium implants, such as dental implants, is cell adhesion and proliferation, especially in the early stages of postsurgical implantation [55]. It is well known that surface roughness in the micro-/sub-metric range leads to increased cell proliferation as well as enhanced protein synthesis compared to a smooth metallic surface, which accelerates the healing process and tissue regeneration [56]. In the last decades, several techniques have been investigated to modify the topography and surface roughness of titanium dental implants, and the most commonly employed approach is sand/grain blasting followed by acid etching. Nevertheless, the treated surfaces require subsequent cleaning steps to remove the ablated particles and for the removal of the etching solution that, disadvantageously, increases the processing time. Therefore, one-step fabrication methods such as stand-alone acid etching, anodizing, plasma spraying, and laser ablation have recently acquired attention [57].

Concerning the use of DLIP for dental implant structure, one study [59] reported improved biological performance of implants in which linear-like patterns were obtained by superimposing two laser beams on biomedical grade Ti samples using a nanosecond pulsed laser. On the linear structured surfaces, the cell viability of human osteoblasts (hOBs) was 16% higher compared to an acid-etched Ti reference surface. A more recent study [58] demonstrates that processing Ti surfaces with picosecond-pulsed lasers (10 ps) can induce in a single-step process the formation of characteristic line-like microstructures together with submicrometric periodic waviness, which is known as Laser-Induced Periodic Surface Structures (LIPSS) (for more information, see Chaps. 5, 23, and 25). These undulations may have a periodicity close to or shorter than the laser wavelength and are generally oriented orthogonally to the polarization vector [60]. Therefore, the topography developed using ps-DLIP has much improved roughness characteristics for cell adhesion in comparison to surfaces treated with nanosecond pulses.

The size of the spatial periods used in this work was chosen based on the typical average size of hOBs cells. In this context, the largest structure period selected was 17 μm. In addition, structures with smaller feature sizes, Ti surfaces with periods of 3 and 10 μm, were selected to analyze the adhesion of the osteoblast cells. For the treatment of implants, a spatial period of 5 μm was chosen to demonstrate the ability of the developed optical configuration to structure 3D geometries while minimizing the processing time. In this way, a three-dimensional cylindrical dental implant piece of 15 mm length by 2 mm diameter (see Fig. 26.8a, b) achieved a structuring time of c.a. 10 min, i.e., with a processing speed of 0.22 cm^2/ min, at a laser power of ~ 5 W. In consequence, higher throughputs can be easily achieved by using laser sources with high power (e.g., 50–200 W). The depth of the structured patterns was further explored using cumulative energy densities ranging from 0.1 to 78.9 J/cm^2.

In vitro cell proliferation assays were performed with hOBs on the laser-treated surfaces to verify the potential of the ultrashort DLIP approach for enhancing osseointegration. Also in this case, standard blasted and etched samples were used for reference. Figure 26.8 shows SEM and fluorescence microscopy images of cell adhesion after 7 days of culture on the Ti reference sample (see Fig. 26.8c) and

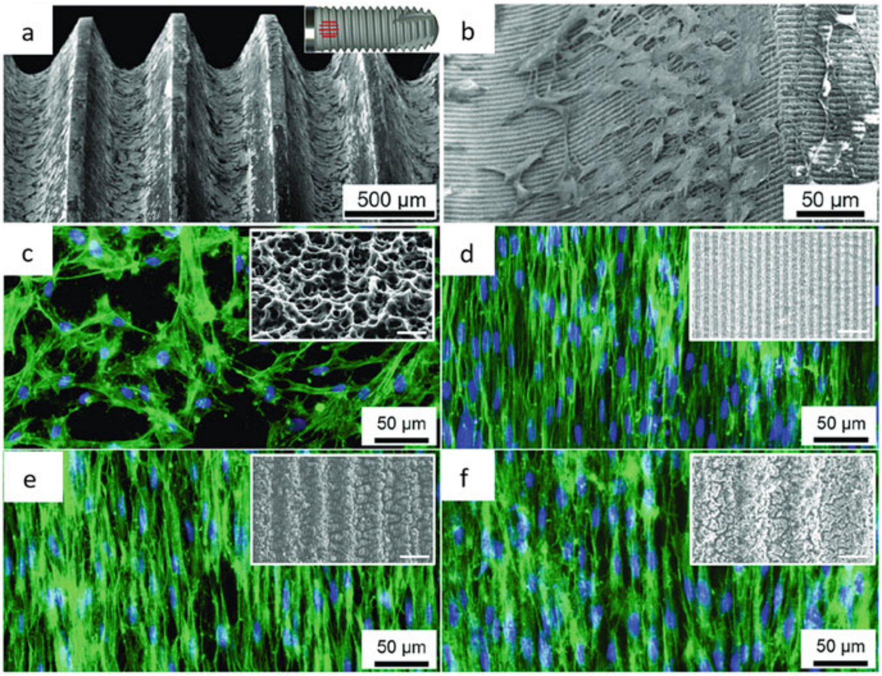

Fig. 26.8 Cell attachment on a 3D Ti dental implant with DLIP pattern: (**a**, **b**) SEM images of the implant with osteoblasts attached on the surface (cumulative fluence: 16 J cm^{-2}, spatial period: 5 μm). The inset in (**a**) shows a model of the implant with the orientation of the linear DLIP pattern. (**c**, **f**) Fluorescence microscopy images of hOBs attached to Ti surfaces after 7 days of culture: (**c**) cells on a sandblasted and acid-etched reference with arithmetical mean height (S_a) = 1.26 μm) and cells on linear patterns with a spatial period of (**d**) 3 μm ($h = 1.3 \pm 0.2$ μm), (**e**) 10 μm ($h = 1.4 \pm 0.3$ μm), and (**f**) 17 μm ($h = 1.7 \pm 0.5$ μm). Actin staining is shown in green and cell nuclei in blue. The top left of each image shows the corresponding SEM images of the surface (scale bar: 10 μm) [58]. (©2019 WILEY-VCH Verlag GmbH & Co. KGaA, Weinheim)

on DLIP-embedded Ti structures (see Figs. 26.8d–f) with spatial periods of 3, 10, and 17 μm and heights of 1.3, 1.4, and 1.7 μm, respectively. As can be seen, the cells adhered and spread randomly on the reference surface, while on all structured surfaces, they aligned parallel to the direction of the microgrooves.

Cell viability was also measured regarding the Ti blasted and etched (set to a relative amount of 100%). In all the samples treated with DLIP, the average relative amount of cells was higher compared to the Ti reference, and the highest value obtained was 250 ± 70% corresponding to the structure with a spatial period of 17 μm.

3.2 Fabrication of Antibacterial Polymer Foils

The presented application example shows how periodic patterns with different sizes can be used for inhibiting the adhesion of bacteria [61]. It is well known from the literature that several strategies can be applied to generate antibacterial properties either by film deposition, smoothening, or roughening of the machined surfaces [62, 63]. Besides biochemically modified surfaces, there is also the possibility of surface structuring, as confirmed in previous studies [64]. Different techniques exist to apply required structures to different surfaces. However, low process costs, high pattern resolution, and complexity for nano- and microscale features represent the current technological challenges. Therefore, the DLIP method was implemented to produce structured metallic stamps (sleeves) to be used as templates in the R2R process to diminish bacteria adhesion on PET foils.

First, nickel sleeves with a thickness of 200 μm, 300 mm wide, and a diameter of 300 mm (Saechsische Walzengravur GmbH, Frankenberg, Germany) were used. The initial surface roughness S_a was 61 nm. The Ni sleeves were processed using the procedure indicated in Sect. 3.3. Line-like structures with spatial periods of 4.3 μm, 3.8 μm, 2.5 μm, and 1.5 μm were produced. The spot diameter was 190 μm, and the employed single pulse laser fluence was 0.36 J/cm^2 for all spatial periods. By changing the pulse-to-pulse overlap, the depth of the periodic structures was varied between 0.1 and 0.5 μm. Later, the PET film samples were processed in R2R hot-embossing system at an embossing temperature of approximately 90 °C and at variable Web speeds between 1 m/min and 12 m/min, reaching throughputs between 0.3 and 3.6 m^2/min. Figure 26.9 shows representative 3D confocal microscopic images of the investigated PET surfaces. In general, the surfaces exhibit a high regularity and homogeneity of the line-like structures, and the structure depths varied between 250 and 800 nm.

The in vitro quantification of *S. aureus* adhesion to the structured PET surfaces revealed the following behavior (Fig. 26.10). The unstructured PET surface, used as a control surface, shows an average value of adherent bacteria of 125 units/mm^2. In the case of the processed PET foils, the number of bacteria adhering to the surfaces differed significantly depending on the roughness (mean value of maximum peak-to-valley height of the profile, R_z) and the spatial period of the surface (detailed information about the methodology employed in the biological assays have been already published elsewhere [61]).

On one hand, the treated PET foils with R_z bellow ~250 nm exhibited a significant reduction of the adhered bacteria as shown in Fig. 26.10b, c (the control surface is shown in Fig. 26.10a). For example, for a spatial period of 4.3 μm (Fig. 26.10b), the number of adherent bacteria was reduced by 54%. On the other hand, higher roughness values (e.g., 550 nm) induced a higher attachment of *S. aureus* bacteria (Fig. 26.10c), similar to the control sample. Taking into account all the surfaces produced, a noticeable decrease of bacterial adhesion was observed for the PET foils with structures that had aspect ratios in the 0.02 and 0.05 range. Hence, the observed bacteria adherence behavior was in agreement with other research works,

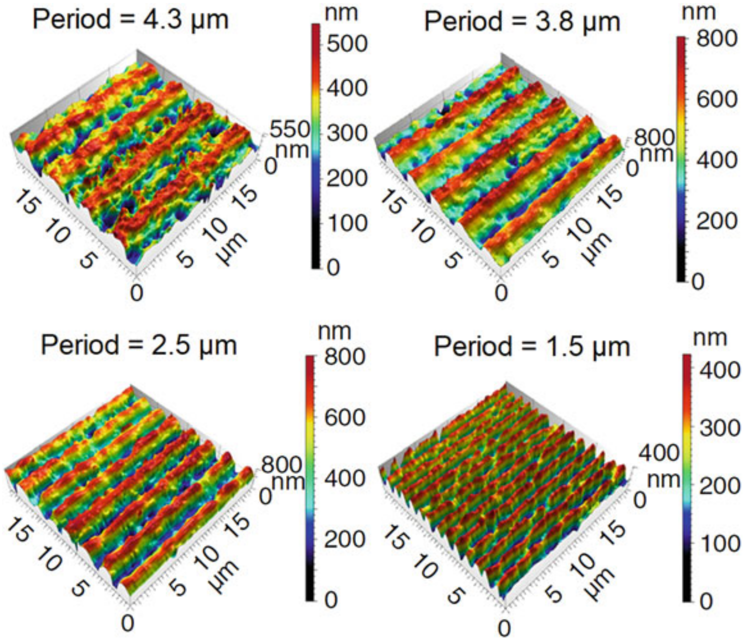

Fig. 26.9 Morphological investigation of the PET tested samples with spatial periods of 4.3 µm, 3.8 µm, 2.5 µm, and 1.5 µm (confocal microscope images) [61]. (©2021 The Authors. Journal of Applied Microbiology published by John Wiley & Sons Ltd. on behalf of Society for Applied Microbiology)

indicating that low surface roughness with a linear-like periodic geometry can be used in order to diminish bacteria adhesion [65–67].

3.3 Efficiency Enhancement of Flexible Perovskite Solar Cells by R2R Hot Embossing

A path to further increase the power conversion efficiency of novel perovskite solar cells is maximizing sunlight absorption, for instance, using patterned substrates with enhanced light-trapping capabilities [68]. However, to be competitive with traditional solar cells, especially in niche markets, low-cost texturing methods have to be developed. In this direction, DLIP patterning combined with roll-to-roll hot embossing appears as a promising solution.

In [46], a proof-of-concept study to assess the technical and economic feasibility of increasing the efficiency of state-of-the-art perovskite solar cells using polymeric substrates structured by R2R hot embossing was introduced. Similar to the previous example (see Sect. 3.2), a 300-mm-long nickel sleeve was structured by DLIP. This

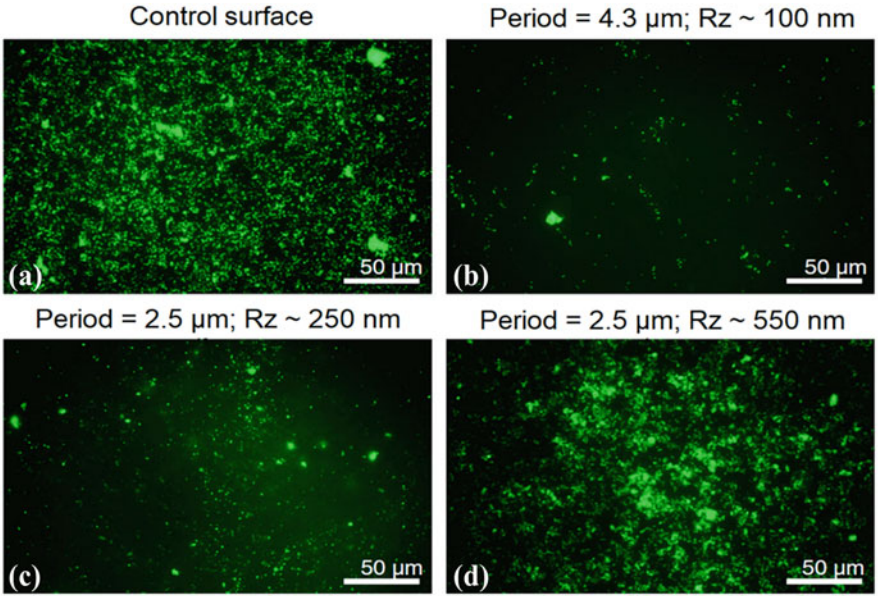
Control surface
Period = 4.3 μm; Rz ~ 100 nm
Period = 2.5 μm; Rz ~ 250 nm
Period = 2.5 μm; Rz ~ 550 nm
(a)
(b)
(c)
(d)
50 μm
50 μm
50 μm
50 μm

Fig. 26.10 In vitro testing of antibacterial properties of structured PET surfaces. The fluorescence microscopy images were taken at a magnification of 630 X [61]. (©2021 The Authors. Journal of Applied Microbiology published by John Wiley & Sons Ltd on behalf of Society for Applied Microbiology)

sleeve was used as a mold in an R2R hot-embossing process to pattern a 200-μm-thick polyethylene terephthalate (PET) foil. The imprinted polymer, shown in Fig. 26.11a, has a rainbow appearance across the entire area due to diffraction of light by the periodic microstructures.

The topography of the R2R imprinted PET foils was characterized by atomic force microscopy (AFM), as shown in Fig. 26.11b. The profile was obtained along the green dotted line. The DLIP-generated periodic line-like structures have a spatial period of 2.7 μm and an average height of 600 nm. In addition, smaller repetitive features were transferred from the sleeve to the polymer.

As reported in previous studies, these structures correspond to LIPSS, which were already observed in many different materials after pulsed picosecond and femtosecond laser radiation [69]. In the case presented here, both low (LSFL) and high-spatial-frequency LIPSS (HSFL) were observed. The LSFL is identified on top of the ridges of the imprinted PET foil and characterized by a lateral length of about 700 nm, which is on the order of the used laser wavelength (1064 nm) and a height between 80 and 150 nm. The HSFL features had an orientation perpendicular to the DLIP grooves and a characteristic length and height of 250 nm and 30 nm, respectively (not shown) [46].

Finally, perovskite solar cells were deposited onto flat and structured PET foils, as well as over a glass substrate (as reference). The current-voltage curves of the

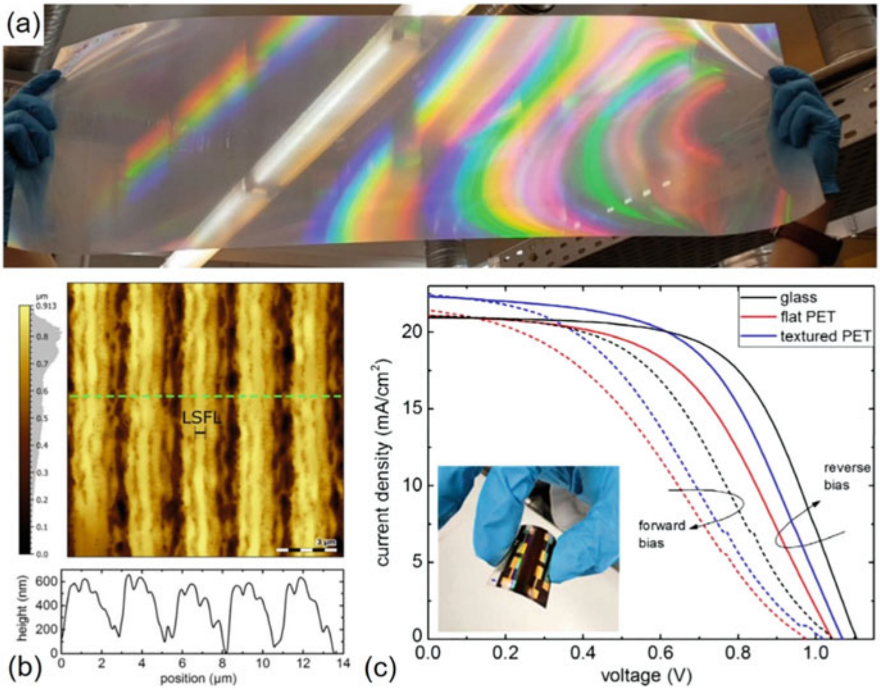

Fig. 26.11 (**a**) Imprinted PET foil by R2R hot embossing showing a high homogeneity over large areas. (**b**) AFM image of the PET-imprinted foil and a profile along the green line (LSFLs with an average spatial period of 700 nm are indicated). (**c**) Current-voltage curves under illumination of flexible perovskite solar cells deposited on glass (as reference), flat, and textured PET foils [46]

best devices deposited on glass, flat, and textured PET are shown in Fig. 26.11c. In the inset of Fig. 26.11c, a photograph of the flexible device deposited on structured PET is shown. The key factor that allows a high efficiency in the textured cell is the increased short-circuit current of 22.3 mA/cm^2, which is 10% higher than the average J_{sc} of the flat PET devices and 8% higher than that of the glass-based cells. In consequence, the obtained results demonstrated the capability of the proposed technology for enhancing the efficiency of perovskite solar cells based on a light-management approach [46].

3.4 Fabrication of Decorative Elements Using Multi-period Structures

The intrinsic periodicity of the DLIP-patterned textures can be exploited for achieving surface relief diffraction gratings. Due to the interaction between incoming white light and the periodic microstructures, light is scattered into multiple diffraction modes providing the surface with a holographic coloration [70]. This trait can be used to engrave motives onto the surface of a good for decoration or even as an anti-counterfeit measure for product protection. To this end, a bitmap image containing the target design is processed with an algorithm and converted to machine code and finally reproduced on the material by DLIP. Furthermore, different colorations or optical appearances can be achieved on the surface by patterning pixels with custom spatial periods or texture geometries, achieving complex microstructures that are hard to replicate by other means.

Examples of different decorative motifs produced on stainless steel by DLIP are shown in Fig. 26.12. In this experiment, the logo and text “CAMP-Center for Advanced Micro-Photonics” (Fig. 26.12a) were patterned with a line-like texture using a scanner-based DLIP system and with a spatial period of 2.4 μm [71]. The engraved image had a size of 6 × 20 mm^2 and was fabricated in 0.82 s. Figure 26.12b displays a photograph of a pattern resembling a chessboard, in which the squares have different colors. This was possible by patterning four spatial periods, namely, 2.4, 2.8, 3.2, and 3.6 μm, for different squares in the chessboard. In the image, 64 squares with a size of 2.5 × 2.5 mm^2 were patterned, resulting in a total area of 20 × 20 mm^2, that was processed in approximately 14 s [71]. However, due to the nature of the diffraction phenomenon and particularly for large areas, it is not possible to achieve a homogeneous coloration by using micropatterns with a single period. Instead, fields with variable spatial periods can be engraved on a surface to obtain a given color over a relatively large area at specific viewing conditions, i.e., for a certain illumination and observation angle.

To illustrate this strategy, photographs of two DLIP-treated steel plates are shown in Fig. 26.12c–e taken at the same illumination and observation angles [72]. Each vertical stripe on the sample shown in Fig. 26.12c was patterned with a different spatial period, ranging from 1.74 μm (left stripe) to 2.37 μm (right stripe). Because of the diffraction of white light, each stripe shows a holographic coloration. In the case of the sample shown in Fig. 26.12d, each stripe was patterned with a variable spatial period as a function of the vertical position so that the observed color is homogeneous along the whole stripe. Furthermore, combining the textures for obtaining red, green, and blue colors, a homogeneous white coloration can be achieved (Fig. 26.12e). This strategy can thus be used for fabricating multicolored motives, like the one shown in Fig. 26.12f [72]. While the image in Fig. 26.12g exhibits homogeneous colors at the designed observation angle of 22° as the target picture, the colors gradually fade as the observation angle changes (Fig. 26.12h).

Due to the complexity of the multi-periodic texture and its singular optical behavior, this patterned logo is significantly harder to reproduce, resulting in a superior product protection feature compared to single-period holograms.

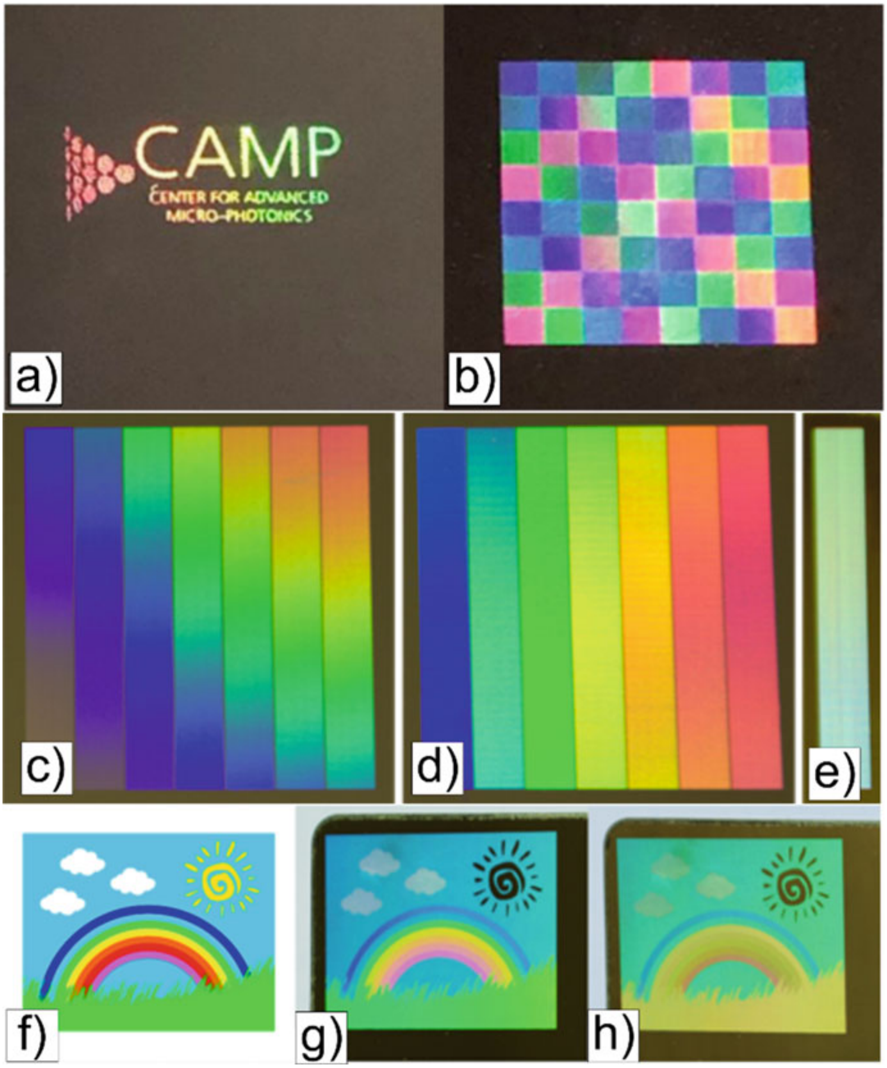

Fig. 26.12 Decorative elements engraved on stainless steel by DLIP. (**a**) Logo featuring a single spatial period of 2.4 μm. (**b**) Chessboard pattern with four different spatial periods (2.4, 2.8, 3.2, and 3.6 μm) providing the squares different colorations. The size of each square is 1.5 mm × 1.5 mm [71]. (**c**) Vertical stripes with a single spatial period ranging from 1.74 μm (left stripe) to 2.37 μm (right stripe). The size of each stripe is 10.5 × 1.5 mm. (**d**) Vertical stripes with variable periods as a function of vertical position to obtain homogeneous colors. (**e**) Homogeneous white color. (**f**) Target picture and observed structural colors under viewing angles of (**g**) 22° (designed observation angle) and (**h**) 25°. The size of the picture is 10.5 × 10.5 mm [72]

4 Challenges and Future Trends

Laser interference micro-/nanoprocessing techniques have their genesis in the laboratory. Being one of the main challenges of these techniques is to cross the barriers of the laboratory workbench and to establish their place in the industry. As with all industrial manufacturing methods, the primary goal is to increase production efficiency: to produce more in less time while maintaining competitive manufacturing costs. Several concepts are currently being developed for boosting the throughput of interference-based patterning technologies.

The high-speed concept for DLIP patterning, pioneered by Fraunhofer IWS/TU Dresden [73], opens up a number of industrial possibilities for laser technology. As with conventional DLIP, it uses a double bi-prismatic system in which the laser beam is split into two sub-beams that are superimposed on the sample surface. But in addition, the laser beams are shaped to form an elongated beam of 5 mm × 100 μm on the sample surface by first expanding the laser beam in one spatial direction using a cylindrical telescope and, secondly, by focusing the sub-beams one-dimensionally with an additional cylindrical lens. The angle of intersection between the overlapping sub-beams is defined by the wedge angles of the bi-prisms, and therefore, the interference spatial period is a fixed feature of the designed optical head. According to the latest findings, this high-speed DLIP configuration was able to produce surface patterns with production speeds of 0.36 m^2/min and 0.9 m^2/min on metal and polymers, respectively, accompanied by low production costs (~ 1.2 US$/$m^2$) [73].

Another strategy involves taking advantage of the high repetition rates, on the order of a few MHz, of ultrashort pulsed lasers in tandem with ultrafast scanners such as polygon scanner systems. In polygon scanners, the laser beam is deflected by a polygonal mirror wheel rotating at high speed. After the mirror wheel, the beam is focused with flat-field optics onto the workpiece. The result is a rapid unidirectional movement of the laser spot on the workpiece reaching scanning speeds beyond 1000 m/s [74]. The rotational speed of the wheel must be very precisely controlled to obtain a constant marking speed and high repeatability. Although polygon scanners are already used in laser ablation technology such as DLW, their implementation in laser interference microprocessing is currently subject of intense research due to their potential for achieving manufacturing throughputs well beyond the 1 m^2/min benchmark [75, 76]. For example, within the EU-funded project "LAMpAS," a DLIP-polygon scanner system is being developed that will be combined with a 1.5 kW pulsed picosecond laser source. Up to now, the proof of principle for this configuration has been demonstrated, permitting to reach throughputs of 1.5 m^2/min on polymers, using approximately 400 W of laser power [77].

Another way to improve the productivity of laser processing is the introduction of in-line monitoring methods to improve the process stability, optimize its reproducibility, and increase the quality of the resulting products. Furthermore, from a more fundamental point of view, these methods can be used in laser processing to generate in-depth knowledge of the underlying physical mechanisms, such as the analysis of the thermal behavior in additive manufacturing, the study of the plasma ignition and development, and the evaluation of the penetration depth of laser radiation [78, 79].

Several strategies have been developed to assess the quality and morphology of surface structures fabricated with DLIP/LIL by recording different signals, such as capturing diffraction patterns by irradiating the textured surface with a low-power laser source [79], monitoring accumulated heat through infrared cameras [80], and collecting photoacoustic signals from acoustic emissions in the air during laser ablation [81]. Once the corresponding signal is detected, it must then be processed using dedicated algorithms, which decide whether the quality of the process or treated workpiece is satisfactory or not.

Machine learning provides a holistic use of the information contained in the acquired data to understand and predict the combined impact of multiple process parameters. The output from learning algorithms is contrasted against back-up libraries containing experimental and/or simulation results with optimized parameters enabling the prediction of quality characteristics. Also, real-time analysis of in situ process data can be performed by artificial neural networks for a wide range of process regimes [82]. Hence, the ultimate goal of implementing these monitoring technologies feeding learning algorithms is the design of artificial intelligence models for Zero Defect Strategy (ZDS) quality control. In this direction, the fabrication of non-defective parts based on a "First-Time-Right" approach will reduce production costs and minimize environmental impacts [83].

As a result of more than two decades of research and development, DLIP technology [23, 84] is now positioned as an industrial-compatible processing technique with a high reproducibility rate for structure periods between 700 nm and 15 μm, offering 24/7 operation, as long as standard periodic maintenance of laser power and beam propagation monitoring is performed. Probably the most important constraint of the technique is the impracticality of achieving large-scale (larger than 100 cm^2) surface homogeneity for nanometric/submicron structure periods due to limitations of the optical elements, such as numerical aperture or lens aberrations. However, for many applications, surface homogeneity has not a significant impact on the surface functionality. For industrial applications requiring submicron structure periods, other direct laser techniques, such as LIPSS, or indirect techniques, such as hot embossing combined with DLIP, are more suitable. Similarly, surface texturing by DLW is technologically simpler when feature sizes larger than 15–20 μm are required.

5 Conclusions and Outlook

Laser-based interferometric methods have been demonstrated to be promising technologies to fabricate defect-free periodic structures on a large variety of materials. Furthermore, DLIP has been successfully implemented utilizing different pulsed laser sources, operating, for instance, with nanosecond or picosecond pulses. Also, different processing systems and configurations using the interference principle have been described, demonstrating the possibility for the fast and precise tailoring of material surface microstructures and topographies on industrial relevant scales as well as to produce tools for roll-to-roll imprint processes. The last allows in the future a significant reduction of costs of imprint tools and, thus, of the fabricated products.

Because of the extreme flexibility of DLIP in terms of geometries that can be produced, sizes, as well as the important number of materials that can be treated, a large number of applications are possible as was shown. In particular, high-throughput processing of dental implants, decorative elements, as well as polymer foils with antibacterial performance and perovskite solar cells has been demonstrated. In the future, due to the significant improvements on stability, performance, and cost reduction of laser sources that can be implemented in DLIP, more applications will arise, and the transfer to the industry of this knowledge will play a relevant role.

Last but not least, the digitization of processes and the deployment of machine learning and artificial intelligence will become key drivers for cutting-edge laser interference technologies. Through the implementation of ZDS, energy consumption will be reduced, system setup times shortened, and environmental impacts minimized, resulting in greener and safer manufacturing.

Acknowledgments The work of A.L. was supported by (i) the German Federal Ministry of Education and Research (BMBF) within the “Unternehmen Region, Innovation and structural transformation/WIR!” program, under contract number 03WIR2003B and implemented by the Project Management Agency Jülich (PTJ); (ii) the Reinhart Koselleck project (323477257), which has received funding from the German Research Foundation (German: Deutsche Forschungsgemeinschaft DFG); and (iii) the German Research Foundation (DFG) under the Excellence Initiative program by the German federal and state government to promote top-level research at German universities. M.S. acknowledges the Alexander von Humboldt Foundation. The authors are especially grateful to Dr. Bogdan Voisiat for fruitful discussions about technological aspects of laser interference setups.

References

1. A.F. Lasagni, T. Kunze, M. Bieda, D. Günther, A. Gärtner, et al., Proc. SPIE **9735**, 973515 (2016)
2. H. van Wolferen, L. Abelmann, *Lithography: Principles, Processes and Materials* (Nova Science Publishers Inc, New York, 2011) ISBN: 978-1-61761-837-6
3. A.F. Lasagni, B.S. Menéndez-Ormaza, Adv. Eng. Mater. **12**, 54–60 (2010)
4. J.H. Seo, J.H. Park, Z. Ma, J. Choi, B.K. Ju, J. Nanosci. Nanotechnol. **14**, 1521–1532 (2014)
5. C.J.M. van Rijn, J. Micro/Nanolithogr. MEMS MOEMS **5**, 011012 (2006)
6. H. Lorenz, M. Despont, N. Fahrni, N. LaBianca, P. Renaud, et al., J. Micromech. Microeng. **7**, 121 (1997)
7. Q. Xie, M.H. Hong, H.L. Tan, G.X. Chen, L.P. Shi, et al., J. Alloys Compd. **449**, 261–264 (2008)

8. F. Watt, A.A. Bettiol, J.A. Van Kan, E.J. Teo, M.B.H. Breese, Int. J. Nanosci. **4**, 269–286 (2005)
9. Y. Chen, Microelectron. Eng. **135**, 57–72 (2015)
10. H. Schift, Appl. Phys. A Mater. Sci. Process. **121**, 415–435 (2015)
11. C. Nebel, S. Christiansen, H.P. Strunk, B. Dahlheimer, U. Karrer, et al., Phys. Status Solidi (a) **166**, 667–674 (1998)
12. A. Lasagni, F. Mücklich, Appl. Surf. Sci. **247**, 32–37 (2005a)
13. A. Lasagni, F. Mücklich, Appl. Surf. Sci. **240**, 214–221 (2005b)
14. F. Yu, F. Mucklich, P. Li, H. Shen, S. Mathur, et al., Biomacromolecules **6**, 1160–1167 (2005)
15. A. Rosenkranz, L. Reinert, C. Gachot, F. Mücklich, Wear **318**, 49–61 (2014)
16. A. Aktag, S. Michalski, L. Yue, R.D. Kirby, S.H. Liou, J. Appl. Phys. **99**, 093901 (2006)
17. L. Guo, H.B. Jiang, R.Q. Shao, Y.L. Zhang, S.Y. Xie, et al., Carbon **50**, 1667–1673 (2012)
18. G. Aichmayr, D. Toet, M. Mulato, P.V. Santos, A. Spangenberg, et al., J. Non-Cryst. Solids **227**, 921–924 (1998)
19. M.K. Kelly, J. Rogg, C.E. Nebel, M. Stutzmann, S. Kátai, Phys. Status Solidi (a) **166**, 651–657 (1998)
20. F. Mücklich, A. Lasagni, C. Daniel, Intermet. **13**, 437–442 (2005)
21. A. Lasagni, F. Mücklich, M.R. Nejati, R. Clasen, Adv. Eng. Mater. **8**, 580–584 (2006)
22. M. Bieda, C. Schmädicke, T. Roch, A. Lasagni, Adv. Eng. Mater. **17**, 102–108 (2015)
23. A.F. Lasagni, C. Gachot, K.E. Trinh, M. Hans, A. Rosenkranz, et al., Laser-based micro-and nanoprocessing XI. Proc. SPIE **10092**, 1009211-1-11 (2017)
24. M. Campbell, D.N. Sharp, M.T. Harrison, R.G. Denning, A.J. Turberfield, Nature **404**, 53 (2000)
25. A.D. Campo, E. Arzt, Chem. Rev. **108**, 911 (2008)
26. K. Ogai, Y. Kimura, R. Shimizu, J. Fujita, S. Matsui, Appl. Phys. Lett. **66**, 1560 (1995)
27. S. Fujita, S. Maruno, H. Watanabe, Y. Kusumi, M. Ichikawa, Appl. Phys. Lett. **66**, 2754 (1995)
28. Y. Shimizu, Nanomanuf. Metrol. **4**, 3–27 (2021)
29. C. Valsecchi, L.E. Gomez Armas, J. Weber de Menezes, Sensors **19**, 2182 (2019)
30. L. Dong, Z. Zhang, R. Ding, L. Wang, M. Liu, et al., Surf. Coat. Technol. **372**, 434–441 (2019)
31. L. Cheng, R. Lu, H. Lipson, Laser Photon. Rev. **4**, 568–580 (2009)
32. N.G. Quilis, M. Lequeux, P. Venugopalan, I. Khan, W. Knoll, et al., Nanoscale **10**, 10268–10276 (2018)
33. J.S. Hwang, M. Yang, Sensors **18**, 4076 (2018)
34. A.J. Wolf, H. Hauser, V. Kübler, C. Walk, O. Höhn, et al., Microelectron. Eng. **98**, 293–296 (2012)
35. B. Bläsi, V. Kübler, H. Hauser, nnt2019 (2019)
36. A. Gombert, K. Forberich, B. Bläsi, J. Mick, W. HoBfeld, et al., Proc. SPIE **5454**(5454), 129–136 (2004)
37. J. Choi, M.H. Chung, K.Y. Dong, E.M. Park, D.J. Ham, et al., J. Nanosci. Nanotechnol. **11**, 778 (2011)
38. M. Hong, L.S. Tan, B. Luk'yanchuk, L. Shi, T. Chong, SPIE News room (2016)
39. A.F. Lasagni, D. Yuan, P. Shao, S. Das, Adv. Eng. Mater. **11**, B20–B24 (2009)
40. Y. Shimizu, R. Aihara, K. Mano, C. Chen, Y. Chen, X. Chen, W. Gao, et al., Precision Eng. **52**, 138–151 (2018)
41. Y. Nakata, Adv. Opt. Technol. **5**, 29–38 (2015)
42. A. Madelung, S. Alamri, T. Steege, B. Krupop, A.F. Lasagni, et al., Adv. Eng. Mat., 202001414 (2021)
43. V. Lang, B. Voisiat, A.F. Lasagni, Materials **12**, 1484 (2019)
44. K. Pelsue, High speed read/write tech. Adv. Print. Data Handl. **0390**, 70 (1983)
45. V. Furlan, M. Biondi, A.G. Demir, G. Pariani, B. Previtali, et al., Appl. Surf. Sci. **423**, 619 (2017)
46. M. Soldera, Q. Wang, F. Soldera, V. Lang, A. Abate, et al., Adv. Eng. Mater., 1901217 (2020a)
47. V. Lang, A.F. Lasagni, Adv. Eng. Mater. **19**, 1700201 (2017)

48. A. Lasagni, S. Alamri, A. Aguilar-Morales, F. Rößler, B. Voisiat, et al., Appl. Sci. **8**, 1260 (2018)
49. M. Soldera, F. Fortuna, S. Teutoburg-Weiss, S. Milles, S. Taretto, et al., J. Laser Micro Nanoeng. **15**, 97–103 (2020b)
50. V. Lang, A. Rank, A.F. Lasagni, Proc. SPIE **10092**, 100920T (2017)
51. Y. Fu, M. Soldera, W. Wang, B. Voisiat, A.F. Lasagni, Materials **12**, 3409 (2019)
52. M. Soldera, Y. Fu, F. Fortuna, W. Wang, A.F. Lasagni, Proc. SPIE **11268**, 1126824 (2020c)
53. Z. Pan, F. Cheng, B. Zhao, Polymers **9**, 725 (2017)
54. W. Liu, S. Liu, L. Wang, Coatings **9**, 249 (2019)
55. L. Le Guéhennec, A. Soueidan, P. Layrolle, Y. Amouriq, Dent. Mater. J. **23**, 844–854 (2007)
56. L. Damiati, M.G. Eales, A.H. Nobbs, B. Su, P.M. Tsimbouri, et al., J. Tissue Eng. **9**, 2041731418790694 (2018)
57. C. Mas-Moruno, B. Su, M.J. Dalby, Adv. Health. Mat. **8**, 1801103 (2019)
58. C. Zwahr, A. Welle, T. Weingärtner, C. Heinemann, B. Kruppke, et al., Adv. Eng. Mat. **21**, 1900639 (2019)
59. C. Zwahr, D. Günther, T. Brinkmann, N. Gulow, S. Oswald, et al., Adv. Health. Mat. **6**, 1600858 (2017)
60. F.H. Rajab, C.M. Liauw, P.S. Benson, L. Li, K.A. Whitehead, Food Bioprod. Process. **109**, 29–40 (2018)
61. A.K. Meinshausen, M. Herbster, C. Zwahr, M. Soldera, T. Halle, et al., J. App. Microbiol. **131**, 1498–1514 (2021)
62. L.A. Gallarato, L.E. Mulko, M.S. Dardanelli, C.A. Barbero, D.F. Acevedo, et al., Colloids Surf. B: Biointerfaces **150**, 1–7 (2017)
63. M. Esposito, L. Murray-Curtis, M.G. Grusovin, P. Coulthard, H.V. Worthington, Cochrane Database Syst. Rev. **4**, Cd003815 (2007)
64. A. Jaggessar, H. Shahali, A. Mathew, P.K.D.V. Yarlagadda, J. Nanobiotechnol **15**, 64 (2017)
65. E.A. Cuello, L.E. Mulko, C.A. Barbero, D.F. Acevedo, E.I. Yslas, Colloids Surf. B: Biointerfaces **188**, 110801 (2020)
66. K.A. Whitehead, J. Colligon, J. Verran, Colloids Surf. B: Biointerfaces **41**, 129–138 (2005)
67. S.D. Ulrich, T.M. Seyler, D. Bennett, R.E. Delanois, K.J. Saleh, et al., Int. Orthop. **32**, 597–604 (2008)
68. M.M. Tavakoli, K.H. Tsui, Q. Zhang, J. He, Y. Yao, et al., ACS Nano **9**, 10287 (2015)
69. J. Bonse, J. Krüger, S. Höm, A. Rosenfeld, J. Laser Appl. **24**, 042006 (2012)
70. T. Tamulevičius, M. Juodėnas, T. Klinavičius, A. Paulauskas, K. Jankauskas, et al., Sci. Rep. **8**, 142451–142411 (2018)
71. V. Lang, A. Madelung, S. Alamri, T. Steege, B. Krupop, et al., Proc. SPIE **11268**, 112680T (2020)
72. B. Voisiat, W. Wang, M. Holzhey, A.F. Lasagni, Sci. Rep. **9**, 78011–78019 (2019)
73. V. Lang, T. Roch, A.F. Lasagni, *Laser-based Micro-and Nanoprocessing X*, vol 9736 (2016)
74. F. Roessler, A. Streek, Adv. Opt. Tech. **10**, 297–304 (2021)
75. B. Jaeggi, B. Neuenschwander, M. Zimmermann, L. Penning, R. de Loor, et al., Laser Applications in Microelectronic and Optoelectronic Manufacturing (LAMOM) XIX, 8967, 89670Q (2014)
76. B. Neuenschwander, B. Jäggi, M. Zimmermann, L. Penning, R. de Loor, et al., International Congress on Applications of Lasers & Electro-Optics, 2013, pp. 677–685 (2013)
77. R. Baumann, F. Ränke, B. Voisiat, A.F. Lasagni, Mater. Lett. (Submitted, 2021)
78. A. Michalek, T. Jwad, P. Penchev, T.L. See, S. Dimov, J. Micro. Nano-Manufact. **8**, 011002-1-7 (2020)
79. S. Teutoburg-Weiss, B. Voisiat, M. Soldera, A.F. Lasagni, Materials **13**, 53 (2020)
80. N. Schröder, S. Teutoburg-Weiss, G. Vergara, A.F. Lasagni, J. Laser Micro Nanoeng. **16**, 130–137 (2021)
81. T. Steege, S. Alamri, A.F. Lasagni, T. Kunze, Sci. Rep. **11**, 1–10 (2021)
82. C. Stadter, M. Schmoeller, L. von Rhein, M.F. Zaeh, J. Laser Appl **32**, 022046 (2020)

83. H. Sohrabpoor, R.T. Mousavian, M. Obeidi, I.U. Ahad, D. Brabazon, Int. J. Adv. Manufact. Tech. **104**, 4571–4580 (2019)
84. L. Mulko, M. Soldera, A.F. Lasagni, Nanophotonics **11**, 203–240 (2022)

Chapter 27
Internal Structuring of Semiconductors with Ultrafast Lasers: Opening a Route to Three-Dimensional Silicon Photonics

David Grojo, Maxime Chambonneau, Shuting Lei, Alexandros Mouskeftaras, Olivier Utéza, and Andong Wang

Abstract Important challenges remain to achieve reliable three-dimensional laser writing inside semiconductors as important as silicon. Experiments show that nonlinear energy deposition with long infrared laser pulses can modify silicon internally. However, the level of controllability is extremely limited compared with the femtosecond laser nanostructuring regimes reported in transparent dielectrics. Recent efforts have concentrated on the specificities of the bulk silicon response to tightly focused ultrashort pulses. The strong propagation nonlinearities inherent to narrow band-gap semiconductors limit the space-time laser energy localization and prevent in most cases material breakdown with the shortest pulses. This chapter proposes an overview of this emerging topic and the practical solutions to this problem. It also discusses the potential of three-dimensional laser nanostructuring in narrow band-gap semiconductors to address applications in different fields. Among them, the first demonstrations of refractive index laser engineering in silicon open the perspective to move silicon photonics from two-dimensional systems to monolithic three-dimensional architectures.

Keywords Femtosecond laser · 3D writing · Silicon · Semiconductor · Waveguide · Refractive index · Silicon photonics

---

D. Grojo (✉) · A. Mouskeftaras · O. Utéza · A. Wang
Aix-Marseille Université, CNRS, LP3 UMR7341, Marseille, France
e-mail: david.grojo@univ-amu.fr; alexandros.mouskeftaras@univ-amu.fr; olivier.uteza@univ-amu.fr; andong.wang@univ-amu.fr

M. Chambonneau
Friedrich Schiller University Jena, Institute of Applied Physics, Abbe Center of Photonics, Jena, Germany
e-mail: maxime.chambonneau@uni-jena.de

S. Lei
Department of Industrial and Manufacturing Systems Engineering, Kansas State University, Manhattan, KS, USA
e-mail: lei@ksu.edu

© The Author(s), under exclusive license to Springer Nature Switzerland AG 2023
R. Stoian, J. Bonse (eds.), *Ultrafast Laser Nanostructuring*, Springer Series in Optical Sciences 239, https://doi.org/10.1007/978-3-031-14752-4_27

1 Introduction

Focused to small focal spots, intense light pulses lead to local nonlinear energy deposition allowing the production of micromodifications at arbitrary location inside transparent materials [1–3]. In a few decades, this has led to the emergence of an alternative to lithography for direct micro-fabrication and rapid prototyping of micro-systems [4–7]. According to experiments in dielectrics described in Chap. 21, there are actually three main types of modifications which can be achieved with femtosecond lasers [8, 9]. First, at low intensities (i.e., slightly above the threshold for permanent modification), repeated bond breaking by multiphoton ionization leads to structural changes [10] and uniform refractive index modification ($\Delta n \approx 10^{-3}$) which allows the fabrication of waveguides and photonic circuits [1, 2, 11, 12]. Second, with repeated irradiations at higher fluences, the modification generally becomes heterogeneous with the formation of defects (from excitons [13] to lattice distortions and reorganization on a subwavelength scale [14]). In fused silica, this culminates with the formation of well-ordered planar nanogratings perpendicular to the laser polarization [15, 16] attracting considerable interest for advanced technologies including photonics [17–22]. Third, when extremely tight-focusing conditions are employed, the extraordinary space-time confinement of the interactions leads to pressure and temperature conditions that are not accessible with other techniques [23, 24]. This latter regime forms void channels for microfluidic applications [25–27]. A particular attention is also given to these microexplosions for the synthesis of new allotropes of solids with unusual physical properties, opening possibilities for future technologies [28]. The physics behind the access of these extreme states in silicon is the subject of Chap. 13.

Taken together, these possibilities in dielectrics allow addressing lab-on-a-chip applications where laser writing can combine different optical, mechanical, and fluidic functionalities, while any required electronic functionality is added by other means (e.g., lithography) so far. For this reason, it is today highly desirable to achieve ultrafast laser internal structuring not only in dielectrics but also in semiconductors—especially silicon—to provide the ability to write directly hybrid devices combining electronics and other functionalities [29]. Due to the band-gap difference between dielectrics and semiconductors, this requires to translate high-power laser experiments in the infrared for accessing the transparency region of narrow-gap materials, where nonlinear ionization processes (e.g., multiphoton ionization) similar to those in dielectrics [30] are predominant.

In this chapter, we review the recent works in this direction thanks to the advent of new high-power laser sources emitting in the infrared (e.g., Er- or Tm-doped fiber lasers) and optical parametric amplifiers (OPA) that become routinely available in research laboratories. We examine experimental results with pulse durations ranging from 60 fs to 150 ns, wavelengths in the 1.03–2.4-μm range, and various sets of control parameters which have been tentatively exploited to achieve high-precision modifications inside crystalline silicon (c-Si) and other semiconductors. We describe the major challenges that remain to demonstrate the same level of controllability as in dielectrics. While the underlying fundamental aspects of high-intensity interaction in semiconductors are today only partially understood from very recent investigations, we review the main physical mechanisms explaining that the only reported modifications under conventional configurations have been achieved in two-photon absorption regimes with pulses or pulse trains with apparent durations from several picoseconds [31, 32] to nanoseconds [33] or more. Producing modifications in silicon with femtosecond pulses is generally doomed to failure, unless unconventional and impractical focusing conditions are employed [34–36]. The common denominator for all these demonstrations is that they aim at limiting the strong prefocal interactions. We will show how this constitutes a key to achieve sufficient energy deposition for producing permanent micromodification inside semiconductors. The most recent successes that will be discussed in this chapter open new and exciting technological perspectives including direct laser writing applied to the rapidly growing field of *silicon photonics* and the advent of laser solutions to meet some of the challenges of future microelectronics.

2 Long-Pulse-Induced Internal Modifications in Semiconductors and Applications

2.1 Nanosecond Laser-Induced Modifications

The topic of laser-induced subsurface modification in semiconductors was pioneered in 2006 by Ohmura et al. who demonstrated confined modifications in c-Si by using 150-ns pulses at the fundamental wavelength of a Nd:YAG laser (wavelength $\lambda = 1064$ nm; photon energy $E_{\mathrm{ph}} = hc/\lambda = 1.16$ eV) [37]. This wavelength is not sufficiently high to access the region of full transparency for Si (band gap $E_g = 1.12$ eV) and, thus, to the production of modifications at arbitrary depths. However, by tightly focusing the pulses at depths less than the penetration depth ($\delta = 1/\alpha \approx 100\,\mu\mathrm{m}$ at 1064 nm [38]), sufficient intensity contrast could be obtained, in turn leading to high absorption (by thermal runaway from near-band-edge absorption) and subsequent material melting in a localized region near the focus. To apprehend the local band-gap closure with progressive temperature rise, one can refer to Varshni's empirical expression [39] which leads to a band gap below 1 eV for a temperature of 600 K, far below the melting threshold of Si ($T_{\mathrm{melt}} = 1687$ K [38]).

The emergence of high-power erbium-doped nanosecond lasers emitting at 1550 nm motivated recent successful studies in the two-photon absorption regime to initiate similar localized thermal runaway [33, 40–42]. For all these heat-driven experiments in the nanosecond regime, the precision is limited by thermal effects—especially, heat diffusion. Simulations of the temperature change [37, 40] as well as images of the modified material [43] show that the melting threshold of c-Si can be largely exceeded in regions with smallest dimensions on the order of

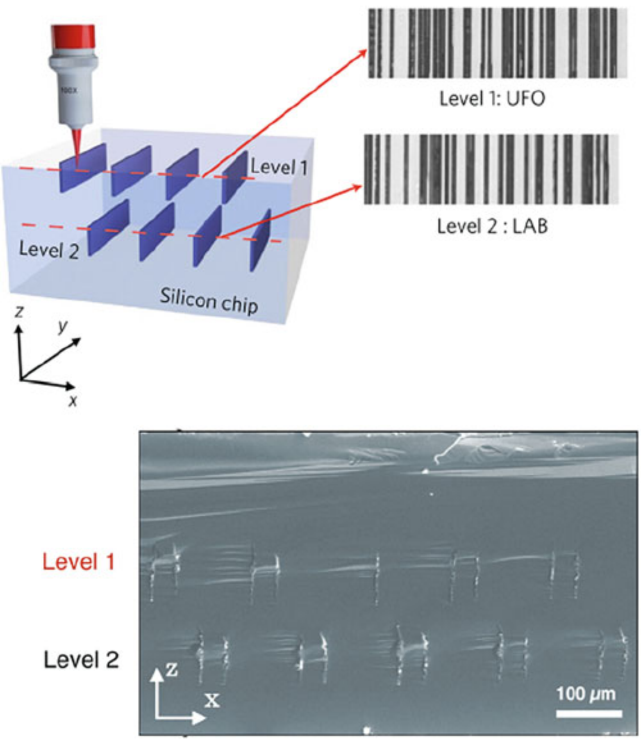

Fig. 27.1 Illustration of multilevel information data of nanosecond laser writing and reading by infrared microscopy inside silicon (NA $= 0.55$, $\tau = 5$ ns, $E = 8\,\mu$J). Bottom image is a cross section of modification produced with the nanosecond pulses as observed by SEM. Level 1 and level 2 are, respectively, at 230 μm and 460 μm from the laser entrance side of the silicon wafer. Adapted with permission [33]

tens of micrometers unless complex multi-beam configurations are used to force a nonlinear collapse of the writing beam [33]. However, as the modifications are governed by thermo-mechanical effects, they remain similar to those reported in the initial paper of Ohmura et al. [37]. The main advantage of two-photon absorption compared to linear absorption is the capacity it provides to deposit the laser energy at arbitrary depths inside silicon. As two-photon absorption depends on the square of the intensity, it remains confined in the focal region at any processing depth. Figure 27.1 shows modifications written at two different depths in a Si wafer [33] with a 1550-nm nanosecond laser and illustrates the 3D capability of this laser writing method.

Nanosecond laser-produced subsurface modifications consist of a melted volume that resolidifies in more or less disordered regions that can take various allotropic forms (amorphous, polycrystalline, or monocrystalline) [44]. For detailed analyses of the modified Si crystal structures, one can refer to the works from Verburg et al. [42] where transmission electron microscopy (TEM) and Raman spectroscopy

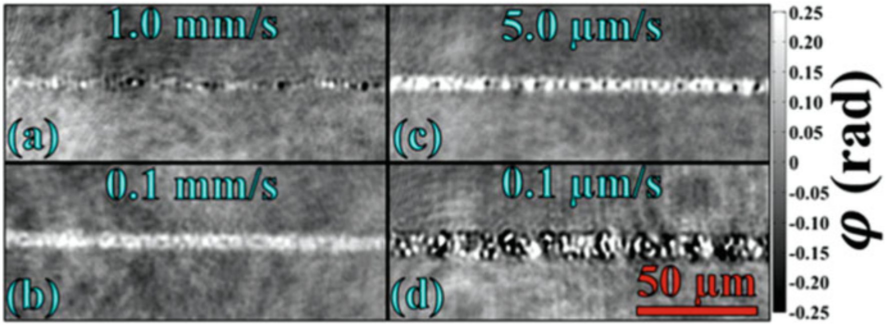

Fig. 27.2 Infrared phase images of lines inscribed longitudinally inside silicon at different scanning speeds (NA = 0.45, $\tau = 5$ ns, $E = 2\,\mu$J). The images reveal regions of positive (bright) and negative (dark) refractive index changes. Reprinted with permission from [48] ©The Optical Society

were applied. The types of modifications that were found in different regions are (i) perfectly resolidified diamond cubic silicon with and without lattice defects, (ii) amorphous material, (iii) cracks and voids [45], and (iv) Si-III/Si-XII phases evidencing high-pressure conditions [46].

By means of infrared quantitative-phase microscopy, Li et al. investigated the refractive index change associated with these transformations depending on the applied laser conditions [43]. Consistent with the abovementioned material analyses, this diagnostic revealed in most cases nonuniform modified zones with coexisting positive and negative refractive index changes. The index variations are reasonably associated with the creation of micro-cavities/porosities and densified regions. The overall apparent index variation is negative due to the important contribution of disruptions and porosities ($n \approx 1$) to the index change [33, 47]. Nevertheless, a study on channel writing [48] revealed interestingly there exists an appropriate scanning speed for which the melted material can redistribute advantageously to achieve a nearly uniform positive index change, as shown in Fig. 27.2b. As shown below, this positive- and negative-tone writing ability depending on the irradiation parameters with the same laser is today largely exploited for technological demonstrations.

2.2 *Potential Applications*

The first laser writing applications inside silicon relied on nanosecond pulses. Hereafter, we present various patented technologies and growing efforts to demonstrate a level of control relevant for the fabrication of photonic microdevices.

Wafer Dicing A major successful application of subsurface modifications by nanosecond lasers is wafer dicing by experimental developments based on the so-called *Stealth dicing* technology originally patented by the Japanese company Hamamatsu [49]. It consists of a two-step method where nanosecond laser pulses are first focused inside the wafer, which results in subsurface modifications along lines inside the wafer. After laser processing, an external force is applied to the wafer which then cleaves the sample along the planes containing the subsurface modifications, thereby separating the wafer into individual chips. This method is especially valuable for the separation of sensitive devices such as microelectromechanical systems (MEMS), as it is dry and debris-free [50] in comparison to conventional laser ablation methods.

Data Inscription Another general application is wafer marking [51] or permanent data encoding in semiconductors [52]. In the example shown in Fig. 27.1, Tokel et *al.* inscribed barcodes buried at different depths inside Si wafers and have demonstrated the possible reading of each independent layer thanks to infrared optical coherence tomography (OCT) [33, 52]. The method is attractive for the semiconductor industry because it is fast and does not damage the surface area of the wafer which fabricated the integrated circuits.

Fabrication of Waveguides and Photonic Microdevices The possibility to control the refractive index of silicon with nanosecond laser pulses makes them attractive for directly integrating various optical functionalities in microelectronic wafers. An important subject is waveguide writing. In 2016, Chambonneau et al. demonstrated the possibility to inscribe longitudinal lines (i.e., along the optical axis) inside the material [48]. As shown by the phase images in Fig. 27.2, the optical properties of the written lines strongly depend on the writing speed. For too high (≥ 1.0 mm s^{-1}) and too low speed (≤ 5.0 µm s^{-1}), the lines consist of a mixture between positive and negative index changes, which is ascribable to the single-pulse configuration and cumulative effects, respectively. Interestingly, for 0.1-mm s^{-1} writing speed, the lines exhibit solely a positive index change $\Delta n = 5.3 \times 10^{-3}$ (assuming a cylindrical symmetry). These structures represent the first laser inscription of waveguides deep inside monolithic crystalline silicon, as confirmed by light injection in the structures. The same group has proposed strategies for optimized writing process for the fabrication of waveguides, gratings [53], and Y-splitters [54]. Process optimizations include the implementation of equivalents of the slit beam shaping technique for transverse writing [54]. In a recent work, Wang et al. first exploited transverse writing thanks to astigmatic beam shaping with a cylindrical telescope and a slit [55]. With this configuration, the authors demonstrated centimeter-long straight and curved waveguides inside silicon as shown in Fig. 27.3. Power measurements showed losses around 3.3 dB cm^{-1} [56].

Besides the regime of gradient-index (GRIN) waveguide writing, the laser-produced modifications generally show a negative index change which can also be advantageously exploited in this context. A remarkable illustration is depressed-cladding waveguides, as demonstrated by Tokel et al. [33], followed by Turnali et al. [47]. They created tubular modifications exhibiting a refractive index change $\Delta n = -3.0 \times 10^{-4}$. Despite the leaky nature of the guiding structures, excellent

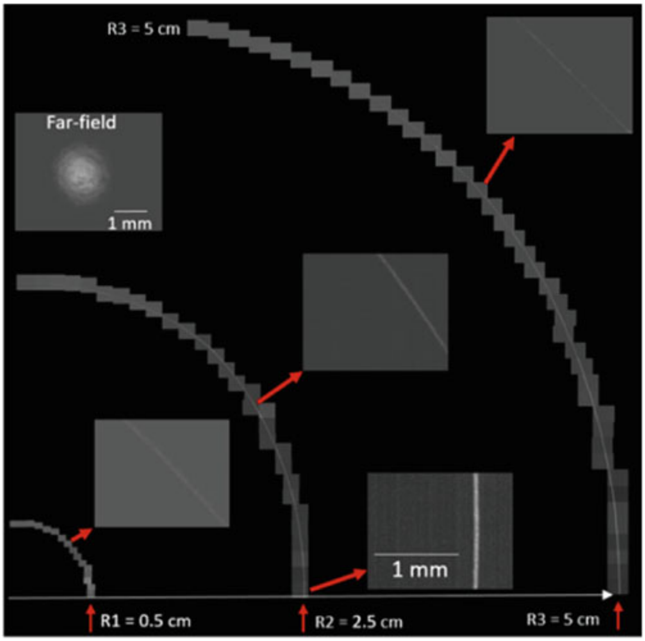

Fig. 27.3 Curved waveguides with different radii written transversely inside a Si wafer with a nanosecond laser. (NA $= 0.85$, astigmatically shaped beam, $\tau = 3.5$ ns, $E < 20\,\mu$J). Infrared light is coupled into each guide from the bottom of the figure shown by the red vertical arrows. The light scatters as it travels along a waveguide arc, and this scattered light is imaged with an infrared camera. Top left image is the far-field light intensity distribution from the curved waveguide (2.5-cm radius). Reprinted with permission from [56] ©The Optical Society

performances were reported since the losses were measured to be as low as $\alpha = 1.4$ dB cm^{-1}. By exploiting this negative index change, the authors demonstrated not only waveguides but also a large panel of optical functionalities including the inscription of Fresnel zone plates (lenses) and holograms [33].

Laser-Assisted Chemical Etching As nanosecond laser pulses can induce both positive and negative index changes, works have demonstrated increased and decreased etching rates for the modified zone as shown with standard potassium hydroxide (KOH) anisotropic etchant for silicon in a recent work [57]. Noteworthy, this holds also for isotropic structuring with hydrofluoric acid (HF) allowing to reach an extremely high etching contrast for negative-tone structuring based on nanosecond laser-produced porosities. This was impressively exploited by Tokel et al. [33] with a plethora of complex structures demonstrated with this method. A major achievement is, for instance, the creation of millimeter-long microfluidic channels inside silicon. Such channels constitute an interesting alternative to standard technologies employed for cooling microelectronic devices (e.g., microprocessors), with direct applications for increasing the clock rates [58].

All these experimental demonstrations concentrate almost exclusively on c-Si due to its technological importance, but it makes no doubt that nanosecond laser subsurface modifications can be extended to any band-gap material (including the various semiconductors exploited by the microelectronic industry) provided that the wavelength is scaled properly with respect to the band gap. However, despite these important developments, the process performance should be improved for a transfer to high-precision applications. An illustration is *silicon photonics* that relies today on silicon-on-insulator (SOI) lithographic fabrication of circuits [59–61] exhibiting losses which can be as low as 0.1 dB cm^{-1} and, thus, much lower than the above-summarized results. In particular, the large heat-affected zone associated with the modifications produced in the nanosecond regime will not reasonably allow one to demonstrate the same level of control as in dielectrics with femtosecond lasers. For this reason, ultrafast laser-produced modifications inside silicon using long-wavelength ultrashort pulses remain a natural option for the most demanding applications (resolution, quality, etc.). However, it requires certain limitations to be circumvented as described in the following sections.

3 Ultrashort-Pulse-Induced Microplasma Formation Inside Silicon and Limitations

3.1 Qualitative Picture and Theoretical Considerations

The nonlinear propagation and energy deposition of intense femtosecond laser beams in dielectrics are a subject of wide investigation for a few decades. In this chapter, we do not intend to repeat the details of theoretical treatments that are described in Chap. 1 of this book or in the literature [3, 62, 63]. However, we would like to highlight here that femtosecond interactions in semiconductors can be expressed with the same set of physical equations usually coupled through the nonlinear Schrödinger equation (under several assumptions) for the description of propagation accounting for diffraction, Kerr effect, group velocity dispersion, and nonlinear ionization with the associated plasma effects [64, 65]. However, a difference is the strong change in the magnitude and the relative importance of the contributing effects. The modified interplay leads to novel nonlinear interaction situations and new observations. As it will be developed below, it is also directly at the origin of the limitations which prevent, in most cases, to reach ultrafast breakdown conditions inside semiconductors [36, 66, 67].

To illustrate the deviation from dielectric studies, we summarize in Table 27.1 the typical values of some important physical parameters for fused silica ($\mathrm{SiO_2}$) (i.e., the most widely studied dielectric material) and Si for comparison. Because most of these parameters are wavelength-dependent, we present a comparison at given multiphoton ionization orders $N_{ph} = \lceil E_g/\hbar\omega \rceil$ from 2 to 4. According to their respective band gaps (1.1 eV for Si and 9 eV for $\mathrm{SiO_2}$), this leads to a comparison

Table 27.1 Important physical parameters for nonlinear interaction experiments in dielectrics and semiconductors. To illustrate the magnitude and relative importance of the different effects in both types of materials, we report the measured values found in the literature for SiO_2 and Si. For a direct comparison, these are sorted according to the multiphoton absorption (up to 4PA) regimes

Materials		Si	SiO_2		
Band gap E_g	Units eV	1.1	9	Ratio	Ref.
2PA					
Wavelength window	nm	1200–2100	150–270		
Refractive index n_0		3.55–3.45	1.55–1.5	≈2.3	
Nonlinear refractive index n_2	$cm^2\ W^{-1}$	$\approx 7 \times 10^{-14}$	$\approx 5 \times 10^{-16}$	≈100	[68, 69]
Critical power for self-focusing P_c	W	$\approx 15 \times 10^3$	$\approx 8 \times 10^5$	≈0.02	
2PA coefficient $\beta^{(2)}$	$cm\ W^{-1}$	$\approx 1.5 \times 10^{-9}$	$\approx 1.7 \times 10^{-11}$	≈100	[68, 70]
Critical plasma density N_c	cm^{-3}	$\approx 6 \times 10^{20}$	$\approx 3.5 \times 10^{22}$	≈0.015	
3PA					
Wavelength window	nm	2300–3200	290–400		
Refractive index n_0		3.45–3.42	1.5–1.45	≈2.3	
Nonlinear refractive index n_2	$cm^2\ W^{-1}$	$\approx 7 \times 10^{-14}$	$\approx 3 \times 10^{-16}$	≈200	[69, 71]
Critical power for self-focusing P_c	W	$\approx 4.5 \times 10^4$	$\approx 4 \times 10^5$	≈0.01	
3PA coefficient $\beta^{(3)}$	$cm^3\ W^{-2}$	$\approx 2 \times 10^{-18}$	$\approx 10^{-23}$	$>10^5$	[72, 73]
Critical plasma density N_c	cm^{-3}	$\approx 1.5 \times 10^{20}$	10^{22}	≈0.015	
4PA					
Wavelength window	nm	3400–4400	420–540		
Refractive index n_0		3.42	1.45	≈2.3	
Nonlinear refractive index n_2	$cm^2\ W^{-1}$	$\approx 3 \times 10^{-14}$	$\approx 2 \times 10^{-16}$	≈100	[69, 71]
Critical power for self-focusing P_c	W	$\approx 2 \times 10^5$	$\approx 10^6$	≈0.2	
4PA coefficient $\beta^{(4)}$	$cm^5\ W^{-3}$	$\approx 3.5 \times 10^{-31}$		>100	[71]
Critical plasma density N_c	cm^{-3}	$\approx 0.8 \times 10^{20}$	5×10^{21}	≈0.015	

of the NIR/MIR domain for Si with that of the UV domain for SiO_2. We indicate the corresponding wavelength windows for which the measured values for each order are given. Because significant discrepancy can be found between measurements in the literature (especially for high-order multiphoton coefficients), we provide typical values for each considered window, a ratio between the values for Si and SiO_2, and the references from which the information has been extracted.

First, we note in Table 27.1 the high refractive index value intrinsic to narrow-gap semiconductors. As we will see later on, this causes a strong index mismatch at air-material interface limiting the achievable focusing conditions inside Si. We can also mention a somehow opposite situation in the time domain for a comparison at a given multiphoton order. In contrary to UV for dielectrics, the NIR/MIR domain is in the near-zero group velocity dispersion (GVD) region for silicon. Therefore, we do not expect significant complication as pulse stretching for situations in semiconductors [74]. When looking for the most important differences with the ratio column in Table 27.1, we note the much stronger nonlinearities in Si. Typically, a difference of two orders of magnitude in the nonlinear refractive index is observed.

The associated critical power for self-focusing given by $P_c \approx 0.15\lambda_{\mathrm{las}}^2/n_0n_2$ for Gaussian beams is then on the order of a few MW for SiO_2, while it is only of a few tens of kW for Si. Considering a 100-fs pulse, this leads to the nanojoule energy level for interactions below the critical power inside Si. Similarly, we note orders of magnitude difference in the multiphoton absorption coefficients that results in increased absorption in the prefocal region for semiconductors. Also, because the critical plasma density N_c is inversely proportional to the square of the wavelength, the long wavelengths associated with multiphoton interactions in semiconductors lead to the occurrence of strong plasma effects (defocusing and absorption) at reduced carrier densities. These become important at typical free-carrier densities of 10^{21}–10^{22} cm^{-3} in dielectrics while they play a role at only 10^{20} cm^{-3} in femtosecond-laser-semiconductor interactions.

A conclusion is that the narrow gap of semiconductors associated to the long-wavelength required to reach multiphoton interactions lead to increased nonlinear propagation effects in comparison to dielectrics. This can be attractive for novel nonlinear propagation and filamentation-induced manipulations. However, it makes also more complex the achievement of controlled and highly concentrated energy deposition in the bulk of materials. Even under the tightest focusing conditions, nonlinear Kerr-induced phase distortions and strong plasma effects must occur in regimes where modifications would be expected in semiconductors. These aspects influence the controllability and complicate technological developments aiming at laser microengineering inside semiconductors.

3.2 Imaging Experiments

The most direct method to study femtosecond laser-induced carrier excitation in transparent materials is ultrafast imaging using pump-probe optical setups [75–77]. Because dielectrics are transparent to visible light which can be sensed with standard Si-based detectors, various pump-probe methods were applied during the last decades for the measurement of all dynamical aspects from ionization, trapping of generated free carriers to material responses [13, 75–80]. This metrology is progressively translated in the infrared to make possible similar measurements inside silicon and other narrow-gap semiconductors [66, 67, 81]. While obviously, the resolution limit decreases with the wavelength, using InGaAs array sensors and microscopy arrangements optimized at telecommunication wavelengths (≈1300 nm or ≈1550 nm) allows one to reach enough precision to extract the free-carrier density and the size of the microplasmas created with tightly focused femtosecond pulses. Figure 27.4 shows an example of amplitude imaging of microplasmas created 1 mm below the surface of a c-Si sample by two-photon ionization with 90-fs 1300-nm pulses [81]. In practice, a beam splitter separates the beam in probe and pump pulses. The probe beam is directed to an optical delay stage and illuminates the Si sample perpendicular to the excitation by the pump pulse. By

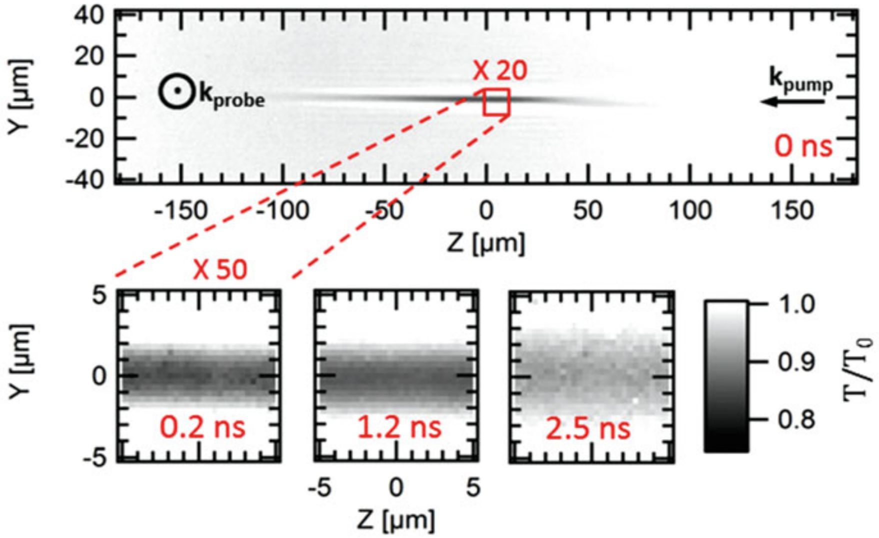

Fig. 27.4 Ultrafast infrared microscopy observation of a femtosecond laser-induced microplasma (E =20 nJ, NA = 0.3, λ = 1300 nm—2PA). The high-resolution images acquired for different delays reveal directly the expansion of the microplasma by free-carrier diffusion. Reprinted with permission [81]

moving the delay stage, the optical path of the probe beam can be adjusted so the time difference between the pump pulse and the probe pulse is changed. The resulting images shown in Fig. 27.4 represent the transmitted probe pulse, corrected for the background intensity measured without laser excitation. Interestingly, the high-mobility and long-lived characteristics of free carriers in Si combined to resolution-limited infrared imaging performances allowed one to observe directly the plasma expansion due to carrier diffusion [81] (which is hard to achieve in dielectrics due to the low mobility of carriers).

To extract the free-carrier densities from the plasma linear transmission images, one can apply a Drude model accounting for inverse bremsstrahlung absorption of the probe. Both experimental works of Kononenko et al. [66] using high-energy focused pulses (>90 µJ) and Mouskeftaras et al. for relatively tight focusing conditions (NA = 0.3) [67] conclude on subcritical plasma densities in all tested femtosecond interactions in c-Si. They observed a clamping of the plasma density at a maximum level that is near or below 10^{20} cm^{-3}. This is significantly below the critical plasma density (≈6×10^{20} cm^{-3} at 1300 nm) and corresponds to absorbed energy density well below the melting point of Si (≈5 kJ cm^{-3}). A major difference with femtosecond-laser dielectric interactions for which much higher absorbed energy densities have been reported [23, 24] is that ultrafast semiconductor interactions are inherently below the thresholds for material modification [31, 36]. The modest plasma density is also confirmed by the relatively long lifetime of

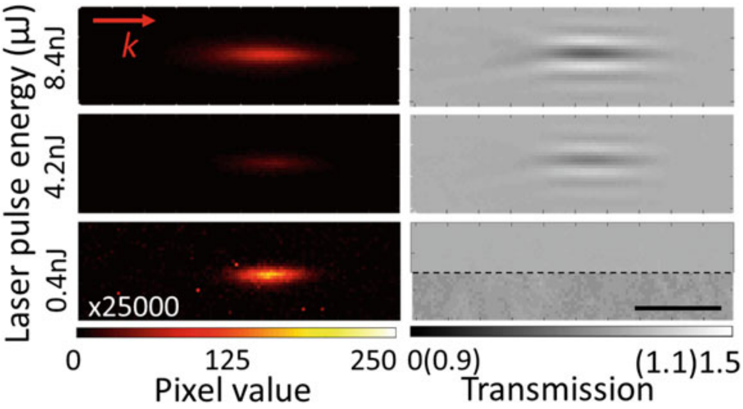

Fig. 27.5 Luminescence imaging compared to pump-probe shadowgraphy for observations of laser-induced plasmas inside GaAs. For the lowest pulse energy (0.4 nJ), the signal is magnified 25,000 times by increasing the exposure time and the digital gain. The scale bar of lower-half of the shadowgraphy image is rescaled between 0.9 and 1.1, showing no visible signal but only noise. The scale bar is 10 μm. The **k** vector marks the laser propagation direction. Reprinted with permission [83]

the measured microplasmas (≈2.5 ns) [81] as the decay of near-critical free-carrier densities should be on the picosecond timescale, according to a dominant Auger recombination mechanism [82].

A major limitation of the technique lies in its sensitivity as the highest dynamic ranges of infrared cameras limit the minimum measurable absorption typically at levels of few percent (performance similar to standard Si-based technologies at best). In practice, this means that only densities exceeding 10^{17} cm^{-3} can be reasonably sensed for micrometer-size plasmas. To overcome this limitation, Wang et al. used luminescence microscopy to measure weak plasmas that are inaccessible with pump-probe method [83]. Their method relies on measurements of the photon emission from the plasma that has a very similar spectrum to what is expected from band-to-band radiative recombination after considering near-band-edge absorption. Figure 27.5 shows the images of microplasmas created inside GaAs measured by both the luminescence and pump-probe methods. At low pulse energy of 0.4 nJ ($\tau = 190$ fs, NA = 0.85), the luminescence image clearly detects locally created free carriers while the pump-probe method fails. This clearly illustrates the advantage of luminescence microscopy for imaging low-density plasmas compared to the pump-probe method.

According to the recombination statistics in undoped semiconductors, the intensity of the luminescence is simply proportional to the square of the produced free-carrier density [84]. Accordingly, densities as low as $\approx 10^{16}$ cm^{-3} were retrieved by this method [83]. This is orders of magnitude lower than what is accessible with probe absorption methods [66, 67, 81]. Another benefit of the luminescence measurement is that it offers an incoherent imaging method that avoids diffraction artifacts as those visible in pump-probe images in Fig. 27.5. This is of importance to assess the details of spatial characteristic excitation in the 3D for situations which may be complicated by beam aberration and/or nonlinear propagation.

Beyond these imaging experiments, new infrared imaging developments will be needed to access more details of femtosecond-laser-semiconductor interactions. In particular, we anticipate that the advanced holographic imaging methodologies developed in the visible domain to study nonlinear interactions in dielectrics can be applied in the infrared domain [80, 85, 86]. It should allow one to retrieve not only the imaginary part of the refractive index with increased sensitivity but also the changes of its real part. These improvements are essential to follow both in time and 3D space the dynamical aspects of ionization, as well as other effects such as the strong Kerr-induced nonlinearities described in the previous section which are inherent to narrow-gap materials.

3.3 *Optical Limitations to Energy Localization*

There are different factors with strong interplays which contribute to the limitation of excitation by multiphoton ionization with femtosecond lasers in bulk semiconductors. Figure 27.6 summarizes those which have been clearly identified with the recent simulation and experimental works concentrating on c-Si, but similar situations apply for other narrow-gap materials as confirmed by experiments turning to other semiconductors [83, 87].

Focusing Limitations First limitations are related to the strong refraction that any beam focused in a high-index material will experience due to the strong index mismatch at the air-material interface. This will cause stronger spherical aberration than in dielectrics ($n \approx 1.5$) and will tend to lower the delivered peak intensity unless focusing optics specially designed to work in semiconductors are used [88]. Another direct consequence of the strong refraction is the relative paraxiality of beam propagation (modest focusing inside materials) even for experiments where beams are focused with high NA objectives. Taking a maximum of $\mathrm{NA} = 1$ for an air-surrounded objective and a refractive index of $n = 3.5$ for Si, it is striking to note that the maximum half-angle of the focused beam inside the material (which is directly given by $\arcsin(\mathrm{NA}/n)$) will not exceed 16°. It is usually admitted that tight focusing leads to strong confinements of interactions and limits the importance of nonlinear propagation effects [4]. While this holds in dielectrics, it is not necessarily the case in some experiments in semiconductors. The strong nonlinearities (see above) combined with inherent paraxial propagation make that nonlinear effects can readily accumulate and transform the pulses before reaching the focus (see hereafter).

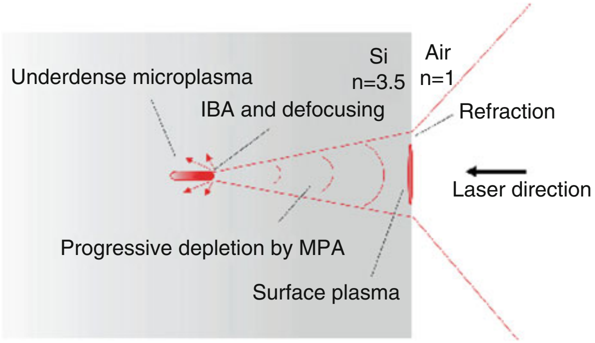

Fig. 27.6 Simplified schematic of physical effects identified as limiting the level of excitation by multiphoton ionization with femtosecond laser pulses in silicon. The strong refraction at the air-material interface leads to spherical aberration and near-paraxial propagation. The delivered intensity at the focus is limited by the progressive depletion due to highly efficient multiphoton absorption in the prefocal region, inverse bremsstrahlung absorption (IBA), and defocusing of the underdense plasma which forms on front of the focus. When increasing the energy, a plasma will form at the surface, affecting the amplitude and the phase of the incoming focused beam until surface damage

Prefocal Beam Energy Depletion Another important effect that lowers the peak intensity at the focus is the progressive depletion of the beam by highly efficient multiphoton absorption in the prefocal region. To reveal the inefficient laser energy deposition caused by this effect, one can compare to the applied pump pulse energy E, the laser energy required to create the plasmas observed in ultrafast imaging experiments [66, 67, 81]. Assuming that each ionization event requires the absorption of two photons, a rough estimate is given by $E = 2\hbar\omega N_e V$ with N_e the free-carrier density and V the plasma volume [30, 67, 88]. Then, one observes that about 30% of femtosecond pulses of 10 nJ contribute to the ignition of the first microplasmas measurable by shadowgraphy [67] and the balance drops rapidly with progressive growth of a low-density plasma in the prefocal region as directly evidenced by luminescence [83]. It reaches less than 1% for pulse energies of $\approx$100 μJ [66], and so very modest energy densities are locally delivered in all conventional focusing cases.

Plasma Defocusing/Screening The increased plasma effects associated with long wavelengths add also a major limitation to bulk excitation. As near-critical plasma densities are approached (see pump-probe imaging described above) and/or significant effects are accumulated by propagation in a large prefocal volume of low-density excitation (see luminescence imaging described above), the importance of inverse bremsstrahlung absorption and plasma defocusing [65, 66] progressively introduces more and more losses in the energy flux. This prevents from further feed any excited region behind a near-critical plasma front. A major difference between surface and bulk interactions is that increasing the pulse energy in the bulk moves the region of maximum plasma density in the backward direction [67] more than it enhances the maximum density produced [36, 64].

Nonlinear Beam Transformations At high-energy levels, all the mentioned effects taken together will cause amplitude and phase distortions on the beam leading to important nonlinear beam transformations. Concerning these aspects, one can refer to the studies of Faccio et al. [89] and Kononenko et al. [90] both comparing measurements with nonlinear propagation simulations. While these papers describe different situations, it is interesting to note that both groups reported a filamentation-like behavior with an elongated beam focus obtained by progressive transformation of the Gaussian profile into a Bessel-like profile with energy increase. To illustrate this aspect, we show in Fig. 27.7 the characterization of the fluence distribution of a femtosecond laser beam focused with a objective lens (NA $= 0.42$) at a depth of 1-mm inside c-Si. The procedure to retrieve the longitudinal fluence distribution (cross section along the optical axis) is similar to that described in Ref. [91]. First, we note the similarity between the shape of the microplasma reported in Fig. 27.4 and the fluence distribution measured for similar conditions (second image in Fig. 27.7). As in previously cited reports [89, 90], a stretching along the optical axis of the fluence distribution according to a filamentation-like behavior is observed. Bessel-like beam profiles are also exhibited for energies exceeding 150 nJ. This adds a third observation (focusing with higher NA compared to previous cases [89, 90]) showing that the spontaneous beam transformation into a Bessel-like beam is likely a general feature of regimes of strong 2PA in semiconductors. This obviously does not help to deliver high-energy densities as the laser energy that is supposed to concentrate on the smallest possible spot spread progressively along the optical axis.

In the experiments, there is also a limit to the pulse energy that can be delivered for bulk processing and which is defined depending on the configuration by the fluence threshold for surface damage. The latter is on the order of 0.1–0.5 J cm^{-2} for regimes dominated by multiphoton absorption and pulse durations near 100-fs [92, 93] (note that this limit is obviously increasing with the NA and the depth at which the focus is placed inside the materials). At the highest energies below surface damage, high-density plasmas are formed on the surface. In this case [90], one can easily understand the transformation because one can draw a parallel with a well-known method to generate Bessel beams consisting of blocking the central portion of a spherical focusing lens [91, 94]. By conserving only the high-order angular components participating in the formation of the focus, a Bessel-like profile naturally forms by constructive interference along the optical axis. Here, the highly refractive and/or reflective plasma at near-critical plasma density acts as the element that prevents the central part of the beam to contribute to the focus and similar transformation is obtained. For energies that do not lead to the formation of surface plasmas, it is important to note that the transformations are observed at pulse energies exceeding by far the intensity level for measurable multiphoton absorption and the critical power for self-focusing. Then, the beam transformations rely on more complex nonlinear accumulated phase changes, absorption, and diffraction in the bulk [89]. However, one can admit that most of the effects affect preferentially

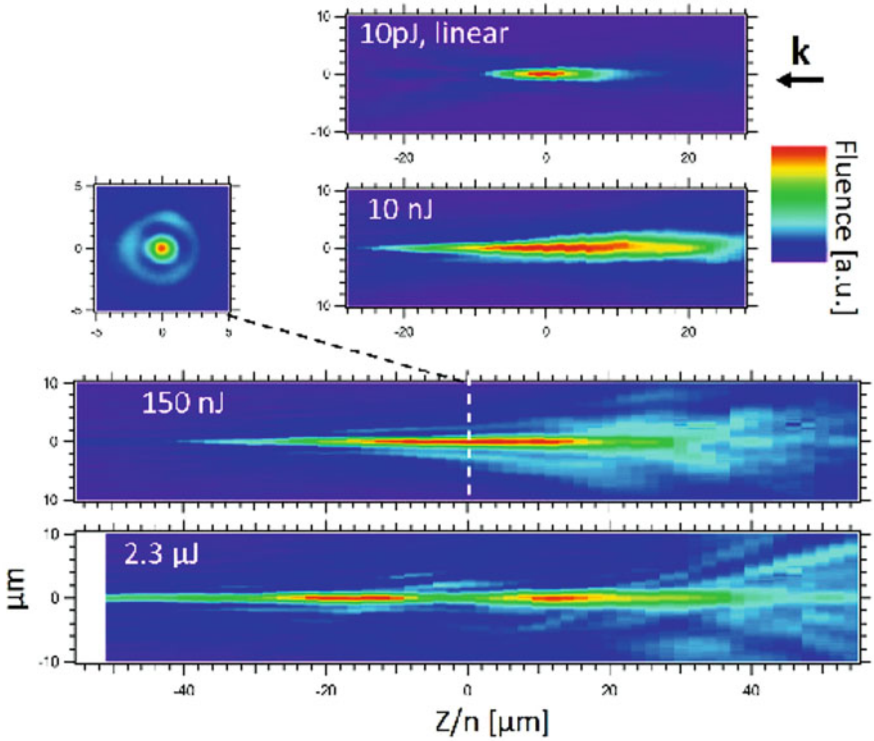

Fig. 27.7 Longitudinal fluence distributions at the focus inside silicon for increasing pulse energy (up to $E = 2.3\ \mu\text{J}$, $\lambda = 1300$ nm, $\tau = 100$ fs, NA = 0.42, and geometrical focus at a depth of 1 mm). When increasing the energy, the symmetry of low-intensity Gaussian focus is rapidly broken due to plasma formation that prevents the pulse energy to pass through the geometrical focus. This is followed by a progressive transformation in a Bessel-like beam associated with a filamentation-like behavior for pulse energy at the micro-Joule level. Each fluence distribution is normalized to their respective maxima

the central and most intense part of the beam leading to a similar transformation, as illustrated in Fig. 27.7. The initial pulse energy of only 10 nJ that reveals already an elongated spot is one order of magnitude higher than the two-photon absorption threshold found under similar conditions [30]. Also, it is interesting to note that most of these experiments report filamentation responses but without catastrophic beam collapse despite beam powers that can exceed by far the critical power for self-focusing. This can be attributed to the strong energy depletion lowering rapidly the apparent power as the beam propagates in the material discussed above. Another important remark on the discussion is also that most of the investigations have concentrated on spatial beam transformations but obviously the spectral and temporal characteristics of the pulses are also subject to important transformations in these situations [95, 96].

4 Strategies for Enhanced Ultrafast Micro-Excitation Inside Silicon

To overcome the limitations to the excitation and to deliver sufficient intensity for femtosecond laser modification, different options have been investigated to date. They can be categorized in terms of optimizations of the interactions in the spectral, spatial, and temporal domains.

4.1 Spectral Optimizations up to the Mid-infrared

An important remark that can be made on the comparison with dielectrics is that interactions at the fundamental wavelength of conventional femtosecond lasers lead to higher-order multiphoton absorption regimes compared to those tested in c-Si so far. For instance, the 800-nm wavelength (1.5 eV) of widely used Ti:sapphire lasers leads to six-photon absorption interactions in fused silica (band gap of 9 eV). However, most of the investigations described here have been performed in the 2PA region of c-Si. This raises important questions: "*Is this difference in nonlinearity related to the limitations in energy densities that can be delivered in semiconductors?*" "*Can we increase the absorbed energy localization in c-Si with higher-order multiphoton interactions?*." This somehow revisits the question of a potential nonlinear resolution applied to in-volume studies, which is also a matter of debate for material surface processing [97].

In practice, femtosecond OPAs are today routinely available in laboratories and should allow to treat this question, but it is hard to repeat ultrafast laser experiments where the wavelength is the only changing parameter [98]. In addition, diagnostics get more complex for wavelengths outside the limited range of sensitivity of InGaAs sensors. In the literature, we find only few experimental studies on laser direct writing in bulk silicon that have been conducted with 3PA getting dominant at wavelength exceeding 2.1 μm [30, 34, 99]. All concluded about difficulties in achieving modifications inside Si very similar to what is reported in the two-photon regime. The work of Nejadmalayeri et al. [34] corresponds to the first attempt made for 3D writing inside silicon with a femtosecond laser. The modification produced at 2.4-μm wavelength could be only written in the subsurface of silicon at very limited depth through an interface with a cover glass. While this does not make possible a true 3D writing, it opens interestingly the perspective of a unique laser method for direct writing of surface waveguides on silicon wafers. This potential alternative to SOI fabrication technologies was explored recently with pulses up the mid-IR in a recent work by Garcia-Lechuga et al. [93].

Interestingly, Zavedeev et al. [65] turned to numerical simulations to study the bulk interactions inside Si for wavelengths in a window from 1.2 μm to 5.25 μm (corresponding to regimes up to 5PA) in which the nonlinear coefficients of Si can be found in the literature [68, 71, 72, 100–103]. Solving the nonlinear

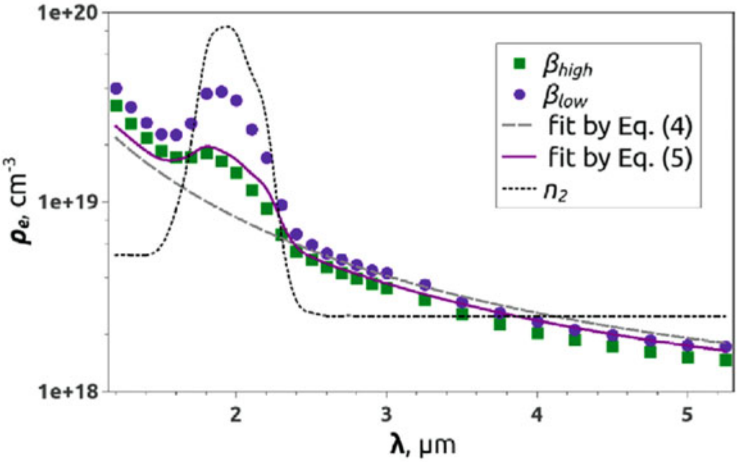

Fig. 27.8 Maximum free-carrier concentration at the focus, $\rho_{\max}$, calculated inside Si as a function of wavelength ($NA = 0.3$). The calculations conclude on a monotonous decrease of the excitation density due to stronger plasma defocusing at increased wavelength. The calculations are performed for the highest and lowest multiphoton absorption coefficients found in the literature. The dashed line represents the wavelength dependence of the nonlinear refractive index (linear ordinate scale) which explains the local peak in the free-carrier density at the maximum Kerr-induced nonlinear focusing. Reprinted with permission [65]

Schrödinger equation accounting for multiphoton absorption, optical Kerr, and plasma effects under the paraxial approximation (NA $= 0.3$ considered), they found the counterintuitive result that the maximum free carrier that can be achieved was decreasing when high-order multiphoton absorption comes into play. The results are illustrated in Fig. 27.8, where the peak free-carrier density in the focal region is plotted as a function of wavelength (for 250-fs pulses of 500-nJ energy that is significantly above the requirement for a saturated delivered intensity in the 2PA regime [36]). A monotonous drop of the excitation down to densities below 10^{18} cm^{-3} is found at the exception of the spectral region exhibiting a peak in n_2 ($\approx$2 µm) which may provide Kerr assistance for the focusing of the pulse. By looking at the space-time characteristics of energy delivery in details, the authors observed that the prefocal depletion of the pulses reported for experiments at 1.3-µm wavelength [67] decreases significantly when increasing the wavelength. However, because plasma defocusing depends on the wavelength (according to Drude model for the permittivity), it actually takes over these prefocal effects near the focus. To simplify, one can easily apprehend that without avalanche ionization which requires longer pulse duration to develop [88], it is difficult to expect the creation of a plasma density approaching the critical density in a nearly paraxial bulk interaction. Therefore, one could intuitively conclude that mid-infrared pulses are unfavorable for achieving breakdown conditions inside silicon. However, another and maybe more important quantity to consider for material modification is the deposited energy density. Rigorously, this adds the consideration of Joule heating of the free carriers in the energy balance. In contrast with the overall decrease in the electron density, the simulations revealed that the delivered energy reaches a minimum in the three-photon absorption regime (at $\approx$2.8-μm wavelength), before growing in the four- and five-photon absorption regime. The benefit predicted in the mid-IR domain can be directly attributed to inverse bremsstrahlung absorption which is more efficient for long wavelengths but has not been confirmed so far by a successful bulk-Si writing experiment in this spectral region.

By taking all these aspects together, a major conclusion is that longer wavelengths would make experiments more complex for a probably modest gain (if any) when aiming at ultrafast laser writing in bulk semiconductors. This likely explains why most experimental efforts have concentrated on optimizations in the spatial and temporal domains, as described hereafter.

4.2 Spatial Optimizations up to Extreme Focusing

On the front of spatial optimizations, interactions inside c-Si with femtosecond micro-Bessel beams have been attempted as the propagation of such beams is known to strongly resist nonlinear distortions. For Bessel beams, the energy flux is directed with a constant angle with respect to the optical axis (conical energy flux) which provides two advantages to deal with the previously listed limitations. First, it makes the interactions free from spherical aberration in comparison with tightly focused Gaussian beams which contain a wide range of angles of incidence [43, 104, 105]. Second, an even more important feature is that the intensity remains modest until the focus is reached. For high-Bessel angle, it is only here that significant nonlinear effects (including nonlinear beam distortions and nonlinear absorption) occur [106]. These beams therefore intrinsically lead to controlled interactions at higher intensities compared to Gaussian beams, and they have been already exploited for fabricating high-aspect ratio nanochannels in glasses using single femtosecond pulses at 800-nm wavelength [26, 74].

High-angle femtosecond micro-Bessel beams ($>20^\circ$) [107] at 1300-nm wavelength have been produced by axicon-based methods and characterized to compare interactions in dielectrics and c-Si. Also, high-energy versions [74] of the beams leading to ultrahigh intensities ($>10^{15}$ W cm^{-2}) over millimeter-long filaments have been tested. A direct comparison of the modifications induced in borosilicate glass and c-Si samples with micro-Bessel and focused Gaussian beams is shown in Fig. 27.9. For glass, it is found that the Bessel beams produce complete through-hole modifications with an efficiency very similar to that of commonly used 800-nm wavelength pulses [26, 108–110]. However, the response in c-Si is drastically different. We note that the surface damage threshold is largely exceeded. The stronger damage in comparison to glass is associated with the high two-photon absorption coefficient of Si. However, for both micro-Bessel and focused Gaussian beams, there is no noticeable material modification in the bulk. In another experimental

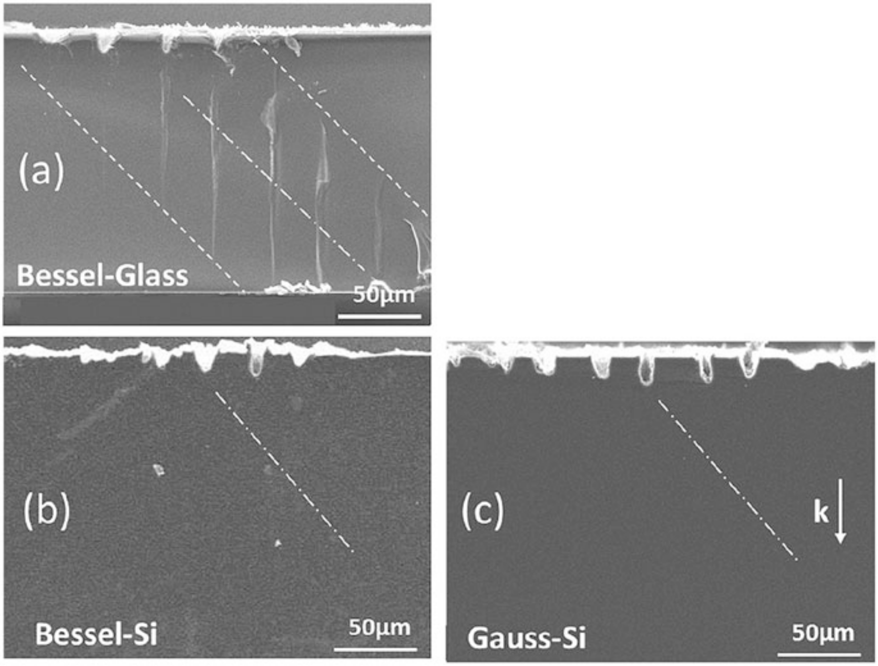

Fig. 27.9 Comparison between modifications induced in glass and silicon for a pulse energy of 12 µJ delivered on the target ($\tau = 100$ fs, $\lambda = 1300$ nm—2PA). For all substrates, lines are written at different depths, and cross sections are observed with scanning electron microscopy (SEM). The material disruption induced by the Bessel beam in glass extends over the entire thickness (**a**) but remains confined at the front surface in Si (**b**). Similarly, there is no confined modification observed in the bulk when Gaussian focusing is applied (**c**). The dashed dotted line shows the evolution of focus position to guide the eyes. Reprinted with permission from Ref [107]

study, He et al. have evidenced the fabrication of high-quality through-silicon vias which constitute an essential building block for vertical electrical connections in 3D integrated electronic circuits using femtosecond Bessel-like beams at 1.5-µm wavelength [111]. The corresponding realizations were nevertheless obtained on ultrathin wafers, employing a percussion drilling technique with sequences of 1200 high-energy (104 µJ) 65-fs duration pulses. Therefore, these conditions are radically different from single-shot drilling experiments in dielectrics.

An interesting complementary measurement achieved in these configurations is the intensity delivered in the bulk which exhibits a clamping at $\approx 4 \times 10^{11}$ W cm^{-2} with $\approx$100-fs pulses [107]. The corresponding fluence (0.05 J cm^{-2}) is well below the typical thresholds for surface modification of silicon ($F_{\text{th}} > 0.1$ J cm^{-2}) [92, 112], but this intensity value exceeds significantly the level for measurable two-photon ionization ($\approx 10^{10}$ W cm^{-2} [30]). Then, we can derive from the measurement a rough estimate of the produced free-carrier density with the relation $N_{\max} = (\tau \beta I_{\max}^2)/(2\hbar\omega)$, where $\tau = 110$ fs, β, and $\hbar\omega = 0.95$ eV are, respectively, the pulse duration, the two-photon absorption coefficient, and the photon energy. This relation assumes again the absence of collision-assisted ionization such as impact ionization leading to avalanche ionization [88]. Using a two-photon absorption coefficient [68, 102, 113] in the range of 0.5–1.5 cm/GW, we find a maximum free-carrier density $N_{\max} = 2.9\text{–}8.1 \times 10^{19}\ \text{cm}^{-3}$ which matches remarkably the value found with the measurements based on ultrafast imaging of the plasma created by Gaussian beams (see previous section). These considerations show that the benefit of Bessel beams on ultrafast Si excitation (if any) remains very modest in the tested situations. One possible reason for this limitation is that significant spatial improvement would require a large-angle cone of light (i.e., breaking the paraxiality). Unless more exotic beams as ring-Airy beams that exhibit a parabolic energy flux and nonlinear collapsing features [114, 115] are implemented, this will always remain particularly challenging due to refraction at the input interface of high refractive index semiconductors. Even if the Bessel beams that have been produced rely on high angles, they do not exceed the highest angle components in tightly focused Gaussian beam experiments.

The identified requirement of high angular components introduces the first methods that has led to the production of modifications in bulk silicon with femtosecond laser pulses. It consists of employing hyper-NA configurations (i.e., numerical apertures well above unity) so that the energy is spread on the largest possible range of angular components and the intensity in the prefocal region is minimized. To do so, Sreenivas et al. have employed an oil immersion microscope objective of numerical NA = 1.25 and index matching liquid of refractive index 1.49 for focusing in bulk silicon 800-fs duration laser pulses at 1.55-μm wavelength and a pulse energy of 50 μJ [35]. The authors reported on buried structures in the material, ascribable to the higher intensity at the focus together with large angles of the cone of light which limit detrimental prefocal nonlinear interactions. While this liquid immersion focusing surely improves the situation, important limitations persist due the limited refractive index that makes it difficult to perform experiment with effective $\text{NA} > 1.5$. To illustrate this aspect, it is interesting to note that the corresponding half-angle of the cone of light in Si is only 25° which remains modest in comparison to what is readily achieved in dielectrics. Therefore, the experiments show that this methodology is insufficient for achieving 3D writing with even-shorter pulses [36].

In order to solve this issue, Chanal et al. have proposed to implement the concept of the solid immersion lens (SIL) technique used in advanced microscopy [116, 117] for a laser writing configuration [36]. As a proof-of-concept experiment, 60-fs laser pulses at 1.3-μm wavelength were focused in the center of a 2-mm-diameter silicon sphere with objective lenses up to a numerical aperture of NA = 0.85. In this configuration schematically depicted in Fig. 27.10, the wave front of the beam matches the air-silicon interface, suppressing refraction. The effective numerical aperture of the laser writing experiment thus becomes one of the objective lens multiplied by the refractive index of silicon $\text{NA}_{\text{eff}} = n_{\text{c-Si}} \times \text{NA}_{\text{obj}} = 2.97$. Supported by nonlinear propagation simulations with the model developed in Ref. [64], these extreme focusing conditions produced the very first modifications

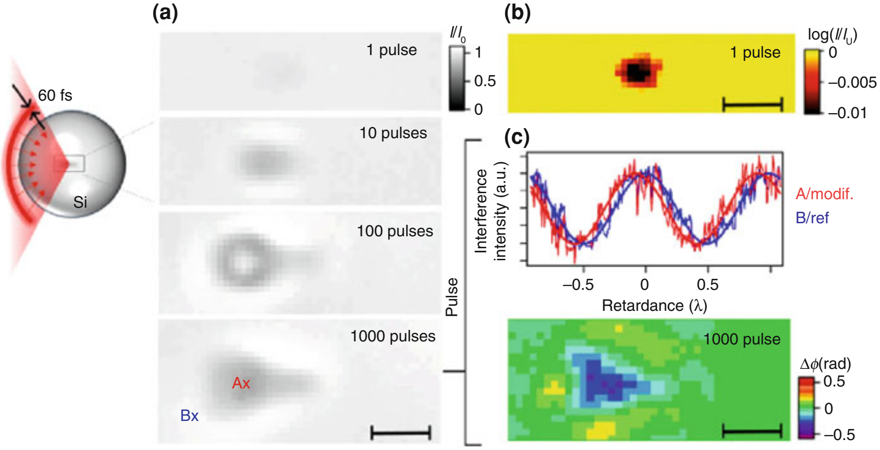

Fig. 27.10 Micromodification produced in bulk silicon with 60-fs duration laser pulses through a spherical interface. (**a**) Bright field infrared images of the modifications for different number of applied pulses. (**b**) Transmission image of a modification induced by a single pulse in logarithmic scale. (**c**) Phase measurements of a modification induced by 1000 pulses including (top) an interferogram comparing the phase on the two points A and B indicated in (**a**) and (bottom) a two-dimensional phase image. Laser wavelength, 1.3 μm; pulse duration, 60 fs. Reprinted with permission from Ref. [36]

in bulk silicon with <100-fs duration pulses. The remarkably low pulse energy sufficient for producing these modifications (20 nJ) as well as the repeatability of experiments when changing the spherical sample confirmed that the laser-produced modifications did not rely on defects inside the material [118]. The refractive index change associated with the modifications is negative, suggesting that these consist of voids or micro-cavities in these tested conditions.

An important conclusion from this success is the absence of a strict physical limit which prevents modification with femtosecond pulses. The introduction of more angular components than those supported by conventional writing configurations provides a solution to circumvent the aforementioned limitations related to nonlinear propagation. However, a practical implementation will remain challenging for wafer processing. This will require an astigmatic solid immersion lens (ASIL) made of silicon (e.g., less than a half-sphere) positioned on a wafer surface to produce modifications similar to those shown in Fig. 27.10 inside the wafer. While such experiments have been successful for microscopy purposes [116, 117], there is no equivalent to date with a material writing beam.

4.3 *Temporal Optimizations for Practical Writing Solutions*

We have introduced the capacity of nanosecond lasers to induce heat-driven damage in the bulk of semiconductors and the relative harmlessness of ultrafast energy deposition. This likely indicates that optimizations of the temporal shape must be possible to achieve stronger energy deposition—and potentially improved controllability on 3D modifications. Several strategies have been proposed to optimize the pulse temporal shape for producing modifications inside silicon.

Picosecond Regime A first consideration is to explore the intermediate picosecond pulse duration that are as short as possible to keep the benefit of ultrafast energy deposition. To this end, several groups have investigated the modification inside Si by using picosecond pulses with variable pulse durations. Kämmer et al. showed that permanent modifications could be produced with infrared 0.8–10-ps pulses at 1.55 μm pulses [119]. However, the maximum damage probability of 95% measured for 10-ps pulses suggested that damage production could not be achieved in a deterministic and repeatable way. At the same wavelength, Das et al. further investigated the 4–21-ps regime for modifying bulk Si. Results in Fig. 27.11 show that a minimum duration of 5.4 ps is required to produce modifications. By employing pulses at the advantageous wavelength of 2 μm for increased energy deposition inside silicon [120], Chambonneau et al. showed that the pulse duration threshold for the production of repeatable modifications could be lowered to 2 ps [57]. Another interesting aspect related to picosecond laser-produced modifications shown in the same study is the non-monotonic evolution of the damage probability and the deposited fluence as a function of the input pulse energy [57]. Such an unusual behavior was measured for 2 ps pulses, but not for longer pulses (9 ps and 400 ps). This phenomenon was confirmed by Das et al., as shown in Fig. 27.11, with a peak power upper limit (energy threshold) above which no damage is formed (Regime D in the map) [32]. These results indicate the persistence of strong nonlinear propagation effects delocalizing the radiation in the picosecond regime.

Multi-Pulse Optimizations A second approach for temporal optimization is to use high repetition rate bursts. If the repetition rate is sufficiently high, accumulation of heat and/or free carriers may lead to the production of permanent modifications. In this way, the energy of each sub-pulse can be much lower—thus avoiding the detrimental intensity clamping induced by high-energy unshaped pulses. Using this approach, Mori et al. and Shimotsuma et al. [121, 122] showed the first internal modifications in semiconductors by using femtosecond pulse trains consisting of two sub-pulses. By using a Cr:Forsterite amplified femtosecond laser system operating at 1.24-μm wavelength with 110-fs pulse duration, they first confirmed that it is impossible to induce any structural changes inside c-Si with repeated single-pulse irradiation despite high-energy pulses (600 μJ) and a large numerical aperture (NA $=$ 0.85) for focusing. However, by repeatedly illuminating silicon with double-pulse trains of $\approx 50 - \mu$J energy, they successfully obtained embedded modifications taking the form of periodic nanostructures. Figure 27.12 shows an electron microscopy image of the modifications captured after polishing the irradiated samples down to the level necessary to have the modifications intercepting the surface. The motivation of applying double pulses to deposit higher energy densities was directly inspired by a method applied in dielectrics to separate and control individually plasma ignition (first pulse) and energy deposition by free-

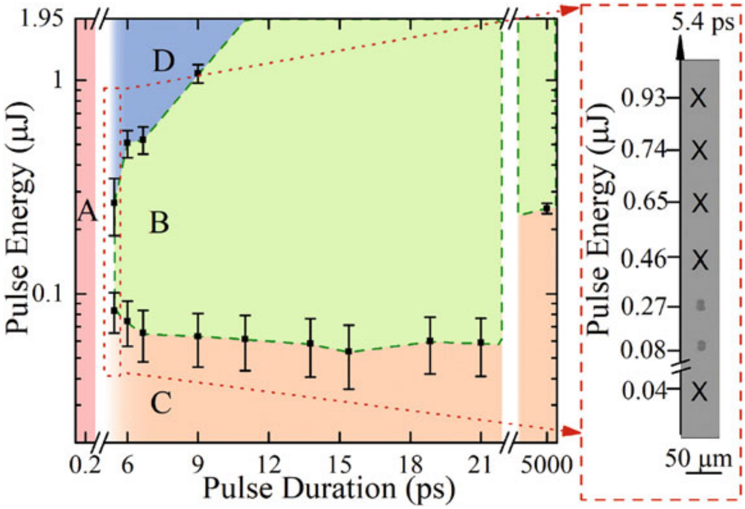

Fig. 27.11 Laser conditions for achieving micromodification inside silicon with a 1550-nm wavelength laser pulses focused with $NA = 0.85$. The pulse energy and pulse duration ranges for modification with 100% probability are shown with region (**b**) in green. The set of parameters leading to the absence of modifications are divided in three zones: (**a**) the region where the pulse duration is too short to achieve modification independently of the pulse energy; (**c**) a region below energy threshold for modification; and (**d**) a region corresponding to high-power regimes where the energy deposition is strongly delocalized leading to local energy densities below the damage threshold. The inserted image (right part) shows the IR microscopy image of modified spots systematically irradiated with 1000 pulses of 5.4-ps duration at different pulse energies where non-damaged parts are symbolized as cross marks. Reprinted with permission from [32] ©The Optical Society

carrier heating and avalanche (second pulse) [123, 124]. Accordingly, the reported modifications were obtained for pulse separations from 1 ps to 1 ns, which is the timescale without significant decay of free-carrier density in Si [81]. The authors found that an appropriate energy ratio between the two pulses is required so that the second arriving pulse can interact with a plasma of adequate density to avoid that most of the energy gets reflected or defocused. Typically, double pulses (of 120 fs each) with equally divided pulse energy were employed. This raises questions on the strongly different results obtained in comparison to previously performed experiments with twice longer pulses (250 fs) in which material modification was impossible [66]. This was only recently understood on the basis of the detailed contrast characteristics of the applied pulses [31] and discussed below.

Recently, Wang et al. generated THz-repetition-rate pulse trains by using a series of birefringent crystals with different thicknesses [125]. This extremely high repetition rate prevents from strong energy dissipation inside silicon between pulses. The situation illustrated in Fig. 27.13a thus enables unique capabilities for accumulation of free carriers generated by nonlinear ionization and heat causing progressive band-gap closure during the applied trains. Space-resolved measurements evidenced

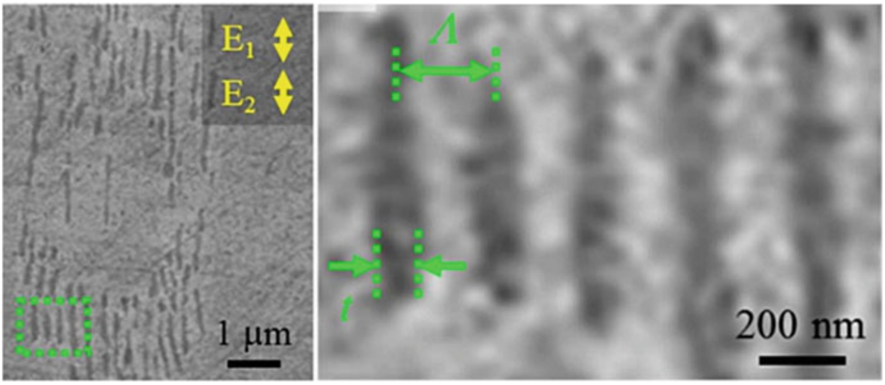

Fig. 27.12 Self-organized nanostructures formed inside c-Si by illumination with pulse trains of two femtosecond pulses. These are secondary electron (SEI) images of polished samples down to the depth of the focus position after laser irradiations with 1000 double pulses of 120-fs duration and ≈25-μJ energy, delayed by ≈1 ps., and focused with NA = 0.85. Adapted with permission [121]

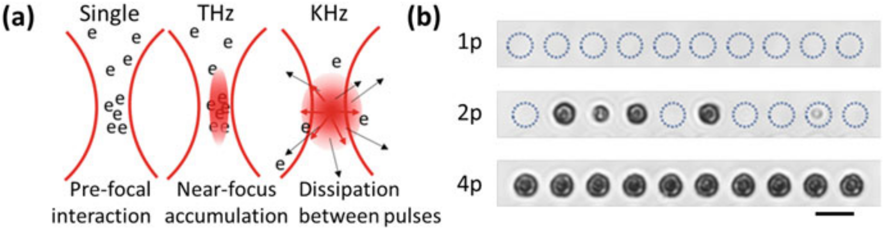

Fig. 27.13 Ultrafast laser writing inside Si with THz-repetition-rate trains of pulses. (**a**) Schematic representation of expected accumulation effects in Si. Single-pulse irradiation leads to strong detrimental prefocal plasmas that prohibit modification. The same energy provided in a terahertz burst irradiation lowers the apparent intensity, but heat and free-carrier accumulation between pulses can be expected. (**b**) Si-bulk writing experiment comparing the results of irradiation at a given energy with trains of 1, 2, and 4 picosecond pulses (NA = 0.85, $E = 2.1\,\mu\text{J}$, $\tau = 4.7\text{ps}$). The irradiation is repeated ten times. Higher delivered energy density is evidenced by progressive improvement of writing reliability when increasing the number of pulses in the trains. The scale bar is 20 μm. Adapted with permission [125]

changes in the interplay between detrimental nonlinearities and accumulation effects depending on the number of pulses in the trains, and a net increase in the level of achievable energy deposition was observed under appropriate conditions. The improvement was also supported by experiments demonstrating high performance for 3D laser writing inside silicon. As shown in Fig. 27.13b, irradiation with trains of only 4-ps pulses with the same total energy (≈2 μJ) leads to drastic improvements of the repeatability and the uniformity of the produced features in comparison to repeated single-pulse irradiations.

Temporal Characteristics of Pulses and Imperfections as Drivers In contradiction with most previous reports, some recent works conducted using fiber lasers have interestingly demonstrated successful waveguide writing inside Si with femtosecond pulses under conventional conditions [126–128]. While the authors mention sometimes the need for a local imperfection to seed the writing process, it tends to show however that more favorable conditions for writing can be found in these particular fiber laser experiments. For instance, Fig. 27.11 shows the incapacity of achieving modification with pulses of durations <4 ps using even higher NA than those used in these waveguide writing experiments. A main difference between the applied laser technologies as pointed out in a recent work is the temporal contrast of the pulses [31]. In an experiment consisting of irradiation of silicon with synchronized femtosecond, picosecond, and nanosecond pulses, Wang et al. could intentionally adjust the apparent temporal contrast of femtosecond irradiations [31]. Figure 27.14 shows a comparison of femtosecond laser modifications obtained while varying the contrast value with a picosecond prepulse. In agreement with previous studies relying on OPAs, these results confirm that highly contrasted femtosecond pulses are inoperative for writing. However, with degraded contrast, modifications can be produced. Interestingly, an optimum for low modification threshold is found at contrast values corresponding very well with those typical for fiber technologies. Overall, by multi-timescale analyses of these aspects (ps and ns contrast), this study reveals a sensitivity to the temporal contrast at an unusually high level for laser material processing applications.

These results on the influence of the temporal contrast have been also observed by Chambonneau et al. who have recently employed temporally distorted 750-fs pulses for achieving ultrafast transverse inscription in the bulk of silicon [105]. In this study, it was shown that repeatable modifications could not be produced with temporally bell-shaped pulses, even by using the beneficial wavelength of 2 μm (where the energy deposition is the highest [65]) in addition to a focus position for which spherical aberrations of different origins mutually balance. In stark contrast, utilizing temporally distorted pulses allows one to increase the energy deposition, leading to repeatable modifications which are the building blocks for transverse inscription. The morphology of the transversely written lines can be discrete, continuous, or erratic and mainly depends on the writing speed and also on the input pulse energy [105].

5 Emerging Three-Dimensional Solutions for the Semiconductor Industry

5.1 *Applications in Microelectronics*

In this chapter, we describe the vision of laser writing contributing to the technological developments in *Silicon Photonics*. However, the associated index engineering

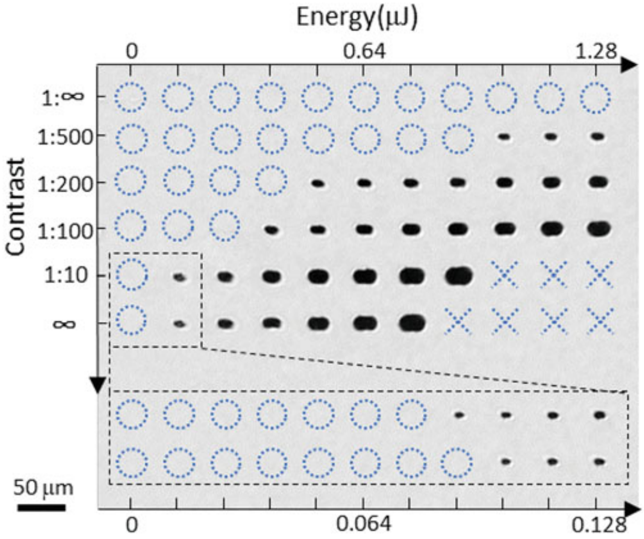

Fig. 27.14 Bulk Si modifications obtained after irradiation with 190-fs pulses and picosecond prepulse contrasts of different energies on separated sites. The duration of the prepulse degrading the contrast is 10 ps. The impacts are made 300 μm below the surface and observed with infrared microscopy. The blue circles indicate irradiations without modifications, and crosses are cases in the matrix that have not been tested because of laser energy limitations. We note the incapacity of achieving modification with high-contrast femtosecond pulses and a contrast-dependent modification threshold given by the transition between the last circle and the first modification on each line. Reprinted with permission from Ref [31]

applications will require an extremely high level of control of laser-induced transformations of silicon. This will need further fundamental and applied efforts for optimizations and can only be seen as a midterm or long-term perspective. It remains that the recent knowledge in the field has led to new approaches immediately applicable in the semiconductor industry.

Electrical Control in Silicon Chips As developed in previous sections, laser direct writing in bulk silicon with femtosecond pulses is extremely challenging. Nevertheless, the transient microplasmas—and thus the induced current—inside silicon in a noninvasive way offers a range of other applications. Some applications are local electrical testing inside integrated circuits by laser. The carrier injection process, namely, photoelectric laser stimulation (PLS), can be synchronized with static or dynamic electrical signals in failure analysis tests [129] or after the fabrication as a parametric measurement, improving the investigation time because of the high repetition rate capability and the simplicity of laser experiments compared to electrical methods. The laser approach is also attractive to emulate more generally accelerated aging or radiative effects to test their robustness in hard condition environments (e.g., space, nuclear). Originally, all these PLS techniques were surface techniques because of the use of laser sources in the near-infrared or visible domain for which silicon is opaque. With the emergence of femtosecond lasers at longer wavelengths for which silicon is transparent, one can initiate the effects by multiphoton ionization and achieve these studies with 3D resolution. At 1.3 μm corresponding to the two-photon ionization regime, local free-carrier injection can be achieved anywhere with beams from the rear-side silicon substrate supporting the integrated circuits. Recent works have revealed that tightly focused femtosecond pulses can inject free-carrier densities exceeding 10^{19} cm^{-3} anywhere inside silicon in a self-limited sub-modification regime [130–135]. This was exploited to develop an induced current imaging technique (the so-called two-photon optical beam-induced current imaging) capable of characterizing integrated circuits through the polished backside of integrated circuits [136–138]. By irradiating nonvolatile FLASH memory cells using pulses of only 100 nJ, the carriers generated in the cell substrate are thus attracted by the inherent vertical electric field induced by the floating gate potential, and the cell could be programmed [131, 133]. For robustness studies, a benefit of laser experiments is that the total ionizing dose [139] can be easily varied with the femtosecond laser parameters (the laser energy density and number of applied pulses). Finally, ionizing radiation or aging tolerance levels for specific region of systems can be derived from test procedures. All these represent the first 3D demonstrations in the field, but one can expect that similar laser effects should be rapidly demonstrated on other silicon semiconductor devices as capacitors, SRAM, etc. We can also expect the emergence of new applications exploiting the inherent speed of the ultrafast laser-based methods. Taking electrical control anywhere locally in a micro-system (micrometer resolution) and with an extreme time precision is obviously a basis for ultrafast electronics.

Backside Wafer Processing As detailed in previous section, the propagation nonlinearities of high-contrast femtosecond laser pulses in silicon prevent sufficient energy deposition to achieve modification in the bulk of the material through a plane interface [36, 64]. Obviously, this holds also when damage is intended at the exit surface of the material due to the bulk effects. Using 100-fs duration pulses at 1.3-μm wavelength, Lei et al. showed however that repeatable modifications could be produced on a gold-coating at the exit surface of a silicon wafer [140]. Despite the optical limitations, the lower damage threshold and higher absorption of the thin metal film compared to silicon made possible to demonstrate back-surface processing. A similar configuration for selective removal of gold films was also used in another study at 2.09-μm wavelength [141]. By employing a single chirped volume Bragg grating for stretching and compressing the pulses, the authors investigated the pulse duration dependence of ablation from 400 fs to 6 ns. The main conclusion was about an optimal ablation obtained with 3.2-ps pulses that can be attributed to a trade-off between the propagation nonlinearities and thermal effects observed with longer pulses. Overall, these laser experiments open the perspective of through-silicon processing of CMOS-processed wafer to trim or adjust locally the functionality of the systems, a situation without any real technological alternative.

Besides these demonstrations, the enhanced absorption at the exit surface of silicon when interfaced with a metal can also lead to new solutions for additive manufacturing. This was recently shown by Chambonneau et al. who achieved the first semiconductor-metal laser welding with 9.8-ps pulses at 1.55-μm wavelength and demonstrated with silicon and copper [142]. The propagation of these short pulses in silicon inevitably leads to the formation of filaments. In order to characterize them, nonlinear propagation imaging in silicon was performed for various input pulse energies. This allowed the authors to determine systematically the experimental value of the nonlinear focal shift (i.e., the distance between the focus positions in the linear and nonlinear propagation regimes on the optical axis), in excellent agreement with theoretical predictions based on a modified Marburger formula [143] accounting for the nonlinear absorption losses. For all tested conditions, a precompensation of the nonlinear focal shift was proposed to optimize the energy deposition at the exit surface of silicon—corresponding to the Si-Cu interface—as shown in Fig. 27.15. Without a precompensation of the nonlinear focal shift [dashed lines in Fig. 27.15b], mediocre shear joining strength values are obtained (<30 kPa). In stark contrast, the precompensation strategy [solid lines in Fig. 27.15b] significantly increases the shear joining strength values. For the highest pulse energies tested (1 μJ), the authors reported shear joining strengths as high as 2.2 MPa, thus compatible with applications [see Fig. 27.15c]. This demonstrates the importance of accounting for the nonlinear propagation in such innovative through-silicon process developments with direct applications in microelectronics, where semiconductors and metals are the backbone materials.

5.2 Toward 3D Silicon Photonics

3D laser writing applicable to silicon may drastically change the design and fabrication in the important field of *silicon photonics*. This field includes, for instance, silicon-on-insulator (SOI) and silicon nitride (SiNx) technologies which are rapidly progressing. However, a limitation is related to the planar lithographic methods used for fabrication. The later confines the possible architectures in two dimensions. Laser writing can provide a unique solution for new 3D designs. At short term, we can expect a flexible tool for prototyping studies which may present a real booster for the emergence of disruptive technologies and new concepts in this context.

Three-Dimensional Refractive Index Engineering and Waveguide Fabrication The critical initial step for the emergence of new fabrication technologies of optical microdevices corresponds obviously to the demonstration of high-performance waveguide structures. This is the question on which process engineering efforts have concentrated recently. A first demonstration of femtosecond laser waveguide writing was provided by Pavlov et al. [126]. Pulses of 350-fs duration, 1.5-μm wavelength, and 250-kHz repetition rate were applied with $\mathrm{NA} = 0.5$. The structures were fabricated in the longitudinal writing configuration starting from the exit surface to the entrance surface (bottom-up writing). The input and output

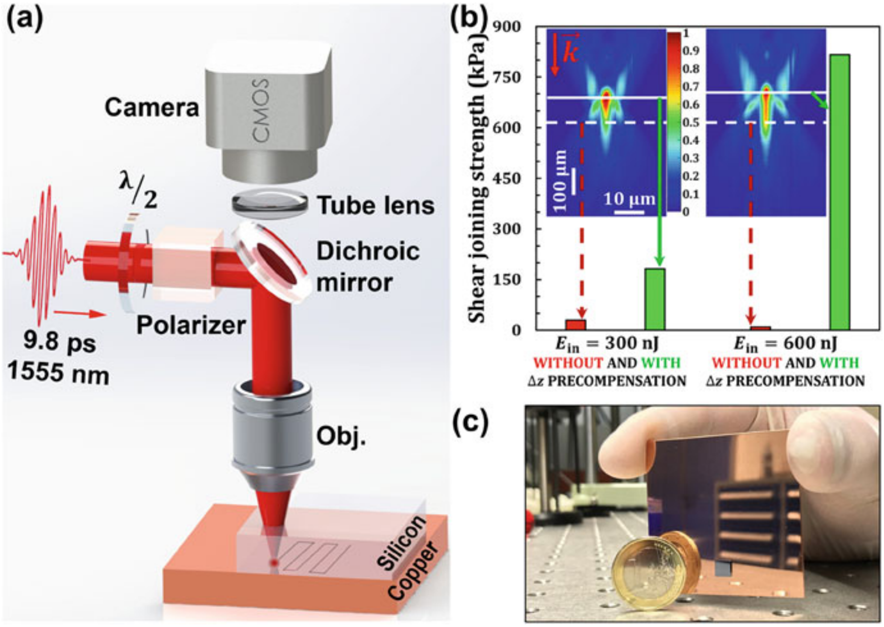
(a)
Camera
CMOS
λ/2
Tube lens
Dichroic mirror
Polarizer
9.8 ps
1555 nm
Obj.
Silicon
Copper
(b)
Shear joining strength (kPa)
900
750
600
450
300
150
0
k
100 µm
10 µm
1
0.9
0.8
0.7
0.6
0.5
0.4
0.3
0.2
0.1
0
E_in = 300 nJ
WITHOUT AND WITH
Δz PRECOMPENSATION
E_in = 600 nJ
WITHOUT AND WITH
Δz PRECOMPENSATION
(c)

Fig. 27.15 Semiconductor-metal ultrafast laser welding (laser wavelength: 1.55 µm, pulse duration: 9.8 ps). (**a**) Schematic of the experimental arrangement. (**b**) Laser-induced shear joining strength between silicon and copper at different pulse energies without (in red) and with (in green) precompensation of nonlinear focal shift. The insets are the corresponding fluence distributions obtained with nonlinear propagation imaging. The solid and dashed white lines indicate the position of the Si-Cu interface in each configuration. (**c**) Photograph of an ultrafast laser welded crystalline silicon sample on copper. Reprinted with permission [142]

facets of the waveguides were then prepared by polishing the surfaces. As illustrated in Fig. 27.16, the injection of continuous light in the 20-µm-diameter and 5.5-mm-long structures revealed their waveguiding properties. This was consistent with an independent measurement of the refractive index changes found to be $\Delta n \approx 5 \times 10^{-4}$ for the modified channel. A comparable technique has been also implemented by Matthäus et al. [127]. In this study, a rough-polishing process was intentionally applied on the exit surface of the sample for generating the necessary seeds for the subsequent waveguide inscription with 800-fs pulses. At an optimum pulse energy to improve the quality of waveguides, a refractive index change as large as $\Delta n = 2.5 \times 10^{-3}$ is obtained. Losses of the waveguides were estimated at 8.7 dB cm^{-1}. This is a critical performance that surely will need improvements for application developments. The light-guiding properties were additionally supported by the inscription of Y-splitters similar to those in Ref. [54]. Complementing this work, the same group has recently carried out in-depth analyses of the waveguide profiles, i.e., its refractive index profile distribution in the xy plane perpendicular to the optical axis z [128]. They also investigated the material science aspects behind the achieved silicon modification by using Raman

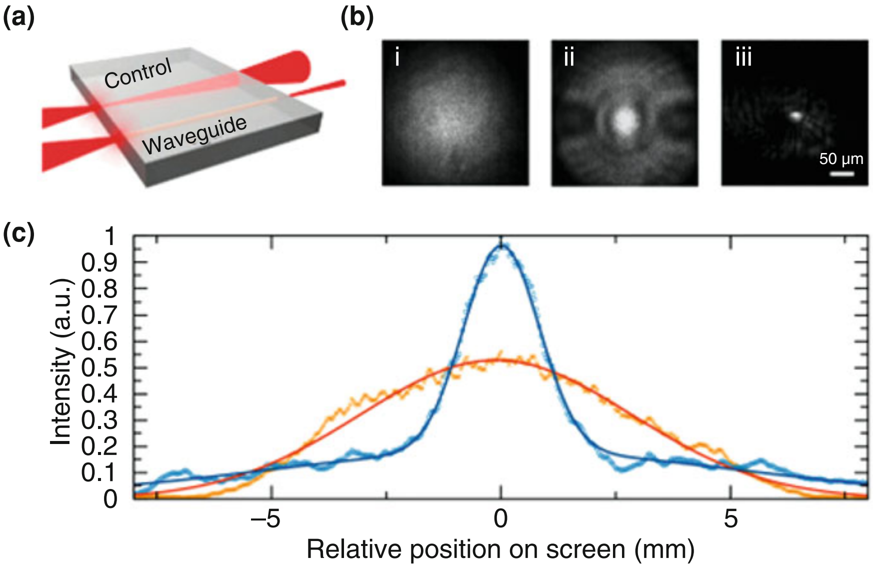

Fig. 27.16 Femtosecond laser waveguide writing inside silicon (laser wavelength, 1.5 μm; pulse duration, 350 fs). (**a**) Schematic illustration of direct coupling of continuous light at 1.5-μm wavelength into the waveguide in bulk silicon and the corresponding control experiment. (**b**) i, far-field image of the light after passing through silicon without waveguide; ii, far-field image of the light exiting from the end facet of the waveguide; iii, near-field image of the light exiting from the end facet of a waveguide. (**c**) Intensity profiles along the vertical axes of the far-field images shown in parts i, ii, and the corresponding numerical fits. Reprinted with permission from [126] ©The Optical Society

spectroscopy [144]. Microspectroscopy images unambiguously exhibit the changes in the spectral ranges of 430–500 cm^{-1} and 930–1040 cm^{-1} associated with amorphous and crystalline features, respectively [145, 146]. The apparent modest decrease in crystallinity was interpreted as a disturbed crystal structure, potentially induced by defects and dislocations.

Ultrafast Optical Signal Switching and Modulation Laser writing of active devices will be likely an important next step for the topic. Integration of optical systems with microelectronics can provide more bandwidth for data transport and switching than any purely electronic approach. Accordingly, silicon photonics and silicon-on-insulator (SOI) waveguide devices are today receiving considerable attention. In these technologies, it is the change in refractive index and absorption due to free-carrier injection by multiphoton ionization which can effectively be exploited, for example, for the development of ultrafast modulators and switches. Different all-optical switching methods have been demonstrated including silicon micro-ring resonators in which switching relies on the detuning of the resonance wavelength of the resonator [147, 148] and photonic crystal structures for which switching is obtained by detuning the optical band gap through carrier injection [149] or by photo-induced carrier injection in one of the arms of interferometric systems [150]. In principle, all these approaches can be translated in 3D systems fabricated by laser writing (see above). However, to really extend signal control and processing at the timescale of the pulse duration, one requires a reversing of the induced effects approximately as fast as they can be induced. In practice, free-carrier lifetime limits the switching or modulation speed of devices based on free-carrier injection. The latter depends strongly on the materials and geometry of the nanostructures/microstructures. We have seen in Sect. 3.2 that reported values for carrier lifetime in silicon are typically on the order of nanoseconds for excited volumes of micrometer dimensions [81], but solutions are envisioned to solve this limitation. Ultimately, light field-induced electron tunneling can be a potential carrier injection mechanism with switching on and off at the timescale of the optical cycle. Looking to the future, this may represent a new route for microelectronics and up to petahertz-bandwidth information processing. Recent high-profile fundamental experiments based on attosecond metrology on dielectrics [151, 152] and silicon [153] pave the way in this new horizon of applications.

6 Summary and Outlook

A major conclusion is the incapacity to achieve ultrafast laser modifications in semiconductors similar to those observed in dielectrics with tightly focused highly contrasted infrared femtosecond pulses. We have reviewed the factors and propagation nonlinearities which lower the apparent intensity inside high refractive index narrow-gap semiconductors. We have also briefly described the results of multiple groups that moved to unconventional configurations (including solid immersion focusing), longer pulses (from picosecond to nanosecond regimes), or ultrashort pulse sequences to demonstrate increased energy deposition and achieve internal modifications in silicon.

It is worth noting that the first attempts of 3D machining with infrared femtosecond pulses were performed a decade ago (for tentative waveguide writing in bulk Si) [34]. However, the door finally opens only recently to the ultrafast regime. It is also interesting to note that the first ever ultrafast modifications deep inside c-Si exhibit a negative index change [36] (exceeding few percent) and some works demonstrated that modifications can take the form of periodic nanostructures [121, 122]. These features are very similar to the results reported with nanograting formation in dielectrics [15, 16] and discussed in Chap. 5.

This definitely tends to show that technologies as the direct writing of photonics microdevices similar to those developed for dielectrics could be translated in semiconductors provided that practical solutions are found to enhance the delivered intensity (and/or energy densities) of long-wavelength femtosecond pulses inside semiconductors. This remains the most important challenge to meet for the future of *silicon photonics*.

For more general perspectives of this work, the plasma characteristics achieved with ultrafast light hold already great promises for studies in microelectronics, ultrafast signal processing, and silicon photonics as described in Sect. 5. When regimes above breakdown will be routinely accessed in semiconductors, we envision that laser writing can become a new booster for innovative developments in the semiconductor sector where microfabrication is largely dominated by lithography methods. The integration of photonic, fluidic, and electronic functionalities by 3D femtosecond laser writing in Si must open the way to hybrid monolithic devices. A potential is already identified to facilitate prototyping studies of emerging new concepts for co-designed electronics and microfluidics seen as solution for critical thermal management in most advanced chip technologies [154, 155].

References

1. K.M. Davis, K. Miura, N. Sugimoto, K. Hirao, Writing waveguides in glass with a femtosecond laser. Opt. Lett. **21**, 1729 (1996)
2. K. Miura, J. Qiu, H. Inouye, T. Mitsuyu, K. Hirao, Photowritten optical waveguides in various glasses with ultrashort pulse laser. Appl. Phys. Lett. **71**(23), 3329 (1997)
3. L. Sudrie, A. Couairon, M. Franco, B. Lamouroux, B. Prade, S. Tzortzakis, A. Mysyrowicz, Femtosecond laser-induced damage and filamentary propagation in fused silica. Phys. Rev. Lett. **89**(18), 186601 (2002)
4. R.R. Gattass, E. Mazur, Femtosecond laser micromachining in transparent materials. Nat. Photon. **2**, 219–225 (2008)
5. K. Sugioka, Y. Cheng, Femtosecond laser three-dimensional micro- and nanofabrication. Appl. Phys. Rev. **1**, 041303 (2014)
6. M. Beresna, M. Gecevičius, P.G. Kazansky, Ultrafast laser direct writing and nanostructuring in transparent materials. Adv. Opt. Phot. **6**(3), 293–339 (2014)
7. K. Sugioka, Y. Cheng, Ultrafast lasers: reliable tools for advanced materials processing. Light: Sci. Appl. **3**, e149 (2014)
8. B. Poumellec, M. Lancry, A. Chahid-Erraji, P.G Kazansky, Modification thresholds in femtosecond laser processing of pure silica: review of dependencies on laser parameters. Opt. Mat. Exp. **1**(4), 766–782 (2011)
9. S.M. Eaton, G. Cerullo, R. Osellame, Fundamentals of femtosecond laser modification of bulk dielectrics, in *Femtosecond Laser Micromachining* (2012), pp. 3–18
10. J.W. Chan, T. Huser, S. Risbud, D.M. Krol, Structural changes in fused silica after exposure to focused femtosecond laser pulses. Opt. Lett. **26**(21), 1726–1728 (2001)
11. F. Chen, J.R. Vazquez de Aldana, Optical waveguides in crystalline dielectric materials produced by femtosecond-laser micromachining. Laser Photon. Rev. **8**(2), 251–275 (2014)
12. T. Meany, M. Gräfe, R. Heilmann, A. Perez-Leija, S. Gross, M.J. Steel, M.J. Withford, A. Szameit, Laser written circuits for quantum photonics. Laser Photon. Rev. **9**(4), 363–384 (2015)
13. D. Grojo, M. Gertsvolf, S. Lei, T. Barillot, D.M. Rayner, P.B. Corkum, Exciton-seeded multiphoton ionization in bulk SiO_2. Phys. Rev. B **81**(21), 212301 (2010)
14. R. Osellame, G. Cerullo, R. Ramponi, *Femtosecond Laser Micromachining: Photonic and Microfluidic Devices in Transparent Materials* (Springer, Berlin, Heidelberg, 2012)
15. Y. Shimotsuma, P.G. Kazansky, J. Qiu, K. Hirao, Self-organized nanogratings in glass irradiated by ultrashort light pulses. Phys. Rev. Lett. **91**(24), 247405 (2003)
16. V. Bhardwaj, E. Simova, P. Rajeev, C. Hnatovsky, R. Taylor, D. Rayner, P. Corkum, Optically produced arrays of planar nanostructures inside fused silica. Phys. Rev. Lett. **96**(5), 057404 (2006)

17. E. Bricchi, B.G. Klappauf, P.G. Kazansky, Form birefringence and negative index change created by femtosecond direct writing in transparent materials. Opt. Lett. **29**(1), 119 (2004)
18. D. Grojo, M. Gertsvolf, H. Jean-Ruel, S. Lei, L. Ramunno, D.M. Rayner, P.B. Corkum, Self-controlled formation of microlenses by optical breakdown inside wide-band-gap materials. Appl. Phys. Lett. **93**(24), 243118 (2008)
19. T. Barillot, D. Grojo, M. Gertsvolf, S. Lei, D.M Rayner, P.B. Corkum, High refractive index modification of SiO2 created by femtosecond laser nanostructuring. J.Phys. B **43**(12), 125401 (2010)
20. J. Zhang, M. Gecevičius, M. Beresna, P.G. Kazansky, Seemingly Unlimited Lifetime Data Storage in Nanostructured Glass. Phys. Rev. Lett. **112**(3), 033901 (2014)
21. G. Corrielli, A. Crespi, R. Geremia, R. Ramponi, L. Sansoni, A. Santinelli, P. Mataloni, F. Sciarrino, R. Osellame, Rotated waveplates in integrated waveguide optics. Nat. Commun. **5**, 4249 (2014)
22. S. Juodkazis, V. Mizeikis, H. Misawa, Three-dimensional microfabrication of materials by femtosecond lasers for photonics applications. J. Appl. Phys. **106**(5), 8 (2009)
23. S. Juodkazis, K. Nishimura, S. Tanaka, H. Misawa, E.G. Gamaly, B. Luther-Davies, L. Hallo, P. Nicolai, V.T. Tikhonchuk, Laser-induced microexplosion confined in the bulk of a sapphire cystal: evidence of multimegabar pressures. Phys. Rev. Lett. **96**(16), 166101 (2006)
24. E.G. Gamaly, B. Luther-Davies, L. Hallo, P. Nicolai, V.T. Tikhonchuk, Laser-matter interaction in the bulk of a transparent solid: confined microexplosion and void formation. Phys. Rev. B **73**(21), 214101 (2006)
25. C. Hnatovsky, E. Simova, P.P. Rajeev, D.M. Rayner, P.B. Corkum, R.S. Taylor, Femtosecond laser writing of porous capillaries inside fused silica glass. Opt. Lett. **32**(11), 1459–1461 (2007)
26. M.K. Bhuyan, F. Courvoisier, P.A. Lacourt, M. Jacquot, R. Salut, L. Furfaro, J.M. Dudley, High aspect ratio nanochannel machining using single shot femtosecond Bessel beams. Appl. Phys. Lett. **97**(8), 4–7 (2010)
27. B.-B. Xu, Y.-L. Zhang, H. Xia, W.-F. Dong, H. Ding, H.-B. Sun, Fabrication and multifunction integration of microfluidic chips by femtosecond laser direct writing. Lab. Chip **13**(9), 1677 (2013)
28. A. Vailionis, E.G Gamaly, V. Mizeikis, W. Yang, A.V Rode, S. Juodkazis, Evidence of superdense aluminium synthesized by ultrafast microexplosion. Nat. Commun. **2**, 445 (2011)
29. M. Chambonneau, D. Grojo, O. Tokel, F.O. Ilday, S. Tzortzakis, S. Nolte, In-volume laser direct writing of silicon—challenges and opportunities. Laser Photon. Rev. **15**, 2100140 (2021)
30. D. Grojo, S. Leyder, P. Delaporte, W. Marine, M. Sentis, O. Utéza, Long-wavelength multiphoton ionization inside band-gap solids. Phys. Rev. B **88**(19), 195135 (2013)
31. A. Wang, A. Das, D. Grojo, Temporal-contrast imperfections as drivers for ultrafast laser modifications in bulk silicon. Phys. Rev. Res. **2**(3), 033023 (2020)
32. A. Das, A. Wang, O. Uteza, D. Grojo, Pulse-duration dependence of laser-induced modifications inside silicon. Opt. Exp. **28**(18), 26623 (2020)
33. O. Tokel, A. Turnali, G. Makey, P. Elahi, T. Çolakoğlu, E. Ergeçen, Ö. Yavuz, R. Hübner, M.Z. Borra, I. Pavlov, A. Bek, R. Turan, D.K. Kesim, S. Tozburun, S. Ilday, F.O. Ilday, In-chip microstructures and photonic devices fabricated by nonlinear laser lithography deep inside silicon. Nat. Photon. **11**(10), 639–645 (2017)
34. A.H. Nejadmalayeri, P.R. Herman, J. Burghoff, M. Will, S. Nolte, A. Tünnermann, Inscription of optical waveguides in crystalline silicon by mid-infrared femtosecond laser pulses. Opt. Lett. **30**(9), 964 (2005).
35. V.V. Parsi Sreenivas, M. Bülters, R.B. Bergmann, Microsized subsurface modification of mono-crystalline silicon via non-linear absorption. J. Eur. Opt. Soc. **7**, 12035 (2012)
36. M. Chanal, V. Yu Fedorov, M. Chambonneau, R. Clady, S. Tzortzakis, D. Grojo, Crossing the threshold of ultrafast laser writing in bulk silicon. Nat. Commun. **8**, 773 (2017)
37. E. Ohmura, F. Fukuyo, K. Fukumitsu, H. Morita, Internal modified-layer formation mechanism into silicon with nanosecond laser. J. Achiev. Mat. Manuf. Eng. **17**(1), 381–384 (2006)

38. D. Lide (ed.), *Handbook of Chemistry and Physics*, 85th edn. (CRC Press, Boca, Raton, 2003)
39. Y.P. Varshni, Temperature dependence of the energy gap in semiconductors. Physica **34**(1), 149–154 (1967)
40. P.C. Verburg, G.R.B.E. Romer, A.J. Huis in ’T Veld, Two-temperature model for pulsed-laser-induced subsurface modifications in Si. Appl. Phys. A **114**(4), 1135–1143 (2014)
41. P.C. Verburg, G.R.B.E. Römer, A.J. Huis in ’t Veld, Two-photon-induced internal modification of silicon by erbium-doped fiber laser. Opt. Exp. **22**(18), 21958 (2014)
42. P.C. Verburg, L.A. Smillie, G.R. B.E. Römer, B. Haberl, J.E. Bradby, J.S. Williams, A.J. Huis in ’t Veld, Crystal structure of laser-induced subsurface modifications in Si. Appl. Phys. A **120**(2), 683–691 (2015)
43. Q. Li, M. Chambonneau, M. Chanal, D. Grojo, Quantitative-phase microscopy of nanosecond laser-induced micro-modifications inside silicon. Appl. Opt. **55**(33), 9577 (2016)
44. H. Kiyota, K. Hara, M. Jankowski, M.M. Fejer, Numerical simulation and validation of subsurface modification and crack formation induced by nanosecond-pulsed laser processing in monocrystalline silicon. J. Appl. Phys. **127**(8), 085106 (2020)
45. H. Iwata, D. Kawaguchi, H. Saka, Electron microscopy of voids in Si formed by permeable pulse laser irradiation. Microscopy **66**(5), 328–336 (2017)
46. H. Iwata, D. Kawaguchi, H. Saka, Crystal structures of high-pressure phases formed in Si by laser irradiation. Microscopy **67**(1), 30–36 (2018)
47. A. Turnali, M. Han, O. Tokel, Laser-written depressed-cladding waveguides deep inside bulk silicon. J. Opt. Soc. Am. B **36**(4), 966 (2019)
48. M. Chambonneau, Q. Li, M. Chanal, N. Sanner, D. Grojo, Writing waveguides inside monolithic crystalline silicon with nanosecond laser pulses. Opt. Lett. **41**(21), 4875 (2016)
49. Y. Fujii, F. Fukuyo, K. Fukumitsu, N. Uchiyama, Method for dicing a substrate (2012). US Patent 8,268,704 B2
50. Y. Izawa, S. Tanaka, H. Kikuchi, Y. Tsurumi, N. Miyanaga, M. Esashi, M. Fujita, Debris-free in-air laser dicing for multi-layer MEMS by perforated internal transformation and thermally-induced crack propagation, in *MEMS 2008. IEEE 21st International Conference on Micro Electro Mechanical Systems* (IEEE, Piscataway, 2008), pp. 822–827
51. M. Finarov, E. Tirosh, G. Dishon, A. Gusarov, A method and apparatus for internal marking of ingots and wafers (2015). Patent WO 125134 A1
52. O. Tokel, A. Turnali, I. Pavlov, S. Tozburun, I. Akca, F.O. Ilday. Laser-writing in silicon for 3D information processing (2014). Arxiv, 1409.2827v
53. M. Chambonneau, D. Richter, S. Nolte, D. Grojo, Inscribing diffraction gratings in bulk silicon with nanosecond laser pulses. Opt. Lett. **43**(24), 6069 (2018)
54. D. Grojo, M. Chambonneau, Methods and systems for optical functionalisation of a sample made of semiconductor material (2019). US Patent 10,509,168
55. X. Wang, X. Yu, H. Shi, X. Tian, M. Chambonneau, D Grojo, B. DePaola, M. Berg, S. Lei, Characterization and control of laser induced modification inside silicon. J. Las. Appl. **31**(2), 022601 (2019)
56. X. Wang, X. Yu, M. J. Berg, P. Chen, B. Lacroix, S. Fathpour, S. Lei, Curved waveguides in silicon written by a shaped laser beam. Opt. Exp. **29**(10), 14201 (2021)
57. M. Chambonneau, L. Lavoute, D. Gaponov, V. Y. Fedorov, A. Hideur, S. Février, S. Tzortzakis, O. Utéza and D. Grojo, Competing nonlinear delocalization of light for laser inscription inside silicon with a 2-μm picosecond laser, Phys. Rev. App. **12**, 024009 (2019)
58. B. Dang, M.S. Bakir, D.C. Sekar, C.R. King, Jr, J.D. Meindl, Integrated microfluidic cooling and interconnects for 2D and 3D chips. IEEE Tr. Adv. Pack. **33**(1), 79–87 (2010)
59. M Lipson, Guiding, modulating, and emitting light on Silicon-challenges and opportunities. J. Lightwave Tech. **23**(12), 4222–4238 (2005)
60. M.A. Foster, A.C. Turner, J.E. Sharping, B.S. Schmidt, M. Lipson, A.L. Gaeta, Broad-band optical parametric gain on a silicon photonic chip. Nature **441**(7096), 960–963 (2006)
61. M.A. Foster, R. Salem, D.F. Geraghty, A.C. Turner-Foster, M. Lipson, A.L. Gaeta, Silicon-chip-based ultrafast optical oscilloscope. Nature **456**(7218), 81–84 (2008)

62. M. Kolesik, J.V. Moloney, Nonlinear optical pulse propagation simulation: From Maxwell's to unidirectional equations. Phys. Rev. E **70**, 036604 (2004)
63. J. Del Hoyo, A. Ruiz de la Cruz, E. Grace, A. Ferrer, J. Siegel, A. Pasquazi, G. Assanto, J. Solis, Rapid assessment of nonlinear optical propagation effects in dielectrics. Sci. Rep. **5**, 7650 (2015)
64. V. Yu. Fedorov, M. Chanal, D. Grojo, S. Tzortzakis, Accessing extreme spatiotemporal localization of high-power laser radiation through transformation optics and scalar wave equations. Phys. Rev. Lett. **117**(4), 043902 (2016)
65. E.V. Zavedeev, V.V. Kononenko, V.I. Konov, Delocalization of femtosecond laser radiation in crystalline Si in the mid-IR range. Laser Phys. **26**(1), 016101 (2016)
66. V.V Kononenko, V.V Konov, E.M Dianov, Delocalization of femtosecond radiation in silicon. Opt. Lett. **37**(16), 3369–71 (2012)
67. A. Mouskeftaras, A.V. Rode, R. Clady, M. Sentis, O. Utéza, D. Grojo, Self-limited underdense microplasmas in bulk silicon induced by ultrashort laser pulses. Appl. Phys. Lett. **105**, 191103 (2014)
68. A.D. Bristow, N. Rotenberg, H.M. van Driel, Two-photon absorption and Kerr coefficients of silicon for 850–2200 nm. Appl. Phys. Lett. **90**(19), 191104 (2007)
69. D. Milam, Review and assessment of measured values of the nonlinear refractive-index coefficient of fused silica. Appl. Opt. **37**(3), 546–550 (1998)
70. A. Dragomir, J.G. McInerney, D.N. Nikogosyan, P.G. Kazansky, Two-photon absorption properties of commercial fused silica and germanosilicate glass at 264 nm. Appl. Phys. Lett. **80**(7), 1114–1116 (2002)
71. X. Gai, Y. Yu, B. Kuyken, P. Ma, S.J. Madden, J. Van Campenhout, P. Verheyen, G. Roelkens, R. Baets, B. Luther-Davies, Nonlinear absorption and refraction in crystalline silicon in the mid-infrared. Laser Photon. Rev. **7**(6), 1054–1064 (2013)
72. S. Pearl, N. Rotenberg, H.M. Van Driel, Three photon absorption in silicon for 2300–3300 nm. Appl. Phys. Lett. **93**(13), 131102 (2008)
73. J. Jasapara, A. Nampoothiri, W. Rudolph, D. Ristau, K. Starke, Femtosecond laser pulse induced breakdown in dielectric thin films. Phys. Rev. B **63**(4), 1–5 (2001)
74. S. Mitra, M. Chanal, R. Clady, A. Mouskeftaras, D. Grojo, Millijoule femtosecond micro-Bessel beams for ultra-high aspect ratio machining. Appl. Optics **54**(24), 7358 (2015)
75. X. Mao, S.S. Mao, R.E. Russo, Imaging femtosecond laser-induced electronic excitation in glass. Appl. Phys. Lett. **82**(5), 697–699 (2003)
76. Q. Sun, H. Jiang, Y. Liu, Z. Wu, H. Yang, Q. Gong, Measurement of the collision time of dense electronic plasma induced by a femtosecond laser in fused silica. Opt. Lett. **30**(3), 320–322 (2005)
77. W. Gawelda, D. Puerto, J. Siegel, A. Ferrer, A. Ruiz de la Cruz, H. Fernandez, J. Solis, Ultrafast imaging of transient electronic plasmas produced in conditions of femtosecond waveguide writing in dielectrics. Appl. Phys. Lett. **93**(12), 2008–2010 (2008)
78. P. Martin, S. Guizard, Ph. Daguzan, G. Petite, P. D'Oliveira, P. Meynadier, M. Perdrix, Subpicosecond study of carrier trapping dynamics in wide-band-gap crystals. Phys. Rev. B **55**(9), 5799–5810 (1997)
79. P. Audebert, Ph Daguzan, A. Dos Santos, J.C. Gauthier, J.P. Geindre, S. Guizard, G. Hamoniaux, K. Krastev, P. Martin, G. Petite, A. Antonetti, Space-time observation of an electron gas in SiO2. Phys. Rev. Lett. **73**(14), 1990–1993 (1994)
80. D.G. Papazoglou, S. Tzortzakis, In-line holography for the characterization of ultrafast laser filamentation in transparent media. Appl. Phys. Lett. **93**(4), 2–5 (2008)
81. A. Mouskeftaras, M. Chanal, M. Chambonneau, R. Clady, O. Utéza, Direct measurement of ambipolar diffusion in bulk silicon by ultrafast infrared imaging of laser-induced microplasmas. Appl. Phys. Lett. **108**, 041107 (2016)
82. M.J. Kerr, A. Cuevas, General parameterization of Auger recombination in crystalline silicon. J. Appl. Phys. **91**(3), 2473–2480 (2002)

83. A. Wang, A. Das, J. Hermann, D. Grojo, Three-dimensional luminescence microscopy for quantitative plasma characterization in bulk semiconductors. Appl. Phys. Lett. **119**(4), 041108 (2021)
84. W. Van Roosbroeck, W. Shockley, Photon-radiative recombination of electrons and holes in germanium. Phys. Rev. **94**(6), 1558 (1954)
85. D. Abdollahpour, D.G. Papazoglou, S. Tzortzakis, Four-dimensional visualization of single and multiple laser filaments using in-line holographic microscopy. Phys. Rev. A **84**(5), 053809 (2011)
86. T. Balciunas, A. Melninkaitis, G. Tamosauskas, V. Sirutkaitis, Time-resolved off-axis digital holography for characterization of ultrafast phenomena in water. Opt. Lett. **33**(1), 58 (2008)
87. O. Tokel, A. Turnali, P. Deminskyi, S. Ilday, F.O. Ilday, Laser writing of nanostructures deep inside gallium arsenide, in *Conference on Lasers and Electro-Optics/Pacific Rim* (Optical Society of America, 2018), p. W1E–2
88. S. Leyder, D. Grojo, P. Delaporte, W. Marine, M. Sentis, O. Utéza, Non-linear absorption of focused femtosecond laser pulses at 1.3 µm inside silicon Independence on doping concentration. Appl. Surf. Sci. **278**, 13–18 (2013)
89. D. Faccio, M. Clerici, A. Averchi, O. Jedrkiewicz, S. Tzortzakis, D.G. Papazoglou, F. Bragheri, L. Tartara, A. Trita, S. Henin, I. Cristiani, A. Couairon, P. Di Trapani, Kerr-induced spontaneous Bessel beam formation in the regime of strong two-photon absorption. Opt. Exp. **16**(11), 8213–8218 (2008)
90. V.V. Kononenko, E.V. Zavedeev, V.M. Gololobov, The effect of light-induced plasma on propagation of intense fs laser radiation in c-Si. Appl. Phys. A **122**, 293 (2016)
91. D. Grojo, N. Sandeau, L. Boarino, C. Constantinescu, N. De Leo, M. Laus, K. Sparnacci, Bessel-like photonic nanojets from core-shell sub-wavelength spheres. Opt. Lett. **39**(13), 3989 (2014)
92. D. Austin, K. Kafka, C.I. Blaga, L.F. Dimauro, E. Chowdhury, Measurement of femtosecond laser damage thresholds at mid IR wavelengths, in *Proc. SPIE*, vol. 9237 (2014), p. 92370V
93. M. Garcia-Lechuga, N. Casquero, A. Wang, D. Grojo, J. Siegel, Deep silicon amorphization induced by femtosecond laser pulses up to the mid-infrared. Adv. Opt. Mat. **9**(17), 2100400 (2021)
94. R.M. Herman, T.A. Wiggins, Production and uses of diffractionless beams. J. Opt. Soc. Am. A **8**(6), 932 (1991)
95. A. Marcinkevičiūtė, V. Jukna, R. Šuminas, N. Garejev, G. Tamošauskas, A. Dubietis, Femtosecond filamentation and supercontinuum generation in bulk silicon. Opt. Lett. **44**(6), 1343 (2019)
96. V. Kadan, S. Pavlova, I. Pavlov, H. Rezaei, Ö. Ilday, I. Blonskyi, Spatio-temporal dynamics of femtosecond laser pulses at 1550 nm wavelength in crystal silicon. Appl. Phys. A **124**(8), 560 (2018)
97. M. Garcia-Lechuga, O. Utéza, N. Sanner, D. Grojo, Evidencing the nonlinearity independence of resolution in femtosecond laser ablation. Opt. Lett. **45**(4), 952 (2020)
98. M. Garcia-Lechuga, D. Grojo, Simple and robust method for determination of laser fluence thresholds for material modifications: an extension of Liu's approach to imperfect beams. Open Res. Eur. **1**, 7 (2021)
99. R.A. Richter, N. Tolstik, S. Rigaud, P.D. Valle, A. Erbe, P. Ebbinghaus, I. Astrauskas, V. Kalashnikov, E. Sorokin, I.T. Sorokina, Sub-surface modifications in silicon with ultra-short pulsed lasers above 2 µm. J. Opt. Soc. Am. B **37**(9), 2543 (2020)
100. R. Dekker, N. Usechak, M. Först, A. Driessen, Ultrafast nonlinear all-optical processes in silicon-on-insulator waveguides. J. Phys. D **40**(14), R249–R271 (2007)
101. F. Gholami, S. Zlatanovic, A. Simic, L. Liu, D. Borlaug, N. Alic, M.P. Nezhad, Y. Fainman, S. Radic, Third-order nonlinearity in silicon beyond 2350 nm. Appl. Phys. Lett. **99**(8), 081102 (2011)
102. Q. Lin, J. Zhang, G. Piredda, R.W. Boyd, P.M. Fauchet, G.P. Agrawal, Dispersion of silicon nonlinearities in the near infrared region. Appl. Phys. Lett. **91**(2), 021111 (2007)

103. T. Wang, N. Venkatram, J. Gosciniak, Y. Cui, G. Qian, W. Ji, D.T.H. Tan, Multi-photon absorption and third-order nonlinearity in silicon at mid-infrared wavelengths. Opt. Exp. **21**(26), 32192–32198 (2013)
104. Q. Li, M. Chambonneau, M. Blothe, H. Gross, S. Nolte, Flexible, fast, and benchmarked vectorial model for focused laser beams. Appl. Opt. **60**(13), 3954 (2021)
105. M. Chambonneau, M. Blothe, Q. Li, V. Yu. Fedorov, T. Heuermann, M. Gebhardt, C. Gaida, S. Tertelmann, F. Sotier, J. Limpert, S. Tzortzakis, S. Nolte, Transverse ultrafast laser inscription in bulk silicon. Phys. Rev. Res. **3**, 043037 (2021)
106. D. Faccio, E. Rubino, A. Lotti, A. Couairon, A. Dubietis, G. Tamošauskas, D. G. Papazoglou, S. Tzortzakis, Nonlinear light-matter interaction with femtosecond high-angle Bessel beams. Phys. Rev. A **85**(3), 033829 (2012)
107. D. Grojo, A. Mouskeftaras, P. Delaporte, S. Lei, Limitations to laser machining of silicon using femtosecond micro-Bessel beams in the infrared. J. Appl. Phys. **117**(15), 153105 (2015)
108. M.K. Bhuyan, P.K. Velpula, J.P. Colombier, T. Olivier, N. Faure, R. Stoian, Single-shot high aspect ratio bulk nanostructuring of fused silica using chirp-controlled ultrafast laser Bessel beams. Appl. Phys. Lett. **104**, 021107 (2014)
109. J. Amako, D. Sawaki, E. Fujii, Microstructuring transparent materials by use of nondiffracting ultrashort pulse beams generated by diffractive optics. J. Opt. Soc. Am. B **20**(12), 2562 (2003)
110. M. Duocastella, C.B. Arnold, Bessel and annular beams for materials processing. Laser Photon. Rev. **6**(5), 607–621 (2012)
111. F. He, J. Yu, Y. Tan, W. Chu, C. Zhou, Y. Cheng, K. Sugioka, Tailoring femtosecond 1.5-μm Bessel beams for manufacturing high-aspect-ratio through-silicon vias. Sci. Rep. **7**(1), 40785 (2017)
112. J. Bonse, S. Baudach, J. Krüger, W. Kautek, M. Lenzner, Femtosecond laser ablation of silicon–modification thresholds and morphology. Appl. Phys. A **74**(1), 19–25 (2002)
113. M. Dinu, F. Quochi, H. Garcia, Third-order nonlinearities in silicon at telecom wavelengths. Appl. Phys. Lett. **82**(18), 2954 (2003)
114. D.G. Papazoglou, N.K Efremidis, D.N Christodoulides, S. Tzortzakis, Observation of abruptly autofocusing waves. Opt. Lett. **36**(10), 1842–1844 (2011)
115. P. Panagiotopoulos, A. Couairon, M. Kolesik, D.G. Papazoglou, J.V. Moloney, S. Tzortzakis, Nonlinear plasma-assisted collapse of ring-Airy wave packets. Phys. Rev. A **93**, 033808 (2016)
116. K.A. Serrels, E. Ramsay, R.J. Warburton, D.T. Reid, Nanoscale optical microscopy in the vectorial focusing regime. Nat. Photon. **2**(5), 311–314 (2008)
117. K. Agarwal, R. Chen, L.S. Koh, C.J.R. Sheppard, X. Chen, Crossing the resolution limit in near-infrared imaging of silicon chips: targeting 10-nm node technology. Phys. Rev. X **5**(2), 021014 (2015)
118. N. Bloembergen, Role of cracks, pores, and absorbing inclusions on laser induced damage threshold at surfaces of transparent dielectrics. Appl. Opt. **12**(4), 661 (1973)
119. H. Kämmer, G. Matthäus, S. Nolte, M. Chanal, O. Utéza, D. Grojo, In-volume structuring of silicon using picosecond laser pulses. Appl. Phys. A **124**(4), 302 (2018)
120. E.V. Zavedeev, V.V. Kononenko, V.I. Konov, Delocalization of femtosecond laser radiation in crystalline Si in the mid-IR range. Las. Phys. **26**(1), 016101 (2015)
121. M. Mori, Y. Shimotsuma, T. Sei, M. Sakakura, K. Miura, H. Udono, Tailoring thermoelectric properties of nanostructured crystal silicon fabricated by infrared femtosecond laser direct writing. Phys. Status Solidi A **212**(4), 715–721 (2015)
122. Y. Shimotsuma, T. Sei, M. Mori, M. Sakakura, K. Miura, Self-organization of polarization-dependent periodic nanostructures embedded in III–V semiconductor materials. Appl. Phys. A **122**(3), 159 (2016)
123. K. Sugioka, M. Iida, H. Takai, K. Micorikawa, Efficient microwelding of glass substrates by ultrafast laser irradiation using a double-pulse train. Opt. Lett. **36**(14), 2734 (2011)
124. J. Peng, D. Grojo, D.M. Rayner, P.B. Corkum, Control of energy deposition in femtosecond laser dielectric interactions. Appl. Phys. Lett. **102**(16), 161105 (2013)

125. A. Wang, A. Das, D. Grojo, Ultrafast laser writing deep inside silicon with THz-repetition-rate trains of pulses. Research **2020**, 8149764 (2020)
126. I. Pavlov, O. Tokel, S. Pavlova, V. Kadan, G. Makey, A. Turnali, Ö. Yavuz, F. Ö. Ilday, Femtosecond laser written waveguides deep inside silicon. Opt. Lett. **42**(15), 3028 (2017)
127. G. Matthäus, H. Kämmer, K.A. Lammers, C. Vetter, W. Watanabe, S. Nolte, Inscription of silicon waveguides using picosecond pulses. Opt. Exp. **26**(18), 24089 (2018)
128. A. Alberucci, N. Alasgarzade, M. Chambonneau, M. Blothe, H. Kämmer, G. Matthäus, C. P. Jisha, S. Nolte, In-depth optical characterization of femtosecond-written waveguides in silicon. Phys. Rev. Appl. **14**(2), 024078 (2020)
129. P. Perdu, R. Desplats, K. Sanchez, F. Beaudoin, D. Lewis, V. Pouget, A. Douin, P. Fouillat, Identification of some key parameters for photoelectric laser stimulation of ic: an experimental approach, in *Proceedings of the 12th International Symposium on the Physical and Failure Analysis of Integrated Circuits, 2005* (IEEE, Piscataway, 2005), pp. 21–26
130. D. McMorrow, W.T. Lotshaw, J.S. Melinger, S. Buchner, R.L. Pease, Subbandgap laser-induced single event effects: carrier generation via two-photon absorption. IEEE Trans. Nuclear Sci. **49**(6), 3002–3008 (2002)
131. M. Chambonneau, S. Souiki-Figuigui, P. Chiquet, V. Della Marca, J. Postel-Pellerin, P. Canet, J.-M. Portal, D. Grojo, Suppressing the memory state of floating gate transistors with repeated femtosecond laser backside irradiations. Appl. Phys. Lett. **110**(16), 6 (2017)
132. P. Chiquet, M. Chambonneau, V. Della Marca, J. Postel-Pellerin, P. Canet, S. Souiki-Figuigui, G. Idda, J.M. Portal, D. Grojo, Phenomenological modelling of non-volatile memory threshold voltage shift induced by nonlinear ionization with a femtosecond laser. Sci. Rep. **9**(1), 1–10 (2019)
133. V. Della Marca, M Chambonneau, S. Souiki-Figuigui, J. Postel-Pellerin, P Canet, P Chiquet, E Kussener, F. Yengui, R. Wacquez, D. Grojo, J.-M. Portal, M. Lisart, NVM cell degradation induced by femtosecond laser backside irradiation for reliability tests, in *2016 IEEE International Reliability Physics Symposium (IRPS)*, vol. 2016 (IEEE, Piscataway, 2016), pp. 7B-4-1–7B-4-7
134. J.M. Hales, J.D. Cressler, D. McMorrow, A. Khachatrian, S. Buchner, J. Warner, A. Ildefonso, G.N. Tzintzarov, D. Nergui, D.M. Monahan, S.D. LaLumondiere, New approach for pulsed-laser testing that mimics heavy-ion charge deposition profiles. IEEE Trans. Nucl. Sci. **67**(1), 81–90 (2020)
135. L.D. Ryder, K.L. Ryder, A.L. Sternberg, J.A. Kozub, H. Gong, E.X. Zhang, D. Linten, J. Mitard, R.A. Weller, R.D. Schrimpf, S.M. Weiss, R.A. Reed, Polarization dependence of pulsed laser-induced SEEs in SOI FinFETs. IEEE Trans. Nucl. Sci. **67**(1), 38–43 (2020)
136. C. Xu, W. Denk, Two-photon optical beam induced current imaging through the backside of integrated circuits. Appl. Phys. Lett. **71**(18), 2578–2580 (1997)
137. P. Parkinson, Y.H. Lee, L. Fu, S. Breuer, H.H. Tan, C. Jagadish, Three-dimensional in situ photocurrent mapping for nanowire photovoltaics. Nano Lett. **13**(4), 1405–1409 (2013)
138. E. Ramsay, N. Pleynet, D. Xiao, R. J. Warburton, D.T. Reid, Two-photon optical-beam-induced current solid-immersion imaging of a silicon flip chip with a resolution of 325 nm. Opt. Lett. **30**(1), 26–28 (2005)
139. E. Simoen, M. Gaillardin, P. Paillet, R.A. Reed, R.D. Schrimpf, M.L. Alles, F. El-Mamouni, D.M. Fleetwood, A. Griffoni, C. Claeys, Radiation effects in advanced multiple gate and silicon-on-insulator transistors. IEEE Trans. Nucl. Sci. **60**(3), 1970–1991 (2013)
140. S. Lei, D. Grojo, J. Ma, X. Yu, H. Wu, Femtosecond laser backside ablation of gold film on silicon substrate. Proc. Manuf. **5**, 594–608 (2016)
141. I. Astrauskas, B. Považay, A. Baltuška, A. Pugžlys, Influence of 2.09-μm pulse duration on through-silicon laser ablation of thin metal coatings. Opt. Las. Tech. **133**, 106535 (2021)
142. M. Chambonneau, Q. Li, V. Yu Fedorov, M. Blothe, K. Schaarschmidt, M. Lorenz, S. Tzortzakis, S. Nolte, Taming ultrafast laser filaments for optimized semiconductor–metal welding. Laser Photon. Rev. **15**(2), 2000433 (2021)
143. J.H. Marburger, Self-focusing: theory. Progr. Quantum Electron. **4**, 35–110 (1975)

144. H. Kämmer, G. Matthäus, K.A. Lammers, C. Vetter, M. Chambonneau, S. Nolte, Origin of waveguiding in ultrashort pulse structured silicon. Laser Photon. Rev. **13**, 1800268 (2019)
145. P.A. Temple, C.E. Hathaway, Multiphonon Raman spectrum of silicon. Phys. Rev. B **7**(8), 3685–3697 (1973)
146. J. Bonse, K.W. Brzezinka, A.J. Meixner, Modifying single-crystalline silicon by femtosecond laser pulses: an analysis by micro Raman spectroscopy, scanning laser microscopy and atomic force microscopy. Appl. Surf. Sci. **221**(1–4), 215–230 (2004)
147. S.F. Preble, Q. Xu, B.S. Schmidt, M. Lipson, Ultrafast all-optical modulation on a silicon chip. Opt. Lett. **30**(21), 2891–2893 (2005)
148. V.R. Almeida, C.A. Barrios, R.R. Panepucci, M. Lipson, All-optical control of light on a silicon chip. Nature **431**, 1081–1084 (2004)
149. F.C. Ndi, J. Toulouse, T. Hodson, D.W Prather, All-optical switching in silicon photonic crystal waveguides by use of the plasma dispersion effect. Opt. Lett. **30**(17), 2254–2256 (2005)
150. Ö. Boyraz, P. Koonath, V. Raghunathan, B. Jalali, All optical switching and continuum generation in silicon waveguides. Opt. Exp. **12**(17), 4094–4102 (2004)
151. M. Schultze, E.M. Bothschafter, A. Sommer, S. Holzner, W. Schweinberger, M. Fiess, M. Hofstetter, R. Kienberger, V. Apalkov, V.S. Yakovlev, M. Stockman, F. Krausz, Controlling dielectrics with the electric field of light. Nature **493**(7430), 75–78 (2013)
152. F. Krausz, M.I. Stockman, Attosecond metrology: from electron capture to future signal processing. Nat. Photon. **8**(3), 205–213 (2014)
153. M. Schultze, K. Ramasesha, C.D. Pemmaraju, S.A. Sato, D. Whitmore, A. Gandman, J.S. Prell, L.J. Borja, D. Prendergast, K. Yabana, D.M. Neumark, S.R. Leone, Attosecond band-gap dynamics in silicon. Science **346**(6215), 1348–1352 (2014)
154. R. van Erp, R. Soleimanzadeh, L. Nela, G. Kampitsis, E. Matioli, Co-designing electronics with microfluidics for more sustainable cooling. Nature **585**(7824), 211–216 (2020)
155. A. Mouskeftaras, S. Beurthey, J. Cogan, G. Hallewell, O. Leroy, D. Grojo, M. Perrin-Terrin, Short-pulse laser-assisted fabrication of a si-sio$_2$ microcooling device. Micromachines **12**(9), 1054 (2021)

Chapter 28
Nanoscale Sampling of Optical Signals: Application to High-Resolution Spectroscopy

Guillermo Martin, Alain Morand, Myriam Bonduelle, Ciro D'Amico, Razvan Stoian, Javier Rodriguez Vazquez de Aldana, and Carolina Romero Vazquez

Abstract Direct laser writing is a powerful technique for the development of photonic devices, namely, by allowing 3D structuring and generation of waveguides and other optical functions in bulk dielectrics by locally changing the material refractive index. One of the main interests of the 3D design is the possibility to avoid in-plane crossings of waveguides that can induce losses and crosstalk in future multi-telescope beam combiners. Another powerful advantage of the direct laser writing technique is the ability to directly photo-write nanoscale dielectric discontinuities, allowing to extract light from a waveguide in a controlled way. This allows to periodically sample an optical signal confined in a waveguide and obtain, by dedicated Fourier transform algorithms, the high-resolution spectrum of the optical source while maintaining a very robust, compact optical device. The versatility of laser writing allows to adapt the technique to different transparency range materials (visible, near-, or mid-infrared) and designs and therefore to address a variety of spectral windows and optical functions with a single technological tool. Finally, direct laser writing allows rapid fabrication of complex optical

---

G. Martin (✉)
Université Grenoble Alpes, CNRS, IPAG, Grenoble, France
e-mail: guillermo.martin@univ-grenoble-alpes.fr

A. Morand
Université Grenoble Alpes, CNRS, Grenoble INP, IMEP-LAHC, Grenoble, France

M. Bonduelle
Université Grenoble Alpes, CNRS, IPAG, Grenoble, France

C. D'Amico · R. Stoian
Laboratoire Hubert Curien, UMR 5516 CNRS, Université de Lyon, Université Jean Monnet, St. Etienne, France

J. Rodriguez Vazquez de Aldana · C. Romero Vazquez
Grupo de Investigacion en Aplicaciones del Laser y Fotonica, Facultad de Ciencias, Universidad de Salamanca, Salamanca, Spain

© The Author(s), under exclusive license to Springer Nature Switzerland AG 2023

R. Stoian, J. Bonse (eds.), *Ultrafast Laser Nanostructuring*, Springer Series in Optical Sciences 239, https://doi.org/10.1007/978-3-031-14752-4_28

chips (photonic functions, material ablation, electrode patterning), without needing multiple lithographic steps.

In this chapter, different techniques will be described for waveguide and nano-scattering center fabrication, and it will be shown how this can be used in integrated optics spectroscopy. After describing the principle of the Fourier transform-integrated optics spectrometer, we will explain how laser writing can address the strong requirements needed to achieve high-resolution, high spectral range spectroscopy. In particular, it will be demonstrated that using laser writing to fabricate 3D nano-antennas, the directivity of the sampled signal can be improved. The development of these techniques in electro-optic crystals is also interesting in order to increase the signal-to-noise ratio and the detected spectral window. In a final paragraph, the use of 3D laser writing of waveguides to achieve pupil remapping will be shown, together with some direct applications: image reconstruction, spectro-imaging, and wavelength filtering.

Keywords Direct laser-written waveguides · Nano-scattering centers · 3D beam combiners · Electro-optic modulation · Stationary wave Fourier transform spectrometry: SWIFTS · Temporal/spatial multiplexing · Arrayed waveguide structures · Spectro-interferometers · Pupil remapping

1 DLW for Waveguide Fabrication

As discussed in the previous chapters, the fundamental result of direct laser writing (DLW) is the possibility to modify the refractive index of the material under exposure [11]. The technique consists in focusing the laser beam into the glass [45], crystal [24], or polymer [58], usually by using high numerical aperture (NA) microscope objectives.

The material is modified in the focal region, where the intensity reached by the focused beam is sufficiently high that strong-field nonlinear ionization processes (multiphoton, tunnel, avalanche) are induced. The locally absorbed laser energy induces a local elevation of the temperature in the material, and eventually thermodynamic and hydrodynamic phenomena of matter modification and rearrangement can happen (phase transitions, material expansion and cavitation, cooling). The permanent change is represented by a local modification of the refractive index, which can be either positive, corresponding to a local smooth densification (the so-called type I refractive index change), or negative, corresponding to a local rarefaction (the so-called type II index change). In the case of smooth type I refractive index changes, straight or curved waveguides can be realized by translating the sample during the irradiation process. For applications using optical waveguides, this will be the first step: Generate a high refractive index core, surrounded by a lower refractive index, so that light can be confined.

The interest of DLW is that provided the material reacts to the high intensity of the laser and the writing parameters (wavelength, fluence, pulse energy), there will be a refractive index modification that could be used for waveguiding, within the transparency window of the material. This gives a wide range of possibilities for single-mode waveguiding, from visible to mid-IR. As an example, the spectral domains of 3–5 μm and 8–12 μm are of great interest for astrophysical observation. Moreover, a large number of molecular organic tracers (water, CO_2, ozone) can be probed at these wavelength ranges. That gives the possibility to realize DLW devices for astronomical research of bio-signatures on exoplanets.

We present hereunder some examples of waveguide fabrication by DLW, to recall the type I or type II fabrications process.

1.1 Waveguides Based on Type I Modification

As an example of waveguide fabrication, we will show the fabrication of WG in commercial GLS glass (transparent up to 10 microns) and use a pulsed femtosecond laser to engrave the optical waveguides [26, 40]. The waveguides were fabricated using an ultrafast laser photoinscription technique described in [36]. GLS material is particularly interesting for laser photoinscription technique as it shows a large processing window of positive type I index changes. A multicore configuration is used to achieve large-mode-area guiding in the NIR and MIR with single-mode characteristics. This is based on a centered hexagonal arrangement of 37 parallel waveguides (and 5 μm radial separation between individual traces) with an index contrast in the range of 10^{-4}–10^{-3}. A view on the multicore waveguide structure and mode diameter at 1550 nm is given in Fig. 28.1. Injection in the central trace and evanescent coupling towards neighboring waveguides ensures coherent modal superposition [9, 55] and the formation and propagation of a single mode at this wavelength [36]. This allows to realize a large area mode, 22 μm FWHM, extending over the physical section of the waveguide.

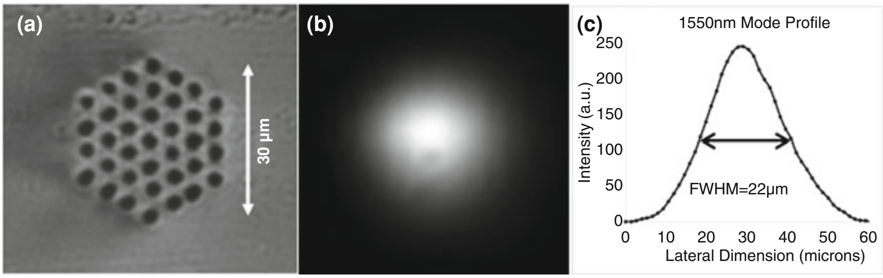

Fig. 28.1 (**a**) Multicore hexagonal single-mode waveguide fabricated in GLS using short laser pulses. (**b**) Image of the mode obtained using a 1550 nm SLED (same scale as (**a**)) and (**c**) mode profile showing large FWHM. (Reproduced from Martin et al. [36])

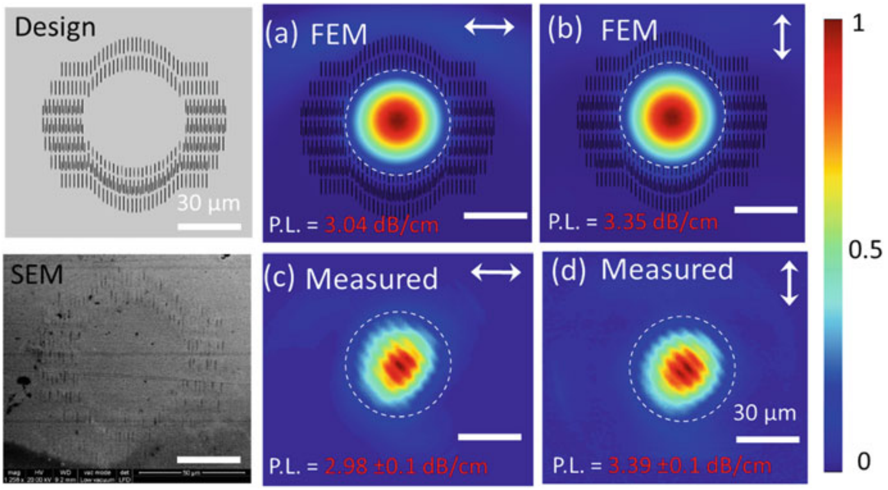

Fig. 28.2 Simulation and experiment of the type II laser-written waveguide: Comparison of near-field TE and TM modes. (**a**) FEM simulation for TE mode (resp. (**b**) for TM mode); (**c**) Experimental measurement of the TE mode (resp. (**d**) for TM mode). Interference fringes in the measured mode images are due to back-reflections in the optical guiding imaging system. (Reproduced from Nguyen et al. [42])

1.2 Waveguides Based on Type II Modification

In this approach, the laser fabrication involves the transversal inscription of tracks to construct a depressed-Δn circular array which supports leaky modes along the tubular channel [25]. Geometrical coordinates of each individual track were extracted from the 2D design and loaded to a script used in the laser inscription process. Trial of writing single tracks was initially conducted in order to specify the track sizes as a function of laser energy and focusing depth.

Using the refractive index profiles obtained [42], simulated TE and TM modes are compared with the measured mode fields, showing good dimensional agreement (Fig. 28.2). The FEM (Finite Element Method) design, obtained from the analysis of the SEM (Scanning Electron Microscopy) image of the cladding structure, is also shown.

Once the waveguide realization has been demonstrated, more complex structures can be investigated: Y junctions, tapers, interferometers (which can be useful for interferometry space observation), and optical sampling (for spectrometry applications). For that, high dielectric discontinuities must be generated using higher energy pulses. The strong interest of DLW relies here in the extension to the third dimension while keeping compact geometries, allowing for very complex and dense optical circuits and scattering centers.

2 DLW for Nano-sampling: Bessel Holes and 3D Antenna

In order to locally extract light from the confining waveguides, a dielectric discontinuity must be generated in the material, sufficiently small to not perturb the main function of the waveguides (confining and propagating light with low losses, without phase modification) but sufficiently contrasted so that enough light can be scattered and subsequently detected by a sensor (typically, a pixel/detector set on top of the waveguide). In order to generate this dielectric discontinuity using laser writing, a non-diffractive irradiation procedure [2, 3, 54] is used to generate a series of one-dimensional voids, transverse to the propagation axis of the waveguides, with a characteristic section below 500 nm and an axial dimension above of 150 µm. An overview of the optical device with side and top views is given in Fig. 28.3.

The main interest of laser writing for making the elongated nanovoids is that we can easily cover a sampling length of 1 cm, without mask replacement, in a very short time (few seconds). Besides, we can adjust the vertical position of the hole with respect to the waveguide, in order to optimize the extraction efficiency. The scattering efficiency depends on the cross-sections of the voids. For cross-sections between 100 and 500 nm and positions in the vicinity of the $1/e^2$ of the mode, scattering efficiencies ranging from 10^{-2} to 10^{-3} were estimated by FDTD calculations.

Using a single sampling center (here, a simple Bessel nanovoid) is of great interest if the detector is really close to the surface and has its active area, where the photon is absorbed, near the physical surface. Although this works properly for visible wavelength applications (CMOS detectors), it is no longer the case in near- and mid-IR (InGaAs, HgCdTe, or similar detectors), as the detector active area is hundreds of microns below the physical surface of the pixel. As seen in Fig. 28.4 [51], this will generate crosstalk and loss of flux detected by the pixel.

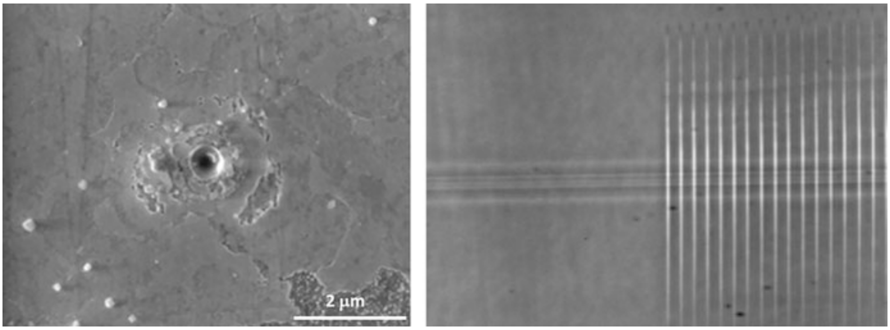

Fig. 28.3 Front view (left) of a Bessel void, using MEB imaging. Top view (right), using simple microscopy, of a set of Bessel voids transverse to the waveguide. (Reproduced from Martin et al. [35])

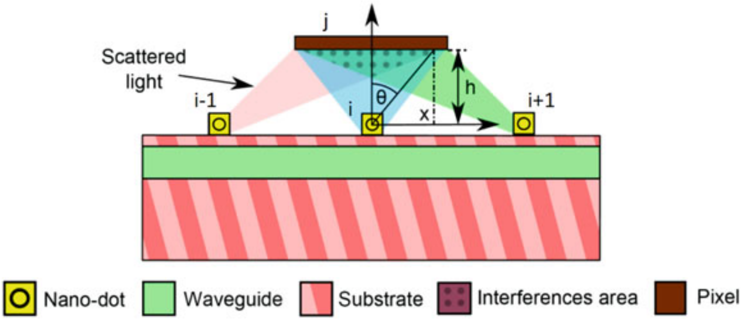

Fig. 28.4 Schematic view of the scattered light extracted from the sample and its angular divergence towards the detector, showing the problem of overlapping between too close sampling centers. (Reproduced from Thomas et al. [51])

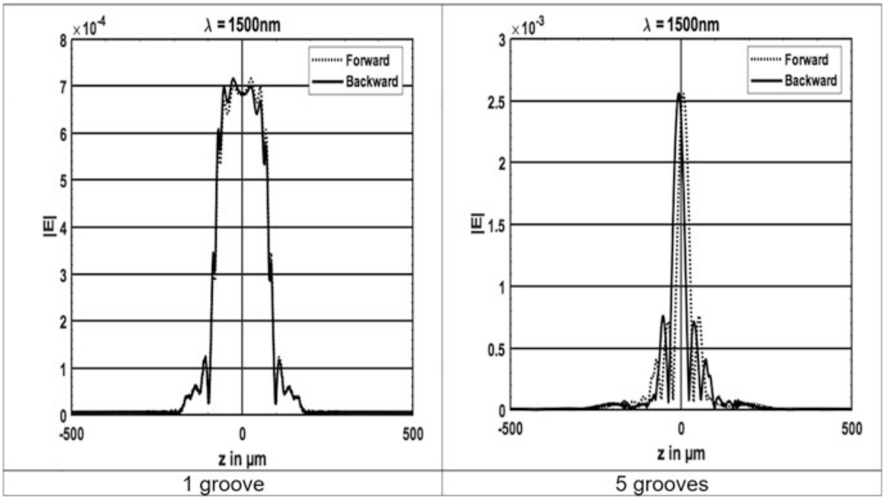

Fig. 28.5 Simulation of the scattered intensity profile issued from an antenna composed of N grooves at the optical wavelength 1500 nm. On the left for $N = 1$ and on the right for $N = 5$. (Reproduced from Bonduelle et al. [6])

An alternative method is to use the versatility of laser writing to inscribe several sampling centers to create a small diffraction grating on top of the waveguide. This way, the extracted flux will follow the laws of diffraction, allowing for higher directivity and narrow angular emission, optimally directed towards the pixel of interest, reducing crosstalk [41].

As seen in Fig. 28.5, the diffracted intensity is larger if we have a single groove, covering around 100 µm on the detector, meaning typical 5 pixels of 20 µm pitch. Therefore, in order to avoid crosstalk, one has to space the following antenna up to 100 µm, which means strongly reducing the spectral etendue. On the contrary, with more periodic grooves, the diffracted intensity is narrower, allowing for a more dense antenna distribution and an increase of the spectral etendue.

2.1 Fundamental Law of Diffraction Using the Nanograting

The first step to achieve a grating that will interact constructively with the optical beam inside the waveguide is to fulfill the following constraint: The spacing between scattering centers of our nanograting must be "in phase" with the optical beam, so that spacing $\Lambda = m \cdot \lambda / n$ with m an integer, and λ and n the wavelength and the effective refractive index of the guided mode, respectively. Of course, the lower the m value, the better, as sampling will be exactly coherent with the optical beam. Higher orders of m mean larger grating period and therefore angularly larger diffracted orders. Despite the performances of DLW, achieving $m = 1$ for $\lambda = 1.5\ \mu\text{m}$ and $n = 1.5$ (typical value in a borosilicate glass) means $\Lambda = 1\ \mu\text{m}$, which is a real challenge in terms of Bessel voids fabrication by DLW. We will focus on a grating using Bessel voids with a spacing of $\Lambda = 3\ \mu\text{m}$, a value that can be easily obtained with good repeatability.

The second step is to calculate the Bragg order created by the nanovoids, acting as a grating, in order to have the maximum diffraction angles that can be covered. The grating law gives us the number of expected Bragg orders in this case. Considering that the optical incident beam is perpendicular to the grating, the angular dependence is simply driven by the output angle, θ, such as:

$$n_{\text{sup}} \cdot \sin(\theta) = n_{\text{eff}} \cdot m \tag{28.1}$$

with $n_{\text{sup}} = 1.444$ (the superstrate refractive index); $-1 < \sin(\theta) < 1$; $n_{\text{eff}} = 1.446$ (the effective index of the guided mode); $\lambda = 1.55\ \mu\text{m}$; and $\Lambda = 3\ \mu\text{m}$.

From this we can deduce that $0.0039 < m < 5.5935$. As m can only be an integer, there are five diffraction orders. However, only three or four are clearly visible because of the total refraction between air and glass that rejects the orders arriving at higher angles. The simulation shown in Fig. 28.6a illustrates how the optical field, for a five-groove sampling center and a wavelength of 1550 nm, will be detected by the pixel array. It is also important to understand that the interaction between the grating and the waveguide is propagation sensitive, as the output angle of the diffracted beams is either positive or negative, depending on the beam propagation direction, either forward or backward, as presented in Fig. 28.6b.

Although a 3 μm grating spacing is not ideal, we can extract some information on the directivity and extraction efficiency of the system. The experimental set-up for the study of the vertical radiation pattern is the following: an IR camera is placed on the sample, above the sampling centers and waveguides. This camera is chosen because its pixel matrix can be uncapsulated, allowing to set the matrix directly in contact with the sample, reducing the light's vertical path. The experiment consists in measuring the radiation pattern for different heights of the camera: First the camera is in physical contact with the sample, and then it is raised step by step from $h = 0$ to $h = 520\ \mu\text{m}$.

In Fig. 28.7, we can observe that depending on the number of grooves (number of nanovoids forming the diffraction grating), the diffracted flux varies from an

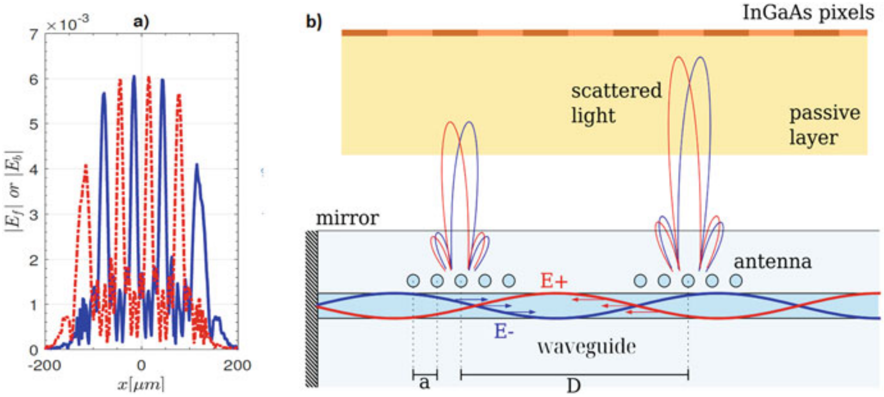

Fig. 28.6 (**a**) Superposition of the incoming wave only (red) and the returning wave (blue) on the pixel array. This figure shows the expected Bragg orders and how they overlap: the signal is not symmetric, and there is a slight angular offset between the incoming and returning wave. (**b**) Sketch of the radiation pattern from two consecutive gratings, as a function of the direct (red, E+) and backward (blue, E−) propagating beams in the waveguide. Depending on the wavelength and the refractive index, the diffracted angle will determine how the direct and backward beams overlap on the pixel array

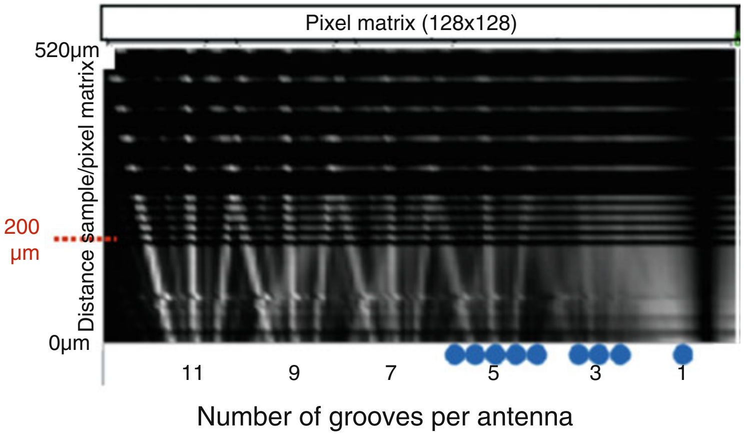

Fig. 28.7 Evolution of the vertical radiation pattern as a function of height between the detector and the sampling center, for different numbers of grooves per diffracting antenna

angularly large and diffused emission cone (for a single groove) to a narrower angle and flux concentrated on the specific Bragg diffraction orders (for 11 grooves), improving the directivity and extraction efficiency. Indeed, having a larger number of grooves not only improves the angular directivity, but it also increases the total extracted flux and, therefore, the signal-to-noise ratio. Let us note however that in the ideal situation (perfect matching $\Lambda = \lambda/n$), only one Bragg order is expected, gathering all the sampled signal, and directed towards a unique pixel.

2.2 *Spectral Dependence on the Extraction Efficiency*

One of the features of these gratings is that the output angular direction is dependent on the wavelength (see (28.1)). Considering that light injected in the waveguide makes a backward beam by reflection on the opposite surface, this implies that the flux extracted from direct and backward beams will overlap, generating interference fringes on the detector. The contrast of this fringes is related again to the wavelength and the total phase mismatch between the direct and backward beams, resulting in a spectral signature that can be used to make accurate spectrometry.

In Fig. 28.8 [6] is shown the simulated intensity detected on the pixel, as a function of the wavelength, for the total optical field extracted from the grating (interference between the direct and backward beams). As seen in the graph, with the increasing number of Bessel nanovoids in the grating, the measured contrast becomes more selective to wavelength.

As seen in the left column of Fig. 28.8, the fringe intensity changes following the optical wavelength used. From the interference fringes, two envelopes are calculated: the envelope of the fringe minima and the envelope of the fringe maxima. From both envelopes, the fringe contrast is then calculated. Increasing the number of grooves reduces the bandwidth of the high contrast fringes (i.e., good spectral sensitivity). This feature will be used to determine an unknown wavelength and use the global system coupling an optical waveguide and the grating as a lambdameter.

We have shown the interest of DLW to generate Bessel voids that allow to extract the signal from a waveguide and improve its directivity towards a detector. We are now going to explore more in detail the principle of spectrometry using DLW for fabrication of the waveguide(s) and the number of nanovoids and nano-gratings needed to achieve high-resolution spectrometry on-chip.

3 Stationary Wave Fourier Transform Spectrometry: SWIFTS

The principle of SWIFTS [31] is based on the generation of a stationary wave inside an optical waveguide and the nanoscale sampling of this stationary wave in order to obtain a discrete interferogram from which, using discrete Fourier transform, the spectrum of the signal is reconstructed. The aim of this section is to show how the DLW Bessel nanovoids are used to periodically sample the signal in the waveguide. Two configurations are proposed: the stationary waves are obtained either from a guided mode being reflected at the opposite facet from the injection (Lippmann mode, Fig. 28.9, right) or from two counterpropagative mode interference (Gabor mode, Fig. 28.9, left).

In the simplest configuration (Fig. 28.9, right), light is coupled into a single-mode waveguide terminated with a mirror. The superposition of the forward wave with the backward wave issued from the mirror reflection gives a stationary wave.

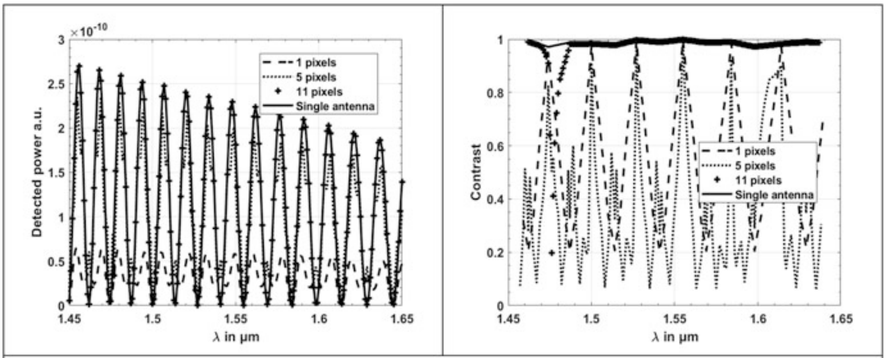

Antenna w. 1 single groove

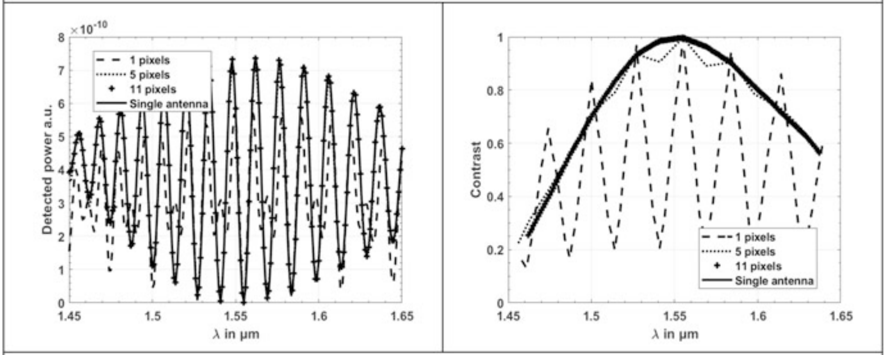

Antenna w. 5 grooves

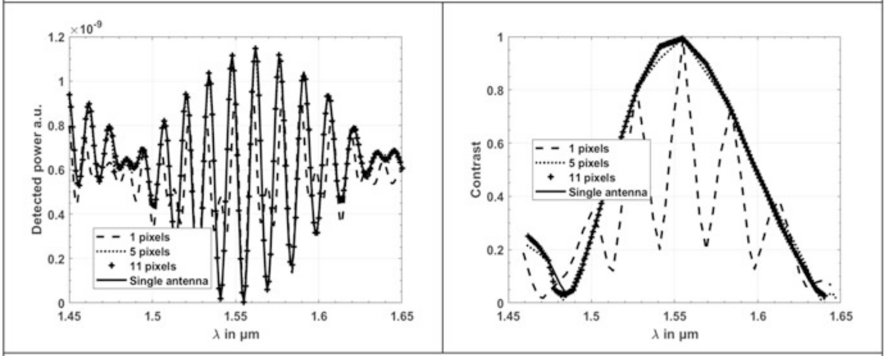

Antenna w. 9 grooves

Fig. 28.8 Trade-off between extraction efficiency and spectral band for high fringe contrast, for three types of antenna, depending on the number of grooves used in one antenna (1, 5, or 9, respectively). On the left, the detected power as a function of wavelength. On the right, the contrast of the fringes. The inset means 1 pixel = an antenna every 20 µm; 5 pixels = an antenna every 100 µm, and 11 pixels = an antenna every 220 µm. Single antenna means integration over the whole detector for a single antenna (ideal case). Therefore, increasing the pixels' spacing improves the contrast and sensitivity spectral range. (Reproduced from Bonduelle et al. [6])

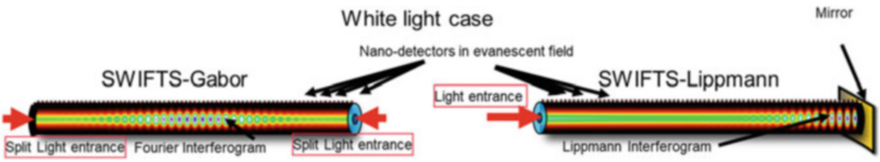

Fig. 28.9 Different configurations to obtain a static interferogram inside an optical waveguide: Left, counterpropagative configuration (Gabor mode); right, Lippmann mode, using reflection at the output facet of the sample. The fringes are sampled using nano-scatterers on the evanescent field of the optical guided mode, generally on top of the waveguide

Miniature localized detectors are placed in the evanescent field of the waveguide mode in order to extract only a small fraction of the guided energy. This peripheral detection approach allows proper sampling of the standing wave using relatively small size detectors in comparison with the quarter wavelength of the guided light. The interferogram resulting from white light illumination is called Lippmann mode. Unlike a classical Fourier interferogram, Lippmann's interferogram starts at the surface of the mirror with a null optical path difference fringe such that only half of the fringe packet is detected. In this way the whole energy is recovered using a minimum number of detectors. This principle thus acts like a spectrometer with simultaneous recorded Fourier transforms, i.e., no moveable part is required to record the information needed to restore the spectrum. However, the drawback of this system is that the interferogram is folded, as seen in the Lippman mode in Fig. 28.9, right so that any asymmetric spectral information (i.e., relative chromatic dispersion) is hidden in the full wideband packet and will be averaged with the Lippmann configuration.

The second SWIFTS configuration (Fig. 28.9, left) is based on the same near-field detection idea, but instead of using a mirror, the light is injected from both sides of the waveguide, and it is known as Gabor configuration. A similar configuration has been proposed by Labeyrie et al. [29] for a data storage system which is an extension of holography [12, 21] or of a Sagnac interferometer [46]. In this configuration, the resulting interferogram is a typical full Fourier interferogram which, in contrast with the mirror configuration, is sensitive to the optical path difference. This type of spectrometer could therefore also be used in metrology.

The interest of SWIFTS spectrometers is their compacity and robustness, as they do not require any relay optics, with the detector directly glued on top of the surface, as shown in Fig. 28.10 (left).

3.1 *Principal Equations of the SWIFTS Spectrometer*

The main equations of the SWIFTS spectrometer [31] state that the spectral resolution SR is related to the sampling length L and the refractive index (or more exactly, the effective index of the guided mode, n) by:

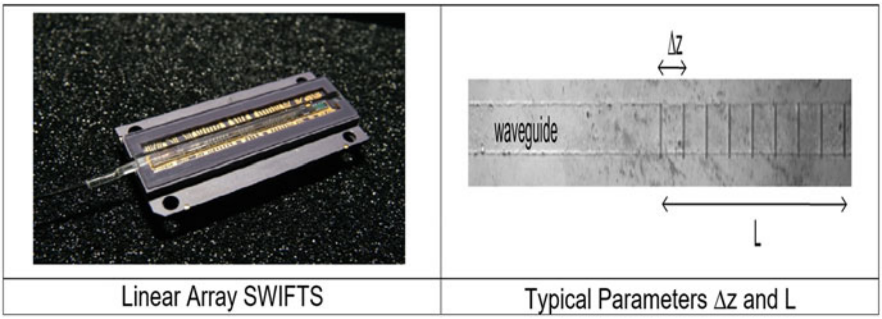

Fig. 28.10 Left: Image of a visible commercial SWIFTS interferometer, showing the optical waveguide (fed by an optical fiber) glued directly to the CMOS linear detector. Right: Image of a waveguide with nano-grooves on the surface, showing the typical parameters of the sampling region (L = total sampling length and Δz = sampling period)

$$\mathrm{SR} = 2\ nL/\lambda \tag{28.2}$$

And that spectral étendue (or spectral range) before aliasing is related to the sampling period (distance between two sampling centers, Δz, see right part of Fig. 28.10).

$$\Delta\lambda = \lambda^2/4n\Delta z \tag{28.3}$$

To have an idea of the orders of magnitude, an example is given for a glass waveguide: $L = 1$ mm, $\lambda = 1.55$ microns, and $n = 1.44$, a spectral resolution of SR = 1858 is obtained so that resolution is rapidly several thousands and the spectral range is $\Delta\lambda = 41$ nm for $\Delta z = 10$ µm, which is a typical pixel pitch. This means that one could expect a thousand resolution in a 1-mm-long sample, with a spectral window of 41 nm, which is sufficient for many applications.

However, in order to expand the spectral range and correctly sample the signal, one has to fulfill the Shannon-Nyquist criteria. If we focus on the Lippmann configuration [50], the intensity equation relating the intensity along the waveguide to the distance to the mirror is:

$$I(\lambda, z) = I_0\left[1 + R - 2\sqrt{R}\cos\left[\frac{4\pi}{\lambda}n_{\mathrm{eff}}(\lambda)\, z\right)\right]\right] \tag{28.4}$$

where z is the distance from the waveguide output facet, n_{eff} is the effective refractive index, and I_0 is the input intensity. Also, R is the reflectivity of the mirror, typically $R > 90\%$ (in case we do not use a mirror, this value is simply the Fresnel reflectivity of the material for a perpendicular incidence, $R = ((n - 1)/(n + 1))^2$). This value can be strong enough to achieve the SWIFTS effect for high refractive index materials such as lithium niobate. Indeed, with $n = 2.2$, $R = 13\%$ can be reached without any technological step for mirror deposition in the output facet.

Knowing that the interferogram has a period of $\lambda/2n$, with λ the wavelength and n the refractive index, the sampling period has to be inferior or equal to $\lambda/4n$ in order to avoid aliasing. This value is therefore the maximum distance that we can have between two sampling centers (two antennas). For a typical borosilicate glass, with a refractive index around 1.444 at $\lambda = 1.55$ μm, the maximum period allowed between two sampling centers is $\Delta z = 268$ nm. This small dimension between sampling centers is not achievable with ultrafast laser writing. But even using complex nano-lithography, the limit of sampling period is the size of the pixel or pixel pitch, which is typically tens of microns. Therefore the stationary wave will necessarily be under-sampled, resulting in a reduced spectral range, typically tens of nanometers for typical pixel pitch of 10 μm. Note that this is not a drawback for laser characterization, where a high resolution is needed over a very narrow window. However, for wide-range spectroscopy (atmospheric detection, mid-infrared molecular analysis, etc.), large bandwidths are required. In order to solve that problem, a phase shift modulation, spatial or temporal, can be introduced. Before exploring these solutions more in detail, let us try to understand the behavior of the static interferogram and the intensity extracted by the DLW grooves, as a function of distance to the mirror, and wavelength, to understand the spectral signature of the signal.

3.2 Dependence of the Signal with the Wavelength and Distance to the Mirror

In (28.4) it can be seen that the intensity along the waveguide depends on the distance z from the waveguide output facet, where reflection occurs and the Lippmann interferogram starts. This dependency can be exploited to make a first simple wavelength meter: Using DLW, we fabricated a set of waveguides, with six antennas [5]. Each antenna consists of five nanovoids, with 3 μm spacing, and each antenna is 400 μm further from the previous one, the first being at 400 μm from the mirror (sketch shown in Fig. 28.11).

As can be seen in Fig. 28.11, the furthest the antenna is from the mirror, the more rapidly the signal oscillates as the wavelength varies (in this case, from 1560 to 1565 nm), being therefore very sensitive to wavelength variations. In order to study the results given by the sample, a high-resolution database is created, consisting on a full scan using a Tunics tunable laser source, between 1510 and 1600 nm, with a wavelength step of 50 pm. The detected intensity of a line of pixels along the six antennas is recorded as a function of wavelength, obtaining a 2D map (see Fig. 28.12).

Then, using this data base as a reference, an unknown wavelength issued from the same source was injected in the sample, and its expected value was retrieved through a comparison algorithm (least squares values search). As an example, the

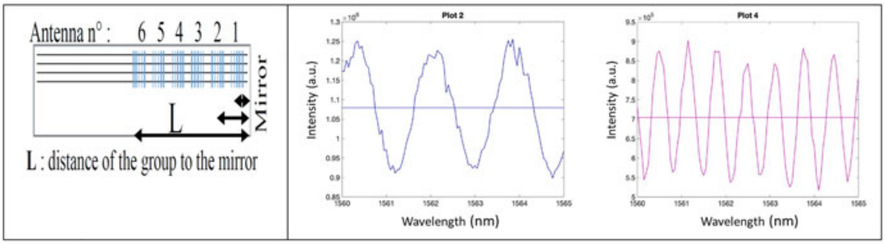

Fig. 28.11 Sketch of the fabricated sample, showing different sets of nano-scattering centers (Bessel voids) at different distances from the mirror. All scattering centers consist of five Bessel voids, to improve flux directivity. On the right, the sampled intensity for antennas number 2 and 4, respectively, showing the influence of the distance to the mirror on the frequency of the fringes. (Reproduced from Bonduelle et al. [5])

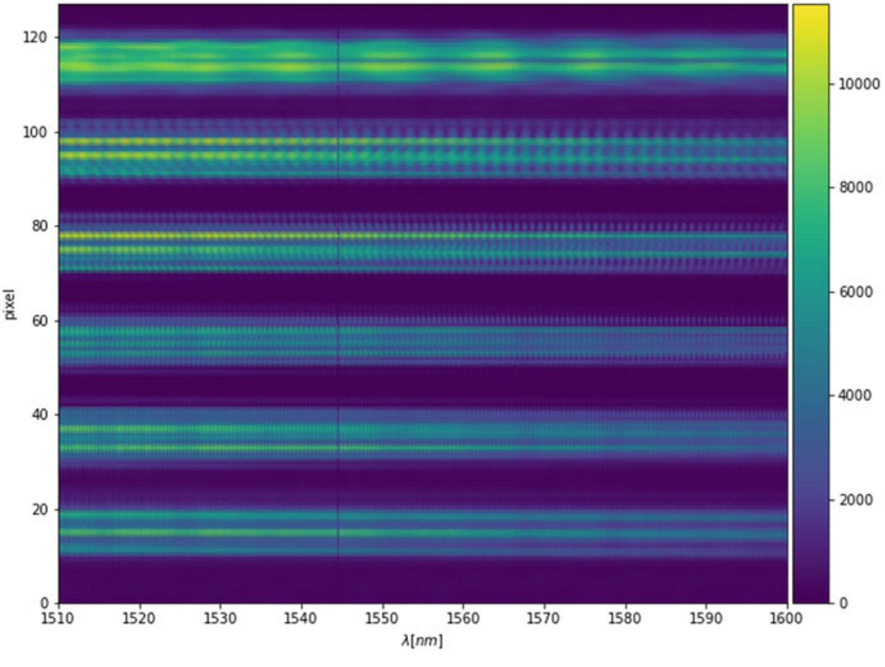

Fig. 28.12 Intensity recorded over each of the antenna while scanning the wavelength from 1510 to 1600 nm with 50 pm step. The top signal comes from the first antenna (closest to the mirror), and the bottom signal comes from the sixth antenna (furthest from the mirror)

recovery of an unknown wavelength, within the spectral window of the system, is shown below.

These results show that the unknown wavelength can be determined with a high accuracy, around 25 pm. However, as seen in Fig. 28.13, there can be two local minima that do not give the same result because of aliasing (secondary guess at

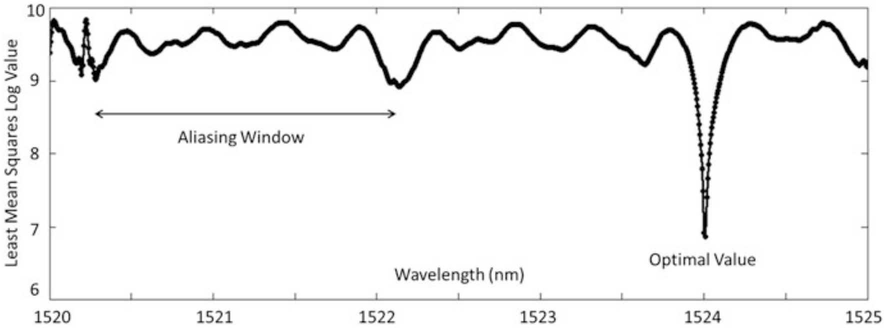

Fig. 28.13 Result of a least squares search for an unknown wavelength (1524.03 nm) injected on the system and comparison with the database (1524 nm), allowing for a guess wavelength with an accuracy around 25 pm

1522.3 nm). However, the global minima is still the accurate one, and the unknown value can still be retrieved.

We are now going to explore how to increase the spectral etendue and work towards the development of large spectral band spectrometers.

4 Laser-Written SWIFTS in Passive Materials: Spatial Multiplexing

As it has been shown in Sect. 2, the main drawback of the SWIFTS approach to spectrometry is that sampling must be done at λ/4n at least, which means hundreds of nanometers between sampling centers, which is not possible actually with commercial detectors. In order to reach a better spectral etendue, a first possibility is to use parallel waveguides where the same interferogram is encoded, but use the accuracy of laser writing nano-scattering fabrication, to set the sampling centers with a spatial shift in each waveguide, so that different parts of the interferogram are sampled. After stitching, the high-density sampling interferogram is recovered.

An example of spatial offset obtained by sampling the wave using several waveguides rather than a single one and introducing a spatial shift is given in Fig. 28.14.

Each waveguide has its own set of sampling centers, with the same spacing but shifted in comparison to the other waveguides. In the example of Fig. 28.14, the shift between each antenna is ¼ of the spacing between two antennas, therefore using four waveguides to complete the set. A fifth waveguide is prepared to check redundancy with the first one. This scheme can be of course increased to a $1/M$ shift, needing M parallel waveguides to work. We will discuss on this later on this chapter, as it raises the problem of how to inject light into M single-mode waveguides simultaneously.

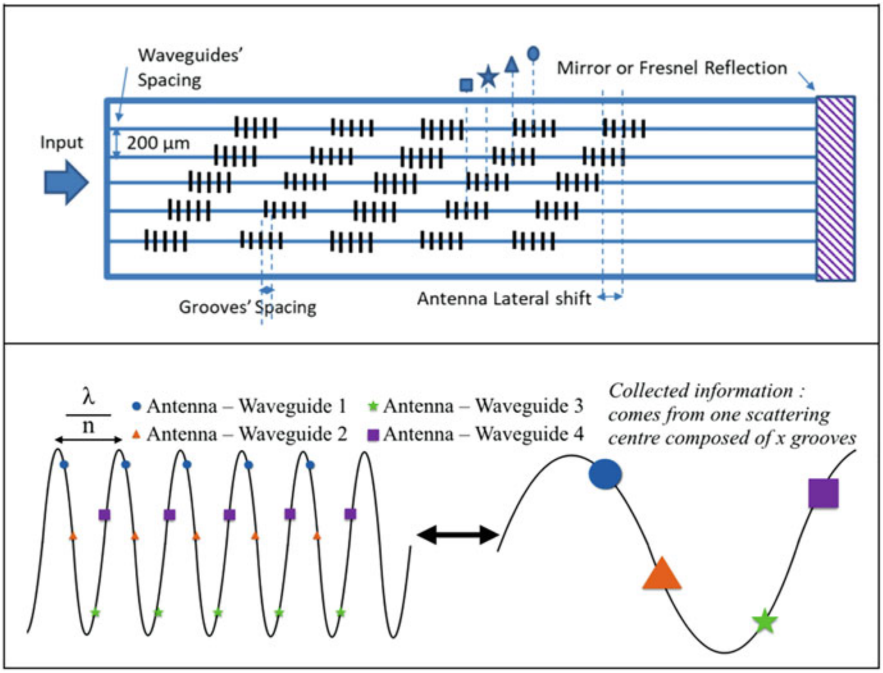
Waveguides' Spacing
Mirror or Fresnel Reflection
Input
200 μm
Grooves' Spacing
Antenna Lateral shift
λ
n
Antenna – Waveguide 1
Antenna – Waveguide 2
Antenna – Waveguide 3
Antenna – Waveguide 4
Collected information : comes from one scattering centre composed of x grooves

Fig. 28.14 Sampling with a spatial offset. Each antenna is set at a different length from the reflecting mirror, sampling a different part of the interferogram. After stitching, an improved sampling of the interferogram is obtained. (Reproduced from Bonduelle et al. [6])

With the multiplexing of the four first waveguides, the sampling can be correctly done (i.e., four sampled values for one optical period).

The numbers are very easy in this case: Increasing to M waveguides implies a increasing of the spectral range by $M \cdot \Delta\lambda$, where $\Delta\lambda$ is still directly related to the spacing Δz between two consecutive antennas in a given waveguide. It is important to note however that as the waveguides have to be single mode, if we want to keep an integrated optic system, one needs a way to inject light to the waveguides simultaneously. This can be done using a photonic lantern that can be also fabricated using DLW [4, 52], followed by the straight parallel waveguides containing the shifted sampling centers (see Fig. 28.15).

The interest of spatial multiplexing is that the signal can be obtained in a single measurement; however, it implies a collecting multimode waveguide and a perfect control of the transition between a (multi) M-mode waveguide to M single-mode waveguides.

Note that an alternative to spatial shift, if increasing the spectral range is not needed, is to keep the photonic lantern for high-efficiency light collection (thanks to its multimode, high numerical aperture behavior) and set the M parallel waveguides with exactly the same position for sampling centers. Therefore, with this square,

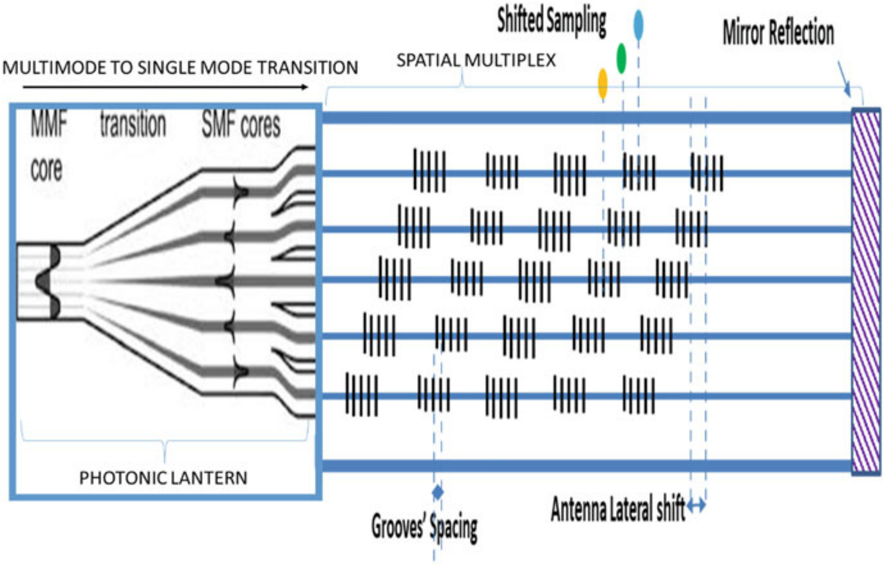
Shifted Sampling
Mirror Reflection
MULTIMODE TO SINGLE MODE TRANSITION
SPATIAL MULTIPLEX
MMF core
transition
SMF cores
PHOTONIC LANTERN
Grooves' Spacing
Antenna Lateral shift

Fig. 28.15 Basic principle of a spatial multiplexer based on a collecting photonic lantern (image extracted from [4]), followed by a set of parallel waveguides with the shifted sampling centers

pixel matrix, one can increase the signal-to-noise ratio, as the signal is distributed between M theoretically identical waveguides and noise can be averaged.

5 Laser-Written SWIFTS in Active Materials: Temporal Multiplexing

An alternative configuration to simplify the system is to fabricate a single-mode waveguide in a material that could observe a phase shift under an external perturbation such as temperature or electric field. With this approach, only one waveguide is needed; therefore the fabrication complexity reduces (no need of photonic lantern or multiple waveguides), and the cost of the detector is lower (no need of 2D matrices, only an array, and eventually, only a single pixel is needed).

As shown in (28.4), the intensity along the waveguide is related to the effective index of the guided mode. If we have a way to vary its value, using a physical property of the optical material, then we are able to temporally shift the fringes under the extracting antenna and, therefore, scan the fringes of the interferogram. However, in order to obtain the temporal shift of the fringes under the detector, it is compulsory to have a relative optical phase modulation between two interacting fields. The intensity along the output waveguide is then given by [33]:

$$I\left(z,\delta\right)=2I_0\left[1+\cos\left(\frac{2\pi}{\lambda}\Delta n\left(\delta\right)L_{\text{elec}}\right)\right]\left[1+R-2\sqrt{R}\cos\left[\frac{4\pi}{\lambda}n_{\text{eff}}z\right]\right] \tag{28.5}$$

As seen in (28.5), the SWIFTS interferogram (right part of the equation) is now coupled to an active modulation term (left part of the equation) that will help us to achieve the desired temporal shift. Two possibilities are going to be presented in the following sections.

5.1 The Electro-Optic Approach

One possibility is to explore the Pockels effect, which occurs in some particular crystals. This electro-optic effect [47] implies that the refractive index of a material (and, therefore, the effective index of the guided mode in a waveguide) can vary under the application of an electric field.

A typical configuration, using the most used electro-optic crystal (lithium niobate, $LiNbO_3$), gives a typical dependence of the refractive index with the electric field E_z such as:

$$\Delta n_{zz}(E)=-\frac{1}{2}n_{zz}^3 r_{zzz}E_z=-\frac{1}{2}n_e^3 r_{33}E_3=-\frac{1}{2}n_e^3 r_{33}\frac{V_{\text{app}}}{d_{\text{elec}}} \tag{28.6}$$

This variation Δn is to be introduced in Eq. (28.5), to understand the intensity variation seen by the pixel above the scattering center. When a voltage ramp is applied, we can scan the fringes, obtaining typically the signal shown in Fig. 28.16.

If several scattering centers are set along the waveguide, as the voltage ramp increases, the wide band fringes will shift from one center to the next one (as shown in Fig. 28.17, left), allowing for a temporal stitching and further reconstruction of an interferogram with increased spectral range (Fig. 28.17, right). An example of a SWIFTS electro-optic spectrometer can be found in [33].

This idea is currently being explored by developing DLW in lithium niobate to achieve simultaneously the waveguides and the scattering centers and, in a second step, fabricate the electrodes. Preliminary results on the waveguides and the nanogratings are shown in Fig. 28.18.

Preliminary results show that the refractive index contrast between the grooves and the waveguides are not strong enough to allow for efficient optical sampling. A new set of samples, with modified parameters and increased laser writing energy, is being studied.

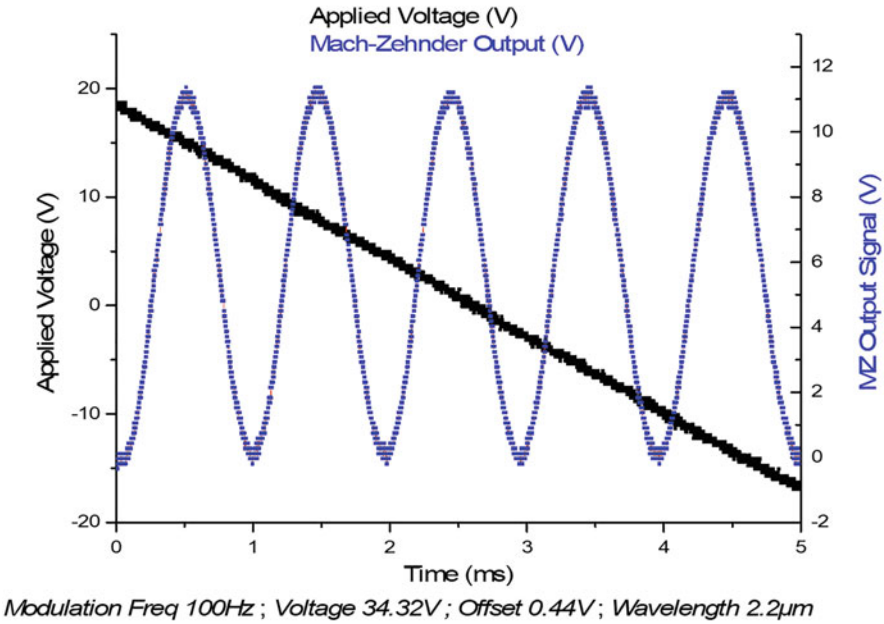

Fig. 28.16 Demonstration of the intensity modulation under an applied electric field in a Mach-Zehnder modulator

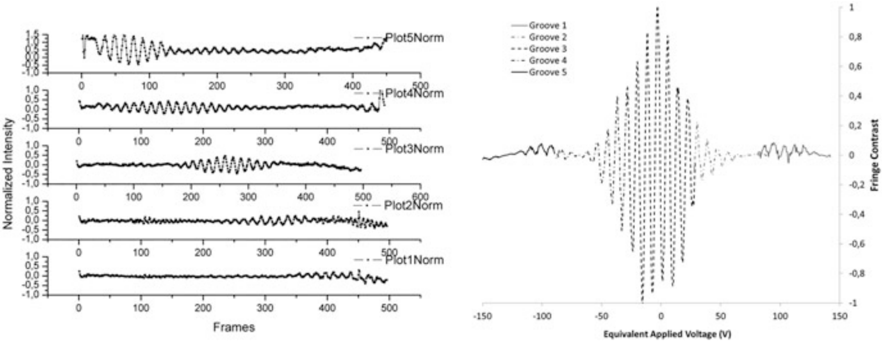

Fig. 28.17 Example of a temporal phase shift introduced in a lithium niobate SWIFTS. The wide band fringes are shifted from a sampling center to the next, thanks to an applied voltage, allowing to reduce the effective sampling step and therefore increasing the spectral range. (Reproduced from Loridat et al. [33]). Note that the source must present a limited coherence length, so that an envelope can be found to identify the relative phase between scattering centers and achieve the stitching

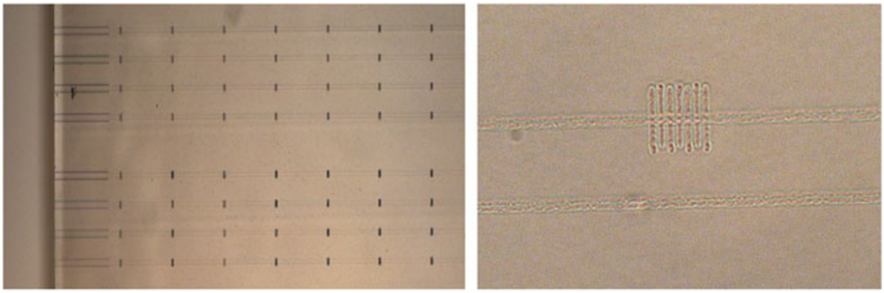

Fig. 28.18 (*Left*) Image of a set of parallel waveguides fabricated by DLW in lithium niobate, with the sampling centers (sets of nano-grooves) also fabricated by laser writing at the Univ. of Salamanca (J. R.V. de Aldana), on the surface of the sample. (*Right*) Zoom on a sampling center showing the seven nano-grooves on top of the waveguide

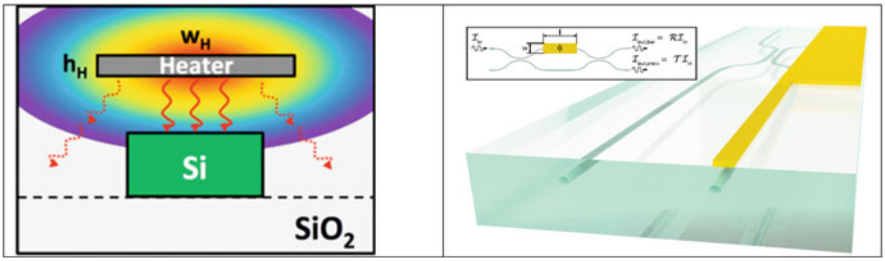

Fig. 28.19 (*Left*) Principle of the micro-heater, showing how the top electrode will diffuse heat through the Joules effect induced by the strong current passing through the metal. (*Right*) Example of a DLW thermo-optic beam coupler. (Reproduced from Ceccarelli et al. [8])

5.2 *Thermo-optic Effect*

A second approach is to actively modify the refractive index by locally changing the temperature of the waveguide. The thermo-optic effect is again related to the thermal constants of the material, but has the interest of being in principle available for any material (glass or crystal), as soon as its thermal constants are strong. Compared to the electro-optic effect that is limited to crystals (not glasses), and only for not-centrosymmetric crystals, the thermo-optic effect can offer a wider range of materials for testing.

The principle is based on the heating of the metallic wire on top of the waveguide (Fig. 28.19 left), resulting from a high current passing through. This will in turn generate a local increase of temperature and, subsequently, the modification of the refractive index of the waveguide, resulting in a phase shift that can be used for intensity modulation (Fig. 28.19 right). Thermal shifters have been demonstrated for several integrated photonics technologies, like silicon photonics [23, 56], silica-on-silicon [37, 39], and, more recently, also for platforms based on DLW of waveguides in transparent substrates [8, 18, 19].

As seen in this section, the advantage of temporal modulation is to call for simpler waveguide and detection construction, but needing more lithographic steps in order to set the electrodes or heaters. Besides, the signal is constructed by temporal phase-shifting, so that there is no snapshot measurement.

6 Perspectives: Image Reconstruction, Spectro-Imaging, and Wavefront Sensing

We have focused on a particular approach for laser-written spectrometers based on the SWIFTS principle. Of course, as long as the laser writing process allows for local modification of the refractive index, and accurate alignment of the laser is achieved to cover large surfaces, one can imagine many other approaches. We will present some of them hereunder. The main driver for the examples shown below is the possibility to achieve spectro-interferometry, that is, to obtain interference fringes from two or more optical inputs (typically astronomical telescopes) and span these fringes as a function of the wavelength to get access to the fringe contrast as a function of wavelength. Two applications are driving these concepts: phase closure studies [44] and image reconstruction using sparse aperture masking [10]. We will discuss this in Sect. 6.3, after briefly presenting two other approaches to spectrometry using direct laser writing.

6.1 Arrayed Waveguide Gratings

Arrayed waveguide gratings (AWG) are based on the concept proposed by Smit and Van Dam [48]. The heart of the system is a set of waveguides with an optical path length that is gradually increased, resulting in an output where different wavelengths superimpose at different lateral positions of a planar output waveguide, obtaining directly the spectrum along the horizontal axis of the sample, as shown in Fig. 28.20. These systems proposed initially in classical waveguide technologies (lithography), have been developed using DLW [14].

The example shown in Fig. 28.21 [16] proposes a horseshoe layout [15, 17]. The input waveguide is single mode at 633 nm and connects to the center of the first FPZ (free propagation zone). The FPZ (7.7 mm × 0.9 mm) confines the light in the vertical direction while allowing it to diffract in the horizontal direction. At the output of the FPZ, 0.7-mm-long linear adiabatic tapers guide the light into an array of 19 single-mode waveguides. Each waveguide has an incrementally longer optical path length (for this design $\Delta L = 11.77\ \mu\text{m}$), with an average length of 12.55 mm. At the end of the waveguide array, linear adiabatic tapers allow the mode size to increase. Light is then recombined in the second FPZ, creating a horizontally dispersed spectrum of the input signal at the output of the chip. More details on the

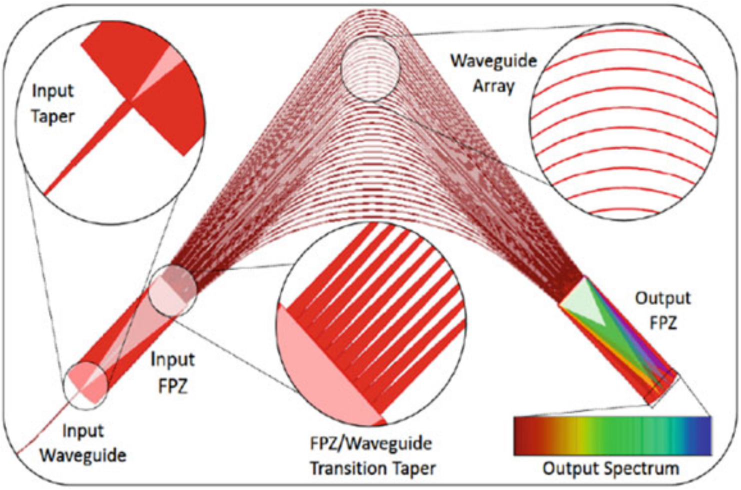
Input
Taper
Waveguide
Array
Output
FPZ
Input
FPZ
Input
Waveguide
FPZ/Waveguide
Transition Taper
Output Spectrum

Fig. 28.20 Principle of an arrayed waveguide grating. (Reproduced from Douglass et al. [14])

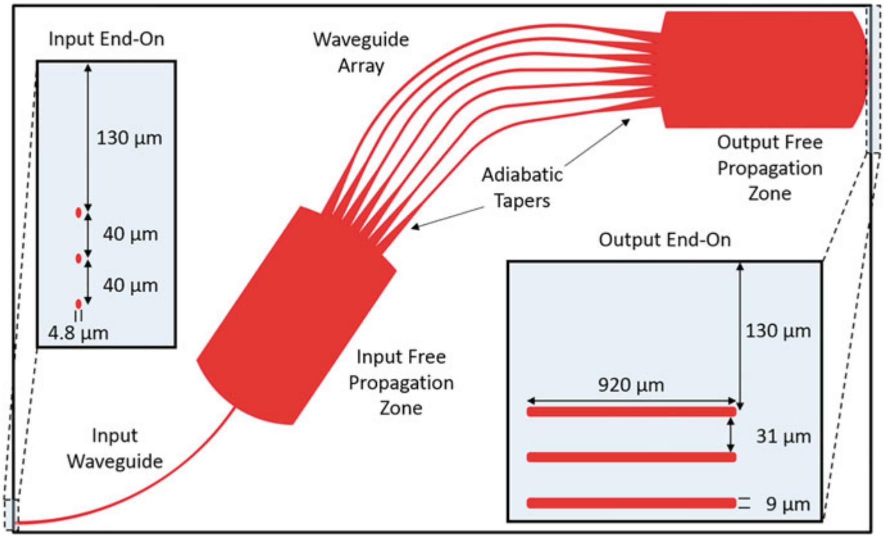
Input End-On
130 µm
40 µm
40 µm
4.8 µm
Waveguide
Array
Adiabatic
Tapers
Output Free
Propagation
Zone
Output End-On
130 µm
920 µm
31 µm
9 µm
Input Free
Propagation
Zone
Input
Waveguide

Fig. 28.21 Top-down schematic of a three-layered AWG sample. Inserts show the input and output end-on. (Reproduced from Douglass et al. [16])

principle of these AWGs can be found in [15, 16]. In order to achieve interference between different inputs, three identical AWGs were stacked vertically separated by 40 µm at three depths 210, 170, and 130 µm. A vertical spacing of 40 µm (center-to-center) was chosen to avoid coupling between AWG layers.

A bright-field microscope image of a tri-layered AWG output facet is shown in Fig. 28.22 (*left*). The thickness of each modification layer is 9 ± 0.2 µm,

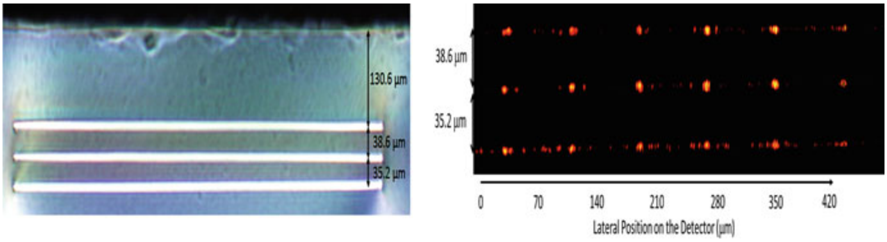

Fig. 28.22 (*Left*) White light image of a tri-layered AWG output facet. (*Right*) Output image of the diffracted modes, for the three layers injected simultaneously, at 790 nm. (Reproduced from Douglass et al. [16])

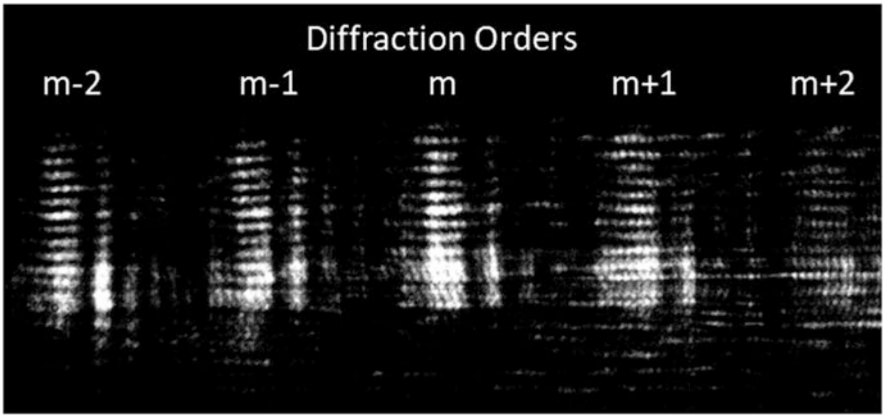

Fig. 28.23 Vertical superposition of the output orders, when the signal is defocused on the detector. (Reproduced from Douglass et al. [16])

which compares well to the designed 9 µm. The spacing between each AWG layer is 35.2 µm (lowest-center) and 38.6 µm (center-highest), which is smaller than the designed spacing of 40 µm. This is due to spherical aberrations affecting the modification depth. All three AWG outputs are 920 µm wide. A previously fabricated AWG with the same design had a measured throughput of 11.5 ± 0.2% at 635 nm across 5 orders [15]. As the wavelength is increased, the throughput was found to decrease due to material absorption.

The three AWGs were tested simultaneously using a near IR Sacher tunable laser centered at 790 nm. The output of the stack of AWG is shown in Fig. 28.23. As the modes are properly arranged vertically, one can play with defocusing, in order to obtain vertical superposition of the flux coming from the waveguides.

We can thus recover the vertical fringe contrast as a function of wavelength, which is the observable we are looking for.

6.2 Far-Field Spectrometers

Another approach is to fabricate several parallel channel waveguides, extract the light from them, and make it interfere, so we can obtain a spectro-interferometer. We fabricated a set of four large-mode-area channel waveguides ([9, 40, 55]; d'Amico 2014) aligned in a plane, with a center-to-center separation of 250 μm, and buried at 800 μm from the surface. In a second step, a non-diffractive irradiation procedure [2, 3] was used to generate a series of one-dimensional voids, transverse to the waveguides, with a characteristic section below 500 nm and an axial dimension above 150 μm, separated by 30 μm (see Fig. 28.24).

Here, as the sampling centers are fabricated inside the material, a symmetric radiation pattern is expected, resulting in a more efficient flux extraction towards the surface. In order to efficiently recover the flux, and discriminate eventually different order modes, we have developed a simple set-up using a cylindrical lens for collecting the wide angle flux and focus different wavelengths at different pixels and a second optical stage to reduce aberrations, disperse laterally diffraction modes, and avoid overlapping.

In order to check proper injection into the waveguides, an image of the waveguide output is obtained on the FLIR camera (Fig. 28.25a) and from above using a simple microscope objective (Fig. 28.25b).

Vertical characterization of the extracted signal (Fig. 28.26, inset B) is achieved using a three-cylindrical lens tube (Fig. 28.26), allowing to image the diffracted signal from the nanovoids to be detected on a Goodrich near IR camera. With this optical set-up, L2 and L3 focus different wavelengths at different areas on the CCD (Fig. 28.26, inset A), along the direction of the channel waveguide.

The equation of the system couples the refractive effective index of the propagating mode, n_{eff}, with the period of the sampling centers Λ and gives the output angle θ as a function of wavelength:

$$n_{\text{eff}} - n_{\text{ext}} \sin\theta = m\frac{1}{\Lambda}\lambda \tag{28.7}$$

The total volume of the spectro-interferometer is thus 320 cm^3 (height 200 mm, width and length 40 mm), including the sample, the relay optics, and the detector. Note that once the flux is injected in the spectrometer (i.e., using a fibered V-groove), there is no moving part up to the detector; interference fringes and spectral dispersion are obtained directly on the detector. In order to reduce the footprint, a trade-off can be obtained by reducing the focal length and therefore the spectral resolution of the device.

We studied a waveguide grating consisting of 330 holes with a period of 30 μm, realized by femtosecond laser writing. In order to determine the resolution of the set-up, a scan between 1560 and 1587 nm was done.

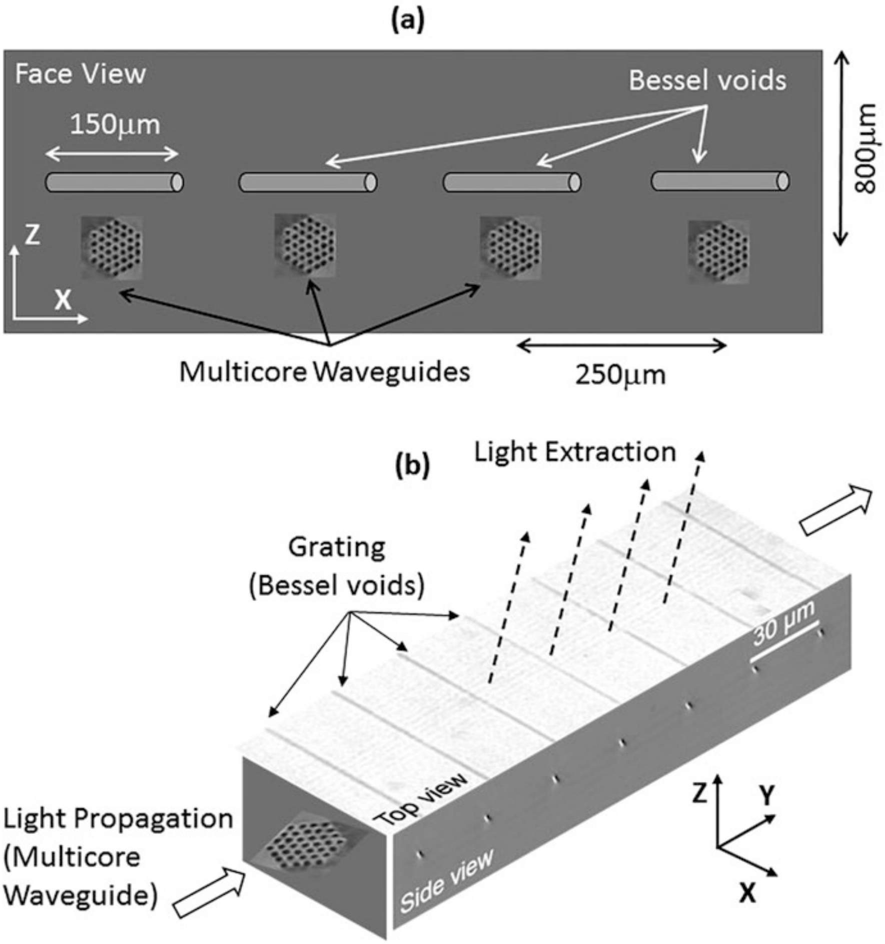
(a)
Face View
150µm
Bessel voids
800µm
Z
X
Multicore Waveguides
250µm
(b)
Light Extraction
Grating
(Bessel voids)
30 µm
Top view
Side view
Light Propagation
(Multicore
Waveguide)
Z
Y
X

Fig. 28.24 (**a**) Face view of the whole structure showing four parallel multicore waveguides and their respective Bessel sampling centers above them. Typical dimensions are given in the figure. (**b**) 3D view of the device showing the disposition of the nanovoid array positioned transverse to the waveguide and the axis orientation. (Reproduced from Martin et al. [36])

As shown in the precedent figure, peak intensity moves on the detector as we scan the wavelength. The images on Fig. 28.27 show the short wavelength peak moving to the right as wavelength is increased. We can verify that a modification of 3 nm implies a peak shift of 30 pixels, that is, each pixel corresponds to 0.1 nm, which is the theoretical expected value.

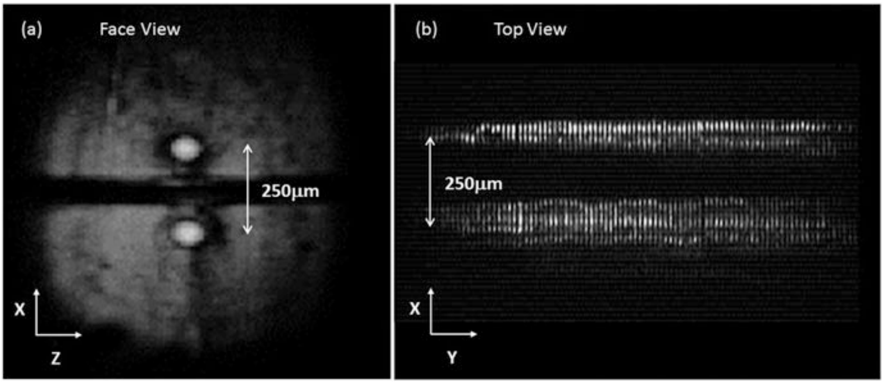

Fig. 28.25 Near IR observation of two parallel waveguides and the sampling centers when illuminated with a 1.56 µm laser. (**a**) Direct transmission on the FLIR camera, showing the two modes of two adjacent channel waveguides. (**b**) Top view as signal is extracted with the sampling centers and imaged on the Goodrich Camera using a simple microscope objective. (Reproduced from Martin et al. [36])

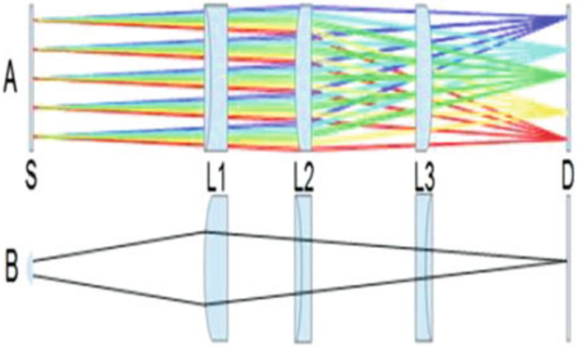

Fig. 28.26 Experimental set-up using a lens triplet, allowing for angular discrimination of the different wavelengths in the optical beam. (**a**) Sketch of optical rays along the vertical waveguide propagation axis. (**b**) Front view sketch, showing how the angular divergence of the signal extracted is focused on the detector. (From Martin et al. [36])

Using two parallel waveguides, one can then superimpose the signal to obtain a spectro-interferometer. The optical scheme is shown in Fig. 28.28.

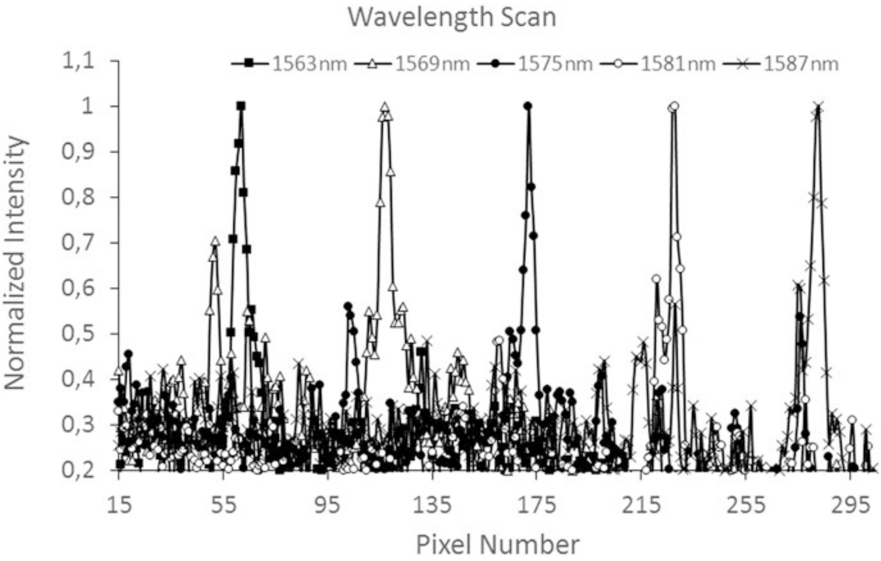

Fig. 28.27 Detected peak on an array of pixels, as the wavelength is scanned within the source tuning range. Side lobes are visible, due to inhomogeneous grating period fabrication, and induce crosstalk (see, e.g., the secondary lobe at 1569 nm (open triangles) close to the main peak at 1563 nm (filled squares)). (Reproduced from Martin et al. [36])

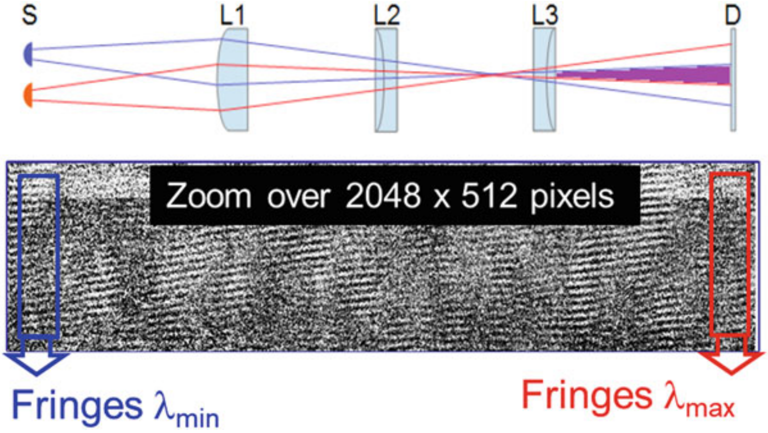

Fig. 28.28 (Top) Experimental set-up using a lens triplet, allowing for imaging two parallel waveguides on the detector and, by slightly defocusing, obtaining an overlap of the optical signals. (Bottom) Fringes obtained on the detector from the superposition of the two waveguides, with the wavelength increasing from left to right

6.3 Other Applications: Image Reconstruction, Pupil Remapping, and Wavelength Filtering (Bragg Filters)

The case of multiple beam recombination is being explored today for image reconstruction in ophthalmology or telecom transmission in order to correct wavefront errors as an alternative to complex adaptive optics systems [20]. Some flagship instruments using multiple sub-aperture recombination like FIRST/SUBARU [10] use this technique for image reconstruction and model fitting in astronomy using complex photonic chips (see Fig. 28.29 left). One can observe that increasing the number of channels to combine implies being rapidly limited by the length of the wafer (typically limited to 5 inches). Besides, two-dimensional (2D) waveguide routing introduces in-plane crossings that imply unwanted phase delays and crosstalk. Therefore, densification of optical functions by accessing the three-dimensional (3D) real space would be a very interesting solution if technologically feasible (see Fig. 28.29 right). Finally, if the full 3D IR photonic instrument is low-energy demanding and has a minimal footprint, avoiding any moving part and going from the collecting aperture to the integrated detector all monolithically, it would be of huge interest for applications in remote sensing: drone or nanosat applications (PICSAT [43]), in particular in the field of gas monitoring (SPOC [13]; NANOCARB [22]).

Some preliminary results on these types of systems are shown here (Fig. 28.30), with a 3D 3T beam interferometer made by DLW in a borosilicate glass [45].

By injecting light in channels 1 and 3 and using and external mirror for relative optical path modulation, we can scan the wideband fringes and, after Fourier transform, recover the spectrum of light. This preliminary results allow to validate the principle of sampling the 3D 3T. More details can be found in [35].

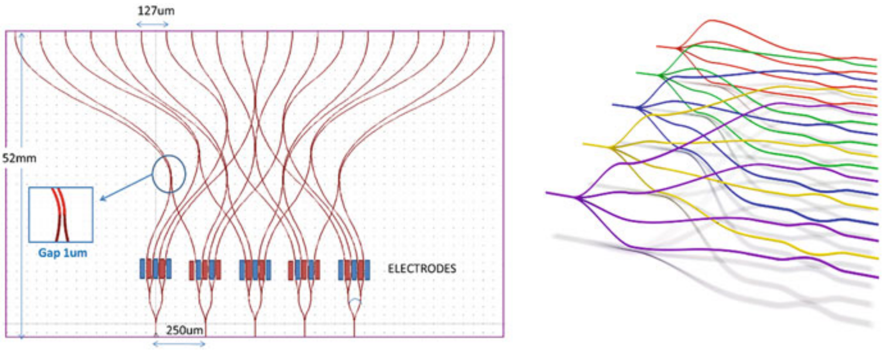

Fig. 28.29 (*Left*) Classical 2D concept of the 5T FIRST beam combiner, implying 20 parallel channel waveguides to be combined by pairs. Note the number of in-plane crossings. (*Right*) Concept of a laser-written 5T FIRST 3D solution, allowing to reduce propagation length and remove in-plane crossings and therefore increasing global transmission

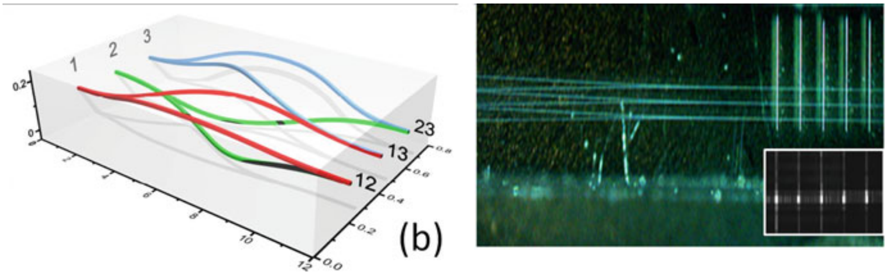

Fig. 28.30 (*Left*) Sketch of a 3D 3T beam combiner. (Reproduced from Rodenas et al. [45]). (*Right*) Image of the fabricated 3D 3T and the sampling centers using DLW. In the inset is shown the image of the radiating sampling centers when an IR laser is injected at the input

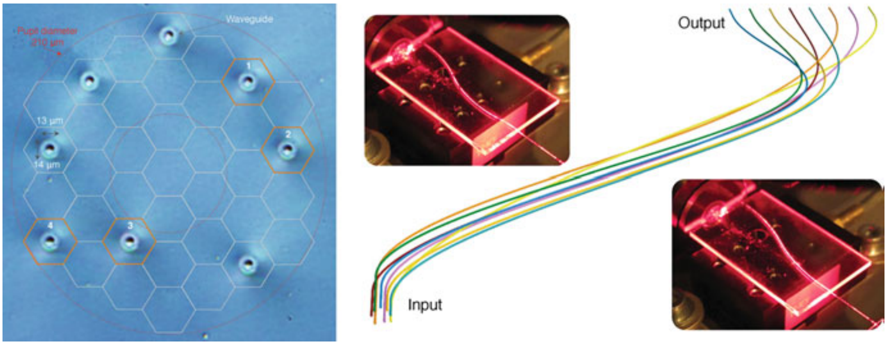

Fig. 28.31 (*Left*) Image of the nonredundant input, fabricated in the sample by DLW. (*Right*) Sketch and images of the optical beam redistribution from a 2D input to a linear 1D output. (Reproduced from Jovanovic et al. [27])

Pupil Remapping

One powerful interferometric technique is aperture masking [53] which offers precise calibration of wavefront structure for angular separations from the target star of around λ/D. This is achieved by recording Fizeau interferograms generated by a nonredundant sparse aperture mask placed in a reimaged telescope pupil plane. Such a scheme has been shown to be highly robust against the degrading effects of atmospheric phase noise, particularly when the self-calibrating closure phase observable [1] is utilized [30, 32].

An example of a pupil remapping system developed for astronomy, using direct laser writing, is Dragonfly [27], which optical waveguide redistribution is shown in Fig. 28.31.

Using DLW, the nonredundant pupil plane is redirected towards a line output that is later reimaged on the detector. The spectrum is obtained by classical prism dispersion in this case.

Waveguide Bragg Gratings (OH Suppression)
A waveguide Bragg grating (WBG) [7, 28, 38] is a type of distributed Bragg reflector constructed in a short segment of optical waveguide that reflects particular wavelengths of light and transmits all others. This is achieved by creating a periodic variation in the refractive index of the waveguide core, which generates a wavelength-specific dielectric mirror. Hence a WBG can be used as an inline optical waveguide to block certain wavelengths, or it can be used as wavelength-specific reflector.

DLW has been used to fabricate fully integrated photonic lanterns with incorporated WBG to provide spectral filtering and discuss potential astronomical applications [49]. Femtosecond laser-written WBG has been demonstrated using various techniques, such as single axial point-by-point [34] or a square-wave modulated pulse train [57]. In a typical example, DLW allows passing from an input photonic lantern to a planar distribution of single-mode waveguides, each with a specific Bragg grating period, and then restructuring an output photonic lantern, where the designed wavelengths will be rejected.

In this chapter we have shown the interest of DLW for its versatility and interest in the fabrication of 3D photonic systems, allowing for accurate fabrication of waveguides, nano-scattering centers, Bragg gratings, and complex interferometers. We have focused on a particular family of Fourier transform spectrometers (SWIFTS approach) and presented also some interesting applications in astronomy. There is no doubt that with the increasing performances of femtosecond laser writing, more complex systems allowing for multiple beam combination and on-chip spectrometry will be developed, paving the way for spectro-imaging at high pixel resolution.

References

1. J. Baldwin, C. Haniff, C. Mackay, et al., Closure phase in high-resolution optical imaging. Nature **320**, 595–597 (1986)
2. M.K. Bhuyan, F. Courvoisier, P.A. Lacourt, M. Jacquot, R. Salut, L. Furfaro, J.M. Dudley, High aspect ratio nanochannel machining using single shot femtosecond Bessel beams. Appl. Phys. Lett. **97**, 081102 (2010)
3. M. Bhuyan, P.K. Velpula, J.P. Colombier, T. Olivier, N. Faure, R. Stoian, Single shot high aspect ratio bulk nanostructuring of fused silica using chirp controlled ultrafast laser Bessel beams. Appl. Phys. Lett. **104**, 021107 (2014)
4. T.A. Birks, I. Gris-Sánchez, S. Yerolatsitis, S.G. Leon-Saval, R.R. Thomson, The photonic lantern. Adv. Opt. Photon. **7**, 107 (2015)
5. M. Bonduelle, G. Martin, I.H. Perez, A. Morand, C. d'Amico, R. Stoian, G. Zhang, G. Cheng, Laser written 3D 3T spectro-interferometer: study and optimisation of the laser-written nano-antenna, in *Proc. SPIE 11446, Optical and Infrared Interferometry and Imaging VII*, (13 December 2020), p. 114462T
6. M. Bonduelle, I. Heras, A. Morand, G. Ulliac, R. Salut, N. Courjal, G. Martin, Near IR stationary wave Fourier transform lambda meter in lithium niobate: Multiplexing and improving optical sampling using spatially shifted nanogroove antenna. Appl. Opt. **60**, D83–D92 (2021)

7. G. Brown, R.R. Thomson, A.K. Kar, N.D. Psaila, H.T. Bookey, Ultrafast laser inscription of Bragg-grating waveguides using the multiscan technique. Opt. Lett. **37**, 491 (2012)
8. F. Ceccarelli, S. Atzeni, A. Prencipe, R. Farinaro, R. Osellame, Thermal phase shifters for femtosecond laser written photonic integrated circuits. J. Light. Technol. **37**(17), 4275–4281 (2019)
9. G. Cheng, C. D'Amico, X. Liu, R. Stoian, Large mode area waveguides with polarization functions by volume ultrafast laser photoinscription of fused silica. Opt. Lett. **38**, 1924 (2013)
10. N. Cvetojevic, et al., FIRST, the pupil-remapping fiber interferometer at Subaru telescope: towards photonic beam-combination with phase control and on-sky commissioning results. Proc. SPIE 10701, Optical and Infrared Interferometry and Imaging VI, 107010A (10 July 2018)
11. K.M. Davis, K. Miura, N. Sugimoto, K. Hirao, Writing waveguides in glass with a femtosecond laser. Opt. Lett. **1024**(21), 1729–1731 (1996)
12. Y.N. Denisyuk, On the reproduction of the optical properties of an object by the wave field of its scattered radiation. Opt. Spectrosc. (USSR) **15**, 279–284 (1963)
13. T. Diard, F. de la Barrière, Y. Ferrec, N. Guérineau, S. Rommeluère, E. Le Coarer, G. Martin, Compact high-resolution micro-spectrometer on chip: spectral calibration and first spectrum, in *Proc. SPIE 9836, Micro- and Nanotechnology Sensors, Systems, and Applications VIII*, (25 May 2016), p. 98362W
14. G. Douglass, F. Dreisow, S. Gross, S. Nolte, M.J. Withford, Towards femtosecond laser written arrayed waveguide gratings. Opt. Express **23**(16), 21392–21402 (2015)
15. G. Douglass, F. Dreisow, S. Gross, M.J. Withford, Femtosecond laser written arrayed waveguide gratings with integrated photonic lanterns. Opt. Express **26**(2), 1497–1505 (2018)
16. G. Douglass, A. Arriola, I. Heras, G. Martin, E. Le Coarer, S. Gross, M.J. Withford, Novel concept for visible and near infrared spectro-interferometry: Laser-written layered arrayed waveguide gratings. Opt. Express **26**, 18470–18479 (2018)
17. C. Dragone, An N × N optical multiplexer using a planar arrangement of two star couplers. IEEE Photon. Technol. Lett. **3**(9), 812–815 (1991)
18. I.V. Dyakonov et al., Reconfigurable photonics on a glass chip. Phys. Rev. Appl. **10**(4), 044048 (2018)
19. F. Flamini et al., Thermally reconfigurable quantum photonic circuits at telecom wavelength by femtosecond laser micromachining. Light Sci. Appl. **4**, e354 (2015)
20. T. Fusco, et al. Optimization of a Shack-Hartmann-based wavefront sensor for XAO systems. Proc. SPIE 5490, Advancements in Adaptive Optics, (25 October 2004)
21. D. Gabor, A new microscopic principle. Nature **161**, 777–778 (1948)
22. S. Gousset, et al., NANOCARB-21: A miniature Fourier-transform spectro-imaging concept for a daily monitoring of greenhouse gas concentration on the Earth surface, in *International Conference on Space Optics—ICSO 2016*, vol. 10562, (International Society for Optics and Photonics, 2017). https://hal.archives-ouvertes.fr/hal-01401371
23. N.C. Harris et al., Efficient, compact and low loss thermo-optic phase shifter in silicon. Opt. Express **22**(9), 10487–10493 (2014)
24. R. He, I. Hernández-Palmero, C. Romero, J.R. Vázquez de Aldana, F. Chen, Three-dimensional dielectric crystalline waveguide beam splitters in mid-infrared band by direct femtosecond laser writing. Opt. Express **22**, 31293–31298 (2014)
25. J. Hu, C.R. Menyuk, Understanding leaky modes: Slab waveguide revisited. Adv. Opt. Photonics **1**, 58–106 (2009)
26. M. Hughes, W. Yang, D. Hewak, Fabrication and characterization of femtosecond laser written waveguides in chalcogenide glass. Appl. Phys. Lett. **90**, 131113 (2007)
27. N. Jovanovic et al., Starlight demonstration of the Dragonfly instrument: An integrated photonic pupil-remapping interferometer for high-contrast imaging. Mon. Not. R. Astron. Soc. **427**, 806–815 (2012)
28. S. Kroesen, W. Horn, J. Imbrock, C. Denz, Electro-optical tunable waveguide embedded multiscan Bragg gratings in lithium niobate by direct femtosecond laser writing. Opt. Express **22**(19), 23339–23348 (2014)

29. A. Labeyrie, J.P. Huignard, B. Loiseaux, Optical data storage in microfibers. Opt. Lett. **23**(4), 301–303 (1998)
30. S. Lacour, P. Tuthill, P. Amico, M. Ireland, D. Ehrenreich, N. Huelamo, A.-M. Lagrange, Sparse aperture masking at the VLT – I. Faint companion detection limits for the two debris disk stars HD 92945 and HD 141569. Astron. Astrophys. **532** (2011). https://doi.org/10.1051/0004-6361/201116712
31. E. le Coarer, S. Blaize, P. Benech, I. Stefanon, A. Morand, G. Lerondel, G. Leblond, P. Kern, J.M. Fedeli, P. Royer, Wavelength-scale stationary-wave integrated Fourier-transform spectrometry. Nat. Photonics **1**, 473 (2007)
32. J.P. Lloyd, F. Martinache, M.J. Ireland, et al., Direct Detection of the Brown Dwarf GJ 802B with Adaptive Optics Masking Interferometry, ApJL **650**, L131 (2006)
33. J. Loridat, S. Heidmann, F. Thomas, G. Ulliac, N. Courjal, A. Morand, G. Martin, All integrated lithium niobate standing wave Fourier transform electro-optic spectrometer. J. Lightwave Technol. **36**, 4900–4907 (2018)
34. G.D. Marshall, M. Ams, M.J. Withford, Direct laser written waveguide Bragg gratings in bulk fused silica. Opt. Lett. **31**, 2690 (2006)
35. G. Martin, J. R. Vázquez de Aldana, A. Rodenas, C. d'Amico, R. Stoian, Recent results on photonic devices made by laser writing: 3D 3T near IR waveguides, mid-IR spectrometers and electro-optic beam combiners, in *Proc. SPIE 9907, Optical and Infrared Interferometry and Imaging V*, (26 July 2016), p. 990739
36. G. Martin, M. Bhuyan, J. Troles, C. D'Amico, R. Stoian, E. Le Coarer, Near infrared spectro-interferometer using femtosecond laser written GLS embedded waveguides and nano-scatterers. Opt. Express **25**, 8386–8397 (2017)
37. J.C.F. Matthews et al., Manipulation of multiphoton entanglement in waveguide quantum circuits. Nat. Photonics **3**(6), 346–350 (2009)
38. B.W. McMillen, M. Li, S. Huang, B. Zhang, K.P. Chen, Ultrafast laser fabrication of Bragg waveguides in chalcogenide glass. Opt. Lett. **39**(12), 3579–3582 (2014)
39. B.J. Metcalf et al., Quantum teleportation on a photonic chip. Nat. Photonics **8**(10), 770–774 (2014)
40. S. Minardi, G. Cheng, C. D'Amico, R. Stoian, A low power threshold photonic saturable absorber in nonlinear chalcogenide glass. Opt. Lett. **40**, 257 (2015)
41. A. Morand, I. Heras, G. Ulliac, E. Le Coarer, P. Benech, N. Courjal, G. Martin, Improving the vertical radiation pattern issued from multiple nano-groove scattering centers acting as an antenna for future integrated optics Fourier transform spectrometers in the near IR. Opt. Lett. **44**, 542–545 (2019)
42. H.-D. Nguyen, A. Ródenas, J.R. Vázquez de Aldana, G. Martín, J. Martínez, M. Aguiló, M.C. Pujol, F. Díaz, Low-loss 3D-laser-written mid-infrared LiNbO3 depressed-index cladding waveguides for both TE and TM polarizations. Opt. Express **25**, 3722–3736 (2017)
43. M. Nowak et al., Reaching sub-milimag photometric precision on Beta Pictoris with a nanosat: The PicSat mission, in *Space Telescopes and Instrumentation 2016: Optical, Infrared, and Millimeter Wave*, vol. 9904, (International Society for Optics and Photonics, Bellingham, 2016)
44. G. Perrin, F. Malbet, J. Monnier, Astrophysics with closure phases. Eur. Astron. Soc. Publ. Ser. **6**, 213–213 (2003)
45. A. Rodenas, G. Martin, B. Arezki, N. Psaila, G. Jose, A. Jha, et al., Three-dimensional mid-infrared photonic circuits in chalcogenide glass. Opt. Lett. **37**(3), 392–394 (2012)
46. G. Sagnac, Sur la preuve de la réalité de l'éther lumineux par l'expérience de l'interférographe tournant. CRAS (Paris) **157**, 708–710, 1410–1413 (1913)
47. B. E. A. Saleh, M. C. Teich (eds.), *Fundamentals of Photonics, Chap. 18* (Wiley & Sons, New York, 1991)
48. M.K. Smit, C. Van Dam, PHASAR-based WDM-devices: Principles, design and applications. IEEE J. Sel. Top. Quantum Electron. **2**(2), 236–250 (1996)
49. I. Spaleniak, S. Gross, N. Jovanovic, et al., Multiband processing of multimode light: Combining 3D photonic lanterns with waveguide Bragg gratings. Laser Photonics Rev. **8**, L1–L5 (2014)

50. F. Thomas, S. Heidmann, M. de Mengin, N. Courjal, G. Ulliac, A. Morand, P. Benech, E. Le Coarer, G. Martin, First results in near and mid IR lithium niobate-based integrated optics interferometer based on SWIFTS-Lippmann concept. J. Lightwave Technol. **32**, 3736–3742 (2014)
51. F. Thomas, S. Heidmann, J. Loridat, M. de Mengin, A. Morand, P. Benech, C. Bonneville, T. Gonthiez, E. Le Coarer, G. Martin, Expanding sampling in a SWIFTS-Lippmann spectrometer using an electro-optic Mach-Zehnder modulator, in *Proc. SPIE 9516, Integrated Optics: Physics and Simulations II*, (1 May 2015), p. 95160B
52. R.R. Thomson, T.A. Birks, S.G. Leon-Saval, A.K. Kar, J. Bland-HawtHorn, Ultrafast laser inscription of an integrated photonic lantern. Opt. Express **19**, 5698–5705 (2011)
53. P.G. Tuthill, J.D. Monnier, W.C. Danchi, Aperture masking interferometry on the Keck I Telescope: New results from the diffraction limit, in *Proc. SPIE 4006, Interferometry in Optical Astronomy*, (5 July 2000)
54. P.K. Velpula, M. Bhuyan, F. Courvoisier, H. Zhang, J.P. Colombier, R. Stoian, Spatio-temporal dynamics in nondiffractive Bessel ultrafast laser nanoscale volume structuring. Laser Photonics Rev. **2**, 230 (2016)
55. M.M. Vogel, M. Abdou-Ahmed, A. Voss, T. Graf, Very-large-mode-area, single-mode multicore fiber. Opt. Lett. **34**, 2876 (2009)
56. J. Wang et al., Experimental quantum Hamiltonian learning. Nat. Phys. **13**(6), 551–555 (2017)
57. H. Zhang, S.M. Eaton, P.R. Herman, Opt. Lett. **32**, 2559–2561 (2007)
58. A. Zoubir, C. Lopez, M. Richardson, K. Richardson, Femtosecond laser fabrication of tubular waveguides in poly(methyl methacrylate). Opt. Lett. **29**, 1840–1842 (2004)

Chapter 29
Ultrafast Laser Volume Nanostructuring of Transparent Materials: From Nanophotonics to Nanomechanics

Razvan Stoian, Ciro D'Amico, Yves Bellouard, and Guanghua Cheng

Abstract The capability of ultrashort laser pulses to generate nonlinear absorption in the transparency window of dielectric materials is at the base of volume structuring. The result is a local change of the refractive index, the building block for generating complex embedded optical functions in three-dimensional geometries within a monolith chip. The nonlinearity determines spatial scales on the order of the wavelength. Depending on the rate and the amount of energy deposition, the local refractive index change can be accurately tuned from positive to negative values on variable scales, generating thus new capabilities for processing light within an optical chip in terms of embedded waveguides and micro-optics. New irradiation strategies and engineered glasses permit to go even further in reaching processing super-resolution, i.e., on spatial scales smaller than the optical resolution. The smallest scales achievable nowadays go well below the diffraction limit approaching and even surpassing the 100 nm value, a tenth of the wavelength. We will discuss in this chapter the possibility of obtaining structural features much smaller than the electromagnetic wavelength and the associated methods. Direct focusing and self-organization phenomena will be analyzed, as well as the optical functions originating from these processes, namely in transporting and manipulating light. Achieving extreme scales in the range of 100 nm generates an additional capability to sample the electrical field within the optical chip and thus to process and read out optical signals. We will discuss emerging applications ranging from photonics, such as sensors, spectro-imagers, actuators, or supports for data storage,

---

R. Stoian (✉) · C. D'Amico
Laboratoire Hubert Curien, UMR 5516 CNRS, Université Jean Monnet, Saint Etienne, France
e-mail: razvan.stoian@univ-etienne.fr; ciro.damico@univ-st-etienne.fr

Y. Bellouard
Galatea Lab, STI/IEM, Ecole Polytechnique Fédérale de Lausanne (EPFL), Neuchâtel, Switzerland
e-mail: yves.bellouard@epfl.ch

G. Cheng
School of Electronics and Information, Northwestern Polytechnical University, Xi'an, China
e-mail: guanghuacheng@nwpu.edu.cn

© The Author(s), under exclusive license to Springer Nature Switzerland AG 2023

R. Stoian, J. Bonse (eds.), *Ultrafast Laser Nanostructuring*, Springer Series
in Optical Sciences 239, https://doi.org/10.1007/978-3-031-14752-4_29

down to nanomechanical systems, and pinpoint the enabling character of extreme nanostructuring scales using ultrafast lasers.

Keywords Laser volume nanostructuring · Optical resolution · 3D photonics · Integrated optical circuits · Sampling electrical fields

1 Introduction

Laser volume structuring of transparent materials is based on a straightforward irradiation concept. This concept implies a capability, firstly, to transport energy to the point of impact (focus location) without losses and, secondly, to deposit the energy from the beam to the material in a restricted spatial domain around the point of impact. In most of the cases, it implies the crossing of a dielectric interface and the focusing inside the volume of the material. A perfectly adapted tool for this task is an ultrashort laser pulse. Typically generated at wavelengths for which the material is intrinsically transparent (mostly in the near-infrared and in the visible range), the propagating ultrashort laser pulse increases its intensity upon focusing, up to the point where a nonlinear absorption process is triggered within the confocal volume. This nonlinear excitation process sustained by high intensities occurs as a combination of multiphoton, field, and collisional ionization events. For intensities in the TW/cm^2 range, free charge carriers are generated across the material forbidden bandgap at densities that approach the material molecular density (10^{22} cm^{-3}), storing enough energy to generate, upon electronic relaxation, strong chemical, structural, and thermodynamic material evolutions. A processing feature is thus created, as illustrated in Fig. 29.1a, a modified material voxel. This comprises first a change of the material dielectric function and thus of its local optical properties, and will represent one of the main topics to be discussed in the chapter. The replication of the focal spot in space and the combination of different scan strategies as shown in Fig. 29.1b can determine a 3D pattern of energy deposition and a complex geometrical assembly of structures with the creation of an optical function. The process, highlighting the strong energy localization by ultrashort laser pulses, was demonstrated in several pioneering works published at the end of the 1990s by Davis et al. [1], Miura et al. [2], and Glezer and Mazur [3], demonstrating the occurrence of positive refractive index changes in silica-based optical glasses for waveguiding applications and, respectively, strong void-like negative index changes potentially useful for data storage. This type of volume nanostructuring relied essentially on the control of the excitation level through the strength of focusing of the laser pulse, with moderate focusing generating soft index increase while a strong focusing enabling a complete breakdown of the material. The technique of ultrafast laser photoinscription based on refractive index engineering experienced, soon after, a strong development, being nowadays a technology capable of uptaking new processing challenges well into the nanoscale [4, 5]. This roadmap driving laser processing on scales smaller than the optical

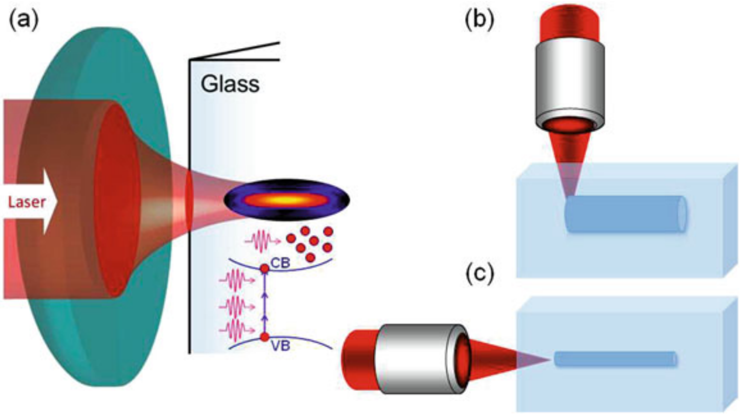

Fig. 29.1 (**a**) The concept of nonlinear laser volume nanostructuring using focused ultrashort laser pulses. (**b**), (**c**) Different scan strategies for volume photoinscription. Adapted with permission from [6] ©Springer Nature. Complex optical functions in three dimensions can be generated by combining the different irradiation geometries [6]. Extrapolating these features, other functionalities beyond the field of optics may be achieved

wavelength leading to a super-resolved processing is the topic of the present chapter. The evolution of 3D ultrafast processing technologies toward miniaturization and packaging of several optical functions on a single chip and with a strong control of the achievable scale is expected to exert a strong impact on the field of photonics. Secondly, a change in the material implies both a variation of the structural bonding and arrangement. A variation of the specific volume generates expansion and thus mechanical movement. An actuator function emerges. Irradiated regions can thus develop new mechanical characteristics, a second application topic of this chapter.

Reviewing the achievements in terms of volume nanostructuring, the chapter will first discuss the basic principles defining optical and processing resolution. Approaching different types of photoinscription results and their thermodynamic conditions, it will then revisit several milestones that define today the field of volume nanostructuring, the process of micro-explosion in direct focusing conditions, the process of self-organization in embedded nanopatterns, and the nonlinear generation of structural and chemical changes in nanoscale domains. Several applications will be reviewed at the end, relying on the use of nanoscale processing features to process and sample optical signals, among these, Bragg grating sensors, astrophotonic spectro-imagers, nonlinear frequency generation in crystalized glasses, or data storage. The fabrication of micromechanical and nanomechanical devices will be discussed.

2 The Laser Process

2.1 Optical Resolution

The capability of generating optical functions relates to an accurate control of the magnitude and of the scale of the refractive index change. This capability of precise structuring has consequences that extend naturally beyond the optical field, to all emerging applications as the majority of generated functions depends on the scale of processing. Let us first focus on the latter and discuss the potential scales in volume structuring. An ultrashort laser pulse (e.g. 100 fs) of spectral bandwidth $\Delta\omega$ and of field $\mathcal{E}(t) \approx \int_{-\infty}^{\infty} \tilde{\mathcal{E}}(\omega)e^{i\omega t}\,\mathrm{d}\omega$ passing through a focusing optical element is characterized in the focal plane mostly by its pulse duration and its spatial dimension [7]. Its multicolor wave packet nature puts forward additional challenges in order to preserve the spatiotemporal characteristics up to the point of impact. In interaction with a transparent solid, these values define the local intensity profile and determine an intricate sequence of propagation and excitation events leading to a permanent modification of the material. This occurs only when the intensity is high enough to generate electronic excitation and to deposit energy at a level above the material modification threshold.

Already recognized in early works of imaging and microscopy of E. Abbe [8] and Lord Rayleigh [9], focusing light encounters the limit of diffraction. Following Rayleigh's concept, an optical plane wave can be focused down to a minimum Airy spot size (radius) of $w = 0.61\lambda/NA$, with NA being the numerical aperture and λ the optical wavelength. As the typical output of a laser system (the lowest order transverse mode) is a Gaussian beam and for optical systems with input pupils comparable to the beam dimension, we can approximate the spot profile with a Gauss function of waist w as $I = I_0 exp(-2r^2/w^2)$, with r being the radial coordinate. Thus, for an optical system of $NA \simeq 1$ (a system that combines resolution power and working distance), the lateral optical resolution is roughly $\lambda/2$, and the axial resolution, approximated by the confocal distance, is $\pi\lambda/2$. Different focusing configurations are depicted in Fig. 29.2a, outlining the lateral spread of energy. The energy is then deposited within a domain given by the optical characteristic length estimated by a volume of $\pi^2\lambda^3/8$, energy diffusion from the interaction area, either thermal or electronic, being negligible for a dielectric material.

It has to be noted that volume interaction involves a propagation that, as intensity increases, becomes nonlinear, culminating at the focal point with nonlinear electronic excitation. An intensity-dependent nonlinear propagation will trigger, above a critical power level (in the range of few MW), self-focusing [10] and the early development of a carrier plasma that will follow in a first approximation a multiphoton ionization process. Due to the presence of carriers, the self-focusing process stops, the beam collapse is arrested [11], the pulse divergence changes, and the propagation becomes quasi-filamentary [12], a situation sketched in Fig. 29.2b.

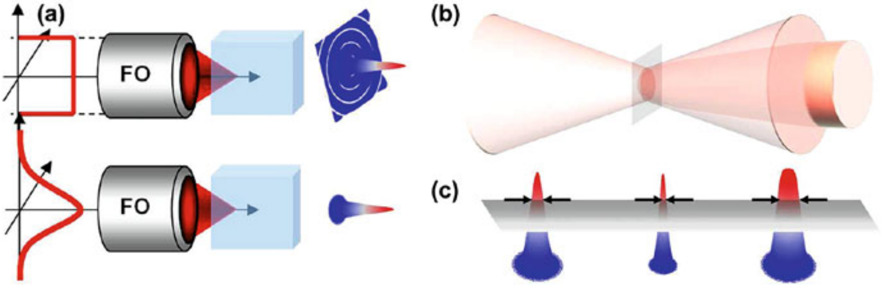

Fig. 29.2 (**a**) Different focusing geometries and relative beam dimensions with respect to the pupil generating Airy and Gauss patterns. (**b**) Nonlinear beam propagation with a change in the beam divergence due to the onset of self-action and excitation processes. The divergence in a linear regime is shown to guide the eye. (**c**) Typical excitation profiles, Gaussian (left), power function of a Gaussian profile (middle), a flatten profile through defocusing (right). They correspond, respectively, to linear interactions, multiphoton processes, and carrier defocusing. The modification threshold is shown as a planar domain, signaling the excitation level from upon which the modification occurs. The resulting above-threshold modifications have smaller sizes than the respective optical beams for the first two cases, giving high accuracies. On the other hand, defocusing delocalize energy increasing the feature size while self-limiting the energy content and thus the strength of the interaction. This provides a stable but less resolved soft interaction regime

These aspects are discussed to a great extent in Chap. 21, and the fundamental bases are reviewed in Chap. 1. If the excitation leading eventually to permanent modification regimes lies at the border between perturbative and strong field processes (see recent reviews of the topic in [6, 13]), we will only retain here for the purpose of the argument two probable evolutions of the excitation profile: a multiphoton-induced narrowing of the profile and a filamentation-induced profile broadening. We note first a potential narrowing of the excitation profile following multiphoton ionization $N_e \sim I^k = (I_0 e^{-\frac{2r^2}{w^2}})^k$, with k being the multiphoton order (the number of photon quanta $h\nu$ required to bridge the gap E_{gap}) and for excitation levels (carrier densities) that do not strongly defocus the light. The new waist becomes $w/\sqrt{k}$. Secondly, with the emergence of carrier plasmas in excess of $10^{16}\,\text{cm}^{-3}$, the carriers oscillating in the field form a negative lens that follows the spatial profile of the carrier density ($\Delta n \sim N_e(r,t)$) modifying the field as $\partial\mathcal{E}/\partial z \sim N_e\mathcal{E}$ [12]. As a side note, it is worth mentioning that carrier defocusing was one of the main reasons for which bulk modifications were not observed in low focusing single-pulse conditions (often applied in surface processing), as they may require higher numerical apertures ($NA > 0.1$) and increased doses. The process may be exacerbated by materials with small electronic effective mass [14], for example, a range of semiconducting materials. With the development of the carrier plasma, the profile of excitation flattens, and the characteristic scale increases, with the process depicted in Fig. 29.2b,c. It is evident from the above considerations that optical resolution alone can hardly provide structural features smaller than 500 nm.

In order to achieve high processing resolutions [15], i.e., small structural features at a high density in space, a different process comes into play. The processing resolution, being related to the onset of a material structure, is in this case determined by a material or an observation threshold. The excitation will produce an observable permanent effect in the processed material if on one hand the energy stored in the electrons matches a structural or thermodynamic threshold of the material (and the required carrier densities in this case are in the range of the critical density $N_e \simeq 10^{21}$ cm^{-3}) or the energy deposition gradient, on the order of ρ_E/w, with ρ_E being the energy density, is sufficient to generate a thermomechanical effect leading to the failure of the material. In this case, the processing resolution can be significantly smaller than the optical resolution. The condition that the energy associated with the excitation exceeds the material threshold requires consideration of the focusing strength and of the locally achieved intensity as the pulse wave packets are affected by chromatic and geometric distortions as it crosses the optical elements and dielectric interfaces [16].

2.2 *Photoinscription Regimes*

The nonlinear focusing and propagation of ultrashort laser pulses within a transparent material have multiple consequences on the spatial domain where optical energy is deposited in the material. The nonlinear excitation quantity, i.e., the free carrier population seeded by multiphoton or field ionization processes and multiplied in collisional events between accelerated electrons and atoms, renders the photoinscription process a predictable, deterministic character, equally observed in the processing results. This implies that the level of excitation does not fluctuate, being set by the seeded carriers and not by randomly localized absorption centers. Based on the morphological aspects of the laser-affected zones, we can first distinguish between (a) soft positive index changes and (b) strong negative index changes. Specific situations may appear where the two of them cohabitate within the same spatial region.

2.2.1 Positive Refractive Index Changes

The process is primarily based on a concept of bond-breaking and structural reorganization of matter [1, 17, 18] in spatial patterns defined by nonlinear propagation [19, 20] and will be discussed in Chap. 21. It lies at the base of volume waveguide photoinscription [1]; an image of a corresponding waveguide is given in Fig. 29.3a. A bond-breaking event represents an increase of the bonding length (e.g., the $Si-O$ bond in a silica-based glass) and occurs following an electronic excitation event which screens the charge and lowers the bonding strength. The consequence is a change in molecular polarizability and a certain structural flexibly where atoms can move to stabilize the internal energy of the molecular ensemble and to accommodate

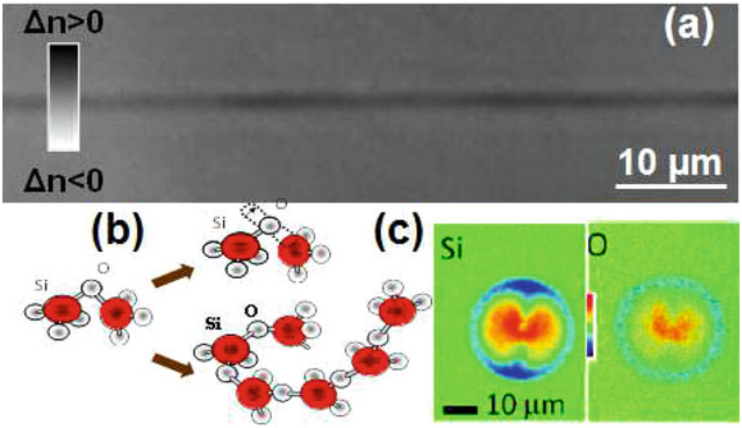

Fig. 29.3 (**a**) Typical positive index change induced by moderately focused ultrashort laser pulses in fused silica (phase contrast microscopy image). The dark color indicates a positive change of the refractive index. (**b**) Schematic representation for bond-breaking with defect generation and rebonding in smaller, hence denser, structural units, characteristic for fused silica [6]. (**c**) Heat-induced ion migration and stoichiometry changes in silicate glasses. Reprinted with permission from [26] ©The Optical Society

the charge redistribution. A strongly polarizable dielectric such as quartz or fused silica with strong electron-vibrational coupling will facilitate the process via the formation and the subsequent self-trapping of excitons in deformation potentials [21]. Such an electronically induced process occurs primarily at low excitation levels in conditions of intensity clamping [22, 23], where the excitation level (carrier density) is stabilized by a balance between self-focusing and defocusing in a range of $10^{19} - 10^{20}\,\text{cm}^{-3}$. Thus, it implies a self-limiting process where any attempt to increase the carrier population via an intensity rise with a non-monotonic profile will accelerate light defocusing, reducing the intensity and decreasing the excitation yield, stabilizing the free carrier density and profile, and regulating the interaction between carriers and the matrix. The follow-up process can be declined in two correlated pathways; the generation of optical defects (broken bonds with charge compensation) and the reorganization of the matrix by rebonding (often in a denser state [17], as, for example, in a largely used support for photoinscription of optical functions, fused silica). This process, illustrated in Fig. 29.3b, results in density and polarizability changes and can be associated with a weak index increase of about $\Delta n \simeq 10^{-5}$ per laser pulse. Repetitive irradiation will thus generate useful index change values in the range of $\Delta n \simeq 10^{-3}$ with a spatial scale related to the excitation profile in the μm range (Fig. 29.3a). Such an index change is called, inspired from Bragg gratings terminology, type I. Other effects may be equally considered for generating similar index values, namely, mechanical densification and changes of the fictive temperature for optical glasses [24, 25] enabling molecular mobility (the sign of the index change depends of the standard or anomalous viscoelastic relaxation), or, provided that the laser repetition allows for an increase of the steady-state level of the temperature, ion migration and changes of stoichiometry [26]. This regime of photochemistry-based photoinscription, first reported by Miura et al. [27] (and categorized here debatable as type I), was recently reviewed in [28]. An illustration of the process, indicating potential of the migration of species, is given in Fig. 29.3c.

To conclude, typical refractive index changes realized in this type I photoinscription regime and often reported for silicon oxide and silicate glasses are summarized in Fig. 29.3a–c. The resulting index change is the base of laser fabrication of embedded optical waveguiding elements, essential for transporting and processing light [1, 29–35], and will be in detail discussed in Chap. 21. It is to be noted that in many cases, as a consequence of heat, the standard thermomechanical behavior will accompany the electronic changes via a counteracting thermomechanical expansion, and if the initial host is a crystal, heating in a liquid phase and rapid cooling can generate local amorphization, with the corresponding density, hence, refractive index change. Nonetheless, in optical glasses, type I waveguiding is leading the conception of optical functions for transmitting, dividing, or amplifying light. If the typical size is in the μm range, in combination with a chemical etching agent, the physical transformation can equally enable extreme nanometric scales. This situation will be discussed in Chapter 20, where nano-lithography concepts based on ultrafast irradiation and chemical etching selectivity will be discussed.

2.2.2 Strong Negative Refractive Index Changes

These types of index changes (called type II), with a much stronger contrast as the previous type, appear once the energy concentration exceeds the mechanical stability of the solid. In this respect, the process allows to fully benefit from a material threshold by tuning the irradiation in its close vicinity and therefore to achieve a small feature size and, consequently, a high processing resolution. Thus, this index type and its characteristic scales will be the main concern of the present chapter. The energy requirements of this type of index change, obtained from more energetic inputs or tighter beam-focusing conditions, come closer to the points of thermodynamic transitions or mechanical failure, suggesting that the energy density allows for the development of molecular decomposition, nucleation of gas bubbles, for the generation of material phases as dense plasma states or low-viscosity states, or for exceeding the mechanical strength limit. All these evolutions are nevertheless intermediated by electronic excitation. Assuming that the energy per electron in the conduction band is limited by a collisional multiplication process at roughly 1.5 times the bandgap energy (up to 10 eV) [36], an estimation of the absorbed energy per unit volume will write as $E_{abs} = N_e E_{gap}$. This value of the absorbed energy density (equivalent to a local pressure), sustained by carrier densities in the range of $10^{21} - 10^{22}\,\text{cm}^{-3}$, should then approach the value of the bulk modulus (in the range of GPa) or determine at least a softening of the material with a temperature increase $\Delta T = E_{abs}/c_p \rho$, with c_p being the specific heat and ρ the material density. In these

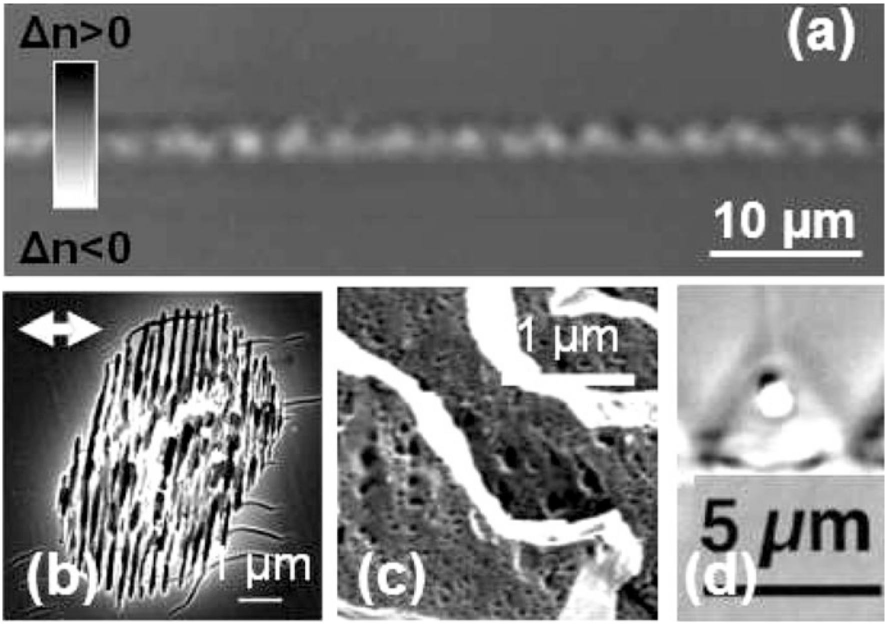

Fig. 29.4 (**a**) Typical negative index change induced by focused ultrashort laser pulses in fused silica (phase contrast microscopy image). The light color indicates a decrease of the refractive index. (**b**), (**c**), (**d**) Different types of type II index change: (**b**) generation of nanogratings in bulk fused silica, oriented perpendicular to the field. Reprinted with permission from [37] ©The Optical Society. (**c**) Generation of nanopores in fused silica in conditions of nanograting formation. Reprinted with permission from [38] ©Wiley. (**d**) Generation of nanovoids via volume micro-explosion. Reprinted with permission from [39] ©American Institute of Physics

conditions, several types of index change can appear, summarized in Fig. 29.4a–d, with scales defined essentially by a material modification threshold.

2.2.3 Genesis and Control of Nanogratings

In 2003, Shimotsuma et al. [40] observed a new form of self-organization of matter in laser-irradiated bulk fused silica in the shape of field-oriented periodic patterns of low index layers with a periodicity of approximately $\lambda/2n$, with n being the refractive index. This first report on nanogratings generation is illustrated in Fig. 29.5a, showing a periodic arrangement perpendicular to the optical field polarization axis, resembling also often reported periodic structures on surfaces. The process corresponds to rather strong excitation conditions just under the void formation threshold, with possible generation of plasma waves [40]. Subject of strong interest from the laser-processing communities (see [41] for a review), these nanogratings emerged as an enabling morphological feature that generates anisotropic optical properties such as from birefringence and directional scattering

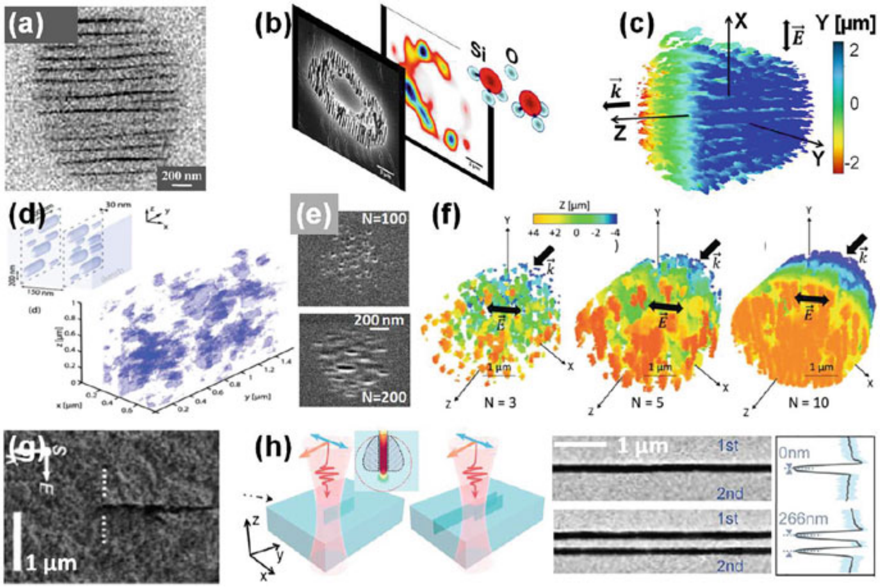

Fig. 29.5 (**a**) Electronic microscopy image of volume nanogratings. Reprinted with permission from [40] ©American Physical Society. (**b**) Correlated distribution of nanogratings (electron microscopy image) and luminescence charts of oxygen deficiency centers [54] signaling internal interfaces and roughness. (**c**) Numerically simulated distribution of layers of electronic charge. Reprinted with permission from [49] ©American Institute of Physics. (**d**) Tomography of nanogratings. X-ray scattering and imaging of bulk nanostructures. Reprinted with permission from [50] ©Wiley. (**e**) Gradual development of nanogratings from isolated inhomogeneities to periodically aligned nanorods with increasing photon dose. Adapted and reprinted with permission from [51] ©Springer Nature. (**f**) Simulated formation of nanogratings with increasing order. Reprinted with permission from [48] ©Wiley. (**g**) Single nanogratings feature generated in porous glass. Reprinted with permission from [55] ©The Optical Society. (**h**) Near-field mediated singular nanoscale features (irradiation sketch and image of results). Reprinted with permission from [56] ©Wiley

[42, 43] as well as selective etching properties [43]. Their formation mechanism and the capacity of self-organization within a volume triggered equally a strong interest. The original plasma wave hypothesis [40] was not reconcilable with the currently reported electron densities and energies, requiring much stronger excitation conditions to form nanogratings. The formation of planar nano-layers was associated with the deformation of nanoplasmas initiated at defect-based nucleation centers [44] in the intense optical field. Structural studies on the periodic layers indicated strong bond-breaking events [18] liberating the oxygen atoms and generating oxygen deficit in the structures (Fig. 29.5b, oxygen-deficiency centers indicating the formation of internal interfaces), as well as the onset of nucleated pores of molecular decomposition [38] (Fig. 29.4c). These observations permitted to link the spatial development of the electric field with the morphological appearance of the modified material [45], determining the local field arrangement. Accounting

for the subsequent generation of nm-scale roughness and volume centers (most probably few nm scaled voids generated by nucleation events or superposed micro-explosion events) that can scatter light generating periodic field and thus excitation patterns [46, 47], recent theoretical models proposed the onset and growth of ordered nanostructures as an interplay of interference of scattered light in near and far fields with the evolution of plasma seeds [43] and the feedback-assisted growth of morphological features in low viscosity domains [48]. Local breakdown and cavitation conditions appear in nm-scale layered zones due to directional scattering, coherence, and near-field enhancement. The increase in the field values takes the form of a regular pattern aligned perpendicular to the field, source of cavitation in the high field zones, and densification in between. With the dose, the order parameter increases and stabilizes. Figure 29.5c,d,e depicts the simulation results on the onset of ordered excitation layers (Fig. 29.5c [49]), experimental detection of evolution stages for nanostructure generation via X-ray scattering measurements (Fig. 29.5d [50]), the transformation from inhomogeneities to periodically aligned nanorods [51] (Fig. 29.5e), and the theoretical description of the process [48] (Fig. 29.5f), illustrating the evolution from random inhomogeneities to fully grown ordered nanogratings. Based on the mutual influence exercised dynamically between light and evolving matter including the competition between light near-field confinement and energy transport, the current model explains the multitude of organizational features within the pattern, including the orientation and the evolution of the periodicity toward smaller values [52]. The capability to observe experimentally the formation of nanostructures using X-ray scattering, electron microscopy, and optical diffraction and to deliver a theoretical frame reproducing the observations represents essential steps into the understanding of a complex physical mechanism dynamically coupling light and matter and the way it can gradually determine their mutual evolution. Light triggers morphological modifications which in turn will reshape light patterns, pushing forward a material self-organization process under light. The flow and dissipation of energy in such dynamical systems and their associated patterns will further reshape and reorganize matter. Within this frame, a common mechanism of organization was identified between surface and volume ordered nanostructures [53], as discussed in Chap. 5.

Recently, the control of such structures became so accurate that single nanoscale features can be induced using near-field enhancement features in diffuse media such as porous glass [55] or even in uniform media [56, 57], with dimensional scales in the range of tens of nm. The process is illustrated in Fig. 29.5g,h. The key element here becomes the directional scattering and the positioning of the near-field spots created by subsequent interference initiated by the intrinsic glass porosity or by existing structures that scatter light. A local cavitation or fracture event in the zone of field concentration enables feature scale in the 10 nm range.

The dependence on laser polarization as well as the dependence on the excitation conditions can be exploited in further nanograting control experiments, either by spatial polarization control [58], by mastering the level of excitation via pulse temporal design [59], via multipulse polarization experiments [60], or by directing the heat flux in relation to the scanning directions [61]. On one hand, nonstandard beams with spatially defined polarization, for example, azimuthal or radial beams but also beams with arbitrary-defined polarization distribution, will then imprint their field structure on the processing result [58], with the local polarization defining the orientation of the nano-layers aligned perpendicular to the field. Circular polarization will generate twisted dot-resembling structures [62], adding chirality. On the other hand, the dispersion design of the laser beam, its chromatic control, as well as mixing different colors (coherently or not) would enable additional flexibility in defining the order degree or the period and, as such, the associated retardance. Mauclair et al. [59] proposed an open-loop pulse duration control associated with a feedback response derived from a diffracting UV beam to increase the nanograting arrangement order by stretching the pulse in time or by the use of double-pulse sequences. Shimotsuma et al. [60] propose a synchronized double-pulse polarization experiment to control the orientation generated by the nanogratings. Using multiple sequences of pulse pairs with orthogonal polarizations and variable interpulse delay in the ps range, they demonstrated to achieve controllable retardance. Multicolor multipulse experiments as used for surface nanoscale periodic patterning [63] may be equally beneficial for bulk nanogratings. If these experiments address the control of the local electric field and excitation yield, energy flow in the sample and transport around excitation anisotropies may provide an additional control knob. A directional heat transport model accounting for anisotropic heat diffusion in the presence of polarized optical fields was proposed by Stankevič et al. [61], intermediated by a direct coupling of the plasma electrons to the laser field to give an additional orientational shift to nanogratings. Ponderomotive torques generated by wavefront tilts were equally suggested to contribute to the orientation of nanogratings [64]. Several examples are depicted in Fig. 29.6a–d showing, respectively, spatial field polarization control [58] (Fig. 29.6a), control via temporal tailoring [59] (Fig. 29.6b), double-pulse polarization control [60] (Fig. 29.6c), and directional heat flux control [61] (Fig. 29.6d). Techniques of temporal and spatial control [65, 66] as those revisited in Chapters 15 and 17 have the potential to

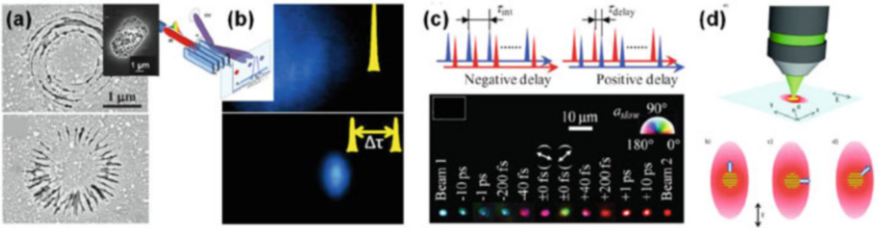

Fig. 29.6 (**a**) Radial and azimuthal field imprinted nanogratings. Reprinted with permission from [58] ©American Physical Society. Inset: nanogratings imprinted by circularly polarized pulses [37]. (**b**) Observation and control of nanostructures induced by temporally tailored irradiation using diffraction feedback [59]. (**c**) Double-pulse control of nanogratings with rotation of the slow axis. Reprinted with permission from [60] ©Wiley. (**d**) Schematic description of anisotropic heat flow generated by the coupling of the electron plasma with the laser field. Reprinted with permission from [61] ©Springer Nature

develop intelligent nanoprocessing techniques assisted by modern machine learning algorithms. The dynamics of the phase itself in topological light beams may enable processes that can twist matter [67, 68] and potentially serve bulk nanostructuring.

In the discussion above, the nanograting structures involved strong negative index modulation with equally strong scattering properties. It is therefore important to note that ordered structures were also obtained in less invasive conditions for the material, i.e., in a more gentle fashion, generating strong enough birefringence with lower scattering losses [51]. These are based on intermediary formation stages resulting less pronounced nanostructured domains. The potential impact in applications will be discussed in the application sections.

2.2.4 Genesis of Single Nanovoids

The original method for the fabrication of embedded void structures (voxels) relied on the concept of micro-explosion [3, 39] that underlined the achievement of high-pressure, high-temperature domains in the focal zone under tight focusing conditions. Building on this concept, Juodkazis et al. [69] indicated the generation of nanoscaled (in the 100 nm range) voids as the consequence of TPa electronic pressures achieved in the bulk [70] and the resulting shock, estimating the achievable scale from an energy conservation law implying that the internal energy within the shocked domain equals the absorbed energy. The void appears whenever the generated pressure exceeds the mechanical strength of the material. As such, a cubic root relation can be determined between the size of the void and the amount of the absorbed energy $D \simeq \sqrt[3]{E_{abs}}$, suggesting the potential to obtain extremely small scales. Hydrodynamic simulations using QEOS and SESAME equations of state [70] supported the shock and failure scenario via an intermediate plasma state. The process is illustrated in Fig. 29.7a,b, showing the resulting voids in different materials (experimental data and simulation results). This scenario demonstrates that the scale of the induced feature can be much smaller than the optical scale when intermediated by a material thermomechanical response. Within this range, in the neighboring areas, the extreme thermomechanical conditions can be the birthplace for generating new densely packed structural phase [71] by overcoming steric hindrance in the densification process (see also Chapter 13).

An important development in the nanoscale void generation technique relies on the extrapolation to one-dimensional geometries as demonstrated by Bhuyan et al. [76, 77] in fused silica glass using non-diffractive Bessel-Gauss beams with high cone angles or dispersion control. This topic is discussed in detail in Chap. 16, which underlines the potential of conical waves to sustain nonlinear and geometrical distortions. A conceptual example is given in Fig. 29.7c. The level of the energy deposition and its gradient can be controlled via a spatiotemporal design of the laser pulse. It is to be noted that if the mechanical strength of the solids should be exceeded in order to generate a void-like structure, the condition can be relaxed if a transition toward lower viscosity states (e.g., liquid states) occurs first. This seems to happen in strongly coupled and polarizable glasses (e.g., fused silica), and the nature

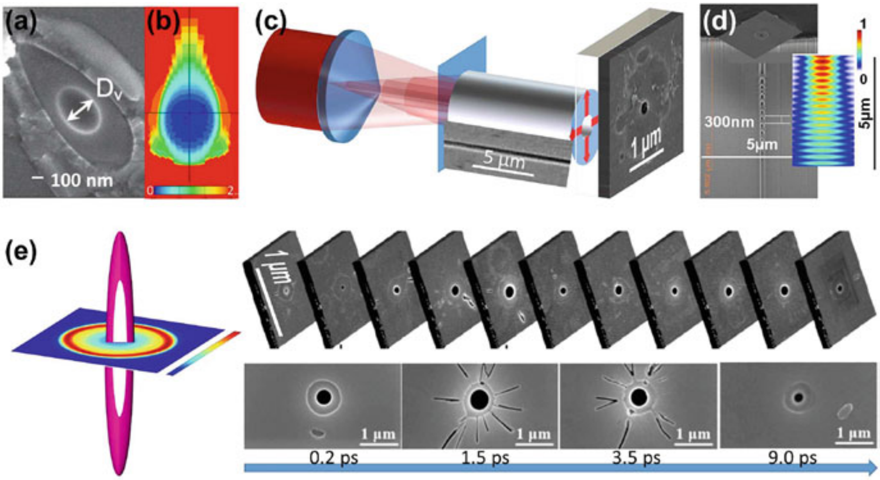

Fig. 29.7 (**a**) Void generation in sapphire using tightly focused ultrashort laser radiation. Reprinted with permission from [69] ©American Physical Society. (**b**) Simulation of density redistribution in fused silica at 600 ps after excitation. The void is formed. Reprinted with permission from [70] ©American Physical Society. (**c**) Bessel-Gauss beam generation of one-dimensional voids. (**d**) Counterpropagating beam interference along the Bessel trace and the formation of nanovoid arrays. Reprinted with permission from [72] ©Wiley. (**e**) Reconstruction of the void and of the affected regions around the voxel with possible cracking under stress [73, 74]. Inset: 2D Compressive stress simulations around a laser-induced heat source. Adapted and reprinted with permission from [75] ©American Institute of Physics

of the process can be determined based on its characteristic times: tens, hundreds of ps for void generation in the solid [69] vs tens, hundreds of ns for void generation in the liquid [78]. This fact underlines a competition between the development of mechanical waves and the rapid achievement of liquid states with rapidly varying viscosities by a fast, potentially sub-ps, vibrational activation. For the latter process, a cavitation phenomenon is at work and defines the ultimate scale of the structural feature to tens of nm. Following spall and cavitation criteria defined by D. E. Grady [79] requiring that the elastic energy surpasses the cohesion energy, the process proceeds, limited by the speed of sound, to achieve a characteristic scale $s = 2ut_{rest}$, with u being the speed of sound and t_{rest} being the relaxation time. A discussion about possible process times and the corresponding resolution was recently given in [80]. It is to be noted that the thermomechanical conditions for cavitation, namely, the achieved temperature in the 3000–4000 K range, are inferior but close to those corresponding to the rapid nucleation of a gas phase by vaporization [80]. The specific irradiation conditions enable further light confinement options. For example, in the vicinity of an interface, the superposition and synchronization of forward and back reflection will enable counterpropagating beam interference generation of nanocavities along the axis. The process, illustrated in Fig. 29.7d [72], is similar to the first reported array by Kanehira et al. [81].

If the processes mentioned above define the size of the laser-induced structures to well below the optical limit, a relevant question relates to the packaging density of such structuring features, i.e., how many nanoscale individual features can be grouped together on a surface unit. The self-organization strategies allow to stich nanostructured domains almost seamlessly on large areas or volumes. However, the strategies for voxel generation, based on extreme thermomechanical conditions, inherently generate mechanically strained areas around the voxel with possible crack generation, generating a limit for dense packing of voxels. If the surrounding area presents intrinsic structural defects or if the stress around the energy deposition volume caused by thermal expansion exceeds the fracturing threshold (a positive Poisson coefficient could create, for example, orthoradial stress with material yielding) [75], cracking occurs, limiting the minimal distance between structural voxels without generating catastrophic fracture connecting the voids. Accurate pulse energy, duration, and positioning are required to reduce the affected region to a minimum size and increase the packaging density [74]. Possible control strategies to limit the affected regions are summarized in Fig. 29.7e.

2.2.5 Photochemical Transformations

The discussion above referred to changes in material density and polarizability generated by electronically induced bond-breaking and extreme thermomechanical effects. The laser-enabled material transformations in domains smaller than the characteristic optical scales are far more numerous, occurring again as a combination of nonlinear excitation and material threshold. In many cases, the resulting transformation is directly related to the use of materials specifically designed for certain operations. Ultrafast laser irradiation of silver-doped glasses determines the formation of Ag clusters and nanoparticles, as it is discussed in Chapter 19 that reviews laser nanoscale photochemistry. The use of structured light inspired by the present super-resolution microscopy techniques enables the photochemical transformation on extreme scales [82]. The laser-enabled photochemistry can equally be used as a triggering step to nucleate crystallization sites, stabilized then by thermal treatment, for example, in photo-thermo-refractive glass [83]. Glass containing nanocrystals can exhibit anisotropic properties, and ultrafast laser radiation can selectively precipitate oriented nanocrystals in 3D. Fan et al. [84] successfully generated oriented $LiNbO_3$ nanocrystalline domains in $34Li_2O$-$33Nb_2O_5$-$33SiO_2$ glass samples. Similarly, three-dimensional luminescent perovskite domains with low formation energy were photoinscribed in Cs, Br, and Pb containing oxide glass [85]. Several examples of photochemistry-mediated laser nanostructuring are given in Fig. 29.8a–d.

The photophysical, photostructural, and photochemical transformations were primarily linked to an optical function based on the local change of the dielectric function. Their roles extend nevertheless beyond optical functions and enable a rich taxonomy of functional features. The laser-induced polymorphism and the local changes in the structure, in the chemical bonding, or in the specific volume will have

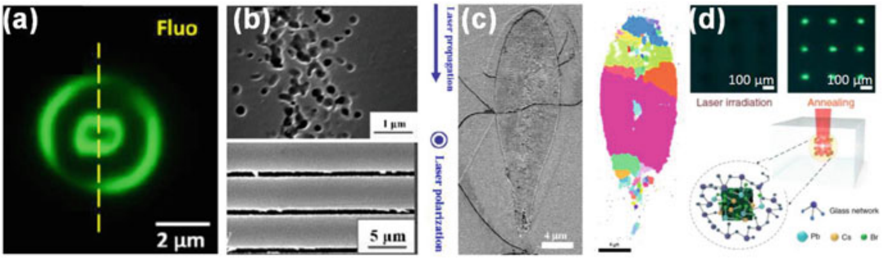

Fig. 29.8 (**a**) Fluorescence patterns of silver clusters in silver-containing zinc phosphate glass. Reprinted with permission from [82] ©The Optical Society. (**b**) Nanocrystal sites in photo-thermal-glass enabled by ultrafast laser irradiation and thermal treatment [83]. (**c**) Precipitation of oriented $LiNbO_3$ nanocrystalline domains in $34Li_2O$-$33Nb_2O_5$-$33SiO_2$ glass. Reprinted with permission from [84] ©The Optical Society. (**d**) Luminescent perovskite domains laser photoinscribed in oxide glass matrix. Reprinted and adapted with permission from [85] ©Springer Nature

consequences in tailoring mechanical properties (Young's modulus, stress states), thermal and electrical transport features (heat and electrical conductivity), or etching selectivity. The coupling of these functional features allows to design sophisticated functional devices coupling optical, electrical, thermal, and mechanical processes.

3 Applications of Volume Nanostructures in Optics, Photonics, Micromechanics, and Nanomechanics

The capability to modify the volume of a transparent material had a strong impact in microfabrication and nanofabrication techniques and related applications, adding to the generated function an intrinsic phase stability. For example, the optical function can be designed based on the structural evolution of matter and equally on the generation of thermomechanical effects (stress, cavitation, etc.). The buildup of an optical function in three-dimensional geometries can be seen as a specific type of additive manufacturing with subtractive features. The present state of the fabrication of embedded features in solid dielectrics for waveguiding using structural and stress-related features is reviewed in Chap. 21 as a technological platform for optical chips. The technique can be extrapolated from solid to liquid environments. Photopolymerization using multiphoton absorption and the associated nanoscale features is discussed in Chap. 22. While giving some conceptual examples in Fig. 29.9a–d, we will be concerned in the following with fabrication features that particularly address the nanoscale of laser-induced structural features in dielectrics with two main field of applications in view: photonics and nanomechanics.

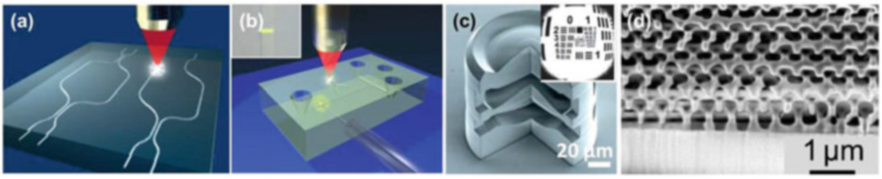

Fig. 29.9 (**a**) Femtosecond laser photoinscribed optical circuit. Reprinted with permission from [86] ©Springer Nature. (**b**) Ultrafast laser-fabricated optofluidic chip. Reprinted with permission from [87] ©Wiley. (**c**) Micro-optics fabrication using direct laser writing of photo-polymerizable additive structures. Reprinted with permission from [88] ©Springer Nature. Inset: simulated image of a resolution test chart. (**d**) Photonic crystal structure obtained by direct laser writing and photopolymerization. Reprinted with permission from [89] ©American Institute of Physics

3.1 Photonics and Optical Technologies

Let us first, based on several examples, illustrate the potential of ultrafast laser fabrication on extreme scales for photonics and optical technologies.

3.1.1 Multifunctionality: Micro-Optics Fabrication, Nano-Optics, and Nanofluidics

A dense packaging of nanoscaled bulk modification features creates a collective function originating in the periodic arrangement of structures. For example, large domains structured with nanogratings enable an optical response sensitive to polarization as a type of form birefringence and anisotropic optical retardation. This optical response is partly similar to what can be expected from a mechanical stress reaction in the form of photoelasticity. This property was already recognized in the first report of Shimotsuma et al. [40]. A first consequence is to be observed in the manipulation of the wave front of the crossing light leading to the fabrication of optical phase plates [90–92]. With a birefringence value in the range of $\delta n_{oe} = 5 \times 10^{-3}$ for the visible range [42], phase retardance can be designed locally and generate wave front engineering systems and phase retarders embedded in solid substrates [91, 92] or polarization gratings [93]. In combination to pulse front tilt, dichroism and chirality functions can be developed [64]. Cheng et al. [94] observed the polarization sensitivity of type I waveguiding and selective division in fused silica associated with type II domains, where only polarization parallel to the nano-layers can be guided. Similar technique leads to the development of waveguide retarders [95]. Associated with optical fiber, the presence of nanogratings can generate controllable polarization effects [96, 97]. Another aspect should be mentioned here that will be developed in Chapter 20, notably the capacity to reach extreme scales by combining laser irradiation and chemical etching selectivity [98]. The dimensional scales enabled by laser structuring ($d < \lambda$), the flexibility of arrangement in periodic patterns, and the strong index contrast enable the

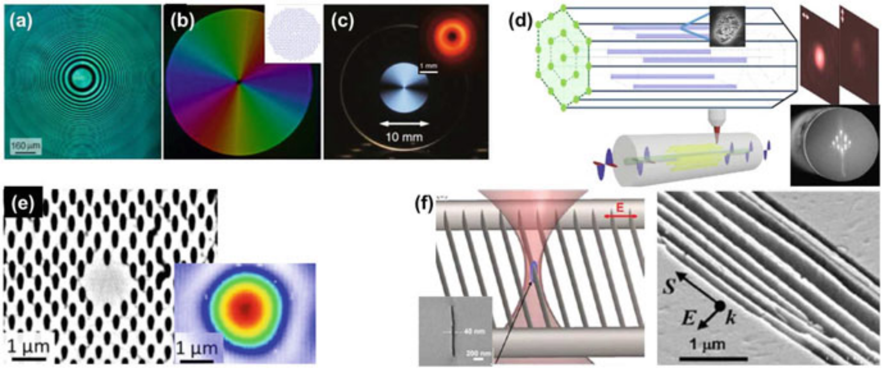

Fig. 29.10 (**a**) Femtosecond laser photoinscribed Fresnel zone plate. Reprinted with permission from [90] ©The Optical Society. (**b**) Polarization converters based on nanograting domains. Reprinted with permission from [90] ©The Optical Society. Inset: direction of nanogratings. (**c**) Low-loss birefringent wavefront converters. Reprinted with permission from [51] ©Springer Nature. Inset: generated vortex beam. (**d**) (Top) polarization large-mode area waveguides consisting of waveguiding traces and nanostructured domain. Evanescent coupling creates a polarized supermode [101]. (Bottom) in-line fiber polarizer. Reprinted with permission from [97] ©Royal Society of Chemistry. (**e**) Light confinement and waveguiding in 2D patterns fabricated by ultrafast laser irradiation and selective chemical etching. Reprinted with permission from [98] ©Springer Nature. (**f**) (Left) nanofluidic device fabricated based on laser fabrication. Reprinted with permission from [102] ©De Gruyter. (Right) favorable direction of nanogratings for efficient etching. Reprinted with permission from [43] ©Wiley

development of optical resonances, the engineering of the dielectric function and of dispersion, and the control of the coherence and, as such, the fabrication of optical bandgap and photonic crystal functions [99, 100]. Several examples relevant to these developments are illustrated in Fig. 29.10a–e, resuming the fabrication of micro-optical elements and polarization-sensitive waveguiding systems with modal control, transporting and manipulating light.

The nanoscale fabrication using nanogratings is not limited to optical fabrication; fluidic micro-systems belong to the potential field of applications (Fig. 29.10e). These will be discussed in Chapter 30. Similarly, associated mechanical functions will be reviewed further below.

3.1.2 Data Storage and Quantum Technologies

The generation of a local change of properties permits the inscription and the readout of information using optical means. The scale achievable in bulk dielectric materials creates the premises of efficient data storage in a solid, resistant, and protective environment. The first example, which will be developed to a large extent in Chapter 19, concerns the laser-mediated chemistry in doped materials and, notably, the generation and aggregation of Ag atoms in photosensitive glass [103], leading to a high packing density of silver cluster dots embedded in the bulk, readable using third harmonic generation microscopy. The advantages of this technique are related to the absence of bleaching and scattering, with directional readout. The variability in the gray level of the read-out signal provides a four dimensionality to the memory support. With the emergence of laser-oriented nanogratings, a different technique of optical storage was proposed, exploiting a multidimensional space defined not only by the X, Y, Z position but also by the orientation of the slow axis and by the value of retardance, as proposed in 2014 by Zhang et al. [104]. The use of nanograting bits allowed thus high capacity storage (potentially up to hundreds of TB per disc). Using the accurate control, similar data storage techniques can be applied to generate layers of field-oriented nanoslits with equivalent capacities [56, 57]. Besides the morphological aspects linking topography and storage functions, laser-assisted structural transitions can further complement the range of data storage techniques with the generation of new structural phases. Going beyond the standard phase change materials, Huang et al. [85] utilized the laser-generated $CsPbBr_3$ perovskite arrangements as reversible quantum dots in inorganic glassy matrices for optical storage and quantum technologies. To illustrate the results, several examples for data storage approaches based on laser microfabrication and nanofabrication are given in Fig. 29.11a–d. Quantum applications foster equally laser techniques for the generation of qubits in quantum information processing systems or spin-based sensing applications. For example, nitrogen vacancies (NV) in diamond were successfully reported using ultrafast laser techniques on surfaces and in the bulk [105–107]. The ultrashort laser pulse was found particularly effective to accurately position the centers in the bulk using pulse spatial control and particularly aberration corrections [107]. Recently, Hadden et al. [108] proposed a laser photoinscription method to generate both waveguiding systems and NV centers as a solution for quantum photonic networks. On a general basis, integrated quantum optical technologies [109, 110] will foster laser-based processing methods for all-optical fabrication including quantum sources, resonant systems, and interconnects able to transport and manipulate photons in three dimensions [111, 112], and a range of laser micromachining applications for quantum photonics were recently reviewed

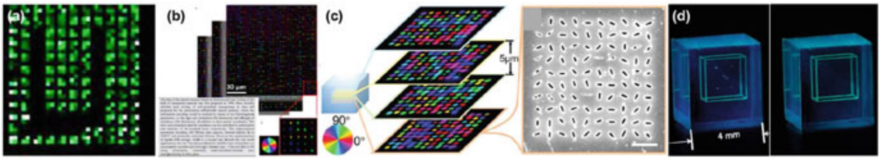

Fig. 29.11 (**a**) Third harmonic generation readout of information bits generated by silver clusters in photosensitive glass. Reprinted with permission from [103] ©IntechOpen. (**b**) Multidimensional (5D) data storage in glass using nanogratings. Inset: retrieved document. Reprinted with permission from [104] ©American Physical Society. (**c**) 5D data storage using single slit-like features oriented in the field with electronic microscopy image of the modification layer. Reprinted with permission from [56] ©Wiley. (**d**) Reversible 3D structure of $CsPbBr_3$ quantum dots in and inorganic glassy matrix. Reprinted with permission from [85] ©Springer Nature

[113] with the prospect of higher levels of miniaturization. It is worth noting that the potential of these techniques was recognized for high-end applications, for example, in cloud computing and media, coupling laser photoinscription, and machine learning-assisted information readout, with ongoing efforts for development and commercialization [114].

3.1.3 Bragg Waveguide Sensors

A powerful field of applications for laser-induced volume nanostructures is the field of sensing and spectral filtering. The Bragg grating [115] insertable in a guiding element (e.g., fiber) represents a nanometer-scale periodic modulation of the refractive index, generating a resonant response (a coherent superposition of individual waves generated by the presence of periodic interfaces of different optical indices) at the wavelength $\lambda_B = 2n_{eff}\Lambda/m$, with n_{eff} being the effective refractive index and Λ the pattern periodicity. This resonant response is defined by a spectrally selective retroreflection peak or transmission dip, making Bragg gratings effective solutions for laser cavity design, spectral filtering, or remote sensing [116]. The Bragg resonance is particularly sensitive to the variation of the effective index to external factors, making it a powerful sensor for detecting, for example, temperature and pressure variation (through thermooptic and piezooptic effects), as well as the presence of ionizing radiation fields (via the generation of relevant optical defects and the associated opacity). The capability to confine light and harvest resolution indicates ultrafast laser pulses of different wavelengths as ideal sources for Bragg photoinscription. If usually interferometric techniques generating fringe patterns are applied [117, 118] to photoinscribe Bragg gratings by side illumination, more recently a direct irradiation technique was considered to take full benefit of the positioning capability of a focused ultrashort laser pulse [119]. The advances in the *point-by-point* techniques were comprehensively reviewed in a recent report by Ams et al. [120] illustrating also emerging applications. In this section, we will pinpoint the most remarkable achievements in terms of the laser-induced modification scale indicating a range of relevant applications as illustrated in Fig. 29.12a–g. If the examples pertain mostly to optical glasses designed for the visible and near-infrared spectral region, the technique can be applied to a large variety of materials in crystalline and amorphous form. From the early developments of the point-by-point technique [119, 121], exploiting the precise positioning Bragg resonances was reported in waveguide bundles [122] (Fig. 29.12a). Slit-shaping techniques [123] (elongation of the focal shape in one dimension in the Fourier plan by truncating the incident beam, giving a disk shape in the focal region) enabled the fabrication of planar patterns as Bragg gratings [124] (Fig. 29.12b). Strong reductions in the periodicity neighboring the 100 nm range were reported in tight focusing conditions allowing resonances in the visible range [120] (Fig. 29.12c). The positioning control including accurate synchronization between the laser source and the sample movement permits a variety of grating designs in terms of periodicity and apodization functions, controlling the spectral

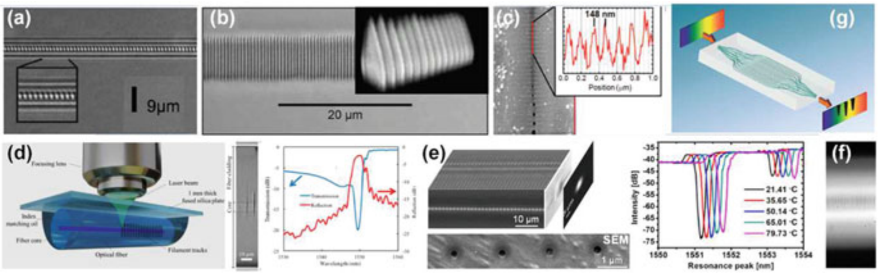

Fig. 29.12 (**a**) Point-by-point dotted Bragg grating fabrication in a laser photowritten waveguide bundle. Reprinted with permission from [122] ©The Optical Society. (**b**) Point-by-point planar Bragg grating fabrication using slit-shaping of the focal region [123] in a laser photowritten waveguide. Reprinted with permission from [120] ©De Gruyter. (**c**) 100 nm range Bragg grating periodicity for the visible domain. Reprinted with permission from [120] ©De Gruyter. (**d**) Utilization of aberrated filament-like beams for nanostructuring Bragg gratings in optical fibers. The reflected and transmitted spectra are given. Reprinted with permission from [129] ©The Optical Society. (**e**) Bessel-written waveguide Bragg gratings in laser photowritten waveguides with strong Bragg resonances in fused silica [131]. The spectral resonance is sensitive to temperature due to a positive thermooptic coefficient ($10^{-5}\,°\mathrm{C}^{-1}$) [130]. Reprinted with permission from [130, 131] ©The Optical Society. (**f**) Bessel-written waveguide Bragg gratings in an optical fiber. (**g**) Spectral filtering of multimode light using photonic lantern and waveguide Bragg gratings. Reprinted with permission from [135] ©Wiley

profile of the resonance. Examples of point-by-point laser techniques include nonstandard fabrications such as apodized [125], chirped [126], phase-shifted [127], or sampled gratings [128] (see [120] for a detailed discussion on various Bragg configurations achieved with fs laser pulses).

The spatial engineering of the beam enabled further progress. Controlled aberrated filaments were used by Ertorer et al. [129] to generate elongated type II structures across an optical fiber (Fig. 29.12d). In order to obtain uniform, highly regulated arrays of one-dimensional voids crossing the core of a laser-fabricated embedded waveguide, Zhang et al. [130] used dispersion-engineered non-diffractive Bessel-Gauss beams to fabricated high-resonance (40 dB/cm in fused silica) waveguide Bragg gratings (WBG) transiting toward the strong coupling regime (Fig. 29.12e), with the technique extendable to optical fibers (Fig. 29.12f). Multiplexing several WBGs on the same waveguide determines several concomitant resonances tuned across the telecom C-band spectrum [131]. Based on the index dependence of temperature (T) and strain (ε) $dn = \frac{\partial n}{\partial T}dT + \frac{\partial n}{\partial \varepsilon}d\varepsilon$ and a similar dependence of the pitch (Λ), the resonance is sensitive to external conditions [132]. An indicative example of temperature measurement is given in Fig. 29.12e. A 3D laser-fabricated sensor network was reported for measuring stress components [133, 134].

With this example, we point out an application field which is particularly large. The monolithic design of optical circuits and Bragg gratings permits to use different optical functions which show chromaticity (e.g., evanescent coupling in arrays or modal separation) in combination with spectral filtering. Spaleniak et al. [135] demonstrated narrowband spectral filtering of multimodal light in a 3D integrated optical chip using photonic lantern, with a conceptual design represented in Fig. 29.12g, and potential applications in astronomy and chemical sensing of various chemical constituents in atmosphere [136]. Their spectral response enables the design of monolith waveguide lasers as distributed Bragg reflectors or gain elements [137]. The Bragg spectral response in connection to modal light transport permits the design of a variety of filters [138]. The ability to process optical signal can design not only optical chips but equally optofluidic chips and lab-on-chip detection systems enabling optical measurements of biochemical fluids [87, 139].

3.1.4 Optical Field Readout in Spectro-Imagers: Potential for Astrophotonics

A powerful consequence of the nanometer-sized cross section of ultrafast laser-induced type II void-like changes and their close packing is the capability to sample and read out optical signals in optical circuits. The 100 nm size with sub-wavelength periodicities can be employed in the fabrication of embedded spectrometers that combine 3D design to augment collection efficiency and the high resolution given by the sampling rate. Stationary-wave integrated Fourier-transform spectrometry (SWIFTS) spectrometers [140] are prominent examples. The basic principle consists in the realization of a standing field by superposing two replicas of the optical signal to be analyzed. Planar systems are already commercially available. A 3D geometry will improve the collection capacity in combination to other facilities in mode conversion, transport, or transformation, coupling imaging with spectral analysis. The nanoscale scattering centers will scatter light (depending on their arrangement as scattering centers or antennas to redirect signals toward a detector) containing the spectral information of the optical signal [141]. Their positioning will set the spectral resolution of the system. The as-designed dispositive is functional in various materials covering different spectral ranges [142]. A conceptual schema [143] with a practical realization of a spectral detector is given in Fig. 29.13a,b. The formalism and the basic principles of such systems are given in Chapter 28, which equally describe a range of applications. Such dispositive that integrates collection design via, for example, large aperture multimodal guides and modal transformations to single-mode transport [144], can be applied for sensing and imaging celestial objects and their spectral signature in astronomy and astrophysics with a compact and robust astrophotonics design [145–147]. Their respond thus to a requirement of manipulating collection and processing weak optical signals comes from remote objects in space.

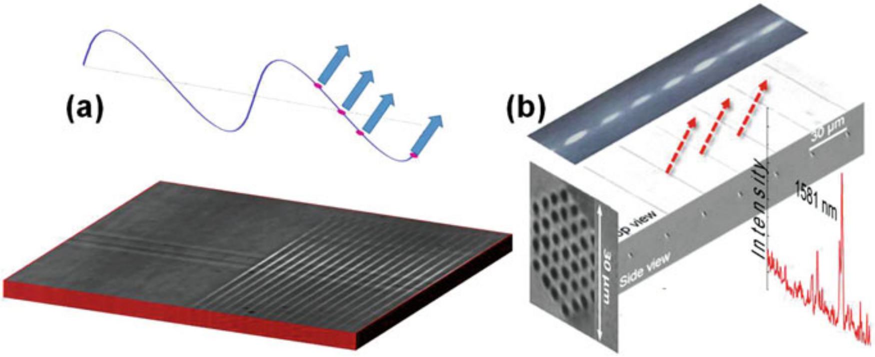

Fig. 29.13 (**a**) Sampling the electrical field with nanoscale scattering centers. (**b**) Spectral detection using scattered radiation of standing patterns developed in the waveguide. Reprinted with permission from [143] ©The Optical Society. These concepts enable the design of embedded spectrometers and imagers

3.2 Nanomechanics

Let us now review the laser-induced modifications from a different perspective, and we will shift the focus from the optical properties to micromechanical characteristics. As discussed in the previous sections and also in different chapters of this book, femtosecond laser exposure in a non-ablative regime induces permanent changes in the material structure. These laser-induced modifications can be of multiscale nature, starting from the molecular scale with the generation of defects and alterations in the molecular bonding to mesoscopic scale with the formation of nanopores, cavities, and nanocracks of tens of nanometers and all the way to micrometer scale bubbles resulting from the inner melting of the material. The nature of the laser modification will inherently depend on the substrate material and on the laser exposure conditions, and we have reviewed before the consequences for the refractive index design [1, 29, 40, 94] but briefly for the enhancement of chemical interactions and notably the selective nature of chemical etching [43, 148–150].

In fact, femtosecond laser pulses do change not only optical and chemical properties but, by the bias of density changes and molecular bonding potentials, also properties such as the thermal transport (e.g., thermal conductivity) [154, 155], the Young's modulus [156], and, recently, thermomechanical properties, such as the coefficient of thermal expansion [151] and the Young's modulus dependence with temperature [157]. One common effect is that these laser-included modifications, be it of nanoscale or microscale, induce localized changes in the material physical properties and, chief of all, localized volume changes in the matter. The process is schematically represented in Fig. 29.14a. Two important consequences emerge. The first one involves the fine positioning and control of mechanical movement with nm resolution [152], as illustrated in Fig. 29.14b, showing an example of fine translation with its equivalent kinematics (a rotational effect is sketched in Fig. 29.14c). The

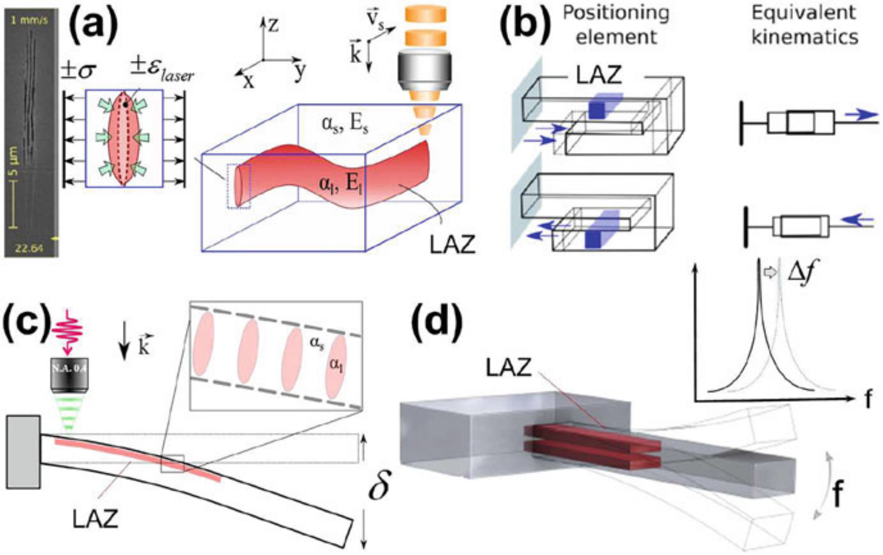

Fig. 29.14 Controlling stress with nanogratings in micromechanical systems. (**a**) Illustration of laser-induced changes in thermomechanical properties. Local arbitrarily written laser-induced modification patterns (laser-affected zone (LAZ)) generate thermomechanical expansion, localized stress, and structural modification, impacting mechanical properties. Via mechanical motion, these modifications determine nm-scale adjustments of position of micromechanical systems (actuator) Adapted from [151] ©American Physical Society. (**b**) Fine-tuning mechanical translation and its equivalent kinematics. Reprinted from [152] ©The Optical Society. (**c**) Probing mechanical properties. Illustration of the use of micromechanical cantilever to probe thermomechanical changes in transparent materials. The tip displacement is measured by interferometry or by using triangulation optical sensing, similar to the methods used in atomic force microscopy. The material changes in terms of density and structural bonding generate variation in the mechanical evolution laws, affecting displacement and oscillation frequency. (**d**) Using cantilevers set in vibration, the monitoring of the natural frequency resonance after laser exposure can be used to access information related to the changes in the Young's modulus. Reprinted with permission from [153] ©The Optical Society

second one involves the challenge to measure micromechanical changes on small scales. To circumvent the difficulty of quantifying thermomechanical changes in extremely small volumes that are often less than a micron-cube [158], a useful technique depicted in Fig. 29.14c,d is to use micro-machined cantilevers to amplify laser-induced changes into measurable displacement in the form of static deformation measurements [159] or frequency resonance shifts, useful for investigating changes of elastic properties [157] and from here evolution laws. Using these methods, it was demonstrated that in fused silica, a regime of densification leads to a decrease of the coefficient of thermal expansion, while the regime of nanogratings has the opposite effect [151]. Interestingly, it was also shown that the nanogratings, whose orientation is governed by the laser light polarization, can be used to create direct write composites in the material [157] and that this realisation can be used to tune the Young's modulus dependence with temperature to an appreciable level [160]. These are just examples reported for femtosecond laser exposure of fused silica. Similar approaches can be used to investigate laser-induced physical property changes in other material systems leading to a capacity to determine and measure mechanical properties of laser-modified materials.

4 Conclusion and Perspectives

This chapter, with its perspective stretching from optics to nanomechanics, outlined the present capability of ultrashort laser pulses to achieve extreme processing scales in bulk transparent materials where a three-dimensional geometry offers extended capabilities to collect, transport, process, and read out light as well as high flexibility to determine and quantify mechanical evolution. An advanced optical design would then rely on the scale, on the geometry, and on the morphology change. This capability of laser processing is based on strong optical nonlinearities and focusing strength and, in parallel, on guided material reaction to light and energy gradients, being fueled by advanced beam spatiotemporal engineering techniques [15]. The thresholded material response to energy gradients can determine extreme feature scales in both direct and self-organized patterning under light. The periodic patterns and the design of anisotropic and wavefront engineering functions follow already an industrial development. A similar industrial uptake concerns 3D optical circuits for remote sensing and telecom applications. High-density optical storage and quantum technologies follow equally a swift development with radical progress in the controllability of the optical design and efficiency. To the mechanical side, the accurate control of structuring allows to design features and micromechanical devices to execute precise mechanical movements as well as to characterize mechanical properties on extreme scales.

The chapter has given several prominent examples of the current advances of laser volume nanostructuring, posing equally the fundamental question of the principal limits of structural modification sizes. Are there fundamental obstacles in pushing the limits of the scale and the self-organization periods beyond the standard scales defined by light? The 100 nm range, a cornerstone in laser processing, is already achieved, with in view 10 nm scale, opening up the route toward photonic metamaterials in optical domains. Given the high resolution and in many cases resonant response, this milestone will enable photonic and sensing techniques in multispectral ranges and with high packaging density, as well as extended means of controlling and engineering light. Exciting opportunities in storing information for cloud computing or in quantum transport are underway. Combination of chemical and optical effects on the nanoscale will push forward the limits of nanostructuring toward a range of coupled functionalities, from sensing to fluidic transport. On the other end, we equally face thriving prospect of controlling mechanical movement with extreme precision, coupling optical and actuating functions.

In parallel, massive progress is achieved in observing the nanoscale [161]. With the implementation of in situ rapid quantitative observation capacity, the concept of control will qualitatively reach a new level. Exploring a complex phase space of irradiation parameters, learning algorithms will help guiding laser processes toward the achievement of higher accuracy and yield, defining the base of smart laser nanoscale manufacturing. A challenging but rewarding pathway of laser extreme nanostructuring lies ahead, correlating scale to pattern, pattern to function, and function to application.

References

1. K.M. Davis, K. Miura, N. Sugimoto, K. Hirao, Opt. Lett. **21**(21), 1729 (1996). https://doi.org/10.1364/OL.21.001729
2. K. Miura, J. Qiu, H. Inouye, T. Mitsuyu, K. Hirao, Appl. Phys. Lett. **71**(23), 3329 (1997). https://doi.org/10.1063/1.120327
3. E.N. Glezer, E. Mazur, Appl. Phys. Lett. **71**(7), 882 (1997). https://doi.org/10.1063/1.119677
4. H. Misawa, S. Juodkazis, *3D Laser Microfabrication: Principles and Applications* (Wiley, New York, 2006). https://doi.org/10.1002/352760846X
5. K. Sugioka, Y. Cheng, Light Sci. Appl. **3**(4), e149 (2014). https://doi.org/10.1038/lsa.2014.30
6. R. Stoian, Appl. Phys. A **126**, 438 (2020). https://doi.org/10.1007/s00339-020-03516-3
7. M. Wollenhaupt, A. Assion, T. Baumert, *Femtosecond Laser Pulses: Linear Properties, Manipulation, Generation and Measurement* (Springer, Berlin, 2007), p. 937. https://doi.org/10.1007/978-0-387-30420-5-12
8. E. Abbe, Arch. mikr. Anat. **9**(1), 469 (1873). https://doi.org/10.1007/BF02956177
9. L.R. F.R.S., Lond. Edinb. Phil. Mag. **8**(49), 261 (1879). https://doi.org/10.1080/14786447908639684
10. J. Marburger, Prog. Quantum. Electron. **4**, 35 (1975). https://doi.org/10.1016/0079-6727(75)90003-8
11. A.L. Gaeta, Phys. Rev. Lett. **84**, 3582 (2000). https://doi.org/10.1103/PhysRevLett.84.3582
12. A. Couairon, L. Sudrie, M. Franco, B. Prade, A. Mysyrowicz, Phys. Rev. B **71**, 125435 (2005). https://doi.org/10.1103/PhysRevB.71.125435
13. D. Tan, K.N. Sharafudeen, Y. Yue, J. Qiu, Prog. Mat. Sci. **76**, 154 (2016). https://doi.org/10.1016/j.pmatsci.2015.09.002
14. V.V. Kononenko, V.V. Konov, E.M. Dianov, Opt. Lett. **37**(16), 3369 (2012). https://doi.org/10.1364/OL.37.003369
15. R. Stoian, J.P. Colombier, Nanophotonics **9**(16), 4665 (2020). https://doi.org/10.1515/nanoph-2020-0310.10.1515/nanoph-2020-0310
16. J. Diels, W. Rudolph, P. Liao, P. Kelley, *Ultrashort Laser Pulse Phenomena*. Optics and photonics (Elsevier Science, Amsterdam, 2006). https://doi.org/10.1016/B978-0-12-215493-5.X5000-9
17. J.W. Chan, T.R. Huser, S.H. Risbud, D.M. Krol, Appl. Phys. A **76**(3), 367 (2003). https://doi.org/10.1007/s00339-002-1822-9
18. K. Mishchik, C. D'Amico, P.K. Velpula, C. Mauclair, A. Boukenter, Y. Ouerdane, R. Stoian, J. Appl. Phys. **114**(13), 133502 (2013). https://doi.org/10.1063/1.4822313
19. L. Sudrie, A. Couairon, M. Franco, B. Lamouroux, B. Prade, S. Tzortzakis, A. Mysyrowicz, Phys. Rev. Lett. **89**, 186601 (2002). https://doi.org/10.1103/PhysRevLett.89.186601
20. I.M. Burakov, N.M. Bulgakova, R. Stoian, A. Mermillod-Blondin, E. Audouard, A. Rosenfeld, A. Husakou, I.V. Hertel, J. Appl. Phys. **101**(4), 043506 (2007). https://doi.org/10.1063/1.2436925

21. P. Martin, S. Guizard, P. Daguzan, G. Petite, P. D'Oliveira, P. Meynadier, M. Perdrix, Phys. Rev. B **55**, 5799 (1997). https://doi.org/10.1103/PhysRevB.55.5799
22. G.N. Steinberg, Phys. Rev. A **4**, 1182 (1971). https://doi.org/10.1103/PhysRevA.4.1182
23. V.P. Kandidov, V.Y. Fedorov, O.V. Tverskoi, O.G. Kosareva, S.L. Chin, Quantum Electron. **41**(4), 382 (2011). https://doi.org/10.1070/qe2011v041n04abeh014486
24. R. Brückner, J. Non-Cryst, Solids **5**(2), 123 (1970). https://doi.org/10.1016/0022-3093(70)90190-0
25. L. Bressel, D. de Ligny, C. Sonneville, V. Martinez, V. Mizeikis, R. Buividas, S. Juodkazis, Opt. Mater. Express **1**(4), 605 (2011). https://doi.org/10.1364/OME.1.000605
26. M. Sakakura, T. Kurita, M. Shimizu, K. Yoshimura, Y. Shimotsuma, N. Fukuda, K. Hirao, K. Miura, Opt. Lett. **38**(23), 4939 (2013). https://doi.org/10.1364/OL.38.004939
27. K. Miura, J. Qiu, T. Mitsuyu, K. Hirao, Opt. Lett. **25**(6), 408 (2000). https://doi.org/10.1364/OL.25.000408
28. T. Fernandez, M. Sakakura, S. Eaton, B. Sotillo, J. Siegel, J. Solis, Y. Shimotsuma, K. Miura, Prog. Mat. Sci. **94**, 68 (2018). https://doi.org/10.1016/j.pmatsci.2017.12.002
29. S. Nolte, M. Will, J. Burghoff, A. Tuennermann, Appl. Phys. A **77**, 109 (2003). https://doi.org/10.1007/s00339-003-2088-6
30. D. Blömer, A. Szameit, F. Dreisow, T. Schreiber, S. Nolte, A. Tünnermann, Opt. Express **14**(6), 2151 (2006). https://doi.org/10.1364/OE.14.002151
31. S.M. Eaton, M.L. Ng, J. Bonse, A. Mermillod-Blondin, H. Zhang, A. Rosenfeld, P.R. Herman, Appl. Opt. **47**, 2098 (2008). https://doi.org/10.1364/AO.47.002098
32. L. Sansoni, F. Sciarrino, G. Vallone, P. Mataloni, A. Crespi, R. Ramponi, R. Osellame, Phys. Rev. Lett. **105**, 200503 (2010). https://doi.org/10.1103/PhysRevLett.105.200503
33. R.R. Thomson, T.A. Birks, S.G. Leon-Saval, A.K. Kar, J. Bland-Hawthorn, Opt. Express **19**(6), 5698 (2011). https://doi.org/10.1364/OE.19.005698
34. S. Gross, M.J. Withford, Nanophotonics **4**(3), 332 (2015). https://doi.org/10.1515/nanoph-2015-0020
35. S. Minardi, G. Cheng, C. D'Amico, R. Stoian, Opt. Lett. **40**(2), 257 (2015). https://doi.org/10.1364/OL.40.000257
36. A. Kaiser, B. Rethfeld, M. Vicanek, G. Simon, Phys. Rev. B **61**, 11437 (2000). https://doi.org/10.1103/PhysRevB.61.11437
37. K. Mishchik, G. Cheng, G. Huo, I.M. Burakov, C. Mauclair, A. Mermillod-Blondin, A. Rosenfeld, Y. Ouerdane, A. Boukenter, O. Parriaux, R. Stoian, Opt. Express **18**(24), 24809 (2010). https://doi.org/10.1364/OE.18.024809
38. M. Lancry, B. Poumellec, J. Canning, K. Cook, J.C. Poulin, F. Brisset, Laser Photonics Rev. **7**(6), 953 (2013). https://doi.org/10.1002/lpor.201300043
39. C.B. Schaffer, A.O. Jamison, E. Mazur, Appl. Phys. Lett. **84**(9), 1441 (2004). https://doi.org/10.1063/1.1650876
40. Y. Shimotsuma, P.G. Kazansky, J. Qiu, K. Hirao, Phys. Rev. Lett. **91**, 247405 (2003). https://doi.org/10.1103/PhysRevLett.91.247405
41. B. Zhang, X. Liu, J. Qiu, J. Materiomics **5**(1), 1 (2019). https://doi.org/10.1016/j.jmat.2019.01.002
42. P.G. Kazansky, Y. Shimotsuma, J. Ceram, Soc. Japan **116**(1358), 1052 (2008). https://doi.org/10.2109/jcersj2.116.1052
43. R. Taylor, C. Hnatovsky, E. Simova, Laser Photonics Rev. **2**(1–2), 26 (2008). https://doi.org/10.1002/lpor.200710031
44. V.R. Bhardwaj, E. Simova, P.P. Rajeev, C. Hnatovsky, R.S. Taylor, D.M. Rayner, P.B. Corkum, Phys. Rev. Lett. **96**, 057404 (2006). https://doi.org/10.1103/PhysRevLett.96.057404
45. F. Liang, J. Bouchard, S. Leang Chin, R. Vallée, Appl. Phys. Lett. **107**(6), 061903 (2015). https://doi.org/10.1063/1.4928551
46. R. Buschlinger, S. Nolte, U. Peschel, Phys. Rev. B **89**, 184306 (2014). https://doi.org/10.1103/PhysRevB.89.184306
47. A. Rudenko, J.P. Colombier, T.E. Itina, Phys. Rev. B **93**, 075427 (2016). https://doi.org/10.1103/PhysRevB.93.075427

48. A. Rudenko, J.P. Colombier, T.E. Itina, R. Stoian, Adv. Opt. Mat. **9**(20), 2100973 (2021). https://doi.org/10.1002/adom.202100973
49. G. Cheng, A. Rudenko, C. D'Amico, T.E. Itina, J.P. Colombier, R. Stoian, Appl. Phys. Lett. **110**(26), 261901 (2017). https://doi.org/10.1063/1.4987139
50. S. Richter, A. Plech, M. Steinert, M. Heinrich, S. Döring, F. Zimmermann, U. Peschel, E. Kley, A. Tünnermann, S. Nolte, Laser Photonics Rev. **6**(6), 787 (2012). https://doi.org/10.1002/lpor.201200048
51. M. Sakakura, Y. Lei, L. Wang, Y.H. Yu, P.G. Kazansky, Light Sci. Appl. **9**(1), 15 (2020). https://doi.org/10.1038/s41377-020-0250-y
52. S. Richter, M. Heinrich, S. Döring, A. Tünnermann, S. Nolte, U. Peschel, J. Laser Appl. **24**(4), 042008 (2012). https://doi.org/10.2351/1.4718561
53. A. Rudenko, J.P. Colombier, S. Höhm, A. Rosenfeld, J. Krüger, J. Bonse, T.E. Itina, Sci. Rep. **7**, 12306 (2017). https://doi.org/10.1038/s41598-017-12502-4
54. R. Stoian, K. Mishchik, G. Cheng, C. Mauclair, C. D'Amico, J.P. Colombier, M. Zamfirescu, Opt. Mater. Express **3**(10), 1755 (2013). https://doi.org/10.1364/OME.3.001755
55. Y. Liao, J. Ni, L. Qiao, M. Huang, Y. Bellouard, K. Sugioka, Y. Cheng, Optica **2**(4), 329 (2015). https://doi.org/10.1364/OPTICA.2.000329
56. Z. Yan, J. Gao, M. Beresna, J. Zhang, Adv. Opt. Mat. **10**(4), 2101676 (2021). https://doi.org/10.1002/adom.202101676
57. Y. Lei, M. Sakakura, L. Wang, Y. Yu, H. Wang, G. Shayeganrad, P.G. Kazansky, Optica **8**(11), 1365 (2021). https://doi.org/10.1364/OPTICA.433765
58. C. Hnatovsky, V. Shvedov, W. Krolikowski, A. Rode, Phys. Rev. Lett. **106**, 123901 (2011). https://doi.org/10.1103/PhysRevLett.106.123901
59. C. Mauclair, M. Zamfirescu, J.P. Colombier, G. Cheng, K. Mishchik, E. Audouard, R. Stoian, Opt. Express **20**(12), 12997 (2012). https://doi.org/10.1364/OE.20.012997
60. Y. Shimotsuma, M. Sakakura, P.G. Kazansky, M. Beresna, J. Qiu, K. Miura, K. Hirao, Adv. Mat. **22**(36), 4039 (2010). https://doi.org/10.1002/adma.201000921
61. V. Stankevič, G. Račiukaitis, F. Bragheri, X. Wang, E.G. Gamaly, R. Osellame, S. Juodkazis, Sci. Rep. **7**, 39989 (2017). https://doi.org/10.1038/srep39989
62. R.S. Taylor, E. Simova, C. Hnatovsky, Opt. Lett. **33**(12), 1312 (2008). https://doi.org/10.1364/OL.33.001312
63. S. Höhm, M. Herzlieb, A. Rosenfeld, J. Krüger, J. Bonse, Appl. Surf. Sci. **374**, 331 (2016). https://doi.org/10.1016/j.apsusc.2015.12.129
64. B. Poumellec, M. Lancry, R. Desmarchelier, E. Hervé, B. Bourguignon, Light Sci. Appl. **5**(11), e16178 (2016). https://doi.org/10.1038/lsa.2016.178
65. R. Stoian, M. Wollenhaupt, T. Baumert, I.V. Hertel, in *Laser Precision Microfabrication*, ed. by K. Sugioka, M. Meunier, A. Piqué (Springer, Berlin, 2010), pp. 121–144. https://doi.org/10.1007/978-3-642-10523-4-5
66. H. Zhang, S. Hasegawa, H. Toyoda, Y. Hayasaki, Opt. Lasers Eng. **151**, 106884 (2022). https://doi.org/10.1016/j.optlaseng.2021.106884
67. S. Syubaev, A. Zhizhchenko, A. Kuchmizhak, A. Porfirev, E. Pustovalov, O. Vitrik, Yu. Kulchin, S. Khonina, S. Kudryashov, Opt. Express **25**(9), 10214 (2017). https://doi.org/10.1364/OE.25.010214
68. T. Omatsu, K. Miyamoto, K. Toyoda, R. Morita, Y. Arita, K. Dholakia, Adv. Opt. Mater **7**(14), 1801672 (2019). https://doi.org/10.1002/adom.201801672
69. S. Juodkazis, K. Nishimura, S. Tanaka, H. Misawa, E.G. Gamaly, B. Luther-Davies, L. Hallo, P. Nicolai, V.T. Tikhonchuk, Phys. Rev. Lett. **96**, 166101 (2006). https://doi.org/10.1103/PhysRevLett.96.166101
70. L. Hallo, A. Bourgeade, V.T. Tikhonchuk, C. Mezel, J. Breil, Phys. Rev. B **76**, 024101 (2007). https://doi.org/10.1103/PhysRevB.76.024101
71. A. Vailionis, E.G. Gamaly, V. Mizeikis, W. Yang, A.V. Rode, S. Juodkazis, Nat. Commun. **2**, 445 (2011). https://doi.org/10.1038/ncomms1449
72. P.K. Velpula, M.K. Bhuyan, F. Courvoisier, H. Zhang, J.P. Colombier, R. Stoian, Laser Photonics Rev. **10**(2), 230 (2016). https://doi.org/10.1002/lpor.201500112

73. T. Chen, G. Zhang, Y. Wang, X. Li, R. Stoian, G. Cheng, Micromachines **11**(7), 671 (2020). https://doi.org/10.3390/mi11070671
74. G. Zhang, R. Stoian, R. Lou, T. Chen, G. Li, X. Wang, Y. Pan, P. Wu, J. Wang, G. Cheng, Appl. Surf. Sci. **570**, 151170 (2021). https://doi.org/10.1016/j.apsusc.2021.151170
75. R. Beuton, B. Chimier, J. Breil, D. Hébert, P.H. Maire, G. Duchateau, J. Appl. Phys. **122**(20), 203104 (2017). https://doi.org/10.1063/1.4993707
76. M.K. Bhuyan, F. Courvoisier, P.A. Lacourt, M. Jacquot, R. Salut, L. Furfaro, J.M. Dudley, Appl. Phys. Lett. **97**(8), 081102 (2010). https://doi.org/10.1063/1.3479419
77. M.K. Bhuyan, P.K. Velpula, J.P. Colombier, T. Olivier, N. Faure, R. Stoian, Appl. Phys. Lett. **104**(2), 021107 (2014). https://doi.org/10.1063/1.4861899
78. M.K. Bhuyan, M. Somayaji, A. Mermillod-Blondin, F. Bourquard, J.P. Colombier, R. Stoian, Optica **4**(8), 951 (2017). https://doi.org/10.1364/OPTICA.4.000951
79. D. Grady, J. Mech. Phys. Solids **36**(3), 353 (1988). https://doi.org/10.1016/0022-5096(88)90015-4
80. R. Stoian, M.K. Bhuyan, A. Rudenko, J.P. Colombier, G. Cheng, Adv. Phys-X **4**(1), 1659180 (2019). https://doi.org/10.1080/23746149.2019.1659180
81. S. Kanehira, J. Si, J. Qiu, K. Fujita, K. Hirao, Nano Lett. **5**(8), 1591 (2005). https://doi.org/10.1021/nl0510154
82. K. Mishchik, Y. Petit, E. Brasselet, A. Royon, T. Cardinal, L. Canioni, Opt. Lett. **40**(2), 201 (2015). https://doi.org/10.1364/OL.40.000201
83. Y. Zhang, X. Wang, G. Zhang, R. Stoian, G. Cheng, Nanomaterials **11**(6), 1432 (2021). https://doi.org/10.3390/nano11061432
84. C. Fan, B. Poumellec, M. Lancry, X. He, H. Zeng, A. Erraji-Chahid, Q. Liu, G. Chen, Opt. Lett. **37**(14), 2955 (2012). https://doi.org/10.1364/OL.37.002955
85. X. Huang, Q. Guo, D. Yang, X. Xiao, X. Liu, Z. Xia, F. Fan, J. Qiu, G. Dong, Nat. Photonics **14**(2), 82 (2019). https://doi.org/10.1038/s41566-019-0538-8
86. F. Flamini, L. Magrini, A.S. Rab, N. Spagnolo, V. D'Ambrosio, P. Mataloni, F. Sciarrino, T. Zandrini, A. Crespi, R. Ramponi, R. Osellame, Light Sci. Appl. **4**(11), e354 (2015). https://doi.org/10.1038/lsa.2015.127
87. R. Osellame, H. Hoekstra, G. Cerullo, M. Pollnau, Laser Photonics Rev. **5**(3), 442 (2011). https://doi.org/10.1002/lpor.201000031
88. T. Gissibl, S. Thiele, A. Herkommer, H. Giessen, Nat. Photonics **10**(8), 554 (2016). https://doi.org/10.1038/nphoton.2016.121
89. M. Thiel, J. Fischer, G. von Freymann, M. Wegener, Appl. Phys. Lett. **97**(22), 221102 (2010). https://doi.org/10.1063/1.3521464
90. M. Beresna, M. Gecevičius, P.G. Kazansky, Opt. Mater. Express **1**(4), 783 (2011). https://doi.org/10.1364/OME.1.000783
91. J. Tian, H. Yao, M. Cavillon, E. Garcia-Caurel, R. Ossikovski, M. Stchakovsky, C. Eypert, B. Poumellec, M. Lancry, Micromachines **11**(2), 131 (2020). https://doi.org/10.3390/mi11020131
92. S. Xu, H. Fan, Z.Z. Li, J.G. Hua, Y.H. Yu, L. Wang, Q.D. Chen, H.B. Sun, Opt. Lett. **46**(3), 536 (2021). https://doi.org/10.1364/OL.413177
93. M. Beresna, P.G. Kazansky, Opt. Lett. **35**(10), 1662 (2010). https://doi.org/10.1364/OL.35.001662
94. G. Cheng, K. Mishchik, C. Mauclair, E. Audouard, R. Stoian, Opt. Express **17**(12), 9515 (2009). https://doi.org/10.1364/OE.17.009515
95. L.A. Fernandes, J.R. Grenier, P.R. Herman, J.S. Aitchison, P.V.S. Marques, Opt. Express **19**(19), 18294 (2011). https://doi.org/10.1364/OE.19.018294
96. C. Hnatovsky, D. Grobnic, D. Coulas, M. Barnes, S.J. Mihailov, Opt. Lett. **42**(3), 399 (2017). https://doi.org/10.1364/OL.42.000399
97. J. Lu, Y. Dai, Q. Li, Y. Zhang, C. Wang, F. Pang, T. Wang, X. Zeng, Nanoscale **11**, 908 (2019). https://doi.org/10.1039/C8NR06078A
98. A. Ròdenas, M. Gu, G. Corrielli, P. Paiè, S. John, A.K. Kar, R. Osellame, Nat. Photonics **13**(2), 105 (2019). https://doi.org/10.1038/s41566-018-0327-9

99. E. Yablonovitch, Phys. Rev. Lett. **58**, 2059 (1987). https://doi.org/10.1103/PhysRevLett.58.2059
100. S. John, Phys. Rev. Lett. **58**, 2486 (1987). https://doi.org/10.1103/PhysRevLett.58.2486
101. G. Cheng, C. D'Amico, X. Liu, R. Stoian, Opt. Lett. **38**(11), 1924 (2013). https://doi.org/10.1364/OL.38.001924
102. F. Sima, K. Sugioka, Nanophotonics **10**(9), 2389 (2021). https://doi.org/10.1515/nanoph-2021-0159
103. M. Bellec, L. Canioni, A. Royon, B. Bousquet, J. Degert, E. Freysz, T. Cardinal, J.F. Letard, in *Data Storage*, ed. by F. Balasa (InTech, New York, 2002), pp. 33–51. https://doi.org/10.5772/8874
104. J. Zhang, M. Gecevičius, M. Beresna, P.G. Kazansky, Phys. Rev. Lett. **112**, 033901 (2014). https://doi.org/10.1103/PhysRevLett.112.033901
105. Y. Liu, G. Chen, M. Song, X. Ci, B. Wu, E. Wu, H. Zeng, Opt. Express **21**(10), 12843 (2013). https://doi.org/10.1364/OE.21.012843
106. V.V. Kononenko, I.I. Vlasov, V.M. Gololobov, T.V. Kononenko, T.A. Semenov, A.A. Khomich, V.A. Shershulin, V.S. Krivobok, V.I. Konov, Appl. Phys. Lett. **111**(8), 081101 (2017). https://doi.org/10.1063/1.4993751
107. Y.C. Chen, P.S. Salter, S. Knauer, L. Weng, A.C. Frangeskou, C.J. Stephen, S.N. Ishmael, P.R. Dolan, S. Johnson, B.L. Green, G.W. Morley, M.E. Newton, J.G. Rarity, M.J. Booth, J.M. Smith, Nat. Photonics **11**(2), 77 (2017). https://doi.org/10.1038/nphoton.2016.234
108. J.P. Hadden, V. Bharadwaj, B. Sotillo, S. Rampini, R. Osellame, J.D. Witmer, H. Jayakumar, T.T. Fernandez, A. Chiappini, C. Armellini, M. Ferrari, R. Ramponi, P.E. Barclay, S.M. Eaton, Opt. Lett. **43**(15), 3586 (2018). https://doi.org/10.1364/OL.43.003586
109. A.G.J. MacFarlane, J.P. Dowling, G.J. Milburn, Philos. Trans. R. Soc. London, Ser. A Math. Phys. Eng. Sci. **361**(1809), 1655 (2003). https://doi.org/10.1098/rsta.2003.1227
110. N. Gisin, R. Thew, Nat. Photonics **1**(3), 165 (2007). https://doi.org/10.1038/nphoton.2007.22
111. T. Meany, M. Gräfe, R. Heilmann, A. Perez-Leija, S. Gross, M.J. Steel, M.J. Withford, A. Szameit, Laser Photonics Rev. **9**(4), 363 (2015). https://doi.org/10.1002/lpor.201500061
112. A.W. Schell, J. Kaschke, J. Fischer, R. Henze, J. Wolters, M. Wegener, O. Benson, Sci. Rep. **3**, 1577 (2013). https://doi.org/10.1038/srep01577
113. G. Corrielli, A. Crespi, R. Osellame, Nanophotonics **10**(15), 3789 (2021). https://doi.org/10.1515/nanoph-2021-0419
114. Microsoft silica project. https://www.microsoft.com/en-us/research/project/project-silica/
115. K.O. Hill, Y. Fujii, D.C. Johnson, B.S. Kawasaki, Appl. Phys. Lett. **32**(10), 647 (1978). https://doi.org/10.1063/1.89881
116. A. Cusano, A. Cutolo, J. Albert, *Fiber Bragg Grating Sensors: Recent Advancements, Industrial Applications and Market Exploitation* (Bentham Science Publishers, Sharjah, 2011). https://doi.org/10.2174/97816080508401110101
117. S.J. Mihailov, C.W. Smelser, P. Lu, R.B. Walker, D. Grobnic, H. Ding, G. Henderson, J. Unruh, Opt. Lett. **28**(12), 995 (2003). https://doi.org/10.1364/OL.28.000995
118. J. Thomas, E. Wikszak, T. Clausnitzer, U. Fuchs, U. Zeitner, S. Nolte, A. Tünnermann, Appl. Phys. A **86**(2), 153 (2007). https://doi.org/10.1007/s00339-006-3754-2
119. A. Martinez, M. Dubov, I. Khrushchev, I. Bennion, Electron. Lett. **40**, 1170 (2004)
120. M. Ams, P. Dekker, S. Gross, M.J. Withford, Nanophotonics **6**(5), 743 (2017). https://doi.org/10.1515/nanoph-2016-0119
121. G.D. Marshall, M. Ams, M.J. Withford, Opt. Lett. **31**(18), 2690 (2006). https://doi.org/10.1364/OL.31.002690
122. M. Thiel, G. Flachenecker, W. Schade, Opt. Lett. **40**(7), 1266 (2015). https://doi.org/10.1364/OL.40.001266
123. Y. Cheng, K. Sugioka, K. Midorikawa, M. Masuda, K. Toyoda, M. Kawachi, K. Shihoyama, Opt. Lett. **28**(1), 55 (2003). https://doi.org/10.1364/OL.28.000055
124. G.D. Marshall, A. Jesacher, A. Thayil, M.J. Withford, M. Booth, Opt. Lett. **36**(5), 695 (2011). https://doi.org/10.1364/OL.36.000695

125. R.J. Williams, C. Voigtländer, G.D. Marshall, A. Tünnermann, S. Nolte, M.J. Steel, M.J. Withford, Opt. Lett. **36**(15), 2988 (2011). https://doi.org/10.1364/OL.36.002988
126. H. Zhang, P.R. Herman, in *Bragg Gratings, Photosensitivity, and Poling in Glass Waveguides* (Optical Society of America, America, 2007), p. BTuD4. https://doi.org/10.1364/BGPP.2007.BTuD4
127. H. Zhang, P.R. Herman, IEEE Photon. Technol. Lett. **21**(5), 277 (2009). https://doi.org/10.1109/LPT.2008.2010717
128. M. Ams, P. Dekker, G.D. Marshall, M.J. Withford, Opt. Lett. **37**(6), 993 (2012). https://doi.org/10.1364/OL.37.000993
129. E. Ertorer, M. Haque, J. Li, P.R. Herman, Opt. Express **26**(7), 9323 (2018). https://doi.org/10.1364/OE.26.009323
130. G. Zhang, G. Cheng, M.K. Bhuyan, C. D'Amico, Y. Wang, R. Stoian, Photon. Res. **7**(7), 806 (2019). https://doi.org/10.1364/PRJ.7.000806
131. G. Zhang, G. Cheng, M. Bhuyan, C. D'Amico, R. Stoian, Opt. Lett. **43**(9), 2161 (2018). https://doi.org/10.1364/OL.43.002161
132. R. Kashyap, in *Fiber Bragg Gratings (Second Edition)*, ed. by R. Kashyap (Academic Press, Boston, 2010), pp. xvii–xviii. https://doi.org/10.1016/B978-0-12-372579-0.00019-3
133. H. Zhang, S. Ho, S.M. Eaton, J. Li, P.R. Herman, Opt. Express **16**(18), 14015 (2008). https://doi.org/10.1364/OE.16.014015
134. K.K. Lee, A. Mariampillai, M. Haque, B.A. Standish, V.X. Yang, P.R. Herman, Opt. Express **21**(20), 24076 (2013). https://doi.org/10.1364/OE.21.024076
135. I. Spaleniak, S. Gross, N. Jovanovic, R.J. Williams, J.S. Lawrence, M.J. Ireland, M.J. Withford, Laser Photonics Rev. **8**(1), L1 (2014). https://doi.org/10.1002/lpor.201300129
136. J. Bland-Hawthorn, M. Englund, G. Edvell, Opt. Express **12**(24), 5902 (2004). https://doi.org/10.1364/OPEX.12.005902
137. G.D. Marshall, P. Dekker, M. Ams, J.A. Piper, M.J. Withford, Opt. Lett. **33**(9), 956 (2008). https://doi.org/10.1364/OL.33.000956
138. J.R. Grenier, L.A. Fernandes, P.R. Herman, Opt. Express **21**(4), 4493 (2013). https://doi.org/10.1364/OE.21.004493
139. V. Maselli, J.R. Grenier, S. Ho, P.R. Herman, Opt. Express **17**(14), 11719 (2009). https://doi.org/10.1364/OE.17.011719
140. E. Le Coarer, S. Blaize, P. Benech, I. Stefanon, A. Morand, G. Lérondel, G. Leblond, P. Kern, J.M. Fedeli, P. Royer, Nat. Photonics **1**(8), 473 (2007). https://doi.org/10.1038/nphoton.2007.138
141. M. Bonduelle, G. Martin, I.H. Perez, A. Morand, C. D'Amico, R. Stoian, G. Zhang, G. Cheng, in *Optical and Infrared Interferometry and Imaging VII*, vol. 11446 (SPIE, New York, 2020), pp. 621–633. https://doi.org/10.1117/12.2562179
142. C. D'Amico, G. Martin, J. Troles, G. Cheng, R. Stoian, Photonics **8**(6), 211 (2021). https://doi.org/10.3390/photonics8060211
143. G. Martin, M. Bhuyan, J. Troles, C. D'Amico, R. Stoian, E.L. Coarer, Opt. Express **25**(7), 8386 (2017). https://doi.org/10.1364/OE.25.008386
144. T.A. Birks, I. Gris-Sánchez, S. Yerolatsitis, S.G. Leon-Saval, R.R. Thomson, Adv. Opt. Photon. **7**(2), 107 (2015). https://doi.org/10.1364/AOP.7.000107
145. R.R. Thomson, A.K. Kar, J. Allington-Smith, Opt. Express **17**(3), 1963 (2009). https://doi.org/10.1364/OE.17.001963
146. J.J. Bryant, R.R. Thomson, M.J. Withford, Opt. Express **25**(17), 19966 (2017). https://doi.org/10.1364/OE.25.019966
147. S. Minardi, R.J. Harris, L. Labadie, Astron. Astrophys. Rev. **29**(1), 6 (2021). https://doi.org/10.1007/s00159-021-00134-7
148. Y. Kondo, J. Qiu, T. Mitsuyu, K. Hirao, T. Yoko, Jpn. J. Appl. Phys. **38**(10A), L1146 (1999). https://doi.org/10.1143/JJAP.38.L1146
149. A. Marcinkevičius, S. Juodkazis, M. Watanabe, M. Miwa, S. Matsuo, H. Misawa, J. Nishii, Opt. Lett. **26**(5), 277 (2001). https://doi.org/10.1364/OL.26.000277

150. Y. Bellouard, A. Said, M. Dugan, P. Bado, Opt. Express **12**(10), 2120 (2004). https://doi.org/10.1364/OPEX.12.002120
151. P. Vlugter, E. Block, Y. Bellouard, Phys. Rev. Materials **3**, 053802 (2019). https://doi.org/10.1103/PhysRevMaterials.3.053802
152. Y. Bellouard, Opt. Express **23**(22), 29258 (2015). https://doi.org/10.1364/OE.23.029258
153. Y. Bellouard, A. Champion, B. McMillen, S. Mukherjee, R.R. Thomson, C. Pépin, P. Gillet, Y. Cheng, Optica **3**(12), 1285 (2016). https://doi.org/10.1364/OPTICA.3.001285
154. Y. Bellouard, M. Dugan, A.A. Said, P. Bado, Appl. Phys. Lett. **89**(16), 161911 (2006). https://doi.org/10.1063/1.2363957
155. J. Morikawa, E. Hayakawa, T. Hashimoto, R. Buividas, S. Juodkazis, Opt. Express **19**(21), 20542 (2011). https://doi.org/10.1364/OE.19.020542
156. Y. Bellouard, T. Colomb, C. Depeursinge, M. Dugan, A.A. Said, P. Bado, Opt. Express **14**(18), 8360 (2006). https://doi.org/10.1364/OE.14.008360
157. P. Vlugter, Y. Bellouard, Phys. Rev. Materials **4**, 023607 (2020). https://doi.org/10.1103/PhysRevMaterials.4.023607
158. R. Lacroix, V. Chomienne, G. Kermouche, J. Teisseire, E. Barthel, S. Queste, Int. J. Appl. Glass Sci. **3**(1), 36 (2012). https://doi.org/10.1111/j.2041-1294.2011.00075.x
159. A. Champion, Y. Bellouard, Opt. Mater. Express **2**(6), 789 (2012). https://doi.org/10.1364/OME.2.000789
160. P. Vlugter, Y. Bellouard, Phys. Rev. Materials **6**, 033602 (2022). https://doi.org/10.1103/PhysRevMaterials.6.033602
161. T. Zhang, C. Godavarthi, P.C. Chaumet, G. Maire, H. Giovannini, A. Talneau, M. Allain, K. Belkebir, A. Sentenac, Optica **3**(6), 609 (2016). https://doi.org/10.1364/OPTICA.3.000609

Chapter 30
Nanofluidics Fabricated by 3D Femtosecond Laser Processing

Koji Sugioka

Abstract Nanofluidics involves miniaturized fluidic devices containing a structure in which at least one dimension is in the nanoscale. Applications of nanofluidics include not only sensing and diagnosis of single molecules and separation of nanoscale objects such as deoxyribonucleic acid (DNA) but also the study of cancer cell migration. For the fabrication of nanofluidics, photolithography-based semiconductor processing and soft lithography are common techniques. Alternatively, femtosecond laser processing is a promising tool due to its distinct features, such as high fabrication resolution, high flexibility, high versatility, and three-dimensional (3D) fabrication capability. In particular, 3D fabrication capability, which enables both top-down (subtractive) and bottom-up (additive) schemes for nanofluidic fabrication, offers a great advantage over other techniques. The top-down scheme involves liquid-assisted femtosecond laser drilling and femtosecond laser-assisted etching (or femtosecond laser irradiation followed by chemical etching). Minimum width of nanochannel fabricated by this scheme is several hundred nanometers. To achieve the width narrower than 50 nm, a new strategy is proposed. The bottom-up scheme is represented by two-photon polymerization, which can create almost arbitrary 3D micro- and nanostructures with a high fabrication resolution of 100 nm or even smaller. This chapter is a comprehensive review of nanofluidics fabricated by 3D processing using femtosecond lasers, focusing on the features and methodologies of femtosecond lasers for nanofluidic fabrication, challenges for downsizing the nanochannel dimensions, and some applications of fabricated nanofluidics with future prospects.

Keywords Nanofluidics · 3D fabrication · Nanofabrication · Additive processing · Subtractive processing · Hybrid femtosecond laser processing · Biological application

---

K. Sugioka (✉)
RIKEN Center for Advanced Photonics, Wako, Saitama, Japan
e-mail: ksugioka@riken.jp

© The Author(s), under exclusive license to Springer Nature Switzerland AG 2023

R. Stoian, J. Bonse (eds.), *Ultrafast Laser Nanostructuring*, Springer Series in Optical Sciences 239, https://doi.org/10.1007/978-3-031-14752-4_30

1 Introduction

Microfluidics is the technology to manipulate a small volume of fluid (on the order of femtoliters to microliters) and typically involves fluidic channels with dimensions of tens to hundreds of micrometers [1]. It can miniaturize a laboratory, reducing systematic labor, expenses, and sample consumption. Thus, microfluidics has revolutionized a variety of fields including chemistry, biology, medicine, physics, and engineering with applications such as microreactors, micro total analysis systems, lab-on-a-chip (LOC) devices, deoxyribonucleic acid (DNA) chips, inkjet printers, and micro-propulsion. Rapid advancement of this technology prompted us to further downsize the dimensions of systems to the nanoscale for challenging the physics of fluid flow in ultrasmall channels and the possibility of single-molecule analysis. Thus, the new field of nanofluidics has emerged and is increasingly attracting attention due to applications of microarrays for DNA sequencing, microfluidic devices for polymerase chain reactions (PCRs), LOC devices for the synthesis and analysis of peptide and oligonucleotide libraries, and microchips for drug screening or for single-cell analysis. Nanofluidics is defined as the study and application of miniaturized microfluidic systems containing a structure in which at least one dimension is in the nanoscale, typically smaller than several hundred nanometers [2]. A typical nanofluidic system consists of nanochannels, nanopipettes, or nanopores, In Fig. 30.1, the length scales and techniques used to fabricate micro- and nanosystems are schematically summarized with applications [3].

Photolithography-based semiconductor processing [4] is among the most common techniques for the fabrication of nanofluidic systems. To create fine structures that are 10 nm in size or smaller, lithography using high-energy beams such as electrons [5] and ions [6] is employed. Soft lithography is an alternative technique that has the advantages of low cost, easy setup, and high throughput while also

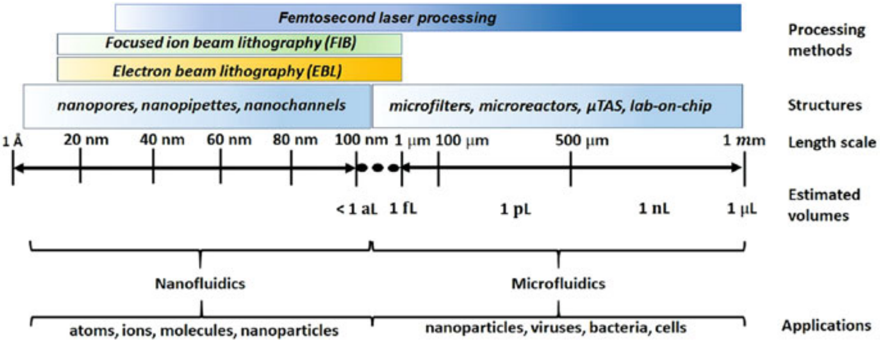
Femtosecond laser processing
Focused ion beam lithography (FIB)
Electron beam lithography (EBL)
Processing methods
nanopores, nanopipettes, nanochannels
microfilters, microreactors, µTAS, lab-on-chip
Structures
1 Å
20 nm
40 nm
60 nm
80 nm
100 nm
1 µm
100 µm
500 µm
1 mm
Length scale
< 1 aL
1 fL
1 pL
1 nL
1 µL
Estimated volumes
Nanofluidics
Microfluidics
atoms, ions, molecules, nanoparticles
nanoparticles, viruses, bacteria, cells
Applications

Fig. 30.1 Description of the length scales and common processing methods with applications used in micro- and nanosystems

enabling resolutions down to tens of nanometers, needed for nanofluidic domains [7]. It involves imprinting, molding, and embossing to replicate various structures on the substrates by using elastomeric stamps or molds. However, soft lithography necessitates the use of the other lithography methods mentioned above to create the stamp or mold masters.

Femtosecond lasers have become a promising technology for the fabrication of microfluidic systems owing to their distinct features such as high fabrication resolution, high flexibility, high versatility, and three-dimensional (3D) fabrication capability [8–13]. Femtosecond laser processing can be then extended to fabrication of nanofluidics. Its fabrication resolution which is defined as a minimum feature size achievable is, however, inferior to semiconductor processing. In fact, the minimum width of nanochannels fabricated by the femtosecond laser is several hundred nanometers [14]. In order to create nanofluidic systems with nanochannels narrower than 50 nm, new strategies were proposed [15]. Meanwhile, femtosecond laser processing offers some advantages over the semiconductor processing for fabrication of nanofluidics. One of the biggest advantages is its capability of true 3D structures, while the semiconductor processing can only create pseudo-3D structures, in other words, 2.5D structures. Another advantage is that the femtosecond laser processing can be adapted to a wide range of processing in terms of size, from nano to micro to even millimeter scale. Nanofluidic system is typically combined with microfluidic structures, and thus such a system can be obtained only by the femtosecond laser processing. Furthermore, the femtosecond laser processing allows the use of both top-down (subtractive) and bottom-up (additive) schemes to directly create 3D micro- and nanostructures. The top-down scheme involves liquid-assisted femtosecond laser drilling [14, 16, 17] and femtosecond laser-assisted etching (FLAE) (or femtosecond laser irradiation followed by chemical etching (FLICE)) [18–21]. The bottom-up scheme is best exemplified by two-photon polymerization (2PP), which can create almost arbitrary 3D micro- and nanostructures with a high fabrication resolution [22–25]. Importantly, performing the different schemes in succession, which is termed hybrid femtosecond laser 3D processing, enables creating much more complex 3D structures with enhanced functionalities [26–31], which are not achievable by the other techniques.

This chapter is a comprehensive review of nanofluidics fabricated by 3D femtosecond laser processing that details the features and methodologies of femtosecond laser processing for nanofluidic fabrication, challenges for downsizing the dimensions of nanofluidic systems, applications of fabricated nanofluidics, and future prospects. Although nanofluidics contains nanopores, nanopipettes, and nanochannels, this chapter focuses on only nanochannels because femtosecond lasers have so far been limited to the fabrication of nanochannels.

2 Features of Femtosecond Laser Processing for Nanofluidic Fabrication

2.1 Fabrication Resolution Far Beyond Diffraction Limit

The ultrashort pulse widths of a femtosecond laser (several tens to several hundreds of femtoseconds) can suppress the diffusion of the laser-induced heat from the exposed region because the deposition of laser energy into a material is completed before thermal diffusion occurs [32–34]. This means that the processed region is confined within the laser-exposed region, resulting in a higher fabrication resolution. The laser beam can be focused to a spot with a diameter comparable to or narrower than the laser wavelength by using an objective lens with a numerical aperture (NA) larger than 1. For example, when using a laser wavelength of around 500 nm, a focused spot size of 400–500 nm can be obtained to perform nanofabrication.

Ideally, the spatial energy distribution of a femtosecond laser beam has a Gaussian-like profile. Meanwhile, there exist threshold intensities only above which the process takes place on the basis of energy absorption. Thus, the processed area can be confined to the central area of the focal spot. Specifically, by adjusting the laser intensity to match the threshold intensity I_{th} indicated by a blue dashed line in Fig. 30.2a, the processed area is significantly narrowed relative to the beam diameter of the focused laser beam, $2W_0$, which is called threshold effect. By decreasing the laser intensity so that it approaches the threshold intensity at the center of the laser beam as shown in Fig. 30.2b, the processed area can be further narrowed.

Another important feature of a femtosecond laser is its extremely high peak intensity associated with the ultrashort pulse width, which easily exceeds 10^{15} W/cm^2. Such a high peak intensity can induce nonlinear absorption by materials whose bandgaps are larger than the photon energy of the laser beam, called multiphoton absorption [35, 36]. Since the absorption cross-section of m-photon absorption is proportional to the m-th power of the laser peak intensity, the effective beam diameter $2W$ for m-photon absorption becomes

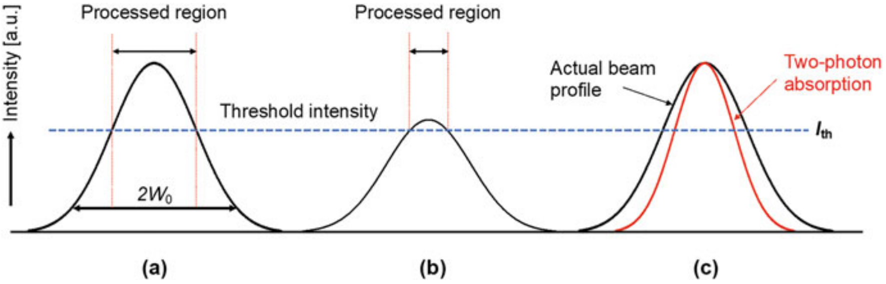

Fig. 30.2 The spatial intensity distributions of a focused Gaussian beam with (**a**) a higher intensity relative to the threshold for processing (dashed blue line) and (**b**) close to the threshold in a plane perpendicular to the beam axis. (**c**) Spatial intensity distributions absorbed by materials through single- (black) and two-photon (red) absorption of the focused Gaussian laser beam

$$2W = 2W_0/m^{1/2} \tag{30.1}$$

Consequently, the multiphoton absorption of a femtosecond laser by materials transparent to the laser beam can further improve the fabrication resolution as compared with single-photon absorption for the same wavelength, as shown in Fig. 30.2c, in which two-photon absorption has a narrower distribution than actual beam profile (single-photon absorption) [23, 37, 38]. Please note that single-photon absorption by half wavelength (second harmonics) provides higher resolution as compared with two-photon absorption by fundamental beam, because the beam diameter of second harmonics is a half that of the fundamental beam.

The synergetic contribution of the threshold effect and multiphoton absorption enabled the fabrication of nanohole arrays with sub-200-nm diameters in GaN substrates by ablation using a 387-nm-wavelength femtosecond laser [39]. The synergetic effect is also conducive to achieving typical fabrication resolutions of approx. 100 nm for 2PP even when using a near-infrared femtosecond laser [23]. These fabrication resolutions, which far exceed the diffraction limit of lasers, mean that femtosecond lasers are likely to find wider application in nanofluidic fabrication than conventional lasers.

2.2 3D Fabrication Capability

One of the most important features of femtosecond laser processing that makes it superior to other fabrication methods of micro- and nanofluidics is the capability of 3D processing, which relies on multiphoton absorption by transparent media including solids, liquids, and gases [38, 40, 41] (also see Chap. 10). As described above, the absorption cross-section of m-photon absorption is proportional to the m-th power of the laser peak intensity, which means the probability of multiphoton absorption depends on the laser peak intensity nonlinearly. Therefore, if the femtosecond laser beam is focused in the transparent medium at a moderate pulse energy, multiphoton absorption can be localized to be induced only at the focal volume where the highest laser intensity is generated in the laser beam path (Fig. 30.3a). As a result, the focal volume of the femtosecond laser inside the transparent medium is processed. 3D scanning of the focused femtosecond laser beam can then perform 3D processing of transparent media, such as glass and polymers, along the scanned trajectory of the focused laser beam (Fig. 30.3b).

The 3D fabrication capability of femtosecond lasers offers three types of schemes in 3D processing: undeformative, subtractive, and additive processing (see Fig. 30.4) [30]. The most common undeformative processing is permanent refractive index change, which is employed in 3D optical waveguide writing [42] and 3D data storage [43]. Subtractive processing can directly create 3D hollow structures at the micro- and nanoscale, typically in glass, by either liquid-assisted femtosecond laser drilling [14, 16, 17] or FLAE [18–21], which are utilized to

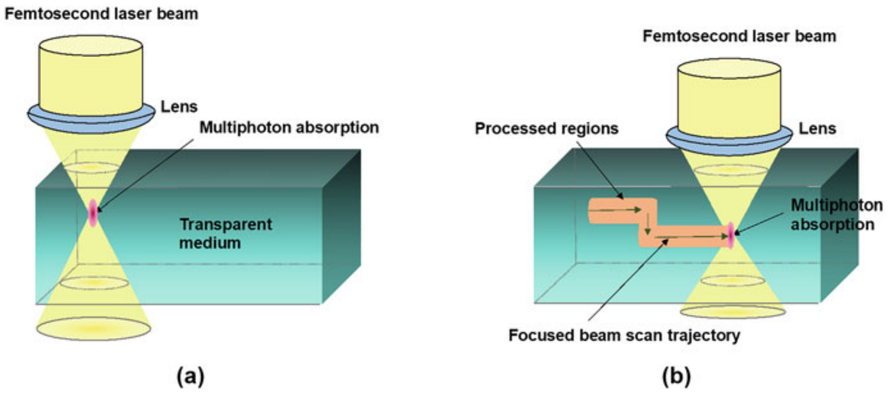

Fig. 30.3 Schematics of 3D fabrication of a transparent medium based on multiphoton absorption processes using a femtosecond laser. (**a**) When the femtosecond laser is focused at an adequate pulse energy inside the transparent medium, multiphoton absorption can be confined to the focal volume. (**b**) 3D scanning of focused femtosecond laser beam in the transparent medium performs 3D processing

fabricate micro- and nanofluidics. 3D polymer microstructure printing performed by TPP exemplifies additive processing and can create 3D micro- and nanostructures made of polymer with almost arbitrary shapes [22–25], which is also useful for nanofluidic fabrication. 2PP can be extended to 3D printing of other materials, such as metals [44, 45] and proteins [46, 47]. In the following section, more details of 3D glass micromachining techniques based on subtractive processing and additive 2PP of polymers are presented to highlight femtosecond laser-based technologies for nanofluidic fabrication.

3 Methods of Nanofluidic Fabrication by Femtosecond Laser

3.1 Top-Down (Subtractive) Method

In the subtractive processing, the laser-exposed regions are removed in a 3D manner. There are two main approaches to fabricating nanofluidic systems by subtractive femtosecond laser processing: liquid-assisted femtosecond laser drilling and FLAE. The former can be applied to a wide variety of materials as long as they are transparent to the laser beam. By contrast, only a limited number of materials can be processed by the latter approach. Femtosecond laser photolithography using positive-tone resists can also perform 3D subtractive processing for the fabrication of micro- and nanofluidic channels [48]. The following two subsections will detail liquid-assisted femtosecond laser drilling and FLAE.

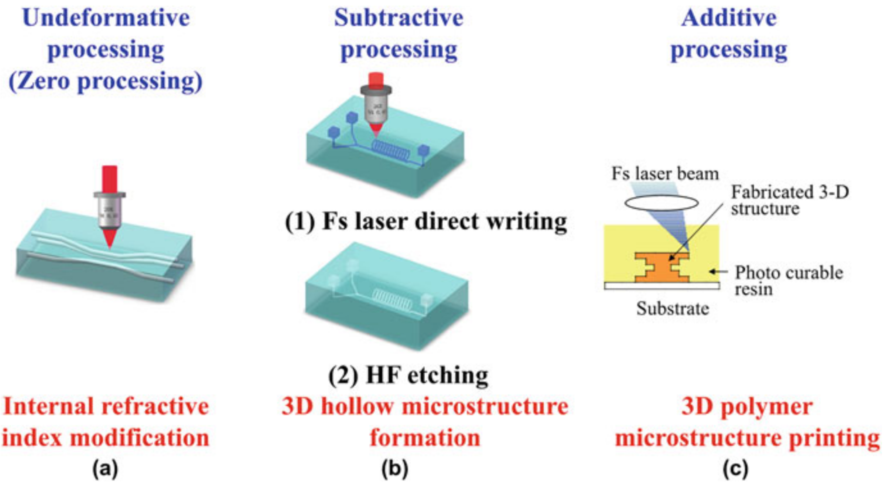
Undeformative processing (Zero processing)
Subtractive processing
Additive processing
(1) Fs laser direct writing
(2) HF etching
Fs laser beam
Fabricated 3-D structure
Photo curable resin
Substrate
Internal refractive index modification
3D hollow microstructure formation
3D polymer microstructure printing
(a)
(b)
(c)

Fig. 30.4 Three different schemes in 3D processing achieved by femtosecond laser: (**a**) undeformative (e.g., internal refractive index modification), (**b**) subtractive (e.g., 3D hollow microstructure formation), and (**c**) additive (e.g., 3D polymer microstructure printing) processing [30]. (Reproduced with permission from the Institute of Physics. ©2019 by IOP)

3.1.1 Liquid-Assisted Femtosecond Laser Drilling

Liquid-assisted femtosecond laser drilling relies on the ablation of transparent materials in liquid, typically water, based on the multiphoton absorption of a femtosecond laser [14, 16, 17]. Specifically, the femtosecond laser beam is first focused on the side or rear surface of the transparent materials immersed in a liquid to initiate ablation and is then scanned toward the material's interior to create 3D drilled holes. This method can be applied to almost any material as long as it is transparent to the laser beam. In this method, the liquid serves the important role of efficiently removing the ablated material from the ablated site and avoiding the redeposition of debris, thus allowing the fabrication of long hollow channels of almost arbitrary shape. The fabrication resolution of this technique is determined by the spatial energy distribution of the focused femtosecond laser beam. The synergetic contribution of the threshold effect and multiphoton absorption enabled the fabrication of nanochannels longer than 200 μm with diameters of less than 700 nm [14].

To create nanochannels narrower than 100 nm, liquid-assisted femtosecond laser drilling of porous glass composed of approximately $95:5SiO_2$-$4B_2O_3$-$0:5Na_2O$ (wt%) was demonstrated using water. The porous glass contained a high density of pores with a mean size of 10 nm, distributed uniformly, forming a 3D connective network. Thus, water could be supplied efficiently to the ablation site through the pores, allowing the formation of long and narrow nanochannels. The ablated sample was finally annealed to form a glass compact by collapsing all the nanopores, while the micro- and nanochannels were trapped inside the glass [49]. Then,

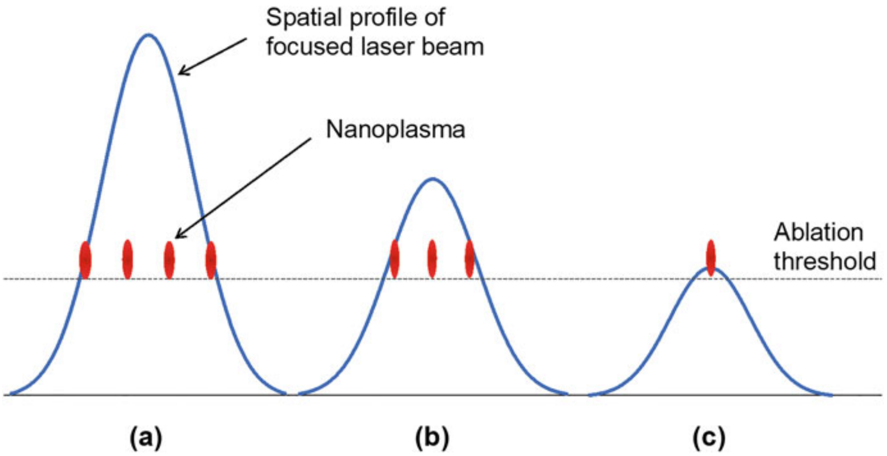

Fig. 30.5 Principle of single nanochannel creation based on nanoripple formation inside glass by femtosecond laser. (**a**) Nanoplasmas are generated at the focal spot due to spatial modulation of the energy deposition in the material with nanoscale periodicity. (**b**) As the laser intensity is reduced, the number of nanoplasmas decreases. (**c**) Further reducing the intensity very close to the ablation threshold at the center of the focused laser beam can generate only a single nanoplasma to create a single nanochannel by ablation [53]. (Reproduced with permission from De Gruyter. ©2016 by De Gruyter)

nanochannels were fabricated in the porous glass by using the phenomenon of nanoripple formation. It is well known that nanoripple structures are formed on the surface of, or inside, materials upon multiple pulse irradiation of a linearly polarized laser beam [50, 51] (also see Chap. 5). The periodicity of the formed ripple is much smaller than the laser wavelength (typically 1/10 to 1/2 of λ). Nanoplasma formation due to spatial modulation of the energy deposition in materials with nanoscale periodicity at the focal spot (see Fig. 30.5a) was proposed as a possible mechanism for nanoripple formation, although this is still under debate [52, 53]. Reducing the laser intensity decreases the number of nanoplasmas (Fig. 30.5b), owing to the threshold effect. Further reducing the intensity very close to the ablation threshold at the center of the focused laser beam can generate only a single nanoplasma (Fig. 30.5c), which ablates the glass to create a single-line nanochannel. Laser direct-write ablation of porous glass in water with well-controlled laser intensities has been employed to fabricate two-layered nanochannel arrays connected to two microchannels embedded 200 μm below the glass substrate, as illustrated in Fig. 30.6a [15]. Figure 30.6b, c shows, respectively, an optical micrograph of the top view of two-layered nanochannel arrays and a cross-sectional scanning electron microscope (SEM) image of the nanochannels cut along the red dashed line in Fig. 30.6b. An SEM image of one of the nanochannels magnified from the white rectangle in Fig. 30.6c shows the formation of a nanochannel with a width of about 40 nm and a height of about 1 μm (aspect ratio of about 25) (Fig. 30.6d).

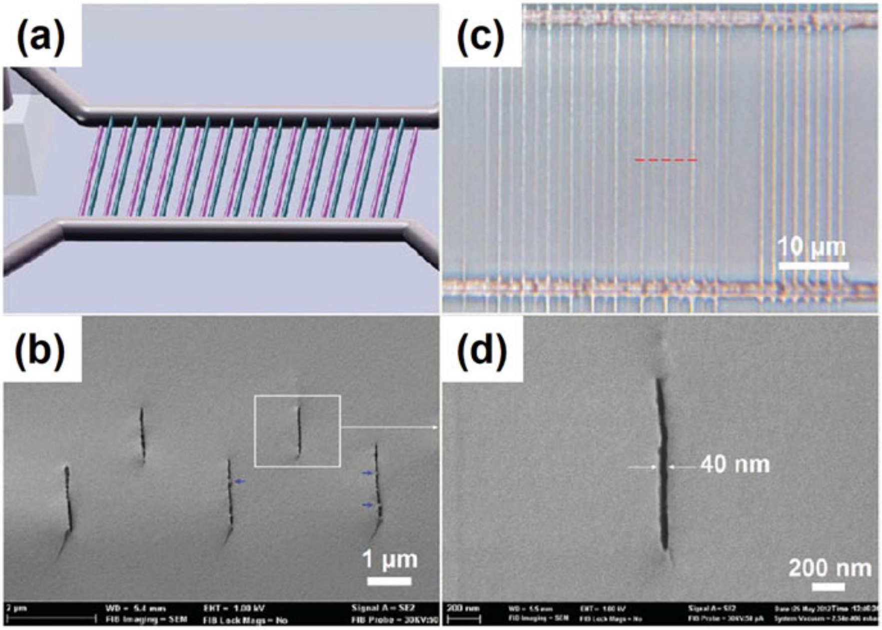

Fig. 30.6 Fabrication of nanochannels in porous glass by liquid-assisted femtosecond laser drilling. (**a**) Schematic of an array of double-layer nanochannels bridging two microchannels. (**b**) Top-view optical micrograph of double-layer nanochannels after post-annealing of drilled glass. (**c**) Cross-sectional SEM micrograph of the nanochannels cleaved along the red dashed line in (**b**). (**d**) Cross-sectional SEM micrograph of a nanochannel magnified from the white rectangle in (**c**) [15]. (Reproduced with permission from the Royal Society of Chemistry. ©2013 by RSC)

3.1.2 Femtosecond Laser-Assisted Etching

FLAE typically involves a two-step process, femtosecond laser 3D direct writing inside transparent materials followed by wet chemical etching, as illustrated in Fig. 30.3b [18–21]. During femtosecond laser direct writing, the chemical properties of the materials are modified as a result of multiphoton absorption, allowing the laser-exposed regions to be selectively etched away by wet chemical etching. The materials that can be processed by FLAE are limited to a few specific types of glass [18–21], sapphire [54], yttrium aluminum garnet crystals [55], and silicon [56]. Glass is used for nanofluidic applications, and there are two types of glass available for FLAE: photosensitive glass and fused silica. In the case of photosensitive glass, thermal treatment must be performed before etching to develop the modified regions in the laser-exposed region. For both types of glass, a diluted hydrofluoric (HF) acid solution (5–10%) is typically used as etchant for selective etching. Although the modification mechanisms of each glass type are completely different, the etching selectivity between the laser-exposed and unexposed regions is approx. 50 for both. The etching selectivity is the most important factor in determining the fabrication resolution, so that the typical fabrication resolution by FLAE using HF is a few microns, which is inferior compared to liquid-assisted femtosecond laser drilling. Thus, it is challenging to fabricate nanofluidic channels by FLAE.

To create nanochannels in fused silica by FLAE, the strategy shown in Figs. 30.5 and 30.6 was employed. Line scanning of a single nanoplasma generated by the linearly polarized femtosecond laser beam created a modified line with a width of less than 100 nm and a length of 55 μm. Subsequent wet etching increased the channel width to 200 nm, which is still much less than 1 μm [57]. In the case of fused silica, selective etching can be performed using a potassium hydroxide (KOH) solution, which provides much higher etching selectivity than HF [58]. Therefore, KOH could improve the fabrication resolution, enabling the fabrication of nanofluidic channels narrower than 100 nm.

Post-thermal treatment is very effective for smoothing the etched surface of photosensitive glass to an average roughness better than 1 nm, which is crucial for some microfluidic applications [59]. Furthermore, the post-thermal treatment can transform the narrow microchannels in photosensitive glass formed by FLAE into nanochannels [60]. To fabricate nanofluidics in photosensitive glass, a microfluidic structure composed of two open microreservoirs connected to an embedded microreservoir with five narrow microchannels was designed. Figure 30.7a shows the optical micrograph of a sample after femtosecond laser direct writing followed by first thermal treatment, where the modified regions show up brown. The modified width of the narrow microchannels was approx. 2 μm. After wet etching in HF, the microchannels became tapered, owing to isotropic etching from both the left- and right-hand side open microreservoirs toward the center-embedded microreservoir (Fig. 30.7b). The narrowest width of the microchannels was measured to be approx. 4 μm at the junction of the center-embedded microreservoir, which was twice the modified width. The post-thermal treatment of the created microfluidic structure significantly deformed the microchannel structure, narrowing the width (Fig. 30.7c). To determine the dimensions of the deformed channels, the fabricated microfluidic structure was filled with a Rhodamine dye solution for fluorescence microscopy. Figure 30.7d, e shows a channel narrower than 1 μm and lower than 7 μm at the channel center. Channel width narrowing is likely responsible for the melting of the shallow glass surface layers during post-thermal treatment. Specifically, the temperature for the post-thermal treatment was set slightly below the glass melting point, which can melt the shallow surface layers of glass thanks to the lower surface energy, as compared to the bulk, needed to induce glass deformation and create architectures down to the nanoscale inside the microfluidic structures.

3.2 *Bottom-Up (Additive) Method*

Additive processing is used to construct solid 3D structures along the scanning trajectory of focused laser beam. The most common additive process using femtosecond lasers is 2PP, for which a photocurable epoxy resin or a negative-tone

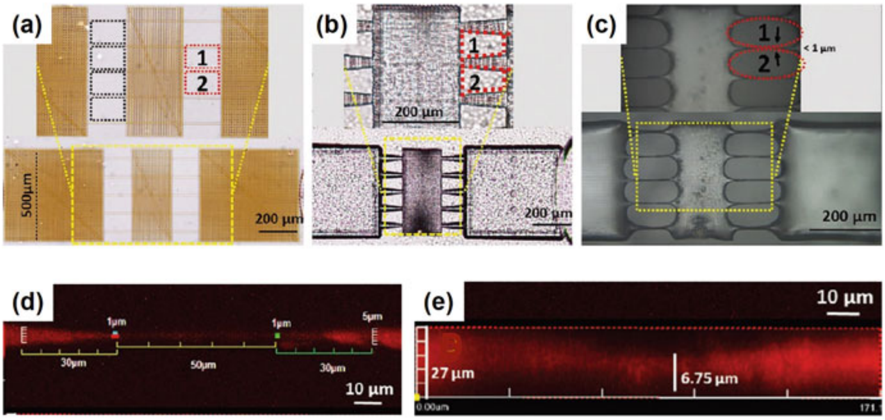

Fig. 30.7 Fabrication of nanofluidics in photosensitive glass by FLAE with post-thermal treatment. (**a**) Optical micrograph of sample after laser direct writing followed by first thermal treatment. Modified regions appear dark brown. (**b**) Optical micrograph of sample after chemical etching. (**c**) Optical micrograph of sample after post-thermal treatment. (**d**) Top and (**e**) cross-sectional fluorescence images of nanochannel filled with Rhodamine inside a microfluidic biochip [60]. (Reproduced with permission from Wiley. ©2020 by Wiley)

resist is utilized as precursor material [22–25] (also see Chap. 22). These precursors are transparent to the wavelength of a femtosecond laser (typically, visible or near-infrared) and solidify (polymerize) by two- (or multi-) photon absorption only at the focal volume. 3D scanning of the focused femtosecond laser in the precursor yields 3D micro- and nanostructures of almost arbitrary shape. Importantly, the fabrication resolution of 2PP is typically approx. 100 nm when using an objective lens with an NA larger than 1, which is much smaller than the diffraction limit of the laser beam, owing to the synergetic contributions of two-photon absorption and the threshold effect [23].

One drawback of 2PP is that it requires an extremely long time to create a volume structure such as a microfluidic chip owing to the nature of bottom-up fabrication using a tightly focused laser spot. Thus, 2PP is only used to integrate nanofluidic channels in microfluidic channels pre-fabricated by other methods. For the fabrication of nanofluidic systems, 2PP was combined with conventional UV photolithography [61]. First, SU-8 photoresist was spin-coated on a Si wafer. Then, UV light was directed through a film mask to create two separated microfluidic structures, followed by femtosecond laser direct writing to connect the two microfluidic channels with an array of nanochannels by 2PP. Finally, the resulting SU-8 structure was used as a mold to produce nanofluidics out of polydimethylsiloxane (PDMS) by soft lithography, as shown in Fig. 30.8. Two microchannels were connected with three arrays of 16 nanochannels with a width of 420 nm and a length of 75 μm.

2PP has been used to integrate nanochannels in a closed glass microfluidic channel for cancer cell migration research [31]. Specifically, a T-shaped glass

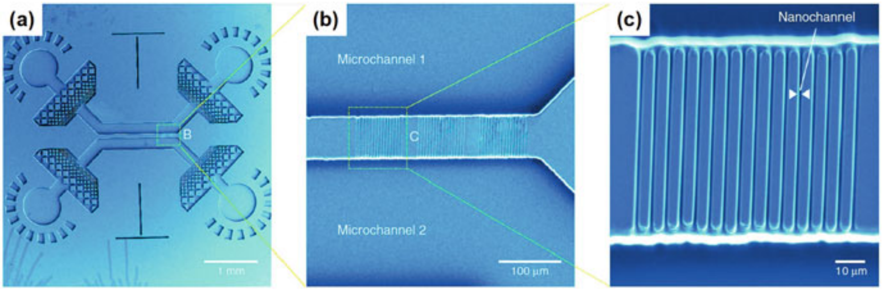

Fig. 30.8 Fabrication of nanofluidics by 2PP combined with conventional UV photolithography. (**a**) SEM micrograph of overview of fabricated nanofluidics. (**b**) SEM micrograph enlarged from the yellow rectangle in (**a**), showing three nanofluidic areas with 75-μm-long nanochannels joining the two microchannels. (**c**) SEM micrograph enlarged from the yellow rectangle in (**b**), showing 420-nm-wide nanochannels imprinted in PDMS [61]. (Reproduced with permission from Springer Nature. ©2019 by Springer Nature)

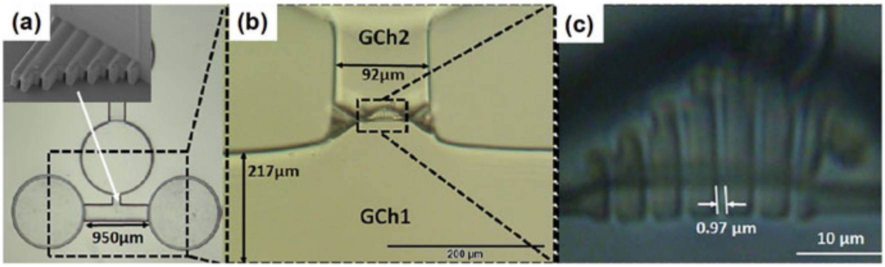

Fig. 30.9 Fabrication of nanofluidics by hybrid subtractive and additive femtosecond laser 3D processing (FLAE + 2PP). (**a**) Optical micrograph of the glass microfluidic platform fabricated by FLAE. Inset is an SEM micrograph of the polymer nanochannel array scaffold integrated at the junction of glass microfluidics by 2PP. (**b**) Optical micrograph enlarged from the dashed rectangle in (**a**). (**c**) Optical micrograph enlarged from the dashed rectangle in (**c**). The panpipe-shaped scaffold, consisting of six nanochannels with lengths of 6, 8, 11, 14, 18, and 21 μm, is integrated by 2PP at the junction of glass microchannels [31]. (Reproduced with permission from the American Chemical Society. ©2018 by ACS)

microfluidic platform (Fig. 30.9a) was fabricated inside photosensitive glass by FLAE. Then, SU-8 was introduced into the glass microfluidic structure to perform 2PP inside the closed microchannel. This two-step process has been termed hybrid subtractive and additive femtosecond laser 3D processing, which combines the best features of each process. However, the fabrication resolution of in-channel 2PP was significantly degraded owing to severe spherical aberration, because the laser beam propagated in three different refractive index media: index-matching oil for the objective lens, glass, and SU-8. To improve the fabrication resolution and thereby fabricate the nanochannels inside the glass microchannel, the wavefront of the laser beam was corrected by using a spatial light modulator so as to compensate for the spherical aberration. As a result, a panpipe-shaped polymer nanochannel array (inset in Fig. 30.9a) was successfully integrated at the junction of the T-shaped glass microfluidic channels (Fig. 30.9b). The width of the integrated nanochannels was measured to be about 900 nm (Fig. 30.9c).

4 Applications of Nanofluidics Fabricated by Femtosecond Laser

The nanoscale fabrication resolution of femtosecond laser processing has yielded material topographies, morphologies, and structures suitable for the fabrication of functional nanofluidics. Nanofluidics fabricated by femtosecond lasers have been used in a variety of applications, such as fabricating fluid mixers in complex 3D microscale analysis systems [14], bacteria trapping [57], DNA stretching [15], and studying cancer cell migration [31, 60].

Liquid-assisted femtosecond laser drilling of fused silica was applied to a simple 3D fluid mixer [14]. Efficient mixing of fluids is crucial for micro- and nanofluidic systems, since a laminar flow is usually generated in the microchannel. For efficient mixing, the two different fluids were divided into four nanochannels (Fig. 30.10a, b). The 3D fabrication capability enables the crisscrossing architecture to interdigitate the two fluids at the outflow of the nanochannels. This architecture increased the area of the fluid-fluid interface to enhance the diffusion of each fluid for mixing. The nanoscale geometry of each fluid stream produced by the nanochannels further accelerated the mixing because the mixing time is proportional to the square of the diffusion distance (Fig. 30.10c).

Fused silica nanochannels with a minor axis of 200 nm fabricated by single-nanoplasma-assisted FLAE were used to trap bacteria [57]. *B. subtilis* was able to be trapped at the nanochannel inlets, since the minor axis of *B. subtilis* (500 nm) was significantly larger than that of the nanochannels.

Single-molecule behavior, specifically DNA stretching, was investigated by using nanochannels fabricated by liquid-assisted femtosecond laser drilling of porous glass based on the nanoplasma shown in Fig. 30.6 [15]. Figure 30.11a, b shows typical images of λ DNA stretched in the nanochannels owing to capillary force. In nanochannels whose cross-sections were elliptical (minor axis, 50 nm; major axis, 1.2 μm), the average stretching lengths of DNA molecules were measured to be about 6.4 ± 1.0 μm (about 30% of dye-adjusted contour length) (Fig. 30.11a); the corresponding figure was about 2.8 ± 0.6 μm (about 13% of dye-adjusted contour length) in nanochannels whose minor and major axes were 200 nm and 1.2 μm, respectively (Fig. 30.11b). Figure 30.11b also shows that some DNA molecules can be stretched to as long as about 15 μm, which is attributable to the clustering of DNA molecules. It was confirmed that the continuous flow ensured uniform stretching of the DNA molecules in the nanochannel arrays thanks to the continuity of the nanochannels and the repeatability of femtosecond laser processing. It is worth mentioning that control of DNA stretching in nanochannels

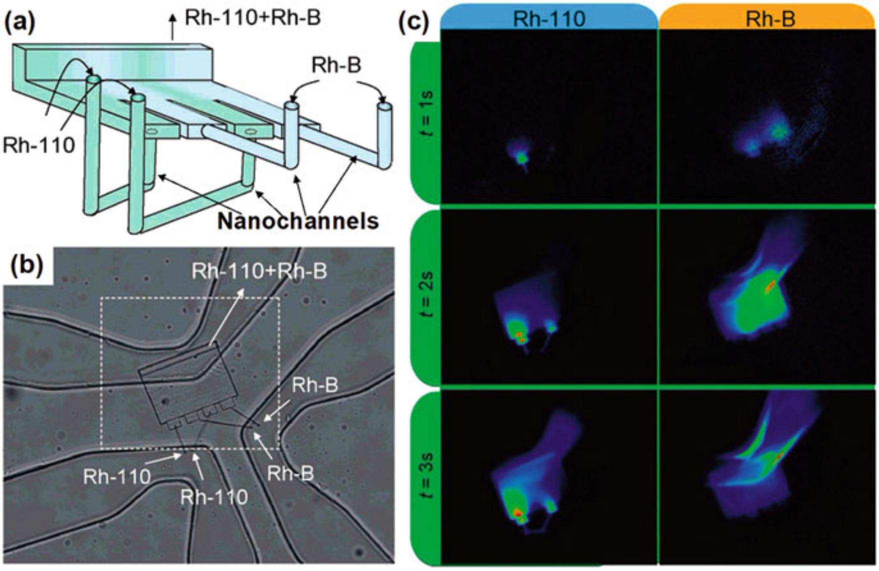

Fig. 30.10 Nanofluidic mixer fabricated by liquid-assisted femtosecond laser drilling of fused silica. (**a**) Schematic of nanofluidic mixer. (**b**) Optical micrograph of the fabricated nanofluidics. The three chevron-shaped channels are microfluidic channels (cast in PDMS, placed atop a glass coverslip) that serve as reservoirs. Fluids are drawn through nanochannels and mixed in the wide, flat, rectangular (65 × 52.5 μm) cavity. Both the nanochannels and the cavity were fabricated by liquid-assisted femtosecond laser drilling. A 10-V potential is applied to the chip reservoirs, creating electroosmotic flows (arrows). (**c**) Time-lapse images taken after the potential is applied, showing mixing of fluorescent dyes Rhodamine-110 (Rh-110) and Rhodamine-B (Rh-B) [14]. (Reproduced with permission from the American Chemical Society. ©2005 by ACS)

has attracted much attention recently because of its potential application to analysis and manipulation of single molecules for DNA mapping and barcoding, for which the dimension of nanochannel narrower than the biomolecule persistence length (~ 50 nm) is essential.

Nanofluidics fabricated by hybrid subtractive and additive femtosecond laser 3D processing (Fig. 30.9) [31] and FLAE of photosensitive glass with post-thermal treatment for channel narrowing (Fig. 30.7) [60] were employed to elucidate the mechanism of human cancer cell migration during metastasis and invasion. In the early stages of metastasis formation and cancer cell invasion, cells must undergo large morphological changes in order to cross the basement membrane and then move through connective tissues to reach blood vessels or lymphatic vessels, since the typical size of cancer cells is several micrometers to several tens of micrometers, which is significantly larger than the space between connective tissues. However, it is still unknown how cancer cells can deform to migrate into narrower spaces, whether the cell nucleus can also be deformed during the migration and, if so, how the cells can survive the migration. Recent research has elucidated the migration behavior of cancer cells in narrow spaces [62, 63]. Femtosecond laser 3D processing

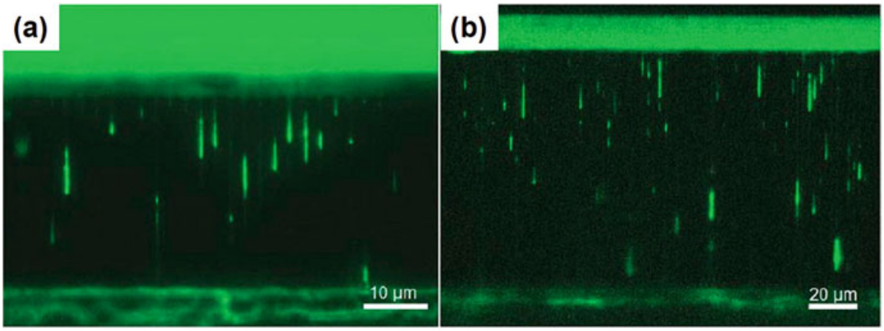

Fig. 30.11 Fluorescence images of λ DNA stretched in nanochannels with widths of (**a**) 50 nm and (**b**) 200 nm, fabricated by liquid-assisted femtosecond laser drilling of porous glass [15]. (Reproduced with permission from the Royal Society of Chemistry. ©2013 by RSC)

is a promising approach to creating platforms for cancer cell migration research, because it can construct true 3D configurations with nanometric dimensions, which could provide an unprecedented biomimetic environment for studying cancer cell migration. Such nanofluidics revealed the capability of human prostate cancer (PC3) cells to penetrate consecutive nanoscale constrictions in vivo. Extensive (approx. 50 μm) nucleus stretching was observed in cells migrating through nanochannels while keeping their viability (Fig. 30.12a, b). It was further observed that the cell body was compressed to a thin sheetlike shape to occupy the entire nanochannel from the entrance to the exit, while the cell nucleus deformed to a disklike shape was pulled into the nanochannel later and migrated. Cancer migration research using nanofluidics revealed many new findings, which include the following:

1. Cells can migrate in nanochannels with a width narrower than 1 μm, which is more than one order of magnitude narrower than the cell size.
2. Cells can migrate in nanochannels even without chemoattractant.
3. Cells are 100% viable and active after migration in nanochannels.
4. Cells can attain speeds of up to 1.5 μm/min, and their speed depends on the channel width: the narrower, the faster.
5. The volume of the cell nucleus is compressed, as it passes through nanochannels, and the cell nuclei can stretch over the length of a 50-μm-long nanochannel with no damage.
6. The cells can divide and proliferate after, and even during, migration. The probability of proliferation remains unchanged after migration.
7. The cells can migrate again through another nanochannel after the first migration, mimicking intravasation and extravasation.

Although ability of cancer cells to migrate in nanochannels narrower than 1 μm has been confirmed, it's very interesting to explore how narrow the channel the cells can migrate. Meanwhile, hybrid femtosecond laser 3D processing can create much more complicated structures to mimic micro- and nanostructures inside the human

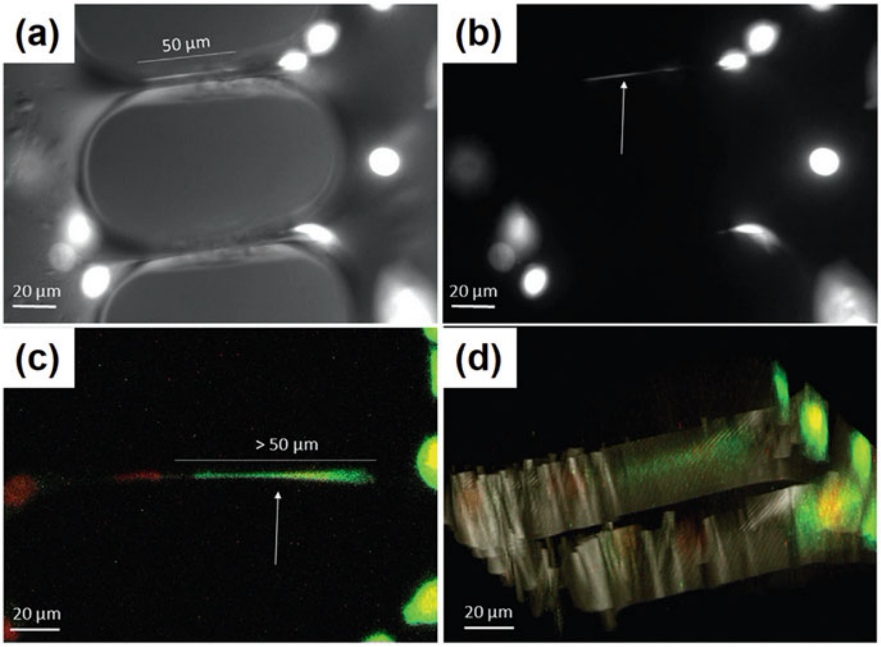

Fig. 30.12 Observation of cancer cells migrating in nanochannels fabricated by FLAE with post-thermal treatment. (**a**, **b**) Grayscale fluorescence micrographs of cell nuclei stained with red fluorescent protein, showing invasion into the narrow regions of the nanochannels. Fluorescence image is merged with optical micrograph in (**a**). The white arrow in (**b**) shows an elongated cell nucleus inside the nanochannel. (**c**) 2D and (**d**) 3D confocal fluorescence micrographs of cells additionally stained with green fluorescent protein as a membrane marker, showing cancer cells migrating in the nanochannels by elongating both their nuclei and entire bodies with no damage to nuclear envelopes or cell membranes [60]. (Reproduced with permission from Wiley. ©2020 by Wiley)

body. Furthermore, 2PP integration of 3D protein structures instead of polymer could provide more biomimetic environment for this study. Further investigation using such functional nanofluidics is expected to be of great help in elucidating the metastasis mechanism of cancer cells.

5 Summary and Outlook

Nowadays, microfluidic systems are widely used for medical, biological, and chemical studies. Downsizing the dimensions to the nanoscale is increasingly demanded to provide a new generation of analytical tools in these fields. Nanofluidic systems with such small spaces offer ultrasensitive analysis at the single-cell and single-molecule level. In fact, they enable label-free identification and characterization of single-stranded genomic DNA or RNA with no amplification procedure, as well as DNA sequencing. Additionally, mass transport in such small spaces can lead to new phenomena, such as enhanced mass flow rate and highly selective molecular transport.

Since critical issues of nanofluidic systems consist of fouling and clogging, future studies may concentrate on design and fabrication of smart geometries for efficient cell/molecule separations and DNA sequencing. Integration of nanofluidic systems with microchannels will become compulsory for many applications. Femtosecond lasers are a promising technology to fulfill those requirements for the fabrication of nanofluidic systems owing to their 3D fabrication capability with a wide range of manufacturable size from several tens of nanometers to several millimeters. Different kinds of femtosecond laser 3D processes, including liquid-assisted femtosecond laser drilling, FLAE, and 2PP, are available for nanofluidic fabrication. Although the fabrication resolution of femtosecond laser processing is inferior to other techniques, such as lithography using electron or ion beam and soft lithography, the fabrication capability of complex 3D structures provides a distinct advantage in creating unique structures and mimicking biological environments. The typical fabrication resolution of femtosecond laser processing is 100 nm for 2PP and several hundred nanometers for ablation. Particular efforts have been made to create nanochannels with widths narrower than 50 nm, for which a single nanoplasma was generated by precise control of the pulse energy in nanoripple formation. Nanofluidics fabricated by femtosecond laser processing has been applied to fluid mixers, bacteria trapping, DNA stretching, and the study of cancer cell migration. One expected application of nanofluidics is single-cell genomic analysis for personalized cancer therapies. Biopsies from cancer tumors harvested from patients will be analyzed using nanofluidic systems. The evaluation of cell population behavior could be correlated with the degree of migration and invasiveness and genomic analysis at a single-cell level. Specific doses of radiation therapy, chemotherapy, immunotherapy, and combinations thereof can then be examined.

The versatility of femtosecond laser processing may enable the fabrication of new nanofluidic systems composed of graded or hierarchical configurations with different dimensions from hundreds of micrometers down to a few tens of nanometers. These systems can be further integrated with functional micro- and nanocomponents such as optics and fluid control components by using different types of femtosecond laser processing. Hybrid approaches will be highly attractive for the fabrication of such functional nanofluidic systems, which will open new avenues for nanofluidic applications for single-cell and single-molecule analysis, drug screening, and the discovery or testing of personalized therapies using patient-derived cells. Further improvement of the fabrication resolution down to a couple of tens of nanometers will diversify nanofluidic applications of femtosecond laser processing.

References

1. E.K. Sackmann, A.L. Fulton, D.J. Beebe, Nature **507**, 181–189 (2014)
2. J.C.T. Eijkel, A. Berg, Microfluid Nanofluidics **1**, 249–267 (2005)
3. F. Sima, K. Sugioka, Nanophotonics **10**, 2389–2406 (2021)
4. J.H. Burnett, S.G. Kaplan, E.L. Shirley, P.J. Tompkins, J.E. Webb, Proc. SPIE **5754**, 611–621 (2005)
5. A.J. Storm, J.H. Chen, X.S. Ling, H.W. Zandbergen, C. Dekker, Nat. Mater. **2**, 537–540 (2003)
6. J. Li, S. Derek, M. Ciaran, B. Daniel, J.A. Michael, A.G. Jene, Nature **412**, 166–169 (2001)
7. D. Qin, X. Younan, M.W. George, Nat. Protoc. **5**, 491–502 (2010)
8. K. Sugioka, Y. Cheng, MRS Bull. **36**, 1020–1027 (2011)
9. K. Sugioka, Y. Cheng, Lab Chip **12**, 3576–3589 (2012)
10. K. Sugioka, J. Xu, D. Wu, Y. Hanada, Z. Wang, Y. Cheng, K. Midorikawa, Lab Chip **14**, 3447–3458 (2014)
11. F. Sima, J. Xu, D. Wu, K. Sugioka, Micromachines **8**, 40 (2017)
12. F. Sima, K. Sugioka, R. Martínez Vázquez, R. Osellame, L. Kelemen, P. Ormos, Nanophotonics **7**, 613–634 (2018)
13. R. Osellame, H.J. Hoekstra, G. Cerullo, M. Pollnau, Laser Photonics Rev. **5**, 442–463 (2011)
14. K. Ke, E.F. Hasselbrink, A.J. Hunt, Anal. Chem. **77**, 5083–5088 (2005)
15. Y. Liao, Y. Cheng, C. Liu, J. Song, F. Hei, Y. Shen, D. Chen, Z. Xu, Z. Fan, X. Wei, K. Sugioka, K. Midorikawa, Lab Chip **13**, 1626–1631 (2013)
16. Y. Li, K. Itoh, W. Watanabe, K. Yamada, D. Kuroda, J. Nishii, Y. Jiang, Opt. Lett. **26**, 1912–1914 (2001)
17. Y. Li, S. Qu, Curr. Appl. Phys. **13**, 1292–1295 (2013)
18. A. Marcinkevičius, S. Juodkazis, M. Watanabe, M. Miwa, S. Matsuo, H. Misawa, J. Nishii, Opt. Lett. **26**, 277–279 (2001)
19. M. Masuda, K. Sugioka, Y. Cheng, N. Aoki, M. Kawachi, K. Shihoyama, K. Toyoda, H. Helvajian, K. Midorikawa, Appl. Phys. **A76**, 857–860 (2003)
20. Y. Bellouard, A. Said, M. Dugan, P. Bado, Opt. Express **12**, 2120–2129 (2004)
21. K.C. Vishnubhatla, N. Bellini, R. Ramponi, G. Cerullo, R. Osellame, Opt. Express **17**, 8685–8695 (2009)
22. S. Maruo, O. Nakamura, S. Kawata, Opt. Lett. **22**, 132–134 (1997)
23. S. Kawata, H.B. Sun, T. Tanaka, K. Takada, Nature **412**, 697–698 (2001)
24. K.K. Seet, V. Mizeikis, S. Matsuo, S. Juodkazis, H. Misawa, Adv. Mater. **17**, 541–545 (2005)
25. S. Maruo, J.T. Fourkas, Laser Photonics Rev. **2**, 100–111 (2008)
26. D. Wu, S. Wu, J. Xu, L. Niu, K. Midorikawa, K. Sugioka, Laser Photonics Rev. **8**, 458–467 (2014)
27. D. Wu, J. Xu, L. Niu, S. Wu, K. Midorikawa, K. Sugioka, Light Sci. Appl. **4**, e228 (2015)
28. L. Jonušauskas, S. Rekštyte, R. Buividas, S. Butkus, R. Gadonas, S. Juodkazis, M. Malinauskas, Opt. Eng. **56**, 094108 (2017)
29. T. Tičkūnas, M. Perrenoud, S. Butkus, R. Gadonas, S. Rekštytė, M. Malinauskas, D. Paipulas, Y. Bellouard, V. Sirutkaitis, Opt. Express **25**, 26280–26288 (2017)
30. K. Sugioka, Int. J. Extreme Manuf. **1**, 012003 (2019)
31. F. Sima, H. Kawano, A. Miyawaki, L. Kelemen, P. Ormos, D. Wu, J. Xu, K. Midorikawa, K. Sugioka, ACS Appl. Bio Mater. **1**, 1667–1676 (2018)
32. W.S. Fan, R. Storz, H.W. Tom, J. Bokor, Phys. Rev. **B46**, 13592–13595 (1992)
33. S.S. Wellershoff, J. Hohlfeld, J. Güdde, E. Matthias, Appl. Phys. **A69**, S99–S107 (1999)
34. K. Sugioka, Y. Cheng, Light Sci. Appl. **3**, e149 (2014)
35. N. Bloembergen, J. Nonlinear Opt. Phys. **6**, 377–385 (1997)
36. B.C. Stuart, M.D. Feit, A.M. Rubenchik, B.W. Shore, M.D. Perry, Phys. Rev. Lett. **74**, 2248–2251 (1995)
37. A.P. Joglekar, H. Liu, E. Meyhöfer, G. Mourou, A.J. Hunt, Proc. Natl. Acad. Sci. **101**, 5856–5861 (2004)

38. K. Sugioka, Y. Cheng, Appl. Phys. Rev. **1**, 041303 (2014)
39. S. Nakashima, K. Sugioka, K. Midorikawa, Appl. Phys. **A101**, 475–481 (2010)
40. K.M. Davis, K. Miura, N. Sugimoto, K. Hirao, Opt. Lett. **21**, 1729–1731 (1996)
41. E.N. Glezer, M. Milosavljevic, L. Huang, R.J. Finlay, T.-H. Her, J.P. Callan, E. Mazur, Opt. Lett. **21**, 2023–2025 (1996)
42. W. Watanabe, T. Asano, K. Yamada, K. Itoh, J. Nishii, Opt. Lett. **28**, 2491–2493 (2003)
43. J. Zhang, M. Gecevičius, M. Beresna, P.G. Kazansky, Phys. Rev. Lett. **112**, 033901 (2014)
44. A. Ishikawa, T. Tanaka, S. Kawata, Appl. Phys. Lett. **89**, 113102 (2006)
45. S. Maruo, T. Saeki, Opt. Express **16**, 1174–1179 (2008)
46. D. Serien, K. Sugioka, Opto-Electron. Adv. **1**, 180008 (2018)
47. D. Serien, K. Sugioka, ACS Biomater Sci. Eng. **6**, 1279–1287 (2020)
48. W.H. Zhou, S.M. Kuebler, K. Braun, T.Y. Yu, J.K. Cammack, C.K. Ober, J.W. Perry, S.R. Marder, Science **296**, 1106 (2002)
49. Y. Liao, Y. Ju, L. Zhang, F. He, Q. Zhang, Y. Shen, D. Chen, Y. Cheng, Z. Xu, K. Sugioka, K. Midorikawa, Opt. Lett. **35**, 3225 (2010)
50. F. Costache, M. Henyk, J. Reif, Appl. Surf. Sci. 208–209, 486–491 (2003)
51. Y. Shimotsuma, P.G. Kazansky, J. Qiu, K. Hirao, Phys. Rev. Lett. **91**, 247405 (2003)
52. V.R. Bhardwaj, E. Simova, P.P. Rajeev, C. Hnatovsky, R.S. Taylor, D.M. Rayner, P.B. Corkum, Phys. Rev. Lett. **96**, 057404 (2006)
53. K. Sugioka, Nanophotonics **5**, 17–37 (2016)
54. M. Hörstmann-Jungemann, J. Gottmann, M. Keggenhoff, J. Laser Micro Nanoeng. **5**, 145–149 (2010)
55. D. Choudhury, A. Rodenas, L. Paterson, F. Díaz, D. Jaque, A.K. Kar, Appl. Phys. Lett. **103**, 041101 (2013)
56. O. Tokel, A. Turnalı, G. Makey, P. Elahi, T. Çolakoğlu, E. Ergeçen, Ö. Yavuz, R. Hübner, M.Z. Borra, I. Pavlov, A. Bek, R. Turan, D.K. Kesim, S. Tozburun, S. Ilday, F.Ö. Ilday, Nat. Photonics **11**, 639–645 (2017)
57. O. Nukaga, S. Yamamoto, K. Tabata, T. Kubota, S. Samukawa, M. Sugiyama, Proc. 14th μTAS 1199–1201 (2010)
58. S. Kiyama, S. Matsuo, S. Hashimoto, Y. Morihira, J. Phys. Chem. **C113**, 11560 (2009)
59. Y. Cheng, K. Sugioka, K. Midorikawa, M. Masuda, K. Toyoda, M. Kawachi, K. Shihoyama, Opt. Lett. **28**, 1144–1146 (2003)
60. F. Sima, H. Kawano, M. Hirano, A. Miyawaki, K. Obata, D. Serien, K. Sugioka, Adv. Mater. Technol. **5**, 2000484 (2020)
61. O. Vanderpoorten, Q. Peter, P.K. Challa, U.F. Keyser, J. Baumberg, C.F. Kaminski, T.P.J. Knowles, Microsyst. Nanoeng. **5**, 40 (2019)
62. C.M. Denais, R.M. Gilbert, P. Isermann, A.L. McGregor, M. Lindert, B. Weigelin, P.M. Davidson, P. Friedl, K. Wolf, J. Lammerding, Science **352**, 353–358 (2016)
63. D. Truong, J. Puleo, A. Llave, G. Mouneimne, R.D. Kamm, M. Nikkhah, Sci. Rep. **6**, 34094 (2016)

Chapter 31
Laser Structuring for Biomedical Applications

Gerda Buchberger, Martina Muck, Cristina Plamadeala, and Johannes Heitz

Abstract Laser structuring enables modification of sample topography, surface chemistry, and/or physical properties of materials. Examples of these processes are ripple, nap or wall formation, surface oxidation, induction of polymerization reactions, or changes in crystallinity or contact angle. These – most of the time – interrelated modifications are exploited widely for biomedical applications. They range from cell-repellent surfaces for easy-to-replace cardiac pacemakers, control of cell proliferation required in regenerative medicine, to increased cell adhesion for cell arrays. Furthermore, ns-laser-induced nanoripples were used for formation of gold nanowires for future surface plasmon resonance sensors directly integrated into biotechnological devices. Additive nano- and microscale manufacturing by two-photon polymerization allows for considerable progress in cell scaffold formation, paving the path for in vitro–grown organs, bones, and cartilages. The very same fs-laser-based technique was also used for biomimetic microneedles with enhanced liquid spreading on their surface. Microneedles are promising candidates for low-cost, high-throughput drug delivery and vaccination applicable even by nonmedically trained personnel. Microfluidic systems fabricated by fs-lasers have enabled progress in 3D microscopy of single cells and in studies on thrombocyte activation with the help of nanoanchors. Explicating the abovementioned and further biomedical applications, the authors put special focus on the achieved limits pointing out what scientists have accomplished so far in their pursuit of extreme scales.

Keywords Microstructures · Nanostructures · Microneedles · Cell scaffolds · Repellent · Adhesion · Activation of cells

---

G. Buchberger (✉) · M. Muck · C. Plamadeala · J. Heitz (✉)
Institute of Applied Physics, Johannes Kepler University (JKU) Linz, Linz, Austria
e-mail: gerda.buchberger@jku.at; martina.muck@jku.at; cristina.plamadeala@jku.at; johannes.heitz@jku.at

© The Author(s) 2023

R. Stoian, J. Bonse (eds.), *Ultrafast Laser Nanostructuring*, Springer Series in Optical Sciences 239, https://doi.org/10.1007/978-3-031-14752-4_31

Abbreviations

AFM	Atomic force microscopy
ALD	Atomic layer deposition
ANN	Artificial neural networks
AOM	Acousto-optical modulator
BG	Bioactive glass
CAD	Computer-aided design
CCD	Charge-coupled device
CHO	Chinese hamster ovary
CNN	Convolutional neural networks
DCM	Dichloromethane
DCP	Dichloropentane
DIMP	Diisopropyl methylphosphonate
DLIP	Direct laser interference patterning
DLW	Direct laser writing
DLW SM	Direct laser writing for subtractive manufacturing
DMMP	Dimethyl methylphosphonate
EBL	Electron beam lithography
ECM	Extracellular matrix
ECSA	Electrochemical surface area
ELI	Extra low interstitial
EUV	Extreme ultraviolet
FEA	Finite element analysis
FEP	Fluorinated ethylene propylene
FLICE	Femtosecond laser irradiation followed by chemical etching
FN	Fibronectin
HA	Hydroxyapatite
HEK	Human embryonic kidney
HMEC	Human microvascular endothelial cell
HUVEC	Human umbilical vein endothelial cell
IR	Infrared
LC	Laser cladding
LIFT	Laser-induced forward transfer
LIL	Laser interference lithography
LIPSS	Laser-induced periodic surface structures
MAPLE	Matrix-assisted pulsed laser evaporation
MIFE	Microelectrode ion flux estimation
MN	Microneedle
MPL	Multiphoton lithography
MSC	Mesenchymal stem cells
NBDS	Nonbulbar dermal sheath
NOA 61	Norland Optical Adhesive 61
OCN	Osteocalcin
OLN-93	Oligodendroglia cell line
OND	Oligonucleotide
OPA	One-photon absorption
PE	Poly(ethylene)
PEG-DA	Poly(ethylene glycol diacrylate)
PET	Poly(ethylene terephthalate)
PETA	Pentaerythritol tetraacrylate
PLA	Poly(lactive) acid
PLD	Pulsed laser deposition

PLGA	Poly(lactive-co-glycolic) acid
PMMA	Poly(methyl methacrylate)
PPy	Poly(pyrrole)
PS	Poly(styrene)
PSF	Point spread function
PU	Poly(urethane)
RIU	Refractive index units
SAW	Surface acoustic wave
SEM	Scanning electron microscopy
SERS	Surface-enhanced Raman scattering
SGC	Spinal ganglion cells
SH	Sodium hyaluronate
SLIPS	Slippery liquid-infused porous surfaces
SLS	Selective laser sintering
SPP	Surface plasmon polariton
STED	Stimulated emission depletion
STL	Stereolithography
TE	Tissue engineering
TPA	Two-photon absorption
TPL	Two-photon lithography
TPP or 2PP	Two-photon polymerization
TRL	Technology readiness level
UV	Ultraviolet
VN	Vitronectin
WGM	Whispering gallery mode
WP	Waveplate

1 Introduction: Overview on Laser Structuring

Section 1 provides a short overview on laser structuring methods commonly used in biomedical applications. Properties like size, shape, and pattern of laser structures as well as the irradiated material type determine the potential for a specific biomedical application. Laser structures come in two different forms: self-organized (Sect. 1.1) or directly written (Sect. 1.2), and can form on various material classes like metals, polymers, and dielectrics. Lasers have also proven to be able to chemically modify surfaces by processes like direct surface irradiation and deposition of thin films. Prominent examples for indirect surface modification with lasers are pulsed laser deposition (PLD) and matrix-assisted pulsed laser evaporation (MAPLE) (Sect. 1.3).

1.1 Self-Organization

Usually, irradiating materials with lasers results in a morphological change of the processed surface, which either leads to self-organized laser-induced structures or direct laser-inscribed structures [1]. For self-organized structures, the laser beam

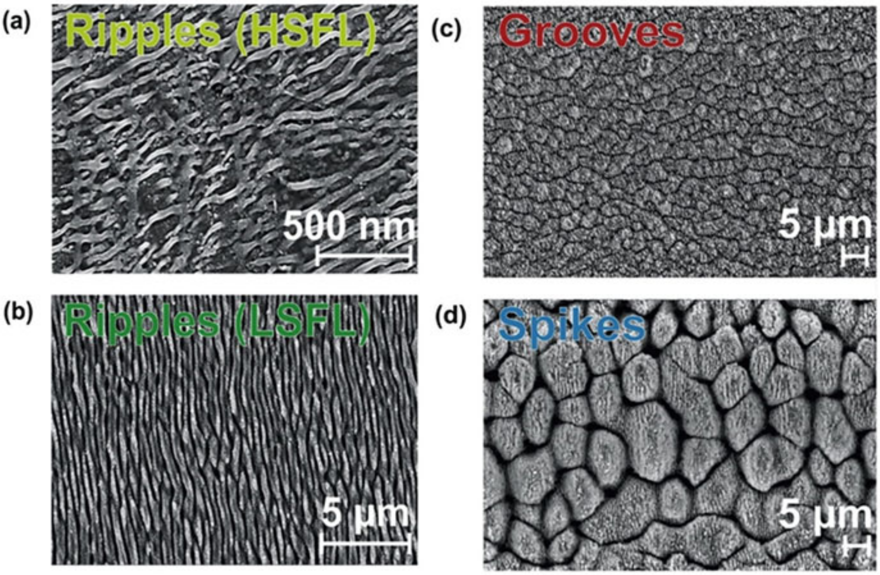

Fig. 31.1 SEM images of LIPSS with (**a**) high and (**b**) low spatial frequency, (**c**) microgrooves, and (**d**) micro-sized spikes with superimposed nanoripples. (Reprinted from Hermens et al. [11], Copyright (2017), with permission from Elsevier)

irradiates the surface in a spot or another scanning geometry, leading to the formation of (quasi-)periodic surface morphologies. An overview of self-organized structures is shown in the scanning electron microscope (SEM) images of Fig. 31.1. These structures can be found on the micrometer as well as on the nanometer range. Microstructures are usually known as grooves and spikes (Fig. 31.1c, d) and nanostructures as laser-induced periodic surface structures (LIPSS) or ripples (Fig. 31.1a, b) [2–4]. The irradiating laser commonly has a Gaussian intensity spatial profile and a spatially homogeneous linear polarization. However, several attempts showed that the complexity of self-organized structures can be increased if inhomogeneous beam profiles and nonlinear laser polarizations are used [5–8]. As an example, it was reported that circularly polarized ultrafast laser pulses can be used to create micro-metric triangular surface structures [9, 10]. Self-organized structures have been reported on various material classes such as metals [1, 11, 12], polymers [13–16], and others [17–19]; however, the types of structures that can form depend on the properties of the irradiated material.

To control the outcome of the structure morphology, a proper selection of the laser processing parameters is required. This includes choosing proper combinations of parameters such as peak fluence Φ_0 and effective number of laser pulses N. For various biomedical applications, it is also necessary that laser-induced structures show a pronounced morphological complexity, which will be discussed in further detail in Sect. 2.1. Only a few approaches on creating complex morphological hierarchies of micro- and nano-metric structures were reported. These include surface irradiation with ultrafast laser pulses in reactive atmosphere [20, 21] or multistep surface processing, which combines both self-organized and directly written laser structures [22, 23]. The process of surface patterning by laser irradiation and formation of laser structures is discussed in detail in Chaps. 12, 13, and 28 of Bäuerle [24]. Self-organized laser-induced structures have been featured on various materials for biomedical applications [25–30], especially in the field of cell behavior control, which will be discussed in Sects. 2.1 and 2.2. An overview of the formation of laser-induced self-organized structures, especially of the ones mimicking biological surfaces, is reported in Stratakis et al. [31].

To get an insight on the precision limit and reproducibility of laser-based nanostructuring, the reader is encouraged to check Chap. 8 of this book. Chapter 23 describes in detail the formation and the wide range of applications of LIPSS. Complex designs of micro- and nanostructures can additionally be achieved by interference pattering methods such as laser interference lithography (LIL) or direct laser interference patterning (DLIP). These methods and their applications, where some of them are of biomedical nature, are described in Chap. 26.

1.2 Direct Writing

Direct laser writing (DLW) for biomedical applications includes subtractive as well as additive laser processing techniques. A special form of direct laser writing is two-photon polymerization (TPP or 2PP), also known as two-photon lithography (TPL or 2PL). TPP is a three-dimensional (3D) additive micro- and nanofabrication technique [32] which is based on the process of simultaneous absorption of two photons (two-photon absorption, TPA) [33]. In TPA, a molecule absorbs one photon and is excited from its ground state to a virtual state. The lifetime of the virtual state is in the order of femtoseconds (10^{-15} s). If within this lifetime the molecule absorbs another photon, the molecule reaches an excited state. If not, the virtual state collapses to the ground state. As TPA depends on the simultaneous absorption of two photons, the probability of the process depends on the second power of the light intensity, which makes the process highly localized. Hence, the polymerization can be confined three-dimensionally, and feature sizes under 200 nm can be obtained [33].

Practically, the simultaneous absorption of two photons and sub-diffraction structures are achieved by setups containing an ultrashort-pulsed laser system (which ensures the absorption of two photons within the lifetime of the virtual state), focusing optics, and sample positioning and/or beam deflection elements (such as linear stages, piezo-systems, and galvanometer scanners). For direct writing of complex 3D structures, a user-defined 3D model is created in a computer-aided design (CAD) software, which is exported into a stereolithography (STL) file. The STL file describes the surface of the 3D object and communicates this information to the elements responsible to translate the laser beam focus relative

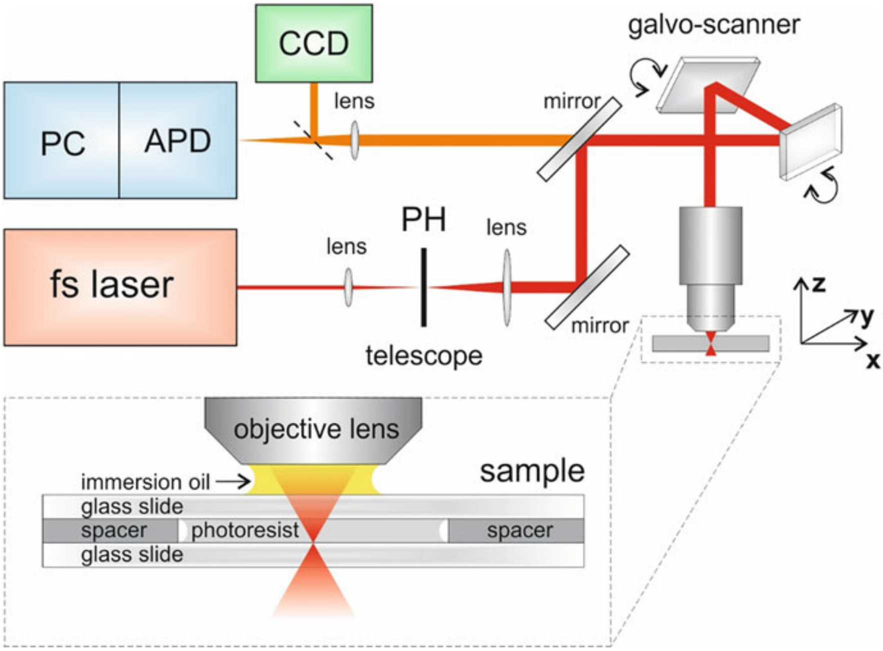

Fig. 31.2 Principle setup for TPP microfabrication of 3D structures. A fs-laser beam is expanded by a telescope and directed into a *xy* galvanometer scanner. The beam is later focused by a high numerical aperture (NA) objective lens into the sample, which is mounted on a 3D piezo-stage. Abbreviations: personal computer (PC), avalanche photodiode (APD), charge-coupled device (CCD), pinhole (PH)

to the substrate and the photoresist [32]. More simple structures can be achieved by any computer controlling the precise movement of the *x, y, z*-stages (or even by moving the stages manually using a joystick). To obtain even smaller features sizes (under 100 nm), stimulated emission depletion (STED) lithography can be employed, where a second laser is used to inhibit the polymerization in the outer rim of the focal point [34]. A principle TPP setup is shown in Fig. 31.2.

Materials used in TPP have to possess the following properties [32]: (1) refractive index close to 1.5, to avoid or minimize aberrations when focusing the laser beam into the resist; (2) transparency for the laser beam wavelength, to avoid one-photon absorption (OPA) processes; (3) fast curing with minimal shrinkage; and (4) good adhesion to the substrate and mechanical strength [35]. Commercially available epoxy- (SU-8 series) and acrylic-based (OrmoComp® series) photoresists, as well as custom-tailored ones, are used for a wide range of applications in photonics, micro-electronics, and micro-mechanics [36], as well as in biomedicine. For the latter one, material selection is even more rigorous, as in some applications not only biocompatibility [37] but also biodegradability is required [38].

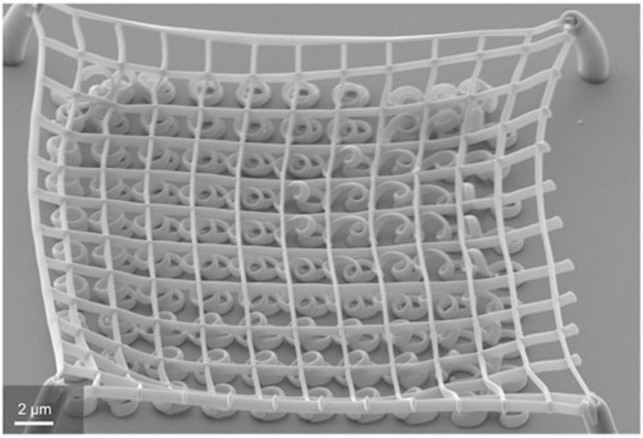

Fig. 31.3 Microstructures of variable geometries written with an acrylate-based photoresist by means of TPP. (By courtesy of Richard Wollhofen, Johannes Kepler University Linz, Austria)

The TPP technique allows the fabrication of micro- and nanostructures of variable geometries in two or three dimensions, which is demonstrated exemplarily in Fig. 31.3.

Besides additive laser processing (such as TPP), subtractive laser processing techniques (also generally known under the term of "laser ablation") are also relevant in biomedical applications. Direct laser writing techniques for subtractive manufacturing (DLW SM) range from material removal and surface modifications [39–41] to laser drilling [42], cutting [43], and welding [44]. Generally, a setup used for these applications contains a laser beam that is shaped by optical elements and focused onto a sample that is mounted onto a translation or rotation stage. DLW SM is used to process polymers [45], zirconia-based ceramics [39], and metals [41], for example, for tissue engineering and biosensing applications.

To get an insight into biological applications of TPP and DLW SM, the reader is encouraged to check Sects. 2.3 and 2.5. The reader is also advised to read the part on subtractive and additive structuring methods in Chap. 8 of this book. Chapter 22 describes multiphoton 3D lithography, which can be used in various fields such as photonics and microfluidics.

1.3 Non-topographical Modifications

Surface modification is often accompanied with the goal of maintaining the bulk material properties. This can be achieved by physically or chemically altering the existing surface or completely changing it by covering it with thin films of a different material [46]. Various thin films on metal alloys such as hydroxyapatite (HA), glass ceramics, and glasses have been employed to change the surface for more biocompatibility. Modifying the surface chemistry plays a key role in the adsorption of proteins such as fibronectin (FN) and vitronectin (VN), which further control cell adhesion. Pulsed laser deposition (PLD) [47] and matrix-assisted pulsed laser evaporation (MAPLE) [48] are examples for laser-assisted cell-biomaterial interaction control (both techniques are described in Chap. 22 of Bäuerle [24]). PLD is often used for deposition of hydroxyapatite or bioactive glass (BG) layers on metallic and polymeric implant surfaces to improve biofunctionality [49–51]. Koch et al. [52] produced bioglass thin films on polished titanium samples by PLD. MAPLE is an extension of the PLD process for growing thin films consisting of polymeric materials, which allows deposition of heat-sensitive molecules with minimal degradation [53, 54]. The possibility to deposit fibronectin molecules with MAPLE, which facilitate the attachment of human osteoprogenitor cells, was reported for silicon substrates [55]. Lactoferrin, an iron-binding glycoprotein, plays an important role in host defense against viral and microbial infections. Constantinescu et al. [56] studied lactoferrin layers produced by MAPLE on different materials to evaluate their biocompatibility and revealed that MAPLE is an excellent process for improved drug delivery due to the possibility of coating drugs with a thin film, thus inhibiting unwanted reaction with a solvent. Additionally, it was reported that biocompatible polymers such as poly(lactive-co-glycolic) acid (PLGA) can be coated by MAPLE for controlled drug delivery [57]. Dinca et al. [58] reported that MAPLE is suitable for obtaining active polymeric-enzymatic interfaces as hybrid or layered coatings for detecting toxic vapors such as dimethyl methylphosphonate (DMMP) and diisopropyl methylphosphonate (DIMP). Electrical stimuli have proven to be of great importance for tissue engineering, and Paun et al. [59] used a MAPLE approach to produce conductive poly(pyrrole) (PPy)-based composite layers to promote new bone formation. These composite layers consist of conductive PPy nanograins in a biocompatible polymeric matrix, such as PLGA or polyurethane (PU).

Chemical modification of surfaces by laser treatment has been used extensively due to its potential of achieving corrosion resistance, self-cleaning, and anti-fouling, which is discussed in detail in Chap. 24 of this book. Corrosion resistance is achieved by surface oxides, which can be formed by laser treatment [24, 60–62] or can be induced by chemical treatments such as anodic oxidation [63, 64]. Laser irradiation can cause bond breaking in polymers, leading to the formation of radicals and subsequent reaction with the surrounding atmosphere. This process is of great importance for biological processes such as cell adhesion [24, 65]. Furthermore, the surface wettability, which is essential for cell growth, can also be modified by laser irradiation [66, 67]. Excimer laser irradiation of poly(ethylene terephthalate) (PET), for example, modifies the surface chemistry of the polymer [68–70] as well as its wettability [68, 70] depending on the applied fluence. Heitz et al. [71] have shown that laser processing of titanium alloy surfaces resulted in a hydrophilic behavior, which changed steadily to a hydrophobic behavior after a few weeks. Subsequent electrochemical anodization of hydrophobic surfaces resulted again in a hydrophilic surface, which also changed back to hydrophobicity after a couple of weeks. The reason for these effects is still an ongoing research topic, but it is believed to result

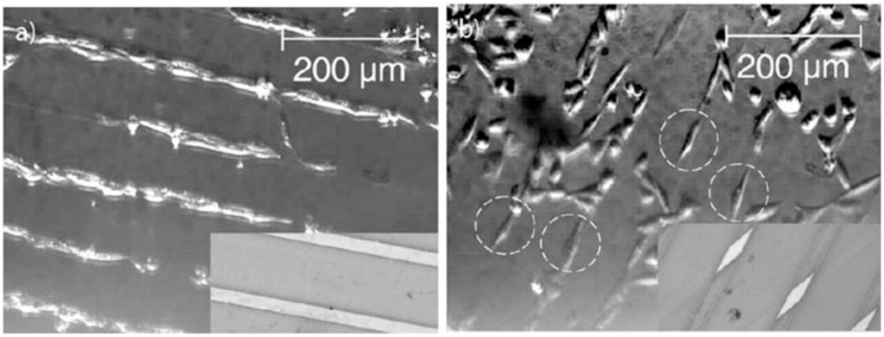

Fig. 31.4 Optical microscopy images of CHO cells seeded on patterned FEP samples: (**a**) lines and (**b**) rhombs (images taken on living cells). Insets are optical microscopy images of the FEP structures before cell seeding (in the same scale). The dashed circles in (**b**) indicate exemplary cells with a shape directly affected by the wettable islands. (Reprinted from Yakunin et al. [73], © 2011 Wiley Periodicals, Inc.)

from chemical bond breaking and reaction with the ambient atmosphere. Ranella et al. [72] investigated how wetting affects fibroblast growth on silicon, concluding that fibroblastic growth is reduced for hydrophobic surfaces.

The combination of the techniques described in this section (i.e., PLD, MAPLE, chemical modification) with laser patterning allows the fabrication of functional micro- and nanostructures. This is illustrated exemplarily in Fig. 31.4, which shows isolated Chinese hamster ovary (CHO) cells grown on a laser-structured photomodified fluorinated ethylene propylene (FEP) surface [73].

2 Biomedical Applications

Section 2 gives an overview on how laser irradiation of different surfaces can be used for biomedical applications. Cell behavior control by physical and chemical modification of surfaces has proven to be of great importance for medical implants and tissue engineering (Sects. 2.1 and 2.2), and 3D support systems such as cell arrays and scaffolds have been shown to create a viable cell environment that replaces the natural surroundings of cells (Sect. 2.3). Microneedles that incorporate directional fluid transport inspired by nature could be employed as minimal-invasive alternatives for commonly used drug delivery systems (Sect. 2.4). Fluidic systems and analysis techniques profit from laser processing, which opens up entirely new possibilities in these fields (Sect. 2.5). Laser structuring is used in the fabrication of biomedical sensors in various ways, for example, in respiratory monitoring or in the detection of cancer cell metabolites, DNA damage, or volatile organic compounds (Sect. 2.6). Section 2.7 gives an introduction on applications where lasers can additionally be used for biomedical purposes, such as bond strengthening and deposition of thin films.

2.1 Micro- and Nanostructures for Adhesion, Alignment, and Activation of Cells

Interactions between cells and surfaces of biomaterials have been proven to be of great importance in the field of biomedicine and tissue engineering [74]. Biomaterials are constituted from a large range of natural and synthetic materials and can be classified into "bio-inert" and "bio-reactive or bioactive". Many studies in the past few years focused on modifying the surface chemistry and morphology to achieve improved biocompatibility and therefore enhance cell attachment, alignment, and proliferation [75–80]. While it was shown that the optimal micro-roughness for enhancing biocompatibility is strongly cell-type dependent, it is known that an additional roughness in the nm range strongly promotes cell adhesion and proliferation [81, 82]. One reason might be that the structured surfaces with nano-sized features resemble the nanostructures found in the extracellular matrix (ECM) of the cells [83], another that protein adsorption from bodily fluids prior to cell colonization is majorly influenced by physical/chemical properties of the underlying surface [84–88]. Recent studies investigated the influence of nano-metric surface structures on protein adsorption that are relevant for further cell attachment processes, which concluded in the assumption that only features in the size range of surface-bound proteins (~10 nm) affect the adsorption [89–93]. When mammalian cells are grown in vitro, adhesion to the cell culture substrate or to the ECM plays a key role for many processes, like proliferation and differentiation. Cells attach to the surface via focal adhesions, which are integrin-containing, multi-protein structures, that connect the ECM to the cytoskeleton [94].

Many researchers investigated the formation of self-organized structures on polymer foils by irradiation with polarized ultraviolet (UV) laser beams [95–99]. Laser-induced periodic surface structures on polymer films have shown to be beneficial for enhanced adhesion and proliferation of cells as well as for cell alignment. Among them are poly(styrene) (PS) foils, a material widely used in cell culture applications. Rebollar et al. [100] investigated human embryonic kidney cells (HEK-293 cells) and CHO-K1 behavior on LIPSS generated on PS foils by UV irradiation. Both cell types showed alignment on LIPSS with periodicities $\Lambda >$ 270 nm, which is demonstrated in Fig. 31.5 for CHO-K1 cells. It was demonstrated that the cells align along the direction of the ripples and show enhanced adhesion and proliferation compared to unmodified PS foils. However, alignment is highly cell-type dependent and only occurs when the periodicity of the ripples is above a critical value.

However, Schernthaner et al. [101] investigated human microvascular endothelial cells (HMECs) on both micro-metric walls and nano-metric LIPSS fabricated on PET foils and reported that the alignment of HMECs is not influenced by structures with periodicities $\Lambda < 1\ \mu\text{m}$, but the proliferation is highly increased by the nano-metric features. Proliferation in endothelial cells is guided by β-catenin, an important transcriptional regulator, which is located within cell-cell contacts in the cell membrane and translocates into the nucleus upon cell activation by proliferative

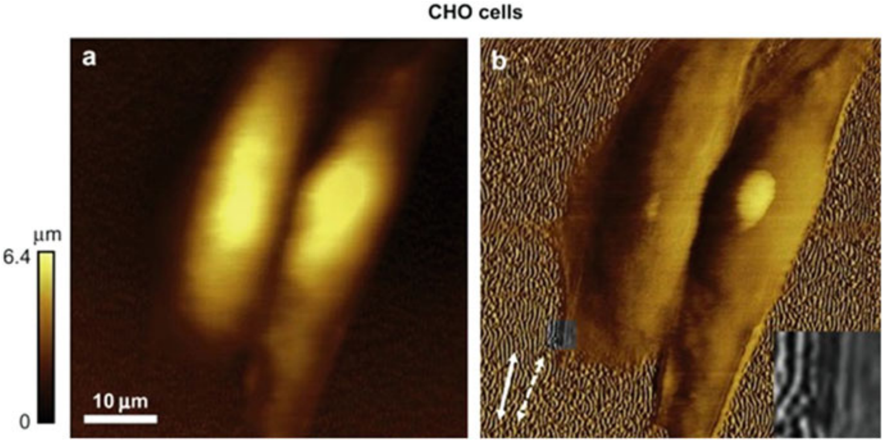

Fig. 31.5 (**a**) Atomic force microscopy (AFM) topographical and (**b**) deflection images of CHO-K1 cells on laser-textured PS foils: The cells align along the ripple direction; in (**b**) the aligned actin filaments of the cells are highlighted in the bottom right corner. (Reprinted from Rebollar et al. [100], Copyright (2008), with permission from Elsevier)

stimuli [102, 103]. This is shown in Fig. 31.6, where HMECs align along the wall-like microstructures, but not on the nano-metric LIPSS, which only enhance cell growth. This effect can also be observed in Fig. 31.7, where a confocal microscope image of vascular progenitor cells was taken on both unstructured and PET surfaces with ripples. The image shows β-catenin located in the interface regions between the cells for the unstructured PET substrate, while β-catenin is extensively found in the nucleus for the surface with ripples.

Additionally, Schernthaner et al. [104] showed that β-catenin activation is guided by enhanced tyrosine phosphorylation involving different types of tyrosine kinases. The type of tyrosine kinase responsible for β-catenin translocation depends on the underlying surface, and this has been shown for HMECs grown on the differently structured PET substrates in the presence of different tyrosine kinase inhibitors.

Even though UV or infrared (IR) laser light is often used to structure material surfaces, extreme ultraviolet (EUV) irradiation has also shown to be able to change the morphology of a treated surface. EUV structures are not as extensively studied as structures fabricated by larger wavelengths due to setup limitations in the past, but are of high interest due to the possibility to create structures that are only a few nanometers large. Reisinger et al. [105] created nano-metric structures with different shapes depending on the peak fluence and the number of applied pulses by EUV irradiation of 50 µm-thick biaxially oriented PET foils (Fig. 31.8). The radiation source was based on a laser-irradiated gas-puff target [106, 107]. But not only was the surface morphology changed by EUV irradiation, also the chemical composition of the surface changed due to photo-induced chemical reactions.

Oxygen content on the surface was reduced by about 8% due to bond breaking and preferential removal of oxygen. The alignment of wall and ripple ridges is

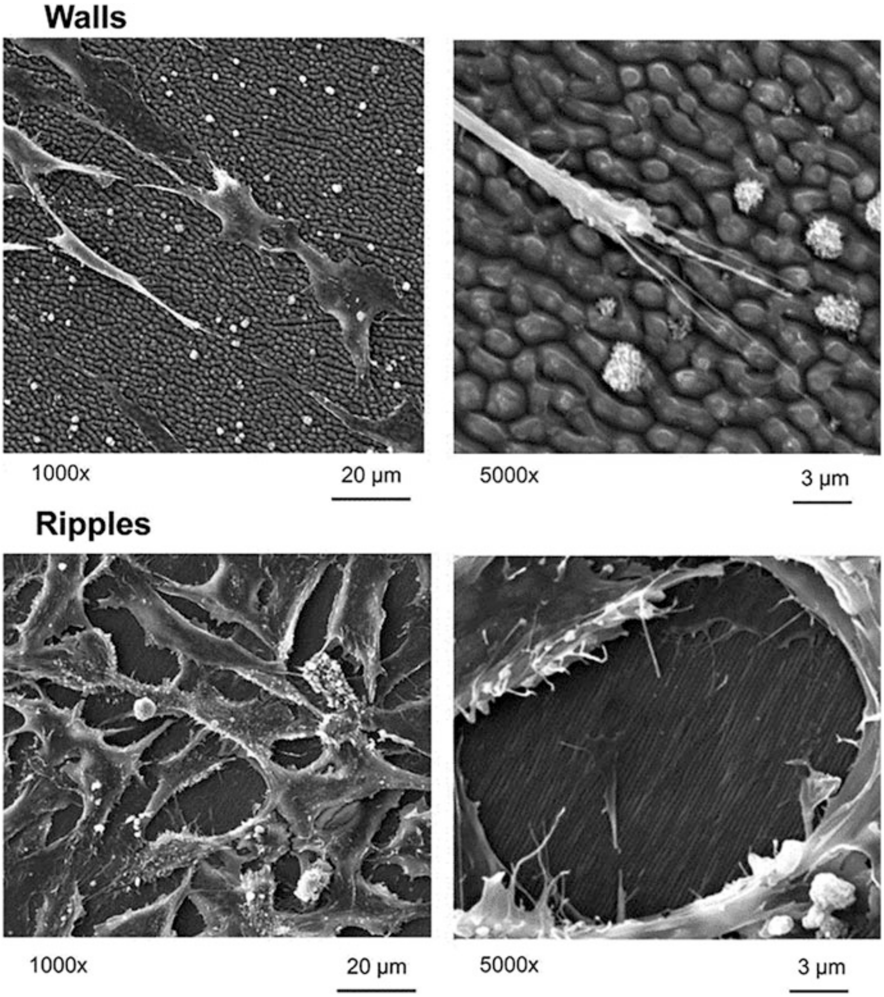

Fig. 31.6 SEM image of HMECs on micro-metric wall-like structures (top) and nano-metric ripple structures (bottom): The cells show alignment on the micro-sized walls, while on the ripples they follow no preferred direction. Even though no alignment is shown for ripples, proliferation of HMECs is nevertheless achieved by relocation of β-catenin to the nucleus instead of the interface regions between the cells. (Reprinted from Schernthaner et al. [101], Copyright (2012), with permission from Elsevier)

perpendicular to the direction of the maximum of the internal stress fields, which originate from the biaxial stretching during the production process of the PET foils. CHO cells align along the direction of the underlying walls and naps and have a spindle-shaped structure.

Guiding cells via micrometer surface texturing has also proven to be an efficient way to increase contact between implanted devices and the surrounding body part.

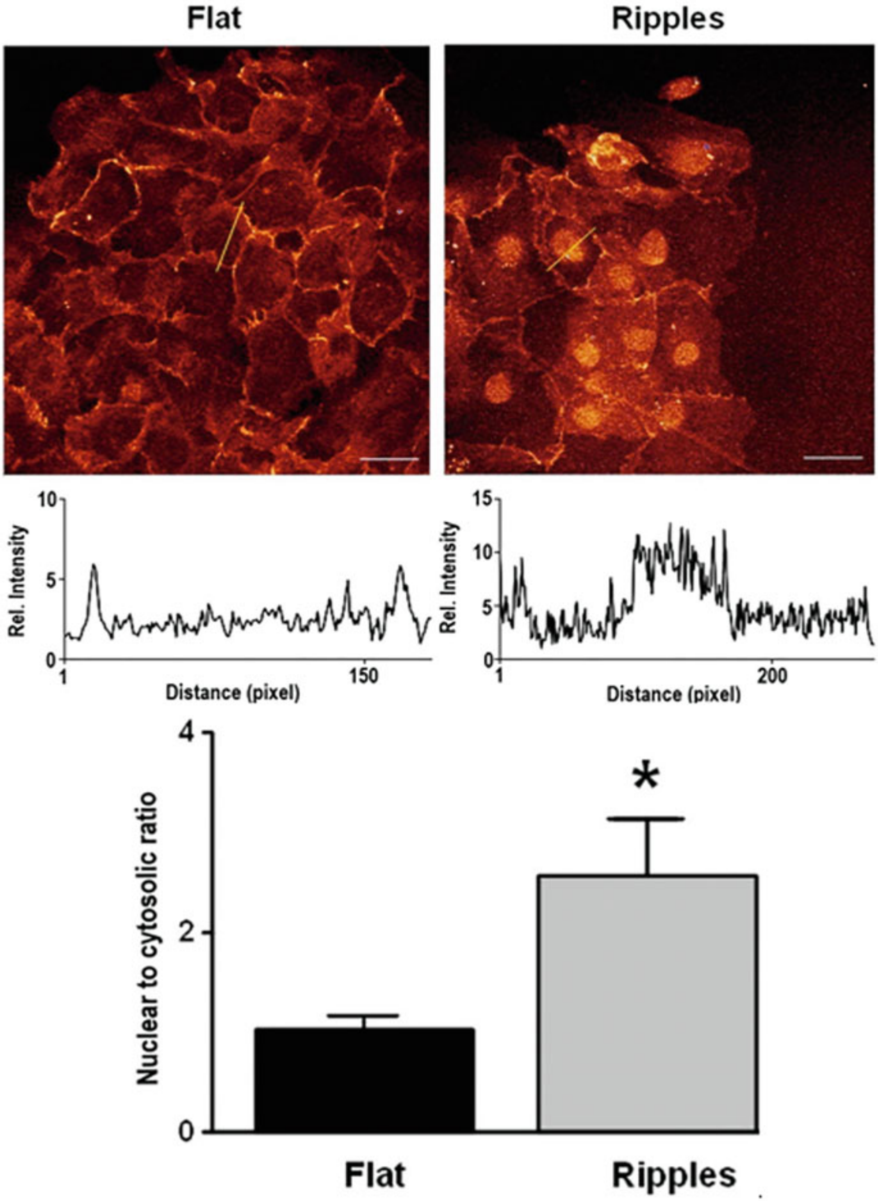
Flat
Ripples
10
5
0
Rel. Intensity
1
150
Distance (pixel)
15
10
5
0
Rel. Intensity
1
200
Distance (pixel)
4
2
0
Nuclear to cytosolic ratio
*
Flat
Ripples

Fig. 31.7 Confocal microscope image of vascular progenitor cells on (left) unstructured and (right) PET foils with ripples: The images and the box plots at the bottom indicate the location of β-catenin in the nucleus for the structured PET substrate. (Reprinted from Schernthaner et al. [101], Copyright (2012), with permission from Elsevier)

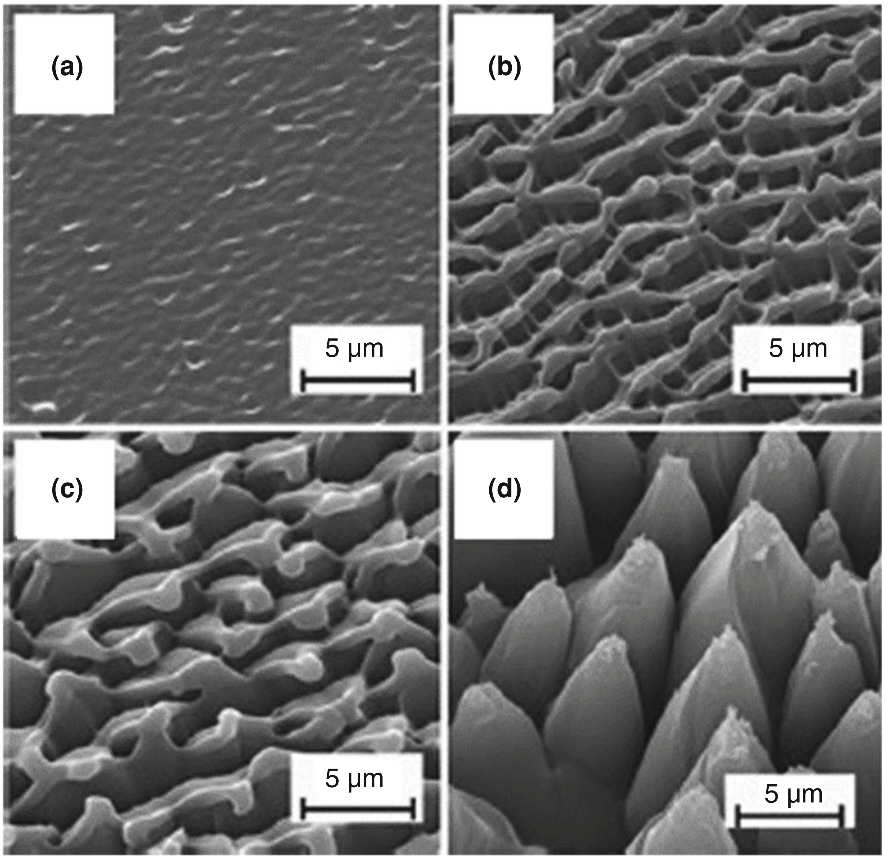

Fig. 31.8 SEM images of (**a**) ripple-like structures (10 pulses), (**b**) wall-like structures (25 pulses), (**c**) nap-like structures (50 pulses), and (**d**) cone-like structures (600 pulses) fabricated by EUV irradiation. (Reprinted by permission from Springer Nature: Reisinger et al. [105], Copyright (2010))

This has been proven to be significant for auditory implants, where a high contact area between the platinum electrodes of the implant and the ear is necessary to provide an excellent hearing experience [108–110]. These implants are constituted from a silicone elastomer which contains several platinum electrode lines that function as inner hair cells, which convert mechanical vibrations into electric signals. Furthermore, auditory implants are also subjected to connective tissue ingrowth, which leads to an increased transitory resistance and interferes with an optimal nerve-electrode interaction [111, 112]. Therefore, Reich et al. [113] investigated the ability of guiding neuronal cells in the direction of the platinum contact material by fabricating linear microgrooves on silicone elastomer and platinum samples by laser irradiation. PC-12 cells (a mixture of neuroblastic and eosinophilic cells) and spinal ganglion cells (SGCs) were seeded on both materials, and the development of neuronal extensions was investigated. Regarding the neuronal extension growth for silicone, it was shown that the molded micro-structured surface has a strong influence on neurite orientation, leading to a growth parallel to the grooves. Laser-ablated micro-structured silicone, however, showed no significant influence on both cell types. It was concluded that micro-structuring offers a possibility of guiding neurites; hereby, the direction of the microgrooves determines the attachment and guidance of the neuronal extensions.

In this subsection, the authors have discussed cell behavior control on various substrates by laser irradiation. Cell behavior control by surface modification has been extensively researched to be used for medical implants. It can be used for alignment of cells in hearing implants [113] and can further be employed in the field of orthopedic and dental implants for better integration into the body [114]. However, laser structuring of implant surfaces can additionally be exploited to achieve a repelling effect, which is in detail discussed in Sect. 2.2.

2.2 Repellent and Anti-adhesive Structures for Medical Implants and Antimicrobiotic Surfaces

As mentioned in Sect. 2.1, biological matter response to a surface can be altered with laser irradiation. This is not only used to align and activate cell growth but also to achieve reduced attachment and growth of cells and bacteria. This, again, is highly favorable in the field of medical implants. Certain implants need to be explanted from the body after a certain amount of time. Examples of implants that need to be removed are pacemakers [115] and bone implants [116]. The effective usage time of pacemakers is limited by the lifetime of the battery, which is several years. For the bone implants, the usage time is limited to several weeks or months, mainly depending on the healing time of the bone fracture. However, by the time of the explantation, these implants are overgrown by confluent multilayers of cells, which, when activated, produce a layer of ECM that encapsulates the implant. This can make the removal difficult due to the possibility of damaging the body part the devices are implanted into [117]. It is therefore desirable to avoid attachment of cells to be able to remove these devices after their respective lifetimes.

As in the case of cell alignment and activation processes, several combinations of physical and chemical modifications of surfaces have been investigated to achieve the desired cell-repellent properties [25, 116, 118, 119]. Qi et al. [118] investigated the blood-biomaterial interaction and evolution of surface modification for cardiovascular devices. In the past several years, the cell behavior on femtosecond laser-induced hierarchical titanium surface micro-/nanostructures was investigated. Titanium and its alloys are the most prominent materials in implant devices [120] and are extensively employed for pacemakers, bone implants, and dental implants [25, 114, 116, 119, 121]. Titanium, like other valve metals, forms a natural thin oxide layer, which can be thickened by anodization [122, 123].

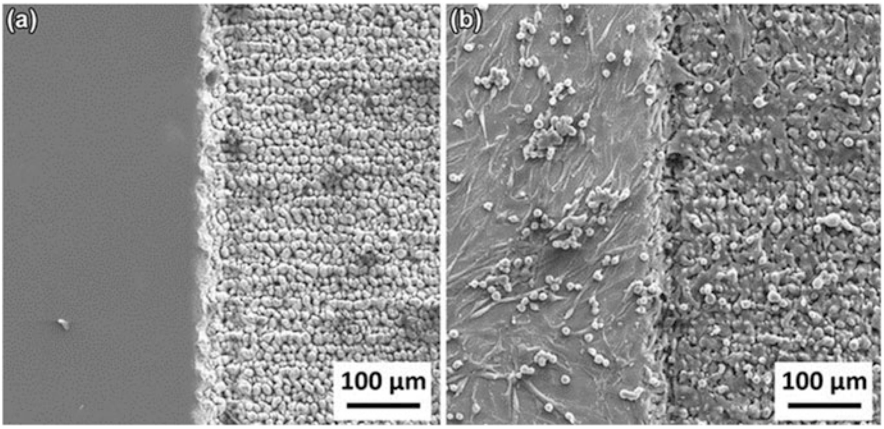

Fig. 31.9 SEM images of the rim between flat, anodized titanium alloy and laser-structured, anodized titanium alloy surface with (**a**) the surface before cell seeding and (**b**) the fibroblasts 1 week after seeding. (Reprinted from Heitz et al. [25], which is licensed under Creative Commons Attribution 4.0 International License (http://creativecommons.org/licenses/by/4.0/))

The interest of using combinations of micro- and nanostructures for cell behavior control on titanium surfaces was sparked by Ranella et al. [72], where femtosecond laser-induced structures were fabricated for cell adhesion tuning on silicon. It is assumed that the combination of both morphological types decreases the effective contact area and limits the number of focal adhesions on the tips of the spikes. Additionally, chemically modifying the surface was found to decrease the adsorption of specific ECM proteins, therefore leading to decreased cell growth (Fig. 31.9). Fibroblast adhesion reduction was successfully achieved on flat titanium samples, which were laser-structured and subsequently electrochemically anodized. In Fig. 31.9, the rim between an unstructured and a laser-structured titanium alloy surface is shown. Both, the unstructured surface and the micro-/nanostructures, were additionally electrochemically anodized. The left image (a) shows the surface before seeding with fibroblasts and the right image (b) the titanium surface 1 week after fibroblast seeding. On the flat, anodized surface the fibroblasts grow in confluent multilayers, while on the laser-structured and anodized surface, only a few adherent cells can be found. It was also reported that the cells change their shape if they do not adhere to the surface below, resulting in spherically shaped cells.

This principle was then used to achieve cell-repellent rings on cylindrical titanium samples. In Fosodeder et al. [119], titanium cylinders with 8 mm diameter were structured by a titanium sapphire (Ti:Sapphire) femtosecond laser system to achieve rings of self-organized structures (Fig. 31.10). These cylinders were subsequently electrochemically anodized by using the sample as a working electrode and dipping it into the electrolyte. This resulted in anodized titanium surfaces surrounding the laser-structured, anodized ring. Fibroblast cell tests were performed by placing the cylinder upright in the Petri dish with the cell culture medium in a

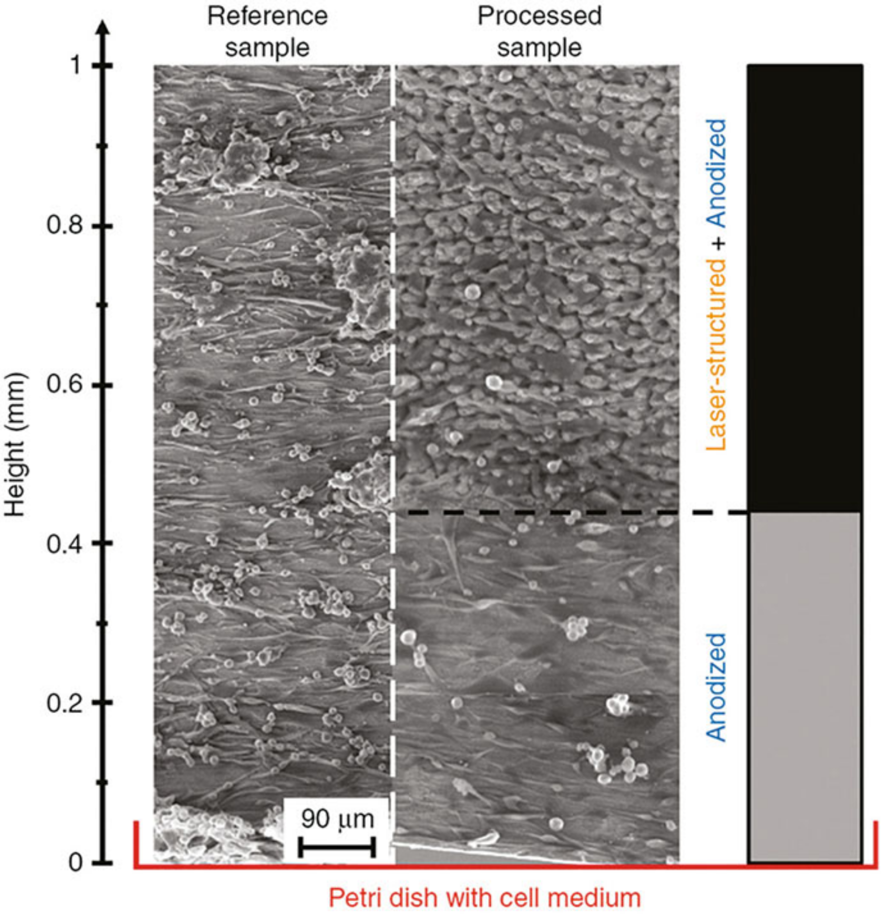

Fig. 31.10 SEM images of a cylindrical control sample (left) and an anodized cylinder with a laser-structured ring at a height of about 400 µm (right). While the control sample shows confluent fibroblast multilayers up to 1 mm height, the laser-structured ring gradually reduces the cell growth until it stops after a few hundreds of micrometers. (Reprinted from Fosodeder et al. [119], which is licensed under Creative Commons Attribution 4.0 Public License)

way that its end closer to the ring is placed in the Petri dish, and an additional control cylinder, which was neither laser-structured nor electrochemically anodized, was also placed in the Petri dish. In Fig. 31.10, it is shown that for the control sample, the cells climb in confluent multilayers up to 1 mm, while on the structured and anodized cylinder, the fibroblast density starts to decrease when they reach the laser-structured ring, up to the point where only a few cells remain after a few hundreds of micrometers. This leads to the assumption that laser-structured and anodized rings can also be used on pacemakers to achieve cell repellency and simplify the removal process.

Lone et al. [63] investigated the electrochemical surface area (ECSA) of structured titanium surfaces. They reported that the ECSA is determined by the voltage used for electrochemical anodization due to electrowetting. At low voltages the electrolyte does not penetrate the structured surface enough to be able to be detected. At higher voltages the electrolyte penetrates the surface structures, leading to an increased ECSA and oxygen evolution. It was also shown that the relative weight percentages of titanium, aluminum, and vanadium in the titanium alloy Ti6Al4V-ELI (extra low interstitial) change after laser treatment and/or anodization due to effects resulting from different evaporation temperatures and passivation.

It is further known that mesenchymal stem cells (MSCs) present in the bone marrow respond to metal implants by forming soft tissue rather than bone, which results in failure of load-bearing prosthesis. Structuring of implant materials such as titanium can be used to differentiate stem cells into the desired cell type. Böker et al. [124] investigated various nano-topographies on PS, stainless steel, and titanium samples. It was observed that a significant reduction of osteocalcin (OCN) expression on structured stainless steel and titanium surfaces occurred compared to non-structured surfaces. It was concluded that the gene expression depends on the underlying structure type. It is also possible to nanopattern surfaces by electron beam lithography (EBL). Dalby et al. [125] produced different nanoscale patterns, concluding that the design and the size of the nanopattern determine the differentiation of MSCs into cells with fibroblastic and osteoblastic morphology.

Due to increased usage of medical implants, implant-associated infections also increased, leading to expensive health-care costs and follow-up treatments for the patient [126, 127]. Implant-associated infections are caused by bacterial biofilms, which form via attachment of bacterial cells and subsequent formation of a polysaccharide matrix, which functions as a protection medium for bacteria. Once biofilms develop, they show exceptional resistance mechanisms against antibiotics and antibacterial coatings applied before implantation [128].

It is therefore desirable to hinder the formation of biofilms by preventing ab initio attachment of bacteria. Several species, such as cicadas and dragonflies, developed nano-sized structures on their wings to hinder the attachment of bacteria [129–131]. Bacterial adhesion is influenced by factors such as species, implant material, environmental aspects, and physical and chemical properties of the implant surfaces [132]. In the process of attachment, bacteria adhere to the surface by increasing the contact area to the underlying substrate as far as possible, extensively stretching the bacteria membrane. Same as cells, bacteria are therefore highly influenced by surface topographies, eventually leading to rupturing of the bacteria membrane if the stretching threshold is exceeded.

An example for bacteria rupturing on two different types of surfaces with ripples is shown in Fig. 31.11 [133]. Furthermore, bacterial attachment is also governed by surface chemistry and wettability, so a combined approach of physical and chemical modification of medical implant surfaces can lead to an antibacterial effect. Nano-sized structures will eventually penetrate the bacteria wall, causing them to rupture, and micro-sized structures will strongly reduce the available flat contact area, preventing the attachment of bacteria.

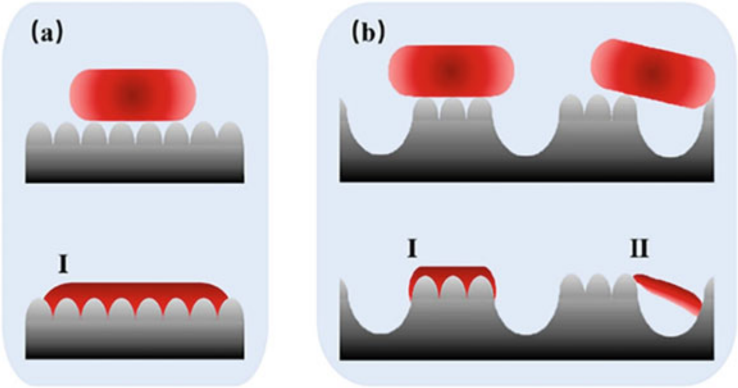

Fig. 31.11 Bacterial cell rupturing mechanism demonstrated on (**a**) a platy form and (**b**) a lacerated form. (Reprinted from Luo et al. [133], Copyright (2020), with permission from Elsevier)

It has been shown that stand-alone chemical modification, for example, by applying antibacterial coatings, fails with respect to long-term performance [134], and therefore a combined approach of both physical and chemical modification is required [135]. Morphologies on the nanometer scale such as nanowires, nanopillars, and nanotubes were investigated and found to increase the antibacterial properties of implants [136–138]. However, it was further proposed that additional treatment of the nano-sized structures, such as heat treatment or polymer coating [139–141], has to be applied to achieve the desired biocompatibility. Laser-induced periodic surface structures (LIPSS) were therefore investigated due to the possibility of producing antibacterial surfaces in a cost-effective and fast way while avoiding surface contamination. Similar as for cells, LIPSS limit the available area for bacterial attachment and are therefore highly promising structures to create antibacterial medical implant surfaces.

Epperlein et al. [142] investigated the adhesion of *Staphylococcus aureus* (*S. aureus*) and *Escherichia coli* (*E. coli*) on LIPSS generated on steel substrates. They found out that *E. coli* adhesion is highly affected by laser-induced structures, while the adhesion of *S. aureus* is not affected by LIPSS. Schwibbert et al. [143] investigated bacterial colonization of *S. aureus* and *E. coli* on femtosecond laser-induced sub-μm structures generated on poly(ethylene) (PE) substrates. However, here the generated structures were no LIPSS. It was shown that *S. aureus* adhesion was not reduced on the fabricated structures, but that the presence of laser-induced structures had a significant effect on the adhesion of *E. coli*. In Richter et al. [70], it was demonstrated that the spatial period of LIPSS on PET polymer foils determines *E. coli* repellence. SEM and biofilm studies using a pili-deficient *E. coli* TG1 strain revealed the role of extracellular appendages in the bacterial repellence.

Slippery, liquid-infused porous surfaces (SLIPS) generated by laser irradiation, chemical modification, and subsequent infusion with lubricants investigated by Doll et al. [144] were introduced as another method to inhibit bacterial attachment (Fig.

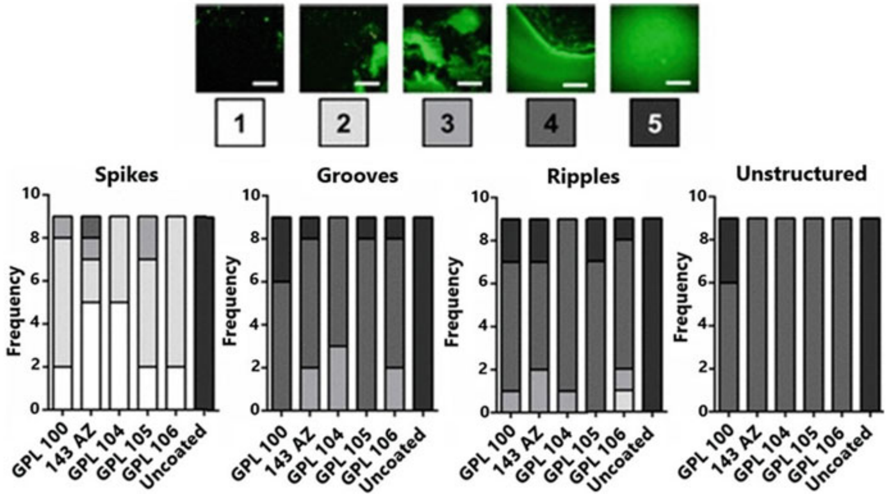

Fig. 31.12 *S. oralis* biofilm formation screening on titanium SLIPS with varying structure/lubricant combinations: The level of biofilm formation is categorized into five groups: level (1) means nearly no bacterial film and level (5) means complete coverage of structures with biofilm. The corresponding levels of coverage for each structure type are demonstrated in the box plots. (Reprinted (adapted) with permission from Doll et al. [144]. Copyright 2017 American Chemical Society)

31.12). Three main criteria have to be fulfilled to achieve the desired outcome: (1) the lubricant has to adhere stably to the surface, (2) the surface must be preferentially wetted by the lubricant rather than by the repellent liquid, and (3) the lubricant and the repellent liquid must be immiscible [145]. Spikes, grooves, and ripples were fabricated on titanium by fs-laser structuring and subsequently dip-coated by a fluorinated polymer as chemical modification. The structures were then spin-coated with five different perfluoropolyether lubricants with varying viscosities. For testing of biofilm-repellent properties, the structures were subjected to *Streptococcus oralis* (*S. oralis*). The level of surface coverage was divided into five groups (1–5), where (1) means nearly no biofilm formation and (5) means complete surface coverage by the biofilm. While spike SLIPS showed nearly no or very small biofilm fragments (level (1)), ripples, grooves, and unstructured surfaces exhibited partially or complete coverage by *S. oralis* biofilms (level (4) or (5)). However, all structured surfaces showed a reduction of biofilm formation compared to the unstructured surface. Additionally, all uncoated structures showed level (5) biofilm formation, meaning that only the combination of structures and lubricants serves as an efficient biofilm-repellent tool. As it can be seen in Fig. 31.12, the biofilm surface coverage for unstructured titanium is almost the same for all lubricants, while all structured surfaces showed at least partial bacteria reduction, with spike structures providing the best results.

It is also worth mentioning that cell-repellent properties have not only been achieved with self-organized structures but also with the process of TPP. Paun et al. [146] created mushroom-like structures that feature ripples in the μm and nm range. They concluded that the nano-metric ripples on top of the mushrooms had much more influence on the cellular attachment than the micrometer-sized structures. They also investigated the influence of wettability on the cell adhesion and found that cell attachment was mostly affected by the surface topography. The cells used in this work were from an oligodendroglia cell line (OLN-93 cells) that has been derived from primary rat brain glial cultures.

2.3 Cell Arrays and Scaffolds for Tissue Engineering Applications

Two-photon lithography (see Sect. 1.2), is a powerful and versatile tool [32, 147, 148], which found multiple applications in the study of cells, as it offers the opportunity to build microenvironments onto which cells can be seeded and their behavior can be analyzed. In this subsection, the authors aim to present an overview on the vast field of possible applications of TPP in the study of cells. Tissue engineering (TE) [149–151], as a biomedical engineering field, uses cells, scaffolds, and appropriate bioactive molecules to produce functional tissue in order to restore, maintain, improve, or replace damaged tissue. Cell scaffolds are responsible to mimic the native ECM of tissue [152]. The ECM is a 3D network of proteins and carbohydrates which provides structural and biochemical support to surrounding cells [153]. Each tissue has a specific ECM composition and topology, but it always regulates cell differentiation, proliferation, migration, and adhesion. In order to artificially produce a functional tissue, the cell supporting structures need to be as close as possible to the natural ECM. Due to its inherent true 3D printing capabilities, TPP is widely used in the production of artificial cell scaffolds [152]. Some of the most common geometries implemented for cell scaffolds are woodpiles [154–156], squares [157–159], honeycombs [160–162], and circular/tubular geometries [163–165]. In these cases, TPP technique offers the possibility to produce scaffolds of arbitrary shapes with control over the pore sizes and feature sizes both in the lateral and axial directions.

Numerous cell types have been studied using TPP scaffolds: osteoblasts [161, 163, 166], fibroblasts [167, 168], chondrocytes [169, 170], endothelial cells [162, 171], neuronal cells [155, 164], stem cells [38, 172], retinal cells [165, 173], etc. For TE applications, the materials used for building the scaffolds have to be biocompatible (the material has to be nontoxic and harmless for the cells) and sometimes biodegradable (the material needs to be decomposable with nontoxic by-products). Commercially available synthetic biocompatible materials that are used for cell studies are Ormocer® such as OrmoComp® and SU-8 [174], acrylate-based SCR500 and epoxy-based SZ2080 (20/80 zirconium-silicon/methacrylate sol-gel, containing 4,4’-bis (diethylaminobenzophenone)), and Norland Optical Adhesive 61 (NOA 61) [37]. Natural materials that can be used for TPL scaffolds are sodium hyaluronate (SH), chitosan [175], hyaluronic acid [37], etc. The synthetic photoresists have outstanding and tunable mechanical properties; therefore, a combination of synthetic and natural photoresists is advantageous.

To study the influence of pore sizes on cell proliferation, OrmoComp® TPP scaffolds with pore sizes varying from 10 to 90 μm were produced, and human dermal fibroblasts were seeded on them [167]. By observing the cell behavior 3, 6, and 9 days after seeding, it has been reported that the scaffolds with larger pores (90 μm) aided to a higher cell growth and proliferation. Also, the scaffolds with 10 μm pores promoted cell alignment along the prominent lines of the scaffold, which was not observed for scaffolds with bigger pore sizes. Comparing the effect of different pore sizes (12 μm, 25 μm, 52 μm, and 110 μm) on cell migration, another study reported that human fibrosarcoma cells of the HT1080 cell line cells move with higher speeds on triacrylate 3D scaffolds compared to the 2D substrate [154]. For smaller pore sizes, a slower speed was observed due to more obstacles the 3D matrix imposed.

The two new biocompatible polymers M10 and BisSR, which can be 3D structured via multiphoton lithography, were tested mechanically by AFM, and their biocompatibilities were compared to pentaerythritol tetraacrylate (PETA) and OrmoComp® [176]. Assessment of biocompatibility of the new resins was done by cultivating human umbilical vein endothelial cells (HUVECs) on 2D grid structures for 4 days; then cell density and presence of apoptotic cells were measured. This analysis indicated a better biocompatibility of the two new photoresists BisSR and M10 compared to PETA and OrmoComp®.

Honeycomb geometries produced with TPP, arranged in a multilayer configuration, are used to aid the 3D attachment and growth of MG-63 osteoblast-like cells, as they mimic the natural bone structure [161]. The authors compared how different distances between consecutive layers affected cells and concluded that for a spacing of 2–10 μm, the cells are able to penetrate between individual layers, interconnect with each other, and promote formation of mineralized tissue. For layer spacings lower than 2 μm and higher than 10 μm, this behavior was not observed. This geometrical configuration is believed to facilitate cell interconnections, to support cellular metabolism through vascularization and nutrient transport to the cells, and to allow easy nerve access to the cells.

In [177], polymer microstructures with one or more levels of quadratic pores were written onto a flexible substrate by TPP (Fig. 31.13). Primary human nonbulbar dermal sheath (NBDS) fibroblast cells served as progenitor cells. They differentiated into an osteogenic lineage and were seeded onto the hydrophilic three-dimensional scaffolds. Due to confinement to the microstructures and/or mechanical interaction with the scaffold, the cells were stimulated to produce high amounts of calcium-binding proteins, such as collagen type I, and show an increased activation of the actin cytoskeleton. The best results were obtained for quadratic pore sizes of 35 μm. Further examples for cell scaffolds produced by laser-assisted techniques for tissue engineering applications are described in the Refs. [178, 179].

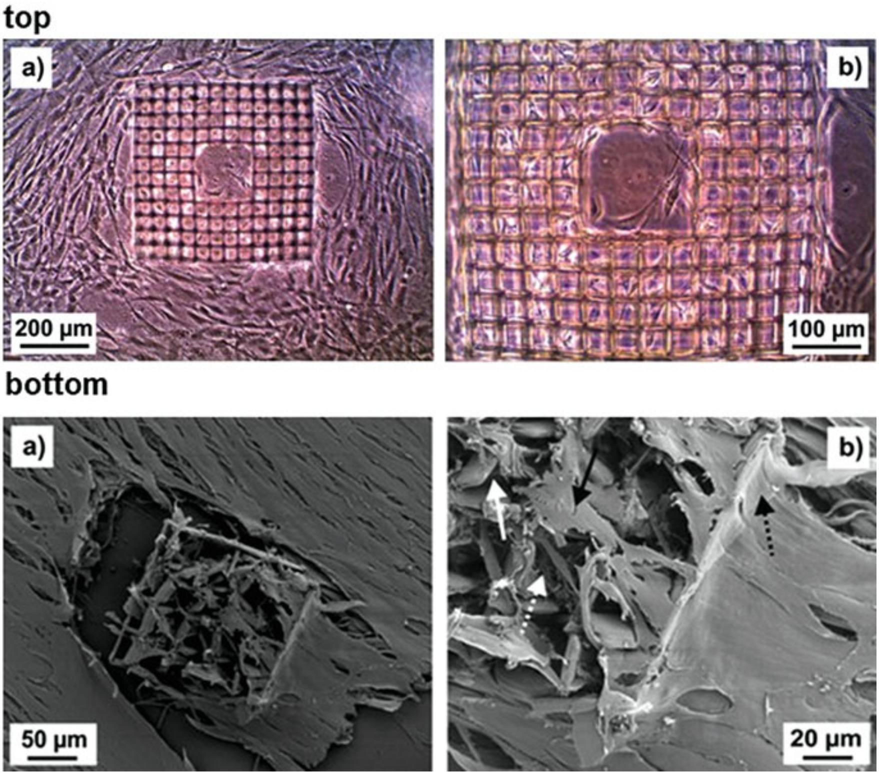

Fig. 31.13 Optical microscope images (top (**a**) and (**b**)) and SEM images (bottom (**a**) and (**b**)) of low (**a**) and high (**b**) magnifications of a cage microstructure with 35 µm square pores on a flexible polymer substrate seeded with NBDS fibroblast cells and cultured in osteogenic culture medium. In (**b**) at the bottom, the solid white arrow points to part of a pore sidewall, the solid black arrow to a cell inside the structure, the dashed white arrow to an area which is rich in fibrous extracellular material, and the dashed black arrow to a cell part at the outer rim of the structure. (Reprinted from Heitz et al. [177] with permission from Wiley. ©2016 The Authors. Journal of Biomedical Materials Research Part A Published by Wiley Periodicals, Inc.)

Three-dimensional blood vessel analogues with a honeycomb cell unit were as well tested for adhesion and proliferation of HUVECs (Fig. 31.14) [162]. The geometrical parameters of the scaffolds were obtained by simulating the mechanical response to external stresses applied to the scaffolds' sidewall structure with a finite element analysis (FEA), and TPP was implemented to create a cylindrical hollow scaffold (100 µm wide and 80 µm tall) with honeycomb wall pattern. A single hexagonal unit cell had a thickness of 5 µm, a side length of 3 µm, and a cell wall width of 1 µm. Upon cell seeding, the artificial vessel proved to sustain large elastic forces. It is expected that in further in vivo studies, the scaffolds would have a proper elastic behavior to withstand the pressure exerted by blood flow.

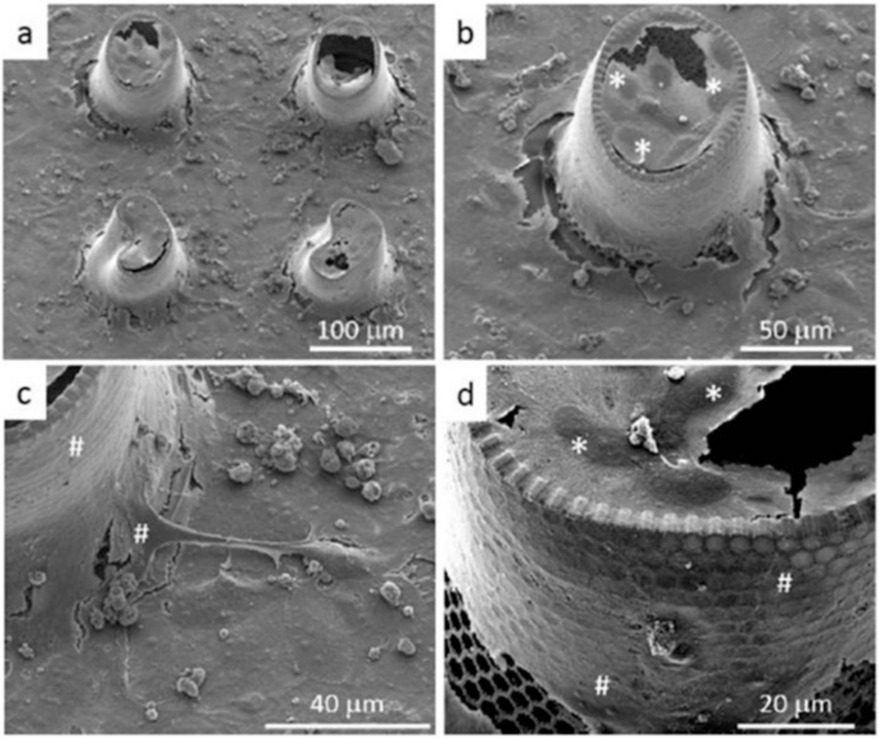

Fig. 31.14 Representative low-magnification (**a**, **b**) and high-magnification (**c**, **d**) SEM images of HUVECs grown in vitro for 9 days on tissue-engineered vascular grafts. (Reprinted from Limongi et al. [162], which is licensed under Creative Commons Attribution 4.0 license; http://creativecommons.org/licenses/by/4.0/)

By repeating the lithographic process with different photoresists, complex micro-sized structures with distinct chemical properties were produced [180]. An array of pillars (≈ 7 µm in diameter, ≈ 23 µm in height) connected by beams (1 µm in diameter) was created using TPP from poly(ethylene glycol diacrylate) (PEG-DA) and PETA mixture. After development of the array, the pillars were cast with a second photoresist (OrmoComp®) and cubes (2.5 µm edge length) were written onto the middle beams connecting two adjacent pillars. After a second developing step, the arrays were incubated in FN solution, which promotes cell adhesion. Upon seeding the arrays with chicken fibroblasts, it was observed that cells bind specifically to the OrmoComp® cubes, as PEG-DA is protein-repellent. The authors proved that by using protein-binding sites embedded on a protein-repellent array, cell adhesion and consequently cell shape can be controlled in a 3D manner.

Besides FN, other chemical treatments and coatings can be used to enhance cell adhesion. As an example, TPP was employed to produce arrays combining hollow posts and rods in order to study the influence of chemically homogeneous

3D topographies on osteoblast-like cell proliferation [181]. The posts were 12 μm high and 10 μm wide, while the rods were about 1.5 μm high and 0.45 μm wide. Commercially available acrylate-based IP-L 780 was used as a photoresist. After the developing step, to assure biocompatibility and homogeneity of the array and its substrate, each sample was coated with a thin layer of titanium oxide using atomic layer deposition (ALD), and osteoblast-like cells were seeded onto the arrays. A 170% increase in proliferation of osteoblasts was observed compared to unstructured titanium dioxide surfaces, when the posts were placed 25 μm apart. The cells also showed a higher content of alkaline phosphatase, which is an enzyme related to bone mineralization.

In conclusion, TPP allows overcoming the major disadvantages of other 3D structuring techniques by enabling the creation of intricate real 3D microenvironments that mimic the ECM. For further information, the reader is encouraged to check the following reviews [147, 148, 152].

2.4 Microneedles for Drug/Vaccine Delivery

Microneedles (MNs) are systems of micron-sized needles [182] organized in arrays covering surfaces up to square centimeters [183]. Due to their short lengths, MNs penetrate only into the top layers of the skin [184], that is, the stratum corneum and the epidermis, without irritating the nerve endings or reaching the blood vessels that lie deeper in the dermis [185]. Hence, MNs are minimally invasive tools, which do neither trigger pain sensations nor induce bleeding [186], used for wide-ranging applications such as transdermal drug and vaccine delivery, drug monitoring [187], sample extraction for diagnosis [188], and real-time monitoring [189, 190]. Depending on the mechanism of drug delivery, MNs are classified in five categories: solid, hollow, coated, dissolving and hydrogel-forming, or swellable [191]. In this subsection the authors focus on the use of TPP in the production of MNs [192, 193]. The authors aim to present a summary of the large amount of MNs and MN arrays that can be fabricated using the TPP technique. TPP is mainly used to produce solid [194], hollow [159, 195], and coated MNs [196] (Fig. 31.15). Furthermore, the solid arrays can be used as master templates for negative molds. The latter ones can be used to mass-produce dissolving [197] and hydrogel-forming MN arrays [192]. Regardless of their more complex geometry, even hollow MNs can be reproduced with high fidelity using micro-molding techniques [196, 198].

MNs with smaller tip diameter were found to penetrate the skin more smoothly than MNs with a larger tip diameter [184]. A decrease in the MN aspect ratio (height to base diameter) also results in an increased mechanical strength [194]. Besides, MN arrays are more resistant to fracturing during penetration than single MN, as the shear stress created by the tissue is distributed over a larger area [199]. These considerations are relevant when designing and producing a MN, since MN patches are desired to be applied with minimal effort and no damage to the skin or to MNs themselves. Furthermore, these requirements translate into parameters

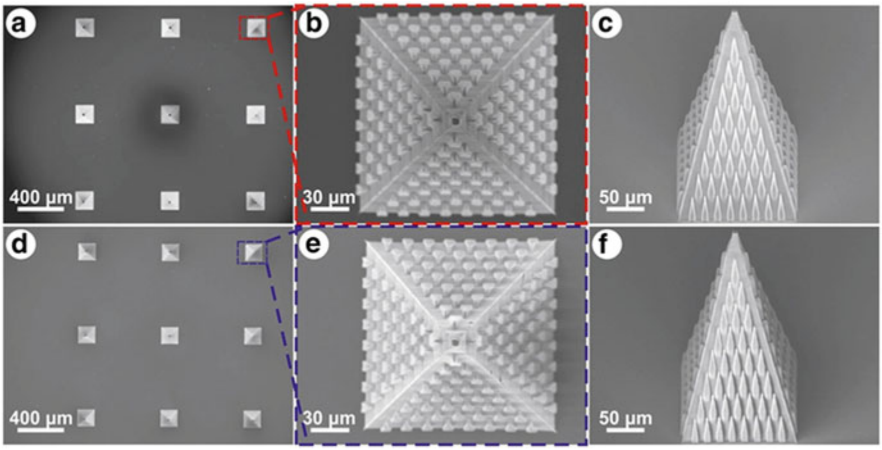

Fig. 31.15 SEM micrographs of a 3 × 3 MN array of (**a**) the TPP original and (**d**) its corresponding epoxy replica. SEM micrograph of a TPP-structured MN from the 3 × 3 array: (**b**) top view and (**c**) side view. SEM micrograph of an epoxy-replicated structured MN: (**e**) top view and (**f**) side view. (Reprinted from Plamadeala et al. [196], which is licensed under Creative Commons Attribution 4.0 International License; http://creativecommons.org/licenses/by/4.0/)

easily controllable through the use of TPP in MN production. This technique offers flexibility in adjusting MN aspect ratios, tip opening angles, and tip diameters [159, 200, 201] as well as adjusting the MN density within the array area.

The excellence of TPP in the production of real 3D structures is evident especially in the achievable designs of hollow MNs [174, 195, 198]. Arrays of in-plane and out-of-plane MNs with different aspect ratios were produced and tested for their fracture and penetration properties [174]. Square arrays of 25 MNs with 500 μm spacing were produced using the Ormocer® photoresist. Three types of MNs with different pore positions were designed: 0 μm (the opening is situated right on the tip of the MN), 1.4 μm, and 20.4 μm off-center, respectively. During penetration tests, the latter MN design proved to exert the lowest resistance upon penetration due to having the sharpest tip. A higher mechanical strength was also observed in MNs with larger base diameter. This study offers practical insights into a proper MN design for an increased mechanical stability during penetration.

Coating MNs with the desired drug formulation implies the use of another setup in an extra production step, which is often time- and finance-consuming [191]. By using TPP, the coating step can be simplified by incorporating microfluidic channels on the MNs and/or in the MN array [196]. Using TPP to create structured guiding channels between MNs and on the MNs’ lateral sides, it has been shown that the latter is easily coated with a liquid formulation compared to a MN with smooth lateral sides. In the case of hollow MNs, TPP proved to be essential in conveniently designing and producing MNs with one open microfluidic channel along its body side [198]. By connecting the open channels of each individual MN into a reservoir, the array can be used for collecting and analyzing body liquids in diagnostic applications. These geometrical features of functional relevance are beyond what is achievable with any other fabrication method.

Concluding this subsection, TPP has allowed creating MNs of user-defined designs with sub-micron features of various complex geometries. For further information, the reader is encouraged to check the following reviews [182, 193].

2.5 *Micro- and Nanostructures for Fluidic Systems and Analysis Techniques*

Three-dimensional photopolymerization techniques such as multiphoton lithography (MPL) and specifically TPP [32, 196, 202–205] and STED [206, 207] are tools for fabricating structures in the sub-μm range (see also "1.2 Direct Writing" for a brief overview on MPL, TPP, and STED). Combining these techniques with microfluidics allows to broaden the range of their applications [196, 202, 203, 207].

Buchroithner et al. [203] developed an improved transwell design for microelectrode ion flux estimation (MIFE), which is a noninvasive electrophysiological method for cellular membrane transport studies (Fig. 31.16a, b). To this end, they modified a standard transwell membrane by subtractive and additive fs-laser manufacturing (Fig. 31.16a): a measurement window was cut out with a fs-laser beam, into which a 3D grid structure was produced by TPP, for cell support. On top of the polymer grid, HMECs efficiently grew and maintained their physiological response to calcium, which was measured by MIFE (Fig. 31.16b, c).

Buchegger et al. [207] manufactured a microfluidic device enhanced with TPP structures carrying STED lithography-written nanoanchors that promoted binding of the von Willebrand factor (vWF) (Fig. 31.17). This allowed the study of the impact of vWF on the activation of thrombocytes, which seemed to decrease with the density of the vWF. To this end, fluorescently labeled antibodies were bound to the activated thrombocytes.

Fluorescent observation of cells generally suffers from the limited axial resolution due to the elongated point spread function (PSF) of the microscope optics [204]. A way to eliminate anisotropic resolution is to fuse images recorded from multiple viewing directions achieved mostly by mechanical rotation of the entire sample. In the approach of Vizsnyiczai et al. [204] (Fig. 31.18), multi-view imaging of single cells was implemented by rotating them around an axis perpendicular to the optical axis by means of holographic optical tweezers, wherefore special microtools were fabricated by TPP. The three spheres of these microtools provide trapping sites for three holographic optical traps, while a concave-shaped attachment disk possesses a binding site for spherical cells. By the proposed technique, significant resolution improvement was measured on mitochondria-stained single cells. Similarly, surface-modified complex SU-8 microstructures were used for indirect optical manipulation

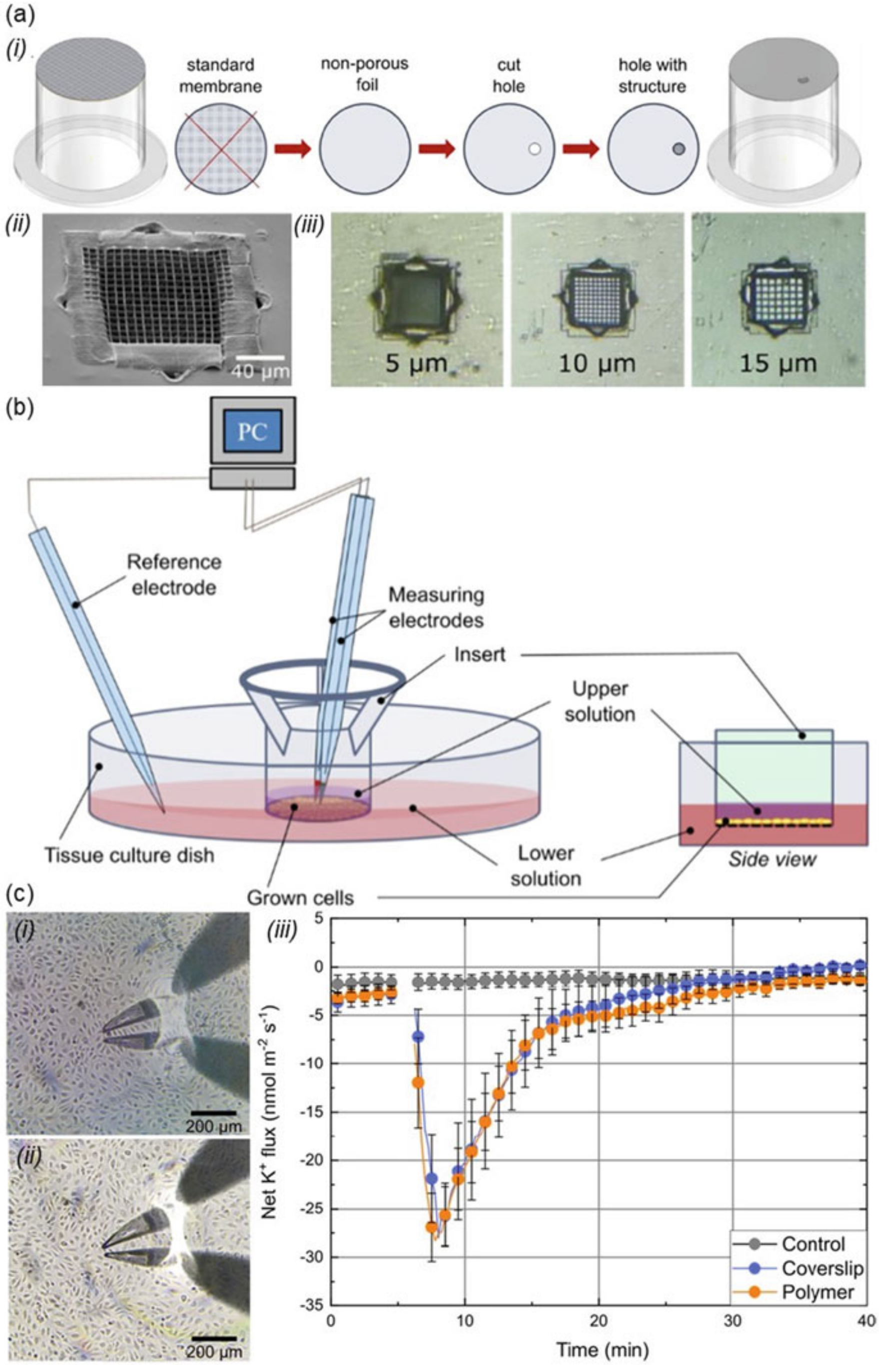
(a)
(i)
standard membrane
non-porous foil
cut hole
hole with structure
(ii)
40 µm
(iii)
5 µm
10 µm
15 µm
(b)
PC
Reference electrode
Measuring electrodes
Insert
Upper solution
Tissue culture dish
Grown cells
Lower solution
Side view
(c)
(i)
200 µm
(ii)
200 µm
(iii)
Net K$^+$ flux (nmol m^{-2} s^{-1})
Time (min)
5
0
-5
-10
-15
-20
-25
-30
-35
0
10
20
30
40
Control
Coverslip
Polymer

of single cells with six degrees of freedom [205]. For interested readers, Chap. 30 provides further overview on how miniaturized fluidic devices with nanofeatures can be employed for sensing and diagnostics.

However, not all biomedical applications aim for a reduction in structure size using TPP or STED lithography. In some cases, there is a need for large structured areas of several square centimeters with the capability of (with)holding microliters of water or for targeted, that is, (uni)directional, liquid transport (Figs. 31.19, 31.20, 31.21, 31.22, and 31.23). To this end, inspiration from nature [11, 196, 202, 208–212] was beneficial, namely, mimicking the liquid transport capability of spermathecae of fleas [212] (Fig. 31.19), of the integument of lizards [11, 211, 213, 214] (Fig. 31.20), and of bugs' cuticle [196, 202, 208, 215] (Fig. 31.21, 31.22, and 31.23). To get an overview on bio-inspired laser-structured surfaces in general, the reader is encouraged to read Chap. 25.

Buchberger et al. [211–213] applied a commercial laser engraver with a CO_2 laser source to render surfaces of some square centimeters able to transport microliters of liquid unidirectionally in asymmetric capillary channels (Figs. 31.19 and 31.20). To a certain extent, these devices were capable of unidirectional water transport even against gravity (Fig. 31.20).

Kirner et al. [215] mimicked bug-like surface structures and their fluid transport using ultrashort laser pulse irradiation of steel (Figs. 31.21 and 31.22). To this end, they applied pulses with durations in the fs to ps range of different wavelengths and systematically varied the laser processing parameters (peak fluence, effective number of pulses per spot diameter, surrounding atmosphere, and angle of incidence); a variety of LIPSS structures with different surface morphologies originated, namely, ripples, grooves, and spikes.

Unidirectional liquid transport was achieved by a gradient structure with different surface morphologies. As a possible biomedical application of directional liquid transport, Plamadeala et al. [196, 202] replicated asymmetric features found on cuticle of flat bugs by TPP and applied them to microneedles (see also Sect. 2.4) for efficient drug/vaccine coating (Fig. 31.23).

Fig. 31.16 (**a**) Transwell design for MIFE measurements: (i) The standard membrane is cut from a transwell insert; a nonporous, non-permeable foil is attached, in which a hole is cut by a fs-laser; a grid is structured inside the hole with TPP. (ii) SEM image of the polymer grid structures inside the hole. (iii) Bright-field microscopy images of grids with grid constants of 5–15 μm. (**b**) Scheme of MIFE setup: modified inserts with grown cells are placed into a culture dish. The ion-selective microelectrode is moved between two positions. From the potential differences, concentration differences and the flux of the specific ion are calculated. (**c**) Two ion-selective electrodes situated above HUVECs grown on a (i) coverslip and (ii) on a polymer grid fixed on a coverslip. (iii) Response of HUVECs to calcium ionophore. Solvent (ethanol, gray dots) or calcium ionophore (to 10 μM, orange and blue dots) was added after 5 min to either cells grown on a coverslip (blue dots) or polymer structures (orange dots). (Adapted from Buchroithner et al. [203], which is licensed under the Creative Commons Attribution (CC BY) license (https://creativecommons.org/licenses/by/4.0/))

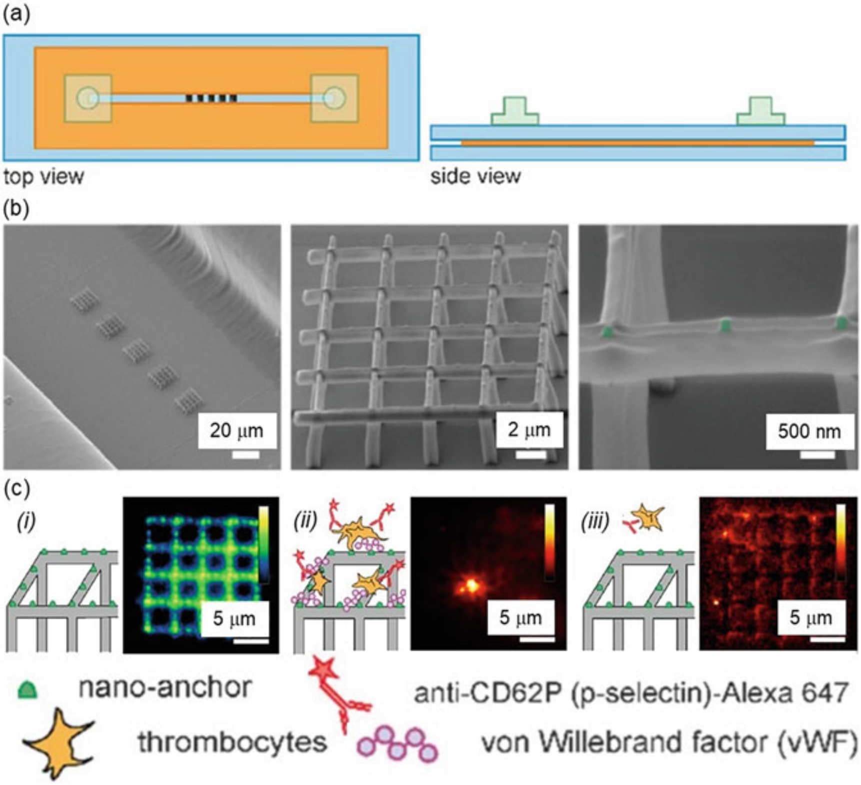

Fig. 31.17 Microfluidic device for thrombocyte activation studies: (**a**) Sketch with top and side view. Blue, glass slides; orange, double-sided adhesive tape; green, in and outlet connectors. (**b**) SEM images of the structures inside the microfluidic channel. Protein-repellent TPP grids on posts (gray) carrying STED lithography-written nanoanchors (green). (**c**) (i) Left: Sketch of the protein-repellent structure (gray) with protein-binding nanoanchors (green). Right: Fluorescence microscopy image of an empty scaffold. (ii) Left: Sketch of the experiment for thrombocyte activation. The protein-binding nanoanchors were labeled with vWf molecules. Subsequently, thrombocytes were added to the microfluidic device. Fluorescently labeled antibodies were bound to the activated thrombocytes. Right: Fluorescence image of activated thrombocytes bound on top of the scaffolds. (iii) Left: Sketch of the control experiment, where vWF molecules were omitted. The structures were incubated with a thrombocyte concentrate under flow conditions and subsequently incubated with fluorescently labeled antibodies. Right: There were no activated thrombocytes present on the structures. (Adapted from Buchegger et al. [207], which is licensed under Creative Commons Attribution 4.0 International License; http://creativecommons.org/licenses/by/4.0/)

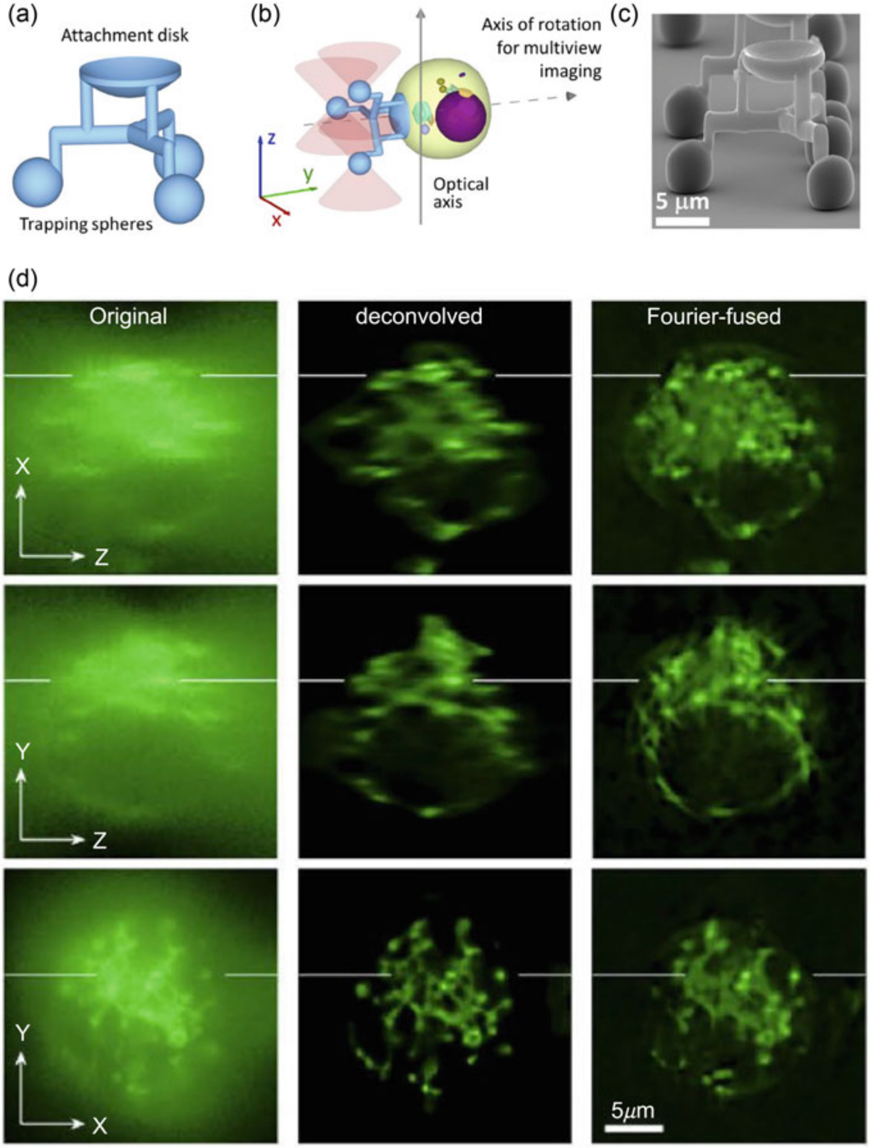
(a)
Attachment disk
Trapping spheres
(b)
Axis of rotation for multiview imaging
z
y
x
Optical axis
(c)
5 µm
(d)
Original
deconvolved
Fourier-fused
X
Z
Y
Z
Y
X
5µm

Fig. 31.18 Scheme of a polymer micromanipulator made by TPP and its application to indirectly manipulate a single cell for multi-view microscopy: (**a**) The model of the manipulator showing its main functional parts. Three spheres provide trapping sites for three holographic optical traps, while a concave-shaped attachment disk possesses a binding site for spherical cells. (**b**) The spatial arrangement of the manipulator-cell couple in the sample space relative to the optical axis of the trapping and observing objective. Pink cones indicate the trapping beams. The cell is rotated around the dashed-line axis for the multi-view microscopic observations (parallel to axis *y*). (**c**) SEM image of the cell manipulator structure. (**d**) Resolution improvement measured on mitochondria-stained single cells: Corresponding single slices taken from the original, deconvolved, and fused 3D data arrays (columns) along the three axes (rows). (Adapted with permission from Vizsnyiczai et al. [204] © The Optical Society)

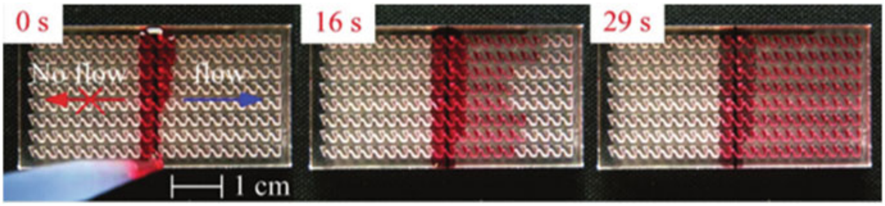

Fig. 31.19 Large-area unidirectional liquid transport bio-inspired by fleas; the capillary channels in poly(methylmethacrylate) (PMMA) were fabricated by means of an industrial CO_2 laser engraver. They are capable of transporting some microliters of liquid. (Reprinted from Buchberger et al. [212], which is licensed under Creative Commons Attribution 4.0 International License (http://creativecommons.org/licenses/by/4.0/))

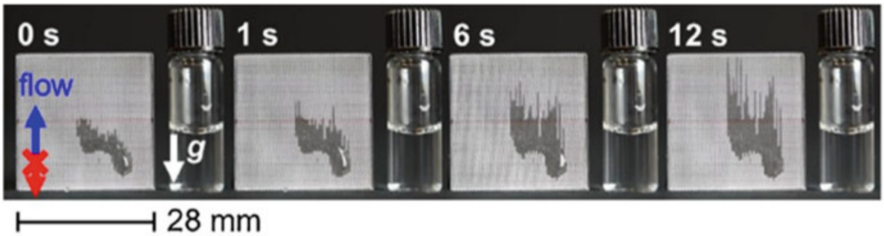

Fig. 31.20 Large-area unidirectional liquid transport mimicking the integument of lizards; the capillary channels in poly(methylmethacrylate) (PMMA) were fabricated by means of an industrial CO_2 laser engraver. They maintain the capability of unidirectional liquid transport even against gravity. (Reprinted from Buchberger et al. [211], Copyright (2019), with permission from Elsevier)

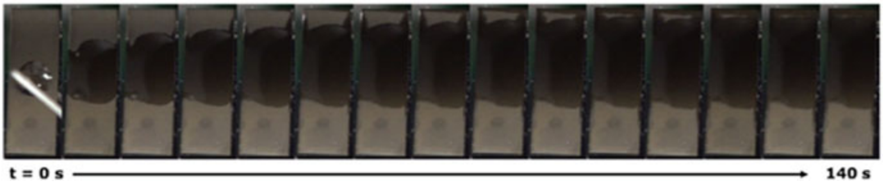

Fig. 31.21 Large-area unidirectional liquid transport bio-inspired by bugs; the image series shows a gradient structure, which possesses different surface morphologies in response to changes in fluence originated from fs-laser processing (area of 8 × 15 mm^2). (Reprinted by permission from Springer Nature: Kirner et al. [215], Copyright (2017))

2.6 Sensors Based on Micro- and Nanostructures for Biomedical Applications

Laser structuring is applied to sensors for biomedical devices in versatile ways: ns-laser processing results in LIPSS for surface-enhanced Raman spectroscopy (SERS) sensors [216–219] and optically active gold nanowires [14, 220]. Furthermore, fs-laser micromachining was used for a microresonator sensor with biosensing capabilities [221] and for a stretchable sensor array for respiration monitoring [222].

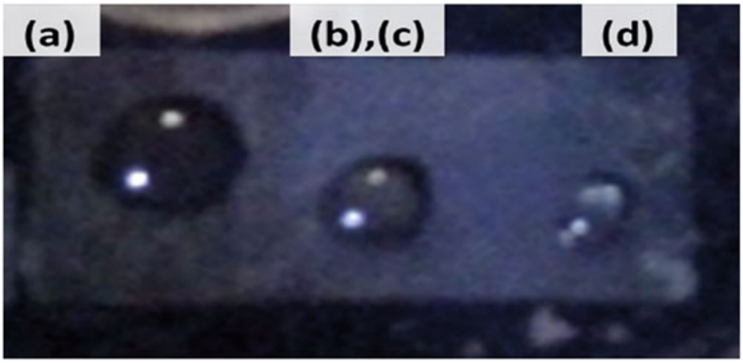

Fig. 31.22 Top-view photograph of 4 μl droplets of deionized water on steel structure taken 14 days after irradiation: (**a**) associated with spikes; (**b**, **c**) associated with grooves; (**d**) associated with low spatial frequency LIPSS (LSFL). The different morphologies lead to unidirectional liquid transport which is shown in the before figure. (Reprinted by permission from Springer Nature: Kirner et al. [215], Copyright (2017))

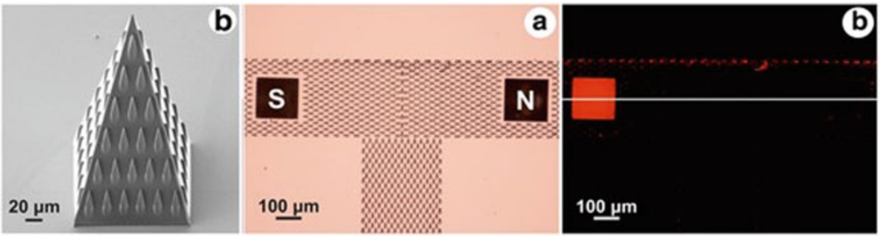

Fig. 31.23 Bio-inspired MN for efficient drug/vaccine coating. (Left) SEM image of MN. (Middle) Optical microscope image of the T-shaped channel and two microneedles after the wetting test with fluorophore solution; the one denoted with "S" is covered by bio-inspired features; the other one ("N") has plain walls. (Right) A fluorescent microscope image taken in the channel after the wetting test shows that the bio-inspired microneedle was coated significantly better with the fluorophore than the plain one. (Reprinted from Plamadeala et al. [196], which is licensed under Creative Commons Attribution 4.0 International License; http://creativecommons.org/licenses/by/4.0/)

In addition, MAPLE and the laser-induced forward transfer (LIFT) process allowed to fabricate e-noses for volatile organic compounds [223–225]. In this section, the respective works will be described in a more detailed way.

LIPSS on SU-8 polymer thin films produced by an excimer laser were sputter-coated in order to form surface plasmon polariton (SPP)-supported gold nanogratings for SERS (Figs. 31.24 and 31.25) [216, 217]. Surface-enhanced Raman spectroscopy labels have proven to be excellent for biosensing because of their merits in many aspects such as flexibility, less interference from biological matrices, high photostability, and easy multiplex encoding [218, 219]. These features make SERS labels particularly suitable for ultrasensitive detection of disease biomarkers

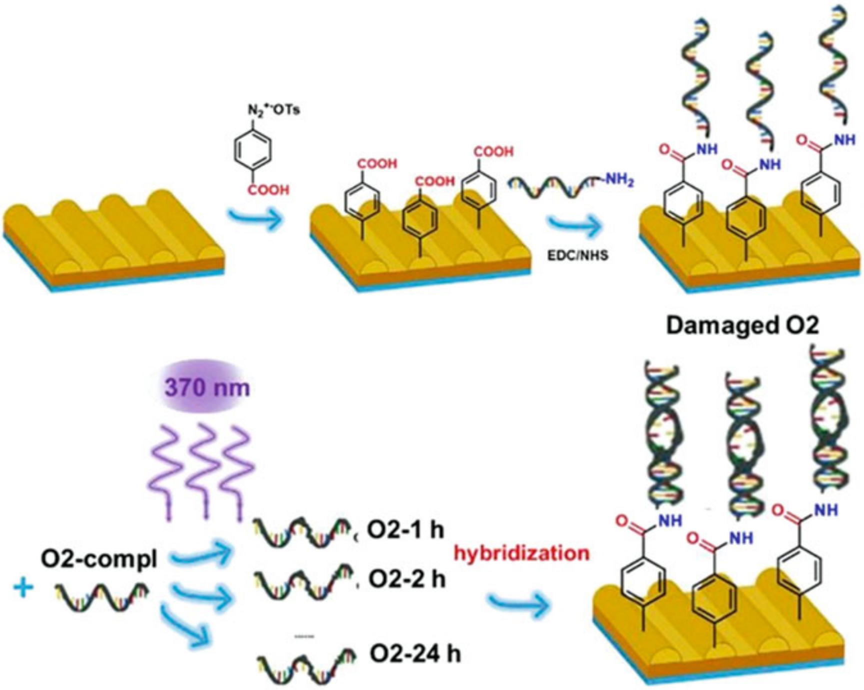

Fig. 31.24 SPP-supported gold nanogratings formed on LIPSS; the ripples were induced on polymer thin films by an excimer laser. These gratings were used for SERS. Spectra were interpreted with the help of ANN. As an explicit example, UV-induced DNA damage in oligonucleotides was detected. (Reprinted from Guselnikova et al. [217], Copyright (2019), with permission from Elsevier)

in body fluids and for targeted imaging of diseased cells and tissues, respectively [218].

Guselnikova et al. [217] combined the functional SERS sensor surface with advanced computing, namely, artificial neural networks (ANN), to collect information about the molecular structure of analytes and to evaluate spectra in the automated regime (Fig. 31.24). As an explicit example, the authors detected UV-induced DNA damage in oligonucleotide (OND) structure by the proposed method, which can be hardly measured by alternative methods [218, 219]. Erzina et al. [216] used plasmonic coupling between specific nanoparticles and underlying periodical plasmonic surface as an interdisciplinary approach for cancer detection and achieved high SERS enhancement factors (Fig. 31.25). Surface-enhanced Raman spectroscopy control spectra of normal and cancer cells' metabolites were classified by trained convolutional neural networks (CNN) and perfectly distinguished with 100% prediction accuracy. For information on other SERS applications, the reader is referred to Chap. 32.

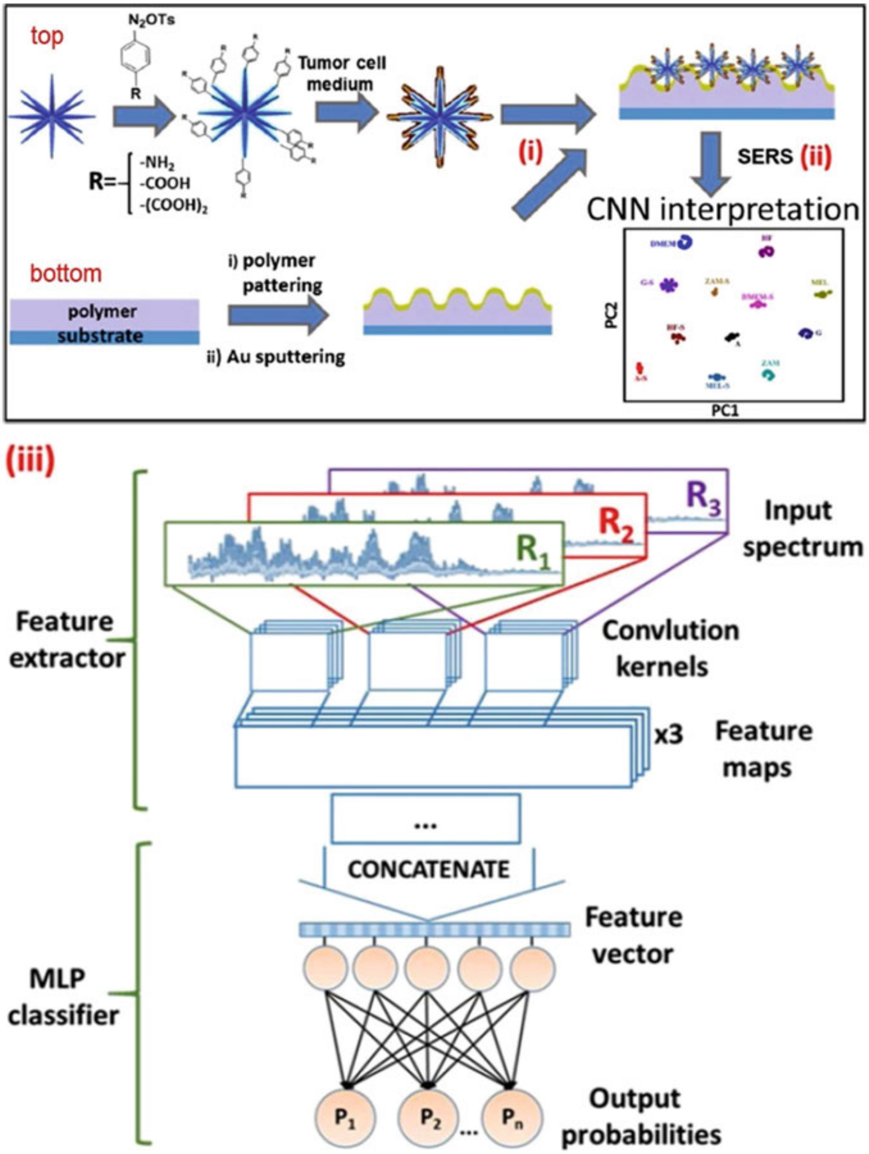
top
N_2OTs
R
R= -NH_2 -COOH -$(COOH)_2$
Tumor cell medium
(i)
SERS (ii)
CNN interpretation
DMEM
BF
G-S
ZAM-S
MEL
DMEM-S
BF-S
A
G
A-S
MEL-S
ZAM
PC2
PC1
bottom
polymer
substrate
i) polymer pattering
ii) Au sputtering
(iii)
Input spectrum
R_1
R_2
R_3
Feature extractor
Convlution kernels
x3
Feature maps
...
CONCATENATE
Feature vector
MLP classifier
P_1
P_2
...
P_n
Output probabilities

Fig. 31.25 Schematic of cancer cell detection method using nanogratings formed by an excimer laser for SERS. Top: Preparation of functional gold multibranched nanoparticles (AuMs) for interaction with tumor cells. (i) Deposition of AuMs on surface of grating. (ii) SERS measurements. Bottom: Fabrication of gold nanograting. (iii) CNN for measurement data interpretation. (Reprinted from Erzina et al. [216], Copyright (2020), with permission from Elsevier)

With a similar fabrication technique, optically active gold nanowires can be created with the help of LIPSS [14, 220, 226]. Steinhauser et al. [226] used them for localized-plasmon voltammetry which bears great potential for electrochemical sensing applications beyond conventional cyclic voltammetry. In order to determine the limitations of this method, they investigated the response toward chemical instability of the plasmonic electrode.

Kelemen et al. [221] reported on a monolithic lab-on-a-chip for label-free biosensing. To this end, they used a hybrid femtosecond laser micromachining approach combining subtractive and additive manufacturing methods. The lab-on-a-chip consists of a polymer whispering gallery mode (WGM) microresonator sensor integrated inside a glass microfluidic chip, presenting a refractive index change sensitivity of 61 nm per refractive index units (RIU). The microfluidic chips from fused silica glass were fabricated by fs-laser irradiation followed by chemical etching (FLICE) technique. A subsequent fs-laser 2PP process created WGM microresonators and coupling waveguides inside the microchannels. The biosensing capabilities of the device have been demonstrated by exploiting the biotin-streptavidin binding affinity, obtaining a measurable minimum surface density increase of 67 × 103 molecules per μm^2.

Koch and Dietzel [222, 227] presented a conformable sensor array to be used for triggering the artificial respiration of premature infants by measuring thorax deformations. The used sensor arrays were transferred into a stretchable format by fs-laser structuring. For the first time, signals from a stretchable sensor array are used to determine trigger points for respiration as well as for surface reconstruction taking artificial respiration to a next level.

For many years, the detection of chemical agents has been a major research topic in order to mitigate the adverse effects on environment and human health [223–225]. Benetti et al. [225] presented an e-nose for the detection of volatile compounds based on an array of six surface acoustic wave (SAW) resonators coated with five different polymers (Fig. 31.26). This e-nose is able to detect a volatile organic compound commonly used in chemical industry, namely, ethyl acetate, and simulants of chemical warfare agents, namely, dimethyl methylphosphonate (DMMP), dichloromethane (DCM), and dichloropentane (DCP). In particular, MAPLE was used to deposit thin polymer layers which were subsequently used as donor films in the laser-induced forward transfer (LIFT) process to selectively cover each SAW resonator of the array. The SAW e-nose was successfully tested upon exposure to vapors of ethyl acetate, DMMP, DCM, DCP, and water.

2.7 Other Applications

As discussed earlier, cell and bacteria behavior can be influenced by directly irradiating the interacting surface with laser light. However, lasers can also be used indirectly to achieve these effects, mainly, by the deposition of coatings onto implant materials via laser light impact. Many methods such PLD [47, 228, 229]

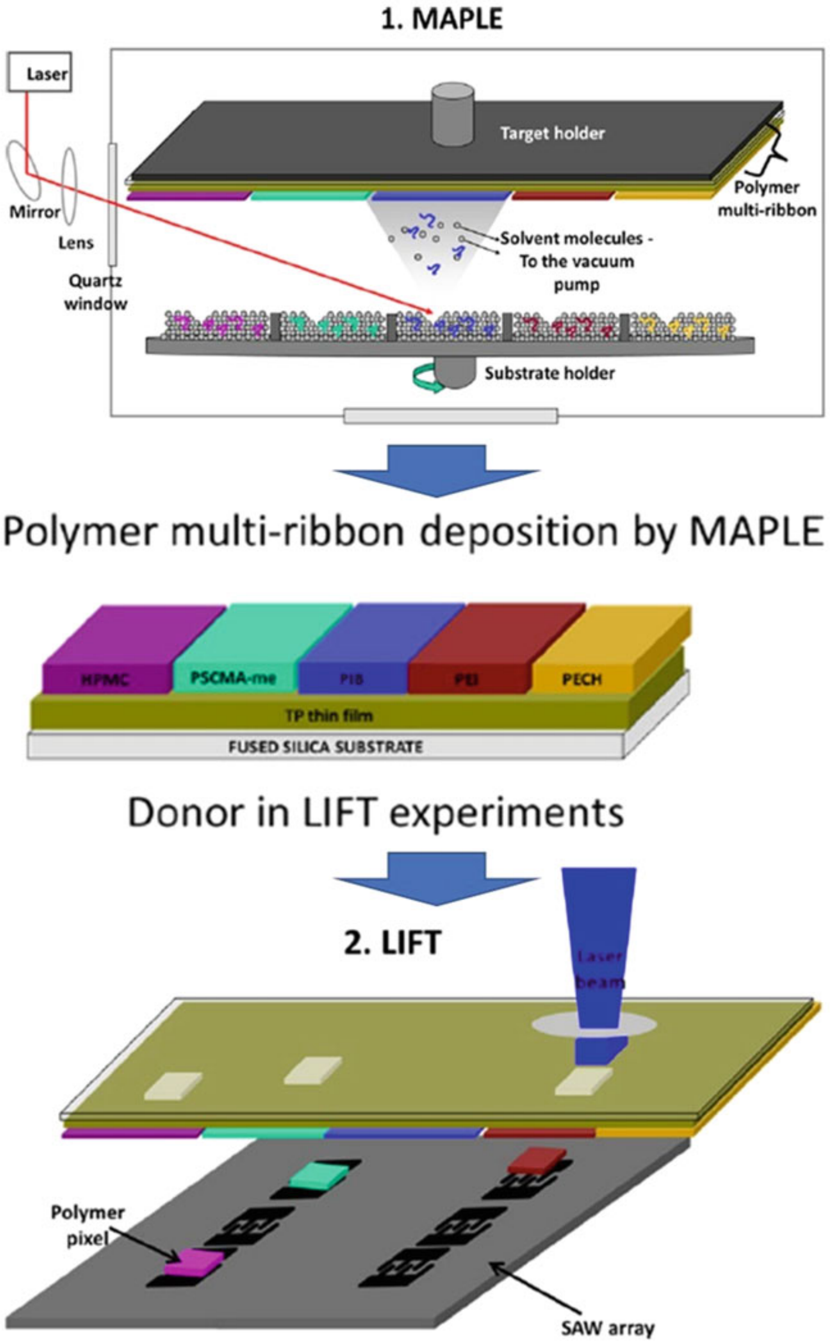
1. MAPLE
Laser
Target holder
Polymer multi-ribbon
Mirror
Lens
Quartz window
Solvent molecules - To the vacuum pump
Substrate holder
Polymer multi-ribbon deposition by MAPLE
HPMC
PSCMA-me
PIB
PEI
PECH
TP thin film
FUSED SILICA SUBSTRATE
Donor in LIFT experiments
2. LIFT
Laser beam
Polymer pixel
SAW array

Fig. 31.26 Scheme of the laser-based methods applied for coating of the SAW devices for an e-nose for chemical agents: MAPLE is used to fabricate a polymer multi-ribbon in one step, which is afterwards used as a donor for printing of polymer pixels onto the SAW resonator by LIFT. (Reprinted from Benetti et al. [225], Copyright (2019), with permission from Elsevier)

or MAPLE [48] have been employed to achieve thin films on implant materials to render the desired surface behavior [27, 230, 231]. Metals show exceptional mechanical strength and are often used for hip replacements and dental implants [232, 233]. However, due to lack of bioactivity, metals can only function in long-term implantations after being coated with a bioactive ceramic material [234–238]. In case of enhanced osseointegration, bioactive ceramic coatings are deposited onto implant substances such as metal alloys. Especially HA coatings, belonging to the calcium phosphate group, are of high interest due to their increased performance regarding the bone-implant contact area, as bulk HA ceramics cannot be employed as implant devices due to their poor mechanical properties [239–241]. Bioactive glasses and BA+PMMA nanocomposites are also broadly used coatings on implant surfaces deposited by the PLD process [242, 243].

Laser surface structuring cannot only be used to apply coatings for biomedical uses, it can also enhance the bond strength between a medical implant and a coating, which generally leads to decreased implant failure. This principle can, for example, be employed in dentistry, where yttria-stabilized zirconia polycrystal substrates are used in dental restoration frameworks [244] and which are veneered with a feldspar-porcelain layer that should mimic the color of natural teeth for aesthetics. However, the applied ceramics are often subjected to chipping due to poor bonding to the zirconia framework, which results in high failure rates in long-term clinical use [245–247]. This problem stems from residual stresses or defects between the two layers [248–251], and this problem was found to be solved by laser structuring the zirconia surface to increase the surface roughness [252, 253] and therefore increase the bonding strength. This was compared to sandblasting, which is a standard surface treatment technique for zirconia-based dental restorations [248, 253, 254]. It was shown that laser patterning of zirconia surfaces resulted in a 75% increase in shear bond strength compared to sandblasting and an additional applied intermediate composite layer further increased the shear bond strength due to increased interlocking of the zirconia surface and veneering porcelain [255].

Besides applying coatings for biocompatibility, laser postprocessing combined with other commonly used fabrication techniques can be used to further improve the effects that are expected from a medical device. Chang et al. [256] used fs-laser post-processing combined with 3D printing to produce biodegradable poly(lactic acid) (PLA) peripheral vascular stents. These biodegradable stents give the advantage of maintaining the physiological function of natural vessels. Selective laser sintering (SLS) is a highly advantageous tool to produce complex 3D structures by computer-generated image-based design techniques [257, 258]. Mangano et al. [259] used SLS to produce titanium blade implants as a nonconventional treatment for extremely atrophied posterior mandibles. The implants showed long-term mechanical stability and good aesthetic integration. Electrosurgical blades often suffer from attachment of overheated soft tissue. To minimize the attachment, surface texturing of the blades to achieve anti-adhesive structures was investigated by Li et al. [260]. It was proposed that the laser-induced blades show hydrophobicity and therefore reduce the adhesion of soft tissue. Lasers can not only be used to structure surfaces for biomedical applications, they further can be employed directly to treat certain diseases. Examples for fields with direct lasers treatment are ophthalmology [261, 262] and dentistry [263–265]. In Chap. 33 of this book, the authors aim to give an insight on how lasers are employed in eye disease treatment.

3 Summary and Outlook

In this chapter, the authors have presented a wide range of biomedical applications where lasers have been successfully employed to achieve a desired outcome. Tables 31.1 and 31.2 give typical examples of works which have been discussed. Lasers are a favorable tool for processing functional surfaces, as they provide the possibility of treating materials in a cost-effective and fast manner. Some laser processing methods also have the advantage of processing without contamination of the irradiated surface, which is desirable in the fields of biomedicine. The mentioned applications and effects are only possible because laser structuring provides a broad range of structure types and materials these structures can be employed on. Self-organized and directly written structures can be fabricated on materials such as metals, polymers, and composites. Metals are extensively used in implanted devices, while polymers are widely used in the field of cell scaffolds, microneedles, sensors, and analytic devices. Limits of laser structures in biomedical fields depend on the application.

While controlling cells and bacteria with laser-induced structures is possible and highly successful, one limitation is given by the fact that the processes are highly cell-dependent. In Sect. 2.1 CHO-K1 cells and HMECs show different behavior on surfaces with ripples: CHO-K1 cells align along the ripples, while HMECs do not show alignment. Instead HMECs only showed increased activation on surfaces with ripples, which was indicated by the relocation of β-catenin into the nucleus. Cell control processes are guided by micro- and nano-metric features, where nano-sized structures in the range of few nanometers interact with surface-bound proteins that guide cell adhesion processes. Self-organized structures in the range of a few nanometers have been fabricated by short wavelength systems in the EUV range, but research on these types of structures has only been conducted in the last years due to device limitations. Self-organized structures fabricated by more commonly used laser systems have sizes in the range of a few hundreds of nanometers. Requiring hierarchical multi-scale surface structuring, bacteria retention is highly favorable in the field of implanted devices.

Direct writing, for instance, TPP or laser ablation, is an important tool to fabricate cell scaffolds and microfluidic devices such as microneedles or analytic tools. Structure sizes of several hundreds of nanometers are achieved with TPP, which can be further reduced when STED is combined with TPP. With STED lithography, the lowest possible structure size is around a few tens of nanometers. This makes it possible to build cell scaffolds, where cell growth can be guided and directed with a combination of micro- and nano-sized structures. Microneedles profit from their size as minimal-invasive meddling with the body is highly desirable. Stability of the

Table 31.1 Overview on exemplary works discussed in the Sects. 2.1, 2.2, and 2.3

	Exemplary works	Authors	Material(s) and laser technique	Achievements and limits
2.1 Micro- and nanostructures for adhesion, alignment and activation of cells	Alignment of HEK-293 cells and CHO-K1 cells	Rebollar et al. [100]	LIPSS on PS by UV ns-laser (KrF excimer laser)	Alignment on ripples with periodicities > 270 nm
	Proliferation/alignment of HMECs	Schernthaner et al. [101]	LIPSS and walls on PET by UV ns-laser (KrF and ArF excimer lasers)	Proliferation increase on both structures following different mechanisms; alignment only on walls (periodicity of 1.5 microns), not on ripples (periodicity of 300 nm)
	Directing neuronal cell growth for auditory implants (pheochromocytoma cell line PC-12 and primary spiral ganglion cells)	Reich et al. [113]	Subtractive direct writing of microgrooves in silicone elastomer and platinum by fs-laser (Ti:Sapphire laser)	Guidance on neurites parallel to laser-processed grooves in platinum and grooves on molded silicone elastomer; no effect on directly laser-ablated silicone
2.2 Repellent and anti-adhesive structures for medical implants and antimicrobiotic surfaces	Repellent structures against fibroblasts for miniaturized pacemakers	Fosodeder et al. [119]	Hierarchical self-organized structures on titanium with LIPSS by fs-laser (Ti:Sapphire laser)	Expansion of the applicability of femtosecond laser processing for cell-repellence from flat samples to cylindric samples with a laser-processed ring serving as barrier for upgrowing cells
	Bacterial adhesion tested for two different test strains	Schwibbert et al. [143]	Nanostructure on PE by fs-laser (Ti:Sapphire laser)	Significant adhesion reduction of *E. coli*
	Adhesion tests of cells on different hierarchical structures (“mushrooms decorated with micro- and nanostructures”)	Paun et al. [146]	2PP of IP-DIP photoresist (Nanoscribe) by fs-laser	Significant reduction of OLN-93 cell adhesion by 55%, which is an oligodendroglia cell line

2.3 Cell arrays and scaffolds for tissue engineering applications	Vascular grafts as blood vessel substitutes	Limongi et al. [162]	2PP of IP-DIP photoresist (Nanoscribe) by fs-laser	HUVECs adhere and grow on the 3D structure
	3D hydrogel cell scaffold variations (photoresist) and mechanical tests/cell growth	Yu et al. [175]	TPP of PEG-DA-based photoresists by fs-laser	High-precision configuration using 40 wt % PEG-DA and 60 wt % PE-3A (80 nm line width), optimizing mechanical stability, SH, and chitosan-assisted hydrogel for study of biocompatibility
	Retinal cell delivery scaffold variations (photoresist) and biocompatibility study	Thompson et al. [173]	TPP by fs-laser (photoresist based on acrylated poly(caprolactone):dioxane solutions)	Increasing the concentration of crosslink-able groups decreased polymerization threshold and the size of resolvable features while increasing fidelity of the scaffold; scaffold supported human retinal progenitor cells in vitro and showed favorable biocompatibility

Table 31.2 Overview on exemplary works discussed in the Sects. 2.4, 2.5, 2.6, and 2.7

	Exemplary works	Authors	Material(s) and laser technique	Achievements and limits
2.4 Microneedles for drug/vaccine delivery	Bio-inspired MN design	Plamadeala et al. [196]	TPP of OrmoComp® and OrmoComp®-based photoresists by fs-laser	Efficient (self-)coating of microneedle with drug/vaccine
	MN design variations (pore-center displacements) and penetration tests	Ovsianikov et al. [174]	TPP of Ormocer® photoresist by fs-laser	Insight in design for improved mechanical strength
	MN array design variations (needle height, shape, base width, interspacing) and insertion tests	Cordeiro et al. [192]	TPP of IPS photoresin (from Nanoscribe) by fs-laser	2PP was used for optimization of master in polymeric hydrogel MN array production
2.5 Micro- and nanostructures for fluidic systems and analysis techniques	Transwell design for MIFE	Buchroithner et al. [203]	TPP of BisSR photoresist and laser ablation of PET by fs-laser	Response of HUVECs grown on modified membranes to calcium ionophore (A23187) measured by MIFE
	Microfluidic device with micro- and nanostructures inside for vWF detection	Buchegger et al. [207]	TPP and STED lithography of PETA-based photoresists by fs-laser and continuous wave laser	Study on the impact of vWF on the activation of thrombocytes with nanoanchors of about 65 nm x 120 nm
	Tools for multi-view microscopy of single cells	Vizsnyiczai et al. [204]	TPP of SU-8 2007 photoresist by fs-laser	Significant resolution improvement by image fusion

2.6 Sensors based on micro- and nanostructures for biomedical applications	Cancer cell detection	Erzina et al. [216]	LIPSS on SU-8 photoresist by UV ns-laser (KrF excimer laser)	100% accuracy in the discrimination of tumor and normal cell’s cultivation media
	Stretchable sensor for respiration monitoring	Koch and Dietzel [222, 227]	Subtractive direct writing (cutting) of polyimide foil with fs-laser	Stretchable sensor array for perfect adaption to complex 3D shapes
	e-nose for volatile organic compounds	Benetti et al. [225]	LIFT (XeCl 308 nm laser system) and MAPLE (ns-pulsed Nd:YAG laser system) of five different polymers onto substrate (fused silica with spin-coated triazene polymer)	Five volatile compounds can be detected based on SAW resonators in good agreement with theoretical sensitivities, usage at room temperature
2.7 Other applications	Biodegradable peripheral vascular stent	Chang et al. [256]	Subtractive direct writing (cutting) of PLA with fs-laser (1030 nm)	Postprocessing of 3D printed peripheral vascular stents for structural uniformity and dimensional precision, i.e., uniform structural widths, smooth edges, and accurate structural dimensions
	Surgical blade	Li et al. [260]	Self-organized surface structures on stainless steel 316L by long-pulse (µs) fiber-laser system (1070 nm)	Anti-adhesive biomimetic scales on blade for adhesion reduction of soft tissue by 16.5% on average

Table 31.3 Further development steps needed to make the methods of this chapter ready for the market

Definition of TRLs	Current status of methods from this chapter and of another exemplary chapter
TRL 1 – Basic principles observed	
TRL 2 – Technology concept formulated	
TRL 3 – Experimental proof of concept	Part of the methods from this chapter
TRL 4 – Technology validated in lab	Part of the methods from this chapter
TRL 5 – Technology validated in relevant environment (industrially relevant environment in the case of key enabling technologies)	
TRL 6 – Technology demonstrated in relevant environment (industrially relevant environment in the case of key enabling technologies)	
TRL 7 – System prototype demonstration in operational environment	
TRL 8 – System complete and qualified	
TRL 9 – Actual system proven in operational environment (competitive manufacturing in the case of key enabling technologies or in space)	Methods from Chap. 33

structure and fluid properties can limit the application of microneedles. TPP as well as DLW SM was also used in the fabrication of microfluidic channels, of analysis platforms, and of various sensors for biomedical applications. Examples of DLW SM are capillary channels capable of unidirectional liquid transport bio-inspired by spermathecae of fleas, by the integument of lizards, and by scent channels of bark bugs. Others are nanoanchors written by STED lithography which help to unravel the role of vWF in thrombocyte activation or tools written by 2PP which increase the resolution in imaging of single cells. On the other hand, also LIPSS are useful in these fields allowing the fabrication of SERS sensors which are employed for a wide range of applications such as the detection of cancer cell metabolites.

As trends in the field of biomedical applications, the authors identify the use of natural materials, laser processing of bio-inspired structures, as well as fast prototyping of personalized medical products. While other related fields presented in this book, especially the ones from Chap. 33, are used in practice with millions of treated patients, the methods presented in this chapter are in a preliminary stage. Using technology readiness levels (TRLs) (Table 31.3) as defined by the European Union[1], one would assign Chap. 33 a “TRL 9 – actual system proven in operational environment” compared to a “TRL 3 – experimental proof of concept” or “TRL 4 –

---

[1] Retrieved from https://ec.europa.eu/research/participants/data/ref/h2020/other/wp/2016_2017/annexes/h2020-wp1617-annex-g-trl_en.pdf on the 6th of December 2021.

technology validated in lab" for the methods of this chapter. The largest challenge for the commercial implementation of these methods, that is, for production of medical implants or medical products with functional surfaces, is probably the fact that medical implants and products face quite strict regulations and standards and that the approval of new concepts is connected with high costs. This applies already for the achievement of "TRL 5 – technology validated in relevant environment" and "TRL 6 – technology demonstrated in relevant environment," which means in many cases animal experiments or pre-clinical studies. This challenge may be balanced by the huge market volume of the related biomedical applications and their advantages compared to the currently applied technologies. Additionally, there is a strong "technology push" by the fact that ultrafast laser systems become rapidly better, that is, more user-friendly, cheaper, and faster.

Acknowledgments Some of the research presented here was performed within the projects BioCombs4nanofibers and LaserImplant. These projects have received funding from the European Union's Horizon 2020 research and innovation program under grant agreement No 862016 and No 95173, respectively. Furthermore, the research was funded in part by the Austrian Science Fund (FWF): T 1270-N in the course of the project "Functional Surfaces with Liquid Diode Characteristics."

References

1. K.M. Tanvir Ahmmed, C. Grambow, A.M. Kietzig, Fabrication of micro/nano structures on metals by femtosecond laser micromachining. Micromachines **5**, 1219–1253 (2014). https://doi.org/10.3390/mi5041219
2. A. Borowiec, H.K. Haugen, Subwavelength ripple formation on the surfaces of compound semiconductors irradiated with femtosecond laser pulses. Appl. Phys. Lett. **82**, 4462–4464 (2003). https://doi.org/10.1063/1.1586457
3. J. Bonse, S. Höhm, S.V. Kirner, A. Rosenfeld, J. Krüger, Laser-induced periodic surface structures – A scientific evergreen. IEEE J. Sel. Top. Quantum Electron. **23**, 9000615 (2017). https://doi.org/10.1007/978-3-319-69537-2_17-2
4. M. Barberoglou, D. Gray, E. Magoulakis, C. Fotakis, P.A. Loukakos, E. Stratakis, Controlling ripples' periodicity using temporally delayed femtosecond laser double pulses. Opt. Express **21**, 18501 (2013). https://doi.org/10.1364/oe.21.018501
5. E. Skoulas, A. Manousaki, C. Fotakis, E. Stratakis, Biomimetic surface structuring using cylindrical vector femtosecond laser beams. Sci. Rep. **7**, 45114 (2017). https://doi.org/10.1038/srep45114
6. G.D. Tsibidis, E. Skoulas, E. Stratakis, Ripple formation on nickel irradiated with radially polarized femtosecond beams. Opt. Lett. **40**, 5172 (2015). https://doi.org/10.1364/ol.40.005172
7. O.J. Allegre, W. Perrie, S.P. Edwardson, G. Dearden, K.G. Watkins, Laser microprocessing of steel with radially and azimuthally polarized femtosecond vortex pulses. J. Opt. (U. K.) **14**, 085601 (2012). https://doi.org/10.1088/2040-8978/14/8/085601
8. O.J. Allegre, Y. Jin, W. Perrie, J. Ouyang, E. Fearon, S.P. Edwardson, G. Dearden, Complete wavefront and polarization control for ultrashort-pulse laser microprocessing. Opt. Express **21**, 21198 (2013). https://doi.org/10.1364/oe.21.021198
9. J.M. Romano, R. Helbig, F. Fraggelakis, A. Garcia-Giron, C. Werner, R. Kling, S. Dimov, Springtail-inspired triangular laser-induced surface textures on metals using MHz ultrashort pulses. J. Micro Nano-Manuf. **7**, 024504 (2019). https://doi.org/10.1115/1.4043417

10. J.M. Romano, A. Garcia-Giron, P. Penchev, S. Dimov, Triangular laser-induced submicron textures for functionalising stainless steel surfaces. Appl. Surf. Sci. **440**, 162–169 (2018). https://doi.org/10.1016/j.apsusc.2018.01.086
11. U. Hermens, S.V. Kirner, C. Emonts, P. Comanns, E. Skoulas, A. Mimidis, H. Mescheder, K. Winands, J. Krüger, E. Stratakis, J. Bonse, Mimicking lizard-like surface structures upon ultrashort laser pulse irradiation of inorganic materials. Appl. Surf. Sci. **418**, 499–507 (2017). https://doi.org/10.1016/j.apsusc.2016.12.112
12. Y. Liu, S. Li, S. Niu, X. Cao, Z. Han, L. Ren, Bio-inspired micro-nano structured surface with structural color and anisotropic wettability on Cu substrate. Appl. Surf. Sci. **379**, 230–237 (2016). https://doi.org/10.1016/j.apsusc.2016.03.234
13. E. Rebollar, M. Castillejo, T.A. Ezquerra, Laser induced periodic surface structures on polymer films: From fundamentals to applications. Eur. Polym. J. **73**, 162–174 (2015). https://doi.org/10.1016/j.eurpolymj.2015.10.012
14. R.A. Barb, C. Hrelescu, L. Dong, J. Heitz, J. Siegel, P. Slepicka, V. Vosmanska, V. Svorcik, B. Magnus, R. Marksteiner, M. Schernthaner, K. Groschner, Laser-induced periodic surface structures on polymers for formation of gold nanowires and activation of human cells. Appl. Phys. A Mater. Sci. Process. **117**, 295–300 (2014). https://doi.org/10.1007/s00339-013-8219-9
15. J. Heitz, B. Reisinger, S. Yakunin, N. Voelcker, Q. Peng, A.L. Hook, C. Romanin, M. Fahrner, Laser-induced micro- and nanostructures at polymer surfaces for applications in cell biology, in *Int. Conf. Transparent Opt. Networks*, (2011), pp. 2–5. https://doi.org/10.1109/ICTON.2011.5970989
16. J. Heitz, B. Reisinger, M. Fahrner, C. Romanin, J. Siegel, V. Svorcik, Laser-induced periodic surface structures (LIPSS) on polymer, in *2012 14th Int. Conf. Transparent Opt. Networks*, (2012), pp. 1–4. https://doi.org/10.1109/ICTON.2012.6253723
17. S. Höhm, A. Rosenfeld, J. Krüger, J. Bonse, Femtosecond diffraction dynamics of laser-induced periodic surface structures on fused silica. Appl. Phys. Lett. **102**, 054102 (2013). https://doi.org/10.1063/1.4790284
18. B.K. Nayak, M.C. Gupta, Ultrafast laser-induced self-organized conical micro/nano surface structures and their origin. Opt. Lasers Eng. **48**, 966–973 (2010). https://doi.org/10.1016/j.optlaseng.2010.05.009
19. D. Dufft, A. Rosenfeld, S.K. Das, R. Grunwald, J. Bonse, Femtosecond laser-induced periodic surface structures revisited: A comparative study on ZnO. J. Appl. Phys. **105**, 034908 (2009). https://doi.org/10.1063/1.3074106
20. V. Zorba, E. Stratakis, M. Barberoglou, E. Spanakis, P. Tzanetakis, S.H. Anastasiadis, C. Fotakis, Biomimetic artificial surfaces quantitatively reproduce the water repellency of a lotus leaf. Adv. Mater. **20**, 4049–4054 (2008). https://doi.org/10.1002/adma.200800651
21. T.H. Her, R.J. Finlay, C. Wu, S. Deliwala, E. Mazur, Microstructuring of silicon with femtosecond laser pulses. Appl. Phys. Lett. **73**, 1673–1675 (1998). https://doi.org/10.1063/1.122241
22. X. Wang, C. Li, W. Hong, C. Ma, Y. Xing, J. Feng, Fabrication of ordered hierarchical structures on stainless steel by picosecond laser for modified wettability applications. Opt. Express **26**, 18998 (2018). https://doi.org/10.1364/oe.26.018998
23. M. Martínez-Calderon, A. Rodríguez, A. Dias-Ponte, M.C. Morant-Miñana, M. Gómez-Aranzadi, S.M. Olaizola, Femtosecond laser fabrication of highly hydrophobic stainless steel surface with hierarchical structures fabricated by combining ordered microstructures and LIPSS. Appl. Surf. Sci. **374**, 81–89 (2016). https://doi.org/10.1016/j.apsusc.2015.09.261
24. D.W. Bäuerle, *Laser Processing and Chemistry* (Springer, Berlin Heidelberg, 2011)
25. J. Heitz, C. Plamadeala, M. Muck, O. Armbruster, W. Baumgartner, A. Weth, C. Steinwender, H. Blessberger, J. Kellermair, S.V. Kirner, J. Krüger, J. Bonse, A.S. Guntner, A.W. Hassel, Femtosecond laser-induced microstructures on Ti substrates for reduced cell adhesion. Appl. Phys. A Mater. Sci. Process. **123**, 734 (2017). https://doi.org/10.1007/s00339-017-1352-0
26. A.Y. Vorobyev, C. Guo, Femtosecond laser structuring of titanium implants. Appl. Surf. Sci. **253**, 7272–7280 (2007). https://doi.org/10.1016/j.apsusc.2007.03.006

27. P. Shukla, D.G. Waugh, J. Lawrence, R. Vilar, Laser surface structuring of ceramics, metals and polymers for biomedical applications: A review, in *Laser Surface Modification of Biomaterials: Techniques and Applications*, (Elsevier Ltd, San Diego, 2016), pp. 281–299
28. A. Riveiro, A.L.B. Maçon, J. del Val, R. Comesaña, J. Pou, Laser surface texturing of polymers for biomedical applications. Front. Phys. **6**, 16 (2018). https://doi.org/10.3389/fphy.2018.00016
29. A.Y. Fasasi, S. Mwenifumbo, N. Rahbar, J. Chen, M. Li, A.C. Beye, C.B. Arnold, W.O. Soboyejo, Nano-second UV laser processed micro-grooves on Ti6Al4V for biomedical applications. Mater. Sci. Eng. C **29**, 5–13 (2009). https://doi.org/10.1016/j.msec.2008.05.002
30. M.P. Fiorucci, A.J. López, A. Ramil, Surface modification of Ti6Al4V by nanosecond laser ablation for biomedical applications. J. Phys. Conf. Ser. **605**, 012022 (2015). https://doi.org/10.1088/1742-6596/605/1/012022
31. E. Stratakis, J. Bonse, J. Heitz, J. Siegel, G.D. Tsibidis, E. Skoulas, A. Papadopoulos, A. Mimidis, A.C. Joel, P. Comanns, J. Krüger, C. Florian, Y. Fuentes-Edfuf, J. Solis, W. Baumgartner, Laser engineering of biomimetic surfaces. Mater. Sci. Eng. R Rep. **141**, 100562 (2020). https://doi.org/10.1016/j.mser.2020.100562
32. J. Stampfl, R. Liska, A. Ovsianikov, *Multiphoton Lithography* (Wiley-VCH Verlag GmbH & Co., Weinheim, Germany, 2016)
33. S. Maruo, O. Nakamura, S. Kawata, Three-dimensional microfabrication with two-photon-absorbed photopolymerization. Opt. Lett. **22**, 132–134 (1997)
34. K. König, A. Ostendorf, *Optically Induced Nanostructures: Biomedical and Technical Applications* (De Gruyter, Berlin, 2015)
35. C. Liao, A. Wuethrich, M. Trau, A material odyssey for 3D nano/microstructures: Two photon polymerization based nanolithography in bioapplications. Appl. Mater. Today **19**, 100635 (2020). https://doi.org/10.1016/j.apmt.2020.100635
36. T. Baldacchini, *Three-Dimensional Microfabrication Using Two-Photon Polymerization: Fundamentals, Technology, and Applications* (William Andrew, Oxford, UK, 2015)
37. X. Wang, Z. Wei, C.Z. Baysah, M. Zheng, J. Xing, Biomaterial-based microstructures fabricated by two-photon polymerization microfabrication technology. RSC Adv. **9**, 34472–34480 (2019). https://doi.org/10.1039/c9ra05645a
38. G. Weisgrab, O. Guillaume, Z. Guo, P. Heimel, P. Slezak, A. Poot, D. Grijpma, A. Ovsianikov, 3D printing of large-scale and highly porous biodegradable tissue engineering scaffolds from poly(trimethylene-carbonate) using two-photon-polymerization. Biofabrication **12**, 045036 (2020). https://doi.org/10.1088/1758-5090/abb539
39. A. Daskalova, L. Angelova, A. Carvalho, A. Trifonov, C. Nathala, F. Monteiro, I. Buchvarov, Effect of surface modification by femtosecond laser on zirconia based ceramics for screening of cell-surface interaction. Appl. Surf. Sci. **513**, 145914 (2020). https://doi.org/10.1016/j.apsusc.2020.145914
40. S. Marimuthu, S. Pathak, J. Radhakrishnan, A.M. Kamara, In-process monitoring of laser surface modification. Coatings **11**, 886 (2021). https://doi.org/10.3390/coatings11080886
41. Z.C. Chen, T.L. Chang, C.C. Liu, W.T. Hsiao, C.H. Huang, Picosecond laser surface modification of aluminum oxide with fish-scale structures for cell culture. Ceram. Int. **46**, 17651–17658 (2020). https://doi.org/10.1016/j.ceramint.2020.04.067
42. A.K. Nath, Chapter 9.06 - laser Drilling of Metallic and Nonmetallic Substrates, in *Comprehensive Materials Processing*, ed. by S. Hashmi, G. F. Batalha, C. J. Van Tyne, B. Yilbas, (Elsevier Ltd., New York, USA, 2014), pp. 115–175. https://doi.org/10.1016/B978-0-08-096532-1.00904-3
43. I. Miyamoto, H. Maruo, Mechanism of laser cutting. Weld. World, Le Soudage Dans Le Monde **29**, 283–294 (1991). https://doi.org/10.22486/iwj.v25i2.148338
44. I. Miyamoto, K. Cvecek, M. Schmidt, Advances of laser welding technology of glass - science and technology. J. Laser Micro Nanoeng. **15**, 63–76 (2020). https://doi.org/10.2961/jlmn.2020.02.1001
45. M. Malinauskas, L. Lukoševičius, D. Mackevičiūtė, E. Balčiūnas, S. Rekštytė, D. Paipulas, Multiscale 3D manufacturing: Combining thermal extrusion printing with additive and

subtractive direct laser writing. Laser Sources Appl. II **9135**, 91350T (2014). https://doi.org/10.1117/12.2051520

46. L. D'Alessio, R. Teghil, M. Zaccagnino, I. Zaccardo, D. Ferro, V. Marotta, Pulsed laser ablation and deposition of bioactive glass as coating material for biomedical applications. Appl. Surf. Sci. **138–139**, 527–532 (1999). https://doi.org/10.1016/S0169-4332(98)00610-2
47. H.-U. Krebs, M. Weisheit, J. Faupel, E. Süske, T. Scharf, C. Fuhse, M. Störmer, K. Sturm, M. Seibt, H. Kijewski, D. Nelke, E. Panchenko, M. Buback, Pulsed laser deposition (PLD)-a versatile thin film technique, in *Advances in Solid State Physics*, (Springer, Berlin, Heidelberg, 2003), pp. 505–518
48. A. Piqué, The matrix-assisted pulsed laser evaporation (MAPLE) process: Origins and future directions. Appl. Phys. A Mater. Sci. Process. **105**, 517–528 (2011). https://doi.org/10.1007/s00339-011-6594-7
49. A. Bigi, B. Bracci, F. Cuisinier, R. Elkaim, M. Fini, I. Mayer, I.N. Mihailescu, G. Socol, L. Sturba, P. Torricelli, Human osteoblast response to pulsed laser deposited calcium phosphate coatings. Biomaterials **26**, 2381–2389 (2005). https://doi.org/10.1016/j.biomaterials.2004.07.057
50. I.N. Zavestovskaya, Laser nanostructuring of materials surfaces. Quantum Electron. **40**, 942–954 (2010). https://doi.org/10.1070/qe2010v040n11abeh014447
51. A. Kurella, N.B. Dahotre, Review paper: Surface modification for bioimplants: The role of laser surface engineering. J. Biomater. Appl. **20**, 5–50 (2005). https://doi.org/10.1177/0885328205052974
52. C.F. Koch, S. Johnson, D. Kumar, M. Jelinek, D.B. Chrisey, A. Doraiswamy, C. Jin, R.J. Narayan, I.N. Mihailescu, Pulsed laser deposition of hydroxyapatite thin films. Mater. Sci. Eng. C **27**, 484–494 (2007). https://doi.org/10.1016/j.msec.2006.05.025
53. A. Piqué, D.B. Chrisey, B.J. Spargo, M.A. Bucaro, R.W. Vachet, J.H. Callahan, R.A. McGill, D. Leonhardt, T.E. Mlsna, Use of matrix assisted pulsed laser evaporation (MAPLE) for the growth of organic thin films. MRS Online Proc. Libr. Arch. **526**, 421–426 (1998). https://doi.org/10.1557/PROC-526-421
54. K.B. Shepard, R.D. Priestley, MAPLE deposition of macromolecules. Macromol. Chem. Phys. **214**, 862–872 (2013). https://doi.org/10.1002/macp.201200621
55. F. Sima, P. Davidson, E. Pauthe, L.E. Sima, O. Gallet, I.N. Mihailescu, K. Anselme, Fibronectin layers by matrix-assisted pulsed laser evaporation from saline buffer-based cryogenic targets. Acta Biomater. **7**, 3780–3788 (2011). https://doi.org/10.1016/j.actbio.2011.06.016
56. C. Constantinescu, A. Palla-Papavlu, A. Rotaru, P. Florian, F. Chelu, M. Icriverzi, A. Nedelcea, V. Dinca, A. Roseanu, M. Dinescu, Multifunctional thin films of lactoferrin for biochemical use deposited by MAPLE technique. Appl. Surf. Sci. **255**, 5491–5495 (2009). https://doi.org/10.1016/j.apsusc.2008.07.163
57. I.A. Paun, A. Moldovan, C.R. Luculescu, M. Dinescu, Biocompatible polymeric implants for controlled drug delivery produced by MAPLE. Appl. Surf. Sci. **257**, 10780–10788 (2011). https://doi.org/10.1016/j.apsusc.2011.07.097
58. V. Dinca, C. Viespe, S. Brajnicov, I. Constantinoiu, A. Moldovan, A. Bonciu, C.N. Toader, R.E. Ginghina, N. Grigoriu, M. Dinescu, N.D. Scarisoreanu, MAPLE assembled acetylcholinesterase– Polyethylenimine hybrid and multilayered interfaces for toxic gases detection. Sensors (Switzerland) **18**, 4265 (2018). https://doi.org/10.3390/s18124265
59. I.A. Paun, A.M. Acasandrei, C.R. Luculescu, C.C. Mustaciosu, V. Ion, M. Mihailescu, E. Vasile, M. Dinescu, MAPLE deposition of polypyrrole-based composite layers for bone regeneration. Appl. Surf. Sci. **357**, 975–984 (2015). https://doi.org/10.1016/j.apsusc.2015.09.083
60. A. Pérez Del Pino, P. Serra, J.L. Morenza, Oxidation of titanium through Nd:YAG laser irradiation. Appl. Surf. Sci. 197–198, 887–890 (2002). https://doi.org/10.1016/S0169-4332(02)00447-6
61. M.T. Mohammed, Z.A. Khan, A.N. Siddiquee, Surface modifications of titanium materials for developing corrosion behavior in human body environment: A review. Procedia Mater. Sci. **6**, 1610–1618 (2014). https://doi.org/10.1016/j.mspro.2014.07.144

62. F.J.C. Braga, R.F.C. Marques, E.d.A. Filho, A.C. Guastaldi, Surface modification of Ti dental implants by Nd:YVO 4 laser irradiation. Appl. Surf. Sci. **253**, 9203–9208 (2007). https://doi.org/10.1016/j.apsusc.2007.05.048
63. S.A. Lone, M. Muck, P. Fosodeder, C.C. Mardare, C. Florian, A. Weth, J. Krüger, C. Steinwender, W. Baumgartner, J. Bonse, J. Heitz, A.W. Hassel, Impact of femtosecond laser treatment accompanied with anodization of titanium alloy on fibroblast cell growth. Phys. Status Solidi Appl. Mater. Sci. **217**, 1900838 (2020). https://doi.org/10.1002/pssa.201900838
64. M.V. Diamanti, B. del Curto, M. Pedeferri, Anodic oxidation of titanium: From technical aspects to biomedical applications. J. Appl. Biomater. Biomech. **9**, 55–69 (2011). https://doi.org/10.5301/JABB.2011.7429
65. O. Nedela, P. Slepicka, V. Švorcík, Surface modification of polymer substrates for biomedical applications. Materials (Basel). **10**, 1115 (2017). https://doi.org/10.3390/ma10101115
66. T. Gumpenberger, J. Heitz, D. Bäuerle, H. Kahr, I. Graz, C. Romanin, V. Svorcik, F. Leisch, Adhesion and proliferation of human endothelial cells on photochemically modified polytetrafluoroethylene. Biomaterials **24**, 5139–5144 (2003). https://doi.org/10.1016/S0142-9612(03)00460-5
67. J. Heitz, M. Olbrich, S. Moritz, C. Romanin, V. Svorcik, D. Bäuerle, Surface modification of polmers by UV-irradition: Applications in micro-and biotechnology. Lasers Appl. **59581U** (2005). https://doi.org/10.1117/12.620816
68. H. Watanabe, T. Takata, M. Tsuge, Polymer surface modification due to excimer laser radiation—Chemical and physical changes in the surface structure of poly(ethylene terephthalate). Polym. Int. **31**, 247–254 (1993). https://doi.org/10.1002/pi.4990310306
69. W. Wong, K. Chan, K.W. Yeung, K.S. Lau, Chemical surface modification of poly (ethylene terephthalate) by excimer irradiation of high and low intensities. Mater. Res. Innov. **4**, 344–349 (2001). https://doi.org/10.1007/s100190000116
70. A.M. Richter, G. Buchberger, D. Stifter, J. Duchoslav, A. Hertwig, J. Bonse, J. Heitz, K. Schwibbert, Spatial period of laser-induced surface nanoripples on PET determines Escherichia coli repellence. Nanomaterials **11**, 3000 (2021). https://doi.org/10.3390/nano11113000
71. J. Heitz, M. Muck, J. Vujovic, W. Baumgartner, A.W. Hassel, S.A. Lone, B. Steinhauser, C. Hrelescu, T.A. Klar, G. Buchberger, A. Weth, D. Baiko, Laser-induced periodic surface structures (LIPSS) for biomedical and sensing applications, in *Int. Conf. Transparent Opt. Networks*, 8–11 July 2020 (2020). https://doi.org/10.1109/ICTON51198.2020.9203402
72. A. Ranella, M. Barberoglou, S. Bakogianni, C. Fotakis, E. Stratakis, Tuning cell adhesion by controlling the roughness and wettability of 3D micro/nano silicon structures. Acta Biomater. **6**, 2711–2720 (2010). https://doi.org/10.1016/j.actbio.2010.01.016
73. S. Yakunin, M. Fahrner, B. Reisinger, H. Itani, C. Romanin, J. Heitz, Laser microstructuring of photomodified fluorinated ethylene propylene surface for confined growth of Chinese hamster ovary cells and single cell isolation. J. Biomed. Mater. Res. – Part B Appl. Biomater. **100**, 170–176 (2012). https://doi.org/10.1002/jbm.b.31935
74. S. Schlie, E. Fadeeva, J. Koch, A. Ngezahayo, B.N. Chichkov, Femtosecond laser fabricated spike structures for selective control of cellular behavior. J. Biomater. Appl. **25**, 217–233 (2010). https://doi.org/10.1177/0885328209345553
75. A.I. Teixeira, P.F. Nealey, C.J. Murphy, Responses of human keratocytes to micro- and nanostructured substrates. J. Biomed. Mater. Res. – Part A **71**, 369–376 (2004). https://doi.org/10.1002/jbm.a.30089
76. C. Xu, F. Yang, S. Wang, S. Ramakrishna, In vitro study of human vascular endothelial cell function on materials with various surface roughness. J. Biomed. Mater. Res. – Part A **71**, 154–161 (2004). https://doi.org/10.1002/jbm.a.30143
77. C.S. Ranucci, P.V. Moghe, Substrate microtopography can enhance cell adhesive and migratory responsiveness to matrix ligand density. J. Biomed. Mater. Res. **54**, 149–161 (2001). https://doi.org/10.1002/1097-4636(200102)54:2<149::AID-JBM1>3.0.CO;2-O
78. Y. Wan, Y. Wang, Z. Liu, X. Qu, B. Han, J. Bei, S. Wang, Adhesion and proliferation of OCT-1 osteoblast-like cells on micro- and nano-scale topography structured poly(L-lactide). Biomaterials **26**, 4453–4459 (2005). https://doi.org/10.1016/j.biomaterials.2004.11.016

79. A.I. Teixeira, G.A. McKie, J.D. Foley, P.J. Bertics, P.F. Nealey, C.J. Murphy, The effect of environmental factors on the response of human corneal epithelial cells to nanoscale substrate topography. Biomaterials **27**, 3945–3954 (2006). https://doi.org/10.1016/j.biomaterials.2006.01.044
80. A.C. Duncan, F. Rouais, S. Lazare, L. Bordenave, C. Baquey, Effect of laser modified surface microtopochemistry on endothelial cell growth. Colloids Surf. B Biointerfaces **54**, 150–159 (2007). https://doi.org/10.1016/j.colsurfb.2006.09.013
81. M. Arnold, E.A. Cavalcanti-Adam, R. Glass, J. Blümmel, W. Eck, M. Kantlehner, H. Kessler, J.P. Spatz, Activation of integrin function by nanopatterned adhesive interfaces. ChemPhysChem **5**, 383–388 (2004). https://doi.org/10.1002/cphc.200301014
82. A. Thapa, T.J. Webster, K.M. Haberstroh, Polymers with nano-dimensional surface features enhance bladder smooth muscle cell adhesion. J. Biomed. Mater. Res. – Part A **67**, 1374–1383 (2003). https://doi.org/10.1002/jbm.a.20037
83. D.J.S. Hulmes, Building collagen molecules, fibrils, and suprafibrillar structures. J. Struct. Biol. **137**, 2–10 (2002). https://doi.org/10.1006/jsbi.2002.4450
84. K. Anselme, Osteoblast adhesion on biomaterials. Biomaterials **21**, 667–681 (2000). https://doi.org/10.1016/S0142-9612(99)00242-2
85. B. Kasemo, Biological surface science. Surf. Sci. **500**, 656–677 (2002)
86. D.A. Puleo, A. Nanci, Understanding and controlling the bone-implant interface. Biomaterials **20**, 2311–2321 (1999)
87. C.J. Wilson, R.E. Clegg, D.I. Leavesley, M.J. Pearcy, Mediation of biomaterial-cell interactions by adsorbed proteins: A review. Tissue Eng. **11**, 1–18 (2005). https://doi.org/10.1089/ten.2005.11.1
88. P. Roach, D. Eglin, K. Rohde, C.C. Perry, Modern biomaterials: A review – Bulk properties and implications of surface modifications. J. Mater. Sci. Mater. Med. **18**, 1263–1277 (2007). https://doi.org/10.1007/s10856-006-0064-3
89. B. Kasemo, J. Gold, Implant surfaces and interface processes. Adv. Dent. Res. **13**, 8–20 (1999). https://doi.org/10.1177/08959374990130011901
90. K. Rechendorff, M.B. Hovgaard, M. Foss, V.P. Zhdanov, F. Besenbacher, Enhancement of protein adsorption induced by surface roughness. Langmuir **22**, 10885–10888 (2006). https://doi.org/10.1021/la0621923
91. M.B. Hovgaard, K. Rechendorff, J. Chevallier, M. Foss, F. Besenbacher, Fibronectin adsorption on tantalum: The influence of nanoroughness. J. Phys. Chem. B **112**, 8241–8249 (2008). https://doi.org/10.1021/jp801103n
92. F.A. Denis, P. Hanarp, D.S. Sutherland, J. Gold, C. Mustin, P.G. Rouxhet, Y.F. Dufrêne, Protein adsorption on model surfaces with controlled nanotopography and chemistry. Langmuir **18**, 819–828 (2002). https://doi.org/10.1021/la011011o
93. L. Richert, F. Variola, F. Rosei, J.D. Wuest, A. Nanci, Adsorption of proteins on nanoporous Ti surfaces. Surf. Sci. **604**, 1445–1451 (2010). https://doi.org/10.1016/j.susc.2010.05.007
94. T. Peterbauer, S. Yakunin, J. Siegel, S. Hering, M. Fahrner, C. Romanin, J. Heitz, Dynamics of spreading and alignment of cells cultured in vitro on a grooved polymer surface. J. Nanomater. **2011**, 413079 (2011). https://doi.org/10.1155/2011/413079
95. B. Zhu, Q. Lu, J. Yin, J. Hu, Z. Wang, Effects of laser-modified polystyrene substrate on CHO cell growth and alignment. J. Biomed. Mater. Res. – Part B Appl. Biomater. **70**, 43–48 (2004). https://doi.org/10.1002/jbm.b.30011
96. W. Xuefeng, C. André Ohlin, Q. Lu, J. Hu, Influence of physicochemical properties of laser-modified polystyrene on bovine serum albumin adsorption and rat C6 glioma cell behavior. J. Biomed. Mater. Res. Part A. **79**, 963–973 (2006). https://doi.org/10.1002/jbm.a
97. B. Zhu, Q. Zhang, Q. Lu, Y. Xu, J. Yin, J. Hu, Z. Wang, Nanotopographical guidance of C6 glioma cell alignment and oriented growth. Biomaterials **25**, 4215–4223 (2004). https://doi.org/10.1016/j.biomaterials.2003.11.020
98. E. Arenholz, J. Heitz, M. Himmelbauer, D. Bäuerle, Laser-enhanced adhesion and thin film formation, in *ALT'95 International Symposium on Advanced Materials for Optics and Optoelectronics*, (1996), pp. 90–97

99. S. Lazare, P. Benet, Surface amorphization of Mylar(R) films with the excimer laser radiation above and below ablation threshold: Ellipsometric measurements. J. Appl. Phys. **74**, 4953–4957 (1993). https://doi.org/10.1063/1.354333
100. E. Rebollar, I. Frischauf, M. Olbrich, T. Peterbauer, S. Hering, J. Preiner, P. Hinterdorfer, C. Romanin, J. Heitz, Proliferation of aligned mammalian cells on laser-nanostructured polystyrene. Biomaterials **29**, 1796–1806 (2008). https://doi.org/10.1016/j.biomaterials.2007.12.039
101. M. Schernthaner, B. Reisinger, H. Wolinski, S.D. Kohlwein, A. Trantina-Yates, M. Fahrner, C. Romanin, H. Itani, D. Stifter, G. Leitinger, K. Groschner, J. Heitz, Nanopatterned polymer substrates promote endothelial proliferation by initiation of β-catenin transcriptional signaling. Acta Biomater. **8**, 2953–2962 (2012). https://doi.org/10.1016/j.actbio.2012.04.018
102. B.T. MacDonald, K. Tamai, X. He, Wnt/β-catenin signaling: Components, mechanisms, and diseases. Dev. Cell **17**, 9–26 (2009). https://doi.org/10.1016/j.devcel.2009.06.016
103. T.P. Rao, M. Kühl, An updated overview on wnt signaling pathways: A prelude for more. Circ. Res. **106**, 1798–1806 (2010). https://doi.org/10.1161/CIRCRESAHA.110.219840
104. M. Schernthaner, G. Leitinger, H. Wolinski, S.D. Kohlwein, B. Reisinger, R.A. Barb, W.F. Graier, J. Heitz, K. Groschner, Enhanced Ca2+ entry and tyrosine phosphorylation mediate nanostructure-induced endothelial proliferation. J. Nanomater. **2013**, 251063 (2013). https://doi.org/10.1155/2013/251063
105. B. Reisinger, M. Fahrner, I. Frischauf, S. Yakunin, V. Svorcik, H. Fiedorowicz, A. Bartnik, C. Romanin, J. Heitz, EUV micropatterning for biocompatibility control of PET. Appl. Phys. A: Mater. Sci. Process. **100**, 511–516 (2010). https://doi.org/10.1007/s00339-010-5845-3
106. A. Bartnik, H. Fiedorowicz, R. Jarocki, J. Kostecki, A. Szczurek, M. Szczurek, Ablation and surface modifications of PMMA using a laser-plasma EUV source. Appl. Phys. B Lasers Opt. **96**, 727–730 (2009). https://doi.org/10.1007/s00340-009-3692-8
107. A. Bartnik, H. Fiedorowicz, R. Jarocki, J. Kostecki, R. Rakowski, A. Szczurek, M. Szczurek, Micro-and nanoprocessing of polymers using a laser plasma extreme ultraviolet source. Acta Phys. Pol. A. **117**, 384–390 (2010). https://doi.org/10.12693/APhysPolA.117.384
108. M.N. Calmels, I. Saliba, G. Wanna, N. Cochard, J. Fillaux, O. Deguine, B. Fraysse, Speech perception and speech intelligibility in children after cochlear implantation. Int. J. Pediatr. Otorhinolaryngol. **68**, 347–351 (2004). https://doi.org/10.1016/j.ijporl.2003.11.006
109. J. Murphy, G. O'Donoghue, Bilateral cochlear implantation: An evidence-based medicine evaluation. Laryngoscope **117**, 1412–1418 (2007). https://doi.org/10.1097/MLG.0b013e318068b594
110. S.C. Peng, J.B. Tomblin, C.W. Turner, Production and perception of speech intonation in pediatric cochlear implant recipients and individuals with normal hearing. Ear Hear. **29**, 336–351 (2008). https://doi.org/10.1097/AUD.0b013e318168d94d
111. J. Xu, R.K. Shepherd, R.E. Millard, G.M. Clark, Chronic electrical stimulation of the auditory nerve at high stimulus rates: A physiological and histopathological study. Hear. Res. **105**, 1–29 (1997). https://doi.org/10.1016/S0378-5955(96)00193-1
112. C. Newbold, R. Richardson, R. Millard, C. Huang, D. Milojevic, R. Shepherd, R. Cowan, Changes in biphasic electrode impedance with protein adsorption and cell growth. J. Neural Eng. **7**, 056011 (2010). https://doi.org/10.1088/1741-2560/7/5/056011
113. U. Reich, E. Fadeeva, A. Warnecke, G. Paasche, P. Müller, B. Chichkov, T. Stöver, T. Lenarz, G. Reuter, Directing neuronal cell growth on implant material surfaces by microstructuring. J. Biomed. Mater. Res. – Part B Appl. Biomater. **100**(B), 940–947 (2012). https://doi.org/10.1002/jbm.b.32656
114. A. Klos, X. Sedao, T.E. Itina, C. Helfenstein-Didier, C. Donnet, S. Peyroche, L. Vico, A. Guignandon, V. Dumas, Ultrafast laser processing of nanostructured patterns for the control of cell adhesion and migration on titanium alloy. Nanomaterials **10**, 864 (2020). https://doi.org/10.3390/nano10050864
115. C. Steinwender, S. Hönig, K. Salch, J. Kammler, H. Blessberger, S. Schwarz, A. Nahler, V. Gammer, M. Grund, A. Kypta, First-in-man experience with a minimally invasive transcatheter pacemaker. Wien. Klin. Wochenschr. **126**, 78 (2014)

116. M. Muck, B. Wolfsjäger, K. Seibert, C. Maier, S.A. Lone, A.W. Hassel, W. Baumgartner, J. Heitz, Femtosecond laser-processing of pre-anodized Ti-based bone implants for cell-repellent functionalization. Nanomaterials **11**, 1342 (2021). https://doi.org/10.3390/nano11051342
117. A. Kypta, H. Blessberger, J. Kammler, M. Lichtenauer, T. Lambert, R. Silye, C. Steinwender, First autopsy description of changes 1 year after implantation of a leadless cardiac pacemaker: Unexpected ingrowth and severe chronic inflammation. Can. J. Cardiol. **32**, 1578.E1–1578.E2 (2016). https://doi.org/10.1016/j.cjca.2015.12.028
118. P. Qi, M.F. Maitz, N. Huang, Surface modification of cardiovascular materials and implants. Surf. Coat. Technol. **233**, 80–90 (2013). https://doi.org/10.1016/j.surfcoat.2013.02.008
119. P. Fosodeder, W. Baumgartner, C. Steinwender, A.W. Hassel, C. Florian, J. Bonse, J. Heitz, Repellent rings at titanium cylinders against overgrowth by fibroblasts. Adv. Opt. Technol. **9**, 113–120 (2020). https://doi.org/10.1515/aot-2019-0070
120. X. Liu, P.K. Chu, C. Ding, Surface modification of titanium, titanium alloys, and related materials for biomedical applications. Mater. Sci. Eng. R Rep. **47**, 49–121 (2004). https://doi.org/10.1016/j.mser.2004.11.001
121. V. Dumas, A. Guignandon, L. Vico, C. Mauclair, X. Zapata, M.T. Linossier, W. Bouleftour, J. Granier, S. Peyroche, J.C. Dumas, H. Zahouani, A. Rattner, Femtosecond laser nano/micro patterning of titanium influences mesenchymal stem cell adhesion and commitment. Biomed. Mater. **10**, 055002 (2015). https://doi.org/10.1088/1748-6041/10/5/055002
122. J.P. Kollender, A.I. Mardare, A.W. Hassel, Direct observation of metal dissolution during anodization of niobium. Electrochem. Commun. **74**, 5–8 (2017). https://doi.org/10.1016/j.elecom.2016.11.011
123. A.I. Mardare, C.D. Grill, I. Pötzelberger, T. Etzelstorfer, J. Stangl, A.W. Hassel, Anodic oxide formation on aluminium-terbium alloys. J. Solid State Electrochem. **20**, 1673–1681 (2016). https://doi.org/10.1007/s10008-016-3139-1
124. K.O. Böker, F. Kleinwort, J.H. Klein-Wiele, P. Simon, K. Jäckle, S. Taheri, W. Lehmann, A.F. Schilling, Laser ablated periodic nanostructures on titanium and steel implants influence adhesion and osteogenic differentiation of mesenchymal stem cells. Materials (Basel). **13**, 3526 (2020). https://doi.org/10.3390/MA13163526
125. M.J. Dalby, N. Gadegaard, R. Tare, A. Andar, M.O. Riehle, P. Herzyk, C.D.W. Wilkinson, R.O.C. Oreffo, The control of human mesenchymal cell differentiation using nanoscale symmetry and disorder. Nat. Mater. **6**, 997–1003 (2007). https://doi.org/10.1038/nmat2013
126. G. Romanos, F. Javed, et al., Peri-implant diseases: A review of treatment interventions. Dent. Clin. N. Am. **59**, 157–178 (2015). https://doi.org/10.1016/j.cden.2014.08.002
127. M.S. Tonetti, Risk factors for osseodisintegration. Periodontol. 2000 **17**, 55–62 (1998). https://doi.org/10.1111/j.1600-0757.1998.tb00123.x
128. S. Ferraris, S. Spriano, Antibacterial titanium surfaces for medical implants. Mater. Sci. Eng. C **61**, 965–978 (2016). https://doi.org/10.1016/j.msec.2015.12.062
129. J. Hasan, H.K. Webb, V.K. Truong, S. Pogodin, V.A. Baulin, G.S. Watson, J.A. Watson, R.J. Crawford, E.P. Ivanova, Selective bactericidal activity of nanopatterned superhydrophobic cicada Psaltoda claripennis wing surfaces. Appl. Microbiol. Biotechnol. **97**, 9257–9262 (2013). https://doi.org/10.1007/s00253-012-4628-5
130. S. Pogodin, J. Hasan, V.A. Baulin, H.K. Webb, V.K. Truong, T.H. Phong Nguyen, V. Boshkovikj, C.J. Fluke, G.S. Watson, J.A. Watson, R.J. Crawford, E.P. Ivanova, Biophysical model of bacterial cell interactions with nanopatterned cicada wing surfaces. Biophys. J. **104**, 835–840 (2013). https://doi.org/10.1016/j.bpj.2012.12.046
131. C.D. Bandara, S. Singh, I.O. Afara, A. Wolff, T. Tesfamichael, K. Ostrikov, A. Oloyede, Bactericidal effects of natural nanotopography of dragonfly wing on Escherichia coli. ACS Appl. Mater. Interfaces **9**, 6746–6760 (2017). https://doi.org/10.1021/acsami.6b13666
132. A. Jaggessar, H. Shahali, A. Mathew, P.K.D.V. Yarlagadda, Bio-mimicking nano and micro-structured surface fabrication for antibacterial properties in medical implants. J. Nanobiotechnol. **15**, 64 (2017). https://doi.org/10.1186/s12951-017-0306-1

133. X. Luo, S. Yao, H. Zhang, M. Cai, W. Liu, R. Pan, C. Chen, X. Wang, L. Wang, M. Zhong, Biocompatible nano-ripples structured surfaces induced by femtosecond laser to rebel bacterial colonization and biofilm formation. Opt. Laser Technol. **124**, 105973 (2020). https://doi.org/10.1016/j.optlastec.2019.105973
134. D. Campoccia, L. Montanaro, C.R. Arciola, A review of the biomaterials technologies for infection-resistant surfaces. Biomaterials **34**, 8533–8554 (2013). https://doi.org/10.1016/j.biomaterials.2013.07.089
135. A. Tripathy, P. Sen, B. Su, W.H. Briscoe, Natural and bioinspired nanostructured bactericidal surfaces. Adv. Colloid Interface Sci. **248**, 85–104 (2017). https://doi.org/10.1016/j.cis.2017.07.030
136. T. Diu, N. Faruqui, T. Sjöström, B. Lamarre, H.F. Jenkinson, B. Su, M.G. Ryadnov, Cicada-inspired cell-instructive nanopatterned arrays. Sci. Rep. **4**, 7122 (2014). https://doi.org/10.1038/srep07122
137. F. Hizal, I. Zhuk, S. Sukhishvili, H.J. Busscher, H.C. Van Der Mei, C.H. Choi, Impact of 3D hierarchical nanostructures on the antibacterial efficacy of a bacteria-triggered self-defensive antibiotic coating. ACS Appl. Mater. Interfaces **7**, 20304–20313 (2015). https://doi.org/10.1021/acsami.5b05947
138. T. Sjöström, A.H. Nobbs, B. Su, Bactericidal nanospike surfaces via thermal oxidation of Ti alloy substrates. Mater. Lett. **167**, 22–26 (2016). https://doi.org/10.1016/j.matlet.2015.12.140
139. A. Mazare, M. Dilea, D. Ionita, I. Titorencu, V. Trusca, E. Vasile, Changing bioperformance of TiO_2 amorphous nanotubes as an effect of inducing crystallinity. Bioelectrochemistry **87**, 124–131 (2012). https://doi.org/10.1016/j.bioelechem.2012.01.002
140. X. Fan, B. Feng, Z. Liu, J. Tan, W. Zhi, X. Lu, J. Wang, J. Weng, Fabrication of TiO2 nanotubes on porous titanium scaffold and biocompatibility evaluation in vitro and in vivo. J. Biomed. Mater. Res. – Part A **100**(A), 3422–3427 (2012). https://doi.org/10.1002/jbm.a.34268
141. K. Gulati, S. Ramakrishnan, M.S. Aw, G.J. Atkins, D.M. Findlay, D. Losic, Biocompatible polymer coating of titania nanotube arrays for improved drug elution and osteoblast adhesion. Acta Biomater. **8**, 449–456 (2012). https://doi.org/10.1016/j.actbio.2011.09.004
142. N. Epperlein, F. Menzel, K. Schwibbert, R. Koter, J. Bonse, J. Sameith, J. Krüger, J. Toepel, Influence of femtosecond laser produced nanostructures on biofilm growth on steel. Appl. Surf. Sci. **418**, 420–424 (2017). https://doi.org/10.1016/j.apsusc.2017.02.174
143. K. Schwibbert, F. Menzel, N. Epperlein, J. Bonse, J. Krüger, Bacterial adhesion on femtosecond laser-modified polyethylene. Materials (Basel) **12**, 3107 (2019). https://doi.org/10.3390/ma12193107
144. K. Doll, E. Fadeeva, J. Schaeske, T. Ehmke, A. Winkel, A. Heisterkamp, B.N. Chichkov, M. Stiesch, N.S. Stumpp, Development of laser-structured liquid-infused titanium with strong biofilm-repellent properties. ACS Appl. Mater. Interfaces **9**, 9359–9368 (2017). https://doi.org/10.1021/acsami.6b16159
145. T.S. Wong, S.H. Kang, S.K.Y. Tang, E.J. Smythe, B.D. Hatton, A. Grinthal, J. Aizenberg, Bioinspired self-repairing slippery surfaces with pressure-stable omniphobicity. Nature **477**, 443–447 (2011). https://doi.org/10.1038/nature10447
146. I.A. Paun, B.S. Calin, C.C. Mustaciosu, E. Tanasa, A. Moldovan, A. Niemczyk, M. Dinescu, Laser direct writing via two-photon polymerization of 3D hierarchical structures with cells-antiadhesive properties. Int. J. Mol. Sci. **22**, 5653 (2021). https://doi.org/10.3390/ijms22115653
147. L. Bourdon, J.C. Maurin, K. Gritsch, A. Brioude, V. Salles, Improvements in resolution of additive manufacturing: Advances in two-photon polymerization and direct-writing electrospinning techniques. ACS Biomater Sci. Eng. **4**, 3927–3938 (2018). https://doi.org/10.1021/acsbiomaterials.8b00810
148. V. Harinarayana, Y.C. Shin, Two-photon lithography for three-dimensional fabrication in micro / nanoscale regime: A comprehensive review. Opt. Laser Technol. **142**, 107180 (2021). https://doi.org/10.1016/j.optlastec.2021.107180

149. A. Atala, R. Lanza, *Methods of Tissue Engineering* (Gulf Professional Publishing, San Diego, 2002)
150. R. Lanza, R. Langer, J. Vacanti, A. Atala, *Principles of Tissue Engineering* (Academic Press, London, 2020)
151. R. Birla, *Introduction to Tissue Engineering: Applications and Challenges* (John Wiley & Sons, Hoboken, 2014)
152. J. Song, C. Michas, C.S. Chen, A.E. White, M.W. Grinstaff, From simple to architecturally complex hydrogel scaffolds for cell and tissue engineering applications: Opportunities presented by two-photon polymerization. Adv. Healthc. Mater. **9**, 1901217 (2020). https://doi.org/10.1002/adhm.201901217
153. C. Frantz, K.M. Stewart, V.M. Weaver, The extracellular matrix at a glance. J. Cell Sci. **123**, 4195–4200 (2010). https://doi.org/10.1242/jcs.023820
154. P. Tayalia, C.R. Mendonca, T. Baldacchini, D.J. Mooney, E. Mazur, 3D cell-migration studies using two-photon engineered polymer scaffolds. Adv. Mater. **20**, 4494–4498 (2008). https://doi.org/10.1002/adma.200801319
155. A. Accardo, M.C. Blatché, R. Courson, I. Loubinoux, C. Vieu, L. Malaquin, Two-photon lithography and microscopy of 3D hydrogel scaffolds for neuronal cell growth. Biomed. Phys. Eng. Express **4**, 027009 (2018). https://doi.org/10.1088/2057-1976/aaab93
156. P. Danilevicius, L. Georgiadi, C.J. Pateman, F. Claeyssens, M. Chatzinikolaidou, M. Farsari, The effect of porosity on cell ingrowth into accurately defined, laser-made, polylactide-based 3D scaffolds. Appl. Surf. Sci. **336**, 2–10 (2015). https://doi.org/10.1016/j.apsusc.2014.06.012
157. R. Schade, T. Weiß, A. Berg, M. Schnabelrauch, K. Liefeith, Two-photon techniques in tissue engineering. Int. J. Artif. Organs **33**, 219–227 (2010). https://doi.org/10.1177/039139881003300406
158. D. Ricci, M.M. Nava, T. Zandrini, G. Cerullo, M.T. Raimondi, R. Osellame, Scaling-up techniques for the nanofabrication of cell culture substrates via two-photon polymerization for industrial-scale expansion of stem cells. Materials (Basel) **10**, 66 (2017). https://doi.org/10.3390/ma10010066
159. A. Trautmann, G.L. Roth, B. Nujiqi, T. Walther, R. Hellmann, Towards a versatile point-of-care system combining femtosecond laser generated microfluidic channels and direct laser written microneedle arrays. Microsyst. Nanoeng. **5**, 6 (2019). https://doi.org/10.1038/s41378-019-0046-5
160. S. Coscoy, S. Baiz, J. Octon, B. Rhoné, L. Perquis, Q. Tseng, F. Amblard, V. Semetey, Micro-topographies control the development of basal protrusions in epithelial sheets. Biointerphases **13**, 041003 (2018). https://doi.org/10.1116/1.5024601
161. I.A. Paun, R.C. Popescu, C.C. Mustaciosu, M. Zamfirescu, B.S. Calin, M. Mihailescu, M. Dinescu, A. Popescu, D. Chioibasu, M. Soproniy, C.R. Luculescu, Laser-direct writing by two-photon polymerization of 3D honeycomb-like structures for bone regeneration. Biofabrication **10**, 025009 (2018). https://doi.org/10.1088/1758-5090/aaa718
162. T. Limongi, L. Brigo, L. Tirinato, F. Pagliari, A. Gandin, P. Contessotto, A. Giugni, G. Brusatin, Three-dimensionally two-photon lithography realized vascular grafts. Biomed. Mater. **16**, 035013 (2021). https://doi.org/10.1088/1748-605X/abca4b
163. A. Koroleva, A. Deiwick, A. Nguyen, S. Schlie-Wolter, R. Narayan, P. Timashev, V. Popov, V. Bagratashvili, B. Chichkov, Osteogenic differentiation of human mesenchymal stem cells in 3-D Zr-Si organic-inorganic scaffolds produced by two-photon polymerization technique. PLoS One **10**, 0118164 (2015). https://doi.org/10.1371/journal.pone.0118164
164. P.S. Timashev, M.V. Vedunova, D. Guseva, E. Ponimaskin, A. Deiwick, T.A. Mishchenko, E.V. Mitroshina, A.V. Koroleva, A.S. Pimashkin, I.V. Mukhina, V.Y. Panchenko, B.N. Chichkov, V.N. Bagratashvili, 3D in vitro platform produced by two-photon polymerization for the analysis of neural network formation and function. Biomed. Phys. Eng. Express **2**, 035001 (2016). https://doi.org/10.1088/2057-1976/2/3/035001
165. K.S. Worthington, L.A. Wiley, E.E. Kaalberg, M.M. Collins, R.F. Mullins, E.M. Stone, B.A. Tucker, Two-photon polymerization for production of human iPSC-derived retinal cell grafts. Acta Biomater. **55**, 385–395 (2017). https://doi.org/10.1016/j.actbio.2017.03.039

166. P.S. Timashev, D. Kuznetsova, A.V. Koroleva, N. Prodanets, A. Deiwick, Y. Piskun, K. Bardakova, N. Dzhoyashvili, S. Kostjuk, E. Zagaynova, Y. Rochev, B. Chichkov, V. Bragatashvili, Novel biodegradable star-shaped polylactide scaffolds for bone regeneration fabricated by two-photon polymerization. Nanomedicine **11**, 1041–1053 (2016). https://doi.org/10.2217/nnm-2015-0022
167. A. Trautmann, M. Rüth, H.D. Lemke, T. Walther, R. Hellmann, Two-photon polymerization based large scaffolds for adhesion and proliferation studies of human primary fibroblasts. Opt. Laser Technol. **106**, 474–480 (2018). https://doi.org/10.1016/j.optlastec.2018.05.008
168. T. Wloka, S. Czich, M. Kleinsteuber, E. Moek, C. Weber, M. Gottschaldt, K. Liefeith, U.S. Schubert, Microfabrication of 3D-hydrogels via two-photon polymerization of poly(2-ethyl-2-oxazoline) diacrylates. Eur. Polym. J. **122**, 109295 (2020). https://doi.org/10.1016/j.eurpolymj.2019.109295
169. S. Engelhardt, E. Hoch, K. Borchers, W. Meyer, H. Krüger, G.E.M. Tovar, A. Gillner, Fabrication of 2D protein microstructures and 3D polymer-protein hybrid microstructures by two-photon polymerization. Biofabrication **3**, 025003 (2011). https://doi.org/10.1088/1758-5082/3/2/025003
170. T. Weiß, R. Schade, T. Laube, A. Berg, G. Hildebrand, R. Wyrwa, M. Schnabelrauch, K. Liefeith, Two-photon polymerization of biocompatible photopolymers for microstructured 3D biointerfaces. Adv. Eng. Mater. **13**, 264–273 (2011). https://doi.org/10.1002/adem.201080090
171. A.K. Nguyen, S.D. Gittard, A. Koroleva, S. Schlie, A. Gaidukeviciute, B.N. Chichkov, R.J. Narayan, Two-photon polymerization of polyethylene glycol diacrylate scaffolds with riboflavin and triethanolamine used as a water-soluble photoinitiator. Regen. Med. **8**, 725–738 (2013). https://doi.org/10.2217/rme.13.60
172. N.A. Bakhtina, M. Müller, H. Wischnewski, R. Arora, C. Ciaudo, 3D synthetic microstructures fabricated by two-photon polymerization promote homogeneous expression of NANOG and ESRRB in mouse embryonic stem cells. Adv. Mater. Interfaces **8**, 2001964 (2021). https://doi.org/10.1002/admi.202001964
173. J.R. Thompson, K.S. Worthington, B.J. Green, N.K. Mullin, C. Jiao, E.E. Kaalberg, L.A. Wiley, I.C. Han, S.R. Russell, E.H. Sohn, C.A. Guymon, R.F. Mullins, E.M. Stone, B.A. Tucker, Two-photon polymerized poly(caprolactone) retinal cell delivery scaffolds and their systemic and retinal biocompatibility. Acta Biomater. **94**, 204–218 (2019). https://doi.org/10.1016/j.actbio.2019.04.057
174. A. Ovsianikov, B. Chichkov, P. Mente, N.A. Monteiro-Riviere, A. Doraiswamy, R.J. Narayan, Two photon polymerization of polymer-ceramic hybrid materials for transdermal drug delivery. Int. J. Appl. Ceram. Technol. **4**, 22–29 (2007). https://doi.org/10.1111/j.1744-7402.2007.02115.x
175. H. Yu, J. Liu, Y.Y. Zhao, F. Jin, X.Z. Dong, Z.S. Zhao, X.M. Duan, M.L. Zheng, Biocompatible three-dimensional hydrogel cell scaffold fabricated by sodium hyaluronate and chitosan assisted two-photon polymerization. ACS Appl. Bio Mater. **2**, 3077–3083 (2019). https://doi.org/10.1021/acsabm.9b00384
176. B. Buchroithner, D. Hartmann, S. Mayr, Y.J. Oh, D. Sivun, A. Karner, B. Buchegger, T. Griesser, P. Hinterdorfer, T.A. Klar, J. Jacak, 3D multiphoton lithography using biocompatible polymers with specific mechanical properties. Nanoscale Adv. **2**, 2422–2428 (2020). https://doi.org/10.1039/d0na00154f
177. J. Heitz, C. Plamadeala, M. Wiesbauer, P. Freudenthaler, R. Wollhofen, J. Jacak, T.A. Klar, B. Magnus, D. Köstner, A. Weth, W. Baumgartner, R. Marksteiner, Bone-forming cells with pronounced spread into the third dimension in polymer scaffolds fabricated by two-photon polymerization. J. Biomed. Mater. Res. – Part A. **105**, 891–899 (2017). https://doi.org/10.1002/jbm.a.35959
178. A. Schober, U. Fernekorn, S. Singh, G. Schlingloff, M. Gebinoga, J. Hampl, A. Williamson, Mimicking the biological world: Methods for the 3D structuring of artificial cellular environments. Eng. Life Sci. **13**, 352–367 (2013). https://doi.org/10.1002/elsc.201200088

179. M. Chatzinikolaidou, S. Rekstyte, P. Danilevicius, C. Pontikoglou, H. Papadaki, M. Farsari, M. Vamvakaki, Adhesion and growth of human bone marrow mesenchymal stem cells on precise-geometry 3D organic-inorganic composite scaffolds for bone repair. Mater. Sci. Eng. C **48**, 301–309 (2015). https://doi.org/10.1016/j.msec.2014.12.007
180. F. Klein, B. Richter, T. Striebel, C.M. Franz, G. Von Freymann, M. Wegener, M. Bastmeyer, Two-component polymer scaffolds for controlled three-dimensional cell culture. Adv. Mater. **23**, 1341–1345 (2011). https://doi.org/10.1002/adma.201004060
181. J.K. Hohmann, G. Von Freymann, Influence of direct laser written 3D topographies on proliferation and differentiation of osteoblast-like cells: Towards improved implant surfaces. Adv. Funct. Mater. **24**, 6573–6580 (2014). https://doi.org/10.1002/adfm.201401390
182. R. Nagarkar, M. Singh, H.X. Nguyen, S. Jonnalagadda, A review of recent advances in microneedle technology for transdermal drug delivery. J. Drug Deliv. Sci. Technol. **59**, 101923 (2020). https://doi.org/10.1016/j.jddst.2020.101923
183. E. Larrañeta, M.T.C. McCrudden, A.J. Courtenay, R.F. Donnelly, Microneedles: A new frontier in nanomedicine delivery. Pharm. Res. **33**, 1055–1073 (2016). https://doi.org/10.1007/s11095-016-1885-5
184. A.M. Römgens, D.L. Bader, J.A. Bouwstra, F.P.T. Baaijens, C.W.J. Oomens, Monitoring the penetration process of single microneedles with varying tip diameters. J. Mech. Behav. Biomed. Mater. **40**, 397–405 (2014). https://doi.org/10.1016/j.jmbbm.2014.09.015
185. S. Dharadhar, A. Majumdar, S. Dhoble, V. Patravale, Microneedles for transdermal drug delivery: A systematic review. Drug Dev. Ind. Pharm. **45**, 188–201 (2019). https://doi.org/10.1080/03639045.2018.1539497
186. H.R. Jeong, H.S. Lee, I.J. Choi, J.H. Park, Considerations in the use of microneedles: Pain, convenience, anxiety and safety. J. Drug Target. **25**, 29–40 (2017). https://doi.org/10.1080/1061186X.2016.1200589
187. T.K.L. Kiang, S.A. Ranamukhaarachchi, M.H.H. Ensom, Revolutionizing therapeutic drug monitoring with the use of interstitial fluid and microneedles technology. Pharmaceutics **9**, 43 (2017). https://doi.org/10.3390/pharmaceutics9040043
188. J. Jin, V. Reese, R. Coler, D. Carter, M. Rolandi, Chitin microneedles for an easy-to-use tuberculosis skin test. Adv. Healthc. Mater. **3**, 349–353 (2014). https://doi.org/10.1002/adhm.201300185
189. P. Miller, M. Moorman, R. Manginell, C. Ashlee, I. Brener, D. Wheeler, R. Narayan, R. Polsky, Towards an integrated microneedle total analysis chip for protein detection. Electroanalysis **28**, 1305–1310 (2016). https://doi.org/10.1002/elan.201600063
190. V. Sachdeva, A. Banga, Microneedles and their applications. Recent Pat. Drug Deliv. Formul. **5**, 95–132 (2011). https://doi.org/10.2174/187221111795471445
191. T.N. Tarbox, A.B. Watts, Z. Cui, R.O. Williams, An update on coating/manufacturing techniques of microneedles. Drug Deliv. Transl. Res. **8**, 1828–1843 (2018). https://doi.org/10.1007/s13346-017-0466-4
192. A.S. Cordeiro, I.A. Tekko, M.H. Jomaa, L. Vora, E. Mcalister, F. Volpe-zanutto, M. Nethery, P.T. Baine, N. Mitchell, D.W. Mcneill, F. Ryan, Two-photon polymerisation 3D printing of microneedle array templates with versatile designs: Application in the development of polymeric drug delivery systems. Pharm. Res. **37**, 174 (2020). https://doi.org/10.1007/s11095-020-02887-9
193. S.N. Economidou, D. Douroumis, 3D printing as a transformative tool for microneedle systems: Recent advances, manufacturing considerations and market potential. Adv. Drug Deliv. Rev. **173**, 60–69 (2021). https://doi.org/10.1016/j.addr.2021.03.007
194. S.D. Gittard, B. Chen, H. Xu, A. Ovsianikov, B.N. Chichkov, N.A. Monteiro-Riviere, R.J. Narayan, The effects of geometry on skin penetration and failure of polymer microneedles. J. Adhes. Sci. Technol. **27**, 227–243 (2013). https://doi.org/10.1080/01694243.2012.705101
195. C. Liao, W. Anderson, F. Antaw, M. Trau, Two-photon nanolithography of tailored hollow three-dimensional microdevices for biosystems. ACS Omega **4**, 1401–1409 (2019). https://doi.org/10.1021/acsomega.8b03164

196. C. Plamadeala, S.R. Gosain, F. Hischen, B. Buchroithner, S. Puthukodan, J. Jacak, A. Bocchino, D. Whelan, C. O'Mahony, W. Baumgartner, J. Heitz, Bio-inspired microneedle design for efficient drug/vaccine coating. Biomed. Microdevices **22**, 8 (2020). https://doi.org/10.1007/s10544-019-0456-z
197. M. Leone, J. Mönkäre, J.A. Bouwstra, G. Kersten, Dissolving microneedle patches for dermal vaccination. Pharm. Res. **34**, 2223–2240 (2017). https://doi.org/10.1007/s11095-017-2223-2
198. Z.F. Rad, R.E. Nordon, C.J. Anthony, L. Bilston, P.D. Prewett, J.Y. Arns, C.H. Arns, L. Zhang, G.J. Davies, High-fidelity replication of thermoplastic microneedles with open microfluidic channels. Microsyst. Nanoeng. **3**, 17034 (2017). https://doi.org/10.1038/micronano.2017.34
199. P. Griss, G. Stemme, Side-opened out-of-plane microneedles for microfluidic transdermal liquid transfer. J. Microelectromech. Syst. **12**, 296–301 (2003). https://doi.org/10.1109/JMEMS.2003.809959
200. M. Kavaldzhiev, J.E. Perez, Y. Ivanov, A. Bertoncini, C. Liberale, J. Kosel, Biocompatible 3D printed magnetic micro needles. Biomed. Phys. Eng. Express **3**, 025005 (2017). https://doi.org/10.1088/2057-1976/aa5ccb
201. A. Aksit, D.N. Arteaga, M. Arriaga, X. Wang, H. Watanabe, K.E. Kasza, A.K. Lalwani, J.W. Kysar, In-vitro perforation of the round window membrane via direct 3-D printed microneedles. Biomed. Microdevices **20**, 47 (2018). https://doi.org/10.1007/s10544-018-0287-3
202. C. Plamadeala, F. Hischen, R. Friesenecker, R. Wollhofen, J. Jacak, G. Buchberger, E. Heiss, T.A. Klar, W. Baumgartner, J. Heitz, Bioinspired polymer microstructures for directional transport of oily liquids. R. Soc. Open Sci. **4**, 160849 (2017). https://doi.org/10.1098/rsos.160849
203. B. Buchroithner, P. Spurný, S. Mayr, J. Heitz, D. Sivun, J. Jacak, J. Ludwig, An improved transwell design for microelectrode ion-flux measurements. Micromachines **12**, 273 (2021). https://doi.org/10.3390/mi12030273
204. G. Vizsnyiczai, A. Búzás, B. Lakshmanrao Aekbote, T. Fekete, I. Grexa, P. Ormos, L. Kelemen, Multiview microscopy of single cells through microstructure-based indirect optical manipulation. Biomed. Opt. Express **11**, 945 (2020). https://doi.org/10.1364/boe.379233
205. B.L. Aekbote, T. Fekete, J. Jacak, G. Vizsnyiczai, P. Ormos, L. Kelemen, Surface-modified complex SU-8 microstructures for indirect optical manipulation of single cells. Biomed. Opt. Express **7**, 45 (2016). https://doi.org/10.1364/boe.7.000045
206. T.A. Klar, R. Wollhofen, J. Jacak, Sub-Abbe resolution: From STED microscopy to STED lithography. Phys. Scr. **T162** (2014). https://doi.org/10.1088/0031-8949/2014/T162/014049
207. B. Buchegger, A. Tanzer, S. Posch, C. Gabriel, T.A. Klar, J. Jacak, STED lithography in microfluidics for 3D thrombocyte aggregation testing. J. Nanobiotechnol. **19**, 23 (2021). https://doi.org/10.1186/s12951-020-00762-8
208. F. Hischen, G. Buchberger, C. Plamadeala, O. Armbruster, E. Heiss, K. Winands, M. Schwarz, B. Jüttler, J. Heitz, W. Baumgartner, The external scent efferent system of selected European true bugs (Heteroptera): A biomimetic inspiration for passive, unidirectional fluid transport. J. R. Soc. Interface **15**, 20170975 (2018). https://doi.org/10.1098/rsif.2017.0975
209. A.C. Joel, G. Buchberger, P. Comanns, Moisture-harvesting reptiles: A review, in *FSurfaces in Biology III. Biologically-Inspired Systems*, ed. by S. Gorb, E. Gorb, vol. 10, (Springer International Publishing AG, part of Springer Nature, Switzerland, 2017). https://doi.org/10.1007/978-3-319-74144-4_4
210. P. Comanns, Passive water collection with the integument: Mechanisms and their biomimetic potential. J. Exp. Biol. **221** (2018). https://doi.org/10.1242/jeb.153130
211. G. Buchberger, R. Baumgartner, A. Kogler, T. Fritz, S. Bauer, W. Baumgartner, Bio-inspired "fluidic diode" for large-area unidirectional passive water transport even against gravity. Sens. Actuators, A Phys. **283**, 375–385 (2018). https://doi.org/10.1016/j.sna.2018.09.070
212. G. Buchberger, A. Kogler, A. Weth, R. Baumgartner, P. Comanns, S. Bauer, W. Baumgartner, Fluidic diode for passive unidirectional liquid transport bioinspired by the spermathecae of fleas. J. Bionic Eng. **15**, 42–56 (2018). https://doi.org/10.1007/s42235-017-0003-7

213. G. Buchberger, F. Hischen, P. Comanns, R. Baumgartner, A. Kogler, A. Buchsbaum, S. Bauer, W. Baumgartner, Bio-inspired microfluidic devices for passive, directional liquid transport: Model-based adaption for different materials. Procedia Eng. **120**, 106–111 (2015). https://doi.org/10.1016/j.proeng.2015.08.576
214. P. Comanns, G. Buchberger, A. Buchsbaum, R. Baumgartner, A. Kogler, S. Bauer, W. Baumgartner, Directional, passive liquid transport: The Texas horned lizard as a model for a biomimetic 'liquid diode'. J. R. Soc. Interface **12**, 20150415 (2015). https://doi.org/10.1098/rsif.2015.0415
215. S.V. Kirner, U. Hermens, A. Mimidis, E. Skoulas, C. Florian, F. Hischen, C. Plamadeala, W. Baumgartner, K. Winands, H. Mescheder, J. Krüger, J. Solis, J. Siegel, E. Stratakis, J. Bonse, Mimicking bug-like surface structures and their fluid transport produced by ultrashort laser pulse irradiation of steel. Appl. Phys. A Mater. Sci. Process. **123**, 754 (2017). https://doi.org/10.1007/s00339-017-1317-3
216. M. Erzina, A. Trelin, O. Guselnikova, B. Dvorankova, K. Strnadova, A. Perminova, P. Ulbrich, D. Mares, V. Jerabek, R. Elashnikov, V. Svorcik, O. Lyutakov, Precise cancer detection via the combination of functionalized SERS surfaces and convolutional neural network with independent inputs. Sens. Actuators B **308**, 127660 (2020). https://doi.org/10.1016/j.snb.2020.127660
217. O. Guselnikova, A. Trelin, A. Skvortsova, P. Ulbrich, P. Postnikov, A. Pershina, D. Sykora, V. Svorcik, O. Lyutakov, Label-free surface-enhanced Raman spectroscopy with artificial neural network technique for recognition photoinduced DNA damage. Biosens. Bioelectron. **145**, 111718 (2019). https://doi.org/10.1016/j.bios.2019.111718
218. B. Shan, Y. Pu, Y. Chen, M. Liao, M. Li, Novel SERS labels: Rational design, functional integration and biomedical applications. Coord. Chem. Rev. **371**, 11–37 (2018). https://doi.org/10.1016/j.ccr.2018.05.007
219. I. Bruzas, W. Lum, Z. Gorunmez, L. Sagle, Advances in surface-enhanced Raman spectroscopy (SERS) substrates for lipid and protein characterization: Sensing and beyond. Analyst **143**, 3990–4008 (2018). https://doi.org/10.1039/c8an00606g
220. J. Siegel, P. Slepička, J. Heitz, Z. Kolská, P. Sajdl, V. Švorčík, Gold nano-wires and nano-layers at laser-induced nano-ripples on PET. Appl. Surf. Sci. **256**, 2205–2209 (2010). https://doi.org/10.1016/j.apsusc.2009.09.074
221. L. Kelemen, E. Lepera, B. Horváth, P. Ormos, R. Osellame, R. Martínez Vázquez, Direct writing of optical microresonators in a lab-on-a-chip for label-free biosensing. Lab Chip **19**, 1985–1990 (2019). https://doi.org/10.1039/c9lc00174c
222. E. Koch, A. Dietzel, Stretchable sensor array for respiratory monitoring, in *19th Int. Conf. Solid-State Sensors, Actuators Microsystems (TRANSDUCERS)*, (IEEE, 2017), pp. 2227–2230. https://doi.org/10.1109/TRANSDUCERS.2017.7994520
223. S. Vucinic, B. Antonijevic, A.M. Tsatsakis, L. Vassilopoulou, A.O. Docea, A.E. Nosyrev, B.N. Izotov, H. Thiermann, N. Drakoulis, D. Brkic, Environmental exposure to organophosphorus nerve agents. Environ. Toxicol. Pharmacol. **56**, 163–171 (2017). https://doi.org/10.1016/j.etap.2017.09.004
224. R.K. Ibrahim, M. Hayyan, M.A. AlSaadi, A. Hayyan, S. Ibrahim, Environmental application of nanotechnology: Air, soil, and water. Environ. Sci. Pollut. Res. **23**, 13754–13788 (2016). https://doi.org/10.1007/s11356-016-6457-z
225. M. Benetti, D. Cannatà, E. Verona, A. Palla Papavlu, V.C. Dinca, T. Lippert, M. Dinescu, F. Di Pietrantonio, Highly selective surface acoustic wave e-nose implemented by laser direct writing. Sens. Actuators B **283**, 154–162 (2019). https://doi.org/10.1016/j.snb.2018.12.005
226. B. Steinhauser, C. Vidal, R.A. Barb, J. Heitz, A.I. Mardare, A.W. Hassel, C. Hrelescu, T.A. Klar, Localized-plasmon voltammetry to detect pH dependent gold oxidation. J. Phys. Chem. C **122**, 4565–4571 (2018). https://doi.org/10.1021/acs.jpcc.7b11355
227. E. Koch, A. Dietzel, Respiratory trigger signal generation by means of a stretchable sensor array. Sens. Actuators A Phys. **273**, 113–120 (2018). https://doi.org/10.1016/j.sna.2018.02.022

228. R. Delmdahl, A. Wiessner, Pulsed laser deposition for coating applications. J. Phys. Conf. Ser. **59**, 28–31 (2007). https://doi.org/10.1088/1742-6596/59/1/006
229. M.J. Aziz, Film growth mechanisms in pulsed laser deposition. Appl. Phys. A Mater. Sci. Process. **93**, 579–587 (2008). https://doi.org/10.1007/s00339-008-4696-7
230. T. Yamaguchi, H. Hagino, M. Takemura, Y. Hasegawa, Y. Michiyama, A. Nakahira, Microstructure of FeTiC composite surface layer on carbon steel formed by laser alloying process. Mater. Trans. **54**, 1755–1759 (2013). https://doi.org/10.2320/matertrans.MAW201304
231. A. Milionis, D. Fragouli, I.S. Bayer, A. Athanassiou, Water adhesion to laser-treated surfaces, in *Laser Surface Modification and Adhesion*, (John Wiley & Sons, Hoboken, 2014), pp. 377–413
232. T. Kokubo, H.M. Kim, M. Kawashita, Novel bioactive materials with different mechanical properties. Biomaterials **24**, 2161–2175 (2003). https://doi.org/10.1016/S0142-9612(03)00044-9
233. M. Mozafari, Bioceramics in the realm of history. Bioceram. Dev. Appl. **4**, e106 (2014). https://doi.org/10.4172/2090-5025.1000e106
234. T. Zhai, X. Fang, M. Liao, X. Xu, H. Zeng, B. Yoshio, D. Golberg, A comprehensive review of one-dimensional metal-oxide nanostructure photodetectors. Sensors **9**, 6504–6529 (2009). https://doi.org/10.3390/s90806504
235. M. Azami, S. Jalilifiroozinezhad, M. Mozafari, M. Rabiee, Synthesis and solubility of calcium fluoride/hydroxy-fluorapatite nanocrystals for dental applications. Ceram. Int. **37**, 2007–2014 (2011). https://doi.org/10.1016/j.ceramint.2011.02.025
236. S. Kargozar, N. Lotfibakhshaiesh, J. Ai, M. Mozafari, P. Brouki Milan, S. Hamzehlou, M. Barati, F. Baino, R.G. Hill, M.T. Joghataei, Strontium- and cobalt-substituted bioactive glasses seeded with human umbilical cord perivascular cells to promote bone regeneration via enhanced osteogenic and angiogenic activities. Acta Biomater. **58**, 502–514 (2017). https://doi.org/10.1016/j.actbio.2017.06.021
237. R. Kamalian, A. Yazdanpanah, F. Moztarzadeh, R. Ravarian, Z. Moztarzadeh, M. Tahmasbi, M. Mozafari, Synthesis and characterization of bioactive glass/forsterite nanocomposites for bone and dental implants. Ceram. – Silik. **56**, 331–340 (2012)
238. M. Mozafari, E. Salahinejad, V. Shabafrooz, M. Yazdimamaghani, D. Vashaee, L. Tayebi, Multilayer bioactive glass/zirconium titanate thin films in bone tissue engineering and regenerative dentistry. Int. J. Nanomedicine **8**, 1665–1672 (2013). https://doi.org/10.2147/IJN.S42659
239. L. Torrisi, S. Trusso, G. Di Marco, P. Parisi, Pulsed laser deposition of hydroxyapatite films by KrF excimer. Phys. Med. **17**, 227–231 (2001)
240. C. Capuccini, F. Sima, E. Axente, E. Boanini, M. Gazzano, A. Bigi, I.N. Mihailescu, Strontium-substituted hydroxyapatite thin films grown by pulsed laser deposition, in *Functionalized Nanoscale Materials, Devices and Systems*, (Springer, Dordrecht, 2008), pp. 389–398
241. E.L. Solla, J.P. Borrajo, P. González, J. Serra, S. Chiussi, C. Serra, B. León, M. Pérez-Amor, Pulsed laser deposition of silicon-substituted hydroxyapatite coatings. Vacuum **82**, 1383–1385 (2008). https://doi.org/10.1016/j.vacuum.2008.03.020
242. L. Floroian, B. Savu, G. Stanciu, A.C. Popescu, F. Sima, I.N. Mihailescu, R. Mustata, L.E. Sima, S.M. Petrescu, D. Tanaskovic, D. Janackovic, Nanostructured bioglass thin films synthesized by pulsed laser deposition: CSLM, FTIR investigations and in vitro biotests. Appl. Surf. Sci. **255**, 3056–3062 (2008). https://doi.org/10.1016/j.apsusc.2008.08.105
243. L. Floroian, M. Florescu, F. Sima, G. Popescu-Pelin, C. Ristoscu, I.N. Mihailescu, Synthesis of biomaterial thin films by pulsed laser technologies: Electrochemical evaluation of bioactive glass-based nanocomposite coatings for biomedical applications. Mater. Sci. Eng. C **32**, 1152–1157 (2012). https://doi.org/10.1016/j.msec.2012.03.001
244. C. Piconi, G. Maccauro, Zirconia as a ceramic biomaterial. Biomaterials **20**, 1–25 (1999). https://doi.org/10.1016/S0142-9612(98)00010-6

245. Z. Pang, A. Chughtai, I. Sailer, Y. Zhang, A fractographic study of clinically retrieved zirconia-ceramic and metal-ceramic fixed dental prostheses. Dent. Mater. **31**, 1198–1206 (2015). https://doi.org/10.1016/j.dental.2015.07.003
246. Z. Zhang, M. Guazzato, T. Sornsuwan, S.S. Scherrer, C. Rungsiyakull, W. Li, M.V. Swain, Q. Li, Thermally induced fracture for core-veneered dental ceramic structures. Acta Biomater. **9**, 8394–8402 (2013). https://doi.org/10.1016/j.actbio.2013.05.009
247. C. Sax, 10-year clinical outcomes of fixed dental prostheses with zirconia frameworks. Int. J. Comput. Dent. **14**(3), 183–202 (2011)
248. M.N. Aboushelib, C.J. Kleverlaan, A.J. Feilzer, Microtensile bond strength of different components of core veneered all-ceramic restorations. Part II: Zirconia veneering ceramics. Dent. Mater. **22**, 857–863 (2006). https://doi.org/10.1016/j.dental.2005.11.014
249. N. De Jager, P. Pallav, A.J. Feilzer, The influence of design parameters on the FEA-determined stress distribution in CAD-CAM produced all-ceramic dental crowns. Dent. Mater. **21**, 242–251 (2005). https://doi.org/10.1016/j.dental.2004.03.013
250. M. Dündar, M. Özcan, B. Gökçe, E. Çömlekoğlu, F. Leite, L.F. Valandro, Comparison of two bond strength testing methodologies for bilayered all-ceramics. Dent. Mater. **23**, 630–636 (2007). https://doi.org/10.1016/j.dental.2006.05.004
251. R.L.P. Santos, F.S. Silva, R.M. Nascimento, J.C.M. Souza, F.V. Motta, O. Carvalho, B. Henriques, Shear bond strength of veneering porcelain to zirconia: Effect of surface treatment by CNC-milling and composite layer deposition on zirconia. J. Mech. Behav. Biomed. Mater. **60**, 547–556 (2016). https://doi.org/10.1016/j.jmbbm.2016.03.015
252. Ç. Ural, T. Külünk, Ş. Külünk, M. Kurt, The effect of laser treatment on bonding between zirconia ceramic surface and resin cement. Acta Odontol. Scand. **68**, 354–359 (2010). https://doi.org/10.3109/00016357.2010.514720
253. D. Liu, J.P. Matinlinna, J.K.H. Tsoi, E.H.N. Pow, T. Miyazaki, Y. Shibata, C.W. Kan, A new modified laser pretreatment for porcelain zirconia bonding. Dent. Mater. **29**, 559–565 (2013). https://doi.org/10.1016/j.dental.2013.03.002
254. H.J. Kim, H.P. Lim, Y.J. Park, M.S. Vang, Effect of zirconia surface treatments on the shear bond strength of veneering ceramic. J. Prosthet. Dent. **105**, 315–322 (2011). https://doi.org/10.1016/S0022-3913(11)60060-7
255. B. Henriques, D. Fabris, J.C.M. Souza, F.S. Silva, Ó. Carvalho, M.C. Fredel, J. Mesquita-Guimarães, Bond strength enhancement of zirconia-porcelain interfaces via Nd:YAG laser surface structuring. J. Mech. Behav. Biomed. Mater. **81**, 161–167 (2018). https://doi.org/10.1016/j.jmbbm.2018.02.031
256. F. Chang, T. Liang, T. Wu, C. Wu, Using 3D printing and femtosecond laser micromachining to fabricate biodegradable peripheral vascular stents with high structural uniformity and dimensional precision. Int. J. Adv. Manuf. Technol. **116**, 1523–1536 (2021). https://doi.org/10.1007/s00170-021-07446-z
257. M.H. Smith, C.L. Flanagan, J.M. Kemppainen, J.A. Sack, H. Chung, S. Das, S.J. Hollister, S.E. Feinberg, Computed tomography-based tissue-engineered scaffolds in craniomaxillofacial surgery. Int. J. Med. Robot. Comput. Assist. Surg. **3**, 206–217 (2007). https://doi.org/10.1002/rcs.143
258. F.G. Mangano, B. Cirotti, R.L. Sammons, C. Mangano, Custom-made, root-analogue direct laser metal forming implant: A case report. Lasers Med. Sci. **27**, 1241–1245 (2012). https://doi.org/10.1007/s10103-012-1134-z
259. F. Mangano, M. Bazzoli, L. Tettamanti, D. Farronato, M. Maineri, A. Macchi, C. Mangano, Custom-made, selective laser sintering (SLS) blade implants as a non-conventional solution for the prosthetic rehabilitation of extremely atrophied posterior mandible. Lasers Med. Sci. **28**, 1241–1247 (2013). https://doi.org/10.1007/s10103-012-1205-1
260. C. Li, Y. Yang, L. Yang, Z. Shi, Biomimetic anti-adhesive surface microstructures on electrosurgical blade fabricated by long-pulse laser inspired by pangolin scales. Micromachines **10**, 816 (2019). https://doi.org/10.3390/mi10120816
261. F. Fankhauser, S. Kwasniewska, *Lasers in Ophthalmology: Basic, Diagnostic, and Surgical Aspects* (Netherlands Kugler Publ, Hague, 2003)

262. M.A. Gilmour, Lasers in ophthalmology. Vet. Clin. North Am. Small Anim. Pract. **32**, 649–672 (2002). https://doi.org/10.1016/S0195-5616(02)00009-8
263. H.A. Wigdor, J.T. Walsh, J.D.B. Featherstone, S.R. Visuri, D. Fried, J.L. Waldvogel, Lasers in dentistry. Lasers Surg. Med. **16**, 103–133 (1995). https://doi.org/10.1002/lsm.1900160202
264. M. Miller, T. Truhe, Lasers in dentistry: An overview. J. Am. Dent. Assoc. **124**, 32–35 (1993). https://doi.org/10.14219/jada.archive.1993.0034
265. C. Fornaini, R. Fekrazad, J. Rocca, E. Merigo, Use of blue and blue-violet lasers in dentistry: A narrative review. J. Lasers Med. Sci. **12**, e31 (2021). https://doi.org/10.34172/jlms.2021.31

Open Access This chapter is licensed under the terms of the Creative Commons Attribution 4.0 International License (http://creativecommons.org/licenses/by/4.0/), which permits use, sharing, adaptation, distribution and reproduction in any medium or format, as long as you give appropriate credit to the original author(s) and the source, provide a link to the Creative Commons license and indicate if changes were made.

The images or other third party material in this chapter are included in the chapter's Creative Commons license, unless indicated otherwise in a credit line to the material. If material is not included in the chapter's Creative Commons license and your intended use is not permitted by statutory regulation or exceeds the permitted use, you will need to obtain permission directly from the copyright holder.

Chapter 32
Laser Nanostructuring for SERS Applications

Xiao Luo and Minlin Zhong

Abstract Surface-enhanced Raman scattering (SERS) is an advanced detecting method, permitting the identification of molecules by their unique vibrational fingerprints presenting in the enhanced Raman spectra. Due to its advantages on rapid detection, label-free, nondestructive, specificity, and excellent sensitivity, SERS is widely used in the fields of food detection, pollutant monitoring, and disease early diagnosis. Correlated to its two enhancement mechanisms – electromagnetic enhancement (EM) and chemical enhancement (CM) – the sensitivity of SERS highly depends on the substrates with well-designed nanostructures. Laser nanostructuring is a promising approach for fabricating versatile functional nanostructures for the SERS substrate needs. It is a one-step, maskless, and no-contact process with sufficient high processing efficiency, uniformity, and stability, which overpasses the available conventional processes for fabricating the nanostructures of SERS substrates. In addition, laser micro-nano structuring is able to fabricate specific wetting surfaces including patterned superhydrophilic center with superhydrophobic surroundings, by which the tested liquids can be concentrated up to 10^5 times by evaporation. Integrated with the hot spot nanostructures and the evaporation enrichment, the nanostructured SERS substrates via ultrafast laser are able to achieve 10^{-18} mol/L detection sensitivity, the highest available detection limit.

This chapter reviews the development and the state of the art on laser nanostructuring for SERS applications, including but not limited to the nanostructures for SERS substrates, the versatile nanostructures formed via ultrafast lasers on metals, the efforts to increase the sensibility of SERS substrates, the laser fabricated patterned superhydrophilic-superhydrophobic surfaces for evaporation concentration, the ultrasensitive SERS detection with patterned platform via evaporation enrichment, and the application cases on laser-nanostructured SERS substrates for

---

X. Luo · M. Zhong (✉)
Laser Materials Processing Research Center, Key Laboratory for Advanced Materials Processing Technology (Ministry of Education), School of Materials Science and Engineering, Tsinghua University, Beijing, P. R. China
e-mail: luox17@mails.tsinghua.edu.cn; zhml@mail.tsinghua.edu.cn

© The Author(s), under exclusive license to Springer Nature Switzerland AG 2023
R. Stoian, J. Bonse (eds.), *Ultrafast Laser Nanostructuring*, Springer Series in Optical Sciences 239, https://doi.org/10.1007/978-3-031-14752-4_32

cancer diagnosis, food safety evaluation, and others. This chapter ends with a summery and prospective section.

Keywords Laser · Nanostructures · Specific wetting surfaces · SERS spectroscopy · Food detection · Cancer diagnose detection

1 Introduction

1.1 Overview of SERS Detecting Technologies

Surface-enhanced Raman Scattering (SERS) is a phenomenon that Raman signal is significantly enhanced when the analytes are adsorbed onto metal surfaces with unique nanostructures, such as Au [1–3], Ag [4–6], and Cu [7–9], or the colloids of their nanoparticles [10]. In 1928, Raman and his co-workers discovered that, when light irradiates sample surfaces, besides the elastic collision (Rayleigh scattering), there occurs inelastic collision for a small amount of photons which results in spectrum lines with altered frequency, named Raman scattering (Fig. 32.1) [11]. Raman scattering is capable of providing the identification information of target molecules. Compared with other spectroscopic techniques based on molecular vibration, Raman scattering spectroscopy possesses unique advantages including simple preparation process, less sample demanded, nondestructive inspection, efficient analysis, and reliable test results. Nevertheless, only about 0.1 percent of the photons will be scattered, and the intensity of Raman scattering is ~10^{-3} times compared with Rayleigh scattering. Thus, the intensity of Raman signal is normally too weak to be applied in practical applications.

In 1974, Fleischmann et al. [12, 13] found that the Raman signal intensity was significantly enhanced when pyridine molecules were attached to a rough silver electrode. They attributed this signal enhancement to more pyridine molecules absorbed on rough silver surfaces compared with smooth surfaces. In 1977, Grant Albrecht et al. [14] and Jeanmaire et al. [15] calculated that the surface area of

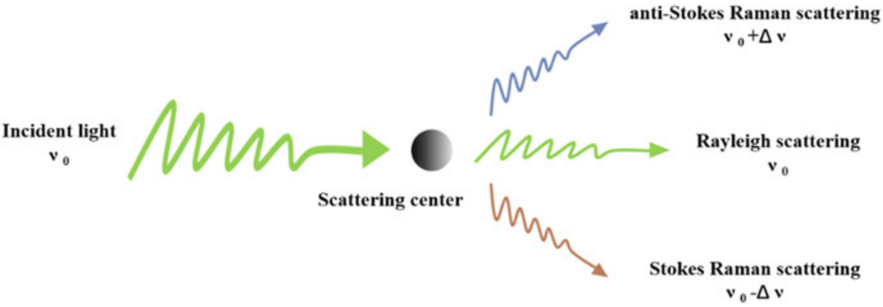

Fig. 32.1 Schematic illustration of the Raman scattering and Rayleigh scattering

rough silver electrode only increased tenfold, while the detected signal strength in experiments was enhanced 10^5 ~ 10^6 times. These results drew global attentions at that time, and scientists named this phenomenon as Surface-enhanced Raman Spectroscopy (SERS). Since then, both the academic researches [16, 17] and practical developments [18, 19] advanced rapidly.

One confusing issue in academic field is the SERS enhancement mechanism. According to the classical electromagnetic theory, Raman scattering generates from the vibration between atoms in the molecular structures, and the scattered intensity (I) is in direct proportion to the square of dipole moments of molecules (P):

$$I \propto P^2 \tag{32.1}$$

$$P = \alpha \times E \tag{32.2}$$

where α is the molecular polarizability and E is the electric field intensity. Therefore, the enhancement effect of SERS mainly comes from two parts: the polarizability of analytic molecules and the intensity of local electric field near the analytic molecules. Each of them corresponds respectively to a theoretical model for the SERS enhancement mechanism.

When the theoretical model focuses on the changes of molecular polarizability, it corresponds to the charge transfer enhancement mechanism (CT) [20], named as chemical enhancement (CM) [21]. Specifically, the analytic molecules interact with the surface metals through chemical bonds to form new compounds, resulting in new excited states. When the substrates are exposed to laser, the electrons transit between the Fermi level and the new excited state, leading to the increase of molecular polarizability. Studies indicate that the chemical enhancement mechanism contributes about 10^2 enhancement factor. The other model focusing on the intensity of local electric field is named as electromagnetic enhancement (EM). The electromagnetic enhancement involves the increase of electric field intensity caused by the local surface plasma resonance (LSPR) [22, 23]. That is, the free electrons on the metal surfaces tend to be excited collectively when exposed to laser, giving rise to the plasma oscillation. When the frequency of plasma oscillation is consistent with that of the incident light, the resonance phenomenon occurs. Significantly, it is widely recognized that EM is the main enhancement mechanism, contributing to the enhancement factor up to 10^6 ~ 10^{12}. LSPR depends highly on the morphology of SERS substrates, especially unique nanostructures, named "hot spots" [24, 25], which will be elaborated in Sect. 1.2. Overall, it remains a challenge to strictly quantify or distinguish the ratios of contribution from EM and CM up to now [26]. Recent researches demonstrated that the two enhancement mechanisms mentioned above usually existed and functioned together [27].

As for the practical applications for SERS, the most important progress is the development of Raman spectrometers. The technique of Raman spectrometer has developed rapidly since laser was invented in 1960 and then used as a light source for Raman spectrometer. Typically, Raman spectrometers are consisted of laser light

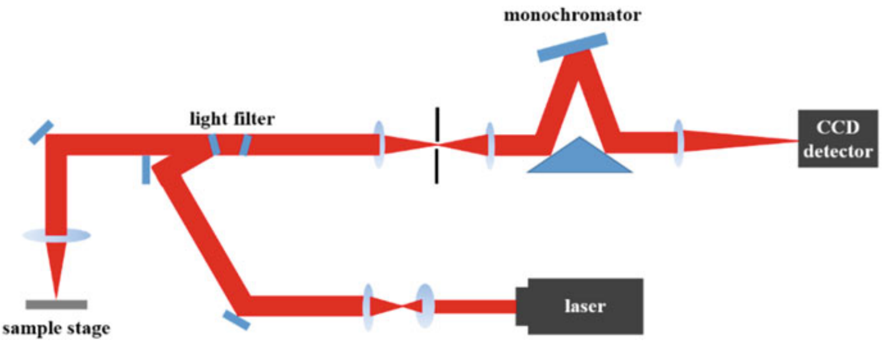

Fig. 32.2 Diagram of dispersive laser Raman spectrometer

source, light filter, monochromator or Michelson interferometer, sample stage, and detecting system [28], as presented in Fig. 32.2. The common wavelengths for the Raman excitation light source contain 325 nm (UV), 488 nm (blue-green), 514 nm (green), 633 nm (red), 785 nm (red), and 1064 nm (IR). Light filter, monochromator, or Michelson interferometer are used to reduce the Rayleigh light and other stray lights to acquire Raman signals with better signal-to-noise ratio (SNR). The detecting system of dispersive Raman spectrometer always uses CCD detector, and FT-Raman spectrometer prefers Ge or InGaAs detector. From the large desktop Raman spectrometer to the handheld Raman spectrometer and portable Raman spectrometer, the rapid developments of Raman spectrometers accelerate the extension of SERS applications.

1.2 Unique Nanostructures for SERS

The sensitivity of SERS substrates is closely related to the “hot spots” – the shape, size, distribution, and density of the nanostructures. Among the nanostructures, nanoparticles (NPs) are the most representative nanostructure for SERS performance. The hot spots formed by nanoparticles mostly come from the nanoscale gaps between the separated nanoparticles. Conventionally, the optimized nanoparticles for SERS application are smaller than 100 nm in diameter [29, 30]. However, recently, Yu Huang et al. [25, 31] reported that the size of NPs could be as large as 200 nm in diameter, and they further demonstrated that along with the increasement of the diameter, the near-field intensity could be strongly enhanced (Fig. 32.3(a1)–(a4)). Besides, the aggregation of nanoparticles induced the hot spots with high density, contributing to the enhancement of Raman signals [32, 33]. L. B. He et al. [34] found that the gaps with an inter-particle spacing of ~3 nm offered 68% of the overall SERS intensity. By simulation, Yu Huang et al. [35] indicated that the local field enhancements in the gap reached up to an order of 10^{10} when the gap was

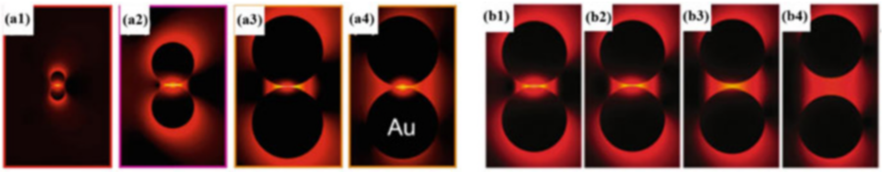

Fig. 32.3 Local electric field distributions when the diameters of NPs are (a1) 20 nm, (a2) 60 nm, (a3) and (a4) 100 nm at different wavelength. (Adapted with permission from Ref. [25] © The Optical Society); local electric field distributions when the gap sizes are (b1) 1 nm, (b2) 2 nm, (b3) 8 nm, and (b4) 30 nm. (Reproduced from Ref. [35] with permission from the Royal Society of Chemistry)

1 nm, while it declined dramatically to 10^4 as the gap distance increased to 30 nm (Fig. 32.3(b1)–(b4)).

Besides the nanoscale gaps, the increased electromagnetic fields occur at the tips of nanostructures according to the lightning rod effect, producing better Raman signals [36–38]. Hence, the nanostructures with abundant tips have been extensively investigated such as nanostars [39–41], nanocubes [42–44], nanotriangles [45–47], nanooctahedras [48], nanoprisms [49], nanoflowers [50–52], and nanopyramids [53–55] (Fig. 32.4(a1)–(a7)). More complex nanostructures were explored along with the rapid development of manufacturing technology, for instance, the slanted nanorods [56], V-shaped nanorods [4], wrinkled nanoporous [57], nanoforests [58], nanowaxberries [59], lotus seedpod-like arrays [60], and nanocages [61] (Fig. 32.4(b1)–(b7)). Furthermore, composite morphologies consisting of structures with different shapes and scales or with various chemical components were also searched for higher sensitivity [62]. Bingyong Lin et al. [63] trapped Au nanobipyramids into the anodic aluminum oxide (AAO) nanoholes (Fig. 32.5a), achieving an average enhancement factor of 1×10^8. Su Yeon Lee et al. [24] decorated Au nanoparticles on the SiO_2 microcylinders for highly active three-dimensional (3D) SERS substrates. Zhendong Zhu et al. [64] generated single gold nanoparticle at the bottom of each nanocavity (Fig. 32.5b), obtaining an experimental SERS enhancement factor of 2×10^7 through Fano resonance boosted cascaded optical field enhancement. The concept of Fano resonances was firstly proposed by Stockman MI et al. [65, 66], meaning that the enhancement of cascaded optical field could be realized via the intercoupling of a chain of self-similar gold nanoparticles. And then the same phenomenon was discovered in nanostars [67] or even composite plasmonic systems such as the arrays of nanoparticles assembled into nanoantennas [68] and the high-quality plasmonic nanoparticle-in-cavity [64]. The cascaded optical field enhancement can lead to stronger local electromagnetic field, benefitting for SERS applications [69].

Recent studies indicated that the composite of noble metals with oxides or semiconductor materials, such as Cu_2O [70], TiO_2 [71], ZnO [72], CdTe [73], Fe_3O_4 [74], WO_3 [75], and graphene [76], strengthened the sensitivity of SERS substrates via tuning the localized electromagnetic field and interfacial charge trans-

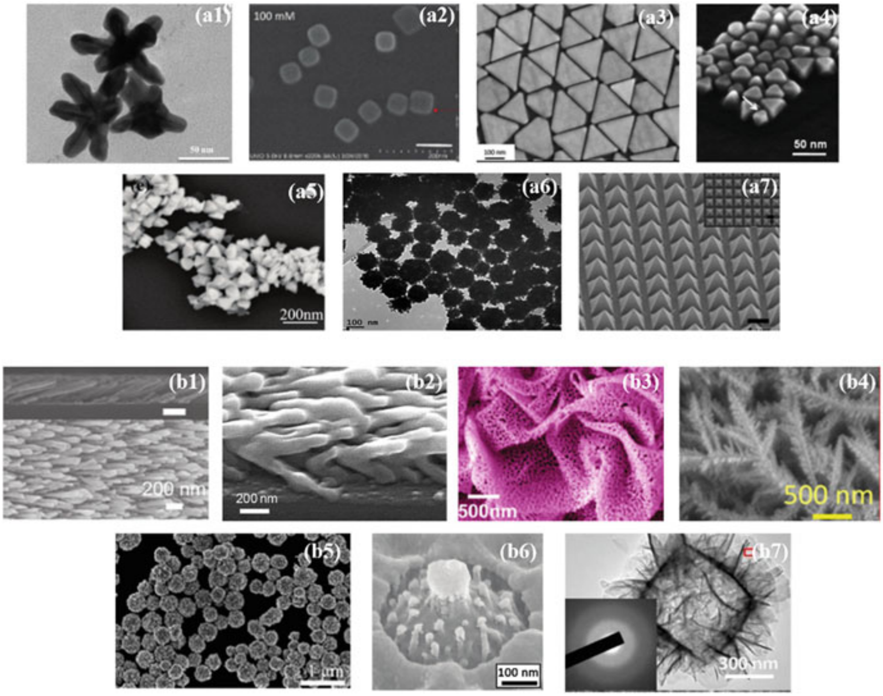

Fig. 32.4 SEM images of nanostructures with abundant tips: (a1) nanostars. (Reproduced from Ref. [39] with permission from the American Chemical Society), (a2) nanocubes. (Reproduced from Ref. [42] with permission from the Royal Society of Chemistry), (a3) nanotriangles. (Reproduced from Ref. [46] with permission from the American Chemical Society), (a4) nanooctahedras. (Reproduced from Ref. [48] with permission from RSC Pub), (a5) nanoprisms. (Reproduced from Ref. [49] with permission from the Royal Society of Chemistry), (a6) nanoflowers. (Reproduced from Ref. [52] with permission from RSC Pub), and (a7) nanopyramids. (Reproduced from Ref. [54] with permission from RSC Pub); the more complex nanostructures: (b1) slanted nanorods. (Reproduced from Ref. [56] with permission from IOP Publishing), (b2) V-shaped Ag nanorods. (Reproduced from Ref. [4] with permission from the Royal Society of Chemistry), (b3) wrinkled nanoporous. (Reproduced from Ref. [57] with permission from the American Chemical Society), (b4) nanoforest. (Reprinted from Ref. [58] which is licensed under Creative Commons Attribution 4.0 International License (https://creativecommons.org/licenses/by/4.0/)), (b5) nanowaxberry. (Reproduced from Ref. [59] with permission from the American Chemical Society), (b6) lotus seedpod-like arrays. (Reproduced from Ref. [60] with permission from John Wiley and Sons), and (b7) nanocages. (Reproduced from Ref. [61] with permission from John Wiley and Sons)

fer (CT). Overall, from the early-stage rough silver electrode to the present diverse nanostructure morphologies and materials, SERS substrates evolve continuously with their nanostructures tending from disordered, large-size, and single structures to ordered, small-size, and composite structures [77].

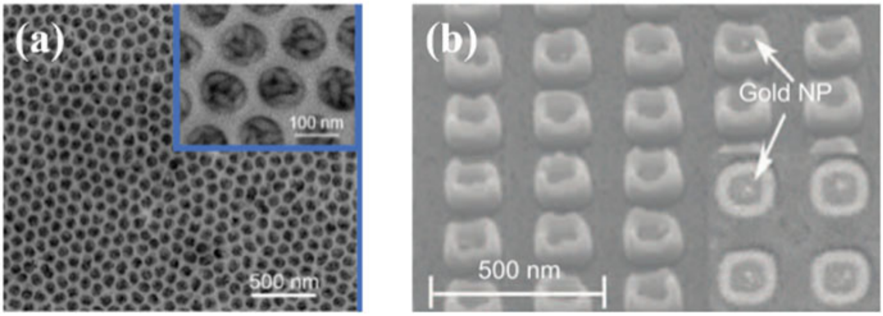

Fig. 32.5 SEM images of (**a**) the gold nanobipyramids trapped into the AAO nanoholes. (Reproduced from Ref. [63] with permission from Elsevier), and (**b**) the nanoparticle-in-cavity nanoantenna arrays. (Reprinted from Ref. [64] which is licensed under Creative Commons CC BY license (https://creativecommons.org/licenses/))

1.3 Fabrication Methods for SERS Substrates

The SERS substrates can be roughly divided into two categories: the colloids and structural solid substrates [78]. Usually, the colloidal nanoparticles are usually made of Au/Ag via chemical reduction method using silver nitrate or auric acid chloride solutions as the precursor and sodium citrate or sodium borohydride as the reducing agent [79–81]. By tuning the types and concentrations of reductants, reaction time, reaction temperature, and surfactant types, the shapes and size of colloidal nanostructures can be optimized [82]. Although this method is convenient, it is still really difficult to accurately control the size and morphology of nanostructures. Meanwhile, the agglomeration of nanoparticles will reduce the sensitivity, limiting the applications of colloidal SERS substrates.

As for the on-chip SERS substrates, the fabrication methods can be divided into three main types: lithography-based approach, non-lithography template approach, and direct formation [18]. The lithography-based approaches contain electron beam lithography (EBL) [83], nanoimprinting lithography (NIL) [84], and nanosphere lithography (NSL) [85]. The SERS substrates fabricated by lithography-based approaches typically possess remarkable performance in repeatability and sensitivity, and the accurate control toward the nanostructure specifications benefits for scientific researches. However, they are difficult for large-area or large-scale fabrication, due to their low fabrication efficiency and high cost. The non-lithography template approach means the un-SERS-active nanopatterned templates coated with the SERS-actives, such as the metal films covered with nanospheres (MFON) [86] and anodic aluminum oxide (AAO) [87]. Compared with lithography-based approaches, the non-lithography template approaches reduce the fabrication cost while maintaining the high sensitivity of SERS substrates. However, the limited morphologies and multiple preparation steps make them unfavorable for large-scale fabrication and practical applications. The last one, direct formation, is to form the

SERS substrates directly by means of approaches such as cyclic voltammetry [88, 89], oblique angle deposition (OAD) [90], dealloying [91], and laser direct ablation [92]. They are undoubtedly the most cost-effective and might be the most viable option for practical applications though their sensitive, uniformity, and stability still need improvements.

2 Overview on Laser Nanostructuring for SERS

This chapter outlines the laser-induced micro-/nanostructures for SERS applications, including materials, morphology, size, shape, and chemical components. When the dielectric constant of a material meets the requirements that the real part is large and negative, and the imaginary part is small and positive, this material can form strong electric field under the excitation of laser and thus generate stronger Raman signals [93]. Au, Ag, and Cu have the above dielectric properties and are the most common SERS substrate materials presently, among which Ag presents the best SERS performance [94, 95]. Thus, silver is the most common laser nanostructuring material for SERS [96–98], and the least used is copper [99]. Considering that gold is relatively expensive, Au layer or Au nanoparticles is often deposited on the laser-textured substrates such as glass [100], silicon [101], polymer [102], Al_2O_3 [103], Ti6Al4V [97], and copper [104] for SERS applications.

As for the laser-induced structures for SERS, the most common structure is laser-induced periodic surface structures (LIPSS), as depicted in Fig. 32.6a, or named as nano-ripples [97, 103, 105, 106]. LIPSS are universal structures formed on the solid substrates via interaction by linearly polarized laser pulses when the adjacent laser tracks are overlapped. More detailed information on the formation mechanism of LIPSS can be found in other chapters of this book. There are two different types of LIPSS: low spatial frequency LIPSS (LSFL) and high spatial frequency LIPSS (HSFL) [107, 108]. The period of LSFL is close to the wavelength of laser, and the period of HSFL is smaller than the wavelength of laser [107].

Based on LIPSS, the microstructures such as grooves (Fig. 32.6b) [97] and smaller-size nanostructures such as nanopillar arrays (Fig. 32.6c) [109] and nanoparticles (Fig. 32.6d) [110] can be fabricated by controlling the laser processing parameters including laser fluence, scanning interval and times, scanning speed, and processing atmosphere. For instance, by increasing the scanning times from 5 cycles to 30 cycles, the morphology of the laser-induced structures changes from LIPSS to hierarchy structures composing of micro-grooves and LIPSS, as shown in Fig. 32.6b [97]. Besides, via appropriately increasing the laser fluence and decreasing the scanning interval and speed, the morphology of micro-grooves and LIPSS can also be acquired [111]. Qianqian Yang et al. [109] generated dense 80-nm-diameter nanopillar arrays on silicon through two-step processing method: firstly to induce LIPSS by a linearly polarized femtosecond laser and then to irradiate the surface with a 90° rotated polarization, as shown in Fig. 32.6c. As for nanoparticles, they can be fabricated by controlling the laser processing parameters or the processing

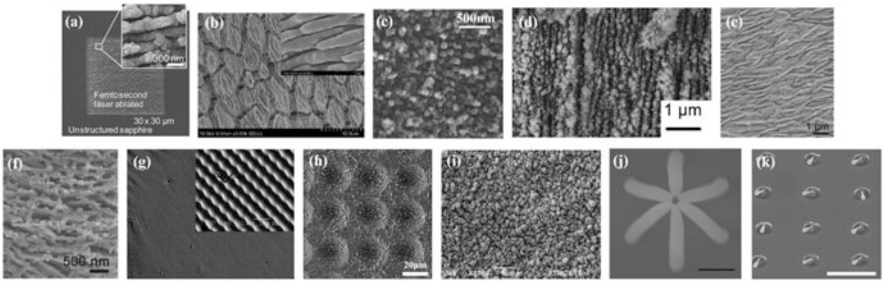

Fig. 32.6 SEM images of (**a**) LIPSS. (Reproduced from Ref. [106] with permission from RSC Pub); (**b**) hierarchy structures composing of micro-grooves and LIPSS. (Reproduced from Ref. [97] which is licensed under Creative Commons Attribution 4.0 International License (https://creativecommons.org/licenses/by/4.0/)); (**c**) nanopillar arrays. (Adapted with permission from Ref. [109] © The Optical Society); (**d**) LIPSS covered by nanoparticles. (Reproduced from Ref. [110] with permission from John Wiley and Sons); (**e**) nanoplates. (Reproduced from Ref. [115] with permission from the Royal Society of Chemistry); (**f**) micro-flowers. (Reproduced from Ref. [116] with permission from the Royal Society of Chemistry (Great Britain)); (**g**) grid-like structures. (Reproduced from Ref. [102] with permission from John Wiley and Sons); (**h**) periodic micropit arrays. (Reproduced from Ref. [98] with permission from Elsevier); (**i**) amorphous nanosphere clusters. (Reproduced from Ref. [120] with permission from Elsevier); (**j**) nanopillar arrays. (Reproduced from Ref. [100] with permission from John Wiley and Sons); (**k**) sub-100 nm antenna arrays. (Reproduced from Ref. [121] with permission from IOP Publishing)

atmosphere. The nanoparticles are induced by the phenomenon of aggregation and redeposition. That is, the laser-induced plasma redeposits back to the substrates after the rapid evaporation and solidification, forming nanoparticles on the surfaces [112]. Studies indicated that the morphology of nanoparticles can be controlled by tuning the ultrafast laser processing parameters [113], and fabricating in an Ar atmosphere rather than air can induce more plentiful nanoparticles as well as their clusters [98]. Except for aggregation and redeposition, the nanoparticles can also be acquired by the laser-induced photoreduction via multiphoton absorption (MPA) when processing the substrates immersed in the solutions such as silver nitrate solutions [114]. The laser-induced photoreduction can also be utilized to fabricate nanoplates [115] and micro-flowers [116], as shown in Fig. 32.6e, f.

Besides, through direct laser interference patterning (DLIP), the grid-like structures with period of about 5.6 μm are processed on commercial polymeric films, as demonstrated in Fig. 32.6g [102]. In DLIP, a single laser beam is split into two, three, or four beams that are overlapped on material surfaces, and an interference pattern related to the energy distribution can be created. The material surface is ablated according to different intensity positions. For two-beam DLIP technique, the spatial period Λ can be calculated using the equation: $\Lambda = \frac{\lambda}{2\sin(\beta/2)}$, where λ refers to the wavelength of the laser beam and β refers to the angle between the two beams [117]. Commonly, the spatial period value is less than 10 μm [117, 118].

In addition to the structures mentioned above, recent studies reported some more complex and elaborate structures for the aim of higher SERS sensitivity.

For instance, Xiao Luo et al. [98] processed periodic micropit arrays covered by interlaced nanorims, nanoprotrusions, and clusters of nanoparticles by laser point-by-point irradiation, as shown in Fig. 32.6h. The diverse nanostructures inside the micropit are induced by the surface multiphoton absorption – when a laser beam irradiates the substrates, the materials generate avalanche ionization and surface plasma and rapidly reunit and deposit as nanostructures after melting and solidification inside the micropit [119]. Aleknavičienė, Indrė et al. [120] acquired amorphous nanosphere clusters with size ranging from tens of nanometers to about 1 μ m using ultrashort-pulse laser-induced plasma-assisted ablation (LIPAA) of soda-lime glass, as depicted in Fig. 32.6i. Zhaoxin Lao et al. [100] fabricated nanopillar arrays with height of 5 μm, 1 μm, and 500 nm by a typical 3D laser printing process on a glass slide, as demonstrated in Fig. 32.6j. Limei Chen et al. [121] reported sub-100 nm antenna arrays on the gold-coated glass substrates consisting of starlike ridges, dome-like heads, and needles in the center, generated by the local melting of gold film and solidification of a liquid metal jet in the laser focus, as shown in Fig. 32.6k.

Laser ablation can not only tune the morphology of surface structures but also control their chemical composition. For example, through a coreduction process of silver ion and palladium ion in a single femtosecond laser direct writing step, Zhuo-Chen Ma et al. [122] integrated silver–palladium (Ag–Pd) alloy nanostructures to protect silver from oxidation.

Chapters 5 and 23 of this book introduce the formation mechanisms and applications of LIPSS and nanoparticles in detail. Chapter 22 descripts the mechanism, detailed process, and applications of laser direct writing method for additive manufacturing. The detailed introduction about direct laser interference patterning (DLIP) can be found in Chap. 26.

3 Laser Nanostructuring of Surfaces for SERS Substrates

Having the unique advantages including one-step, fast, maskless, and direct processing, laser nanostructuring is one of the most promising techniques for the fabrication of diverse nanostructures needed for SERS substrates [113]. According to the fabrication process, laser-nanostructured SERS substrates can be divided into two types: SERS substrates fabricated by one-step laser direct ablation and SERS substrates fabricated by laser direct ablation and then Au/Ag deposition. The laser-nanostructured SERS substrates typically show excellent performances in stability, activity, reproducibility, high fabrication efficiency, and low cost, which is capable of practical applications including food safety evaluation and environmental pollutant monitoring.

3.1 SERS Substrates Fabricated by One-Step Laser Nanostructuring

Ultrafast laser possesses outstanding properties such as high power density and short pulse duration, leading to direct and controllable fabrication of micro-/nanostructures on the bulk material. Han-Wei Chang et al. [96] applied a commercial Ti:sapphire femtosecond laser system to process Ag surfaces to form periodic nanostructure, also known as ripples, covered by random nanocavities and nanospheres. This SERS structure realized 15 times enhancement on Raman signal strength when detecting Rhodamine 6G (R6G), as shown in Fig. 32.7a. Libin Lu et al. [97] used a Yb:KGW solid-state laser with the pulse duration of 230 fs to fabricate Ti6Al4V surfaces for hierarchical LIPSS consisting of micro-grooves, nano-ripples, and nanoparticles, as exhibited in Fig. 32.6b. The textured Ti6Al4V SERS substrate showed high sensitivity for crystal violet (CV) with a limit of detection (LOD) of 10^{-11} mol/L and an enhancement factor (EF) of 7.85×10^5, which was about 22 times higher than the EF of LIPSS, as demonstrated in Fig. 32.7b. Limei Chen et al. [121] used femtosecond laser with wavelength of 632.8 nm to process sub-100 nm antenna arrays on the gold-coated glass substrates, as shown in Fig. 32.6k, and achieved two orders of magnitude of Raman signal compared with plain gold film. Xiao Luo et al. [98] employed Trumpf TruMicro5000 femtosecond laser to process Ag substrates in the atmosphere of Argon to form unique micro-nano structure consisting of micropits covered by interlaced nanorims, nanoprotrusions, microparticles, and clusters of nanoparticles (referring to S-Ag-Ar). This Ag SERS substrate exhibited higher sensitivity (LOD = 10^{-8} mol/L) and enhancement factor (EF = 5.3×10^6). Aimed at practical applications, they further evaluated the uniformity to be RSD = 11.97% and the storage time more than 7 months in vacuum. Therefore, the S-Ag-Ar substrate demonstrated good comprehensive properties on sensitivity, uniformity, stability, and universality, as demonstrated in Fig. 32.7c. Chandu et al. [123] applied a femtosecond Ti:sapphire laser system delivering ~50 fs pulses at a wavelength of 800 nm, to process silver-based substrates in acetone liquid atmosphere. They obtained two kinds of SERS structures-groove-type morphology on the substrates (Ag NS) and Ag nanoparticles in acetone (Ag NPs) at the same time. The resultant enhancement factors were 2.3×10^4 and 8.1×10^3 for Ag NS and Ag NPs, respectively. Moreover, the combination of Ag NS and Ag NPs (depositing Ag NPs on Ag NSs) provided an enhancement factor of ~1×10^5. Except for Ag, the Au nanoparticle SERS substrates, processed directly by a femtosecond laser with the pulse duration of 35 fs and a repetition rate of 1 kHz in a grid-like scanning, were reported to detect analytic molecules of R6G, Rhodamine B, and malachite green (MG) with concentrations down to 10^{-9} mol/L [124]. Moreover, Syed Hamad et al. [99] fabricated random nanostructures with typical size of ∼100 nm by ultrafast laser ablation in chloroform with the fluence of ∼2.5 J/cm and achieved the EF in the range of 10^6–10^8 for R6G and explosive molecules of 5-amino-3-nitro-1,2,4-triazole and 1,1-diamino-2,2-dinitroethene, as illustrated in Fig. 32.7d.

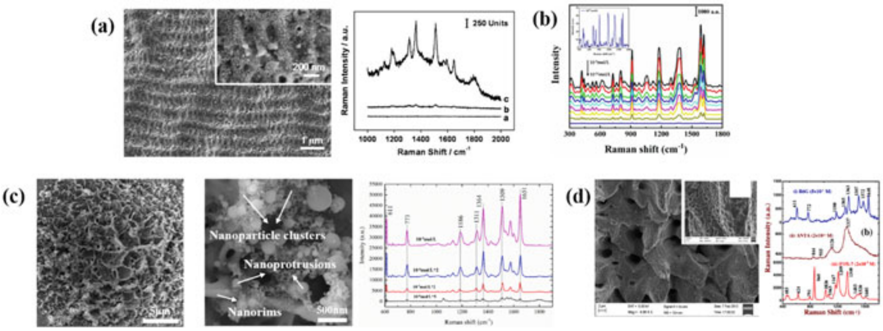

Fig. 32.7 (**a**) SEM images of ripples covered by random nanocavities and nanospheres and the Raman spectra of 10^{-6} mol/L R6G in aqueous solution on the laser-irradiated Ag substrate. (Reproduced from Ref. [96] with permission from Elsevier); (**b**) SERS spectra of CV with the concentration decreased from 10^{-3} to 10^{-11} mol/L. (Reproduced from Ref. [97] which is licensed under Creative Commons Attribution 4.0 International License (https://creativecommons.org/licenses/by/4.0/)); (**c**) SEM images of S-Ag-Ar and the Raman spectra of R6G solutions on S-Ag-Ar substrates with different concentrations. (Reproduced from Ref. [98] with permission from Elsevier); (**d**) SEM image of random nanostructures and their SERS performance. (Reproduced from Ref. [99] with permission from Elsevier)

Direct laser processing can also induce photoreduction via multiphoton absorption (MPA), in addition to ablate the micro-/nanostructures, which is able to further enhance the Raman effect. Hai-lung Tsai et al. [114] used a femtosecond laser with pulse energy of 0.3 J/cm^2 to process silicon in 0.1 M silver nitrate solutions. They obtained grating-like nanostructures covered by silver nanoparticles via the laser-induced photoreduction effect (Fig. 32.8a) and achieved an enhancement effect about 10^9. The same group processed $AgNO_3$-coated silicon surfaces to create 20–100 nm silver particles distributed on nanostructured surfaces (Fig. 32.8b) again based on photoreduction effect and to achieve an enhancement effect of 5×10^5 measured by 10^{-6} mol/L R6G [125]. Qianqian Yang et al. [109] firstly processed ripples on silica by a linearly polarized femtosecond laser and then fabricated 80-nm-diameter nanopillar arrays covered by silver nanoparticles via a 90° rotated polarization, femtosecond double-pulse train in silver nitrate solution, as demonstrated in Fig. 32.6c. They achieved a LOD of 125 ppb and an EF of 1.1×10^9 for melamine. This approach can be combined with microfluidic channel for in situ SERS monitoring, called integrated microfluidic SERS substrates. For instance, Bin-Bin Xu et al. processed crystallized silver nanoplates [115] and silver microflower arrays attached by nanoparticles [116] inside glass microchannel beds via femtosecond laser (wavelength = 800 nm, pulse width = 120 fs, and repetition rate = 80 MHz) (Figs. 32.8c and 32.6f). They realized real-time monitoring of chemical reactions through in situ detection of target analytes at different positions in the microchannel, both achieving an enhancement factor (EF) about 10^8 for p-aminothiophenol (p-ATP). Rajasimha Kurnoothala et al. [126] integrated silver nanoparticles onto a fused silica-based microfluidic channel by femtosecond fiber

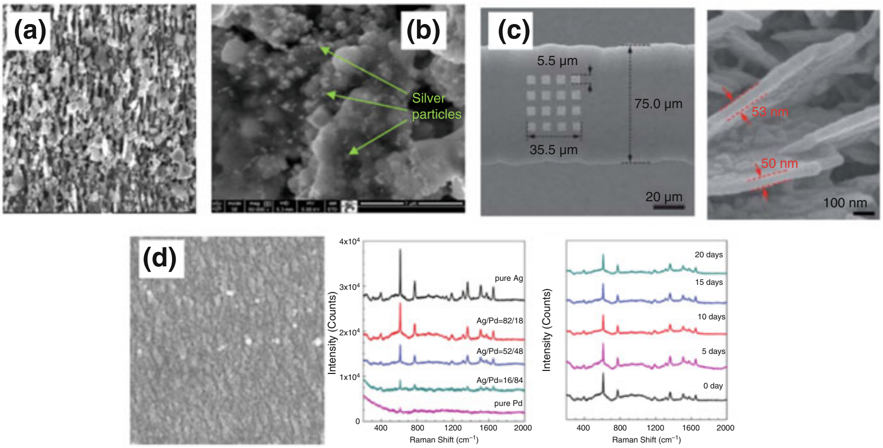

Fig. 32.8 (**a**) Surface morphologies of the machined silicon wafer substrates in 0.1 M silver nitrate solutions. (Adapted with permission from Ref. [114] © The Optical Society); (**b**) SEM image of silver nanoparticles on laser-machined substrate with $AgNO_3$ coating. (Reproduced from Ref. [125] with permission from Springer Nature); (**c**) SEM images of the silver nanoplates on the substrate integrated in the microfluidic channel. (Reproduced from Ref. [115] with permission from the Royal Society of Chemistry); (**d**) SEM images of Ag–Pd alloy nanostructures (18% Pd), SERS spectra of Ag–Pd alloy nanostructures with various metal ratios, and SERS spectra of Ag–Pd alloy nanostructures (18% Pd) with increasing exposure time under ambient conditions within 20 d. (Reproduced from Ref. [122] with permission from John Wiley and Sons)

laser (BlueCut) micromachining, achieving an average EF of 10^4. Zhuo-Chen Ma et al. [122] explored Ag–Pd alloy nanostructures with various compositions by femtosecond laser direct writing via Ti:sapphire laser system (Spectra-Physics Tsunami) with an output wavelength of 800 nm, achieving a LOD of 10^{-9} mol/L and an EF of 2.62×10^8 for R6G. They concluded that the Ag–Pd alloy with 18% content of Pd could protect the silver from oxidation and prolong the lifetime for about 20 days (Fig. 32.8d).

3.2 SERS Substrates Fabricated by Laser Nanostructuring and Ag/Au Deposition

Typical SERS substrate materials are metals such as gold, silver, and copper with gold and silver showing better effect; however these materials are normally expensive. To be cost-effective, silver and gold coatings were sometimes deposited onto bulk solid-state materials, such as silicon [127], glass [120, 128, 129], aluminum sheets [130], Al_2O_3 [103, 106], and polymeric plate [102]. Laser nanostructuring these bulk materials with gold and silver coatings or Ag/Au nanoparticle deposition resulted in more plentiful micro-/nanostructures as "hot spots" and lower cost

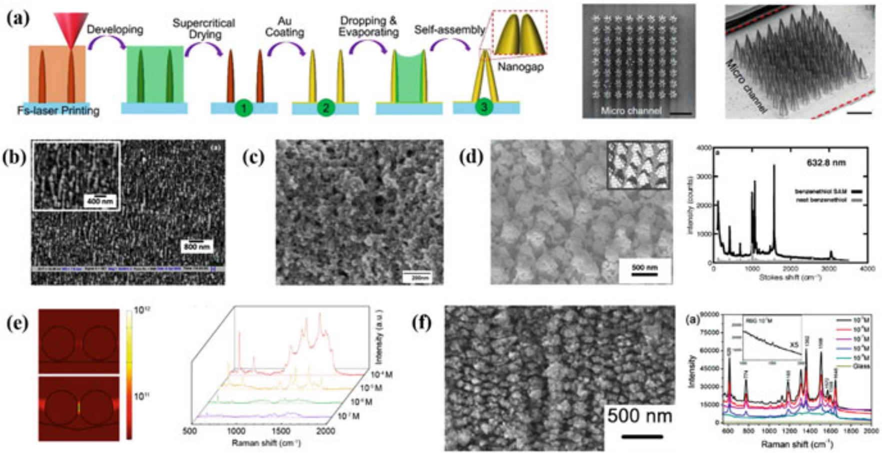

Fig. 32.9 (**a**) Fabrication illustration of microstructures in channels and the SEM images of nanogap plasmonic structures fabricated with the switchable CFSA method. (Reproduced from Ref. [100] with permission from John Wiley and Sons); (**b**) SEM image of nanostructured Si surface obtained from femtosecond laser irradiation. (Reproduced from Ref. [101] with permission from Elsevier); (**c**) SEM image of the Cu substrate covered by AuNPs. (Reproduced from Ref. [104] with permission from Springer Nature); (**d**) SEM images of the nanostructured substrate coated with 80 nm of silver and Raman spectra of benzenethiol. (Reproduced from Ref. [132] with permission from the American Chemical Society); (**e**) COMSOL simulations of local electrical field distribution on flatten and structured SERS substrates and the SERS spectra of R6G molecules. (Reproduced from Ref. [133] which is licensed under Creative Commons Attribution 4.0 International License (https://creativecommons.org/licenses/by/4.0/)); (**f**) SEM images of periodic metal nanostructures fabricated using a femtosecond laser and the SERS spectra of R6G solutions on the periodic Cu-Ag nanostructured surfaces. (Reproduced from Ref. [110] with permission from John Wiley and Sons)

of raw materials. Zhaoxin Lao et al. [100] applied a femtosecond laser to form plasmonic polymer micropillar arrays inside glass microchannels and then used the supercritical drying and the capillary force-driven self-assembly (CFSA) to acquire 3D nanogap structures, as shown in Fig. 32.9a. They subsequently coated Au film on the resultant structures and realized the in situ sensing for anticancer drugs with a maximum enhancement factor of 8×10^7. Jing Yang et al. [131] used a nanosecond laser (wavelength = 1064 nm, pulse duration = 5 ns, and pulse repetition rate = 100 kHz) to create micro-grooves on a silicon substrate and then deposited Ag film on it. They further optimized the thickness of Ag film and found that 20 nm Ag film coating exhibited the best with an enhancement factor up to 5.5×10^6.

As for the deposition of Ag/Au nanoparticles, Vinod Parmar et al. [101] used a Ti:sapphire femtosecond laser (pulse energy = 70 mJ, wave length = 800 nm, pulse duration = 120 fs, repetition rate = 1 kHz) to fabricate LIPSS on silicon substrate and deposited Au nanoparticles on the LIPSS subsequently (Fig. 32.9b). The resultant composite structures obtained a LOD of 2.5×10^{-8} mol/L and an

EF about 10^4 for R6G. Binh Nguyen et al. [104] applied a nanosecond laser to irradiate Cu surfaces and then deposited Ag or Au nanoparticles on the textured Cu, as shown in Fig. 32.9c. Both of them achieved a LOD of 10^{-7} mol/L and an enhancement factor about 10^6 for R6G. Eric D. Diebold et al. [132] utilized amplified titanium:sapphire laser with the pulse duration of 100 fs to process quasi-uniform pillar arrays with a spatial period about 505 nm on a n-type crystalline silicon wafer and then thermally deposited silver nanoparticles on the pillars (Fig. 32.9d), achieving an enhancement factor of 10^7 for benzenethiol.

To enhance the SERS sensitivity, some scientists explored the influence of laser-induced morphology on it. For example, laser-processed microstructures with shallow depth as well as small curvature shorten the distance between the adjacent deposited Ag/Au nanostructures, enhancing the intensity of electrical field and leading to a higher sensitivity (Fig. 32.9e) [133]. When the depth of microstructures reached tens of microns, the intensity of SERS signals drops down dramatically owing to the trap of light inside the microstructures [131, 134]. Other works optimized the quantity, size, and distribution of the laser-induced nanostructures to improve the SERS sensitivity. Kaichen Xu et al. [134] tuned the incident angle between the Si surface and nanosecond laser beam (the laser wavelength is 1064 nm and the pulse duration is 10 ns) to obtain different nanoparticle distributions and sizes. They indicated that nanoparticles with diameter of 100 ~ 200 nm achieved the best enhancement factor of 160 for 4-MBT. Adam Hamdorf et al. [105] applied a femtosecond laser to fabricate LIPSS on silicon and then deposited a 50 nm gold film. Subsequently, the gold film was melted by a nanosecond laser to acquire numerous gold nanoparticles on the substrate. The obtained more abundant nanostructures benefited the enhancement factor up to 2×10^7 for Rhodamine 6G. Shi Bai et al. [110] utilized a femtosecond laser amplifier system with a pulse duration of 457 fs to irradiate the deposited Cu-Ag thin film on the photosensitive-glass substrate. They acquired LIPSS covered with arrays of Cu-Ag nanodots (Fig. 32.9f), which was installed in a 3D microfluidic chip and detected Cd^{2+} ions with a concentration of 10 ppb.

4 Laser Fabricated Specific Wetting Surfaces for Ultrasensitive SERS Detection via Evaporation Enrichment

As discussed in Part 3, the sensitivity of laser-nanostructured SERS substrates typically ranges from 10^{-6} mol/L to 10^{-9} mol/L, which can meet the basic needs of most application areas including food safety evaluation and water quality monitoring. However, as for the diagnose detection, the sensitivity of laser-nanostructured SERS substrates still needs improvements. Studies indicate that the concentrations of biomolecular analytes are mostly lower than 10^{-9} mol/L [135]. Especially, the concentrations of bacterial blood infections, circulating tumor cells (CTCs) which can mark cancers, and the viral targets such as hepatitis C virus (HCV) and human immunodeficiency virus (HIV) are even down to 10^{-17} mol/L ~ 10^{-18} mol/L [135]. Hence, it is necessary to further improve the sensitivity of SERS substrates mentioned above. To integrate SERS substrates with laser-textured superhydrophobic surfaces for the aim of improving sensitivity through evaporation enrichment is one of the most promising strategies.

There are two kinds of sample preparation methods for SERS detection: soaking the SERS substrates into a solution [136, 137] or dropping the liquid onto the SERS substrates [138]. Specifically, the former one is to soak the substrate into a solution and take it out after a period of time. After drying in the air, the target molecules are adsorbed on the surfaces. However, most of the analytic molecules are left in the solution, resulting in the diffusion limiting effect. The latter preparation method is to drop a certain volume of analyte liquid onto the surface of SERS substrates, and then the target molecules deposit on the SERS substrates after the droplet evaporation. Since the SERS substrates are normally hydrophilic or even superhydrophilic, the analytic molecules disperse to a large area on the SERS surfaces, thus resulting in a lower density. Considering that the Raman intensity is always in direct proportion to the concentration or the number of analyte detected [139], the analytic molecules in the solution with low concentration are normally too disperse to be detected, which significantly limits the sensitivity of SERS substrates. Superhydrophobic surfaces, enabling the enrichment of target molecules in the droplets via evaporation process, are considered to break the diffusion limits and to achieve much lower detection limits. Therefore, they are capable of realizing ultrasensitive SERS detection via evaporation enrichment. Based on this idea, there are two strategies: the superhydrophobic surfaces (Sect. 4.1) and patterned hydrophobic/superhydrophilic-superhydrophobic surfaces (Sect. 4.2). Although it's better to prepare SERS structures with specific wettability characteristics during the same laser writing process, fabricating them in different steps is also accepted because the colloids of Au/Ag nanoparticles can be added into the target droplets as the "hot spots" for SERS performance.

4.1 Ultrasensitive SERS Detection with Laser Fabricated Superhydrophobic Surfaces

Superhydrophobic surfaces are defined as the surfaces with contact angle (CA) greater than 150° and sliding angle (SA) smaller than 10° [140–142]. When a droplet evaporates on superhydrophobic surfaces, the contact area will decrease continuously leading to the enrichment of analyte molecules and thus realize higher sensitivity of SERS substrates [143–145]. Due to the ability of fabricating various micro-/nanostructures on almost any kind of materials, laser is one of the most promising techniques for fabricating superhydrophobic surfaces [146, 147]. Meanwhile, laser ablation is also an effective method to process micro-

/nanostructures with SERS performance as discussed previously. Therefore, it is natural to come up with the idea of fabricating superhydrophobic SERS substrates for higher sensitivity by laser processing.

Zhao-Xu Yan et al. [148] used a frequency-tripled, Q-switched, single-mode Nd:YAG laser to fabricate hierarchical reduced graphene oxide (RGO) grating structures with microscale gratings and nanoscale folders through laser ablation and photoreduction process. They then deposited silver and removed the hydrophilic oxygen-containing groups; the resultant material, named as Ag-RGO, was superhydrophobic with contact angle of 152°. It showed high SERS performance with LOD of 10^{-10} mol/L and EF of 2×10^7, as illustrated in Fig. 32.10a. Jijo Easo George et al. [149] applied femtosecond laser to generate grid patterns on polymethylmethacrylate (PMMA) with periodic sharp structures. This patterned PMMA was used as mold to replicate the structures onto polydimethylsiloxane (PDMS). Subsequently, Ag nanoparticles were deposited on the patterned PDMS via in situ reduction. Owing to the low surface energy of PDMS and the diverse micro-/nanostructures, this SERS substrate exhibited superhydrophobic property with a contact angle of 150 ± 3° and at the same time achieved a LOD of 10^{-14} mol/L and an EF of ~10^{10} for R6G solutions, as shown in Fig. 32.10b. Andong Wang et al. [150] utilized a regenerative amplified Ti:sapphire femtosecond laser with the pulse duration of 35 fs and wavelength of 800 nm to process silicon substrates and then deposited 60 nm silver film. The deposition of silver thin film reduced the surface energy and increased hydrophobicity. After evaporation enrichment on this SERS substrate, the target molecules in the droplet mostly shrank to an area with diameter of 0.42 mm, and the laser structured array of conical-shaped spikes and small protrusions led to a detection limit as low as 10^{-14} mol/L for R6G (Fig. 32.10c). Pei Fu et al. [151] produced superhydrophobic micro-/nanostructures on Cu substrates (Fig. 32.10d) via femtosecond laser ablation and chemical treatment. The contact angle of this SERS platform reached 149°, and the resultant deposited area was 0.385 mm^2 for 12 μL mixed solution droplet (10 μL of target molecular solution and 2 μL of Ag nanoparticles solution) after evaporation enrichment, achieving a LOD of 10^{-13} mol/L for R6G.

After the evaporation enrichment on superhydrophobic SERS substrates, the smaller the deposition area of target analytes, the higher the sensitivity. That is, the evaporation shrunk area of the analytic molecules should be as small as possible. It is widely accepted that the wetting of a droplet on a superhydrophobic surface can be divided into two states: the Cassie state and the Wenzel state [152]. In the Cassie state, a droplet wets only part of the micro-nano structured surface since thousands of gasbags will be trapped between thousands of valleys of the micro-/nanostructures and the water droplet. During evaporation, the contact angle keeps constant, while the three-phase contact line keeps moving and shortening, called constant contact angle (CCA) mode. In the Wenzel state, the water droplet penetrates into thousands of the micro-nano valleys and thus completely wets the surface; the water droplet is strongly pinned to the surface. During evaporation in this case,

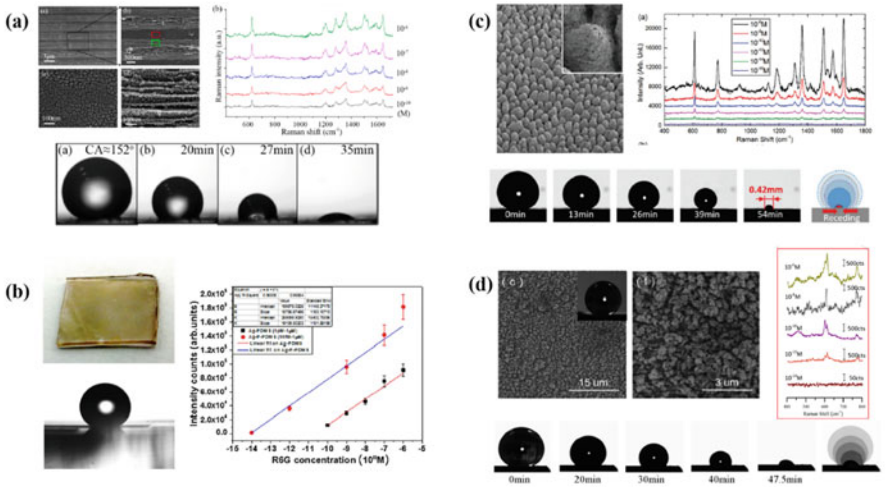

Fig. 32.10 (**a**) SEM images of Ag-RGO gratings, the optical images during the evaporation of the RhB droplet, and the SERS spectra of RhB solution with different concentrations, from 10^{-6} to 10^{-10} mol/L. (Reproduced from Ref. [148] with permission from the American Chemical Society); (**b**) optical images of in situ-reduced silver nanoparticle-grown PDMS substrate and a water droplet (10 μL) on it and the average Raman band intensity with different concentrations of R6G solutions. (Reproduced from Ref. [149] with permission from Elsevier); (**c**) SEM images of the superhydrophobic SERS substrates, the lateral images of the droplet during evaporation at different times, and Raman scattering spectra of solutions with different concentrations from 10^{-6} mol/L to 10^{-16} mol/L, respectively. (Reproduced from Ref. [150] with permission from the Royal Society of Chemistry); (**d**) typical surface morphologies obtained after laser irradiation, the evaporation process of a 12 μL droplet on the SERS substrates, and SERS spectra of R6G with concentrations ranging from 10^{-6} to 10^{-14} mol/L. (Reproduced from Ref. [151] with permission from Elsevier)

the contact line keeps constant, while the contact angle continuously decreases, called constant contact line (CCL) mode. The evaporation process decreases the diameter of the water droplet and increases the Laplace pressure; thus the CCA mode tends to transform to the CCL mode. To be specific, firstly, the contact angle keeps constant, and the three-phase contact line is moving inward, and then, after the pinning of three-phase contact line, the contact angle decreases continuously until the end of evaporation. Thus, the Cassie state, which features the CCA evaporation mode, benefits for the evaporation enrichment. As mentioned, the Laplace pressure keeps increasing during evaporation until a critical pressure when the Cassie state transits eventually to Wenzel state. The more stable the Cassie state, the higher pressure it endures and the smaller the water droplet diameter, thus the better evaporation enrichment. Therefore, a stable Cassie state of a superhydrophobic surface is the key issue for evaporation enrichment. Jiangyou Long et al. [153] studied the relationship between Cassie state stability of metallic superhydrophobic surfaces and the laser fabricated various micro-/nanostructures. They demonstrated that the surfaces with micrometer-scale structures as well as abundant nanoscale

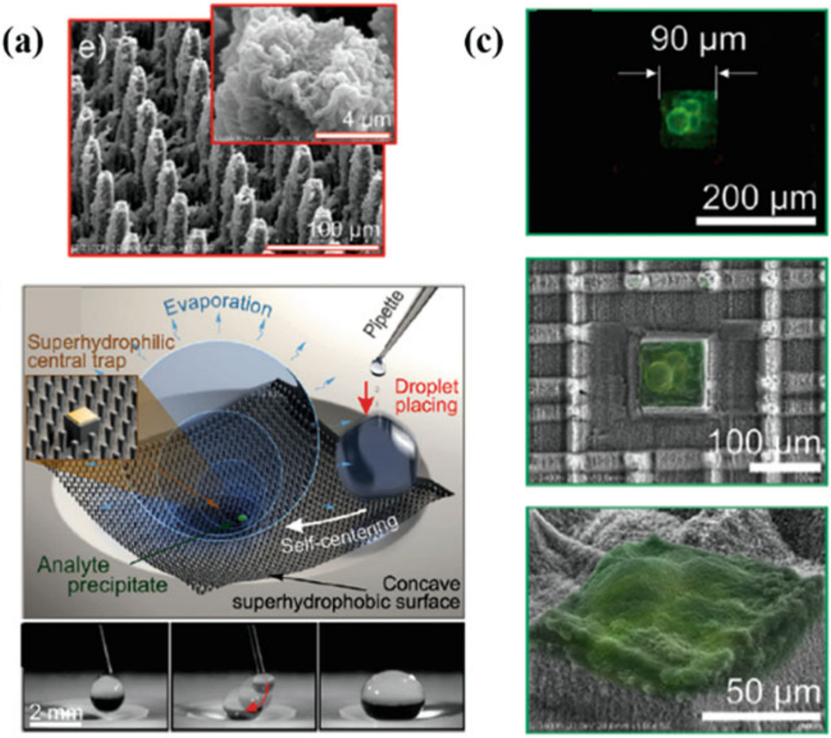
(a)
e)
4 µm
100 µm
(b)
Evaporation
Pipette
Superhydrophilic central trap
Droplet placing
Self-centering
Analyte precipitate
Concave superhydrophobic surface
2 mm
(c)
90 µm
200 µm
100 µm
50 µm

Fig. 32.11 (**a**) SEM images of the PTFE surfaces textured by femtosecond laser; (**b**) schematic illustration of the self-centering and deposition of the water drop onto the pillared PTFE surface with a central trap; (**c**) deposition of 10^{-10} mol/L of R6G analyte molecules dissolved in 5 μL drop onto the central trap. (Reproduced from Ref. [155] with permission from RSC Pub)

structures exhibited stable Cassie state. Furthermore, Rui Pan et al. [154] indicated that the increased hierarchical level and structural complexity contributed to the Cassie state stability. Alexey Zhizhchenko et al. [155] applied femtosecond laser with the pulse duration of 100 fs, wavelength of 400 nm, and repetition rate of 1 kHz to form specific micro-nano structure on polytetrafluoroethylene (PTFE) substrate surface, containing pillar arrays with height of 70 μm and submicron drop-shaped protrusions covered by spherical-shape 50-nm-diameter globules. This structure enabled the PTFE surface a contact angle (CA) up to 170° and a stable Cassie state, which was capable of evaporating a 5 μL water droplet dissolved with analytic molecules completed into a 90 × 90 μm^2 area (Fig. 32.11).

4.2 Ultrasensitive SERS Detection with Laser Fabricated Patterned Hydrophobic/Superhydrophilic-Superhydrophobic Surfaces

Generally, a superhydrophobic surface with high Cassie state stability has its sliding angle typically close to zero, meaning that the droplets roll off rapidly when they are dropped onto such surface. During evaporation, the droplet may locate at anywhere of the superhydrophobic surfaces or not the structured area with SERS signal enhancement. Therefore, in spite of many achievements toward the superior sensitivity on superhydrophobic SERS substrates, there is an urgent need for the spatial localization of solution droplets to be detected in view of practicability [156]. In order to insure the analytic molecules localizing on the sensitive area as predicted, scientists made attempts on the patterned nonuniform superhydrophobic surfaces [157, 158], hydrophobic-superhydrophobic surfaces [159], and superhydrophilic-superhydrophobic surfaces [160]. Again, laser nanostructuring shows its excellent flexibility for fabricating of patterned hybrid wetting surfaces, including hydrophobic-superhydrophobic surfaces [161], superhydrophilic-superhydrophobic surfaces [154], and slippery liquid-infused porous surfaces (SLIPS)-superamphiphobic surfaces [162, 163]. Therefore, laser nanostructuring is the most promising fabrication method for ultrasensitive patterned wetting SERS platform.

In terms of the hydrophobic-superhydrophobic platform, Xinyu Hu et al. [161] fabricated arrays of micro-pillars on polytetrafluoroethylene (PTFE) surfaces via a femtosecond laser. They investigated the relationships among the processing parameters (laser power, scanning times, and scanning intervals), the morphology (column height and column intervals), and the superhydrophobic properties (contact angle and sliding angle) and optimized the structures for better superhydrophobic property (CA $\geq$ 150°). In order to trap the droplet, a tiny square area (0.36 mm^2–0.49 mm^2) remained unprocessed. They mixed the Rhodamine 6G (R6G) with gold nanoparticles and dropped the mixture solution on the textured surface. Compared with the plat PTFE surface, the intensity of Raman signal increased 1–2 orders of magnitude on this textured hydrophobic-superhydrophobic PTFE platform. Similarly, Fangjia Chu et al. [159] applied CO_2 laser engraving technology to change the wettability of PTFE surfaces and obtained hydrophobic microarrays (the diameter of circle: 0.5 mm) surrounded by superhydrophobic area on PTFE substrate. Based on evaporation enrichment, they detected target molecules including methylene blue (10^{-14} mol/L), R6G (10^{-14} mol/L), and bovine serum albumin (BSA, 0.002 μg/ml), as demonstrated in Fig. 32.12.

As for the superhydrophilic-superhydrophobic surfaces, Xiaodan Ma et al. [164] used a femtosecond laser beam with a pulse duration of 35 fs and the repetition rate of 1000 Hz to process sputtered PDMS film on silicon surfaces through laser-induced forward transfer (FLIFT), obtaining superhydrophobic surfaces. Then they used the same femtosecond laser to ablate and remove part of

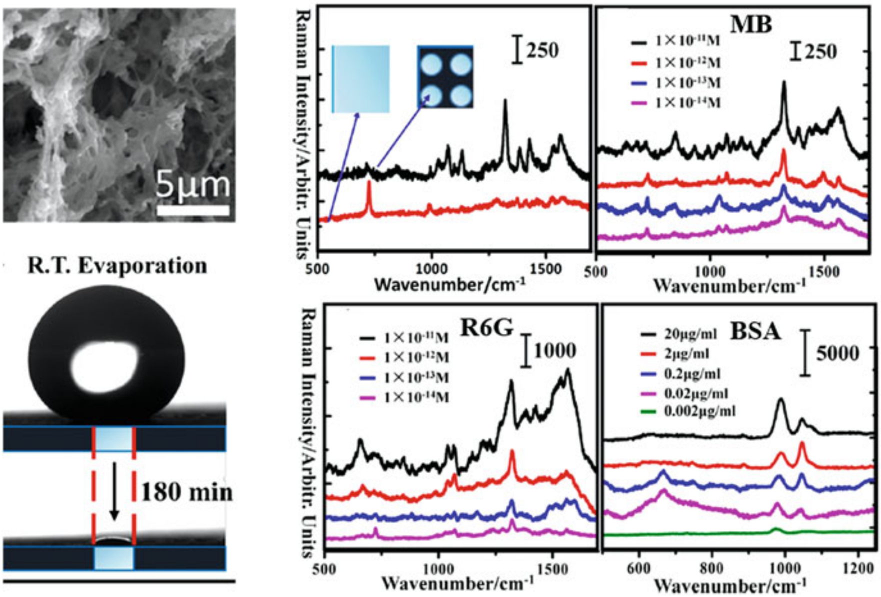

Fig. 32.12 SEM images of the laser-induced structures on PTFE, the evaporation profiles of solution on the engraved PTFE, and the SERS spectra of MB, R6G, and BSA with various concentrations, respectively. (Reproduced from Ref. [159] which is licensed under Creative Commons CC BY license (https://creativecommons.org/licenses/))

PDMS to form patterned superhydrophilic structures on silicon (Fig. 32.13a). This hybrid superhydrophilic-superhydrophobic SERS (HS-SERS) platform was heated to promote a smaller concentration area of 0.013 mm^2, achieving a detected limit concentration as low as 10^{-16} mol/L for R6G. Huan Yang et al. [165] processed stainless steels via a femtosecond laser to fabricate a circular superhydrophilic area with LIPSS covered by nanoparticles and surrounding superhydrophobic region with deep micro-groove structures, as exhibited in Fig. 32.13b. This platform realized a concertation area only 0.09 mm^2 of a 5 μL droplet and detected 10^{-14} mol/L R6G with a good uniformity (RSD = 6.98%) and the SERS enhancement factor of 5.7×10^8. Georgii Pavliuk et al. [166] utilized a regenerative amplified Yb:KGW femtosecond laser system to fabricate superhydrophobic periodically arranged pillars on PTFE, as they reported in the former work [140]. Then they applied the same laser to process the central rectangular-shaped area with size of 80×80 μm^2 to be superhydrophilic. This superhydrophilic central area functioned as SERS with morphology of multiple-nanoscale spiky features randomly arranged within circular-shaped craters, as shown in Fig. 32.13c. The SERS platform can identify various analytes including organic dye and medical drugs (levofloxacin, ciprofloxacin, pefloxacin, diphenhydramine hydrochloride, ibuprofen sodium, diclofenac sodium, 4-acetamidophenol) at a concentration down to 10^{-12} mol/L. Xiangyun Guan et al. [167] used femtosecond laser to process

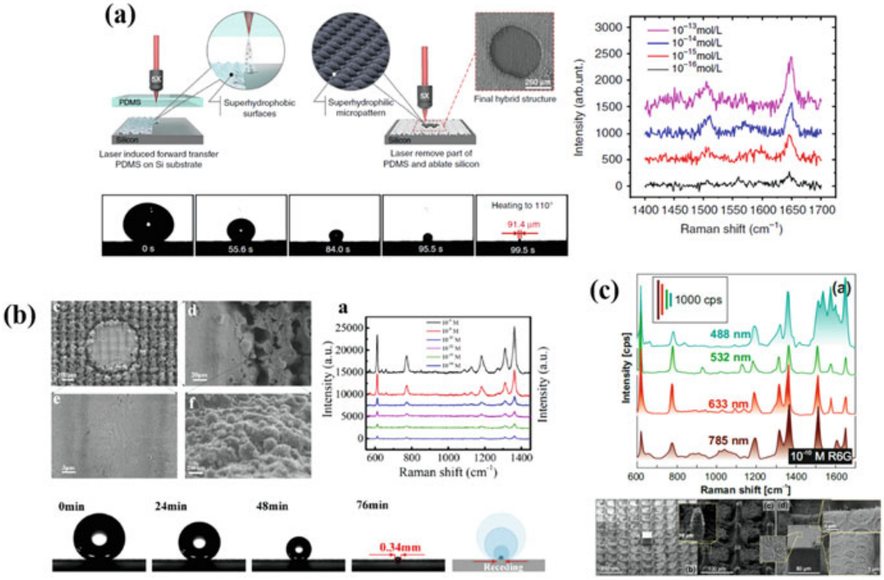

Fig. 32.13 (**a**) Schematic of the fabrication process of the HS-SERS substrate, lateral images of the concentration process of a droplet on the HS-SERS surface with a diameter of 100 μm and heated to 110 °C, and the Raman spectra of 10^{-13} ~ 10^{-16} mol/L R6G solutions on the HS-SERS substrate. (Reproduced from Ref. [164] which is licensed under Creative Commons CC BY license (https://creativecommons.org/licenses/)); (**b**) morphology of the femtosecond laser-patterned surface, evaporation process of 5 μL drops containing 0.1 mg/mL polystyrene, and the Raman spectra of R6G at different concentrations. (Adapted with permission from Ref. [165] © The Optical Society); (**c**) SEM images of the surface morphology of the hydrophobic pillars and laser-patterned plasmonic site and the SERS spectra measured from Rhodamine 6G (R6G) molecules at different pump wavelengths. (Reproduced from Ref. [166] which is licensed under Creative Commons CC BY license (https://creativecommons.org/licenses/))

micropillar array on copper; after chemical modification, the surface with micro-pillars became superhydrophobic with contact angle of 151.2° and sliding angle of 2.4°. Then they used the same laser to irradiate an area with diameter of 0.4 mm to destroy the micro-pillars and chemicals with low surface energy to acquire superhydrophilic area with contact angle close to 0°, realizing the detection of 10^{-13} mol/L R6G after evaporation enrichment. Xiao Luo et al. [160] applied a femtosecond laser to fabricate superhydrophobic copper surfaces with multiple structures of micro-pillars, micro-flowers, and nano-sheets, by hybrid of laser ablation, oxidation, and fluorination. These surfaces showed extremely high Cassie stability. However, a central rectangular region on the surface kept was unprocessed, and then unique micro-/nanostructures for SERS functions were formed by the same femtosecond laser; they were composed of periodic micropit arrays covered by nanorims as well as nanoparticles. The second laser processing removed the fluoride layer in the central region and thus made it superhydrophilic together

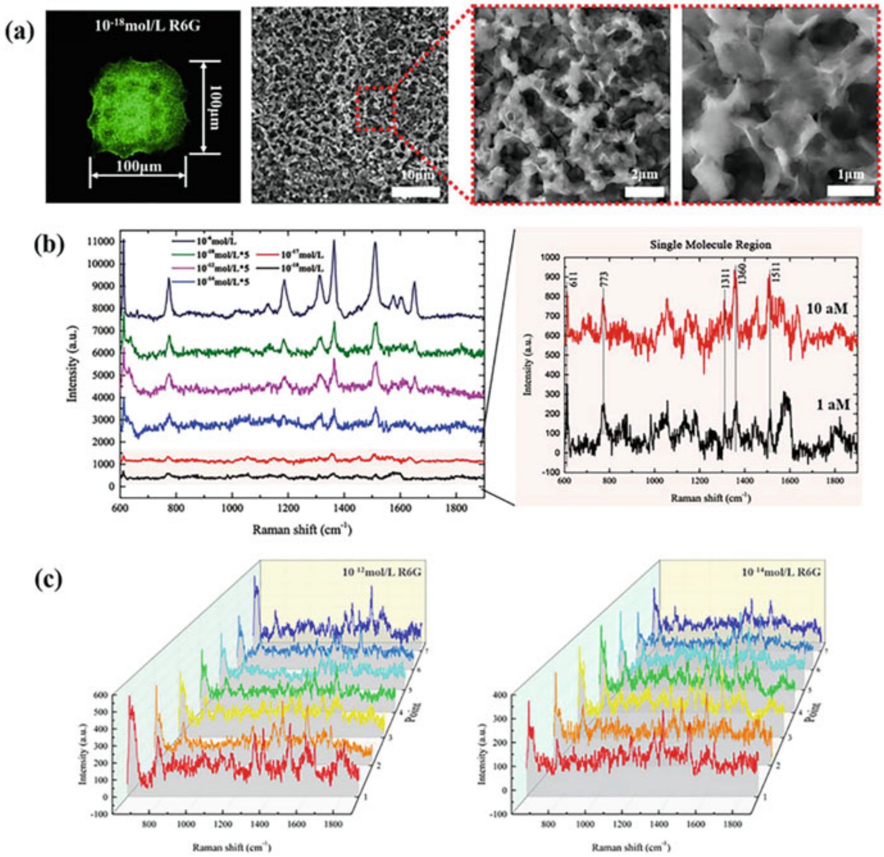

Fig. 32.14 Patterned superhydrophilic-superhydrophobic platform fabricated by femtosecond laser. (**a**) SEM images of the R6G and AuNSs aggregating on the central area after evaporation concentration; (**b**) Raman spectra of R6G@AuNSs with different concentrations; (**c**) Raman signals of seven random points on the central area with 10^{-12} mol/L and 10^{-14} mol/L R6G solutions. (Reproduced from Ref. [160] with permission from Elsevier)

with its micro-/nanostructures. This surface then had a superhydrophilic SERS central region and extra-stable superhydrophobic surroundings. As a result, after evaporation enrichment, almost all of the target molecules deposited on the central superhydrophilic area of 0.01 mm^2, as shown in Fig. 32.14a. Meanwhile, the authors further mixed the analyte solutions with three kinds of colloids (silver nanoparticles, gold nanoparticles, and gold nanostars) to enhance the SERS effect. They observed that the gold nanostar addition performed the best results with a LOD of 10^{-18} mol/L for R6G and an EF of ~1.09×10^{14}, which was the highest available SERS detection limit as reported (Fig. 32.14b). In addition, this platform exhibited good uniformity with the relative standard deviation (RSD) to be 11.7% at 10^{-14} mol/L for R6G (Fig. 32.14c).

In conclusion, the laser nanostructuring technology can fabricate SERS platforms with patterned superhydrophilic-superhydrophobic structures for extremely high sensitivity and uniformity, excellent comprehensive performances, and high fabrication efficiency, which enables the trace detection of chemicals in many fields including disease early diagnosis.

5 Applications of SERS Detection

Raman spectrum can provide the fingerprint information of molecular structures and then realize the identification of unknown components based on the spectrums about the vibration or rotation mode of molecules. The ordinary Raman spectroscopy shows the advantages of simple preparation process, less sample demanded, nondestructive inspection, efficient analysis, and reliable test results. In addition to inheriting those advantages, SERS has many extra unique virtues such as high sensitivity, quantitative analysis potential, real-time monitoring, and so on. Thus, it can be broadly applied in food safety evaluation [168], environment monitoring [169], drug testing [170], biomedicine [171], and disease diagnosis [172]. The following part introduces the potential applications of laser-nanostructured SERS substrates, especially in the food safety evaluation and cancer diagnose detection.

5.1 SERS for Food Safety Evaluation

Some unscrupulous businesses, for various illegal purposes, may add harmful additives into the foods during the production and processing procedures, such as melamine [173], sudan [174], malachite green [175], crystal violet [176], methylene blue [177], thiram [178], and clenbuterol [179], which brings enormous harms to the human health. Recently, the incidents about food safety affairs make the supervision on the food additives the focus both at home and abroad. To realize the efficient and rapid monitoring, the scientists pay attention not only to the adequate sensitivity but also to the cost-effective and reliable detection technologies [180]. Numerous testing methods have been developed including colorimetric analysis [181], high-performance liquid chromatography (HPLC) [182], mass spectra (MS) [183], HPLC-MS [184], and spectroscopic imaging [185]. However, deficiencies such as complicated pretreatment process, long detection time, expensive equipment, lack of field testing capability, as well as inconveniency on real-time analysis are available to different extent in those methods. SERS is thus considered an attractive way for food safety assurance, especially the rapid field testing in production line [180], based on its merits of excellent sensitivity, rapid, nondestructive, label-free, and fingerprint detection [186–188].

The sensitivity required for food safety evaluation usually ranges from 10^{-6} mol/L to 10^{-8} mol/L, which can be met by most of the SERS substrates processed by laser ablation. For instance, the SERS substrate composing of laser-induced periodical surface structures (LIPSS) detected the crystal violet with a concentration of 10^{-11} mol/L, and the high uniformity with relative standard deviation value of 5.15% was achieved [97] (Fig. 32.15a). Wending Zhang [124] realized the detection of 10^{-9} mol/L malachite green by using the SERS substrates fabricated via femtosecond laser irradiation (Fig. 32.15b). Raju Botta et al. [130] detected a concentration of 27 ppb of paraquat dissolved in the water from rice field and vegetable field using the laser-textured aluminum sheet decorated with gold nanoparticles (Fig. 32.15c). Xiao Luo et al. [98] reported that the silver-based SERS substrates (referring to S-Ag-Ar) processed by a femtosecond laser detected the common food additives such as malachite green (1 ppm), crystal violet (10^{-7} mol/L), sudan I (1 ppm), melamine (1 ppm), brilliant blue (1 ppm), and tartrazine (1 ppm) (Fig. 32.15d). Therefore, high sensitivity of SERS substrates may not be a challenging issue; however, from the perspective of practical applications, it remains a crucial issue for SERS substrates to have good comprehensive properties on low cost, uniformity, stability, and universality [189]. Hence, laser nanostructuring offers a promising approach for SERS substrates with better uniformity and stability aiming at quantitative determination.

5.2 SERS for Cancer Diagnose Detection

Raman spectroscopy is a molecular vibrational spectroscopic technique that is capable of optically probing the biomolecular changes associated with disease transformation. Due to its advantages on convenient operation, high sensitivity, and reliability of the molecular information, SERS is being extensively developed to be a potential method for disease diagnose detection, especially the cancer diagnose detection including lung cancer [190], gastric cancer [191], breast cancer [192], prostate cancer [193], oral cancer [194], and nasopharynx cancer [195]. Generally, as a cancer grows, the relevant cells emit or overconsume some chemicals. SERS with enough high sensibility is able to detect the variation of the quantity of these chemicals in breath [196], saliva [197], urine [198], and blood [199, 200]. For example, Vlad Moisoiu et al. [201] tested the SERS spectroscopy on serum samples from the patients of five leading malignancies: breast, colorectal, lung, ovarian, and oral cancer. The results demonstrated that the accuracy was 88% for oral cancer, 86% for colorectal cancer, 80% for ovarian cancer, 76% for breast cancer, and 59% for lung cancer via principal component analysis–linear discriminant analysis (PCA-LDA). Considering that these detections always require a large number of samples for data analysis, the stability and reproducibility of the SERS substrates become particularly important. Moreover, the recent studies indicated that the concentrations of cancer biomarkers – the circulating tumor cells (CTCs) – in clinical samples ranged from 0.5×10^{-13} mol/L to 10^{-17} mol/L [202]. That is, once the sensitivity of SERS technique is better than 10^{-17} mol/L, like the reported patterned superhydrophilic-superhydrophobic platform with a LOD of 10^{-18} mol/L

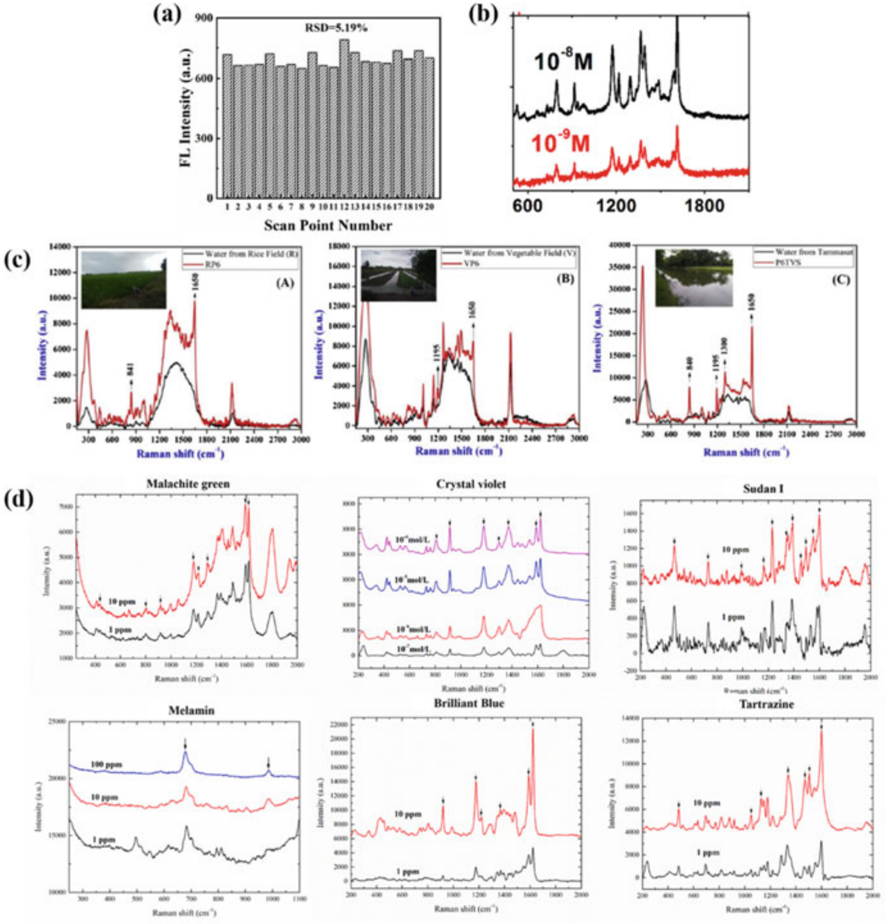

Fig. 32.15 (**a**) RSD of the integrated fluorescence intensity of CV at 880 cm^{-1}. (Reproduced from Ref. [97] which is licensed under Creative Commons Attribution 4.0 International License (https://creativecommons.org/licenses/by/4.0/)); (**b**) Raman spectra of MG with the concentrations of 10^{-8} and 10^{-9} mol/L on the laser fabricated Au-NP substrates. (Reproduced from Ref. [124] with permission from IOP Publishing); (**c**) SERS spectra of paraquat dissolved in the water from rice field, vegetable field, and Thammasat University with the concentration of 27 ppb. (Reproduced from Ref. [130] with permission from Elsevier); (**d**) SERS spectra of the common food additives. (Reproduced from Ref. [98] with permission from Elsevier)

[160], it is possible to detect the CTCs in the blood and to realize more accurate diagnosis. Therefore, the detection of cancer biomarkers is considered as the most important potential application field for the laser fabricated superhydrophilic-superhydrophobic patterned SERS substrates with the ability of single molecule detection.

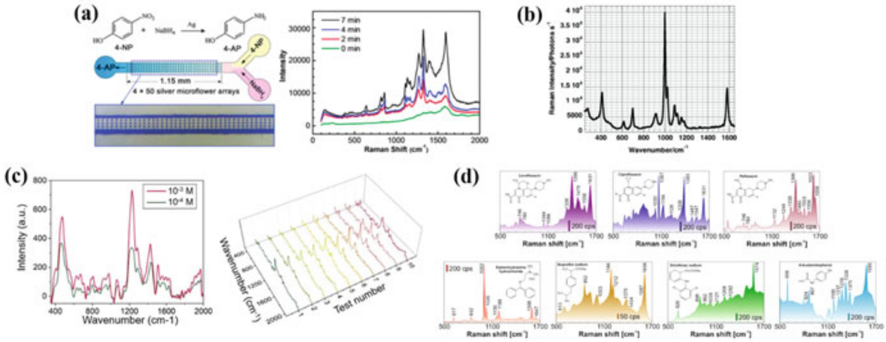

Fig. 32.16 (**a**) Scheme for catalytic microfluidic channel and the Raman spectra detected after different reaction times. (Reproduced from Ref. [116] with permission from the Royal Society of Chemistry (Great Britain)); (**b**) Raman spectrum of benzenethiol. Reproduced from Ref. [127] with permission from John Wiley and Sons); (**c**)The Raman spectra of anticancer drugs (DOX) with different concentrations on self-assembled patterns and Raman signals of ten random points on the SERS substrates – the RSD is about 8.1%. (Reproduced from Ref. [100] with permission from John Wiley and Sons); (**d**) ERS spectra of levofloxacin, ciprofloxacin, pefloxacin, diphenhydramine hydrochloride, ibuprofen sodium, diclofenac sodium, and 4-acetamidophenol with the concentration of 10^{-8} mol/L. (Reproduced from Ref. [166]. Reproduced from which is licensed under Creative Commons CC BY license (https://creativecommons.org/licenses/))

5.3 SERS for Other Applications

Except for the food safety evaluation and cancer diagnose detection, scientists also researched other application areas for laser-nanostructured SERS substrates such as the real-time observation of chemical reactions, monitoring of hazardous chemicals, drug testing, and the detection of pollutants in water. For instance, Bin-Bin Xu et al. [116] observed the reduction of 4-nitrophenol (4-NP) to 4-aminophenol (4-AP) via laser fabricated silver microflower arrays on microfluidic channels (Fig. 32.16a). The toxic, flammable, and reactive chemicals such as benzenethiol were detected through silver-covered laser-induced nanopillar arrays, as demonstrated in Fig. 32.16b [127]. Moreover, as for the drug testing, Zhaoxin Lao [100] fabricated 3D nanogap plasmonic structures via laser printing, allowing the localized sensing for anticancer drugs (doxorubicin) with the relative standard deviation (RSD) of about 8.1%, as depicted in Fig. 32.16c. Georgii Pavliuk et al. [166] detected seven kinds of biologically active organic pollutants (pefloxacin, ciprofloxacin, levofloxacin, diphenhydramine hydrochloride, ibuprofen, diclofenac, and 4-acetamidophenol) in water with a concentration of 10^{-8} mol/L by using superhydrophilic-superhydrophobic platform with analyte-enrichment system, as shown in Fig. 32.16d. There are still many potential applications waiting to be explored for laser-nanostructured SERS substrates, especially the laser-induced ultrasensitive superhydrophilic-superhydrophobic patterned SERS substrates.

6 Summary and Perspectives

SERS is currently a research hotspot in the field of substance detection due to its inherent molecular fingerprint specificity and potential for single molecule detection, possessing rich research connotations and broad application potentials. Along with the advances in ultrafast laser processing technologies, laser nanostructuring becomes one of the most promising methods to overcome the difficulties of current SERS-active substrates. Furthermore, the integration of SERS substrates with superhydrophobic surfaces significantly increases the SERS sensitivity and extends the detection limit through the evaporation enrichment of analytic solutions, thus making single molecule detection more realistic. All the above enable SERS technology a bright future, especially in the disease diagnose detection.

This chapter begins with SERS concept, its enhancement mechanisms, unique nanostructures, and versatile fabrication methods for SERS substrates. Then we focus on laser nanostructuring for SERS substrate fabrication, including the one-step laser nanostructuring and laser nanostructuring with Ag/Au deposition (Table 32.1). Furthermore, we elaborate the laser fabricated superhydrophobic surfaces and patterned superhydrophilic-superhydrophobic surfaces for the ultrasensitive SERS detection via evaporation enrichment. Tables 32.1 and 32.2 give the overview of typical works mentioned in the Sects. 3.1, 3.2, 4.1, and 4.2. Meanwhile, for comparison, the typical SERS substrates processed by other fabrication methods are discussed in Sect. 1.3, as illustrated in Table 32.3. According to the merits of laser fabricated SERS substrates, we explored their applications, including but not limited to food safety evaluation, cancer diagnose detection, real-time observation of chemical reactions, monitoring of hazardous chemicals, drug testing, and detection of pollutants in water. Based on the developments of the laser-textured SERS substrates up to now, this field is undoubtedly expected to continuously produce more achievements in the future. However, there are still many challenges for the development of laser-nanostructured SERS substrates:

1. Systematic researches on optimization of nanostructures for better SERS performance, especially the composite structures consisting of nanostructures with different shapes and scales or with various chemical components.
2. The controllable fabrication of more plentiful nanostructures with smaller size according to the theoretical researches on enhancement mechanisms and simulation results. Notably, as for the laser nanostructuring method, how to break the diffraction limit and realize the free fabrication of typical nanostructures with size of 1–100 nm remains a big challenge.
3. To further improve the sensitivity and realize the detection of solutions with concentration even lower than 10^{-18} mol/L, it deserves further studies on the fabrication of more stable superhydrophobic surfaces to ensure the target molecules deposited on the smaller desired central area through evaporation enrichment.
4. As for the practical applications, it needs further efforts to fabricate uniform and reproducible SERS nanostructures, the semi-quantitative analysis and quantita-

Table 32.1 Overview on exemplary works discussed in the Sects 3.1 and 3.2

	Authors	Material(s)	Laser technique	Micro-/nanostructures	Sensitivity for SERS		
					Analyte	LOD	EF
3.1 SERS substrates fabricated by one-step laser nanostructuring	Han-Wei Chang et al. [96]	Ag	Commercial Ti:sapphire femtosecond laser system	Ripples covered by random nanocavities and nanospheres	R6G	10^{-8} mol/L	1.2×10^6
	Libin Lu et al. [97]	Ti6Al4V	Yb:KGW solid-state laser with the pulse duration of 230 fs	Hierarchical LIPSS consisting of micro-grooves, nano-ripples, and nanoparticles	CV	10^{-11} mol/L	7.85×10^5
	Limei Chen et al. [121]	Gold-coated glass	Femtosecond laser with wavelength of 632.8 nm	Sub-100 nm antenna arrays consisting of starlike ridges, dome-like heads, and needles in the center	Rhodamine	–	10^2
	Xiao Luo et al. [98]	Ag	Trumpf TruMicro5000 femtosecond laser, processed in Ar	Micropit arrays covered by interlaced nanorims, nanoprotrusions, microparticles, and clusters of nanoparticles	R6G	10^{-8} mol/L	5.3×10^6
	B. Chandu et al. [211]	Ag	Femtosecond Ti: sapphire laser system delivering ~50 fs pulses at a wavelength of 800 nm, processed in acetone	Groove-type morphology on the substrates (Ag NS)	2, 4-dinitrotoluene	–	2.3×10^4
				Ag nanoparticles in acetone (Ag NPs)		–	8.1×10^3
				The combination of Ag NS and Ag NPs		–	$\sim 1 \times 10^5$

(continued)

Table 32.1 (continued)

	Authors	Material(s)	Laser technique	Micro-/nanostructures	Sensitivity for SERS		
					Analyte	LOD	EF
	Wending Zhang et al. [124]	Au	A femtosecond laser with the pulse duration of 35 fs and a repetition rate of 1 kHz	Au nanoparticles	R6G, Rhodamine B, and MB	10^{-9} mol/L	–
	Syed Hamad et al. [99]	Cu	Ultrafast laser with the fluence of ~2.5 J/cm	Random nanostructures with typical size of ~100 nm	R6G and explosive molecules	–	10^6–10^8
	Hai-lung Tsai et al. [114]	Si	Femtosecond laser with pulse energy of 0.3 J/cm^2, processed in 0.1 M silver nitrate solutions	Grating-like nanostructures covered by silver nanoparticles	R6G	–	10^9
	Hai-lung Tsai [125]	$AgNO_3$-coated silicon	Femtosecond laser	20–100 nm silver particles	R6G	10^{-6} mol/L	5×10^5
	Qianqian Yang et al. [109]	Silica	A linearly polarized femtosecond laser, processed in silver nitrate solution	80-nm-diameter nanopillar arrays covered by silver nanoparticles	Melamine	125 ppb	1.1×10^9
	Bin-Bin Xu et al. [115]	Glass	Femtosecond laser (wavelength = 800 nm, pulse width = 120 fs, and repetition rate = 80 MHz), processed in silver nitrate solution	Silver nanoplates	p-ATP	10^{-9} mol/L	~10^8

	Bin-Bin Xu et al. [116]	Glass	Femtosecond laser (wavelength = 800 nm, pulse width = 120 fs, and repetition rate = 80 MHz)	Silver microflower arrays	p-ATP	–	10^8
	Rajasimha Kurnoothala et al. [126]	Silica	Femtosecond fiber laser (BlueCut)	Silver nanoparticles	R6G	–	10^4
	Zhuo-Chen Ma et al. [122]	Ag, Pd	Ti:sapphire laser system (Spectra- Physics Tsunami) with wavelength of 800 nm	Ag–Pd alloy nanostructures	R6G	10^{-9} mol/L	2.62×10^8
3.2 SERS substrates fabricated by laser nanostructuring and Ag/Au deposition	Alison Chou et al. [106]	Gold, sapphire	Ti:sapphire femtosecond pulse laser with wavelength of 800 nm and pulse duration of 150 fs	Gold-coated ripple	2,4-DNT	–	5.5
	Ricardas Buividas et al. [129]	Gold, sapphire	Femtosecond laser	Gold-coated ripple	Thiophenol	10 nM	–
	Indrė Alek-navičienė et al. [120]	Silver, glass	Ultrashort-pulse laser-induced plasma-assisted ablation (LIPAA)	170 nm silver layer-coated amorphous nanostructures with diameter of 100 nm	Thiophenol	–	3×10^5
	Zhaoxin Lao et al. [100]	Polymer, glass, Au	Femtosecond laser	Au-coated 3D nanogap structures	Doxorubicin	–	8×10^7

(continued)

Table 32.1 (continued)

					Sensitivity for SERS		
	Authors	Material(s)	Laser technique	Micro-/nanostructures	Analyte	LOD	EF
	Jing Yang et al. [131]	Silicon, Ag	Nanosecond laser (wave-length = 1064 nm, pulse duration = 5 ns, and pulse repetition rate = 100 kHz)	Ag-coated micro-grooves	4-Methylbenzenethiol	–	5.5×10^6
	Vinod Parmar et al. [101]	Silicon, Au	Ti:sapphire femtosecond laser (pulse energy = 70 mJ, wave length = 800 nm, pulse duration = 120 fs, repetition rate = 1 kHz)	LIPSS covered by Au nanoparticles	R6G	2.5×10^{-8} mol/L	10^4
	Binh Nguyen et al. [104]	Cu, Ag, Au	Nanosecond laser	Gold/silver nanoparticle-covered laser-textured Cu	R6G	10^{-7} mol/L	~10^6
	Eric D. Diebold et al. [132]	Silicon, Ag	Amplified titanium:sapphire laser with the pulse duration of 100 fs	Silver nanoparticle-covered quasi-uniform pillar arrays with a spatial period about 505 nm	Benzenethiol	–	10^7
	Kaichen Xu et al. [134]	Silicon, Ag	Nanosecond laser beam (the laser wavelength is 1064 nm and the pulse duration is 10 ns)	Nanoparticles with diameter of 100 ~ 200 nm covered by silver	4-MBT	–	160
	Adam Hamdorf et al. [105]	Silicon, Au	Femtosecond laser	LIPSS covered by Au nanoparticles	R6G	–	2×10^7
	Shi Bai et al. [110]	Glass, Cu, Ag	Femtosecond laser amplifier system with a pulse duration of 457 fs	LIPSS covered with arrays of Cu-Ag nanodots	Cd^{2+}	10 ppb	–

R. L. Aggarwal et al. [127]	Silicon, Ag	A regeneratively amplified titanium: sapphire laser with wavelength of 800 nm, pulse duration of 50 fs, and repetition rate of 1 kHz	Random nanopillars coated with 80 nm silver layer	Benzenethiol	–	$0.8 \pm 0.3 \times 10^6$
Li-Nan Fang et al. [133]	PTFE, Ag	Femtosecond laser: $\lambda = 1030$ nm, the pulse duration = 290 fs, the repetition rate = 200 kHz, the laser power ≈ 1500 mW	Grating microstructures and nanoporous structures covered by silver	R6G	10^{-7} mol/L	–
Yukun Han et al. [128]	Glass, Ag	Femtosecond laser with repetition rate of 1 kHz, wavelength of 800 nm, and pulse duration of 80 fs	Silver-coated hollow holes with diameter of 100 nanometers and depth of 700 nm	R6G	10^{-7} mol/L	2.5×10^6
Raju Botta et al. [130]	Al, Ag	Laser with wavelength of 1064 nm, power of 12 W, frequency of 30 kHz, and scanning space of 20 µm	Nanostructured roughness Al surfaces covered by Ag nanoparticles	Paraquat	2.7 ppb	5×10^9
Ricardas Buividas et al. [103]	Sapphire, Ag	Ti:sapphire femtosecond laser system with wavelength of 800 nm, pulse duration of 150 fs, and repetition rate of 1 kHz	Ripples covered by silver layer	Thiophenol	–	10^3 - 10^4
Diego Acevedo et al. [102]	PC, Au, and Pt	Direct laser interference patterning (DLIP)	Hexagonal grid-like microstructures covered with 500 nm of Au and Pt	2-Thioaniline	–	10^3

Table 32.2 Overview on exemplary works discussed in Sects. 4.1 and 4.2

					Sensitivity for SERS		
	Authors	**Material(s)**	**Laser technique**	**Micro-/nanostructures**	**Analyte**	**LOD**	**EF**
4.1 Ultrasensitive SERS detection with laser fabricated superhydrophobic surfaces	Zhao-Xu Yan et al. [148]	Graphene, silver	Frequency-tripled, Q-switched, single-mode Nd:YAG laser	Hierarchical reduced graphene oxide (RGO) grating structures with microscale gratings and nanoscale folders covered by silver	Rhodamine B	10^{-10} mol/L	2×10^{7}
	Jijo Easo George et al. [149]	PMMA, PDMS, silver	Femtosecond laser direct writing (LDW) and replication of master structure using soft lithography	Grid patterns with periodic sharp structures covered by Ag nanoparticles	R6G	10^{-14} mol/L	6×10^{10}
	Andong Wang et al. [150]	Silicon, Ag	A regenerative amplified Ti:sapphire femtosecond laser with pulse duration of 35 fs and wavelength of 800 nm	An array of conical-shaped spikes covered by small protrusions started and LIPSS and then coated with 60 nm silver film	R6G	10^{-14} mol/L	6×10^{6}
	Pei Fu et al. [151]	Cu	Femtosecond laser with the laser fluence of 151 J/cm^2	The unorganized and broken nano-ripples	R6G	10^{-13} mol/L	1.2×10^{5}

				Hydrophobic/ superhydrophilic area	**Superhydrophobic area**	**Analyte**	**LOD**	**EF**
4.2 Ultrasensitive SERS detection with laser fabricated patterned hydrophobic/ superhydrophilic-superhydrophobic surfaces	Xinyu Hu et al. [161]	PTFE	A Trumpf TruMicro5000 laser system with 800 fs pulses and 1030 nm central wavelength	Unprocessed	Arrays of micro-pillars	R6G	–	10 ~ 100
	Fangjia Chu et al. [159]	PTFE	CO_2 laser (the output power, 16–24%; the engraving speed, 35–75 mm/s; the engraving step length, 0.02–0.10 mm)	Microarrays	–	Methylene blue and Rhodamine 6G	10^{-14} mol/L	–
	Xiaodan Ma et al. [164]	PDMS, silicon	A femtosecond laser beam with a pulse duration of 35 fs and the repetition rate of 1000 Hz	Convex morphology	–	R6G	10^{-16} mol/L	–

(continued)

Table 32.2 (continued)

Authors	Material(s)	Laser technique	Micro-/nanostructures		Sensitivity for SERS		
					Analyte	LOD	EF
Huan Yang et al. [165]	Stainless steels	A 520 nm femtosecond laser with a pulse width of 300 fs and repetition frequency of 250 kHz	LIPSS covered by nanoparticles	Deep micro-groove structures	R6G	10^{-14} mol/L	5.7×10^8
Georgii Pavliuk et al. [166]	PTFE	A regenerative amplified Yb:KGW femtosecond laser system	Multiple-nanoscale spiky features randomly arranged within circular-shaped craters	Periodically arranged micro-pillars	Medical drugs	10^{-12} mol/L	–
Xiangyun Guan et al. [167]	Cu	A femtosecond laser with wavelength of 520 nm, pulse duration of 800 fs, and repetition rate of 250 kHz	–	Micropillar array	R6G	10^{-13} mol/L	–
Xiao Luo et al. [160]	Cu	Femtosecond laser with the wavelength of 1030 nm and pulse duration of 800 fs	Multiple structures of micro-pillars, micro-flowers, and nano-sheets	Micropit arrays covered by interlaced nanorims, nanoprotrusions, microparticles	R6G	10^{-18} mol/L	1.09×10^{14}

Table 32.3 Overview on typical SERS substrates processed by other fabrication methods discussed in the Sect. 1.3

							Sensitivity for SERS		
	Types	Fabrication methods		Authors	Material(s)	Micro-nanostructures	Analyte	LOD	EF
1.3 Fabrication methods for SERS substrates	Colloids	Chemical reduction	Ag mirror reaction conditions that included 20 mM $AgNO_3$, 5 min reaction time, and 0.5 M glucose	Rajapandiyan Panneerselvam et al. [78]	$AgNO_3$, glucose	Ag NP colloids with an average size of 319.1 nm (s.d ± 128.1)	Nucleotides adenosine 5′-mono-phosphate (AMP)	5×10^{-7} mol/L	–
			Modified hydrothermal method	Longyun Zhao et al. [203]	$HAuCl_4 \cdot 3H_2O$, NaOH, graphene oxide (GO)	The colloid of Au nanoparticles (AuNPs)/reduced graphene oxide (rGO)	Pb^{2+}	10^{-9} mol/L	–
			A 30 mM aqueous metal chloride solution ($HAuCl_4$ or Na_2PdCl_4, 30 mL) was added to a 25 mM solution of tetraoctylammonium bromide in toluene (80 mL)	David I. Gittins at al [204].	$HAuCl_4$, Na_2PdCl_4, tetraoctylammonium bromide	The colloid of Au nanoparticles	R6G and crystal violet	10^{-6} mol/L	–
	Structural solid substrates	Lithography-based	EBL, metal deposition, liftoff, reactive ion etching (RIE), and gold deposition	Nahla A. Hatab et al. [83]	Si, Au	Suspended gold bowtie nanoantenna	p-Mercaptoaniline	–	10^{11}
			Nanoimprint lithography (NIL)	Wei Wu et al. [205]	Si, Au	Au-coated 3D cone arrays	Trans-1,2-bis(4-pyridyl)-ethylene (BPE)	10 nM	–

(continued)

Table 32.3 (continued)

	Types	Fabrication methods		Authors	Material(s)	Micro-/ nanostructures	Sensitivity for SERS		
							Analyte	LOD	EF
			Thermal nanoimprint litho-graphy (NIL) with a laser interference lithography-assisted stamp	Seung-Woo Lee et al. [206]	Glass, Au	Au nanodisk arrays	Prostate-specific antigen (PSA)	10^{-15} mol/L	–
		Non-lithography template	Anodized alumina template method and magnetron sputtering	Guochao Shi et al. [207]	Al, Ag	Nanoflower-like Ag/AAO nanoarray	Crystal violet	10^{-12} mol/L	3.677×10^7
			Physical vapor deposition (PVD) technology	Jianghao Li et al. [56]	Si, Ag, Al	Slanted Ag-Al alloy nanorod arrays	MB	10^{-9} mol/L	1.7×10^9
			Metal film over nanospheres (MFON)	L. Baia et al. [208]	Si, polystyrene, Au	Gold-coated polystyrene nanospheres	p-Aminothiophenol	–	1.23×10^{6}
		Direct formation	Galvanic displacement process	Xianzhong Sun et al. [209]	Cu, Ag	Highly branched Ag dendritic nanostructures and Ag nanoparticles	R6G	10^{-6} mol/L	–
			Thermal contraction of the NPG/PS composites	Ling Zhang et al. [57]	PS, glass, Au	Wrinkled nanoporous gold films	CV	10^{-8} mol/L	0.7×10^8
							R6G	10^{-11} mol/L	
			Chemical dealloying of Ag-Al precursor alloys	Huajun Qiu et al. [210]	Ag, Al	Stable monolithic nanoporous silver (NPS)	R6G		1.6×10^8

tive analysis of target molecules via the analysis of Raman signals in complex detection conditions, and the more concise and standard pretreatment processes for different samples.

5. The laser-nanostructured SERS substrates have excellent comprehensive properties including high sensitivity, uniformity, stability, universality, fabrication efficiency, and low cost. Nevertheless, more efforts are needed for future researches such as ultrasensitive superhydrophilic-superhydrophobic patterned SERS platforms, commercial applications in the fields of food safety, homeland security, environmental monitoring, process control, criminal forensics, drug testing, and disease diagnose.

References

1. T. Tezcan, I.H. Boyaci, A new and facile route to prepare gold nanoparticle clusters on anodic aluminium oxide as a SERS substrate. Talanta **232**, 122426 (2021)
2. L. Zhang, T. Liu, K. Liu, L. Han, Y. Yin, C. Gao, Gold nanoframes by nonepitaxial growth of Au on AgI nanocrystals for surface-enhanced Raman spectroscopy. Nano Lett. **15**(7), 4448–4454 (2015)
3. G. Zheng, L. Polavarapu, L.M. Liz-Marzan, I. Pastoriza-Santos, J. Perez-Juste, Gold nanoparticle-loaded filter paper: A recyclable dip-catalyst for real-time reaction monitoring by surface enhanced Raman scattering. Chem. Commun. **51**(22), 4572–4575 (2015)
4. J. Li, Y. Fan, X. Xue, L. Ma, S. Zou, Z. Fei, Z. Xie, Z. Zhang, Fabrication and simulation of V-shaped Ag nanorods as high-performance SERS substrates. Phys. Chem. Chem. Phys. **20**(40), 25623–25628 (2018)
5. L. Ma, H. Wu, Y. Huang, S. Zou, J. Li, Z. Zhang, High-performance real-time SERS detection with recyclable Ag Nanorods@HfO2 substrates. ACS Appl. Mater. Interfaces **8**(40), 27162–27168 (2016)
6. Q. Zhou, Y. Yang, J. Ni, Z. Li, Z. Zhang, Rapid detection of 2, 3, 3', 4, 4 '-pentachlorinated biphenyls by silver nanorods-enhanced Raman spectroscopy. Physica E **42**(5), 1717–1720 (2010)
7. X. Zhao, M. Deng, G. Rao, Y. Yan, C. Wu, Y. Jiao, A. Deng, C. Yan, J. Huang, S. Wu, High-performance SERS substrate based on hierarchical 3D Cu nanocrystals with efficient morphology control. Small **14**(38), 1802477 (2018)
8. R.-C. Wang, C.-H. Li, Cu, Cu-Cu2O core-shell, and hollow Cu2O nanodendrites: Structural evolution and reverse surface-enhanced Raman scattering. Acta Mater. **59**(2), 822–829 (2011)
9. Y. Tan, J. Gu, W. Xu, Z. Chen, D. Liu, Q. Liu, D. Zhang, Reduction of CuO butterfly wing scales generates Cu SERS substrates for DNA Base detection. ACS Appl. Mater. Interfaces **5**(20), 9878–9882 (2013)
10. B. Sharma, R.R. Frontiera, A.-I. Henry, E. Ringe, R.P. Van Duyne, SERS: Materials, applications, and the future. Mater. Today **15**(1–2), 16–25 (2012)
11. C.V. Raman, K.S. Krishnan, A new type of secondary radiation. Nature **121**(3048), 501 (1928)
12. M. Fleischmann, P.J. Hendra, A.J. McQuillan, Raman spectra of pyridine adsorbed at a silver electrode. Chem. Phys. Lett. **26**(2), 163–166 (1974)
13. M. Fleischmann, P.J. Hendra, A.J. McQuillan, Raman spectra from electrode surfaces. J. Chem. Soc. Chem. Commun. **3**, 80–81 (1973)
14. M.G. Albrecht, J.A. Creighton, Anomalously intense Raman spectra of pyridine at a silver electrode. J. Am. Chem. Soc. **99**(15), 5215–5217 (1977)

15. D.L. Jeanmaire, R.P. Van Duyne, Surface Raman spectroelectrochemistry: Part I. Heterocyclic, aromatic, and aliphatic amines adsorbed on the anodized silver electrode. J. Electroanal. Chem. Interfacial Electrochem. **84**(1), 1–20 (1977)
16. X. Wang, W. Shi, G. She, L. Mu, Surface-Enhanced Raman Scattering (SERS) on transition metal and semiconductor nanostructures. Phys. Chem. Chem. Phys. **14**(17), 5891–5901 (2012)
17. Z. Xian, Z. Qin, H. Yu, L. Zhengcao, Z. Zhengjun, The nanofabrication and application of substrates for surface-enhanced Raman scattering. Int. J. Spectro. **35068**, 4 (2012)
18. X. Sun, H. Li, A. Review, Nanofabrication of Surface-Enhanced Raman Spectroscopy (SERS) substrates. Curr. Nanosci. **12**(2), 175–183 (2016)
19. J. Jiang, S. Zou, L. Ma, S. Wang, J. Liao, Z. Zhang, Surface-enhanced Raman scattering detection of pesticide residues using transparent adhesive tapes and coated silver nanorods. ACS Appl. Mater. Interfaces **10**(10), 9129–9135 (2018)
20. J.R. Lombardi, R.L. Birke, A unified view of surface-enhanced Raman scattering. Acc. Chem. Res. **42**(6), 734–742 (2009)
21. X. Yu, H. Cai, W. Zhang, X. Li, N. Pan, Y. Luo, X. Wang, J.G. Hou, Tuning chemical enhancement of SERS by controlling the chemical reduction of graphene oxide nanosheets. ACS Nano **5**(2), 952–958 (2011)
22. E. Hutter, J.H. Fendler, Exploitation of localized surface plasmon resonance. Adv. Mater. **16**(19), 1685–1706 (2004)
23. E.C.L. Ru, M. Meyer, E. Blackie, P.G. Etchegoin, Advanced aspects of electromagnetic SERS enhancement factors at a hot spot. J. Raman Spectrosc. **39**(9), 1127–1134 (2008)
24. S.Y. Lee, S.-H. Kim, M.P. Kim, H.C. Jeon, H. Kang, H.J. Kim, B.J. Kim, S.-M. Yang, Freestanding and arrayed nanoporous microcylinders for highly active 3D SERS substrate. Chem. Mater. **25**(12), 2421–2426 (2013)
25. Y. Huang, Y. Chen, X. Xue, Y. Zhai, L. Wang, Z. Zhang, Unexpected large nanoparticle size of single dimer hotspot systems for broadband SERS enhancement. Opt. Lett. **43**(10), 2332–2335 (2018). https://doi.org/10.1364/ol.43.002332
26. M.V. Canamares, C. Chenal, R.L. Birke, J.R. Lombardi, DFT, SERS, and single-molecule SERS of crystal violet. J. Phys. Chem. C **112**(51), 20295–20300 (2008)
27. M.M. Dvoynenko, J.-K. Wang, Finding electromagnetic and chemical enhancement factors of surface-enhanced Raman scattering. Opt. Lett. **32**(24), 3552–3554 (2007)
28. M. Sidorova, S.G. Pavlov, A.D. Semenov, M. Gensch, H.W. Huebers, Fiber-dispersive Raman spectrometer with single-photon sensitivity. Opt. Express **29**(13), 20941–20951 (2021)
29. J. Prinz, C. Heck, L. Ellerik, V. Merk, I. Bald, DNA origami based Au-Ag-core-shell nanoparticle dimers with single-molecule SERS sensitivity. Nanoscale **8**(10), 5612–5620 (2016)
30. G.C. Schatz, Theoretical-studies of surface enhanced Raman-scattering. Acc. Chem. Res. **17**(10), 370–376 (1984)
31. Y. Huang, L. Ma, J. Li, Z. Zhang, Nanoparticle-on-mirror cavity modes for huge and/or tunable plasmonic field enhancement. Nanotechnology **28**(10), 105203 (2017)
32. M.J. Vesga, D. McKechnie, S. Laing, H. Kearns, K. Faulds, K. Johnston, J. Sefcik, Effect of glycine on aggregation of citrate-functionalised gold nanoparticles and SERS measurements. Colloids Surf. A Physicochem. Eng. Asp. **621**, 126523 (2021)
33. H. Zhang, F. Zhou, M. Liu, D. Liu, D. Men, W. Cai, G. Duan, Y. Li, Spherical nanoparticle arrays with tunable nanogaps and their hydrophobicity enhanced rapid SERS detection by localized concentration of droplet evaporation. Adv. Mater. Interfaces **2**(9), 1500031 (2015)
34. L.B. He, Y.L. Wang, X. Xie, M. Han, F.Q. Song, B.J. Wang, W.L. Chen, H.X. Xu, L.T. Sun, Systematic investigation of the SERS efficiency and SERS hotspots in gas-phase deposited Ag nanoparticle assemblies. Phys. Chem. Chem. Phys. **19**(7), 5091–5101 (2017)
35. Y. Huang, Q. Zhou, M. Hou, L. Ma, Z. Zhang, Nanogap effects on near-and far-field plasmonic behaviors of metallic nanoparticle dimers. Phys. Chem. Chem. Phys. **17**(43), 29293–29298 (2015)

36. E.N. Esenturk, A.R.H. Walker, Surface-enhanced Raman scattering spectroscopy via gold nanostars. J. Raman Spectrosc. **40**(1), 86–91 (2009)
37. G. Lu, T.Z. Forbes, A.J. Haes, SERS detection of uranyl using functionalized gold nanostars promoted by nanoparticle shape and size. Analyst **141**(17), 5137–5143 (2016)
38. M. Chirumamilla, A. Gopalakrishnan, A. Toma, R.P. Zaccaria, R. Krahne, Plasmon resonance tuning in metal nanostars for surface enhanced Raman scattering. Nanotechnology **25**(23), 7 (2014)
39. X.-B. Huang, S.-H. Wu, H.-C. Hu, J.-J. Sun, AuNanostar@4-MBA@Au core-shell nanostructure coupled with exonuclease III-assisted cycling amplification for ultrasensitive SERS detection of ochratoxin A. ACS Sens. **5**(8), 2636–2643 (2020)
40. X. Meng, J. Dyer, Y. Huo, C. Jiang, Greater SERS activity of ligand-stabilized gold nanostars with sharp branches. Langmuir **36**(13), 3558–3564 (2020)
41. Y. Ran, P. Strobbia, V. Cupil-Garcia, T. Vo-Dinh, Fiber-optrode SERS probes using plasmonic silver-coated gold nanostars. Sens. Actuators B Chem. **287**, 95–101 (2019)
42. R. Omar, A.E. Naciri, S. Jradi, Y. Bettie, J. Toufaily, H. Mortada, S. Akil, One-step synthesis of a monolayer of monodisperse gold nanocubes for SERS substrates. J. Mater. Chem. C **5**(41), 10813–10821 (2017)
43. H. Wang, K.B. Li, C. Xu, S.C. Xu, G.H. Li, Large-scale solvothermal synthesis of Ag nanocubes with high SERS activity. J. Alloys Compd. **772**, 150–156 (2019)
44. L. Liu, Y. Wu, N. Yin, H. Zhang, H. Ma, Silver nanocubes with high SERS performance. J. Quant. Spectrosc. Radiat. Transf. **240**, 106682 (2020)
45. C. Kuttner, M. Mayer, M. Dulle, A. Moscoso, J.M. Lopez-Romero, S. Foerster, A. Fery, J. Perez-Juste, R. Contreras-Caceres, Seeded growth synthesis of gold nanotriangles: Size control, SAXS analysis, and SERS performance. ACS Appl. Mater. Interfaces **10**(13), 11152–11163 (2018)
46. F. Liebig, R.M. Sarhan, M. Sander, W. Koopman, R. Schuetz, M. Bargheer, J. Koetz, Deposition of gold nanotriangles in large scale close-packed monolayers for X-ray-based temperature calibration and SERS monitoring of plasmon-driven catalytic reactions. ACS Appl. Mater. Interfaces **9**(23), 20247–20253 (2017)
47. C. Wu, E. Chen, J. Wei, Surface enhanced Raman spectroscopy of Rhodamine 6G on agglomerates of different-sized silver truncated nanotriangles. Sens. Actuators A Phys. **506**, 450–456 (2016)
48. M.A. Casado-Rodriguez, M. Sanchez-Molina, A. Lucena-Serrano, C. Lucena-Serrano, B. Rodriguez-Gonzalez, M. Algarra, A. Diaz, M. Valpuesta, J.M. Lopez-Romero, J. Perez-Juste, R. Contreras-Caceres, Synthesis of vinyl-terminated Au nanoprisms and nanooctahedra mediated by 3-butenoic acid: Direct Au@pNIPAM fabrication with improved SERS capabilities. Nanoscale **8**(8), 4557–4564 (2016)
49. X. Geng, W. Leng, N.A. Carter, P.J. Vikesland, T.Z. Grove, Protein-aided formation of triangular silver nanoprisms with enhanced SERS performance. J. Mater. Chem. B **4**(23), 4182–4190 (2016)
50. S. Roy, C.M. Ajmal, S. Baik, J. Kim, Silver nanoflowers for single-particle SERS with 10 pM sensitivity. Nanotechnology **28**(46), 465705 (2017)
51. S. Zhen, T. Wu, X. Huang, Y. Li, C. Huang, Facile synthesis of gold nanoflowers as SERS substrates and their morphological transformation induced by iodide ions. Sci. China Chem. **59**(8), 1045–1050 (2016)
52. V.M. Kariuki, J.C. Hoffmeier, I. Yazgan, O.A. Sadik, Seedless synthesis and SERS characterization of multi-branched gold nanoflowers using water soluble polymers. Nanoscale **9**(24), 8330–8340 (2017)
53. P. Wang, M. Xia, O. Liang, K. Sun, A.F. Cipriano, T. Schroeder, H. Liu, Y.-H. Xie, Label-free SERS selective detection of dopamine and serotonin using Graphene-Au nanopyramid heterostructure. Anal. Chem. **87**(20), 10255–10261 (2015)

54. K.-H. Tsui, X. Li, J.K.H. Tsoi, S.-F. Leung, T. Lei, W.Y. Chak, C. Zhang, J. Chen, G.S.P. Cheung, Z. Fan, Low-cost, flexible, disinfectant-free and regular-array three-dimensional nanopyramid antibacterial films for clinical applications. Nanoscale **10**(22), 10436–10442 (2018)
55. P. Zheng, S. Kasani, X. Shi, A.E. Boryczka, F. Yang, H. Tang, M. Li, W. Zheng, D.E. Elswick, N. Wu, Detection of nitrite with a surface-enhanced Raman scattering sensor based on silver nanopyramid array. Anal. Chim. Acta **1040**, 158–165 (2018)
56. K. Liu, S. Jin, Z. Song, L. Jiang, L. Ma, Z. Zhang, Label-free surface-enhanced Raman spectroscopy of serum based on multivariate statistical analysis for the diagnosis and staging of lung adenocarcinoma. Vib. Spectrosc. **100**, 177–184 (2019)
57. L. Zhang, X. Lang, A. Hirata, M. Chen, Wrinkled nanoporous gold films with ultrahigh surface-enhanced Raman scattering enhancement. ACS Nano **5**(6), 4407–4413 (2011)
58. H.J. Huang, M.-H. Shiao, Y.-W. Lin, B.-J. Lin, J. Su, Y.-S. Lin, H.-W. Chang, Au@Ag dendritic nanoforests for surface-enhanced Raman scattering sensing. Nano **11**(7), 1736 (2021)
59. D. Chen, X. Zhu, J. Huang, G. Wang, Y. Zhao, F. Chen, J. Wei, Z. Song, Y. Zhao, Polydopamine@Gold nanowaxberry enabling improved SERS sensing of pesticides, pollutants, and explosives in complex samples. Anal. Chem. **90**(15), 9048–9054 (2018)
60. Y. Wang, M. Zhang, L. Feng, B. Dong, T. Xu, D. Li, L. Jiang, L. Chi, Tape-imprinted hierarchical lotus seedpod-like arrays for extraordinary surface-enhanced Raman spectroscopy. Small **15**(19), 1804527 (2019)
61. X. Wang, W. Shi, Z. Jin, W. Huang, J. Lin, G. Ma, S. Li, L. Guo, Remarkable SERS activity observed from amorphous ZnO nanocages. Angew. Chem. Int. Ed. **56**(33), 9851–9855 (2017)
62. G. Song, J. Li, Y. Yuan, L. Yao, J. Gu, Q. Liu, W. Zhang, Y. Su, D. Zhang, Large-area 3D hierarchical superstructures assembled from colloidal nanoparticles. Small **15**(18), 1805308 (2019)
63. B. Lin, P. Kannan, B. Qiu, Z. Lin, L. Guo, On-spot surface enhanced Raman scattering detection of Aflatoxin B1 in peanut extracts using gold nanobipyramids evenly trapped into the AAO nanoholes. Food Chem. **307**, 125528 (2019)
64. Z. Zhu, B. Bai, O. You, Q. Li, S. Fan, Fano resonance boosted cascaded optical field enhancement in a plasmonic nanoparticle-in-cavity nanoantenna array and its SERS application. Light Sci. Appl. **4**, e296 (2015)
65. M.I. Stockman, S.V. Faleev, D.J. Bergman, Coherent control of femtosecond energy localization in nanosystems. Phys. Rev. Lett. **88**(6), 067402 (2002)
66. K.R. Li, M.I. Stockman, D.J. Bergman, Self-similar chain of metal nanospheres as an efficient nanolens. Phys. Rev. Lett. **91**(22), 227402 (2003)
67. M. Chirumamilla, A. Toma, A. Gopalakrishnan, G. Das, R.P. Zaccaria, R. Krahne, E. Rondanina, M. Leoncini, C. Liberale, F. De Angelis, E. Di Fabrizio, 3D nanostar dimers with a Sub-10-nm gap for single-/few- molecule surface-enhanced Raman scattering. Adv. Mater. **26**(15), 2353–2358 (2014)
68. V.G. Kravets, G. Zoriniants, C.P. Burrows, F. Schedin, C. Casiraghi, P. Klar, A.K. Geim, W.L. Barnes, A.N. Grigorenko, Cascaded optical field enhancement in composite plasmonic nanostructures. Phys. Rev. Lett. **105**(24), 246806 (2010)
69. A. Dutta, K. Alam, T. Nuutinen, E. Hulkko, P. Karvinen, M. Kuittinen, J.J. Toppari, E.M. Vartiainen, Influence of Fano resonance on SERS enhancement in Fano-plasmonic oligomers. Opt. Express **27**(21), 30031–30043 (2019)
70. L. Chen, H. Sun, Y. Zhao, Y. Zhang, Y. Wang, Y. Liu, X. Zhang, Y. Jiang, Z. Hua, J. Yang, Plasmonic-induced SERS enhancement of shell-dependent Ag@Cu2O core-shell nanoparticles. RSC Adv. **7**(27), 16553–16560 (2017)
71. Y. Wang, J. Liu, Y. Ozaki, Z. Xu, B. Zhao, Effect of TiO2 on altering direction of interfacial charge transfer in a TiO2-Ag-MPY-FePc system by SERS. Angew Chem Int Ed **58**(24), 8172–8176 (2019)
72. Q. Huang, J. Li, Enhanced photocatalytic and SERS properties of ZnO/Ag hierarchical multipods-shaped nanocomposites. Mater. Lett. **204**, 85–88 (2017)

73. S. Shen, B. Zhao, H. Wang, Z. Li, G. Qu, Z. Guo, T. Zhou, W. Song, X. Wang, W. Ruan, CdTe quantum dots modified polystyrene spheres with Ag nanoparticle caps: Applications both in fluorescence and in SERS. Colloids Surf., A **443**, 467–472 (2014)
74. C. Sun, W. Dong, J. Peng, X. Wan, Z. Sun, D. Li, S. Wang, Dual-mode fluorescence-SERS sensor for sensitive and selective detection of uranyl ions based on satellite Fe3O4-Au@CdTe nanostructure. Sens. Actuators B Chem. **325**, 128644 (2020)
75. B. Zhang, X. Yin, D. Zhen, W. Gu, Y. Liu, Q. Cai, Au nanoparticle-modified WO3 nanoflowers/TiO2 nanotubes used for the SERS detection of dyes. New J. Chem. **41**(22), 13968–13973 (2017)
76. G. Neri, E. Fazio, P.G. Mineo, A. Scala, A. Piperno, SERS sensing properties of new graphene/gold nanocomposite. Nano **9**(9), 1236 (2019)
77. S.-C. Luo, K. Sivashanmugan, J.-D. Liao, C.-K. Yao, H.-C. Peng, Nanofabricated SERS-active substrates for single-molecule to virus detection in vitro: A review. Biosens. Bioelectron. **61**, 232–240 (2014)
78. R. Panneerselvam, L. Xiao, K.B. Waites, T.P. Atkinson, R.A. Dluhy, A rapid and simple chemical method for the preparation of Ag colloids for surface-enhanced Raman spectroscopy using the Ag mirror reaction. Vib. Spectrosc. **98**, 1–7 (2018)
79. A. Zielinska, E. Skwarek, A. Zaleska, M. Gazda, J. Hupka, Preparation of silver nanoparticles with controlled particle size, in *22nd conference of the european colloid and interface society, ECIS 2008*, ed. by Z. Adamczyk, P. Warszynski, (2009), pp. 1560–1566
80. R. He, X.F. Qian, J. Yin, Z.K. Zhu, Preparation of polychrome silver nanoparticles in different solvents. J. Mater. Chem. **12**(12), 3783–3786 (2002)
81. W. Zhang, X. Qiao, J. Chen, Synthesis of silver nanoparticles – Effects of concerned parameters in water/oil microemulsion. Mater. Sci. Eng., B **142**(1), 1–15 (2007)
82. J.-K. Yang, I.-J. Hwang, M.G. Cha, H.-I. Kim, D. Yim, D.H. Jeong, Y.-S. Lee, J.-H. Kim, Reaction kinetics-mediated control over silver nanogap shells as surface-enhanced Raman scattering nanoprobes for detection of Alzheimer's disease biomarkers. Small **15**(19), 1900613 (2019)
83. N.A. Hatab, C.-H. Hsueh, A.L. Gaddis, S.T. Retterer, J.-H. Li, G. Eres, Z. Zhang, B. Gu, Free-standing optical gold bowtie nanoantenna with variable gap size for enhanced Raman spectroscopy. Nano Lett. **10**(12), 4952–4955 (2010)
84. W. Wu, M. Hu, F.S. Ou, Z. Li, R.S. Williams, Cones fabricated by 3D nanoimprint lithography for highly sensitive surface enhanced Raman spectroscopy. Nanotechnology **21**(25), 255502 (2010)
85. T.R. Jensen, M.D. Malinsky, C.L. Haynes, R.P. Van Duyne, Nanosphere lithography: Tunable localized surface plasmon resonance spectra of silver nanoparticles. J. Phys. Chem. B **104**(45), 10549–10556 (2000)
86. L.A. Dick, A.D. McFarland, C.L. Haynes, R.P. Van Duyne, Metal film over nanosphere (MFON) electrodes for surface-enhanced Raman spectroscopy (SERS): Improvements in surface nanostructure stability and suppression of irreversible loss. J. Phys. Chem. B **106**(4), 853–860 (2002)
87. B. Mondal, S.K. Saha, Fabrication of SERS substrate using nanoporous anodic alumina template decorated by silver nanoparticles. Chem. Phys. Lett. **497**(1–3), 89–93 (2010)
88. S.H. Macomber, T.E. Furtak, T.M. Devine, Surface-enhanced raman-scattering magnified by photochemical activation of the silver electrode in aqueous halide electrolytes. Chem. Phys. Lett. **90**(6), 439–444 (1982)
89. D. Thierry, C. Leygraf, The influence of photoalteration on surface-enhanced raman-scattering from copper electrodes. Surf. Sci. **149**(2–3), 592–600 (1985)
90. J.D. Driskell, S. Shanmukh, Y. Liu, S.B. Chaney, X.J. Tang, Y.P. Zhao, R.A. Dluhy, The use of aligned silver nanorod arrays prepared by oblique angle deposition as surface enhanced Raman scattering substrates. J. Phys. Chem. C **112**(4), 895–901 (2008)
91. L.H. Qian, M.W. Chen, Ultrafine nanoporous gold by low-temperature dealloying and kinetics of nanopore formation. Appl. Phys. Lett. **91**(8), 083105 (2007)

92. K. Christou, I. Knorr, J. Ihlemann, H. Wackerbarth, V. Beushausen, Fabrication and characterization of homogeneous surface-enhanced Raman scattering substrates by single pulse UV-laser treatment of gold and silver films. Langmuir **26**(23), 18564–18569 (2010)
93. K.L. Kelly, E. Coronado, L.L. Zhao, G.C. Schatz, The optical properties of metal nanoparticles: The influence of size, shape, and dielectric environment. J. Phys. Chem. B **107**(3), 668–677 (2003)
94. L.M. Liz-Marzan, Tailoring surface plasmons through the morphology and assembly of metal nanoparticles. Langmuir **22**(1), 32–41 (2006)
95. M. Rycenga, K.K. Hou, C.M. Cobley, A.G. Schwartz, P.H.C. Camargo, Y. Xia, Probing the surface-enhanced Raman scattering properties of Au-Ag nanocages at two different excitation wavelengths. Phys. Chem. Chem. Phys. **11**(28), 5903–5908 (2009)
96. C. Han-Wei, T. Yu-Chen, C. Chung-Wei, L. Cen-Ying, L. Yen-Wen, W. Tzong-Ming, Nanostructured Ag surface fabricated by femtosecond laser for surface-enhanced Raman scattering. J. Colloid Interface Sci. **360**(1), 305–308 (2011)
97. L. Lu, J. Zhang, L. Jiao, Y. Guan, Large-scale fabrication of nanostructure on bio-metallic substrate for surface enhanced Raman and fluorescence scattering. Nano **9**(7), 916 (2019)
98. X. Luo, W. Liu, C. Chen, G. Jiang, X. Hu, H. Zhang, M. Zhong, Femtosecond laser micro-nano structured Ag SERS substrates with unique sensitivity, uniformity and stability for food safety evaluation. Opt. Laser Technol. **139**, 106969 (2021)
99. S. Hamad, G.K. Podagatlapalli, M.A. Mohiddon, S.V. Rao, Surface enhanced fluorescence from corroles and SERS studies of explosives using copper nanostructures. Chem. Phys. Lett. **621**, 171–176 (2015)
100. Z. Lao, Y. Zheng, Y. Dai, Y. Hu, J. Ni, S. Ji, Z. Cai, Z.J. Smith, J. Li, L. Zhang, D. Wu, J. Chu, Nanogap plasmonic structures fabricated by switchable capillary-force driven self-assembly for localized sensing of anticancer medicines with microfluidic SERS. Adv. Funct. Mater. **30**(15), 1909467 (2020)
101. V. Parmar, P.K. Kanaujia, R.K. Bommali, G.V. Prakash, Efficient surface enhanced Raman scattering substrates from femtosecond laser based fabrication. Opt. Mater. **72**, 86–90 (2017)
102. D. Acevedo, H. Salavagione, A. Lasagni, E. Morallon, F. Muecklich, C. Barbero, SERS active surface in two steps, patterning and metallization. Adv. Eng. Mater. **15**(5), 325–329 (2013)
103. R. Buividas, P.R. Stoddart, S. Juodkazis, Laser fabricated ripple substrates for surface-enhanced Raman scattering. Ann. Phys. **524**(11), L5–L10 (2012)
104. T.B. Nguyen, N.A. Nguyen, T.D. Tran, Production of SERS substrates using ablated copper surfaces and gold/silver nanoparticles prepared by laser ablation in liquids. J. Electron. Mater. **49**(10), 6232–6239 (2020)
105. A. Hamdorf, M. Olson, C.-H. Lin, L. Jiang, J. Zhou, H. Xiao, H.-L. Tsai, Femtosecond and nanosecond laser fabricated substrate for surface-enhanced Raman scattering. Opt. Lett. **36**(17), 3353–3355 (2011)
106. A. Chou, E. Jaatinen, R. Buividas, G. Seniutinas, S. Juodkazis, E.L. Izake, P.M. Fredericks, SERS substrate for detection of explosives. Nanoscale **4**(23), 7419–7424 (2012)
107. S. Hoehm, M. Herzlieb, A. Rosenfeld, J. Krueger, J. Bonse, Dynamics of the formation of laser-induced periodic surface structures (LIPSS) upon femtosecond two-color double-pulse irradiation of metals, semiconductors, and dielectrics. Appl. Surf. Sci. **374**, 331–338 (2016)
108. P. Fan, R. Pang, M. Zhong, Ultrafast laser enabling hierarchical structures for versatile superhydrophobicity with enhanced cassie-baxter stability and durability. Langmuir **35**(51), 16693–16711 (2019)
109. Q. Yang, X. Li, L. Jiang, N. Zhang, G. Zhang, X. Shi, K. Zhang, J. Hu, Y. Lu, Nanopillar arrays with nanoparticles fabricated by a femtosecond laser pulse train for highly sensitive SERRS. Opt. Lett. **40**(9), 2045–2048 (2015). https://doi.org/10.1364/ol.40.002045
110. S. Bai, D. Serien, A. Hu, K. Sugioka, 3D microfluidic surface-enhanced Raman spectroscopy (SERS) chips fabricated by all-femtosecond-laser-processing for real-time sensing of toxic substances. Adv. Funct. Mater. **28**(23), 1706262 (2018)
111. L. Xiao, C. Mingyong, L. Weijian, C. Changhao, P. Rui, Z. Hongjun, Z. Minlin, Flexible control over optical reflection property of metallic surfaces via pulse laser. J. Laser Appl. **31**(2), 022502 (2019)

112. J. Long, Z. Cao, C. Lin, C. Zhou, Z. He, X. Xie, Formation mechanism of hierarchical micro- and nanostructures on copper induced by low-cost nanosecond lasers. Appl. Surf. Sci. **464**, 412–421 (2019)
113. P. Fan, M. Zhong, B. Bai, G. Jin, H. Zhang, Tuning the optical reflection property of metal surfaces via micro–nano particle structures fabricated by ultrafast laser. Appl. Surf. Sci. **359**, 7–13 (2015)
114. C.-H. Lin, L. Jiang, Y.-H. Chai, H. Xiao, S.-J. Chen, H.-L. Tsai, One-step fabrication of nanostructures by femtosecond laser for surface-enhanced Raman scattering. Opt. Express **17**(24), 21581–21589 (2009). https://doi.org/10.1364/oe.17.021581
115. B.-B. Xu, Z.-C. Ma, L. Wang, R. Zhang, L.-G. Niu, Z. Yang, Y.-L. Zhang, W.-H. Zheng, B. Zhao, Y. Xu, Q.-D. Chen, H. Xia, H.-B. Sun, Localized flexible integration of high-efficiency surface enhanced Raman scattering (SERS) monitors into microfluidic channels. Lab Chip **11**(19), 3347–3351 (2011)
116. B.-B. Xu, R. Zhang, X.-Q. Liu, H. Wang, Y.-L. Zhang, H.-B. Jiang, L. Wang, Z.-C. Ma, J.-F. Ku, F.-S. Xiao, H.-B. Sun, On-chip fabrication of silver microflower arrays as a catalytic microreactor for allowing in situ SERS monitoring. Chem. Commun. **48**(11), 1680–1682 (2012)
117. S. Milles, M. Soldera, T. Kuntze, A.F. Lasagni, Characterization of self-cleaning properties on superhydrophobic aluminum surfaces fabricated by direct laser writing and direct laser interference patterning. Appl. Surf. Sci. **525**, 146518 (2020)
118. J.T. Cardoso, A.I. Aguilar-Morales, S. Alamri, D. Huerta-Murillo, F. Cordovilla, A.F. Lasagni, J.L. Ocana, Superhydrophobicity on hierarchical periodic surface structures fabricated via direct laser writing and direct laser interference patterning on an aluminium alloy. Opt. Lasers Eng. **111**, 193–200 (2018)
119. Y. Lin, J. Han, M. Cai, W. Liu, X. Luo, H. Zhang, M. Zhong, Durable and robust transparent superhydrophobic glass surfaces fabricated by a femtosecond laser with exceptional water repellency and thermostability. J. Mater. Chem. A **6**(19), 9049–9056 (2018)
120. I. Aleknavičienė, E. Pabrėža, M. Talaikis, M. Jankunec, G. Račiukaitis, Low-cost SERS substrate featuring laser-ablated amorphous nanostructure. Appl. Surf. Sci. **571**, 151248 (2022)
121. L. Chen, T. Zhai, X. Zhang, C. Unger, J. Koch, B.N. Chichkov, P.J. Klar, Polarization-dependent SERS effects of laser-generated sub-100 nm antenna structures. Nanotechnology **25**(26), 265302 (2014)
122. Z.-C. Ma, Y.-L. Zhang, B. Han, X.-Q. Liu, H.-Z. Zhang, Q.-D. Chen, H.-B. Sun, Femtosecond laser direct writing of plasmonic Ag/Pd alloy nanostructures enables flexible integration of robust SERS substrates. Adv. Mater. Technol. **2**(6), 1600270 (2017)
123. B. Chandu, M.S.S. Bharati, S.V. Rao, Ieee, Ag nanoparticles coupled with Ag nanostructures as efficient SERS platform for dtection of 2, 4-dinitrotoluene, 3rd Biennial IEEE Workshop on Recent Advances in Photonics (WRAP), Mahindra Ecole Centrale, Hyderabad, India (2017)
124. W. Zhang, C. Li, K. Gao, F. Lu, M. Liu, X. Li, L. Zhang, D. Mao, F. Gao, L. Huang, T. Mei, J. Zhao, Surface-enhanced Raman spectroscopy with Au-nanoparticle substrate fabricated by using femtosecond pulse. Nanotechnology **29**(20), 205301 (2018)
125. Y. Han, Z. Liang, H. Sun, H. Xiao, H.-L. Tsai, Nanostructured substrate with nanoparticles fabricated by femtosecond laser for surface-enhanced Raman scattering. Appl. Phys. A-Mater. Sci. Process. **102**(2), 415–419 (2011)
126. R. Kurnoothala, S.V. Muthukumar, K.C. Vishnubhatla, Facile fabrication of integrated microfluidic SERS substrate by femtosecond laser sintering of silver nano particles. Opt. Mater. **111**, 110518 (2021)
127. R.L. Aggarwal, L.W. Farrar, E.D. Diebold, D.L. Polla, Measurement of the absolute Raman scattering cross section of the 1584-cm(-1) band of benzenethiol and the surface-enhanced Raman scattering cross section enhancement factor for femtosecond laser-nanostructured substrates. J. Raman Spectrosc. **40**(9), 1331–1333 (2009)

128. Y. Han, X. Lan, T. Wei, H.-L. Tsai, H. Xiao, Surface enhanced Raman scattering silica substrate fast fabrication by femtosecond laser pulses. Appl. Phys. A-Mater. Sci. Process. **97**(3), 721–724 (2009)
129. R. Buividas, N. Fahim, J. Juodkazyte, S. Juodkazis, Novel method to determine the actual surface area of a laser-nanotextured sensor. Appl. Phys. A-Mater. Sci. Process. **114**(1), 169–175 (2014)
130. R. Botta, P. Eiamchai, M. Horprathum, S. Limwichean, C. Chananonnawathorn, V. Patthanasettakul, R. Maezono, A. Jomphoak, N. Nuntawong, 3D structured laser engraves decorated with gold nanoparticle SERS chips for paraquat herbicide detection in environments. Sens. Actuators B Chem. **304**, 12 (2020)
131. J. Yang, J. Li, Z. Du, Q. Gong, J. Teng, M. Hong, Laser hybrid micro/nano-structuring of Si surfaces in air and its applications for SERS detection. Sci. Rep. **4**, 6657 (2014)
132. E.D. Diebold, N.H. Mack, S.K. Doom, E. Mazur, Femtosecond laser-nanostructured substrates for surface-enhanced Raman scattering. Langmuir **25**(3), 1790–1794 (2009)
133. L.N. Fang, J.C. Li, J.R. Zhang, D.D. Han, Femtosecond laser structuring for flexible surface-enhanced Raman spectroscopy substrates. IEEE Photonics J. **13**(2), 6800908 (2021)
134. K. Xu, C. Zhang, R. Zhou, R. Ji, M. Hong, Hybrid micro/nano-structure formation by angular laser texturing of Si surface for surface enhanced Raman scattering. Opt. Express **24**(10), 10352–10358 (2016)
135. J.D. Spitzberg, A. Zrehen, X.F. van Kooten, A. Meller, Plasmonic-nanopore biosensors for superior single-molecule detection. Adv. Mater. **1900422** (2019)
136. P.E. Sheehan, L.J. Whitman, Detection limits for nanoscale biosensors. Nano Lett. **5**(4), 803–807 (2005)
137. P.R. Nair, M.A. Alam, Performance limits of nanobiosensors. Appl. Phys. Lett. **88**(23), 233120 (2006)
138. Z. Huang, A. Nagpal, S. Siddhanta, I. Barman, Leveraging coffee-ring effect on plasmonic paper substrate for sensitive analyte detection using Raman spectroscopy. J. Raman Spectrosc. **49**(9), 1552–1558 (2018)
139. F. Gentile, G. Das, M.L. Coluccio, F. Mecarini, A. Accardo, L. Tirinato, R. Tallerico, G. Cojoc, C. Liberale, P. Candeloro, P. Decuzzi, F. De Angelis, E. Di Fabrizio, Ultra low concentrated molecular detection using super hydrophobic surface based biophotonic devices. Microelectron. Eng. **87**(5–8), 798–801 (2010)
140. S. Wang, L. Jiang, Definition of superhydrophobic states. Adv. Mater. **19**(21), 3423–3424 (2007)
141. E. Bormashenko, O. Gendelman, G. Whyman, Superhydrophobicity of lotus leaves versus birds wings: Different physical mechanisms leading to similar phenomena. Langmuir **28**(42), 14992–14997 (2012)
142. M. Gross, F. Varnik, D. Raabe, I. Steinbach, Small droplets on superhydrophobic substrates. Phys. Rev. E **81**, 051606 (2010)
143. F. Guo, H. Yang, J. Mao, J. Huang, X. Wang, Y. Lai, Bioinspired fabrication SERS substrate based on superwettable patterned platform for multiphase high-sensitive detecting. Compos. Commun. **10**, 151–156 (2018)
144. Y. Song, T. Xu, L.-P. Xu, X. Zhang, Superwettable nanodendritic gold substrates for direct miRNA SERS detection. Nanoscale **10**(45), 20990–20994 (2018)
145. B. Shang, Y. Wang, P. Yang, B. Peng, Z. Deng, Synthesis of superhydrophobic polydopamine-ag microbowl/nanoparticle array substrates for highly sensitive, durable and reproducible surface-enhanced Raman scattering detection. Sens. Actuators B Chem. **255**, 995–1005 (2018)
146. J. Long, M. Zhong, H. Zhang, P. Fan, Superhydrophilicity to superhydrophobicity transition of picosecond laser microstructured aluminum in ambient air. J. Colloid Interface Sci. **441**, 1–9 (2015)
147. J. Long, P. Fan, D. Gong, D. Jiang, H. Zhang, L. Li, M. Zhong, Superhydrophobic surfaces fabricated by femtosecond laser with tunable water adhesion: From lotus leaf to rose petal. ACS Appl. Mater. Interfaces **7**(18), 9858–9865 (2015)

148. Z.-X. Yan, Y.-L. Zhang, W. Wang, X.-Y. Fu, H.-B. Jiang, Y.-Q. Liu, P. Verma, S. Kawata, H.-B. Sun, Superhydrophobic SERS substrates based on silver-coated reduced graphene oxide gratings prepared by two-beam laser interference. ACS Appl. Mater. Interfaces **7**(49), 27059–27065 (2015)
149. J.E. George, V.K. Unnikrishnan, D. Mathur, S. Chidangil, S.D. George, Flexible superhydrophobic SERS substrates fabricated by in situ reduction of Ag on femtosecond laser-written hierarchical surfaces. Sens. Actuators B Chem. **272**, 485–493 (2018)
150. A. Wang, L. Jiang, X. Li, Q. Xie, B. Li, Z. Wang, K. Du, Y. Lu, Low-adhesive superhydrophobic surface-enhanced Raman spectroscopy substrate fabricated by femtosecond laser ablation for ultratrace molecular detection. J. Mater. Chem. B **5**(4), 777–784 (2017)
151. P. Fu, X. Shi, F. Jiang, X. Xu, Superhydrophobic nanostructured copper substrate as sensitive SERS platform prepared by femtosecond laser pulses. Appl. Surf. Sci. **501**, 144269 (2020)
152. L. Jiang, Bio-inspired, smart, multiscale interfacial materials. J. Biol. Inorg. Chem. **19**, S153–S153 (2014)
153. J. Long, L. Pang, P. Fan, D. Gong, D. Jiang, H. Zhang, L. Li, M. Zhong, Cassie-state stability of metallic superhydrophobic surfaces with various micro/nanostructures produced by a femtosecond laser. Langmuir **32**(4), 1065–1072 (2016)
154. W. Liu, P. Fan, M. Cai, X. Luo, C. Chen, R. Pan, H. Zhang, M. Zhong, An integrative bioinspired venation network with ultra-contrasting wettability for large-scale strongly self-driven and efficient water collection. Nanoscale **11**(18), 8940–8949 (2019)
155. A. Zhizhchenko, A. Kuchmizhak, O. Vitrik, Y. Kulchin, S. Juodkazis, On-demand concentration of an analyte on laser-printed polytetrafluoroethylene. Nanoscale **10**(45), 21414–21424 (2018)
156. F. De Angelis, F. Gentile, F. Mecarini, G. Das, M. Moretti, P. Candeloro, M.L. Coluccio, G. Cojoc, A. Accardo, C. Liberale, R.P. Zaccaria, G. Perozziello, L. Tirinato, A. Toma, G. Cuda, R. Cingolani, E. Di Fabrizio, Breaking the diffusion limit with super-hydrophobic delivery of molecules to plasmonic nanofocusing SERS structures. Nat. Photonics **5**(11), 683–688 (2011)
157. F. Gentile, M.L. Coluccio, E. Rondanina, S. Santoriello, D. Di Mascolo, A. Accardo, M. Francardi, F. De Angelis, P. Candeloro, E. Di Fabrizio, Non periodic patterning of super-hydrophobic surfaces for the manipulation of few molecules. Microelectron. Eng. **111**, 272–276 (2013)
158. W. Song, D. Psaltis, K.B. Crozier, Superhydrophobic bull's-eye for surface-enhanced Raman scattering. Lab Chip **14**(20), 3907–3911 (2014)
159. F. Chu, S. Yan, J. Zheng, L. Zhang, H. Zhang, K. Yu, X. Sun, A. Liu, Y. Huang, A simple laser ablation-assisted method for fabrication of superhydrophobic SERS substrate on teflon film. Nanoscale Res. Lett. **13**(1), 244 (2018)
160. X. Luo, R. Pan, M. Cai, W. Liu, C. Chen, G. Jiang, X. Hu, H. Zhang, M. Zhong, Atto-Molar Raman detection on patterned superhydrophilic-superhydrophobic platform via localizable evaporation enrichment. Sens. Actuators B Chem. **326**, 128826 (2021)
161. X. Hu, R. Pan, M. Cai, W. Liu, X. Luo, C. Chen, G. Jiang, M. Zhong, Ultrafast laser micro-nano structured superhydrophobic teflon surfaces for enhanced SERS detection via evaporation concentration. Adv. Opt. Technol. **9**(1–2), 89–100 (2020)
162. W. Liu, R. Pan, M. Cai, X. Luo, C. Chen, G. Jiang, X. Hu, H. Zhang, M. Zhong, Oil-triggered switchable wettability on patterned alternating air/lubricant-infused superamphiphobic surfaces. J. Mater. Chem. A **8**(14), 6647–6660 (2020)
163. W. Liu, X. Luo, C. Chen, G. Jiang, X. Hu, H. Zhang, M. Zhong, Directional anchoring patterned liquid-infused superamphiphobic surfaces for high-throughput droplet manipulation. Lab Chip **21**(7), 1373–1384 (2021)
164. X. Ma, L. Jiang, X. Li, B. Li, J. Huang, J. Sun, Z. Wang, Z. Xu, L. Qu, Y. Lu, T. Cui, Hybrid superhydrophilic-superhydrophobic micro/nanostructures fabricated by femtosecond laser-induced forward transfer for sub-femtomolar Raman detection. Microsyst. Nanoeng. **5**(1), 48 (2019)

165. H. Yang, X. Gun, G. Pang, Z. Zheng, C. Li, C. Yang, M. Wang, K. Xu, Femtosecond laser patterned superhydrophobic/hydrophobic SERS sensors for rapid positioning ultratrace detection. Opt. Express **29**(11), 16904–16913 (2021). https://doi.org/10.1364/oe.423789
166. G. Pavliuk, D. Pavlov, E. Mitsai, O. Vitrik, A. Mironenko, A. Zakharenko, S.A. Kulinich, S. Juodkazis, S. Bratskaya, A. Zhizhchenko, A. Kuchmizhak, Ultrasensitive SERS-based plasmonic sensor with analyte enrichment system produced by direct laser writing. Nano **10**(1), 49 (2020)
167. X. Guan, G. Feng, Patterned superhydrophobic/superhydrophilic SERS sensors fabricated by femtosecond laser for precise positioning and ultra-sensitive detection. Chem. Phys. Lett. **783**, 139065 (2021)
168. L. Wu, H. Pu, L. Huang, D.-W. Sun, Plasmonic nanoparticles on metal-organic framework: A versatile SERS platform for adsorptive detection of new coccine and orange II dyes in food. Food Chem. **328**, 127105–127105 (2020)
169. C. Song, B. Yang, Y. Zhu, Y. Yang, L. Wang, Ultrasensitive sliver nanorods array SERS sensor for mercury ions. Biosens. Bioelectron. **87**, 59–65 (2017)
170. K. Dana, C. Shende, H. Huang, S. Farquharson, Rapid analysis of cocaine in saliva by surface-enhanced Raman spectroscopy. J. Anal. Bioanal. Tech. **6**(6), 1000289 (2015)
171. N.D. Kline, A. Tripathi, R. Mirsafavi, I. Pardoe, M. Moskovits, C. Meinhart, J.A. Guicheteau, S.D. Christesen, A.W. Fountain III, Optimization of surface-enhanced Raman spectroscopy conditions for implementation into a microfluidic device for drug detection. Anal. Chem. **88**(21), 10513–10522 (2016)
172. A.-M. Hada, M. Potara, S. Suarasan, A. Vulpoi, T. Nagy-Simon, E. Licarete, S. Astilean, Fabrication of gold-silver core-shell nanoparticles for performing as ultrabright SERS-nanotags inside human ovarian cancer cells. Nanotechnology **30**(31), 315701 (2019)
173. A. Kim, S.J. Barcelo, R.S. Williams, Z. Li, Melamine sensing in milk products by using surface enhanced Raman scattering. Anal. Chem. **84**(21), 9303–9309 (2012)
174. Y. Ou, L. Pei, K. Lai, Y. Huang, B.A. Rasco, X. Wang, Y. Fan, Rapid analysis of multiple sudan dyes in chili flakes using surface-enhanced Raman spectroscopy coupled with Au–Ag Core-Shell nanospheres. Food Anal. Methods **10**(3), 565–574 (2017)
175. D. Zhang, H. You, L. Yuan, R. Hao, T. Li, J. Fang, Hydrophobic slippery surface-based surface-enhanced Raman spectroscopy platform for ultrasensitive detection in food safety applications. Anal. Chem. **91**(7), 4687–4695 (2019)
176. L. Li, W.S. Chin, Rapid fabrication of a flexible and transparent Ag Nanocubes@PDMS film as a SERS substrate with high performance. ACS Appl. Mater. Interfaces **12**(33), 37538–37548 (2020)
177. G. Yang, X. Fang, Q. Jia, H. Gu, Y. Li, C. Han, L.-L. Qu, Fabrication of paper-based SERS substrates by spraying silver and gold nanoparticles for SERS determination of malachite green, methylene blue, and crystal violet in fish. Microchim. Acta **187**(5), 310 (2020)
178. A.M. Dowgiallo, D.A. Guenther, Determination of the limit of detection of multiple pesticides utilizing gold nanoparticles and surface-enhanced Raman spectroscopy. J. Agric. Food Chem. **67**(46), 12642–12651 (2019)
179. J. Cheng, S. Wang, S. Zhang, P. Wang, J. Xie, C. Han, X.-O. Su, Rapid and sensitive determination of clenbuterol residues in animal urine by surface-enhanced Raman spectroscopy. Sensors Actuators B Chem. **279**, 7–14 (2019)
180. T. Yaseen, H. Pu, D.-W. Sun, Functionalization techniques for improving SERS substrates and their applications in food safety evaluation: A review of recent research trends. Trends Food Sci. Technol. **72**, 162–174 (2018)
181. C.-H. Ko, C.-C. Liu, K.-H. Chen, F. Sheu, L.-M. Fu, S.-J. Chen, Microfluidic colorimetric analysis system for sodium benzoate detection in foods. Food Chem. **345**, 128773–128773 (2021)
182. M. Esteki, Z. Shahsavari, J. Simal-Gandara, Food identification by high performance liquid chromatography fingerprinting and mathematical processing. Food Res. Int. **122**, 303–317 (2019)

183. J.N. Damico, The mass spectra of some organophosphorus pesticide compounds. J. AOAC Int. **49**(5), 1027–1045 (1966)
184. J.W. Wong, J. Wang, W. Chow, R. Carlson, Z. Jia, K. Zhang, D.G. Hayward, J.S. Chang, Perspectives on liquid chromatography-high-resolution mass spectrometry for pesticide screening in foods. J. Agric. Food Chem. **66**(37), 9573–9581 (2018)
185. C. Wang, R. Zhou, Y. Huang, L. Xie, Y. Ying, Terahertz spectroscopic imaging with discriminant analysis for detecting foreign materials among sausages. Food Control **97**, 100–104 (2019)
186. H. Pu, W. Xiao, D.-W. Sun, SERS-microfluidic systems: A potential platform for rapid analysis of food contaminants. Trends Food Sci. Technol. **70**, 114–126 (2017)
187. S. Kumar, T. Fukuoka, R. Takahashi, M. Yoshida, Y. Utsumi, A. Yamaguchi, K. Namura, M. Suzuki, Highly stable and reproducible Au nanorod arrays for near-infrared optofluidic SERS sensor. Mater. Lett. **129106** (2020)
188. W. Zhengkun, S. Ning, Z. Yong, Z. Jie, AgNPs decorated volcano-like Ag arrays for ultrasensitive Raman detection. Opt. Mater. Express **10**(12), 3393–3402 (2020)
189. M. Liszewska, B. Bartosewicz, B. Budner, B. Nasilowska, M. Szala, J.L. Weyher, I. Dziecielewski, Z. Mierczyk, B.J. Jankiewicz, Evaluation of selected SERS substrates for trace detection of explosive materials using portable Raman systems. Vib. Spectrosc. **100**, 79–85 (2019)
190. H. Wen, H. Wang, J. Hai, S. He, F. Chen, B. Wang, Photochemical synthesis of porous CuFeSe2/Au heterostructured nanospheres as SERS sensor for ultrasensitive detection of lung cancer cells and their biomarkers. ACS Sustain. Chem. Eng. **7**(5), 5200–5208 (2019)
191. G. Eom, H. Kim, A. Hwang, H.-Y. Son, Y. Choi, J. Moon, D. Kim, M. Lee, E.-K. Lim, J. Jeong, Y.-M. Huh, M.-K. Seo, T. Kang, B. Kim, Nanogap-rich Au nanowire SERS sensor for ultrasensitive telomerase activity detection: Application to gastric and breast cancer tissues diagnosis. Adv. Funct. Mater. **27**(37), 1701832 (2017)
192. Z. Zheng, L. Wu, L. Li, S. Zong, Z. Wang, Y. Cui, Simultaneous and highly sensitive detection of multiple breast cancer biomarkers in real samples using a SERS microfluidic chip. Talanta **188**, 507–515 (2018)
193. Q. Wu, G. Chen, S. Qiu, S. Feng, D. Lin, A target-triggered and self-calibration aptasensor based on SERS for precise detection of a prostate cancer biomarker in human blood. Nanoscale **13**(16), 7574–7582 (2021)
194. A. Falamas, H. Rotaru, M. Hedesiu, Surface-enhanced Raman spectroscopy (SERS) investigations of saliva for oral cancer diagnosis. Lasers Med. Sci. **35**(6), 1393–1401 (2020)
195. S. Feng, R. Chen, J. Lin, J. Pan, G. Chen, Y. Li, M. Cheng, Z. Huang, J. Chen, H. Zeng, Nasopharyngeal cancer detection based on blood plasma surface-enhanced Raman spectroscopy and multivariate analysis. Biosens. Bioelectron. **25**(11), 2414–2419 (2010)
196. Y. Huang, T. Xie, K. Zou, Y. Gu, G. Yang, F. Zhang, L.-L. Qu, S. Yang, Ultrasensitive SERS detection of exhaled biomarkers of lung cancer using a multifunctional solid phase extraction membrane. Nanoscale **13**(31), 13344–13352 (2021)
197. H. Yang, Y. Xiang, X. Guo, Y. Wu, Y. Wen, H. Yang, Diazo-reaction-based SERS substrates for detection of nitrite in saliva. Sens. Actuators B Chem. **271**, 118–121 (2018)
198. T. Yang, X. Guo, Y. Wu, H. Wang, S. Fu, Y. Wen, H. Yang, Facile and label-free detection of lung cancer biomarker in urine by magnetically assisted surface-enhanced Raman scattering. ACS Appl. Mater. Interfaces **6**(23), 20985–20993 (2014)
199. S. Dong, Y. Wang, Z. Liu, W. Zhang, K. Yi, X. Zhang, X. Zhang, C. Jiang, S. Yang, F. Wang, X. Xiao, Beehive-inspired macroporous SERS probe for cancer detection through capturing and analyzing exosomes in plasma. ACS Appl. Mater. Interfaces **12**(4), 5136–5146 (2020)
200. D. Lin, Q. Wu, S. Qiu, G. Chen, S. Feng, R. Chen, H. Zeng, Label-free liquid biopsy based on blood circulating DNA detection using SERS-based nanotechnology for nasopharyngeal cancer screening. Nanomedicine **22**, 102100 (2019)
201. V. Moisoiu, A. Stefancu, D. Gulei, R. Boitor, L. Magdo, L. Raduly, S. Pasca, P. Kubelac, N. Mehterov, V. Chis, M. Simon, M. Muresan, A.I. Irimie, M. Baciut, R. Stiufiuc, I.E. Pavel, P. Achimas-Cadariu, C. Ionescu, V. Lazar, V. Sarafian, I. Notingher, N. Leopold, I.

Berindan-Neagoe, SERS-based differential diagnosis between multiple solid malignancies: Breast, colorectal, lung, ovarian and oral cancer. Int. J. Nanomedicine **14**, 6165–6178 (2019)

202. J.D. Spitzberg, A. Zrehen, X.F. van Kooten, A. Meller, Plasmonic-nanopore biosensors for superior single-molecule detection. Adv. Mater. **31**(23), 1900422 (2019)
203. L. Zhao, W. Gu, C. Zhang, X. Shi, Y. Xian, In situ regulation nanoarchitecture of Au nanoparticles/reduced graphene oxide colloid for sensitive and selective SERS detection of lead ions. J. Colloid Interface Sci. **465**, 279–285 (2016)
204. D.I. Gittins, F. Caruso, Spontaneous phase transfer of nanoparticulate metals from organic to aqueous media. Angew. Chem. Int. Ed. **40**(16), 3001–3004 (2001)
205. W. Wu, M. Hu, F.S. Ou, Z.Y. Li, R.S. Williams, Cones fabricated by 3D nanoimprint lithography for highly sensitive surface enhanced Raman spectroscopy. Nanotechnology **21**(25), 255502 (2010)
206. S.W. Lee, K.S. Lee, J. Ahn, J.J. Lee, M.G. Kim, Y.B. Shin, Highly sensitive biosensing using arrays of plasmonic Au nanodisks realized by nanoimprint lithography. ACS Nano **5**(2), 897–904 (2011)
207. G.C. Shi, M.L. Wang, Y.Y. Zhu, X.Y. Yan, S.Y. Pan, A.Q. Zhang, Nanoflower-like Ag/AAO SERS platform with quasi-photonic crystal nanostructure for efficient detection of goat serum. Curr. Appl. Phys. **19**(11), 1276–1285 (2019)
208. L. Baia, M. Baia, J. Popp, S. Astilean, Gold films deposited over regular arrays of polystyrene nanospheres as highly effective SERS substrates from visible to NIR. J. Phys. Chem. B **110**(47), 23982–23986 (2006)
209. X. Sun, L. Lin, Z. Li, Z. Zhang, J. Feng, Novel Ag-Cu substrates for surface-enhanced Raman scattering. Mater. Lett. **63**(27), 2306–2308 (2009)
210. H. Qiu, Z. Zhang, X. Huang, Y. Qu, Dealloying Ag-Al alloy to prepare nanoporous silver as a substrate for surface-enhanced Raman scattering: Effects of structural evolution and surface modification. ChemPhysChem **12**(11), 2118–2123 (2011)
211. B. Chandu, M.S.S. Bharati, S.V. Rao, AG nanoparticles coupled with AG nanostructures as efficient SERS platform for detection of 2,4-dinitrotoluene, in *2017 IEEE Workshop on Recent Advances in Photonics (WRAP)*, (IEEE, 2017), pp. 1–3

Chapter 33
Laser Micro- and Nanostructuring for Refractive Eye Surgery

Norbert Linz, Sebastian Freidank, Xiao-Xuan Liang, and Alfred Vogel

Abstract Every year, more than a million refractive eye operations using femtosecond (fs) laser procedures are performed, and yet the cutting process in corneal tissue remains an area for development. In this chapter, we first review the state of the art of infrared (IR) fs laser dissection in laser in situ keratomileusis (LASIK) and small incision lenticule extraction (SMILE) and formulate the challenges for an improvement of precision and reduction of side effects. Since overcoming these challenges requires better knowledge of the cutting mechanisms, the plasma-mediated corneal dissection process is analyzed by high-speed photography of laser-induced bubble dynamics with up to 50 Mio frames/s, histological analysis of the cuts, and gas chromatography of the dissection products. Based on these results, we show that cutting efficiency and precision are improved through focus shaping by means of a helical phase plate, which converts the linear polarized Gaussian fs laser beam into a Laguerre-Gaussian vortex beam. The focus of the vortex beam has a ring shape with the same length in axial direction as the focus of a Gaussian beam but larger diameter. This greatly facilitates cleavage along the corneal lamellae, enabling cutting with low plasma energy density, higher precision, and fewer mechanical side effects. A shortening of the laser plasma length at constant focusing angle by use of UV-A laser pulses instead of IR pulses further improves precision. To compare the performance of UV and IR Gaussian and vortex beams, the incident and absorbed laser energy needed for easy removal of flaps created in porcine corneas are determined at various pulse durations and the smoothness of cuts is evaluated by scanning electron microscopy. Overall, vortex beams perform better than Gaussian beams for all wavelengths and can be easily implemented in clinical systems. Finally, we discuss a novel concept for refractive correction based on the introduction of refractive index changes in the corneal stroma by localized low-density plasma formation. Experimental findings that UV wavelengths work better for this purpose than IR wavelengths are explained through an analysis of

---

N. Linz · S. Freidank · X.-X. Liang · A. Vogel (✉)
Institut für Biomedizinische Optik, Universität zu Lübeck, Lübeck, Germany
e-mail: norbert.linz@uni-luebeck.de; sebastian.freidank@uni-luebeck.de;
x.liang@uni-luebeck.de; alfred.vogel@uni-luebeck.de

© The Author(s), under exclusive license to Springer Nature Switzerland AG 2023

R. Stoian, J. Bonse (eds.), *Ultrafast Laser Nanostructuring*, Springer Series
in Optical Sciences 239, https://doi.org/10.1007/978-3-031-14752-4_33

the wavelength dependence of free electron density and energy spectrum that are obtained by numerical simulations.

Keywords Refractive eye surgery · Laser in situ keratomileusis (LASIK) · Small incision lenticule extraction (SMILE) · Laser-induced refractive index change (LIRIC) · Ultrashort laser pulses · Vortex beam

1 Introduction: State of the Art of Femtosecond Laser Refractive Eye Surgery and Concepts for Improvement

Laser dissection in transparent tissue relies on energy deposition by nonlinear absorption through plasma formation (optical breakdown) at the laser focus [1–4]. The laser-induced plasma features a high volumetric energy density going along with high pressure in the kilobar range and a high temperature of several thousand Kelvin [5]. Therefore, plasma expansion results in shock wave emission and the formation of a cavitation bubble that locally disrupts the corneal tissue, as described in detail in Sect. 2. Application of a raster pattern of laser exposures produces an intrastromal cut. The smoothness of this cut and the amount of side effects produced during dissection relies on an appropriate choice of laser and irradiation parameters. Based on an analysis of the dissection mechanisms, we discuss known strategies and novel approaches for process optimization (Sects. 3 and 4) and present an alternative method of refractive correction via laser induction of corneal refractive index changes (Sect. 5).

1.1 IR fs Laser Refractive Surgery

Femtosecond (fs) laser refractive corneal surgery of shortsightedness (myopia) and farsightedness (hyperopia) has been introduced in the late 1990s [6, 7]. In laser in situ keratomileusis (LASIK), fs laser pulses are tightly focused in a raster pattern into the corneal stroma at numerical apertures between 0.2 and 0.5 to create a corneal dissection. This way, a circular flap with ≥5 mm diameter is created by producing a cut parallel to the corneal surface in about 100 µm depth followed by a side cut from the flap bed to the surface. On one side, a hinge is left to keep the flap connected to the cornea. The flap is lifted, and the refractive correction is then performed by reshaping the intrastromal surface via excimer laser ablation. After surgery, the flap is repositioned and covered for some time by a therapeutic contact lens until the flap adheres again to the stromal bed. Flap cuts with a laser enable precise repositioning of the flap, which is not so easy after dissection with a sharp knife (microkeratome), where no side cut is produced and the flat can laterally move. Exact repositioning is essential if wavefront-guided correction of higher-order aberrations is performed in conjunction with myopic or hyperopic correction.

Excimer laser ablation must be performed within the corneal stroma because after surface ablation, the top layer of the cornea (corneal epithelium) would regrow within a few days, and the ablative correction would not last. Moreover, the cut must be performed at a certain depth because injuries of Bowman's layer (the uppermost stromal layer next to the epithelium) may result in corneal haze. These requirements together with the thinning of the corneal stroma by the excimer laser ablation for refractive correction imply a weakening of the mechanical stability of the cornea [8].

In 2010, small incision lenticule incision (SMILE) was introduced into the clinic. Here, two intrastromal incisions produce a lenticule that is then removed through a 2–4-mm-long incision on one side [9, 10]. The concept had been introduced ten years earlier by Lubatschowski et al. [7]. The lenticule is $\approx 20\ \mu\text{m}$ high at its rim to provide the necessary thickness and mechanical stability that enables to remove it easily with forceps. SMILE compromises the corneal stability less than LASIK because it avoids the 100-μm-high circular flap side cut required in LASIK. This reduces the "dry eye" syndrome frequently observed after LASIK, which originates from a dissection of corneal nerves that interrupts the feedback circle controlling the tear flow [11]. Corneal nerves run horizontally from the nasal towards the temporal side of the cornea. The nerves are interrupted by the circular flap side cut but not by the small incision for lenticule removal that is usually located at the upper side of the excised lenticule where it does not cross nerve fibers. SMILE can be performed completely with the femtosecond laser system, whereas in LASIK two complex laser systems are needed. This reduces treatment time and costs.

Both LASIK and SMILE work best for correction of myopia, which involves a flattening of the corneal curvature. Hyperopic corrections require a steepening of the central cornea. In LASIK or SMILE, this is achieved either by creating a ringlike indentation around the center via excimer laser ablation or through an appropriate shape of the extracted lenticule. However, epithelial regrowth tends to fill the indentation, which compromises the stability of the refractive correction [12]. Therefore, filler techniques are now under investigation in which a transparent biocompatible material is injected into a laser-generated corneal pocket to steepen the curvature of the central cornea [13–15].

In all commercially available refractive laser systems, ultrashort infrared (IR) laser pulses are employed for dissection [16]. IR wavelengths do not dazzle the patient and cause minimum heating of the retina because melanin absorption in the retinal pigment epithelium decreases strongly with increasing wavelength (it drops from $\approx 50\%$ at 500 nm to less than 3% above 1000 nm [1, 17]). Model simulations predicted a peak retinal temperature rise of ≤ 0.6 K for all investigated clinical laser systems [18].

In recent years, the spectrum of refractive laser surgeries has been expanded by femtosecond laser-assisted cataract surgery (FLACS) [19–21]. State-of-the-art cataract surgery involves creating a small incision in the cornea, a circular tear (capsulorhexis) in the anterior lens capsule, and emulsification of the turbid lens. Then an artificial intraocular lens (IOL) is implanted into the remaining capsular bag. The first three steps can be assisted by FLACS laser systems. Lasers can perform steplike corneal incisions, which facilitate sealing of the cut by intraocular pressure after surgery and IOL implantation. The sutureless technique reduces the risk of postoperative astigmatism. Moreover, lasers can perform a precise and well-centered incision of the anterior lens capsule, which is otherwise one of the most difficult tasks in cataract surgery. Well-centered capsulotomies with predictable diameter are a prerequisite for the implantation of toric IOLs for astigmatic correction and multifocal IOLs that enable to focus at near and far distances (with a trade-off of reduced contrast visibility) [22]. Finally, the shock waves and cavitation bubbles arising from laser-induced plasma formation can also be employed for lens fragmentation. Since plasma generation does not work well in strongly scattering lenses, FLACS has promoted a trend towards early cataract surgery on clear lenses, often in conjunction with the implantation of multifocal intraocular lenses for presbyopia correction.

The above laser-surgical procedures require guidance by optical coherence tomography (OCT) or another 3D imaging technique and a delivery optics capable of providing good focus quality at different depths [19]. Overall, the design of FLACS systems is more challenging than the design of LASIK or SMILE systems and relies on the experience gathered in these areas. However, laser tissue interactions are similar as in corneal surgery. In the following, we will focus attention on corneal refractive surgery because it involves high challenges on precision that can be optimally met by advanced laser micro- and nanostructuring techniques, which will be introduced in this chapter.

1.2 Challenges for Precision and Predictability

The thinning of the cornea needed for myopic correction is 9 μm per diopter in the center for an optical zone with 5 mm diameter and progressively less towards the periphery of the zone [23]. Larger optical zones increase the thickness of ablated material but do not reduce the requirements on shape accuracy and surface quality within the optical zone. The necessary precision is in LASIK provided by argon-fluoride (ArF) excimer laser ablation at a wavelength of 193 nm, where the optical penetration depth is $\approx$ 0.3 μm, and the thermal damage zone is only $\approx$100-nm thin [1].

Precise and smooth femtosecond laser dissection requires a minimization of the spatial extent of individual laser effects. The numerical aperture (NA) of the focusing beam must be as large as possible to minimize the focus length. Optics design for achieving this goal is challenging because the field of view must have $\approx$ 10 mm diameter. Therefore, NAs in clinical instruments usually range between 0.2 and 0.35. A value of NA $\approx$ 0.5 can be achieved when the optics is moved during treatment and the field of view is covered by stitching individual tiles [24].

SMILE imposes particular challenges on cutting precision since the predictability of refractive correction relies completely on the precision of lenticule cutting. This precision is compromised by long plasmas generated at small NAs and by high pulse energies producing large cavitation bubbles (see Sect. 2.2). Large bubbles created during cutting of the lower lenticule face distort the overlying corneal stroma and compromise the cutting precision of the upper face.

1.3 Potential Improvements by Focus Shaping, Use of Shorter Wavelengths, and Refractive Index Modifications by Low-Density Plasma

Cutting precision and efficacy can be improved by the use of shorter wavelengths that go along with a shorter focus length and, thus, a thinner zone affected by the dissection process (Fig. 33.1a). Suitable wavelengths must be outside the visible range to avoid dazzling of the patient and long enough to avoid photochemical damage to the cornea and lens. At the same time, they must be short enough to be largely absorbed by the lens of adult patients because the retina is very vulnerable to photochemical damage. These requirements are fulfilled by UV-A wavelengths around 350 nm, such as provided by the third harmonic of Nd:YAG and Yb:YAG laser emission (355 nm and 348 nm, respectively) [25, 26]. Nevertheless, safety aspects remain critical, as will be discussed further in Sect. 4.

Focus shaping is a novel concept for improving cutting precision and efficacy that can be employed at any laser wavelength [27, 28]. The focus of a Gaussian beam is elongated, and the orientation of the forces acting on the corneal collagen lamellae by the expanding laser plasma is not very effective for producing a cut or cleavage parallel to the corneal surface, i.e., perpendicular to the laser beam axis.

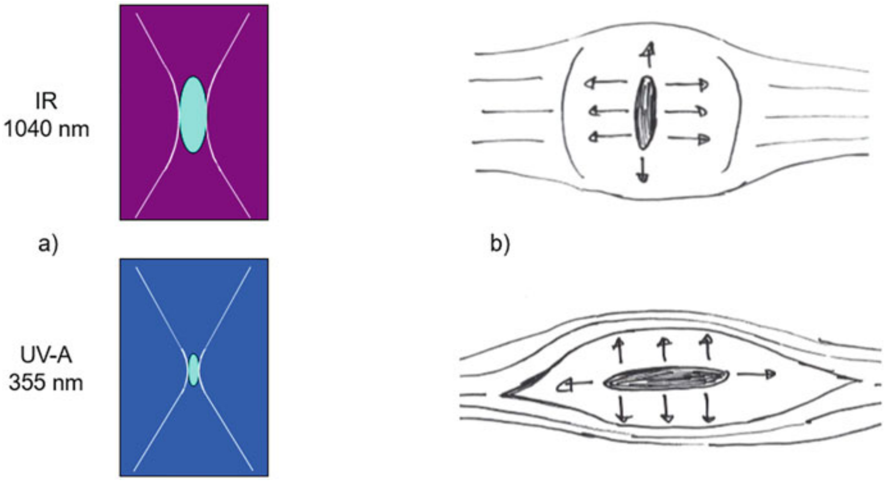

Fig. 33.1 (**a**) Comparison of focal length and diameter for IR and UV wavelengths, (**b**) schematic drawing of rod- and disklike foci in layered corneal stroma and of the forces exerted during plasma expansion

A disklike focus would be much better suited to cleave the corneal lamellae, as illustrated in Fig. 33.1b. We will see in Sect. 3 that ring foci produced by optical vortex beams have the same length as that of a Gaussian beam focused at the same NA but a larger diameter. Thus, vortex beams are promising tools for improving cutting efficacy, which, in turn, minimizes mechanical side effects. Moreover, the better aspect ratio improves cutting precision.

Another novel approach is femtosecond laser-induced refractive index change (LIRIC) of corneal stroma [29]. A similar technique is also under investigation for modification or fine-tuning of the refractive power of intraocular lenses that have been implanted after cataract surgery [30–32]. These approaches involve no dissection, and the corneal mechanical integrity is maintained. The change of refractive power relies on the inscription of diffractive lenses or Fresnel lenses by laser-induced refractive index changes, as will be discussed in more detail in Sect. 5.

2 Mechanisms of Corneal Dissection

Precise knowledge about the mechanisms of corneal dissection helps to optimize the cutting process and surgical outcome. Investigations by physicists have mostly focused on the physics of plasma formation and the parameter dependence of optical breakdown thresholds in water and cornea and the bubble size in water [6, 33]. Biomedical investigations focused on the refractive outcome, surgical complications, and histological and histochemical studies of the tissue effects and the size of the laser-induced damage zone [34, 35]. However, the dynamics of the cutting process itself has hardly been studied because time-resolved studies of plasma formation and bubble dynamics in corneal stroma are very challenging. In the following, we will focus on these dynamical aspects.

2.1 *Modes of Corneal Dissection*

Two modes of corneal dissection are used in clinical practice. In the most commonly used “cleavage mode,” laser pulses are applied in a raster pattern with several micrometer spot separation. To achieve a homogeneous cut, the laser pulse energy must be large enough to produce disruptive effects (shock waves and cavitation bubbles) that can cleave the corneal lamella between the individual laser spots. In the cleavage mode, one scan covers the entire surgical field, and the NA is moderate. The maximum possible pulse repetition frequency (PRF) is determined by the possible scan speed in conjunction with the desired spot separation. In present clinical systems, the spot separation is 2–6 μm and the PRF 150–500 kHz [16].

One manufacturer uses an alternative approach in which laser pulses of lower energy are applied at large NA and a much higher PRF in the MHz range. Here, the focusing/scanning unit is moved to cover the entire flap area. The individual laser spots overlap [16] and each location in the dissection plane is hit by several low-energy laser pulses. Cutting does not rely on the disruptive action of laser-induced plasma expansion but rather on free-electron-mediated disintegration of biomolecules in the collagen fibers, as described in [4]. High-rep-rate, low-energy dissection has been extensively covered in two recent review papers [24, 36], and we will focus further attention on the cleavage mode.

2.2 Bubble Dynamics in the Cornea

Heisterkamp et al. [37] and Arnold et al. [38] studied the influence of nonlinear beam propagation on plasma formation in the cornea at moderate NAs. They found that filamentation results in a prolongation of the spatial extent of the laser effects, which compromises cutting precision and increases the potential of undesired side effects. Vogel et al. showed that the volume of laser-induced cavitation bubbles in corneal stroma is considerably smaller than in water but much larger than the plasma volume [39, 40]. This explains why concepts of flattening the corneal curvature by vaporization-induced removal of corneal tissue that were pursued in the 1990s [41, 42] failed. The disruptive effects from shock wave and bubble by far dominated over the effect of tissue vaporization within the plasma volume [5, 40]. A reproducible introduction of refractive changes by tissue removal proved to be possible only by dissection and extraction of a stromal lenticule, as first proposed by Lubatschowski et al. [7].

In the abovementioned studies, photographs of intrastromal bubbles were taken several seconds after laser exposure, when bubble oscillations had ceased. The first time-resolved studies of the bubble dynamics in corneal stroma were performed in 1996 by Juhasz and coworkers [43]. Time-resolved photography with illumination by a collimated picosecond laser beam enabled to take shadow pictures of the bubble but allowed no view into the bubble interior. Bubbles appeared round, possibly because experiments were performed on bovine eyes that had been stored overnight in cold saline solution, which softens the tissue. These results have influenced artist's views on the process dynamics that for many years showed round bubbles in the corneal stroma. However, the bubble shape should actually not be spherical considering that bubbles expand within a layered corneal stroma. The stroma consists of 2–3-μm-thick corneal lamella in which collagen fibrils extend from opposite sides of the corneal periphery (limbus) across the center, whereby the fibrils in successive layers are oriented at an angle of about 45° with respect to each other. Recently, we performed ultrafast photographic investigations of the bubble dynamics in fresh porcine cornea, with speckle-free white-light Köhler illumination from a plasma discharge flash lamp [44]. A typical image series is shown in Fig. 33.2. The bubble has a lobular structure with lobes expanding along the direction of the collagen fibrils in the individual lamellae. The fact that a stack of 4–5 lobes is seen on the images indicates that the plasma producing the bubble extends across several lamella and is 10–15 μm long.

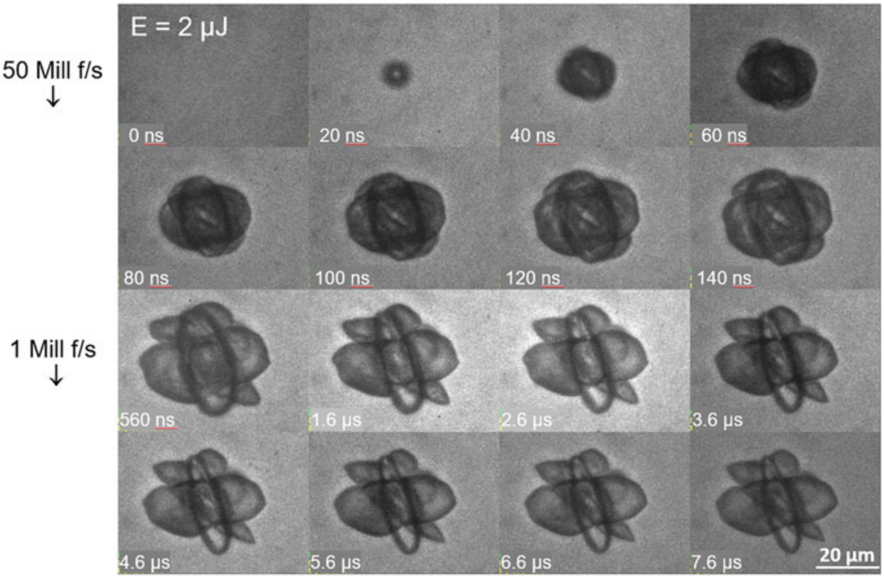

Fig. 33.2 High-speed photographical picture series of laser-induced bubble dynamics in porcine corneal stroma recorded with up to 50 Mio frames per second at 10 ns exposure time per frame. The bubble was produced by a 355-nm, 560-ps laser pulse of 2 µJ energy that was focused at NA = 0.75 into the stroma at a depth of 150 µm. (Reprinted with permission from Freidank et al. [44] © The Optical Society)

In order to form a homogeneous cut, the bubble lobes from adjacent bubbles must meet each other and merge. If this is not everywhere the case, tissue bridges between flap and flap bed remain that must be severed by the surgeon, which is usually done with a blunt instrument. Cutting modalities that minimize the thickness of the bubble layer and the amount of tissue bridges create the smoothest cuts with the least side effects.

2.3 Histology: Tissue Bridges and Bubble Content

Figure 33.3a shows a histological section of a laser-induced cut in corneal stroma in which one can infer the location of dissections (arrows) and a tissue bridge between flap and flap bed. Tissue bridges occur particularly easily at locations, where the lamellae are oriented under a small angle with regard to the direction of laser dissection. Such "suture lamellae" are frequently found in the anterior stroma where they increase mechanical stability by connecting the lamellae running parallel to the corneal surface [45, 46].

The large bubbles visible in histology coalesce from the large number of smaller bubbles produced during laser tissue interaction, whereby the coalescence is driven

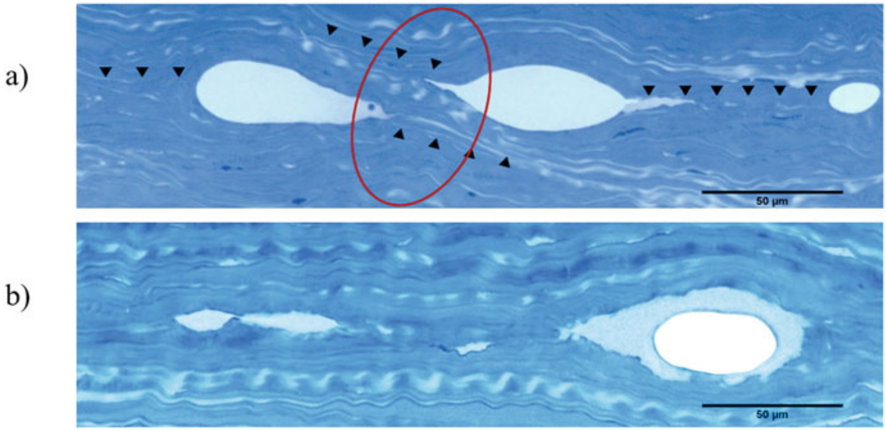

Fig. 33.3 Histologic sections through toluidine-blue stained, araldite resin-embedded corneal stroma after dissection by 0.8-µJ pulses. Pulses were focused at NA = 0.28, with 4 µm spot separation. (**a**) Dissections are marked by arrowheads; a tissue bridge is marked by the red oval. Cuts close locally after dissection, and gas produced by tissue disintegration and water dissociation in the plasma collects in large bubbles. (Adapted with permission from Freidank et al. [44]. © The Optical Society). (**b**) Cavities are filled with gas, debris, and probably exudates

by surface tension. The bubble interior contains some solid debris, as seen in Fig. 33.3b. Gas chromatography revealed that the gaseous content of the bubble consists mainly of hydrogen and some oxygen [47]. This is somewhat surprising, considering the large collagen content of corneal stroma. An explanation could be that the small volatile gas molecules arise from free-electron-mediated cleavage of side chains from collagen peptide chains, as described in [48, 49], while larger chain fragments form the debris observed in histology. Besides that, dissociation of water in the plasma volume produces molecular hydrogen [47, 50], which contributes to the gaseous bubble content.

2.4 Interplay of Consecutive Pulses

The image series in Fig. 33.2 shows the dynamics of a single cavitation bubble, but the actual cutting dynamics is characterized by the interaction of successively generated bubbles during laser scanning, which is even more complex. Experimental investigation of this process at high pulse repetition frequency and high spatial resolution is very challenging. With a fixed target, the laser interaction rapidly moves out of the field of view, and for cutting with fixed focus position and moving corneal specimen, the PRF is limited because the scan speed is smaller than with flying focus. To date, only two-bubble interactions in a tissue phantom have been investigated [51] but not the cutting dynamics of laser dissection of corneal stroma. First experimental results of cutting dynamics in the cornea at 1 kHz repetition rate are reported in [44].

Avoiding the abovementioned difficulties, one can study the role of PRF for flap dissection by comparing clinical reports published during the evolution of the IntraLase system, which was the first commercially available system for femto-LASIK. The PRF started in 2001 at 6 kHz [52] and was then increased to 15 kHz, 30 kHz, 60 kHz, and finally to 150 kHz [53–55]. It turned out that the pulse energy required for flap cutting dropped considerably from 2.0 μJ at 15 kHz through 1.2 μJ at 30 kHz [53] to $\leq$0.9 μJ at 60 kHz and 150 kHz [54, 55]. This indicates that the cutting process relying on the cleavage of stromal lamellae becomes more effective with higher PRF. Studies of damage zone and healing response and of the refractive outcome also showed an improvement with higher PRF and smaller pulse energies [35].

With increasing PRF, the cutting process evolves from a series of individual disruptive events into laser-driven crack propagation driven by the consecutive expansion of bubbles generated along the laser beam track. At an optimum combination of scan speed and PRF, the front bubble has already expanded to a certain size when the next pulse is released but has not yet reached its maximum size or started to collapse. The energetics and speed of crack propagation in solids can be described using the Griffith theory [44, 56] that is well presented in a book by Gordon [57]. It's applicability is supported by the fact that cornea has strain-stiffening features, i.e., it's elastic modulus strongly increases during deformations at high strain rate as occurring in laser dissection [1]. To date, no systematic study on corneal dissection dynamics based on the Griffith theory is yet available, but that would be a promising venture.

3 Focus Shaping by Gaussian and Vortex Beams

A Gaussian beam with linear polarization can be transformed into a Laguerre-Gaussian vortex beam by means of a helical phase plate as illustrated in Fig. 33.4a (see also [58, 59] and Chap. 15 in this book). The ring focus arising from this transformation is illustrated in (a) and compared with the focus from a Gaussian beam. An experimental result achieved with a commercially available fused-silica phase plate with 16 steps is shown in Fig. 33.4b. For equal *NA*, both foci have the same length; only the diameter differs [58, 60]. Since Laguerre-Gaussian beams are propagation invariant, the phase plate can be inserted anywhere in the beam path before the scanning device.

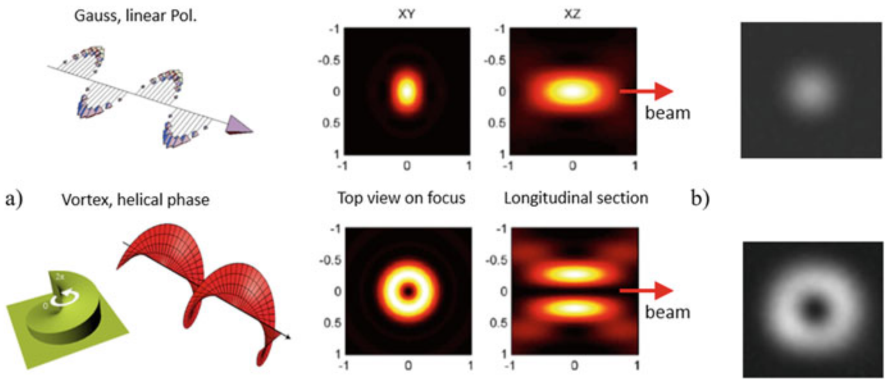

Fig. 33.4 (**a**) Transformation of a Gaussian beam into a vortex beam with ring focus by means of a helical phase plate. (Adapted from Ref. [59], and taken from Ref. [60], with permission). (**b**) Experimental results for Gaussian and ring focus, respectively. The phase plate used was a 16-step fused-silica phase plate. The diameter of the ring focus depends on the order m of the vortex beam and increases with increasing m. Here, we see the focus of a beam with $m = 1$

3.1 Cutting Precision and Bubble Layer Formed During Dissection

Figure 33.5 demonstrates the improvement of dissection quality with smoother flap bed that can be achieved by converting a Gaussian beam into a vortex beam [28].

Pulse energies required for easy flap lifting are slightly larger with the vortex beam than with the Gaussian beam because the focal area is four times larger. However, the distance between neighboring spots that needs to be bridged by lamellae cleaving is smaller and the focus shape is better suited to produce cleavage parallel to the corneal surface. Therefore, cutting is more efficient. The threshold energy for easy flap lifting was for the vortex beam identical with the bubble threshold in water, but for Gaussian beam it was 60–80% higher [28]. As a result, a pronounced bubble layer is visible in cuts produced by the Gaussian beam that persists for more than 10 minutes, whereas with the vortex beam, bubbles are much smaller and disappear shortly after dissection although the flap can be easily lifted (Fig. 33.6). The only trace visible from dissection is the raster pattern of the laser pulses, with dots that are only slightly larger than the laser plasma and possibly arise from the disruptive interaction in the immediate plasma vicinity. The images in the left column shows that bubbles from the individual pulses coalesce shortly after dissection, forming much larger bubbles that are also seen in histology (Fig. 33.3).

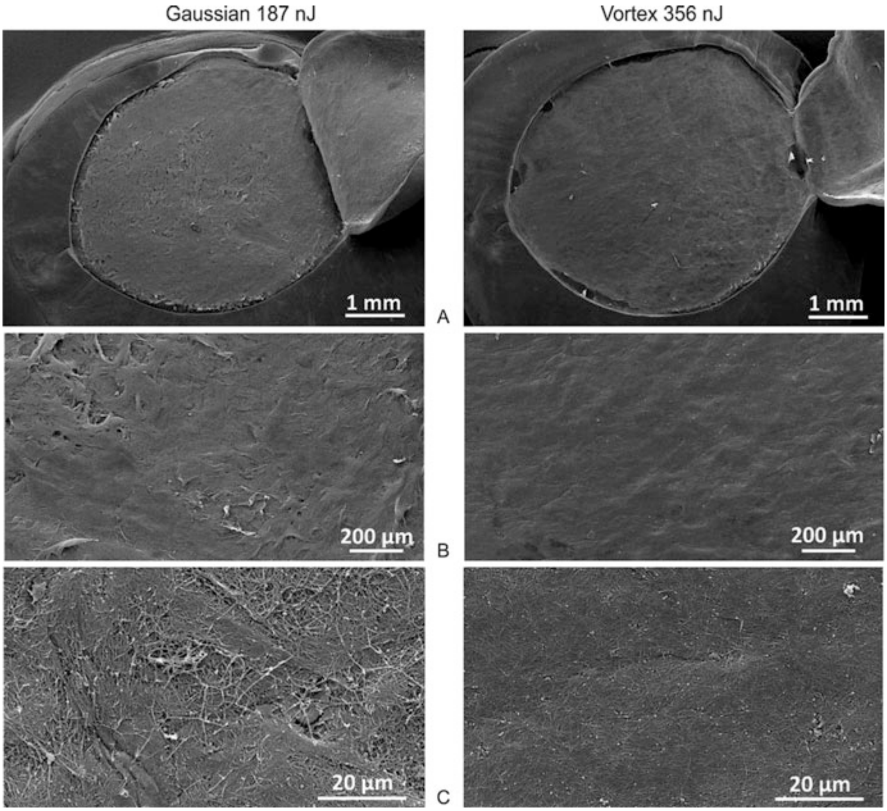

Fig. 33.5 SEM images of 6-mm flaps in a porcine cornea specimen that were cut using Gaussian (*left*) and vortex (*right*) beams with 1030-nm wavelength and 480-fs laser pulse duration. (Reprinted from Freidank et al. [28]). NA = 0.38, spot separation 6 µm. In (**a**) to (**c**), the flap bed is shown with increasing magnification

3.2 Improved Cutting Efficiency of Vortex Beams Reduces Mechanical Side Effects

Figure 33.7 shows the dependence of laser energy transmission during intrastromal cutting on the incident laser pulse energy from which the absorbed energy at the flap dissection threshold, $E_{\text{th,cut}}$, can be derived. Below the threshold for visible bubble formation in the cornea, the transmission through the porcine cornea stays constant at 100%. After bubble formation sets in, the transmission decreases with increasing laser pulse energy, because ever more laser energy is absorbed and available for vaporisation and conversion into mechanical energy of the bubbles and acoustic transients. At $E_{\text{th,cut}}$, the transmission for the Gaussian beam was 72.2%, corresponding to an absorbed energy fraction of 27.8%. For the vortex beam, the incident energy for flap cutting was higher, but only 2.0% were absorbed at $E_{\text{th,cut}}$.

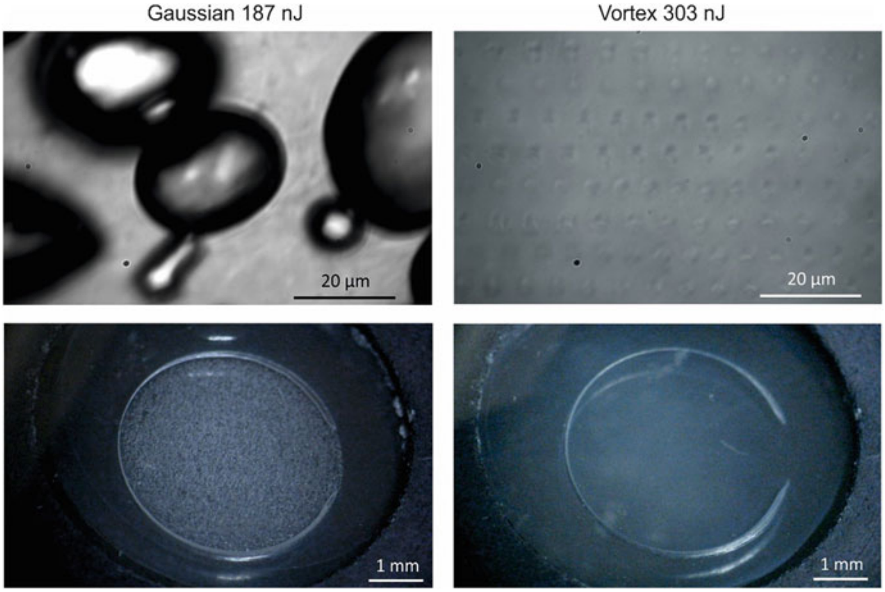

Fig. 33.6 Laser-induced gas bubble layer after flap dissection with Gaussian (left column) and vortex (right column) beams with 1030-nm wavelength and 480-fs laser pulse duration. Photographs in the upper row were taken through the focusing objective less than 1 minute after flap cutting. Photographs in the lower row were taken 10 minutes after flap cutting using a stereo microscope. (Reprinted from Freidank et al. [28])

The absorbed energy values were 6 nJ for the vortex beam versus 52 nJ for the Gaussian beam [28]. The above estimate neglects scattering at the laser plasma, and the absorbed energy values are thus upper estimates. Scattering at bubbles from previous pulses plays no role because a low repetition rate of 4 Hz and a large spot distance was employed for the energy measurements to avoid disturbances by bubbles from previous pulses. We conclude that the use of a vortex beam does not only improve cutting precision and smoothness (Fig. 33.5) and diminish the bubble layer (Fig. 33.6), but the strong reduction of absorbed energy required for dissection also leads to a substantial reduction of mechanical side effects.

For ultrashort laser pulses, energy deposition is stress confined, and thermoelastic stress lowers the bubble threshold well below the superheat limit [1, 4, 61]. The coincidence of $E_{\mathrm{th,cut}}$ with the bubble threshold suggests that the ring-shaped focus of the vortex beam facilitates cleavage along the corneal lamellae to such a degree that an explosive vaporization is not necessary for dissection but the thermoelastic stress produced at the bubble threshold is sufficient. Therefore, cutting is less disruptive than for a Gaussian beam.

With a Gaussian beam, the absorbed energy is 8.7 times higher than with the vortex beam, and the focal volume is much smaller. Therefore, the plasma density and temperature rise in the focal volume are much greater, and peak temperatures can well exceed 1000 °C. This favors pyrolysis as well as free-electron-mediated

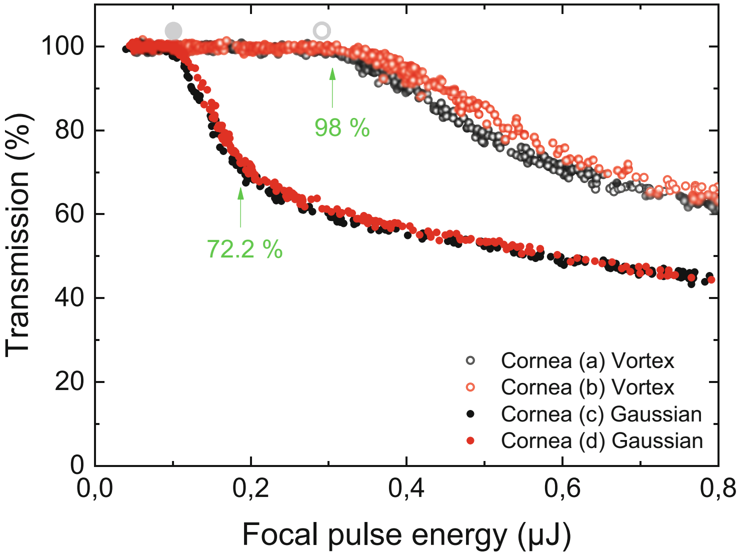

Fig. 33.7 Laser energy transmission during intrastromal flap cutting for Gaussian and vortex beams at 480 fs laser pulse duration. (From Freidank et al. [28]). For each parameter set, two different porcine corneas were investigated (red and black dots). The thresholds for visible bubble formation in the cornea are shown as gray dots (Gaussian) and gray circles (vortex). The energy values required for flap cutting are marked with green arrows, and the corresponding transmission values are indicated

molecular disintegration and explains the large amount of non-condensable gas that forms the layer of long-lived gas bubbles [4, 47].

Freidank et al. assessed the mechanical stress on keratocytes close to the cut and on epithelial cells approximately 100 μm from the dissection plane (as often used clinically) [28]. For 480-fs pulses and pulse energies at $E_{\text{th,cut}}$, they arrived at pressure estimates of 0.57 MPa for the vortex beam and 4.3–6.0 MPa for the Gaussian beam (i.e., 7.6–10.6 times larger). Use of a vortex beam also reduces pressure and thermoelastic tensile stress in the immediate vicinity of the cut such that the mechanical damage zone, which amounts to ≈10 μm for Gaussian fs laser beams [34, 35], is diminished.

3.3 Improvements of LASIK and SMILE by Focus Shaping

An opaque bubble layer in the anterior stroma during LASIK is a well-known intraoperative finding seen with all clinical femtosecond laser systems [62, 63]. An excessive opaque bubble layer can lead to complications during flap creation, and bubble remnants remaining in the corneal stroma after flap lifting may compromise measurements of the residual stromal thickness and the reliability of pupil tracking

[62, 64]. The increased precision and reduction of mechanical side effects in intrastromal cutting by the use of a vortex beam make it a promising tool for flap cutting in LASIK and intrastromal pocket dissection for hyperopia correction [13, 14]. It offers even greater potential for improving SMILE, where formation of an opaque bubble layer is a known complication that compromises the predictability of the lenticule thickness [65–67].

4 Effect of Wavelength and Pulse Duration on Surgical Precision with Gaussian and Vortex Beams

We have discussed in Sect. 1.3 that the use of UV-A wavelengths may improve precision of corneal dissection for both Gaussian and vortex beams because of the much shorter plasma length compared to IR breakdown at the same *NA* (Fig. 33.1a). Besides this, nanosecond (ns) UV-A laser pulses with well-reproducible temporal shape offer to produce deterministic nano- and microeffects in a similar way as femtosecond laser pulses [25, 68, 69]. This is possible because both UV ns pulses and high-power fs pulses produce abundant seed electrons via multiphoton ionization that enable to fine-tune the endpoint of the subsequent ionization avalanche by varying the laser irradiance. By contrast, in IR ns breakdown, the multiphoton-induced generation of seed electrons determines the breakdown threshold, and a high irradiance is needed to initiate breakdown due to the high order of multiphoton processes [2, 4, 70]. At such high irradiance values, the avalanche progresses very rapidly once started, which is further promoted by the quadratic increase of the avalanche ionization rate with increasing wavelength, $\eta_{\mathrm{AI}} \propto \lambda^2$. Therefore, a “big bang” occurs immediately at the threshold of ns IR breakdown, which makes it impossible to achieve precise surgical effects. However, the strength of laser effects can be precisely tuned when using fs pulses or UV-A ns pulses with reproducible temporal shape [69]. Nanosecond pulses emitted from regular Nd:YAG laser oscillators have a spiky temporal shape originating from statistical mode beating of the longitudinal laser modes. Here, pulse-to-pulse variations of the mode beating go along with variations of peak intensity that result in statistical variations of breakdown effects. By contrast, single-longitudinal-mode (slm) pulses exhibit a reproducible Gaussian temporal shape with reproducible breakdown characteristics. They can be produced by seeding large Nd:YAG laser resonators but are genuinely emitted from microchip lasers with short resonator. Thus, such lasers emitting UV-A pulses could offer the possibility to produce precise corneal dissection in a cost-effective way. Therefore, we have explored the effect of wavelength and pulse duration on surgical precision. Measurements were performed with both Gaussian and vortex beams.

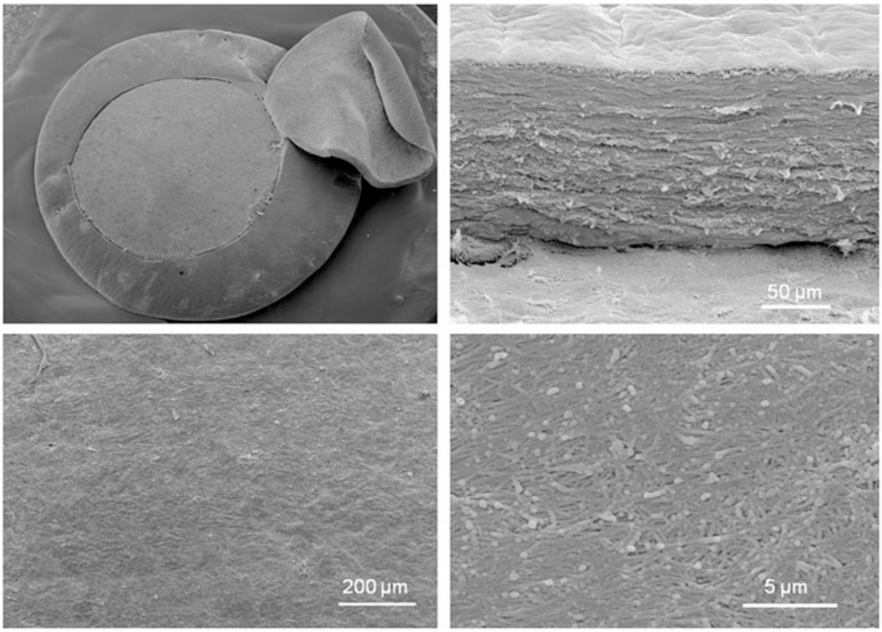

Fig. 33.8 Scanning electron microscopic images of a flap with 5 mm diameter in porcine cornea. The flap was produced with 1.0-μJ UV-A laser pulses ($\lambda = 355$ nm, $\tau_L = 560$ ps) focused at NA = 0.28 with 6 μm spot separation. The cutting energy per unit area averaged over the corneal surface was 2.8 J/cm^2. The side cut (upper right image) was produced with 0.8-μJ pulses focused at NA = 0.75 with 2 μm spot separation

4.1 High Cutting Precision with UV-A Wavelengths

Figure 33.8 shows a 5-mm flap created by Gaussian UV-A laser pulses from an amplified slm microchip Nd:YAG laser emitting pulses of 560 ps duration at $\lambda = 355$ nm. The flap bed is very smooth, and the flap side cut is very precise with little distortions of the tissue structure. Even individual lamellae can be recognized in the electron micrograph.

4.2 Pulse Duration Dependence of Cutting Energies for UV and IR Wavelengths

Figure 33.9 shows the pulse duration dependence of the absorbed laser energy required for easy flap lifting, E_{abs}, together with the influence of the focus shape and laser wavelength.

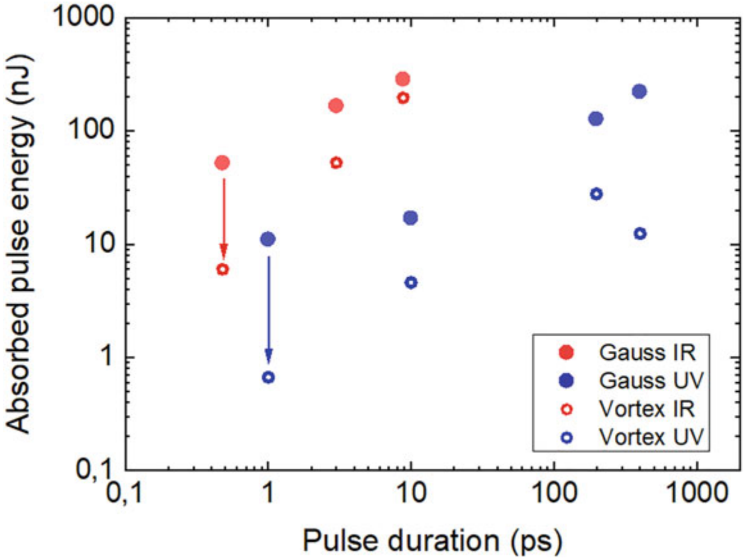

Fig. 33.9 Absorbed laser energy necessary for easy flap lifting after dissection of porcine cornea with IR (1030 nm) and UV-A (343 nm/355 nm) laser pulses, applied at 6 × 6 μm spot separation (NA = 0.38)

The required cutting energy is considerably lower for UV-A pulses than for IR laser pulses and also considerably lower for the vortex beam compared to the Gaussian beam. Moreover, we find that $E_{\mathrm{th,cut}}$ decreases with decreasing laser pulse duration, regardless of wavelength and focus shape. The first two findings prove the validity of the approaches outlined in Sect. 1.3, but the understanding of the pulse duration dependence requires a deeper analysis (see Freidank et al. [28]).

At first sight, one may be tempted to relate to the cumulated pulse energies needed for corneal dissection per unit area to the work required for mechanical separation of corneal lamellae by (slow) tearing, which has been investigated by Smolek and McCarey [71]. This hypothesis is compatible with the observed wavelength and focus shape dependence because at shorter wavelengths, cleavage occurs in a thinner stromal layer, and with a ring focus, forces are orientated in a more favorable fashion (Fig. 33.1). Thus, less energy is exerted for unnecessary lamella cleavage and dislocation in cutting direction. However, the hypothesis cannot explain the strong dependence on laser pulse duration. Hence, we must look at the pulse duration dependence of thermomechanical effects in bulk media to find an explanation. Moreover, we must consider that the ultimate tensile stress of the tissue must be overcome for disruptive tearing of corneal lamellae by ultrashort laser effects.

At laser pulse durations ≤1 ns, energy deposition is obviously *thermally confined* [1], and losses by heat diffusion play no role in the entire investigated parameter range. By contrast, the degree of *stress confinement* increases with decreasing pulse duration [1, 72]. For the sound velocity in water or tissue of ≈1.5 µm/ns and a plasma diameter of ≈1.5 µm, stress confinement sets at pulse durations around 1 ns but becomes more effective at shorter pulse durations. The degree of stress confinement is only about 30%, when the nominal condition for stress confinement is just fulfilled (i.e., when laser pulse durations equals the acoustic propagation time through the region of energy deposition) and reaches 100% for fs pulses. Stress confinement does not only increase the peak compressive stress produced in the region of energy deposition but also goes along with the generation of a tensile stress wave following the compressive pulse. The tensile wave will certainly contribute to the tearing of collagen fibrils necessary for corneal dissection. However, we must concede that an increase of the degree of stress confinement from ≈30% to 100% is not strong enough to fully explain the drop of absorbed dissection energy by one order of magnitude from $\tau_L = 560$ ps to $\tau_L = 1$ ps in Fig. 33.9.

Another factor that comes into play during the cavitation bubble expansion after the initial tearing of collagen fibrils is *inertial confinement*. Depending on laser pulse enrgy, we can distinguish between three regimes: a purely thermoelastic regime at small pulse energies, in which collagen fibrils are not ruptured and no cavity forms; a dominantly thermoeleastic regime, in which the restoring elastic forces around the bubble prevent its expansion to a size, where effective cutting may occur; and the cutting regime, in which the maximum bubble size must exceed the distance between laser spots to produce a homogeneous cut. In the latter regime, the initial bubble wall velocity that builds up during the laser pulse is in the order of several hundred m/s [5, 73]. For very small plasma volumes, a significant movement of the bubble wall during the laser pulse will reduce the peak pressure that can be reached for a given pulse energy and thus the disruptive force of the laser pulse. Since inertial confinement increases with decreasing laser pulse duration, higher peak pressures are reached in fs breakdown than with 560-ps pulses. This will contribute to the observed pulse duration dependence of cutting energy.

While the degree of stress confinement and inertial confinement increases when the pulse duration is shortened from 560 ps to about 10 ps, it remains approximately constant when it is further reduced into the femtosecond regime. Nevertheless, the pulse energy required for flap dissection continues to decrease. This could be caused by an increase of plasma energy density at constant levels of energy absorption leading to higher plasma peak pressure [28]. Experimental investigations by Vogel et al. revealed that the plasma absorption coefficient for breakdown in bulk water first decreases when the pulse duration is decreased below the ns regime, reaches a minimum at durations of a few ps, and increases again for fs pulses [74]. Numerical simulations showed that this behavior is due to changes in the plasma formation dynamics: With ns pulses the electron concentration reaches high values already early during the pulse because avalanche ionization progresses rapidly once multiphoton-generated seed electrons are available. With ps pulses the maximum is achieved much later during the pulse, which leads to a decrease of the average absorption coefficient. With fs pulses, a high electron density is again reached earlier due to the increasing role of multiphoton ionization [3].

The above explanations imply an increase of the disruptive action of laser pulses with decreasing pulse duration. This seems to contradict earlier findings that the conversion of laser pulse energy into bubble energy was larger for ns pulses than for fs pulses [74]. However, these findings applied to a regime well above the bubble threshold, while the results in Fig. 33.9 refer to the threshold $E_{\mathrm{th,cut}}$ for easy flap lifting. Moreover, the earlier findings refer to laser-induced cavitation in water rather than to corneal laser surgery, where a minimum stress amplitude is required to overcome the rupture strength of the tissue matrix and initiate dissection.

4.3 Safety Considerations

The results in Sect. 4.1 suggest that a vortex beam of UV-A fs laser pulses may provide the optimum solution for precise and gentle corneal dissection. However, we must consider the photochemical damage potential of UV laser light that may be enhanced if the light interacts with the tissue in conjunction with the mechanical stresses involved in cutting.

Safety aspects must consider the wavelength dependence of the transmission into and through the human cornea, the wavelength dependence of photokeratitis (damage to corneal epithelium, endothelium, and keratocytes), the age- and wavelength-dependent transmission through the lens, and potential photochemical damage to the retina [75]. A detailed discussion of these subjects goes beyond the topic of this chapter, and the reader is referred to Ref. [25]. It turns out that at 355 nm, light still penetrates well into the cornea (70% transmission through the entire cornea) and can produce optical breakdown. Photokeratitis thresholds are three to four orders of magnitude higher at 355 nm than at the peak of the action spectrum around 260 nm. Less than 0.1% of the applied light at the cornea will reach the retina in a 20-year-old eye, and this fraction decreases further with age. Histological investigations in rabbit eyes showed no damage of any of the corneal layers even with $\tau_L = 850$ ps and 2.5 μJ pulse energy and 6 μm spot separation, corresponding to a total radiant exposure of 6.9 J/cm^2 [25]. This value remained below the maximum permissible exposure limit of 19 J/cm^2 recommended by the International Commission on Non-Ionizing Radiation Protection (ICNIRP) in 2004 [76]. However, punctuate epithelial edema was observed in clinical trials with these parameters, which may be related to the combined UV and mechanical stress that is not considered in the ICNIRP recommendations. Those recommendations were later changed to a considerably lower limit of 1 J/cm^2 in the entire region between 320 and 400 nm to exclude any possibility of photochemical damage [77, 78]. For corneal dissection, this creates some difficulties in staying below the maximum permissible UV exposure values with sufficient buffer for clinical practice.

5 Fs Laser-Induced Refractive Index Changes

In 2008, a group led by Wayne Knox began to work on a femtosecond laser-based procedure for intra-tissue refractive index shaping (IRIS), which was later developed into a non-ablative, nonincisional, laser refractive correction procedure for human applications named laser-induced refractive index change (LIRIC). The technique is based on free-electron-mediated modifications on corneal biomolecules by low-density plasma below the cavitation threshold.

5.1 Creation of Fresnel Lenses Via Patterned Low-Density Plasma Formation

Femtosecond laser induction of refractive index changes was originally demonstrated on hydrogels in 2006 [79]. Creation of such changes in the cornea was first attempted in 2008 using a laser system emitting 27-fs pulses at 800-nm wavelength [80]. However, it turned out later that 400-nm fs laser pulses were more efficient at locally increasing the refractive index of corneal stromal tissue [81, 82]. Series of tightly focused, 400-nm fs laser pulses with 80 MHz repetition rate were used to inscribe small (2.5 mm wide) gradient index (GRIN) Fresnel lenses of positive refractive change in cat corneas and hydrogel lenses, as shown in Fig. 33.10. Depending on the type of the Fresnel lens, the refractive change of the treated eye can be made both positive and negative. The present state of the LIRIC technique is described in detail in [29].

LIRIC was first tested in humans in 2019 by inscribing a 3-mm-diameter gradient index lens in the corneal mid-stroma [84], and it was recently shown that generation

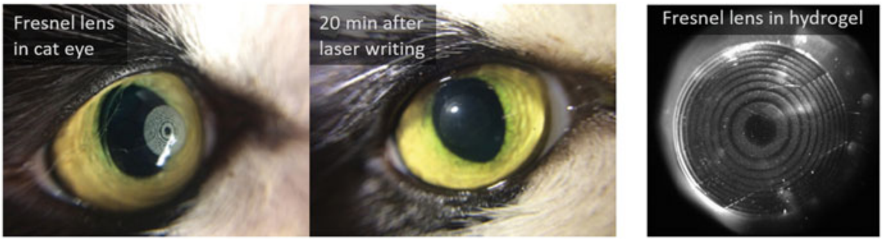

Fig. 33.10 Direct writing of Fresnel lenses into living cornea and hydrogel lenses by fs laser generation of refractive index changes. (Adapted from Knox [83], with permission). 80-MHz series of 100-fs pulses at $\lambda = 400$ nm (dwell time: ≈ 50 µs) were used to create local refractive index changes. Pulse energies were below the single-pulse cavitation threshold but slightly above the threshold at which long-lived bubbles of non-condensable gas are created by biomolecular disintegration in low-density plasma [4]. Bubbles dissolved within 10–20 min, and a refractive index change of up to 0.037 remained. The refractive change in the cat eye caused by the Fresnel lens was stable during an 18 months follow-up time

of a +2.5 D gradient index Fresnel lens in the mid-stromal region of live rabbit corneas induced little-to-no disruption to corneal structure and biology for 3 months after the procedure [29].

The refractive index changes arise through the cumulative action of about 4000 laser pulses hitting each spot during the laser scan, but the underlying mechanisms are still under exploration. Since they involve modifications of living tissue, they must differ from the creation of refractive index changes in glass (Chap. 21 of this book) that goes along with high pressures and temperatures in the modified regions. By contrast, refractive index changes in the cornea are achieved with negligible temperature and pressure rise through free-electron-mediated chemical modifications of biomolecules in low-density plasmas. Yu et al. showed that irradiation of ex vivo rabbit corneas at the laser parameters used for IRIS and LIRIC causes hyperfluorescence and a decrease of SHG signal [85]. Both observations indicate collagen changes originating from the cumulative action of free electrons in the laser-induced low-density plasma. It is interesting to note that hyperfluorescence has been also observed above the damage threshold in multiphoton microscopy of various tissues [86, 87]. The SHG signal arises from the parallel orientation of stacked, long molecules in the collagen fibrils [45, 88], and SHG loss indicates a loss of structural integrity of the native fibrils due to the breakage of molecular bonds [85]. The observation of long-lived gas bubbles in the treated areas (Fig. 33.10) supports the conclusion that some molecular bonds are broken. We hypothesize that the collagen changes may consist of a helix-coil transition that arises when weak bonds in the collagen protein break but most covalent bonds in the peptide chains and between collagen molecules still remain intact. Gaseous products likely arise from bond breaking in peptide side chains as discussed in Sect. 2.3. Helix-coil transitions have previously been observed after thermally induced breakage of weak bonds in laser thermo-keratoplasty [89, 90]. They result in local fibril contraction and thickening, which will displace some aqueous ground substance from the space between the fibrils. Since the refractive index of collagen is larger than that of water [1, 91], this increases the average refractive index in the treated regions. Our hypothesis relies on the assumption of a direct interaction of laser-produced electrons with collagen molecules that is supported by a host of literature on electron capture dissection of proteins for mass spectroscopy [92, 93]. This reasoning differs from the explanation given by Wang et al. that relates refractive changes to the induction of crosslinks between tyrosine amino acids caused by free-electron-generated reactive oxygen species originating from the dissociation of tissue water [94]. It seems unlikely that such crosslinks can *cause* refractive index modifications; in our opinion they can, at best, *stabilize* them after they have been induced by another mechanism.

5.2 *Relation of Electron Energy Spectra to the Wavelength Dependence of fs Laser-Induced Refractive Index Changes*

Our hypothesis on the mechanism of fs laser induction of corneal refractive index changes is supported by numerical simulations of the laser-induced free electron density and the energy spectra of the quasi-free conduction band (CB) electrons in water at 400-nm and 800-nm wavelength that were performed using the multi-rate-equation model (2) of Ref. [95]. Figure 33.11a presents simulation results for the parameters of the first experimental investigations that were performed with 27-fs, 800-nm pulses [80], and Fig. 33.11b shows the results for 100-fs, 400-nm pulses employed in a study on Blue-IRIS tissue effects [85]. Finally, Fig. 33.11c shows CB electron energy spectra for 100-fs, 800-nm pulses and a pulse energy E_{pulse} that would produce the same CB electron density as the 100-fs, 400-nm pulses in (b). In all three cases, the electron density remains four orders of magnitude below the value of 1.8×10^{20} cm^{-3} corresponding to the single-pulse bubble threshold in water [2], and the temperature rise is negligible.

CB electrons with relatively low energy can break weak bonds but leave strong covalent bonds intact. The simulations reveal that such electrons dominate both with 27-fs, 800-nm pulses ($E_{\mathrm{e.avg}} = 2.4$ eV) and 100-fs, 400-nm pulses ($E_{\mathrm{e.avg}} = 1.2$ eV). However, the number of electrons produced per pulse in the focal volume, which determines the effectivity of refractive index modifications, is three orders of magnitude larger with the shorter wavelength and longer pulse duration. On the other hand, 100-fs IR pulses that generate the same electron density as the blue fs pulses in (b) would produce more energetic electrons ($E_{\mathrm{e.avg}} = 7.3$ eV), which can more easily break covalent bonds. With such laser parameters, molecular disintegration and the generation of non-condensable gas is expected to quench the generation of stable refractive index changes. Altogether, the simulations explain why blue IRIS is advantageous - in agreement with our hypothesis on the mechanisms underlying the fs laser induction of refractive index changes.

The above considerations show that it is not sufficient to look at the free electron density produced by ultrashort laser pulses to understand their effect on biomolecules and biological tissues. Especially for low-density plasmas, the wavelength and irradiance dependence of the interplay between multiphoton absorption and avalanche ionization goes along with strong changes in the electron energy spectrum. At higher irradiance values close to the single-pulse cavitation threshold, spectral shape and $\varepsilon_{\mathrm{avg}}$ converge against an asymptotic limit and then remain constant until full ionization is reached, and it shoots up with further energy deposition [95]. In the future, it may be useful to introduce action spectra for the analysis and description of laser-induced electron-mediated molecular changes, in analogy to the photonic action spectra which are already used in photobiology and photochemistry [96].

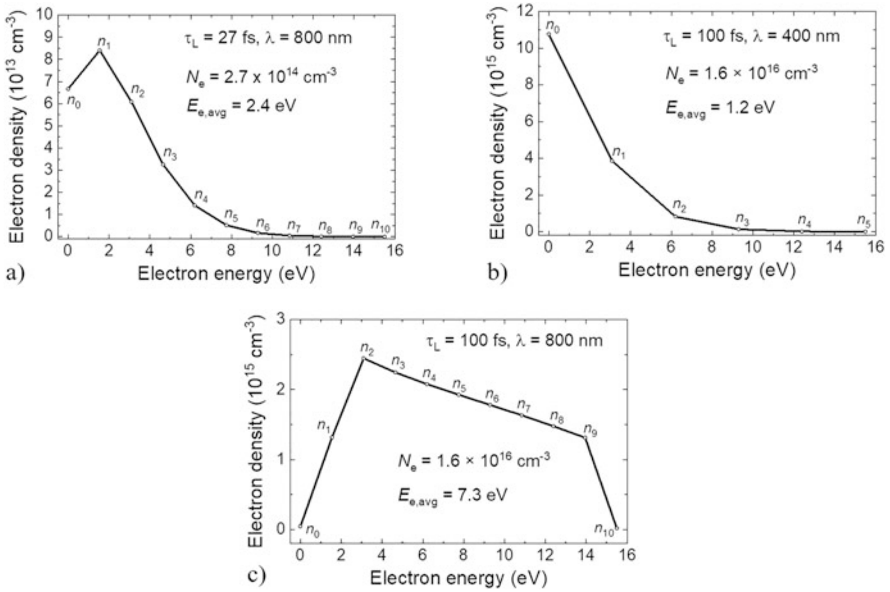

Fig. 33.11 Energy spectra of fs laser-induced conduction band electrons in water at different pulse durations and wavelengths. (**a**) $\lambda = 800$ nm, $\tau_L = 27$ fs, $E_{\text{pulse}} = 0.32$ nJ, NA = 0.7 as in Ref. [80]. (**b**) $\lambda = 400$ nm, $\tau_L = 100$ fs, $E_{\text{pulse}} = 1.03$ nJ, NA = 0.26 as in Ref. [85]. (**c**) $\lambda = 800$ nm, $\tau_L = 100$ fs, NA = 0.26 as in (**b**), $E_{\text{pulse}} = 14.1$ nJ. The pulse energy in (**c**) was selected such that simulations yield the same electron density as for the 400-nm, 100-fs pulses in (**b**). The number density of the quasi-free CB electrons, N_e, and their average kinetic energy, $E_{e.avg}$, is given in the individual graphs. The number of free electrons produced in the focal volume by every pulse at the given electron densities and *NA*s is 208 in (**a**), 1.88×10^5 in (**b**), and 6.9×10^5 in (**c**). The value in (**c**) is larger than in (**b**) in spite of equal N_e because the focal volume is larger due to the longer wavelength

6 Conclusion

Based on an analysis of the mechanisms of fs laser corneal dissections, we presented novel approaches for its improvement. Minimization of the plasma length by use of UV-A wavelengths and plasma shaping by use of vortex beams both improve cutting precision and reduce mechanical side effects. Innovative application of fundamental physical principles for the optimization of surgical precision and minimization of side effects is the medical equivalent to the pursuit of extreme scales in nanostructuring of nonliving matter.

While photochemical side effects may hinder the introduction of UV-A wavelengths into refractive surgery, the vortex beam approach works for all wavelengths. Because of the propagation invariance of a Laguerre-Gaussian beam, its vortex characteristics is retained along the entire beam path. This feature enables easy implementation of the phase plate into a beam delivery system and is compatible with beam scanning after the plate. The phase plate can be swung in and out to switch between Gaussian and vortex beams [27]. Although the vortex beam is advantageous for lenticule cutting in SMILE and the flap bed in LASIK, the Gaussian beam, with its more elongated plasma shape, may be better suited for the vertical side cuts of the LASIK flap.

Intrastromal writing of Fresnel lenses via refractive index modifications promises to maintain corneal integrity and mechanical stability, and fs laser-induced refractive index modifications in hydrogels offer the potential for postsurgical modifications of the refractive power of lens implants after cataract surgery. However, refractive corneal surgery based on this novel technique still needs to undergo clinical trials, whereas focus shaping is a modification of approved techniques, and phase plates for generating vortex beams can be easily implemented in clinical systems. Therefore, the introduction of vortex beams could result in substantial improvements already for the next generation of clinical refractive laser systems.

References

1. A. Vogel, V. Venugopalan, Mechanisms of pulsed laser ablation of biological tissues. Chem. Rev. **103**, 577 (2003). https://doi.org/10.1021/cr010379n
2. N. Linz, S. Freidank, X.X. Liang, A. Vogel, Wavelength dependence of femtosecond laser-induced breakdown in water and implications for laser surgery. Phys. Rev. B **94**, 024113 (2016). https://doi.org/10.1103/PhysRevB.94.024113
3. J. Noack, A. Vogel, Laser-induced plasma formation in water at nanosecond to femtosecond time scales: Calculation of thresholds, absorption coefficients, and energy density. IEEE J. Quantum Electron. **35**, 1156 (1999). https://doi.org/10.1109/3.777215
4. A. Vogel, J. Noack, G. Huttman, G. Paltauf, Mechanisms of femtosecond laser nanosurgery of cells and tissues. Appl. Phys. B-Lasers Opt. **81**, 1015 (2005). https://doi.org/10.1007/s00340-005-2036-6
5. A. Vogel, S. Busch, U. Parlitz, Shock wave emission and cavitation bubble generation by picosecond and nanosecond optical breakdown in water. J. Acoust. Soc. Am. **100**, 148 (1996). https://doi.org/10.1121/1.415878
6. T. Juhasz, F. Loesel, R.M. Kurtz, C. Horvath, J.F. Bille, G. Mourou, Corneal refractive surgery with femtosecond lasers. IEEE J. Sel. Top. Quantum Electron. **5**, 902 (1999). https://doi.org/10.1109/2944.796309
7. H. Lubatschowski, G. Maatz, A. Heisterkamp, U. Hetzel, W. Drommer, H. Welling, W. Ertmer, Application of ultrashort laser pulses for intrastromal refractive surgery. Graefes Arch. Clin. Exp. Ophthalmol. **238**, 33 (2000). https://doi.org/10.1007/s004170050006
8. T. Kohnen, A. Strenger, O.K. Klaproth, Basic knowledge of refractive surgery: Correction of refractive errors using modern surgical procedures. Dtsch. Arztebl. Int. **105**, 163 (2008). https://doi.org/10.3238/arztebl.2008.0163
9. W. Sekundo, K.S. Kunert, M. Blum, Small incision corneal refractive surgery using the small incision lenticule extraction (smile) procedure for the correction of myopia and myopic astigmatism: Results of a 6 month prospective study. Br. J. Ophthalmol. **95**, 335 (2011). https://doi.org/10.1136/bjo.2009.174284
10. M. Blum, K. Taubig, C. Gruhn, W. Sekundo, K.S. Kunert, Five-year results of small incision lenticule extraction (relex smile). Br. J. Ophthalmol. **100**, 1192 (2016). https://doi.org/10.1136/bjophthalmol-2015-306822
11. R.M. Shtein, Post-lasik dry eye. Expert Rev. Ophthalmol. **6**, 575 (2011). https://doi.org/10.1586/eop.11.56

12. R. Dave, D.P. O'Brart, V.K. Wagh, W.S. Lim, P. Patel, J. Lee, J. Marshall, Sixteen-year follow-up of hyperopic laser in situ keratomileusis. J Cataract Refract Surg **42**, 717 (2016). https://doi.org/10.1016/j.jcrs.2016.03.028
13. S. Freidank, A. Vogel, R.R. Anderson, R. Birngruber, N. Linz, Correction of hyperopia by intrastromal cutting and liquid filler injection. J. Biomed. Opt. **24**, 1 (2019). https://doi.org/10.1117/1.JBO.24.5.058001
14. C.M. Wertheimer, K. Brandt, S. Kaminsky, C. Elhardt, S.A. Kassumeh, L. Pham, H. Schulz-Hildebrandt, S. Priglinger, R.R. Anderson, R. Birngruber, Refractive changes after corneal stromal filler injection for the correction of hyperopia. J. Refract. Surg. **36**, 406 (2020). https://doi.org/10.3928/1081597X-20200429-01
15. A. Vogel, N. Linz, S. Freidank, R. Birngruber, Apparatus for changing the refractive power of the cornea (International filing date 31.05.2017 2017)
16. H. Lubatschowski, Overview of commercially available femtosecond lasers in refractive surgery. J. Refract. Surg. **24**, 102 (2008). https://doi.org/10.3928/1081597x-20080101-18
17. W.Y. Song, L. Zhang, S. Ness, J. Yi, Wavelength-dependent optical properties of melanosomes in retinal pigmented epithelium and their changes with melanin bleaching: A numerical study. Biomed. Opt. Express **8**, 3966 (2017). https://doi.org/10.1364/Boe.8.003966
18. H. Sun, N. Hosszufalusi, E.R. Mikula, T. Juhasz, Simulation of the temperature increase in human cadaver retina during direct illumination by 150-khz femtosecond laser pulses. J. Biomed. Opt. **16**, 108001 (2011). https://doi.org/10.1117/1.3631788
19. D.V. Palanker, M.S. Blumenkranz, D. Andersen, M. Wiltberger, G. Marcellino, P. Gooding, D. Angeley, G. Schuele, B. Woodley, M. Simoneau, N.J. Friedman, B. Seibel, J. Batlle, R. Feliz, J. Talamo, W. Culbertson, Femtosecond laser-assisted cataract surgery with integrated optical coherence tomography. Sci. Transl. Med. **2** (2010). https://doi.org/10.1126/scitranslmed.3001305
20. Z. Nagy, A. Takacs, T. Filkorn, M. Sarayba, Initial clinical evaluation of an intraocular femtosecond laser in cataract surgery. J. Refract. Surg. **25**, 1053 (2009). https://doi.org/10.3928/1081597x-20091117-04
21. K.E. Donaldson, R. Braga-Mele, F. Cabot, R. Davidson, D.K. Dhaliwal, R. Hamilton, M. Jackson, L. Patterson, K. Stonecipher, S.H. Yoo, A.R.C.S. Subcommittee, Femtosecond laser-assisted cataract surgery. J Cataract Refract Surg **39**, 1753 (2013). https://doi.org/10.1016/j.jcrs.2013.09.002
22. R. Montes-Mico, E. Espana, I. Bueno, W.N. Charman, J.L. Menezo, Visual performance with multifocal intraocular lenses: Mesopic contrast sensitivity under distance and near conditions. Ophthalmology **111**, 85 (2004). https://doi.org/10.1016/S0161-6420(03)00862-5
23. C.R. Munnerlyn, S.J. Koons, J. Marshall, Photorefractive keratectomy: A technique for laser refractive surgery. J Cataract Refract Surg **14**, 46 (1988)
24. C. Latz, T. Asshauer, C. Rathjen, A. Mirshahi, Femtosecond-laser assisted surgery of the eye: Overview and impact of the low-energy concept. Micromachines-Basel **12** (2021). https://doi.org/10.3390/mi12020122
25. A. Trost, F. Schrodl, C. Strohmaier, B. Bogner, C. Runge, A. Kaser-Eichberger, K. Krefft, A. Vogel, N. Linz, S. Freidank, A. Hilpert, I. Zimmermann, G. Grabner, H.A. Reitsamer, A new nanosecond UV laser at 355 nm: Early results of corneal flap cutting in a rabbit model. Invest. Ophthalmol. Vis. Sci. **54**, 7854 (2013). https://doi.org/10.1167/iovs.13-12580
26. J. Menzel-Severing, C. Petsch, T. Tourtas, N. Polisetti, J. Klenke, K. Skerl, C. Wullner, C. Donitzky, F.E. Kruse, J. Kremers, C.M. Hammer, Evaluation of a 345 nm femtosecond laser for corneal surgery with respect to intraocular radiation hazard. PLoS One **10** (2015). https://doi.org/10.1371/journal.pone.0137638
27. A. Vogel, S. Freidank, N. Linz, Device for laser cutting within transparent materials. European patent 2760622 b1, us patent 9795511 b2, chinese patent 104703563 b, japanese patent 6005290 b2 (2015)
28. S. Freidank, A. Vogel, N. Linz, Optical vortex beam for gentle and ultraprecise intrastromal corneal dissection in refractive surgery. Transl. Vis. Sci. Technol. **9** (2020). https://doi.org/10.1167/tvst.9.10.22

29. K.T. Wozniak, S.C. Butler, X. He, J.D. Ellis, W.H. Knox, K.R. Huxlin, Temporal evolution of the biological response to laser-induced refractive index change (LIRIC) in rabbit corneas. Exp. Eye Res. **207** (2021). https://doi.org/10.1016/j.exer.2021.108579
30. R. Sahler, J.F. Bille, S. Enright, S. Chhoeung, K. Chan, Creation of a refractive lens within an existing intraocular lens using a femtosecond laser. J. Cataract. Refract. Surg. **42**, 1207 (2016). https://doi.org/10.1016/j.jcrs.2016.05.005
31. J.F. Bille, J. Engelhardt, H.R. Volpp, A. Laghouissa, M. Motzkus, Z.X. Jiang, R. Sahler, Chemical basis for alteration of an intraocular lens using a femtosecond laser. Biomed. Opt. Express **8**, 1390 (2017). https://doi.org/10.1364/Boe.8.001390
32. J. Nguyen, L. Werner, J. Ludlow, J. Aliancy, L. Ha, B. Masino, S. Enright, R.K. Alley, R. Sahler, Intraocular lens power adjustment by a femtosecond laser – In vitro evaluation of power change, modulation transfer function, light transmission, and light scattering in a blue light-filtering lens. J. Cataract. Refract. Surg. **44**, 226 (2018). https://doi.org/10.1016/j.jcrs.2017.09.036
33. F.H. Loesel, M.H. Niemz, J.F. Bille, T. Juhasz, Laser-induced optical breakdown on hard and soft tissues and its dependence on the pulse duration: Experiment and model. IEEE J. Quantum Electron. **32**, 1717 (1996). https://doi.org/10.1109/3.538774
34. M.V. Netto, R.R. Mohan, F.W. Medeiros, W.J. Dupps, S. Sinha, R.R. Krueger, W.M. Stapleton, M. Rayborn, C. Suto, S.E. Wilson, Femtosecond laser and microkeratome corneal flaps: Comparison of stromal wound healing and inflammation. J. Refract. Surg. **23**, 667 (2007)
35. F.W. de Medeiros, H. Kaur, V. Agrawal, S.S. Chaurasia, J. Hammel, W.J. Dupps Jr., S.E. Wilson, Effect of femtosecond laser energy level on corneal stromal cell death and inflammation. J. Refract. Surg. **25**, 869 (2009). https://doi.org/10.3928/1081597X-20090917-08
36. B. Pajic, B. Pajic-Eggspuehler, C. Rathjen, M. Resan, Z. Cvejic, Why use ultrashort pulses in ophthalmology and which factors affect cut quality. Medicina-Lithuania **57** (2021). https://doi.org/10.3390/medicina57070700
37. A. Heisterkamp, T. Ripken, T. Mamom, W. Drommer, H. Welling, W. Ertmer, H. Lubatschowski, Nonlinear side effects of fs pulses inside corneal tissue during photodisruption. Appl. Phys. B-Lasers Opt. **74**, 419 (2002). https://doi.org/10.1007/s003400200825
38. C.L. Arnold, A. Heisterkamp, W. Ertmer, H. Lubatschowski, Streak formation as side effect of optical breakdown during processing the bulk of transparent kerr media with ultra-short laser pulses. Appl. Phys. B-Lasers Opt. **80**, 247 (2005). https://doi.org/10.1007/s00340-004-1701-5
39. A. Vogel, M.R.C. Capon, M.N. Asiyovogel, R. Birngruber, Intraocular photodisruption with picosecond and nanosecond laser-pulses – Tissue effects in cornea, lens, and retina. Invest. Ophthalmol. Vis. Sci. **35**, 3032 (1994)
40. A. Vogel, T. Gunther, M. Asiyo-Vogel, R. Birngruber, Factors determining the refractive effects of intrastromal photorefractive keratectomy with the picosecond laser. J. Cataract. Refract. Surg. **23**, 1301 (1997). https://doi.org/10.1016/S0886-3350(97)80107-1
41. M.S. Habib, M.G. Speaker, R. Kaiser, T. Juhasz, Myopic intrastromal photorefractive keratectomy with the neodymium-yttrium lithium fluoride picosecond laser in the cat cornea. Arch. Ophthalmol. **113**, 499 (1995). https://doi.org/10.1001/archopht.1995.01100040121037
42. V. Marchi, A. Gualano, G. Zumbo, S. Marchi, Intrastromal photorefractive keratectomy for myopia by Nd:YLF picosecond laser. J. Refract. Surg. **12**, S284 (1996)
43. T. Juhasz, G.A. Kastis, C. Suarez, Z. Bor, W.E. Bron, Time-resolved observations of shock waves and cavitation bubbles generated by femtosecond laser pulses in corneal tissue and water. Laser Surg. Med. **19**, 23 (1996). https://doi.org/10.1002/(Sici)1096-9101(1996)19:1
44. S. Freidank, A. Vogel, N. Linz, Mechanisms of corneal intrastromal laser dissection for refractive surgery: Ultra-high-speed photographic investigation at up to 50 million frames per second. Biomed. Opt. Express **13** (2022). https://doi.org/10.1364/boe.455926
45. J.V. Jester, M. Winkler, B.E. Jester, C. Nien, D. Chai, D.J. Brown, Evaluating corneal collagen organization using high-resolution nonlinear optical macroscopy. Eye Contact Lens **36**, 260 (2010). https://doi.org/10.1097/ICL.0b013e3181ee8992

46. M. Winkler, D. Chai, S. Kriling, C.J. Nien, D.J. Brown, B. Jester, T. Juhasz, J.V. Jester, Nonlinear optical macroscopic assessment of 3-d corneal collagen organization and axial biomechanics. Invest. Ophthalmol. Vis. Sci. **52**, 8818 (2011). https://doi.org/10.1167/iovs.11-8070
47. G. Maatz, A. Heisterkamp, H. Lubatschowski, S. Barcikowski, C. Fallnich, H. Welling, W. Ertmer, Chemical and physical side effects at application of ultrashort laser pulses for intrastromal refractive surgery. J. Opt. A-Pure Appl. Opt. **2**, 59 (2000). https://doi.org/10.1088/1464-4258/2/1/311
48. N. Leymarie, C.E. Costello, P.B. O'Connor, Electron capture dissociation initiates a free radical reaction cascade. J. Am. Chem. Soc. **125**, 8949 (2003). https://doi.org/10.1021/ja028831n
49. E. Alizadeh, S. Massey, P.A. Rowntree, L. Sanche, Low-energy electron-induced dissociation in condensed-phase L-cysteine I: Desorption of anions from chemisorbed films. J. Phys. Conf. Ser. **635** (2015). https://doi.org/10.1088/1742-6596/635/1/012001
50. C.G. Elles, I.A. Shkrob, R.A. Crowell, S.E. Bradforth, Excited state dynamics of liquid water: Insight from the dissociation reaction following two-photon excitation. J. Chem. Phys. **126** (2007). https://doi.org/10.1063/1.2727468
51. N. Tinne, B. Kaune, A. Krüger, T. Ripken, Interaction mechanisms of cavitation bubbles induced by spatially and temporally separated fs-laser pulses. PLoS One **9**, e114437 (2014). https://doi.org/10.1371/journal.pone.0114437
52. L.T. Nordan, S.G. Slade, R.N. Baker, C. Suarez, T. Juhasz, R. Kurtz, Femtosecond laser flap creation for laser in situ keratomileusis: Six-month follow-up of initial U.S. Clinical series. J. Refract. Surg. **19**, 8 (2003)
53. M.A. Sarayba, T.S. Ignacio, P.S. Binder, D.B. Tran, Comparative study of stromal bed quality by using mechanical, intralase femtosecond laser 15- and 30-khz microkeratomes. Cornea **26**, 446 (2007). https://doi.org/10.1097/ICO.0b013e318033e7cc
54. P.S. Binder, M. Sarayba, T. Ignacio, T. Juhasz, R. Kurtz, Characterization of submicrojoule femtosecond laser corneal tissue dissection. J Cataract Refract Surg **34**, 146 (2008). https://doi.org/10.1016/j.jcrs.2007.07.056
55. G.D. Kymionis, G.A. Kontadakis, I. Naoumidi, V.P. Kankariya, S. Panagopoulou, A. Manousaki, M.A. Grentzelos, I.G. Pallikaris, Comparative study of stromal bed of lasik flaps created with femtosecond lasers (intralase fs150, wavelight fs200) and mechanical microkeratome. Br. J. Ophthalmol. **98**, 133 (2014). https://doi.org/10.1136/bjophthalmol-2013-304023
56. A.A. Griffith, G.I. Taylor, Vi. The phenomena of rupture and flow in solids. Philos. Trans. R. Soc. Lond. Ser. A **221**, 163 (1921). https://doi.org/10.1098/rsta.1921.0006
57. J.E. Gordon, *The Science of Structures and Materials* (Scientific American Books, New York, 1988)
58. Q.W. Zhan, Cylindrical vector beams: From mathematical concepts to applications. Adv. Opt. Photonics **1**, 1 (2009). https://doi.org/10.1364/Aop.1.000001
59. A.M. Yao, M.J. Padgett, Orbital angular momentum: Origins, behavior and applications. Adv. Opt. Photonics **3**, 161 (2011). https://doi.org/10.1364/Aop.3.000161
60. X.A. Hao, C.F. Kuang, T.T. Wang, X. Liu, Effects of polarization on the de-excitation dark focal spot in sted microscopy. J Opt. – UK **12** (2010). https://doi.org/10.1088/2040-8978/12/11/115707
61. A. Vogel, N. Linz, S. Freidank, G. Paltauf, Femtosecond-laser-induced nanocavitation in water: Implications for optical breakdown threshold and cell surgery. Phys. Rev. Lett. **100**, 038102 (2008). https://doi.org/10.1103/PhysRevLett.100.038102
62. C.H. Liu, C.C. Sun, D. Hui-Kang Ma, J. Chien-Chieh Huang, C.F. Liu, H.F. Chen, C.H. Hsiao, Opaque bubble layer: Incidence, risk factors, and clinical relevance. J Cataract Refract Surg **40**, 435 (2014). https://doi.org/10.1016/j.jcrs.2013.08.055

63. D.N. Shah, S. Melki, Complications of femtosecond-assisted laser in-situ keratomileusis flaps. Semin. Ophthalmol. **29**, 363 (2014). https://doi.org/10.3109/08820538.2014.959194
64. A.M. dos Santos, A.A. Torricelli, G.K. Marino, R. Garcia, M.V. Netto, S.J. Bechara, S.E. Wilson, Femtosecond laser-assisted lasik flap complications. J. Refract. Surg. **32**, 52 (2016). https://doi.org/10.3928/1081597X-20151119-01
65. L. Mastropasqua, R. Calienno, M. Lanzini, N. Salgari, S. De Vecchi, R. Mastropasqua, M. Nubile, Opaque bubble layer incidence in femtosecond laser-assisted lasik: Comparison among different flap design parameters. Int. Ophthalmol. **37**, 635 (2017). https://doi.org/10.1007/s10792-016-0323-3
66. G. Son, J. Lee, C. Jang, K.Y. Choi, B.J. Cho, T.H. Lim, Possible risk factors and clinical effects of opaque bubble layer in small incision lenticule extraction (smile). J. Refract. Surg. **33**, 24 (2017). https://doi.org/10.3928/1081597X-20161006-06
67. L. Li, J.M. Schallhorn, J. Ma, L. Zhang, R. Dou, Y. Wang, Risk factors for opaque bubble layer in small incision lenticule extraction (smile). J. Refract. Surg. **33**, 759 (2017). https://doi.org/10.3928/1081597X-20170821-02
68. A. Vogel, S. Freidank, N. Linz, Method for laser machining transparent materials, us patent 8,350,183, publication date 2013/1/8 (2003)
69. A. Vogel, N. Linz, S. Freidank, J. Noack, G. Paltauf, Femtosecond and nanosecond laser-inducec nanoeffects for cell surgery and modification of glass. Conference on Lasers and Electro-Optics/Quantum Electronics and Laser Science, OSA Technical Digest (CD), paper CMHH1 (2008). https://opg.optica.org/abstract.cfm?URI=CLEO-2008-CMHH1
70. N. Linz, S. Freidank, X.X. Liang, H. Vogelmann, T. Trickl, A. Vogel, Wavelength dependence of nanosecond infrared laser-induced breakdown in water: Evidence for multiphoton initiation via an intermediate state. Phys. Rev. B **91**, 134114 (2015). https://doi.org/10.1103/PhysRevB.91.134114
71. M.K. Smolek, B.E. McCarey, Interlamellar adhesive strength in human eyebank corneas. Invest. Ophthalmol. Vis. Sci. **31**, 1087 (1990)
72. G. Paltauf, P.E. Dyer, Photomechanical processes and effects in ablation. Chem. Rev. **103**, 487 (2003). https://doi.org/10.1021/cr010436c
73. X.X. Liang, N. Linz, S. Freidank, G. Paltauf, A. Vogel, Comprehensive analysis of spherical bubble oscillations and shock wave emission in laser-induced cavitation. J. Fluid Mech. **940** (2022). https://doi.org/10.1017/jfm.2022.202
74. A. Vogel, J. Noack, K. Nahen, D. Theisen, S. Busch, U. Parlitz, D.X. Hammer, G.D. Noojin, B.A. Rockwell, R. Birngruber, Energy balance of optical breakdown in water at nanosecond to femtosecond time scales. Appl. Phys. B-Lasers Opt. **68**, 271 (1999). https://doi.org/10.1007/s003400050617
75. D. van Norren, T.G.M.F. Gorgels, The action spectrum of photochemical damage to the retina: A review of monochromatic threshold data. Photochem. Photobiol. **87**, 747 (2011). https://doi.org/10.1111/j.1751-1097.2011.00921.x
76. A.F. McKinlay, J.H. Bernhardt, A. Ahlbom, J.P. Cesarini, F.R. de Gruijl, M. Hietanen, R. Owen, D.H. Sliney, P. Soderberg, A.J. Swerdlow, M. Taki, T.S. Tenforde, P. Vecchia, B. Veyret, R. Matthes, M.H. Repacholi, B. Diffey, M.A. Mainster, T. Okuno, B.E. Stuck, I.C.N. Radiati, Guidelines on limits of exposure to ultraviolet radiation of wavelengths between 180 nm and 400 nm (incoherent optical radiation). Health Phys. **87**, 171 (2004)
77. K. Schulmeister, D.H. Sliney, J. Mellerio, D.J. Lund, B.E. Stuck, J.A. Zuclich, Review of exposure limits and experimental data for corneal and lenticular damage from short pulsed uv and ir laser radiation. J. Laser Appl. **20**, 98 (2008). https://doi.org/10.2351/1.2900539
78. ICNIRP, Icnirp guidelines on limits of exposure to laser radiation of wavelengths between 180 nm and 1,000 µm. Health Phys. **105**(271) (2013). https://doi.org/10.1097/HP.0b013e3182983fd4
79. L. Ding, R. Blackwell, J.F. Kunzler, W.H. Knox, Large refractive index change in silicone-based and non-silicone-based hydrogel polymers induced by femtosecond laser micromachining. Opt. Express **14**, 11901 (2006). https://doi.org/10.1364/oe.14.011901

80. L. Ding, W.H. Knox, J. Buhren, L.J. Nagy, K.R. Huxlin, Intratissue refractive index shaping (IRIS) of the cornea and lens using a low-pulse-energy femtosecond laser oscillator. Invest. Ophthalmol. Vis. Sci. **49** (2008). https://doi.org/10.1167/iovs.08-1921
81. L.S. Xu, W.H. Knox, M. DeMagistris, N.D. Wang, K.R. Huxlin, Noninvasive intratissue refractive index shaping (IRIS) of the cornea with blue femtosecond laser light. Invest. Ophthalmol. Vis. Sci. **52**, 8148 (2011). https://doi.org/10.1167/iovs.11-7323
82. D.E. Savage, D.R. Brooks, M. DeMagistris, L.S. Xu, S. MacRae, J.D. Ellis, W.H. Knox, K.R. Huxlin, First demonstration of ocular refractive change using blue-IRIS in live cats. Invest. Ophthalmol. Vis. Sci. **55**, 4603 (2014). https://doi.org/10.1167/iovs.14-14373
83. W.H. Knox, Femtosecond lasers and nonlinear optics: New approaches solve old problems in ophthalmology. Laser Focus World **54**, 22 (2018)
84. L. Zheleznyak, S.C. Butler, I.G. Cox, K.R. Huxlin, J.D. Ellis, W. Knox, K. Waltz, J.A. Vukich, G. Quesada, R. Quesada, A. Melendez, J.J. Machat, S.M. MacRae, First-in-human laser-induced refractive index change (liric) treatment of the cornea. Invest. Ophthalmol. Vis. Sci. **60**, 5079 (2019)
85. D. Yu, E.B. Brown, K.R. Huxlin, W.H. Knox, Tissue effects of intra-tissue refractive index shaping (IRIS): Insights from two-photon autofluorescence and second harmonic generation microscopy. Biomed. Opt. Express **10**, 855 (2019). https://doi.org/10.1364/Boe.10.000855
86. K. Koenig, P.T.C. So, W.W. Mantulin, B.J. Tromberg, E. Gratton, Two-photon excited lifetime imaging of autofluorescence in cells during UVA and NIR photostress. J. Microsc. Oxford **183**, 197 (1996)
87. R. Orzekowsky-Schroeder, A. Klinger, B. Martensen, M. Blessenohl, A. Gebert, A. Vogel, G. Huttmann, In vivo spectral imaging of different cell types in the small intestine by two-photon excited autofluorescence. J. Biomed. Opt. **16** (2011). https://doi.org/10.1117/1.3655587
88. P.J. Campagnola, A.C. Millard, M. Terasaki, P.E. Hoppe, C.J. Malone, W.A. Mohler, Three-dimensional high-resolution second-harmonic generation imaging of endogenous structural proteins in biological tissues. Biophys. J. **82**, 493 (2002). https://doi.org/10.1016/S0006-3495(02)75414-3
89. M.N. Asiyo-Vogel, R. Brinkmann, H. Notbohm, R. Eggers, H. Lubatschowski, H. Laqua, A. Vogel, Histologic analysis of thermal effects of laser thermokeratoplasty and corneal ablation using sirius-red polarization microscopy. J Cataract Refract Surg **23**, 515 (1997). https://doi.org/10.1016/s0886-3350(97)80208-8
90. J.C. Allain, M. Le Lous, S. Cohen, S. Bazin, P. Maroteaux, Isometric tensions developed during the hydrothermal swelling of rat skin. Connect. Tissue Res. **7**, 127 (1980). https://doi.org/10.3109/03008208009152104
91. G.B. Benedek, Theory of transparency of the eye. Appl. Opt. **10**, 459 (1971). https://doi.org/10.1364/AO.10.000459
92. R.A. Zubarev, Electron-capture dissociation tandem mass spectrometry. Curr. Opin. Biotechnol. **15**, 12 (2004). https://doi.org/10.1016/j.copbio.2003.12.002
93. K.O. Zhurov, L. Fornelli, M.D. Wodrich, U.A. Laskay, Y.O. Tsybin, Principles of electron capture and transfer dissociation mass spectrometry applied to peptide and protein structure analysis. Chem. Soc. Rev. **42**, 5014 (2013). https://doi.org/10.1039/c3cs35477f
94. C. Wang, M. Fomovsky, G.X. Miao, M. Zyablitskaya, S. Vukelic, Femtosecond laser crosslinking of the cornea for non-invasive vision correction. Nat. Photonics **12**, 416 (2018). https://doi.org/10.1038/s41566-018-0174-8
95. X.X. Liang, Z.X. Zhang, A. Vogel, Multi-rate-equation modeling of the energy spectrum of laser-induced conduction band electrons in water. Opt. Express **27**, 4672 (2019). https://doi.org/10.1364/Oe.27.004672
96. R.B. Setlow, The wavelengths in sunlight effective in producing skin cancer: A theoretical analysis. Proc. Natl. Acad. Sci. U. S. A. **71**, 3363 (1974). https://doi.org/10.1073/pnas.71.9.3363